

PAC

Proceedings of the

2003

Particle Accelerator Conference



DISTRIBUTION STATEMENT A
Approved for Public Release
Distribution Unlimited

Volume 5 of 5
pp. 2835-3569



REPORT DOCUMENTATION PAGE

Form Approved
OMB No. 0704-0188

Public reporting burden for this collection of information is estimated to average 1 hour per response, including the time for reviewing instructions, searching existing data sources, gathering and maintaining the data needed, and completing and reviewing the collection of information. Send comments regarding this burden estimate or any other aspect of this collection of information, including suggestions for reducing this burden, to Washington Headquarters Services, Directorate for Information Operations and Reports, 1215 Jefferson Davis Highway, Suite 1204, Arlington, VA 22202-4302, and to the Office of Management and Budget, Paperwork Reduction Project (0704-0188), Washington, DC 20503.

1. AGENCY USE ONLY (Leave Blank)		2. REPORT DATE		3. REPORT TYPE AND DATES COVERED Final	
4. TITLE AND SUBTITLE 2003 Particle Accelerator Conference Vol. 5				5. FUNDING NUMBERS G	
6. AUTHORS variou					
7. PERFORMING ORGANIZATION NAME(S) AND ADDRESS(ES) IEEE 445 Hoes Lane, PO Box 1331 Piscataway, NJ 08855-1331				8. PERFORMING ORGANIZATION REPORT NUMBER	
9. SPONSORING / MONITORING AGENCY NAME(S) AND ADDRESS(ES) Office of Naval Research Ballston Centre Tower One 800 North Quincy Street Arlington, VA 22217-5660				10. SPONSORING / MONITORING AGENCY REPORT NUMBER N00014-04-1-0417	
11. SUPPLEMENTARY NOTES					
12a. DISTRIBUTION / AVAILABILITY STATEMENT DISTRIBUTION STATEMENT A Approved for Public Release Distribution Unlimited				12b. DISTRIBUTION CODE	
13. ABSTRACT (Maximum 200 words) The twentieth biennial Particle Accelerator Conference on Accelerator Science and Technology was held May 12 - 16, 2003 at the Hilton Hotel in Portland, Oregon. The Stanford Linear Accelerator Center and the Lawrence Berkeley National Laboratory organized PAC 2003, and it was held under the auspices of the Nuclear and Plasma Sciences Society of the Institute of Electrical and Electronics Engineers and the Division of Physics of Beams of the American Physical Society. The attendance was 1025 registrants from 21 countries. The Program Committee was co-chaired by Alan Jackson and Ed Lee. The program they arranged had opening and closing plenary sessions that covered the most important accomplishments, opportunities, and applications of accelerators. During the remainder of the conference there were parallel sessions with oral and poster presentations. In addition, there was an industrial exhibit during the first three days. The Proceedings present a total of 1154 papers from the invited, contributed orals, and poster sessions.					
14. SUBJECT TERMS Particle Accelerators and Colliders, Beam Dynamics, Magnets, RF Systems, Synchrotron radiation sources, Free Electron Lasers, Energy Recovery Linacs, Instabilities, Feedback Instrumentation, Pulsed Power, High Intensity Beams, Accelerator Applications, Advanced Accelerators.				15. NUMBER OF PAGES 3571	
				16. PRICE CODE	
17. SECURITY CLASSIFICATION OF REPORT Unclassified	18. SECURITY CLASSIFICATION OF THIS PAGE Unclassified	19. SECURITY CLASSIFICATION OF ABSTRACT Unclassified	20. LIMITATION OF ABSTRACT		

NSN 7540-01-280-5500

Standard Form 298 (Rev. 2-89)
Prescribed by ANSI Std. Z39-1
298-102

PAC 2003

PROCEEDINGS OF THE 2003 PARTICLE ACCELERATOR CONFERENCE

Portland, Oregon U.S.A.
May 12-16, 2003

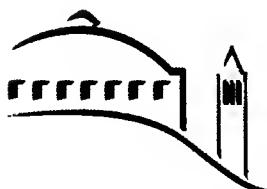
Joe Chew, Peter Lucas, and Sara Webber, editors

Volume 5 of 5

Organized by
Stanford Linear Accelerator Center
Lawrence Berkeley National Laboratory

Held under the joint auspices of
Institute of Electrical and Electronics Engineers
(Nuclear and Plasma Sciences Society)
American Physical Society
(Division of Physics of Beams)

Sponsored by
U.S. Department of Energy
Office of Naval Research
National Science Foundation



20040311 163

ACKNOWLEDGEMENTS

Cover Design: Terry Anderson

Photographs: Edmund Keene Photographers

Funding for these proceedings was provided under DOE Grant No. DE-FG03-01ER41233 by the following U.S. Department of Energy offices:

- Office of High Energy and Nuclear Physics
- Office of Basic Energy Sciences
- Office of Fusion Energy Sciences

This work related to Department of Navy grant N00014-03-1-0417 issued by the Office of Naval Research. The United States Government has a royalty-free license throughout the world in all copyrightable material contained herein.

Funding for student and postdoctoral associate travel to attend the conference was provided by National Science Foundation Grant No. PHY-0225358.

Proceedings of the 2003 Particle Accelerator Conference

Copyright and Reprint Permission: Abstracting is permitted with credit to the source. Libraries are permitted to photocopy beyond the limit of U.S. copyright law for private use of patrons those articles in this volume that carry a code at the bottom of the first page, provided the per-copy fee indicated in the code is paid through Copyright Clearance Center, 222 Rosewood Drive, Danvers, MA 01923. For other copying, reprint, or republication permission, write to IEEE Copyrights Manager, IEEE Operations Center, 445 Hoes Lane, P.O. Box 1331, Piscataway, NJ 08855-1331. All Rights reserved. Copyright ©2003 by the Institute of Electrical and Electronics Engineers, Inc.

IEEE Catalog Number: 03CH37423

ISBN: 0-7803-7738-9

Library of Congress: 88-647453

Additional copies of this publication are available from
IEEE Operations Center
445 Hoes Lane
Piscataway, NJ 08855-1331 USA
+1 800 678 IEEE
+1 732 981 9667 (FAX)
email: customer.service@ieee.org

Volume 5

Tuning of the RF Field of the DTL for the J-PARC

F. Naito, M. Ikegami, T. Kato, E. Takasaki, H. Tanaka (KEK), T. Ito (Japan Atomic Energy Research Institute).....2835

High-Gradient Tests on S-Band 2m-Long Accelerating Structures for KEKB Injector Linac

Y. Igarashi (The Graduate University for Advanced Studies), A. Enomoto, Y. Higashi, K. Kakihara, S. Ohsawa, T. Oogoe, S. Yamaguchi (KEK), H. Hanaki, T. Taniuchi, H. Tomizawa (SPRING-8)2838

Mechanical Design of the Drift-Tube Linac (DTL) for the Spallation Neutron Source

T. Ilg, S. Ellis, W. Fox, R. Gentzlinger, R. Martineau, L. Rowton, J. Sims (LANL), G. Johnson (ORNL).....2841

Fabrication and Tuning of the SNS CCL Hot Model

N. Bultman, J. Billen, Z. Chen, M. Collier, D. Richards, L.M. Young (LANL).....2844

RIA Fragmentation Line Beam Dump

W. Stein (LLNL)2847

Analysis of a Multi-Spoke Option for the RIA Driver Linac

D. Gorelov, T. Grimm, W. Hartung, F. Marti, X. Wu, R. York (National Superconducting Cyclotron Laboratory)..2849

Numerical Design and Optimization of Cooling System for 2 MeV Traveling Wave Accelerator

L. Shen, L. Cao, Shaoqing Li, Xiaoguang Li, J. Yao (University of Science and Technology of China), D. Jiang, Y.J. Pei (National Synchrotron Radiation Lab)2852

Impact of Cavity RF Field Phase and Amplitude Control Uncertainties on the SNS Linac

D. Jeon (ORNL), J. Stovall, H. Takeda (LANL), K. Crandall (TechSource, Inc.)2855

The Low Level RF System for 100MV Proton Linac of KOMAC

I.H. Yu, M.H. Chun, K.M. Ha, Y.J. Han, W.H. Hwang, H.S. Kang, D.T. Kim, S.C. Kim, S.H. Nam, J.S. Yang (Pohang Accelerator Laboratory), Y.S. Cho, J.M. Han, H.J. Kwon, K.T. Seol (Korea Atomic Energy Research Institute)2857

Status of the Production Electropolishing System at JLAB

J. Mammoser, J. Delayen, J. Gordon, L. Phillips, A.-M. Valente, T. Wang, A.T. Wu (Thomas Jefferson National Accelerator Facility), J. Saunders (ORNL)2860

Gradient Optimization for SC CW Accelerators

W.J. Schneider, P. Kneisel, C.H. Rode (Thomas Jefferson National Accelerator Facility)2863

Mechanical Cavity Design for 100MV Upgrade Cryomodule

K.M. Wilson, E. Daly, J. Henry, J. Hogan, D. Machie, J. Sekutowicz, T. Whitlatch (Thomas Jefferson National Accelerator Facility).....2866

Commissioning-Results of the REX-ISOLDE Linac

S. Emhofer, F. Ames, J. Cederk  ll, D. Habs, O. Kester, K. Rudolph (Sektion Physik der LMU M  nchen), T. Sieber (CERN)2869

An Energy Upgrade of the REX-ISOLDE Linac

O. Kester, H. Bongers, W. Carli, S. Emhofer, D. Habs, K. Rudolph, T. Sieber (Sektion Physik der LMU M  nchen)2872

Front End Design of the RIA Driver Linac

A.A. Kolomiets (Institute for Theoretical and Experimental Physics), V.N. Aseev, P.N. Ostroumov, R.C. Pardo (ANL)2875

High Power Electron S-band Linac for Industrial Purposes

V.A. Kushnir, M.I. Ayzatsky, E.Z. Biller, V.N. Boriskin, A.N. Dovbnya, V.V. Mitrochenko (NSC KIPT), V.I. Beloglasov, N.V. Demidov, L.K. Myakushko, T.F. Nikitina, V.A. Popenko, G.D. Pugachev, G.D. Repikhov, L.V. Reprintzev, V.A. Shendrik, D.L. Stepin, G.E. Tarasov, Yu.D. Tur, V.L. Uvarov (Kharkov Institute of Physics and Technology)2878

Pulsed Heating Experiments at 34 GHz

O.A. Nezhevenko, V.P. Yakovlev (Omega-P, Inc.), J.L. Hirshfield (Omega-P, Inc. and Yale University), G.V. Serdobintsev (Yale University)2881

The Vacuum Systems for PEPF Linac

M.Y. Park, Y.S. Cho, J.M. Han, J.H. Jang, K.K. Jeong, Y.J. Kim, H.J. Kwon (Korea Atomic Energy Research Institute)2884

Series Production of Copper and Niobium Cavities for the Spallation Neutron Source

M. Pekeler, S. Bauer, K. Dunkel, B. Griep, C. Piel, H. Vogel, P. vom Stein (ACCEL Instruments GmbH)2887

Continued Development of the RFI Linac Structure

D.A. Swenson, K.R. Crandall, F.W. Guy, W.J. Starling (Linac Systems)2889

Upgrades of Linac System at CAMD

Y. Wang, M. Fedurin, P. Jines, T. Miller, T. Zhao (Center for Advanced Microstructures and Devices)2892

Linear Coupling of RMS Emittances

L.C. Teng (ANL)2895

Proposal of Partial Siberian Snake based on Helical Magnets for AGS

Yu.M. Shatunov, I.A. Koop, A.V. Otboev, E.A. Perevedentsev, P.Yu. Shatunov (BINP)2898

Action and Phase Analysis to Determine Sextupole Errors in RHIC and the SPS

J. Cardona, S. Peggs, T. Satogata (BNL), R. Tom_s (CERN)2901

Beam Diffusion Measurements at RHIC

R. Fliller III, A. Drees, D. Gassner, G. McIntyre, S. Peggs, D. Trbojevic (BNL)2904

Measurement of the Nonlinear Momentum Compaction Factor in RHIC

C. Montag (BNL)2907

Adiabatic Capture of Charged Particles in Stable Islands: a Novel Approach to Multi-Turn Extraction

M. Giovannozzi, R. Capi (CERN)2910

Optics Studies for the CERN Proton Synchrotron: Linear and Nonlinear Modelling Using Beam Based Measurements

M. Giovannozzi, R. Capi, E. M_tral, G. M_tral, M. Martini, R. Steerenberg (CERN), A.-S. M  ller (Forschungszentrum Karlsruhe)2913

Measurements of Transverse Space-Charge Effects in the CERN Proton Synchrotron

E. M_tral, M. Giovannozzi, G. M_tral, M. Martini, R. Steerenberg (CERN)2916

Beam-Based BPM Alignment

R. Talman, N. Malitsky (BNL)2919

Barrier RF Stacking at Fermilab

W. Chou, J. Griffin, K.Y. Ng, D. Wildman (FNAL), H. Zheng (California Institute of Technology), A. Takagi (KEK)2922

Fermilab Booster Modeling and Space Charge Study

W. Chou, A. Drozhdin, P. Lucas, J.-F. Ostiguy (FNAL)2925

Ion Production and Tune Shift in the Recycler Ring

K. Gounder, J.P. Marriner, C.S. Mishra (FNAL)2928

Analysis and Measurements of Emittance Dilution from Vacuum Windows in the Fermilab Recycler Transfer Lines

C. Johnstone, C. Gattuso, D. Johnson, M. Syphers (FNAL), K. Paul (University of Illinois)2931

Automatic Beamline Correction	
<i>T. Kobilarcik, J. DeVoy, C. Moore (FNAL)</i>	2934
Increasing the Intensity of the Fermilab Booster	
<i>E.J. Prebys, C. Ankenbrandt, W. Chou, A. Drozhdin, P.H. Kasper, J.R. Lackey, N.V. Mokhov, W.A. Pellico, R. Tomlin, R.C. Webber (FNAL)</i>	2936
Space Charge in the FNAL Booster: Experiment and Modeling	
<i>P. Spentzouris, J. Amundson (FNAL)</i>	2939
End-to-End Simulations of a Superconducting Deuteron CH-DTL for IFMIF	
<i>A. Sauer, H. Deitinghoff, H. Klein, H. Liebermann, H. Podlech, U. Ratzinger, R. Tiede (Institut für Angewandte Physik)</i>	2942
Developments in Linear and Non-Linear DAFNE Lattice	
<i>C. Milardi, G. Benedetti, M. Biagini, C. Biscari, M. Boscolo, S. Guiducci, M.A. Preger, P. Raimondi, C. Vaccarezza, M. Zobov (INFN)</i>	2945
Jitter Control and Scraping in the 12-View AHF HEBT	
<i>B. Blind, A. Jason (LANL)</i>	2948
The Use of Electric Multipole Lenses for Bending and Focusing Polar Molecules, with Application to the Design of a Rotational-State Separator	
<i>J.G. Kalnins (LBNL)</i>	2951
Space-Charge Driven Emittance Growth in a 3D Mismatched Anisotropic Beam	
<i>J. Qiang, R.D. Ryne (LBNL), I. Hofmann (Gesellschaft für Schwerionenforschung mbH)</i>	2954
Pulse Compression Via Velocity Bunching with the LLNL Thomson X-Ray Source Photoinjector	
<i>S.G. Anderson, W. Brown, A.M. Tremaine (LLNL), P. Musumeci, J.B. Rosenzweig (University of California, Los Angeles)</i>	2957
Eliminating the Spot Dilution due to Kicker Switching in DARHT-II	
<i>Y.-J. Chen, F. Chambers, A.C. Paul, J.A. Watson, J. Weir (LLNL)</i>	2960
RF Focusing Methods for Heavy Ions in Low Energy Accelerators	
<i>E.S. Masunov, S.M. Polozov (MEPhI), P.N. Ostroumov, N.E. Vinogradov (ANL)</i>	2963
Image-Charge Effects on the Envelope Dynamics of an Unbunched Intense Charged-Particle Beam	
<i>B.L. Qian, C. Chen, J. Zhou (MIT Plasma Science and Fusion Center)</i>	2966
Random-Regular Accelerating Structures	
<i>K. Kramarenko, M.I. Ayzatsky (NSC KIPT)</i>	2969
The Beam Dynamics Studies of Combined Misalignments and RF Errors for RIA	
<i>X. Wu, D. Gorelov, T. Grimm, W. Hartung, F. Marti, R. York (National Superconducting Cyclotron Laboratory)</i> ..	2972
Plasma Neutralization Models for Intense Ion Beam Transport in Plasma	
<i>I.D. Kaganovich, S. O'Rourke (Princeton University), E.P. Lee (LBNL), R.C. Davidson, E.A. Startsev (Plasma Physics Laboratory, Princeton University)</i>	2975
Intense Sheet Beam Stability Properties for Uniform Phase-Space Density	
<i>E.A. Startsev, R.C. Davidson (Plasma Physics Laboratory, Princeton University)</i>	2978
RF Modes in the PEP-II Shielded Vertex Bellows	
<i>A. Novokhatski, S. Weathersby (SLAC)</i>	2981
Characteristics of Pulse Compression in Laser Pulse Amplification by Stimulated Raman Backscattering	
<i>J.B. Kim (KERI and POSTECH), H.J. Lee, H. Suk (Korea Electrotechnology Research Institute), I.S. Ko (Pohang Accelerator Laboratory)</i>	2984

Effect of Preplasmas on High-Energy Ion Generation by an Intense Laser Pulse Irradiated on Overdense Plasmas	
<i>H.J. Lee, C. Kim, G.H. Kim, J.U. Kim, H. Suk (Korea Electrotechnology Research Institute), J.B. Kim (KERI and POSTECH)</i>	2987
New Regions of Stability for Periodically Focused Particle Beams	
<i>R. Pakter, J.S. Moraes, F.B. Rizzato (Universidade Federal do Rio Grande do Sul)</i>	2990
Coupling Impedances for Corrugated Beam Pipes from Impedance Boundary Conditions	
<i>S. Petracca, Th. Demma (University of Sannio and INFN)</i>	2993
The Gaussian Approximation for a Purely Inductive Wake Function	
<i>S. Petracca, Th. Demma (University of Sannio and INFN), K. Hirata (The Graduate University for Advanced Studies)</i>	2996
Electromagnetic Fields in the Toroidal Region of LHC-Like Rings	
<i>S. Petracca, Th. Demma (University of Sannio and INFN)</i>	2999
Non-Coulomb Perturbations Influence on Beam Dynamics in Extended Accelerating/Focusing Channels	
<i>B.I. Bondarev, A.P. Durkin (Moscow Radiotechnical Institute)</i>	3002
Acceleration and Self-Focused Particle Beam Drivers	
<i>V. Zadorozhny (Institute of Cybernetics, Ukraine), Z. Parsa (BNL)</i>	3005
Vertical Coupling Impedance of the APS Storage Ring	
<i>Y.-C. Chae, K. Harkay, X. Sun (ANL)</i>	3008
Horizontal Coupling Impedance of the APS Storage Ring	
<i>Y.-C. Chae, K. Harkay, X. Sun (ANL)</i>	3011
Longitudinal Coupling Impedance of the APS Storage Ring	
<i>Y.-C. Chae, K. Harkay, X. Sun (ANL)</i>	3014
The Impedance Database and its Application to the APS Storage Ring	
<i>Y.-C. Chae (ANL)</i>	3017
Bunch Length Measurements at BESSY	
<i>P. Kuske, M. Abo-Bakr, W. Anders, G. Ẅestefeld (BESSY)</i>	3020
Coherent Emission of Synchrotron Radiation and Longitudinal Instabilities	
<i>P. Kuske, M. Abo-Bakr, J. Feikes, K. Holldack, G. Ẅestefeld (BESSY)</i>	3023
Transverse Instabilities in RHIC	
<i>M. Blaskiewicz, J.M. Brennan, P. Cameron, C. Dawson, C. Degen, K. Drees, W. Fischer, E. Koropsak, R. Michnoff, C. Montag, T. Roser, T. Satogata (BNL), N. Catalan-Lasheras (CERN)</i>	3026
Longitudinal Solitons in RHIC	
<i>M. Blaskiewicz, J.M. Brennan, P. Cameron, W. Fischer, J. Wei (BNL), A. Luque, H. Schamel (University of Bayreuth)</i>	3029
Effects of Space Charge and Nonlinearities on Collective Instabilities of a Long Bunch	
<i>A. Fedotov, J. Wei (BNL), V. Danilov (ORNL)</i>	3032
Coupling Impedance Measurements of the SNS RF Cavity and Extraction Kicker Magnet	
<i>H. Hahn, M. Blaskiewicz, D. Davino (BNL)</i>	3035
The Electron Cloud Instability of the LHC Beam in the CERN SPS	
<i>G. Arduini, K. Cornelis, W. Ḧafle, G. Rumolo, F. Zimmermann (CERN)</i>	3038
Investigation of Space Charge Effects in the SPS	
<i>H. Burkhardt, G. Rumolo, F. Zimmermann (CERN)</i>	3041

Coherent Tune Shifts Measured with Few Bunches in the SPS and Comparison with Resistive Wall Theory	
<i>H. Burkhardt, A. Koschik, G. Rumolo, F. Zimmermann, B. Zotter (CERN)</i>	3044
Longitudinal Microwave Instability in Lepton Bunches	
<i>E. M. Tral (CERN)</i>	3047
Nominal Longitudinal Parameters for the LHC Beam in the CERN SPS	
<i>E. Shaposhnikova, P. Baudrengnien, T. Bohl, T. Linnecar, J. Tuckmantel (CERN)</i>	3050
Transverse 'Monopole' Instability Driven by an Electron Cloud?	
<i>F. Zimmermann, E. Benedetto, D. Schulte (CERN), Y. Papaphilippou (European Synchrotron Radiation Facility), G. Rumolo (Gesellschaft für Schwerionenforschung mbH), K. Ohmi (KEK)</i>	3053
Simulation Study of Coupled-Bunch Instabilities due to Resistive Wall, Ions, or Electron Cloud	
<i>F. Zimmermann (CERN), H. Fukuma, K. Ohmi, Y. Ohnishi, S.S. Win (KEK)</i>	3056
Instability Threshold Currents vs. Energy in CESR	
<i>M. Billing, J. Sikora (Cornell University)</i>	3059
Head-Tail Instability at Tevatron	
<i>P.M. Ivanov, G. Annala, A. Burov, V.A. Lebedev, E. Lorman, V. Ranjbar, V. Scarpine, V. Shiltsev (FNAL)</i>	3062
Impedances of Tevatron Separators	
<i>K.Y. Ng (FNAL)</i>	3065
A 1.7 GHz Waveguide Schottky Detector System	
<i>R.J. Pasquinelli, E. Cullerton, D. Peterson, P. Seifrid, J. Steimel, D. Sun, D. Tinsley (FNAL)</i>	3068
The Tevatron Bunch by Bunch Longitudinal Dampers	
<i>C.Y. Tan, J. Steimel (FNAL)</i>	3071
The Tevatron Transverse Dampers	
<i>C.Y. Tan, J. Steimel (FNAL)</i>	3074
Bunch Lengthening Recently Observed at PF-AR	
<i>T. Ieiri, T. Kasuga, Y. Minagawa, T. Obina (KEK), T. Fujita (Hiroshima University)</i>	3077
Transverse Sawtooth Instability Observed in Photon Factory Advanced Ring	
<i>Y. Minagawa, T. Ieiri, T. Kasuga, T. Obina (KEK), T. Fujita (Hiroshima University)</i>	3080
Study of ep Instability for a Coasting Proton Beam in Circular Accelerators	
<i>K. Ohmi, M. Tomizawa, T. Toyama (KEK)</i>	3083
An Experimental Study of Microwave Stability near Transition in the PSR	
<i>P. Colestock, C. Beltran, A. Browman, J.D. Gilpatrick, R.J. Macek, R. McCrady, F. Neri, L.J. Rybarczyk, T. Spickermann (LANL), M. Schulze (General Atomics)</i>	3086
Status of the Experimental Studies of the Electron Cloud at the Los Alamos Proton Storage Ring	
<i>R.J. Macek, M. Borden, A. Browman, D. Fitzgerald, R. McCrady, T. Spickermann, T. Zaugg (LANL)</i>	3089
A Three-Dimensional Kinetic Theory of Continuous-Beam Stability	
<i>T.S. Wang (LANL)</i>	3092
A Numerical Study of Bunched Beam Transverse Electron-Proton Instability Based on the Centroid Model	
<i>T.S. Wang (LANL)</i>	3095
RF Impedance Measurements on the DARHT-II Accelerator Intercell Assembly	
<i>W. Fawley, S. Eylon (LBNL), R. Briggs (Science Applications International Corporation)</i>	3098

The Stabilization of Budker-Chirikov Instability by the Spread of Longitudinal Velocities <i>Yu.Ya. Golub (Moscow Radiotechnical Institute)</i>	3101
New Vortices in Axisymmetric Inhomogeneous Beams <i>Yu.Ya. Golub (Moscow Radiotechnical Institute)</i>	3103
Beam Instabilities at the PLS Storage Ring <i>E.-S. Kim (Pohang Accelerator Laboratory)</i>	3105
Simulations on Wakefield Effects in the Electron Beam at the 2.5 GeV PLS Linac <i>E.-S. Kim, H. Heo, S.H. Nam (Pohang Accelerator Laboratory)</i>	3108
Design Considerations for SASE-FEL at PLS <i>E.-S. Kim (Pohang Accelerator Laboratory)</i>	3111
Operational Performance in 2.5 GeV Full Energy Injection at PLS <i>E.-S. Kim, Y.J. Han, S.-H. Jeong, M.G. Kim, S.C. Kim, S.-S. Park, J.-H. Seo (Pohang Accelerator Laboratory)</i>	3114
Instability Driven by Wall Impedance in Intense Charged Particle Beams <i>R.C. Davidson, H. Qin (Plasma Physics Laboratory, Princeton University), G. Shvets (Illinois Institute of Technology)</i>	3117
Delta-f Simulation Studies of the Ion-Electron Two-Stream Instability in IBX <i>H. Qin, R.C. Davidson, E.A. Startsev (Plasma Physics Laboratory, Princeton University)</i>	3120
Kinetic Studies of Temperature Anisotropy Instability in Intense Charged Particle Beams <i>E.A. Startsev, R.C. Davidson, H. Qin (Plasma Physics Laboratory, Princeton University)</i>	3123
Measurement of the Longitudinal Wakefield in the SLAC Linac for Extremely Short Bunches <i>K. Bane, F.-J. Decker, P. Emma, L. Hendrickson, P. Krejcik, C.L. O'Connell, H. Schlarb, J. Welch, M. Woodley (SLAC)</i>	3126
Measurements of Transverse Emittance Growth due to Coherent Synchrotron Radiation in the SLAC SPPS Bunch Compressor Chicane <i>P. Emma, F.-J. Decker, P. Krejcik, C.L. O'Connell, M. Woodley (SLAC), H. Schlarb, F. Stulle (DESY)</i>	3129
Single-Mode Coherent Synchrotron Radiation Instability <i>S. Heifets, G.V. Stupakov (SLAC)</i>	3132
Nonlinear Regime of a Single-Mode CSR Instability <i>S. Heifets, G.V. Stupakov (SLAC)</i>	3135
Effects of Linac Wakefield on CSR Microbunching in the Linac Coherent Light Source <i>Z. Huang, P. Emma (SLAC), M. Borland, K.-J. Kim (ANL)</i>	3138
An Over-Damped Cavity Longitudinal Kicker for the PEP-II LER <i>P. McIntosh, R. Akre, D. Anderson, S. DeBarger, M. Dormiani, J. Fox, K. Jobe, H. Schwarz, D. Teytelman, U. Wienands, A. Young (SLAC), F. Marcellini (INFN), M. Tobiya (KEK)</i>	3141
Evolving Bunch and Retardation in the Impedance Formalism <i>R. Warnock (SLAC), M. Venturini (LBNL)</i>	3144
Robinson Modes at Aladdin <i>R.A. Bosch, J.J. Bisognano, K.J. Kleman (Synchrotron Radiation Center, University of Wisconsin)</i>	3147
The Effects of Temperature Variation on Electron Beams with RF Voltage Modulation <i>P.J. Chou, M.H. Wang (Synchrotron Radiation Research Center), S.Y. Lee (Indiana University)</i>	3150
A Fast Method to Estimate the Gain of the Microbunch Instability in a Bunch Compressor <i>S. Reiche, J.B. Rosenzweig (University of California, Los Angeles)</i>	3153

Experimental Study of Energy Spread in a Space-Charge Dominated Electron Beam	
<i>Y. Cui, I. Haber, R.A. Kishek, P.G. O'Shea, M. Reiser, A. Valfells, Y. Zou (University of Maryland)</i>	3156
Alternative Bunch Formation for the Tevatron Collider	
<i>G. Jackson (Hbar Technologies, LLC)</i>	3159
Longitudinal Emittance Growth in the Fermilab Booster Synchrotron	
<i>G. Jackson (Hbar Technologies, LLC)</i>	3162
Two-Stream Studies for Heavy Ion Beam Propagation in a Reactor Chamber	
<i>D.R. Welch, T.C. Genoni, D.V. Rose (Mission Research Corporation), C.L. Olson (Sandia National Laboratories)</i>	3165
Simulated Growth Rates for Single-Bunch Instabilities Driven by a Resistive Impedance	
<i>N. Towne (BNL)</i>	3168
Analytical and Time-Domain Computations of Single-Bunch Loss-Factor in a Planar Structure	
<i>D. Yu, A.V. Smirnov (DULY Research Inc.)</i>	3171
Simulation of Beam-Electron Cloud Interactions in Circular Accelerators Using Plasma Models	
<i>A.Z. Ghalam, T.C. Katsouleas (University of Southern California), V. Decyk, C. Huang, W.B. Mori (University of California, Los Angeles)</i>	3174
Booster's Coupled Bunch Damper Upgrade	
<i>W.A. Pellico, D. Wildman (FNAL)</i>	3177
Beam Dynamics Simulations for the Fermilab Recycler Ring Barrier Buckets	
<i>C.M. Bhat, J.A. MacLachlan, J.P. Marriner (FNAL), H. Kang (Stanford University)</i>	3180
Studies of a Generalized Beam-Induced Multipacting Resonance Condition	
<i>K. Harkay, R.A. Rosenberg (ANL), L. Loiacono (Loyola University)</i>	3183
Simulation of Magnetized Beams	
<i>D. Wang, I. Ben-Zvi, X. Chang, J. Kewisch, C. Montag (BNL), F. Zhou (University of California, Los Angeles)</i>	3186
Probing the Non-Linear Dynamics of the ESRF Storage Ring with Experimental Frequency Maps	
<i>Y. Papaphilippou, L. Farvacque, A. Ropert (European Synchrotron Radiation Facility), J. Laskar (BDL, Paris)</i>	3189
Non-Linear Longitudinal Beam Dynamics with Harmonic RF Systems for Bunch Lengthening	
<i>V. Serriere, J. Jacob (European Synchrotron Radiation Facility)</i>	3192
Synergia: A Hybrid, Parallel Beam Dynamics Code with 3D Space Charge	
<i>J. Amundson, P. Spentzouris (FNAL)</i>	3195
Flat Beam Production in Low Energy Injectors	
<i>S.-H. Wang (Indiana University), J. Corlett, S.M. Lidia, J. Staples, A. Zholents (LBNL)</i>	3198
Low Emittance Optics at the Photon Factory	
<i>K. Harada, M. Izawa, Y. Kobayashi, T. Obina, A. Ueda (KEK)</i>	3201
Injection Performance with a Traveling Wave Kicker Magnet System at the Photon Factory Storage Ring	
<i>Y. Kobayashi, T. Mitsuhashi, A. Ueda (KEK)</i>	3204
Measurement of the Transverse Quadrupole-Mode Frequencies of an Electron Bunch in the KEK Photon Factory Storage Ring	
<i>S. Sakanaka, T. Mitsuhashi, T. Obina (KEK)</i>	3207

Simulation Results of Corkscrew Motion in DARHT-II	
<i>K.C.D. Chan, C. Ekdahl (LANL), Y.-J. Chen (LLNL), T. Hughes (Mission Research Corporation)</i>	3210
Coupling Correction and Beam Dynamics at Ultralow Vertical Emittance in the ALS	
<i>C. Steier, D. Robin, A. Wolski (LBNL), G. Portmann, J. Safranek (SLAC)</i>	3213
Comparison of PARMELA Simulations with Longitudinal Emittance Measurements at the SLAC Gun Test Facility	
<i>C.G. Limborg, P.R. Bolton, J. Clendenin, D. Dowell, S. Gierman, B.F. Murphy, J.F. Schmerge (SLAC)</i>	3216
Recent Electron-Cloud Simulation Results for the Main Damping Rings of the NLC and TESLA Linear Colliders	
<i>M. Pivi, T.O. Raubenheimer (SLAC), M. Furman (LBNL)</i>	3219
Mitigation of the Electron-Cloud Effect in the PSR and SNS Proton Storage Rings by Tailoring the Bunch Profile	
<i>M. Pivi (SLAC), M. Furman (LBNL)</i>	3222
Derivation of FEL Gain Using Wakefield Approach	
<i>G.V. Stupakov, S. Krinsky (SLAC)</i>	3225
Coherent Synchrotron Radiation Effects in the Electron Cooler for RHIC	
<i>J. Wu (SLAC), D. Wang (BNL), F. Zhou (University of California, Los Angeles)</i>	3228
Impact of the Wiggler Coherent Synchrotron Radiation Impedance on the Beam Instability	
<i>J. Wu, Z. Huang, T.O. Raubenheimer, G.V. Stupakov (SLAC)</i>	3231
Electron Beam Motion Observed in Infrared Synchrotron Radiation at NSRRC	
<i>D.S. Hung, C.I. Chen, C.H. Kuo, Y.C. Lo (Synchrotron Radiation Research Center)</i>	3234
Experimental Measurements of 2-Dimensional Nonlinear Resonances	
<i>T.S. Ueng, J. Chen, K.T. Hsu, K.H. Hu, C.H. Kuo (Synchrotron Radiation Research Center)</i>	3237
First Experimental Test of Emittance Measurement Using the Quadrupole-Mode Transfer Function	
<i>M.H. Wang (Synchrotron Radiation Research Center), S.Y. Lee, Y. Sato (Indiana University)</i>	3240
Beam Characterization in the CEBAF-ER Experiment	
<i>C. Tennant, Y. Chao, D. Douglas, A. Freyberger, M. Tiefenback (Thomas Jefferson National Accelerator Facility)</i>	3243
A Beam Breakup Instability in a Recirculating Linac Caused by a Quadrupole Mode	
<i>B. Yunn (Thomas Jefferson National Accelerator Facility)</i>	3246
The Short-Range Transverse Wakefields in TESLA Accelerating Structure	
<i>I. Zagorodnov, T. Weiland (Technische U. Darmstadt)</i>	3249
Calculation of Collimator Wakefields	
<i>I. Zagorodnov, T. Weiland (Technische U. Darmstadt), K. Bane (SLAC)</i>	3252
Focusing Horn System for the BNL Very Long Baseline Neutrino Oscillation Experiment	
<i>S.A. Kahn, A. Carroll, M. Diwan, J.C. Gallardo, H. Kirk, C. Scarlett, N. Simos, B. Viren, W. Zhang (BNL)</i>	3255
Beam Shaping and Compression Scheme for the UCLA Neptune Laboratory	
<i>R.J. England, P. Musumeci, J.B. Rosenzweig, R. Yoder (University of California, Los Angeles)</i>	3258
Detection of Wake Field Using Test-Bunch Method at Photon Factory Advanced Ring	
<i>T. Fujita (Hiroshima University), T. Kasuga, Y. Minagawa, T. Obina (KEK)</i>	3261
Bunch Transverse Emittance Increases in Electron Storage Rings	
<i>J. Gao (Laboratoire de L'Accelérateur Lineaire [LAL])</i>	3264

Analytical Estimation of Dynamic Apertures Limited by the Wigglers in Storage Rings	
<i>J. Gao (Laboratoire de L'Accelerateur Lineaire [LAL])</i>	3267
Lattice Design of Saga Synchrotron Light Source	
<i>Y. Iwasaki, S. Koda, T. Tomimasu (Saga Synchrotron Light Source), H. Ohgaki (Kyoto University), H. Toyokawa, M. Yasumoto (National Institute of Advanced Industrial Science and Technology), Y. Hashiguchi, T. Kitsuka, Y. Ochiai, Y. Yamatsu (Saga Prefectural Government)</i>	3270
Linear and Nonlinear Optics Studies in the ANKA Storage Ring	
<i>A.-S. M��ller, I. Birkel, E. Huttel, F. Perez, M. Pont, R. Rossmanith (Forschungszentrum Karlsruhe)</i>	3273
Beam Size and Bunch Length Measurements at the ANKA Storage Ring	
<i>F. Perez, I. Birkel, E. Huttel, A.-S. M��ller, M. Pont (Forschungszentrum Karlsruhe)</i>	3276
Single-Bunch Injection System for the LNL Booster Injector	
<i>P.F. Tavares, S.R. Marques, H.J. Onisto (Laborat��rio Nacional de Luz S��ncrotron, Brazil)</i>	3279
Polarized H⁺ Ion Source Performance During the 2003 RHIC Run	
<i>J. Alessi, B. Briscoe, O. Gould, A. Kponou, Vincent LoDestro, D. Raparia, J. Ritter, A. Zelenski (BNL), V. Klenov, S. Kokhanovski, V. Zubets (Institute for Nuclear Research, Moscow)</i>	3282
The SPARC Project: A High Brightness Electron Beam Source at LNF to Drive a SASE-FEL Experiment	
<i>L. Palumbo, A. Cianchi, A. D'Angelo, R. Di Salvo, A. Fantini, D. Moricciani, C. Schaerf (University of Rome), R. Bartolini, F. Ciocchi, G. Dattoli, A. Doria, F. Flora, G.P. Gallerano, L. Giannessi, E. Giovenale, G. Messina, L. Mezi, P.L. Ottaviani, L. Picardi, M. Quattromini, A. Renieri, C. Ronsivalle (Ente Nazionale per le Nuove Tecnologie l'Energia e l'Ambiente), D. Alesini, F. Alessandria, A. Bacci, S. Bertolucci, M. Biagini, C. Biscari, R. Boni, I. Boscolo, M. Boscolo, F. Broggi, M. Castellano, L. Catani, E. Chiadroni, S. Cialdi, A. Clozza, C. De Martinis, G. Di Pirro, A. Drago, A. Esposito, M. Ferrario, V. Fusco, A. Gallo, F.S. Gamma, A. Ghigo, D. Grove, S. Guiducci, M. Incurvati, D. Levi, C. Ligi, F. Marcellini, C. Maroli, M. Mattioli, G. Medici, C. Milardi, L. Pellegrino, V. Petrillo, M.A. Preger, P. Raimondi, R. Ricci, M. Rom��, C. Sanelli, L. Serafini, M. Serio, B. Spataro, A. Stecchi, A. Stella, S. Tazzari, F. Tazzioli, C. Vaccarezza, M. Vescovi, C. Vicario, M. Zobov (INFN), J.B. Rosenzweig (University of California, Los Angeles)</i>	3285
A Simulation Study of the JLC Positron Source	
<i>T. Kamitani, Y. Ohnishi (KEK), S. Kashiwagi (Waseda University)</i>	3288
Diffusion of Alkali Species in Porous Tungsten Substrates Used in Contact-Ionization Sources	
<i>E. Chacon-Golcher (LANL), J. Kwan (LBNL), E.C. Morse (University of California, Berkeley)</i>	3291
Fabrication of Large Diameter Alumino-Silicate K⁺ Sources	
<i>D. Baca, J. Kwan, J.K. Wu (LBNL), E. Chacon-Golcher (LANL)</i>	3294
Beam Optics of a 10-cm Diameter High Current Heavy Ion Diode	
<i>J. Kwan, F.M. Bieniosek, J.-L. Vay (LBNL), E. Halaxa, G. Westenskow (LLNL), I. Haber (University of Maryland)</i>	3297
Characterization of an RF-Driven Plasma Ion Source for Heavy Ion Fusion	
<i>G. Westenskow, E. Halaxa, R.P. Hall (LLNL), J. Kwan (LBNL)</i>	3300
Stability of Electron Beam Parameters in Sources with Cold Secondary-Emission Cathodes	
<i>A.N. Dovbnya, N.I. Aizatsky, V.N. Boriskin, M.A. Krasnogolovets, V.A. Kushnir, V.A. Mitrochenko, N.G. Reshetnyak, Yu.Ya. Volkolupov, V.V. Zakutin (NSC KIPT)</i>	3303
Development and Status of the SNS Ion Source	
<i>R.F. Welton, S.N. Murray, M.P. Stockli (ORNL), R. Keller (LBNL)</i>	3306
Proof-of-Concept Experiments for Negative Ion Driver Beams for Heavy Ion Fusion	
<i>L. Grisham (Plasma Physics Laboratory, Princeton University), S.K. Hahto, S.T. Hahto, J. Kwan, K.N. Leung (LBNL)</i>	3309

3D Modeling Activity for Novel High Power Electron Guns at SLAC	
<i>A. Krasnykh, V. Ivanov, G. Scheitrum, D. Sprehn (SLAC), L. Ives, G. Miram (Calabazas Creek Research, Inc.)</i>	3312
An Improved Version of TOPAZ 3D	
<i>A. Krasnykh, V. Ivanov, G. Scheitrum (SLAC), A. Jensen (Oregon Institute of Technology)</i>	3315
First Test of the Charge State Breeder BRIC	
<i>V. Variale, V. Valentino (INFN), P. Bak, Y. Boimelshtein, P. Logatchov, B. Skarbo, M. Tiunov (BINP), A. Boggia, G. Brautti, T. Clauser, A. Raino (Dipartimento di Fisica di Bari and INFN)</i>	3318
Design and Operation of Pegasus Thermionic Cathode	
<i>P. Frigola, G. Andonian, S. Reiche, J.B. Rosenzweig, S. Telfer, G. Travish (University of California, Los Angeles)</i>	3321
Development of Dispenser Photocathodes for RF Photoinjectors	
<i>D. Feldman, P.G. O'Shea, M. Virgo (University of Maryland), K.L. Jensen (Naval Research Laboratory)</i>	3323
The Research on the Carbon Nano Tube Cathode	
<i>A. Yamamoto, N. Kaneko, H. Nakai, T. Nakashizu (Ishikawajima-Harima Heavy Industries Co.,Ltd.), M. Ikeda, S. Ohsawa, T. Sugimura (KEK)</i>	3326
Crystal-Based Spin Analyzer for Fast Neutron Beams	
<i>N. Bondarenko, N. Shul'ga (Kharkov Institute of Physics and Technology)</i>	3329
Pulsed HV Electron Gun with Thermionic Cathode for the Soft X-Ray FEL Project at SPring-8	
<i>K. Togawa, K. Onoe, T. Shintake (SPring-8), H. Baba (RIKEN Harima Institute in SPring-8), T. Ishizuka (Sumitomo Heavy Industries)</i>	3332
Ion and Neutral Beam Generation by 1TW, 50fs Laser Irradiation of Thin Foils	
<i>Y. Wada, T. Kubota, A. Ogata (Hiroshima University)</i>	3335
Topology for a DSP Based Beam Control System in the AGS Booster	
<i>J. DeLong, J.M. Brennan, T. Hayes, Tuong N. Le, K.S. Smith (BNL)</i>	3338
A Bunch to Bucket Phase Detector Using Digital Receiver Technology	
<i>J. DeLong, J.M. Brennan, T. Hayes, Tuong N. Le, K.S. Smith (BNL)</i>	3341
Progress on the SNS Ring LLRF Control System	
<i>K.S. Smith, M. Blaskiewicz, J.M. Brennan, J. DeLong, F. Heistermann, A. Zaltsman (BNL), T.L. Owens (ORNL)</i>	3344
A New Digital Control System for CESR-c and the Cornell ERL	
<i>M. Liepe, S. Belomestnykh, J. Dobbins, R. Kaplan, C.R. Strohman (Cornell University)</i>	3347
Longitudinal Damping System with Two Transverse Kickers	
<i>A. Mikhailichenko (Cornell University)</i>	3350
53 MHz Feedforward Beam Loading Compensation in the Fermilab Main Injector	
<i>J. Dey, I. Kourbanis, J. Reid, J. Steimel (FNAL)</i>	3353
2.5 MHz Feedforward Beam Loading Compensation in the Fermilab Main Injector	
<i>J. Dey, I. Kourbanis, J. Steimel (FNAL)</i>	3356
Tune and Coupling Drift Compensation during the Tevatron Injection Porch	
<i>M. Martens, G. Annala, P. Bauer (FNAL)</i>	3359
Beam Loading Compensation for Slip Stacking	
<i>J. Steimel, T. Berenc, C. Rivetta (FNAL)</i>	3362
Analysis of the Feedback System Used to Damp Longitudinal Quadrupole-Mode Bunch Oscillations	
<i>S. Sakanaka, T. Obina (KEK)</i>	3365

Two-Bunch Orbit Correction Using the Wake Field Kick	
<i>M. Satoh, K. Furukawa, M. Kikuchi, H. Koiso, Y. Ogawa, T. Suwada (KEK)</i>	3368
Newly Designed Field Control Module for the SNS	
<i>A. Regan, K. Kasemir, S. Kwon, J. Power, M. Prokop, H. Shoaee, M. Stettler (LANL), C. Swanson (Alpha Cad, Inc.), L. Doolittle, A. Ratti (LBNL), M. Champion (ORNL)</i>	3371
Commissioning Results of the Fast Orbit Feedback at the ALS	
<i>C. Steier, A. Biocca, E. Domning, S. Jacobson, G. Portmann, T. Scarvie, E. Williams (LBNL)</i>	3374
The Spallation Neutron Source Accelerator Low Level RF Control System	
<i>M. Champion, M. Crofford, H. Ma, M. Piller (ORNL), K. Kasemir, S. Kwon, J. Power, M. Prokop, A. Regan, H. Shoaee, M. Stettler, D. Thomson (LANL), S. De Santis, L. Doolittle, M. Monroy, A. Ratti (LBNL)</i>	3377
Control of Heavily-Beam-Loaded SNS-Ring Cavities	
<i>T.L. Owens (ORNL), K.S. Smith, A. Zaltsman (BNL)</i>	3380
Analysis of Slow Orbit Movement in PLS Storage Ring	
<i>H.S. Kang, J. Choi, Y.J. Han, H.J. Park (Pohang Accelerator Laboratory)</i>	3383
Commissioning of the Fast Orbit Feedback at SLS	
<i>M. Boege, B. Keil, T. Schilcher, V. Schlott (Paul Scherrer Institut)</i>	3386
Low-Mode Coupled Bunch Feedback Channel for PEP-II	
<i>J. Fox, L. Beckman, N. Hassanpour, L. Sapozhnikov, D. Teytelman (SLAC)</i>	3389
Upgrading the Orbit Feedback System in the Taiwan Light Source	
<i>C.H. Kuo, J. Chen, K.T. Hsu, K.H. Hu (Synchrotron Radiation Research Center)</i>	3392
Operation of the Digital Multi-Bunch Feedback Systems at ELETTRA	
<i>D. Bulfone, V. Forchi', M. Lonza, L. Zambon (Sincrotrone Trieste), M. Dehler (Paul Scherrer Institut)</i>	3395
Strong-Strong Simulation of Beam-Beam Interaction for Round Beams	
<i>A. Valishev, E.A. Perevedentsev (BINP), K. Ohmi (KEK)</i>	3398
Macroparticle Simulations of Antiproton Lifetime at 150 GeV in the Tevatron	
<i>J. Qiang, R.D. Ryne (LBNL), T. Sen, M. Xiao (FNAL)</i>	3401
Parallel Computation of Beam-Beam Interactions Including Longitudinal Motion	
<i>F.W. Jones (TRIUMF), W. Herr (CERN)</i>	3404
Measurement and Application of Betatron Modes with MIA	
<i>C.X. Wang (ANL)</i>	3407
Spatial-Temporal Modes Observed in the APS Storage Ring Using MIA	
<i>C.X. Wang (ANL)</i>	3410
FFAGs for Muon Acceleration	
<i>J.S. Berg, S.A. Kahn, R.B. Palmer, D. Trbojevic (BNL), C. Johnstone, E. Keil (FNAL), M. Aiba, S. Machida, Y. Mori, T. Ogitsu, C. Ohmori (KEK), A.M. Sessler (LBNL), S. Koscielniak (TRIUMF)</i>	3413
Beam Dump Optics for the Spallation Neutron Source	
<i>D. Raparia, Y.-Y. Lee, J. Wei (BNL), S. Henderson (ORNL)</i>	3416
Beam Scrubbing Strategy for Electron-Cloud Suppression in the Spallation Neutron Source Ring	
<i>S.Y. Zhang, M. Blaskiewicz, H. Hseuh, J. Wei (BNL), R.J. Macek (LANL)</i>	3419
The AGS Electrostatic Septum	
<i>J. Hock, K.A. Brown, J. Glenn, T. Russo (BNL)</i>	3422
Beam Based Characterization of a New 7-Pole Superconducting Wiggler at CESR	
<i>A. Temnykh, J. Crittenden, D. Rice, D.L. Rubin (Cornell University)</i>	3425

Status of the Cooler Synchrotron COSY-Juelich

D. Prasuhn, U. Bechstedt, J. Dietrich, R. Gebel, K. Henn, A. Lehrach, B. Lorentz, R. Maier, A. Schnase, H. Schneider, R. Stassen, H.J. Stein, H. Stockhorst, R. Toelle (Forschungszentrum Juelich)3428

Fermilab Recycler Stochastic Cooling Commissioning and Performance

D. Broemmelsiek, R.J. Pasquinelli (FNAL)3431

Time Evolution of Beam Current in the Recycler Ring

K. Gounder, J.P. Marriner, C.S. Mishra (FNAL)3434

Residual Gas Pressure Profile in the Recycler Ring

K. Gounder, T.G. Anderson, J.P. Marriner, C.S. Mishra (FNAL)3437

Lattice Function Measurements of Fermilab Recycler Ring

M.J. Yang, A. Marchionni, C.S. Mishra (FNAL)3440

Linac Optics Optimization for Energy Recovery Linacs

R. Nagai, R. Hajima, N. Kikuzawa, E.J. Minehara, N. Nishimori, M. Sawamura (Japan Atomic Energy Research Institute)3443

Performance and Upgrade of the JAERI ERL-FEL

M. Sawamura, R. Hajima, N. Kikuzawa, E.J. Minehara, R. Nagai, N. Nishimori (Japan Atomic Energy Research Institute)3446

Cost Estimation of an Energy Recovery Linac Light Source

M. Sawamura, R. Hajima, N. Kikuzawa, E.J. Minehara, R. Nagai, N. Nishimori (Japan Atomic Energy Research Institute)3449

Status of 150MeV FFAG Synchrotron

T. Yokoi, S. Machida, Y. Mori, A. Muto, J. Nakano, C. Ohmori, I. Sakai, Y. Sato, A. Takagi, T. Uesugi, A. Yamazaki, M. Yoshii, M. Yoshimoto, Y. Yuasa (KEK), M. Matoba, Y. Yonemura (Kyushu University), M. Aiba, M. Sugaya (University of Tokyo)3452

Stripper Foil Temperatures and Electron Emission at the Los Alamos Proton Storage Ring

T. Spickermann, M. Borden, A. Browman, D. Fitzgerald, R.J. Macek, R. McCrady, T. Zaugg (LANL)3455

Testing and Commissioning of the ALS Adjustable, Hysteresis-Free Chicane Magnet

J.Y. Jung, S. Marks, R. Schlueter (LBNL)3458

SDDS-Based Software Tools for Accelerator Design

L. Emery, M. Borland, H. Shang, R. Soliday (ANL)3461

Application of Model-Independent Analysis Using the SDDS Toolkit

L. Emery (ANL)3464

Beam Dynamics Optimization in the Rare Isotope Accelerator Driver Linac

Eliane S. Lessner, P.N. Ostroumov (ANL)3467

New Features in the SDDS-Compliant EPICS Toolkit

H. Shang, M. Borland, L. Emery, R. Soliday (ANL)3470

New Features in the SDDS Toolkit

R. Soliday, M. Borland, L. Emery, H. Shang (ANL)3473

Use of a Simple Storage Ring Simulation for Development of Enhanced Orbit Correction Software

R. Soliday, M. Borland, L. Emery, H. Shang (ANL)3476

Evaluation of the Horizontal to Vertical Transverse Impedance Ratio for LHC Beam Screen Using a 2D Electrostatic Code

U. Iriso-Ariz (BNL), F. Caspers (CERN), A. Mostacci (University of Rome)3479

Configurable UAL-Based Modeling Engine for Online Accelerator Studies	
<i>N. Malitsky, T. Satogata (BNL), R. Talman (Cornell University)</i>	3482
A Comparison of Several Lattice Tools for Computation of Orbit Functions of an Accelerator	
<i>D. Trbojevic, J.S. Berg, E.D. Courant (BNL), R. Talman (Cornell University), A.A. Garren (LBNL)</i>	3485
LIONS_LINAC: A New Particle in Cell Code for Linacs	
<i>P. Bertrand (Grand Accelérateur National d'Ions Lourds)</i>	3488
New Implement in TraceWIN/PARTRAN Codes: Integration in External Field Map	
<i>N. Pichoff (French Atomic Energy Commission), D. Uriot (CE Saclay)</i>	3491
Tools for Predicting Cleaning Efficiency in the LHC	
<i>R. Assmann, M. Brugger, M. Hayes, J.-B. Jeanneret, F. Schmidt (CERN), I. Baichev (Institute of High Energy Physics, Protvino), D. Kaltchev (TRIUMF)</i>	3494
MAD-X -- An Upgrade from MAD8	
<i>F. Schmidt, H. Grote (CERN)</i>	3497
Recent Improvements to the ASTRA Particle Tracking Code	
<i>S.M. Lidia (LBNL), K. Floettmann (DESY), P. Piot (FNAL)</i>	3500
PyORBIT: A Python Shell for ORBIT	
<i>J.-F. Ostiguy (FNAL), J. Holmes (ORNL)</i>	3503
A Framework Design for a Cyclotron Virtual Control Platform Based on Object-Oriented Methodology	
<i>B. Qin, D. Chen, M. Fan, X. Jian, Y. Xiong, T. Yu (HuaZhong University of Science and Technology)</i>	3506
Modeling and Beam Dynamic Visualization in Cyclotron Virtual Prototyping	
<i>X. Jian, D. Chen, M. Fan, B. Qin, Y. Xiong, T. Yu (HuaZhong University of Science and Technology)</i>	3509
Self-Consistent 3D PIC Code for the Modeling of High Brightness Beams	
<i>L. Serafini, A. Bacci, C. Maroli, V. Petrillo (INFN)</i>	3512
RF Coupler for High-Power CW FEL Photoinjector	
<i>S. Kurennoy, L.M. Young (LANL)</i>	3515
Recent Improvements in the PARMILA Code	
<i>H. Takeda, J. Billen (LANL)</i>	3518
The Particle Tracking Code PARMELA	
<i>L.M. Young, J. Billen (LANL)</i>	3521
PARSEC: Parallel Self-Consistent 3D Electron-Cloud Simulation in Arbitrary External Fields	
<i>A. Adelmann, M. Furman (LBNL)</i>	3524
A Modular On-line Simulator for Model Reference Control of Charged Particle Beams	
<i>C.K. Allen, C.A. McChesney (LANL), C. Chu, J. Galambos, T.A. Pelaia, A. Shishlo (ORNL), W.-D. Klotz (ORNL and ESRF), N.D. Pattengale (Sandia National Laboratories)</i>	3527
Monte-Carlo Simulation Module for LIDOS.RFQ.Designer Code	
<i>I.V. Shumakov, B.I. Bondarev, A.P. Durkin, Yu.D. Ivanov, S.V. Vinogradov (Moscow Radiotechnical Institute)</i>	3530
Template Potentials Technique with Fully-Parameterized Field Solver for High-Current Beams Simulation	
<i>L.G. Vorobiev, R. York (National Superconducting Cyclotron Laboratory)</i>	3533
On-Line Model of the SNS Medium Energy Beam Transport Line	
<i>A. Aleksandrov (ORNL), V. Alexandrov (Branch of INP, Protvino)</i>	3536
Particle Tracking and Bunch Population in TraFiC4 2.0	
<i>A.C. Kabel (SLAC)</i>	3539

A Parallel Code for Lifetime Simulations in Hadron Storage Rings in the Presence of Parasitic Weak-Strong Beam-Beam Interactions	
<i>A.C. Kabel, Y. Cai (SLAC), B. Erdelyi, T. Sen, M. Xiao (FNAL)</i>	3542
Parallel Simulation Algorithms for the Three-Dimensional Strong-Strong Beam-Beam Interaction	
<i>A.C. Kabel (SLAC)</i>	3545
Code Comparison for Simulations of Photo-Injectors	
<i>C.G. Limborg, Y.K. Batygin (SLAC), J.-P. Carneiro, K. Floettmann (DESY), L. Giannessi, M. Quattromini (Ente Nazionale per le Nuove Tecnologie l'Energia e l'Ambiente), M. Boscolo, M. Ferrario, V. Fusco, C. Ronsivalle (INFN)</i>	3548
Simulation of Particle Dynamics in Accelerators Using the Ensemble Model	
<i>W. Ackermann, W. Beinhauer, H.-D. Graef, M. Krasilnikov, A. Richter, T. Weiland (Technische U. Darmstadt)</i>	3551
Periodic Boundary Conditions in the Parallel Eigensolver OM3P: Application of the Inexact Lanczos Process to Hermitian Systems	
<i>J.F. DeFord, B. Held (Simulation Technology & Applied Research, Inc.)</i>	3554
Simulation Tools for High-Intensity Radiographic Diodes	
<i>S. Humphries (Field Precision), J. McCarrick, T. Orzechowski (LLNL)</i>	3557
Development of 3D Finite-Element Charged-Particle Code with Adaptive Meshing	
<i>L. Ives, T. Bui, W. Vogler (Calabazas Creek Research, Inc.), D. Datta, M. Shephard (Rensselaer Polytechnic Institute)</i>	3560
Conformal Modelling of Space-Charge-Limited Emission from Curved Boundaries in Particle Simulations	
<i>E. Gjonaj, T. Lau, T. Weiland (Technische U. Darmstadt)</i>	3563
Simulation of Dark Currents in a FEL RF-Gun	
<i>S. Setzer, W. Ackermann, T. Weiland (Technische U. Darmstadt), M. Krasilnikov (DESY)</i>	3566
Investigation of Dark Currents in the S-DALINAC Superconducting Cavity	
<i>S. Setzer, M. Gopych, H.-D. Graef, U. Laier, M. Platz, A. Richter, A. Stascheck, S. Wazlawik, T. Weiland (Technische U. Darmstadt)</i>	3569

TUNING OF THE RF FIELD OF THE DTL FOR THE J-PARC

F. Naito*, H. Tanaka, M. Ikegami, T. Kato, E. Takasaki, KEK, Tsukuba, Japan
T. Ito, JAERI, Tokai, Japan

Abstract

Tuning of the accelerating field of the DTL first tank for the Japan Proton Accelerator Research Complex (J-PARC) has been done. The first DTL tank consists of 75 full drift tubes, 37 post-couplers and 10 fixed tuners. The resonant frequency of the tank is 324 MHz. An uniform accelerating field has been achieved by the fine adjustment of the post-couplers and the fixed tuners. The field stabilization by the post-couplers against perturbations has been confirmed also. In order to achieve the stabilized-uniform distribution of the average field for each accelerating gap, the following techniques have been applied for the post-coupler tuning: (1) non-uniform insertion length of the post-coupler from the tank wall; (2) increment of the diameter of several post-couplers. The recipe of the fine post-coupler tuning is described.

INTRODUCTION

The construction of Japan Proton Accelerator Research Complex (J-PARC) has been started[1]. The J-PARC consists of a 181-MeV linac, a 3-GeV rapid cycle synchrotron and a 50-GeV synchrotron. The 181-MeV injection linac is comprised of a H^- ion source, a radio-frequency quadrupole (RFQ) linac, a drift-tube linac (DTL), a separated DTL (SDTL) and several beam transport lines. The linac will be extended to obtain the a 400-MeV beam by adding the annular coupled structure (ACS) linac at the downstream of the SDTL in the next phase of the project.

The Alvarez-type DTL accelerates the H^- ion beam from 3 to 50 MeV. It consists of the three independent tanks of which the length is about 9 m. Furthermore each tank is comprised of three short unit tanks (~ 3 m in length). The inside diameter of the tank is 560 mm. The resonant frequency is 324 MHz. Each drift tube (DT) accommodates the tunable electromagnetic quadrupole.

For the first tank (DTL-1), which accelerates the beam from 3 MeV to 20 MeV, the assembling of the tube and the tuning of the post-coupler have been completed.

The tuning of the post-couplers were not so simple. In the following section we describe the situation of our DTL-1 rf properties and the tuning procedure of the post-couplers in detail.

* fujio.naito@kek.jp

STRUCTURE OF DTL-1

The DTL-1 has 75 full-size DTs and two half-size DTs. The drift tube is 140 mm in diameter. Bore diameter of the DT is 13 mm till the lower energy side of the 57th DT, and it changes to 18 mm from the higher energy side of the DT to the last DT in DTL-1.

The layout of the tuners and the input couplers are shown in figure 1. The first and third unit tanks have four fixed tuners. The second unit tank has two fixed tuners and also has two movable tuners. Diameter of the tuner is 80 mm. There are two power input ports in the tank in order to reduce the rf power per coupler. Each coupler is located at one fourth of the total length from the end plate in order to suppress the excitation of the TM_{011} mode.

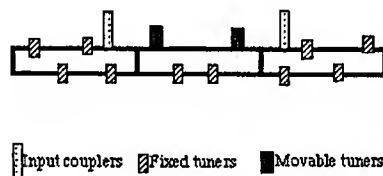


Figure 1: Layout of the tuners and the input couplers.

ADJUSTMENT OF THE TUNERS

The accelerating field measurement has been done by using a bead-pull perturbation technique[2]. Initial field distribution of the TM_{010} mode without the tuner and the post-coupler is shown in figure 2 and the bullets (•) in figure 3. The former is the raw data and the latter is the calculated average field for each cell. The ordinate of figure 2 shows the frequency shift at each point on the beam axis. (The left side of the abscissa is the beam injection side.) The results show the non-uniform distribution of the field. One of the reason for the non-uniformity is the systematic increment of the inside diameter of the unit tank. However more precise investigation is required to explain the field distribution.

The DTL tank has two movable tuners and 10 fixed tuners as described above. The length of each fixed tuners was adjusted in order to obtain the uniform accelerating field along the beam axis. (During the tuning, the "fixed" tuners are replaced by the "movable" model tuners.) The circles (o) in figure 3 show the accelerating field for each

gap along the beam axis after the adjustment of the tuners. Here, no post-couplers are used. The resonant frequency is 323.72 MHz which is approximately 100 kHz lower than the desired value. The length of each fixed tuner is shown by bullets (●) in figure 4. As shown in figure 5, which plots the frequency shift of the tank by a tuner, the length of the last four tuners are almost maximum. Because the last four tuners can not be inserted more, other 7 tuners have to be inserted more in order to increase the tank frequency. Consequently the accelerating field distribution tilts by the unbalanced tuner effect along the tank.

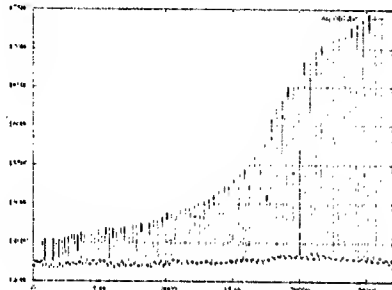


Figure 2: Measured frequency shift along the beam axis. (TM₀₁₀ mode. No post-couplers and tuners)

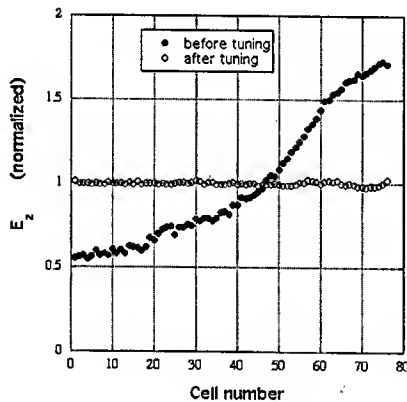


Figure 3: Accelerating field for each cell.
●: without tuners, calculated from data of figure 2.
○: after tuner tuning.

There are three methods to decrease the length of the last four tuners: (1) decrease the diameter of the third unit tank; (2) increase the diameter of the tuners; (3) increase the diameter of the post-couplers. Although the first and the second methods are standard techniques, it was very hard to apply to our cavity since the tank has been assembled. Thus the last 13 post-couplers have been rebuilt with a modified design shown in figure 6. Finally the distribution of the tuner length has been improved as shown by circles (○) in figure 4. In this case, the resonant frequency is 323.81 MHz with the correction of the volume increment of the post-coupler[3].

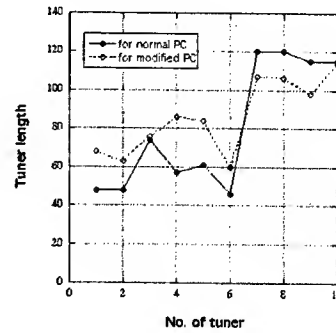


Figure 4: Length of the tuners.
●: for normal post-couplers.
○: for modified post-couplers.

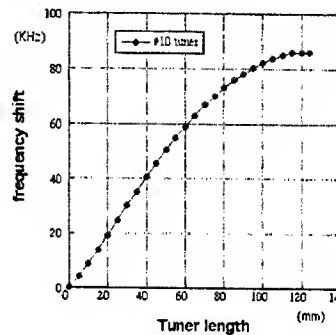


Figure 5: Frequency shift by a tuner.

TUNING OF THE POST-COUPLES

The length of the post-couplers, which include the modified-shape ones, has been adjusted by the measurement of the distribution of the average electric field for each gap along the beam axis. The initial adjustment of the post-couplers has been done by keeping up the length of all post-couplers constant.

For the field stabilization of the TM₀₁₀, the field distributions on the beam axis of the nearest neighbor modes, which are TM₀₁₁ and the mode of the highest resonant fre-

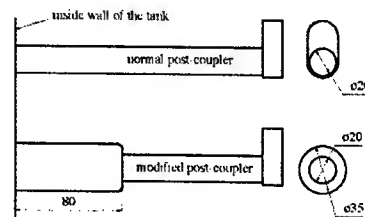


Figure 6: Design of the post-coupler.
(upper) normal post-coupler.
(lower) modified post-coupler.

quency in the post-coupler modes (it is called PC_1 mode in this report), should be almost same as each other. However, both modes have different field distributions on the axis as shown in figure 7 after the adjustment by the post-couplers with the uniform length. As a result, it has been confirmed by the measurement that the field stabilization of the TM_{010} is not so strong against perturbation in this case.

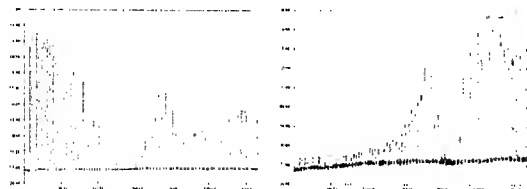


Figure 7: Measured frequency shift along the beam axis with the post-couplers of the uniform length. (left): TM_{011} (right): PC_1

Consequently it was known that the tuning of the post-coupler has to achieve the following two subjects simultaneously: (1) close the stop band between the dispersion curve of the post-mode and that of the TM -mode[4]; (2) increase the similarity between the field distribution of the TM_{011} and that of PC_1 mode along the beam axis.

As the tuning of the post-couplers with uniform length did not succeed, the length of the post-coupler was varied along the beam axis. During the tuning, the resonant frequency of the localized post-coupler mode in each cell calculated by MAFIA was very useful as the initial values of the setting. The adjusted length of the post-couplers is summarized in figure 8. The distribution of the TM_{011} and PC_1 modes was improved as shown in figure 9.

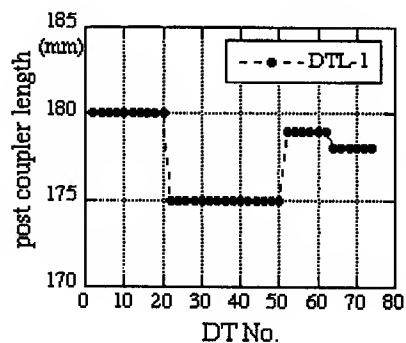


Figure 8: Final insertion length of the post-couplers.

After the fine adjustment of the post-couplers length, the tub of several post-couplers was tilted in order to improve the uniformity of the field distribution. The final result of the field distribution is shown in figure 10. The maximum deviation and the standard deviation of the distribution are approximately 2% and 0.6%, respectively. The distribution is not changed even if the tuner perturbation is applied.

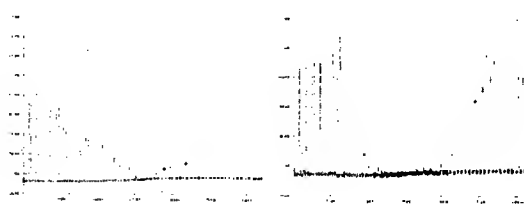


Figure 9: Measured frequency shift along the beam axis with non-uniform insertion of the post-couplers. (left): TM_{011} (right): PC_1

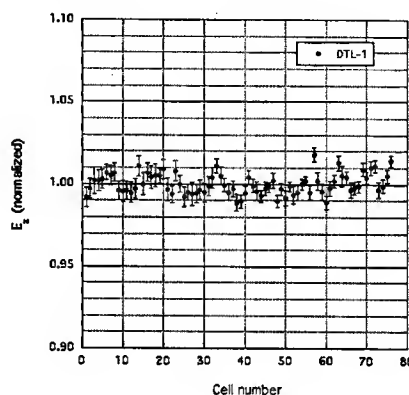


Figure 10: Accelerating field for each cell. (Error bar: 1σ)

CONCLUSION

The post-coupler tuning has been done for the DTL-1 of the J-PARC project. The tuning required the fine adjustment of post-couplers. The good measure of the tuning is the similarity between the shape of the field distribution of the TM_{011} and that of PC_1 along the beam axis. The tank has been installed in the tunnel of the test facility in KEK for the high-power test and the beam experiment.

REFERENCES

- [1] F. Naito, et al, "The KEK/JAERI joint project; Status of design and development", Proc. of LAC2002, Gyeongju, Korea, to be published.
- [2] S. Okumura and A. Swenson, "Bead perturbation measurement for the KEK linac cavity", KEK-report, KEK-74-15 (1975).
- [3] F. Naito, et al, "Mechanical and rf properties of the DTL for the JAERI/KEK joint project", Proc. of LAC2002, Gyeongju, Korea, to be published.
- [4] J. Ungrin, S. O. Schriber and R. A. Vokes, "Post-coupler and stem current measurements for high current cw drift-tube linac", IEEE Trans. Nucl. Sci. NS-30, 3013 (1983).

HIGH-GRADIENT TESTS ON S-BAND 2M-LONG ACCELERATING STRUCTURES FOR KEKB INJECTOR LINAC

Y. Igarashi[†], The Graduate University for Advanced Studies (SOKENDAI)
 S. Yamaguchi, Y. Higashi, A. Enomoto, T. Oogoe, K. Kakihara, and S. Ohsawa, KEK
 1-1 Oho, Tsukuba, Ibaraki, 305-0801 Japan
 H. Tomizawa, T. Taniuchi, H. Hanaki, Spring-8
 1-1-1 Kouto, Mikazuki-cho, Sayo-gun, Hyogo 679-5198, Japan

Abstract

In this paper, we describe high-gradient test results performed on S-band 2m-long accelerating structures for KEKB injector linac. High-gradient tests were performed on three types of accelerating structures: (1) a conventional accelerating structure for KEKB injector linac, (2) an accelerating structure whose input and output couplers were replaced by ones without a crescent-shaped cut, and (3) a conventional accelerating structure which was rinsed with high-pressure ultrapure water. As a result of the tests, an average accelerating gradient of more than 40 MV/m was obtained in all structures. Especially, 45 MV/m was achieved in a structure rinsed with high-pressure ultrapure water with a short rf processing time and a low breakdown rate (this gradient was limited by the klystron output power). Black patterns were observed at a crescent-shaped cut and the iris of the coupler cells. The simulated surface current densities were higher by about 10 times than that of the other surfaces of the cells. The measured momentum spectra were reproduced qualitatively by a simulation. It was found that the breakdown rate decreased significantly after conditioning.

1 HIGH-GRADIENT TEST OF THE ACCELERATING STRUCTURE

1.1 Tested structures

The 2m-long accelerating structure for KEKB injector linac is of a quasi-constant gradient type and has 54 regular cells with 2 coupler cells (Fig. 1). It is operated in the $2\pi/3$ mode at 2856 MHz. This structure is fabricated using a high-precision turning lathe with a diamond byte and a electroplating fabrication method. There is a crescent-shaped cut at the opposite side of the waveguide iris to correct for any asymmetry of the electromagnetic fields in coupler cell. High-gradient tests were performed on three types of accelerating structures:

Type (1): The conventional accelerating structure for KEKB injector linac [1].

Type (2): The accelerating structure whose input and output couplers were replaced with those without a crescent-shaped cut. After a high-gradient test of Type (1), a black pattern was observed at the crescent-shaped cut of the output coupler cell.

Type (3): The conventional accelerating structure which

[†]yasuhito.igarashi@kek.jp

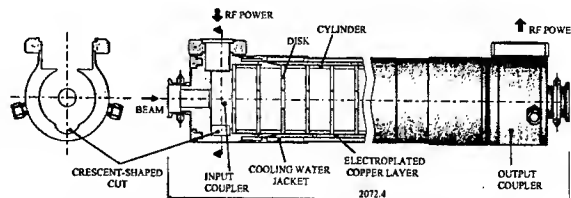


Fig. 1: Schematic of the 2m-long accelerating structure for KEKB injector linac.

was rinsed with high-pressure ultrapure water. The high-pressure ultrapure water rinsing technique (HPR) is very effective to improve the field gradients for normal conducting and superconducting rf cavities. HPR eliminates surface contamination, such as dust particles, that is thought to be one of the causes of field emission. We applied this technique to the 2m-long accelerating structure (Fig. 2). It was observed in preliminary tests that HPR could reduce dust particles to 1/10 or less on a disk surface[1].

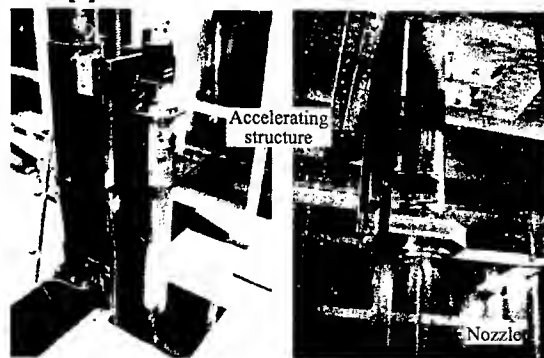


Fig. 2: High-pressure ultrapure water rinsing of the 2m-long accelerating structure.

1.2 Experimental results

The pulse width and repetition rate of the rf pulse were 4.0 μ sec and 50 Hz, respectively. At first, a test was carried out with the SLED detuned; next, it was carried out with the SLED tuned. Reflection of the rf power from the accelerating structure or waveguides, and the vacuum pressure of the ion pumps were used as an interlock. The total amount of dark current caused by the field-emitted electrons was measured by two Faraday cups set upstream and downstream of the accelerating structure. The vacu-

um pressure of the accelerating structure was maintained at around 1×10^{-6} Pa during rf conditioning.

Table 1 summarizes the high-gradient test results. The average accelerating field vs. the number of shots is shown in Fig. 3. The field enhancement factor (β) can be obtained from a modified Fowler-Nordheim (F.N.) plot. F.N. plots are shown in Fig. 4, and the β values are shown in Fig. 5 (only Type (3)). As a result of the tests, an average accelerating gradient of 45 MV/m was achieved.

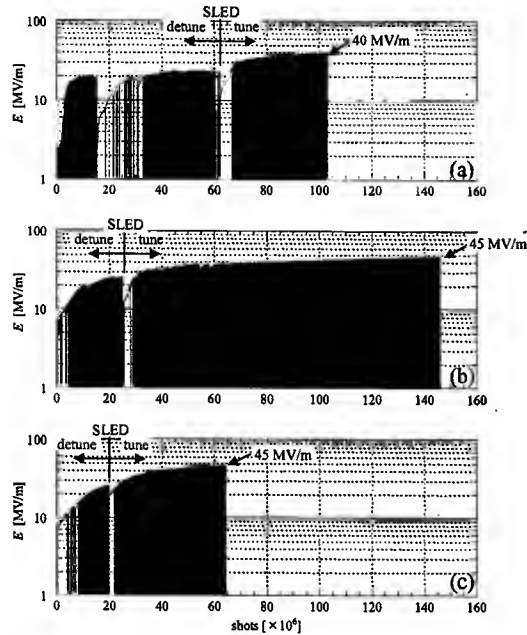


Fig. 3: Average field vs. number of shots. (a) Type(1), (b) Type(2), (c) Type(3).

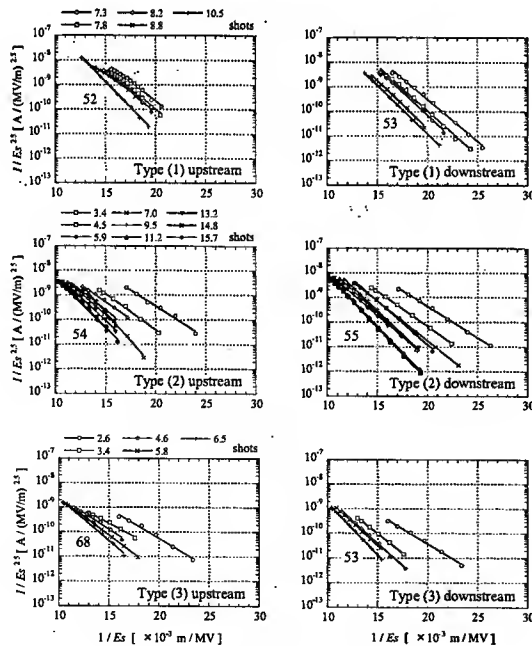


Fig. 4: Modified F. N. plot (SLED tune).

Especially, a structure rinsed with high-pressure ultra-pure water reached 45 MV/m with a short rf processing time, low breakdown rate and low dark currents compared with the others. Although this gradient was limited by the klystron output power, we are expecting that more than 45 MV/m can be achieved.

Table 1: Test results of three types of structures.

Type	Time [hour]	Shot [$\times 10^7$]	Maximum average field [MV/m]	Peak dark current [μ A]		β	
				up	down	up	down
(1)	542	10.0	40*	570	630	52	53
(2)	812	15.0	45	720	1130	54	55
(3)	356	6.4	45	300	237	68	53

*: Terminated due to a time limit

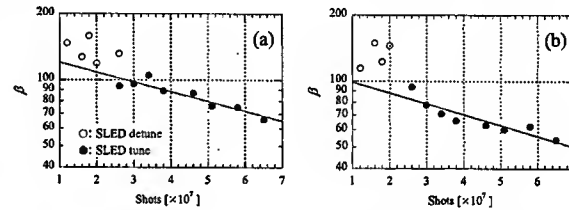


Fig. 5: Field enhancement factor (β) vs. number of shots. (a) upstream, (b) downstream.

2 BLACK PATTERNS INSIDE THE COUPLER CELLS

When we confirmed that inside of the conventional accelerating structure after the high-gradient test, a black pattern was observed at the crescent-shaped cut of the output coupler cell. Also, when we cut the accelerating structure used for the accelerator operation, in order to confirm inside of the input coupler cell, a black pattern was observed at the coupler iris.

We performed simulations of the surface electric field strength and the surface current density on the coupler cell using HFSS. The surface current densities on the crescent-shaped cut and on the coupler iris are shown in Figs. 6 and 7, respectively. From these results, the surface current densities at the location of black patterns were higher by about 10 times than that of the other surfaces of the cells.

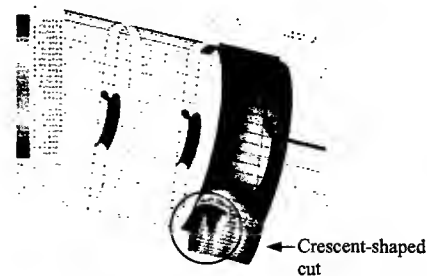


Fig. 6: Simulated surface current density on the crescent-shaped cut.

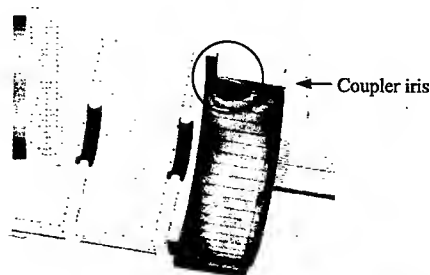


Fig. 7: Simulated surface current density on the coupler iris.

3 MOMENTUM SPECTRA OF DARK CURRENTS

The momentum spectra of the dark currents were measured by a bending magnet with a Faraday cup. The slit aperture was 20 mm. The measured result of Type (3) for an average accelerating gradient of 42 MV/m after 5.7×10^7 shots is shown in Fig. 8 (dotted line). The dashed line is the simulated momentum spectrum. The simulations were calculated by the ETS code (The simulated structures were constant-impedance types) [2]. An example of the simulated trajectories of the field-emitted electrons is shown in Fig. 9. (In this example, the number of primary electrons is 200. In the actual calculation, it was set to 720,000.) In Fig. 8, the measured momentum spectrum has a slope at the low-energy region, but the simulated momentum spectrum does not have a slope. The phase-space distribution of the field-emitted electrons that arrived at the end of structure was calculated. Fig. 10 shows the relation with the momentum and the position x and the angle x' . Most of the electrons are within the aperture size ($a = 11.875$ mm), and the low-energy electrons have a large angle. The momentum spectrum, recalculated by the electrons with $x < a$ mm and $x' < 0.02$ rad, is shown in Fig. 8 (solid line). The electrons with $x' < 0.02$ rad are captured at the cavity disks (collimator) and the slit. The simulation results were qualitatively consistent with the measurement results.

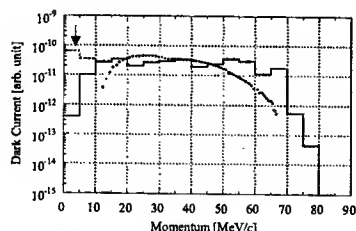


Fig. 8: Momentum spectra of the dark current.

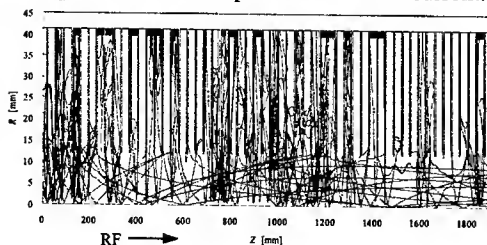


Fig. 9: Example of the field-emitted electrons trajectories.

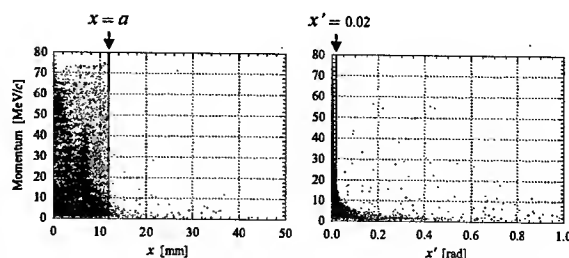


Fig. 10: Momentum vs. the position x and the angle x' of the field-emitted electrons that arrived at the end of the structure.

4 RELATION WITH THE AVERAGE ACCELERATING GRADIENT AND THE BREAKDOWN RATE

At the end of high-gradient tests, we examined the relation between the breakdown rate and the average accelerating gradient. The test result of Type (2) is shown in Fig. 11. The breakdown rate was significantly decreased after conditioning.

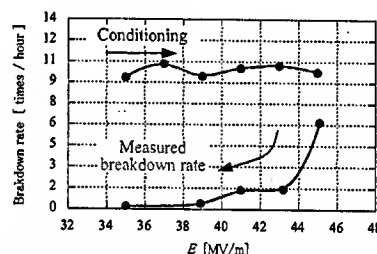


Fig. 11: Relation between the breakdown rate and the average accelerating gradient.

5 SUMMARY

An average accelerating gradient of 45 MV/m was obtained in a structure rinsed with high-pressure ultrapure water with a short rf processing time, a low breakdown rate and low dark currents. Black patterns were observed at a crescent-shaped cut and the iris of the coupler cells. As a result of simulations, the surface current densities were found to be higher by about 10 times than that of the other surfaces of the cells. The measured momentum spectra were qualitatively reproduced by the simulation. It was found that the breakdown rate decreased significantly after conditioning.

6 REFERENCES

- [1] Y. Igarashi, et al., "High-gradient Tests on an S-band Accelerating Structure", Proc. of the 21st International Linac Conference, LINAC2002, Korea, 2002.
- [2] S. Yamaguchi, "Simulation Studies on High-Gradient Experiments", LAL/RT 92-18, 1992.

MECHANICAL DESIGN OF THE DRIFT-TUBE LINAC (DTL) FOR THE SPALLATION NEUTRON SOURCE *

T. Ilg, R. Martineau, J. Sims, W. Fox, S. Ellis, R. Gentzlinger, L. Rowton, LANL, Los Alamos, NM 87545, USA

G. Johnson, ORNL, Oakridge, TN 37830, USA

Abstract

The Spallation Neutron Source (SNS) utilizes a linac to accelerate H^+ ions to 1 GeV at an average beam power of 1.4 MW. The linac consists of four RF structures: a 2.5-MeV RFQ, an 87-MeV DTL, a 186-MeV CCL, and a 1-GeV SRF linac. The DTL is divided into six RF structures, each powered by a 2.5-MW klystron. Design and fabrication of the DTL has been completed, and LANL has aligned and tuned the first structure (Tank #3) to be installed at ORNL. The description of the design and fabrication process, including machining and copper plating of the tank sections, machining and welding of the drift tubes. Also, design and fabrication of the post couplers, slug tuners, endwalls, Iris waveguide, and support structure is discussed. In addition, the assembly and alignment of the RF components using the Leica Laser Tracker System Coordinate Measuring Machine are also discussed.

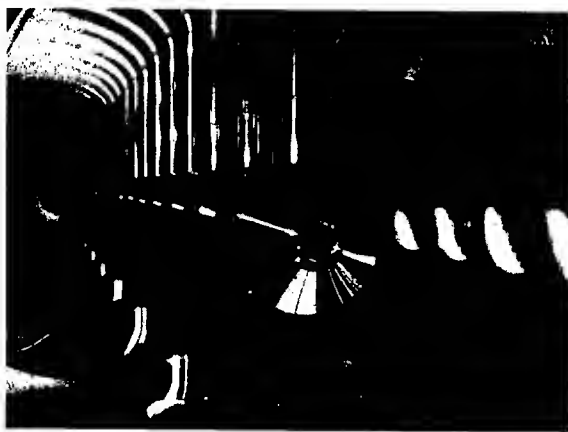


Figure 1: Photo of Drift tubes inside DTL tank 3

INTRODUCTION

The 402.5-MHz DTL is based on the Transverse magnetic (TM) Alvarez design. Cells are of length $\beta\lambda$ and the transverse focusing period is $6\beta\lambda$ in length. Focusing is accomplished with permanent magnet quadrupoles (PMQs) positioned within specific drift tubes. The focusing lattice is Focus-Focus-Empty-Defocus-Defocus-Empty, (FFODDO). The magnets are internal to the drift tube bodies and are orientated (clocked) in either of two positions to produce the focusing or defocusing field. Empty drift tubes do not contain a magnet and are left as solid copper. Some empty drift tubes will incorporate

electromagnet dipoles (EMDs) for beam steering or beam position monitoring (BPM) diagnostics. The EMD drift tubes are usually at the end of each DTL tank while the BPM drift tubes are at the beginning. The DTL will have post couplers to stabilize and adjust the longitudinal field distribution along the tank. Slug tuners will be used to provide static frequency adjustment to RF cavity.

DTL RF STRUCTURE

The DTL RF structure includes drift tubes tanks, endwalls, slug tuners, post couplers, and the waveguide iris assemblies. See figure 2 for a general layout of a DTL tank 3.

DTL Tank

The primary DTL structure is the tank or RF cavity. The tank is a vacuum vessel that provides a RF envelope and a mechanically stable platform for the array of drift-tube assemblies, post couplers, and slug tuners. The tank also provides support and interfaces to other beam-line components such as the RF system, the cooling system and the vacuum pumping system. Each tank incorporates coolant passages to flow temperature controlled water used to adjust the electro-magnetic resonant frequency of the DTL. Varying the temperature will change the dimensional characteristics of the DTL which will change its capacitance and inductance, thus changing the electro-magnetic resonant frequency.

For ease of fabrication and assembly each DTL tank assembly consist of 2 or 3 sections bolted together to form one long assembly. Each tank section is approximately 7 feet long and is fabricated from medium carbon forged (per ASTM A266 [1]) steel. Component penetrations, fastener holes, vacuum seal grooves, RF seal grooves, coolant channels, and interface surfaces are all integrally machined into each tank section. This eliminates the need for welding on any additional components to the tank section. Eliminating welding on the tank sections increases the material uniformity and reduces plating and other fabrication risks.

Steel was chosen over other potential materials such as aluminum, stainless steel, and copper because of lower material and fabrication costs.

Tank Plating

Each DTL tank section was Copper plated to increase the electrical conductivity of the tank RF surfaces. The Tank sections were plated at Gesellschaft für Schwerionenforschung (GSI) in Darmstadt Germany using

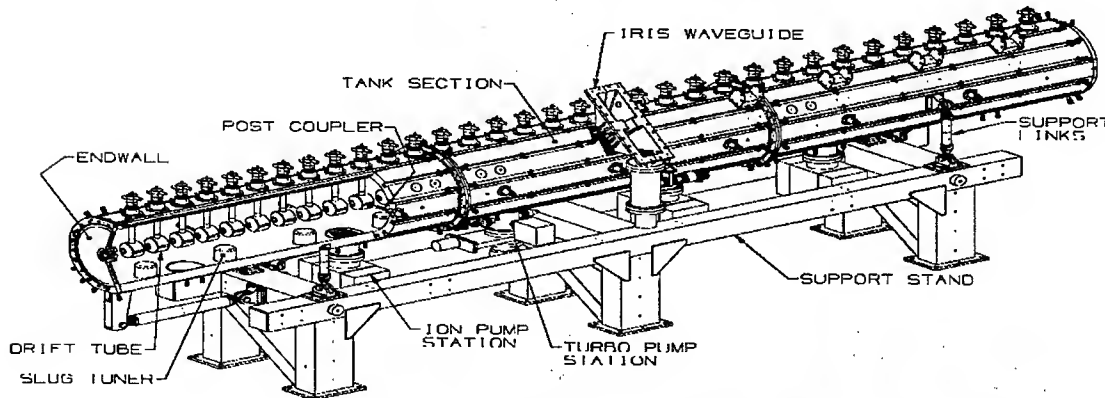


Figure 2: Partial cut-away isometric view of DTL tank 3

GSI's standard plating process for accelerator components. Their process provides a high-conductivity, ductility, high-brightness and a relatively good hardness for a plated surface. GSI was chosen because of their vast experience in copper plating accelerator components and the relatively short time they require to plate a tank section. Including preparation, each tank section was plated in approximately 2 days.

The plating process is proprietary to GSI however it is similar to the Udytite Bright Acid Copper (UBAC) bath process used on prior accelerator tanks such as the Ramp Gradient DTL and the Accelerator Test Stand (ATS) at LANL.

Drift Tubes

Each drift tube assembly is comprised of a body and stem, see figure 3. The body is made up of oxygen free electronic grade copper (OFE) parts and electron beam (EB) welded together. The stem is fabricated from concentric stainless steel tubing and is welded to the drift tube body. OFE copper was chosen for the body material because of its high electrical and thermal conductivity. The stem is constructed of stainless steel due to its strength and modulus properties. The Stainless steel stem exterior is Copper plated using the UBAC plating process. Due to high RF heating each Drift tube will be water-cooled. Drift tube fabrication methods and issues are discussed in [2].

Most Drift tubes will house a 16 segment Samarium Cobalt ($\text{Sm}_2\text{CO}_{17}$) Permanent Magnet Quadrupole (PMQ). The PMQ's provide transverse beam focusing with a gradient of 3.70 kG/cm.

Some Drift tubes will house an Electro-Magnet Dipole (EMD) required for transverse beam steering. Each DTL tank assembly will have 2 sets of the "x" and "y" EMD steering magnets. Two Drift tubes downstream of the EMD Drift tubes will house a Beam Position Monitor (BPM), which will provide beam location feedback.

Post Couplers

Post couplers are used to provide longitudinal electric field adjustment and stability. Post couplers are located in every DTL tank along the horizontal axis. They are

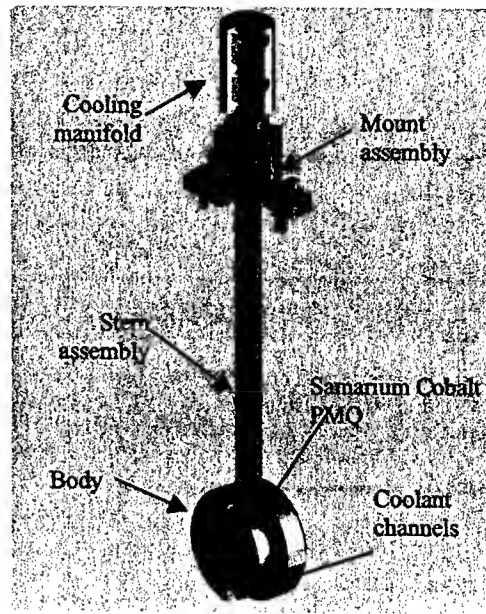


Figure 3: Cut away view of a typical Drift tube

alternately spaced from one side to the other. On tanks 1 thru 3 the post couplers are located at every other drift tubes. In tanks 4 thru 6, post couplers are located at every drift tube position. Post couplers are constructed of OFE copper and are EB welded together. Each post coupler is water-cooled and requires a unique stem length and a rotational orientation on the tank wall.

Slug Tuners

Slug tuners provide static frequency adjustment to the RF cavity. Each DTL tank incorporates 12 tuners approximately equally spaced. Each slug tuner is constructed of OFE copper components and furnace brazed. The tuning range for each tuner is approximately 110 kHz to 440 kHz for a flush to a 3" cavity penetration respectively. The penetration length was determined during low power testing on the DTL cold model.

Endwalls

Endwalls are bolted-on components that enclose each end of the DTL tank assembly. A PMQ may be installed in the half of drift tube body protruding from the endwall internal surface. The endwalls are fabricated from OFE copper parts and furnace brazed together. In some location the endwalls provide enclosures for diagnostic equipment such as a current monitor (toriod). Each endwall is water cooled to compensate for high RF heating.

Iris Waveguide

The Iris waveguide provides RF coupling to the tank cavity from the waveguide. The Iris interfaces to the air-filled waveguide thru a 402.5 MHz window. The Iris waveguide is a brazed assembly using Dispersion Strengthened (DS) copper GlidCop® AL-15 material. The DS copper was chosen because of its high strength and high thermal conductivity properties. The high strength is required due to the structural loading caused by gravity and possible seismic activity.

ALIGNMENT

Accurate transverse magnetic alignment of each drift tube PMQ is essential for proper beam focusing and beam dynamics. Typical transverse magnetic alignment between drift tubes is ± 0.005 inches (± 0.13 mm). To achieve this alignment requirement a two-step process is used, drift tube fiducialization followed by drift tube alignment. Both processes utilize the Lecia laser tracker system coordinate measure machine, LTD 500.

Drift Tube Fiducialization

A pulsed taut wire system is used to locate the transverse magnetic center of the PMQ located within the drift tube. The Lecia laser tracker system will be used to measure and record the magnetic center of the PMQ relative to references (fiducials) located on the outside of each drift tube.

A short rectangular pulse accelerates the wire transversely at the PMQ by an amount proportional to the displacement of the wire from the magnetic center. The transverse wave propagates along the wire to sensors where they are measured. The PMQ is translated transversely using x-y translation stages until the signal measured in the wire is minimized. Displacing the PMQ by known amounts using translation stages gives an accurate calibration of signal size versus misalignment. When the wire is located at the magnetic center of the PMQ the laser tracker system will be used to measure the transverse location of the wire magnetic center to the external features (fiducials). This process is also used to fiducialize the DTL endwalls that have PMQ's installed.

Drift Tube Alignment

After the drift tube fiducialization is completed each drift tube is installed into the DTL tank assembly. Using the fiducialization data each drift tube is aligned to a

common axis. This axis is the beamline axis. The axis is established using the magnetic centers of the upstream endwall PMQ and the downstream endwall PMQ. If either endwall does not have a PMQ installed the geometric center of the endwall bore tube is used. The Lecia laser tracker system coordinate measure machine aides in the construction of the alignment axis as well as the drift tube alignment.

DTL SUPPORT STRUCTURE

The DTL support structure provides support for the DTL tanks and sub-systems including the vacuum system and the water-cooling system. Each DTL tank assembly is supported by a kinematic support link system connected to a welded steel frame. The support system is designed to provide each drift tube with a structural dynamic stability of less than 200 μ -inch transverse RMS. The support structure also provides seismic restraint for the DTL tank assemblies.

REFERENCES

- [1] ASTM A 266/A266M -99, "Standard specification for carbon steel forgings for pressure vessel components".
- [2] W. Fox, "Manufacturing issues related to the fabrication of the SNS DTL drift tubes and how they were resolved", PAC2003, May 2003.

FABRICATION AND TUNING OF THE SNS CCL HOT MODEL*

N. Bultman, J. Billen, Z. Chen, M. Collier, D. Richards, L. Young,
Los Alamos National Laboratory, Los Alamos, NM 87545, USA

Abstract

A full-scale powered model of the SNS CCL was completed in August 2001. The manufacturing processes and tuning procedures used in the CCL Hot Model formed the basis of the main manufacturing contract for the SNS CCL system later placed in private industry. In this paper we summarize the design basis for the CCL and the manufacturing and process steps required to fabricate and of the various tooling and lifting and handling fixtures utilized in the process at the various machining, brazing, welding, and tuning steps. The tooling utilized in the fabrication and tuning process is discussed in detail. The ultimate successful testing of the CCL hot model was key to development of a manufacturing plan for the CCL system.

1 INTRODUCTION

The Spallation Neutron Source has the goal of designing, fabricating, installing and commissioning a complete high-energy H⁻ linac system at Oak Ridge National Laboratory to be used for the purpose of generating neutrons for materials research. The high-energy Linac spans an energy range from 2.5 MeV to 1 GeV and is composed of a room temperature section consisting of a Drift Tube Linac (DTL), and a Coupled Cavity Linac (CCL), and a Superconducting section. The

tune the Hot Model for high power testing. In particular the machining, brazing and welding steps are discussed for both the CCL Segment assembly and the powered Bridge Coupler. In addition we discuss transfer of the information and some specific modifications that were made to the basic design at the point of starting full scale manufacture in industry. One critical area to the overall success of the Hot Model was the type and specific design CCL configuration of four modules, each containing 12 accelerator segments and 11 bridge couplers. A cross-section view of the first two segments and the first bridge coupler is shown in Figure 1. The segments are Side-Coupled Cavity accelerating structures joined by offset bridge-couplers to form a continuous RF resonator. Electromagnet quadrupoles and beam diagnostic devices also occupy the spaces between the segments. The focusing period selected is $13\text{-}B\lambda$ in a FDFD configuration, giving $6.5\text{-}B\lambda$ between magnet centers. Each segment occupies $4\text{-}B\lambda$ and the remaining $2.5\text{-}B\lambda$ is available for magnets, diagnostics, and the bridge couplers.

2.1 RF Cavity Configuration

Each segment has 8 accelerating cells and 7 internal side-coupling cells. The 10 internal segments of each module have an additional flanged half-coupling cell that

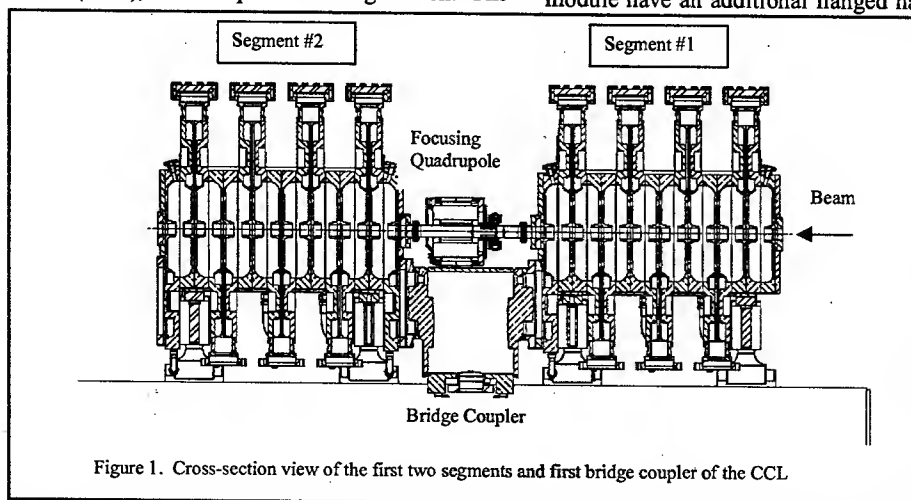


Figure 1. Cross-section view of the first two segments and first bridge coupler of the CCL

CCL section is a RF Linac, operating at 805 MHz that accelerates the beam from 87 to 186 MeV and has a physical installed length of slightly over 55 meters.

2 SYSTEM CONFIGURATION

The accelerator is modularized around a 5 MW RF power amplifier system. This requirement produces a

provides mechanical interface and power coupling with the bridge coupler. The bridge coupler has a mating end flange and cavity that forms the remaining half-coupling cell. It also has a larger powered center cell. In total each module consists of 213 cells. The module RF power is supplied through bridge couplers 3 and 9 using iris coupling into the powered center cell. This configuration

* Work supported by the Office of Basic Energy Science, Office of Science of the US Department of Energy, and by Oak Ridge National Laboratory.

provides even power distribution within the module and helps minimize field non-uniformities.

Several engineering and manufacturing simplifications were imposed on the RF cavity design to reduce the complexity and cost of fabrication. These include constant cell length within each segment, identical segment end coupling cells throughout the system, and constant outer corner radius on all accelerating cells. The latter feature also provides constant coupling slot geometry along the structure [1]. The bridge coupler end half-cells are also constant geometry throughout; the varying overall length with increasing beta is taken in the length of the center cell.

3 RF SEGMENT MANUFACTURING OVERVIEW

The CCL Hot Model segments are manufactured from simple hot rolled plate stock, machined to thickness with the cooling channels and side coupling cell cut into one surface (septum). The septum surfaces of plate pairs are vacuum-furnace brazed together to form the water cooling passages and coupling cells. The outer surfaces of the plate pairs are then machined to form the accelerating cells. The accelerating cell sides (equator planes) of the plates are stacked together to form groups of 8 accelerating cells called segments. The resonant frequency of the stacked segment is measured and adjusted by un-stacking and machining on a tuning ring inside each cell. After machining the segment is restacked and checked. When the proper tune is achieved, the stack of plates is furnace brazed together at the equator plane of each cell to form a monolithic segment having all internal cooling. After brazing fine-tuning of the segment cells is accomplished by deforming the wall of the segment in thinned "dimpling ports". The dimpling raises the frequency of the dimpled cell slightly to achieve the final cell frequency and accelerating mode frequency desired. The concept of a monolithic halfcell is utilized to allow incorporation of cooling water passages into the septum surfaces between cells while simultaneously eliminating the need for braze joints between the side coupling cell and the main accelerating cell. In addition this design approach allows the machinist to work with mostly wide, flat plates during the precision machining steps. The plate is easily held to the machine tool (mill or lathe) accurately and with minimal clamping force distortion.

3.1 Manufacturing Steps Utilized

a) Manufacturing begins with the production of the cell blanks from hot-rolled copper plate stock. The material is high purity Oxygen Free Electronic Grade (OFE) Copper that is certified to comply with the ASTM F-68 specification of Class II or Class I. This specification controls primarily oxygen content limits (less than 5 PPM oxygen) and the wrought properties of the material.

b) The cell blanks are then finish machined on the septum side, Figure 2, to produce the coupling cell geometry and the septum cooling channels. The individual plates are called "half-cells".

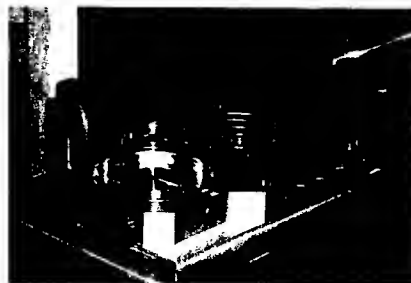


Figure 2. Septum Side Geometry

c) In the next step, the half-cells are vacuum furnace brazed together in pairs along the septum surfaces to produce "half-cell" assemblies, Figure 3. Alloy 50% Au - 50% Cu is utilized at a braze temperature of 1850 F. To this point all half-cell assemblies for each module are identical and interchangeable.



Figure 3. Septum Brazing

d) After helium leak testing, the accelerating cell sides of the plates are machined, Figure 4, to produce "finished half-cell-assemblies". The accelerating cells are rough machined in a mill and finished on a lathe using counterweights attached to the lathe chuck for balance.



Figure 4. Accelerating cell machining

e) Following cavity finish machining the parts are again vacuum leak tested, cleaned thoroughly with a water-detergent solution and dried with clean dry nitrogen. At this point the cells belong to a specific segment and are not interchangeable between segments. The $\frac{1}{2}$ accelerating cells are then frequency measured

individually and then all segment cells are stacked together in a special handling fixture, Figure 5, and the collective accelerating mode frequency is measured.



Figure 5. Measuring the Segment Frequency

The offset between the individual cell frequency and the accelerating mode frequency is then determined. The difference is a result of nearest neighbor coupling between adjacent accelerating cells directly through the coupling slot. The required accelerating mode frequency is set to a value slightly below (-200kHz) the final operating mode value of 805 MHz by removing material (machining on lathe or milling machine) (Figure 4) from the tuning ring mentioned earlier. The parts are then thoroughly cleaned and stacked for vacuum furnace brazing.

- f) The stacked assembly is vacuum furnace brazed using a copper-silver eutectic alloy at 1450 F, Figure 6. This braze produces a mechanically finished but not completely tuned segment assembly. It's complete with all water and vacuum fitting tube connections. The assembly is again vacuum leak tested and the final welds are made to the vacuum connection flanges.

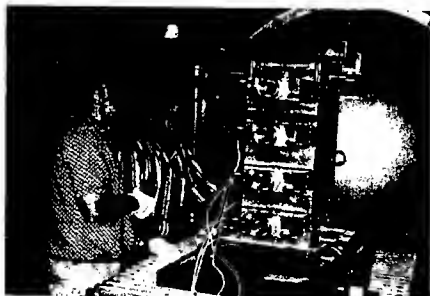


Figure 6. Stack brazing of tuned segment assembly in the vacuum furnace

- g) Following flange welding the segments are finish tuned. First the frequency of the side coupling cells must be adjusted to 805 MHz by squeezing or expanding the cell across the noses. This is done using a special wedge shaped tool to force the noses apart or by squeezing the outside with a clamp or tapping the cell nose region lightly with a hammer.

When the side cells are complete the accelerating cells are adjusted in frequency (raised) by dimpling in the wall of the thin ports for each cell located on the sides of the segment. During the pre-braze tuning step the accelerating cells are intentionally set about 200 kHz low to allow room for raising the frequency at this step by dimpling. The final adjustment then must raise the frequency of the accelerating cells about 150 to 200 kHz during the dimpling process. The dimple ports are able provide a total tuning range of about +400 kHz if needed. Figure 7 shows the dimpling being done on the first Hot Model Segment located on the support stand in the test bay.



Figure 7. Tuning the Accelerating Cells

- h) Following the dimpling process the segments and the bridge coupler are joined and the frequency of the group is adjusted. Particularly the frequency of the segment end cells and the end coupling cell must be done with the entire unit assembled. When this is completed an electric field measurement is made in the cells by pulling a metal bead through the gaps and recording the effect on a phase-locked loop. The field distribution must be correct or some tuning steps are repeated as required. Figure 8 shows the Hot Model assembly and a bead pull measurement.



Figure 8. Bead Pull measurement on the Hot Model

4 CONCLUSIONS

The manufacturing and tuning steps have been successfully demonstrated on the CCL Hot Model. The manufacturing and tuning steps as well as the specialized tooling and handling fixtures have been critical to the success of the process. These same processes have been incorporated into the contract and work procedures for the construction of the full-scale CCL accelerator.

RIA FRAGMENTATION LINE BEAM DUMP

W. Stein, Lawrence Livermore National Laboratory, Livermore, CA 94551, USA

Abstract

The Rare Isotope Accelerator project involves generating heavy element ion beams for use in a fragmentation target line to produce selected ion beams for physics research experiments. The main beam and fission fragments, after passing through the target, are collected and passed along by a series of collecting magnets and a dipole magnet. In the first dipole magnet, the main beam impacts onto a beam dump located on each side of the magnet vacuum chamber. A dump design that involves rotating cylinders and internal water cooling passages has been designed to absorb the glancing impact of the main beam. The beam power designed for is 100 kW and water cooling is by turbulent sub-cooled forced convection.

INTRODUCTION

The RIA accelerator beams consist of particles in a range from protons to uranium ions which are impacted on either ISOL or fragmentation line targets. The power along one fragmentation line is expected to be 100 kW for a uranium ion beam. The beam after passing through the fragmentation target is dumped along the sides of the first dipole magnet.

The beam dump that can absorb the main beam has been designed to fit inside the first dipole magnet of the fragment separator. As the beam is curved through the dipole magnet it may impact either side of the magnet vacuum chamber.

The dump physical design consists of rotating cylinders placed along the sides of the magnet vacuum chamber. The beam is assumed to impact the dump at an angle of 15 degrees and the beam deposited heat is removed by water coolant in the dump copper channels.

BACKGROUND

The beam for the fragmentation line impacting the fragmentation target has a nominal diameter¹ of 1 mm and a power of 100 kW with an energy of 400 MeV per nucleon. After passing through the fragmentation target the beam emerges with a slight angle spread and passes through the first dipole magnet. The beam is estimated to be at a diameter of 2 cm as it impacts the beam dump. Selection of desired fission fragments by adjustments in the magnet results in the beam striking either side of the magnet vacuum chamber.

When the beam strikes the metal of the beam dump, the energy of the particles penetrate and deposit energy according to the relationship:

$$I = I_0 e^{-x/a} \quad (1)$$

With I_0 equal to the initial intensity, "x" equal to penetration depth, and "a" equal to the interaction length for uranium ions in copper. For 400 MeV per nucleon uranium ions into copper, "a" equals 0.42 cm.

Beam Dump Geometry

The arrangement of the fragmentation target and the fragment separator is as shown in Fig. 1. The beam dump is located in the first dipole magnet of the separator and consists of two rotating cylinders on each side of the dipole magnet vacuum chamber and is shown schematically in Fig. 2.

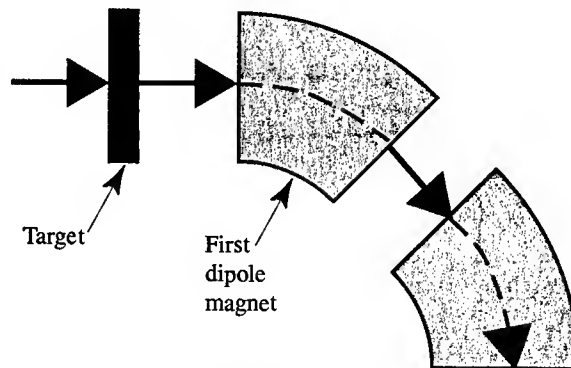


Figure 1: Fragment separator and target schematic.

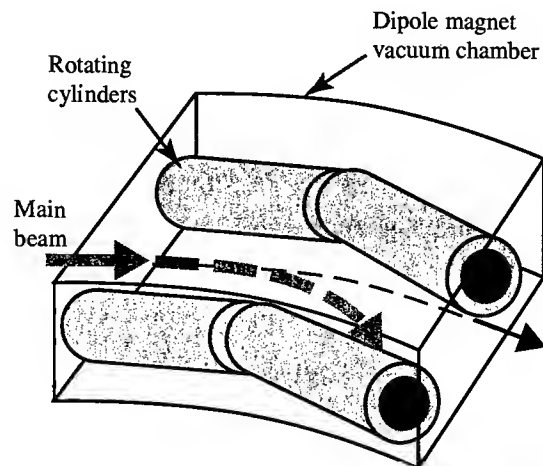


Figure 2: Beam dumps located in the first dipole magnet cavity.

* Work sponsored by the U.S. Department of Energy under Contract Nos. DE-AC03-76SF00515 (SLAC) and by Lawrence Livermore National Laboratory under Contract W-7405-Eng-48. Neither the U.S. Government nor the University of California makes any warranty or assumes any legal liability for the accuracy, completeness, or usefulness of the work performed.

The dump material is chosen to be copper because of its high thermal conductivity. The figure shows schematically the beam striking the side of the rotating cylinder at an angle estimated to be 15 degrees.

The beam dump cylinders consist basically of a cylinder with coolant channels as shown in Fig. 3. The cylinder outside diameter is 12 cm and the inner diameter is 11.3 cm. The longitudinal channels are 1 mm wide, 2 mm high, and spaced 1 mm apart.

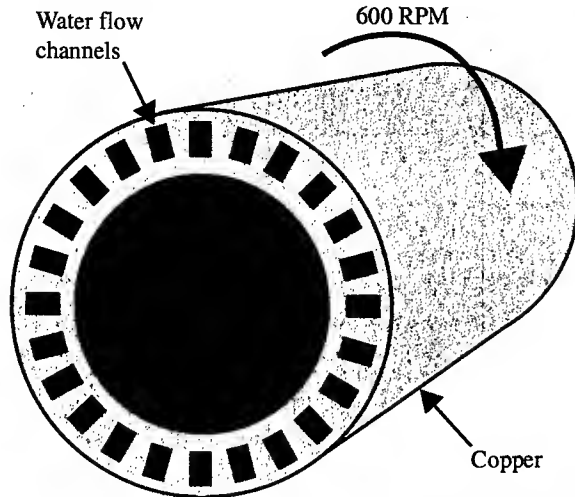


Figure 3: Schematic cross-section of beam dump cylinder design.

The cylinder is assumed to be rotating in order to spread out the beam energy over the greatest possible dump surface area. A rotation speed of 600 RPM will effectively accomplish this.

Heat transfer analyses

The impact of the 2 cm diameter beam with a 15 degree angle on the rotating surface will result in the 100 kW beam spread out over a cylindrical surface that has a diameter of 12 cm and a length of 7.5 cm. The surface flux is thus 3.6 MW/m² and this power is deposited into the copper exponentially varying to zero over a depth of 0.5 cm. The water cooling is assumed to have a velocity of 10 m/s and a turbulent convective heat transfer coefficient of 20000 W/m²°K. The heat transfer coefficient is calculated from Nusselt number, Nu, correlations² for turbulent water flow with applicable Reynolds, Re, and Prandtl, Pr, numbers:

$$Nu = 0.023(Re)^{0.8} Pr^{1/3} \quad (2)$$

Inlet water pressure is assumed at 3 atmospheres and the water inlet temperature is 20 °C. For 100 kW power, the water heats up less than 3 °C over its flow length.

A two dimensional heat transfer analysis was made to determine peak copper surface temperatures and also annulus water/copper surface temperatures. The LLNL two-dimensional finite element heat transfer code, TOPAZ2D³, was used to make the calculations. The code modeled the energy deposition rate per unit volume on the outside region of the copper dump, the thermal conduction heat transfer in the copper, and the convection heat transfer to the 20 °C water with a convection heat transfer coefficient. Fig. 4 shows a color fringe plot of the temperature profile in a cross section of the beam dump.

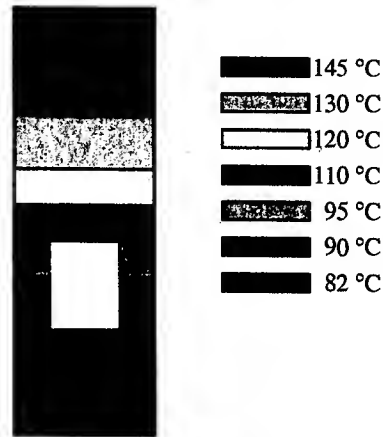


Figure 4: Calculated temperature profile in a dump cross section (20 °C water).

The plot shows that the peak surface temperature of the copper is 145 °C and the peak channel wall temperature is 110 °C with a water bulk temperature of 20 °C.

SUMMARY

A beam dump for the RIA fragmentation line can be designed to fit inside the first dipole magnet vacuum chamber. The dump consists of rotating cylinders that absorb the 100 kW beam energy as the beam strikes the cylinders at a small angle. The dump is cooled with forced convection turbulent water flow that maintains coolant channel wall temperatures below the water boiling temperature.

REFERENCES

- [1] J.A. Nolen, et al., "Liquid-lithium cooling for 100 kW ISOL and fragmentation targets," *Nuclear Physics A 701* (2002) 312c-322c.
- [2] Frank Kreith, *Principles of Heat Transfer*, Intex Press, Inc., 3rd edition, 1973, p. 431.
- [3] A.B. Shapiro, A.L. Edwards, *TOPAZ2D Heat Transfer Code Users Manual*, Lawrence Livermore National Laboratory, Livermore, California, UCRL-ID-104558 (Rev 1), May 1990.

ANALYSIS OF A MULTI-SPOKE OPTION FOR THE RIA DRIVER LINAC*

D. Gorelov[†], T. Grimm, W. Hartung, F. Marti, X. Wu, and R.C. York
National Superconducting Cyclotron Laboratory, MSU, East Lansing, MI 48824, USA

Abstract

Beam dynamics simulations of the proposed Rare Isotope Accelerator (RIA) [1] driver linac have been done. The RIA driver linac is designed to accelerate stable ion beams from proton to uranium to final energies of 400 MeV/u for the heaviest and about 900 MeV/u for the lightest ions with beam powers of 100 to 400 kW. Two stripping sections are used to increase the charge state of heavy ions and minimize the total accelerating voltage required. To achieve the final beam power and to reduce the ion source requirements, multi-charge state beam acceleration is used. Multi-spoke structures [2] in the high-energy part of the driver linac have been proposed as an alternative to the baseline design of 6-cell elliptical structures [3]. A comparative analysis of this alternative is explored including beam dynamics, error constraints, and manufacturing issues.

INTRODUCTION

The baseline RIA driver linac design uses 805 MHz 6-cell elliptical cavities with geometric β_g of 0.47, 0.61 and 0.81 to accelerate beam from the 2nd charge-stripping chicane at ~85 MeV/u to final energies of ≥ 400 MeV/u [3]. (An alternative design without the $\beta_g = 0.81$ cavities is also being evaluated, but would not affect these results.) Figure 1 shows a section view of a $\beta_g = 0.47$, 805 MHz 6-cell elliptical cavity. A prototype $\beta_g = 0.47$, 805 MHz 6-cell elliptical cavity was completed and tested in 2002, exceeding design goals [4].



Figure 1: $\beta_g = 0.47$ 805 MHz 6-cell elliptical cavity.

An option of using 322 MHz triple-spoke cavities in lieu of the 805 MHz 6-cell elliptical cavities was proposed in 2002 [2]. Because of the lower operating frequency of the triple-spoke structures, the required number of cavities in the driver linac for the spoke cavity option will be smaller. Two types of triple-spoke cavities are required, with optimum $\beta = 0.48$ and $\beta = 0.62$. Figure 2 shows a section view of a 322 MHz, triple-spoke cavity for $\beta = 0.62$. No prototype has been made of this cavity.

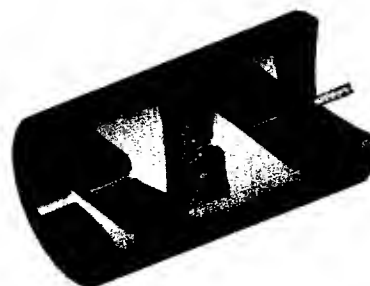


Figure 2: $\beta = 0.62$ 322 MHz triple-spoke cavity.

Longitudinal and transverse beam dynamics studies were performed to compare these two alternative designs in the high- β section of the RIA driver linac using the computer codes LANA [5] and DIMAD [6].

LONGITUDINAL BEAM DYNAMICS

The longitudinal acceptance of the elliptical structure linac with average reference particle phase in the accelerating gaps $\phi_s \sim 30^\circ$ is comparable in size with the longitudinal acceptance of a triple-spoke structure linac with $\phi_s \sim 15^\circ$, as shown in Figure 3. For the 6-cell elliptical cavities an accelerating gradient of $E_0 T = 8.28$ MV/m was used, corresponding to a peak electric field of $E_p = 27.5$ MV/m and requiring 192 cavities. For the triple-spoke structures, $E_0 T = 7$ MV/m was used, corresponding to a peak electric field of $E_p = 20$ MV/m and requiring 152 triple-spoke cavities for $\phi_s \sim 15^\circ$. (Note that a 6-cell elliptical cavity system with a frequency of 644 MHz (8th harmonic of initial frequency) would require 154 cavities, but, like the triple-spoke, this cavity has never been prototyped.)

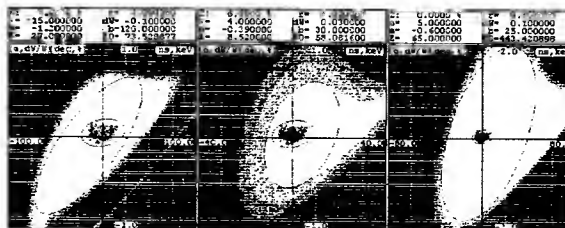


Figure 3: Longitudinal beam acceptances for 6-cell elliptical cavities with $\phi_s \sim 30^\circ$ (left), triple-spoke cavities with $\phi_s \sim 15^\circ$ (middle), and $\phi_s \sim 30^\circ$ (right, doubled scale). A multi-charge longitudinal beam emittance of $\sim 9 \pi$ keV/u nsec is shown for comparison.

TRANSVERSE BEAM DYNAMICS

Three transverse focusing lattices were established. The rf defocusing from both cavity types was found to be

*Work supported by MSU and NSF PHY 0110253.

[†]gorelov@nsl.msu.edu

similar, with strength an order of magnitude smaller than that of the lattice focusing elements. As a consequence, the transverse beam dynamics are predominantly determined by the focusing elements and the lattice layout and not the cavity choice.

The cryostat dimensions for all three focusing lattices are based on the rectangular cryomodule design with cryogenic alignment rail proposed for RIA at Michigan State University [7]. A prototype cryomodule for the elliptical cavities with geometric $\beta_g = 0.47$ is under construction and easily extends to the other cavity types.

Solenoid Focusing Lattice

The layout of a solenoid focusing lattice is shown in Figure 4, with each cryostat containing four cavities and a superconducting solenoid magnet for transverse focusing. The effective lengths of the solenoids range from 0.5 to 1.25 m, with a maximum magnetic field of about 9 T. The transverse phase advance of each cryostat is about 90° . Two extra solenoids are necessary to match the beam condition from the 2nd charge-stripping chicane to a periodic solenoid focusing lattice. Figure 5 shows the beam envelopes for ^{238}U with three charge states, 87+ to 89+. The initial beam emittance for all charge states was assumed to be $2.9 \pi \text{ mm mrad}$. The maximum beam size for all three charge states is about 8.6 mm.

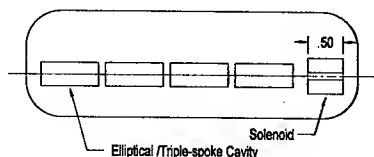


Figure 4: Layout of solenoid focusing lattice.

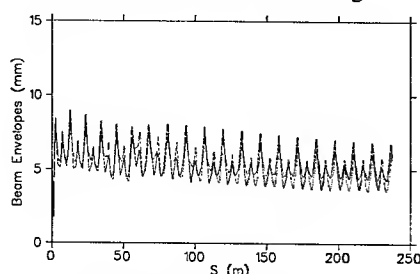


Figure 5: Multi-charge beam envelopes of ^{238}U in the solenoid focusing lattice with Triple-spoke cavities.

Two-Quadrupole Focusing Lattice

In this energy range, quadrupoles can provide a more efficient and less costly focusing system than superconducting solenoids. A layout with two superconducting quadrupoles per cryostat is shown in Figure 6. The effective lengths of the quadrupole magnets are 0.25 m with an aperture of 5 cm. For a 90° transverse phase advance per cryostat, the maximum pole face magnetic field is about 0.5 T. A short section with four quadrupole magnets is required to match the beam from the 2nd charge-stripping chicane to the regular focusing

lattice. Figure 7 shows the beam envelopes for the same beam as Figure 5. The maximum beam size for all the three charge states is about 11.3 mm significantly larger than that of the solenoid focusing lattice. The focusing properties of this lattice are virtually identical to those of a previously presented doublet-focusing lattice [3,8].

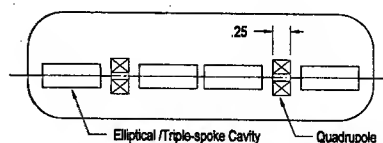


Figure 6: Layout of the two-quadrupole focusing lattice.

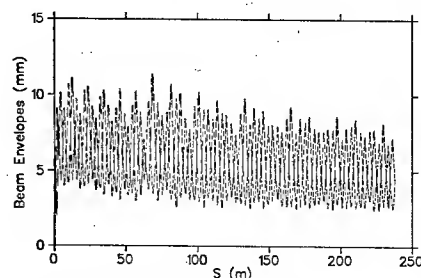


Figure 7: Multi-charge beam envelopes of ^{238}U in the two-quadrupole focusing lattice with Triple-spoke cavities.

Five-Quadrupole Focusing Lattice

To reduce the beam size to less than that of the two-quadrupole focusing lattice, a lattice with more transverse focusing and a larger phase advance was explored. The five-quadrupole focusing lattice is shown in Figure 8.

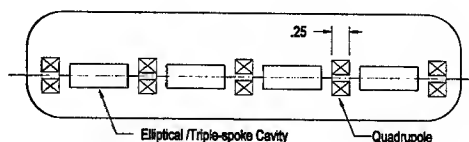


Figure 8: Layout of cryostat of the five-quadrupole focusing lattice.

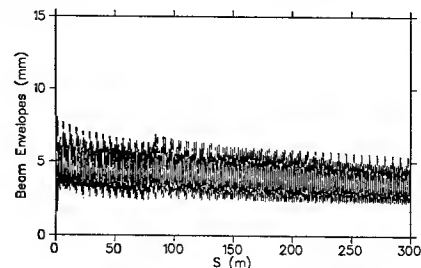


Figure 9: Multi-charge beam envelopes of ^{238}U in the five-quadrupole focusing lattice with Triple-spoke cavities.

The effective lengths of the quadrupole magnets remain 0.25 m with an aperture of 5 cm. The maximum pole face magnetic field required for these quadrupole magnets to maintain each cryostat with a transverse phase advance of about 235° is about 0.75 T. Similarly, a short section with

four quadrupole magnets is required to match the beam from the 2nd charge-stripping chicane to the regular focusing lattice. Figure 9 shows the similar multi-charge beam envelopes for ²³⁸U beam. The maximum beam size for all the three charge states is about 8 mm. However, the additional quadrupoles increase the required cryostat length by about 20%.

MISALIGNMENT AND CORRECTIONS

The lattice sensitivity to misalignment of focusing elements and cavities was investigated using DIMAD for all three transverse focusing lattices and for both elliptical and triple-spoke cavity types. The cavity choice has little impact on the lattice sensitivity based on our simulations. All accelerating structures and focusing elements were misaligned assuming a Gaussian distribution ($\pm 2\sigma$). The same correction scheme was used for all three lattices. A package in front of each cryostat consisting of a pair of horizontal and vertical orbit correctors and a beam position monitor (BPM) was assumed for the orbit correction scheme. A least-square-fit algorithm was used to obtain the horizontal and vertical corrector values that minimized the orbit distortions at all BPMs. Multi-charge beam simulations were then done to evaluate the impact on the lattice performance.

Figure 10 shows the misalignment simulation results for all three focusing lattices, considered showing a nearly linear dependence on focusing element misalignment. (The position errors for the cavities were fixed at 1.0 mm.) The triple-spoke cavity will have a much smaller aperture with 3 cm or possibly 4 cm, being considered, while the 805 MHz 6-cell elliptical cavities have a much larger aperture (7.7 cm). To avoid uncontrollable beam halo formation due to nonlinear radial accelerating field dependence in the cavities, 1/3 of the cavity aperture was assumed to be an exclusion zone for the beam as shown in shaded areas in Figure 10.

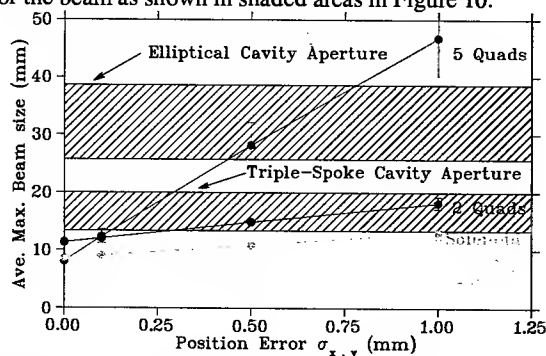


Figure 10: Average maximum beam sizes vs. misalignment errors for all three focusing lattices. The apertures of elliptical and triple-spoke cavities are also shown. The shaded areas are exclusion zones for each cavity type.

Due to the large phase advance and unfavorable ratio of correctors and BPMs vs. quadrupoles, the five-quadrupole focusing lattice is the most sensitive to the misalignment

errors and will require unreasonable alignment requirements to maintain the beam inside the exclusion zones for both types of the cavities. The solenoid focusing lattice has the smallest maximum beam size, and with misalignment position errors of 1.0 mm for both the solenoids and cavities, is adequate for either cavity option. The 2-quadrupole focusing lattice has sensitivities to the misalignment errors similar to the solenoid focusing lattice, and would be adequate for the 6-cell elliptical cavity option. However with a reasonable misalignment tolerance, it will not be suitable for even a 4 cm aperture triple-spoke cavity option.

CONCLUSION

Both the 805 MHz 6-cell elliptical and 322 MHz triple-spoke cavities would in principle provide the necessary acceleration. Due to its lower frequency and therefore longer effective accelerating gap, fewer cavities are needed for the 322 MHz triple-spoke cavity option. However, the triple-spoke cavity will have a much smaller aperture, as the result, requires more expensive superconducting solenoid focusing lattice. No triple-spoke cavity has been built so far and its performance is untested. The 805 MHz 6-cell elliptical cavities have a much larger aperture and have been successfully tested in 2002. A cost effective 2-Quadrupole focusing lattice (superconducting or room-temperature) with reasonable misalignment tolerances for both quadrupoles and cavities will be an adequate choice with the elliptical structure linac.

REFERENCES

- [1] C.W. Leemann, "RIA Facility Project", Proc. of LINAC 2000, Monterey, CA, 2000.
- [2] K.W. Shepard, "The RIA Driver Linac", Proc. of LINAC 2002, Gyeongju, Korea, 2002.
- [3] D. Gorelov, T. Grimm, W. Hartung, F. Marti, H. Podlech, X. Wu and R.C. York, "Beam Dynamics Studies at NSCL of the RIA Superconducting Driver Linac", Proc. of EPAC 2002, Paris, France, 2002.
- [4] W. Hartung, C.C. Compton, T.L. Grimm, R.C. York, G. Ciovati, P. Kneisel, "Status Report on Multi-Cell Superconducting Cavity Development for Medium-Velocity Beams", *these proceedings*.
- [5] D.V. Gorelov and P.N. Ostroumov, "Application of LANA Code for Design of Ion Linac" Proc. of EPAC 1996, Sitges, June 1996.
- [6] R. Servranckx, K. Brown, L. Schachinger, and D. Douglas, "User's Guide to the Program Dimad", SLAC Report 285, UC-28, May 1985.
- [7] T.L. Grimm, W. Hartung, M. Johnson, R.C. York, P. Kneisel, L. Turlington, "Cryomodule Design for the Rare Isotope Accelerator", *these proceedings*.
- [8] X. Wu, D. Gorelov, T. Grimm, W. Hartung, F. Marti, and R.C. York, "The Misalignment and RF Error Analyses for the RIA Driver Linac", Proc. of LINAC 2002, Gyeongju, Korea, 2002.

NUMERICAL DESIGN AND OPTIMIZATION OF COOLING SYSTEM FOR 2MeV TRAVELING WAVE ACCELERATOR

SHEN Lianguan, LI Shaoqing, YAO Jianping, LI Xiaoguang, CAO Lei,
Department of Precision Machinery & Precision Instrumentation, USTC, Hefei
230026, China

JIANG Daoman, Y.J. Pei

Hefei National Synchrotron Radiation Lab., USTC, Hefei 230029, China

Abstract

Eliminating or reducing thermal deformation of an accelerator structure (caused by microwave power dissipated on the walls of RF cavities) to insure resonance frequency is an important topic in the design of the structure. A civil accelerator for killing anthrax bacilli must be small and compact, and so must its cooling system. This paper introduces the design and optimization of a cooling structure for an 0.57 m long, 2 kW, disk-loaded waveguide accelerator structure, for which the temperature distribution is required to be $30 \pm 3^\circ \text{C}$. All the parameters have been calculated and optimized by means of FEM (the Finite Element Method). The simulation is accomplished with software called I-DEAS (Integrated Design, Engineering, Analysis System). An optimized structure with a jacket style cooling chamber has been designed. The outside wall of the jacket is made of stainless steel and its external diameter is $\phi 118 \text{ mm}$. The flux of the cooling water is as small as 0.45 ton/hour. As a result, the temperature nonuniformity of the accelerator tube is better than $\pm 2.5^\circ \text{C}$. The system is also very robust against surrounding temperature shifts. The cooling system has been installed in a 2 MeV accelerator, and the facility is running well.

INTRODUCTION

The requirements for accelerators in the world market are diverse and changeable, which demands rapid response by the designers and manufacturers. Traditional procedures have not acclimatized themselves to these circumstances. Advanced technologies are emerging as the times require in this era of ours. Numerical simulation based on CAD/CAM (Computer aided Design /Computer aided Manufacture) is a most promising technology for rapidly designing new machines as market requirements change and for making them reliable.

The 2-kW traveling wave accelerator is used for scanning mail and killing potential anthrax bacilli, etc. Accelerating cavities are key parts of the accelerator.

Thermal deformation of them, caused by dissipation of microwave power, deeply affects the operating frequency of the machine. Therefore, a cooling structure that can keep temperature distribution within a tolerance region is important. This paper describes an approach to designing the cooling structure by means of the TMG Thermal Analysis module of I-DEAS, which allows people to carry out sophisticated thermal analysis as part of a collaborative engineering process and get solid reliability. All of the thermal design attributes and operating conditions can be applied as history-supported entities in a 3D model geometry. Thus an optimized design of the system is possible.

COOLING STRUCTURE DESIGN

The accelerator will serve in a post office, a location that requires it to be as compact as possible. The design should have good adaptability to its surroundings, and the cooling water flux should be kept small in order to minimize both the whole-system cost of the cooling system and the operating expense. As a design goal, the flux of cooling water should be less than 0.5 ton per hour and the temperature nonuniformity should be better than $\pm 3^\circ \text{C}$.

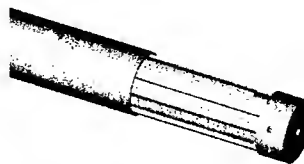


Fig. 1: Jacket type cooling structure



Fig. 2: Tube type cooling structure

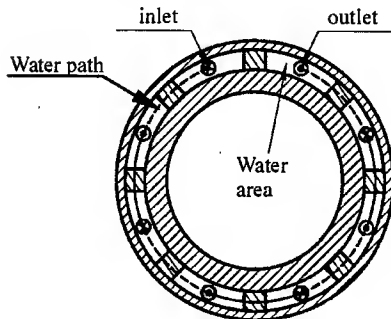


Fig. 3: Profile of the water jacket

The accelerating tube, composed of 19 cavities, is a constant impedance traveling wave accelerating structure. Generally, there are two types of cooling structures: jacket and welded tubes, as shown in Figures 1 and 2. Here certain things should be given attention. In order to diminish the inside diameter of the focus coil, a single-inlet waterway was chosen as early as possible in the design process. Considering its environment (a post office), the system must be able to deal with shifts in the ambient temperature. Because of the highly suitable manufacturing technology and the high stiffness of the structure, jacket type cooling structure has been adapted. the jacket is made of stainless steel. Calculation has shown that it is very robust against shifts in room temperature.

OPTIMIZATION OF THE PARAMETERS

The shape of the section of the water jacket

The shape and size of the water channels is an important factor, not only for small flux but also for good cooling effect and even temperature field distribution. Comparing different sections, a profile of eight chambers is chosen. It is shown in Fig. 4. The simulation calculating results show that almost all of the 2 kW power dissipated is carried away by the water. The parameters in the bold-face column are important to the requirement.

Table 1 Calculating result of the eight-chamber structure (ambient 25° C, inlet water temperature 23° C)

Mass flux of water (kg/s)		0.10	0.12	0.14	0.16	0.18	0.20
Outlet water temperature (°C)		27.76	26.97	26.40	25.98	25.65	25.39
Temperature of the accelerator structure (°C)	MAX	32.72	31.60	30.78	30.15	29.64	29.23
	MIN	28.00	27.17	26.58	26.14	25.79	25.51
	T	4.72	4.43	4.20	4.01	3.85	3.72
Energy carried by water (W)		1991	1994	1996	1997	1998	1999

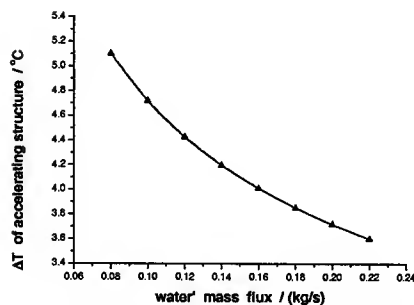


Fig. 4: Influence of mass flux on temperature distribution

Determination of the water flux

In order to cut the construction and operating costs of the cooling system, optimization of the mass flux of the water is another target. Fig. 5 shows that the relationship between the temperature distribution of the accelerating structure vs. the mass flux of the water is nonlinear. The mass flux of 0.12 Kg/s fits within the limit of 0.5 ton/h. In this case the temperature distribution is $\pm 2.2^{\circ}\text{C}$.

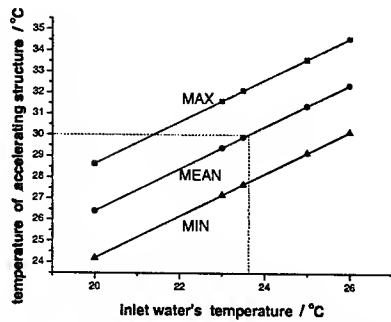


Fig. 5: Influence of inlet water's temperature on temperature of accelerating structure

Selection of Inlet water temperature

The distribution of the temperature should be kept around $30 \pm 8^\circ \text{C}$ (which we consider the mean temperature) when the machine runs. Calculation shows that the mean temperature of the accelerating structure is almost a linear function of inlet water temperature (see Fig. 6). The results also indicate that the influence of ambient temperature on temperature dispersion can be ignored.

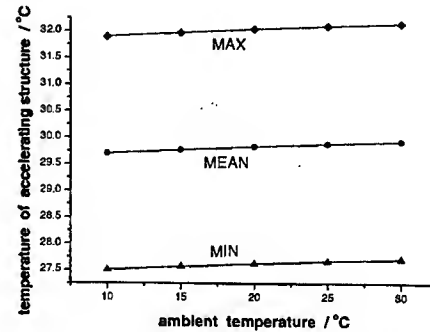


Fig. 6: Influence of ambient temperature on temperature of accelerating structure

Table 2 Simulation results under different ambient temperatures

(Mass flux 0.12 kg/s, inlet water temperature 23.5°C)

Ambient temperature (° C)		10	15	20	25	30
Outlet water temperature (° C)		27.33	27.38	27.42	27.46	27.50
Temperature of accelerator structure (°C)	MAX	31.90	31.97	32.04	32.10	32.15
	MIN	27.51	27.57	27.62	27.67	27.71
	T	4.39	4.40	4.42	4.43	4.44
Energy carried by water (W)		1924	1949	1972	1992	2008

CONCLUSION

Integrating the above numerical simulations, a set of satisfactory parameters for the cooling system has been achieved. The system has been constructed and commissioned in the accelerator, which is running well.

REFERENCES

- [1]. Tian Z, Pei Y J. Finite Element Analysis of RF Cavity for HLS Storage Ring [J], Nuclear Techniques, 1999, Vol. 22, No.2: 107-113.
- [2]. Y.J. Pei, D.F. Wang, D.H. He, 200MeV LINAC-inject for storage ring of HESYRL [J], Review of Scientific Instruments, 1989, Vol. 60, No. 7: 1701-1704.
- [3]. Shen L G, Qian X B. Finite Element Analysis of RF Cavity for HLS Storage Ring [A], in Proceedings of the Second Conference on Technology of Accelerator[C], 1998.7, Ning Bo.
- [4]. Hu Defang, Tian Baoying, Ouyang Xiaotao, et al., The MACSYM-350 Computer System for Thermal Parameters Measurement and Control for HESYRL [A], in Proceedings of the International Conference on Synchrotron Radiation Application [C], May 9-1, 1989, Hefei, China.

IMPACT OF CAVITY RF FIELD PHASE AND AMPLITUDE CONTROL UNCERTAINTIES ON THE SNS LINAC*

D. Jeon[#], SNS Project, ORNL, Oak Ridge, TN37830, USA

J. Stovall, H. Takeda, LANL, Los Alamos, NM87545, USA

K. Crandall, TechSource, Santa Fe, NM87594, USA

Abstract

There is an accuracy limit of LLRF control over cavity rf phase and amplitude. This limited accuracy of control gives rise to beam energy and phase jitter, emittance growth, and beam loss. In the case of the SNS linac [1], there are a few limiting factors such as minimizing injection foil miss, acceptable ring injection painting, and beam loss in the linac which are related with the LLRF control errors. We studied the impact of $\pm 1^\circ / \pm 1\%$ and $\pm 0.5^\circ / \pm 0.5\%$ rf phase and amplitude uncertainties to the linac using the Ltrace and Parmila codes.

BEAM CENTROID ENERGY AND PHASE JITTER

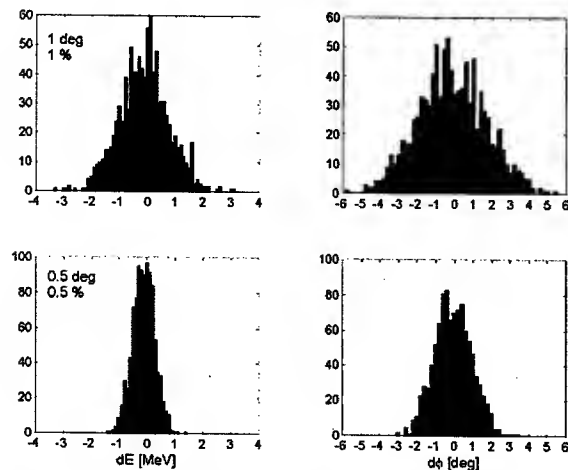


Figure 1: Histograms of beam centroid energy and phase jitters at the SCL end for $\pm 1^\circ$ and $\pm 1\%$ rf phase and amplitude control (upper plots) and for $\pm 0.5^\circ$ and $\pm 0.5\%$ rf phase and amplitude control.

As a direct consequence of cavity rf phase and amplitude control uncertainties, the beam energy and phase jitters are induced. If these jitters exceed a certain limit, it may lead to ring injection problem. The injection beam energy and phase jitters are assumed to be zero. Figure 1 shows histograms of beam centroid energy and phase jitters at the SCL end for $\pm 1^\circ$ and $\pm 1\%$ rf phase and amplitude uncertainties (upper plots) and for $\pm 0.5^\circ$ and $\pm 0.5\%$ rf

phase and amplitude uncertainties. These are the results of 1000 linac runs using the Ltrace code. When the LLRF control uncertainties increase by factor two, the centroid energy and phase jitters almost doubles.

There is an energy corrector cavity (ECC) in the HEBT just before the achromat bend to reduce the beam energy jitter to facilitate the ring injection painting. What really counts is the beam centroid energy jitter after the ECC. Figure 2 shows the beam centroid energy jitters at the SCL end (left column) and after the ECC (right column) for the two sets of rf control uncertainties. As is shown, beam centroid energy jitter after the ECC degrades from $\pm 0.2\text{MeV}$ to $\pm 0.4\text{MeV}$. 99 (90)% of beam is within $\pm 0.2\text{MeV}$ for the $\pm 0.5^\circ / \pm 0.5\%$ [$\pm 1.0^\circ / \pm 1.0\%$] rf control uncertainties. This is a minor degradation. So from the viewpoint of beam centroid energy and phase jitters, $\pm 1.0^\circ$ and $\pm 1.0\%$ rf control uncertainties make little difference after the energy corrector cavity.

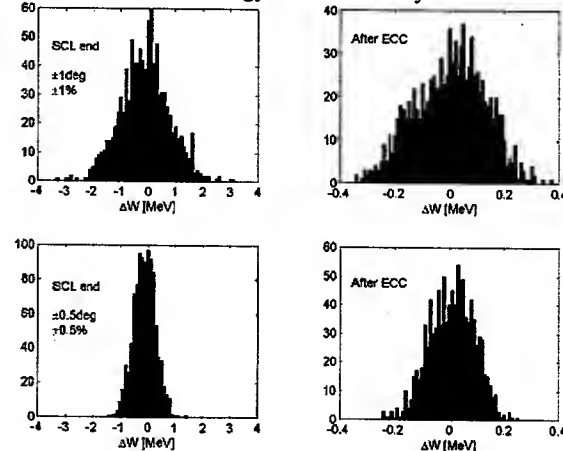


FIG. 2: Histograms of beam centroid energy at the end of SCL and after the ECC for the two sets of rf control.

BEAM EMITTANCE GROWTH IN THE LINAC

Beam emittances grow due to the rf control errors. This is important because it affects the injection foil miss and beam loss in the linac. To see the impact, 1000 Parmila [2] runs were made with 10 000 macro particles. The injected beam to DTL is an ideal water bag beam with a 0.22 (0.30) $\pi\text{mm-mrad}$ transverse (longitudinal) rms emittance. So attention should be paid to the relative difference between emittance values for the two sets of rf control uncertainties.

* SNS is a collaboration of six US National Laboratories: Argonne National Laboratory (ANL), Brookhaven National Laboratory (BNL), Thomas Jefferson National Accelerator Facility (TJNAF), Los Alamos National Laboratory (LANL), Lawrence Berkeley National Laboratory (LBNL), and Oak Ridge National Laboratory (ORNL). SNS is managed by UT-Battelle, LLC, under contract DE-AC05-00OR22725 for the U.S. Department of Energy.

[#]jeond@ornl.gov

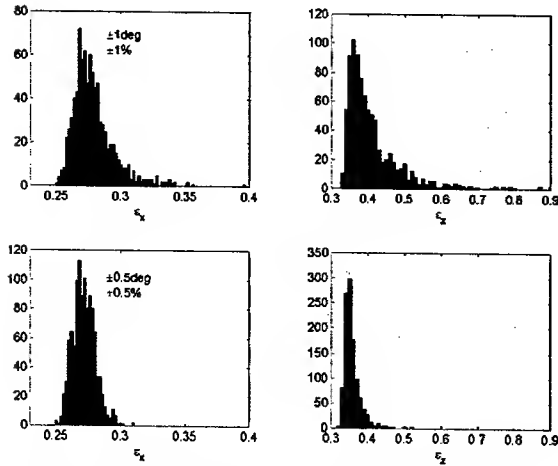


Figure 3: Histograms of x and z rms emittances [π mm-mrad] at the SCL end for the two sets of rf control errors.

Figure 3 shows the histograms of x and z rms emittances [π mm-mrad] at the end of SCL for the two sets of rf control errors. Clearly the transverse emittance ϵ_x degrades modestly even though the longitudinal rms emittance ϵ_z significantly degrades. So the injection foil miss and beam loss due to the transverse emittance growth will increase only modestly compared with the

$\pm 0.5^\circ$ and $\pm 0.5\%$ rf phase and amplitude uncertainties. This is a result of the weak space charge coupling between transverse and longitudinal dimension of the SNS linac design. For some of the beams, the transverse emittance increases by more than 15%. This is an indication of the increase of beam loss when the rf control uncertainties increase. Even though this is acceptable for the current CD-4 commissioning goal, $\pm 0.5^\circ$ and $\pm 0.5\%$ rf phase and amplitude uncertainties are recommended for the post CD-4 operation.

CONCLUSION

We can commission the SNS linac with $\pm 1.0^\circ$ rf phase and $\pm 1.0\%$ rf amplitude control uncertainties. However $\pm 0.5^\circ$ rf phase and $\pm 0.5\%$ rf amplitude control uncertainties are required for routine operation after the commissioning.

REFERENCES

- [1] J. Stovall et al, Proc. of 2001 Particle Accelerator Conference (Chicago, 2001) p. 446.
- [2] H. Takeda, Parmila code.

THE LOW LEVEL RF SYSTEM FOR 100MV PROTON LINAC OF KOMAC*

I. H. Yu, D. T. Kim, J. S. Yang, H. S. Kang, W. H. Hwang, M. H. Chun, K. M. Ha, Y. J. Han,
S. C. Kim, and S. H. Nam, PAL, Pohang, Kyungbuk 790-784, Korea.
J. M. Han, H. J. Kwon, Y. S. Cho, K. T. Seol, PEFR, KAERI, Daejeon 305-353, Korea

Abstract

At the 100MeV proton linac of the KOMAC(Korea Multi-Purpose Accelerator Complex), the low level RF system provides field control for the entire KOMAC proton linac, including an RFQ and a DTL1 at 350MHz as well as 7 DTL cavities at 700MHz. In addition to field control, it provides cavity resonance control, and incorporates the personnel and machine protection functions. An accelerator electric field stability of $\pm 1\%$ in amplitude and $\pm 1^\circ$ in phase is required for the RF system. In order to accomplish these requirements, a digital feedback control technique is adopted for flexibility of the feedback and feed forward algorithm implementation.

In this paper, the detailed description of the low level RF system will be described.

1 INTRODUCTION

The KOMAC accelerator has been designed to accelerator a 20mA cw proton/H⁻ with the final energy 1GeV CW super-conductive linear accelerator. As the 2nd phase of the project, we are developing cw accelerating structure up to 20MeV, and operate the accelerator in 10% duty pulse mode. After the initial operation, we will challenge the cw operation of the linear accelerator. The 20MeV proton accelerator is constructing in the KTF(KOMAC Test Facility), and will be commissioned in 2005. After the commissioning, KTF will provide the proton beam for the many industrial applications. With the technologies developed in KTF, the 2nd phase accelerator of 100MeV final energy will be constructed in 2010. The final goal of this phase is 100MeV proton accelerator.

In the 100MeV proton linear accelerator(LINAC) for KTF, the RF source will power two accelerator cavities (an RFQ, a DTL1) operated at a frequency of 350MHz, and five cavities(DTL2) operated at a frequency of 700MHz.

The low level RF(LLRF) system for 100MeV proton linear accelerator provides field control including an RFQ and a DTL at 350MHz as well as 7 DTL cavities at 700MHz. In addition to field control, it provides cavity resonance control, and incorporates the personnel and machine protection functions. An accelerator electric field stability of $\pm 1\%$ in amplitude and $\pm 1^\circ$ in phase is required for the RF system. In order to accomplish these requirements, we will employ digital feedback control

technique adopting flexibility of the feedback and feed-forward algorithm implementation.

2 MASTER OSCILLATOR & RF GENERATOR

Figure 1 shows the block diagram of the master oscillator and RF generator included clock. The 10MHz RF reference is distributed to 9 low level RF systems. As shown in the figure, the electrical RF reference signal (10MHz, sine) generated by a master oscillator (external reference oscillator) is divided into 18 way by divider and amplified individually.

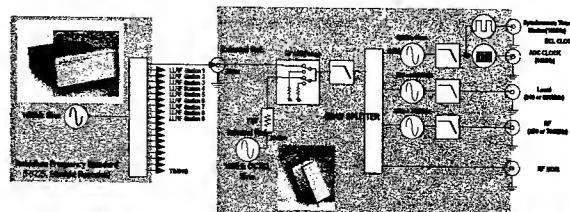


Fig. 1. A block diagram of the master oscillator and RF generator included 40MHz ECL clock for 100MeV linear accelerator

In order to maintain the correct accelerating field of RF source within an amplitude error of $\pm 1\%$, and a phase error of $\pm 1^\circ$, a digital feedback and feed-forward control system with high intelligence is required. Therefore, the RF reference signal, which is distributed to all of the RF stations included klystrons, should be more highly stable.

	Internal(LLRF)	External (Master Oscillator)
Model No./Mfg's name	SC10/SRS	FS725/SRS
Output Frequency	10MHz Sine	10MHz Sine
Phase Noise(SSB)	< -120dBc(10Hz)	< -120dBc(10Hz)
	< -150dBc(100Hz)	< -140dBc(100Hz)
	< -155dBc/Hz(1kHz)	< -150dBc/Hz(1kHz)
Stability	< ± 0.002 ppm	< ± 0.00005 ppm
Operating Temp.	0 to +50°C	+10 to +40°C
Freq. Tuning	± 3 Hz	± 0.02 Hz(0 to 5VDC)
Spatious		< -100dBc(100kHz BW)
Harmonics		< -60dBc

Table 1. The characteristics of the internal RF reference and external RF reference

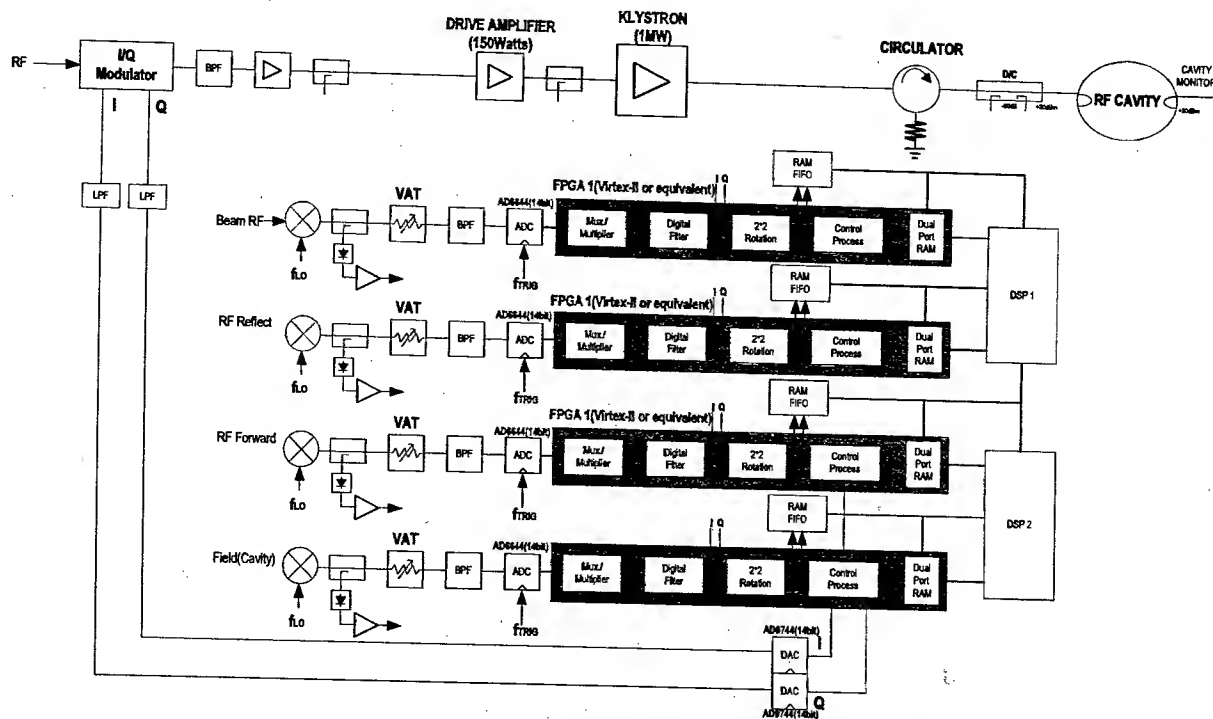


Fig. 2. A block diagram of the digital feedback hardware

Our goal for the RF reference is at within $\pm 0.1^\circ$ for the phase stability. The characteristics of the internal RF reference and external RF reference are shown in table 1. One stabilized coaxial line provides the RF reference for each RF stations (RFQ, DTL1, DTL2). The LLRF system was designed to make use of a 350MHz (or 700MHz) RF, 340MHz (or 690MHz) LO, 40MHz ECL clock, 10MHz synchronization. The accelerator source RF (klystron driving signal) of 350MHz or 700MHz is generated by a VCO with PLL synchronizing with the distributed 10MHz reference at each local station.

3 DIGITAL FEEDBACK HARDWARE

For the 100MeV proton LINAC of the KOMAC, the error of the accelerating field must be within $\pm 1^\circ$ in phase and $\pm 1\%$ in amplitude. To stabilize the amplitude and phase of the field in the accelerator cavity, a digital feedback and feed-forward technique is used in the LLRF system. Figure 2. shows a block diagram of the digital feedback hardware in the LLRF. This system controls I/Q components of the RF signal as shown in Fig. 2. The feedback and feed-forward control is performed by a combination of FPGAs (Field Programmable Gate Array) for fast and simple then feed to the appropriate carrier RF signal prior to amplification by the klystron. As shown in Figure 2., the RF signals from the cavity field probe, forward power, and reflected power are down-converted to 10MHz IF and sampled at 40MS/s by individual 14bit ADCs with 40MHz ECL clock in order to produce quadrature I, Q, -I, -Q samples. These are then properly updated at 20MS/s by two multipliers, and filtered. Once

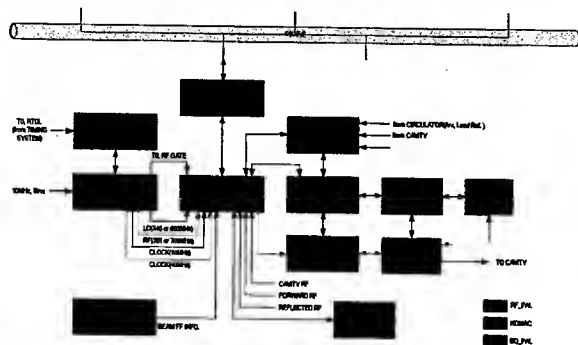
filtered, they are compared to set-point tables and control algorithms are performed to control an RF vector (I/Q) modulator.

	XCV1000E (Virtex-E)	XC2V1000 (Virtex-II)	XC2VP30 (Virtex-II Pro)
System Gate	1.57M	1M	
Logic Gate	331,776		30,816 Logic Cells
CLB Array	64x96	40x32	
CLB Slice		5120	13,696
CLB Max. Distributed RAM Kbits	393	160	428
Multiplier Blocks		40	136 (18x18Bit)
SelectRAM Blocks Max. RAM (Kbit s)	393	720	2,448
Features	*fast high density *high flexible select I/O *0.18um 6layer metal process	*selectRAM memory hierarchy *Select I/O-ultra *PCI/XPCL compliant *0.15um 8layer metal process 0.1um high speed transistor	*high performance platform *selectRAM memory hierarchy *power pC RISC block *Select I/O-ultra *PCI/XPCL compliant *0.13um 9layer copper process 90nm high speed transistor

Table 2. Xilinx FPGA's comparison

The digital feedback hardware relies on FPGA (Field Programmable Gate Array) and digital signal processors optimised for real-time signal processing. Table 2. shows the Xilinx FPGA's comparison. The digital feedback hardware performs feedback and feed-forward algorithms on the field signal, resulting in control in phase and quadrature (I/Q) outputs, which are processing and DSPs (Digital Signal Process) for slow and complicate

The control parameters are set through the EPICS(Experimental Physics Interface Control System) interface allows the operator to set up the LLRF system, in a variety ways. Registers on the module provide access to all manners of control – set points, thresholds, mode selection, controller type, etc, and the DSPs provide the direct interface to the control register and hardware. A network host computer connects the fast signal processing chip to outside world via Ethernet. Timing and interlocks are routed through an FPGA. Fig. 3. shows the interface of the RF station for the RFQ, DTL1, DTL2.



5 SUMMARY

6 ACKNOWLEDGMENT

The Korea Ministry of Science and Technology (MOST) supports this work

- [1] Y. S. Cho, et al., "Development of 100MeV Proton Accelerator for KOMAC 2nd Phase", LINAC'02, Kyungju, August 2002.
- [2] H. J. Kwon, et al., "RF System of KOMAC RFQ", LINAC'02, Kyungju, August 2002..
- [3] T. Kobayashi, et al., "RF Reference Distribution System for the 400-MeV Proton Linac of the KEK/JAERI Joint Project," LINAC'02, Kyungju, August 2002.
- [4] S. Michizono, et al., "Digital RF Control System for 400-MeV Proton Linac of JAERI/KEK Joint Project", LINAC'02, Kyungju, August 2002.
- [5] A. Regan, et al., "The SNS Linac RF Control System", LINAC'02, Kyungju, August 2002.
- [6] L. Doolittle, et al., "The SNS Front End LLRF System", LINAC'02, Kyungju, August 2002.
- [7] S. Yamaguchi, et al., "Overview of the RF System for the JAERI/KEK High-Intensity Proto Linac", LINAC'02, Kyungju, August 2002.
- [8] S. N. Simlock, "Achieving Phase and Amplitude Stability in Pulsed Superconducting Cavities. Proc. Of the 2001 Particle Accelerator Conf (PAC2001)
- [9] Sasa Bremec, et.al., "Advantages of Implementing Digital Receivers in Field Programmable Gate Arrays(FPGA)", DIPAC2003, Mainz, Germany, May 2003

STATUS OF THE PRODUCTION ELECTROPOLISHING SYSTEM AT JLAB*

J. Mammosser[#], J. Delayen, J. Gordon, L. Phillips, A. M. Valente, T. Wang, A.T. Wu, Jefferson Lab,
Newport News, VA 23606, USA

J. Saunders, SNS, Oak Ridge, TN 37830, USA

Abstract

Jefferson Lab has installed, and is in the process of commissioning, a production electropolish system, sized for 805MHz SNS cavities. This paper describes the basic system design, plans for studying the effectiveness of polishing SNS high- β cavities and early results from cavity tests.

INTRODUCTION

Historically, producing high field and Q-values in superconducting RF cavities of niobium has required the removal of a substantial layer of the inner cavity surface, typically of the order of 100 microns in depth. Two methods have commonly been used: electropolishing (EP) or immersion in a buffered chemical polish (BCP)[1]. Both methods have occasionally produced cavities exhibiting exceptionally good performance. However, some studies have demonstrated, by direct comparison under controlled conditions, substantial advantages of EP over BCP [2,3,4], both in terms of Q-value and accelerating gradient. To take advantage of high performance levels obtainable with this technique, a system was installed at Jefferson Lab for the preparation of SNS cavity surfaces. A highly valuable feature of this system (Figure 1) is that it is fully automated, providing a high level of process repeatability. An additional advantage of process automation is the ability to study the process under controlled conditions, providing opportunity for rapid process optimisation and improvement. Although the reasons for the superior performance of EP over BCP are not fully understood, electropolishing produces smoother surfaces, which could conceivably increase both Q-values and maximum gradients by mechanisms suggested by Knobloch et. al. [5]. Typical values for surface roughness in one study are given as 1.5 microns for BCP and 0.2 microns for EP samples from the same material [6]. These are small sample studies, which might not reflect varying conditions over a cavity surface, such as differing current densities or electrolyte velocity between iris and equator especially for the deep cells of SNS cavities.

We have instituted a program with the following goals: commission the EP system; establish the adequacy of the

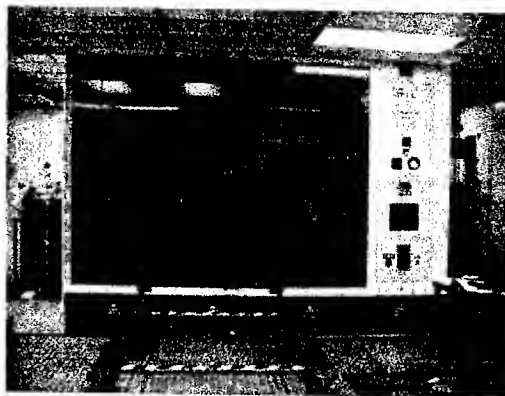


Figure 1. EP System at Jefferson Lab.

EP system for SNS cavity surface preparation; and process SNS cavities for production. The commissioning phase has been successfully completed.

The first prototype cavity result shown in figure 3, exceeds SNS requirements for high beta cavities and establishes the effectiveness of the system.

Production processing will start when the cavities begin to arrive in June. An additional goal of the program is to understand many of the issues referred to above, which are relevant to cavity performance and specifically to SNS cavities. A prototype cavity with replaceable niobium buttons (HB-button), has been fabricated and tested and will be used to measure local current densities, roughness and chemistry of the niobium surface, etc., at different cavity locations. Such understanding is valuable in achieving the highest levels of performance possible.

SYSTEM DESIGN

The electropolishing system consists of a self-contained processing cabinet, a remotely located chiller and direct current power supply variable up to 600 amperes and 50 volts. The process cabinet is installed in one of the production process rooms, next to the cavity production cleanroom complex in the Testlab, Building 58, at Jefferson Lab. The EP cabinet was procured from industry [7] and consists of three separate compartments: plumbing, electronic and main process chamber. The plumbing compartment houses the pumping systems, valves, acid sump and instrumentation for process control. The electronic compartment contains the main process programmable logic controller and all electronic controls and wiring. The main process chamber (Figure 2) has a frame, designed for inserting and holding the

*Work supported by United States Department of Energy under contract DE-AC05-84ER40150
[#]mammosse@jlab.org

cavity tilt/rotation tooling. This frame transfers the weight of the tooling to the floor and has two insertion rails that penetrate the front of the cabinet for insertion of the tooling into the process chamber. The insertion rails extend eight feet (2.44m) in front of the main process chamber doors, allowing for assembly and disassembly of cavities into and out of the tilt/rotation tooling. The cabinet has a sub-frame that is constructed of stainless steel tubing wrapped with polypropylene plastic. All cabinet walls and surfaces are fabricated from fire-retardant polypropylene sheet. The rotary sleeves that allow for horizontal rotation of the cavity during processing and serve as a primary seal. The rotary sleeves, cavity holding frame and the cathode were purchased from industry [8]. All other tooling was designed and built at Jefferson Lab.

System Features

The Jefferson Lab EP processing system, Figure 1 and 2, is designed with the following features:

- Fully automated controls – programmable logic controller with a personal computer interface
- Processing horizontally while rotating
- Rinsing horizontally while rotating
- Draining vertically for the electrolyte and rinse water
- Straight aluminium cathode with electrolyte fill ports located at cell centres
- Tooling variable up to a 60 inch cavity length
- Direct current power supply rated at 50 volts and 600 amperes
- Onboard chemical sump that holds 70 gallons of electrolyte and an onboard heat exchanger
- Six ton chiller for electrolyte temperature control
- An integrated CO₂ fire suppression system that covers all compartments

The following are programmed steps for a typical cavity process run:

- Lock door and start nitrogen leak test
- Cavity nitrogen purge
- Filter/mix acid
- Rotate cavity
- Fill/overflow cavity
- Sweep voltage
- Start polishing
- Stop polishing
- Tilt to vertical and drain
- Tilt to horizontal and rinse
- Rinse to Resistivity and pH
- Tilt to vertical and drain
- Tilt to horizontal and unlock doors

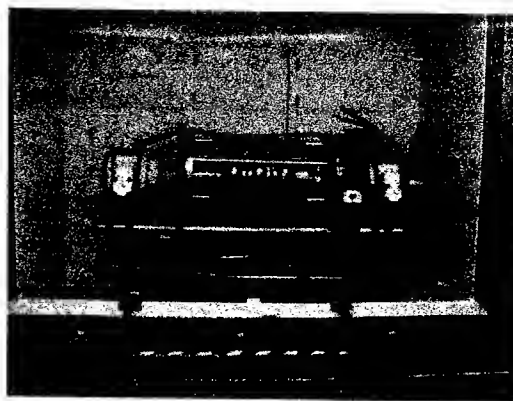


Figure 2. Three Cell 700 MHz Cavity Installed in the EP Tooling.

EARLY TEST RESULTS

During commissioning of the EP systems, a 700MHz three-cell cavity was processed to test system functionality and gain understanding of the control system operability. This cavity was processed for 5 ½ hours at 350 amperes and 25-40 volts. The material removal as determined by ultrasonic thickness gauging averaged over four samples at each of seven locations along the cavity. The material removal for this cavity was quite uniform with the equators having approximately 20% less material removed than the beam-tubes. A visual inspection of the cavity showed a smooth interior surface that was bright but not shiny. This cavity was not RF tested.

Two additional cavities were prepared for processing, both high- β (HB) prototype cavities built at Jefferson Lab. One of these HB cavities (Figure 5) was modified to allow for small niobium buttons (HB-button) to be inserted at various locations. The second HB prototype cavity (HB-proto) will be used for feedback of RF performance as a function of the process parameters used.

During processing of the HB-button cavity several leaks occurred at the button locations, forcing the run to be ended early. The current was increased up to the 600 amperes and approximately 30 volts during this test and buttons were removed for inspection.

The HB-proto cavity was also processed for four hours at approximately 445 amperes and 18-20 volts. After processing a visual inspection of each end of the cavity interior surfaces showed a difference in appearance from one end to the other. This cavity was then high pressure (HP) rinsed for three hours in the production cleanroom. The cavity was dried over night and all test flanges assembled with the exception of the evacuation flange.

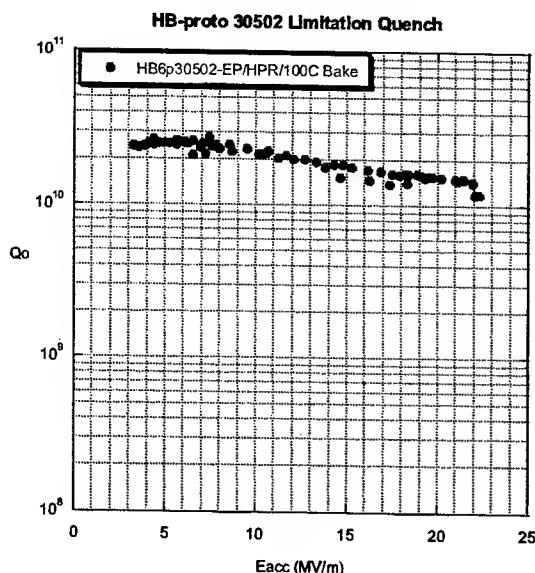


Figure 3. Vertical Test Results of Cavity HB-proto.

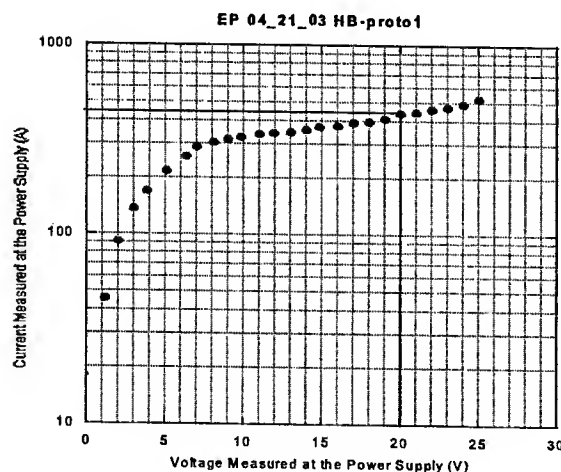


Figure 4. Current-Voltage Curve Taken After Two Hours Into The EP Run.

The cavity was HP rinsed six more hours before assembly of the final flange and evacuation. It was then vacuum baked for 44 hours at 100°C and inserted into vertical dewar for RF testing. Figure 3 shows the test result from this cavity with the limitation of a thermal quench at 22.5 MV/m. Figure 4 shows the current-voltage curve taken after two hours into the run and the operating point for the run. A current-voltage curve was also taken at the beginning of the run before the electrolyte temperature was at 34°C. This curve did not show the rapidly increasing potential area where process current increases slowly.

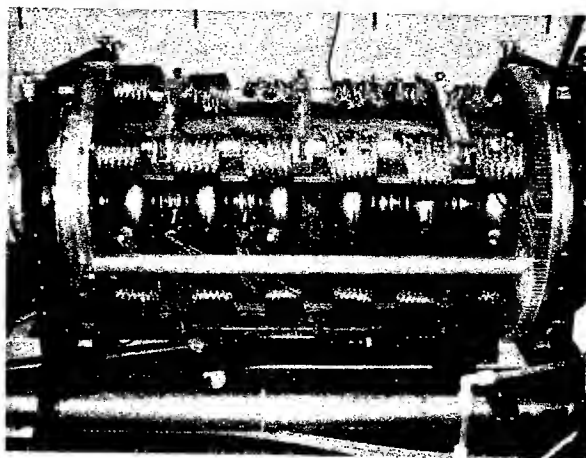


Figure 5. HB-button Cavity Installed Into The Cavity Tilt/Rotation Tooling.

CONCLUSION

In parallel with production processing of high- β cavities, further process optimisation and understanding will be pursued. In particular, surfaces roughness, current density and surface chemistry will be examined at iris, equator, and sidewall locations. The HB-proto cavity (Figure 1) will be alternately processed by EP and BCP and RF tested for comparative evaluation of performance and superconducting parameters. Although existing studies indicate that hydrogen absorption will not be a problem [9], we will verify this through RF testing for the absence of Q-disease.

REFERENCES

- [1] Padamsee, Knobloch, and Hays, "RF Superconductivity for Accelerators", John Wiley and Sons, 1998.
- [2] K. Saito, et. al., "Superiority of Electropolishing Over Chemical Polishing on High Gradients", Proceeding of 8th SRF Workshop, Abano, 1997.
- [3] E. Kako, et. al., "Improvement of Cavity Performance in the Seclay/Cornell/DESY SC Cavities", 9th SRF Workshop, p.179, SanteFe, 1997.
- [4] K. Saito, "High Gradient Performance by Electropolishing with 1300 MHz Single and Multi-cell Superconducting Cavities", ibid p.288..
- [5] J. Knobloch, et. al., "High-Field Q Slope in Superconducting Cavities due to Magnetic Field Enhancement at Grain Boundaries", p. 77, 9th SRF Workshop. SanteFe, 1999.
- [6] N. Steinhilber-Kuhl, et. al., "Basic Studies for the Electropolishing Facility at DESY.
- [7] Polyflow Engineering Inc., Sylmar, CA.
- [8] Nomura Plating Co. Ltd., Tochigi-ken, Japan
- [9] Saito, et. al., "Discovery of the Needless of Outgas Annealing after Horizontally Continuously Rotated Electropolishing with Niobium Superconducting RF Cavities", p. 283, 9th SRF Workshop. SanteFe, 1999.

GRADIENT OPTIMIZATION FOR SC CW ACCELERATORS*

W. J. Schneider[†], P. Kneisel, C. H. Rode and the Jefferson Lab SRF Staff
Jefferson Lab, 12000 Jefferson Avenue, Newport News VA 23606, USA

Abstract

The proposed rare isotope accelerator (RIA) design consists of a normally conducting radio frequency quadrupole (RFQ) section, a superconducting (SC) drift tube cavity section, a SC elliptical multi-cell cavity section and two charge strippers with associated charge state selection and beam matching optics. The SC elliptical section uses two or three multi-cell beta cavity types installed into cryomodules to span the energy region of about 84.5 MeV/nucleon up to 400 MeV/nucleon. This paper focuses on the gradient optimization of these SC elliptical cavities that provide a significant portion of the total acceleration to the beam. The choice of gradient coupled with the cavity quality factor has a strong affect on the overall cost of the accelerator. The paper describes the optimization of the capital and operating cost associated with the RIA elliptical cavity cryomodules.

1. INTRODUCTION

Last May [1] a workshop at Argonne National Laboratory (ANL) reviewed the design of a superconducting (SC) ion linac driver for a proposed rare isotope accelerator (RIA). The driver for RIA was originally outlined in 1999, updated at an earlier workshop in 2000 and formally costed for the Harrison Review on behalf of National Science Foundation (NSF) in 2001 [2,3]. Requirements for RIA are to produce and accelerate ions over the full mass range from protons to uranium up to 400 MeV/u. The continuous wave (CW) beams produced are to have at least 100 kW up to a maximum of 400 kW of beam power. The machine is to be able to irradiate two targets simultaneously and produce a beam spot size of less than 1 mm wide on fragmentation targets. The elliptical portion of the superconducting linac (SCL), discussed here, contains eighteen (18) beta (β) 0.47 cryomodules, twenty-three (23) β 0.61 cryomodules and seven (7) β 0.81 cryomodules for the Michigan State University (MSU) design and fifteen (15) β 0.47 cryomodules, twenty (20) β 0.61 cryomodules and seven (7) β 0.81 cryomodules for the Argonne National Laboratory (ANL) design [4, 5]. ANL is also investigating another low frequency option. The cavities are currently designed for a peak gradient of 27.5 MV/m with a cavity quality factor (Q_0) of $5.0 \cdot 10^9$ at 2.1 K. Raising the peak gradient while maintaining the cavity quality factor, Q_0 allows one to reach the desired machine energy with fewer modules and a concomitant reduction

in overall length, but requires additional RF power and refrigeration capacity to counter the increased cavity power dissipation. For pulsed accelerator like SNS and TESLA with low duty factors, one can afford to push the peak gradient (E_{peak}) much higher. The SNS β 0.81 cavities are being pushed to 35 MV/m while TESLA is working at 45 MV/m. The cryomodule (CM) is based on the CEBAF CM with improvements borrowed from LHC, TESLA, SNS and the JLab 12 GeV upgrade and uses the frequency scaled KEK fundamental power coupler (FPC). Figure 1 is the elevation view of the β 0.81 CM, while Figure 2 is the flow schematic.

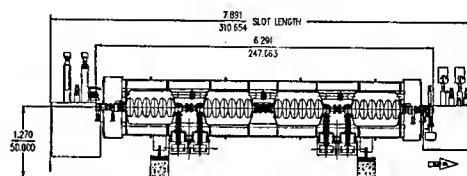


Figure 1. High Beta Cryomodule

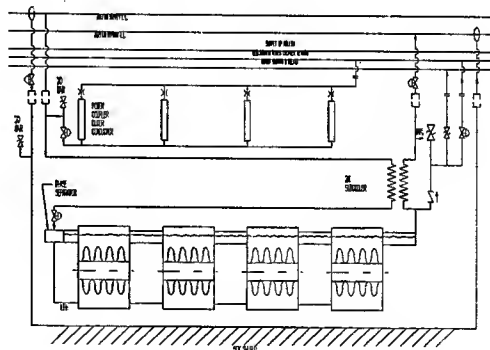


Figure 2. Flow Schematic

The refrigerator produces a 3 bar, 4.5 K stream, which feeds two Joule-Thompson (JT) valves in parallel. The first supplies a small sub-cooler in the CM and then cools the cavity. The second feeds the power coupler outer conductor. The CM shield is cooled by a 4 bar, 35 K stream, which first cools the supply transfer line (TL) shield, then the CM shield, and finally the return TL shield before returning to the refrigerator at 52 K. The bayonet design permits replacement of a CM in less than a day if needed without warming up the entire linac. In the ten years since the initial CEBAF cooldown, the linacs have never been warmed and only four CM have been replaced during scheduled accelerator shutdowns.

*Work supported by US DOE Contract No. DE-AC05-84ER40150

[†]schneide4@cox.net

The relevant parameters for low, medium and high beta cavity cryomodules are given in Table 1.

Table 1. CM Baseline Parameters/ 4 cavities per CM

Beta	0.47	0.61	0.81
Slot length	6.34 m	7.00 m	7.891 m
CM length	4.74 m	5.4 m	6.291 m
Ea Gradient	8 MV/m	10.1	12.3
		MV/m	MV/m
Q_0	$5.0 \cdot 10^9$	$5.0 \cdot 10^9$	$5.0 \cdot 10^9$
CM cost	\$1300 k	\$1350 k	\$1400 k

The costs indicated are in 2003 dollars and assume scaling from SNS experience. Note that for the 27.5 MV/m peak gradient, the current design for β 0.47, 0.61 and 0.81 is respectively Eacc 8, 10.1 and 12.3 MV/m. As E peak increases, Eacc scales. For example, at an E peak of 32.5 MV/m Eacc is respectively 9.5, 12 and 14 MV/m. For purposes of this optimization, the average gradient of 10.1 MV/m is equivalent to an E_{peak} of 27.5 MV/m i.e we will use the β 0.61 cavity, the most common cavity as a baseline.

2. HEAT LOADS

There are three sources of heat that govern the cryomodule primary circuit power dissipation. The first is the static heat load, associated with the bore tube, power couplers, tuners, bayonets, etc. The cavity dynamic heat load is made up of two components – the temperature independent resistance caused by localized resistive areas where defects, impurities or surface dirt affect the SC properties; and the temperature dependent surface resistance or the Bardeen, Cooper, and Schrieffer (BCS) theory, which is due to unbound Cooper Pairs of electrons. In the earlier work [6] discussing cavity optimization, the following approximations were used for total power in W/m:

$$P_{total} = P_{static} + P_{res} + P_{bcs} \text{ (W/m)}$$

$$P_{total} = 8 / (f / 500)^{0.5} + E^2 / 380 (f / 500)^{0.9} Q_{res} + E^2 (f / 500)^{1.1} 0.0000223 \text{ Exp}^{-17.67/T} / 380 280 T \text{ (W/m)}$$

Where f is frequency in MHz, E is accelerating gradient in V/m, T is absolute temperature in Kelvin and Q_{res} is the temperature independent resistive component of cavity losses. [$Q = g/R$, g = geometry factor ~ 200 Ohm]

The change in refrigerator efficiency as a function of temperature is factored into the overall heat load, as shown on figure 3. At 4.4 K one can achieve 30 % of Carnot while below 1.8 K the efficiency is less than half of this value. As reported previously [7], there is a significant shift in Q_0 the quality factor across the Lambda line at higher gradients as a result of the slope in Q_0 vs. Eacc above Lambda. This change is attributable to the heat transfer associated with the superfluid. To account for this shift Q_0 in the optimization, the Q_{res} is

reduced by a factor of three once the temperature exceeds Lambda to match experimental results shown in figure 4.

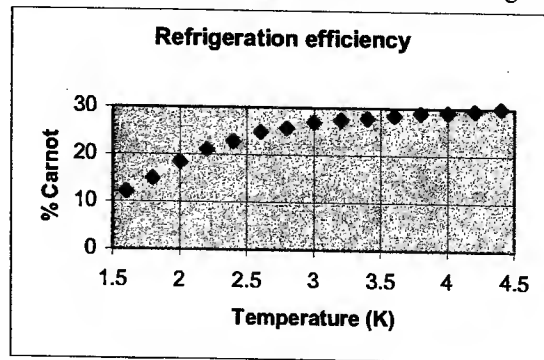


Figure 3 Refrigerator Efficiency

Linac capital cost consists primarily of the tunnel, cryomodules, RF, and cryogenics, while the operating cost consists primarily of the RF and cryogenics. The tunnel and cryomodule cost vary as $1/G$ (Gradient). The total RF power increases proportional to G and therefore its operating cost since this is a low current accelerator, but the number of RF systems decreases as $1/G$. Therefore we will model the RF capital cost as a constant. The dynamic refrigeration wattage varies proportional to G ; for CW machine above a gradient of 5 MV/m this is the predominant load. The capital and operating cost for the refrigerator vary to the 0.7 and 0.85 power of total wattage respectively.

3. DISCUSSION

A typical Q_0 versus accelerating gradient for a β 0.47 RIA recently measured at JLab is shown in figure 4. At 2.1 K this curve drops from 15 to about 4 E_{09} . As the temperature increases over lambda the Q_0 drops by a factor of two to three. We know the optimal temperature for cavities operating at 805 MHz is 2.1 K. Figure 5 shows this temperature optimization for a cavity with a Q_0 $5.0 \cdot 10^9$ at 2.1 K, the base line design.

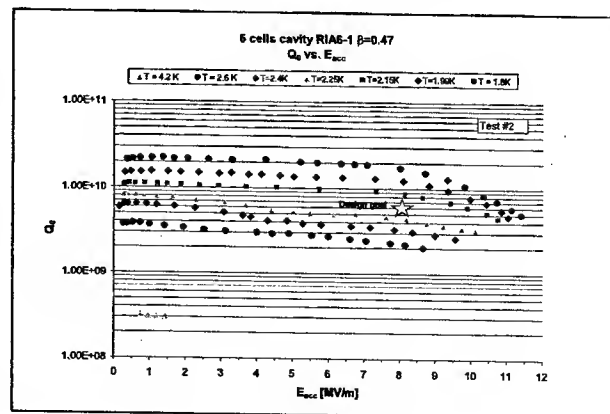


Figure 4. β 0.47 Gradients vs. Q_0 Performance

The assumed baseline costs, scaled from CEBAF to the RIA accelerator [8] for the refrigerator is \$40 million, RF is \$21.1 million, cryomodule is \$ 70.9 M and tunnel is \$ 15 M. Operating costs for the refrigerator over a ten year period are 49 million and RF is 8.4 million. As the temperature increases the refrigerator efficiency increases from 12 to 30 %; this together with the 1/T effect generates another minimum above Lambda. It is believed that above Lambda and above 15 MV/m peak there is severe turbulence and therefore the RF system will require large amounts of power to compensate for microphonics. Suffice to say that cavities at higher frequencies, greater than 800 MHz, the optimum is below lambda.

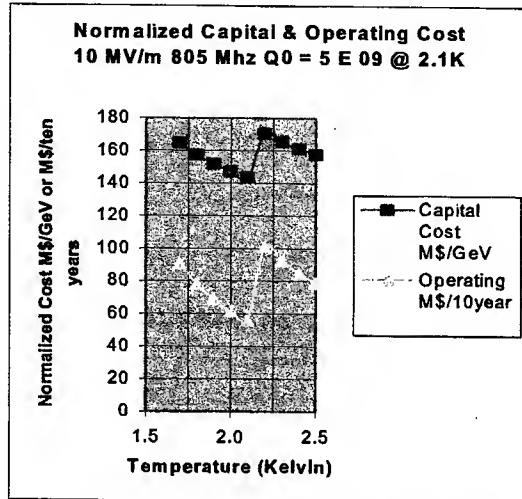


Figure 5. Temperature optimization at baseline

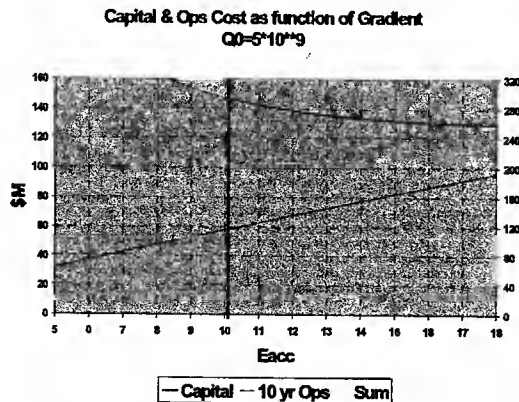


Figure 6 Optimization for Q_0 5 E 09 @ 2.1K

The optimizations show a minimum in capital cost for a given gradient at a particular Q_0 . This minimum shifts to a higher gradient as the Q_0 improves. With a Q_0 of 5 E 09 the optimum is 10 MV/m, the design for the RIA project. As Q_0 increases to 10 E 09, the optimum shifts to a gradient of 14 MV/m. The higher value would represent an E peak of 37.5 MV/m, a major challenge. The overall cost of the project, for both capital and operating, decreases as the Q_0 is improved. Referring to

figures 6 and 7, as the Q_0 increases from 5 to 10 E 09 at 10 MV/m, equivalent to the 27.5 MV/m peak, the capital costs decreases from 147 M\$ to 132 M\$ and the operating cost decreases from 58 to 36 M\$ during the 10 year operating period. This is a net saving of 37 M\$.

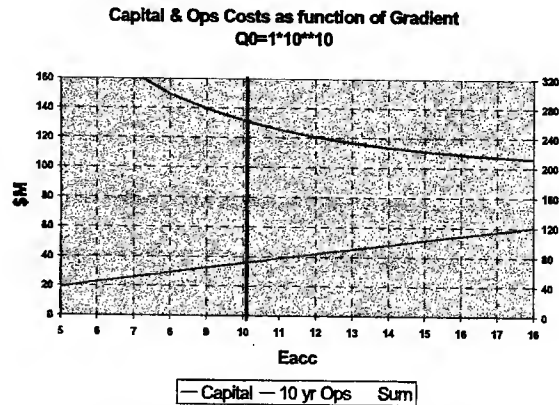


Figure 7. Optimization for Q_0 10 E 09

4. CONCLUSION

As shown above, the cost optimised gradient for an accelerator like RIA is determined by the achievable Q-value at the design gradient. Improving the Q-value from the present design value of 5 E 09 at a peak surface field of E peak = 27.5 MV/m to a value beyond 1 E 10 will significantly reduce the construction and operating costs. Therefore improvement of the Q-value at high gradients through proven techniques must become the primary focus of the cavity R&D program.

5. ACKNOWLEDGEMENTS

This work is supported by US DOE under Contract No. DE-AC05-584ER40150. Thanks to the JLab Cryomodule design group and the cavity prototyping team for their efforts. Additional thanks to the teams at Argonne National Laboratory and NSCL at East Lansing.

6. REFERENCES

1. "The RIA driver Workshop II", May 22-24, 2002, Organized by J. Delayen - JLab, T. Grimm- NSCL, K. Shepard -ANL, held at Argonne National Laboratory.
2. "The Rare Isotope Accelerator (RIA) Facility Project" C.W. Leemann, in Proc. 20th International Linac Conference, August 21-25, 2000, Monterey, California.
3. "The US Rare Isotope Accelerator Project", G. Savard, in Proc. 2001 Particle Accelerator Conference, June 18-22 2001, Chicago, Illinois, p561 (2001).
4. Personal Communication K. Shepard ANL DESIGN
5. Personal Communication T. Grimm MSU DESIGN
6. C.H. Rode and D. Proch. "Cryogenic Optimization for Cavity Systems" Proceedings of the IEEE Particle Accelerator Conference, March 1989, p589.
7. C. H. Rode and the JLab SRF staff, "Temperature Optimization for Superconducting Cavities" Proceedings of the IEEE Particle Accelerator Conference, March 1999.
8. J.R. Specht and W.C. Chronis "Cryogenics for the Rare Isotope Accelerator Project" Proceedings of the CEC 2001

MECHANICAL CAVITY DESIGN FOR 100MV UPGRADE CRYOMODULE*

K. M. Wilson[†], E. F. Daly, J. Henry, J. Hogan, D. Machie, J. Sekutowicz, T. Whitlatch
Thomas Jefferson National Accelerator Facility, Newport News, VA 23606

Abstract

To achieve up to 6 GeV, each cryomodule in the CEBAF accelerator currently provides about 30 MV of acceleration. To raise the accelerator energy to 12 GeV, ten additional cryomodules, each capable of providing over 100 MV of acceleration, are required. A prototype of the 100 MV cryomodule has been designed, is presently under construction, and will be completed in 2004. This prototype cryomodule comprises two new cavity designs, four cavities of the low loss design and four cavities of the high gradient design [1,2].

Although the cavity shapes were designed for their RF properties, the mechanical implications must be considered. In addition to the new cavity shapes, changes have also been made to the cavity end dish assemblies, weld joints, and stiffening rings. This paper will present the results of the stress and vibration analyses used for designing the cavity string.

STRESS ANALYSIS

Two critical load cases were examined, one for the warm cavities and one for the cold. The highest stresses in the cold cavity will result from the superposition of tuning and pressure loads. The cavity may be displaced outwards by as much as 2 mm during tuning, placing the cavity in tension; in theory, this could coincide with a pressure load of up to 4 atmospheres in case of system failure.

For the warm cavity, the greatest stresses will most likely occur during alignment. The cavities are held just outside the end cells and force is applied to the beam pipe flange to bring the beam pipe into alignment for assembly.

Model Description

During the course of the cavity design, several different configurations were considered and analyzed for both the low-loss (LL) and high-gradient (HG) cavities. Figure 1 reflects the final design of the low-loss cavity.

For the analysis of the cold cavity, a two-dimensional part was meshed with axisymmetric parabolic elements. As shown in Figure 1, blue elements are titanium, red elements are niobium-titanium, and green elements are RRR niobium.

For the warm analysis, only the beam pipe was modeled (Figure 4) since it was assumed the cavity would be fully fixed just outside the cells and only the beam pipe would deform. A half-model was used and meshed with parabolic solid elements.

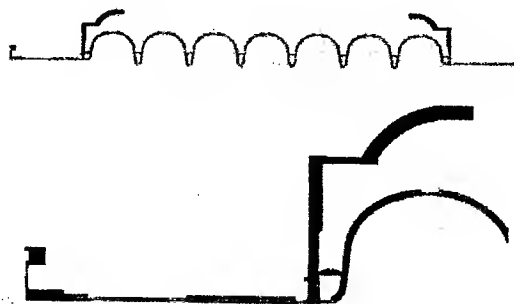


Figure 1: Low loss cavity mesh

Material Properties

Material properties used in the models are shown in the tables below.

Table 1: Material Properties of Niobium [3,4,5,6]

Property	SI Units	English Units
Modulus - Room Temp	1.03 E+11 Pa	1.49 E+07 psi
Modulus - Cryo Temp	1.23 E+11 Pa	1.79 E+07 psi
Poisson's Ratio	0.38	
Density	8.58E-03 g/mm ³	0.31 lb/in ³
Yield - RT	4.83 E+07 Pa	7.0 ksi
Yield - Cryo	5.77 E+08 Pa	83.7 ksi

Table 2: Material Properties of Titanium [7]

Property	SI Units	English Units
Modulus - Room Temp	1.02 E+11 Pa	1.48 E+07 psi
Modulus - Cryo Temp	1.25 E+11 Pa	1.81 E+07 psi
Poisson's Ratio - RT	0.338	
Poisson's Ratio - Cryo	0.305	
Density	4.51E-03 g/mm ³	0.163 lb/in ³

In the absence of data on the cryogenic properties of niobium-titanium, an assumption was made that the modulus would follow the same trend as niobium and titanium and increase by about 21% over the room temperature modulus.

* Supported by US DOE Contract No. DE-AC05-84ER40150
[†]kwilson@jlab.org

Table 3: Material Properties of Niobium-Titanium

Property	SI Units	English Units
Modulus - Room Temp	7.31 E+10 Pa	1.06 E+07 psi
Modulus - Cryo Temp	8.83 E+10 Pa	1.28 E+07 psi
Poisson's Ratio	0.38	
Density	6.36E-03 g/mm ³	0.23 lb/in ³

Boundary Conditions

For the cold cavity, a 2 mm outwards deflection was applied to one of the dished heads on the cavity model while the other was held fixed, representing the maximum displacement during cavity tuning. In addition, a 4-atmosphere pressure load, the maximum failure load the cavity could experience, was applied to the outside of the cavity. (The operational pressure load is actually much lower, only 0.034 atmospheres.)

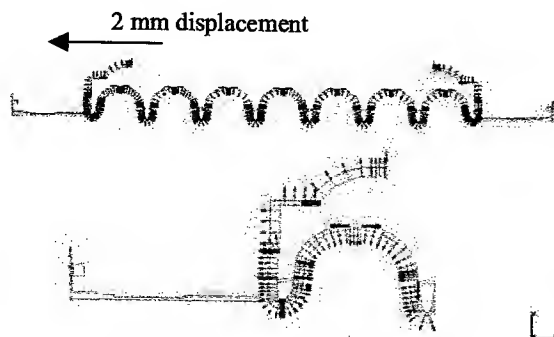


Figure 2: Loads on cold cavity

For the warm cavity, the primary concern was stress and plastic deformation from alignment, which might cause distortions in the field. The half model shown in Figure 4 was restrained in its plane of symmetry and fully fixed at the end adjacent to the cavity. The beam pipe flange was displaced vertically 1.5 mm and rotated slightly as indicated by the arrows in Figure 4. This was the largest estimated displacement of the flange during alignment.

Results

On the cold cavity, the greatest stress is at the intersection of the stiffener and the end cell, as shown in Figure 3. The yield strength of niobium under cryogenic conditions is about 84 ksi. The maximum Von Mises stresses in this area are under 20 ksi.

For the warm cavity, the maximum alignment stresses occur due to bending in the beam pipe. Since the analysis involves plastic deformation of the material, the stress-strain relationship is no longer linear. Figure 4 therefore shows the strains, which are proportional to the deflection, rather than the stresses, which are dependent on the stress-strain graph of the particular material.

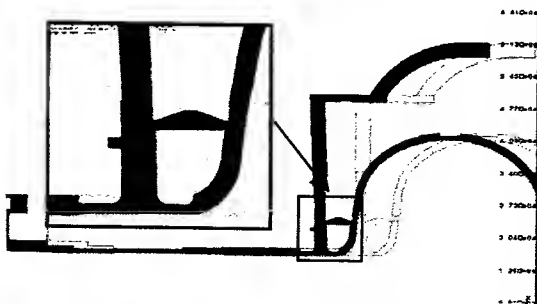


Figure 3: Low Loss - 2 mm deflection + 4 atm load

The ultimate tensile strength of niobium is much smaller warm than cold, about 20 ksi [8]. The stress-strain properties of this particular material are still being investigated. Graphs of typical niobium properties show that, for the worst-case material located, failure (i. e., ultimate tensile strength) would occur at 0.026 in/in of strain. With the given deflections, the maximum Von Mises strains in the cavity beam pipe are about 0.007 in/in.

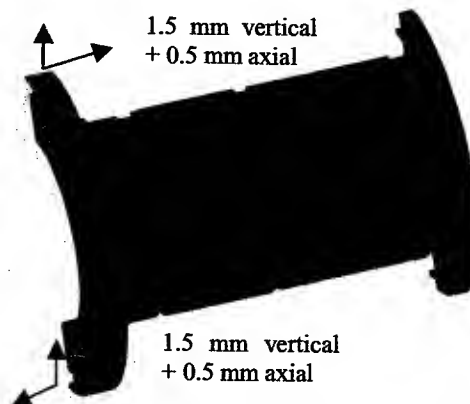


Figure 4: Alignment strains

NORMAL MODES ANALYSIS

The natural frequencies of the cavities are of interest as any external vibrations which operate at the same frequencies as the natural frequencies could induce system resonance, an undesirable condition.

Model Description

Both the high gradient and low loss cavities consist of seven cells with stiffeners between them. Additional stiffeners connect the end cells to the end dishes on each end. At both the axis and equator of each cell, weld preps result in somewhat thinner material, and this was included in the model.

A full three-dimensional model of the cavities only (without beam pipes) was meshed with parabolic shell elements. Elements shown in green are niobium and elements in red are the niobium-titanium end dishes.

The material properties used are shown in Tables 1 and 3, above.

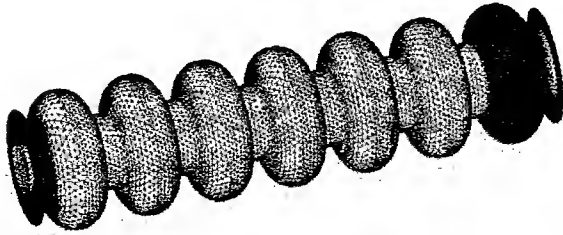


Figure 5: Shell mesh on high gradient cavity

Boundary Conditions

The stiffnesses of both the high gradient and low loss cavities were determined, using both room temperature and cryogenic material properties, to verify that these correlate with the natural frequencies. A nominal load of 100 lb was applied to one end of the cavities and the other was held fixed to determine the resulting deflection. The spring constant was calculated from this.

The fundamental frequencies of the cavities were then determined with both ends fully fixed.

Results

The cavity stiffnesses are more strongly influenced by the temperature of the cavities than by the difference in shape between the high gradient and low loss cavities, as shown in Table 4.

Table 4: Cavity Spring Constants (lb/in)

	Room Temp.	Cryogenic
High Gradient	32,400	38,900
Low Loss	32,500	39,000

The stiffnesses are also largely driven by the location of the stiffeners. For comparison, at room temperature the spring constant of a low loss cavity with no stiffeners is 8,000 lb/in and of the high gradient cavity with no stiffeners is about 17,000 lb/in. The addition of stiffeners increases the spring constants of both cavity designs several times, to about the same value.

The fundamental frequencies of the cavities are shown in Table 5. The second and third bending modes are significantly higher, as expected; for a beam, the natural frequency of the second bending mode is nearly three times higher than the first mode and the third mode is about five times higher. These are shown in Table 6.

Table 5: Cavity Frequencies, First Mode (Hz)

	Room Temp.	Cryogenic
High Gradient	114	125
Low Loss	112	123

In addition, an axial mode exists between the second and third bending modes.

Table 6: High Gradient Cavity Frequencies (Hz)

	Second Mode	Third Mode
Room Temperature	285	494
Cryogenic	312	541

For comparison, hand calculations (assuming the cavity can be treated like a beam) for the high gradient cavity at room temperature give the first three bending modes as 99, 270, and 530 Hz.



Figure 6: Fundamental mode of high gradient cavity

CONCLUSIONS

The current cavity design meets stress and frequency requirements, and manufacturing of the prototypes is underway.

Efforts to verify these analyses experimentally are ongoing. Tests on other cavities suggest that alignment within these limits will not damage the cavities and has a minimal effect on field flatness. Tests of the cavity stiffnesses and natural frequencies are currently being performed on a prototype high gradient cavity, with similar tests planned for the low loss cavities in the future.

Plans for future analyses include a study of the effects of Lorentz force detuning.

REFERENCES

- [1] J. Sekutowicz, et al. "Cavities for JLab's 12 GeV Upgrade." Proceedings of PAC2003.
- [2] E. F. Daly, et al. "Improved Prototype Cryomodule for the CEBAF 12 GeV Upgrade." Proceedings of PAC2003.
- [3] Mark Wiseman, "Normal Mode Analysis of the CEBAF Accelerator Cavity." TN-89-144, dated 7/17/89.
- [4] *Metals Handbook*, 10th Ed., Vol. 2. (USA: ASM International, 1990): 1144-1145.
- [5] Technical Specification for Niobium for Use in Superconducting Accelerators (RRR Grade). Specification 1111ISO144, Rev. 7. 1 October 1999.
- [6] Peter Kneisel and Ganapati Rao Myneni, "Preliminary Results of Tensile Test on Niobium at Room Temperature and 4.2K." TN-88-097. (October 1988): Table 2.
- [7] Email from Russ Mitchell to Katherine Wilson dated 6 December 2002.
- [8] Ganapati Myneni and Peter Kneisel, "High RRR Niobium Material Studies" TN-02-01.

COMMISSIONING-RESULTS OF THE REX-ISOLDE LINAC*

S. Emhofer, F. Ames, J. Cederkäll, D. Habs, O. Kester, K. Rudolph, Sektion Physik der LMU, München, Germany
T. Sieber, CERN, Geneva, Switzerland

Abstract

At REX-ISOLDE at ISOLDE/CERN radioactive ions are post accelerated with a 10 meters linac for experiments in nuclear-, astro- and solid state physics. For the efficient acceleration to energies between 0.8 and 2.3 MeV/u the principles of charge breeding of radioactive ions by an electron beam source was introduced at REX. The linac in its current stage consists of a 4-rod RFQ, a 20-gap IH drift tube cavity and three seven-gap splitting resonators. It is able to accelerate up to a mass to charge ratio of 4.5. 2002 has been the first year of nuclear physics experiments with REX-ISOLDE. The experiments done so far using Coulomb excitation and particle transfer reactions require good beam quality at the two target stations. Therefore commissioning measurements of the linac were made and are still being done. The results of those measurements will be presented showing the current energy spreads and radial emittances of the different cavities.

INTRODUCTION

2002 was a successful year for REX-ISOLDE as several experiments took place with different accelerated Mg-, Na- and Sm- and Li-isotopes. The beam energy range of those beam times was starting from 300 keV/u for implantation using just the RFQ up to 2.3 MeV/u using the RFQ, buncher, IH-cavity and all three 7-gap resonators. As an experience of the different beam times it had also been discovered how sensitive the system is on small changes of amplitude and phases of the different cavities. The requirements at the target are to deliver the full beam through a 3 to 5 mm aperture on the target. Losses had to be minimized and the beam size reduced. Therefore one had to focus mainly on a smaller energy distribution of the beam in front of the bender. The energy dispersion could otherwise lead to a broad beam in the dispersive plane which can result in an activation of the target edges. This paper focuses on the recent measurements on the first part of the linac namely the RFQ, the buncher and the IH-cavity.

MEASUREMENTS OF THE SEPARATOR'S EMITTANCE

In order to examine the beam quality in front of the linac emittance measurements in front of the RFQ were done. Two EBIS operation modes have been tested, one with highly charged ions from residual gas and one using He-ions to reach higher beam currents needed for emittance measurements of the linac at higher energies. The emittances with ions from residual gas fulfil very

well the expected values with a transverse phase space of 10π mm mrad in x-direction and 15π mm mrad in y-direction. The emittances measured with higher currents have grown due to the fact that one had to saturate the EBIS electron beam with helium to get enough current for the high energy emittance measurements. Therefore the transverse phase space increased to 35π mm mrad in x-direction and 90π mm mrad in y-direction.

MEASUREMENTS ON THE MATCHING SECTION

A very sensitive region regarding the beam quality is the matching section between the REXRFQ and the IH-cavity. After being accelerated from 5 keV/u to 300keV/u by the RFQ a re-buncher is needed to match the phase-space to the phase acceptance of the IH-cavity of $\pm 8^\circ$.

Beam energy spreads

The RFQ itself is rather uncritical as the amplitude is well known and its phase is the reference for the other cavities. The energy spread was measured to $\pm 1.5\%$ in agreement to PARMTEQ calculations and recent measurements [1,2]. A more detailed analysis had to be done regarding the buncher's properties. As the rf-low level-system was modified several times the buncher had to be re-calibrated in phase and amplitude. By using the 0° accelerating phase and acceleration at different power levels we could gain an effective shunt impedance of $19.9 \text{ M}\Omega/\text{m}$, which is in good agreement with the results from low level measurements [3]. Measuring the energy-spread of the buncher at different power levels which correspond to certain effective voltages one received a curve shown in figure 1. Just in the range from about 10 to 40 kV effective resonator voltage there is a discrepancy due to the energy resolution of the bending magnet, which is about 0.4-0.6% for a 1mm slit in front of the magnet. The shape of the energy-curves for different buncher power-levels is shown in figure 2. The typical three peak shape of the RFQ energy distribution is preserved. The ideal injection condition for the following IH structure is the curve with a tank loop level (A_{tank}) of 1.42V which corresponds to an effective buncher voltage of 70kV for a mass to charge ratio of four. One can see that the buncher broadens the RFQ energy distribution and shifts the maxima slightly. In order to get a more realistic simulation, the RFQ beam energy distribution has to be taken into account regarding simulations of the longitudinal emittance for the other cavities behind the buncher.

*This work has been supported by the BMBF

Emittance measurements of the matching section

Emittance measurements of the linac took place at the 20°-beam line of the REX-ISOLDE linac. As the energy spread is increasing the x-emittance values due to the bending magnet's dispersion, one should concentrate on the values in the non dispersive plane (y). The normalized y-emittance of the RFQ was measured to $0.16 \pi \text{ mm mrad}$ and of the buncher to $0.17 \pi \text{ mm mrad}$. So there is no significant emittance growth in the re-buncher.

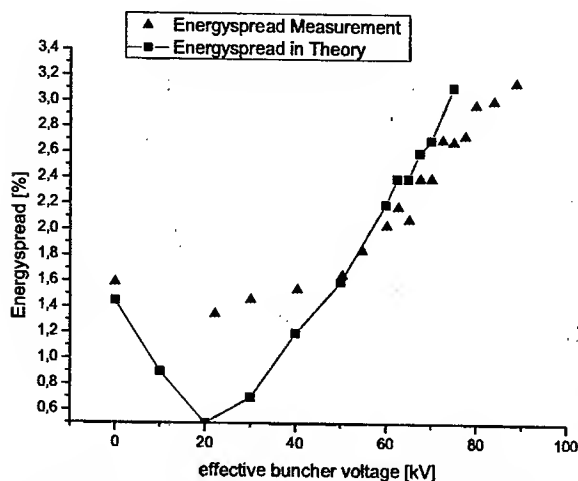


Figure 1: The measured energy spread of the buncher in dependence of effective voltage levels compared to simulation results.

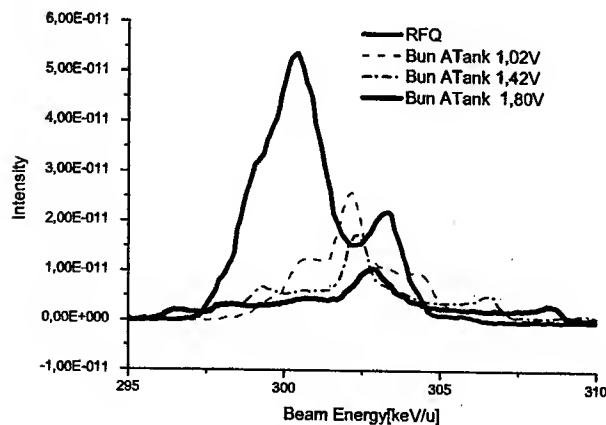


Figure 2: The energy-distribution of the RFQ beam compared to the one of the beam with different power levels of the buncher.

MEASUREMENTS ON THE IH-DRIFT TUBE CAVITY

The IH-cavity is the booster accelerator of REX-ISOLDE accelerating the bunched beam from the RFQ-energy of 300keV/u to an energy of max. 1.2MeV/u. There are 20 gaps which produce an effective acceleration

voltage of 4.05MV meaning an effective voltage in the gaps of 4.16MV for the maximum A/q-value of 4.5. The difference of those two values is used for re-bunching using the KONUS-beam dynamics [4].

Tuning of the proper amplitude and phase

The main goal for the IH-drift-tube-cavity was to set the proper phase and amplitude. Therefore simulation calculations with different phases and amplitude levels for the IH were done using the LoraSR computer code [4]. The bunch of results has been compared to measurements of energy spectra from the IH-cavity. The proper IH amplitude was mainly set by reducing the amplitude of the IH until the energy spread of the beam was reduced to the expected value. Figure 3 shows the simulation for 95% of the IH-voltage amplitude and the suiting measurement-curve. The upper edge of this curve is in well agreement with the LORASR calculations.

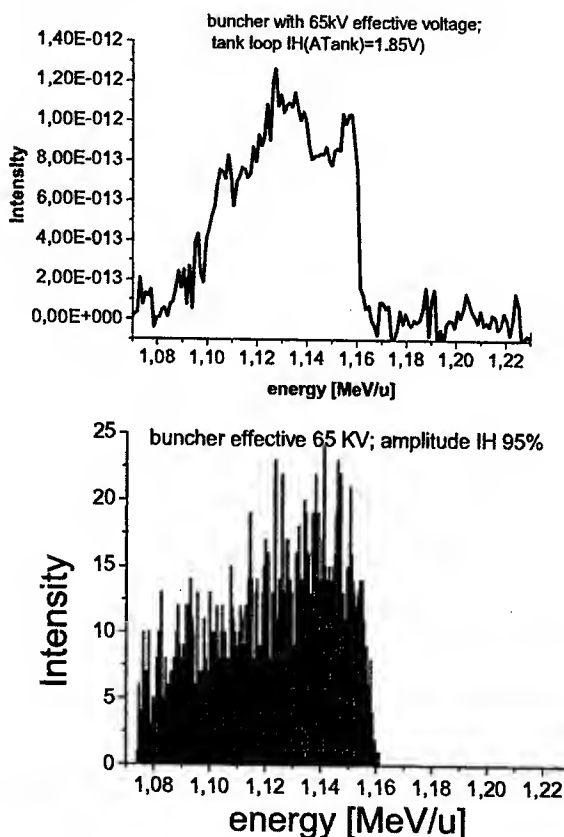


Figure 3: The measured energy-spread of the IH at a tank loop voltage of 1.85V compared to theory for 95% of amplitude.

With those measurement it could be proved that 1.95V of tank loop amplitude is the proper operation mode for the IH at a mass to charge ratio of 4. This level is reached with 43kW rf-power. The resulting absolute shunt impedance was calculated to 330 MΩ/m and is in exact agreement with results from X-Ray measurements of the gap-voltages and low level measurements. There one obtained 300 to 330 MΩ/m [5]. With this amplitude

energy-distributions at different phase settings were measured and compared to theoretical ones. The proper phase was identified. The energy-spectra and the calculated spectra at the optimal phase are shown in figure 4. They agree very well in width and in the overall shape. At the proper phase (0°) the measured energy spread is $\pm 0.8\%$ while from calculations it was expected to be $\pm 1\%$. The energy spreads at different phases agree well over the full measurable range. Figure 5 shows the energy spread over a phase range of more than 40° . First analysis of this discrepancy led to the following explanation: The simulations were done using waterbag distribution of particles in all three phase spaces (6-d). In reality the longitudinal emittance is injected into the IH-structure does not coincide with a waterbag distribution, it is filled less at the edges. This can be concluded from the shape of the energy distribution in figure 2. Calculations using the simulation results of the longitudinal emittance from the RFQ and the matching section will be carried out in the next step to proof the agreement with the measurements.

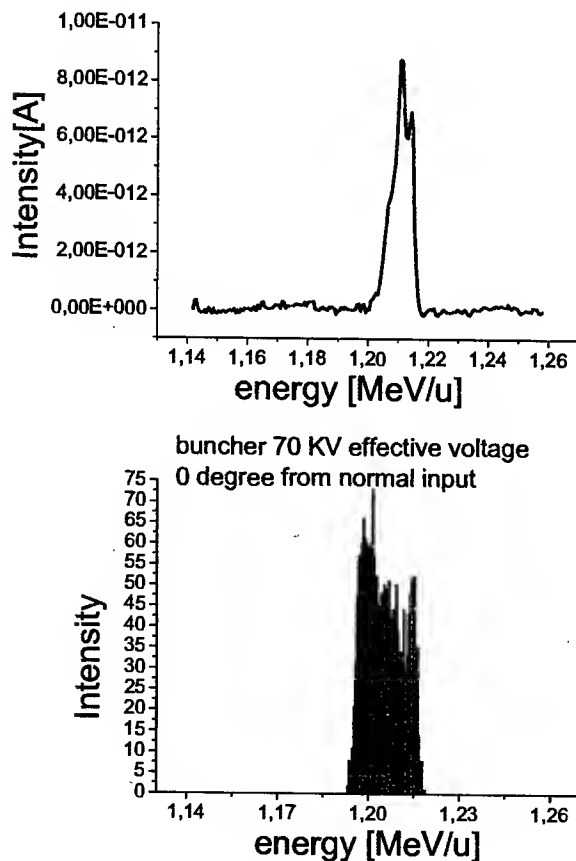


Figure 4: In the upper part of the figure the measured energy-spectra of the IH-cavity is shown, in the lower part the simulated one.

Emittance measurements

Beam emittances from the IH-structure were already taken last year, but at that time the amplitude was not

tuned properly which was resulting in a large emittance growth. At that time the normalised emittance was measured to $0.27 \pi \text{ mm mrad}$ which would mean an emittance growth factor of 1.6 within the IH-cavity. The following measurements carried out at known phase and amplitude will be done together with the measurement of the other cavities in the following beam period in 2003.

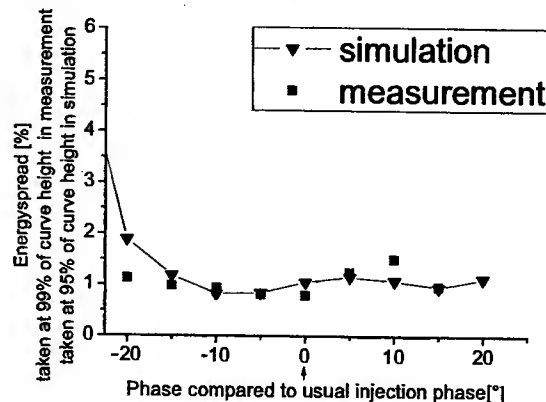


Figure 5: The measured energy-spread of the IH compared to theory in dependence on the phase. The proper phase is marked at 0° .

The emittance measurement device will be placed at the zero degree beam line to be able to measure the x- and y-emittances without the dispersion problem of energy spread being transformed into radial emittance. One expects an emittance growth factor less than 30% comparing with the exit emittances from the buncher. In the following run the commissioning of the RFQ, buncher, IH-cavity and 7-gap resonators will be finished. This year experiments are scheduled in July and September/October accelerating different Na- and Mg-isotopes with the new improved beam quality. In between the radioactive beam experiments a new 202.56 MHz 9-gap cavity will be installed to energy upgrade the REX-ISOLDE linac. With it one will be able to reach a beam energy of approximately 3.0 MeV/u.

REFERENCES

- [1] T.Sieber et al., "Acceleration of Radioactive Ions at REX-ISOLDE", Proc. of the LINAC 2002
- [2] T. Sieber, PhD thesis, "Entwicklung von 4-Rod- und IH-Radio-Frequenz-Quadrupol (RFQ) Beschleunigern für radioaktive Strahlen bei REX-ISOLDE und MAFF", LMU München, Mai 2001
- [3] K.-U. Kühnel, „Aufbau eines Splittingsesonators als Rebuncher für das REX-ISOLDE Projekt“, diploma thesis, Universität Frankfurt, September 1999
- [4] U. Ratzinger, Habilitation, Universität Frankfurt, July 1998
- [5] S. Emhofer, diploma thesis, „Aufbau und Vermessung der HF-Eigenschaften des REX-ISOLDE IH-Beschleunigers“, LMU München, December 1999

AN ENERGY UPGRADE OF THE REX-ISOLDE LINAC*

O. Kester, T. Sieber, H. Bongers, S. Emhofer, K. Rudolph, W. Carli, D. Habs
LMU München and the MLL München, 85748 Garching, Germany

Abstract

In 2002 the dominant experiment at CERN-ISOLDE was REX-ISOLDE. The LINAC delivered beams of radioactive isotopes at energies of 0.3, 2 and 2.2 MeV/u towards the two target stations. Due to the charge state breeder very different mass regions of the nuclear chart could be addressed from Li to Sm. In order to perform Coulomb excitation and particle transfer experiments in the mass region up to $A = 150$, an energy of the LINAC is required, which is foreseen in two steps. The first step of the upgrade to 3.1 MeV/u will be done by using the MAFF 202.56 MHz IH-cavity. The second step to energies close to 4.2 MeV/u will be a mayor change of the LINAC structure. There two 7-gap spiral resonators of REX-ISOLDE will be exchanged by a 202 MHz IH-cavity. Design calculations, cavity design and first measurements with the cavity dedicated for the first step of the upgrade will be presented.

INTRODUCTION

The radioactive beam experiment REX-ISOLDE at ISOLDE/CERN delivers post accelerated radioactive ion beams with a variable energy between 0.8 and 2.2 MeV/u [1]. In order to address many nuclear physics aspects, the full variety of beams available at ISOLDE should become accessible as accelerated beams for experiments. The method of charge state multiplication, which was introduced for the first time at REX-ISOLDE allows to access the different regions of the nuclear chart [2]. The charge-state breeder defines the time structure of the beam delivered to the LINAC and it adjusts the A/q of the ions below 4.5. The higher charge states of the radioactive ions allow a moderate size of the accelerator.

In 2002 first experiments with radioactive nuclear beams have been carried out with REX-ISOLDE. Beams have been delivered to the γ -detector array MINIBALL and to small experiments in the second beam line at a maximum energy of 2.3 MeV/u. In addition the commissioning of the LINAC has been performed in order to improve the beam quality and to reduce the beam energy spread [3]. It has been demonstrated that ions with masses up to $A=150$ could be accelerated with an overall efficiency of 2-3% from the ISOLDE target to the MINIBALL target. Until now the REX-ISOLDE LINAC could accelerate charge bred ions of $^{23}\text{Na} - ^{28}\text{Na}$ and ^7Li to 2.3 MeV/u with a transmission through the LINAC of about 75%. In the beam time with ^{30}Mg the beam could be delivered with smaller energy spread at 2.2 MeV/u and could be focussed through the target aperture of 5 mm. Slightly lowering of the final energy and adjustment of the 7-gap cavities 2 and 3 to negative synchronous phases

the best longitudinal beam quality could be reached so far. For the Lithium run the second beam line was installed in the target area. With the successful acceleration of $^9\text{Li}^{2+}$ to 2.3 MeV/u, REX-ISOLDE proved for the first time operation at the maximum A/q of 4.5 above design energy.

Towards the energy upgrade of REX-ISOLDE and the planned acceleration of isotopes in the mass range of Uranium fission products, measurements have been taken to test the breeding efficiency of the EBIS in the vicinity of $A=150$. Therefore, a ^{133}Cs beam from the test source of REXTRAP was injected into the EBIS. The acceleration tests performed so far had to be done with $^{133}\text{Cs}^{32+}$ ($A/q=4.16$) at a breeding efficiency of about 1%. Earlier measurements with Cs have shown a maximum charge state at 32+ for a breeding time of 160 ms.

THE ENERGY UPGRADE

To use the full range of isotopes from ISOLDE for nuclear physics experiments with Coulomb excitation and transfer reactions, higher beam energies are required. An increased energy of approx. 3 MeV/u allows studies of nuclear reactions up to mass $A=85$ on deuterium targets. A beam energy of 4.2 MeV/u would be suitable up to mass $A=145$. Therefore an energy upgrade of the REX-ISOLDE LINAC to increase the maximum particle energy at the target has been started. In two steps it is foreseen to raise the beam energy to approx. 4.2 MeV/u by maintaining the beam quality.

The structure of the REX-ISOLDE LINAC for the two energy upgrade scenarios is shown in fig.1. In order to reach 3.1 MeV/u the simplest solution is to include a 9-gap IH-cavity operating with 202.56 MHz resonance frequency. Due to the delay of the final permission to run FRM II, it was proposed to modify the prototype of the Munich accelerator for Fission Fragments (MAFF) IH-7-Gap resonator into such an IH-9-Gap cavity [4]. A major change of the LINAC structure will be required in order to reach energies of approximately 4.2 MeV/u. Thus two of the 7-gap spiral resonators with 101.28 MHz resonance frequency have to be replaced by a 1.5 m IH-cavity with 202.56 MHz resonance frequency to boost the energy to required region of 3.75 MeV/u. Then a 7-gap IH-resonator of the MAFF type cavity can be used to accelerate to final energies above 4 MeV/u. The rf-parameter of the 7-gap set-up and the 9-gap set-up are specified in table 1.

The MAFF IH-7gap resonator

For the MAFF-LINAC an efficient 7-gap structure compared to the split ring resonators of REX-ISOLDE is required for the energy variation. Hence the 7-gap

*supported by the BMBF and the DFG

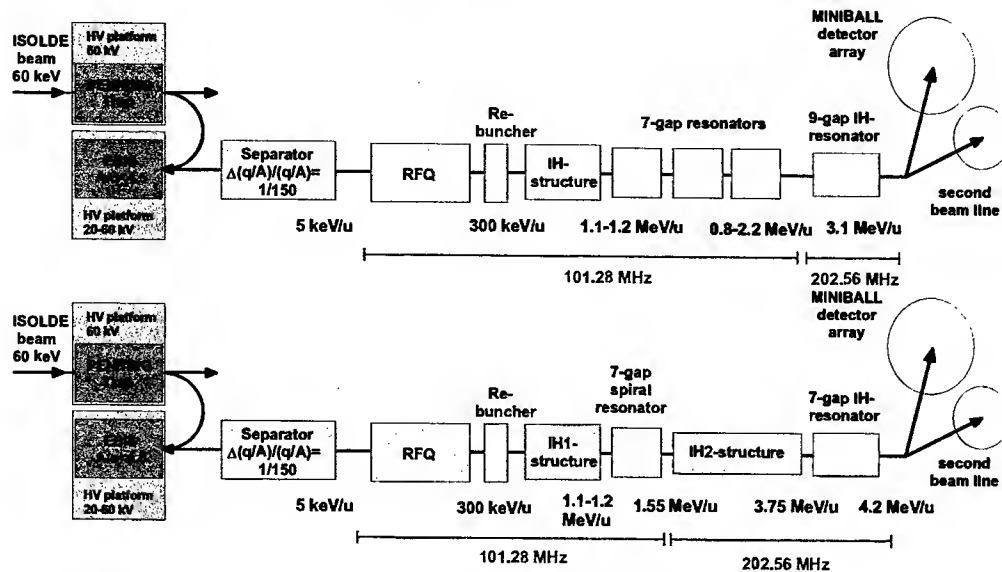


Figure 1: Structure of the REX-ISOLDE LINAC for the two upgrade scenarios. Several IH-structures with 202.56 MHz resonance frequency have to be included in order to raise the final beam energy.

structure has been designed as an IH-structure. Due to the higher shunt impedance of IH-structures a higher resonator voltage in combination with a very compact design can be achieved with the same rf-power compared to split ring resonators. Since the resonator is used both for acceleration and deceleration respectively, the cell length is kept constant. Based on the fact that the beam energy at MAFF will be varied between 3.7 MeV/u and 5.9 MeV/u a cell length of 74 mm was chosen, which corresponds to a design speed of $\beta = 0.1$. This results in an total length of 518 mm for the seven cells. The inner tank length therefore is 520 mm and the overall outside length is 646 mm. Low level measurements have been carried out to determine Q-values and shunt impedance (table 1) of both set-ups.

Table 1: Specification of the 7- and 9-gap IH-cavity

	7-gap	9gap
cell length [mm]	74	55
gap length [mm]	24	22-26
drift tube length [mm]	50	32
drift tube diameter [mm]	20 / 26	16 / 22
max. A/q	6.3	4.5
synchronous particle β	0.1	0.073
shunt impedance [MΩ/m] (low level measurements)	129	218
Q (measured)	9800	10100

Fig.2 shows the power resonator tank in the 7-gap set-up ready for beam tests at the MLL tandem. On a high energy beam line of the MLL a test bench for high power and beam measurements was installed. It was possible to obtain momentum spectra of a dc beam at different amplifier power and spectra for beam pulses at different

phases, using a 70° bending magnet positioned behind the resonator tank. The spectra with a dc-beam from the tandem were used to determine the effective shunt impedance. The measurement with pulsed beam injected into the 7-gap structures have been done to determine the ability to vary the beam energy by tuning the resonator's phase and amplitude.

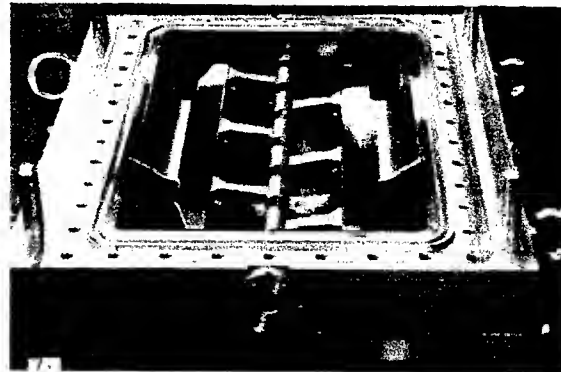


Figure 2: The resonator of the 202.56 MHz IH cavity.

Since the tandem can not deliver ions with $A/q = 6.3$ and an energy of 4.15 MeV/u or 5.40 MeV/u respectively, a 66.4 MeV $^{16}\text{O}^{5+}$ beam was used ($A/q = 3.2$). Hence the rf-power could be reduced by a factor of 3.9. This way, the worst case scenario of deceleration and acceleration from 4.15 MeV/u could be examined. Fig.3 shows the results of the power measurements. The effective shunt impedance remains constant although the calculated transit time factor (TTF) increases from 0.81 to 0.87 in the range of the rf-power level we have measured. Hence the absolute shunt impedance decreases, although the resonator's Q-value does not change significantly. Due to

the acceleration far of the synchronous particle velocity, local changes of the gap voltage distribution lead to a drastic change in the TTF, which can compensate the expected increase of the TTF from calculations. However the requirements for MAFF of 82 M Ω /m effective shunt impedance are exceeded by far.

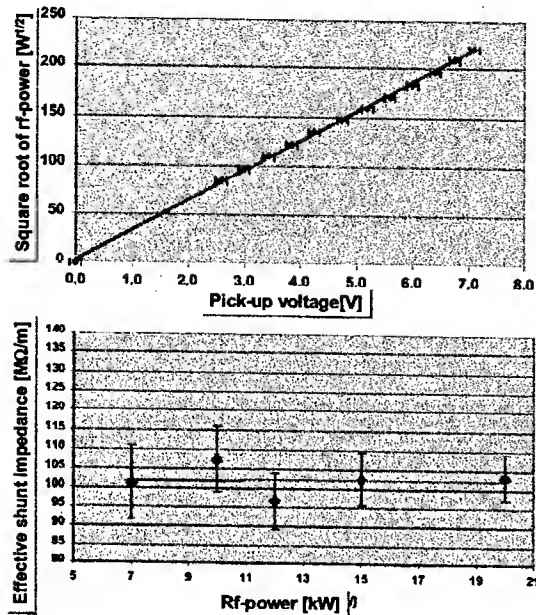


Figure 3: Measurements of the IH-7-gap resonator amplitude and shunt impedance.

The IH-9-gap resonator

The 9-gap set-up required for the first step energy upgrade has been examined with oxygen beams at the MLL test bench as well. A O^{5+} -beam at 2.2, 2.25 and 2.3 MeV/u from the Munich tandem was used to test the ability of the 9-gap IH-structure to post accelerate at power levels from 5 to 70 kW. An energy spectrum is shown for 70 kW rf-power in fig.4. The tandem peak has been used for energy calibration. The drift tube structure was adjusted with constant cell length of 55 mm.

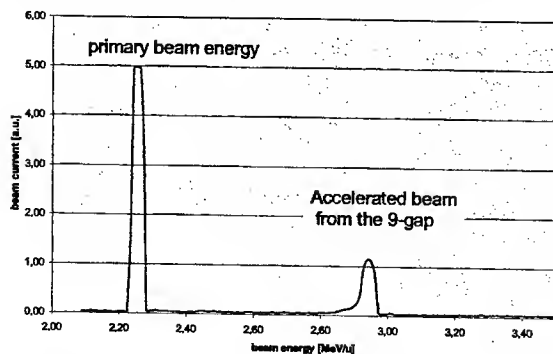


Figure 4: Adjustment of the gap voltage distribution.

The measured effective shunt impedance (fig.5) shows changes with the rf-power level, which corresponds to

small values of the TTF below 0.8. This is a result of the cell length which was kept constant at 2.5 MeV/u synchronous particle energy. Therefore a higher injection energy led to higher effective shunt impedances shown in fig.5. As a result the drift tube structure has to be installed according to the velocity profile in case of the 9-gap set-up, otherwise the required energy gain for REX-ISOLDE will not be possible.

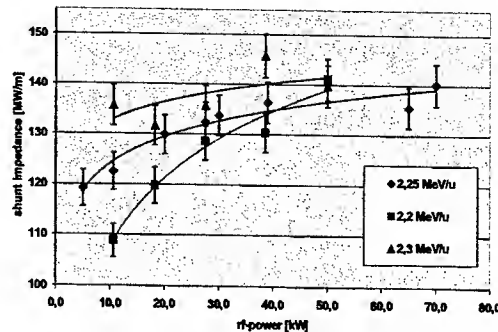


Figure 5: Effective shunt impedance of the 9-gap resonator for different injection energies.

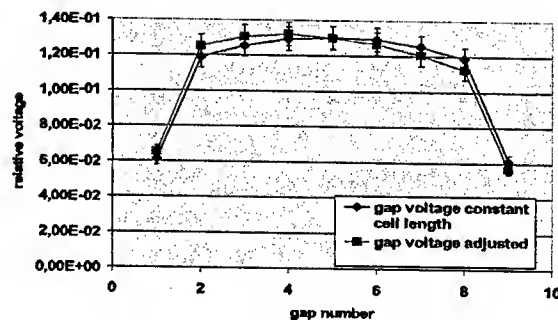


Figure 6: Adjustment of the gap voltage distribution.

With MAFIA the gap voltage distribution has been calculated for the constant cell length and the adjusted velocity profile. Taking that distribution shown in fig.6 into account, beam dynamic calculations deliver a TTF of 0.87 and an effective shunt impedance of 165 M Ω /m, which is sufficient to reach 3 MeV/u at REX-ISOLDE with 90 kW rf-power.

REFERENCES

- [1] O. Kester et al., "Accelerated radioactive beams from REX-ISOLDE", Proc. of EMIS14, Victoria, Canada, 2002, to be published in NIM
- [2] O. Kester and D. Habs, "Charge breeding of intense radioactive beams", 8. Symp. on EBIS sources, AIP Conf. Proc. 572, p. 217
- [3] S. Emhofer et al., "Beam measurements at the REX-ISOLDE LINAC", these proceedings
- [4] O. Kester et al., "A short IH-cavity for the Energy Variation of Radioactive Ion Beams", Proc. of the EPAC2002, 3.-7. Juni, Paris, Frankreich, 2002.

FRONT END DESIGN OF THE RIA DRIVER LINAC*

A.A. Kolomiets, ITEP, Moscow 117259, Russia
V.N. Aseev, P.N. Ostroumov, R.C. Pardo, ANL, Argonne, IL, 60439,

Abstract

This paper describes the front end design for the RIA driver linac which is able to select, separate and accelerate in the RFQ the required ion species of one- or two-charge states. The front end consists of an ECR ion source located on a 100 kV platform, LEBT, RFQ and MEBT. The first section of the LEBT is an achromatic bending system for charge-to-mass analysis and selection. For the heaviest ions with masses above 180, the transport system is able to deliver to the entrance of the first buncher a two-charge-state beam with similar Twiss parameters for both charge states. In order to match two-charge-state ions with different mass to charge ratios, the straight section of the LEBT upstream of the RFQ will be placed on a high-voltage platform. A voltage ~30 kV is required in order to match velocities of ions with mass to charge ratio less than the design value and to maintain the possibility accelerating two charge states simultaneously. Several beam matching schemes in the transitions LEBT-RFQ and RFQ-MEBT have been studied.

INTRODUCTION

The RIA driver linac will deliver a wide range of ions to secondary beam targets. The linac is designed for simultaneous acceleration of ions with different charge states to obtain the required beam power, up to 400 kW, even with limited intensity of highly charged heavy ions available from present ECR ion sources. The dynamics of multiple-charge-state beams have to be designed to prevent emittance growth in all sections of the linac. It is especially important to form high quality two-charge-state beam in the front end of the linac. To achieve this goal the front end has been designed taking into account higher order terms of focusing and accelerating fields and space charge of multi-component heavy-ion beams extracted from the ECR. Finally, the design has been analyzed and corrected with the help of beam dynamics simulation codes in realistic 3D fields.

LEBT DESIGN

The LEBT performs two main tasks: 1) an achromatic bending system for charge-to-mass analysis selects one or two charge state heavy ion beams; 2) a straight section forms longitudinal emittance and matches the beam to the following RFQ. The design of the straight section which comprises a multi-harmonic buncher (MHB), velocity equalizing resonator and focusing elements has been reported in ref [1]. The schematic layout of the LEBT is shown in Fig. 1. According to ref. [1] the lowest possible longitudinal emittance of a two charge state beam

accelerated through an RFQ can be obtained using an external MHB. A resonator installed immediately upstream of the RFQ entrance equalizes the average velocity of ions with different charge states.

Achromatic bending system

This section consists of two 60° bending magnets, two electrostatic quadrupole lenses, four sextupoles and a solenoid. A high dispersion area is formed by the first magnet where the required one- or two-charge state beam can be defined and transported to the RFQ. The baseline design of the RIA driver linac calls for 100 kW uranium beam that requires ~2 μ A in charge states 28 and 29. The estimated total beam current extracted from the ECR will be ~2 mA. The space charge of this multi-component ion beam effects the uranium beam parameters. To compensate the linear component of the space charge forces a solenoid magnet between the ECR and bending magnet is used. It has been found that changing solenoid position and field level provides required beam matching to the location of the horizontal slits.

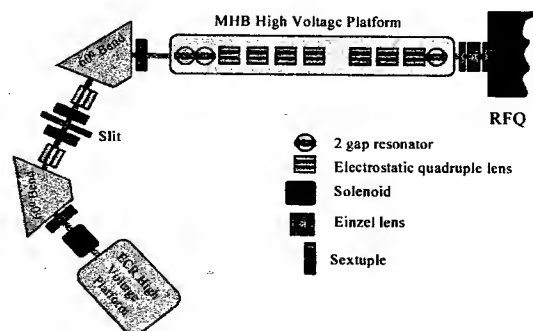


Figure1: Schematic layout of RIA driver LEBT

Straight section

The straight section of the LEBT includes a MHB, a velocity equalizer (VE), electrostatic quadrupoles and Einzel lens. All elements of this section except the Einzel lens are placed on a high voltage platform. The MHB consists of two quarter wave resonators. The first resonator provides the required voltage at the fundamental operating frequency, 28.75 MHz, and the third harmonic. The second resonator is operated at the second harmonic.

The distance between MHB and VE is determined by the need to separate the two charge states into adjacent RF buckets of the RFQ and is defined by the following expression:

* Work supported by the U. S. Department of Energy under contract W-31-109-ENG-38.

$$L = \lambda \sqrt{\frac{2e \cdot V_0}{Am_0 c^2} \frac{\sqrt{q_0(q_0-1)}}{\sqrt{q_0} - \sqrt{q-1}}},$$

where e is the elementary charge, V_0 is the accelerating voltage, A is the mass number, m_0 is the nucleon rest mass, q_0 is the highest charge state of ions, c is the speed of light. The distance depends on the charge-to-mass ratio and is equal to 1.507 m for the heaviest ions U^{29+} and U^{28+} at $V_0=100$ kV.

The LEBT can be tuned to accept any two-charge-state ions with masses $A \geq 180$ by satisfying two conditions: 1) provide the design velocity at the RFQ entrance for the average charge state; 2) provide the same time difference between the two charge states over the distance L , between the MHB and VE. The first condition is fulfilled if the voltage of the ECR ion source is

$$V_{01} = 2\beta_{av}^2 \frac{Am_0 c^2}{e \cdot (\sqrt{q_0} + \sqrt{q_0-1})^2}.$$

The second condition can be satisfied if the MHB and VE are biased by the voltage $\Delta V = V_{01} - V_{02}$, where

$$V_{02} = \left(\frac{L}{\lambda}\right)^2 \frac{Am_0 c^2}{2 \cdot e} \left(\frac{1}{\sqrt{q_0}} - \frac{1}{\sqrt{q_0-1}}\right)^2.$$

This value varies as a function of the charge to mass ratio of ions. This dependence is shown in Figure 2 which plots the voltage ΔV as a function of the charge state q_0 for three different mass number.

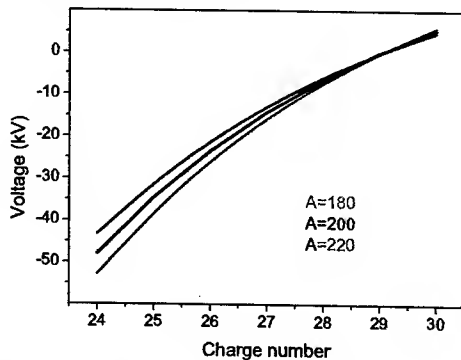


Figure 2: LEBT bias voltage as a function of charge state.

The electrostatic quadrupoles are used for beam focusing in this section of the LEBT and form a round beam waist in the VE. Matching of the low-velocity beam to the RFQ acceptance is a challenging task due to the large difference in the focusing strength of the LEBT and RFQ. The distance between the VE and RFQ should be as short as possible in order to have effective bunching of two-charge-state beams. To minimize this space a relatively short Einzel lens is used for the matching of the axially symmetric beam to the RFQ acceptance which is defined by the RFQ radial matcher.

MODIFICATIONS OF THE RFQ DESIGN

The detailed description of the RIA RFQ is given in [2]. The main goal of the beam dynamics design of the RFQ was to match the parameters of the RFQ with the longitudinal emittance formed by the MHB, eliminate halo particles from the acceleration process and keep the transverse emittance of a two-charge-state beam unchanged. The basic RFQ parameters are given in Table 1. To address the beam matching in the transitions LEBT-RFQ and RFQ-MEBT the entrance and exit radial matchers have been carefully analysed and modified designs of these sections of the RFQ have been proposed.

Table 1: The main RFQ parameters.

Average radius R_0	0.6 cm
Vane-to-vane voltage U_0	68.5 kV
Output beam energy	199 keV/u
Synchronous phase ϕ_s	-25°
Normalized trans. acceptance	>1.8 π mm-mrad
Vane length	392 cm

Entrance radial matcher

The external buncher forms a very short bunch length $\sim 40^\circ$ at the entrance of the RFQ. For such a short bunch there is no need for a standard radial matcher which provides dynamic matching over 360° and requires convergent beam to be matched. As was pointed out in ref. [3], by providing an appropriate RFQ vane profile it is possible to form matched conditions of the beam waists in both planes at the RFQ entrance. For this modified matcher there is no need to have any focusing elements between VE and RFQ because the matched parameters can be easily provided by quadrupoles placed upstream of the VE. The parameters of the conventional and modified matchers are given in Table 2.

Table 2: Parameters of the conventional and modified radial matcher.

	Conventional	Modified
Length	170 mm	300 mm
Mismatch factor	1.15	1.107
Emittance growth in the upstream LEBT	14%	-
Twiss parameters α	1.3737	-0.048
β (cm/mrad)	0.088	0.093

The quoted length of the conventional matcher includes Einzel lens. In spite of the fact that the modified matcher is longer, it does not increase the total length of the RFQ because electrodes behind the horn are modulated so the number of accelerating cells is the same as in the initial design. The modified matcher mitigates emittance growth in the LEBT.

Exit radial matcher

We have found that solenoid focusing in the MEBT produces a minimal mismatch of two-charge state beams compared with any other type of focusing. There is a need to match beam between the RFQ and this axially symmetric transport channel. One solution is using electromagnetic or electrostatic triplet quadrupole lenses immediately after the RFQ. A short transition cell at the end of the RFQ vanes is used in this case to obtain the beam waists in both transverse planes. The second option is using a 4-cell RFQ radial matcher which can form an axially symmetric beam as was proposed in ref. [4]. As was found both solutions provide required beam matching to the MEBT based on solenoid focusing.

BEAM DYNAMICS SIMULATIONS

The first order design of the LEBT has been carried out using TRACE-2D and -3D codes [5]. Higher order optimization has been done using the code GIOS [6]. The RFQ has been designed using code DESRFQ [7]. Further optimization of the LEBT has been based on simulations of multi-component heavy-ion beam dynamics using multiparticle codes TRACK [8] and DYNAMION [9].

TRACK has been especially developed for the RIA driver design and allows us to perform end-to-end simulations beginning from the ECR ion source. The main feature of the code is the use of a realistic preliminary calculated 3D representation of external accelerating and focusing fields. DYNAMION has been primarily used for the beam dynamics simulations in the RFQ.

Beam simulations starts with a multi-component heavy-ion beam exiting the ECR. To produce 60 μ A total uranium two-charge-state beam at the RFQ entrance the ECR extracts >2 mA multi-component heavy-ion beam. In our design and simulation we have assumed the same Twiss parameters for all ion species exiting the ECR. Most ion species are eliminated by the first bending magnet. Figure 3 shows phase space plots at the location of the slits shown in Fig. 1. It presents the design uranium ions and nearest unwanted ions O^{2+} simulated for a total input total current 2 mA. The simulations show the system separates charge states reliably over full range of total input beam current and provides at MHB similar Twiss parameters of transverse emittances for both charge states.

The Fig. 4 shows simulated beam envelopes in a modified and conventional radial matcher. The envelope for the last case is shown for Einzel lens and RFQ matcher. The simulations confirm that the modified matcher provides perfect matching not only for short bunches, but also in case of unbunched beam.

The results for both exit matchers are presented in Table 2. It shows that the both options solve the task of matching the RFQ output beam with a solenoid channel but the option with a short transit cell seems more practical because it simplifies the RFQ design and allows more flexible control of beam parameters.

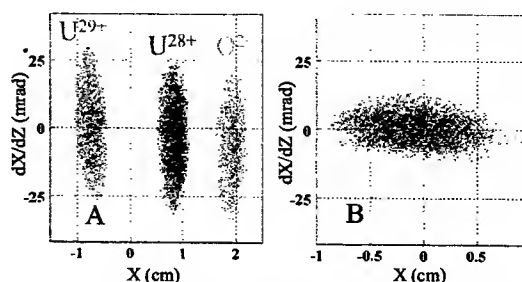


Figure 3: Transverse phase space plots in bending section. (A) at slit position shown in Fig.1. (B) – at MHB entrance.

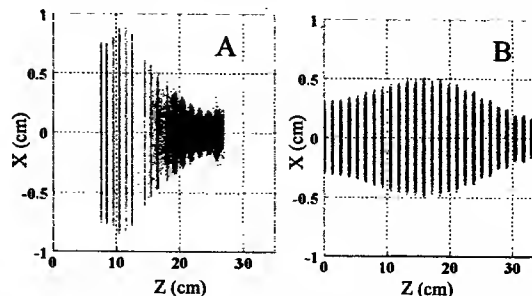


Figure 4: Envelopes in conventional (A) and modified (B) RFQ entrance radial matcher.

Table 2: Beam parameters of the beam at RFQ exit for both charge state

Twiss parameters	4-cell matcher		Short transition cell	
	X	Y	X	Y
α	-0.446	-0.37	0.04	0.05
β (cm/mrad)	0.029	0.030	0.019	0.010

REFERENCES

- [1] P.N. Ostroumov, K. W. Shepard, V.N. Aseev and A.A. Kolomiets, Proc of the 2000 Linac Conf., Monterey, August 2000, SLAC-R-561, p. 202.
- [2] P.N. Ostroumov et al., Phys. Rev. ST Accel. Beams 5, 060101 (2002).
- [3] D.G. Koshkarev and L.G. Vorobiev, Nuclear Instruments and Methods in Nuclear Research, A 336 (1993), p. 291.
- [4] K. Crandall, Proc. of the 1994 LINAC Conf., Tsukuba, August 1994, p. 227.
- [5] K. Crandall, Report LA-11054-MS. Los Alamos, 1987.
- [6] H. Wollnik, J. Brezina and M. Berz, NIM, A258, (1987) 408
- [7] A. Kolomiets, S. Yaramishev, ITEP report, Moscow, 1998 (unpublished).
- [8] P. N. Ostroumov and K. W. Shepard, Phys. Rev. ST. Accel. Beams 11, 030101 (2001).
- [9] A.Kolomiets, V.Pershin, I.Vorobyov, S.Yaramishev, Ju.Klabunde, Proc.,of the 6 EPAC Conf., Stokholm, June 1998.

HIGH POWER ELECTRON S-BAND LINAC FOR INDUSTRIAL PURPOSES

M.I. Ayzatsky, E.Z. Biller, V.N. Boriskin, V.I. Beloglasov, N.V. Demidov, A.N. Dovbnya, V.A. Kushnir, V.V. Mitrochenko, L.K. Myakushko, T.F. Nikitina, V.A. Popenko, G.D. Pugachev, L.V. Reprintzev, G.D. Repikhov, V.A. Shendrik, D.L. Stepin, G.E. Tarasov, Yu.D. Tur, V.L. Uvarov, National Science Center 'Kharkov Institute of Physics & Technology', 1, Academicheskaya St., NSC KIPT, 61108 Kharkov, Ukraine

Abstract

The high-power S-band linac KYT-20 with electron energy 20 MeV and average beam power up to 20 kW was designed and fabricated in the NSC KIPT. The linac was put into operation in 2002. The accelerator is devoted to irradiation applications mainly for radioisotope production for medicine. The KYT-20 consists of two accelerating structures with variable geometry and the injector system. The wave phase velocity in the structures is equal to the velocity of the light. Length of the accelerating section is 1.23 m. The linac is equipped with different output systems to extract the beam. The paper contains a detailed description of the main linac systems. The results of KYT-20 testing and the beam parameters measurement are presents.

INTRODUCTION

Development of advanced radiation technologies requires designing of a proper accelerator technique. In the last few years at the NSC KIPT several types of technological linacs with an electron energy of 10-20 MeV and an average beam power up to 20 kW were developed [1]. One of such installations is the powerful S-band electron linac KYT-20 [2]. The main purpose of the KYT-20 is to produce isotopes for medical needs. The accelerator design and accelerated beam parameters make it possible to use it for other tasks, for example, radiation treatment of materials, gamma-activation analysis, carrying out of experiments in the field of radiation physics etc. The linac consists of a small-sized injector and two accelerating sections with a moving wave. For realization of radiation technologies the accelerator is provided with different output units. Below the description of basic accelerator systems and results of their testing are presented.

INJECTOR

The injector system of the linac KYT-20 comprises a low-voltage diode electron gun, a bunching cavity and an accelerating cavity. The diode electron gun with an impregnated cathode of 14 mm in diameter was used as an electron source. The micropervance of the source was $0.58 \text{ A/V}^{3/2}$, that ensured, at an anode voltage of 25 kV, a pulse current of 2.3 A. The density of an emission current did not exceed 1.6 A/cm^2 .

The self-frequency, quality factor and the shunt resistance of the bunching cavity were 2797.15 MHz, 3000 and 0.39 MOhm, respectively. The accelerating

cavity is a cylindrical E_{010} cavity. The quality factor and the shunt resistance were $1.1 \cdot 10^4$ and 1.1 MOhm, respectively. The coefficient of coupling with the waveguide transmission line was equal to 4.5. The cavity is provided with a device for frequency tuning within $\pm 3 \text{ MHz}$. At the 1 MW microwave power the maximum field strength along the axis of the cavity without field was 56.5 MV/m. At the accelerating cavity exit an induction monitor of the pulse beam current was installed. The magnetic system of the injector is composed of two axially symmetrical magnetic lenses. The first of them, arranged between the gun and the bunching cavity, can be used for control of the pulse beam current value. The total length of the injector is 20 cm.

Experimental investigations of the injector were carried out on a special test bench. The investigations included measuring the energy spectrum and the emittance, evaluating the phase length of bunches. The methods of evaluating the phase length of bunches was based on a supposition that the phase portrait of particles at the phase-energy plane can be represented in the form of a line. The phase spread of particles at a given energy is substantially less than the phase length of bunch. The line thickness depends, in our case, only on the energy spread that occurs due to the action of the space charge force and electric field force in the bunching cavity. As it follows from the simulation results (see Fig.1) this spread is rather insignificant.

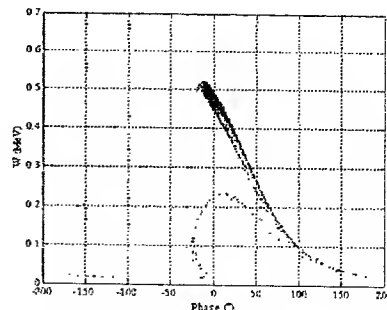


Figure.1: The calculated phase portrait of the beam at the injector output (70% of particles are within the phase and energy intervals being 24° and 18%, respectively)

To evaluate the phase length of bunches we have used a E_{010} cavity at the exit of the magnetic analyzer. It permitted to measure the phases of the centers of gravity for particle bunches that passed through the magnetic analyzer aperture at different magnetic field values, and thus to plot the phase-energy relation of particles. Fig.2

shows the measured phase-energy relation and the energy beam spectrum for one of realizations of injector performances. The data for the plot were taken in the time point corresponding to the middle of the current pulse. In this case the microwave power supply was 1.26 MW, the current at the injector output was 1.25 A. One can see that the results obtained are in a good agreement with the computer simulation data.

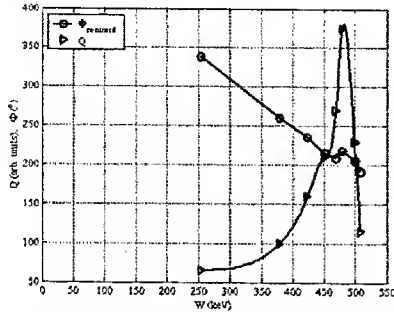


Figure 2: The phase-energy distribution of particles at the injector output and the energy spectrum

As is seen from Fig.2, the beam has a core. The FWHM energy spectrum is 13%, the phase length is near 25%. Nevertheless, the beam contains the particles with sufficiently high energy whose phase differs, at least, by 150°. Since the accelerator is not large and the field strength in the beginning of sections is sufficiently high, the particle from the bunch "tail" can lead to forming the low-energy halo at the linac exit.

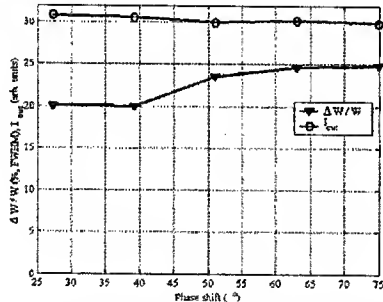


Figure 3: The beam current and the integral energy spectrum width as a function of the phase shift between the bunching and accelerating cavities.

The energy spectrum width at the injector output depends on the phase shift between the bunching and accelerating cavities, while the output current depends slightly on changing this parameter in wide ranges. The value of the integral energy spectrum width was determined with taking into account the particle energy changing during transitional processes in the injector cavities.

The transversal emittance was measured by the three gradients method. The results of measurements of the vertical beam profile width as a function of the quadrupole current with a beam current at the injector output equal to 0.8 A are presented in Fig.4.

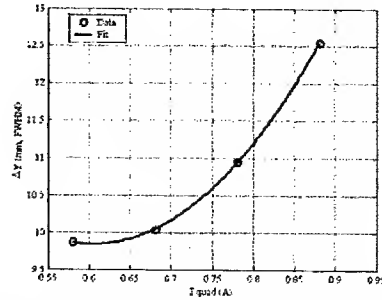


Figure 4: The half-width of the vertical particle density distribution as a function of the quadrupole current.

In this case the normalized emittance was 22π -mm-mrad. It should be noted, that as the current at the injector output increases up to 1.4 A, then the transversal emittance increases insignificantly and equals to 30π -mm-mrad. In the course of injector testing, a beam autobunching was observed – electron bunching was observed even in the case when the microwave power was not supplied into the bunching cavity. The effect can be explained by the following manner. A part of electrons being not captured into the acceleration mode fall into the slowing-down phase and are accelerated in the reverse direction. The reverse electron flow consists in a sequence of bunches following with an operating frequency. The flow of "reverse" electrons passes through the bunching cavity and excites in it electromagnetic oscillations. In turn, the beam coming from the gun interacts with the field excited by these electrons that results in grouping the electron bunches. In more details this effect is described in [3].

ACCELERATING SECTIONS

To reach a maximum efficiency the accelerator is provided with two accelerating sections of 1.23 m length having a variable geometry of the accelerating structure. The phase wave velocity in the accelerating structures of the sections is equal to the light velocity. The developed novel mathematical model of coupled cavities and diaphragmatic waveguides, as well as, the proposed methods of tuning [4, 5, 6] allowed us to solve completely the problem of tuning the cells in the nonhomogeneous accelerating structures. The $2\pi/3$ mode sections with a variable geometry were created using these methods. In the first section of the KYT-20 the radius of coupling holes is decreased linearly from the entry to the exit of the section. The second section has a quasi-constant law of changing the radii of coupling holes linearly with decreasing the radii in transition cells. The chosen sequence of arranging the sections with different sizes of accelerating cells decreases a possibility for occurrence of BBU effect. At the input power of 15 MW and the accelerating current 1.0 A each of the accelerating sections provides an energy gain of 12.2 MeV.

OUTPUT UNITS

In connection with that the accelerator can be used for different purposes requiring diverse spatial electron distributions on the target we have developed and tested a set of systems for the beam extraction.

The first of them is a magnetic system designed for the beam scanning with a 3 Hz frequency. Here the beam is extracted via the air-cooled titanium foil. The beam dimensions on the foil are 10x100 mm. When scanning the beam at the pulse repetition rate exceeding the scanning frequency, there is the considerable particle density nonhomogeneity in time and space. For a number of applications such a situation is not acceptable. The use of the secondary system eliminates these disadvantages. The beam is extracted from the accelerator via the double water-cooled foil and incomes into the special quadrupole lens where the beam defocusing in the vertical plane and focusing in the horizontal plane occur. A required electron beam distribution on the target is formed after placing it at the distance exceeding the focal length of the lens. The design of the device makes it possible to perform remotely the quadrupole lens replacement with a special target unit designed for target irradiation according to the program of radionuclide production. The unit comprises a special converter, a system for cooling the converter and remotely operated mechanism for removing of the irradiated target and its further transporting. For carrying out of experiments requiring an insignificant energy spread a magnetic system of "chicane" type was designed. The system consists of four permanent magnets with a field of 0.18 T in the 3.5cm clearance. To release the energy of a necessary range, in the place of maximum system dispersion a collimator was disposed.

RESULTS OF ACCELERATOR TESTS

In the course of accelerator tests we have adjusted all its systems and determined basic beam parameters at the accelerator exit as well as their relations. For measurement of the pulse beam current there are installed three beam current monitors. One of them (at the accelerator exit) is combined with the induction monitor for measuring the position of the beam center of gravity [7]. The system of secondary-emission monitors was used for monitoring of the irradiation field [8]. The particle energy was determined using a magnetic system of the scanning device. The tests showed that the beam parameters satisfy, in main, the specifications on intensity, power and efficiency. Fig.5 presents the electron energy v.s. the pulsed beam current at the RF power supply of 14.5 MW to each of accelerating sections.

At a pulse repetition rate of 200 Hz, a current pulse duration of 3.6 μ s and a pulse current of 1.2 A, the mean beam power equals \approx 18 kW. The electron efficiency is about 87%. From the analysis of beam current passage along the accelerator it follows that more than 75% of

particles injected into the first accelerating section arrive to the accelerator exit. This value increases with pulse current decreasing.

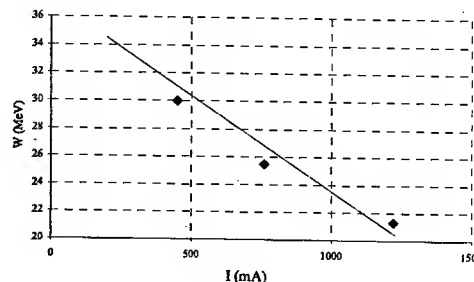


Figure 5: Electron energy versus pulse current. Points - experimental data, curve - calculation.

It has been found that at a pulse current exceeding 800 mA in the electron energy spectrum at the accelerator exit the low-energy halo is observed. Its occurrence is related, probably, with features of the injector operation in the heavy current mode. We plan to conduct a series of investigations aimed to removing this phenomenon.

To date the accelerator has gained the operating time more than 2000 hours for applied and research programs.

ACKNOWLEDGE

The work is fulfilled under the support of the Scientific-Technology Center in Ukraine, Project #2185.

REFERENCES

- [1] V.A. Kushnir et al., Proc. of the 2001 Asian Particle Accelerator Conference, Beijing, 2001, p.150.
- [2] K.I. Antipov et al., Proc. of the 2001 Particle Accelerator Conference, Chicago, 2001, p. 2805.
- [3] M.I. Ayzatsky et al, Journal of Kharkov National University, Ser.: "Nuclei, Particles, Fields", № 569, 3/19/, (2002), p.69. (in Russian)
- [4] M.I. Ayzatsky, Proc. of the 1996 EPAC, 1996, v. 3, p. 2023.
- [5] M.I. Ayzatsky, Proc. of the 1996 EPAC, 1996, v. 3, p. 2026.
- [6] M.I. Ayzatsky, E.Z. Biller, Proc. of the 1996 LINAC Conference, Geneva, Switzerland, p. 119.
- [7] V.N. Boriskin et al., Proc. of the Int. Particle Acceleration Conf. (PAC-99), New York, 1999, vol. 2, p.753.
- [8] V.N. Boriskin et al., Proc. of the Int. Conf. Large Experimental Physics Systems (ICALEPS-97), Beijing, 1997, p. 569.
- [9] V.N. Boriskin et al., Problems of Nuclear Science and Technology, Ser.: "Nuclear Physics Experiments", 2001, vol. 5 (39), p. 147.

PULSED HEATING EXPERIMENTS AT 34 GHZ*

O.A. Nezhevenko¹, V.P. Yakovlev¹, J.L. Hirshfield^{1,2}, and G.V. Serdobintsev^{2,#}

¹Omega-P, Inc., New Haven, CT 06511, USA,

²Physics Department, Yale University, New Haven, CT 06520, USA

Abstract

Pulsed heating is one of the main factors that limit accelerating gradient in normal conducting linear accelerators. In this paper a special test device is described that is designed to determine the maximum achievable surface electric field limit due to pulsed heating and metal fatigue. The power source for driving the test device is to be the Omega-P 34 GHz pulsed magnicon. Utilization of a few MW of μ sec pulse width should allow one to obtain pulsed heating excursions exceeding 600° C. The test device is designed with a to allow measurements for copper, for other materials, and for different procedures of surface preparation.

INTRODUCTION

Two phenomena limit the practical utility of accelerating structures: rf breakdown that limits the acceleration gradient, and surface fatigue due to pulsed heating that limits the structure lifetime. #

Pulsed heating [1] is caused by the eddy currents created by a high-power rf pulse. Mechanical stress appears in the thin surface layer of metal due to a temperature rise ΔT . When the rise in temperature is above a "safe" value ΔT_s , the mechanical stress grows large enough to create microscopic damages in the metal. The damage accumulates with each succeeding pulse and the cavity surface is destroyed after a certain number of pulses. In practice, the destruction of the metal surface occurs when the mechanical stress exceeds its elastic limit, which allows one to estimate a safe temperature threshold [1,2], namely $\Delta T_s \approx 2\sigma/\alpha E$, where σ is the yield stress, α is the coefficient of linear thermal expansion, and E is the elastic modulus. For copper this estimate gives a safe threshold for temperature rise ΔT_s of about 110 C°.

At present, pulse heating experiments using 11.424 GHz cavities have been carried out at SLAC [3]. The experiments demonstrated that pulsed heating with a temperature rise of 120°C showed modification and damage of the copper surface after 5.5×10^7 pulses. It also showed that significant damage had occurred to the coupler aperture of the test cavity, where the temperature rise was about 250 C°.

However, for practical needs it is important to know the temperature rise threshold and material life-time more exactly, because even at the moderately high gradients in the NLC design it is hard to reduce the local temperature rise to an acceptable level of about 100 C° [4]. Possible

progress in increasing the accelerating gradient will make pulsed heating even more serious.

The structure life-time drops exponentially when the temperature rise increases; [1,2] thus in order to make reliable measurements within a reasonable time one has to have a high temperature rise, up to 500-600 C°. Tests at 34 GHz can produce such temperature rises. The asymptotic behavior of the surface degradation may be determined based on measurements for different temperature rises that will allow firm conclusions to be drawn as to structure life-time.

In present paper a test device is described, to be driven with power from the 34.272 GHz magnicon, [5] to determine the maximum achievable surface field limit imposed by pulsed heating.

TEST CAVITY DESIGN

The TE₀₁₁ test cavity schematic layout and the rf magnetic field pattern are shown in Fig. 1. The cavity consists of two main parts, the cavity body which is coupled to an input waveguide, and the removable end cap, the left-most element in Fig. 1.

The cavity design has to satisfy two main requirements: (a) the cavity geometry including input coupling must be axially symmetric in order to keep surface electric fields negligibly small, and consequently to avoid breakdown problems, and (b) in order not to damage the main part of the cavity surface, the temperature rise at any point (except for the end cap) should not exceed the "safe" value of 110°C. Because the end cap has to be tested up to 500 C°, the maximum current density on its tip must be at least 2 – 2.5 times higher than at any other point on the cavity surface.

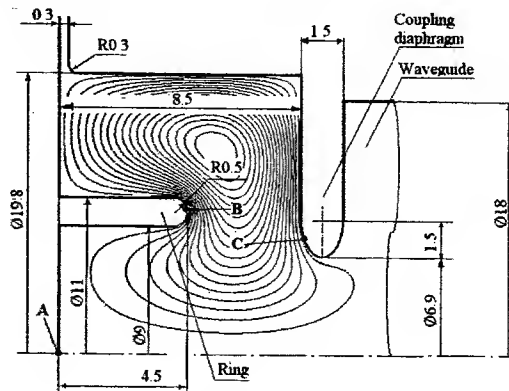


Fig. 1. The cavity schematic layout and the rf magnetic field pattern. All dimensions are in mm.

The test cavity geometry shown in Fig. 1 has been developed in order to satisfy both requirements. In Fig 1.

* Work supported by US DoE

Permanent address: Budker INP, Novosibirsk 630090, Russia

one can see that the input coupling diaphragm is elliptical in cross section with an eccentricity (i.e., ratio of the axial-to-radial semi-axes.) of 0.5, in order to reduce surface current density at the iris edge. The end cap has a ring with diameter of ~ 1 cm to achieve the required enhancement in surface current density (e.g., RF magnetic field). The RF magnetic field distribution along the cavity surface and the corresponding temperature rise are shown in Fig. 2.

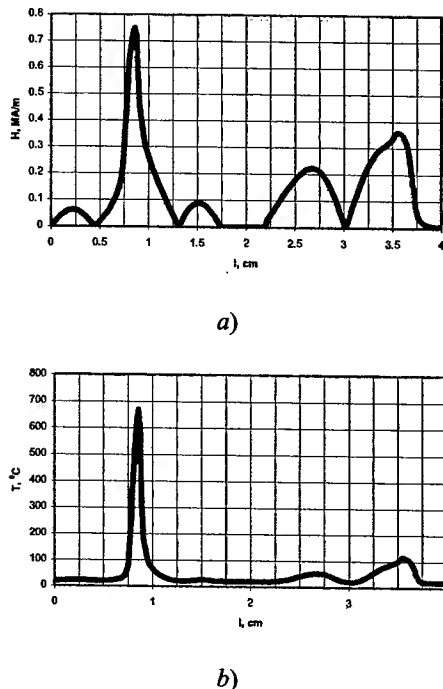


Fig. 2. The magnetic field (a) and temperature rise (b) distributions over the cavity surface. Input power is 1.5 MW; pulse width is 1 μsec .

The axial point $l = 0$ is the center of end cap (point A in Fig. 1). The highest maximum surface magnetic field is at point B on the ring, and the last maximum (at l of about 35 mm) is at point C at the coupling iris. One can see that the magnetic field near the ring is at least two times greater than anywhere else in the cavity. The temperature distribution in Fig. 2b is given for copper taking into account the increase in copper resistivity with temperature [6].

In Fig. 3, the maximum surface temperature of this cavity vs. the input power for a pulse width of 1 μsec is presented. The lower curve corresponds to calculations without taking into account temperature dependence of the copper resistivity. The upper curve corresponds to calculations taking into account the cavity surface resistivity change during the pulse. The incident power reflection due to a mismatch, caused by decrease in the cavity quality factor is also taken into account. Note that this effect can be used as a technique for direct

measurement of the temperature rise, which is difficult to do any other way.

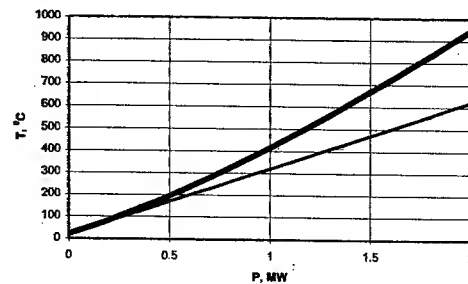


Fig. 3. Maximum surface temperature vs. input power for an initial temperature of 20 $^{\circ}\text{C}$. See text for details.

The design parameters of the test cavity are listed in Table I.

Table I. Cavity parameters.

operating frequency	34.272 GHz
operating mode	TE ₀₁₁
quality factor (unloaded)	7000
input power	1.5 MW
maximum surface current density	0.82 MA/m
RF pulse duration	1 μsec
temperature rise	650 $^{\circ}\text{C}$
input waveguide mode	TE ₀₁

One can see that in order to achieve a temperature rise of 650 $^{\circ}\text{C}$ on the cavity surface during a 1 μsec rf pulse at 34.272 GHz, an rf power level of 1.5 MW is sufficient.

The test cavity mechanical design is shown in Fig. 4.

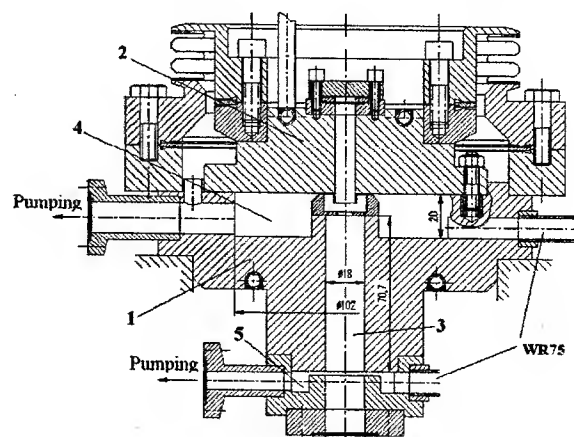


Fig. 4. Test cavity design. 1- cavity body; 2- end cap; 3- input waveguide; 4- coaxial chamber; 5- measuring chamber

The cavity is constituted of two main parts: cavity body (1) with coupling iris, and end cap (2). The end cap is separated from the cavity body by a gap, which allows

one to replace the end cup, pump out the cavity and provide the possibility of microwave diagnostics. The end cap (2) is water cooled, which allows one to maintain constant temperature at before the pulse starts by regulating the water flow. One of the important parts of the experiment is the means for diagnosis of surface degradation due to metal fatigue. The major criterion that allows an indication of the state of the cavity surface is the Q -factor. It is necessary to make periodic measurements of the Q -factor without disassembling the cavity, so as to maintain high vacuum conditions. A hybrid dipole mode is used for this diagnosis. This mode has a resonant frequency of about 14 GHz. A substantial fraction of its Ohmic loss (~20%) is at the end of the field enhancement ring, which makes this mode sensitive to small changes in the damaged material conductivity. The mode is coupled to both coaxial chamber (4) and input waveguide (3). For this measurement the cavity can be excited through one WR-75 waveguide and measured through a second one (see Fig. 4). The test cavity input waveguide is not cut-off for the 14 GHz dipole mode, and in order to prevent propagation of the test signal back to the input mode converter, the "measuring chamber" (5) is designed to constitute a choke for 14 GHz.

The schematic arrangement for pulsed heating experiment is shown in Fig. 5. All the magnicon ports are to have directional couplers. Because the minimum required RF power is about 2 MW, only one magnicon port will be used in the experiments. The three other ports will be connected to vacuum loads. The TE_{01} - TE_{10} mode converter [7] is used to match the cylindrical waveguide in the TE_{01} mode with the WR28 rectangular waveguide at the magnicon output. A ceramic window separates the cavity from the magnicon in order to isolate high vacuum in the magnicon during the experiments with the cavity, e.g. when the cavity end cap is replaced.

Different materials can sustain different pulsed temperature rises, but the most important and common material for accelerating cavities is copper. Consequently, the first experiments will be done with copper. It is planned to perform experiments and assess damage to the cavity surface at different temperatures (from 500 °C to 200 °C), which will allow one to extrapolate results to lower temperatures. After a certain number of pulses the end cap will be removed and investigated using facilities of the Yale Electron Microprobe Laboratory. Two major methods will be used for the end cap autopsy, Scanning Electron Microscopy (SEM), and Energy-Dispersive X-ray analysis (EDX), the latter to provide elemental concentration analysis.

CONCLUSIONS

At present the test cavity and the waveguide components are in construction. The 34 GHz magnicon is undergoing initial tests [8]. Pulsed heating experiments are expected to begin within a year.

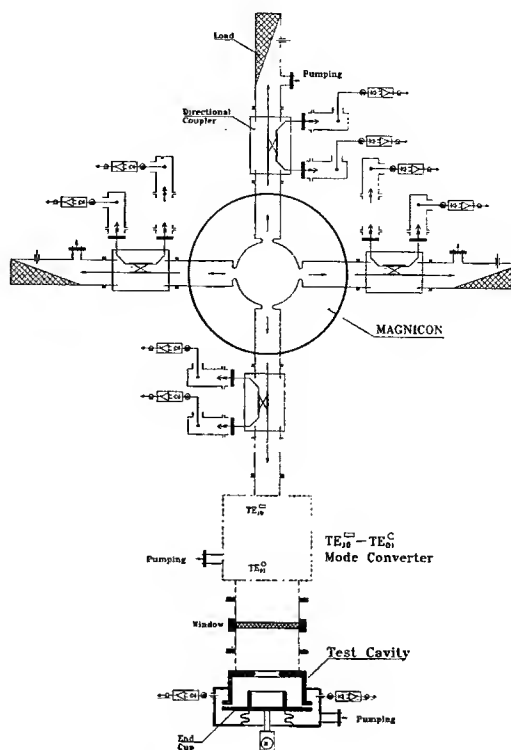


Fig. 5. Test bed layout (14 GHz diagnostics are not shown).

REFERENCES

- [1] O.A. Nezhevenko, PAC97, Vancouver, 1997, p.3013.
- [2] V.F. Kovalenko, "Physics of Heat Transfer and Electrovacuum Devices", (Sovetskoe Radio, Moscow, 1975).
- [3] D.P. Pritzkau and R.H. Sieman, Phys. Rev., v.5, 112002 (2002).
- [4] J.W. Wang, et.al., LINAC2002, TH464.
- [5] O.A. Nezhevenko, et al, AAC2002, AIP 647, p. 433 (2002).
- [6] Handbook on Physics, I.K. Kikoin ed., Atomizdat, Moscow, 1976.
- [7] G.G. Denisov, et al., AAC2002, AIP 647, p. 476 (2002).
- [8] O.A. Nezhevenko, et al., "34 GHz, 45 MW Pulsed Magnicon: First Results," Present Conference, TPAE024.

THE VACUUM SYSTEMS FOR PEFP LINAC*

M.Y. Park[#], Y.S. Cho, J.M. Han, Y.J. Kim, H.J. Kwon, J.H. Jang, K.K. Jeong
KAERI, Dae-Jeon, Korea

Abstract

The frontier project for high power proton accelerator including the proton injector, LEBT, RFQ and DTL has been launched in Sep. 2002. The fabrication and installation of the front-end system completed and the engineering design of the DTL has been ended. Now we are fabricating the 1st tank and RF components for the DTL. The purpose of this paper is to overview the installed vacuum systems of the front-end system, and to check out the designation of the DTL vacuum system.

- Output current : 20 mA
- RF power : 225/225/224/221 kW

FRONT END

The layout of the front-end vacuum system is presented in figure 1. The PEFP linac is designed to accelerate to 20 MeV both H⁺ and H⁻ beams and at the front-end the beam energy is 3.0 MeV. As showing in the figure, every structure has respective vacuum system and they'll be operate independently.

INTRODUCTION

The high power proton accelerator has been developed at KAERI (Korea Atomic Energy Research Institute) for basic researches and industrial applications. In the 1st step of the project we're plan to develop the system for acceleration to 20 MeV until 2005 and will provide beam to users in the middle of 2007[1-2].

The main design scope of the vacuum system is to select the proper vacuum components and install locations to lower the system pressure efficiently. At first for this, we understood the vacuum characters and estimated the gas loads for respective accelerating structure. And then we selected the pumps in which have the sufficient pumping speed in order to overcome the gas loads evolved from the beam loss, surface out-gassing and leak, etc. The required pressures of respective structure are decided to limit the beam losses by resident neutral gases. The main gas loads on front-end are hydrogen gases from beam losses amount of 10 mA, and are surface outgassed and leaked gases on the DTL. Another factor to select the components is the easiness of operation and maintenance. Also the counter-plan for problems of sudden failure of the pumps is to be prepared.

LINAC PARAMETERS

The main parameters of the linac are listed in table 1.

Table 1. The Linac parameters

Injector	- Energy : 50 keV
	- Current : 30 mA
	- Proton ratio : > 80%
LEBT	- Energy : 50 keV
	- Current : 10 ~ 40 mA(variable)
	- Transfer efficiency : > 92%
RFQ	- Energy : 3.0 MeV
	- Output current : 20 mA
	- RF power : 417.9 kW
DTL	- Energy : 20.0 MeV

*This work is done supported by the Ministry of Science & Technology
ex-mypark@kaeri.re.kr

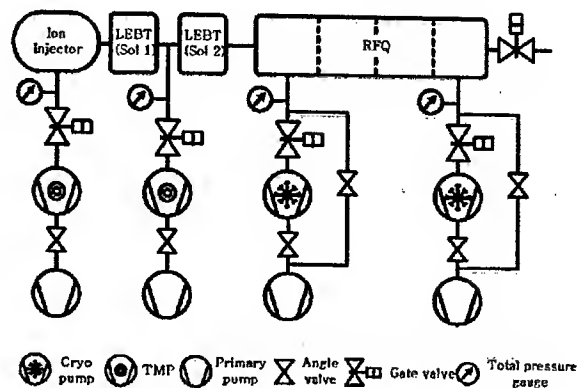


Figure 1 : The layout of the front-end vacuum system

Injector and LEBT

The duo-plasmatron type proton source to produce the H⁺ beam is installed (refer to the figure 2). The neutral hydrogen gas is injected into the source through the MFC (mass flow controller) about 4 sccm. The large amount of the proton and H₂⁺, H₃⁺ beam about 7 mA vanishes at the end of the source and the LEBT. The demanded pressure on these parts is about 1x10⁻⁵ mbar, we installed pumps at the injector and LEBT respectively. The stainless steel chamber was fabricated to evacuate the hydrogen gas evolved from these beam loss and installed at the end of the source. The LEBT is the long stainless steel pipe having two solenoid magnets. Inner diameter of the LEBT is 160 mm and the total length is 2.2 m. The conductance of the entire pipe is 887.3 L/sec. We installed the TMPs on injector of 720 L/sec pumping speed of H₂ and on LEBT of 370 L/sec of H₂. We selected the TMP for these parts in spite of the high H₂ loads since the required pressure is a little high about 10⁻⁵ order and the regeneration process of the cryo pump will give rise to the problems during the beam operation in this operational pressure range.



Figure 2. Picture of the installed ion injector. The vacuum system consists of gate valve, TMP with rotary pump and penning gauge.

RFQ

The pumping efficiency of the RFQ is not good because of the low conductance in the accelerating space, large surface area and high rate of beam loss. The PEFP 3 MeV RFQ divided into 4 sections, and all sections are bolted with fluorocarbon sealants [3]. The total length of the RFQ including a coupling plate located between 2nd and 3th section is 324 cm and aperture diameter is 6 mm. The OFHC copper was machined and brazed to shape the 4 vane cavities, and the 16 elements of the vacuum ports are located in 1st and 4th section.

Due to the particular geometry of the RFQ, we installed the pumping station made of stainless steel pipe at the respective cavities to raise the pumping speed at the cavity wall (refer to figure 3).

We performed the He leak tests on the fabricated systems and the leak rate were measured below 2×10^{-10} mar L/sec at every joints except the o-ring parts.

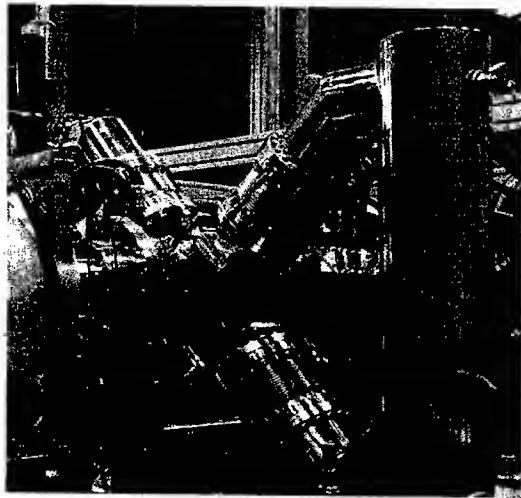


Figure 3. Installed RFQ vacuum pumping station.

The expected gas loads on the RFQ are estimated.

- Outgassing ($41,500 \text{ cm}^2$) : $> 8 \times 10^{-6}$ mbar L/sec
- Joint leaks : $> 2.8 \times 10^{-6}$ mbar L/sec
- Beam loss (H^+ , 3 mA) : 7.2×10^{-4} mbar L/sec

The main pump for the RFQ is cryo-pump. The cryo pump has several advantages such as high H_2 pumping

speed vs. inlet flange and pumping performances of other gases are also excellent. For PEFP RFQ, 2 sets of 5000 L/sec (H_2 speed) cyro pumps are installed at the 1st and 4th section. The regeneration period is calculated as 65 days when operate the pump at 1×10^{-6} mbar, so we're planning to install a concurrent cryo pump in parallel in each pumping station. The 2 sets of the 250 L/min scroll pumps are used to rough the system from atm. to 2×10^{-2} mbar and to back up during cryo pump regeneration.

DTL

The goal of the project is to end the development of the 20 MeV DTL in the first step. We finished the DTL engineering design and now fabricating the 1st tank [4]. The PEFP DTL consists of 4 tanks – each tank divided two sections – made by Cu plated steel pipes. The total length of the DTL is 18.61 m and inner diameter is 54.44 cm. Ports for the DTL are mentioned in the table 3.

The pressure requirement of the DTL is calculated from the minimizing the beam loss due to the residual gases [5-6]. In table 2, the calculation results are presented.

Table 2. Beam loss due to stripping in the DTL

Tank (No.)	Exit beam energy (MeV)	Tank length (m)	Beam loss due to stripping		Max. allowable pressure (mbar)
			$\mu\text{A/m}$	μA	
1	6.9	4.45	0.882	3.66	3.00E-07
2	11.4	4.61	0.488	2.25	3.00E-07
3	15.7	4.54	0.406	1.84	3.00E-07
4	20.2	4.74	0.364	1.72	3.00E-07
Total loss (μA)			9.47		

Seal

We divide the vacuum and RF seal as fluorocarbon and canted coil spring. The compression set of the viton is about 20% at below 200 C, and required compression force is about 1.6 kg/cm. The force for compression for viton is higher than the coil spring, so we considered to

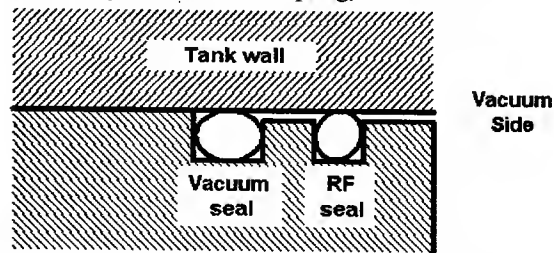


Figure 4. RF and vacuum seal groove design of ports

this point when designing the groove. The material of the coil is silver coated BeCu produce by Bal Seal engineering. Seal geometries of each port are similar to figure 4.

Gas loads

In the table 3 and 4, the gas loads due to outgassing and leak on the DTL are presented. The outgassing rate of the OFHC copper is assumed to reach 1.33×10^{-10} mbar L/sec/cm² after 100 hrs of vacuum and RF conditioning [5]. Despite of the low outgassing rate of the copper, the main gas loads on DTL was the outgassed gas on the large surface area as shown in the table. So we choose the PR (periodic reverse) method to plate the inner surface of tank [7].

Table 3. Gas loads on DTL due to the surface outgassing

	Qty.	Area (cm ²)	Outgas load (mbar L/sec)
Tank	1	75739.10	1.01E-05
End wall	2	341.88	4.55E-08
Drift tube	50	18809.86	2.50E-06
Stem	50	8449.74	1.12E-06
Post coupler	17	2872.91	3.82E-07
Slug tuner	8	3818.24	5.08E-07
Vacuum spool	1	1431.84	1.90E-07
			1.48E-05

Table 4. Summary of ports for 1st tank and gas loads due to the leaks

Seal Name	Qty.	Nominal seal dia.(cm)*	Gas load (mbarL/sec)	Remarks
Tank	2	55.8(54.2)	8.27E-06	Endwall
	1	57.1(55.5)	4.24E-06	Intertank
Stem	50	2.6(2.6)	6.75E-06	
Post couplers	17	2.6(2.6)	2.30E-06	
Slug tuners	8	15.8(14.5)	9.56E-06	
Vacuum ports	4	17.6(15.8)	5.31E-06	
RF coupler	1	14.9(13.1)	1.12E-06	
RF pick up	5	3.5(2.2)	8.55E-07	
Pump spool	1	15.24	1.36E-07	
Total			3.85E-05	

Viton O-ring (Coil spring)

Vacuum components

The SIP (sputter ion pump) is adopted as the main pump for the DTL. Ion pump is reliable, has no moving part, using the low outgassing material, and has long life. We plan to install the 3 sets of 300 L/sec SIP per one tank, and a set of TMP and scroll pump will be used to rough the a cavity to 1×10^{-5} mbar.

The pirani gauges and penning gauges will be installed at the pumping spool pipe to measure the total pressure of the cavity. They cover the range from atmospheric pressure to 1×10^{-10} mbar.

RF GRILL DESIGN

RF grills for RFQ and DTL are showed in the figure 5. These grills are installed to less the RF attenuation through the pumping ports, but they also reduce the conductance. The calculation results are listed in table 5.

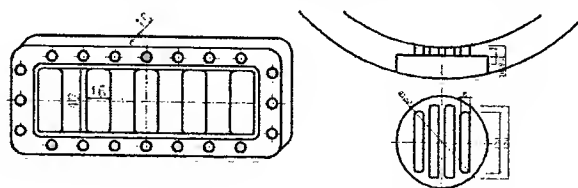


Figure 5. The RF grills for RFQ and DTL

Table 5. Conductance calculation of the RF grills.

	RFQ	DTL	
		SIP	TMP
Pumping speed (L/sec)	3,000	300	400
Grill conductance (L/sec)	4,224 (16896)	2,854	
Spool conductance (L/sec)	2,822	-	1,945
Effective pumping speed (L/sec)	1339	271.5	297

CONCLUSION

- The status of the vacuum systems of PEFP proton linac was overviewed.
- The expected difficulties of DTL vacuum system are the stem installation of vacuum tight and the plating of the copper to reduce the outgassing
- We will design the vacuum systems for the RF window region for next plan

REFERENCES

- [1] J. M. Han, et al., "Development of a low-energy proton accelerator system for the proton engineering frontier project (PEFP)", at this conference
- [2] K. R. Kim, et al., "Construction of user facilities for the proton beam utilization of PEFP", at this conference
- [3] J. M. Han, et al., "3.0 MeV KTF RFQ Linac", LINAC2002, Gyeongju, Aug. 2002
- [4] Y. S. Cho, et al., "PEFP DTL (3-20 MeV) Preliminary design report", PE-30000-DD-P001, 2002
- [5] J. D. Bernardin, et al., "SNS Drift tube linac vacuum system", SNS-104020400-DE0001-R00
- [6] G. H. Gillespie, Phys. Rev. A, 15, 563 page, 1977
- [7] H. Ino, et al., "Advanced copper lining for accelerator components", Proceedings of the XX international Linac conference, Monterey, 2000

SERIES PRODUCTION OF COPPER AND NIOBIUM CAVITIES FOR THE SPALLATION NEUTRON SOURCE

S. Bauer, K. Dunkel, B. Griep, M. Pekeler, C. Piel, P. vom Stein, H. Vogel

ACCEL Instruments, Bergisch Gladbach, Germany, accel@accel.de

Abstract

Since about one and a half year ACCEL is working on two large scale cavity series production: The normal conducting CCL type copper cavities [1] and all superconducting 6-cell cavities for the linac of the Spallation Neutron Source SNS [2]. For both projects, the prototype phase is finished and we are in the middle of the series production. Tuning results on the normal conducting cavities will be presented as well as the cold RF test results of the superconducting medium beta cavity production. Experiences gained for future large scale cavity production will be presented.

1 CCL CAVITIES

Since October 2001 ACCEL manufactures the cavity coupled linac segments for the normal conducting part of the proton linear accelerator from energies of 87 MeV to 185 MeV for the SNS project in Oak Ridge.

The contract has been concluded with Los Alamos National Laboratory and covers the production of 4 modules, each consisting out of 12 segments (Figure 2) and 11 bridge couplers (Figure 1). Each cavity coupled linac segment consists of 8 accelerating cells, coupled to each other by 7 coupling cells. Two segments are coupled by one bridge coupler, which forms together with the two endplates of the segments a three cell coupling structure.

The scope of work covers machining, brazing and RF tuning of all segments and bridge couplers. In addition module assembly, mapping and tuning is within ACCEL's responsibility.

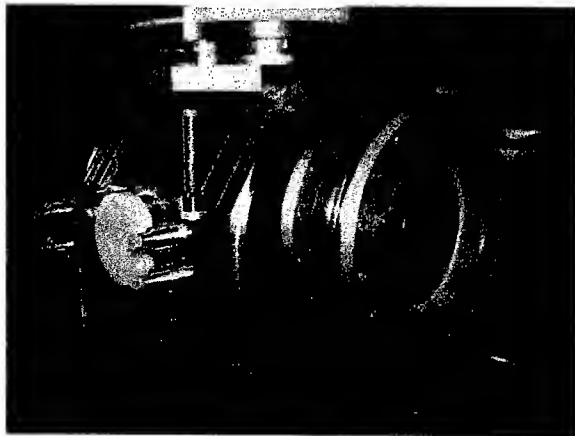


Figure 1: Bridge Coupler at final machining



Figure 2: Segment at final dimension control

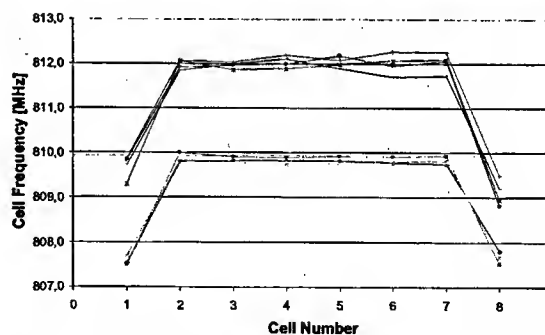


Figure 3: RF measurements before (upper curve) and after (lower curve) tuning

Comparing pre and post tuning results show RF measurement on Segment and Bridge Coupler level show good reproducibility within the entire manufacturing sequence which will allow easy tuning of brazed assemblies.

2 SC ELLIPTICAL CAVITIES

The production of the superconducting cavities of both types, medium beta ($\beta = 0,61$) and high beta ($\beta = 0,81$) is proceeding well (Figure 4). After an intense time of tooling development and establishing all the work procedures for both type of cavities, the series production was launched.



Figure 4: Series production of medium beta cavities is finalised

All 35 medium beta cavities have been delivered to Jefferson Laboratory from October 2002 until April 2003 and test results are exceeding well the design value.

For the high beta cavity production, the majority of the single part production is finished. A first article high beta cavity was delivered to Jefferson Lab in February 2003. This cavity was tested in the meantime and exceeded the design specifications. The production of the high beta cavities is now ramping up with a production rate of at least one cavity per week. This rate can be established with the current infrastructure of two electron beam welding machines. Both machines are used in a one shift operation with an occupation of about 80 % for this project. Tooling is used that allows to perform 3 similar welds within one pumpdown of the welding chamber.

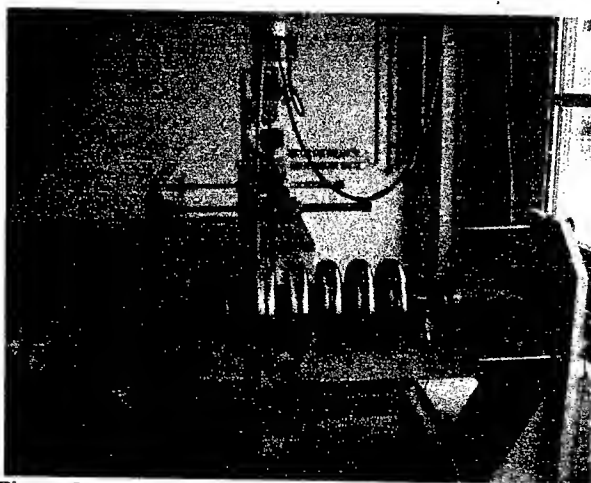


Figure 5: SNS medium beta cavity during field flatness tuning.

All cavities are delivered with guaranteed frequency and the field flatness tuned to an accuracy of 5 % in

Amplitude (Figure 5). Additionally the external Q of the fundamental mode of the HOM couplers is tuned and the cavities are chemically polished from the inside and outside in order to remove the so called damage layer. Therefore at Jefferson Laboratory only the final preparation and the cold rf-test needs to be done.

Figure 6 shows the cold RF test results of the first delivered medium beta cavities. The cold RF test was performed at Jefferson Lab after final chemical preparation and high pressure rinsing. Up to now all cavities delivered reached the specified performance.

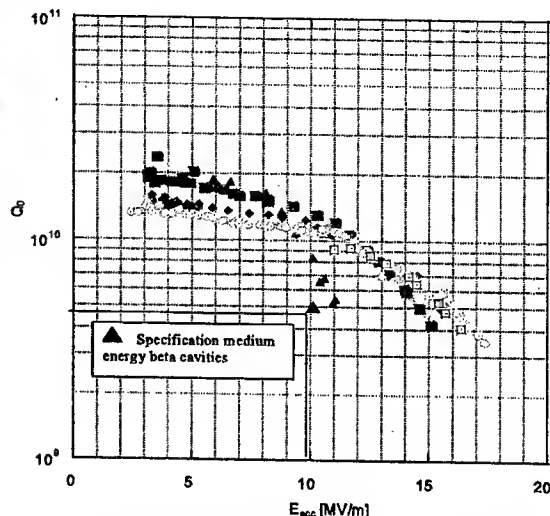


Figure 6: Cold test results of first cavities delivered (Courtesy JLab)

3 CONCLUSIONS

Both projects have been successfully started with development of tooling, optimisation of procedures and assembly deliveries. The series production of a total number of 109 s.c. cavities and 48 n.c. cavities is well on track for the SNS project.

Based on this experience (completion of 4 to 6 cavities per month) we conclude that production rates of about 40 sc. cavities per month as may be required e.g. DESY X-FEL project can be handled. An analysis in view of such future projects shows that production rates can be easily handled with specially designed electron beam welding machines and the surrounding appropriate infrastructure for chemical processing within the frame of existing infrastructure.

REFERENCES

- [1] N. Bultman, MECHANICAL DESIGN OF THE SNS COUPLED CAVITY ACCELERATOR, Proceedings of the 2001 Particle Accelerator Conference, Chicago
- [2] G. Ciovati et al., "Superconducting Prototype Cavities for the Spallation Neutron Source (SNS) Project," Proceedings of the 2001 Particle Accelerator Conference, Chicago

CONTINUED DEVELOPMENT OF THE RFI LINAC STRUCTURE*

D.A. Swenson, W.J. Starling, F.W. Guy, and K.R. Crandall
Linac Systems, LLC Albuquerque, NM 87109, USA

Abstract

The Rf-Focused Interdigital (RFI) linac structure is under development at Linac Systems. It promises very efficient acceleration of protons, light ions, and heavy ions to tens of MeV in relatively small packages. Recent developments include the discovery of effective geometries for the support of the two-part drift tubes, which provide the rf focusing, and efficient geometries for the end terminations of the interdigital linac tanks. These developments required extensive use of our 3d rf cavity calculational capability. A "cold model" of an RFI linac has been fabricated and tested. The measured and calculated field distributions are in reasonable agreement. The beam dynamics of the structure has been studied with TRACE-3D and a modified version of PARMILA. The structure is capable of remarkably high beam currents (space charge limits). The results of these studies will be presented. The high rf efficiency of the structure promotes the possibility of cw operation. A prime application for the RFI linac structure is the challenging job of providing intense fluxes of epithermal neutrons for the boron neutron capture therapy (BNCT) application. Mechanical designs of the RFI linac structure for that application will be presented. Other applications for the RFI linac structure will be described.

INTRODUCTION

The Rf-Focused Interdigital (RFI) linac structure^[1,2] represents an effective combination of the interdigital (Wideröe) linac structure^[3] and the rf electric quadrupole focusing used in the Radio Frequency Quadrupole (RFQ) and Rf-Focused Drift tube (RFD) linac structures^[4,5]. This linac structure is two-to-six times more efficient and three times smaller than the conventional Drift Tube Linac (DTL) structure in the energy range from 0.75 to 6 MeV. It is ten times more efficient than the RFQ linac structure in the 0.75 to 6 MeV range. A comparison of the rf efficiencies for these three structures is shown in Fig. 1.

The rf efficiency and size advantages of this new structure will reduce the capital and operating costs of small proton, deuteron, and heavy ion linac systems. The high efficiency will reduce the rf power dissipation in their structures, thereby promoting the prospect for cw operation, which in turn, offers the possibility of large increases in their average beam currents. These features will increase the number and types of applications for which small linac systems are suitable.

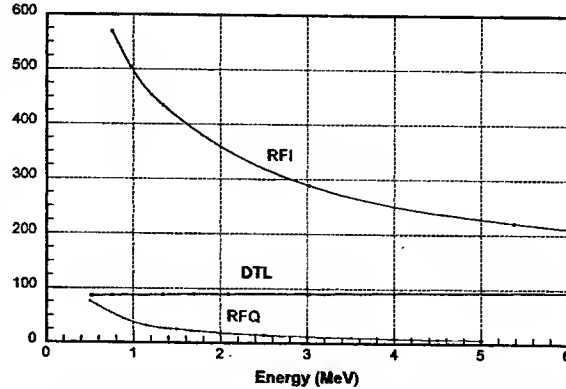


Fig. 1. Effective Shunt Impedance (MΩ/m) for the RFI, DTL and RFQ Linac Structures at 200 MHz.

THE RFI LINAC STRUCTURE

In an interdigital linac structure, the electric fields in the gaps between drift tubes alternate in direction along the axis of the linac. The longitudinal dimensions of the structure are such that the particles travel from the center of one gap to the center of the next gap in one half of the rf cycle. Hence, particles that are accelerated in one gap will be accelerated in the next gap because, by the time the particles arrive there the fields have changed from decelerating fields into accelerating fields. In the interdigital linac structure, it is common to support the drift tubes alternately from the top and bottom (or left and right side) of the cavity to achieve the desired alternation in field direction. This same practice has been adopted for the RFI linac structure.

As in the RFD linac structure, rf focusing is introduced into the RFI linac structure by configuring the drift tubes as two independent pieces operating at different electrical potentials as determined by the rf fields of the linac structure. Each piece (or electrode) supports two fingers pointed inwards towards the opposite end of the drift tube forming a four-finger geometry, which produces an rf quadrupole field along the axis of the linac for focusing the beam.

The longitudinal distribution of the acceleration, focusing, and drift actions are quite different between the RFD and RFI linac structures. In the RFI structure, when the accelerated particles are two thirds of the way between the centers of the gaps, the electric fields are passing through zero strength as they change sign and are not suitable for focusing the beam. As a result, the focusing action must be pushed upstream to lie as close to the accelerating gap as possible, leaving the latter portion of the drift tube solely as a drift action (no focusing, no

* Work supported by the U.S. Department of Energy.

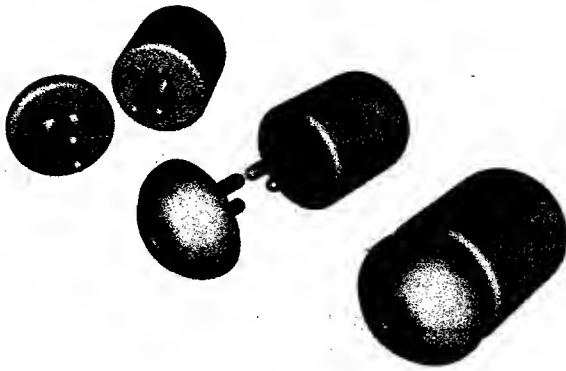


Fig. 2 RFI Drift Tubes, Exploded and Assembled.

acceleration). Hence, the drift tubes of the RFI linac structure are asymmetrical, consisting of a minor piece and a major piece as shown in Fig. 2.

The analysis of the RFI linac structure breaks conveniently into two parts, namely the analysis of the interdigital feature of the structure and the analysis of the rf focusing feature. For the first part, we analyzed and optimized the interdigital feature of the structure with simple, one-part drift tubes, having no provisions for rf focusing. For the second part, we incorporated two-part drift tubes into the optimized interdigital structure in order to analyze the rf focusing properties of the structure. As the RFI linac structure is highly three dimensional, these analyses made heavy use of the 3D rf cavity calculational program, SOPRANO^[6].

THE INTERDIGITAL FEATURE

One form of the interdigital linac structure is a cylindrical tank, loaded with drift tubes, positioned along the axis of the tank and spaced by one half of the particle wavelength, supported on drift tube stems extending alternately from the top and bottom (or left and right sides) of the tank. Of concern are the rf field distribution

within the structure, the stability of this rf field distribution, the cavity mode spectra in the vicinity of the operating mode, and the rf efficiency of the structure.

The analysis and optimization of the interdigital feature of this structure involved studies of the structure properties as a function of the rf frequency, the beam particle, the particle velocity, and the geometry. We chose to optimize the structure for proton acceleration at an rf frequency of 200 MHz in the energy range of 1 to 20 MeV. These results can be scaled to other beam particles and rf frequencies.

The significant features of the geometry that we chose to study are the cell length (L), the cavity radius (R_c), the drift tube length, the drift tube radius (R_d), and the support stem radius (R_s). For a given proton energy and rf frequency, the cell length is equal to $\beta\lambda/2$ and the drift tube length is three quarters of the cell length. The cavity radius is used to satisfy the frequency constraint. Hence, for a given proton energy and rf frequency, the geometrical parameters to be optimized are R_d and R_s .

Figure 3 presents an array of data for an interdigital linac structure at 200 MHz for cell lengths of 4, 6, 8, 10, 12, 14, and 16 cm, corresponding to proton energies of 1.34, 3.02, 5.38, 8.45, 12.25, 16.79, and 22.11 MeV, a drift tube radius of 1.2 cm, and a stem radius of 2.0 cm. Two important features of the RFI linac structure, resulting in part from its interdigital configuration, are immediately obvious from this data, namely its exceptionally high effective shunt impedance (ZT^2) and its small transverse size (cavity radius).

THE RF FOCUSING FEATURE

The acceleration gaps (between the drift tubes) and the focusing gaps (within the drift tubes) form capacitive dividers that place a portion of the rf acceleration voltage on each rf focusing lens. In order not to short out this focusing potential, the two pieces of each drift tube are supported on separate stems, a major stem for the major piece and a minor stem for the minor piece. These stems form inductive dividers that couple to the rf magnetic

Cell Length (cm)	4	6	8	10	12	14	16
Beta (velocity/c)	0.0533	0.0800	0.1067	0.1333	0.1600	0.1867	0.2133
Proton Energy (MeV)	1.34	3.02	5.38	8.45	12.25	16.79	22.11
Cavity Radius (cm)	14.0	16.1	17.7	18.7	19.4	19.9	20.2
Stored Energy (J)	0.0011	0.0026	0.0047	0.0074	0.0107	0.0147	0.0194
Shunt Impedance ($M\Omega/m$)	468.2	313.5	240.5	188.9	155.3	130.5	111.3
Transit Time Factor	0.960	0.960	0.960	0.960	0.960	0.960	0.960
ZT^2 ($M\Omega/m$)	431.5	288.9	221.6	174.1	143.1	120.3	102.6
Quality Factor	15738	16961	17542	17581	17439	17214	16925
Power Loss (Total) (W)	85.4	191.4	332.6	529.5	772.9	1073.2	1437.9
Power Loss (Outer Wall)	49.5	104.2	168.0	250.2	342.6	448.5	571.6
Power Loss (Bars)	34.6	85.2	160.5	171.1	415.1	597.7	821.7
Power Loss (Drift Tubes)	1.3	2.0	4.1	8.2	15.2	27.0	44.6

Fig. 3. Geometrical and Rf Properties of the Interdigital Structure.

fields of the structure. The geometry of these stems must be configured to yield the same potential difference to the rf lenses that the capacitive dividers do. This prevents the drift tube supports from shorting out the rf focusing lenses.

It is convenient to describe the rf lens excitation as the ratio of the lens voltage (V_L) to the cell voltage (V_C). The desired lens voltage is beam dynamics dependent. A good choice is to have a constant lens voltage throughout the linac. With a constant acceleration gradient (a common design choice), the cell voltage is proportional to the cell length. With these choices, the V_L/V_C ratio decreases throughout the linac. In some of our designs, this ratio begins as high as 40% and decreases to something like 10% at the end of the structure.

Originally, we had planned to couple to the magnetic field surrounding each major stem. This lent itself to a two stem configuration emanating from a single base, with the minor stem being located a short distance upstream from the major stem. This would allow the two pieces of each drift tube to be accurately aligned in the manufacturing process and to be installed as a single unit in a "hard socket" in the outer wall of the linac tank. After considerable study, we found that the total flux surrounding the major stem was not sufficient to yield the lens excitations that we needed.

At this point, we realized that we needed to couple to some of the longitudinal magnetic fields in the structure. This requires that the minor stem be offset to one or both sides of the major stem. For symmetry and mechanical rigidity, we choose a minor stem geometry that extended symmetrically on both sides of the major stem. Once again, we tried to achieve a design where both stems (major and minor) emanated from a single base to facilitate the manufacture and installation of the drift tubes. However, these geometries, when pushed to the maximum desired lens excitations, had detrimental effects on the rf efficiency of the structure.

This led to a radial stem approach, where the minor stems are essentially radial members extending from the tank wall, and offer unlimited coupling (from 0% to nearly 100% of the cell voltage) to the magnetic fields of the structure. The coupling is a simple function of the angle between the radial stems and the major stem – the greater the angle, the greater the coupling. In one design that we have considered, the desired coupling, ranging from 29% at 0.75 MeV to 16% at 2.5 MeV, can be achieved by radial stem angles ranging from 51 to 33 degrees.

To facilitate the fabrication of the RFI linac structure under this radial stem approach, we have adopted what we call the "Stacked Cell" approach, shown in Fig. 4, where the basic unit of the structure is a single cell, complete with a two-piece drift tube, supported by major and minor stems in a short section of the outer wall. The linac structure is assembled by stacking up a sequence of these cells, each with the proper dimensions. The stack can be held together either by tie-bolts running along the structure or by welding the cells together into a single unit as shown in Fig. 5.

REFERENCES

- [1] D.A. Swenson, "An Rf-Focused Interdigital Linac Structure", 2002 Intern. Linac Conf., Korea, 2002.
- [2] D.A. Swenson, "An Rf-Focused Interdigital Ion Accelerating Structure", CAARI 2002, Denton, TX.
- [3] Krietenstein, Weiland, Ratzinger, Tiede, and Minaev, "Numerical Simulation - ", 1996 Linac Conf. CERN.
- [4] D.A. Swenson, "RF-Focused Drift Tube Linac Structure", 1994 Linac Conf., Tsukuba, Japan, 1994.
- [5] D.A. Swenson, "Applications for the RFD Linac Structure", CAARI 2000, Denton, TX.
- [6] Vector Fields, SOPRANO version 8.700, Oxford, UK

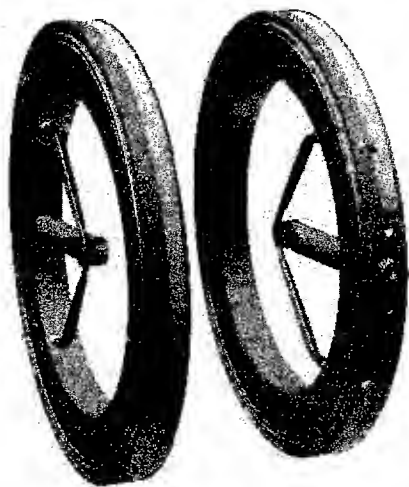


Fig. 4. The "Stacked Cell" Approach.

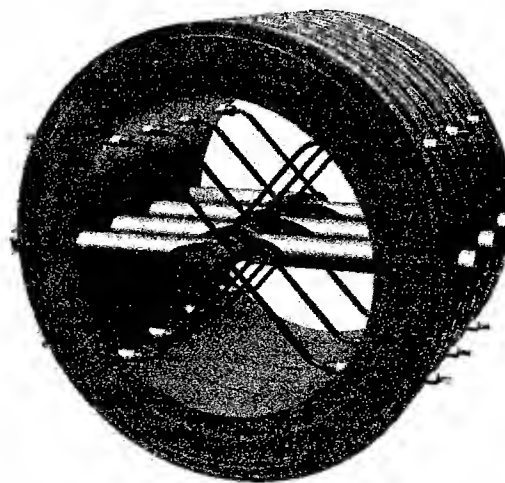


Fig. 5. The RFI Linac Structure.

UPGRADES OF THE LINAC SYSTEM AT CAMD*

Y. Wang#, M. Fedurin, P. Jines, T. Miller, T. Zhao, CAMD/LSU, Baton Rouge, LA 70806, USA

Abstract

The 180 - 200 MeV linac is an injector of Center of Advanced Microstructures and Devices (CAMD) 1.3 or 1.5 GeV accelerator, and was configured, installed and commissioned more than 10 years ago[1]. CAMD has pursued the upgrades of linac due to the bad reliability and performance of linac. In the paper, the latest operation parameters of linac are introduced, the results of recent upgrades of linac, such as the linac control system upgrade, the linac timing system upgrade, the master oscillator upgrade, and the klystron focusing power supply upgrades are presented, and the linac energy increase is discussed.

1 INTRODUCTION

The linac at CAMD as shown in Figure 1 consists of a 50kV triode electron gun, a 500MHz chopper-prebuncher, a 4MeV, 3GHz standing wave buncher, and two 6-meter long traveling wave accelerating sections. The RF system which drives the linac consists of two 35MW, 3GHz Klystrons and modulators, RF drivers, master oscillator, and so on. The linac can be operated in either a 2.5 nS pulse of electrons or a 50-500 nS pulse. The current operation parameters are below:

Energy	180 MeV
Energy Spread	$\pm 0.25\%$
RF frequency	2998.2MHz
Repetition rate	1 Hz
Pulse Length	150 nS
Current	50 mA
Current stability	$\pm 15\%$

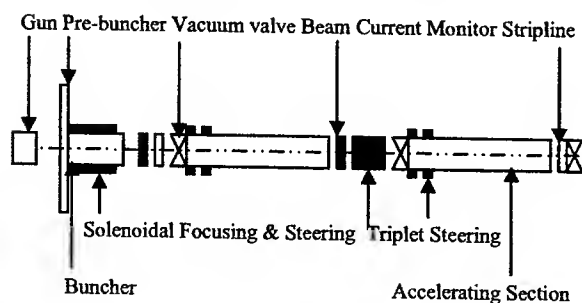


Figure 1: Linac at CAMD

2 THE CONTROL SYSTEM UPGRADE

The old linac control system consists of a 68020 microprocessor board and a VME interface board which

* Work supported by the State of Louisiana
wangysh@lsu.edu

makes the link between the VME bus and the I/O bus. Due to the poor reliability and the poor performance of the old control system, we replace it with the PLC as shown in Figure 2[2].

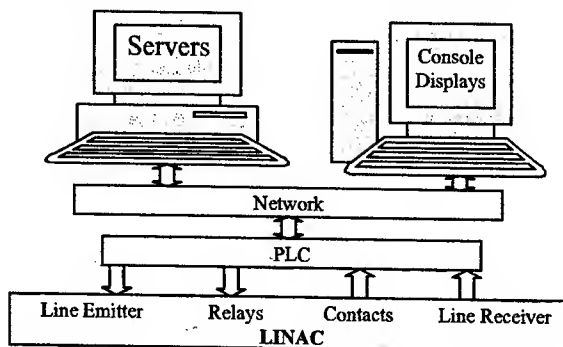


Figure 2: The linac control system

In the new control system, the servers and console display communicate PLC through network. The PLC controls linac by analog inputs/outputs which are connected to line emitter/line receiver and logic inputs/outputs which are connected to relays and contacts.

3 THE TIMING SYSTEM UPGRADE

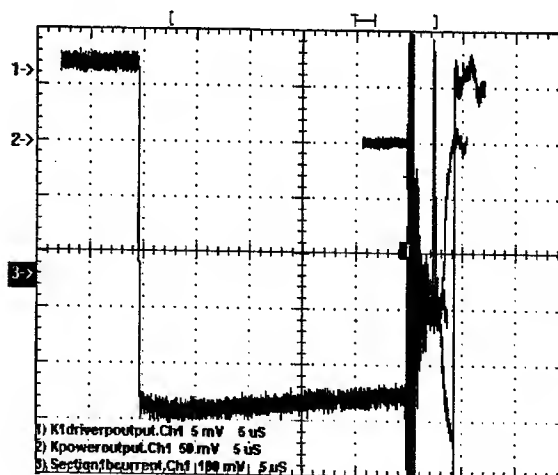


Figure 3: The time relation between prebuncher input(1), klystron output(2) and beam(3)

Three Stanford Research Systems' DG535 Digital Delay / Pulse Generators in the timing system in linac are used to realize the time relation between prebuncher input, klystron output and beam as shown in Figure 3 and to function the protection for the system under abnormal

operation conditions. The old timing system is made of a timing board in the VME crate. In order to protect the system from noise, TTL to fiber transducers are used; therefore, fiber to TTL transducers are used at the equipments.

4 THE MASTER OSCILLATOR UPGRADE

The master oscillator consists of three main parts: an EMF phase locked oscillator, two CTT APN/032-3840 amplifiers, and a LORCH phase shifter as shown in Figure 4. A 499.7 MHz is multiplied by six in the EMF phase locked oscillator to 2998.2 MHz as shown in Figure 5. There is a CW output port which parameters are listed in Table 1 as the reference signal to measure the phase ripple for the master oscillator output [3, 4]; moreover, the phase ripple of klystron output power can be measured.

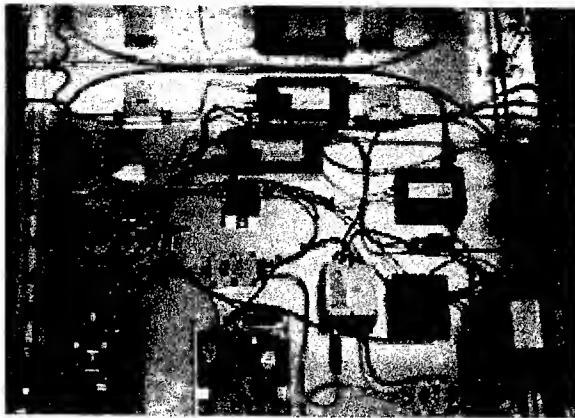


Figure 4: Layout of the master oscillator of linac

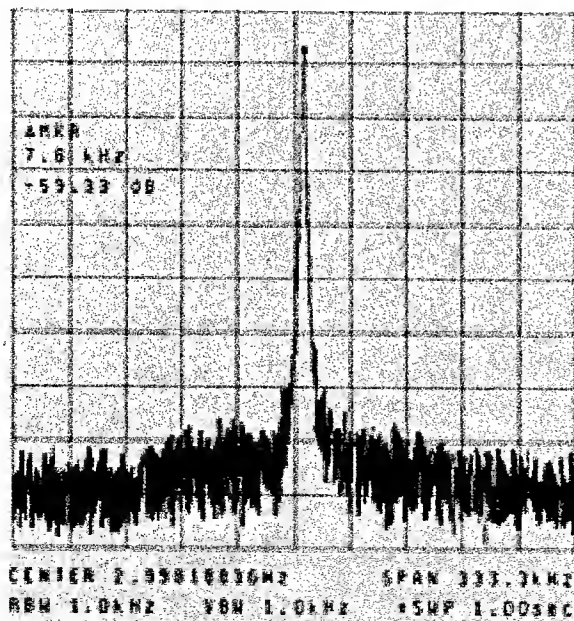


Figure 5: 3 GHz, CW output measured by spectrum analyzer from master oscillator

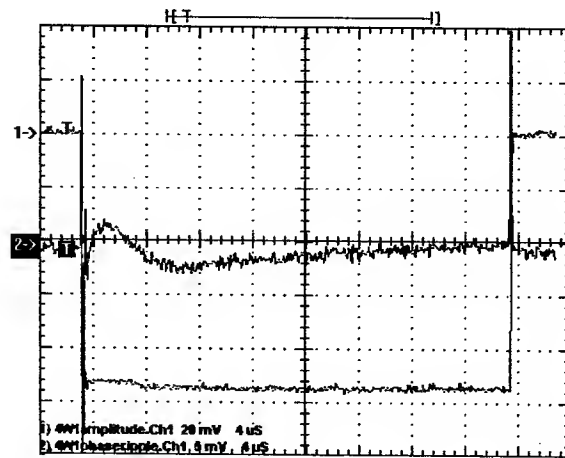


Figure 6: Amplitude and phase-ripple at 4W1 output of master oscillator at linac

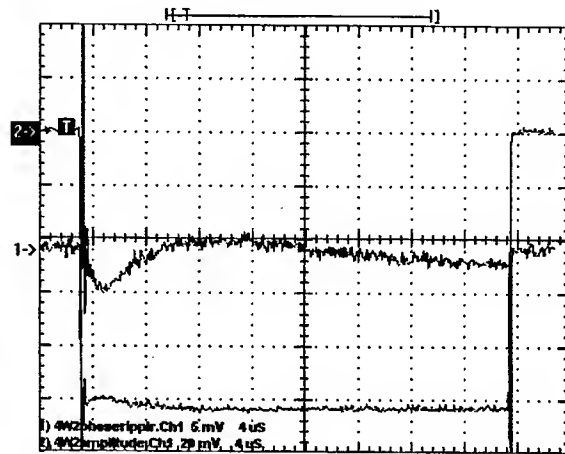


Figure 7: Amplitude and phase-ripple at 4W2 output of master oscillator at linac

Table 1: The test parameters of the CW output port

Output Power	10 dBm,
Frequency	2998.1883 MHz
Phase Noise	100 dBc

Table 2: The output parameters of the master oscillator

Output	Power	Phase Ripple
4W1	36 dBm	± 0.3 Degrees
4W2	36.6 dBm	± 0.3 Degrees

As mentioned in the introduction, there are two klystrons are used at CAMD linac, so the master oscillator has two ports to drive the preamplifiers of the klystrons. The tested results are shown in Figure 6 and Figure 7, and the parameters are listed in Table 2.

5 THE UPGRADE OF KLYSTRON FOCUSING POWER SUPPLIES

There are six power supplies for klystron focusing in the linac. Due to the sense of impending failure of major components which is not easy to get them in spare because of the age of power supplies, the six new POWER TEN power supplies are used to replace the old power supplies. All new power supplies are installed in a cabinet and tested. They will be used in case of the failure of old power supplies. The parameters of power supply's current are listed in Table 3.

Table 3: The current in coils of klystrons

Klystron 1	Coil 1	178.4 A
	Coil 2	120.8 A
	Coil 3	157.1 A
Klystron 2	Coil 1	172.7 A
	Coil 2	102.8 A
	Coil 3	180.6 A

6 INCREASE ENERGY

The purpose to increase energy is to increase the beam current in the storage ring at CAMD. Through careful study, the 200MeV can be achieved from 180MeV based on the measured data.

The variable voltage-controlled attenuator has been installed to the RF loop to the buncher to adjust the input power. The characteristics of the attenuator are shown in Figure 8 & Figure 9.

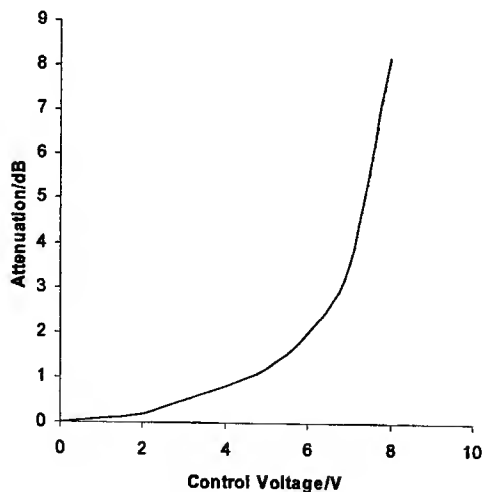


Figure 8: The attenuation of the attenuator at buncher

The RF system at linac is optimized during the last shutdown. We should calibrate the output voltage of the high voltage power supply for the modulators of klystron in the RF system because the power supply is saturated when the voltage is increased.

There is another way to increase energy to 250MeV by adding another accelerating section in the linac tunnel.

This proposal was discussed by the Machine Advisory Committee for CAMD/LSU. The transport line is also needed to upgrade because its limitation is a little over 200MeV.

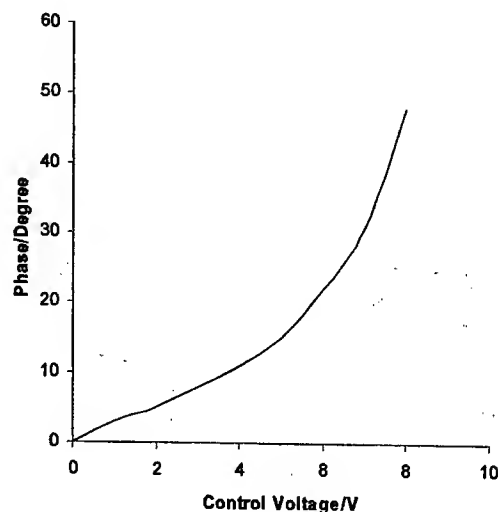


Figure 9: The phase of the attenuator at buncher

7 FUTURE PLAN

The linac at CAMD can be used as a user facility to generate a coherent light in DUV or VUV range when the injection is completed [5]. We also hope the linac can be re-circulated one time to achieve electron beam energy more than 300 MeV by used current RF system and accelerating sections.

ACKNOWLEDGEMENTS

The authors are grateful to the late Deputy Director Dr. B. Craft for the suggestions of the linac upgrades; to Mr. A Crappell, Mr. D. Dixon, Mr. D. Launey, Mr. S. LeGrand, and Mr. M. Smiths for their hard work in the linac upgrades; to the Machine Advisory Committee for CAMD/LSU for reviewing the projects; to Dr. G. Vignola (LNF) & Mr. K. Morris for discussions; to all other CAMD staffs for the support and encouragement.

REFERENCES

- [1] CGR MeV, 200MeV Electron Linac for Louisiana State University, Baton Rouge, LA, USA, April 1989.
- [2] P. Jines et al., Proc. of the Particle Accelerator Conference, 2003.
- [3] J. Xie, et al., Nuclear Physics and Method A407, 1998, p. 146-150.
- [4] J. Fox & H. Schwarz, IEEE Transactions on Nuclear Science, 30(4), 1983, p2264-2266.
- [5] L. Yu et al., Proc. of the Particle Accelerator Conference, 2001, p2719-2721.

LINEAR COUPLING OF RMS EMITTANCES*

L.C. Teng[#], Argonne National Laboratory, Argonne, IL 60439 USA

Abstract

A general formulation of the linearly coupled rms emittances in two degrees of freedom is given. This formulation shows clearly what can be done to the emittances and how best to design for the necessary coupling.

NOTATION AND DEFINITIONS

The phase point of the i^{th} particle in a distribution (beam) is represented by a column vector

$$X_i = \begin{pmatrix} x_i \\ x'_i \end{pmatrix}. \quad (1)$$

(The index i is often omitted as being understood.) Its symplectic conjugate (a row vector) is defined as

$$X^+ \equiv \tilde{X}\tilde{S} = (x \ x') \begin{pmatrix} 0 & -1 \\ 1 & 0 \end{pmatrix} = (x' - x), \quad (2)$$

where as shown S is the unit symplectic matrix. The symplectic conjugate of a row vector such as X^+ is defined as

$$(X^+)^+ \equiv S\tilde{X}^+ = -X. \quad (3)$$

For a distribution of phase points (particles) the second-moment matrix is defined as the outer product

$$E \equiv \overline{XX^+} = \begin{pmatrix} -\overline{xx'} & \overline{x^2} \\ -\overline{x'^2} & \overline{xx'} \end{pmatrix}, \quad (4)$$

where a bar means averaging over the distribution. We see immediately $\text{Tr}(E) = 0$ and $E^+ = -E$. We can parameterize E as

$$E = \varepsilon \begin{pmatrix} \alpha & \beta \\ -\gamma & -\alpha \end{pmatrix} \equiv \varepsilon J. \quad (5)$$

Matrix J is the Courant-Snyder "imaginary" unit matrix with $|J| = 1$ and $J^2 = -I$. The rms emittance ε is then given by

$$\varepsilon^2 \equiv |E| = \overline{x^2} \overline{x'^2} - \overline{xx'}^2. \quad (6)$$

We write the transfer matrix for the motion as

$$M = \begin{pmatrix} a & b \\ c & d \end{pmatrix} \quad (7)$$

and define its symplectic conjugate as

$$M^+ \equiv \tilde{S}M\tilde{S} = \begin{pmatrix} d & -b \\ -c & a \end{pmatrix}. \quad (8)$$

Then $(M^+)^+ = M$, and

$$MM^+ = M^+M = |M|I, \quad M+M^+ = [\text{Tr}(M)]I. \quad (9)$$

If $M^+M = M^+M = I$, M is called symplectic and $|M| = 1$.

The transformations given by M are

$$X_T = MX, \quad X_T^+ = X^+M^+ \quad (10)$$

and

$$E_T = MEM^+, \quad \varepsilon_T^2 = |E_T| = |M|^2 \varepsilon^2. \quad (11)$$

Thus, the emittance is invariant for a symplectic transformation.

The second-moment (rms) phase ellipse is defined as

$$X^+E^{-1}X = -1, \quad (12)$$

where X (without index i) is now the running variable.

Since $E^{-1} = \frac{E^+}{|E|} = \frac{-E}{|E|}$ we can also write the ellipse as

$$X^+EX = |E| \quad (13)$$

or

$$X^+JX = \gamma x^2 + 2\alpha xx' + \beta x'^2 = \varepsilon. \quad (14)$$

We can diagonalize E^{-1} to get the area of the ellipse and show that

$$\varepsilon = |E|^{\frac{1}{2}} = \frac{1}{\pi} (\text{area of ellipse}). \quad (15)$$

TWO DEGREES OF FREEDOM

With two degrees of freedom (dof) we will write all 4-dimensional (4-D) vectors and matrices in the "block form." The phase-point position vector is now

$$X_i \equiv \begin{pmatrix} x_i \\ x'_i \\ y_i \\ y'_i \end{pmatrix} \equiv \begin{pmatrix} X_i \\ Y_i \end{pmatrix}. \quad (16)$$

The symplectic conjugate is then

$$X^+ = (\tilde{X} \ \tilde{Y}) \begin{pmatrix} \tilde{S} & 0 \\ 0 & \tilde{S} \end{pmatrix} = (X^+ \ Y^+). \quad (17)$$

As before,

$$(X^+)^+ \equiv \begin{pmatrix} S & 0 \\ 0 & S \end{pmatrix} \begin{pmatrix} \tilde{X}^+ \\ \tilde{Y}^+ \end{pmatrix} = -X. \quad (18)$$

For a distribution, the second-moment matrix is

*Work supported by the U.S. Department of Energy, Office of Basic Energy Sciences, under Contract No. W-31-109-ENG-38.

[#]teng@aps.anl.gov

$$\mathbf{E} = -\overline{\mathbf{X}\mathbf{X}^+} = \begin{pmatrix} -\overline{\mathbf{X}\mathbf{X}^+} & -\overline{\mathbf{X}\mathbf{Y}^+} \\ -\overline{\mathbf{Y}\mathbf{X}^+} & -\overline{\mathbf{Y}\mathbf{Y}^+} \end{pmatrix} \equiv \begin{pmatrix} \mathbf{E} & \mathbf{K} \\ -\mathbf{K}^+ & \mathbf{F} \end{pmatrix}, \quad (19)$$

where \mathbf{E} and \mathbf{F} retain their 1-dof forms and the coupling block is

$$\mathbf{K} \equiv -\overline{\mathbf{X}\mathbf{Y}^+} = \begin{pmatrix} -\overline{\mathbf{x}\mathbf{y}'} & \overline{\mathbf{xy}} \\ -\overline{\mathbf{x}'\mathbf{y}'} & \overline{\mathbf{x'y}} \end{pmatrix}, \quad \text{Tr}(\mathbf{K}) \neq 0. \quad (20)$$

The projection of all the phase points on the, say, \mathbf{X} -plane will have a distribution given simply by \mathbf{X}_i , hence the “projection” rms emittance and second-moment ellipse are as given in Eqs. (6) and (13).

We can define the 4-D second-moment “ellipsoid” (bounded by a closed 3-D surface) as

$$\mathbf{X}^+ \mathbf{E}^{-1} \mathbf{X} = -1. \quad (21)$$

In block form we have

$$\mathbf{E}^{-1} = \frac{1}{e} \begin{pmatrix} \mathbf{A} & -\mathbf{C}^+ \\ \mathbf{C} & \mathbf{B} \end{pmatrix}, \quad (22)$$

where

$$\begin{cases} \mathbf{A} = |\mathbf{F}| \mathbf{E}^+ + \mathbf{K} \mathbf{F} \mathbf{K}^+ = -\mathbf{A}^+ \\ \mathbf{B} = |\mathbf{E}| \mathbf{F}^+ + \mathbf{K}^+ \mathbf{E} \mathbf{K} = -\mathbf{B}^+ \\ \mathbf{C} = |\mathbf{K}| \mathbf{K}^+ + \mathbf{F} \mathbf{K}^+ \mathbf{E} \end{cases} \quad (23)$$

and

$$e = \frac{|\mathbf{A}|}{|\mathbf{F}|} = \frac{|\mathbf{B}|}{|\mathbf{E}|} = \frac{|\mathbf{C}|}{|\mathbf{K}|} = |\mathbf{E}| |\mathbf{F}| + |\mathbf{K}|^2 + \text{Tr}(\mathbf{E} \mathbf{K} \mathbf{F} \mathbf{K}^+).$$

The equation of the “ellipsoid” in block form is then

$$\mathbf{X}^+ \mathbf{A} \mathbf{X} - \mathbf{X}^+ \mathbf{C}^+ \mathbf{Y} + \mathbf{Y}^+ \mathbf{C} \mathbf{X} + \mathbf{Y}^+ \mathbf{B} \mathbf{Y} = -e. \quad (24)$$

The Liouville invariant is defined as

$$\mathcal{L} \equiv |\mathbf{E}|^{\frac{1}{2}} = \frac{2}{\pi^2} \quad (4\text{-D volume of the ellipsoid}) \quad (25)$$

but has nothing to do with emittances. The “projection” ellipses are the projections of the ellipsoid on the \mathbf{X} and \mathbf{Y} planes, and their areas are related to the “projection” emittances as before.

PROPOGATION OF EMITTANCES AND INVARIANTS

The linearly coupled 2-dof motion is given by a transfer matrix

$$\mathbf{M} \equiv \begin{pmatrix} \mathbf{M} & \mathbf{m} \\ \mathbf{n} & \mathbf{N} \end{pmatrix}. \quad (26)$$

The symplectic conjugate of \mathbf{M} is defined as

$$\mathbf{M}^+ \equiv \begin{pmatrix} \mathbf{S} & \mathbf{0} \\ \mathbf{0} & \mathbf{S} \end{pmatrix} \begin{pmatrix} \tilde{\mathbf{M}} & \tilde{\mathbf{n}} \\ \tilde{\mathbf{m}} & \tilde{\mathbf{N}} \end{pmatrix} \begin{pmatrix} \tilde{\mathbf{S}} & \mathbf{0} \\ \mathbf{0} & \tilde{\mathbf{S}} \end{pmatrix} = \begin{pmatrix} \mathbf{M}^+ & \mathbf{n}^+ \\ \mathbf{m}^+ & \mathbf{N}^+ \end{pmatrix}. \quad (27)$$

Thus,

$$(\mathbf{M}^+)^+ = \mathbf{M}. \quad (28)$$

\mathbf{M} is symplectic if

$$\mathbf{M} \mathbf{M}^+ = \mathbf{M}^+ \mathbf{M} = \mathbf{I}. \quad (29)$$

This gives in terms of the block matrices

$$\begin{cases} |\mathbf{M}| = |\mathbf{N}|, & |\mathbf{m}| = |\mathbf{n}|, & |\mathbf{M}| + |\mathbf{m}| = 1 \\ \mathbf{m}^+ \mathbf{M} + \mathbf{N}^+ \mathbf{n} = 0 \end{cases} \quad (30)$$

The propagated (transformed) second-moment matrix is then

$$\mathbf{E}_T = \mathbf{M} \mathbf{E} \mathbf{M}^+. \quad (31)$$

This gives in block form

$$\begin{cases} \mathbf{E}_T = \mathbf{M} \mathbf{E} \mathbf{M}^+ + \mathbf{m} \mathbf{F} \mathbf{m}^+ + \mathbf{M} \mathbf{K} \mathbf{m}^+ - \mathbf{m} \mathbf{K}^+ \mathbf{M}^+ \\ \mathbf{F}_T = \mathbf{N} \mathbf{F} \mathbf{N}^+ + \mathbf{n} \mathbf{E} \mathbf{n}^+ - \mathbf{N} \mathbf{K}^+ \mathbf{n}^+ + \mathbf{n} \mathbf{K} \mathbf{N}^+ \\ \mathbf{K}_T = \mathbf{M} \mathbf{K} \mathbf{N}^+ - \mathbf{m} \mathbf{K}^+ \mathbf{n}^+ + \mathbf{M} \mathbf{E} \mathbf{n}^+ + \mathbf{m} \mathbf{F} \mathbf{N}^+ \end{cases}, \quad (32)$$

which then gives

$$\begin{cases} \epsilon_{xT}^2 = |\mathbf{E}_T| = |\mathbf{M}|^2 \epsilon_x^2 + |\mathbf{m}|^2 \epsilon_y^2 + 2|\mathbf{M}||\mathbf{m}|\kappa \\ \quad - 2|\mathbf{M}|\text{Tr}(\mathbf{E} \mathbf{K} \mathbf{m}^+ \mathbf{M}) - 2|\mathbf{m}|\text{Tr}(\mathbf{K} \mathbf{F} \mathbf{m}^+ \mathbf{M}) \\ \quad - \text{Tr}(\mathbf{E} \mathbf{M}^+ \mathbf{m} \mathbf{F} \mathbf{m}^+ \mathbf{M}) - \text{Tr}(\mathbf{K} \mathbf{m}^+ \mathbf{M} \mathbf{K} \mathbf{m}^+ \mathbf{M}) \\ \epsilon_{yT}^2 = |\mathbf{F}_T| = |\mathbf{N}|^2 \epsilon_y^2 + |\mathbf{n}|^2 \epsilon_x^2 + 2|\mathbf{N}||\mathbf{n}|\kappa \\ \quad - 2|\mathbf{n}|\text{Tr}(\mathbf{E} \mathbf{K} \mathbf{n}^+ \mathbf{n}) - 2|\mathbf{N}|\text{Tr}(\mathbf{K} \mathbf{F} \mathbf{n}^+ \mathbf{n}) \\ \quad - \text{Tr}(\mathbf{E} \mathbf{n}^+ \mathbf{N} \mathbf{F} \mathbf{n}^+ \mathbf{n}) - \text{Tr}(\mathbf{K} \mathbf{n}^+ \mathbf{n} \mathbf{K} \mathbf{n}^+ \mathbf{n}) \\ \kappa_T = |\mathbf{K}_T| = |\mathbf{M}||\mathbf{n}|\epsilon_x^2 + |\mathbf{N}||\mathbf{m}|\epsilon_y^2 + (|\mathbf{M}||\mathbf{N}| + |\mathbf{m}||\mathbf{n}|)\kappa \\ \quad - |\mathbf{M}|\text{Tr}(\mathbf{E} \mathbf{K} \mathbf{n}^+ \mathbf{n}) - |\mathbf{m}|\text{Tr}(\mathbf{K} \mathbf{F} \mathbf{n}^+ \mathbf{n}) \\ \quad - |\mathbf{n}|\text{Tr}(\mathbf{E} \mathbf{K} \mathbf{m}^+ \mathbf{M}) - |\mathbf{N}|\text{Tr}(\mathbf{K} \mathbf{F} \mathbf{m}^+ \mathbf{M}) \\ \quad - \text{Tr}(\mathbf{E} \mathbf{n}^+ \mathbf{N} \mathbf{F} \mathbf{m}^+ \mathbf{M}) - \text{Tr}(\mathbf{K} \mathbf{n}^+ \mathbf{n} \mathbf{K} \mathbf{m}^+ \mathbf{M}) \end{cases}, \quad (33)$$

where we have defined $|\mathbf{K}| \equiv \kappa$ as the “coupliance.” (Note that $|\mathbf{K}|$ is not always ≥ 0 as are $|\mathbf{E}|$ and $|\mathbf{F}|$.)

If \mathbf{M} is symplectic, Eqs. (33) are simplified by Eqs. (30) to

$$\begin{cases} \epsilon_{xT}^2 = |\mathbf{M}|^2 \epsilon_x^2 + |\mathbf{m}|^2 \epsilon_y^2 + 2|\mathbf{M}||\mathbf{m}|\kappa - 2|\mathbf{M}|a - 2|\mathbf{m}|b + c \\ \epsilon_{yT}^2 = |\mathbf{m}|^2 \epsilon_x^2 + |\mathbf{M}|^2 \epsilon_y^2 + 2|\mathbf{M}||\mathbf{m}|\kappa + 2|\mathbf{m}|a + 2|\mathbf{M}|b + c, \\ \kappa_T = (|\mathbf{M}|^2 + |\mathbf{m}|^2)\kappa + |\mathbf{M}||\mathbf{m}|(\epsilon_x^2 + \epsilon_y^2) + (|\mathbf{M}| - |\mathbf{m}|)(a - b) - c \end{cases} \quad (34)$$

where

$$\begin{cases} a \equiv \text{Tr}(\mathbf{E} \mathbf{K} \mathbf{W}), & \mathbf{W} \equiv \mathbf{m}^+ \mathbf{M} \\ b \equiv \text{Tr}(\mathbf{K} \mathbf{F} \mathbf{W}) \\ c \equiv -\text{Tr}(\mathbf{E} \mathbf{W}^+ \mathbf{F} \mathbf{W}) - \text{Tr}(\mathbf{K} \mathbf{W} \mathbf{K} \mathbf{W}) \end{cases}. \quad (35)$$

Equations (34) show directly

$$\epsilon_{xT}^2 + \epsilon_{yT}^2 + 2\kappa_T = \epsilon_x^2 + \epsilon_y^2 + 2\kappa, \quad (36)$$

a well-known invariant for symplectic transformations.

EXAMPLES OF APPLICATION

There are two classes of x-y coupled beam transports—the skew quadrupole train and the solenoid.

Class 1 Skew Quadrupole Train

This is a case of symplectic “deformation” propagation. The transfer matrix is

$$\mathbf{M} = \begin{pmatrix} I \cos \frac{\pi}{4} & -I \sin \frac{\pi}{4} \\ I \sin \frac{\pi}{4} & I \cos \frac{\pi}{4} \end{pmatrix} \begin{pmatrix} P & 0 \\ 0 & Q \end{pmatrix} \begin{pmatrix} I \cos \frac{\pi}{4} & I \sin \frac{\pi}{4} \\ -I \sin \frac{\pi}{4} & I \cos \frac{\pi}{4} \end{pmatrix} \\ = \frac{1}{2} \begin{pmatrix} P+Q & P-Q \\ P-Q & P+Q \end{pmatrix}, \quad (37)$$

where P and Q are the principal 2-D transfer matrices along the quadrupole axes and the end matrices rotate the quadrupole train 45°. In this case

$$\begin{cases} |M| = \frac{1}{4} |P+Q| = \frac{1}{2} \left[1 + \frac{1}{2} \text{Tr}(P^*Q) \right] \\ |m| = \frac{1}{4} |P-Q| = \frac{1}{2} \left[1 - \frac{1}{2} \text{Tr}(P^*Q) \right] \\ W = m^* M = \frac{1}{4} (P^* - Q^*) (P+Q) = \frac{1}{4} (P^*Q - Q^*P) \end{cases} \quad (38)$$

We parameterize the symplectic matrix P^*Q as

$$P^*Q \equiv \cos 2\phi + J \sin 2\phi, \quad (39)$$

then

$$\begin{cases} |M| = \cos^2 \phi, & |m| = \sin^2 \phi \\ W = m^* M = (\sin \phi \cos \phi) J \end{cases} \quad (40)$$

Substituting Eqs. (40) in Eqs. (34) we get the transformed emittances.

Class 2A Solenoid – Whole

The transport through a whole solenoid (from exterior to exterior where the vector potential is zero) is a symplectic “rotation.” The transfer matrix is

$$\mathbf{M} = \begin{pmatrix} R \cos \psi & R \sin \psi \\ -R \sin \psi & R \cos \psi \end{pmatrix} \quad (41)$$

with the 2-D

$$R \equiv \begin{pmatrix} \cos \psi & \frac{1}{k} \sin \psi \\ -k \sin \psi & \cos \psi \end{pmatrix}, \quad (42)$$

where

$$\psi \equiv \left(\frac{1}{2} \frac{B_z}{B\rho} \right) \ell \equiv k\ell,$$

and B_z and ℓ are the solenoid field and length and $B\rho$ is the rigidity of the beam. This gives

$$\begin{cases} |M| = \cos^2 \psi, & |m| = \sin^2 \psi \\ W = m^* M = (\sin \psi \cos \psi) I \end{cases} \quad (43)$$

Compared to Eqs. (40) we see that J is here replaced by I. This distinguishes the “deformation” of a skew-quadrupole train from the “rotation” of a solenoid.

Class 2B Solenoid – Ends

The only easily available nonsymplectic case is when either (or both) end of the transport is in the interior of the solenoid where the transverse vector potential $A_\perp \neq 0$. We give here the thin “entry” of a solenoid. The transfer matrix is

$$M = N = I \quad m = -m^* = n^* = -n = \begin{pmatrix} 0 & 0 \\ k & 0 \end{pmatrix}. \quad (44)$$

In this case we have to go back to the general (nonsymplectic) formulas in Eqs. (33). We have $|M| = |N| = 1$ and $|m| = |n| = 0$. For the emittances Eqs. (33) give

$$\begin{cases} \epsilon_{xT}^2 = \epsilon_x^2 + 2a + c \\ \epsilon_{yT}^2 = \epsilon_y^2 + 2b + c \\ \kappa_T = \kappa + a + b + c \end{cases} \quad (45)$$

where

$$\begin{cases} a = -\text{Tr}(E K m^* M) = k \left(\overline{x^2 x' y'} - \overline{xy x x'} \right) \\ b = -\text{Tr}(K F m^* M) = -k \left(\overline{y^2 x y'} - \overline{xy y y'} \right) \\ c = -\text{Tr}(E M^* m F m^* M) - \text{Tr}(K m^* M K m^* M) \\ = k^2 \left(\overline{x^2 y^2} - \overline{xy}^2 \right) \end{cases} \quad (46)$$

This shows the noninvariance of

$$\epsilon_{xT}^2 + \epsilon_{yT}^2 + 2\kappa_T = \epsilon_x^2 + \epsilon_y^2 + 2\kappa + 4(a + b + c). \quad (47)$$

The “exit” is identical to the “entry” except with the sign of k reversed.

With these three classes of transport one should be able to obtain most desired emittance transformations. If, indeed, there is a transformation that cannot be obtained from combinations of these cases (plus uncoupled transports), some yet unknown coupled transports must be invented.

THREE DEGREES OF FREEDOM

For 3-dof the phase-point position is given by a 1×3 block vector. The second-moment matrix and the transfer matrix are both 3×3=9 block matrices. The inverse second-moment matrix and the conditions for symplecticity are more complex than the 2-dof case, but can be given in a straightforward manner.

PROPOSAL OF PARTIAL SIBERIAN SNAKE BASED ON HELICAL MAGNETS FOR AGS

I.A.Koop, A.V.Otboev, E.A.Perevedentsev, P.Yu.Shatunov, Yu.M.Shatunov
Budker Institute of Nuclear Physics, Novosibirsk, Russia

Abstract

A scheme of partial Siberian snake is considered for polarized proton acceleration at AGS. The snake consists of four identical helical magnets with the field amplitude about 4.0 T on axis and provides proton spin rotation by about 32 degrees per one pass at the injection energy 2.5 GeV. Orbit distortions do not exceed 2 cm inside the insertion. The influences of the snake fields' nonlinearities on the beam dynamics are discussed.

INTRODUCTION

Adiabatical crossing of imperfection spin resonance with a partial Siberian snake has been suggested, tested and successfully used already 30 years ago [1]. The application of this method at AGS has provided an acceleration of polarized protons up to 21 GeV with the 50% beam polarization [2]. Introduction of an RF dipole field inducing a coherent vertical betatron oscillation results in adiabatical spin flip on four strong intrinsic spin resonances with vertical tune at AGS. However, a coupling of the betatron oscillations introduced by the strong snake solenoid enhances depolarizing resonances with the horizontal tune and dramatically reduces the polarization level during acceleration up to the top energy of 25 GeV. To avoid these problems, a design of the partial snake based on the room temperature helical magnet was suggested in 1998 [3]. It was shown that the helical snake approach creates much smaller coupling with the same snake strength 5%.

The helical approach for the partial snake has an evident advantage. In contrast to the solenoid, a DC current in the helix coil will rotate spin approximately on the same angle during entire AGS acceleration cycle.

This paper considers a scheme of partial Siberian snake which consists of four 0.5-meter identical helical magnets with the field value up to 4.0 T. An analysis of particle and spin motions yielded a configuration of the helical magnets that can provide proton spin rotation by 32 degrees per one pass. At that, orbit distortions are zero outside the snake and do not exceed 2.2 cm inside the insertion on the injection energy 2.5 GeV.

MAIN PARAMETERS OF THE SNAKE AND MAGNETIC FIELD DISTRIBUTION

It's clear that the 4.0 T magnetic field level can be realized only in a superconducting helix. Main parameters of the helix are determined by a number of simple requirements. The total length of the snake insertion is 10 feet; the aperture of the magnet does not restrict the AGS acceptance; a number of the helixes results from symmetry. Taking into account fringe fields, we need to

insert four identical helixes to exclude outside orbit excursions in both transverse directions. So we come to the parameters: period of the helix is 50 cm; internal diameter is 10 cm, end conductors are each 10 cm in length.

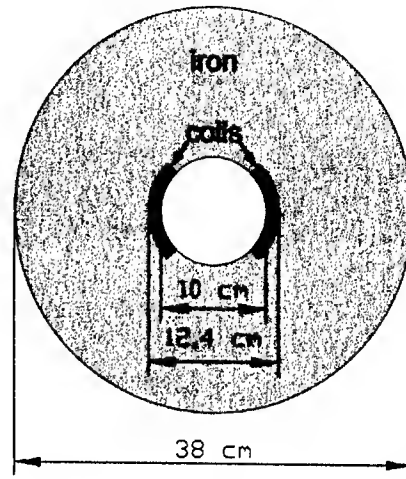


Fig. 1 A cross section view of the MERMAID input file model.

A practical design of the helical magnet has to be based on the realistic fields including edges of coils. A calculation of the field configuration was done by computer code MERMAID [4]. The helix was presented as a number of consecutive slices in the transverse cross section. The coil size was optimized for coils wound by 1.26 mm NbTi wire with well known critical parameters. Fig. 1 shows a cross section view of the helix. 2-D distributions of transverse (B_x , B_y) and longitudinal (B_z) components of the magnetic field in the middle cross section are presented in Figs. 2-4.

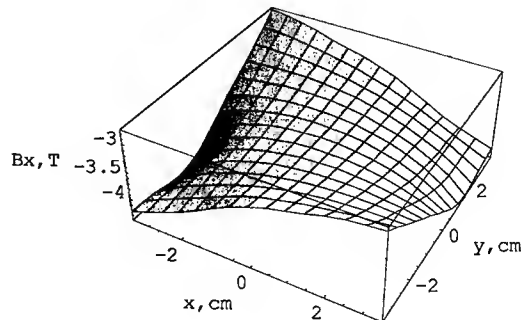


Fig. 2 Transverse distribution of B_x component.

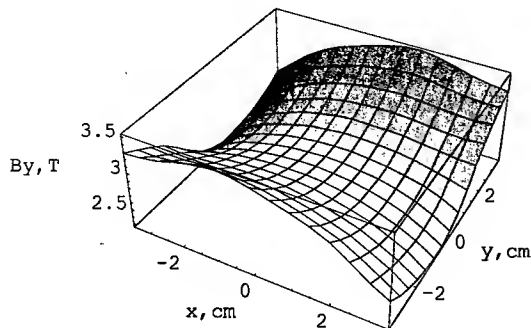


Fig. 3 Transverse distribution of By component.

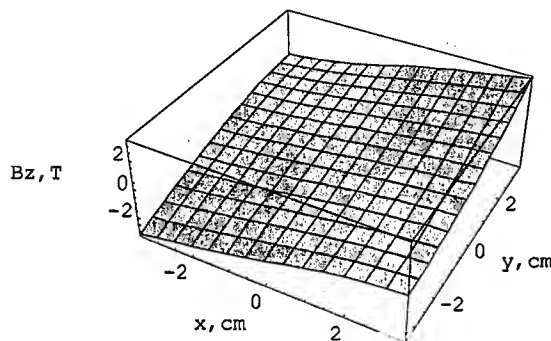


Fig. 4 Transverse distribution of Bz component.

An interpolated behaviour of the on-axis transverse components along the helix is shown in Fig. 5.

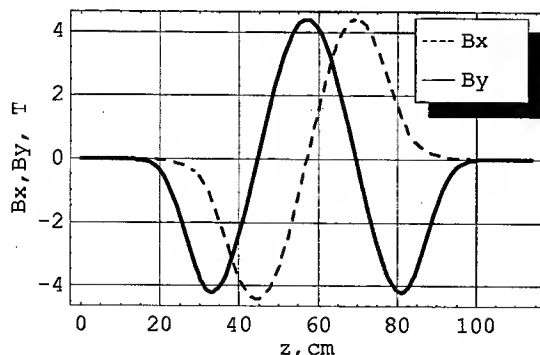


Fig. 5. Longitudinal distribution of the Bx and By components on axis.

Our analysis has shown that the spin rotation is not very sensitive to the initial field direction. For simplicity we always consider the magnetic field on the helix entrance along "y"-axis.

EQUATIONS OF THE ORBITAL MOTION

Consideration of the particle and spin motions in the calculated fields was done in the rectangular Cartesian frame with z-coordinate along the helix axis. Exact equations of particle trajectory excursions $x(z)$ and $y(z)$ are:

$$x''(z) = \frac{1}{B\rho} q \left(x'(z)y'(z)B_x - (1+x'(z)^2)B_y + y'(z)B_z \right)$$

$$y''(z) = -\frac{1}{B\rho} q \left(x'(z)y'(z)B_y - (1+y'(z)^2)B_x + x'(z)B_z \right)$$

$$q = \sqrt{1+x'(z)^2 + y'(z)^2} \quad (1)$$

We calculated two options of the snake with four helices with the right helicity but different polarities. The first set of helices had the polarities: "+ - - +". More serious orbit excursions appear at the AGS injection energy of 2.5 GeV. Some residual mismatching of the trajectory can be adjusted by existing steering coils in the ring.

The other snake option can be constructed by the helix sequence: "+ - + -". This option has no symmetry. It results in a big enough x-angle at the snake exit. To compensate this angle we calculated dipole correctors incorporated in the helix module above the edge commutations. Fig. 6 presents a picture of the field on the axis with correctors "on".

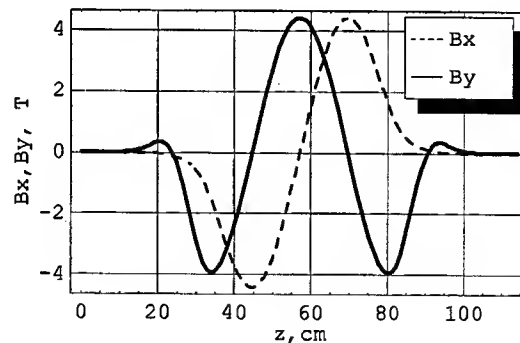


Fig. 6 Longitudinal distribution of the Bx and By components with correctors.

The particle trajectory in the 2nd snake option, when the first and last helices are equipped by the correctors is given in Fig. 7.

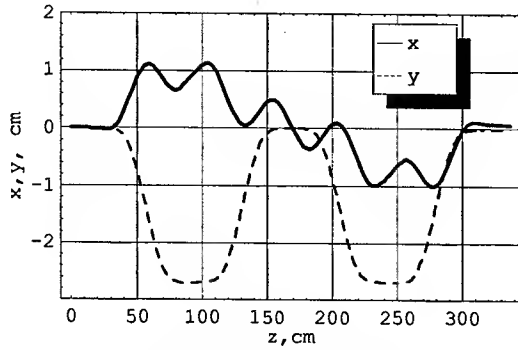


Fig. 7 Particle's trajectory at 2.5 GeV in case of "+ - + -" scheme. 1st and 4th snakes have correctors.

EQUATIONS OF SPIN ROTATION

Similarly to the particle motion, the BMT-equation for the spin vector \vec{S} can be presented in the same frame in the form:

$$\begin{aligned} S_x' &= S_y \frac{q}{B\rho} \left[(1 + \gamma a) B_z - \frac{a}{q} \left(1 - \frac{1}{\gamma} \right) (x' B_x + y' B_y + B_z) \right] - \\ &- S_z \frac{q}{B\rho} \left[(1 + \gamma a) B_y - \frac{a}{q} \left(1 - \frac{1}{\gamma} \right) y' (x' B_x + y' B_y + B_z) \right] \\ S_y' &= S_z \frac{q}{B\rho} \left[(1 + \gamma a) B_x - \frac{a}{q} \left(1 - \frac{1}{\gamma} \right) x' (x' B_x + y' B_y + B_z) \right] - \\ &- S_x \frac{q}{B\rho} \left[(1 + \gamma a) B_z - \frac{a}{q} \left(1 - \frac{1}{\gamma} \right) (x' B_x + y' B_y + B_z) \right] \\ S_z' &= S_x \frac{q}{B\rho} \left[(1 + \gamma a) B_y - \frac{a}{q} \left(1 - \frac{1}{\gamma} \right) y' (x' B_x + y' B_y + B_z) \right] - \\ &- S_y \frac{q}{B\rho} \left[(1 + \gamma a) B_x - \frac{a}{q} \left(1 - \frac{1}{\gamma} \right) x' (x' B_x + y' B_y + B_z) \right] \\ q &= \sqrt{1 + x'^2 + y'^2} \end{aligned}$$

Here γ is the relativistic factor, $a = 1.7928$ is the proton magnetic anomaly; all derivatives are taken with respect to longitudinal coordinate and field components are taken along the particle trajectory given by solution of Eq. (1).

As one can see from the Fig. 8, the final spin rotation corresponds to precession around the longitudinal axis by

the angle: $\arccos[S_y(z = L)] \approx 32^\circ$. This angle practically does not depend on the beam energy and gives snake strength ≈ 0.18 .

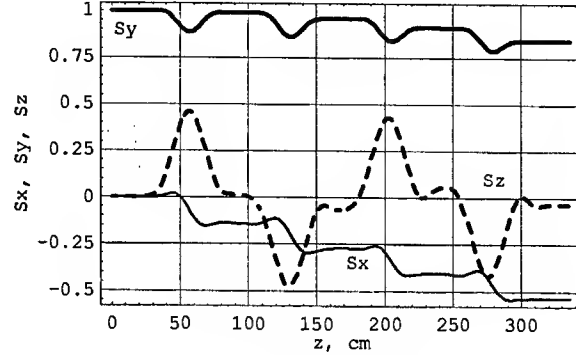


Fig. 8 Spin rotation along the snake.

CONCLUSION

Presented snake design requires a more detailed analysis before the realization phase. Numerical estimations shown that the tune shifts are quite moderate, ≈ 0.02 . Since the snake occupies about 1% of the machine circumference we hope that relatively high local field nonlinearities in the helices can be easily compensated by existing correctors. In any case further investigations of particle and spin dynamics should be done.

REFERENCES

- [1] Ya.Derbenev, A.Kondratenko, A.Skrinsky, Yu.Shatunov, "Study of Spin Resonance Crossing", Proc. of X Int. PAC, Protvino, 1977, vol. 2, p. 76.
- [2] H.Huang et al., Polarized Proton Experiment in the AGS with a Partial Snake, Proc. of SPIN'96, Amsterdam, p. 528.
- [3] T.Roser et al., Spin Note AGS/RHIC/SN 072 (March 1998).
- [4] A.Dubrovin, MERMAID User Guide, Novosibirsk, 1994.

ACTION AND PHASE ANALYSIS TO DETERMINE SEXTUPOLE ERRORS IN RHIC AND THE SPS *

Javier Cardona, Steve Peggs, Todd Satogata, BNL, Upton, NY 11973, USA
Rogelio Tomas, CERN, Geneva, Switzerland

Abstract

Success in the application of the action and phase analysis to find linear errors at RHIC Interaction Regions [1] has encouraged the creation of a technique based on the action and phase analysis to find non linear errors.

In this paper we show the first attempt to measure the sextupole components at RHIC interaction regions using the action and phase method. Experiments done by intentionally activating sextupoles in RHIC and in SPS [2] will also be analyzed with this method.

First results have given values for the sextupole errors that at least have the same order of magnitude as the values found by an alternate technique during the RHIC 2001 run [3].

INTRODUCTION

Under ideal conditions, the action J and phase φ of betatron oscillations of a particle should remain constant all around the ring. Magnetic errors in the different elements of the ring can lead to a change of these two constants of motion. These changes are used to determine the location of such errors and their strengths.

Action and phase associated with particle orbits at particular position in the ring are obtained from pairs of adjacent Beam Position Monitor (BPM) measurements. BPM measurements are converted into action and phase by inverting the equations:

$$\begin{aligned} x_1 &= \sqrt{2J\beta_1} \sin(\psi_1 - \varphi) \\ &= \dots \\ x_2 &= \sqrt{2J\beta_2} \sin(\psi_2 - \varphi) \end{aligned} \quad (1)$$

where, x_1 and x_2 correspond to any two adjacent BPM measurements, β_1 , β_2 , ψ_1 and ψ_2 are their corresponding beta functions and phase advances.

Eq. 1 is applied to all adjacent BPM measurements in the ring to obtain functions of action and phase with respect to s , the azimuthal location.

During the RHIC 2000 run, studies of action and phase indicated significant coupling errors at the RHIC IRs. A method based on first-turn orbit measurements and action and phase analysis was developed to find the magnitude of the coupling errors and to perform the corresponding correction [1].

The positive results obtained from the previous studies stimulate the development of a general method able to de-

termine not only skew quadrupole errors but also gradient errors and non linear errors. This method was used during the RHIC 2001 run to confirm the skew error measurements done with orbits taken in the RHIC 2000 run (see [4]). The action and phase analysis was then used to measure integrated gradient errors giving very precise results (see [5]). The accuracy of the method to determine skew quadrupole errors and gradient errors as well as also demonstrated with a series of experiments performed during the RHIC 2001 run (see [5]). This paper covers experiments performed during the RHIC 2001 proton run and the experiments performed during the RHIC 2003 dAu run to determine sextupole errors with the action and phase analysis method. Results obtained with SPS orbits with sextupoles intentionally introduced in the accelerator are also presented.

DETERMINATION OF ERRORS FROM THE ACTION AND PHASE ANALYSIS

The magnitude of the magnetic kick that particles experience due to the presence of an optical error located at some arbitrary position s_0 is given by:

$$\Delta x'(s_0) = \sqrt{\frac{(J_x^L + J_x^R - 2\sqrt{J_x^L J_x^R} \cos(\psi_x^L - \psi_x^R))}{\beta_x(s_0)}} \quad (2)$$

where J_x^L , J_x^R , ψ_x^L and ψ_x^R correspond to the action and phases for $s < s_0$ (superindice L) and $s > s_0$ (superindice R) respectively. There is an equivalent expression for $\Delta y'(s_0)$.

On the other hand, $\Delta x'(s_0)$ and $\Delta y'(s_0)$ can also be expressed as function of A_1 and B_1 , the skew quadrupole and gradient errors present at s_0 , and all other non linear components like A_2 and B_2 , the skew and normal sextupole errors. Such expression is given by:

$$\begin{aligned} \Delta x' &= (A_1 y_0 - B_1 x_0 \\ &\quad + 2A_2 x_0 y_0 + B_2(-x_0^2 + y_0^2) + \dots) \\ \Delta y' &= (A_1 x_0 + B_1 y_0 \\ &\quad + 2B_2 x_0 y_0 + A_2(x_0^2 + y_0^2) + \dots) \end{aligned} \quad (3)$$

where x_0 and y_0 are the horizontal and vertical positions of the beam at s_0 . The expansion shown in Eq. 3 is valid only for an error localized in a single point or in good approximation for a single magnet. When magnet structures like the RHIC triplets or the RHIC interaction regions are responsible for the now so called integrated magnetic kick $\Delta x'$ the

* Work performed under Contract No. DE-AC02-76CH00016 with the U.S. Department of Energy

new expressions are [5]:

$$\begin{aligned}\Delta x' &= A_1^{eq} y_0 - B_1^a x_0 + 2A_2^b x_0 y_0 - B_2^a x_0^2 + B_2^b y_0^2 + \dots \\ \Delta y' &= A_1^{eq} x_0 + B_1^b y_0 + 2B_2^b x_0 y_0 + A_2^a x_0^2 - A_2^b y_0^2 + \dots\end{aligned}\quad (4)$$

where the superindices employed in the coefficients point to the fact that except for the equivalent skew error, A_1^{eq} , all the other coefficients are not longer symmetric and hence they have to be splitted in two, one with superindice a and one with superindice b . It is possible to evaluate the different multipoles components in Eq. 3 if a set of measurements of the delta kicks versus the beam position at s_0 are available. The procedure to obtain such measurements is basically to record orbits with significant betatron oscillations (usually produced by adjusting a dipole corrector to strengths several times bigger than its normal setting); create the so called difference orbits by subtracting the baseline from the orbits created with the different settings of the dipole corrector; apply Eq. 1 to the difference orbits to obtain action and phases before and after s_0 , and finally apply Eq. 2 to obtain $\Delta x'$ and $\Delta y'$ with an equivalent equation. The beam position (x_0, y_0) at s_0 it is usually approximated with the nearest beam position monitor.

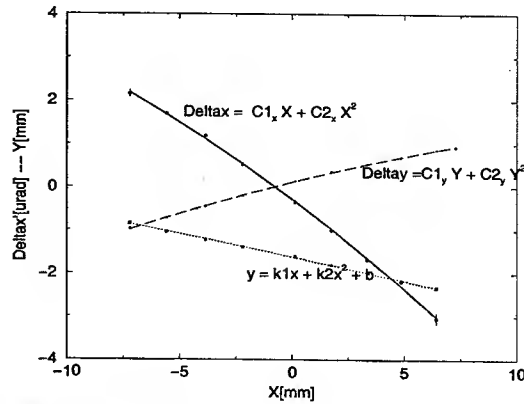
NON LINEAR ANALYSIS OF RHIC 2001 PROTON EXPERIMENTS

During the RHIC 2001 proton run, difference orbits were taken to study non linearities at one of the interaction regions of RHIC with the action and phase method. The orbits were taken by changing the strength of a horizontal and a vertical dipole correctors 10 times which allows to have 10 points in the graphs of magnetic kick versus beam position. A fitting of the graphs (see the graphs obtained with the horizontal dipole corrector in Fig. 1) obtained in both cases give the coefficients defined in Fig. 1. Those coefficients are related with the multipole errors by linear formulas (see [5]) that were used to obtain Table 1.

Table 1: Equivalent multipole errors obtained from the fits of Fig. 1 and its corresponding figure in the vertical plane.

A_1^{eq}	0.122 ± 0.003
B_1^x	0.386 ± 0.001
B_1^y	-0.142 ± 0.002
A_2^{ya}	0.0121 ± 0.0003
A_2^{yb}	-0.0012 ± 0.0011
B_2^y	0.0061 ± 0.0011
B_2^{xa}	0.0037 ± 0.0025

Table 1 indicates that the linear components can be precisely extracted from data and also sextupolar components can be extracted but not with the same precision as linear errors can be determined. Even though the precision of the sextupole errors determined in this experiment is



Tue May 13 15:08:58 2003

Figure 1: Graphs of magnetic kick vs beam position extracted from orbits obtained by changing the strength of a horizontal dipole corrector in RHIC. Even though the linear errors dominated these curves, nonlinear behavior is also present and it is possible to determine such nonlinearities from polynomial fits.

not completely satisfactory, these errors are still comparable with the corresponding values found by an alternate method used during the RHIC 2001 run [3].

CALIBRATION OF THE TECHNIQUE TO FIND NON LINEAR ERRORS

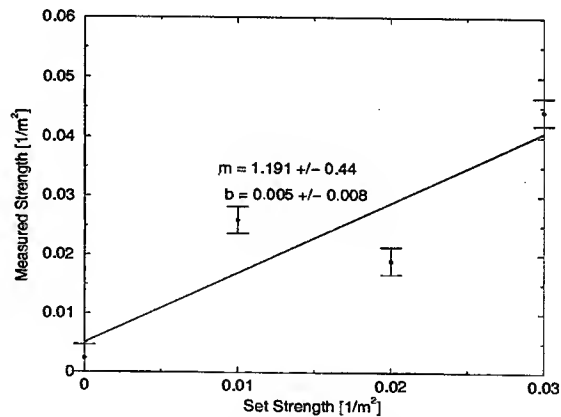


Figure 2: Sextupole calibration curve obtained with difference orbits collected during the RHIC 2003 dAu run.

Experiments to calibrate the action and phase method to determine sextupole errors were done during the RHIC 2003 dAu run. The experiment is basically to set a sextupole corrector to some known strength and then take a series of orbits with different strengths of a particular dipole corrector, first in the horizontal plane and then in the vertical plane. The experiment is then repeated for other 3 different sextupole corrector strengths. From every series

of orbits it is possible to measure a sextupole component with the method described earlier and a calibration curve like the one shown in Fig. 2 can be obtained. The errors shown are propagated errors derived from the estimated errors of the graphs of magnetic kick versus position from which the calibration curve was obtained. The calibration curve follows the expected trend but the propagated errors seem to be very small when compared with the general deviation of the points from the model. There are evidence that errors associated with the magnetic kicks from which the sextupole were extracted were underestimated. Indeed the quadratic fits done to the curves of magnetic kick versus the beam position give values for χ^2 equal to 2.3, an indication of too small uncertainties. Apart from this problem the general deviation of the data points is still significant and more experimentation will be needed to reduce this deviation. The uncertainties associated with RHIC 2001 proton experiments magnetic kicks were 4 times smaller than the ones found in the RHIC 2003 dAu experiments. This might be due to some temporary condition of the machine but also might be related with the particle used. If this is the case, then it will be convenient to repeat this experiment with protons. Another factor that will reduce the errors is increasing the number of points used to determine each sextupole strength. Due to the time limitations only 4 points per sextupole strength were used in the RHIC 2003 dAu experiment. Increasing the amplitude of the betatron oscillation will definitively help to resolve the strength with better precision but the feasibility of increasing the amplitude beyond the maximum amplitude used of about 10 mm must be carefully examined.

ACTION AND PHASE ANALYSIS WITH SPS ORBITS

Orbits taken originally in the SPS to study resonance driving terms [2] were also analyzed with the action and phase method. The graphs of phase (see Fig. 3) obtained by inverting Eq. 1 show regular behavior of the phase with jumps at some places. Most of these places exactly correspond to the places where strong sextupole were on during the data taking of orbits at the SPS. The jumps are more or less clear depending on the turn that is being analyzed.

The graphs of phase also have a tilt (the phase graphs are expected to be horizontal lines with jumps at the places where the errors are located) that probably is due to the fact that the model used for the analysis and the machine model were tuned slightly different. The next step in the analysis of the SPS orbits with the action and phase method is to numerically determine the magnitude of the sextupole strengths and compare them with the set sextupole strengths in the control room.

CONCLUSIONS

Very precise measurements of linear components were obtained in the first experiment presented in this article (RHIC 2001 proton run) and the feasibility of extracting

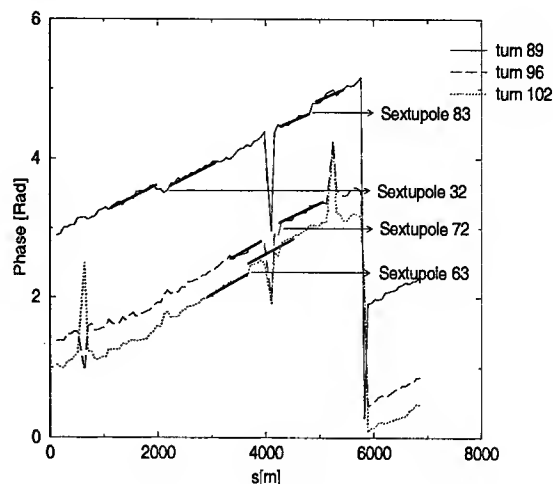


Figure 3: Phase analysis of SPS orbits. The sextupoles that were introduced intentionally in the accelerator can be clearly identified by the jumps in phase.

non linear errors has been demonstrated with the same data.

Data collected during the RHIC 2003 dAu run has allowed to test the calibration of the action and phase analysis to determine sextupole components. The calibration curve obtained is in agreement with the expected curve but more experimental data will be necessary to improve the precision of the measurements.

Application of the action and phase analysis in turn by turn orbits of the SPS has allowed to identify clearly the places where sextupoles were intentionally turned on. Future analysis will also give the strengths of such sextupoles.

ACKNOWLEDGMENTS

We are grateful to Fulvia Pilat, Vadim Ptitsyn, Steven Tepikian and Johannes Van Zeijts for valuable discussions, suggestions and help in the realization of the experiment.

REFERENCES

- [1] V. Ptitsyn, J. Cardona, F. Pilat, J. P. Koutchouk, *Measurement and Correction of Linear Effects in the RHIC Interaction Regions*, PAC 2001, Chicago Illinois, (2001).
- [2] M. Hayes, F. Schmidt and R. Tomas, *Direct Measurements of Resonance Driving Terms at SPS at 26 GeV*, EPAC 2002, Paris - France (2002).
- [3] F. Pilat, P. Cameron, V. Ptitsyn, J. P. Koutchouk, *Linear and Nonlinear Corrections in the RHIC Interaction Regions*, EPAC 2002, Paris - France, (2002).
- [4] J. Cardona, S. Peggs, T. Satogata, F. Pilat, V. Ptitsyn, *Determination of Linear and Non Linear Components in RHIC Interaction Regions from Difference Orbit Measurements*, EPAC 2002, Paris - France (2002).
- [5] J. Cardona, *Linear and Non Linear Studies at RHIC Interaction Regions and Optical Design of the Rapid Medical Synchrotron*, Ph.D. thesis, Stony Brook University, to be published, (2003).

BEAM DIFFUSION MEASUREMENTS AT RHIC *

R. P. Fliller III [†], A. Drees, D. Gassner, G. McIntyre, S. Peggs, D. Trbojevic, BNL, Upton, NY, 11793

Abstract

During a store, particles from the beam core continually diffuse outwards into the halo through a variety of mechanisms. Understanding the diffusion rate as a function of particle amplitude can help discover which processes are important to halo growth. A collimator can be used to measure the amplitude growth rate as a function of the particle amplitude. In this paper we present results of diffusion measurements performed at the Relativistic Heavy Ion Collider (RHIC) with fully stripped gold ions, deuterons, and protons. We compare these results with measurements from previous years, and simulations, and discuss any factors that relate to beam growth in RHIC.

1 INTRODUCTION

The understanding of beam halo is important for current and future accelerators. Beam halo can be a major source of detector background. Halo can also reduce component lifetime through induced radiation. Understanding beam halo is very important for the next generation of accelerators[1]. In superconducting machines, significant halo can induce magnet quenches. All of these effects can ultimately limit accelerator performance by reducing the amount of beam that can be injected.

Beam halo grows because various processes slowly move particles from the core of the beam into the halo. One way to measure this halo growth is using a collimator to measure the diffusion rate of the beam. By measuring the loss rate at a collimator after it moves relative to the beam, it is possible to reconstruct the diffusion coefficient as a function of the particle action. In this paper we discuss experiments carried out at RHIC to measure the diffusion coefficient with gold, deuteron, and proton beams at 100 GeV/u.

2 THEORY

The theory of how to measure beam diffusion with a collimator is treated in detail in references [2] and [3]. A shortened treatment is given here. The diffusion equation is

$$\frac{\partial}{\partial t} f(J, t) = \frac{1}{2} \frac{\partial}{\partial J} B(J) \frac{\partial}{\partial J} f(J, t) \quad (1)$$

where $f(J, t)$ is the beam distribution as a function of the particle action J and time, and $B(J)$, given by

$$B(J) = \frac{\langle \Delta J^2 \rangle}{\Delta t} \quad (2)$$

is the diffusion coefficient to be measured. $B(J)$ is generally postulated to be a monomial. If it is assumed that only particles that are initially close to the collimator will eventually hit the collimator, or equivalently, that $B(J)$ is not "too large", then near the collimator $B(J)$ can be written,

$$B(J) = b_0 \left(\frac{J}{J_c} \right)^n \quad (3)$$

where J_c is the action of a particle that just touches the collimator, $J_c = x_c / \sqrt{2\beta}$, x_c is the distance between the collimator and the beam center, and β is the β function at the collimator. $b_0 = b J_c^n$ is the diffusion coefficient at $J = J_c$. Assuming that $f(J_c, t)$ vanishes at the collimator, and that $f(J_c, 0)$ increases linearly away from the collimator, then the left hand side of Eqn. 1 is just the particle loss rate due to the collimator, $\dot{N}(t)$. For actions near the collimator action, $B(J \approx J_c) \approx b_0$ one can introduce the variables

$$z = \frac{J_c - J}{J_c} \quad (4)$$

$$R = \frac{b_0}{2J_c^2} \quad (5)$$

the fractional change in the collimator action, and the normalized diffusion rate to be determined by a fit, and solve Eqn. 1 for the loss rate at the collimator. For the instance when the collimator moves towards or away from the beam, one obtains:

$$\dot{N}^{(1)}(t) = a_0 \left\{ 1 + \frac{\Delta z}{\sqrt{\pi R(t - t_0)}} \right\} + a_1 \quad (6)$$

$$\dot{N}^{(2)}(t) = a_0 \operatorname{erfc} \left(\frac{\Delta z}{\sqrt{4R(t - t_0)}} \right) + a_1 \quad (7)$$

$\Delta z = 2|\Delta x_c|/x_c$ is the absolute change in z due to the change in collimator position Δx_c , a_1 is the count rate from background or an activated collimator, measured when the collimator is fully retracted, and a_0 is an arbitrary constant. By fitting one of these solutions to the loss rate after moving the collimator, it is possible to obtain the normalized diffusion coefficient R and then $B(J_c) = 2J_c^2 R$. Sampling over many collimator positions, it is possible to reconstruct the diffusion coefficient for the beam halo.

3 EXPERIMENT

The RHIC collimator system is shown in Fig. 1. The collimators are 450 mm long copper blocks with an inverted L shape residing downstream of the PHENIX detector in both the blue (clockwise) and yellow (counterclockwise) rings. Downstream of each collimator there are

* Work performed under the auspices of the U.S. Department of Energy
[†] rfiller@bnl.gov

four PIN diodes that are used to monitor the beam losses due to the collimator. The crystal collimator and its associated detectors were not used for these studies.

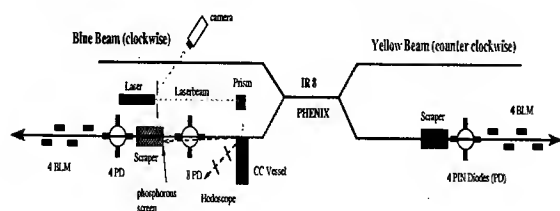


Figure 1: The RHIC collimation system

The collimators were inserted into the beam and rotated to align the face of the collimator to the beam to minimize the secondary halo due to particles scattering from the collimator. Then the collimator was stepped horizontally into and out of the beam varying the collimator position and the stepsize. This way, various actions are sampled, and self-consistency is checked by using different step sizes and/or directions to measure at the same action.

Fig. 2 shows the loss rate at the PIN diodes for the collimator moving toward and away from the beam with fits to the data. The left picture shows how the losses respond with the collimator moving toward the beam. An initial scraping of the beam occurs as it contacts the collimator, with a reduction in the losses to a steady state as beam is removed. The right picture shows the losses when the collimator is moved away from the beam. Diffusion slowly pushes particles toward the scraper, eventually filling up the available space in typically 30s.

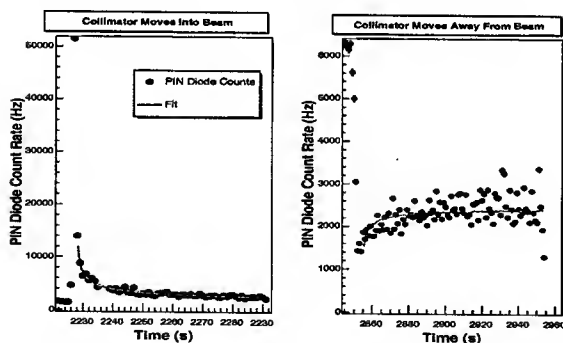


Figure 2: The effect of the collimator motion on beam loss rates with fit.

For each type of movement of the collimator, the loss rate is fit to either of Eqns. 6 or 7. As one can see from Fig. 2, the fit to the loss rate when the collimator is retracted yields a higher R value than the data indicate. This was found in some fills during the last RHIC run as well [3].

The normalized diffusion coefficient, R is averaged over the four PIN diodes. This is used to reconstruct $B(J_c)$ and the results are fit to $B(J) = b_0 J^n$. Fig. 3 shows the re-

construction of the $B(J)$ for fill 02797. The horizontal and vertical error bars are dominated by the uncertainty in the collimator action. This uncertainty is equally due to the uncertainty in the distance between the collimator and the beam and the knowledge of the β function at the collimator [4].

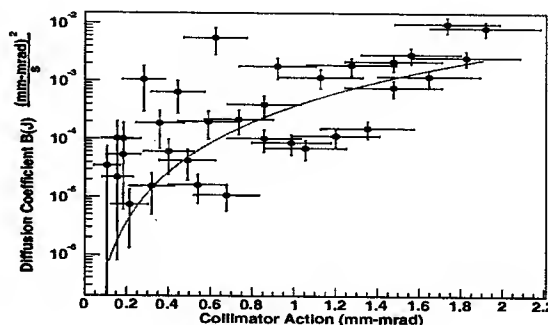


Figure 3: Reconstructed diffusion coefficient for Fill 02797. Note the vertical axis has a log scale.

Fig. 4 shows the reconstructed diffusion coefficient for the first data set of Fill 03155. There is a large variation in the diffusion coefficient for this data set that is not yet understood.

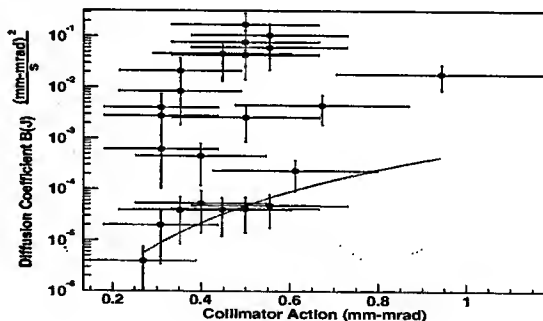


Figure 4: Reconstructed diffusion coefficient for first data set of Fill 03155. Note the vertical axis has a log scale.

4 RESULTS

Table 1 shows the preliminary results of the fits for all runs. There are two data sets missing from the analysis. Both were taken in the blue (clockwise) ring of RHIC with a deuteron beam. Because of a missing BPM and time constraints it was not possible to analyze the data. For Fill 03155, two data sets were taken, the first immediately after the ramp to storage energy. The second was taken two and a half hours later. For this fill, the diffusion measurement was done in the vertical plane because of an oscillation of the beam orbit caused by the AGS Booster cycle seen in

Table 1: Results of Fit to $B(J) = bJ^n$

Store Number	Year	Ring	Beam	$b \mu\text{m}^{2-n}\text{s}^{-1}$	n
01413	2001	yellow	Au	0.17 ± 0.09	10.3 ± 1.2
02797(i)	2003	yellow	Au	$(3.6 \pm 0.8) \times 10^{-4}$	2.8 ± 0.3
02959	2003	yellow	Au	0.0081 ± 0.0014	8.3 ± 0.8
03155-01	2003	yellow	Au	$(5.3 \pm 4.4) \times 10^{-4}$	3.5 ± 1.0
03155-02	2003	yellow	Au	1.8 ± 1.12	8.7 ± 0.8
01874(i)	2002	yellow	p	0.045 ± 0.026	8.5 ± 1.5
01924(i)	2002	blue	p	0.06 ± 0.02	7.0 ± 0.8
02136	2002	yellow	p	7.8 ± 5.5	5.7 ± 0.6
02175	2002	blue	p	0.0036 ± 0.0005	3.0 ± 0.3

(i) indicates injection energy

the horizontal plane. All other measurements were done in the horizontal plane. Three data sets were taken at injection energy.

The data for the 2003 run were fit with a slightly different method than the other data. We are in the process of reanalyzing the data.

We are still in the process of determining the systematic errors and correlations in the data. Fig. 5 shows the distribution of n in all of the data sets. The average $\langle n \rangle = 5.7 \pm 1.3$ is fairly constant between the data sets.

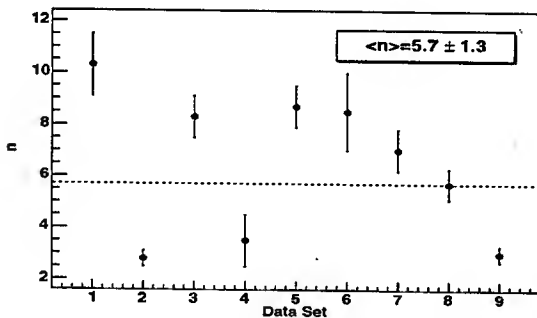


Figure 5: $B(J)$ exponents in same order as Table 1. The dotted line is the weighted average.

The b coefficient generally has a large relative error, this is because of the large error in the action. There seems to be no consistent change in b with different beams. However, there is one interesting correlation. Before the data was taken in Fill 02136, a van der Meer scan was done in the PHENIX IR [5], and before the second data set in Fill 03155, orbit bumps were done through the same IR [6]. Both of these measurements have a large b as compared to all other measurements. In these cases, the beam passes off center through the IR triplet magnets and samples non-linear magnetic fields. This may cause the relatively large b in these cases. However, we are still investigating other possible reasons such as pressure rises, tune shifts, and chromaticity changes.

5 CONCLUSION

Diffusion measurements were performed in RHIC with Au, proton, and deuteron beams. The data does show that n is relatively constant over the variety of measured conditions. Data analysis will continue, with the emphasis on understanding the errors in the measurements and finding correlations between the measurements and the configuration of the machine.

6 REFERENCES

- [1] R. Abman *et al.* "Requirements for the LHC Collimation System" Proceeding of the 2002 European Particle Accelerator Conference, Paris, France (2002).
- [2] M. Seidel. "The Proton Collimation System of HERA", Ph.D. thesis, Universität Hamburg, 1994 (DESY Report 94-103).
- [3] R. P. Fiiller III, *et al.* "Beam Diffusion Studies at RHIC" Proceeding of the 2002 European Particle Accelerator Conference, Paris, France (2002).
- [4] T. Satogata, *et al.* "Linear Optics Measurement and Correction in the RHIC 2003 Run" These Proceedings; M. Bai *et al.* "Measurement of Betatron Functions and Phase Advances in RHIC with AC Dipoles" These Proceedings. T. Satogata, *et al.* "Linear Optics during the RHIC 2001-2 Run", Proceeding of the 2002 European Particle Accelerator Conference, Paris, France (2002).
- [5] A. Drees, *et al.* "Results from Vernier Scans at RHIC During Runs 2000-2003", these Proceedings.
- [6] F. Pilat, *et al.* "Nonlinear Effects in the RHIC Interaction Regions: Modeling, Measurements, Correction", these Proceedings.

MEASUREMENT OF THE NONLINEAR MOMENTUM COMPACTION FACTOR IN RHIC *

C. Montag[†], BNL, Upton, NY 11973, USA

Abstract

During gold beam acceleration in the Relativistic Heavy Ion Collider (RHIC), the transition energy has to be crossed at $\gamma_t \approx 23$. Since close to γ_t the longitudinal slip factor $\gamma_t^{-2} - \gamma^{-2}$ becomes very small, the longitudinal momentum compaction factor α_1 becomes significant. Measurements of this factor using longitudinal phase space tomography will be reported.

INTRODUCTION

The Relativistic Heavy Ion Collider (RHIC) consists of two superconducting storage rings, capable of accelerating hadron beams from protons to fully stripped gold ions up to energies of 100 GeV/nucleon in the case of gold. Ion species other than protons have to cross transition energy around $\gamma_t = 23.2$ during acceleration in RHIC, which is accomplished by a set of γ_t -quadrupoles equipped with special power supplies that can switch the sign of the magnetic field within 30 msec, thus providing a γ_t jump of $\Delta\gamma_t = 1.0$.

To minimize longitudinal emittance blow-up during the γ_t jump due to bucket mismatch, a detailed understanding of the beam dynamics is required. Here we report an attempt to measure the nonlinear momentum compaction factor α_1 using tomographic phase space reconstruction.

TOMOGRAPHIC PHASE SPACE RECONSTRUCTION

To fully reconstruct the n -dimensional picture of an object, tomography requires a set of $n - 1$ -dimensional projections of this object, taken at different angles spanning at least 180 degrees. In the case of tomographic reconstruction of the longitudinal phase space in a storage ring, this rotation is provided by phase space dynamics. However, this dynamics is not just a simple rotation of a rigid object, but is intrinsically nonlinear with the rotation frequency (synchrotron frequency) being a function of the phase space amplitude. This difficulty can be overcome by taking into account the exact equations of motion which can be arbitrarily complex [1].

Taking the exact equations of motion, a set of test particles launched on a regular grid in phase space are tracked and sorted into N_{bins} bins that correspond to the binning of the

measured profiles each time a longitudinal bunch profile i was obtained by the wall current monitor. Each particle k is therefore assigned a bin number $N_i^{\text{bin}}(k)$. Next, the number $N_{i,j}^{\text{population}}$ of test particles in the j th bin at the time the i th profile was taken is determined.

During the reconstruction process an intensity i is assigned to each test particle by an iterative back-projection algorithm according to the measured bunch profiles. This process increases the intensity I_k of all test particles that fall into a certain profile bin j at a specific time when the i th profile was taken by

$$\Delta I_{k:N_{\text{bin}}(k)=j} = \frac{1}{N_{\text{profiles}} N_{i,j}^{\text{population}}} \sum_{i=0}^{N_{\text{profiles}}} h_{i,j}^{\text{meas}}, \quad (1)$$

where $h_{i,j}^{\text{meas}}$ is the measured profile height of the j th bin in the i th profile, and N_{profiles} is the total number of profiles used for the reconstruction.

When this has been done for all profiles, the algorithm calculates the projections of the resulting distribution that correspond to the profiles measured by the wall current monitor. The difference between measured and reconstructed profiles is then iteratively back-projected.

The remaining discrepancy between measured and reconstructed profiles after a fixed number of iterations is then used as a quantitative measure of the quality of the reconstruction, which allows for parameter fitting [1].

THE NONLINEAR MOMENTUM COMPACTION FACTOR

The frequency-slip factor η which characterizes the chromatic behavior in the longitudinal phase space is defined as the relative change of revolution frequency ω per unit change of the relative momentum $\delta = \Delta p/p$,

$$\eta = -\frac{1}{\omega_s} \frac{d\omega}{d\delta}. \quad (2)$$

Here ω_s denotes the revolution frequency of the synchronous particle.

In general, the slip-factor η is a nonlinear function of δ ,

$$\eta = \eta_0 + \eta_1 \delta + \mathcal{O}(\delta^2), \quad (3)$$

with [2]

$$\eta_0 = \alpha_0 - \frac{1}{\gamma_s^2}, \quad (4)$$

$$\eta_1 = 2\alpha_0\alpha_1 - 2\eta_0\alpha_0 + 3\frac{\beta_2^2}{\gamma_s^2}, \quad (5)$$

* Work performed under contract number DE-AC02-98CH10886 with the auspices of the US Department of Energy

[†] montag@bnl.gov

where $\gamma_s = (1 - \beta_s^2)^{-1/2}$ is the Lorentz factor of the synchronous particle, $\beta_s = v_s/c$, and $\alpha_0 = 1/\gamma_t^2$. In the vicinity of γ_t , $1/\gamma_s^2 = 1/\gamma_t^2 = \alpha_0$, and therefore

$$\eta_1 = 2 \frac{\alpha_1}{\gamma_t^2} + 3 \frac{\beta_s^2}{\gamma_t^2}. \quad (6)$$

While the linear part η_0 of the slip factor η changes sign when the transition energy is crossed, the nonlinear contribution η_1 does not. This effect leads to bucket mismatch at the transition jump unless α_1 can be specifically chosen. With $\beta_s = 1$ for relativistic beams, the contribution of η_1 vanishes for $\alpha_1 = -3/2$.

SIMULATIONS

To test the feasibility of measuring the nonlinear momentum compaction factor α_1 tomographically, simulations were performed. A set of 100000 particles with gaussian distributions in phase ϕ and energy deviation δ were tracked using the parameter setpoints as given in Table 1. To potentially improve the convergence of the subsequent parameter fit, a quadrupole oscillation was induced by launching the particles with a deliberate bucket mismatch, namely $\sigma_\delta = 0.2 \cdot \delta_{\max}$ and $\sigma_\phi = 0.1 \cdot \phi_{\max} = 0.1 \cdot \pi$, where δ_{\max} denotes the bucket height. Projections (wall current monitor profiles) of the evolving distribution were calculated every 125 turns. First, a one-parameter fit for the nonlinear momentum compaction factor α_1 was performed, assuming all other parameters as exactly known. As shown in Figure 1, several local minima exist in the vicinity of the correct value of $\alpha_1 = 0.35$, which may be explained by the limited number of particles used to generate the profiles, and/or the binning of those profile data. Smoothing the curve shown in Figure 1 by regarding those small fluctuations as some sort of noise results in a nonlinear momentum compaction factor around $\alpha_1 \approx -0.8$, which significantly differs from the correct value.

In a second step, the profiles were used to reconstruct the initial phase space distribution, simultaneously fitting for three unknown parameters as it is required in the case with measured data, the nonlinear momentum compaction factor α_1 , the RF voltage U_{RF} , and the bin position of the synchronous phase in the profiles using a simulated annealing technique [3, 4].

The nonlinear momentum compaction factor was fitted as $\alpha_1 = 0.32 \pm 0.14$, where the error is taken as the rms deviation from the average over several fitting runs with different initial parameters. This showed that phase space tomography together with simultaneous fitting of the three unknown parameters may indeed be a feasible method to measure the nonlinear momentum compaction factor α_1 .

MEASUREMENTS

For the measurements, two RF voltage jumps were introduced 1.0 sec and 0.5 sec before the transition jump to

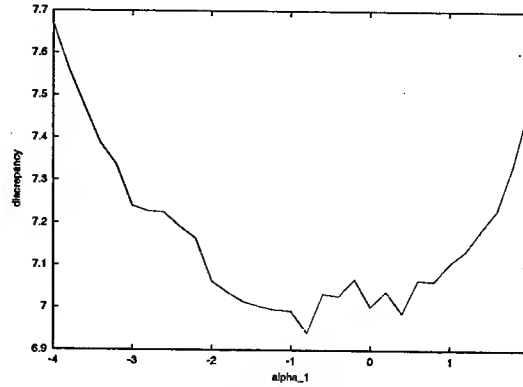


Figure 1: Remaining discrepancy as function of α_1 , using simulated data. The RF voltage is set to the exact value during this one-parameter fit.

Table 1: Parameter table for the simulation test. All parameters are set according to the situation in the “blue” RHIC ring. α_1 is chosen according to model calculations with both chromaticities set to $\xi_{x,y} = -2$.

γ_t	23.7647
γ_i	22.85775
$d\gamma/dt$	0.4556/sec
U_{RF}	145 kV
n_{harm}	360
α_1	0.35

create some longitudinal quadrupole oscillation, as shown in Figure 2. 50 profiles taken every 125 turns were used for the α_1 measurement, starting 0.1 seconds after the second RF jump.

As in the simulation test, a simulated annealing technique was applied to simultaneously fit for the three unknown parameters α_1 , U_{RF} , and the position of the synchronous phase in the wall current monitor profiles. The resulting value for the nonlinear momentum compaction factor is $\alpha_1 = -1.37 \pm 0.11$, which significantly differs from the value calculated by the model, $\alpha_1 = 0.35$.

This discrepancy may have several causes. First of all, tomographic phase space reconstruction may not be sensitive enough to changes of α_1 on the order of ± 1 . This explanation is backed by a similar observation during the simulation tests, where α_1 was found with a similar discrepancy during one-parameter fits.

A poor sensitivity of the resulting discrepancy to small changes in α_1 leads to additional problems during multi-parameter fits. As Figure 3 shows, different values of α_1 result in different local minima for different setpoints of the RF voltage during the reconstruction. In the vicinity of $\alpha_1 \pm 1$, the remaining discrepancy is clearly dominated by fluctuations, which may be interpreted as noise.

Finally, the nonlinear momentum compaction factor de-

BLUE bunch length around transition, fill 02797

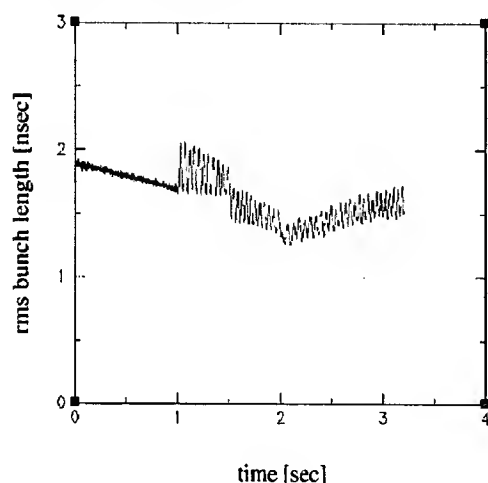


Figure 2: Measured bunch length with two RF voltage jumps (at 1.0 sec and 1.5 sec, respectively) to induce a quadrupole oscillation. The transition jump occurs at 2.0 sec, indicated by the minimum bunch length.

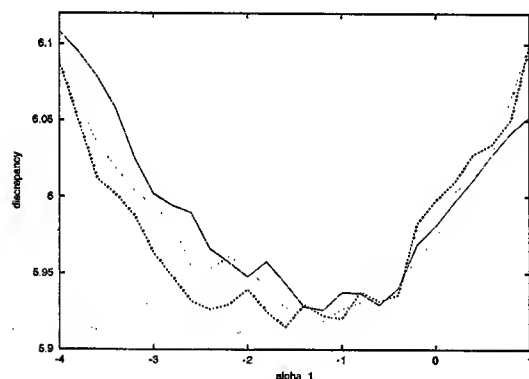


Figure 3: Remaining discrepancy as function of α_1 for different RF voltages. The red line corresponds to $U_{RF} = 140$ kV, the green one to $U_{RF} = 145$ kV, and the blue one to $U_{RF} = 150$ kV.

depends on various machine parameters such as the chromaticity, as Figure 4 shows. Since the superconducting RHIC dipoles have a non-negligible field-dependent sextupole component, exact modeling of the machine is not trivial. This sextupole component contributes to the chromaticity, leading to a different setting of the regular sextupoles than in an ideal machine without sextupole contributions from the dipoles. Furthermore, the sextupole component of the dipoles also results in tune change due to an overall radial orbit shift of about 1.3 mm, which in turn requires adjustment of the tune quadrupoles to keep the tunes at their target values [5]. All these corrections to the ideal

model contribute to changes in the nonlinear momentum compaction factor.

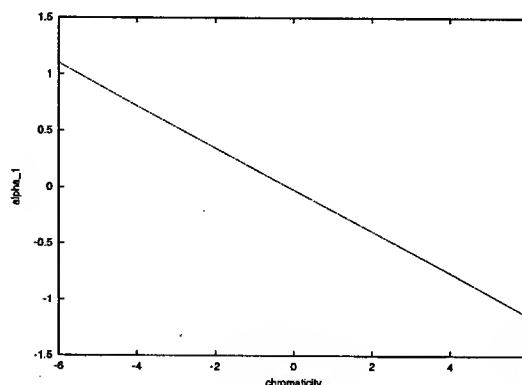


Figure 4: Nonlinear momentum compaction factor α_1 as calculated from the model, for different chromaticities, $\xi_x = \xi_y$.

CONCLUSION

An alternative approach to measuring the nonlinear momentum compaction factor α_1 of RHIC has been made, namely the use of tomographic reconstruction of the longitudinal phase space. The discrepancies with the model may be due to discrepancies between the model and the real machine itself as well as due to insufficient sensitivity of the quality factor of those parameters fits to small changes in α_1 .

ACKNOWLEDGEMENTS

The author would like to thank J. Kewisch, J. van Zeijts, and M. Blaskiewicz for stimulating discussions.

REFERENCES

- [1] S. Hancock, M. Lindroos, S. Koscielniak, Longitudinal Phase Space Tomography with Space Charge, PRST-AB 3, 124202 (2000)
- [2] J. Wei, Longitudinal Dynamics of the Non-Adiabatic Regime on Alternating-Gradient Synchrotrons, Ph. D. thesis, Stony Brook, 1990
- [3] C. Montag, N. D'Imperio, R. Lee, J. Kewisch, T. Satogata, Longitudinal Phase Space Tomography in RHIC, Proc. EPAC2002, Paris, 2002
- [4] C. Montag, N. D'Imperio, R. Lee, J. Kewisch, Tomographic Phase Space Reconstruction During Rebucketing in the Relativistic Heavy Ion Collider, PRST-AB 5, 082801, (2002)
- [5] J. van Zeijts, private communication

ADIABATIC CAPTURE OF CHARGED PARTICLES IN STABLE ISLANDS: A NOVEL APPROACH TO MULTI-TURN EXTRACTION

R. Cappi and M. Giovannozzi, CERN, Geneva, Switzerland

Abstract

Recently a novel approach has been proposed aimed at performing multi-turn extraction from a circular machine. Such an approach consists of splitting the beam by means of stable islands created in transverse phase space by nonlinear magnetic elements such as sextupoles and octupoles. Provided a slow time-variation of the linear tune is applied, adiabatic with respect to the betatron motion, the islands can be moved in phase space and eventually charged particles may be trapped inside the stable structures. This generates a certain number of well-separated beamlets. Originally, this principle was successfully tested using a fourth-order resonance. In this paper the approach is generalised to other type of resonances and some examples of adiabatic capture performed by using various low-order resonances are presented and described in detail.

INTRODUCTION

A special technique is normally used to fill the CERN Super Proton Synchrotron (SPS) with a high-intensity proton beam from the Proton Synchrotron (PS), the so-called Continuous Transfer (CT) [1]. The beam is sliced using an electrostatic septum: by properly defining a closed orbit perturbation and by setting the horizontal tune equal to $Q_H = 6.25$ the beam is extracted from the PS over five consecutive turns. A continuous ribbon four-turn long is extracted first, while the remaining central core is extracted last thus generating a proton spill five-turn long (see Refs. [1, 2] for more details). Such a multi-turn extraction might not be the best choice for the planned CERN Neutrino to Gran Sasso (CNGS) proton beam [3], especially in case of an intensity upgrade [4], due to the intrinsic losses (of the order of 15 – 20 % of the overall proton intensity) onto the electrostatic septum as well as the poor betatron matching of the resulting slices.

An alternative method was proposed [5, 6]. The beam is split in the transverse horizontal phase space by the combined effect of a slow tune variation and the presence of stable islands created by nonlinear elements: the beam is trapped inside stable islands, creating a number of beamlets corresponding to the order of the resonance used. For the specific CERN application the fourth-order resonance was studied [5]. Following the encouraging results, numerical simulations were performed also for the third-order resonance [6] showing the validity of the method even in that case.

Preliminary experimental results obtained during the 2002 run of the PS machine allowed observing the trapping process into stable islands of phase space in real machines [7].

In this paper the latest results of numerical simulations are presented, showing how to perform multi-turn extraction for a small number of turns (2 – 6) using adiabatic trapping inside a properly chosen resonance.

NUMERICAL MODEL

By assuming that the nonlinear magnets are located at the same place in the ring, that they are represented in the single-kick approximation [9], and that the vertical motion can be neglected, the one-turn transfer map can be expressed as $\hat{X}_{n+1} = M_n(\hat{X}_n)$:

$$\begin{pmatrix} \hat{X}_{n+1} \\ \hat{X}'_{n+1} \end{pmatrix} = R(2\pi\nu_n) \begin{pmatrix} \hat{X}_n \\ \hat{X}'_n + \kappa \hat{X}_n^3 \end{pmatrix}, \quad (1)$$

where (\hat{X}, \hat{X}') are obtained from the Courant-Snyder coordinates [8] (\hat{x}, \hat{x}') by means of the non-symplectic transformations [9]

$$(\hat{X}, \hat{X}') = \frac{K_2 \beta_H^{3/2}}{2} (\hat{x}, \hat{x}') \quad K_l = \frac{L}{B_0 \rho} \frac{\partial^l B_y}{\partial x^l}, \quad (2)$$

K_2 (K_3) being the integrated sextupole (octupole) strength, L the length of the nonlinear element, B_y the vertical component of the magnetic field, $B_0 \rho$ the magnetic rigidity, and β_H the value of the horizontal beta-function at the location of the nonlinear elements. $R(2\pi\nu_n)$ is a 2×2 rotation matrix of angle ν_n , the fractional part of Q_H , and κ is expressed as

$$\kappa = \frac{2}{3} \frac{K_3}{\beta_H K_2^2}. \quad (3)$$

RESULTS OF NUMERICAL SIMULATIONS

Two-Turn Extraction

The case of a two-turn extraction is considered first, as it deserves special consideration. In fact, the map (1) does not possess any stable islands related to a resonance of order two (more details on this point can be found in Ref. [10]). To overcome this difficulty, a solution consists in assuming that the sextupoles and octupoles are not placed in the same location in the ring. In the numerical simulations they have been located $\pi/2$ apart in betatron phase advance. Figure 1 reports the tune as a function of turn number. The four points labelled with letters refer to the tune values at which the beam distribution is shown in Fig. 2. The adiabatic capture inside the two stable islands is clearly visible. A small fraction of particles remains near the origin of phase space,

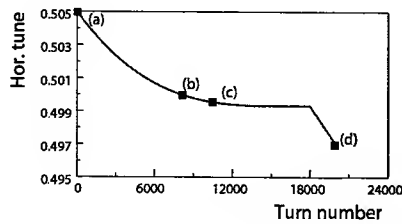


Figure 1: Evolution of the tune for a two-turn extraction.

while the majority of them migrates to the islands as the tune is swept through the half-integer resonance. Once the two beamlets are created, it is possible to move the islands towards higher-amplitudes, hence increasing the beamlets separation so to prepare for extraction.

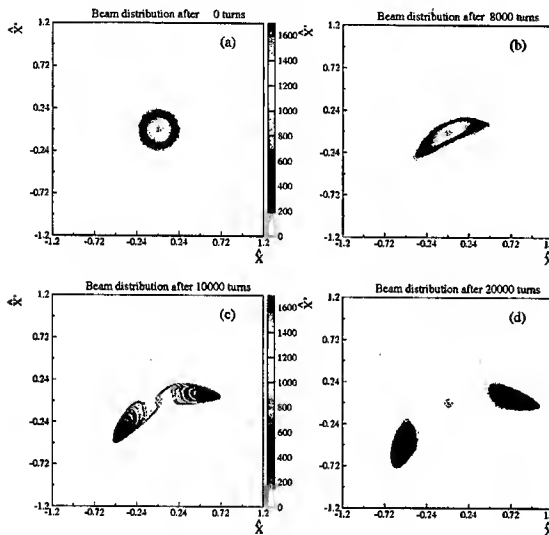


Figure 2: Beam distribution during the trapping process with two islands (8.1×10^5 initial condition). The initial distribution is a Gaussian centred on zero, with a standard deviation $\sigma = 0.11$. Only a few particles are left near the origin of phase space.

Three-Turn Extraction

In this case the model (1) is used in the numerical simulations without any modification. The time-evolution of the linear tune is presented in Fig. 3, while the evolution of the beam distribution is shown in Fig. 4. The fact that

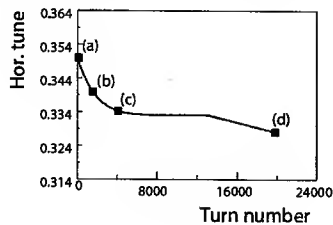


Figure 3: Evolution of the tune for a three-turn extraction. the resonance is intrinsically unstable makes it possible to

deplete almost perfectly the region near the origin of phase space, thus generating three beamlets as a final result of the capture process.

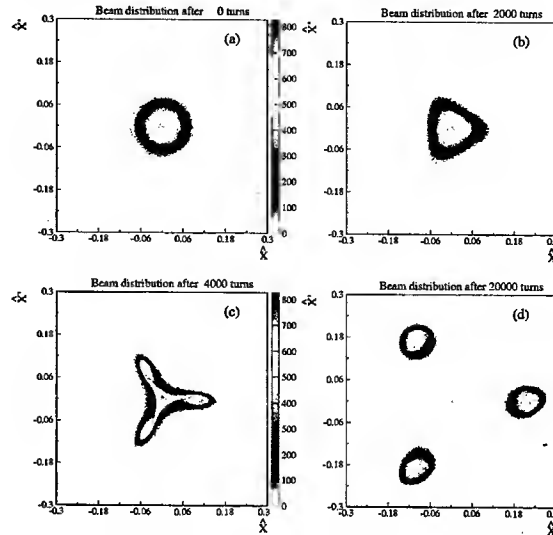


Figure 4: Beam distribution during the trapping process with three islands (8.1×10^5 initial conditions). The initial distribution is a Gaussian centred on zero, with standard deviation $\sigma = 0.04$. Even in this case very few particles are left in the central part of phase space.

Five-Turn Extraction

The fourth-order resonance is the one used in the original proposal [5] for a novel multi-turn extraction to replace the present CT extraction mode. As the fourth-order resonance is stable for the system (1), the beam will be split into five beamlets. The evolution of the beam distribution is plotted

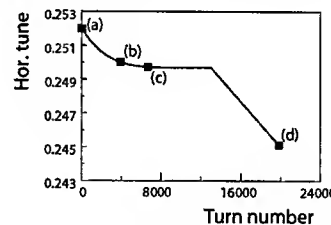


Figure 5: Evolution of the tune for a five-turn extraction. in Fig. 6. The four outermost beamlets are created by adiabatic trapping inside the stable islands, while the fifth one is generated by those particles left unperturbed near the origin of phase space. This fact has deep implications on the properties of the beamlets. In fact, for the previous multi-turn extraction processes (two- and three-turn) the various beamlets had the same number of particles trapped inside as they represent a unique ribbon of length two or three times the machine circumference. However, when the central part of phase space is filled at the end of the capture process, the beamlets need not be equally populated, unless a dedicated optimisation of the free parameters is performed.

Such an optimisation concerns mainly the sigma of the initial beam distribution, the nonlinear elements strength, and the properties of the tune-variation.

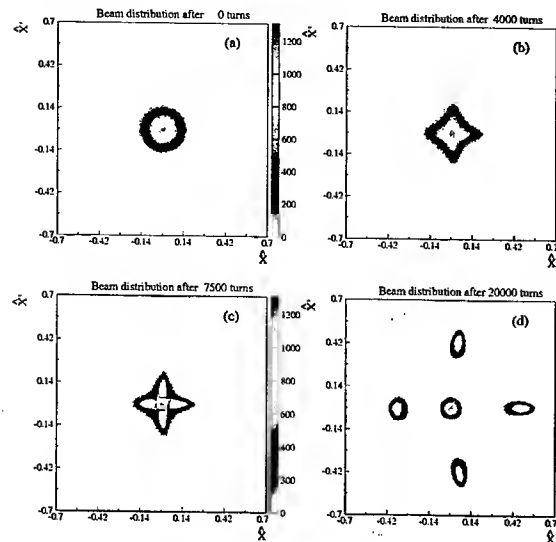


Figure 6: Beam distribution during the trapping process with four islands (8.1×10^5 initial conditions). The initial distribution is a Gaussian centred on zero, with standard deviation $\sigma = 0.073$.

Six-Turn Extraction

By using even higher-order resonances it is possible to increase further the length of the extracted spill. Here, the case of a resonance of order five is shown in Figs. 7 and 8. However, it is clear that there are intrinsic limitations on the resonance order. In fact, the higher the order, the smaller will be the islands, thus enhancing the difference between the first turns and the last one, represented by the particles left around the origin in phase space at the end of the capture process. Furthermore, it will be more and more difficult to create enough free space between the beamlets to accommodate the blade of an extraction septum.

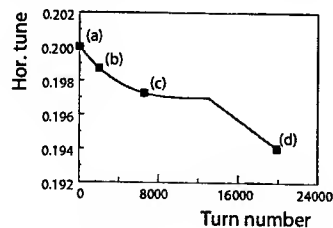


Figure 7: Evolution of the tune for a six-turn extraction.

CONCLUSIONS

In this paper various schemes for multi-turn extraction based on adiabatic capture of charged particles in stable islands of phase space were presented. By choosing the appropriate resonance, two-, three-, five-, and six-turn extraction have been computed. In all the cases shown here, par-

ticles can be trapped inside islands without any loss. Furthermore, it is possible to move the beamlets by acting on the tune so to increase their separation, which is the necessary condition to allow the actual beam extraction to take place. Further studies are in progress to quantify a number of issues such as the adiabaticity of the process and the dependence of the extracted beam parameters on the strength of the nonlinear elements.

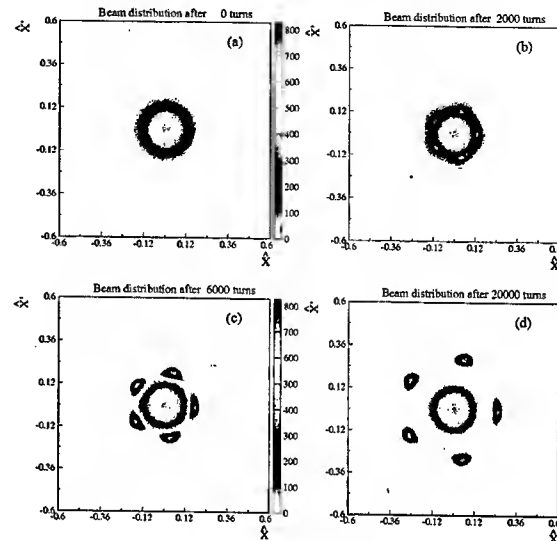


Figure 8: Beam distribution during the trapping process with five islands (8.1×10^5 initial conditions). The initial distribution is a Gaussian centred on zero, with standard deviation $\sigma = 0.08$.

REFERENCES

- [1] C. Bovet et al., in *1973 Particle Accelerator Conference*, edited by D. W. Dupen (IEEE, New York, 1973) p. 438.
- [2] R. Capii, M. Giovannozzi, "Computation of Betatron Mismatch and Emittance Blow-up for Multi-Turn Extraction", *CERN PS (AE) 2002-083* (2002).
- [3] K. Elsener (Ed.) et al., "The CERN Neutrino Beam to Gran Sasso (Conceptual Technical Design)", *CERN 98-02* (1998).
- [4] R. Capii (Ed.) et al., "Increasing proton intensity of PS and SPS", *CERN-PS (AE) 2001-041* (2001).
- [5] R. Capii, M. Giovannozzi, *Phys. Rev. Lett.* **88**, (2002) 104801.
- [6] R. Capii, M. Giovannozzi, in *Eighth Particle European Accelerator Conference*, edited by J. Poole and C. Petit-Jean-Genaz (Institute of Physics, UK London, 2002) p. 1250.
- [7] R. Capii et al., "Adiabatic Beam Trapping in Stable Islands of Transverse Phase Space: Measurement Results at CERN Proton Synchrotron", these proceedings.
- [8] E. Courant and H. Snyder, *Ann. Phys.* **3**, (1958) p. 1.
- [9] A. Bazzani et al., *CERN 94-02* (1994).
- [10] R. Capii, M. Giovannozzi, "Multi-turn Extraction and Injection by Means of Adiabatic Capture in Stable Islands of Phase Space", in preparation.

OPTICS STUDIES FOR THE CERN PROTON SYNCHROTRON: LINEAR AND NONLINEAR MODELLING USING BEAM BASED MEASUREMENTS

R. Cappi, M. Giovannozzi, M. Martini, E. Métral, G. Métral, R. Steerenberg, CERN
A.-S. Müller, ISS, Forschungszentrum Karlsruhe, Germany

Abstract

The CERN Proton Synchrotron machine is built using combined function magnets. The control of the linear tune as well as the chromaticity in both planes is achieved by means of special coils added to the main magnets, namely two pole-face-windings and one figure-of-eight loop. As a result, the overall magnetic field configuration is rather complex not to mention the saturation effects induced at top-energy. For these reasons a linear model of the PS main magnet does not provide sufficient precision to model particle dynamics. On the other hand, a sophisticated optical model is the key element for the foreseen intensity upgrade and, in particular, for the novel extraction mode based on adiabatic capture of beam particles inside stable islands in transverse phase space. A solution was found by performing accurate measurement of the nonlinear tune as a function of both amplitude and momentum offset so to extract both linear and nonlinear properties of the lattice. In this paper the measurement results are presented and the derived optical model is discussed in detail.

PS LATTICE AND MAIN MAGNET

The PS lattice consists of ten super-periods each made of ten combined function magnets 4.4 m long, interlaced with eight 1.6 m and two 3.0 m drift spaces [1]. Every magnet is composed of two half-units, each made of five blocks with small gaps in between, with gradients of opposite sign ($|G| = 5.2 \text{ T/m}$), separated by a central junction. The control of the tunes and chromaticities is obtained by means of the three currents of the pole-face winding and figure-of-eight loop devices located on the magnet poles. As an example, the layout of a PS magnet unit in the extraction region is shown in Fig. 1. The latest PS magnetic field measurements using Hall probes were undertaken in 1992 [2] for different settings of the currents in the main coil, pole-face and figure-of-eight loop windings. The data of the vertical field, including measurements of the central field, the end and lateral stray fields, as well as the field in the junction between the two half-units, produced a discrete 2D field map [2].

The field measurements were carried out in a Cartesian co-ordinate frame (see Fig. 1 for its definition). In this reference system a regular mesh is defined and for each point in the mesh the value of B_y was measured in the median plane. The step size is 20 mm along the longitudinal z -axis and 10 mm along the radial x -axis. The mesh extends

from -2.55 m to 2.73 m and from -70 mm to 310 mm in the longitudinal and radial directions respectively. As an example, the fitted 2D field map for the 26 GeV/c working point is shown in Fig. 2 (see Ref. [3] for more details). When the effect of the additional coils is taken into account,

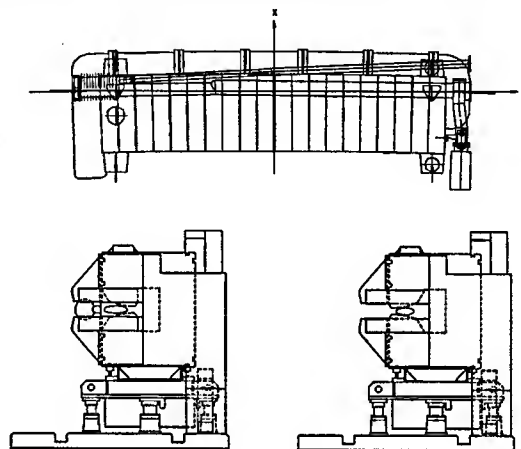


Figure 1: Layout of the PS magnet unit 16 (upper part). The vacuum pipes for both the circulating beam and the extracted one are visible. The cross sections of the entry face (open gap) and exit face (closed gap) are shown on the lower left and lower right respectively.

nonlinear field components have to be considered. Multipolar components may be derived from the measured field map to model the machine lattice. However, they hold only for the specific set of currents in the pole-face and figure-of-eight loop windings. Unfortunately, these values change according to the machine setting, thus a magnetic measurement is required for each new working point, which is not possible in practise.

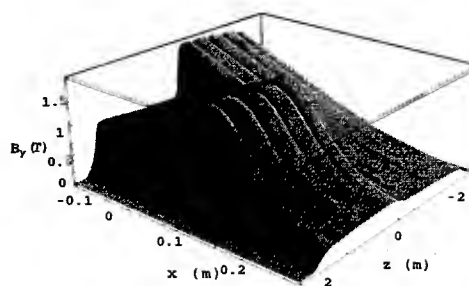


Figure 2: Polynomial field map fitted to the measured field values $B_y = B_y(x, z, 0)$ for the 26 GeV/c working point.

MEASUREMENT RESULTS

Measurement Technique

The technique used resembles that one used to derive the nonlinear field components using beam based measurements for the Super Proton Synchrotron (SPS) [4]. The tunes, both horizontal and vertical, are measured as functions of the momentum offset generated by a proper rf-perturbation. A polynomial fit of the measured curve is performed to extract numerical information on the different orders. Then, virtual nonlinear elements, represented by thin lens elements, are inserted in the machine lattice model and they are used as fit parameters to reproduce the fitted polynomial. This procedure is applied order-by-order, i.e. the quadrupole components are used to reproduce the constant term in the polynomial, the sextupole components the linear term and so on, up to the dodecapolar components. Due to the structure of the PS main magnet, the virtual nonlinear elements are located at both dipole ends, thus giving two free parameters per each element type. The computations on the PS model were performed by using the MAD program [5].

Injection Plateau - 2.14 GeV/c

The first case considered here, refers to the modelling of the injection flat-bottom. Although the tunes at injection are normally controlled by means of the low-energy quadrupoles, in recent years it was tried out to use the additional coils, i.e. pole-face windings and figure-of-eight loop, to improve the machine control, also including the chromaticity. Of course, this might lead to introducing unwanted nonlinear effects, particularly harmful for a high-intensity (hence large emittance) proton beam at injection. The measurement results shown in Fig. 3 show clearly a third-order effect on top of the expected linear behaviour. The coefficients of the best fitting polynomial are:

$$Q_x(\delta) = -3.92 \times 10^4 \delta^3 - 96.94 \delta^2 - 4.49 \delta + 6.179$$

$$Q_y(\delta) = -2.64 \times 10^4 \delta^3 - 146.26 \delta^2 - 4.62 \delta + 6.222$$

In the model, nonlinear elements have been added up to

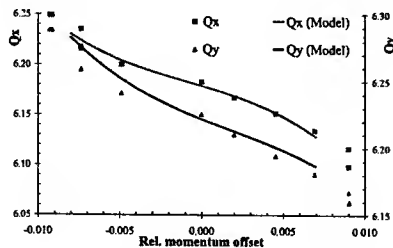


Figure 3: Tune vs. momentum offset: experimental data (markers) are compared with curves obtained using the lattice model with the fitted virtual thin lens multipoles.

decapoles only, as the agreement with measurement results is already quite good (see Fig. 3).

Intermediate Plateau - 14 GeV/c

High-intensity proton beams are normally extracted towards the SPS at 14 GeV/c. A detailed model of the PS machine for such energy is crucial for the proposed multi-turn extraction based on adiabatic capture inside stable islands of phase space using nonlinear magnets [6, 7] and also for the experimental measurements of this novel technique [8]. To this end, two main configurations were considered, i.e. standard working point (ST) and a special setting (SP) with reduced horizontal chromaticity (see Ref. [8] for more details). For each configuration, two sets of measurements were performed, namely with and without the sextupoles and octupoles necessary to create the stable islands for capturing and splitting the beam in the transverse phase space. Figure 4 refers to the normal working point and the results of the fitted PS model are directly compared with the measurements. A rather good agreement is visible for the horizontal tune curve, while a slightly worse situation (particularly for negative values of momentum offset) is visible for the vertical tune curve. The same considerations hold when the strong nonlinear elements are excited. It is worthwhile stressing that no fitting procedure was applied in this second case, i.e. the virtual kicks obtained without dedicated sextupoles and octupoles were kept unchanged when the special nonlinear elements were excited in the PS model. A somewhat different situation occurs

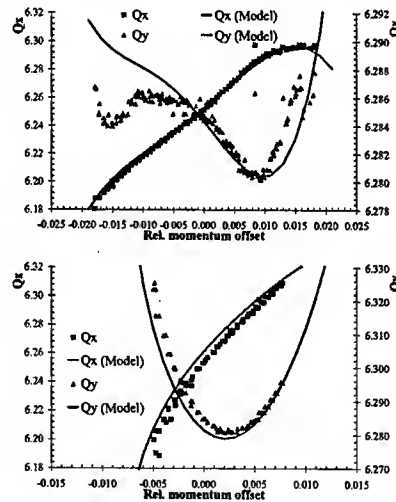


Figure 4: Tune vs. momentum offset: experimental data (markers) and fitted model (curves) without (upper) and with (lower) nonlinear elements used for the adiabatic capture tests. The standard working point is used.

when a special working point is used (see Fig. 5). The fitted model agrees quite well to measurement results without the dedicated nonlinear elements. However, the same virtual kicks do not give good enough results when comparing with measurements performed with dedicated sextupoles and octupoles. Two considerations might explain this observation. Firstly, the fitting procedure produces only an *effective model*: the details are not exactly reproduced, but the average behaviour is well described. Secondly, the non-

linear effects in the dynamics break the superposition principle. Therefore, in some cases, the final result of combining a good fitted model (computed without dedicated nonlinear elements) with the effect of dedicated sextupoles and octupoles might not be in good agreement with experimental results. The fitted polynomials for the two configurations, including dedicated sextupoles and octupoles are

$$Q_x^{ST}(\delta) = -1.96 \times 10^7 \delta^4 + 1.97 \times 10^5 \delta^3 - 362.15 \delta^2 - 6.79 \delta + 6.255$$

$$Q_y^{ST}(\delta) = 3.60 \times 10^6 \delta - 4.30 \times 10^4 \delta^3 + 688.01 \delta^2 - 2.88 \delta + 6.285$$

$$Q_x^{SP}(\delta) = -1.40 \times 10^4 \delta^3 - 249.90 \delta^2 + 1.26 \delta + 6.243$$

$$Q_y^{SP}(\delta) = 1.76 \times 10^4 \delta^3 + 599.03 \delta^2 + 5.43 \delta + 6.282$$

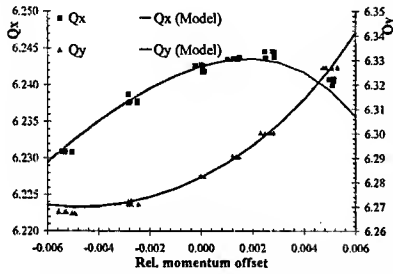


Figure 5: Tune vs. momentum offset: experimental data (markers) and fitted model (curves) with nonlinear elements used for the adiabatic capture tests. The special working point with low horizontal chromaticity is used.

Top Plateau - 26 GeV/c

Finally, the model of the PS machine at top energy (26 GeV/c) is considered. This is particularly interesting as the main PS magnet shows signs of saturation effects at high-energy that could enhance the nonlinear components introduced by the special coils used to control the working point. The measurement results are shown in Fig. 6, where the good agreement with the fitted model is clearly visible. The best fit polynomials for the measured tune curves are:

$$Q_x(\delta) = 1.72 \times 10^6 \delta^4 - 1.97 \times 10^4 \delta^3 - 317.10 \delta^2 + 2.27 \delta + 6.239$$

$$Q_y(\delta) = 4.57 \times 10^5 \delta^4 + 9.03 \times 10^2 \delta^3 - 63.67 \delta^2 + 0.27 \delta + 6.266$$

In this case magnetic field components up to dodecapole have been used in the model. The summary of the values of the fitted multipolar components is presented in Table 1, the expansion of the magnetic field in multipoles being:

$$B_y + iB_x = B_0 \rho_0 \sum_{n=1}^M [K_n + iJ_n] \frac{(x + iy)^n}{n!} - B_0$$

$$K_n = \ell \frac{1}{B_0 \rho_0} \frac{\partial^n B_y}{\partial x^n}, \quad J_n = \ell \frac{1}{B_0 \rho_0} \frac{\partial^n B_x}{\partial x^n},$$

where ρ_0 is the nominal bending radius and ℓ the length of the magnetic element.

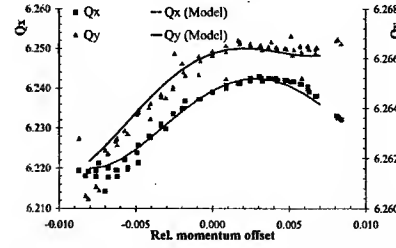


Figure 6: Tune vs. momentum offset: experimental data (markers) are compared with curves obtained using the lattice model with the fitted virtual thin lens multipoles.

GeV/c		K_1 (10^{-4})	K_2	K_3	K_4	K_5
2.14	F	-10.3	0.013	0.026	-105.53	—
	D	10.2	-0.0014	-0.17	150.79	—
14	F	-0.96	0.04	0.07	-1.79	-478.81
(ST)	D	1.29	-0.03	-0.06	0.11	462.27
14	F	-2.51	0.06	0.02	1.05	—
(SP)	D	2.21	-0.05	0.01	-2.04	—
26	F	-3.29	0.04	-0.63	-36.21	5013.04
	D	3.50	-0.03	0.69	39.89	-7239.44

Table 1: Summary of virtual kick values in units of m^{-n} (F, D stands for the half-unit type of the PS magnet).

CONCLUSIONS AND OUTLOOK

A model of the PS machine derived from measurements of the tune as a function of the momentum offset was successfully computed for various situations, i.e. injection energy, intermediate extraction energy and top-energy, including different configurations of dedicated nonlinear elements. The outcome of these studies will be beneficial for many other topics under investigation, such as the nonlinear resonance benchmarking experiment [9], the measurements [8] as well as the simulations concerning the adiabatic trapping inside stable islands of phase space [7].

REFERENCES

- [1] T. Risselada, "Beam Optics Data for the PS Ring and its Transfer Lines", *CERN PS (PA) Note 92-04* (1992).
- [2] D. Cornuet, Z. Sharifullin, "Magnetic Measurements on the PS Magnet Unit U17 with Hall Probes", *CERN AT (MA) Note 92-23* (1992).
- [3] D. Manglunki, M. Martini, "Beam Optics Modelling at CPS Extraction Throughout a non-linear Fringe field", *CERN PS (CA) 97-018* (1997).
- [4] G. Arduini et al., these proceedings.
- [5] H. Grote, F. C. Iselin, "The MAD Program, User's Reference Manual", *CERN SL (AP) 90-13* (1990).
- [6] R. Cappi, M. Giovannozzi, *Phys. Rev. Lett.* **88**, (2002) 104801.
- [7] R. Cappi, M. Giovannozzi, these proceedings.
- [8] R. Cappi et al., these proceedings.
- [9] I. Hofmann et al., these proceedings.

MEASUREMENTS OF TRANSVERSE SPACE-CHARGE EFFECTS IN THE CERN PROTON SYNCHROTRON

M. Giovannozzi, M. Martini, E. Métral, G. Métral, R. Steerenberg, CERN, Geneva, Switzerland

Abstract

Several beam dynamics codes are used in the design of the next generation of high beam power accelerators. They are all capable of simulating the full six-dimensional motion through a machine lattice in the presence of strong space-charge effect and beam-to-wall interaction. A key issue is the validation of these codes. This is usually accomplished by comparing simulation results against available theories, and more importantly, against experimental observations. To this aim, a number of well-defined test cases, obtained by accurate measurements made in existing machines, are of high interest. This paper reports and discusses precise measurements of transverse emittance blow-up due to space-charge induced crossing of the integer or half-integer stop band.

1 INTRODUCTION

Space-charge tune shifts can drive the beam onto linear and/or non-linear resonances generating transverse emittance blow-up and sometimes subsequent beam loss. Depending on how the space-charge tune spread overlaps the resonance, i.e. whether the centre or the tail of the particles distribution is in the stop-band, the beam behaviour will be completely different. The first case leads to a loss-free (if the mechanical aperture is sufficiently large) core-emittance blow-up, where the distribution is almost conserved. The second case leads to diffusion of the tail particles into a halo of increasing size, which may lead to particle losses due to the reduced dynamic aperture close to the resonance, extracting the halo particles [1].

Benchmarking experiments, which have been carried out in the CERN Proton Synchrotron (PS) for the transverse emittance blow-up due to space-charge induced crossing of the integer or half-integer stop band, are presented in this paper.

2 MEASUREMENTS

Three cases have been examined in detail, recording the evolution of the transverse beam profiles and emittances. All the measurements have been performed with no measurable loss. The study has been made on the long 1.2 s injection flat-bottom at 1.4 GeV kinetic energy,

using a single-bunch beam of 1.7×10^{12} protons, with nominal horizontal and vertical rms normalised emittances of $3.3 \mu\text{m}$ and $2.6 \mu\text{m}$ respectively, and varying both the bunch length and the working point. A small amount of linear coupling due to skew quadrupoles

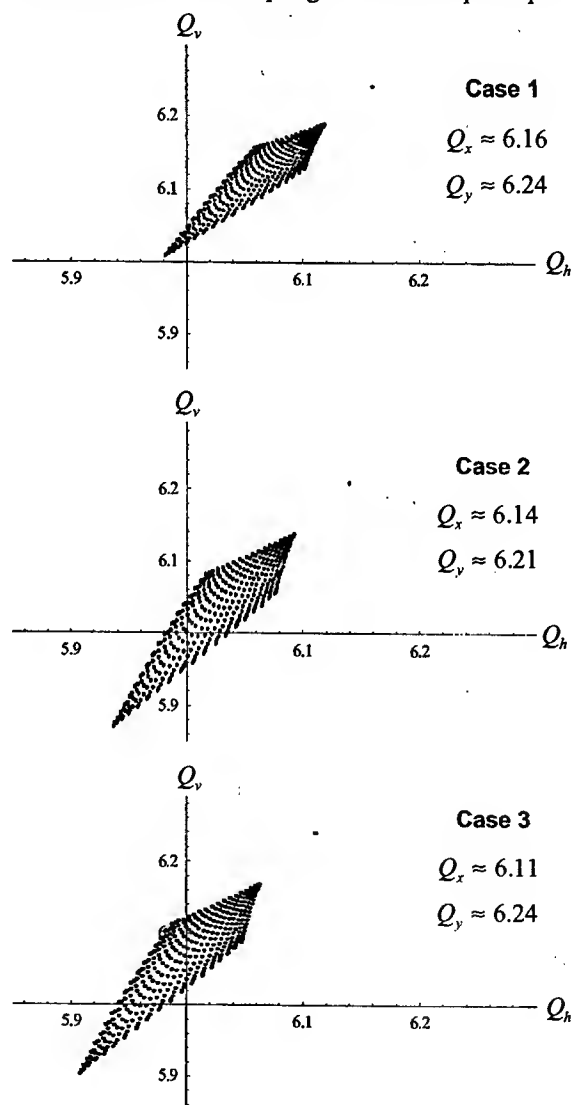


Figure 1: Plots of the computed necktie-shaped area in the tune diagram for the three cases of space-charge tune spreads considered. Case 1: full (4σ) bunch length of 180 ns, and relative momentum spread (2σ) of 2.15×10^{-3} . Cases 2 and 3: full (4σ) bunch length of 106 ns, and relative momentum spread (2σ) of 4×10^{-3} .

was introduced to damp a horizontal head-tail instability [2]. The skew quadrupole current was -0.33 A, which corresponds to a closest tune approach of 0.043 [2]. The three cases of space-charge tune spreads are represented in Fig. 1.

Note that the space-charge tune spreads of Fig. 1 have been computed using the Keil formula, which considers a bi-Gaussian in the horizontal and vertical plane [3]. A gap without particles between the low-intensity working point and the incoherent working points is observed as the third (longitudinal) distribution is not taken into account (see Ref. [4] where a tri-Gaussian in the horizontal, vertical and longitudinal plane is considered).

2.1 First case

The first case has been chosen to be close to the emittance blow-up limit. Figure 2 shows the evolution of the horizontal and vertical rms normalised emittances (in μm) vs. time (in ms). The horizontal axis is labelled "C Time", as all the processes in the machine are referenced with respect to a certain timing C0. In this notation, the injection is at C170. The vertical scale on the right-hand side of the picture is used for three parameters, the RF voltage (in kV), and the fractional part of the horizontal and vertical tunes ($\times 10^3$). In this first case, the RF voltage is kept constant at 25 kV, as well as the horizontal and vertical tunes, which are equal to 6.16 and 6.24 respectively. Three data have been recorded for each measurement point. It is seen in Fig.2 that there is no emittance blow-up in this case.

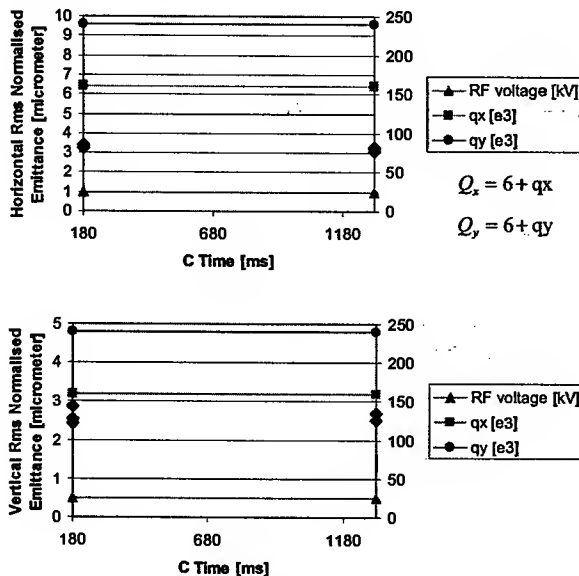


Figure 2: Horizontal and vertical rms normalised emittance vs. time, from C180 (i.e. 10 ms after injection, which is at C170) to C1300 (i.e. 1120 ms after).

The transverse beam profiles with a Gaussian fit are represented in Fig. 3. It can be seen that there is no core-emittance blow-up and that the particle distribution is conserved.

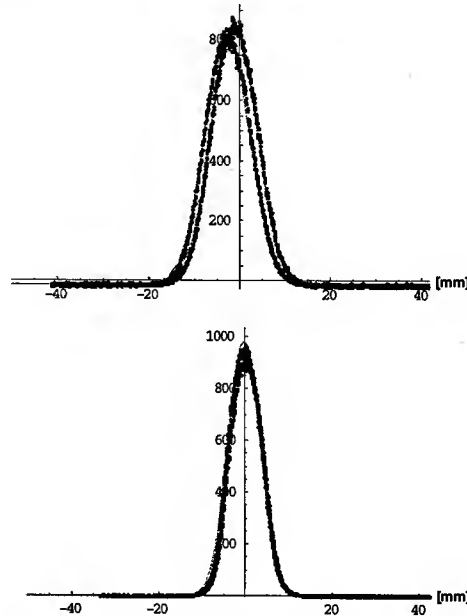


Figure 3: Initial (C180) and final (C1300) horizontal and vertical beam profiles with a Gaussian fit.

2.2 Second case

In the second case, the initial (at C180) parameters are the same as in the first case. Then, steps in the RF

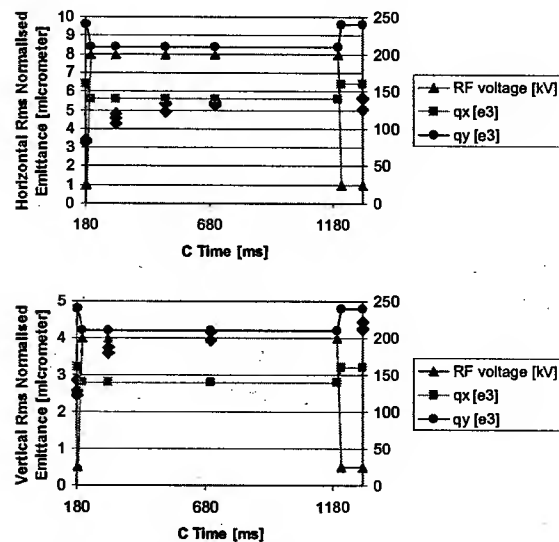


Figure 4: Horizontal and vertical rms normalised emittance vs. time, from C180 to C1300.

voltage and the transverse tunes are programmed between C185 and C200, and C1200 and C1215 (the steps are

performed at the same time for the three parameters). The results for the transverse emittance blow-up and beam profiles are summarized in Figs. 4 and 5 respectively.

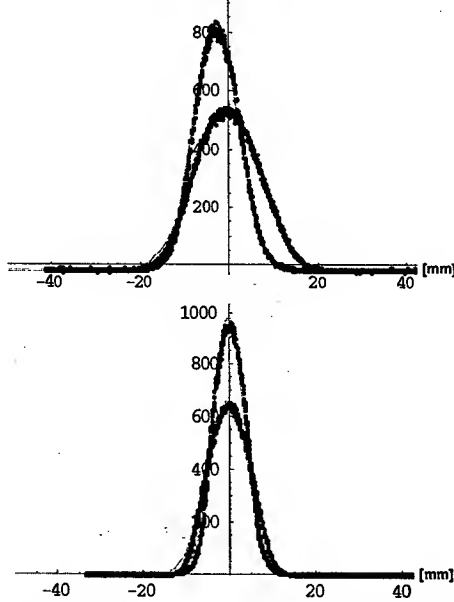


Figure 5: Initial (C180) and final (C1300) horizontal and vertical beam profiles with a Gaussian fit.

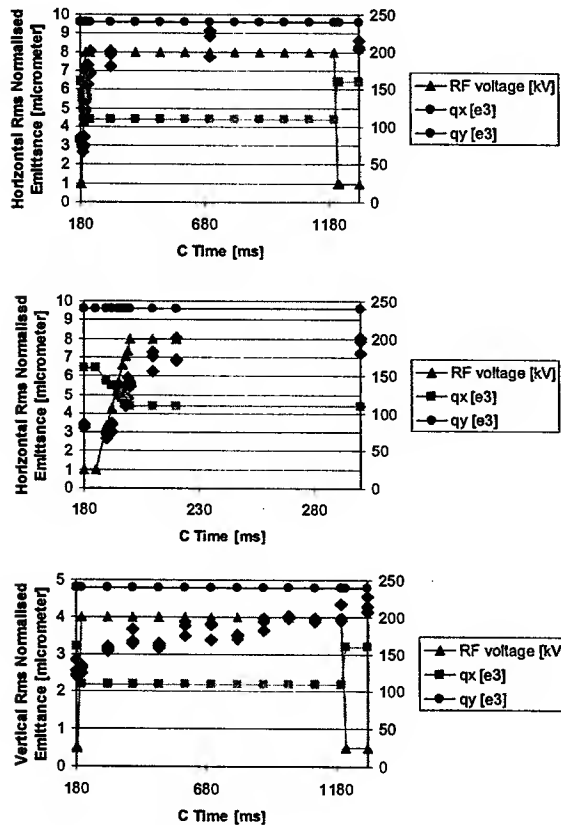


Figure 6: Horizontal and vertical rms normalised emittance vs. time.

2.3 Third case

The results for the third case are summarized in Figs. 6 and 7.

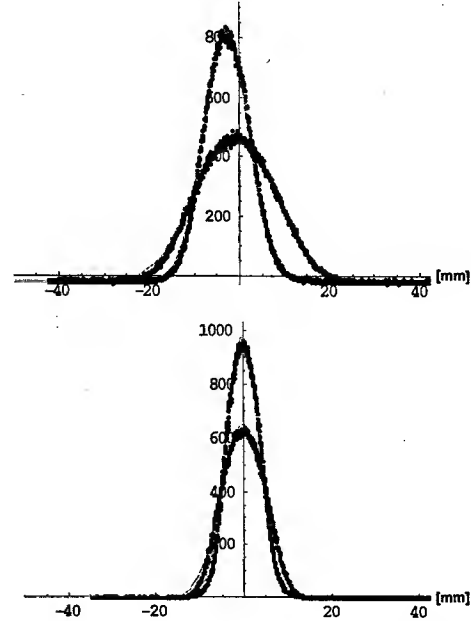


Figure 7: Initial (C180) and final (C1300) horizontal and vertical beam profiles with a Gaussian fit.

Flat bunches with reduced peak line density have also been looked at, expecting a higher transverse space-charge limit. Unfortunately, no measurable improvement has been observed. This may be due to the fact that the increase of bunching factor was less significant than what has been already achieved ($\sim 10\%$ during these measurements, compared to $\sim 20\text{-}30\%$ during the 2001 run). Furthermore, the bunching factor was already very good due to the longitudinal blow-up. These measurements have to be re-done.

3 CONCLUSION

Measurements of transverse emittance blow-up due to space-charge induced crossing of the integer or half-integer stop band, have been performed in the CERN PS. These results could be used to benchmark the beam dynamics codes, which are used in the design of the next generation of high beam power accelerators.

REFERENCES

- [1] I. Hofmann et al., "Nonlinear Resonance Benchmarking Experiment at the CERN Proton Synchrotron", these proceedings.
- [2] R. Cappi, R. Garoby and E. Métral, "Collective Effects in the CERN-PS beam for LHC", CERN/PS 99-049 (CA), 1999.
- [3] E. Keil, "Non-Linear Space Charge Effects I", CERN/ISR-TH/72-7, 1972.
- [4] M. Martini, "An Exact Expression for the Momentum Dependence of the Space Charge Tune Shift in a Gaussian Bunch", CERN-PS-93-23-PA, 1993.

BEAM-BASED BPM ALIGNMENT

R. Talman and N. Malitsky, Collider Accelerator Development Department
Spallation Neutron Project, Brookhaven National Laboratory

Abstract

An operational, beam-based, null-measurement, control room procedure designed to steer the closed orbit through the effective (no steer) center of every quadrupole is described. Performance of the procedure is simulated using UAL (Unified Accelerator Libraries). Matching SNS hardware availability, quadrupole strengths are assumed to be trimmable, but only in families, not individually. The accuracy of the procedure is unaffected by geometric and/or electrical misalignment of BPM's (beam position monitors) but calibration of their misalignments is a byproduct of the procedure. Some of the many possible failure mechanisms have been modeled, and have been found not to invalidate the procedure.

DEFINITION OF THE TASK

We are concerned with steering the closed orbit through the centers of all quadrupoles. Magnet imperfection may cause significant displacement of the effective quadrupole center (position of no particle deflection) from its geometric center and electronic imperfection may cause significant displacement of the effective BPM center (position the data acquisition system reports to be zero) relative to *its* center.

In this report, to avoid ambiguity, when "center" is used, be it quad center or BPM center, the meaning will always be *effective* center that is meant. From the control room the absence of steering is the determinant of beam passage through effective quadrupole center and output of zero from the BPM is the determinant of beam passage through the effective center of the BPM. The present paper describes a control room, beam-based, procedure that is independent of the installed BPM alignment and can therefore corroborate, or even supercede, the installation accuracy.

An ideal arrangement would supply every quadrupole with a full "detector/adjuster package" consisting of trim winding, horizontal and vertical kickers, and horizontal and vertical BPM. There is a natural "null measurement" operational procedure that can be performed using a quadrupole (call it quad i , and let its inverse focal length be q_i) endowed with such a package. Taking the quad effective center as origin, let the closed orbit position be (x_i, y_i) . The effect of the quadrupole is to cause angular orbit deflections

$$\Delta x'_i = -q_i x_i, \quad \Delta y'_i = q_i y_i. \quad (1)$$

The effect of making fractional change f (absolute change $f q_i$) in the quadrupole's strength is to introduce a further kink ($\delta \Delta x'_i = -f q_i x_i$, $\delta \Delta y'_i = f q_i y_i$) that changes the closed orbit. This changes not only local position (x_{di}, y_{di}) but also the complete set of closed orbit measurements at

all N_d BPM locations, (x_{dj}, y_{dj}) , $j = 1, 2, \dots, N_d$. A simple operational procedure is then to adjust the local kicker values to "null out" this closed orbit change; the kicker strengths will be $\delta x'_i = -\delta \Delta x'_i$, $\delta y'_i = -\delta \Delta y'_i$. In principle the nulling could employ a single BPM (which need not be the i 'th) but a more robust (less subject to noise) procedure would be to average numerous BPM's. From the available data one obtains

$$x_i = \frac{\delta x'_i}{f q_i}, \quad y_i = -\frac{\delta y'_i}{f q_i}. \quad (2)$$

This information can be used to center the beam on the quad, or more practically, if there is a local BPM, to calibrate the BPM so that its electrical center coincides with the quad center, both horizontally and vertically. The BPM will then serve as a secondary, or transfer, standard. After all BPM's have been calibrated in this way they can be used for a grand smoothing that puts the beam through the centers of all quads. Even if a quad lacks a BPM the closed orbit can be adjusted to pass through the quad center, provided there is a local steering elements that can be used for the null measurement.

Unfortunately, in practice, all quadrupoles are not necessarily supplied with the full detector/adjuster package. In the case of SNS, though there are trim windings on all quadrupoles, the quadrupole trims are not individually powered. Rather the quadrupoles are grouped in families of 8 having trim windings powered from a single power supply. The purpose of this report is to generalize the null calibration procedure in this circumstance and to simulate its performance using UAL.

ORBIT SMOOTHING ALGORITHMS

It has to be assumed that there is a control program which uses N_d detectors (BPM's) and N_a adjusters to smooth the orbit, say horizontally, where "smooth" may mean that all measured offsets are zero. More commonly there is a redundantly generous distribution of BPM's so that $N_d > N_a$, so the "badness"

$$B(\delta x'_1, \delta x'_2, \dots, \delta x'_{N_d}) = \sum_{i_d=1}^{N_d} \frac{x_{i_d}^2}{\beta_{i_d}^{(x)}} \quad (3)$$

can be minimized but not be made to vanish. Here B is expressed as a function of the adjuster deflections $\delta x'_1, \delta x'_2, \dots, \delta x'_{N_a}$ since they are the quantities to be varied in order to minimize B . Mathematically this leads to the equations

$$\frac{\partial B}{\partial (\delta x'_{i_a})} = 0, \quad i_a = 1, 2, \dots, N_a. \quad (4)$$

In this report the UAL algorithm (TEAPOT module) that simulates orbit smoothing is called *hsteer* and the corresponding vertical algorithm is *vsteer*. Programs like this rely on the optical model of the lattice to calculate an "influence function" $T_{i_a}(i_d)$ which is the closed orbit displacement at detector i_d caused by unit deflection at adjuster location i_a . Starting from closed orbit displacements $x_{i_d}^{(0)}$, the effect of applying kicks $\delta x'_{i_a}$ is to produce displacements $x_{i_d}^{(x)}$ given by

$$\frac{x_{i_d}}{\sqrt{\beta_{i_d}^{(x)}}} = \frac{x_{i_d}^{(0)}}{\sqrt{\beta_{i_d}^{(x)}}} + \sum_{i_a=1}^{N_a} \delta x'_{i_a} T_{i_a}(i_d). \quad (5)$$

Letting $Q = (\delta x'_1, \delta x'_2, \dots, \delta x'_{N_a})^T$ be the (transpose of the) vector of unknowns and substituting Eq. 5 into Eq. 4 yields equations (in matrix form)

$$MQ = V, \quad (6)$$

where

$$M_{ab} = \sum_{i_d=1}^{N_d} T_a(i_d) T_b(i_d), \quad V_a = - \sum_{i_d=1}^{N_d} \frac{x_{i_d}^{(0)}}{\sqrt{\beta_{i_d}^{(x)}}} T_a(i_d). \quad (7)$$

Solving Eq. 6 yields kicker values which minimize the badness.

BPM ALIGNMENT AT SNS WITH QUADRUPOLES GANGED IN FAMILIES

Consider, for example, the family consisting of the $N_q (=8)$ quadrupoles labeled QFH in the SNS lattice shown in Fig. 1 for which the MAD lattice description file is *BmBasedBPMAAlign.mad*. This file differs only from file *ff_sext_latnat.mad* by name changes made for the present simulation. Both files are available at <http://www.ual.bnl.gov>, along with a detailed description of the simulation. The task is to measure all N_d horizontal misalignments and all N_d vertical misalignments. Of course there are also many other quadrupoles, grouped in other families. The procedure described here is immediately applicable to all such families. It is not even required that all nominal quadrupole strengths in the same family be equal or that the fractional trim strengths be equal. But, for this report, these simplifications have been made.

The strategy to be followed is much the same as with a single quadrupole trim. An intentional systematic change of the strengths of the quadrupoles in a single family causes the closed orbit to shift because of the (random and unknown) displacements of the quadrupoles in the family. Using an orbit smoothing algorithm the associated kicker magnets can be adjusted to undo this change. Then the individual quad misalignments can be inferred from the kicker strengths and the nominal quadrupole strengths using Eq. 2. At that time all BPM offsets would be recorded to enable subsequent use of the BPM's as "secondary standards".

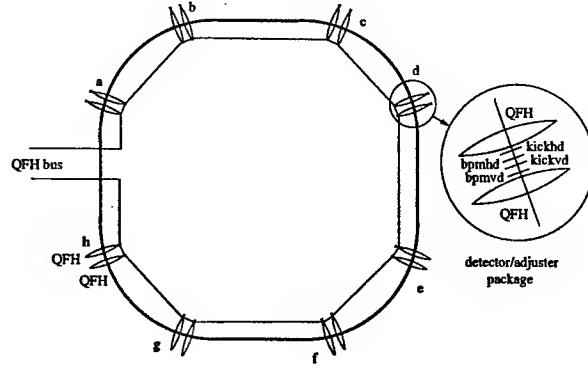


Figure 1: SNS lattice showing the particular family of quadrupoles used in the paper to illustrate beam-based quadrupole alignment when quadrupoles cannot be trimmed individually. The QFH elements are half-quads. In real life the BPM's and kickers would be somewhat displaced from the actual full quads.

Concentrating first on the horizontal measurement, it is essential now to restrict the adjusters being used to precisely those associated with the quadrupoles in the QFH family. Therefore $N_a = N_q$. For noise suppression it would be appropriate to use $N_d \gg N_q$ but, for simplicity, we assume $N_d = N_q$. So from here on the term "perfectly smooth closed orbit" is equivalent to $B = 0$ where B is given by Eq. 3 with $N_d = N_q$. Because $N_a = N_d$, the number of Eqs 4 is equal to the number of unknowns. Therefore the equations have a unique solution. If the lattice were ideal (except for the misalignments being investigated) this would be the end of the story. But because of coupling and nonlinearity, when the calculated kicker values are installed the value of B is still found to differ from zero. This may necessitate proceeding by successive approximation.

In any case one eventually achieves the result $B = 0$, be it in simulation or in the control room. Repeating, for emphasis, what has already been implied, this only means that the orbit is perfect *as far as the QFH detectors are concerned*. Let us refer to this restricted closed orbit as the "QFH closed orbit". The orbit shown by all BPM's in the ring will not necessarily improve in the successive approximations described in the previous paragraph. In fact, our simulation shows that the closed orbit at points outside the QFH family frequently is made worse by a next approximation. Though disconcerting this is what is to be expected.

In the control room the QFH closed orbit *appears to be* perfectly smooth when all BPM outputs from the QFH family are zero. But this only means that the closed orbit has been adjusted to pass through the electrical centers of every QFH detector.

Next we apply the systematic fractional strength change f to all quadrupoles in the QFH family. This causes the QFH closed orbit to be no longer smooth. Applying *hsteer* and *vsteer* again yields the kicker strengths needed to re-smooth the orbit. Finally the misalignments

being sought are given by Eq. 2. This completes the determination of closed orbit displacement relative to quad centers at all quads in the family.

FUNDAMENTAL LIMITATIONS

As with all operational procedure, the BPM calibration can be compromised by world realities. Some BPM's may not function at all and electronic noise will cause fluctuation of the measured positions. These effects are perhaps the ones most likely to limit the practicality of the procedure being described here. For this procedure the absolute accuracy of BPM's is irrelevant, but it is important that their least count correspond to a very small distance—or rather that they be capable of stably and reproducibly recording very small beam position *changes*.

Another practical complication is that BPM's, though physically close to their associated quadrupoles, cannot be precisely superimposed. But, provided they are reasonably close and that signals are available from other nearby BPM's, values can be accurately interpolated to the precise quadrupole locations. Even if vertical quads are restricted to vertical focusing quad locations, and horizontal to horizontal (as is common) there are reliable interpolation procedures to produce the signals assumed in this report. Similarly, even though kickers are not precisely in their ideal locations, the kicker strengths can be appropriately adjusted.

There are other more fundamental effects that potentially limit the practicality of the proposed method. The effect of increasing a quadrupole strength is not just to cause a steering effect proportional to the quad offset. There are also changes in the lattice optics, both tunes and beta functions. At worst the change in quad strength could make the lattice unstable and, at a minimum, the changes in lattice optics will cause the closed orbit fitting programs to be somewhat inaccurate. Such a limitation is already present in the single quadrupole procedure. In the interest of increased signal to noise ratio one wishes to make the quad strength increment $f q_i$ as large as possible, but the need to limit lattice distortion forces one to compromise. Nonlinear elements present in the ring also limit the accuracy of the procedure. Nonlinear elements would not affect the one quadrupole, null measurement, but their presence reduces the accuracy of the closed orbit algorithms. All effects mentioned in this paragraph are subject to investigation using UAL or another simulation code. Our (very limited) investigations started with the guess that a one percent alteration of quad strengths ($f = 0.01$) would be satisfactory. At this level we find the algorithm to be essentially unaffected by changing the chromaticities from their natural (all chromaticity sextupoles off) values to being zero in both planes. Similarly the procedure is little affected by the inclusion or exclusion of magnet imperfections at anticipated levels.

The achievable accuracy can be estimated as follows. Let us concentrate on vertical orbit smoothing. If the lattice is taken to consist of nothing but 90 degree FODO cells and the tune is Q there will be $8Q$ quads altogether, each

with its local BPM. But of these only half are close to vertical quads where their accuracy is high and only about half of those are favorably located relative to a particular vertical steering that is being nulled. If the r.m.s. position error at a quad of strength q_i is σ_y , the r.m.s. deviation of the deflection to be nulled for trim factor f is $f q_i \sigma_y$. The downstream displacement caused by such a deflection is

$$\sigma_d \lesssim \beta_{typ} f q_i \sigma_y \quad (8)$$

For individually trimmed quads the $2Q$ "useful" detectors would improve the nulling precision by a factor $1/\sqrt{2Q}$. The effect of being forced to trim the N_q quads in a family will exact a loss of accuracy which will erode this factor to $1/\sqrt{2Q/N_q}$. Incorporating this estimate in Eq. 8, using the estimate $\beta_{typ} q_i \approx 1$ and solving for σ_y yields

$$\sigma_y \gtrsim \frac{\sigma_d}{f} \sqrt{\frac{N_q}{2Q}}, \quad (9)$$

as the estimated accuracy with which the closed orbit can be steered through the quadrupole center. Taking the square root factor as 1, the precision with which the orbit can be steered through the quad is approximately the BPM precision eroded by factor $1/f$. With f being of order 0.01 the steering accuracy is 100 times worse than the measurement accuracy. To achieve 0.1 mm steering accuracy will require something like 1 μ m BPM reproducibility. Note, though, that it is *short term reproducibility* not absolute or even long term relative accuracy that is required. Perhaps the required precision could be attained using very low frequency excitation with lock-in detection. Least count precision of the steering power supplies may also be an issue, as the required deflections are very small.

CONCLUSIONS AND COMMENTS

An algorithm for centering the beam on all quadrupoles has been described. The algorithm is applicable even when multiple quad trims are powered from the same bus. Some effects that could potentially cause the algorithm to fail have been investigated. Sextupoles of strength needed to adjust chromaticities to zero have negligible effect. So also do the random and systematic magnetic field errors assumed in the only lattice file investigated.

Other effects, potentially more limiting, have not been investigated. A simulation such as this one could, however, anticipate the degree to which this calibration procedure would be reliable. Electronic noise and stability could be estimated and included. Also instrumentation issues such as the required least count precision of analog to digital conversion could be addressed.

BARRIER RF STACKING AT FERMILAB*

W. Chou[#], J. Griffin, K.Y. Ng, D. Wildman, FNAL, Batavia, IL 60510, USA
A. Takagi, KEK, Tsukuba, Japan, H. Zheng, Caltech, Pasadena, CA 91125, USA

Abstract

A key issue to upgrade the luminosity of the Tevatron Run2 program and to meet the neutrino requirement of the NuMI experiment at Fermilab is to increase the proton intensity on the target. This paper introduces a new scheme to double the number of protons from the Main Injector (MI) to the pbar production target (Run2) and to the pion production target (NuMI). It is based on the fact that the MI momentum acceptance is about a factor of four larger than the momentum spread of the Booster beam. Two RF barriers - one fixed, another moving - are employed to confine the proton beam. The Booster beams are injected off-momentum into the MI and are continuously reflected and compressed by the two barriers. Calculations and simulations show that this scheme could work provided that the Booster beam momentum spread can be kept under control. Compared with slip stacking, a main advantage of this new method is small beam loading effect thanks to the low peak beam current. The RF barriers can be generated by an inductive device, which uses nanocrystal magnet alloy (Finemet) cores and fast high voltage MOSFET switches. This device has been designed and fabricated by a Fermilab-KEK-Caltech team. The first bench test was successful. Beam experiments are being planned.

MOTIVATION

A major performance parameter of the Fermilab Tevatron collider program Run2 is the total integrated luminosity. The goal is $10\text{-}15\text{ fb}^{-1}$ by 2007. There is also a neutrino program NuMI at Fermilab. It uses the 120-GeV proton beams from the MI to generate high intensity neutrino beams for a long baseline experiment at Soudan, Minnesota. This experiment will start in early 2005.

In order to reach the goals of the luminosity in Run2 and the neutrino flux in NuMI, one needs to increase the proton intensity on the production targets. In the present Fermilab accelerator complex, the Booster is a bottleneck that limits the proton intensity on the targets. The number of protons per cycle from the Booster cannot exceed 6×10^{12} . Otherwise the beam loss would become prohibitive.

To get around this bottleneck, one method is to use stacking. Namely, to put more than one Booster bunch into a Main Injector RF bucket. This is possible because the longitudinal acceptance of the Main Injector (0.4 eV-s) is larger than the longitudinal emittance of the Booster beam (0.1 eV-s). There are several possible ways to perform stacking. This paper introduces a new method based on employing a barrier RF system. The goal is to double the number of protons per bunch in the Main Injector, which would then give twice as many protons on the production targets per cycle. The average production rate of antiprotons and neutrinos would increase 50-60%.

For more information about this study the readers are referred to Ref. [1].

METHOD

A straightforward way to do barrier RF stacking is as follows. Inject two Booster batches into the MI, confine them by RF barriers, and then move the barriers to compress the beam. When the beam size is reduced to half of its original length (i.e., to the size of one Booster batch), the main RF system (53 MHz) in the MI is turned on to capture the beam and starts acceleration. The drawback of this approach is that the compression must be slow (adiabatic) in order to avoid emittance growth. This would lengthen the injection process and thus reduce the number of protons on the targets per unit time.

A better way, which was first proposed by J. Griffin [2], works as follows. Inject the Booster beams into the MI with a small energy offset (a few tens of MeV). Two RF barriers are employed. One is stationary, another moving. The stationary barrier serves as a firewall preventing particles from penetrating. The moving barrier bends the beam of successive injections so that the total beam length is continuously compressed. A detailed analysis and simulations have been performed by K.Y. Ng and can be found in Ref. [3].

There is a difference between the barrier RF stacking for Run2 and that for NuMI. In Run2, the stacking process is 2-to-1, that is, two Booster batches compressed to the size of one. In NuMI, it is 12-to-6, that is, twelve Booster batches compressed to the size of six. Figs. 1 and 2 illustrate the two different stacking processes.

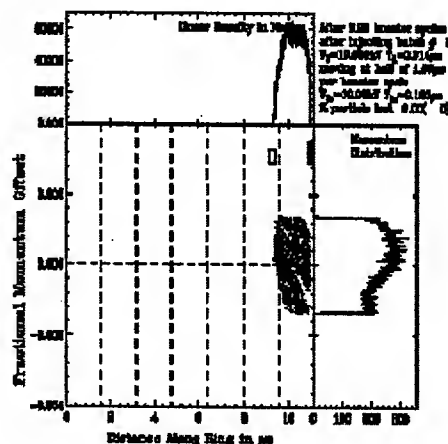


Figure 1: Barrier RF stacking for Run2. Two Booster batches are confined and compressed to the length of one. The two small rectangles, one red and one white, represent the two RF barriers.

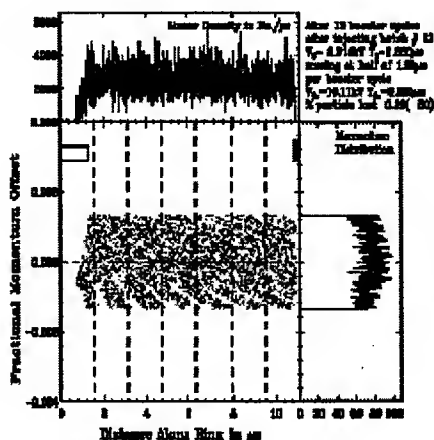


Figure 2: Barrier RF stacking for NuMI. Twelve Booster batches are confined and compressed to the length of six. The two small rectangles, one red and one white, represent the two RF barriers.

A BARRIER RF SYSTEM

An ideal barrier RF system is a wideband system rather than a resonant one, although the latter has also been used for this purpose [4,5]. One can use a wideband amplifier driving a 50 Ω gap to generate the required isolated voltage pulses, as is done in the Fermilab Recycler [6]. But this is an expensive approach. Instead, we adopt the design using an inductive device with a low quality factor, which is driven by high voltage solid-state switches.

System Description and Parameters

The system consists of an RF cavity and a power supply. It generates isolated square voltage pulses of both polarities. There are two different types of RF barriers:

- **Stationary barrier:** This is a series of bipolar pulses (+ and -) generated once every MI turn (11.2 μ s), as shown in Fig. 3 (top). This barrier is similar to the one that was built and tested by a Fermilab-KEK-HIMAC team for an RF chopper [7].
- **Moving barrier:** This is a series of separated bipolar pulses shown in Fig. 3 (bottom). The spacing between +V and -V pulses varies from 0 up to 11 μ s. They are also generated once every MI turn.

This barrier RF system works in burst mode. It generates a burst of pulses for a short period (150 ms for Run2). The time between two bursts is fairly long (about 2.2 sec). Therefore, the duty factor of this system is low. This makes the use of solid-state switches possible. Table 1 is the design parameters of this system.

Cavity

The cavity uses 7 Finemet cores. Finemet is a nanocrystal magnetic alloy developed by Hitachi. Compared with

ferrite, it has higher permeability in the frequency range of several MHz and can stand a much higher magnetic field. Its Q value is less than one.

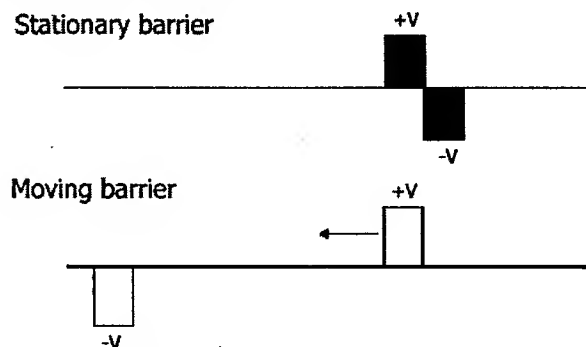


Figure 3: Two types of barriers.

Table 1: Barrier RF System Parameters

Pulse peak voltage	± 6 kV
Pulse maximum length	0.3 μ s
Pulse gap	0 - 11 μ s
Max pulse repetition rate	100 kHz
Burst length	150 ms
Burst repetition rate	0.5 Hz

High-Voltage Fast Switch Circuit

The switches need to have high peak voltage and high peak current. Because the load is inductive, the switches must be bipolar in order to avoid flyback when the pulse is terminated. The HTS 161-06-GSM solid-state switches made by Behlke Co. are chosen. Fig. 4 is the circuit designed using SPICE. It has four switches forming a full bridge circuit. Snubber and damper circuits are applied to reduce the voltage flyback and peak current.

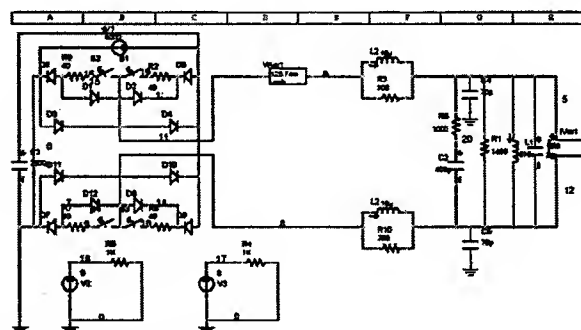


Figure 4: SPICE model of the circuit for the barrier RF power supply.

Bench Test

A bench test (with no beam) has been carried out on this system. The pulse pattern and peak voltage meet the specifications. The burst width reaches 200 ms. Fig. 5 shows the results.

*Work supported by Universities Research Association, Inc. under contract No. DE-AC02-76CH03000 with the U.S. Dept. of Energy.

[†]chou@fnal.gov

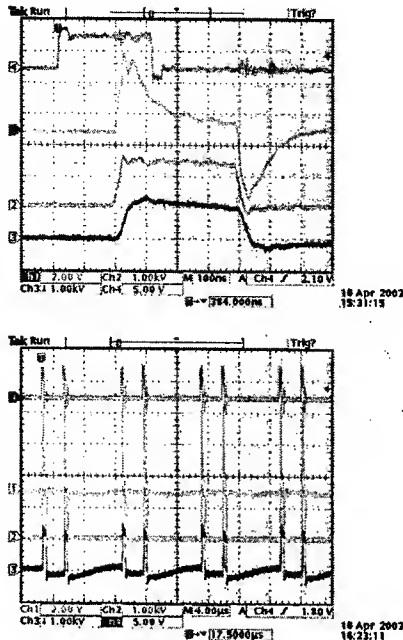


Figure 5: The four traces are, respectively, green – trigger, yellow – current, blue – switch output voltage, purple – cavity gap voltage. Top: single pulse. Bottom: a pair of pulses with a period of 10 μ s. The distance between the twin peaks can be varied, forming a moving barrier.

DISCUSSIONS

Comparison with Slip Stacking

Stacking beams in the longitudinal phase space can also be achieved by the slip stacking method, which was first proposed at CERN in 1979 for the PS [8,9]. A main problem was beam loading. It caused large particle loss and emittance blowup at high beam intensities. This method is being reinvestigated at the Fermilab with an improved beam loading compensation technique [10].

The barrier RF stacking has smaller beam loading effects, because the peak beam current is lower and its 53 MHz component much smaller thanks to a debunched beam. This is a main advantage of this new method.

Emittance Dilution and Particle Loss

The simulation assumes 0.1 eV-s for the incoming Booster bunch longitudinal emittance. During the process, the Booster beam is debunched, compressed, stacked, rebunched and captured by the 53 MHz RF bucket. The final bunch has an emittance of 0.32 eV-s. So the blowup factor is 3.2, which is tolerable, because the MI acceptance is 0.4 eV-s. The particle loss in the simulation is negligible.

A Key Issue

In order to make the barrier RF stacking work, a key issue is to keep the energy spread ΔE of the injected beam small. Simulation shows that ΔE of the Booster beam must be below ± 6 MeV so that the beam will be contained

in the RF bucket after stacking. However, the ΔE of the present Booster beam is 2-3 times larger due to coupled bunch instabilities. Several measures are being tested to reduce the energy spread: (1) a longitudinal feedback system, (2) RF frequency modulation to provide Landau damping [11,12], and (3) bunch rotation.

Other Issues

This system will be installed in the MI for beam experiments. A potential concern is the radiation hardness of the switch, because it must be placed next to the cavity in order to minimize stray inductance and capacitance. Data are being collected.

Switch power dissipation for NuMI stacking is another concern, because the duty factor will be higher. One may use oil-cooled switches as a possible solution.

ACKNOWLEDGEMENT

This project is partially funded by the US-Japan collaboration in high-energy physics.

REFERENCES

- [1] <http://www-bd.fnal.gov/pdriver/barrier/>
- [2] <http://www-bd.fnal.gov/pdriver/barrier/pdf/griffin.pdf>
- [3] K.Y. Ng, "Doubling Main Injector Beam Intensity using RF Barriers," AIP Conference Proc. 642, p. 226 (2002); also see FERMILAB-FN-715, FERMILAB-TM-2183 (2002).
- [4] M. Blaskiewicz et al., "Barrier Cavities in the Brookhaven AGS," Proc. 1999 PAC (New York, USA), p. 2280.
- [5] M. Fujieda et al., "Magnetic Alloy Loaded RF Cavity for Barrier Bucket Experiment at the AGS," Proc. 1999 PAC (New York, USA), p. 857.
- [6] G. Jackson, "The Fermilab Recycler Ring Technical Design Report," FERMILAB-TM-1991 (1996).
- [7] W. Chou et al., "Design and Measurements of a Pulsed Beam Transformer as a Chopper," KEK Report 98-10 (September 1998); W. Chou et al., Proc. 1999 PAC (New York, USA), p. 565; Y. Shirakabe et al., Proc. 2000 EPAC (Vienna, Austria), p. 2468.
- [8] D. Boussard and Y. Mizumachi, "Production of Beams with High Line-Density by Azimuthal Combination of Bunches in a Synchrotron," IEEE Vol. NS-26, No. 3, p. 3623 (1979).
- [9] J.P. Delahaye et al., "Improved Recombination of the 20 PSB Bunches and Merging into 5 Dense Bunches in the CERN Proton Synchrotron," IEEE Vol. NS-26, No. 3, p. 3565 (1979).
- [10] K. Koba and J. Steimel, "Slip Stacking," AIP Conference Proc. 642, p. 223 (2002).
- [11] C. Ankenbrandt et al., "Longitudinal Motion of the Beam in the Fermilab Booster," IEEE Vol. NS-24, No. 3, p. 1449 (1977).
- [12] B. Zotter, "Damping of Coupled Bunch Instabilities by RF Frequency Modulation," FERMILAB-TM-2189 (November 2002).

FERMILAB BOOSTER MODELING AND SPACE CHARGE STUDY*

W. Chou[#], A. Drozhdin, P. Lucas, F. Ostiguy, FNAL, Batavia, IL 60510, USA

Abstract

The Fermilab Booster is a bottleneck limiting the proton beam intensity in the accelerator complex. A study group has been formed in order to have a better understanding of this old machine and seek possible improvements [1]. The work includes lattice modeling, numerical simulations, bench measurements and beam studies. Based on newly obtained information, it has been found that the machine acceptance is severely compromised by the orbit bump and dogleg magnets. This, accompanied by emittance dilution from space charge at injection, is a major cause of the large beam loss at the early stage of the cycle. Measures to tackle this problem are being pursued.

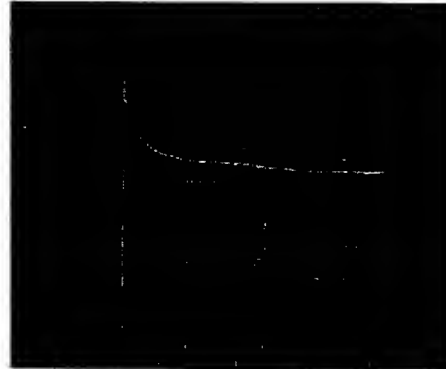
INTRODUCTION

The Fermilab Booster is a 30 years old machine and the only machine at Fermilab that has never been upgraded. It is the bottleneck in the accelerator complex limiting the proton beam intensity. The linac upstream from the Booster can deliver 5 times more protons than it does now. The Main Injector downstream from the Booster can also accept 5 times more protons. However, the Booster, which sits in between, can provide no more than 6×10^{12} protons per cycle. Otherwise the loss would be prohibitive (Fig. 1). Most of the losses occur at the early stage of the cycle (about 25-30%); in particular during the first few ms. (The cycle time is 66.7 ms.) In order to understand the cause of the early loss, a study group was formed about 6 months ago. It launched a systematic investigation on the Booster. A comprehensive lattice model using MAD is established. The space charge codes ESME (authored by J. MacLachlan) and ORBIT (authored by J. Holmes) are employed. With the help of the Proton Source Department and other departments/divisions, a series of beam studies and magnet field measurements are also carried out.

PERTURBATION ON LINEAR OPTICS: THE DOGLEG EFFECT

One surprise in this study (first discovered by A. Drozhdin) is that the linear optics of the Booster is significantly perturbed by the edge focusing of the injection and extraction orbit bumps. The latter is termed "dogleg" at Fermilab. As can be seen in Figure 2, in the horizontal plane, the maximum beta function is increased from 33 m to 47 m, maximum dispersion from 3 m to 6 m; in the vertical plane, the maximum beta from 20 m to 26 m. The edge focusing strength of a bending magnet is:

$$1/f = \tan\theta/\rho \cong \theta^2/L \quad (1)$$



For 0, 2, 4, 6, 8, 10, 12, 14 Injected Turns

Figure 1: Proton intensity (in green) and integrated beam power loss (in red) during the cycle. (courtesy R. Webber)

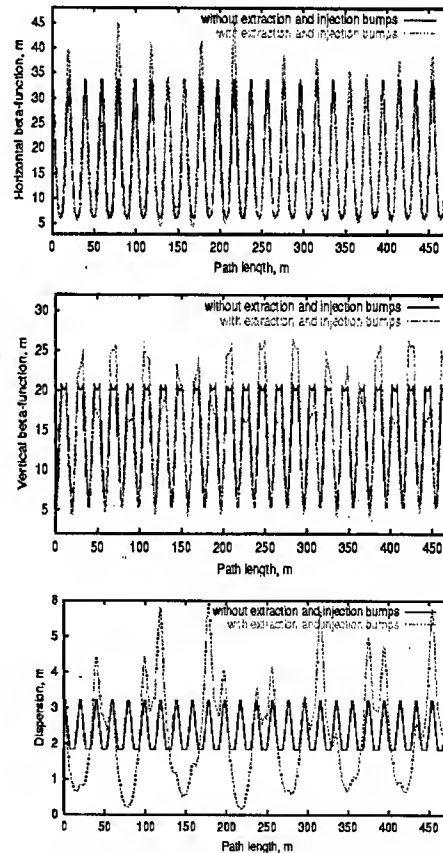


Figure 2: Lattice function perturbation due to edge focusing of the orbit bump and dogleg. Red: original, green: perturbed. Top - β_x , middle - β_y , bottom - D_x .

in which θ is the bending angle, ρ the bending radius, L the magnet length. For the Booster doglegs, L is small (0.2 m) and θ large (60 mrad). There are two doglegs, each with 4 bending magnets. The focusing effects are additive, giving rise to a significant amount of extra focusing (0.1152 m^{-1} , close to one main magnet which has $1/f = 0.1567 \text{ m}^{-1}$) and leading to a big perturbation to the linear lattice. Both the injection orbit bump (horizontal bend) and extraction doglegs (vertical bend) are rectangular bends. Therefore, their edge focusing acts in the non-deflecting plane. That is, vertical for the injection orbit bump and horizontal for the dogleg. The former is pulsed (pulse length about 150 μs), while the latter DC. Hence, the doglegs cause more damage to the beam.

This effect was quickly confirmed in a beam study. The measured tune shift and dispersion perturbation are in good agreement with the MAD prediction. When one of the doglegs was removed in a machine experiment, the beam transfer efficiency showed a considerable improvement (Fig. 3). A milestone of the MiniBooNE neutrino program (5e16 protons per hour) was reached. There was a champagne celebration.

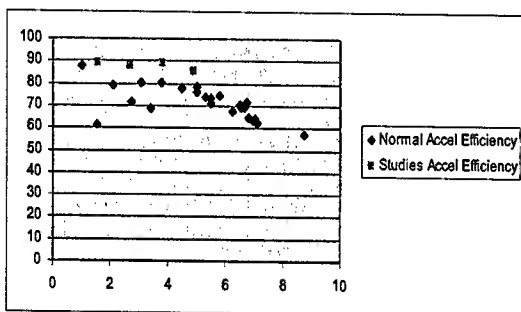


Figure 3: The beam transfer efficiency is improved when one of the doglegs is removed during a machine study. The x-axis is the injected number of protons ($\times 10^{12}$). Blue – normal operation; pink – one dogleg removed. (courtesy J. Lackey)

CHROMATICITY MODELING

The present setting of the chromaticity during the cycle is somewhat confusing. For instance, the horizontal chromaticity is positive below transition, which could cause the head-tail instability that has not been seen. It is decided to try other chromaticity ramp curves by compiling a spreadsheet relating the sextupole setting with the machine chromaticity. There are four major contributors to the chromaticity: lattice (main quads), dogleg (edge focusing), sextupole of the main magnets and chromaticity sextupoles.

$$\xi = \xi(\text{lat}) + \xi(\text{dogleg}) + \xi(\text{mag sext}) + \xi(\text{chrom sext}) \quad (2)$$

The direct contribution from the dogleg is small. However, it has big impact on the chromaticity, because it changes the local beta and dispersion functions at the chromaticity sextupoles. One unknown parameter in this

equation is the sextupole component of the main magnets, which comes not only from the body but also from the ends. In order to get a reliable value of this parameter, a “blind check” method was applied. Two teams, one working on the chromaticity and another on the field, carried out the measurements independently without communication between them. The results were then put on the table for a comparison. The agreement is very good, as listed in Table 1. It is seen that the ends compensate the body sextupole of the F magnet almost perfectly, but nearly doubles that of the D magnet.

Table 1: Sextupole component of the main magnets

Magnet type	Body only	Body + Ends field meas.	Body + Ends chrom meas.
F	0.026	0.0045	-0.003
D	-0.021	-0.0413	-0.0454

SPACE CHARGE STUDY

Space charge is a dominant factor limiting the beam intensity in low energy proton machines. It causes tune shift, emittance growth and resonance. Analytical tools have limited use for this complicated phenomenon. Therefore, we invoke numerical simulations. Two codes, ESME (longitudinal) and ORBIT (transverse) are employed for this purpose. (Another group also uses a code called Synergia.)

Figure 4 shows 805 MHz micro-bunch injected into the Booster simulated by ESME. The energy spread matches the measured value ($\pm 0.88 \text{ MeV}$). Figure 5 is the tune footprint obtained from ORBIT. The tune spread (-0.3) agrees with that predicted by the Laslett formula. Figure 6(a) is the transverse emittance growth simulated by ORBIT. It shows two distinct regions. One is a fast growth during the 10-turn injection, another a slow growth after injection. Measurement from the ion profile monitor (IPM) seems to support this observation, see Figure 6(b). (Note: The IPM data processing is complicated and sometimes even controversial. Fig. 6(b) shows the raw data. But the processed data demonstrates a similar qualitative behavior, namely, a fast growth during injection and a slowdown after that [2].)

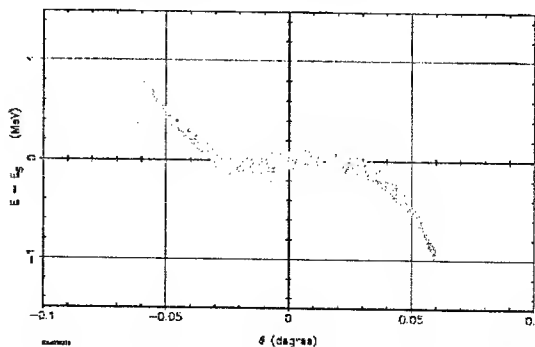


Figure 4: 805 MHz micro-bunch simulated by ESME.

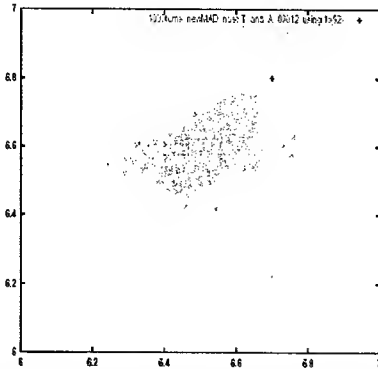


Figure 5: Tune footprint due to space charge simulated by ORBIT. The red point is the nominal tune (6.7, 6.8).

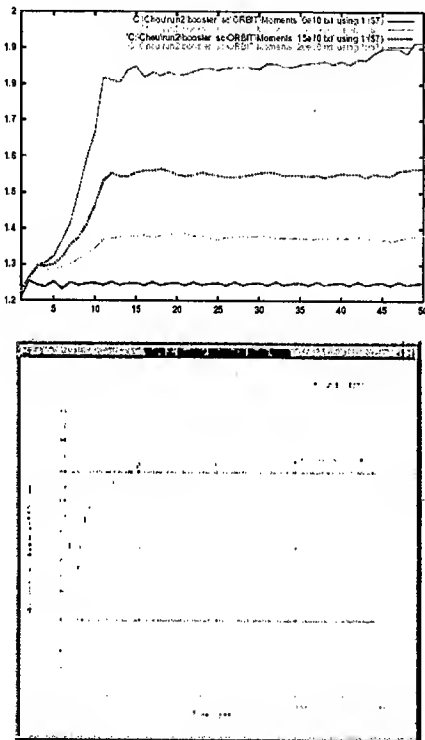


Figure 6: (a) Top: Emittance dilution during the first 50 turns from ESME. The injection time is 10 turns. From the bottom trace to the top, the space charge effect (beam intensity) is increased. (b) Bottom: Emittance dilution during the first 50 turns from IPM measurement. The first injection starts at the valley of the curve. The injection time is 10 turns.

BEAM LOSS IN THE FIRST FEW MS

Based on the results in the previous sections, one can develop a coherent picture of what happens in the first few ms in the Booster and why the large beam loss should occur.

Longitudinal Loss

The measured Booster longitudinal acceptance is small (± 0.15 - 0.2%). It is about the same as the linac beam momentum spread ($\pm 0.13\%$). When the RF is turned on to capture the beam adiabatically, the momentum spread of the bunched beam will increase to about $\pm 0.3\%$ and exceed the acceptance, resulting in loss.

Transverse Loss

The machine transverse acceptance is:

$$A = \{\beta_{\max} \times \epsilon_N / \beta\gamma\}^{-1/2} + D_{\max} \times \Delta p/p + \text{c.o.d.} \quad (3)$$

in which c.o.d. is the closed orbit distortion. Take the horizontal plane as an example. The magnet good field region is small ($\sim \pm 1.2$ inches). For the regular values of β_{\max} and D_{\max} , the maximum allowable ϵ_N is about 16π mm-mrad. However, the dogleg effect blows up the lattice functions and reduces the acceptable ϵ_N to 8π , whereas the incoming linac beam is about 7π . The situation is worsened by the space charge. It dilutes the emittance during multi-turn injection. The beam is scraped transversely, resulting in loss.

These losses are most severe in the first few ms. When beam energy goes up, the situation improves rapidly due to a number of factors: the relative momentum spread $\Delta p/p$ becomes smaller, the dogleg effect ($\propto 1/\gamma^2$) and space charge effect ($\propto 1/\beta\gamma^2$) reduce quickly, the beam size also shrinks from adiabatic damping.

A systematic investigation of various measures for correcting the dogleg effect, reducing the space charge and increasing the machine acceptance is under way. This will be the content of another paper that will be published later.

ACKNOWLEDGEMENT

This study is a collaboration involving physicists and engineers from the Beam Physics Department, Proton Source Department, Operation Department, Technical Division and Computer Division. The authors would like to express their thanks to the following people for their help and stimulating discussions: J. Amundson, C. Ankenbrandt, J. DiMarco, M. Foley, D. Harding, J. Lackey, J. MacLachlan, E. Malamud, E. McCrory, M. Popovic, E. Prebys, P. Schlabach, P. Spentzouris, M. Syphers, L. Teng, R. Tomlin, D. Wolff and X. Yang.

REFERENCES

- [1] <http://www-bd.fnal.gov/pdriver/booster/>
- [2] P. Spentzouris, http://www-bd.fnal.gov/pdriver/booster/meetings2/spentz_24apr03.pdf

*Work supported by the Universities Research Association, Inc. under contract No. DE-AC02-76CH03000 with the U.S. Dept. of Energy.
*chou@fnal.gov

ION PRODUCTION AND TUNE SHIFT IN THE RECYCLER RING

K. Gounder *, J. Marriner, and S. Mishra
FNAL, Batavia, IL 60510, USA.

Abstract

We calculate the ion production rate for a beam of 2×10^{12} antiprotons in the Recycler Ring using the known vacuum residual gas composition. We study the effect of ion buildup around the antiproton beam on beam lifetime and stability. We compare the ion production rate with the actual measurement using the beam tune shifts when the RF gap in the circulating beam is removed. Work supported by the U.S. Department of Energy under contract No. DE-AC02-76CH03000.

INTRODUCTION

The Recycler Ring [1] located in the upper portion of the Main Injector tunnel at Fermilab is designed as a storage ring for antiprotons. Antiprotons transferred from the Accumulator and the residual Tevatron stores will be cooled and stored in the Recycler Ring before reinjection into the Tevatron. The stacking rate of the antiprotons in the Accumulator is improved by steady transfer of antiprotons to the Recycler Ring when the stack size becomes sufficiently large. Thus, as a part of Run II upgrade, the Recycler Ring is expected to provide a factor of 2-3 improvement in luminosity. Presently, the Recycler Ring (RR) is being commissioned using protons as well as antiprotons. As a beginning phase of the integration of RR in the Fermilab collider complex, we expect to have a circulating beam of 2×10^{12} antiprotons. From the known residual gas composition of the RR vacuum, we study the ion production rates and the effects of ion trapping by the antiproton beam on lifetime and transverse tunes. The relevant RR parameters used are listed in Table 1. More detailed description of the Recycler Ring can be found elsewhere [1].

Table 1: The basic Recycler Ring parameters relevant for the computations detailed in this note.

Parameter	Value
Acceptance (mm-mr)	40.0π
Average β (m)	40.0
Average beam pipe radius (in m)	0.023
Beam energy (GeV)	8.89
Average beam β	0.998
Average beam γ	9.48
Maximum energy loss (GeV)	0.089

*gounder@fnal.gov

RECYCLER RING VACUUM RESIDUAL GASES

The RR ultra high vacuum is maintained by arrays of Titanium sublimation pumps (TSP) and Ion pumps has a total pressure of a fraction of a nano Torr. The types of gases present in the vacuum and their partial pressures can be obtained from RGA measurements and Ion gauge readings done often around the ring. The major constituents of the vacuum (average of RGA measurements normalized by Ion gauge readings) are listed below. We have also detected some very minor quantities of hydrocarbons such as Ethane, Ethylene etc. and denoted them as the 'unknown' component. The observed gases and the relevant parameters are listed in Table 2.

Table 2: The Recycler Ring vacuum residual gases as measured by RGA and Ion gauges located around the ring. The 'unknown' component will be treated as Nitrogen for computational purposes.

Gas	Avg. Pres. [Torr]	Gas Density [M^{-3}]
H_2	0.354E-09	1.25E+13
H_2O	0.380E-10	1.35E+12
CO	0.190E-10	6.73E+11
Ar	0.010E-10	3.54E+10
CH_4	0.050E-10	1.77E+11
CO_2	0.150E-10	5.31E+11
Unknown	0.105E-09	3.72E+12
Total	0.537E-09	1.90E+13

ION PRODUCTION RATES

The rate of ionization R_j for a given gas type can be written as [3]:

$$R_j = n_j n_b \sigma_j v$$

with n_j density of the gas type, n_b beam particle density, σ_j ionization cross section and v the beam particle velocity. The σ_j can be parametrized:

$$\sigma_j = 4\pi \left(\frac{\hbar}{m_e c} \right)^2 \left\{ M_j^2 \left[\frac{1}{\beta^2} \ln \left(\frac{\beta^2}{1 - \beta^2} \right) - 1 \right] + \frac{C_j}{\beta^2} \right\}$$

where \hbar is Planck's constant, m_e the electron mass, c the speed of light and β associated with the ionizing beam.

The parameters M_j^2 and C_j have been tabulated for various types of gases [4]. Knowing the partial pressure of each gas as given Table 2 and beam distribution for a beam of 2×10^{12} antiprotons, the total ion production rate can be computed. The rate for the above composition of gases considered is 5.0×10^8 /meter/second. Now for the whole ring, this becomes 1.7×10^{12} ions/second - or each beam particle roughly creates an ion per second in the ring.

THE TUNE SHIFT DUE TO IONS

The presence of ion cloud around the beam can induce an incoherent tune spread due to the static transverse electrostatic field generated by the cloud. For a gaussian beam of longitudinal density λ_b , the transverse beam density $n_b(r)$ is given by:

$$n_b(r) = \frac{-\lambda_b}{2\pi\sigma_r^2} e^{-\frac{r^2}{2\sigma_r^2}}$$

where σ_r is the radial width of the distribution. Assuming similar distribution for the ion cloud, the electric field (beam fully neutralized) generated by the ions is given by:

$$E_r(r) = \frac{-q^2\lambda_b}{2\pi\epsilon_0 r} \left\{ 1 - e^{-\frac{r^2}{2\sigma_r^2}} \right\}$$

where ϵ_0 is the permittivity for free space and q , unit charge. The radial space charge force $F_r(r)$ for small distances can be by obtained using Lorentz equation as:

$$F_r(r) = \frac{q^2\lambda_b}{4\pi\epsilon_0\sigma_r^2} r$$

Converting this result into the form of a quadrupole gradient error ΔK as:

$$\Delta K = \frac{r_0\lambda}{\gamma\beta^2\sigma^2}$$

The tune shift due to this gradient error can be cast as:

$$\Delta\nu = \frac{1}{4\pi} \int ds \beta(s) \Delta K$$

where r_0 is the classical proton radius. For simplicity, we assume an average beta of 40 meters around the ring, and for a beam of 1.0×10^{12} antiprotons with total ionization case, the transverse tune shift will be:

$$\Delta\nu = \frac{N\beta_{avg}r_0}{\gamma\beta^24\pi\sigma^2} \approx 0.021$$

MEASUREMENT RESULTS

Measurements were carried out with a beam of $\approx 2 \times 10^{11}$ antiprotons in the Recycler Ring. The longitudinal gap usually left in the beam is 64 RF buckets. The transverse tunes and beam lifetime were measured using Schottky and beam current monitors. After turning off the gap, lifetime and transverse tunes were remeasured. Then the tune Trambone was used to reset the tunes to its original values. The transverse tune and lifetime measurements were repeated. The measurement results are summarized in Table 3.

Table 3: Antiproton lifetime (τ_{ap}) and transverse tunes (horizontal, vertical) measurements with and with out the longitudinal gap in the circulating beam of $\approx 2.0 \times 10^{11}$ antiprotons in the Recycler Ring. The measurements indicate tune shifts due to ion trapping.

Scenario	τ_{ap} [hours]	Transverse Tunes [Fractional]	Beam
Longitudinal beam gap on	135	(0.4166, 0.4193)	2.00E+11
No longitudinal beam gap	86	(0.4180, 0.4215)	1.91E+11
No longitudinal beam gap but tunes reset	120	(0.4166, 0.4193)	1.90E+11

THE EFFECT OF IONS ON BEAM LIFETIME

To study the additional beam-gas scattering due to ion trapping, let us assume that about 2.0×10^{12} antiprotons circulating in RR with a gaussian beam shape of $\sigma_r = 0.005$ m. Now assuming the ionization rate is complete that each antiproton traps an ion, there will be 2.0×10^{12} ions trapped along the beam with a similar gaussian distribution. To estimate the maximum effect, the ions are taken to have a similar composition as the normal vacuum shown in Table 2. Using the convention that all the beam resides in the $\pm 3\sigma_r$ region, we expect all the ions to be contained in a tube of radius $3\sigma_r$ along the ring (3320 meters in length). Therefore the average ion density for each gas can be written as in Table 4.

Table 4: Average Ion densities trapped around the beam assuming the extreme case of full neutralization of a beam of 2.0×10^{12} antiprotons. The ion distribution is assumed to be same as that of the beam - Gaussian with a $\sigma_r = 0.005$ meters. The vacuum gas composition given in Table 2 is used here.

Ions	Gas Fraction	Ion Density [M^{-3}]	Par. Pres. [Torr]
H_2	0.66	5.62E+11	1.59E-11
H_2O	0.07	0.60E+11	1.69E-12
CO	0.04	0.34E+11	0.96E-12
Ar	0.00	0.00E+11	0.00E-12
CH_4	0.01	0.09E+11	0.03E-12
CO_2	0.03	0.26E+11	0.07E-12
Unknwon	0.19	1.61E+11	0.45E-11
Total	1.00	8.52E+11	2.31E-11

Comparing two tables above we see that the partial pressures are roughly two orders of magnitude smaller for ions compared to that of normal gases. At this level we can assume that this additional density the particles see along with normal gas densities. On the otherhand, if we assume that we can stack an order of magnitude higher, then we may not be able to treat the ion densities as independent of the normal gas densities! But in this case, we assume that they are independent, and compute the lifetime to compare with the case of no ion trapping.

The lifetime due to beam-gas scattering has four components: (a) Single coulomb scattering where a particle is lost due to a single scattering of beam particle with a gas atom; (b) Multiple coulomb scattering when particle is lost at the beam pipe limiting aperture due to emittance growth of the beam attributed to multiple scattering of beam with gas atoms; (c) Nuclear scattering when a beam particle is absorbed by the nucleus of a gas atom; and (d) Inelastic scattering when a particle is lost due to energy loss from gas atom ionization, bremsstrahlung etc. All four types of processes of beam loss can be combined to produce the total lifetime of the beam. The lifetime due to multiple scattering process is computed for the asymptotic case when the beam is already grown and filled the whole beam pipe aperture. More details of the lifetime computations can be found elsewhere [5]. We use RR parameters listed in Table 1 along with gas densities shown in Tables 2 and 4. The results of lifetime estimations are summarized in Table 5.

Table 5: The lifetime comparisons with full neutralization of the 2.0×10^{12} antiproton beam with case of no neutralization. The vacuum residual gas composition in Table 2 and ion densities shown in Table 4 were used for the above lifetime estimations.

Physical Process	No Ions (Normal Case) [hours]	Neutralization (100%) [hours]
Single Coloumb	4.64×10^2	4.62×10^2
Inelastic Scatt.	8.06×10^2	8.02×10^2
Mult. Coloumb	5.55×10^1	5.53×10^1
Nuclear Scatt.	1.61×10^3	1.60×10^2
Total Life Time	4.54×10^1	4.50×10^1

From Table 5, the effect of full neutralization is small on lifetime due to beam-gas scattering for a beam of 2.0×10^{12} antiprotons, less than 1%! For a beam of 2.0×10^{13} antiprotons, this could become easily noticeable - about 8%!

ION CLEARING IN THE RECYCLER RING

If the ions produced are not effectively cleared from beam pipe, this will affect the beam stability by tune shifts, induce coherent ion-beam transverse oscillations etc. The ion cloud will increase the concentration of gas molecules near the beam and can cause additional beam-gas scattering affecting beam lifetime adversely. This effect as shown above may be considerable for higher intensity low emittance beams. The trapped ions are cleared in the RR using two sets of ion clearing electrodes located in each half cell. In addition to the clearing electrodes, a longitudinal gap in the circulating antiproton beam is maintained using RF cavities. Also transverse dampers will be installed in the RR to combat coherent instabilities due to beam-ion oscillations. They are designed to have electronics capable of exciting the beam at the resonant frequency of the ion oscillations about the beam centroid.

REFERENCES

- [1] Gerry Jackson, "The Fermilab Recycler Ring Technical Design Report", November 1996, Fermilab-TM-1991; Mishra, "Status of Fermilab Recycler Ring", EPAC2002, Paris, June 2002.
- [2] J. Marriner et. al., "Run II Handbook", at <http://www-bd.fnal.gov/runII/index.html>; Also see K. Gounder, "The Status of Run II at Fermilab", in the 2002 proceedings of ICHEP, Amsterdam, July 2002, Fermilab-Conf-02-233-E.
- [3] A. Poncet in the Proceedings of CERN Accelerator School, Vol. 2, 859-878, CERN-95-06.
- [4] Rudd et al., Rev. Mod. Phys., Vol. 57, No.4, 1985; F Rieke and W. Prepejchal, Phys. Rev. A, 6, 1507 (1972).
- [5] K. Gounder et al., "Recycler Ring Beam Lifetime", Fermilab-Conf-01-186-E, PAC-2001-RPPH055, July 2001.

ANALYSIS AND MEASUREMENTS OF EMITTANCE DILUTION FROM VACUUM WINDOWS IN THE FERMILAB RECYCLER TRANSFER LINES*

C. Johnstone[#], C. Gattuso, D. Johnson, M. Syphers, FNAL, Batavia, IL 60510, USA
K. Paul, UIUC, Urbana, IL 61801, USA

Abstract

Round-trip beam transfers between the Fermilab Main Injector and Recycler (antiproton accumulator) have been plagued by an emittance dilution of about a factor of 2 with corresponding beam loss. The source of the large dilution was traced to two Ti vacuum windows, one installed in each of the two transfer lines that connect the machines for beam injection/extraction. The dilution can be accounted for by calculating the increase in beam divergence due to multiple scattering in the windows followed by an amplitude mismatch that serves to further enhance the instantaneous dilution immediately downstream of the window. This work presents the analytical basis for the phase-space, or emittance, dilution due to the window, the subsequent optics mismatch, and then presents an analysis of beamline measurements that evidences the effect and validates the analytical argument. The data showed a strong skew quadrupole component in the transfer line optics that initially complicated the analysis, but was effectively eliminated in some of the data samples acquired under specific beam conditions.

INTRODUCTION

For some time beam transfers of 8-GeV protons between the Main Injector synchrotron and the Recycler permanent-magnet storage ring were plagued by beam loss and immediate emittance dilution, with evidence of an amplitude function mismatch between the accelerators presumably generated in the transfer lines. Of concern were Titanium (originally beryllium) vacuum windows, estimated to be ~3 mil thick, installed in each transfer line. The effects on emittance and subsequent second-moment oscillation amplitudes due to beam passing through these windows will be first derived followed by experimental verification in a later section.

The emittance dilution can be derived in several forms. All forms depend on solving the linear equations of motion (linear magnetic fields: quadrupole and dipoles fields) piecewise which results in constraining the coordinates of particle motion to an elliptical envelope given by:

$$\varepsilon = \gamma x^2 + 2\alpha x x' + \beta x'^2$$

where β , α , and γ (which is $(1+\alpha^2)/\beta$) are the so-called Courant-Snyder parameters and ε is the area of the ellipse. These lattice parameters evolve according to the optical solutions along the line, but the area of the ellipse, or total phase space, remains conserved, and in a predominately linear system, particles remain on their respective

elliptical contour. Further, if the system is periodic, the phase ellipse is also repetitive, and particles move around the given contour according to the phase advance of the lattice.

EMITTANCE DILUTION FROM MULTIPLE SCATTERING

When beam passes through material, the dominant process is Coulomb multiple scattering, which changes the direction but not the energy or position of the incident beam particle if the material is thin. Multiple scattering is a statistical process which is azimuthally symmetric about the particle's trajectory (this symmetry will be exploited later). The phase space of a distribution immediately after a thin window is expanded in one coordinate only, x' .

The change in a particle's phase coordinates is represented by a discrete jump to a different ellipse generating, on average, a clearly different aspect ratio; the change in the distribution is governed by the statistics of the scattering process. Since the original distribution is an even function in x and x' , and the scattering process is an even-function convolution of the original distribution, the rms of the distribution is a particularly powerful description—there is not only an rms value for x and x' , but also an rms emittance, ε , and an rms multiple scattering angle specific to the composition and thickness of the window (values for multiple scattering angles will be given later in this paper).

Statistical Ensemble Description

This derivation is facilitated by conversion to "normalized" coordinates which always reduces the ellipse to a circle; the phase space of the beam just upstream of the vacuum window is circular when expressed in $\{x, (\beta x' + \alpha x)\}$ coordinates. (One plane conveniently remains the original transverse coordinate.) Initially we assume an otherwise perfectly matched beam between the two accelerators, and look at the effect of the particles passing through a vacuum window. The process is depicted in Figure 1.

**Work supported by the Universities Research Association, Inc., under contract DE-AC02-76CH00300 with the U.S. Department of Energy.

*cjj@fnal.gov

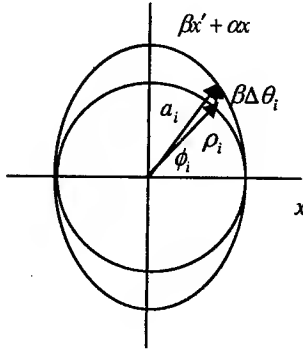


Figure 1. Phase space in normalized coordinates showing the new oscillation amplitude a_i a single particle may acquire after multiple scattering in a window.

The particles are initially following trajectories around the inner circle, each has a radius ρ_i , with a corresponding transverse amplitude of:

$$\sigma_0(x) = \langle x^2 \rangle^{1/2} = \langle \rho^2 / 2 \rangle^{1/2}.$$

Upon passing through the window, the i th particle's amplitude will change from ρ_i to a_i according to:

$$a_i^2 = \rho_i^2 + (\beta \Delta \theta_i)^2 - 2\beta \rho_i \Delta \theta_i \cos \phi_i$$

where β is the amplitude function at the window, and $\Delta \theta_i$ is the final scattering angle through the material due to multiple Coulomb interactions. The phase angle, ϕ_i , depends upon the phase of the particle in its phase space oscillation, and is randomly distributed among all the particles, and is thus uncorrelated with either ρ or scattering angle. Therefore, after averaging over all the particles in the beam, we have

$$\begin{aligned} \langle a^2 \rangle &= \langle \rho^2 \rangle + \beta^2 \langle \Delta \theta^2 \rangle - 2\beta \langle \rho \Delta \theta \cos \phi \rangle \\ &= \langle \rho^2 \rangle + \beta^2 \langle \Delta \theta^2 \rangle - 2\beta \langle \rho \rangle \langle \Delta \theta \rangle \langle \cos \phi \rangle \\ &= \langle \rho^2 \rangle + \beta^2 \langle \Delta \theta^2 \rangle \end{aligned}$$

Note that the scattering angle, $\Delta \theta$, and $\cos \phi$ independently average to zero, as there is no preferred direction. The resulting phase space distribution subsequently tumbles through the lattice of the beamline and through the downstream machine, resembling an amplitude function mismatch in that a transverse beam profile monitor will see a "quadrupole oscillation" ensue at twice the betatron tune until the coherent oscillation amplitude dies away due to filamentation. Filamentation, as depicted in Figure 2, proceeds through unavoidable field nonlinearities, which simply implies differences exist in phase advance as a function of particle amplitude. (Chromatic correction sextupoles are usually the largest contributor to this effect.)

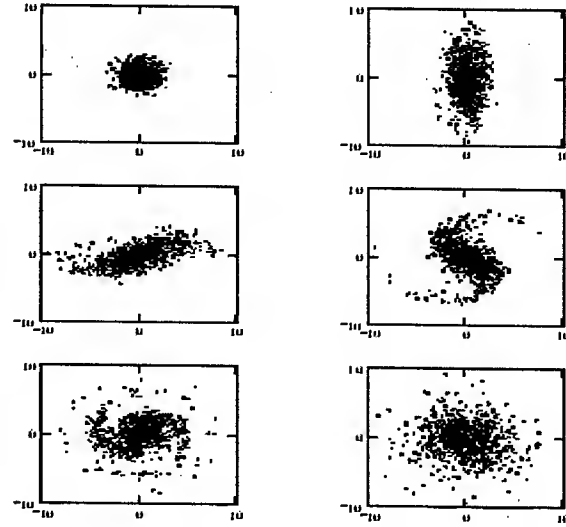


Figure 2. From top left to bottom right: phase space distributions, a) before undergoing scattering in the window, c)-e) during filamentation, and f) after filamentation is complete. For each plot the horizontal axis is x and the vertical axis is $(\beta x' + \alpha x)$. The scales are arbitrary units.

Each particle now oscillates in phase space with its new betatron amplitude (or single particle invariant ellipse) acquired in the scattering process. If the new phase space distribution has not been "re-matched" after the window, then, through filamentation, a final equilibrium distribution is reached within a larger matched ellipse concentric to the original one (or circle in normalized coordinates). In normalized coordinates, the new amplitude $\langle \alpha^2 \rangle^{1/2}$ describes the final redistribution. Again, since the new envelope is circular,

$$\sigma_f^2(x) = \langle x^2 \rangle_{final} = \langle \rho^2 / 2 \rangle + \frac{1}{2} \beta^2 \langle \Delta \theta^2 \rangle.$$

or

$$\sigma_f^2(x) = \sigma_0^2(x) + \frac{1}{2} \beta^2 \theta_{rms}^2.$$

In the second equation, θ_{rms} is the rms scattering angle due to multiple Coulomb interactions in the window material as projected into a transverse plane (the specific equation used to compute this angle is given later in the text.) The rms emittance enhancement then follows from:

$$\Delta \varepsilon_{rms} = \frac{\Delta \sigma^2}{\beta} \pi = \frac{1}{2} \beta \theta_{rms}^2,$$

or

$$\Delta \varepsilon_N = 3\beta \theta_{rms}^2 (\beta \gamma) \pi$$

for the 95% normalized emittance (this derivation can also be found in references [1]). One observation which

stands out is that the increase in emittance is not dependent on the incoming emittance upstream of the window, only on the β function, or optics, at the vacuum window itself. This is an interesting result and derives from the fact that the scattering angle adds in quadrature to the beam divergence--thus the higher the beam divergence, or the smaller the beam size as indicated by the beta function, the lower the increase in emittance.

Coulomb Multiple Scattering

The projected rms scattering angle resulting from multiple Coulomb interactions in a material can be estimated using[2]

$$\theta_{rms} = \frac{13.6 \text{ MeV}}{p\beta} \sqrt{\frac{l}{L_{rad}}} [1 + 0.038 \ln(\frac{l}{L_{rad}})]$$

where l is the thickness of the material, L_{rad} is the radiation length (which is 3.56 cm for Ti), p the momentum of the particle, and β here is the relativistic velocity.

With 3 mil Ti windows the predicted emittance blowup at 8 GeV is 1.1π and 4.2π mm-mr horizontally and vertically, due to the 13 m and 50 m beta functions, respectively, at the location of the windows.

EXPERIMENTAL MEASUREMENTS

In the following data, the beam emittance has been measured using flying wires in the Fermilab Main Injector before and after completing a round-trip transfer to and from the Fermilab Recycler. The beam passes through two Ti windows in the process. The measured blowup was $\Delta\epsilon = 7.6\pi(\text{horz}) + 7\pi(\text{vert}) = 14.6\pi$ mm-mr total--(blowup in both planes ~60%). No asymmetry was observed in the blowup. If the vertical and horizontal planes were completely mixed by the time of the measurement, then the combined expected blowup of at least 10.6π mm-mr is, in fact, completely consistent with the observed dilution (about $3-4\pi$ mm-mr can be attributed to nonlinearities in the accelerator systems). The mixing of the two planes was, in fact, verified through a pencil-beam measurement which evidenced blowup in the vertical plane only. Strong skew quadrupole components in the transfer line have been identified.

In a shutdown last winter the vacuum windows were completely removed and the flying wire data retaken. The large dilution disappeared leaving only the expected $3-4\pi$ mm-mr.

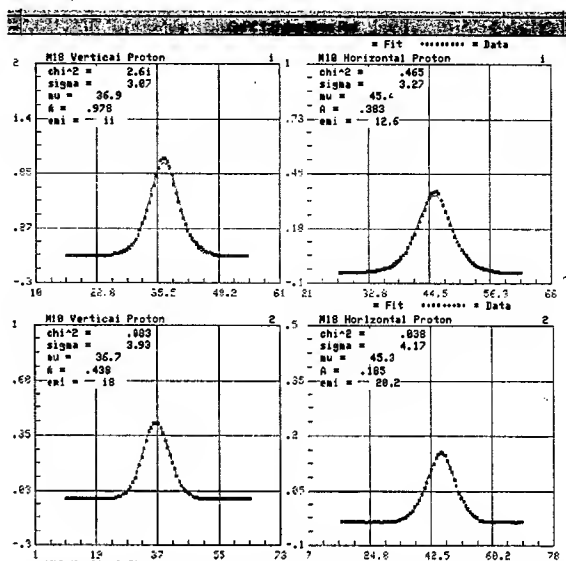


Figure 3. Flying wire data taken before and after transfer to the Recycler. The last number is the 95% normalized emittance as calculated from the data and the optics.

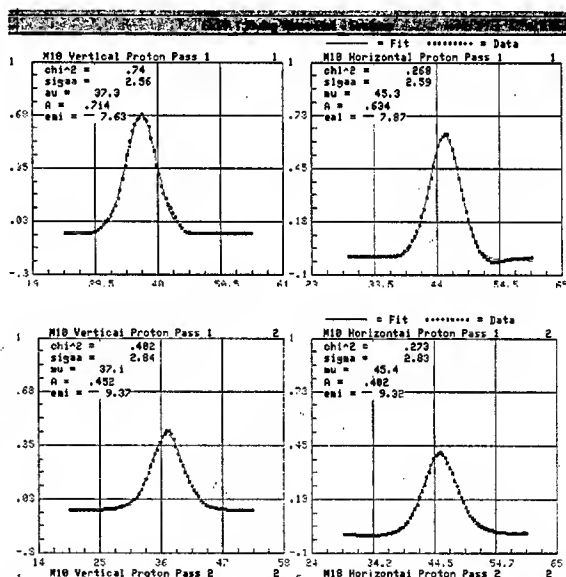


Figure 4. Flying Wire data as in previous figure with vacuum window removed.

REFERENCES

- [1] D. A. Edwards and M. J. Syphers, An Introduction to the Physics of High Energy Accelerators, J. Wiley, & Sons, Inc., New York (1993).
P. J. Bryant, Introduction to Transfer Lines and Circular Machines, CERN-84-04.
- [2] Phys. Rev. D, Vol. 66, Review of Particle Physics, July 2002, 1998.

AUTOMATIC BEAMLINE CORRECTION

T. Kobilarcik, J. DeVoy and C. Moore
FNAL, Batavia, IL 60510, USA*

Abstract

In the MiniBooNE experiment, a simple linear algorithm is used to maintain the correct beam position throughout the beamline and at the target. The algorithm is explained, and key features of the implementation are discussed.

INTRODUCTION

Experience has shown that in any fixed target experiment at Fermilab, the primary beam tends to "drift" over time. There are many causes for this drift, such as diurnal variation in temperature affecting control cards. Traditionally, it was the role of the operations group to monitor the beam position and make appropriate corrections.

When several HEP programs are run simultaneously, the number of operators needed to monitor the beamlines becomes large. Additionally, the work is extremely tedious—watching several monitors, making small corrections (and usually only being able to correct one position at a time). Even when features such as "three bumps" are incorporated in the control system, an operator can only adjust one position at a time.

Thus, making corrections to a beamline is a job well suited to automation. The response of the beam to changing individual magnets can be well characterized; the beam can be continuously monitored; appropriate limits can be placed so that the program "calls an expert" (for example, by setting an alarm) if conditions change too severely.

THE ALGORITHM

The algorithm used is simply the inversion of a set of linear equations.

A set of magnets, b , and a set of beam position monitors, x , are chosen. As each magnet is varied, the change in beam position at each beam position monitor is recorded. This leads to the linear expression:

$$\delta x = M \delta b \quad (1)$$

To implement the algorithm, one simply inverts the equation. Note that cross-plane coupling is naturally accommodated in this algorithm.

Exact Solution versus Least Squares Fit

One will note that in order to implement the algorithm, the matrix, M , must be invertible. A commonly asked question is "Why not implement a least-squares fit?" There are several reasons to choose an exact solution over a least-squares fit:

- An exact solution is just that—it always puts the beam where it should be, not just close.
- Having more beam position monitors than adjustable magnets provides no additional usable information.
- Having more adjustable magnets than beam position monitors implies that at some point along the beamline the trajectory is not known.
- The algorithm will fail if any one BPM fails. This is good—when instrumentation breaks it must be fixed.

Reasonable people may disagree with the relative merits of an exact solution versus least squares fit. Ultimately, one must make a decision and evaluate the outcome. Experience with the exact solution algorithm at Fermilab has shown that it is highly reliable [1], and thus was chosen for MiniBooNE.

General Implementation Concerns

Although inverting the set of equations gives an exact solution, the measured changes in beam position are never exact. Thus, one should never implement the full calculated change every spill. The present correction program also allows the user to specify a tolerance and a convergence factor for each beam position.

Thus, the corrections will not be applied unless the beam position is out of tolerance at one or more locations. The tolerance is usually 2 to 3 times the RMS position change during stable running, although at tight apertures the tolerance is smaller. Furthermore, only a fraction of the correction (typically 80%) is made.

Additionally, one must check that beam is actually present when the measurement is made, and that no magnet will beset beyond its operating limit.

IMPLEMENTATION SPECIFIC TO MINIBOONE

The generic name of the program is "Autotune". Variations of this program will be implemented for various beamlines as needed; the MiniBooNE autotune is the first. Autotune written in Java using a client-server model. The server part runs inside an Apache Tomcat servlet engine. The client runs on a user's desktop and communicates with the server via Xml-Rpc.

The Autotune Server

The Autotune server runs continuously inside an Apache Tomcat servlet engine. In simplest terms, it is an infinite loop that monitors the position of each beam pulse and, if

* Operated by Universities Research Association, Inc. under contract number DE-AC02-76CH03000 with United States Department of Energy.

necessary, computes and makes new settings for the trim magnets.

For the MiniBooNE beam, a complication is the fact that the beam is composed of a series of "pulse trains". Each pulse train contains a set of pulses arriving at 15 Hz intervals, with the trains separated by 2-3 seconds. Trying to correct each individual pulse at that rate is not feasible. Consequently, the pulses in each train are averaged and the correction applied before the next pulse train arrives.

The average of the pulses is a weighted average of the positions of each pulse in the train. The weight for each pulse is determined by a combination of the intensity and position of that pulse. Three weighting algorithms are currently defined:

- Use the intensities only. All pulses below a threshold intensity are given a weight of zero; those above are given a weight of one. Note that if all the weights are zero, we effectively assume that no beam is present.
- Compute an initial set of weights and the average position using the above algorithm. Any pulses farther from this average than a threshold distance are reassigned a weight of zero, and the average position recalculated.
- Like the above, but the threshold distance is based on a multiple of the rms of the initial average, rather than being a simple constant.

The parameters used for monitoring and controlling the beam (averaging algorithms, cut thresholds, lists of BPMs and trims to monitor, the matrix, etc.) are stored in a set of "control files" (implemented as a set of relational database tables). Any number of control files may be kept. The operators may load, unload, and modify the files as necessary.

The control loop operates as follows:

1. Initialize. Load the control file designated as "active", and initiate data acquisition.
2. Wait for a pulse train to arrive.
3. Get the position and intensity of each pulse as returned by each position/intensity monitor.
4. If any returned an error code, goto step 2. Else calculate the average position of the beam at each monitor.
5. If the average position of each pulse is within tolerance at each monitor, then no tuning is necessary. Goto step 2.
6. If the average position of any pulse is farther from the nominal than a given limit then we will not move the beam. Goto step 2. Rationale: if the beam is too far from the desired position at any point, it is assumed that the operating conditions have changed, or that something is seriously amiss. In either case operator intervention is indicated.

7. We will attempt to move the beam. Compute the change in trim magnet settings using the algorithm described in section 2. Note that the deltas in the settings are multiplied by the convergence factor (section 2.2). The convergence factor is currently a constant; in the future it may be made a function of the distance of the beam from the nominal. This would effectively merge steps 6 and 7.

8. Get the current setting of each magnet and add the delta computed above.

9. Set the new current for each trim magnet. Note that the operators have the option to suppress this step. This allows them to confirm that the calculations are correct before taking the program "live".

10. Goto step 2.

Testing indicates that the above loop takes about 200-300 ms.

The Autotune Client

The autotune client runs on a user's desktop and graphically displays the progress of the above loop. The horizontal and vertical position of the beam between adjacent monitors is indicated by a color-coded line: Green if the position is within tolerance at both monitors, Yellow if the intensity is low (at either monitor), Red if the position is out of tolerance (at either monitor).

Control buttons and dialog boxes are provided to allow the user to:

- Tell the server to suppress the setting of the trims (step 9) in the above loop.
- View the current readings (and possibly settings) in tabular format. This provides a more analytic view than the graphical display on the main screen.
- Create, modify, delete and load control files.
- Designate certain individuals (e.g., operators) as having the authority to make changes to the control files.
- View a log file of beam settings. That is, the server will keep a log of the times it has moved the beam. This gives an operator the opportunity to restore the trims to a prior state.

CONCLUSION

A simple algorithm has been implemented to correct for beam motion in the MiniBooNE experiment. The algorithm is easily extended to other beamlines.

REFERENCES

- [1] T. Kobilarcik, "Preliminary results of Stability Study for the KTeV Beam", FERMLAB-TM-2037

INCREASING THE INTENSITY OF THE FERMILAB BOOSTER

E. Prebys, C. Ankenbrandt, W. Chou, A. Drozhdin, P. Kasper, J. Lackey, N. Mokhov, W. Pellico, R. Tomlin, R. Webber
FNAL, Batavia, IL 60510

Abstract

The Fermilab Booster is a fast-cycling synchrotron which accelerates protons from 400 MeV to 8 GeV of kinetic energy. Until recently, the primary demand for protons was for antiproton production, which typically uses about $7E15$ protons per hour. Over the next few years, the Fermilab neutrino program will increase that demand dramatically, possibly beyond $1.8E17$ protons per hour. This paper discusses the issues involved in reaching these intensities, and the plan for achieving them.

- Maximum average repetition rate: $\sim 7.5\text{Hz}$, limited by heating of the RF cavities and the magnets in the injection dogleg. This may have to be increased to 10 Hz or more by 2006 or so.
- Aboveground radiation: limited by shielding and the occupancy classes of the buildings above.
- Beam loss in the tunnel. This is discussed in detail shortly.

INTRODUCTION

Overview

The Fermilab Booster [1] is the synchrotron which takes 400 MeV protons from the Fermilab Linac and accelerates them to 8 GeV for use by all of the lab's physics programs. It is 472 m in circumference and has a harmonic number of 84. The 96 combined function magnets which form its 24-fold symmetric lattice are configured in an offset 15 Hz resonant circuit.

Projected Proton Demand

Figure 1 shows the projected proton demand through the next few years. The primary users of protons are the two major neutrino experiments: MiniBooNE and NuMI/Minos.

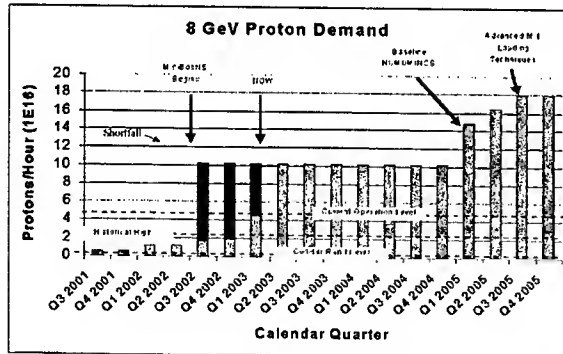


Figure 1: Projected Proton Demand

Limiting Factors

There are several factors that limit the total flux from the Booster:

- Maximum batch size: $\sim 5E12$ protons, limited by beam stability. At the moment, there is no plan for increasing this.

PREPARATIONS FOR HIGH INTENSITY

A great deal of work has been done to prepare the Booster for high intensity.

Longitudinal Damping System

At high batch intensities, coupled-bunch oscillations become a problem, so a longitudinal damping system [2] was developed which is crucial to high-intensity operation.

Shielding and Shielding Assessment

Initially, aboveground radiation was a severe limitation to total Booster flux, primarily because of the office space located above the ring. To address this problem, a large amount of shielding was added and a number of offices were moved and their space reclassified "minimum occupancy".

As a result, we believe we can meet even the ultimate requirements of the Booster without exceeding the aboveground limits.

Extraction Septum

Formerly, heating in the Booster's primary extraction septum limited the average repetition rate to about 2.5 Hz. Recently, both the septum and its power supply were replaced with a system which is capable of operating at the full 15 Hz rate.

MONITORING BEAM LOSS

The Booster is now physically capable of delivering the protons that are requested of it, and intensity is limited by the maximum acceptable beam loss in the tunnel. This is of concern both because of potential radiation damage to accelerator components and because activation of these components makes it difficult to service them.

We have generally attempted to keep the activation at key locations in the Booster tunnel to within a factor of two of what it was prior to the start of the neutrino program. Recall that we hope to achieve this while

ultimately increasing the total proton flux by more than a factor of 40.

We have two methods for monitoring beam loss during Booster operation. The first involves a system of 60 beam loss ionization monitors arranged around the ring. For each of these, a 100 second running sum is calculated, which is compared to a limit. Broadly speaking, limits have been set to be roughly twice the loss levels observed prior to the start of the neutrino program, but they have also been fine tuned based on observed activation in the tunnel. Booster operation is inhibited if any of these exceeds its limit.

In addition to the individual beam losses, the average beam power loss is calculated by measuring the derivative of the number of protons in the ring, weighting it by beam energy, and integrating it through the cycle. Presently, we limit this power loss to 400W. The limit was chosen in similar manner to the individual loss limits, but it is remarkably close to the 1W/m limit specified for the SNS.

KNOWN LATTICE PROBLEMS

Both of the Booster's extraction regions involve a four magnet dogleg to vertically steer the beam around the extraction septum during acceleration. These doglegs operate at fixed current, and bend the beam by 42 mrad at injection. It has recently been discovered that edge focusing effects in these doglegs cause severe lattice distortions [3], which are worst at injection and fall off as $1/p^2$. Figure 2 shows the effect of these doglegs at injection. It is now believed that these lattice distortions are a major cause of losses early in the cycle.

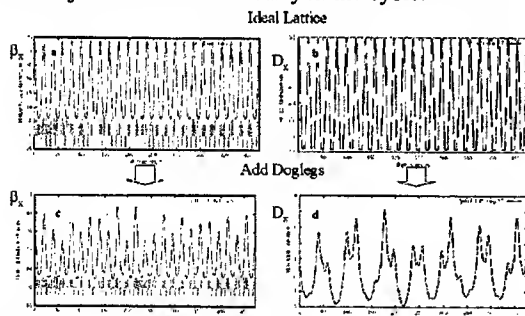


Figure 2: Lattice distortions due to the extraction doglegs. The ideal horizontal lattice functions are shown in (a) and (b), respectively, while (c) and (d) show these functions including the effects of the extraction doglegs.

RECENT PERFORMANCE

Figure 3a shows the output of the Booster in protons per minute starting in August, 2002. Although the proton flux has increased by more than a factor of 12 during this period, the average activation in the Booster tunnel has only increased by about a factor of two to three. This is illustrated in figure 3b, which shows the energy loss per proton over the same period. The primary reasons for this

improved performance are increased attention to beam losses, and specific tuning to minimize the dogleg current.

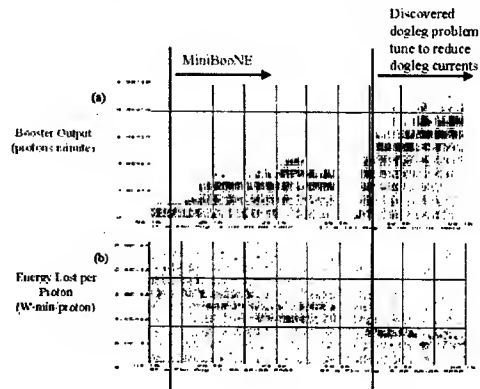


Figure 3: Booster performance since Aug. 2002.

MAJOR UPGRADE PROJECTS

Collimator Project

The biggest single project to increase the Booster intensity is the implementation of a collimation system [4]. Figure 4 illustrates the principle. High amplitude particles are intercepted by a thin primary foil, and subsequently absorbed by thick stainless steel secondary collimators. Each of the secondary collimators intercepts the beam on one edge in each plane.

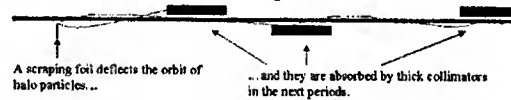


Figure 4: Collimation principle of operation.

The otherwise simple design is complicated by the need for fairly extensive shielding of the secondary collimators. We lack a quantitative model for Booster beam loss, so the shielding needs were calculated based on the assumption that the collimation system would intercept more or less all of the beam which is currently observed to be lost during the acceleration cycle. For the sake of calculation, the loss was taken to be 30% of the beam at injection energy (400 MeV) and 2% near extraction energy (8 GeV) with the Booster delivering the maximum proton flux which is foreseen.

This leads to a shielding requirement of about 4' long steel 2' thick around each of the three secondary collimators. To avoid the need for moveable parts or vacuum seals in the extreme radiation environment inside the shielding, we settled on a design in which the secondary collimator jaws are fixed within monolithic steel shielding blocks. Each block is attached to the beam pipe on either end with bellows, allowing the *entire assembly* to move over the range required by collimator operation.

The design of the collimator system is more or less complete and construction is underway. Installation is planned for the 2003 summer shutdown.

Large Aperture RF System

The 18 cavities of the Booster RF system have 2¼" drift tubes. This aperture restriction is of particular concern because it results in activation of the cavities themselves, which are a high maintenance item.

A powered prototype of a new cavity with a 5" aperture was built and tested last year. Based on the success of these tests, work is proceeding on two vacuum prototypes. In order to reduce the cost of these cavities and expedite the fabrication, a substantial number of the parts have been machined at universities involved in the lab's neutrino program.

All the major parts have now been completed and assembly of the cavities has begun. We are on schedule to replace two of the existing cavities with these new cavities on the summer shutdown. Based on our evaluation of the effectiveness of these prototypes, we will make the decision whether to proceed with the complete replacement of the RF system over the next few years.

Extraction Dogleg Improvements

As mentioned before, ameliorating the dogleg problem has become one of our primary goals.

In the fairly near term, there's a plan to stretch out the distance between the magnets of the doglegs. Over the summer shutdown, we hope to increase the distance between the dogleg magnets of the primary extraction region from 18" to 41". Because the effect goes as the square of the bending angle, this will be almost a factor of five reduction for this dogleg. Ultimately, we hope to do the same for the second extraction region.

We are also considering ways to completely eliminate the need for the doglegs. These include:

- Putting large aperture lattice magnets upstream of the extraction septum, so that the septum blade may be moved completely out of the beam.
- Adding a pulsed bump within the extraction period which is only energized near extraction time.
- Develop a septum that mechanically moves into the beam near extraction. This would involve motion of about 2-3 cm at 15 Hz.

Beam Orbit Control

While the main lattice elements of the Booster ramp sinusoidally, the correction dipoles have historically been operated DC. This means that the beam position moves on the order of several millimeters over the acceleration cycle. Among other things, this will complicate the use of the collimation system.

A system has been designed to use ramped current controllers to maintain beam position during acceleration. Details are described elsewhere [5], but the basic idea is that beam positions will be measured at discrete times in

the cycle and corrections will be calculated to move these orbits to the ideal orbit, subject to the limitations of the power supplies.

This system is currently in the commissioning phase.

Lattice Improvements and Space Charge Mitigation

Recently, there has been a dramatic increase in the effort to accurately model the Booster, with particular interest in space charge issues [6].

One immediate result of the improved model was the discovery of the dogleg problems.

This effort continues on a number of fronts, which are too numerous to mention here, but we have hopes that other problems and solution will be found.

CONCLUSIONS

The 30 year old Fermilab Booster has made impressive progress toward meeting the demands of the Fermilab neutrino program. The proton flux has increased by roughly a factor of 12 over that prior to the start of the MiniBooNE experiment in August, 2002. This has been accomplished with only roughly a factor of two increase in the activation of tunnel components.

On the other hand, we are still delivering only about 45% of the MiniBooNE baseline request. With this, the turn-on of the NuMI beamline in 2005, and proposed increases in the needs for antiproton production, the Booster flux will have to increase by about another factor of five over the next few years.

A number of improvements are planned which make us optimistic that we can reach these goals.

ACKNOWLEDGEMENTS

These dramatic improvements in Booster performance would not have been possible without the efforts and dedication of the Fermilab operations department and technical support departments.

This work was supported by the U.S. Department of Energy, under contract DE-AC02-76CH03000.

REFERENCES

- [1] Fermilab Technical Memo TM-405 (1973).
- [2] See minutes of Fermilab Booster Modeling Group, www-bd.fnal.gov/pdriver/booster/meetings.html, Jan 23, 2003.
- [3] D.A. Herrup, D.McGinnis, J. Steimel, and R. Tomlin, "Analog Dampers in the Fermilab Booster", 1995 PAC Proc., p. 3010.
- [4] N. Mokhov, *et al* "Fermilab Beam Collimation and Shielding", 2003 PAC, TPAG033 (2003).
- [5] L. Coney and E. Prebys "Booster Orbit Correction", 2003 PAC, TPPE017 (2003)
- [6] W. Chou, *et al* "Space Charge Studies in the Fermilab Booster", 2003 PAC, RPAG017 (2003).

FNAL BOOSTER: EXPERIMENT AND MODELING

P. Spentzouris*, J. Amundson, FNAL, Batavia, IL 60510, USA

Abstract

We present measurements of transverse and longitudinal beam phase space evolution during the first two hundred turns of the FNAL Booster cycle. We discuss the experimental technique, which allowed us to obtain turn-by-turn measurements of the beam profile. The experimental results are compared with the prediction of the Synergia 3D space charge simulation code.

INTRODUCTION

The Fermilab Booster is a rapid-cycling, 15 Hz, alternating gradient synchrotron with a radius of 75.47 meters. The lattice consists of 96 combined function magnets in 24 periods, with nominal horizontal and vertical tunes of 6.7 and 6.8 respectively. The Booster accelerates protons from a kinetic energy of 400 MeV to 8 GeV, at a harmonic number $h=84$, using 17 rf cavities with frequency which slews between 37.7 MHz (at injection) and 52.8 MHz (at extraction). The revolution time at injection is $2.2 \mu s$. A comprehensive technical description of the Booster as built can be found in reference [1]. The injection system utilizes the H^- charge-exchange injection technique. The typical linac peak-current is 45 mA; usually up to eleven turns of H^- beam are injected in the booster. The injected beam is a stream of bunches equally spaced at the linac rf frequency of 201.2 MHz. During injection, a pulsed orbit bump magnet system (ORBUMP) is used to superimpose the trajectories of the circulating (protons) and injected (H^-) beams.

There are many factors affecting the behavior of the Booster beam, including the energy and emittance of the incoming beam, nonlinear field errors and space charge effects, which are believed to be responsible for a significant fraction of the observed losses in the Booster [2] during the first 2 ms of the cycle (injection, capture, and bunching phase). Since the performance of the Booster is what makes or breaks the FNAL neutrino program, and its stable operation is required for the FNAL collider program, it is essential to study and quantify these effects. In order to achieve this goal, we have developed a fully three dimensional (3D), Particle In Cell (PIC) model of the booster, based on the package Synergia [3]. The Synergia package has been developed under the DOE SciDAC initiative for accelerator modeling, *Advanced Computing for 21st Century Accelerator Science and Technology*. Synergia incorporates existing packages for modeling 3D space charge and computing transfer maps using Lie algebraic techniques. It utilizes a split operator technique for particle propagation, includes a parser of the *Methodical Acceler-*

ator Design (MAD) language, and has multi-turn injection modeling capabilities. The code has the capability to compute higher order transfer maps, but linear maps were used for the simulations presented in this paper.

In the following sections, we describe measurements of Booster beam evolution during the first 200 turns after injection, and present comparisons with the Synergia model.

EXPERIMENTAL DATA AND COMPARISON TO SIMULATION

The objective of the experiments was to study the beam evolution in the first few hundred turns after injection, by comparing transverse and longitudinal beam widths to the simulation, with single turn time resolution, for different beam currents. The FNAL Booster has two measuring devices capable of measuring of beam widths with such resolution: the *Ion Profile Monitor* detector (IPM) [4], which utilizes the ions from ionization of the residual gas by the proton beam to measure transverse beam profiles, and the *Resistive Wall Monitor* (RWM) device, which utilizes the induced current on the beam pipe by the particle beam, to measure the longitudinal beam profile. Since the response of the IPM depends on the charge of the beam, and since the goal of the experimental program is to use this detector for a quantitative study of space charge effects, we installed a third measuring device, the "flying beam" wire, in order to check and calibrate the performance of the IPM.

IPM calibration

The IPM detector measures the projection of the beam distribution on each one of the transverse coordinates. An applied transverse clearing field of 8 kV causes the ions to drift to a micro-channel plate (MCP). (The beam direction defines the longitudinal coordinate). The detector is 0.5 m long, with a transverse gap of 12 cm. The MCP plate is $8 \times 10 \text{ cm}^2$ and has strip spacing 1.5 mm. For an ideal measurement of one projection, the ions' drift should be parallel to the other (non-measured) coordinate. The external clearing field is applied on the beam along the non-measured coordinate to achieve this objective. The response of detector is complicated by the effect of the fields of the beam itself. The field due to the beam is not transverse, so it distorts the behavior from the ideal. As a result, the response of the IPM depends on the charge of the beam, so it has to be calibrated as a function of the injected number of protons.

In order to perform an experimental measure of the IPM calibration, we took width measurements simultaneously with the Booster IPM, the MI-8 extraction line wire cham-

* spentz@fnal.gov

ber and the so-called “flying beam” wire [5]. The “flying beam” wire is a single wire measuring device at the Booster Long 1 section, which can be parked just outside the beam envelope of the *injected* beam, i.e. beam envelope with the ORBUMP magnets on. At injection, the ORBUMP magnets keep the beam trajectory displaced by ~4 cm with respect to the nominal beam orbit, so that the injected H^- ions will pass through a stripping foil. The wire is placed between the displaced and nominal orbits. As the ORBUMP current decays, the beam sweeps through the wire, providing a measure of the horizontal beam profile. By recording the ORBUMP current as a function of time, $I(t)$, and the response of the wire as a function of time, $a(t)$, we can reconstruct the horizontal profile, $a(x)$, as measured by the wire by using the known beam position as a function of current, $x(I)$. The result of the calibration is a parameteri-

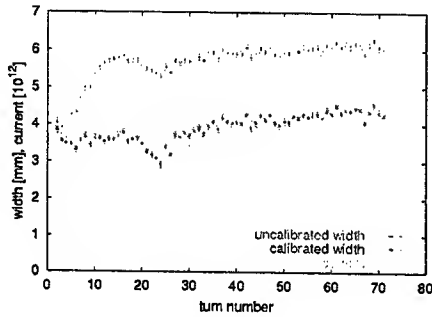


Figure 1: IPM horizontal beam width in the Booster (mm) as a function of time (in Booster turns -2.2 micro seconds), at injection. Both the calibrated (blue) and uncalibrated (red) widths are shown. Also shown (green curve) is a simultaneous measurement of the beam current in the machine, in units of 10^{12} protons/turn.

zation of the true width as a function of the measured width and the charge injected in the machine.

The importance of the calibration for the Booster IPM detector and the size of the beam self-field induced effects is demonstrated in Fig. 1, where both the calibrated and uncalibrated IPM beam profiles are shown, together with the beam current, as a function of time. The effect is most dramatic during the first eleven turns in the machine (injection time), since the beam current is changing. The change of the uncalibrated beam width clearly tracks the beam current change. The calibrated width shows a much smaller variation during the injection period.

IPM transverse profile measurements

We collected data with the IPM detector in three different time periods and for different configurations of the Booster injection bump magnets (ORBUMP). The different data sets were collected on November and December 2002, and April and May of 2003. We took measurements for different injected beam currents, for different timings of the injected beam with respect to the ORBUMP current pulse

flattop, and for different shapes of the ORBUMP pulse (this change was implemented in 2003 to reduce heating problems). For each setting we took at least ten different measurements of beam profiles and beam currents over the full machine cycle. The data were corrected using the IPM calibration obtained with the procedure described in the previous section. There is a correlation between beam losses and beam envelope perturbations early in the cycle and the ORBUMP timing [6]. In Fig. 2 the horizontal and vertical beam widths are shown as a function of time, together with the normalized beam current. The different curves correspond to different injection timings with respect to the ORBUMP (averaging the corresponding data sets). All data sets were taken with 11×40 mA of beam injected in the Booster. Both the beam width perturbations and the losses move in time with the change of timing with the same offset used in the trigger. One of the data sets averaged in

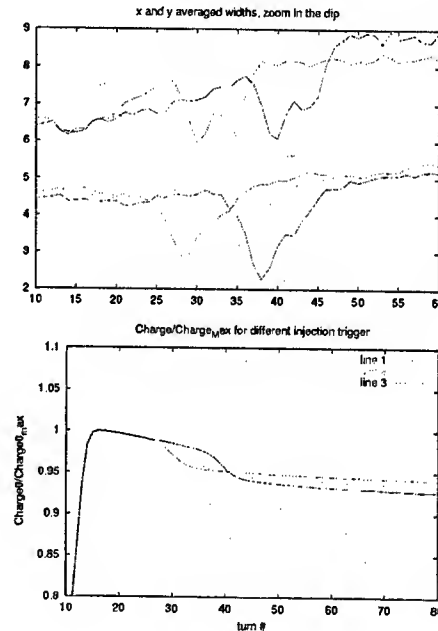


Figure 2: Top: IPM horizontal and vertical beam widths (mm) versus time (turn number). Bottom: Normalized charge, to the maximum charge in the machine), versus time (turns). The time window is around the time that the ORBUMP turns off.

Fig. 2 is shown in Fig. 3 compared to the *Synergia* prediction (run with an input emittance two times smaller than the nominal). The model describes the data well, except of the region of the beam perturbation due to the injection bump, which was not included in the model. To verify that the injection bump fringe field can cause such effects we included a very simple model of this field in our simulation. A comparison of the prediction of the model to the data is shown in Fig. 4. The model includes just a quadrupole term in the non bending view of the bump magnet, with strength which has the same time dependence as the current pulse

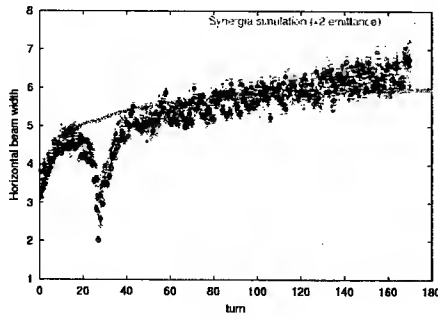


Figure 3: Comparison of horizontal beam width as a function of time, measured with the IPM, to the prediction of *Synergia*.

of the magnet. The model seems to reproduce the general

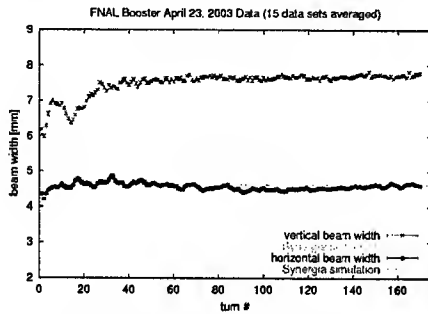


Figure 4: *Synergia* model, including the ORBUMP effect compared to horizontal and vertical beam widths as a function of time.

features of the data.

Longitudinal profile measurements

The purpose of these measurements were to obtain a data set under well defined conditions in order to check the model implementation. The data set was obtained with the Booster running DC (rf system off and no ramping of the magnet power supplies). This was done in order to simplify the running conditions and reduce the number of parameters in the comparisons. To further reduce complications in the initial conditions, only a single turn worth of Linac beam was injected in the machine. The current of the Linac beam was controlled by detuning one of the Linac quadrupoles. Under these conditions, we took data with injected beam of 11, 20, and 42 mA, and recorded the evolution of the longitudinal beam profile using the RWM. Already, after ~ 5 turns in the machine, the beam distribution in time is almost flat within the 200 MHz time slices (the injected beam has the structure of the 200 MHz Linac rf system). In Fig. 5 the RMS of the time distribution of the beam in a 200 MHz time slice is plotted versus the turn number. The data (points) are compared to the simulation (lines) for the different values of injected beam current.

There is good qualitative agreement between data and sim-

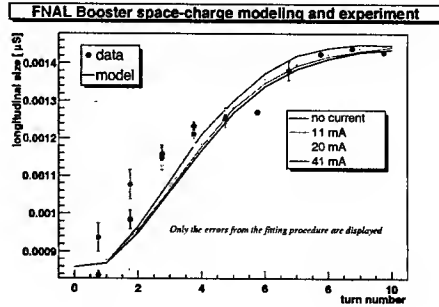


Figure 5: Longitudinal phase space evolution. Beam distribution RMS width in time as a function of turn number. The data from the RWM measurements (points with error bars) is compared to the model prediction from *Synergia* (lines).

ulation. The model predicts very small effects due to the different beam currents, well within the uncertainty of the measurement. Both the data and simulation extracted RMS widths tend to a constant value, since they are calculated within a 200 MHz time slice. Note that in the simulation we only model one 200 MHz bunch with periodic boundary conditions. This is an accurate representation of the main body of the beam (see discussion in [3]).

REFERENCES

- [1] Booster Staff 1973 *Booster Synchrotron* ed E L Hubbard Fermi National Accelerator Laboratory Technical Memo TM-405
- [2] Popovic P and Ankenbrandt C 1998 *Workshop on Space Charge Physics in High intensity Hadron Rings* ed A U Lucio and W T Weng (Woodbury, New York: AIP Conference Proceedings) p 128
- [3] J. Amundson and P. Spentzouris, "A Hybrid, Parallel 3D Space Charge Code with Circular Machine Modeling Capabilities", Proc. International Computational Accelerator Physics Conference (ICAP 2002), Michigan State University, Oct. 2002; see also J. Amundson and P. Spentzouris *this proceedings*
- [4] Zagel J, Chen D, and Crisp J 1994 *Beam Instrumentation Workshop* (AIP Conference Proceedings 333) p 384
- [5] J. Amundson, J. Lackey, P. Spentzouris, G. Jungman, and Linda Spentzouris, "Calibrating the Booster Ionization Profile Monitor: Preliminary Summary", FNAL Beams Document 495-v2, <http://beamdocs.fnal.gov/>, 2003.
- [6] P. Spentzouris and J. Amundson "Booster beam profiles and losses before and after dog leg and ORBUMP magnet changes", FNAL Beams Document 581-v1, <http://beamdocs.fnal.gov/>, 2003.

END-TO-END SIMULATIONS OF A SUPERCONDUCTING DEUTERON CH-DTL FOR IFMIF*

A. Sauer, H. Deitinghoff, H. Klein, H. Liebermann, H. Podlech, U. Ratzinger, R. Tiede
J.W. Goethe-University, Frankfurt/Main

Abstract

The IFMIF project (International Fusion Materials Irradiation Facility) requests two cw linacs operated in parallel. Each of them is designed to provide a 5 MW 125 mA deuteron beam at 40 MeV for the production of an intense neutron flux with an energy around 14 MeV. This paper presents an alternative linac design for this project. The acceleration is completely based on H-type cavities. The room temperature (rt) 4-Vane-RFQ and a short IH-DTL (Interdigital-H-DTL) are followed by 4 superconducting (sc) CH-DTL (Crossbar-H) cavities. The operating frequency is 175 MHz, the designed section lengths are 13 m for the RFQ (Radio-Frequency-Quadrupole) (5 MeV), 1 m for a compact MEBT (Middle Energy Beam Transport), 2 m for the IH-cavity (10 MeV) and 9 m for the sc CH-DTL (40 MeV). The structure parameters and end-to-end multiparticle beam dynamics calculations with and without DTL errors of the whole linac will be presented and the results will be discussed.

1 INTRODUCTION

Extended particle dynamics investigations of the reference IFMIF DTL layout (Four-Vane-RFQ+Alvarez-DTL) showed a very robust beam behaviour for the Alvarez-type DTL. Even with the reduction of the input energy – to reduce the length of the RFQ – and the favourable lower input power per tank gave in all cases stable solutions, good emittance conservation, strong transverse and longitudinal focusing, no particle losses and sufficient large aperture factors even with including standard quadrupole and rf errors and mismatched input beams [1]. This layout has an overall length of 46 m. The rf power consumption per linac is estimated around 7.5 MW. Technical challenges in case of the Alvarez-DTL are the high thermic load per meter in combination with a quadrupole singlet channel where each magnet is housed in a drift tube on a slim stem. Beam dynamics studies for a corresponding rt IH-type DTL showed its capability for high intensity acceleration with good power efficiency. Investigations on beam stability against matching, field and quadrupole errors showed however, that the IH-DTL is due to the KONUS-dynamics (Kombinierte – Nullgrad – Struktur) more sensitive to errors than the Alvarez [2,3]. Both rt structures showed in combination with a special compact MEBT no particle loss and smooth beam behaviour, but the RFQ+Alvarez-DTL combination gave higher aperture factors and lower emittance growth [1].

Due to the mandatory cw operation mode of the IFMIF facility the combination of a short rt IH structure and a

chain of sc CH resonators with inter tank focusing has also been made which in addition fulfills the requirements for a high current IFMIF DTL. The sc CH DTL part provides very high rf and acceleration efficiency and due to its special cell geometry high mechanical robustness. The sc drift tube linac has a total length of ≈ 11 m only, the cryostat length is ≈ 8 m. The estimated total plug power (including all cryostat losses) per meter of this design study is ≈ 1.5 kW/m (for comparison the rt linacs need ≈ 50 kW/m assuming 50 % amplifier efficiency), which demonstrates the high rf efficiency of the sc CH modules. In connection with large drift tube apertures the risk of particle losses in the sc part is reduced. Detailed simulations showed also a low sensitivity of the beam behaviour and beam quality against all combinations of statistic and mechanical errors, i.e. transverse quadrupole triplet displacement errors ± 0.1 mm and a rotation of $\pm 1^\circ$, rf phase errors $\pm 1^\circ$, rf amplitude errors $\pm 1\%$ and quadrupole gradient errors $\pm 1\%$ [1].

2 THE FOUR-VANE-RFQ

For all DTL studies the same reference design of an RFQ has been used to be comparable between all design versions for the IFMIF linac. Table 1 gives a summary of the RFQ structure and beam parameters. The main goal was a lowered Kilpatrick factor of 1.7 to reduce the sparking probability due to the required cw operation. Nevertheless the transmission should be high as well as the beam quality at the RFQ output to allow good matching to the following DTL. In the design the recipe of equipartitioning has been applied leading to a parameter set, which fulfills the IFMIF requirements [4].

Table 1: Structure parameters of a Four-Vane-RFQ for IFMIF.

RFQ-Parameters	Values
A/q	2 (D^+)
RF-frequency f [MHz]	175
In / Out energy W [MeV]	0.1 / 5.0
P_{tot} [MW]	1.506
Peak field E_{peak} [MV/m]	23.77
Cells / length [m]	659 / 12.31
In / Out current [mA]	140 / 132.7
In / Out $\epsilon^{N,rms}_{trans}$ [cm \times mrاد]	0.020 / 0.023
In / Out $\epsilon^{N,rms}_{long}$ [cm \times mrاد]	0 / 0.043

In Fig 1. the matched output distribution of the RFQ at 5 MeV calculated with PARMTEQM® (multipole effects and image charges included) is plotted. The transmission

*Work supported by the EU, BMBF (number: 060F998) and GSI.

is about 95 % with good beam quality. The transverse rms emittance growth is less than 10 % and the beam is well confined with a few halo particles only.

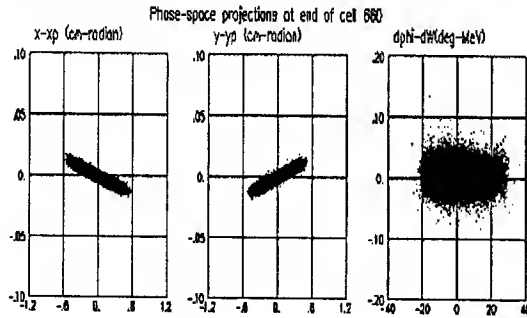


Fig. 1: Output distribution at 5.0 MeV of the Four-Vane-RFQ, calculated with 50000 macro particles.

It should be mentioned, that the matching to the RFQ can be accomplished by a conventional partly space charge compensated magnetic LEBT (Low Energy Beam Transport) with low influence on transmission and beam quality. Therefore the output emittances of Fig. 1 have been taken for the beam dynamics simulations through the DTL, aiming for preliminary results for the beam behaviour from source to 40 MeV to ensure stable and loss free operation in the whole IFMIF accelerator facility.

3 BEAM DYNAMICS DESIGN OF A SC CH-DTL

The sc CH-version (design and structure parameters of table 2 and Fig. 2 made with LORASR©) turned out to be superior to the rt IH-design with respect to the following critical issues: a) no cooling problems in cw operation b) reduced linac length and less tanks, i.e. higher efficiency and lower structure periods c) larger drift tube diameters up to 8 cm. The beam behaviour is smooth, no losses along the linac occurred and a good safety margin could be reached in the sc linac against losses due to mismatch and standard DTL errors. Extended electromagnetic simulations have been performed with Microwave Studio® to optimize the parameters of the first and last superconducting CH cavity for IFMIF. It was possible to further reduce the electric and magnetic peak fields to modest values which is important for reliable routine operation. Fig. 3 gives a real 3D sketch of the optimized 175 MHz sc CH tanks 1 and 4 in the critical low energy part and at the high energy end of the DTL, calculated with Microwave Studio®.

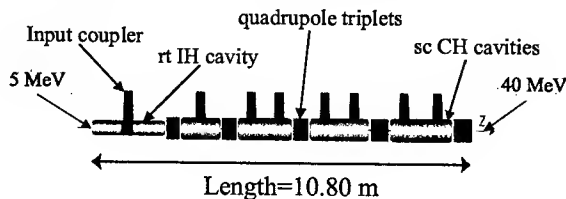


Fig. 2: Scheme of a 175 MHz sc IH/CH-DTL.

Table 2: Design parameter of a 175 MHz sc IH/CH-DTL for IFMIF + Cavity parameters of sc CH tank 1 and 4.

Design parameters	SC CH-DTL	Units	
A/q	2 (D ⁺)		
In-/out current	125.0 / 125.0	mA	
Frequency	175.0	MHz	
Number of tanks	5 (INC+4SC)		
P _{tot}	4.44	MW	
W _{in} / W _{out}	5.0 / 40.1	MeV	
Cells / Length	73 / 10.8	m	
a ₀ of DT	NC:1.5 SC:2.4 - 4.0	cm	
In- / Out rms ε ⁿ _{trans}	0.035 / 0.091	cm×mrad	
In- / Out rms ε ⁿ _{long}	0.070 / 0.097	cm×mrad	
Cavity parameters	CH 1	CH 4	Units
Beta	0.1	0.2	
Frequency	175.00	175.00	MHz
E _{acc} (=E ₀)	5.00	4.3	MV/m
Tank length	1.20	2.30	m
Tank diameter	52.9	67.3	cm
Gaps	12	12	
E _{peak} /E _{acc}	4.01	3.75	
B _{peak} /E _{acc}	7.73	8.46	mT/MV/m

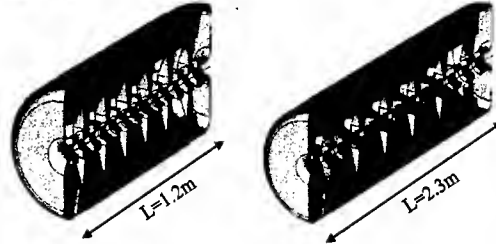


Fig. 3: 3D view of the first and last 175 MHz sc CH-cavities (tank 1 and 4) calculated with Microwave Studio®.

4 END-TO-END SIMULATIONS

As a last method for testing the global stability of the complete injector facility against particle losses integrated overall multiparticle simulation studies of the whole 25 m long sc linac (RFQ+MEBT+sc IH/CH-DTL) were performed with the programs PARMTEQ® and LORASR©. Fig. 4 plots the 100 % transverse beam envelopes along the whole linac in the nominal case without assuming mechanical and rf tolerances. Fig. 5 displays the phase space distribution in this case at the exit of the linac at 40.1 MeV. The beam behaviour is smooth, no losses after the RFQ occurred, a good safety margin could be reached throughout the sc part of the H-DTL against losses. The output distribution is well confined with a quasi elliptic dense core.

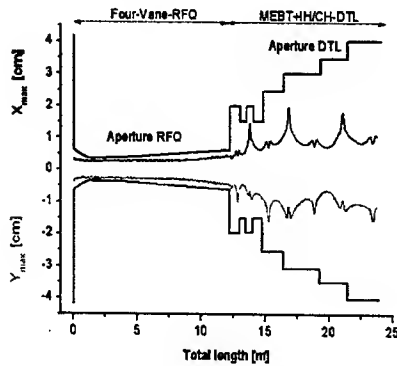


Fig. 4: 100 % transverse beam envelopes along the whole linac (RFQ+MEBT+H-DTL) in the nominal case.

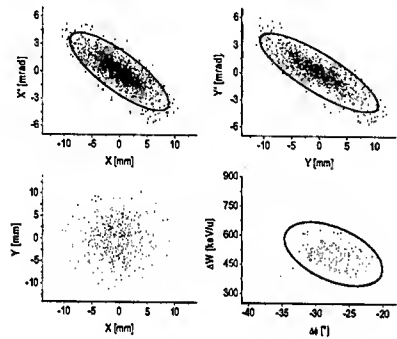


Fig. 5: Output distribution of the linac at 40.1 MeV in the nominal case, 2000 macro particles used.

At least the overall simulations were repeated, but now with applied combined statistically distributed standard mechanical, rf and quadrupole triplet gradient errors for the MEBT and the following H-DTL, i.e. transverse quadrupole triplet displacement errors ± 0.1 mm and a rotation of $\pm 1^\circ$, rf phase errors $\pm 1^\circ$, rf amplitude errors $\pm 1\%$ and quadrupole gradient errors $\pm 1\%$. The Figs. 6 and 7 show the results of the numerical multiparticle calculations of the IFMIF linac for this case. The 100 % beam envelopes are still smooth. No further losses occur after the RFQ and the phase space at the exit of the H-DTL at 40.1 MeV is still quasi elliptic and well confined.

5 CONCLUSION

The superconducting CH-structure in combination with the KONUS beam dynamics layout is well suited for the efficient acceleration of intense light ion beams. Extended beam dynamics simulations gave high transmission, also in case of statistically distributed mechanical, rf, quadrupole gradient and matching errors due to a low number of rf and structure periods of the H-DTL with KONUS dynamics. Also integrated overall simulations of the whole linac (RFQ+H-DTL) with and without mechanical and optical tolerances showed a smooth beam behaviour, moderate emittance growth and a non-chaotic beam be-

haviour without particle loss. A downscaled 1:2 room temperature copper model has been built and tested in order to investigate basic rf properties, tuning methods and to validate the simulations. There was an excellent agreement between the simulations and the measurements [5]. The order for a 350 MHz superconducting prototype of bulk niobium has been placed already. The prototype will be tested in the new cryo lab at the IAP Frankfurt which has been equipped with a cryostat, a magnetic shielding, dewars and a class 100 laminar flow box [6].

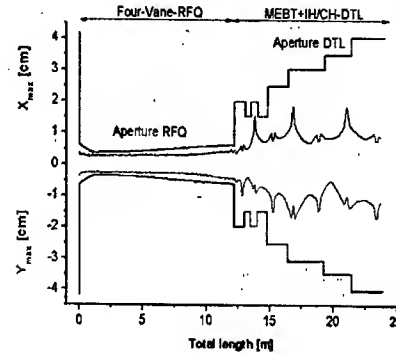


Fig. 6: 100 % transverse beam envelopes along the linac with combined errors for the MEBT and H-DTL.

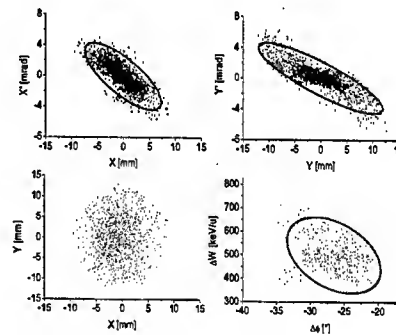


Fig. 7: Output distribution of the linac at 40.1 MeV with combined errors of the MEBT and H-DTL, 2000 macro particles used.

6 REFERENCES

- [1] A. Sauer, PhD. Thesis, JWGU-Uni. Frankfurt, March 2003.
- [2] A. Sauer et al. "Investigation of a normal conducting 175 MHz Linac design for IFMIF", EPAC 2002, Paris, France, June 2002.
- [3] U. Ratzinger, "Effiziente HF-Linacs für leichte und schwere Ionen", JWGU-Univ. Frankfurt, July 1998.
- [4] R. A. Jameson, "Some Characteristics of the IFMIF RFQ KP1.7 Designs", Int.-Rep, Frankfurt, Germany, May 2000.
- [5] H. Podlech et al., this conference.
- [6] H. Liebermann et al., this conference.

DEVELOPMENTS IN LINEAR AND NON-LINEAR DAΦNE LATTICE

C. Milardi, G. Benedetti, M. E. Biagini, C. Biscari, M. Boscolo, S. Guiducci, M. Preger,
P. Raimondi, C. Vaccarezza, M. Zobov, INFN-LNF, Frascati, Italy

Abstract

The agreement between the DAΦNE model and the measured machine parameters (betas, dispersion etc) has further improved in the 2002 runs. A better dispersion function control has been obtained by modifying the closed orbit correction algorithm, which now includes corrector strength minimization.

The model has been integrated in the accelerator control system, providing a faster and reliable tool for fine and on-line machine optics tuning.

New measurements, such as the machine second order dispersion, have proved to be very effective in studying the second order terms in the rings.

Measurements of second order chromaticity and tune shift on amplitude have extended our knowledge about the lattice up to the third order.

INTRODUCTION

DAΦNE [1], the Frascati electron-positron collider working at the energy of the Φ resonance, has run in year 2002 mainly for providing luminosity to the physics experiments. Nevertheless, 10% of its uptime has been used for machine optics studies aimed at improving the machine model understanding as well as the machine performances.

DAΦNE has two Interaction Regions (IRs), each housing an experiment: KLOE studies CP violation in kaon decays and DEAR investigates exotic atoms. The two experiments cannot run at the same time and have different collision optics, due to the strong differences in their IRs magnetic structures and in their experimental setups.

LINEAR MODEL

As a matter of fact, the model of an operating accelerator evolves continuously. At DAΦNE during the past year the lattice model experienced a remarkable evolution due to a deeper understanding of the machine behaviour.

The model is based on the MAD design program [2]. The machine element description has been completely reorganized in order to make file sharing and evolution easier. The agreement between measured and simulated Twiss parameters (betas, dispersion, tunes) has been improved. The same model describes now, using the same set of model parameters, the two collider rings. These parameters have been moved back to their nominal values, with the exception of those few, describing situations really different from the nominal one. It's worth recalling that DAΦNE is a very compact machine (97.98 m long), with no periodicity at all, running with the KLOE strong detector solenoid always on

($Bds = 2.4$ Tm, to be compared with a magnetic rigidity $B\rho = 1.7$ Tm). As a consequence the model parameters are far from being independent.

The description of the machine quadrupoles has been improved and their focusing strength related directly to the magnet power supply readout. The same has been done for the splitter magnets.

Procedures have been written, using the MAD formalism, to easily change scalar quantities such as tunes, momentum compaction and energy at constant optical functions. The same has been done for optical variables such as betatron functions, horizontal and vertical dispersion and phase advances. Special care has been dedicated to the beta functions at the IPs to investigate their impact on luminosity and beam-beam behaviour and at the position of sextupoles to optimize their efficiency and therefore the dynamic aperture. All these procedures can start from any operating point of the ring, calculate the required variations, returning the results in terms of current changes to be set on the magnetic elements specified.

The upgraded model has been ported on the Control System [3] and almost completely integrated in the Control System Software. A first version of model interface has been developed allowing comparison among different simulated optics and between simulated and measured optical functions, see Fig. 1.

The on-line model has demonstrated to be a flexible tool not only in computing, but also in exploring efficiently different machine configurations, even during experiment data taking.

DEAR Optics

ONE of the most relevant modifications to the DAΦNE optics concerns the DEAR IR [4].

The original design of the DEAR IR is based on quadrupole triplets (FDF) placed at both sides of the Interaction Point (IP) and providing a low vertical beta. In this configuration at the end of 2001, the optical functions at the IP were $\beta_x^* = 4.4$ m and $\beta_y^* = .04$ m.

By switching off the inner focusing quadrupole and by retuning the other two (FD), it has been possible to reach $\beta_x^* = 1.7$ m and $\beta_y^* = .038$ m (see Fig. 1) thus reducing the DEAR IR contribution to the chromaticity. The optics of the two rings has been kept almost unchanged outside the DEAR IR, avoiding a time consuming optimization due to different phase advances between sextupoles, between injection kickers and different beta values at the feedback pick-ups.

Last but not least, the new configuration has provided 50% reduction of β_x at the first parasitic crossing (occurring .405 m from the IP), making collisions with

100 bunches out of 120 buckets possible [5] (20 empty buckets are necessary to neutralize ion trapping effects).

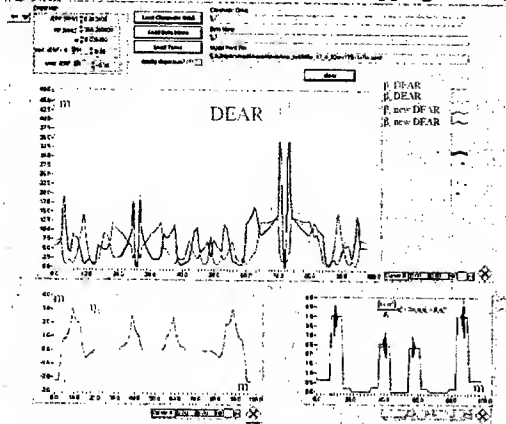


Figure 1: DEAR optics evolution presented by the Control System model interface.

Before such modifications DAΦNE was operated with interleaved bunches (one full and one empty bucket), with a maximum number of 50 bunches in collision. Further modifications in the DEAR IR optics have included an increase of the crossing angle, (from 25 to 29 mrad), and 10% reduction in the beam horizontal emittance.

In a four months run the collider has provided an integrated luminosity $L_{2002} = 68 \text{ pb}^{-1}$ (to be compared with $L_{2001} = 3 \text{ pb}^{-1}$), enough for the DEAR experiment to go through its preliminary phase with the observation of kaonic Nitrogen, and to make the first experimental test of the hydrogen target.

KLOE Optics

The extension of the β_x reduction adopted for the DEAR optics to the KLOE one has not been straightforward since low- β at the KLOE IP is realized with a couple of permanent quadrupole triplets embedded in the field of the experimental solenoid, whose field is compensated by two superconducting solenoids, one at each side of the IP. In this context it is not possible to locally modify the IR optics.

The KLOE horizontal beta has been modified by changing the currents of the quadrupoles closest to the IR, going, in successive steps, from $\beta_x^* = 5.7 \text{ m}$ to $\beta_x^* = 2.7 \text{ m}$, the minimum compatible with the β_x limitation imposed, at the splitter magnets by stay-clear requirements. β_y^* has been only slightly changed, from .03 to .026 m, the minimum value compatible with the hour-glass effect. The horizontal emittance has been reduced by 10% in both rings also for the KLOE optics.

The reduction in β_x^* has been remarkable (~ 50%), but not enough to avoid parasitic crossing, in fact during 100 bunches operations problems such as bunch pattern degradation, beam blow-up and peak luminosity limitation have been still observed. Nevertheless the modified KLOE optics has given a relevant contribution to the luminosity improvement summarized in Table 1. The peak luminosity has reached $L_{\text{peak}} = .8 \cdot 10^{32} \text{ cm}^{-2} \text{ s}^{-1}$,

the best integrated luminosity over a day $L_{\text{day}} = 4.8 \text{ pb}^{-1}$ and the luminosity lifetime $\tau_L = .6 \text{ hours}$.

Table 1: DAΦNE luminosity

	2001	2002
KLOE $L_{\text{peak}} \text{ cm}^{-2} \text{ s}^{-1}$	$.5 \cdot 10^{32}$	$.8 \cdot 10^{32} \text{ } n_b=49$
KLOE $L_{\text{day}} \text{ pb}^{-1}$	3.2	4.8 $n_b=49$
DEAR $L_{\text{peak}} \text{ cm}^{-2} \text{ s}^{-1}$	$.1 \cdot 10^{32}$	$.7 \cdot 10^{32} \text{ } n_b=100$
DEAR $L_{\text{day}} \text{ pb}^{-1}$.24	2.2 $n_b=100$

CLOSED ORBIT CORRECTION

The closed orbit correction application has been upgraded and now includes explicitly a steering strength minimization procedure [6]. The steering strength minimization is beneficial in avoiding stray dispersion bumps as well as local orbit deviations due to the presence of couples of strong nearby perturbations; at DAΦNE it has proved to be powerful in minimizing parasitic dispersion and as well as in limiting the background rate seen from the experimental detectors.

NON LINEAR MODEL

Non-linearities at DAΦNE have been observed and studied from the beginning of machine operation; they essentially come from higher order components in the field of the wigglers [7]. Their negative influence affects machine dynamic aperture and beam lifetime and therefore the integrated luminosity. Moreover, non-linearities influence beam-beam behaviour inducing beam blow-up, thus reducing the achievable peak luminosity.

In 2002 three octupole magnets have been installed in each ring in order to provide non-linearities tuning [8].

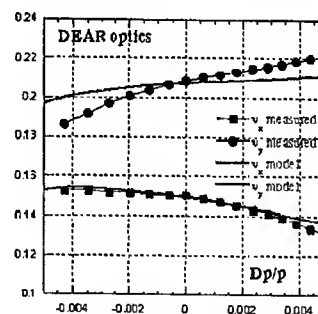


Figure 2: Tune shift versus energy for the DEAR optics.

The non-linear model has been upgraded to include the new elements and sextupole terms detected during the wiggler magnetic measurements have been included in the wiggler model.

The agreement between measured and computed chromaticity has been improved both at the first and second order, as shown in Fig. 2 for the DEAR optics and in Fig. 3 for the KLOE one. Still there is some discrepancy in the vertical plane, but it is small when

compared to the machine chromaticity without sextupoles. The tune shift on amplitude predicted from the model is very close to the measured one [9], see Table 2.

Table 2: Strength of the cubic non-linearity

	C_{11} measured m^{-1}	C_{11} model m^{-1}
Sextupole on	-175.	-187.5
Sextupole off	-73.11	-98.5

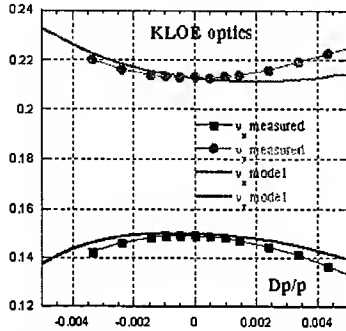


Figure 3: Tune shift versus energy for the KLOE optics

The second order dispersion η_{1x} has been measured as orbit shift versus energy and it is quite similar, for the KLOE optics (see Fig. 4), to the one predicted by the model.

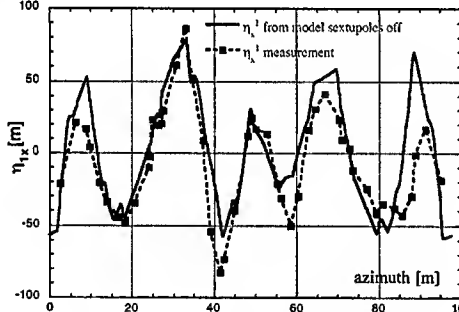


Figure 4: η_{1x} (sextupole off).

Even the computed sextupole contribution to η_{1x} agrees with the measured one (Fig. 5) confirming once more that the betatron functions predicted by the model at the sextupoles are the same as the real ones in the machine.

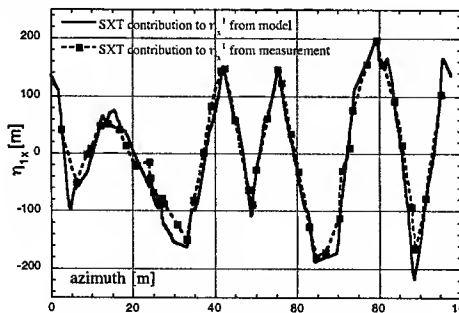


Figure 5: Sextupole contribution to η_{1x} .

Collider operation has shown that the reduction of η_{1x} is beneficial for dynamical aperture and beam-beam behaviour, since the best luminosity results have been obtained after cancelling, almost completely η_{1x} in the KLOE IR (IP at 25.72 m), see Fig. 6.

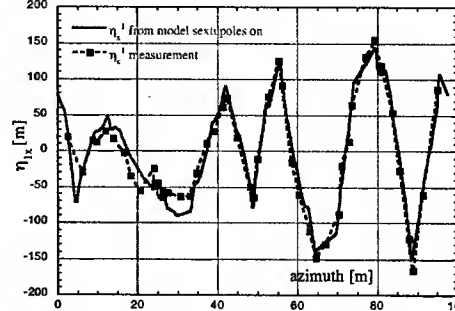


Figure 6: η_{1x} (sextupole on).

CONCLUSIONS

The linear and non-linear model has been extensively used to optimize DAΦNE optics, contributing to a gain of 60% in the peak luminosity and 50% in the daily integrated luminosity, with respect to the year 2001.

The improvements obtained in decreasing β_x^* at DEAR have suggested a new design in which the two IRs are rebuilt substituting quadrupole triplets with doublet ones. With this new configuration it will be possible to reach β_x^* as low as 1.5 m and collide with 100 bunches at both IPs, which could allow, assuming a current per bunch $I_b = 20$ mA, a total current per beam $I_t = 2$ A.

In this context it seems quite reasonable to expect further luminosity increases.

REFERENCES

- [1] G. Vignola and DAΦNE Project Team, "DAΦNE the Frascati Φ Factory", PAC 93, Washington, May 1993.
- [2] H. Grote and F. C. Iselin "The MAD program".
- [3] G. Di Pirro et al., "DANTE Control System for DAΦNE based on Macintosh and LabView", PCaPAC 2002, Frascati, Italy.
- [4] C. Biscari et al., "Half β_x^* at DEAR", DAΦNE Technical Note, BM-9, April 2002.
- [5] A. Drago et al. "100 Bunches Operations at DAΦNE", this conference.
- [6] P. Raimondi et al., "Emittance Optimization with Dispersion Free Steering at LEP", CERN-SL-2000-YY OP, DAΦNE May 2000.
- [7] C. Milardi, "Effects of non-linear terms in the wiggler magnets at DAΦNE", PAC 01, Chicago, June 2001.
- [8] C. Vaccarezza et al., "Preliminary results on DAΦNE operation with octupoles", EPAC 02, Paris, June '01.
- [9] A. Drago et al., "The dynamic tracking acquisition system for e^+e^- collider", DIPAC 01, Grenoble, France.

JITTER CONTROL AND SCRAPING IN THE 12-VIEW AHF HEBT*

Barbara Blind and Andrew J. Jason, LANL, Los Alamos, NM 87545, USA

Abstract

The HEBT of the proposed Advanced Hydrotest Facility (AHF) [1] is designed to deliver 50-GeV protons to an object from 12 directions, 15° apart. Individual beam bunches extracted from a synchrotron are split with 11 sets of septa such that, nominally, the same number of particles arrives from each direction. Extraction-kicker jitter can be expected, and can result in beam-intensity fluctuations in the 12 lines to the object. The HEBT tune is chosen to minimize this effect, with interesting consequences for the beam-splitting process. Beam splitting in each set of septa is initiated by a wire septum, with some particles hitting the wires. Particle-tracking simulations predict that activation of beamline components due to these affected particles can be kept low with sets of scrapers. They also predict that the scraping scheme is not sensitive to beam-position jitter from extraction-kicker jitter, or to average-energy jitter. Details of the jitter study and the scraping study are discussed.

which can change the splitting ratios (percentages of beam entering the two channels of a septum set) and thus the beam intensities in the 12 lines to the object.

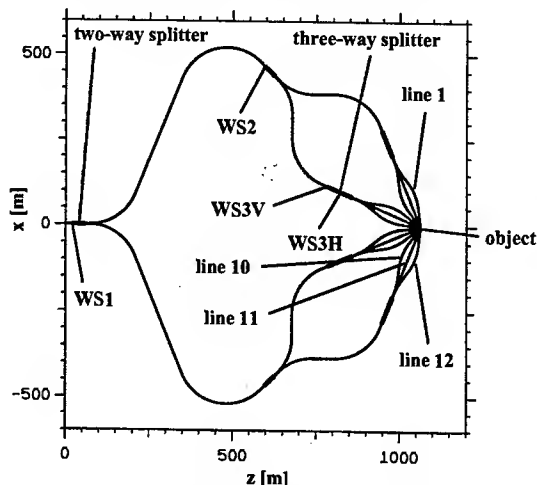


Figure 1: Layout of 50-GeV AHF HEBT.

OVERVIEW

The jitter study assessed the problems caused by jitter, identified possible remedies, and provided a means for establishing tolerances. The scraping study assessed the feasibility and effectiveness of a scraping scheme. Both studies relied heavily on code developed at LANL.

The HEBT layout is shown in Fig. 1. Each set of septa splits the beam into two parts. Beam splitting is initiated by wire septa and each set of septa will be referred to by its wire septum (WS). Septum sets WS1 and WS2 split the impinging beam in half. The vertically oriented septum sets WS3V send 2/3 of the impinging beam into the lower channel, where it is subsequently split in half by septum sets WS3H, and 1/3 into the upper channel. A septum set WS1 or WS2 is referred to as a two-way splitter, while a unit composed of a septum set WS3V and a septum set WS3H is referred to as a three-way splitter.

JITTER STUDY

To minimize beam-intensity fluctuations in the 12 lines to the object, corrective measures must be taken. In the about 1748 m from the start of the extraction line to the entrance of the line-12 lens system [1] the particles encounter 126 dipoles and 182 quadrupoles, and beamline errors lessen the effectiveness of the corrective measures.

Extraction-Kicker Jitter

The synchrotron has two extraction kickers. Kicker jitter causes horizontal beam-position jitter in the HEBT,

All jitter is made up of correlated (same magnitude, same sign) and anti-correlated (same magnitude, opposite sign) deflection-angle errors in the two kickers. Correlated (anti-correlated) errors of 0.01 mrad per kicker move the beam centroid to the 0.298-rms (0.055-rms) ellipse of the nominal beam and can conceivably change the splitting ratio of WS1 from 50/50 to 60/40 (52/48), and thus cause significant beam-intensity fluctuations.

HEBT Tune

There are two possible methods for dealing with kicker jitter, an active method and a passive method.

The active method returns the beam to the axis with two additional kickers in the synchrotron or extraction line, so that there is no beam-position jitter due to kicker jitter in the HEBT. This is conceptually easy, but it may only be possible in case the kicker jitter is reproducible.

The passive method employs a nominal HEBT tune where correlated kicker jitter does not cause position jitter at any of the horizontal wire septa, by setting $R_{12}=0$ from the symmetry point of the kickers to WS1, from WS1 to WS2, and from WS2 to WS3H. This passive method only protects against beam-intensity fluctuations due to correlated components of kicker jitter and causes the maximum possible fluctuations due to anti-correlated components, and the method is not fully effective in the presence of beamline errors. Also, with constraints imposed on the transfer-matrix elements a larger number of independently adjusted quadrupoles is needed than without.

*Work supported by the US Department of Energy under contract W7405-ENG-36

Beam-intensity fluctuations due to average-energy fluctuations are minimized by setting $R_{16}=R_{26}=0$ at WS1, WS2 and WS3H. This does not guard against fluctuations due to second-order chromatic aberrations.

Description of Simulations

The 47,825-particle input beam used had a momentum distribution with momentum deviations of up to $\pm 0.175\%$. The transverse coordinates were Gaussian distributed, with 0.047π -cm-mrad $\sqrt{6}$ -rms emittances. The beam was tracked from the synchrotron extraction region through line 12 (see Fig. 1), which provides information about the beam intensities in lines 10, 11 and 12.

Random sets of beamline errors were assumed. The (uniformly distributed) errors that do not cause beam steering were quadrupole rolls to $\pm 0.2^\circ$, gradient errors in strings of quadrupoles to $\pm 0.1\%$ and gradient errors in individually powered quadrupoles to $\pm 0.01\%$, as well as multipole errors (normal and skew sextupoles, octupoles, decapoles and duodecapoles) in quadrupoles to $\pm 0.1\%$ of the quadrupole field at 80% of the 1.0-inch or 1.5-inch aperture radius and in dipoles to $\pm 0.01\%$ of the dipole field at 80% of the 0.75-inch half gap. The (Gaussian distributed) errors that do cause beam steering were dipole-field errors of 0.1% (rms), dipole rolls of 1.0 mrad (rms), and quadrupole transverse misalignments of 0.25 mm (rms). Steerers periodically returned the beam to the axis, and beam-position monitor readings had errors of 0.25 mm (rms). The code removed the particles not being sent to line 12. Each beamline with a set of errors was tuned so that, in the absence of jitter, 8.333% of the input beam arrived in each of lines 10, 11, and 12.

Jitter-Study Results

The simulations showed that the beam-intensity fluctuations are roughly proportional to the amount of jitter. Without beamline errors, the fluctuations are only about $\pm 1\%$ per 0.01 mrad of correlated kicker jitter, but $\pm 10\%$ per 0.01 mrad of anti-correlated kicker jitter. With beamline errors, the fluctuations can reach $\pm 5\%$ per 0.01 mrad of correlated kicker jitter and again $\pm 10\%$ per 0.01 mrad of anti-correlated kicker jitter. Without (with) beamline errors, the fluctuations are around $\pm 2\%$ ($\pm 5\%$) per 10 MeV of energy jitter.

The simulations showed that the beam-intensity fluctuations due to several types of jitter can roughly be added up. Kicker baseline shifts act like a turn-dependent combination of correlated and anti-correlated kicker jitter. Persistent 300-V baseline shifts in the 50-kV kickers act like 3.0% of anti-correlated kicker jitter and 0.8% of correlated kicker jitter and can lead to fluctuations of up to $\pm 30\%$. Short-term 300-V baseline shifts act like 4.1% of anti-correlated kicker jitter and 0.8% of correlated kicker jitter and can lead to fluctuations of up to $\pm 34\%$.

With all types of jitter, factor-of-two beam-intensity fluctuations are easily possible. Thus, an active method for dealing with kicker jitter is strongly recommended.

SCRAPING STUDY

To minimize the number of particles interacting with the wires of the wire septa, the beam is focused with large spot sizes transverse to the wires. Nevertheless, a fraction of the beam hits the wires of WS1, WS2, WS3V and WS3H. Scrapers are planned to, ideally, remove those of these affected particles that would otherwise be lost in downstream beamline elements, without removing any of the unaffected particles.

Description of Simulations

The beam was tracked from the upstream end of WS1 through each of the 12 lines to the respective lens-system entrance. Particles hitting the wires experienced multiple Coulomb scattering, and energy loss and straggling. Particles undergoing nuclear interactions were simply dropped from the beam. They should be easy to scrape, due to their large scattering angles. The scrapers were described as zero-length elements that cleanly remove all particles hitting them. Particles outside the magnet apertures were also simply removed.

The scraping scheme was developed using a HEBT without beamline errors. To facilitate the effort, poor-quality wire septa that generate large numbers of affected particles were assumed. The 2,362 2-mil-wide 2-mil-deep wires of each 3-m-long wire septum were randomly misaligned by up to ± 5 mil.

First, effective scraper locations were established. Later, the minimum number of scrapers needed to avoid losses in downstream elements was determined. In the final configuration, there were four one-plane scrapers and four two-plane scrapers in each two-way splitter, and eight one-plane scrapers and ten two-plane scrapers in each three-way splitter.

Some Peculiarities of Beam Splitting

The first wire septum splits the beam in half. Affected particles lie at the edges of the two beam halves. Those particles that are given only small scattering angles will remain close to these edges. They are impossible to remove but do not cause activation.

Because of the tune of the HEBT, chosen to minimize the effects of kicker jitter, the edges generated by upstream wire septa re-emerge at downstream wire septa. Fig. 2 shows the beam entering WS2 of lines 1 through 6. The particles are shown looking upstream. Unaffected particles are shown in gold, affected particles generated by WS1 are shown in red. All affected particles from WS1 will be routed towards lines 4 through 6.

Fig. 3 (left) shows the beam entering the second scraper downstream of WS2 of lines 1 through 6, a one-plane scraper. Affected particles generated by WS2 are shown in blue. This scraper removes particles that would otherwise hit the downstream deflectors of the two-way splitter. Fig. 3 (right) shows the beam entering the third scraper downstream of WS2 of lines 1 through 3, a two-plane scraper. As predicted, there are no affected particles generated by WS1 (red particles).

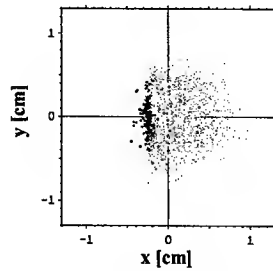


Figure 2: Beam entering WS2 of lines 1 through 6.

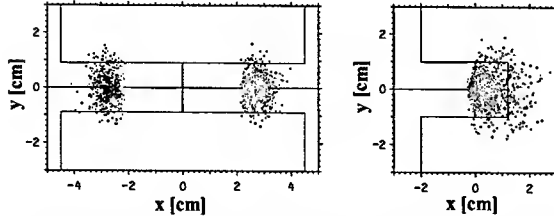


Figure 3: Beam entering a one-plane scraper downstream of WS2 of lines 1 through 6 (left) and a two-plane scraper downstream of WS2 of lines 1 through 3 (right).

Fig. 4 shows the beam entering WS3H of lines 4 and 6 (left) and the beam entering WS3H of lines 1 and 3 (right). Affected particles generated by WS3V are shown in black. The two equivalent locations have very different beams. To cut the beams in half, they need to be cut along lines with different intensities and more particles of the beam shown at left interact with the wires than of the beam shown at right. Thus, unequal numbers of particles must be sent into equivalent channels in order to achieve equal numbers of particles in all 12 lines. This effect should be less pronounced for good-quality wire septa than for the wire septa assumed for the study. As a further consequence of the HEBT tune, some equivalent scrapers have different apertures and some beamlines can be scraped more efficiently than others, with fewer affected particles surviving.

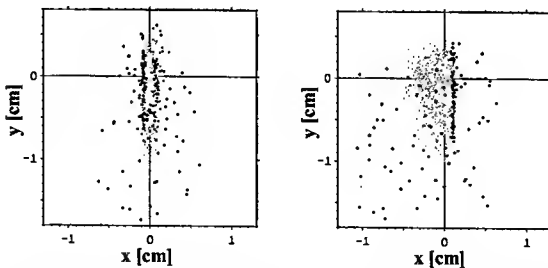


Figure 4: Beam entering WS3H of lines 4 and 6 (left) and WS3H of lines 1 and 3 (right).

Fig. 5 shows the beam entering the line-4 lens system. Affected particles generated by WS3H are shown in turquoise. The location, in phase space, of each set of affected particles indicates its origin at either a horizontally or a vertically oriented wire septum.

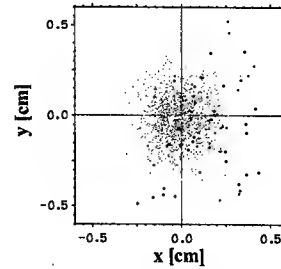


Figure 5: Beam entering line-4 lens system.

Scraping-Study Results

The simulations showed that the scraping scheme should perform acceptably well. Of the input-beam particles, some 20.3% became affected particles. Of these, only about 11.1% arrived at the lens systems, and many were near the unaffected beam. Only one unaffected particle hit a scraper. Two affected particles were lost in arc dipoles, but 90 of them unavoidably hit the septum material of the septa immediately downstream of the wire septa. As possibly unacceptable consequence of the three-way-splitter tune, 16 unaffected particles hit the septa immediately downstream of wire septa WS3H. Each particle represents some 5 pA of average beam current.

PERFORMANCE OF HEBT WITH SCRAPERS AND JITTER

The scraping-study simulations were repeated, with the input beam shifted to represent extraction-kicker jitter and average-energy jitter. It was found that the scraping scheme is not sensitive to such jitter. About the same fraction of the affected particles is removed by scrapers as without jitter. The number of affected particles hitting beamline elements and the number of unaffected particles removed by scrapers remain small. Unaffected-particle hits of the septa immediately downstream of wire septa WS3H increase and are observed at other such septa. The beam-intensity fluctuations agree with the results of the jitter study, for beamlines without errors.

REFERENCES

- [1] Andrew J. Jason et al., "Beam-Distribution System for Multi-Axis Imaging at the Advanced Hydrotest Facility," Proceedings of the 2001 Particle Accelerator Conference, 3374 (2001).

THE USE OF ELECTRIC MULTIPOLE LENSES FOR BENDING AND FOCUSING POLAR MOLECULES, WITH APPLICATION TO THE DESIGN OF A ROTATIONAL-STATE SEPARATOR*

Juris G. Kalnins, LBNL, Berkeley, CA 94720, USA

Abstract

The dipole interaction (Stark effect) of a polar molecule allows one to use an inhomogeneous electric field to bend and focus a neutral beam in a transport line. The dependence of the optics on the Stark potential energy is discussed and we describe the type of multipole-field lenses that are needed. The special features that differ from charged particle optics are discussed. The RMS envelope equations are used to design a rotational-state separator to be built at LBNL. Its performance is simulated using the non-linear trajectory equations (with off-energy molecules included) and we find good state selection.

STARK POTENTIAL ENERGY

The Hamiltonian for a non-relativistic neutral beam in an electric lens-field is $H = \frac{1}{2} m_0 v^2 + W_S(E)$, where W_S is the Stark potential energy which depends only on the magnitude E of the electric field and not its direction. If the derivative of the potential with respect to the field is negative $dW_S/dE < 0$, then the neutral particle is strong-field-seeking. This includes neutral atoms and polar molecules in the ground state, as well as all rotational states in the limit of large fields. Excited rotational states for which $dW_S/dE > 0$, are weak-field-seeking.

Two simple forms of the Stark interaction energy are:

$$(I) \text{ A constant dipole moment } (\mu_d): W_S = -\mu_d E \quad (1)$$

$$(II) \text{ A constant polarizability } (\alpha_p): W_S = -\frac{1}{2} \alpha_p E^2 \quad (2)$$

Neutral atoms are strong-field-seeking, with induced dipole moments and a quadratic field dependence.

The Stark energy for polar molecules is not as simple – for methyl fluoride, an analytic approximation for the ground state gives [1]

$$W_S = -W_C(E/E_C)^2/[1 + (E/E_C)] \quad (3)$$

where $W_C = 4.3$ K and $E_C = 11$ MV/m. This molecule is strong-field-seeking, and the Stark energy starts from a quadratic (type-II) dependence at low fields, to a linear one (type-I) at high fields.

We do not have this variability in the interaction energy for charged particles, for which the interaction energy is the same $W_S = q_0 \Phi$, and the charge state q_0 is constant.

*Supported by the Director, Office of Science of the U.S. Department of Energy, under Contract No. DE-AC03-76SF00098.

ELECTROSTATIC LENS FIELD

A charged particle we can deflect with a dipole field and focus with a quadrupole field.

For a neutral beam, we need a quadrupole field to bend it and a sextupole field to focus it, in combination with a dipole field to provide a non-zero field on axis [2]. There is an exception for weak-field-seeking molecules, where a pure sextupole field will focus the beam linearly in both transverse planes. A disadvantage is that the field is zero at the beam center and molecules can drop out of their excited rotational state.

Choosing skew multipoles for greater horizontal clearance, the lens potential, to order (r^3) , is:

$$-\Phi = E_{y0}(z)[y + (\sigma_2/r_0)xy + (a_3/r_0^2)(x^2y - 1/3y^3) - 1/6(\sigma_2/r_0\rho_0)y^3] - 1/6E''_{y0}(z)y^3 \quad (4)$$

where E_{y0} is the vertical dipole field on midplane and $E'_{y0} = dE_{y0}/dz$, etc. The quadrupole field polarity is given by $\sigma_2 = \pm 1$, and the sextupole field strength is a_3 . The curvature of the electrodes is specified by r_0 , the lens-field scaling length. This length r_0 also determines the range of the non-linear fields which arise from the coupling between the multipole fields [1]. For example, in a simulation of a long 60°-FODO transport line [1], the dynamic aperture was found to be about 40% of the scaling length r_0 . The curvature ρ_0 of the optic axis in a sector bend-lens with local coordinates, $x = r - \rho_0$, $y = -Z$ and $z = \rho_0\theta$, contributes the ρ_0 -term to the potential. The lens end fields contribute the E''_{y0} -term to the potential, and affect only the vertical motion.

The total electric field in the lens to order (r^2) is

$$E^2 = E_{y0}^2 \{1 + 2(\sigma_2/r_0)x + [(\sigma_2^2 + 2a_3)/r_0^2]x^2 + [(\sigma_2^2 - 2a_3 - \sigma_2 r_0/\rho_0)/r_0^2]y^2\} + [E'_{y0}{}^2 - E_{y0}E''_{y0}]y^2 \quad (5)$$

and contains all the terms needed for linear optics. For calculating non-linear trajectories, the field to order (r^4) was used.

LINEAR OPTICS

From the Stark potential energy and the total lens field, we can now obtain the equations of motion for neutral particle linear optics.

Trajectory Equations

These, with dispersion included, have the usual form

$$x'' + K_x x + \delta_0/\rho_0 = 0 \quad y'' + K_y y = 0 \quad (6)$$

where the lens focusing strengths are

$$K_x = a_x K_0 \quad K_y = a_y K_0 - U_0 k_{ye} \quad (7)$$

and k_{ye} is the contribution from the end field. Table 1 gives the bend and focusing parameters for the two types of Stark potential considered here.

Table 1: Lens parameters for field E_0 ($\sigma_2^2 = 1$).

Type	(I) Linear	(II) Quadratic
W_0	$-\mu_d E_0$	$-\frac{1}{2} \alpha_p E_0^2$
$1/\rho_0$	$\sigma_2 U_0 / 2r_0$	$\sigma_2 U_0 / r_0$
K_0	$U_0 / r_0^2 = 2 / \sigma_2 r_0 \rho_0$	$U_0 / r_0^2 = 1 / \sigma_2 r_0 \rho_0$
a_x	$+a_3 + \sigma_2(r_0/2\rho_0)$	$+2a_3 + \sigma_2^2 + \sigma_2(r_0/\rho_0)$
a_y	$-a_3 + \sigma_2^2/2 + \sigma_2(r_0/2\rho_0)$	$-2a_3 + \sigma_2^2 - \sigma_2(r_0/\rho_0)$
k_{ye}	$[E'_{y0}{}^2 - E_{y0}E''_{y0}] / 2E_0E_{y0}$	$[E'_{y0}{}^2 - E_{y0}E''_{y0}] / E_0^2$

The bend radius and the focusing strengths are proportional to the energy ratio $U_0 = W_0/T_E$, where W_0 is the Stark energy and $T_E = \frac{1}{2} m_0 v_E^2$ is the kinetic energy. If the lens field is static then the Hamiltonian is conserved and the kinetic energy inside is $T_E = T_0 - W_s(E_0)$. Strong-field-seeking molecules gain energy upon entering a field while weak-field-seeking ones lose it (this is reversed on leaving). This effect with pulsed fields is used to decelerate [3] and bunch neutral beams. The inverse energy ratio $|U_0^{-1}|$ can also be taken as a measure of the rigidity of a neutral beam, and the dispersion term in Eq.(6) is given in terms the deviation $\delta_0 = \delta U_0 / U_0$.

In the bend lenses the total dimensionless multipole field strengths (a_x, a_y), plotted in Fig.1, are controlled by the sextupole component a_3 – equivalent to the field-index in a gradient bend magnet. If $a_3 > 0$, a strong-field-seeking molecule ($U_0 < 0$) is defocused in the x-plane, while a weak-field-seeking will be focused.

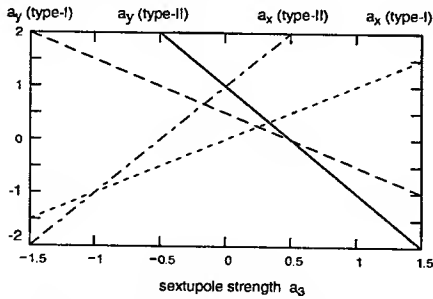


Figure 1: Total multipole strengths a_x and a_y .

We see that for $a_3 = \frac{1}{4}$ (type-I), or 0 (type-II), a bend lens has equal defocusing for strong-field-seeking molecules, but equal focusing for weak-field-seeking ones. This can be used to make the size of a synchrotron ring much smaller for a weak-field-seeking molecule [4].

The vertical focusing by the end field is significant, since the field goes to zero over a short distance. A complication is that the end fields are affected by the location and potential of neighboring electrodes. For example, by using a short lens spacing and equal fields, we can make the end-field focusing negligible between the two lenses.

As a model for the lens end field next to a drift space, we can use the field of two parallel plates with half-gap r_p . The axial field E_{y0} with its derivatives, and the resulting vertical focusing field k_{ye} (type-I), are plotted in Fig.2.

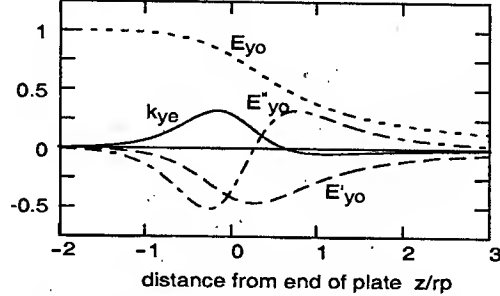


Figure 2: Parallel plate end fields (normalized to 1).

The first term $E'_{y0}{}^2$ is the dominant one and is always positive, so both ends act the same, with focusing for weak-field-seeking and defocusing for strong-field-seeking molecules. In general k_{ye} can have a number of focusing regions of different sign, such as the negative tail in Fig.2.

Since the lens field scales with the half-gap r_p , we can approximate the end-field focusing by a constant strength $k_{ye} \approx a_{ye}/r_p^2$ over an effective length $L_{ye} \approx \lambda_{ye} r_p$. The parameters a_{ye} and λ_{ye} will depend on the electrode shape, and for the separator electrodes with curved ends (radius $\frac{1}{2} r_p$) we estimate $a_{ye} = 0.175$ and $\lambda_{ye} = 1$.

RMS Envelope Equations

A beam can be characterized by the second moments of the distribution function

$$\begin{aligned} \sigma_x^2 &= \epsilon_x \beta_x & -\sigma_{xx'} &= \epsilon_x \alpha_x & \sigma_x'^2 &= \epsilon_x \gamma_x \\ \sigma_y^2 &= \epsilon_y \beta_y & -\sigma_{yy'} &= \epsilon_y \alpha_y & \sigma_y'^2 &= \epsilon_y \gamma_y \end{aligned} \quad (8)$$

which we can express in terms of the associated envelope functions (β, α, γ), and the invariant RMS emittances

$$\epsilon_x = (\sigma_x^2 \sigma_x'^2 - \sigma_{xx'}^2)^{1/2} \quad \epsilon_y = (\sigma_y^2 \sigma_y'^2 - \sigma_{yy'}^2)^{1/2} \quad (9)$$

with the envelope functions related by

$$\gamma_x \beta_x - \alpha_x^2 = 1 \quad \gamma_y \beta_y - \alpha_y^2 = 1 \quad (10)$$

This gives us the RMS envelope equations, F. J. Sacherer [5], in a form independent of the emittance,

$$\begin{aligned} \beta_x' + 2\alpha_x &= 0 & \beta_y' + 2\alpha_y &= 0 \\ \alpha_x' + \gamma_x - K_x(z)\beta_x &= 0 & \alpha_y' + \gamma_y - K_y(z)\beta_y &= 0 \end{aligned}$$

$$\gamma_x' - 2K_x(z)\alpha_x = 0 \quad \gamma_y' - 2K_y(z)\alpha_y = 0 \quad (11)$$

which apply to all phase-space particle distributions.

BERKELEY MOLECULAR SEPARATOR

The Berkeley molecular separator (BMS) consists of a jet source followed by a triplet of focusing lenses Q1F-Q2D-Q3F, that transport the beam to a focusing doublet Q4D-Q5F and a horizontal-bend lens BH1. The design optics with the acceptance beam sizes (σ_x , σ_y) and the horizontal dispersion η_x , is shown in Fig.3.

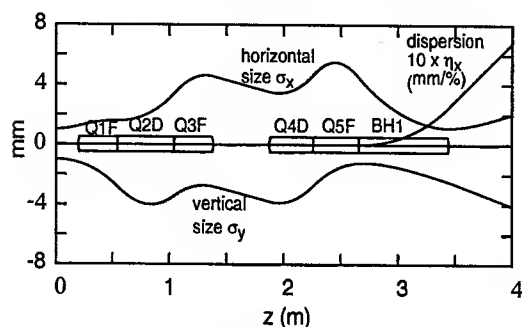


Figure 3: Berkeley Molecular Separator (BMS).

Table 2, lists the BMS separator elements, together with their focusing parameters. The lens fields given are for the ground state of the 196.5 K (310 m/s) methyl flouride beam that will be used to test the separator.

Table 2: BMS separator parameters

	L_{eff} cm	E_0 MV/m	K_0 m^{-2}	a_3	r_0 mm	r_p mm
Drift	19.80					
End	0.40		17.9			
Q1F	34.05	2.51	7.26	-1	15	4
Q2D	49.80	2.51	7.24	+1	15	4
Q3F	34.05	2.51	7.26	-1	15	4
End	0.40		17.9			
Drift	49.60					
End	0.40		17.5			
Q4D	38.25	2.48	7.10	+1	15	4
Q5F	40.00	2.74	8.45	-1	15	3.5
BH1	78.74	3.00	7.96	0.5	16.74	3
End	0.30		43.1			

The horizontal bend-lens BH1 deflects the beam 3° , with a bend radius of 15 m and a sextupole field $a_3 = 0.5$, so vertically it's a drift space (Fig.1). There are cleanup collimators just upstream of the triplet and doublet lenses and a final one 16 cm downstream of BH1.

The lens apertures and non-linear forces, limit us to beam acceptances of about 3.5 mm-mr in both planes. The initial jet-source aperture radius is 1 mm, so the angular acceptance is ± 3.5 mr. The kinetic energy acceptance, from the simulations, is about 2 % RMS.

At the last collimators ($z = 3.6$ m), the horizontal mono-energetic beam size is 1.3 mm and the dispersion is 0.373

mm/%. This should allow us to separate rotational states that differ in rigidity by 10 to 20%. The lens fields for CH_3F are low enough that we can scan over rotational states three times as rigid.

The BMS separator performance was simulated using the nonlinear trajectory equations with beam energy spread included. Fig.4 shows the transverse particle distribution just after the last collimators ($z = 3.6$ m), for three rotational states with rigidity $\delta_0 = 0, \pm 10\%$, and an initial 2 % RMS energy spread. Here, Fig.4(a) is the distribution for no collimators, and Fig.4(b) with them – resulting in a well separated beam.

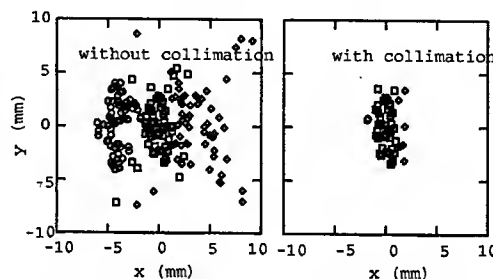


Figure 4: Separation of rotation states with $\delta_0 = -10\%$ (circles), 0 (squares), $+10\%$ (diamonds).

CONCLUSIONS

Neutral beam optics is significantly affected by the sign and the electric field dependence of the Stark potential. Electric multipole lenses can be used to bend and focus beams of neutral atoms or polar molecules, but they have inherent non-linear fields that limit the acceptances. Optics for strong-field-seeking molecules is made more difficult by the defocusing in the end fields and from the quadrupole component in the bend field.

ACKNOWLEDGEMENTS

I would like to thank H. Gould for the opportunity to work on the separator design optics, and G. Lambertson, H Nishimura and J. Maddi for useful discussions.

REFERENCES

- [1] J. G. Kalnins, G. Lambertson, and H. Gould, "Improved Alternating Gradient Transport and Focusing of Neutral Molecules", Rev. Sci. Instr. 73, 2557 (2002); LBNL-49088
- [2] G. Lambertson, "Beam Dynamics in a Storage Ring for Neutral (Polar) Molecules", in this proceedings, Portland, May 2003.
- [3] J. A. Maddi, T. P. Dinneen, and H. Gould, Phys. Rev. A 60, 3882 (1999).
- [4] H. Nishimura, G. Lambertson, J. G. Kalnins, and H. Gould, "Lattices for Milli-eV Neutral Molecules", in this proceedings, Portland, May 2003.
- [5] F. J. Sacherer, IEEE Trans. Nucl. Sci., NS-18, 1105 (1971)

SPACE-CHARGE DRIVEN EMITTANCE GROWTH IN A 3D MISMATCHED ANISOTROPIC BEAM

J. Qiang*, R. D. Ryne, LBNL, Berkeley, CA 94720, USA
I. Hofmann, GSI Darmstadt, Planckstrasse 1, 64291 Darmstadt, Germany

Abstract

In this paper we present a 3D simulation study of the emittance growth in a mismatched anisotropic beam. The equipartitioning driven by a 4th order space-charge resonance can be significantly modified by the presence of mismatch oscillation and halo formation. This causes emittance growth in both the longitudinal and transverse directions which could drive the beam even further away from equipartition. The averaged emittance growth per degree of freedom follows the upper bound of the 2D free energy limit plus the contributions from equipartitioning.

INTRODUCTION

Emittance growth is one of the most fundamental issues in accelerator beam dynamics studies. In a constant focusing channel (smooth approximation of the real machine), the energy anisotropy of the beam is defined as the ratio of the longitudinal temperature to transverse temperature, $\frac{T_z}{T_x} = \frac{\epsilon_z k_z}{\epsilon_x k_x}$, where z is correlated to the longitudinal direction and x is the transverse direction. For a collisionless anisotropic beam in the accelerator, the nonlinear space-charge forces coupling the longitudinal and transverse directions cause emittance exchange among different degrees of freedom when the internal resonance conditions are satisfied. This will be further enhanced by the collective space-charge instability which can grow out of the noise in an anisotropic beam. In this case, the emittance grows in a plane that receives energy, and decreases in a plane that loses energy. A major fourth order difference resonance band in the vicinity of the symmetric focusing has been identified and studied [1, 2, 3, 4]. It was found that within this fourth order resonance band, the anisotropic beam will approach to equipartition within a few betatron oscillation periods. Outside the stopband of the coupling resonance, the emittance exchange is small. An initial anisotropic beam can remain anisotropic for a long time without progressing to an equipartitioned beam.

On the other hand, in accelerators, the change of focusing lattice can cause the mismatch between the input beam and the transport system. The mismatch will result in the oscillation of beam envelope and excite the envelope eigenmodes. These envelope modes possess additional free energy compared with the stationary distribution. Individual particles with right oscillation frequency can resonate with these envelope modes through the so-called parametric resonance, e.g. 2 : 1 resonance, and attain large amplitude to form halo [5, 6]. These halo particles extract the energy

from the envelope modes and convert the free energy from mismatch into thermal energy, which causes beam emittance growth.

In recent years, studies have been focused on the understanding of the emittance exchange of an rms matched beam with initial energy anisotropy [2, 3, 4, 7, 8] or the mismatched halo formation without the presence of energy anisotropy [9]. For a mismatched anisotropic beam, the final rms emittance growth is more complicated depending on the longitudinal to transverse tune ratio and the longitudinal to transverse emittance ratio of the beam. In this paper, we have carried out a detailed parameter study of the final emittance growth in a constant focusing channel as a function of longitudinal to transverse tune ratio for two longitudinal to transverse emittance ratios. The simulations have been done using the 3D particle-in-cell code IMPACT [10]. In the simulations, which include a self-consistent space-charge calculation, we used one million particles on a $64 \times 64 \times 64$ Cartesian grid. We have assumed that in the 3D simulation the initial distribution in y is identical to that in x . The numerical convergence of the simulation has been checked using a larger number of macroparticles, more grid points, and a smaller step size.

SPACE-CHARGE DRIVEN EMITTANCE GROWTH

We first discuss the emittance growth without the presence of the major fourth order coupling resonance in a mismatched beam. In this case, we have chosen $\epsilon_z/\epsilon_x = 1$, $k_z/k_{0x} = 0.6$ and a symmetric mismatch factor of 1.3 in all three directions. The emittance exchange around the fourth order difference resonance $2k_z - 2k_x \approx 0$ is negligible since there is no free energy available to transfer for a beam with equipartitioned temperature ratio $T_z/T_x = 1$. Fig. 1 shows the final relative rms emittance growth as a function of k_z/k_x for fixed transverse tune depression. The simulations were done through 100 zero current betatron oscillation periods to reach saturated amplitudes. The initial distribution is a 6D Gaussian distribution. For $0.56 < k_z/k_x < 1$, the relative emittance growth in the transverse direction is larger than that in the longitudinal direction. Above $k_z/k_x = 1$, the emittance growth in the longitudinal direction becomes dominant. In both cases, the emittance growth is predominately in the direction with stronger focusing. Such anisotropic emittance growth could make the beam move further away from equipartition. It has been shown by Franchetti et. al. that around $k_z/k_x = 1$, with stronger focusing in that plane, the fixed point in that plane

*jqiang@lbl.gov

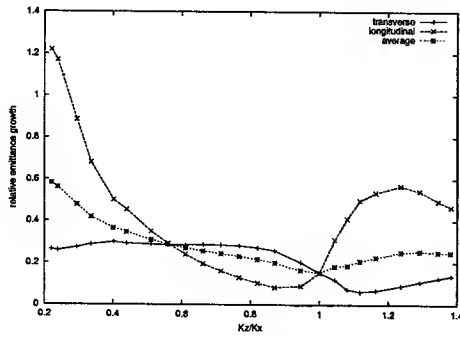


Figure 1: Final relative rms emittance growth in the longitudinal direction, transverse direction, and averaged per degree of freedom as a function of tune ratio k_z/k_x ($k_x/k_{x0} = 0.6$, $\epsilon_z/\epsilon_x = 1$) for an initial mismatched ($M = 1.3$) Gaussian distribution.

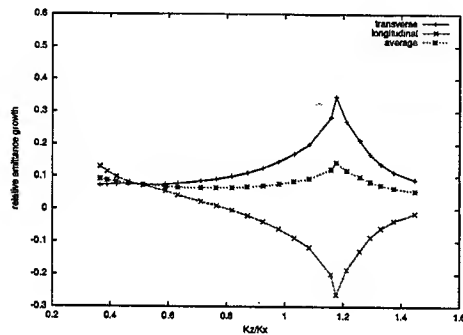


Figure 2: Final relative rms emittance growth in the longitudinal direction, transverse direction, and averaged per degree of freedom as a function of tune ratio k_z/k_x ($k_x/k_{x0} = 0.6$, $\epsilon_z/\epsilon_x = 2$) for an initial matched Gaussian distribution.

for the typical 2 : 1 parametric resonance moves closer to the core [9]. This results in more particles being involved in the parametric resonance in that plane and larger emittance growth. Additional final emittance growth in the longitudinal direction is observed for $0.2 < k_z/k_x < 0.56$. The large final longitudinal emittance growth is associated with the contributions from the halo formations and from the equipartitioning driven by the higher order modes.

Next, we are going to discuss the emittance growth of an anisotropic beam with the presence of the major fourth order coupling resonance. Within the resonance band of $2k_z - 2k_x \approx 0$, there will be pronounced emittance exchange between the transverse direction and the longitudinal direction even though the beam is initially rms matched. Fig. 2 shows the final relative emittance growth as a function of the longitudinal to transverse tune ratio for an initial rms matched Gaussian beam with $k_x/k_{x0} = 0.6$ and $\epsilon_z/\epsilon_x = 2$. Within the resonance band $2k_z - 2k_x \approx 0$, the maximum longitudinal emittance decreases by about 26%, while the maximum transverse emittance increases

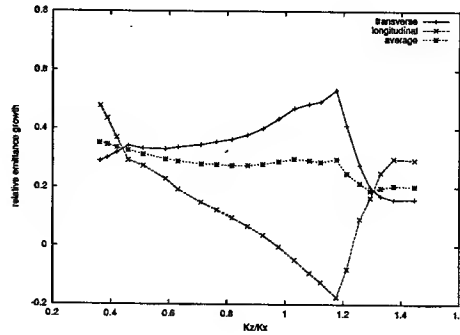


Figure 3: Final relative rms emittance growth in the longitudinal direction, transverse direction, and averaged per degree of freedom as a function of tune ratio k_z/k_x ($k_x/k_{x0} = 0.6$, $\epsilon_z/\epsilon_x = 2$, and $M = 1.3$) for an initial Gaussian distribution.

by about 34%. The energy anisotropy T_z/T_x has dropped from initial 2.3 to 1.1 at the peak of resonance.

With the presence of initial mismatch in above anisotropic beam, the final emittance growth within the fourth order resonance band $2k_z - 2k_x \approx 0$ for the rms matched beam is significantly modified. The mismatch causes the envelope oscillations and halo formation in both transverse and longitudinal directions. As a result, the emittances grow in both directions even with the presence of initial emittance exchange. This process pushes the final state of the mismatched anisotropic beam away from equipartition. Fig. 3 shows the final relative emittance growth as a function of k_z/k_x for an initial Gaussian distribution with a fixed $k_x/k_{x0} = 0.6$, $\epsilon_z/\epsilon_x = 2$, and an initial 1.3 mismatch in all three directions. The mismatched anisotropic beam shows both equipartitioning and anisotropic emittance growth. Comparing with the case of emittance growth around $2k_z - 2k_x \approx 0$ ($0.6 < k_z/k_x < 1.4$) for a mismatched beam with $\epsilon_z/\epsilon_x = 1$, there exists a regime of equipartitioning ($0.97 < k_z/k_x < 1.24$) for the mismatched beam with $\epsilon_z/\epsilon_x = 2$. Comparing with the matched anisotropic beam with $\epsilon_z/\epsilon_x = 2$, the peak of the resonant emittance exchange occurs at the same tune ratio. However, the range of tune ratio for the final emittance exchange has been reduced from $0.8 < k_z/k_x < 1.45$ to $0.97 < k_z/k_x < 1.24$. Within this range, the fourth order resonance driven equipartitioning is stronger than the halo driven emittance growth. There is a net final emittance exchange between longitudinal direction and transverse direction. Outside this range, the opposite is true. The emittance growth from the mismatched halo overcomes the initial equipartitioning process. The final state of the beam can be driven further away from equipartition.

Even though the emittance growth along the transverse and longitudinal direction shows strong dependence on the longitudinal to transverse tune ratio, the averaged rms emittance growth per degree of freedom, is found to be relatively insensitive to the ratio of the tune within the range

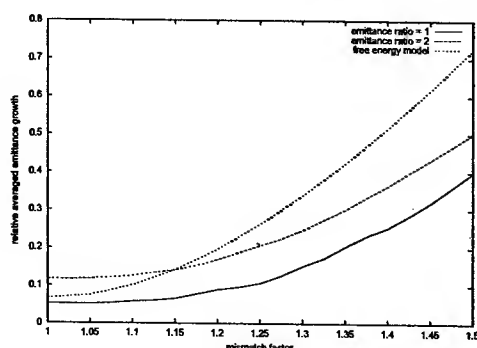


Figure 4: Relative averaged rms emittance growth with $\epsilon_z/\epsilon_x = 1$, $\epsilon_z/\epsilon_x = 2$, and compared with free energy theory, as a function of mismatch factor for Gaussian beams ($k_x/k_{x0} = 0.6$, $k_z/k_{z0} = 1.0$).

$0.6 < k_z/k_x < 1.4$ as shown in Figs. 1-3. This makes it feasible to estimate the average emittance growth and to compare with the "free energy" limit derived by Reiser for symmetrically focused beam [11]. The latter is a "2D" approximation understood as the maximum possible rms emittance growth, if all of the energy added to an axially symmetric beam by radial mismatch is "decohered" and a new matched uniform beam is obtained - regardless of the actual driving mechanism. Fig. 4 shows the averaged rms emittance as a function of mismatch factor for an initial Gaussian beam with $k_{z0}/k_{x0} = 1$, $\epsilon_z/\epsilon_x = 1$ and 2 together with the emittance growth calculated from the free energy model. The emittance growth using the 2D free energy model includes the contributions from the initial charge redistribution of the Gaussian beam and from the initial envelope mismatch. For $\epsilon_z/\epsilon_x = 1$, the averaged emittance growth per degree of freedom from simulation rises slower than that from the free energy model as the mismatch factor increases. For $\epsilon_z/\epsilon_x = 2$, the averaged emittance growth from simulation is larger than that from the free energy model for mismatch factor less than 1.15. This extra-emittance growth is due to contributions from equipartitioning. For mismatch factor greater than 1.15, the emittance growth calculated from the free energy model quickly takes over. The general function dependence of the averaged emittance growth on the mismatch factor for $\epsilon_z/\epsilon_x = 2$ and $\epsilon_z/\epsilon_x = 1$ is similar except an upshift for the $\epsilon_z/\epsilon_x = 2$ case due to the equipartitioning within the coupling resonance. The smaller averaged emittance growth from simulations is due to the fact that there is an incomplete transfer of free energy of envelope oscillation to the emittance growth. The free energy model tends to overestimate the emittance growth since it does not take into account the field energy associated with nonuniform density in the final stationary distribution. Including the contributions from the energy anisotropy, the 2D free energy model represents an upper bound for the averaged emittance growth per degree of freedom in a mismatched

anisotropic beam.

CONCLUSIONS

In summary, the final equipartitioning state of an anisotropic beam within the fourth order coupling resonance has been significantly modified with the presence of the rms mismatch. The anisotropic beam within the resonance band can be pushed further away from the equipartitioning by the mismatch halo induced emittance growth. For a mismatched anisotropic beam, the emittance growth shows a superposition of the contribution from the equipartitioning and from the mismatched halo formation. Even though the emittance growth along the transverse and longitudinal directions shows strong dependence on the longitudinal to transverse tune ratio, The averaged rms emittance growth per degree of freedom is relatively insensitive to the tune ratio and follows the bound of free energy model plus the equipartitioning contributions.

ACKNOWLEDGMENTS

The research used resources of the National Energy Research Scientific Computing Center, which is supported by the Office of Science of the U.S. Department of Energy (US DOE/SC) under Contract No. DE-AC03-76SF00098. This work was performed under the auspices of a Scientific Discovery through Advanced Computing project, "Advanced Computing for 21st Century Accelerator Science and Technology, which is supported by the US DOE/SC Office of High Energy and Nuclear Physics and the Office of Advanced Scientific Computing Research.

REFERENCES

- [1] B. W. Montague, CERN Report No. 68-38, 1968.
- [2] R. A. Kishek, P. G. O'Shea, and M. Reiser, Phys. Rev. Lett. **85**, 4514 (2000).
- [3] I. Hofmann, J. Qiang, and R. Ryne, Phys. Rev. Lett. **86**, 2313 (2001).
- [4] I. Hofmann and O. Boine-Frankenheim, Phys. Rev. Lett. **87**, 034802 (2001).
- [5] R. L. Gluckstern, Phys. Rev. Lett. **73**, 1247 (1994).
- [6] J. Qiang and R. D. Ryne, Phys. Rev. ST Accel. Beams **3**, 064201 (2000).
- [7] I. Hofmann, Phys. Rev. E **87**, 4713 (1998).
- [8] I. Hofmann, G. Franchetti, O. Boine-Frankenheim, J. Qiang, and R. Ryne, Phys. Rev. ST Accel. Beams **6**, 024202 (2003).
- [9] G. Franchetti, I. Hofmann, and D. Jeon, Phys. Rev. Lett. **88**, 254802 (2002).
- [10] J. Qiang, R. Ryne, S. Habib, V. Decyk, J. Comput. Phys. **163**, 434 (2000).
- [11] M. Reiser, "Theory and Design of Charged Particle Beams," John Wiley & Sons, 1994, New York, NY 10158.

PULSE COMPRESSION VIA VELOCITY BUNCHING WITH THE LLNL THOMSON X-RAY SOURCE PHOTOINJECTOR

S.G. Anderson*, W.J. Brown, A.M. Tremaine, LLNL, Livermore, CA 94550, USA
P. Musumeci, J.B. Rosenzweig, UCLA, Los Angeles, CA 90095, USA

Abstract

We report the compression of a high brightness, relativistic electron beam to rms lengths below 300 femtoseconds using the velocity compression technique in the LLNL Thomson X-ray source photoinjector. The results are consistent with analytical and computational models of this process. The emittance evolution of the beam during compression is investigated in simulation and found to be controllable with solenoid focusing.

INTRODUCTION

Fourth generation light sources [1] and future high energy physics accelerators [2] will require beams with both very low emittance, and sub-picosecond rms lengths. The need for high brightness motivates the use of radio frequency (rf) photoinjectors, the highest brightness electron sources. However, the brightness of these sources results in space-charge forces which are large enough to dominate the transverse beam dynamics. The method of maintaining the low emittance of photoinjector beams, termed emittance compensation [3, 4], balances the defocusing space-charge forces with external focusing and accelerating forces. This process defines the optimal dimensions of the beam and typically limits the minimum rms bunch length to a few picoseconds.

This limit coupled with the needs of advanced beam applications has produced much interest in the topic of pulse compression of high brightness beams. Specifically, magnetic compression schemes [5], in which a longitudinal position/momentum correlation is created by running off-crest in an rf accelerator and then removed by path-length/momentum correlation in a magnet system, have been studied extensively [6, 7]. These studies have revealed distortions, and corresponding emittance growth, in both the longitudinal and transverse phase space arising from magnetic compression. At moderate to high energy (≥ 40 MeV) coherent synchrotron radiation (CSR) is the most significant source of emittance growth [7], while at lower energies space-charge forces can play an important role [8].

To avoid the effects of magnetic compression on the transverse beam quality, a new rectilinear compression technique, termed velocity bunching, has been proposed [9], and recently studied experimentally [10, 11]. In this paper we review the velocity bunching mechanism and present data produced by its implementation at the LLNL

Thomson X-ray source photoinjector [12]. In addition, we examine the beam dynamics in the compression process with PARMELA simulations and find the emittance behavior consistent with that predicted by emittance compensation theory.

VELOCITY BUNCHING

For compression with velocity bunching, the required time of flight difference between the beam head and tail, $\Delta t/t = \Delta L/L - \Delta v/v$, is provided solely by the velocity difference, $\Delta v/v$, imparted by the time dependent rf fields in the accelerating structure. This method, therefore, is more easily applied at lower energies, since $\Delta v/v = \frac{1}{\gamma^2} (\Delta p/p)$, and the imparted momentum spread required for compression is lower, and may be more easily reduced by acceleration.

To understand the basic mechanism of velocity compression, consider the interaction of an electron with the sinusoidal, accelerating rf wave given by $E_z = E_0 \sin(\Psi)$, where $\Psi = \omega t - kz + \phi_0$ is the particle phase with respect to the wave, and E_0 is the peak accelerating electric field of the wave. With a field of this form, the particle equations of motion are given (as in Ref. [11]) by

$$\frac{d\gamma}{dz} = \alpha k \sin \Psi \quad (1)$$

$$\frac{d\Psi}{dz} = k \left[\frac{\gamma}{\sqrt{\gamma^2 - 1}} - 1 \right], \quad (2)$$

where $\alpha = eE_0/m_e c^2 k$ is the dimensionless vector potential amplitude of the wave. These equations can be used to plot electron trajectories in (Ψ, γ) phase space, as illustrated in Fig. 1b. In this space particles follow lines of constant Hamiltonian and, as the figure illustrates, a beam injected near the rf zero crossing ($\Psi = 0$) will initially slip back in phase as a strong Ψ - γ correlation is produced. As the beam slips in phase, it samples a stronger electric field and accelerates as the phase space correlation begins to bunch the beam. At the end of this process the beam has slipped into a strongly accelerating phase and the phase space orientation of the beam has rotated by 90° from that of the injected beam.

EXPERIMENTAL MEASUREMENTS

The LLNL Thomson X-ray source photoinjector and linac consists of a BNL/SLAC/UCLA/LLNL 1.625 cell photo-cathode rf gun [13] followed by four SLAC style 2.5

* anderson131@llnl.gov

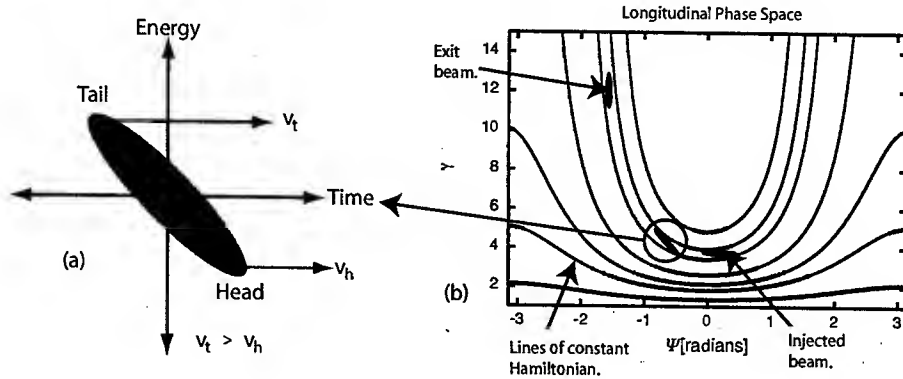


Figure 1: Phase space particle trajectories illustrate the velocity compression mechanism.

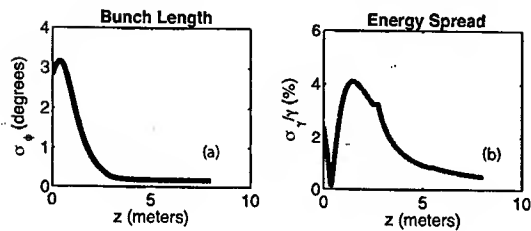


Figure 2: Simulation of the (a) pulse length, and (b) energy spread in the compression experiment.

meter, S-band traveling wave sections. The linac is capable of producing 100 MeV electrons, and is typically run in an energy range of 20-70 MeV for Thomson scattering X-ray production [14]. The gun and each of the accelerator sections are independently powered and phased, allowing us to study velocity compression. The beam charge for this study was 250 pC, again the typical amount produced in X-ray production experiments.

A simulation of longitudinal beam dynamics is shown in Fig. 2. Here the initial phase space configuration is taken from a PARMELA simulation of the rf gun and injected into the first linac section at a phase of -17° (107° ahead of crest). The next two sections are phased in this simulation for on-crest acceleration of the beam up to a final energy of 50 MeV. As the figure shows, the bunch length decreases in the first accelerator section reaching a minimum rms value of 160 femtoseconds. Simultaneously, the energy spread increases to a peak rms value of $\sim 4\%$. As the beam begins to accelerate at the end of the first section and in the following sections the relative energy spread decreases to a final value of 0.5%. Note also that these simulations predict a final energy of 57 MeV and energy spread of 0.2% when the beam is injected into the first accelerator section at 70° , consistent with experimental measurements performed with a spectrometer magnet.

The bunch length diagnostic we employed is a polarizing

Michelson interferometer which analyzes coherent transition radiation (CTR) emitted from the electron beam's impact on a metal foil [15]. The device uses $100 \mu\text{m}$ spaced wire grids to polarize the coherent THz radiation, which limits the highest frequencies that can be measured and therefore, limits the shortest measurable pulses to ~ 300 femtoseconds, rms.

The first traveling wave section was phased as indicated above to perform the velocity bunching measurement. The phase was adjusted to maximize the CTR detector signal at the end of the linac and thus, minimize the pulse length, since the radiated energy, $E_{CTR} \propto Q^2/\sigma_t$ [16]. The interferometer was then used to obtain the autocorrelation of the electron pulse, shown in Fig 3. Analysis of the interferometer data is complicated somewhat by the fact that longer wavelengths ($\lambda > 1 \text{ mm}$) are not adequately measured due to diffraction and finite apertures in the device. The measured data is in fact the filtered autocorrelation of the beam temporal profile. The pulse length was extracted

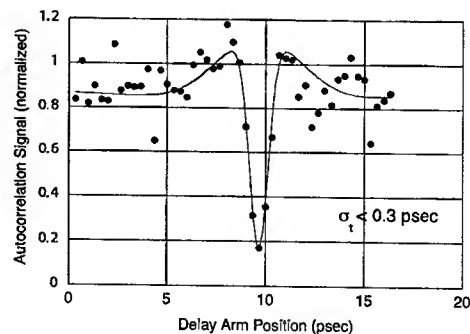


Figure 3: Autocorrelated CTR data for a fully compressed bunch. The measured bunch length is limited by the wavelengths detectable by the diagnostic.

from the data through the use of a time domain fitting algorithm which takes into account the loss of low frequencies, as described in Ref. [15].

The shortest measured pulse length was 300 femtoseconds, rms. This number is consistent with the wire grid spacing limit of the diagnostic and as simulations indicate, the actual bunch length may be significantly shorter. In addition, space-charge inclusive PARMELA and HOMDYN simulations of this system give minimum pulse lengths below 200 fsec.

EMITTANCE DYNAMICS

As mentioned above, velocity bunching has the potential to compress while avoiding the emittance growth observed in bending systems. The possibility for emittance growth in this case comes from space-charge forces. Because the bunch is compressing — increasing in current, in this measurement approaching 1 kA — at relatively low energy, the normal emittance compensation process must be altered to control the emittance.

The nominal emittance compensation process in the case of a split injector [17] is to focus the beam out of the gun to a waist, and matched onto the invariant envelope [4],

$$\sigma_{IE} = \frac{2}{\gamma} \sqrt{\frac{I}{(1 + \eta/2) I_0 \gamma}}, \quad (3)$$

at the entrance of the accelerator section. Here γ is the normalized accelerating gradient, γ the energy, $I_0 = 17\text{kA}$ the characteristic current, and η is a unitless function of the external focusing forces. In the case of velocity compression, the current increases with z , and we may choose to match the beam to and equilibrium size, $\sigma_{eq} (\sigma'' = \sigma' = 0)$,

$$\sigma_{eq} = \frac{2}{\gamma'(z)} \sqrt{\frac{2I(z)}{\eta(z) \gamma(z) I_0}} \quad (4)$$

If we make the approximation that $I(z)/\gamma(z)$ is constant, then it is clear that the applied external focusing must increase as γ' increases. This process is shown in Fig. 4, where the beam envelope is kept roughly matched by increasing the external solenoid field while it compresses. Here the emittance oscillates, as expected by compensation theory, but does not increase beyond this oscillation.

ACKNOWLEDGEMENTS

This work was performed under the auspices of the U.S. Department of Energy by the University of California, Lawrence Livermore National Laboratory under contract No. W-7405-Eng-48.

REFERENCES

- [1] The LCLS Design Study Group, Tech. Rep. SLAC-R-0521, Stanford Linear Accelerator Center (1998).

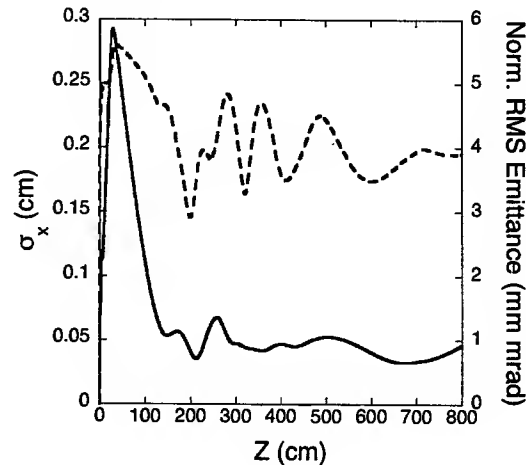


Figure 4: PARMELA simulation of the RMS beam size (solid line) and emittance (dashed line) evolution for the compressing scenario.

- [2] International Study Group, Tech. Rep. SLAC-R-559, Stanford Linear Accelerator Center (2000).
- [3] B. E. Carlsten, Nucl. Instrum. Methods Phys. Res., Sect. A **285**, 313 (1989).
- [4] L. Serafini and J. B. Rosenzweig, Phys. Rev. E **55**, 7565 (1997).
- [5] M. James *et al.*, IEEE Trans. Nucl. Sci. NS-**30**, 2992 (1983).
- [6] H. Braun, *et al.*, Phys. Rev. Lett. **84**, 658 (2000).
H. Braun, *et al.*, Phys. Rev. ST Accel. Beams **3**, 124402 (2002).
- [7] ICFA Beam Dynamics mini workshop (2002), see http://www.desy.de/csr/csr_workshop_2002/csr_workshop_2002_index.html.
- [8] S. G. Anderson, Ph. D. thesis, University of California, Los Angeles (2002).
- [9] L. Serafini, A. Bacci, and M. Ferrario, in *Proceedings of the PAC 2001, Chicago*, (IEEE, Piscataway, NJ, 2001), pp. 2242-2244.
- [10] P. Musumeci *et al.*, these proceedings.
- [11] P. Piot *et al.*, Phys. Rev. ST Accel. Beams **6**, 033503 (2003).
- [12] G. P. LeSage *et al.*, in *Advanced Accelerator Concepts: Ninth Workshop*, edited by P.L. Colestock and S. Kelly (AIP, New York, 2001), AIP Conf. Proc. No. 569.
- [13] D. T. Palmer, Ph. D. thesis, Stanford University (1998).
- [14] W. J. Brown *et al.*, these proceedings.
- [15] A. Murokh *et al.*, Nucl. Instrum. Methods Phys. Res., Sect. A **410**, 452 (1998).
- [16] A. Murokh, Ph. D. thesis, University of California, Los Angeles (2002).
- [17] L. Serafini and J.B. Rosenzweig, in *Proceedings of the PAC 1997*, (IEEE, Piscataway, NJ, 1997), p. 2876.

ELIMINATING THE SPOT DILUTION DUE TO KICKER SWITCHING IN DARHT-II*

Yu-Jiuan Chen, Frank W. Chambers, Arthur C. Paul, James A. Watson and John T. Weir
Lawrence Livermore National Laboratory, Livermore, CA 94550, USA

Abstract

To produce four short x-ray pulses for radiography, the second-axis of the Dual Axis Radiographic Hydrodynamic Test facility (DARHT-II) will use a fast kicker to select current pulses out of the 2- μ s duration beam provided by the accelerator. Beam motion during the kicker voltage switching could lead to dilution of the time integrated beam spot and make the spot elliptical. A large elliptical x-ray source produced by those beams would degrade the resolution and make radiographic analysis difficult. We have developed a tuning strategy to eliminate the spot size dilution, and tested the strategy successfully on ETA-II with the DARHT-II kicker hardware.

1 INTRODUCTION

The second-axis of the Dual Axis Radiographic Hydrodynamic Test facility (DARHT-II) will perform multiple-pulse (1 - 4 pulses) x-ray flash radiography [1]. The downstream [2] consists of a high-speed, high-precision kicker system [3] and an x-ray converter target assembly [4]. The kicker will be used to select four short current pulses out of the 2- μ s duration beam provided by the accelerator. In general, the beam motion introduced by the kicker voltage switching could lead to a large smeared elliptical time integrated beam spot even though each beam slice is focused to a small round spot [5]. To achieve good x-ray resolution, we can simply focus every beam slice to a spot tighter than the design specifications to accommodate beam motion during switching. However, the DARHT-II facility uses a static x-ray converter target to preserve the radiographic axis, and having enough target material for all four beam pulses to generate the required X-ray doses provides a big challenge. A tighter beam will put the multi-pulse, static target's confinement at risk. Furthermore, an elliptical x-ray source would make radiographic analysis difficult. We have explored a tuning strategy to eliminate the spot size dilution, and tested the strategy successfully on ETA-II with the DARHT-II kicker hardware.

This paper presents the ETA-II kicker experimental results for minimizing the spot dilution in Sec. 2. The beam transport for the kicked beam with elimination of spot size dilution during kicker switching is discussed in Sec. 3. Finally, conclusions are given in Sec. 4.

2 BEAM TRANSPORT

The DARHT-II kicker ensemble consists of the kicker

* This work was performed under the auspices of the U.S. Department of Energy by University of California Lawrence Livermore National Laboratory under contract No. W-7405-Eng-48.

with a DC bias dipole, a large quadrupole magnet serving as a septum, four Collins quadrupole magnets, a septum dipole and a beam dump. When the kicker is off, the DC bias dipole deflects the beam, and the magnetic field of the quadrupole septum, set by the beam energy, sends the unkicked portion of the 2- μ s beam to the beam dump. When the kicker is on, the net deflecting field is reduced to zero. The beam transports through three Collins quadrupoles, which are needed to re-establish the beam to round, onto the straight target line. The fourth Collins quadrupole incorporated into the design was originally included to provide flexibility in the tuning if needed. The nominal beam envelope without using the 4th quadrupole in the target line is shown in Fig. 1. For an 18-MeV beam, the net dipole field from the kicker and the DC bias dipole during the kicker switching varies from 8 to zero Gauss. The beam centroids corresponding to the net field of zero to 2 Gauss (with a 0.2-Gauss increment) during the kicker switching are also shown in Fig. 1 (dashed curves). Although the nominal net deflecting field during the kicker switching varies from zero to 8 Gauss, only the slice with a deflecting field no greater than 2 Gauss would reach the target. Figure 1 indicates that the beam arriving the target will have a few nanoseconds of rise and fall. The beam phase space at the converter target is presented in Fig. 2. For simplicity, we have ignored the coupling in the x-y plane due to the beam rotation in solenoid field. Hence, the beam motion during the kicker switching only appears in the x direction. Therefore, the y-y' phase space plots are the same for all the beam slices during the kicker switching. The x-y plot clearly shows the beam spot moves with the net deflecting field during the switching. The time integrated spot would be a large elongated spot. The x-x' plot also indicates that there is large beam motion during the switching.

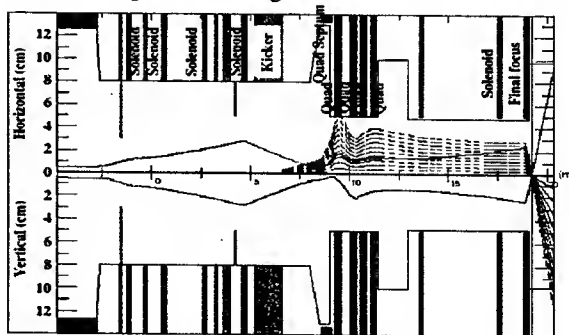


Figure 1. The nominal beam envelope and the beam centroid during the kicker switching in the DARHT-II transport line from the accelerator exit to the target.

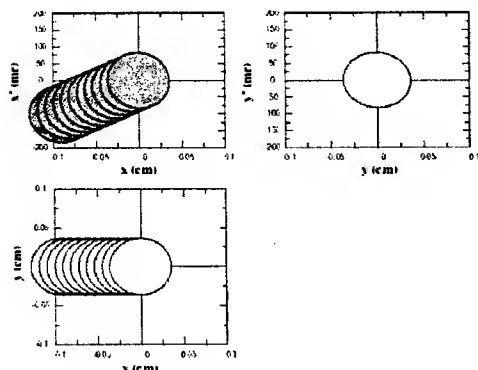


Figure 2. Phase space of the nominal beam at the converter target with the net deflecting field at the kicker varying from 0 to 2 Gauss

To fix the beam motion of an individual beam slice during the kicker switching, we need to apply a set of dipole fields linearly proportional to its residual deflecting field from the kicker and the bias dipole. We have noticed that a beam slice during the kicker pulser's rise and fall will experience a dipole field linearly proportional to its transverse displacement in a quadrupole, and its beam displacement is linearly proportional to the residual field strength. Therefore, we can eliminate the transverse beam displacement on the converter target by using the additional fourth Collins quadrupole with a proper magnetic tune. There are several ways to tune the quadrupoles. We have explored a tuning strategy, which uses four constraints; $x = y$ (round beam), $x' = y' = 0$ and $x_c = 0$ at the converter to set the field strength of those four quadrupoles. By letting the beam round and focused at the target, we have found that scanning the beam radius at the view port downstream from the quadrupoles effectively rotates the kicker sweep in the x - x' phase space (Fig. 3). Double values at the small radii for both curves in Fig. 3 are due to the fact that two different envelopes can give the same beam radius at the view port. There is a wide operation range, which can provide $x_c/a < 10\%$. We have found three quadrupoles tunes with 1.05-cm, 2.19-cm and 2.76-cm beam radii at the view port, which can eliminate spot dilution while the beam angle sweeps either down or up. The beam x - x' phase spaces at the converter target for these tunes are presented in Fig. 4. The x - y plots indicate that there is no spot dilution during the kicker switching.

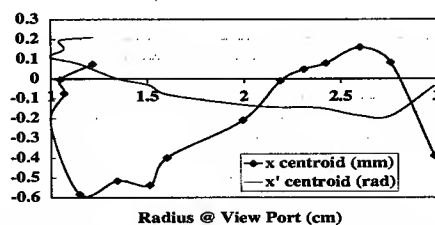


Figure 3. Beam motion at the target of a beam slice with a 1-Gauss residual dipole field during the kicker switching

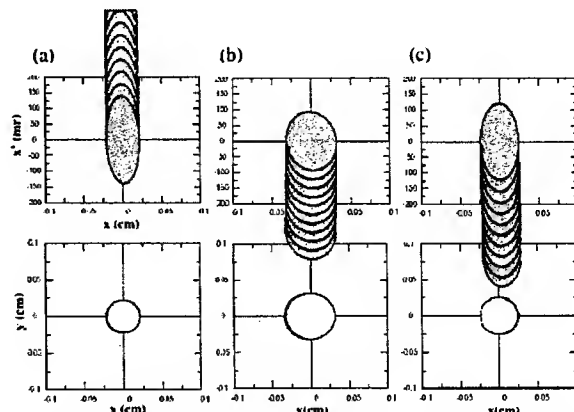


Figure 4. Beam phase spaces at the target for the three optimal tunes that minimize spot dilution. The beam radii at the view port are (a) 1.05 cm, (b) 2.19 cm and (c) 2.76 cm. The net kicker field varies from 0 to 2 Gauss.

3 KICKER EXPERIMENT

We tested the spot size dilution optimization on the ETA-II accelerator at LLNL with the DARHT-II kicker hardware (Fig. 5). The experimental setup is given in Fig. 6. A removable Cherenkov foil was used to examine beam profile past the last quadrupole. Current and beam position were measured with a beam bug placed upstream of the viewing foil. At the end of the setup, we installed a second viewing foil followed by a permanent magnet dipole and beam dump. A camera set with a wide time gate relative to the ETA-II beam was used to observe the time integrated beam profile at this location.



Figure 5. The DARHT-II kicker system being tested on the ETA-II accelerator

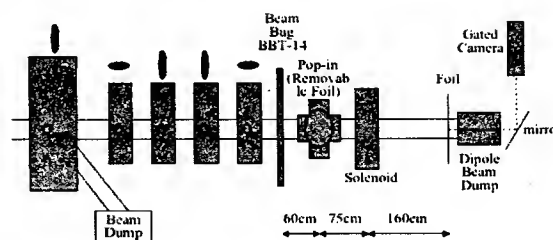


Figure 6. The ETA-II Kicker experimental setup after the kicker

Although the kicker pulser's amplitude modulation and control system can provide precision beam manipulation, such as compensating for transverse beam motion at the kicker input as well as the dynamic response and beam-induced steering effects associated with the kicker structure during the flat-top portion of the kicker pulse for high current electron beams [6], the transverse beam motion during the kicker switching will not be compensated. The beam motion during the kicker switching should not be an issue for a long pulse since its time integrated spot size on the target will be mainly determined by the beam flat-top instead of by the beam head and tail. However, as demonstrated on the ETA-II (Fig. 7), kicker switching can potentially lead to severe dilution of the time integrated spot size for a short pulse. Fortunately, the spot size dilution can be eliminated with proper tuning of the Collins quadrupoles. The data for kicked beams in Fig. 7 were taken when 20-ns kicker pulses were applied to the center of the 40-ns ETA-II beam. The beam was set to be round at the pop-in foil upstream of the solenoid and at the end of the beam line. Without an optimized tune, the time integrated beam over 100 ns shows the beam being kicked away from and back to its original spot. This beam motion resulted a large elongated time integrated spot size. With an optimized tune to minimize the beam motion during the switching, there was little net beam motion over the entire beam even though the kicker pulser was on, and the 100 ns gated beam image looked similar to the un-kicked round beam.

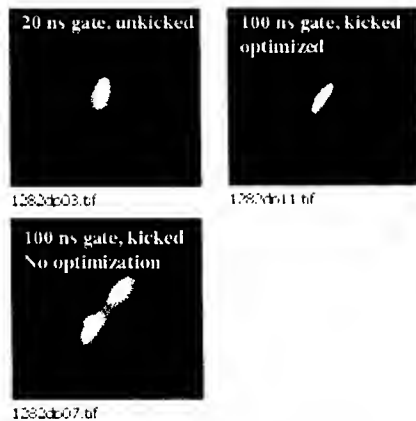


Figure 7. The time integrated ETA-II beam spots without the kicker pulser, and during the entire kicker switching with and without implementing the tuning optimization scheme.

4 CONCLUSIONS

Spot size dilution caused by beam motion during the kicker switching can degrade the DARHT-II radiography facility's performance. We have demonstrated both computationally and experimentally that the beam spot dilution can be removed by tuning the kicker quadrupole system properly. We have noticed that the beam centroid angle at the target during the switching is large for all

cases presented in Fig. 4 even though the beam spatial displacement vanishes. Our transport modelling results indicate that only the beam with a 1-Gauss or less net kicker deflecting field will reach the target for those tunes, and that the centroid slope for the beam with a 1-Gauss net deflecting field is about ± 200 mr. There are two solenoids after the quadrupoles on the DARHT-II beamline. One serves as the final focus lens, and the other is for the tuning flexibility. The modelling results presented in Sec. 2 were done without using the additional solenoid. Using the extra solenoid would change the steepest centroid angle roughly to ± 100 mr. The nominal beam has a -65 -mr centroid angle (Fig. 2), which indicates that the spot minimization tunes do not trade the beam displacement with the centroid angle. A large beam centroid angle during the kicker switching is a concern. The x-rays produced by large angle electrons may smear the x-ray spot while the beam spot is small and round. Some end-to-end particle simulations should be performed to estimate the impact of the large beam angle to the x-ray spot and on-axis dose. If it is needed, adding an additional quadrupole to the beamline may fix the problem. As discussed in Sec. 2, we have used four constraints to tune four Collins quadrupoles. It is possible that the additional quadrupole would allow us to set an additional constraint, i. e., a zero centroid angle.

5 REFERENCES

- [1] M. J. Burns, et. al., "Status of the Dual Axis Radiographic Hydrodynamics Test (DARHT) Facility", *Proc. of BEAMS 2002*, Albuquerque, NM, June 24-28, 2002.
- [2] Y.-J. Chen, et. al., "Downstream System for the Second Axis of the DARHT Facility", *Proc. of the XXI LINAC*, Gyeongju, South Korea, August 19-23, 2002.
- [3] Y. J. Chen, et. al., "Precision Fast Kickers for Kiloampere Electron Beams", *Proc. Of the 1999 IEEE PAC*, New York, NY, March 27 - April 2, 2002, p. 627.
- [4] D. D.-M. Ho, et. al., "Hydrodynamic Modelling of a Multi-Pulse X-Ray Converter Target for DARHT-II", LLNL Report. UCRL-JC-1442, July 26, 2001.
- [5] B. R. Poole and Y.-J. Chen, "Particle Simulations of DARHT-II Transport System", *Proc. of the 2001 IEEE PAC*, Chicago, IL, June 18-22, 2001, p. 3299.
- [6] J. A. Watson, et. al., "Control System for the LLNL Kicker Pulse Generator", *Proc. of the 2002 IEEE Power Modulator Conference*, Hollywood, CA July 1-3, 2002.
- [7] Y.-J. Chen, et. al., "Final Focusing System for the Second Axis of the Dual-Axis Radiographic Hydrodynamic Test Facility", *Proc. of the 14th High-Power Particle Beams*, Albuquerque, NM, June 24-28, 2000.

RF FOCUSING METHODS FOR HEAVY IONS IN LOW ENERGY ACCELERATORS*

E.S. Masunov[#], S.M. Polozov, MEPHI, Moscow, 115409, Russia,
P.N. Ostroumov, N.E. Vinogradov, ANL, Argonne, IL 60439, USA

Abstract

A new type of axially symmetric RF field focusing (ARF) in a drift-tube accelerating structure is proposed and studied. Beam stability in both transverse and longitudinal directions is achieved by the variation of drift tube aperture and appropriate phasing. An analysis of 3D beam dynamics is performed using the smooth approximation technique. Beam dynamics in an APF structure and in a conventional RFQ are compared. An universal method is suggested to choose a voltage V and aperture in the APF structure designed for heavy-ions with charge-to-mass ratio $q/A \geq 1/66$ in the energy range above 20 keV/u. The proposed structure and analysing technique can be useful in the design of a post-accelerator for the Rare Isotope Accelerator Facility being designed in the U.S. [1].

INTRODUCTION

Transverse stability of beam motion in an accelerating structure can be ensured either by external focusing elements or by applying a special configuration of the accelerating RF field (RF focusing). The latter is especially effective for low energy ion linacs. Several types of RF focusing such as alternating phase focusing (APF) [2], radio frequency quadrupole (RFQ) [3] and undulator RF focusing (RFU) [4] have been proposed and investigated. In some applications the ARF focusing [5] may be preferable. In RFQ and ARF structures the beam is accelerated by a synchronous wave of RF field, in which case the acceleration gradient must be set to provide particle stability in both transverse and longitudinal directions.

BEAM DYNAMICS IN ARF LINAC

The ARF accelerating cavity can be designed as an interdigital structure. The longitudinal and transverse electric RF field components $E_{z,r}$ in a periodical resonant structure can be described by:

$$\begin{aligned} E_z &= E_n I_0(h_n r) \cos\left(\int h_n dz\right) \cos(\omega t), \\ E_r &= E_n I_1(h_n r) \sin\left(\int h_n dz\right) \cos(\omega t), \end{aligned} \quad (1)$$

where $h_n = h_0 + 2\pi m / D$, $h_0 = \mu / D$, μ are the propagation factors and phase advance per period D of

RF structure, n is the harmonic number, I_0 , I_1 are the modified Bessel functions. A nonsynchronous harmonic can only focus the beam when its phase velocity $v_{ph,n} = \omega / h_n$ significantly differs from the average velocity of the particles v_b . The TF structure with a single nonsynchronous harmonic can be examined as a periodical sequence of axially symmetric electrostatic lenses. The synchronous s -th harmonic ($v_{ph,s} = v_b$) can be provided by modulation of the inner radius of the drift tubes. A configuration of the accelerating structure is characterized by the radii a_i of the drift tubes, the modulation factor m and structure period D , as is shown in Fig.1. Together with the electrode voltage $\pm V/2$, applied to neighbouring drift tubes, these parameters determine the acceleration and focusing fields.

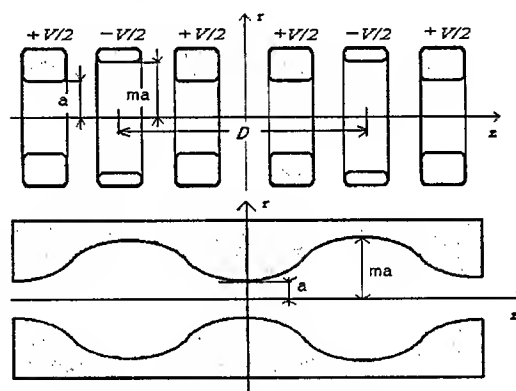


Figure 1: ARF and RFQ channels.

Let us consider particle acceleration in the two-wave approach when $\mu=\pi$, and a synchronous, $s=0$, and one nonsynchronous, $n=1$, harmonics are taken into account. In general, individual particles trajectories are complicated but can be represented as the sum of a slow variation \bar{r} and rapid oscillation \tilde{r} . Accordingly, the beam momentum p can be represented as the sum of a slowly varying and a rapidly oscillating components, $p = \bar{p} + \tilde{p}$. Following ref. [4] one can apply averaging over the rapid oscillations and obtain a time-averaged equation of motion for a non-relativistic ion:

$$\frac{d^2 R}{dt^2} = -\frac{d}{dR} \tilde{U}_{\text{eff}}, \quad (2)$$

* Work is partially supported by the U. S. Department of Energy under contract W-31-109-ENG-38.

[#] masunov@dinus.mephi.ru

where $R = 2\pi\bar{r}/\lambda\beta_s$ is a dimensionless coordinate and $\tau = \omega t$. \tilde{U}_{eff} is the effective potential function determined by dimensionless field harmonics amplitudes of on the axis $e_{s,n} = eE_{s,n}\lambda/(2\pi mc^2\beta_s)$:

$$\tilde{U}_{eff} = -\frac{1}{2}e_0[I_0(\rho)\sin(\psi_s + \chi) - \chi\cos(\psi_s)] + \frac{1}{16}\left\{5\left(\frac{e_1}{4}\right)^2 g(3\rho) + \left(\frac{e_0}{2}\right)^2 g(\rho)\right\}, \quad (3)$$

where $R = [\chi, \eta]$, $\chi = 2\pi(\bar{z} - \bar{z}_c)/\lambda\beta_s$, $\rho = 2\pi\bar{r}/\lambda\beta_s$, $g_{s,n}(\rho) = I_0^2(\rho) + I_1^2(\rho) - 1$; ψ , z_c , $\beta_s = \omega/h_s c$ are the phase, coordinate, and velocity of the synchronous particle.

The effective potential function can be rewritten as:

$$\tilde{U}_{eff,a} = -A_a \frac{qV}{8W_s} [I_0(\rho)\sin(\psi_s + \chi) - \chi\cos(\psi_s)] + X_a^2 \left(\frac{qV}{8W_s} \right)^2 \left\{ \frac{45}{64} g(3\rho) + \left(\frac{3A_a}{4X_a} \right)^2 g(\rho) \right\}, \quad (4)$$

where W_s is the energy of the synchronous particle, A_a and X_a determine acceleration and focusing gradients which are mutually coupled. If geometrical parameters a , D , m are known, A_a and X_a are defined as

$$A_a = \frac{2[I_0(3m\rho_m) - I_0(3\rho_m)]}{I_0(m\rho_m)I_0(3\rho_m) + 2I_0(3m\rho_m)I_0(\rho_m)}, \quad (5)$$

$$X_a = \frac{1 - A_a I_0(\rho_m)}{I_0(3\rho_m)}, \quad \rho_m = \frac{\pi a}{D}. \quad (6)$$

The effective potential function $U_{eff,a}$ describes the 3-D particle dynamics completely. In addition, it determines the system Hamiltonian

$$H = \frac{1}{2} \left(\frac{dR}{d\tau} \right)^2 + U_{eff}. \quad (7)$$

Using the Hamiltonian (7) and analyzing the bunch form in the 4-dimensional phase space one can find the relationship between the longitudinal and transverse acceptances.

A necessary condition for simultaneous transverse and longitudinal focusing is the existence of a global minimum of \tilde{U}_{eff} . In this case the effective potential function is 3-D potential well in the beam frame. In the two-wave approach, the transverse stability condition (5) results in

$$\frac{qV}{mc^2} \left(\frac{\lambda}{2\pi a} \right)^2 > F_a = \frac{64}{135} \Phi_a(\rho) \frac{A_a}{X_a^2 \rho_m^2} \sin(\psi_s + \chi), \quad (8)$$

where the form-factor Φ_a is

$$\Phi_a = \frac{I_1(\rho)}{I_1(3\rho)} \left[I_0(3\rho) - \frac{I_1(3\rho)}{6\rho} \right]^{-1} \quad (8a)$$

As it is seen in Eq. (8), the ARF efficiency depends significantly on the parameter X_a^2/A_a . Amplitudes of the RF field harmonics must be chosen to satisfy Eq. (8) along the structure. Eq. (8) also shows that for the considered range of beam energy the transverse focusing with an arbitrary synchronous phase can be achieved only if the amplitude of non-synchronous wave is larger than the amplitude of the synchronous one. The accelerating gradient is proportional to $A_a(qV/8W_s)$. Thus the RF focusing effectiveness is limited by the acceleration gradient and sets restrictions on the parameter A_a . It also means that the ARF structure is effective for low energy beams. The ARF structure can be created by a special design of the focusing period consisting of two or more accelerating gaps.

BEAM DYNAMICS IN RFQ LINAC

The longitudinal and transverse electric RF field components E_v in an RFQ structure are described by:

$$E_z = \frac{h}{2} A_q V I_0(\rho) \sin(\psi + \tau) \sin\tau, \quad h = 2\pi/\beta\lambda, \quad (9)$$

$$E_r = -hV \left[X_q \rho \cos(2\theta) + \frac{1}{2} A_q I_1(\rho) \cos(\psi + \tau) \right] \sin\tau,$$

where

$$A_q = \frac{m^2 - 1}{m^2 I_0(m\rho_m) + I_0(m\rho_m)}, \quad X_q = \frac{1 - A_q I_0(\rho_m)}{\rho_m^2}. \quad (10)$$

In this case, the effective potential function can be written as follows:

$$U_{eff,q} = -A_q \frac{qV}{8W_s} [I_0(\rho)\sin(\psi_s + \chi) - \chi\cos(\psi_s)] + X_q^2 \left(\frac{qV}{8W_s} \right)^2 \left\{ 4\rho^2 + \left(\frac{A_q}{4X_q} \right)^2 g(\rho) \right\}. \quad (11)$$

The existence of the global minimum of the potential U_{eff} is a condition for simultaneous transverse and longitudinal stability. The oscillations will be stable if the condition

$$\frac{qV}{mc^2} \left(\frac{\lambda}{2\pi a} \right)^2 > F_q = \frac{1}{2} \Phi_q(\rho) \frac{A_q}{X_q^2 \rho_m^2} \sin(\psi_s + \chi) \quad (12)$$

is satisfied, where the form-factor $\Phi_q = I_1(\rho)/\rho$. This inequality is very similar to the condition (8) and allows a detailed comparison of two methods of RF focusing.

COMPARISON OF ARF AND RFQ LINACS

The analysis of the 3D effective potential function allows us to find the conditions under which focusing and acceleration of the particles occur simultaneously. Universal curves which are described by the functions $\Phi_{a,q}$ in the right side of the inequalities (8), (12) allow to choose V , and λ/a at the given q/m , and a range of ion velocity change β_s .

In a RFQ linac the amplitude of rapid transverse oscillations \tilde{r} is comparable with \bar{r} , and in an ARF linac, $\tilde{r} \ll \bar{r}$. As a consequence aperture of an RFQ linac a_q must be larger than for an ARF structure. The accelerating gradient, $A_{a,q}$, as function of a dimensionless aperture $\rho_m = a\omega/\nu$ for $m=2$ is shown in Fig. 2. In an ARF linac the acceleration gradient is larger than for a RFQ if $a_q \approx 2a_a$. The transverse focusing conditions (8) and (13) depend on the ratio A/X^2 as function of channel aperture ρ_m and form-factor $\Phi(\rho)$. The functions of $\Phi_{a,q}(\rho)$ for different ion beam radii are shown in Fig. 2. The magnitude of $\Phi_a(\rho)$ is smaller than $\Phi_q(\rho)$ and drops as radius ρ increases. The latter means that the focusing condition (8) is easier to satisfy for non-axis particles in an ARF structure. For given V and λ the velocity range where the transverse stability conditions are satisfied is different for ARF and RFQ. For an RFQ structure one can find a minimal value of the normalized voltage

$$\tilde{V} = \frac{qV}{mc^2} \left(\frac{\lambda}{2\pi a} \right)^2 \quad (\text{left part of the inequalities (12)})$$

that provides transverse stability independently from the particle velocity. In an ARF structure transverse stability is achieved only for particle velocities above a lower limit of the voltage. The values of $\tilde{V}_{a,q}$ in Fig. 3 were calculated for heavy ions with $q/m=1/66$, $V=100$ kV, $\lambda=25$ m, $\psi_s = 20^\circ$ and radius $a=1$ cm for RFQ and $a=0.5$ cm for ARF. For these parameters in ARF structure beam stability is provided if $\nu > 1.8\omega a$.

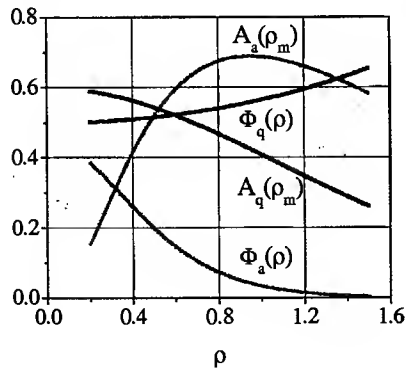


Figure 2: Accelerating gradients and form-factors as a function of unitless aperture, ρ_m , and radius, ρ .

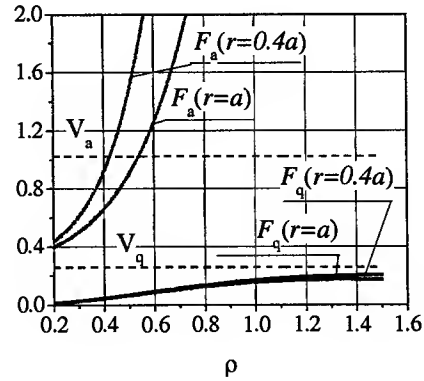


Figure 3: Transverse stability conditions.

CONCLUSION

New methods for axial-symmetric RF focusing and acceleration of heavy ions are studied and compared with the well-known RFQ structure. Universal curves are established to choose a voltage V and λ/a for a given q/m and ion velocity β_s in RFQ and ARF linacs. The acceleration gradient in ARF linac is larger than in the RFQ structure. Aperture of the RFQ linac must be larger due to large amplitudes of rapid transverse oscillations. Transverse stability in both ARF and RFQ structures depends on beam velocity range. For the same a/λ and V , the focusing properties of the ARF structure are extended to higher velocities. This result is especially interesting for the design of the RIA post accelerator [7] where ions with low charge-to-mass ratio $q/m=1/66$ are accelerated prior to injection into the superconducting linac.

REFERENCES

- [1] G. Savard. Proc. of the PAC2001, Chicago, IL, June 18-21, 2001, p. 561.
- [2] I.B. Fynberg, Sov. Phys. Tech. Phys. v.4, p506, 1959.
- [3] I.M. Kapchinskiy, V.A. Teplyakov, Prib. Tekh. Eksp., v.119, No.2, p.17, 1970.
- [4] E.S. Masunov, Sov. Phys.-Tech. Phys., vol. 35, No. 8, p. 962, 1990.
- [5] V.S. Tkach, Sov. Phys. JETP, v.32, p.538, 1957.
- [6] E.S. Masunov, N.E. Vinogradov, Phys. Rev. ST Accel. Beams, 2001, No 7, 070101.
- [7] P.N. Ostroumov and et. al., Proc. of the PAC2001, Chicago, IL, June 18-21, 2001, p. 4080.

IMAGE-CHARGE EFFECTS ON THE ENVELOPE DYNAMICS OF AN UNBUNCHED INTENSE CHARGED-PARTICLE BEAM

B. L. Qian, J. Zhou, and C. Chen

Plasma Science and Fusion Center, Massachusetts Institute of Technology, Cambridge, MA 02139

Abstract

The root-mean-squared (rms) envelope equations are derived and analyzed for an unbunched intense charged-particle beam in an alternating-gradient focusing field and a cylindrical conducting pipe. All higher-order image-charge effects from the cylindrical pipe are expressed in terms of so-called multiple moment factors in the rms beam envelope equations, and the multiple moment factors are evaluated. Numerical results show that for vacuum phase advance $\sigma_v < 90^\circ$, the image-charge effects on the matched and slightly mismatched beam envelopes are negligibly small, at all orders, for all beams with arbitrary beam density profiles (including hollow density profiles) as well as for arbitrary small apertures (including beams with large aspect ratios). However, the main unstable region for the envelope evolution with image-charge effects, which occurs for $90^\circ < \sigma_v < 270^\circ$, depending on the value of the normalized beam intensity SK/ε , is found to be narrower than its counterpart without image-charge effects.

INTRODUCTION

High-intensity accelerators with alternating-gradient focusing systems have many applications in basic scientific research and nuclear physics. In the research and development of high-intensity accelerators, a key issue is to minimize the aperture of the transport system for intense charge-particle beams, while preventing the beams from developing large-amplitude charge density and velocity fluctuations as well as subsequent emittance growth and halo formation. In order to understand the collective behavior of charged-particle beams, it is important to examine the beam envelope evolution under the influence of both the beam space-charge and the image charges induced on the conducting walls of accelerator structures.

The earliest works on the beam envelope equations without image-charge effects can be found in Refs. [1-4]. These works are very important for understanding the beam envelope dynamics. Recently, Lee, Close and Smith [5] and Allen and Reiser [6,7] extended Sacherer's 2-D results to include the image-charge effects due to the cylindrical conducting pipe. They analyzed the *first-order* image-charge effects.

In this paper, we extend the previous 2-D envelope equations [5-7] to include all higher-order image-charge

effects from the cylindrical conducting pipe [8]. We treat the density distribution using the self-similar model, though the normal-mode analysis (i.e., small-signal theory) was used to describe the density evolution in a charged-particle beam for understanding the collective oscillations and instabilities in the beam. In particular, the self-electric and self-magnetic fields are calculated for an unbunched beam with elliptic symmetry and an arbitrary transverse dependence in the self-similar beam density model. The root-mean-squared (rms) envelope equations are derived, including all higher-order image-charge effects from the cylindrical conducting pipe. Useful numerical results on the beam envelope dynamics are presented.

BEAM ENVELOPE EQUATIONS WITH IMAGE-CHARGE EFFECTS

We consider an unbunched elliptical beam propagating in an alternating-gradient focusing field and a cylindrical metal pipe with radius R , as shown in Fig. 1. The beam has an envelope $a(s)$ in the x -direction and an envelope $b(s)$ in the y -direction, where $s = z$. The beam drift velocity in the z direction is $v_z \approx \beta_b c$, where c is the speed of light in vacuum. Following the analysis of Sacherer [3], we have derived the generalized envelope equations with image-charge effects, which can be expressed as [8]

$$\frac{d^2 X}{ds^2} + \kappa_q(s)X - 2K \left[\frac{1}{X+Y} + \sum_{l=1}^{\infty} \frac{X(X^2 - Y^2)^{2l-1}}{R^{4l}} N_l \right] = \frac{e^2}{X^3} \quad (1)$$

and

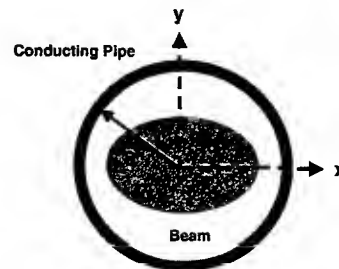


Fig. 1 Elliptical unbunched charged particle beam in a cylindrical conducting pipe.

$$\frac{d^2 Y}{ds^2} - \kappa_q(s)Y - 2K \left[\frac{1}{X+Y} + \sum_{l=1}^{\infty} \frac{Y(Y^2 - X^2)^{2l-1}}{R^{4l}} \right] N_l = \frac{\epsilon_y^2}{Y^3}. \quad (2)$$

In Eq. (2), $X = 2\tilde{x}$ and $Y = 2\tilde{y}$; $\tilde{x} = \sqrt{\langle x^2 \rangle}$ and $\tilde{y} = \sqrt{\langle y^2 \rangle}$ are the rms envelopes in the x - and y -directions, respectively; ϵ_x and ϵ_y are 4 times the beam rms emittances in the x - and y -directions, respectively;

$$N_l = 2 \left(\frac{(2l)!}{4^l (l!)^2} \right)^2 \frac{\left[\int_0^{\infty} 2\pi ab n(\tilde{r}^2) \tilde{r}^{2l+1} d\tilde{r} \right]^2 \left[\int_0^{\infty} 2n(\tilde{r}^2) \tilde{r} d\tilde{r} \right]^{2l}}{N_b^2 \left[4 \int_0^{\infty} n(\tilde{r}^2) \tilde{r}^3 d\tilde{r} \right]^{2l}} \quad (3)$$

is a multiple moment factor related to the beam density profile of $n = n[(x^2/a^2) + (y^2/b^2)]$.

Unlike the previous results [5-7], which include only the $l=1$ contribution, the present envelope equations (1) and (2) are complete, including both the $l=1$ contribution and all of the higher-order image-charge effects with $l \geq 2$.

EVALUATION OF MULTIPLE MOMENT FACTORS

The multiple moment factor N_l contains the information about the higher-order image-charge effects in the envelope equations (1) and (2). We can assess these effects by evaluating N_l as a function of l . In particular, we consider the following parabolic density profile,

$$n = \begin{cases} n_0 + \delta n_0 \left[1 - 3 \left(\frac{x^2}{a^2} + \frac{y^2}{b^2} \right)^2 \right], & \frac{x^2}{a^2} + \frac{y^2}{b^2} \leq 1, \\ 0, & \frac{x^2}{a^2} + \frac{y^2}{b^2} > 1, \end{cases} \quad (4)$$

where $N_b = \int_{-\infty}^{\infty} \int_{-\infty}^{\infty} n dx dy = \pi ab n_0 = \text{constant}$ and δn_0 is independent of x and y and satisfies $-n_0 \leq \delta n_0 \leq n_0/2$.

Using Eq. (4) and the moment definition, we can obtain the simplified expressions of envelopes X and Y . They are written in the form of $X^2 = a^2(1-g/2)$ and $Y^2 = b^2(1-g/2)$. In addition, substituting Eq. (4) into Eq. (3), we obtain

$$N_l = 2 \left(\frac{(2l)!}{4^l (l!)^2} \right)^2 \left(\frac{1}{1-0.5g} \right)^{2l} \left(\frac{1-2gl/(l+3)}{l+1} \right)^2 \quad (5)$$

where $g = \delta n_0/n_0$. Note in Eq. (5) that $N_1 = 1/8 = 0.125$ is independent of the factor g . Figure 2 shows a plot of N_l

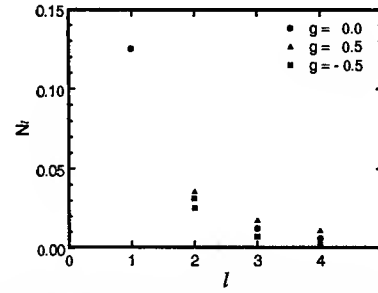


Fig. 2 The dimensionless multiple moment factor N_l versus l for several densities with $g = 0, 0.5$, and -0.5 .

as a function of l for three cases corresponding to $g = 0, 0.5$, and -0.5 .

IMAGE-CHARGE EFFECTS ON RMS MATCHED BEAMS

In this section, we show that for vacuum phase advance $\sigma_v < 90^\circ$, the higher-order image-charge effects on the matched beam envelopes are negligibly small for all beams with arbitrary beam density profiles (including hollow density profiles) as well as for arbitrary small apertures (including beams with large aspect ratios). We pay special attention to a hollow beam observed in a recent heavy ion beam experiment.

For present purposes, we assume that the rms emittances ϵ_x and ϵ_y are constant, i.e., $\epsilon_x = \epsilon_y = \epsilon$, and that the beam density profile is given in Eq. (4). We also assume that the alternating-gradient transport system is presented a step-function lattice defined by [9]

$$\kappa_q(s) = \begin{cases} +\kappa_{q0}, & 0 \leq s/S < 0.25\eta, \\ 0, & 0.25\eta \leq s/S < 0.5(1-0.5\eta), \\ -\kappa_{q0}, & 0.5(1-0.5\eta) \leq s/S < 0.5(1+0.5\eta), \\ 0, & 0.5(1+0.5\eta) \leq s/S < 0.5(2-0.5\eta), \\ +\kappa_{q0}, & 0.5(2-0.5\eta) \leq s/S < 1, \end{cases} \quad (6)$$

where κ_{q0} is a constant and η ($0 < \eta < 1$) is the filling factor.

In the numerical analysis of the beam envelope equations (1) and (2), it is convenient to use the dimensionless parameters and normalized variables defined by $\hat{s} = s/S$, $\tilde{a} = X/\sqrt{S\epsilon}$, $\tilde{b} = Y/\sqrt{S\epsilon}$, $\hat{K} = KS/\epsilon$, $\hat{R} = R/\sqrt{S\epsilon}$, and $\tilde{\kappa}_q(s) = S^2 \kappa_q(s)$. For example, Fig. 3 shows the matched beam envelope functions for beam propagation in free space as well as in a cylindrical conducting pipe. It is evident in Fig. 3 that the image-charge effects, including the contributions from all orders, are negligibly small for a hollow beam whose maximum

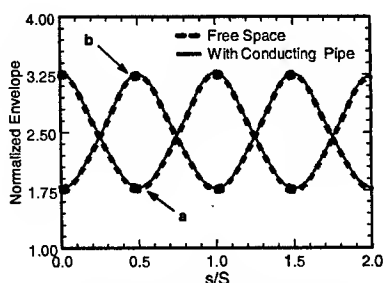


Fig. 3 Plot of the normalized envelope functions \tilde{a} and \tilde{b} versus normalized propagating distance s/S for vacuum phase advance $\sigma_v = 80^\circ$, $\hat{K} = 10$, $g = -0.5$, $\eta = 0.5$, and $\hat{R} = 4.0$.

envelopes are very close to the wall of the cylindrical pipe ($\tilde{a}_{\max} = \tilde{b}_{\max} \approx 3.25$ and $\hat{R} = 4.0$).

IMAGE-CHARGE EFFECTS ON SLIGHTLY MISMATCHED BEAMS AND ENVELOPE INSTABILITIES

In a real device, it is almost impossible to obtain a precisely matched beam because there are some perturbations on the beam propagation. These perturbations may cause beam envelope instabilities, and the unstable beam envelopes may result in particle beam losses. The beam envelope instability has already been investigated in free space [9]. However, the image-charge effects of the cylindrical conducting pipe on the mismatched beams and the beam envelope instability have not been studied until the present paper. In this section, the envelope equations (1) and (2) are solved, assuming $\varepsilon_x = \varepsilon_y = \varepsilon$, for slightly mismatched beams to find the unstable regions in the parameter space.

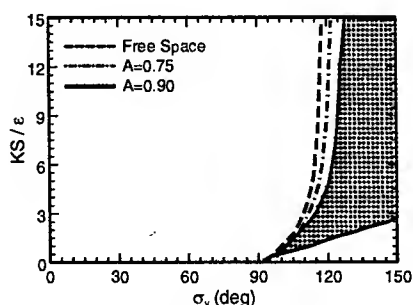


Fig. 4 Plot of the unstable regions in the dimensionless parameter space for the beam envelope evolution with $\eta = 0.5$ and $g = 0$ for three cases corresponding to (a) $R = \infty$ (free space), (b) $A = \tilde{a}_0 / \hat{R} = 0.75$, and (c) $A = \tilde{a}_0 / \hat{R} = 0.90$. Here, the shaded region is the unstable region for the beam envelope evolution with image-charge effects and $A = \tilde{a}_0 / \hat{R} = 0.90$.

In order to obtain slightly mismatched beam envelopes, following the method employed in Ref. [9], the initial conditions for $\tilde{a}(s)$ and $\tilde{b}(s)$ at $s=0$ are chosen to be $\tilde{a}(0) = \tilde{a}_0(1+\delta)$ and $\tilde{b}(0) = \tilde{b}_0(1-\delta)$, where \tilde{a}_0 and \tilde{b}_0 are the matched beam envelopes at $s=0$ and δ is chosen to be in the region of $0 \leq |\delta| \leq 0.01$. Here, δ represents the perturbations caused by the noise in the beam. In the numerical calculations, the particle beams are allowed to propagate over 40 periods.

Figure 4 is a plot of $\hat{K} = KS / \varepsilon$ versus σ_v , showing the unstable regions of the slightly mismatched beam envelopes. As can be seen from Fig. 5, the unstable regions for all the three cases start around $\sigma_v = 90^\circ$. The solid lines indicate the boundary of the unstable region with image-charge effects from the cylindrical pipe for $A = \tilde{a}_0 / \hat{R} = 0.90$, whereas the dashed lines represent the boundary of unstable region without image-charge effects in free space. The unstable region with image-charge effects for $A = \tilde{a}_0 / \hat{R} = 0.90$ is shaded in Fig. 4. Although the lower boundaries for the three cases almost coincide, there is an observable difference between their upper boundaries. The unstable region for cylindrical pipe case (i.e., with image-charge effects) is obviously narrower than that in free space situation (i.e., without image-charge effects).

This research was supported by the U. S. Department of Energy, Division of High-Energy Physics, Grant No. DE-FG02-95ER40919, and Office of Fusion Energy Science, Grant No. DE-FG02-01ER54662.

REFERENCES

- [1] I. M. Kapchinskij and V. V. Vladimirkij, in *Proceedings of the International Conference on High Energy Accelerators and Instrumentation* (CERN, Geneva, 1959), p. 274.
- [2] P. Lapostolle, CERN Report AR/Int. SG/65-15, (1965).
- [3] F. J. Sacherer, IEEE Trans. Nuclear Sci. NS-18, 1105 (1971).
- [4] P. Lapostolle, IEEE Trans. Nuclear Sci. NS-18, 1101 (1971).
- [5] E. P. Lee, E. Close, and L. Smith, in *Proceedings of the 1987 IEEE Particle Accelerator Conference*, edited by E. R. Lindstorm and L. S. Taylor (Institute for Electrical and Electronic Engineers, New York, 1987), p. 1126.
- [6] C. K. Allen and M. Reiser, Phys. Rev. E 54, 2884(1996).
- [7] C. K. Allen, Ph. D. dissertation, University of Maryland, (1996).
- [8] B. L. Qian, J. Zhou, and C. Chen, Phys. Rev. ST-AB 6, 014201(2003).
- [9] Q. Qian and R. C. Davidson, Phys. Rev. E53, 5349 (1996).

RANDOM-REGULAR ACCELERATING STRUCTURES

M. Ayzatsky*, K. Kramarenko#, NSC KIPT, Kharkov, 61108, Ukraine

Abstract

In this work we present results of investigation of the characteristics of inhomogeneous sections on the base of a disk-loaded waveguide with different laws of hole radius variation. We have shown that in the case when coupling of cavity fields is small there is a traveling wave in a waveguide even for the non-smooth laws of hole radius variation. But the traveling wave regime exists only at a certain frequency (operating frequency). Unlike the homogeneous accelerating structures, where reflections can arise only from the couplers, in the case of inhomogeneous structures there is no a pure traveling wave regime inside the waveguide at the frequencies different from the operating one. We investigate the RF – properties of different accelerating structures with random distribution of the hole sizes.

INTRODUCTION

The calculations performed by us on the base of a new disk-loaded waveguide model (coupled cavity chain) [1] indicate that for waveguides with the period $D \geq \lambda/3$, where λ is the free-space wavelength, the “remote” coupling influences weakly on the phase shift per cell. For $\varphi = 2\pi/3$, taking into account the “cross-cavity coupling” $((n, n-1), (n, n+1), (n-1, n+1), n$ is the cavity number) at $a/\lambda < 0.14$ (a is the coupling hole radius), one can expect to achieve an accuracy of forming a phase shift per cell of the order of $\Delta\varphi = 0.05$. If one restricts oneself only “paired coupling” $((n, n-1), (n, n+1))$, then, the accuracy of phase shift per cell is getting worse - $\Delta\varphi = 0.5$. Development of the techniques of disk-loaded waveguide cell tuning that should allow making feasible the cross-cavity coupling is a difficult task, since during tuning of the n -th cavity one has to take into account, somehow, the effect from the $(n+1)$ -th cavity which has not yet been tuned.

In the paper [2] we present the results of our research on the technique of cell-tuning in a strongly inhomogeneous disk-loaded waveguides which realizes paired coupling.

This paper presents the simulation results of our research on the technique of cell-tuning which realizes paired coupling.

UNDERLYING THEORY

It follows from the paper [2] that an infinite chain of cylindrical cavities of the length d and the radii b_n , coupled through co-axial cylindrical holes with the radii a_n in the cavity dividing walls of thickness t (inhomogeneous disk-loaded waveguide with the period

$D = d + t$) at $D \geq \lambda/3$ can be, with a definite accuracy, described by a set of coupled equations

$$\left[\omega_n^2 \left(1 + \alpha_n^{(+)} + \alpha_n^{(-)} \right) - \omega^2 \right] u_n = \omega_n^2 \beta_{n,n-1} u_{n-1} + \omega_n^2 \beta_{n,n+1} u_{n+1} \quad (1)$$

where u_n is the amplitude of E_{010} -mode in the n -th cavity, ω_n is the n -th cavity eigenfrequency, $\alpha_n^{(+)}$, $\alpha_n^{(-)}$ are the relative eigenfrequency shifts due to the coupling with $(n+1)$ -th and $(n-1)$ -th cavities, $\beta_{n,n-1}$, $\beta_{n,n+1}$ are the coupling coefficients. If $\alpha_n^{(+)}$ and $\beta_{n,n+1}$ are determined by geometrical dimensions of only the n -th and $(n+1)$ -th cavities, as well as by the coupling hole radius a_{n+1} ($\alpha_n^{(-)}$, $\beta_{n,n-1}$ are determined by geometrical dimensions of the n -th, $(n-1)$ -th cavities and the hole radius a_n), then we shall say that the cavity coupling is paired. If these coefficients depend on geometrical dimensions of three cavities (n -th, $(n-1)$ -th and $(n+1)$ -th), as well as two coupling hole radii a_n , a_{n+1} , then, such coupling we shall call “cross-cavity coupling”.

Let's find the conditions when the set (1) at $\omega = \omega_*$ (ω_* is the operating frequency) has the solution of such form

$$u_n = u_{n,0} \exp(in\varphi)$$

where $u_{n,0}$ is the real value. It follows from (1) that in order to achieve this the following condition is to be fulfilled

$$\beta_{n,n-1} u_{n-1,0} = \beta_{n,n+1} u_{n+1,0}$$

For the n -th cavity eq. (1) will take the form

$$\left[\omega_n^2 \left(1 + \alpha_n^{(+)} + \alpha_n^{(-)} \right) - \omega_*^2 \right] u_{n,0} = 2\omega_n^2 \beta_{n,n-1} u_{n-1,0} \cos \varphi \quad (2)$$

and for the $(n-1)$ -th cavity

$$\left[\omega_{n-1}^2 \left(1 + \alpha_{n-1}^{(+)} + \alpha_{n-1}^{(-)} \right) - \omega_*^2 \right] u_{n-1,0} = 2\omega_{n-1}^2 \beta_{n-1,n} u_{n,0} \cos \varphi \quad (3)$$

From (2) and (3) it follows that if $\alpha_n^{(+)}$ is independent from the parameters of the $(n+1)$ -th cavity, $\alpha_{n-1}^{(-)}$ - from the parameters of the $(n-2)$ -th cavity and $\beta_{n-1,n}$, $\beta_{n,n-1}$ depend only upon the parameters of the n -th and $(n-1)$ -th cavities, then, two equations (2) and (3) become closed and determine fully the relation of geometrical dimensions of the n -th and $(n-1)$ -th cavities. In this case, having tuned the $(n-1)$ -th cavity, one can find the condition, which must satisfy the geometrical dimensions of the n -th cavity, and, consequently, allow tuning consecutively all waveguides cavities. It can be shown

*ayzatsky@kipt.kharkov.ua

#kramer@kipt.kharkov.ua

that at the paired coupling $\beta_{n-1,n} = \beta_{n,n-1}$ and these coefficients are determined by the geometrical dimensions of the n -th and $(n-1)$ -th cavities, only. Things are more complicated with the dependence of coefficients $\alpha_n^{(+)}$ on the parameters of the $(n+1)$ -th cavity and $\alpha_n^{(-)}$ on the parameters of the $(n-2)$ -th cavity. Such dependence exists even under the assumption of paired coupling. However, our calculations shown that this dependence is considerably weaker than the dependence on the parameters of the n -th $((n-1)$ -th) cavity, and can be neglected, as a result.

Quasi-static approach

Let's consider the simplest model of coupling cavities that is based on the quasi-static approach [3]. We shall consider the thickness of the disk to be zero and the radius of the hole to be small. Then the coupling coefficients will have the form

$$\alpha_n^{(+)} = \xi \frac{a_{n+1}^3}{b_n^2 d}, \quad \alpha_n^{(-)} = \xi \frac{a_n^3}{b_n^2 d} \quad (4)$$

$$\beta_{n,n-1} = \beta_{n-1,n} = \xi \frac{a_n^3}{b_n b_{n-1} d} \quad (5)$$

where $\xi = 2/3\pi I_1^2(\rho_{01})$, ρ_{01} is the first root of the zero order Bessel function J_0 .

To achieve the travelling wave mode in an inhomogeneous disk-loaded waveguide with the mode type $\varphi = 2\pi/3$ the parameters of $(n-1)$ -th and n -th cavities should be connected via the relationship (it follows from Eqs. (2), (3))

$$\left[\omega_n^2 (1 + \alpha_n^{(+)} + \alpha_n^{(-)}) - \omega_*^2 \right] \times \left[\omega_{n-1}^2 (1 + \alpha_{n-1}^{(+)} + \alpha_{n-1}^{(-)}) - \omega_*^2 \right] = \omega_n^2 \omega_{n-1}^2 \beta_{n,n-1}^2 \quad (6)$$

From (6) and (4)-(5) we can find

$$b_n = b_0 \sqrt{0.5(1 + \sqrt{1 + 4Z_n})} \quad (7)$$

where $b_0 = c\rho_{01}/\omega_*$,

$$Z_n = \xi \frac{(a_n^3 + a_{n+1}^3)}{b_0^2 d} - 4 \cos^2 \varphi \xi^2 \frac{a_n^6}{b_0^2 b_{n-1}^2 d^2} \times \left[1 - b_{n-1}^2 / b_0^2 + \xi(a_{n-1}^3 + a_n^3) / (b_{n-1}^2 d) \right]^{-1}$$

Suppose we have placed the n -th and $(n-1)$ -th cavity into some sort of a cavity stack. It can be shown that the condition (6) is fulfilled in the case, when in the cavities, adjoining the cells under consideration, the amplitudes of E_{010} - modes equal to zero. Such cavity stacks have already been used for tuning separate parts of quasi-constant impedance sections for LIL accelerator [4]. However, there the cells were tuned not consecutively,

i.e. beginning from the entrance (or exit), but in different stacks being then simply joined one-to-one.

Stability of tuning technique

Our results [2] indicate that it is possible to use a consecutive tuning of all cells for disk-loaded waveguide with an arbitrary law of the coupling hole radius variation. With that, at the operating frequency $\omega = \omega_*$ the travelling wave mode with the phase shift of the order of $2\pi/3$ with a certain accuracy is guaranteed in a waveguide.

Consecutive tuning feasibility is determined by the stability of this technique. Our numerical analysis show that small errors in the tuning of individual cells should not lead to the exponential growth of subsequent deviations, i.e. the technique is stable.

RANDOM STRUCTURE

Using such tuning technique we can consider accelerating structures with various laws of the hole radius variation, which will operate in a travelling wave mode at $\omega = \omega_*$.

We give the random deviations of the hole sizes in the constant impedance accelerating structure ($a = 1.25$ cm). The random sizes of the holes are uniformly distributed in the interval 1.25 ± 0.05 cm. The cavity radii and the parameters of the couplers are tuned depending on the hole sizes and operating frequency $f_* = 2.7972$ GHz. The cavity radii are tuned according to the considered technique. The cavity length is $d = \lambda/3$. We tune the structure by such a way that the phase shift per cell equals $2\pi/3$. So, we can consider such structure as random - regular accelerating structure.

Let's compare the random-regular accelerating structure with the constant impedance one, which already has been tuned according to the described above technique (see Fig. 1).

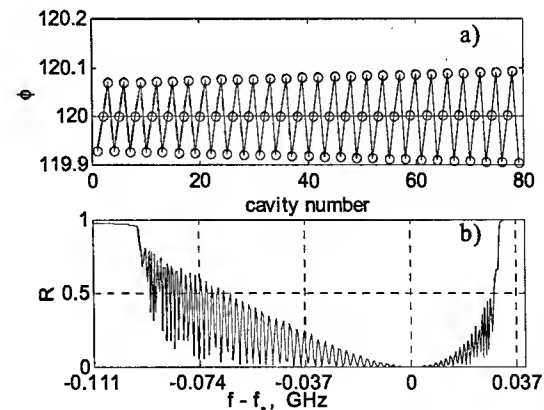


Figure 1: constant impedance structure - a) phase shift per cell; b) reflection coefficient $R = P^{(r)}/P_0$ versus the frequency.

In the random-regular structure the phase deviation from the phase shift per cell $\varphi_0 = 2\pi/3$ is small $\approx 0.5^\circ$ and the amplitudes of electric field take strongly different values in various cells (see Fig. 2). The energy gain in such random-regular structure is even a bit greater then in constant impedance one.

In the case of constant impedance structure reflection can arise only from the couplers within the passband (see Fig. 1b). Unlike the constant impedance structure, in the random-regular structure there is no pure traveling wave regime at the frequencies different from the operating one (see Fig. 3).

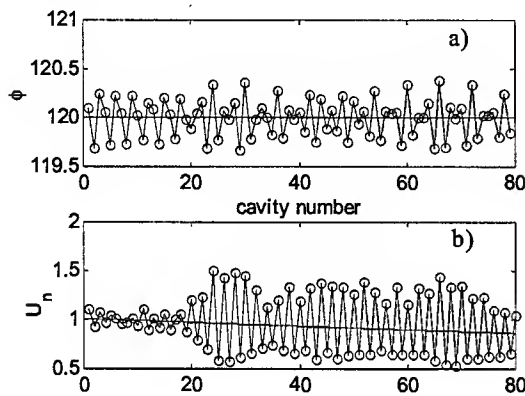


Figure 2: random (constant impedance) structure - a) phase shift per cell; b) amplitude distribution.

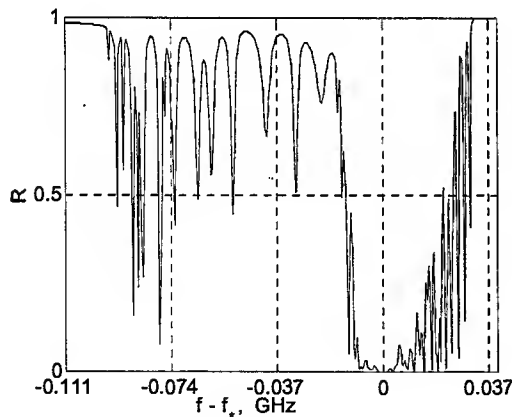


Figure 3: reflection coefficient $R = P^{(r)}/P_0$ in the random (constant impedance) structure versus the frequency.

The constant gradient accelerating structure is more useful in comparison with the constant impedance one. The radii of the holes in the constant gradient structure decrease from entrance to exit. They decrease by the value 0.002 cm from cell to cell. We give the random deviations of the hole sizes in such constant gradient accelerating structure. As in the previous case, the random sizes of the holes are uniformly distributed in the interval ± 0.05 cm. The characteristics of such random-

regular accelerating structure are shown in figures 4 and 5.

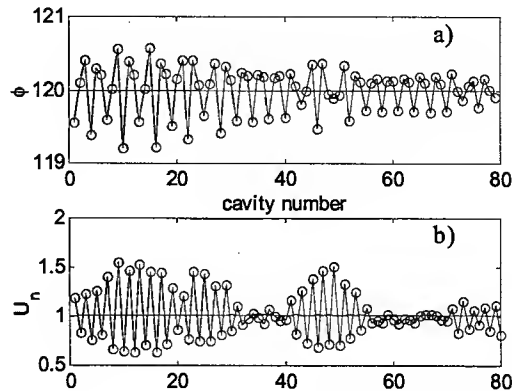


Figure 4: random (constant gradient) structure - a) phase shift per cell; b) amplitude distribution.

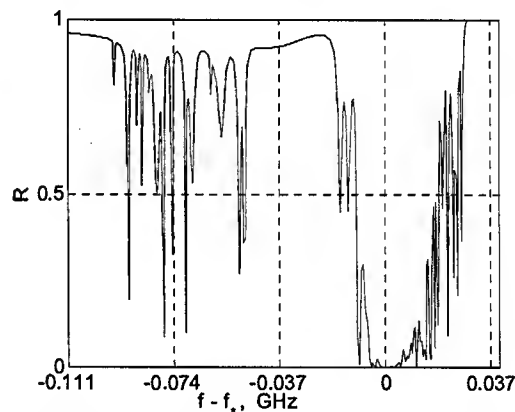


Figure 5: reflection coefficient $R = P^{(r)}/P_0$ in the random (constant gradient) structure versus the frequency.

There is "detuning" of the first dipole passband in the considered random-regular structures. These structures can find application in high current accelerators and in the travelling wave klystron output circuits.

REFERENCES

- [1] M.I. Ayzatsky, "New Mathematical Model of an Infinite Cavity Chain", EPAC'96, Sitges, June 1996, p. 2026.
- [2] M.I. Ayzatsky, E.Z. Biller, "Development of Inhomogeneous Disk-Loaded Accelerating Waveguides and RF-coupling", LINAC'96, Geneva, August 1996, p. 119.
- [3] H.A. Bathe, Phys. Rev. 66 (1944) 163.
- [4] G. Bienvenu, J.C. Bourdon, P. Brunet et al., "Accelerator Structure Developments for the LEP Injector Linac", LINAC'84, Seeheim, 1984.

THE BEAM DYNAMICS STUDIES OF COMBINED MISALIGNMENTS AND RF ERRORS FOR RIA*

X. Wu[†], D. Gorelov, T. Grimm, W. Hartung, F. Marti, and R.C. York
National Superconducting Cyclotron Laboratory, MSU, East Lansing, MI 48824, USA

Abstract

The National Superconducting Cyclotron Laboratory (NSCL) design for the Rare Isotope Accelerator (RIA) driver linac [1] uses superconducting quarter-wave, half-wave and 6-cell elliptical cavities with rf frequencies ranging from 80.5 MHz to 805 MHz with two charge-stripping chicanes. The driver linac requirements include acceleration of light and heavy ions to final beam energies of ≥ 400 MeV/nucleon with final beam powers of 100 to 400 kW. The impact of simultaneous misalignment and rf errors for the full RIA driver linac, including the charge-stripping chicanes, on the 6-dimensional beam emittance was evaluated by simulation. Beam loss and large-amplitude beam behaviors were also studied.

INTRODUCTION

Misalignment and rf errors were previously evaluated for the Rare Isotope Accelerator (RIA) driver linac [2,3]. The NSCL design for this linac [4] is considered in the present study using the computer codes DIMAD [5] and LANA [6,7]. The misalignment and rf error tolerances for the RIA driver linac from the previous analysis are given in Tables 1 and 2.

Table 1: Alignment tolerances.

RIA Driver Linac	Cavity Misalignment		Focusing Element Misalignment	
	$\sigma_{x,y}$ (mm)	σ_z (mrad)	$\sigma_{x,y}$ (mm)	σ_z (mrad)
Part I	1.0	-	0.25	-
Part II	1.0	-	0.50	-
Part III	1.0	-	1.00	5.0

Table 2: RF error tolerances.

RF Errors	Maximum Value
Phase	0.5°
Amplitude	0.5%

These tolerances were based on the separate beam simulations using DIMAD for misalignment with orbit corrections, and using LANA for rf errors. These evaluations found that the beam centroid distortion is limited and stays within ± 5 mm for the specified misalignment margins using the proposed correction scheme. It also was found that beam loss of $\leq 10^{-4}$ is achievable with rf errors of $\Delta\phi \leq 0.5^\circ$ in phase and $\Delta E_0 \leq 0.5\%$ in amplitude.

*Work supported by MSU and NSF PHY 0110253.

[†]xwu@nsl.msu.edu

To study the impact of the combined misalignment and rf errors in the 80.5 MHz-based RIA driver linac [4] a procedure was established to combine DIMAD and LANA simulations. First, the rf defocusing matrices were generated using LANA and imported into DIMAD. With the inclusion of these matrices, DIMAD was used to establish the transverse focusing lattice for the reference charge beam, to implement misalignment errors, and to apply the orbit correction scheme. The misalignment analysis included all SRF cavities and focusing elements assuming a Gaussian distribution ($\pm 2\sigma$). The alignment correction scheme used least square fitting to minimize orbit deviations at the beam position monitors. The focusing lattice, misalignment errors for cavities and focusing elements, and corresponding corrections were then imported into LANA to perform the final 6-dimensional particle tracking, combining the rf jitter with the misalignment errors. Extensive tracking comparisons were performed to ensure the proper data translation between the two codes. LANA and DIMAD models applied for RIA driver linac were found to be in excellent agreement.

SIMULATIONS WITH MISALIGNMENTS AND RF ERRORS

Part I – Low β Section

Part I of the RIA driver linac accelerates two charge states, 28+ and 29+, of uranium beams from the RFQ to the 1st stripping chicane. A total of 153 low β superconducting quarter-wave cavities with frequencies of 80.5 MHz and 161 MHz, and 81 superconducting solenoid magnets were positioned in 18 cryomodules. The SRF cavities in Part I all have an aperture of 30 mm. The initial normalized beam emittance was assumed to be 0.6π mm mrad. The errors were applied with the values given in Tables 1 and 2. Figure 1 shows the two-charge state uranium beam envelope resulting from a typical set of errors after orbit correction in the Part I of the linac. Figure 2 shows the corresponding transverse rms beam emittances along this part. Simulations were performed for multiple seeds and the statistical confidence plots for maximum of the multi-charge beam envelopes, as well as horizontal and longitudinal rms emittances, at the end of this part of the linac are shown in Figure 3. The vertical emittance is the same as horizontal within small statistical error. With 90% confidence, the maximum radial beam size will be about 11-12 mm, well within the SRF cavity aperture. The transverse and longitudinal rms beam emittance growths were $\sim 30\%$ and $\sim 25\%$, respectively.

No beam loss was observed for the 2×10^5 particles tracked.

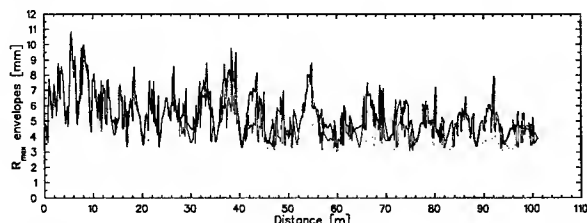


Figure 1: Beam envelopes for multi-charge uranium beam in Part I of the RIA driver linac (red – $^{238}\text{U}^{29+}$, green – $^{238}\text{U}^{28+}$, black – all charge states) with errors of Tables 1 and 2 after orbit correction.

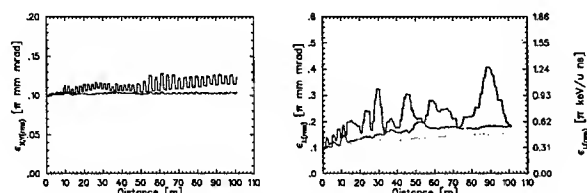


Figure 2: Horizontal (left) and longitudinal (right) rms emittances for ^{238}U beam in Part I of the linac (red – $^{238}\text{U}^{29+}$, green – $^{238}\text{U}^{28+}$, black – all charge states) with errors of Tables 1 and 2 after orbit correction.

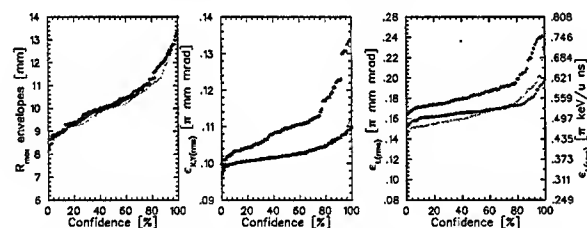


Figure 3: Maximum beam envelopes in Part I of the linac (left), horizontal (middle) and longitudinal (right) rms emittances at the end of Part I vs. statistical confidence (red – $^{238}\text{U}^{29+}$, green – $^{238}\text{U}^{28+}$, black – all charge states) with errors of Table 1 and 2 after orbit correction.

Simulations were done for misalignment only and for misalignment with rf errors together. Between these two cases, only the longitudinal rms beam emittance growth increased, indicating weak coupling between the transverse and longitudinal motion.

Part II – Medium β Section

Part II of the RIA driver linac will accelerate five charge states, 73^+ to 77^+ , of the uranium beam from the 1st to the 2nd stripping chicane. It consists of 32 cryomodules containing 257 SRF cavities with frequencies of 161 MHz and 322 MHz. A total of 66 superconducting solenoid magnets were used to provide the transverse focusing. The misalignment tolerances, $\sigma_{x,y}$, in this section of driver linac are 1.0 mm for all SRF cavities and 0.5 mm for the solenoid magnets. The random rf errors of $\Delta\phi \leq 0.5^\circ$ in phase and $\Delta E_0 \leq 0.5\%$ in

amplitude were also included, and a similar multi-seed simulation with LANA performed. The statistical confidence plots for multi-charge beam envelopes, and for transverse and longitudinal rms emittances, are shown in Figure 4. Of 100 seeds, no beam loss was observed in all but 2 pathological cases.

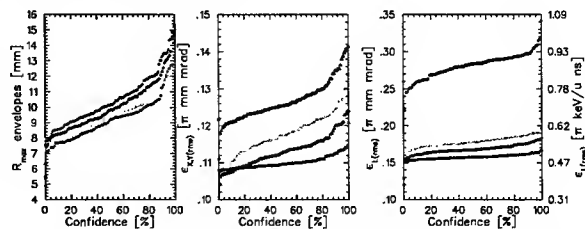


Figure 4: Maximum beam envelopes in Part II of the linac (left), horizontal (middle) and longitudinal (right) rms emittances at the end of Part II with combined misalignment and rf errors vs. statistical confidence (red – $^{238}\text{U}^{75+}$, green – $^{238}\text{U}^{73+}$, blue – $^{238}\text{U}^{77+}$, black – all charge states).

Part III – High β Section

Part III of the RIA driver linac uses 192 6-cell elliptical cavities to accelerate three charge states, 87^+ to 89^+ , U^{238+} beams to a final energy of 400 MeV/u. A total of 100 superconducting quadrupole magnets were used to provide the transverse focusing. The misalignment tolerances, $\sigma_{x,y}$, in this section of the driver linac are 1.0 mm for all SRF cavities and 1.0 mm for quadrupole magnets. In addition, quadrupole magnets have a skew error (rotation about beam axis) specification of σ_π of 5.0 mrad. The statistical confidence plots for multi-charge beam envelopes, and for transverse and longitudinal rms emittances with combined misalignment and rf errors are shown in Figure 5. No beam loss was observed in any simulated case in this part of the linac.

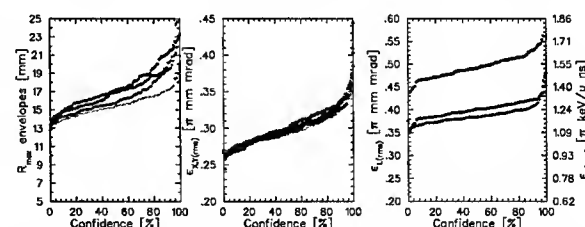


Figure 5: Maximum beam envelopes in Part III of the linac (left), horizontal (middle) and longitudinal (right) rms emittances at the end of Part III with combined misalignment and rf errors vs. statistical confidence (red – $^{238}\text{U}^{88+}$, green – $^{238}\text{U}^{87+}$, blue – $^{238}\text{U}^{89+}$, black – all charge states).

MISALIGNMENT TOLERANCES FOR CHARGE STRIPPING CHICANES

The two charge-stripping chicanes in the RIA driver linac have similar magnetic configurations, each with 8 dipoles, 24 quadrupoles and 16 sextupoles forming a complete 2nd order achromat [8]. Chicane #1 has a

stripping energy of 12.7 MeV/u and transports five charge states, 73+ to 77+, of the uranium beam. Chicane #2 strips at 79.0 MeV/u and only transports three charge states, 87+ to 89+. Different position errors, $\sigma_{x,y}$, and rotation errors, σ_z for all magnets in chicanes were added together with corrections using correctors in front of each focusing quadrupoles, and multi-charge beam simulations were then performed for both chicanes using DIMAD. The results of the simulations are shown in Figures 6 and 7.

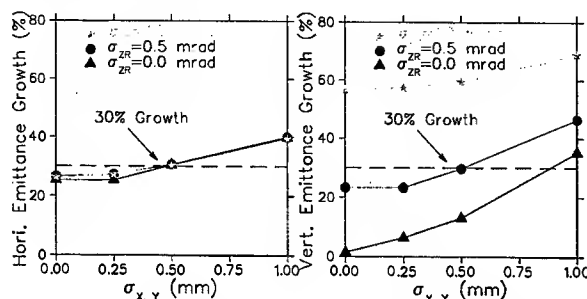


Figure 6: Horizontal (left) and vertical (right) beam emittance growths in charge-stripping chicane #1 due to transverse misalignment errors. Three curves for three different rotational errors (σ_z) are shown. The dashed line indicates a 30% emittance increase.

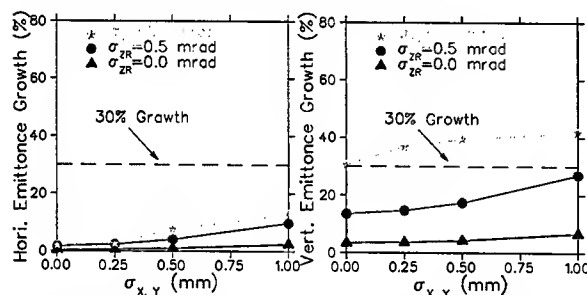


Figure 7: Horizontal (left) and vertical (right) beam emittance growths in charge-stripping chicane #2 due to transverse misalignment errors. Three curves for three different rotational errors (σ_z) are shown. The horizontal dashed line indicates a 30% emittance increase.

Table 3: Misalignment tolerances for two charge-stripping chicanes in the RIA driver linac

Chicane	Position $\sigma_{x,y}$	Rotation σ_z
#1	0.5 mm	0.5 mrad
#2	1.0 mm	0.5 mrad

The transverse emittance of both planes increase nearly linearly with the magnet position errors for both stripping chicanes. However, the rotation error (σ_z) strongly impacts the vertical emittance, while the effect is small in the horizontal plane. This can be understood from the x - y coupling caused by the rotation error and the large dispersion used to implement the charge state selection. The misalignment tolerances are listed in Table 3, using

as a criterion that the average transverse emittance growth is to be smaller than ~30% in each chicane.

SUMMARY AND CONCLUSIONS

The impact of combined transverse misalignment and rf errors on the multi-charge beam envelope and transverse, longitudinal emittance growths for different segments of RIA driver linac were investigated by simulation. The results show that the misalignment and rf jitter specifications given are adequate, and that the proposed correction scheme works well for the RIA driver linac. The coupling between the longitudinal and transverse motion in the RIA driver linac is negligible. Although limited transverse and longitudinal emittance growths for multi-charge beam were observed, the impact on the RIA driver linac beam operation should be minimal. Further beam dynamics studies for RIA at NSCL will involve a complete beam simulation from the RFQ through the entire RIA driver linac, with combined rf and misalignment errors, improving LANA's misalignment correction abilities. Better understanding of the charge-stripping process, and modification of the charge selection chicane design to limit contamination of the superconducting cavities from the stripping process is also needed.

REFERENCES

- [1] C.W. Leemann, "RIA Facility Project", Proc. of LINAC 2000, Monterey, CA, 2000.
- [2] X. Wu, D. Gorelov, T. Grimm, W. Hartung, F. Marti, and R.C. York, "The Misalignment and RF Error Analyses for the RIA Driver Linac" Proc. of LINAC 2002, Gyeongju, Korea, 2002.
- [3] P.N. Ostroumov, "Development of a medium-energy superconducting heavy-ion linac", Phys. Rev. ST-AB Vol. 5, 030101 (2002).
- [4] D. Gorelov, T. Grimm, W. Hartung, F. Marti, H. Podlech, X. Wu and R.C. York, "Beam Dynamics Studies at NSCL of the RIA Superconducting Driver Linac", Proc. of EPAC 2002, Paris, France, 2002.
- [5] R. Servranckx, K. Brown, L. Schachinger, and D. Douglas, "User's Guide to the Program Dimad", SLAC Report 285, UC-28, May 1985.
- [6] D.V. Gorelov and P.N. Ostroumov, "Application of LANA Code for Design of Ion Linac", Proc. of EPAC'96, Sitges, June 1996.
- [7] D.V. Gorelov and P.N. Ostroumov, "Simulation of Beam Dynamics Including Space Charge in Proton Linac with Errors", Proc. of LINAC'98, Chicago, August 1998.
- [8] X. Wu, D. Gorelov, T. Grimm, W. Hartung, F. Marti, H. Podlech, and R.C. York, "The Design of the Isochronous and Achromatic Charge-Stripping Sections for the Rare Isotope Accelerator", Proc. of EPAC 2002, Paris, France, 2002.

PLASMA NEUTRALIZATION MODELS FOR INTENSE ION BEAM TRANSPORT IN PLASMA

Igor D. Kaganovich, Edward A. Startsev, Ronald C. Davidson and Sean O'Rourke
Plasma Physics Laboratory, Princeton University, Princeton, New Jersey 08543
Edward P. Lee, Lawrence Berkeley National Laboratory, Berkeley, California 94720

Abstract

Plasma neutralization of an intense ion pulse is of interest for many applications, including plasma lenses, heavy ion fusion, cosmic ray propagation, etc. An analytical electron fluid model has been developed based on the assumption of long charge bunches ($l_b \gg r_b$). Theoretical predictions are compared with the results of calculations utilizing a particle-in-cell (PIC) code. The cold electron fluid results agree well with the PIC simulations for ion beam propagation through a background plasma. The analytical predictions for the degree of ion beam charge and current neutralization also agree well with the results of the numerical simulations. The model predicts very good charge neutralization (>99%) during quasi-steady-state propagation, provided the beam pulse duration τ_b is much longer than the electron plasma period $2\pi/\omega_p$, where $\omega_p = (4\pi e^2 n_p / m)^{1/2}$ is the electron plasma frequency, and n_p is the background plasma density. In the opposite limit, the beam pulse excites large-amplitude plasma waves. The analytical formulas derived in this paper can provide an important benchmark for numerical codes, and provide scaling relations for different beam and plasma parameters.

INTRODUCTION

Neutralization of the ion beam charge and current by a background plasma is an important issue for many applications involving the transport of positive charges in plasma, including heavy ion inertial fusion, positrons for electron-positrons colliders, high-density laser-produced proton beams for the fast ignition of inertial confinement fusion targets, etc.

There are many critical parameters for ion beam transport in the target chamber, including beam current, type of ion species, radial and longitudinal profiles of the beam density, chamber gas density, stripping and ionization cross sections, etc. This necessitates an extensive study for a wide range of parameters to determine the conditions for optimum beam propagation. To complement numerical simulation studies, a number of reduced models have been developed. Based on well-verified assumptions, reduced models can yield robust analytical and numerical descriptions and provide important scaling laws for the degrees of charge and current neutralization.

The electron response frequency is of order the electron plasma frequency, $\omega_p = (4\pi n_p e^2 / m_e)^{1/2}$, where

n_p is the background plasma density. For heavy ion fusion applications, the ion pulse propagation time through the chamber is much longer than the inverse electron plasma frequency ω_p^{-1} . Therefore, a beam-plasma quasi-steady state forms during beam propagation. The initial step of the study is to describe the steady-state propagation (in the beam frame) of an ion beam pulse through a background plasma.

The case where the beam propagates through a cold plasma, with the plasma density large compared with the beam density, can be studied by the use of linear perturbation theory [1]. Here, we focus on the nonlinear case where the plasma density has an arbitrary value compared with the beam density, and correspondingly, the degrees of current and charge neutralization are arbitrary. The transport of stripped, pinched ion beams has also been discussed in [2], where the assumptions of current and charge neutrality were made to determine self-consistent solutions for the electric and magnetic fields. Rosenbluth, *et al.*, have considered the equilibrium of an isolated, charge-neutralized, self-pinched ion beam pulse in the absence of background plasma [3]. In contrast, we consider here the case where "fresh" plasma is always available in front of the beam, and there are no electrons co-moving with the beam.

In a recent calculation [4,5], we studied the nonlinear quasi-equilibrium properties of an intense ion beam pulse propagating through a cold background plasma, assuming that the beam pulse duration τ_b is much longer than the inverse electron plasma frequency, i.e., $\omega_p \tau_b \gg 1$. In the present study, we generalize the previous results to general values of the parameter $\omega_p \tau_b$.

BASIC EQUATIONS FOR ION BEAM PULSE PROPAGATION IN BACKGROUND PLASMA

In most applications, the background plasma electrons are cold – the electron thermal velocity is small compared with the directed beam velocity. Particle-in-cell simulations show that in most cases the electron flow is laminar and does not form multistreaming. Thus, the electron cold-fluid equations can be used for the electron description, and thermal effects are neglected in the present study. The electron fluid equations together with Maxwell's equations comprise a complete system of equations describing the electron response to a propagating ion beam pulse. The electron cold-fluid equations consist of the continuity equation,

$$\frac{\partial n_e}{\partial t} + \nabla \cdot (n_e \mathbf{V}_e) = 0, \quad (1)$$

and the force balance equation,

$$\frac{\partial \mathbf{p}_e}{\partial t} + (\mathbf{V}_e \cdot \nabla) \mathbf{p}_e = -e \left(\mathbf{E} + \frac{1}{c} \mathbf{V}_e \times \mathbf{B} \right), \quad (2)$$

where $-e$ is the electron charge, \mathbf{V}_e is the electron flow velocity, $\mathbf{p}_e = \gamma_e m_e \mathbf{V}_e$ is the average electron momentum, m_e is the electron rest mass, and γ_e is the relativistic mass factor. Maxwell's equations for the self-generated electric and magnetic fields, \mathbf{E} and \mathbf{B} , are given by

$$\nabla \times \mathbf{B} = \frac{4\pi e}{c} (Z_b n_b \mathbf{V}_b - n_e \mathbf{V}_e) + \frac{1}{c} \frac{\partial \mathbf{E}}{\partial t}, \quad (3)$$

$$\nabla \times \mathbf{E} = -\frac{1}{c} \frac{\partial \mathbf{B}}{\partial t}, \quad (4)$$

where \mathbf{V}_b is the ion beam flow velocity, n_e and n_b are the number densities of the plasma electrons and beam ions, respectively (far a way from the beam $n_e \rightarrow n_p$), and Z_b is the ion beam charge state. The plasma ions are assumed to remain stationary with $\mathbf{V}_i = 0$ and $n_i = n_p$. The assumption of immobile plasma ions is valid for sufficiently short ion pulses with $2l_b < r_b \sqrt{M/m_e}$ [4]. Here, r_b and $2l_b$ are the ion beam radius and length, respectively, and M is the plasma ion mass.

Considerable simplification can be achieved by applying the conservation of generalized vorticity Ω [4]. If Ω is initially equal to zero ahead of the beam, and all streamlines inside of the beam originate from the region ahead of the beam, then Ω remains equal to zero everywhere, i.e.,

$$\Omega \equiv \nabla \times \mathbf{p}_e - \frac{e}{c} \mathbf{B} = 0. \quad (5)$$

Substituting Eq.(5) into Eq.(2) yields

$$\frac{\partial \mathbf{p}_e}{\partial t} + \nabla K_e = -e \mathbf{E}, \quad (6)$$

where $K_e = (\gamma_e - 1) m_e c^2$ is the electron kinetic energy. Note that the inertia terms in Eq.(6) are comparable in size to the Lorentz force term and cannot be omitted. Estimating the self-magnetic field from Eq.(5), we conclude that the electron gyroradius is of order the beam radius. This is a consequence of the fact that the electrons originate from the region of zero magnetic field in front of the beam. If most electrons are dragged along with the beam and originate from the region of large magnetic field, the situation may be different [3, 6].

APPROXIMATE SYSTEM OF EQUATIONS FOR LONG CHARGE BUNCHES ($l_b \gg r_b$)

We use the assumption of a long ion pulse ($l_b \gg r_b$), but relax the assumption of a dense beam used in [4,5], i.e., the condition $V_b/\omega_p \ll l_b$.

The typical longitudinal scale of electron density perturbations is V_b/ω_p . If $V_b/\omega_p \gg r_b$, the main variations are in the radial direction, and longitudinal derivatives can be neglected in comparison with the radial derivatives in Poisson's equation. This gives for steady-state beam propagation

$$(V_{ez} - V_{bz}) \frac{\partial n_e}{\partial z} + \frac{1}{r} \frac{\partial}{\partial r} (r n_e V_{ez}) = 0, \quad (7)$$

$$\frac{1}{r} \frac{\partial}{\partial r} (r E_r) = 4\pi e (Z_b n_b + n_p - n_e), \quad (8)$$

$$(V_{ez} - V_{bz}) \frac{\partial}{\partial z} p_{ez} + \frac{\partial K_e}{\partial r} = -e E_r. \quad (9)$$

It follows from Eq.(5) for cylindrically symmetric beams that the azimuthal self-magnetic field is determined in terms of the longitudinal flow velocity, which gives

$$B = -\frac{c}{e} \frac{\partial p_{ez}}{\partial r}, \quad (10)$$

$$-\frac{1}{r} \frac{\partial}{\partial r} r \frac{\partial}{\partial r} p_{ez} = \frac{4\pi e}{c} (Z_b n_b V_{bz} - n_e V_{ez}). \quad (11)$$

Equation (11) describes the longitudinal electron flow velocity and determines the degree of current neutralization of the beam. In Eq. (11), we neglected the displacement current. The displacement current can be comparable with the electron current if V_b/ω_p is comparable with l_b . However, in this case both the displacement current and the electron current are small compared with the other terms in Eq. (11).

Numerical solutions of the system of equations consisting of Eqs. (7) - (9) and Eq.(11) are presented in [7] and [8]. In Fig.1, we present a detailed comparison of the fluid and PIC results. The fluid results of Eqs. (7) - (9) and Eq. (11) agree well with the results of the two-dimensional electromagnetic PIC simulations described in [4].

In the linear case, when $n_p \gg Z_b n_b$, the equation for electron plasma oscillations is given by [4]

$$V_{bz}^2 \frac{\partial^2}{\partial z^2} n_e + \omega_p^2 (n_e - Z_b n_b - n_p) = 0. \quad (12)$$

Equation (12) is readily recovered from the linearized version of Eqs.(1) and (2) and Poisson's equation, and is not restricted by any requirements on the beam radius. It can also be derived from Eqs. (7) - (9) when the nonlinear terms are neglected. Because the reduced model consisting of Eqs. (7) - (9) and Eq. (11) gives the same results in the limit $V_b/\omega_p \gg r_b$, and in the linear case where $n_p \gg Z_b n_b$, it also works well in the intermediate case where $V_b/\omega_p \sim r_b$, as can be seen in Fig.1. For $n_b > n_p$, the plasma waves break [4] as shown in Figure 2. The utilization of the cold-fluid model is therefore limited by the wave-breaking condition.

The approach used here can be generalized to the case of a nonuniform, nonstationary, warm electron fluid, and forms the basis for a hybrid, semi-analytical approach

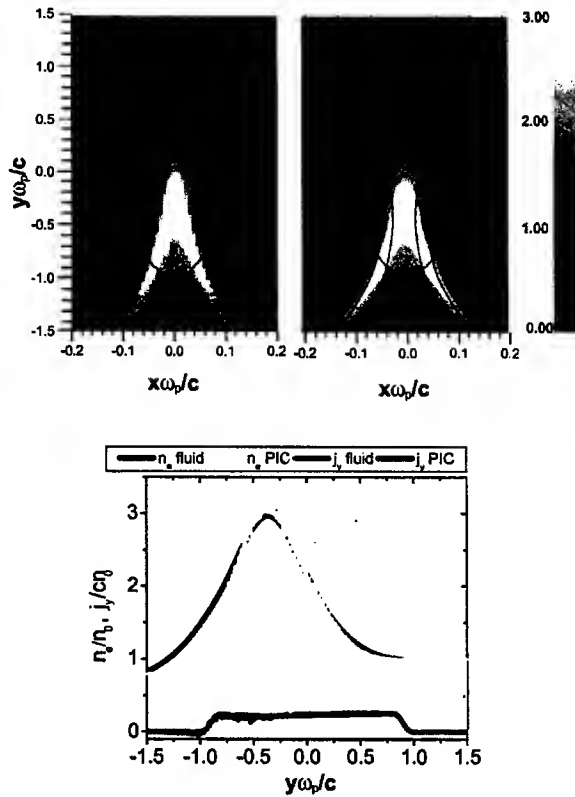


Figure 1 Neutralization of an ion beam pulse during steady-state propagation of the beam pulse through a cold, uniform, background plasma. The figure shows comparisons between the PIC simulations and the fluid description. The beam propagates in the y -direction. The beam density has a flat-top profile, and the red lines show the beam pulse edge. Shown in the figure are color plots of the normalized electron density (n_e/n_p) for particle-in-cell simulations (top left) and the fluid model consisting of Eqs. (7) - (9) and Eq. (11) (top right) in $(x\omega_p/c, y\omega_p/c)$ space. The lower figure shows the normalized electron density (n_e/n_p), and the normalized longitudinal current ($j_z/en_p c$) in the beam cross-section at $x=0$ (lowest curves). The brown contours in the upper figure show the electron trajectories in the beam frame. The beam velocity is $V_b=0.5c$, and the beam density is $n_b=0.5n_p$. The beam dimensions correspond to $r_b=0.1 c/\omega_p$ and $l_b=1.0 c/\omega_p$.

to be used for calculations of beam propagation in the target chamber. This research is now underway.

In summary, the analytical results agree well with the results of PIC numerical simulations for ion beam charge and current neutralization. The visualization of the data obtained in the numerical simulations shows complex collective phenomena during beam entry into and exit from the plasma, and will be described in future publications. Further visualization is also available on the website [9].

ACKNOWLEDGEMENTS

This research was supported by the U.S. Department of Energy Office of Fusion Energy Sciences and the Division of High Energy Physics.

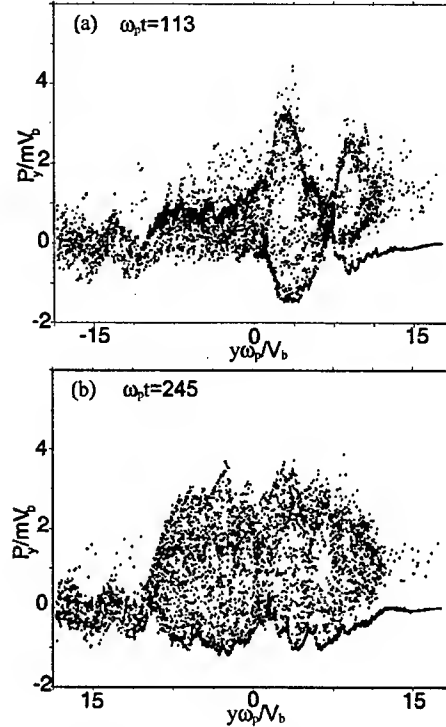


Figure 2 Electron phase space for 1D simulation of beam entering the plasma at $t=0$. Here, $l_b=30V_b/\omega_p$ and $n_b = 2n_p$. The times after entering the plasma plug correspond to (a) $t=113/\omega_p$ and (b) $t=245/\omega_p$.

REFERENCES

- [1] P. Chen, J.M. Dawson, R. W. Huff and T. Katsouleas, Phys. Rev. Lett. **51**, 693 (1985).
- [2] K. Hahn and E. P. Lee, J. Fusion Engineering and Design **32-33**, 417 (1996).
- [3] M. Rosenbluth, E.P. Lee and R. Briggs, private communication (2001).
- [4] I. D. Kaganovich, G. Shvets, E. Startsev and R. C. Davidson, Physics of Plasmas **8**, 4180 (2001).
- [5] I. D. Kaganovich, E. Startsev and R. C. Davidson, Laser and Particle Beams **20**, 497 (2002).
- [6] D. R. Welch, D. V. Rose, B. V. Oliver, T. C. Genoni, R. E. Clark, C. L. Olson and S. S. Yu, Phys. Plasmas **9**, 2344 (2002).
- [7] I. D. Kaganovich, E. Startsev, S. Klasky and R. C. Davidson, Special Issue on Images in Plasma Science, IEEE Trans. Plasma Science **30**, 12 (2002).
- [8] I. D. Kaganovich, G. Shvets, E. Startsev and R. C. Davidson, Proc. 2001 Particle Accelerator Conference; http://pacwebserver.fnal.gov/papers/Tuesday/PM_Poster/TPPH317.pdf.
- [9] High Intensity Particle Beams and Nonneutral Plasma, Division, Plasma Physics Laboratory, Princeton University; <http://w3.pppl.gov/~nnp/>.

INTENSE SHEET BEAM STABILITY PROPERTIES FOR UNIFORM PHASE-SPACE DENSITY*

Edward A. Startsev and Ronald C. Davidson,
Plasma Physics Laboratory, Princeton University, Princeton, New Jersey 08543

Abstract

A self-consistent one-dimensional waterbag equilibrium $f_b^0(x, p_x)$ for a sheet beam propagating through a smooth focusing field is shown to be exactly solvable for the beam density $n_b^0(x)$ and space-charge potential $\phi^0(x)$. A closed Schrodinger-like eigenvalue equation is derived for small-amplitude perturbations, and the WKB approximation is employed to determine the eigenfrequency spectrum as a function of the normalized beam intensity $s_b = \hat{\omega}_{pb}^2 / \gamma_b^2 \omega_{\beta\perp}^2$, where $\hat{\omega}_{pb}^2 = 4\pi\hat{n}_b e_b^2 / \gamma_b m_b$ is the relativistic plasma frequency-squared and $\hat{n}_b = n_b(x=0)$ is the on-axis number density of beam particles.

SHEET BEAM EQUILIBRIUM WITH UNIFORM PHASE-SPACE DENSITY

We consider an intense sheet beam [1], made up of particles with charge e_b and rest mass m_b , which propagates in the z -direction with directed kinetic energy $(\gamma_b - 1)m_b c^2$ and average axial velocity $V_b = \beta_b c = \text{const}$. Here, $\gamma_b = (1 - \beta_b^2)^{-1/2}$ is the relativistic mass factor, c is the speed of light *in vacuo*, and the beam is assumed to be uniform in the y - and z -directions with $\partial/\partial y = 0 = \partial/\partial z$. The beam is centered in the x -direction at $x = 0$, and transverse confinement is provided by an applied focusing force, $F_x^{\text{foc}} = -\gamma_b m_b \omega_{\beta\perp}^2 x$, with $\omega_{\beta\perp}^2 = \text{const}$ in the smooth focusing approximation. The transverse dimension of the sheet beam is denoted by $2x_b$, and planar, perfectly conducting walls are located at $x = \pm x_w$. The particle motion in the beam frame is assumed to be nonrelativistic, and we introduce the effective potential $\psi(x, t)$ defined by

$$\psi(x, t) = \frac{1}{2} \gamma_b m_b \omega_{\beta\perp}^2 x^2 + \frac{1}{\gamma_b} e_b \phi(x, t). \quad (1)$$

The Vlasov-Maxwell equations describing the self-consistent nonlinear evolution of $f_b(x, p_x, t)$ and $\psi(x, t)$ can be expressed as [2]

$$\left(\frac{\partial}{\partial t} + v_x \frac{\partial}{\partial x} - \frac{\partial \psi}{\partial x} \frac{\partial}{\partial p_x} \right) f_b = 0, \quad (2)$$

and

$$\frac{\partial^2 \psi}{\partial x^2} = \gamma_b m_b \omega_{\beta\perp}^2 - \frac{4\pi e_b^2}{\gamma_b^2} \int_{-\infty}^{\infty} dp_x f_b. \quad (3)$$

As an equilibrium example ($\partial/\partial t = 0$) that is analytically tractable, we consider the choice of distribution function

$$F_b(H_{\perp}) = \frac{\hat{n}_b}{(8\gamma_b m_b \hat{H}_{\perp})^{1/2}} \Theta(H_{\perp} - \hat{H}_{\perp}), \quad (4)$$

where $H_{\perp} = p_x^2 / 2\gamma_b m_b + \psi^0(x)$ is the transverse Hamiltonian, $\Theta(x)$ is the Heaviside step-function, and $\hat{n}_b, \hat{H}_{\perp}$ are positive constants. Evaluating the number density $n_b^0(x) = \int_{-\infty}^{\infty} dp_x F_b(H_{\perp})$, we readily obtain

$$n_b^0(x) = \begin{cases} \hat{n}_b \left[1 - \psi^0(x) / \hat{H}_{\perp} \right]^{1/2}, & -x_b < x < x_b, \\ 0, & |x| > x_b. \end{cases} \quad (5)$$

Here, the location of the beam edge ($x = \pm x_b$) is determined from

$$\psi^0(x = \pm x_b) = \hat{H}_{\perp}, \quad (6)$$

where $\psi^0(x = 0) = 0$ is assumed. It is useful to introduce the effective Debye length λ_D defined by

$$\lambda_D^2 = \frac{\gamma_b^3 \hat{H}_{\perp}}{4\pi \hat{n}_b e_b^2} = \frac{1}{2} \frac{\gamma_b^2 \hat{v}_0^2}{\hat{\omega}_{pb}^2}. \quad (7)$$

Here, $\hat{v}_0 = (2\hat{H}_{\perp} / \gamma_b m_b)^{1/2}$ is the maximum speed of a particle with energy \hat{H}_{\perp} as it passes through $x = 0$. Substituting Eq. (5) into Eq. (3) then gives

$$\frac{\partial^2}{\partial x^2} \left(\frac{\psi^0(x)}{\hat{H}_{\perp}} \right) = \frac{1}{\lambda_D^2} \left(\frac{1}{s_b} - \left[1 - \frac{\psi^0(x)}{\hat{H}_{\perp}} \right]^{1/2} \right) \quad (8)$$

in the beam interior ($-x_b < x < x_b$). Equation (8) is to be integrated subject to the boundary conditions $[\psi^0]_{x=0} = 0 = [\partial\psi^0/\partial x]_{x=0}$. For physically acceptable solutions to Eq. (8), the condition $[\partial^2\psi^0/\partial x^2]_{x=0} > 0$ imposes the requirement that s_b lies in the interval $0 < s_b < 1$, where $s_b = \hat{\omega}_{pb}^2 / \gamma_b^2 \omega_{\beta\perp}^2$. The regime $s_b \ll 1$ corresponds to a low-intensity, emittance-dominated beam, whereas the regime $s_b \rightarrow 1$ corresponds to a low-emittance, space-charge-dominated beam. In solving Eq. (8), it is convenient to introduce the dimensionless variables defined by

$$X = \frac{x}{\lambda_D}, \quad \hat{\psi}^0(X) = \frac{\psi^0(x)}{\hat{H}_{\perp}}. \quad (9)$$

Substituting Eq. (9) into Eq. (8), integrating once, and enforcing $[\psi^0]_{x=0} = 0 = [\partial\psi^0/\partial x]_{x=0}$, gives

$$\frac{1}{2} \left(\frac{d\hat{\psi}^0}{dX} \right)^2 = \frac{1}{s_b} \hat{\psi}^0 + \frac{2}{3} \left[(1 - \hat{\psi}^0)^{3/2} - 1 \right] \quad (10)$$

in the interval $-x_b/\lambda_D \leq X \leq x_b/\lambda_D$. Equation (10) can be integrated exactly to determine X as a function of $(1 - \hat{\psi}^0)^{1/2} = n_b^0(X) / \hat{n}_b$ [see Eq. (5)]. We express $X =$

* This research was supported by the U. S. Department of Energy.

$\int_0^{\psi^0} d\psi^0 / (d\psi^0/dX)$, change variables to $z = (1 - \psi^0)^{1/2}$, and make use of Eq. (10). This gives [1, 3]

$$X = 3^{1/2} \int_{(1-\psi^0)^{1/2}}^1 \frac{z dz}{[(1-z)(a^+ - z)(z - a^-)]^{1/2}}, \quad (11)$$

where a^+ and a^- are defined by

$$a^\pm = \frac{1}{4s_b} \{3 - 2s_b \pm [3(3 + 4s_b - 4s_b^2)]^{1/2}\}. \quad (12)$$

From Eqs. (6) and (11) we obtain a closed expression for x_b/λ_D in terms of the normalized beam intensity s_b for the choice of equilibrium distribution function in Eq. (4). The areal density of the beam particles, $N_b = \int_{-x_b}^{x_b} dx n_b^0(x)$, for the density profile in Eq. (5) can be expressed as

$$N_b = 2\hat{n}_b \int_0^{x_b} dx [1 - \psi^0(x)/\hat{H}_\perp]^{1/2}. \quad (13)$$

Some algebraical manipulation that make use of Eqs. (9), (10) and (13) gives

$$\frac{N_b}{2\hat{n}_b x_b} = 3^{1/2} \frac{\lambda_D}{x_b} \int_0^1 \frac{z^2 dz}{[(1-z)(a^+ - z)(z - a^-)]^{1/2}}, \quad (14)$$

where x_b/λ_D is determined from Eq. (11). Note that $N_b/2\hat{n}_b x_b$ depends only on the dimensionless intensity parameter s_b . Typical normalized density profiles

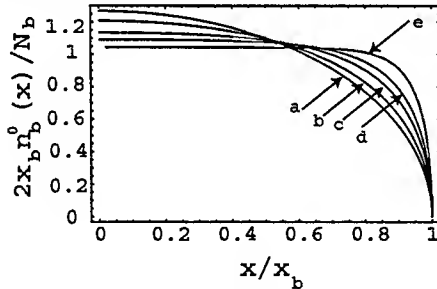


Figure 1: Plots of the normalized density profile $2x_b n_b^0(x)/N_b$ versus x/x_b for different values of the normalized beam intensity s_b corresponding to (a) $s_b = 0.2$, (b) $s_b = 0.9$, (c) $s_b = 0.99$, (d) $s_b = 0.999$, (e) $s_b = 0.999999$.

$2x_b n_b^0(x)/N_b$ are illustrated in Fig.1 for values of s_b ranging from $s_b = 0.2$ to $s_b = 0.999999$ [1]. Finally, defining the equilibrium transverse pressure profile by $P_b^0(x) = \int_{-\infty}^{\infty} dp_x (p_x^2/\gamma_b m_b) f_b^0$, we readily obtain

$$P_b^0(x) = \frac{4}{3} \hat{n}_b \hat{H}_\perp \left[1 - \frac{\psi^0(x)}{\hat{H}_\perp} \right]^{3/2}. \quad (15)$$

Comparing Eqs. (5) and (15), note that $P_b^0(x) = \text{const}[n_b^0(x)]^3$, which corresponds to a triple-adiabatic pressure relation.

LINEARIZED EQUATIONS AND STABILITY ANALYSIS

The linearized Vlasov-Maxwell equations can be expressed as [2]

$$\left(\frac{\partial}{\partial t} + v_x \frac{\partial}{\partial x} - \frac{\partial \psi^0}{\partial x} \frac{\partial}{\partial p_x} \right) \delta f_b = v_x \frac{\partial \delta \psi}{\partial x} \frac{\partial F_b}{\partial H_\perp}, \quad (16)$$

and

$$\frac{\partial^2}{\partial x^2} \delta \psi = -\frac{4\pi e_b^2}{\gamma_b^2} \delta n_b, \quad (17)$$

where $\delta n_b(x, t) = \int_{-\infty}^{\infty} dp_x \delta f_b$ is the perturbed number density of beam particles. In analyzing Eqs. (16) and (17), it is convenient to change variables from (x, p_x, t) to the new variables (x', H_\perp, τ) defined by [1]

$$x' = x, \quad \tau = t, \quad H_\perp = \frac{1}{2\gamma_b m_b} p_x^2 + \psi^0(x). \quad (18)$$

Substituting Eqs. (18) into Eqs. (16) and (17) gives for the evolution of the perturbations $\delta f_b(x', H_\perp, \tau)$ and $\delta \psi(x', \tau)$,

$$\left(\frac{\partial}{\partial \tau} + v_x \frac{\partial}{\partial x'} \right) \delta f_b = v_x \frac{\partial \delta \psi}{\partial x'} \frac{\partial F_b}{\partial H_\perp}, \quad (19)$$

$$\frac{\partial^2}{\partial x'^2} \delta \psi = -\frac{4\pi e_b^2}{\gamma_b^2} \delta n_b. \quad (20)$$

In Eq. (19), $v_x = +v(H_\perp, x')$ for the forward-moving particles with $v_x > 0$, and $v_x = -v(H_\perp, x')$ for the backward-moving particles with $v_x < 0$, where

$$v_x = \pm v(H_\perp, x') \equiv \pm \left(\frac{2H_\perp}{\gamma_b m_b} \right)^{1/2} \left[1 - \frac{\psi^0(x')}{H_\perp} \right]^{1/2}. \quad (21)$$

Furthermore,

$$\frac{\partial F_b}{\partial H_\perp} = -\frac{\hat{n}_b}{2\gamma_b m_b \hat{v}_0} \delta(H_\perp - \hat{H}_\perp), \quad (22)$$

where $\hat{v}_0 = (2\hat{H}_\perp/\gamma_b m_b)^{1/2}$. Using Eqs. (19)-(22) and introducing $\delta E_x(x', \tau) = -(\partial/\partial x') \delta \phi(x', \tau) = -(\gamma_b^2/e_b)(\partial/\partial x') \delta \psi(x', \tau)$, after some algebraic manipulation we obtain [1]

$$\begin{aligned} \frac{\partial^2}{\partial \tau^2} \delta E_x - \hat{v}_0^2 N(x') \frac{\partial}{\partial x'} \left[N(x') \frac{\partial}{\partial x'} \delta E_x \right] \\ = -\frac{\hat{\omega}_{pb}^2}{\gamma_b^2} N(x') \delta E_x, \end{aligned} \quad (23)$$

where $N(x')$ is the (dimensionless) profile shape function defined by

$$N(x') = \left[1 - \frac{\psi^0(x')}{\hat{H}_\perp} \right]^{1/2}. \quad (24)$$

In the analysis of Eq. (23), we make use of a normal-mode approach and express $\delta E_x(x', \tau) =$

$\delta \hat{E}_x(x', \omega) \exp(-i\omega\tau)$, where ω is the (generally complex) oscillation frequency. Equation (23) can be represented in a convenient form by introducing the angle variable α defined by

$$\alpha = \frac{\pi}{2} \frac{X'}{X_b} = \frac{\omega_0}{\hat{\omega}_0} X', \quad (25)$$

where X' and ω_0 are defined by

$$X' = \int_0^{x'} \frac{dx'}{N(x')}, \quad \omega_0 = \frac{\pi}{2} \frac{\hat{\omega}_0}{X_b}, \quad (26)$$

where $X_b = X'(x_b)$. Substituting Eq. (25) into Eq. (23) gives the eigenvalue equation

$$\omega_0^2 \frac{\partial^2}{\partial \alpha^2} \delta \hat{E}_x + \left[\omega^2 - \frac{\hat{\omega}_{pb}^2}{\gamma_b^2} N(\alpha) \right] \delta \hat{E}_x = 0. \quad (27)$$

Equation (27) is to be solved over the interval $-\pi/2 < \alpha < \pi/2$ subject to the boundary conditions $\delta \hat{E}_x(\alpha = \pm\pi/2, \omega) = 0$. Substituting Eqs. (10) and (24) into Eq. (25) gives

$$\alpha = \frac{\pi}{2} \frac{\lambda_D}{X_b} 3^{1/2} \int_N \frac{dz}{[(1-z)(a^+-z)(z-a^-)]^{1/2}}, \quad (28)$$

where a^\pm is defined in Eq. (12). Some algebraical manipulation gives exactly for the inverse function $N(\alpha)$

$$N(\alpha) = \frac{\left[1 - a^+ \kappa^2 \operatorname{sn}^2 \left(\frac{\alpha}{\pi} \frac{X_b}{\lambda_D} \left[\frac{a^+ - a^-}{3} \right]^{1/2}, \kappa \right) \right]}{\left[1 - \kappa^2 \operatorname{sn}^2 \left(\frac{\alpha}{\pi} \frac{X_b}{\lambda_D} \left[\frac{a^+ - a^-}{3} \right]^{1/2}, \kappa \right) \right]}, \quad (29)$$

where $\operatorname{sn}(\beta, \kappa)$ is the Jacobi elliptic sine function and $\kappa = [(1-a^+)/(a^+-a^-)]^{1/2}$. In Eqs. (28)-(29), the "stretched" half-layer thickness (X_b) measured in units of the Debye length (λ_D) is given by

$$\frac{X_b}{\lambda_D} = \frac{2 \cdot 3^{1/2}}{(a^+ - a^-)^{1/2}} F \left(\arcsin(\kappa^2/a^+)^{-1/2}, \kappa \right), \quad (30)$$

where F is the elliptic integral of the first kind. Using the expression for $N(\alpha)$ in Eq. (29), the eigenvalue equation (27) can be solved numerically for $\delta \hat{E}_x(\alpha, \omega)$ and the eigenvalues ω^2 subject to the boundary conditions $\hat{E}_x(\alpha = \pm\pi/2, \omega) = 0$. An approximate expression for the eigenvalues of the Schroedinger-like equation (27) can be obtained in the WKB approximation. The Born-Zommerfeld formula, when applied to Eq. (27), gives

$$\frac{\hat{\omega}_{pb}}{\gamma_b \omega_0} \int_{-\pi/2}^{\pi/2} d\alpha \left[\left(\frac{\gamma_b \omega_m}{\hat{\omega}_{pb}} \right)^2 - N(\alpha) \right]^{1/2} = \pi m, \quad (31)$$

where ω_m is the m th-mode eigenfrequency with m half-wavelength oscillations of $\delta \hat{E}_x$ over the layer thickness.

Making use of Eq. (28), the result in Eq. (31) can be rewritten as

$$6^{1/2} \int_0^1 \frac{dz (q_m^2 - z)^{1/2}}{[(1-z)(a^+ - z)(z - a^-)]^{1/2}} = \pi m, \quad (32)$$

where q_m and r are defined by $q_m = \omega_m/(\hat{\omega}_{pb}/\gamma_b)$ and $r = \kappa[(q_m^2 - a^+)/(q_m^2 - 1)]^{1/2}$. Equation (32) has been

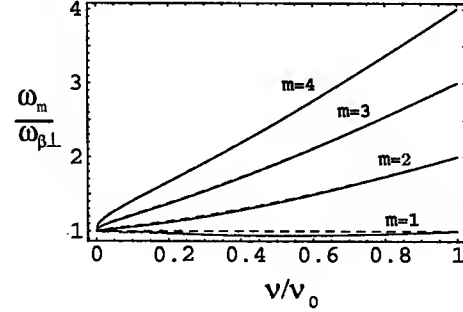


Figure 2: Plots of the normalized mode frequencies $\omega_m/\omega_{\beta\perp}$ versus the on-axis ($x = 0$) tune depression $\nu/\nu_0 = (1 - s_b)^{1/2}$ for several values of mode numbers $m = 1, 2, 3, 4$. The dotted curves are the numerical solutions of the eigenvalue equation (27); the solid curves are the solutions obtained in the WKB approximation [Eq. (32)].

solved numerically [1] for ω_m^2 , and the results have been compared with the numerical solutions of the eigenvalue equation (27) (Fig. 2). In Fig. 2, the convention is such that there are m half-wavelength oscillations of $\delta \hat{E}_x$ over the layer thickness. Note that low beam intensity ($s_b \ll 1$) corresponds to $\nu/\nu_0 \rightarrow 1$, with $\omega_m \simeq m\omega_{\beta\perp}$, whereas the space-charge-dominated regime ($s_b \rightarrow 1$) corresponds to $\nu/\nu_0 \rightarrow 0$, with $\omega_m \simeq \omega_{\beta\perp} \simeq \hat{\omega}_{pb}/\gamma_b$.

To summarize, we have demonstrated that the self-consistent waterbag equilibrium f_b^0 satisfying the steady-state ($\partial/\partial t = 0$) Vlasov-Maxwell equations is exactly solvable for the beam density $n_b^0(x)$ and electrostatic potential $\phi^0(x)$. In addition, we derived a closed Schroedinger-like eigenvalue equation for small-amplitude perturbations ($\delta f_b, \delta \phi$) about the self-consistent waterbag equilibrium in Eq. (4). In the eigenvalue equation, the density profile $n_b^0(x)$ plays the role of the potential $V(x)$ in the Schroedinger equation. The eigenvalue equation was investigated analytically and numerically, and the eigenfrequencies were shown to be purely real.

REFERENCES

- [1] E. A. Startsev and R. C. Davidson, Phys. Rev. Special Topics on Accelerators and Beams **6**, 044401 (2003).
- [2] R. C. Davidson and H. Qin, *Physics of Intense Charged Particle Beams in High Energy Accelerators* (World Scientific, Singapore, 2001), and references therein.
- [3] The integrals in Eqs. (11), (14), (28), (32) can be expressed in terms of elliptic functions (see Ref. 1).

RF MODES IN THE PEP-II SHIELDED VERTEX BELLOWS*

A. Novokhatski** and S. Weathersby, SLAC, Stanford, CA 94309, USA

Abstract

Experimental and simulation study of RF modes were carried out for the complicated geometry of the shielded vertex bellows near the IP region of the PEP-II B-factory. A beam position monitor button electrode located 50 cm from the bellows provides a signal for spectrum measurement. Calculations indicate monopole, dipole and quadrupole modes can exist in the bellows structure near the experimentally observed frequency region of 5 GHz. The observed modes are correlated to the bellows heating. The beam-generated fields are scattered by the masks, taper and axial offsets and heat the bellows by coupling through the RF shield fingers.

INTRODUCTION

The PEP-II B-Facility collides 1.7 A of 3 GeV positrons with 1.0 A of 10 GeV electrons, in trains of several hundred bunches. The bunch length is 1.3 cm. Within the BaBar detector near the IP, where the two beams share a common vacuum chamber, anomalous heating is observed at thermocouples situated on a shielded bellows structure at the juncture of a beryllium beam pipe with a copper vacuum chamber. The heating is determined to be due to higher order modes [1]. A signal from a nearby BPM was used to measure the spectrum of the fields excited by the beams. These observations reveal several high Q modes correlated with the bellows temperature. Computer calculations have found eigenmodes which can exist in the bellows structure near the observed frequencies. Further calculations are performed modelling the vacuum chamber and bellows together in 3D as coupled cavities from which coupling parameters are obtained for the dipole and quadrupole modes. This study complements and extends the pioneering work carried out by Stan Ecklund et al. [1] during the last physics run.

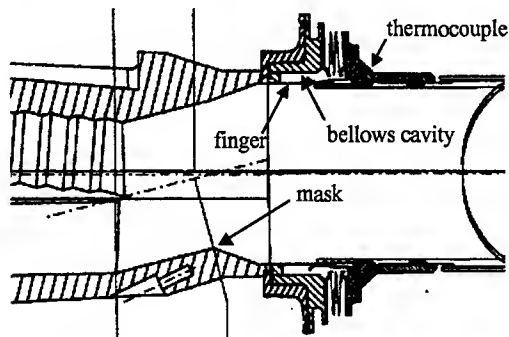


Figure 1: Bellows structure and vacuum chamber showing synchrotron masks and site of thermocouple with high temperature readings.

THE BELLOWS STRUCTURE

Figure 1 gives an overview of the bellows area. Positrons are incident from the left, electrons from the right. The IP is located roughly 20 cm to the right of the bellows. The bellows are shielded from the beam chamber by a series of 16 metal fingers azimuthally separated by gaps or slots. The variations in the beam pipe vertical cross section couple the beam field and high order transverse modes. It is the transverse modes which are expected to couple into the bellows through slots between the fingers. The slots are made to vary in length from 10 to 13 mm in response to thermal expansion and contraction of surrounding structures. During a recent maintenance period the vertex chamber was extracted from the BaBar detector and the slots were found to be fully extended at 13 mm.

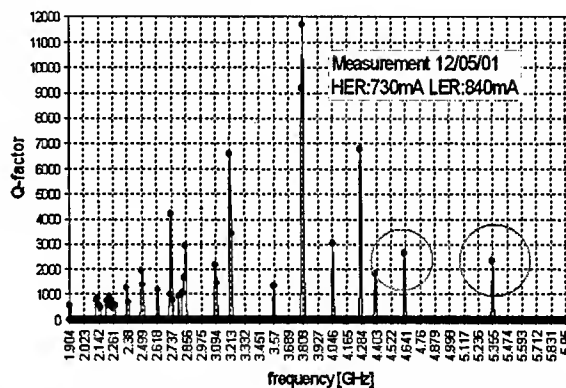


Figure 2: FFT of a gated oscilloscope BPM button signal in the gap between trains. The circled peaks show amplitude correlation with the thermocouple temperature.

SPECTRUM MEASUREMENTS

The colliding bunch trains have an intervening gap of about 350 ns required for the ramp-up of an abort kicker and the clearing of ions for the electron ring. A beam position monitor button electrode located 50 cm from the bellows provides a signal to a HP54120 high frequency oscilloscope and a R&S gated spectrum analyzer. The signal is gated in time to coincide with the gap where no beam is present. An FFT of the oscilloscope signals is shown in figure 2. To calculate the equivalent Q-factor the amplitudes are measured in small time windows at the beginning and the end of the gap.

The same spectrum was also observed with the gated spectrum analyzer. Within a forest of peaks in the 5 GHz region several modes are identified as having amplitudes correlated with the bellows temperature. The amount of

Work supported by Department of Energy contract DE-AC03-76SF00515.
**novo@slac.stanford.edu

thermal power dissipated in the bellow vs. time was calculated from the temperature data. In figure 3 this calculation is compared with the amplitude of one of the peaks.

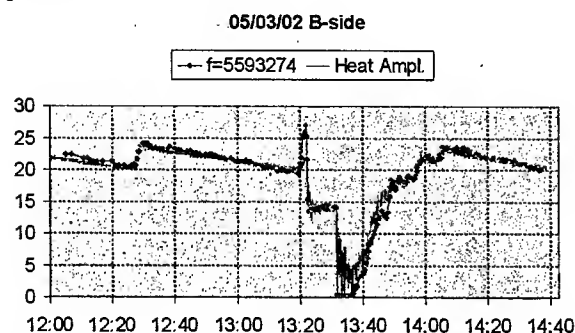


Figure 3: Estimated thermal power (pink) from thermocouple data and measured peak amplitude (blue) of a 5.6 GHz mode vs. time.

The figure includes data from a beam abort in which one of the beams was lost followed by a subsequent loss of the remaining beam. The slow rise after the beam loss reflects filling the rings back to nominal currents. The data indicate contributions from both beams to the heating and mode power.

MAIN MODES

Two dimensional eigenmode calculations are performed for the bellows cavity. The fingers and beam chamber are not modelled in this calculation. We found several modes in frequency range of 5-6 GHz. They are: monopole, dipole and quadrupole modes. Frequencies of first modes are given in table 1.

Monopole	4.75 GHz	7.22 GHz	8.05 GHz
Dipole	5.46 GHz	8.37 GHz	9.44 GHz
Quadrupole	6.19 GHz	8.82 GHz	9.78 GHz

Table 1: Eigenmode frequencies.

IP Bellows model (open 13 mm between flanges)

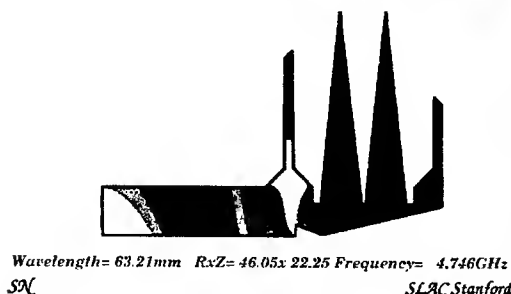


Figure 4: Monopole 4.75 GHz. Magnetic energy density.

The monopole mode is computed using a proprietary code NOVO [2]. The magnetic field energy density for the monopole mode integrated over the azimuthal angle is shown in figures 4.

Dipole and quadrupole modes are obtained with MAFIA [3]. The magnetic field energy density for dipole and quadrupole modes are shown in figures 5-6. There is high energy density at the bottom of the bellows convolutions for the dipole and quadrupole case. This magnetic energy density corresponds to large longitudinal magnetic flux.

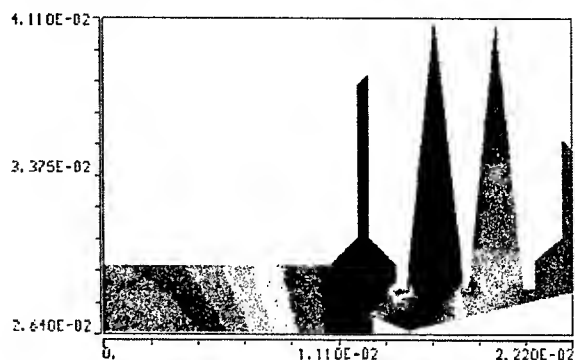


Figure 5: Dipole 5.46 GHz. Magnetic energy density.

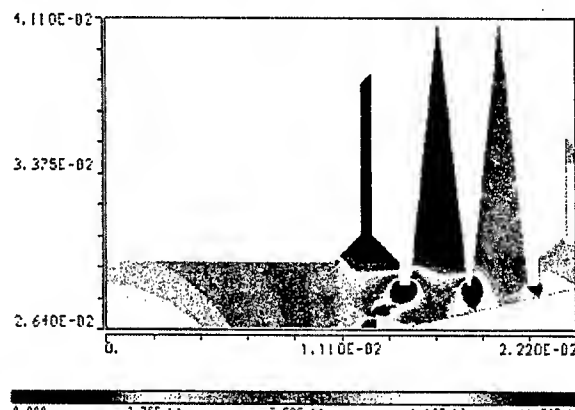


Figure 6: Quadrupole 6.19 GHz magnetic energy density. The scale is truncated at the high end to enhance the density pattern in the hot spots.

COUPLING STUDIES

So far we have determined the existence of modes in the bellows cavity which are likely responsible for the observed heating. To examine a possible excitation mechanism we now construct an inner beam cavity with slots in its outer walls linking the outer bellows cavity in its simple coaxial configuration. The evolution of a particular mode in each cavity is observed as the longitudinal dimension of the beam cavity is varied. The bellows cavity dimensions are held fixed in these studies. Furthermore, the slots are kept at the center of the longitudinal dimension of the beam cavity, to minimize the effect of the cavity walls. Within the regime where no coupling is present, the bellows cavity frequency remains constant while the beam cavity frequency changes with the change in length. If there is no coupling, the change in

the beam cavity frequency will have no effect on the fixed frequency of the bellows cavity. If there is coupling, one expects a shift in the bellows cavity frequency as the beam cavity frequency approaches the bellows cavity frequency. The closest approach of the two frequencies yields the degree of coupling. The larger the closest approach, the larger the coupling. We give the coupling as the minimum frequency separation over the average frequency. Monopole mode coupling is not considered since the magnetic field lines are purely azimuthal, however, if the beam axis and the cavity axis are not parallel, a longitudinal coupling component will be introduced. The result for the dipole case is shown in figure 7. For a given slot size, frequencies of the dipole mode for both cavities and their difference are plotted as a function of beam cavity length. The minimum frequency separation is 75 MHz yielding a 1% coupling.

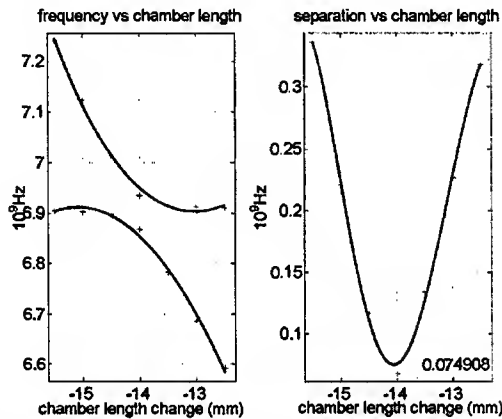


Figure 7: Dipole mode frequency for the beam and bellows cavities and their difference as a function of beam cavity length for a slot width.

Typical plot for the dipole modes in the beam chamber and bellows cavity is shown in figure 8.

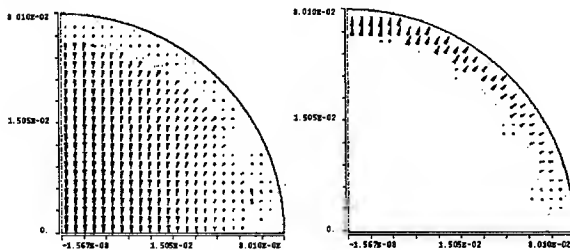


Figure 8: Dipole electric field in the beam cavity (left) and bellows cavity (right).

As shown in figure 9 for the quadrupole case, a minimum difference in frequency of 229 MHz indicates a higher degree of coupling of roughly 2%.

To extrapolate, we investigate coupling for different slot widths. The minimum frequency separation as a function of slot size for the quadrupole modes is shown in

figure 10, where the horizontal axis is the fractional width of the real slot width of 0.81 mm.

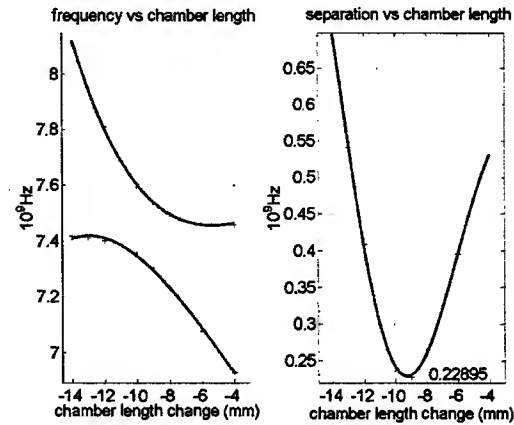


Figure 9: Quadrupole mode frequency for the beam and bellows cavities and their difference as a function of beam cavity length.

The data is fitted with an analytic expression derived from electric and magnetic polarizabilities of small apertures [4] which is given in terms of slot width w and length l and inversely proportional to $\ln(4l/w) - 1$. Both the data and fit are fairly linear and flat in the region of interest. Practically speaking, reduction of coupling for the quadrupole modes by narrowing the slots is not feasible.

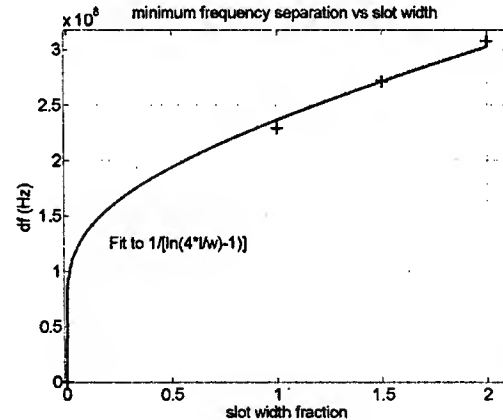


Figure 10: Coupling (+) and analytic expression (solid line) vs. fractional slot width.

REFERENCES

- [1] F. Decker et al., PAC2001, Chicago, June 2001, p.
- [2] A. Novokhatski, "Code 'NOVO' for wake field calculations", in preparation.
- [3] The MAFIA collaboration "User Guide", CST GmbH, Darmstadt, Germany.
- [4] B. Zotter and S. Kheifets, "Impedances and Wakes in High - Energy Particle Accelerators", 1998, World Scientific.

CHARACTERISTICS OF PULSE COMPRESSION IN LASER PULSE AMPLIFICATION BY STIMULATED RAMAN BACKSCATTERING*

Jincheol B. F. Kim ^{a,b}, Hae June Lee ^b, Hyyong Suk ^b, In Soo Ko ^a

^a Department of Physics, POSTECH, San-31, Hyoja-dong, Pohang, Kyungbuk, 790-784, South Korea

^b Center for Advanced Accelerators, Korea Electrotechnology Research Institute, Seongju-dong 28-1, Changwon, 641-120, South Korea

Abstract

The characteristics of pulse compression during the laser pulse amplification using a counter-propagating pump and plasmas have been investigated using a one-dimensional fluid model of stimulated Raman backscattering. The pulse widths of the amplified laser at the front and rear half are examined in terms of the initial amplitudes of the pump and the seed, and the ratio of the electron plasma frequency to the laser frequency. The pulse widths have a common scaling behaviour in time over the considered parameter regime. The scaling exponents of the pulse widths during broadening and compression are all the same as 1.0. The pulse compression scaling shows a reciprocal behaviour to the peak energy growth.

INTRODUCTION

It was suggested that a short laser pulse (seed) of low energy can be amplified with a counter-propagating long laser pulse (pump) and a plasma by stimulated Raman backscattering (RBS) [1-4]. In this paper, we present simulation results on the characteristics of pulse compression during the amplification.

ONE-DIMENSIONAL FLUID MODEL

One-dimensional (1D) fluid model was used for the study of seed pulse amplification by RBS. The model follows the formulation of RBS in [1] and assumes a cold plasma. We do not consider the detuning term in this model. The governing equation for RBS for the case is

$$\begin{aligned} \frac{\partial a_p}{\partial t} - v_{g,0} \frac{\partial a_p}{\partial x} &= \frac{c}{4} k_f \frac{\omega_p}{\omega_0} a_s f, \\ \frac{\partial a_s}{\partial t} + v_{g,1} \frac{\partial a_s}{\partial x} &= -\frac{c}{4} k_f \frac{\omega_p}{\omega_1} a_p f^*, \\ \frac{\partial f}{\partial t} - v_{g,2} \frac{\partial f}{\partial x} + \Gamma f + i \frac{3}{8} \omega_p |f|^2 f &= -\frac{c}{4} k_f a_s * a_p, \end{aligned} \quad (1)$$

where $f = eE_x/mc\omega_p$ is the normalized longitudinal electric field, and $a_s = eE_1/mc\omega_1$ and $a_p = eE_0/mc\omega_0$ are the normalized electric fields for the seed and the pump, respectively. ω_j and k_j meet the matching condition, $k_f = k_0 + k_1$ and $\omega_0 = \omega_1 + \omega_p$, where ω_j and k_j are the angular frequency and the wave number of the pump ($j = 0$) and the seed ($j = 1$), respectively. $v_{g,j} = c^2 k_j / \omega_j$ is the group velocities for the seed ($j=1$) and the pump ($j=0$). In this study, we neglect the damping term and the relativistic nonlinear detuning term since $|f|$ is much smaller than 1.

A moving window was used to make computations faster. The moving window is on the frame of the seed and advances with the speed of $v_{g,1}$. The size of the moving window is about 500 μm to 2000 μm . The used grid size (Δx) ranges from 0.2 to 0.4 μm . It is small enough to observe the essential behaviour of 1D fluid model using a quasi-static eikonal approximation to analyze the slowly varying amplitudes. The confronting boundary condition of the moving window to the pump is the initial amplitude of the pump (a_{p0}). The trailing boundary condition at the end of the moving window is just to discard the previous quantities as ordinary moving window simulations do.

The initial spatial profile was set up in the moving window as the situation when the collision between the seed and the pump starts. It means that the interaction of the seed or the pump only with a plasma is negligible, which is valid for a non-relativistic low intensity laser pulses.

The time step is determined from the spatial grid size as $\Delta t = \zeta (\Delta x / v_{g,1})$ with an appropriate complement factor ζ , which is typically close to 1.0.

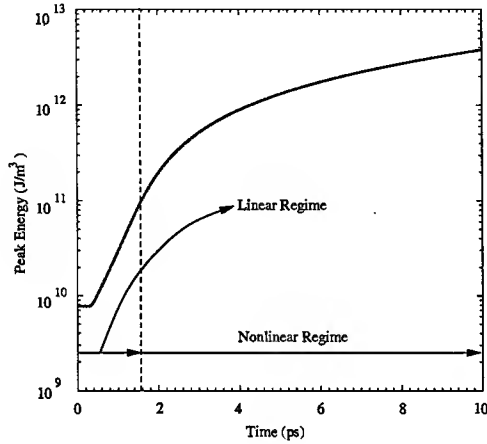
We investigated the time evolutions of the full width at the half maximum (FWHM), the peak energy, and the widths of the front and rear half of the seed, D_f and D_r , respectively. The wavelength of the pump (λ_0) was set to be 0.532 μm . The seed and the plasma wavelengths were set to meet the matching condition. The parameter ω_p / ω_1 ranges from 0.02 to 0.25 by changing the plasma density. The initial pump amplitude, a_{p0} , has a value from 0.003 to 0.020 which corresponds to the laser intensities of 40 TW/cm² and 2 PW/cm² with $\lambda_0 = 0.532 \mu\text{m}$. a_{p0} can be adjusted by changing the laser intensity or spot sizes in experiments. The pump is assumed to be a long square pulse with a pulse length (τ_p) of 20 ps. The initial seed amplitude was chosen to be from 0.001 to 0.020. The seed was assumed to be a Gaussian pulse in time domain, $\exp(-t^2/\tau_s^2)$, where τ_s is from 0.2 to 1.0 ps. The initial FWHM is $1.18\tau_s$.

SIMULATION RESULTS

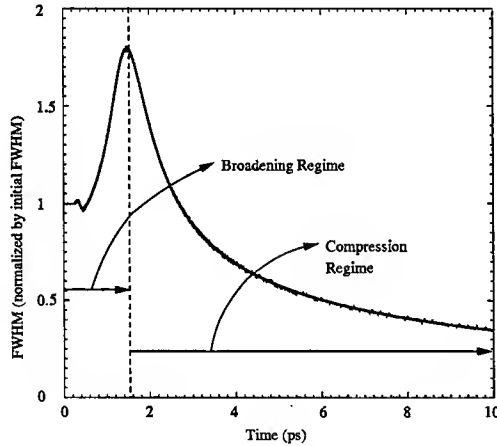
Linear and Nonlinear Growth Regime and Pulse Compression

Figure 1 shows the time evolutions of the peak energy of the seed and the compression of the seed during the amplification. It is known that the peak energy grows in two stages. First, the seed is amplified exponentially,

which is classified as a linear regime. In this regime, the seed broadens and the semi-log plot of the peak energy vs. time shows linear behaviour [Fig. 1(a)]. After the linear regime, the peak energy grows as t^δ , which is classified as a nonlinear regime. The seed is compressed simultaneously in the nonlinear regime. The difference between the linear and the nonlinear regimes is associated with the depletion of the pump. The start of the nonlinear regime corresponds to the local depletion of the seed, which is followed, by the 100% depletion of the pump.



(a)



(b)

Figure 1: Time evolutions of (a) the peak energy and (b) the FWHM showing the linear and nonlinear regime of the seed amplification ($a_{p0} = 0.01$, $a_{s0} = 0.001$, $\omega_p/\omega_l = 0.002$, $\tau_p = 20$ ps, $\tau_s = 0.2$ ps)

Characteristics of the Pulse Compression

The seed amplification happens along with the pulse compression in the nonlinear regime. It means that the characteristics of the pulse compression give us much information about the amplification of the seed.

In order to investigate the characteristics of the pulse compression, we define two quantities, D_f and D_r , which are the normalized half width of the seed as follows:

$$D_f = \frac{|x_s - x_{\max}|}{\sigma_i}, \quad (2)$$

$$D_r = \frac{|x_{\max} - x_{f,1}|}{\sigma_i}, \quad (3)$$

where x_s is the position of the starting point of the seed, x_{\max} is the maximum point of the seed, and $x_{f,1}$ is the first zero-crossing position of the normalized vector potential of the seed (a_s). σ_i is the initial FWHM of the seed.

Figure 2 shows the pulse broadening and compression in the front and rear half. Figure 2(a) shows the log-log plot of D_f vs. time. The slope of these curves in compression phases does not vary much. Figure 2(b) describes the log-log plot of D_r vs. time. D_r grows in t^δ in the broadening regime. After then, D_r drops sharply at the start of the compression, and decreases as t^η . The sharp drop of D_r comes from the local depletion of the seed.

The broadening and the compression behaviours appear in common throughout parameter ranges of the initial seed amplitude a_{s0} , the initial pump amplitude a_{p0} , and ω_p/ω_l . However, D_f with variation of a_{s0} shows slightly different behaviours from those with the variation of other parameters.

Figure 2 shows D_f and D_r with different values of initial pump amplitude a_{p0} . The larger a_{p0} results in the shorter broadening regime. For D_f , the slopes of the curve during the compression are the same for every a_{p0} . The curve runs parallel to each other for different a_{p0} 's. The phenomenon is also shown for D_r in Fig. 2(b). However, in case of D_r curve, the slopes of the curves do not change during both the compression and the broadening phases. We can express these relationships as

$$D_f = t^{-\nu}, \quad (\text{during compression})$$

$$D_r = t^\delta, \quad (\text{during broadening}) \quad (4)$$

$$D_r = t^{-\eta}, \quad (\text{during compression})$$

where ν , δ , and η were measured to be the same as 1.0.

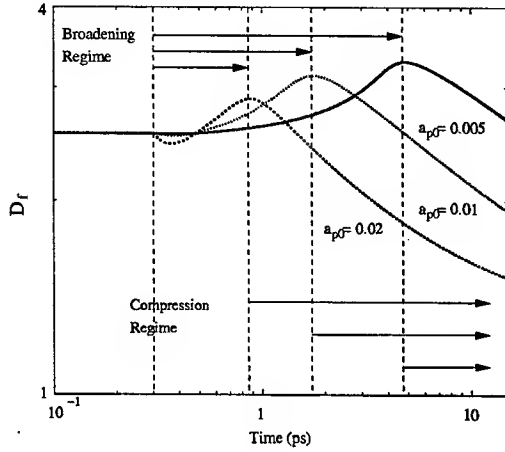
The difference between the behaviours of D_f and D_r comes from the first local depletion of the seed following that of the pump. The front part of the seed is not affected by the depletion, and there is no discontinuity in the derivative of D_f . At the rear part of the seed, there appear the zero-crossing points following the pump depletion. Emergence of the zero-crossing points is featured as the discontinuous derivative of D_r .

It takes some time until D_f and D_r follow the relationship explained in Eq. (4) because of transient behaviours. The relationship is satisfied when the seed is separated into two pulses and enters the nonlinear regime.

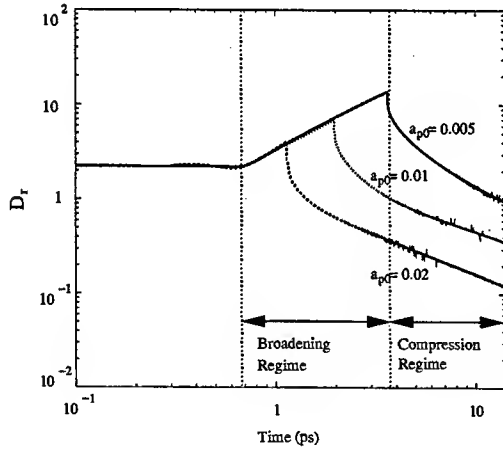
One more feature we should note in D_r is the linear behaviour during pulse broadening. D_r grows linearly with respect to time. It is connected with the counter-propagating pump with a constant velocity $v_{g,0}$. As the pump evolves through the seed in the opposite direction, the rear end of the seed moves backward following the

front end of the pump by stimulated RBS before the pump is totally depleted. It is the reason why D_r in broadening regime grows linearly.

Figure 3 presents the time evolutions of D_f and D_r in terms of ω_p/ω_l . As ω_p/ω_l becomes larger, the broadening regime becomes shorter and the compression starts earlier. In this case also, ν , δ and η become constant to be 1.0 with the variation of ω_p/ω_l .



(a)



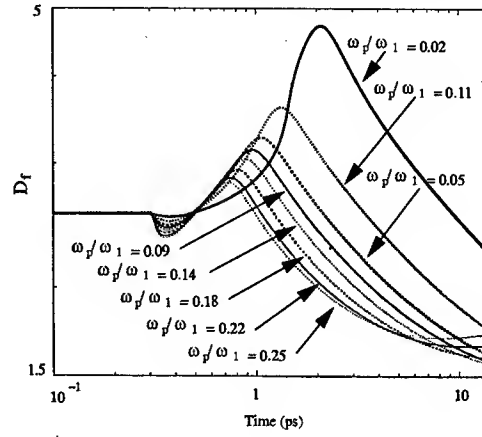
(b)

Figure 2: Broadening and compression regimes in (a) D_f and (b) D_r with the variation of initial pump amplitudes, a_{p0} ($a_{s0} = 0.005$, $\omega_p/\omega_l = 0.002$, $\tau_p = 20$ ps, $\tau_s = 0.2$ ps)

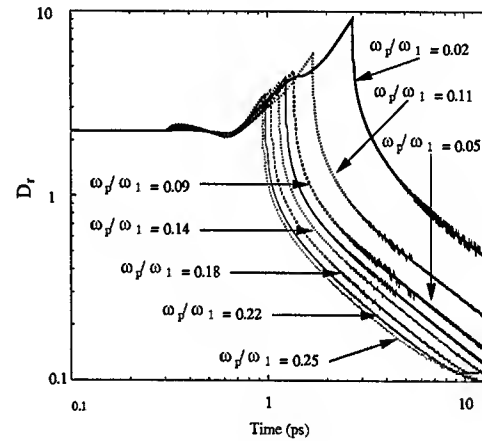
The variations of a_{p0} , a_{s0} , and ω_p/ω_l are associated only with the starting time of compression. The larger a_{p0} , a_{s0} and ω_p/ω_l result in the shorter broadening regimes, the more seed amplification, and the more pulse compression under the same interaction length.

We observed that the exponents ν , δ and η are constant throughout the parameter ranges of the simulation. From our simulations, ν , δ and η are all equal to 1.0 in average. The fact is associated with that the growth rate of the peak energy in nonlinear regime is equal to 1.0. It means that

the peak energy in nonlinear regime grows reciprocally to the compression of the seed. Therefore, the total energy proportional to the product of the peak intensity and the pulse width is saturated for the amplified seed pulse.



(a)



(b)

Figure 3: (a) D_f and (b) D_r curves in terms of different ω_p/ω_l 's with the initial condition of $a_{p0} = 0.01$, $a_{s0} = 0.001$, $\tau_p = 20$ ps, and $\tau_s = 0.2$ ps.

REFERENCES

- [1] V. M. Malkin, G. Shvets, and N. J. Fisch, Phys. Plasma 7, No. 5, 2232, 2000.
- [2] V. M. Malkin, G. Shvets, and N. J. Fisch, Phys. Rev. Lett. 82, No. 22, 4448, 1999.
- [3] G. Shvets, N. J. Fisch, A. Pukhov and J. Meyer-ter-Vehn, Phys. Rev. Lett. 81, No. 22, 4879, 1998.
- [4] V. M. Malkin, G. Shvets, and N. J. Fisch, Phys. Rev. Lett. 84, No. 6, 1208, 2000.
- [5] P. Mardahl, H. J. Lee, G. Penn, J. S. Wurtele, and N. J. Fisch, Phys. Lett. A 296, 109, 2002.
- [6] H. J. Lee, P. J. Mardahl, G. Penn, and J. S. Wurtele, IEEE. Trans. Plasma. Sci. (Special Issue) 30, No. 1, 2002.

EFFECT OF PREPLASMAS ON HIGH-ENERGY ION GENERATION BY AN INTENSE LASER PULSE IRRADIATED ON OVERDENSE PLASMAS

Hae June Lee * Jincheol B. Kim, Changbum Kim, Guang-Hoon Kim, Jong-Uk Kim, Hyyong Suk,
Korea Electrotechnology Research Institute, Changwon, 641-120, Republic of Korea

Abstract

High-energy ion generation from the interaction of an ultrashort intense laser pulse with an overdense plasma slab is studied with fully electromagnetic and relativistic particle-in-cell simulation. With a properly designed underdense preplasma, we observed that the forward ion acceleration from the front surface can be enhanced. The momentum distribution functions of the accelerated ions are investigated with respect to the laser pulse intensity and the preplasma profile.

INTRODUCTION

With the fast development of laser technology, the relativistic interaction of a super intense laser pulse with plasmas attracted lots of interests in the society of particle accelerators. Advanced acceleration concepts using a laser pulse can be applied for the generation of ions [1, 2, 3, 4] as well as electrons [5, 6, 7] due to the enhancement in the intensity and the pulse duration with the help of chirped pulse amplification (CPA) technique.

Two mechanisms of forward ion acceleration from a solid target irradiated by an ultrashort intense laser pulse were introduced recently. One is the ion generation from the rear surface [1, 2], and the other is that from the front surface [3, 4]. The former is generated by hot electrons penetrating through the slab and has low emittance and high maximum energy. However, the energy spread of the accelerated ions is large. The latter is produced by a shock wave produced by the ponderomotive force of the laser pulse and has low energy spread. It was also reported that the advantages of both of them can be combined as the ions initially formed in the shock wave at the front surface reach the rear side of the exploding plasma layer and are further accelerated by the electric field produced by the hot electrons [8].

In this study, we investigate the effect of preplasmas on the formation of the ion shock wave in the front surface by using one-dimensional (1d) electromagnetic particle-in-cell (PIC) code (1D-XOOPIC) [9] and two-dimensional (2d) one (OSIRIS) [10] in order to achieve high maximal ion energy.

SIMULATION PARAMETERS

For 1d simulation, we use a linearly polarized plane wave with a Gaussian profile,

$$E_z(x, t) = E_0 \exp[-(x - x_c)^2 / c^2 \tau_L^2] \sin(kx - \omega_0 t), \quad (1)$$

where E_z is the transverse electric field, E_0 is the maximum electric field, $x_c(t)$ is the center position of the laser pulse, ω_0 is the frequency, k is the wavenumber, and τ_L is the pulse duration of the laser pulse. The wavelength in vacuum is set to $\lambda_0 = 2\pi/k = 1 \mu\text{m}$ and the full width at half maximum (FWHM) is calculated as $1.18 c\tau_L$, where c is the speed of light. For 2d simulation, the laser pulse is linearly polarized and has a Gaussian profile also in the transverse direction.

The laser intensity is represented as a normalized vector potential,

$$a = \frac{eE_0}{mc\omega_0}, \quad (2)$$

which can be expressed with the laser intensity (I) as

$$a = 0.85 \times 10^{-9} \lambda_0 \sqrt{I}. \quad (3)$$

Here, I is in W/cm^2 and λ_0 is in μm . The target is assumed to be a fully ionized cold plasma slab with thickness of $2 \mu\text{m}$ composed of protons and electrons with density of n_e . Mainly $n_e = 10^{23} \text{ cm}^{-3} = 90 n_c$ is used in the simulation, where n_c is the critical density of the laser pulse. The electron plasma frequency for this case is, $\omega_p = (n_e e^2 / \epsilon_0 m)^{1/2}$, which is about ten times larger than the laser frequency, ω_0 . Here, e , ϵ_0 , and m are the elementary charge, the vacuum permittivity, and the electron mass, respectively.

For 1d simulation, The simulation domain was set to have a length of $100 \mu\text{m}$ and the target is located at $x_0 = 50 \mu\text{m}$. A laser pulse is launched from the left side of the simulation domain at $t = 0$ and propagates toward the target. The grid size is $\Delta x = 3.9 \text{ nm}$ (256 cells per one wavelength) and the time step is $\Delta t = 0.0065 \text{ fs}$ ($\Delta x / \Delta t = 2c$). Note that $\omega_p \Delta t \approx 0.12 < 1.0$, which is small enough to simulate the electron motions in the overdense plasma regime.

For 2d simulation, however, simulation time becomes very long to calculate with the same size of simulation domain as that of 1d case. Therefore, we simulated the case of $n_e = 10^{22} \text{ cm}^{-3} = 9 n_c$ instead of $n_e = 10^{23} \text{ cm}^{-3}$ just in order to confirm that the tendency of 1d and 2d simulation results are almost similar. The grid size is $\Delta x = 31.3 \text{ nm}$ (32 cells per one wavelength), and the time

* E-mail address : leehj@keri.re.kr. This work is supported by the Creative Research Initiatives of the Korea Ministry of Science and Technology.

step is $\Delta t = 0.076$ fs ($\Delta x/\Delta t = 1.38c$) for 2d simulation. In this case, $\omega_p \Delta t \approx 0.44 < 1.0$. For a higher plasma density, the grid size should be reduced.

In order to represent wide density ranges of the preplasma, we used varying ratios of the simulation particles to real particles. Because of small collision cross sections for fast moving particles, the collisions of electrons and ions with neutrals are neglected.

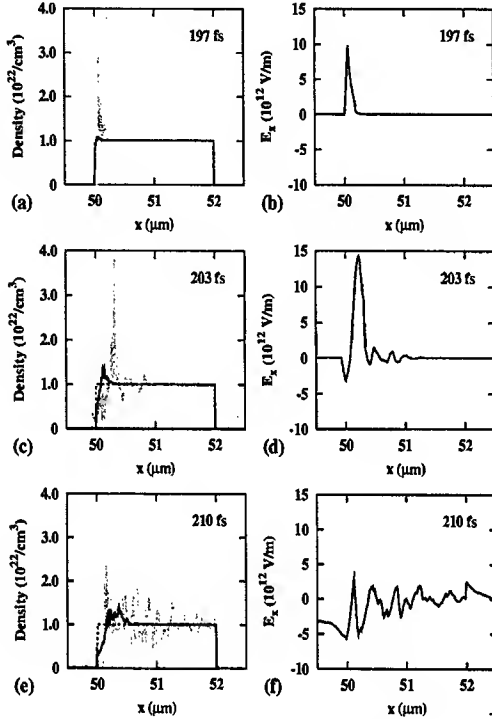


Figure 1: Shown are the profiles of the ion (solid) and electron (dashed) densities [(a), (c), and (e)] and the longitudinal electric field [(b), (d), and (f)] at different time. The dotted line in the density profiles shows the initial plasma profile. Simulation parameters are $a = 10$, $\tau_L = 10$ fs, and $n_e = 9 n_c$.

RESULTS

Figure 1 shows the evolution of plasma density and longitudinal electric field in 1d simulation. When the laser pulse has been incident on the plasma slab, electrons are pushed by the ponderomotive force of the intense laser pulse and the charge separation produces strong longitudinal electric field as shown in Figs. 1(a) and 1(b). Due to the strong electric field, ions begin to move, and some electrons are pulled backward while hot electrons propagate inside the slab as shown in Figs. 1(c) and 1(d). Even after the laser pulse has been reflected back, the hot electrons penetrate through the plasma slab and make strong electric field also in the rear side. Finally, there are three types of ion acceleration which are the backward ion acceleration (BIA) at the front side, the forward ion acceleration

at the rear side (FIAR), and the forward ion acceleration at the front side (FIAF) [8]. As shown in Fig. 1(e), the ion density in FIAF is high, and thus it is possible to increase the total amount of charges of the ion beam if we can utilize FIAF properly.

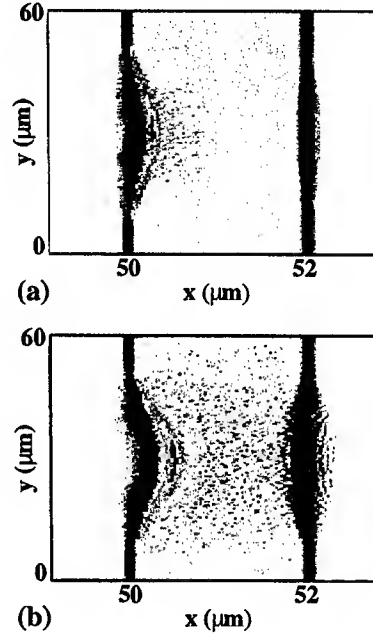


Figure 2: Density profile of the ions at (a) $t = 239$ fs and (b) $t = 292$ fs. Simulation parameters are $a = 5$, $\tau_L = 10$ fs, and $n_e = 9 n_c$.

With the same parameters, we observed that the 2d simulation results at the center plane of the Gaussian laser pulse agree qualitatively well with those shown in Fig. 1. Figure 2 shows the 2d ion density profiles at later time far after the laser pulse has been reflected. BIA, FIAR, and FIAF are clearly recognized in Fig. 2(b).

We investigated the effect of underdense preplasmas which can be generated by a prepulse. The preplasma is formed in front of the target and assumed to have an exponential density profile, $n(x) = n_1 e^{\kappa(x-x_0)}$, over range of $10 \mu\text{m}$. Here, n_1 is the maximum density of the preplasma, x_0 is the location of the plasma slab, and κ is the scale factor of the preplasma profile. In the simulations, we set κ to be $0.69 \mu\text{m}^{-1}$, and varied n_1 from $10^{-3} n_c$ to $0.9 n_c$. Note that the collisionless skin depth is $\approx c/\omega_p = 0.0168 \mu\text{m}$ for $n_e = 10^{23} \text{ cm}^{-3}$, which is much shorter than the target thickness of $2 \mu\text{m}$.

Figure 3 shows the enhancement of the ion acceleration at the front surface with the maximum preplasma density close to the critical density, n_c . The maximum value of the ion momentum in the longitudinal direction, p_x , does not change much when n_1 is small, but it increases more than 30% when $n_1 = 0.9 n_c$ compared with the case without the preplasma. The enhancement is caused by the electrons

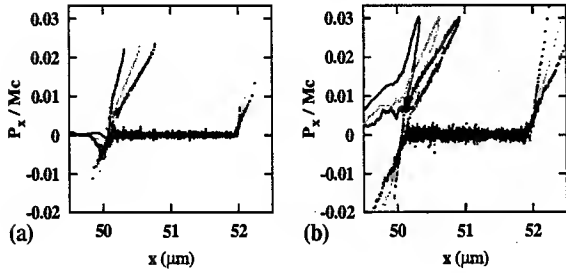


Figure 3: Momentum-position phase space for the cases of (a) $n_1 = 10^{-3}n_c$ and (b) $n_1 = 0.9n_c$ at $t = 253$ fs, 287 fs, and 320 fs. Simulation parameters are $a = 5$, $\tau_L = 10$ fs.

which is accelerated from the preplasma and penetrate into the plasma slab. They produce more strong longitudinal electric field at the front surface where the laser pulse is reflected. It was observed that not only the maximum energy of FIAF but also that of FIAR increases with the preplasma.

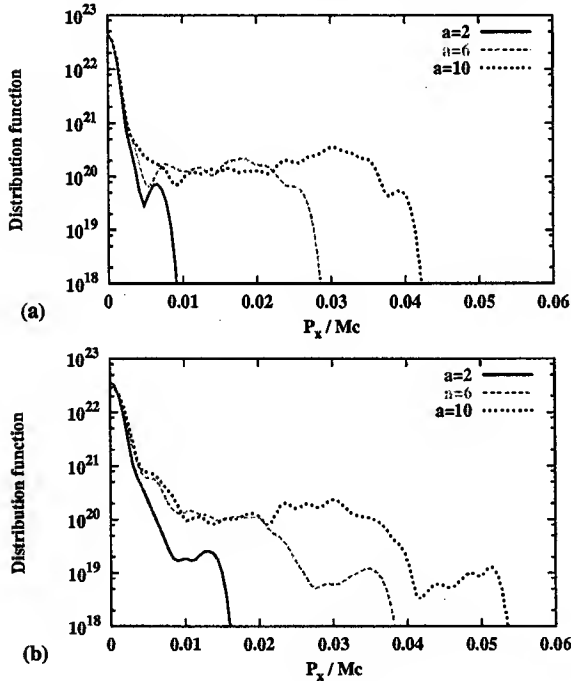


Figure 4: Momentum distribution functions of the accelerated ions for different laser intensities (a) without preplasmas and (b) with an exponential-profiled preplasma for $n_1 = 0.9n_c$. The profiles are measured at $t = 247$ fs.

Figure 4 shows the comparison of the momentum distribution function with and without preplasmas. For both the cases, the maximal ion momentum increases as the laser intensity increases. Here, a is proportional to $I^{1/2}$ with the relation of Eq. (3). As shown in Fig. 4(b), the distribution functions have a high energy tail and thus the maximal ion momentum increases when there is a preplasma with a proper density profile.

CONCLUSION

We simulated high-energy ion generation from the interaction of ultrashort intense laser pulse with an overdense plasma slab which has exponential-profiled preplasmas. The forward ion acceleration from the front surface with the formation of an ion shock wave is investigated. The one-dimensional and the two-dimensional simulation results show the same tendency for the profile evolution of the plasma density and the induced longitudinal electric field. With a preplasma of which maximum density is close to the critical density of the laser pulse, the accelerated ion energy has been enhanced more than 30% compared with the case without preplasma.

REFERENCES

- [1] S. P. Hatchett *et al.*, Phys. Plasmas **7**, 2076 (2000).
- [2] Y. Murakami *et al.*, Phys. Plasmas **8**, 4138 (2001).
- [3] A. Maksimchuk *et al.*, Phys. Rev. Lett. **84**, 4108 (2000).
- [4] T. Zh. Esirkepov *et al.*, JETP Lett. **70**, 82 (1999).
- [5] T. Tajima and J. M. Dawson, Phys. Rev. Lett. **43**, 267 (1979).
- [6] M. Everett, A. Lal, D. Gordon, C. E. Clayton, K. A. Marsh, and C. Joshi, Nature **368**, 527 (1994).
- [7] K. Nakajima *et al.*, Phys. Rev. Lett. **74**, 4428 (1995).
- [8] A. Zhidkov *et al.*, Phys. Rev. Lett. **89**, 215002, (2002).
- [9] J. P. Verboncoeur, A. B. Langdon, and N. T. Gladd, Comp. Phys. Comm., **87**, 199 (1995); H. J. Lee, P. J. Mardahl, G. Penn, and J. S. Wurtele, IEEE Trans. Plasma Science **30**, 40 (2002).
- [10] R. G. Hember *et al.*, Phys. Rev. E **57**, 5920 (1998).

NEW REGIONS OF STABILITY FOR PERIODICALLY FOCUSED PARTICLE BEAMS*

R. Pakter[†], F. B. Rizzato, J. S. Moraes

Instituto de Física, Universidade Federal do Rio Grande do Sul, Brazil

Abstract

In this paper we perform a comprehensive analysis of the transport of periodically focused particle beams within the new regions of stability recently found [R. Pakter and F. B. Rizzato, Phys. Rev. Lett., **87**, 044801 (2001)] for vacuum phase advances well above the 90 degrees threshold. In particular, we investigate the stability as a function of the relevant parameters of the system, such as beam intensity and focusing field profile. Self-consistent numerical simulations are used to verify the findings.

INTRODUCTION

The physics of intense beams in periodically focusing systems is an active area of theoretical and experimental research where one looks for external field configurations capable of confining high-current, low emittance ion or electron beams [1, 2]. The area is crucial for the development of several advanced particle accelerator applications, as well as applications in basic science.

A key aspect of periodically focused beams is their equilibrium and stability properties. Up until recently, it was believed that only one matched solution – equilibrium solution where the beam transverse radius oscillates with the same periodicity of the focusing field – is present for a given set of beam and focusing parameters and that this solution becomes unstable as the focusing field intensity is raised above a certain threshold [1, 2]. The threshold corresponds to a vacuum-phase advance of 90 degrees. Recently, however, it was shown that new regions of stability that lead to much tighter beam confinement are present for vacuum-phase advances well above 90 degrees [3, 4]. In fact, the scenario as the focusing field increases is the appearance of successive regions of stability which are interrupted by gaps where either the matched solutions are unstable or simply do not exist. The dynamical mechanism responsible for the onset of the gaps is analyzed in Ref. [5].

In this paper, we perform a detailed investigation of beam envelope stability as a function of the relevant parameters of the system, such as beam intensity and focusing field profile.

THE MODEL

In the paraxial approximation the envelope equation that dictates the envelope evolution of a particle beam propagat-

ing with average axial velocity $\beta_b c \hat{e}_z$ through a periodic solenoidal focusing magnetic field is given, in its dimensionless form, by

$$\frac{d^2 r_b}{ds^2} + \kappa_z(s) r_b - \frac{K}{r_b} - \frac{1}{r_b^3} = 0. \quad (1)$$

In Eq. (1), $s = z/S = \beta_b ct/S$ is the dimensionless coordinate along the beam axis, $r_b(s) = r_{b, \text{dimensional}} / (S\epsilon)^{1/2}$ is the normalized beam envelope radius and $K = 2q^2 N_b S / \epsilon \gamma_b^3 \beta_b^2 m c^2$ is the normalized perveance of the beam where c is the speed of light in *vacuo*, S is the periodicity length of the magnetic focusing field, ϵ is the unnormalized emittance of the beam, N_b is the number of particles per unit axial length, and q , m and $\gamma_b = (1 - \beta_b^2)^{-1/2}$ are, respectively, the charge, mass and relativistic factor of the beam particles. The focusing field is characterized by the normalized focusing strength parameter $\kappa_z(s+1) = \kappa_z(s)$ related to the magnetic field by $\kappa_z(s) = q^2 B_z^2(s) S^2 / 4 \gamma_b^2 \beta_b^2 m^2 c^4$.

In order to investigate the role of the focusing field profile on beam transport, we consider a focusing field parameter of the form

$$\kappa_z(s) = \sigma_0^2 \left[\frac{1 + \cos \theta(s)}{N} \right], \quad (2)$$

with the phase function given by

$$\theta(s) = \pi \left\{ \frac{\tan^{-1} [\Delta(\bar{s} + \eta/2)] + \tan^{-1} [\Delta(\bar{s} - \eta/2)]}{\tan^{-1} [\Delta(1 + \eta)/2] + \tan^{-1} [\Delta(1 - \eta)/2]} \right\}, \quad (3)$$

where $\sigma_0 = [\int_0^1 \kappa_z(s) ds]^{1/2}$ is the vacuum phase advance in the smooth-beam approximation, which is proportional to the rms focusing field, $N = 1 + \int_0^1 \cos \theta(s) ds$ is used to normalize the function, $\bar{s} = \text{mod}(s + 1/2, 1) - 1/2$ is periodic in s and lies always in the range $-1/2 \leq \bar{s} \leq 1/2$, $\Delta > 0$ is the focusing field profile parameter, and $0 < \eta \leq 1$ is the filling factor. The function $\kappa(s)$ in Eq. (2) is constructed such that for small Δ it resembles a smooth sinusoidal function of period 1 in s , while for increasing Δ it starts developing sharper edges, eventually turning into a discontinuous periodic step function of filling factor η for infinite Δ . In fact, in the limit $\Delta \ll 1$ the arguments of the inverse tangent functions in Eq. (3) are small, allowing the approximation $\tan^{-1}(x) = x$ which leads to $\theta(s) = 2\pi\bar{s}$ and to the sinusoidal focusing field profile $\kappa_z(s) = \sigma_0^2 [1 + \cos(2\pi s)]$, studied in Refs. [3, 4]. Note that in this limit, η plays no role in focusing field profile. On the other hand, when $\Delta \gg 1$ the inverse

* Work supported by CNPq and CAPES, Brazil

[†] pakter@ifufrgs.br. The author would like to thank the partial support from the PAC03 Organizing Committee.

tangent functions present an abrupt change from $-\pi/2$ to $\pi/2$ as their arguments change sign, allowing the approximation $\tan^{-1}(x) = (\pi/2)\text{sign}(x)$ which leads to a discontinuous phase function with $\theta(\bar{s} < -\eta/2) = -\pi$, $\theta(-\eta/2 < \bar{s} < \eta/2) = 0$ and $\theta(\bar{s} > \eta/2) = \pi$, and to a step-function focusing field lattice with filling factor η . Note that for all Δ , the denominator in Eq. (3) guarantees that the phase function completes a full cycle from $\theta = -\pi$ to $\theta = \pi$ as \bar{s} goes from $-1/2$ to $1/2$, and consequently $\kappa_z(s)$ is always continuous at the lattice boundaries.

BEAM STABILITY ANALYSIS

In this section, we analyse the stability of beams propagating through the focusing field given in Eq. (2), as the relevant parameters of the system are varied, paying special attention to the new regions of stability. To perform the analysis we use a Newton-Raphson method to search for and verify the stability of envelope matched solutions obtained from Eq. (1). The stability is determined with the aid of the stability index α defined as $\alpha = \cos(k_{fix})$, where k_{fix} is the wavenumber of small linear oscillations around the periodic trajectory, obtained with the Newton-Raphson method. For stable orbits where k_{fix} is a real number, $|\alpha| < 1$; if α crosses the lower boundary $\alpha = -1$ it undergoes a period doubling bifurcation losing stability, and if the orbit crosses the upper boundary $\alpha = +1$ the orbit undergoes an inverse tangent bifurcation with a previous unstable fixed point.

Generally, the bifurcation scenario for the matched solutions as one increases the vacuum phase advance is as follows; detailed description is found in Refs. [3, 4]. Stable matched solutions are born in the phase space with $\alpha = +1$. For the original matched solution, this occurs exactly at $\sigma_0 = 0^\circ$, whereas for the new regions of stability it occurs at different $\sigma_0 > 180^\circ$. As the vacuum phase advance is increased, the respective α moves towards $\alpha = -1$. When $\alpha = -1$ is reached, the matched solution suffers a period doubling bifurcation and becomes unstable. We define as a region of stability, the range of σ_0 that goes from the onset of the corresponding stable matched solution with $\alpha = +1$ until it bifurcates with $\alpha = -1$. As a matter of fact, before eventually disappearing permanently from the phase space, the matched solutions cross back the $\alpha = -1$ line and recover their stability as σ_0 is further increased. However, as shown in Ref. [4] the matched solution is not useful for beam confinement after its re-stabilization because beam emittance growth was observed in self-consistent numerical simulations for these parameter regions.

To determine the role of a particular parameter on the beam transport stability we construct parametric space plots of σ_0 as a function of the parameter displaying the locations of the different regions of stability. The plots are obtained by using the Newton-Raphson method to numerically determine the curves in the parameter space for which a bifurcation with $\alpha = \pm 1$ occurs.

Dependence on the Beam Intensity

In Fig. 1 we analyze the dependence of the beam stability on the beam intensity by plotting the parameter space plot of $K \times \sigma_0$, for a sinusoidal field with $\Delta \ll 1$. The white regions in the figure correspond to parameter values for which at least one stable matched solution with $|\alpha| < 1$ exists. The gray regions correspond to the existence of a single matched solution with $\alpha < -1$ which is unstable because a period doubling bifurcation has taken place. The black regions correspond to the gaps where no matched solution is found.

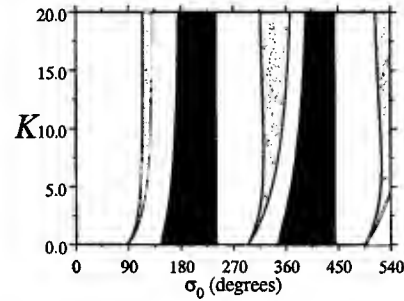


Figure 1: $K \times \sigma_0$ parameter space plot: stable regions are the white regions

Figure 1 shows that the perveance plays a tricky role on the characteristics of the new regions of stability. In particular, the size of the instability gap caused by the period doubling bifurcation (gray regions) tends to increase with increasing K . On the other hand, the size of the gap where matched solutions are absent (black regions) tends to decrease as K and/or n increases. Therefore, there is a particular values of K (around $K = 7.5$ for the specific sinusoidal focusing field used in Fig. 1) for which the new regions of stability are wider in the parameter space. Another interesting feature is that the onset of the new stable matched solutions, which are the bifurcations leading to the lines that limit the black regions to the right, is essentially independent of the perveance K . This can be understood based on the fact that the new matched solutions enter the phase-space as solutions that oscillate from $r_b = 0$ to $r_b \rightarrow \infty$ [4]. Because in this case the particles of the beam spend most of the time far away from each other, space charge effects introduced by K are unimportant.

Dependence on the Focusing Field Profile

Recalling from the model, Δ determines the overall shape of the focusing field: as Δ is increased from small values $\Delta \ll 1$, the focusing field profile continuously goes from a smooth sinusoidal function to a sharp-edged step-function as $\Delta \rightarrow \infty$. In Fig. 2, it is shown the parameter space plot of $\sigma_0 \times \Delta$, for a *small* filling factor $\eta = 0.2$, and a beam intensity corresponding to $K = 5.0$. The

black regions correspond to stable regions; the region below $\sigma_0 \approx 100^\circ$ is the original region of stability (ORS) and the other one is the second region of stability (SRS). Here, we consider as stable regions only those preceeding the respective period doublings. Higher order new regions of stability were also investigated and the results are qualitatively the same as for the SRS.

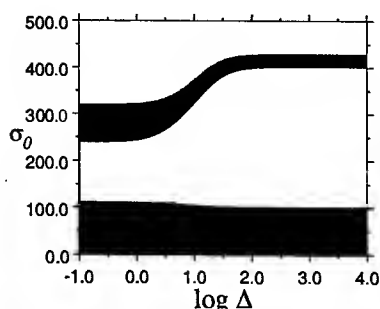


Figure 2: $\sigma_0 \times \Delta$ parameter space plot: stable regions are the black regions.

It is seen in Fig. 2 that the focusing field profile plays an important role in the beam stability and as Δ increases two effects are clearly seen regarding the SRS. (i) First, there is an increase in the vacuum phase advance necessary to reach the SRS. Since σ_0 is proportional to the rms focusing field, this reveals that the peak magnetic field has to be raised considerably as the profile becomes more localized with *small* η not only because its average has to increase, but also because the spatial region where the field is effectively applied is smaller. In the case depicted in Fig. 2(b), for instance, taking into account that σ_0 for the SRS increases roughly 50% as Δ goes from 10^{-1} to 10^4 , the increase in the peak magnetic field has to be about 3.75 times. However, if one now looks at the minimum value attained by the matched beam envelope as it oscillates in the focusing lattice one notes that it is noticeably reduced as the peak magnetic field for the SRS increases with Δ . (ii) Second, the SRS becomes much narrower as Δ is increased. The range in vacuum phase advance for which the SRS exists goes from 80° to 25° as Δ is increased. Not only this reveals that a more accurate field intensity tuning is necessary as the focusing channel becomes more localized for $\eta = 0.2$, but it also suggests that more nonlinear resonances may appear in the phase space because the variation of α with σ_0 , and hence the range of orbital frequencies in the phase space, is larger. The resonances may affect the beam transport nonlinear stability.

Other values of the filling factor η were also investigated and the overall conclusion is that $\eta = 0.5$ may be seen as a midpoint in the sense that at this value the new regions of stability are not greatly affected by the variations in the focusing field profile parameter. This is probably connected to the fact that exactly at $\eta = 0.5$ the sinusoidal ($\Delta \rightarrow 0$)

and the step-function ($\Delta \rightarrow \infty$) limits of the focusing profile present the same norm $N = 1 + \int_0^1 \cos \theta(s) ds = 1.0$, such that the peak magnetic field is the same in both cases. For $\eta > 0.5$ it was found that the new regions tend to increase in size as Δ is increased from 0, getting closer to the ORS. In fact, one may eventually find parameter sets for which two stable matched solutions coexist in the phase space. On the other hand, as shown in detail for $\eta = 0.2$, when $\eta < 0.5$ the new regions become narrower and occur at higher vacuum phase advances as Δ is increased. In particular, for the thin lens regime where $\eta \rightarrow 0$, $\Delta \rightarrow \infty$, and $\kappa_z(s)$ tends to a series of Dirac-delta functions, the onset of the new regions of stability only occur at $\sigma_0 \rightarrow \infty$, which in practice means that these regions are absent. However, this limit is not realistic due to the restrictions imposed by Maxwell's equations on the focusing field profile.

CONCLUSIONS

The new regions of stability found for vacuum phase advance well above 90 degrees are sensitive to variations in the relevant parameters of the system, specially to variations in the shape of the focusing field profile. However, they are always present and are robust against parameter changes.

REFERENCES

- [1] I. Hofmann, L. J. Laslett, L. Smith, and I. Haber, Part. Accel., **13**, 145 (1983).
- [2] C. Chen and R. C. Davidson, Phys. Rev. Lett., **72**, 2195 (1994); Phys. Rev. E., **49**, 5679 (1994).
- [3] R. Pakter and F.B. Rizzato, Phys. Rev. Lett., **87**, 044801 (2001).
- [4] R. Pakter and F.B. Rizzato, Phys. Rev. E, **65**, 056503 (2002).
- [5] F.B. Rizzato and R. Pakter, Phys. Rev. Lett., **89**, 184102 (2002).

COUPLING IMPEDANCES FOR CORRUGATED BEAM PIPES FROM IMPEDANCE BOUNDARY CONDITIONS

S. Petracca, Th. Demma, University of Sannio at Benevento, Italy and INFN

Abstract

An equivalent wall impedance describing the electromagnetic boundary conditions at corrugated pipe walls is introduced in the context of a general perturbative approach for computing the longitudinal and transverse beam coupling impedances in complex heterogeneous pipes.

INTRODUCTION

Coupling impedances are a powerful tool for studying the interaction between a charged particle beam and the surrounding chamber. Unfortunately, coupling impedances can be usually computed only by numerical methods leading to computationally intensive design optimization procedures.

The combined occurrence of complex geometrical features and/or the use of several different wall materials, make the electromagnetic boundary value problem analytically almost untractable. As a matter of fact, only a few analytic solutions for coupling impedances are available, for simple cases where, e.g., the Laplacian is separable in the pipe cross-section coordinates, and the boundary conditions are very simple too (e.g., perfect conductors).

In this paper we estimate the longitudinal and transverse coupling impedances for a pipe with corrugated walls using the general framework presented in [1] and summarized below, using an impedance boundary condition (b.c.) of the Leontovich type, to account for the corrugations. An application to a candidate LHC geometry is included.

COUPLING IMPEDANCES IN COMPLEX PIPES

According to [1] the longitudinal and transverse beam coupling impedances $Z_{0,\parallel}(\omega)$ and $\bar{Z}_{0,\perp}(\omega)$ of a *simple, unperturbed* pipe (e.g., circular, perfectly conducting) assumed known, can be related to those $Z_{\parallel}(\omega)$, $\bar{Z}_{\perp}(\omega)$ of another pipe differing from the former by some *perturbation* in the boundary geometry and/or constitutive properties, as follows (beam at $\vec{r} = 0$)¹:

$$Z_{\parallel}(\omega) - Z_{0,\parallel}(\omega) = \frac{\epsilon_0}{\beta_0 c Q^2 k} \left\{ Y_0 \oint_{\partial S} Z_{wall} E_{0n}^{(irr)*}(\vec{r}) \right. \\ \left. \left[\beta_0 E_n^{(irr)}(\vec{r}) + \beta_0^{-1} E_n^{(sol)}(\vec{r}) \right] d\ell - \oint_{\partial S} E_{0z}^*(\vec{r}) E_n^{(irr)}(\vec{r}) d\ell \right\}, \quad (1)$$

¹The beam impedances are obviously independent of the total beam charge, as the field in (1) is proportional to Q .

$$\bar{Z}_{\perp}(\omega) - \bar{Z}_{0,\perp}(\omega) = \frac{\epsilon_0}{\beta_0 c Q^2 k} \left\{ Y_0 \oint_{\partial S} Z_{wall} \nabla_{\vec{r}_0} E_{0n}^{(irr)*}(\vec{r}, \vec{r}_0) \otimes \right. \\ \left. \otimes \nabla_{\vec{r}_1} \left[\beta_0 E_n^{(irr)}(\vec{r}, \vec{r}_1) + \beta_0^{-1} E_n^{(sol)}(\vec{r}, \vec{r}_1) \right] d\ell + \right. \\ \left. - \oint_{\partial S} \nabla_{\vec{r}_0} E_{0z}^*(\vec{r}, \vec{r}_0) \otimes \nabla_{\vec{r}_1} E_n^{(irr)}(\vec{r}, \vec{r}_1) d\ell \right\}_{\vec{r}_1 = \vec{r}_0 = 0}, \quad (2)$$

where $c = (\epsilon_0 \mu_0)^{-1/2}$ is the speed of light in vacuum, $Y_0 = (\epsilon_0 / \mu_0)^{1/2}$ is the vacuum characteristic admittance, ϵ_0 and μ_0 being the vacuum permittivity and permeability, β_0 is the relativistic factor, Q is the total beam charge, $\vec{E}^{(sol)}$, $\vec{E}^{(irr)}$ are the solenoidal and irrotational parts of the electric field, a suffix "0" identifies the *unperturbed* quantities, and an impedance (Leontovich) boundary condition is assumed to hold at the (perturbed) pipe wall ∂S :

$$\hat{u}_n \times (\hat{u}_n \times \vec{E} - Z_{wall} \vec{H})_{\partial S} = 0, \quad (3)$$

where Z_{wall} is the pipe-wall complex characteristic impedance and \hat{u}_n is the unit vector normal to ∂S .

The first integral term on the r.h.s of (1) and (2) is nonzero if and only if Z_{wall} is not identically zero on ∂S , and accounts for the effect of the (complex) wall conductivity. The second integral term on the r.h.s. of (1) and (2), on the other hand, accounts for the effect of the geometrical perturbation of the boundary, and is non-zero if and only if the *unperturbed* axial field component E_{0z} is not identically zero on ∂S . Letting \vec{E}_0 in place of \vec{E} in (1) and (2), one obtains a first order perturbative formula for the beam coupling impedances in the *perturbed* pipe.

CORRUGATED BEAM PIPES

Let

$$\vec{r} = \vec{r}_b(\theta) = \vec{R}_b(\theta) + \delta \vec{R}(\theta), \quad (4)$$

the (transverse) position of a point on the (perturbed) pipe boundary ∂S , where $\vec{R}_b(\theta)$ defines the unperturbed boundary ∂S_0 , $\delta \vec{R}(\theta)$ describes the z -independent roughness, and θ is the polar angle. To first order in the corrugations,

$$E_{0z}^*(\vec{r}_b) \sim E_{0z}^*(\vec{R}_b) + \nabla E_{0z}^*|_{\vec{R}_b} \cdot \delta \vec{R}. \quad (5)$$

The first term in (5) is obviously zero (the unperturbed boundary is by assumption a perfect conductor). The unperturbed longitudinal field is related to the potential Φ_0 ,

$$E_{0z}^* = -jk(1 - \beta_0^2)\Phi_0^*, \quad (6)$$

whereby

$$\vec{E}_0^* = -\nabla\Phi_0^*, \quad (7)$$

so that (5) becomes

$$E_{0z}^*(\vec{r}_b) \sim jk(1 - \beta_0^2)E_{0n}^*(\vec{R}_b)\hat{u}_{n0}(\theta) \cdot \delta\vec{R}. \quad (8)$$

since the tangential component of \vec{E}_0 at the unperturbed boundary (perfect conductor) is zero.

Accordingly, the integral in (1) which accounts for the effects of the geometrical perturbation of the pipe boundary can be written, to first order:

$$\parallel = -jk(1 - \beta_0^2) \oint_{\delta S_0} \hat{u}_n(\ell) \cdot \delta\vec{R}(\ell) |E_{0n}^*(\ell)|^2 d\ell \quad (9)$$

where ℓ is a curvilinear coordinate on δS_0 .

Similarly, to first order in the corrugation term $\delta\vec{R}$,

$$\begin{aligned} & \nabla_{\vec{r}_0} E_{0z}^*(\vec{r}_b, \vec{r}_0) \otimes \nabla_{\vec{r}_1} E_{0n}(\vec{r}_b, \vec{r}_1) \\ & \approx jk(1 - \beta_0^2) \delta\vec{R} \cdot \hat{u}_{n0}(\theta) \\ & \cdot \left[\nabla_{\vec{r}_0} E_{0n}^*(\vec{R}_b, \vec{r}_0) \otimes \nabla_{\vec{r}_1} E_{0n}(\vec{R}_b, \vec{r}_1) \right]. \end{aligned} \quad (10)$$

Accordingly, the integral in (2) which accounts for the effects of the geometrical perturbation of the pipe boundary can be written, to first order:

$$\begin{aligned} \perp & = -jk(1 - \beta_0^2) \oint_{\delta S_0} \hat{u}_n(\ell) \cdot \delta\vec{R}(\ell) \\ & \cdot \{ \nabla_{\vec{r}_0} E_{0n}^*(\ell, \vec{r}_0) \otimes \nabla_{\vec{r}_1} E_{0n}(\ell, \vec{r}_1) \}_{\vec{r}_1=\vec{r}_0=0} d\ell \end{aligned} \quad (11)$$

Comparison of (9), (11) to (1) and (2) shows that the roughness $\delta\vec{R}(\theta)$ is "equivalent" to a non-uniform, purely reactive impedance loading

$$Z_{wall}^{(equiv.)} = -jk(1 - j\beta_0^2)Z_0\hat{u}_{n0}(\theta) \cdot \delta\vec{R}(\theta), \quad (12)$$

laid down on the unperturbed pipe wall. It is also seen that, for the special case where $\delta\vec{R}(\theta)$, is a random process, its statistical moments are simply related to those of the equivalent wall-impedance (12). These findings are more or less obviously related to the general formalism developed in [3] for describing (weakly) irregular surfaces in terms of impedance boundary conditions.

CORRUGATED CIRCULAR PIPE

As a simplest example, we refer to a corrugated perfectly conducting circular pipe. The unperturbed geometry is a smooth perfectly conducting pipe of radius R . The unperturbed field produced at \vec{r} by a beam at \vec{r}_0 is ²

$$\vec{E}_0(\vec{r}, \vec{r}_0) = \frac{Q}{2\epsilon_0} \left\{ \frac{\vec{r} - \vec{r}_0}{|\vec{r} - \vec{r}_0|^2} - \frac{\vec{r} - \vec{r}_0(R/r_0)^2}{|\vec{r} - \vec{r}_0(R/r_0)^2|^2} \right\}, \quad (13)$$

²The field (13) is the vacuum field produced by beam at \vec{r}_0 , and its image at $\vec{r}_0(R/r_0)^2$.

From (13) one readily obtains

$$\vec{E}_0(\vec{r}) = \frac{Q}{2\epsilon_0} \frac{\vec{r}}{|\vec{r}|^2} \quad (14)$$

and:

$$\lim_{\vec{r}_0 \rightarrow 0} \nabla_{\vec{r}_0} \vec{E}_0(\vec{r}, \vec{r}_0) = \lim_{\vec{r}_1 \rightarrow 0} \nabla_{\vec{r}_1} \vec{E}_0(\vec{r}, \vec{r}_1) = \frac{Q}{\epsilon_0} \frac{\vec{r}}{r^3}. \quad (15)$$

Now consider the perturbed case of a circular pipe with uniform wall impedance Z_{wall} . Using eq.s (1) and (2) with $\vec{E} = \vec{E}_0$ together with (14) and (15), one readily obtains

$$Z_{\parallel} = \frac{Z_{wall}}{2R}, \quad \bar{Z}_{\perp} = \frac{Z_{wall}}{k_0 R^3} (\hat{u}_x \hat{u}_x + \hat{u}_y \hat{u}_y), \quad (16)$$

in agreement with the known exact result [2]. One is therefore led to guess that eq.s (9), (11) should be likewise accurate for computing the coupling impedances contributed by corrugations. Hence, for a perfectly conducting pipe

$$Z_{\parallel} = \frac{\langle Z_{wall}^{(equiv.)} \rangle}{2R}, \quad \bar{Z}_{\perp} = \frac{\langle Z_{wall}^{(equiv.)} \rangle}{k_0 R^3} (\hat{u}_x \hat{u}_x + \hat{u}_y \hat{u}_y), \quad (17)$$

where

$$\langle Z_{wall}^{(equiv.)} \rangle = -jk(1 - \beta^2)Z_0 \frac{\oint_{\delta S_0} \hat{r} \cdot \delta\vec{R}(\ell) d\ell}{2R} \quad (18)$$

is the circumferential average of (12). It is seen that suitable (z -independent) corrugations can be used to compensate the remaining reactive terms in the beam coupling impedance at a specific frequency.

LHC IMPEDANCE BUDGET

The candidate LHC geometry includes two corrugated sections as shown in Fig.1 below. The corrugations con-

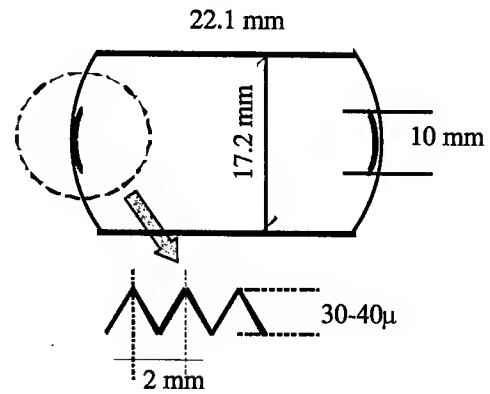


Figure 1: A simplified candidate LHC geometry.

tributions to the (reactive) impedance budget can be easily computed using (13) for the unperturbed field, with $R \approx 14$ mm. Assuming $\beta \approx 0.987$, it is found from (18) and Fig.1 that $\langle Z_{wall}^{(equiv.)} \rangle \approx -1.467 \cdot 10^{-8}$ ohm at the beam circulation frequency (≈ 11 KHz).

REFERENCES

- [1] S. Petracca, *Particle Accel.*, **50**, 211, 1995.
- [2] A.W. Chao, *Physics of Collective Beam Instabilities in High Energy Accelerators*, J. Wiley & Sons, 1993.
- [3] T.B.A. Senior, *Appl. Sci. Res.* **B8**; 437, 1960.

THE GAUSSIAN APPROXIMATION FOR A PURELY INDUCTIVE WAKE FUNCTION

S. Petracca, Th. Demma, University of Sannio, Benevento, Italy and INFN,
K. Hirata, Sokendai, The Graduate University for Advanced Studies, Hayama, Japan

Abstract

The equilibrium bunch length in electron storage rings with a purely inductive localized wake function has been studied, assuming the Gaussian approximation of the distribution function in phase space. The localized wake describes more general cases, even uniformly distributed wakes, described by the Haissinski equation. The comparison of our results with those obtained from Haissinski equation shows good agreement and helps understanding the validity of the Gaussian approximation.

INTRODUCTION

The wake force describes the electromagnetic interaction between particles and environment and affects the particles distribution in a bunch. In the conventional analytic approach one assumes that the source of the wake force is uniformly distributed along the ring, and the equilibrium bunch distribution at low current is a solution of the Haissinski equation, the so-called Potential Well Distortion (PWD) equation. A linear stability analysis around this static solution gives the threshold for turbulent bunch lengthening. Obviously this method tells us very little about the behavior of the unstable solutions. On the other hand it is more realistic for large machines to consider the many sources of wake fields along the ring as localized objects, as usually assumed in the Multi-Particle Tracking (MPT) codes.

In a previous paper [1], the authors studied an analytical model which incorporates the time dependence of the wake force, assuming that if the initial distribution function in synchrotron phase space is Gaussian, it can still be approximated by a Gaussian after the effect of the wake force, represented as a 'kick'. The distribution function can be accordingly always represented by its only first and second order moments, describing the beam envelope in synchrotron phase space. The evolution of these moments from turn to turn can be obtained by applying a non linear mapping at each turn. The equilibrium bunch length can have stable solutions with period-one fixed points as well as multistable states or a cusp-catastrophe behavior, depending on the parameters values. The results obtained in [1] show a good agreement with those obtained from MPT.

The localized wake can be extended to more general cases, even to uniformly distributed wakes, described by the Haissinski equation. To do so one should introduce the superperiodicity N_s and let it grow to infinity.

In this paper we study the validity of the Gaussian ap-

proximation with respect to the existence of the equilibrium longitudinal distribution of electrons in circular accelerators in the case of a purely inductive localized wake function.

THE MOMENT MAPPING

The longitudinal beam dynamics in electron storage rings can be described by the stochastic equations of motion for a single particle (Langevin equations). Introducing the canonical variables:

$$x_1 = \frac{\text{longitudinal displacement}}{\text{natural bunch length}},$$

$$x_2 = \frac{\text{relative energy spread}}{\text{natural energy spread}}.$$

and integrating the Langevin equations over one turn, we obtain the following stochastic mapping:

$$\begin{pmatrix} x_1 \\ x_2 \end{pmatrix}' = U \begin{pmatrix} x_1 \\ \Lambda x_2 + \hat{r} \sqrt{1 - \Lambda^2} - \phi(x_1) \end{pmatrix},$$

where $\vec{X}' = (x_1', x_2')$ is $\vec{X} = (x_1, x_2)$ after one turn. Here U is the rotation matrix:

$$U = \begin{pmatrix} \cos \mu & \sin \mu \\ -\sin \mu & \cos \mu \end{pmatrix}, \quad (1)$$

$\mu = 2\pi\nu_s$, ν_s being the synchrotron tune, $\Lambda = \exp(-2/T)$, T being the synchrotron damping time measured in units of the revolution period, \hat{r} is a Gaussian random variable with $\langle \hat{r} \rangle = 0$ and $\langle \hat{r}^2 \rangle = 1$. The wake force $\phi(x_1)$ is represented by:

$$\phi(x_1) = \frac{Q_{tot}}{\sigma_0 E_0} \int_0^\infty \rho(x - u) W(u) du. \quad (2)$$

where E_0 is the nominal beam energy, σ_0 is the nominal relative energy spread ($\sigma_0 E_0$ is the natural energy spread), $W(x)$ is the wake potential and $\rho(x)$ is the charge density normalized to one. Note that synchrotron oscillations have been linearized, and radiation is localized at one point of the ring [3]. The above stochastic mapping is equivalent to an infinite hierarchy of deterministic mappings in the following statistical quantities: $\bar{x}_i = \langle x_i \rangle$, $\sigma_{ij} = \langle (x_i - \bar{x}_i)(x_j - \bar{x}_j) \rangle$, and so on, which are the moments of the distribution function $\psi(\vec{x})$, $\langle * \rangle$ indicating an average over all particles. Our main assumption

is that the distribution function in phase space is always a Gaussian, even in the presence of a wake force:

$$\psi(x_1, x_2) = \frac{\exp[\frac{1}{2} \sum_{i,j} \sigma_{i,j}^{-1} (x_i - \bar{x}_i)(x_j - \bar{x}_j)]}{2\pi \sqrt{d} \sigma} \quad (3)$$

We consider a purely inductive wake function

$$W(x) = \sigma'(x) \quad (4)$$

and split the mapping for the second order moments into three parts, representing the effect of radiation, wake-force and synchrotron oscillation, as it follows:

radiation:

$$\begin{aligned} \sigma'_{11} &= \sigma_{11} \\ \sigma'_{12} &= \Lambda \sigma_{12} \\ \sigma'_{22} &= \Lambda^2 \sigma_{22} + (1 - \Lambda^2), \end{aligned} \quad (5)$$

wake force:

$$\begin{aligned} \sigma'_{11} &= \sigma_{11} \\ \sigma'_{12} &= \sigma_{12} + \frac{\sigma_{12}}{4\sqrt{\pi\sigma_{11}}} \\ \sigma'_{22} &= \sigma_{22} + \frac{\sigma_{12}^2}{2\sigma_{11}\sqrt{\pi\sigma_{11}}} + \frac{2}{6\sigma_{11}^2\pi\sqrt{3}}, \end{aligned} \quad (6)$$

synchrotron oscillation:

$$\sigma'_{ij} = \sum_{h,k=1}^2 U_{ih} \sigma_{hk} U_{kj}^t. \quad (7)$$

The stability of the system depends on the values of the synchrotron tune ν_s , the damping time (measured in number of turns) T_0 and the strength of the wake force. We studied a wide range of parameters values and found stable solution of period-one and period-two, multi-stable states and coexistence of solutions with different periodicity. These results are in very good agreement with those obtained in [4], but in addition to them we found fine structures of bifurcations and chaotic regions, depending on parameters values.

As an example we plot σ_{11} versus b in Fig. 1 (top) for $T = 30$ and $\nu_s = 0.085$ with $N_S = 1$. In the parameter space a chaotic region shows up and this behavior mainly depends on the b value but is almost independent on ν_s and T .

The localized wake can be extended to more general cases, even to uniformly distributed wakes, described by the Haissinski equation. To do so one should introduce the superperiodicity N_s and let it grow to infinity. This is done introducing in the mapping the following substitutions:

$$\nu_s \rightarrow \nu_s/N_s, \quad T_0 \rightarrow T_0 N_s, \quad b \rightarrow b/N_s \quad (8)$$

In Fig. 1 (bottom) we show $\sigma_{11}(b)$ with $N_S = 150$: the chaotic behavior exists also for $N_s \gg 1$. In Fig. 2 we plot σ_{11} versus b for different N_s and $b > 0$. As N_s increases the mapping curves become more closely spaced and $\sigma_{11}(b)$ converges to the solution of the PWD equation.

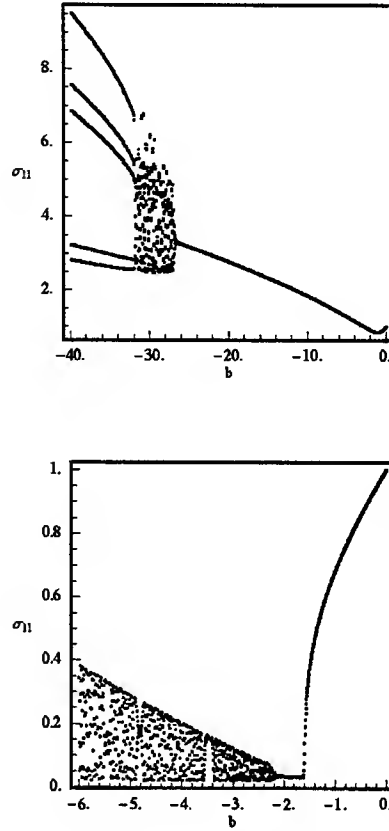


Figure 1: σ_{11} versus b for $T = 30$, $\nu_s = 0.085$ and with (top) $N_S = 1$ and (bottom) $N_S = 150$.

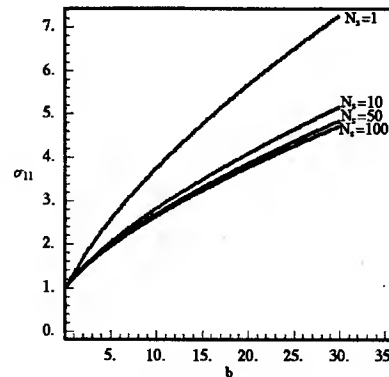


Figure 2: σ_{11} versus b for different N_s and $T = 30$, $\nu_s = 0.085$.

HAISSINSKI EQUATION

Introducing the variables $x = x_1, x_2$ the Haissinski equation can be written as [5]:

$$u(x) = \exp\left\{-\frac{x^2}{2} - \int_0^{+\infty} u(x-d) d\right\} \quad (9)$$

with the normalization condition

$$\int_{-\infty}^{+\infty} u(x) dx = 1 \quad (10)$$

and the following parameter definitions: $\sigma = 2\pi/T_0, \sigma = \sqrt{2} \sigma, \sigma = 2N \sigma_{RF}(0)/RF(0)^2$,

$$W(x) = \frac{e}{RF(0)} \int_0^x W(x-d) d \quad (11)$$

where N is the total bunch particles and σ the bunch length. Following [2] we rewrite equation (4) and (9) as

$$\log u(x) + u(x) = \log -\frac{x^2}{2}, \quad (12)$$

with $u = eNb/RF(0)\sigma^2$. For $u \geq 0$ the solution exists always, but not for $u \leq 0$, in particular for

$$-u \leq -\int_0^1 \frac{1-x}{\sqrt{x-\log x-1}} \sim -1.55061 \quad (13)$$

no value of u can satisfy the normalization condition (10). This fixes a critical value for our parameter b : if $b < b_{min}$ the system is unstable. Therefore the solution of Haissinski does not exist and the mapping gives a chaotic behavior for the second order moments. The value of b_{min} in the mapping depends on the values of the physical parameters. Increasing the superperiodicity accordingly to (8) the value of b_{min} shifts.

In order to compare the results obtained from the mapping with $N_s \gg 1$ and those from the Haissinski equation, we consider the longitudinal density

$$u(x) = \int_{-\infty}^{+\infty} \psi(x, d) d \quad (14)$$

and compare that one obtained from the mapping with $N_s = 150$ and the solution of the Haissinski equation (9). The comparison of the longitudinal densities for different b is shown in Fig 3. We found that approaching the threshold value b_{min} the comparison becomes more and more meaningless.

CONCLUSIONS

For $b > 0$ and superperiodicity $N_s \gg 1$, the mapping of the second order moments shows stable solutions of period 1 and period 2, accordingly to what happens with $N_s = 1$ [4]. For $b < 0$ and $N_s \gg 1$ the solution is stable only in a

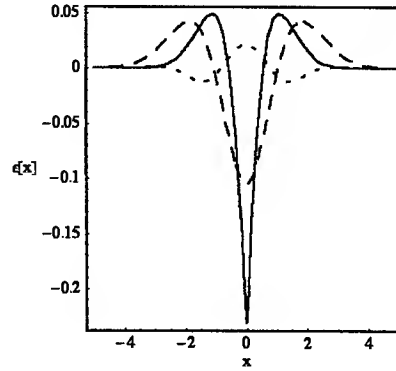


Figure 3: The comparison of the longitudinal densities $u_H(x) - u_m(x)$ for different b : $b = 0.4$ (dotted line), $b = -0.1$ (dashed line), $b = -0.416$ (solid line). $u_m(x)$ is computed from the mapping with $N_s = 150$ and $u_H(x)$ numerically from the PWD equation.

small interval of b values: below a critical value of b the solution of the mapping is unstable and furthermore a chaotic behavior appear; correspondingly the Haissinski equation does not have solution. This result is obtained by numerical iteration of the mapping and it should be discussed more carefully.

While the Haissinski equation can give stable solutions and predict only the nonexistence of stable solutions, the mapping (the Gaussian approximation) shows also what kind of instability (successive period-doubling bifurcations, coexistence of multi-periodic states or chaos) can occur in the parameter space for the bunch length and the energy spread.

As further application of the Gaussian approximation we plan to consider a regularized inductive wake function (which restores the existence of solutions of Haissinski equation below threshold) as recently discussed in [6].

Moreover we will compare our mapping results with those obtained from MPT, as done in [1] and [7], where in the simplest case of constant wake function a good agreement with MPT was found.

REFERENCES

- [1] K. Hirata, S. Petracca and F. Ruggiero, Phys. Rev. Lett., **66**, N. 13, 1991, 1693
- [2] A.W. Chao, *Physics of Collective Beam Instabilities in High Energy Accelerators*, J. Wiley & Sons, 1993.
- [3] K. Hirata and F. Ruggiero, Part. Acc., **28**, 1990, 137 and LEP Note 611 (1988).
- [4] K. Hirata, E.S. Kim, KEK Report 95-5 (1995).
- [5] S. Petracca, Part. Acc. 1993, vol. 42(1), p. 45-64.
- [6] Y. Shobuda, K. Hirata, KEK Preprint 99-37, July 1999, A.
- [7] K. Hirata, Part. Acc. 1987, vol. 22, p. 57-59.

ELECTROMAGNETIC FIELDS IN THE TOROIDAL REGION OF LHC-LIKE RINGS

S. Petracca, Th. Demma, University of Sannio, Benevento, Italy, and INFN

Abstract

We develop an analytic solution for the electromagnetic field in the toroidal region between the liner and the vacuum chamber in LHC-like rings.

INTRODUCTION

In a closed ring machine, the region between the external wall of the liner and the internal wall of the surrounding vacuum chamber is a toroidal resonator. In the steady regime, the particle bunches circulating in the liner set up stationary field in the toroidal region through the pumping holes. In this paper we outline the procedure for deriving a full analytic solution for the field in the toroidal region, for a multibunch beam. We consider the simplest case of a ring of (axial) length L with circular cross section liner and vacuum chamber. The (external) radius of the liner and the (internal) radius of the vacuum chamber will be denoted as a and b , respectively.

TEM FIELDS IN A TOROIDAL RESONATOR

Under usual conditions, the spectral content of the circulating bunch current is well below the lowest higher order TE and TM cutoff frequency of the coaxial region between the liner and the vacuum chamber. The time-harmonic TEM fields in the toroidal region can be accordingly written (phasor notation, $\exp(j\omega t)$ time factor dropped):

$$\begin{cases} \vec{E} = \frac{1}{\log(b/a)} \sum_{m=1}^{\infty} [V_m \vec{E}_m^{(e)} + \mathcal{V}_m \vec{E}_m^{(h)}], \\ \vec{H} = \frac{1}{\log(b/a)} \sum_{m=1}^{\infty} [I_m \vec{H}_m^{(e)} - \mathcal{I}_m \vec{H}_m^{(h)}], \end{cases} \quad (1)$$

where $k_0 = 2\pi/L$, and the (complex) constants V_m , \mathcal{V}_m , I_m and \mathcal{I}_m having the dimensions of voltages and currents, respectively, are to be determined. The basis "fields" in (1)

$$\begin{cases} \vec{E}_n^{(h)} = \frac{\vec{u}_r}{r} \cos(nk_0 z), \\ \vec{H}_n^{(h)} = -\frac{\vec{u}_\phi}{r} \sin(nk_0 z), \end{cases} \quad (2)$$

$$\begin{cases} \vec{E}_n^{(e)} = \frac{\vec{u}_r}{r} \sin(nk_0 z), \\ \vec{H}_n^{(e)} = \frac{\vec{u}_\phi}{r} \cos(nk_0 z), \end{cases} \quad (3)$$

are solutions of

$$\begin{cases} \nabla \times \vec{E}_n^{(e,h)} = nk_0 \vec{H}_n^{(e,h)}, \\ \nabla \times \vec{H}_n^{(e,h)} = nk_0 \vec{E}_n^{(e,h)}, \end{cases} \quad (4)$$

where $k_0 = \omega_0/c$, describe free-field oscillations with angular frequency $\omega = n\omega_0$, $\omega_0 = 2\pi/T$, $T = L/c$ being the light round-trip time. They satisfy the following conditions

$$\begin{cases} \vec{E}_n^{(e)} = 0, \\ \vec{H}_n^{(h)} = 0 \end{cases} \quad \text{at } z = 0, L, \quad (5)$$

and earn the following orthogonality properties:

$$\begin{cases} \int_V \vec{E}_n^{(i)} \cdot \vec{E}_m^{(i)} dV = \int_V \vec{H}_n^{(i)} \cdot \vec{H}_m^{(i)} dV = \\ = \iint_{\partial V} \vec{H}_n^{(i)} \cdot \vec{H}_m^{(i)} dS = 0, \quad m \neq n, \quad i = e, h \\ \int_V \vec{E}_n^{(e)} \cdot \vec{E}_m^{(h)} dV = \int_V \vec{H}_n^{(e)} \cdot \vec{H}_m^{(h)} dV = \\ = \iint_{\partial V} \vec{H}_n^{(e)} \cdot \vec{H}_m^{(h)} dS = 0, \quad \forall m, n. \end{cases} \quad (6)$$

Moreover, $\forall n$

$$\begin{cases} \int_V \vec{E}_n^{(i)} \cdot \vec{E}_n^{(i)} dV = \int_V \vec{H}_n^{(i)} \cdot \vec{H}_n^{(i)} dV = \pi L \log(b/a), \\ \iint_{\partial V} \vec{H}_n^{(i)} \cdot \vec{H}_n^{(i)} dS = \pi L \frac{a+b}{ab}, \end{cases} \quad (7)$$

where V and ∂V are the coax ring volume and its (complete) boundary, consisting of the outer surface of the liner ($r = a$) and inner surface of the vacuum chamber ($r = b$).

The unknown constants V_m , \mathcal{V}_m , I_m , \mathcal{I}_m can be determined in terms of the source terms, represented by Bethe equivalent electric and magnetic dipoles sitting at the holes connecting the beam pipe to the vacuum chamber, discussed in the next section. The fields (1) obey Maxwell equations:

$$\begin{cases} \nabla \times \vec{E} = -j\omega\mu_0 \vec{H} - j\omega\mu_0 \vec{M}, \\ \nabla \times \vec{H} = j\omega\epsilon_0 \vec{E} + j\omega \vec{P}, \end{cases} \quad (8)$$

We dot-multiply the first equation in (8) by $\vec{H}_n^{(i)}$, ($i = e, h$), use the obvious vector identity, $\nabla \cdot (\vec{a} \times \vec{b}) = \nabla \times \vec{a} \cdot \vec{b} - \vec{a} \cdot \nabla \times \vec{b}$, together with equations (4), and the Leontovich boundary conditions:

$$\hat{n} \times [\hat{n} \times \vec{E} - Z_{wall} \vec{H}]_{\partial V} = 0 \quad (9)$$

\hat{n} being the outward unit vector normal to ∂V , and $Z_{wall} = (\omega\mu_0/2)^{1/2}$ the appropriate wall impedance. Hence ($i = e, h$):

$$\begin{aligned} & \int_V (\nabla \times \vec{E}) \cdot \vec{H}_n^{(i)} dV = \\ & = \int_{\partial V} Z_{wall} \vec{H} \cdot \vec{H}_n^{(i)} dS + nk_0 \int_V \vec{E} \cdot \vec{E} dV = \\ & = -j\omega\mu_0 \int_V \vec{H} \cdot \vec{H}_n^{(i)} dV - j\omega\mu_0 \int_V \vec{M} \cdot \vec{H}_n^{(i)} dV, \end{aligned} \quad (10)$$

whence, using eq.s (1), and (6), (7),

$$\begin{cases} (-j)I_n - jnk_0 V_n = -i_n^{(e)}, \\ (-j)I_n + jnk_0 V_n = i_n^{(h)}, \end{cases} \quad (11)$$

where:

$$i_n^{(e,h)} = \frac{1}{\pi L} \int_V \vec{M} \cdot \vec{H}_n^{(e,h)} dV, \quad (12)$$

and:

$$= \omega/c, \quad = Z_{wall} \frac{a+b}{ab \log(b/a)} \quad (13)$$

are the TEM propagation and attenuation constant in the toroidal region.

Similarly, we dot-multiply the second equation in (8) by $\vec{E}_n^{(i)}$, and proceed as before to get ($i = e, h$):

$$\begin{aligned} & \int_V (\nabla \times \vec{H}) \cdot \vec{E}_n^{(i)} dV = nk_0 \int_V \vec{H}_n^{(i)} \cdot \vec{H} dV = \\ & = j\omega\epsilon_0 \int_V \vec{E} \cdot \vec{E}_n^{(i)} dV + j\omega \int_V \vec{P} \cdot \vec{E}_n^{(i)} dV, \end{aligned} \quad (14)$$

whence,

$$\begin{cases} -jnk_0 Z_0 I_n = V_n + i_n^{(e)}, \\ jnk_0 Z_0 I_n = V_n + i_n^{(h)}, \end{cases} \quad (15)$$

where:

$$i_n^{(e,h)} = \frac{Z_0 c}{\pi L} \int_V \vec{P} \cdot \vec{E}_n^{(e,h)} dV. \quad (16)$$

From (11) and (15) we finally get:

$$\begin{cases} I_n = -\frac{2i_n^{(e)} + jnk_0 V_n}{2-j - (nk_0)^2}, \\ V_n = \frac{jnk_0 Z_0 i_n^{(e)} - (2-j) i_n^{(e)}}{2-j - (nk_0)^2}, \\ I_n = -\frac{2i_n^{(h)} + jnk_0 V_n}{2-j - (nk_0)^2}, \\ V_n = \frac{jnk_0 Z_0 i_n^{(h)} - (2-j) i_n^{(h)}}{2-j - (nk_0)^2}. \end{cases} \quad (17)$$

THE HOLE COUPLING

In the frame of Bethe's approximation [1], the electromagnetic coupling between the beam field in the liner and the toroidal region through the pumping holes (assumed identical) can be described by the (spectral) source terms

$$\begin{aligned} \vec{P} &= \epsilon_0 \sum_p (\vec{r} - \vec{r}_p) \hat{u}_r \hat{u}_r \cdot \vec{E}_i \\ \vec{M} &= \sum_p (\vec{r} - \vec{r}_p) (\vec{I} - \hat{u}_r \hat{u}_r) \cdot \vec{H}_i, \end{aligned} \quad (18)$$

where ϵ and m are the hole electric and magnetic polarizabilities [1], \vec{E}_i, \vec{H}_i is the (spectral mate of) the beam field in the liner, discussed in the next section, and $\{\vec{r}_p\}$ are the holes positions. These are the source terms in (8), (12) and (16). Note that in view of the azimuthal invariance of the basis fields in (12) and (16), the azimuthal coordinates of the holes are irrelevant, and can be set to zero. Hence

$$\vec{r}_p = a\hat{u}_r + z_p\hat{u}_z \quad (19)$$

where, for regularly spaced holes $z_p = \Lambda$, Λ being the hole spacing.

BUNCHED BEAM FIELD IN LINER

The charge density of a b equispaced point-like bunches of equal charge circulating on axis along a ring-liner can be written:

$$(\vec{r}, t) = (r) (z - ct \bmod (L/b)). \quad (20)$$

The corresponding field can be written:

$$\vec{e}_i(\vec{r}, t) = \frac{b}{\pi\epsilon_0 L} \frac{\vec{u}_r}{r} \left\{ \frac{1}{2} + \sum_{m=1}^{\infty} e^{jmN_b(\omega_b t - k_b z)} \right\}, \quad (21)$$

where

$$T_b = \frac{L}{c}, \quad \omega_b = \frac{2\pi}{T_b}, \quad k_b = \frac{\omega_b}{c}, \quad (22)$$

are the bunch circulation time, (angular) frequency and wavenumber, and we used the Fourier representation of the periodic δ -function.

Real world bunches can be better described by a gaussian charge distribution, viz.:

$$\begin{aligned} (\vec{r}, t) &= (r) (z - ct \bmod (L/b)) * (z), \\ (z) &= (2\pi)^{-1/2} \sigma^{-1} e^{-z^2/2\sigma^2}, \end{aligned} \quad (23)$$

where $*$ denotes convolution, σ is the r.m.s. bunch-length, and we assume that $L/b \gg \sigma$. Hence¹

$$\begin{aligned} \vec{e}_i(\vec{r}, t) &= \frac{b}{\pi\epsilon_0 L} \frac{\vec{u}_r}{r} \cdot \left\{ \frac{1}{2} + \sum_{m=1}^{\infty} e^{jmN_b(\omega_b t - k_b z)} \right\}. \end{aligned} \quad (24)$$

¹Equation follows taking the $z \rightarrow k$ Fourier transform of eq. (23), using Borel theorem, and then switching back to the z -domain

where:

$$F(k) = \pi^{1/2} e^{-\sigma^2 k^2 / 2} \quad (25)$$

is the Fourier transform of the gaussian distribution.

This field is a superposition of time-harmonic forward (counterclockwise) propagating waves, at $\omega = mN_b\omega_b$, with complex (phasor) representation:

$$\vec{E}_{i,m} = \frac{F(mN_b k_b)}{1 + \delta_{m0}} \frac{N_b Q}{\pi \epsilon_0 L} \frac{\vec{u}_r}{r} e^{-jmN_b k_b z}, \quad (26)$$

δ_{hk} being the Kronecker function.

CONCLUSIONS

We outlined a general framework for computing the fields in the toroidal region between the liner and the vacuum chamber in ring machines. The main relevant quantities of interest (peak field amplitudes, parasitic losses) can be accordingly readily computed. Numerical results pertinent to LHC will be reported elsewhere. It can be anticipated that these are possibly more accurate than those obtained either for the case of an infinite straight structure [2], or from an impedance boundary condition at the liner's wall which takes consistently into account the presence of the hole-coupled co-axial vacuum chamber [3]. This work has been sponsored in part by INFN.

REFERENCES

- [1] R.E. Collin, *Field Theory of Guided Waves*, Wiley, 1983.
- [2] S. de Santis et al., *Phys. Rev.* **E56**, 5990, 1997.
- [3] S. Petracca, *Phys. Rev.* **E60**, 6030, 1999.

NON-COULOMB PERTURBATIONS INFLUENCE ON BEAM DYNAMICS IN EXTENDED ACCELERATING/FOCUSING CHANNELS

Boris Bondarev, Alexander Durkin

Moscow Radiotechnical Institute

113519, Russia, Moscow, Warshawskoe shosse 132, lidos@aha.ru

It is generally taken that the main source of particle losses in extended linac channel is the Coulomb field of space charge dominated beam. However there are the non-Coulomb effects concerned with external field perturbations (external perturbations) and their influence on beam dynamic is comparable with the action of space charge.

It is convenient to split external perturbations into two groups: constructive (regular) perturbations caused by distinction of a real structure from an ideal one and perturbations caused by random parameter deviations within given tolerances. In the last case only the probability that the beam size would be no more than given value can be found. In connection with strict requirements for channel transparent and also with the complex procedure for channel retuning and readjustment, the confidence level must be chosen sufficiently large.

The calculation of the accelerating/focusing channel always based on the specific mathematical model involving description of external accelerating and focusing forces.

In this model as a rule, the focusing field linear dependence on transverse coordinates and accelerating field axis distribution is used. The channel based on such models will be called ideal. Of course, there are no unprojected losses in the ideal channel.

Output beam parameters degradation including transverse size and emittance growths is caused by channel and beam parameter perturbations (not always small). The influence of perturbations upon the beam output parameters determines by quantity, which have come to be known as the channel sensitivity. The goals of beam dynamics investigations are:

- knowledge about channel sensitivity - each perturbing factor influences output beam parameters,
- perturbing factors compensation possibilities,
- redundant factor determination guaranteed the beam passing throughout the real channel without losses.

From strategy standpoint, the major goal of the investigation is determination of the generalized parameters whose numerical values permit to judge about channel sensitivity as well as about beam parameter degradation. The confidence level must be sufficient for intolerable beam loss estimation. The cardinal problem is to choose the channel with minimum sensitivity in order to minimize the beam losses during the process of accelerating.

Mathematical foundation and the main treatments are given in the works [1-6] as well as the tolerance estimation for various types of focusing and accelerating channel. Below we will investigate the parameters determining the sensitivity of long channel to external perturbations.

Let us consider as example motion of particles in focusing channel with random errors in focusing field gradients

$$x'' + \tilde{G}(z) \cdot x = 0$$

Let us consider $\tilde{G}(z)$ as $\tilde{G}(z) = G(z) \cdot (1 + \alpha(z))$, where $G(z)$ is non-perturbed field gradient, $\alpha(z)$ is function for perturbation description.

As is shown in above cited works we need to do transformation of variables $x, dx/dz$ to phase variables r, η . r^2 is quadric in $x, dx/dz$, describing the ellipses matched with the ideal periodical channel. η is an addition due to external perturbations. We obtain as a result the main equation in form

$$\begin{cases} r' = r \cdot \alpha \cdot G \cdot \rho^2 \cdot \sin^2(\mu z + \eta + \psi) \\ \eta' = \alpha \cdot G \cdot \rho^2 \cdot \cos^2(\mu z + \eta + \psi) \end{cases}$$

Here μ is phase advance, ρ is the envelope of beam with the emittance of unity in the ideal channel.

The right part of the second equation does not depend on r , so it can be solved separately. If $\eta(z)$ is solution of the second equation, then solution of the first equation has the following form

$$\frac{r(z)}{r_0} = \theta(z) = \exp\left(\int_0^z \alpha G \rho^2 \sin(\mu t + \eta + \psi) \cos(\mu t + \eta + \psi) dt\right) = \exp(F(z))$$

It can be seen from obtained relation that distribution of random value $\theta(z)$ is determined by distribution of random value $F(z)$.

If focusing channel contains N periods, then $F(z)$ can be presented as sum of statistical independent components adequate to corresponding periods L_k

$$F(N) = \sum_{k=1}^N F_k = \sum_{k=1}^N \int_{L_k} \alpha G \rho^2 \sin(\mu t + \eta + \psi) \cos(\mu t + \eta + \psi) dt$$

Using approximate solution of the second equation

$$\begin{aligned} \eta(N) &= \varphi_0 + \int_0^N \alpha G \rho^2 \cos^2(\mu t + \varphi_0 + \psi) dt = \\ \varphi_0 + \sum_{k=1}^N \eta_k &= \varphi_0 + \sum_{k=1}^N \int_{L_k} \alpha G \rho^2 \cos^2(\mu t + \varphi_0 + \psi) dt \end{aligned}$$

we obtain with an accuracy of α^3

$$F_k = \int_{L_k} \alpha G \rho^2 (0.5 \sin 2(\mu t + \varphi_0 + \psi) - \cos 2(\mu t + \varphi_0 + \psi) \cdot \sum_{i=1}^k \eta_i) dt$$

Suppose $\alpha(z)$ is piecewise constant function that is equal the relative error of field gradient inside any element of channel. In this case integral is calculated only along the part of period, containing perturbation. If σ^2 is mean square value of field gradient tolerance, then using statistical independence of errors for different focusing periods and averaged over oscillations we obtain relations for the mean value and dispersion for $F(N)$

$$M[F(N)] = D[F(N)] = \frac{\sigma^2}{8} \sum_{k=1}^N \langle G \rho^2 \rangle_k^2 = \frac{\sigma^2}{8} \sum_{k=1}^N S_k$$

As shown in [4] if σ^2 is mean square value of focusing field gradient relative error then the probability that effective emittance growth would be no more than x is determined by function $P(x) = 1 - e^{-(\ln x)^2 / \Delta^2}$, where

$$\Delta^2 = \frac{\sigma^2}{4} \sum_{k=1}^N S_k. \text{ If } \sigma^2 \text{ is error of axis transverse}$$

displacement then the probability that center of output beam displacement would be no more than x is determined by function $P(x) = 1 - e^{-x^2 / \Delta^2}$, where

$$\Delta^2 = \sigma^2 \sum_{k=1}^N S_k. \text{ We can give the definition of } S_k \text{ as a}$$

sensitivity of period numbered k . Then total sensitivity of channel will be sum of period sensitivities $S = \sum_{k=1}^N S_k$.

The regions of stability diagrams for RFQ and some types of quadrupole channels are shown in Fig. 1-4. In this regions the isolines of transverse oscillation frequency μ and sensitivity $S = \overline{Q \rho^2}^2$ are plotted. We use traditional coordinates: focusing

parameter $B = \frac{eU}{m_0 c^2} \kappa \left(\frac{\lambda}{a} \right)^2$ and defocusing parameter

$$A = \frac{\pi^2 e U \sigma}{4 W_s} |\sin \varphi_s| \text{ for RFQ diagram. For quadrupole}$$

channels we use focusing parameter $Q = \frac{e G L^2}{m_0 c \beta \gamma}$, where G

- focusing field gradient, L - length of focusing period, and defocusing parameter $A = \frac{\pi e E_m L^2}{m_0 c^2 (\beta \gamma)^2 \lambda} |\sin \varphi_s|$, where

E_m - accelerating wave amplitude, λ - RF field wave length. In figures 1-4 μ -isolines are corresponded to values (from bottom to top) $\mu = 0$, $\mu = \pi/3$, $\mu = \pi/2$, $\mu = 2\pi/3$, $\mu = \pi$.

As is seen from these diagrams even within the boundaries of operating region of stability diagram the channel sensitivity can be varied two times by value. So for choice and calculations parameters of long linac channel the reported results would be taken into account necessary.

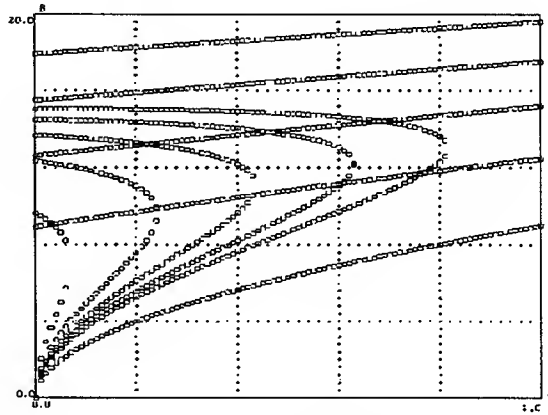


Fig.1. Sensitivity S of RFQ channel.
1 - 40, 2 - 50, 3 - 60, 4 - 70, 5 - 80 (from left to right)

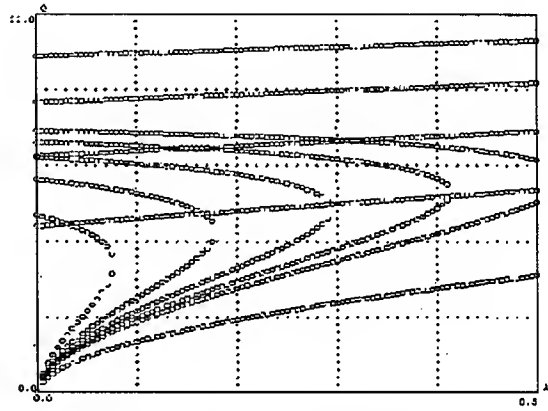


Fig.2. Sensitivity S of FODO channel.
1 - 30, 2 - 35, 3 - 40, 4 - 45, 5 - 60
(from left to right; Gap/Period = 0.5)

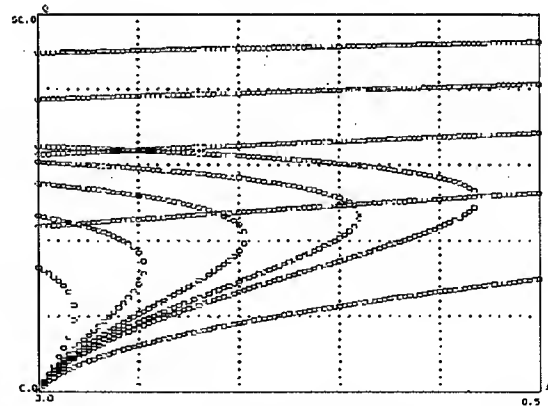


Fig.3. Sensitivity S of FDO channel.
1 - 70, 2 - 85, 3 - 100, 4 - 115, 5 - 130
(from left to right; Gap/Period = 0.8)

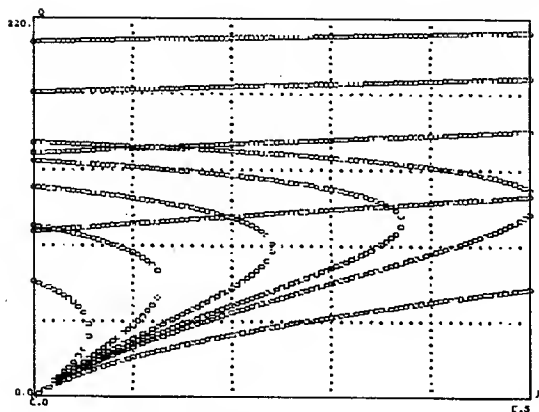


Fig.4. Sensitivity S of FDO channel.
1 - 100, 2 - 130, 3 - 160, 4 - 190, 5 - 220
(from left to right; Gap/Period = 0.9)

REFERENCES

- [1] B.I.Bondarev, A.P.Durkin, B.P.Murin, L.Yu.Soloviev. Random Perturbation of the Transverse Motion of Protons in a Linear Accelerator and Their Correction, Particle Accelerators, 1974, Vol.6, N 1, pp.27-40.
- [2] A.P.Durkin. The Investigation of Transverse Particles Motion in Linac by the Perturbation Theory Techniques, Dr. Ph. Theses, Russia, Moscow, 1978 (in Russian).
- [3] B.I.Bondarev, A.P.Durkin, L.Yu.Soloviev. Influence of Focusing Fields Errors on the Particles Motion in Linac. Journal of Technical Physics, 1979, v.49, No 8, p.1662-1672. (in Russian)
- [4] B.P.Murin, B.I.Bondarev, A.P.Durkin An Approach to the Design of a Robust Focusing Channel. *Proceedings of 1992 Linear Accelerator Conference*, v.2, pp.731-733. (1992, August 24-28, Ottawa, Ontario, Canada).
- [5] B.P.Murin, B.I. Bondarev, A.P.Durkin, L.G.Lomize, L.Yu.Soloviev. Some Aspects of Simultaneous Acceleration of Proton and H⁻ Beams in a Linac, Particle Accelerators, 1975, v.6, No 3, p.133-139.
- [6] B.I.Bondarev, A.P.Durkin, B.P.Murin. Effective Emittance Growth. Contract 9-XG3-5167H-1 between LANL and MRTI, Phase 1, Moscow 1993.

ACCELERATION AND SELF-FOCUSED PARTICLE BEAM DRIVERS *

Z. Parsa[†], BNL, Physics Department, 510 A, Upton, NY 11973, USA
V.Zadorozhny[‡], Institute of Cybernetics of NASU, Ukraine

Abstract

Here it is shown that the Vlasov equation is an adequate model in case of high-intensity charged-particle beams.

Several instances are analyzed when it is possible to construct an integral basis of the operator, associated with the dynamic system under study. This is the case, in particular, for the two-dimensional dynamic systems, just such systems describing the longitudinal motion of a perturbed system. For systems of more general structure we advance a method of reduction of the quasilinear Vlasov equation to an integral Fredholm equation. The main cases are examined when it is possible to construct kernels of corresponding integral operators. In particular, a feasibility to employ Feier - Chesaro kernels is demonstrated. Using the universality (according to V.I.Zubov) of Maxwell equations the problem of a search for stabilizing and focusing fields is reduced to the construction of Toeplitz matrix.

Also conditions are analyzed, ensuring initiating of a continuous spectrum points within the spectrum of a dynamic system. Physically, this phenomenon is related to the chaotic motion of the particles. Also, the dispersion equation, expressed in terms of solutions to the Fredholm equation, is deduced.

Keywords: Vlasov-Maxwell equation, kernel operator, self-focused particle beams, asymptotic stability.

INTRODUCTION

In this paper we propose a new approach for solving the Vlasov-Maxwell equations on the basis of optimal control theory. With the help of control algorithms solution of the nonlinear wave equations can be essentially simplified.

Many analytical studies and computer experiments are devoted to analysis of these system of equations. Our earlier works [1-5] contain fresh analytic results on this subject. In this paper we outline an approach to study some problems of beam acceleration and strong focusing. This approach appears as the development of previous results of the authors [1-5] and essentially use the universality of Maxwell equations and some methods of optimal control theory. It is based on the fundamental result of V.Zubov on the necessary and sufficient conditions for asymptotic stability and the well known Halmos theorem concerning Hilbert-Schmidt integral operator. This approach made it

feasible to apply the direct Lyapunov method to essentially nonlinear problems. The Lyapunov function generates a certain kernel operator in the domain of asymptotic stability of the system under analysis. Thus the Lyapunov equation can be reduced to the Fredholm equation [1]. The self-focused and accelerating particle beams are studied using analytic solution of the self-consistent Vlasov equation. In so doing the Lorentz force is substituted with some vector parameter describing the controlling field. As a result we come to some problem on the optimal control solving which we find the charge and the current densities. Substituting the latter into the Maxwell equations and solving this equation we obtain the electromagnetic field (E, H) .

PROBLEM STATEMENT. SIMULATION METHOD

In this paper we treat standing wave solutions $f(t, x, v) = f_0(x, v)e^{i\omega t}$ to the self-consistent Vlasov equation

$$\frac{\partial f}{\partial t} + \partial_x f \cdot v + \partial_v f \cdot \left[E + \frac{1}{c} v \times H \right] = 0, \quad (1)$$

under the initial condition $f(0, x, v) = \phi(x, v)$. Evidently,

$$\partial_x f_0 \cdot v + \partial_v f_0 \cdot \left(E + \frac{1}{c} v \times H \right) = i\omega f_0. \quad (2)$$

The fields E, H are functions of (t, x) , $x = (x_1, x_2, x_3) \in R^3$, and satisfy the Maxwell equations:

$$\text{rot} E + \frac{1}{c} \frac{\partial H}{\partial t} = 0, \quad \text{div} E = 4\pi q e^{i\omega t} \int f_0(x, v) dv, \quad (3)$$

$$\text{rot} H - \frac{1}{c} \frac{\partial E}{\partial t} = \frac{4\pi}{c} q e^{i\omega t} \int v f_0(x, v) dv, \quad \text{div} H = 0. \quad (4)$$

In view of the universality of the Maxwell equations we introduce the control parameter $U = E + \frac{1}{c} v \times H$. Then, using (2) we deduce the following equation

$$\partial_x f_0 \cdot v + \partial_v f_0 \cdot U = i\omega f_0. \quad (5)$$

Problem Statement

Let $\eta = \eta(U)$ be a performance criterion. For example, such criterion may be selected in the case of self-focusing of the longitudinal motion.

Thus, we can find (f_0, ω) from the equation (5). In order to construct a solution to (3), (4) we will treat electric and magnetic fields in the wave form

$$E(t, x) = E_0(x) e^{i\omega t}, \quad H(t, x) = H_0(x) e^{i\omega t}.$$

* This work was supported by the Science and Technology Center in Ukraine, grant No. 1746

[†] pars@bnl.gov

[‡] zvf@umex.istrada.net.ua

Then

$$\begin{aligned}\operatorname{div} E_0 &= 4\pi q \int f_0(x, v) dv, \\ \operatorname{rot} H_0 - \frac{i\omega}{c} &= -\frac{4\pi q}{c} \int v f_0(x, v) dv.\end{aligned}\quad (6)$$

This subject has attracted considerable interest in recent years. Only few cases are known when it is possible to obtain analytic solution in explicit form. Recall the pioneer paper of R. Davidson where the wave propagation is analyzed in symmetric structure of self-consistent equations (6). We treat this problem as a problem of control, to be specific, we seek the solution U^0 from the condition for minimum: $\eta(U^0) = \min \eta(U)$, where η is a norm in some functional space.

Simple example

Let $x \in R$ and $\omega = 0$. Then $\frac{\partial f}{\partial t} = 0$ and there exists a general solution to the equation

$$\partial_x f_0 \cdot v + \partial_v f_0 \cdot U(x) = 0,$$

which is an arbitrary function of the integral basis $\Psi(\int U(x) dx - \frac{1}{2}v^2)$. Now we obtain a unique solution that satisfies the initial condition $f_0(x, v) = \phi(x, v)$. Unfortunately, an integral basis can be constructed in rare instances. The approach outlined below makes it possible to overcome this difficulty.

In case of the long-time asymptotics our method is based on the reduction of equation (1) to the Fredholm integral equation (see [2]):

$$\begin{aligned}i\omega f_0 &= \int L w(x, v; y, u) f_0(y, u) dy du, \\ x, y &\in \Omega_x \subset R^3, v, u \in \Omega_v \subset R^3,\end{aligned}$$

where L is a differential operator

$$L = v \frac{\partial}{\partial x} + (E + \frac{1}{c} v \times H) \frac{\partial}{\partial v}$$

and $w(x, v; y, u)$ is a symmetrical kernel such that

$$\int [w(x, v; x, v)]^2 dx dv < \infty.$$

Here Ω_x and Ω_v are domains in $R^3(x)$ and $R^3(v)$ respectively, on which boundaries $f(t, x, v) = 0$ vanishes ($x \in \partial\Omega_x$ or $v \in \partial\Omega_v$), i. e. the beam is restricted in a phase space.

SELF-FOCUSING

In this paper we investigate the long-time asymptotics of a longitudinal electron motion in a ring accelerator.

Let f_0 be a solution to the equation

$$L f_0 = 0 \quad (7)$$

for $f_0(x, v) = \eta_0(x, v)|_{t=0}$.

If $f_0 \notin L^2$ then zero belongs to the continuous spectrum.

Assume that f is a solution of equation (7) under the arbitrary initial value $\eta(x, v)$. Obviously, function $\psi = f - f_0$ is a solution to the equation (7) too.

Definition. A solution $\psi = 0$ of the system $L\psi = 0$ is called asymptotically stable, if for any $\varepsilon > 0$ and arbitrary fixed $t_0 > 0$ there exist a number $\delta > 0$ such that for any $t \geq t_0$ and ψ_0 that $\rho(\psi_0, 0) < \delta$ the inequality holds: $\rho(\psi(\psi_0, t), 0) < \varepsilon$, and, moreover, $\rho(\psi(\psi_0, t), 0) \rightarrow 0$, as $t \rightarrow \infty$.

The case 4D phase space that include, in particular, the most important problem of stationary two-dimensional self-focusing is called critical. It is well known that this case is especially difficult both for analytical and numerical investigation (see, for example, [6]).

Let the motion of a beam be described (in polar coordinates (r, θ)) by the following partial differential equation

$$\frac{\partial f}{\partial t} + v_r \frac{\partial f}{\partial r} + \frac{v_\theta}{r} \frac{\partial f}{\partial \theta} + \left[\frac{v_\theta^2}{r} - \frac{e}{m} \frac{\partial U}{\partial r} \right] \frac{\partial f}{\partial v_r} - \frac{v_\theta v_r}{r} \frac{\partial f}{\partial \theta} = 0$$

under the condition $f(r_0, v_{\theta 0}) = \eta(r_0, v_{\theta 0})$. Here η is a given initial distribution function, r_0 and $v_{\theta 0}$ – initial values.

We can construct the integral basis for this equation and the function f can be expressed in terms of this basis as follows:

$$f\left(\frac{r}{r_0} - \frac{v_\theta}{v_{\theta 0}}; 3v^2 - c \frac{r^3}{r_0^2} + 6 \frac{e}{m} U(r); \frac{mv^2}{2} + CU(r)\right).$$

Let us take into consideration a quadratic form

$$[\psi, \psi] = (L\psi, \psi) + (\psi, L\psi).$$

Assume that the following condition holds

$$[\psi, \psi] \leq 0$$

for $\psi \in D(L)$ and some set of initial values $\{\eta(x, v)\}$.

Denote by \bar{L} the closure of the operator L in Hilbert space L^2 . We see that the operator $-\bar{L}$ is positively defined:

$$-[\psi, \psi] = \operatorname{Re}(-\bar{L}\psi, \psi) \geq 0, \quad \psi \in D(\bar{L}).$$

From this it follows that the domain $D(\bar{L})$ is a dense subset in the space L^2 and the quadratic form $[\cdot, \cdot]$ is symmetric. In view of the known F. Riesz theorem the operator \bar{L} is a co-generator of some contraction semigroup R_t in the Hilbert space:

$$\|R_t \psi\| \leq \alpha \|\psi\|, \quad 0 < \alpha \leq 1,$$

where $\|\cdot\|$ is a norm in L^2 .

It is easy to show that

$$\|R_t \psi\| \leq \varepsilon(\delta), \quad \text{for } \psi \in L^2: \|\psi\| < \delta,$$

and, moreover,

$$\lim_{t \rightarrow \infty} \|R_t \psi\| \rightarrow 0.$$

From this we conclude that the search of focusing fields can be reduced to problem on asymptotic stability of solutions ψ . Whence follows that if

$$\operatorname{Re} \sigma(\bar{L}) < \alpha < 0$$

then the original problem can be solved.

REFERENCES

- [1] Z. Parsa, V. Zadorozhny, Focusing and Acceleration of Bunched Beams, Book ed. Bruce J. King. Colliders and Collider Physics at the Highest energies.- New York, - 1999, - Pp. 249-259.
- [2] Z. Parsa, V. Zadorozhny, Nonlinear Dynamics on Compact and Beam Stability, Nonlinear Analysis, - 2001. - 47, - Pp. 4897-4904.
- [3] Z. Parsa, V. Zadorozhny, Formalism for chaotic Behavior of the Bunched Beam, Problems of Automatic Science and Technology. - 2001. - 6 (2). - Pp. 53-61
- [4] Z. Parsa, V. Zadorozhny, The Chaotic Behavior of the Bunched Beam, PAC2001, Chicago, IL.
- [5] Parsa Z., Zadorozhny V.F., Goncharov A.A. and Litovko J.V. Stationary equilibrium orbits of compensated charged beams in curvilinear magnetic field, Cybernetics and systems analysis, -2002. - No.5. - Pp. 122-132.
- [6] Kosmatov N.E., Shvets V.F. and Zakharov V.E. Computer simulation of wave collapses, Phisica D. -1991. -52. -Pp. 16-35.

VERTICAL COUPLING IMPEDANCE OF THE APS STORAGE RING*

Yong-Chul Chae[†], Katherine Harkay, Xiang Sun

Advanced Photon Source, Argonne National Laboratory, Argonne, IL 60439 USA

Abstract

The three-dimensional wake potentials of the APS storage ring have been reconstructed according to the impedance database concept. Every wakefield-generating component in the ring was considered including small-gap insertion device (ID) chambers, rf cavities, shielded bellows, beam position monitors, synchrotron radiation absorbers, scrapers, flags, various chamber transitions, septum chambers, and pulsed kickers. In this paper the result for the vertical wake potentials and its impedance are presented. Dominant contributors are the ID chambers whose heights are 5 mm and 8 mm. Since more small-gap chambers are envisioned for installation in the APS storage ring, prediction of their effect on the beam is very important not only for the APS but also for all third-generation light sources. We used the vertical impedance reported here to investigate the measured tune slope and single-bunch current limit in the APS storage ring. The program *elegant* was used for particle tracking, and its results are presented. We also report that we observed a vertical focusing in the calculated wake potential of the shallow transition without rotational symmetry.

IMPEDANCE DATABASE

The concept of an impedance database is described in the companion paper [1]. We report highlights of building the database for the vertical impedance. The horizontal and longitudinal impedance are reported separately [2,3].

Insertion Device

The small gap chambers for insertion devices have been identified as having the most significant effect on the single-bunch current limit [4]. Therefore, the investigation of ID chamber effects is important and requires an accurate estimate of the impedance. Only the geometric impedance is considered in the impedance database; the resistive impedance is computed from analytical expressions and is not included.

Since the impedance calculation was performed using numerical simulation (we used the program MAFIA), the mesh size is one of the important parameters to be determined. For the bunch length of 5 mm we could use a 1-mm mesh. However, we found that we need a finer mesh of 0.5 mm in order to avoid numerical instability. A total of 17 million mesh points was required.

The impedance of ID chambers with 5-mm and 8-mm gaps are shown in Fig. 1. In the simulation we used two boundary conditions at the symmetry plane; one is that the electric field is equal to zero (E-wake) and the other is that the magnetic field is equal to zero (H-wake). The

total wake is $(E\text{-wake} + H\text{-wake})/2$. The Fourier transform of the total wake divided by the bunch spectrum is the impedance shown in Fig. 1. Among the two boundary conditions, E-wake dominates and is always positive (defocusing). However, the H-wake is small and could be negative (focusing).

The magnitude of the impedance for the different gap sizes, b , shows a b^{-3} dependence similar to resistive-wall impedance.

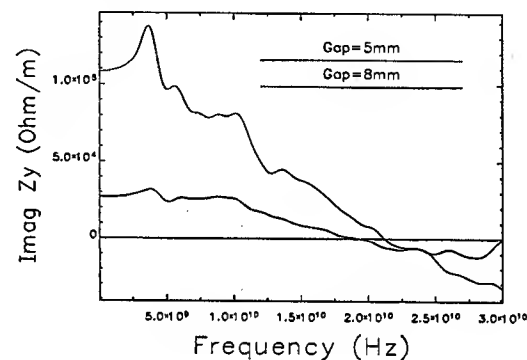


Figure 1: Impedance of ID chamber.

We knew that it was difficult to verify the accuracy of the numerical calculation of wake potentials for a 3-D transition because no reference exists with which to compare it. In order to increase our confidence in the 3-D calculation, we adopted a 2-D calculation as the reference that could be benchmarked later.

We constructed transitions for a circular chamber whose dimensions are comparable to the ID chamber; the geometry is shown in Fig. 2. We used two different programs, ABCI and MAFIA, to calculate the wake potential for the same geometry. The results from the two programs are compared in Fig. 3; it shows good agreement. Since the results from the 2-D program (ABCI) were highly accurate, we considered the results by MAFIA's simulations to be as accurate and reliable. This gave us confidence in the results presented in Fig. 1.

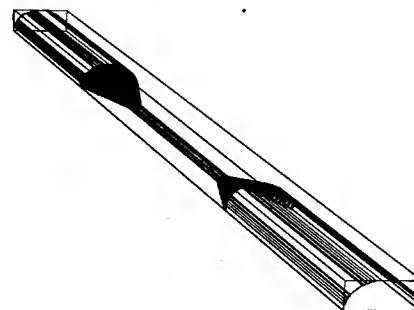


Figure 2: Circular transition.

* Work supported by the U.S. Department of Energy, Office of Basic Energy Sciences under Contract No. W-31-109-ENG-38.

[†] chae@aps.anl.gov

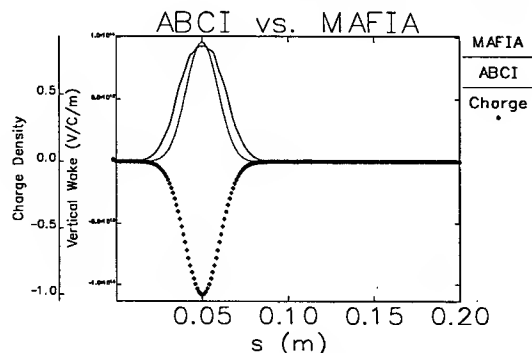


Figure 3: Vertical wake potentials by ABCI and MAFIA.

Synchrotron Radiation Absorber

In the APS storage ring, there are five synchrotron radiation absorbers per sector totaling 200 installed in the ring. They are all similar and one of them is shown in [3]. Since the absorber material intrudes on the horizontal side of the chamber without altering the vertical chamber dimension significantly, we expected a negative wake in the vertical plane if the empirical rule conjecture in [3] is true.

The MAFIA simulation resulted in a negative wake as shown in Fig. 4. Since the vertical beta function at the absorber location is high, the focusing effect of the negative wake is beneficial to the APS storage ring.

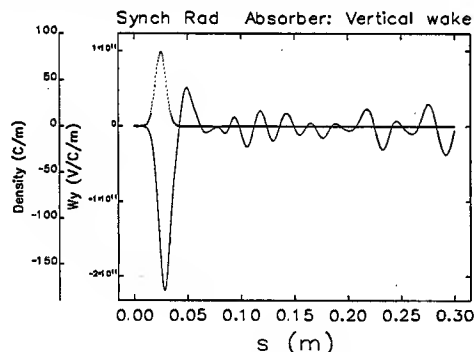


Figure 4: Vertical wake potential of absorber showing negative wake.

Other Components

Among the many components in the ring, one of the surprise was the flag chamber, of which there are ten in the ring. It has an rf screen in the chamber that forms a cavity-like structure; this contributes more than the anticipated impedance to the total. In addition, the mini-BPMs installed at the ID chamber also showed a negative wake potential, which was totally unexpected.

TOTAL IMPEDANCE

The total wake potential for a 5-mm bunch and the corresponding impedance are shown in Fig. 5. The shape of the wake is nearly proportional to the charge distribution. The impedance at low frequency is about 1.2 MΩ/m. A broad band resonator (BBR) was used to fit the imped-

ance; its parameters were found to be shunt impedance $R_s=0.5 \text{ M}\Omega$, quality factor $Q=0.4$, and resonant frequency $f_r=20 \text{ GHz}$.

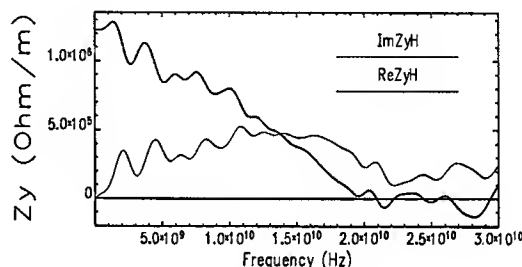
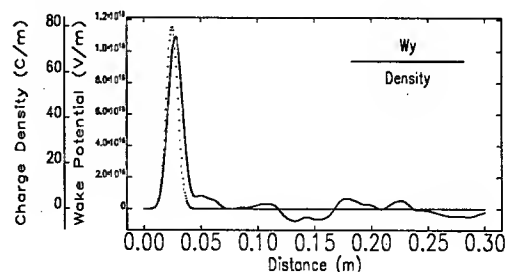


Figure 5: Total wake potential of the APS storage ring (top); the impedance (bottom).

The breakdown of the total impedance is presented in Fig. 6, which clearly shows that the dominant contributions are from 22 ID chambers of 8-mm gap together with 2 ID chambers of 5-mm gap.

Vertical Impedance (kOhm/m)

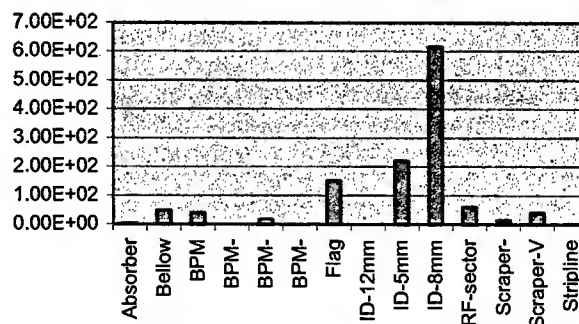


Figure 6: Breakdown of vertical impedance of the ring.

APPLICATION

We applied the total impedance to the APS storage ring in order to explain the various beam behaviors observed in the ring. A few examples are presented.

Tune Slope

Recently, the response matrix fit method [5] was used to measure the tune slope; the measured value was

$2.4 \times 10^{-3}/\text{mA}$, which was obtained by fitting the data in the range of current from 2 mA to 10 mA.

In order to estimate the tune slope by utilizing the total calculated impedance, we used the tune slope formula:

$$\frac{dv}{dI} = \frac{R}{2\pi\sigma_s E/e} \sum_{\text{Elements}} \beta Z_{\text{eff}},$$

where β_i is the betatron function at the location of the impedance element. The recently measured bunch length data were incorporated in the calculation, using the 2.5-nm lattice. The tune slope as a function of current is shown in Fig. 7. It shows that the resistive-wall contribution is much smaller than the geometric impedance. The average tune slope over a range of currents is found to be $2.6 \times 10^{-3}/\text{mA}$. This is in good agreement with the measured data.

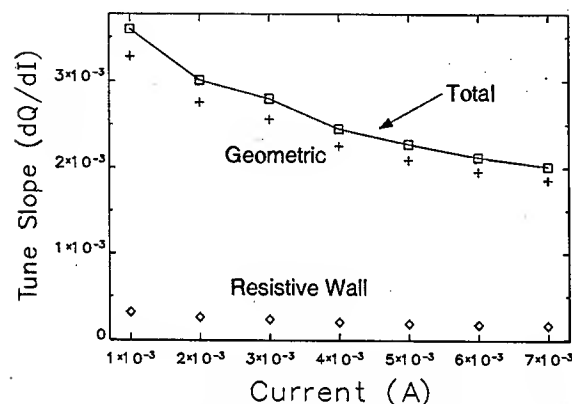


Figure 7: Tune slope as function of stored current in the 2.5-nm lattice with vertical chromaticity at 7.

Tracking Study

To understand the single-bunch current limit, we investigated the beam dynamics in the vertical plane by tracking multiple particles. We used the program *elegant* [6] to model a fully nonlinear lattice; the total impedance element is included at the location of the ID chamber.

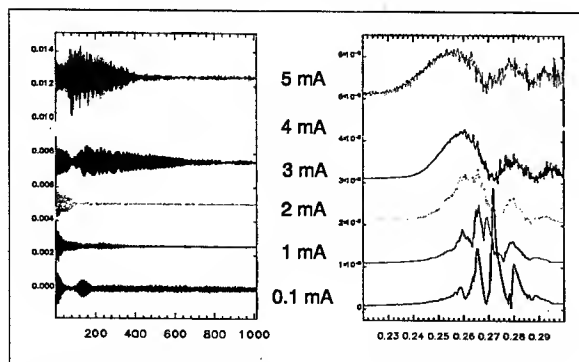


Figure 8: Turn-by-turn history of beam center (left); its Fourier transform (right).

In the simulation we kicked the beam once in the vertical plane and then recorded turn-by-turn histories of a number of beam parameters. One is the beam centroid as

shown in Fig. 8; several traces of various currents are depicted in a single graph. Also shown is the corresponding power spectrum, which reveals mode-coupling at 3 mA. We can see the effect of chromaticity modulation in the trace of low current of 0.1 mA. Above the mode-coupling threshold current of 3 mA the beam centroid is excited but subsequently damped fast. The amplitude of motion is not large enough to cause the particle loss

However, the history of the modeled beam size in Fig. 9 shows the significant blowup above the mode coupling. Since the dynamic aperture of the lattice is less than 10 mm, this blowup could cause the particle loss at 5 mA. The loss of particles was recorded in the simulation at the current 5 mA; the loss rate increased as the current increased. This may explain the observed limit of 8-10 mA in accumulating the current in a single bunch in the ring.

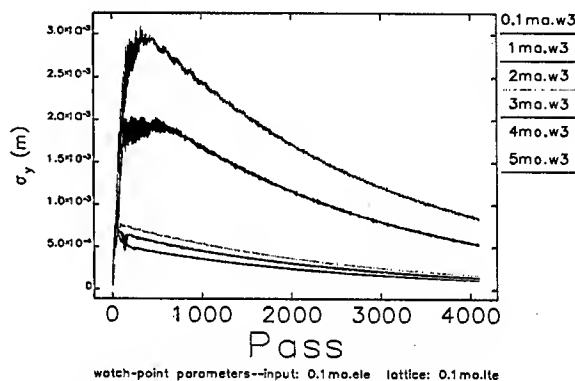


Figure 9: Turn-by-turn history of beam size showing blowup above the mode-merging current of 3 mA.

CONCLUSION

The impedance database concept was utilized to construct the total impedance of the ring. Modeling the APS ring using this impedance characterized well some of the observed beam behavior. The dominance of the small-gap chamber for ID has prompted research in reducing the vertical impedance through a new design of the chamber transitions.

REFERENCES

- [1] Y.-C. Chae, "The impedance database and its application to the APS storage ring," these proceedings.
- [2] Y.-C. Chae et al., "Horizontal coupling impedance of the APS storage ring," these proceedings.
- [3] Y.-C. Chae et al., "Longitudinal coupling impedance of the APS storage ring," these proceedings.
- [4] K.H. Harkay et al., Proc. 1999 PAC, 1644 (1999).
- [5] V. Sajaev, "Transverse impedance distribution measurements using the response matrix fit method at APS," these proceedings.
- [6] M.Borland, "elegant: A flexible SDDS-compliant for accelerator simulation," Advanced Photon Source Light Source Note 287, 2000.

HORIZONTAL COUPLING IMPEDANCE OF THE APS STORAGE RING*

Yong-Chul Chae[†], Katherine Harkay, Xiang Sun

Advanced Photon Source, Argonne National Laboratory, Argonne, IL 60439 USA

Abstract

The three-dimensional wake potentials of the APS storage ring have been reconstructed according to the impedance database concept. Every wakefield-generating component in the ring was considered including small-gap insertion device (ID) chambers, rf cavities, shielded bellows, beam position monitors, synchrotron radiation absorbers, scrapers, flags, various chamber transitions, septum chambers, and pulsed kickers. In this paper the result for the horizontal wake potentials and its impedance are presented. The numerically obtained impedance has been used to investigate the experimental results. Tune shift was calculated and compared with the measurement. We also observed a horizontal focusing in the calculated wake potential of the shallow transition without rotational symmetry.

IMPEDANCE DATABASE

The concept of impedance database is described in the companion paper [1]. We report highlights of building the database for the horizontal impedance. The longitudinal and vertical impedance are reported separately [2,3].

Insertion Device

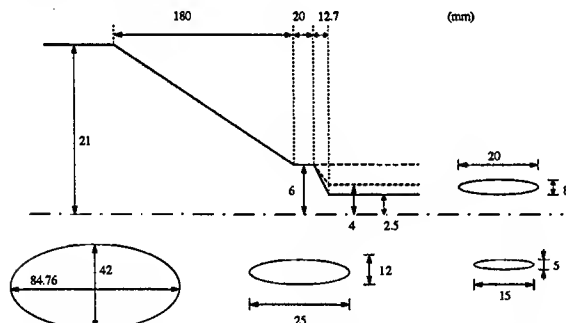


Figure 1: Transition between regular and ID chambers.

At the APS, the vacuum chamber for an insertion device is 5 m long with a small gap; its schematic diagram is shown in Fig. 1, which shows the transition from the regular chamber (8.4 cm by 4.2 cm) to the small-gap chambers whose vertical dimensions are 5 mm or 8 mm. There are 22 chambers with 8-mm gap and 2 chambers with 5-mm gap installed in the storage ring (there are no longer any 12-mm chambers).

The ID chambers have a detrimental effect on the single-bunch current limit in the vertical plane due to beam-chamber interaction. However its horizontal effects

seemed to be small and were not well known.

We used the program MAFIA in order to calculate the wake potential for a bunch of 5 mm. The simulation conditions are described in detail in the companion papers [1,3]. The results show that the horizontal wake is 100 times smaller than the vertical wake.

The smallness of the horizontal wake was found to be due to the cancellation between the wakes obtained by two different boundary conditions imposed on the symmetry plane. The electric boundary condition is $E=0$ (E-wake), and the magnetic boundary condition is $H=0$ (H-wake). The two wake potentials, E-wake and H-wake, shown in Fig. 2, were found to be opposite in the sign but nearly equal in magnitude. Therefore, the total horizontal wake, which is $(E\text{-wake} + H\text{-wake})/2$, becomes small.

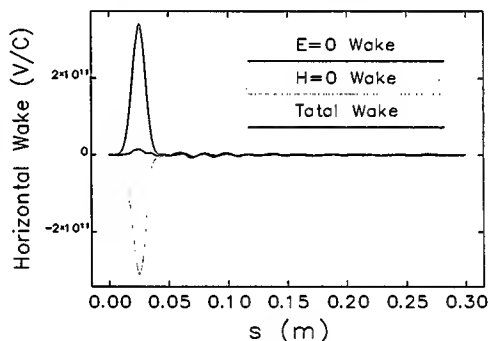


Figure 2: Total horizontal wake is the sum of E-wake and H-wake.

Beam Position Monitor (BPM)

Two main types of BPMs are installed in the ring: 1) 400 BPMs with standard buttons installed at the regular chambers, and 2) 24 BPMs with mini-buttons installed at the ID chambers. These are called the P0-BPMs. We will show later that these BPMs contribute the most to total horizontal impedance. The P0-BPM has an especially strong influence on the beam because of its proximity to the beam.

The geometry of the P0-BPM used in the MAFIA simulation is shown in Fig. 3. The long coaxial conductor above the button characterizes a large resonance peak at 22 GHz in the total impedance.

The results from MAFIA simulation are shown in Fig. 4. The top graph shows the long-ranged wake modulated by the 22 GHz wavelength. The impedance is shown in the bottom graph and exhibits a few resonant peaks.

* Work supported by the U.S. Department of Energy, Office of Basic Energy Sciences under Contract No. W-31-109-ENG-38.

[†] chae@aps.anl.gov

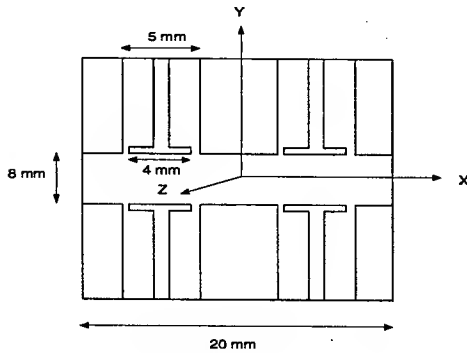


Figure 3: P0-BPM geometry used in the MAFIA simulation.

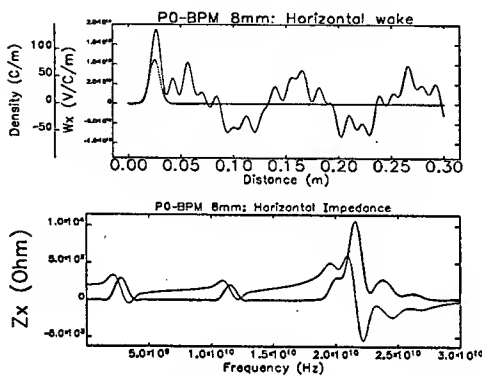


Figure 4: P0-BPM's wake (top); its impedance (bottom).

Bellow (Focusing Wake Potential)

The bellows in the APS storage ring are shielded by sliding contacts. Figure 5 is a drawing of the B1 bellow, one of six different types of bellows. The transition in the horizontal dimension varies from 8.4 cm to 9.3 cm, giving a transition angle of 4 deg. The transition angle in the vertical dimension is slightly greater, varying from 4.07 cm to 5.39 cm, giving 5.7 deg.

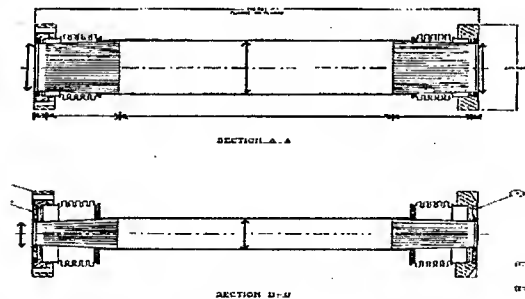


Figure 5: Drawing of the B1-bellow: horizontal plane (top), vertical plane (bottom).

The results from the initial simulation by MAFIA showed a slightly negative kick factor; this implies that the bunch traversing the bellows would receive a focusing kick instead of a defocusing kick. The longitudinal equivalent of this phenomenon would be gaining energy

instead of losing energy by the beam. The small magnitude of wake potential, as well as the negative sign, was unexpected. In order to verify the simulation result, we carried out a series of phenomenological investigations to study the mesh effect, bunch-length effect, 2-D simplification, angle effect, etc. The results from a systematic case study of the transition geometry is presented below.

We devised the structure similar to the bellows depicted in Fig. 5. The cross section is an ellipse whose taper and aspect ratio are varied. The semimajor axis is varied from 2 cm to one of 2, 2.25, 2.5, 2.75, or 3.0 cm and back to 2 cm. The tapering of the semiminor axis is not varied; tapering is from 1 cm to 1.3 cm and back to 1.0 cm. The semimajor axis in the middle section, a_m , identifies each case.

A half chamber is used in the simulation with two boundary conditions, E-wake and H-wake. The total wakes, the E-wakes, and the H-wakes are shown in Fig. 6. Each case for the different value of a_m is represented by a different curve. From the E-wake plot, we observe that the sign of the wake is always positive, and its magnitude decreases as the variation of the aperture is reduced. However, from the H-wake plot, we clearly see that the sign changes; a transition occurs at $a_m=2.5$ cm, and the wake becomes more negative as a_m is further reduced. The total wake, then, eventually becomes negative at $a_m=2.0$ cm. Transition from positive to negative occurs for the total wake at $a_m=2.25$ cm.

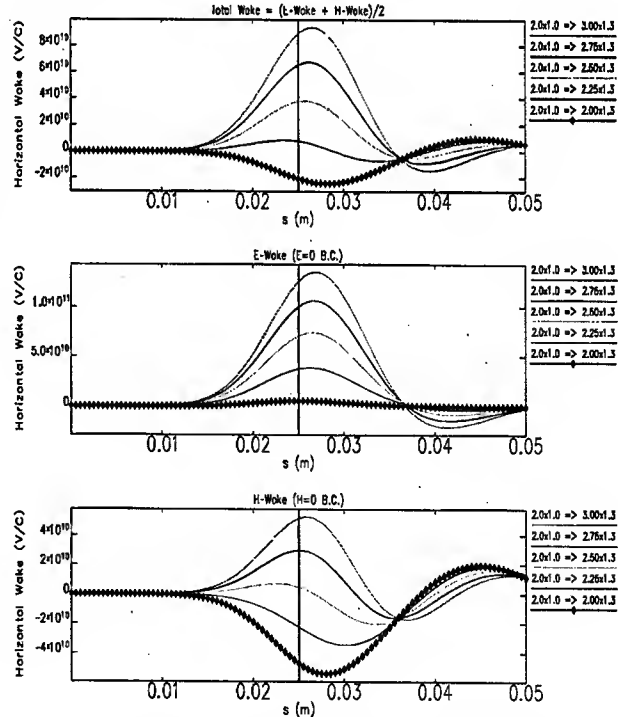


Figure 6: Horizontal wake potentials of 3-D elliptical taper: total wake (top), electric boundary condition (middle), magnetic boundary condition (bottom).

Based on the above study we conjecture that:

- 1) the negative wake potential is a completely three-dimensional phenomena,
- 2) it can occur when the degree of perturbation in one dimension is greater than in the other,
- 3) the negative wake potential is in the plane of the smaller perturbation.

In our bellows example, the smaller perturbation is in the horizontal plane where the negative wake occurred.

TOTAL IMPEDANCE

The total wake potential for the bunch of 5 mm and the impedance derived from it are shown in Fig. 7. The shape of the wake potential follows the charge profile at the head but is distorted near the tail and then followed by an extended wake. The impedance at low frequency is about 0.22 MΩ/m; the previous estimate based on the tune slope measurement also predicted a similar result [4]. A broadband resonator (BBR) was used to model the impedance; its parameters were found to be shunt impedance $R_s=0.6$ MΩ, quality factor $Q=4$, and resonant frequency $f_r=22$ GHz.

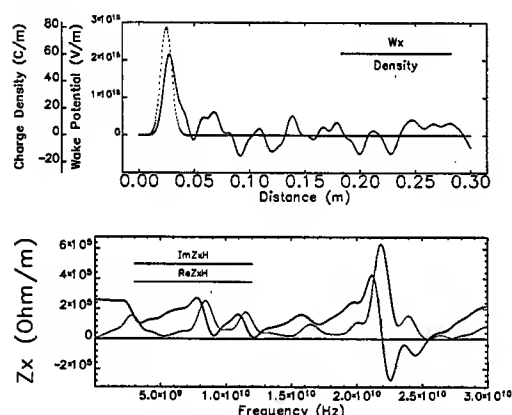


Figure 7: Horizontal wake potential and impedance of the ring

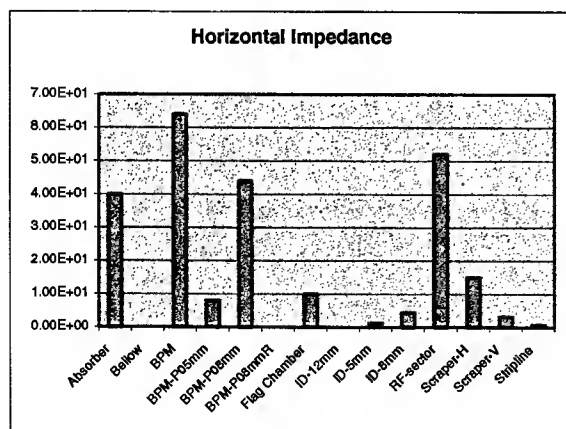


Figure 8: Horizontal impedance breakdown.

The breakdown of total impedance is presented in Fig. 8. From the figure we identify the major contributors, which are the BPM, P0-BPM, rf sector, and synchrotron radiation absorber.

APPLICATION

We used the total impedance in order to investigate the current-dependent beam dynamics observed in the ring. We chose the tune slope to compare. The recently measured value was $8 \times 10^{-4}/\text{mA}$, which was fitting tune shifts over the current from 2 mA to 10 mA [4,5].

The numerical estimate is based on the well-known formula:

$$\frac{dv}{dl} = \frac{R}{2\pi\sigma_s E/e} \sum \beta_i Z_{eff},$$

where β_i is the betatron function at the location of the impedance element. Note that the tune slope depends on the bunch length and chromaticity.

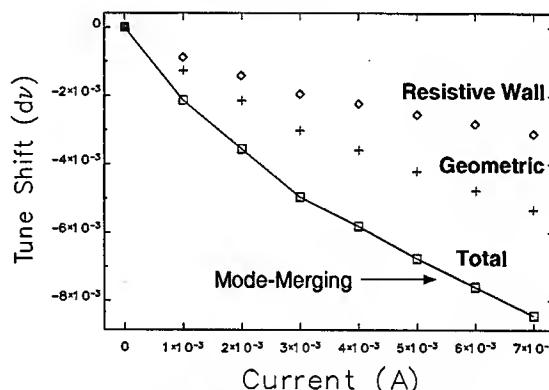


Figure 9: Tune slope as function of chromaticity for the 2.5-nm lattice.

The resultant tune shift as a function of current is shown in Fig. 9. We used the impedance shown in Fig. 7 and incorporated the measured bunch lengths (42 ps at 5 mA, for example) in the calculation. The tune slope, by fitting over 2 mA to 7 mA, is $9 \times 10^{-4}/\text{mA}$, which is slightly larger than the measured value. The horizontal tune is reduced by the amount of synchrotron tune, $\nu_s=0.007$, at the current 5.5 mA, which is close to mode-merging current observed in the ring. Contrary to results in the vertical plane, the resistive-wall impedance constitutes 1/3 of the total in the horizontal plane, so that its effect is expected to be dominant. An investigation is under way.

REFERENCES

- [1] Y.-C. Chae, "The impedance database and its application to the APS storage ring," these proceedings.
- [2] Y.-C. Chae et al., "Longitudinal coupling impedance of the APS storage ring," these proceedings.
- [3] Y.-C. Chae et al., "Vertical coupling impedance of the APS storage ring," these proceedings.
- [4] K.C. Harkay et al., *Proc. 1999 PAC*, 1644 (1999).
- [5] V. Sajaev, private communication.

LONGITUDINAL COUPLING IMPEDANCE OF THE APS STORAGE RING*

Yong-Chul Chae[†], Katherine Harkay, Xiang Sun

Advanced Photon Source, Argonne National Laboratory, Argonne, IL 60439 USA

Abstract

The three-dimensional wake potentials of the APS storage ring have been reconstructed according to the impedance database concept. Every wakefield-generating component in the ring was considered including small-gap insertion device (ID) chambers, rf cavities, shielded bellows, beam position monitors, synchrotron radiation absorbers, scrapers, flags, various chamber transitions, septum chambers, and pulsed kickers. In this paper the result for the longitudinal wake potentials and its impedance are presented. The total impedance is not model-based but the direct sum of numerical functions. The fit parameters for the broadband resonator model are also included as a convenient representation. We used this impedance model to investigate the observed microwave instability, namely bunch lengthening, anomalous energy spread, and coherent excitation at high synchrotron sideband.

note that there exists significant interference effect between the transition and cavities.

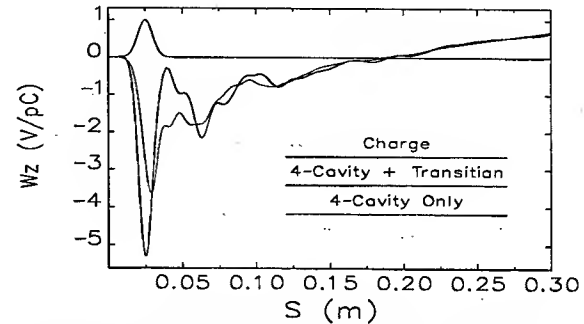


Figure 2: Total wake potential of rf sector. Wake potential of four cavities only is also shown for comparison.

IMPEDANCE DATABASE

The concept of impedance database is described in the companion paper [1]. We report highlights of building the database for the longitudinal impedance. The horizontal and vertical impedance are reported separately [2,3].

Rf-Sector (rf-cavities and transition)

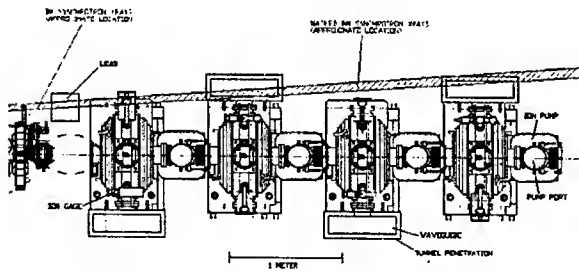


Figure 1: Rf sector showing four cavities.

The rf cavities at the APS storage ring provide energy to the beam with 9.5 MV of gap voltage distributed in sixteen cavities in four sectors. One of the rf sectors is shown in Fig. 1.

An rf sector consists of four cavities and the transition of vacuum chamber at both ends. The complexity is simplified in the simulation to axially symmetric geometry. We used the program ABCI in order to calculate wake potential. The wake potential of one rf sector for a 5 mm bunch is shown in Fig. 2; the cavity-only wake potential is also included for comparison. We

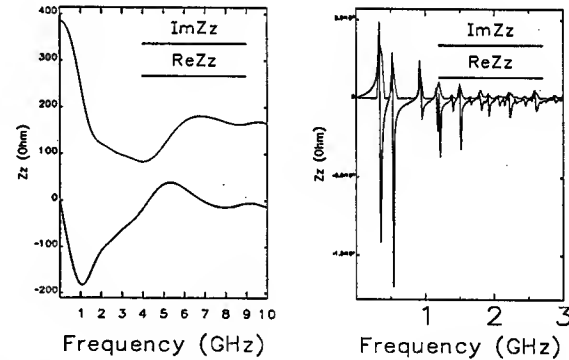


Figure 3: Impedance of the wake over 30 cm (left); impedance of the wake over 10 m (right).

The impedance, the Fourier transform of the wake potential divided by the bunch spectrum, is shown in Fig. 3. The graph on the left shows the impedance of short-ranged wake over 30 cm, which shows the characteristic cavity-type impedance in the form of $(1-j)/\sqrt{\omega}$. This short-ranged wake potential is included in the total wake potential. Note the imaginary part of the impedance is negative.

The impedance of long-ranged wake over 10 m is also shown in Fig. 3 on the right. Higher-order modes (HOMs) as well as the fundamental mode resonating at 352 MHz are clearly shown. The total HOM contribution to Z/n is 0.2 Ω , which was estimated by using the formula

$$(Z/n)_{HOM} = \sum_{j=2} (R_s / Q/n)_j,$$

where R_s is the shunt impedance, Q is the quality factor, and n is the harmonic number. This $(Z/n)_{HOM}$ is included in the impedance breakdown for Z/n .

* Work supported by the U.S. Department of Energy, Office of Basic Energy Sciences under Contract No. W-31-109-ENG-38.

[†] chae@aps.anl.gov

Synchrotron Radiation Absorber

In the APS storage ring there are 200 absorbers of five types; one of them, C2 type, is in a crotch shape that intrudes into the vacuum chamber. The schematic used in the simulation is shown on the top of Fig. 4. The device-under-test (DUT) depicted on the top requires the "DIRECT" method in the MAFIA simulation whose result depends on the chamber length. Accurate simulation could require a length that is often prohibitively long.

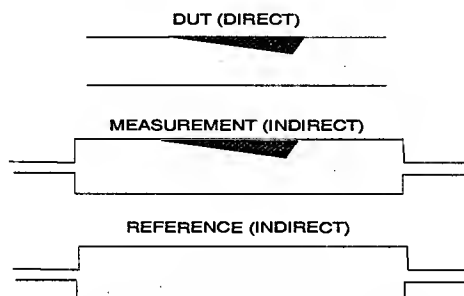


Figure 4: DUT = MEASUREMENT - REFERENCE.

In order to overcome this constraint we used a technique similar to the coaxial wire method, which can be described as DUT=MEASUREMENT-REFERENCE as shown in Fig. 4. The reference chamber is necessary in order to make the simulation geometry suitable for the "INDIRECT" method, whose result doesn't depend on the chamber length and is less susceptible to numerical noise.

The improved result, derived by comparing the new method with the "DIRECT" method, is shown in Fig. 5. The oscillatory wake after the bunch, which could be misread as a "trapped mode," disappeared when a proper simulation technique was applied to the problem.

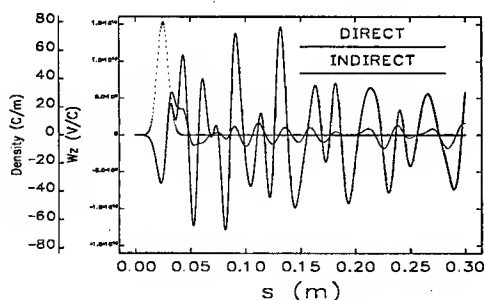


Figure 5: Wake potentials comparing the DIRECT and INDIRECT methods.

TOTAL IMPEDANCE

The total wake potential of the ring and its impedance are shown in Fig. 6. The important parameter Z/n is about 0.22Ω , which is constant up to 22 GHz. The breakdown of Z/n is presented in Fig. 7, where the rf sector dominates by its 0.2Ω impedance due to the HOMs.

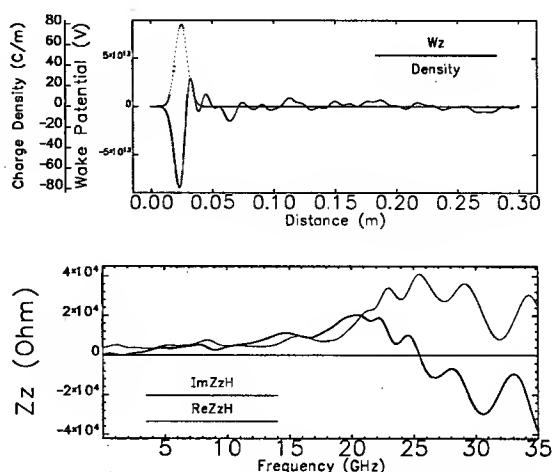


Figure 6: Longitudinal wake potential and impedance of the ring.

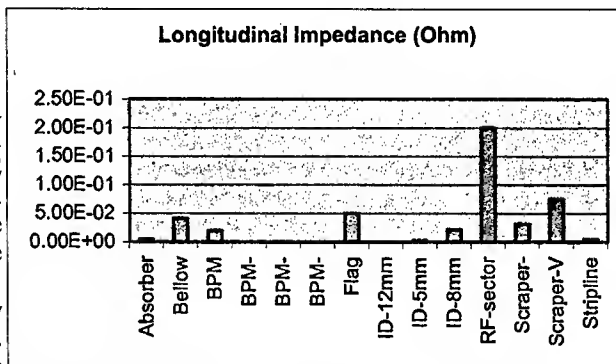


Figure 7: Longitudinal impedance breakdown.

APPLICATION

The longitudinal microwave instability in the APS storage ring had been measured and reported [4]. As an application of the impedance database we used the total impedance in Fig. 6 as the input to the particle-tracking program *elegant* [5] in order to reproduce the measured results.

In the simulation we tracked 10,000 particles over 10,000 turns. At each turn the parameters of beam distributions were calculated; two of them were bunch length and energy spread. The average and rms value over 5000 turns for each current level were calculated and their results are shown in Fig. 8. The bunch length (black curve) varies as $I^{1/3}$ over the whole range of current. But the energy spread (red curve) shows a threshold behavior at a current of 6 mA or 7 mA. This is consistent with the threshold observed experimentally [4]. The rms values depicted as error bars in Fig. 8 also reveal the important information. Above the threshold the rms values increase dramatically, indicating dynamic motion of the bunch in the phase space.

The nature of dynamics above the threshold is revealed by its power spectrum, which is shown in Fig. 9. Each

trace represents the fast Fourier transform of turn-by-turn bunch length data. The bottom two traces below threshold show the coherent signal at the synchrotron frequencies f_s and $2*f_s$, representing $m=1$ and $m=2$ mode, respectively. However, above the threshold the coherent signal near $4*f_s$ is excited; it was also observed experimentally [4].

The simulation using the total impedance reproduced three important aspects of longitudinal phenomena, which are bunch lengthening, energy spread, and synchrotron sideband at $4*f_s$. However, this occurred only when the impedance was increased by 80% of the total impedance, as shown in Fig. 6.

When the maximum frequency of the total impedance was extended to 200 GHz instead of a nominal 100 GHz, we observed microbunching of the beam in the simulation as shown in Fig. 10. Apparently buckets formed by the impedance at high frequency trap the particles. We observed that the energy spread increases as the current increases. Unlike the phenomena shown in Figs. 8 and 9, the deformation of bunch was static without a coherent signal at $4*f_s$ or higher. This tantalizing phenomenon is under investigation.

DISCUSSION

The good agreement between the simulation and the experimental results were obtained by increasing the calculated impedance by 80%. The total inductive impedance at the low frequency expressed as Z/n is 0.22 Ω without *ad hoc* inclusion of HOM contribution, which is 80% lower than the estimated value based on the bunch-length measurement [4].

We searched for the missing impedance source to make up for such big differences. We did not miss the impedance source in our impedance database, but perhaps we didn't include the HOM contribution properly in the total impedance.

We show Z/n with and without rf-sector contribution in Fig. 11. The rf sector reduces the total impedance in the low frequency range, but the broad and constant Z/n didn't change with and without the rf sector, which implies that a HOM contribution of 0.2 Ω is not included in the total impedance. The proper treatment of the rf cavity might be to subtract the wake potential due to the fundamental mode to make a HOM-only wake potential. Thus pure HOM wake should contribute to the total wake.

REFERENCES

- [1] Y.-C. Chae, "The impedance database and its application to the APS storage ring," these proceedings.
- [2] Y.-C. Chae et al., "Horizontal coupling impedance of the APS storage ring," these proceedings.
- [3] Y.-C. Chae et al., "Vertical coupling impedance of the APS storage ring," these proceedings.
- [4] Y.-C. Chae et al., "Measurement of the longitudinal microwave instability in the APS storage ring," 2001 Part. Accel. Conf., 1817 (2001).

- [5] M.Borland, "elegant: A flexible SDDS-compliant for accelerator simulation," Advanced Photon Source Light Source Note 287, 2000.

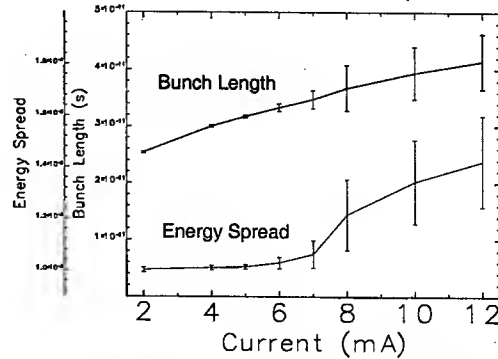


Figure 8: Bunch length and energy spread.

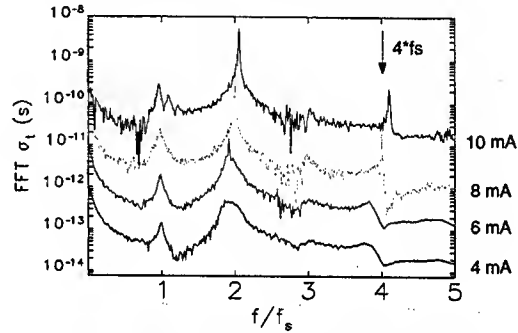


Figure 9: Spectrum of bunch-length oscillation.

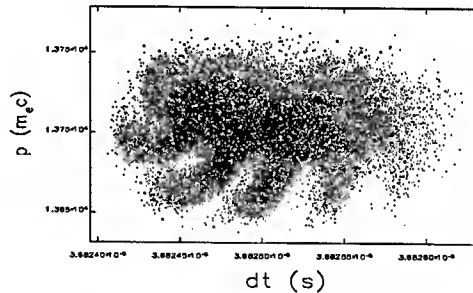


Figure 10: Microbunching of the beam by a high-frequency impedance.

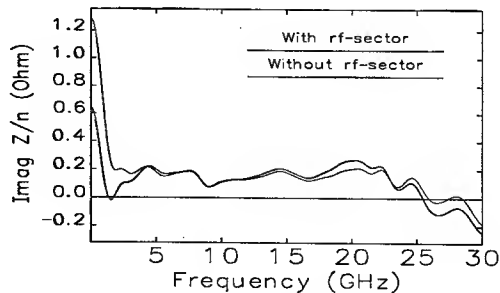


Figure 11: Imaginary part of total Z/n with and without rf sector.

THE IMPEDANCE DATABASE AND ITS APPLICATION TO THE APS STORAGE RING *

Yong-Chul Chae[†]

Advanced Photon Source, Argonne National Laboratory, Argonne, IL 60439 USA

Abstract

Since the operation of the APS storage ring, we have observed instabilities of different kinds. Some of them are not well understood and need further investigation; transverse saw-tooth instability and anomalous energy spread are examples. Quantitative understanding of these instabilities requires detailed knowledge of impedance of the ring. For this purpose we developed the concept of the impedance database, where the wake potential of each vacuum component in the ring is deposited and maintained in a standard form. These standardized wake-potentials can be manipulated with high flexibility by utilising the Self Describing Data Sets (SDDS) toolkit developed at Argonne National Laboratory. In this paper we will present the total impedance of the APS storage ring obtained by using the impedance database. Then we report the application of the total impedance to investigate the currently observed instabilities in the APS storage ring.

INTRODUCTION

In the development of the APS storage ring, the information of impedance had been estimated and collected as an Impedance Budget. This tabular data had been not only useful for characterizing the total impedance of the ring but also convenient because of its simplicity.

However, as we installed small-gap chambers for insertion devices (ID) in the ring, we observed that the single-bunch current reduced dramatically. The maximum current we could stably store in the ring is about 5 mA, limited by the mode-coupling instability in vertical plane [1,2,3]. In addition, we also observed saw-tooth excitation in the horizontal plane [2,3] and microwave instability in the longitudinal plane [4]. Understanding these instabilities required a more accurate estimate of the impedance over a broad frequency range because the bunch length in the APS storage ring is as short as 5 mm at low current.

Understanding and curing the instabilities so that we could improve the performance of the ring was the motivation to extend the idea of the Impedance Budget into an Impedance Database, where we collect the impedance function for all impedance elements installed in the ring. The impedance function was used in the simulation by tracking the multiple particles traversing the lattice magnets and impedance elements.

In subsequent sections we introduce the Impedance Database concept and then present highlights of the

results including the total impedance of the ring and some of the simulation results. More complete results are presented in the companion papers [5,6,7].

IMPEDANCE DATABASE

Goal

The goal of the Impedance Database is an accurate estimation of the total impedance in the ring. In practice, since we usually obtain the impedance via wake potential, the goal could be expressed as:

$$W_{total} = \sum_{Element} N_i * W_i * \alpha_i,$$

where

W_{total} = total wake-potential of the ring,

N_i = number of the element in the ring,

W_i = wake-potential of the element,

α_i = weight of the element.

This expression shows that the total wake potential of the ring is the weighted sum of the individual wake potential. A convenient choice of the weight for each element is the lattice function.

Then, the total impedance, Z_{total} , will be obtained via fast Fourier transform (FFT).

Method

We standardize the data format in order to combine and process the wake potentials obtained by the different methods. For this purpose we use the SDDS file format, which is column oriented, and data are accessed by name only for robustness. Standard wake potential requires at least four column data, which are the distance, s , and the wake potentials of three planes, W_x , W_y , and W_z .

We also adopted uniform simulation conditions for all impedance elements in order to assure the even quality for each simulation; those were:

1. bunch length=5 mm,
2. longitudinal mesh size=0.5 mm or smaller,
3. wake length of simulation=0.3 m or longer.

We desire short-bunch simulation because, the shorter the bunch length, the broader the valid frequency range of impedance. However, the numerical instability limits the mesh size depending on the bunch length and the wake length, which in turn is limited by the available computer resources. The above simulation conditions reflect a balancing act of desire and limitations.

We had used LINUX pc-clusters at APS, where we could perform 3-D MAFIA simulation up to 17 million

* Work supported by the U.S. Department of Energy, Office of Basic Energy Sciences under Contract No. W-31-109-ENG-38.

[†] chae@aps.anl.gov

mesh points, which was enough to simulate the insertion device chambers for a bunch length of 5 mm.

We used the programs ABCI and MAFIA for calculation of wake potential. Both programs had been modified to be SDDS compliant so that their output is in SDDS format. The wake potential obtained for each impedance element was deposited in the designated directory within the APS computer network.

Since the Impedance Database should be available to all APS personnel, we developed a script to add and remove the impedance elements easily so that whoever has access to the Impedance Database directory can construct the total wake potential and its impedance at any time for his/her own use.

Results

We recently completed building the first phase of the Impedance Database for the storage ring. Some of the results and highlights are summarized here.

The Impedance Database includes ID chambers with 5 mm and 8 mm gap, rf sectors including rf cavities and chamber transitions, three types of beam position monitors installed at the regular chambers and ID chambers, six types of shielded bellows, five types of synchrotron radiation absorbers, flag chambers for the fluorescent screens, vertical scrapers, horizontal scrapers, and strip line monitors.

The Impedance Budget showing the contributions of each impedance element is shown in the Table 1. Impedance in the table is an absolute value at the low-frequency near origin. In the table we used an average value for an element having multiple types.

Table 1. Impedance Budget of the APS storage ring.

Name	Qty	Z_x (k Ω /m)	Z_y (k Ω /m)	Z/n (Ω)
Absorber	200	4.00E+01	4.00E+00	5.00E-03
Bellow	240	0.00E+00	4.80E+01	4.20E-02
BPM	400	6.40E+01	4.00E+01	2.00E-02
BPM-P05mm	2	8.00E+00	4.00E-01	1.00E-04
BPM-P08mm	22	4.40E+01	1.76E+01	1.10E-03
Flag Chamber	10	1.00E+01	1.50E+02	2.00E-02
ID-5mm	2	1.20E+00	2.20E+02	2.40E-03
ID-8mm	22	4.40E+00	6.16E+02	2.20E-02
RF-sector	4	5.20E+01	6.00E+01	2.00E-01
Scraper-H	2	1.50E+01	1.40E+01	3.20E-02
Scraper-V	2	3.20E+00	4.00E+01	7.50E-02
Strip line	4	8.00E-01	1.20E+00	6.00E-03
Total		2.43E+02	1.21E+03	4.20E-01

The major contributors to the total impedance were identified. The ID chambers dominate vertical impedance with 80% contribution, rf sectors and flag chambers containing fluorescent screens contribute 50% of longitudinal impedance, and the beam position monitors

(BPM) and synchrotron radiation absorbers contribute the most to horizontal impedance.

The total impedance of the ring, which is the Fourier transform of the total wake potential divided by the bunch spectrum, is shown in Fig. 1. The result shown was obtained with the unit weight for every impedance element. Horizontal, vertical and longitudinal impedances of both real and imaginary parts are shown from top to bottom. For the longitudinal impedance, Z/n are presented, where n is the harmonic number.

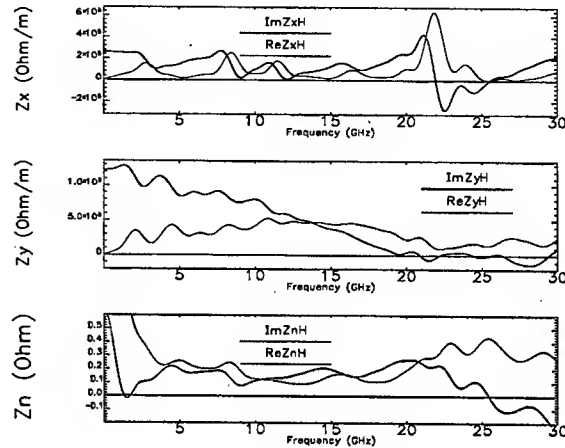


Figure 1: Total impedance of the ring.

We used a broadband resonator (BBR) model in order to parameterize the total impedance. The results are shown in Table 2. In the table, Z/n has two values; one is 0.22 Ohm without rf sector, and the other is 0.42 Ω , which includes 0.2 Ω from higher order modes (HOMs). This is discussed more in ref. 5.

Table 2: Broadband Resonator Model.

	R_s (Ω)	Q	f_r (GHz)
Z_x	0.6e6	4.0	22
Z_y	0.5e6	0.4	20
Z/n	0.22/0.42	2.0	25

APPLICATION

As the initial application of the Impedance Database, we carried out multiparticle tracking with a goal of reproducing the beam behaviors observed in the ring. The program elegant [8] was used for all tracking simulations, and some of the results are presented.

Longitudinal Phenomena

We observed microwave instability in the ring characterized by bunch lengthening, energy spread, and the coherent signal excitation at $4*f_s$ above the threshold current [4].

We used the 7.5 nm lattice whose natural bunch length is 20 ps, and natural energy spread is 1×10^{-3} . The 10,000 particles were initially loaded in the equilibrium phase space and then tracked 10,000 turns. After 2000 turns of initial transient, we took an average of 5000 turns. The

average value of bunch length and energy spread together with standard deviation are shown in Fig. 2. The results in Fig. 2 are in good agreements with experiment [4], however, we had to increase the impedance in Fig. 1 by 80%.

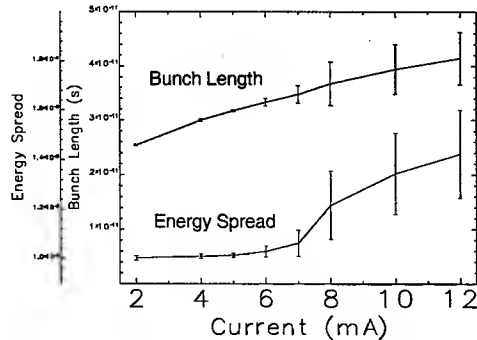


Figure 2: Bunch length and energy spread.

Vertical Phenomena

In the APS storage ring we observed mode-coupling instability in the vertical plane [2,3]. The observations include the modes couple at about 3 mA, the beam is vertically stable up to 5 mA, and we could accumulate a single bunch up to 8-10 mA.

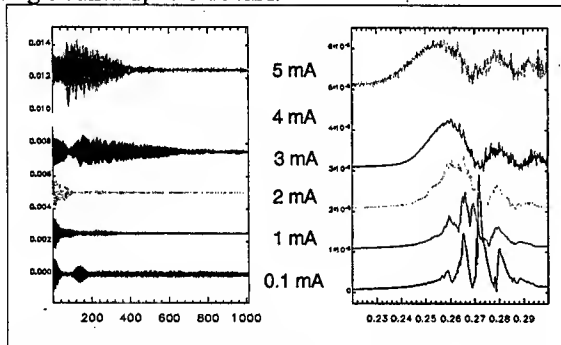


Figure 3: Turn-by-turn history of vertical beam center (left); its Fourier transform (right).

In the simulation we used a 7.5 nm lattice whose chromaticities were set to 4 and 7 in the horizontal and vertical planes, respectively. We used the BBR impedance with $R_s=0.9 \text{ M}\Omega$, $Q=0.6$, $f_r=20 \text{ GHz}$. Compared with the most up-to-date parameters in Table 2, this resulted in a larger wake potential by 20%. We show the beam history and its Fourier transform of several currents in Fig. 3. We find that the beam centroids are stable up to 5 mA, the modes couples at 3 mA. In a companion paper [6], we show the beam size blowup after mode coupling, which could reduce the lifetime.

Horizontal Phenomena

In the horizontal plane, a saw-tooth instability was observed in the ring [2,3]. One of the characteristics was the sequence of stable, steady state, bursting, and steady state as the single bunch current increased.

The simulation study of this phenomenon is still in its infancy, but we made some progress to report. We found two types of impedance sources that could excite the

bursting mode, namely, a narrowband source and a broadband source.

The resistive wall impedance was used as a narrowband source. The horizontal excitations of different currents are shown in Fig. 4. On the left are the traces excited by the narrowband impedance. As the current increases, the amplitude of bursting increases too. On the right are the traces excited by the broadband impedance, which is offset by 1 mm horizontally. Even though the bursting modes are not as clean as observed in the experiment or in the narrowband simulation, the characteristic mode changes are well reproduced.

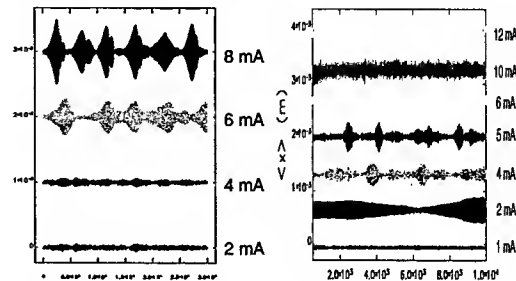


Figure 4: Turn-by-turn history of horizontal beam center excited by narrowband resistive-wall impedance (left) or by broadband impedance (right).

CONCLUSION

The Impedance Database was useful in constructing the total impedance of the ring. When it was applied to the APS storage ring, the initial simulation results showed good agreement with measurement, encouraging a more realistic simulation for the real machine.

ACKNOWLEDGEMENT

We thank S. Sharma, L. Morrison, A. Barcikowski from Mech. Eng., E. Rossi, P. Choi from Design/Drafting, X. Sun, G. Decker, O. Singh from Diagnostics, S. Milton, K. Harkay from Accel. Physics, L. Emery, M. Borland, N. Sereno from Operations Analysis. Without LINUX cluster and numerous software supports from B. Soliday it may not be possible to finish this project in time.

REFERENCES

- [1] N. Sereno et al., Proc. 1997 PAC, 1700 (1997).
- [2] K.C. Harkay et al., Proc. 1999 PAC, 1644 (1999).
- [3] K.C. Harkay et al., Proc. 2001 PAC, 1919 (2001).
- [4] Y.-C. Chae et al., Proc. 2001 PAC, 1817 (2001).
- [5] Y.-C. Chae et al., "Longitudinal coupling impedance of the APS storage ring," these conference proceedings.
- [6] Y.-C. Chae et al., "Vertical coupling impedance of the APS storage ring," these conference proceedings
- [7] Y.-C. Chae et al., "Horizontal coupling impedance of the APS storage ring," these conference proceedings.
- [8] M. Borland, "elegant: A flexible SDDS-compliant for accelerator simulation," Advanced Photon Source Light Source Note 287, 2000.

BUNCH LENGTH MEASUREMENTS AT BESSY*

M. Abo-Bakr, W. Anders, P. Kuske, G. Wüstefeld, BESSY, Berlin, Germany

Abstract

In the range from 2 ps to 40 ps the rms bunch length and the bunch shapes have been measured with a streak camera as a function of the beam current. Short bunches were produced by reducing the momentum compaction factor of the storage ring lattice. An attempt is made to distinguish between vacuum chamber and radiation impedance effects.

INTRODUCTION

BESSY is a high brilliance VUV to soft X-ray synchrotron light source [1]. After 3 years of operation 13 out of 16 straight sections are equipped with insertion devices (ID) with gaps of the vacuum chamber down to 11 mm. Four IDs are strong superconducting devices which have an impact on the bunch length. The storage ring is operated usually at 1.72 GeV. The low emittance double bend lattice already produces short bunches due to the small momentum compaction factor, α . In addition, the bunch length can be reduced even further by nearly a factor of 10 by changing the optics and reducing α by a factor of 100. The shape and the length of these short bunches have been measured with a streak camera (SC) as a function of beam current. The technique, analysis, and very little interpretation of the observations will be presented. For comparison results will be given of further measurements related to the longitudinal dynamics of high current bunches in a storage ring like the current dependent energy spread and the current dependent shift of the longitudinal quadrupole mode.

EXPERIMENTAL SETUP

For the bunch length measurements the Hamamatsu dual sweep SC model C5680 connected to a stand alone PC is used. Bending magnet radiation (± 1 mrad in both planes) is guided out of the radiation safety area, passes through a colour glass filter which transmits radiation below 420 nm, and is focussed with a single quartz lens onto the 30 μm entrance pin hole of the camera. The camera's static time resolution was found by operating the SC in the focussing mode. Depending on the sweep speed the resolution with a 30 μm pin hole can reach 1.5 ps. The fast 250 MHz sweep voltage for the SC is taken from the RF master oscillator frequency of 500 MHz divided by two. The long term phase stability is thus assured. Short term phase noise reduces the time resolution of the SC operated in the dual sweep mode. The contributions stem from the phase noise of the master oscillator, the fast sweep voltage, and the noise in the accelerating RF voltage. In addition, the RF voltage contains small spikes

which induce coherent synchrotron oscillations of the bunch. Therefore, the slower sweep speed of the SC is always chosen such that these coherent bunch oscillations occurring between 1 and 10 kHz can be resolved. A full sweep takes 1 to 10 ms. With a bunch revolution time of 800 ns many images of the bunch are superimposed in order to collect sufficient intensity. Usually a single bunch is stored, however, at extremely low beam current of the order of 1 μA , corresponding to $N=5 \cdot 10^6$ electrons in the bunch, all 400 buckets are filled as equally populated as possible.

ANALYSIS OF THE STREAK CAMERA DATA

In the top of Fig. 1 raw data from the CCD camera at the end of the SC is shown. The slow horizontal time span is 1 ms and the fast vertical time span is 275 ps. There are 640 pixels in the slow sweep direction and 512 in the fast direction. Slices of pre-chosen horizontal width are analysed and the data is averaged horizontally over the slice first. Then the background is subtracted based on the signal at the beginning and the end of the fast sweep (top and bottom of Fig. 1).

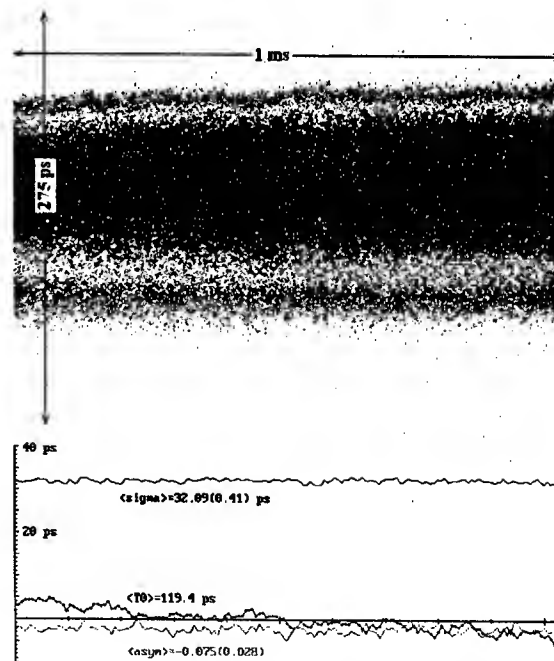


Fig. 1: Streak camera taken image in dual sweep mode (top) and results of the data analysis of the sliced image along the slow sweep direction.

* Work supported by the Bundesministerium für Bildung, Wissenschaft, Forschung und Technologie and by the Land Berlin

The remaining signal is analysed in terms of centred statistical moments, M_i . This starts with the determination of $\langle T_0 \rangle$, the centre of gravity (COG), of the intensity distribution in the slice, $I(t)$. In the next step up to the forth centred moment of $I(t)$ is calculated. The final results are the averages of the following quantities:

- $\langle T_0 \rangle = M_1/M_0$
- $\sigma = \text{sqr}(M_2/M_0)$
- $\text{Asymmetry} = (M_3/M_0)/\sigma^3$

Since each image contains up to 640 slices a corresponding number of results is obtained. With these samples, averaged values and their standard deviations are calculated. Channel numbers are translated into time with the scaling factors provided by the manufacturer of the camera. The slice wise results of the above analysis are shown at the bottom of Fig. 1.

The time resolution of the SC in the dual sweep mode is not only determined by the static time resolution which depends on the size of the entrance pin hole and the quality of the streak tube. There is an even larger uncertainty introduced by the phase noise and the fact that many images are superimposed. The phase noise of the master oscillator and of the 250 MHz fast sweep voltage was measured with a Rohde & Schwarz spectrum analyser FSE30. The analysis showed that these noise sources add a random contribution of ≈ 2.4 ps to the bunch length. The measured bunches appear enlarged due to the statistically independent effects and the actual bunch length can therefore be obtained by:

$$\sigma_{\text{act}} = \sqrt{\sigma_{\text{meas}}^2 - \sigma_{\text{ph.noise}}^2 - \sigma_{\text{stat.res.}}^2}$$

In order to check this approach the bunch length was measured with the SC as a function of the synchrotron frequency, F_{syn} , by changing the optics and reducing the momentum compaction factor. This can be done without beam loss at very low beam current. The measured as well as the corrected results are shown in Fig. 2 and these values agree well with the theoretical expectations:

$$\sigma(F_{\text{syn}}) = \text{const} \cdot F_{\text{syn}}$$

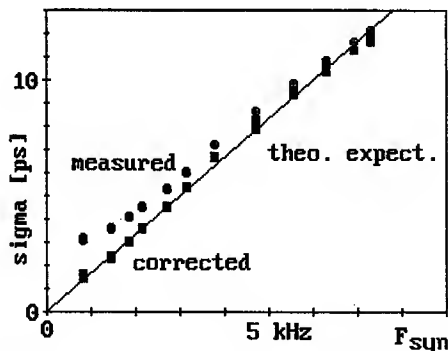


Fig. 2 Result of bunch length measurements as a function of the synchrotron frequency F_{syn} .

At small synchrotron frequencies the directly measured uncorrected bunch length saturates around 3 ps and the resolution limitations of the SC become dominant. The

simultaneously observed increased shift of the COG, the synchronous phase, as a function of bunch current is however a clear indication that the bunch length really is shorter than observed. The accuracy of the COG determination is not influenced by the resolution limitations of the SC.

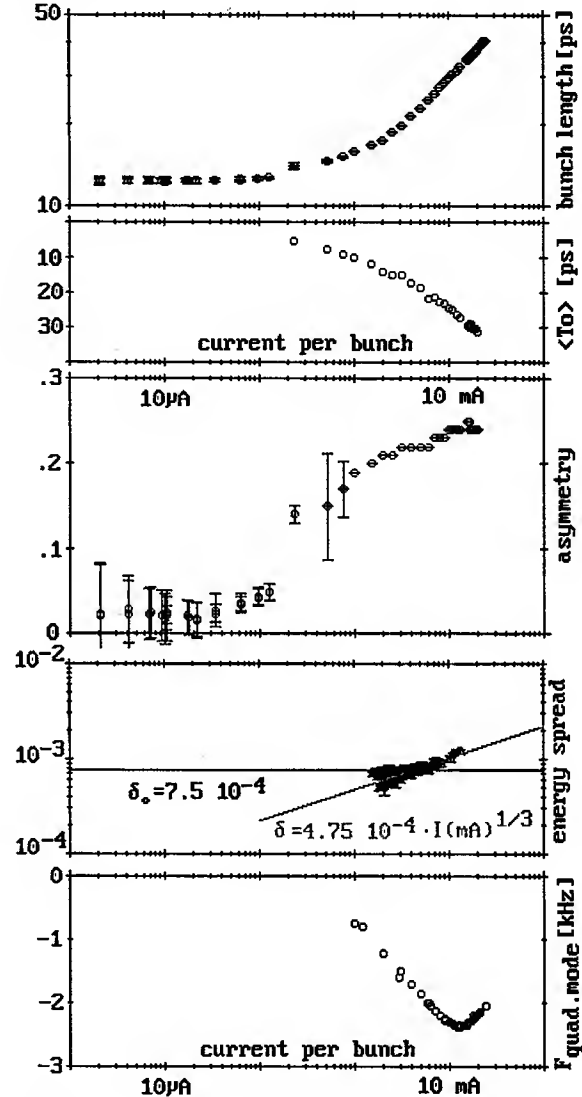


Fig. 3: Results of measurements with the nominal BESSY optics.

Most extensive studies were performed with the nominal optics and the results are shown in Fig. 3. In the case of long bunches the resolution limitation of the SC is not important. The top three curves are the bunch length, the shift of the synchronous phase, and the asymmetry of the distribution as measured with the streak camera. The bunch leans forward with a steeper leading edge of the distribution and moves up the RF voltage in order to compensate for the increased current dependent energy loss. This is consistent with a resistive interaction of the bunch with its surroundings. The observed phase shift

corresponds to 5 ps/mA. Other experimental results are included in Fig. 3 for comparison. The fourth trace shows the outcome of direct absolute measurements of the rms energy spread by Compton back scattering a CO₂-laser beam [2]. With this technique also the nominal momentum compaction factor was determined with high accuracy and found to be in agreement with the expectations based on the linear model of the storage ring lattice. The onset of the turbulent bunch lengthening shows up around 3 mA not as clearly as desired. The accuracy of this measurement suffers from the low rate of back scattered high energy photons obtained with a small beam current in the single bunch. At the bottom of Fig. 3 is shown the frequency shift of the quadrupole mode which is for very small beam current equal to $2 \cdot F_{\text{syn}}$. The quadrupole mode shifts down with beam current. The beam was excited by an amplitude modulation of the RF cavity voltage with a swept frequency and the quadrupole mode was detected as a sideband to the 500 MHz-component of the beam. A shift of 0.7 kHz/mA is found at low beam current. This result is close to the more direct determination of the incoherent synchrotron tune shift by looking at the shifts of the transverse $m=\pm 1$ -modes in the vertical plane [3]. The measured tune shift can be used to estimate the inductive impedance.

In Fig. 4 the current dependence of the bunch length is shown for different values of the momentum compaction factor (the synchrotron frequency). The asymptotic slope of the rms bunch length is proportional to $I^{1/3}$ which is close to $I^{1/3}$ as expected from a purely inductive impedance. An inductive impedance alone would however not produce energy widening.

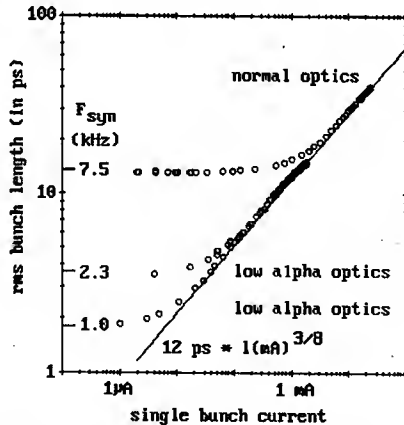


Fig. 4: Bunch length as a function of beam current for three different momentum compaction factors.

INTERPRETATION

These measurements are traditionally interpreted in terms of the vacuum chamber related geometrical impedance. Especially with very short bunches the radiation impedance can play a significant role in the longitudinal dynamics of a bunched beam. Fig. 5 shows the shielded coherent synchrotron radiation (CSR) impedance for the BESSY parameters and calculated with

equ. (B7) of Murphy, et al. [4]. Included in the figure is the spectral power density of a Gaussian bunch.

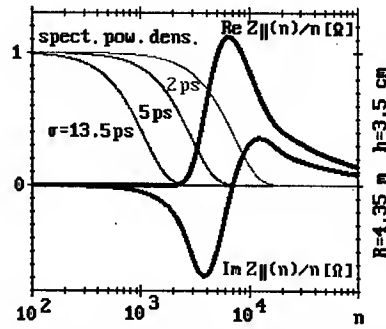


Fig. 5: CSR impedance for BESSY. The frequency is given by $\omega = n \cdot R/c$, with R the dipole bending radius, and c the speed of light.

There is hardly any overlap between the real and imaginary parts of impedance and the bunch modes for the nominal bunch length of 13.5 ps. Therefore, at least the shift of the synchronous phase and of the quadrupole mode presented in Fig. 3 must be attributed to the impedance of the vacuum chamber. So far only a very simple impedance model has been used to explain the observations:

$$Z_{\text{par}}(\omega) = R - i\omega L$$

It consists out of a resistive part $R=850 \Omega$ and an inductive part, L . The resulting predictions are not yet in acceptable agreement with all the measurements.

In summary, a variety of experimental results has been presented which are related to the longitudinal beam dynamics taking place in the storage ring BESSY. Comparison of these results with the estimated impedance of the BESSY vacuum chamber based on two and three dimensional calculations [5] and modelling with more advanced impedance models [6] including the shielded CSR effects will take place in the near future.

REFERENCES

- [1] Highlights 2002, published by BESSY
- [2] R. Klein, et al., Nucl. Instrum. Meth. A 486 (2002) 545-551, and private communication
- [3] P. Kuske, DIPAC 2001 Proceedings, pp. 31-35, ESRF, Grenoble
- [4] J. Murphy, et al. Part. Acc. 1997, Vol. 57, pp. 9-64
- [5] S. Khan, private communication
- [6] B.W. Zotter, S.A. Kheifets, in "Impedances and Wakes in High-Energy Particle Accelerators", World Scientific, 1997

COHERENT EMISSION OF SYNCHROTRON RADIATION AND LONGITUDINAL INSTABILITIES*

M. Abo-Bakr, J. Feikes, K. Holldack, P. Kuske, G. Wüstefeld, BESSY, Berlin, Germany

Abstract

At BESSY bursts of coherent synchrotron radiation around 20 cm^{-1} have been observed above a certain threshold current. The repetition rate of these bursts depends on the beam current and the thresholds vary strongly with the bunch length. Observed thresholds are in agreement with the theory of beam instability and microbunching due to coherent synchrotron radiation (CSR) [1].

INTRODUCTION

In storage rings the longitudinal beam dynamics of a bunched beam can be described with the Haissinski equations [2] as a distortion of the potential well as long as the energy distribution of particles remains Gaussian and is independent of the beam intensity. Above a threshold current longitudinal bunch shape variations are accompanied by energy widening and are called 'turbulent bunch lengthening' or 'microwave instability'. Based on the description of the particle distribution within a bunch in the two dimensional longitudinal phase space in terms of azimuthal and radial modes it is believed that the mixing of modes causes the instability. Whether and at which beam intensity modes are mixed so strongly that an instability sets in depends on the interaction of the particles. The interaction is either expressed by the longitudinal delta function wakefield or equivalently by the longitudinal coupling impedance. Until recently the contribution of the vacuum chamber and the influence of leading particles on trailing particles was seen as the dominating effect. However, with shorter and shorter bunches, the CSR interaction and the impact of the trailing on leading particles becomes more and more important for the stability of a bunched beam.

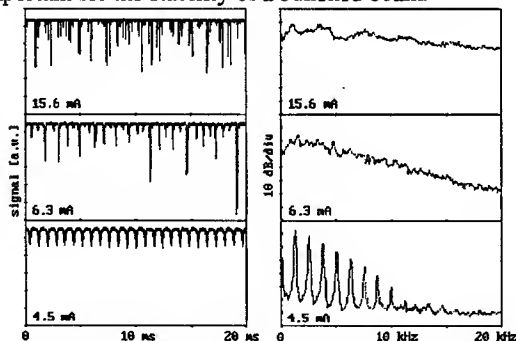


Fig. 1: Appearance of the radiation bursts in time and frequency domain.

* Work supported by the Bundesministerium für Bildung, Wissenschaft, Forschung und Technologie and by the Land Berlin

This paper presents observations made at the 3rd generation light source BESSY, a 1.7 GeV electron storage ring. Experiments were performed with bunches having a rms-length in the range from 2 ps up to 40 ps [3] by operating the storage ring lattice with reduced momentum compaction factor. The stability of single bunches was determined by looking at the time dependent emission characteristics of radiation around 10 cm^{-1} . Parts of the experimental results are compared to analytical and numerical calculations.

OBSERVATIONS

Bursts of Radiation

At the infrared beamline [4] $60 \times 40\text{ mrad}^2$ synchrotron radiation is focussed onto the input window of an InSb-FIR detector model HDL-5 from QMC Instruments Ltd. This detector is most sensitive around 20 cm^{-1} and is capable of resolving the passage of a single circulating bunch every 800 ns. The detector is internally coupled to an AC-amplifier so that only the input power variations of the radiation can be seen. For the results presented here the output of the detector was connected either to a digital scope or to a spectrum analyser. Figure 1 shows a comparison of the signals in time and frequency domain for single bunch currents above a clear, bunch length dependent threshold. In this case the zero current bunch length was 14.5 ps. Individual bursts of radiation are very short, can occur in groups, and appear more or less randomly. The average burst rate, the timing jitter between the bursts, or the randomness of the emission of bursts is more clearly seen in the frequency domain. At low beam currents the average rate is around 1 kHz and there is strong correlation between bursts and many multiples of the fundamental burst frequency. At medium intensity the pulses are less correlated and the spectrum becomes broad. The characteristics of the time domain data is very similar to the observations at the ALS [5].

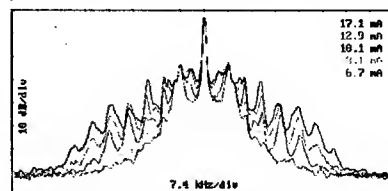


Fig. 2: Longitudinal beam spectra taken at 10 GHz as a function of single bunch current with $F_{\text{syn}}=7.4\text{ kHz}$

Longitudinal Beam Spectra

The synchrotron sideband spectra were acquired with a Rohde & Schwarz spectrum analyser FSEK30 connected to a stripline. Measurements were performed as a function

of beam current at 10 GHz and are shown in Fig. 2. More and more, and strongly shifted, harmonics of the synchrotron frequency appear as the beam current goes up. The first synchrotron sideband is always visible and presumably excited by phase noise of the RF system. The appearance of the quadrupole mode seems to be correlated with the radiation bursts.

Comparison of Burst rates and Spectra

Fig. 3 shows a comparison of longitudinal sidebands and radiation bursts observed simultaneously with two spectrum analysers. Opposite to what was claimed for the ALS [5] sidebands at a fraction of the synchrotron frequency ($F_{syn}=7.4$ kHz) are observed and identical to the repetition rates of radiation bursts. The conclusion is that the density modulations inside the bunch of electrons (microbunching) responsible for the bursting emission of radiation in the THz range are correlated with bunch shape variations showing up at 10 GHz.

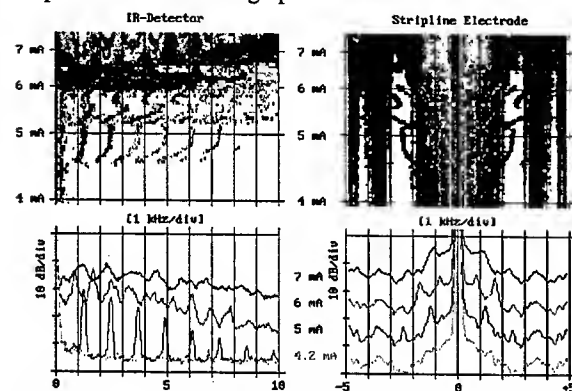


Fig. 3: Comparison of bursts of THz radiation and low frequency longitudinal sidebands at 10 GHz. The longitudinal stripline spectra are shifted by 10 dB each.

The measurement was taken during the natural decay of the intensity over many hours. Even though a spectrum is acquired every minute and the intensity does not change much during this time the burst's average repetition rate as well as the sideband frequencies can change slowly or can jump suddenly to a new value. At low beam intensity there seem to be typical rational relations between the burst frequencies before and after a jump: 2 to 3 and 3 to 4. This behaviour is very reproducible and better seen in Fig. 4. Below a threshold beam current no bursts of radiation can be detected. In the case shown in Fig. 3 and 4 two superconducting wavelength shifters were operated at 7 and 6 Tesla and the bursts set in at a single bunch current of 4.5 and 3.8 mA. Without these strong field insertion devices the threshold is 2.3 mA presumably due to the smaller natural energy spread in this case.

With shorter bunches the results are very similar, however, the first line appearing in the spectra of the bursts is close to three times the natural synchrotron frequency and also visible in the longitudinal spectra at 10 GHz. These lines shift strongly upwards with beam current. Well above the instability threshold the overall

behaviour is rather similar and independent of the bunch length: Regions of more or less correlated bursts with repetition times around 1 ms (the natural longitudinal damping time is 8 ms) and eventually at very high intensity random and chaotic bursts. By inserting a cut-on filter at 10 cm^{-1} in front of the IR-detector it could be verified that the more regularly appearing bursts are connected to radiation below the cut-on whereas the chaotic region is related to radiation above it.

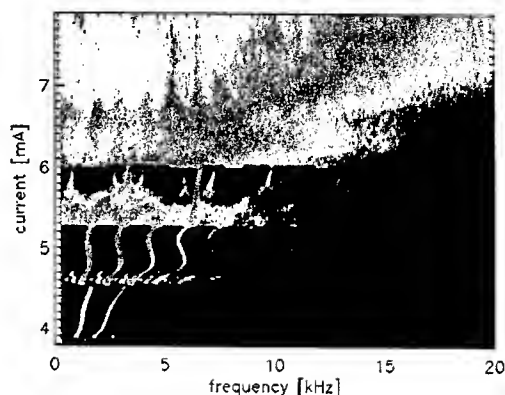


Fig. 4: Spectra of the FIR radiation bursts as a function of single bunch current.

COMPARISON OF OBSERVED AND CALCULATED THRESHOLDS

Thresholds are found either by looking at the appearance of bursts on the oscilloscope, appearance of lines in the spectra of the bursts, or by the sudden power increase observed with a lock-in amplifier with the revolution frequency as a reference [6]. The results of the experiments together with analytical and numerical calculations are presented in Fig. 5 as a function of the synchrotron frequency which is proportional to the bunch length. 1 kHz corresponds to a σ of 1.9 ps.

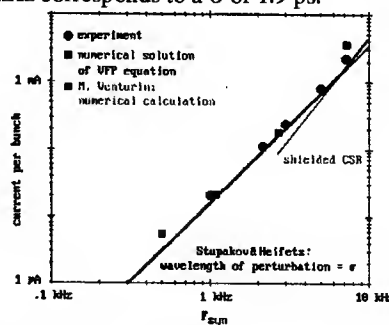


Fig. 4: Comparison of observed and calculated threshold currents as a function of the bunch length.

The predictions of the analytical theory [1] are shown as straight lines and the agreement with the observations and the calculations based on the numerical solution of the Vlasov-Fokker-Planck [7] equation is excellent. The analytical instability model extends a coasting beam result to bunched beams and it turns out that good agreement

with the observations is obtained if the wavelength of the perturbation is chosen equal to the rms bunch length. This conditions seems more stringent than the shielding. In general, coasting beam results are applicable to bunched beams if the bunch length is much larger than this wavelength.

Recently the interaction of a bunch with its own radiation field including shielding was investigated by the numerical solution of the VFP equations [7]. Similar calculations were performed for the BESSY case based on the original approach [8] and with the radiation wakefield between perfectly conducting parallel plates as given by Murphy, et al. as their equ. (9.10) [9]. In Fig. 6 an attempt is made to visualise the delta function wakefield. Note that the interaction goes forward as well as backwards. In the calculations the wakefield is used to determine the wakepotential of the bunch. Venturini [7] does this with the help of the shielded CSR impedance. His and our results concerning the threshold do agree especially if one takes into account that he assumes a distance between the plates 5 mm smaller than in reality ($H=3.5$ cm).

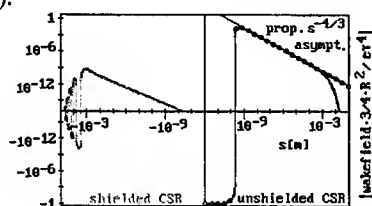


Fig. 6: Wakefield as used in the numerical solution of the VFP equations. In case of the free space radiation the wake acts only in the forward direction (shown in green and to the right) with the asymptotic dependence displayed in red. If the radiation takes place in between perfectly conducting parallel plates then the wakefield (yellow) drops to zero a few mm in front of the electron and additional oscillating contributions occur behind the electron (to the left).

The results of our calculations are collected in Fig. 7 as a function of the scaled intensity, Γ , where c is the speed of light, Z_0 is the vacuum impedance of $120\pi \Omega$, R is the dipole bending radius, $T_0 \cdot I$ is the total charge, V'_{rf} is the derivative of the accelerating voltage, and σ_{z0} is the rms-bunch length. δ_0 , δ and σ_0 , σ are the natural and the actual rms-width of the distribution function in momentum and time. These quantities, the shift of the centre of gravity, COG, $\langle T_0 \rangle / \sigma_0$, corresponding to the synchronous phase shift, and the asymmetry (skewness) of the distribution were determined from the statistical moments of the distribution functions that solve the VFP equation. Results for very short bunches which is identical to assuming no shielding are in agreement with the solution of the Haissinski equation given by Bane, et al. [10]. The other results have to be taken with some caution since the positive shift of the COG is related to an energy gain of the bunch as the current increases which is impossible in reality. This point has to be clarified before more detailed

comparisons of the numerical results with the observations can be made more faithfully. Nevertheless the current at which the energy spread starts to increase is taken as the onset of the instability and are in very good agreement with the observations and displayed in Fig. 5 as red squares.

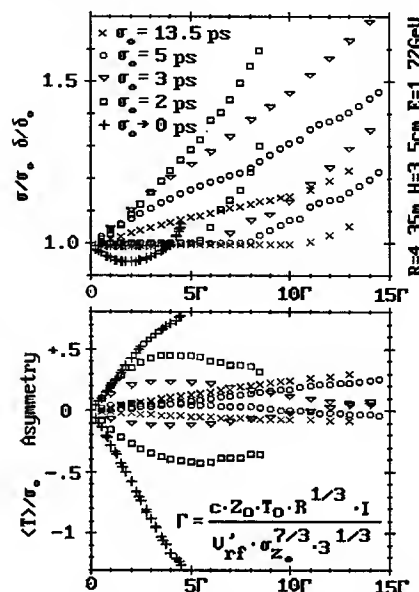


Fig. 7: Results of the numerical solution of the VFP equation for the wakefield due to shielded CSR.

The numerical solution of the VFP equation is valid also in the unstable region of intensities. There are indications that the observed time dependence of the more regular as well as the chaotic bursts do show up in these calculations. Studies in this direction including attempts to model the longitudinal spectra will be made in the future and as soon as the problems with the chosen wakefield have been removed.

In conclusion, a rich variety of observations on the dynamics of bunches in storage rings can be made at 10 GHz and well above into the THz region. The theoretical understanding of bunched beams well into the region of microwave instability is still incomplete.

REFERENCES

- [1] G. Stupakov, S. Heifets, Phys. Rev. ST AB **5**, 054402 (2002)
- [2] J. Haissinski, Il Nuovo Cimento, **18B**, no. 1, p. 72 (1973)
- [3] M. Abo-Bakr, et al., these proceedings
- [4] U. Schade, et al., Rev. Sci. Instr. **73**(3), 1568 (2002)
- [5] J. M. Byrd, et al., Phys. Rev. Lett. **89**, 224801 (2002)
- [6] K. Holldack, et al., these proceedings
- [7] M. Venturini and R. Warnock, Phys. Rev. Lett. **89**, 224802 (2002)
- [8] R. L. Warnock and J. A. Ellison, SLAC-PUB-8404
- [9] J. Murphy, et al. Part. Acc. 1997, Vol. 57, pp. 9-64
- [10] K. Bane, et al., AIP Conf. Proc. **367**, 191 (1996)

TRANSVERSE INSTABILITIES IN RHIC*

M. Blaskiewicz[†], J.M. Brennan, P. Cameron, C. Dawson, C. Degen, K. Drees, W. Fischer, E. Koropsak, R. Michnoff, C. Montag, T. Roser, T. Satogata, BNL, Upton NY 11973, USA
N. Catalan-Lasheras, CERN, Geneva, Switzerland

Abstract

The beam quality in RHIC can be significantly impacted by a transverse instability which can occur just after transition[1]. Data characterizing the instability are presented and analyzed. Techniques for ameliorating the situation are considered.

DATA

During the run of 2003 a button beam position monitor was used to measure instabilities in the deuteron beam. During the injection process the most intense bunch was determined. Beginning at transition, triggers were generated every 100 turns (1.28 ms) for this bunch. A total of 4000 triggers were generated each acceleration cycle and sent to a digital oscilloscope (Lecroy waverunner) in segmented memory mode. Each trigger generated 200 ns of data sampled at 2 GHz. Instabilities were observed in the vertical plane. Horizontal signals were much smaller.

Figure 1 shows a mountain range plot of sum (blue) and difference (red) signals from the buttons. The spacing between the buttons is 7 cm. The RC time constant of the button is 0.5 ns and has been ignored in the analysis. Trigger jitter was removed by integrating the sum signal, fitting a parabolic cap to the peak, and shifting the data using linear interpolation. Next, closed orbit effects were removed by subtracting the same fixed multiple of the sum signal from all the difference signals. Finally, each difference trace was viewed as a vector and a principle component analysis was done. This technique is referred to as canonical variables in the statistical literature [2]. In brief, one starts with a set of vectors $v_m(n)$, where $m = 1, 2, \dots, M$ is the index within a vector, and $n = 1, 2, \dots, N$ denotes the vector in the set. In Fig 1, each red trace corresponds to a different n , and m varies from 1 to $M = 30$ within a trace. The question is whether it takes all 30 indices to characterize the data. Toward this end assume the existence of a vector x_m and consider the Lagrangian

$$L = \sum_{n=1}^N \left(\sum_{m=1}^M v_m(n) x_m \right)^2 - \lambda \sum_{m=1}^M x_m^2,$$

where λ will be an eigenvalue. Demanding that $\partial L / \partial x_k = 0$ for $k = 1, 2, \dots, M$ leads to the equations of principle

*Work performed under contract numbers #DE-AC02-98CH10886 and #DE-AC05-00OR2275 with the auspices of the United States Department of Energy. Additional support from CERN

[†]blaskiewicz@bnl.gov

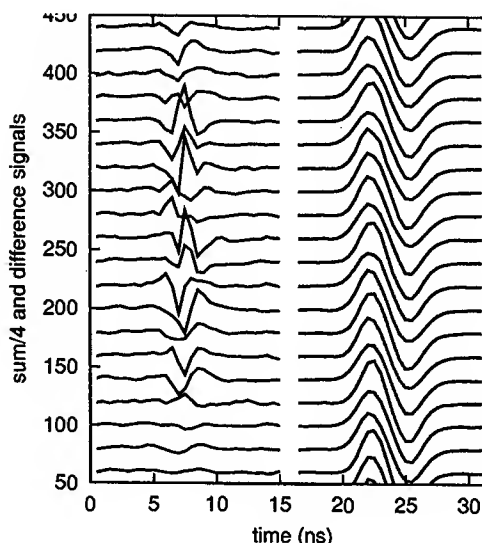


Figure 1: Difference (red, left) and sum (blue, right) data from a pair of vertical buttons. The sum data have been divided by 4.

component analysis. A principle component analysis corresponds to changing the set of basis vectors, and this new set of basis vectors concentrates the signal power in a natural way. A similar technique has been used to great benefit in various steering algorithms at the SLC [3]. Fig. 2 shows the 3 strongest principle components for the data in Fig. 1.

Using the raw button signals leads to the least noise in the principle component analysis but the eigenvectors are not intuitive. Integrating the eigenvectors with respect to time yields a basis that is proportional to the product of the offset and the instantaneous current. Fig. 3 shows the integrals of the principle components as well as the reconstructed beam current pulse from the average of the sum signal. The three strongest principle components are concentrated near the middle of the beam pulse. This is not a rigid or head-tail mode. The time series of the principle components are shown in Fig. 4. The envelope over-plotted on component 1 has an e-folding time of $\tau = 15.4$ ms. During the exponential phase, the amplitude of vertical oscillations evolves as $\hat{y} \propto \exp(t/\tau)$. The synchrotron frequency was $f_s = 14$ Hz, and the e-folding time of the transverse mode coupling instability should satisfy $\tau_{TMC} \gtrsim 1/\pi f_s = 23$ ms. After the instability saturates, the signal for component 1 beats with a ~ 30 ms period. This

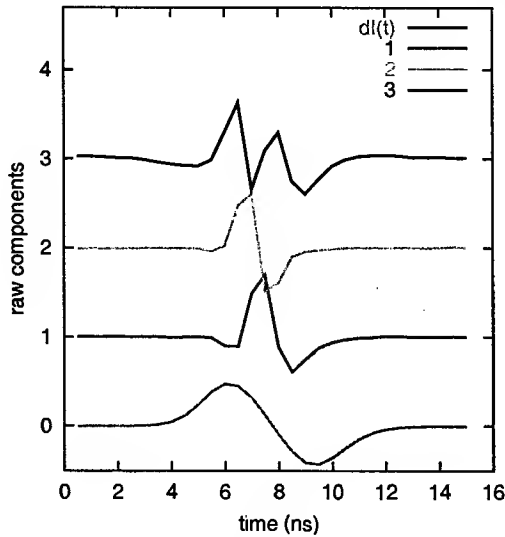


Figure 2: Average of sum signal and 3 strongest principle components for data in Fig 1. Component 1 accounted for most of the variation, then 2, then 3. The traces are offset vertically to improve clarity.

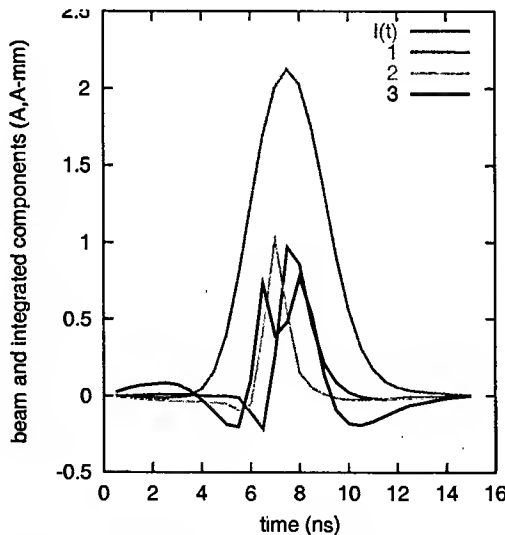


Figure 3: Integrals of the average sum signal and the 3 strongest principle components for data in Fig 1.

is about $1/2$ of the synchrotron period. One would expect a beating period $\gtrsim 1/f_s$ for two, recently decoupled, head-tail modes. Analyzing the sum data provides no evidence of longitudinal dipole or quadrupole oscillations.

Slower growing instabilities were also seen. Fig. 5 shows the integrated eigenmodes and the reconstructed beam current pulse when such an instability was present. While the integrated mode 1 is narrower than the average profile, the effect is small compared to that shown in Fig. 3. Also, a strong, longitudinal, quadrupole oscillation was present when this instability occurred. The time series of the two

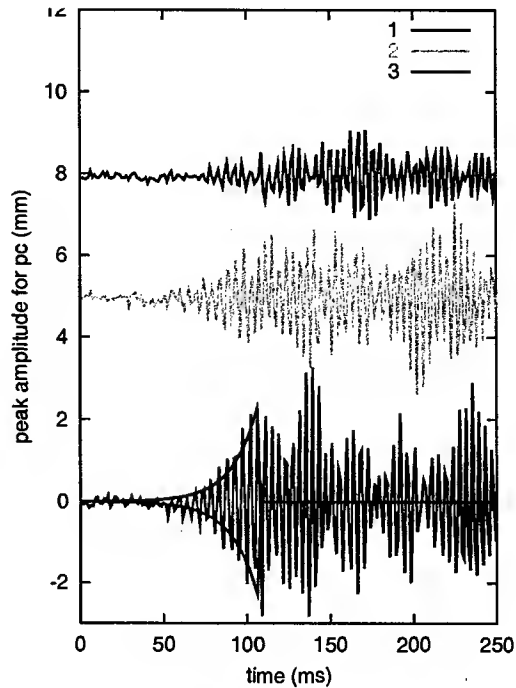


Figure 4: Time series of the 3 strongest principle components for the data in Fig 1. The traces are offset vertically to improve clarity.

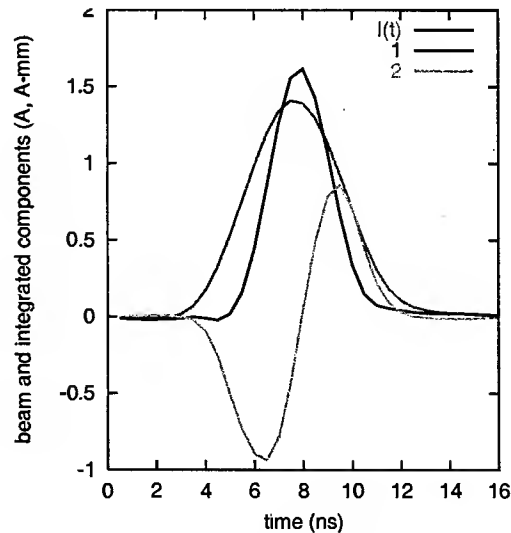


Figure 5: Integrals of the average sum signal and the strongest principle components for a slower instability.

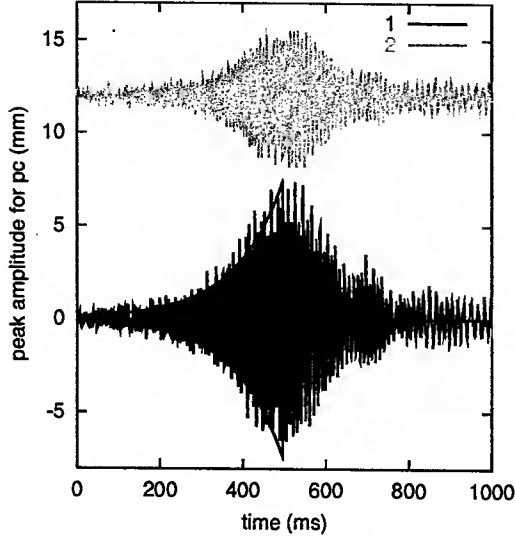


Figure 6: Time series of the 2 strongest principle components for a slower instability. The traces are offset vertically to improve clarity.

strongest principle components are shown in Fig 6. The envelope over-plotted on the time series for component 1 has an e-folding time of $\tau = 118$ ms.

While instabilities are fascinating from an intellectual point of view, they are a menace in the control room. The technique described above is not useful as a tool for tuning the machine so a new technique was developed. The coherence monitor takes data gated around the most intense bunch in the ring. The sum and difference voltages $V_s(t)$ and $V_d(t)$ are from a stripline BPM. On each turn n , a single number is generated,

$$S_n \approx C \int_{\text{bunch}} V_s(t) V_d(t) dt.$$

In actuality the product signal is low passed and then sampled, but parameters are such that the result is effectively identical. Next this discrete time series is put through a chip that calculates rms averages, and the control system samples the output at 720 Hz. This 720 Hz signal can be viewed through any operations console. Figure 7 displays the output during a vertical instability. Once the coherence monitor was commissioned, instabilities were readily identified and addressed. In fact, single bunch currents that are twice those shown in Figures 3 and 5 are now routine.

A few words on the tuning required to cure these instabilities is in order. First, since RHIC goes through transition, the chromaticity $\xi = \Delta Q / (\Delta p/p)$ must pass from negative to positive in the vicinity of transition. The initial configuration had ξ passing through zero a second or two after transition and the rate of $\dot{\xi} \approx 3\text{s}^{-1}$ was as fast as the magnets allowed. However, it was found that ξ passing through zero before transition worked better. In fact, because of the transition jump and other considerations, the chromaticities

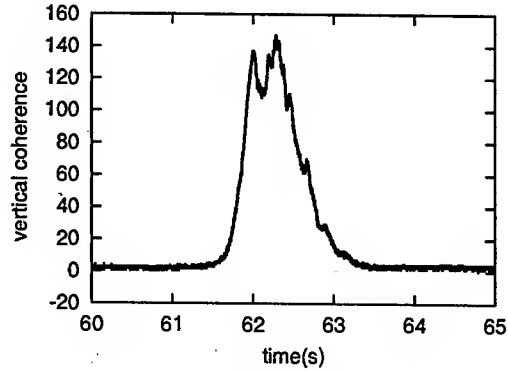


Figure 7: Vertical coherence signal used in the control room.

are not smooth, monotonic functions but exhibit excursions of order $\Delta\xi \sim 1$. By passing through ξ before transition the possibility of nearing $\xi = 0$ again, after transition, was reduced. However, why is having ξ pass through zero well before transition better than well after?

Along with tuning the chromaticity, octupoles were used to increase the tune spread. To leading order the tune shifts with betatron action are $\Delta Q_x = a_{xx}J_x + a_{xy}J_y$ and $\Delta Q_y = a_{xy}J_x + a_{yy}J_y$. For RHIC parameters

$$\begin{aligned} \delta Q_N &\equiv \langle a_{xx}J_x \rangle \approx \langle a_{yy}J_y \rangle \approx 5.6 \times 10^{-4}, \\ \delta Q_S &\equiv \langle a_{xy}J_x \rangle \approx \langle a_{xy}J_y \rangle \approx -8.8 \times 10^{-4}, \end{aligned}$$

where $\langle \rangle$ denotes averaging over the beam.

Since $\delta Q_S > \delta Q_N$, any theoretical treatment of octupole detuning should include both transverse dimensions. So far, only one transverse dimension has been modeled, but a few points are of interest. Firstly, even though $\gamma_t = 23.8$, the space charge tune shift, ΔQ_{sc} is many times larger than the synchrotron tune, Q_s . Neglecting space charge in our simulations, yields stable beams. However, when space charge is included, the unstable modes don't look like the figures, and the calculated growth time is $\tau \sim 100$ ms. Measurements of the transverse impedance [4] suggest that the actual transverse impedance is about 3 times larger than the our impedance model. It is possible that using the correct impedance in the simulations will yield agreement with the data, in Fig. 1 but impedance measurements of higher resolution are required.

REFERENCES

- [1] C. Montag, J. Kewisch, D. Trbojevic, F. Schmidt, PRSTAB, 5, 084401, (2002).
- [2] M. Kendall, A. Stuart, K. Ord, *The Advanced Theory of Statistics*, Vol. 3, Charles Griffin & Co. Ltd. London & High Wycombe (1983).
- [3] J. Irwin et. al., *Phys. Rev. Lett.*, **82** (8), 1684 (1999).
- [4] S.Y. Zhang, P. Cameron, A. Drees, R. Fliller III, H. Huang, T. Satogata, EPAC02, p1112.

LONGITUDINAL SOLITONS IN RHIC*

M. Blaskiewicz[†], J.M. Brennan, P. Cameron, W. Fischer, J. Wei
BNL, Upton NY 11973, USA

A. Luque, H. Schamel

University of Bayreuth, 95440 Bayreuth, Germany

Abstract

Stable, coherent, longitudinal oscillations have been observed in the RHIC accelerator. Within the context of perturbation theory, the beam parameters and machine impedance suggest these oscillations should be Landau damped. When nonlinear effects are included, long lived, stable oscillations become possible for low intensity beams. Simulations and theory are compared with data.

INTRODUCTION

Solitary waves in the form of notches or hotspots have been observed in coasting beams and the theory of solitary waves in plasmas [1] and coasting beams have been discussed in [2, 3, 4, 5, 6]. As an introduction we will use a very simple model due to Sacherer[7]. Consider a coasting beam with a phase space density that is piecewise constant. Figure 1 shows a simple picture in the frame comoving with the soliton, where the phase space density is either 0, f_0 , or $f_0 + f_1$; and the distribution is independent of time. We use x as the longitudinal coordinate and $p = dx/dt$. The coasting beam Hamiltonian is

$$H = p^2/2 + \ell/2 \int dp f(p, x)$$

where ℓ is negative for a focusing impedance. Since the phase space density is constant on contours of constant H one obtains algebraic equations, $H(x = 0, p = p_1) = H(x = L, p = 0)$ and $H(x = 0, p = p_0 + p_2) = H(x = L, p = p_0)$. While Sacherer resorted to numerical methods these equations are straightforward if one assumes $p_1 \ll p_0$ which results in

$$p_1 \approx \frac{-2\ell f_1}{1 + \ell f_0/p_0}.$$

If the correction term $\ell f_0/p_0$ is set to zero, the condition is identical to that for a phase space density of f_1 to self bunch. The change in the line density due to soliton is $\approx -p_1^2/\ell$. For an inductive impedance above transition $\ell > 0$ and one observes a notch, or hole in a wall current monitor (WCM) signal.

* Work performed under contract numbers #DE-AC02-98CH10886 and #DE-AC05-00OR2275 with the auspices of the United States Department of Energy. Additional support from the Deutsche Forschungsgemeinschaft (DFG)

[†] blaskiewicz@bnl.gov

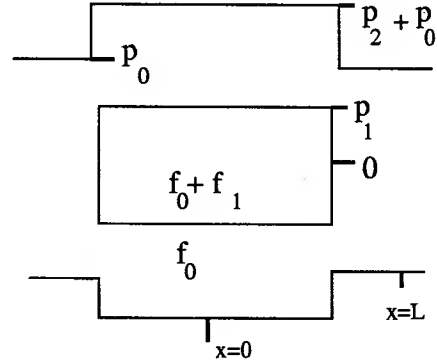


Figure 1: Simple picture of a soliton in a coasting beam. The horizontal axis is x , the longitudinal position within the bunch. The vertical axis is $p = dx/dt$.

DATA

Long lived coherence has been observed in the SPS[8], the Tevatron[9], and now the RHIC. Figure 2 shows a mountain range plot of the WCM for freshly injected protons with $\gamma = 25.9$. The amplitude of the coherent oscillation increased steadily, and Figure 3 shows the same bunch, still at injection energy, 17 minutes later. Figures 4 and 5 show different bunches at flattop with $\gamma = 107$. In all the cases shown, only the 28 MHz accelerating cavities were operating and the total acquisition time was 4000 turns ≈ 50 milliseconds. RHIC's transition energy is $\gamma_T = 23.8$, so all the data are above transition. All the data show a coherent oscillation which corresponds to a region of overdensity, or hot spot, in the longitudinal phase space. This behavior is commonplace in RHIC and we have never observed a stable hole. Measurements of RHIC's broad band impedance[10] give $Z/n = j(3 \pm 1)\Omega$ for the inductive wall contribution. The longitudinal space charge impedance at $\gamma = 25.9$ is $Z/n = j1.3\Omega$ and the space charge impedance becomes negligible at store. Therefore, we see hotspots with a defocusing impedance, which is just the reverse of what one expects for coasting beams.

THEORY

Attempts to understand the "dancing bunches" in the Tevatron[9] are based on the linearized theory of coherent instabilities[11]. The main idea is that the coherent tune shift due to the broad band impedance is larger than the synchrotron tune spread. This results in undamped coher-

ent modes. If this was the case in RHIC, the data shown in Figure 5 would require many modes and one would expect to see all kinds of coherent oscillations for different bunch lengths and intensities. We always see one, perhaps two, hotspots. In the rest of this section we develop an alternate theory which yields stable, long lived hotspots[12].

Let ϕ denote the position of a particle in the bunch, measured in units of RF radians; $\omega_{s,0}$ denote the small amplitude angular synchrotron frequency; and use $s = \omega_{s,0}t$ as the evolution variable. Let $\rho(\phi, s)$ be the normalized line density of the particles so that $\int d\phi \rho(\phi, s) = 1$. Take a simple broad band impedance model $Z = j\omega L$. Let $V(\phi) = V_{rf} \sin \phi$ be the RF voltage and let ω_{rf} be the angular RF frequency. Note that our definitions give $V_{rf} > 0$ below transition and $V_{rf} < 0$ above transition. Let Q denote the total charge within the bunch. Then the equation of motion for ϕ is

$$\frac{d^2\phi}{ds^2} + \sin \phi = \frac{LQ\omega_{rf}^2}{V_{rf}} \frac{\partial \rho(\phi, s)}{\partial \phi}, \quad (1)$$

To simplify notation set $\ell = -LQ\omega_{rf}^2/V_{rf}$. For a steady state, matched bunch, a positive value of ℓ defocuses the beam and leads to an incoherent synchrotron frequency that is less than the synchrotron frequency for $\ell = 0$. We have done multi-particle drift-kick simulations and have verified that equation (1) creates high density solitons for $\ell > 0$.

Equation (1) describes a Hamiltonian system, and we make a canonical transformation to the action angle variables for a simple harmonic oscillator J and Ψ . We make the ansatz that the phase space density undergoes a rigid rotation $f(J, \Psi, s) = g(J, \Psi - (1 - \beta)s)$ where the coherent frequency of the soliton is $\omega_c = (1 - \beta)\omega_{s,0}$. The Hamiltonian is then phase averaged over s resulting in

$$K = \beta J + \alpha(J) + V(J, \Psi), \quad (2)$$

where $\alpha(J) \approx -J^2/16$, generates detuning with synchrotron action and the coherent forces are generated by

$$V(J, \Psi) = \frac{\ell}{\pi} \int \frac{g(J_1, \Psi_1) d\Psi_1 dJ_1}{\sqrt{2J + 2J_1 - 4\sqrt{JJ_1} \cos(\Psi - \Psi_1)}}. \quad (3)$$

The Vlasov equation is

$$\frac{\partial K}{\partial J} \frac{\partial g}{\partial \Psi} - \frac{\partial K}{\partial \Psi} \frac{\partial g}{\partial J} = 0, \quad (4)$$

The simplest solutions of equation (4) are of the form $g(J, \Psi) = G(K(J, \Psi))$, without regard to separatrices. Both analytic and numerical solutions have been obtained. It is easiest to switch to Cartesian variables $A = \sqrt{2J} \sin \Psi$, $B = \sqrt{2J} \cos \Psi$. The analytic work relies on approximating the unperturbed Hamiltonian $K_0 = \beta J + \alpha(J) \approx \tilde{K} - \lambda(A - A_0)^2$ where $A = A_0$, $B = 0$ is the center of the soliton; and $\lambda \approx A_0^2/16$. Consider a phase space density of the form

$$g(A, B) = \frac{3}{2\pi ab} \sqrt{1 - (A - A_0)^2/a^2 - B^2/b^2} \quad (5)$$

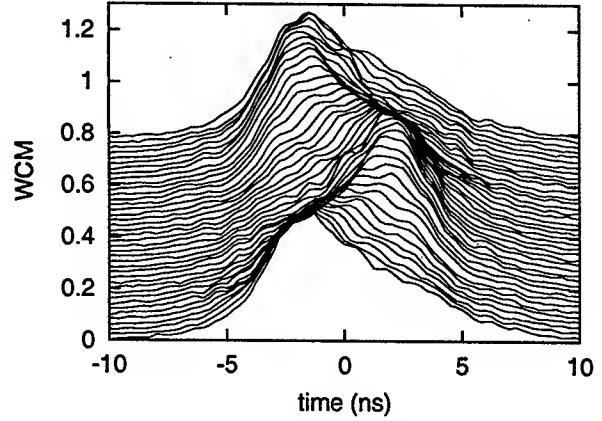


Figure 2: WCM data for a freshly injected bunch

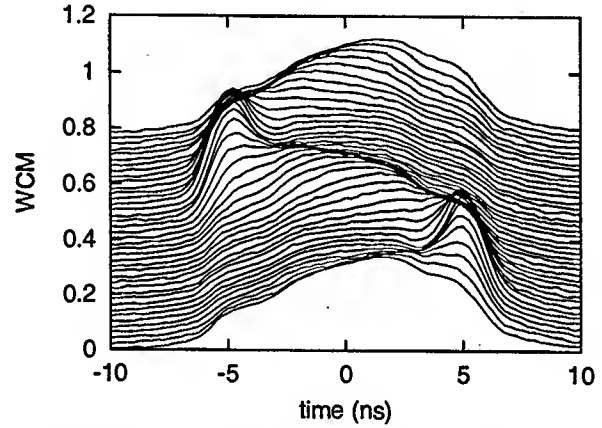


Figure 3: WCM data at injection for the same bunch as in Figure 2, but 17 minutes later.

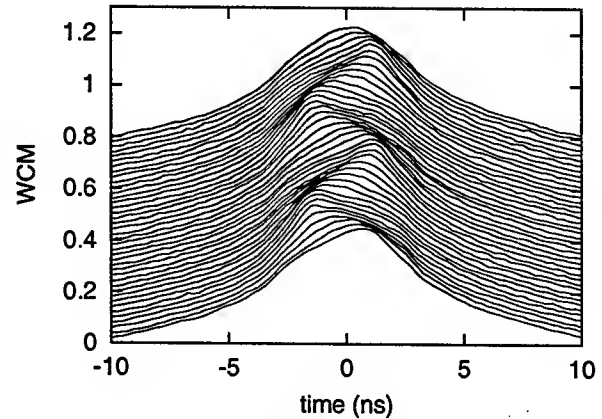


Figure 4: WCM data for a bunch at the beginning of flattop

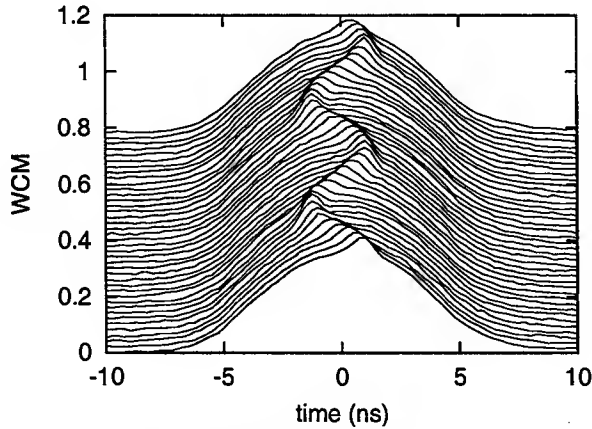


Figure 5: WCM data for a different bunch at flattop.

where a and b are the half widths of an ellipse and the solution is zero outside this ellipse. With this density $\partial V/\partial A = C_A(A - A_0)$ and $\partial V/\partial B = C_B B$, for points inside the ellipse. When combined with the previous approximation, the Vlasov equation is solved if

$$a^2(C_A - 2\lambda) = b^2 C_B. \quad (6)$$

Letting $r = a/b$ one finds that $0 \leq r < 1$ and

$$\frac{a^3 \lambda}{\ell} = \sum_{n=0}^{\infty} \left[\frac{(2n-1)!!}{2^n n!} \right]^2 (1-r^2)^n \left[\frac{3r}{4} - \frac{3nr^3}{1-r^2} \right], \quad (7)$$

$$\equiv R(r) \approx -0.464r \ln r - 0.285r(1-r) \quad (8)$$

where $(-1)!! \equiv 1$, $0 \leq R \leq 0.10$, and the fractional error of the approximate expression is $\leq 5\%$. Positive values of ℓ are needed for self bunching. Also, since $a < b$, the peak of the line density is largest when the soliton is farthest from the bunch center, as in Figure 3.

We have also done iterative solutions. We search for solutions of the form $g(A, B) = G(K(A, B))$. Start by choosing a value of β and take an initial distribution $g_0(A, B)$. Iterate using $g_{n+1}(A, B) = G(K_0(A, B) + V_n(A, B))$, where $V_n(A, B)$ is calculated using equation (3) with g_n . Figures 6 and 7 show solutions for $G(K) = C_0 \theta(K - K_0) \sqrt{K - K_0}$ which is the same as was used for the analytic solution.

REFERENCES

- [1] H. Schamel, Phys. Rep. **140**, 161, (1986).
- [2] H. Schamel, Phys. Rev. Lett. **79** 2811, (1997).
- [3] H. Schamel, DESY 97-161 (1997).
- [4] H. Schamel, R. Fedele, Phys. Plasmas **7**, 3421, (2000)
- [5] S. Koscielniak, S. Hancock, M. Lindroos, PRSTAB **4** 044201 (2001)
- [6] J-M. Griessmeier, H. Schamel, R. Fedele, PRSTAB, **5** 024201, (2002)
- [7] E. Raka *private communication*.
- [8] D. Boussard, L. Evans, J. Gareyte, T. Linnekar, W. Mills, E.J.N. Wilson, IEEE TNS, NS-26, 3484, (1979)
- [9] V. Lebedev, Presentation to the Fermilab Accelerator Advisory Committee, February 4, 2003.
- [10] M. Blaskiewicz, J.M. Brennan, P. Cameron, W. Fischer, EPAC02, 1488, (2002).
- [11] V.I. Balbekov, S.V. Ivanov, IHEP preprint 91-14, Protvino, 1991.
- [12] M. Blaskiewicz, A. Luque, H. Schamel, J. Wei *in preparation*.

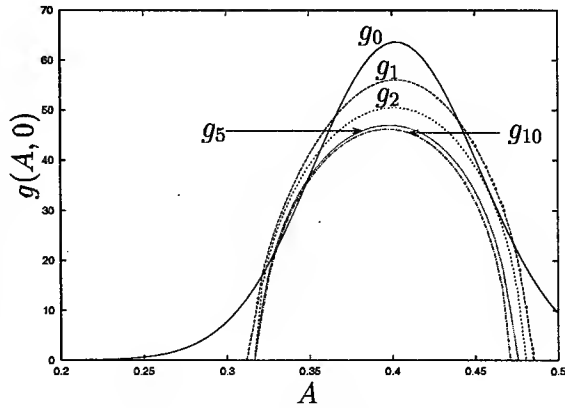


Figure 6: Values of the distribution taken through the line containing the coordinate origin and the peak of the soliton, during the iterative solution.

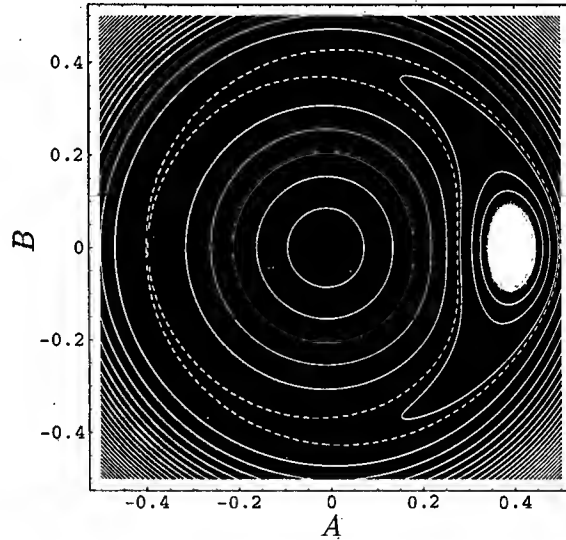


Figure 7: Final solution after 10 iterations.

EFFECTS OF SPACE CHARGE AND NONLINEARITIES ON COLLECTIVE INSTABILITIES OF A LONG BUNCH *

A.V. Fedotov, J. Wei
BNL, Upton, NY 11973, USA
V. Danilov
ORNL, Oak Ridge, TN 73831 USA

Abstract

We start with discussion of the effects of space charge and nonlinearities on the transverse microwave instability. A possibility of Landau damping with octupole correctors, using an example of the SNS ring, is explored. We also discuss the required strength of such nonlinearities for a bunched beam in the presence of the space-charge tune spread, as well as their effect on dynamic aperture and emittance dilution.

INTRODUCTION

Recently, the intensity limitation in the SNS associated with the transverse instability due to the extraction kickers was explored [1]. In this paper, we explore damping of the instability with the octupole correctors. Although some analytic theories on this subject exist, their application to a realistic situation may be limited. A complicated dynamics in a real machine can be studied in a more self-consistent way using computer simulations. In such an approach, many effects which influence dynamics of the beam can be accurately included. As a result of such studies for the SNS, we find a substantial damping of the instability even when the octupoles introduce very small tune spread, which is not expected based on the existing theories. A possible physical explanation is given, although ultimate conclusions are driven based on the simulations.

TRANSVERSE INSTABILITY IN THE SNS

The instability due to the extraction kickers in the SNS was studied using the UAL code [1]. It was found that even with the chromaticity of $\xi = -7$, the growth rate of the unstable harmonics below 10 MHz were relatively large ($\tau^{-1} \approx 4ms^{-1}$ for a 2 MW beam). This is despite the fact that such a chromaticity introduces the tune spread much bigger than the growth rate of the instability. An incomplete compensation happens because of the space charge tune shift. The onset of the instability with some halo growth was observed by the end of the accumulation in the SNS, which takes about 1 ms [1]. Since that studies, the impedance of the extraction kickers was reduced by a factor of two, due to the aperture increase of the magnets [2]. As a result, the instability growth rate for the present impedance budget was reduced to just below

$\tau^{-1} = 2 ms^{-1}$. Here, we present studies of the instability damping using the old impedance of the SNS [1], which was chosen in order to observe a noticeable growth of the unstable harmonics by the end of the accumulation process.

THRESHOLDS AND SPACE CHARGE

For a long bunch in the SNS and a very slow synchrotron motion, a coasting beam model becomes a good approximation. The growth rate of the instability, due to the coupling impedance (in the absence of any damping mechanism), can be obtained from

$$\tau^{-1} = -Im(\Omega) = \frac{qcI_p}{4\pi E_0\nu_0} Re(Z_{\perp}), \quad (1)$$

where q is the charge of a proton, I_p is the peak current, $E_0 = \gamma mc^2$, ν_0 is the zero-current betatron tune, and Ω is the coherent dipole frequency.

To damp the growth rate with the frequency spread $\Delta\omega$, one should have $\Delta\omega > Im(\Omega)$. When $\Delta\omega$ comes from the momentum spread in the distribution, the stability condition is written, using Eq. 1, as [3]:

$$|Z_{\perp}| < F \frac{4E_0\nu_0\gamma\beta}{IR} \frac{\Delta p}{p} \left[(n - \nu_0)\eta - \xi \right], \quad (2)$$

where R is the average machine radius, η is the slippage factor, $\xi = (\delta\nu)/(\Delta p/p)$ is the chromaticity, and F is the form factor which depends on the distribution. Since η is small in the SNS, the low n harmonics, which sample the peak of the extraction kicker impedance, can be effectively damped only by the chromatic term in Eq. 2. It was shown that one gets some chromatic damping even for the bunched beam in the SNS [1].

If there is also a frequency spread from the nonlinear elements, it contributes to the total spread $\Delta\omega$ required for damping. The stability condition in Eq. 2 does not take into account the effect of the space charge, which shifts the tunes of the incoherent particles even in the absence of the beam-pipe surroundings. A typical statement, which could be found in the literature, is that a tune spread due to the nonlinear elements, required for damping, should be comparable to the space-charge tune shift. Such a large spread may destroy the dynamic aperture. Here, we explore to what extent such guidelines are valid.

First, we review the role of the space charge in the stability of a collective dipole motion. Obviously, the fact that the particles inside the bunch have strong space-charge tune

* Work supported by the SNS through UT-Battelle, LLC, under contract DE-AC05-00OR22725 for the U.S. Department of Energy.

shift cannot influence the dipole oscillation of the beam, in the absence of the wall images. When one takes into account the effect of the images, both the incoherent frequencies and the dipole coherent frequency have the intensity-dependent shifts. In fact, the difference between the coherent dipole and incoherent self-field shifts is called the space-charge impedance. However, such an impedance should not be used in the stability condition directly. First, its incoherent part does not influence the coherent motion, and, more importantly, it has a pure imaginary contribution which is not directly responsible for the growth rate of the instability (see Eq. 1). On the other hand, the shift due to the imaginary space-charge impedance can influence the stability condition. Its effect will be different depending whether there exists a strong $Re(Z_{\perp})$ contribution from other sources of the impedance. In the SNS, there is a large $Re(Z_{\perp})$ from the extraction kickers. One can assume the stability diagram obtained from the dispersion relation without the space charge and then take into account the effect of space charge by introducing a shift along the imaginary axis. A more self-consistent approach is to derive the dispersion relation with the space charge [4]. With both approaches, one finds that, for the SNS case, the space charge has a destabilizing effect on the transverse instability, which was confirmed in simulations [1].

OCTUPOLES AND DAMPING

The octupole correctors in the SNS are intended for correction of the resonances, and thus produce only small tune spread of about 0.01. This is much smaller than the space-charge incoherent tune shift of 0.15 for a 2MW beam. However, the simulation studies with a full-intensity full-size beam showed that such weak octupoles may be effective in the damping process, which warranted further investigation. In addition, it was realized that, for the octupole spread to be effective, there should be a large amplitude particles within the beam. As a result, the spread becomes less effective because of the dynamic painting in the SNS, where the large size beam is reached only by the end of the accumulation. Such a finding forced us to perform a realistic study with a full 1060-turn injection process.

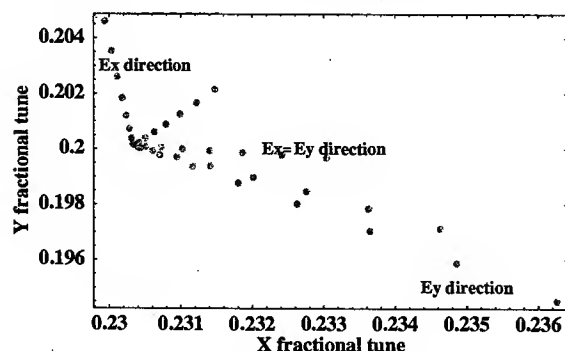


Figure 1: Tune spread by octupoles placed at large β_y .

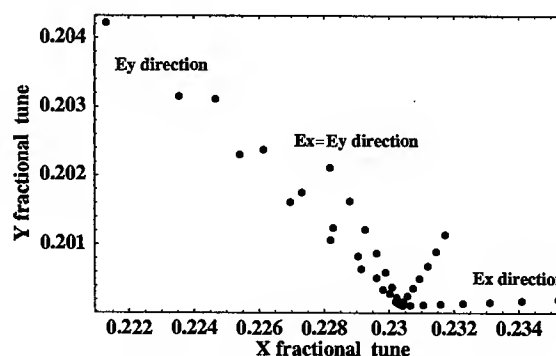


Figure 2: Tune spread by octupoles placed at large β_x .

EFFECTIVE SPREAD

Not surprisingly, one polarity of octupoles gave a stabilizing effect while the other did not, since a proper sign is necessary to introduce the incoherent spread in the direction where it overlaps the coherent spectrum. The damping effect from the octupoles was strongly influenced by their location because the octupole tune spread depends on the particle emittances and beta-functions. It is necessary to generate a spread which affects most of the particles in the transverse distribution. In the SNS, where we use the correlated painting, a substantial portion of the particle distribution has equal emittances. As a result, the most effective location and combination of the octupoles is the one which introduces the largest tune spread in the direction of $\epsilon_x = \epsilon_y$. We refer to such a spread as "effective".

For simplicity, in Figs. (1, 2, 4), only five values of $\alpha = 0, 0.25, 0.5, 0.75, 1.0$, which represent the correlation between the particle emittances, are shown. Here, the correlation is defined as $\alpha = \epsilon_x / (\epsilon_x + \epsilon_y)$, with $\alpha = 0$ corresponding to the particles in the y direction (indicated in Figs. as "Ey direction") with only ϵ_y emittances, and $\alpha = 1$ corresponding to the x direction (indicated in Figs. as "Ex direction"). Note that, due to the space-charge redistribution, the particles occupy all the emittances between the pure ϵ_x and ϵ_y motions. In each line, the dots correspond to eight different amplitudes of the particles within the beam. Only fractional tunes for the working point $(\nu_{0x}, \nu_{0y}) = (6.23, 6.20)$ are shown. The instability due to the extraction kicker impedance of the SNS occurs in the vertical direction, which requires (for damping) the incoherent spread to overlap the vertical coherent spectrum.

Figure 1 shows the tune spread due to a family of 4 octupoles located at large β_y . The strength of all correctors was taken equal with a negative polarity. The effective spread is not in the right direction, and no damping of collective oscillation is observed. A positive polarity gave spread in a proper direction but it was not sufficient. For the octupoles at the location of a large β_x and negative polarity, the effective spread (shown in Fig. 2) has a significant impact on the instability. Figure 3 shows the growth rates

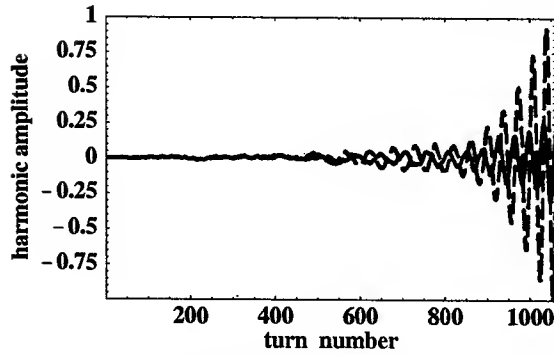


Figure 3: Time evolution for unstable harmonic: wrong sign of octupoles (red - dash line), right sign (blue - solid).

of the unstable harmonic at 6 MHz. The red (dash) line indicates the growth rate for the octupoles with the incorrect polarity, corresponding to Fig. 1, while the blue (solid) line corresponds to the octupole spread of Fig. 2. In addition, Fig. 4 shows that a more effective tune spread can be obtained with the two families of octupoles. In this example, the octupoles at large β_y locations had positive polarity while the octupoles at large β_x had negative polarity. Both families were powered at a nominal current of 10 Amp. The corresponding damping of the unstable harmonic at 6 MHz is shown in Fig. 5. The damping rates were comparable to the case when only one family was used but powered at a maximum current of 17 Amp.

Note that simulations were done for the impedance which is a factor of two larger than the present impedance budget. For a presently expected impedance and the SNS base-line intensity of $N = 1.5 \times 10^{14}$ (rather than 2×10^{14} used here), the growth rate of the instability was found to be only about $\tau^{-1} = 1 \text{ ms}^{-1}$, which was damped with the corrector settings corresponding to Fig. 4.

EFFECT ON DYNAMIC APERTURE

Although the strength of the octupoles was small, there is still a question whether they can effect the dynamic aperture. We suggest that, if the choice of correctors is done in a proper way, the effect on dynamic aperture may be minimized. For example, four correctors were placed one per superperiod of the SNS with the same phase advance between them. The strength and sign of all correctors in the family were the same so that only the systematic harmonics were driven. For the w.p. (6.23,6.20), the octupole resonances above the working point are driven by the $n = 25$ imperfection harmonic. As a result, we did not see emittance growth associated with these resonances when we used the correctors for Landau damping.

MECHANISMS OF DAMPING

We observed that the instability can be effected or even damped with the frequency spread from the octupoles be-

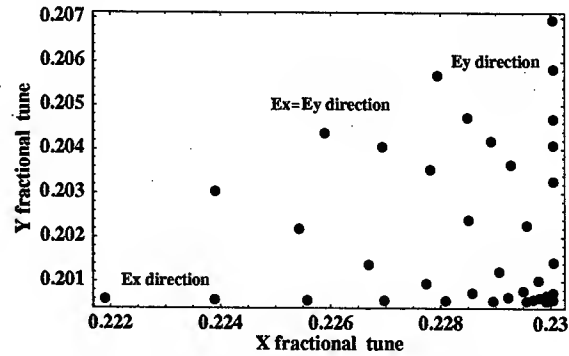


Figure 4: Tune spread with two families of octupoles.

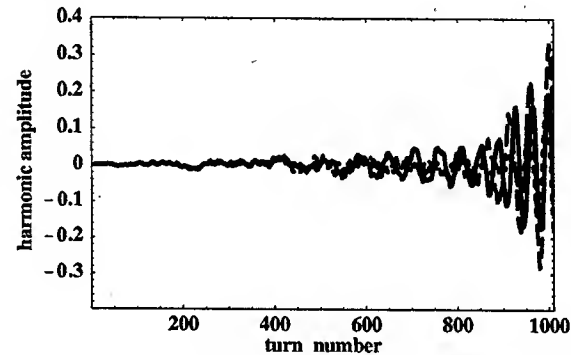


Figure 5: Time evolution for unstable harmonic: β_y family with positive sign (pink, long-dash), β_x family with negative sign (blue, solid), two families (black, short-dash).

ing much smaller than the space-charge tune shift. To understand such effect one needs to take into account the tunes of the particles in the head and tail of the bunch correctly. These tunes are only weakly depressed by the space charge so that even small frequency spread in the right direction can influence the coherent rigid oscillation of the bunch. Also, the coherent shift due to the wall images for the head and tail of the bunch is different from the shift at the longitudinal bunch center which results in the effective spread along the bunch [1].

ACKNOWLEDGMENT

We are indebted to M. Blaskiewicz for useful discussions on the subject. We also thank Accelerator Physics groups of the SNS for numerous comments and useful suggestions.

REFERENCES

- [1] A.V. Fedotov et al, Proc. of EPAC'02, p. 1350 (2002).
- [2] D. Davino et al., BNL/SNS Tech Note 112 (2002).
- [3] W. Schnell and B. Zotter, CERN-ISR-GS-RF/76-26 (1976).
- [4] M. Blaskiewicz, Phys. Rev. ST AB, V. 4, 044202 (2001).

COUPLING IMPEDANCE MEASUREMENTS OF THE SNS RF CAVITY AND EXTRACTION KICKER MAGNET*

H. Hahn, M. M. Blaskiewicz, D. Davino[#], SNS Project, BNL, Upton, NY 11973, USA

Abstract

The Spallation Neutron Source (SNS) is a high intensity machine with peak currents in the accumulator ring reaching ~50 A at the 1.4 MW design level. This unprecedented beam intensity necessitates a careful investigation of coupling impedances posing as potential performance limitations. Impedance estimates of accelerator components pointed to the RF cavities and extraction kickers as the major contributors to the impedance budget and extensive measurements were performed on their prototypes. Impedance measurements were performed using the standard wire method.

INTRODUCTION

The Spallation Neutron Source consists of a linear accelerator, accumulator ring, and a mercury target [1]. A 1 GeV H⁺ beam is charge-exchange injected into the ring, where it is maintained as one bunch by the rf system, and extracted by a fast kicker magnet. The SNS RF system is based on three cavities operating at the fundamental frequency, ~1 MHz and one cavity at the second harmonic. The single turn beam extraction is achieved by means of fourteen kicker magnets.

At extraction time, there are 1.5×10^{14} protons corresponding to a ~50 A peak current. Maintaining stability of the high intensity beam until extraction is essential to minimize beam losses. Impedance driven instabilities are a potential source of beam loss and preventing them by establishing and enforcing the impedance budget represents a crucial design challenge. Impedance estimates from some sources such as space charge, beam position monitors, resistivity of the beam pipe, ceramic pipe coatings, bellows, steps, ports and vacuum valves can be calculated from handbook formulas with sufficient confidence. Other components, in particular the RF cavities and the extraction kicker magnets requires verification by measurement [2]. The estimates indicated that the performance of the SNS will largely depend on reducing the longitudinal impedance of the rf cavities and the transverse impedance of the extraction kickers [3,4]. Instability thresholds for longitudinal and transverse instabilities are established by the total impedance but the growth rate is determined by the resistive part and needs special care. In view of their importance, cavities and kickers were extensively measured. In this paper, the impedance measurement

techniques using the single wire for the longitudinal impedance and the twin-wire for the transverse impedance are discussed and the experimental results are presented. The results from the RF cavity and extraction kicker prototypes generate the confidence that the design performance is achievable.

RF CAVITIES

The SNS RF system consists of four cavities, three of them are operating on the fundamental and one on the second harmonic, with the rotation frequency being 1.058 MHz [5]. The reentrant cavity has two RF gaps and is driven by the power amplifier in parallel by means of side bus-bars. The inductance is provided by coaxial stacks of Philips 4M2 ferrite rings. The total length of the unit is about 2.7 m and the gaps are spaced ~1.3 m apart. The cavity is placed into a covering box, from which it is DC isolated by ceramic rings at each end. The preliminary coupling impedance measurements of the cavity showed a series of strong longitudinal resonances which were caused by the ceramic rings [6]. Shorting the ceramic rings, to simulate the operational capacitors, suppressed most of the resonances with the remaining analyzed in this paper.

The construction of the cavities is identical, and the operating frequency is adjusted by adding four gap capacitors of 750 pF for the fundamental or by adding only one 750 pF capacitor for the first harmonic. A view of the cavity end showing the placement of the capacitors is given in Fig.1. It was found that the radially concentrated capacitor arrangement resulted in a dipole mode responsible for a sharp horizontal transverse impedance resonance. Placing four 40 Ω carborundum rods (glow-bars) on top and bottom of each gap damped the resonances by a factor of two. The resonance appears only in the cavity with the fundamental capacitors. It is worth noting that the impedance contribution is only horizontal and not additive to the extraction kicker vertical impedance.

Longitudinal Impedance Measurement

The longitudinal coupling impedance of a component is conveniently measured on the bench by inserting a wire in the center of the beam pipe to form a coaxial transmission line. The forward scattering coefficient S_{21} is measured both for the device under test and a reference tube of the same length. The coupling impedance is then obtained from the ratio $S_{21}^{DUT} / S_{21}^{REF} = S_N e^{j\phi}$ [7].

*SNS is managed by UT-Batelle, LLC, under Contract No. DE-AC05-00OR22725 for the U.S. Department of Energy.

[#]Now at: Dipartimento di Ingegneria, Universita' del Sannio, Piazza Roma, 82100 Benevento, Italy.

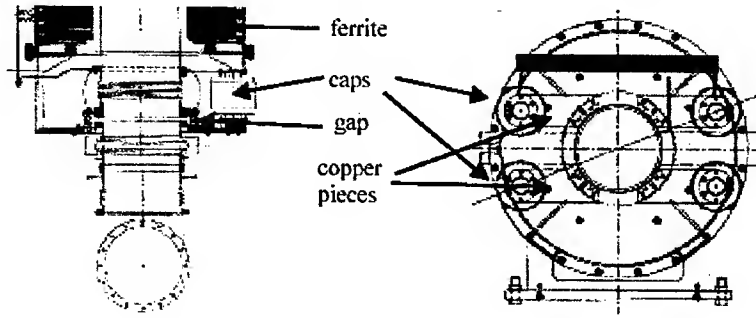


Fig. 1. Cavity end seen from the top (left) and from the end (right). Also shown is the carborundum rod.

In the typical situation, the characteristic impedance, R_C , of the line is different from the standard impedance of the network analyzer, R_0 . Consequently a matching network, such as an impedance transformer, must be inserted. Often, for simplicity's sake, a resistive matching is applied. On the input side, forward and backward matching is achieved with a series and parallel resistor,

$$R_p = G_p^{-1} = R_C \frac{\eta}{\sqrt{1-\eta}}, R_{IN} = R_C \left(\frac{\eta}{1-\sqrt{1-\eta}} - 1 \right) \quad (1)$$

with $\eta = R_0/R_C$. Furthermore, on the output side, forward matching is achieved with a series resistor $R_{OUT} = R_C(1-\eta)$. As example for the present measurement, the characteristic impedance of the 1.25 mm \varnothing wire in the ~15 cm beam tube is

$$R_C = \frac{Z_0}{2\pi} \ln \frac{r_o}{r_i} \approx 288 \Omega \quad (2)$$

(vs. 265 Ω measured) requiring the matching resistors, $R_p \approx 55 \Omega$, $R_{IN} \approx 262 \Omega$, and $R_{OUT} \approx 238 \Omega$.

Depending on the configuration of the DUT, the scattering coefficient is interpreted according to the log or HP formula. The log formula is only applicable to distributed impedances, small compared to R_C , thus precluding strong resonances. Here, the impedance is seen by the beam at the two cavity gaps. At sufficiently low frequencies, the two cavity gaps act as lumped impedances and the scattering coefficient is interpreted via the modified HP formula,

$$Z_0 = 2R_C \left\{ \left(\frac{\cos \Phi}{S_N} - 1 \right) - j \frac{\sin \Phi}{S_N} \right\} \quad (3)$$

The measurements were performed with the network analyzer, Agilent 8753ES. The ratio can be stored in the instrument as data/memory, and by using the conversion from scattering to impedance format, the real and imaginary part of the coupling impedance is directly obtained. The longitudinal coupling impedance of the RF cavity is shown in Fig. 2. with the ceramic rings shorted [8]. The remaining small resonances can be parameterized by fitting the measured results to

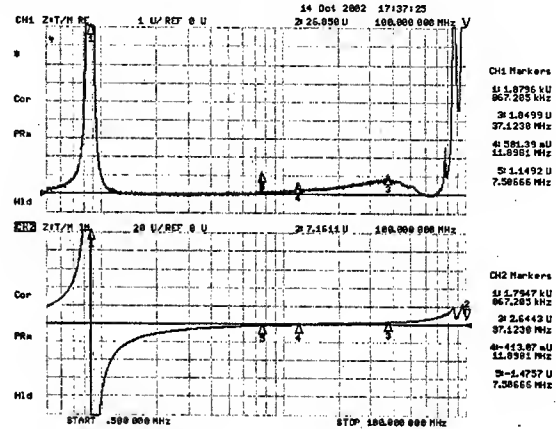


Fig. 2. Longitudinal impedance of RF cavity

$$Z_0 = \sum_i \frac{R_i}{1 + jQ(f/f_0 - f_0/f)} \quad (4)$$

with the parameters given in Table I.

Table I. Spurious Cavity Resonances

f (MHz)	R (Ω)	Q	Z/n
7.49	4.5	88	0.6
11.4	2.17	59	0.2
35	3.8	1	0.1
87	74	20	0.9
100	98	19	1

Transverse RF Cavity Impedance

The transverse coupling impedance of the RF cavity is measured by means of a homemade twin-wire (TW) line, driven by commercial wide-band transformers (North Hills NH15880) with a center-tapped secondary serving as 180° hybrid. The TW line has a spacing of $\Delta = 41$ mm and a characteristic impedance of $R_C = 215 \Omega$ as measured with the communication signal analyzer, Tektronix CSA 803.

The transverse cavity modes are excited at the gaps and represent lumped impedances. Since they are small compared to R_C , the scattering coefficients can be interpreted with the log formula,

$$Z_1 = \frac{cZ^{DUT}}{\omega\Delta^2} = -2 \frac{cR_C}{\omega\Delta^2} \ln S_N \quad (5)$$

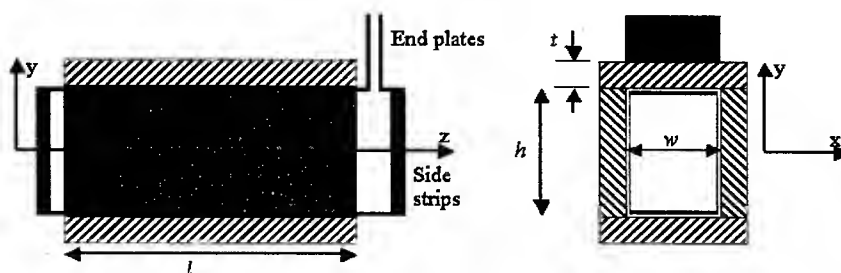


Fig. 4. Schematic View of SNS Extraction Kicker Magnet, $h = 248$ mm, $w = 159$ mm, $l = 360$ mm.

No impedance is generated in vertical direction which thus allows an in-situ reference measurement [6]. The horizontal impedance with the gaps set for the first harmonic is shown in Fig. 3. The glow-bars (red curve) give a factor ~ 2 damping.

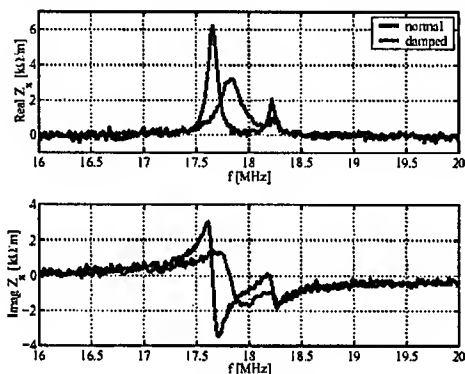


Fig. 3. Transverse impedance of the RF cavity

EXTRACTION KICKER MAGNET

A schematic view of the extraction kicker is shown in Fig. 4. Since the 14 kickers make the biggest contribution to the transverse impedance budget, a prototype was constructed and extensively measured [9]. The longitudinal impedance is minimized by placing copper (so-called eddy current) stripes at the middle plane of the side ferrite bricks, thereby keeping the real $Z/n \leq 1\Omega$.

The transverse impedance is measured via the standard twin-wire method as described above. At low frequencies, from ~ 50 MHz down to below 1 MHz, the signals are small and the data is noisy, even after averaging and smoothing. Clean results were obtained by directly measuring the Z^{DUT} at the bus-bar gap and interpreting it by taking $\Delta = h$ in the conversion from longitudinal to transverse impedance [10].

The vertical transverse impedance is composed of a intrinsic value, obtained with the gap shorted, and the coupled value determined by the external termination. The kicker prototype was measured with feed-thru and the 25Ω termination simulating the operational condition. The real part of the kicker impedance, obtained with the wire (W) and direct (D) method, is shown on top and with expanded frequency scale at the bottom of Fig. 5.

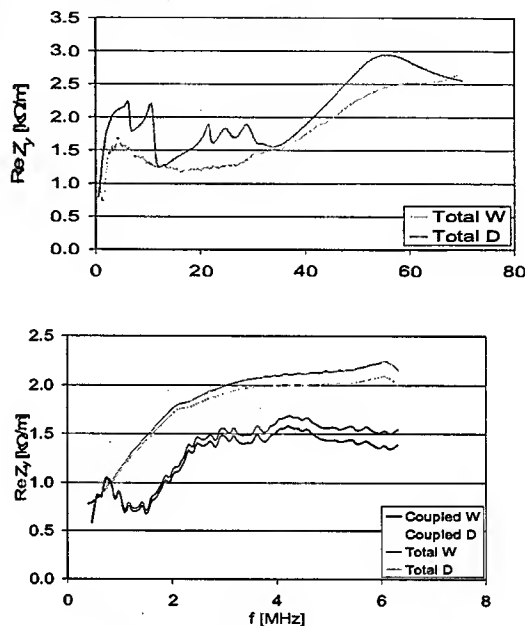


Fig. 5. Vertical impedance of kicker with 25Ω

ACKNOWLEDGEMENTS

Advice and support from M. Brennan and A. Zaltsman and the members of the RF group is acknowledged.

REFERENCES

- [1] J. Wei, Proc. EPAC 2002, Paris, France, p. 1064
- [2] J. G. Wang & S.Y. Zhang, EPAC 2000, Vienna, p. 672
- [3] M. Blaskiewicz, BNL/SNS Tech. Note No. 42 (1998)
- [4] J. Wei et al., (ref. 1) p. 1067
- [5] M. Blaskiewicz, et al., Proc. 2001 PAC, Chicago, IL, p. 490
- [6] D. Davino, H. Hahn, M. Blaskiewicz, BNL/SNS Tech. Note No. 115 (2002)
- [7] F. Caspers, in *Handbook of Accelerator Physics and Engineering*, A. W. Chao and M. Tigner, eds., (World Scientific, Singapore, 1998), p. 570.
- [8] H. Hahn, M. Blaskiewicz & A. Zaltsman, BNL/SNS Tech. Note No. 117 (2002)
- [9] D. Davino & H. Hahn, Phys. Rev. ST Accel. Beams **6**, 012001 (2003), and ref. 1, p. 1067.
- [10] H. Hahn, BNL/SNS Tech. Note No. 120, (2003).

THE ELECTRON CLOUD INSTABILITY OF THE LHC BEAM IN THE CERN SPS

G. Arduini, K. Cornelis, W. Höfle, G. Rumolo, F. Zimmermann, CERN, Geneva, Switzerland

Abstract

The electron cloud induced by the LHC beam in the SPS occurs mainly in the dipoles and it is responsible for strong transverse instabilities. In the horizontal plane a coupled bunch mode instability develops in a few tens of turns at injection. Tune shift measurements, mode number and phase space analyses have been performed at different energies and provide information about the electron cloud distribution and its dynamics. In the vertical plane a single bunch head-tail like instability occurs. The equivalent 'electron-cloud wake field' is inferred from the analysis of the head-tail motion of the bunches of the LHC beam train.

INTRODUCTION

Because of the large bunch population (N_{bunch}) and of the bunch spacing the LHC beam [1][2], when injected in the SPS, induces electron multipacting for N_{bunch} higher than a given threshold (N_{th}) depending on the secondary emission yield of the vacuum chamber. Above the multipacting threshold the following phenomena are observed when the LHC beam is injected:

- dramatic dynamic pressure increases (by more than a factor 100), mainly in the arcs, and build-up of an electron cloud along the LHC beam bunch train (72 bunches) [3];
- in the dipoles (covering 70% of the SPS circumference) the electron cloud surrounds the beam for $N_{\text{th}} < N_{\text{bunch}} < 5 \cdot 6 \times 10^{10}$ p. For larger N_{bunch} electrons concentrate in two stripes centred on the beam and parallel to the magnetic

field lines and for $N_{\text{bunch}} > 11 \times 10^{10}$ p a third stripe centred on the beam appears [4];

- horizontal and vertical transverse instabilities [5][6].

TRANSVERSE INSTABILITIES

The transverse instabilities developing for $N_{\text{bunch}} > N_{\text{th}}$ start from the tail and progress to the head of the batch. For a single batch with nominal bunch population all the bunches except the first 10-15 are affected. The lower the bunch population is, the smaller will be the number of bunches affected by the instability. When more batches are injected with nominal batch spacing the instability affects a larger and larger number of bunches as we move from the first to the last (fourth) batch. These observations are compatible with the measured build-up and decay of the electron cloud density along and between successive bunch trains [3].

The properties of the instability are significantly different in the horizontal and vertical plane. In the horizontal plane it manifests itself as a coupled-bunch instability while in the vertical plane a single bunch head-tail like instability occurs [7].

Horizontal plane

Fig. 1 shows the two most important spatial and temporal patterns of the horizontal oscillations of the batch obtained by Singular Value Decomposition of the 72 bunch positions recorded over 1000 consecutive turns for $N_{\text{bunch}} = 3 \times 10^{10}$ p, just above the multipacting threshold [8].

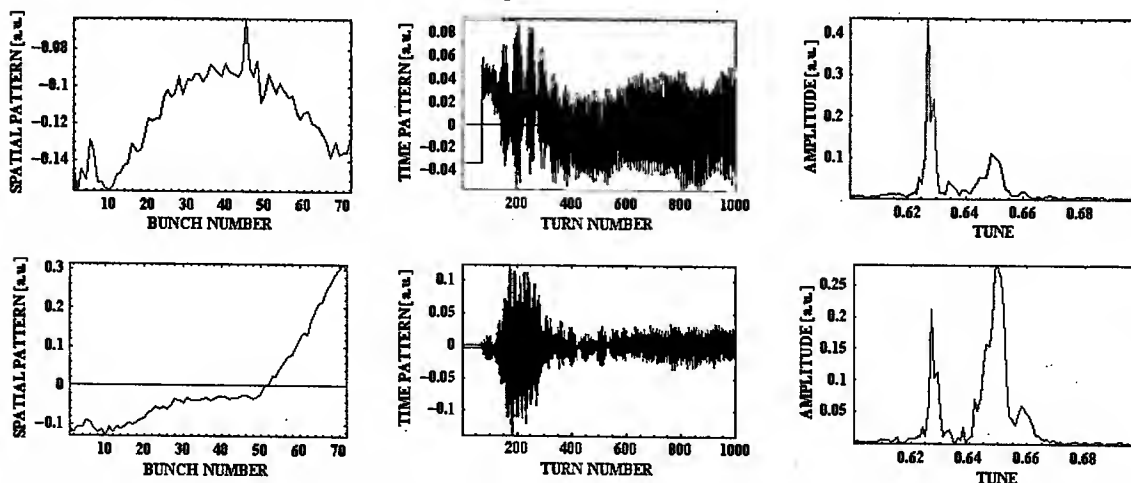


Figure 1. Two dominant spatial and temporal patterns together with the Fourier transform of the temporal patterns of the horizontal oscillation. $N_{\text{bunch}} = 3 \times 10^{10}$ p and $q_H = 0.18$, $q_V = 0.13$. Injection occurs 71 turns after the start of the acquisition.

Only low order coupled-bunch modes contribute to the above spatial patterns that oscillate with two main tunes:

the unperturbed fractional tune (0.627) and 0.65. The transverse feedback is designed to damp these low

frequency modes (few MHz). A “knee” is clearly visible in the second spatial pattern at about bunch 50 where the oscillations start to have significant amplitude. This corresponds with the position along the batch where the electron cloud starts to build-up.

The rise time of the instability is a few tens of turns and is only weakly dependent on the bunch population. Measurements at 5×10^{10} p/bunch show that the rise time is even by about 50% longer than at 3×10^{10} p/bunch while at the nominal bunch population (11×10^{10} p) the rise time is again comparable with that measured at 3×10^{10} p/bunch.

At higher intensity the two well-separated frequencies of oscillation are no more visible. Measurements of the tune of each bunch as a function of its amplitude of oscillation evidence an important detuning (Fig. 2). At the nominal intensity a significant positive detuning is measured for low amplitudes (~ 0.01 in 1 beam sigma for nominal beam emittance) followed by a negative detuning. A sort of hysteresis is also observable. These are clear indications of non-linear behaviour of the coupling force between bunches in the tail of the LHC batch.

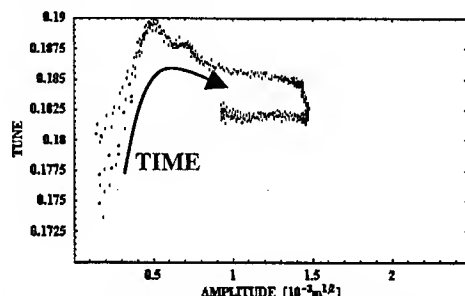


Figure 2. Tune vs. amplitude of oscillation for a bunch in the tail of the batch and $N_{\text{bunch}} = 11 \times 10^{10}$ p. This measurement was performed with the LHC beam high intensity working point ($q_H = 0.18$, $q_V = 0.13$). The data for the first 700 turns after injection are plotted (each point represents a sliding average over 32 turns of the amplitude and phase advance per turn). $\beta_H \sim 21$ m at the monitor.

The characteristics of the electron cloud instability in the SPS are a consequence of the fact that multipacting mainly occurs in the arcs. In a dipole field electrons are bouncing up and down in the vacuum chamber and are tightly bound to the magnetic field lines around which they spiral. For the lower intensities ($N_{\text{th}} < N_{\text{bunch}} < 5-6 \times 10^{10}$ p/bunch) the electron cloud can be approximated as a vertical ribbon of uniform density developing along the batch and starting from a given bunch n . Any transverse movement of the bunch, or of a slice of it, affects the electron cloud distribution which, in turn, affects the trailing bunches, or trailing slices, generating bunch-to-bunch or head-tail coupling. Due to the presence of the magnetic field no net horizontal motion is imparted to the electrons during the bunch passage. Consequently no significant distortion of the electron cloud distribution

occurs in the horizontal plane during the bunch passage and the electron cloud can couple only subsequent bunches. When a bunch has a horizontal displacement with respect to the preceding one, it will go through the electron cloud ribbon off-centre and will experience a linear force F (in the approximation of a uniform electron cloud distribution with density ρ_{ec}) [7]:

$$F = -\frac{e\rho_{ec}}{\epsilon_0}(x_{j+1} - x_j)\chi(j-n)$$

where x_j and x_{j+1} are the horizontal positions of bunch j and $j+1$, respectively and χ is the step function. The strength of the electron cloud coupling does not depend directly from the bunch population but only indirectly via ρ_{ec} which depends on N_{bunch} . In general the range of the coupling due to the electron cloud can be longer than the bunch spacing and one bunch can couple to more than one trailing bunch. The behaviour of the 72 bunches can therefore be described by a set of coupled linear differential equations of second order. The solution of such a system, including terms approximating the effect of the resistive wall wake, allows determining the most unstable modes. A tune shift of $+0.025$ (with respect to the unperturbed tune) and a growth time of 60 turns are estimated assuming that the electron cloud has a density $\rho_{ec} = 1 \times 10^{12}$ e/m³ and develops after 50 bunches (as observed experimentally for $N_{\text{bunch}} = 3 \times 10^{10}$ p). This is in good agreement with the observations.

For $N_{\text{bunch}} > 5 \times 10^{10}$ p the electron cloud distribution takes the form of two stripes symmetrically placed with respect to the beam and the uniform approximation is no longer valid, except for small amplitudes where the electron cloud density is nevertheless reduced as compared to the lower intensity case. This explains why the growth time for $N_{\text{bunch}} = 5 \times 10^{10}$ p is longer than that measured for $N_{\text{bunch}} = 3 \times 10^{10}$ p. Significant detuning with amplitude is expected for oscillation amplitudes comparable with the electron stripe half-separation (few mm for the $N_{\text{bunch}} = 5 \times 10^{10}$ p). The non-linear behaviour is exacerbated for the nominal bunch intensity where an additional central stripe appears.

The growth rate of the instability has been measured at different energies and decreases almost linearly with the momentum of the beam. This is in good agreement with the simple model described above.

Vertical plane

In the vertical plane the electron cloud instability is a single bunch instability: a measurement of the position of the bunches of the batch over several turns does not show any phase correlation among subsequent bunches. The instability mainly affects the tail of the batch and the rise time is decreasing with increasing N_{bunch} (the maximum amplitude of oscillation is achieved in ~ 600 turns for $N_{\text{bunch}} = 3 \times 10^{10}$ p and in 300 turns for 5×10^{10} p). Several sidebands are visible close to the main tune line with separation close to the synchrotron frequency $Q_s \sim 0.004$ indicating the head-tail nature of the instability. The comparison of the spectra of the signals provided by a

wide-band strip-line coupler for a bunch of the head and one of the tail of the batch reveals vertical motion inside the bunch at frequencies of about 700 MHz (full bunch length = 4 ns) particularly enhanced in the trailing bunch as a result of the electron cloud.

The difference with respect to the horizontal plane is due to the fact that in the vertical plane the motion of the electrons under the influence of the electric field of the bunch is not constrained by the presence of the magnetic field as for the horizontal plane. For that reason any motion of the head of the bunch will couple to the tail similarly to what a short-range wake field does.

Electrons are pinched during the bunch passage and the density of the cloud in the region traversed by the bunch is significantly enhanced. The density evolution of the electron cloud with time depends strongly on the bunch population and this explains the dependence of the growth rate of the instability on the bunch population.

Because of the strong electron cloud density modulation during the bunch passage the effect is very different from that of conventional wake fields, the electron cloud wake depends strongly on the position along the bunch from where it is excited and cannot be expressed simply in the form $W(z_s - z_w)$, where z_s and z_w are the longitudinal positions of the source and witness particles, respectively [9][10].

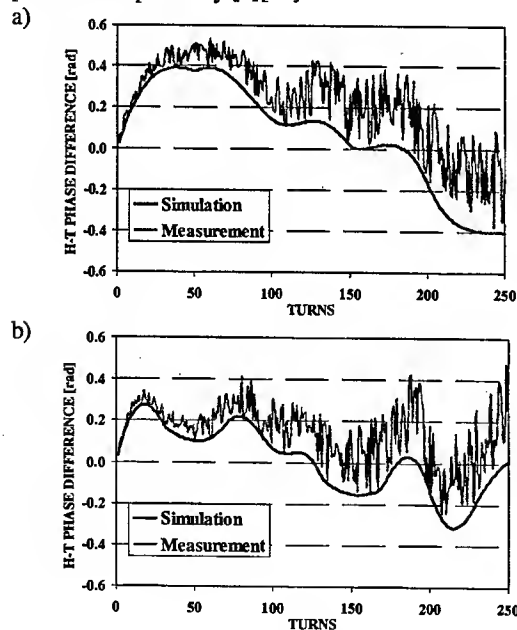


Figure 3. Calculated and measured head-tail phase difference for a bunch of the head (a) and a bunch of the tail (b) of the LHC batch [7].

Within this approximation an effective wake field associated with the electron cloud can be inferred by comparing the head-tail phase difference evolution with time for a bunch with and without electron cloud. Fig. 3 presents such a comparison for a bunch of the head of the

batch (no electron cloud) and a bunch of the tail (electron cloud).

The measurement can be reproduced if a wake field with interaction length 0.3 to 0.5 times the bunch length is introduced to model the electron cloud head-tail coupling.

Simulations taking into account the interaction of electron cloud with the beam [9] and simple head-tail models based on the effective electron cloud wake seem to indicate that the electron cloud enhances the effects of the machine impedance and that the combination of the electron cloud and impedance wake is responsible for the fast growth rate of the vertical instability.

Simulations confirm also the beneficial effect of high positive chromaticity to fight the vertical instability as observed experimentally [9].

SUMMARY

In the SPS the different behaviour of the electron cloud instability of the LHC beam in the horizontal and vertical planes is a consequence of the confinement of multipacting in the dipoles. In the horizontal plane low order coupled bunch instabilities are observed and can be cured by the transverse feedback. In the vertical plane a single bunch head-tail instability develops as a result of the interplay of the electron cloud and of the machine impedance, coupling the motion of the head and the tail of the bunch. The only cure found so far is running at high positive vertical chromaticity ($\xi = (\Delta Q/Q)/(\Delta p/p) > 0.1$).

REFERENCES

- [1] P. Collier ed., "The SPS as Injector for the LHC - Conceptual Design", CERN/SL/97-07 DI.
- [2] G. Arduini et al., "The LHC Proton Beam in the SPS: an Update", these Proceedings.
- [3] J.-M. Jimenez et al., "Electron Cloud Studies and Analyses at SPS for LHC-Type Beams", these Proceedings.
- [4] G. Arduini et al., "Measurement of the Electron Cloud Properties by means of a Multi-Strip Detector in the CERN SPS". Proc. of EPAC '02, p. 1437.
- [5] G. Arduini et al., "Transverse Instabilities of the LHC Proton Beam in the SPS", Proceedings of EPAC2000, p. 341.
- [6] G. Arduini et al., "Transverse Behaviour of the LHC Proton Beam: an Update", Proceedings of PAC2001, p. 1883.
- [7] K. Cornelis, "The Electron cloud Instability in the SPS", CERN-2002-001, p. 11.
- [8] Y. Ohnishi et al., "Study of the Fast Ion Instability at KEKB Electron Ring", Proc. of EPAC2000, p. 1167.
- [9] G. Rumolo and F. Zimmermann, "Electron Cloud Simulations: Beam Instabilities and Wake Fields", CERN 2002-001, p. 147.
- [10] E. Perevedentsev, "Head-Tail Instability Caused by Electron Cloud", CERN-2002-001, p. 171.

INVESTIGATION OF SPACE CHARGE EFFECTS IN THE SPS

H. Burkhardt, G. Rumolo, F. Zimmermann, CERN, Geneva, Switzerland

Abstract

Space charge effects generally play a rather minor role in high energy machines like the SPS. Rather high space charge tune shifts may however become unavoidable in the SPS for the heavy ion beams required by the LHC. We describe recent measurements performed with intense proton beams in the SPS. The space charge effects were enhanced by a reduction of the injection energy from 26 to 14 GeV.

1 INTRODUCTION

Space charge effects are strongly energy dependent ($\sim 1/\gamma^3$). High space charge tune shifts in excess of 0.5 have been observed in smaller machines [1–3]. Such high space charge tune shifts are typically accompanied by blow-up and short lifetimes, well below a second.

In larger, high energy machines like the SPS, space charge effects usually play a rather minor role. Space charge tune shifts in the SPS generally remain well below 0.1 and do not cause any lifetime problems or blow-up [4, 5]. For the LHC heavy ion program, it is planned to inject lead ions into the SPS at $\gamma \approx 5.5 - 7.3$ [6, 7]. Space charge tune shifts above 0.1 may become unavoidable. In addition, good lifetimes and little blow-up during the about 40 seconds long injection plateau will be important. The required heavy ion beams will only become available in several years from now after an upgrade of the injector chain.

We describe here an investigation performed with high intensity proton beams. To enhance space charge effects, the injection energy in the SPS was lowered from 26 GeV to 14 GeV.

2 SPACE CHARGE TUNE SHIFT

We used the maximum single bunch intensity currently available from the PS for low emittance single bunch operation of $N = 1.2 \times 10^{11}$ protons. The relevant beam parameters are summarized in Table 1. Beam dimensions and the momentum spread are given in terms of single σ r.m.s values.

Table 1: Measured beam parameters.

Proton momentum	14 GeV/c
Initial proton intensity	$N = 1.2 \times 10^{11}$
Relative momentum spread	$\sigma_{\Delta p/p} = 1.9 \times 10^{-3}$
Normalized emittances	$\epsilon_{x,N} = 3.43 \mu\text{m}$
	$\epsilon_{y,N} = 3.75 \mu\text{m}$
Bunch length	$\sigma_t = 0.75 \text{ ns}$

The emittances were obtained from transverse profile measurements using a wire scanner (WS51995 in the SPS

in a place without dispersion). The measurements generally showed approximately Gaussian beams and no significant blow-up over time scales of about a second. Bunch lengths were measured using a longitudinal pickup and a digital oscilloscope.

The beam dimensions in x, y around the ring were calculated from

$$\sigma_{x,y} = \sqrt{\epsilon_{x,y} \beta_{x,y} + (D_{x,y} \sigma_{\Delta p/p})^2}. \quad (1)$$

where $\beta_{x,y}$ and $D_{x,y}$ are the beta-functions and dispersions. Geometrical emittances $\epsilon_{x,y}$ and normalized emittances are related by

$$\epsilon = \epsilon_N / (\beta\gamma).$$

The incoherent space charge tune shift parameters $\Delta Q_{x,y}$ are calculated according to

$$\begin{aligned} \Delta Q_x &= -\frac{r_c}{2\pi\beta^2\gamma^3} \frac{N}{\sqrt{2\pi}\sigma_z} \int_0^L \frac{\beta_x}{\sigma_x(\sigma_x + \sigma_y)} ds \\ \Delta Q_y &= -\frac{r_c}{2\pi\beta^2\gamma^3} \frac{N}{\sqrt{2\pi}\sigma_z} \int_0^L \frac{\beta_y}{\sigma_y(\sigma_x + \sigma_y)} ds \end{aligned} \quad (2)$$

by numerical integration around the ring using nominal values of the β functions and dispersion (here on average $\beta_x = 41.5 \text{ m}$, $\beta_y = 41.6 \text{ m}$, $\sigma_x = 3.48 \text{ mm}$, $\sigma_y = 1.9 \text{ mm}$). r_c is the classical proton radius and σ_z the bunch length.

With the (measured) beam parameters of Table 1, we obtain for the conditions of the experiments described here the rather substantial space charge tune shifts of

$$\Delta Q_x = -0.14$$

$$\Delta Q_y = -0.18$$

It is likely that the beam sizes obtained from the wire scanner were overestimated by 30% (due to a problem in the low level software of the instrument). This would imply even 30% larger tune shifts.

3 LIFETIME DEPENDENCE ON TUNE

We performed scans in the vertical and horizontal tune and observed the decay of the proton intensity over times of up to 10 seconds from injection. For the vertical tune scan, the horizontal tune was kept at a fixed value of $Q_x = 0.2^\dagger$. For the horizontal scan, the vertical tune was kept at $Q_y = 0.234$. Chromaticities were set to small negative values in both planes (14 GeV is below the transition, $\gamma_{tr} \approx 23.2$).

[†]we refer to the non-integer part; integer tunes are 26 in both planes

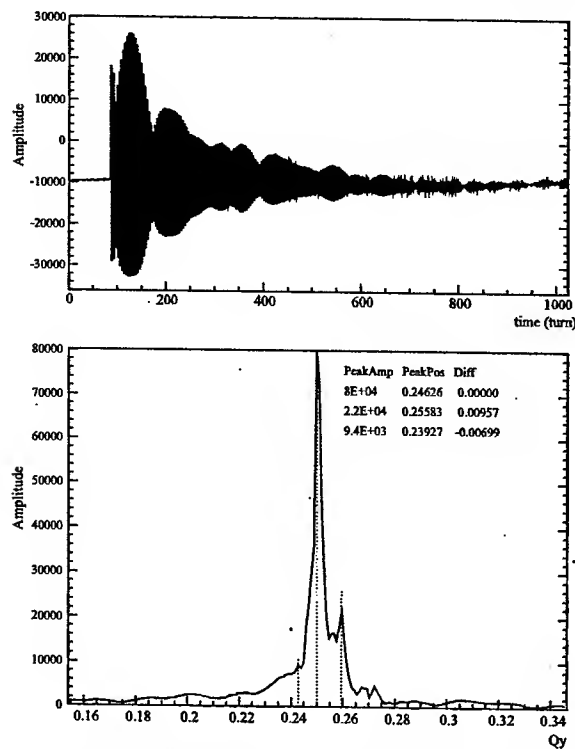


Figure 1: Example of a tune measurement, here $Q_y = 0.2462$, which gave a good lifetime. The beam was kicked 3 s after injection at an intensity of 1.1×10^{11} protons. Vertical centre of gravity oscillations recorded by the tune meter are shown on top and the spectrum after fast Fourier transform (FFT) on the bottom.

An example of a tune measurement is shown in Fig. 1. The tune meter records the coherent (centre of gravity) motion of the bunch. To first order, the central tune value obtained is not effected by the substantial internal space charge tune spread.

Intensities as function of time over the first 10 s from injection are shown in Figures 2 and 3 for various tunes. Losses of less than 10% over 10 s corresponding to over 100 s lifetime were observed for "good" tune settings. The observed decay however, particularly for the "poor" tune settings, is not always exponential. Transitions between slow decay and rapid losses and nearly linear decay were also observed.

Rather than using lifetime, we are now going to present the same data in terms of transmission (ratio of final over initial intensity) over 10 s as a measure of stability. The results as function of tune are shown in Figures 4 and 5. Stability is poor for low (< 0.2) and very high (> 0.4) vertical tunes. There is more freedom in the choice of the horizontal tunes (as expected due to the lower space charge tune spread in this plane). Poor stability in the horizontal plane was observed for very low (< 0.1) tunes.

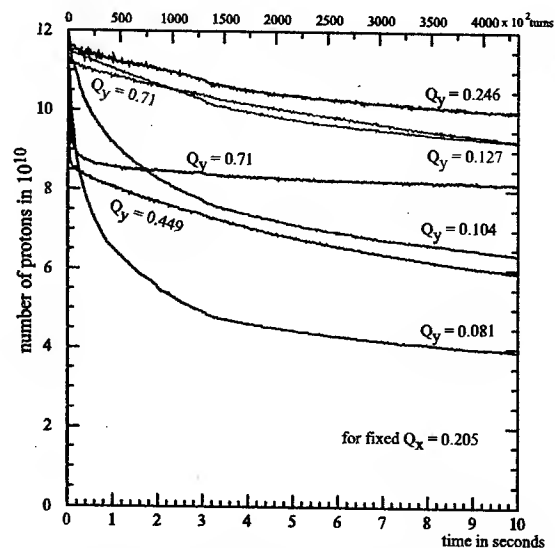


Figure 2: Single bunch intensities in the SPS over 10 s from injection for various vertical tunes Q_y and a fixed $Q_x = 0.2$.

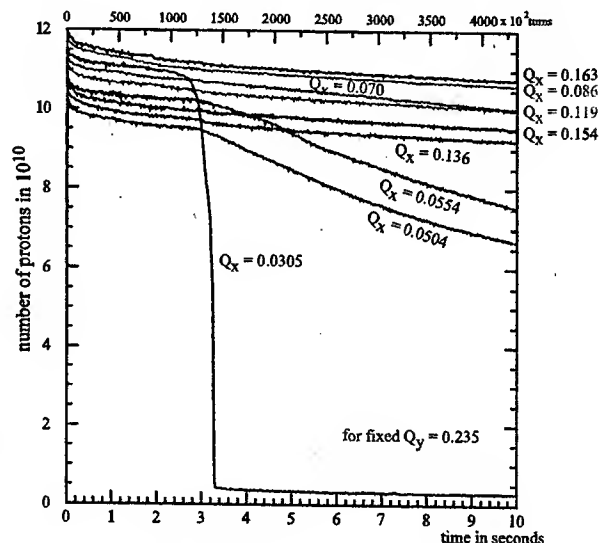


Figure 3: Single bunch intensities in the SPS over 10 s from injection for various horizontal tunes Q_x and a fixed $Q_y = 0.234$.

4 TESTS WITH OCTUPOLES

The measurements reported so far were obtained for a rather linear machine. This was verified by measurements of detuning with kick amplitude.

It is known that octupoles improve the stability under certain conditions [8]. The last hour of available beam time was used for a first quick test on the effect of the two octupole families ("vertical and radial") on the stability in the presence of space charge. Losses increased whenever the octupoles were run at strong negative excitation which

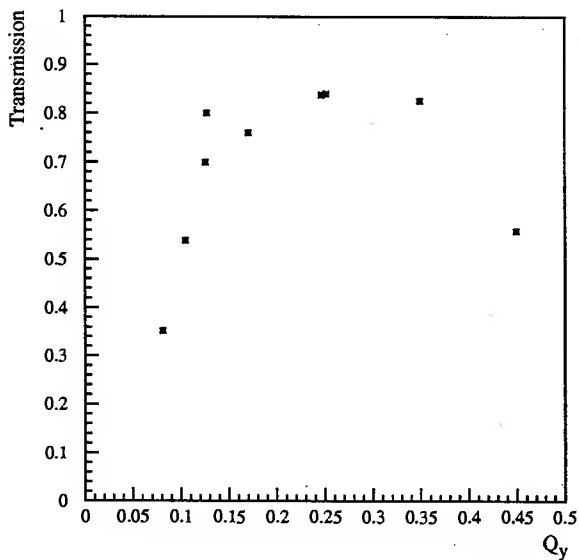


Figure 4: Results of the vertical tune scan in terms of transmission over 10 s.

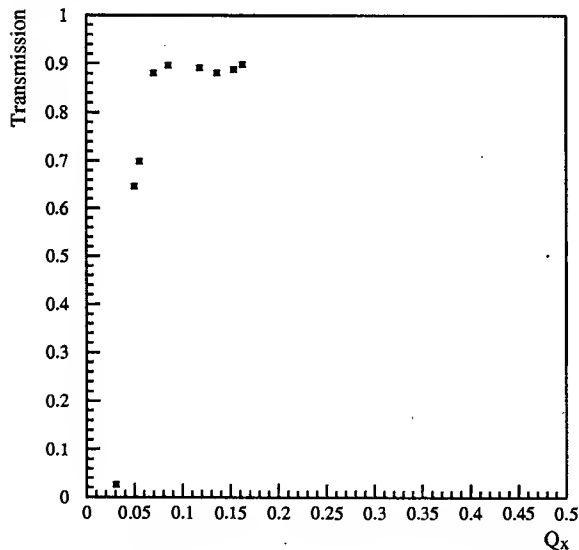


Figure 5: Results of the horizontal tune scan in terms of transmission over 10 s.

corresponds to positive detuning with amplitude. Positive radial settings had no visible effect. Strong positive vertical octupole excitation ("settings of +6 or better +11") appeared to improve the stability. Using these settings, we were able to reduce the bunch length (by an increase of the rf-voltage from 1.5 to 5 MV) without major losses.

5 SUMMARY AND OUTLOOK

Studies with high intensity single bunch proton beams injected at 14 GeV allowed a first investigation in the SPS

of the behaviour of beams at space charge tune shifts of 0.14 to 0.18. Good stability with lifetimes of over 100 s were observed over a rather broad range of tunes. This is encouraging and leaves some margin for an overall optimization of beam parameters in the injector chain for heavy ion operation of the LHC. Further measurements including systematic studies with octupoles are foreseen.

6 REFERENCES

- [1] G. Gelato, L. Magnani, N. Rasmussen, K. Schindl, and H. Schonauer, "Progress in Space Charge Limited Machines: Four times the design intensity in the CERN Proton Synchrotron Booster", Proc. PAC. 1987 p. 1298 and CERN-PS/87-36 (1987).
- [2] R. Cappi, R. Garoby, D. Möhl, J.L. Vallet, and E. Wildner, "Experiments to Test Beam Behaviour Under Extreme Space Charge Conditions", Proc. EPAC 1994 p. 279.
- [3] R. Cappi, "Emittance issues in the CERN-PS", CERN/PS 95-05 (PA), CERN Geneva 1995.
- [4] L. Vos, "Decoherence from space-charge", Proc. of the 17th International Conference on High Energy Accelerators - HEACC '98, Dubna, Russia, 7 - 12 Sep 1998, CERN-SL-98-056-AP.
- [5] H. Burkhardt, G. Rumolo, and F. Zimmermann, "Measurements of SPS Single-Bunch Coherent Tune Shifts and Head-Tail Growth Rates in the Year 2001", CERN, SL Note 2001-043 (MD), 7-12-2001.
- [6] D. Manglunki, "Status of what has been and what has to be done on SPS", Chamonix XII proceedings, p. 81, CERN AB/2003-008 ADM (2003).
- [7] J. Jowett, "Heavy Ions in the LHC", this conference.
- [8] Möhl, D., "On Landau damping of dipole modes by nonlinear space charge and octupoles", Part. Accel. 50 (1995) 177-187.

COHERENT TUNE SHIFTS MEASURED WITH FEW BUNCHES IN THE SPS AND COMPARISON WITH RESISTIVE WALL THEORY

H. Burkhardt, A. Koschik, G. Rumolo, F. Zimmermann, B. Zotter, CERN, Geneva, Switzerland

Abstract

Coherent tune shifts with current have been measured in the SPS with single bunches and two bunches at varying distances between them. The measurements showed the usual negative slope with intensity in the vertical plane and a small positive one in the horizontal direction. The results are compared with theoretical predictions which include estimates of tune shifts due to the impedance of resistive vacuum chambers with non-circular geometry and finite wall thickness.

1 INTRODUCTION

Coherent tune shifts with current have been measured precisely on single bunches in the SPS for several years [1, 2]. This allowed to monitor the decrease of the SPS impedance by hardware improvements [3].

The usual negative slope with intensity, corresponding to a defocusing effect of the wake fields is observed in the vertical plane. In the horizontal plane instead, a very small positive slope is observed. Most of the SPS beam pipe consists of flat chambers with horizontal to vertical aspect ratios of 2.5 – 4. This asymmetry results in quadrupolar forces. They approximately cancel the focusing effect of the dipole wake fields in the horizontal plane and increase instead the detuning with intensity in the vertical plane [4].

We were motivated to extend the SPS studies to more than one bunch by observations in other machines (PEP2), in which positive slopes have only been observed with multiple bunches. The measurements were done on single bunches and two bunches at various distances. The restriction to very few bunches avoids any complication by electron cloud effects present for many bunches.

2 MEASUREMENTS

The measurements were performed in summer 2002, with a single bunch or two bunches of protons injected into the SPS. The relevant beam parameters are summarized in Table 1.

The SPS was operated in a special 20.7 s long cycle with a 10.86 s long injection plateau. The first bunch was injected at the beginning of the cycle and its intensity varied by scraping in the vertical plane at 1.5 s. The second bunch (if present), was injected at 9.6 s. The delay between the two bunches around the ring was chosen by rf-bucket selection. For the main measurements presented here, the distance between the two bunches was selected to be half a turn (about 12 μ s). Additional measurements in which the second bunch preceded the first by 2 and 4 μ s were also performed.

Table 1: Relevant SPS parameters

variable	symbol	value
momentum	p	26 GeV/c
revolution frequency	f_{rev}	43347 Hz
	$1/f_{\text{rev}}$	23.07 μ s
betatron tunes	$Q_{x,y}$	~ 26.2
synchr. tune (at 2 MV)	Q_s	5.6×10^{-3}
momentum compaction	α_c	1.86×10^{-3}
bunch population	N	$(1 - 12) \times 10^{10}$
rms bunch length	σ_t	~ 0.7 ns

The tune measurements were done on the first bunch towards the end of the injection plateau, at 10 s from the cycle start (after the injection of the second bunch). Bunch lengths were monitored using a longitudinal pick-up and a digital scope. The bunch length was observed to increase slightly with intensity, from $\sigma_t = 0.65$ ns at the lowest to 0.83 ns at the highest intensities. Figures 1,2 show the results in terms of the coherent tune shift with intensity, normalized to $\sigma_t = 0.5$ ns. The slope of the curves in the horizontal and vertical plane is a measure of the effective transverse impedance in these planes.

Table 2: Coherent tune shift results, normalized to 0.5 ns bunch length.

	$\Delta Q_x / \Delta N_p [10^{10}]$	$\Delta Q_y / \Delta N_p [10^{10}]$
single	$(+1.1 \pm 0.3) \times 10^{-4}$	$(-24.2 \pm 0.4) \times 10^{-4}$
two	$(+1.1 \pm 0.2) \times 10^{-4}$	$(-24.8 \pm 0.6) \times 10^{-4}$

The results obtained by straight line fits are shown in the figures and summarized in Table 2. The uncertainties quoted are obtained from the scattering of the data points around the fitted lines.

No significant difference between the single and two bunch case was observed. This was still the case for 2 and 4 μ s delay between the bunches.

3 PREDICTIONS

The coherent transverse tune shift $\Delta\Omega$ due to the finite resistivity of a circular symmetric vacuum chamber wall can be expressed by the functions $g(q) + if(q)$,

$$\Delta\Omega_{\text{coh.}} \propto g(q) + if(q), \quad (1)$$

where q is the non-integer part of the betatron tune in either of the transverse planes x or y . These functions are defined as an infinite sum over all previous revolutions k , and in

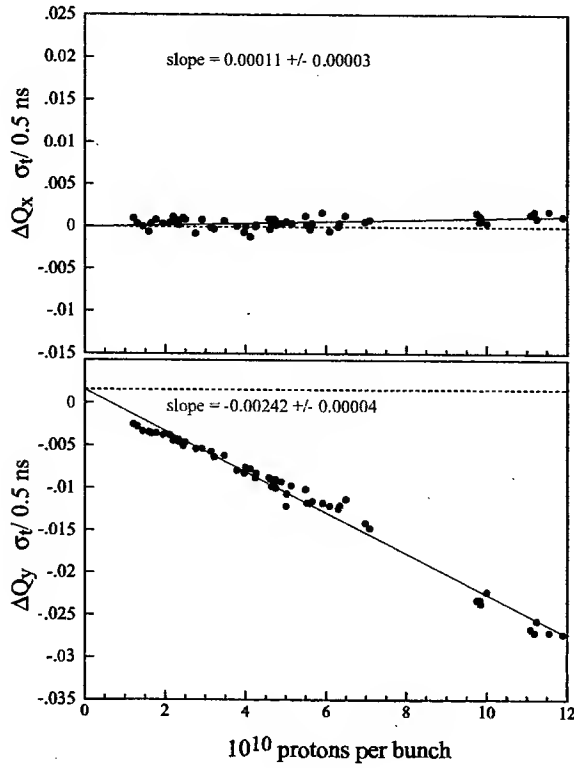


Figure 1: Coherent tune shift with intensity measured for a single bunch in the SPS.

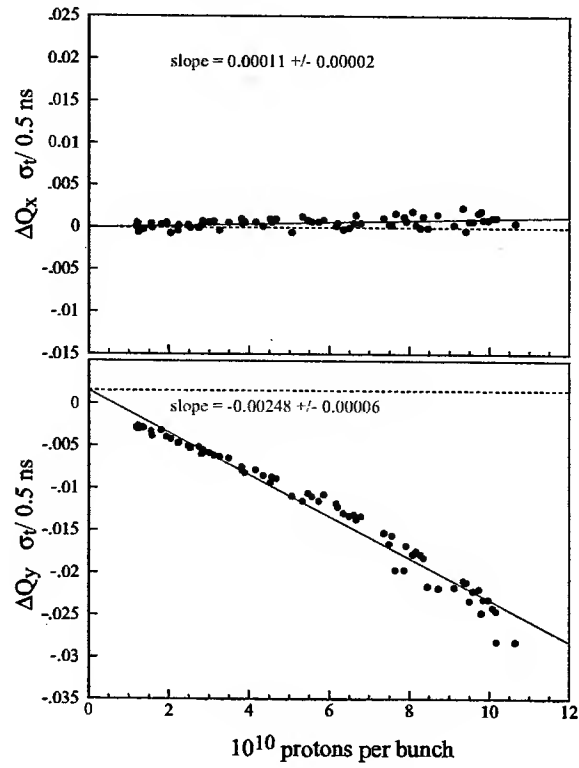


Figure 2: Coherent tune shift with intensity measured on the first of two bunches spaced by half a turn (12 μsec).

the case of multiple bunches as an additional sum over all bunches,

$$g(q) + if(q) = \frac{1}{n_b} \sum_{m=0}^{n_b-1} \sum_{k=1}^{\infty} \sqrt{\frac{2}{k'}} \exp(2\pi i q k'), \quad (2)$$

with

$$\begin{aligned} k' &= k + m \cdot S_b / C \\ n_b &\dots \text{number of bunches} \\ 0 \leq m < n_b &\dots \text{coupled bunch mode number} \\ S_b &\dots \text{bunch spacing} \\ C &= 2\pi R \dots \text{circumference.} \end{aligned}$$

The single bunch case (see e.g. [5, p.177]) is included by setting $n_b = 1$.

In non-circular symmetric vacuum chambers additional quadrupolar wakes must be added [6, 7], which are proportional to the offset of the test bunch itself

$$g(q) + if(q)_{\text{non-circular}} = \frac{1}{n_b} \sum_{m=0}^{n_b-1} \sum_{k=1}^{\infty} \left[\sqrt{\frac{2}{k'}} \exp(2\pi i q k') \mp \sqrt{\frac{2}{k'}} \right]. \quad (3)$$

In the circular symmetric case both horizontal and vertical tune shifts are of equal (negative) size. The additional

term $h = \mp \frac{1}{n_b} \sum_{m=0}^{n_b-1} \sum_{k=1}^{\infty} \sqrt{\frac{2}{k'}}$ appears only for *non-circular symmetric* chambers. It reduces or even compensates the horizontal tune shift, while it further increases the vertical one.

The infinite sum h diverges, but a natural truncation occurs when the electromagnetic fields penetrate the chamber wall of finite thickness t . In that case the wake function transforms into an exponentially decaying one [8], hence h becomes

$$h = \mp \frac{1}{n_b} \sum_{m=0}^{n_b-1} \left(\sum_{k=1}^{\hat{k}} \sqrt{\frac{2}{k'}} + \sqrt{\frac{2}{\hat{k}'}} \sum_{k=\hat{k}+1}^{\infty} \exp(-\alpha k') \right), \quad (4)$$

where $\alpha = \pi \delta_0 / (\kappa b t)$, δ_0 the skin depth at revolution frequency ω_0 , b the vacuum chamber radius, and

$$\kappa = 1 + b^2/d^2 \quad (5)$$

for a perfect magnet at radius d [8]. The “cut-off turn number” \hat{k} can be determined approximately by equating the square-root and the exponential wakes,

$$\hat{k} \approx t^2 / (\pi \delta_0)^2 \quad (6)$$

In the SPS, where $\delta_0 \approx t \rightarrow \hat{k} \approx 1/\pi^2 < 1$, therefore the summation over k starts immediately with the exponen-

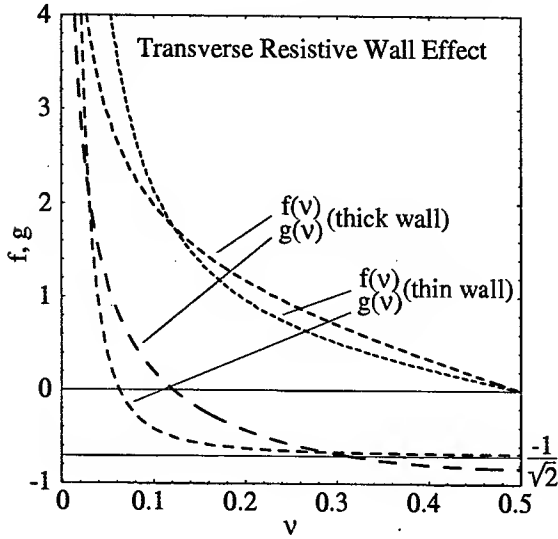


Figure 3: The functions $g(q)$ and $f(q)$ of Eq.(2) and (7). The thin wall graph is drawn for SPS parameters ($\delta_0 = t = 2\text{mm}$, $b = 20\text{mm}$)

tial terms. The infinite sum can now be evaluated analytically as geometric series, and we obtain for a single bunch ($n_b = 1$ and $k' = k$):

$$\begin{aligned} g(q) + if(q) &= \sqrt{\frac{2}{k}} \sum_{k=1}^{\infty} \exp(-\alpha k + 2\pi i q k) \\ &= \sqrt{\frac{2}{k}} \frac{1}{\exp(\alpha - 2\pi i q) - 1} \end{aligned} \quad (7)$$

For very small $\alpha \ll 1$, the real part of the infinite sum becomes approximately $-1/\sqrt{2}$, as can be seen from Fig.(3). Furthermore one finds

$$g(q) = -1/\sqrt{2k} \approx -\pi\delta_0/(\sqrt{2}t), \quad (8)$$

independent of the tune. However, for q close to zero this approximation breaks down and one has to use the exact expression to obtain

$$h = g(0) = \frac{\sqrt{2}}{\sqrt{k} [e^\alpha - 1]} \approx \sqrt{2} \frac{\kappa b}{\delta_0}, \quad (9)$$

where the last approximation is valid for $\alpha \ll 1$.

For the SPS, we get $g \approx -2.2$, while $h \approx 28.3$ is the dominant term. Hence the horizontal tune shift for a single bunch is close to zero or even slightly positive as already reported in [8].

4 CONCLUSION

We have measured coherent tune shifts with current in the SPS. The usual negative slope is found in the vertical plane and a small positive slope in the horizontal plane.

A much smaller slope in the horizontal plane is expected for a flat chamber geometry, in which quadrupolar wake fields enhance the vertical tune shift and largely cancel the horizontal tune shift.

Positive slopes have already been seen for bunch trains in PEP-II [8] and have been explained in terms of long range resistive quadrupolar wakes which add up coherently over successive bunches and several turns.

In the SPS, we already observe a small positive slope in the horizontal plane for a single bunch and did not see a significant change in case of the presence of a second bunch.

A reduced multi-bunch effect in the SPS compared to PEP-II is in fact expected due to the larger skin depth at revolution frequency in the stainless steel vacuum chamber and the larger SPS-circumference. For the SPS, the wake function changes from the usual inverse square-root dependence on distance to an exponentially decaying one in less than one turn.

5 REFERENCES

- [1] H. Burkhardt, G. Rumolo, and F. Zimmermann, "Measurements of SPS Single-Bunch Coherent Tune Shifts and Head-Tail Growth Rates in the Year 2001", CERN, SL Note 2001-043 (MD), 7-12-2001.
- [2] H. Burkhardt, G. Rumolo, and F. Zimmermann, "Coherent beam oscillations and transverse impedance in the SPS", Proc. EPAC 2002 pp. 1449 - 1451 and CERN-SL-2002-030.
- [3] P. Collier, M. Ainoux, *et al.*, "Reducing the SPS Machine Impedance", Proc. EPAC 2002 pp. 1458 - 1460 and CERN-SL-2002-026-MR.
- [4] J. Gareyte, "Impedances: Measurements and Calculations for Non-symmetric Structures", Proc. EPAC 2002 pp. 89 - 93 and CERN-SL-2002-028.
- [5] A. Chao, *Physics of Collective Beam Instabilities in High Energy Accelerators*, John Wiley & Sons, 1993.
- [6] R. L. Gluckstern, J. van Zeijts, and B. Zotter, "Coupling impedance of beam pipes of general cross-section", *Phys. Rev. E* 47 (1993) 656-663.
- [7] S. Heifets, A. Wagner, and B. Zotter, "Generalized impedances and wakes in asymmetric structures", SLAC-AP-110, Jan. 1998.
- [8] A. Chao, S. Heifets, and B. Zotter, "Tune shifts of bunch trains due to resistive vacuum chambers without circular symmetry", *Phys. Rev. ST Accel. Beams* 5 (2002) 111001.

LONGITUDINAL MICROWAVE INSTABILITY IN LEPTON BUNCHES

E. Métral, CERN, Geneva, Switzerland

Abstract

The stability criterion for the longitudinal microwave instability in bunched lepton beams is derived using the mode-coupling formalism and taking into account the potential-well distortion. The new formula yields an intensity threshold which can be higher than the one given by the Keil-Schnell-Boussard approximation by a large factor. This result may explain why the classical instability threshold has been exceeded in some lepton machines.

1 INTRODUCTION

The longitudinal microwave instability for coasting beams is well understood [1-4]. It leads to a stability diagram, which is a graphical representation of the solution of the dispersion relation depicting curves of constant growth rates, and especially a threshold contour in the complex plane of the driving impedance. When the real part of the driving impedance is much greater than the modulus of the imaginary part, a simple approximation, known as the Keil-Schnell (or circle) stability criterion, may be used to estimate the threshold curve [3]. For bunched beams, it has been proposed by Boussard [5] to use the coasting-beam formalism with local values of bunch current and momentum spread. This approximation was expected to be valid in the case of instability rise-times shorter than the synchrotron period, and wavelengths of the driving wake field much shorter than the bunch length. This empirical rule is widely used for estimations of the tolerable impedances in the design of new accelerators. A first approach to explain this instability, without coasting-beam approximations, has been suggested by Sacherer through Longitudinal Mode-Coupling (LMC) [6]. The equivalence between LMC and microwave instabilities has been pointed out by Sacherer [6] and Laclare [7] in the case of broad-band driving resonator impedances, neglecting the Potential-Well Distortion (PWD). The complete theory describing the microwave instability for bunched beams is still under development [4,8].

It has been shown in Refs. [9,10], using the mode-coupling formalism for the case of proton bunch with a parabolic line density interacting with a broad-band resonator impedance, that a new stability criterion can be derived taking into account the PWD due to both space-

charge and resonator impedances. This new formula reveals in particular that it is better to operate the machine below transition (as already found in Ref. [11]). It also predicts a stability area below transition even in the presence of large space-charge impedances, without coasting-beam considerations of stability diagrams.

The case of a lepton bunch with a Gaussian amplitude density is discussed in this paper. Space charge is negligible in this case and the machine is operating above transition.

2 THEORY

Applying Sacherer's formula for LMC between modes m and $m+1$ yields the following intensity threshold condition [9]

$$I_b \leq \frac{3}{2} \times \frac{h \hat{V}_T B^3 |\cos \phi_s|}{F_1 \left| \frac{Z_l^{BB}}{p} \right|}, \quad (1)$$

with

$$F_1 = \frac{|m|}{|m|+1} \times \left| \frac{Z_l^{BB}}{p} \right|^{-1} \times \left\{ \left| j(Z_l^{eff})_{m,m+1} \times \frac{|m|+1}{\sqrt{|m|(|m|+2)}} \right| + \frac{j}{2} \times \frac{|\cos \phi_s|}{\cos \phi_s} \right\} \times \left[(Z_l^{eff})_{m,m} - \frac{(|m|+1)^2}{|m|(|m|+2)} \times (Z_l^{eff})_{m+1,m+1} \right] \quad (2)$$

$$(Z_l^{eff})_{m,n} = \frac{\sum_{p=-\infty}^{p=+\infty} \frac{Z_l(\omega_p')}{p} h_{m,n}(\omega_p')}{\sum_{p=-\infty}^{p=+\infty} h_{m,m}(\omega_p')} \quad (3)$$

Here, $I_b = N_b e f_0$ is the current in one bunch with N_b the number of protons in the bunch, e the elementary charge, and $f_0 = \Omega_0/2\pi$ the revolution frequency, h is the harmonic number, \hat{V}_T is the total (effective) peak voltage taking into account the PWD (the peak RF voltage is

\hat{V}_{RF}), $B = \tau_b f_0$ is the bunching factor with τ_b the total bunch length (in seconds) taking into account the PWD (the unperturbed total bunch length is τ_{b0}), ϕ_s is the RF phase of the synchronous particle ($\cos \phi_s < 0$ above transition) taking into account the PWD (the unperturbed synchronous phase is ϕ_{s0}), $|Z_l^{BB}/p|$ is the peak value of the Broad-Band (BB) resonator impedance, $m = \dots, -1, 0, 1, \dots$ is the longitudinal coherent bunch mode number, $j = \sqrt{-1}$ is the imaginary unit, Z_l is the longitudinal coupling impedance, $\omega_p^l = p \Omega_0 + m \omega_s$ with $-\infty \leq p \leq +\infty$, where $\omega_s = 2\pi f_s$ is the synchrotron angular frequency taking into account the PWD (the unperturbed synchrotron angular frequency is $\omega_{s0} = 2\pi f_{s0}$), and $h_{m,n}$ describes the cross-power densities of the m th and n th line-density modes. The broad-band resonator impedance is defined by

$$\frac{Z_l^{BB}(p)}{p} = \frac{\Omega_0}{\omega} R_s \left[1 - j Q_r \left(\frac{\omega_r}{\omega} - \frac{\omega}{\omega_r} \right) \right], \quad (4)$$

where R_s is the shunt impedance (in Ω), $Q_r = 1$ is the quality factor and $\omega_r = 2\pi f_r$ is the resonance angular frequency.

Considering a lepton bunch with Gaussian amplitude density, the following relations are obtained when PWD is taken into account [7]

$$g_0(\hat{\tau}) = \frac{8}{\pi \tau_b^2} e^{-8 \left(\frac{\hat{\tau}}{\tau_b} \right)^2}, \quad (5)$$

$$\phi_s = \phi_{s0} + \frac{2\pi I_b}{\hat{V}_{RF} \cos \phi_{s0}} \times \sum_{p=-\infty}^{p=+\infty} \text{Re}[Z_l(p)] \sigma_0(p), \quad (6)$$

$$\sigma_0(p) = \int_{\hat{\tau}=0}^{\hat{\tau}=+\infty} J_0(p \Omega_0 \hat{\tau}) g_0(\hat{\tau}) \hat{\tau} d\hat{\tau}, \quad (7)$$

$$\Delta = \frac{\omega_{s1}^2 - \omega_{s0}^2}{\omega_{s0}^2} = -\frac{2\pi I_b}{h \hat{V}_{RF} \cos \phi_{s0}} \sum_{p=-\infty}^{p=+\infty} j \frac{Z_l(p)}{p} p^2 \sigma_0(p) = -\frac{6 I_b}{\pi^2 h \hat{V}_{RF} \cos \phi_{s0} B^3} j \left[\frac{Z_l(p)}{p} \right]_{\text{Im,eff}}, \quad (8)$$

$$\left[\frac{Z_l(p)}{p} \right]_{\text{Im,eff}} = \frac{\pi^3 B^3}{3} \sum_{k=-\infty}^{k=+\infty} \frac{Z_l(k)}{k} k^2 \sigma_0(k), \quad (9)$$

$$\omega_{s1}^2 = \omega_{s0}^2 \times \frac{\hat{V}_T}{\hat{V}_{RF}}, \quad (10)$$

$$\Delta_0 = \Delta \left(\frac{B}{B_0} \right)^3, \quad (11)$$

$$\left(\frac{B}{B_0} \right) \times \left| \frac{\cos \phi_{s0}}{\cos \phi_s} \right| = \left(\frac{B}{B_0} \right)^3 + \Delta_0, \quad (12)$$

where J_0 is the Bessel function of first kind and 0th order, and $g_0(\hat{\tau})$ is the stationary distribution of the synchrotron oscillation amplitude $\hat{\tau}$. The stability criterion of Eq. (1) can then be re-written

$$I_b \leq \frac{3}{2} \times \frac{h \hat{V}_{RF} B_0^3 |\cos \phi_{s0}|}{\left| \frac{Z_l^{BB}}{p} \right|} \times \frac{F_2}{F_1}, \quad (13)$$

where $F_2 = B/B_0$ is a factor found by equating the intensity at threshold of Eq. (13) to the one due to PWD (see Eq. (8)), which is given by

$$F_2 = \frac{B}{B_0} = \left\{ \frac{|\cos \phi_{s0}|}{|\cos \phi_s|} + \frac{9}{\pi^2 \frac{\cos \phi_{s0}}{|\cos \phi_{s0}|} F_1} \times \frac{j \left[\frac{Z_l^{BB}}{p} \right]_{\text{Im,eff}}}{\left| \frac{Z_l^{BB}}{p} \right|} \right\}^{1/2}. \quad (14)$$

Note that for sufficiently long bunches ($\tau_{b0} \gg 2/f_r$), the factor F_1 is independent of the bunch length and is given by $F_1 \approx 0.6$. In this case, the factor F_2 is given analytically by Eq. (14). This is not the case for shorter bunches, where Eq. (14) has to be solved numerically.

Neglecting the synchronous phase shift, the stability criterion for the longitudinal microwave instability can be written

$$I_{p0} \leq F \times I_{p0}^{KSB}, \quad (15)$$

with

$$I_{p0}^{KSB} = \frac{1}{\ln 2} \times \frac{(E/e) \alpha_p}{\left| \frac{Z_l^{BB}}{p} \right|} \times \left(\frac{\Delta p}{p_0} \right)_{\text{FWHH},0}^2, \quad (16)$$

where I_{p0}^{KSB} is the initial (low-intensity) peak intensity threshold from the Keil-Schnell-Boussard criterion for

Gaussian bunches [12], E is the beam energy, $\alpha_p = \gamma^{-2}$ is the momentum compaction factor, and $(\Delta p/p_0)_{FWHM,0}$ is the initial (low-intensity) relative momentum spread (full width at half height). The factor F , which is given by

$$F = \frac{6}{\pi \sqrt{2\pi}} \times \frac{F_2}{F_1}, \quad (17)$$

is solved numerically and represented in Fig. 1.

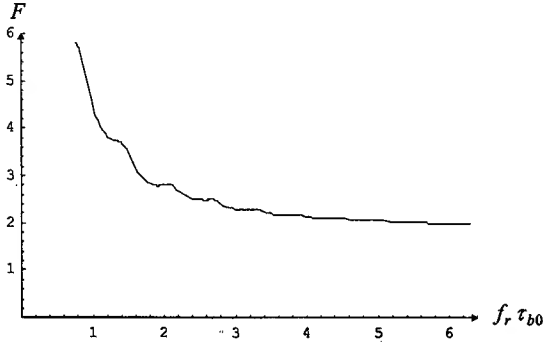


Figure 1: Plot of the factor F vs. $f_r \tau_{b0}$.

It is seen from Fig. 1 that for long (compared to the inverse of the resonance frequency of the impedance) bunches, the intensity threshold is ~ 2 times larger than from the Keil-Schnell-Boussard criterion. Furthermore, when the bunch length gets smaller, the threshold intensity increases, and if $f_r \tau_{b0} \leq 0.75$ there is no instability anymore (with this model...).

3 MEASUREMENTS

Microwave instability measurements made in the CERN SPS in 1993 for long proton bunches produced a value for the longitudinal impedance $|Z_l/p| \approx 20 \Omega$, with $Q_r \approx 1$ and $f_r \in [1.3-1.6 \text{ GHz}]$, using the Keil-Schnell-Boussard criterion [13]. To explain the absence of longitudinal microwave instability for short lepton bunches at high energies, i.e. when $\sigma_z \leq 5 \text{ cm}$, an effective longitudinal impedance 5 times lower than the long bunch value was needed, which was not understood.

Applying the new criterion for the case of the short bunch with $\sigma_z = 5 \text{ cm}$, i.e. $f_r \tau_{b0} \approx 1$, one sees that a factor of ~ 5 is predicted, in perfect agreement with the above (non) observations.

4 CONCLUSION

A new stability criterion for the longitudinal microwave instability of lepton bunches is given. For a sufficiently long bunch, the intensity threshold is found to be ~ 2 times larger than from the Keil-Schnell-Boussard

criterion. When the bunch length gets smaller, the threshold intensity increases. It is ~ 5 times larger than from the Keil-Schnell-Boussard criterion when $f_r \tau_{b0} \approx 1$, which is in perfect agreement with the (non) observations made in Ref. [13]. The new stability criterion may explain why the classical (Keil-Schnell-Boussard) instability threshold can be exceeded in lepton machines.

REFERENCES

- [1] J.L. Laclare, CERN Accelerator School, CERN 85-19, 1985.
- [2] V.K. Neil, A.M. Sessler, Rev. Sci. Instr. 6, 429, 1965.
- [3] E. Keil, W. Schnell, CERN Report ISR-TH-RF/69-48, 1969.
- [4] T. Roser, S.Y. Zhang, Workshop on Instabilities of High Intensity Hadron Beams in Rings, AIP Conference Proceedings 496, 412 p, Upton, New York, June/July 1999.
- [5] D. Boussard, CERN Report LabII/Rf/Int./75-2, 1975.
- [6] F.J. Sacherer, "Bunch Lengthening and Microwave Instability", IEEE Trans. Nucl. Sci., Vol. NS-24, No. 3, June 1977.
- [7] J.L. Laclare, CERN Accelerator School, CERN 87-03, 1987.
- [8] E. Shaposhnikova, "Signatures of Microwave Instability", CERN-SL-99-008 HRF, 1999.
- [9] E. Métral, "Stability Criterion for the Longitudinal Mode-Coupling Instability in the Presence of Both Space-Charge and Resonator Impedances", CERN/PS 2001-063 (AE), October 2001.
- [10] E. Métral, "Stability Criteria for High-Intensity Single-Bunch Beams in Synchrotrons", CERN/PS 2002-022 (AE) or Proc. 8th EPAC, Paris, France, 3-7 June 2002.
- [11] K. Ng, "Potential-Well Distortion and Mode-Mixing Instability in Proton Machines", FERMILAB-FN-630, 1995.
- [12] A. Hofmann, "Single Beam Collective Phenomena-Longitudinal", Proc. First Course Int. School on Accelerators, Erice, 1976: Theoretical Aspects of the Behaviour of Beams in Accelerators and Storage Rings, CERN 77-13, p. 176, 1977.
- [13] T. Linnecar and E.N. Shaposhnikova, "Analysis of the Transverse Mode Coupling Instability of the Leptons in the SPS", CERN/SL/93-43 (RFS).

NOMINAL LONGITUDINAL PARAMETERS FOR THE LHC BEAM IN THE CERN SPS

P. Baudrenghien, T. Bohl, T. Linnecar, E. Shaposhnikova and J. Tuckmantel,
CERN, Geneva, Switzerland

Abstract

A proton beam with the basic structure defined by the LHC requirements, was first available for injection into the SPS in 1998. At the end of 2002, following a significant beam-studies and RF hardware upgrade programme, a beam having both the nominal LHC intensity and the correct longitudinal parameters was obtained at top energy for the first time. This beam, characterised by high local density, must satisfy strict requirements on bunch length, longitudinal emittance and bunch to bunch phase modulation for extraction to the LHC, where only very limited particle losses are acceptable. The problems to be solved came mainly from the high beam loading and microwave and coupled bunch instabilities which led both to beam losses and to unacceptably large longitudinal emittance on the flat top. In this paper the steps taken to arrive at these nominal beam parameters are presented.

INTRODUCTION

The preparation of the CERN SPS for its future role as an injector of LHC started well before the first LHC type beam was available from the PS injector. At the beginning work concentrated on single bunch stability. During the studies of microwave instability, which started in 1995, the guilty impedances were identified and then the sources shielded two years ago. Single bunch reference measurements before and after the impedance reduction are summarised below together with final results for the whole LHC beam. The nominal LHC beam consists of 3 or 4 batches with 72 bunches each. Bunches are spaced by 25 ns and batches by 220 ns. Nominal bunch intensity at top energy is 1.1×10^{11} .

To cope with expected large longitudinal emittances, it was suggested in 1998 to install an additional 200 MHz RF system in the LHC for beam capture and injection damping. In this case bunches with an emittance ϵ around 1 eVs would be acceptable. For loss-free capture in the LHC with the main 400 MHz RF system alone, in the presence of expected energy and phase errors, ϵ should be less than 0.7 eVs and the bunch length $\tau < 2$ ns. At injection into the SPS (26 GeV) $\epsilon = 0.35$ eVs.

The LHC beam was first injected with bunch and total intensity much lower than nominal. Even so it was unstable first on the flat bottom, then during the ramp after 5 s of acceleration (280 GeV), and again on the flat top (450 GeV).

The continuous emittance blow-up due to the microwave instability, leading to beam losses on the flat bottom, had disappeared in 2001, after the impedance reduction. From then on the main efforts to obtain nominal LHC beam concentrated on commissioning new hardware to cope

with strong beam loading and instabilities caused by the impedance of the main 200 MHz RF system, and on cures for the coupled bunch instabilities observed at the end of the acceleration ramp.

IMPEDANCE REDUCTION

The impedance reduction programme in the SPS was completed during the shutdown of 2000/2001. Around 1000 vacuum ports were shielded [1], different types of kickers and septa were screened, and all lepton equipment including 3 RF systems was removed from the ring.

The single bunch reference measurements in 2001 have demonstrated significantly improved stability [2]. The change of quadrupole synchrotron frequency shift with intensity by a factor 2.5 agrees well with that expected from the reduction in the low frequency inductive impedance estimated from the impedance budget (from 12.4 Ohm to 5.6 Ohm). The space charge impedance at 26 GeV is -1 Ohm. The slope of the bunch lengthening curve is reduced by a factor 7; emittance blow-up due to the microwave instability is seen before the impedance reduction but bunch lengthening due to the potential well distortion after. In the measurements of bunch spectra with RF off, the resonant peaks due to the vacuum ports (above 1.3 GHz) and kickers (at 400 MHz) have disappeared.

For the LHC type beam, no emittance blow-up is observed now on the flat bottom, and even some controlled emittance blow-up is necessary as a cure for coupled bunch instabilities at high energies (see below).

The impedance of the main RF system around the fundamental (200 MHz) frequency had long been recognized to be a serious problem not only for beam loading but also for coupled-bunch instability [3]. The One-Turn-Delay Feedback (1tFB) in operation since the early eighties [4] and acting on the 4 cavities in parallel did not provide sufficient impedance reduction for the LHC beam. By April 2001 all cavities had been equipped with a Feedforward system providing a (10-15) dB impedance reduction in a 1 MHz band on each side of the RF frequency [5]. By the end of 2001 an upgraded 1tFB had also been installed on each cavity (~ 20 dB impedance reduction at the RF frequency, 1 MHz single-sided bandwidth). However a coupled-bunch instability (dipole mode) with frequency < 2 MHz was still observed on the flat bottom at half nominal intensity. In 2002 the feedback bandwidth was therefore increased (2 MHz single-sided) and two cavities were equipped with a longitudinal damping system capable of damping dipole modes up to 3 MHz during the full acceleration ramp.

In 2003 three of the 200 MHz cavities will have new

power couplers. They are rated for more than 1 MW continuous power per cavity. With improved multipactoring control they should also allow low voltage without counterphasing, thus easing operation under beam loading [7].

In 2002, after the scrubbing run at the beginning of the operation year, the nominal intensity could be reached without serious problems from vacuum pressure increase due to e-cloud [6]. As a result of all upgrades to the 200 MHz RF system, this beam was stable on the flat bottom. However a coupled bunch instability was observed at 280 GeV (16 s) for a single batch with an intensity as low as 2×10^{12} . The source of this instability is not yet clear; one of the high order modes (with mode frequency outside the bandwidth of the longitudinal damper) in the 200 MHz cavities is suspected.

INSTABILITY AT HIGH ENERGY

Effect of voltage programme

The main purpose of these studies was to optimise the 200 MHz voltage (V_1) through the cycle to obtain minimum emittance and bunch length on the flat top. As a basis we used a voltage programme for $\epsilon = 0.5$ eVs with a constant filling factor in momentum of 0.95.

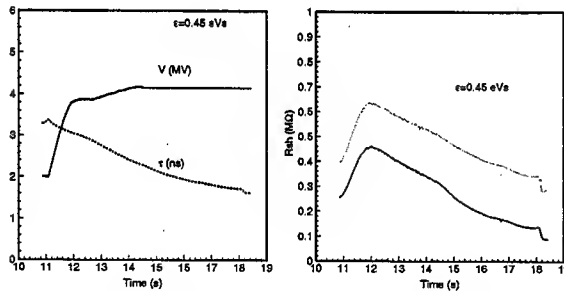


Figure 1: Left: the 200 MHz voltage programme used during studies together with the expected variation of bunch length for $\epsilon = 0.45$ eVs. Right: the minimum threshold impedance for coupled bunch instabilities for this voltage programme with 800 MHz off (bottom curve) and on (top).

In all the cases studied the beam was unstable well below the nominal intensity. The emittance measured on the flat top was larger for higher voltage during the cycle, and increased also with intensity. For the voltage programme in Fig. 1 (left), $\epsilon = 0.73$ eVs was obtained at 450 GeV for a single batch with nominal intensity at injection ($\sim 10\%$ lower at 450 GeV). Measurements of bunch length (averaged over the last 5 bunches in the batch, which are the most unstable ones and can have up to 50% more emittance blow-up than the first bunches) through this cycle are presented in Fig. 2 (top left) and should be compared with the expected behaviour during the cycle from Fig. 1 (left).

Measurements in 2000 for 48 bunches with intensity 8.3×10^{10} /bunch ($V_1 = 3.5$ MV at the end of the ramp),

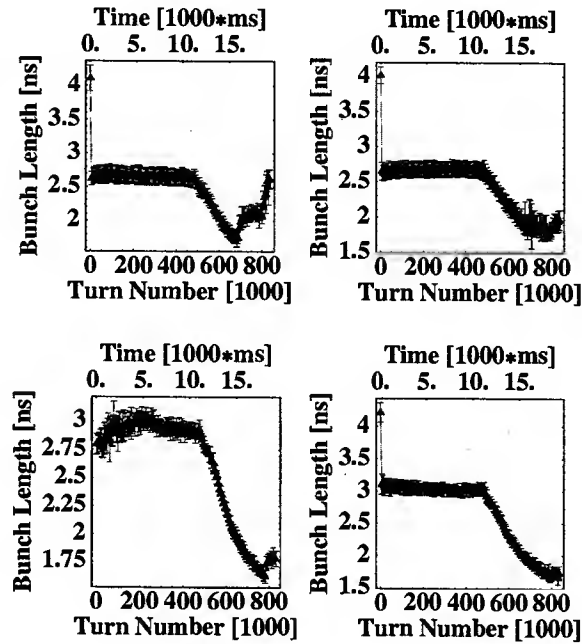


Figure 2: The average bunch length during the cycle with V_1 from Fig. 1 and 800 MHz off (top left), 800 MHz on during the ramp (top right), 800 MHz on from injection (bottom left) and 800 MHz on during the ramp plus emittance blow-up due to mismatched injection (bottom right). Single batch with injected intensity 7.5×10^{12} .

gave $\epsilon = 1.1$ eVs [8]. This should be compared with 0.53 eVs obtained under similar conditions in 2002.

On the flat bottom an increase of voltage improves the beam stability. This is why the matched voltage of 0.75 MV used for beam capture was adiabatically raised to 2 MV, this being repeated 4 times (for each injection). Increasing the voltage up to 7 MV on the flat top, necessary to shorten the bunches before transfer to LHC, has the opposite effect. The beam is more stable at lower voltage. This can be explained by the fact that at 26 GeV the instability is due to the 200 MHz impedance, while at the top energy it is due to a higher frequency impedance, so that reducing the bunch length has the opposite effect [9]. The decrease of the threshold towards the end of the cycle and the sharp drop on the flat top in Fig. 1 explain very well the instability observed at 16 s and then later again on the flat top.

High harmonic RF system

The stabilising effect of the 800 MHz RF system can be seen in Fig. 1 (right) and Fig. 2 (top right). The total voltage seen by the beam in the presence of two RF systems is:

$$V = V_1 \sin \phi + V_2 \sin (4\phi + \Delta\phi). \quad (1)$$

The phase shift $\Delta\phi$ was programmed through the cycle to increase the synchrotron frequency spread using the bunch

shortening (BS) mode: $\Delta\phi = \pi - 4\phi_s$. The 800 MHz voltage was limited through the cycle to the level $V_2/V_1 \simeq 0.1$ [10] to avoid creation of a flat zone in the synchrotron frequency distribution outside the bunch center, where Landau damping can be lost.

Until the effect of beam loading in the idling 800 MHz cavity was taken into account, there was a large difference in the phase shift $\Delta\phi$ required for BS mode between the flat bottom and flat top due to the beam induced voltage. Correction of this phase shift eliminated additional emittance blow-up, Fig. 2 (bottom left). As a result the beam became unstable on the flat top and a small controlled emittance blow-up had to be introduced.

Controlled emittance blow-up

The optimum (minimum) controlled emittance blow-up in the SPS should ensure at the same time both beam stability and minimum loss at the SPS-LHC bunch to bucket transfer. A first blow-up on the flat bottom by mismatched injection ($V = 2$ MV instead of 0.75 MV) gives an increase of emittance from 0.35 eVs to 0.4 eVs, Fig. 2 (bottom right). This was sufficient to stabilise the beam with injected intensities up to nominal. To obtain nominal intensities with 7 MV on the flat top an additional emittance blow-up was needed, see Fig. 3.

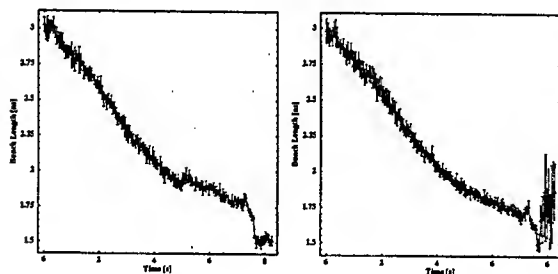


Figure 3: Effect of controlled emittance blow-up on beam stability. The average (of the 5 last bunches in the batch) bunch length during the ramp with bunch excitation (left) and without (right). 1.07×10^{11} /bunch at 450 GeV.

Two methods were used for emittance blow-up during acceleration. First, by phase modulation of the 800 MHz voltage, see (1),

$$\Delta\phi(t) = \alpha \sin(2\pi f_{mod} t + \psi_0) + \Delta\phi_0. \quad (2)$$

The resonant excitation at 16 s during 10 ms (bucket area 0.75 eVs) provided an emittance increase to 0.6 eVs. This was done using parameters optimised for the 4th harmonic [11] $f_{mod} = 3f_s$, $\alpha = 1.05$ and $\Delta\phi_0 = \pi$, where f_s is the linear synchrotron frequency.

Second, pink noise excitation of the 200 MHz amplitude was also tried. It was applied with the 800 MHz in BS mode (to affect the bunch center more than the tails) at 15.8 s at frequency $2f_s$ with bandwidth $\pm\Delta f/f_s \simeq 0.125$.

It was less effective (a blow-up to 0.54 eVs after 0.5 s) but could be useful for LHC, where a high harmonic RF system will not be available. Small beam losses at the time of excitation were observed for both methods. Decreasing the time or strength of excitation eliminated losses but then the emittance blow-up was insufficient to stabilise beam on the flat top. A possibly better technique using a programmable excitation frequency is planned for 2003.

SUMMARY

Bunch lengths (4σ Gaussian fit) in the range (1.51 - 1.58) ns, depending on the batch number, and averaged over 50 bunches, were finally obtained on the flat top for 4 batches in the ring with the nominal bunch intensity 1.1×10^{11} . These bunch lengths correspond to emittances of (0.52 - 0.56) eVs, well below our initial target. These bunch parameters together with the bunch to bunch phase modulation of ± 0.065 ns achieved ($V_1 = 7$ MV), the expected energy error ± 50 MeV and reserve for an eventual synchronisation error (say ± 0.13 ns) should provide minimum particle loss at injection into the LHC even in the absence of the 200 MHz RF system, which consequently will not be installed in the LHC at least for nominal intensities.

These results have been achieved due to the SPS impedance reduction, the commissioning of improved feedback, feedforward and damping systems based on the 200 MHz RF system and the use of the 4-th harmonic RF system both for beam stabilisation by increasing synchrotron frequency spread through the cycle and controlled emittance blow-up during the ramp.

We are grateful to the operation teams for their help, to G. Lambert, R. Olsen, D. Stellfeld and U. Wehrle for their assistance and the considerable electronics development and to E. Montesinos for excellent collaboration.

REFERENCES

- [1] P. Collier et al., Proceed. of EPAC 2002, Paris, p. 1458.
- [2] T. Bohl, T. Linnecar, E. Shaposhnikova, Proceed. of EPAC 2002, Paris, p. 1446.
- [3] D. Boussard, G. Dome, T.P.R. Linnecar, IEEE Transactions on Nuclear Science, Vol. NS-26, No. 3, June 1979.
- [4] D. Boussard, G. Lambert, IEEE Transactions on Nuclear Science, Vol. NS-30, No. 4, August 1983.
- [5] P. Baudrenghien, G. Lambert, Proc. LHC Workshop Chamonix XI, CERN-SL-2001-003 DI, p. 63, 2001.
- [6] G. Arduini et al., The LHC Proton Beam in the CERN SPS, these Proceed.
- [7] T. Bohl, Proc. Workshop Chamonix X, CERN-SL-2000-007 DI, p. 56, 2000.
- [8] T. Bohl, Proc. LHC Workshop Chamonix XI, CERN-SL-2001-003 DI, p. 73, 2001.
- [9] E. Shaposhnikova, CERN SL-Note-2001-031 HRF, 2001.
- [10] T. Bohl, T. Linnecar, E. Shaposhnikova, J. Tuckmantel, Proceed. EPAC 1998, Stockholm, p. 978.
- [11] T. Bohl et al., CERN SL-MD Note 221, 1996.

TRANSVERSE 'MONOPOLE' INSTABILITY DRIVEN BY AN ELECTRON CLOUD?

E. Benedetto, D. Schulte, F. Zimmermann, CERN, Geneva, Switzerland; K. Ohmi, KEK, Japan;
Y. Papaphilippou, ESRF Grenoble, France; G. Rumolo, GSI Darmstadt, Germany

Abstract

We simulate the long-term emittance growth of a proton beam due to an electron cloud of moderate density. This emittance growth is sometimes characterized by a rapid blow up of the bunch tail, and it appears to be different from the strong head-tail instability, which is observed at higher electron densities. We study whether this instability can occur in the absence of transverse dipole motion along the bunch, and its sensitivity to various simulation parameters, such as the number of beam-electron interaction points (IPs) and the phase advances between them. Using a frozen-potential model, we compute tune footprints, which reveal the resonances contributing to the incoherent part of the emittance growth.

1 INTRODUCTION

A beam blow up and vertical instability caused by an electron cloud in the KEK B factory and in the CERN SPS have been explained by a mechanism similar to the strong head-tail (or TMCI) instability [1]. However, at the PEP-II B factory the beam already blows up below the 'TMCI' threshold. A similar phenomenon was seen in simulations by Cai [2]. At EPAC 2002, Lotov and Stupakov reported a new type of 'monopole' instability for PEP-II, that occurs in the absence of any dipole motion and is characterized by a fast blow up of the bunch tail [3].

Recent simulations of the beam-electron interaction for the LHC proton beam using the codes HEADTAIL [4] and PEHTS [5] indicate a significant long-term emittance growth, already at low electron densities [6, 7]. Since the LHC beam has to be stored for several hours, even a few percent emittance growth over one hour can be a concern. The emittance increase observed in our simulation could be related to that observed by Cai or Lotov and Stupakov. Below we present the results of a simulation campaign which explored the nature of the emittance growth.

2 SIMULATIONS

Throughout this paper, we discuss only the effect of the electron cloud, and do not take into account additional space-charge forces or conventional impedances. The simulation parameters are those listed in Table 1, unless noted otherwise. In the simulation, the proton beam and the electron cloud interact at a few discrete 'interaction points' (IPs) around the ring, where we compute the integrated effect of a large number of electrons, which in reality are spread out over a long section of the ring. The implicit assumption is that the electrons introduce only a small perturbation.

Figure 1 shows simulations using the HEADTAIL code

Table 1: Simulation parameters, representing an electron cloud at injection into the LHC.

parameter	symbol	value
electron cloud density	ρ_e	$6 \times 10^{11} \text{ m}^{-3}$
bunch population	N_b	1.1×10^{11}
beta function	$\beta_{x,y}$	100 m
rms bunch length	σ_z	0.115 m
rms beam size	$\sigma_{x,y}$	0.884 mm
rms momentum spread	δ_{rms}	4.68×10^{-4}
synchrotron tune	Q_s	0.0059
momentum compaction	α_c	3.47×10^{-4}
circumference	C	26.659 km
nominal tunes	$Q_{x,y}$	64.28, 59.31
chromaticity	$Q'_{x,y}$	2, 2
relativistic factor	γ	479.6

[4] for the LHC, where we consider a single IP per turn. The various curves refer to different average electron-cloud densities. The growth rates are significant for most of the cases. The saturation after a ten- or twenty-fold increase in emittance is due to the finite size of the grid used in the simulation, which here extends over $\pm 10\sigma$ (± 8.84 mm). Figure 2 compares results from HEADTAIL and PEHTS for different cloud sizes. The curves obtained from the two codes are similar.

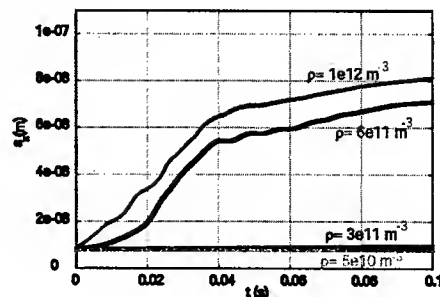


Figure 1: Evolution of LHC emittance vs. time in seconds for an LHC bunch at injection simulated by HEADTAIL for different densities.

Simulations in Fig. 3 illustrate the stabilizing effect of increasing the synchrotron tune Q_s . Above a threshold value for Q_s , the sudden large emittance growth disappears and only a continuous much smaller growth remains. This transition is the threshold of the TMCI instability. However, even the much reduced growth below the TMCI threshold could dilute the LHC proton beam. Comparing the two pictures we observe that for a two times increased electron density the threshold synchrotron tune is also two times larger, consistent with the TMCI model of [1].

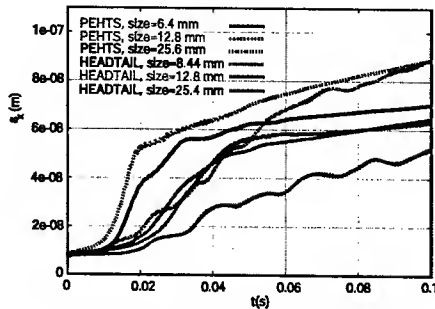


Figure 2: Comparison of HEADTAIL and PEHTS results for various grid sizes, considering a single IP.

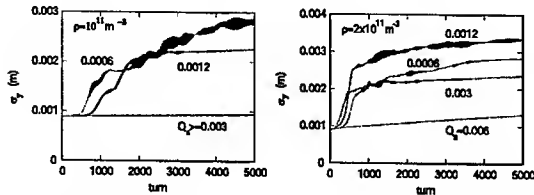


Figure 3: Evolution of LHC vertical beam size vs. time in turns, simulated by the code PEHTS for $\rho_e = 10^{11} \text{ m}^{-3}$ (left) and $\rho_e = 2 \times 10^{11} \text{ m}^{-3}$ (right). The curves correspond to different synchrotron tunes as indicated.

From basic considerations, for a constant ratio of density and synchrotron tune, the emittance growth should look similar, if we scale the time axis with the density (or with Q_s). Figure 4 illustrates that this scaling is nearly fulfilled.

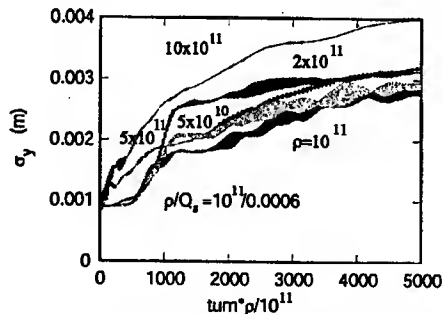


Figure 4: Evolution of LHC vertical beam size vs. the normalized product of turns and electron density, simulated by PEHTS for different ρ_e and Q_s , keeping a constant ratio ρ_e/Q_s .

Repeating the simulation of Fig. 1 for different numbers of IPs, we obtain the results in picture (a) of Fig. 5. By increasing the number of IPs from 1 to 5 (and above), we do not observe any clear convergence of the simulated emittance evolution, but instead we find a rather erratic and non-monotonic dependence. A tentative explanation is that, as we increase the number of IPs and distribute them uniformly around the ring, the phase advance between successive IPs changes abruptly, and for different numbers of IPs the beam experiences resonances of unequal strength.

Figure 6 compares snap shots of the slice centroids and

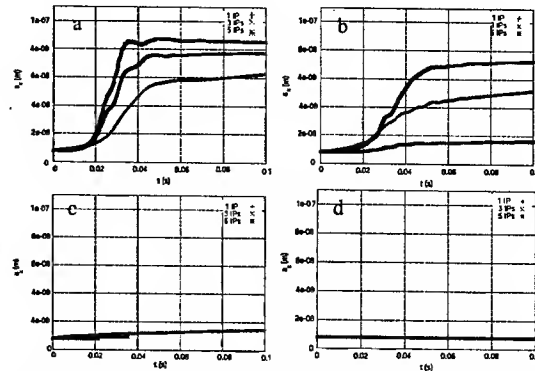


Figure 5: Simulated evolution of LHC emittance vs. time in seconds for $\rho_e = 6 \times 10^{11} \text{ m}^{-3}$, the curves correspond to different numbers of IPs. (a) full simulation with fixed phase advances between IPs; (b) bunch centroid motion suppressed at each IP; (c) bunch-slice centroid motion suppressed; (d) perfect symmetrization of beam and electron macro-particles.

the local beam size after 20 and 40 ms in simulations with 1 and 5 IPs. For the case of a single IP, there is less motion along the bunch. In the vertical plane (not shown), the behaviour for 1 IP is different, and all bunch slices blow up steadily starting from time zero. A possible interpretation is that for 1 IP the stronger nonlinear forces and the larger tune spread induced by the electrons during the bunch passage lead to a more rapid filamentation than for 5 IPs.

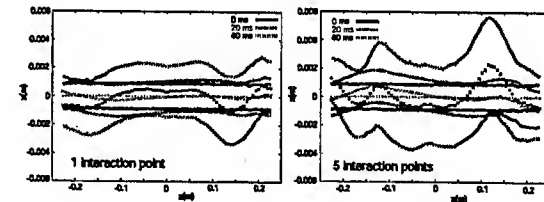


Figure 6: Simulated horizontal bunch shape (centroid and rms beam size) after 0, 20 ms, and 40 ms in the LHC, assuming an electron density of $\rho_e = 6 \times 10^{11} \text{ m}^{-3}$ and either 1 (left) or 5 (right) beam-cloud interactions per turn.

In order to better reveal the character of the instability, the simulation was modified, by (1) removing the bunch centroid oscillation once per IP, (2) removing the centroid of each longitudinal bunch slice once per IP, and (3) completely symmetrizing the initial distribution of macro-particles representing beam and electrons, so that for each particle at position (x, y) there are equivalent partners at $(x, -y)$, $(-x, y)$, and $(-x, -y)$. In this way, any dipole motion is completely removed. The results of these three changes are illustrated in pictures b-d of Fig. 5. Suppressing the centroid bunch motion reduces the emittance growth, but does not eliminate it. Removing the slice centroids is much more efficient, but a small emittance growth remains, especially for 1 IP. Symmetrization fully removes any emittance growth. This rules out the existence of a pure monopole instability, for the parameters considered.

To reduce the sensitivity to resonances in the original model including full dipolar motion, we have introduced a random phase advance between successive IPs, always maintaining the correct average tune. The result is shown in the left picture of Fig. 7. The simulated emittance growth now monotonically approaches smaller values as the number of IPs is increased. For few IPs, the overall level of the emittance growth is higher than in the case of constant phase advance (compare the top left picture of Fig. 5). The larger growth is probably due to noise from the randomization. Plotting the initial linear growth rate as a function of IP number, we observe an inversely linear dependence, which suggests that the emittance growth may approach zero in the limit of infinitely many IPs.

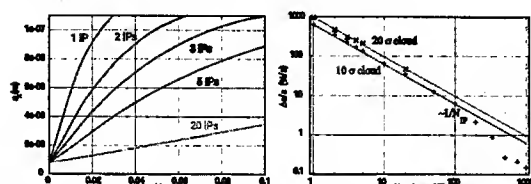


Figure 7: Left: simulated evolution of LHC emittance vs. time in seconds for $\rho_e = 6 \times 10^{11} \text{ m}^{-3}$ with a random phase advances between IPs; the different curves correspond to different numbers of interaction points as indicated. Right: initial linear growth rate in the left plot as a function of the number of IPs; a $1/N$ dependence is superimposed.

In the usual multi-particle simulation the motion of individual protons is not governed by a Hamiltonian. We constructed a Hamiltonian system as follows. First, we computed the electric field of the electrons during a single bunch passage, we stored these values for each time step of the bunch passage, and next, in a separate simulation, we applied these stored fields at either 1 or 5 IPs per turn to simulate the motion of protons over a few thousand turns. For this frozen field, the simulated emittance growth was much smaller than for the complete simulations above. This confirms that the emittance growth is mainly a dynamic effect due to a (dipolar) two-stream instability, and it also demonstrates that diffusive single-particle motion is of secondary importance.

Figure 8 shows a tune footprint obtained from the corresponding frequency-map analysis for a case when the synchrotron motion was switched off (synchrotron motion adds an additional degree of freedom, making it difficult to determine the fundamental frequencies). For 1 IP, there is a multitude of excited resonances, with most importantly the (0, 3), (1, -4) and some of higher order (especially 10th). By contrast, the 5-IP case does not show any resonance excitation. A similar resonant behaviour appears in the equivalent 6-dimensional simulation (not shown), but here the synchrotron motion is obscuring the picture. The line of points formed in the left corner of the two diagrams is not a resonance, but reflects particles far ahead or behind the bunch, which do not interact with the electron cloud. It

is an artifact of our simulation.

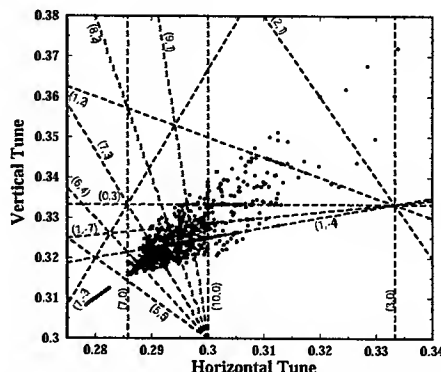


Figure 8: Tune footprint obtained from tracking through a frozen electron potential with 1 IP per turn by a frequency-map analysis [8].

The tune shift expected from the unperturbed cloud is [9] $\Delta Q_{x,y} \approx r_p / (2\gamma) \beta_{x,y} \rho_e C$, which amounts to about 0.003 in our example. The spread of the tune footprints in Fig. 8 is about 20 times larger, evidence of the highly nonlinear field of the electron cloud during a bunch passage.

3 CONCLUSIONS

A slow long-term emittance growth caused by an electron cloud of low density could be important for proton storage rings like the LHC. Our simulations show that the emittance growth observed in the simulations is not due to a monopole instability. It depends strongly on the number of interaction points and on the inter-IP phase advances. Non-linear resonances, of order 3–10, can be excited by the field of the electron cloud and may also contribute to the emittance growth. Preliminary results for a random phase advance suggest that below the TMCI threshold the simulated emittance growth converges towards zero, as the number of IPs is increased. In the future, we plan to calibrate our simulation against the code QUICKPIC [10], which models a continuous electron cloud instead of discrete IPs.

We thank A. Ghalam, T. Katsouleas and F. Ruggiero for helpful discussions.

4 REFERENCES

- [1] K. Ohmi, F. Zimmermann, PRL 85, p. 3821 (2000).
- [2] Y. Cai, ELOUD'02, CERN-2002-001, p. 141 (2002).
- [3] K.V. Lotov, G.V. Stupakov, EPAC 2002, Paris, p. 1643.
- [4] G. Rumolo et al., ELOUD'02, CERN-2002-001, 147.
- [5] K. Ohmi, Proc. PAC2001, Chicago, p. 1895 (2001).
- [6] E. Benedetto et al., Chamonix'03, CERN-AB-2003-008.
- [7] G. Arduini et al., "Present Understanding of Electron Cloud Effects in the Large Hadron Collider," these proceedings.
- [8] J. Laskar, Astron. Astrophys. 198, 341 (1988).
- [9] K. Ohmi et al., Proc. APAC'01, p. 445 (2001).
- [10] G. Rumolo, A. Ghalam, T. Katsouleas et al., to be published.

SIMULATION STUDY OF COUPLED-BUNCH INSTABILITIES DUE TO RESISTIVE WALL, IONS, OR ELECTRON CLOUD

F. Zimmermann, CERN, Geneva, Switzerland

H. Fukuma, K. Ohmi, Y. Ohnishi, S.S. Win, KEK, Tsukuba, Japan

Abstract

We simulate the interaction of a bunch train with either an external wake field, (semi-)trapped ions in a field-free region or in a dipole field, or an electron cloud, on successive turns, using a simplified algorithm with only a small number of macro-particles. We present simulated mode spectra and rise times for the ensuing coupled-bunch instabilities, and show that observations at the KEKB HER are consistent with a horizontal instability driven by carbon-monoxide ions in a region without magnetic field.

1 INTRODUCTION

A horizontal instability may limit the beam current in the KEKB HER. The instability growth rate depends nonlinearly on the beam current, shows almost a threshold behavior, and is about a factor of 2 faster than the corresponding instabilities in the vertical plane [1]. The measured unstable multi-bunch frequencies, as viewed at a fixed location, were found to be close to the revolution harmonics 7 and 1 [1], and, for another set of data, roughly equal to 17 [2]. In [3] we explored if this instability could be a manifestation of an electron cloud instability in the electron ring. However, the fairly low order of the unstable modes is not easily explained by an electron-driven instability. It appears more compatible with an instability caused by ions (the ion 'oscillation' frequency is much lower than that of the electrons). In addition to ions, low frequencies are also expected for the resistive-wall instability. We have developed a simple simulation model for coupled-bunch instabilities driven by ions, resistive wall, and electron cloud, respectively. For each driving mechanism, the simulation provides growth rates and mode patterns. In the case of ions, we can also vary the ion mass and the magnetic field. After a brief review of the experimental data, we describe the simulation model and present example results.

2 EXPERIMENTAL DATA

Figure 1 shows an example measurement. The left picture in Fig. 1 displays raw data (after subtracting the average BPM offset for each bunch) of the 1280 horizontal bunch positions measured on the 2000th turn after turning off the transverse feedback. A gap of 80 missing bunches is visible at the end. We see about ten oscillations, whose amplitudes increase along the train. The right picture illustrates the mode spectrum of the instability computed over 4095 turns, by applying a complex fast Fourier transform to the BPM data. This spectrum shows the lower betatron sidebands as a function of the revolution harmonic. Only the sidebands of the 80 lowest revolution frequencies (from

a total of 1280) are displayed here, since the higher-order modes are not excited. The peak corresponds to the lower sideband of the 11th revolution harmonic. This indicates that the 'ion tune' or 'wake tune', *i.e.*, the local oscillation frequency of the wake normalized to the revolution harmonic, is about 11. The number 11 lies between the numbers 7 and 17 determined in [1] and [2].

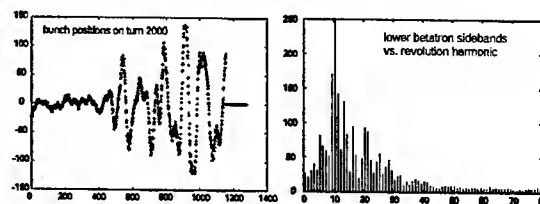


Figure 1: Left: measured horizontal position along the bunch train after 2000 turns; right: amplitude of lower betatron sidebands as a function of the revolution harmonic.

3 SIMULATION MODEL

In the simulation, we consider n_{step} uniformly spaced locations around the ring. The train of n_{bunch} bunches passes each of these locations, on n_{turn} successive turns. Each bunch creates a 'wake', which can act on the following bunches in the train or on later turns.

In the case of an ion instability, at each location the 'wake' left behind by a passing bunch is represented by a 'macro-ion'. A similar model was first employed by S. Heifets [4]. The effective charge weight of a newly created macro-ion is $q = \sigma_{\text{ion}} \rho_{\text{gas}} C / n_{\text{step}}$, where ρ_{gas} is the residual-gas density and σ_{ion} the ionization cross section, which we take to be equal to 2 Mbarn for CO molecules at multiple GeV beam energies. In the simulation, to enhance the instability, we consider a vacuum pressure up to 10^{-6} Torr (the real average pressure is less than 1 nTorr).

The ions are generated at a random transverse position within $\pm 1\sigma_{x,y}$ from the bunch centre. During the passage of a bunch, a macro-ion is accelerated (it receives kicks $\Delta x'_{\text{ion}}$ and $\Delta y'_{\text{ion}}$) and the passing (j th) bunch is deflected as well, by an amount $\Delta x'_j = -\Delta x'_{\text{ion}} q A_{\text{ion}} r_e / (r_p N_b)$, where A_{ion} is the ion mass in units of the proton mass, and N_{bunch} the bunch population. An analogous relation applies to the vertical plane. The kicks $\Delta x'_{\text{ion}}$ and $\Delta y'_{\text{ion}}$ are computed from the transverse distance between the macro-ion and the bunch centroid, using the Bassetti-Erskine formula [5] for the electric field of a Gaussian distribution. After a bunch passage the macro-ion either drifts, without magnetic field, or, inside a bending magnet, it performs a cyclotron oscillation in the horizontal plane, until the next

bunch arrives. The ion motion in a dipole field is

$$x = x_0 + \kappa(CSx'_0 + S^2z'_0), \quad x' = (C^2 - S^2)x'_0 + 2SCz'_0,$$

$$z = z_0 + \kappa(CSx'_0 - S^2z'_0), \quad z' = (C^2 - S^2)z'_0 - 2SCx'_0,$$

where the quantities with subindex 0 are the initial coordinates just after passage of a bunch, and we have used the abbreviations $\kappa \equiv 2E/(eBc)$, where B is the dipole field and E the beam energy, $C \equiv \cos(L_{\text{sep}}/\kappa)$, and $S \equiv \sin(L_{\text{sep}}/\kappa)$. Between the n_{step} interaction points, the bunches perform a free betatron oscillation. The ions can survive for many bunches or even several turns. Light hydrogen are overfocused within the train and are lost in the vertical direction. Heavier ions, such as CO, are overfocused only in the gap at the end of the train. In a dipole field, the ions can be stabilized by cyclotron motion. The typical decay constant n_{decay} for each case was determined by a separate simulation, where we tracked groups of different ions in various field configurations during repeated passages of the KEKB bunch train [6]. The decay constants so obtained vary between one hundred and several thousand bunch passages (up to a few turns). In [4], each passing bunch generated a new macro-ion at each of the n_{step} locations. To limit the total number of macro-ions, we here merge the charges, positions and momenta of all (macro-)ions that would be generated at the same location into those of a single 'super macro-ion'. Taking into account ion losses, at each bunch passage the effective contribution from old ions to the 'super macro-ion' is reduced by a factor $n_{\text{decay}}/(n_{\text{decay}} + 1)$. The total number of macro-ions around the ring is always equal to n_{step} . The charge of a 'super macro-ion' initially increases until it saturates at a value qn_{decay} . The above simplification may not correctly represent the ion dynamics at large amplitudes, but we still expect to obtain a fairly accurate image of the excited multi-bunch mode patterns and a reasonable estimate of the instability rise times.

The simulation of the resistive-wall instability proceeds analogously. We employ the same type of 'macro-particles' to store the offset of all bunches passing a certain location and their longitudinal position along the train as well as the turn number. For each bunch a resistive-wall wake-field deflection is computed as

$$\begin{bmatrix} \Delta x'_j \\ \Delta y'_j \end{bmatrix} \approx \begin{bmatrix} 0.5 \\ 0.8 \end{bmatrix} \sum_{i < j} \frac{2r_e N_b}{\gamma \pi b^3} \sqrt{\frac{c}{\sigma_0 (s_i - s_j)}} \begin{bmatrix} x_i \\ y_i \end{bmatrix},$$

where $(s_i - s_j)$ is the longitudinal distance between two bunches, $\sigma_0 \approx 5.4 \times 10^{17} \text{ s}^{-1}$ the conductivity of copper, b the vertical beam-pipe half gap, and the coefficients 0.5 or 0.8 for an elliptical chamber follow from [9]. We should add the contributions from all previous bunches, but in practice we often truncate the sum after two turns. The convergence can be checked easily. Unlike for the ion case, the 'macro-particles' are static and do not move between bunch passages. Here all the bunches are initially offset transversely by the same constant value of $10^{-3}\sigma_{x,y}$. The

Table 1: KEKB HER electron-beam parameters.

variable	symbol	value
beam energy	E	8 GeV
rms bunch length	σ_z	6 mm
transv. rms beam sizes	$\sigma_{x,y}$	687, 73 μm
average beta function	$\beta_{x,y}$	15 m
bunch spacing	s_b/c	8 ns (4 buckets)
bunch population	N_b	3.5×10^{10}
total no. of bunches	n_b	1200
missing bunches (gap)	n_{gap}	80
ring circumference	C	3016 m
half aperture	$h_{x,y} (b)$	52, 28.5 (25) mm

constant offset is chosen, because it is close to the asymptotic multi-bunch pattern of the resistive-wall instability, which is driven at low frequency.

Finally, in the case of the electron cloud, we consider a short-range wake coupling only consecutive bunches, and zero electron memory from turn-to-turn. This case is similar to the resistive-wall case, but the number of macro-particles needed is much smaller, since only a single preceding bunch contributes to the wake, $\Delta x'_j \approx (r_e N_b / \gamma) W_{xx} x_{j-1}$. The initial transverse bunch centroid positions are chosen randomly within $\pm 10^{-3}\sigma_{x,y}$. For the electron-cloud case, we assume a bunch-to-bunch wake field of strength $W_{x,y} \approx 10^5 \text{ m}^{-2}$, about a factor 10 smaller than typical for positron or proton beams [7].

The other simulation parameters are listed in Table 1.

4 RESULTS

Figure 2 shows the simulated horizontal bunch positions along the train, and Fig. 3 the oscillations of a few selected bunches as a function of turn number, for various cases exhibiting an instability. In the resistive-wall case, the oscillation amplitudes of all bunches grow with a similar rate, while, both with CO ions in a field-free region and with an electron cloud, the growth rate increases towards the end of the train. The case of H ions in a dipole shows a faint instability, with three 'bursts' along the train. For two other examples (not shown), *i.e.*, hydrogen ions without magnetic field, and carbon monoxide ions in a dipole field, the beam appears stable. Figure 4 presents the mode spectra computed for the same 4 simulations as above. The case of carbon-monoxide ions in a field-free region (top left picture) is the only one that — nearly perfectly — matches the observation. The unstable mode number of 13 is almost the same as measured (11). This number is more than 2 times smaller than expected from the angular ion oscillation frequency near the center of the beam $\omega_{ix} \approx (2N_b r_p c^2 / (L_{\text{sep}} \sigma_x (\sigma_x + \sigma_y) A))^{1/2}$, which for CO would yield an 'ion tune' of 28. We attribute this frequency reduction to the finite size of the beam and the ion cloud, and to the nonlinearity of the force acting between them. The 15% difference between 13 (simulated) and 11 (measured) can be explained by a 30% difference in bunch population between this particular experimental data

set ($N_b \approx 2.7 \times 10^{10}$) and the simulation. In the top left picture of Fig. 4, also the mode 2 is strongly excited, which is not seen in the experimental data of Fig. 1, but resembles those presented in Ref. [1]. This mode likely is a consequence of the nonlinear beam-ion force, causing detuning with amplitude and saturation.

None of the other 3 cases yields a simulation result which even remotely resembles the observed spectrum. However, the mode spectrum simulated for the electron-cloud wake is similar to that observed in the KEKB LER positron ring without a solenoid field [1].

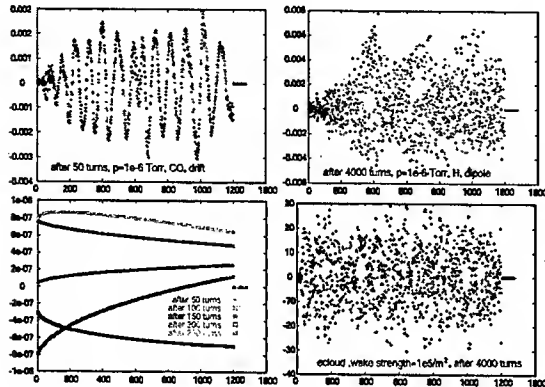


Figure 2: Simulated horizontal position along the bunch train for carbon monoxide without magnetic field after 50 turns (top left), for hydrogen in a dipole field after 4000 turns (top right), for the resistive wall instability after various numbers of turns (bottom left) and for the electron cloud after 4000 turns (bottom right).

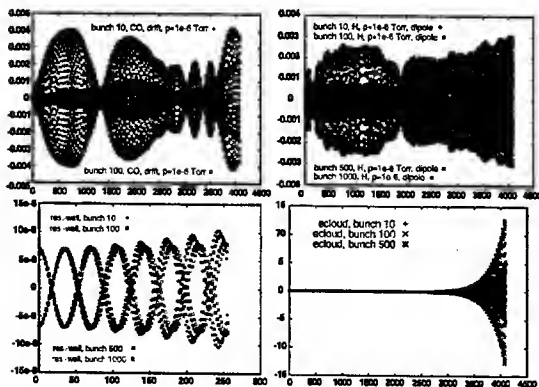


Figure 3: Simulated horizontal position of different bunches as a function of turn number, for the same four cases as in Fig. 2.

From Fig. 3 we can estimate the growth rates at the end of the train. To this end, for the ion instabilities, we scale with the square of the bunch position and extrapolate linearly from 1 μ Torr to the actual pressure of 1 nTorr. We then find rise times of 1 ms for carbon monoxide ions without field, 5 ms for the resistive wall, 2 ms for the electron cloud, and 4 s for hydrogen ions inside a dipole. The

growth rates for the resistive wall and electron cloud are consistent with analytical estimates. The horizontal growth rate for carbon-monoxide ions fits the observation. Additional simulations suggest that it is larger than the vertical growth rate, which would resolve another 'puzzle'.

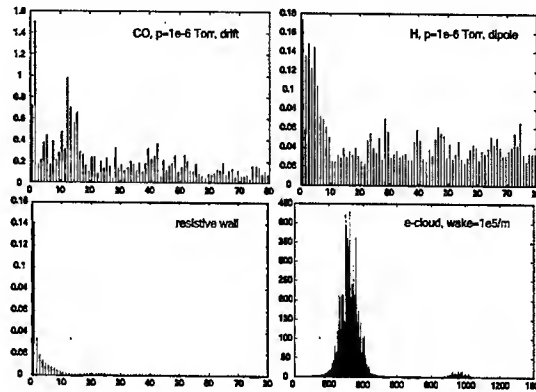


Figure 4: Amplitudes of lower betatron sidebands as a function of the revolution harmonic for the same four cases as in Fig. 2. The last picture (for the electron-cloud wake) shows the full spectrum; in the other three cases, where higher modes are not excited, only the harmonics 1–80 are displayed.

5 CONCLUSION

A fast computer simulation was written to model coupled-bunch instabilities driven by various sources. Application to the KEKB HER suggests that the observed horizontal instability is caused by carbon monoxide ions in field-free regions. For this case the simulated mode patterns and growth rates almost exactly match the observations. On the other hand, electron cloud, resistive wall, hydrogen ions, or ions trapped inside dipoles are all incompatible with the measurements.

6 REFERENCES

- [1] S.S. Win, H. Fukuma, E. Kikutani, M. Tobiya, "Observation of Transverse Coupled Bunch Instability at KEKB," Proc. 2nd APAC Beijing (2001).
- [2] Y. Ohnishi, "Analysis of Horizontal Oscillations in the KEKB HER Measured in May 2002," unpublished presentation.
- [3] F. Zimmermann, "Accelerator Physics Studies for KEKB," CERN-SL-Note-2002-017 (AP).
- [4] S. Heifets, "Saturation of the Ion Transverse Instability," SLAC-PUB-7411 (1997).
- [5] M. Bassetti, G.E. Erskine, "Closed Expression for the Electrical Field of a Two-Dimensional Gaussian Charge," CERN-ISR-TH/80-06 (1980).
- [6] F. Zimmermann, "Horizontal Instability in the KEKB HER, KEK, Oct. 19–Nov. 1, 2002, and March 16–29, 2003," unpublished note.
- [7] F. Zimmermann, "Electron-Cloud Effects in High-Luminosity Colliders," 1997 Advanced ICFA Workshop, Frascati Physics Series X (1998) p. 419
- [8] A. Chao, "Physics of Collective Beam Instabilities in High Energy Accelerators," J. Wiley (1993).
- [9] K. Yokoya, "Resistive Wall Impedance of Beam Pipes of General Cross Section," Part. Acc. 41, p. 221 (1993).

INSTABILITY THRESHOLD CURRENTS VS. ENERGY IN CESR*

M. Billing, J. Sikora, LEPP, Cornell University, Ithaca, NY 14850, USA

Abstract

CESR has been observed to have two coupled bunch instabilities, one horizontal and the other longitudinal, which can limit the total beam current when operating with trains of bunches. Feedback has been employed for some time to counter these instabilities. This paper reports on the threshold current for the onset of the longitudinal instability when feedback is turned off vs. beam energy over a range from 1.9 GeV to 5.2 GeV and compares the change in threshold current with that expected from the change in radiation damping. Operating performance with feedback in use will also be reported for both longitudinal and horizontal instabilities.*

INTRODUCTION

CESR is an electron-positron storage ring collider, generating luminosity at 4.7 to 5.5 GeV beam energies and operating with both beams circulating in the same vacuum chamber throughout the entire ring. In 1983 CESR began operating with multiple bunches in the ring with head on collisions; in 1994 it progressed to 9 trains of from 1 to 5 bunches with a crossing angle in the interaction region. In 1983 a horizontal, coupled bunch dipole instability was observed for the positron beam only[1]. This instability was countered with feedback and the cause ultimately determined to be due to the action of the distributed ion pumps in use in CESR[2]. The mechanism is believed to be photo-electrons trapped inside the beam chamber by weak electric fields, which have "leaked" through the pumping slots[3]. In 1996 a coupled bunch longitudinal dipole instability was first observed when CESR was operating at higher beam currents with 9 trains of 2 bunches. The threshold current for this instability initially had a strong dependence on the number and spacing of bunches in each train. Subsequent studies had identified the dominant source of the offending impedance as the 20 cells of the normal-conducting RF accelerator cavities. Simulations of the growth rates used results from beam induced signals on field probes in each cell, and predicted the variation of instability threshold currents for all of the various filling patterns of bunches in 9 trains[4].

Over the course of several years the four 5-cell normal conducting RF cavity structures have been replaced with four single cell, superconducting RF cavities, having very low loaded Q's for all higher order modes. As the superconducting RF cavities began replacing the normal conducting cavities, the instability threshold currents increased on the average and the large variation of these currents due to changes in the filling pattern lessened substantially[4]. Now the dominant impedance causing the longitudinal dipole coupled bunch instability is

suspected to be due to the 4 horizontal and 2 vertical separators in use in CESR for beam separation.

Shortly after this instability was observed, longitudinal feedback was added to stabilize the beams. The latest implementation of this feedback uses a very low-Q RF cavity as the longitudinal feedback system kicker[5]. In the range of 4.7 to 5.5 GeV the feedback system is able to stabilize the beams at all operating currents and in all desired filling patterns of 9 trains of bunches.

During the next several years CESR will be operating part of the time at lower beam energies (1.5-2.5 GeV) to produce luminosity in the charm physics energy range[6]. The plan is to operate with approximately 20 m of superconducting wiggler magnets to increase the emittance and the radiation damping rate. During the summer of 2002 a single 1.6 m superconducting wiggler was installed in CESR for studies at or near 1.88 GeV beam energy. This allowed for measurements to test the beam stability at low energies with and without the wiggler being powered. Also at lower energies the pumping from the distributed ion pumps, which use the lower dipole magnetic fields, will be ineffective and these will be turned off for operations. As a result the horizontal dipole coupled bunch instability for positrons should not be important, however the longitudinal stability will not be affected by turning off the distributed vacuum pumps and, therefore, will continue to be a concern for operations.

THEORY

As the beam energy in a storage ring is lowered, the longitudinal or transverse deflection, felt by the beam, from the vacuum chamber's impedance or from a feedback kicker increases inversely proportional to the beam energy. Also if no additional source of radiation loss is added to the ring (such as the wiggler magnets), the radiation damping rate should decrease proportional to the beam energy to the third power. The time evolution of an oscillation amplitude, $A(t)$, for any particular mode in CESR will have the general form,

$$\frac{dA}{dt} = [\alpha_Z' I + \alpha_{FB}' I + \alpha_R] A(t) + e(t) \quad (1)$$

where I is the total beam current, $\alpha_Z' I$ is the growth rate due to the vacuum system impedance, $\alpha_{FB}' I < 0$ is the damping rate due to feedback, $\alpha_R < 0$ is the radiation damping rate and $e(t)$ is any excitation applied to the beam. Notice particularly that the damping rate from feedback in CESR grows proportional to beam current (by design) over a fairly large range in current per bunch. As was stated above, also note that beam energy, E_b , dependence is

* Work supported by the NSF.

$$\alpha_z' \text{ and } \alpha_{FB}' \propto \frac{1}{E_b} \quad \text{while} \quad \alpha_R \propto E_b^3$$

assuming (for the last proportionality) fixed bending radii for all of the dipole magnets. During the entire machine studies CESR has operated with two permanent magnet wigglers closed to increase the damping at low energy. The field in these magnets did not scale with energy, but instead remained constant. An approximate fit to the total radiation growth (damping) rate calculated from the design of the optics vs. energy yields a dependence which scales as $E_b^{2.7}$. Unstable motion will occur when the term in brackets in equation 1 is greater than zero, so the instability threshold current, I_{thresh} , will then be given by

$$I_{\text{thresh}} = -\frac{\alpha_R}{\alpha_z' + \alpha_{FB}'} \quad (2)$$

With Feedback

For modes of oscillation that are damped by feedback, i.e. $\alpha_{FB}' I < 0$, if the feedback damping exceeds the instability growth rate, $-\alpha_{FB}' I > \alpha_z' I$, then the bracket in equation 1 will always be negative and the amplitude of oscillation will damp. This is true independent of energy since both the instability growth rate and the feedback damping rate have the same beam energy dependence.

Without Feedback

For the case when the mode of oscillation is not damped by feedback ($\alpha_{FB}' = 0$), from equation 2 the threshold current will be proportional to $-\alpha_R / \alpha_z'$, which in turn for CESR is proportional to $E_b^{3.7}$. (For storage rings, which have magnets with fields that scale with energy, this dependence would be E_b^4 .) Therefore, instabilities from modes without any feedback will become much more important at low energy.

OBSERVATIONS

Measurements of the longitudinal dipole coupled bunch instability thresholds were made at several different energies. For longitudinal dipole oscillations, the onset of the instability was determined by observing the amplitudes of the synchrotron sidebands of the rotation harmonics from a phase detected, beam position monitor signal. (Because of the unequal spacing of the trains of bunches in CESR, it is only necessary to observe the lowest 10 sidebands.) At the instability threshold some of the sideband frequency amplitudes increase, indicating larger displacements of the bunches. Generally the oscillation amplitude will increase several orders of magnitude before it reaches a limiting value, thought to be caused by the motion becoming non-linear due to the nonlinearities of the RF restoring force. The threshold current is defined as the current at which this growth of the oscillation amplitude first begins. Generally it has been observed that there is some variation over time with a measured threshold current for a particular filling

pattern for the bunches. This is thought to be caused by changes in the dimensions of the vacuum chamber structures in the ring adjusting the frequencies of parasitic modes in the structures. If more than one set of measurements has been performed, the data presented here will always use the highest threshold current that has been measured for a given set of conditions.

Figure 1 shows the dependence of the instability threshold current vs. beam energy when the longitudinal feedback and the superconducting wiggler magnet were turned off. Data was taken at different energies with different numbers of bunches in the 9 trains. The spacing between the bunches within the train is always 14 nsec. The data was limited to RF settings, which gave design bunch lengths between 12.5 and 16.5 mm at zero current. Figure 1 also contains a solid curve proportional to the expected dependence for CESR of the instability threshold current on beam energy to the 3.7 power as a reference to guide the eyes. A second, dotted curve is plotted, which is the least squares fit of the log of the threshold current to the beam energy raised to a power. This fit gives the beam energy to the 3.36 power in reasonable agreement with the expected 3.7 power dependence. The figure shows that there are some variations in the threshold currents for different filling patterns at the same energy, however this variation is fairly small compared to the almost factor of 30 which is expected for the range of beam energy. When the longitudinal feedback system is turned on and the wiggler was not powered, no instability was observed up to total single beam current of 160mA.

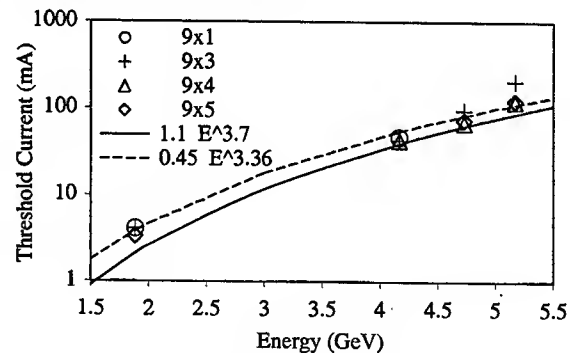


Figure 1. Instability threshold currents for different filling patterns vs. energy. The filling pattern 9xN designates 9 trains of N bunches.

The effect of turning on and off the superconducting wiggler on the instability threshold may be seen in table 1. These measurements were taken at 1.88 GeV with the longitudinal feedback off and at two RF voltages for several different filling patterns. For the conditions used, the bunch length at zero current is computed and displayed as part of table 1. The ratio of the instability thresholds for the wiggler being on and off is also given in table 1. Notice that although there is some variation from fill pattern to fill pattern, the average increase in the instability threshold current was a factor of 2.2-2.3. From

the optics and the measured synchrotron oscillation frequency, the calculated increase in damping rate is expected to be a factor of 1.6. The measured values give a result that is about 40% larger than expected.

An explanation for this enhanced damping rate may be that, as the wiggler was turned on, the bunch length also increased producing a longer, more stable bunch. The size of this effect may be estimated as follows. If the data in table 1 is compared for wiggler off conditions for filling patterns 9x1, 9x3 and 9x5, the average instability threshold increased by a factor of 1.4 ± 0.5 as the bunch length changed from 6.4 mm to 8.3 mm (a factor of 1.38.) Similarly for the wiggler on conditions, the thresholds increased an average factor of 1.4 ± 0.2 as the bunch length changed from 9.6 mm to 13.0 mm (a factor of 1.35.) These results suggest the instability threshold varies roughly inversely as the bunch length and when taken with the calculation of the change of the bunch length, as the wiggler turns on, yields a factor of 1.4 in agreement with the 40% larger threshold current seen above.

Fill Pattern	I_{thresh} (mA) Wiggler OFF $\sigma_z = 8.8\text{mm}$	I_{thresh} (mA) Wiggler ON $\sigma_z = 13.0\text{mm}$	Ratio
1 bunch	1.0 ± 0.2	2.2 ± 0.2	2.2 ± 0.5
9x1	4.1 ± 0.5	6.0 ± 0.5	1.5 ± 0.2
9x3	4.1 ± 0.6	10.5 ± 0.5	2.6 ± 0.4
9x4	3.2 ± 0.3	7.3 ± 0.3	2.3 ± 0.2
9x5	3.3 ± 0.7	8.0 ± 0.2	2.2 ± 0.5
Average			2.2 ± 0.4
Fill Pattern	I_{thresh} (mA) Wiggler OFF $\sigma_z = 6.4\text{mm}$	I_{thresh} (mA) Wiggler ON $\sigma_z = 9.6\text{mm}$	Ratio
9x1	2.6 ± 0.5	5.1 ± 0.5	2.0 ± 0.4
9x3	2.7 ± 0.5	6.4 ± 0.4	2.4 ± 0.5
9x5	3.0 ± 0.4	6.5 ± 0.5	2.2 ± 0.3
Average			2.3 ± 0.4

Table 1. Longitudinal instability threshold currents for different filling patterns, for the wiggler magnet on and off, and for two different zero current bunch lengths, σ_z . The filling pattern 9xN designates 9 trains of N bunches.

OPERATIONAL EXPERIENCE

CESR has operated at beam energies near 1.9 GeV with one 1.6 m superconducting wiggler and the two permanent magnet wigglers in use. In these conditions and with the distributed ion vacuum pumps in the normal bending magnets turned off, horizontal feedback was not needed to stabilize the positron beam, as expected. Generally horizontal and vertical feedback systems were used to damp the coherent oscillations caused by injection transients imparted to the beams. However, it was found necessary to limit the horizontal feedback gain setting to less than 15% of its value at 4.7-5.3 GeV. It was found that raising the feedback gain significantly for electrons, during injection reduced the accumulation rate into CESR. Although this effect has not been studied in depth,

it is suspected that low level noise in the feedback system may be exciting beam motion at low per bunch currents, effectively reducing the injection aperture. It has been found that horizontal and vertical feedback loop gain settings in the range of 15-20% of their maximum levels are useful for stabilizing the beams especially during injection. The longitudinal feedback system is needed for operations with either one or two beams above the instability threshold currents presented above. There is no difficulty in operating this system at full gain during injection and HEP operation.

Lastly a vertical instability has been observed for 8 and 9 trains of electrons. This happens for electrons only. The instability threshold current can be raised first by using 8 trains of bunches rather than 9 and then further by using 7 trains of bunches. Vertical, dipole beam motion occurs at the onset of the instability, which is similar to some ion related events seen in the past. Operating with 7 trains has not been a problem thus far, but further study of this instability is needed.

FUTURE STUDIES

A number of machine studies of beam stability and feedback system operation are planned for the next several months. One question is why does the horizontal feedback gain need to be limited to approximately 15% of maximum gain during injection? If this is caused by low-level noise driving the beam at low current (where the loop gain and, hence, damping is lower), what modifications can be made to the feedback system to correct this effect? The electron transverse instability needs further study to determine the cause and whether it may be countered without needing to remove as many bunches from the ring. Another question is will the beam remain stable as the beam current is increased, especially when both beams are stored? Since CESR at low energy will operate with the current in both beams well above the maximum current achieved at 5.3 GeV scaled to low energy by E_b^4 , quadrupole coupled bunch modes or other higher modes of oscillation may become unstable as the currents increase.

REFERENCES

- [1] L. Sakazaki et al, " 'Anomalous,' Nonlinear Current-Dependent Damping in CESR," IEEE Trans. Nuc. Sci. 32, 2353, 1985.
- [2] M. Billing et al, "Interaction of CESR Vacuum Pumps with the Stored Beam," PAC89, March 1989.
- [3] J. Rogers, "Photoemission Instabilities: Theory and Experiment," PAC97, May 1997.
- [4] M. Billing, et al, "Observation of Longitudinal Coupled Bunch Instability in CESR," PAC99, March 1999.
- [5] M. Billing, et al, "Performance of the Beam Stabilizing Feedback Systems at CESR," PAC01, June 2001
- [6] D. Rice et al, "Parameters for the Low Energy Operation of CESR," PAC01, June 2001.

HEAD-TAIL INSTABILITY AT TEVATRON*

P. M. Ivanov[#], J. Annala, A. Burov, V. Lebedev, E. Lorman, V. Ranjbar, V. Scarpine, V. Shiltsev
FNAL, Batavia, IL 60510, USA

Abstract

Tevatron performance suffers from a coherent transverse instability. Experimental and theoretical studies allow identifying the instability as a weak head-tail, driven by the short-range wake fields in presence of the space charge. Growth rates and coherent tune shifts are measured at injection of single high-intensity proton bunch using a fast strip-line pickup. Landau damping through the octupole-generated betatron tune spread for all unstable head-tail modes has been demonstrated.

INTRODUCTION

In order to prevent developing a transverse coherent instability for high intensity proton beam, the Tevatron lattice chromaticities should be set above $\xi_{x,y} \approx 8$ at the injection (150 GeV) and above $\xi_{x,y} \approx 26$ at the collision energy (980 GeV). Although it suppresses the instability, it results in a degradation of the machine performance due to reduction of beam lifetime. Observation of the particle loss in vicinity of the CDF-detector clearly demonstrates that the minimum loss is achieved at $\xi_{x,y} = 0$ [1], and the loss increases with growth of absolute value of the chromaticity. That stimulated us to investigate a driving mechanism for this instability, as well as to search for possible solutions to operate at zero chromaticities. The measurements performed in November 2002 exhibited that the transverse impedance significantly exceeds the Run II transverse impedance budget [2]. The source of the excessive impedance was tracked to two laminated Lambertson magnets. The removal one of them in January 2003 shutdown significantly reduced the chromaticities required for the beam stabilization. This summer we plan to insert a shielding liner into the remaining injection Lambertson magnet.

INSTABILITY OBSERVATION

A fast digital oscilloscope, connected to the horizontal and vertical 1-meter long strip-line pickups, records turn-by-turn data for 2000 turns. Each turn data are sampled during 80 ns with 0.4 ns rate so that the transverse head-tail dynamics of single bunch could be observed. After the measurement, the signal is deconvoluted and transverse positions along the bunch are computed. The measurements are synchronized with the beam injection. Chromaticities are set below zero so that the mode $l=0$ would be unstable.

At $N_{ppb}=2.6 \cdot 10^{11}$ and chromaticity values of $\xi_{x,y} \approx -2$,

we identified that the coherent mode with $l=0$ was developed with the coherent tune shift $\Delta\nu=0.0011 \pm 0.0001$ and the growth rate $1/\tau_0=120 \pm 5 \text{ s}^{-1}$. The coherent tune shift for the strongest mode is smaller than the synchrotron tune, $\Delta\nu \approx 0.7\nu_s$. That classifies the instability as a weak head-tail.

To crosscheck the measurements we also measured the chromaticity by pinging the beam and measuring the phase shift between head and tail. The chromaticity was calculated from this phase difference according to [3]:

$$\xi_{x,y} = -\eta \frac{\Delta\Psi_{x,y}}{\omega_0 \Delta\tau (\cos(2\pi n\nu_s) - 1)} \quad (1)$$

Here $\Delta\Psi$ is the head-tail phase difference, η is the slip-page factor, ω_0 is the revolution frequency, and $\Delta\tau$ is the time length of the bunch. Comparison of the head-tail chromaticity measurement with the traditional RF technique is presented in Figure 1.

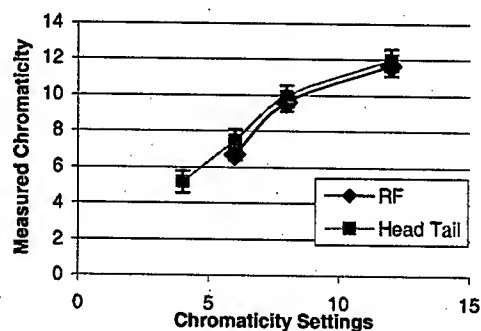


Figure 1. Comparison of the Head-Tail chromaticity measurement with the traditional RF technique.

To compute the transverse impedance with good accuracy we build a computer model of the instability. An ensemble of macro-particles with the Gaussian longitudinal distribution has been tracked many turns for particles interacting through the resistive wake field. The Landau damping was not taken into account in the model, and therefore matching the measurements and simulations yields the low boundary for the transverse impedance. The measurements were performed at the injection orbit where the growth rate is 120 s^{-1} . That results in $Z_{Lmin} \approx 4-5 \text{ M}\Omega/\text{m}$.

Tevatron stainless steel vacuum chamber has a square cross section with $2h=6 \text{ cm}$, the transverse impedance of which amounts to $\sim 0.9 \text{ M}\Omega/\text{m}$ at 100 MHz [2]. That is about 5 times smaller than the measured value. After careful examination it was suggested that a major source of impedance is the Lambertson injection magnet. Its value can be estimated by integrating the resistance over

*Work supported by the Universities Research Assos., Inc., under contract DE-AC02-76CH03000 with the U.S. Dept. of Energy.
[#]pmivanov@fnal.gov

the low frequency current pass through the laminas [4]:

$$Z_{\perp} \approx \frac{2Z_0}{\pi b^2} \cdot \frac{\mu}{\kappa} \cdot F \cdot \frac{L}{d} \quad (2)$$

where $\kappa^2 = -4\pi i \sigma \mu \omega / c^2$, $Z_0 \approx 377 \Omega$, $\mu \approx 100$, $F = 0.5 - 1.0$ is a geometry form-factor, $L = 11.2 m$ is a total length of the magnet, $d = 1 mm$ is the lamination thickness, and b is the distance from the beam to the wall.

To prove that the injection Lambertson magnet makes dominant contribution into the transverse impedance the stability bounds in chromaticity space have been measured for the three local beam orbit offsets (see Fig.2). The results are presented in Figure 3. As one can see the beam displacement in the magnet strongly affects the stability bounds. Using Eq. (2) one can find the following values for the Lambertson transverse impedance at different locations inside the magnet: (1) injection local orbit bump, $b_1 \approx 6 mm$, $Z_{\perp} \approx 5 M\Omega/m$; (2) central regular orbit, $b_2 \approx 9 mm$, $Z_{\perp} \approx 1.8 M\Omega/m$; (3) local orbit bump with respect to the central orbit, $\Delta Y = -3 mm$, $\Delta X = -10 mm$, $b_3 \approx 18 mm$, $Z_{\perp} \approx 0.6 M\Omega/m$.

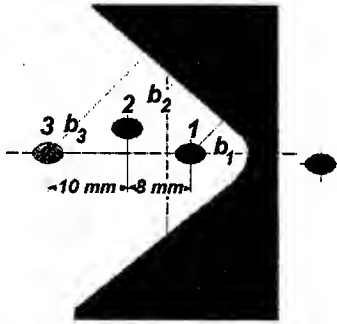


Figure 2. Layout of the local orbit bumps.

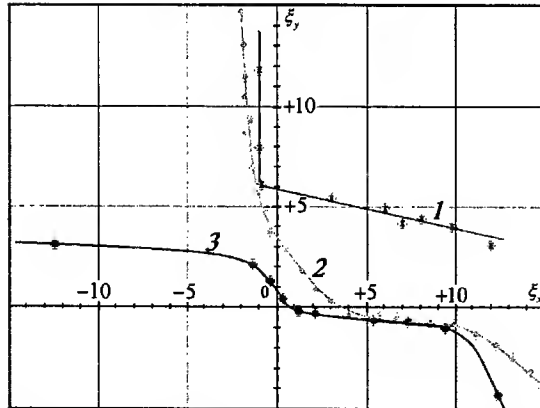


Figure 3. The stability regions for the head-tail modes in the chromaticity space. All measurements are performed with single proton bunch ($N_{ppb} = 2.65 \cdot 10^{11}$). The thresholds of the excitation correspond to an increase in the coherent component of the Schottky spectrum as the chromaticities were smoothly decreased.

On the injection orbit, the head-tail instability is polar-

ized in the vertical plane at positive chromaticities. Stability is limited by excitation of the quadrupole mode with longitudinal number $l=2$ (see Fig. 4). The coherent mode with the monopole longitudinal configuration $l=0$ limits stability in horizontal plane when $\xi_x \approx -1$.

Horizontal and vertical impedances of Eq. 2 are approximately equivalent, but the stability bounds for the vertical and horizontal modes are different (Fig.3). A possible reason could be related to the space charge tune shifts, which are different for the two planes because of dispersion. The vertical incoherent shift is two times larger than the horizontal shift. Calculated coherent tune shifts for the first two horizontal modes are found to be comparable with the incoherent space-charge tune shift that promotes Landau damping due to a synchrotron tune spread. The vertical modes are in worse conditions because the space-charge shift is higher. At Tevatron injection energy the synchrotron tune and rms-tune spread are: $\nu_{s0} = 1.8 \cdot 10^{-3}$, $\delta\nu_s \approx 2.2 \cdot 10^{-4}$.

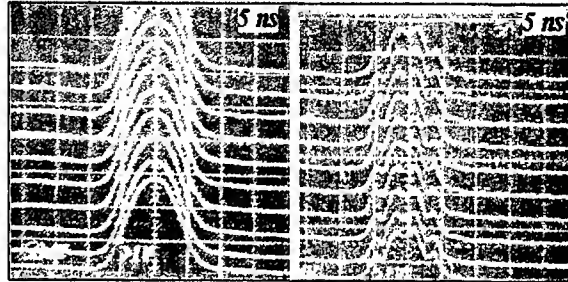


Figure 4. Longitudinal density profiles of the initial ($N_{ppb} = 2.65 \cdot 10^{11}$) and remaining ($N_{ppb} = 1.03 \cdot 10^{11}$) proton bunches before and after self-stabilization of the vertical instability due to the particle losses. The particles were lost in accordance with the longitudinal configuration of the coherent vertical oscillations that points qualitatively at excitation of the head-tail mode with $l=2$.

The Tevatron tunes $\nu_x = 20.585$ and $\nu_y = 20.575$ are located in vicinity of the coupling resonance $\nu_x - \nu_y = 0$. At crossing the resonance both the vertical and horizontal coherent modes become unstable that can be caused by a repartition of the direct space-charge tune shift between two normal betatron modes with the coupling increased.

On central orbit (curve 2 in Figure 3), a single coherent vertical mode with dipole longitudinal configuration is observed at the chromaticity threshold $\xi_y \leq 3$. The horizontal higher order head-tail modes are stable out of the resonance $\nu_x - \nu_y = 0$.

At the orbit bump ($\Delta Y = -3 mm$, $\Delta X = -10 mm$) with negative chromaticities (curve 3), the unstable mode $l=0$ can be easily stabilized by means of octupoles. Similar stability conditions are expected after installation of planned shielding of the magnet bare lamination.

These experimental studies clearly identified the transverse coherent instability as a single bunch head-tail effect, driven by resistive wall impedance [5].

SPACE CHARGE EFFECT

The space charge effect results in a non-linear incoherent detuning and plays important role in coherent head-tail dynamics. Laslett tune shifts due to electric- and magnetic-image fields are not included in our consideration because for the Tevatron performance parameters, the image terms are negligibly small as compared with a contribution of the electromagnetic self-fields. For the 3D-Gaussian charge distribution the direct space-charge linear tune shifts are given by:

$$\Delta\nu_{x,y}^{sc} = -\frac{N_{ppb} r_0 R_0}{\sqrt{2\pi} \beta^2 \gamma^3 \sigma_z} \left\langle \frac{\beta_{x,y}}{\sigma_{x,y}(\sigma_x + \sigma_y)} \right\rangle \quad (3)$$

where $\sigma_{x,y}(s) = \sqrt{\epsilon_{x,y} \beta_{x,y}(s) + D_{x,y}^2(s) \sigma_{dp/p}^2}$ are the transverse beam sizes, the $\langle \dots \rangle$ -denotes averaging over the machine. For $N_{ppb} = 2.6 \cdot 10^{11}$ and $\sigma_s = 90 \text{ cm}$, it comes out as:

$$\Delta\nu_x^{sc} \approx -0.36 \cdot 10^{-3}, \quad \Delta\nu_y^{sc} \approx -0.7 \cdot 10^{-3}$$

DAMPING OF THE HEAD-TAIL MODES

Presently, in order to work at low chromaticities ($\xi_x \approx 6$, $\xi_y \approx 4$), the transverse dampers are used to prevent an excitation of the transverse instability at the multi-bunch mode of operation [7].

An universal method for damping the instability is to introduce a betatron frequency spread that is larger than the growth rates. Landau damping is effective when the following approximate condition is satisfied:

$$\sqrt{(\delta\nu_{x,y}^{oct})^2 + (\delta\nu_{x,y}^{sc})^2} + \left| \langle \delta\nu_{x,y} \rangle \right| \geq \left| \Delta\nu_{x,y}^{sc} - \Delta\nu_{x,y}^{coh}(l) \right| \quad (4)$$

The two Tevatron regular octupole families are used to provide Landau damping for the head-tail modes:

$$OZD(n=12, \beta_x > \beta_y), \quad OZD(m=24, \beta_y > \beta_x).$$

There are two sources of the octupole-driven tune spread: first due to the betatron amplitude spread, and second due to the dispersion in the octupole locations.

$$\delta\nu_{x,y}^{\beta} = \frac{1}{16\pi B\rho} \left[J_{x,y} \sum_{n,m} \left(\bar{K}_3 \beta_{x,y}^2 \right)_{n,m} - 2J_{y,x} \sum_{n,m} \left(\bar{K}_3 \beta_x \beta_y \right)_{n,m} \right] \quad (5)$$

$$\delta\nu_{x,y}^D = \frac{\sigma_{dp/p}^2}{16\pi B\rho} \sum_{n,m} \left(\bar{K}_3 \beta_{x,y} D_x^2 \right)_{n,m} \quad (6)$$

where $J_{x,y} = a_{x,y}^2 / \beta_{x,y}$ are single particle Courant-Snyder invariants and

$$\bar{K}_3(n, m) = I_{n,m}(\text{Amps}) \int_0^L \frac{\partial^3 B_y}{\partial x^3} ds / 1 \text{ Amp}$$

$$\bar{K}_3(n, m) = 616 \cdot I_{n,m}(\text{Amps}) [T/m^2]$$

are the normalized octupole strengths with I_n and I_m as the OZF- and OZD-family octupole currents. On the central orbit, damping the vertical mode $l=1$ required currents $I_{OZD} \approx 4.2 \text{ A}$ and $I_{OZF} = 0$ with the estimated tune spreads as:

$$\langle \delta\nu_y^{Oct} \rangle \approx 0.28 \cdot 10^{-3}, \quad \langle \delta\nu_x^{Oct} \rangle \approx 1 \cdot 10^{-4}.$$

At the chromaticity of $\xi_{x,y} \approx -2$ the coherent mode $l=0$ has been stabilized at $I_{OZD} \approx 5.0 \text{ A}$ and $I_{OZF} \approx 2.0$ with $\langle \delta\nu_y^{Oct} \rangle \approx 0.52 \cdot 10^{-3}$, $\langle \delta\nu_x^{Oct} \rangle \approx 0.38 \cdot 10^{-3}$.

In both cases the widths of betatron spectra measured by Schottky monitor are in a reasonable agreement with this calculation taking into account the contributions from the synchrotron and direct space-charge tune spreads. The octupole cubic non-linearity has the positive sign that is better from dynamic aperture point of view since the vertical tune is slightly above the resonance $\nu_y = 4/7$. Besides, it has the "right" sign to minimize the octupole strengths of the OZD-family in consequence of:

$$(\Delta\nu_y^{sc} - \Delta\nu_y^{coh}(l=0)) > 0$$

In the horizontal plane the incoherent and coherent tune shifts are comparable but the space-charge tune spread does not promote Landau damping without octupoles.

CONCLUSION

The observed single-bunch head-tail instability has been found to be driven by the resistive impedance of laminated Lambertson magnets. To reduce the impedance, the insertion of a thin shielding liner inside the magnet is planned. It is expected that it will stabilize the higher order head-tail modes at positive chromaticities and significantly reduce the growth time at negative chromaticities.

Landau damping through the octupole-generated betatron tune spread for all of the unstable head-tail modes at positive and negative chromaticities has been seen. After performing additional experimental studies, this method is planned to be involved in the routine machine operations. That will result in an enhancement of the peak and integrated luminosity.

ACKNOWLEDGMENTS

We would like to thank V. Danilov (ORNL) for useful discussions of the instability problems and Dean Still (FNAL) for helping in machine studies.

REFERENCES

- [1] X. Zhang, *et al.*, Experimental Studies of Beam-Beam Effects in Tevatron, Proc. of this conference.
- [2] Tevatron Run-II Handbook, FNAL 1998.
- [3] D. Cocq *et al.*, The measurement of chromaticity via a head-tail phase shift, BIW98, Stanford CA, 1998.
- [4] A. Burov, V. Danilov, unpublished note, 2003.
- [5] A.W. Chao, Physics of Collective Beam Instabilities in High Energy Accelerators, John Wiley & Sons, New York, 1993
- [6] D. Mohl, Part. Acc., v.50, p.177, 1995.
- [7] C.Y. Tan, J. Steimel, The Tevatron Transverse Dampers, Proc. of this conference, RPPB025, 2003.

IMPEDANCES OF TEVATRON SEPARATORS

K.Y. Ng,* FNAL, Batavia, IL 60510, USA

Abstract

The impedances of the Tevatron separators are revisited and are found to be negligibly small in the few hundred MHz region, except for resonances at 22.5 MHz. The latter are contributions from the power cables which may drive head-tail instabilities if the bunch is long enough.

I INTRODUCTION

Large chromaticities (~ 12 units) were required to control the vertical transverse head-tail instabilities observed recently in the Tevatron. Application of the head-tail growth expression [1] reveals that the necessary transverse impedance to drive such instabilities has to be at least twice the amount estimated in the Run II Handbook. [2] This underestimation becomes thrice when it was suggested [3] that the transverse impedance of the Lambertson magnets have been overestimated by ten fold.¹ It was further suggested that most of the transverse impedance actually comes from the static separators: the vertical transverse impedance should be $5.33 \text{ M}\Omega/\text{m}$ assuming 27 separators while the Run II Handbook estimate has been only $0.082 \text{ M}\Omega/\text{m}$ assuming 11 separators.² This 26-time difference for each separator prompts us to review the impedances in detail by numerical computation, theoretical reasoning, and experimental measurement. The conclusion points to the fact that the separators actually contribute negligibly when compared with other discontinuities in the Tevatron vacuum chamber, except for the rather large resonances at 22.5 MHz due to the power cables.

II NUMERICAL COMPUTATIONS

We model a separator without the power cables as two plates 6 cm thick, 20 cm wide, 2.57 m long, separated by 5 cm inside a circular chamber of length 2.75 m and radius 18 cm (Fig. 1). The beam pipe is circular in cross section with radius 4 cm. The 3-D code MAFIA in the time domain [4] has been used to obtain the longitudinal and transverse impedances shown in Fig. 2. We find that, at low frequencies, the longitudinal impedance per harmonic and the vertical transverse impedance are, respectively, $Z_0^{\parallel}/n \sim 0.019j \Omega$ and $Z_1^V \sim 0.0075j \text{ M}\Omega/\text{m}$, which agree with the estimates given in the Run II Handbook.

In many cases, a 2-D approximation, assuming cylindrical symmetry of the 3-D problem, should give us a good insight as to the physics of the problem. The advantage is obvious; we can use more mesh points to better represent the geometry. The first 50 resonant modes computed by

* Email: ng@fnal.gov. Work supported by the U.S. Department of Energy under contract No. DE-AC02-76CH03000.

¹The Run II Handbook estimate has been rather rough, but reasonable. The C0 Lambertson magnet removed recently shows very large transverse impedance.

² $0.82 \text{ M}\Omega/\text{m}$ quoted in the Run II Handbook is a misprint.

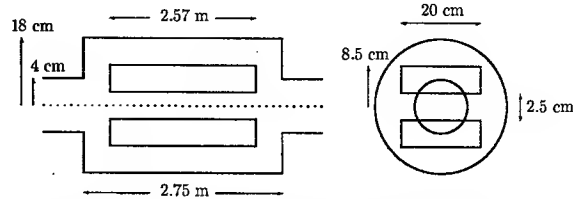


Figure 1: The simplified separator model used in MAFIA computation of longitudinal and transverse wake potentials.

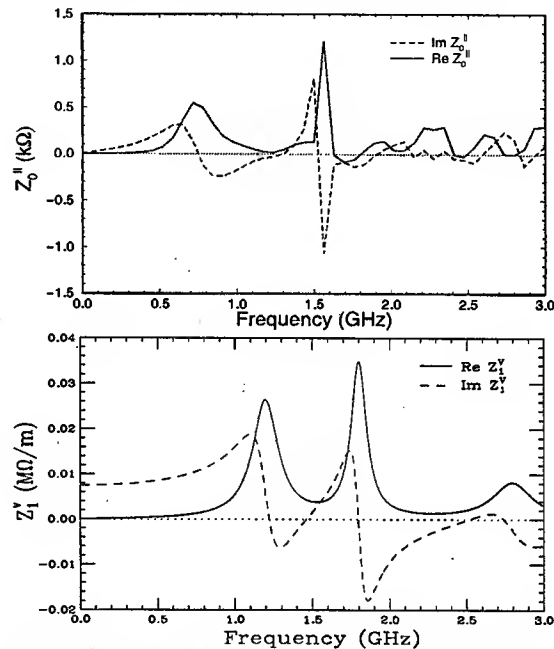


Figure 2: The real and imaginary parts of Z_0^{\parallel} (top) and Z_1^V (bottom) of one separator as computed by MAFIA.

the 2-D URMEL code [4] are shown in Fig. 3 (top). They are well below the cutoff frequency of 4.59 GHz and therefore appear as narrow resonances. The separator can be viewed as two pill-box cavities joined by a coaxial waveguide. The coaxial waveguide resonates when its length equals to an integral number of half wavelengths. Thus, the lowest mode has a frequency of $c/(2\ell) = 54.5 \text{ MHz}$ and successive modes are separated also by 54.5 MHz, where c is the velocity of light and $\ell = 2.75 \text{ m}$ is the length of separator. To excite these standing TEM modes in the coaxial waveguide, electromagnetic fields must penetrate into the separator, and penetration is only efficient when the frequency is near the resonant frequencies of the cavities at each end of the separator. These pill-box-like cavities have a radial depth of $d = 18 \text{ cm}$ with the first resonance at 637 MHz, and we do see coaxial-guide modes excited very much stronger near this frequency. The next pill-box-cavity mode is at 1463 MHz with a radial node at 7.84 cm

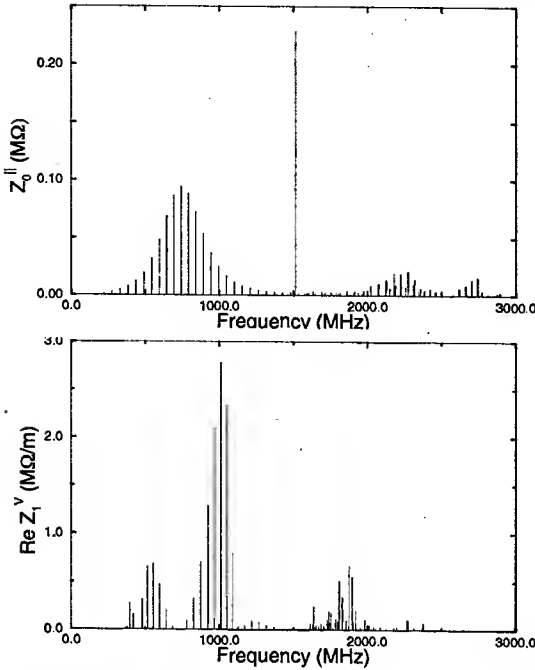


Figure 3: $\text{Re } Z_0^{\parallel}$ (top) and $\text{Re } Z_1^V$ (bottom) as obtained from 2-D URMEL computation.

which is very near the outer radius of 8.5 cm of the cylindrical plates. Thus a rather pure cavity mode is excited with very little contamination from the coaxial guide. This explains why we see a very strong excitation of this mode without many coaxial-guide modes at nearby frequencies. The third pill-box-cavity mode at 2294 MHz can also be seen in the figure with coaxial-guide modes at surrounding frequencies. Because excitation decreases with frequency, the shunt impedances are much smaller.

Due to the finite mesh size and rms bunch length used in the computation, MAFIA broadens all these sharp resonances. If all quality factors are broadened to $Q = 15$, the results look very similar to those in Fig. 2, implying that our interpretation of the longitudinal impedance of the separator is correct.

Similar analysis applies to the transverse dipole modes. The lowest 50 resonances computed by URMEL are shown in Fig. 3 (bottom). The first two transverse resonances in the pill-box cavities are 1016, 1860 MHz. We do see coaxial-guide modes enhanced near these frequencies. There is a special mode when one wavelength of the magnetic field wraps around the "cylindrical plate" between the plate and the encasing outer shield. The radius is from $r = 8.5$ to 18 cm. The wavelength will be $\lambda = 2\pi r$ and the frequency will be between 265 and 562 MHz. This explains the cluster of low-frequency coaxial-guide modes in the URMEL results. There is no cylindrical symmetry in the actual separator and this low-frequency cluster is therefore not present in the MAFIA results. Again if we broaden the sharp resonances until the quality factor reaches 15, the real and imaginary parts of the transverse impedance will look similar to the MAFIA results of Fig. 2.

III COMPARISON WITH BPM

Although the Tevatron stripline beam-position monitor (BPM) is similar in structure to the separator, however, its impedance is completely different. Here, the striplines play the role of the separator plates. The main difference is that each end of the striplines is terminated with a resistor of $Z_c = 50 \Omega$, which is equal to the characteristic impedance of the transmission line formed from the stripline and the enclosing outer shield. As a pulse of protons crosses the upstream gap, it creates on the beam-side of the stripline negative image charges, which move forward with the beam pulse. Since the stripline is neutral, positive charges will be created at the underside of the stripline. These positive charges, seeing a termination Z_c in parallel with a transmission line of characteristic impedance Z_c , split into two equal halves: one half flows down the termination while the other half travels along the transmission line and flows down the termination Z_c at the other end of the stripline. When the beam pulse crosses the downstream gap of the BPM, the negative image charges on the beam-side of the stripline wrap into the underside of the stripline; one half flows down the downstream termination while the other half flows backward along the transmission line and eventually down the upstream termination. Assuming the transmission line velocity to be the same as the beam velocity, the current in the downstream termination vanishes between one half of the stripline underside positive charges and one half of the wrap-around negative image charges. At the upstream termination, we see first a positive signal followed by a negative signal delayed by twice the transit time of traveling along the stripline. Thus the potential across the upstream gap is

$$V(t) = \frac{1}{2} Z_c [I_0(t) - I_0(t - 2\ell/c)] , \quad (1)$$

where ℓ is the length of the stripline and $I_0(t)$ is the beam current. The factor $\frac{1}{2}$ occurs because only one half of the current flows down the upstream termination each time. The impedance of one stripline in the BPM becomes

$$Z_0^{\parallel}(\omega) = \frac{1}{2} Z_c \left(\frac{\phi_0}{2\pi} \right)^2 \left(1 - e^{-j2\omega\ell/c} \right) , \quad (2)$$

where ϕ_0 is the angle the stripline subtends at the beam pipe axis. The added factor, $[\phi_0/(2\pi)]^2$, indicates that only a fraction of the image current flows across the gap into the stripline and only this fraction sees a gap potential.

For a separator plate, there are no terminations on either end. As a result, while the negative image charges flow along the beam-side of the plate, all the positive charges needed to balance the neutrality of the plate flow along the underside of the plate. These negative and positive charges just annihilate each other when the beam pulse reaches the downstream end of the plate. Thus there is no dissipation if the plates are considered perfectly conducting. Therefore, the impedance in Eq. (2) does not apply. The only contribution to the impedance come from the resonances in the cavity gaps. Since these resonant frequencies are high, there is little contribution in the few hundred MHz range.

IV MEASUREMENT

The coupling impedances of a separator have recently been measured [5] via the attenuation S_{21} by stretching a 0.010" tin-plated copper wire through the separator for the longitudinal mode and two wires for the transverse mode. The impedances are derived from

$$Z_0^{\parallel} = 2Z_c \left(\frac{1}{S_{21}} - 1 \right), \quad Z_1^{\vee} = \frac{2Z_c c \ln S_{21}}{\omega \Delta^2}, \quad (3)$$

where $\Delta = 1$ cm is the separation of the two wires and $Z_c = 50 \Omega$ is the characteristic impedance of the cables connected to the network analyzer, to which the wires have been matched. In Fig. 4, we plot³ the measured $\text{Re} Z_0^{\parallel}/n$ and $\text{Re} Z_1^{\vee}$. We see that both $\text{Re} Z_0^{\parallel}/n$ and $\text{Re} Z_1^{\vee}$ con-

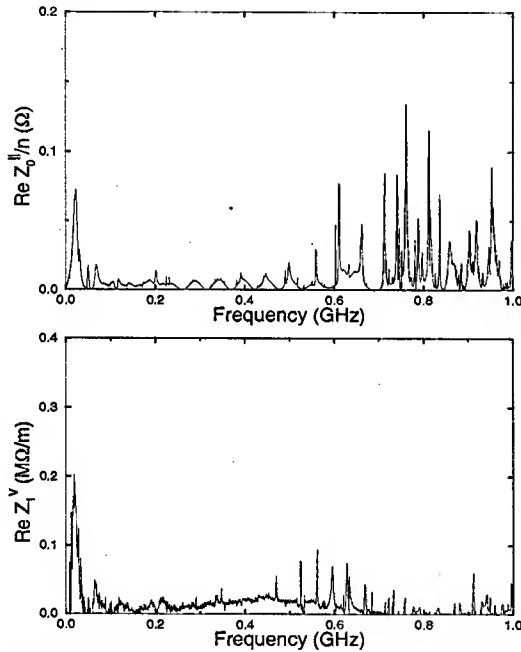


Figure 4: $\text{Re} Z_0^{\parallel}/n$ (top) and $\text{Re} Z_1^{\vee}$ (bottom) as measured by stretching wires.

tain the resonant structures determined by MAFIA and are small in the few hundred MHz region. However, we do see a large resonance at 22.5 MHz, which can be traced to coaxial power cables attached about 12 1/2" from one end of the plate through a 50 Ω resistor. Typically, the cables are two-meter long and terminate into a 1 M Ω impedance. These cables extend the electric lengths of the plates and the first waveguide mode is shifted from 54.5 MHz to 22.5 MHz. The function of the series 50 Ω resistor is to remove any sparks if present. Actually, this resistor, being situated near the end of a plate, absorbs the oscillatory current of this resonant mode. Without this resistor, the 22.5-MHz peak in both Z_0^{\parallel}/n and Z_1^{\vee} will be almost tripled. On the other hand, these peaks will disappear if the power cables are removed. There are 24 separators, giving

³If we plot $\text{Re} Z_0^{\parallel}$ instead of $\text{Re} Z_0^{\parallel}/n$, the 22.5 MHz resonant peak will not be visible.

in total $\text{Re} Z_0^{\parallel}/n \sim 1.73 \Omega$ and $\text{Re} Z_1^{\vee} \sim 4.10 \text{ M}\Omega/\text{m}$, which are rather large. The longest Tevatron bunch has been $\sigma_t = 95$ cm rms. Considering $\pm \sqrt{6} \sigma_t$, the lowest head-tail mode will have a frequency of $c/(4\sqrt{6} \sigma_t) = 32$ MHz. Thus this 22.5 MHz mode may pose a danger. There are ways to alleviate the effect. One is to increase the length of the power cables so as to further reduce the resonant frequency. A second way is to increase the damping resistors to about 500 Ω , [5] hoping that the peak impedances will be damped by a factor of ten. The designed Tevatron rms bunch length is only $\sigma_t = 37$ cm. If this shorter bunch length can be achieved, the lowest head-tail mode will have a frequency of 82.8 MHz, too high to be affected by the power cables.

V OTHER ESTIMATION

Ref. [3] suggests the vertical transverse separator wake,

$$W_1(z) = \frac{Z_0 c}{4\pi b^2} \frac{2}{12} \left[\theta(z) - \theta(z-2\ell) \right] \frac{\pi^2}{12}, \quad (4)$$

based on two plates separated by $2b = 5$ cm without any outer shield, where Z_0 is the free-space impedance. The vertical transverse impedance is

$$Z_1^{\vee} = \frac{Z_0 c}{2\pi b^2} \frac{\pi^2}{12} \frac{1}{\omega} \left(1 - e^{-2j\omega\ell/c} \right), \quad (5)$$

and becomes, at low frequencies,

$$\text{Im} Z_1^{\vee} = \frac{Z_0 \ell}{2\pi b^2} \frac{\pi^2}{12}, \quad (6)$$

which gives the large estimate cited earlier in the Introduction. The wake resembles the stripline BPM wake [cf Eq. (1)] with a reflected current at the downstream end of the separator plate. As we have discussed earlier, there is no reflected current because the positive and negative charges created on the plate annihilate when the beam pulse crosses the downstream separator gap. An outer shield is very essential for a separator model, because a waveguide/transmission line will be formed. For the BPM, the transmission line characteristic impedance Z_c enters into the impedance expression of Eq. (2). Without the transmission line, here in Eq. (6), the much larger free-space impedance Z_0 enters instead.

REFERENCES

- [1] A.W. Chao, *Physics of Collective Beam Instabilities in High Energy Accelerators*, Wiley, 1993, Section 6.3.
- [2] *Run II Handbook*, Beams Division, Fermilab, Section 6.7; see web address: http://www-bd.fnal.gov/lug/runIIhandbook/RunII_index.html; King-Yuen Ng, *Impedances and Collective Instabilities of the Tevatron at Run II*, Fermilab TM-2055, 1998.
- [3] Alexey Burov and Valeri Lebedev, *Head-Tail Instability in the Tevatron*, talk given at Fermilab on November 14, 2002.
- [4] *MAFIA User Guide*, DESY, LANL and KFA, May 3, 1988; *URMEL and URMEL-T User Guide*, DESY M-17-03, 1987.
- [5] James L. Crisp and Brian J. Fellenz, *Measured Longitudinal Beam Impedance of a Tevatron Separator*, Fermilab TM-2194, 2003; *Tevatron Separator Beam Impedance*, Fermilab TM-2202, 2003.

A 1.7 GHZ WAVEGUIDE SCHOTTKY DETECTOR SYSTEM

R.J. Pasquinelli, E. Cullerton, D. Sun, D. Tinsley, P. Seifrid, D. Peterson, J. Steimel,

FNAL*, Batavia, IL 60510, USA

Abstract

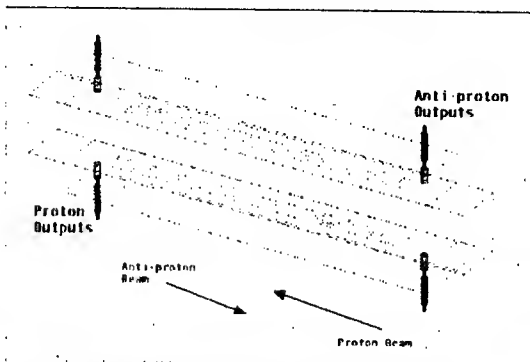
A 1.7 GHz waveguide Schottky detector system has been designed and built for each of the Fermilab Tevatron and Recycler accelerators. The waveguide detector is designed to measure the betatron sideband and longitudinal Schottky signals of the accelerators at a frequency high enough to avoid coherent effects. Two detectors are used for each machine, one for horizontal and one for vertical betatron signals. Each detector is bi-directional providing both proton and antiproton signals. This paper describes the details of the waveguide design and construction as well as the design of the electronic system of the detector. Sensitivity calculations and bandwidth models are included. The electronic system utilizes down conversion to frequencies less than 10 MHz, so that the signals may be analyzed by standard instrumentation, such as a Vector Signal Analyzer. The electronic system includes electronic gates to measure single or multiple bunches of protons or antiprotons with the RF as a source for tracking up and down energy ramps. The electronic system also includes a continuous beam emittance monitor.

INTRODUCTION

With the successful installation and commissioning of the Debuncher and Accumulator Core Stochastic Cooling upgrades, it was decided that the use of slow wave slotted waveguide pickups would be the perfect solution to high frequency Schottky detectors for both the Tevatron and Recycler accelerators. [1,2] A means of non-destructive measurement of beam emittance and tune was necessary for both accelerators. In the case of the Tevatron, the existing low frequency Schottky pickups suffer from the effects of coherent beam signals. Bunched Beam cooling tests in the Tevatron indicated that clean transverse Schottky signals were observed at 4 GHz and above. [3,4] For the Recycler, this Schottky system provides the necessary continuous beam emittance monitor and tune measurement capability. Both systems employ a gating circuit that allows distinguishing protons from antiprotons in the Tevatron and sections of warm and cold antiprotons in the Recycler.

* Work supported by the Universities Research Association, Inc., under contract DE-AC02-76CH03000 with the U.S. Department of Energy.

Schottky Pickup Waveguide Structure



Waveguide Assembly

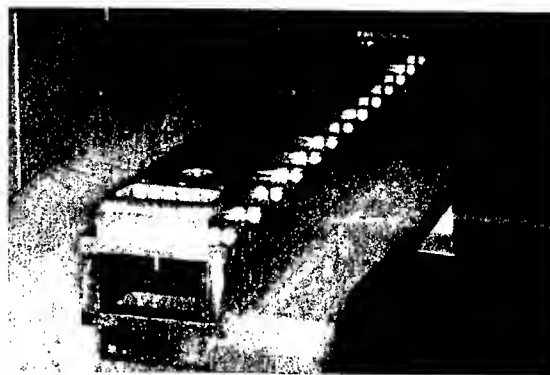


Figure 1. Schottky Pickup design top, fabricated pickup array bottom.

Schottky Pickup Frequency Response

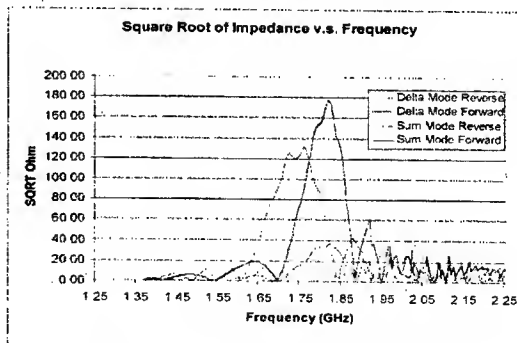


Figure 2. Calculated transfer impedance.

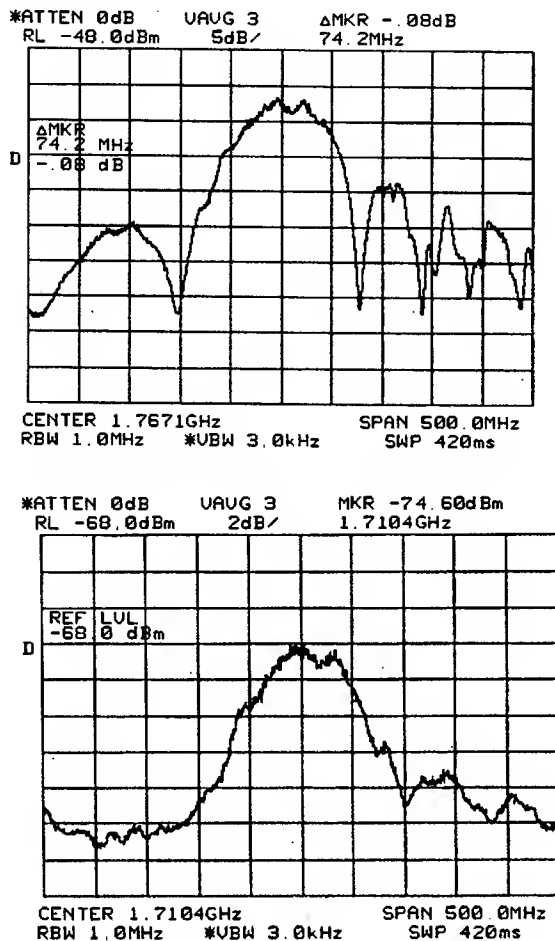


Figure 3. Measured response with 1.4×10^{11} protons in the Recycler. Top: sum mode; Bottom: difference mode.

SCHOTTKY PICKUPS

A Schottky pickup consists of a rectangular beam pipe with two waveguides on either side of the beam pipe (Figure 1). The septum wall between waveguide and beam pipe is made of slotted thin aluminum foil for coupling signal into the waveguide. The designed operating frequency is approximately 1.745 GHz (DELTA mode) and 1.813 GHz (SUM mode.) For these frequencies, dimensions of beam pipe are chosen as 4.3" wide and 2.953" high (close to the aperture of the beam pipe in Recycler). Dimensions of waveguide are 4.3" wide and 2.15" high. The design goal of these Schottky pickups is to obtain high impedance with a bandwidth of 100 MHz. To achieve this goal, 216 equally spaced slots are utilized in each foil.

A waveguide to coax launcher couples the signals at each end of the waveguides. All launchers are matched with better than -27 dB reflections. Microwave absorbers (TT2-111R from Trans-Tech Inc.) are placed on the walls of the beam pipe (end area) to prevent microwave signals

from propagating into or out of the pickup. Thickness and length of these absorbers are designed to provide adequate absorption (-25 dB) as well as minimum reflection (-23 dB). Figure 2 depicts the calculated transfer impedance. The actual pickup was measured with beam to have a response some 50 MHz below that predicted by the computer model, Figure 3.

RECYCLER

The Recycler beam is maintained in barrier buckets to facilitate the frequent transfer of beams from the Accumulator. As such, it is not a truly coasting beam. It is possible to have a cooled core of beam in the Recycler and freshly injected batches of antiprotons in an adjacent longitudinal portion of the ring. As the particles are cooled, they will be merged before the next transfer. A gating system was developed to allow measurement of the two different beams.

Signal processing includes a preamp followed by down conversion electronics that obtain the local oscillator signal from a phase locked microwave oscillator. The base band signal is shipped from the MI 62 service building (location of the pickups) to the MI 60 service building where a multiplexer and vector signal analyzer (VSA) are located for the Recycler diagnostic system.

The down converted signal is split with one input to the VSA, the other to a second down converter and on line continuous emittance monitor. The DC-89Khz signal is further processed through an active fourth order band pass filter that integrates the betatron sideband signal followed by an RMS to DC converter that generates a voltage proportional to emittance. The emittance monitor is calibrated against the newly installed transverse scrapers. Typical measurement results depicted in Figure 4, installation of pick up in Figure 5.

Recycler Measurement Program

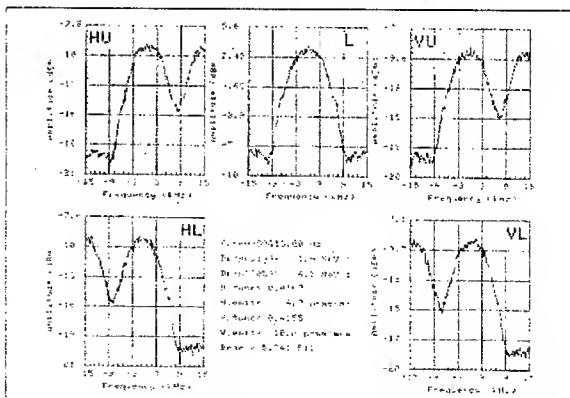


Figure 4. Automated Vector Signal Analyzer measurement of Recycler Schottky signals. Displays tune, momentum spread, revolution frequency, and calculated emittance.

TEVATRON

The Tevatron Schottky signals differ substantially from those observed in the Antiproton Source and Recycler rings. As was observed in the bunched beam cooling experiments, a large coherent signal is evident. (Figure 6) In the absence of front end filtering, this longitudinal line saturated the preamplifier. A different means of signal processing was necessary to keep active components in the linear operation range. A 100 MHz wide at 1.7 GHz cavity band pass filter is installed before the first preamp. This limited the peak signal seen by the first amplifier. The 100 MHz width allows sufficient bandwidth necessary to allow bunch-by-bunch gating. At the E17 location in the Tevatron where the pickups reside, beam separation is one hundred nanoseconds at 980 GeV. The directivity of the pickup was measured at 12 dB. Proton intensities are typically a factor of ten larger than antiproton intensities, hence gating is mandatory to dis segregate the antiproton from the proton signals.

An additional narrow band pass filter, 5 MHz wide at 1.7 GHz follows the gate reducing the signal level before additional gain and down conversion to base band. Down conversion is synchronous by phase locking to the Tevatron 53 MHz RF to generate the 1.7 GHz local oscillator. This technique allows monitoring the base band signal from injection at 150 GeV through the ramp to 980 GeV. An emittance monitor similar to that described will be added, except that the Tevatron will require a recursive digital FIR filter to remove the revolution components before integrating the betatron side bands.

Horizontal Schottky Pickup - Recycler

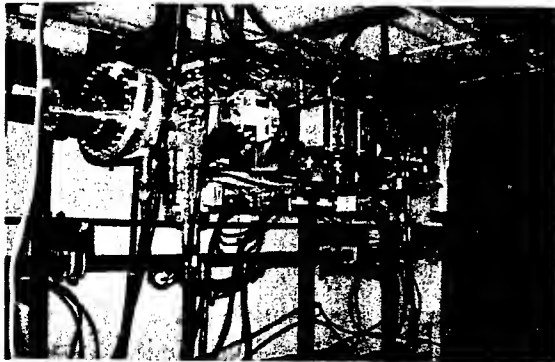


Figure 5. Recycler Horizontal Schottky Pickup Installation.

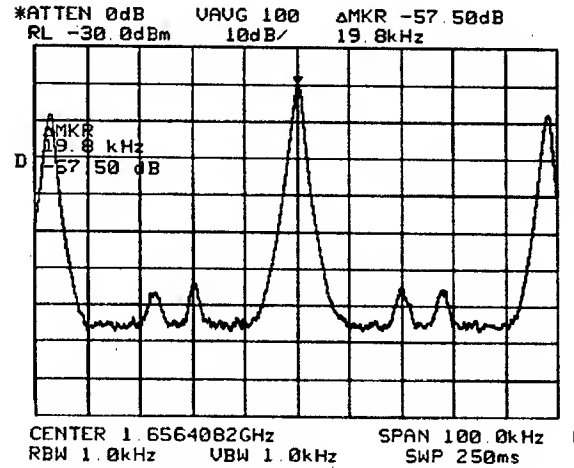


Figure 6. Microwave Spectrum of Tevatron Proton Horizontal Schottky. Large coherent longitudinal signal requires high system dynamic range.

Date: 04-17-03 Time: 07:57 AM

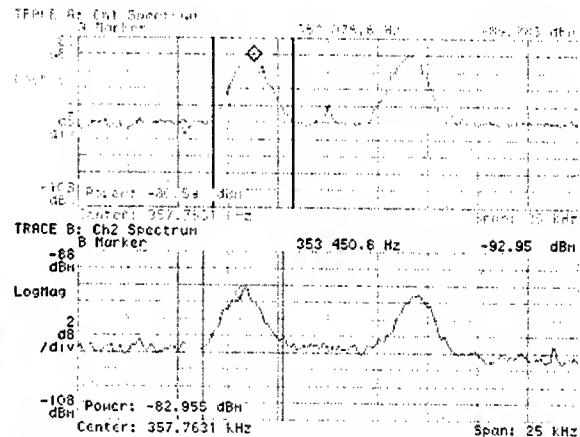


Figure 7. VSA display of Tevatron Antiproton transverse Schottky signals 6.1×10^{11} Pbars. Top: Horizontal; Bottom: Vertical.

REFERENCES

- [1] D. McGinnis, Slotted Waveguide Slow-Wave Stochastic Cooling Arrays, PAC '99, New York
- [2] D. McGinnis, The 4-8 GHz Stochastic Cooling Upgrade for the Fermilab Debuncher, PAC '99, New York,
- [3] G. Jackson, et al, A Test of Bunched Beam Stochastic Cooling in the Fermilab Tevatron, PAC '91, San Francisco, May 1991.
- [4] R. J. Pasquinelli, "Bunched Beam Cooling for the Fermilab Tevatron," PAC'95, Dallas, May 1995.

THE TEVATRON BUNCH BY BUNCH LONGITUDINAL DAMPERS

C.Y. Tan, J. Steimel
FNAL, Batavia, IL 60510, USA*

Abstract

We describe in this paper the Tevatron bunch by bunch longitudinal dampers. The goal of the dampers is to stop the spontaneous longitudinal beam size blowup of the protons during a store. We will go through the theory and also show the measured results during the commissioning of this system. The system is currently operational and have stopped the beam blowups during a store.

INTRODUCTION

As Run II begins its first year, unforeseen problems have started appearing which need to be fixed before higher luminosities can be achieved. One of the problems which started to appear at the beginning of 2002 is the rapid blowup of the longitudinal beam size during a store. See Figure 1. Although these blowups do not appear in every store, they seem to be weakly correlated with beam current. There are conjectures by the authors that the blowups are due to coupled bunch mode instabilities which arise from coupling to the higher order parasitic modes of the RF cavities. As these higher modes move as a function of temperature, the coupled bunch modes can be stable or unstable depending on where and how the higher order parasitic modes line up.

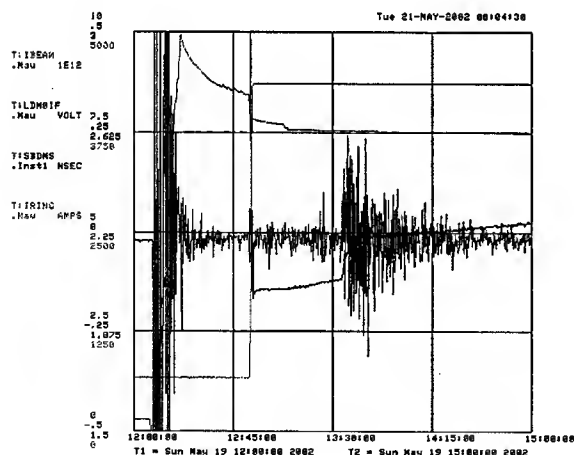


Figure 1: The beam blows up longitudinally (T:SBDMS) at about 1340hrs during the store which started at about 1300hrs. We see that when it blows up the phase signal of the bunch oscillates w.r.t. RF (T:LDM0IF). Plotted also are beam current T:IBeam and the bus current T:IRING.

* Work supported by the U.S. Department of Energy under contract No. DE-AC02-76CH03000.

After much discussion, it was decided that the best course of action is to build a bunch by bunch longitudinal damper system. At first glance, the idea of using the RF cavity themselves as the source of longitudinal kicks on the beam seems to be difficult. This is because each of the four proton RF cavities has a high Q ($\sim 10^4$) near its resonance and thus its impedance falls off rapidly away from it. Therefore, the amplitude and phase response is not flat at all synchrotron sideband pairs and thus the dampers are not bunch by bunch. The solution to this problem is to build an equalizer that lifts up the impedance so that it looks constant away from the resonance. Besides the equalizer, the damper also needs a notch filter which suppresses the revolution harmonics (otherwise these harmonics will limit the gain of the loop) and differentiates in time the synchrotron sidebands. Lastly, we also have to time in the system so that the error signal of bunch n is applied exactly one turn later to kick bunch n .

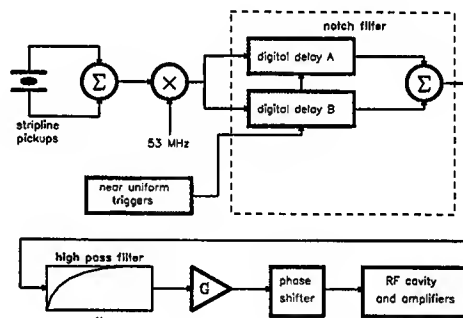


Figure 2: This figure shows the block diagram of the setup used for the longitudinal dampers.

SETUP

Figure 2 is a block diagram of the setup. The damper system starts at the stripline pickups which sum the beam signals at the two plates to produce a signal which is proportional to the longitudinal position of the beam. This signal is then mixed down with the Tevatron RF to produce a phase error (or quadrature) signal w.r.t. it. The error signal is then processed with electronics which perform the following:

- Equalize the impedance of the RF cavity.
- Suppress the revolution harmonics and differentiate the synchrotron sidebands around the revolution lines.

- One turn delay so that when the dampers pick up the signal of bunch 1 it will kick bunch 1 one turn later.

Equalizer

The idea of using a hpf to equalize the impedance of the RF cavity comes from observing that if we model the RF cavity impedance Z_{RF} using an RLC circuit and define R_s as its shunt impedance, L as its inductance and C as its capacitance, then

$$Z_{RF} = \frac{R_s}{1 - iQ \left(\frac{\omega_R}{\omega} - \frac{\omega}{\omega_R} \right)} \quad (1)$$

If $\omega_R = 1/\sqrt{LC}$ is its resonant frequency and $Q = R_s\sqrt{C/L}$ is its quality factor, then the magnitude $|Z_{RF}|$ is

$$|Z_{RF}| = \frac{R_s}{Q \left| \frac{\omega_R}{\omega} - \frac{\omega}{\omega_R} \right|} \quad \text{when } Q \rightarrow \infty \quad (2)$$

which means that $|Z_{RF}|$ has a $1/\delta\omega$ type dependence when $Q \rightarrow \infty$ and $\delta\omega/\omega_R \ll 1$.

Next, let us examine the response of a hpf. We introduce first a new variable $\Delta\omega = (\omega - \omega_{RF})$ where ω_{RF} is the RF drive frequency and $\omega_{RF} \approx \omega_R$. For a hpf with a 3dB response at $\Delta\omega_{3dB}$, its response function R_{hpf} is

$$R_{hpf}(\Delta\omega) = \frac{1 + i \frac{\Delta\omega_{3dB}}{\Delta\omega}}{1 + \frac{\Delta\omega_{3dB}^2}{\Delta\omega^2}} \quad (3)$$

and thus $|R_{hpf}|$ has a $\Delta\omega$ dependence. At base band, the mixed down impedance of the RF cavity will have a $|Z_{RF}(\Delta\omega)| \sim \Delta\omega$ dependance from (2) and when multiplied with $R_{hpf}(\Delta\omega)$ will have a constant impedance in the region around $\omega_R \approx \omega_{RF}$ and $|\omega_{RF} - \omega| \ll \omega_{3dB}$.

Notch Filter

The notch filter used in the electronics serves a two fold purpose. First, it suppresses the revolution harmonics. Second, it differentiates the synchrotron sidebands around the revolution harmonics which tells the damper which direction to kick. In our setup, the notch filter is created with two digital delay lines. Its response is given by

$$R_{notch}(\omega) = 1 - e^{-i\omega NT} \quad (4)$$

where T is the revolution period and N is the number of revolution periods in the delay. The choice of N is a compromise between the Tevatron's injection energy at 150 GeV and its top energy at 980 GeV and the phase and amplitude responses at these two energies. We chose $NT = 1/6f_s$ where $f_s \approx 88$ Hz is the synchrotron frequency at 150 GeV. Therefore, $N = 90$ when $T = 21 \mu s$. (Note: we have actually set $N = 91$ in the actual setup).

Triggers

In order for the digital delays to work they have to be triggered. The triggers which we use are uniform in time and spaced 7 buckets apart. These triggers also appear in the abort gap where there is no beam. The reason for having this pattern of triggers rather than having triggers where the bunches are is to allow us to use reasonable cable delays to ensure that the correct bunches are kicked. In the worst case scenario using equally spaced triggers, the cable length will be $7 \text{ buckets}/2 \approx 66 \text{ ns}$ for correctly hitting the right bunch. While for triggers where there are bunches only, the worst case scenario will be $140 \text{ buckets}/2 \approx 1.3 \mu s$ of cable!

RESULTS

Finally, we get to look at the open loop response of the dampers. The first set of measurements are performed with delay B disconnected. See Figure 2. This is to get the delay to be exactly 1 turn, i.e. $\Delta t = 2\pi/\omega_0$. When the delay is made exactly right, we get nice anti-symmetric imaginary responses for all the modes. Three of the modes are shown as examples in Figure 3.

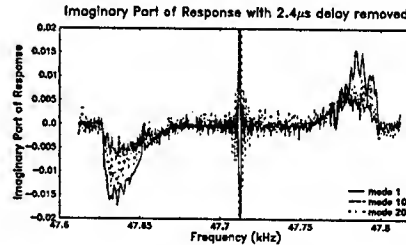


Figure 3: This graph shows the imaginary part of the response of modes 1, 10 and 20 after the delay is corrected. We have superimposed all the three graphs on top of each other by shifting the frequency of mode 10 by $-10f_0$ and mode 20 by $-20f_0$.

With the delay set in Delay A, we can now make the notches by reconnecting back Delay B and by setting the delay in this card by $N (= 91)$ revolution periods w.r.t. Delay A. See Figure 4. With the the notch filter in the circuit, the real part of the open loop response is negative and symmetric which implies that when the loop is closed, we get damping. These results are shown in Figures 5 at 150 GeV and Figure 6 at 980 GeV.

To test whether the dampers indeed work, we excite the beam at 980 GeV by switching the sign of the gain. This is a good sign because we can actually excite the beam which means that there is sufficient gain in the loop. When we switch the sign of the gain back to damping, we find that the excitation can be damped. The results of these actions are shown in Figure 7. Although the dampers do perform their job, we find that damping takes 2 to 3 minutes in this example.

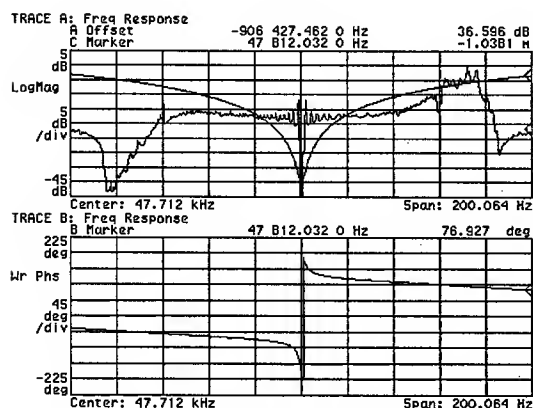


Figure 4: With both delays in the loop, we get notches near the revolution harmonics. The uncorrected imaginary response with one digital delay is superimposed for reference.

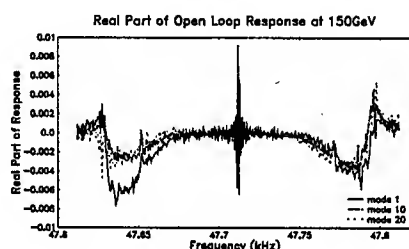


Figure 5: This graph shows the real part of the open loop response of modes 1, 10 and 20 at 150 GeV. We have superimposed all the three graphs on top of each other by shifting the frequency of mode 10 by $-10f_0$ and mode 20 by $-20f_0$.

CONCLUSION

After installing the dampers, the problem of sudden beam size growth during a store discussed in *Introduction*, is no longer observed. To prove to ourselves that the dampers definitely stopped the problem, we deliberately turned the dampers off for one store. In this store the beam blew up longitudinally as before. This conclusively showed us that the longitudinal dampers solved the problem. However, the underlying cause of the blowup is still not understood. There are speculations that higher order parasitic modes in the RF cavity, phase noise from microphonics etc. are the source of these blowups. For intellectual satisfaction, a hunt for the source will be the next thing to do. However, operationally, the dampers are a success.

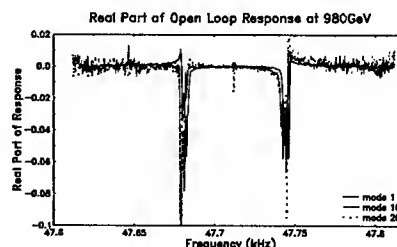


Figure 6: Similar to Figure 5 but at 980 GeV.

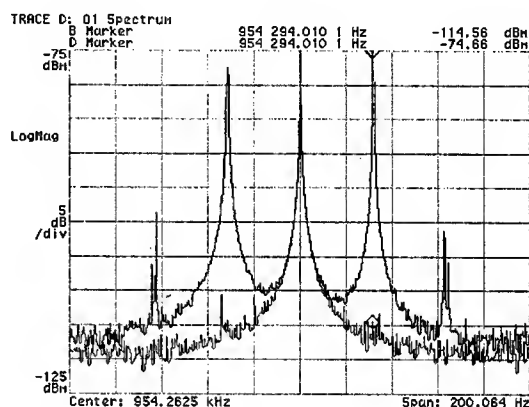


Figure 7: When we closed the loop at 980GeV, we excited the beam by anti-damping it. Then we turned on damping and clearly the synchrotron lines of mode 20 were damped.

REFERENCES

- [1] C.Y. Tan, J. Steimel, "The Tevatron Bunch by Bunch Longitudinal Dampers" (unabridged), Fermilab Technical Memo, TM-2184.
- [2] A.W. Chao, "Physics of Collective Beam Instabilities in High Energy Accelerators", Wiley Series in Beam Physics, 1993.

THE TEVATRON TRANSVERSE DAMPERS

C.Y. Tan, J. Steimel
FNAL, Batavia, IL 60510, USA*

Abstract

We describe in this paper the Tevatron transverse dampers. The goal of these dampers is to keep the beam stable when we operate at lower chromaticities. The reason for operating at lower chromaticities is to improve the beam lifetime. However, the beam becomes unstable at low chromaticities and thus dampers are required. Also included in this paper are the damper commissioning notes and their real-life performance.

INTRODUCTION

The motivation for building transverse dampers for the Tevatron is to improve the lifetime of the proton and pbar beam on their helices during pbar injection. Previous studies by Y. Alexahin *et al* [2], showed that when octupoles were used to stabilize the beam, and chromaticities lowered, the lifetime of the beam of both species on the helix is improved. However, due to great difficulties in using octupoles in operations because of drifts in tunes, coupling and chromaticities at 150 GeV, this method was abandoned from use in operations. Therefore, when it was decided to resurrect the idea of lowering the chromaticity to improve beam lifetimes, we had to come up with some other way of keeping the beam stable and transversely damping the beam immediately came to mind.

The idea behind lowering the chromaticity ξ comes from the simple observation that the tune spread ΔQ is related to the energy spread dp/p by

$$\Delta Q = \xi dp/p \quad (1)$$

Thus, if the chromaticity is lowered, ΔQ is smaller and the beam will occupy a smaller footprint in the tune plane. A smaller footprint means that the beam will enclose fewer resonances which means that less beam will be lost and thus the lifetime is improved. However, there is a competing mechanism which throws a spanner into this. As long as there is a non-zero transverse impedance, the beam naturally becomes more unstable when the tune spread becomes smaller because Landau damping becomes weaker. Stability is determined by the Keil-Schnell stability criteria which is given by

$$|(\Delta\omega_q)_{coh}| \lesssim (\Delta\omega_q)_{HWHM} F \quad (2)$$

where $(\Delta\omega_q)_{coh}$ is the coherent betatron tune shift which comes from the transverse impedance, $(\Delta\omega_q)_{HWHM}$ is the betatron tune spread measured at half-width half-max and

F is the form factor depending on distribution. $F = 1/\sqrt{3}$ for an elliptic distribution. This tells us that when we lower the chromaticity, which decreases $(\Delta\omega_q)_{HWHM}$, at some point $|(\Delta\omega_q)_{coh}|$ becomes larger than the rhs of (2), and the beam becomes unstable. Therefore, in order to keep the beam stable when we lower the chromaticity, we have to have a stabilization mechanism and in this case we choose to use active transverse damping.

In practice, for (36×36) bunch high energy physics operations after August of 2002, with both the horizontal and vertical dampers in service, the chromaticities of the horizontal plane is lowered by 6 units and the vertical plane by 4 units from their nominals which is about 8 for both planes on the central orbit and about 12 units for horizontal and 8 units for the vertical on the proton helix.

SETUP

In this section, we will go through each part of our setup used for our bunch by bunch transverse dampers and show that the open loop response < 1 . Figure 1 is a block diagram of the setup. The damper system starts at the stripline pickups working in difference mode. A transverse kicker is installed at a position in the Tevatron so that it has a phase advance of an odd multiple of $\pi/2$ w.r.t. pickup after 1 turn. In order to improve the dynamic range of the damper system, a method developed by McGinnis called the autozero circuit shown in Figure 2, is used to virtually centre the beam in the pickup. This signal is mixed down with the Tevatron RF and low pass filtered to produce a transverse position error signal. The error signal is processed with electronics which perform the following:

Autozero Circuit

The autozero circuit was developed by D. McGinnis to improve the dynamic range of the damper system. If the closed orbit of the beam is not in the electrical centre of the striplines in Figure 2, then clearly the induced voltage on the top plate is not equal to the voltage on the bottom plate. However, by changing the value of the attenuator connected on the bottom plate, we can make the induced voltages equal. Thus, the beam is now virtually centred in the stripline pickup and the dynamic range is immediately improved because we have essentially removed the DC component of the error signal, i.e. we can have much more gain downstream without saturating the amplifiers due to the DC component.

* Work supported by the U.S. Department of Energy under contract No. DE-AC02-76CH03000.

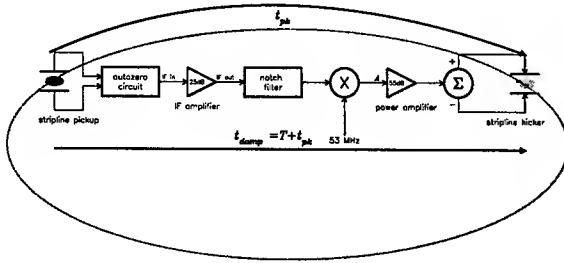


Figure 1: This is a block diagram which shows the overall setup of the transverse damper system. Note that the signal of the bunch which is detected at the stripline pickup is applied approximately one turn later to the same bunch at the stripline kicker. Each block is expanded further in Figures 2

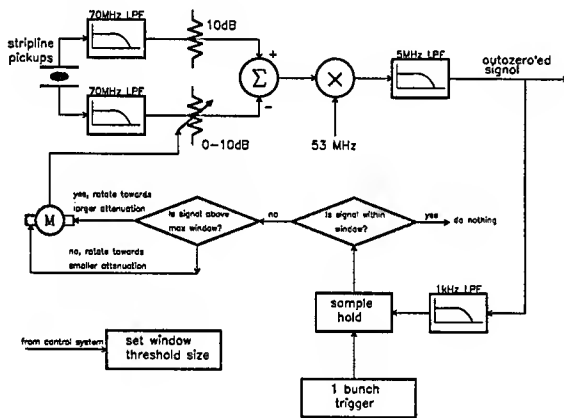


Figure 2: This figure shows the block diagram of the autozero circuit.

Digital Notch Filter

The digital notch filter consists of two digital delay lines when summed together produces notches at the revolution harmonics. Its response is given by

$$R_{\text{notch}}(\omega) = 1 - e^{-i\omega NT} \quad (3)$$

where T is the revolution period and N is the number of revolution periods in the delay.

Uniform Triggers

In order for the digital delays to work they have to be triggered. The triggers which we use are uniform in time and they trigger in places even when the beam is not present. The reason will become apparent later in the discussion. At present, in Tevatron operation, there are three

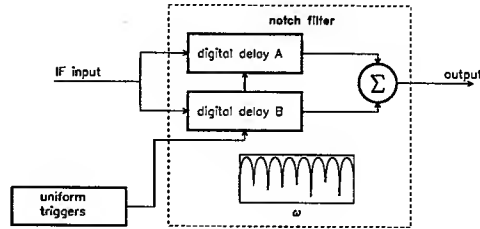


Figure 3: The digital notch filter.

trains of 12 bunches each. In each train, the bunches are spaced 21 buckets apart. The spaces between the trains are the abort gaps and they take up 140 buckets each.

Notice that all bucket spacings are divisible by 7. Therefore, if we have triggers which are spaced exactly 7 buckets apart, the digital delays will sample all the bunches as well as a lot of empty space. The reason for having more triggers than necessary is to allow us to use reasonable cable delays to fine tune the system delay to ensure that the correct buckets are kicked. In the worst case scenario for this trigger pattern, the cable length will be 7 buckets/2 \approx 70 ns for correctly hitting the right bucket. While for triggers where there are bunches only, the worst case scenario will be 140 buckets/2 \approx 1.3 μ s of cable! (Recall that 1 ns is about 1 foot of cable.)

RESULTS

We measured the open loop response of the damper system by breaking the loop as shown in Figure 4. The Tevatron is filled with 36 bunches of protons in the pattern discussed in *Uniform Triggers*. After we add in 17 μ s of delay, the frequency response becomes nice and symmetric about half the revolution frequency $f_r/2$ as shown in Figure 5

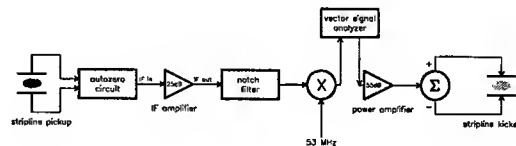


Figure 4: The loop is broken just downstream w.r.t. mixer and a vector signal analyzer (VSA) is connected there.

Closing the Loop

Finally, we can close the loop and damp. We injected 36 bunches into the Tevatron and sat at 150 GeV for this set of experiments. Figure 6 shows the effect of closing the loop. The red curve is the noise spectrum measured at A of

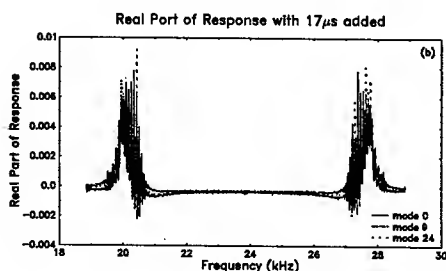


Figure 5: This graph shows real part of the response after adding $17 \mu s$ to the digital delay. To get the real part of the response to be negative, we have to multiply by -1 in the electronics. We have superimposed three graphs on top of each other by shifting the frequency of mode 9 by $-9f_r$ and mode 24 by $-24f_r$.

Figure 1 with the power amplifier off. The power amplifier is turned on, thus closing the loop, and we see that there is a suppression at the horizontal tune sidebands of about 6 dB (the purple curve). The noise floor is increased by about 2 dB in the middle of the spectrum. The closed loop gain of the damper is 6 dB at the horizontal tune. The full width at half min (fwhm) of the absorption line gives the damping time of the damper for the 361.6 kHz tune line which is $0.55 \text{ ms} \approx 26$ turns in the Tevatron.

Date: 10-27-00 Time: 01:24 AM

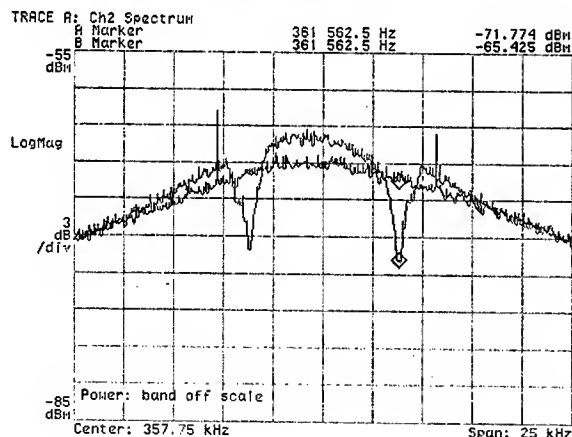


Figure 6: The suppression of the horizontal tune sidebands (purple curve) when the loop is closed compared to the red curve when it is open.

Operations

In operations, we lower the horizontal chromaticity by about 6 units and vertical chromaticity by about 4 units from their nominals of 8 units for both planes on the cen-

tral orbit and 12 units for the horizontal and 8 units for the vertical on the proton helix. For store #1868 shown in Figure 7 which had the horizontal chromaticity lowered by 5 units and vertical lowered by 2 units, the effect of the lower chromaticity is dramatic. Before the dampers are turned on, beam lifetime T:IBEAM (total beam current) and C:FBIPNG (proton beam current) is poor. The $1/e$ time is about 1 hr for C:FBIPNG at this time. When the dampers are turned on for pbar injection and chromaticities lowered, we see that the C:FBIPNG $1/e$ lifetime is improved by a factor of 3 to 3 hr. At the completion of pbar injection, just before we ramp, the dampers are turned off and chromaticities restored to nominal. Again, we see that the T:IBEAM and C:FBIPNG lifetime reverts back to being poor again.

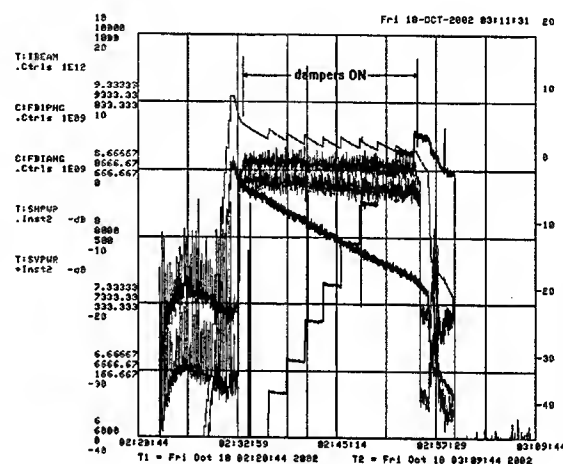


Figure 7: This plot shows the damper in action. Total beam current is T:IBEAM (the sawtooth shape comes from pbars being injected). C:FBIPNG shows the increase in pbar current as they are being injected. C:FBIPNG is the proton beam current only. T:SHUPWR and T:SVPWR are the horizontal and vertical Schottky powers which rise up by about 30 dB when the dampers are turned on.

CONCLUSION

The transverse dampers have been used in high energy physics operations and enough data have been gathered to show that the dampers do no harm to the protons or pbars at 150 GeV. With low chromaticity the lifetime of the pbars is always improved, although the proton lifetime is improved some of the time on the helix. Thus the value of the dampers for high energy operations is mainly for keeping pbars in the Tevatron during injection.

REFERENCES

- [1] C.Y. Tan, J. Steimel, "The Tevatron Transverse Dampers" (unabridged), Fermilab Technical Memo, TM-2204.
- [2] Y. Alexahin, *et al*, "2002 Tevatron Log Book", 2002.

BUNCH LENGTHENING RECENTLY OBSERVED AT PF-AR

T. Ieiri*, T. Kasuga, Y. Minagawa, T. Obina, KEK, Tsukuba, Japan
T. Fujita, Hiroshima University, Hiroshima, Japan

Abstract

The PF-AR (Photon Factory Advanced Ring for pulse X-rays) at KEK has been renewed to upgrade the performance. In this project, new vacuum ducts were installed with shielding bellows instead of non-shielding aluminium bellows. Thus, the coupling impedance of the ring was improved due to the shields. Measuring the bunch lengthening before and after the installation, we evaluated the longitudinal impedance of the bellows in a low bunch current. When the bunch current was high enough, a longitudinal instability was observed, accompanied by higher-order coherent synchrotron oscillations. We discuss the instability and the impedance issues based on various phenomena and calculations.

INTRODUCTION

In electron storage rings, the natural bunch length is determined by the lattice parameters. As the bunch current increases, a bunch is distorted by the interaction with its environments. A change in a bunch shape would provide information on the coupling impedance. The resistive component of the impedance induces an additional energy loss. As a result, the center of a bunch is shifted with changing its profile. According to a numerical calculation [1], it was found that the bunch length did not change very much due to the resistive impedance. On the other hand, the imaginary part of the impedance changed the bunch length due to a potential-well distortion. When a purely inductive impedance is assumed, bunch lengthening is analytically derived. We can estimate the inductive impedance from the bunch lengthening.

When the bunch current increases further, a microwave or turbulent instability takes place above the threshold, which results in increasing the energy spread. The instability appeared not only with abnormal bunch lengthening, but also with curious phenomena related to nonlinearity. Sawtooth phenomena [2] in the bunch lengthening; for example, were observed in the damping ring at SLAC. The bunch length was unstable and entered into a cycle of damping followed by blow-up. In the PF-AR, hysteresis phenomena [3] were observed, *i.e.* two bunch-lengths existed depending on the directions changing the bunch current or the cavity voltage. Two bunch lengths in the hysteresis region exhibited different synchrotron sideband patterns. It was found that the hysteresis depended on the number of cells of the accelerating cavity, *i.e.*, the strength of the cavity impedance. These phenomena are closely related to the impedance or the wakes of the rings.

* Email: takao.ieiri@kek.jp

PF-AR

The PF-AR was originally constructed as a booster of the TRISTAN electron-positron collider. The beam energy was increased to 8.0 GeV to inject a bunch into the TRISTAN ring. After completion of the TRISTAN project in 1995, the PF-AR was converted into a storage ring dedicated to pulse X-ray research at a beam energy of 6.5 GeV. However, its performance as a light source was not satisfactory. In order to improve the performance, the vacuum ducts were renewed with shielding bellows. The upgrading project for changing the impedance was completed at the end of 2001 after a one-year shutdown.

The PF-AR is a storage ring of 377 m in circumference. There are four long straight sections, each with a length of approximately 20 m. Two straight lines, east and west parts, are prepared for accelerating cavities. Alternating periodic structure (APS) cavities with multi-cells [4] were installed there to increase the beam energy up to 6.5 GeV from injection energy of 2.5 GeV. The PF-AR usually runs with a single bunch operation. The main parameters at the injection energy of 2.5 GeV are listed in Table 1.

Table 1: Main parameters at injection beam energy*

RF Accelerating Frequency, f_{rf}	508.58 MHz
Number of Particles per Bunch, N_b	7.8×10^9 / mA
Synchrotron Frequency, f_s	24 – 32 kHz
Momentum Compaction, α	0.0128
Energy Spread, δ_e	4.4×10^{-4}
Longitudinal Damping Time, τ_d	21.6 ms
Natural Bunch Length, σ_0	8.3 – 11.7 mm

*) The energy has changed to 3.0 GeV since October 2002.

MEASUREMENT

The bunch length was measured using a method based on the beam spectrum. A bunch-length monitor detecting two frequency components in the beam spectrum under the condition of $\omega_d \sigma_t < 1$, where ω_d is the detected angular frequency and σ_t is the rms bunch length in time, indicates the rms length of a bunch in real-time, even if the bunch shape changes [5].

The bunch-length measurement was performed for the old chamber before the upgrade in 1998. Figure 1 shows that the bunch length increases slowly up to a bunch current of 8 mA, and abruptly increases by 50% together with increasing the energy spread. The jump in the bunch length indicated a clear instability threshold. Though the jump did not indicate the hysteresis region observed in

1993 [3], the bunch length was bistable around the threshold [6]. There was a difference between the two stages in 1993 and in 1998, in that the number of cavity cells was 88 cells in 1993 and reduced to 66 cells in 1998. Figure 1 also shows the calculated bunch length, assuming that the inductive impedance is 1.0Ω . The measured bunch length agrees with the calculation in a region of relatively low current. Thus, the inductive impedance at the stage in 1998 is estimated to be $1.0 \pm 0.05 \Omega$. On the other hand, the synchrotron sidebands were observed around a carrier of 4.29 GHz using a spectrum analyzer. The frequencies were observed at $2f_s$ and near $3f_s$ just below the threshold. The spectrum was changed above the threshold, where the fundamental synchrotron sideband, f_s , was excited together with $2f_s$, $3f_s$ and so on.

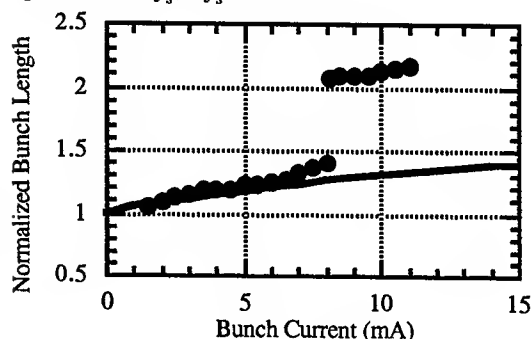


Figure 1: Bunch length normalized by the natural bunch length as a function of the bunch current for an old chamber measured in 1998 at 2.5 GeV. Dots are measured one and line is calculated bunch length based on the potential well. $\sigma_0 = 12.2$ mm.

A similar measurement was performed for the new chamber after the upgrade. Figure 2 shows the measured bunch length together with the calculated bunch length. The measured bunch length agrees with the calculation in a low-current region when the inductive impedance is assumed to be $0.25 \pm 0.05 \Omega$. The measured bunch length, however, tends to deviate from the calculation above a current of 14 mA. We observed a jump in the bunch lengthening above a bunch current of 30 mA, where the specific current is much higher than that observed in the old chamber. In the high-current region, a horizontal instability was also observed, which may be discussed elsewhere [7]. On the other hand, the synchrotron sidebands were measured with the bunch current during an injection. As shown in Fig. 3, we observed a sideband frequency of 62 kHz at a current of 12 mA, which shifted to a higher frequency as the bunch current increases. The observed frequencies correspond to a synchrotron sideband of between $2.2f_s$ and $2.5f_s$. When the bunch current reached 30 mA, sidebands around fundamental synchrotron frequency were excited in addition to the higher-order synchrotron sideband.

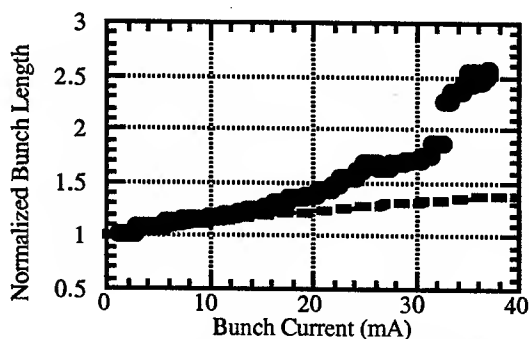


Figure 2: Normalized bunch length vs. bunch current for the new chamber measured in 2002 at 2.5 GeV. The dashed line is the calculated bunch length, assuming that the impedance is 0.25Ω . $\sigma_0 = 10.5$ mm.



Figure 3: Sideband spectra for various bunch currents. The horizontal scale is frequency and the vertical scale is the bunch current. The spikes are the horizontal oscillation due to an injection error. $f_s = 28$ kHz.

DISCUSSION

Let us consider the longitudinal impedance. In the old chamber, the impedance was dominated by the APS cavities and non-shielding bellows. In the new chamber, the impedance of the bellows is negligible because of the shield; note that the cavities are the same in both stages. The wake of the cavity shows a resistive type for bunch lengths of 10 mm to 20 mm. Other dominant impedance sources are radiation masks and tapered chambers. The wakes of the masks and the tapers are inductive and contribute to bunch lengthening.

The bunch-length measurement in a low current indicates that the inductive impedance is 1.0Ω for the old chamber and 0.25Ω for the new one. Since the impedance of shielding bellows is negligible in the new

chamber and other components, such as masks and tapers, do not much change in the upgrade, the reduction in the impedance is caused by the non-shielding bellows installed in the old chamber. Thus, the impedance of the non-shielding bellows is estimated to be 0.75Ω from the bunch lengthening. On the other hand, the impedance of the bellows can be analytically estimated. The bellows are approximated by small cavities. Such a small cavity as illustrated in Fig. 4 behaves as inductive impedance in a region of low frequency. The impedance is given by

$$\frac{Z}{n} = -j \frac{Z_0 \omega_0 g h}{2\pi c b}, \quad (1)$$

where $n = \omega/\omega_0$ is an integer, ω_0 is the angular revolution frequency, Z_0 is the impedance of free space and c is the velocity of light. The PF-AR had about 130 bellows and each of the bellows had 12 cavities. The total impedance of the bellows is estimated to be $620 \text{ m}\Omega$ using the geometric parameters captioned in Fig. 4. The calculation is consistent with the measurement.

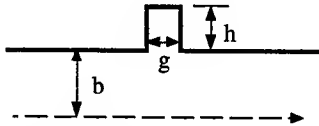


Figure 4: Sketch of a small cavity as a part of bellows, where $b=40 \text{ mm}$, $g=2 \text{ mm}$ and $h=8 \text{ mm}$. Note that a circular chamber is assumed instead of the actual racetrack type.

A code of the ABCI [8] calculates the wakes of the vacuum components. The masks and the tapers were modified to symmetric structures to match with the ABCI. A computer program developed by Oide [9] solves a time-dependent distribution function of a bunch using a Vlasov equation. Eigenvalues of a matrix derived from a linearized Vlasov equation were calculated using the calculated wakes. Figure 5 shows an example of the eigen-frequencies normalized by the synchrotron frequency as a function of the bunch current using the calculated wakes of the new chamber. When the bunch current reaches 10 mA, higher-order synchrotron sidebands appear with frequencies of $1.8f_s$ and $2.6f_s$. The frequencies change as the bunch current increases. The frequency of near f_s appears above 17 mA. On the other hand, the measurement indicated that the coherent sideband was observed between $2.2f_s$ and $2.5f_s$ above a current of 12 mA. Though the calculation is not precisely consistent with the measurement, excitation with higher-order synchrotron oscillation is common to both cases.

The injection energy has been lifted to 3.0 GeV from 2.5 GeV. The threshold current based on a deviation from the potential-well increased about twice, comparing Fig. 6 with Fig. 2. Considering the radiation-damping rate increases 1.73 times and the energy spread increases by 20%, the increase in the threshold current is reasonable. The deviation in the bunch lengthening from the calculation coincided with excitation of the higher-order synchrotron of $2.2f_s$.

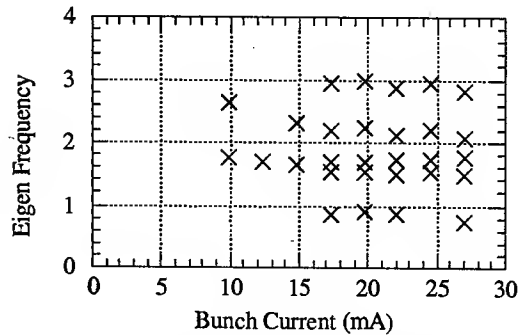


Figure 5: Imaginary part of eigenvalues normalized by synchrotron frequency as a function of the bunch current for the impedance of the new chamber. $\sigma_0=8.75 \text{ mm}$. Values for $\text{Re/Damp} > 0.001$ are plotted.

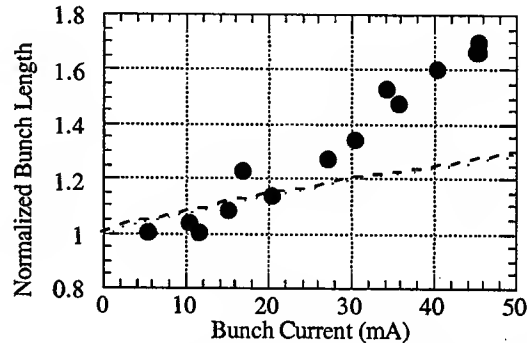


Figure 6: Normalized bunch length at a energy of 3.0 GeV. The dots are the measured bunch length; the dashed line is the calculated bunch length, assuming that the impedance is 0.25Ω . $\sigma_0=11.3 \text{ mm}$.

In summary, the relation among the impedance, the bunch lengthening and the longitudinal instability was experimentally investigated in the PF-AR. The estimated impedance of non-shielding bellows is consistent with the calculation. The longitudinal instability was observed before and after the upgrade. The jump in the bunch length shifted to a higher current due to the shielding effect of the bellows. The higher-order synchrotron signal was observed in both stages. The effect is not fully understood. Increasing the beam energy increased the instability threshold.

REFERENCES

- [1] K. Bane, 1989 PAC, Chicago (1989) 789.
- [2] P. Krejcik et al., 1993 PAC (1993) 3240.
- [3] T. Ieiri, Nucl. Instrum. Methods A329 (1993) 371.
- [4] T. Higo et al., 1984 SAST, Tsukuba, (1984) 114.
- [5] T. Ieiri, EPAC 2000, Vienna (2000) 1735.
- [6] T. Ieiri and T. Obina, PAC'99, NY (1999) 1135.
- [7] Y. Minagawa et al., RPPB029, in these proceedings.
- [8] Y. Chin, LBL-35258, UC-414 (1994).
- [9] K. Oide and K. Yokoya, KEK Report 90-10 (1990).

TRANSVERSE SAWTOOTH INSTABILITY OBSERVED IN PHOTON FACTORY ADVANCED RING

Y. Minagawa*, T. Ieiri, T. Obina and T. Kasuga, KEK, Tsukuba, Japan
T. Fujita, Hiroshima University, Hiroshima, Japan

Abstract

This paper reports a curious instability observed at the Photon Factory Advanced Ring for pulse X-rays (PF-AR). In a low bunch current, the horizontal betatron oscillation induced by an injection error was suppressed well by the beam feedback system. However, when the bunch current was high, the horizontal oscillation grew over several milliseconds and damped again like a sawtooth, after an injection process was finished. To investigate the mechanism of the sawtooth instability, we measured the horizontal beam size turn by turn as well as the dipole oscillation when the parameters (octupole magnets, the beam feedback and RF voltage) were changed. It was found that the transverse feedback for damping the dipole oscillation was suspicious for the instability, when the dipole oscillation and increase of the beam size coexisted.

INTRODUCTION

The PF-AR is an electron storage ring dedicated to pulse X-ray research [1]. The users require a single bunch current as high as possible. The beam injected from the KEK linac at the energy of 2.5 GeV or 3.0 GeV is raised up to the energy of 6.5 GeV for the users by the accelerating cavities. Since a high bunch current of more than 50 mA is expected, we need to take countermeasures against a single bunch instability at the injection energy. Octupole magnets are installed, which makes tune spread depending on the the beam size or the oscillation amplitude and would stabilize the beam. The transverse feedback system is employed to suppress coherent dipole oscillations. Though the bunch current of 47 mA at the energy of 2.5 GeV and of 65 mA at 3.0 GeV was achieved by tuning both the beam feedback and the octupole fields, we observed a curious instability during the injection process. It is important to investigate the cause of the instability from the views of the beam dynamics and the operation.

TRANSVERSE SAWTOOTH INSTABILITY

We observed horizontal bunch oscillations during the injection process. As shown in Fig. 1, a betatron oscillation induced by an injection error damps due to the beam feedback system. The betatron oscillation, however, continues to grow over several milliseconds and damps rapidly, when the bunch current is high enough, greater than about 20 mA. The phenomena appeared repeatedly every injection. We call the phenomena a *transverse sawtooth instability*.

* yasuyuki.minagawa@kek.jp

At a storage mode with the injection energy, the sawtooth instability was also observed, after an artificial kick was given to a bunch. This result suggests that the sawtooth instability is excited by a stored bunch itself rather than an interaction between an injected beam and a stored bunch. To investigate the cause and the mechanism of the instability, we measured the abnormal growth of the betatron oscillation in details, when the parameters (octupole fields, feedback gain, RF voltage etc.) were changed.

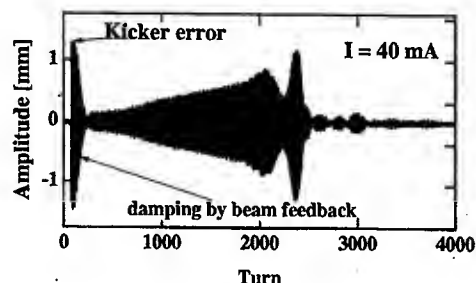


Figure 1: Transverse sawtooth instability. Horizontal betatron oscillations are shown at the injection at the beam energy of 3.0 GeV as a function of turn number. The bunch current is 40 mA. The revolution period is 1.258 μ s.

MEASUREMENT OF DIPOLE OSCILLATION

Experimental setup

The monitor system measuring the horizontal beam oscillation consists of a stripline, the *Bunch Oscillation Detector* (B.O.D.) [2] and an ADC module. A beam signal was picked up by the stripline horizontally mounted in a vacuum chamber. A picked-up signal was fed into the B.O.D, where the dipole oscillation was detected. The output signal of the B.O.D. was recorded by the ADC module with a memory. The oscillation data were taken turn by turn, after a bunch was horizontally excited by a kicker magnet prepared for the injection.

Influence of RF voltage

We measured a range of the bunch current at which the sawtooth instability appeared, while the voltage of the RF cavity (V_c) changed. The measurement was performed under constant octupole fields and a constant feedback gain. A result is shown in Fig. 2. The maximum amplitude of the oscillation was 1.1 mm and the growth time was about

3.75 ms at $V_c=2.95$ MV. The sawtooth instability, however, appeared intermittently when the V_c exceeded 3.0 MV and it did not appear when the voltage was over 4.0 MV. These results suggest that the sawtooth instability is influenced by a longitudinal bunch shape.

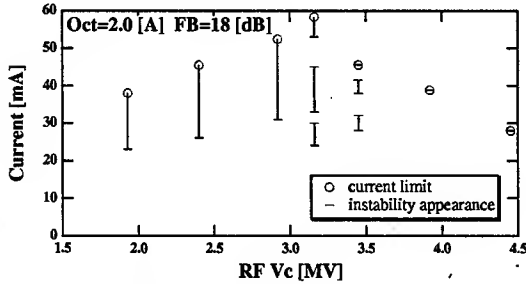


Figure 2: Appearance of the sawtooth instability is shown by bars as a function of the voltage of the RF cavity. A small circle attached with the bars at each voltage shows the maximally stored current. In this experiment, the current of 2 A for the octupole magnets and a relative feedback gain, $FB=18$ dB are constant.

Influence of octupole fields and beam feedback

An effect of the octupole fields was measured under a constant feedback gain. Figure 3 shows the sawtooth instability for varying the octupole current. The sawtooth instability appears clearly when the octupole current is 1A, however, it eliminates at the current of 3A. This result indicates that octupole magnets contribute to suppress the sawtooth instability. But, there was a trouble in the injection at a low current, when the octupole current was set to be 3 A.

On the other hand, the gain of the beam feedback was changed under a constant octupole current. Figure 4 shows the sawtooth instability for various feedback gains. The appearance time of the instability tends to be shorter and the maximum amplitude of the oscillation is larger as the feedback gain increases. A higher gain of the beam feedback seems to excite the sawtooth instability. The injection was performed with a lower feedback gain, however, we could not store the bunch current of more than 15 mA.

Since some doubts in the feedback system [2] were arisen, the hardware was checked. In this system, a dipole oscillation is picked up by a single stripline and it is fed to deflector electrodes composed of four striplines via power amplifiers. Another method for detecting the bunch oscillation was tried using four button electrodes, where the BOD and a phase shifter were replaced by an amplitude modulation to phase modulation (AM/PM) detector and a 2-tap FIR filter module [3][4]. The sawtooth instability was still observed in the modified system. Moreover, we confirmed that the instability occurred regardless of saturation of the power amplifiers and also regardless of unbalance of deflection. The feedback system itself seems to work well.

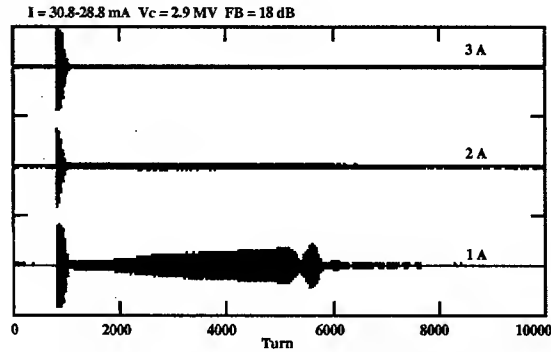


Figure 3: The horizontal oscillations as a function of turn number when the current of the octupole magnets changes. The current of 2 A corresponds to the K_3 -value of 90 m^{-3} .

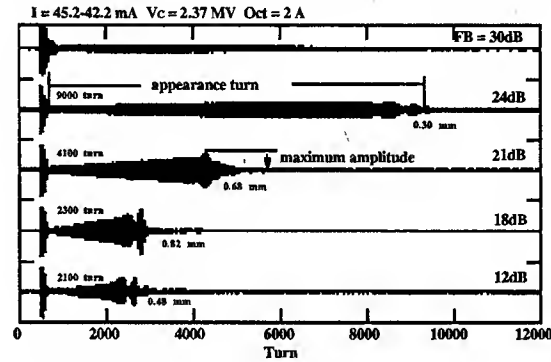


Figure 4: The horizontal oscillations as a function of turn number are shown for various feedback gains. The value of FB shows a value of the attenuators in the feedback loop and the gain of the beam feedback becomes large in inverse proportional to the FB value. The damping rate of the beam feedback is about 0.01 turn^{-1} for $FB=18\text{dB}$.

BEAM SIZE MEASUREMENT

The maximum amplitude of the dipole oscillation is relatively small, about 1 mm and damps quickly, that may not be a serious problem. Other effects should be considered for the instability. Thus, the beam size was measured turn by turn with an electrical method. The beam size can be obtained by measuring the quadrupole moment of the beam [5]. The setup of the beam size monitor is shown in Fig. 5. The signals indicated by A and by B, signals from each button electrode are added horizontally and the vertically, respectively, are expressed as

$$A \propto \frac{I}{\pi R} \left\{ 1 - \frac{2}{R^2} [(\sigma_x^2 - \sigma_y^2) + (x_0^2 - y_0^2)] \right\}$$

$$B \propto \frac{I}{\pi R} \left\{ 1 + \frac{2}{R^2} [(\sigma_x^2 - \sigma_y^2) + (x_0^2 - y_0^2)] \right\}, \quad (1)$$

where I is the bunch current, R is the duct radius, σ_x and σ_y are the horizontal and vertical rms sizes of the

beam, x_0 and y_0 are the charge center of the bunch and ($\sigma_x, \sigma_y \ll R$). The AM/PM detector compares the signals A and B and the detector outputs a signal proportional to the rms beam size regardless of the bunch current. Assuming the vertical beam size is constant or negligibly small, this signal indicates a change of the horizontal beam size.

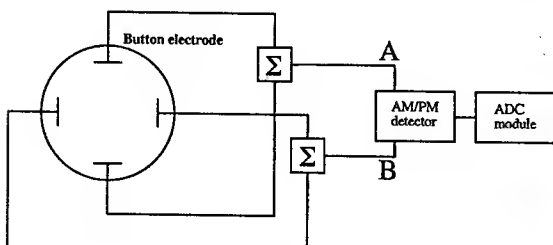


Figure 5: Block diagram of the beam size monitor.

The horizontal dipole oscillation and the beam size were measured at the same time as shown in Fig. 6. While the amplitude of the betatron oscillation grows, the beam size also grows without any oscillations. The time at which the amplitude is maximum corresponds to the maximum of the size. However, the size remains enlarged and shrinks slowly, even after the amplitude of the dipole oscillation fully damps. The size goes back to an initial value with a scale of the radiation damping time.

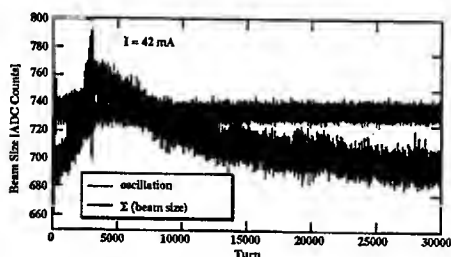


Figure 6: Beam size and the dipole oscillation are shown as a function of turn number. The ADC value in the size corresponds to a change of the rms size, 0.06 mm/count. The radiation damping time is 25 ms.

The beam size was directly measured using a streak camera [6]. Figure 7 shows horizontal beam profiles taken by the streak camera with the bunch oscillations. It is impossible that the beam size data over several ten of thousands of turns are continuously obtained at one time. Thus, sampled data of the beam profile are shown. We confirmed that the horizontal beam size and the oscillation amplitude grow together and the size shrinks slowly after the oscillation fully damps, as measured by the electrical size monitor.

DISCUSSION

From the behavior of the sawtooth instability for the changes of the various parameters, it is found that the beam

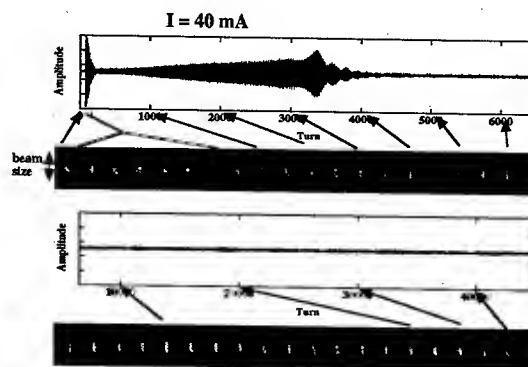


Figure 7: Horizontal beam profiles taken by the streak camera and the horizontal oscillation are shown as a function of turn number. For the beam profiles, the vertical axis indicates a beam size and the bunch goes from left side to right side. The bunch current is 40mA.

feedback is related to the sawtooth instability. Though the feedback system works well, the question remains why the feedback system cannot suppress the slowly growing betatron oscillation with the increase of the beam size. We had similar experiences in the early stage of the PF-AR. A vertical instability was observed [7], where blow-up of the beam size and dipole oscillation appeared at the same time. The beam feedback system for damping the dipole oscillation had no effect on the vertical instability. In the current PF-AR, we observed that the head and the tail of a bunch oscillated individually like a strong head-tail instability using a streak camera at a high bunch current. The different oscillations at the head and the tail of a bunch may influence the detection of the bunch oscillation in the beam feedback. We will clarify a detailed mechanism of the sawtooth instability by a computer simulation including an inside structure of a bunch.

ACKNOWLEDGEMENT

The authors would like to thank Prof. T. Mitsuhashi and Mr. M. Tadano who set up the measurement of the optical beam profile using the streak camera.

REFERENCES

- [1] Photon Factory Activity Report 1999-2000 and K. Ebihara et al., in these proceedings.
- [2] J.-L. Pellegrin et al., KEK 82-10, 1982 or T. Ieiri et al., Proc. 5th Symp. Accelerator Science and Technology, p.157, 1984.
- [3] M. Arinaga et al., KEK Preprint 93-104, 1993.
- [4] Y. Minagawa et al., Nucle. Instr. Meth. A416, p.193, 1998.
- [5] R. H. Miller et al., SLAC-PUB-3186, 1983.
- [6] T. Mitsuhashi, in these proceedings.
- [7] A. Ogata et al., IEEE Trans. Nuclear Sci. NS-32, p.1944, 1985.

STUDY OF EP INSTABILITY FOR A COASTING PROTON BEAM IN CIRCULAR ACCELERATORS

K. Ohmi, T. Toyama, M. Tomizawa
KEK, 1-1 Oho, Tsukuba, 305-0801, Japan

Abstract

We discuss interactions between a coasting proton beam and electrons. The electrons, which are created near the beam position, are considered in this paper. A coasting proton beam traps the electrons eternally, if there is not perturbations nor diffusion mechanisms. Therefore electrons are accumulated and their density could arrive above a threshold value for the instability, finally: i.e., a coasting proton beam is always unstable. However the instability affects both of the beam and electrons. Electrons may be diffused by the instability, in which the beam still has a small oscillation amplitudes, with the result that the beam amplitude may be kept in the small level, and may be stable in actual operations of accelerators. We study the ep instability with focusing the electron diffusion using a computer simulation method.

INTRODUCTION

We study ep instability for a coasting beam, in which the charged distribution is uniform along the longitudinal axis z . A static electric potential is formed by the coasting beam, when there is no transverse motion. Electrons created near the beam are trapped eternally, while electrons created at the chamber wall are absorbed with the same energy as those at the creation. Proton beam, which ionizes residual gas, creates electrons near the beam. The electrons, which are trapped, are accumulated, and their density arrives a threshold of the ep instability. Above the threshold, both of the beam and electron cloud become unstable. To be precise, amplitude of electrons is much larger than that of the beam, as is shown in later. The beam-electron force is strongly nonlinear. The electrons with a large amplitudes due to the instability are smeared by the nonlinear force. The size of the electron cloud is enlarged, and electrons are absorbed into the chamber wall.

Electrons are also created at the chamber wall due to proton beam loss and secondary electron. The energy of the electrons is the order of 10 eV, except some portion with an energy equal to incident one. Therefore the multipacting does not develop naively in the coasting beam, because the initial energies of electrons are kept at their absorption. The beam with a perturbation traps the electrons created at the chamber during a short period or accelerates them to higher energy than initial one. Therefore the multipacting may be important even in the coasting beam. This is the same physics in the meaning of the transition between the trapping and diffusion.

We focus the ionization electrons and their diffusion in

this paper, and will discuss somewhere the extension to surface electrons and multipacting for the coasting beam.

Ionization cross-section for CO and H₂ is estimated to be $\sigma(\text{CO}) = 1.3 \times 10^{-22} \text{ m}^2$ and $\sigma(\text{H}_2) = 0.3 \times 10^{-22} \text{ m}^2$ using the Bethe formula [1]. The molecular density d_m is related to the partial pressure in nPa using the relation at 20°C, $d_m(\text{m}^{-3}) = 2.4 \times 10^{11} P_m (\text{nPa})$. The electron production rate is $7.7 \times 10^{-9} e^- / (\text{m} \cdot \text{p})$ at $2 \times 10^{-7} \text{ Pa}$.

The instability is characterized by the frequency of electron in the potential of the coasting beam,

$$\omega_e = \sqrt{\frac{\lambda_p r_e c^2}{2\sigma_{x(y)}(\sigma_x + \sigma_y)}} \quad (1)$$

Landau damping, which is caused by the longitudinal slippage, is conjectured to be very strong, since the frequency is very rapid, $n \equiv \omega_e / \omega_0 \gg 1$.

Linear theory is reviewed in Sec.2, and beam stability and the electron diffusion using a particle tracking method is discussed in Sec.3.

LINEAR THEORY AND THRESHOLD OF THE INSTABILITY

We survey linear theory of ep instability [2], and estimate the threshold at some high intensity proton rings in the world. The interactions between the beam and electron cloud is represented by a wake force [3]. The wake force is expressed by

$$W_1(z) = c \frac{R_S}{Q} \frac{\omega_e}{\tilde{\omega}} \exp\left(\frac{\alpha}{c} z\right) \sin\left(\frac{\tilde{\omega}}{c} z\right), \quad (2)$$

where

$$cR_S/Q = \frac{\lambda_e}{\lambda_p} \frac{L}{(\sigma_x + \sigma_y)\sigma_y} \frac{\omega_e}{c}. \quad (3)$$

in the language of impedance, we would say that the Q factor is infinite. Actually the frequency spread of ω_e should be taken into account. By taking into the frequency spread of ions, $\Delta\omega_e = \omega_e/2Q$, the impedance is given by

$$\begin{aligned} Z_1(\omega) &= \frac{c}{\omega} \frac{R_S}{1 + iQ \left(\frac{\omega_e}{\omega} - \frac{\omega}{\omega_e} \right)} \\ &= \frac{\lambda_e}{\lambda_p} \frac{L}{\sigma_y(\sigma_x + \sigma_y)} \frac{\omega_e}{\omega} \frac{Z_0}{4\pi} \frac{Q}{1 + iQ \left(\frac{\omega_e}{\omega} - \frac{\omega}{\omega_e} \right)}, \end{aligned} \quad (4)$$

where Z_0 is the vacuum impedance 377Ω.

We discuss the stability of a beam which experiences the effective impedance. The stability criterion for the coasting beam is given by the dispersion relation as follows [4],

$$U \equiv \frac{\sqrt{3}\lambda_p r_p \beta \omega_0 |Z_1(\omega_e)|}{\gamma \omega_e \eta \sigma_{\delta E/E} Z_0}, \quad (5)$$

where β is a typical value of the beta function in a ring, and r_p is the classical proton radius. This formula is the same as that given by Keil and Zotter for e-p instability [2]. For $U > 1$, the beam is unstable. The thresholds of the neutralization factor are given by

$$f_{th} = \frac{2\pi\gamma n \eta \sigma_{\delta} \sigma_{x(y)}(\sigma_x + \sigma_y)}{\sqrt{3}\lambda_p r_p \beta Q L} \quad (6)$$

We put 5 and 10 m for Q and β , respectively, and the threshold values for various rings are shown in Table 1.

SIMULATION USING BEAM TRACKING

Before going to beam tracking we study electron motion trapped in the beam potential. Fig. 1 shows samples of electron trajectories for (a) static beam potential and for (b) including a perturbation due to a coherent motion of beam. Motion of three samples of electrons are depicted in Fig. 1(a). It shows that electrons are trapped in the potential. Fig. 1(b) depicts motion of an electron in a perturbed potential. The amplitude of the electron gradually increase as time goes by.

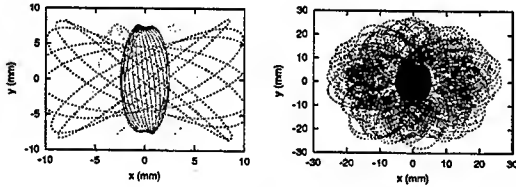


Figure 1: Trajectory of electrons. (a) Three electrons are tracked without perturbation. (b) An electrons are tracked with perturbation. Green and blue points are phase space coordinate of electron during 10 turns and 100 turns, respectively. Red points are those without perturbation as a reference.

We study the motion of proton beam interacting with the electron cloud using a tracking simulation.

A coasting proton beam is represented by macro-particles which are located along z with equal spacing. Each macro-particle has a charge and a mass corresponding to the proton line density. The macro-particle (proton) can undergo dipole motion with a dipole moment characterized by $\bar{x}_{p,i}(z_i, s) = (\bar{x}_p, \bar{y}_p)$, but the emittance (size) is kept constant. The number of macro-protons should be more $\omega_e L/c$, because electrons in the cloud oscillate smoothly by the force from the macro-protons. The electron cloud is created at some positions in the ring, and is represented by a

large number of point-like macro-particles denoted by $x_{e,a}$ ($a = 1, N_e$). The electrons are created in every passage of the proton beam. The transverse position of electrons is randomly generated with the same rms size as the beam.

The motion of the macro-electrons and macro-protons is tracked during the beam passage. After that, macro-protons are transported by the lattice magnets. This procedure is repeated in every interaction of the bunch with the cloud. Electrons are absorbed at the chamber wall surface. The number of macro-electrons increases except their disappear at the wall.

We take into account the Landau damping caused by the longitudinal motion, which disturbs the coherence of the dipole motion. The Landau damping rate per one revolution is given by $\alpha = n \eta \sigma_{\delta E/E} / \sqrt{3}$ for the coasting beam, where $n = \omega_e / \omega_0$. In the simulation, the Landau damping is treated by a simple way as

$$\bar{x}_{p,i} = (1 - \alpha) \bar{x}_{p,i}. \quad (7)$$

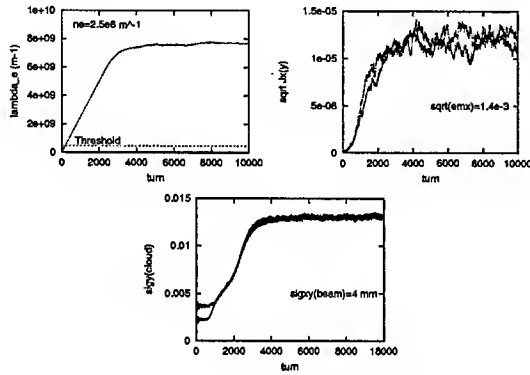
We performed the simulation for J-PARC 50 GeV rings at the flat top. The damping rate is 1.1×10^{-3} . The threshold line density is $\lambda_e = 4.5 \times 10^8 \text{ m}^{-1}$. Electron production rate per one revolution time T_0 is $7.7 \times 10^{-9} e^- / (\text{m} \cdot \text{p}) \times 21.2 \times 10^{10} \times 1567 = 2.5 \times 10^6 \text{ m}^{-1} T_0^{-1}$ for $P = 2 \times 10^{-7} \text{ Pa}$. The production rate linearly depends on the vacuum pressure. The build up time up to the threshold is 180 turns (0.9 ms) in linear theory. We put 10 interaction points in the ring. The dipole motion is assumed to be periodic for the 1/10 divided part of the whole ring: that is, the beam (macro-proton train) with 1/10 length is tracked. The beam (1/10 part) is represented by 1000 macro-protons. $\omega_e L / 10c = 774$ is $\gg 1$ and < 1000 .

The simulations were performed for several electron production rates. Amplitudes of each macro-proton ($J_{x(y),i}$), electron line density (λ_e), electron rms. size (σ_e), etc. were obtained by the simulation. There was no significant result for the production rate of $2.6 \times 10^5 \text{ m}^{-1} T_0^{-1}$, correspond to $P = 2 \times 10^{-7} \text{ Pa}$. Fig. 2 shows λ_e , maximum amplitude of $\sqrt{J_{x(y)}}$ and σ_e for the electron production rate, $2.6 \times 10^6 \text{ m}^{-1}$ ($P = 2 \times 10^{-6} \text{ Pa}$). All of them increase and is saturated at 3000 turn. The saturation of the beam amplitude is $\sigma_r / 100$. We may not observe the instability due to the small amplitude.

Fig. 3 shows electron line density λ_e and maximum amplitude $\sqrt{J_{x(y)}}$ for various electron production rates of $2.6 \times 10^7 \text{ m}^{-1} T_0^{-1}$, $2.6 \times 10^8 \text{ m}^{-1} T_0^{-1}$ and $2.6 \times 10^9 \text{ m}^{-1} T_0^{-1}$. Converting to the vacuum pressure, the rates are $P = 2 \times 10^{-5} \text{ Pa}$, $2 \times 10^{-4} \text{ Pa}$ and $2 \times 10^{-3} \text{ Pa}$, respectively. The saturation levels are $\sigma_r / 30$, $\sigma_r / 10$ and σ_r , respectively. If we can observe the instabilities with a resolution of 10% of σ_r , the production rate should be more than $10^8 \text{ m}^{-1} T_0^{-1}$, which corresponds to 10^{-4} Pa . This value is too high for the vacuum pressure.

Table 1: Basic parameters and threshold of the neutralization factor of the proton rings

variable	symbol	JPARC-MR	KEK-PS	PSR	ISIS	AGS-Bst.	AGS	FNAL-MI
circumference	L (m)	1567.5	339	90	163	202	800	3319
relativistic factor	γ	54.	12.8	1.85	1.07	1.2	3.0	128
beam line density	$\lambda_p (\times 10^{10}) \text{ m}^{-1}$	21.2	0.74	33.3	18.4	82.7	8.75	0.90
rms beam sizes	σ_r (cm)	0.35	0.5	1.0	3.8	1	0.7	0.17
rms energy spread	$\sigma_{\delta E/E}$ (%)	0.25	0.3	0.4	0.5	0.5	0.28	0.03
transition energy	γ_t	31.6	6.76	3.08	5.07	4.88	8.5	21.8
slippage factor	η	-0.0013	0.016	-0.187	-0.83	-0.652	0.0122	0.0020
	$\omega_e L/c$	7740	225	195	69	226	2012	6930
Threshold	$f_{th}(\%)$	0.21	4.0	2.5	45.	15.	2.6	0.06

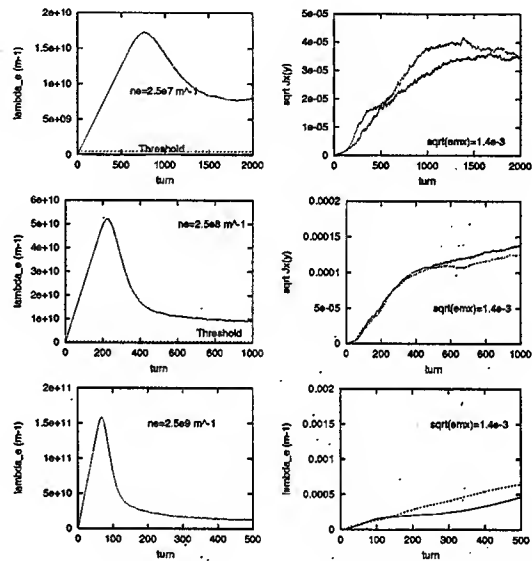

 Figure 2: Evolution of line density of electron cloud (λ_e [m^{-1}]), maximum amplitude of beam ($J_{x(y)}^{1/2}$ [$\text{m}^{1/2}$]) and size of electron cloud ($\sigma_{x(y)}$ [m]) for the electron production rate of $2.6 \times 10^6 \text{ m}^{-1} T_0^{-1}$.

CONCLUSION

We have studied ep instability for a coasting proton beam. Electrons created by ionization are treated in this paper. The instability is not caused by electron cloud for slow production rate. Production rate is important whether the instability grow to visible amplitudes. The production rate more than $10^8 \text{ m}^{-1} T_0^{-1}$ is required to be unstable for JPARC-MR ring. The rate corresponds to 10^{-4} Pa, which is quite nonsense. Ionization may not be a direct candidate of the instability. Electron sources with a higher production rate, for example, proton loss and/or multipacting have an essential role even for the coasting beam instability.

Similar analysis and discussion can be extended to the beam-ion instability in electron storage rings straightforwardly.

The authors thank the members of the electron-proton instability working group of J-PARC, N. Hayashi, S. Kato, K. Satoh, S. Machida, K. Oide K. Yokoya for fruitful discussions.


 Figure 3: Evolution of line density of electron cloud (λ_e [m^{-1}]) and maximum amplitude of beam ($J_{x(y)}^{1/2}$ [$\text{m}^{1/2}$]) for the electron production rates of $2.6 \times 10^7 \text{ m}^{-1} T_0^{-1}$, $2.6 \times 10^8 \text{ m}^{-1} T_0^{-1}$ and $2.6 \times 10^9 \text{ m}^{-1} T_0^{-1}$.

REFERENCES

- [1] Y. Baconnier, CERN report 85-19, pp.267 (1985).
- [2] E. Keil and B. Zotter, CERN-ISR-TH/71-58 (1971).
- [3] K. Ohmi, T. Toyama, C. Ohmori, Phys. Rev. ST-AB.,5, 124402 (2002).
- [4] E. Keil and W. Schnell, CERN Report TH-RF/69-48 (1969).

AN EXPERIMENTAL STUDY OF MICROWAVE STABILITY NEAR TRANSITION IN THE PSR*

Patrick Colestock, Chris Beltran, Andrew Browman, Douglas Gilpatrick, Robert Macek, Rodney McCrady, Filippo Neri, Larry Rybarczyk, and Thomas Spickermann, *Los Alamos National Lab, Los Alamos, NM, USA* and Martin Schulze, *General Atomics, Los Alamos, NM, USA**

Abstract

We have undertaken a study of microwave stability in the PSR storage ring under a variety of beam conditions near transition, including variable intensity and machine impedance, which can be independently controlled in the PSR. Results indicate that the general features of a linear stability model are valid, namely that the instability threshold becomes very small sufficiently close to transition. In addition, many nonlinear features are apparent and the results suggest an extended operating regime is possible with saturated, but otherwise benign, longitudinal fluctuations. Details of the linear model experimental results and corresponding simulations will be presented.

INTRODUCTION

Beams in circular accelerators that must cross transition have long been observed to suffer significant, though often manageable, emittance growth. While the cause for the emittance growth is not completely understood, it is a widely-held belief that it arises from a longitudinal microwave instability at or near transition energy.

Recent theoretical work [1] has suggested that beams are always unstable longitudinally near transition. Since the first-order frequency dispersion goes to zero at transition, it is necessary to include second-order effects to determine the stability properties. For a Gaussian beam, the following dispersion relation is found:

$$Z_m / m = \frac{2\pi^{1/2} \epsilon_o^2 i \sqrt{k_o^2 - 4 \frac{k_1}{m} (m\omega_o - \Omega)}}{N \left(\frac{\epsilon\omega_o}{2\pi} \right)^2 \left(\Xi' \left[\frac{\epsilon_1}{\epsilon_o} \right] - \Xi' \left[\frac{\epsilon_2}{\epsilon_o} \right] \right)}$$

where the first and second-order frequency dispersion is given by

$$\epsilon_{1,2} = -\frac{k_o}{k_1} \pm \sqrt{\frac{k_o^2}{4k_1^2} - \frac{m\omega_o - \Omega}{mk_1}}$$

$$k_o = -\omega_o \frac{\eta_o}{\beta^2 E_o}$$

$$k_1 = -\frac{\omega_o}{2} \left(\alpha_o - \alpha_1 - \frac{3}{2} \eta_o \alpha_o \frac{\beta^2}{\gamma^2} \right) \frac{1}{\beta^4 E_o^2}$$

with $\Delta\omega = k_o \Delta E + k_1 \Delta E^2$ and where Ξ is the complex error function and ϵ_o is the RMS beam energy spread. Other parameters are given in ref. [1]. We note that the higher-order correction to η effectively adds another branch to the stability criterion, such that whenever it exists there is a region of instability. The stability criterion formally is found by imposing $\text{Im}(\Omega) = 0$ and solving for the associated complex impedance. This is parameterized by the quantity $\alpha = k_1 \epsilon / k_o$, which denotes the proximity to transition. $\alpha = \infty$ occurs at transition. The stability boundary is plotted on the impedance plane in Fig. 1.

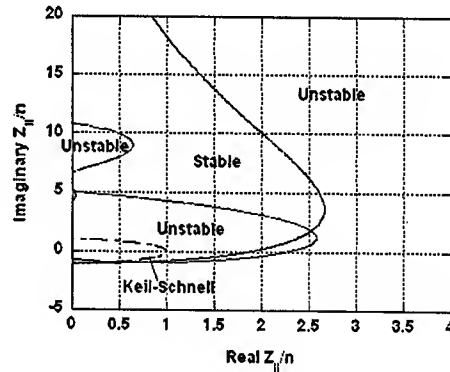


Fig. 1 Stability boundaries in the complex impedance plane near transition. As transition is approached, a new unstable region appears within the familiar Keil-Schnell boundary. Plot is for $\alpha \sim 0.15$.

It is seen that for η sufficiently small, there is always a region of instability near transition, as evidenced by the branch internal (smaller impedance) to the usual Keil-Schnell limit. At issue, however, is the growth rate and the relevant emittance growth. Solving for the growth rate associated with the Keil-Schnell impedance limit, we find the growth rate approaches a constant value as transition is approached (Fig. 2). We note, in particular, that the entire impedance plane is expected to be unstable, but the growth rates are bounded by the isochronicity of the dynamics.

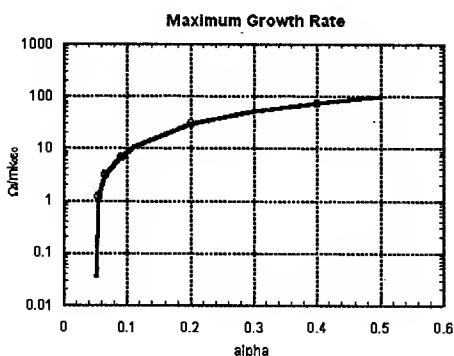


Fig. 2 Maximum growth rate for longitudinal modes normalized to revolution harmonic as a function of the parameter α , i.e. proximity to transition. Transition occurs at $\alpha = \infty$. Instability occurs for $\alpha > 0.05$.

EXPERIMENTAL SETUP

We have designed an experiment to quantify longitudinal stability near transition on the Proton Storage Ring (PSR) at LANL. The experimental setup is shown schematically in Fig. 3. Longitudinal oscillations are picked up by a pair of beam position monitor strip lines and summed. In addition, the capability for beam transfer function measurements exists using an amplified network analyzer and pick-up as shown.

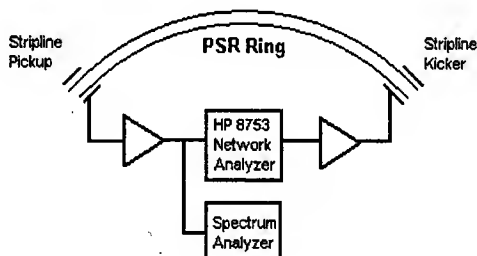


Fig. 3 Experimental setup on the PSR. Approximately 90 db of gain was used in the circuit.

Care was taken to ensure that the lattice was tuned so that γ_t was close to the injection energy ($\gamma = 1.85$), which required careful tuning of the injection orbit and lattice quadrupoles. Subsequent measurements showed that the operating point was within 0.05 units of transition for the data shown in this paper. To facilitate a sufficiently long storage time, the buncher cavity ($h=1$) was detuned and unpowered. Moreover, the ring was filled with multiplet injection, allowed to debunch and was extracted after 1 msec.

EXPERIMENTAL RESULTS

A primary result of this study is that we found the beam to be longitudinally unstable for very small beam currents when the beam was within 0.2 units of transition. In Fig.

4, we show the envelope of longitudinal oscillations following injection and debunching. It is characterized by a rapid growth followed by saturation and envelope oscillation at much lower frequencies. The corresponding frequency spectrum in Fig. 5 shows a broad range over which oscillations occur.

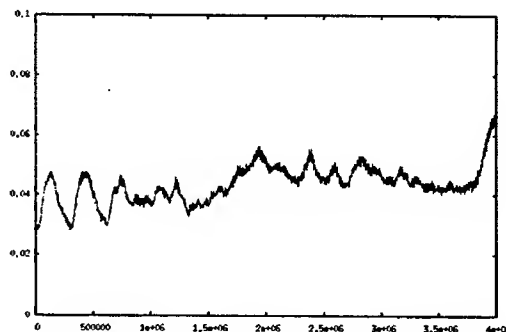


Fig. 4 Envelope of longitudinal oscillations near transition. $I = 7$ mA. Initial growth is followed by low-frequency oscillations. Vertical scale is signal amplitude in arbitrary units. Horizontal scale is in samples. Sample rate is at 2 Gs/sec.

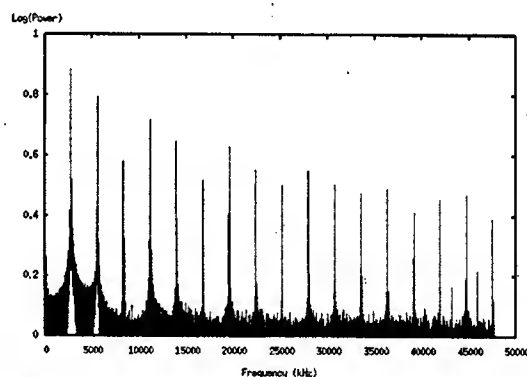


Fig. 5 Frequency domain signature of longitudinal oscillations near transition for the above time domain data. $I = 7$ mA. The main machine impedance occurs at $h=1$. Vertical scale is 10 db/div.

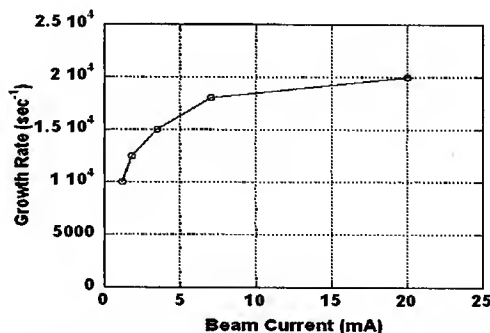


Fig. 6 Measured initial growth rate as a function of beam current. The associated beam momentum width is not measured.

We conjecture that the rapid growth at the onset is the linear part of the instability growth, and should be comparable to the theoretical model presented in the first section. The low-frequency oscillation, we assert, is due to nonlinear wave overturning and self-trapping, and occurs at the lower synchrotron frequency of the trapped particles [2]. In Fig. 6, we show the scaling of the growth rates with beam intensity, and in Fig. 7, we show the associated scaling of the saturated fluctuation amplitudes.

Performing a beam transfer function measurement leads to the surprising result that the beam has bifurcated into several beamlets, as shown in Fig. 8. As the tune is moved away from transition, approximately 0.3 units, we find that these beamlets merge back into a single beam.

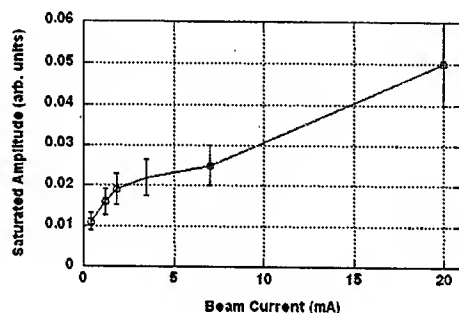


Fig. 7 Saturated longitudinal fluctuation amplitude as a function of beam current.

DISCUSSION

It is clear that the growth rate saturates with increasing beam current, as does the saturated fluctuation amplitude. It is found that there is essentially no mode growth if the tune is moved to 0.5 units from transition, qualitatively confirming our theoretical model. However, without a direct measure of the momentum distribution, we are unable to make a quantitative comparison.

We also note that while the saturated amplitude increases with beam current, the increase is only approximately linear, indicating that nonlinear behavior may render the instability benign. The importance of nonlinearity in the dynamics is underscored by the bifurcation of the beam into beamlets, suggested by the beam transfer function measurement, and the results of the simulation (Fig. 9). Further work is planned to quantify the stability properties with a simultaneous measurement of momentum distribution.

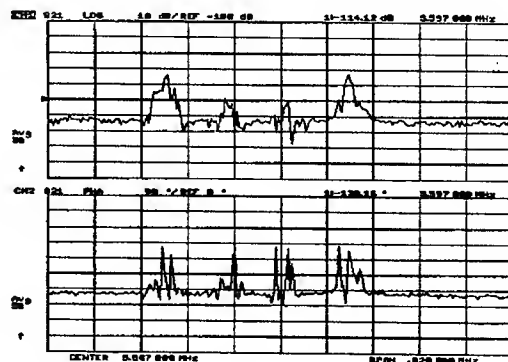


Fig. 8 Beam transfer function measurement within approximately 0.07 units of transition. Top trace is the magnitude of the BTF; bottom trace is the corresponding phase. 2 kHz/div centered at $h=2$.

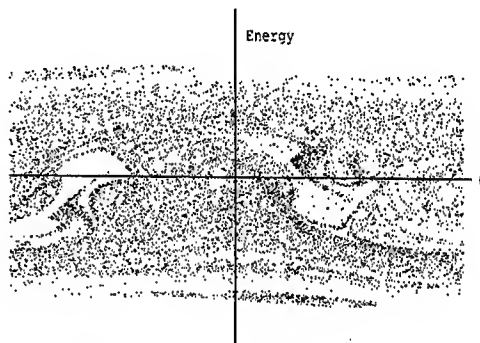


Fig. 9 Longitudinal phase space from a simulation near transition with a resonator wakefield, $Z/n = 10$ ohms, $Q = 100$. Beamlets form on both the high and low energy sides of the core.

* LA-UR - 03-3073

REFERENCES

- [1] J. A. Holt and P. L. Colestock, Microwave Stability at Transition, Proc. IEEE Particle Accelerator Conference, Dallas, Tx., 5, p. 3016 (1995)
- [2] P. L. Colestock and L. K. Spentzouris, Nonlinear Wave Phenomena and Emittance Growth in Coasting Beams, Tamura Symposium, Univ. of Texas, Austin, Nov.(1994)

STATUS OF THE EXPERIMENTAL STUDIES OF THE ELECTRON CLOUD AT THE LOS ALAMOS PROTON STORAGE RING*

R.J. Macek[#], A. Browman, M. Borden, D. Fitzgerald, R. McCrady, T. Spickermann, T. Zaugg,
LANL, Los Alamos, NM 87545, USA

Abstract

The electron cloud (EC) at the Los Alamos Proton Storage Ring (PSR) has been studied extensively for the past several years with an overall aim to identify and measure its important characteristics, the factors that influence these characteristics, and to relate these to the two-stream (e-p) transverse instability long observed at PSR. Some new results since PAC2001 are presented.

INTRODUCTION

Experimental studies of the electron cloud at PSR during the past two years were undertaken to consolidate the understanding gained from earlier exploratory studies [1],[2] and to determine the important characteristics that are needed to adequately explain the e-p instability at PSR. In addition, we sought to understand how well the instability might be cured by suppression of the electron cloud. To accomplish this, our studies aimed to resolve several important issues which include:

1. Will sufficient electrons from the "prompt" pulse emerging at the end of the bunch passage survive the gap (between successive passages of the bunch) to be captured by the bunch and cause the instability?
2. Will electron suppression by TiN coating of the vacuum chamber surfaces or the use of weak solenoids provide a cure?
3. A beam "conditioning effect" on the e-p instability threshold intensity curves had been observed in prior years. Is this effect caused by a reduction in the electron cloud from "beam scrubbing" i.e., does this effect correlate with a reduction in the EC density?
4. What are the important source terms for the initial or "seed" electrons that get amplified by the beam-induced, trailing-edge multipactor process?
5. What causes the electron "burst" phenomenon in PSR?

ELECTRONS SURVIVING THE GAP

Electrons left in the pipe just after passage of the beam pulse will degrade by secondary emission processes to a few eV after the next collision with the wall. The retarding field analyzing detector (RFA) is not suited to the task of measuring these electrons as it only measures those striking the walls not those left in the pipe. To solve this problem, the electron sweeping diagnostic (ESD) was developed to measure low energy electrons lingering in

the pipe. Basically it is an RFA with an electrode opposite the RFA. The electrode is pulsed with a short fast pulse (up to 1kV) to sweep low energy electrons from the pipe into the detector. It is described in more detail in reference [3] and the references therein.

The observed swept electron signal which was pulsed at the end of the ~90 ns gap (shown in Figure 1) implies an average neutralization of ~1-2% at the location of this detector (section 4 of PSR). This is approximately the value needed to explain the observed e-p instability threshold curves, assuming this represents the average neutralization of the beam [4].

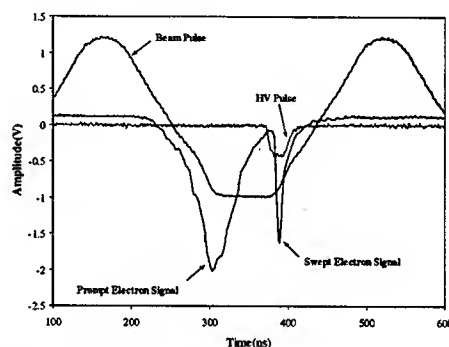


Figure 1. Swept electron signal from ESD plotted in time relationship to the HV and beam pulses.

Another important feature of the swept electron signal at the end of the ~90 ns beam-free gap is that it saturates above a certain level (possibly from space charge effects) as illustrated in Figure 2 while the prompt electron signal continues its rapid increase with intensity.

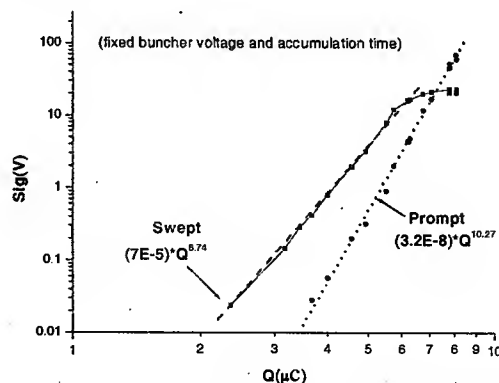


Figure 2. Prompt electron and "swept" electron signal amplitudes plotted as a function of stored beam intensity.

With the electron sweeper it was possible to measure the electrons in the beam pipe as a function of time after single turn extraction from PSR. Some early results for a 5 μC/pulse beam are plotted in Figure 3 and show the

* Work conducted at the Los Alamos National Laboratory, operated by the University of California for the U.S. Department of Energy under Contract No. W-7405-ENG-36.

#macek@lanl.gov

unexpected feature that significant numbers of electrons are still observed 1 μ s after the end of the beam pulse. The long exponential tail (~ 180 ns time constant) implies a relatively high reflectivity (~ 0.5) for low energy electrons (2-5 eV) at the peak of the secondary emission spectrum.

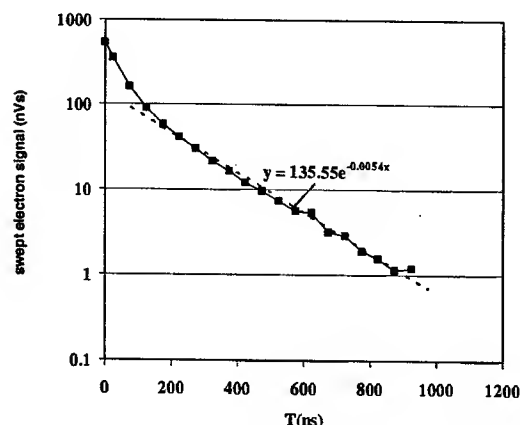


Figure 3. Swept electron signal (integral of pulse) plotted as a function of time after the end of the beam pulse.

TESTS OF ELECTRON SUPPRESSION

We have tested the effect of TiN coatings on the electron cloud signal in three regions of PSR and obtained mixed results, which are summarized in Table I. The most encouraging test was the first one in 1999 where a comparison test of a 2.5 m vacuum chamber coated with TiN and one that was not coated showed a good factor of 100 reduction of the prompt electron signal for the TiN coated chamber. This was carried out in straight section 5 of PSR, which is the region of lowest beam loss in PSR. The comparisons were made for the same beam intensity (within $\sim 5\%$) to limit the effect of the strong dependence of the electron signal on beam intensity.

Table I. Results of TiN coating tests.

Test Location	Date	Beam Intensity	Prompt e reduction factor	Swept e reduction factor
Sect. 5	1999	8.5 μ C	>100	N. A.
Sect. 4	2002	8 μ C	no initial reduction	none
Sect. 9	2002	7 μ C	~ 40	N. A.
Sect. 4 **	2002	8 μ C	~ 5	None

**Plus 2 months of operational beam scrubbing.

In the past year we tested TiN coatings in two more sections; section 4 and section 9, a high loss region near the extraction septa. Section 9 showed a factor of ~ 40 reduction in prompt electrons with the TiN coating. The test in section 4 included an electron-sweeping detector and showed no change in either the prompt or swept electrons signal with and without TiN coating. It should be noted that the prompt electron signal for the TiN coated chamber in section 4 did show a conditioning effect in which the prompt signal (at a fixed intensity) was

reduced by a factor ~ 5 after a few weeks of continuous beam operation at 100 μ A.

Weak solenoids with an embedded RFA were tested in two locations in PSR, section 9 (2001) and section 2 (2002). Results are shown in Figure 4 where a factor of ~ 50 reduction is seen with a magnetic field of 20 G.

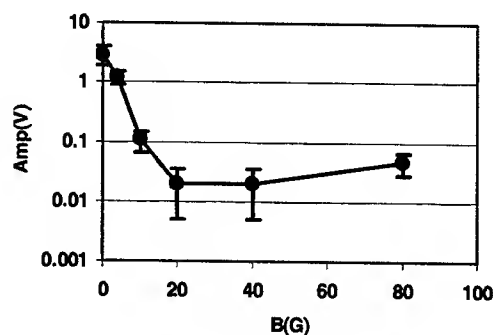


Figure 4. Effect of a weak solenoid field on the prompt electron peak amplitude.

Studies in the 2002 run cycle showed a significant reduction (factor of ~ 5) in the prompt electron signal with time. It is presumably due to beam scrubbing [5]. A related phenomenon is the aptly named 1st pulse instability. For a time after beam operations are resumed following a several month shutdown, a high intensity pulse accumulated in ring after a several minute wait is unstable while the same intensity pulses that follow a short time later are stable. Instability threshold curves for the "first pulse" instability (after a wait time of 3 minutes) are plotted in Figure 5 and compared with the threshold curves for subsequent pulses that follow in a regular pattern (~ 1 Hz). The reduction in threshold for the first pulse is evident. The other characteristics of the instability are identical with the standard e-p instability. The disappearance of the first pulse instability after a few weeks of operation is additional evidence that beam scrubbing is beneficial.

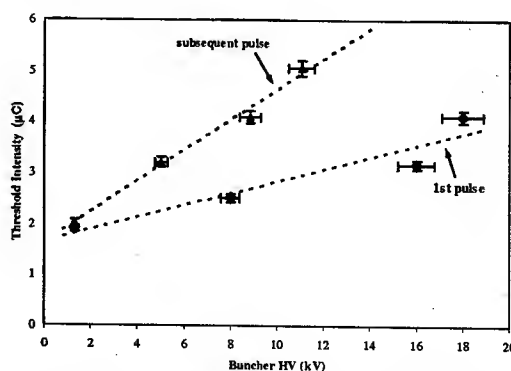


Figure 5. Plots of the instability threshold curves for the 1st pulse after a several minute wait and for the subsequent pulses for a small emittance beam in PSR.

SOURCES OF INITIAL ELECTRONS

The numbers of initial or primary electrons from the various sources e.g., beam losses, residual gas ionization, the stripper foil etc, are important parameters needed as inputs to the EC simulation codes [6]. We found evidence that both residual gas ionization and beam losses make significant contributions to the initial electrons, with somewhat more from beam losses under typical operating conditions. Experiments showed that the prompt electron signal varies linearly with either residual gas pressure or beam losses while the swept electron signal is constant. The results for the variation with gas pressure are shown in Figure 6. Normal operating vacuum range is 10-100 nTorr for section 4 of PSR.

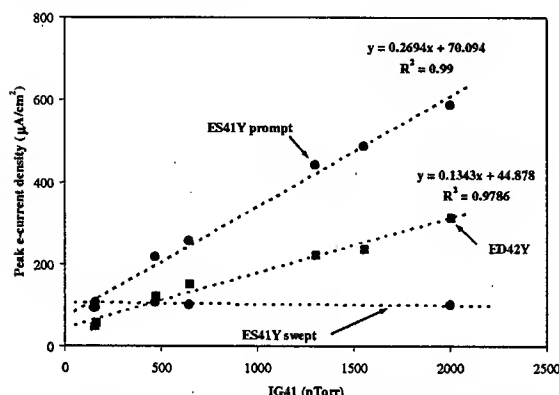


Figure 6. Prompt and swept electron signals amplitudes at the end of accumulation are converted to peak current density at the wall for two detectors in section 4 and plotted as a function of vacuum pressure as measured at ion gauge, IG41. Beam intensity was a fixed 8.2 μC/pulse.

ELECTRON BURSTS

Electron bursts are the name given to the rapid turn-to-turn variations in the prompt electron signal amplitude. This puzzling phenomenon is illustrated in Figure 7 where signals for a train of pulses (120 turns) are shown.

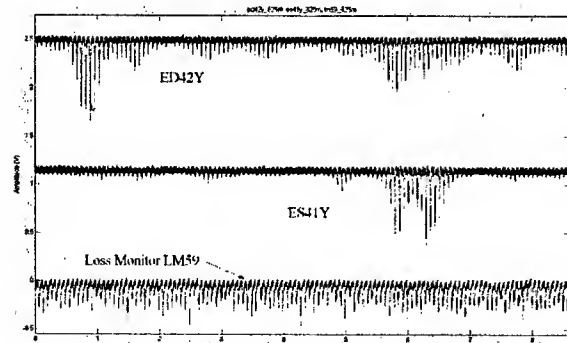


Figure 7. Simultaneous signal traces for two electron detectors (ES41Y, ED42Y) and a local loss monitor (LM59) for 120 turns.

The lack of significant correlation of the bursts with the local loss monitor signal (LM59) in Figure 7 suggests that fluctuations in the local losses are not the cause of the

bursts. However, some correlation has been observed between detectors in other locations and suggests some aspect of the beam structure drives the bursts.

The electron burst phenomena, which has become more pronounced with time, is the least understood aspect of the electron cloud in PSR. Perhaps this should not be a surprise, given that beam-induced multipacting is a cascade or avalanche-like process. The fluctuations from the bursts complicate data collection on the electron cloud and necessitate considerable averaging to get reproducible results. It is unclear what impact the bursts have on the instability or other beam dynamics.

SUMMARY AND CONCLUSIONS

Data obtained using the electron sweeping diagnostic (ESD) show that a surprisingly large number of electrons survive passage of the beam-free gap and implies ~1% average neutralization during the beam pulse passage for nominal operating beam intensities. This is approximately the fractional neutralization needed to account for the observed e-p thresholds. The long exponential survival curve for electrons in a beam free region is another important result obtained with the electron sweeping diagnostic and is evidence for a relatively high (~0.5) reflectivity or secondary emission yield, $\delta_e(E)$, from very low energy electrons (2-5 eV peak of the secondary emission distribution).

Our tests of TiN coatings gave mixed results which are not well understood but which suggest caution in assuming that this coating is a universal cure for ECE. The prompt electron peak was reduced by a factor ~40-50 by ~20 G field in tests in two sections of the ring. However, there was no measurable effect on the instability threshold when weak solenoids covering ~10% of the ring circumference were excited.

Operating experience at PSR since 1999 provides evidence that beam scrubbing has been effective in significantly raising the threshold for the e-p instability. Studies in the 2002 run cycle showed a significant reduction (factor of ~5) in the prompt electron signal with time and are presumably due to beam scrubbing. The disappearance of the first pulse instability after a few weeks of operation is additional evidence that beam scrubbing is beneficial.

Our studies also provide evidence that both the residual gas and beam losses make significant contributions to the initial electrons that are then amplified by the beam-induced multipacting processes.

REFERENCES

- [1] R. Macek et al., FOAB007, PAC'01, 688(2001).
- [2] R. Macek, ECLLOUD'02 Proceedings, CERN-2002-001, 259(2002).
- [3] R. Macek et al., ROAB003, PAC'03.
- [4] D. Neuffer et al., NIM A321, p.1-12(1992).
- [5] S.Y. Zhang et al., FPAB066, PAC'03.
- [6] M. Pivi and M. Furman, PRST-AB 6, 034201 (2003).

A THREE-DIMENSIONAL KINETIC THEORY OF CONTINUOUS-BEAM STABILITY *

Tai-Sen F. Wang[†], LANL, Los Alamos, NM 87545, USA

Abstract

This work is a three-dimensional stability study based on the modal analysis for a continuous beam with a Kapchinskij-Vladimirskij (KV) distribution. The analysis is carried out self-consistently within the context of linearized Vlasov-Maxwell equations and electrostatic approximation. The emphasis is on investigating the coupling between longitudinal and transverse perturbations in the high-intensity region. The interaction between the transverse modes supported by the KV distribution and those modes sustainable by the cold beam is examined. We found two classes of coupling modes that would not exist if the longitudinal and the transverse perturbations are treated separately. The effects of wall impedance on beam stability is also studied and numerical examples are presented.

INTRODUCTION

In a customary stability analysis of a continuous beam in an accelerator or storage ring, longitudinal and transverse effects are treated separately, an approximation that is valid because space-charge forces are relatively weak and characteristic frequencies differ by orders of magnitude. For a very intense beam like the one in the proposed heavy ion fusion facilities, the space-charge forces are large and all frequencies are of the order of the plasma frequency, the separated treatment of longitudinal and transverse perturbations may not be applicable. Such a concern was raised more than two decades ago in the heavy ion fusion studies. Since then, some investigations have been exploited in attempt to address the issue by improving the earlier stability theories for laminar beams or nearly laminar beams. In a study of two-dimensional, axisymmetric perturbations in a beam with a KV distribution, an instability caused by the coupling between the longitudinal and transverse motion was discovered in theory.[1] Later computer simulations confirmed the prediction and found this kind of instability to be a mechanism for energy exchange between the longitudinal and transverse motions in the beams with high anisotropy in temperature.[2-4] These findings and many fine papers published afterward[5-11] mark a success in exploring the intense beam stability. However, to date, the rigorous theory, though not necessarily computer simulations, is still left in the axisymmetric geometry and the three-dimensional theory remains to be improved. The purpose of this work is to extend the earlier investigation of axisymmetric modes in a KV beam to a full three-dimensional stability study. It is hoped that the approach

and the results of this work will be helpful in the exploring and understanding of beam stability in non-axisymmetric geometry.

THEORETICAL MODEL

We consider a continuous, nonrelativistic beam of circular cross section with radius a and constant particle density ρ_0 propagating inside a conducting pipe of radius b and arbitrary wall impedance. A cylindrical coordinate system (r, φ, z) is chosen such that the beam is propagating in the positive z direction and the z axis coincides with the central axis of the beam. The equilibrium state of the beam is maintained by a constant linear external transverse focusing force which can be represented as $M\nu_0^2 r$ where M is the mass of a beam particle and ν_0 is the betatron frequency in the absence of the beam's self-field. Taking the self-field of the beam into account, one finds the relation $\nu^2 = \nu_0^2 - (\omega_p^2/2)$, between the effective betatron frequency of particles ν , and the plasma frequency $\omega_p = (4\pi q^2 \rho_0 / M)^{1/2}$, where q is the charge of a beam particle. We assume the equilibrium distribution of beam particles in the phase space is described by the distribution function $f_0(\mathbf{x}, \mathbf{v})$ that is a product of the KV distribution in the transverse direction and a delta function of the longitudinal speed, i.e.

$$f_0(\mathbf{x}, \mathbf{v}) = \frac{\rho_0}{\pi} \delta[v_\perp^2 - \nu^2(a^2 - r^2)] \delta_z(v_z - v_0), \quad (1)$$

where $v_\perp^2 = v_r^2 + v_\varphi^2$, v_r , v_φ and v_z are particles' radial, azimuthal and axial speeds, respectively, v_0 is the averaged axial speed of particles, and $\delta(x)$ is the delta function.

STABILITY ANALYSIS

The stability study here is carried out within the context of the Vlasov-Maxwell equations and the electrostatic approximation for small perturbations evolving in the linear regime. Thus, we consider small perturbations in the distribution function $f_1(\mathbf{x}, \mathbf{v}, t)$ and in the electric potential $\phi_1(\mathbf{x}, t)$ described by the linearized Vlasov-Poisson equations

$$\frac{\partial f_1}{\partial t} + \mathbf{v} \cdot \frac{\partial f_1}{\partial \mathbf{x}} + \frac{d\mathbf{v}}{dt} \cdot \frac{\partial f_1}{\partial \mathbf{v}} = \frac{q}{M} \nabla \phi_1 \cdot \frac{\partial f_0}{\partial \mathbf{v}}, \quad (2)$$

and

$$\nabla^2 \phi_1 = -4\pi q \int_{-\infty}^{\infty} \int_{-\infty}^{\infty} \int_{-\infty}^{\infty} f_1(\mathbf{x}, \mathbf{v}, t) d^3v. \quad (3)$$

Assuming the perturbed quantities vary in space and time according to $\{f_1, \phi_1\} = \{\tilde{f}, \tilde{\phi}\} e^{i(\omega t + m\varphi - kz)}$, the linearized Vlasov-Poisson equation can be treated by integrating over the unperturbed particle orbit to yield the following differential-integral equation in the region of $r \leq a$,

* Research supported by Los Alamos National Laboratory under the auspices of the US Department of Energy.

[†] TWANG@LANL.GOV

$$\begin{aligned}
 & \frac{1}{r} \frac{\partial}{\partial r} \left(r \frac{\partial \tilde{\phi}}{\partial r} \right) - \left(\frac{m^2}{r^2} + k^2 \right) \tilde{\phi} \\
 &= \frac{\omega_p^2}{a\nu^2} \tilde{\phi}(a) \delta(r-a) + \frac{2\omega_p^2}{\pi} \left[i\Omega \int_{-\infty}^{\infty} \int_{-\infty}^{\infty} dv_r dv_\varphi \frac{d\delta_\perp}{dv_\perp^2} \right. \\
 & \quad \times \int_0^\infty \tilde{\phi}(r') \left(\frac{1}{r'} \right)^m (\xi_1 e^{i\theta} + \xi_2)^m e^{-i\Omega\tau} d\tau \\
 & \quad + \frac{k^2}{2} \int_{-\infty}^{\infty} \int_{-\infty}^{\infty} dv_r dv_\varphi \delta_\perp \int_0^\infty \tau \tilde{\phi}(r') \left(\frac{1}{r'} \right)^m \\
 & \quad \left. \times (\xi_1 e^{i\theta} + \xi_2)^m e^{-i\Omega\tau} d\tau \right], \quad (4)
 \end{aligned}$$

where $\delta_\perp = \delta[v_\perp^2 - \nu^2(a^2 - r^2)]$, $\xi_1 = (v_\perp/\nu) \sin(\nu\tau)$, $\xi_2 = r \cos(\nu\tau)$, $\Omega = \omega - kv_o$ is the Doppler-shifted frequency, $r' = (\xi_1^2 + \xi_2^2 + 2\nu r \xi_1 \xi_2 / v_\perp)^{1/2}$, and $m = 0, 1, 2, \dots$ denotes the azimuthal harmonic number. The right hand side of Eq. (4) is zero in the region of $a < r \leq b$.

Expanding the perturbed electric potential in Eq. (4) as a sum of Jacobi polynomials $P_l^{(m,0)}(x)$ according to

$$\tilde{\phi}(r) = \left(\frac{r}{a} \right)^m \sum_{l=0}^{\infty} G_l P_l^{(m,0)} \left(1 - \frac{2r^2}{a^2} \right), \quad (5)$$

we can derive a recursion relation

$$W_l A_{l+1} + (W_l + W_{l-1} + U_l) A_l + W_{l-1} A_{l-1} = 0, \quad (6)$$

for $l = 1, 2, 3, \dots$, where G_j is independent of r , $A_l = \sum_{j=l}^{\infty} (-1)^{j+l} G_j$,

$$U_l = 2(m+2l) + (\omega_p/\nu)^2 (B_{l-1} - B_l), \quad (7)$$

$$W_l = \frac{a^2 k^2}{2(m+2l+1)} \left[1 + \left(\frac{\omega_p}{\nu} \right)^2 \frac{\partial B_l}{\partial \alpha} \right], \quad (8)$$

$$B_l = i \int_0^\infty e^{-i\alpha x} \cos^m x P_l^{(0,m)}(\cos 2x) dx, \quad (9)$$

and $\alpha = \Omega/\nu$. Applying the proper boundary conditions at $r = a$ together with Eq. (6) leads to the dispersion relation

$$\frac{a}{\tilde{\phi}_0} \frac{d\tilde{\phi}_0}{dr} \Big|_{r=a} = m + \left(\frac{\omega_p}{\nu} \right)^2 (1 - B_0) + W_0 + \frac{W_0 A_1}{A_0}, \quad (10)$$

where the ratio A_1/A_0 can be expressed in terms of infinite determinants or a continuous fractions, and

$$\begin{aligned}
 \tilde{\phi}_0(r) \sim & I_m(kr) K_m(kb) - I_m(kb) K_m(kr) \\
 & - iZ [I_m(kr) K'_m(kb) - K_m(kr) I'_m(kb)], \quad (11)
 \end{aligned}$$

is the potential external to the beam derive from solving Eq. (4) in the region of $a < r \leq b$. Here, $I_n(x)$ and $K_n(x)$ are the n th order modified Bessel functions of the first and the second kinds, respectively, the prime indicates the derivative with respect to the argument, $Z = \omega Z/(ck)$, Z is the wall impedance, and c is the speed of light.

For $k = 0$, the recursion relation (6) reduces to the dispersion relation $U_j = 0$ for the transverse modes discussed earlier in Ref. 12. When $m = 0$, the Jacobi polynomials in

Eq. (5) become Legendre polynomials and Eq. (10) reduces to the dispersion relation for axisymmetric modes studied in Ref. 1. Taking the limit of $\nu \rightarrow 0$ in Eq. (10), one finds the cold-beam dispersion relation[13]. The customary dispersion relation of the "usual dipole mode"[14] in a continuous nonrelativistic beam without axial momentum spread can be obtained from Eq. (10) by considering the limit of $kb \ll 1$ for $m = 1$.

The roots of the dispersion relation (10) fall into three classes: (i) the ones that approach the pure transverse modes, i.e., the solutions of $U_j = 0$, when $k \rightarrow 0$, (ii) the "high-frequency coupling modes" having the limit of $\Omega \rightarrow n\nu$ when $\omega_p \rightarrow 0$, and (iii) the "low-frequency coupling modes" with $\Omega \rightarrow 0$ when $\omega_p \rightarrow 0$. Both types of "coupling modes" are full three-dimensional perturbations and therefor vanish when $k = 0$ or $m = 0$ or when the longitudinal and the transverse perturbations are treated separately. The high-frequency coupling modes do not exist in the axisymmetric perturbations, and the low-frequency coupling modes exist only in the perturbations of even and zero m . The "usual transverse modes" found in the customary analyses[14] are similar to the lowest radial modes in class (i). When there is no strong necessity to distinguish the roots among the solutions of $U_j = 0$, we shall use the notation $T_{m,j}$ to represent the whole family of solutions associated with $U_j = 0$ for the m th azimuthal harmonic. The usual transverse modes will be referred to as the $T_{m,0}$ modes, the high-frequency coupling modes will be designated as $C_{m,j}$ modes, and the low-frequency coupling modes will be referred to as $L_{m,n}$ modes for $n \geq 1$, in the order of their first appearance in solving the dispersion relation using the $(2n-1) \times (2n-1)$ determinants.

NUMERICAL EXAMPLE

Here, we present a numerical example of the solutions to the dispersion relation (10) for some low radial modes associated with the dipole ($m = 1$) perturbation. Readers are referred to Ref. 1 for the numerical results of the axisymmetric modes. We consider only the case of $b/a = 1.5$ and $ka = 1$. The infinite determinants in the dispersion relation have to be truncated to finite ranks for a practical numerical computation. We limit our study to the first sixteen transverse modes, up to the $T_{1,3}$ modes, out of the sequence of an infinite number of the roots of Eq. (10). The real part of Ω/ν_o is shown in Fig. 1 as a function of tune depression ν/ν_o . Figure 2 shows the real part of Ω^2/ν_o^2 as a function of ν/ν_o in the high-intensity region. As shown in Fig. 1, that for all modes, the values of Ω/ν_o start from the solutions of $U_j = 0$ ($j = 1, 2$, and 3), i.e. from 1, 3, 5, and 7, at $\nu = \nu_o$, and decrease when the beam intensity increases. When $\nu \rightarrow 0$, the $T_{1,0}$ mode approaches the cold-beam limit, while the Ω/ν_o of the upper $T_{1,2}$ and $T_{1,1}$ modes approach 2, and the Ω of all other modes approach zero.

A kind of obvious mode interaction appears in the high-intensity region as confluences of modes where two or more modes have the same real part of frequencies. Among

the first sixteen roots, three confluences are found: the confluence of $T_{1,0}$ and $T_{1,2}$ near $\nu = 0.38\nu_0$, the confluence of $C_{1,1}$ and $T_{1,2}$ between $\nu = 0$ and $\nu = 0.26\nu_0$, and the confluence of two upper $T_{1,3}$ s between $\nu = 0.118\nu_0$ and $\nu = 0.52\nu_0$. The frequencies in the confluence regions are complex conjugate pairs indicating possible instability. In addition, the lowest $T_{1,1}$ mode, the two lower $C_{1,2}$ modes, and the two upper $T_{1,3}$ modes are unstable in the high-intensity region. The two upper $T_{1,3}$ s have the highest growth rate, about $0.72\nu_0$ at $\nu = 0.118\nu_0$ in the confluence and reaching $1.4\nu_0$ around $\nu \approx 0$. The lowest $T_{1,1}$ has the next highest growth rate of $0.088\nu_0$ near $\nu = 0.23\nu_0$. The confluence of $T_{1,0}$ and $T_{1,2}$ has a maximum growth rate of $0.001\nu_0$. We investigated the effect of resistive wall impedance and found that only the usual dipole mode, the $T_{1,0}$ mode, is appreciably influenced by the resistive wall impedance. The highest growth rate occurs near $\nu \approx 0$. In the case considered here, the maximal $|\text{Im}(\Omega/\nu_0)|$ of the $T_{1,0}$ mode has the values of 0.0, 0.034, 0.066, and 0.092, for $Z = 0.0, 0.1, 0.2$, and 0.3 , respectively.

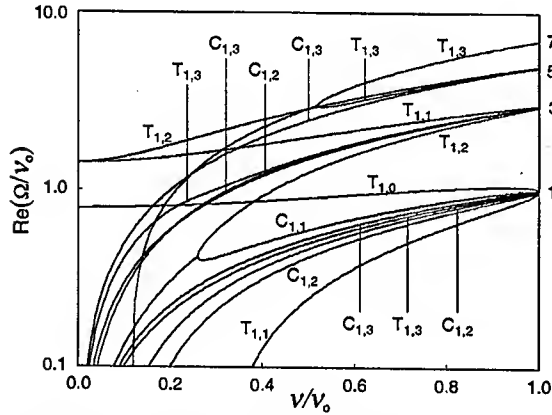


Figure 1: The real part of Ω/ν_0 for the first sixteen $m = 1$ modes versus ν/ν_0 for $ka = 1.0$, $b/a = 1.5$, and $Z = 0$.

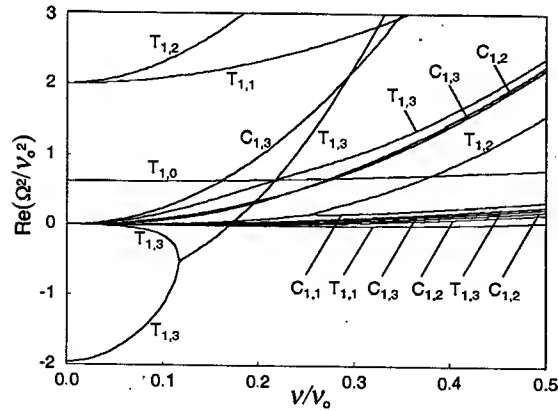


Figure 2: The real part of Ω^2/ν_0^2 for the first sixteen $m = 1$ modes as a function of ν/ν_0 in the high-intensity region for $ka = 1.0$, $b/a = 1.5$, and $Z = 0$.

CONCLUSIONS

We have studied the three-dimensional stability of a continuous beam with a KV distribution within the context of linearized Vlasov-Maxwell equations and electrostatic approximation. A dispersion relation has been derived to facilitate the investigation of any azimuthal mode. Two classes of coupling modes were discovered. The occurrence of mode confluences in the high-intensity region indicates possible instability. We have examined some lower radial modes of dipole perturbation and identified some unstable modes. In particular, we have found a confluence of the usual dipole mode and a previously studied transverse mode may cause weak instability. The highest growth rate of the dipole modes are higher than that of the axisymmetric modes previously studied. Since not all instability in a KV beam are realized, computer simulations are suggested for further investigation. The effect of resistive wall impedance was also studied for dipole modes. It was found that only the usual dipole mode is appreciably affected by the resistive wall impedance.

REFERENCES

- [1] T. F. Wang and L. Smith, *Particle Accelerators*, **12** (1982) 247.
- [2] I. Haber, D. A. Callahan, A. Friedman, D. P. Grote and A. B. Langdon, *Fusion Engn. and Design*, **32-33** (1996) 169.
- [3] S. M. Lund, D. A. Callahan, A. Friedman, D. P. Grote, I. Haber and T. F. Wang, *Proc. of the XIX Int. Linear Accelerator Conf.*, 1998, p. 372.
- [4] I. Haber, D. A. Callahan, A. Friedman, D. P. Grote, S. M. Lund and T. F. Wang, *Nucl. Instrum. Methods in Phys. Res.*, **A415** (1998) 405.
- [5] S. M. Lund and R. C. Davidson, *Phys. Plasmas*, **5** (1998) 3028.
- [6] I. Haber, A. Friedman, D. P. Grote, S. M. Lund and R. A. Kishek, *Phys. Plasmas*, **6** (1999) 2254.
- [7] R. C. Davidson and S. Strasburg, *Phys. Plasmas*, **7** (2000) 2657.
- [8] H. Qin, R. C. Davidson, W. W.-L. Lee and R. Kolesnikov, *Nucl. Instrum. Methods in Phys. Res.*, **A464** (2001) 477.
- [9] I. Haber, A. Friedman, D. P. Grote, S. M. Lund, S. Bernal and R. A. Kishek, *Nucl. Instrum. Methods in Phys. Res.*, **A464** (2001) 343.
- [10] R. C. Davidson, H. Qin, W. W.-L. Lee and S. Strasburg, *Nucl. Instrum. Methods in Phys. Res.*, **A464** (2001) 358.
- [11] E. A. Startsev, R. C. Davidson and H. Qin, *Phys. Plasmas*, **9** (2002) 3138.
- [12] R. L. Gluckstern, *Proc. 1970 Proton Linear Accelerator Conf.*, National Accelerator Laboratory, 1970, p. 811.
- [13] W. C. Hahn, *Gen. Elec. Rev.*, **42**, 258 (1939), and *S. Ramo, Phys. Rev.*, **56**, 276 (1939).
- [14] For example, see the discussion in SLAC Report SLAC-76, 1967, by M. J. Lee, F. E. Mills and P. L. Morton.

A NUMERICAL STUDY OF BUNCHED BEAM TRANSVERSE e-p INSTABILITY BASED ON THE CENTROID MODEL *

Tai-Sen F. Wang[†], LANL, Los Alamos, NM 87545, USA

Abstract

In a recent theoretical study of the transverse electron-proton (e-p) instability, an asymptotic solution has been found for the equations describing the centroid motion of the traversing proton bunch and the stationary background electrons.[1] It was shown that the combination of finite proton bunch length, non-uniform proton line density, and the single-pass e-p interaction cause the instability to evolve intricately in space and time even in the linear regime. This paper reports a numerical study of the e-p instability based on the same centroid equations. The purpose of the work is to compare the numerical solution with the analytic solution and to use the numerical approach to investigate the early development of the instability not covered by the asymptotic solution. In particular, the instability threshold and the initial growth of the instability are studied for various proton-beam conditions, fraction of charge neutralization, and initial perturbations.

INTRODUCTION

In recent years, there has been a growing interest in studying the transverse electron-proton (e-p) two-stream instability in intense proton beams. One of the focuses is on the e-p instability observed in the long proton bunch like the one in the Proton Storage Ring (PSR) at Los Alamos National Laboratory [2]. Although the basic mechanism of the instability has been well known, the theory for a bunched beam e-p instability is still under developing. In a recent theoretical study of transverse e-p instability, an asymptotic solution has been found for the equations describing the centroid motion of the traversing proton bunch and the stationary background electrons.[1] The growth rate and the stability threshold were estimated based on the asymptotic solution. As discussed in Ref. 1, the results derived from this kind of approach are applicable to special cases only. The initial evolution of the perturbations and the instability threshold still need more investigation. The work reported in this paper is a numerical study based on the centroid equations discussed in Ref. 1. We will compare the numerical results with the analytic solution and study the early development of perturbations in the proton bunch by investigating various proton-beam conditions, fraction of charge neutralization, and initial conditions. Since the numerical approach inevitably lacks generality, the intention here is to extract some qualitative understanding in a limited parameter space only.

* Research supported by Los Alamos National Laboratory under the auspices of the US Department of Energy.

[†] TWANG@LANL.GOV

CENTROID MODEL

We consider a bunched proton beam of full length L and circular cross section of radius a , propagating with a constant velocity v through a stationary electron background of infinite extent in the direction of beam propagation. The protons are confined in the transverse direction by a linear external focusing force. We assume that in the equilibrium state, particles are distributed uniformly in the transverse direction and the electrons experience a linear transverse focusing force due to the space charge of the proton bunch. A Cartesian coordinate system is chosen such that the z axis is pointing opposite to the direction of proton propagation, and the origin coincides with the center of the beam cross section. The line densities of the protons and electrons, λ_p and λ_e , generally depend on z . The synchrotron motion of the protons and the axial motion of the electrons in the laboratory frame are neglected for simplicity. We also neglect the impedance due to the beam environment, and consider the transverse motion in only one direction, say the y direction. The stability study is based on a model in which each electron interacts with the proton beam only once, i.e., a "one-pass" interaction between the electrons and protons.

The centroid of the proton beam $Y_p(z, t)$ and the centroid of electrons $Y_e(z, t)$ are defined by

$$Y_q(z, t) = \int_{-\infty}^{\infty} y_q(z, t, \omega_q) F_q(\omega_q) d(\omega_q / \Delta_q), \quad (1)$$

where the subscripts q stands for p (protons) or e (electrons), $y_q(z, t, \omega_q)$ is the particle displacement at the position z and time t , ω_q is the oscillation frequency, $F_q(\omega_q)$ is the frequency distribution function, and Δ_q characterizes the frequency spread of ω_q . We consider a Lorentzian distribution function $F_q(\omega_q) = (\Delta_q^2 / \pi) [\Delta_q^2 + (\omega_q - \omega_{q0})^2]^{-1}$, where ω_{q0} is the mean value of ω_q . Averaging over the equations of single particle motion yields

$$D^2 Y_p + 2\Delta_p D Y_p + (\omega_\beta^2 + \Delta_p^2) Y_p = \omega_\beta^2 \xi(z) Y_e, \quad (2)$$

and

$$\ddot{Y}_e + 2\Delta_e \dot{Y}_e + [\Omega^2(z) + \Delta_e^2] Y_e = \Omega^2(z) Y_p, \quad (3)$$

where $D = \partial/\partial t - v(\partial/\partial z)$, and ω_β is the undepressed betatron frequency, $\xi(z) = 2r_p c^2 \lambda_e(z) / (a^2 \omega_\beta^2 \gamma)$, $\Omega(z) = (c/a) \sqrt{2r_e \lambda_p(z)}$, is the electron bounce frequency, c is the speed of light, $\gamma = (1 - v^2/c^2)^{-1/2}$; r_p and r_e are the classical radii of a proton and an electron, respectively. In deriving Eqs. (2) and (3), we have also assumed that the incoherent betatron frequency shift due to the self-fields of the proton beam is negligible, and that the maximal value of λ_e is much smaller than that of λ_p , so that $\omega_{p0} = \omega_\beta$. The

perturbing forces are assumed to be $m_e \Omega^2(z) Y_p$ for electrons and $m_p \omega_\beta^2 \xi(z) Y_e$ for protons, where m_q is the relativistic mass of a proton or an electron. Note that Eqs. (2) and (3) depend on the choice of the frequency distribution functions.

An approximate asymptotic solution for Eqs. (2) and (3) in the beam frame is found to be

$$Y_p(z', t) \approx C_p M_p(z') e^{-\Delta_p t} \left\{ \left[\frac{I_1(u)}{u} - \frac{\mathcal{J}^2 I_2(u)}{8u^2} \right] \times \cos T_p - \left[\frac{J_1(u)}{u} - \frac{\mathcal{J}^2 J_2(u)}{8u^2} \right] \cos S_p \right\}, \quad (4)$$

where z' is the distance from the head of the proton bunch, $J_n(x)$ and $I_n(x)$ are Bessel functions, $u = \sqrt{2\theta} \mathcal{J}$, $\theta = \theta(z', t) = \omega_\beta(t - z'/v)$, $M_p(z') = \mathcal{J} \xi(z') R(z') \exp[(\Delta_p - \Delta_e)z'/v]$, $T_p = P - \theta$, $S_p = P + \theta$, $P = \sigma_p + \Theta(z') - \mathcal{J}/4$, C_p and σ_p are constants, $R(z')$ and $\Theta(z')$ are determined by $\Phi(x) = R(x)e^{i\Theta(x)}$ and $\Psi(x) = R(x)e^{-i\Theta(x)}$,

$$\mathcal{J} = \mathcal{J}(z') = i \int_0^{z'/v} \frac{\Omega^2(x) \xi(vx)}{W(x)} [R(x)]^2 dx, \quad (5)$$

$i = \sqrt{-1}$, $\Phi(x)$ and $\Psi(x)$ are the linearly independent solutions of the equation $d^2 Y/dx^2 + \Omega^2(x) Y = 0$, and $W(x)$ is the Wronskian of $\Phi(x)$ and $\Psi(x)$. In deriving Eq. (4), we have assumed that $Y_e = dY_e/dt = 0$ for $z' \leq 0$. The solution for Y_e is very similar to Eq. (4). The growth (or damping) rate $\Gamma_p(z', t)$, and the stability threshold of the proton motion $(\Delta_p)_t$, can be estimated from Eq. (4) as

$$\Gamma_p(z', t) \approx -\Delta_p + \frac{\omega_\beta \mathcal{J} [8u I_2(u) - \mathcal{J}^2 I_3(u)]}{u [8u I_1(u) - \mathcal{J}^2 I_2(u)]}, \quad (6)$$

and

$$(\Delta_p)_t \approx \text{Max} \left[\frac{\omega_\beta \mathcal{J}}{4} \left(\frac{1 - \mathcal{J}^2/48}{1 - \mathcal{J}^2/32} \right) \right], \quad (7)$$

where $[Y_p(z', t)]_a$ denotes the amplitude of $Y_p(z', t)$, and $\text{Max}[f(z')]$ indicates the maximum of $f(z')$. For $u \gg 1$, we have $\Gamma_p(z', t) \approx \omega_\beta \sqrt{\mathcal{J}/(2\theta)} - \Delta_p$. Typically, $\mathcal{J} < 1$ for a small fractional charge neutralization, $\Gamma_p(z', t)$ is a monotonically decreasing function of time, and the highest growth rate occurs at the tail of the proton bunch. Eqs. (6) and (7) are valid only when the centroid motion can be described by the asymptotic solution given in Eq. (4).

NUMERICAL STUDY

The study here is based on the numerical solution of Eqs. (2) and (3). Earlier numerical studies as well as simulations using the similar equations, including the variations that cover multi-electrons and electron production, have yielded reasonable agreement with experimental data.[3,4]

Comparison between numerical results at large time and the asymptotic solution given in Eq. (4) shows good qualitative agreements: the growth rate depends linearly on Δ_p as a consequence of choosing the Lorentzian frequency spreads, the perturbation wavelength along the proton bunch is roughly proportional to the square root of the

proton line density, and the damping of instability in the long time as described in the analytic solution. At large t , the numerical solutions show that the growth or the damping rate depends weakly on Δ_e .

Our main interest is to investigate the initial evolution of perturbations. The following is a summary of general characteristics observed in the numerical solutions:

(i) The initial growth or damping rate does depend on Δ_e . The dependence diminishes as time increases. This result is not covered by the asymptotic solution in Eq. (4).

(ii) The dependence of the growth rate on Δ_p is not affected by the initial conditions.

(iii) Since the growth rate given in Eq. (6) is a local quantity, and because we are considering the one-pass interaction between the electrons and the protons, initial perturbations with quarter wavelength comparable to the bunch length have strong influence on the initial growth rate. Further, the growth rate at any location is not affected by the perturbations behind. Typically, constant-amplitude (or constant-envelope) sinusoidal perturbations with wavelength substantially smaller than the bunch length are initially damped at a rate near Δ_p . For similar perturbations having tilted envelope, the initial damping rate is shifted from Δ_p by certain amounts with a sign opposite to that of envelope's slope. The initial slope of the damping rate also shows the same kind of dependence on the envelope of initial perturbations.

(iv) In the beginning, there is a transient period before the centroid motion, and hence the growth rate, is evolved into the asymptotic regime. During this transient period, the evolution of the growth rate depends on the density profile and other parameters in a complicated way, e.g. the growth rate may oscillate. The system stability can not be judged base on the momentary sign of the growth rate.

(v) The length of the transient period for the growth rate to evolve into the asymptotic regime appears to be independent of Δ_p . Variations of other parameter values, like the fraction of neutralization, that make the system less stable tend to shorten the transient period.

(vi) The initial growth rate estimated in Eq. (6) is usually much higher than the simulation results. Estimates of stability threshold made by using Eq. (7) appear to be too conservative in general.

As an example, we focus our study here on a few specific density profiles and initial conditions with Δ_p and proton intensity chosen near the stability threshold. Thus, we consider a constant λ_e and four types of λ_p : constant, elliptical, parabolic, and quartic (parabolic squared). Four initial perturbations on the proton centroid are investigated: wavelength proportional to $\sqrt{\lambda_p}$, noise, 100 MHz, and 250 MHz. All four initial perturbations have a same constant envelope. The electron centroid was assumed to be unperturbed when entering the proton bunch. The following PSR parameter values were used for computation: $\gamma = 1.85$, $a = 1.5$ cm, the circumference $C = 90$ m, 2.74×10^{13}

protons per bunch, $\omega_\beta = 40$ MHz, and $L/v = 200$ ns (for a short bunch). We assume $\Delta_p = 0.125\% \omega_\beta$, $\Delta_e = 1.25\omega_\beta$, and a flat amount of electrons corresponding to a 2% of charge neutralization in the case of constant proton line density. For the four types of λ_p considered here, the peak electron bounce frequency in the proton bunch is between 100 MHz and 200 MHz.

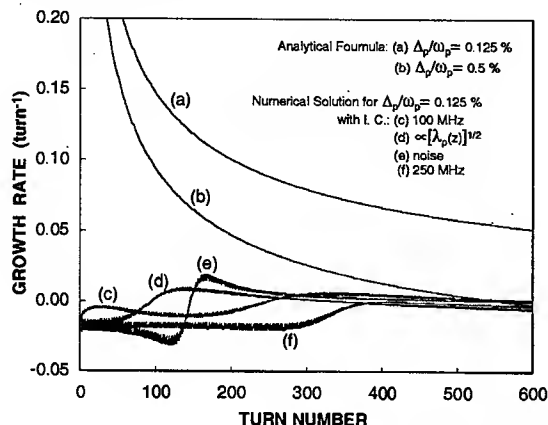


Figure 1: The growth rate at the tail of the proton bunch as a function of the turn number in PSR for different initial conditions and the growth rate computed using Eq. (6). Parabolic proton line density is considered here.

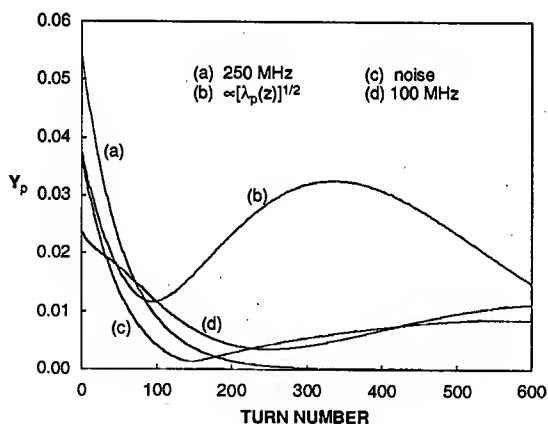


Figure 2: The amplitude of oscillation for the proton centroid is shown as a function of the turn number in PSR for the cases considered in Fig. 1. The ordinate has an arbitrary unit.

Shown in Fig. 1 is the growth rate at the tail of the proton bunch as a function of the turn number in PSR for different initial conditions and parabolic proton line density. The growth rate computed using Eq. (6) is also shown for comparison. The corresponding amplitude of proton centroid oscillation is shown in Fig. 2. Figure 3 shows the growth rate at the tail of the proton bunch as a function of the turn number for different proton line densities and a same noise initial condition. It is seen that the initial perturbation with wavelength proportional to $\sqrt{\lambda_p}$ is the least

stable one among the four initial conditions considered.

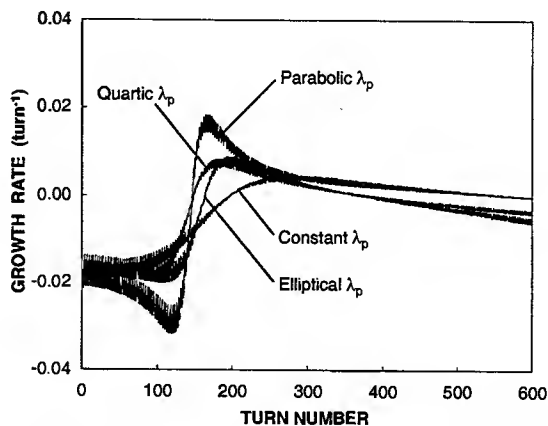


Figure 3: The growth rate at the tail of the proton bunch as a function of the turn number in PSR for different proton line densities and a same noise initial condition.

CONCLUSIONS

We have carried out a numerical study of the transverse e - p instability using the centroid equations derived from Lorentzian distribution of particles' oscillation frequencies and the model of one-pass interaction between the stationary electrons and traveling proton bunch. Numerical results were compared with the asymptotic solution. Good qualitative agreements were found when the initial perturbation in the numerical solution is evolved into the asymptotic regime at large time. The initial evolution of perturbations was investigated for various proton line densities and initial conditions of the proton bunch. Some qualitative understanding has been acquired from these numerical solutions. Notably, we found that the asymptotic solution tend to overestimate the growth rate and the frequency spread of proton oscillation required for stability in general. Thus, unlike the situation in analyzing a usual beam stability, the extrapolation of the growth rate from the asymptotic regime to the initial state is much more restricted for the e - p instability in a bunched beam of non-uniform line density. We also found that the perturbations with frequency below the peak electron bounce frequency have stronger influence on the initial growth rate than the high-frequency perturbations.

REFERENCES

- [1] T. Wang, P. J. Channell, R. J. Macek, and R. C. Davidson, Phys. Rev. ST Accel. Beams, **6**, 014204 (2003).
- [2] Articles in Two Stream Special Collection, Phys. Rev. STAB, Ed. R. C. Davidson and R. J. Macek, and the references cited therein.
- [3] T. Wang, AIP Conf. Proc. 496, p. 305 (1999).
- [4] T. Wang, Proc. of 1995 Particle Accelerator Conf., p. 3143.

RF IMPEDANCE MEASUREMENTS ON THE DARHT-II ACCELERATOR INTERCELL ASSEMBLY*

W.M. Fawley[#] and S. Eylon, LBNL, Berkeley, CA 94720-8211 USA
R. Briggs, SAIC, Walnut Creek, CA 94596 USA

Abstract

We report upon recent experimental measurements made of RF properties of the intercell assembly of the second axis accelerator[1] of Dual Axis Radiographic Hydrodynamic Test (DARHT) facility at LANL. The intercells provide both pumping and diagnostic access to the main DARHT-II beamline. Their design includes a pumping plenum separated from the main beam pipe by return current rods together with RF shielding provided by a copper-coated stainless steel mesh. Measurements using the twin lead technique (see Ref. [2]) at low frequencies ($f \leq 200$ MHz) suggest a constant value for the ratio η of the radial and azimuthal magnetic field components to which the transverse impedance is linearly related. We find that these results compare favorably to predictions from a simple analytic, lumped circuit model which includes the effects of the mesh and return current rods. We also present RF loop-to-loop frequency scans above beam pipe cutoff (~ 600 MHz) showing the existence of many RF modes with relatively high Q 's.

INTRODUCTION

The main function of the intercell assemblies on the DARHT-II accelerator is to provide both adequate pumping and diagnostic access to the beamline between cell blocks. The intercell design also must provide a low impedance path for the electron beam return current, and adequate RF shielding of the beam from possible high Q RF modes in the pumping plenum box. In this paper we describe recent measurements of both the impedance and the RF mode structure of the intercell assembly. We first describe the intercell design and then summarize analytic predictions for the effective impedance of the wire mesh. We then describe our measurement setup and technique followed by the twin lead impedance results at low and high frequencies.

EVOLUTION OF THE DARHT-II INTERCELL DESIGN

Originally, the intercells in DARHT-II were to be spaced every eight accelerator cells but then, due to ion hose growth concerns, the spacing was reduced to every six, thus increasing the pumping effectiveness by a ratio $(8/6)^2$. The electron beam current return path across the intercell is provided by eight, 1/4"-diameter, stainless steel return current rods spaced uniformly in azimuthal angle around the pumping plenum opening at the beam tube radius ($\approx 5"$). Then non-specific concerns about the

possible existence of high frequency, high Q , RF modes in the pumping plenum led to a request that RF shielding consisting of a conducting mesh be placed around the return current bars. The selection of wire mesh parameters involved tradeoffs, since the "geometrical transparency" of this mesh needed to be as high as possible for pumping effectiveness but the larger the mesh holes, the larger the effective RF impedance. Some initial analysis and calculations were then done concerning the impedance of a mesh. The mesh chosen was a square 20-mm grid composed of 0.56-mm diameter stainless steel wire resulting in a geometrical transparency of about 94%. It was then speculated that since the (effective) dipole L/R time of the SS mesh might be less than one microsecond, transverse resistive wall type amplification of low frequency corkscrew displacements, *etc.*, might be an issue and the mesh was coated with approximately 1 mil of copper to reduce its resistance. In all, there are 11 intercells in DARHT-II, 4 with and 7 without solenoid magnets. Figure 1 shows a CAD representation of the intercell structure and its components.

ANALYTIC RF IMPEDANCE MODEL FOR THE WIRE MESH

We developed a simple analytic model to estimate the effective RF impedance of the wire mesh/return current rod assembly. First, we presume that at RF wavelengths much greater than the wire spacing s , the mesh impedance is dominated by the self-inductance (which is associated with the time-dependent magnetic field in the mesh openings) and the wire resistance. The transverse interaction impedance of a gap region of length w

$$Z_{\perp} = -j \sqrt{\frac{\mu}{\epsilon_0}} \frac{w}{\pi b^2} \eta$$

where b is the beam pipe radius and η is a complex dimensionless number giving the ratio of radial magnetic field in the gap to azimuthal magnetic field at the wall several beam pipe radii away from the gap. For a mesh-covered gap at relatively low frequencies, η scales as:

$$\eta \approx -\frac{H_r|_{r=b}}{K_{z0}} = -\frac{s\Lambda_m}{2\pi b}$$

Here K_{z0} is the surface-area-averaged dipole return current, s is the mesh spacing, and Λ_m is a logarithmic factor relating the magnetic energy around the mesh wires (with radius ρ) to their lumped inductance:

$$\Lambda_m \approx \ln\left(\frac{s}{2\rho}\right)$$

*Work supported by U.S. DOE under Contract No. DE-AC03-76SF00098.
[#]IWMFawley@lbl.gov

Note that this formulation is for TM-like modes; since E_θ is shorted out by the wire mesh, TE-like modes should be strongly suppressed. The 8 thick, return current rods also contribute to the inductance; putting this in parallel with the mesh inductance reduces η by ~ 1.5 resulting in an estimated final value of $|\eta| = 0.045$. A key result here is that the low frequency impedance is predicted to be independent of frequency in the range of validity of the model.

EXPERIMENTAL SETUP AND TECHNIQUE

A "twin-lead/twin loop" technique was used to measure the transverse RF impedances of the intercell structure, similar to that previously used to measure DARHT-II accelerator cell transverse impedances (see Refs. 2 and 3). A production intercell was mounted on a support stand with 3-foot long, 10"-inner diameter "surrogate" beam tube sections clamped on both ends. A 2-meter long twin lead made of two, 1/2"-diameter copper tubes with their centers transversely spaced 1.5" apart was placed on the longitudinal axis of the system. The twin lead was excited by the +/- output from a balun, itself driven by output from a HP-8751A network analyzer. The twin lead was terminated at the other end in its characteristic (TEM mode) impedance (about 214 ohms). A "spider" of resistors connected the midpoint of the 214-ohm resistor to the tube (ground) in order to match any "monopole" (*i.e.* common mode) currents (+,+) that might be generated (see Ref. [3]). Termination in the characteristic impedance ensures that the dipole RF fields will be in the form of a traveling wave, which simulates the transverse fields of a relativistic beam with a transverse displacement oscillating (in the laboratory frame) at frequency f .

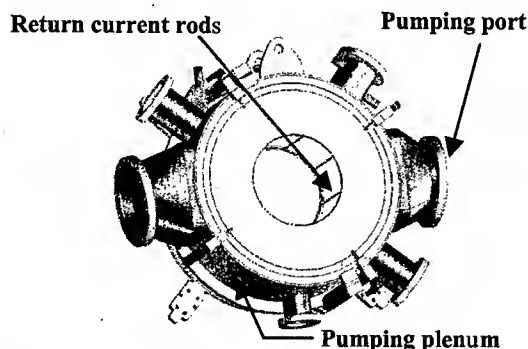


Fig. 1 – Depiction of DARHT-II Intercell Assembly

A small loop (a 3/8" ID loop made with a miniature coax wrapped in a circle) was used for the impedance measurements over the full frequency range (*i.e.* 1-2000 MHz) highlighted in the following section. Each loop was attached in one of two possible configurations to the end of a solid copper coax and then inserted into the pumping plenum through the one of the diagnostic ports (see Fig. 1). One configuration had the loop axis perpendicular to

the coax line and was used to detect the B_θ or B_z field components. The other configuration involved the loop being bent at 90 degrees in order to detect B_r . Each type of loop could be inserted through the wire mesh to measure fields on the inside "beam tube" region as well as the outside pumping plenum region. The twin lead was oriented azimuthally in the tube so that one of the diagnostic ports would be aligned with the maximum B_r component (perpendicular to the plane of the twin lead), while another (*i.e.* orthogonal) diagnostic port would be located at the maximum of B_θ . In order to measure the low level RF signals in the plenum region, we had to wrap tin foil shields over the twin lead input and termination ends to minimize stray RF emission.

To make a quick survey of the resonant frequencies and Q 's of RF modes localized primarily in the plenum pumping box region, we used the usual loop-to-loop coupling method (see, *e.g.*, Ref. [3]). The B_r and B_θ loops were each inserted radially about halfway into the plenum through different diagnostic ports, with the feed coax clamped to the side of the port (the twinlead assembly was removed for these particular measurements). The B_θ loop was driven by the network analyzer while the B_r loop was used as the pickup.

RESULTS

Figures 2&3 show typical frequency scan data obtained with the B_θ and B_r loops. The RF field amplitude scale changed by a factor of 20-40 between the measurements made inside the mesh compared with those made outside.

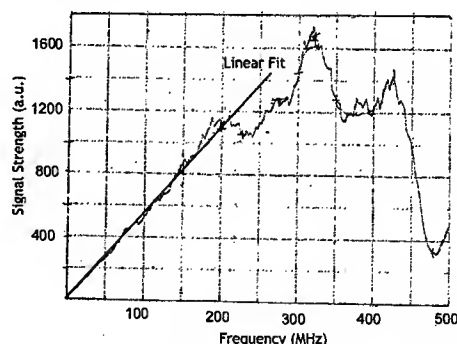


Fig. 2 - B_θ measured inside wire mesh at $r = 4.625$ ".

Both inside and outside the mesh,, the loop signals rose linearly with frequency up to about 200 MHz at all radial positions. This behavior implies that η is independent of frequency over this "lower frequency band", in agreement with the predictions of the simple analytic model discussed above. At frequencies above ~ 200 MHz, the RF magnetic fields of the twin lead inside the mesh showed both a general decrease in amplitude and an oscillatory structure versus frequency. These oscillations are likely

due to a combination of mismatches at the higher frequencies and excitation (possibly due to stray inductances) of common mode currents on the twinlead.

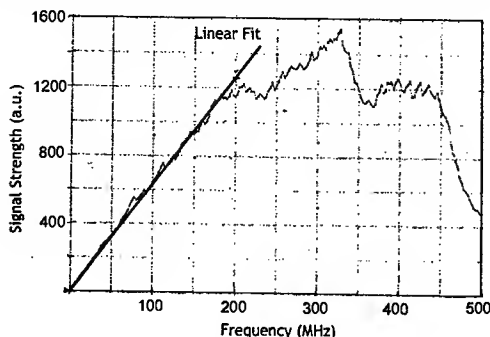


Fig. 3 - B_r measured inside wire mesh at $r = 2.875''$.

The fields deep inside the plenum, on the other hand, drop little at higher frequency. This implies that the RF field penetration through the mesh and the magnitude of the transverse impedance ($\propto \eta$) both increase with frequency in this range.

A value for η may be determined by extrapolating a value for B_r inward to the mesh radius from data outside the mesh and a value for B_θ outwards to the mesh from data inside the mesh. The result as a function of frequency is displayed in Fig. 4 and shows virtual no dependence upon f below 200 MHz as expected analytically.

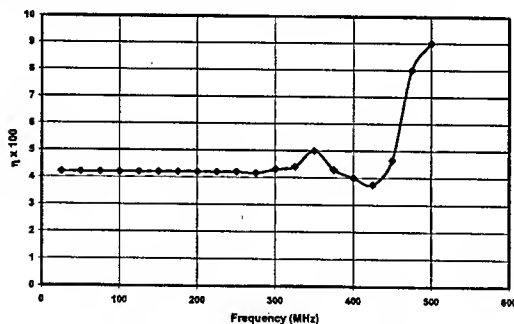


Fig. 4 - Reduced η factor from twinlead data

HIGH FREQUENCY MEASUREMENTS

We made several twin lead high frequency (0.5 to 2.5 GHz) scans of the network analyzer pickup signal (S_{12}) in the intercell plenum. For some of the "stronger" resonances, Q 's were measured and found to be as large as ~ 800 . As might be expected from applying a simple analytic pillbox model with the 6.5" radial separation of the mesh from the outer plenum boundary at 11.5", the resonant frequencies of the modes appearing in these scans are all above 800 MHz. Figure 5 shows a sample measurement; in this particular case, conducting plates were clamped over the pumping ports. When the conducting plates were removed, the Q 's dropped ~ 4 -fold. The 1.69 GHz mode was common to both cases with a Q

value of (680, 140) for plates (on,off). Since the actual pump boundary is relatively far away, we believe the "plate-off" case is more likely to be representative of the actual situation in a working DARHT-II intercell. Due to time constraints, we were unable to investigate the mode field structure and could not determine the relevant Z_{11} .

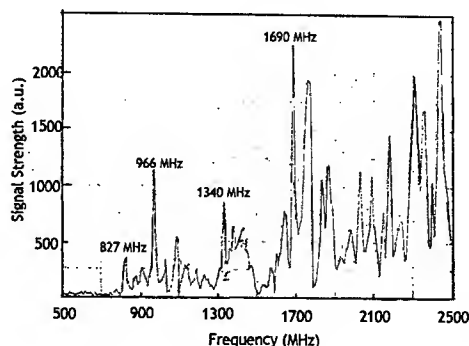


Fig. 5 - High frequency scans of the intercell plenum

CONCLUSIONS

Our twin lead measurements at frequencies below beam pipe cutoff (690 MHz) show no indication of dangerous resonant modes. In general the impedances are low with η values ranging from 0.04 to 0.08. Compared with an individual accelerator cell, each intercell has a reactive impedance ~ 3 times smaller. At the lower frequencies the measurements are in good agreement with simple analytic models of the shielding effects of the wire mesh.

From our preliminary RF mode studies at frequencies above cutoff we found that there is a "forest" of relatively high Q modes in the intercell above 800 MHz or so. It is possible (but not at all certain!) that one of these could couple to the beam (although early commissioning results at ~ 1.3 kA do not show any obvious beam transport difficulties from such high frequency modes). We suggest that the DARHT-II commissioning team insert some RF loops in diagnostic ports of one or more of the intercells to monitor the RF behavior.

REFERENCES

- [1] C. Ekdahl *et al.*, "DARHT-II Commissioning Results", Paper ROAC008, this conference.
- [2] R. Briggs *et al.*, "Transverse Impedance Measurements of the DARHT-2 Accelerator Cell", PAC2001, Chicago, June 2001, p.1850.
- [3] D. Bix, R. Briggs, and L. Reginato, "BBU Impedance Measurements on the DARHT-2 Cell", LBNL-42876, 1999.

THE STABILIZATION OF BUDKER-CHIRIKOV INSTABILITY BY THE SPREAD OF LONGITUDINAL VELOCITIES

Yu.Ya. Golub,

Moscow Radiotechnical Institute, 132 Warshavskoye shosse, 113519 Moscow, Russia,

E-mail: yurigolub@mtu-net.ru

Abstract

The two-beams electron - ion system consists of a nonrelativistic ion beam propagating co-axially with a high-current relativistic electron beam in a longitudinal homogeneous magnetic field [1]. The effect of spread of longitudinal velocities of an electron beam on instability Budker-Chirikov (BCI) in the system is investigated by the method of a numerical simulation in terms of the kinetic description of both beams. The investigations are development of investigations in [2].

Is shown, that the increasing of spread of longitudinal velocities of electron beam results in the decreasing of an increment of instability Budker-Chirikov and the increasing of length of propagation of a electron beam.

1 BASIC EQUATIONS

We investigate a two-beam electron-ion system consisting of a nonrelativistic ion beam propagating co-axially with a high-current relativistic electron beam. The both beams are injected in equilibrium into drift tube. The spread of longitudinal velocities of an electron beam are took place. The kinetic description- of both beams is provided by means of solutions of the Vlasov equations for the electron and ion distributions functions, $f_{e,i}(t, z, r, v_z, v_r, v_\theta)$. The equations for the scalar potential and the three component of the vector potential are used for finding the electromagnetic fields. The equations are solved in the long-wave ($\partial^2/\partial z^2 \ll \Delta_\perp$), low-frequency ($\partial^2/\partial t^2 \ll c^2 \Delta_\perp$), axial-symmetric ($\partial/\partial \theta = 0$) case. where Δ_\perp is the transverse part of the Laplace operator. Boundary conditions for the potentials fellow from the system's axial symmetry, the presence of conducting tube with radius R and the gauge condition $\text{div } A = 0$. The Vlasov equations are solved by the macroparticle method. It is assumed that the steady-state process is periodic in time set with a frequency ω . In this case it is convenient to use the longitudinal coordinate z as the independent variable, using the relation $d/dt = (1/v_z) d/dz$, where v_z is the velocity of a given macroparticle. The problem is then reduced to the evolution of a periodic-in-time system on z .

The periodic in time (with frequency ω) potential function are of the form

$$G(t, z, r) = \bar{G}(z, r) + \text{Re} \left\{ \sum_j \bar{G}_j(z, r) \cdot e^{i j \omega t} \right\}$$

which is substituted into the equations for the potential components and integrated over a time period. The equations for the four components of the 4-potential A_i , ($\Delta_\perp A_i = 4\pi \rho_i$, $i = 1, 2, 3, 4$ Δ_\perp is the radial parts of the Dalmber operator, and ρ_i are the components of the 4-density) are solved at every z -cross-section by the grid method.

The electron beam was divided into a number of fractions, which have different longitudinal velocities. The amount of fraction is odd number. Each fraction distinguish from another on the same velocity. One from the fractions have velocity, which is equal to the average electron beam velocity. The others fractions are symmetrical arrangement in pairs around of the fraction with average velocity. The quantity of the spread of longitudinal velocities of an electron beam is equal to difference between the last fraction and average velocity divided on average velocity and multiply on 100%.

2 BCI INSTABILITY

The important of the instabilities in the two-beam electron-ion system are the Budker-may be solved by using of ion beam undulator. We investigate the ion - beam undulator which Chirikov instability (BCI) [3,4]. They are connected with the resonance of the slow-cyclotron wave of tile electron beam and the fast Langmure wave and fast betatron wave of the ion beam, respectively. Unlike [1], the spread of longitudinal velocities of an electron beam are took place.

The Budker-Chirikov instability take place in that case. The instability in the time periodic regime is displayed in the growth of the radial modulation amplitude of both beams along the longitudinal coordinate. Also the BCI is developed in exponential growth of the potential amplitude. The BCI increment decreases with the increase in spread of longitudinal velocities of an electron beam.

The dependence of space increment E of BCI on the spread of longitudinal velocities of an electron beam is shown in Fig. 1. The electron beam current $J = 0.5$ kA, ion longitudinal velocity $b = 0.03$, average relativistic factor $\gamma = 3$, longitudinal magnetic field 1 kG, the drift tube radius $R = 1.5$ cm, ion beam density $n_i = f \cdot n_e$, $f = 1/9$, the electron and ion beam radii $= 0.6 \cdot R$. The resonance frequency is to the increment maximum.

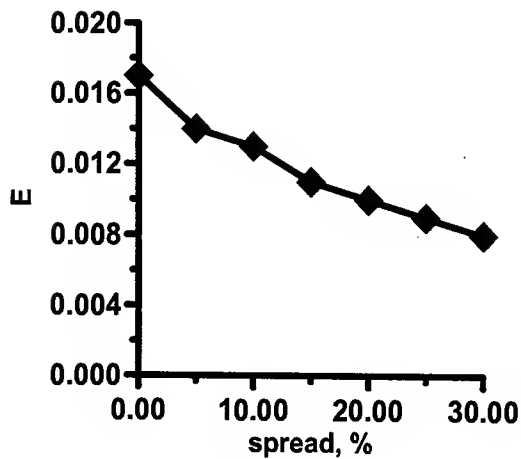


Fig.1: The dependence of space increment E of BCI on the spread of longitudinal velocities of an electron beam is shown in Fig. 1.

We see in Fig.1, that the BCI increment is decreased with decreasing of the ion beam radius. Because amount of electrons in resonance is increased.

If the spread of longitudinal velocities of an electron beam are large than 15%, BCI is saturation by nonlinear mechanism [1]. Electron beam don't destroy, if the spread of longitudinal velocities of an electron beam are large than 15%. Thus electron beam with the spread of longitudinal velocities must propagate without destruction with the ion beam.

REFERENCES

- [1]. Yu.Ya. Golub, N.E.Rozanov, Nuclear Instruments and Methods in Physics Research, A358 (1995) 479
- [2] Yu.Ya. Golub, Proceedings of EPAC 2002, Paris, France, 1497
- [3] G.I. Budker. Atomnaya energiya 1 (1956) 9
- [4] B.V. Chirikov, Atomnaya energiya 19 (1965) 239

NEW VORTICES IN AXISYMMETRIC INHOMOGENEOUS BEAMS

Yu.Ya. Golub,

Moscow Radiotechnical Institute, 132 Warshavskoye shosse, 113519 Moscow, Russia,

E-mail: yurigolub@mtu-net.ru

Abstract

We analyzed localized vortices in non-neutral inhomogeneous by density and velocity electron beams propagating in vacuum along the external magnetic field. These vortices distinguish from well-known vortices of Larichev-Reznik or Reznik types, which used in [1]. New types of vortex are obtained by new solution method of nonlinear equations. The new method is development of a method described in [2]. That method distinguish from standard Larichev-Reznik or Reznik method, which used in [1]. It has been found new expression for electric field potential of vortex in a wave frame. The expression is axisymmetric in a wave frame. New vortices are new solitons. New vortices are the result of external disturbances or the appearance and development of instabilities like for example a diocotron instability in hollow beams and a slipping-instability in solid beams.

1 BASIC EQUATIONS

We investigate the nonrelativistic electron beam, which propagating in vacuum along the external homogeneous magnetic field B_0 in z -direction of cylindrical coordinate system (r, θ, z) . An equilibrium and homogeneous by θ and z state of the system is characterized by radial distributions of electron density $n_0(r)$ and velocity $v_0[0, v_{0\theta}(r), v_{0z}(r)]$ and the electron field potential $\phi_0(r)$. We assume $\omega_c^2 \gg \omega_p^2$, where ω_p - the plasma electron frequency, ω_c - the electron cyclotron frequency.

We investigate the nonsteady state of the system characterized by the deviations n, v, ϕ from equilibrium values of n_0, v_0, ϕ_0 . The solution of the motion and continuity equations for the particles and Poisson equation for the electric fields potential we choose in the form of a travelling wave in which all the parameters are functions of the variables r and $\eta = \theta + k_z z - \omega t$ with the constant wave number k_z and frequency ω . If we neglect by inertial drift of the electrons due to large value of ω_c , we obtain equation as in [3]:

$$\left\{ \Delta_{\perp} \phi - \Lambda \phi + S \phi^2, \phi - \frac{\omega_d B_0}{2c} r^2 \right\}_{r, \eta} = 0 \quad (1)$$

where

$$\{f, g\}_{r, \eta} = \frac{1}{r} \left(\frac{\partial f}{\partial r} \frac{\partial g}{\partial \eta} - \frac{\partial f}{\partial \eta} \frac{\partial g}{\partial r} \right)$$

$$\Lambda = -\frac{k_z(k_z + k_v)\omega_p^2}{\omega_d^2} - \frac{k_n \omega_p^2}{v_0 \omega_d}$$

$$S = \frac{k_z}{2} \left(\frac{(k_z + k_v)e}{m \omega_d^2} \right)^2$$

$$k_v = \frac{1}{\omega_c r} \frac{dv_{0z}}{dr}$$

$$k_n = \frac{v_0}{\omega_c r} \frac{dn_0}{dr} \quad v_0 = v_{0z}(0)$$

$$\omega_d = \omega - k_z v_{0z} - \frac{v_{0\theta}}{r}$$

m and $-e$ - the electron mass and charge, c - is the speed of light. Δ_{\perp} is the transverse part of the Laplace operator.

2 LOCALIZED VORTICES

In [4-5] Larichev V.D. and Reznik G.M. solved the equation (1) only then, when neglected term $S \phi^2$. Thus they obtain solution known as Larichev-Reznik. But we don't neglect that nonlinear term. We obtain nonlinear equation

$$\frac{\partial^2 \phi}{\partial r^2} + \frac{1}{r} \frac{\partial \phi}{\partial r} - \Lambda \phi + S \phi^2 = 0. \quad (2)$$

The nonlinear equation (2) is distinguish from KdV and Bessel. We obtain the approximate solution the equation (2) by original method. The method is the functional iteration method. The next $(n+1)$ iteration obtain from equation:

$$\phi^{(n+1)} = \phi^{(n)} + \text{sign}(\tau^{(n)}(0)) * \frac{1}{\Lambda} (\tau^{(n)}(r)) \quad (3)$$

where $\tau^{(n)}$ - the residual of $\phi^{(n)}$ in (2):

$$\tau^{(n)} = \left(\frac{\partial^2 \varphi^{(n)}}{\partial r^2} - \Lambda \varphi^{(n)} + \frac{1}{r} \frac{\partial \varphi^{(n)}}{\partial r} + S(\varphi^{(n)})^2 \right),$$

$\varphi^{(0)}$ is the solution for KdV equation:

$$\varphi^{(0)} = \frac{3\Lambda}{2S} \frac{1}{\left(\operatorname{ch} \left(\frac{\sqrt{\Lambda}}{2} r \right) \right)^2}$$

The equation for first iteration:

$$\varphi^{(1)} = \varphi^{(0)} - \frac{1}{\Lambda} \left(\frac{\partial^2 \varphi^{(0)}}{\partial r^2} - \Lambda \varphi^{(0)} + \frac{1}{r} \frac{\partial \varphi^{(0)}}{\partial r} + S(\varphi^{(0)})^2 \right)$$

First iteration $\varphi^{(1)}$

$$\varphi^{(1)} = \frac{3\sqrt{\Lambda} \left(\sec h \left(\frac{\sqrt{\Lambda} r}{2} \right) \right)^2 \left(\sqrt{\Lambda} r + \tanh \left(\frac{\sqrt{\Lambda} r}{2} \right) \right)}{2Sr}$$

That iteration $\varphi^{(1)}$ is the approximate solution the equation (2). We can obtain $\varphi^{(2)}$, then $\varphi^{(3)}$, et al. The iterations $\varphi^{(2)}$ and $\varphi^{(3)}$ is the approximate solution the equation (2). The second iteration equation $\varphi^{(2)}$

$$\varphi^{(2)} = \frac{1}{\Lambda} \left(\frac{\partial^2 \varphi^{(1)}}{\partial r^2} + \frac{1}{r} \frac{\partial \varphi^{(1)}}{\partial r} + S(\varphi^{(1)})^2 \right)$$

The dependence of $\varphi^{(0)}$ - dot line, $\varphi^{(1)}$ - solid line, $\varphi^{(2)}$ - dash dot line, $\varphi^{(3)}$ - dash line - on the radius r is shown in Fig. 1 for $\Lambda=1 \text{ cm}^{-2}$ and $S=1 \text{ cm}^{5/2} \text{ g}^{-1/2} \text{ sec}$. We see that the maximum amplitude $\varphi^{(n)}$ approach to constant with increase n .

We see that the $\varphi^{(1)}$ and $\varphi^{(2)}$ are closely to $\varphi^{(3)}$. Thus the functional iteration method for the approximate solution have convergence.

Thus we obtain the approximate solution, which exponentially decreases with radius r . That approximate solution is continuous function in first differential in contrast to Larichev-Reznik solution. That approximate solution is near KdV solution at large r . It has been found new expression for electric field potential of vortex in a wave frame. The expression is axisymmetric in a wave frame. New vortices are the result of external disturbances or the appearance and development of instabilities like for example a diocotron instability in hollow beams and a slipping-instability in solid beams.

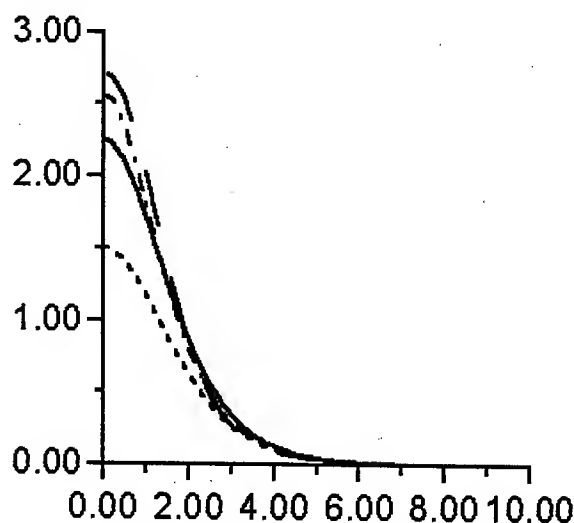


Fig.1: The dependence of $\varphi^{(0)}$ - dot line, $\varphi^{(1)}$ - solid line, $\varphi^{(2)}$ - dash dot line, $\varphi^{(3)}$ - dash line - on the radius r .

REFERENCES

- [1]. Golub Yu.Ya., Nikulin M.G., Rozanov N.E. In: Nonlinear world: IV Intern. Workshop on Nonlin. and Turbul. Proc. in Phys., (ed. by V.G. Bar'yakhtar et al) World Scientific Publishing Co. Pte. Ltd., Singapore, 1990, vol. 2, p.857
- [2] Golub Yu.Ya., Proceedings of EPAC 2002, Paris, France, 1253
- [3]. Aburdzhaniya G.D., Kamenetz F.F., Lakhin V.P., Mikhailovskii A.B. and Onishchenko O.G. Phys. Lett. 105A (1984) 48
- [4] Larichev V.D. and Reznik G.M. Dokl.Akad. Nauk SSSR 231 (1976) 1077
- [5] Reznik G.M. Dokl.Akad. Nauk SSSR 282 (1985) 981

BEAM INSTABILITIES AT THE PLS STORAGE RING

Eun-San Kim, Pohang Accelerator Laboratory, POSTECH, Pohang, 790-784 Korea

Abstract

A simulation method to obtain beam tail distribution and beam lifetime in electron storage rings has been applied to the 2.5 GeV Pohang Light Source. The simulations were performed to obtain transverse and longitudinal tail distributions due to beam-residual gas bremsstrahlung, beam-residual gas scattering and intra-beam scattering at the Pohang Light Source. The beam lifetime that is obtained by the simulation is estimated to be around 19 hours in beam current of 180 mA. It is shown that the simulated beam lifetimes well agree with those of on normal operation.

INTRODUCTION

The distribution of particles in a bunch can be divided into two regions: the core region at small amplitudes and the tail region at large amplitudes. The core distribution determines the brilliance in the synchrotron light source and the tail distribution may affect the beam lifetime. A simple and fast simulation method was proposed to obtain the beam tail due to rare random processes[1][2]. The simulation method investigates the beam tail distributions generated by rare and large-amplitude processes from the core distribution. In this paper, the same simulation method was applied to the 2.5 GeV Pohang Light Source (PLS). To see the effects of beam tails in the transverse and longitudinal distributions, we considered the cases of beam-residual gas scattering, intra-beam scattering and beam-residual gas bremsstrahlung. The beam lifetime at the PLS is also estimated in a simulation and the beam lifetimes obtained from the simulation show good agreements with those of on normal operation.

DESCRIPTION OF THE SIMULATION METHOD

This section reviews the simulation method which follows from earlier work[1][2]. The simulation starts with n macroparticles that are given randomly with specified variances in six-dimensional phase space. Each macroparticle (i) has a particle number (N_i). Let p be the probability that an electron undergoes a random process during one turn. Once an electron in a macroparticle undergoes this process (the probability P is $N_i p$), we create a new macroparticle ($n+1$)th. This new macroparticle has one particle ($N_{i+1} = 1$) and the macroparticle which has undergone a random process now has a number of particles ($N_i - 1$).

We assume that the variation in the random variable due to a random process is limited to a range between a minimum and a maximum value. To obtain the variation, first, calculate the probability (P), and generate

one uniform random number ($0 \leq x \leq 1$). If $x < P$, a random process occurs for the macroparticle. Second, generate a uniform random number (θ_1) in the interval between the minimum value (θ_c) and the maximum value (θ_m) and one uniform random number in the interval $0 < y < (d\sigma(\theta)/d\theta)_{max}$, and compare y and $(d\sigma(\theta)/d\theta)_{\theta=\theta_1}$. Here θ is the scattering-angle random variable and $(d\sigma(\theta)/d\theta)_{\theta=\theta'}$ is the cross section corresponding to θ' . If $y < (d\sigma(\theta)/d\theta)_{\theta=\theta_1}$, a random variation corresponding θ_1 is given to an electron. If $y > (d\sigma(\theta)/d\theta)_{\theta=\theta_1}$, discard these θ_1 and y , and generate new θ_1 and y until the relation $y < (d\sigma(\theta)/d\theta)_{\theta=\theta_1}$ holds.

Each macroparticle in the simulation is tracked as follows:

1. *Input* We use the following normalized variables in tracking:

$$X = \frac{x}{\sigma_x^o}, P = \frac{\beta_x P_x}{\sigma_x^o}, Y = \frac{y}{\sigma_y^o} \quad (1)$$

$$Q = \frac{\beta_y P_y}{\sigma_y^o}, Z = \frac{z}{\sigma_z^o}, E = \frac{\epsilon'}{E_o \sigma_\epsilon^o} \quad (2)$$

Here, the σ_x^o , σ_y^o , β_x and β_y are nominal horizontal beam size, nominal vertical beam size, horizontal and vertical betatron functions, respectively. E_o , σ_z^o , σ_ϵ^o and $\epsilon' (= E - E_o)$ are the nominal beam energy, nominal bunch length, relative energy spread and energy deviation due to a random process, respectively.

2. *Random process* When a transverse random process, such as beam-residual gas scattering, occurs, the momenta of a particle are varied by

$$P = P - \frac{\theta}{\sigma'_x}, Q = Q - \frac{\theta}{\sigma'_y} \quad (3)$$

Here, the scattering angle (θ) is given by values between the minimum cutoff angle and the transverse aperture of the beam. $\sigma'_x = \sigma_x^o/\beta_x$ and $\sigma'_y = \sigma_y^o/\beta_y$.

3. *Betatron oscillation*

4. *Synchrotron oscillation*

5. *Synchrotron radiation*

In the simulation program, it is assumed that new macroparticles do not undergo the random processes and are not tracked after they are produced by the random processes, although the original macroparticles are continuously tracked. CPU time at this simulation can be reduced by this method, and we can perform long-term runs.

BEAM TAIL DISTRIBUTIONS BY A SIMULATION MODEL

It was shown that there is no great differences in their equilibrium states if we track over around 20000 macroparticles. We performed a weak-strong simulation with 30000 macroparticles in the phase spaces.

Beam-Residual Gas Bremsstrahlung

The differential cross section for an energy loss due to bremsstrahlung between E and $E + dE$ is given by[4]

$$d\sigma = 4\alpha r_e^2 Z(Z+1) \frac{du}{u} \frac{E'}{E_0} \left[\left(\frac{E_0^2 + E'^2}{E_0 E'} - \frac{2}{3} \right) \log \frac{183}{Z^{1/3}} + \frac{1}{9} \right], \quad (4)$$

where Z , α and r_e denote the atomic number, the fine-structure constant and the classical electron radius, respectively. If we expand Eq.(5) by $\frac{u}{E_0}$ and take first-order term, we obtain

$$d\sigma = 4\alpha r_e^2 Z(Z+1) \left(\frac{4}{3} \log \frac{183}{Z^{1/3}} + \frac{1}{9} \right) \frac{du}{u}. \quad (5)$$

We assume that one type of molecule uniformly exists in the ring.

Beam-Residual Gas Scattering

The cross section of the elastic scattering with an atom is given by[4]

$$\frac{d\sigma}{d\Omega} = \left(\frac{2Zr_e}{\gamma} \right)^2 \frac{1}{(\theta^2 + \theta_{min}^2)^2}, \quad (6)$$

where Ω is the solid angle, θ the scattering angle, Z the atomic number, r_e the classical electron radius, γ the Lorentz factor and the screening of the atomic electrons is accounted by the angle θ_{min} .

To obtain scattering angle, first, calculate the probability(P) that is scattered at higher angles θ than minimum scattering angle θ_a , and generate one uniform random number ($0 \leq x \leq 1$) each turn to decide whether the scattering occurs or not. If $x < P$, the scattering angle is defined by

$$\theta = \theta_a / \sqrt{R}, \quad (7)$$

where R ($0 < R < 1$) is the other uniform random number. On the other hand, beam-residual gas scattering causes the changes of momenta of a particle in the horizontal and the vertical directions. Then, third random number is used to define azimuthal angle ϕ which is the angle between the horizontal and scattering planes. To obtain the changes of momenta due to the scattering in the normalized momenta, we have to multiply $\theta_x = \theta \cos \phi$ and $\theta_y = \theta \sin \phi$ with the value β_x/σ_x , β_y/σ_y , respectively, taken at the position where the elastic scattering takes place. We use 4 m and 5.5 m as the average values of β_x and β_y in the ring, respectively.

Intra-beam Scattering

The Touschek effect describes collision processes which lead to loss of both colliding particles. In reality, however, there are many other collisions with only small exchanges of momentum. Due to a scattering effect, two particles can transform their transverse momenta into longitudinal momenta. If the new longitudinal momenta of the two particles are outside the momentum acceptance, the particles will be lost. The differential cross section for Coulomb scattering of two particles with equal but opposite momenta in the non-relativistic approximation is given by the Möller formula[5]:

$$\frac{d\sigma}{d\Omega} = \frac{4r_e^2}{(v/c)^2} \left[\frac{4}{\sin^4 \theta} - \frac{3}{\sin^2 \theta} \right], \quad (8)$$

where v is the relative velocity in the center of mass system and θ is the scattering angle. Note that the scattering angle is measured in the laboratory system, while intra-beam scattering cross section is evaluated in the center of mass system. Accordingly, in order to obtain the scattering angle in the center of mass system, we have to perform a Lorentz transformation of the momentum and energy of a particle from laboratory system to the center of mass system. Then the new momenta are transformed back to the laboratory system.

Fig.1 shows the horizontal, vertical and longitudinal beam distributions due to beam-residual gas bremsstrahlung, beam-residual gas scattering and intra-beam scattering, respectively.

BEAM LIFETIMES AS A FUNCTION OF APERTURES

We obtain the lifetime by using average $\beta_{x,y}$ in stead of $\beta(s)$ in the ring. The pressure-levels in total beam currents of 180 mA and 120 mA on normal operation at the PLS are 0.6×10^{-9} Torr and 0.45×10^{-9} Torr, respectively. The number of bunches on the operation is 400. Table 1 shows simulated beam lifetimes due to the bremsstrahlung as a function of the energy apertures. The lifetimes are obtained when the horizontal and the vertical apertures are set to $100\sigma'_x$ and $100\sigma'_y$, respectively. Table 2 shows the simulated beam lifetimes that result from the beam-residual gas scattering and intra-beam scattering as a function of vertical aperture. The lifetimes are obtained when the horizontal and the energy apertures are set to $100\sigma'_x$ and 1.5%, respectively.

Comparison with operational beam lifetime

If we estimate the beam lifetime due to above considered three random processes, it gives the beam lifetime around 18.9 hours in the single bunch with beam current of 0.45 mA under of vacuum pressure of 0.6×10^{-9} Torr for the transverse apertures of $100\sigma'_x$, $100\sigma'_y$ and energy aperture of 1.5%. Fig.2 shows the beam lifetimes as a function of beam current on normal operation at the PLS which includes 400

bunches. It is shown that the beam lifetimes obtained from the simulation show good agreements with ones obtained on normal operation.

DISCUSSION AND CONCLUSION

We have established the simulation method to obtain beam tail distributions due to the incoherent random processes. This simulation method provides a simple and fast means to obtain the tail distributions due to various random processes in the storage rings. Intra-beam scattering at the PLS more affects transverse tails than the beam-residual gas scattering. The tail distributions due to the beam-residual gas and intra-beam scatterings are obtained by considering relative large angle scatterings for the case of the PLS. These relative large angle scatterings only contribute a tail of large amplitude particles and do not affect the core of the beam distribution. Random processes influence the lifetimes as well as the tails of the beam distribution. The simulation study on the lifetime was performed as a function of the apertures. This simulation method for beam tails is also used to obtain the beam lifetime. This simulation showed good agreements with the operational beam lifetime.

REFERENCES

- [1] Eun-San Kim, Part. Accel. **56**, 249 (1997).
- [2] Eun-San Kim, Part. Accel. **63**, 13 (1999).
- [3] Pohang Light Source Design Report (1992).
- [4] Heiliter, W., The Quantum Theory of Radiation, Oxford Univ. Press (1995).
- [5] A. Piwinski, DESY 98-179 (1998).

Table 1: Lifetimes due to the beam-residual gas bremsstrahlung

Energy aperture	1.2 %	1.5 %	1.8 %
Lifetime(h)	297.4	461	797.6

Table 2: Lifetimes due to the beam-residual gas scattering and intra-beam scattering.

Vertical aperture	$80\sigma'_y$	$100\sigma'_y$	$120\sigma'_y$
Gas scattering(h)	319	487.4	731
Intra-beam scattering(h)	19.4	20	20.5

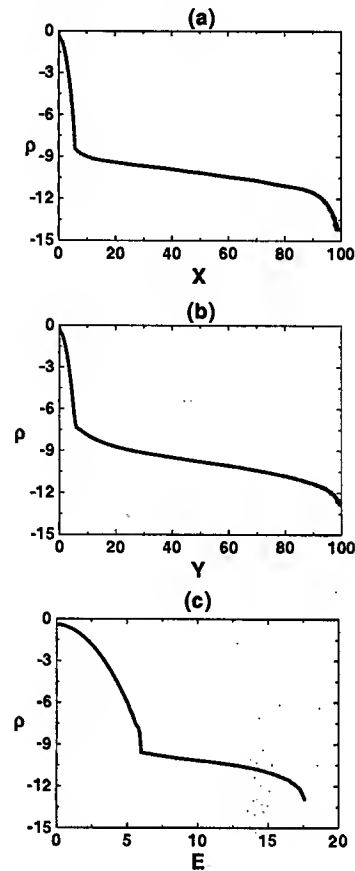


Figure 1: (a) Horizontal, (b) vertical and (c) longitudinal beam distributions due to the beam-residual gas bremsstrahlung, beam-residual gas scattering and intra-beam scattering after 560,000 turns. The horizontal axes are X and Y , the distance normalized by the nominal horizontal and vertical beam sizes and E , the energy deviation normalized by the relative energy spread. The vertical axes represent the distribution in X , Y and E measured using the logarithmic scale.

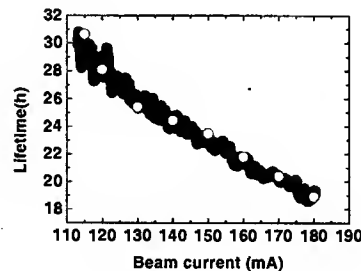


Figure 2: Circles show the simulated beam lifetimes that are obtained from the tracking of the beam-residual gas bremsstrahlung, beam-residual gas scattering and intra-beam scattering. Black line shows the beam lifetime verse beam current on normal operation.

SIMULATIONS ON WAKEFIELD EFFECTS IN THE ELECTRON BEAM AT THE 2.5 GeV PLS LINAC

Hoon Heo[#], Eun-San Kim, Sang-Hoon Nam, Pohang Accelerator Laboratory, Pohang, Korea

Abstract

We investigated simulations on the effects of the wakefield on emittance growth at the 2.5 GeV PLS linac. The effects of initial beam offset, bunch charge, misalignments of an accelerating structure and magnets on the emittance growth are considered in the simulation. It is shown that BNS damping effectively reduces emittance growths due to these causes. Based on the simulation results, maximum possible beam current per bunch for the stable beam operation of linac is estimated to be 3 nC.

INTRODUCTION

Since the October 2002, PLS linac has been served as a 2.5 GeV full energy injector. In the injector linac, a high-intensity, stable single bunched electron beam is required. It is well known that wake fields affect on the emittance growth and energy spread [1]. The longitudinal wake field causes an energy spread within a bunch as well as a decrease in beam energy, depending on the bunch length and the acceleration phase, while the transverse wake field induces an emittance growth related with a beam instability due to injection errors and cavity misalignments [2][3]. Therefore, it is valuable to estimate both the longitudinal and transverse effects of a wake field concerning the 2.5 GeV PLS linac for optimum stable beam operation. Using a simulation code LIAR [4], we estimated the wake field effects on the PLS linac. We also considered the BNS damping to reduce the emittance growths due to the several causes.

PLS LINAC

The 2.5 GeV PLS consists of the storage ring as a 2.5 GeV storage ring and a full energy linear accelerator as an injector. The 160 meter-long linac has a 44 accelerating columns powered by 12 klystrons. A total of 7 quadrupole triplets guide the accelerated electron beam through the linac. The pre-injector, which is the first 100 MeV section of the PLS linac, consists of an thermionic triode electron gun, an S-band prebuncher, an S-band buncher, and two accelerating columns powered by a klystron. The electron beams from the pre-injector are accelerated to 2.5 GeV by 42 accelerating columns powered by 11 klystrons of 200 MW maximum output power. The 3m long accelerating column has a SLAC-type constant gradient structure with $2\pi/3$ operating mode [5].

The main simulation parameters of the 2.5 GeV PLS linac are listed in table 1. We assumed that the initial normalized emittance is 295 mm mrad referring the designed value, and calculated the initial Twiss

parameters. Concerning the designed value of the bunch length of 2mm [5], the bunch length in the simulation is varied from 0.5 mm to 6 mm to see the effects of bunch length. In order to estimate the wake field effects, we used the short-range wake function of the SLAC type accelerating structure. The bunch in the simulation was represented with 20 slices having 2 macroparticles per slice.

Table 1: Used parameters in this simulation

E_0	0.1	[GeV]
E_f	2.5	[GeV]
I	1~20	nC
$\gamma E_x, \gamma E_y$	295×10^{-6}	[m rad]
β_x, β_y	8.32	M
α_x, α_y	-0.9	

LONGITUDINAL WAKE FIELD EFFECTS

Figure 1 shows dependence of bunch length on optimum off-crest phase, which is determined by the phase minimizing the final energy spread for the given bunch charge and the bunch length.

The energy spread is estimated as a function of the bunch length, which is shown in Figure 2. In order to obtain the energy spread below 1 %, the bunch length should be below 3 mm. These results well agree with the Ogawa's Gaussian longitudinal wake field model [2].

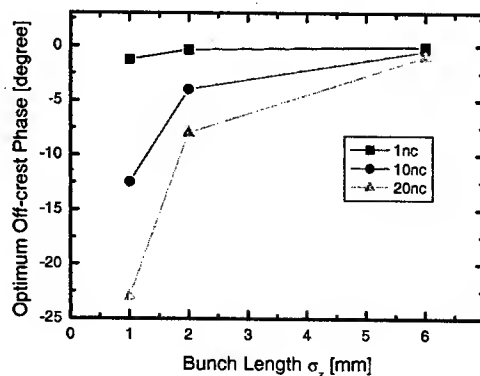


Figure 1: Optimum off-crest phase vs bunch length.

[#]heoon@postech.ac.kr

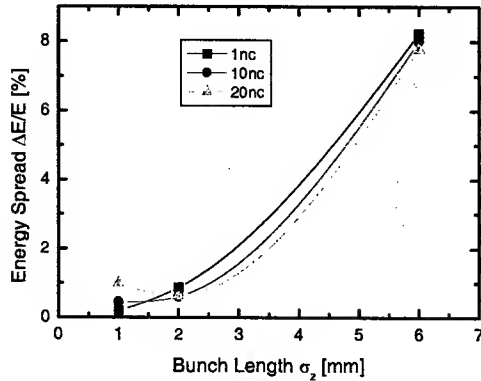


Figure 2: Dependence of bunch length dependence on the energy spread.

TRANSVERSE WAKE FIELD EFFECTS

Initial offset of the injected beam or beam defections along the linac causes emittance growth from the transverse wake field, as shown in figure 3. It is well known that the single bunch instability caused by a short-range transverse wake field can be cured effectively by BNS damping[6]. The BNS damping is done with a position-correlated energy spread in the bunch, that is, $\Delta E/E > 0$ in the head and $\Delta E/E < 0$ in the tail, which makes the quadrupole lattices focus the tail particles, and hence compensates the defocusing wake field force by the head particles [7]. The energy spread is generated by creating a slope on the accelerating gradient over the bunch length through adjusting the rf phase with respect to the bunch. At the high-energy end, the klystron phase are shifted to make the bunch arrive early for final correction of the longitudinal energy spread.

Figure 4 shows that when BNS damping is applied, the energy spread increases at the low energy position of the 2.5 GeV PLS linac, but that decreases at the high-energy region. We empirically found the BNS configuration for PLS linac satisfying final beam energy spread of $\sim 0.9\%$.

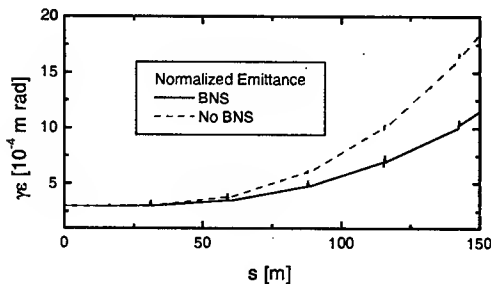


Figure 3: Typical normalized emittance profile.

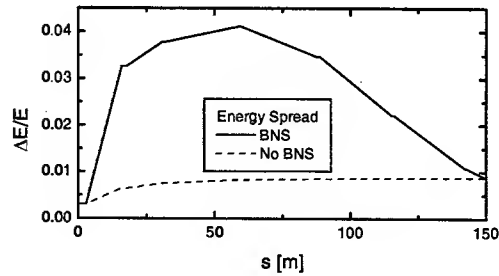


Figure 4: Typical energy spread profile.

Figure 5 shows the emittance growths due to initial beam offsets. The BNS damping effectively reduces the emittance growths due to the initial beam offset effects, depending on the RF phase configurations. The RF settings for the BNS I and the BNS II are shown in Table 2.

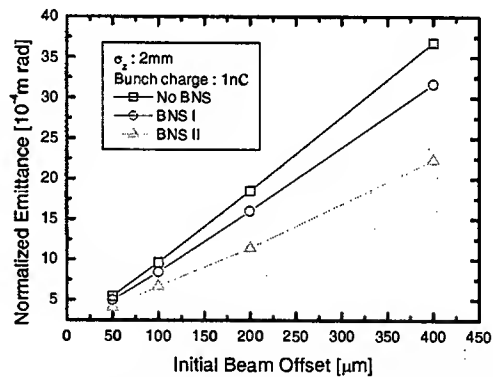


Figure 5: Dependence of initial beam offset on the $\gamma\epsilon$.

Table 2: Several BNS damping conditions for PLS linac.

	1 st phase	1 st sw	2 nd phase	2 nd sw	3 rd phase
BNS I	20°	Accel. 24	-10°	Accel. 40	-60°
BNS II	20°	Accel. 24	-10°	Accel. 40	-110°

Figure 6 and 7 show the emittance growths caused by the misalignments of accelerating structures and quadrupoles, respectively. They show that the cavity misalignments cause larger emittance growth than the quadrupoles' case. It is also shown that the corrections well cured these emittance growths. BNS damping also

reduced the emittance growth induced by the quadrupole misalignments.

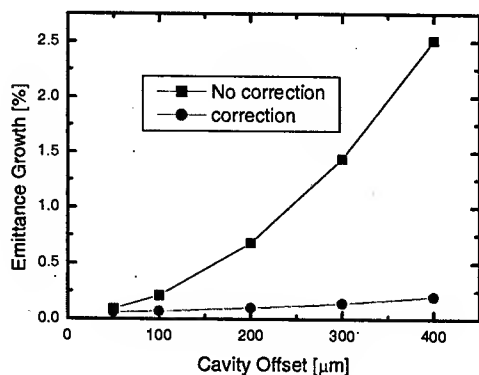


Figure 6: Dependence of cavity misalignment on $\Delta(\gamma\epsilon)/(\gamma\epsilon)$.

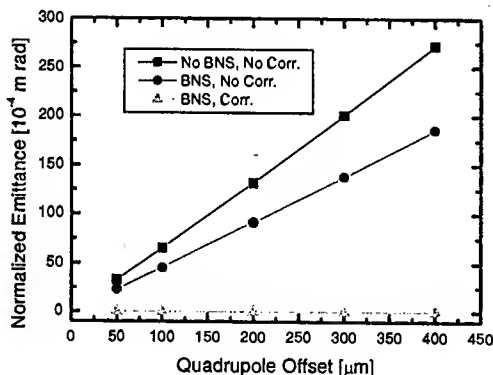


Figure 7: Dependence of quadrupole misalignment on $\gamma\epsilon$.

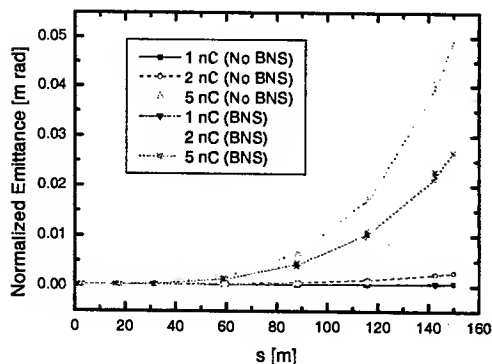


Figure 8: Dependence of bunch charge on $\gamma\epsilon$.

The emittance growths that are caused by an initial beam offset of 50 μm for the different bunch charges are shown in Figure 8. When the bunch charge is 5 nC/bunch, emittance grows over 500 mm mrad resulting to the beam breakup.

DISCUSSIONS AND CONCLUSION

We simulated the effects of the wake field on the emittance growth and energy spread in the 2.5 GeV PLS linac. Initial beam offsets, accelerating structure offsets and quadrupole misalignments induce severe emittance growth. However, it was shown that the corrections for misalignments and the BNS damping method could cure sufficiently the emittance growth. In order to obtain low emittance and low energy spread electron beam, the bunch length and the bunch current act as crucial beam parameters. The simulation indicated that it is possible to operate the linac up to 3 nC/bunch without showing the emittance growth. The simulation results show that longer bunch length than 2 mm induces larger energy spread than 1%, which invokes the chromatic effects.

REFERENCES

- [1] A. W. Chao, et al, Nucl. Inst. Methods, p. 178 1980.
- [2] Y. Ogawa, et al, KEK preprint 94-94, Sept. 1994.
- [3] Y. Kamitani, et al, KEK preprint 2000-4, April. 2000.
- [4] R. Assmann, et al, "LIAR- A computer program for the modelling and simulation of high performance linacs", SLAC/AP-103, April 1997.
- [5] Design Report, Pohang Light Source, revised edition, Pohang Accelerator Laboratory, POSTECH, 1992.
- [6] V. Balakin, et al, "VLEPP: Transverse Beam dynamics", 1983 International Accelerator Conf., FNAL, p. 119. 1983
- [7] J. T. Seeman, et al, SLAC-PUB-6204, Jun. 1993.

DESIGN CONSIDERATIONS FOR SASE-FEL AT PLS

Eun-San Kim, Pohang Accelerator Laboratory, POSTECH, Pohang, 790-784 Korea

Abstract

The infrared (IR) free-electron laser (FEL) which is in design stage at Pohang Light Source is a self-amplified spontaneous emission (SASE) system that is driven by a 60 MeV to 100 MeV test linac facility. We present results of the numerical simulation for the design of the IR SASE-FEL at the PLS. It is shown that high-gain SASE-FEL with 1.5 μm radiation wavelength is driven by a 61 MeV electron beam from the S-band rf linac and a about 5 m long undulator. The generation of third harmonic from bunching at the fundamental wavelength is also investigated as a purpose toward enhancing the usefulness of the IR SASE-FEL facility at the PLS. In this paper, we investigate sensitivity of the beam parameters, emittance, energy spread, beam energy and peak beam current, to the performance of the designed IR SASE-FEL by a simulation code GINGER. We also investigate the influence of beam parameters on the bunching of fundamental and nonlinear third harmonic, and show that the third harmonic emission results in the same trend as that of the fundamental.

INTRODUCTION

SASE is driven by the random longitudinal bunching on an electron beam that is traversing along the undulator[1,2]. The fundamental radiation wavelength is determined by parameters of the electron beam energy and the strength of the undulator. A method to obtain shorter wavelengths at given beam energy is to utilize coherent bunching at higher harmonics. It may be generated by nonlinear harmonic bunching in the exponential gain regime starting from either SASE or a weak input signal[3,4].

Pohang Light Source (PLS) is designing a SASE-FEL system by using a test linac facility. The system is based on an existing electron linac that consists of a thermionic RF gun, an alpha magnet for bunch compression, and two S-band linac sections to provide electron energies from 60 MeV to 100 MeV. In this paper, we investigate the sensitivity of emittance, energy spread, beam energy and peak beam current to the performance of the designed IR SASE-FEL. Achievable values for the normalized emittance and the peak beam current are considered as boundaries for the design of the system. The design study is centered to achieve saturation at the radiation wavelength of 1.5 μm . For this design, we consider a 5 m long undulator with a period length of 15 mm and peak magnetic field value of 1.37 T.

It was known that for radiation emission, odd harmonics are favored as they couple effectively to the natural undulating motion of the electron beam through a linearly polarized undulator. It was shown that nonlinear harmonic

bunching and radiation could serve as a seed for further FEL amplification at the regions such as x-ray (LCLS), (LEUTL and VISA) and far-infrared (ISIR) [5,6]. In particular, we investigate characteristics of third harmonic in the our designed SASE-FEL system because it may be a promising way to produce radiation power at the regime of shorter wavelength. It is shown in our simulation that the third harmonic experience similar trend in gain and saturation similar to the fundamental. One purpose of this paper will be to predict the usefulness of the third harmonic output in the our IR SASE-FEL. A numerical simulation code is used to investigate the influence of electron beam parameters (i.e., emittance, energy spread, beam energy and peak beam current) on the field energy at the fundamental, and on the bunching of the fundamental and third harmonic, by using basic parameters corresponding to the SASE-FEL at the PLS.

CODE DESCRIPTION

A simulation study for the IR SASE-FEL at the PLS is carried out using the time-dependent code GINGER[7]. The main parameters of the electron beam and the undulator are given in Table I. GINGER is a direct descendent of the FEL code FRED which modeled the interaction between particles in one ponderomotive well and a monochromatic, r- and z-dependent electromagnetic wave. The electron beam is modeled by discrete slices, each containing numerous macroparticles, to simulate the particle distribution in one ponderomotive well. GINGER also uses a moderate number of macroparticles (512-8192) per slice to represent the actual electrons in each beam slice. The equations of motion are averaged over an undulator period following the standard Kroll-Morton-Rosenbluth formulation while an eikonal approximation in time and space is used for field propagation. For nonwaveguide simulations, GINGER used an expanding radial grid whose spacing is approximately constant near the origin but grows exponentially near the outer boundary. For polychromatic SASE simulations, GINGER can be initiated with either electron beam shot noise or, alternatively, photon noise.

SIMULATION

In simulations with the time dependent GINGER code, we have chosen an electron beam with a parabolic distribution in longitudinal direction and with a Gaussian distribution in the transverse direction. We use 2048 macroparticles per slice and 60 slices to represent an electron beam in the simulation. For simplicity, we adopted a single-segment planar undulator with curved pole-face focusing.

We also injected an input power of $1 \mu\text{W}$ at the fundamental. GINGER calculates the output radiation energy at the fundamental, and beam bunching at both the fundamental and third harmonic. For this analysis, we first compare the longitudinal locations of saturation of the output field energy and the fundamental bunching. It is shown that peak in the bunching occurs at almost the same position with the output field energy saturates. Note that the third harmonic does saturate at the same position where the fundamental saturates.

Table 1: Basic IR SASE-FEL Parameters at the PLS.

Electron beam energy	61.3 MeV
Normalized beam emittance	5 mm mrad
Peak beam current	300 A
Beam energy spread	0.1 %
Radiation wavelength	$1.5 \mu\text{m}$
Undulator period	15 mm
FEL parameter	0.0046
Peak undulator magnetic field	1.37 T
Power gain length	17.8 cm
Undulator parameter	1.918

Emittance scans

For the emittance sensitivity scans, the normalized emittance was varied between 1 mm mrad and 10 mm mrad, which results in the saturation distance approximately doubling. Figure 1 shows the field energy as a function of undulator distance versus beam emittance at the fundamental wavelength. The field energies for smaller emittances than 6 mm mrad show saturation in smaller distance than about 5 m long undulator. The field energies for larger emittances than 6 mm mrad show slow increases of the field energy up to the 15 m long undulator. Larger emittances requires much longer saturation lengths and shows decreased outputs, even though the FEL operation is kept. Over this limited range, the field energy at the fundamental shows significant sensitivity to emittance.

Energy spread scans

For the energy spread scans, the initial beam energy spread was varied between 1 % and 0.001 %. Figure 2 shows the field energy versus energy spread at the fundamental. For the energy spreads smaller than 0.1%, the field energies saturate in smaller distance than 5 m long undulator. For the energy spreads larger than 0.5%, the field energies do not show peak value up to 15 m long undulator.

Peak beam current scans

For the beam current scans, the peak beam current was varied between 200 A and 1000 A. Figure 3 shows the field energy at the fundamental versus the peak beam current.

For peak beam currents larger than 300 A, the field energies show saturation in smaller distance than 5 m long undulator. For the peak beam current of 200 A, the field energy shows trend of increasing up to 15 m long undulator. Over this limited range, the field energy at the fundamental shows significant sensitivity to peak beam current.

Electron beam energy scans

For the electron beam energy scans, the beam energy was varied between $\gamma=120$ and $\gamma=200$. Figure 4 shows the field energy at the fundamental versus beam energy. Over this limited range, the field energy does not show significant sensitivity to the beam energy.

Performance of the IR SASE-FEL at PLS test linac facility

For the nominal parameters that are given in Table I, the simulation results show that saturation can be reached at about 4.5 m long undulator, as shown in Figure 5(a). The peak bunchings at the fundamental and the third harmonic also occur at about 4.5 m, as shown in Figure 5(b). Figure 5(b) shows the ratio of the bunching fraction of the third harmonic to fundamental is about 15% at 4.5 m long undulator. From these simulation results, we note that an undulator of a length of about 5 m is required to achieve saturation in the designed IR SASE-FEL.

In a one-dimensional model, the FEL parameter ρ is given by [16]

$$\rho = \left[\frac{I \gamma \Lambda^2}{I_A 16 \pi^2 \sigma^2} \frac{K^2}{(1 + K^2/2)} (J_0(\xi) - J_1(\xi))^2 \right]^{1/3}, \quad (1)$$

where I is the peak beam current, $I_A=17,045$ A is the Alfvén, $J_{0,1}$ are Bessel functions, and σ is the rms beam size. $\xi = \frac{K^2}{2(1+K^2)}$, where K is the undulator parameter. Under the nominal designed parameters, the FEL parameter is given by 0.0046.

The gain in the SASE-FEL can be estimated. Defining the gain as $G = E/E_0$ where E is the total energy when the saturation occurs and E_0 is the energy at the first gain length, we calculate a gain, $G \simeq 1.0 \times 10^7$. The gain length in one-dimensional model is given by $L_G = \lambda_u / 4\sqrt{3\pi\rho}$ where λ_u is fundamental radiation wavelength and the calculated gain length is given by 0.15 m. The three-dimensional gain length obtained from the numerical simulation was 0.17 m, which is good agreement with the one-dimensional calculated one.

CONCLUSIONS

In this paper, we presented the results of numerical simulation for the design of the IR SASE-FEL at the PLS. The FEL will be a $1.5 \mu\text{m}$ SASE system that is driven 61 MeV electron beam from S-band linac and a about 5 m long undulator. We have examined the influence of electron

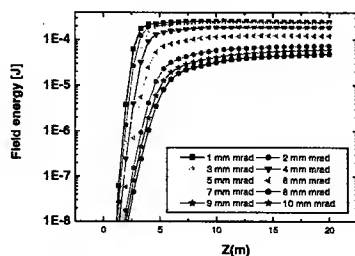


Figure 1: shows the field energy at the fundamental versus beam emittance as a function of the distance.

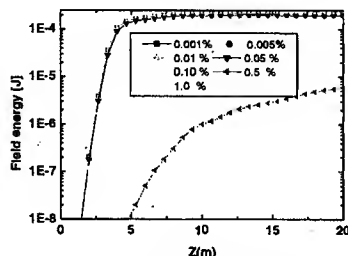


Figure 2: shows the field energy at the fundamental versus energy spread as a function of the distance.

beam parameters on performance of the high-gain SASE-FEL by using a numerical simulation code GINGER. We have also investigated the sensitivities of the radiation output energy to variations in beam emittance, energy spread, beam energy and peak current centered around the nominal designed parameters for IR SASE-FEL at the PLS. It is shown that the nonlinear third harmonic generation in the designed IR SASE-FEL at the PLS can be used to achieve shorter wavelengths and characteristics of its growth and saturation vary along with the fundamental. Since the nonlinear third harmonic is driven by the growth of the fundamental wavelength, the sensitivity of the nonlinear third harmonic to the beam parameters is shown to be comparable to that of the fundamental. That is, if the bunching is sufficient at the fundamental, the bunching for the third harmonic will also be sufficient.

REFERENCES

- [1] A. M. Kondratenko and E.L. Saldin, Sov. Phys. Dokl. **24**, 986 (1979).
- [2] Linac Coherent Light Source Design Study Report, SLAC-R-521 (1998).
- [3] J. Rossbach, Nucl. Instrum. & Methods Phys. Res. A **375**, 269 (1996).
- [4] A. Tremaline et al., SLAC-PUB-9583 (2002).
- [5] H. P. Freund et al., Nucl. Instrum. & Methods Phys. Res. A **445**, 53 (2000).
- [6] S. G. Biedron et al., Nucl. Instrum. & Methods Phys. Res. A **483**, 101 (2002).
- [7] W. M. Fawley, LBNL-49625, 2002.

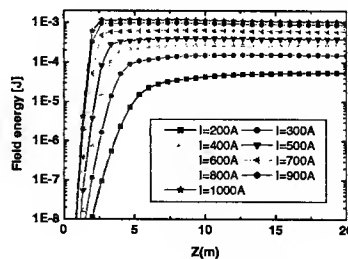


Figure 3: shows the field energy at the fundamental versus beam current as a function of the distance.

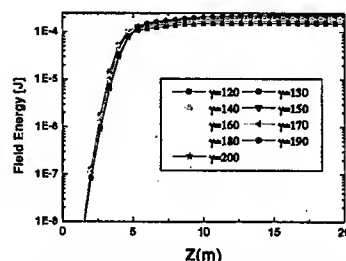


Figure 4: shows the field energy at the fundamental versus beam energy as a function of the distance.

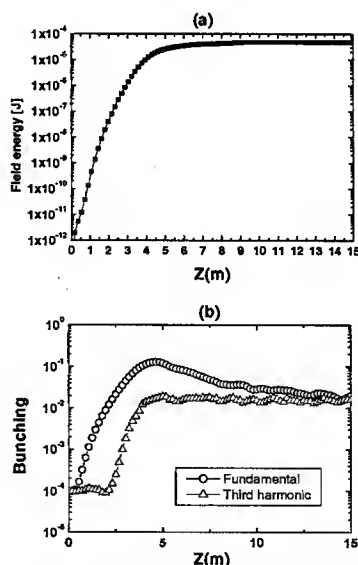


Figure 5: (a) shows the field energy at the fundamental. (b) shows the bunching fraction for the fundamental and third harmonic.

OPERATIONAL PERFORMANCE IN 2.5 GeV FULL ENERGY INJECTION AT PLS

E.-S. Kim, Y.-J. Han, S.-H. Jeong, M.-G. Kim, S.-C. Kim, S.-S. Park and J.-H. Seo
Pohang Accelerator Laboratory, POSTECH, Pohang, 790-784 Korea

Abstract

The PLS has provided 2.5 GeV electron beam to users of beam lines since Jan. 2000. During Jan. 2000 to Oct. 2002, 2 GeV electron beam was injected from the linac to the storage ring and the storage ring had used energy ramping process to increase the beam energy to 2.5 GeV. Instead of energy ramping process, we have used the 2.5 GeV full energy injection from the linac to the storage ring since Oct. 2002. We present the activities on the stability and reliability of the linac for 2.5 GeV operation, stabilities of injection kicker and septum magnets in the storage ring, orbit correction of COD due to leakage field of the septum magnet, and a DC bump for beam injection. Orbit stabilities and global orbit correction on the operation of 2.5 GeV full energy injection are also presented.

INTRODUCTION

In September 1995, PLS started to operate with 2 GeV electron beam in the range of 100 mA of the beam current. Since then, the operation of PLS has aimed to realize stable operation with higher beam current and higher beam energy. One of the major factors to limit the operation with higher beam current was the coupled-bunch instabilities driven by the HOMs of rf cavities. By optimizing of the cavity temperature, betatron tune, bunch filling pattern and chromaticity, it was possible to suppress the instabilities. During Jan. 2000 to October 2002, the beam energy in the storage ring was raised from 2 GeV to 2.5 GeV by energy ramping. PLS has been operating successfully by 2.5 GeV full energy injection from the linac since October 2002. The issue about the energy ramping to achieve the 2.5 GeV beam will be discussed. The operational performance and beam parameters that are related to the 2.5 GeV full energy injection are presented.

LINAC

PLS linac had injected 2 GeV electron beams to storage ring from September 1994 to October 2002. During that time, linear accelerator had used as 2 GeV injector to the storage ring. At the end of 1997 one klystron modulator system and two accelerating columns were installed to the linac to add energy of 150 MeV. The module consists of one klystron of 80 MW peak, a modulator of 200 MW peak and one pulse compressor. The linac has been continuously improved to raise stability and reliability in the system, as well as to raise injection energy to 2.5 GeV. Current overall system availability is around 95 %. PLS linac has total 12 modules with 44 accelerating structures. Accordingly, PLS

linac could increase injection energy to 2.5 GeV by using the 12 accelerating modules. However, several issues had to be realized before performing the 2.5 GeV full energy injection: stability and reliability of the linac in 2.5 GeV, optics optimization and energy stability of the linac in 2.5 GeV. The linac includes 13 beam current monitors and 12 beam profile monitors for the diagnostics of the beam. The delivery rate of the beam mainly depends on the beam optics and RF phase control. The beam loss rate on 2.5 GeV full energy injection shows around 30% in the linac.

Beam dynamics issues affect the PLS linac performance. Figure 1 shows beam sizes in optics of the present 2.5 GeV linac. Investigation on tolerance for beam injection and alignment of accelerator components is also being performed[2]. In the early period of 2.5 GeV operation, the RF phase due to changes of temperature and cooling water influenced beam energy and beam quality. The RF phase variation of high power is being controlled by adjusting the RF phase of the driving signal for klystron through IPA system. The PLS 2.5 GeV linac has satisfactorily served as full energy injector to the storage ring since the October 2002.

STORAGE RING

The PLS was designed to store the electron beam up to 2.5 GeV. There are two ways to store the beam of 2.5 GeV: first way is to ramp the beam of 2 GeV in the storage ring to 2.5 GeV and second way is to perform the full energy injection from the linac.

The full energy injection way has merits in several facts: in machine stability, shorter injection time, orbit stability and so on. However, several issues in the storage ring had to be solved to realize the 2.5 GeV full energy injection: power stabilities in the injection kicker magnet and septum magnet, and effect of leakage field in the septum magnet on the beam orbit. In the following subsections we will discuss these issues that are investigated to perform the 2.5 GeV full energy injection.

Energy Ramping and De-ramping

During January 2000 to April 2001, 2 GeV beam was injected from the linac to the storage ring and then the beam was ramped to 2.5 GeV. In order to re-fill the beam current at 2.0 GeV, a 2.5 GeV beam was dumped and degaussing was performed. Then the 2.0 GeV beam was injected and ramped to 2.5 GeV. In the ramping process the energy increment rate in bending and Q2 power supplies varied as the beam energy increases. This is because the relationship

of magnet field strength and MPS current is not linear due to insufficient synchronization. It also showed large variations in betatron tunes during the ramping process. Both vertical and horizontal betatron tunes were merged at approximately 0.25 at the starting of ramping in order to prevent beam loss during the ramping process because the betatron tunes hit the third-order resonance. Energy ramping under on resonance also caused significant changes in beam lifetime due to enlarged vertical beam sizes.

During May 2001 to October 2002, it was possible for 2.5 GeV beam to de-ramp without beam dumping to 2.0 GeV in the new energy ramping system. The energy increment rate per step in the new energy ramping system is constant per step during the energy ramping: 0.32% per step for bending and 0.30% per step for other magnets. New energy ramping control system showed better synchronization than the previous energy ramping control system. In addition to the energy ramping, the new ramping control system could also decrease the beam energy from 2.5 GeV to 2.0 GeV (de-ramping), at the same rate but in the reverse direction with the energy ramping. The operation could be performed without merging the betatron tunes at approximately 0.25 at the start of ramping. The variation of closed orbit distortion during energy ramping was reduced by a factor of 1.5 compared to that of the previous ramping system. Practically no beam loss was noted during the ramping at the speed which requires 1.3 min to increase from 2 GeV to 2.5 GeV. The ramping speed was about four times faster in the new ramping system than in the previous ramping system.

Magnet Power Supply

The LC resonance frequency of 18 Hz in the bending magnet power supply was observed in beam position monitors and an undulator beam line. When the LC values in the filter were changed, beam signal with the same components were also observed in the beam position monitor and the undulator beam line on normal operation. Then, the LC filter was changed to structure of the $(LC+RC)$ filter. The circuit has the values of $L1=2\text{ mH}$, $L2=1\text{ mH}$, $C1=34000\text{ }\mu\text{F}$, $C2=6800\text{ }\mu\text{F}$ and $R=0.6\Omega$. Then we could observe that the ripple component of 18 Hz was greatly reduced. By decreasing integral constant of error amplifier from $10\text{ }\mu$ to $1\text{ }\mu$, we increased bandwidth of current-control loop. Then the current stability was improved from 100 ppm to 50 ppm. Further, current stability was also improved from 50 ppm to 15 ppm as DCCT of current-control loop was replaced.

Injection

The injection system in the PLS storage ring consists of a Lambertson-type septum magnet and four injection kicker magnets. When we perform the 2.5 GeV full energy injection, leakage field of the septum magnet is increased and rms value of the vertical COD increases about five times.

Orbit correction to reduce the orbit deviations due to the leakage field was sufficiently performed.

The four kicker magnets are operated by single power modulator for local bump orbit. The current requirement in the kicker magnets is 22500 A for 2.5 GeV, while it is 19500A for 2 GeV operation. The maximum capacity of the modulator is 24000A. On the other hand, when we utilized a DC bump that was consisted of two bendings and two correctors, it was shown that beam injection was could be performed with current of the kicker magnet of 19500A.

Beam Lifetime

In the present operation of the 2.5 GeV, Touschek effect is a dominant factor that determines the beam lifetime. The gas scattering and gas-bremsstrahlung give minor effect on the beam lifetime. If we estimate the beam lifetime due to the gas-scattering, gas-bremsstrahlung and intra-beam scattering processes, it gives the beam lifetime around 18.9 hours in beam current of 180 mA under the vacuum pressure of 0.6 nTorr. Horizontal and vertical apertures are $100\sigma_x/\beta_x$ and $100\sigma_y/\beta_y$, respectively. Energy aperture is 1.5%. It is shown that the beam lifetimes obtained from the simulation well agree with ones obtained on normal operation.

Beam Instabilities

During the user operation between Jan. 2000 and July 2000, the number of bunches was 468 that was equal to the harmonic number. Operated tune was 14.26 and 8.15 in horizontally and vertically, respectively. We observed resonant frequency of 831.8 MHz in beam spectrum due to transverse higher order mode in rf cavities.

Since September 2000, we have changed the number of bunches and betatron tune for the user operation. At present, the number of bunches is 400 and operating tune is 14.28 and 8.18 in horizontally and vertically, respectively. We don't observe resonant frequency in beam spectrum due to rf HOMs. The beam at the 2.5 GeV can be stably stored up to 200 mA. At present higher beam current than 200 mA is limited by total rf power. On the other hand, the beam current of 450 mA at 2 GeV could be stored without using of transverse and longitudinal feedback systems.

Orbit Stability

The dominant source of orbit fluctuation in the storage ring is slow drift due to temperature variations and gap change of insertion device. There are three major causes of thermal variations: 1) variation in air temperature of the ring tunnel, 2) variation in the low conducting water temperature, and 3) variation in underground movement. Gap change in the insertion device is the next largest source of slow orbit distortion. The horizontal orbit is mainly affected by the gap of insertion device. Without orbit feedback, orbit drifts of rms 30 micron to rms 100 micron have been observed on normal operation of 10 days period.

Global Orbit Correction

A global orbit feedback system was installed on the PLS storage ring to correct horizontal and vertical orbit distortion. The system that consists of 96 BPMs and 140 correctors has been tested to suppress orbit fluctuation due to the orbit drift. The closed orbit distortion was measured and excitation currents of the correctors were calculated with the SVD method. Rms horizontal and vertical closed orbit distortion before the global orbit correction were 1.1 mm and 1.2 mm, respectively. After global orbit corrections the rms orbits were reduced to 0.2 mm and 0.4 mm, respectively. The difference orbit (orbit drift) relative to the operational orbit of the PLS storage ring was around rms 70 micron and it was also corrected by using of the global orbit correction. Then the orbit drift could be suppressed to the level of less than rms 10 micron. It means that the global orbit feedback system is demonstrated and is effective to suppress the orbit drift in the PLS. Global orbit correction will be applied every after beam injection. The real-time feedback system will be prepared to provide more stable beam. With the global orbit correction on the operation, we expect that orbit drift will be greatly decreased and photon beam stability at the beam lines will be more improved.

Beta function

Beta-function correction that includes compensation of gradient error, correctors error and BPMs error is being performed to minimize the horizontal and vertical beam sizes and to restore design periodicity of the storage ring. Measured horizontal beta function before and after the correction in the present 2.5 GeV lattice is shown in Figure 2.

Linear Coupling and Chromaticity

Linear coupling constant is estimated by measuring tunes close to the coupling resonance. The minimum separation of tunes are obtained by measuring of the horizontal and vertical tune variations as a function of quadrupole power supply current. The coupling constant is shown to be 0.8 % on operation. When skew quadrupoles are excited, minimum achievable coupling constant is around 0.15 %. Measured natural horizontal and vertical chromaticities are -16.6 and -12.3, respectively. Chromaticity is 0.7 and 1.1 in horizontal and vertical directions, respectively.

Broadband Ring Impedance

Broadband ring impedance was estimated by measuring bunch-lengthening in the ring. Longitudinal impedance was analyzed through a $R+L$ model. The results are estimated to be around $R=800\Omega$ and $L=14 nH$.

CONCLUSION

In this report, we presented various activities that were performed to achieve the 2.5 GeV full energy injection operation in the PLS storage ring and linac. Operational per-

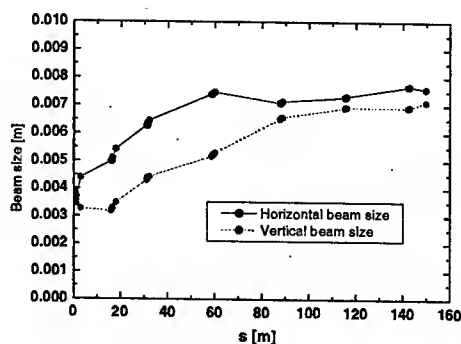


Figure 1: Beam sizes in the optics of the present 2.5 GeV linac.

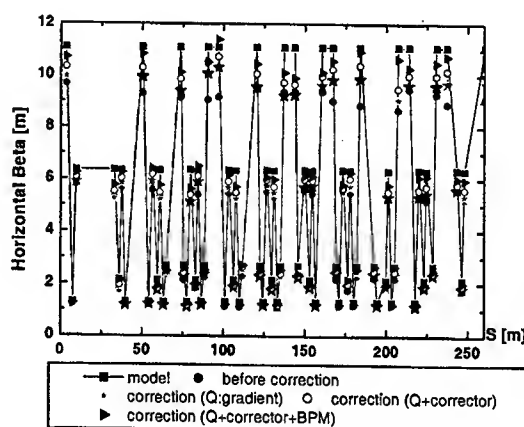


Figure 2: Horizontal beta-functions in the present 2.5 GeV storage ring

formance and beam parameters of the linac and the storage ring are also described.

REFERENCES

- [1] Pohang Light Source Design Report 1992.
- [2] Eun-San Kim, PAC2001, p.1945, Chicago, June 2002.
- [3] H. Heo, E.-S. Kim and S.-H. Nam, In these Proceedings.

INSTABILITY DRIVEN BY WALL IMPEDANCE IN INTENSE CHARGED PARTICLE BEAMS

Ronald C. Davidson and Hong Qin

Plasma Physics Laboratory, Princeton University, Princeton, NJ 08543*

Gennady Shvets

Center for Accelerator and Particle Physics, Illinois Institute of Technology, Chicago, IL 60616

Abstract

The linearized Vlasov-Maxwell equations are used to investigate properties of the wall-impedance-driven instability for a long charge bunch with flat-top density profile propagating through a cylindrical pipe with radius r_w and wall impedance $\tilde{Z}(\omega)$. The stability analysis is valid for general value of the normalized beam intensity $s_b = \hat{\omega}_{pb}^2 / 2\gamma_b^2 \omega_{\beta\perp}^2$ in the interval $0 < s_b < 1$.

INTRODUCTION AND MODEL

High energy ion accelerators, transport systems and storage rings [1] have a wide range of applications ranging from basic research in high energy and nuclear physics, to applications such as spallation neutron sources, heavy ion fusion, and nuclear waste transmutation. Considerable recent analytical progress has been made in applying the Vlasov-Maxwell equations to investigate the detailed equilibrium and stability properties of intense charged particle beams [1]. Building on these advances, the present analysis reexamines the classical wall-impedance-driven instability [2-5], making use of the linearized Vlasov-Maxwell equations [1] for perturbations about a Kapchinskij-Vladimirskij (KV) beam equilibrium [6, 7] with flat-top density profile. Compared with previous work, the present analysis based on the Vlasov-Maxwell equations constitutes a much more general approach. In particular, it enables us to solve for the dispersion relations and mode structures for arbitrary azimuthal mode number ℓ in the transverse direction [8].

To summarize, the present analysis considers a very long charge bunch (bunch length $\ell_b \gg$ bunch radius r_b) with directed axial kinetic energy $(\gamma_b - 1)m_b c^2$ propagating in the z -direction through a cylindrical pipe with constant radius r_w and (complex) wall impedance $\tilde{Z}(\omega)$. The analysis is carried out in the smooth-focusing approximation, where the applied transverse focusing force is modeled by $\mathbf{F}_{foc} = -\gamma_b m_b \omega_{\beta\perp}^2 \mathbf{x}_\perp$. Here, $\gamma_b = (1 - \beta_b^2)^{-1/2}$ is the relativistic mass factor, $V_b = \beta_b c$ is the directed axial velocity of the charge bunch, m_b is the particle rest mass, $\omega_{\beta\perp} = \text{const.}$ is the applied focusing frequency, and $\mathbf{x}_\perp = x\hat{\mathbf{e}}_x + y\hat{\mathbf{e}}_y$ is the transverse displacement of a beam particle from the cylinder axis. Denoting the number density of beam particles by \hat{n}_b and the particle charge

by e_b , it is convenient to introduce the relativistic plasma frequency $\hat{\omega}_{pb}$ defined by $\hat{\omega}_{pb} = (4\pi\hat{n}_b e_b^2 / \gamma_b m_b)^{1/2}$ and the normalized (dimensionless) beam intensity s_b defined by $s_b = \hat{\omega}_{pb}^2 / 2\gamma_b^2 \omega_{\beta\perp}^2$ [1].

An important feature of the analysis is that it is carried out for arbitrary value of s_b in the interval $0 < s_b < 1$, assuming perturbations about a KV equilibrium with flat-top density profile. Illustrative parameters for intense beam systems range from the very small value $s_b = 1.36 \times 10^{-4}$ in the Tevatron, where the particles are highly relativistic, to the intermediate value $s_b = 0.08$ in the low-energy, moderate-intensity Proton Storage Ring (PSR) experiment, to $s_b \simeq 0.98$ in the low-emittance, space-charge-dominated beams for heavy ion fusion. Finally, the present analysis considers the case where the axial momentum spread is negligibly small. Furthermore, the functional form of the wall impedance $\tilde{Z}(\omega)$ is not specified, although the case of small impedance ($|\tilde{Z}| \ll 1$) is considered.

To describe stability properties of the charge bunch, we make use of a kinetic description based on the Vlasov-Maxwell equations [1]. For simplicity, the analysis considers small-amplitude perturbations about the axisymmetric, axially uniform, quasi-steady-state equilibrium distribution function [6, 7]

$$f_b^0(r, \mathbf{p}_\perp) = \frac{\hat{n}_b}{2\pi\gamma_b m_b} \delta(H_\perp - \hat{T}_{\perp b}) \delta(p_z - \gamma_b m_b \beta_b c). \quad (1)$$

In Eq. (1), \hat{n}_b and $\hat{T}_{\perp b}$ are positive constants, and H_\perp is the transverse Hamiltonian defined by

$$H_\perp = \frac{1}{2\gamma_b m_b} p_\perp^2 + \frac{1}{2} \gamma_b m_b \omega_{\beta\perp}^2 r^2 + e_b [\phi^0(r) - \beta_b A_z^0(r)], \quad (2)$$

where $r = (x^2 + y^2)^{1/2}$ is the radial distance from the cylinder axis, and $p_\perp = (p_x^2 + p_y^2)^{1/2}$ is the transverse momentum. In Eq. (2), the equilibrium self-field potentials are determined self-consistently in terms of $f_b^0(r, \mathbf{p})$ from the steady-state Maxwell equations. Note that the distribution function in Eq. (1) is *cold* in the axial direction. An attractive feature of the choice of $f_b^0(r, \mathbf{p})$ in Eq. (1) is that the corresponding equilibrium number density, $n_b^0(r) = \int d^3p f_b^0(r, \mathbf{p})$, has the flat-top profile [6, 7]

$$n_b^0(r) = \begin{cases} \hat{n}_b = \text{const.}, & 0 \leq r < r_b, \\ 0, & r_b < r \leq r_w. \end{cases} \quad (3)$$

Here, $\hat{n}_b = \text{const.}$ is the number density of beam particles,

* This research was supported by the U.S. Department of Energy under contract AC02-76CH03073. It is a pleasure to acknowledge the benefit of useful discussions with Edward Lee.

and the edge radius r_b is determined self-consistently from

$$\frac{2\hat{T}_{\perp b}}{\gamma_b m_b} = \left(\omega_{\beta\perp}^2 - \frac{1}{2\gamma_b^2} \omega_{pb}^2 \right) r_b^2 \equiv \nu_b^2 r_b^2. \quad (4)$$

In Eq. (4), we have introduced the quantity ν_b^2 defined by

$$\nu_b^2 = \omega_{\beta\perp}^2 - \frac{1}{2\gamma_b^2} \omega_{pb}^2 = \omega_{\beta\perp}^2 (1 - s_b), \quad (5)$$

where $s_b = \omega_{pb}^2 / (2\gamma_b^2 \omega_{\beta\perp}^2)$ is a dimensionless measure of the normalized beam intensity. Note from Eq. (5) that $\nu_b = \omega_{\beta\perp} (1 - s_b)^{1/2}$ corresponds to the (depressed) betatron frequency for transverse particle oscillations in the equilibrium field configuration.

LINEARIZED EQUATIONS

To investigate the instability, we express $f_b(\mathbf{x}, \mathbf{p}, t) = f_b^0(r, \mathbf{p}) + \delta f_b(\mathbf{x}, \mathbf{p}, t)$, and make use of the linearized Vlasov-Maxwell equations [1, 8] to determine the self-consistent evolution of $\delta f_b(\mathbf{x}, \mathbf{p}, t)$, $\delta \mathbf{E}^s(\mathbf{x}, t)$ and $\delta \mathbf{B}^s(\mathbf{x}, t)$ for small-amplitude perturbations. The perturbed fields are expressed as $\delta \mathbf{E}^s = -\nabla \delta \phi - c^{-1} \partial \delta A / \partial t$ and $\delta \mathbf{B}^s = \nabla \times \delta \mathbf{A}$, and use is made of the Lorentz gauge condition, $\nabla \cdot \delta \mathbf{A} = -c^{-1} \partial \delta \phi / \partial t$, to relate $\delta \mathbf{A}$ and $\delta \phi$. The linearized Vlasov-Maxwell equations are analyzed [8] for perturbations of the form

$$\delta \psi(\mathbf{x}, t) = \delta \psi^\ell(r) \exp(i\ell\theta + ik_z z - i\omega t), \quad (6)$$

where $\ell = 1, 2, \dots$ is the azimuthal mode number of the perturbation, k_z is the axial wavenumber, and ω is the oscillation frequency. We consider perturbations with sufficiently low frequency and long axial wavelength that

$$\frac{|\omega| r_b}{c} \ll 1, \quad |k_z| r_b \ll 1, \quad \text{and} \quad \left| k_z^2 - \frac{\omega^2}{c^2} \right| r_w^2 \ll 1. \quad (7)$$

The linearized Vlasov-Maxwell equations can be simplified within the context of the inequalities in Eq. (7). Without presenting algebraic details [1, 8], it follows that the perturbed transverse force $\delta \mathbf{F}_\perp$ on a beam particle can be approximated by

$$\delta \mathbf{F}_\perp = -e_b \nabla_\perp \left(\delta \phi - \frac{1}{c} v_z \delta A_z \right). \quad (8)$$

Similarly, for the low-frequency, long-wavelength perturbations consistent with Eq. (7), it can be shown that the perturbed longitudinal force can be neglected [7, 8]. Moreover, because the axial momentum spread is negligibly small for the distribution function in Eq. (1), we approximate $\int d^3 p v_z \delta f_b = \beta_b c \int d^3 p \delta f_b$.

In summary, making use of the approximations outlined above, the linearized Vlasov-Maxwell equations can be approximated by [8]

$$\begin{aligned} & \left(\frac{\partial}{\partial t} + \mathbf{v} \cdot \frac{\partial}{\partial \mathbf{x}} - \gamma_b m_b \nu_b^2 \mathbf{x}_\perp \cdot \frac{\partial}{\partial \mathbf{p}} \right) \delta f_b \\ &= \frac{e_b}{\gamma_b m_b} \mathbf{p}_\perp \cdot \nabla_\perp \left(\delta \phi - \frac{1}{c} v_z \delta A_z \right) \frac{\partial f_b^0}{\partial H_\perp}, \end{aligned} \quad (9)$$

where $\delta \phi$ and δA_z are determined from

$$\nabla_\perp^2 \delta \phi = -4\pi e_b \delta n_b, \quad (10)$$

$$\nabla_\perp^2 \delta A_z = -4\pi e_b \beta_b \delta n_b. \quad (11)$$

Here, $\nabla_\perp^2 = \partial^2 / \partial x^2 + \partial^2 / \partial y^2$, $V_b = \beta_b c$ is the average axial velocity, and the perturbed number density is defined by $\delta n_b = \int d^3 p \delta f_b$.

Equations (9)–(11) are to be solved in the beam interior ($0 \leq r < r_b$) and in the vacuum region ($r_b < r \leq r_w$) outside the beam, enforcing the appropriate boundary conditions at the conducting wall located at radius $r = r_w$. For present purposes, we describe the wall impedance by a complex scalar function, $\tilde{Z}(\omega) = \tilde{Z}_r + i\tilde{Z}_i$, where ω is the oscillation frequency in Eq. (6). The boundary condition on the perturbed tangential electric and magnetic fields at $r = r_w \equiv [r_w(1 - \epsilon)]_{\epsilon \rightarrow 0+}$ can be expressed as [2-5, 8]

$$[\delta \mathbf{E}_t]_{r_w} = \tilde{Z}(\omega) \hat{\mathbf{n}} \times [\delta \mathbf{B}_t]_{r_w}. \quad (12)$$

Here, $\hat{\mathbf{n}} = -\hat{\mathbf{e}}_r$ is a unit vector pointing outward from the cylindrical conducting wall surface. In what follows we assume that the metal wall is almost perfectly conducting, implying that $|\tilde{Z}(\omega)| \ll 1$. Making use of $(\nabla \times \delta \mathbf{B})_r = c^{-1} \partial \delta E_r / \partial t$ in the vacuum region, the boundary conditions in Eq. (12) can be expressed for $|\tilde{Z}| \ll 1$ as

$$\begin{aligned} k_z [\delta \phi^\ell]_{r_w} - \frac{\omega}{c} [\delta A_z^\ell]_{r_w} &= i\tilde{Z} \left[\frac{\partial}{\partial r} \delta A_z^\ell \right]_{r_w}, \\ \frac{\ell}{r_w} [\delta \phi^\ell]_{r_w} &= -i\tilde{Z} \left\{ \frac{\omega}{c} \left[\frac{\partial}{\partial r} \delta \phi^\ell \right]_{r_w} + k_z \left[\frac{\partial}{\partial r} \delta A_z^\ell \right]_{r_w} \right\}. \end{aligned} \quad (13)$$

Equation (13) expresses the boundary conditions at the conducting wall in terms of the impedance $\tilde{Z}(\omega)$ and the perturbed potentials, $\delta \phi$ and δA_z . In the limit of zero impedance, $\tilde{Z} \rightarrow 0$, Eq. (13) reduces to $[\delta \phi^\ell]_{r_w} = 0 = [\delta A_z^\ell]_{r_w}$, corresponding to the boundary conditions expected for a perfectly conducting, cylindrical wall. Depending on the frequency regime, there are several models of wall impedance $\tilde{Z}(\omega)$ that can be used in the boundary conditions in Eq. (13) [4].

STABILITY ANALYSIS

In the analysis of Eqs. (9)–(11), we introduce the new independent variables τ and Z defined by $\tau = t - z/V_b$ and $Z = z$. The perturbation in Eq. (6) can be expressed as

$$\delta \psi(\mathbf{x}, Z, \tau) = \delta \psi^\ell(r) \exp[i\ell\theta - i\omega\tau - i(\Omega/V_b)Z], \quad (14)$$

where $\ell = 1, 2, \dots$, is the azimuthal mode number, ω is the oscillation frequency, and

$$\Omega/V_b = (\omega - k_z V_b)/V_b \quad (15)$$

is the effective axial wavenumber of the perturbation in the new variables (Z, τ) . If the charge bunch experiences a perturbation for $\tau > 0$ with real oscillation frequency ω , it

is evident from Eqs. (14) and (15) that Ω/V_b represents the spatial oscillation and growth (or damping) of the perturbation as a function of axial position Z .

Assuming perturbations of the form in Eq. (14) for $\text{Im}\Omega > 0$ and integrating Eq. (9), it is found that a class of solutions exists with density perturbation amplitude $\delta n_b^\ell(r) = \int d^2p \delta f_b^\ell(r, \mathbf{p}_\perp)$ localized at the surface of the charge bunch ($r = r_b$). Without presenting algebraic details [8], we obtain

$$4\pi e_b \delta n_b^\ell(r) = -\frac{2\ell}{r_b} \chi_b^\ell(\Omega) [\delta\phi^\ell(r) - \beta_b \delta A_z^\ell(r)] \delta(r - r_b). \quad (16)$$

Here, the response function $\chi_b^\ell(\Omega)$ is defined by

$$\chi_b^\ell(\Omega) = -\frac{\hat{\omega}_{pb}^2}{2\ell 2^\ell \nu_b^2} \sum_{m=0}^{\ell} \frac{\ell!}{m!(\ell-m)!} \frac{(\ell-2m)\nu_b}{\Omega - (\ell-2m)\nu_b}, \quad (17)$$

where $\Omega = \omega - k_z V_b$ is the Doppler shifted frequency, $\hat{\omega}_{pb} = (4\pi n_b e_b^2 / \gamma_b m_b)^{1/2}$ is the relativistic plasma frequency, and $\nu_b = (\omega_{\beta\perp}^2 - \hat{\omega}_{pb}^2 / 2\gamma_b^2)^{1/2}$ is the depressed betatron frequency. As expected, the response function in Eq. (17) has a rich harmonic content at harmonics of ν_b . We define $\delta\psi^\ell(r) = \delta\phi^\ell(r) - \beta_b \delta A_z^\ell(r)$, and denote $\delta\hat{\psi}^\ell = \delta\psi^\ell(r_b)$, $\delta\hat{\phi}^\ell = \delta\phi^\ell(r_b)$ and $\delta\hat{A}_z^\ell = \delta A_z^\ell(r_b)$. Substituting Eq. (16), Maxwell's equations (10) and (11) become [8]

$$\left(\frac{1}{r} \frac{\partial}{\partial r} r \frac{\partial}{\partial r} - \frac{\ell^2}{r^2} \right) \delta\phi^\ell(r) = \frac{2\ell}{r_b} \chi_b^\ell(\Omega) \delta\hat{\psi}^\ell \delta(r - r_b), \quad (18)$$

$$\left(\frac{1}{r} \frac{\partial}{\partial r} r \frac{\partial}{\partial r} - \frac{\ell^2}{r^2} \right) \delta A_z^\ell(r) = \frac{2\ell}{r_b} \beta_b \chi_b^\ell(\Omega) \delta\hat{\psi}^\ell \delta(r - r_b), \quad (19)$$

for azimuthal mode numbers $\ell = 1, 2, \dots$.

Equations (18) and (19), derived for perturbations about the equilibrium distribution in Eq. (1) with flattop-density profile, constitute the final forms of the eigenvalue equations used in the present stability analysis. Here, Eqs. (18) and (19) are to be solved over the interval $0 \leq r \leq r_w$ for the eigenfunctions $\delta\phi^\ell(r)$ and $\delta A_z^\ell(r)$ and eigenvalue Ω , subject to the condition that $\delta\phi^\ell(r)$ and $\delta A_z^\ell(r)$ be regular at the origin ($r = 0$), and satisfy the boundary conditions in Eq. (13) at the conducting wall ($r = r_w$).

Equations (18) and (19) can be solved exactly for the eigenfunctions $\delta\phi^\ell(r)$ and $\delta A_z^\ell(r)$ in the interval $0 \leq r \leq r_w$, and the boundary condition (13) enforced at the conducting wall [8]. We introduce

$$\begin{aligned} \Delta' &= -2 \frac{\omega r_w}{\ell c} \left(1 + \frac{k_z V_b}{\omega} \right) i \tilde{Z}(\omega), \\ \Delta &= -2 \frac{\ell c}{\omega r_w} \left[1 + \frac{k_z^2 r_w^2}{\ell^2} \left(1 + \frac{\omega}{k_z V_b} \right) \right] i \tilde{Z}(\omega), \end{aligned} \quad (20)$$

where Δ' and Δ are treated as small parameters with $|\Delta'|, |\Delta| \ll 1$. Some straightforward algebra [8] then leads to

the dispersion relation

$$\begin{aligned} D_b^\ell(\Omega) &= 1 + \frac{1}{\gamma_b^2} \left[1 - \left(\frac{r_b}{r_w} \right)^{2\ell} \right] \chi_b^\ell(\Omega) \\ &+ \left(\frac{r_b}{r_w} \right)^{2\ell} \chi_b^\ell(\Omega) [\beta_b^2 \Delta - \Delta'] = 0. \end{aligned} \quad (21)$$

Equation (21) is the final form of the dispersion relation derived from the linearized Vlasov-Maxwell equations for perturbations about the equilibrium distribution function in Eq. (1) with corresponding flattop density profile in Eq. (3). The dispersion relation (21) is valid for low-frequency long-wavelength perturbations consistent with Eq. (7), and can be applied over a wide range of normalized beam intensity in the range $0 < s_b = \hat{\omega}_{pb}^2 / 2\gamma_b^2 \omega_{\beta\perp}^2 < 1$.

The dispersion relation (21) can be used to investigate detailed stability properties for azimuthal mode numbers $\ell = 1, 2, 3, \dots$. As an example, we consider dipole-mode perturbations with $\ell = 1$. In this case, it follows from Eq. (17) that the response function $\chi_b^{\ell=1}(\Omega)$ is given by

$$\chi_b^{\ell=1}(\Omega) = -\frac{\hat{\omega}_{pb}^2/2}{\Omega^2 - \nu_b^2}, \quad (22)$$

where $\nu_b^2 = \omega_{\beta\perp}^2 - \hat{\omega}_{pb}^2 / 2\gamma_b^2$. Substituting Eq. (22) into Eq. (21), the dispersion relation reduces to

$$\Omega^2 = \omega_{\beta\perp}^2 - \left(\frac{r_b^2}{r_w} \right)^2 \frac{\hat{\omega}_{pb}^2}{2\gamma_b^2} - \left(\frac{r_b}{r_w} \right)^2 \beta_b^2 \hat{\omega}_{pb}^2 \frac{c}{\omega r_w} i \tilde{Z}(\omega), \quad (23)$$

where use has been made of $\nu_b^2 = \omega_{\beta\perp}^2 - \hat{\omega}_{pb}^2 / 2\gamma_b^2$, and we have approximated $\beta_b^2 \Delta - \Delta' = -(2i\beta_b^2 c \ell / \omega r_w) \tilde{Z}(\omega)$.

The dipole-mode dispersion relation (23) is valid over the entire allowed range of normalized beam intensity ($0 < s_b < 1$) and can be used to investigate detailed stability properties for a wide variety of choices of impedance function $\tilde{Z}(\omega)$. The application of Eq. (23) is discussed in more detail in Ref. 8.

REFERENCES

- [1] R. C. Davidson and H. Qin, *Physics of Intense Charged Particle Beams in High Energy Accelerators* (World Scientific, Singapore, 2001), and references therein.
- [2] V. K. Neil and A. M. Sessler, *Rev. Scientific Instr.* **36**, 429 (1965).
- [3] E. P. Lee, in *Proceedings of the 1981 Linear Accelerator Conference*, Los Alamos National Laboratory Report LA-9234-C, pp. 263-265.
- [4] E. P. Lee, *Part. Accel.* **37**, 307 (1992).
- [5] J. D. Lawson, *The Physics of Charged-Particle Beams* (Oxford Science Publications, New York, 1988).
- [6] T. -S. Wang and I. Smith, *Part. Accel.* **12**, 247 (1982).
- [7] R. C. Davidson, H. Qin, P. Stoltz and T. -S. Wang, *Phys. Rev. ST Accel. Beams* **2**, 054401 (1999).
- [8] R. C. Davidson, H. Qin and G. Shvets, submitted for publication (2003).

δf SIMULATION STUDIES OF THE ION-ELECTRON TWO-STREAM INSTABILITY IN IBX*

Hong Qin, Ronald C. Davidson, and Edward A. Startsev
Plasma Physics Laboratory, Princeton University, Princeton, NJ 08543, USA

Abstract

The ion-electron two-stream instability is studied numerically for the high intensity heavy ion beams envisioned in the Integrated Beam Experiment (IBX). We consider a 1.7 MeV K^+ beam with 0.25 microcoulombs/m line density propagating through a small background electron population. The detailed linear properties of the ion-electron two-stream instability are studied using a 3D low-noise delta- f particle simulation method implemented in the Beam Equilibrium, Stability and Transport (BEST) code.

INTRODUCTION

In typical linear induction accelerators for heavy ion fusion drivers, the beam current is much higher than that in contemporary accelerators and storage rings in order to obtain sufficient fusion energy gain. For a given focusing lattice, most designs of heavy ion fusion drivers operate near the space-charge limit. Large space-charge forces inevitably induce a strong interaction among the beam particles, and in some regimes can result in collective instabilities [1, 2]. One of the major objectives in the Integrated Beam Experiment (IBX) proposed by the U.S. Heavy Ion Fusion Virtual National Laboratory is to study collective effects in a space-charge-dominated beam [3]. In particular, it is proposed to use IBX to investigate the ion-electron two-stream instability, which has been observed experimentally in high intensity accelerators and storage rings [4–6]. A well-documented example is the electron-proton (e-p) instability observed in the Proton Storage Ring experiment [4, 5]. Theoretical studies [1, 7–15] suggest that the relative streaming motion of the high-intensity beam particles through a background charge species provides the free energy to drive the classical *two-stream* instability, appropriately modified to include the effects of dc space charge, relativistic kinematics, presence of a conducting wall, etc. A background population of electrons can result by secondary emission when energetic beam ions strike the chamber wall [16–18], or through ionization of background neutral gas by the beam ions.

When electrons are present, two-stream interactions in IBX are expected to be stronger than the two-stream instabilities observed so far in proton machines because of the much larger beam intensity. In this paper, we study the ion-electron two-stream instability in IBX using a per-

turbative particle simulation method (δf method) for solving the Vlasov-Maxwell equations. As a low-noise nonlinear particle simulation technique, the δf method has been implemented in the recently developed Beam Equilibrium, Stability and Transport (BEST) code [19–21], which has been applied to a wide range of important collective processes in intense beams. We consider a K^+ IBX beam with $m = 39.1$ au and kinetic energy 1.72 MeV in the low energy regime. Other beam parameters are: line density $N = 1.50 \times 10^{12}$ /m; RMS radius $R_b = 1.3$ cm; and beam transverse thermal speed $v_{th} = 0.054\beta_c$. For the focusing lattice, the vacuum phase advance is $\sigma_v = 72^\circ$, and the applied betatron frequency is $\omega_{\beta b} = 1.21 \times 10^7 \text{ s}^{-1}$.

δF SIMULATION METHOD

The theoretical model employed here is based on the nonlinear Vlasov-Maxwell equations. We consider a thin, continuous, high-intensity ion beam ($j = b$), with characteristic radius r_b propagating in the z -direction through background electrons ($j = e$), with each component described by a distribution function $f_j(\mathbf{x}, \mathbf{p}, t)$ [1, 7]. The nonlinear Vlasov-Maxwell equations for $f_j(\mathbf{x}, \mathbf{p}, t)$ and the self-generated fields can be approximated by [1, 7]

$$\left\{ \frac{\partial}{\partial t} + \mathbf{v} \cdot \frac{\partial}{\partial \mathbf{x}} - [\gamma_j m_j \omega_{\beta j}^2 \mathbf{x}_\perp + e_j (\nabla \phi - \frac{v_z}{c} \nabla_\perp A_z)] \cdot \frac{\partial}{\partial \mathbf{p}} \right\} f_j(\mathbf{x}, \mathbf{p}, t) = 0, \quad (1)$$

$$\begin{aligned} \nabla^2 \phi &= -4\pi \sum_j e_j \int d^3 p f_j(\mathbf{x}, \mathbf{p}, t), \\ \nabla^2 A_z &= -\frac{4\pi}{c} \sum_j e_j \int d^3 p v_z f_j(\mathbf{x}, \mathbf{p}, t). \end{aligned} \quad (2)$$

To solve the Vlasov-Maxwell equations, we use a low-noise δf method [19–21], where the total distribution function is divided into two parts, $f_j = f_{j0} + \delta f_j$. Here, $\omega_{\beta j}$ is the applied smooth-focusing frequency, f_{j0} is a *known* equilibrium solution ($\partial/\partial t = 0$) to the nonlinear Vlasov-Maxwell equations (1) and (2), and the numerical simulation is carried out to determine the detailed nonlinear evolution of the perturbed distribution function δf_j . This is accomplished by advancing the weight function defined by $w_j \equiv \delta f_j / f_j$, together with the particles' positions and momenta. The dynamical equations for w_{ji} is given by [21]

$$\begin{aligned} \frac{dw_{ji}}{dt} &= -(1 - w_{ji}) \frac{1}{f_{j0}} \frac{\partial f_{j0}}{\partial \mathbf{p}} \cdot \delta \left(\frac{d\mathbf{p}_{ji}}{dt} \right), \\ \delta \left(\frac{d\mathbf{p}_{ji}}{dt} \right) &\equiv -e_j \left(\nabla \phi - \frac{v_{zji}}{c} \nabla_\perp A_z \right), \end{aligned} \quad (3)$$

* Research supported by the U.S. Department of Energy. We thank Drs. Ron Cohen, Christine Celata, Art Molvik, John Barnard, and Alex Freidman for many productive discussions.

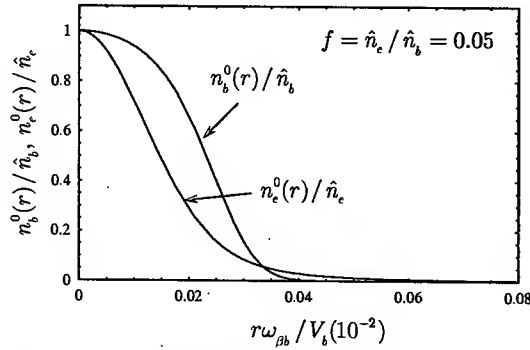


Figure 1: Normalized equilibrium beam ion and background electron density profiles.

where the subscript “ j ” labels the i ’th simulation particle of the j ’th species, $\delta\phi = \phi - \phi_0$, and $\delta A_z = A_z - A_{z0}$. Here, the equilibrium solutions (ϕ_0, A_{z0}, f_{j0}) solve the steady-state Vlasov-Maxwell equations (1) and (2). A detailed description of the nonlinear δf method can be found in Ref. [21].

SIMULATION RESULTS

In the present simulations of the two-stream instability, instead of using the theoretically-convenient KV distribution [1], we assume that the background equilibrium distribution ($\partial/\partial t = 0$) is the more realistic *bi-Maxwellian* distribution with temperature $T_{j\perp} = \text{const.}$ in the transverse plane, and temperature $T_{j\parallel} = \text{const.}$ in the longitudinal direction. That is,

$$f_{j0}(r, \mathbf{p}) = \frac{\hat{n}_j}{(2\pi m_j)^{3/2} \gamma_j^{5/2} T_{j\perp} T_{j\parallel}^{1/2}} \times \exp \left\{ -\frac{(p_z - \gamma_j m_j \beta_j c)^2}{2\gamma_j^3 m_j T_{j\parallel}} - \frac{p_\perp^2}{2\gamma_j m_j T_{j\perp}} \right\} \times \exp \left\{ -\frac{\gamma_j m_j \omega_{\beta j}^2 r^2/2 + e_j(\phi_0 - \beta_j A_{z0})}{T_{j\perp}} \right\}, \quad (4)$$

where \hat{n}_j is the density on axis ($r = 0$) of the j ’th species, and ϕ_0 and A_{z0} are the equilibrium self-field potentials, determined self-consistently from the nonlinear Maxwell equations

$$\frac{1}{r} \frac{\partial}{\partial r} r \frac{\partial \phi_0(r)}{\partial r} = -4\pi \sum_j e_j \int d^3p f_{j0}(r, \mathbf{p}), \quad (5)$$

$$\frac{1}{r} \frac{\partial}{\partial r} r \frac{\partial A_{z0}(r)}{\partial r} = -\frac{4\pi}{c} \sum_j e_j \int d^3p v_z f_{j0}(r, \mathbf{p}).$$

The equilibrium density profile for each species, $n_j^0(r)/\hat{n}_j = (1/\hat{n}_j) \int d^3p f_{j0}(r, \mathbf{p}, t)$ ($j = b, e$), can be readily obtained once the equilibrium potentials ϕ_0 and A_{z0} are determined numerically from Eqs. (4) and (5). If the beam particles are the only species in the system,

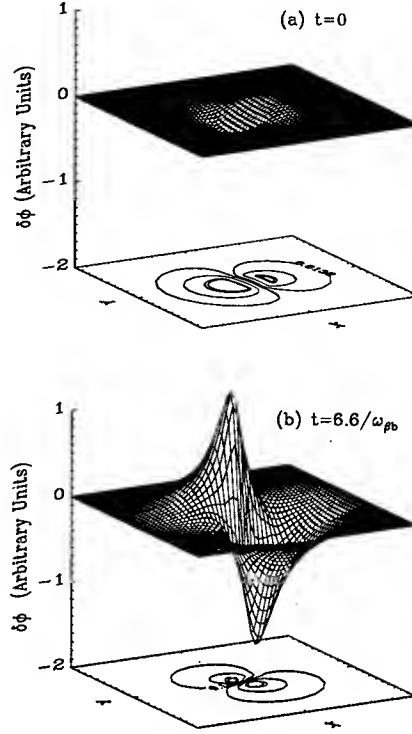


Figure 2: The x - y projection (at fixed value of z) of the perturbed electrostatic potential $\delta\phi(x, y, t)$ for the ion-electron two-stream instability growing from a small initial perturbation, shown at (a) $t = 0$, and (b) $\omega_{\beta b} t = 6.6$.

the equilibrium can be characterized by a single dimensionless parameter $s_b \equiv \hat{\omega}_{pb}^2 / (2\gamma_b^2 \omega_{\beta b}^2)$, where $\hat{\omega}_{pb}^2 = 4\pi\hat{n}_b e_b^2 / (m_b \gamma_b)$ is the beam plasma frequency on axis. The parameter s_b , which measures the self-field intensity relative to the applied focusing force, satisfies $0 \leq s_b \leq 1$, with $s_b = 0$ corresponding to the zero space-charge limit, and $s_b \rightarrow 1$ to the space-charge-dominated limit. For IBX, we take $s_b = 0.996$, and the density profile is close to a flat-top profile, because s_b is very close to the space-charge dominated limit. If there is a small background electron population, the space-charge force will be partially neutralized, and the beam density profile relaxes to a bell-shape. Plotted in Fig. 1 are the density profiles for an ion-electron two-species equilibrium with fractional charge neutralization $f \equiv \hat{n}_e/\hat{n}_b = 0.05$, and $V_e = 0$ and $\omega_{\beta e} = 0$ for stationary background electrons.

To simulate the ion-electron two-stream instability, we perturb the two-species equilibrium discussed above with a small initial perturbation, and use the *linearized* version of the BEST code to simulate the dynamics of the system for many thousands of wave periods. In Fig. 2, the $x - y$ projection of the perturbed potential $\delta\phi$ at a fixed longitudinal position is plotted at $t = 0$ and $t = 6.6/\omega_{\beta b}$. Clearly, $\delta\phi$ grows to a moderate amplitude by $t = 6.6/\omega_{\beta b}$, and

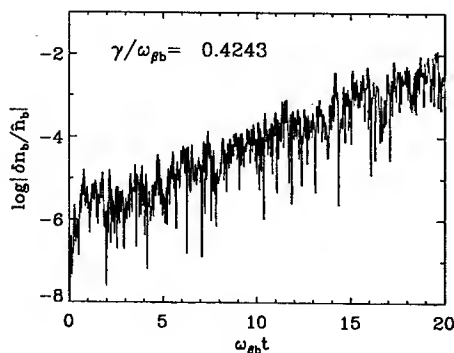


Figure 3: Time history of perturbed density $\delta n_b/\hat{n}_b$ at a fixed spatial location.

the $l = 1$ dipole mode is the dominant unstable mode, for which the growth rate is measured to be $\text{Im } \omega = 0.42\omega_{pb}$. Plotted in Fig. 3 is the time history of the beam density perturbation at one spatial location. Evidently, after an initial transition period, the perturbation grows exponentially, which is the expected behavior of an instability during the linear growth phase.

In the simulation results for the two-stream instability presented above, we have assumed initially cold beam ions in the longitudinal direction ($\Delta p_{b\parallel}/p_{b\parallel} = 0$) to maximize the growth rate of the instability. Here, $p_{b\parallel} = \gamma_b m_b V_b$. In general, when the longitudinal momentum spread of the beam ions is finite, Landau damping by parallel ion kinetic effects provides a mechanism that reduces the growth rate. Shown in Fig. 4 is a plot of the maximum linear growth rate $(\text{Im } \omega)_{\max}$ versus the normalized initial axial momentum spread $\Delta p_{b\parallel}/p_{b\parallel}$ obtained in the numerical simulations for the cases where $f \equiv \hat{n}_e/\hat{n}_b = 5\%$ and $f = 2.5\%$. As evident from Fig. 4, the growth rate decreases dramatically as $\Delta p_{b\parallel}/p_{b\parallel}$ is increased. When $\Delta p_{b\parallel}/p_{b\parallel}$ is high enough, the mode is completely stabilized by longitudinal Landau damping effects by the beam ions. This result agrees qualitatively with theoretical predications [9]. For a fixed value of $\Delta p_{b\parallel}/p_{b\parallel}$, the growth rate obtained from the simulation is several times smaller than the theoretical value predicted by the dispersion relation derived for a KV beam with flat-top density profile [7, 8]. This difference can be attributed to the fact that the present simulations are carried out for more realistic thermal equilibrium beams with bell-shape density profiles. The nonlinear space-charge potential due to the bell-shape density profiles induces substantial tune spread in the transverse direction, which provides an additional damping mechanism, and reduces the growth rate of the two-stream instability [20].

REFERENCES

[1] R. C. Davidson and H. Qin, *Physics of Intense Charged Particle Beams in High Energy Accelerators* (World Scientific, 2001).

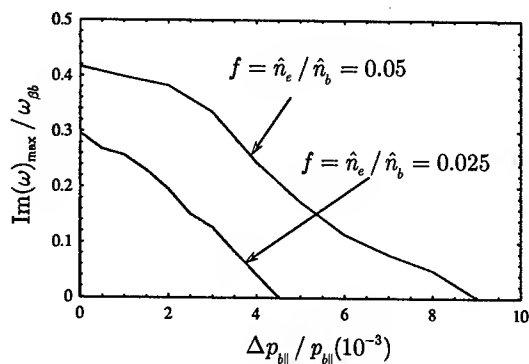


Figure 4: The maximum linear growth rate $(\text{Im } \omega)_{\max}$ of the ion-electron two-stream instability decreases as the longitudinal momentum spread of the beam ions increases.

- [2] A. W. Chao, *Physics of Collective Beam Instabilities in High Energy Accelerators* (Wiley, New York, 1993).
- [3] J. J. Barnard et al., *Laser and Particle Beams* **21**, in press (2003).
- [4] D. Neuffer et al., *Nucl. Instr. Methods Phys. Res. A* **321**, 1 (1992).
- [5] R. J. Macek et al., in *Proc. 2001 Particle Accelerator Conference*, pp. 668–672 (2001).
- [6] M. Giovannozzi, E. Mtral, G. Mtral, G. Rumolo and F. Zimmermann, *Phys. Rev. ST Accel. Beams* **6**, 010101 (2003).
- [7] R. C. Davidson, H. Qin, P. H. Stoltz and T. S. Wang, *Phys. Rev. ST Accel. Beams* **2**, 054401 (1999).
- [8] R. C. Davidson, H. Qin and T. S. Wang, *Physics Letters A* **252**, 213 (1999).
- [9] R. C. Davidson and H. Qin, *Phys. Lett. A* **270**, 177 (2000).
- [10] T.-S. F. Wang, P. J. Channell, R. J. Macek and R. C. Davidson, *Phys. Rev. ST Accel. Beams* **6**, 014204 (2003).
- [11] P. J. Channell, *Phys. Rev. ST Accel. Beams* **5**, 114401 (2003).
- [12] K. Ohmi, T. Toyama and C. Ohmori, *Phys. Rev. ST Accel. Beams* **5**, 114402 (2002).
- [13] D. G. Koshkarev and P. R. Zenkevich, *Particle Accelerators* **3**, 1 (1972).
- [14] E. Keil and B. Zotter, CERN-ISH-TH/71-58, Technical report, CERN (1971).
- [15] L. J. Laslett, A. M. Sessler and D. Möhl, *Nucl. Instr. Methods Phys. Res.* **121**, 517 (1974).
- [16] R. H. Cohen et al., in *Proc. 2003 Particle Accelerator Conference* (2003).
- [17] A. W. Molvik et al., in *Proc. 2003 Particle Accelerator Conference* (2003).
- [18] M. T. F. Pivi and M. A. Furman, *Phys. Rev. ST Accel. Beams* **6**, 034201 (2003).
- [19] H. Qin, E. A. Startsev, R. C. Davidson and W. W. Lee, *Laser and Particle Beams* **21**, 1 (2003).
- [20] H. Qin, E. A. Startsev and R. C. Davidson, *Phys. Rev. ST Accel. Beams* **6**, 014401 (2003).
- [21] H. Qin, R. C. Davidson and W. W. Lee, *Phys. Rev. ST Accel. and Beams* **3**, 084401 (2000).

KINETIC STUDIES OF TEMPERATURE ANISOTROPY INSTABILITY IN INTENSE CHARGED PARTICLE BEAMS *

Edward A. Startsev, Ronald C. Davidson and Hong Qin

Plasma Physics Laboratory, Princeton University, Princeton, New Jersey 08543

Abstract

This paper extends previous analytical and numerical studies [E. A. Startsev, R. C. Davidson and H. Qin, *Phys. Plasmas* 9, 3138 (2002)] of the stability properties of intense nonneutral charged particle beams with large temperature anisotropy ($T_{\perp b} \gg T_{\parallel b}$) to allow for non-axisymmetric perturbations with $\partial/\partial\theta \neq 0$. The most unstable modes are identified, and their eigenfrequencies and radial mode structure are determined.

LINEAR STABILITY THEORY

It is well known that in neutral plasmas with strongly anisotropic distributions ($T_{\parallel b}/T_{\perp b} \ll 1$) a collective Harris instability [1] may develop if there is sufficient coupling between the transverse and longitudinal degrees of freedom. Such anisotropies develop naturally in accelerators. For particles with charge q accelerated by a voltage V , the longitudinal temperature decreases according to $T_{\parallel bf} = T_{\parallel bi}^2/2qV$ (for a nonrelativistic beam). At the same time, the transverse temperature may increase due to nonlinearities in the applied and self-field forces, non-stationary beam profiles, and beam mismatch. These processes may provide the free energy to drive collective instabilities, and lead to a deterioration of beam quality. The instability may also result in an increase in the longitudinal velocity spread, which will make the focusing of the beam difficult, and may impose a limit on the minimum spot size achievable in heavy ion fusion experiments.

We briefly outline here a simple derivation [2] of the Harris-like instability in intense particle beams for electrostatic perturbations about the thermal equilibrium distribution with temperature anisotropy ($T_{\perp b} > T_{\parallel b}$) described in the beam frame by the self-consistent axisymmetric Vlasov equilibrium [3]

$$f_b^0(r, \mathbf{p}) = \frac{\hat{n}_b}{(2\pi m_b)^{3/2} T_{\perp b} T_{\parallel b}^{1/2}} \exp\left(-\frac{H_{\perp}}{T_{\perp b}} - \frac{H_{\parallel}}{T_{\parallel b}}\right). \quad (1)$$

Here, $H_{\parallel} = p_z^2/2m_b$, $H_{\perp} = p_{\perp}^2/2m_b + (1/2)m_b\omega_f^2 r^2 + e_b\phi^0(r)$ is the single-particle Hamiltonian for transverse particle motion, $p_{\perp} = (p_x^2 + p_y^2)^{1/2}$ is the transverse particle momentum, $r = (x^2 + y^2)^{1/2}$ is the radial distance from the beam axis, $\omega_f = \text{const.}$ is the transverse frequency associated with the applied focusing field in the smooth-focusing approximation, and $\phi^0(r)$ is the equilibrium space-charge potential determined self-consistently

from Poisson's equation,

$$\frac{1}{r} \frac{\partial}{\partial r} r \frac{\partial \phi^0}{\partial r} = -4\pi e_b n_b^0, \quad (2)$$

where $n_b^0(r) = \int d^3p f_b^0(r, \mathbf{p})$ is the equilibrium number density of beam particles. A perfectly conducting wall is located at radius $r = r_w$.

For present purposes, we consider small-amplitude electrostatic perturbations of the form

$$\delta\phi(\mathbf{x}, t) = \widehat{\delta\phi}(r) \exp(im\theta + ik_z z - i\omega t), \quad (3)$$

where $\delta\phi(\mathbf{x}, t)$ is the perturbed electrostatic potential, k_z is the axial wavenumber, m is the azimuthal mode number and ω is the complex oscillation frequency, with $\text{Im}\omega > 0$ corresponding to instability (temporal growth). Without presenting algebraic details, using the method of characteristics [2, 3], the linearized Poisson equation can be expressed as

$$\left(\frac{1}{r} \frac{\partial}{\partial r} r \frac{\partial}{\partial r} - k_z^2 - \frac{m^2}{r^2}\right) \widehat{\delta\phi}(r) = -4\pi e_b \int d^3p \widehat{\delta f}_b, \quad (4)$$

where

$$\begin{aligned} \widehat{\delta f}_b = & e_b \frac{\partial f_b^0}{\partial H_{\perp}} \widehat{\delta\phi} + e_b \left[(\omega - k_z v_z) \frac{\partial f_b^0}{\partial H_{\perp}} + k_z v_z \frac{\partial f_b^0}{\partial H_{\parallel}} \right] \\ & \times i \int_{-\infty}^t dt' \widehat{\delta\phi}[r'(t')] \exp[i(k_z v_z - \omega)(t' - t) + im\theta'(t')], \end{aligned} \quad (5)$$

for perturbations about the choice of the anisotropic thermal equilibrium distribution function in Eq. (1). In the orbit integral in Eq. (5), $\text{Im}\omega > 0$ is assumed, and $r'(t') = [x'^2(t') + y'^2(t')]^{1/2}$ and $\theta'(t')$ are the transverse orbits in the equilibrium field configuration such that $[\mathbf{x}_{\perp}'(t'), \mathbf{p}_{\perp}'(t')]$ passes through the phase-space point $(\mathbf{x}_{\perp}, \mathbf{p}_{\perp})$ at time $t' = t$ [2, 3].

In Eq. (4), we express the perturbation amplitude as $\widehat{\delta\phi}(r) = \sum \alpha_n \phi_n(r)$, where $\{\alpha_n\}$ are constants, and the complete set of vacuum eigenfunctions $\{\phi_n(r)\}$ is defined by $\phi_n(r) = A_n J_m(\lambda_n r/r_w)$. Here, λ_n is the n 'th zero of Bessel function $J_m(\lambda_n) = 0$, and A_n is a normalization constant [2]. This gives the matrix dispersion equation

$$\sum_n \alpha_n D_{n,n'}(\omega) = 0. \quad (6)$$

The condition for a nontrivial solution to Eq. (6) is

$$\det\{D_{n,n'}(\omega)\} = 0, \quad (7)$$

*RESEARCH SUPPORTED BY THE U. S. DEPARTMENT OF ENERGY

which plays the role of a matrix dispersion relation that determines the complex oscillation frequency ω [2].

In the present analysis, it is convenient to introduce the effective *depressed* betatron frequency $\omega_{\beta\perp}$. It can be shown [3] for the equilibrium distribution in Eq. (1), that the mean-square beam radius $r_b^2 = \langle r^2 \rangle = N_b^{-1} 2\pi \int_0^{r_w} dr r^3 n_b^0(r)$ is related *exactly* to the line density $N_b = 2\pi \int_0^{r_w} dr r n_b^0(r)$, and the transverse beam temperature $T_{\perp b}$, by the equilibrium radial force balance equation

$$\omega_f^2 r_b^2 = \frac{N_b e_b^2}{m_b} + \frac{2T_{\perp b}}{m_b}. \quad (8)$$

Equation (8) can be rewritten as

$$\left(\omega_f^2 - \frac{1}{2} \bar{\omega}_{pb}^2 \right) r_b^2 = \frac{2T_{\perp b}}{m_b}, \quad (9)$$

where we have introduced the effective *average* beam plasma frequency $\bar{\omega}_{pb}$ defined by

$$r_b^2 \bar{\omega}_{pb}^2 \equiv \int_0^{r_w} dr r \omega_{pb}^2(r) = \frac{2e_b^2 N_b}{m_b}, \quad (10)$$

where $\omega_{pb}^2(r) = 4\pi n_b^0(r) e_b^2 / \gamma_b m_b$ is the relativistic plasma frequency-squared. Then, Eq. (9) can be used to introduce the effective *depressed* betatron frequency $\omega_{\beta\perp}$ defined by

$$\omega_{\beta\perp}^2 \equiv \left(\omega_f^2 - \frac{1}{2} \bar{\omega}_{pb}^2 \right) = \frac{2T_{\perp b}}{m_b r_b^2}, \quad (11)$$

and the normalized tune depression $\bar{\nu}/\nu_0$ defined by

$$\frac{\bar{\nu}}{\nu_0} \equiv \frac{\omega_{\beta\perp}}{\omega_f} = (1 - \bar{s}_b)^{1/2}. \quad (12)$$

If, for example, the beam density were uniform over the beam cross section, then Eq. (11) corresponds to the usual definition of the depressed betatron frequency for a Kapchinskij – Vladimirskij (KV) [3] beam, and it is readily shown that the radial orbit $\hat{r}(\tau)$ occurring in Eq. (5) can be expressed as [2]

$$\hat{r}^2(\tau) = \frac{H_{\perp}}{m_b \omega_{\beta\perp}^2} \left[1 - \sqrt{1 - \left(\frac{\omega_{\beta\perp} P_{\theta}}{H_{\perp}} \right)^2} \cos(2\omega_{\beta\perp} \tau) \right]. \quad (13)$$

In general, for the choice of equilibrium distribution function in Eq. (1), there will be a spread in transverse depressed betatron frequencies $\omega_{\beta\perp}(H_{\perp}, P_{\theta})$, and the particle trajectories will not be described by the simple trigonometric function in Eq. (13). For present purposes, however, we consider a simple *model* in which the radial orbit $\hat{r}(\tau)$ occurring in Eq. (5) is approximated by Eq. (13) with the constant frequency $\omega_{\beta\perp}$ defined in Eq. (11), and the approximate equilibrium density profile is defined by $n_b^0(r) = \hat{n}_b \exp(-m_b \omega_{\beta\perp}^2 r^2 / 2T_{\perp b})$. For a nonuniform beam, $\omega_{\beta\perp}^{-1}$ is the characteristic time for a particle with thermal speed $v_{th\perp} = (2T_{\perp b}/m_b)^{1/2}$ to cross the rms radius

r_b of the beam. In this case $D_{n,n'}(\omega)$ can be evaluated in closed analytical form [2] provided the conducting wall is sufficiently far removed from the beam ($r_w/r_b \geq 3$, say). In this case, the matrix elements decrease exponentially away from the diagonal, with

$$\left| \frac{D_{n,n+k}}{D_{n,n}} \right| \sim \exp \left(-\frac{\pi^2 k^2}{4} \frac{r_b^2}{r_w^2} \right), \quad (14)$$

where k is an integer. Therefore, for $r_w/r_b \geq 3$, we can approximate $\{D_{n,n'}(\omega)\}$ by a *tri-diagonal* matrix. In this case, for the lowest-order radial modes ($n = 1$ and $n = 2$), the dispersion relation (7) can be approximated by [2]

$$D_{1,1}(\omega) D_{2,2}(\omega) - [D_{1,2}(\omega)]^2 = 0, \quad (15)$$

where use has been made of $D_{1,2}(\omega) = D_{2,1}(\omega)$.

Typical numerical results [2] obtained from the approximate dispersion relation utilizing Eq. (15) are presented in Figs. 1 – 2 for the case where $r_w = 3r_b$. Only the leading-order nonresonant terms and one resonant term at frequencies $\omega \approx \pm 2\omega_{\beta\perp}$ for even values of m , and $\omega \approx \pm \omega_{\beta\perp}$ for odd values of m , have been retained in the analysis [2]. Note from Fig. 1 that the critical values of $k_z r_w$ for the onset of instability and for maximum growth rate increase as the azimuthal mode number m is increased. As expected, finite $-T_{\parallel b}$ effects introduce a finite bandwidth in $k_z r_w$ for instability, since the modes with large values of $k_z r_w$ are stabilized by Landau damping [2, 3]. Also, the unstable modes with odd azimuthal number are purely growing.

Note from Fig. 2 that the $m = 1$ dipole mode has the

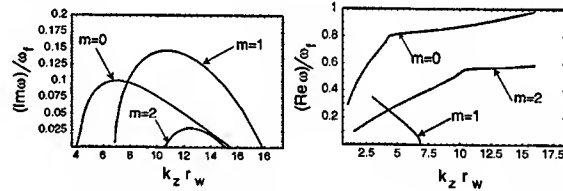


Figure 1: Plots of normalized growth rate $(Im\omega)/\omega_f$ and real frequency $(Re\omega)/\omega_f$ versus $k_z r_w$ for $\bar{\nu}/\nu_0 = 0.53$ and $T_{\parallel b}/T_{\perp b} = 0.02$ [2].

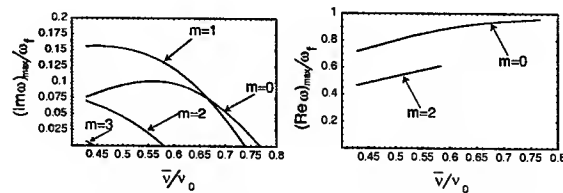


Figure 2: Plots of normalized growth rate $(Im\omega)_{max}/\omega_f$ and real frequency $(Re\omega)_{max}/\omega_f$ at maximum growth versus tune depression $\bar{\nu}/\nu_0$ for $T_{\parallel b}/T_{\perp b} = 0.02$ [2].

highest growth rate, $(Im\omega)/\omega_f \approx 0.15$, for $\bar{\nu}/\nu_0 \approx 0.45$, and that the critical value of $\bar{\nu}/\nu_0$ for the onset of the instability, and the value of $(\bar{\nu}/\nu_0)_{max}$ with maximum growth

rate, decrease with azimuthal mode number m . The instability is absent for $\bar{\nu}/\nu_0 > 0.77$ for the choice of parameters in Fig. 2. The real frequency $(Re\omega)/\omega_f$ of the unstable modes with odd azimuthal numbers $m = 1, 3, \dots$ are zero and are not plotted in Fig. 2. Moreover, the real frequency is plotted only for the unstable modes.

BEST SIMULATION RESULTS

Typical numerical results obtained with the *linearized* version of the 3D BEST code [4] are presented in Figs. 3-5 [2] for the case where $r_w = 3r_b$ and $T_{||b}/T_{\perp b} = 0.02$, and for perturbations with a spatial dependence proportional to $\exp(ik_z z + im\theta)$, where k_z is the axial wavenumber, and m is the azimuthal mode number. Random initial perturbations are introduced to the particle weights, and the beam is propagated from $t = 0$ to $t = 200\omega_f^{-1}$. Note from Fig.

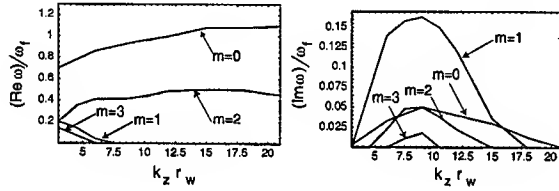


Figure 3: Plots of normalized real frequency $(Re\omega)/\omega_f$ and growth rate $(Im\omega)/\omega_f$ versus $k_z r_w$ for $\bar{\nu}/\nu_0 = 0.53$ and $T_{||b}/T_{\perp b} = 0.02$ [2].

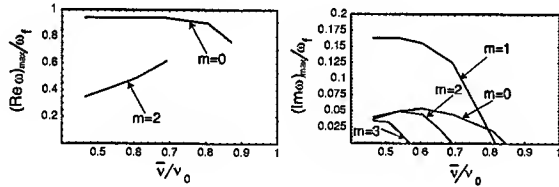


Figure 4: Plots of normalized real frequency $(Re\omega)_{max}/\omega_f$ and growth rate $(Im\omega)_{max}/\omega_f$ at maximum growth versus normalized tune depression $\bar{\nu}/\nu_0$ for $T_{||b}/T_{\perp b} = 0.02$ [2].

3 that the instability has a finite bandwidth with maximum growth rate occurring at $k_z r_w \simeq 9$. From Fig. 4, the critical value of $\bar{\nu}/\nu_0$ for the onset of the instability decreases with azimuthal mode number m . The real frequency $(Re\omega)/\omega_f$ of the unstable modes for odd azimuthal numbers $m = 1, 3$ are zero and are not plotted. Moreover, the real frequency is plotted only for the unstable modes. Consistent with the analytical predictions, note that the dipole mode ($m = 1$) has the largest growth rate. Furthermore, all modes are found to be stable in the region $\bar{\nu}/\nu_0 \geq 0.85$. The simulation results presented in Figs. 3 and 4 are in good qualitative agreement with the theoretical model (see Figs. 1 and 2). Moreover, Fig. 5 shows that instability is absent for $T_{||b}/T_{\perp b} > 0.08$.

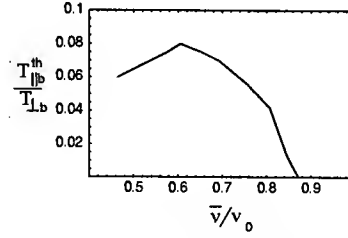


Figure 5: Longitudinal threshold temperature $T_{||b}^{th}$ normalized to the transverse temperature $T_{\perp b}$ for onset of instability plotted versus normalized tune depression $\bar{\nu}/\nu_0$ [2].

CONCLUSIONS

To summarize, the BEST code [4] was used to investigate the detailed stability properties of intense charged particle beams with large temperature anisotropy ($T_{||b}/T_{\perp b} \ll 1$) for three-dimensional perturbations with several values of azimuthal wave number $m = 0, 1, 2, 3$. An analytical model, which generalizes the classical Harris-like instability to the case of an intense charged particle beam with anisotropic temperature, has been developed [2]. Both the simulations and the analytical results clearly show that moderately intense beams with $s_b \geq 0.5$ are linearly unstable to short wavelength perturbations with $k_z^2 r_b^2 \geq 1$, provided the ratio of longitudinal and transverse temperatures is smaller than some threshold value.

REFERENCES

- [1] E. G. Harris, Phys. Rev. Lett. **2**, 34 (1959).
- [2] E. A. Startsev, R. C. Davidson and H. Qin, Phys. Plasmas **10** submitted (2003); Phys. Plasmas **9**, 3138 (2002);
- [3] R. C. Davidson and H. Qin, *Physics of Intense Charged Particle Beams in High Energy Accelerators* (World Scientific, Singapore, 2001), and references therein.
- [4] H. Qin, R. C. Davidson and W. W. Lee, Phys. Rev. Special Topics on Accelerators and Beams **3**, 084401 (2000); **3**, 109901 (2000).

MEASUREMENT OF THE LONGITUDINAL WAKEFIELD IN THE SLAC LINAC FOR EXTREMELY SHORT BUNCHES*

K. Bane, F.-J. Decker, P. Emma, L. Hendrickson, P. Krejcik, C.L. O'Connell, H. Schlarb,[†]
J. Welch, M. Woodley: Stanford Linear Accelerator Center, Stanford, CA 94309, USA

INTRODUCTION

The Linac Coherent Light Source (LCLS) [1] is an x-ray FEL project with a 1-nC electron bunch compressed to an rms length of 20 microns at 4.5 GeV, accelerated in 500 meters of SLAC linac to 15 GeV, and then injected into an undulator to generate SASE radiation. The longitudinal wakefield generated by the short bunch in the (S-band) linac is very strong, and is relied upon to cancel the energy chirp left in the beam after bunch compression.

Up to now, both the average [2] and the shape [3] of the longitudinal wake of the SLAC linac have been measured and confirmed using bunches ranging down to an rms 500-microns in length. The recent installation of a chicane in the SLAC linac for the Sub-Picosecond Photon Source (SPPS) [4, 5, 6], however, allows compression of a 3.4-nC bunch down to 50 μm rms length. We present measurements of the average wakefield, for bunch lengths down to this, LCLS-type scale, and compare with theory.

THEORY

For a periodic, disk-loaded structure the steady-state longitudinal wakefield can be obtained numerically. The result over the very short-range can be approximated by [7]

$$W(s) = \frac{Z_0 c}{\pi a^2} H(s) e^{-\sqrt{s/s_0}}, \quad (1)$$

where s is the longitudinal separation between drive and test particles ($s > 0$ if the drive particle leads); with $Z_0 = 377 \Omega$, c the speed of light, a the (average) structure iris radius; with $H(s) = 1$ (0) if $s > 0$ (< 0). The parameter $s_0 = 0.41g^{1.6}a^{1.8}/p^{2.4}$ with g the gap length and p the period length. For the SLAC linac structure, $a = 1.16$ cm, $g = 2.92$ cm, and $p = 3.50$ cm; $s_0 = 1.47$ mm and the model is valid for $s \lesssim 5$ mm. Note that Eq. (1) gives the steady-state solution, valid after the distance $L_{crit} \approx \frac{1}{2}a^2/\sigma_z$, after which initial transients have died down. For $\sigma_z = 50 \mu\text{m}$, $L_{crit} = 1.4$ m, which is very small compared to the total structure length; thus, the transient contribution is small and can be ignored.

We will describe measurements that depend on the average wake. For a Gaussian bunch with rms length σ_z , the loss factor—the average wake-induced energy loss per unit charge per unit length of structure—is given by

$$\kappa(\sigma_z) = \frac{1}{2\sqrt{\pi}\sigma_z} \int_0^\infty W(s) e^{-(s/\sigma_z)^2/4} ds. \quad (2)$$

* Work supported by U.S. Department of Energy, contract DE-AC03-76SF00515.

[†] Visitor from DESY.

Substituting Eq. (1) into Eq. (2) we obtain a result that can be approximated (for $\sigma_z \lesssim s_0$ to 2% accuracy) by

$$\kappa(\sigma_z) \approx \frac{Z_0 c}{2\pi a^2} e^{-0.88\sqrt{\sigma_z/s_0}}. \quad (3)$$

The average energy gain of a bunch after passing through a linac is given by a combination of the applied rf and the wakefield effect. The average gain of a Gaussian bunch is

$$\Delta E = \hat{E}_{acc} \cos \phi e^{-k_{rf}^2 \sigma_z^2/2} - eNL\kappa(\sigma_z), \quad (4)$$

with \hat{E}_{acc} the crest energy change, ϕ the average bunch phase (with respect to crest), k_{rf} the rf wave number, eN the bunch charge, and L the total structure length. Note that increasing the bunch length will decrease the first and increase the second term contributions, and the converse is also true. Note also that when $\sqrt{\sigma_z/s_0} \ll 1$ we lose sensitivity in ΔE to bunch length.

To estimate the range of energy change that we can expect to measure, consider first that, for a point charge, the total wake effect is $(eNLZ_0c)/(2\pi a^2)$, which in our experiment is ~ 850 MeV (3% of the final beam energy). For a bunch length range between 50 and 600 μm this quantity is reduced by the difference of $e^{-0.88\sqrt{\sigma_z/s_0}}$ at the two bunch lengths, yielding an energy change of ~ 240 MeV (a 0.8% effect). Eqs. (3-4) can be used to estimate the wakefield effect for the measurements to be discussed. In reality the beams are not exactly Gaussians, however, and in the simulations used in comparisons to follow, no such assumption is made.

MACHINE LAYOUT

A new four-dipole bunch compressor chicane was installed in sector-10 of the SLAC linac in October of 2002 [4, 5]. The chicane is located at the 1-km point in the 3-km linac, at 9 GeV. The electron bunch is extracted from a damping ring which is followed by an existing ring-to-linac (RTL) bunch compressor beamline at 1.2 GeV. The RTL includes a 2.1-m long S-band rf accelerating structure operated at the zero-crossing phase, followed by a series of bends which generate an R_{56} of 590 mm. The RTL structure is operated at a nominal voltage (V_{RTL}) of 42 MV, which can vary with machine configuration.

A 3.4-nC bunch is compressed from 6-mm rms in the ring to 1.2-mm in the RTL, accelerated to the chicane at 9 GeV through 810-m of linac at an rf phase of -19° (crest at 0), and then further compressed in the new chicane to as short as 50- μm rms (up to 9-kA peak current). The time-correlated energy spread at chicane entrance is 1.6% rms,

with bunch head at lower energy than its tail. The bunch is then accelerated to 28.5 GeV in 1870 meters of S-band rf accelerating structures, where in order to save power, only ~ 90 of the 160 available klystrons beyond the chicane are presently switched on. Figure 1 shows the machine layout.

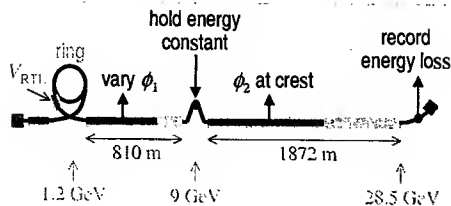


Figure 1: Layout of ring, RTL, linac, and chicane. Linac sections highlighted in red are rf-powered.

The longitudinal wakefield of the post-chicane linac generates an energy loss and spread which reaches a maximum for the shortest bunch length. This dependence can be used to find the minimum bunch length by maximizing the energy loss. This is done by varying the pre-chicane rf phase (ϕ_1), composed of the first 40 klystrons in sectors 2-6, several degrees around its nominal setting of -19° , while the chicane energy is held constant. The varying phase changes the correlated energy spread in the chicane, which changes the final bunch length, passing through a minimum near -19° with over- and under-compression on either side.

The energy in the chicane is held constant by a pair of "feedback" klystrons in sector-9, each operated symmetrically around opposing zero-crossing phases (at $\pi/2 \pm \Delta\phi_f$ and $-\pi/2 \pm \Delta\phi_f$). This allows energy control without changing the correlated energy spread. A beam position monitor (BPM) at the center of the chicane is used to drive this micro-processor based chicane energy-feedback system. With a peak x -dispersion of 450 mm in the chicane and a 50- μ m BPM resolution, the single-shot energy resolution is 0.01%, or 1 MeV. The actual pulse-to-pulse energy stability in the chicane is typically 0.05%, or 5 MeV rms.

A second BPM, located after a bend at the end of the linac, is used to record energy change as a function of ϕ_1 . The 5-MeV chicane energy stability, and its R_{56} of -76 mm, contributes to post-chicane rf phase (ϕ_2) errors of $< 0.2^\circ$ around crest phase. This tiny error is < 0.2 MeV at the end of the linac. Therefore, any significant energy change at the end of the linac, which is correlated with ϕ_1 , minus the chicane energy error, is due to the bunch-length dependent wakefield in the post-chicane linac.

The shortest bunch length is produced at the ϕ_1 phase where the energy loss is maximized. This simple procedure has become a standard optimization and diagnostic tool to quickly (2-3 minutes) minimize the bunch length after the chicane, at any bunch charge and with any V_{RTL} setting.

SIMULATIONS

Particle tracking from ring extraction to end-of-linac has been done in 2D (longitudinal only), and also confirmed in 6D. More tracking details are shown in reference [5]. Machine and beam parameters are given in Table 1. The tracking starts at ring extraction with a gaussian energy profile and a slightly asymmetric-gaussian temporal profile, due to resistive ring vacuum chamber impedance [6, 9].

Table 1: Machine and electron bunch parameters.

bunch population	N	1.8-2.1	10^{10}
e^- energy in ring	E_0	1.19	GeV
ring rms energy spread	σ_E/E_0	0.08	%
ring rms bunch length	σ_{z0}	6.0	mm
pre-chicane rf phase	ϕ_1	-19	deg
post-chicane rf phase	ϕ_2	0	deg

The tracking includes 1st, 2nd, and 3rd-order momentum compaction (R_{56} , T_{566} , and U_{5666}) in the RTL and chicane. It also includes sinusoidal rf, and longitudinal geometric wakefields of all rf structures: before and after the chicane, and in the RTL. Figure 2 shows simulated longitudinal phase space, energy, and temporal distributions after the chicane and after the full linac, for the minimum bunch length. A gaussian-fit (in red) is used to determine the core bunch length at $\sigma_z \approx 40 \mu\text{m}$ rms. The energy spread is uncorrelated immediately after the chicane, but the wakefield of the post-chicane linac induces a large correlated spread and a mean loss of $\sim 1\%$ (bunch head at left here).

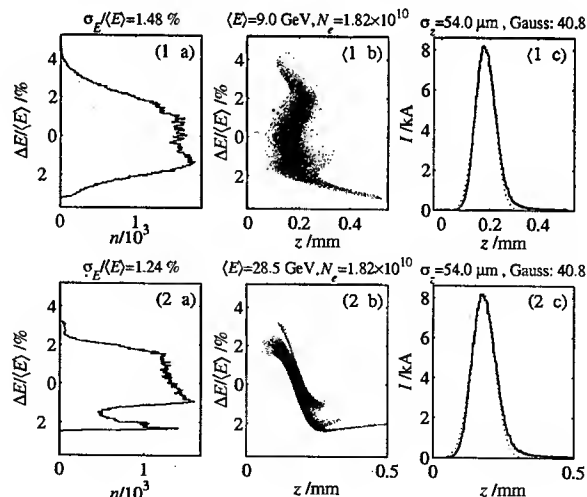


Figure 2: Beam at chicane exit (top) and end of linac (bottom), showing longitudinal phase space (1-b & 2-b), energy (1-a & 2-a), and temporal (1-c & 2-c) distributions (gaussian-fit in red: $\sigma_z \approx 40 \mu\text{m}$ rms).

Incoherent synchrotron radiation in the 9-GeV chicane bends is also included, but is a small effect producing an rms energy spread of 0.006% and a loss of 0.02% at 9 GeV.

The effects of coherent synchrotron radiation (CSR) in the chicane have also been calculated and, although there is a small effect on the x -emittance [10], the maximum rms energy spread and mean loss due to CSR is very small at 0.02 and 0.03%, respectively (at 9 GeV with 3.4 nC).

Finally, a small V_{RTL} -dependent beam loss in the narrow-aperture RTL beamline is also included in the simulations. Transmission measurements at various V_{RTL} settings (various x beam sizes in the RTL) show the energy-aperture at $\pm 2\%$. At 3 nC and $V_{RTL} = 42$ MV, this results in a 9% particle loss (7% at 40 MV and 12% at 45 MV).

The simulations are run multiple times with ϕ_1 varied $\pm 7^\circ$ in 0.5° steps, around the nominal phase of -19° , with chicane energy held constant. The energy change at the end of the linac vs. ϕ_1 is compared with measurements.

MEASUREMENTS

The energy loss of the compressed bunch is measured by reading the computations of a second micro-processor based energy-feedback system which nominally holds the electron energy constant at the end of the linac. This system uses three BPMs, one placed after a bend magnet with (x)-dispersion $\eta_x \approx -86$ mm, and the other two, prior to the bend, at $\eta_x = 0$, to accommodate trajectory variations initiated upstream of the bend. BPM calibration was verified accurate to 5%. The feedback loop is switched to "compute-only" mode during the wake-loss scans, which calculates energy, but applies no correction.

As described above, the rf phase, ϕ_1 , is varied while the chicane energy is held constant, and the end-of-linac energy is monitored. The final energy is typically stable to 8 MeV rms (0.03%) and five beam pulses (10 Hz) are averaged per ϕ_1 setting for a measurement error of 4 MeV.

The final bunch length was confirmed using a transverse deflecting rf structure to 'streak' the beam on an off-axis screen [11]. The absolute bunch length is measured from the streaked vertical beam size and independently demonstrates a minimum rms bunch length of 60 ± 10 μ m.

The measured and simulated energy loss vs. ϕ_1 settings are shown in Figures 3. Each scan is at a different RTL voltage (40 to 45 MV). The error bars show the estimated rms energy stability at each point. For this data taken at 3.0 nC, an RTL voltage other than 42 MV results in a longer minimum bunch length and a different correlated energy spread in the chicane. Therefore, the depth of the energy loss and the phase at the minimum will change for each RTL voltage setting. The (c) plot (42 MV) also shows the rms simulated bunch length (dotted), with scale at far right.

No fitting parameters are used, except the arbitrary offset on the vertical (energy) scale. The measurements and simulations are simply overlaid. The nominal 42 MV case (c) agrees quite well, but the 40 and 41 MV settings, (a) and (b), show a flat-bottomed area which is not understood. There also appears to be a slight RTL-saturation effect at $V_{RTL} > 42$ MV. The dashed curves in (d), (e) and (f) show the simulation at the actual V_{RTL} settings, but the data suggests that the RTL klystron was beginning to saturate here.

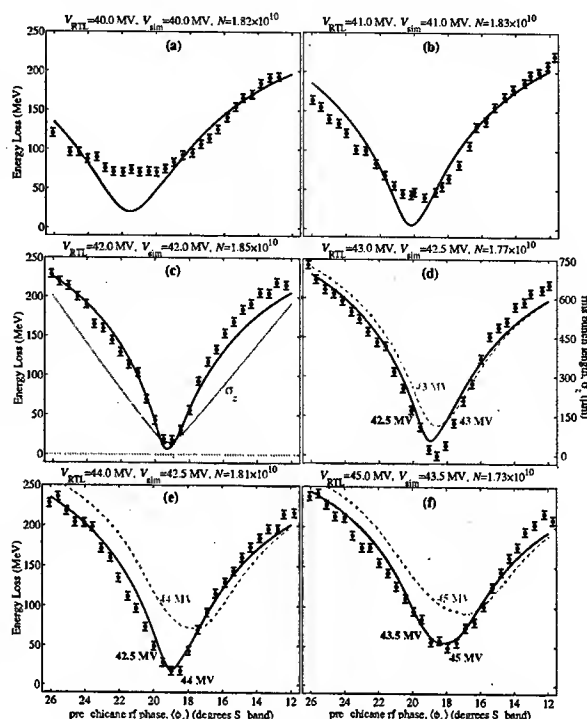


Figure 3: Wake-loss scans (the vertical scale has an arbitrary offset) with varying V_{RTL} from 40 to 45 MV, (a) to (f), respectively. The 42-MV case (c) also plots the simulated rms bunch length: scale at far right.

At the setting of 43 MV in (d), the data fits slightly better to 42.5 MV (solid). Likewise, at 44 and 45 MV settings in (e) and (f), the data fits much better to 42.5 and 43.5 MV, respectively. Note especially the measurements at 42 (c), 43 (d), and 44 MV (e) are almost identical, yet the simulations (dashed) at 43 and 44 MV suggest a clear change should have occurred. Unfortunately, this klystron saturation possibility was not confirmed by any independent technique. Further measurements, including wakefield-induced energy spread, will be made in the near future.

REFERENCES

- [1] LCLS CDR, SLAC Report No. SLAC-R-593, 2002.
- [2] K. Bane, *et al.*, EPAC'90, Nice, France, June 1990, p. 1762.
- [3] K.L.F. Bane, *et al.*, PAC'97, Vancouver, May 1997, p. 1876.
- [4] P. Krejcik, *et al.*, Commissioning of the SPPS Linac Bunch Compressor, PAC'03, Portland, OR, May 2003.
- [5] L. Bentson *et al.*, EPAC'02, Paris, France, June 2002, p. 683.
- [6] P. Emma, *et al.*, PAC'01, Chicago, USA, June 2001, p. 4038.
- [7] K.L.F. Bane, *et al.*, ICAP'98, Monterey, Sept. 1998, p. 137.
- [8] K.L.F. Bane, *et al.*, PAC'97, Vancouver, May 1997, p. 515.
- [9] K. Bane, *et al.*, PAC'95, Dallas, TX, June 1995, p. 3109.
- [10] P. Emma, *et al.*, Measurements of Transverse Emittance Growth due to ..., PAC'03, Portland, OR, May 2003.
- [11] R. Akre, *et al.*, EPAC'02, Paris, France, June 2002, p. 1882.

MEASUREMENTS OF TRANSVERSE EMITTANCE GROWTH DUE TO COHERENT SYNCHROTRON RADIATION IN THE SLAC SPPS BUNCH COMPRESSOR CHICANE

P. Emma, F.-J. Decker, P. Krejcik, C.L. O'Connell, M. Woodley
SLAC, Stanford, CA 94309, USA*
H. Schlarb, F. Stulle, DESY, 22603 Hamburg, Germany

Abstract

A four-dipole bunch compressor chicane has recently been installed in the SLAC linac at 9 GeV and is capable of compressing a 3.4-nC electron bunch to an rms length of 50 microns, resulting in a peak current of nearly 10 kA [1]. The electron bunch is extracted from a damping ring with normalized horizontal emittance of $\sim 30 \mu\text{m}$. We present preliminary measurements of the initial and final emittance in the chicane and compare these to 1D and 3D calculations of the effects of coherent synchrotron radiation (CSR).

INTRODUCTION

A four-dipole bunch compressor chicane was installed in sector-10 of the SLAC linac in October of 2002 [2]. The new chicane is located at the 1-km point in the 3-km linac, at 9 GeV, in order not to interfere with present PEP-II operations. The electron bunch is extracted from a damping ring which is followed by an existing ring-to-linac (RTL) bunch compressor beamline at 1.2 GeV. The 3.4-nC bunch is compressed from 6-mm rms in the ring to 1.2-mm in the RTL, and then further compressed in the new chicane to as short as 50- μm rms (9-kA peak current).

The existing FFTB (final focus test beam) beamline, which follows the 3-km linac, has been adjusted to produce another stage of compression, for a possible final bunch length of 12 μm rms, or 30 kA of peak current. The very short bunch (80 fsec FWHM) will be used to produce high-brightness spontaneous x-rays at 28 GeV in a 2.5-m long undulator. This sub-picosecond photon source (SPPS) [3], will be commissioned in June of 2003. The chicane compressor also enhances FFTB plasma-wakefield experiments by increasing the accelerating gradient a factor of ~ 36 [4].

Finally, the new compressor provides an opportunity for machine R&D toward the linac coherent light source (LCLS) project [5], especially by allowing measurements of transverse emittance growth possibly induced by CSR.

With the large bend-plane emittance from the damping ring, and limited time, the data collected is not yet exhaustive, but does provide an upper limit to the measured CSR emittance growth. Since few CSR emittance growth measurements exist at present, these results are published in their preliminary state. Future measurements should ultimately be more conclusive and more comprehensive.

* Work supported by U.S. Department of Energy, contract DE-AC03-76SF00515.

Table 1: Chicane and beam parameters [2].

parameter	symbol	value	unit
Bunch charge	N_e	3.0-3.4	nC
e^- energy	E_0	9.00	GeV
rms corr. energy spread	σ_E/E_0	1.55	%
init. rms bunch length	σ_{s0}	1.15	mm
final rms bunch length	σ_{sf}	50	μm
x norm. emittance	$\gamma\epsilon_x$	27-45	μm
momentum compaction	R_{56}	-76	mm
bend angle per dipole	$ \theta $	97	mrads
bend magnet length	L_B	1.80	m
drift from bend-1 to 2	ΔL	2.80	m
drift from bend-2 to 3	ΔL_c	1.50	m
peak dispersion	η_{pk}	449	mm
initial x beta-func.	β_x	56.3	m
initial x alpha-func.	α_x	3.29	

CSR CALCULATIONS

The chicane is shown in Fig. 1 with symbol values listed in Table 1. Bending is in the horizontal (x) plane, and a limited aperture constrains the R_{56} adjustment to just $\pm 5\%$ (no changes made here). The simulated longitudinal phase space at chicane entrance and exit is shown in Fig. 2 (bunch head at $s < 0$), with the total CSR-induced relative energy variation along the bunch at lower right. The final rms bunch length is 74 μm , but the rms is dominated by tails and the core bunch length is $\text{FWHM}/2.355 \approx 36 \mu\text{m}$.

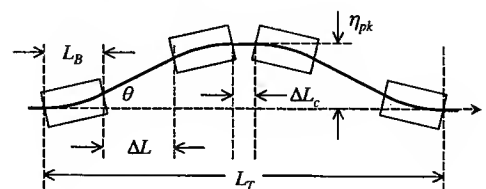


Figure 1: SPPS chicane at 9 GeV ($L_T \approx 14.3\text{m}$).

The CSR-wakefield alters each particle's energy as it passes through the chicane, generating x -kicks which become projected (bunch-length integrated) emittance growth in the bend-plane. A 1D line-charge transient field calculation, which is based on references [6, 7], is used here to generate these plots and evaluate the emittance growth. In the code, bends and drift sections are split 20 times each and the evolving non-gaussian temporal beam distribution is continually re-binned in 500 slices at each step, with

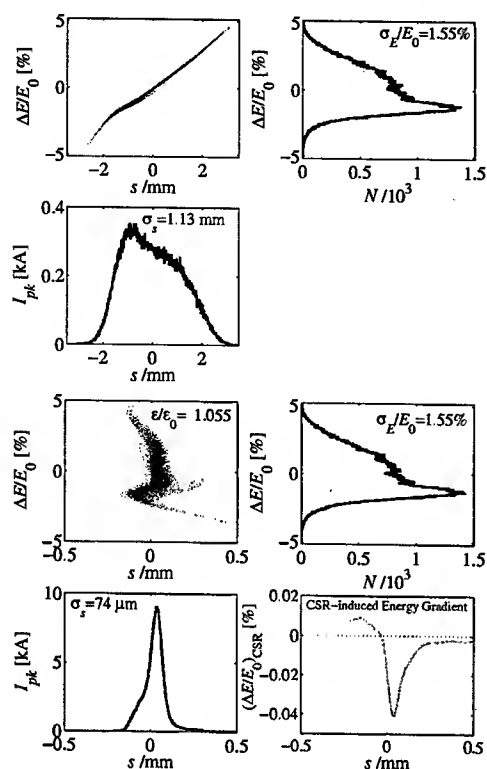


Figure 2: Simulated longitudinal phase space before (top 3-plots) and after chicane (bottom 4-plots) at 9 GeV.

2×10^5 macro-particles. The macro-particles are taken from a previous 2nd-order tracking run, using *Elegant* [8], through the entire RTL beamline and the 1-km of SLAC linac leading up to the chicane, including the longitudinal wakefield of the linac structures and 2nd-order optics. The emittance growth in the chicane has also been calculated using the 3D CSR code *TraFiC*⁴ [9], which includes transverse effects and agrees reasonably well with the 1D code. With a vacuum chamber full-height of 13-mm, shielding effects are not important for $\sigma_s \lesssim 100 \mu\text{m}$.

A calculation (1D) of the CSR-induced energy spread, energy loss, and the normalized projected horizontal emittance is shown evolving along the chicane in Fig. 3, using the phase space of Fig. 2. The larger of the two emittance curves includes incoherent synchrotron radiation (ISR) in the chicane. The calculation shows the emittance is expected to grow from $\gamma\epsilon_x = 27 \mu\text{m}$ to $30 \mu\text{m}$ (10% increase) due to CSR alone at 3.4 nC, and up to $33 \mu\text{m}$ (22% increase) when also including ISR at 9 GeV. The CSR-induced rms energy spread is $< 0.02\%$, including a 2-m long drift section after the chicane.

BUNCH LENGTH MEASUREMENTS

The bunch length after the chicane is measured using a 2.4-m long S-band (2856 MHz) transverse rf vertical-

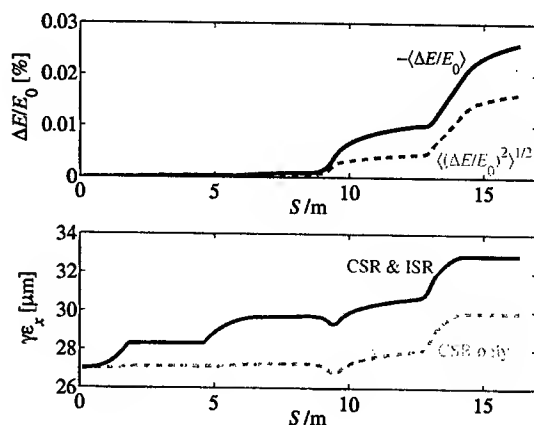


Figure 3: Simulated CSR-induced relative energy loss (top-solid), rms relative energy spread (top-dash), and bend-plane emittance along chicane, with (solid) and without ISR effect (dash) at 3.4 nC.

deflecting structure located at 28.5 GeV [10]. An off-axis screen is placed downstream of the structure ($\sim 60 \text{ m}$) by $\Delta\psi_y \approx \pi/2$, vertical betatron phase advance. A pulsed horizontal magnet is used to kick the vertically-streaked beam onto the screen. The absolute bunch length is calculated from the vertical beam size by using data from both zero-crossing rf phases as well as the rf-off setting. This 3-point measurement with parabolic fit allows for a finite vertical emittance and for initially tilted (pitched) beams, possibly induced by upstream transverse wakefields.

The transverse deflector is powered by a single 50-MW klystron and applies up to 22 MV (at crest phase) allowing 10-20% resolution (at zero-crossing phase) of a 50- μm rms bunch length. A calibration is made by scanning the beam position vertically across the span of the screen, varying rf phase a few degrees around the zero-crossing. The calibration, in screen-pixels per S-band degree of phase change, allows direct conversion of beam size, in pixels, to bunch length in degrees S-band (or psec). Therefore, no apriori calibration is needed, except the rf phase shifter, and this is separately scanned $\pm\pi$ reading a nearby BPM to ensure the phase calibration is accurate to better than 1%. The minimum measured RMS bunch length is from 50 to 70 μm .

The bunch length is independently verified by measuring the longitudinal wakefield energy loss of the compressed bunch across 1872 meters of SLAC rf structures [11]. For a 50- μm rms bunch length and 3 nC of charge, the wake-field energy loss at the end of the linac is nearly 250 MeV (1%) which is easily measured using an end-of-linac BPM with $|\eta_x| \approx 85 \text{ mm}$ (the chicane CSR energy loss should be only $\sim 0.01\%$ at 28 GeV). It is a simple matter to adjust the pre-chicane rf phase until this energy-loss is maximized, resulting in a minimum post-chicane bunch length. These wake-loss scans with rf phase are a routine diagnostic and are in good agreement with tracking calculations. They further verify the minimum bunch length at 50-60 μm rms.

EMITTANCE MEASUREMENTS

Horizontal emittance measurements are made using four consecutive wire scanners (well used over last 10 yrs), all of which are located within 80 m of the chicane. The four wires (x rms beam sizes from 100 to 300 μm) allow some redundancy for the 3-parameter measurement of ϵ_x , β_x , and α_x . The beam sizes are taken from asymmetric gaussian fits, which allow for reasonably distorted beams. A profile measurement requires 50 pulses at 10-30 Hz, or 2-5 seconds plus some overhead. One emittance measurement requires about 2 minutes. Figure 4 shows two measured x -profiles with asymmetric gaussian fits. The narrower profile is with chicane off, and the wider is chicane on. The asymmetries are fairly insensitive to the bunch length (i.e., CSR power) in both the tracking and the measurements. No simultaneous vertical emittance measurements were made.

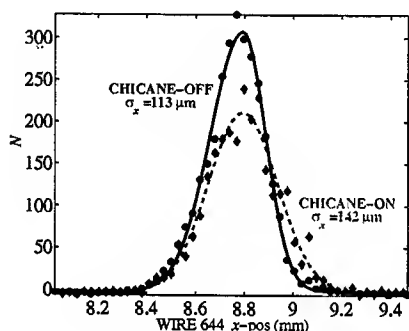


Figure 4: Measured x -profiles (points) on one of four wire-scanners with asymmetric gaussian fits, for chicane-ON (dash-red) and chicane-OFF (solid-blue).

The emittance measurements are precise to a level of about 4%, over periods < 1 hour, but the linac is quite sensitive to changes in charge, rf phase, and trajectory. This makes controlled changes of the compression difficult without altering the initial emittance prior to the chicane. For these reasons we present data taken only at the minimum bunch length, and as a control, with the chicane switched completely off. The data were taken on two separate days (Feb. 5 and May 4, 2003) at 3.0 nC and 3.4 nC, respectively. The 3.4-nC data has a smaller initial emittance achieved by coupling the damping ring tunes.

Efforts were also made to correct all x -dispersion errors after the chicane. Tight quality control was placed on field quality of the dipole magnets [2], and two weak 'tweaker' quadrupole magnets were located inside the chicane and used to empirically correct the x -dispersion by minimizing the measured emittance to a precision of $\Delta\epsilon_x/\epsilon_x \approx 1\%$. In addition, impedance effects inside the chicane beam-pipe were minimized, including copper plating [2].

Figure 5 shows two sets of x -emittance measurements made downstream of the chicane on two separate days, each time with "chicane-ON" and also "chicane-OFF", at 3.0 nC (Feb. 5) and 3.4 nC (May 4). The "tracking" values

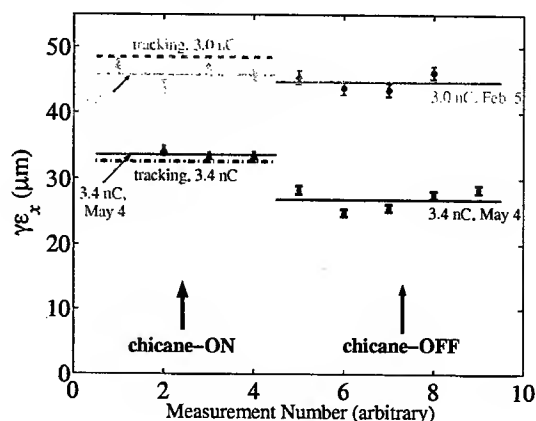


Figure 5: Emittance measurements with chicane ON and OFF at 3.0 nC (Feb. 5) and 3.4 nC (May 4). Tracking results, including ISR, are shown for both 3.0 nC (dash) and 3.4 nC (dash-dot) at $\sigma_s \approx 50 \mu\text{m}$.

(including CSR and ISR) are also shown (for both days) at 3.0 nC (dash) and 3.4 nC (dash-dot) and $\sigma_s \approx 50 \mu\text{m}$. These are calculated by tracking with the average "chicane-OFF" measured emittance as an input. With 3.4 nC, the mean "chicane-OFF" emittance is $\langle\gamma\epsilon_{x0}\rangle \approx 26.9 \pm 0.7 \mu\text{m}$ and the tracking result after the chicane is: $\gamma\epsilon_x = 32.9 \mu\text{m}$. The "chicane-ON" measurements at 3.4 nC have a mean value of $\langle\gamma\epsilon_x\rangle \approx 33.6 \pm 0.3 \mu\text{m}$, which is in reasonable agreement with tracking. Measurements (not shown) were also made of the β_x and α_x functions and confirm, within a few percent, the values in Table 1.

CONCLUSIONS

The observed bend-plane emittance growth after the SPPS chicane, with a 50- μm rms bunch length and up to 3.4 nC of charge, is reasonably consistent with 1D and 3D CSR tracking calculations and sets a clear upper limit on the scale of the effect. Measurements will continue and might be improved in the future by using a larger β_x in the final bend to amplify the relative growth, and perhaps a 6-GeV chicane energy to remove ISR effects.

REFERENCES

- [1] P. Krejcik et al., PAC'03, Portland, OR, USA, May 2003.
- [2] L. Bentson, et al., EPAC'02, Paris, Fr., June 2002.
- [3] P. Emma et al., PAC'01, Chicago, IL, June 2001.
- [4] M. Hogan et al., PAC'03, Portland, OR, USA, May 2003.
- [5] LCLS CDR, SLAC Report No. SLAC-R-593, 2002.
- [6] E. L. Saldin et al., TESLA-FEL 96-14, Nov. 1996.
- [7] G. Stupakov, P. Emma, EPAC'02, Paris, France, June, 2002.
- [8] M. Borland, APS LS-287, Sep. 2000.
- [9] M. Dohlus et al., FEL'97, Beijing, China, Aug. 1997.
- [10] R. Akre et al., EPAC'02, Paris, France, June 2002.
- [11] K. Bane et al., PAC'03, Portland, OR, USA, May 2003.

SINGLE-MODE COHERENT SYNCHROTRON RADIATION INSTABILITY

S. Heifets and G. Stupakov

Stanford Linear Accelerator Center, Stanford University, Stanford, CA 94309

INTRODUCTION

A relativistic electron beam moving in a circular orbit in free space can radiate coherently if the wavelength of the synchrotron radiation exceeds the length of the bunch. In accelerators coherent radiation of the bunch is usually suppressed by the screening effect of the conducting walls of the vacuum chamber [1, 2, 3]. The screening effect is much less effective for short wavelengths, but if the wavelength is shorter than the length of the bunch (assuming a smooth beam profile), the coherent radiation becomes exponentially small. However, an initial density fluctuation with a characteristic length much shorter than the screening threshold would radiate coherently. If the radiation reaction force is directed so that it drives the growth of the initial fluctuation, one can expect an instability that leads to micro-bunching of the beam and an increased coherent radiation at short wavelengths.

In Ref. [6], the growth rate of the beam instability driven by the coherent synchrotron radiation (CSR) was found using the so called "CSR impedance" [4, 5] that neglects the shielding effect of the walls and assumes a continuous spectrum of radiation. In many cases, the instability is limited to relatively long wavelengths, and it may be affected by the wall shielding effect [1]. Close to the shielding threshold, one has to take into account that the spectrum of the synchronous modes of radiation is discrete, and the instability may be driven by a single synchronous mode rather than a continuous spectrum.

In this paper we study a linear regime of single-mode CSR instability. As in Ref. [6], we assume that the bunch is much longer than the wavelength of the modulation and consider a coasting beam model. The nonlinear regime of the instability is described in accompanying paper [7].

SYNCHRONOUS MODES IN TOROIDAL BEAM PIPE CLOSE TO SHIELDING THRESHOLD

A relativistic beam moving in a toroidal beam pipe interacts with synchronous modes that have phase velocity equal to the speed of light. For a perfectly conducting walls of the toroid, those modes have discrete frequencies. Such modes have been extensively studied in the past [3, 8]. Recently, a new approach to the problem [9] extended the previous analysis and allowed to treat arbitrary cross sections of the toroid.

Following Ref. [9], we assume that the characteristic size of the pipe cross section a is much smaller than

the toroid radius R , so that the ratio $\sqrt{a/R}$ is a small parameter. For a given toroid, the synchronous modes have wavenumbers k greater than a minimal value $k_{\min} = \omega_{\min}/c$:

$$k \geq \frac{\omega_{\min}}{c} \sim \frac{R^{1/2}}{a^{3/2}} \gg a^{-1}.$$

Each mode is characterized by its frequency ω_n , the wavenumber $q_n = \omega_n/c$, and the group velocity v_{gn} . The wake of each mode is

$$w_n(z) = 2\chi_n \cos(q_n z), \quad (1)$$

where χ_n is the loss factor. The total wake is the sum of partial contributions of all modes: $w(s) = \sum_n w_n(s)$.

The lowest synchronous mode wavenumber is of order of k_0 , where

$$k_0 = \frac{\pi}{a} \sqrt{\frac{R}{a}}.$$

For example, for a beam pipe of a square cross-section with the side a , $k_{\min} = 1.52 k_0$. The loss factor per unit length χ_1 and the group velocity v_{g1} for this mode are $\chi_1 = 4.94/a^2$, $1 - v_{g1}/c = 0.62 a/R$. Note that such modes propagate with the group velocity close to the speed of light. The next mode with a nonzero loss factor has a frequency $\omega_2 = 2.79 ck_0$ and the loss factor $\chi_2 = 3.01/a^2$. We emphasize here that the distance between the synchronous modes in the vicinity of ω_{\min} is of the order of their frequency, and in that sense the modes are well separated on the frequency scale. Similar results hold for the round toroidal pipe [9].

INTERACTION OF THE BEAM WITH A SINGLE SYNCHRONOUS MODE IN LINEAR APPROXIMATION

The interaction of the beam with electromagnetic waves is usually described in terms of the beam impedance (see, e.g., [10]). For discrete synchronous modes, the beam impedance has singularities centered at the mode frequencies. In this case, a direct application of the standard approach may give an incorrect result. In Ref. [11], a derivation of equations for beam-wave interaction is given based on the Maxwell-Vlasov system of equations without using the concept of the impedance. In this section, we obtain the equations of Ref. [11] using a simple heuristic argument that "fixes" the conventional approach by taking into account the effect of retardation.

We use a one dimensional model for the beam, neglecting effect of the finite transverse emittance and considering

a distribution function $f(z, \delta, t)$, where z is the longitudinal coordinate measured from a reference particle moving with the speed of light, and δ is the energy offset relative to the nominal energy E_0 , $\delta = (E - E_0)/E_0$. We also assume that the modulation wavelength is small compared to the bunch length and consider a coasting beam with the linear density n_b equal to the local linear density of the bunch.

In the linear approximation, the perturbation due to the electromagnetic field can be considered as small: $f = f_0(\delta) + f_1(z, \delta, t)$, with $|f_1| \ll f_0$. The linearized Vlasov equation for f_1 is

$$\frac{\partial f_1}{\partial t} - \eta c \delta \frac{\partial f_1}{\partial z} + \frac{e}{\gamma m c} \mathcal{E}(z, t) \frac{\partial f_0}{\partial \delta} = 0, \quad (2)$$

where η is the momentum compaction factor, $\gamma m c^2$ is the nominal beam energy, and $\mathcal{E}(z, t)$ is the longitudinal component of the electric field. The function f is normalized so that $\int f dz d\delta$ gives the number of particles in the beam.

The usual formula for the electric field in terms of the wake function is [10]:

$$\mathcal{E}(z, t) = -e \int_z^\infty dz' \int d\delta w(z' - z) f_1(z', \delta, t). \quad (3)$$

However, it misses an important effect of the wake retardation that we need to take into consideration here. Indeed, the wave radiated at position s' at time t' and propagating in the forward direction to s , such that $s > s'$, will take time $t - t' = (s - s')/v_g$ to arrive at the destination, where v_g is the group velocity of the wave. Since $s' = z' + ct'$ and $s = z + ct$ we find from the above relation the retardation time between the emission and arrival in terms of coordinate z : $t - t' = (z' - z)/(c - v_g)$. To include the effect of the retardation in Eq. (3), we need to take the distribution function in Eq. (3) at the time of emission of the wave:

$$\begin{aligned} \mathcal{E}(z, t) = & -e \int_z^\infty dz' \int d\delta w(z' - z) \\ & \times f_1 \left(z', \delta, t - \frac{z' - z}{c - v_g} \right). \end{aligned}$$

This equation replaces Eq. (3) in our derivation. Contrary to the usual case of the geometric impedance, where the group velocity is small, effect of retardation here is important because v_g is close to the speed of light.

Note, that for the free space CSR, the retardation time is equal to $[24R^2(z' - z)]^{1/3}$ defined by the difference of the path length along the circle for the beam and the straight line for the radiation. A more detailed study of the retardation effect for the CSR wake in vacuum can be found in Ref. [12].

For what follows, it is convenient to introduce the Fourier transform g_1 of the perturbation of the distribution function $g_1(\omega, q, \delta) = \int dt dz e^{i(\omega t - q z)} f_1(z, \delta, t)$. It follows from Eq. (2):

$$g_1(\omega, q, \delta) = -\frac{ie}{\gamma m c} \frac{E(\omega, q)}{\omega + \eta c \delta q} \frac{\partial f_0}{\partial \delta}, \quad (4)$$

where $E(\omega, q) = \int dt dz e^{i(\omega t - q z)} \mathcal{E}(z, t)$. The quantity $E(\omega, q)$ can be found by Fourier transforming Eq. (4) and using the wake from Eq. (1):

$$E(\omega, q) = \sum_n \frac{-ie \chi_n (c - v_{gn})}{\omega + (c - v_{gn})(q - q_n)} \int d\delta g_1(\omega, q, \delta). \quad (5)$$

To obtain the above equation, we assumed that the frequency $|\omega| \sim (1 - \beta_g)|q - q_n| \ll \omega_n$, which is equivalent to using only the synchronous part of the wake: $\cos(q_n z) \rightarrow e^{-iq_n z}/2$. Combining Eqs. (4) and (5) yields the dispersion relation

$$1 = - \sum_n \frac{\lambda_n}{\omega/c + (1 - \beta_{gn})\Delta q_n} \int d\delta \frac{\partial f_0/\partial \delta}{\omega + \eta c q \delta}, \quad (6)$$

where $\lambda_n = r_e c (1 - \beta_{gn}) \chi_n / \gamma$, $\Delta q_n = q - q_n$, with $r_e = e^2/mc^2$. In Eq. (6) we took into account that $v_{gn} \approx c$. As always in stability theory, the integration in Eq. (6) goes in the complex plane above the pole $\delta = -\omega/\eta c q$. For a real value of q , Eq. (6) defines a complex frequency ω the imaginary part of which gives the growth rate of the instability. Alternatively, we can consider real ω and find a complex wavenumber q describing a periodic perturbation growing or decaying along the beam pipe.

Note that the frequency of the mode Ω observed in the laboratory frame, where it has a dependence $e^{i(qs - \Omega t)}$, is equal to $\Omega = \omega + qc$.

DISPERSION RELATION FOR A SINGLE MODE

In the single-mode approximation, we leave only one term in the dispersion equation Eq. (6) corresponding to the lowest synchronous mode with frequency ω_n and $q_n = \omega_n/c$. Let us assume that the distribution function $f_0(\delta)$ is Gaussian with the rms energy spread δ_0 , $f_0 = (n_b/\delta_0)\rho_0(\delta/\delta_0)$ with $\rho_0(\xi) = e^{-\xi^2/2}/\sqrt{2\pi}$. Eq. (6) takes the form

$$\frac{\omega}{c} - (1 - \beta_{gn})\Delta q_n = -\frac{n_b \lambda_n}{\eta \omega_n \delta_0^2} \int \frac{d\xi \frac{d\rho_0}{d\xi}}{\frac{\omega}{\eta \omega_n \delta_0} + \xi}, \quad (7)$$

where we replaced q under the integral by q_n and used $q_n = \omega_n/c$. Depending on the ratio $\omega/\eta \omega_n \delta_0$, there are two possible regimes for the instability: a large energy spread regime, when $|\omega| \ll |\eta \omega_n \delta_0|$, and a "cold beam" approximation when the opposite inequality holds. We consider here the latter case only, as a more relevant to the parameters of the existing accelerators (see below). In this case, we can evaluate the integrand in Eq. (7) asymptotically in the limit $|\omega/\eta \omega_n \delta_0| \gg 1$, which results in the cubic dispersion equation:

$$\omega^2 \left[\frac{\omega}{c} - (1 - \beta_{gn})\Delta q_n \right] = -n_b \lambda_n \eta \omega_n. \quad (8)$$

For $\Delta q_n = 0$, one of the roots has a positive imaginary part:

$$\omega = \mu e^{i\pi/3}, \quad (9)$$

where we introduced the parameter μ

$$\mu = (n_b \lambda_n c \eta \omega_n)^{1/3} = c \left[\frac{r_e n_b \omega_n \eta \chi_n}{c \gamma (1 - \beta_{gn})} \right]^{1/3}$$

Note that for a cold beam there is no threshold for the instability. The estimate of the integral term in the dispersion equation used above neglects the Landau damping and is valid provided $|\mu| \gg \eta \omega_n \delta_0$.

For a general case of arbitrary detuning Δq_n , Eq. (8) can be written in the dimensionless form as

$$x^2(x + y) + 1 = 0, \quad (10)$$

by introducing $x = \omega/\mu$, $y = c\Delta q_n(1 - \beta_{gn})/\mu$. Eq. (10) can be easily solved numerically—it has three roots one of which corresponds to the instability. The maximum growth rate is achieved at zero detuning, $\Delta q_n = 0$ and is equal to $\text{Im } \omega = \sqrt{3}/2\mu$.

Table 1 gives parameters and compares the growth rate for four accelerators: the Low Energy Ring (LER) and the High Energy Ring (HER) of PEP-II accelerator at SLAC, Advanced Light Source at the Berkeley National Laboratory, and the VUV ring at the National Synchrotron Light Source at BNL. For the ALS, we used beam parameters for the regime in which bursts of infrared radiation were observed [13]. Calculations were made for the lowest synchronous mode (which frequency is denoted by ω_1) assuming a square cross section of the vacuum chamber with the size a equal to the vertical full gap of the beam pipe. Since the real shape of the cross section usually differs from the square, the results in the table should be considered as a rough estimate of the instability parameters. For the linear density of the beam n_b , we used the quantity $N_p/\sqrt{2\pi}\sigma_z$, which gives the maximum linear density in a gaussian bunch (N_p is the number of particles in the bunch, σ_z is the rms bunch length). Note that the ratio $\mu/\eta\omega_1\delta_0$ in the last line of the table related the cold beam approximation—it is large in all cases except for the HER PEP-II where it is close to one.

DISCUSSION

The model developed in this paper considers a ring as a perfect toroid with a constant bending radius. We derived equations for the beam-mode interaction, found the growth rate for the instability, and estimated it for several machines. We have shown that in this case, due to the persistent interaction with a resonant mode, the beam becomes unstable even at low currents.

In real lattice, bending magnets are usually separated by straight sections, which also have a different cross section of the vacuum chamber. The beam-mode interaction ceases in the straight sections and the amplitude and phase of the mode will most likely change after the passage through the straights. The beam density modulation induced in one bend, after passage through a straight section, will serve as a seed for the instability in the next one. We expect that

Table 1: Parameters relevant to the instability for PEP-II low energy (LER) and high energy (HER) rings, ALS, and VUV NSLS ring.

Parameter	LER	HER	ALS	VUV NSLS
Energy, GeV	3.1	9.0	1.5	0.81
η , 10^{-3}	1.3	2.1	1.4	2.4
δ_0 , 10^{-4}	8.1	6.1	7.1	5.0
n_b , 10^{10} cm^{-1}	3.7	0.82	7	3.6
a , cm	5	5	4	4.2
R , m	13.7	165.0	4.0	1.9
$\omega_1/2\pi$, GHz	75.5	260	57	36.6
χ , V/pC/m	18	18	28	25
μ , 10^6 s^{-1}	7.5	2.5	18	22
n_{cr} , 10^{10} cm^{-1}	13	140	3	0.8
$\mu/(\eta\omega_1\delta_0)$	15	1.2	84	50

in a real lattice the instability would develop with a growth rate smaller than in an ideal toroid. A study of this case will be published in a separate paper.

ACKNOWLEDGEMENTS

We thank S. Krinsky and Z. Huang for useful discussions. This work was supported by the Department of Energy, contract DE-AC03-76SF00515.

REFERENCES

- [1] J. Schwinger, *On radiation by electrons in a betatron* (1945).
- [2] L. Schiff, *Rev. Sci. Instr.* **17**, 6 (1946).
- [3] R. L. Warnock and P. Morton, *Part. Accel.* **25**, 113 (1990).
- [4] J. B. Murphy, S. Krinsky, and R. L. Gluckstern, in *Proc. of PAC 1995*.
- [5] Y. S. Derbenev, et al. DESY FEL Report TESLA-FEL 95-05, September 1995.
- [6] S. Heifets and Stupakov G. V., *Phys. Rev. ST Accel. Beams* **5**, 054402 (2002).
- [7] S. Heifets and G. Stupakov, in *PAC03* (2003).
- [8] K.-Y. Ng, *Part. Accel* **25**, 153 (1990).
- [9] G. V. Stupakov and I. A. Kotelnikov, *Phys. Rev. ST Accel. Beams* **6**, 034401 (2003).
- [10] A. W. Chao, *Physics of Collective Beam Instabilities in High Energy Accelerators* (Wiley, New York, 1993).
- [11] S. Heifets and G. Stupakov, Preprint SLAC-PUB-9627, SLAC (2003).
- [12] S. Heifets, Preprint SLAC-PUB-9054, SLAC (2001).
- [13] J. Byrd, et al. *Phys. Rev. Lett.* **89**, 224801 (2002).

NONLINEAR REGIME OF A SINGLE-MODE CSR INSTABILITY

S. Heifets and G. Stupakov

Stanford Linear Accelerator Center, Stanford University, Stanford, CA 94309

INTRODUCTION

In Ref. [1] the growth rate of the beam instability driven by the coherent synchrotron radiation (CSR) was found using the so called "CSR impedance" [2, 3] that neglects the shielding effect of the walls and assumes a continuous spectrum of radiation. In many cases, the instability is limited to relatively long wavelengths where it may be affected by the wall shielding effect [4]. Close to the shielding threshold, one has to take into account that the spectrum of synchronous modes of radiation is discrete, and the instability may be driven by a single mode rather than a continuous spectrum.

The linear theory of single-mode CSR instability is developed in Refs. [1, 5]. In this paper, we study nonlinear regime of the instability. As in Ref. [1], we assume that the bunch is much longer than the wavelength of the modulation and consider a coasting beam model.

NONLINEAR REGIME OF THE INSTABILITY

In Refs. [1, 5] we calculated the growth rate for a single-mode instability as a function of detuning $q - q_n$, where q is the wavenumber of the perturbation and q_n is the wavenumber of the n th synchronous mode in a toroidal waveguide. The growth rate is localized in a small vicinity of q_n with a maximum at $q = q_n$.

When the amplitude of the unstable mode becomes large, the linear theory is not valid any more and one has to use the full Vlasov equation for the distribution function $f(z, \delta, t)$:

$$\frac{\partial f}{\partial t} - \eta c \delta \frac{\partial f}{\partial z} + \frac{e}{\gamma m c} \mathcal{E}(z, t) \frac{\partial f}{\partial \delta} = 0. \quad (1)$$

Here z is the longitudinal coordinate measured relative to a reference particle moving with the speed of light, δ is the energy offset relative to the nominal energy E_0 , $\delta = (E - E_0)/E_0$, η is the momentum compaction factor, $\gamma m c^2$ is the nominal beam energy, and $\mathcal{E}(z, t)$ is the longitudinal component of the electric field. The function f is normalized so that $\int f dz d\delta$ gives the number of particles in the beam.

An important approximation that we make in the nonlinear regime is that the evolution of the instability is governed by a single mode with a wavenumber q . One would expect that this wavenumber is equal to q_n —the mode that has the maximum growth rate in the linear regime—however, for the sake of generality, we treat q as arbitrary (but close to

q_n). The derivation of the equation for $\mathcal{E}(z, t)$ describing the interaction of the beam with the mode is given in Ref. [6]. Together with Eq. (1), they constitute a system that describes nonlinear evolution of the beam with the single mode of the field. Here we formulate this system of equation without derivation.

It is convenient to introduce dimensionless variables τ , ζ , and p instead of t , z and δ , respectively, where

$$\tau = \mu t, \quad \zeta = qz, \quad p = -\frac{\eta \omega_n}{\mu} \delta,$$

and

$$\mu = c \left[\frac{r_e n_b \omega_n \eta \chi_n}{c \gamma (1 - \beta_{gn})} \right]^{1/3},$$

where ω_n , χ_n and $c \beta_{gn}$ are the frequency, loss factor and the group velocity of the synchronous mode, respectively, ($\omega_n = c q_n$), and $r_e = e^2/mc^2$. We introduce the amplitude $A(\tau)$ such that,

$$\mathcal{E} = -\frac{\gamma m c \mu}{e \eta \omega_n} [A(\tau) e^{i q z} + \text{c.c.}],$$

and the dimensionless distribution function

$$F(\zeta, p, \tau) = \frac{1}{2\pi n_b} \frac{\mu}{\eta \omega_n} f,$$

normalized by the condition $\int_{-\infty}^{\infty} dp \int_0^{2\pi} d\zeta F(\zeta, p, \tau) = 1$. In these variables, the beam dynamics is described by the following equation,

$$\frac{\partial F}{\partial \tau} + p \frac{\partial F}{\partial \zeta} + [A(\tau) e^{i\zeta} + \text{c.c.}] \frac{\partial F}{\partial p} = 0, \quad (2)$$

and the amplitude $A(\tau)$ satisfies the equation

$$\frac{\partial A(\tau)}{\partial \tau} = \langle e^{-i\zeta} \rangle + i u A, \quad (3)$$

with

$$\begin{aligned} \langle e^{-i\zeta} \rangle &= \int_{-\infty}^{\infty} dp \int_0^{2\pi} d\zeta F(\zeta, p, \tau) e^{-i\zeta}, \\ u &= \frac{c}{\mu} (q - q_n) (1 - \beta_{gn}). \end{aligned} \quad (4)$$

Characteristics of Eq. (2) are equations of motion for a single particle:

$$\frac{d\zeta}{d\tau} = p, \quad \frac{dp}{d\tau} = [A(\tau) e^{i\zeta} + \text{c.c.}]. \quad (5)$$

Eq. (2), (3) and Eq. (5) constitute a full system of equations. These equations have an integral of motion:

$$C = |A|^2 - \langle p \rangle, \quad (6)$$

which reflects conservation of energy—the sum of the wave energy and the beam energy is constant during the interaction.

The system of equations (2), (3), and Eq. (5) is encountered in other problems of nonlinear beam-wave interaction, *e.g.*, in the one-dimensional FEL theory [7, 8], with the parameter μ being equivalent to the Pierce parameter ρ . The solution of the system on a limited time interval can be obtained by numerical methods. In the numerical approach, the beam is represented by a finite number M of macroparticles, and the average $\langle e^{i\zeta} \rangle$ is approximated by the sum $(1/M) \sum_1^M e^{-i\zeta_k}$ over all particles' coordinates ζ_k . The result of such a solution—the absolute value $|A|$ of the amplitude of the wave—is shown in Fig. (1). The amplitude of an initial small perturbation saturates after an initial exponential growth and exhibits oscillations at frequency of the order of the bounce frequency of particles in the bucket of the excited wave. Fig. 1 agrees with a similar solution obtained earlier in Ref. [7].

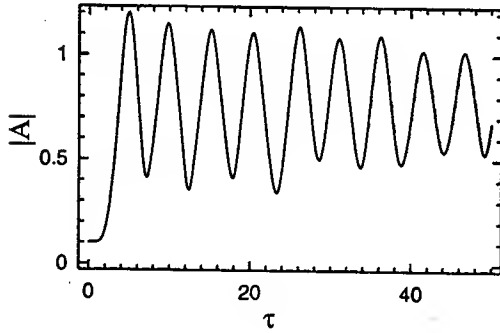


Figure 1: The dependence of the amplitude $|A|$ versus τ in the nonlinear regime of the instability.

SYNCHROTRON DAMPING AND QUANTUM DIFFUSION

Contrary to the FEL theory, where it usually suffices to track the solution on several gain lengths only, for a beam in the storage ring we may be interested in time comparable to the synchrotron damping time. The analysis in this case has to include the synchrotron damping and diffusion due to quantum fluctuations effects. One of the difficulties of such analysis is that the damping time typically is larger than the synchrotron oscillation period in the damping right so that one has also take into account synchrotron oscillations of a particle in the bunch. Here, however, we will consider an idealized formulation which neglects synchrotron

oscillations, but includes synchrotron damping and diffusion due to quantum fluctuations in synchrotron radiation. A more detailed study, with account of synchrotron motion, can be found in Ref. [9].

To include the effects of synchrotron damping and quantum diffusion into the interaction of the wave with the beam, we need to use the Vlasov-Fokker-Planck equation [10]. In our dimensionless variables it has the following form

$$\begin{aligned} \frac{\partial F}{\partial \tau} + p \frac{\partial F}{\partial \zeta} + [A(\tau)e^{i\zeta} + \text{c.c.}] \frac{\partial F}{\partial p} \\ = \Gamma \frac{\partial}{\partial p} \left(\Delta^2 \frac{\partial F}{\partial p} + pF \right), \end{aligned}$$

where Γ and Δ are related to the synchrotron radiation damping γ_{SR} and the rms energy spread δ_{SR} due to the quantum fluctuations in the synchrotron radiation:

$$\Gamma = \frac{\gamma_{SR}}{\mu}, \quad \Delta = \frac{\eta \omega_n \delta_{SR}}{\mu}.$$

Note that with damping the integral C in Eq. (6) is not conserved any more: $\frac{d}{d\tau} (|A|^2 - \langle p \rangle) = \Gamma \langle p \rangle$ instead of Eq. (6).

In order to carry out numerical simulation of the Vlasov-Fokker-Planck equation, we note that this equation is equivalent to a set of single-particle equations of motion with damping and an external force $\kappa(\tau)$:

$$\frac{d\zeta}{d\tau} = p, \quad \frac{dp}{d\tau} = [A(\tau)e^{i\zeta} + \text{c.c.}] - \Gamma p + \kappa(\tau).$$

where $\kappa(\tau)$ is a random function of time τ with zero average value $\langle \kappa \rangle = 0$ and the correlation function

$$\langle \kappa(\tau) \kappa(\tau') \rangle = 2\Gamma\Delta^2 \delta(\tau - \tau').$$

In our simulation, we used a discrete time mesh τ_i with the time step $\tau_s = \tau_{i+1} - \tau_i$ and a finite number of particles M . On each interval, we first solved the system of the differential equations Eqs. (5) and (3) without damping and fluctuations. The damping and fluctuations were taken into account at the end of each step by changing the variable p for each particle:

$$p_k \rightarrow p_k - \Gamma \tau_s p_k + \sqrt{24\tau_s \Gamma \Delta^2} \xi,$$

where ξ is a random number uniformly distributed in the range $[-1/2, 1/2]$. This algorithm was tested on the case without the wave, $A = 0$, and also for the case of an external wave with constant amplitude $A = \text{const}$, when the Vlasov-Fokker-Planck equation has analytical solutions. In both cases we found a good agreement between the numerical and analytical solutions.

The simulations were carried out for the parameters close to that of ALS: $\mu = 3.2 \cdot 10^7 \text{ s}^{-1}$, $\omega_n = 1.0 \cdot 10^{12} \text{ s}^{-1}$, $\Delta = 0.032$. However, to speed up the tracking, we increased the parameter Γ from the ALS value $2.0 \cdot 10^{-6}$ to $2.0 \cdot 10^{-2}$. We expect that such a rescaling of Γ accelerates

the manifestation of the synchrotron damping effects without qualitatively changing the solution. Typically we used from 200 to 800 particles in the simulation.

The results of the tracking for $\tau \approx 1000$ (corresponding to approximately 20 damping times) are shown in Fig. 2 and Fig. 3. Fig. 2 shows the amplitude $|A(\tau)|$, and

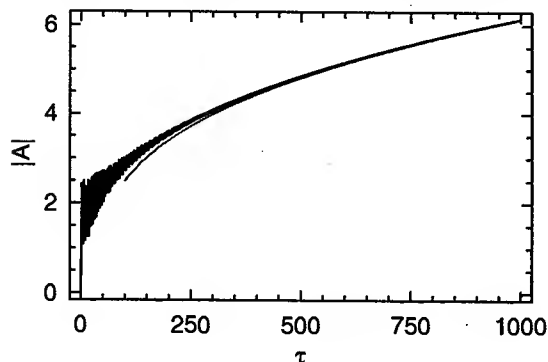


Figure 2: The absolute value of the amplitude $|A(\tau)|$ as a function of τ . Black curve shows the result of simulation, red curve—analytical solution of Eq. (8).

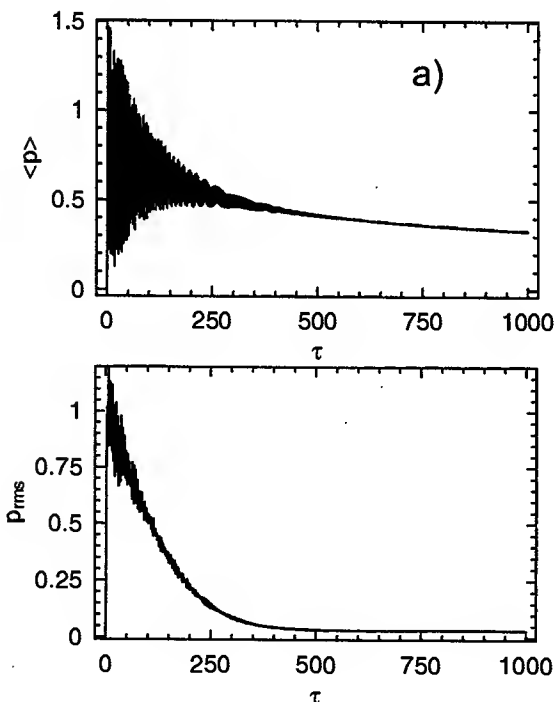


Figure 3: Numerical simulation of nonlinear regime of the instability: a)—the average momentum $\langle p \rangle$, b)—the rms momentum spread Δp_{rms} . The red line shows the result of the analytical model.

Fig. 3 shows the average over distribution function momentum $\langle p \rangle$ and the rms spread in p , Δp_{rms} , as functions

of time. For the time interval small compared with the damping time $\tau \lesssim 50$, results of tracking reproduce Fig. 1. For larger time intervals, $\tau \gg 50$, the amplitude $|A|$ keeps growing, and the beam comes to a quasi equilibrium, with a slowly changing values of $\langle p \rangle$ and Δp_{rms} . Note also a relatively small value of Δp_{rms} , which means that particles of the beam are well localized in the p -space.

The numerical results shown in Figs. 2 and 3 give us an indication of an analytical solution to the problem in the limit of large τ . In this solution we assume that

$$A(\tau) = \frac{1}{2} i A_0(\tau) e^{-i\nu(\tau)\tau}, \quad (7)$$

where the function $A_0(\tau)$ and frequency $\nu(\tau)$ are slow functions of time. Particles are trapped by the wave $e^{i(\zeta - \nu\tau)}$ and drift with the rate $d\zeta/d\tau = \nu$. It can be shown [6] that the amplitude $A_0(\tau)$ grows in time due to damping with the rate

$$\frac{dA_0}{d\tau} = \frac{2}{\sqrt{1 + A_0^4/(2\Gamma)^2}}. \quad (8)$$

Since this equation determines asymptotic behavior of A in the limit $\tau \rightarrow \infty$, the initial condition for it is not defined. For the purpose of comparison with the numerical solution, we considered an initial condition $A(\tau_0) = A_*$, with A_* as a fitting parameter. The result of integration of Eq. (8) with $A(100) = 2.5$ is shown in Fig. 2 in red color, in good agreement with the numerical solution. It is straightforward to show that for large τ it follows from Eq. (8) that $A_0 \propto \tau^{1/3}$. The averaged momentum of the particles $\langle p \rangle$ in this model can also be found and is shown as a red line in Fig. 3a.

ACKNOWLEDGMENTS

We thank S. Krinsky and Z. Huang for useful discussions. This work was supported by the Department of Energy, contract DE-AC03-76SF00515.

REFERENCES

- [1] S. Heifets and Stupakov G. V., Phys. Rev. ST Accel. Beams **5**, 054402 (2002).
- [2] J. B. Murphy, S. Krinsky, and R. L. Gluckstern, in *Proc. of PAC 1995*.
- [3] Y. S. Derbenev, et al. DESY FEL Report TESLA-FEL 95-05, (September 1995).
- [4] J. Schwinger, (1945), unpublished.
- [5] S. Heifets and G. Stupakov, in *PAC03* (2003).
- [6] S. Heifets and G. Stupakov, Preprint SLAC-PUB-9627, SLAC (2003).
- [7] R. Gluckstern, S. Krinsky, and H. Okamoto, Phys. Rev. **E47**, 4412 (1993).
- [8] N. A. Vinokurov, et al. NIM A **475**, 74 (2001).
- [9] S. Heifets, Preprint SLAC-PUB-9626, SLAC (2003).
- [10] A. Piwinski, in *Proc. CERN Accelerator School, Gif-sur-Yvette, 1984* no. 85-19 in CERN Yellow Report, pp. 432-462, (1985).

EFFECTS OF LINAC WAKEFIELD ON CSR MICROBUNCHING IN THE LINAC COHERENT LIGHT SOURCE

Z. Huang^{a*}, M. Borland^b, P. Emma^a, K.-J. Kim^b

^aSLAC, Stanford, CA 94309, USA

^bANL, Argonne, IL 60439, USA

Abstract

The design of the Linac Coherent Light Source (LCLS) requires two-stage bunch compression for stability against timing and charge jitters. Coherent synchrotron radiation (CSR) induced in these bunch compressors can drive a microbunching instability that may degrade the beam brightness. In this paper, we study effects of the longitudinal wakefield in the accelerator on this instability. We show that significant energy modulation can be accumulated in the linac through the geometrical wakefield and can enhance the CSR microbunching in these compressors. Analytical calculations are compared with numerical simulations to evaluate the gain of microbunching for the entire LCLS accelerator system.

INTRODUCTION

Magnetic bunch compressors are designed to increase the peak current while maintaining the small emittance for the electron beam necessary to drive an x-ray free-electron laser (FEL) [1, 2]. Recent simulation studies [3] and theoretical investigations [4, 5, 6] have shown that such a bend system is subject to a microbunching instability driven by coherent synchrotron radiation (CSR) and hence can be very sensitive to any density or energy modulation of the incoming beam distribution. Multiple stage compressions are often employed in x-ray FELs to partially offset the effect of rf phase jitters and to reach a peak current of a few kA. In this case, both density and energy modulations induced in the first-stage compressor can be further amplified in the next-stage compressor, leading to a large gain in overall modulation amplitudes [6, 7]. In this paper, we show that in an S-band linac such as the Stanford linear accelerator, the geometric wakefield of the accelerating structures can also induce significant energy modulation and enhance the CSR microbunching in the subsequent bunch compressor. We determine the total gain in density modulation for the Linac Coherent Light Source (LCLS) [1] and compare with numerical simulations that model the entire accelerator system.

CSR MICROBUNCHING

A magnetic bunch compressor introduces a linear path length dependence on the electron energy (characterized by the momentum compaction factor R_{56}). An incoming electron beam with an energy chirp will be compressed if

the tail of the bunch catches up the head by going through a shorter trajectory. CSR emitted by a very short bunch in the bends of a compressor can interact with the bunch itself and increase both correlated energy spread and projected emittances in the bending plane [8]. Furthermore, if the longitudinal density of the bunch is not smooth but is modulated at a wavelength $\lambda = 2\pi/k$ that is much smaller than the bunch length, CSR will be emitted at the same wavelength and induce energy modulation. Such energy modulation can be turned into additional density modulation through R_{56} of the compressor, leading to a microbunching instability. This process can also be initiated by energy modulation of the incoming beam. If this effect is large, both the "sliced" energy spread and the "sliced" emittance on the scale of the wavelength will be increased, directly affecting the FEL performance which depends critically on these "sliced" quantities.

Given the electron distribution function $f(\mathbf{X}; s)$ in the horizontal and longitudinal phase space denoted by $\mathbf{X} \equiv (x, x', z, \delta \equiv \Delta\gamma/\gamma)$, we can quantify both density and energy modulations by

$$\begin{aligned} b(k; s) &= \frac{1}{N} \int d\mathbf{X} e^{-ikz} f(\mathbf{X}; s), \\ p(k; s) &= \frac{1}{N} \int d\mathbf{X} e^{-ikz} \delta f(\mathbf{X}; s), \end{aligned} \quad (1)$$

where $N = \int d\mathbf{X} f(\mathbf{X}; s)$ is the total number of electrons. Considering the evolution of the distribution function in the presence of CSR, one can show that the bunching spectrum $b(k; s)$ is governed by an integral equation [5, 6]

$$\begin{aligned} b[k(s); s] &= [b_0(k_0) - ik(s)R_{56}(s)p_0(k_0)] L(0, s) + ik(s) \\ &\times \int_0^s d\tau R_{56}(\tau \rightarrow s) \frac{I(\tau)}{\gamma I_A} Z[k(\tau); \tau] b[k(\tau); \tau] L(\tau, s), \end{aligned} \quad (2)$$

where $b_0(k_0)$ and $p_0(k_0)$ are the initial density and energy spectra, respectively, $I(\tau)$ is the peak current at τ , $I_A \approx 17$ kA is the Alfvén current, $Z(k; s) = (1.63 + 0.94i)k^{1/3}/R(s)^{2/3}$ is the steady-state CSR impedance for a bending radius $R(s)$ [9], $L(\tau, s)$ denotes Landau damping from τ to s due to the beam emittance and energy spread. The integral equation can be solved numerically [5] or analytically for a typical bunch compressor chicane [6] to obtain $b(k; s)$. The energy modulation spectrum is then

*zrh@slac.stanford.edu

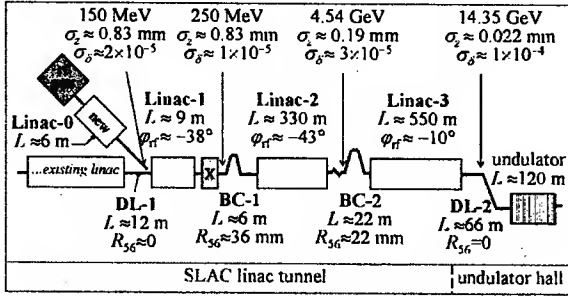


Figure 1: Layout of the LCLS accelerator system.

determined by [6]

$$p[k(s); s] = p_0(k_0)L(0, s) - \int_0^s d\tau \frac{I(\tau)}{\gamma I_A} Z[k(\tau), \tau] \times b[k(\tau), \tau] L(\tau, s). \quad (3)$$

We note that Eqs. (2) and (3) can be used not only for a bunch compressor but also for any beam transport system with a given impedance.

In Ref. [7], the analytical solutions of Eqs. (2) and (3) are applied to study the gain of density modulation for the LCLS bend systems (see Fig. 1). The results agree reasonably well with tracking studies of these bend systems. Furthermore, elegant simulations of the entire accelerator system show a peak gain almost a factor of 2 larger than the gain of just these bend systems. In what follows, we extend this study to consider wakefield in the accelerator that can enhance CSR microbunching.

LINAC WAKEFIELD AND IMPEDANCE

As was pointed out in Refs. [4, 6], wakefield upstream of a bunch compressor can accumulate energy modulation for a density-modulated beam and induce additional density modulation in the bunch compressor. For a periodic, cylindrically symmetric accelerating structure such as the SLAC S-band linac, Gluckstern has derived the high-frequency behavior of the longitudinal impedance as [10]

$$Z_L(k) \approx \frac{4i}{ka^2} \left[1 + (1+i) \frac{\alpha L}{a} \left(\frac{\pi}{kg} \right)^{1/2} \right]^{-1}, \quad (4)$$

where a is the average iris radius, L is the cell (period) length, g is the gap distance between irises and is comparable to L in normal structures, and the parameter α is a function of g/L and is about 0.5 for $g/L \sim 1$. Fourier transformation of Eq. (4) yields a very short-range wakefield $W(z)$ (valid for $z < 100 \mu\text{m}$). A wakefield fitting formula valid for a larger distance (up to a few mm) is given by [11]

$$W(z) = \frac{Z_0 c}{\pi a^2} \exp \left(-\sqrt{\frac{z}{z_0}} \right), \quad (5)$$

where $Z_0 = 377 \Omega$ and $z_0 \approx 0.41 a^{1.8} g^{1.6} / L^{2.4}$. Eqs. (4) and (5) are steady-state solutions of a periodic accelerating

structure and can be applied to a linac longer than the catch up distance $\alpha k a^2$ [10, 11]. For the SLAC linac, $a = 11.6 \text{ mm}$, $L = 3.5 \text{ cm}$, $g = 2.9 \text{ cm}$, and $z_0 \approx 1.32 \text{ mm}$, and the catch up distance varies from a few meters to a few hundred meters for $\lambda = 100 \mu\text{m}$ down to $1 \mu\text{m}$, the wavelength range of interest for CSR microbunching.

Equation (4) indicates that the linac impedance decreases with λ . Let us compare magnitudes of the leading term of the linac impedance with the steady-state CSR impedance, say, at $\lambda = 100 \mu\text{m}$:

$$|Z_L| \sim \frac{4}{ka^2} \approx 0.5 \text{ m}^{-1}, \quad |Z_{\text{CSR}}| \sim \frac{k^{1/3}}{R^{2/3}} \approx 9 \text{ m}^{-1} \quad (6)$$

for $a = 11.6 \text{ mm}$ and $R = 10 \text{ m}$. We see that the wakefield effect per unit length is much smaller than the CSR effect at these short modulation wavelengths. However, the net effect of the impedance on a beam is integrated over the interaction distance. For CSR, the interaction distance is the total length of dipoles and is on the order of a few meters. For the linac wakefield, the interaction distance is the total length of the linac and is on the order of a few hundred meters. Thus, the net effect of CSR and linac impedances on the microbunching instability can be comparable for the LCLS. Since $R_{56} \approx 0$ in the linac, and the Landau damping due to beam emittance and energy spread is negligible, Eqs. (2) and (3) reduce to

$$b[k(s); s] = b_0(k_0), \quad \gamma(s)p[k(s); s] = \gamma_0 p_0(k_0) - \frac{I}{I_A} Z_L(k_0) b_0(k_0) s. \quad (7)$$

Here we have multiplied Eq. (3) by γ on both sides to include the adiabatic damping due to acceleration.

LCLS TOTAL GAIN

We can now evaluate the amplification of a small current modulation in the initial beam distribution through the entire LCLS accelerator by taking into account both CSR and wakefield effects. Here we take the normalized emittance at $1 \mu\text{m}$ and keep track of the change of the incoherent energy spread σ_δ due to acceleration and compression (see Fig. 1). The peak currents are obtained by assuming a 1-nC Gaussian bunch with rms bunch lengths σ_z given in Fig. 1 at various stages of compression. We also use the steady-state CSR impedance and the high-frequency linac impedance (i.e., Eq. (4)) for simplicity. First, we calculate the induced density and energy modulations in DL-1 and BC-1 through the analytical solutions of Eqs. (2) and (3) as was done in Ref. [7]. For the given density modulation at the exit of BC-1, the linac wakefield induces additional energy modulation through Eq. (7) in Linac-2 (its effect in Linac-0 and Linac-1 is negligible). Finally, Eq. (2) is again applied to BC-2 to calculate the final density modulation amplified from both density and energy modulations at the entrance of BC-2. Two cases are considered: (1) the incoherent energy spread at the entrance of BC-2 (at 4.54 GeV)

is 3×10^{-6} without the superconducting wiggler; (2) the incoherent energy spread at the entrance of BC-2 is increased to 3×10^{-5} by the superconducting wiggler as indicated in Fig. 1. Since $R_{56} \approx 0$ in DL-2, the density modulation after BC-2 is unchanged, and its ratio to the initial density modulation is defined as the total gain. In Fig. 2, we show the total gain as a function of the initial modulation wavelength with and without the damping wiggler. For comparison, we also plot elegant simulation results from Ref. [7]. Note that elegant uses the transient CSR model [12] and Eq. (5) for the linac wakefield. Nonlinearities in the machine lattice are also included. While theory predicts that the modulation wavelength should compress according to the bunch length compression (by about a factor of 38 after BC-2), simulation shows less wavelength compression than expected. Nevertheless, we see that the gain calculation including the linac wakefield agrees roughly with the elegant results. The peak gain is increased by about a factor of 2 compared to previous studies that did not take into account the linac wakefield [7].

It is very important to design the LCLS to have a low gain in CSR microbunching. Typical drive laser of the photocathode rf gun can have structures on the order of a few hundred femtosecond. Suppose such structures cause 1% density modulation of electron beam at $\lambda = 60 \mu\text{m}$ in the injector, a total gain close to 100 (in the absence of the damping wiggler, see Fig. 2) implies nearly 100% final density modulation at $\lambda_f \approx 60/38 \approx 1.6 \mu\text{m}$. When the density modulation is close to 100% or $|b_f| \approx 1$, nonlinear effects of CSR instability can significantly increase the incoherent energy spread and sliced emittance on the scale of the modulation wavelength, which is not treated in the present linear theory. Furthermore, we can estimate the induced energy modulation by the linac impedance in Linac-3 and the CSR impedance in DL-2 for the given b_f :

$$\Delta p_f \approx \left| \frac{I_f}{\gamma_f I_A} \left[Z_L L_{\text{Linac3}} + Z_{\text{CSR}} L_{\text{DL2}} \right] b_f \right|, \quad (8)$$

where $L_{\text{Linac3}} \approx 550 \text{ m}$ is the length of Linac-3 and $L_{\text{DL2}} = 4 \times 2.62 \text{ m} \approx 10.5 \text{ m}$ is the total dipole length in DL-2. For $\lambda_f = 1.6 \mu\text{m}$, $I_f \approx 5 \text{ kA}$, $\gamma_f \approx 28077$, $|b_f| \approx 1$, and the bending radius of DL-2 dipoles $R = 231 \text{ m}$, we have the final energy modulation $\Delta p_f \approx 9 \times 10^{-4}$, almost a factor of 2 larger than the FEL parameter $\rho \approx 5 \times 10^{-4}$ for the LCLS [1]. In such cases, the high gain in the absence of the damping wiggler would mean that the FEL may not reach saturation for a 100-m undulator.

CONCLUSION

We have extended previous studies of CSR microbunching instability to include the effect of geometric wakefield in the accelerator. Using the analytical model for the high-frequency, periodic accelerating structure and the analytical solutions of the integral equation for the CSR instability in a bunch compressor chicane, we have evaluated the

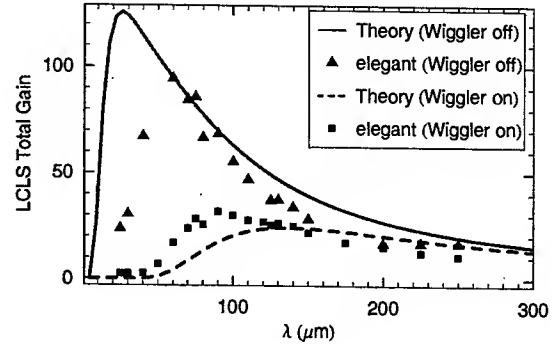


Figure 2: LCLS total gain of density modulation as a function of the initial modulation wavelength.

total gain of density modulation in the LCLS accelerator system and found the linac wakefield can increase the gain by about a factor of 2. The gain in shorter wavelength modulations may be more detrimental to the FEL performance and can be strongly suppressed by the damping wiggler incorporated in the LCLS design.

We thank K. Bane for useful discussions on geometric wakefield and impedance in a linac. This work was supported by the U. S. Department of Energy Contract Nos. DE-AC03-76SF00515 and W-31-109-ENG-38.

REFERENCES

- [1] Linac Coherent Light Source Conceptual Design Report, SLAC-R-593, UC-414 (2002).
- [2] TESLA Technical Design Report, DESY 2001-011, TESLA Report 2001-23, TESLA-FEL 2001-05 (2001).
- [3] M. Borland *et al.*, in *Proc. of PAC 2001*, 2707 (IEEE, Piscataway, NJ, 2001); Nucl. Instrum. Methods Phys. Res., Sect. A **483**, 268 (2002).
- [4] E.L. Saldin, E.A. Schneidmiller, M.V. Yurkov, DESY TESLA-FEL 2002-02 (2002); Nucl. Instrum. Methods Phys. Res., Sect. A **490** 1 (2002).
- [5] S. Heifets, G. Stupakov, S. Krinsky, Phys. Rev. ST Accel. Beams **5**, 064401 (2002); Phys. Rev. ST Accel. Beams **5**, 129902 (2002).
- [6] Z. Huang, K.-J. Kim, Phys. Rev. ST Accel. Beams **5**, 074401 (2002); Phys. Rev. ST Accel. Beams **5**, 129903 (2002).
- [7] Z. Huang *et al.*, SLAC-PUB-9538, in *Proc. of FEL2002*, to appear in Nucl. Instrum. Methods Phys. Res., Sect. A, 2003.
- [8] Y.S. Derbenev *et al.*, DESY TESLA-FEL 95-05 (1995).
- [9] J.B. Murphy, S. Krinsky, R.L. Gluckstern, in *Proc. of PAC 1995*, 2980 (IEEE, Piscataway, NJ, 1995); Particle Accelerators **57**, 9 (1997).
- [10] R.L. Gluckstern, Phys. Rev. D **39**, 2780 (1989).
- [11] K. Bane *et al.*, SLAC-PUB-7862, in *Proceedings of ICAP98* (1998).
- [12] G. Stupakov, P. Emma, in *Proc. of EPAC 2002*, 1479 (2002).

AN OVER-DAMPED CAVITY LONGITUDINAL KICKER FOR THE PEP-II LER*

P. McIntosh, R. Akre, D. Anderson, S. DeBarger, M. Dormiani, J. Fox, K. Jobe, H. Schwarz, D. Teytelman, U. Wienands, A. Young, SLAC, Stanford, CA 94025, USA. F. Marcellini, INFN-Frascati, Italy. M. Tobiyama, KEK, Japan

Abstract

Both rings of PEP-II use drift tube kickers in the longitudinal bunch-by-bunch feedback system. Efforts are now underway to increase the stored beam currents and luminosity of PEP-II, and beam-induced heating of these structures, particularly in the Low Energy Ring (LER) is of concern. An alternative kicker design based on the over-damped cavity kicker, first developed by INFN-Frascati is being built for PEP-II. This low loaded Q (or wide bandwidth) structure is fed by a network of ridged waveguides coupled to a simple pill-box cavity. Beam induced RF power is also coupled out of the cavity to external loads, so that the higher order modes (HOMs) excited in the structure are well-damped. This paper details the kicker design for PEP-II and discusses some of the design trade-offs between shunt impedance and bandwidth, as well as the influence of the feedthroughs on the kicker parameters. Estimates of the expected power deposition in the cavity are also provided.

INTRODUCTION

The longitudinal bunch-by-bunch feedback systems at PEP-II use wide-band drift-tube kickers [1] that have performed very well at beam currents up to 1.9 A and 6.3 ns bunch spacing and roughly 1000 bunches in the LER. However, with plans to substantially increase the beam currents, with bunch currents much higher than originally anticipated, the thermal stresses in these kickers will become quite high. The drift tube kickers are difficult to cool since the drift-tubes are supported only by rather thin electrodes. In order to prevent these kickers from becoming a beam current limit we are building new feedback kickers based on the successful design of an over-damped cavity developed at INFN-Frascati [2] and used elsewhere [3][4] to replace the existing feedback kickers in the LER. The new structure is easily cooled from the outside and expected to more than double the current capability of the LER kickers.

THE NEW LFB CAVITY KICKER DESIGN

The bandwidth requirement for the new kicker derives from the spectrum of modes in the beam. At PEP-II, every 2nd RF bucket can be filled, the bandwidth required to perform efficient damping is then equal to $f_{RF}/4$, or 119 MHz. A bandwidth of $\sim f_{RF}/2$ or 238 MHz has been chosen to provide more linearity over its operating band. The cavity fundamental TM_{010} mode therefore has to be

very broadband with a low loaded Q , which is contrary to traditional RF cavity design requirements. A simple pill-box cavity is employed, strongly coupled to which are four large waveguides (see Figure 1) which are terminated externally to 50 Ω , reducing the Q to give a $Q_L \sim 5$.

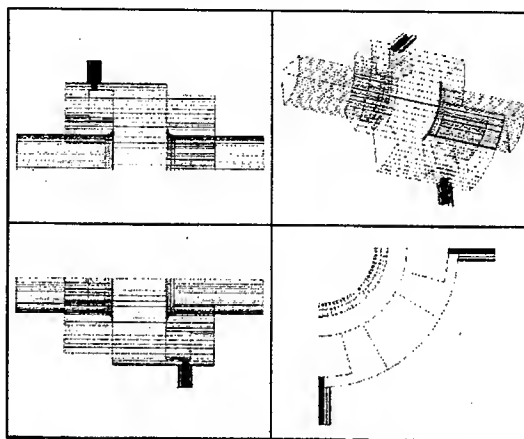


Figure 1 HFSS Longitudinal Feedback Kicker Geometry

The frequency chosen for the new kicker is $9/4 f_{RF}$ or 1.071 GHz as this gives the highest shunt impedance solution of the options available ($13/4$ and $9/4 f_{RF}$) [5]. The existing longitudinal feedback system also operates at 1.071 GHz and has enough power to drive the new kickers, so infrastructure modifications are minimal. The HOM spectrum of the kicker is shown in Table 1 and the fundamental mode shunt impedance is ~ 1.5 times as much as the drift-tube kicker so that some voltage kick increase is expected from the same amplifier power. The TM_{01} mode cut-off frequency of the 89 mm beam pipe is 2.6 GHz and modes above that are highly damped as confirmed by MAFIA simulations.

Table 1 Kicker Fundamental and HOM Characteristics

Mode	Freq (GHz)	Q_L	BW (MHz)	$R_s (\Omega)$
TM_{010}	1.071	4.8	224	626
TM_{110}	1.5151	22	69	16.7 k
TE_{111}	1.7114	210	8	19.2 k
TM_{011}	2.0507	13	157	65
TM_{020}	2.4117	116	21	76

The new kicker cavity has been developed using the Ansoft finite element, electro-magnetic solver – HFSS [6]. A bandwidth response of 224 MHz, centered at 1.071 GHz (see Figure 2), has been achieved by optimization of the waveguide profile and coupling transitions.

* Work supported by Department of Energy contract DE-AC03-76SF00515

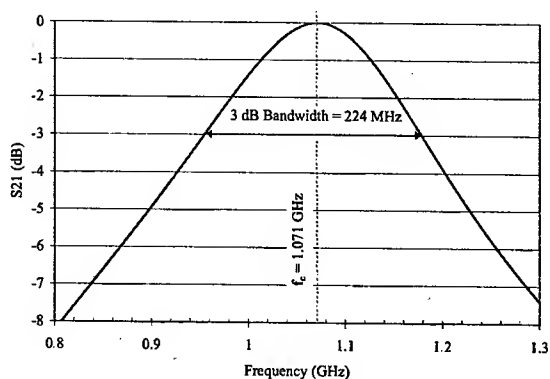


Figure 2 Transmission Frequency Response of Kicker

The kicker structure (see Figure 3) is being fabricated from OFHC copper for efficient cooling and to avoid multipactor problems that can arise in aluminium structures without Titanium Nitride coating.

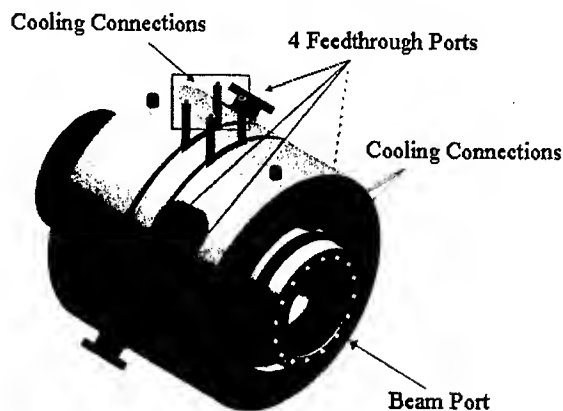


Figure 3 New Kicker Mechanical Assembly

KICKER BEAM INDUCED POWER

Both the existing drift-tube and cavity kickers present impedances that absorb power from the circulating beam. The center frequencies of both designs are selected to minimize the impedance at multiples of the RF frequency for which there are very strong harmonic content in the circulating current. However, due to gaps in the filling patterns and unequal charges in the stored buckets, there is significant power deposited by the beam in both structures. As seen in figures 4 and 5, the 3A nominal fill in the LER would deposit roughly 14 kW in the cavity kicker and 12 kW in the drift-tube kicker.

One important difference between the structures is seen in the periodic impedance of the drift tube, which absorbs power from the beam at high frequencies as well as in the operating band. The drift-tube structure has a finite directivity in the 1 - 2 GHz band, so that the bulk of the power in this band is coupled out of only two load ports. Therefore the power to the drift tube load ports is higher, by almost a factor of 2, than in each of the 4 symmetric ports on the cavity kicker.

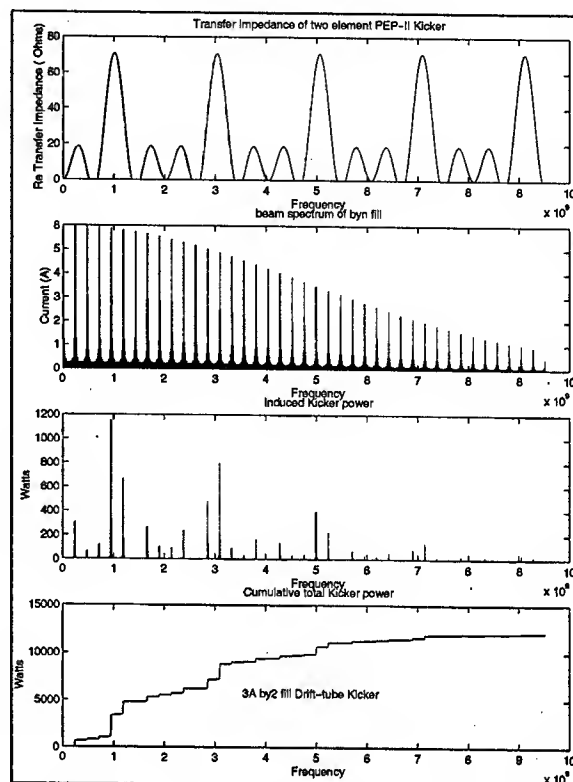


Figure 4 Beam Induced Power for Existing Drift-tube Kicker

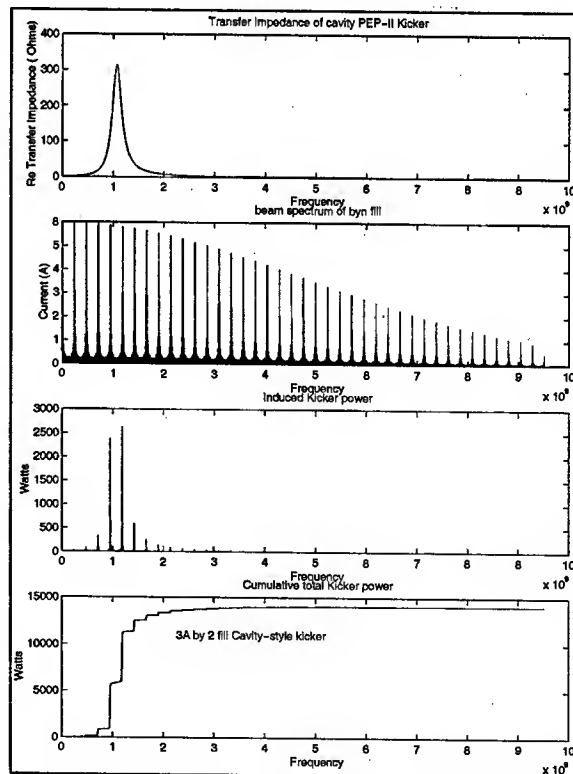


Figure 5 Beam Induced Power for New Cavity Kicker

On the other hand, the cavity kicker requires the installation of high power circulators between power amplifier and kicker. The most important advantage of the cavity kicker is thermal management, as it has no internal structure, and the cavity itself can be water-cooled on surfaces outside the vacuum chamber.

A NEW RF FEEDTHROUGH

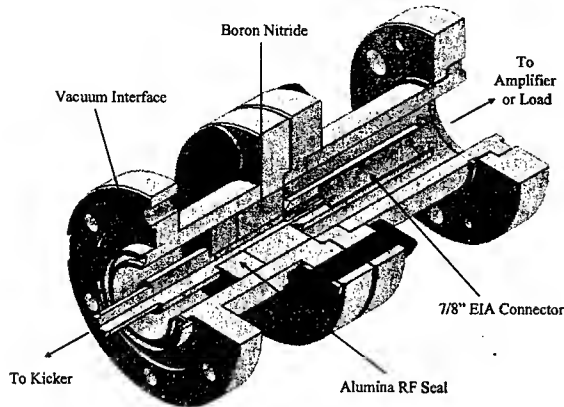


Figure 6 The New High Power RF Feedthrough Design

Each feedthrough has to be able to handle at least $\frac{1}{4}$ of the total beam induced power (plus $\sim\frac{1}{4}$ of the amplifier power). To have some safety margin in the power handling capability and allow beam current increases to 4.5 A in the future, a new high power RF feedthrough has been developed at SLAC. The design may also be an attractive solution for other high power feedthrough applications. The feedthrough is being built by industry (see Figure 6) and is specified to handle 10 kW at 1 GHz, although we expect some leakage of frequencies up to 8 GHz due to excitation of HOMs.

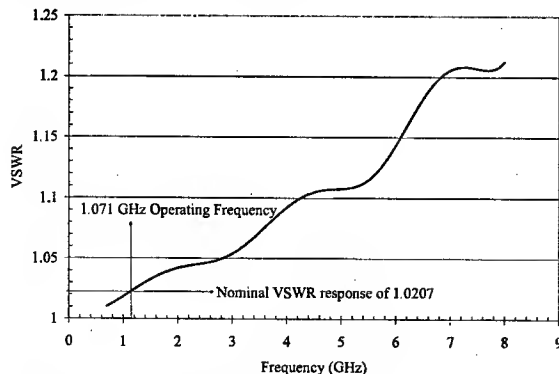


Figure 7 HFSS RF Feedthrough Frequency Response

HFSS has again been utilized to optimize the feedthrough to have a good VSWR response over a wide bandwidth, extending up to 8 GHz (see Figure 7). The new feedthrough comprises a $\frac{7}{8}$ " EIA interface and incorporates an alumina ceramic vacuum seal; it also has a boron nitride ceramic which is used to dissipate some of the thermal energy generated in the inner coax. There are

optimized impedance transformations at either side of the ceramics which control the VSWR response up to this high frequency. The output coax then has a smooth 50 Ω impedance transition to the cavity kicker.

Attaching the feedthroughs to the cavity kicker has the effect of perturbing the fundamental mode bandwidth. The magnitude of the perturbation is intrinsically related to the mismatch the feedthrough presents. Experience at both DAΦNE and KEK, who also use this type of cavity kicker and feedthrough configuration, albeit with different operating characteristics, has shown that the operational bandwidth perturbation can be as much as 20% [7][8]. With this in mind, by having a low VSWR at its fundamental operating frequency, HFSS simulations predict that when attached to the new kicker, the induced perturbation from this new feedthrough is only $\sim 5\%$ (see Table 2).

Table 2 TM_{010} Mode Perturbation Due to Feedthroughs

TM_{010}	Freq (GHz)	Q_L	BW (MHz)	$R_s (\Omega)$
w/o f/thru	1.071	4.8	224	626
with f/thru	1.071	4.6	235	620

CONCLUSIONS

This collaboration has developed a new 4-port longitudinal feedback kicker which should not limit the LER operation on PEP-II up to 4.5 A. The increased shunt impedance of the structure enables a larger voltage kick to be applied to the bunch than with the present drift-tube kicker, for the same amplifier power. Operation of the LER at 4.5 A will generate more beam-induced power which is extracted from the structure through the RF feedthroughs. A new high-power feedthrough design will be able to fulfill this requirement. Two kicker cavities are currently being manufactured at SLAC and the associated feedthroughs manufactured by industry, for installation on the PEP-II LER this summer.

REFERENCES

- [1] J. N. Corlett et al, "Longitudinal and Transverse Feedback Kickers for the ALS", Proc. EPAC'94, London, June 1994.
- [2] R. Boni et al, "A waveguide Overloaded Cavity as a Longitudinal Kicker for the DAΦNE Bunch-by-Bunch Feedback System", Particle Accelerators, 1996, Vol. 52, pp 95 - 113.
- [3] M. Tobiyama et al, "Bunch-by-Bunch Feedback System for KEKB Rings", Proc. APAC'98, Tsukuba, March 1998, pp 540 - 542.
- [4] T. Knuth et al, "Longitudinal and Transverse Feedback Kickers for the BESSY II Storage Ring", Proc. PAC'99, New York, March 1999, pp 1147 - 1149
- [5] F. Marcellini et al, "Study and Design of a New Over-Damped Cavity Kicker for the PEP-II Longitudinal Feedback System", BIW'02, Brookhaven, May 2002.
- [6] HFSS is licensed to Ansoft Corporation, Pittsburgh, USA.
- [7] Private communication M. Tobiyama, KEK.
- [8] Private communication F. Marcellini, INFN Frascati.

EVOLVING BUNCH AND RETARDATION IN THE IMPEDANCE FORMALISM*

R. Warnock[†], SLAC, Stanford, CA 94309 and M. Venturini, LBNL, Berkeley, CA 94720

Abstract

The usual expression for the longitudinal wake field in terms of the impedance is exact only for the model in which the source of the field is a rigid bunch. To account for a deforming bunch one has to invoke the *complete impedance*, a function of both wave number and frequency. A computation of the corresponding wake field would be expensive, since it would involve integrals over frequency and time in addition to the usual sum over wave number. We treat the problem of approximating this field in an example of current interest, the case of coherent synchrotron radiation (CSR) in the presence of shielding by the vacuum chamber.

Consider a rigid bunch moving on a circular trajectory of radius R . A test particle feels a voltage

$$V(\theta, t) = \omega_0 Q \sum_{n=-\infty}^{\infty} e^{in(\theta - \omega_0 t)} Z(n) \lambda_n, \quad (1)$$

where $\theta - \omega_0 t$ is the azimuthal angle between the test particle and the reference particle, the latter having revolution frequency $\omega_0 = \beta_0 c/R$. The impedance at azimuthal mode number n (wave number n/R) is $Z(n)$. The mode amplitude λ_n is the Fourier transform of the line density $\lambda(\theta)$ in the bunch rest frame. With $\int \lambda(\theta) d\theta = 1$ the total charge is Q . For the case of a deforming bunch one's first inclination is merely to replace λ_n in (1) by $\lambda_n(t)$. The resulting formula (or its equivalent statement in terms of a wake potential) has been used in dynamical calculations based on the Vlasov-Fokker-Planck equation [1, 2, 3, 4], and in earlier macroparticle simulations. In such work λ_n (or $\lambda(\theta)$) is updated at each time step according to the values of external and coherent forces at the previous step. Although the calculations seem successful in many respects, the simple replacement $\lambda_n \rightarrow \lambda_n(t)$ is a first approximation of uncertain accuracy, especially in an unstable regime of rapid bunch evolution.

Our object here is to derive this first approximation and systematic corrections. We do so in an analytically solvable model, the case of particles on circular trajectories between two infinite parallel plates, perfectly conducting. The plates represent the vacuum chamber, which suppresses CSR at wavelengths greater than a certain "shielding cutoff". This model has considerable utility in spite of its simplified view of a real system; it led to interesting re-

sults on instabilities induced by CSR in the work of Refs. [2, 3].

The field equations are solved in cylindrical coordinates (r, θ, y) , with y -axis perpendicular to the plates and origin midway between the plates of separation h . We allow an arbitrary but fixed distribution of charge in the y -direction, with density $H(y)$, $\int H(y) dy = 1$. The full charge density has the form $\rho(\theta, t) = Q \lambda(\theta - \omega_0 t) H(y) \delta(r - R)/R$. We make a Laplace transform of the Maxwell equations and the charge/current density in time, assuming that the charge and the fields are zero before $t = 0$. We also make Fourier transforms in θ and y , the Fourier series in y chosen to satisfy the boundary conditions of fields on the plates. Then the transformed field equations can be solved in terms of Bessel functions. The Fourier/Laplace transform of the longitudinal electric field (averaged over the vertical distribution $H(y)$) will be denoted as $\hat{E}(n, \omega)$. Here $\omega = u + iv$, $v > 0$ is a complex frequency, while the Laplace transform variable conjugate to time is $s = -i\omega$. By linearity of the field equations, $-2\pi R \hat{E}$ is proportional to the corresponding transform of the current, with a proportionality constant $Z(n, \omega)$ called the *complete impedance*: $-2\pi R \hat{E}(n, \omega) = Z(n, \omega) \hat{I}(n, \omega)$.

The transform of the current is

$$\hat{I}(n, \omega) = \frac{Q \omega_0}{2\pi} \int_0^\infty dt e^{i(\omega - n\omega_0)t} \lambda_n(t), \quad (2)$$

$$\lambda_n(t) = \frac{1}{2\pi} \int_0^{2\pi} d\theta e^{-in\theta} \lambda(\theta, t). \quad (3)$$

Compare the case of a rigid bunch existing for all time, for which

$$\hat{I}(n, \omega) = Q \omega_0 \delta(\omega - n\omega_0). \quad (4)$$

The impedance has the form

$$Z(n, \omega) = \frac{Z_0 (\pi R)^2}{\beta_0 h} \sum_{p=1}^{\infty} \Lambda_p \left[\frac{\omega \beta_0}{c} J'_{|n|}(\gamma_p R) H_{|n|}^{(1)'}(\gamma_p R) + \left(\frac{\alpha_p}{\gamma_p} \right)^2 \frac{n}{R} J_{|n|}(\gamma_p R) H_{|n|}^{(1)}(\gamma_p R) \right]. \quad (5)$$

Here $H_n^{(1)} = J_n + iY_n$, where J_n and Y_n are Bessel functions of the first and second kinds, $Z_0 = 120\pi \Omega$ in m.k.s. units, and $\alpha_p = \pi p/h$, $\gamma_p^2 = (\omega/c)^2 - \alpha_p^2$. The sum on p corresponds to modes in the Fourier expansion with respect to y . The factor Λ_p depends on the vertical distribution $H(y)$, and is zero for even p if H is even. For a Gaussian distribution with r.m.s. width $\sigma_y \ll h$, and the y -average to define \hat{E} taken over $[-\sigma_y, \sigma_y]$, we have $\Lambda_p = 2 \sin(x) e^{-x^2/2}/x$, $x = \alpha_p \sigma_y$.

* Work supported in part by Department of Energy contract DE-FG03-99ER41104

[†] e-mail: warnock@slac.stanford.edu

The impedance at fixed integer n is defined as an analytic function of ω in the upper half-plane by first defining $\gamma_p(\omega) = ((\omega/c)^2 - \alpha_p^2)^{1/2}$ as an analytic function. We take $\gamma_p(u)$ to be positive for $u > \alpha_p c$, then define $\gamma_p(\omega)$ by analytic continuation to $\text{Im } \omega \geq 0$; it follows that $\gamma_p(-u) = -\gamma_p(u)$, $u > \alpha_p c$. This specification makes $Z(n, \omega)$ analytic and bounded for $\text{Im } \omega \geq v > 0$. The boundedness follows from integral representations and asymptotic formulas [3]. On the real axis Z is not bounded, having poles at the wave guide cutoffs, $\omega = \pm \alpha_p c$. These points are frequency thresholds for the advent of propagating waves with transverse mode number p . In (5) the poles are from γ_p^{-2} in the coefficient of $J_{|n|} Y_{|n|}$ and from $J'_{|n|} Y'_{|n|}$. The poles alone make the following contribution to the impedance, for $|n| > 0$:

$$Z_*(n, \omega) = i \frac{Z_0 \pi c}{2 \beta_0 h} \sum_p \Lambda_p \times \left[\frac{|n| \beta_0 - \text{sgn}(n) \alpha_p R}{\omega - \alpha_p c} + \frac{|n| \beta_0 + \text{sgn}(n) \alpha_p R}{\omega + \alpha_p c} \right], \quad (6)$$

where $\text{sgn}(n)$ is the sign of n . There is no pole for $n = 0$. The poles do not show up as infinities or even sharp peaks in $Z(n) = Z(n, n\omega_0)$, since $Z_*(n, n\omega_0) = i Z_0 (\pi R / \beta_0 h) \sum_p \Lambda_p$ is bounded and independent of n .

From (2) and the definition of Z we get the wake voltage V by the inverse Fourier/Laplace transform as

$$V(\theta, t) = -2\pi R \mathcal{E}(\theta, t) = \omega_0 Q \sum_n e^{in\theta} \int_{\text{Im } \omega=v} d\omega e^{-i\omega t} Z(n, \omega) \times \frac{1}{2\pi} \int_0^\infty dt' e^{i(\omega - n\omega_0)t'} \lambda_n(t'). \quad (7)$$

If we substitute the rigid bunch current instead of (2) in (7), we get (1) with the identification $Z(n) = Z(n, n\omega_0)$. We cannot be sure that the ω -integral in (7) exists without some assumption on λ_n , since $Z(n, u + iv)$ is bounded but nonvanishing as $|u| \rightarrow \infty$; see [3]. We assume that $\lambda_n(t) \in C^{(2)}(-\infty, \infty)$, i.e., it has a continuous second derivative on the real line. Then since $\lambda_n(t) = 0$, $t < 0$, it follows that $\lambda_n^{(k)}(0) = 0$, $k = 0, 1, 2$. This allows two partial integrations with vanishing boundary terms, so that the t' -integral takes the form

$$-\frac{1}{(\omega - n\omega_0)^2} \left(\int_0^t + \int_t^\infty \right) dt' e^{i(\omega - n\omega_0)t'} \lambda_n''(t'), \quad (8)$$

which is $\mathcal{O}(u^{-2})$, $u \rightarrow \infty$. Consequently, the ω -integral converges absolutely. Moreover, the second term in (8) contributes nothing to (7), since it is analytic for $\text{Im } \omega = v > 0$ and is less in magnitude than $M \exp(-vt)/|\omega|^2$ for some constant M . Since $Z(n, \omega)$ is analytic and bounded for $\text{Im } \omega > 0$, we can replace the ω -integral by an integral over the semi-circle at infinity, which is zero, thanks to decay of the integrand as $|\omega|^{-2}$. Thus causality is satisfied,

since future values of the charge density do not enter:

$$V(\theta, t) = -\omega_0 Q \sum_n e^{in\theta} \int_{\text{Im } \omega=v} d\omega e^{-i\omega t} Z(n, \omega) \times \frac{1}{(\omega - n\omega_0)^2} \frac{1}{2\pi} \int_0^t dt' e^{i(\omega - n\omega_0)t'} \lambda_n''(t'). \quad (9)$$

One could attempt a calculation of V by direct numerical evaluation of the two integrals in (9), but that would be expensive and would involve many insignificant contributions. Instead we note that the t' -integral is expected to be concentrated (for small v) near $u = n\omega_0$. Outside such a neighborhood the integral is small by virtue of oscillations. Moreover, the second order pole at $\omega = n\omega_0$ also tends to concentrate the ω integral (i.e., u -integral) near $u = n\omega_0$. Consequently, it makes sense as a first approximation to replace $Z(n, \omega)$ by $Z(n, \omega_0)$, and that allows us to compute the ω -integral by closing the contour in the lower half-plane. The factor

$$-\frac{1}{2\pi} e^{-i\omega t} \int_0^t e^{i(\omega - n\omega_0)t'} \lambda_n(t') dt' \quad (10)$$

is an entire function of ω , bounded in the lower half-plane, and the residue of the second order pole is just the derivative of (10), evaluated at $n\omega_0$. An integration by parts using $\lambda_n(0) = \lambda_n'(0) = 0$ then gives the expected lowest approximation, namely (1) with $\lambda_n \rightarrow \lambda_n(t)$, and $Z(n) = Z(n, n\omega_0)$.

For the next approximation one might think of expanding $Z(n, \omega)$ in (9) in a Taylor series about $\omega = n\omega_0$. This cannot succeed for $n\omega_0$ close to $\pm \alpha_p c$, because of the poles of (6). We can, however, write $Z(n, \omega) = \tilde{Z}(n, \omega) + Z_*(n, \omega)$ and compute the contribution of the pole term Z_* to the ω -integral by the method of residues. The smooth remainder \tilde{Z} can later be expanded in a Taylor series about $n\omega_0$. For the integral of the pole term it is best to first undo the two partial integrations in t' , so that the ω -integral of (9) has just first order poles at $\pm \alpha_p c$. The boundary terms vanish as is seen by closing their integrals by a circle at infinity in the upper half-plane. The integral over Z_* is then found by closing the contour in the lower half plane, and the result is

$$-\frac{Z_0 \pi R e^{-in\omega_0 t}}{2 \beta_0 h} \sum_p \Lambda_p \int_0^t \lambda_n(t') dt' \times \left[A(p, n) e^{iA(p, n)(t'-t)} + B(p, n) e^{iB(p, n)(t'-t)} \right], \quad (11)$$

where $A(p, n) = \alpha_p c - n\omega_0$, $B(p, n) = -\alpha_p c - n\omega_0$.

Having accounted exactly for the poles, we account approximately for the remainder \tilde{Z} by a Taylor expansion, $\tilde{Z}(n, \omega) = \tilde{Z}(n, n\omega_0) + \partial \tilde{Z}(n, n\omega_0) / \partial \omega (\omega - n\omega_0) + \dots$. To evaluate the contribution of the k -th order term of the expansion to (9), we have to assume $\lambda_n(t) \in C^{(k+2)}(-\infty, \infty)$. Taking the expansion just to the first order, we suppose that λ_n has a continuous third derivative,

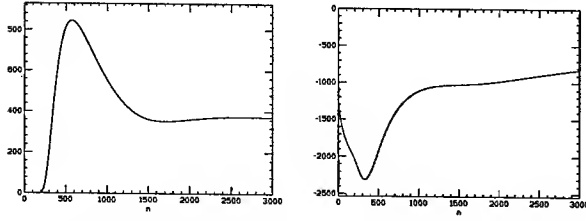


Figure 1: Real and imaginary parts of $\omega_0 \partial \tilde{Z}(n, n\omega_0) / \partial \omega$ in ohms, plotted versus n

and do an additional integration by parts on t' to get a factor $(\omega - n\omega_0)^{-3}$, thus a behavior $\mathcal{O}(|\omega|^{-2})$ in the lower half-plane for the first order Taylor term, enough to close the contour in the lower half-plane. The zeroth order Taylor term contains a contribution from $-Z_*(n, n\omega_0)$ which is finite but alarmingly large. This caused a headache until we realized that it is exactly cancelled by a part of (11), namely the boundary term in an partial integration in which the integral over λ_n is replaced by an integral on λ'_n . Invoking this cancellation, we state our proposal for the wake voltage with main corrections to the lowest approximation:

$$\begin{aligned}
 V(\theta, t) = & 2\omega_0 Q \operatorname{Re} \sum_{n=1}^{\infty} e^{in(\theta - \omega_0 t)} \left[Z(n, n\omega_0) \lambda_n(t) \right. \\
 & + i \frac{\partial \tilde{Z}}{\partial \omega}(n, n\omega_0) \lambda'_n(t) - i \frac{Z_0 \pi R}{2\beta_0 h} \sum_p \Lambda_p \\
 & \left. \times \int_0^t dt' \lambda'_n(t') \left(e^{iA(p,n)(t'-t)} + e^{iB(p,n)(t'-t)} \right) \right]. \quad (12)
 \end{aligned}$$

The integral in (12) represents retardation effects associated with wave guide cutoffs. It is expected to be largest at those (p, n) for which $A(p, n) = \alpha_p c - n\omega_0$ is small, giving a primarily reactive effect. The presence of the integral does not add a lot to the cost of a dynamical calculation, since one can store each of the integrals as a matrix $M(p, n)$, and update that matrix at each time step δt by adding the integral from t to $t + \delta t$. This requires a few floating point operations for each (p, n) . Fig. 1 shows the function $\partial \tilde{Z}(n, n\omega_0) / \partial \omega$ that appears in the first order Taylor term, multiplied by ω_0 . Parameters are for a compact storage ring studied in [3]: $R = 25$ cm, $h = 1$ cm, $E_0 = 25$ MeV.

In Fig.2 we report a first attempt at evaluating formula (12) in the context of a time-domain integration of the Vlasov equation. Beside the r.f. bucket, the force is entirely from (12). The machine parameters are those of [3]. The time parameter is $\tau = \omega_s t$, where ω_s is the circular synchrotron frequency. To model the smooth switching on of the current assumed above, we increase the charge from zero, multiplying the final charge Q by the function $f(\tau) = (1 - (\tau - 1)^4)^4$. The final charge at $\tau = 1$ is close to the value for onset of a CSR-induced instability ($I = 0.98$ pC/V in the notation of [3]). We assume that

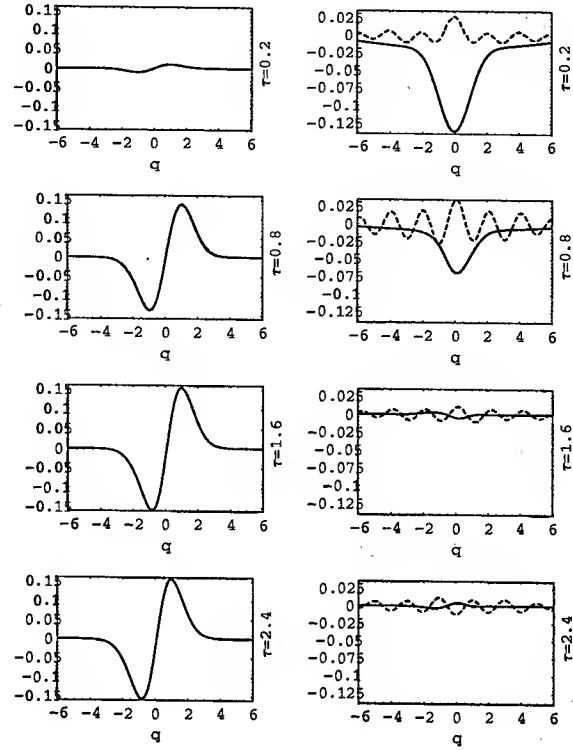


Figure 2: Dimensionless wake force $IF(q)$ (in notation of [3]) proportional to (12), at successive times. First term on left graph, second (solid) and third (dashed) on right. $q = (\theta - \omega_0 t)R/\sigma_z$, σ_z = bunch length.

$\lambda'_n(t)$ is given by a simple divided difference, the time increment being that of the Vlasov integration. The curves on the left in Fig.2 are from the first term in (12) at successive times (up to about 4/10 of a synchrotron period). The solid and dashed curves on the right are from the second and third terms, respectively. The period of oscillations in the third term is exactly what one expects from peaking of the integral at n such that $A(1, n) = 0$. After initial transients the corrections to the first term are fairly small. It remains to be seen whether they remain small during full development of the instability, at somewhat later times.

REFERENCES

- [1] R. Warnock and J. Ellison, in *Proc. 2nd ICFA Workshop on High Brightness Beams*, (World Sci., Singapore, 2000).
- [2] M. Venturini and R. Warnock, *Phys. Rev. Lett.* **89**, 224802 (2002).
- [3] M. Venturini, R. Warnock, and R. D. Ruth, to be submitted to *Phys. Rev. E*; R. Warnock and M. Venturini, in preparation.
- [4] N. Towne, *Phys. Rev. ST Accel. Beams* **4**, 114401 (2001).

ROBINSON MODES AT ALADDIN*

R. A. Bosch,[#] K. J. Kleman and J. J. Bisognano,
Synchrotron Radiation Center, University of Wisconsin-Madison,
3731 Schneider Dr., Stoughton, WI 53589, USA

Abstract

A fourth harmonic radiofrequency (RF) cavity improves the beam lifetime of the Aladdin electron storage ring. When the harmonic cavity is operated with a low-emittance lattice, coupling between the dipole and quadrupole Robinson modes may cause instability. During stable operation, damped Robinson modes are observed in the spectrum of phase noise upon the beam.

1 PASSIVE HARMONIC CAVITY

The Aladdin 800-MeV 300-mA electron storage ring is now being operated with a low-emittance lattice [1]. When the bunches are lengthened by a fourth harmonic RF cavity, the small value of the momentum compaction results in coupling of the dipole and quadrupole Robinson modes [2]. A Robinson instability may result, in which all bunches oscillate longitudinally in unison.

The operation of a harmonic cavity may be described by a parameter ξ that is proportional to its voltage, where ξ equals 1 for an "optimally lengthened" bunch whose linear synchrotron frequency is zero [2, 3]. For $\xi \ll 1$, a quadratic synchrotron potential provides a Gaussian bunch shape, while $\xi > 1$ describes a double-hump bunch shape in a double-well synchrotron potential.

To analytically model Robinson instabilities with two RF cavities, the calculated frequency of a rigid bunch oscillation may be substituted for the synchrotron frequency in a formula describing Robinson instabilities in a quadratic RF potential [2]. For $\xi \leq 1$, quantitative agreement with simulations and measurements is obtained when coupling between the dipole and quadrupole Robinson modes is included in the analytic model. For double-hump bunches with $\xi > 1$, qualitative agreement is obtained in which some instabilities may occur that are not predicted by the analytic model.

For passive operation of a harmonic cavity, varying its resonant frequency (characterized by a "tuning angle" [2]) changes the value of ξ . Instability predictions for passive operation are shown in Fig. 1(a), for the case where an RF circulator (required for active operation) is attached to the harmonic cavity. An RF-coupling β_2 of 1.5 describes the circulator, while a momentum compaction of 0.006 (obtained from the measured low-current synchrotron frequency) describes the imperfect experimental implementation of the low-emittance lattice. The remaining parameters are theoretical low-emittance parameters given in Table 1 of Ref. [2]. We consider the case where power is supplied to the fundamental RF

cavity by operation in the "compensated condition," in which the RF generator current is in phase with the cavity voltage [4].

In Fig. 1, a curved line shows the harmonic-cavity tuning angle that gives an optimally lengthened bunch with $\xi = 1$; double-hump bunches with $\xi > 1$ occur on the right hand side of this curve. For optimally lengthened bunches, a fast mode-coupling instability is predicted. Figure 1(b) shows instabilities observed in 500,000-turn longitudinal simulations of 900 macroparticles, which are injected at the synchronous phase within a single revolution [2]. An energy spread that exceeds the natural value by more than 10% is taken to indicate instability. Approximate agreement between analytic modeling and simulations is obtained.

The modeling and simulations agree with experimental observation of Robinson instabilities [2]. Experiments show that bunches with $\xi \ll 1$ also suffer from coupled-bunch instabilities driven by parasitic modes of the RF cavities. For ring currents exceeding ~100 mA, double-hump bunches with $\xi \approx 1.2$ do not suffer from Robinson

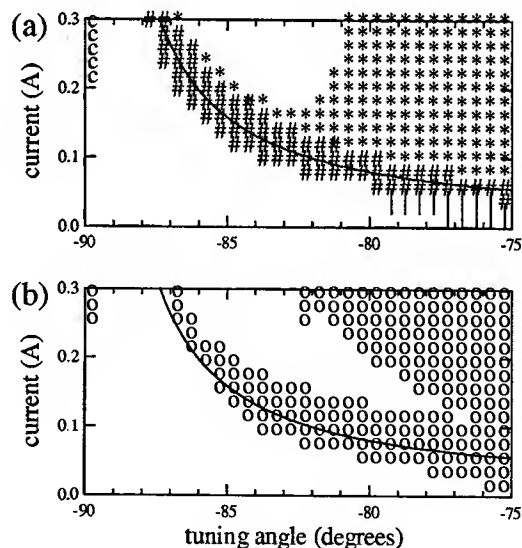


Figure 1. (a) Analytic instability predictions for passive harmonic-cavity operation with a low-emittance lattice. A solid curve shows the parameters for optimal bunch lengthening. |: coupled dipole Robinson instability; *: coupled quadrupole Robinson instability; #: fast mode-coupling Robinson instability; c: coupled-bunch instability with longitudinal mode number of 1. (b) Instabilities observed in 500,000 turn simulations.

* Work supported by NSF grant DMR-0084402.

[#] bosch@src.wisc.edu

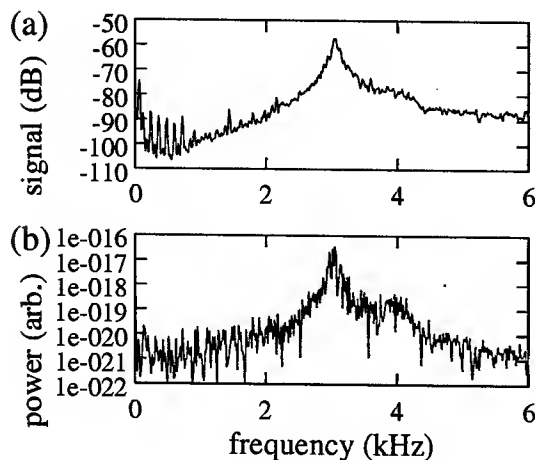


Figure 2. (a) Experimental spectrum of phase noise for a double-hump bunch with $\xi = 1.2$ and current of 144 mA. (b) Spectral power density of the average bunch centroid position in a simulation.

instabilities or parasitic coupled-bunch instabilities. These double-hump bunches are used routinely for stable operation with a long Touschek lifetime.

For ring parameters where stability is attained, the damped Robinson modes influence the beam's response to noise generated by the RF master oscillator and power supply. A large response is expected at the frequency of the Robinson modes, resulting in a peak in the phase noise on the beam [5, 6]. When a fourth harmonic RF cavity is used to increase the Aladdin low-emittance bunch length, coupling between the dipole and quadrupole Robinson modes gives two noise peaks in the longitudinal phase spectrum [2]. Figure 2(a) shows the spectrum of phase noise observed under normal operating conditions ($\xi = 1.2$) with a beam current of 144 mA, when an Agilent E4400B signal generator is used as our master oscillator.

We performed a 900-macroparticle simulation of 500,000 turns with $\alpha = 0.006$ for the parameters of Fig. 2(a). A fast Fourier transform was performed of the bunches' average centroid position, sampled every 100 turns during the final 409,600 turns. The simulation's spectral power density, shown in Fig. 2(b), is similar to the experimental noise spectra. This suggests that damped Robinson oscillations are excited in simulations by transients and "shot" noise from the finite number of macroparticles.

The spectrum of phase noise was observed experimentally when the resonant frequency of the passive fourth harmonic cavity was varied, for a ring current of 150 mA. For $0.88 < \xi < 1.08$, the beam is unstable and a large-amplitude 3 kHz signal is observed, consistent with a fast mode-coupling Robinson instability [2]. For harmonic-cavity voltages where Robinson instability is not observed, the frequency of peaks in the experimental phase noise spectrum are plotted in Fig. 3.

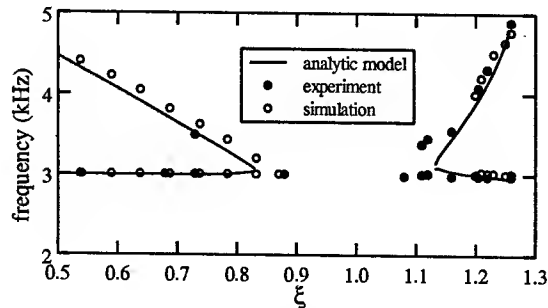


Figure 3. Measured noise peaks on a phase detector circuit agree with noise peaks observed in macroparticle simulations and with calculations of the coupled dipole and quadrupole Robinson modes.

The coupled dipole and quadrupole Robinson frequencies calculated for $\alpha = 0.006$ are also plotted in Fig. 3, in agreement with the measured peaks.

The spectral power density in simulations was also studied. Unstable simulations with $0.88 < \xi < 1.18$ display a large 3 kHz peak. Stable simulations with $\xi < 0.88$ or $\xi > 1.18$ display two peaks. The higher-frequency peak is more prominent in fast Fourier transforms of the RMS bunch length. The peaks observed in stable simulations are plotted in Fig. 3, in agreement with the measured peaks and the calculated Robinson frequencies.

We performed simulations to study feedback that counteracts Robinson oscillations of the bunch centroids. Simulations show that an ideal feedback system with damping time of 0.5 ms reduces phase noise at 3 kHz by 20 dB, with much less effect upon the coupled-quadrupole-mode noise around 4 kHz. This agrees with experimental tests of such a feedback system, which is now routinely employed.

2 ACTIVE HARMONIC CAVITY

By powering the harmonic cavity in the "compensated condition" [4], one may attempt to produce an optimally lengthened bunch at all values of the ring current. Initially, the RF feedback at Aladdin was insufficient to prevent dipole-quadrupole Robinson mode coupling in this case [2]. To overcome this limitation, we installed additional feedback that produces an effective coupling of $\beta_2 \approx 750$ for bunch oscillation frequencies below ~ 5 kHz.

Figure 4(a) displays analytic predictions for $\beta_2 = 750$. For currents > 200 mA, a coupled bunch instability excited by the harmonic cavity is predicted for short bunches with $\xi \ll 1$; Robinson instability is predicted to disrupt optimally lengthened bunches with $\xi = 1$.

Figure 4(b) shows instabilities observed in simulations. An "o" is plotted when the energy spread at the end of a simulation exceeds the natural value by $> 10\%$. However, this criterion does not detect an equilibrium phase Robinson instability where the bunches move to a different phase and then attain a stable equilibrium [7].

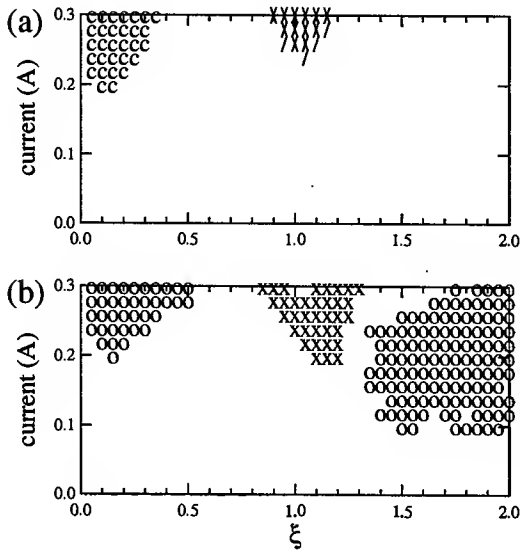


Figure 4. (a) Instability predictions for active harmonic-cavity operation with a low-emittance lattice. /: equilibrium phase instability; \: zero-frequency coupled dipole-quadrupole Robinson instability; c: coupled-bunch instability with longitudinal mode number of 1. (b) Instabilities observed in 500,000 turn simulations.

To detect this manifestation of instability, an "x" is plotted when the energy spread is within 10% of its natural value and the bunch centroids are shifted from their initial synchronous phase by more than 2.35 times the RMS bunch length. For a Gaussian bunch shape, this corresponds to a change in bunch position exceeding the FWHM of the bunch length. When the equilibrium phase instability occurs in simulations, the bunch becomes much shorter than a stable optimally lengthened bunch.

For single-hump bunch shapes, the simulations and analytic predictions are in agreement. For double-hump bunch shapes, instabilities that are not predicted by the analytic model may occur. Consistent with the modeling

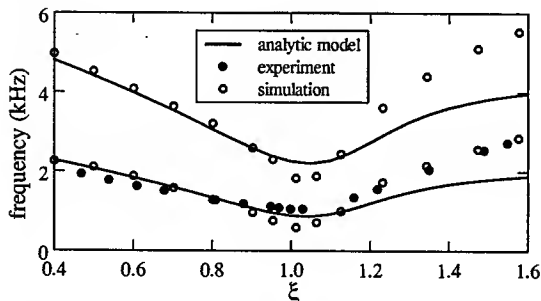


Figure 5. Measured noise peaks on a phase detector circuit are compared with noise peaks observed in simulations and with calculations of the coupled dipole and quadrupole Robinson modes.

and simulations, active harmonic-cavity operation with currents exceeding 200 mA has been unsuccessful.

For a ring current of 155 mA, the peaks in the experimental spectrum of phase noise are plotted in Fig. 5. Double peaks were not observed. Also shown are the calculated coupled dipole and quadrupole Robinson frequencies for $\alpha = 0.006$. From simulations, we plot the noise peaks from fast Fourier transforms of bunch position and length. Quantitative agreement is obtained for single-hump bunches, while the calculated frequencies for double-hump bunches differ significantly from those observed in simulations and experiment.

The phase noise observed in active operation exceeds that in passive operation. This may be a result of the low Robinson-mode frequency of ~ 1 kHz in active operation. The fundamental cavity's RF oscillator and power supply are expected to produce more noise at lower frequencies [5], while the power supply for the harmonic cavity provides additional noise during active operation. With a low Robinson frequency, the beam responds to this noise.

It is expected that the equilibrium phase instability may be avoided in active operation by using a higher RF voltage [2], but the Touschek lifetime will be reduced. The reduced lifetime and increased noise make active operation unattractive.

3 SUMMARY

For passive harmonic-cavity operation with a low-emittance lattice, optimally lengthened bunches are destabilized by coupling of the dipole and quadrupole Robinson modes, necessitating the use of stable double hump bunches. In this case, the coupled dipole and quadrupole Robinson frequencies are around 3–4 kHz. Active operation of the higher harmonic cavity gives a lower coupled dipole Robinson frequency (~ 1 kHz) with increased noise. We routinely employ passive operation with double-hump bunches, reducing noise with feedback that damps oscillations of the bunch centroids.

REFERENCES

- [1] J. J. Bisognano, R. A. Bosch, D. E. Eisert, M. A. Green, K. J. Kleman and W. S. Trzeciak, in *Proc. 2001 PAC* (IEEE, Piscataway, NJ, 2001), p. 2671.
- [2] R. A. Bosch, K. J. Kleman and J. J. Bisognano, *Phys. Rev. ST Accel. Beams* **4**, 074401 (2001).
- [3] Tai-Sen F. Wang, in *Proc. 1993 PAC* (IEEE, Piscataway, NJ, 1993), p. 3500.
- [4] M. Sands, Institut National de Physique Nucleaire et de Physique des Particules, Rapport technique 2-76, 3-76, and 4-76, 1976.
- [5] J. M. Byrd, in *Proc. 1999 PAC* (IEEE, Piscataway, NJ, 1999), p. 1806.
- [6] J. M. Byrd, M. Martin and W. McKinney, in *Proc. 1999 PAC* (IEEE, Piscataway, NJ, 1999), p. 495.
- [7] Y. Miyahara, S. Asaoka, A. Mikuni and K. Soda, *Nucl. Instr. and Meth. A* **260**, 518 (1987).

THE EFFECTS OF TEMPERATURE VARIATION ON ELECTRON BEAMS WITH RF VOLTAGE MODULATION

P.J. Chou*, M.H. Wang, SRRC, Hsinchu, Taiwan
S.Y. Lee#, Indiana University, IN 47405, USA

Abstract

The correlation between the horizontal beam size vs. the cavity temperature, observed at the Taiwan Light Source (TLS), is explained by the combined effects of (1) cavity resonance frequency shift resulting from temperature change, (2) cavity voltage and synchronous phase angle change resulting from uncompensated beam loading in the low-level rf-feedback system, and (3) rf cavity voltage modulation for alleviating the coupled bunch instability. This experimental method can be used to evaluate the intrinsic resolution of the low-level rf-feedback system.

INTRODUCTION

At TLS, high brightness beam bunches in the storage ring have encountered longitudinal coupled-bunch instabilities (CBI), which have been suppressed by applying a sinusoidal rf voltage modulation [1]. The beam lifetime and beam stability have been substantially improved in routine operation. However, the beam bunches in the storage ring may become more sensitive to small perturbations to the rf cavities.

In a recent experiment at TLS, it was observed that a variation of 0.5 °C (1.5%) in the peak-to-peak rf cavity body temperature can induce 20 μm correlated peak-to-peak variation in the horizontal beam size, measured by a synchrotron light monitor using a CCD camera from a dispersive location. This amounts to about 3% variation in the horizontal beam size with no associated vertical beam size variation. Thus, the horizontal beam size variation is related to the momentum spread of the beam. Since the single beam intensity is much less than the microwave-instability threshold, the momentum spread should be independent of the rf cavity voltage. The observed horizontal beam size variation vs. rf cavity temperature is indeed puzzling because the rms momentum spread of electron beam depends only on the radiation damping and quantum fluctuation. This experiment sets a tight limit of the cavity cooling-water temperature control, which has attained the accuracy of ± 0.1 °C.

In this paper, we will analyze this phenomenon and show that it is related to the combined effects of cavity frequency shift, the change of effective accelerating voltage resulting from partially compensated low-level rf-feedback system (LLRF), and the rf-voltage modulation used to combat the CBI. We will also demonstrate how to evaluate the intrinsic resolution of the low-level rf-feedback system with this experimental method.

*pjchou@srcc.gov.tw

#S.Y. Lee would like to thank grant support from DOE and NSF.

EXPERIMENTAL MEASUREMENTS

A dedicated experiment was conducted to measure the sensitivity of electron beam size stability vs. the temperature of cavity cooling-water. The local feedback system of cavity cooling-water was adjusted so that a periodic variation of cavity temperature was possible. The horizontal beam size, measured by a synchrotron light monitor recorded by a CCD camera from a dispersive location, was observed to undergo periodic variation correlated with the cavity temperature as shown in Fig. 1. This phenomenon was observed while rf voltage modulation was applied to stabilize the CBI for electron beams. Table 1 lists relevant accelerator parameters for this experiment.

Table 1: Operation parameters associated with the archived data in Figure 1

Parameter	Value
rf frequency f_{rf} (MHz)	499.648
rf voltage V_0 (kV)	800
modulation frequency f_m (kHz)	49.663
modulation amplitude ε	0.026
synchrotron tune ν_s	0.0100716
synchronous phase ϕ_s	169°
synchrotron frequency f_s (kHz)	24.929
momentum compaction α_c	5.97×10^{-3}
emittance (nm . rad)	19.5
natural momentum spread σ_E	7.5×10^{-4}

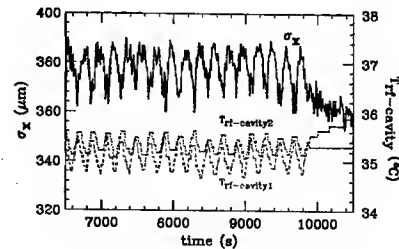


Figure 1: The temporal correlation between the horizontal beam size and the body temperature of rf cavities observed in the TLS storage ring. The data was recorded at a rate of 0.1 Hz.

At TLS, the electron beam size can be measured by using a synchrotron light monitor with CCD camera, which is located at a beam line of the 3rd bending magnet of the three bend achromatic lattice where $\beta_x = 0.5544$ m and the dispersion function is $D_x = 0.15036$ m. At a dispersive location, the effective rms beam size is $\sigma_{x0} = (\beta_x \epsilon_x + D_x^2 \sigma_\delta^2)^{1/2}$, where ϵ_x and σ_δ are the rms emittance and fractional momentum-spread of the beam. Since ϵ_x and σ_δ depend only on the synchrotron radiation damping and quantum fluctuation, σ_{x0} should be independent of the cavity temperature.

In the presence of rf voltage modulation at $f_m \approx 2f_s$, the invariant Hamiltonian tori coherently rotate at a frequency of $f_m/2$. The signal from the CCD camera of the synchrotron light monitor is a standard NTSC signal at 33 Hz. Let $\hat{\delta}$ be the coherent bunch oscillation amplitude of the beam bunch. The effective beam size is

$$\sigma_x^2 = \sigma_{x0}^2 + \frac{1}{2} D_x \hat{\delta}^2 \quad (1)$$

The horizontal beam size under the normal operational conditions with voltage modulation was $\sigma_x \approx 385$ μ m. For a fixed modulation frequency, the effective rms horizontal beam size will change if the synchrotron frequency is changed. We will review the effect of rf voltage modulation on particle motion and study mechanisms that can change $\hat{\delta}$.

BEAM DYNAMICS WITH RF VOLTAGE MODULATION

When the rf voltage is modulated at a frequency near the second harmonic of the synchrotron frequency, the Hamiltonian tori may be divided into stable islands driven by parametric resonances [2]. Those tori coherently rotate in the longitudinal phase space at exactly one half of the modulation frequency. Since the measured horizontal beam size is the time average of the quadrature of the betatron and momentum beam sizes, the increase in the energy spread of beam distribution may result in a larger measured horizontal beam size (see Fig. 2). At TLS, the rf cavity voltage is sinusoidally modulated with $V_{rf} = V_0(1 + \epsilon \sin(\omega_m t + \chi))$, where $\omega_m = 2\pi f_m$ is the modulation angular frequency, ϵ is the fractional rf voltage modulation amplitude, and χ is an arbitrary phase factor. As the modulation frequency is near the 2nd order synchrotron sidebands, there exist solutions of stable fixed points (SFPs) [1] if $v_m < v_{bif+}$

$$J_{sfp} = \frac{24v_s |\cos \phi_s|^{1/2} - 12v_m + 2\epsilon v_s |\cos \phi_s|^{1/2} (3 + \tan^2 \phi_s)}{v_s (3 + 5 \tan^2 \phi_s)} \quad (2)$$

; $J_{sfp} = 0$ if $v_m < v_{bif-}$ or $v_m > v_{bif+}$

where the bifurcation frequencies are

$$f_{bif \pm} = f_s \left[2 \pm \frac{\epsilon}{2} \left(1 + \frac{1}{3} \tan^2 \phi_s \right) \right] \quad (3)$$

The peak fractional energy deviation $\hat{\delta}$ of coherent

motion, associated with a Hamiltonian torus, is related to the action by

$$\hat{\delta}^2 = \frac{2v_s^2}{h^2 \eta^2} |\cos \phi_s|^{1/2} J_{sfp} \quad (4)$$



Figure 2: The images of synchrotron light monitor with (top) and without (bottom) rf voltage modulation.

Since the modulation frequency was in the region of $v_{bif-} < v_m < v_{bif+}$ for the experimental data, the resulting bunch length in the longitudinal phase space would become larger [1]. The effective horizontal beam size measured at a location of nonzero dispersion function is given by Eq. (1). Using Eqs. (1), (2), and (4), we find the variation of horizontal beam size due to the change of energy spread as

$$\begin{aligned} \Delta \sigma_x &= \frac{D_x^2}{4\sigma_x} \Delta(\hat{\delta}^2) \\ &= \frac{D_x^2}{2\sigma_x h^2 \eta^2} \Delta(v_s^2 |\cos \phi_s|^{1/2} J_{sfp}) \end{aligned} \quad (5)$$

Since the resonance frequency depends on the cavity size, the effective acceleration voltage may be changed through the cavity tuning angle through the partially compensated low-level rf-feedback system. The change of the horizontal beam size is

$$\Delta \sigma_x = \frac{D_x^2}{2\sigma_x h^2 \eta^2} (A - B \tan \phi_s) \frac{\Delta V_0}{V_0} \quad (6)$$

where

$$A = [24v_s^2 |\cos \phi_s| - 6v_m v_s |\cos \phi_s|^{1/2} + 2\epsilon v_s^2 |\cos \phi_s| (3 + \tan^2 \phi_s)] (3 + 5 \tan^2 \phi_s)^{-1} \quad (7)$$

$$\begin{aligned} B = & [24v_s^2 |\sin \phi_s| - 6v_m v_s |\tan \phi_s \sin \phi_s|^{1/2} + \\ & 2\epsilon v_s^2 |\sin \phi_s| (3 + \tan^2 \phi_s) + 4\epsilon v_s^2 \tan \phi_s |\cos \phi_s|^{-1} (3 + \\ & 5 \tan^2 \phi_s)^{-1} - [240v_s^2 |\cos \phi_s| - 120v_m v_s |\cos \phi_s|^{1/2} + \\ & 20\epsilon v_s^2 |\cos \phi_s| (3 + \tan^2 \phi_s)] \tan \phi_s \sec^2 \phi_s (3 + \\ & 5 \tan^2 \phi_s)^{-2} \end{aligned} \quad (8)$$

ANALYSIS OF BEAM SIZE VARIATION

The cavity detuning angle ψ is related to the resonance frequency ω_r by

$$\psi = \tan^{-1} \left[\frac{2Q_L(\omega - \omega_r)}{\omega_r} \right] \quad (10)$$

where Q_L is the loaded quality factor of cavities. We assume a uniform expansion/contraction of the cavity radius when the temperature was changed. With a small temperature variation ΔT , the fractional deviation of resonance frequency for a cylindrical cavity is given by

$$\frac{\Delta\omega_r}{\omega_{r0}} = -\frac{\Delta b}{b} = -\alpha\Delta T \quad (11)$$

where α is the coefficient of linear thermal expansion ($\alpha=16.668 \times 10^{-6}$ per $^{\circ}\text{C}$ for copper). Considering a small variation of Eq. (10) with respect to the resonance frequency ω_r , we arrive at

$$\Delta\psi \approx 2\alpha Q_L \cos^2 \psi \Delta T \quad (12)$$

For a steady state beam loading the expression of accelerating voltage in terms of complex phasor is [3]

$$\tilde{V}_0 = \left[I_g e^{j(\theta+\theta_g)} - I_i \right] R_{sh} \cos \psi e^{-j\psi} \quad (13)$$

where I_i is the rf beam image current, R_{sh} is the cavity shunt impedance. The fractional change of effective accelerating voltage due to the temperature change is given by

$$\frac{\Delta V_0}{V_0} = -2\alpha Q_L \sin \psi \cos \psi \Delta\psi \quad (14)$$

Using Eqs. (6) and (14), we find the relation between the change of horizontal beam size vs. the cavity temperature as

$$\Delta\sigma_x = -\frac{\alpha Q_L D_x^2 \sin \psi \cos \psi}{\sigma_x h^2 \eta^2} (A - B \tan \phi_s) \Delta T \quad (15)$$

Here, the parameter A and B of Eqs. (7) and (8) are both positive, the cavity detuning angle ψ is also positive due to the Robinson stability, and $\tan \psi_s < 0$ for electron storage rings. Therefore, the deviation of horizontal beam size is of opposite sign to the temperature change. Based on Eq. (15), the calculated variation of horizontal beam size vs. cavity temperature variation is shown in Fig. 3(C), while the experimental data for temperature variation is reproduced in Fig. 3(A) and the measured rms horizontal beam size variation is shown in Fig. 3(B). Note that the calculated beam size variation is larger than the measured data, i.e. the effect of temperature variation has been partially compensated by the LLRF.

In fact, the LLRF is designed to compensate changes in cavity operational conditions so that the acceleration voltage would remain constant. The rf tuning angles are changed by the LLRF in response to temperature variation at 0.1 Hz. The top and middle plots of Fig. 4 show the data of cavity tuning angles recorded in response to the temperature variation for cavities 1 and 2 respectively. The required tuning angle derived from the observed data is shown in the bottom plot of Fig. 4. If the LLRF is perfect, we would not observe beam size variation.

According to the technical specification of TLS low level system [4], the accuracy of phase detector in the feedback system is ± 1 degree. One can use Eqs. (14) and (6) to estimate the uncompensated variation of horizontal beam size with rf voltage modulation. Using the worst

estimate for the phase error of 2 degrees, we obtain $25 \mu\text{m}$ peak-to-peak variation in the horizontal beam size. The peak-to-peak value of measured data is $20 \mu\text{m}$.

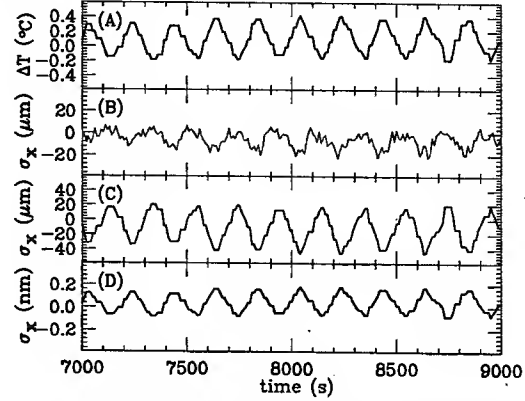


Figure 3: (A) the average temperature variation of rf cavities. (B) the measured variation of horizontal beam size. (C) the calculated variation of horizontal beam size arising from the change of rf resonance frequency. (D) the calculated variation of horizontal beam size due to the change of higher order parasitic loss factor.

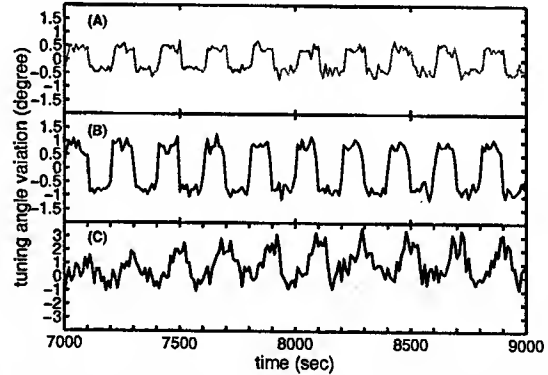


Figure 4: Top and middle plots show the rf tuning angles for cavities 1 and 2 adjusted by the LLRF. The bottom plot shows the tuning angle derived from the observed horizontal data in Fig. 3(B).

Finally, we also have analysed the effect of higher-order parasitic-mode losses on the beam size variation and found its effect small. Because the beam size is very sensitive to small perturbations in the rf cavities in the presence of rf voltage modulations, this rf voltage modulation has applications in testing the intrinsic resolution of LLRF to various cavity perturbations.

REFERENCES

- [1] M.H. Wang and S.Y. Lee, J. Appl. Phys. 92 (2002) 555.
- [2] D. Li, et al., NIM A 364 (1995) 205.
- [3] see e.g. S.Y. Lee, "Accelerator Physics" (World Scientific, Singapore, 1999), p. 328.
- [4] H. Schwarz, SLAC Circuit Description 125-306-00 R1, 1992 (unpublished).

A FAST METHOD TO ESTIMATE THE GAIN OF THE MICROBUNCH INSTABILITY IN A BUNCH COMPRESSOR

S. Reiche and J.B. Rosenzweig

University of California Los Angeles – Department of Physics, CA 90095-1547, USA

Abstract

To reach high peak currents driving Free-Electron Lasers an initial chirped electron bunch is compressed in a bunch compressor. The interaction of the electron beam with its radiation field can yield a collective instability, which amplifies any initial modulation in the current profile. We present a model, which allows one to derive an explicit analytical expression for the gain of the microbunch instability. The results are compared to those of the more complex analytical models.

INTRODUCTION

Many FEL experiments [1] requires a bunch compressor to increase the peak current. The magnetic chicane resembles a single period of an undulator and like the bunching effect in an FEL [2, 3] the interaction between the coherent synchrotron radiation (CSR) [4] and the electron beam can enhance the amplitude of an initial current modulation[5]. The mechanism has striking similarity to the FEL process, although the electron motion is more complex than the averaged motion needed for the FEL model. The interaction with the CSR field is expressed by a potential, acting instantaneously on the electrons.

MOTION IN A MAGNETIC CHICANE

A magnetic chicane consists typically of bending magnets, drifts, and, optionally, focusing quadrupoles. For a simpler comparison to the FEL we exclude the latter two components from the discussion.

Because the electron beam interacts with the spontaneous radiation, the dispersion function η has to be calculated for all positions, where the electron energy changes. We sum up all contributions to the longitudinal position, resulting in

$$\zeta(s) = \zeta(s_0) + \int_{s_0}^s \delta(s') \tilde{R}_{56}(s, s') ds'. \quad (1)$$

Here s and s_0 denote the final and initial position on the design orbit, respectively, $\zeta = ct$ is the position in the frame of the moving bunch and $\delta = (\gamma - \gamma_0)/\gamma_0$ is the normalized deviation of the electron energy from the mean energy γ_0 .

We consider an idealized chicane, which consists of three bending magnets with a bend radius R and no drift space separating them. The outer magnets have a length of L while the inner one, which bends in the opposing direction of the outer two, is twice as long. With the initial

conditions $\eta(s') = 0$ and $\eta'(s') = 0$ and a small bending angle $\theta_b \approx L/R \ll 1$, the dispersion function is

$$\frac{\eta}{R} = \begin{cases} \frac{1}{2} \left(\frac{s-s'}{R} \right)^2 & \text{(I,I), (II,II),} \\ & \text{(III,III)} \\ \left(\frac{s-L}{R} \right)^2 - \frac{1}{2} \left(\frac{s-s'}{R} \right)^2 & \text{(II,I)} \\ \left(\frac{s-3L}{R} \right)^2 - \frac{1}{2} \left(\frac{s-s'}{R} \right)^2 & \text{(III,II)} \\ \frac{1}{2} \left(\frac{s-3L}{R} \right)^2 + \frac{1}{2} \left(\frac{3L-s'}{R} \right)^2 - \left(\frac{2L}{R} \right)^2 & \text{(III,I)} \\ - \left(\frac{s-3L}{R} \right) \left(\frac{L-s'}{R} \right) & \end{cases} \quad (2)$$

where the pair of Roman numbers indicates, in which dipole the end and start positions s and s' , respectively, are located. We incorporated the bend direction of the dipoles into the sign of the bend radius with $R(s) = R$ in the first and third dipole and $R(s) = -R$ in the second dipole.

The differential equation for the longitudinal motion ($s_0 = 0$) becomes

$$\frac{d\zeta}{ds} = \int_0^s \delta(s') \frac{s-s'}{R(s)R(s')} ds'. \quad (3)$$

To describe a microbunched distribution of electrons, we assume a coasting beam with a small modulation

$$I(\zeta, s) = I_0 [1 + |b(s)| \cos(k\zeta + \phi(s))] \quad (4)$$

where k is the modulation wavenumber. The potential [4] seen by the electrons is

$$W(\zeta) = -\frac{2}{(3R^2)^{\frac{1}{3}}} \frac{1}{\zeta^{\frac{1}{3}}} \frac{\partial}{\partial \zeta} \quad (5)$$

for $\zeta < 0$, and zero otherwise. The energy change of any given electron is

$$\frac{d\delta}{ds} = -\frac{I_0}{I_A \gamma_0} \frac{2\Gamma(\frac{2}{3})k^{\frac{1}{3}}}{(3R^2)^{\frac{1}{3}}} |b(s)| \sin \left(k\zeta + \phi(s) + \frac{\pi}{3} \right). \quad (6)$$

The growth of the energy modulation scales linearly with the modulation of the current.

THE LOW GAIN MODEL

A change in the particle energy has a delayed effect on the particle's longitudinal position, which grows with the third power in s . In addition, the change in the longitudinal position is also inhibited by the change in the polarity of

the bending magnets. Particles with higher energy fall behind due to the larger bend radius, but catch up due to the shorter path length after a polarity change. Thus, for short time scales, and low gain, $\delta(s')$ can be expected to change linearly in s' . This assumption of klystron-like behavior is invalid for high currents. We discuss this limit further in the following section.

We model the initial current by a equidistant distribution plus an added sinusoidal modulation in the positions with $\Delta\zeta_j = \Delta\zeta \sin(k\zeta_{0,j} + \phi)$ for the j th electron, where ζ_0 is the initial position of the electron. Because the effective radiation potential is harmonic in ζ , the resulting modulation in the longitudinal position is harmonic as well with $\delta\zeta = Z(s) \sin(k\zeta_{j,0} + \psi)$, with $Z(0) = 0$. In our low gain model the initial offset $\Delta\zeta$ and the modulation amplitude $Z(s)$ are much smaller than the modulation wavelength, thus, the bunching factor can be approximated with $b(s) = k[\Delta\zeta e^{i\phi} + Z(s)e^{i\psi}]$.

As long as $Z(s)$ is comparable to the initial modulation amplitude $\Delta\zeta$, the bunching factor can be taken as constant and Eq. 6 can easily be integrated, giving a linear dependence on s . Inserting $\delta(s)$ into Eq. 3, the longitudinal position evolves in the chicane as

$$\zeta_j(s) = \zeta_j(0) - \frac{I_0}{IA\gamma_0} \frac{2\Gamma(\frac{2}{3})}{(3R^2)^{\frac{1}{3}}} k^{\frac{1}{3}} |b(0)| \cdot \sin\left(k\zeta_j(0) + \phi + \frac{\pi}{3}\right) \Phi(s), \quad (7)$$

with

$$\begin{aligned} \Phi(s) &= \int_0^s \left[\int_0^{s''} \frac{s'(s'' - s')}{R(s'')R(s')} ds' \right] ds'' \\ &= \begin{cases} \frac{1}{24} \frac{s^4}{R^2} & \text{(I)} \\ \frac{1}{24} \frac{s^4}{R^2} - \frac{1}{2} \frac{L^2}{R^2} s^2 + \frac{2}{3} \frac{L^3}{R^2} s - \frac{1}{6} \frac{L^4}{R^2} & \text{(II)} \\ \frac{1}{24} \frac{s^4}{R^2} - \frac{4}{3} \frac{L^2}{R^2} s^2 + \frac{52}{3} \frac{L^3}{R^2} s - \frac{56}{3} \frac{L^4}{R^2} & \text{(III).} \end{cases} \end{aligned}$$

The Roman numerals indicate the dipole in which the position s lies. The final, normalized amplitude of the sine-term in Eq. 7 is

$$\xi = \frac{I_0 \Gamma(\frac{2}{3})}{2IA\gamma_0} \left(\frac{8L^3 k}{3R^2} \right)^{\frac{1}{3}}. \quad (8)$$

With $kZ(4L) = \xi |b(0)| \ll 1$ the gain, defined as the ratio between final and initial amplitude of modulation, becomes

$$G = \frac{|b(4L)|}{|b(0)|} = \sqrt{1 + \xi + \xi^2}. \quad (9)$$

As an example of a generic magnetic chicane, modeling the first LCLS bunch compressor ($\gamma = 500$, $I_0 = 100$ A, $R = 12$ m and $L = 1.5$ m), an initial modulation with a period of $5\mu\text{m}$ would grow by a factor of 25.

The gain growth (Eq. 9) has a singularity at a zero modulation period length. This artifact is removed if energy spread is included in the model. For a Gaussian energy distribution with rms spread σ_δ the current modulation evolves

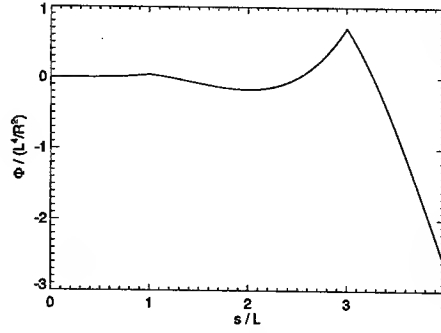


Figure 1: The function Φ (Eq. 8).

as

$$I = I_0 \left[1 + e^{-\frac{1}{2}(\sigma_\delta R_{56} k)^2} |b(0)| \cos(k\zeta + \phi) \right] \quad (10)$$

The modulation decays if the spread in the longitudinal position $\sigma_\delta R_{56}$ is comparable with the modulation period length. The initial modulation is sheared mainly in the second dipole, where the value of matrix element R_{56} changes significantly. Because the seed for the microbunch instability – the accumulated change in the electron energy – occurs before that, the change in the longitudinal position (Eq. 8) is hardly effected. We can just apply the damping factor due to the energy spread to the previous results of Eq. 9. With $R_{56}(4L, 0) = -(4/3)L^3/R^2$, the final gain is now given by

$$G = e^{-\alpha |\xi|^{\frac{2}{3}}} \sqrt{1 + \xi + \xi^2}, \quad (11)$$

defining the normalized energy spread as

$$\alpha = \sqrt{\left(\frac{IA\gamma_0}{2I_0 \Gamma(\frac{2}{3})} \right)^3 \sigma_\delta^2}. \quad (12)$$

For the LCLS case with an energy spread of 0.01% ($\alpha = 0.05$), the gain at $5\mu\text{m}$ would be reduced by 7 orders of magnitudes.

THE HIGH GAIN MODEL

In our low gain model we assumed that the CSR microbunching instability does not drive any bunching within the first dipole. To qualitatively place a limit on this assumed scenario, we develop here a high-gain, exponential growth model as well. There may be situations where the exponential gain does not assert itself in the first dipole, but may, by compression and thus higher current, become notable in the last dipole.

We define the collective variables $B = -ik < e^{-i\Psi} \zeta >$ and $\Delta = < e^{-i\Psi} \delta >$, where $\Psi_j = k\zeta_{0,j}$ is the initial phase of the j th electron of a uniform distribution. The equations

of motion for a cold beam become

$$\frac{d\Delta}{ds} = -\frac{\rho_{CSR}^4}{kR^2} e^{i\frac{\pi}{3}} B \quad (13)$$

$$\frac{dB}{ds} = -i\frac{k}{R^2} \int_0^s \Delta(s-s') ds', \quad (14)$$

with the definition of the dimensionless ρ_{CSR} -parameter expressed as

$$\rho_{CSR} = \left[\frac{I_0}{I_A \gamma_0} 4^{\frac{1}{3}} \Gamma\left(\frac{2}{3}\right) \right]^{\frac{1}{4}} (kR)^{\frac{1}{3}}. \quad (15)$$

The equations can be combined into a fourth order differential equation. Using the ansatz $B \propto \exp[i\Lambda s]$ we obtain the dispersion relation $\Lambda^4 = (\rho_{CSR}/R)^4 \exp(i5\pi/6)$. Two of the four roots have a negative imaginary part, corresponding to an exponentially growing instability. The growth rates are $(\rho_{CSR}/R) \sin(7\pi/24)$ and $(\rho_{CSR}/R) \sin(5\pi/24)$, respectively. The gain length of the high-gain CSR instability is roughly R/ρ_{CSR} . Because the calculations are based on a relatively small deflection angle ($L \ll R$) exponential gain within a single dipole becomes significant only for $\rho_{CSR} > \frac{R}{L} \gg 1$.

The start-up regime determines after how many gain lengths the exponential growth becomes dominant. The two growing modes have similar growth rate but different phase slippages (real part of Λ), so that the interference between these two is still noticeable after several gain lengths (Fig. 2). It takes at least 5 gain lengths before the bunching factor has grown by one order of magnitude, compensating an initial amplitude drop.

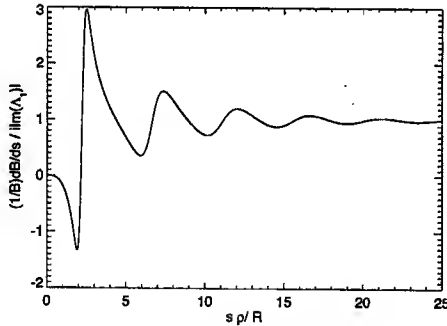


Figure 2: Growth rate of the bunching factor, normalized to the growth rate of the dominant growing mode.

For a characteristic spread σ_δ in energy the momentum dispersion couples it to a phase spread of approximately $(k/6R^2)\sigma_\delta s^3$. In units of the gain length ($\hat{s} = s\rho_{CSR}/R$) the normalized phase spread $\hat{\sigma}_\delta = (kR/6\rho_{CSR}^3)\sigma_\delta$ is independent on the bend radius and wavelength. An estimate on the mitigation of the instability by the energy spread is $\hat{\sigma}_\delta < 0.02$ by this criterion – any value larger than 0.02 would smear out the modulation and completely suppress the exponential growth of this instability.

CONCLUSIONS

We have derived a simple low-gain model to calculate the growth of an initial current modulation within a magnetic chicane. As in a klystron, the physics is split into the initial modulation in beam energy, and a change in the longitudinal position (followed by an enhanced emission level of radiation). The major assumption in our low-gain model is that the beam current modulation, which generates the coherent synchrotron radiation, is held constant over the entire chicane. The klystron-like assumption implies that the system does not have an exponential gain, but rather acts as a linear amplifier where the gain coefficient is dependent on the physical details of the beam and chicane. Fig. 3 shows the difference, however, between our klystron-like model and a self-consistent, more complex model [5].

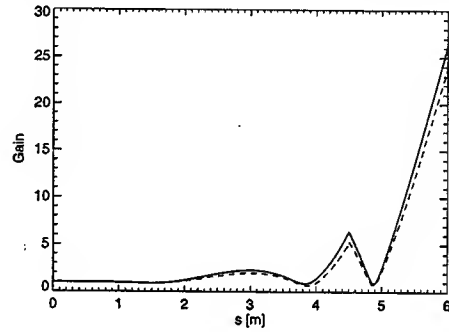


Figure 3: Evolution of the gain along the chicane, using the low gain model (Eq. 9) and a self-consistent numerical simulation (solid and dashed line, respectively). The input parameters are $I_0 = 100$ A, $\gamma_0 = 500$, $R = 12$ m and $L = 1.5$ m.

In order to extend the low-gain model to account for self-consistent behavior, we have developed a high gain model with a gain-length proportional to R/ρ_{CSR} . The parameter ρ_{CSR} must have a value in excess of unity, so that exponential gain occurs within a single dipole.

REFERENCES

- [1] E.g. *Linac Coherent Light Source (LCLS) Design Study Report*, SLAC-R-521, UC-414 (1998) and *TESLA - Technical Design Report TESLA-FEL 2001-05*, DESY, Hamburg, Germany (2001)
- [2] R. Bonifacio, C. Pellegrini, L.M. Narducci, *Opt. Comm.* **50** (1984) 373
- [3] A.M. Kondratenko and E.L. Saldin, *Par. Acc.* **10** (1980) 207
- [4] Y.S. Derbenev *et al.* *TESLA-FEL 95-05*, DESY, Hamburg, Germany (1995)
- [5] S. Heifets *et al.* *SLAC-PUB-9165*, SLAC, Stanford, USA (2002)

EXPERIMENTAL STUDY OF ENERGY SPREAD IN A SPACE-CHARGE DOMINATED ELECTRON BEAM *

Y. Cui[†], Y. Zou, A. Valfells, I. Haber, R. Kishek, M. Reiser, P. G. O'Shea
Institute for Research in Electronics and Applied Physics,
University of Maryland, College Park, Maryland 20742

Abstract

Characterization of beam energy spread in a space-charge dominated beam is very important to understand the physics of intense beams. It is believed that coupling between transverse and longitudinal direction via Coulomb collisions will cause an increase of the beam longitudinal energy spread. At the University of Maryland, experiments have been carried out to study the energy evolution in such intense beams. To measure the energy spread, a high-resolution retarding field energy analyzer has been developed. In this paper, we present the initial experimental results using this energy analyzer. The temporal beam energy profile along the beam pulse has been characterized at the exit of the electron gun. It is the first time that we measure the energy profile of the head and tail of the bunched beams in the experiment. The measured mean energy variation along the beam pulse is in excellent agreement with direct measurement of the cathode-grid pulse waveform. The measured rms energy spread is very close to the theoretical prediction of Coulomb scattering.

1 EXPERIMENTAL SETUP

The experimental setup as shown in Figure 1, consists of a gridded thermionic electron gun, a solenoidal magnetic lens and a diagnostic chamber. The energy analyzer is located in the diagnostic chamber after a solenoid. The solenoid is used to control the beam current into the energy analyzer. The distances of the solenoid and energy analyzer from the gun are 11 cm and 24 cm,

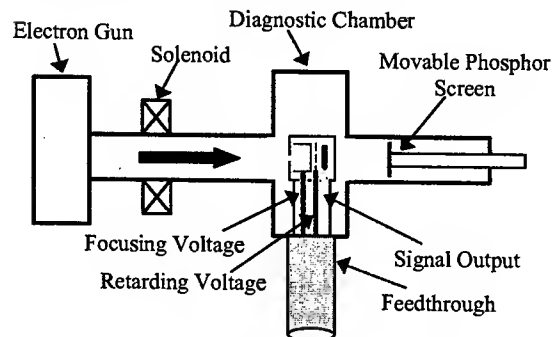


Figure 1. Experimental Setup

*Work supported by the Department of Energy
[†]Email: cuiyp@glue.umd.edu

respectively. The magnetic fringe field extends less than 10 cm from the solenoid center, so magnetic field has no influence inside the energy analyzer and electron gun. The energy analyzer as shown in Figure 2 is cylindrical with a focusing electrode that is insulated with the retarding mesh. The focusing voltage on the focusing cylinder is independently adjustable to provide proper focusing strength to overcome the defocusing force due to space-charge force and beam trajectories etc. A collector is located downstream of the retarding mesh. We developed a computer-controlled automated system. By automatically controlling the retarding voltage and oscilloscope this system can take the energy analyzer data with very fine step. The smallest step to change the retarding voltage is 0.16 V on top of several kilo volts. In the ground shielding there is a 2mm diameter pinhole at the front for beam entry. With a diameter of 5.1 cm and a length of 4.8 cm, this energy analyzer can be easily inserted at any place in the beam line. The energy analyzer can be aligned by a linear feedthrough with three connectors for retarding voltage, focusing voltage and output signal respectively. We also have the ability to insert a movable phosphor screen into the plane of the energy analyzer so that we may obtain an image of the beam at that axial position.

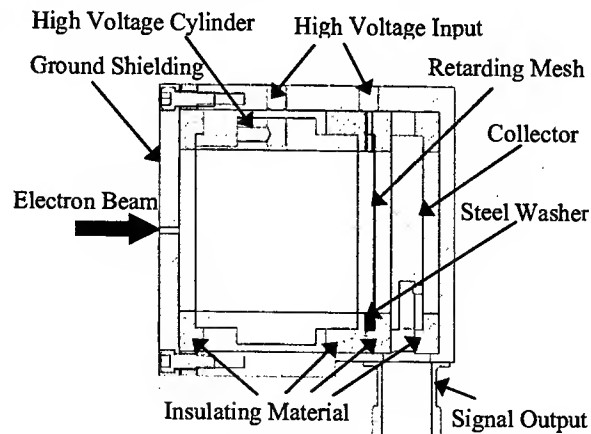


Figure 2. Schematic of the energy analyzer with variable-focusing cylindrical electrode

2 EXPERIMENTAL RESULTS AND ANALYSIS

In the experiment, the nominal beam energy is 5 keV and beam current is 135 mA with pulse width 100ns and

rise time 2ns. Figure 3 shows different signal profiles corresponding to different retarding voltages. For a given retarding voltage, 16 current pulses are sampled and averaged to remove noise effect. The signal from the energy analyzer ($\sim 10\text{mV}$) is deliberately generated by a small injected beam current ($\sim 0.2\text{mA}$) to avoid the space-charge effect in the energy analyzer [1,2]. The focusing voltage is set to 120V to measure the optimum energy spread [2]. The wiggles on the waveform may be related to the oscillation of the virtual cathode formed in the energy analyzer and other effects.

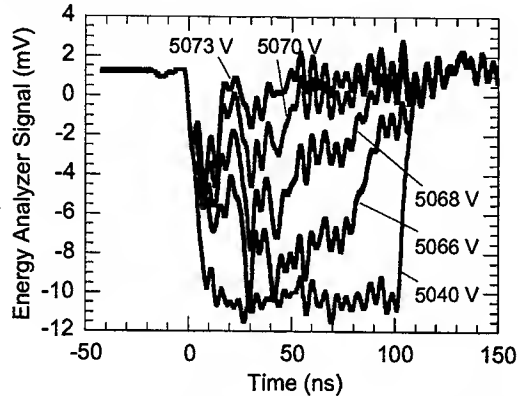


Figure 3. Energy analyzer outputs at different retarding voltages

By differentiating the energy analyzer output with respect to the retarding voltage, we can get the beam energy profile information at a given time in the pulse. Figure 4 shows the energy distribution function curve taken at mid-pulse. From the energy distribution function, we can get temporal mean energy and rms energy spread along the beam pulse.

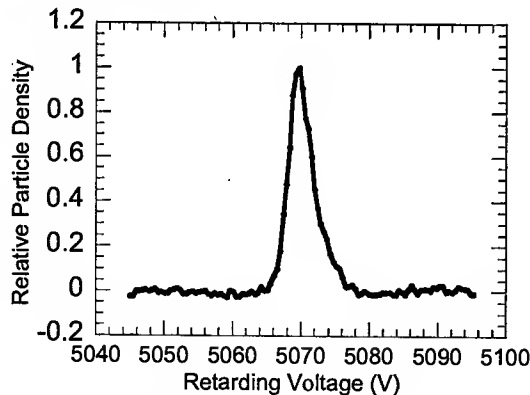


Figure 4. Beam energy spectrum for a beam with energy of 5 keV and current of 135 mA. The rms energy spread is 2.2 eV

Figure 5 shows the measured mean energy as a function of time along the beam pulse. The measured mean energy of the main beam is about 5070 eV. This is 50 eV higher than the beam energy from the gun. It is believed that this DC energy shift is due to the use of mesh and focusing voltage in the energy analyzer. The head of the beam with a length of about 6 ns has a higher mean energy, up to

5200 eV. The tail of the beam with about the same length has a lower energy, down to 4940 eV. The head and the tail of the beam are caused by the longitudinal space-charge effect in the bunched beam [3]. It is the first time that we clearly observed the temporal mean energy information including the head and tail along the beam pulse in the experiment.

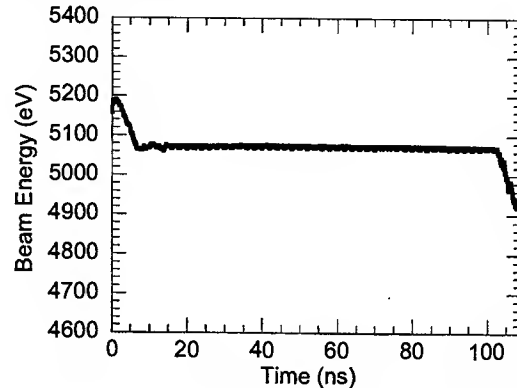


Figure 5. Mean energy along the beam pulse for a beam with energy of 5 keV.

When we zoom out to see the Figure 5, we note the mean energy of the beam has an about 4 eV droop from 30 ns to 100 ns in time region as shown in Figure 6 in the solid line. This is due to the droop in the cathode-grid pulse, as shown in Figure 6 in the dotted line, when we directly measure the pulse waveform between cathode and grid in the electron gun. Although the measured pulse waveform has some noise due to high voltage probe's resolution, we still can see the excellent agreement using two experimental methods. The energy analyzer has better resolution ($<0.25\text{eV}$) than the high voltage probe when measuring beam mean energy.

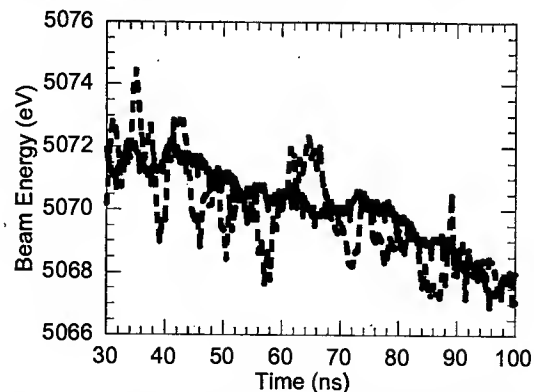


Figure 6. Zoomed mean energy along beam pulse (red solid line) compared with pulse voltage between cathode and grid of the electron gun (blue dotted line).

Figure 7 shows the measured energy spread as a function of time along the aforementioned beam. It is clear that there is higher energy spread at the beam head. The energy spread decreases from $\sim 12\text{ eV}$ at the head to \sim

2.2 eV at the main beam, then goes up at the tail of the beam. The wiggle in the head of the beam may be caused by plasma oscillation with a plasma period of ~ 5 ns. When beam energy and other experimental condition are kept the same except that the beam current reduced to ~ 13 mA by decreasing the aperture size in the electron gun, the temporal energy spread of the beam drops from ~ 10 eV at the head to ~ 1.7 eV of the main beam as shown in Figure 8. We note there is no wiggle in the small current case.

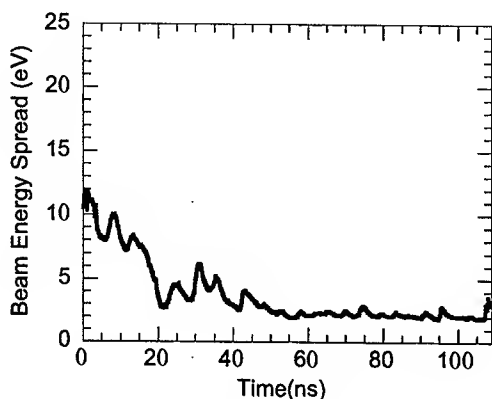


Figure 7. Beam Energy Spread Along Beam Pulse for a beam with energy of 5 keV and current of 135 mA. Average energy spread of the main beam is 2.2 eV

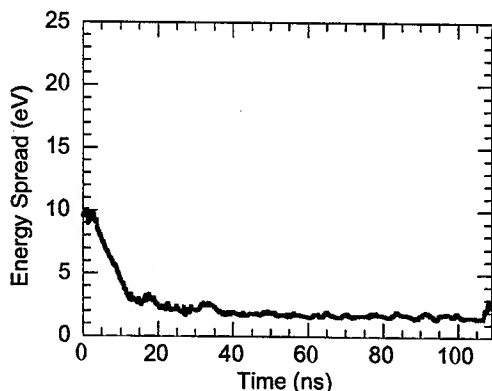


Figure 8. Beam Energy Spread Along Beam Pulse for a beam with energy of 5 keV and current of 13 mA. Average energy spread of the main beam is 1.7 eV

It is very interesting to compare the measured energy spread with theoretical prediction considering the longitudinal-longitudinal effects and the Boersch effect [4,5,6]. According to the theoretical prediction, the rate of evolution of energy spread depends on the current density of the beam. A Higher current density makes energy spread in the longitudinal direction increase faster via Coulomb collisions and other effects after the beam is accelerated. In our experiment, beam energy is 5 keV and beam current is 135 mA. Current density of the beam can be varied by changing the focusing strength of the solenoid. When we use weak focusing, the measured energy spread is ~ 2.2 eV, which is very close to

theoretical prediction, ~ 2.0 eV. However, when we use strong focusing and get high current density, the measured energy spread increases to ~ 2.5 eV, also very close to theoretical prediction, ~ 2.6 eV. We also measured the energy spreads with beam energies of 3 keV and 4 keV. Beam current is 70 mA for the 3 keV beam and 100 mA for the 4 keV beam. Figure 9 shows the measured energy spread compared with the theoretical prediction for different beam energies for both weak and strong focusing of the beam. Triangles with solid line are the theoretical values for weak focusing. Diamonds with dotted line are the theoretical values for strong focusing. Circles are the measured energy spreads for weak focusing and squares are for strong focusing. Error bars added on the measured energy spread are determined by the resolution of the energy analyzer [2].

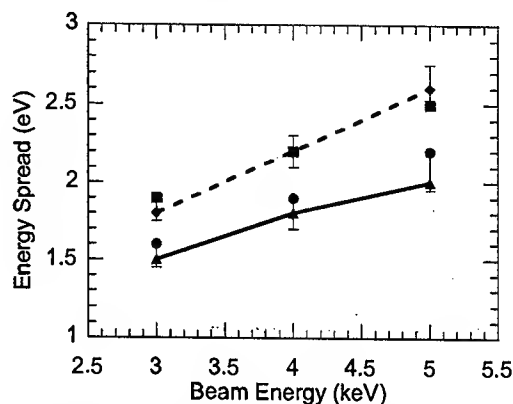


Figure 9. Measured beam energy spreads are compared with the theoretical predictions for different beam energies.

3 FUTURE WORK

We already characterized the energy profiles of the beam at the exit of the electron gun for different energy and different beam current. We will set up a long transport line with a length of 2 m to study the energy spread evolution and other interesting physics.

4 REFERENCES

- [1] Y. Zou, Y. Cui etc, Theoretical study of Longitudinal Space-Charge Effects in a Retarding Field Energy Analyzer in PAC 03
- [2] Y. Cui, Y. Zou etc, Design and Test of a Variable-Focusing Retarding Field Energy Analyzer for Space Charge Dominated Electron Beam to be submitted to RSI
- [3] A. Valfells, J. Harris etc, Initial Studies of Longitudinal Dynamics on UMER in PAC 03
- [4] M. Reiser, Theory and Design of Charged Particle Beams (John Wiley & Sons, Inc, New York, 1994).
- [5] Y. Zou, Y. Cui etc, Physical Review Special Topics, Volume 5, 072801(2002)
- [6] Y. Cui, A. Valfells etc, Proceedings of the 2001 Particle Accelerator Conference, p. 2076

ALTERNATIVE BUNCH FORMATION FOR THE TEVATRON COLLIDER

G. Jackson, Hbar Technologies LLC, West Chicago IL 60185, USA

Abstract

Both the proton and antiproton bunches in the Fermilab Tevatron Collider have longitudinal emittances that are so large as to introduce serious limitations to operations. Poor beam lifetime, narrower horizontal aperture, and 30% lower luminosities are just a few examples. Theoretically, these 36 protons and 36 antiproton bunches could have longitudinal emittances roughly 6-10 times smaller if the formation of these bunches did not involve emittance dilution. In this paper, alternative longitudinal manipulations are discussed that reduce or eliminate this nonadiabatic longitudinal emittance growth. The measured results of accelerator studies in the Fermilab accelerator chain are presented and compared with theoretical and numerical calculations.

MOTIVATION

The formation of the 36 proton and 36 antiproton bunches required for Fermi National Accelerator Laboratory (Fermilab) Tevatron Collider operations [1] presently requires that several bunches spaced at 53 MHz are coalesced [2] into a single high intensity bunch with correspondingly large longitudinal emittance. It was proposed over six years ago to reduce the longitudinal emittance of antiproton bunches by directly transferring and accelerating antiprotons at a lower RF frequency until acceleration reduced the bunch length and increased the RF bucket area sufficiently to directly capture the beam in a single 53 MHz RF bucket. It is proposed in this paper to reduce the longitudinal emittance of the Collider proton bunches by performing an alternative coalescing scheme at injection of the Main Injector. Because of large coherent longitudinal oscillations in the bunches from the Booster ring [3], this alternative method is awaiting Booster beam improvements.

ANTIPROTON BUNCHES

Protons are injected from the Fermilab Booster into the Main Injector at a kinetic energy of 8 GeV. Antiprotons are injected at 8 GeV from either the Fermilab Accumulator or Recycler rings. The Main Injector accelerates both beams to 150 GeV for eventual injection into the Tevatron Collider.

The Tevatron Collider needs 36 antiproton bunches. At present the Accumulator ring performs 9 transfers of antiproton beam to the Main Injector, and Tevatron. Each transfer consists of 4 groups of between 7 and 11 bunches spaced at 53 MHz. This charge distribution is accelerated to 150 GeV and then coalesced [2] into 4 monolithic bunches and transferred into the Tevatron Collider. The 4 bunches each have a longitudinal emittance between 2 and 3 eV-sec, whereas the initial distributions extracted

from the core of the Accumulator antiproton beam was 0.4-0.6 eV-sec. The longitudinal emittance dilution is suffered at the time the beam is bunched at 53 MHz in the Accumulator, and when the 53 MHz structure is again removed during the coalescing process.

The original reason for this arrangement was the fact that the old Main Ring synchrotron had a very limited longitudinal emittance aperture at transition. The new Main Injector ring has been shown during the work described in this paper to have a longitudinal acceptance in excess of 0.7 eV-sec. As described in the Recycler technical design report [4], it is possible to completely bypass the coalescing process by performing bucket-to-bucket transfers between the Accumulator (or Recycler) and Main Injector at 2.5 MHz. After some acceleration to get closer to transition, direct adiabatic transfer of beam from the 2.5 MHz RF system and the 53 MHz RF system can take place to form the Tevatron Collider bunches. In principle no longitudinal emittance growth is incurred in this scenario and a reduction of bunch length and momentum spread of more than a factor of two is realized. Such a reduction would significantly improve Collider operations.

PROTON BUNCHES

The goal of the research described in this paper was to generate proton bunches for the Tevatron Collider with longitudinal emittances less than 1 eV-sec. The tactic proposed to accomplish this goal was to perform the coalescing process on the Booster bunches at 8 GeV in the Main Injector just after injection. Traditional 150 GeV coalescing [2] incurs significant particle loss, and the concept for this alternative formation process is to invoke particle loss at the very beginning of the coalescing process in order to increase the phase space density of the initial Booster bunch distributions.

Simulation of the Process

The author wrote a multiparticle simulation using Microsoft Excel to assess numerically the viability of this alternative formation process. Using 7000 test particles to simulate 7 Booster bunches, the initial distribution was generated assuming a bi-Gaussian longitudinal phase space density distribution with a 95% invariant longitudinal emittance of 0.2 eV-sec per bunch. Figure 1 shows an example of such a distribution in phase space, where the vertical axis is fractional energy deviation and the horizontal axis is RF phase in radians.

The first step is to snap down the RF bucket height such that only the core of the bunch distribution is still within the bucket. As seen in figure 2, after 90 degrees of phase advance the distribution has lost the low density protons in one phase space dimension.

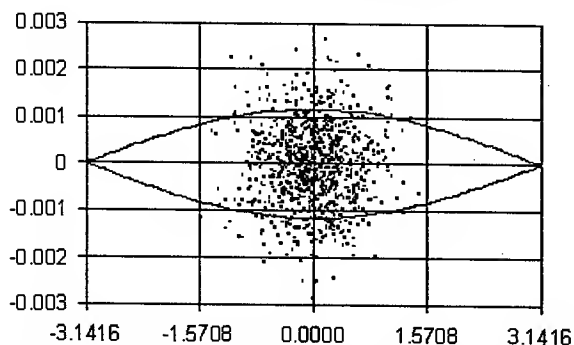


Figure 1: Initial distribution of the test particles in one of seven bunches simulating this alternative form of proton coalescing at 8 GeV in the Main Injector.

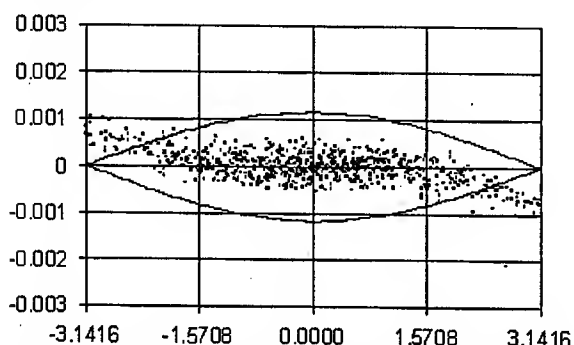


Figure 2: Distribution after 90 degrees of synchrotron phase advance in the RF bucket formed after instantaneously snapping down the RF voltage to 100 kV.

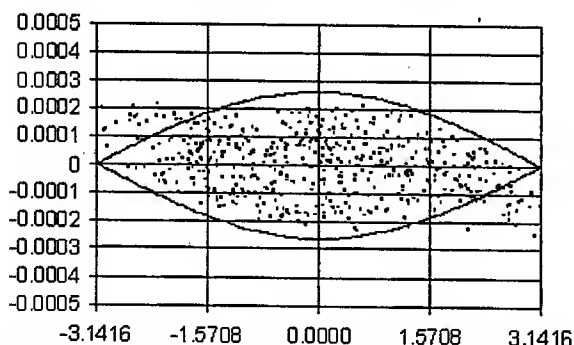


Figure 3: The result of stepping the RF voltage down to 5 kV and waiting another 90 degrees of synchrotron phase advance in the newly reduced RF bucket.

In order to cut away the low density protons in the other projection of phase space, the RF bucket height was again snapped down to bisect the energy distribution shown in figure 2. Figure 3 presents the result of waiting 90 degrees in synchrotron phase advance after this second voltage reduction. Note the reduction in energy spread as compared to figure 1. Figure 4 is an expanded view of the phase space distribution of the entire group of 7 Booster bunches. Note that the low density protons are streaming away while the dense distribution cores of the bunches form a high density line charge ready for coalescing with the Main Injector 2.5 MHz RF system.

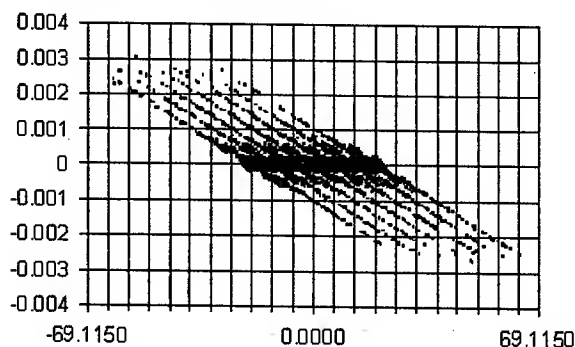


Figure 4: Expanded view of figure 3, showing the phase space distribution of all 7 Booster bunches. The dense central line charge is now ready for coalescing.

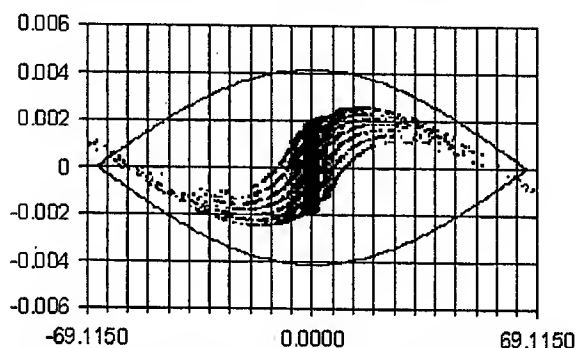


Figure 5: Phase space distribution of the protons after rotation in the 2.5 MHz RF system bucket by 90 degrees in synchrotron phase.

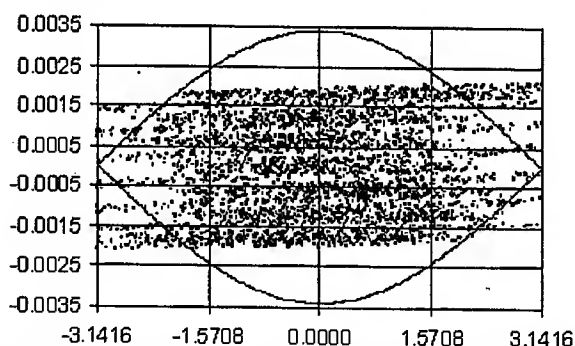


Figure 6: Same view as figure 5 but restricted to the central 53 MHz RF bucket that recaptures the beam for later synchronous transfer to the Tevatron Collider.

The 2.5 MHz RF system has a maximum voltage of 60 kV. In addition, there is a lower voltage 5.0 MHz system capable of partially linearizing the sinusoidal waveform in order to rotate up to 11 bunches uniformly. Figure 5 shows the effect of this RF system on the proton distribution after 90 degrees of synchrotron phase advance. At this stage the 2.5 MHz is turned off and 850 kV capture voltage at 53 MHz is snapped on.

Figure 6 shows the capture RF bucket superimposed on the central charge distribution shown in figure 5. Figure 7 shows the steady state charge distribution in the central bucket a few milliseconds after the recapture process.

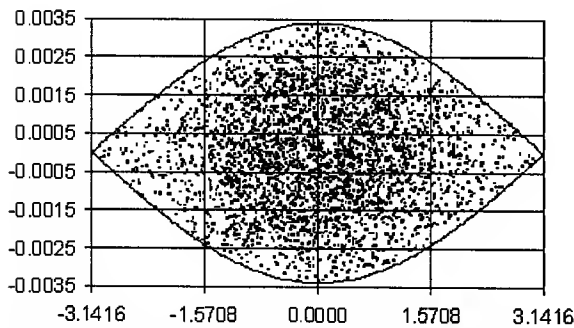


Figure 7: The distribution in figure 6 after a few milliseconds of storage in the 850 kV RF bucket.

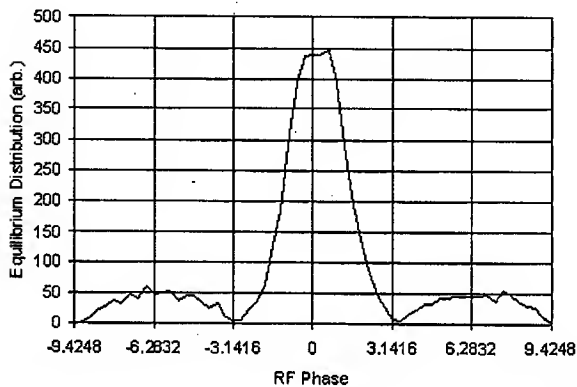


Figure 8: Histogram of the data in figure 7 simulating the longitudinal beam profile measured using a wall current monitor in the Main Injector. The central bunch plus the two neighboring RF buckets are shown.

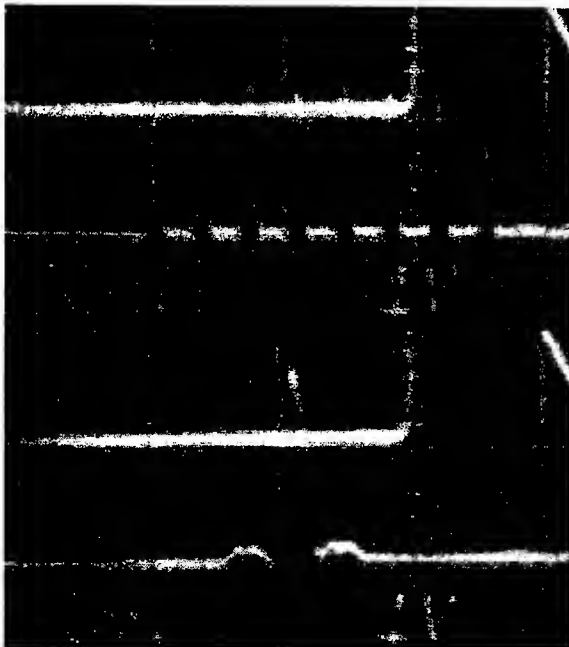


Figure 9: Measured beam profile after testing this alternative form of proton bunch formation at 8 GeV in the Fermilab Main Injector. Note the similarity to fig. 8.

Measurement of the Process

Figure 8 was generated by histogramming the RF phase coordinates of all the test particles trapped in the RF buckets. This alternative bunch formation process was tested in the Main Injector at 8 GeV using the same proton longitudinal emittance and RF voltages that were simulated. The measured beam profile using the Main Injector resistive wall detector is shown in figure 9. Note the accuracy with which the simulation predicted the final bunch shape for the core and satellite RF buckets.

Unfortunately, at higher intensities relevant for Tevatron Collider operations the reproducibility and accuracy of the simulation disappeared. It was noted that although the single bunch longitudinal emittance from the Booster had not increased with intensity, the size of the coherent longitudinal oscillations was dramatic. Figure 10 contains a measurement of such oscillations. Until these oscillations are reduced in the Booster, this alternative proton bunch formation scheme for the Tevatron Collider is not possible.

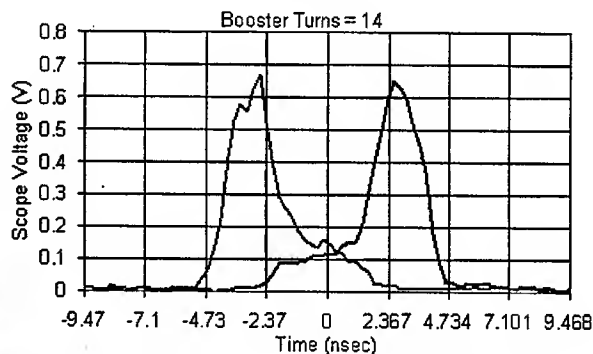


Figure 10: Same bunch measured twice separated by approximately one half synchrotron oscillation. The full width of the plot is an entire RF bucket.

ACKNOWLEDGEMENTS

This work was supported by the U.S. Department of Energy through the high energy physics contract of the University of Michigan physics department and the concurrence of Fermilab.

Main Injector department head Shekhar Mishra supervised this project. Operations specialist Dave Capista and RF engineers Brian Chase, Joe Dey, and John Reid provided valuable advice.

REFERENCES

- [1] S.Mishra, "High Luminosity Operation of the Fermilab Accelerator Complex", this conference.
- [2] I.Kourbanis, J.Dey, J.Reid; "Performance of Main Injector Bunch Coalescing during Fermilab's Current Collider Run", this conference.
- [3] G.Jackson, "Longitudinal Emittance Growth in the Fermilab Booster Synchrotron", this conference.
- [4] G. Jackson, ed., "Recycler Ring Technical Design Report", Internal Fermilab Memo TM-1991 (1996).

LONGITUDINAL EMITTANCE GROWTH IN THE FERMILAB BOOSTER SYNCHROTRON

G. Jackson, Hbar Technologies LLC, West Chicago IL 60185, USA

Abstract

In order to shorten the proton bunches in the Fermilab Tevatron Collider, it would be quite helpful to reduce the longitudinal emittance for proton bunches generated by the Booster Synchrotron. A study was undertaken to re-evaluate the sources of longitudinal instability and resultant longitudinal emittance growth as a function of Booster beam and bunch currents. Employing a novel technique for generating partially populated circumferences of protons, the Booster was tested to understand whether increased longitudinal emittance growth was correlated with total current in the synchrotron, consistent with coupled-bunch instability, or with the number of protons per individual bunch. This paper will present findings that indicate that the instability responsible for poor Booster emittance performance is consistent with single bunch (or low cavity-Q) instabilities.

MOTIVATION

The formation of the 36 proton bunches required for Fermi National Accelerator Laboratory (Fermilab) Tevatron Collider operations [1] requires that several proton bunches spaced at 53 MHz are coalesced [2] into a single high intensity bunch with correspondingly large longitudinal emittance. It was proposed to reduce the longitudinal emittance of the Collider proton bunches by performing an alternative coalescing scheme at injection of the Main Injector [3]. Because of large coherent longitudinal oscillations in the bunches from the Booster ring [4], it was necessary to step back into the Booster to understand the origin of these oscillations and to find methods of reducing them.

BOOSTER BACKGROUND

Negatively charged atomic hydrogen is injected from the Fermilab Linac into the Booster at a kinetic energy of 400 MeV. The Linac pulse length is equal to an integer number of Booster revolution periods, or "turns". By stripping the electrons during the injection process, multiturn injection of protons is accomplished without significant emittance dilution.

The Booster ramps to a peak kinetic energy of 8 GeV in 33 msec due to the resonant 15 Hz power supplies driving the magnet system. The RF frequency that accelerates the beam swings from 37.6 MHz to 52.8 MHz. The beam feedback loops that control the RF frequency and synchronous phase ramps rely on the fact that all 84 RF buckets are filled with beam (with the recent upgrade that a few bunches can be empty to accommodate an extraction kicker risetime gap to minimize beam losses

and reduce tunnel losses. Transition crossing occurs at roughly halfway through the ramp.

FULL BATCH OPERATIONS

It was found in the Main Injector [3] that the bunch length and coherent longitudinal oscillations increase little as the ring intensity increases from one to four turns, but after that, they grow quickly to the operational maximum of 12 Booster turns.

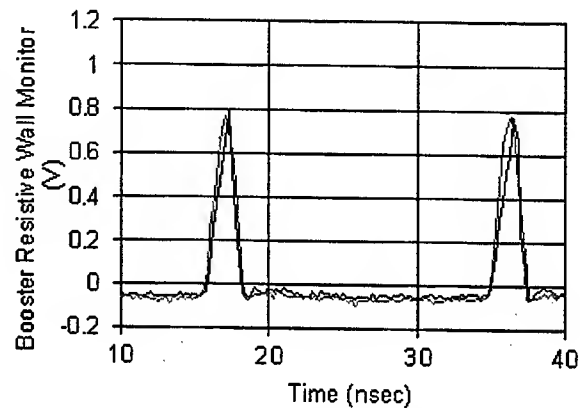


Figure 1: Two bunches on a single revolution before transition crossing. The black trace corresponds to two Booster turns. The red trace corresponds to twelve Booster turns, with the bunch area scaled down to that of two turns. Note that the 95% bunch lengths are identical.

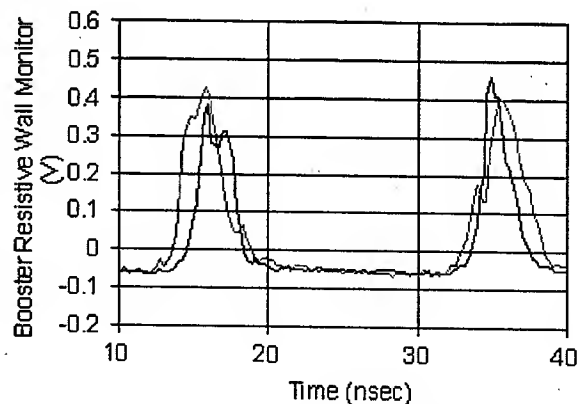


Figure 2: Two bunches on a single revolution after transition crossing. The black trace corresponds to two Booster turns. The red trace corresponds to twelve Booster turns, with the bunch area scaled down to that of two turns. Note that the 95% bunch lengths are now quite different, with the higher intensity bunches being wider.

Figures 1 and 2 show the difference in bunch length with beam intensity before and after transition. Clearly the problem of increasing longitudinal emittance with beam intensity occurs near transition crossing.

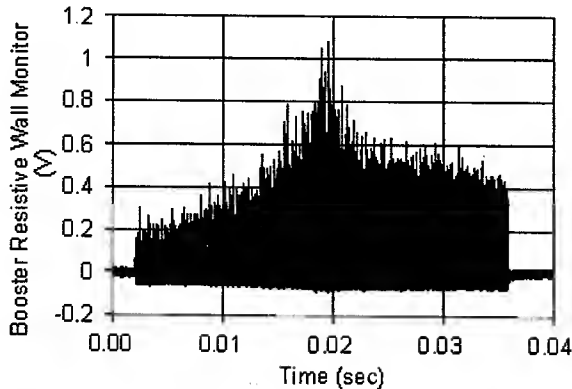


Figure 3: Peak current throughout the Booster acceleration cycle for two Booster turns. The noisiness of the data is not instrumental.

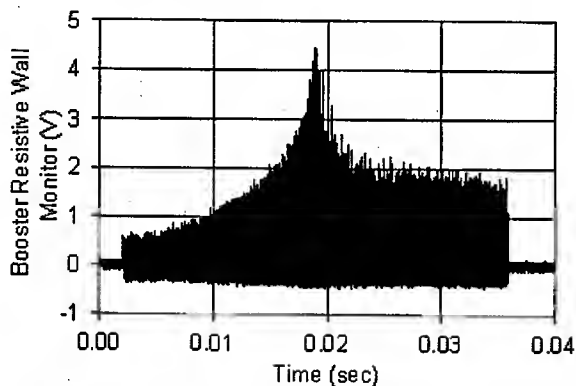


Figure 4: Peak current throughout the Booster acceleration cycle for twelve Booster turns.

Figures 3 and 4 are measurements of the peak bunch current throughout the Booster acceleration cycle. From this resolution, the difference in bunch length is not apparent. On the other hand, note that the ratio of final to initial peak current is nearly 2x for both two and twelve Booster turns of intensity.

Figures 5 and 6 show the variation of peak current with time after transition. Note that these oscillations are caused by bunch length oscillations, and violent ones at that. There are two conclusions that can be gleaned from these figures. First, the relative amplitudes of these oscillations is quite similar between two and twelve Booster turns, suggesting that it is not an intensity dependent effect. Second, the existence of such large low-intensity mismatches through transition should be a key priority in any future effort to minimize the longitudinal emittance of proton bunches injected into the Main Injector. Unfortunately, these investigations were terminated by Fermilab before the cause of this effect was fully understood.

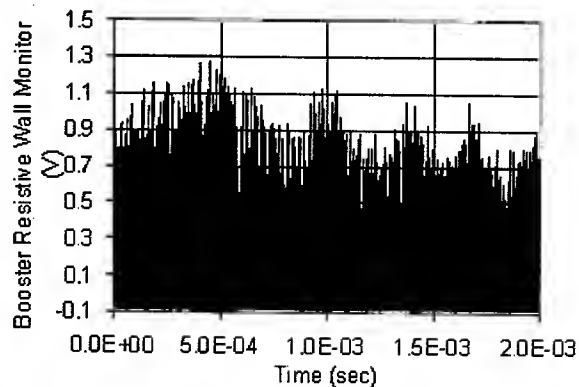


Figure 5: Peak bunch current after transition (which occurs at 0.5 msec in the figure) at a beam intensity of 2 Booster turns.

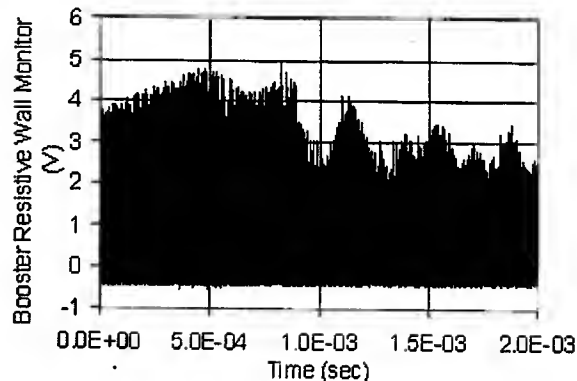


Figure 6: Peak bunch current after transition (which occurs at 0.5 msec in the figure) at a beam intensity of 12 Booster turns.

PARTIAL BATCH OBSERVATIONS

In order to diagnose the cause of the high intensity emittance dilution in figure 2, the author suggested a novel method for determining whether the intensity dependence was due to the total current in the Booster or the intensity per bunch.

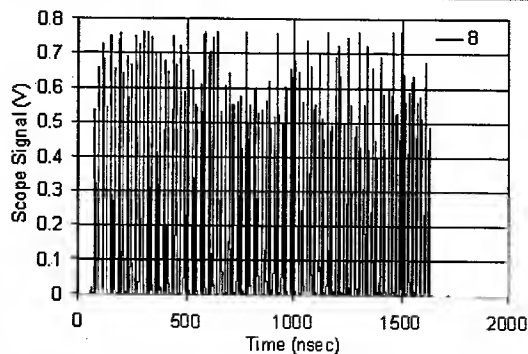


Figure 7: Full batch injection into the Main Injector at eight Booster turns of intensity. Note the variation of peak bunch current over the 82 (out of 84) bunches that are transferred by the extraction kickers.

It is known that the RF feedback loops can operate at one Booster turn of intensity, and that they have sufficient dynamic range to also accelerate twelve Booster turns. Therefore, with injection controls set for 12 Booster turns, one of the extraction kickers was fired just after turn 11. In comparison to full batch (a batch is a set of 84 bunches extracted from the Booster) injection into the Main Injector shown in figure 7, figure 8 shows the result of partial batch acceleration and extraction in the Booster.

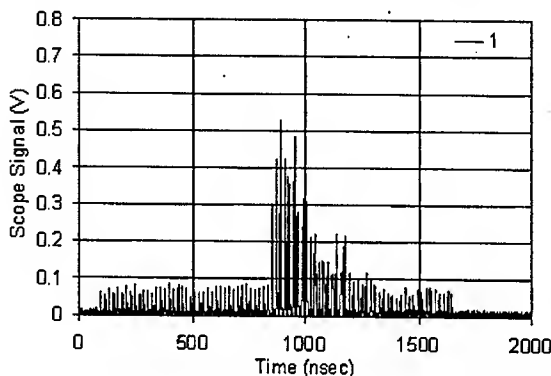


Figure 8: Partial Booster batch injection into the Main Injector. Booster injection was set to eight turns, and the extraction kicker allowed one turn to remain in the full circumference to allow the low level RF feedback loops to operate. Note that the peak current is lower than in the full batch case of figure 7.

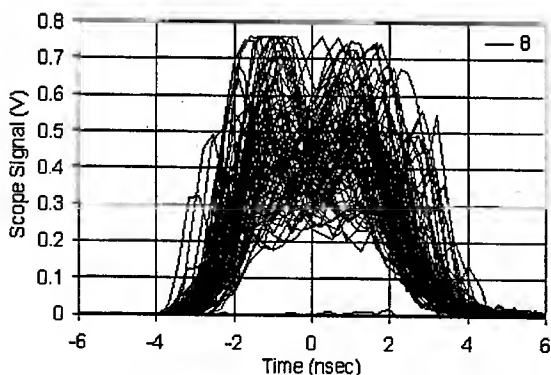


Figure 9: Overlap of 82 bunches injected into the Main Injector after normal full batch acceleration of eight Booster turns of intensity.

Individual bunches were resolved by recording the first turn in the Main Injector using a LeCroy digital scope connected to a resistive wall monitor. By knowing that the injection RF frequency is 52.811400 MHz, Microsoft Excel was used to overlap their profiles. For example, a full batch at eight Booster turn intensity is shown in figure 9. The number of intense bunches during partial batch operations is determined by the fact that the extraction kickers are shorter than a single revolution at the injection revolution frequency. The extraction kicker

was fired on revolution 7 out of 8 during the Booster injection sequence. It was observed that the dozen intense bunches had the same bunch length and erratic shape as a full batch of beam at the same bunch intensities. This suggests that the cause of the longitudinal emittance problems above four Booster turns depends on the intensity per bunch, and not the total current in the Booster. This further suggests that the standard blame on longitudinal coupled bunch instabilities is incorrect. Because the bunch lengths are independent of intensity before transition, space charge at injection is clearly also not the culprit.

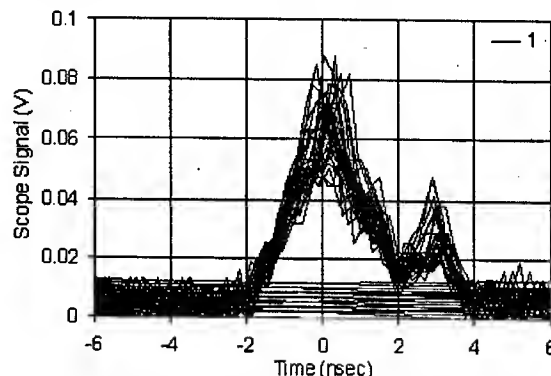


Figure 10: Low intensity stabilization bunches after the intense bunches during partial batch operations.

One outstanding mystery is the distortion of the low intensity stabilization bunches directly after the intense bunches. One unlikely explanation is a wakefield at the third harmonic of the RF frequency at half its amplitude.

ACKNOWLEDGEMENTS

This work was supported by the U.S. Department of Energy through the high energy physics contract of the University of Michigan physics department and the concurrence of the Fermilab.

Main Injector department head Shekhar Mishra supervised this project. Booster department head Robert Webber provided logistical support. Jim Lackey implemented the partial batch operation of the Booster, and Bill Pellico provided RF system advice and support. Ray Tomlin provided control room support and was a valuable resource for information on Booster operations and instrumentation.

REFERENCES

- [1] S.Mishra, "High Luminosity Operation of the Fermilab Accelerator Complex", this conference.
- [2] I.Kourbanis, J.Dey, J.Reid, "Performance of Main Injector Bunch Coalescing during Fermilab's Current Collider Run", this conference.
- [3] G.Jackson, "Alternative Bunch Formation for the Tevatron Collider", this conference.
- [4] E.Prebys, "Increasing the Intensity of the Fermilab Booster", this conference.

TWO-STREAM STUDIES FOR HEAVY ION BEAM PROPAGATION IN A REACTOR CHAMBER*

D. V. Rose,[†] T. C. Genoni, and D. R. Welch, Mission Research Corp., Albuquerque, NM 87110
C. L. Olson, Sandia National Laboratories, Albuquerque, NM 87185

Abstract

Growth rates for the two-stream instability for a heavy-ion beam propagating in a collisionless plasma are analyzed analytically and numerically using particle-in-cell simulations. Good agreement between the analytic and simulation results is found for a wide range of parameters consistent with heavy-ion driven inertial fusion energy chamber designs.

INTRODUCTION

Heavy-ion inertial-fusion-energy requires beams of high-energy, heavy-ions to be focused and propagated across a gas and plasma filled reactor chamber. The robust point design [1] uses the neutralized ballistic transport scheme which requires that the focusing force be applied to the ion beams outside of the reactor chamber. Prior to entering the chamber, the beams pass through a pre-ionized plasma region which provides charge neutralization. Target designs require lower energy "foot" beams to preheat the target prior to the arrival of the high energy beams which provide the final target impulse. The chamber environment for the foot beams includes a low density (~ 3 mtorr) background gas. The main beams propagate through gas which is partially ionized near the target by photo-ionization due to the preheated target. In addition, aerosols may be present along all or part of the beam path lengths, possibly impacting the transport properties [2].

A previous analysis [3] of two-stream instability growth and saturation for converging heavy ion beams propagating in a reactor chamber considered the rate of change of the maximum growing wave-number with increasing beam and plasma densities as the converging beam crosses the chamber. That analysis concluded that for a specific range of parameters, a reasonable propagation window existed in part because of the changing instability mode as the beams propagated across the chamber.

One goal of this work is to revisit the assumptions made for the analysis of Ref. [3] in light of the recent robust point design [1] parameters. As a first step towards this goal, a study of both 1-D and 2-D two-stream instability modes is examined in this paper.

* This work is supported by the U.S. Department of Energy through the Lawrence Berkeley National Laboratory, the Princeton Plasma Physics Laboratory, and the ARIES Program.

[†] drose@mrcaq.com

1-D STUDIES

The growth rate of the electrostatic two-stream instability is investigated in 1-D for the case of cold electron and heavy-ion streams propagating through a stationary background ion population. The electron and ion beams are moving in the same direction with (possibly) different speeds. Charge neutralization is enforced in all cases by setting $n_b + n_p = n_e$, where $n_{b,e,p}$ are the beam ion, electron, and plasma ion densities, respectively.

The electrostatic dispersion relation for an ion beam propagating along with an electron stream through a stationary background ion population can be written as (see, for example, Ref. [4])

$$\frac{\omega_b^2}{(\omega - kv_b)^2} + \frac{\omega_e^2}{(\omega - kv_e)^2} + \frac{\omega_p^2}{\omega^2} = 1, \quad (1)$$

where $\omega_{b,e,p}$ are the beam ion, electron, and plasma ion plasma frequencies, respectively, and $v_{b,e}$ are the beam ion and electron speeds.

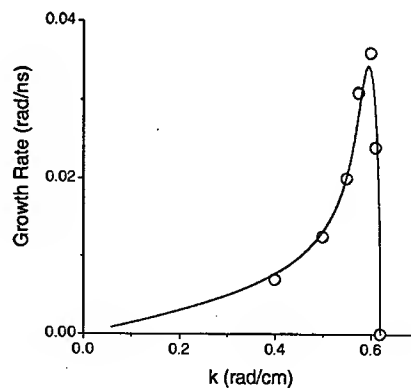


Figure 1: 1-D two-stream growth rate from dispersion relation (solid line) and 1-D LSP simulations (open circles). The parameters are $n_e = 10^9 \text{ cm}^{-3}$, $n_e/n_b = 2$, $n_b = n_p$, and $v_e = 0.1c$.

Electrostatic particle-in-cell simulations using LSP [5] have been carried out in 1-D with periodic boundary conditions for direct comparison to the solutions of Eq. (1). The simulation length is set to be $2\pi/k$, where k is the wave number of interest. The instability growth is stimulated by an initial sinusoidal perturbation of wave-number k and amplitude $0.0001v_e$ applied to the electron velocity.

Comparisons were carried out over a wide range of parameters, including electron speed, density, and wavenumbers. Very good agreement over all parameter ranges was found. A sample comparison is shown in Fig. 1 for the specific case of $v_e = 0.1c$, and ion masses of $200M$ for the beam ions and $12M$ for the initially stationary plasma ions, where M is the mass of a proton. (These mass values are used throughout this paper.) Note that the beam ion speed, v_b , is fixed at $0.2c$ throughout this work. The solid line is the maximum growth rate as a function of k , with peak growth found for $k \sim \omega_e/v_e$. The data points are individual LSP simulations carried out for different periodic lengths $2\pi/k$. The peak growth rate in the simulations is slightly different than that found from Eq. (1), but the overall k -dependence is reproduced.

2-D SURFACE MODE

Surface wave two-stream growth is assessed for the limit of a "hard-edge" ion beam propagating with an electron stream through a background ion density. In the electrostatic limit, an eigenfunction analysis leads to the dispersion relation

$$1 - \frac{\omega_b^2}{(\omega - kv_b)^2} - \frac{\omega_{e1}^2}{(\omega - kv_e)^2} - \frac{\omega_p^2}{\omega^2} = -\alpha \left(1 - \frac{\omega_{e2}^2}{\omega^2} - \frac{\omega_p^2}{\omega^2} \right), \quad (2)$$

where α is a geometric factor given by

$$\alpha = \frac{I_0(ka)}{I_1(ka)} \left[\frac{I_0(kR)K_1(ka) + I_1(ka)K_0(kR)}{I_0(kR)K_0(ka) - I_0(ka)K_0(kR)} \right]. \quad (3)$$

(A fully electromagnetic formulation for an annular relativistic electron beam in a background plasma has been given by Jones [6]. In the electrostatic limit, a dispersion relation similar to Eq. (2) was obtained by Fukano, *et al.* [7] for the case of no outer radial boundary.) The electron density is again set such that $n_e = n_p + n_b$, which leads to a higher electron density inside the beam ("e1") than outside ("e2"). The outer conducting wall is at R and the beam radius is a . These values are fixed at $R = 2$ cm and $a = 1$ cm throughout this paper.

For the case of a smooth density gradient at the edge of the beam a simple analytic dispersion relation such as Eq. (2) no longer applies. In this more general case, the dispersion analysis is carried out by setting the determinant of the discretized system of linearized electrostatic equations equal to zero. We choose a simple form for the ion beam density profile as a function of radius

$$n_b(r) = n_{b0}g(r) = n_{b0} \frac{1}{e^{(r-a)/f} + 1}, \quad (4)$$

where n_{b0} is approximately the on-axis value of the beam density and f determines the inclination angle of the normalized beam density profile $g(r)$ at $r = a$ [this angle in

radians is $\tan^{-1}(0.25/f)$]. The radial profile of the axial electron velocity is obtained from the condition for current neutralization

$$v_e(r) = \frac{n_b(r)v_b}{n_b(r) + n_p}. \quad (5)$$

In the limit of very small values of f , this analysis converges to the same result as obtained from the solution of Eq. (2), the "hard-edge" limit.

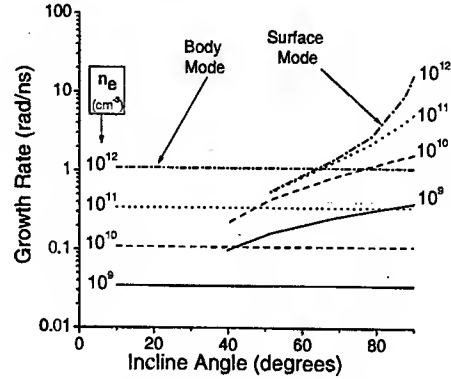


Figure 2: The maximum two-stream growth rates for the 1-D "body" and 2-D "surface" modes as a function of density and inclination angle. The parameters are $n_e = 10^9 \text{ cm}^{-3}$, $n_{e1}/n_b = 2$, $n_b = n_p$, and $v_e = 0.1c$.

A comparison between the body mode given by the solution of Eq. (1) and the surface mode is shown in Fig. (2) for $v_e = 0.1c$. The maximum body mode growth rate (continuous spectrum) is independent of inclination angle while the maximum surface mode growth rate increases with increasing inclination angle. For the range of parameters considered here, the maximum growth rate of the surface mode at large inclination angle is always greater than the maximum body mode growth rate for a given value of n_e .

2-D SIMULATIONS

Periodic, electrostatic, 2-D LSP simulations were carried out for direct comparison with the results presented above. The simulations are periodic in the axial direction with a conducting boundary at R . All velocities are initialized in the axial direction only. The axial electron velocity is perturbed as described above.

Figure 3 compares the calculations and simulations for the hard-edge beam limit at $n_e = 10^9 \text{ cm}^{-3}$ and $v_e = 0.1c$ as a function of k . Qualitative agreement in the overall k -spectrum is found, which is significantly broader than the similar k -spectrum found in the 1-D or body mode results (Fig. 1). The disagreement between the calculations and the simulation results around the maximum growth values is attributed to the finite radial zoning in the LSP simulations that gives an effective inclination angle to the beam once the electrons gain some radial velocity spread. Finer

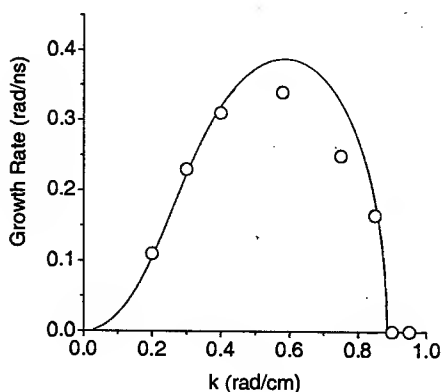


Figure 3: 2-D two-stream growth rate from dispersion relation (solid line) and 2-D LSP simulations (open circles) as a function of k . The parameters are $n_e = 10^9 \text{ cm}^{-3}$, $n_{e1}/n_b = 2$, $n_b = n_p$, and $v_e = 0.1c$.

resolution radial zoning and better particle statistics produces growth rates which tend towards the calculated values.

A comparison of the calculated and simulated surface mode growth rate as a function of inclination angle is shown in Fig. 4 for $n_e(0) = 10^9 \text{ cm}^{-3}$ and $v_e(0) = 0.1c$. The calculated growth rate increases linearly with inclination angle for our choice of beam radial profile, as given in Eq. (4).

DISCUSSION

Simulations presented here are idealized in order to facilitate direct comparison to analytic models of two-stream growth. Future work will examine the impact of a converging ion beam on these growth rates.

Recent analysis of current neutralization for ion beams propagating in a background plasma [8, 9] shows limits on the degree to which current neutralization can be obtained. These limits may be related to the growth and saturation of the two-stream instability for the electron return current.

Also, we note that recent simulation results [8] show a beneficial ion beam pinching effect near the target driven by a reduction in the return current near the beam focus. Again, the growth and saturation of the two-stream instability may be partially responsible for the abrupt decrease in the electron return current in this region. Extensions to the work presented here are being directed towards examining this issue.

We note that a considerable body of work on two-stream instabilities for heavy ion beams propagating through low density background plasmas, applicable to a variety of periodic focusing accelerators and transport systems, can be found in the literature; see, for example, Ref. [10], and references therein.

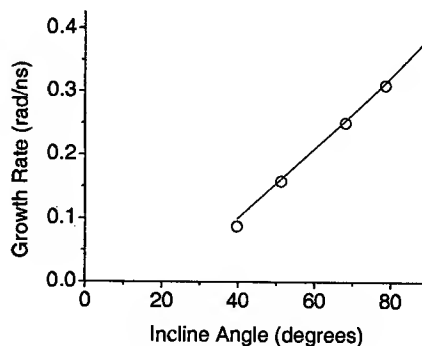


Figure 4: Two-stream surface mode growth rate calculations (solid line) and 2-D LSP simulations (open circles). The parameters are $n_e = 10^9 \text{ cm}^{-3}$, $n_e/n_b = 2$, $n_b = n_p$, and $v_e = 0.1c$.

REFERENCES

- [1] S. S. Yu, *et al.*, submitted to Fusion Sci. Technol. (2003).
- [2] D. V. Rose, *et al.*, submitted to Fusion Sci. Technol. (2003).
- [3] P. Stroud, Lasers and Part. Beams **4**, 261 (1986).
- [4] R. Briggs, in Advances in Plasma Physics, edited by A. Simon and W. B. Thompson (Interscience, New York, 1971), p. 43.
- [5] LSP is a software product of Mission Research Corp., Albuquerque, NM 87110 (<http://www.mrcabq.com>).
- [6] M. E. Jones, Phys. Fluids **26**, 1928 (1983).
- [7] A. Fukano, *et al.*, J. Phys. Soc. Jap. **60**, 2627 (1991).
- [8] D. R. Welch, *et al.*, Phys. Plasmas **9**, 2344 (2002).
- [9] I. Kaganovich, *et al.*, Phys. Plasmas **8**, 4180 (2001).
- [10] R. C. Davidson, *et al.* Nucl. Instrum. Meth. Phys. Res. A **464**, 493 (2001).

SIMULATED GROWTH RATES FOR SINGLE-BUNCH INSTABILITIES DRIVEN BY A RESISTIVE IMPEDANCE

N. Towne*, National Synchrotron Light Source
Brookhaven National Laboratory, Bldg. 725B, Upton, NY 11973-5000†

Abstract

Vlasov simulations of instabilities driven by resistive impedance are used to determine growth rates of single-bunch instabilities. A method for measuring synchrotron tunes and growth rates from simulated synchrotron sidebands is described. Simulated growth rates are compared with Oide's calculation [K. Oide, Part. Accel. **51**, 43 (1995)].

INTRODUCTION

Vlasov-based and particle-tracking [1], and Perron-Frobenius [2] methods exist for the numerical calculation of single-bunch instabilities. These methods are capable of simulating the growth of modes arising from a few coupled synchrotron modes as well as instabilities in the microwave regime. Oide used a Vlasov-mode-based computer code to calculate growth rates for the first four synchrotron modes in the presence of a resistive impedance and in the absence of radiation damping [3]. He found that these rates are approximately proportional to the square of the beam current over a wide range of currents. This paper describes the time-domain simulation of growth of these instabilities and compares the simulated growth rates with Oide's calculations. These simulations are performed by integrating the Vlasov equation using the method of Warnock and Ellison [2] in a code written in Mathematica [4]. Nonlinear terms coming from potential-well distortion are simulated. Simulated quadrupole-mode growth rates agree very well with Oide's results while the dipole-mode growth rates are lower than Oide's results.

CALCULATION OF SIMULATED TUNES AND DAMPING RATES

A simulated bunch above threshold for instability that initially has the Haissinski distribution will not, in principle, change with time. In computational practice, however, perturbations of the bunch distribution exist and these perturbations serve to seed the growth of unstable modes. In the model under consideration, the unstable modes Oide described [3] grow exponentially in time, each mode with its own growth rate. Each mode contributes a finite-width line to a synchrotron sideband reflecting the synchrotron tune of the mode and its growth rate.

*Email: townen@bnl.gov

† Work performed under the auspices of the U.S. Department of Energy, under contract DE-AC02-76CH00016.

In this study, the tunes and damping rates of dipole and quadrupole modes are calculated from simulations in the linear regime by first Fourier transforming the simulated line density $\lambda(\phi, t)$ with respect to the phase coordinate ϕ at some revolution line n to obtain an approximation of a transformed pickup signal $\lambda_n(t)$.

$$\lambda_n(t) = \frac{1}{2\pi} \int d\phi \lambda(\phi, t) e^{-in\phi} \quad (1)$$

The expression is approximate to the degree that the line density does not change significantly during the time the bunch traverses the pickup. This function is Fourier transformed with respect to t to obtain the spectral signal $\lambda_n(\omega)$, with ω the offset from the n th revolution line. It is assumed that that offset is small compared to ω_0 . One then fits this function to resonances of multipole modes in the synchrotron sidebands. The resonances are each functions

$$\tilde{f}_j(\omega) = \left[1 - i \frac{\omega_j}{2\Gamma_j} \left(\frac{\omega}{\omega_j} - \frac{\omega_j}{\omega} \right) \right]^{-1}, \quad (2)$$

where ω_j and Γ_j are the resonant frequency and damping rate of the j th mode. These functions are the Fourier transforms of the wake functions

$$f_j(t) = 2\Gamma_j e^{-\Gamma_j t} \left(\cos \bar{\omega}_j t - \frac{\Gamma_j}{\bar{\omega}_j} \sin \bar{\omega}_j t \right), \quad (3)$$

where $\bar{\omega}_j = \sqrt{\omega_j^2 - \Gamma_j^2}$. One then constructs a model $S(\omega)$ of the spectrum of the bunch as the superposition of N of these resonances and corrects for the finite duration of the simulations.

$$S(\omega) = \sum_{j=1}^N a_j \tilde{f}_j(\omega) \left[1 - e^{i\omega t_{\max}} \left(\frac{f_j(t_{\max})}{2\Gamma_j} + i \frac{\omega_j^2}{\omega \bar{\omega}_j} e^{-\Gamma_j t_{\max}} \sin \bar{\omega}_j t_{\max} \right) \right] \quad (4)$$

In this expression, t_{\max} is the duration of the simulation and the coefficients a_j are complex-valued weights. This differs significantly from a simple superposition of resonances (Eq. (2)) for a given mode if few e -folds growth of the mode are simulated, which is the case for the slow-growing dipole modes. The $4N$ real parameters embedded in Eq. (4) are all varied to fit the model to the simulated sidebands $\lambda_n(\omega)$ in a frequency range encompassing the synchrotron lines, i.e., the function

$$\int_{\min}^{\max} d\omega |\lambda_n(\omega) - S(\omega)|^2 \quad (5)$$

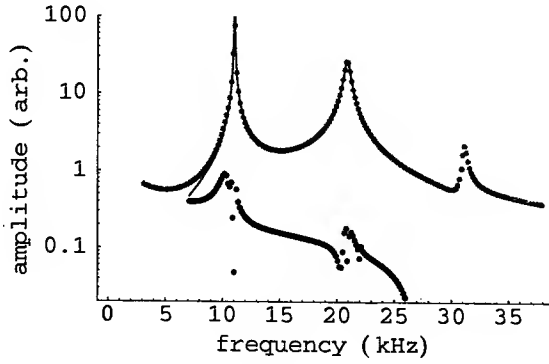


Figure 1: Example spectrum of a simulated bunch at 118 mA and corresponding fit as a function of frequency offset from a revolution line. The synchrotron frequency is 11 kHz and the revolution harmonic n is 55. The green points are of the simulated spectrum $\lambda(\omega)$, the blue trace is the fit function $S(\omega)$ covering the dipole and quadrupole lines, and red is the residual error. The sextupole line is also visible in the simulated spectrum.

is minimized. Figure 1 shows an example of a spectrum and its corresponding fit for $N = 2$.

SEEDING INSTABILITIES

A perturbation $\delta\Psi$ of the Haissinski distribution $\Psi_{\text{Ha}}(\phi, p)$ [5], where ϕ and p are phase-space variables, serves to seed instability in the bunch. Using a seed ensures that mode signals are above the noise background in the synchrotron sidebands at the start of the simulation, a background that originates from an imperfectly calculated Haissinski distribution. It was found that the quadrupole mode grows large more quickly than the dipole mode and nearly any seed results in strong quadrupole oscillations in the time there is significant growth of the dipole mode. So a perturbation that seeds the dipole mode preferentially was used. This allowed sufficient time that the growth rate of the dipole mode could be estimated before quadrupole-mode oscillations swamp the dipole mode.

The seed used has the form

$$\delta\Psi(\phi, p; t = 0) = \varsigma p \Psi_{\text{Ha}}(\phi, p), \quad (6)$$

where ς is the real constant chosen so that $\varsigma p_{\text{max}} \ll 1$, where p_{max} is the value of p at the edge of the grid (this ensures that $\delta\Psi$ is a small perturbation).

Oide and Warnock and Ellison discuss the 'trivial' dipole solution, which is the solution of the Vlasov equation where the Haissinski solution translates in phase space in an orbit determined by the rf Hamiltonian. This translational solution exists only for hamiltonians harmonic in both the configuration and momentum variables. It exists because of the degeneracy of the frequencies (divided by the multipole orders) of the synchrotron modes and that the wake induced by the bunch has short range and tracks

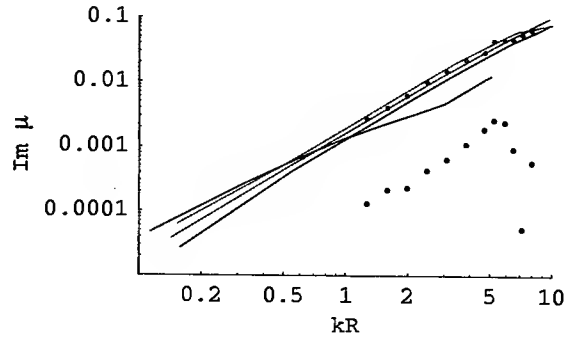


Figure 2: Simulated growth rates (dots) plotted on top of Oide's Fig. 2. Red represents dipole-mode growth rates while pale green represents quadrupole-mode growth rates. Sextupole and octupole modes are represented by aqua and violet traces without simulated data points.

the bunch [3, 2]. This translation is not a dipole mode in the sense of the dipole term of a multipole expansion of the distribution. So this solution is an inappropriate initial condition for seeding dipole oscillations: it results in undamped oscillations.

RESULTS

Oide expresses complex-valued synchrotron frequencies Ω normalized with respect to ω_s ,

$$\mu = \Omega / \omega_s, \quad (7)$$

when referring to a coherent frequency of any synchrotron harmonic. The synchrotron tune is the real part of $\omega_s \mu$ and the damping rate Γ is

$$\Gamma = \omega_s \text{Im } \mu. \quad (8)$$

The beam intensity is represented by the dimensionless parameter product

$$kR \equiv e I_{\text{av}} R / \alpha \sigma_e^2 E_0, \quad (9)$$

where I_{av} is the average single-bunch beam current, α is the momentum compaction, σ_e is the fractional natural energy spread of the ring, E_0 is the beam energy, and the ring impedance is the resistance R . While the product kR of Eq. (9) is the same as Oide's, there is a different convention for the dimension of R (a resistance) in Eq. (9) that changes the exact form of Eq. (9).

Simulations were performed at 12 beam currents with kR ranging from 1.27 to 7.95. Growth rates of the simulations are plotted together with Oide's results in Fig. 2. Figure 3 shows the corresponding synchrotron tunes.

There is good agreement between the quadrupole-mode growth rates predicted by Oide and my simulations. In these simulations, there are many e -folds growth of the mode and analysis of their synchrotron lines is very clean.

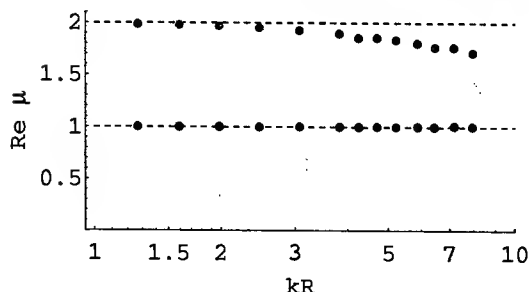


Figure 3: Simulated synchrotron tunes for the dipole (red) and quadrupole (green) modes.

A separate time-domain analysis of these growth rates gives the same results as the frequency-domain analysis described above.

Simulated dipole-mode growth rates are much lower than predicted by Oide, however. Calculations of this parameter using the method above were confirmed by inspection of time-domain plots of the intensity of dipole oscillations from a separate calculation based on the same simulations, which serves as a check of the method. Also by inspection of these plots, extraction of the three dipole-mode growth rates at the highest-current data points of Fig. 2 is compromised by the fast growth and intensity of the quadrupole-mode oscillations. The low growth rates of the dipole modes at these currents were not determined precisely due to the rapid growth of the quadrupole mode.

Errors in the simulation of growth rates result from, in part, the finite time step and the finite spacing of the grid in phase space. In most of these simulations, the time step is $\delta t = 2\pi/90\omega_s$ and the phase-space grid is 81×81 . I then varied these parameters to check convergence. Figure 4 shows the dipole- and quadrupole-mode growth rates for a $kR = 5.87$ beam for varying number of grid points. The time step is $1.0 \mu s$. Figure 5 shows the effect of varying the time step from 0.5 to $2.0 \mu s$ for 81×81 grids. Both plots show that the quadrupole-mode growth-rate predictions show little variation with these parameters except with the coarsest grids. So these calculations are robust. But the plot varying the time step shows that the dipole-mode growth-rate predictions have not seen enough exponential growth to accurately estimate the growth rate. At best, the calculations provide an upper limit that is a fraction of the quadrupole-mode rate.

There is still uncertainty regarding the appropriate seed for the dipole mode. If the 'trivial' dipole mode, as well as the 'true' dipole mode, is seeded, the growth rate appears artificially low until the 'true' dipole mode overpowers the 'trivial' one. Furthermore, one must see substantial exponential growth of the dipole mode before the quadrupole mode overpowers the dipole mode. A better estimate of the dipole coherent mode is necessary to better suppress the quadrupole mode and enhance the dipole mode. So the source of the discrepancy in the dipole-mode growth rates (compared with Oide's calculation) is not determined.

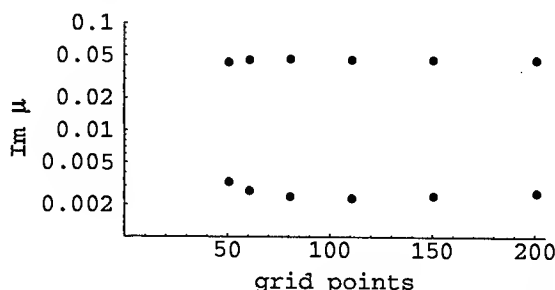


Figure 4: Variation of simulated dipole- and quadrupole-mode (red and green, respectively) growth rates with number of grid points. $kR = 5.87$ and the time step is $1.0 \mu s$.

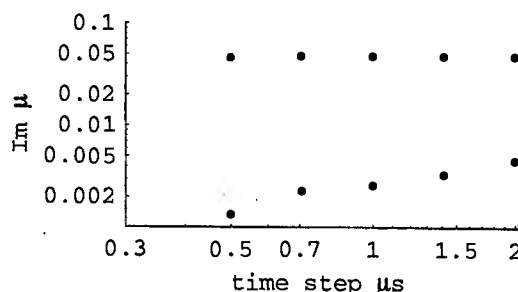


Figure 5: Variation of simulated dipole- and quadrupole-mode (red and green, respectively) growth rates with integration time step. $kR = 5.87$ and the number of grid points is 81×81 .

CONCLUSION

Vlasov simulations of bunch instability driven by a resistive impedance were used to determine growth rates of the dipole and quadrupole modes. The method for determining these growth rates from simulated synchrotron sidebands was described. These simulations resulted in very good agreement with Oide's calculations [3] for the quadrupole mode but lower growth rates for the dipole mode.

I would like to thank Boris Podobedov for suggesting this study.

REFERENCES

- [1] K. L. F. Bane and K. Oide Presented at 16th IEEE Particle Accelerator Conference (PAC 95) and International Conference on High Energy Accelerators, Dallas, Texas, 1-5 May 1995.
- [2] R. L. Warnock and J. A. Ellison (2000), presented at 2nd ICFA Advanced Accelerator Workshop on the Physics of High Brightness Beams, Los Angeles, California, 9-12 Nov 1999; SLAC-PUB-8404.
- [3] K. Oide, Part. Accel. **51**, 43 (1995).
- [4] N. Towne, Phys. Rev. ST Accel. Beams **4**, 114401 (2001).
- [5] J. Haissinski, Nuovo Cimento **18B**(1), 72 (1973).

ANALYTICAL AND TIME-DOMAIN COMPUTATIONS OF SINGLE-BUNCH LOSS-FACTOR IN A PLANAR STRUCTURE

A. Smirnov, D. Yu, *DULY Research Inc., Rancho Palos Verdes, CA 90275*

Abstract

An analytical formulation is developed for a Gaussian bunch loss-factor in a periodic planar ("muffin-tin") structure. The short-range wakefield contribution is modeled with diffraction pattern expanded in a sum of quasi-eigenmodes of an equivalent open waveguide, which is excited by charge "image" fields induced on the iris edges. Comparisons with GdfidL time-domain multi-cell 3D simulations demonstrate a good accuracy of the model. Transverse wakes are computed numerically.

1 INTRODUCTION

Planar structures are of growing potential for application in linear colliders based on mm-wave structures [1]. Along with current projects based on state-of-the-art circular accelerating structures, planar accelerators may be the next evolutionary step in the development of accelerator technology of multi-TeV linear colliders and compact accelerators. It would be based on modern microfabrication technologies [2] that have already been significantly advanced [3,4,5] towards mass-production of planar accelerating structures in the future.

Similar to conventional structures, short-range wakefields can be a potential source of instabilities, excessive bunch energy loss and phase-space distortions. However, unlike circular structures the short-range wakefields in planar structures are not yet studied comprehensively. Earlier we introduced extended models that allow describing the wakefields in the high-frequency domain [6]. The monopole short-range fields induced by a point charge in both periodic and single-cell, circular and rectangular structures were characterized analytically on the solid ground of Green-function and "image" field methods, diffraction and excitation theories of open cavities and waveguides [6,7,8]. Another semi-analytical approach employed in parallel [7] was based on matched field technique.

In this paper, wakefields induced by a Gaussian bunch are considered for a periodic planar structure (analytically) and corresponding for a multi-cell structure (numerically).

2 ANALYTICAL FORMULATION

Convenient form for practical calculation of bunch loss-factor per unit length k_{qL} in an arbitrary non-tapered slow-wave guide can be represented as follows:

$$k_{qL} = \sum_{s=0}^{s=s_1} \frac{\omega_s}{4} \frac{r_s(z, \bar{\rho}_\perp) |\tilde{\Phi}_s|^2}{Q_s |1 - v_{grs}/v|} + \frac{1}{\pi q^2} \int_{\omega_2}^{\omega_\infty} \tilde{\eta}^2 r_\parallel(\omega, \bar{\rho}_\perp) d\omega, \quad (1)$$

where v is the bunch velocity, $\bar{\rho}_\perp$ is the bunch transverse displacement, ω_s are the modal synchronous frequencies at $v = v_{phs} = \omega_s / h'_s$, v_{grs} is the modal group velocity at this point of synchronism, $r_s(z, r_\perp) = E_{zs}^0(z, r_\perp)^2 / |dP_s/dz|$ is the longitudinal modal shunt impedance per unit length, ω_2 is the next modal frequency after ω_s at $s = s_1$, $\tilde{\eta} = \tilde{\eta}(\omega)$ is the Fourier-transform of the longitudinal space charge linear density $\eta(z)$, $\tilde{\Phi}_s = q^{-1} \int dz' \eta(z') \exp(-i\tilde{h}_s z')$ is the bunch modal formfactor, $\tilde{h}_s = h'_s - ih''_s / (v/v_{grs} - 1)$ is the complex dynamical wavenumber, $h''_s = \omega_s / 2Q_s v_{grs}$ is the modal attenuation constant, and $r_\parallel(\omega, \bar{\rho}_\perp)$ is the real part of longitudinal impedance per unit length at higher frequencies $\omega \geq \omega_2$.

For a Gaussian bunch with rms length σ we have in (1):

$$\tilde{\Phi}_s = \exp(-\tilde{h}_s \sigma^2 / 2), \quad \tilde{\eta}(\omega) = q \exp(-(\omega \sigma / v)^2 / 2). \quad (2)$$

The expression (1) consists of modal term, which describes usually low-frequency wakes having discrete spectrum, and short-range term written as integrated quasi-continuous wake impedance. The first (resonant) term now takes into account the group velocity effect correctly (see [9,10]). Note, HOM group velocity grows in (1) with frequency: $\max |v_{grs}| \xrightarrow{\omega \rightarrow \infty} c$, keeping $(r_s/Q_s) / |1 - v_{grs}/v|$ a finite value [11].

The smoothed wake resistance r_\parallel is defined by spectral density of the point charge losses $dU/d\omega$. For the planar structure with period Λ it was found with systematic approach and diffraction model [7]:

$$r_\parallel(\omega, 0) = \frac{\pi}{\Lambda q^2} \frac{dU}{d\omega} = \frac{Z_0 B}{4\pi^2 \Lambda} \sum_{s=1,2} \alpha_s C_s, \quad (3)$$

where $1 \ll (kb)^2 \ll (\beta\gamma)^2$, $k = \omega/c$, $\beta = \sqrt{1 - \gamma^{-2}}$,

$$Z_0 = 120\pi \text{ Ohms}, \quad B = A + (1 + A^2) \arctg A - \pi A^2 / 2,$$

$$\alpha_{1,2} = \frac{2\pi^2}{\beta_\eta^2} \left\{ \frac{m_{1,2}^2 (M_x / \beta_\eta + 1)}{[(M_x / \beta_\eta + 1)^2 + 1]^2} + \frac{n_{1,2}^2 (M_y / \beta_\eta + 1)}{[(M_y / \beta_\eta + 1)^2 + 1]^2} \right\},$$

$$\frac{C_1}{C_2} = \frac{-A + (1 - A^2) \arctg A + \pi / 2}{3A - (3 + A^2) \arctg A^{-1} + \pi / 2}, \quad C_1 + C_2 = 1, \quad m_{1,2} = (2, 1);$$

$$n_{1,2} = (1, 2); \quad \beta_\eta = 0.824, \quad M_{x,y} = \sqrt{8\pi N_{x,y}},$$

$N_{x,y} = \omega(d, b)^2 / 2\pi c(\Lambda - t)$ are the Fresnel numbers, t is the iris thickness, $2d$ is the horizontal dimension of the aperture (including side openings), $A = a/b$ is the aspect ratio, $2b$ is the vertical gap, and $2a$ is the horizontal dimension of each cavity. For high frequencies

$M_{s,v} \gg \beta_\eta$ of short-range wakefields the wake resistance (3) varies as $\sim \omega^{-3/2}$. The practical option for the transition frequency ω_2 is based on the validity of Fresnel diffraction approximation ($b\omega_2/c \geq 3$, see [8]). An additional criterion is smoothness of the function $k_{qL}(\sigma)$ (especially in the vicinity of the transition $\sigma \approx c/\omega_2$).

Note, cavity depth (i.e. maximum vertical dimension) is meaningful only for the trapped (discrete low-frequency) part of the full longitudinal coupling impedance (through the ω_s , r_s/Q_s and v_{grs}), and does not have significant effect on the smoothed, short-range wake impedance (3) which is dominated by fields induced and diffracted only in the vicinity of the aperture [6]. A similar situation takes place with the dimension d .

3 NUMERICAL MODEL

The key problem in time-domain numerical simulation of quasi-periodic structures is the RAM (and CPU time) limitations. To make correct comparison between periodical and multi-cell models the minimum (or critical) number of cells to be included in simulations. It is defined by the dominant Fresnel number (see [12 and 13]):

$$N_{per} > N_{cr} = 2N_y. \quad (4)$$

For a Gaussian bunch in the time domain this condition results in the same form as known for circular structures:

$$N_{cr} \approx b^2 / \Lambda \sigma. \quad (5)$$

Taking into account of Eq. (5), the total number of mesh elements scales as $\sim \sigma^{-4}$ as the bunch length decreases. An alternative numerical approach is eigenmode summation (see the first term in (1)) with modal characteristics calculated with 3D codes or matched field 3D models. However, to date there are still no eigenmode 3D finite-element solvers capable of computing the characteristics only for the *synchronous* modes (\sim thousand of them for short bunches) using a single cell only, each mode having proper phase advance depending on its frequency. Note, such a code would have more affordable scaling factor $\sim \sigma^{-3}$ (similar to eigenmode problem for a single cell with periodical boundaries). The matched field model has, instead, a different problem: "missing zeros" and instability in solving the transcendent equation with matrix of big ranks [7] to find "proper" roots for HOMs in 3D structure. Nevertheless, the matched field model is very useful for the first few modes in (1) that make the computation of short-range wakefields very effective and completely analytical.

Time-domain simulations are performed here to verify analytical formulation (1-3) for a Gaussian, ultrarelativistic bunch of variable length using the GdfidL code with indirect algorithm [14]. The planar geometry considered here corresponds to the 37-cell 30 GHz $2\pi/3$ section that was manufactured [5] and successfully tested [15]. A few cells of the model are depicted in Fig. 1.

Parameters used in calculations are the following: $b=1.8\text{mm}$, $\Lambda=3.332\text{mm}$, $a=3.344\text{mm}$, $t=0.7\text{mm}$. We use here reduced side openings (horizontal dimension $d=5.016\text{mm}$) compared to the prototype [5,15] ($d=21\text{mm}$) to reduce memory requirements. According to theory [7] it should not affect HOM losses significantly. Numerically we have only 0.08% difference in $\sigma=62.5\mu\text{m}$ bunch loss-factor (and 0.04%, 0.09% for transverse factors) while d was reduced further by 27%.

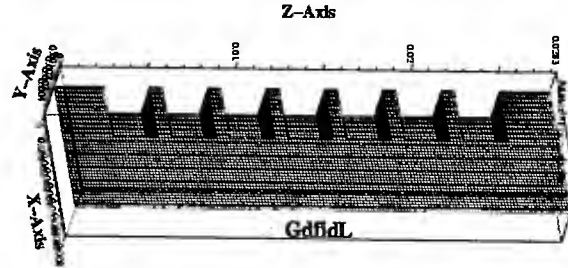


Figure 1: One-quarter of structure fragment model.

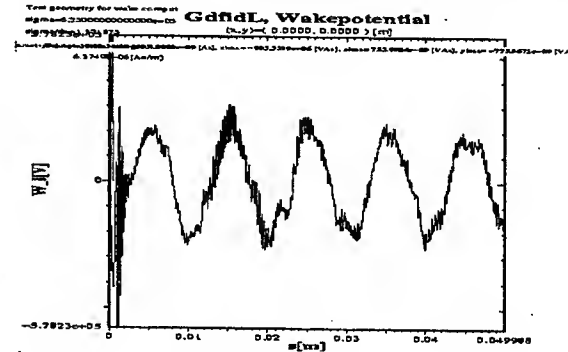


Figure 2: Longitudinal wake-function at $\sigma = 62.5\mu\text{m}$.

For long bunches ($\sigma > 200\mu\text{m}$), with a system RAM of $< 800\text{MB}$ it is possible to simulate the wakefields along the whole length (37 cells). Unfortunately, limited memory implies reduced number of cells for shorter bunches. Figs. 2 and 3 demonstrate the wake potential plots in a 7-cell structure for a short bunch. The transverse wake-potentials are about the same for X and Y directions (1.15 and -1.17 V/nC-mm per cell for $\sigma = 62.5\mu\text{m}$), in agreement with the initial design and the "symmetric" transverse force concept [15]. Loss-factors calculated analytically and numerically are plotted versus bunch length in Fig. 4. The upper frequency in (1) is assumed $\omega_\infty \approx 3c/\sigma$, $s_1=0$, and the transition frequency chosen, $\omega_2=2\pi \cdot 42\text{ GHz}$ is one that immediately follows the fundamental one, $\omega_{s1}=2\pi \cdot 30\text{ GHz}$. Direct integration is performed in (1) instead of analytical approximation with Gamma-function (see [16]), which introduces too high an inaccuracy in the model compared to the small difference between the original formulation (1) and time domain simulations (see Figs. 4). Growing discrepancy (Fig. 5) for bunch lengths $< 65\mu\text{m}$ indicates too few cells

($N_{\text{cells}} < N_{\text{cr}}$) as well as mesh lines per bunch length (σ/dz in Fig. 4).

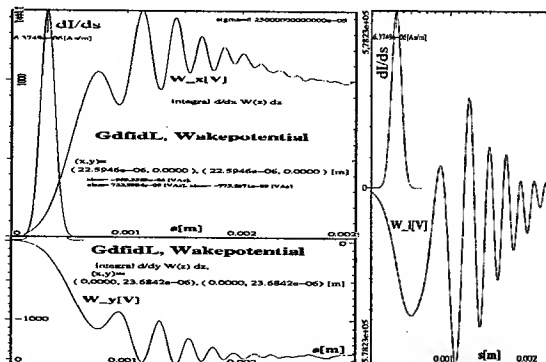


Figure 3: Short-range transverse (on the left) and longitudinal (on the right) wake-functions in 7-cell structure for $\sigma = 63 \mu\text{m}$ and $q = 4\text{nC}$.

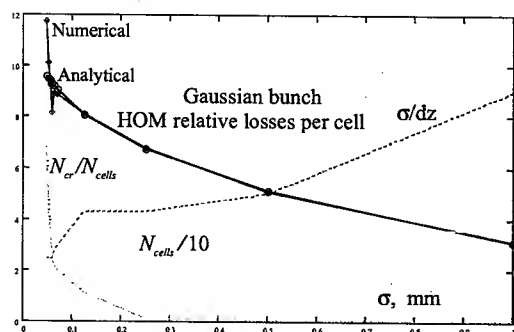


Figure 4: Monopole HOM energy losses related to fundamental mode loss per cell vs rms bunch length σ .

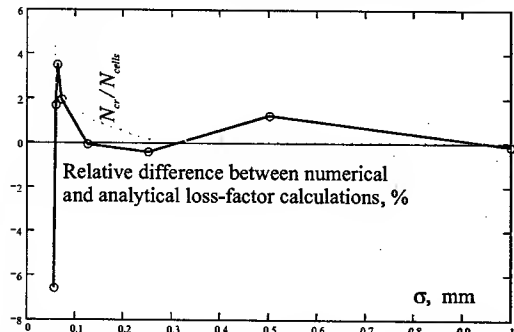


Figure 5: Relative difference [%] between numerical and analytical calculation of total energy losses per cell.

4 CONCLUSION

Comparison of analytical and time-domain modeling demonstrates very good agreement of bunch loss-factor calculations (\sim a few percentages for ~ 200 fs bunch) and gives additional confirmation of the extended diffraction model.

Computations based on the approach of Eq. 1 can be completely analytical for conventional (e.g., cylindrical and planar) structures that makes it extremely fast and accurate. Practical benefits of this method can be

extended to the asymmetric wakefields and some other types of structures.

5 ACKNOWLEDGMENTS

The authors are very appreciative to Drs. Warner Brunes and Manfred Filtz for very helpful comments.

6 REFERENCES

- [1] D. Yu, S. Ben-Menahem, P. Wilson, R. Miller, R. Ruth, A. Nassiri, in AIP Conf. Proc., AIP 335, Edited by P. Schoessow, (1994) 800.
- [2] P. Chou et al., SLAC-PUB-7339, November, 1996
- [3] H. Henke, Proc. of the 1995 Particle Accelerator Conference, p. 1750, Dallas, Texas, May 1995.
- [4] H. Henke, in Proc. of the 7th Workshop on Advanced Accelerator Concepts, Lake Tahoe, October 12-18, (1996) 485.
- [5] D. Yu, H. Henke, H.H. Braun, S. Döbert, W. Wuensch, in Proc. of the 2001 Part. Acc. Conf., Chicago, (2001) 3858
- [6] A.V. Smirnov, Preliminary study of wake-fields in non-circular structures, a talk given on BIG seminar, SLAC, 04/30/00.
- [7] A.V. Smirnov, D. Yu, in Proc. of the 2001 Part. Acc. Conf., Chicago, (2001) 2994
- [8] L.A. Vainshtein, Open Resonators and Open Waveguides, Izdatelstvo "Sovetskoe Radio", Moscow (1966).
- [9] A. V. Smirnov, Ph. D. Dissertation, Moscow, Moscow Engineering Physics Institute, MEPhI (1985).
- [10] A.V. Smirnov, D. Yu, in Proc. of the 2001 Part. Acc. Conf., Chicago, (2001) 2994
- [11] K. Bane, G.V. Stupakov, SLAC-PUB-8559 (2000)
- [12] S. A. Heifets, S. A. Kheifets, SLAC-PUB-4625 (1988).
- [13] A.V. Smirnov, in Proc. of Particle Accelerator Conference, (PAC'95), Dallas, Texas, (1999) 3615
- [14] W. Bruns, in Proc. of Particle Accelerator Conf. (PAC'97), Vancouver, B.C., Canada 12-16 May 1997, p. 2651.
- [15] R. Merte, H. Henke, M. Peikert, D. Yu, in Proc. of 1999 Part. Acc. Conf., New York, (1999) 815
- [16] K. Bane, M. Sands. SLAC-PUB-4441, Nov. 1987

SIMULATION OF BEAM-ELECTRON CLOUD INTERACTIONS IN CIRCULAR ACCELERATORS USING PLASMA MODELS

A.Z. Ghalam, T. Katsouleas, USC, Los Angeles, USA
C. Huang, V. Decyk, W. B. Mori, UCLA, Los Angeles, USA

Abstract

In this paper we study the effect of low-density electron clouds on intense positively charged beams in circular accelerators. We apply one of the simulation tools we have been developing for the study of plasma-based accelerators to the problem of wake production and beam propagation in electron clouds. Particularly, we apply it to the electron cloud wakefields in the SPS proton synchrotron at CERN. We explore physics of beam-electron cloud interactions, particularly we present results on electron cloud effects on the long term beam dynamics. We present simulation results on the effects of bending magnets on the beam centroid oscillation, spot size and compare them to the case where bending magnets are not present.

INTRODUCTION

Electron clouds have been shown to be associated with limitations in particle accelerators performance in several of the world's largest circular proton and positron machines [1]. Electrons accumulate in the vacuum chamber where a positively charged bunched particle beam propagates because of a multipacting process which involves primary electron generation (e.g., from residual gas ionization) and their multiplication through secondary emission at the wall [2]. The detailed physics of electron cloud build up process has been extensively discussed elsewhere [1,2,3]. The presence of an electron cloud inside the beam chamber can deteriorate the vacuum [4], causing interference on the electrodes of beam pick up monitors and make the beam unstable via bunch-to-bunch or head-tail coupling [5,6].

Although a number of beam-cloud interaction models that can satisfactorily explain many of the observations have been developed [7], the exact dynamics that leads to beam degradation (e.g., emittance growth, beam loss) is still under study. In particular, previous models have been limited in that they treat the cloud in an impulse approximation [8] (giving a single kick per turn) and they have not included conducting boundaries (and hence image forces of the cloud and beam charge) into the treatment of the beam dynamics.

In this paper we apply techniques from plasma wake field accelerator models to the study of the non-neutral plasma-beam interaction. We describe analytic and numerical models for the interaction between a positively charged beam and an electron cloud in a circular accelerator. Our model takes into account the effect of cloud image charges from the conducting beam pipe on the beam dynamics for the first time.

In second section we briefly describe the simulation model (QuickPIC). More detail can be found in [11]. In the third section we discuss different forces acting on the beam from the electron cloud and their effects on the beam dynamics. In the fourth section we study the effects of bending magnets on the cloud dynamics and its consequent impacts on the beam stability. Throughout the entire paper we adapt our physical parameters to the CERN-SPS parameters. These parameters can be found in Table 1.

BRIEF DESCRIPTION OF THE SIMULATION MODEL (QUICKPIC)

QuickPIC is a 3-D PIC code using a quasi-static or frozen field approximation [9,10]. This approximation is specifically useful for studying wakes. It requires that the beam does not evolve significantly on the time scale that it takes the plasma to pass through it. The quasi-static approximation assumes that the wakes are functions of $z-ct$ only and leads to equations for the wake potentials φ and $\Psi \equiv \varphi - A_{\parallel}$ that involve only solving 2-D Poisson equations. The Poisson equations are solved on a 2-D slab of electron cloud with conducting boundary conditions. The wakes are stored and used to update the plasma in the slab and the slab is then pushed back a small step through the beam. After transiting the beam, the stored values of ψ are used to find the force on the beam (treated as a 3-D PIC model) and it is pushed through a large step (of the order $\beta/30$). As mentioned, the code is used for modeling plasma wakefield accelerators. In order to enable QuickPIC to simulate a bunch in a circular accelerator, some extra features needed to be added to correctly model the bunch evolution. In particular, betatron and synchrotron oscillations of the beam particles are introduced. These oscillations are due to the external fields of the magnets and RF power in the accelerator. Under the effect of these forces, individual particles (and the bunch as a whole, if off-centered) execute oscillations in all 3 spatial coordinates. All different aspects of the code have been fully discussed in [11].

FORCES FROM THE ELECTRON CLOUD ACTING ON THE BEAM

There are three different forces from the cloud acting on the beam. First, there is a direct force from the uniform cloud to the beam.

When a positively charged bunch passes through an electron cloud it sucks in the cloud towards its axis, creating cloud compression near the axis of the beam. The pinched cloud exerts a force to an unperturbed beam and focuses the beam toward its own axis. The

situation becomes different when the beam is slightly tilted from its axis. In this case, the pinched cloud exerts a force on the tail of the beam so as to pull it back to the un-tilted axis.

When we have conducting boundary conditions, there is yet another restoring force acting on the displaced beam. The pinched cloud on the axis of the beam produces its own image charges of like sign of the beam in a conducting pipe and hence in a direction as to restore the beam to the pipe axis.

Expressions for these forces are given in [11].

Fig.1 shows a beam off-centered D mm from the pipe axis and slightly tilted (α) from the beam axis. Looking at the forces exerted on a particle at the tail of the beam, first, there is a force from the uniform cloud density, this force contributes to the coherent betatron tune shift. Second, there is a force due to the image charges of the pinched cloud ($F_{cl,y}$), exerted on the tail of the beam pulling it toward the pipe axis. The last force exerted to the tail by electron cloud is a force due to direct pinched cloud ($F_{image,y}$) pulling it toward the beam axis. Based on this simple observation, we can say for any displacement of the beam (D) there is always an equilibrium tilt angle at which these two forces cancel each other at the tail of the beam. Therefore the long term propagation of the beam can be pictured as follows: No matter how the beam is initially perturbed, it will oscillate around the axis of the pipe with the tail slightly tilted toward the center line with respect to the head toward the axis.

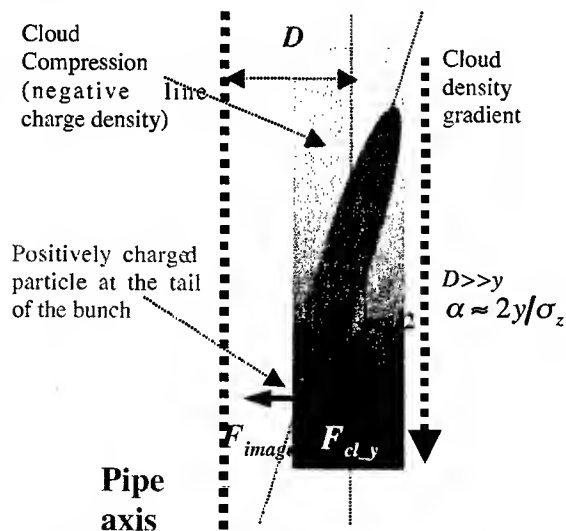


Fig.1. A cartoon showing a tilted beam and the electric field on the tail of the beam due to cloud compression on the axis

To verify the above hypothesis, two different simulations are performed by QuickPIC. In the first simulation, the beam is off-centered by 1mm from the vertical axis as an initial perturbation to the beam while in the second run, the beam is tilted but not displaced in the vertical plane. Simulation results are shown in Fig.2.

The figure shows two snapshots of the beam in each of these two runs. Fig.2-a and Fig.2-b show the initial beam, displaced and tilted from the pipe axis respectively and Fig.2-c and Fig.2-d are the corresponding snap shots of the beam after 18 and 35 turns of beam propagation over CERN-SPS ring. It is seen that the beam performs betatron oscillation around the pipe with its tail slightly tilted from its unperturbed axis.

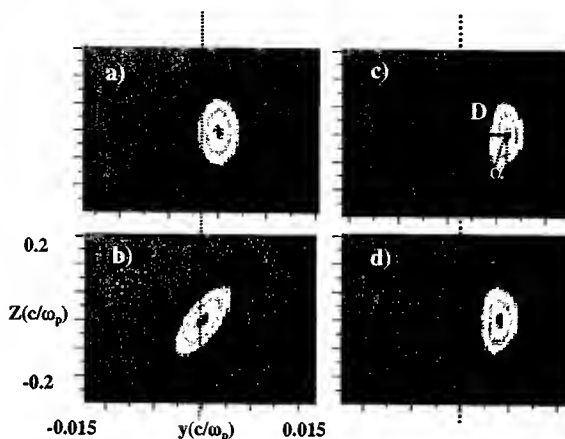


Fig.2. a) and b) initially displaced (1mm) and tilted beam respectively. c) A snap shot of the initially displaced beam after 0.4ms (18 turns of SPS ring). d) A snap shot of the initially tilted beam after 0.6ms(36 turns of CERN-SPS ring)

A lower bound on the equilibrium tilt angle can be found by writing the total force by cloud on the tail and setting it to zero [11].

A detailed analysis of the beam dynamics and machine tune shift due to the electron cloud is discussed in [13].

EFFECTS OF BENDING MAGNETS ON BEAM INSTABILITY

In this section we study the effects of magnet systems on cloud dynamics and their consequent effects on the beam dynamics. We mentioned earlier that the cloud is sucked in toward the axis as the positive bunch passes. The situation is different when there is a magnetic field in the vertical direction. Electrons, rushing toward the axis feel a strong Lorentz force and perform cyclotron motion in horizontal plane with a small Larmor radius. This cyclotron motion prevents them from being sucked in toward the axis and lowers the density of line charge on the pipe axis. Fig.3 shows QuickPIC simulations for the cloud density in horizontal plane. Fig.3-a shows the density when there is a magnetic field of 0.117T(CERN-SPS ring specification) in vertical direction and Fig.3-b is the cloud density when there is no magnetic field. As can be seen there is a high concentration of cloud density close to the axis in Fig.3-b while that of Fig.3-a is much shallower.

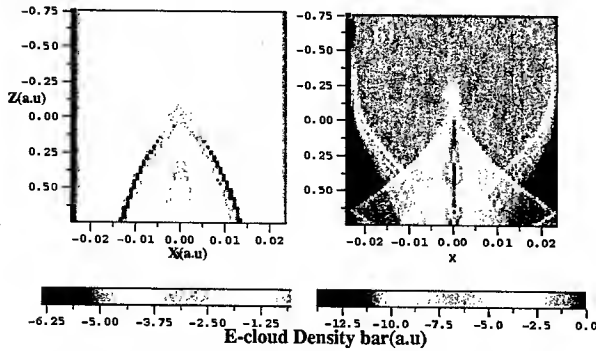


Figure 3: a) Cloud density in horizontal plane with $B=0.117T$. b) Cloud density in horizontal plane without magnetic field.

In order to study the impacts of the bending magnets on the beam dynamics, we look at the long-term propagation of the beam in CERN-SPS ring. Fig.4 shows the horizontal spot size of the beam for both cases of magnetic field on (Fig.4-a) and off (Fig.4-b). We perform the simulations over 125 turns of the ring. As can be seen there is a significant spot size growth in the no magnetic field case while there is almost no growth observed in the case with the bending magnets. We note that in the actual ring, the magnetic field is present in only 2/3 of the ring.

The fact that the spot size growth is significantly suppressed, shows that bending magnets have a great stabilizing effect.

Further work is directed to modelling beam dynamics in this case of varying fields and cloud densities.

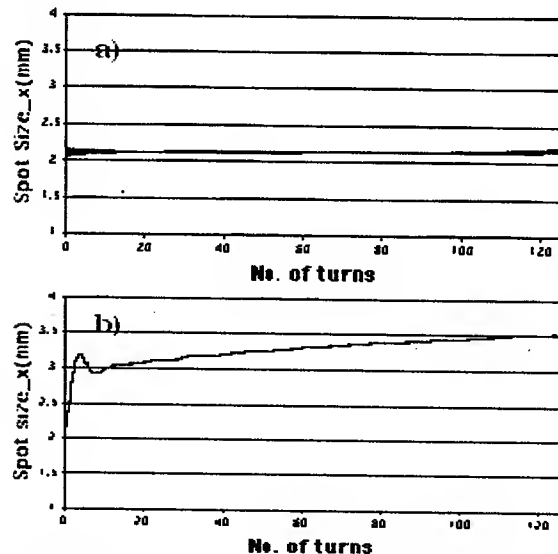


Figure 4: a) Horizontal spot size with $B=0.117T$. b) Horizontal spot size without magnetic field.

ACKNOWLEDGEMENT

This work is supported by:
USDOE #DE-FG03-93ER40745, NSF-PHYS-00787815, DE-FC02-01ER41192, DE-FG03-92ER40727, DE-FC02-01ER41179, PHY-0078508

Table 1: Physical Parameters used in the Simulations

Momentum Spread	2.48E-3
Beam Momentum(Gev/c)	26
Circumference(km)	6.9
Horizontal Betatron Tune	26.41
Vertical Betatron Tune	26.41
Synchrotron Tune	0.005
Electron Cloud Density(cm^{-3})	10^6 - 10^7
Horizontal Spot Size(mm)	2
Vertical Spot Size (mm)	2
Bunch Length (cm)	30
Horizontal Box Size (mm)	80
Vertical Box Size (mm)	40
Bunch Population	10^{11}
Horizontal Emittance(μm)	0.1
Vertical Emittance(μm)	0.1

REFERENCES

- [1] H. Fukuma, K. Cornelis, F.-J. Decker, R. Macek, E. Metral, W. Fischer in *Proceedings of ECLLOUD'02*, CERN, Geneva 15-18 April 2002, edited by G. Rumolo and F. Zimmermann, Yellow Report CERN-2002-001
- [2] G. Rumolo, F. Ruggiero and F. Zimmermann, Phys. Rev. ST Accel. Beams, **4**, 012801 (2001).
- [3] M. T. F. Pivi and M. A. Furman, Phys. Rev. ST Accel. Beams **6**, 034201(2003)
- [4] A. Rossi, G. Rumolo, and F. Zimmermann, in *Proceedings of ECLLOUD'02*, CERN, Geneva 15-18 April 2002, edited by G. Rumolo and F. Zimmermann, Yellow Report CERN-2002-001
- [5] G. Arduini, K. Cornelis, W. Hoefle, G. Rumolo, and F. Zimmermann, in *Proceedings*
- [6] K. Oide, "Observation and Cure of the Electron Cloud Effect at the KEKB Low Energy Ring", Chamonix XI, CERN SL-2001-003 (DI)
- [7] K. Ohmi and F. Zimmermann, Phys. Rev. Lett. **85**, 3821 (2000)
- [8] G. Rumolo and F. Zimmermann, "Electron Cloud Simulations: Beam Instability and Wakefields" in *Proceedings of ECLLOUD'02*, CERN, Geneva 15-18 April 2002, edited by G. Rumolo and F. Zimmermann, Yellow Report CERN-2002-001
- [9] C. Huang *et.al*, *proceedings*, 18th Annual Review of Progress in Computational Electromagnetics, p 557(2002)
- [10] D.H. Whittum, Phys. Plasmas, **4**, 1154(1997)
- [11] G. Rumolo, A.Z. Ghalam *et.al.*, "Electron Cloud Effects on Beam Dynamics evolution in a Circular Accelerator" Submitted to PR-STAB.

BOOSTER'S COUPLED BUNCH DAMPER UPGRADE

W. A. Pellico*, D. W. Wildman,
FNAL^o, Batavia, IL 60510, USA

Abstract

A new narrowband active damping system for longitudinal coupled bunch (CB) modes in the Fermilab Booster has recently been installed and tested. In the past, the Booster active damper system consisted of four independent front-ends. The summed output was distributed to the 18, $h=84$ RF accelerating cavities via the RF fan-out system. There were several problems using the normal fan-out system to deliver the longitudinal feedback RF. The high power RF amplifiers normally operate from 37 MHz to 53 MHz whereas the dampers operate around 83 MHz. Daily variations in the tuning of the RF stations created tuning problems for the longitudinal damper system. The solution was to build a dedicated narrowband, $Q \approx 10$, 83 MHz cavity powered with a new 3.5 kW solid-state amplifier. The cavity was installed in June 2002 and testing of the amplifier and damper front-end began in August 2002.

A significant improvement has been made in both operational stability and high intensity beam damping. At present there are five CB modes being damped and a sixth mode module is being built. The new damper hardware is described and data showing the suppression of the coupled-bunch motion at high intensity is presented.

HISTORY

For almost three decades, longitudinal coupled-bunch motion in the Fermilab Booster has been a limiting factor in determining the extracted beam's longitudinal emittance. Various methods of damping the coupled-bunch oscillations have been developed to keep pace with the steadily increasing proton intensities in the machine. The Booster coupled-bunch oscillations were first observed at a proton intensity of 1.2×10^{12} ppp. The two dominant modes near $m=16$ and $m=36$ (for $h=84$, mode 34, 35 and 36 is the same as mode 50, 49 and 48) were correctly identified in 1977 [1] but were not associated with any particular RF cavity mode or other resonator in the machine. The solution at that time was to create a bunch by bunch spread in synchrotron periods by operating one of the 18 $h=84$ RF cavities at a harmonic number of $h=83$. This increased Landau damping, successfully reducing the coupled bunch motion.

By 1993 the $m=16$ and $m=36$ modes were identified with three specific resonances in the RF cavities [2,3]. The modes near $m=16$ correspond to the 3rd and 5th "harmonics" of the Booster cavity at 165 MHz and 217 MHz. Both modes move in frequency as the bias on the

cavity ferrite tuners changes during acceleration. Modes near $m=36$ correspond to a non-tuning (<30 kHz shift) RF cavity mode near 83 MHz. The $m=36$ mode frequency, primarily determined by the physical length of the RF cavity drift tube, has both acceleration gap voltages oscillating in phase. Once the offending modes were identified, two passive dampers were installed in each Booster RF cavity. These passive dampers eliminated the $m=16$ line and decreased the $m=36$ line by about an order of magnitude. This resulted in stable bunch motion and a factor of three reduction in the longitudinal emittance of the extracted beam at an intensity of 1.9×10^{12} ppp. Further reduction in the $m=36$ mode line was accomplished by reducing the RF bucket area during acceleration to increase Landau damping [4] and by using a narrowband active damper at mode $m=35$ to drive a wideband kicker [5].

The narrowband damper approach was later extended to include modes 1, 34, 35, and 36 [6]. In this instance, the low level damping signal was applied to the beam through the 18, $h=84$ RF cavities. Using the 18 RF cavities as kickers had the disadvantage that the RF power amplifiers when driven around 83 MHz were being operated well outside their normal operating frequency range of 30 to 53 MHz. A more serious drawback of this method was that the RF fanout is optimized to deliver properly phased RF signals at $h=84$, not at 83 MHz. The amplitude and phase of the damping kick delivered to an individual proton bunch relied on the net vector sum of all 18 cavities at 83 MHz. This system required frequent manual tuning of the low level damping signal and proved to be difficult to operate on a daily basis. For example, if one of the 18 RF cavities failed or had a reduced output, the amplitude and phase of the damping kick would no longer be correct and both the gain and phase of the low level damping drive signal would have to be re-adjusted. The gain of the active system was adequate when Booster was below 4×10^{12} protons per pulse, the present Booster intensities are now around 5×10^{12} with higher intensities planned.

To alleviate these problems, a dedicated longitudinal kicker cavity was installed in the Booster to damp the coupled-bunch modes near $m=36$. The individual RF cavities have a range of resonances between 82.0 MHz and 82.8 MHz with an average value of 82.45 MHz. The Q of these cavity modes was initially ≈ 3300 but was reduced to ≈ 170 by the addition of the passive dampers. To reduce the necessary drive power but still maintain a conservative design, the new CB damper cavity has a center frequency of 82.6 MHz and a loaded $Q = 11$.

* Email: pellico@fnal.gov

^o Operated by the URA, under contract No. DE-AC02-76CH03000 with the U.S. DOE.

DAMPER FRONT END ELECTRONICS

The previous CB damper system used a direct digital synthesizer (D.D.S) that could be clocked up to 800MHz. This allowed a clock that was eight times the Booster VCO frequency (422 MHz.) to be used [4]. The D.D.S's provided quadrature outputs to be mixed with the beam signal band-pass filtered at 83MHz. Each mode module did it's own front end processing. This required each mode module to do it's own frequency transposition around 83 MHz. The new CB design has a single module (CB front-end module) that downconverts the beam signal to baseband then splits the output eight ways (we use only 5 at present.) With the common baseband error signal (approximately 21 MHz) the individual mode modules can use a D.D.S unit clocked at only twice the Booster VCO to do the necessary frequency transposition. The mode module outputs are then summed, upconverted, filtered and pre-amplified in the front-end module. The correction signal is then applied to a 3.5 KW amplifier (see next section.) The layout of the new system is shown in Fig 1. The mode modules are similar to the old design with superheterodyne and single side-band mixing allowing for detection and phase correction of the CB mode error. The modules all have internal wide dynamic range phase shifters.

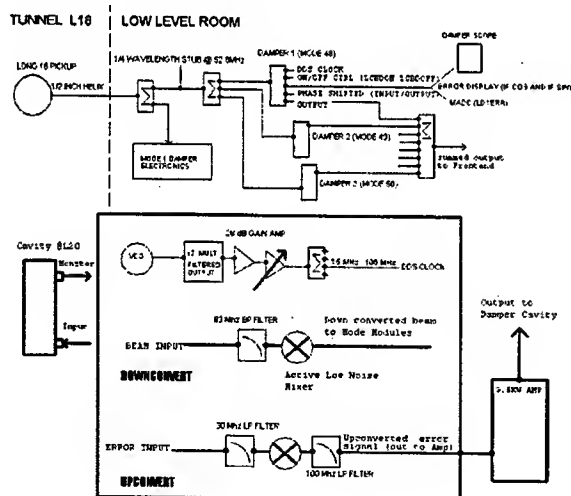


Figure 1. CB Damper Layout

DAMPING CAVITY

Figure 2 is a drawing of the new damping cavity. It is a single gap, quarter wave, coaxial aluminum resonator with an inner conductor diameter of 4.5" and an outer conductor diameter of 10". The center frequency is 82.6 MHz. The loaded Q value of 11 is obtained by over-coupling the power amplifier drive loop to the cavity. A

4" diameter, 4" long ceramic gap was chosen so that the cavity would be operated below the calculated multipacting threshold of 4.3 kV. The ceramic gap is welded to a 4" diameter stainless steel beam pipe that slides through the center conductor of the cavity. The electrical connection between the aluminum cavity and the stainless beam pipe is made with two strips of BeCu finger stock.

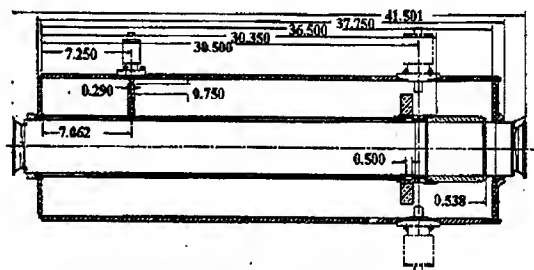


Figure 2. 83 MHz Damping Cavity

To reduce the impedances of higher order modes (HOM's) in the damping cavity, a single 8" OD X 5" ID X 1" thick ferrite core (Stackpole Ceramag 2285) is inserted around the cavity's inner conductor, 2.5" from the accelerating gap. The 2285 core has a Curie temperature of 510°C, $\mu' = 12.5$ and a $Q \approx 150$ at 83 MHz which drops sharply above 120 MHz. The unloaded cavity Q is 268 and the shunt impedance is 15.9 k Ω with the input coupling loop disconnected from the drive-line. The HOM frequencies and loaded Q values are: 233MHz (Q=55.5), 251.3 MHz (Q=28), and 521.2 MHz (Q= 70.8).

The damper cavity is driven by an Amplifier Research 3500A100 solid-state amplifier (maximum output power greater than 3500 watts at 83 MHz.) The RF power is transmitted to the cavity through 74.5 m of 7/8" Helix coaxial cable with ≈ 1 dB attenuation. A maximum cavity peak gap voltage of 3670 volts was measured using a capacitively coupled (1000:1) gap monitor. This value is in good agreement with the measured forward and reflected power into the cavity from a dual directional coupler inserted in the 7/8" coaxial line.

RESULTS

The new damping cavity was installed in June 2002 and the existing CB mode 34,35 and 36 signals were switched over from the Booster fanout to the new amplifier and cavity. Mode 33 and 37 modules were built and tested several months later using the new front end module. The beam measurements shown in this paper are with the new electronics, cavity and 3.5KW amplifier damping CB modes 34,35 and 36. A phase signal generated by mixing the signal from a wall current monitor in the MI-8 line (MI-8 line is the extraction line from Booster to Main Injector/MinibooNE) with the Booster RF is used as a

measure of the Booster's beam quality. Figure 3 is a display of the extracted beam's phase measurement with dampers off and on.

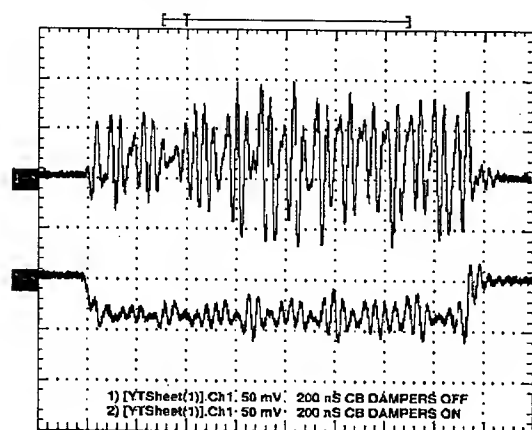


Figure 3. Scope Display of Phase 1)CB Off 2)CB

With dampers off, beam loss in the high dispersion regions of the MI-8 line will trip the Mini-BooNE^{*} beam permit. Figure 4 shows the loss pattern on two downstream loss monitors with the dampers off/on. Booster CB dampers also play a critical role in the proton intensities used in colliding beams.

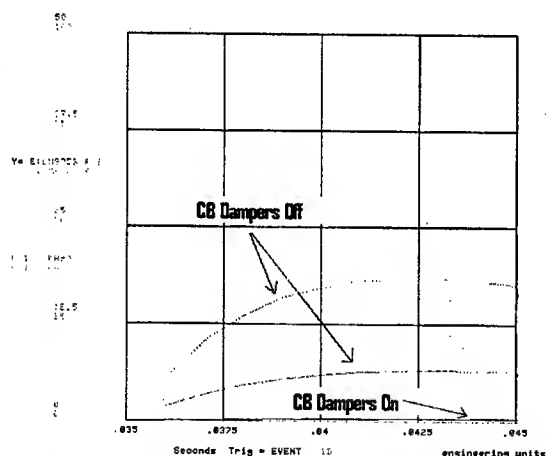


Figure 4. Loss Monitors in MI-8 Line: CB OFF/ON

The Main Injector proton coalescing efficiency/intensity is greatly improved (intensity dependent) when the dampers are on. The large dipole oscillations associated with bunch to bunch phase oscillations create an effective longitudinal emittance blowup. This problem also

impacts performance in the Main Injector cycle used for making antiprotons.

CONCLUSION

Higher Booster proton intensities have required CB damper upgrades. The success of this CB damper system allows Booster to meet current proton demands. However, the requested proton intensity will be required to increase. The Booster CB system will require additional damping power and additional mode modules. The new modules are being built, as is a new damper cavity. The additional cavity will be used to damp mode 16. The plan is to install the new cavity sometime this summer.

REFERENCES

- [1]C.M. Ankenbrandt, J.E.Griffin, R.P. Johnson, J. Lackey and K. Meisner, "Longitudinal Motion of the Beam in the Fermilab Booster," IEEE Trans. Nucl. Sci. NS-24 1449 (1977).
- [2]D. Wildman and K. Harkay, "HOM RF Cavity Dampers for Suppressing Coupled Bunch Instabilities in the Fermilab Booster," 1993 PAC Proc. Washington, DC., p.3528A.
- [3]K. Cecelia Harkay "A Study of longitudinal Instabilities and Emittance Growth in the Fermilab Booster Synchrotron." FERMILAB-THESIS-1993-65 (Dec 1993) 211p.
- [4]J.P. Shaw, D. McGinnis, and R. Tomlin, "Reducing the Coupled-Bunch Oscillation in the Fermilab Booster by Optimizing RF Voltage," 1993 PAC Proc. Washington, DC., p.3787
- [5]J.M. Steimel and D. McGinnis, "Damping in The Fermilab Booster," 1993 PAC Proc. Washington, DC., p. 2100
- [6]D.A. Herrup, D. McGinnis, J. Steimel, and R. Tomlin, "Analog Dampers in the Fermilab Booster," 1995 PAC Proc. Dallas, Texas, p.3010

* The MiniBooNE experiment uses 8GeV protons from Booster to create a Neutrino beam.

BEAM DYNAMICS SIMULATIONS FOR THE FERMILAB RECYCLER RING BARRIER BUCKETS

H. Kang¹, C. M. Bhat², J. P. Marriner² and J. Maclachlan²

¹ Stanford University, Stanford, CA 94305 USA*

² FNAL, Batavia, IL 60510, USA #

Abstract

The Recycler Ring (RR) is an 8 GeV pbar storage ring for future ppbar collider operations at Fermilab. By design, the beam in the Recycler is stored in three segments (hot, cold and newly transferred beam) azimuthally, using barrier buckets. Properties of the beam in the Recycler are found to be affected by stray magnetic field caused by the Main Injector acceleration ramping process. Here we present results of our measurements of the longitudinal emittance growth of the beam in the Recycler Ring due to the Main Injector ramp and the results of model simulation of this effect using a multi-particle beam dynamics simulation program (ESME).

INTRODUCTION

The purpose of the Recycler [1] at Fermilab is to increase luminosity for the Tevatron experiments by injecting low emittance high intensity antiprotons bunches in each store. The Recycler is also used as a high intensity antiproton accumulator. When the stack size of antiprotons in the Fermilab Accumulator Ring reaches about 40E10 the beam will be transferred to Recycler barrier buckets and stored and cooled in the Recycler. We plan to stack >200E10 antiprotons in the Recycler and cool them over a period of several hours before they are transferred to the Tevatron for ppbar collision. Since antiprotons are stored in the Recycler for an extended time, even a small disturbance of the beam caused by any rf noise, rf base-line shift (or slope) or any external electromagnetic field will result in emittance growth of the beam and may be of concern.

Several measurements indicate that a beam in the Recycler is influenced by stray magnetic fields mainly from magnetic ramping in the MI. The emittance of the beam increases as the beam is exposed to the time varying electromagnetic fields generated during MI ramping. Here an attempt has been made to simulate beam emittance growth. The result of the apparent effect due to the field is qualitatively reproduced by a 2-D beam simulation program (ESME) [2]. The barrier bucket system in the RR has been previously described [3].

THE CHANGE OF BEAM DYNAMICS DUE TO ASTRAY MAGNETIC FIELD

Initial beam distribution

The wide band RF system in the RR is capable of generating arbitrary waveforms with a maximum pulse height of ± 2 kV in each polarity. We use a rectangular barrier pulse of about 908 ns width.

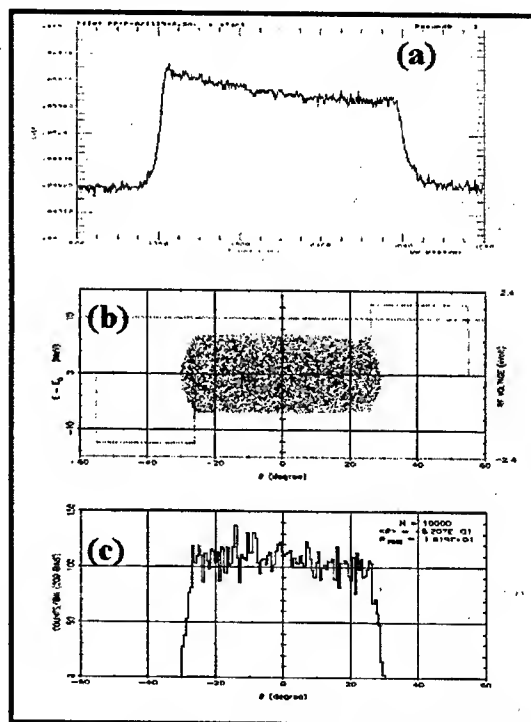


Figure 1: The initial distribution of the beam measured from (a) Wall Current Monitor (WCM) and, (b) and (c) simulation results in $(\Delta E, \Delta\theta)$ -space and its projection on θ -axis

Ideally the base-line of the middle segment of the barrier bucket should not have any residual voltage, but we observed that there is a shift of the baseline up to ~ 50 V. The existence of baseline voltage offset causes non-uniformity in the spatial distribution of the beam as shown in Fig.1(a), which is the measured beam

distribution from a Wall Current Monitor (WCM). Figs (b) and (c) show simulation results.

Beam distribution with existence of ramping in the MI

The Recycler and the MI share the same tunnel. The lattice of the both of these synchrotrons are similar at most places except with some small differences at their long straight sections. The MI is designed to accelerate protons from 8 GeV to 120 GeV at a maximum repetition rate of 40 cycles per minutes during pbar stacking and is just about 1.7 meters below the Recycler. At the time of beam transfers from the MI to the Tevatron, the MI ramps from 8 GeV to 150 GeV and the MI dipole magnets saturate for energy above 120 GeV. Since the Recycler is very close to the MI, a non-negligible quantity of time varying magnetic field resulting from the MI acceleration penetrates the relatively thin shielding of the Recycler. The growth of the longitudinal emittance is primarily due to non-adiabatic changes in the orbit length of the beam induced by MI ramping. The change in the orbit length causes a shift of the relative position of the beam with respect to the barrier pulses. The shift of the beam position generates inconsistent energy reduction and acceleration for the beam when the beam passes through each barrier pulse, and this causes an increase in the energy spread of the beam and thereby an increase in the longitudinal emittance. We expect that a large longitudinal beam emittance make an even beam distribution throughout $\Delta\theta$. The MI magnetic field also gives a small acceleration and deceleration to the beam through induction.

Fig.2 presents the beam distribution in $\Delta\theta$ measured at 4 min (Fig.2(a)) and 30 min (Fig.2(b)) in the presence of MI 120 GeV cycles with a repetition rate of about 20cycles/minutes. The Fig.2 shows wider distributions in $\Delta\theta$ than that shown in Fig. 1(a) (initial distribution). The longitudinal beam emittance corresponding to the beam distribution in Fig.2(b) is found to be $\sim 20\%$ larger than the one shown in Fig.1(a). The change in energy spread of the beam and the deviation from the initial value (25 eV-s) of the longitudinal beam emittance as a function of time is shown in Fig. 3(a) and 3(b), respectively. The growth in the longitudinal emittance and the energy spread of the beam is very rapid in the first few minutes after the beam gets injected into the RR, but the growth becomes slower as time increases.

To attempt to simulate the measured beam distribution, we model the effect of MI ramping as if there were an extra time varying voltage in the barrier bucket system instead of a time varying magnetic field. The simulation comprises of increasing and decreasing the voltages of the barrier pulses as well as the baseline by a certain amount during the cycle times of magnetic ramping. The purpose of the simulation is to estimate the amount of the extra voltage in the barrier bucket by comparing the WCM data and the predictions from the simulations.

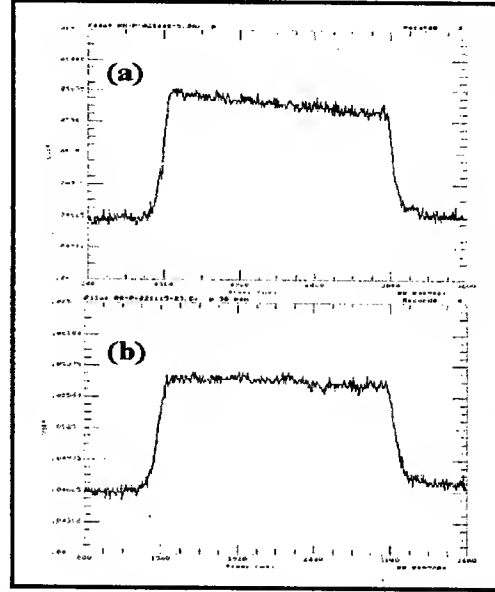


Figure 2: WCM data for the beam after (a) 4min and (b) 30min later in the presence of 120 GeV MI acceleration cycle at a rate of 20 cycles/min.

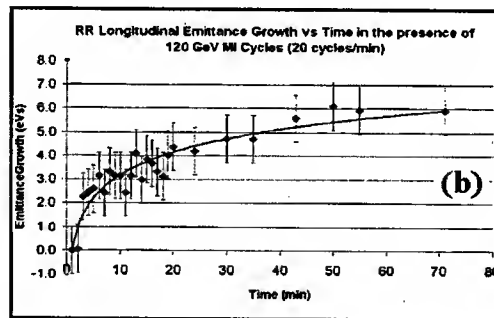
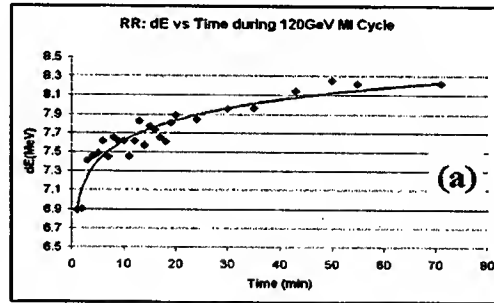


Figure 3: Measured (a) ΔE and (b) longitudinal emittance growth of the beam as a function of time in the presence of the MI 120GeV acceleration cycles

For this paper, the simulation is performed during the first four minutes of MI ramping. The predicted (ΔE , $\Delta\theta$)-

space distribution of the beam and the projection of the beam in $\Delta\theta$ are presented in Fig.4. The simulation reproduces the shape of the projected beam distribution in $\Delta\theta$ but the rate of emittance growth is not well modelled. The measured growth rate of the distribution in $\Delta\theta$ is $\sim 7\%$ in 30 minutes and the result from the simulation shows similar amount of increase in the beam distribution. The simulation shows a halo in $(\Delta E, \Delta\theta)$ -space distribution and illustrates that the enlargement of the longitudinal emittance is significantly larger than the one measured using WCM but the growth of the distribution in $\Delta\theta$ is comparable to the measured value. A plausible explanation for the difference between the measured and the simulated value of the growth of longitudinal emittance is that the WCM might not be sensitive enough to detect the extreme wings of the halo of the beam distribution in time $(\Delta\theta)$.

More sophisticated follow-up studies are required with a longer simulation time to attempt to quantitatively reproduce the measurement.

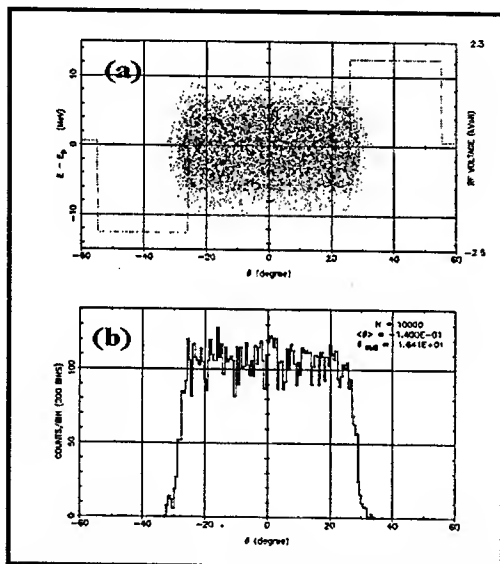


Figure 4: Simulation results for the effects of ramping of the barrier waveform for the first four minutes. Total of 73 ramps in four minutes. The initial distributions for this case are shown in Fig. (b) and (c).

CONCLUSIONS

Measurements of the longitudinal emittance of proton beams stored in the RR show that there is time dependence of the growth of the emittance in the presence of MI magnetic ramping. The residual field appears to cause a shift of the beam position relative to the barrier pulses. The position shift of the beam is the primary source of the growth of the longitudinal emittance.

We have made an initial attempt to model this emittance growth in a 2-D beam dynamic simulation. The simulated rate of the emittance growth is considerably larger than the observed value.

Further study is required to quantitatively estimate the induced voltage and the rate of emittance growth.

REFERENCES

- * Work supported by the US National Science Foundation (NSF) under grant number PHY0089116.
- # Work supported by the US Department of Energy (DOE) under contract number DE-AC02-76CH03000.
- [1] G. Jackson, "The Fermilab Recycler Ring Technical Design Report", FERMILAB-TM-1991 (1996).
- [2] <http://www-ap.fnal.gov/ESME>: J. MacLachlan and J-F Ostiguy, "Enhancements to the longitudinal dynamics code ESME", IEEE PAC'97 conference proceeding (p.2556)
- [3] C.M.Bhat, "Barrier bucket system in the Recycler Ring at Fermilab", 20th ICFA Advanced Beam Dynamics Workshop, 2002. (p.229)

STUDIES OF A GENERALIZED BEAM-INDUCED MULTIPACTING RESONANCE CONDITION*

K.C. Harkay[†], L. Loiacono[‡], and R.A. Rosenberg,
Argonne National Laboratory, Argonne, IL, 60439, USA
[‡] Loyola University, Chicago, IL, 60611, USA

Abstract

At certain bunch intensities and bunch spacings, beam-induced multipacting (BIM) was observed during experiments performed at the Advanced Photon Source. Dedicated diagnostics known as retarding-field analyzers (RFAs) were used to directly measure the electron flux on the vacuum chamber walls. The peak signals were observed at a bunch spacing other than that predicted in the classical form of BIM, which assumes cold secondary electron emission. Using a simple computer model, we studied the effect of including an energy distribution for the emitted secondary electrons. We found that the experimental data can be explained by a resonance condition in which the secondary electron energy and surface emissivity properties are included. Results for positron beams are presented.

INTRODUCTION

Experiments were carried out in the 7-GeV Advanced Photon Source third-generation x-ray light source using dedicated diagnostics to measure the properties of the background, low-energy electron cloud [1]. The diagnostic is based on the planar retarding-field analyzer (RFA) [2], and both the time-averaged flux and energy spectrum were measured for electrons striking the vacuum chamber wall for varying machine conditions. A main goal of the experiments was to acquire data to provide realistic limits on key parameters relating to electron-cloud production, improving the predictive capabilities of computer models. The electron cloud was very sensitive to the bunch intensity and spacing. Maximum amplification for positrons was observed for bunches spaced at 7λ (20 ns), where λ is the rf wavelength. The enhancement was clearly seen for bunch intensities above 1.5 mA (5.5 nC).

These experimental results were compared with the code POSINST, developed by M. Furman and M. Pivi. The position of the peak and width of the resonance curve (RFA signal vs. bunch spacing) were found to be sensitive to the secondary electron energy (SEE) [3,4]. In the code, the distribution assumes the form: $E \exp(-E/E_s)$, where E_s is a constant. Good agreement was found for $E_s = 1$ eV.

If secondary electron emission processes dominate, the electron cloud can build up significantly if a BIM resonance condition is satisfied. In its classical form [5], cold electrons at the wall are accelerated by the beam and traverse the chamber in precisely the time between bunch passages. It was noted by M. Furman [3] that the range of

bunch spacings over which amplification was observed for APS positrons (4λ to 16λ) is consistent with the classical BIM condition for trajectories ranging between the minor and major chamber axes. However, the cold electron assumption is clearly incomplete, since the peak at 7λ cannot be readily explained. M. Furman and S. Heifets proposed a general BIM resonance that includes a non-zero SEE; this general form of BIM appeared to explain the data [1]. A simple computer model was written in order to study the dependence of the general BIM resonance condition on the emitted SEE. The model is described and the results are compared with the APS experimental data.

MODEL

The interaction between an electron and a train of bunches is modeled as a series of drifts and instantaneous kicks. The electron is constrained to move on a trajectory that crosses the chamber center. In the "impulse kick" approximation [5], the electron momentum gain is given by $\Delta p = m_e c r_e N_b / r \hat{r}$, where m_e is the electron mass, c is the speed of light, $r_e = 2.82 \times 10^{-13}$ cm is the classical electron radius, N_b is the bunch population, and r is the distance between the electron and the bunch. \hat{r} is a unit vector pointing towards a positron beam and away from an electron beam. Between bunch passages, the electron drifts under its momentum. If the electron strikes the wall before the next kick, a secondary electron is created with a nonzero energy and assumed to drift towards the beam. At the next kick, the electron's new position is calculated, and its new momentum is given by $\mathbf{p} = \Delta \mathbf{p} + \mathbf{p}_0$, where \mathbf{p}_0 is the momentum just prior to the kick.

For improved accuracy, since it is not exactly an ellipse, the APS vacuum chamber shape was modeled according to design drawings. The chamber schematic is shown in Fig. 1, where θ is an angle measured from the vertical. The available path length for a given electron will vary according to θ . The mounted RFA position is between 49 and 67 deg. The antechamber (between 80 and 90 deg) was not taken into account in the model.

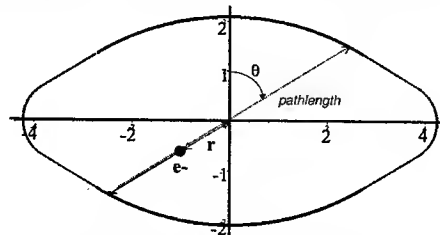


Figure 1: Vacuum chamber geometry used in the model. The chamber half-dimensions are 4.25×2.1 cm.

* Work supported by the U.S. Department of Energy, Office of Basic Energy Sciences under Contract No. W-31-109-ENG-38.

[†] harkay@aps.anl.gov

At a given bunch spacing, an electron with initial (r_0, θ, p_0) is tracked for N kicks, and its new (r, p) are recorded for each kick (θ is constant). The calculations are repeated for a range of values of θ and SEE. The output is checked for a resonance condition as follows: If the electron energies on three successive kicks are within 0.5 eV of each other, the resonant values of (r, θ, p) , SEE, and kick details are recorded. The secondary emission at resonance depends on the electron incident energy $KE = p^2/2m_e$. The secondary electron yield coefficient $\delta(KE)$ corresponding to the resonant condition is also recorded.

Input Parameters

δ is a critical input parameter. Figure 2 shows the values of δ measured as a function of incident electron energy for a APS aluminum chamber sample [6]. If δ is greater than unity for the resonant electron striking the walls, amplification can occur. The measured energy dependence of the data very nearly fits the universal δ curve for true secondary electrons, using an empirical formula developed by Furman [7]. The maximum value of δ occurs at $\delta_{\max} = 2.8$ for an incident energy $E_{\max} = 330$ eV. It should be noted that there was $\sim 10\%$ variation in δ_{\max} among the measured samples.

The final resonant energy is not sensitive to the electron starting position and energy, but the number of kicks before falling into resonance is. The most probable "seed" electron is a secondary created at the wall. Rather than use a secondary electron (SE) distribution from the literature, we used the APS data [1] to choose an initial SEE that is near the mean value. We differentiated the RFA signal for a case where the bunches were far apart: 128λ (360 ns)

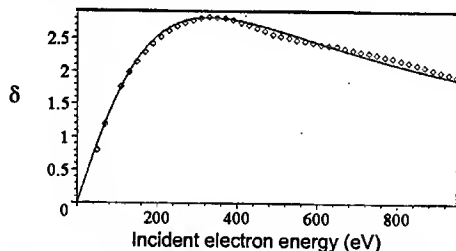


Figure 2: Measured secondary-electron yield coefficient δ for Al APS chambers, fitted to empirical formula in [7].

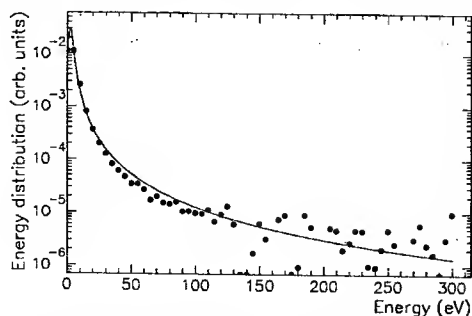


Figure 3: Measured electron-cloud energy distribution fitted with a Lorentzian function (data for 10 positron bunches spaced at 128λ , with 2 mA (7.4 nC) per bunch).

(see Fig. 3). In this case, there is no electron amplification. A Lorentzian function, $(\Gamma/2)/\{\Gamma/2 + (E - \langle E \rangle)^2\}$, fits the data well, where the width Γ is 4 eV and the mean (most probable) energy $\langle E \rangle$ is 2.5 eV. For this distribution, 90% of the SEs are within 10 eV, and about 50% are within $\langle E \rangle \pm \Gamma/3$ (i.e., SEs ranging from 1.2 to 3.8 eV). Note the Lorentzian tail falls off more slowly than the exponential function assumed in POSINST.

RESULTS

Calculations of resonance conditions for a range of SEEs comprising 50% of the distribution were performed for bunch spacings ranging from 4 to 9λ . The bunch intensity is 2 mA to compare with the experimental data. In the examples shown in Figs. 4 and 5, the bunch spacing is 7λ . In Fig. 4, the resonant electron energy after 50 kicks is shown as a function of SEE at two angles: 0 deg (vertical plane) and 56 deg (RFA location). The inset in the figure shows the kinetic energy as a function of kick number for SEE = 2.5 eV. The resonance is reached after about 5-10 and 10-20 kicks for 0 and 56 deg, respectively. In the vertical plane, the resonant energy is 10 keV or more for SEEs between 2.9 and 3.7 eV. For these cases, the resonant condition corresponds to an electron position

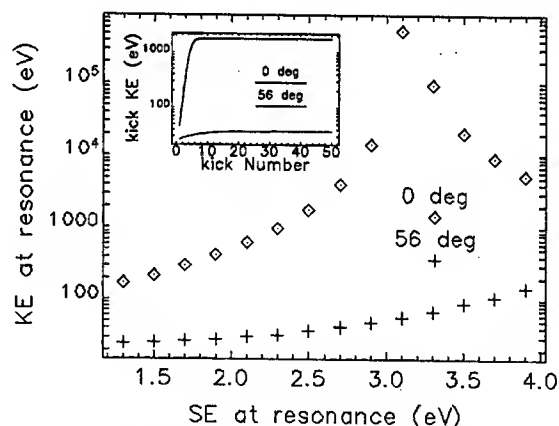


Figure 4: Resonant energy of an electron after 50 kicks for a range of SEEs (a) in the vertical plane (0 deg) and (b) at the location of the RFA (56 deg).

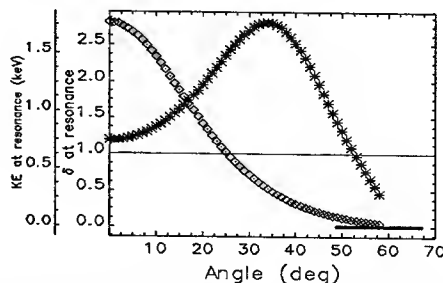


Figure 5: Electron kinetic energy (\diamond) and δ ($*$) at resonance as a function of the angle θ ; the SEE is 2.5 eV. The RFA location is represented by the thick line.

r that is very close to the beam. Here, the energy gain is likely to be overestimated by the impulse kick approximation. This is because the bunches are no longer short ($\sigma_z \approx 30$ c ps) compared to the electron drift distance during the bunch passage. In these cases, δ is negligible and these resonances do not contribute to the electron cloud.

In Fig. 5, the resonance conditions are shown as a function of angular position θ for an SEE of 2.5 eV, showing the electron kinetic energy and corresponding δ . There are no resonances for $\theta > 60$ deg; this includes part of the RFA area. However, δ is greater than unity for angles up to just past the edge of the RFA.

The full space of resonance solutions in (r, θ) are shown graphically in Fig. 6 for different bunch spacing values. The δ corresponding to each resonance is marked in color. It can be seen that while few resonances exist for 4λ , a successively larger area is resonant up to 7λ , after which the area diminishes. Notably, 7λ has the largest area of resonances corresponding to $\delta \geq 2.0$, followed by 6λ . This is consistent with the experimental data, and could help explain the strong peak at 7λ [1]. There were no resonance solutions for 1-3 λ in this range of SEEs.

The results shown in Fig. 6 suggest that since the solutions were found using secondary electrons starting from the wall, it is likely that electrons will populate these regions in the chamber after 5-20 bunches (from Fig. 4). Synchrotron radiation reflecting from the chamber surfaces above and below the antechamber (not shown, 0.5 cm half height) can strike virtually anywhere on the surface, producing both photoelectrons and secondary electrons. Interestingly, in the simulations for the APS at 7- λ bunch spacing using POSINST, a snapshot of the electron cloud spatial distribution after the 9th bunch passage shows a clumping of electrons in a region approximately in agreement with Fig 6 [3].

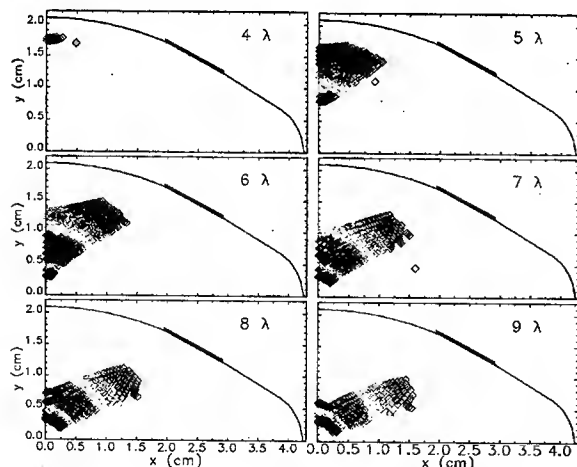


Figure 6: Resonance conditions as a function of bunch spacing for SEE between 1.2 and 3.8 eV. The color legend is: $1.0 \leq \delta < 1.5$ (black), $1.5 \leq \delta < 2.0$ (red), $2.0 \leq \delta < 2.5$ (green), and $2.5 \leq \delta$ (blue).

Verification of Cold Electron Model

We verified that the model gives the expected result in the limit that the secondary emitted electrons have zero energies. In Fig. 7, the positions of the resonant conditions for a bunch spacing of 4λ are shown, assuming that the SEE ≤ 0.1 eV (2 mA/bunch). As expected, only the electrons at the wall near 0 deg satisfy the BIM resonance. Figures 6 and 7 show that the area in the chamber covered by resonantly multipacting electrons is significantly underestimated by the cold secondary-electron BIM model.

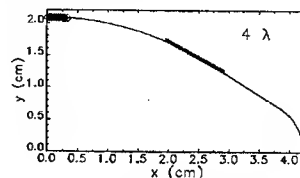


Figure 7: Resonance conditions for 4- λ bunch spacing for SEE ≤ 0.1 eV. The corresponding δ is ~ 0.7 .

CONCLUSIONS/FUTURE WORK

A simple computer model was written to study the dependence of a general beam-induced multipacting resonance condition on the secondary electron energy distribution. The results are consistent with the experimental data at the APS and help explain the peak observed in the electron cloud signal at a bunch spacing of 7λ (20 ns). Preliminary modeling has been performed for electron beams (currently in operation) and will be presented in the future. Of recent interest is a possible installation in the APS of a superconducting (SC) undulator. The heat deposition from electron bombardment is being analyzed. Also planned is modifying the model to allow different chamber dimensions; e.g., for the SC undulator chamber and other rings. In addition, a more realistic, nonimpulse kick will be implemented, taking the bunch longitudinal profile into account, as suggested in [8].

REFERENCES

- [1] K.C. Harkay and R.A. Rosenberg, Phys. Rev. ST Accel. Beams 6, 034402 (2003).
- [2] R.A. Rosenberg and K.C. Harkay, Nucl. Instrum. Methods A 453, 507 (2000).
- [3] M.A. Furman, M. Pivi, K.C. Harkay and R.A. Rosenberg, Proc. 2001 PAC, 679 (2001).
- [4] K.C. Harkay, R.A. Rosenberg, M.A. Furman, M. Pivi, Proc. of Mini-Workshop on Electron-Cloud Simulations for Positron and Proton Beams, CERN Yellow Report No. CERN-2002-001, 69 (Apr. 2002).
- [5] O. Gröbner, Proc. 10th Int'l. Conf. on High-Energy Accel., Protvino, 277 (1977); Proc. of 1997 PAC, 3589 (1997).
- [6] R.A. Rosenberg et al., to be published in J. Vac. Sci. Technol., (2003).
- [7] M.A. Furman and M.T.F. Pivi, Phys. Rev. ST Accel. Beams 5, 124404 (2002).
- [8] J.S. Berg, LHC Project Note 97, CERN (1997).

SIMULATION OF MAGNETIZED BEAMS

Dong Wang*, Ilan Ben-Zvi, Xiangyun Chang, Jorg Kewisch, Christoph Montag, Brookhaven National Laboratory, Upton, NY 11973, Feng Zhou, UCLA, Los Angeles, CA 90095

Abstract

The angular momentums of particles in a bunch of beam are of importance in many applications. Usually the angular momentums are related to the end field of solenoids. In electron cooling facilities the solenoid fields are widely used as they are found very helpful not only in focusing and guiding the charge particle beams but also in enhancing the cooling rates. The RHIC electron cooler is a challenging project because it requires a high performance facility including a solenoid with high quality strong field (1 Tesla). Issues cause by the end fields of the solenoid have been studied to minimize the extra temperature and coherent motions. In this paper we report recent results in simulating the angular momentums of the electron beam and its application on the RHIC electron cooler.

INTRODUCTIONS

The Relativistic Heavy Ion Collider (RHIC) [1] is an accelerator complex consisting The main goal of the RHIC is to provide head-on collisions at energies up to 100 GeV/u per beam for very haevy ions, which are defined to be gold $^{197}\text{Au}^{79+}$, but the program also calls for lighter ions all the way down to protons and polarized protons. Luminosity requirements for the heaviest ions are specified to be in the $10^{26}\sim 10^{27}\text{cm}^{-2}\text{s}^{-1}$ range. A first upgrade of the luminosity by about a factor four consists of increasing the number of bunches from about 60 to about 120 and decreasing beta* from 2m to 1m. Luminosity can be further enhanced by decreasing the beam emittance by the electron cooling the gold beams at storage energy. With electron cooling [2] [3] the beam emittance can reduced and maintained throughout the store and the luminosity increased until non-linear effects of the two colliding beams on each other limit any further increase (beam-beam limit).

An electron beam is considered magnetized when its radius of transverse Larmor oscillations is much smaller than beam radius. If the solenoid field lines are perfectly parallel, these oscillations can increase the duration of an electron-ion interaction thus increasing the friction force (assuming that there are several Larmor oscillations in the cooler). In this case the cooling rate is mainly determined by the electron longitudinal energy spread, which can be made much smaller than the transverse one.

The calculations of electron cooling for RHIC show that a strong longitudinal field, among other requirements, is needed to achieve required cooling rate. Figure 1 shows the layout of this energy recovery linac (ERL) machine. Table 1 gives major parameters of the RHIC electron cooler.

* Email: dongwang@rocko.mit.edu

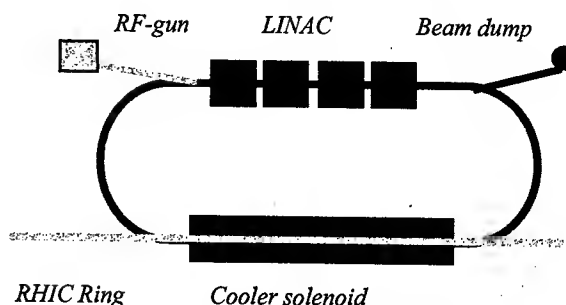


Figure 1: is the sketch of the RHIC e-cooling facility

Table 1: Parameters of electron beam for RHIC cooler

Final Beam energy	55MeV
Solenoid field	1 Tesla
Length of solenoid	~ 30 m
Charge per bunch	10 nc
Repetition rate	9.4MHz
Average current	94 mA
Bunch length at Linac	~5~10 mms
Injection energy	2.5 MeV

However, the end fields of a solenoid have radial components and can give beam extra angular momentum.

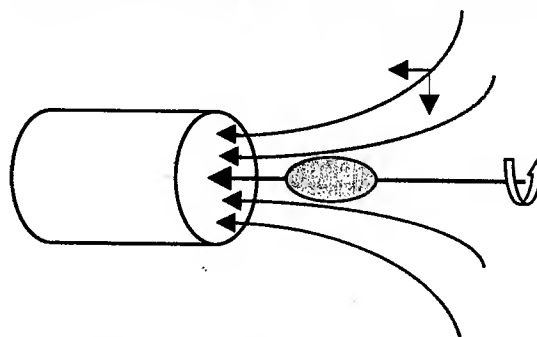


Figure 2: Beam acquires angular momentum from end field of solenoid

There are two main effects in cooler solenoid due to the angular momentum,

- 1) angular momentum itself means certain transverse temperature .
- 2) it will cause coherent radial motion in longitudinal magnetic field in the cooler.

Particle tracking show clearly above two major effects. In this simulation the modified PARMELA [4] is used to include major fields and forces, i.e., cavities(gun, lianc, buncher, rotation), magnets (dipole, quads, sextupole, solenoid), space charge, etc.

MUTLI-PARTICLE TRACKING

The canonical angular momentum can be expressed in following ways,

$$M = pr^2\theta' - e\Phi(r, z) / 2\pi c \quad \text{or,}$$

$$M = xp_y - yp_x$$

Here, x, y, p_x, p_y , are the transverse Cartesian coordinates and their canonically conjugated momenta, r, θ, z are the cylindrical coordinates, the prime denotes a derivative along the axis z , $p = \gamma\beta mc$ is the total momentum, Φ is the magnetic flux inside a circle enclosed by the electron offset r , e is the charge of electrons. Different phase spaces of magnetized beam are exploited to find best way to reveal the behavior of this kind of beam. See Figure 3.

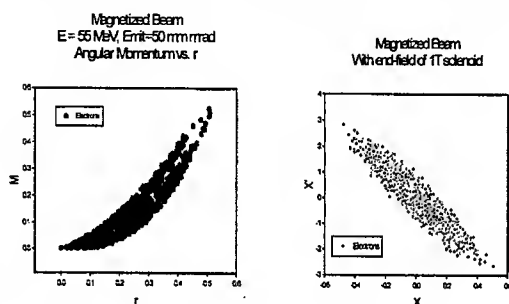


Figure 3: Angular Momentum Figure 4: (x, x')

The horizontal axis is r and the vertical axis is M . Figure 4 is normal (x, x') phase space. To better observe the evolution of the angular momentum several other methods are explored, say, $r\theta'$ vs. r , x' vs. y or y' vs. x , xy' vs. r , or yx' vs. r , xy' vs. x (or y), see Figures 5 to 10.

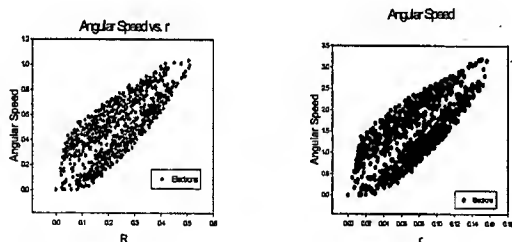


Figure 5: $r\theta'$ at start

Figure 6: $r\theta'$ after a drift

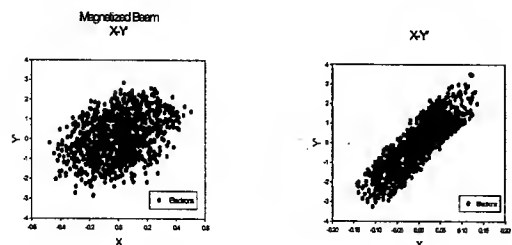


Figure 7: (x, y') at start

Figure 8: (x, y') after a drift

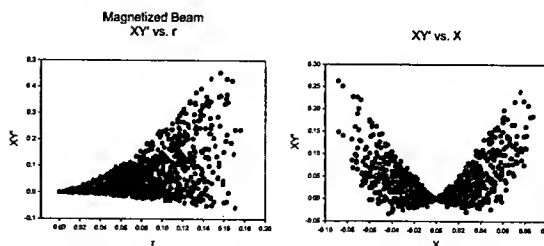


Figure 9: xy' vs. r

Figure 10: xy' vs. x

Besides the M itself (Figure 3), the $r\theta'$ is found very useful since it has pretty concise and certain shape (linear correlation, thermal AM is flat in this phase space) in phase space therefore easy for comparing the its amount and distribution of a bunch at different locations. The (x, y') or (y, x') also has some patterns for magnetized beam. They might be useful in measuring the magnetized beam with (x, y) tomography technique. What is different from the $(r\theta', r)$ phase space is that their shape vary along the beam line as shown in Figure 7 and 8. Other phase spaces have rather complicated patterns and are not invariants.

MATCHING AND START-TO-END SIMULATION

The basic principle of matching or eliminating the angular momentum in a solenoid can be illustrated by the Busch's theorem.

$$\dot{\phi} = -\frac{e}{2\pi\gamma m_e r^2(s)} [\Phi(s) - \Phi_{cathode}]$$

It shows that one needs to give electrons certain amount of angular momentums which may exactly cancel the effects of the end field of cooler solenoid. The traditional electron coolers don't have this issue since the continuous solenoids are adopted from the start to the end. For high energy cooler like one for the RHIC one has to use discrete elements (sc linac etc.) to accelerator intense beam (10 nc) to 55 MeV. For this purpose some detailed analytical approaches have been performed under some assumptions (linear optics, zero energy spread, etc.) [5] [6]. The point is that the beam must be magnetized when it was born on the cathode and the angular momentum must be preserved through the whole beam line, gun, linac, transport, then canceled by the end field of cooler solenoid. In reality the situation are more complicated than linear single particle dynamics. The questions then become what kind angular momentum distributions are needed for a bunch of electrons and how significant the distortions due to various reasons could be.

The simplest case of matching is the cancellation of the angular momentums caused the same end field but with opposite field directions. Electrons acquire the angular momentum from a solenoid with opposite field then enter the cooler solenoid. The angular momentums would be canceled if the beam is focused properly at the entrance of

solenoid. For a global matching one needs to make the transform as a rotationally invariant mapping.

Based on above studies on illustrating the angular momentums of a electron bunch, a start-to-end simulation is carried out for the RHIC electron cooling project. Beam is magnetized on the cathode (non-aero magnetic field at cathode) then accelerated through the RF gun and sc linac followed by a transport line to stretch the bunch before it is sent to the cooler solenoid. The Figure 11 is beam envelope along the beam line. Figure 12 and 13 show that the angular momentums of electrons in the bunch are mostly preserved (left bottom plot) but some distortions are observed, possibly due to the energy spread (the largest in RF gun where beam energy is the lowest).

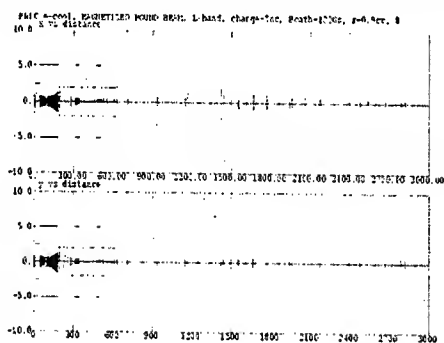


Figure 11: beam envelopes along the beam line

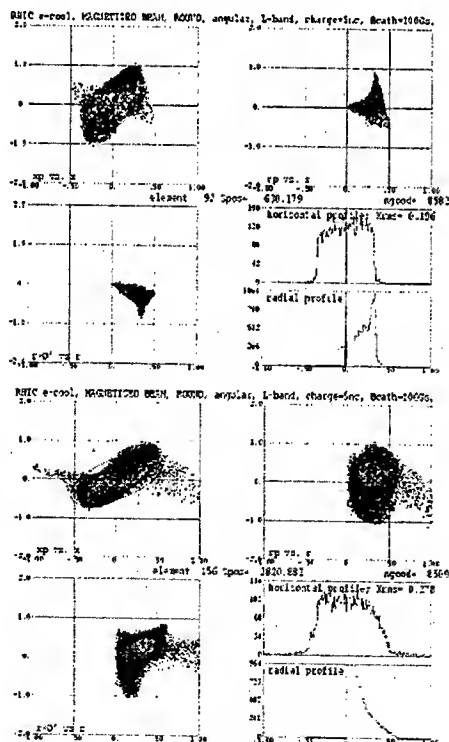
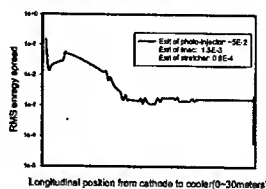


Figure 12 and 13: magnetization (left-bottom ones) at the exit of linac and entrance of the cooler solenoid

The magnetic field on the cathode is about 100 Gs while beam spot size is about 10 mm radius. In RF-gun the beam is accelerated to about 2.5 MeV then directed to the linac by a small angle bending magnet. Three sc cavities (L-band, now likely to use four or five 700MHz cavities) will further accelerate beam up to 55 MeV energy. A transport line is designed [7] to stretch the bunch to a few cm and energy spread is lowered by a rotation cavity.

RHIC e-cool, magnetized beam transport optimization of beam energy spread



RHIC e-cool, magnetized beam transport (photo-injector, linac, stretcher) Transverse emittance preservation

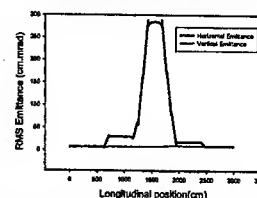


Figure 14 (left) and 15 (right): Evolutions of energy spread and beam emittances for the RHIC electron cooling beam

SUMMARY

The simulations of angular momentums have been studied. Different ways to describe the distributions of the angular momentums in a bunch beam are explored. It is found that some of them, M , transverse velocity and (x, y') or (y, x') are the best ways to understand the issue. The evolutions of angular momentums in solenoid, cathode, acceleration cavity and other beam line elements are simulated. The simulation has included more effects than the existing theory (space charge, energy spread, etc.) It proved that the magnetized beam in the RHIC cooler with strong solenoid magnetic field can be produced and transported to the cooler solenoid smoothly while keeping their angular momentums mostly preserved. The distortions observed need to be further minimized with fine compensations.

ACKNOWLEDGMENTS

We'd like to thank Lloyd Young and his coworkers in LANL for their discussions and helps in the PARMELA codes. We also thank the participants of RHIC e-cooling meetings for their discussions.

REFERENCES

- [1] See, for example, T. Roser, these proceedings
- [2] I. Ben-Zvi et al., these proceedings
- [3] S. Nagaitsev (Fermilab). FERMILAB-CONF-01-171-E, PAC-2001-FOAC002, Jul 2001
- [4] L. Young, et al., LANL, PARMELA
- [5] Y. Derbenev, Nucl.Instrum.Meth.A441:223-233, 2000
- [6] A. Burov, et al., Physical Review Special Topics on Accel. Beams 3:094002, 2000
- [7] J. Kewisch, et al., these proceedings

PROBING THE NON-LINEAR DYNAMICS OF THE ESRF STORAGE RING WITH EXPERIMENTAL FREQUENCY MAPS

Y. Papaphilippou, L. Farvacque, A. Ropert, ESRF, Grenoble, France
J. Laskar, ASD-IMCEE, Paris, France

Abstract

A key issue for improving the performance of third generation light sources like the ESRF storage ring is the identification and correction of resonances that have a detrimental effect in the machine performance. Frequency analysis of experimental data, recorded on BPMs around the ring, is a powerful tool for studying the non-linear dynamics of an accelerator in operation. In a series of experiments, experimental frequency maps were produced using the 1000-turns measurement system. These maps revealed the resonance structure in the vicinity of the nominal working point which was limiting the dynamic aperture. Their comparison with maps produced by simulations was used as a guide for understanding the storage ring non-linear model. The possibility of using the quasi-periodic approximations of the experimental data for testing the efficiency of resonance correction schemes was finally investigated.

INTRODUCTION

The beam lifetime, determined by the electron beam loss rate, is one of the key parameters for evaluating the performance of a synchrotron light source. It depends strongly on collision mechanisms with other electrons or residual gas, effects which are associated with the collective behaviour of the beam and its interaction with the environment (e.g. the vacuum quality). On the other hand, single particle motion, dominated by the applied non-linear magnetic fields, can become chaotic and particles may diffuse to large amplitudes through non-linear resonances, enhancing the particle loss. It is the interplay of these two mechanisms that reduces the beam lifetime [1]. In recent years, methods coming principally from celestial mechanics [2], such as the frequency map analysis (FMA), have been successfully used in order to study the single particle non-linear dynamics in accelerators. Apart from the already established power of the methods when applied in simulations in order to display and understand the global beam dynamics [3], they have been very successfully applied for analysing experimental data of excited transverse beam oscillations, recorded turn by turn on beam position monitors [1, 4, 5]. In this paper, we will present the first feasibility test made at the ESRF storage ring, in order to produce experimental frequency maps, by using the 1000-turn measurement system [6]. These tests are the first step towards studying and understanding the limitations of the horizontal dynamic aperture observed at the storage ring in various experimental machine studies [7].

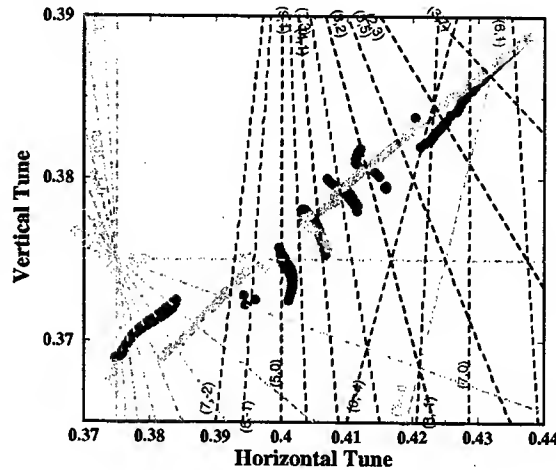


Figure 1: Experimental frequency map of the ESRF ring. The red curve corresponds to the frequencies computed by an analysis of all 252 turns, whereas the green curve corresponds to the frequencies computed for a time-span equal to the decoherence time.

FREQUENCY MAP ANALYSIS

In brief, the FMA enables the derivation of a quasi-periodic approximation $f'(t) = \sum_{k=1}^N a_k e^{i2\pi\nu_k t}$, truncated to order N , of a complex function $f(t) = q(t) + ip(t)$, formed by a pair of conjugate variables, which are determined numerically or experimentally. The frequency ν_1 of the first term is associated with the fundamental frequency of motion. Applying the method to a large number of orbits with different initial conditions enables the creation of a very detailed tune footprint, the frequency map. Due to the very high precision of the tune determination through a refined Fourier analysis using the NAFF algorithm [2], all the excited resonances appear as line distortions of this map. The application of the method to experimental data can reveal the complex network of resonances associated with non-linear motion in a real accelerator [4]. A second aspect of the method, is the study of the quasi-periodic approximation itself for each excited orbit [5]. All terms of this approximation are decomposed as a linear combination of the fundamental frequencies $\nu_k = k_x\nu_x + k_y\nu_y$. The amplitudes $a_k \equiv a_{(k_x, k_y)}$ of these terms are associated with the driving terms of a resonance $m_x\nu_x + m_y\nu_y = c$ with: a) $(m_x, m_y) = (-k_x + 1, -k_y)$ for horizontal and b) $(m_x, m_y) = (-k_x, -k_y + 1)$ for vertical motion. Thereby, the excitation of an individual resonance can be determined by computing or measuring these amplitudes.

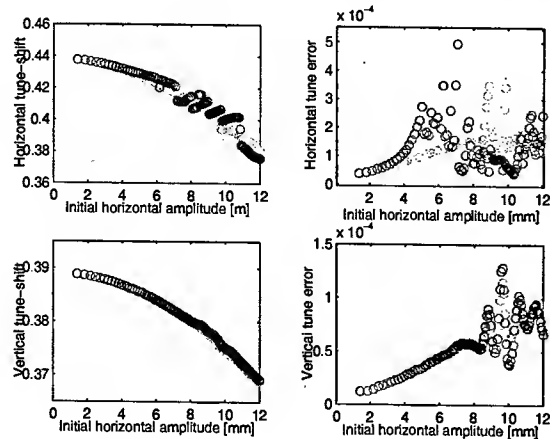


Figure 2: Horizontal [top] and vertical [bottom] tune-shift [right] and tune-error [left] with amplitude. The colour-code of the two curves is the same as in Fig. 1.

EXPERIMENTAL FREQUENCY MAPS

In a series of experiments, we have performed several tests for setting up and automating the procedure for the production of experimental frequency maps. We used an electron bunch train of around 5mA total current, filling 1/3 of the machine circumference. The machine tunes were set to the nominal ones (36.44, 14.39) and the chromaticity was set to zero in order to limit the beam decoherence time. The beam was excited synchronously with one of the four horizontal fast injection kickers and a vertical shaker. The kicker and shaker currents were automatically controlled and 104 horizontal times 3 vertical kicks were applied, giving a total of 312 orbits. The whole experiment lasted about 4 hours. The maximum horizontal kicker current was set to a value where beam losses start to occur. This corresponds to an horizontal displacement of 12 mm in the middle of the straight section where $\beta_x = 35.1$ m. The shaker was limited by technical problems giving a maximum vertical displacement of 0.8 mm in the middle of the straight section, where $\beta_y = 2.5$ m (40% of the vertical physical aperture).

The data was recorded on the 214 BPMs of the storage ring for 256 turns and post-processed with a MatLab [8] version of the frequency analysis algorithm. The tunes were extracted on each BPM and the results of the average tune from all the BPMs for each measurement are plotted in the frequency map of Fig. 1. The red curve corresponds to the tunes obtained by an application of the frequency analysis algorithm to the full length of data (252 turns). However, for high amplitudes, due to the amplitude dependent tune-shift, the beam decoheres very rapidly leaving a few tens of turns available to be analysed. The green curve corresponds to the analysis of the data of the oscillations that are still coherent. The two curves are roughly the same apart from the obvious deviation at large amplitude and the fact that the second one is more linear and less distorted. Due to the fact that the vertical amplitudes are very small, the tune-shift in both directions is mostly due to the hor-

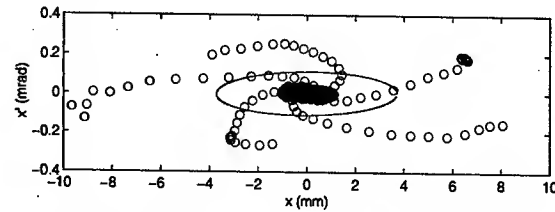


Figure 3: Horizontal phase space plot in the vicinity of the (5,0) resonance.

izontal excursion of the beam, as can be seen in Fig. 2, where the horizontal and vertical tune-shift is plotted as a function of the horizontal initial amplitude in the middle of the straight section. In the same figure, the statistical error in the tune determination is also displayed, defined through the standard deviation over the measured tune values on all the BPMs. As this error is a measure of the tune precision, it depends on the length of the analysed data but also on the regularity of the phase space for each measured orbit. Indeed, the tune error is less than 10^{-4} for most cases, whereas in the vicinity of a resonance it gets higher. Finally, note that the statistical error in the determination of the horizontal tune is higher than the one of the vertical tune, as the beam excursion and thus the influence of non-linear fields is stronger in the horizontal plane.

The map can be roughly separated in three regions: For small amplitudes and up to 7 mm amplitude, the detuning with amplitude seems to have a regular behaviour. Between 7 and 11 mm amplitudes, there is a zone of instability characterised by the accumulation of points on resonant lines or gaps. Most of the resonances are of the fifth or tenth order: (5,0), (4,1), (3,2), (9,1), (7,3), (6,4) and (5,5). A projection of the phase space motion on the horizontal plane, in the vicinity of the (5,0) resonance, is presented in Fig. 3. The resonant behaviour of motion is obvious. Finally, for bigger amplitudes (from 11 up to 12 mm amplitude), the tune path is regular, crossing a multitude of 8th order resonances that are not excited. The last point, where losses begin to occur, approaches an area of potential instability, the crossing point of all third order resonances and the coupling resonances (1, -1). A frequency map resulting from a numerical simulation of a model, with measured focusing and coupling errors included and corrected, is presented in Fig. 4. These first numerical results suggest that the excited zone in the vicinity of the 3rd order resonance is large enough to induce beam loss as far as the last measured tunes in this experiment.

RESONANCE DRIVING TERMS

In Fig. 5, the strength of the fifth order resonance (5,0) driving term is plotted, for initial conditions in its vicinity, as measured by the corresponding $a_{(-4,0)}$ amplitude of the quasi-periodic approximation. In the top plot, the driving term mean values over the measurements given by all the BPMs with error-bars representing their standard deviation are plotted versus the initial horizontal amplitudes of the kicked beam. The resonance driving term is increasing

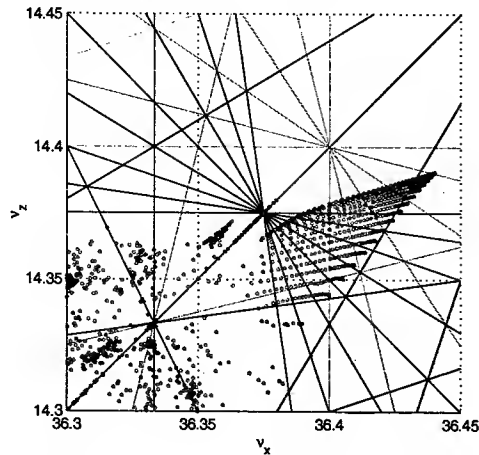


Figure 4: Frequency map for the ESRF model.

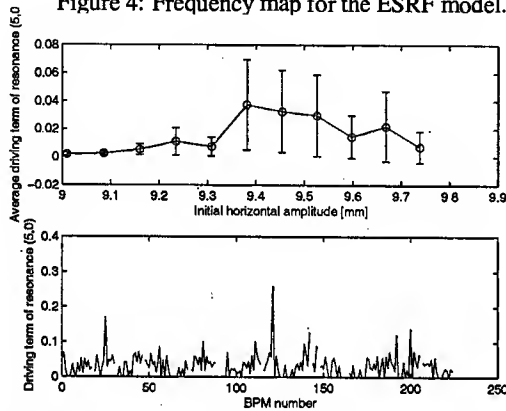


Figure 5: Average (5,0) resonance driving term and its variation along the ring for one particular beam excitation.

as the particles approach the resonance and then decreases gradually to very small values after the resonance has been crossed. In the bottom plot, the behaviour of the resonance driving term along the ring is displayed. The maximum values of the driving term are reached in areas where the horizontal beta function takes large values (higher than 25 m).

Another driving term associated with the horizontal 3rd integer resonance is plotted in Fig. 6. In order to increase the measurement's sensitivity, the lattice was matched to a working point close to this resonance and 4 small kicks of increasing horizontal amplitude were applied. The two curves correspond to measurements before and after switching on the sextupole corrector and, indeed, the resonance driving term drops, after the correction.

CONCLUSIONS AND PERSPECTIVES

We presented the first results from the application of the frequency map analysis technique to experimental beam data of the ESRF storage ring. This was mostly a feasibility study for testing the efficiency of the method with respect to the available hardware and diagnostics. The preliminary results revealed many unknown features of the electron dynamics for the nominal working point of the ESRF storage ring. Moreover, it was confirmed that the limitation of the

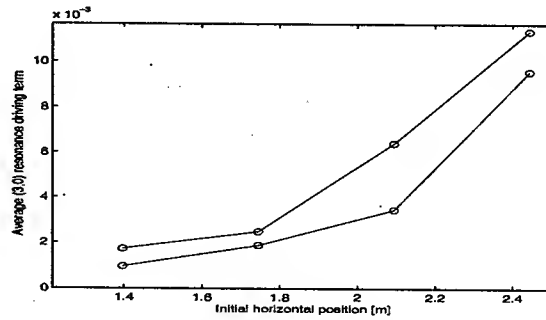


Figure 6: Comparison between the normal sextupole (3,0) resonance driving term along the ring with (green) and without (blue) sextupole correction.

horizontal dynamic aperture is due to an interplay between third order resonances. At the same time, a variety of questions were raised with respect to the reason for this resonance excitation. A detailed non-linear dynamics' analysis assisted by particle tracking is underway in order to refine the non-linear model. One of the practical limitations of the method is the long acquisition time [6]. A dedicated "frequency map" BPM has been tested and the first results were very promising [9]. The development of this system in addition with the installation of a strong vertical kicker will enable the construction of a frequency map for beam amplitudes up to the full ring aperture in a few minutes. Finally, the problem of beam decoherence and the ambiguity it introduces in the tune determination is being currently under careful study. One of the perspectives is establishing a method for a very accurate tune determination using the information from all the BPMs, for a few turns.

We would like to thank P. Elleaume, E. Plouviez, J.-L. Revol, K. Scheidt and the ESRF operation group for their help in the course of these experiments.

REFERENCES

- [1] C. Steier, et al., PRE 65, 056506, 2002; Nadolski et al., submitted to PRST-AB.
- [2] J. Laskar, Astron. Astroph. 198, 341, 1988; Icarus 88, 266, 1990; Physica D 67, 257 1993; NATO-ASI, S'Agaro, Spain, 1996; J. Laskar, et al., Physica D 56, 253, 1992; Y. Papaphilippou et al., Astron. Astroph. 307, 427, 1996; Astron. Astroph. 329, 451, 1998.
- [3] H.S. Dumas et al., Phys. Rev. Let. 70, 2975, 1993; J. Laskar et al., Part. Accel. 54, 183, 1996; Y. Papaphilippou, PAC'99, New York, 1999; PAC'01, Chicago, 2001; Y. Papaphilippou et al., PRST-AB 2, 104001, 1999; PRST-AB 5, 074001, 2002;
- [4] D. Robin et al., Phys. Rev. Let. 85, 558, 2000; L. Nadolski, PhD thesis, CEA, 2001; A.L. Robinson, CERN Courier, Vol 41, N.1, 2001.
- [5] R. Bartolini et al., PAC'99, New York, 1999; Schmidt et al., PAC'01, 2001; Hayes et al., EPAC'02, 2002; R. Tomas, PhD Thesis, CERN 2003.
- [6] L. Farvaque et al., DIPAC 2001, Grenoble, 2001.
- [7] A. Ropert, ESRF notes 13-98/MDT, 20-98/MDT, 12-01/MDT, 1301/MDT, 12-02/MDT.
- [8] MatLab, The MathWorks, Natick, MA
- [9] E. Plouviez, private communication.

NON-LINEAR LONGITUDINAL BEAM DYNAMICS WITH HARMONIC RF SYSTEMS FOR BUNCH LENGTHENING

V. Serrière, J. Jacob, ESRF, Grenoble, France

Abstract

Harmonic cavities have been installed on various storage ring light sources to increase the Touschek lifetime by a factor of 2 to 4 by lengthening bunches. Several side effects have been observed, which limit the gain in lifetime. In the worst case, the beam stability can be altered, but harmonic cavities can also provide Landau damping of coherent motion. A multibunch multiparticle tracking code has been developed to evaluate the performance of harmonic RF systems under consideration of all longitudinal beam dynamics issues. Bunches with high intensities are already elongated by the interaction with the ring impedance. The computations indicate that a harmonic RF system provide significant additional lengthening. The application to the ESRF shows that an active superconducting harmonic system would constitute the only appropriate solution. Such a system would be useful in single bunch and sixteen-bunch operation to improve the beam lifetime by a factor of 2 and 3, respectively.

1 INTRODUCTION

Touschek scattering is the dominant factor that limits the beam lifetime in many low transverse emittance storage rings. Harmonic RF systems have been used in several low-medium energy synchrotron light storage rings to improve the beam lifetime by lengthening bunches. Side effects such as transient beam loading or Robinson instabilities can significantly limit the gain in lifetime [1]. On the other hand, the additional Landau damping that is provided by a harmonic RF system gives a reduction of the amplitude of longitudinal coupled bunch instabilities (LCBI), as for instance at MAX-II [2]. As described in [1], transient effects have been studied with a multibunch single particle model. However, for an accurate evaluation of Landau damping as well as a prediction of LCBI thresholds and Robinson AC instability, non-linear intrabunch effects needed to be included in the computation. In order to evaluate the performance of a harmonic RF system at the ESRF, a multibunch multiparticle tracking code has been developed, which computes the longitudinal dynamic with a harmonic RF system by taking into account all longitudinal instability mechanisms. This code has been used to predict the thresholds of Robinson instabilities and LCBI in the case of the ESRF and the main results were presented at EPAC02 [3]. To further understand the influence of a harmonic RF system on longitudinal instabilities, the beam response to a harmonic excitation was computed and results are presented in section 2. For single and few bunch operation, the effect of the

longitudinal impedance must be taken into account for the evaluation of the possible gain in lifetime. A study of the bunch elongation in both potential well and microwave instability regimes is presented in section 3. The conclusion for the implementation of a harmonic RF system at the ESRF is given in section 4.

2 NON-LINEARITY OF THE RF WAVEFORM

2.1 Beam spectrum

To understand further the influence of the non-linear accelerating voltage on the longitudinal beam dynamics, a harmonic excitation $f(\omega) = a_f \times \cos(\omega t)$ was injected into the multibunch multiparticle tracking code. The bunch spectrum was then computed by taking the discrete inverse Fourier transform of the time-dependent beam intensity. For the example of the ESRF with its 352.2 MHz RF system, $\omega_{RF} = 2.21295$ GHz, the beam was excited at the synchrotron frequency f_{s0} obtained at zero current with a main accelerating voltage of 8 MV. As expected, the beam spectrum shows lines at the angular resonant frequency of the main RF system and the lower and upper sidebands at $\omega_{s0} = \pm 2\pi f_{s0}$. As shown in [4], in the case of optimum bunch lengthening, the average synchrotron frequency amounts to $\langle f_{s,opt} \rangle = 0.2 \times f_{s0}$. Computing the time response of the beam to an excitation at $\langle f_{s,opt} \rangle$ yields the beam spectrum in figure 1.

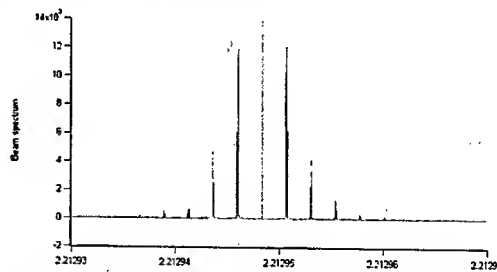


Figure 1: Beam spectrum for $V_h = V_{h,opt}$ around the main RF frequency.

The signal is at its maximum at the main angular RF frequency and exhibits several sideband at $m \times \langle f_{s,opt} \rangle$ with $m=1,2,3,\dots$ on either side of ω_{RF} . Simulations carried out with an excitation slightly below and above $\langle f_{s,opt} \rangle$ have confirmed that the maximum amplitude of the response is obtained by exciting the beam at exactly $\langle f_{s,opt} \rangle$. The occurrence of sidebands at multiples m of the excitation frequency is the signature of the non-linear total accelerating voltage seen by the bunches. The simulations have also shown that the number of sidebands

increases with growing amplitude a_f of the excitation. While more and more new sidebands appear, the amplitudes of the lower order sidebands do not increase linearly with a_f but show some saturation effect. This splitting of the excitation power over several sidebands already indicates that Landau damping will limit the amplitude of unstable coherent motion such as the AC Robinson instability or HOM driven LCBI.

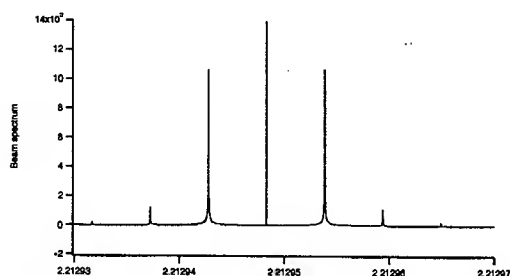


Figure 2: Beam spectrum for $V_h=0.8 \times V_{h,opt}$ around the main RF frequency.

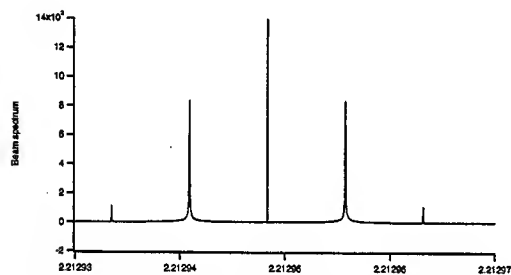


Figure 3: Beam spectrum for $V_h=0.6 \times V_{h,opt}$ around the main RF frequency.

Figures 2 and 3 show the beam spectrum obtained for $V_h=0.8 \times V_{h,opt}$ and $V_h=0.6 \times V_{h,opt}$, respectively. In each case, the beam was excited at the corresponding average synchrotron frequency. The number of sidebands on either side of ω_{RF} decreases by lowering the harmonic voltage. These computations indicate that the non-linearity of the RF voltage needs to be considered in the prediction of coherent collective effects, and that a linear approximation cannot provide a correct model for the amplitude dependent beam response. In order to evaluate the performance of a harmonic RF system, the intrabunch particle motion as well as the multibunch collective response must be included in the analysis of coherent multibunch oscillations, which can lead to the AC Robinson instability or HOM driven LCBI.

2.2 Landau damping

A thorough analysis of various system configurations has shown that the AC Robinson instability is generally encountered, when a passive harmonic cavity is tuned close to the corresponding beam harmonic in order to provide the required voltage for low beam intensities. It

turned out to be a key design element, which imposes a minimum number of passive harmonic cavities, in particular in the case of the ESRF, where harmonic cavities are expected to be operated in single bunch mode. As mentioned in [3], the multibunch multiparticle model constitutes a powerful tool, which allows the prediction of the observed spectacular Landau damping of strong HOM driven LCBI at currents 10 to 100 times the threshold intensity in the case of MAXII. Numerical computations in the case of the ESRF and MAXII allowed the comparison of the LCBI behaviour for both machines. They confirm the experimental observation that for low and medium energy storage rings, harmonic RF systems do not only provide an increase in Touschek lifetime, but that they can also be used to almost suppress the energy blow-up of HOM driven LCBI. For higher energy machines such as the ESRF, only a slight increase in LCBI thresholds is predicted.

3 SINGLE BUNCH EFFECTS

3.1 Potential well regime

The interaction between the beam and the longitudinal broadband impedance of the storage ring produces a local short-range voltage distortion. The wake potential of a given bunch simultaneously acts back on all particles of this particular bunch. At moderate bunch intensities, the voltage induced in the mainly inductive longitudinal impedance locally flattens the voltage waveform and leads to bunch lengthening. In this potential well regime, which is a single bunch effect, the natural energy spread remains unaffected. The longitudinal particle distribution $\Psi(\phi, \Delta E)$ for a given bunch intensity I_0 satisfies the Haissinsky equation [5]

$$\Psi(\phi, \Delta E) = K_I \Psi_0(\phi, \Delta E) \exp \left[-C_1 \times h \left| \frac{Z_L \omega_0}{\omega} \right| (I(\phi) - I(0)) \right],$$

where ϕ and ΔE are the phase advance and the energy deviation relative to the synchronous phase, Z_L is the impedance of the storage ring, K_I is a constant of normalisation and

$$C_1 = -\frac{1}{2} \left(\frac{Q_s}{ch \sigma_E / E} \right)^2.$$

The function $\Psi_0(\phi, \Delta E)$ is the "zero-current" longitudinal particle distribution and $I(\phi)$ is given by

$$I(\phi) = 2\pi I_0 \int \Psi(\phi, \Delta E) d\Delta E.$$

Resolving numerically Haissinski's equation gives the longitudinal particle distribution and thus the bunch length at a given beam intensity. As a result, figure 4 shows the computed evolution of $\Psi(\phi)$ for various bunch intensities with a harmonic RF system at the ESRF tuned for optimum bunch lengthening. The longitudinal distribution is stretched with increasing bunch intensity due to the interaction with the longitudinal inductive impedance. Both the numerical resolution of Haissinski's

equation and the results given by the tracking show that in the potential well regime the total bunch length increase is very close to the value obtained by multiplying the elongation from the harmonic voltage and from the potential well effect.

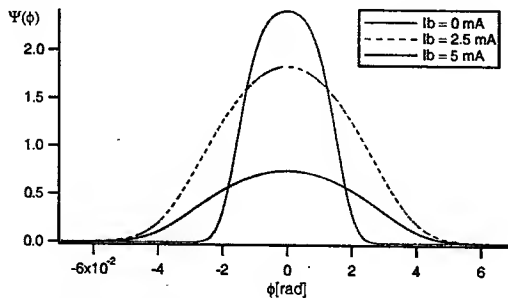


Figure 4: Longitudinal distribution for various bunch intensities in the potential well regime – Prediction with a harmonic RF system at the ESRF tuned for optimum bunch lengthening.

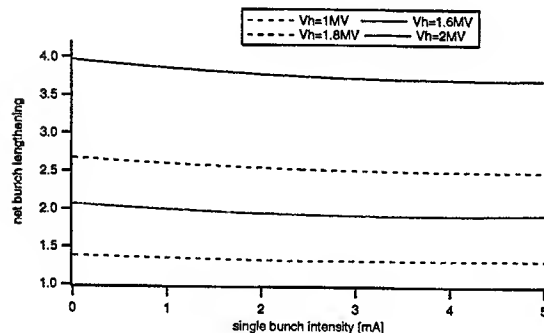


Figure 5: Net bunch lengthening from various harmonic voltages vs bunch intensity in the potential well regime.

In figure 5 the ratio between the total bunch length obtained for various harmonic voltages and the bunch length without harmonic voltage is plotted as a function of the bunch intensity. For any given harmonic voltage, these ratios are almost independent from the bunch intensity. For example $V_h = 2.0$ MV, the ratio decreases only from 4.0 at 0 mA to 3.7 at 5 mA.

Below the limit of the potential well regime of about 5 mA at the ESRF, the effect of the BBR does not limit the possible gain in bunch length and consequently the achievable Touschek lifetime improvement from a harmonic RF system.

3.2 Microwave instability

In the microwave instability regime, both the energy spread and the bunch length increase. In the case of the ESRF, with a microwave instability threshold of 5 mA, a single bunch of 20 mA is lengthened by a factor of 6 and its energy spread increases by a factor of 2, with respect to the “zero-current” values. The computations show that

a harmonic RF system allows the improvement of the bunch length by a further factor of 3 and to reduce the energy spread to a factor of 1.7.

4 CONCLUSION ON THE IMPLEMENTATION OF A HARMONIC RF SYSTEM AT THE ESRF

The implementation of a harmonic RF system on the ESRF storage ring is envisaged for operation modes with a high intensity per bunch such as the 20 mA single bunch and the 90 mA 16-bunch filling modes. For optimum bunch lengthening, a harmonic voltage of 2 MV would be required.

As many as 150 normal conducting passive cavities would be needed to obtain good harmonic voltage and phase conditions for a significant bunch lengthening at low intensity: this is not a realistic solution. For an active normal conducting cavity, the maximum field gradient would impose a minimum of 12 cavities: again not a practical solution. It was therefore decided to concentrate on a more modern approach using superconducting technology.

As presented in [3], with a passive superconducting harmonic RF system, the criterion of AC Robinson stability imposes the implementation of four Super3-HC modules. However, only one active superconducting module, powered with up to 100 kW, would suffice to obtain both beam stability and optimum bunch lengthening. Taking into account possible operational difficulties, we could realistically expect that the beam lifetime in 16-bunch operation mode would be increased from the current 10 hours to 30 hours. Concerning the single bunch operation mode dominated by the microwave instability, the lifetime would be doubled from 5 hours to 10 hours.

ACKNOWLEDGEMENTS

Special thanks to John Byrd (ALS) and Patrick Marchand (SLS/SOLEIL) for many fruitful discussions.

5 REFERENCES

- [1] J. Byrd, S. De Santis, J. Jacob, V. Serrière, “Transient beam loading effects in harmonic RF systems for light sources”, Phys. Rev. ST Accel. Beams, vol 5, 09001, 2002.
- [2] M. Georgson et al. “Landau Cavities at MAX II”, Nucl. Inst. and Meth. in Phys. Res. A 416, 1998.
- [3] V. Serrière, J. Jacob, “Expected Lifetime Improvement with a Superconducting harmonic RF system at the ESRF”, EPAC’02, Paris, 2002.
- [4] A. Hofmann, S. Myers, “Beam dynamics in a double RF system”, Proc. of the 11th Int. Conf. on High Energy Acc. ISR-TH-RF/80-26 (1980).
- [5] A. Hofmann, “Kinetic Theory”, CAS 95-06, CERN, Switzerland.

SYNERGIA: A HYBRID, PARALLEL BEAM DYNAMICS CODE WITH 3D SPACE CHARGE

J. Amundson* and P. Spentzouris†, FNAL, Batavia, IL 60510, USA

Abstract

We describe Synergia, a hybrid code developed under the DOE SciDAC-supported Accelerator Simulation Program. The code combines and extends the existing accelerator modeling packages IMPACT and beamline/mxyzptlk. We discuss the design and implementation of Synergia, its performance on different architectures, and its potential applications.

INTRODUCTION

Synergia is an accelerator physics simulation code with a fully three-dimensional space-charge model and circular and linear machine modeling capabilities. The implementation is fully parallel. Development of Synergia has been funded by the Department of Energy's SciDAC Advanced Accelerator Modeling Project. The goals of this project include building upon existing simulations and creating distributable code. Synergia is compatible with these goals because it is a hybrid code; the primary accelerator physics components are taken from existing, although possibly modified, codes. In the interests of distributability, we have taken care to ensure that Synergia is easy to build on various architectures.

Below, we give a brief description of the components used in Synergia as well as the details involved in combining them into a single product. We pay close attention to the build system, in keeping with the "distributable" goal mentioned above. We also describe how we have taken advantage of Python to give us a flexible, humane user interface with very little effort. Since space-charge calculations are computationally intensive, we present benchmarks for our code running on various parallel clusters. Finally, we compare Synergia simulation results with results from a recent accelerator study.

COMPONENTS

The two packages at the core of Synergia are IMPACT[1] and the mxyzptlk/beamline libraries[2]. We have added glue code and a human-interface wrapper to these packages to form the Synergia package.

Impact

Synergia uses IMPACT for its parallel implementation of particle propagation, RF modeling and, most importantly, parallel space-charge calculations. IMPACT contains a fully three-dimensional space charge model utiliz-

ing the split-operator technique. The split-operator technique is applicable for Hamiltonian of the form

$$H = H_{\text{ext}} + H_{\text{sc}}, \quad (1)$$

where, in our case, H_{ext} is the Hamiltonian for the magnetic optics part of the problem and H_{sc} is the Hamiltonian for the space-charge part of the problem. If the transfer maps corresponding to the individual Hamiltonians H_{ext} and H_{sc} are \mathcal{M}_{ext} and \mathcal{M}_{sc} , respectively, then

$$\mathcal{M}(t) = \mathcal{M}_{\text{ext}}(t/2)\mathcal{M}_{\text{sc}}(t)\mathcal{M}_{\text{ext}}(t/2) + \mathcal{O}(t^2) \quad (2)$$

is the transfer map for H to leading order in t . The problem of calculating beam propagation including space-charge effects therefore factorizes into the problem of calculating the two effects one at a time and combining them as above. The space-charge effects in IMPACT are calculated by solving the Poisson-Vlasov Equation using particle-in-cell (PIC) methods. The magnetic optics effects vary quickly, but require little CPU time to compute. The space-charge effects vary slowly, but require a great deal of CPU time to compute. Without the factorization above, we would be forced to calculate the space-charge effects on the time scale set by the magnetic optics effects, which would be computationally prohibitive.

Mxyzptlk/Beamline Libraries

The mxyzptlk/beamline package is a set of C++ libraries covering a wide range of accelerator physics computations. This package was the first C++ library for accelerator physics. Even though the original code is over 10 years old, the libraries are written in a modern style, including real objects with encapsulation and well-considered interfaces. The package includes *basic toolkit*, a set of useful utility classes such as Vector, Matrix, etc., *beamline*, objects for modeling elements of a beamline including a full parser for the Methodological Accelerator Design (MAD) language, *mxyzptlk*, automatic differentiation and differential algebra, and *physics toolkit*, a set of classes for analysis and computation.

One of most important features of the mxyzptlk/beamline package for our purposes is the ability to read accelerator descriptions in the MAD language. Since MAD has become the *lingua franca* of accelerator description, being able to directly use MAD files greatly enhances the usability of Synergia. The flexibility of the beamline/mxyzptlk libraries made it easy for us to utilize the features we needed, namely the MAD parser and generalized propagator functors. Synergia passes a mad file and beamline name to beamline and beamline returns an array of transfer maps divided into an arbitrary number of slices.

* amundson@fnal.gov

† spentz@fnal.gov

SYNERGIA

Synergia is the combination of IMPACT, mxyzptlk/beamline, glue code to get the two packages talking to each other and a wrapper providing a simple, yet powerful, human interface. Figure 1 shows the relationship between Synergia components as well as the role MAD files, studies and analysis tools play in producing results.

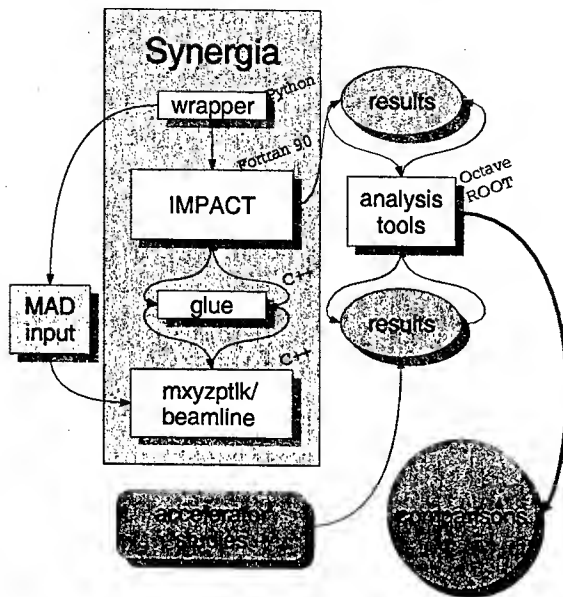


Figure 1: Synergia components and their relation to outside inputs.

Build System

Portability has been a major design concern in creating Synergia. We rely on multiple components written in multiple languages. While using multiple components allows us to quickly put together a powerful package, it also creates a configuration management problem. Multiple-language issues are particularly problematic because calling conventions vary from platform to platform. We solve the multiple language part of the problem by writing all of the inter-language wrapper code in terms of macros that can be redefined for various platforms. We solve configuration management problem by incorporating a modern build system based on the GNU Autotools to provide consistent builds on all platforms.

In principle, building Synergia is as simple as executing “./configure && make && make install” in the mxyzptlk directory followed by “./configure && make” in the Synergia directory. In practice, many options to configure are available. The two principles we have followed in constructing the build system are (1) modifying the source (including Makefiles) should never be necessary, and (2) all options should come with reasonable defaults.

To date, Synergia builds without modifications on Linux systems using either the Portland Group F90 compiler or the Intel F90 compiler, g++, and either MPICH or lam. Synergia also builds without modifications on AIX, using XL Fortran, Visual Age C++ and POE. Compiling Synergia on other platforms should be a straightforward exercise.

Human Interface

The user-level interface to Synergia consists of a set of Python classes that wrap the low-level interfaces to the code. To run Synergia, the user writes a short Python script utilizing these classes. An example script excerpt is shown in Figure 2. The use of Python has several advantages: There is no specialized syntax to learn. A user familiar with Python will be able to understand the entire interface easily. A user unfamiliar with Python will be able to copy an example script and modify it with little difficulty. Although most examples will only use Python trivially, the full power of the language is available should it be needed. Last, but not least, the use of an existing scripting language greatly simplifies our implementation, meaning we were able to write it quickly with a minimum of opportunities for introducing bugs.

```
p = impact_parameters.Impact_parameters()
ip.processors(16,4)
ip.space_charge_BC(
    "trans finite, long periodic round")
ip.input_distribution("6d gaussian")
ip.pipe_dimensions(0.04,0.04)
ip.kinetic_energy(0.400)
ip.scaling_frequency(201.0e6)
ip.x_params(sigma = .004 , lam = 1.0e-4)
ip.y_params(sigma = .004 , lam = 1.0e-4)
pz = ip.gamma() * ip.beta()*ip.mass_GeV
ip.z_params(sigma = 0.10, lam = 3.0e-4 * pz)
ip.particles(2700000)
ip.space_charge_grid(65,65,65)
booster = impact_elements.External_element(
    length=474.2,kicks=100, steps=1,
    radius=0.04,
    mad_file_name="booster.mad")
for turn in range(1,11):
    ip.add(booster)
```

Figure 2: Example excerpt of a Python script showing the Synergia user interface.

Parallel Performance

We have run benchmarks of our code on four different clusters under a variety of configurations. Our benchmark is a simulation of a single revolution of the FNAL Booster (see the following section.) The simulation included 2.7 million particles undergoing 100 space-charge kicks on a $65 \times 65 \times 65$ grid.

Three of the clusters are Linux clusters: lqcd[4], heimdall[5] and Alvarez[6]. Our benchmarks include a sampling of the range of currently-available networking options for Linux: 100 Mbit Ethernet, Gigabit Ethernet and Myrinet 2000. We also compared the performance of the Intel fortran compiler (ifc) with the Portland Group fortran compiler (pgf90). For the former, the code was compiled with the optimization setting "-O2". For the latter the code was compiled with the setting "-fast". The fourth cluster we used for benchmarking was Seaborg[7], the 6,080-processor IBM SP at NERSC.

The results of our benchmarks are displayed in Figure 3. Overall, we find that Synergia scales very well up to a certain scale set by the networking used. The clear winner in scaling is the specialized configuration found in Seaborg. The fastest Linux clusters, however, showed overall superior performance. We can also see that Gigabit or Myrinet is necessary for a Linux cluster to effectively take advantage of more than a few processors. These tests were insufficient to distinguish between Gigabit and Myrinet. Somewhat surprisingly, we also see that the Intel compiler produced significantly better performance than the Portland compiler for our application.

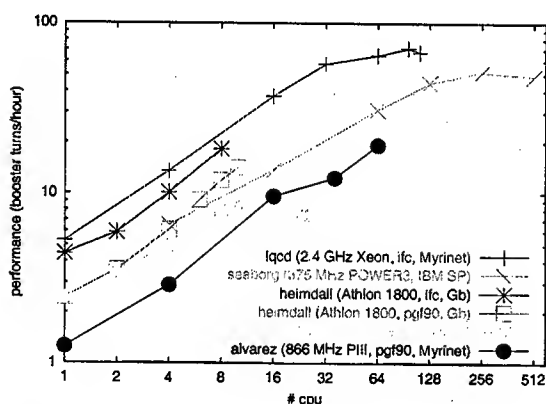


Figure 3: Performance on various parallel machines.

APPLICATION TO FNAL BOOSTER

The first important application of Synergia has been to model the FNAL Booster[3]. The Booster is an alternating gradient synchrotron with a radius of 75.47 meters. It accelerates protons from 400 MeV to 8 GeV with a typical injected current of over 450 mA. Since space-charge effects are expected to be significant in the Booster it is an excellent testing ground for Synergia.

As an example, Figure 4 shows a comparison between measured vertical and horizontal beam widths in the Booster with a Synergia simulation. Here 42 mA of current was injected in each of the 11 initial turns. For a more detailed discussion of recent FNAL Booster studies including comparisons to Synergia, see Reference [8].

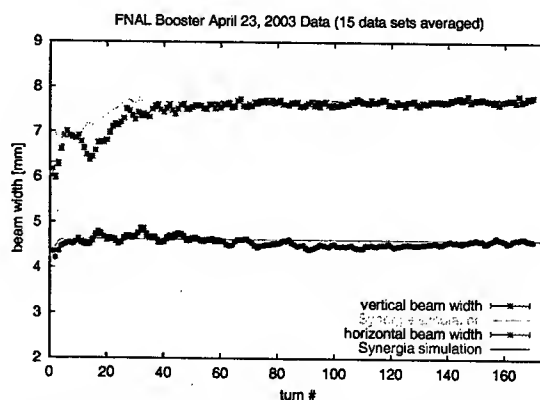


Figure 4: Synergia simulations compared to beam width measurements from the FNAL Booster.

REFERENCES

- [1] J. Qiang, R. D. Ryne, S. Habib and V. Decyk, J. Comput. Phys. 163, 434 (2000).
- [2] L. Michelotti, FERMILAB-CONF-91-159 Presented at 14th IEEE Particle Accelerator Conf., San Francisco, CA, May 6-9, 1991.
L. Michelotti, FERMILAB-FN-535-REV.
L. Michelotti. Published in Conference Proceedings: *Automatic Differentiation of Algorithms: Theory, Implementation, and Application*. Society for Industrial and Applied Mathematics. First International Workshop on Computational Differentiation. 1991.
L. Michelotti. Published in Conference Proceedings: *Advanced Beam Dynamics Workshop on Effects of Errors in Accelerators, their Diagnosis and Correction*. Corpus Christi, Texas. October 3-8, 1991. American Institute of Physics: Proceedings No.255. 1992.
- [3] Booster Staff 1973 *Booster Synchrotron* ed E L Hubbard *Fermi National Accelerator Laboratory Technical Memo TM-405*
- [4] <http://lqcd.fnal.gov/>
- [5] Linux cluster in the beams theory department at Fermilab.
- [6] <http://www.nersc.gov/alvarez/>
- [7] <http://hpcf.nersc.gov/computers/SP/>
- [8] P. Spentzouris and J. Amundson, "Space charge studies and comparison with simulations using the FNAL Booster," Proc. International Computational Accelerator Physics Conference (ICAP 2002), Michigan State University, Oct. 2002; see also P. Spentzouris and J. Amundson, *these proceedings*.

FLAT BEAM PRODUCTION IN LOW ENERGY INJECTORS

S.-H Wang*, Indiana University, IN 47408, USA

J. Corlett, S. Lidia, J. Staples, A. Zholents, LBNL, Berkely, CA 94720, USA

Abstract

A source of ultra-fast synchrotron radiation pulses based on a recirculating superconducting linac is proposed at LBNL[1]. A flat beam will be produced in the low energy phase. High-brightness photocathode rf gun will produce electron beams in a solenoidal magnetic field. The electron beam will be transformed into flat beam with a large x/y emittance ratio by a skew-quadrupole-sequence adaptor[2]. A theoretical model is shown and simulations have been done with PARMELA. Space charge effect and possible solenoid setup are reported.

FLAT BEAM PRODUCTION

Beam Dynamics in Magnetic Field

For the production of flat beam, the cathode is immersed in solenoid magnetic field, hence, the beam is born with finite canonical angular momentum. Considering only the linear term of z component of solenoid field, B_z , we have equations of motion like:

$$x'' - Sy' - \frac{1}{2}S'y = 0 \quad (1)$$

$$y'' + Sx' + \frac{1}{2}S'x = 0 \quad (2)$$

where $S = \frac{eB_z}{P_z}$, P_z is the Z component of the particle momentum, prime indicates the derivative with respect to Z. Equations (1), (2) can be combined into a single complex equation:

$$\xi'' + iS\xi + \frac{iS'\xi}{2} = 0 \quad (3)$$

if we let:

$$\xi = x + iy$$

Equation (3) can be further simplified in Larmor frame

$$u'' - \phi'^2 u = 0 \quad (4)$$

by making a rotation transformation, letting:

$$u = \xi e^{i\phi}, \quad \text{where } \phi' = \frac{S}{2}$$

ϕ is a non-periodic function of Z. There are two fundamental phase-amplitude form solutions exist for equation (4) [3]:

$$u = W(z) e^{i(\pm\psi(z))} \quad (5)$$

*shaowang@indiana.edu

If we substitute this solutions into equation (4), we can get following relations:

$$\psi' = \frac{1}{W^2} \quad (6)$$

$$W'' + \phi'^2 W - \frac{1}{W^3} = 0 \quad (7)$$

For equation (4), the general solution can be written as:

$$u = AW e^{i(\psi+\delta_+)} + BW e^{i(-\psi+\delta_-)} \quad (8)$$

Where A, B, δ_+ and δ_- are constants decided by initial conditions. In phase space of u and u' , we can get expressions for A as

$$\sqrt{2}A e^{i(\psi+\delta_++\frac{\pi}{2})} = \frac{1}{\sqrt{2}}(u'W - uW' + \frac{iu}{W}) \quad (9)$$

Note, the modulus of the lhs of equation (9) is a constant, so will be the rhs. If we take the modulus of both sides and use the real and image part of u and u' to express the result, we will get:

$$\epsilon_+ = \frac{1}{2}\epsilon_r + \frac{1}{2}\epsilon_i + L_u \quad (10)$$

where

$$\begin{aligned} \epsilon_+ &= 2A^2 \\ \epsilon_r &= \frac{u_r^2}{W^2} + (W'u_r - Wu'_r)^2 \\ \epsilon_i &= \frac{u_i^2}{W^2} + (W'u_i - Wu'_i)^2 \\ L_u &= u_ru'_i - u'_ru_i \end{aligned}$$

similarly, from expression of B, we have

$$\epsilon_- = \frac{1}{2}\epsilon_r + \frac{1}{2}\epsilon_i - L_u \quad (11)$$

where

$$\epsilon_- = 2B^2$$

Here, we can introduce the Twiss parameter in Larmor frame,

$$\beta_l = W^2, \quad \alpha_l = -WW', \quad \gamma_l = \frac{1 + \alpha_l^2}{\beta_l} \quad (12)$$

and get ϵ_r and ϵ_i in new expressions,

$$\epsilon_r = \gamma_l u_r^2 + 2\alpha_l u_r u'_r + \beta_l u_r'^2 \quad (13)$$

$$\epsilon_i = \gamma_l u_i^2 + 2\alpha_l u_i u'_i + \beta_l u_i'^2 \quad (14)$$

The real and image components of u and u' correspond to the movements in x and y dimensions in Larmor frame, respectively. When particles get out of the solenoid field region, the Larmor frame is same as lab frame, then ε_r becomes ε_x , and ε_i becomes ε_y . If we combine equation (10), (11), we can get following simple relations:

$$\varepsilon_+ + \varepsilon_- = \varepsilon_x + \varepsilon_y \quad (15)$$

$$\varepsilon_+ - \varepsilon_- = 2L_u \quad (16)$$

Note, ε_+ and ε_- are constants decided by initial conditions, no matter within or outside the solenoid field region. ε_x and ε_y are measured outside the solenoid field region, and they are regular emittances. Experimentally, we can get the value of ε_+ and ε_- by measuring the ε_x , ε_y and L_u .

Initial Conditions

So, What initial conditions decide ε_+ and ε_- ? Let's simplify the problem by assuming uniform $\frac{B_z}{P_z}$ at the very first moment after electrons are emitted. Then we have:

$$\phi' = \text{constant}$$

$$W = \text{constant}$$

$$\psi = \phi'Z$$

$$\alpha_l = 0$$

$$\beta_l = \frac{1}{\psi'} = \frac{1}{\phi'} = \frac{2P_z}{eB_z}$$

Then, in Lab frame, we have

$$x = \sqrt{\frac{\varepsilon_+\beta_l}{2}} \cos(\delta_+) + \sqrt{\frac{\varepsilon_-\beta_l}{2}} \cos(-2\phi'Z + \delta_-)$$

$$x' = \sqrt{\frac{2\varepsilon_-}{\beta_l}} \sin(-2\phi'Z + \delta_-)$$

$$y = \sqrt{\frac{\varepsilon_+\beta_l}{2}} \sin(\delta_+) + \sqrt{\frac{\varepsilon_-\beta_l}{2}} \sin(-2\phi'Z + \delta_-)$$

$$y' = -\sqrt{\frac{2\varepsilon_-}{\beta_l}} \cos(-2\phi'Z + \delta_-)$$

In above equations, two terms on rhs involve ε_+ , and these two terms describe the position of the center of the cyclotron motion. All other terms are ε_- related, they describe the cyclotron motion itself.

From above equations, we can get the expressions for ε_+ and ε_- in uniform $\frac{B_z}{P_z}$ region,

$$\varepsilon_+ = \frac{r_0^2 e B}{P_z} \quad (17)$$

$$\varepsilon_- = \frac{P_z v_\perp^2}{e B} \quad (18)$$

where $v_\perp^2 = x'^2 + y'^2$. r_0 is the distance from the center of the cyclotron motion to solenoid axis. Multiply both sides with P_z , we get two normalized quantities,

$$\varepsilon_+ = r_0^2 e B \quad (19)$$

$$\varepsilon_- = \frac{P_z^2}{e B} \quad (20)$$

where P_\perp is the transverse momentum. Hence, acceleration along solenoid axis is included. From here, we know that initial transverse distribution combined with B_z decide ε_+ , and initial transverse momentum combined with B_z decide ε_- .

The Transformation

Since after particles leave the solenoid field region, ϕ won't change any more, we can combine it with another constant phase δ_\pm :

$$\chi_+ = \delta_+ - \phi$$

$$\chi_- = \delta_- - \phi$$

And in Lab frame, we can get the matrix form of solutions of equation (4)

$$\begin{pmatrix} x \\ x' \\ y \\ y' \end{pmatrix} = V \begin{pmatrix} \sqrt{\varepsilon_+} \cos \chi_+ \\ \sqrt{\varepsilon_+} \sin \chi_+ \\ \sqrt{\varepsilon_-} \cos \chi_- \\ \sqrt{\varepsilon_-} \sin \chi_- \end{pmatrix}, \quad \text{or: } \vec{X} = V \vec{a} \quad (21)$$

$$V = \begin{pmatrix} \frac{\sqrt{\beta_l} c}{-\alpha_l c - s} & -\sqrt{\beta_l} s & \frac{\sqrt{\beta_l} c}{-\alpha_l c + s} & \frac{\sqrt{\beta_l} s}{-\alpha_l c - s} \\ \frac{\sqrt{\beta_l}}{\sqrt{\beta_l}} & \frac{\sqrt{\beta_l}}{\sqrt{\beta_l}} & \frac{\sqrt{\beta_l}}{\sqrt{\beta_l}} & \frac{\sqrt{\beta_l}}{\sqrt{\beta_l}} \\ \frac{\sqrt{\beta_l} s}{-\alpha_l c + s} & \frac{\sqrt{\beta_l} c}{-\alpha_l c - s} & \frac{\sqrt{\beta_l} s}{-\alpha_l c + s} & \frac{\sqrt{\beta_l} c}{-\alpha_l c - s} \end{pmatrix} \quad (22)$$

where $c = \cos \psi$, $s = \sin \psi$. The transformation from round beam to flat beam is to block-diagonalize matrix V by passing such a beam described by equation (21) through the adaptor. The quantities in \vec{a} are constants during the transformation, and after transformation, ε_+ and ε_- are recognized as the emittances of x and y dimension, respectively. Because of the special initial conditions (the cathode is immersed in solenoid field), ε_+ is usually much larger than ε_- . Hence, we finally get a flat beam.

After the transformation, for the flat beam, we can use regular Twiss parameters to describe the beam. It can be derived that the Twiss parameters at the exit of the adaptor satisfy:

$$\beta_x = \beta_y \quad \alpha_x = \alpha_y \quad (23)$$

and phase advance of the adaptor section satisfy:

$$\Delta \Phi_y = \Delta \Phi_x + \frac{\pi}{2} \quad (24)$$

Skew-quadrupole-triplet has been used as the adaptor in experiments to realize the transformation [4] for the capability of skew quadrupole to remove the canonical angular momentum. A0 group at FNAL has achieved flat beam production experimentally.

SIMULATIONS

We have done some simulations with PARMELA[5]. The space charge effect is not included in the above theoretical model, although it definitely contributes in experiments. We simulate A0 beamline at FNAL[4]. The bunch

charge is about 1 nC, and the energy at the adaptor is about 15 MeV. In simulations, We let electron bunch travel until it arrive at the entrance of the adaptor. In this part 2D space charge effect is included in simulation. According to the particle distribution in 6D phase space, we can calculate ε_{\pm} and search for the skew quadrupole gradients which can provide suitable transformation according to the above model. Then we set the skew quadrupole gradients and let the bunch resume travelling. If we turn off space charge calculation, we do get a flat beam with $\varepsilon_{x,y}$ very close to ε_{\pm} , by "very close" I mean the discrepancy is less than 3%. But if we turn 3D space charge calculation, the final $\varepsilon_{x,y}$ of the flat beam is 20 to 30 percent higher, while we can fine-tune the skew quadrupole gradients to get the final $\varepsilon_{x,y}$ about 10% higher than ε_{\pm} .

FUTURE WORK

Simulations also show that, the transformation is very sensitive to the energy spread of the bunch. One possible way to reduce the energy spread is to reduce the longitudinal space charge force by increasing the bunch transverse size in strong space charge effect region. If we look at the solenoid field distribution of the typical solenoid setup for flat beam production, Fig. 1, we noticed that the solenoid provides a strong focusing at initial accelerating phase.

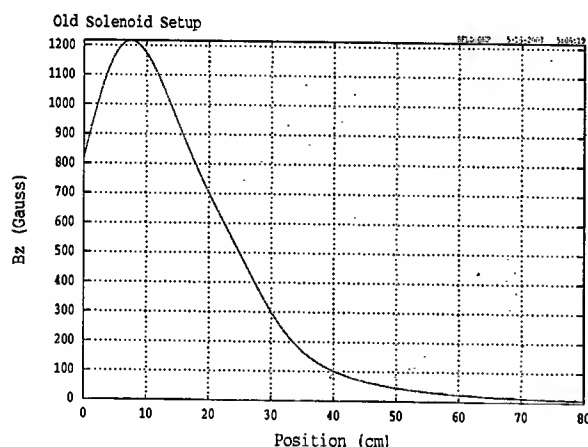


Figure 1: Bz from old solenoid setup

If we change the currents of the solenoid setup and get a new magnetic field distribution like in Fig. 2, the beam transverse size will be larger with weaker solenoid focusing. Simulations has shown obvious energy spread reduction for this new solenoid setup. Experiments need to be done to verify it. And possible side effect of the new solenoid setup need to be investigated.

REFERENCES

- [1] J. Corlett et al, This conference, TOAC003

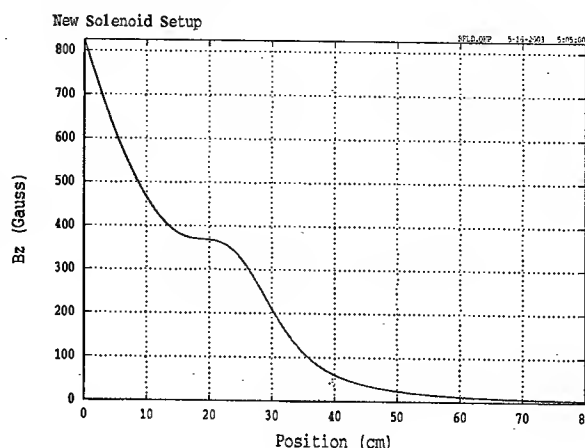


Figure 2: Bz from new solenoid setup

- [2] R. Brinkmann, Ya. Derbenev, K. Flottmann, "A low emittance, flat -beam electron source for linear colliders" Phys. Rev. ST Accel. Beams 4, 053501, 2001
- [3] M. Reiser, "Theory and Design of Charged Particle Beams", John Wiley & Sons, Inc. 1994
- [4] D. Edwards et al, "Status of Flat Electron Beam Production", Proceedings of IEEE Particle Accelerator Conference, 2001
- [5] L. Young, "PARMELA", LANL

LOW EMITTANCE OPTICS AT THE PHOTON FACTORY

K. Harada, Y. Kobayashi, T. Obina, A. Ueda and M. Izawa
Photon Factory, High Energy Accelerator Research Organization,
1-1 Oho, Tsukuba, 305-0801, Ibaraki, Japan

Abstract

We successfully reduced the emittance of the Photon Factory storage ring (PF ring) to as low as 28 nm-rad, which is very close to the theoretical minimum (27.3 nm-rad) under the present lattice configuration. The new low emittance optics had been already tried, however, we could not examine it sufficiently because of a poor injection rate. Recently, new kicker magnets developed for the new optics were installed in the ring. Since the injection rate of more than 1 mA/sec became steady, the new optics was fully examined. No difficulty was found up to the stored current of 500 mA. The operation with the new optics for users' experiments will start in near future.

INTRODUCTION

Figure 1 shows the lattice configuration of PF ring which was reconstructed in order to realize the low emittance optics in 1997 [1]. Since then, the ring has been operated with the optics having the emittance of 35.7 nm-rad at 2.5 GeV, which is one-fourth smaller than previous one (130 nm-rad). It was clearly known that we could reduce the emittance by increasing the horizontal phase advance of normal cell in the arc sections of the ring. However, the stronger focusing makes the dispersion function smaller, therefore, the strength of sextupole magnets should be larger in order to correct the chromaticity, resulting in a very narrow dynamic aperture due to the large non-linearity produced by the sextupole magnets [2]. This makes the beam injection very difficult. In order to improve the injection rate, we designed new travelling wave kicker magnets, and installed them in October 2002 [3]. In this paper, we will introduce the optics with the emittance of 28.0 nm-rad, and show the results of measurements carried out in the machine development.

LOW EMITTANCE OPTICS

The horizontal phase advance of normal cell in present optics is set to be 105 degree. The emittance is 35.7 nm-rad. If the phase advance is set to be 125 degree, the emittance is reduced to 28.0 nm-rad. We call the optics as low emittance optics in this paper. Figure 2 shows the comparison of optical functions between present and low emittance optics in some normal cells. It is clearly found that the dispersion function of low emittance optics is much smaller than that of present optics. Both of optical functions of the ring measured using the response matrix methods [3] are shown in Fig. 3. The comparisons of dynamic apertures are shown in Fig. 4. It is clear that the

horizontal aperture of the low emittance optics is only one-half of that of present optics. This is reason why the beam injection is quite difficult.

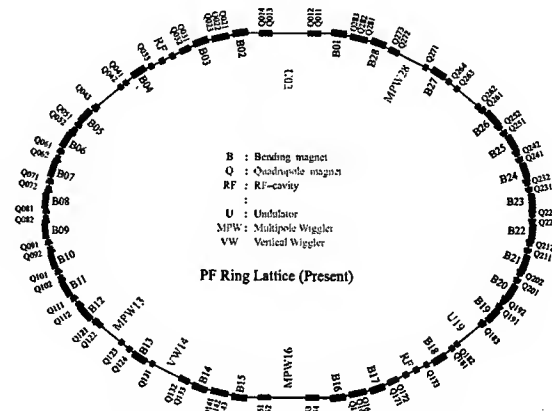


Figure 1: Lattice configuration of PF ring.

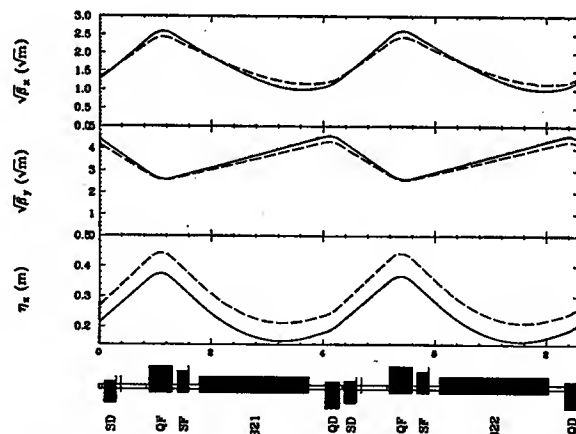
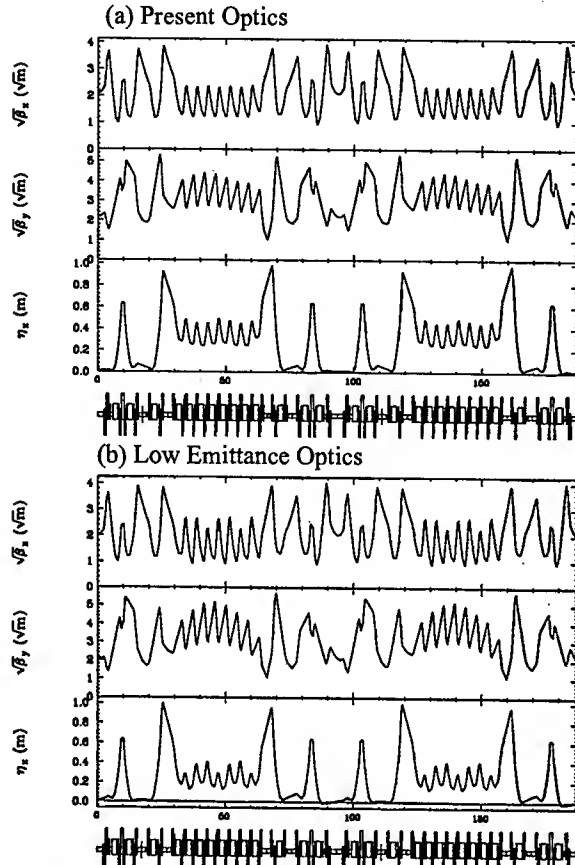


Figure 2: Comparison of optical functions between present and low emittance optics in some normal cells. The solid line shows low emittance optics, and the dashed line present optics.

INJECTION PARAMETERS

A set of parameters of the injection magnets is given in Table 1. The maximum kick angle of previous kicker magnets was limited to 3 mrad. As shown in Table 1, the kick angle of K3 and K4 magnets reached almost maximum value even in present optics. Since the kick angle required for the low emittance optics had been estimated to be more than 3 mrad, the beam injection was expected to be quite severe in the use of the same parameters. Actually, the injection rate was less than 0.2

mA/sec at a repetition rate of 25 Hz. New kicker magnets were designed to have maximum kick angle up to 3.5 mrad. They enabled us to set new injection parameters over 3 mrad for low emittance optics as shown in Table 1.



Figures 3: Fig. (a) shows optical functions of the ring for present optics, and (b) for low emittance optics.

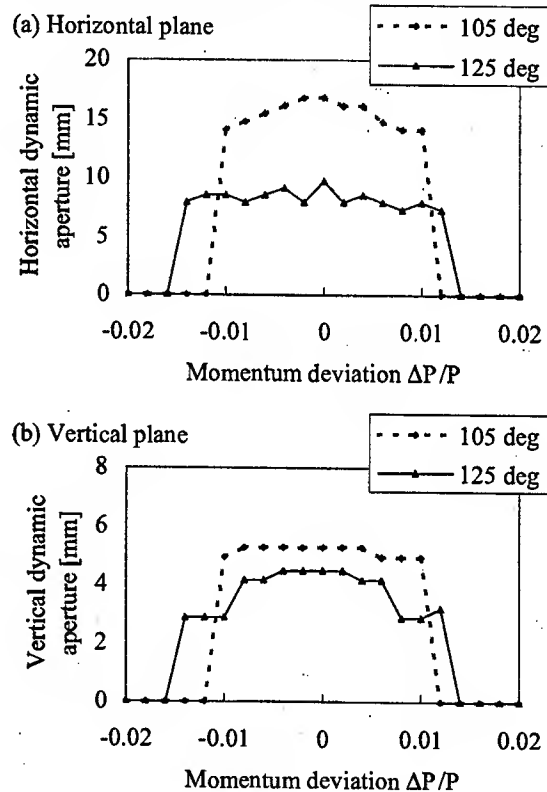
Table 1: Set parameter of the injection magnets. The first initial K and S indicate kicker magnets and septum magnets, respectively.

	105 deg	125 deg
K1 (mrad)	2.507	3.107
K2 (mrad)	-1.649	-2.549
K3 (mrad)	2.928	3.428
K4 (mrad)	2.912	2.812
S1 (mrad)	117.74	117.64
S2 (mrad)	101.7	102.8

COHERENT OSCILLATION OF THE INJECTED BEAM

We measured the coherent oscillation of injected beam using turn-by-turn position monitor [5]. Before the measurement, the kicker parameters were roughly adjusted so as to increase the injection rate. Typical results of the measurement are shown in Figs. 5. During

several turns just after the injection, the amplitude of the injected beam is so large to be scraped by the septum wall and about 10% of the injected beam is lost, indicated as region(i) in Fig. 5 (a). The damping time is about 11000 turns but the amplitudes of the injected beam rapidly decrease by the smear effect due to the non-linear fields, as shown in figures (b) and (c). The part of the beam indicated as region (ii) is injected outside of the dynamic aperture and lost in several hundred turns. In the region (iii), the beam current seems to be decreased, however, in this region, the bunch length may become long and it may cause the lower sensitivity of the beam monitor. The stored beam is cleared by the RF knock out before the next measurement. The optimization was done so as to minimize the beam loss in the region(i). The improvement of the injection rate is about 10% in this case.

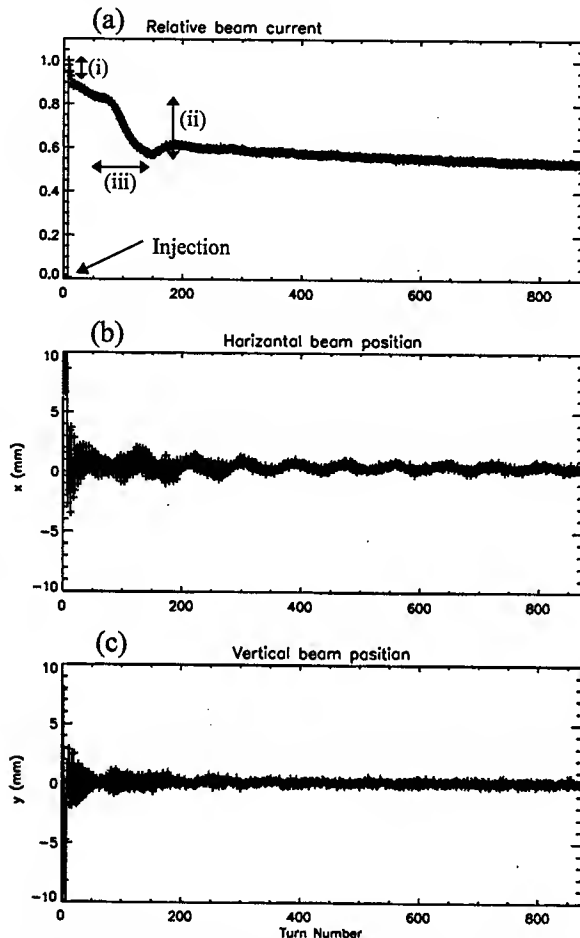


Figures 4: Fig. (a) shows dynamic aperture at a center of 5m long straight in the horizontal plane, and (b) in the vertical plane. The solid line indicates the aperture for low emittance optics, and the dashed line for present optics.

OPTICS TUNING

Since the injection rate was strongly sensitive for the betatron tunes, we carried out the tune survey around the designed tune. The tune point giving the injection rate of 1 mA/sec at a repetition rate of 25 Hz was found and fixed. In this point we measured the response matrix of all steering magnet to investigate the beta functions, and also dispersion function as shown in Fig. 2(b). Through the

analysis of the response matrix, we estimated that the emittance was 28.0 nm-rad, and that betatron tunes were $(\nu_x, \nu_y) = (10.42, 4.37)$. The values of tunes agreed well with those obtained from the tune measurement. The typical injection history is shown in Fig. 6.



Figures 5: Coherent oscillation of the injected beam: (a) shows the turn-by-turn relative beam current, (b) the horizontal beam position and (c) the vertical one. The horizontal axis indicates the turn number from the injection.

FUTURE PLAN

Even in low emittance optics the beam lifetime was quite long. When the beam current (I) was stored up to 450 mA, the beam lifetime (τ) was over 45 hours, and $I \cdot \tau$ was over 1200 (A·min). These values are comparable for the present optics. It might be due to the XY coupling. In the next step, we challenge to minimize the emittance, which is 27.3 nm-rad. The minimum emittance will be realized when the horizontal phase advance of the normal cell is set to be 135 degree. We had tried this optics before installing new kickers, however, only the current of 4.6 mA could be stored without excitation of sextupole magnets. The dynamic aperture is, therefore, extremely

small. It will be interesting to study this optics with the new kicker magnets.

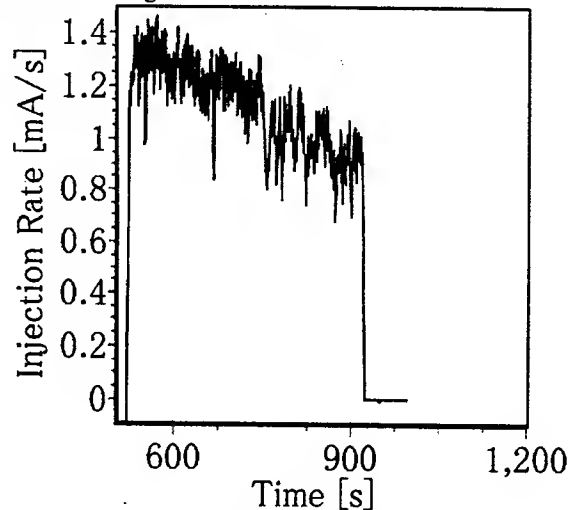


Figure 6: Typical injection history is shown when beam was stored from a current of 0 mA to 450 mA.

SUMMARY

We tried to reduce emittance much less. The emittance of as low as 28.0 nm-rad was achieved under the new low emittance optics using new kicker system. Though the dynamic aperture was one-half of that of the present optics, the kicker system enabled us to improve the injection rate over 1 mA/sec at a repetition rate of 25 Hz. We measured the coherent oscillation of the injected beam, and found that over 50% of them were captured. Consequently, we could smoothly store the beam current up to 450 mA, the nominal beam current at present PF ring.

REFERENCES

- [1] M. Katoh et al., J.Synchrotron 5, 1998, p.366
- [2] E. Kim et al., Jpn.J.Appl.Phys. 36, 1997, p.7415
- [3] Y. Kobayashi et al., in this proceedings.
- [4] J. Safranek, Nucl.Instr.Meth. A388, 1997, p.27
- [5] Y. Kobayashi et al., Proc. of EPAC, Spain, 1996, p.1666

INJECTION PERFORMANCE WITH A TRAVELING WAVE KICKER MAGNET SYSTEM AT THE PHOTON FACTORY STORAGE RING

Y. Kobayashi, T. Mitsuhashi, and A. Ueda
Photon Factory, High Energy Accelerator Research Organization
1-1 Oho, Tsukuba, Ibaraki 305-0801, Japan

Abstract

At the Photon Factory storage ring (PF-ring), four traveling wave kicker magnets were installed to obtain a wide acceptance for the injected beam in the high brilliant optics. The pulse shape and the excitation curve of the kick angles were measured using the stored beam. The phase-space motion of the stored beam after the excitation of the injection bump kick was measured. We achieved an injection speed more than 1.0 mA/s at a repetition rate of 12.5 Hz.

INTRODUCTION

The Photon Factory (PF) ring is a 2.5 GeV electron storage ring as a dedicated synchrotron radiation source. In 1994, we started the high-brilliant project. In this project, we modified the optics of ring to reduce the horizontal emittance from 130 nm-rad to 27 nm-rad [1]. The dynamic aperture was reduced to four times smaller than previous optics by this modification [2]. Due to the narrow dynamic aperture, we encountered some difficulties in the design of the injection with existed kicker magnets. To solve the difficulties, we applied kicker magnets having a shorter pulse length and a larger kick angle. We designed and constructed new travelling-wave type kicker magnets to realize these requests [3]. In October 2002, the kicker magnets were installed in the ring and started the operation. In this paper, it is described about the performance of the kicker magnets and the measured coherent oscillations of the stored beam using the actual beam.

OPTICS AROUND THE KICKER MAGNETS AND INJECTION BUMP

The square root of horizontal beta function (upper part) and the designed injection bump (lower part) with the lattice configuration in the injection section are shown in Fig. 1. The kicker magnets are named K1, K2, K3 and K4 from the upper stream of the ring. The principal parameters are listed in Table 1.

Table 1: The parameters of the kicker magnets.

Pulse length	1.3 μ sec
Total magnet length	400 mm
Gap height	60 mm
Maximum voltage	15 kV
Maximum kick angle at 2.5 GeV	4 mrad

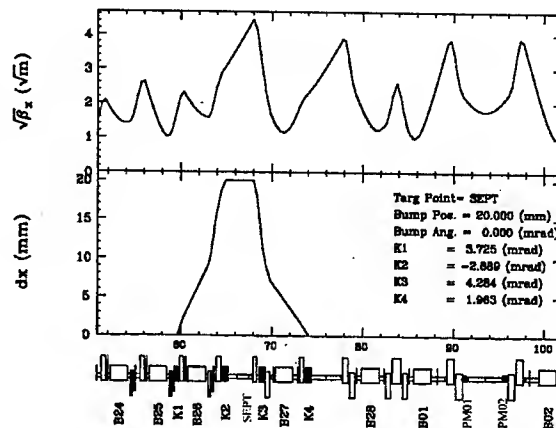


Figure 1: The square root of horizontal beta function (upper part) and the designed injection bump (lower part) are shown with the lattice configuration in the injection section.

PHASE-SPACE MONITOR

A pair of the beam position monitors (BPMs) is used for a phase-space monitor. The monitors are installed at the both end of long straight section. The distance between the monitors is 4.3 m [4]. The each monitor has six button-type electrodes, and the electrode is independently connected to the turn-by-turn detection circuit. The block diagram of the circuit is shown in Fig. 2.

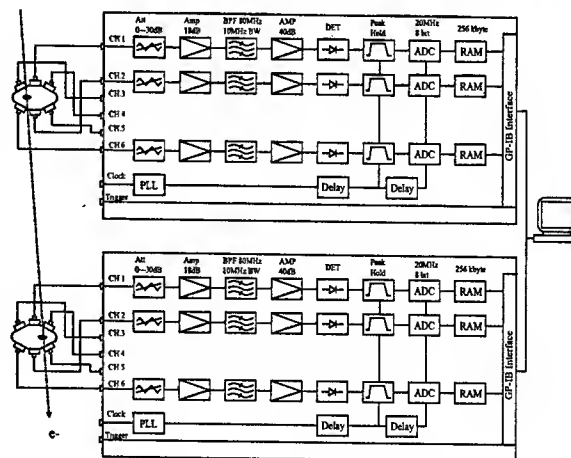


Figure 2: Block diagram of the turn-by-turn detection circuit.

The circuits consist of variable attenuators, RF amplifiers, band-pass filters, peak detectors with a sample hold, 8-bit 20MHz ADCs and 256 kbyte memories. The data acquisition is started with the external trigger. The analog signals from the electrodes are desitized within a revolution period of 624 nsec. The desitized data are stored in the memories and sent to on-line computer through GP-IB when the memories become full.

MEASUREMENT OF THE PULSE SHAPES AND EXCITATION CURVES

We measured the pulse shapes and the excitation curves of the kicker magnets through the coherent oscillation of the stored beam. The oscillation was produced by the excitation of the magnets. The measurements were carried out using the single-bunch beam of 5 mA. The turn-by-turn position and angles of coherent oscillation were measured using the phase-space monitor. Figure 3 shows the block diagram of the trigger circuits for four kicker magnets. The timings of trigger pulses are controlled using independent four delay modules. The measurements of pulse length were carried out by changing the delay time of trigger pulses from 0 nsec to 650 nsec by 50 nsec step. The excitation curves of the kick angle were measured by changing the output voltage of power supplies from 2 kV to 5 kV by 1 kV step.

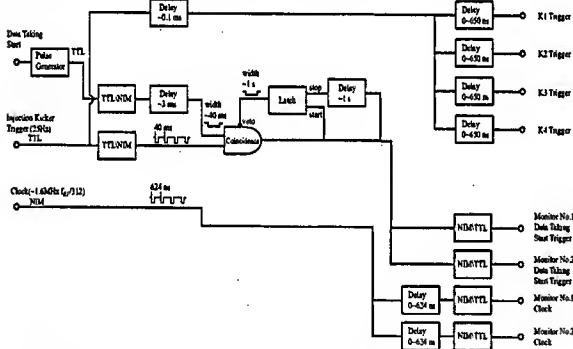


Figure 3: Block diagram of the trigger circuits for the kicker magnets, which is controlled by independent delay modules. The block diagram of data taking timing is also shown.

MEASUREMENT RESULTS

The turn-by-turn beam positions are evaluated by the following equations,

$$\begin{cases} U(n) = \frac{v_1(n) - v_3(n) - v_4(n) + v_6(n)}{v_1(n) + v_3(n) + v_4(n) + v_6(n)} \\ V(n) = \frac{v_2(n) - v_5(n)}{v_2(n) + v_5(n)} \end{cases} \quad (1)$$

$$x(n) = \sum_{i=0}^6 \sum_{j=0}^6 k_x(i, j) U^i(n) V^j(n) \quad (2)$$

where $v_i(n)$ is the digitized data of i -th channel of the BPM, n turn number, and k_x the two-dimensional transfer

coefficients to the beam position. The coefficients are calculated using a mapping data of the BPM. Since only the drift space exists between the monitors, the positions and the angles of the beam at the center of the monitors are simply calculated by the following equation,

$$\begin{cases} x_M(n) = \frac{x_{1M}(n) + x_{2M}(n)}{2} \\ x'_M(n) = \frac{x_{2M}(n) - x_{1M}(n)}{\ell_M} \end{cases} \quad (3)$$

where ℓ_M is the distance. The results plotted until 3rd turn after the kick of K4 magnet are shown in Fig. 4.

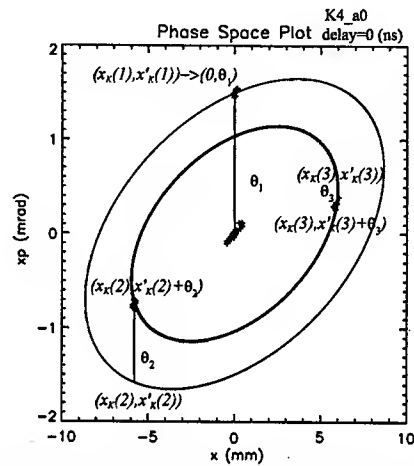


Figure 4: Phase-space plots after the kick by K4 magnet. The crosses display the measured data. The solid lines represent the calculated ellipse.

The solid line in the Fig. 4 calculated by the following equation with the Twiss parameters listed in Table 2,

$$\begin{cases} \gamma_K x_K(n)^2 + 2\alpha_K x_K(n)x'_K(n) + \beta_K x'_K(n)^2 = \beta_K \theta_n^2 \\ n=1, 2, 3 \end{cases} \quad (4)$$

Table 2: Twiss parameters at the kicker magnets and the center between two monitors. The horizontal phase advances $\Delta\psi_x$ from the monitors are also listed.

	K1	K2	K3	K4	C.Mon.
β_x (m)	4.000	6.840	6.206	5.781	5.220
α_x	-2.111	-0.8378	3.960	-0.4671	0.110
$\Delta\psi_x$	-9.665	-8.129	-7.712	-5.770	0.000

where θ_n is the kick angle of n^{th} turn. During this calculation, we assume that the betatron oscillation after the kick is linear. Using the Eq. 4, we can easily evaluate the kick angle. The measured result of the pulse shape in the kicker magnets is shown in Fig.5. The horizontal axis denotes the time t , which is calculated as follows,

$$\begin{cases} t = n \times \tau_{rev} - m \times \tau_{delay} \\ n = 1, 2, 3 \\ m = 1, 2, \dots, 14 \end{cases}$$

τ_{rev} : revolution period (624 nsec)

τ_{delay} : delay time (50 nsec)

n: turn number

m: number of the measurements

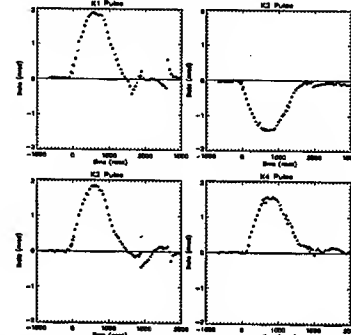


Figure 5: Pulse shapes of kicker magnets measured at the voltage of 5 kV. The crosses display the measured data and solid line show the normalized pulse shape obtained by the field measurement.

The excitation curve of the kicker magnets is shown in Fig. 6. The results of the pulse length and kick angles at 5kV are summarized in Table 3. From the Fig. 5, we found the timing of the K4 magnet is delayed by 200 nsec from that of the other magnets. The pulse length of K2 magnet was about 200 nsec longer. We adjusted the timing of K4 magnet to those of other magnets. We do not understand the cause of the longer pulse length. From the Fig. 6, the kick angles of four magnets varied up to 20% in this measurement.

Table 3: Kick angles, and pulse lengths measured at the voltage of 5 kV.

	K1	K2	K3	K4
θ_k (mrad) at 5 kV	1.88	1.41	1.84	1.56
τ_{total} (nsec)	1626	1874	1611	1611

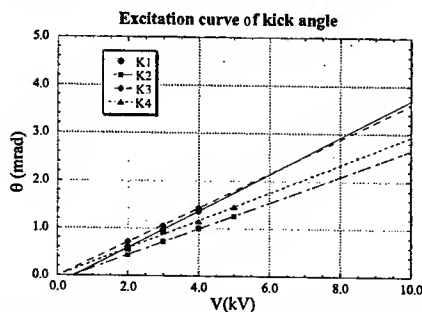


Figure 6: Excitation curves of the kick angle. The closed circles display the measured data and solid line shows the excitation curve obtained by fitting the data.

COHERENT OSCILLATION OF THE STORED BEAM

The phase-space motion of the stored beam after the excitation of the injection bump kick was measured. The result is shown in Fig. 7. Since the injection bump was not completely closed, the coherent oscillation of the stored beam was exited. However, this coherent oscillation quickly damped turn by turn. Actually, we found that the coherent oscillation of the stored beam had no influence to the beam injection.

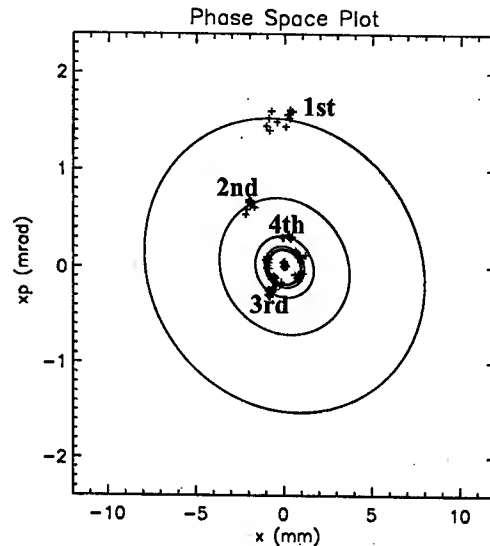


Figure 7: The phase-space plot of the coherent oscillation measured after the excitation of the injection bump.

CONCLUSIONS

Four traveling wave kicker magnets were installed in October 2002. The performance of injection bump was investigated using the stored beam. The pulse shapes and the excitation curves of the kick angle were individually measured using the phase-space monitor. We found the timing of K4 magnets was delayed by 200 nsec. The pulse lengths of K1, K3 and K4 agreed to each other except K2. The kick angles varied up to 20%. In fact, these variations were no problem in the beam injection. Since these variations has not observed in the magnetic field measurement [3], we do not understand the cause of the variations now, and we will investigate it in the future. Consequently, we achieved an injection speed more than 1.0 mA/s at a repetition rate of 12.5 Hz.

REFERENCES

- [1] M. Katoh et al., J. Synchrotron 5,1998, p.366
- [2] E. Kim et al., Jpn. J. Appl. Phys. 36, 1997, p.7415
- [3] A. Ueda et al., Proc. of PAC, Chicago, 2001, p.4050
- [4] Y. Kobayashi et al., Proc. of EPAC, Spain, 1996, p.1666

MEASUREMENT OF THE TRANSVERSE QUADRUPOLE-MODE FREQUENCIES OF AN ELECTRON BUNCH IN THE KEK PHOTON FACTORY STORAGE RING

S. Sakanaka*, T. Mitsuhashi, T. Obina, Photon Factory, High Energy Accelerator Research Organization (KEK), 1-1 Oho, Tsukuba, Ibaraki 305-0801, Japan

Abstract

In order to extend our knowledge on the collective beam behavior, we measured the transverse quadrupole-mode frequencies of an electron bunch in the Photon Factory storage ring at KEK. The transverse quadrupole oscillations were excited by applying oscillating quadrupole magnetic fields. The responses of the excited oscillations were recorded by detecting visible synchrotron light using a photo multiplier and a spectrum analyzer. As a result, we found remarkable dependences of the horizontal and the vertical quadrupole frequencies on the bunch current.

INTRODUCTION

According to the perturbation formalism [1] for the collective beam dynamics, the motion of a bunched beam can be described by a superposition of many normal-modes of oscillation. The coherent frequency of each oscillation mode can be affected by some collective effects due to wake forces or to other mechanisms.

It has been reported in many electron storage rings [2, 3] that the transverse dipole-mode (barycentric oscillation) frequency shifts down as the bunch current increases. This effect has been explained by the following mechanism [4]. When an electron bunch passes some components with a transverse offset, the particles generate a transverse wakefield behind them. The succeeding particles in the same bunch are kicked by the short-range wakefield in the same direction to the bunch offset. Then, an integrated kick gives a defocusing force to the motion of the bunch center.

On the other hand, there have been few measurements on the coherent, quadrupole or higher-mode oscillations in the electron storage rings. We expect that such a measurement will extend our knowledge on the collective beam behavior. In this paper, we report our measurement results of the coherent quadrupole frequencies, which were carried out in the 2.5-GeV Photon Factory (PF) storage ring at KEK.

EXPERIMENTAL METHOD

Basic technique for exciting the transverse quadrupole oscillation was described in references [5, 6]. Our setup for the measurement is shown in Fig. 1. While storing a single bunch of electrons in the PF storage ring, we applied a small tune modulation using a high-frequency quadrupole magnet (HFQM). An excitation signal for the HFQM was produced by a spectrum/tracking analyzer

*shogo.sakanaka@kek.jp

(Advantest R3162). In order to measure the horizontal quadrupole frequencies, we swept the excitation frequency around a frequency of $2 \cdot f_{\beta x}$, where the $f_{\beta x}$ is a fractional horizontal betatron frequency (i.e. fractional tune times the revolution frequency). For the other measurement of the vertical quadrupole frequency, we used a slightly different setup as described later.

Excited bunch oscillations were then detected using an optical monitor system. Visible synchrotron light from the bunch was imaged on a slit. A fast photo multiplier (Hamamatsu H5783) behind the slit detected the quadrupole oscillations as the intensity modulation of the synchrotron light from the central part of the bunch. A signal from the photo multiplier was analyzed by the spectrum/tracking analyzer. At the same time, we used a dual-sweep streak camera (Hamamatsu C5680) in order to confirm that the excited oscillations were really the transverse quadrupole mode.

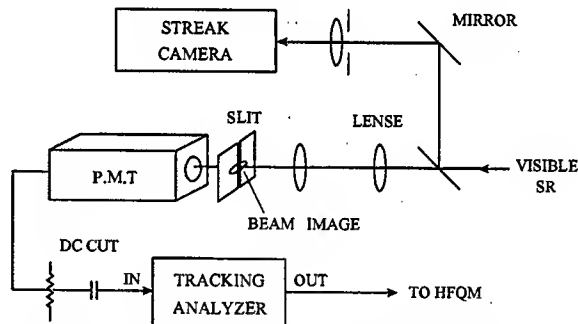


Figure 1: Experimental setup for measuring the transverse, coherent quadrupole frequencies. P.M.T.: photo multiplier.

MEASUREMENT RESULTS

Horizontal Quadrupole Frequency

We swept the excitation frequency around a frequency of about 1.915 MHz ($\approx 2 \cdot f_{\beta x}$), where a fractional horizontal betatron frequency ($f_{\beta x}$) was about 957.5 kHz at low currents. The responses of the bunch oscillations were then measured using the spectrum/tracking analyzer. A peak excitation current of the HFQM was about 3.96 A, which gave an estimated horizontal-tune modulation of about 5.2×10^{-5} . An estimated growth rate of oscillation was about 260 s^{-1} , which was about twice the radiation damping rate of 128 s^{-1} . Other parameters were the beam energy of 2.5 GeV, the revolution frequency of 1.602904 MHz (harmonic number: 312), and a fractional vertical betatron frequency of 456 kHz (at low currents),

respectively. Octupole magnets were almost turned off.

Some of the measured beam responses are shown in Fig. 2. Each trace showed a peak where the quadrupole oscillation was excited most strongly. Then, we could consider that the frequency of each peak indicated the coherent quadrupole frequency. During this measurement, we checked using the streak camera that the quadrupole oscillations were really excited at around the peak frequencies; an example of the measurement is shown in Fig. 3. We could clearly observe the quadrupole oscillations at low currents (below 10 mA), while the quadrupole oscillations were not very clear at high currents (more than about 10-15 mA).

We can see from Fig. 2 that the horizontal quadrupole frequency shifted up as the bunch current increased. Figure 4 shows a summary of the measured quadrupole frequencies as a function of the bunch current. Fitting these data linearly (except for the first two points) gave the following current dependence:

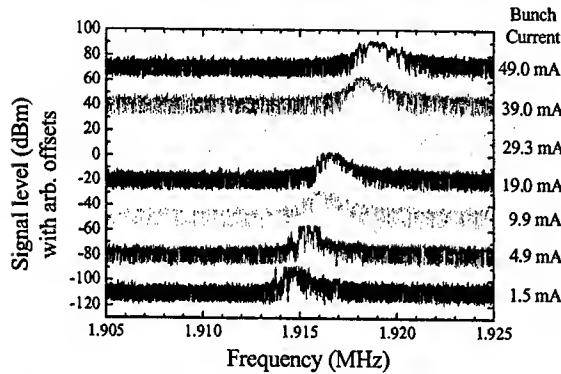


Figure 2: Frequency responses of the horizontal quadrupole oscillation, which were measured under different bunch currents. Abscissa: excitation frequency, ordinate: spectrum intensity of the photo-multiplier signal. The neighboring traces were separated by adding an offset of 30 dB. The excitation frequency was swept upward.

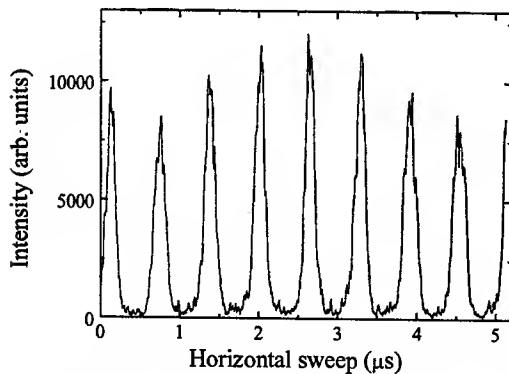


Figure 3: Measured turn-by-turn change in the horizontal beam profile due to a horizontal quadrupole oscillation. Bunch current: 1.5 mA.

$$f_{qx}[\text{kHz}] \approx 1915.2 + 0.0769 \times I_b[\text{mA}], \quad (1)$$

where the f_{qx} is the horizontal quadrupole frequency and the I_b is the bunch current, respectively.

During the above measurement, we also measured the dipole-mode frequencies using an rf knockout method. The results are shown in Fig. 5 (in horizontal) and in Fig. 6 (in vertical), respectively. Linear fits of these data

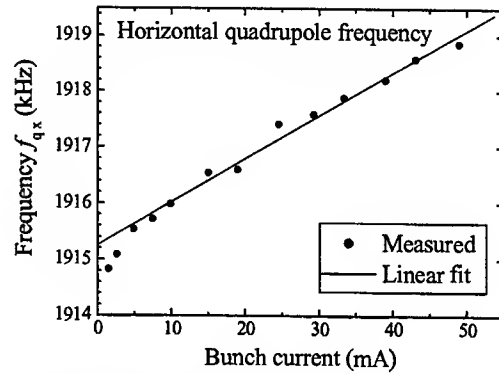


Figure 4: Measured coherent frequencies of the horizontal quadrupole oscillation. Peak current of the HFQM: 3.96 A.

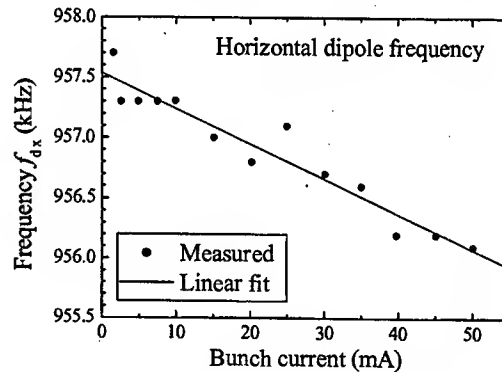


Figure 5: Measured frequencies of the horizontal dipole oscillation as a function of the bunch current.

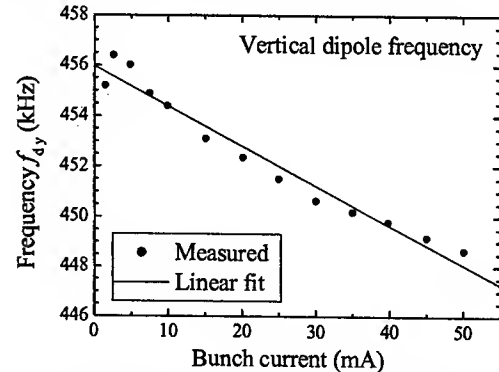


Figure 6: Measured frequencies of the vertical dipole oscillation as a function of the bunch current.

resulted in

$$f_{dx}[\text{kHz}] \approx 957.5 - 0.0290 \times I_b[\text{mA}], \quad (2)$$

and

$$f_{dy}[\text{kHz}] \approx 456.0 - 0.158 \times I_b[\text{mA}], \quad (3)$$

where the f_{dx} and the f_{dy} are the horizontal and the vertical dipole frequencies, respectively.

Vertical Quadrupole Frequency

Due to limited bandwidth (1.4 - 2 MHz) of the HFQM power supply used in the above experiment, we could not excite it at twice the vertical betatron frequency. Instead, we used another HFQM power supply (bandwidth: 3.3-5.9 MHz), and excited the HFQM at a frequency of $(3f_r + 2f_{\beta y}) \approx 5.72$ MHz, where the $f_{\beta y}$ is the fractional vertical betatron frequency and the f_r is the revolution frequency, respectively.

An initial measurement was carried out using the similar setup to the one in Fig. 1, with a 90°-rotation of the beam image. However, it was found that the measurement was considerably affected by an rf noise from the HFQM. Then, we changed the measurement method; the HFQM was excited by a signal from a function generator at a frequency around $(3f_r + 2f_{\beta y})$, and then, an induced beam oscillation was detected at a different sideband frequency of about $(2f_r + 2f_{\beta y})$.

The result of our preliminary measurement is shown in Fig. 7. The frequency of the function generator was changed by a step of 0.1 kHz within 10 kHz. For each frequency, we measured a signal spectrum at a center frequency of about $(2f_r + 2f_{\beta y}) \approx 4.118$ MHz within a span of 20 kHz, and then, recorded the maximum (peak) amplitude. Each trace in Fig. 7 indicates the measured peak amplitudes as a function of the excitation frequency.

Although the above measurement was still preliminary, we can see in Fig. 7 that the vertical quadrupole frequency, which was indicated by a peak in each trace, tended to shift down as the bunch current increased. The current dependence was, roughly, -0.095 kHz/mA.

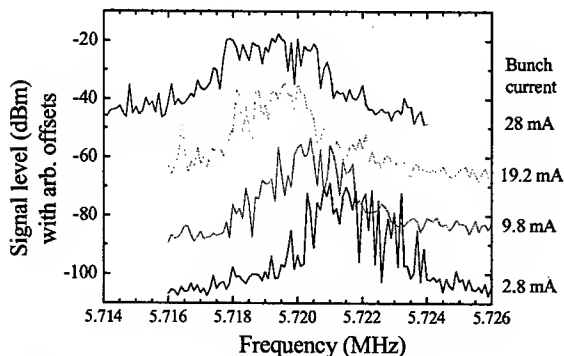


Figure 7: Measured responses of the vertical quadrupole oscillation at different bunch currents. Offsets of 20 dB were added between neighboring traces.

DISCUSSIONS

It can be seen from Figs. 4 and 5 that the horizontal quadrupole frequency was very close to two-times the dipole frequency at the limit of low current. This agrees with a single particle model [6]. As the bunch current increased, the horizontal quadrupole frequency shifted up, while the horizontal dipole frequency shifted down. An absolute slope of the current dependence for the quadrupole oscillation was roughly 2.6 times larger than that of the dipole oscillation. Moreover, the preliminary measurement for the vertical quadrupole frequency indicated that the frequency tended to shift down with the bunch current. The above dependences of the quadrupole frequencies should be due to some collective effects.

In a usual manner, the observed shifts in the dipole frequencies should be attributed to the transverse wake forces [1] which were induced by a dipole ($m=1$) moment of the charge distribution in the bunch. Similarly, the shift in the quadrupole frequencies may be attributed to the wake forces, which were induced by a quadrupole ($m=2$) moment of the charge distribution. However, we still have a question why the quadrupole-frequency shift was so large; we usually expect that the effect of the higher-moment wake forces would be smaller than the fundamental mode ($m=1$, for the transverse case) wakes.

CONCLUSIONS

We measured the horizontal and the vertical quadrupole frequencies in the PF storage ring. The measured quadrupole frequencies showed remarkable dependences on the bunch intensity. The horizontal quadrupole frequency shifted up with the bunch current, while the vertical quadrupole frequency shifted down. These frequency shifts may be attributed to the transverse wake forces of higher moment. However, there remains a question why the quadrupole-frequency shift was so large as compared to that of the dipole-frequency.

REFERENCES

- [1] A.W. Chao, *Physics of Collective Beam Instabilities in High Energy Accelerators*, John Wiley & Sons, New York, 1993.
- [2] J.C. Denard *et al.*, IEEE Trans. on Nucl. Sci. NS-28 (1981) 2474.
- [3] D. Rice *et al.*, IEEE Trans. on Nucl. Sci. NS-28 (1981) 2446.
- [4] R. Klatt, R.D. Kohaupt, T. Weiland, IEEE Trans. on Nucl. Sci. NS-32 (1985) 2356.
- [5] S. Sakanaka *et al.*, PAC2001, Chicago, 2001, p. 393.
- [6] S. Sakanaka, Y. Kobayashi, T. Mitsuhashi, T. Obina, Jpn. J. Appl. Phys. 42 (2003) 1757.

SIMULATION RESULTS OF CORKSCREW MOTION IN DARHT-II

K. C. Dominic Chan, Carl A. Ekdahl, Los Alamos National Laboratory, Los Alamos, NM 87545,
Yu-Juan Chen, Lawrence Livermore National Laboratory, Livermore, CA 94550, Thomas P.
Hughes, Mission Research Corporation, 5001 Indian School Road, Albuquerque, NM 87110

Abstract

DARHT-II, the second axis of the Dual-Axis Radiographic Hydrodynamics Test Facility, is being commissioned. DARHT-II is a linear induction accelerator producing 2-microsecond electron beam pulses at 20 MeV and 2 kA. These 2-microsecond pulses will be chopped into four short pulses to produce time resolved x-ray images. Radiographic application requires the DARHT-II beam to have excellent beam quality, and it is important to study various beam effects that may cause quality degradation of a DARHT-II beam. One of the beam dynamic effects under study is "corkscrew" motion. For corkscrew motion, the beam centroid is deflected off axis due to misalignments of the solenoid magnets. The deflection depends on the beam energy variation, which is expected to vary by $\pm 0.5\%$ during the "flat-top" part of a beam pulse. Such chromatic aberration will result in broadening of beam spot size. In this paper, we will report simulation results of our study of corkscrew motion in DARHT-II. Sensitivities of beam spot size to various accelerator parameters and the strategy for minimizing corkscrew motion will be described. Measured magnet misalignment is used in the simulation.

INTRODUCTION

Recently, we have completed the Phase-I commissioning by successfully accelerating beam in DARHT-II [1]. We are proceeding to Phase-II commission (Long-Pulse Beam Optimization) when the minimization of the effective beam-spot size increase due to corkscrew motion is one of the major objectives.

A general analysis of corkscrew motion in induction linacs and their minimization was given in Ref. 2 and 3 by Chen. Such analysis was applied to DARHT-II and showed, using simulation, that corkscrew motions can be controlled using the "tuning-V" algorithm [4]. In this algorithm, transverse steering fields are added to cancel the effect of the error transverse field due to solenoid misalignments, leading to the minimization of the corkscrew motion.

Recently, we have performed more computer simulations in preparation of the Phase-II commissioning of DARHT-II. We have calculated the sensitivity of corkscrew motion to various beam parameters and improved the simulations by using the measured magnet misalignment data derived last year while testing the induction cell modules [5]. In addition, measured steerer fields were used in these simulations. The results of these simulations are described in this paper.

DETAILS OF SIMULATIONS

DARHT-II consists of an injector (between 0 and 100 cm, with the cathode at 0 cm) and a main accelerator (between 100 and 4860 cm). We have simulated the corkscrew motion in the main accelerator using the computer code LAMDA [6]. LAMDA represents the beam pulse with slices along the pulse. It calculates the development of beam size by solving the envelope equation and tracks the beam centroids of the slices under the influence of solenoids, steerers, and beam induced transverse fields. The code can be used to calculate magnet misalignment effects, the beam breakup instability, and the resistive-wall instability.

For the simulations, the injector beam entering the main accelerator has an energy of 2.5 MeV and a current of 1.24 kA. The energy spread of the injector beam is 0.5%, represented by one cycle of a sine wave with amplitude of 12.5 keV on top of the 2.5 MeV, over the pulse length of 200 ns. The magnets were randomly misaligned. The standard deviations in x and y offsets and in rotation and tilts of magnet misalignments are, respectively, 0.1 cm and 1 mrad. Such misalignment is slightly worse than the measured misalignment data of 0.05 cm and 1 mrad respectively. Ten sets of random magnet misalignments were generated to cover the actual misalignment after installation.

Beam centroid data were recorded at 1500-, 3000-, and 4860-cm locations. Figure 1 shows a typical output from LAMDA. It shows the beam centroid location in y direction along the length of the pulse. Data for the first 50-ns were not used because they would be part of the transient and were impacted by the beam breakup modes. Using data between 50 and 200 ns, we obtained y_{\max} and y_{\min} and calculated the average (y_0) and ranges of centroid offsets (dy) in y-direction.

$$y_0 = (y_{\max} + y_{\min}) / 2$$

$$dy = (y_{\max} - y_{\min})$$

Together with x_0 and dx similarly obtained for the x-direction, we calculated the average beam offset R and the equivalent corkscrew radius r:

$$R = \sqrt{x_0^2 + y_0^2}$$

$$r = \sqrt{dx^2 + dy^2}$$

The quantity r is equivalent to the effective increase in beam radius.

BASELINE CALCULATIONS

As a baseline for later comparison, we used the beam parameters listed in the last section to calculate R and r for the ten magnet-misalignment sets. The beam was

injected into the accelerator on axis. At the exit of the accelerator (4850 cm), we obtained:

$$R = 0.61 \pm 0.32 \text{ cm}, \quad r = 0.058 \pm 0.028 \text{ cm}$$

The effective increase of beam radius, r , is slightly higher than the DARHT-II requirement of 0.05 cm (10% of beam size). Our results are similar to previous calculation reported [7].

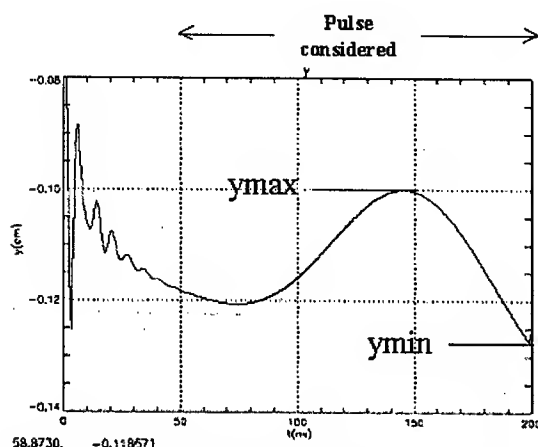


Figure1: Typical LAMDA data showing the beam centroid position along the pulse

SENSITIVITY CALCULATIONS

To understand the effects of different beam parameters on the effective increase in beam radius, we calculated r for beam conditions modified from the baseline calculations. The results are summarized in Table 1.

Table 1: Increase of effective beam radius with modified beam parameters compared to baseline calculations

Beam Condition	Effective radius increase (cm)
Baseline calculation	0.058
0.3 cm input beam offset	0.065
3 mrad input beam tilt	0.121
37.5 keV beam energy spread (3x baseline)	0.177
0.3 cm magnet offset (3x baseline)	0.160
3 mrad magnet rotation and tilt (3x baseline)	0.076

TUNING-V ALGORITHM

LAMDA simulations were used to obtain experience for applying the "tuning-V" algorithm to minimize corkscrew motions. In order to see the changes in beam radius more clearly, the simulations in this section were performed with an energy spread of 37.5 keV, which is three times larger than the baseline beam energy spread. The same set of magnet misalignments was used in all the simulations in this section and the centroid motions were recorded at the end of the accelerator. We systematically applied steering fields using each of the steerers installed

on the cell blocks along the accelerator. These steerers have a current carrying capability of at least 8 amperes. Figure 2 shows an ideal V-shaped "tuning curve" with a minimum r of 0.02 cm achieved with a steerer in cell-block 1 (CB1) at the beginning of the accelerator operating at a current of 2.5 A.

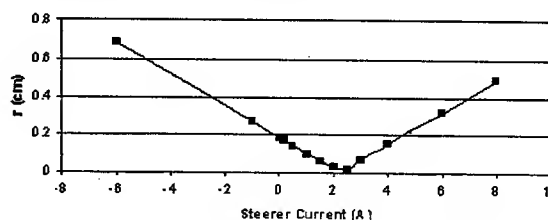


Figure 2; An ideal V-shaped tuning curve

Figure 3 shows the R and r at three locations in the accelerator as a function of steerer current using the same steerer as used in Figure 2. Figure 4 shows the dx and dy that were used to calculate r at location 1500 cm. Figure 5 is a tuning curve using a steerer at 3657 cm and observed at the end of the accelerator. Data in Figures 3 to 5 show:

1. Although most the tuning curves show the typical V-shape, there are deviations from this shape, particularly at steerer currents far from the minimum of r .
2. Because of the V-shape, which is different from a parabola, using a parabola fit to a few data points on the tuning curve can only locate the minimum r location approximately.
3. The effectiveness of a steerer to change r decreases towards the high-energy end of the accelerator. The minimization of r is most effectively done with steerers at the low-energy end of the accelerator.
4. While the value r is being minimized, the average centroid of the beam R also changes along the accelerator.
5. The minima of dx , dy , and r do not necessarily fall on the same values of steerer currents.

PROPOSED PROCEDURE TO MINIMIZE COCKSCREW MOTION

We propose the following procedure for minimizing corkscrew motion in the DARHT-II accelerator. Beam positions in x and y directions, equivalent to centroid data shown in Figure 1, will be measured using BPM's (Beam Position Monitor) installed along the accelerator. We will begin tuning for minimum r starting with steerers at the beginning of the accelerator.

1. We will obtain three points on the tuning curve with steerer currents -6 , 0 and 6 A. A parabola will be fitted to these three points to estimate the steerer current for minimum r .
2. Around this initial estimate, we will look for minimum in r by measuring r in steerer-current steps of 0.5 A. This search usually takes not more than 4 current steps.

After finding the minimum r , we will leave that steerer at that current and repeat the process with the next steerer downstream. This procedure have been tried using

LAMDA simulations and was found to be able to obtain a r satisfying the requirement of 0.05 cm using less than three steerers. While minimizing the corkscrew motion in the accelerator, we have to monitor the average beam offset R along the accelerator, to insure that beam is not too far off axis. A limit on beam centroid displacement should be set administratively.

After the corkscrew motion has been minimized, we will use steerers near the end of the accelerator to steer the beam centroid back on axis in the beam line following the accelerator. Experiment showed that this would take less than five shots.

With our proposed procedure, we will take 26 shots to have a beam on axis with minimum corkscrew motion. The number of shots actually needed will depend on other practical consideration and 26 shots should be considered an optimistic estimate.

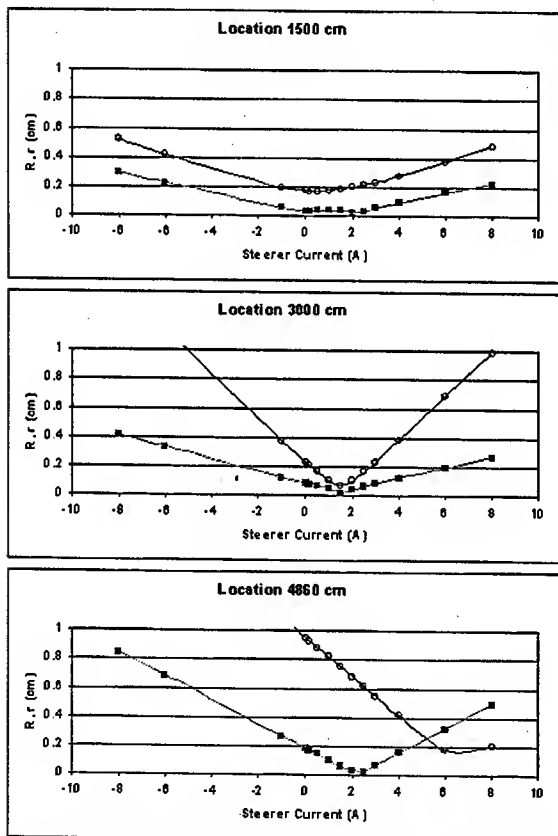


Figure 3: R (open) and r (solid) at three locations as a function of steerer current of a steerer in cell block 1

CONCLUSION

Increase of beam spot size in DARHT-II due to corkscrew motion has been studied using computer simulations. Using baseline accelerator parameters, the increase in beam spot size is only slightly larger than allowed by DARHT-II requirements. The sensitivities of the beam spot size to different accelerator parameters

were calculated. A procedure that might need only 26 shots to accomplish has been proposed.

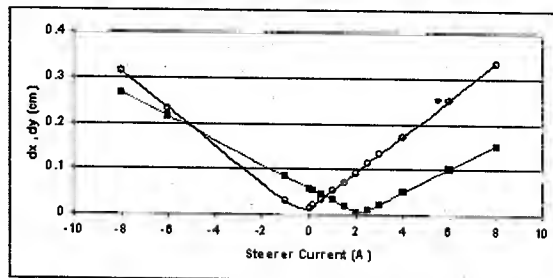


Figure 4: dx (open) and dy (solid) at location 1500-cm as a function of steerer current of a steerer in cell block 1

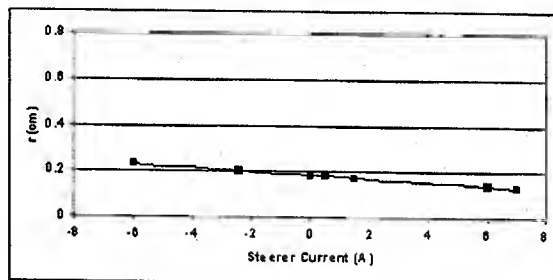


Figure 5: Tuning curve using a steerer at the high-energy end of the accelerator (2287 cm)

ACKNOWLEDGEMENT

This work was supported by the US Department of Energy.

REFERENCES

1. C. Ekdahl, et al., DARHT-II Commissioning Results, presented in this conference
2. Y. J. Chen, Corkscrew Modes in Linear Accelerators, NIM A292 (1990) 455-464
3. Y. J. Chen, Control of Transverse Motion Caused by Chromatic Aberration and Misalignments in Linear Accelerators, NIM A 398 (1997) 139-146
4. Y. J. Chen and W. M. Fawley, BBU and Corkscrew Growth Predictions for the DARHT Second Axis Accelerator, Proceedings of the 2001 Particle Accelerator Conference, Chicago, 3490-3492.
5. M. Kang, private communication.
6. T. P. Hughes, LAMDA User's Manual, May 1996, Prepared by Mission Research Corporation, 1720 Randolph Road, SE, Albuquerque, NM 87106-4245.
7. Y. J. Chen, Corkscrew and Tuning-V Algorithm, presented to DARHT-II Integrated Beam Dynamics Final Design Review at Los Alamos National Laboratory, August 15-16, 2000.

COUPLING CORRECTION AND BEAM DYNAMICS AT ULTRALOW VERTICAL EMITTANCE IN THE ALS*

C. Steier†, D. Robin, A. Wolski, LBNL, Berkeley, CA94720, USA

G. Portmann, J. Safranek, SLAC, Menlo Park, CA94025, USA

Abstract

For synchrotron light sources and for damping rings of linear colliders it is important to be able to minimize the vertical emittance and to correct the spurious vertical dispersion. This allows one to maximize the brightness and/or the luminosity. A commonly used tool to measure the skew error distribution is the analysis of orbit response matrices using codes like LOCO. Using the new Matlab version of LOCO and 18 newly installed power supplies for individual skew quadrupoles at the ALS the emittance ratio could be reduced below 0.1% at 1.9 GeV yielding a vertical emittance of about 5 pm. At those very low emittances, additional effects like intra beam scattering become more important, potentially limiting the minimum emittance for machine like the damping rings of linear colliders.

INTRODUCTION

The Advanced Light Source (ALS) is a third-generation source located at Lawrence Berkeley National Laboratory that has been operating for almost a decade and is generating forefront science over a broad area. However, the ALS was one of the first third-generation machines to be designed, and its performance will be outstripped by newer, more advanced machines. Accelerator and insertion device technology have changed significantly since the conception of the ALS, and in order to remain competitive in the core areas of high-resolution spectroscopy, high-spatial-resolution soft x-ray microscopy, and experiments that exploit coherence, an upgrade plan is in place to enhance the performance.

The main possibilities to increase the brightness of the ALS are increasing the time-averaged current, reducing the beam size, and reducing the insertion device gaps. Currently those changes would result in (unacceptably) short lifetime. With continuous injection (top-off), the importance of this lifetime impediment will become significantly reduced in the future. Fig. 1 shows a comparison of the brightness of planned, new ALS insertion devices with the upgraded beam parameters to the typical brightness of a current ALS undulator. One of the main improvements comes from a smaller vertical emittance and the smaller physical gaps of the undulators.

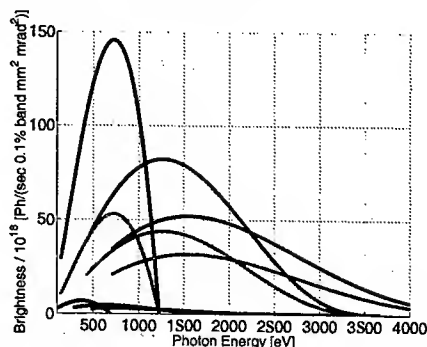


Figure 1: Comparison of brightness of new ALS insertion devices with 750 mA and 10 pm vertical emittance (red/blue) to the typical brightness of a current U5 undulator (black).

SIMULATION OF EMITTANCE CORRECTION

A number of simulations was performed to find the smallest number of individual skew quadrupoles which still allows an effective emittance correction, as well as a good distribution of those skew quadrupoles and finally an optimum correction algorithm. The result was that 12 skew quadrupoles (one in each sector) were sufficient, six of them located at high dispersion points and six of them at lower dispersion points with a larger product of horizontal and vertical beta-functions. In the simulations many different minimization algorithms were used, but it turned out, that orbit response matrix analysis (using Matlab LOCO [1, 2]) to fit an effective skew quadrupole distribution gave results as good as the best other minimization algorithm. Since it has the advantage of requiring very few iterations and automatically providing a measurement of the local coupling everywhere along the ring it is perfectly suited to be used with measurement data on the real machine. The simulations were also used to optimize the parameters of LOCO like the weight factor of the dispersion function, the outlier rejection tolerance, and the number of singular values. Fig. 2 shows the results of one of those simulation runs for 100 random seeds of misaligned machines. In this particular case it was possible to correct the vertical emittance below 5 pm for 25% of the error seeds.

The skew quadrupoles at the ALS are integrated in the sextupoles and used to be connected in 4 chains. Based on the simulations, individual power supplies were installed last year, powering 18 individual skew quadrupoles - at least one in every sector. Two sectors have four skew quadrupoles each to generate a closed dispersion bump for

* This work was supported by the U.S. Department of Energy, under Contract No. DE-AC03-76SF00098 and DE-AC03-76SF00515.

† CSteier@lbl.gov

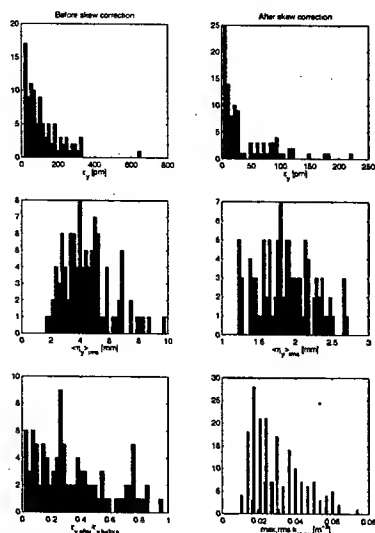


Figure 2: Histograms showing the results of simulated vertical emittance and dispersion correction for 100 randomly misaligned error seeds.

the fs-slicing experiments [3].

MEASUREMENTS

Because of the resolution limit even of x-ray beamlines it is quite difficult to measure emittances in the few pm range accurately. The primary beamline to measure emittances at the ALS uses an imaging optics with a KB-mirror pair, carbon filters to select the x-ray wavelength (1.5 keV) and to attenuate, a BGO crystal to convert to visible light and a microscope with CCD. Even though the fundamental resolution limit would allow a direct measurement of emittances of a few pm, aberrations of the optics create a larger limit. Therefore we used three somewhat indirect but independent methods to measure the very small vertical emittances.

The first method was to determine the resolution of the beamline using Touschek lifetime measurements for various beamsizes. We then corrected the beamsizes measurements for the beamline resolution to deduct the real vertical emittance. The second method was based on the analysis of an orbit response matrix, using a large number of skew gradient error fit parameters. With the calibrated machine model one can then calculate the vertical emittance using a lattice code. The final method used a scan of the RF-acceptance while measuring the Touschek lifetime. For low RF amplitudes, the Touschek lifetime is strictly proportional to the bunch volume. Therefore one can deduct a very small emittance from a beamsizes measurement at moderate coupling.

All three methods gave consistent results. In the best case, the measured vertical emittance as determined by the three methods was 4-7 pm, corresponding to an emittance ratio of less than 0.1% at 1.9 GeV (natural emittance is 6.75 nm). Fig. 3 shows an example of the change in beam-

size and local tilt angle in one iteration of the emittance correction. The mean value of the emittance measurements of about 5 pm is to our knowledge a world record for vertical emittances in electron/positron storage rings and is virtually identical to the design value for the NLC damping rings (references to vertical emittances achieved elsewhere are listed in [4]). It is interesting to note that emittances this small are within one order of magnitude of the theoretical limit due to the finite opening angle of the synchrotron radiation emission.

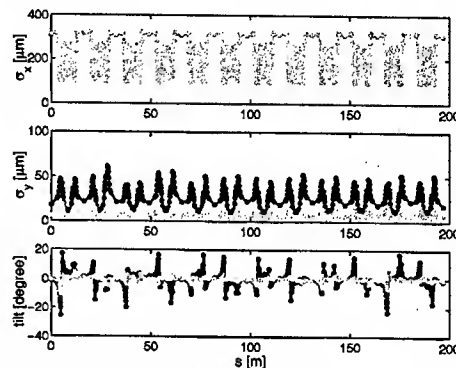


Figure 3: Horizontal/vertical beamsizes and beam tilt as calculated from calibrated machine model using orbit response matrix analysis. The blue case is before coupling correction, the green one after one iteration.

EMITTANCE CONTROL

Until the full energy injector upgrade at the ALS is finished to allow top-off injection, it is important to still operate with artificially increased vertical emittance to achieve reasonable beam lifetimes for users. Historically at the ALS a controlled excitation of the nearby linear coupling resonance has been used to increase the vertical beamsizes. After installing the individual skew quadrupoles, we switched to a different scheme. The emittance and vertical dispersion is corrected and then 12 skew quadrupoles are used such as to introduce a global vertical dispersion wave, without introducing coupling. In that case, the vertical emittance is generated directly via quantum excitation. The local emittance ratio around the ring can be made fairly flat and all local tilt angles are small.

The main advantages of this method are a better beamsizes stability (especially for scanning undulators/wigglers), better dynamic (momentum) aperture and less sensitivity of the momentum aperture to the vertical physical aperture. An example of the improvement in longtime beamsizes stability can be seen in Fig. 4.

BEAM DYNAMICS AT LOW EMITTANCE

Single Particle Dynamics

Since the lifetime at all (low energy) third generation light sources is (strongly) Touschek limited, the momentum

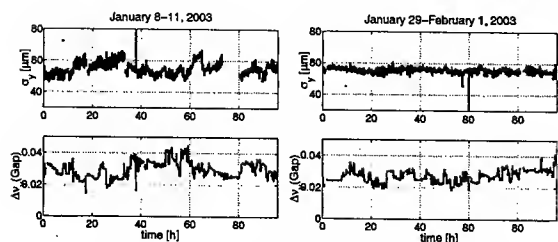


Figure 4: Vertical beam size for two four day periods. Using a global vertical dispersion wave to increase the vertical emittance (right) leads to a much better beam size stability than excitation of the coupling resonance (left).

aperture of the ring is very important [5]. For top-off operation, injection efficiency becomes very important as well (i.e. on-energy dynamic aperture). For most light sources the dominant factor for the momentum aperture is the transverse single particle dynamics and in most cases the particles are lost on the narrowest vertical apertures. Therefore it is important to understand and optimize the dependence of the momentum aperture on the vertical physical aperture.

We found that for the current ALS lattice the dependence of the momentum aperture (lifetime) on the vertical physical aperture became much weaker both for the case with corrected vertical emittance and the case with vertical dispersion wave, compared to the case with artificially excited coupling resonance (compare Fig. 5). Combined with the improvements in the lattice implemented two years ago and better correction of lattice symmetry errors this will enable the ALS to reduce the physical gap of insertion devices from the current 8-9 mm down to about 5 mm.

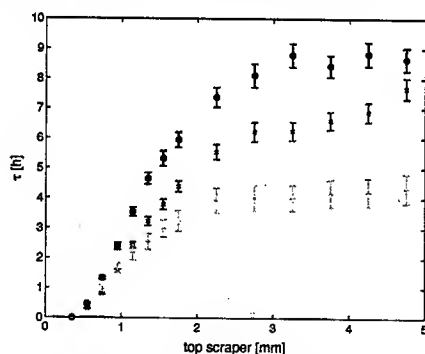


Figure 5: Measured lifetime of the ALS versus half aperture in one straight for three different cases: excited coupling resonance (red), corrected coupling and vertical dispersion (green), vertical dispersion wave (blue). The two cases with excited coupling resonance and dispersion wave were measured for identical vertical emittance.

Simulating the effects in tracking, we found good agreement between measurements and simulations. The simulations showed that a correction of the coupling reduces the sensitivity of the dynamic momentum aperture to the vertical physical aperture [6]. The injection efficiency for smaller vertical gaps was studied as well and no show stoppers were found so far. It is planned to install a collimator

system to protect all insertion devices in the ALS from injection losses during top-off operation.

Intra beam scattering

Although it is not an important effect for the ALS, intra beam scattering is important for the damping ring designs for linear colliders or future light sources with smaller natural emittance than the ALS. To verify the accuracy of intra beam scattering calculations, a measurement program was started a few years ago mostly at the ATF [7] and also at the ALS [8]. At the ALS at that time only chains of skew quadrupoles were available, limiting the minimum vertical emittance at which the measurements could be performed. With an emittance ratio of about 0.75% at 1.5 GeV, no effects of IBS could be seen. At lower energies, significant effects of IBS were found, but since the minimum vertical emittances were relatively large, the quantitative separation of IBS effects and potential well distortion/microwave instability effects was difficult.

Since the installation of the individual skew quadrupoles it is now possible to achieve much smaller vertical emittances, so it should be possible to measure IBS effects in a much cleaner way. Therefore the IBS measurement program at the ALS has been restarted.

SUMMARY

It is planned to upgrade the performance of the ALS significantly over the coming years by upgrading the injector for full energy (top-off) injection, upgrading the rf-system to allow for higher current operation and installing new insertion devices (in-vacuum and superconducting). Studies to correct and control the vertical emittance were carried out with the goal to improve the brightness once the full energy injector is installed. Vertical emittances as small as 5 pm were achieved which to our knowledge is currently the best value achieved worldwide. In addition studies were carried out which lead to big improvements in the vertical beam size stability and dependence of the momentum aperture on the physical vertical aperture.

REFERENCES

- [1] J. Safranek et al., Proceedings of EPAC2002, Paris (2002).
- [2] A. Terebilo, et al., Proceedings of PAC2001, Chicago p. 3203 (2001).
- [3] C. Steier et al., Accelerator Physics Challenges of the fs-Slicing Upgrade at the ALS, these proceedings
- [4] K. Kubo et al., Phys. Rev. Lett. 88:194801 (2002).
- [5] C. Steier et al., Phys. Rev. E 65, 056506 (2002).
- [6] D. Robin et al., Impact of Narrow Gap Chambers on the Lifetime at the ALS, these proceedings.
- [7] K. Bane et al., Phys. Rev. STAB 5, 084403 (2002).
- [8] C. Steier et al., Proceedings of PAC2001, Chicago p. 2938 (2001).

COMPARISON OF PARMELA SIMULATIONS WITH LONGITUDINAL EMITTANCE MEASUREMENTS AT THE SLAC GUN TEST FACILITY

C.Limborg*, P.R. Bolton, J.E.Clendenin, D.Dowell, S.Gierman, B.F. Murphy, J.F.Schmerge
MS 69 SLAC 2275 Sand Hill Road, Menlo Park CA, USA

INTRODUCTION

At the Gun Test Facility (GTF), we have been testing an S-band RF gun similar to the one to be used in the Linac Coherent Light Source (LCLS) Photo-Injector. The beam transverse properties have been extensively characterized on that gun and it was shown that this gun is capable of providing slice emittances of less than 1 mm.mrad for 100A slices [1]. The longitudinal beam properties are now also being investigated for 2 principal reasons:

- the transverse beam properties are correlated to the longitudinal one; an excessively large correlated energy spread at the gun exit would damage the emittance compensation
- the uncorrelated rms energy spread as small as 10keV at the gun exit is required for a good lasing in the LCLS

To measure the longitudinal emittance, the booster phase scan technique has been used at the GTF as described in [2]. We have now performed simulations of this experiment to better understand the non-linear effects and to reconstitute the longitudinal emittance.

Set-Up

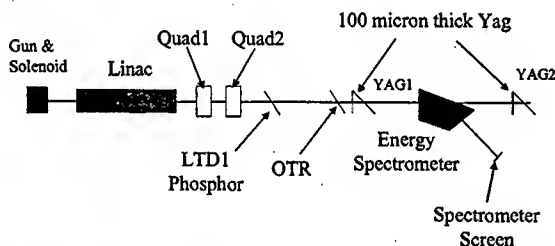


Figure 1: Layout of the GTF- The 1.6 cell S-Band RF Gun is operated at 110MV/m; the Linac is located at 89cm from the cathode.

LOW CHARGE

We first studied the low charge case. At 16 pC, the space charge effects are very small for a bunch with a FWHM close to 2ps. The RF effects in the gun are dominant. By comparing with PARMELA simulations, we could deduce the initial injection phase and bunch length. Those values were then compared with experimental parameters.

Bunch Compression

In figure 2, the evolution of bunch length and energy spread as a function of injection phase shows that:

- the bunch is compressed for injection phase smaller

than 70 degrees (from zero-crossing)

- the rms bunch length does not depend on the shape of the bunch
- the energy spread (correlated) is very small for phases between 0 and 35 degrees

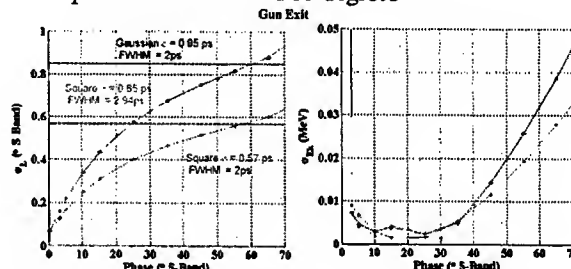


Figure 2: rms bunch length and energy spread as a function of injection phase

The rms bunch length reconstituted from the linear analysis of the booster phase scan at low charge, as shown in figure 5 of reference [2], was 0.4 ps. The experimental injection phase is 30 degrees. We conclude that the initial UV laser pulse had an rms close to 0.57 ps.

Booster Phase Scan

The booster phase scan measurement technique is described in detail in [2]. We use a reference phase of zero for the crest of the Linac RF sinusoidal field. This phase corresponds to the case where a maximum energy is reached for any particle. This is equivalent to the definition used in the experiment.

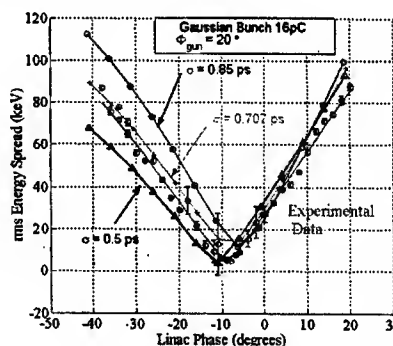


Figure 3: rms energy spread vs booster phase; Comparison experimental data with PARMELA simulations for 20° injection phase, for different initial laser pulse lengths

The 20 degrees injection phase seemed to give a better agreement for longer pulses as shown in figure 3. It was checked experimentally that the injection phase was 30 degrees, by measuring the output charge vs injection

(*) Contact: C.Limborg
e-mail: limborg@slac.stanford.edu

phase at low current. Rms bunch length of between 0.5ps and 0.6 ps gave a good match to the experimental data as shown in figure 5. It was also checked that the rms energy spread only depends on the initial rms laser pulse length and not on its shape.

HIGH CHARGE

The next series of measurements compared with the simulation corresponds to 290pC. It corresponds to a peak current close to 130 A for the core of the bunch. This is slightly larger than the LCLS requirements [1].

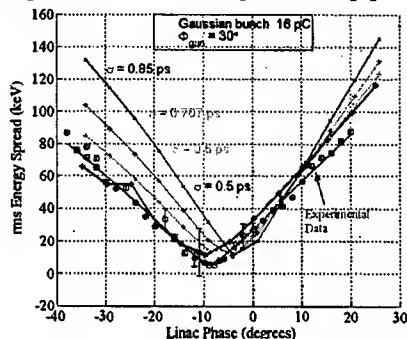


Figure 4: same as Figure 3 but for 20° injection phase.

Bunch Length

In figure 5, the evolution of bunch length and energy spread as a function of phase, for 200pC (not 290pC) shows:

- bunch lengthening occurs within the gun
- strong bunch lengthening and energy spread increase appears in the drift between the gun and entrance of the linac
- again the rms bunch length and rms energy spread are independent of the shape of the bunch and depend only of the initial rms laser pulse length; this is not true for the total energy spread which gets larger for a square pulse than for a Gaussian pulse having the same initial rms value

For 30 degrees injection phase, the bunch has lengthened by 40% at the gun exit and by 70% at the linac entrance with respect to the laser pulse length.

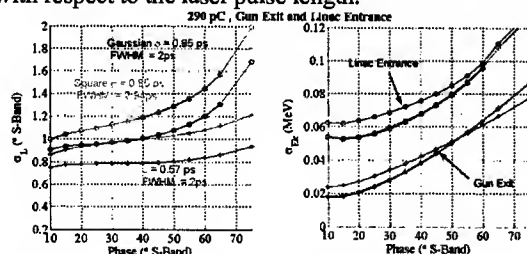


Figure 5: rms bunch length and energy spread as a function of injection phase for 290pC

Booster Phase Scan (no wakefield)

A first analysis was done ignoring the effect of wakefield in the linac. It could be concluded, as in the low charge case, that the evolution of rms energy spread as a

function of booster only depends on the original rms bunch length but not on the shape of the bunch. This is illustrated in figure 6. For all the pulse lengths chosen, the slopes of the PARMELA curves do not match the measurements.

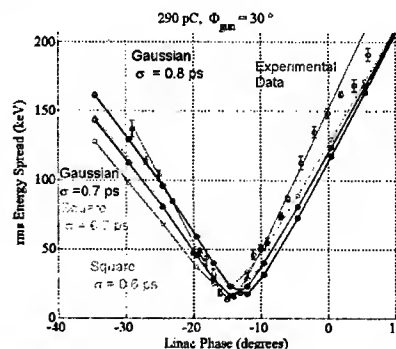


Figure 6: rms energy spread vs booster phase

Booster Phase Scan (with wakefield)

In any event, for peak currents close to 100 A, wakefields cannot be neglected anymore. The longitudinal wakefield in the SLAC S-Band section can be approximated by:

$$W(s) = \frac{Z_0 c}{\pi a^2} e^{-s/\sigma_0}$$

with $Z_0 = 377 \text{ Ohms}$, $a = 11.6 \text{ mm}$ and $\sigma_0 = 1.32 \text{ mm}$

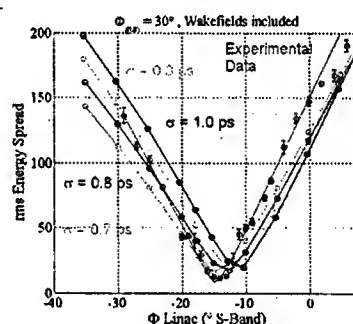


Figure 7: rms Energy spread vs booster Phase for various initial rms bunch length; wakefields are included

Longitudinal wakefield calculations were added to the PARMELA computations. It was checked that there was little difference applying the wakefield at a single point either at the end of the linac or at 20 locations along the linac. When including wakefields, it was not possible either to obtain a good match of PARMELA results with the experimental curve by varying the pulse length as shown in figure 7.

None of the solutions were satisfactory. However, we knew that we were neglecting wakefield effects in the drift from gun to linac. More particularly, we fear that the entrance port for the laser beam located at 50 cm from the cathode, generates strong longitudinal wakefields. This port hosts the last mirror for steering the laser beam to the RF gun cathode. We plan to compute this wakefield using ABCI. But, in the meantime to include some additional energy spread on the bunch, we simply unbalanced the

gun field ratio between the two cells. This generates some additional energy spread on the bunch as plotted in figure 8.

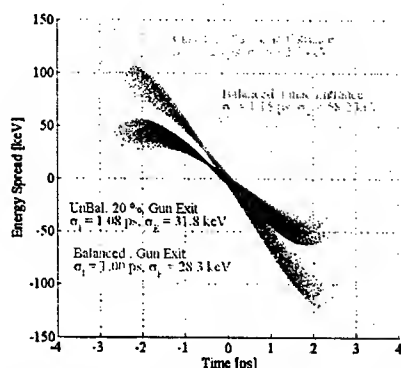


Figure 8: Longitudinal phase space from PARMELA output at gun exit and entrance Linac for Balanced and Unbalanced cases initial; the rms pulse length is 0.9ps

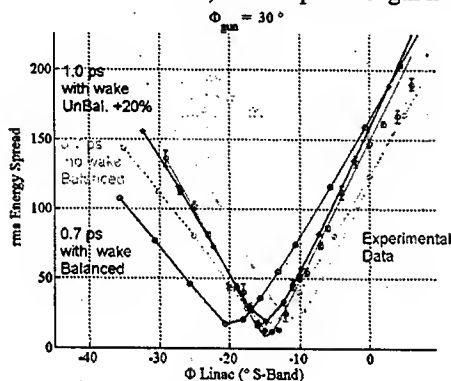


Figure 9: rms Energy Spread vs booster Phase w/o wakefields, w/o additional energy chirp. (UnBal. = ratio field amplitudes of the 2 cells different by 20 %)

The most satisfying fit corresponds to the case of an initial pulse of 1ps and a gun unbalanced by 20%. Thorough measurements of the gun field balance on the GTF gun have been performed and show that the gun was not unbalanced when the experiment was done [3]. However, we believe that an additional wakefield effect increases the correlated energy spread of the bunch in the drift between the gun exit and the linac entrance.

We deduce that the rms bunch length and the rms energy spread are respectively 1.26 ps and 62.7 keV at the entrance of the linac. The measurement of the bunch length will be performed at the entrance of the linac using an Electro-Optic device next summer and the booster phase scan experiment will be repeated.

The uncorrelated energy spread along the bunch can be extracted after removal of the correlation as plotted in figure10. All the slices have an uncorrelated rms energy spread smaller than 10 keV. This confirms what has been measured at other facilities[4].

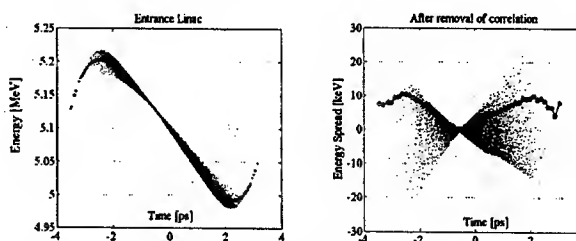


Figure10- Longitudinal Phase Space at linac entrance (1) – Uncorrelated energy spread (2)

CONCLUSION

From the low charge studies, we reconstitute the initial rms bunch length to be 0.5-0.6 ps. The high charge case leads us to an initial rms close to 1ps. This increase in uv pulse duration with pulse energy is possible since the uv conversion (from ir) is a two stage second harmonic generation process. Furthermore, we had not fully implemented uv pulse energy control that was independent of the ir pulse energy. Producing electron bunches with 15 pC and 290 pC charge levels required uv pulse energies of 1.2 μ J and 23 μ J respectively. At lowest ir and uv energy levels, the uv pulse duration can be half of that for higher ir and uv levels. The temporal profile of single uv pulses needs to be directly measured. Measuring the temporal profile of a single ir laser pulse is done using a FROG technique. A similar technique will implemented to enable single uv pulse measurements.

REFERENCES

- [1] C.Limborg "New Optimization for the LCLS injector", EPAC02, Paris, June 2002
- [2] D.Dowell et al. "Longitudinal Emittance Measurements At the SLAC Gun Test Facility " D.Dowell, FEL02, ANL, Chicago, August 02, (SLAC-PUB-9541)
- [3] S.Gierman, Private Communications, LCLS Tech note to be released
- [4] H.Schlarb, Private Communications, Measurements of energy spread on L-Band Gun at the TTF

SLAC is operated by Stanford University for the Department of Energy under contract number DE-AC03-76SF00515

RECENT ELECTRON-CLOUD SIMULATION RESULTS FOR THE MAIN DAMPING RINGS OF THE NLC AND TESLA LINEAR COLLIDERS*

M. Pivi†, T. O. Raubenheimer, SLAC, Menlo Park 94025, California, USA
M. A. Furman, LBNL, Berkeley 94720, California, USA

Abstract

In the beam pipe of the Main Damping Ring (MDR) of the Next Linear Collider (NLC), ionization of residual gasses and secondary emission give rise to an electron-cloud which stabilizes to equilibrium after few bunch trains. In this paper, we present recent computer simulation results for the main features of the electron cloud at the NLC and preliminary simulation results for the TESLA main damping rings, obtained with the code POSINST that has been developed at LBNL, and lately in collaboration with SLAC, over the past 7 years. Possible remedies to mitigate the effect are also discussed. We have recently included the possibility to simulate different magnetic field configurations in our code including solenoid, quadrupole, sextupole and wiggler.

INTRODUCTION

Beam induced multipacting, driven by the electric field of successive positively charged bunches, may arise from a resonant motion of electrons, generated by secondary emission, bouncing back and forth between opposite walls of the vacuum chamber. The electron-cloud effect (ECE) has been observed or is expected at many storage rings [1]. In all results presented, the positron beam is assumed to be a static distribution of given charge and shape moving at the center of the vacuum chamber, while the electrons are treated fully dynamically. We defer issues like the instability threshold, growth rate and frequency spectrum to future studies.

PHYSICAL MODEL

Sources of Electrons

In this article we consider what we believe to be the two main sources of electrons for the positron damping rings: (1) residual gas ionization and (2) secondary emission from electrons hitting the walls.

Secondary Emission Process

The secondary electron yield (SEY) $\delta(E_0)$ and the corresponding emitted-electron energy spectrum $d\delta/dE$ (E_0 = incident electron energy, E = emitted secondary energy) are represented by a detailed model described elsewhere [2]. The parameters have been obtained from detailed fits to the measured SEY of various materials [3]. Due to electron

Table 1: Simulation parameters for the NLC and TESLA positron damping rings.

Parameter	Symbol	NLC	TESLA
Beam energy	E, GeV	1.98	5.0
Bunch population	$N_p \times 10^{10}$	0.75	2
Ring circumference	C, m	299.8	17000
Dipole field	B, T	0.67	-
Quadrupole gradient	$G, \text{T/m}$	35	-
Wiggler field at max.	B_y, T	2.1	-
Wiggler period	λ_w, m	0.27	-
Bunches per train	N_b	192	2820
Train gap	τ_g, ns	65	-
Bunch spacing	b_s, ns	1.4	20
Bunch length ($\pm 5\sigma_z$)	σ_z, mm	5.5	6.0
Gauss. tr. bunch size	$\sigma_x, \sigma_y, \mu\text{m}$	49, 6	230, 230
Beam pipe semi-axes	a, b, cm	2, 2	5, 5
Antechamber gap	h, mm	10	none
No. slices/bunch	N_k	250	300
Steps during bunches	N_g	1400	200

scrubbing, the secondary electron yield is expected to decrease according to [4]. The main SEY parameters are the energy E_{max} at which $\delta(E_0)$ is maximum, the peak value $\delta_{\text{max}} = \delta(E_{\text{max}})$ and the elastic backscattered and rediffused components of the secondary emitted-electron energy spectrum $d\delta/dE$ at $E_0 \simeq 0$.

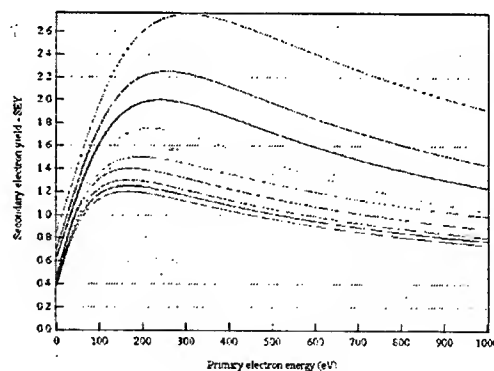


Figure 1: Secondary electron yield model used for the simulations.

Simulation Model

The NLC positron MDR stores 3 trains, separated by 65 nsec with each train consisting of 192 bunches having a 1.4

*Work supported by the US DOE under contracts DE-AC03-76SF00515 and DE-AC03-76SF00098.

†mpivi@slac.stanford.edu

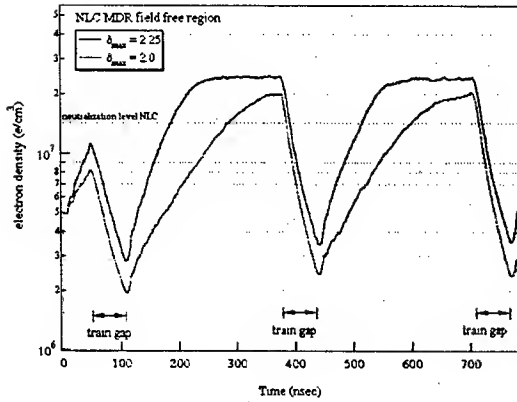


Figure 2: Development of the electron cloud during the passage of two bunch trains in a NLC Main Damping Ring field free region. Simulations for secondary yield δ_{\max} 2.25 and 2.0, with an initial seed of the electrons $5 \times 10^6 / \text{cm}^3$. The dependence of the saturation level with the SEY is shown in Fig 3.

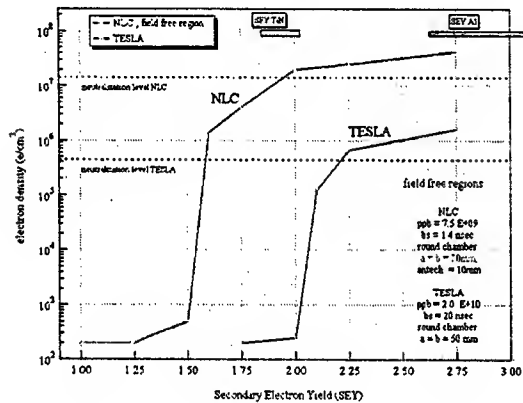


Figure 3: Dependence of the saturation density level with the peak SEY in a field free region of the NLC and TESLA Main Damping Ring. Typical value ranges for the SEY of Aluminum and TiN coated *as received* samples are shown above in the figure.

nsec bunch spacing. The aluminum vacuum chamber is assumed to be a cylindrical perfectly-conducting round pipe with a 20 mm radius and includes an antechamber to remove most of the synchrotron radiation. The TESLA main damping ring stores 2820 bunches with a 20 nsec bunch spacing. The vacuum chamber in the long TESLA straight sections is a round aluminum pipe with a 50 mm radius without an antechamber.

Typically, the electrons are simulated by macro-particles, each one representing a defined number of electrons and carrying a fixed charge. The secondary electron emission mechanism adds to these a variable number of macro-particles, generated according to the SEY model mentioned above. The bunch is divided up into N_k slices

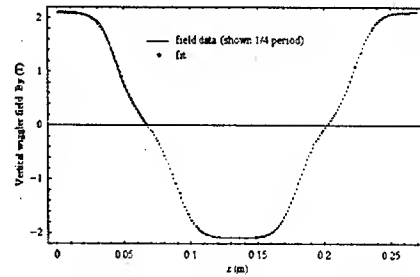


Figure 4: Wiggler vertical field model, NLC MDR.

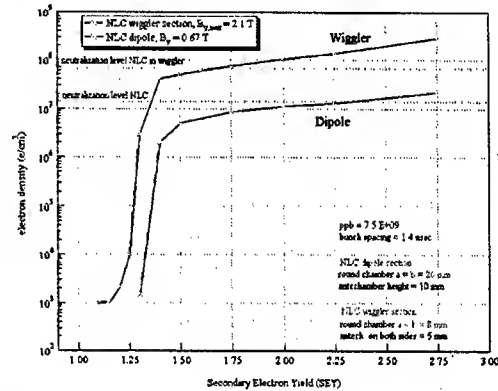


Figure 5: Saturation density as a function of δ_{\max} in a NLC wiggler (above) and a dipole section. Thresholds for the development of the electron cloud are respectively $\delta_{\max} \sim 1.3$ and 1.4. Note that the neutralization level in a wiggler is higher due to a smaller beam pipe cross section.

and the inter-bunch gap into N_g intermediate steps. The image and space charge forces are computed and applied at each slice in the bunch and each step in the gap. Typical beam and vacuum chamber parameters are listed in Table 1.

Since each bunch generates a small number of electrons by ionization of residual gases, a simulation of the entire process, up to the saturation level, would require a large number of macro-particles and long computer processing time. The saturation density level depends on the electron cloud space charge forces, the secondary electron yield and is independent of the initial seed. Thus, we generate a large number of electrons at the first bunch passage and let the electron cloud develops until a saturation density is reached, see Fig. 2.

SIMULATION RESULTS

NLC and TESLA Ring Field Free Regions

In our study, we are mainly interested in the estimate of the saturation electron density as a function of the secondary yield. The simulation results for the field free regions in both damping rings are shown in Fig. 3. The threshold for the development of the electron cloud in a field free region is $\delta_{\max} \sim 1.6$ and 2.1 for NLC and TESLA,

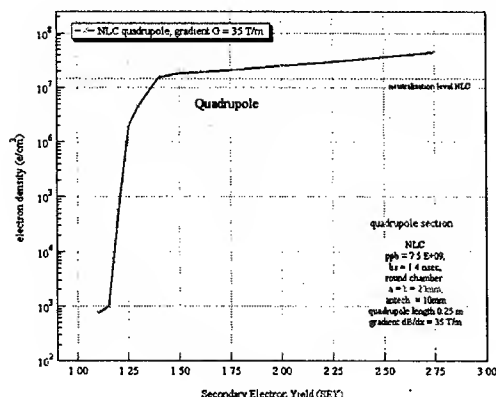


Figure 6: Saturation density as a function of the peak secondary yield in an NLC MDR quadrupole.

respectively. The threshold should occur under the conditions where the production rate of secondary electrons exceeds the decay rate of the electron cloud. The neutralization levels are also shown in figure.

NLC Dipole, Quadrupole and Wiggler

We have recently included in our code the possibility to simulate different magnetic field configurations. We present simulation results for the electron cloud in the wiggler, quadrupole and dipole regions of the NLC positron main damping ring.

For analysis of the electron dynamics in a wiggler, we have used a cylindrical mode representation of the field [5] and a model for the wiggler field used in our simulation is shown in Fig. 4. In the wiggler, an 8mm radius round beam pipe is provided with antechamber on both sides $h_w=5$ mm. We simulate a four period section of the wiggler. The results are compared with the results for a dipole region in Fig. 5.

The saturation density as a function of the secondary yield in a quadrupole are shown in Fig. 6. We generate the electrons in a 0.25 m long quadrupole with field gradient $G=35$ T/m. Previous studies and simulations [6] indicate that electrons may be trapped in a quadrupole, therefore surviving a long gap between bunch trains. The electron cloud decay times for three different sections are shown in Fig. 7. Note that, in these simulations, our code does not consider longitudinal variation of the quadrupole field which is treated as infinitely long¹. Refined quadrupole simulations are underway.

CONCLUSIONS

We present electron cloud simulation results suggesting that the SEY threshold for the development of the electron cloud in the main damping rings field free regions is

¹This is a good approximation, if the effective net flow of electrons leaving the quadrupole region is small.

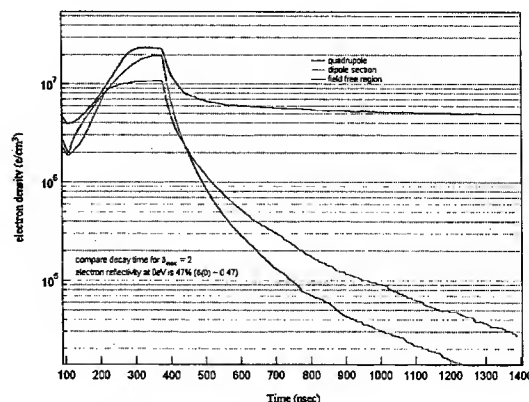


Figure 7: Decay time of the electron cloud compared for three different sections of the NLC MDR. Trapping of the electrons in the quadrupole field may result in a long decay time. Note that, in these simulations, our code does not consider the longitudinal variation of the quadrupole field, the quadrupole should be considered infinitely long.

$\delta_{max} \sim 1.6$ and 2.1 respectively for the NLC and TESLA. Furthermore, we simulate the electron cloud effect in the dipole, wiggler and quadrupole of the NLC main damping ring. A demanding SEY threshold is given by $\delta_{max} \sim 1.3$ in the wigglers. Simulations confirm the electron trapping mechanism in quadrupoles. More simulations are needed to estimate the longitudinal drift of the electrons in quadrupoles.

We are considering TiN as a possible coating material to reduce the secondary yield of aluminum. An experimental program, to measure the secondary yield of TiN coating materials and study the reduction of the SEY due to ion sputtering of the TiN surface, has started at SLAC. Furthermore, the solenoid field is a possible way to suppress the electron cloud in a limited fraction of the damping rings.

We are particularly grateful to our colleagues for many stimulating discussions, especially to A. Wolski, F. Le Pimpec and R. Kirby. We are grateful to NERSC for supercomputer support.

REFERENCES

- [1] For an updated summary and links on electron cloud studies, see ECLLOUD02: <http://slap.cern.ch/collective/ecloud02/>. In particular, see contributions from: N. Hilleret, R. Macek, K. Harkay, M. Blaskiewicz, K. Ohmi, F. Zimmermann.
- [2] M.A. Furman, M. Pivi Phys.Rev. ST AB 5, 124404, 2002.
- [3] R. Kirby, private communication.
- [4] J.M. Jimenez et al. LHC-Project-Report-632.
- [5] M. Venturini, A. Wolski, A. Dragt these proceedings RPAB023.
- [6] L. Wang presentation <http://conference.kek.jp/two-stream/>; F. Zimmermann, CERN SL-Note-2002-017 (AP); P. J. Channell and A. J. Jason, LANL AOT-3 Tech. Note 94-11.

MITIGATION OF THE ELECTRON-CLOUD EFFECT IN THE PSR AND SNS PROTON STORAGE RINGS BY TAILORING THE BUNCH PROFILE*

M. Pivi[†], SLAC, Menlo Park 94025, California, USA
M. A. Furman, LBNL, Berkeley 94720, California, USA

Abstract

For the storage ring of the Spallation Neutron Source (SNS) at Oak Ridge, and for the Proton Storage Ring (PSR) at Los Alamos, both with intense and very long bunches, the electron cloud develops primarily by the mechanism of trailing-edge multipacting. We show, by means of simulations for the PSR, how the resonant nature of this mechanism may be effectively broken by tailoring the longitudinal bunch profile at fixed bunch charge, resulting in a significant decrease in the electron-cloud effect. We briefly discuss the experimental difficulties expected in the implementation of this cure.

INTRODUCTION

It is becoming progressively clear that the electron-cloud effect plays an important role in the high-intensity instability which has been observed in the PSR at the Los Alamos National Laboratory (LANL) for more than 13 years. This instability is now believed to be due to the collective coupling between an electron cloud and the proton beam [1]. Such instability is a particular manifestation of the electron-cloud effect (ECE) that has been observed or is expected at various other machines. In this article we present simulation results for the SNS ring obtained with the ECE code that has been developed at LBNL, and lately in collaboration with SLAC, over the past 7 years. Besides other possible mitigation effects including Landau damping, TiN coating, clearing electrodes, solenoid windings and electron conditioning [2], we investigate the possibility to suppress the electron formation by tailoring the longitudinal beam profile.

PHYSICAL MODEL

Sources of Electrons

The electron production may be classified into: (1) electrons produced at the injection region stripping foil (2) electrons produced by proton losses incident on the vacuum chamber at grazing angles (3) secondary electron emission process and (4) electrons produced by residual gas ionization. The two main sources of electrons considered for proton storage rings at the SNS and the PSR, are lost protons hitting the vacuum chamber walls, and secondary emission from electrons hitting the walls.

*Work supported by the US DOE under contracts DE-AC03-76SF00515 and DE-AC03-76SF00098.

[†] mpivi@slac.stanford.edu

Table 1: Simulation parameters for the PSR and SNS.

Parameter	Symbol, unit	PSR	SNS
Ring parameters			
Proton beam energy	E , GeV	1.735	1.9
Dipole field	B , T	1.2	0.78
Bunch population	N_p , $\times 10^{13}$	5	20.5
Ring circumference	C , m	90	248
Revolution period	T , ns	350	945
Bunch length	τ_b , ns	254	700
Gauss. tr. beam size	σ_x, σ_y , mm	10, 10	
Flat tr. beam size	r_x, r_y , mm		28, 28
Beam pipe semi-axes	a, b , cm	5, 5	10, 10
Simulation parameters			
Proton loss rate	p_{loss} , $\times 10^{-6}$	4	1.1
Proton-electron yield	Y	100	100
No. kicks/bunch	N_k	1001	10001
No. steps during gap	N_g	400	1000
Max sec. yield	δ_{max}	2.0	2.0
Energy at yield max	E_{max} , eV	300	250
Yield low energy el.	$\delta(0)$	0.5	0.5
Rediffused component	$P_{1,r}(\infty)$	0.74	0.2

Secondary Emission Process

When a primary electron impinges on the beam pipe surface generates secondary electrons. The main secondary electron yield (SEY) parameters are the energy E_{max} at which $\delta(E_0)$ is maximum, and the peak value itself, $\delta_{\text{max}} = \delta(E_{\text{max}})$, see Table 1 and Fig. 1. For the results shown below, we do take into account the elastic backscattered and rediffused components of the secondary emitted-electron energy spectrum $d\delta/dE$.

Simulation Model

The SNS proton storage ring stores a single proton bunch of length τ_b followed by a gap of length τ_g with a typical current intensity profile shown in Figs. 3 and 5. The transverse beam distribution for the SNS is assumed to be constant with $r_x=r_y=28$ mm. The vacuum chamber is assumed to be a cylindrical perfectly-conducting pipe. The number of electrons generated by lost protons hitting the vacuum chamber wall is $N_p \times Y \times p_{\text{loss}}$ per turn for the whole ring, where Y is the effective electron yield per lost proton, and p_{loss} is the proton loss rate per turn for the whole ring per beam proton. The lost-proton time distribution is proportional to the instantaneous bunch intensity. The electrons are then simulated by macroparticles. The secondary electron mechanism adds to these a variable number

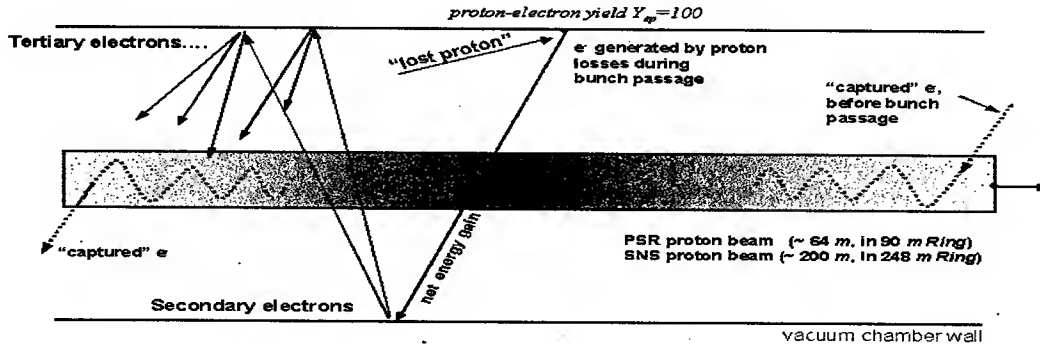


Figure 2: Electron multiplication mechanism in long proton bunches.

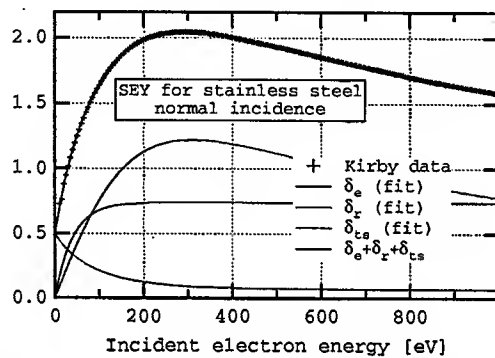


Figure 1: (Color) The SEY for stainless steel for a SLAC standard 304 rolled sheet, chemically etched and passivated but not conditioned (data courtesy R. Kirby).

of macroparticles, generated according to the SEY model mentioned above. The bunch is divided up into N_k kicks, and the interbunch gap into N_g intermediate steps. The image and space charge forces are computed and applied at each slice in the bunch and each step in the gap.

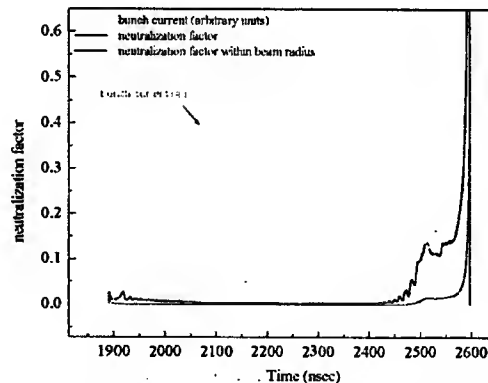
RESULTS AND DISCUSSIONS

An electron present in the vacuum chamber before the bunch passage oscillates in the beam well potential. The oscillation amplitude most likely remains smaller than the chamber radius during the beam passage and the electron is released at the end of the beam passage. On the other hand, electrons generated at the wall by proton losses near the peak of the beam pulse are accelerated and decelerated by the beam potential and hit the opposite wall with a net energy gain, producing secondary electrons, see Fig. 2. Electrons which survive the gap between two bunch passages will increase in number. The electrons gradually increase in number during successive bunch passages until, owing to the space-charge forces, a balance is reached between emitted and absorbed electrons. See also an animation of the PSR electron cloud dynamic during the beam passage at [4].

The estimated build-up of the electron cloud in a PSR field free region gives ~ 75 nC/m or 6×10^7 e/cm³ [1].

The SNS beam pipe chamber will be coated with TiN. Recent measurements of an as-received sample of the TiN coated stainless steel SNS vacuum chamber, has shown a secondary electron yield $\delta_{\max} = 1.9 \pm 0.2$ [5, 6].

Due to the large electron multiplication, we have used a relatively small number of macroparticles generated per bunch passage, which leads, nevertheless, to reasonably stable results in terms of the turn-by-turn electron density. The amplification factor per macroparticle may exceed 10^4 during a single bunch passage when $\delta_{\max} = 2$. Simulation results for the SNS obtained with a different code [7] show a qualitative agreement with our results, although they yield a lower estimated electron density at this SEY value [5]. We assume in these simulations that pro-


 Figure 3: Simulated electron neutralization factor in a SNS field-free region. The fractional charge neutralization computed within the beam radius region is $\sim 1\%$ during the bunch passage, and it exceeds 10% at the tail of the bunch.

ton losses corresponding to 1.1×10^{-6} protons loss per proton per turn are expected in the SNS ring. The build-up of the electron cloud results in an average line density of 100 nC/m with a line density within the beam radius region exceeding 10 nC/m. These imply neutralization factors as shown in Fig. 3. In particular the neutralization factor dur-

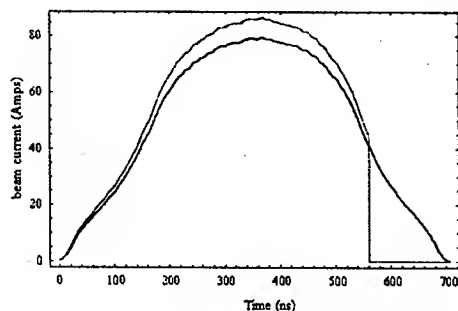


Figure 4: SNS beam current profile cut at 560 ns, compared to the nominal beam profile.

ing the bunch passage is 1%, and most of the electrons are contained in the beam radius region.

The possible amplification mechanism which may take place in long-beam storage rings suggest interesting considerations. Electrons generated at the wall by proton losses near the peak of the beam pulse are accelerated and decelerated by the beam potential and hit the opposite wall with a net energy gain, producing secondary electrons. Many generations of secondary electrons may occur during a single bunch passage leading to an high electron cloud density owing to trailing-edge multipacting. In order to verify this assumption, in the simulations, we have artificially truncated the tail of the bunch, while maintaining the same integrated beam charge. In particular, Fig. 4 shows the modified SNS beam current profile, compared to the nominal beam current profile. The effect of the modification of the beam profile on the formation of the electron cloud is shown in the lowest curves of Fig. 5. The density of the electron cloud decreases as the tail of the beam is progressively truncated. Tailoring the 700ns long beam at 560ns and 500ns reduces the peak electron density by a factor 20 and 200 respectively. A reduction of the beam head profile has the opposite effect of increasing the electron cloud density. Simulation results for the PSR have shown a similar behavior.

CONCLUSIONS

We have presented electron cloud simulations for the SNS. When considering proton losses of 10^{-6} and $\delta_{\max} = 2$, a line density of ≥ 100 nC/m should be expected in an SNS field-free region, with a density exceeding 10 nC/m within the beam radius region. Although the neutralization factor may exceed 10% near the tail of the beam, the resulting electron cloud tune shift is moderate. Linear stability studies and current threshold estimates are deferred to a separate publication [5]. Many generations of secondary electrons may occur during a long bunch passage leading to an high electron cloud density owing to trailing-edge multipacting. In order to verify this assumption, in the simulations, we have artificially truncated the tail of the bunch, while maintaining the same integrated beam charge.

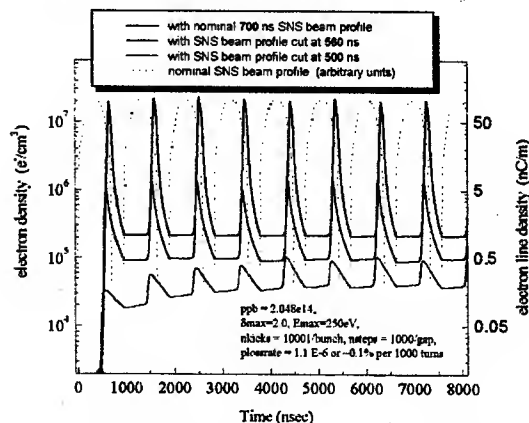


Figure 5: Simulated electron density in an SNS field-free region, assuming $\delta_{\max} = 2$ and $N_p = 2.05 \times 10^{14}$. We have artificially truncated the tail of the bunch, while maintaining the same integrated beam charge. The density of the electron cloud decreases as the tail of the beam is progressively reduced.

The density of the electron cloud decreases, more than to 2 orders of magnitude, as the tail of the beam is progressively truncated. Although tailoring the beam is difficult to achieve in practice as alternative method to suppress the formation of the electron cloud, it has been considered as a possible experiment at the PSR. More investigations are needed.

ACKNOWLEDGMENTS

We are indebted to M. Blaskiewicz, K. Harkay, R. Davidson, H. Qin, P. Channell, T. S. Wang for many stimulating discussions. We are especially grateful to R. Macek for kindly providing us the experimental data and for many valuable discussions. Thanks to R. Kirby, A. Alexandrov, V. Danilov. We are grateful to NERSC for supercomputer support.

REFERENCES

- [1] Various contributions <http://slap.cern.ch/collective/eccloud02/>, especially the surveys by M. Blaskiewicz and R. Macek.
- [2] J. Wei et al., these proceedings (WPPG004).
- [3] For an updated on the self consistent treatment of the instability see Physical Review Special Topic, [http://prst-ab.aps.org/Two-Stream/Special Collection Edition](http://prst-ab.aps.org/Two-Stream/Special%20Collection%20Edition).
- [4] Movie of the electron-cloud in the PSR by M. Pivi at <http://slap.cern.ch/collective/eccloud02/newschedule.html>
- [5] M. Blaskiewicz et al. Phys. Rev. ST Accel. Beams 6, 014203 (2003).
- [6] T. Toyama, K. Ohmi, in *Proceedings of the ECLLOUD-02 workshop*.
- [7] M. Blaskiewicz, in *Proceedings of the ECLLOUD-02 workshop*.

DERIVATION OF FEL GAIN USING WAKEFIELD APPROACH

G. Stupakov and S. Krinsky

Stanford Linear Accelerator Center, Stanford University, Stanford, CA 94309

Abstract

We describe the one-dimensional SASE FEL instability using the wake approach. First, we obtain an expression for the longitudinal 1-D wake in a helical undulator. We then show that taking into account the retardation effect in the Vlasov equation with the proper wake leads to the correct result for the FEL instability, in agreement with the traditional theory.

INTRODUCTION

Coherent instabilities arise when the electromagnetic field produced by an electron beam, interacts with the environment, generating new fields which act back on the electrons. It is conventional to describe such phenomena by using the Vlasov equation, with the electromagnetic forces represented by a wakefield [1]. In the high-gain free-electron laser (FEL), the radiation emitted by an electron beam passing through a long undulator acts back on the electrons. This interaction is often described using the Vlasov-Maxwell equations [2-4]. In this paper, we discuss the FEL using the wakefield approach and emphasize the necessity of including the effects of retardation [5].

WAKE IN THE UNDULATOR

Consider a helical undulator with the undulator parameter K . A beam of density n_0 (per cubic cm) and relativistic factor γ propagates along the axis of the undulator. The transverse velocity v_\perp of a particle in the undulator is equal to

$$v_\perp = v_\perp (e_x \cos k_w s + e_y \sin k_w s), \quad (1)$$

where

$$v_\perp = c \frac{K}{\gamma},$$

with $k_w = 2\pi/\lambda_w$, λ_w the undulator period, e_x and e_y the unit vectors in x and y directions, respectively, and s the distance along the undulator. The longitudinal velocity of the particle in the undulator is $v_z \approx c[1 - (1 + K^2)/(2\gamma^2)]$, corresponding to the longitudinal gamma-factor γ_z

$$\gamma_z = \left(1 - \frac{v_z^2}{c^2}\right)^{-1/2} = \frac{\gamma}{\sqrt{1 + K^2}}.$$

To derive a wake in 1-D theory we consider an infinitely thin sheet of electrons in the $x - y$ plane with the charge

density σ per unit area. The longitudinal position of the sheet is $s = v_z t$. Due to the transverse motion, the sheet radiates electromagnetic field. To find the radiation field, we first calculate it in the beam frame. In this frame, the sheet rotates with the frequency $\gamma_z \omega_w$, where $\omega_w = ck_w$, and its transverse velocity is

$$\hat{v}_\perp = \gamma_z v_\perp [\hat{e}_x \cos(\gamma_z \omega_w \hat{t}) + \hat{e}_y \sin(\gamma_z \omega_w \hat{t})], \quad (2)$$

where the hat indicates variables in the beam frame. The sheet radiates two circularly polarized plane electromagnetic waves—one in the direction of the beam propagation, and the other in the opposite direction—with equal amplitudes and the frequency $\gamma_z \omega_w$. From the symmetry of the problem, the directions of the magnetic field vector in these waves at the location of the sheet ($s = v_z t$) are opposite. To find the amplitude of the magnetic field, we use Ampere's law:

$$2\hat{H}(t)|_{\text{sheet}} = \frac{4\pi}{c} \sigma \hat{v}_\perp \times \hat{e}_z,$$

from which it follows that the amplitude \hat{H}_0 of the field is

$$\hat{H}_0 = \frac{2\pi}{c} \sigma \hat{v}_\perp = \frac{2\pi}{c} \gamma_z \sigma v_\perp.$$

Note that the amplitude of the electric field \hat{E}_0 is also equal to \hat{H}_0 . Returning to the lab frame we find that the frequency of the wave propagating in the forward direction is

$$\omega_0 = 2\gamma_z^2 \omega_w = 2 \frac{\gamma^2}{1 + K^2} \omega_w, \quad (3)$$

and the amplitudes of the electric and magnetic fields are

$$E_0 = H_0 = 2\gamma_z \hat{H}_0 = \frac{4\pi}{c} \sigma v_\perp \gamma_z^2.$$

The electric field in this wave is

$$\mathbf{E}(s, t) = -E_0 [e_x \cos(\omega_0(t - s/c)) + e_y \sin(\omega_0(t - s/c))]. \quad (4)$$

The magnetic and electric fields in the backward wave, in the limit $\gamma_z \gg 1$, are much smaller than H_0 , and we neglect them below in the calculation of the wake.

To calculate the longitudinal wake, we consider a test sheet of particles, with a unit charge per unit area, moving in front of the source sheet in the undulator, at distance z , with the same velocity given by Eq. (1). For the test sheet we have $s = v_z t + z$. The radiated electromagnetic wave

will exert a force on the test sheet, and the work of the force per unit time (and per unit area) is

$$\begin{aligned} \mathbf{E} \left(s, \frac{s-z}{v_z} \right) \cdot \mathbf{v}_\perp(s) \\ \approx -\frac{4\pi}{c} \sigma v_\perp^2 \gamma_z^2 \cos(\omega_0 z/v_z) \\ = -4\pi \sigma \frac{K^2}{1+K^2} \cos(\omega_0 z/v_z), \end{aligned} \quad (5)$$

where we used Eqs. (2), (4), and (3). If we define the longitudinal wake $w(s, z)$ as the energy loss of the test sheet per unit area per unit length of path and per unit σ , then

$$w(s, z) = \begin{cases} 2\kappa \cos\left(\frac{\omega_0 z}{v_z}\right), & \text{for } 0 < z < \frac{c-v_z}{c}s \\ \kappa, & \text{for } z = 0 \\ 0, & \text{otherwise} \end{cases}, \quad (6)$$

where the loss factor κ is:

$$\kappa = 2\pi \frac{K^2}{1+K^2}. \quad (7)$$

This wake is localized in front of the sheet because the radiated wave overtakes the particles. Positive wake corresponds to the energy loss, and negative wake means an energy gain. Note that the wake is a function of two variables: the distance z between the source and the test sheets, and the current position s of the source.

The product $\kappa\sigma^2$ is the spontaneous radiation emitted per unit area per unit length of path. It is interesting to note, that usually in accelerators the longitudinal wake is associated with the longitudinal component of the electric field E_z , with the energy gain for the test particle given by $eE_z v_z$. In undulator, as expressed by Eq. (5), the work is done by the transverse component of the electric field coupled with the wiggling motion of the particle.

VLASOV EQUATION

Having derived the longitudinal wake, we can now apply the standard formalism of accelerator theory to describe dynamics of the beam [1]. The one-dimensional Vlasov equation in a coasting beam approximation is

$$\begin{aligned} \frac{\partial f}{\partial s} - \eta \delta \frac{\partial f}{\partial z} - \frac{r_0}{\gamma} \frac{\partial f}{\partial \delta} \\ \times \int_{-\infty}^{\infty} dz' \int_{-\infty}^{\infty} d\delta' w(s, z-z') f(\delta', z', s) = 0, \end{aligned} \quad (8)$$

where η is the slip factor per unit length, $\delta = \Delta\gamma/\gamma$ is the energy deviation relative to the nominal value γmc^2 , and $r_0 = e^2/mc^2$ is the classical electron radius. The distribution function f is normalized so that $\int f dz d\delta$ gives the particle density (per cm^3).

It turns out, however, that the standard form of the Vlasov equation (8) should be corrected by taking into account the retardation effect in the last term on the left hand

side¹:

$$\begin{aligned} \int_{-\infty}^{\infty} dz' \int_{-\infty}^{\infty} d\delta' w(s, z-z') f(\delta', z', s) \rightarrow \\ \int_{-\infty}^{\infty} dz' \int_{-\infty}^{\infty} d\delta' w(s, z-z') f\left(\delta', z', s - c \frac{z-z'}{c-v_z}\right). \end{aligned} \quad (9)$$

Indeed, the wake that is generated at coordinate z' moves relative to the beam with the velocity $c-v_z$, and if it reaches the point z at time t , it should have been emitted at position $s - c(z-z')/(c-v_z)$. Taking into account that in the undulator

$$\eta = -\frac{1+K^2}{\gamma^2}, \quad (10)$$

we obtain

$$\begin{aligned} \frac{\partial f}{\partial s} + \frac{\delta(1+K^2)}{\gamma^2} \frac{\partial f}{\partial z} - \frac{r_0}{\gamma} \frac{\partial f}{\partial \delta} \int_{-\infty}^{\infty} dz' \int_{-\infty}^{\infty} d\delta' \\ \times w(s, z-z') f\left(\delta', z', s - c \frac{z-z'}{c-v_z}\right) = 0. \end{aligned} \quad (11)$$

It is convenient to introduce new variables: $\bar{s} = k_w s$ and $\theta = \omega_0 z/v_z$ and consider f as a function of \bar{s} and θ . We linearize Eq. (11) assuming that $f = f_0(\delta) + f_1(\delta, z, s)$ with $|f_1| \ll f_0$. Using notation $f_0(\delta) = n_0 h(\delta)$, we find [2-4]

$$\begin{aligned} \frac{\partial f_1}{\partial \bar{s}} + 2\delta \frac{\partial f_1}{\partial \theta} - (2\rho)^3 h'(\delta) \int_{\theta-\bar{s}}^{\theta} d\theta' \\ \times \int_{-\infty}^{\infty} d\delta' \cos(\theta - \theta') f_1(\delta', \theta', \bar{s} - \theta + \theta') = 0, \end{aligned} \quad (12)$$

where ρ is the Pierce parameter [6] given by

$$(2\rho)^3 = \frac{2n_0 \kappa c r_0}{k_w \gamma \omega_0} = \frac{2\pi K^2 r_0 n_0}{\gamma^3 k_w^2}, \quad (13)$$

and we have used the relation

$$\frac{k_0}{k_w} = \frac{v_z}{c-v_z}.$$

FEL DISPERSION RELATION

We introduce a new variable $\bar{s}' = \bar{s} - \theta + \theta'$, and rewrite Eq. (12) in the following form

$$\begin{aligned} \frac{\partial f_1}{\partial \bar{s}} + 2\delta \frac{\partial f_1}{\partial \theta} - (2\rho)^3 h'(\delta) \int_0^{\bar{s}} d\bar{s}' \\ \times \int_{-\infty}^{\infty} d\delta' \cos(\bar{s} - \bar{s}') f_1(\delta', \theta - \bar{s} + \bar{s}', \bar{s}') = 0. \end{aligned} \quad (14)$$

Assume sinusoidal modulation of the distribution function with frequency ω , $f_1 \propto e^{i\omega z/c} = e^{i(1+\nu)\theta}$, where $\nu = (\omega - \omega_0)/\omega_0$. We then define functions Φ_ν and K_ν such that

$$\begin{aligned} f_1(\delta, \theta, \bar{s}) &= e^{i(1+\nu)\theta} \Phi_\nu(\delta, \bar{s}), \\ K_\nu(\bar{s}) &= e^{-i(1+\nu)\bar{s}} \cos \bar{s}. \end{aligned}$$

¹A similar modification of the Vlasov equation is invoked in the derivation of a single-mode CSR instability in rings, [5].

Then Eq. (14) takes the form

$$\frac{\partial \Phi_\nu}{\partial \bar{s}} + 2i\delta(1+\nu)\Phi_\nu = (2\rho)^3 h'(\delta) \int_0^{\bar{s}} d\bar{s}' K_\nu(\bar{s} - \bar{s}') \times \int_{-\infty}^{\infty} d\delta' \Phi_\nu(\delta', \bar{s}') = 0. \quad (15)$$

Laplace transforming Eq. (15) we find

$$-\Phi_\nu(\delta, 0) + [\beta + 2i\delta(1+\nu)]\tilde{\Phi}_\nu(\delta, \beta) = (2\rho)^3 h'(\delta) \tilde{K}_\nu(\beta) \int_{-\infty}^{\infty} d\delta' \tilde{\Phi}_\nu(\delta', \beta), \quad (16)$$

where

$$\begin{aligned} \tilde{\Phi}_\nu(\delta, \beta) &= \int_0^{\infty} d\bar{s} e^{-\beta\bar{s}} \Phi_\nu(\delta, \bar{s}), \\ \tilde{K}_\nu(\beta) &= \int_0^{\infty} d\bar{s} e^{-\beta\bar{s}} K_\nu(\bar{s}) \\ &= \frac{1}{2} \left[\frac{1}{\beta + i\nu} + \frac{1}{\beta + i\nu + 2i} \right]. \end{aligned} \quad (17)$$

Dividing Eq. (16) by $\beta + 2i\delta(1+\nu)$ and integrating over δ yields

$$\int_{-\infty}^{\infty} d\delta \tilde{\Phi}_\nu(\delta, \beta) = \frac{\int_{-\infty}^{\infty} d\delta \frac{\Phi_\nu(\delta, 0)}{\beta + 2i\delta(1+\nu)}}{1 - (2\rho)^3 \tilde{K}_\nu(\beta) \int_{-\infty}^{\infty} d\delta \frac{h'(\delta)}{\beta + 2i\delta(1+\nu)}}.$$

The dispersion relation that defines the frequency ν of modes is given by zeros of the denominator on the right hand side of this equation:

$$(2\rho)^3 \tilde{K}_\nu(\beta) \int_{-\infty}^{\infty} d\delta \frac{h'(\delta)}{\beta + 2i\delta(1+\nu)} = 1. \quad (18)$$

Rapid growth will be seen to correspond to $|\nu| \lesssim 2\rho$ and $\beta \sim 2\rho$. The second term in expression for \tilde{K}_ν on Eq. (17) is not resonant and can be neglected, which gives

$$\frac{1}{2} (2\rho)^3 \frac{1}{\beta + i\nu} \int_{-\infty}^{\infty} d\delta \frac{h'(\delta)}{\beta + 2i\delta} = 1,$$

where we neglected ν relative to unity in the denominator of the integrand of Eq. (18).

For a cold beam, $h(\delta) = \delta(\delta)$ (where the first δ stands for the delta-function), and we obtain

$$\beta^2(\beta + i\nu) = i(2\rho)^3 \quad (19)$$

in agreement with conventional result of the FEL theory [2-4].

DISCUSSION

In order to clarify the effect of retardation introduced in Eq. (9), we will analyze here the dispersion relation that would result from using the Vlasov equation Eq. (8), without retardation. In this analysis, we will neglect the s dependence of the wake in Eq. (6). Linearizing Eq. (8), and

assuming the dependence $f_1(\delta, z, s) \propto e^{\beta k_w s + i(1+\nu)\omega_0 z/c}$ we obtain a well known Keil-Schnell dispersion relation [1] for a coasting beam instability:

$$\frac{cr_0}{\gamma} Z \left(\frac{\omega_0(1+\nu)}{c} \right) \int_{-\infty}^{\infty} \frac{d\delta(\partial f_0/\partial \delta)}{\beta k_w - i\eta\delta(1+\nu)\omega_0/c} = 1, \quad (20)$$

where the impedance $Z(k)$ is related to the wake by the following equation

$$Z(k) = \frac{1}{c} \int_{-\infty}^{\infty} w(z) e^{-ikz} dz.$$

For a cold beam, with the distribution function $f_0 = n_0\delta(\delta)$, Eq. (20) reduces to

$$-\frac{i\eta n_0 r_0 \omega_0 (1+\nu)}{\gamma \beta^2 k_w^2} Z \left(\frac{\omega_0(1+\nu)}{c} \right) = 1. \quad (21)$$

To illustrate our point, we will use the wake given by $w = 2\kappa \cos(\omega_0 z/v_z)$ for arbitrary $z > 0$ (that is we neglect the condition $0 < z < \frac{c-v_z}{c}s$ in Eq. (6)). We then find

$$Z(k) = \frac{2\kappa}{c} \int_0^{\infty} \cos\left(\frac{\omega_0 z}{c}\right) e^{-ikz} dz \approx \frac{i\kappa}{c} \frac{1}{k - \omega_0/c}, \quad (22)$$

where we left only the resonant term, dominant when kc is close to the FEL frequency ω_0 . Substituting Eq. (22) into Eq. (21) and using equations Eq. (7) and (10) for κ and η , and Eq. (13) for ρ we find

$$\beta^2 = \frac{(2\rho)^3}{\nu}. \quad (23)$$

According to this dispersion relation, the quantity β diverges when $\nu \rightarrow 0$. This result is due to the fact that $\nu = 0$ corresponds to the exact resonance with the wake, when the impedance $Z = \infty$. Comparing with the correct dispersion relation Eq. (19), we see that the retardation effectively detunes and broadens the resonance in Eq. (23) changing $\nu \rightarrow \nu - i\beta$, and effectively eliminates the divergence at the resonance.

ACKNOWLEDGMENTS

This work was supported by the Department of Energy, contract DE-AC03-76SF00515.

REFERENCES

- [1] A. W. Chao, *Physics of Collective Beam Instabilities in High Energy Accelerators* (Wiley, New York, 1993).
- [2] N. M. Kroll and W. A. McMullin, *Physical Review A* **17**, 300 (1978).
- [3] K.-J. Kim, *Nuclear Instruments and Methods in Physics Research A* **250**, 396 (1986).
- [4] J. M. Wang and L. H. Yu, *Nuclear Instruments and Methods in Physics Research A* **250**, 484 (1986).
- [5] S. Heifets and G. Stupakov, in *PAC03* (2003).
- [6] R. Bonifacio, C. Pellegrini, and L. M. Narducci, *Opt. Commun.* **50**, 373 (1984).

COHERENT SYNCHROTRON RADIATION EFFECTS IN THE ELECTRON COOLER FOR RHIC

Juhao Wu^{1*}, Dong Wang^{2,3†} and Feng Zhou^{2,4‡}

¹SLAC, Stanford University, Stanford, CA 94309; ²BNL, Upton, NY 11973

³Bates Linear Accelerator Center, MIT, Middleton, MA 01949; ⁴UCLA, Los Angeles, CA 90095

Abstract

The Coherent Synchrotron Radiation (CSR) could be a concern in many modern accelerator projects. In the proposed electron-cooling project for the Relativistic Heavy Ion Collider (RHIC), the electron cooler is designed to cool 100 GeV/nucleon bunched ion-beam using 55 MeV electrons. The electron bunch length will be on the order of cm, and the charge per bunch would be around 5 - 10 nC. We study the CSR effect in this paper.

INTRODUCTION

Because the synchrotron radiation damping mechanism is essentially absent for the heavy particles, electron cooling was proposed as the method to cool the particle beams in the storage ring of heavy particles [1, 2] based on the heat-energy transfer from the beam to an electron stream with lower temperature. Without additional perturbations, the electron cooling of ion beams stops when the ion beam and the cooling electron beam reach the equilibrium temperature. For a planed luminosity upgrade for the Relativistic Heavy Ion Collider (RHIC) operated by BNL, an important component is the electron cooling of the RHIC gold ion beams [3]. The luminosity increase for the RHIC II upgrade would be about 40, of which a factor of 10 is anticipated to come from the electron cooling, and the other 4 comes from beta function reduction at the interaction point and increasing (doubling) the number of bunches.

To cool the 100 GeV/u gold beam, the single bunch charge of the electron bunch has to be on the order of 10 nC. In one scenario, this charge is compressed to a rms bunch length of approximately 12 mm to be accelerated by a LINAC. Later the electrons will be debunched from 12 mm to about 50 mm before entering the cooling region. Since the electrons need be debunched, during the acceleration, the electron beam is chirped. The transport line then consists of three components [4]: a decompressor which will debunch the electrons; a rotation cavity which will reverse the chirp on the electron bunch; and finally a compressor which will bunch the electrons and safely transport the electrons back to the LINAC and then after energy recovery the electrons are dumped. The requirement on the electron beam quality directly affect the efficiency of cooling the gold beam, it is of great importance to make sure that the transport line will preserve the electron beam qual-

ity. Though the bunch length is relatively long, the single bunch charge is high, one question is whether the coherent synchrotron radiation (CSR) [5, 6] in the decompressor and compressor would be a concern. In this paper, we study the CSR effects.

CONSIDERATION AND PARAMETERS

CSR is mostly a longitudinal effect, and due to the chromatic transfer function, the transverse phase space volume is also affected. For a transversely thin beam with a Gaussian distribution in the longitudinal density, the energy loss gradient along the bunch is equal to [5, 6]

$$\frac{d\mathcal{E}}{cdt} = \frac{2Ne^2}{\sqrt{2\pi}(3\rho^2\sigma_s^4)^{1/3}} F\left(\frac{s}{\sigma_s}\right), \quad (1)$$

with

$$F(\xi) = - \int_{-\infty}^{\xi} \frac{d\xi'}{(\xi - \xi')^{1/3}} \frac{d}{d\xi'} e^{-\xi'^2/2}, \quad (2)$$

where N is the bunch population, ρ is the bending radius, σ_s is the rms bunch length. Compared with the high brightness electron beam for the Linear Collider (LC) or the Free-Electron Laser (FEL), the bunch length here is longer, but the bunch charge is also higher, the scaling $d\mathcal{E}/(cdt) \propto N(\sigma_s)^{-4/3}$ tells us that CSR effects here in the e-cooler could be a concern as that in the LCs and the FELs. In the lattice design, each piece of magnet has a length of $L = 0.75$ m and the bending angle is $\theta = \pi/4$, hence the path length difference between the trajectory taken by the electron and that of the radiation is $\Delta L = L - 2L \sin(\pi/8)/(\pi/4) \approx 1.9$ cm. Normally, the vacuum chamber cut-off wavelength is on the order of a few millimeters and, we know the steady-state CSR impedance is applicable to wavelength down to the cut-off wavelength. Therefore, in our calculation, it would be fine, if we take the steady state CSR impedance. Of course, the free-space CSR impedance will overestimate the CSR effect and we will come back to this point in the following.

As the nominal set of parameters, the reference kinetic energy is 55 MeV, the emittance is on the order of 30 to 60 mm-mrad. In our calculation here, we set the initial rms bunch length to be $\sigma_{zi} = 12$ mm. Since we want to stretch it to a rms length of $\sigma_{zf} = 50$ mm at the e-cooler point, and the lattice provides a $R_{56} = -32.8$ m, we need chirp the electron beam so that the head will have higher energy, and the tail lower energy. The corresponding initial chirp we need is $\sigma_{\xi}^2 = 1.16 \times 10^{-3}$. At the e-cooler point, we then

*jhwu@SLAC.Stanford.EDU

†wangd@bnl.gov

‡zhouf@bnl.gov

need a cavity to reverse the chirp, so that the electrons in the head will have lower energy than the electrons in the tail would. Since at the e-cooler point, the rms bunch length is already 50 mm, a linearizer is probably a requirement. In our calculation, we implement a linearizer to correct the RF curvature. At the end of the compress arc, we also add a cavity to remove the residual correlated energy chirp. At the e-cooler, the intrinsic energy spread $\sigma_{\delta f}$ is on the order of 10^{-4} to ensure good cooling efficiency. If we assume that $\sigma_{\delta f} \approx 1.0 \times 10^{-4}$ and, there is no phase space volume degradation, we would require the initial intrinsic energy spread to be less than $\sigma_{\delta i} = \sigma_{\delta f} \sigma_{zf} / \sigma_{zi} \approx 4.17 \times 10^{-4}$.

PRELIMINARY RESULTS

We take the optic for the bunch decompression and compression arc from Ref. [4], with the beta-function and dispersion function shown in Fig. 1. Before we calculate

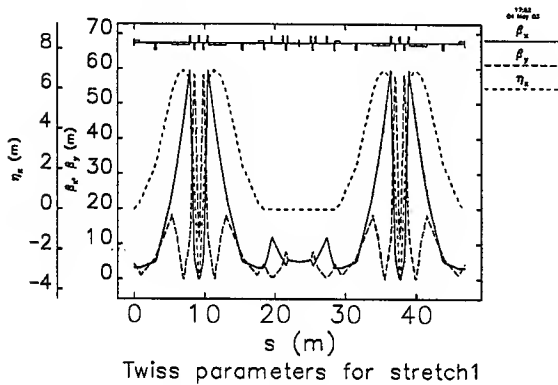


Figure 1: The β_x , β_y and η_x in the beam line.

the CSR effect, let us have a look at the electron beam parameters in such transport line. Shown in Fig. 2 is the evolution of the rms bunch length and the rms energy spread (including the chirp). In Fig. 2, $\sigma_5 = \sigma_z$ is the rms bunch length, and $\sigma_6 = \sigma_\delta$ is the rms energy spread. As we find, the electron bunch was initially 12 mm long, and it stretched to be 50 mm at the e-cooler, then it is compressed back to its original bunch length. In this special case, we take $\sigma_{\delta i} = 1.0 \times 10^{-4}$, and we chirp the bunch to have enough correlated energy spread for debunching. The correlated energy spread is recovered at the end of the beam line, and no longitudinal degradation.

After studying the beam line, in the following, we will focus on the beam quality at the e-cooler point, taking into account the degradation due to the CSR in the transport line. The requirements at the e-cooler point are that: $\sigma_{\delta f} \sim 10^{-4}$, $\sigma_{zf} \sim 50$ mm and the normalized emittance $\epsilon_{nf} < 60 \pi$ mm-mrad. In Table 1, we set $\sigma_{zi} = 12$ mm, charge $Q = 10$ nC and, vary ϵ_{nxi} and $\sigma_{\delta i}$ to study the initial value dependency. In Fig. 3, we show a typical case for the evolution of the emittance growth and in Fig. 4 for

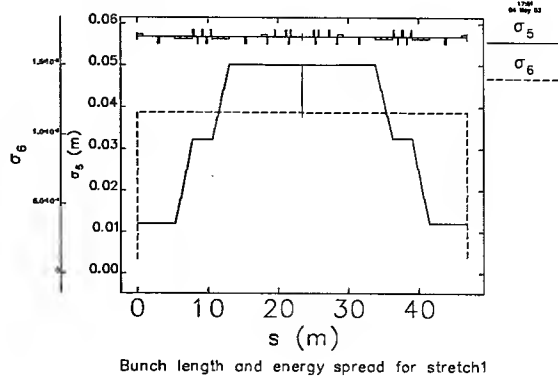


Figure 2: The evolution of the rms bunch length and the energy spread in the beam line.

Table 1: The units are the following: 10^{-4} for rms energy spread σ_δ ; π mm-mrad for normalized emittance ϵ_n and mm for rms bunch length σ_{zf} .

$\sigma_{\delta i}$	$\epsilon_{n(x,y)i}$	ϵ_{nxf}	ϵ_{nyf}	$\sigma_{\delta f}$	σ_{zf}
1.0	10	23.6	12.6	2.09	56.6
	20	36.1	25.1	2.03	56.6
	30	48.6	37.7	2.00	56.6
	40	61.8	50.2	1.99	56.5
2.0	10	23.6	12.6	2.10	57.0
	20	37.0	25.2	2.07	57.0
	30	50.1	37.8	2.04	56.9
	40	63.2	50.4	2.03	56.8
3.0	10	25.2	12.7	2.15	57.4
	20	39.5	25.3	2.13	57.4
	30	53.0	38.0	2.12	57.3
	40	66.2	50.6	2.10	57.3

the rms bunch length and the energy spread. In Fig. 3 and Fig. 4, the initial $\sigma_{\delta i} = 2.0 \times 10^{-4}$ and $\epsilon_{n(x,y)i} = 40 \pi$ mm-mrad.

The results show that the final bunch length and energy spread are almost independent of the initial energy spread or the emittance within the range we studied. The net amount of growth in the transverse emittance is also almost independent on the initial conditions. Within the range we studied, it seems to us that the CSR will cause some phase space degradation, but the degradation is not dramatic. Of course, compensation scheme on the lattice would be a plus.

OTHER POSSIBLE SCENARIO

Now, let us look at the other possible scenario, e.g. a L-band cavity. The initial electron rms bunch length is then about $\sigma_{zi} = 6$ mm, and the charge is around $Q = 5$ nC. Ac-

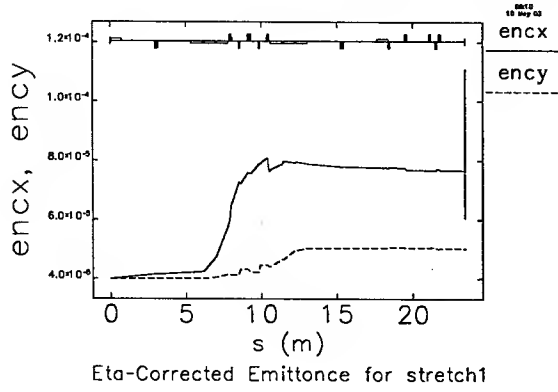


Figure 3: The evolution of the emittance $\epsilon_{n(x,y)}$ growth in the beam line.

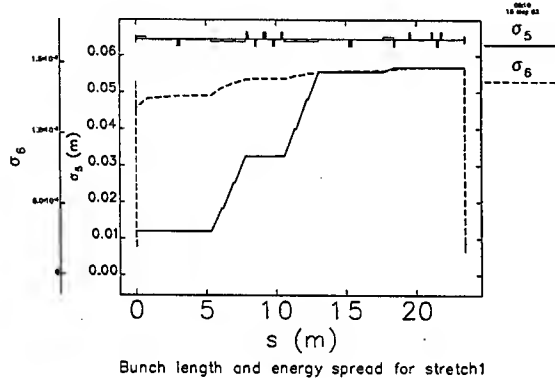


Figure 4: The evolution of the rms bunch length σ_5 and the energy spread σ_6 in the beam line.

cording to the scaling we just discussed, i.e., $d\mathcal{E}/(cdt) \approx N(\sigma_s)^{-4/3}$, then the situation would be similar to what we discussed above for the case of $\sigma_{zi} = 12$ mm, and $Q = 10$ nC.

To study a different case for future design reference, we set the initial bunch length $\sigma_{zi} = 3$ mm. Accordingly, the require energy chirp is $\sigma_{\delta}^i = 1.43 \times 10^{-3}$ to ensure that at the e-cooler point $\sigma_{zf} = 50$ mm. Assuming that there is no longitudinal phase space degradation, then if we want to ensure that at the e-cooler point, the final energy spread $\sigma_{\delta f} < 10^{-4}$, then the initial energy spread should be smaller than $\sigma_{\delta i} = \sigma_{\delta f} \sigma_{zf} / \sigma_{zi} \approx 1.67 \times 10^{-3}$.

The results are summarized in Table 2. We find similar fact that the amount of degradation is almost independent of the initial conditions. However, the net effect is larger as we expected, since in this extreme case, though the charge is only half, the bunch length is four times shorter. According to the scaling we discussed previously, i.e. $d\mathcal{E}/dt \propto N(\sigma_s)^{-4/3}$, we would expect larger net effect in this case based on the parameters we used. Of course, in real life the initial bunch length $\sigma_{zi} \approx 6$ mm, and the situ-

Table 2: The units are the following: 10^{-4} for rms energy spread σ_{δ} ; π mm-mrad for normalized emittance ϵ_n and mm for rms bunch length σ_{zf} .

$\sigma_{\delta i}$	$\epsilon_{n(x,y)i}$	ϵ_{nxf}	ϵ_{nyf}	$\sigma_{\delta f}$	σ_{zf}
1.0	10	51.2	14.5	1.10	65.0
	20	67.6	28.9	1.09	64.6
2.0	10	52.2	14.5	1.09	65.2
	20	67.8	28.9	1.08	64.9
3.0	10	53.5	14.5	1.09	65.6
	20	70.2	29.0	1.09	65.3

ation would be much better as what we studied for the case of $\sigma_{zi} = 12$ mm and $Q = 10$ nC.

DISCUSSION

In this paper, we study the CSR effect for the proposed electron cooler for the RIHC II in BNL. The results presented in this paper are based on Borland's Elegant code [7]. We find that the CSR effect will bring some effect at the e-cooler point, but the effect is not dramatic. As we mentioned before, we adopted the free space CSR impedance and, we did not implement the shielding cut-off due to the vacuum chamber. Should we take this into account, the CSR effect would be even smaller. The results presented here are only the starting point for looking into this problem. Further study is needed.

ACKNOWLEDGMENTS

The authors thank Dr. I. Ben-Zvi of BNL and Dr. T.O. Raubenheimer of SLAC for many discussions and encouragement for the work. The authors thank Dr. M. Borland for helping them in using his Elegant code. The work was supported by the U.S. Department of Energy under Contract No. DE-AC03-76SF00515 (Juhao Wu) and Contract No. DE-AC02-98CH10886 (Dong Wang and Feng Zhou).

REFERENCES

- [1] G.I. Budker, *Atomic Energy*, Vol. 22, No. 5 (1967).
- [2] Ya.S. Derbenev and A.N. Skrinsky, *Part. Accel.* **8**, 1 (1977).
- [3] I. Ben-Zvi *et al.*, PAC2001, p. 48, Chicago, IL, June 2001.
- [4] J. Kewisch *et al.*, "Layout and Optics for the RHIC Electron Cooler", these proceedings.
- [5] J.B. Murphy, S. Krinsky, and R.L. Gluckstern, PAC95, p. 2980, Dallas, TX, May 1995; *Part. Accel.* **57**, 9 (1997).
- [6] Ya.S. Derbenev, J. Rossbach, E.L. Saldin, and V.D. Shiltsev, DESY-TESLA-FEL-95-05 (1995).
- [7] M. Borland, *Phys. Rev. ST Accel. Beams* **4**, 070701 (2001).

IMPACT OF THE WIGGLER COHERENT SYNCHROTRON RADIATION IMPEDANCE ON THE BEAM INSTABILITY*

Juhao Wu[†], G.V. Stupakov, T.O. Raubenheimer, and Zhirong Huang
SLAC, Stanford University, Stanford, CA 94309

Abstract

Previous studies of the (Coherent Synchrotron Radiation) CSR induced longitudinal instability have been made using the CSR impedance due to dipole magnets, however, many storage rings include long wigglers where a large fraction of the synchrotron radiation is emitted. In this paper, the instability due to the CSR impedance from a wiggler is studied assuming a large wiggler parameter K . The primary consideration is a low frequency microwave-like instability, which arises near the pipe cut-off frequency. Finally, the optimization of the relative fraction of damping due to the wiggler systems is discussed for the damping rings in future linear colliders.

LONGITUDINAL BEAM INSTABILITY

When the electron bunch passes the curved trajectory inside a dipole, the CSR induces an impedance [1]. The CSR impedance is known to impact single pass bunch compressors where the beam currents are extremely high but it is also possible that CSR might cause a microwave-like beam instability in storage rings. A theory of such an instability in a storage ring has been recently proposed in Ref. [2] where the impedance is generated by the synchrotron radiation of the beam in the storage ring bending magnets. A similar instability may arise due to coherent synchrotron radiation in long wigglers. Many storage rings have used large wiggler systems to reduce the damping times and control the beam emittance. In particular, the high luminosity colliding beam factories, such as DAPHNE, KEK-B, PEP-II, and CESR-C, as well as the damping ring designs for future linear colliders. In a previous study, we have obtained the wakefield and impedance in a wiggler with large parameter K [3] and, in this paper, we study the impact of the wiggler synchrotron radiation impedance on the beam longitudinal dynamics in rings with dipoles and wigglers.

We will consider the longitudinal dynamics of a thin coasting beam. The beam can be described with a longitudinal distribution function $\rho(\nu, s, z)$. The positive direction for the internal coordinate s is the direction of motion, and $\nu = (E - E_0)/E_0$. The position of the reference particle in the beam line is $z = ct$ with c the speed of light. We assume that the initial energy distribution function is a Gaussian, i.e., $\rho_0 = n_0/(\sqrt{2\pi}\nu_0) \times \exp(-\nu^2/2\nu_0^2)$, where n_0 is the linear density, i.e., the number of particles per unit length. In this case, the instability is determined by the following dispersion relation [2],

$$1 = -\frac{iZ(k)\Lambda}{\sqrt{2\pi}k} \int_{-\infty}^{\infty} dp \frac{p e^{-\frac{p^2}{2}}}{\Omega \pm p} \quad (1)$$

where, ω and k are the perturbation frequency and wavenumber respectively; $\Lambda = n_0 r_0 / (|\eta| \gamma \nu_0^2)$; $\Omega = \omega / (ck|\eta|\nu_0)$; $p = \nu/\nu_0$; η is the slippage factor and $r_0 \approx 2.82 \times 10^{-15}$ m is the classical electron radius and γ is the Lorentz factor. In addition, $Z(k) = \int_0^\infty ds w(s) \exp\{-iks\}$, is the CSR impedance and $w(s)$ is the wake Green function.

	NLC	TESLA	ATF
Circumference C/km	0.3	17	0.14
Dipole radius R/m	5.5	80	5.7
Total bending angle $\Theta/2\pi$	1	5/3	1
Moment. comp. $\alpha/10^{-4}$	2.95	1.2	19
Energy E/Gev	1.98	5	1.3
Energy rms spread $\nu_0/10^{-4}$	9.09	9	6
Bunch rms length σ_z/mm	3.6	6	5
Particles per bunch $N_e/10^{10}$	0.75	2	1
Wiggler peak field B_w/T	2.15	1.5	1.88
Wiggler period λ_w/m	0.27	0.4	0.4
Wiggler total length L_w/m	46.24	432	21.2
Pipe radius b/cm	1.6	2	1.2
F_w	2.2	13.4	1.8
Cut-off wavelength λ_c/mm	4.9	1.8	3.1
Threshold (off) $N_t/10^{10}$	0.60	27.44	0.95
Threshold (on) $N_t/10^{10}$	0.52	24.56	0.76
Growth time (off) $\tau/\mu\text{s}$	54.9	N/A	34.3
Growth time (on) $\tau/\mu\text{s}$	32.9	N/A	6.5

Table 1: Parameters and results.

STORAGE RINGS WITH WIGGLERS

As concrete examples, we study the NLC main damping ring [4], the TESLA damping ring [5], and the KEK ATF prototype damping ring [6]. Parameters are given in Table 1. In our model, we use the steady state CSR impedance and assume a distributed model. For a dipole, the steady state CSR impedance is [1]: $Z_D(k) = -iA k^{1/3} R^{-2/3}$, with $A = 3^{-1/3} \Gamma(2/3)(\sqrt{3}i - 1) \approx -0.94 + 1.63i$. The wiggler impedance $Z_W(k)$ is computed in Ref. [3]. Hence, the total impedance is then: $Z(k) = Z_D(k)\Theta R/C + Z_W(k)L_W/C$, where, R , Θ , L_W and C are the dipole bending radius, the total bending angle, the wiggler total length and the damping ring circumference given in Table 1 respectively. To study the instability, we numerically solve the dispersion relation Eq. (1). In Fig. 1, the imaginary part of Ω is plotted as a function of the instability wavenumber

* The work was supported by the U.S. Department of Energy under Contract No. DE-AC03-76SF00515.

[†] jhwu@SLAC.Stanford.EDU

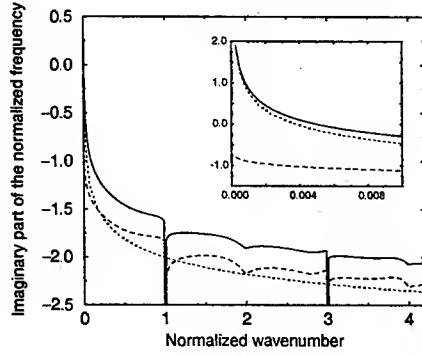


Figure 1: The imaginary part of the normalized frequency Ω as a function of the normalized wavenumber k/k_0 for the NLC main damping ring [4]. The solid curve includes the entire CSR impedance while the dotted and dashed curves include either the steady state dipole CSR impedance or the wiggler CSR impedance, respectively. The inset shows a blow up of the low frequency unstable region.

for the NLC main damping ring using the parameters listed in Table 1. At low frequencies, the dipole CSR impedance dominates while at shorter wavelengths the wiggler CSR impedance is usually more important. In the region where $\text{Im}(\Omega) < 0$, the beam is stable and this is true for all regions except at the longest wavelengths as shown in the inset. This low frequency instability will be discussed subsequently. Based on similar calculations, we find that with the design current in the TESLA damping ring, the impedance from the dipoles and wigglers will not drive an instability while the results for the ATF are very similar to those of the NLC damping ring shown in Fig. 1.

As seen in Fig. 1, the instability is most important at relatively low frequency. We can use a simple scaling analysis to understand this. The dipole CSR impedance scales as $Z_D(k) \propto k^{1/3}$. Similarly, the low frequency behavior of the wiggler impedance is [3]: $Z_W(k) = \pi k_w(k/k_0)[1 - (2i/\pi)\log(k/k_0)]$; which is accurate for $k \in [0, 0.1k_0]$, where $k_0 = 2\gamma^2 k_w / (1 + K^2/2)$ is the wiggler fundamental radiation wavenumber and the wiggler parameter $K \approx 93.4 B_w \lambda_w$, with B_w the peak magnetic field of the wiggler in units of Tesla and λ_w the period in meters. Thus, the wiggler CSR impedance scales as $\text{Re}[Z_W(k)] \propto k$, and $\text{Im}[Z_W(k)] \propto k \log(k)$, which is a weaker scaling than k over the range of interest. Hence, the CSR induced energy modulation has a scaling no-stronger than k . On the other hand, the Landau damping due to the phase mixing is more serious for short wavelength perturbations and the resulting damping is proportional to k . Since the growth due to the CSR impedance is weaker than the linear scaling of the phase mixing effect, it is expected that the threshold is determined by the perturbation with the longest wavelength.

The vacuum chamber causes an exponential suppression of the synchrotron radiation at wavelengths λ greater than the 'shielding cutoff' [7] $\lambda_c \leq 4\sqrt{2}b(b/R)^{1/2}$. Here, R is

the dipole bending radius, and b is the vacuum chamber half height. We assume that the vacuum chamber is made up of two infinitely wide plates. Given the previous discussion, the threshold will be the lowest at the smaller of the bunch length or the "shielding cutoff" wavelength.

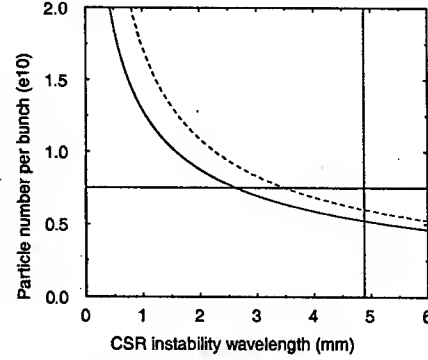


Figure 2: The threshold as a function of the CSR wavelength for the NLC main damping ring. The dashed curve is the result for the dipoles only; the solid curve for both the dipoles and the wigglers. The vertical straight line is the approximate cutoff wavelength; the horizontal straight line is the nominal number of particles per bunch: 0.75×10^{10} .

For the NLC main damping ring, we find that perturbations with wavelengths $\lambda \approx 3.5$ mm are not stable due to the dipole CSR impedance alone. Adding the CSR impedance from the wiggler causes perturbations with wavelengths $\lambda \approx 2.6$ mm to be unstable. In Fig. 2, the threshold particle number is plotted as a function of the perturbation wavelength. Next, in Fig. 3, the growth time, $\tau \equiv (\text{Im}(\Omega)ck|\eta|\nu_0)^{-1}$, is plotted versus the perturbation wavelength. It is clearly seen that the threshold current decreases as we approach the longer wavelength perturbations as expected from our scaling analysis. Based on the parameters in Table 1, the "shielding cutoff" wavelength is $\lambda_c \approx 4.9$ mm. At this cutoff wavelength, the threshold currents and growth time are summarized in Table 1. The growth time is significantly faster than the synchrotron period, in consistent with the analysis for a microwave-like instability.

For the KEK ATF prototype damping ring, the cut-off wavelength would be about $\lambda_c \approx 3.1$ mm. Taking the dipole CSR impedance alone, the instability sets in for perturbations with wavelengths $\lambda \approx 2.8$ mm. Adding the wiggler CSR impedance, the electron beam would be unstable for perturbations with wavelengths $\lambda \approx 1.9$ mm. Other results are summarized in Table 1.

It is interesting to note that in both the NLC and the ATF damping rings roughly twice as much synchrotron radiation power is emitted in the wiggler as in the arc dipoles. However, the instability threshold is not dramatically impacted by the additional radiation and decreases by less than a factor of two in each case. This arises because of the very different low frequency scaling of the impedances. It

also suggests an optimization of the damping ring design where a larger fraction of radiation is emitted in the wigglers as will be discussed subsequently.

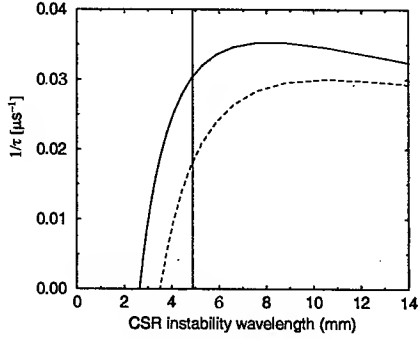


Figure 3: The growth rate as a function of the CSR wavelength for the NLC main damping ring. The dashed curve is the result for the dipoles only; the solid curve for both the dipoles and the wigglers. The vertical straight line is the approximate cutoff wavelength.

DAMPING RING OPTIMIZATION

To study the ring optimization, we use expressions derived in Ref. [8] for the damping ring parameters. The primary constraint is the damping times. Because all linear collider designs presently only consider flat beams with $\sigma_x \gg \sigma_y$, the tightest requirement is on the vertical damping time which, using Eq. (11) of Ref. [8], can be written $\tau_y \approx ((2.89 \times 10^{12} \text{ kG})C|\Theta|/(|B_a|\gamma^2(1+F_w)c2\pi))$, where B_a is the arc bending field, C is the ring circumference, Θ is the total bending angle of the arcs, and F_w is defined as the ratio of the damping due to the wiggler over the damping due to the arc bending magnets: $F_w \equiv 2w/2a$. Here, $2a$ and $2w$ are the second synchrotron integrals calculated over the arcs and the wigglers respectively.

Since $B_a \propto 1/(1+F_w)$, for a given ring size and damping time and, given a maximum wiggler field, the required wiggler length can be found. At this point, we can calculate the other ring parameters. According to the dispersion relation in Eq. (1), we will need the momentum compaction factor α , the energy spread ν_0 , and the bunch rms length σ_z . Using Eqs. (37), (39) and (40) from Ref. [8], the scaling can be written: $\alpha \propto (1+F_w)^{5/3}$, $\nu_0 \propto \sqrt{(B_a + B_w F_w)/(1+F_w)}$, and $\sigma_z \propto \nu_0 \sqrt{\alpha}$. Using these relations, we estimated parameters for NLC ring with $F_w = 0$ and $F_w = 6.5$. These parameters are summarized in Table II along with the nominal $F_w = 2.2$.

At this point, we can study the threshold. Based on our previous studies, we expect the CSR impedance from the wiggler to be small compared to the CSR impedance of dipoles in the low frequency region of interest. Hence,

the threshold is essentially determined by the dipole CSR impedance. According to the dipole CSR impedance, and the relation between B_a and F_w , the total impedance should scale as $Z(k) \propto Z_D(k)R \propto R^{1/3} \propto (1+F_w)^{1/3}$, at a fixed wavenumber k . Clearly, this is an increasing function with F_w however, according to the dispersion relation in Eq. (1), the threshold will scale as: $N_t \propto \alpha \nu_0^2 \sigma_z / Z(k) \propto (1+F_w)^{13/6}$, where it was assumed that $B_a \sim B_w$, so ν_0 is roughly constant. Thus, it is expected that increasing F_w will increase the threshold significantly. In addition, the cutoff wavelength λ_c scales as $R^{-1/2}$, i.e. scales as $(1+F_w)^{-1/2}$ and the cutoff wavelength will decrease as F_w increases and B_a decreases. Since, the threshold is lowest at long wavelength, the threshold will increase as F_w is increased due to both the shift in the cutoff wavelength as well as the change in the ring parameters. The above scaling analysis has been compared to numerical calculations for the NLC damping ring. The results are given in Table 2. Clearly, the threshold increases rapidly as F_w is increased as expected. Integrated with other considerations [9], the result here led to a redesign for the NLC damping which increases the threshold to more than four times the nominal charge per bunch [10].

F_w	0	2.2	6.5
Dipole field B_a/T	3.8	1.2	0.55
Dipole radius R/m	1.7	5.5	12.0
Wiggler length L_w/m	0	46.24	66
Momentum compaction $\alpha/10^{-4}$	0.69	2.95	14
Energy rms spread $\nu_0/10^{-4}$	13	9.09	8.4
Bunch rms length σ_z/mm	2.4	3.6	5.5
Cutoff wavelength λ_c/mm	8.7	4.9	3.3
Threshold at cutoff $N_t/10^9$	2.0	5.2	31.3

Table 2: Parameters and results for the NLC main damping ring when $F_w=0, 2.2$ and 6.5 .

REFERENCES

- [1] J.B. Murphy, S. Krinsky, and R.L. Gluckstern, Part. Accel. **57**, 9 (1997).
- [2] G. Stupakov, S. Heifets, Phys. Rev. ST Accel. Beams **5**, 054402 (2002).
- [3] J. Wu, T.O. Raubenheimer, G.V. Stupakov, Phys. Rev. ST Accel. Beams **6**, 040701 (2003).
- [4] A. Wolski, URL: <http://awolski.lbl.gov/nlcdrlattice/default.htm>.
- [5] W. Decking, "The TESLA Damping Ring", in *Snowmass 2001*, July 2001.
- [6] <http://www-jlc.kek.jp/atf/ATF.overview-e.html>.
- [7] R.L. Warnock and P. Morton, Part. Accel. **25**, 113 (1990).
- [8] P. Emma, T. Raubenheimer, Phys. Rev. ST Accel. Beams **4**, 021001 (2001).
- [9] M. Venturini, "Wigglers and Single-Particle Dynamics in the NLC Damping Rings", these proceedings.
- [10] A. Wolski *et al.*, "A Lattice With Large Momentum Compaction for the NLC Main Damping Rings", these proceedings.

ELECTRON BEAM MOTION OBSERVED IN INFRARED SYNCHROTRON RADIATION AT NSRRC

D. S. Hung, Y. C. Lo, C. I. Chen and C. H. Kuo
National Synchrotron Radiation Research Center, Hsinchu, Taiwan

Abstract

Noise existing between 1000 to 4000 cm^{-1} in FTIR spectrum is degrading the signal to noise ratio in infrared (IR) microscopy beam line at SRRC. This is mainly because the interferometer detection is very sensitive to the electron beam motion. Through the RF modulation, the noise spectrum of the infrared interferometry was observed to change as the electron beam motion was modulated. Some of the noise sources were identified in terms of electron beam motion. The analysis indicated that their contribution decided the performance of the IR synchrotron radiation.

INTRODUCTION

Noise generated by the electron beam in storage ring has been regarded as a hurdle of enhancing the performance of IR beam line. It has been known that the IR noise was very sensitive to the mechanical vibration, electrical system and electron beam motion etc. [1,2,3]. Over the past years, these issues were readily improved by adding the active mirror feedback system, replacing the master oscillation and adjusting the power supply, etc., at several IR beamlines. Efforts of improving the S/N ratio of IR beam line at NSRRC, Taiwan light source, were given by tracing the noise from IR-related system, including mechanical and electronic systems. A considerable achievement was given by reducing its RMS of IR noise down to 0.03% over the mid-IR region.

The IR signal affected by the electron beam motion took a special care at ALS and BESSY II over the past years [4,5], due to some behaviors in IR beamline were still an enigma. Interest of tracing the IR noise generated by the electron beam motion is given by observing the beam motion and IR spectrum at NSRRC. According to the observation at IR beamline on the last quarter season, a statistics of RMS in IR spectrum is showed in Fig. 1. As can be seen, the performance of IR beamline is quite similar for both high (~190mA) and low (~100mA) beam current. However, the IR beamline performance became worse during some operation periods. Particularly, after the shut down period, the IR noise was growing up and the beamline performance became poor. The situation was usually improved after 3 to 7-days user-shift operation. The beam spectrum taken from the storage ring was also analyzed during the observed period. The consistency of the beam spectrum indicated

that the spectrum was not sensitive enough for detecting a small electron beam motion, which damaged the IR beam quality. How to find out the relation of IR noise with the small beam motion could be important role at the early stage of improving the IR beamline performance at NSRRC.

In this study, we observed the IR beamline spectrum via adjusting the RF modulation. As it has been well known, the RF modulation is one of the mechanisms of stabilizing the electron beam motion. Through the RF modulation system, we observed that some of IR noises came from the beam instability motion.

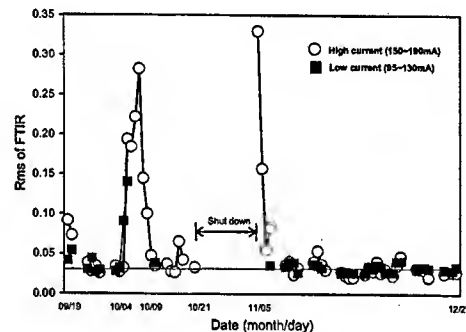


Figure 1: The RMS of IR spectra at transmittance mode

IR SIGNAL MEASUREMENT SETUP

The IR beamline has been developed at the National Synchrotron Radiation Research Center (NSRRC). As shown in Fig. 2, this beamline collects 70 x 35 mrad of synchrotron radiation in the horizontal and vertical directions, respectively, and covers a wavelength range from 2 to 30 μm . The optical design consists of one water-cooled plane mirror, two high-order corrected polynomial bendable mirrors and a set of steering and collimating mirrors. For the consideration of vibration, the first mirror is 45 degree face-downward and its support is fixed to massive dipole magnet. In order to focus effectively the extended arc source of bending magnet, a newly special designed optical system including so-called "Kirkpatrick-Baez" mirrors which use two high-order polynomial mirrors has been adopted, designed and fabricated. The average brightness of this

beamline is found to be greater than 10^{16} photons/sec/0.1%bw/mm²/ 200mA. A wedged CVD diamond window is used to separate the up-stream UHV section from the down-stream low vacuum section. Three off-axis paraboloid mirrors of different focal lengths are employed to facilitate different experimental setups which require different IR objectives. Table 1 lists the parameters of the mirror elements adopted in our IR beamline. The beamline has been installed, commissioned and now is open to the all users.

In IR noise study, the spectrum was taken through the Nicolet 860 FTIR bench and a continuum IR microscope. The scanning speed of the interferometer is down to the lowest (0.00158mm/sec). The interferometer signal is then taken from the spectrum analyzer.

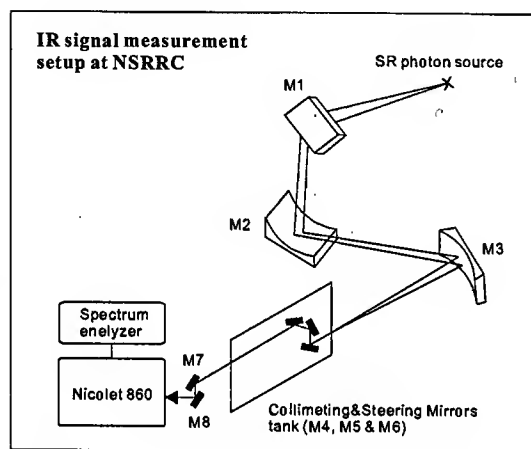


Figure 2: Schematic Diagram of Optical Layout of IR beamline at NSRRC

Table 1: The optical parameter of 14A IR Beamline (70mrad x 30 mrad)

Mirror	M1	M2	M3	M4	M5
PARAMETER					
Source-Element distance (mm)	1206.8	1706.8	3776.8	7981	8345
eviation angle (°)	90	90	100	9.5	99.5
Facing	Downward	Upward	Horizontal	Upward	Downward
Coating	Au	Au	Au	Ag(or Au)	Ag(or Au)
Distance (mm)	---	r1=1706.8 r2=5670	r1=3776.8 r2=3600	r1=604.2 r2=∞	---

SPECTRAL NOISE STUDY

Investigation of IR noise generated by electron beam motion, we adjusted the RF voltage modulation to observe the IR noise. As it has been known, the modulation of RF system is an important mechanism of

stabilizing beam motion in the storage ring. At NSRRC, RF voltage modulation is operated by a sinusoidal wave with 51.08kHz modulation frequency. The beam stability $\Delta I/I_0$ lower than 0.2% takes 80% at the user shift. Under such a condition, the IR spectrum was observed by fixing the moving mirror in the interferometer and measured by the spectrum analyzer on the output of MCT detector. Fig. 3 demonstrates the RMS of FTIR spectrum over the mid-IR is 0.024% at 122mA. The measurement also taken by switching off the RF modulation system. A visible beam shacking was immediately observed on beam monitor. The RMS of FTIR spectrum raises to 0.23% at 119 mA. This is more

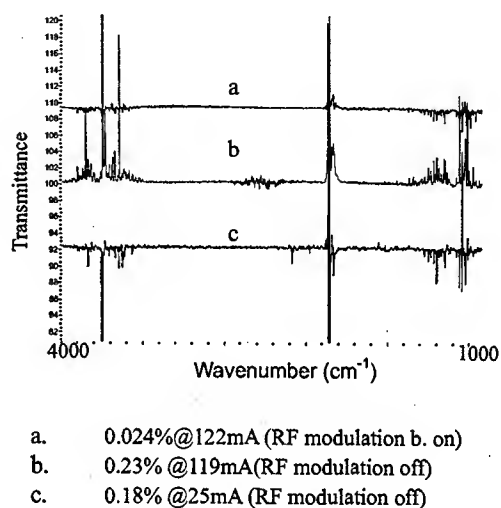


Figure 3: The FTIR spectrum

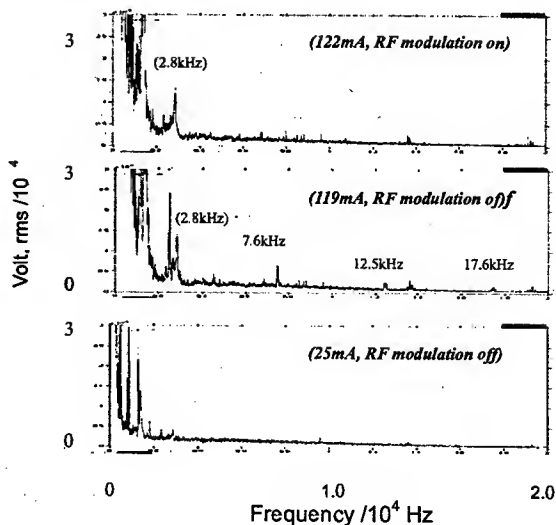


Figure 4: The IR spectrum taken from the MCT detector

one order increasing in IR noise. Comparing the results shown in Figs. 4, 2.8kHz noise always exists in IR beamline. Obviously, it doesn't matter with the beam motion. As can be seen in Fig. 4, the peaks at 7.6kHz, 12.5kHz and 17.6kHz were come into view after the RF modulation off. It indicates that these noises were generated by the electron beam motion but suppressed by the RF modulation. In order to further demonstrate the effect of beam instability on IR beam line, the beam current was down to 25mA, where the electron beam was observable stability without the RF voltage modulation. The RMS is shifted to 0.18% at 25mA, The noise peaks including 2.8kHz disappear at the stable beam motion. It can be said that 2.8kHz noise peak is current dependent. Very flat noise figure implied that part of IR noise indeed generated by the electron beam motion.

CONCLUSIONS

IR noise driven by the electron beam instability has been identified in terms of the RF voltage modulation. As the case study at NSRRC, some specific IR noises (eg., 2.8kHz) are excited by the electron beam after a threshold current is reached. They are not affected by the beam instability. However, some other IR noises are driven by the beam instability and reduced after the beam

is stabilized. The sources of exciting these IR noises through the beam motion are still unknown. They could be generated by the IR-related systems, merged into the electron beam motion and then spoil the IR signal. The further study of IR noise could need to trace the sources step by step in the whole system and analysis their effects. Additionally, due to the IR noise is very sensitive to the beam motion, the analysis may be used as a tool of diagnosing the beam quality.

ACKNOWLEDGEMENTS

We would like to thanks Drs. K.T.Hsu and K.K.Lin and the operation group at NSRRC for their very helpful advice and assistance.

REFERENCES

- [1] Michael C. Martine et al., ALS IR news, Sep.,1998.
- [2] Michael C. Martine et al., ALS IR news, July,2001.
- [3] S. Heifets and G. Stupakov, Proc. 2001 PAC. 1856.
- [4] J. M. Byrd et al., Proc. 2002 EPAC 659.
- [5] M. Abo-Bakr et al., Proc. 2002 EPAC 778.

EXPERIMENTAL MEASUREMENTS OF 2-DIMENSIONAL NONLINEAR RESONANCES

T. S. Ueng, Jenny Chen, K. T. Hsu, K. H. Hu, C. H. Kuo, SRRC, Hsinchu, Taiwan

Abstract

The measurements on both horizontal and vertical coherent betatron oscillations at nonlinear resonances have been performed with turn-by-turn method. Besides the systematic errors, the magnet misalignments and other imperfections could drive the nonlinear resonances. Experiments were conducted in the region close to the working tunes of the Taiwan Light Source electron storage ring to study their effects. The typical measurement results are reported. The phenomena of these 2-dimensional resonances are investigated.

1 INTRODUCTION

The Taiwan Light Source (TLS) electron storage ring of NSRRC is a third generation synchrotron radiation source. In order to provide a low emittance electron beam strong transverse focusing and defocusing quadrupoles are used. The sextupoles are used to correct the large chromatic aberrations generated by quadrupole magnets. The nonlinear effects produced by the chromaticity correcting sextupoles, sextupole fields in dipoles and other small higher order random error multipoles can perturb the beam orbit and give the phase space significantly different from that with linear lattice elements when the betatron tunes are near a resonance condition. A series of experiments have been conducted on the one-dimensional nonlinear resonances in the horizontal plane at TLS[1,2,3], also in other facilities[4,5,6]. Since the 2-dimensional nonlinear resonances could have more effects on the growth in amplitudes of betatron oscillations, experimental measurements were performed recently to investigate their effects.

In a circular accelerator, the betatron oscillations $x(s)$ and $y(s)$ of particles around a closed orbit are given by Hill's equation:

$$\frac{d^2 x}{ds^2} + K_x(s)x = \frac{\Delta B_y}{B\rho}; \quad \frac{d^2 y}{ds^2} + K_y(s)y = -\frac{\Delta B_x}{B\rho}$$

$$\text{with } \Delta B_y + i\Delta B_x = B_0 \sum_{n=0}^{\infty} (b_n + ia_n)(x + iy)^n,$$

where b_n and a_n are the normal and the skew multipole components, respectively. $K_x(s)$, $K_y(s)$ are the quadrupole strength functions, which can be varied in order to adjust the horizontal and the vertical betatron tunes, ν_x and ν_y . $B\rho = p/e$ is the momentum rigidity and s is the longitudinal particle coordinate. ΔB_x and ΔB_y are linear or nonlinear magnetic multipole field errors. Both $K_{x,y}$ and the anharmonic term, $\Delta B_{x,y}/B\rho$, are periodic functions of s with period of the circumference of circular accelerator. Normally, the higher order anharmonic term, $\Delta B_{x,y}/B\rho$, arising from higher order multipoles is small. When the

betatron tune is near a resonance condition, $m\nu_x + n\nu_y = 1$, where $m, n, 1$ are integers, respectively, particles in the accelerator can encounter coherent kicks from these multipoles. Its effect will show up as beam diffusion, halo or beam loss. In the phase space map it shows deviation from a simple ellipse.

In this paper, we will present recent experimental measurement results of single resonance at 2-dimensional nonlinear resonance condition. Several problems encountered during the measurements are also discussed.

2 EXPERIMENTAL PROCEDURE

The data acquisition system for the turn-by-turn beam position measurement is similar to that used in the previous studies. At present, the electron beam can only be kicked in the horizontal direction by one of the injection kickers, which were also configured for the turn-by-turn experiments. The centroids of kicked beam were measured in both horizontal and vertical direction by two beam position monitors. Various kicking strengths have been applied to kick the electron beam. The signals corresponding to measured beam positions were passed through a hybrid junction and Bergoz's Log-Ratio beam position monitor electronics, Fig. 1, to the VME based transient digitizers, then to a workstation for online analysis. The turn-by-turn beam positions were also saved for further detailed analysis.

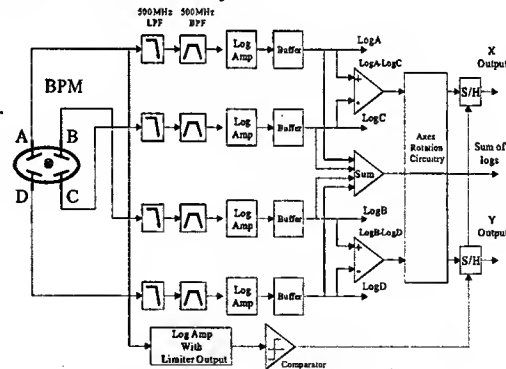


Fig. 1: The block diagram of the turn-by-turn beam position measurement system.

Due to the time consuming single bunch beam injection process and an unsolved hardware problem that gives poor signal/noise ratio in the vertical beam position measurement at low beam current, at present, the multi-bunch beam was used for the experiment. During the experiment the chromaticity was also adjusted to near zero for minimizing the tune spread in the beam bunch. Several 2-dimensional single resonance conditions that were close to the working tunes in regular operation have

been selected for the measurements. During the experiment the betatron tunes were adjusted to near resonance condition by adjusting the strength of one of the quadrupoles manually. It was found that the stop band and also the strength of higher order resonance seemed to be small. The setting of quadrupole power supply was adjusted each step very close to the minimum resolution of hardware.

3 RESULT AND DISCUSSION

3.1 $3\nu_x + 2\nu_y = 30$

The TLS storage ring is a storage ring with superperiodicity of 6. At the nonlinear resonance of $3\nu_x + 2\nu_y = 30$, the order of azimuthal harmonic is just a multiple of its superperiodicity. Thus, this resonance deserves special attention, because it should be sensitive to the systematic errors in the lattice elements. In the resonance frame this nonlinear resonance has $J_1 = J_x/3$ and the constant of motion $J_2 = J_y - 2J_x/3$. It implies that this sum resonance is an unstable resonance and the motion of particles is unbound. Fig. 2 shows the measured beam position spectra of both horizontal and vertical plane. Since the motion of electrons is unbound when the resonance condition meets, one would suppose to see an ever increasing betatron oscillation amplitude and the kicked beam would be lost eventually. During the experiment, it was very difficult to knock all of the electrons out of the chamber through this nonlinear resonance after kicking the beam in the horizontal direction. Because the strong decoherence effect, it was also difficult to see the horizontal turn-by-turn beam positions reached a maximum and back to zero. During the experiment we adjusted the quadrupole strength to tune the horizontal and vertical tune to very close to this resonance condition, then, kicked the beam starting from smaller kicking strength and increased gradually. Due to decoherence the beam positions would decohere and reach to about zero some turns after the start. As the kicking strength increased, one saw the turn number of beam position approaching zero amplitude decreased. But when the sum resonance occurred, one would see the turn number of beam position approaching zero amplitude increased, and the amplitude of beam position at each turn increased also. It indicated that some of the beam was moving away from the center of orbit due to the resonance. Also, the tune could be measured to justify that the resonance occurred. In Fig. 2, one of the typical raw data is shown. The beam positions representing the sum resonance are clearly seen from the start to about 600th turn. An FFT result of this first 600 turns of beam positions shows $\nu_x = 0.2400$ and $\nu_y = 0.1400$, which makes $3\nu_x + 2\nu_y = 30$. Also, the beam current changed from 72 mA to 17 mA after the kick. The remnant oscillations after 600th turn in the horizontal beam positions in figure 2 should be from the electrons that were not knocked out of the orbit. The two peaks in the

remnant oscillation. The vertical beam positions after 650th turn shows only the noise when small signals corresponding to the beam positions were detected. Further study of this sum resonance is underway.

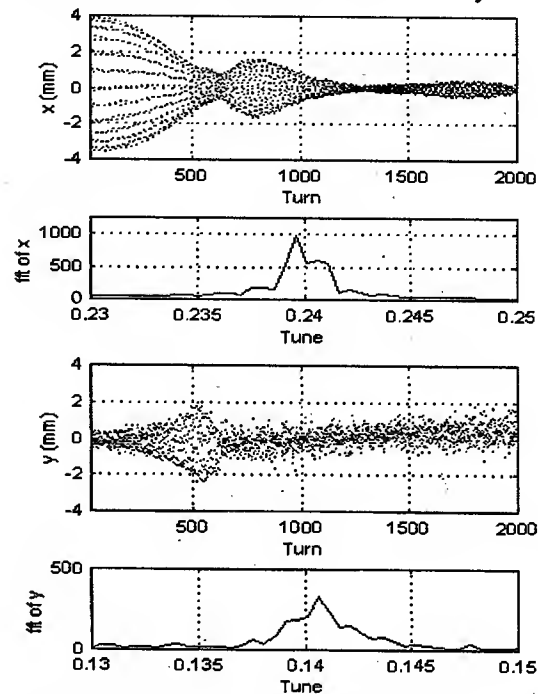


Fig. 2: The measured horizontal and vertical turn-by-turn beam positions at resonance of $3\nu_x + 2\nu_y = 30$. The corresponding tune spectrum is shown under its beam position spectrum.

3.2 $\nu_x - 2\nu_y = -1$

The difference resonance $\nu_x - 2\nu_y = -1$ is intrinsically stable and does not lead to instable particle motion. At the resonance the energy exchanges between the horizontal and vertical plane. A set of typical measured turn-by-turn beam positions in both horizontal and vertical plane with a horizontal kick and their corresponding tune (FFT) spectra are shown in Fig. 3. In the figure the horizontal turn-by-turn beam positions decohere rapidly in about 700 turns due to a large tune spread within the multi-bunched electron beam. Even though, one sees a dip in the horizontal position spectrum at around 400th turn, and a corresponding nonlinear coupling peak appears clearly at about the same turn numbers in the vertical position spectrum. For the larger turn numbers the horizontal beam positions strongly suppressed by the decoherence effect. But, the remnant oscillations still can be seen with small amplitude. In the vertical plane the beam positions show clearly the oscillations after the energy transformed from the horizontal plane due to the nonlinear coupling. The corresponding sidebands are also shown clearly in the vertical tune spectrum. From the sidebands of the tune spectrum one can estimate the island tune is about 0.0016. If the FFT spectrum of horizontal beam positions from 750th turn to 2250th turn are obtained, two small sidebands appear at both sides of the main peak, $Q_x = 0.2674$, and

with larger intensity than the main peak. The island tune obtained from these sidebands seems smaller than that from Fig. 3. This seems to result from a smaller detune effect.

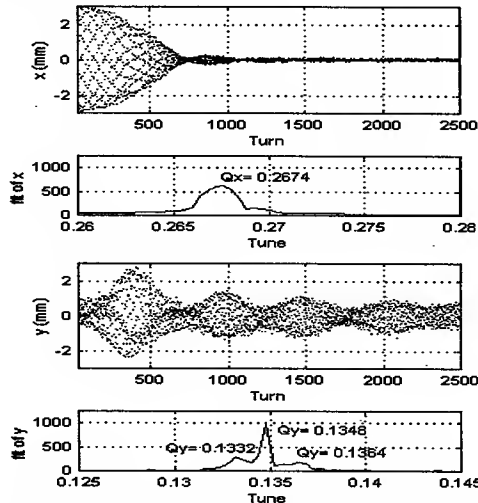


Fig. 3: The measured horizontal and vertical turn-by-turn beam positions at resonance of $v_x - 2v_y = -1$. The corresponding tune spectrum is shown under its beam position spectrum.

3.3 $4v_x - v_y = 25$

The horizontal beam position spectrum and its corresponding FFT spectrum taken at $4v_x - v_y = 25$ resonance line are shown in Fig. 4. It shows oscillations produced by this resonance. This resonance is a difference resonance. Thus, its invariant actions $J_x + 4J_y = \text{constant}$. Changes in J_x could only result in a very small change in J_y . At present, our hardware did not have enough resolution to let us see the betatron oscillation in the vertical plane.

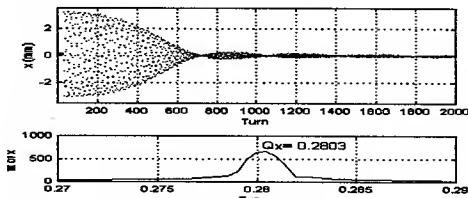


Fig. 4: The horizontal turn-by-turn beam positions and the tune spectrum at resonance of $4v_x - v_y = 25$.

3.5 $2v_x - 3v_y = 2$

The horizontal beam position spectrum and its corresponding FFT spectrum taken at $2v_x - 3v_y = 2$ resonance are shown in Fig. 5. Its vertical beam positions are also not seen clearly due to the hardware resolution.

4 CONCLUSION

The effects of 2 dimensional single nonlinear resonances were measured recently at TLS. Besides using the present acquired data to study their mechanism, we

are also investigating better methods to improve our beam position measurement. At present the multi-bunch beam has been used, which had a larger beam size and could also have a larger intrinsic tune spread due to the transverse non-linearity. Thus, even the chromaticity was adjusted to about zero, the decoherence effect was still large, especially when the beam was kicked to a larger amplitude. This made the interpretation of the experimental data very difficult. In our later experiment, we are considering running the experiments with a single bunch beam or with a multi-bunch beam of fewer buckets. Also, a plan to install a vertical pinger is considered in order to excite the electron beam in the vertical direction. The data acquisition electronics is also under major improvement recently in order to achieve a much better resolution and accuracy in beam position measurement in both horizontal and vertical plane. After these improvements, we hope the 2 dimensional resonances can be studied much easier.

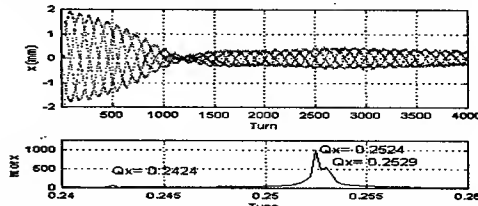


Fig. 5: The horizontal turn-by-turn beam positions and the FFT spectrum at resonance of $2v_x - 3v_y = 2$.

5 ACKNOWLEDGMENTS

The authors are always very appreciated the assistance in operating the accelerator from the members of SRRC's Operation Group during experiments. Special thanks should give to Prof. S. Y. Lee of IUCF for his motivation and useful discussions.

6 REFERENCES

- [1] T. S. Ueng et al., "Experimental Study on the 5th Order Nonlinear Resonance at Taiwan Light Source," PAC 2001, Chicago, June 2001.
- [2] C. C. Kuo et al., "Nonlinear Beam Dynamics Experiments at the SRRC," PAC 2001, Chicago, June 2001.
- [3] T. S. Ueng et al., "Experimental Study on the Higher Order Nonlinear Resonance at Taiwan Light Source," EPAC 2002, Paris, June 2002
- [4] J. Liu et al., "Difference Resonance Study on the Electron Storage Ring Aladdin at SRC," Part. Accel. 41, 1, 1993.
- [5] Y. Yang et al., "Experimental Results of the Betatron Sum Resonance," Proc. of 1993 PAC, 227, 1993
- [6] M. Ellison et al., "Experimental Measurements of a Betatron Difference Resonance," Phys. Rev. E 50, 4501, 1993

FIRST EXPERIMENTAL TEST OF EMITTANCE MEASUREMENT USING THE QUADRUPOLE-MODE TRANSFER FUNCTION

M. H. Wang¹, Y. Sato², and S.Y. Lee²

¹Taiwan Light Source, NSRRC, Hsinchu, Taiwan

²Department of Physics, Indiana University, Bloomington, IN 47405

Abstract

We carried out the first experimental test of the emittance (thermal energy) measurement using the quadrupole-mode transfer function. We show that this method can be applied to measure the intrinsic thermal energy dynamical systems nondestructively. Since the QTF does not depend on the beam distribution, this method can be used to measure the rms emittance of different dynamical systems.

INTRODUCTION

Measurements of the thermal energy (or the rms emittance) are important in the study of the dynamical systems. Tools in the measurement of the rms beam emittance in high energy accelerators include the flying wire, ionization profile monitor, laser wire interference methods, synchrotron light monitor with CCD camera, etc. Most of these methods can cause beam dilution.

Recently, the quadrupole-mode transfer function has been proposed to measure the rms beam emittance of beams in storage rings [1]. The idea is to modulate the beam with an rf quadrupole field and detect the beam quadrupole-mode response function. From the beam quadrupole-mode transfer function, one can determine the rms emittance, betatron tune, or provide mismatch correction to the injected beams.

As the rf quadrupole field is adiabatically excited, particle motion is deformed according to the Hamiltonian contour without changing the phase space area (Liouville theorem). Since the Hamiltonian contour executes coherent motion under external harmonic modulation, the rms beam emittance can be more accurately measured by fast Fourier transform (FFT) method. Hardware for the measurement of QTF are the driver with rf quadrupole electromagnetic field, e.g. ferrite quadrupole magnet [2] or strip-line electrodes [3], and the quadrupole-mode monitors [4]. Even though the signal of the quadrupole moment is weak, the amplitude of the coherent beam shape oscillations can be enhanced by FFT analysis or a spectrum analyzer.

The aim of this quadrupole mode transfer function is intended to measure the transverse phase space area. However, the hardware for the transverse phase space measurement is not currently available in all accelerator laboratories. While the development of this measurement is going on, we study the feasibility of the quadrupole-mode transfer function measurement in the longitudinal phase space.

In fact, the longitudinal rms phase space area can be eas-

ily obtained from measuring the rms bunch length with a wall-gap monitor and then employing the well-known dynamics of the synchrotron motion to derive its conjugate phase space variable [5]. However, we will use the quadrupole-mode transfer function to measure the longitudinal rms phase space area in order to experimentally test the applicability of the method in the transverse phase space. This paper discusses the first experimental test of the longitudinal quadrupole transfer function for the measurement of the longitudinal rms emittance. Our experiment was carried out at the Taiwan Light Source, located in Hsinchu, Taiwan.

THE LONGITUDINAL QUADRUPOLE MODE TRANSFER FUNCTION

When the rf cavity voltage with angular frequency $h\omega_0$ is applied to charged particles in the accelerator, where h is the harmonic number and ω_0 is the angular revolution frequency of a synchronous particle, beam particles will execute stable synchrotron motion around the synchronous particle. Let ϕ and $\delta = \Delta p/p_0$ be the rf phase and the fractional off-momentum coordinates of a non-synchronous particle, and ϕ_s be the rf phase angle of a synchronous particle. The equations of motion are

$$\dot{\phi} = h\omega_0\eta\delta, \quad (1)$$

$$\dot{\delta} = \frac{\omega_0}{2\pi\beta^2 E} eV (\sin \phi - \sin \phi_s), \quad (2)$$

where the overdot is the derivative with respect to time t , η is the phase slip factor, V is the rf cavity voltage, β is the Lorentz velocity factor, and E is the beam energy. The small amplitude synchrotron tune is $Q_s = \sqrt{h|\eta \cos \phi_s| eV / 2\pi\beta^2 E}$.

To excite the longitudinal quadrupole mode, the rf cavity voltage is sinusoidally modulated around twice the synchrotron frequency with modulation amplitude ratio b , i.e. $V = V_0(1 + b \sin \omega_m t)$ with $\omega_m \approx 2\omega_s$. The longitudinal quadrupole mode transfer function can be measured by using a spectrum analyzer with signal from a wall-gap monitor (or a beam position monitor).

In the presence of harmonic modulation near twice the synchrotron frequency, the synchrotron motion is coherently excited. In terms of the conjugate action-angle variables (J, ψ) , defined by

$$\varphi = \phi - \phi_s = -\sqrt{2J} |\cos \phi_s|^{-1/4} \sin \psi, \quad (3)$$

$$\mathcal{P} = -\frac{h|\eta|}{\nu_s} \delta = \sqrt{2J} |\cos \phi_s|^{1/4} \cos \psi, \quad (4)$$

with $\nu_s = \sqrt{h|\eta|eV/2\pi\beta^2E}$ as the small amplitude synchrotron tune at $\phi_s = \pi$, the Hamiltonian can be approximated by [6]

$$H = \Delta J - \frac{1}{2}\alpha J^2 + GJ \cos(2\psi). \quad (5)$$

Here the resonance proximity parameter Δ , nonlinear detuning parameter α , and the resonance strength G are

$$\Delta = \left(\nu_s |\cos \phi_s|^{1/2} - \frac{\nu_m}{2} \right), \quad (6)$$

$$\alpha = \frac{\nu_s}{8} \left(1 + \frac{5}{3} \tan^2 \phi_s \right), \quad (7)$$

$$G = \frac{1}{4} b \nu_s |\cos \phi_s|^{1/2} \left(1 + \frac{1}{3} \tan^2 \phi_s \right), \quad (8)$$

where $\nu_m = \omega_m/\omega_0$ is the modulation tune. The Hamiltonian Eq. (5) closely resembles the quadrupole-mode Hamiltonian of the betatron phase space.

The parameters of the TLS are circumference $C = 120$ m; dipole bending radius $\rho = 3.495$ m; harmonic number $h = 200$; betatron and synchrotron tunes: $\nu_x = 7.22$, $\nu_z = 4.18$, $\nu_s = 0.010156$; phase slip factor $\eta_c \approx 6.1 \times 10^{-3}$; the cavity voltage $V_0 = 800$ kV, and $\phi_s \approx 166^\circ$. Electrons in synchrotrons radiate electromagnetic fields. An equilibrium beam emittance is attained from the effects of quantum fluctuation and synchrotron radiation damping. The damping time was $\tau_E = 3.1$ ms for the longitudinal phase space. The equilibrium distribution function obeying the Fokker-Planck equation is [7]

$$\rho(J, \psi) = \mathcal{N} e^{H(J, \psi)/E_{th}}, \quad (9)$$

where the normalization and the thermal energy \mathcal{N} and E_{th} are determined by

$$\int \rho(J, \psi) dJ d\psi = 1, \quad (10)$$

$$\sqrt{\langle \varphi^2 \rangle \langle \mathcal{P}^2 \rangle - \langle \varphi \mathcal{P} \rangle^2} = \epsilon_{||}. \quad (11)$$

Here, $\epsilon_{||}$ is the longitudinal rms emittance: [5]

$$\epsilon_{||} = \left(\frac{h\eta}{\nu_s} \right)^2 |\cos \phi_s|^{-1/2} C_q \frac{\gamma^2}{J_E \rho}, \quad (12)$$

where $C_q = 3.84 \times 10^{-13}$ m, $J_E \approx 2$ is the damping partition number. The theoretical longitudinal rms emittance of the TLS is expected to be $\epsilon_{||} \approx 8.243 \times 10^{-3}$, which will increase slightly resulting from synchrotron radiation in undulators and wigglers.

Now, we consider the coherent synchrotron mode of the beam. When a charged particle passes a wall-gap monitor, the image current can be expressed as

$$I_e(t) = e \sum_{\ell=-\infty}^{\infty} \delta(t - \hat{\tau} \cos(\omega_s t + \psi) - \ell T_0)$$

$$= \frac{e}{T_0} \sum_{n=-\infty}^{\infty} \sum_{m=-\infty}^{\infty} j^{-m} J_m(n\omega_0 \hat{\tau}) e^{j[(n\omega_0 + m\omega_s)t + m\psi]}, \quad (13)$$

where e is the charge, $\hat{\tau}$ and ψ are the synchrotron amplitude and phase of the particle, T_0 is the revolution period, and J_m is the Bessel function of order m . The resulting spectra of the particle motion are classified into synchrotron modes, i.e. there are synchrotron sidebands around each orbital harmonic n . The amplitude of the m -th synchrotron sideband is proportional to the Bessel function J_m .

A bunch is made of particles with different synchrotron amplitudes and phases, the coherent synchrotron modes of the bunch can be obtained by averaging the synchrotron mode over the bunch distribution, i.e.

$$\begin{aligned} I(t) &= N_B \int I_e(t) \rho(\hat{\tau}, \psi) \hat{\tau} d\hat{\tau} d\psi \\ &= \sum_{n,m} A_{n,m} e^{i(n\omega_0 + m\omega_s)t}. \end{aligned} \quad (14)$$

The amplitude $A_{n,m}$ is called the coherent beam mode of the n -th revolution harmonic and m -th synchrotron sideband. When the beam distribution is only a function of $\hat{\tau}$, there exists only the revolution harmonics. Measuring all revolution harmonics, one can determine the beam distribution via inverse Hankel transformation [5]. Unfortunately, the detection system and the spectrum analyzer are limited by the bandwidth and intrinsic noises, it is difficult to carry out this type of analysis. Here, we demonstrate the method of QTF for the measurement of the rms beam emittance.

When the beam distribution is given by Eq. (9) with Hamiltonian given by Eq. (5), the amplitude of even order synchrotron sideband $m = 2\ell$ is

$$\begin{aligned} A_{n,2\ell} &= \frac{2\pi N_B \mathcal{N} e}{T_0} (-1)^\ell \int J_{2\ell} \left(\frac{n}{h} |\cos \phi_s|^{-1/4} \sqrt{2J} \right) \\ &\quad I_\ell \left(\frac{G}{E_{th}} J \right) \exp \left\{ \frac{\Delta J - \frac{1}{2} \alpha J^2}{E_{th}} \right\} dJ, \end{aligned} \quad (15)$$

where I_ℓ is the modified Bessel function of order ℓ . All odd order synchrotron sidebands vanish for the coherent quadrupole mode excitation.

Figure 1 shows a beam spectrum with center frequency at $n = h$ with a span of 130 kHz, a resolution bandwidth of 300 Hz, video bandwidth of 300 Hz, and a modulation frequency of $f_m = \omega_m/2\pi = 54$ kHz with the voltage modulation amplitude ratio at $b = 2.6\%$. Note that the spectrum shows the main rf peak of the revolution harmonic, and its coherent mode power at ± 54 kHz sidebands. In fact, the high intensity beam bunches in TLS suffer collective coupled bunch instabilities induced by the parasitic high order modes in the rf cavities. The resulting beam spectrum shows f_s , $2f_s$ and other noise harmonics. Choosing the rf voltage modulation frequency properly can effectively suppress the coupled bunch instability [6]. In this experiment,

we measure only the power spectra of $P_{h,0}$ and $P_{h,\pm 2}$ at $\omega = h\omega_0$ and $\omega = h\omega_0 \pm \omega_m$ respectively. Thus we can simultaneously measure the powers of the revolution harmonic $P_{h,0}$ and the quadrupole mode synchrotron sideband $P_{h,\pm 2}$ as a function of the modulation frequency ω_m . The quadrupole-mode transfer function (QTF), defined by

$$q_2(n, \omega_m, b) = P_{n,\pm 2}/P_{n,0}, \quad (16)$$

should be independent of the beam intensity.

At the maximum voltage modulation amplitude ratio of about 2.6%, the two-beamlet bifurcation of the synchrotron bucket occurs at about 51.5 kHz [6]. To avoid complication of hysteresis in our measurement resulting from nonlinear resonances [5], we vary the modulation frequency from 60 kHz downward till 50 kHz. The dependence of q_2 on the modulation frequency ω_m and modulation amplitude ratio b can be used to derive the rms emittance of the beam distribution.

Theoretically, the QTF is given by $q_2(n, \omega_m, b) = |A_{n,\pm 2}/A_{n,0}|^2$. Figure 2 shows a one-parameter fit to the experimentally data, where the modulation amplitude ratio varies from 0.26% to 2.6%. The solid lines show the fit with a longitudinal emittance of $\epsilon_{\parallel} = 0.18 \pm 0.01$ using the thermal distribution of Eq. (9). The fit is much larger than the theoretical rms emittance of $\epsilon_{\parallel 0} \approx 0.008$.

CONCLUSION

In conclusion, we have carried out experiments to test the applicability of using QTF to determine the longitudinal rms beam emittance. The derived rms beam emittance is much higher than the theoretical value. The possible reason for the enlargement may cause by the coupled bunch instability as shown in Figure 1. Figure 1 shows that there are synchrotron sidebands, i.e. the beam has been excited by parasitic modes. A new calculation including rigid dipole mode oscillations would be necessary to resolve the discrepancy between the derived emittance and the actual beam emittance. A single bunch experiment that can avoid the couple bunch mode excitation of the unwanted synchrotron sidebands would be very useful.

REFERENCES

- [1] W.E. Guo and S.Y. Lee, Phys. Rev. E, **65**, 066505 (2002).
- [2] J. Budnick *et al.*, Design, fabrication, and experimental test of a multi-purpose Panofsky magnet, Nucl. Inst. and Methods, **A368**, 572 (1996).
- [3] Beam Instrumentation workshop
- [4] S.J. Russell *et al.* in the Proc. Particle Accelerator Conference, p. 2580 (IEEE, Piscataway, 1995); A. Jansson *et al.*, in the Proc. of Part. Acc. Conf., p. 528 (IEEE, Piscataway, 2001).
- [5] see e.g. S.Y. Lee, Accelerator Physics, (World Scientific Inc., Singapore, 1999).

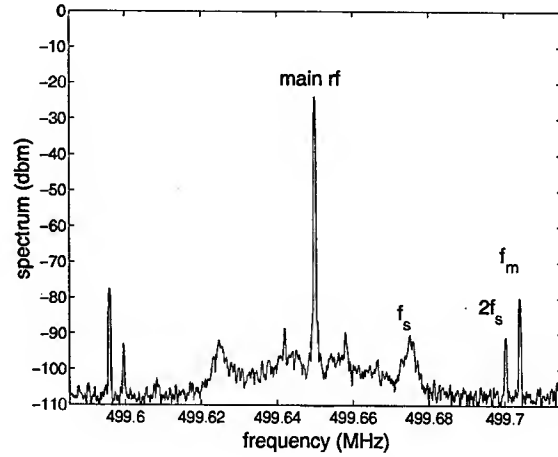


Figure 1: The beam spectrum obtained from a spectrum analyzer at the center frequency $hf_0 = 499.6649062$ MHz, span 130 kHz, resolution bandwidth 300 Hz, video bandwidth 300 Hz. The beam current is about 185 mA at the Taiwan Light Source. The rf voltage modulation frequency is $f_m = \omega_m/2\pi = 54$ kHz with modulation amplitude ratio $b = 2.6\%$. Besides the coherent mode frequencies at hf_0 and $hf_0 \pm f_m$, we also observe noise spectra at $2f_s$, $1f_s$, etc, arising from the parasitic modes in the rf cavities.

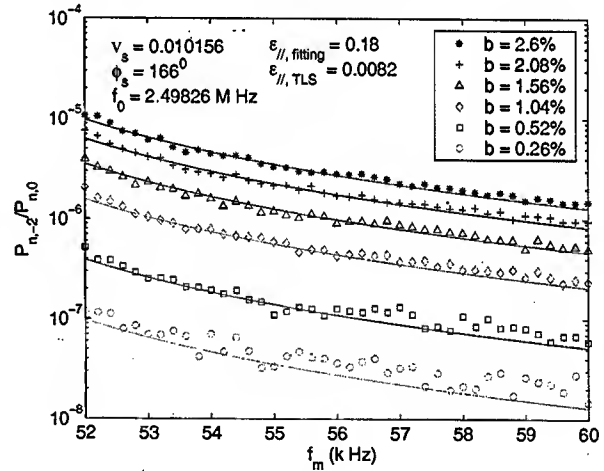


Figure 2: The QTF, $P_{n,-2}/P_{n,0}$, is shown as a function of modulation frequency f_m for different modulation amplitude ratio b from 2.6% to 0.26%. The symbols present the measured data and the solid lines are the fitting result of longitudinal rms emittance 0.18.

- [6] M.H. Wang and S.Y. Lee, Journal of Applied Physics, **92**, 555 (2002); D. Li *et al.*, Phys. Rev. E **48**, R1638 (1993); Nucl. Instrum. Methods Phys. Res. A **364**, 205 (1995).
- [7] M. Bai *et al.*, Phys. Rev. E **55**, 3493 (1997).

BEAM CHARACTERIZATION IN THE CEBAF-ER EXPERIMENT*

C. Tennant[#], Y. Chao, D. Douglas, A. Freyberger, M. Tiefenback
Thomas Jefferson National Accelerator Facility, Newport News, VA 23606, USA

Abstract

Energy recovering a 1 GeV beam through CEBAF (Continuous Electron Beam Accelerator Facility) presents many operational challenges. As a result, it is important to have a quantitative understanding of the beam behavior throughout the machine. The emittance provides a figure of merit in this context inasmuch as it characterizes the extent to which beam quality is preserved during energy recovery. A solution to the problem of obtaining a high-resolution emittance measurement in the extraction region of the CEBAF-ER experiment (CEBAF with Energy Recovery) is presented. The method makes use of a single scanning quadrupole and a downstream wire scanner. In addition, by using multiple wire scans, a scheme for measuring the emittance and momentum spread of the first pass beam in the injector and Arcs 1 and 2 was implemented. And by using a novel technique employing wire scans in conjunction with PMTs (Photomultiplier Tubes) to accurately measure the beam profile at the dump, we can quantify the extent to which we have successfully transported beam to the energy recovery dump.

INTRODUCTION AND MOTIVATION

With several proposals world-wide for machines based on Energy Recovery Linacs (ERLs), there are still important accelerator physics and technological issues that must be resolved before any of these applications can be realized. The Jefferson Lab FEL (Free Electron Laser) upgrade, presently under construction and designed to accelerate 10 mA up to 210 MeV and then subject it to energy recovery will be an ideal test bed for the understanding of high current phenomena in ERL devices. In an effort to address the issues of energy recovering high energy beams, Jefferson Lab has successfully completed a minimally invasive energy-recovery experiment utilizing the CEBAF accelerator [2]. The experiment's goal was to demonstrate the energy recovery of a 1 GeV beam while characterizing the beam phase space at various points in the machine and to measure the RF system's response to energy recovery. Once satisfactory measurements were obtained using the nominal 55 MeV injection energy, the measurements were repeated for low injection energy (20 MeV) to study the parametric dependence on low injection energy to final energy ratios.

PHASE SPACE MEASUREMENTS

To gain a quantitative understanding of the beam behavior through the machine, an intense effort was made to characterize the 6D phase space during the CEBAF-ER experimental run. A scheme has been implemented to measure the geometric emittance of the energy recovered beam prior to being sent to the dump, as well as in the injector and in each arc. In this way we can understand how the emittance evolves through the machine. In addition to describing the transverse phase space, the momentum spread was measured in the injector and arcs to characterize the longitudinal phase space.

Emittance and Momentum Spread in the Injector and Arcs

The emittance and momentum spread of the first pass beam were measured in the injector, Arc 1, and Arc 2 utilizing a scheme involving multiple optics and multiple wire scanners. Two wire scanners were placed in each arc, one at the beginning of the arc in a non-dispersive region and the second in the middle of the arc at a point of high dispersion (6 m). The emittance in the injector was measured using five wire scanners along the injector line.

One of the unresolved difficulties with this measurement was finding a scheme for which the emittance and momentum spread of the *recirculated* beam could be measured in Arc 1. During the measurement an insertable, downstream dump was used to prohibit the transport of a recirculated beam. But it is unclear how to resolve each beam from a wire scanner that is sampling two co-propagating beams; even more so in the case of Arc 1 where, notionally, both the first pass and second pass energy recovered beam have the same energy. This is not an issue for Arc 2; since the energy recovered beam is sent to the dump immediately upon exiting the South Linac, there is at all times only one beam being transported through Arc 2.

Emittance in the Extraction Region

Of great interest is the beam emittance of the energy recovered beam prior to delivery to the dump. Whereas the previous section described the use of multiple wire scanners and multiple optics to obtain the emittances in the injector and Arcs, the emittance in the extraction region relied on a single scanning quadrupole and a wire scanner. The quadrupole at region 2L21 (just after the exit of the South Linac) was scanned and used to obtain the emittance in the horizontal plane while the adjacent, downstream quad at 2L22 was scanned to obtain the vertical emittance. Because of the presence of the two co-propagating beams in the extraction region (the first pass beam at 1055 MeV and the second pass, energy recovered

*supported by US DOE Contract No. DE-AC05-84ER40150
[#]tennant@jlab.org

beam at 55 MeV), care was taken to produce compensatory optics using a family of downstream quads to ensure the first pass beam would be unaffected and transported unaffected through the machine.

By the end of the CEBAF-ER run, data were collected to calculate the emittance in each transverse plane for injection energies of 55 and 20 MeV. All the analysis was done off-line. First, the signals of the raw wire scans were fit with a Gaussian distribution and the sigmas of each extracted. For the case of a quadrupole-drift-wire scanner configuration, one can show that the beam size squared depends quadratically on the quadrupole strength,

$$\sigma_{\text{measured}}^2 = \beta_{\text{wire}} \epsilon = (1 + kL)^2 (\beta_{\text{quad}} \epsilon) - 2L(1 + kL)(\alpha_{\text{quad}} \epsilon) + L^2 (\gamma_{\text{quad}} \epsilon)$$

where L is the distance from the quadrupole to the wire scanner and k is the quadrupole strength in the thin lens approximation. By plotting the sigmas squared versus the quadrupole strength and performing a least-squares fit, the emittance as well as the Twiss functions at the entrance of the scanning quadrupole can be extracted [3].

There were several challenges in analyzing the data. The first obstacle, as mentioned above, was that all the analysis had to be done off-line. Whereas in normal operation of CEBAF the wire scanner software calculates the sigmas of the signals immediately, due to the fact that the wire was now picking up six distinct signals (a three-wire scanner in the presence of two beams), the software simply fit the first three it encountered. Consequently, it was not immediately known if we had scanned far enough away from the nominal gradient integral to pass through a minimum in spot size. In fact, in two out of our four emittance measurements, we were fitting one-half of a parabola because the quadrupole had not been scanned sufficiently far. A second difficulty we encountered was a fit of the data that resulted in an unphysical (i.e. complex) solution for the emittance. This occurred when the fitting parameters led to the condition that the determinant of the sigma matrix was less than zero, $\epsilon^2 = (\sigma_{11}\sigma_{22} - \sigma_{12}^2) < 0$.

To illustrate these complications, consider the data taken for calculating the emittance in the vertical plane for a beam energy of 55 MeV as shown in Figure 1. It is clear that the quadrupole was not scanned sufficiently far and we are relegated to fitting one-half of a parabola. However, simply fitting all 12 of the data points results in an unrealizable, complex emittance. Yet by removing three outlying data points and fitting the remaining points, a physically acceptable emittance was obtained.

At the time of this writing, the analysis of the emittance data is still in progress. However initial estimates suggest that the geometric emittance in the transverse planes with an injector energy of 55 MeV with 10 μA of pulsed beam is on the order of $(0.5\text{--}2.5) \times 10^{-8}$ m-rad, while for an injector energy of 20 MeV the transverse emittances are roughly 2-5 times larger (see Tables 1 and 2 for normalized emittances).

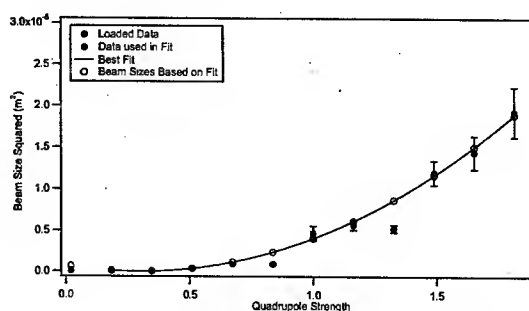


Figure 1: Vertical emittance data for $E_{\text{inj}} = 55$ MeV.

BEAM PROFILE MEASUREMENTS

Wire scanners are used throughout the CEBAF accelerator to measure the beam profile. The wire scanner mechanism drives 25 μm tungsten wires through the electron beam, oriented in the X, XY and Y axes. The standard CEBAF wire scanner measures the induced current on the wire due to secondary emission of electrons from the wire. These induced currents tend to be in the nA range and this system is well suited to measuring the core σ of beam and have a dynamic range of about 100. To improve on the dynamic range of the wire scanner for beam profile measurements of the energy recovered beam, instrumentation was added to the wire scanner just upstream of the beam dump. This instrumentation relies on photomultiplier tubes to detect the scattered electron or the subsequent shower from the incident beam intercepting the wire [3]. The beam currents for the energy recovery experiment are large (tens of μA) compared to those previously measured using this method in CEBAF's Hall-B (nA range) where photomultipliers are used routinely.

The beam profiles for the energy recovered beam are processed in a manner similar to that described in Reference [4]. Instead of merging data from wires of different diameters, the photomultipliers were operated with different gains. The data are combined to yield a beam profile with greater dynamic range than one would obtain using a single photomultiplier or by measuring the induced current on the wire. Fits were performed with the data. The Y (vertical) profile for both the 55 MeV and 20 MeV recovered beam are well represented by a single Gaussian over the complete dynamic range. The X (horizontal) profile for the 55 MeV beams shows a small additional contribution on the left side of the plot (see Figure 2) while the 20 MeV X profile is quite broad, but Gaussian, for this portion of the experiment.

RF MEASUREMENTS

In addition to the beam based measurements presented in the previous sections, another important class of measurements deals with the RF system's response to energy recovery [5]. These measurements are intended to test the system's response by measuring the gradient and

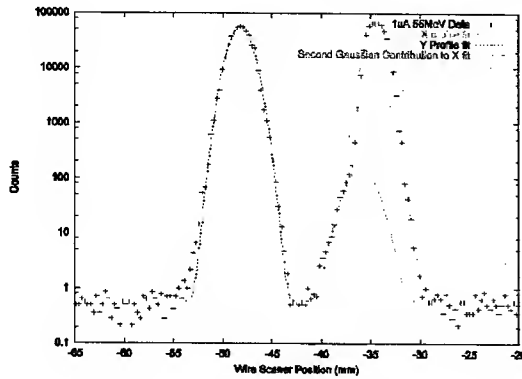


Figure 2: Large dynamic range X and Y beam profile measurement of energy recovered beam with E=55 MeV.

phase stability with and without energy recovery in several cavities throughout the north and south linac. As an example, consider Figure 3 which illustrates the RF system gradient modulator drive signal during pulsed beam operation. Without energy recovery this signal is nonzero when a 250 μ s beam pulse enters the RF cavity, indicating power is drawn from the cavity. This occurs either when the recirculation of the beam is completely impeded (as in the long pulse train) or in the period during which the head of the pulse train does not close on the machine circumference (at the leading edge of the long pulse). With energy recovery, the signal is zero once the initial transient passage of the leading edge of the pulse is over, indicating no additional power draw is required by the cavity.

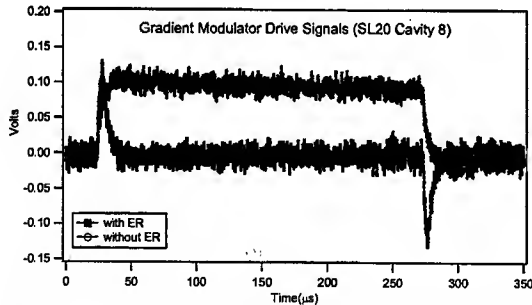


Figure 3: Gradient modulator drive signals during pulsed mode operation with and without energy recovery.

PRELIMINARY RESULTS

Although further analysis is required, several conclusions can be made based upon the available data. The first is that we were able to measure the beam profile of the energy recovered beam with up to 10^5 dynamic range with no measurable halo (i.e. particles outside a Gaussian core). The second, based upon the phase space measurements in Tables 1 and 2, is that the emittance is degraded by passage through the linacs. Possible causes are [6] cavity fundamental power coupler dipole mode driven steering and cavity higher order mode coupler

induced transverse coupling. The third and perhaps the most salient conclusion is that the energy recovery process does not contribute significantly to the emittance degradation since the degradation of the recirculating pass is consistent with that of the accelerating pass.

Location	Normalized Emittance (mm-mrad)	$\delta p/p$ (10^{-3})	E_{beam} (MeV)
Injector (1 st pass)	$\epsilon_x = 0.119798$ $\epsilon_y = 0.188577$	0.029010	55
Arc 1 (1 st pass)	$\epsilon_x = 0.434472$ $\epsilon_y = 0.256338$	0.007980	555
Arc 2 (1 st pass)	$\epsilon_x = 2.393010$ $\epsilon_y = 2.064720$	0.019811	1055
Extraction (2 nd pass)	$\epsilon_x \sim (0.538 - 1.184)$ $\epsilon_y \sim (1.184 - 2.799)$		55

Table 1: Phase space measurements for $E_{inj} = 55$ MeV.

Location	Normalized Emittance (mm-mrad)	$\delta p/p$ (10^{-3})	E_{beam} (MeV)
Injector (1 st pass)	$\epsilon_x = 0.100796$ $\epsilon_y = 0.090427$	0.036966	20
Arc 1 (1 st pass)	$\epsilon_x = 0.280880$ $\epsilon_y = 0.253402$	0.007155	520
Arc 2 (1 st pass)	$\epsilon_x = 0.674722$ $\epsilon_y = 0.451146$	0.010000	1020
Extraction (2 nd pass)	$\epsilon_x \sim (0.899 - 0.978)$ $\epsilon_y \sim (1.956 - 5.869)$		20

Table 2: Phase space measurements for $E_{inj} = 20$ MeV.

ACKNOWLEDGMENTS

We would like to thank H. Dong, A. Hofler, C. Hovater, L. Merminga, and T. Plawski for performing the required RF measurements and J. Bengsston for assistance with the emittance and energy spread measurements.

REFERENCES

- [1] Bogacz, A. et al. Proceedings of this conference.
- [2] *Ibid.*
- [3] C. Tennant, "An Overview of Emittance Measurements in CEBAF-ER", TN-03-004, 2003.
- [4] A. Freyberger, "Large Dynamic Range Beam Profile Measurements" Proceedings of this conference.
- [5] Bogacz, A. et al. Proceedings of this conference.
- [6] Z. Li, "Beam Dynamics in the CEBAF Superconducting Cavities", PhD Thesis, William and Mary, 1995.

A BEAM BREAKUP INSTABILITY IN A RECIRCULATING LINAC CAUSED BY A QUADRUPOLE MODE*

Byung C. Yunn[†]

Thomas Jefferson National Accelerator Facility, Newport News, VA 23606, USA

Abstract

Following the successful demonstration of energy recovery in a recirculating linac with superconducting cavities at the Jefferson Lab FEL[1], several ambitious electron accelerator projects have recently been proposed or are in study for either a light source or a collider based on this novel technology. These projects all intend to utilize a high quality linac electron beam generated with an average beam current typically in the range of 100's of mA. As is well known, a recirculating linac suffers from a beam breakup instability of a regenerative type caused by a Higher Order Mode (HOM) in an accelerating cavity, which can have a very high Q (quality factor) when superconducting. The instability can degrade the beam quality significantly. We investigate one such beam breakup instability in a recirculating linac that could arise as a result of high Q quadrupole modes excited in the cavity. In a simple model we derive a relation which allows one to deduce the upper limit on tolerable Q values for such modes. The results should provide a useful guide in setting the HOM damping requirement among others.

1 INTRODUCTION

A recirculating linac with an energy recovery is especially suitable for a high beam power accelerator project. While preserving the outstanding beam quality which the linac can provide it shows a way to substantially reduce costs involving RF power generation and consumption. Also significantly less are environmental problems and high cost associated with the construction of high power beam dumps necessary for such a high beam power project.

In order to take a full advantage of energy recovery feature superconducting cavities are preferred for acceleration in such a linac. Extremely high Q values for HOMs in the order of 10^9 to 10^{10} are commonly observed for a superconducting RF (SRF) cavity when not damped. As is well known damping of HOMs in a SRF cavity is a major research field in developing SRF technology for the application in accelerator projects.

It is also well acknowledged that high Q HOMs are causes of various beam quality degradations. Among them the most debilitating ones are so called multipass beam breakups[2,3,4] unique to recirculating linacs. Several ambitious recirculating electron accelerator

projects[5,6,7] have recently been proposed and many more are under intensive study. Typical average beam current required for these future projects are very high indeed in the neighborhood of a few 100 mA. At such high currents it is very likely that one of these multipass beam breakups will become the limiting factor of the accelerator performance. It should be noted that the multipass dipole beam breakup phenomenon has been investigated quite extensively as a part of design study of the 5-pass CEBAF superconducting accelerator and Jefferson Lab IR FEL. In both cases we had an ample safety margin (a factor of 100 for CEBAF machine and a factor of 10 for IR FEL) for beam breakups. Therefore, we didn't have to face the beam breakup directly. But the situation may be quite different in some of these new projects being proposed.

In this note we draw an attention to one more kind of multipass beam breakup phenomenon which has a potential to be very destructive. This is a beam breakup induced by a quadrupole HOM of cavity. We present an analysis of a quadrupole beam breakup for designers of future high current projects with energy recovering linac.

2 QUADRUPOLE WAKE

At high energies a beam bunch passes through a cavity without its trajectory being perturbed much. Under such a circumstance it is very useful to consider integrated impulses in order to introduce wake functions to describe interactions between the beam and the beam induced electromagnetic fields. Quite generally one can derive following relations for an axially symmetric structure in the cylindrical coordinate system[8],

$$\int F_{parallel} ds = -eI_m W_m'(z) r^m \cos m\theta$$

$$\int F_{perp} ds = -eI_m W_m(z) m r^{m-1} (\hat{r} \cos m\theta - \hat{\theta} \sin m\theta)$$

where the integration is for the length of the structure and I_m is the m-th moment of the beam bunch. The function $W_m(z)$ is the wake function. Here $m = 0$ is the monopole, $m = 1$ the dipole, and $m = 2$ the quadrupole wake function.

Our concern here is with $m = 2$ wake functions which couple with the quadrupole moments I_2 . When the transverse beam shape is not round, the beam bunch may in general possess normal and skew quadrupole moments. However, we will exclude the skew quadrupole moment

*Work supported by the U. S. Department of Energy under contract DE-AC05-84-ER40150, the Office of Naval Research, the Commonwealth of Virginia, and the Laser Processing Consortium.

[†]yunn@jlab.org

in the following analysis. In linacs this is usually a good assumption. It should be noted that one can easily include the skew moment in the analysis when necessary.

3 A BEAM BREAKUP ANALYSIS

Let us consider a simple model of a 2-pass recirculating accelerator consisting of just a single cavity. Let us assume that a bunch enters the cavity with some quadrupole moment on its 1st pass for acceleration. The bunch will excite more quadrupole HOMs to be added to already existing HOMs in the cavity. While being accelerated in the cavity the bunch will also interact with the quadrupole wakes excited by all preceded bunches. Subsequently the induced quadrupole moments will in turn add to the existing HOM fields on its 2nd pass through the cavity. Thereby a feedback loop is closed, an exponential increase of the wakes is possible when the beam current exceeds a threshold by providing more wakes than the amount decreased which is typically quantified by the external Q_s of HOMs.

First, we remember that the integrated quadrupole wake potential $G_2(t)$ is obtained from

$$G_2(t) = \int_{-\infty}^t W_2(t-t') Q_n(t') dt'$$

where $W_2(t)$ is the delta functional quadrupole wake function and $Q_n(t)$ is the normal component of beam bunch quadrupole moment when the bunch passes the cavity at time t . We note that $Q_n = \langle x^2 \rangle - \langle y^2 \rangle = \epsilon(\beta_x - \beta_y)$, where ϵ is the transverse emittance which we assume to be the same in x and y directions for the sake of simplicity.

For a single quadrupole mode with an angular frequency ω , the wake $W_2(t)$ is given by

$$W_2(t) = 2 \frac{ck_{loss}}{\omega} \exp\left(-\frac{\omega t}{2Q}\right) \sin \omega t$$

for $t > 0$, and $W_2(t)$ is equal to 0 for $t < 0$ by causality. Here k_{loss} is the usual loss factor for the quadrupole mode defined as follows,

$$k_{loss} = \frac{\omega R}{4Qb^4}$$

where b is the beam pipe radius and R/Q is to be evaluated at b .

Second, we notice that a bunch entering the cavity with an accumulated wake excited by all previous bunches will receive a transverse kick given by

$$F_x i + F_y j = -2Ne^2(xi - yj) \frac{G_2(t)}{L}$$

where i and j represent unit vectors along x and y and L is the length of cavity and N is the number of electrons in a single bunch.

Consequently, we may regard that the action of the excited cavity wake on the beam is equivalent to a regular quadrupole lens with the focal length,

$$f = \frac{\gamma}{2Nr_0 G_2(t)L}$$

where r_0 is the classical radius of the electron, $r_0 = e^2/m_e c^2 = 2.818 \times 10^{-13}$ cm.

To proceed further without being overwhelmed by too many variables to keep track we need to simplify the problem a bit. We will assume that in the absence of quadrupole wakes the transverse cross sections of the bunch entering the cavity on its 1st and 2nd pass are perfectly round, which means that there will be no excitation of quadrupole wake by the design beam. Furthermore we will assume that the lattice has no x-y coupling. Let $\beta_1 = \beta_x = \beta_y$ at the 1st pass and $\beta_2 = \beta_x = \beta_y$ at the 2nd pass for the beam at the cavity location and also let $\phi_x(\phi_y)$ be the phase advance in x (and in y respectively) from the cavity to the cavity for one recirculation.

Third, we are now able to calculate changes in β 's from the design value at the 2nd pass at the cavity location induced by the quadrupole wake following the perturbation formula worked out by T. Collins[9]. We obtain

$$\Delta\beta_{x,y}(t) = -2 \frac{Nr_0 G_2(t)}{\gamma} \beta_1 \beta_2 \sin 2\phi_{x,y}$$

We can now compute bunch quadrupole moment at the cavity on its 2nd pass

$$Q_n(t) = -2 \frac{Nr_0}{\gamma} \epsilon \beta_1 \beta_2 (\sin 2\phi_x - \sin 2\phi_y) \\ \times G_2(t - t_r) \Sigma \delta(t - t_r - mt_0)$$

where t_r is the recirculation path length in time and t_0 is the fundamental bunching period and the summation Σ is over all integer values of m . $\delta(t)$ is the Dirac delta function.

Finally, we are now in a position to construct a homogeneous integral equation for the integrated wake

function $G_2(t)$ by inserting the quadrupole moments back into the first equation of this section. We obtain

$$G_2(t) = -2 \frac{Nr_0}{\gamma} \epsilon \beta_1 \beta_2 (\sin 2\phi_x - \sin 2\phi_y) \times \int W_2(t-t') G_2(t'-t_r) \Sigma \delta(t'-t_r - mt_0) dt'$$

Searching for an exponentially growing solution for $G_2(t)$ we find the following expression for the threshold current, I_{th}

$$I_{th} = \frac{\omega E \exp(-\frac{\omega t_r}{2Q})}{ec(\frac{R}{Qb^4}) Q \epsilon \beta_1 \beta_2 (\sin 2\phi_x - \sin 2\phi_y) \sin \alpha t_r}$$

where the beam energy $E = \gamma mc^2$. We should note that the above relationship has been derived in a perturbation expansion.

As an example, let us consider a 7-cell CEBAF cavity which is being designed for the 12 GeV upgrade of the CEBAF accelerator. The lowest pass band start at 2568 MHz and the strongest quadrupole mode in that pass band has $R/Q = 32.6 \Omega$ at the beam pipe radius according to URMEL. We may get an appreciation of the relevance of the quadrupole mode beam breakup from a simple exercise with following parameters

$$\begin{aligned} f &= 2575 \text{ MHz} \\ R/Q &= 32.6 \Omega \\ b &= 3.5 \text{ cm} \\ E &= 100 \text{ MeV} \\ \epsilon &= \sim 1 \text{ mm-mrad} \\ \beta_1, \beta_2 &= \sim 10 \text{ m} \\ \sin 2\phi_x, \sin 2\phi_y &= \sim 1 \\ \sin \alpha t_r &\sim 1 \end{aligned}$$

Inserting these numbers into the threshold formula we get I_{th} as a function of the loaded Q

$$I_{th} = 2.5 \times 10^5 / Q \text{ (in A)}$$

We can see that the quality factor of 2575 MHz mode should be down to $10^6 \sim 10^7$ when designing a 100 mA machine with only one 7-cell CEBAF cavity. It is to be reminded that this is for an accelerator with only a single 7-cell cavity of CEBAF type.

4 CONCLUSIONS

In high energy accelerators beam focusing is achieved mainly with quadrupoles. Consequently the beam can't be

round in accelerating cavities in general and the quadrupole beam breakup instability presented in this paper is unavoidable at some point when we are pushing the current limit higher. Furthermore one should be aware that this instability will show up even after one has achieved a perfect alignment of all beamline elements. Despite many simplified assumptions made which require a future detailed study I hope that the present analysis has clearly shown the possible importance of higher order quadrupole modes in a future very high current recirculating linac and should be looked at carefully in a design stage when setting the damping requirement of HOMs, etc., for example.

5 ACKNOWLEDGMENT

I am grateful to D. Douglas for providing Reference [9] and many helpful discussions.

6 REFERENCES

- [1] G. R. Neil et al., "Sustained Kilowatt Lasing in a Free-Electron Laser with Same-Cell Energy Recovery", *Phys. Rev. Lett.*, **84**, 662 (2000).
- [2] J. J. Bisognano and M. L. Fripp, *Proc. of 1988 Linear Accelerator Conf.*, 388 (1988).
- [3] J. J. Bisognano and R. L. Gluckstern, *Proc. of 1987 Particle Accelerator Conf.*, 1078 (1987).
- [4] B. C. Yunn, *Proc. of 1991 Particle Accelerator Conf.*, 1785 (1991).
- [5] S. Gruner et al., *Rev. Sci. Inst.*, **73**, 1402 (2002).
- [6] M. W. Poole et al., *Proc. of the 2002 Euro. Part. Acc. Conf.*, 733 (2002).
- [7] E. Steffens and U. Schindler, editors, *Proc. of the ERLSYN 2002 Workshop*, Universitat Erlangen (2002).
- [8] A. W. Chao, "Physics of Collective Beam Instabilities in High Energy Accelerators", John Wiley & Sons, Inc. (1993).
- [9] D. Douglas, A. Garren, and F. Dell, "The Collins' Scheme for the Local Correction of Chromatic Aberrations due to Insertions", LBID-911 (1984).

THE SHORT-RANGE TRANSVERSE WAKEFIELDS IN TESLA ACCELERATING STRUCTURE

I. Zagorodnov*, T. Weiland, Fachbereich 18, TU Darmstadt, 64287 Darmstadt, Germany

Abstract

The operation of a Free Electron Laser in TESLA project requires very short bunches. This results in a very long interaction length between the bunch and the wakefields. From this fact severe problems for computer simulations arise. The longitudinal case was recently studied intensively by Novokhatski et al. [1]. In this paper we study mainly the transverse forces. Using a recently developed time domain numerical approach, we calculate the short-range transverse wakefields of the TESLA linac accelerating structure. We also consider behaviour of transverse wake potential in a periodic array of cavities and compare it with wake potential of the TESLA quasi-periodic structure.

INTRODUCTION

For the operation of the Free Electron Laser in the TESLA project very short bunches of length $\sigma = 50$ micrometers or less are required. This bunch length is very short compared to the iris radius a of the accelerating structure ($\sigma/a \sim 0.0014$). This induces severe problems for computer simulations. The longitudinal case was recently studied intensively by Novokhatski et al. [1]. It was shown that as for periodic structures and very short bunches the loss factor becomes independent of the bunch length. In this paper we study mainly the transverse forces. Using a recently developed time domain numerical approach [2], we calculate the short-range transverse wakefields in the TESLA accelerating structure of three cryomodules with total length ~ 36 m. Wakefields in the TESLA cryomodule and corresponding integral parameters are given for bunches of different length. We also consider behaviour of transverse wake potential in a periodic array of cavities and compare it with wake potential of the TESLA quasi-periodic structure. The numerical results are compared with analytical estimations and it is shown that, the same as for periodic structure [3], for very short bunches the kick factor decreases linear with the bunch length.

ANALYTICAL ESTIMATIONS

We consider an axially symmetric structures and bunch with charge Q moving parallel to the axis. The bunch with longitudinal distribution $q(s)$ travels near the axis, and thus the longitudinal loss is dominated by monopole fields

$$L_{\parallel} \approx \langle W_{\parallel}^0 \rangle = \frac{1}{Q} \int_{-\infty}^{\infty} W_{\parallel}^0(s) q(s) ds = \frac{1}{Q^2} \int_{-\infty}^{\infty} \int_{-\infty}^s W_{\parallel}^0(s-s') q(s') q(s) ds' ds$$

* Work supported in part by the Deutsche Forschungsgemeinschaft, project 1239/22-1

and the transversal kick by dipole fields

$$L_{\perp} \approx \langle W_{\perp}^1 \rangle = \frac{1}{Q} \int_{-\infty}^{\infty} W_{\perp}^1(s) q(s) ds = \frac{1}{Q^2} \int_{-\infty}^{\infty} \int_{-\infty}^s W_{\perp}^1(s-s') q(s') q(s) ds' ds.$$

Short bunches interact with single cavity and periodical structure in a different way. However, in both cases the wake functions $w_{\parallel}^0(s)$ and $w_{\perp}^1(s)$ at short distance s are approximately related in the simple way [4]

$$w_{\perp}^1(s) \approx \frac{2}{a^2} \int_0^s w_{\parallel}^0(z) dz. \quad (1)$$

For short bunches in a single cavity the well known result of K. Bane and M. Sands [5] reads as

$$w_{\parallel}(s) = -\frac{Z_0 c}{\sqrt{2} \pi^2 a} \sqrt{\frac{g}{s}}, \quad w_{\perp}(s) = \frac{2}{a^2} \frac{\sqrt{2} Z_0 c}{\pi^2 a} \sqrt{g s}, \quad (2)$$

where a is the iris radius and g is the cavity gap. As we see relation (1) holds for the wakes (2).

In the periodic structure the short range wake functions can be approximated by the relations [4]

$$w_{\parallel}(s) = A \frac{Z_0 c}{\pi^2 a} \exp(-\sqrt{s/s_0}), \quad (3)$$

$$w_{\perp}(s) = \frac{2}{a^2} A \frac{Z_0 c}{\pi^2 a} 2s_1 \left(1 - \left(1 + \sqrt{s/s_1} \right) \exp(-\sqrt{s/s_1}) \right), \quad (4)$$

where A, s_0, s_1 are fit parameters to be defined. If $s_0 = s_1$ then relation (1) holds exactly. However, in the common case $s_0 \neq s_1$ we have only

$$\partial_s w_{\perp}^1(0) = \frac{2}{a^2} w_{\parallel}^0(0). \quad (5)$$

This corresponds to a small difference of the right hand and left- hand sides in (1) for short distances s .

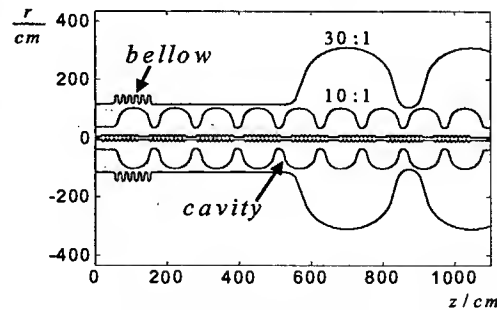


Fig. 1: Geometry of the TESLA cryomodule.

The TESLA linac consists of a long chain of cryomodules. One cryomodule of total length 12 m contains 8 cavities and 9 bellows as shown in Fig.1. The iris radius is 35 mm and beam tubes radius is 39 mm.

The wakefields for Gaussian bunches up to $\sigma = 50 \mu\text{m}$ are studied. To reach steady state solution the structure of 3 cryomodules with total length 36 m considered.

SINGLE-CELL STRUCTURE

As the first step we study wake fields in one middle cell of 9-cell TESLA cavity with aperture $a = 35\text{mm}$. From the fit of numerical data to formulas (2) we obtain

$$w_0(s) = \frac{Z_0 c}{\sqrt{2\pi^2 a}} \sqrt{\frac{\bar{g}}{s}} = 0.072 s^{-0.5} [\text{V/pC}],$$

$$w_1(s) = \frac{2}{a^2} \frac{\sqrt{2} Z_0 c}{\pi^2 a} \sqrt{\bar{g} s} = 235 s^{0.5} [\text{V/pC/m}],$$

where \bar{g} is "effective" cavity gap, $\bar{g} = 0.84L$, expressed through the cell period $L = 10.54\text{cm}$ in the TESLA cavity. As we see relation (1) holds exactly.

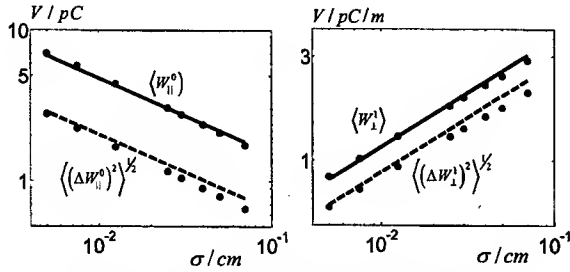


Fig. 2: Comparison of numerical and analytical integral parameters for a TESLA single-cell structure.

Fig.2 (left) shows the analytical (solid line) and numerical (points) loss factors and energy spreads (dashed line and points). On the right side of the figure the transversal kick and kick spread are shown. As we see the longitudinal loss factor scales as $O(\sigma^{-0.5}), \sigma \rightarrow 0$, and transversal kick factor scales as $O(\sigma^{0.5}), \sigma \rightarrow 0$.

PERIODIC STRUCTURE

In the case of a periodic structure the induced by short bunches wake fields can not be simply calculated as the sum of the single cell contributions, because the field traveling with the bunch is strongly modified and reach the steady state solution only after $\sim N = 2a^2/(\sigma L)$ cells. To study the steady state solution in the periodic structure we calculate wake fields in the chain of 144 cells.

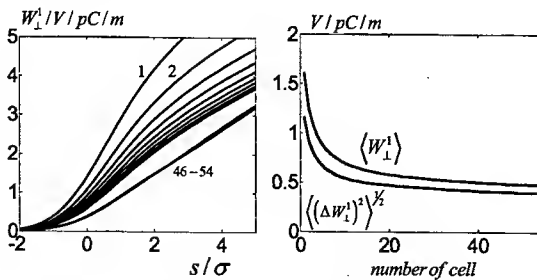


Fig. 3: Modification of the transverse wake potentials and the kick factor in periodic structure.

Fig. 3. shows the transverse wake potentials in the first nine cells (left) and the kick factor per cell for bunch with

$\sigma = 200\mu\text{m}$ (right) as a function of the number of cells. The kick factor converges to the steady state value.

From the fit of numerical data to formulas (3), (4) we obtain with $A = 1.025$, $a = 35\text{mm}$, wake functions per cell period $L = 10.54 [\text{cm/cell}]$

$$w_0(s) = 3.47 \exp(-\sqrt{s/s_0}) [\text{V/pC/cell}],$$

$$w_1(s) = 15.64 \left(1 - \left(1 + \frac{s}{s_1} \right) \exp\left(-\frac{s}{s_1}\right) \right) \left[\frac{V}{\text{pC} \times \text{m} \times \text{cell}} \right],$$

where $s_0 = 3.46 \cdot 10^{-3}$ and $s_1 = 1.4 \cdot 10^{-3}$. Thus, for $s_0 \neq s_1$ relation (1) is not fulfilled exactly but relation (5) holds.

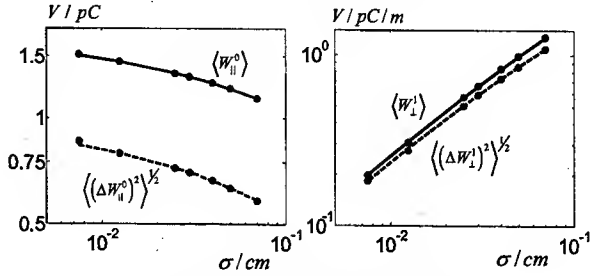


Fig. 4: Comparison of numerical and analytical integral parameters for periodic structure.

Fig. 4(left) shows the analytical (solid line) and numerical (points) loss factors and energy spreads (dashed line and points) for cell number 144. On the right side of the figure the transversal kick and kick spread are shown. As we see in the periodic case longitudinal loss factor becomes independent from the bunch length and transversal kick factor scales as $O(\sigma), \sigma \rightarrow 0$.

TESLA ACCELERATING STRUCTURE

The TESLA linac can be considered as multi-periodic structure: the first elementary period is the cavity cell, the second one is the 9-cell cavity with bellow and beam tubes and the third one is the cryomodule, housing 8 cavities with 9 bellows. In addition, some extra effects, like the larger tube diameter with respect to the aperture and different form of end cells of the cavity have to be taken into account. To reach steady state solution we calculate wake fields in the chain of 3 cryomodules.

From the fit of the numerical data to formulas (3), (4) we obtain with $A = 1.46$ and active length of cryomodule $L_c = 8 \cdot 1.036 [\text{m/module}]$ the wake functions per cryomodule

$$w_0(s) = 344 \exp(-\sqrt{s/s_0}) [\text{V/pC/module}],$$

$$w_1(s) = 10^3 \left(1 - \left(1 + \frac{s}{s_1} \right) \exp\left(-\frac{s}{s_1}\right) \right) \left[\frac{V}{\text{pC} \times \text{m} \times \text{module}} \right],$$

where $s_0 = 1.74 \cdot 10^{-3}$ and $s_1 = 0.92 \cdot 10^{-3}$. In formulas (3), (4) we used "effective" iris radius $a = \bar{a} = 35.57\text{mm}$. It was chosen as value between the pipe and iris radii to fulfill relation (5) for the above given wake functions. Thus, for $s_0 \neq s_1$ relation (1) is not fulfilled exactly but

relation (5) holds again (with $a = \bar{a}$). Like in the periodic case the transversal wake function scales as $O(s), s \rightarrow 0$.

To obtain the formulas for the wake function on the unit of active length the above relations should be divided by $L_a = 8.288$ [m/module].

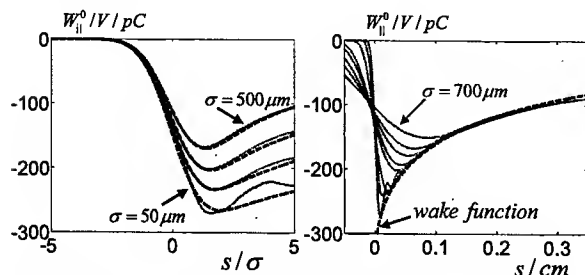


Fig. 5: Comparison of analytical and numerical longitudinal wakes in the third cryomodule ($\sigma = 50 \div 700 \mu\text{m}$).

Fig. 5 (left) shows numerical (gray solid lines) and analytical (black dashed lines) wake potentials for bunches with $\sigma = 500, 250, 125, 50 \mu\text{m}$. The deviation of the curves for the shortest bunch can be explained by the insufficiency of the 3 cryomodules to reach the steady-state solution. Fig. 5 (right) shows the wakes (gray lines) together with the analytical wake function (black dashed line) which tends to be the envelope function to all wakes.

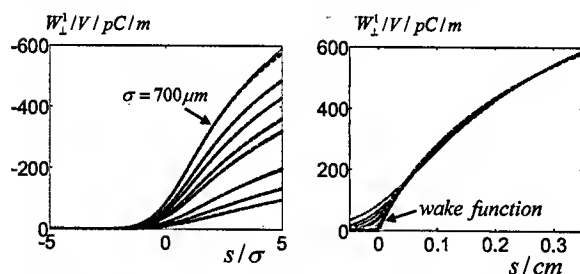


Fig. 6: Comparison of analytical and numerical transversal wake potentials in the third cryomodule ($\sigma = 50 \div 700 \mu\text{m}$).

Fig. 6 shows likewise the results for transversal wakes. Again, the analytical wake function (black dashed line) tends to be the envelope function to all wakes (see Fig. 6 right).

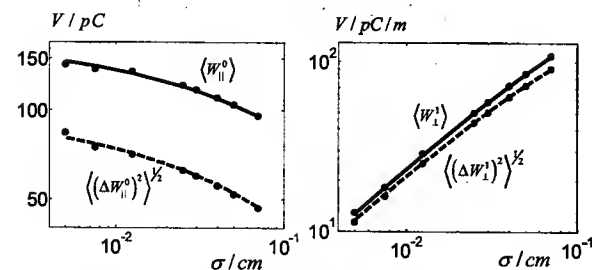


Fig. 7: Comparison of numerical and analytical integral parameters for the third TESLA cryomodule.

Fig. 7 (left) shows the analytical (solid line) and

numerical (points) loss factors and energy spreads (dashed line and points) in the third TESLA cryomodule. On the right side of the figure transversal kick and kick spread are shown.

Table 1. Comparison of the numerical and analytical loss factors.

$\sigma / \mu\text{m}$	Loss factor/V/pC		
	Numerical	Analytical	TDR
1000	86.4	90.2	90.4
700	95.9	95.8	95.6
500	105	104	103
400	110	110	108
300	117	116	114
250	122	120	117
125	135	133	128
75	138	141	134
50	143	146	138

Table 2. Comparison of the numerical and analytical kick factors.

$\sigma / \mu\text{m}$	Kick factor/V/pC/m		
	Numerical	Analytical	TDR
1000	138	137	153
700	109	108	130
500	85.4	85.1	111
400	72.5	72.2	99.6
300	58.1	57.9	86.8
250	50.2	50.1	79.6
125	28.8	28.3	56.9
75	18.2	18.1	44.3
50	12.8	12.6	36.3

Finally, in Tables 1,2 we compare numerical values with analytical ones obtained from the above formulas ("analytical") and the formulas given in [6] ("TDR"). As we see for the longitudinal case the results agree inside of the 5% level. For the transversal case the TDR formula

$$w_{\perp}(s) = L_a \left(1290\sqrt{s} - 2600s \right) \left[\frac{V}{pC \times m \times \text{module}} \right]$$

shows for the short bunches wrong $O(s^{0.5}), s \rightarrow 0$, behavior and overestimates the kicks.

ACKNOWLEDGEMENTS

The authors thank K. Bane and M. Dohlus for helpful discussions.

REFERENCES

- [1] Novokhatski A., Timm M., Weiland T., DESY TESLA-99-16, 1999.
- [2] Zagorodnov I., Weiland T., Proc. of ICAP 2002.
- [3] Fedotov A.V., Gluckstern R.L., Venturini M., Phys. Rev. STAB, Vol.2, 064401, 1999.
- [4] Bane K.L.F., SLAC-PUB-9663, LCC-0116, 2003.
- [5] Bane K., Sands M., SLAC-PUB-4441, 1987.
- [6] TESLA Technical Design Report, DESY 2001-011.

CALCULATION OF COLLIMATOR WAKEFIELDS*

I. Zagorodnov, T. Weiland, Fachbereich 18, TU Darmstadt, 64287 Darmstadt, Germany
K. Bane, SLAC, Stanford University, Stanford, CA 94309, USA

Abstract

We present longitudinal and dipole wakefield simulations of TESLA and NLC collimator designs using a newly developed numerical algorithm, one that allows for the accurate calculation of the combination of very short bunches and very long, gently tapered structures. We demonstrate that the new algorithm is superior to the standard method of such calculations. For small taper angles our results agree with analytical formulas of Yokoya. In addition, we optimize the TESLA TTF2 "step+taper" collimator design, and compare with collimator test measurements carried out at SLAC.

INTRODUCTION

In future linear colliders, such as the TESLA [1] and the NLC project [2], in order to remove halo particles, the beams pass through a series of collimators before entering into collision. With the high current, low emittance beams envisioned, however, short-range transverse wakefields, generated when passing even slightly off-center through the collimator region, can spoil the projected emittance of the beams, and therefore the luminosity of the collider. Therefore, optimizing the collimator design to reduce wakefields is an important task for such projects.

A collider collimator can be described as a shallow transition from a beam pipe to a smaller aperture and then back again. Among the features making it difficult to find the wake for such structures are their finite wall conductivity, their complicated (non-cylindrically symmetric) geometry, and their long, gentle transitions. To simplify the calculation, cylindrically symmetric models are often used. In addition, for the purpose of design, the wakefields of such collimators are separated into two components, a resistive-wall component and a geometric component, where the geometric component is the wake assuming perfectly conducting walls [2].

In this report we study the geometric component of the wake of cylindrically symmetric collider collimators, using a time domain numerical method to obtain the dipole, and also the longitudinal, wakes. A main difficulty in such calculations is that—due to the short bunch length and the long, shallow tapers of the collimator—grid dispersion and errors in geometry (e.g. a shallow taper ends up with stair steps) can arise.

Using a recently developed numerical approach [3], one that is able to model arbitrary, cylindrically symmetric boundaries faithfully and does not suffer from longitudinal dispersion, we are able to calculate accurately the short-range wakefields of TESLA and NLC collimator

designs. Our numerical results are compared to those of a standard time domain program, ABCI [4], to analytical estimates, and to measurements. Optimization of the TESLA TTF2 collimator geometry is also performed.

CALCULATIONS

New Time-Domain Program

We will study the wakefield effects of collider collimators using the computer program ECHO. This program incorporates a newly developed finite difference, time-domain algorithm [3]. With a time step $c\Delta t = \Delta z$ (where c is the speed of light, t is time, and z is longitudinal position) allowed by the numerical stability condition, the algorithm has no longitudinal dispersion, allowing, with the use of a moving mesh, for the solution of very short bunches in very long structures. In addition, the "stair step" problem is avoided by means of the boundary approximation method of Ref. [5], a method that allows for accurate calculation in arbitrarily shaped, cylindrically symmetric structures. For longitudinal case (monopole mode) and staircase geometry approximation our scheme is reduced to the one presented in [6].

In this report we focus on perfectly conducting, cylindrically symmetric collimators of the form sketched in Fig. 1. A tube of smaller radius b and length l is connected to beam pipes of larger radius a by symmetric tapers of angle α and length L .

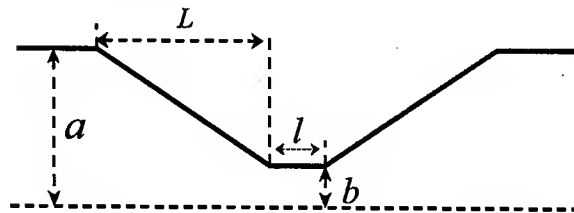


Fig.1. Collimator geometry.

For the TESLA and NLC collimators the angle α is small. K. Yokoya has shown that, if α and $\rho = \tan(\alpha)\omega b/c$ are small compared to 1 (ω is frequency), the longitudinal (monopole) and transverse (dipole) impedances of such structures are given by [7]

$$Z_0^0 = \Theta \frac{i\omega}{c^2} \int_{-\infty}^{\infty} (f')^2 dz, \quad (1)$$

$$Z_1^1 = \Theta \frac{2i}{c} \int_{-\infty}^{\infty} (f'/f)^2 dz, \quad (2)$$

$f(z)$ is the beam pipe radius variation, and $\Theta = Z_0 c/4\pi$, with Z_0 the free space impedance. Note that the two impedances are purely inductive and resistive, respectively. Table 1 gives sample parameters of TESLA

*Work supported by the Deutsche Forschungsgemeinschaft, project 1239/22-1, and by the U.S. Department of Energy, contract DE-AC03-76SF00515.

and NLC collimators and beams. The beams of charge Q have longitudinal distributions that are Gaussian, with rms length σ . Since the typical frequency excited $\omega \sim c/\sigma$, we see that for TESLA $\rho = 0.03$, for NLC $\rho = 0.04$; therefore, in both cases we are in the small angle regime where Yokoya's formulas apply.

Table 1. Typical TESLA and NLC collimator and bunch properties.

	α [mrad]	a [mm]	b [mm]	l [mm]	Q [nC]	σ [mm]
TESLA	20	17.5	0.4	20	1.	0.3
NLC	20	17.5	0.2	20	1.	0.1

In the time domain, Yokoya's formulas imply that the longitudinal bunch wake, $W_{||}$, will be proportional to the derivative of the bunch shape, and the transverse bunch wake, W_{\perp} , will be proportional to the bunch shape itself. We can quantify the time domain results by the average wake ($\kappa_{||}$ the loss factor or κ_{\perp} the kick factor) and the rms of the wake, W_{rms} . Note that Yokoya's formulas imply: $\kappa_{||} = 0$ and [for small b/a] $\kappa_{\perp} = 2\alpha/(\sqrt{\pi}\sigma b)$, $(W_{||})_{rms} \approx 0.35\alpha/\sigma^2$, $(W_{\perp})_{rms} \approx 0.44\alpha/(\sigma b)$.

Parameter Study

We begin our numerical study with the parameters in Table 1 for TESLA, and study the dependence of the results on α . Longitudinal results— $\kappa_{||}$ and $(W_{||})_{rms}$ —are shown in Fig. 2. The solid black curves give results obtained by ECHO with $\sigma/h = 5$ (h is the mesh size). The wake was calculated for angles down to $\alpha = 0.5^\circ$, in which case the total collimator length ~ 4 m. To test the accuracy of the numerical results, at sample points ($\alpha = 5^\circ, 10^\circ, 20^\circ$), the mesh was made finer, and the result changed by less than 1%. Yokoya's formula predicts $\kappa_{||} = 0$, and $(W_{||})_{rms}$ as given by the dot-dashed curve in the figure (the right plot). We see that the ECHO results approach the analytical solutions for small α ; at $\alpha = 10^\circ$ the difference is $\sim 10\%$, at $\alpha = 5^\circ$ it is $< 3\%$. Finally, in Fig. 2, for comparison, we also display results obtained by the time-domain program, ABCI, for cases $\sigma/h = 5, 10, 20$ (gray curves); we see that for large α a much finer mesh is needed than by ECHO, and for small α the dependence is not correct.

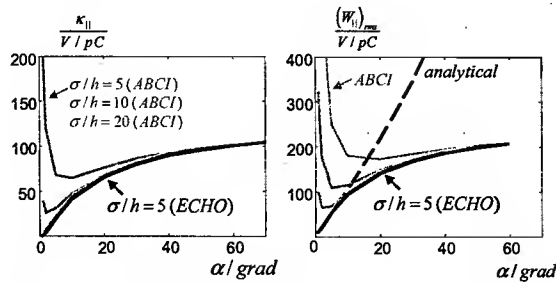


Fig. 2. Longitudinal wake dependence on collimator angle.

In Fig. 3 we plot the transverse results of ECHO— κ_{\perp} and $(W_{\perp})_{rms}$ —and compare to the analytical results, and we see that the numerical results have the correct small α behavior.

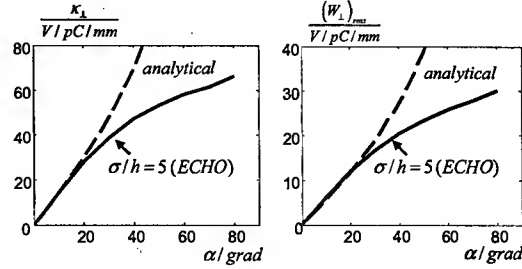


Fig. 3. Transverse wake dependence on collimator angle.

In Fig. 4 we give the wakes themselves, W_{\perp} (left) and $W_{||}$ (right), as obtained by ECHO, for the case $\alpha = 20$ mrad and for several cases of σ/h (gray lines). We see that the numerical results approach the analytical curves (black dashes) as the mesh becomes finer.

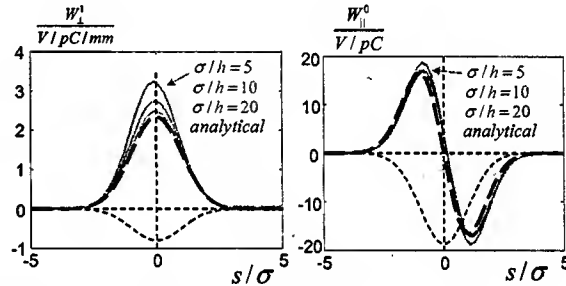


Fig. 4. Transverse (left) and longitudinal (right) wakes when $\alpha = 20$ mrad.

In Table 2 we give $\kappa_{||}$ and κ_{\perp} , for TESLA and NLC collimators with $\alpha = 20$ mrad (near the nominal value), as obtained by ECHO. Also given are some results of ABCI (in parentheses) and the analytical asymptotic values. We clearly see that, for a given mesh, ECHO is much more accurate than ABCI. We note also that the absolute error for ECHO remains nearly unchanged as the length of the collimator is increased, unlike a program like ABCI, which requires an ever increasingly dense mesh.

Table 2: Dependence of $\kappa_{||}$ and κ_{\perp} on mesh density when $\alpha = 20$ mrad, as obtained by ECHO. ABCI results are given in parentheses.

σ/h	$\kappa_{ }$ [V/pC]		κ_{\perp} [V/pC/mm]	
	TESLA	NLC	TESLA	NLC
5	1.46	33.6	2.24 (135)	12.8
10	1.42	32.9	1.91 (44.3)	11.2
20	1.42	-	1.74 (13.4)	10.6
Analytical	0		1.65	10

Collimator Shape Optimization

We have seen that reducing the taper angle decreases the wakefield effect. However, to obtain a significant effect, the types of collimator that we have studied so far may need to be meters long. An alternative solution is to consider a type of collimator that we call a "step+taper" collimator [8]. An example is shown in Fig. 5 where the parameters correspond to the TESLA TTF2 collimator [9]. We perform ECHO calculations for a very short bunch, $\sigma = 0.05$ mm.

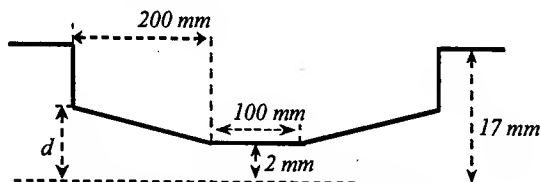


Fig. 5. Geometry of the TESLA TTF2 "step+taper" collimator.

Fig. 6 displays κ and W_{rms} , both longitudinal and transverse, as functions of collimator parameter d . As can be seen all functions have a minimum; the overall minimum can be taken to be $d \approx 4.5$ mm.

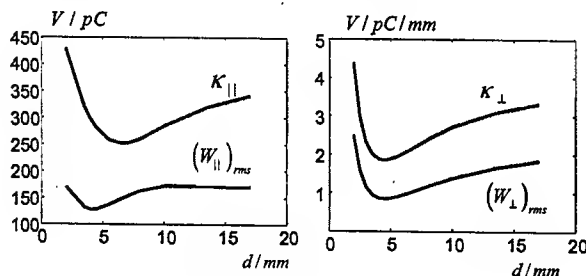


Fig. 6. Collimator geometry optimization.

Comparison with Measurement

Finally, we compare ECHO numerical results with experimental data. At SLAC dedicated test chambers with collimators were constructed, installed in the SLAC linac, and then the transverse wakefield effect was measured with beam [10]. One chamber has a square collimator that we will assume has a wakefield that is similar to that of a round chamber. The parameters are: $\alpha = 335$ mrad, $a = 19$ mm, $b = 1.9$ mm, $l = 0$ mm, and $L = 51$ mm. (Note that the taper angle α is much larger than will be the case in future colliders.) The measured, simulated, and analytical small angle asymptotic results are given in the Table 3.

The ECHO results were checked by refining the mesh, and were found to be accurate to better than 1%. Note that $\rho = 0.55(1.02)$ for the case $\sigma = 1.2(0.65)$ mm, and it is therefore not surprising, in the latter case, that simulated and analytical results are in disagreement. Measurement and simulation agree well for the former case, but significantly disagree in the latter, shorter bunch case, a disagreement that is not understood.

Table 3. SLAC collimator measurement comparison. Given are kick factors, κ_L , in units of V/pC/mm.

σ [mm]	Measured	Simulated	Analytical
1.2	1.2 ± 0.1	1.268	1.34
0.65	1.4 ± 0.1	1.908	2.48

ACKNOWLEDGEMENTS

The authors thank M. Dohlus and G. Stupakov for helpful discussions.

REFERENCES

- [1] "TESLA: Technical Design Report," DESY, 2001.
- [2] "NLC Design Report," SLAC Report 474, SLAC, 1996.
- [3] I. Zagorodnov and T. Weiland, "Calculation of Transversal Wake Potential for Short Bunches," Proc. ICAP 2002, East Lansing, MI, Oct. 2002 (to appear).
- [4] Y.H. Chin, "User's Guide for ABCI Version 8.7," CERN-SL-94-02-AP, CERN, 1994.
- [5] I. Zagorodnov, R. Schuhmann, T. Weiland, "A Uniformly Stable Conformal FDTD-Method on Cartesian Grids," *Int. J. Numer. Model.*, **16**, Issue 2 (2003) 127.
- [6] A. Novokhatski, M. Timm, T. Weiland, "Transition Dynamics of the Wake Fields of Ultra Short Bunches," ICAP 1998, Monterey, California, 1998.
- [7] K. Yokoya, "Impedance of Slowly Tapered Structures," Tech. Rep. SL/90-88 (AP), CERN, 1990.
- [8] K. Bane and P. Morton, "Deflection by the Image Current and Charges of a Beam Scraper," LINAC'86, SLAC, June 1986, p. 490 and SLAC-PUB-3983.
- [9] M. Körfer, "Layout and Functionality of Collimator System," TESLA Coll. Meeting, Salza, 21 Jan. 2003.
- [10] P. Tenenbaum, *et al.*, "Transverse Wakefields from Tapered Collimators: Measurement and Analysis," PAC'01, Chicago, June 2001, p. 418.

FOCUSING HORN SYSTEM FOR THE BNL VERY LONG BASELINE NEUTRINO OSCILLATION EXPERIMENT

S. A. Kahn, A. Carroll, M. V. Diwan, J. C. Gallardo, H. Kirk, C. Scarlett, N. Simos, B. Viren,
W. Zhang

Brookhaven National Laboratory, Upton, NY 11973, USA

Abstract

This paper describes the focusing horn system for the proposed very long baseline neutrino oscillation experiment using a neutrino beam from BNL to an underground facility such as the Homestake Mine in South Dakota. The proposed experiment uses a 1 MW upgraded AGS. In order to achieve this performance the AGS will operate with a cycle time of 2.5 Hz and 8.9×10^{13} protons on target at 28 GeV. This paper discusses the design criteria of a horn system necessary to handle this intense beam and the optical geometry to achieve the desired flux distribution at the detector.

INTRODUCTION

Recent results show evidence for neutrino oscillations has kindled interest in experiments that can provide precise measurements of the neutrino mixing parameters. A bold proposal to send a neutrino beam from Brookhaven National Laboratory to the Homestake Mine in South Dakota, a distance of 2540 km, could provide sensitivity to the mixing angles, mass splittings and CP violating phase that describe the neutrino oscillation matrix. The physics potential of this proposed long baseline experiment is described elsewhere [1, 2]. In order to provide a sufficient event rate at the far detector, an upgraded AGS would be required to provide the necessary proton intensity. The AGS upgrade would increase the repetition rate of the machine from the current 0.5 Hz to 2.5 Hz with 8.9×10^{13} protons per pulse providing an average beam power of 1 MW. The expected integrated intensity for a typical year of operation (10^7 sec) is expected to be 2.2×10^{21} 28 GeV protons on target. A description of the accelerator and target system design of the AGS Super Neutrino Beam Facility is given in a report [3]. The target and horn system must be designed to handle this intense proton beam. A solid target made of a low Z material is needed to survive a beam of this power. The target material selected is a woven carbon-carbon composite that has a very small coefficient of thermal expansion up to 1000°C. The expected temperature rise in the target from the deposited proton beam energy is 280°C. This extends the life of the target by reducing the thermo-mechanical stresses induced by the beam. The target itself is cooled by pumping helium gas into the space between the target and the inner surface of the horn. The description of the target system and its integration into the horn is discussed in another paper submitted to this conference [4]. Table 1 summarizes the important target parameters. In order to

reach the Homestake mine, the neutrino beam must be directed into the earth with an 11.3° incline with respect to the ground level. To produce a sufficient flux of neutrinos a channel of 200 meters is needed to allow the secondary pions to decay. The target-horn ensemble must be located at an elevation of 38.5 meters to avoid possible contamination of the ground water. The neutrino beamline, target, horn and decay channel will be located on a 48 m high hill built for that purpose.

Table 1: Parameters that describe the proton target

Parameter	Value
Normalized X, Y Emittance	100π mm-mrad
Target Radius	3.2 mm
Target Length	60 cm
Beam Radius	0.8 mm
Material Density	1.9 g/cm^3
Interaction Length	46 cm

HORN REQUIREMENTS

Table 2 shows the parameters that describe the horn system. The horn current is selected to produce a toroidal field, $B_\phi = 5$ T at the inner conductor of the first horn, which both captures and focuses the π and K mesons produced in the target. The second horn provides additional focusing for the higher energy component of the beam that is relatively forward. The starting point for the geometrical design of this horn system was that proposed by Palmer for horns that were designed for previous neutrino experiments at BNL[5, 6]. The first horn had to be elongated to contain the longer carbon-carbon target. Also additional modifications to the inner surface of the downstream part of the first horn were made to capture more of the higher energy part of the meson spectrum. The next section will describe the results of the simulation of the horn geometry. Figure 1 shows an illustration of the geometry of the first horn.

The following issues are important in the design of the horn:

- Heat generation in the horn and its removal.
- Irradiation and corrosion effects on the horn materials.
- Mechanical response and fatigue in the horn.
- The proper capture and focusing of π and K mesons to produce the desired neutrino beam.

The heat generation is a greater problem for the first horn than the second because of its proximity to the target. The two major contributions to the heat generation are the

energy deposited in the horn from the secondary particles produced in the target and the Joule heating from the current in the horn conductor. The heat produced for both of these processes is maximal on the inner conductor of the horn of the first horn. The heat deposited from secondary particles on the inner conductor of the horn is estimated to be 8.39 ± 1.9 kw. The contribution from the time averaged Joule heating on the first horn is 9.375 kw. An additional heat load due to heat radiation from the target is estimated at 1.36 kw. This heat load can be removed by spraying water onto the interior surface of the horn inner conductor. The material used for the horn conductor must have low resistivity, high yield strength and high resistance to corrosion. We have assumed that conductor material can be an aluminum alloy with resistivity of $3.7 \times 10^{-8} \Omega\text{-m}$. The aluminum corrosion issue could be minimized by coating the surfaces with nickel in a manner similar to the NuMi horn.

Table 2: Table of Horn System Parameters

Parameter	Value
Material	Aluminum
Horn Current	250 kA
Horn 1 Inner Radius	7 mm
Horn 1 Inner Conductor Thickness	2.5 mm
Horn 1 Length	217 cm
Horn 1 Inductance	779 nH
Horn 1 Resistance	248 $\mu\Omega$
Horn 2 Inner Radius	58.4 mm
Horn 2 Inner Conductor Thickness	1.6 mm
Horn 2 Length	150 cm
Horn 2 Inductance	287 nH
Horn 2 Resistance	30 $\mu\Omega$
Stripline Inductance	480 mH
Stripline Resistance	30 $\mu\Omega$
Pulse Width	1.2 ms
Repetition Rate	2.5 Hz
Distance Betw. Horn Fronts Plates	8.17 m

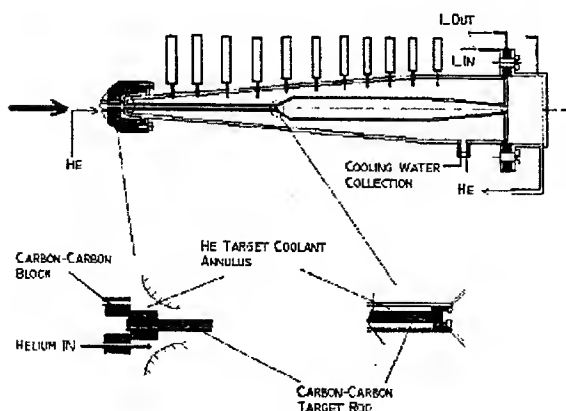


Figure 1: Sketch of First Horn with target inserted.

SIMULATIONS

The focusing performance of the horn can be examined by simulating the particle production in the target, tracking those particles through the horn field and allowing them to decay using the GEANT program. In this study a 28 GeV proton beam with a transverse profile of $\sigma_r=0.8$ mm and $\sigma_z=0$ is incident on a carbon target with 3.2 mm radius, 60 cm length (1.1 interaction lengths) and $\rho=1.6\text{g/cm}^3$ (in this calculation). Because of its length the target is not a point source. The GEANT program has several options available for production of hadrons. We have compared pion production rates using GFluka, Gheisha and MARS [7, 8]. Table 3 shows the particle production rate from the target for these different hadron shower programs. Figure 2

Table 2: Particle production rate from carbon target. Rates are particles per proton on target.

Particle	Gfluka	Gheisha	Mars
π^+	1.72	2.17	1.68
π^-	1.39	1.73	1.34
K^+	0.083	0.072	0.105
K^-	0.037	0.022	0.001
K^0	0.058	0.044	

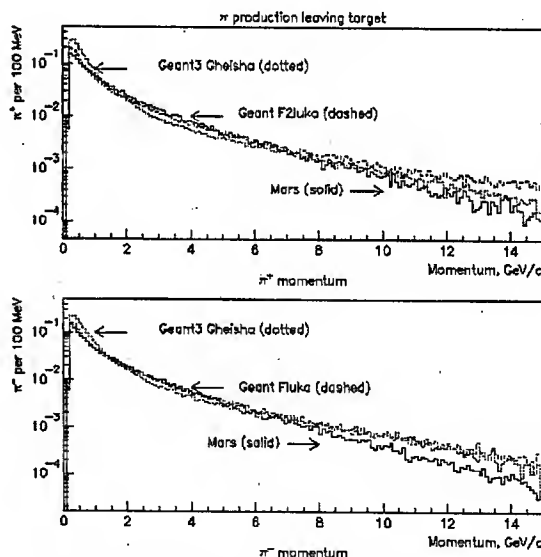


Figure 2: π^+ (upper) and π^- (lower) production from carbon target. Rates are per 100 MeV per 10^5 protons on target.

shows π^+ and π^- production from the carbon target. The figure shows different curves corresponding to the different hadron production options. The Mars program shows a production rate similar to Gfluka for $P_\mu < 7$ GeV/c. At very large P_μ the Mars rates are significantly lower than that which Gfluka or Gheisha predict. These rates will affect the event estimates expected at the detector. The Gfluka program overestimates the π^+ production by 50% in comparison with Mars for $P_\mu > 7$ GeV/c.

NEUTRINO FLUXES

We have chosen to use the Gfluka program for hadron production in order to make the neutrino flux calculations. The π 's and K 's produced in the target are tracked through the magnetic field of the horns until they decay or interact.

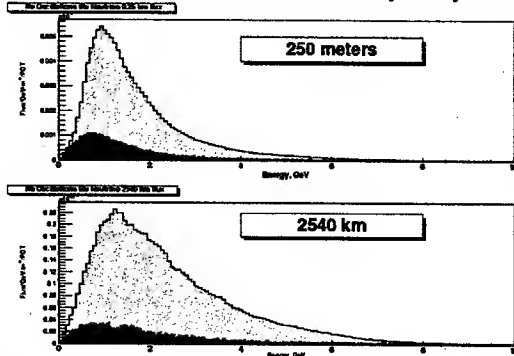


Figure 3: Neutrino Flux Distributions at the close (upper) and far (lower) detectors. Each plot shows the dominant ν_μ with the ν_e distribution superimposed in a darker color. The ν_e flux is scaled by a factor of 20 to be visible.

The horns are followed by a 200 meter (measured from the target) decay channel. Each meson is allowed to decay many times to obtain a reasonable number of neutrinos at the far detectors for a meaningful flux calculation. Each neutrino produced is weighted to account for these multiple decays. The various species of neutrinos from the decays of π , K and μ are counted as they pass the detectors. The location of the close detector, which is positioned at 250 m from the target, is constrained by the steep inclination of the neutrino beam line. The purpose of the near detector is to measure accurately the flux of the various neutrino species so that a prediction of the neutrino flux without oscillations can be made at the far detector. Figure 3 shows the expected flux at the near detector and at the far detector positioned at the Homestake mine. Since the distance to the close detector is comparable to the length of the decay tunnel the spectrum for that detector is different from the spectrum of the far detector which sees the neutrinos originating at a point source. Techniques will have to be developed to extract the predicted non-oscillated far detector spectrum from the observed near detector spectrum. Also, Figure 3 shows the ν_e flux spectrum expected at each location. (This spectrum is scaled by a factor of 20 in order to be visible on the same graph.) The ν_e contamination in the beam comes from the decay of K^+ , K^0 and μ that are present. This is a background to the appearance signal of ν_e that come from oscillations of $\nu_\mu \rightarrow \nu_e$ and is $\sim 1\%$ of the non-oscillated ν_μ flux.

One can obtain an estimate of the number of non-oscillated events that would be seen at the near and far detectors by integrating the flux over the appropriate neutrino cross sections. To make these estimates it is

assumed that the detector at BNL has a mass of 0.33 kton and that a water Cherenkov detector with a mass of 0.5 megatons would be built at the far location. Table 3 shows the number of events that would be seen after a five year running period (5×10^7 sec.)

Table 3: Estimates of the number of events that would be seen after a 5×10^7 sec running period if no oscillations occurred.

Channel	Near Detector	Far Detector
$\nu_\mu N \rightarrow \mu^- X$	3.5×10^9	51800
$\nu_\mu N \rightarrow \nu_\mu X$	1.1×10^9	16908
$\nu_e N \rightarrow e^- X$	4.5×10^7	380
$\nu_\mu n \rightarrow \mu^- p$	1.1×10^9	11767
$\nu_e n \rightarrow e^- p$	1.4×10^7	84

ACKNOWLEDGEMENTS

This work was performed with the support of the US DOE under Contact No. DE-AC02-98CH10886.

REFERENCES

- [1] *Report of the BNL Neutrino Working Group: Very Long Baseline Neutrino Oscillation Experiment for Precise Determination of Oscillation Parameters and Search for $\nu_\mu \rightarrow \nu_e$ Appearance and CP Violation*, BNL Report 69395 (2002).
- [2] M.V. Diwan et al., *Very Long Baseline Neutrino Oscillation Experiment for Precise Measurements of Mixing Parameters and CP Violation Effects*, hep-ph/0303081v1 (2003) submitted to Phys Rev D.
- [3] *The AGS-Based Super Neutrino Beam Facility, The BNL Neutrino Working Group Report II*, BNL-71228-2003-IR.
- [4] N. Simos, *Concept Design of the Target/Horn System for the BNL Neutrino Oscillation Experiment*, TPPB044, submitted to this conference.
- [5] R. B. Palmer, *Proceedings of Informal Conference on Experimental Neutrino Physics*, Edit. C. Franzinetti, CERN, Geneva, p141 (1965)
- [6] A. Carroll, *Overview of Recent Focusing Horns for the BNL Neutrino Program*, p1731, Proc of the 1987 Particle Accelerator Conference.
- [7] *GEANT, Detector Description and Simulation Tool*, CERN Program W5013.
- [8] N.V. Mokhov, *The MARS Code System User's Guide*, Fermilab-FN-628 (1995)

BEAM SHAPING AND COMPRESSION SCHEME FOR THE UCLA NEPTUNE LABORATORY*

R. J. England, P. Musumeci, R. Yoder, J. B. Rosenzweig, UCLA, Los Angeles, CA 90095, USA

Abstract

We have recently added a dispersionless translating section to the UCLA Neptune linear accelerator beamline. This new section of beamline will serve as a venue for beam shaping and compression experiments using the 14MeV electron beam produced by the UCLA Neptune PWT linac and newly installed photoinjector. An examination of the first and second-order optics indicates that when certain nonlinear effects are minimized through the use of sextupole magnets, the longitudinal dispersion is dominated by a negative R_{56} which, for an appropriately chirped initial beam, can be used to create a ramped beam of a few picosecond duration that would be ideal for driving large amplitude wake fields in a plasma and producing high transformer ratios. The beamline is now in operation. Preliminary data indicate that the beamline optics are well-predicted by simulation and that sextupoles can be used successfully to eliminate nonlinear horizontal dispersion. Future experiments are planned for measuring beam compression (using CTR autocorrelation) and doing longitudinal phase space tomography (using a transverse deflecting cavity).

INTRODUCTION

Recently, a scheme was proposed [1] for the creation of a beam which approximates an asymmetrical "doorstep" current profile using first and second order beam optics. The proposed method takes advantage of the RF curvature in the longitudinal phase space distribution of a positively chirped (i.e. back-of-crest) driving beam. Under a pure negative R_{56} compression of the longitudinal phase space (i.e. with negligible higher order contributions), such a phase space distribution results in a ramp-shaped current profile of a few picosecond to sub-picosecond duration, which is ideal for use as a driving beam for large amplitude plasma wake-fields with high transformer ratios [2,3].

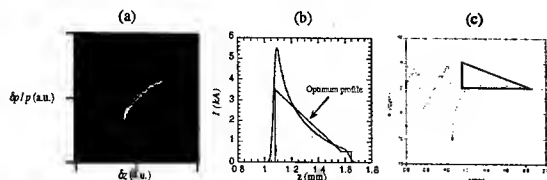


Figure 1. Plots showing the longitudinal phase space (a) and density profile (b) of a ramped beam produced by negative R_{56} compression, as well as a PIC simulation (c) of the wake field produced by such a beam in a plasma of density $2 \times 10^{16} \text{ cm}^{-3}$.

* Work funded by Department of Energy Grant DE-FG03-92ER40693.

The simulated longitudinal phase space for such a beam is shown in Fig. 1(a). The current profile associated with the phase space in Fig. 1(a), and a comparison of it to the optimized "doorstep" current profile, are shown in Fig. 1(b). The wake fields produced by this beam distribution, shown in Fig. 1(c), were obtained from a particle-in-cell simulation of a proposed wake field accelerator experiment for the ORION project at the Stanford Linear Accelerator Laboratory. The *S-Bahn*, a new section of beamline installed at the UCLA Neptune laboratory in the Fall of 2002 has been designed, using sextupoles to cancel nonlinear effects, to produce a nearly linear negative R_{56} compression capable of creating a ramped beam of the sort shown in Fig. 1. A diagram of this beamline is shown in Fig. 2.

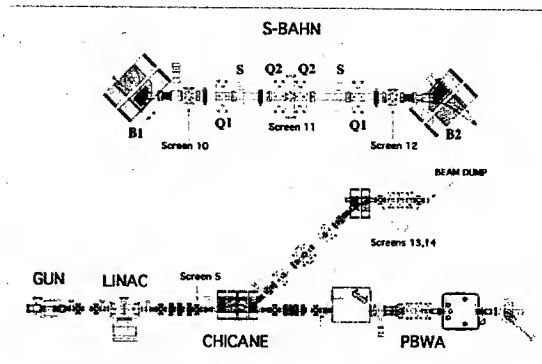


Figure 2. UCLA Neptune beamline with S-Bahn.

BACKGROUND

The S-Bahn beamline is a dispersionless translating section exhibiting a widely used geometry known as a "dogleg." The two pairs of bending dipoles (B1 and B2) are separated by symmetrically positioned focusing optics (Q1 and Q2) and sextupole magnets (S1 and S2) for performing nonlinear corrections. Pursuant to the discussion of reference [1], the optics of this device are optimized under the conditions that (1) the quadrupole field settings be symmetric about the midpoint, (2) the beamline be operated in a nondispersive mode, and (3) there be a focus at the midpoint (Screen 11 in Fig. 2). If satisfied, the aforementioned conditions ensure that transverse emittance growth is minimized and that the beam size is well-controlled. In addition, elimination of the horizontal dispersion to linear order was shown to predictably determine the (negative) value of the longitudinal dispersion element (R_{56}) of the transport matrix, which is the primary mechanism for compression.

Compression requires that an RF curvature and momentum chirp be imposed upon the beam's distribution in the longitudinal phase plane by injecting it into the linac off-crest. When acted upon by a negative longitudinal dispersion (R_{56}), a beam with a positive momentum chirp (i.e. injected back-of-crest) will experience a rotation in the trace space plane of the longitudinal coordinate z and the fractional momentum error δ . This transformation results in a net longitudinal compression of the beam and a hook-shaped distribution of the sort shown in Fig. 1 (a) which has a ramped density profile.

This mechanism is dependent upon the z phase space transformation being *linear*. However, since a beam injected off-crest tends to have a larger energy spread, the longitudinal dispersion may be expected to contain significant nonlinear contributions from terms proportional to various powers of the momentum error. For the beamline geometry and RMS energy spread particular to the Neptune S-Bahn, these nonlinearities are dominated by the second order transport matrix elements T_{566} and to a lesser degree by T_{561} and T_{562} . The longitudinal transport equation to second order is therefore approximated by

$$z = z_0 + R_{56}\delta + T_{566}\delta^2 + T_{561}x_0\delta + T_{562}x_0'\delta \quad (1)$$

Analytical calculations and simulations using the codes PARMELA and ELEGANT predict that the dominant T_{566} contribution can be eliminated and the other two reduced by a factor of approximately one-half by effective use of sextupoles. To this end, two sextupole magnets (labeled S in Fig. 2) have been included in the S-Bahn lattice.

RECENT EXPERIMENTAL RESULTS

Between recent shutdowns of the Neptune laboratory for RF work (January-February) and for installation of a new magnesium cathode photoinjector (April 2003), several runs were performed for the purposes of determining the running parameters and upstream optics for proper matching of the beam into the S-Bahn, and for optimizing the optics of the S-Bahn for operation in a nondispersive mode suitable for negative R_{56} compression.

The various conditions on the S-Bahn optics discussed above constrain the allowed transverse Twiss parameters and emittance of the beam entering the dogleg section. In particular, the normalized emittance should be less than 10 mm mrad, the beta function should be relatively large (at least 1m) and the beam should be highly convergent at the entrance to the first bend (B1). However, various technical and spatial constraints required that the upstream optics be operated in a mode with somewhat smaller beta functions and larger emittance. The empirical values for the Twiss parameters and normalized emittance obtained from quadrupole scans are shown in Table 1.

Table 1: Empirical Parameters

Parameter	Value	Location
Q_{beam}	35.4 ± 3.8 pC	Faraday Cup
U (Energy)	11.5 MeV	Screen 10
σ_δ	$< 0.5\%$	
α_0	-0.94 ± 0.43	Upstream Quads
β_0	0.77 ± 0.43 m	Upstream Quads
$\epsilon_{N,0}$	6.03 ± 1.8 mm mrad	Upstream Quads

Since no diagnostic is currently in place for measuring beam compression, the linac phase was set to minimize energy spread rather than to produce a chirped beam. Previous measurements have indicated an energy spread of less than 0.5% under these operating conditions. A stable nondispersive operating point was determined empirically by observing the beam on the six profile monitors (Screens 5, 10-14 in Fig. 2). The horizontal dispersion function η (or R_{16}) was minimized by observing the beam centroid position at the S-Bahn midpoint (Screen 11) under a variation of the fields of all magnetic elements on the dogleg (B1, B2, Q1, Q2) by a fractional offset ζ from those field values corresponding to the desired operating configuration. For a beam of constant central energy, the resultant shift in the centroid position is the same as that which would be observed due to a change in the central momentum by the same fractional amount and is given to second order in ζ by

$$\Delta x_{cen} = R_{16}\zeta + T_{166}\zeta^2 + O(\zeta^3) \quad (2)$$

Consequently, the first and second order horizontal dispersion terms R_{16} and T_{166} can be obtained by fitting the measured centroid position data to a quadratic in ζ . The values of T_{166} at the exit of the S-Bahn (Screen 13) obtained by this method are shown in Table 2 at three different settings of the sextupole field strength. Simulation values from the transport code ELEGANT [4] are provided for comparison.

Table 2. Measured vs. Simulated Dispersion Values

Sextupole (T/m ²)	T_{166} (m) Experiment	T_{166} (m) Simulation
0.00	2.59 ± 0.59	2.54
22.4	0.23 ± 0.77	0.67
32.9	-1.27 ± 0.93	-2.07

The R_{16} for all three cases has the same simulated value of -0.013 m, to be compared with the measured value of -0.009 ± 0.015 m. Experimental errors listed correspond to 95% confidence level. The T_{166} values match to within 20% relative error for the case where the sextupoles are turned off. The larger discrepancies for the sextupole-corrected cases are due in part to the fact that the sextupole magnets have not yet been characterized and the

field values listed are those predicted by RADIA simulations of their field profiles.

The input beam for the ELEGANT simulation was obtained by modeling the gun and linac using the particle transport code PARMELA and matching the simulated output beam to the empirical values of emittance, energy, Twiss parameters, and energy spread in Table 1. The magnetic field parameters used in ELEGANT were set to match the experimental running conditions as closely as possible, given the available calibration information for the various magnetic elements on the beam line. The transverse beam profiles predicted at the locations of the six profile monitors are shown in Fig. 3.

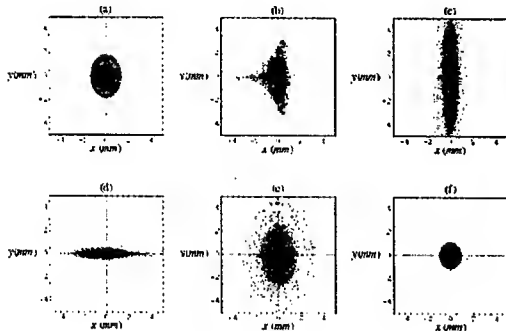


Figure 3. Beam profiles from ELEGANT simulations at locations corresponding to the six profile monitors labeled in Fig. 2: (a) Screen 5, (b) Screen 10, (c) Screen 11, (d) Screen 12, (e) Screen 13, (f) Screen 14.

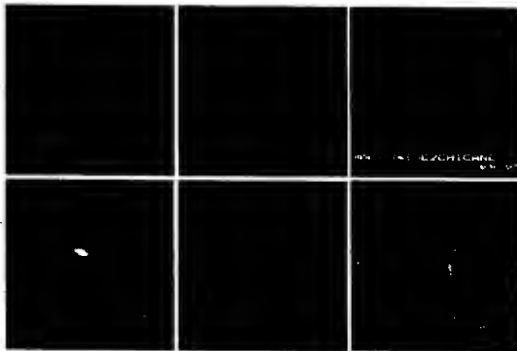


Figure 4. Matrix of images from the six profile monitors corresponding to the locations in Fig. 3.

The ELEGANT simulation successfully reproduces the experimentally observed root mean square (RMS) beam sizes on all six screens to within 30%, with the exception of screen 14, where the vertical beam size is underestimated by 70%. For a visual comparison, images of the beam captured on the various screens are shown in Fig. 4. The scales and positions of the images within the matrix correspond with those of the plots in Fig. 3.

In order to judge the suitability of this operating point for negative R_{56} compression, the ELEGANT simulation was rerun using the same lattice file but with a chirped

input beam of 1.8% RMS energy spread (obtained by setting the linac phase in the PARMELA simulation to 20° back-of-crest) and with the sextupole field strengths set appropriately for cancellation of nonlinear longitudinal dispersion (T_{566}). Plots of the longitudinal trace space and density profile of the simulated beam are shown in Fig. 5. The density plot shows a ramped beam of the sort indicated in Fig. 1 as being an ideal drive beam for plasma wake-field experiments.

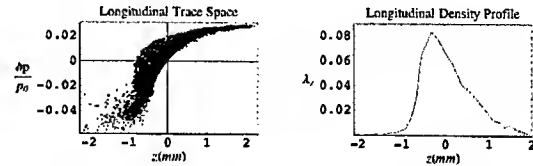


Figure 5. Ramped beam as predicted by ELEGANT simulation for the operating parameters of the present experiment.

CONCLUSIONS

The preliminary results reported above indicate that the UCLA Neptune S-Bahn beamline has been successfully operated in a configuration in which the measured beam sizes and nonlinear *horizontal* dispersion are in good agreement with simulation. The same simulation results also predict a ramped beam at the output of the S-Bahn, indicating that this would be a suitable operating point for negative R_{56} beam compression.

Following the installation and conditioning of the new Neptune photoinjector (currently in progress), coherent transition radiation (CTR) interferometry will be used to measure the final bunch length of the beam. In addition, a transverse mode deflecting cavity is currently being developed as a tool for experimental verification of beam shaping. This diagnostic method imposes upon the beam a time-dependent transverse momentum kick that is proportional to longitudinal position within the bunch. The beam's distribution in the longitudinal phase space is thereby deflected transversely so that it can be observed on a simple profile monitor [5-7].

REFERENCES

- [1] R. J. England, J. B. Rosenzweig, M. Thompson, AIP Conf. Proc. **647**, 884 (2002).
- [2] K. L. F. Bane, P. Chen, and P. B. Wilson, SLAC PUB-3662 (1985).
- [3] P. Chen, J. J. Su, J. M. Dawson, K. L. F. Bane, and P. B. Wilson, Phys. Rev. Lett. **56**, 1252 (1986).
- [4] M. Borland, APS LS-287 (2000).
- [5] G. A. Loew, O. H. Altenmueller, SLAC PUB-135 (1965).
- [6] R. H. Miller, R. F. Koontz, D. D. Tsang, IEEE Trans. Nucl. Sci. June, 804 (1965).
- [7] P. Emma, J. Frisch, P. Krejcik, SLAC PUB LCLS-TN-00-12, August (2000).

DETECTION OF WAKE FIELD USING TEST-BUNCH METHOD AT PHOTON FACTORY ADVANCED RING

T. Fujita*, Hiroshima University, Higashi-Hiroshima, 739-8526, Japan
T. Kasuga, Y. Minagawa and T. Obina, KEK, Tsukuba, 305-0801, Japan

Abstract

Curious phenomena which depend on the beam current have been appeared during injection into PF-AR. In order to get information on the wake field, a test-bunch method has been carried out: a main bunch with a large current and a test bunch with a smaller current are stored and wake field excited by the main bunch is estimated from the motion of the test bunch. Experimental results and an analytical calculation suggest that the wake field excited in rf cavities influence the injection rate. The wake field estimated by the test bunch method is compared with the calculated field and the motions of the stored and injected beam are discussed.

INTRODUCTION

PF-AR (Photon Factory Advanced Ring) is an electron storage ring dedicated to a Pulsed X-ray source. Electrons at the energy of 2.5GeV are injected in a single bunch and are accelerated up to 6.5GeV or 5.0GeV, and synchrotron radiation is delivered to users' stations. Main parameters of PF-AR at the energy of 2.5GeV are shown with symbols used in this paper in Table 1. After the completion of

Table 1: Main parameters of PF-AR

injection energy	E_0	2.5GeV
circumference	L	377m
acceleration frequency	f_{rf}	508.58MHz
harmonic number	h	640
revolution frequency	f_{rev}	794kHz
betatron tune (H/V)	ν_H/ν_V	10.15/10.21
radiation damping rate (transverse)	α_x	23/sec

the upgrading project of PF-AR [1], several phenomena are observed during injection. One of them is sudden decrease in an injection rate. Typical change of the beam current and the injection rate are shown in Fig.1. The injection rate of 1mA/sec can be achieved at a low beam current, but the rate decreases suddenly around the beam current of 35mA. After a while, the injection rate recovers a little bit but low injection rate continues up to 40mA that is a usual beam current in users' operation. The other phenomenon is an anomalous oscillation in horizontal plane observed during injection. We call the oscillation as a transverse sawtooth instability [2]. To ease the effect of instabilities during injection, the injection energy was raised to 3.0GeV

*fujita@post.kek.jp

from 2.5GeV since Oct. 2002. Although the raise of the injection energy increased the maximum stored current to 65mA, instabilities still have been appeared during injection. These phenomena suggest that the wake field excited in components of the ring affects the motion of the beam. We have tried to detect the wake field using a test-bunch method. In this paper, we report the test-bunch method and preliminary results. We also discuss the motion of the beam stored in the ring and the beam injected into the ring during injection.

THE TEST-BUNCH METHOD

In the test-bunch-method, two bunches called a "main bunch" and a "test bunch" are injected. The bunch current of the test bunch is small enough compared with that of the main bunch. When oscillation of the main bunch is excited artificially, a wake field excited in the ring affects the motion of the test bunch. From the motion of the test bunch, information of the wake field can be obtained. In this method, it is essential that only the main bunch is excited and the test bunch is not affected by the excitation.

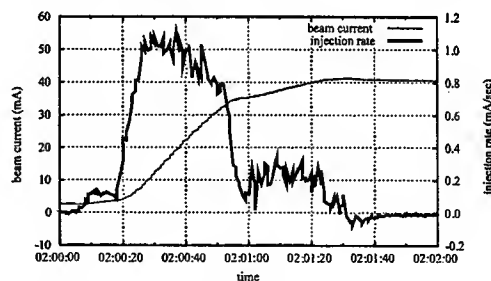


Figure 1: Typical change of beam current and injection rate during injection.

Selective excitation of bunch oscillation

The excitation of the main bunch oscillation without any effect on the test bunch is realized by an excitation signal modulated by a pulse train synchronized to the bunch revolution, however, spectrum lines are scattered in a wide frequency range. In the test-bunch method, we used only three frequency components to excite the main bunch oscillation without any effect on the test bunch as mentioned below.

At first, we define the bucket of the main bunch as the 0-th bucket, and successive buckets as 1st, 2nd and so on.

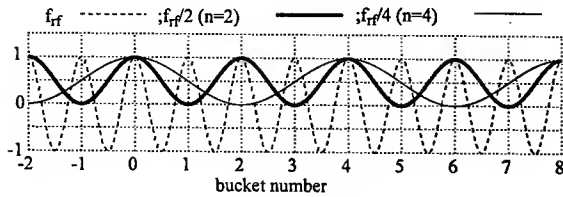


Figure 2: sinusoidal signals with DC offset at the frequency of f_{rf} divided by an integer n

Consider a sinusoidal signal at the frequency of f_{rf} divided by an integer n which is a small even factor of the harmonic number. When a DC offset is added to the signal as shown in Fig.2, and fed to the kicker a bunch at the m -th bucket is deflected. The deflection angle is given by

$$\Delta\theta \propto l \left(\frac{nc}{\omega_{rf}l} \sin \frac{\omega_{rf}l}{nc} \cos \frac{2m\pi}{n} + 1 \right), \quad (1)$$

where l is a length of the kicker and c is a speed of light. Then the signal is modulated by the betatron frequency. The betatron oscillation of bunches at the $(1+2m)$ -th $((2+4m)$ -th) bucket are not excited by the signal when $n=2$ ($n=4$), i.e., the $(n/2+nm)$ -th bunch are not excited, while the bunch at the 0-th bucket is excited.

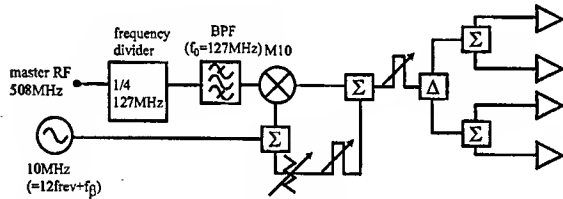


Figure 3: Block diagram of the circuit for main bunch excitation

Fig.3 is a block diagram of the main bunch exciter. The master rf signal is converted to signals with frequencies of $f_{rf}/2$, $f_{rf}/4$ or $f_{rf}/8$ and modulated by the betatron frequency. In order to correct frequency characteristics of transmission line and power amplifier and to cancel out a residual deflection due to a finite length of the kicker, we adjusted the phase and the amplitude of the lowest sideband of the excitation signal observing the betatron sideband. We obtained an isolation, which is defined as the amplitude ratio of test bunch oscillation to main bunch one, of about -40dB.

Detection of test bunch oscillation

We used a strip-line type beam position monitor with a length of 30cm to detect the oscillation of the test bunch. DBMs (Double Balanced Mixer) were used to separate the designated signal from the test bunch in mixture of the signals from the test bunch and the main bunch. The selected signal is filtered by a band-pass filter with the center frequency of 250MHz, and fed to a SA (Spectrum Analyzer).

The oscillation amplitude of each bunch was obtained from the bunch spectrum.

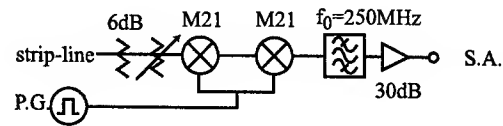


Figure 4: Detection circuit to observe the oscillation of bunches separately

EXPERIMENTAL RESULTS

A feedback damper that suppresses horizontal/vertical instabilities is indispensable for the usual operation. We cannot store the beam current larger than 15mA without the damper. We carried out test-bunch measurement at low beam current with the damper off in order to avoid effects of the damper on the test bunch. The bunch current of the main bunch and the test bunch was 2.0mA and 0.2mA respectively. We adjusted the amplitude of the main bunch oscillation to about 1.0mm adjusting the power of the excitation signal.

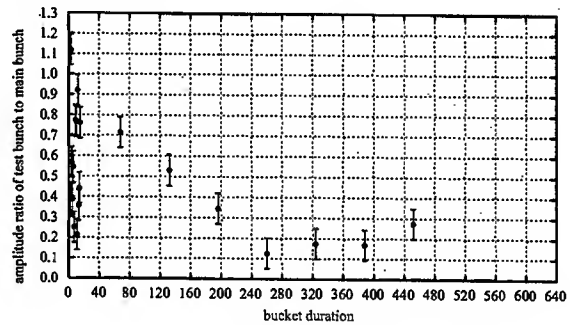


Figure 5: Result of measurement for whole the ring

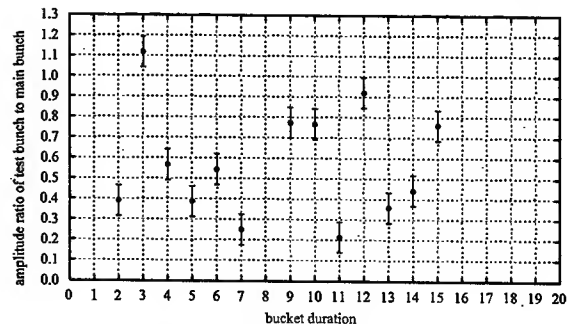


Figure 6: Result of measurement for whole 20 bunches after the main bunch

Results of measurement are shown in Fig.5 and Fig.6. Abscissa and ordinates indicate the bucket number of the test bunch and the amplitude ratio of the test bunch to

the main bunch, respectively. The larger value means the stronger wake field at the bucket of the test bunch. In Fig.5, the ratio for whole the ring is shown, and tends to decrease as a whole. In Fig.6, the ratios for 20 buckets after the main bunch are shown. The effect of the wake field is scattered about one order depending on the bucket. But, that is much larger than the measurement error. The frequency component of the wake field is supposed to be higher than the sampling frequency, which is f_{rf} , therefore no periodicity can be extracted by aliasing.

DISCUSSION

Simple analysis of test-bunch method

In the analysis, the motion of each bunch is described by a damped oscillation with an external force. A bunch feels two kinds of wake fields, one is a short range wake which vanishes in one turn, another is a long range wake which does not decay in one turn. We regarded the long range wake as a decrease in radiation damping rate. Then equations of motion are given by

$$x_m'' + \left(\frac{\nu}{R}\right)^2 x_m + 2\frac{\alpha - gq_m}{c} x_m' = \frac{\theta}{L} \sin \frac{\nu}{R} z + \frac{q_t x_t W_n}{E_0 L} \quad (2)$$

$$x_t'' + \left(\frac{\nu}{R}\right)^2 x_t + 2\frac{\alpha - gq_t}{c} x_t' = \frac{q_m x_m W_n}{E_0 L}, \quad (3)$$

where x , q , g , θ and W_n are the displacement, the bunch charge, the growth rate due to long range wake per coulomb, the deflection angle by the excitation and the wake potential normalized by the beam energy at a distance of n buckets from the main bunch to the test bunch. Subscripts m and t indicate the main bunch and the test bunch, respectively. Motion of bunches, after enough time that is longer than the radiation damping time, is harmonic. From Eqn.2 and Eqn.3, the amplitude ratio is written by

$$\frac{\hat{x}_t}{\hat{x}_m} = \frac{cq_m W_n}{4\pi E_0 \nu (\alpha - gq_t)}. \quad (4)$$

When single bunch of 10mA was stored, self-induced oscillation was observed without the external excitation signal. We get g as 1.98 (1/sec/nC). From g and the test-bunch result, W_n is obtained for each buckets.

We calculated wake potential by an electro-magnetic code MAFIA for the acceleration cavity. In PF-AR, there are 6 cavities called APS (Alternating Periodic Structure), each of which has 11 cells for acceleration and 10 cells for coupling. The calculated wake potential multiplied by 6 is consistent with that obtained from test-bunch measurement and simple analysis in a factor of 2.

Numerical simulation on injection

In order to investigate the motion of the stored beam and the injected beam, we performed a numerical simulation. In this simulation the stored beam is described by one

macro-particle with a current of 35mA, and the injected beam is described by 3 macro-particles with a current of 0.08mA. Time separation between the macroparticles is set to be 350ps which is the acceleration period of the injector LINAC. The initial amplitude of the stored beam and the injected beam at the injection point are 4mm and 20mm respectively. The feedback damper is also considered with the damping time of about 0.2ms. We used the wake potential obtained by MAFIA calculation as a short range wake, which vanishes completely after the beam rotates the ring.

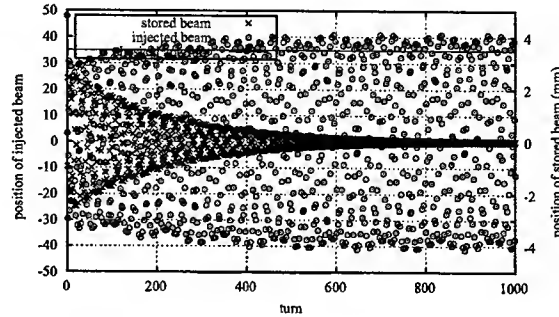


Figure 7: Result of numerical simulation assuming a wake potential

The result of the simulation is shown in Fig.7. In the figure, because the motions of all macro-particles of the injected beam are similar, the macro-particle corresponding to the stored beam and one macro-particle corresponding to the injected beam are shown. The solid line indicates physical aperture by the septum magnet. The injected beam is lost in about 200 turns.

The stored beam oscillates in horizontal plane with betatron frequency and excites wake field. Injected beam which consists of a few bunches from the LINAC with large amplitude of betatron oscillation is kicked by the wake field and lost from the ring aperture. The behavior of the injection beam depends on the initial condition of the stored beam.

SUMMARY

In this paper, we reported the test-bunch method. Devices to excite the main bunch and to observe the test bunch were worked with a good isolation. Wake field detected by the method indicated that about 20 buckets after the main bunch are affected by the wake field. From the numerical simulation, it was found that the injected beam could be lost by the wake field excited by the stored beam.

REFERENCES

- [1] K. Ebihara et.al., Present Status of PF-AR, in these proceedings
- [2] Y. Minagawa et.al., Transverse Sawtooth instability observed in Photon Factory Advanced Ring, in these proceedings

BUNCH TRANSVERSE EMITTANCE INCREASES IN ELECTRON STORAGE RINGS

J. Gao, Laboratoire de L'Accélérateur Linéaire, B.P. 34, 91898, Orsay cedex, France

Abstract

In this paper a theoretical framework to estimate the bunch transverse emittance grow up in electron storage rings due to short range transverse wakefield of the machine is established. The new equilibrium emittance equations are derived and applied to explain the experimentally obtained results in ATF damping ring.

INTRODUCTION

Required by the future e^+e^- linear colliders, damping rings are needed to provide the main linacs with extremely small transverse emittance beams. In an electron storage ring, it is observed that with the increasing bunch current not only a bunch suffers from bunch lengthening, increase in energy spread, but also transverse emittance growth. The usual explanation to the transverse emittance grow up is based on the intrabeam scattering theory [1][2][3] which has its origin from H. Bruck's idea [4]. Comparison of the emittance grow up between experimental results and those from intrabeam scattering theory shows, however, that in the vertical plane the agreement is not satisfactory [5][6]. In this paper we will draw attention to another important physical cause for the transverse emittance grow up in addition to the intrabeam scattering, i.e. the short range transverse wakefield of the machine.

EQUATION OF TRANSVERSE MOTION

The differential equation of the transverse motion of a bunch with zero transverse dimension is expressed as

$$\frac{d^2 y(s, z)}{ds^2} + \frac{2}{\tau_y c} \frac{dy(s, z)}{ds} + k(s, z)^2 y(s, z) = \frac{1}{m_0 c^2 \gamma(s, z)} e^2 N_e W_{\perp, y}(s, z) Y(s, z) \quad (1)$$

where $y(s, z)$ is the particle's transverse deviation from the closed orbit, s is the longitudinal coordinate of the particle located at the center of a bunch, z denotes a particle's longitudinal position inside the bunch with respect to the bunch center, $k(s, z)$ describes the linear lattice focusing strength, $W_{\perp, y}(s, z) = \int_{-\infty}^{\infty} \rho(z') \mathcal{W}_{\perp, y}(s, z' - z) dz'$, $\mathcal{W}_{\perp, y}(s, z)$ is the point charge wakefield, the bunch line charge density $\rho(z)$ is normalized as $\int_{-\infty}^{\infty} \rho(z') dz' = 1$, c is the velocity of light, τ_y is the synchrotron radiation damping time in transverse y direction, m_0 is the rest mass of the electron, e is the electron charge, and $Y(s, z)$ is the deviation between particles and the geometric center of vacuum chamber. Due to synchrotron radiation effect, one can treat the particles in a bunch on the same footing by multiplying $\rho(z)$ on both

sides of eq. 1 and make the integration from $-\infty$ to ∞ over z . Consequently, one gets

$$\frac{d^2 y(s)}{ds^2} + \Gamma \frac{dy(s)}{ds} + k(s)^2 y(s) = \Lambda \quad (2)$$

where $\Gamma = \frac{2}{\tau_y c}$, $\Lambda = \frac{e^2 N_e k_{\perp, y}(s) Y(s)}{m_0 c^2 \gamma l_s}$, l_s is the circumference of the storage ring, $k_{\perp, y}(s) = \int_0^{l_s} \left\{ \int_{-\infty}^{\infty} \rho(z) W_{\perp, y}(s, z) dz \right\} ds$, and $\rho(z) = \frac{1}{\sqrt{2\pi}\sigma_z} e^{-\frac{z^2}{2\sigma_z^2}}$. $Y(s)$ is a random variable due to vacuum chamber misalignment error and close orbit distortion with $\langle Y(s) \rangle = 0$ ($\langle \rangle$ denotes the average over s). Eq. 2 can be regarded as Langevin equation which governs the Brownian motion of a molecule.

To make an analogy between the movement of the transverse motion of an electron and that of a molecule, we define $P = \frac{e^2 N_e k_{\perp, y}(s)}{m_0 c^2 \gamma}$, and regard $Y(s)P$ as the particle's "velocity" random increment ($\Delta \frac{dy}{ds}$) over the distance l_s . We assume that the random variable $Y(s)$ follows Gaussian distribution:

$$f(Y(s)) = \frac{1}{\sqrt{2\pi}\sigma_Y} \exp\left(-\frac{Y(s)^2}{2\sigma_Y^2}\right) \quad (3)$$

and the velocity (u) distribution of the molecule follows Maxwellian distribution:

$$g(u) = \sqrt{\frac{m}{2\pi kT}} \exp\left(-\frac{mu^2}{2kT}\right) \quad (4)$$

where m is the molecule's mass, k is the Boltzmann constant, and T is the absolute temperature. The fact that the molecule's velocity follows Maxwellian distribution permits us to get the distribution function for Λl_s [7]:

$$\phi(\Lambda l_s) = \frac{1}{\sqrt{4\pi q l_s}} \exp\left(-\frac{\Lambda^2 l_s^2}{4q l_s}\right) \quad (5)$$

where

$$q = \Gamma \frac{kT}{m} \quad (6)$$

By comparing eq. 5 with eq. 3, one gets:

$$2\sigma_Y^2 = \frac{4q l_s}{P^2} \quad (7)$$

or

$$\frac{kT}{m} = \frac{\sigma_Y^2 P^2}{2l_s \Gamma} \quad (8)$$

Till now one can use all the analytical solutions concerning the random motion of a molecule governed by eq. 2 by a

simple substitution described in eq. 8. Under the condition, or $k^2(s) \gg \frac{\Gamma^2}{4}$ (adiabatic condition), one gets [7]:

$$\begin{aligned} \langle y^2 \rangle &= \frac{kT}{mk^2(s)} + \left(y_0^2 - \frac{kT}{mk^2(s)} \right) \\ &\times \left(\cos(k_1 s) + \frac{\Gamma}{2k_1} \sin(k_1 s) \right)^2 \exp(-\Gamma s) \\ &= \frac{\sigma_Y^2 \tau_y}{4T_0 k^2(s)} \left(\frac{e^2 N_e k_{\perp,y}(\sigma_z)}{m_0 c^2 \gamma} \right)^2 \\ &+ \left(y_0^2 - \frac{\sigma_Y^2 \tau_y}{4T_0 k^2(s)} \left(\frac{e^2 N_e k_{\perp,y}(\sigma_z)}{m_0 c^2 \gamma} \right)^2 \right) \\ &\times \left(\cos(k_1 s) + \frac{\Gamma}{2k_1} \sin(k_1 s) \right)^2 \exp(-\Gamma s) \quad (9) \end{aligned}$$

$$\begin{aligned} \langle y'^2 \rangle &= \frac{kT}{m} + \frac{k(s)}{k_1^2} \left(y_0^2 - \frac{kT}{mk^2(s)} \right) \sin^2(k_1 s) \exp(-\Gamma s) \\ &= \frac{\sigma_Y^2 \tau_y}{4T_0 k^2(s)} \left(\frac{e^2 N_e k_{\perp,y}(\sigma_z)}{m_0 c^2 \gamma} \right)^2 \\ &+ \frac{k(s)}{k_1^2} \left(y_0^2 - \frac{\sigma_Y^2 \tau_y}{4T_0 k^2(s)} \left(\frac{e^2 N_e k_{\perp,y}(\sigma_z)}{m_0 c^2 \gamma} \right)^2 \right) \\ &\times \sin^2(k_1 s) \exp(-\Gamma s) \quad (10) \end{aligned}$$

$$\langle yy' \rangle = \frac{k(s)^2}{k_1}$$

$$\begin{aligned} &\times \left(\frac{kT}{mk(s)^2} - y_0^2 \right) \left(\cos(k_1 s) + \frac{\Gamma}{2k_1} \sin(k_1 s) \right) \exp(-\Gamma s) \\ &= \frac{k(s)^2}{k_1} \left(\frac{\sigma_Y^2 \tau_y}{4T_0 k^2(s)} \left(\frac{e^2 N_e k_{\perp,y}(\sigma_z)}{m_0 c^2 \gamma} \right)^2 - y_0^2 \right) \\ &\times \left(\cos(k_1 s) + \frac{\Gamma}{2k_1} \sin(k_1 s) \right) \exp(-\Gamma s) \quad (11) \end{aligned}$$

where $k_1 = \sqrt{k(s)^2 - \frac{1}{4}\Gamma^2}$. The asymptotical values for $\langle y^2 \rangle$, $\langle y'^2 \rangle$, and $\langle yy' \rangle$ as $s \rightarrow \infty$ are easily obtained:

$$\langle y^2 \rangle = \frac{kT}{mk^2(s)} = \frac{\sigma_Y^2 \tau_y}{4T_0 k^2(s)} \left(\frac{e^2 N_e k_{\perp,y}(\sigma_z)}{m_0 c^2 \gamma} \right)^2 \quad (12)$$

$$\langle y'^2 \rangle = k^2(s) \langle y^2 \rangle = \frac{\sigma_Y^2 \tau_y}{4T_0} \left(\frac{e^2 N_e k_{\perp,y}(\sigma_z)}{m_0 c^2 \gamma} \right)^2 \quad (13)$$

$$\langle yy' \rangle = 0 \quad (14)$$

Inserting eqs. 12, 13, and 14 into the definitions of the r.m.s. emittance shown in eq. 15:

$$\epsilon_{w,y} = (\langle y^2 \rangle \langle y'^2 \rangle - \langle yy' \rangle^2)^{1/2} \quad (15)$$

one gets

$$\epsilon_{w,y} = \frac{\sigma_Y^2 \tau_y}{4T_0 k(s)} \left(\frac{e^2 N_e k_{\perp,y}(\sigma_z)}{m_0 c^2 \gamma} \right)^2 \quad (16)$$

$$\epsilon_{w,y} = \frac{\sigma_Y^2 \tau_y \langle \beta_y(s) \rangle}{4T_0} \left(\frac{e^2 N_e k_{\perp,y}(\sigma_z)}{m_0 c^2 \gamma} \right)^2 \quad (17)$$

where $\langle \beta_y(s) \rangle$ is the average beta function of the machine in y plane. Before going on further, we have to remind the reader that at the beginning of this section it is assumed that the bunch has zero transverse dimension (the bunch is represented as a soft line), in reality, however, a bunch has finite transverse dimension. A particle inside the bunch can move like a molecule in a gas due to quantum effect of synchrotron radiation. In electron storage rings, the "banana" shape of the bunch cannot be sustained due to "mixing", quite different from what happens in a linac and a hadron storage ring where there is no, or little, synchrotron radiations. Mathematically to take this fact into account, one can rewrite eq. 17 as follows

$$\epsilon_{w,y} = \frac{\sigma_Y^2 \tau_y \langle \beta_y(s) \rangle}{4T_0 \mathcal{R}_{\epsilon,y}^3} \left(\frac{e^2 N_e k_{\perp,y}(\sigma_z)}{m_0 c^2 \gamma} \right)^2 \quad (18)$$

where $\mathcal{R}_{\epsilon,y} = \epsilon_{total,y}/\epsilon_{0,y}$, $\epsilon_{total,y}$ is the final emittance at a given bunch population N_e , $\epsilon_{0,y}$ is the emittance zero current, and the cubic functional dependence on $\mathcal{R}_{\epsilon,y}$ can be regarded as an Ansatz. Finally, we find the expression for the emittance of a bunch corresponding to a given bunch population

$$\epsilon_{total,y} = \epsilon_{0,y} + \epsilon_{w,y}$$

$$= \epsilon_{0,y} + \frac{\sigma_Y^2 \tau_y \langle \beta_y(s) \rangle}{4T_0} \left(\frac{e^2 N_e k_{\perp,y}(\sigma_z)}{m_0 c^2 \gamma} \right)^2 \quad (19)$$

If we distinguish now the horizontal plane denoted by the subscript x and the vertical plane denoted by the subscript y , one gets the two emittance equations

$$\mathcal{R}_{\epsilon,x} = \frac{\epsilon_{total,x}}{\epsilon_{0,x}}$$

$$= 1 + \frac{\sigma_X^2 \tau_x \langle \beta_x(s) \rangle}{4T_0 \epsilon_{0,x} \mathcal{R}_{\epsilon,x}^3} \left(\frac{e^2 N_e k_{\perp,x}(\sigma_{z0})}{m_0 c^2 \gamma \mathcal{R}_z^\Theta} \right)^2 \quad (20)$$

$$\mathcal{R}_{\epsilon,y} = \frac{\epsilon_{total,y}}{\epsilon_{0,y}}$$

$$= 1 + \frac{\sigma_Y^2 \tau_y \langle \beta_y(s) \rangle}{4T_0 \epsilon_{0,y} \mathcal{R}_{\epsilon,y}^3} \left(\frac{e^2 N_e k_{\perp,y}(\sigma_{z0})}{m_0 c^2 \gamma \mathcal{R}_z^\Theta} \right)^2 \quad (21)$$

where σ_{z0} is the bunch length of zero current, $\mathcal{R}_z = \sigma_z/\sigma_{z0}$, and $\Theta = 0.7$, which corresponds to SPEAR scaling for transverse loss factor [8]. Since \mathcal{R}_z is also a function of N_e , it is obvious that one can start to solve eqs. 20 and 21 only when $\mathcal{R}_z(N_e)$ has been solved from the bunch lengthening equation [9].

APPLICATION TO THE ANALYSIS OF ATF DAMPING RING EXPERIMENTAL RESULTS

ATF damping ring is a machine dedicated for the feasibility studies of future e^+e^- linear colliders [10]. In this section, by applying our theory established above and neglecting intrabeam scattering effects, we try to explain the ATF damping ring experimental results [6] with the following machine parameters: $E_0 = 1.3$ GeV, $\langle \beta_x \rangle = 4.2$ m, $\langle \beta_y \rangle = 4.6$ m, $\tau_x = 18.2$ ms, $\tau_y = 29.2$ ms, $\epsilon_{x0} = 1.1 \times 10^{-9}$ mrad, $\epsilon_{y0} = 5.8 \times 10^{-11}$ mrad, and the information about the bunch lengthening with respect to N_e can be obtained either from experimental results [11][12] or from analytical results [9]. Assuming $k_{\perp,x}(\sigma_{z0}) = k_{\perp,y}(\sigma_{z0}) = 1020$ V/pC/m, for $\sigma_X = 0.42$ mm and $\sigma_Y = 0.163$ mm, by using eqs. 20 and 21 one fits the experimentally measured emittance grow ups vs the bunch population as illustrated in Figs. 1 and 2, where the experimental results correspond to the values denoted in ref. [6] as "Wire scanner 2001/2/8". It is seen clearly that both the horizontal and vertical emittances' functional dependences on the bunch population fit well with the experimental results. We stress that $\sigma_{X,Y}^2 = \sigma_{x,y,chamber}^2 + \sigma_{x,y,co}^2$, where $\sigma_{x,y,chamber}$ are the vacuum chamber misalignment errors and $\sigma_{x,y,co}$ are the closed orbit distortion errors. It is obvious that to avoid excessive emittance grow ups, both the closed orbit distortions and the vacuum chamber misalignment errors should be under careful controls with the same rigour.

To check further the validity of this theory one has to do more experiments by varying $\sigma_{X,Y}$ and to have more accurate values for $k_{\perp,x}(\sigma_{z0})$ and $k_{\perp,y}(\sigma_{z0})$.

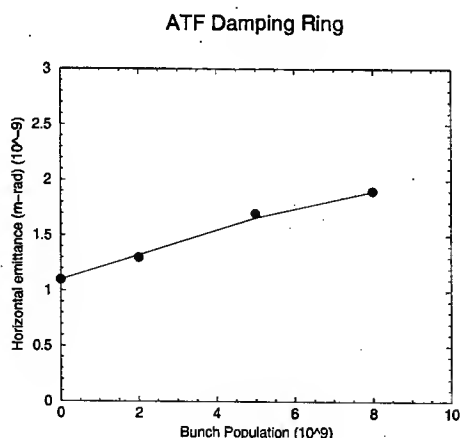


Figure 1: Horizontal emittance vs bunch population. The dots and solid line correspond to the experimental and theoretical values, respectively.

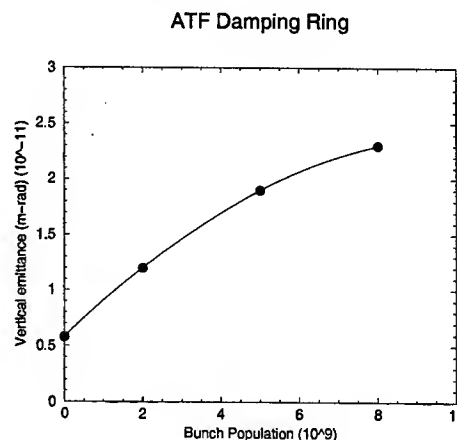


Figure 2: Vertical emittance vs bunch population. The dots and solid line correspond to the experimental and theoretical values, respectively.

CONCLUSION

In this paper we have established a theoretical framework to explain the bunch transverse emittance growth vs the bunch population in an electron storage ring. The new equilibrium emittance equations are given and applied to explain the experimental results from the ATF damping ring. More quantitative works need to be done in the future.

ACKNOWLEDGEMENT

The author thanks J. Haissinski for discussions.

REFERENCES

- [1] A. Piwinski, Proceedings of the IXth international conference on high energy accelerators, May 2-7, 1974, SLAC, p. 405.
- [2] J.D. Bjorken and S.K. Mtingwa, *Particle Accelerators*, Vol. 13 (1983), p. 115.
- [3] J. Le Duff, CERN 95-06, Vol. 2, p. 573.
- [4] H. Bruck and J. Le Duff, Proceedings of the 5th Int. Conf. on High Energy Accelerators, INFN, Frascati, Italy, 1965.
- [5] A. Piwinski, DESY 90-113, Sept. 1990.
- [6] K. Kubo, et al, KEK Preprint 2001-126, Sept. 2001.
- [7] S. Chandrasekhar, *Rev. of Modern Physics*, Vol. 15, No. 1 (1943), p. 1.
- [8] J. Gao, *Nucl. Instr. and Methods*, A491 (2002) p. 346.
- [9] J. Gao, *Nucl. Instr. and Methods*, A491 (2002) p. 1.
- [10] J. Urakawa, Proceedings of EPAC2000, Vienna, Austria (2000), p. 63.
- [11] K.L.F. Bane, et al, SLAC-AP-135, AFT-00-14, Dec. 2000.
- [12] K.L.F. Bane, et al, SLAC-PUB-8875, June 2001.

ANALYTICAL ESTIMATION OF DYNAMIC APERTURES LIMITED BY THE WIGGLERS IN STORAGE RINGS

J. Gao, Laboratoire de L'Accélérateur Linéaire, B.P. 34, 91898, Orsay cedex, France

Abstract

By applying the general dynamic aperture formulae for the multipoles in a storage ring developed in ref. [1] (J. Gao, *Nucl. Instr. and Methods A* **451** (2000), p. 545), in this paper, we give the analytical formulae for the dynamic apertures limited by the wigglers in storage rings.

INTRODUCTION

Wiggler as an insertion device finds many applications in damping rings [2], synchrotron radiation facilities [3] [4], and storage ring colliders [5]. Intrinsically, as a nonlinear device, together with the perturbations to the linear optics it brings additional limitations to the general performance of the machines, such as reducing dynamic apertures. In this paper, we will estimate in an analytical way the dynamic apertures limited by wigglers. Firstly, in section 2, we make a brief review of the beam dynamics inside a wiggler, and secondly, in sections 3 a wiggler is inserted into a storage ring as a perturbation. By applying the general dynamic aperture formulae of multipoles in a storage ring developed in ref. [1], in section 4 we derived analytical formulae of the wiggler limited dynamic aperture. Finally, in section 5 some numerical examples will be given.

PARTICLE'S MOTION INSIDE A WIGGLER

Considering a wiggler of sinusoidal magnetic field variation, one can express the wiggler's magnetic fields, which satisfies Maxwell equations, as follows:

$$B_x = \frac{k_x}{k_y} B_0 \sinh(k_x x) \sinh(k_y y) \cos(ks) \quad (1)$$

$$B_y = B_0 \cosh(k_x x) \cosh(k_y y) \cos(ks) \quad (2)$$

$$B_z = -\frac{k}{k_y} B_0 \cosh(k_x x) \sinh(k_y y) \sin(ks) \quad (3)$$

with

$$k_x^2 + k_y^2 = k^2 = \left(\frac{2\pi}{\lambda_w}\right)^2 \quad (4)$$

where B_0 is the peak sinusoidal wiggler magnetic field, λ_w is the period length of the wiggler, and x , y , s represent horizontal, vertical, and beam moving directions, respectively.

The Hamiltonian describing particle's motion can be written as [3]:

$$H_w = \frac{1}{2} (p_z^2 + (p_x - A_x \sin(ks))^2 + (p_y - A_y \sin(ks))^2) \quad (5)$$

where

$$A_x = \frac{1}{\rho_w k} \cosh(k_x x) \cosh(k_y y) \quad (6)$$

$$A_y = -\frac{k_x \sinh(k_x x) \sinh(k_y y)}{k_y \rho_w k} \quad (7)$$

and ρ_w is the radius of curvature of the wiggler peak magnetic field B_0 , and $\rho_w = E_0/ecB_0$ with E_0 being the electron energy. After making a canonical transformation to betatron variables, averaging the Hamiltonian over one period of wiggler, and expanding the hyperbolic functions to the fourth order in x and y , one gets:

$$\begin{aligned} \mathcal{H}_w = & \frac{1}{2} (p_x^2 + p_y^2) \\ & + \frac{1}{4k^2 \rho_w^2} (k_x^2 x^2 + k_y^2 y^2) + \frac{1}{12k^2 \rho_w^2} (k_x^4 x^4 + k_y^4 y^4 + 3k^2 k_x^2 x^2 y^2) \\ & - \frac{\sin(ks)}{2k \rho_w} (p_x (k_x^2 x^2 + k_y^2 y^2) - 2k^2 p_y x y) \end{aligned} \quad (8)$$

After averaging the motion over one wiggler period, one obtains the differential equations for particle's transverse motions [6]:

$$\frac{d^2 x}{ds^2} = -\frac{k_x^2}{2k^2 \rho_w^2} \left(x + \frac{2}{3} k_x^2 x^3 + k^2 x y^2 \right) \quad (9)$$

$$\frac{d^2 y}{ds^2} = -\frac{k_y^2}{2k^2 \rho_w^2} \left(y + \frac{2}{3} k_y^2 y^3 + \frac{k_x^2 k^2}{k_y^2} x^2 y \right) \quad (10)$$

Considering the wigglers are built with plane poles, one has $k_x = 0$.

WIGGLER AS AN INSERTION DEVICE IN A STORAGE RING

Now we insert a "wiggler" of only one period (or one cell) into a storage ring located at s_w . The total Hamiltonian of the ring in the vertical plane can be expressed as follows:

$$H = H_0 + \frac{1}{4\rho^2} y^2 + \frac{k_y^2}{12\rho^2} y^4 \lambda_w \sum_{i=-\infty}^{\infty} \delta(s - iL) \quad (11)$$

where H_0 is the Hamiltonian without the inserted wiggler, L is the circumference of the ring, and $k_y = k$. It is obvious that the perturbation is a delta function octupole.

Now, let's recall some useful results obtained in ref. [1] where we have studied analytically the one dimensional dynamic aperture of a storage ring described by the following Hamiltonian:

$$\mathcal{H} = \frac{p^2}{2} + \frac{K(s)}{2} x^2 + \frac{1}{3!B\rho} \frac{\partial^2 B_z}{\partial x^2} x^3 L \sum_{k=-\infty}^{\infty} \delta(s - kL)$$

$$+ \frac{1}{4!B\rho} \frac{\partial^3 B_z}{\partial x^3} x^4 L \sum_{k=-\infty}^{\infty} \delta(s - kL) + \dots \quad (12)$$

where

$$B_z = B_0(1 + xb_1 + x^2b_2 + x^3b_3 + \dots + x^{m-1}b_{m-1} + \dots) \quad (13)$$

The dynamic aperture corresponding to each multipole is given as:

$$A_{dyna,2m,x}(s) = \sqrt{2\beta_x(s)} \left(\frac{1}{m\beta_x^{2m}(s_{2m})} \right)^{\frac{1}{2(m-2)}} \times \left(\frac{\rho}{|b_{m-1}|L} \right)^{1/(m-2)} \quad (14)$$

where s_{2m} is the location of the $2m$ th multipole, $\beta_x(s)$ is the beta function in x plane, and x here stands for either horizontal or vertical plane.

Comparing eq. 11 with eq. 12, by analogy, one finds easily that:

$$\frac{b_3}{\rho} L = \frac{k_y^2 \lambda_w}{3\rho_w^2} \quad (15)$$

and the dynamic aperture limited by this one period "wiggler":

$$A_{1,y}(s) = \frac{\sqrt{\beta_y(s)}}{\beta_y(s_w)} \left(\frac{3\rho_w^2}{k_y^2 \lambda_w} \right)^{1/2} \quad (16)$$

where $\beta_y(s)$ is the unperturbed beta function. In fact, a wiggler is an insertion device which is composed of a large number of cells, say, N_w , and the wiggler length $L_w = N_w \lambda_w$. Now, the first question which follows is what the combined effect of these N_w cells will be. According to ref. [1], one has:

$$\frac{1}{A_{N_w,y}^2(s)} = \sum_{i=1}^{N_w} \frac{1}{A_{i,y}^2} = \sum_{i=1}^{N_w} \left(\frac{k_y^2}{3\rho_w^2 \beta_y(s)} \right) \beta_y^2(s_{i,w}) \frac{L_w}{N_w} \quad (17)$$

where the index i indicates different cell. When N_w is a large number, Eq. 17 can be simplified as:

$$\frac{1}{A_{N_w,y}^2(s)} = \frac{k_y^2}{3\rho_w^2 \beta_y(s)} \int_{s_{w0}-L_w/2}^{s_{w0}+L_w/2} \beta_y^2(s) ds \quad (18)$$

where s_{w0} correspond to the center of the wiggler. If the variation of the unperturbed beta function inside the wiggler is approximated as linear, one gets

$$A_{N_w,y}(s) = 3 \sqrt{\frac{\beta_y(s)(\beta_{y,2} - \beta_{y,1})}{\beta_{y,2}^3 - \beta_{y,1}^3}} \frac{\rho_w}{k_y \sqrt{L_w}} \quad (19)$$

where $\beta_{y,1}$ and $\beta_{y,2}$ correspond to the beta function values at the two extremities of the wiggler. As is well known, the inserted wiggler perturbs linear optics also, such as tune shifts and beta functions. In our specific case [7], we have $\Delta\nu_x = 0$, $\Delta\beta_x = 0$, and

$$\Delta\nu_y \approx \frac{L_w \beta_{av,y}}{8\pi \rho_w^2} \quad (20)$$

$$\frac{\Delta\beta_y}{\beta_y} \approx - \frac{L_w \beta_{av,y} \cos(2\nu_y(\pi - |\phi - \phi_w|))}{4\rho_w^2 \sin(2\pi\nu_y)} \quad (21)$$

or

$$\left(\frac{\Delta\beta_y}{\beta_y} \right)_{max} \approx |2\pi \Delta\nu_y / \sin(2\pi\nu_y)| \quad (22)$$

where $\beta_{av,y}$ is the averaged beta function within the wiggler. The fact that the tune shift and the beta function inside the wiggler vary in a complex way makes us assume that the octupole like cells of the wiggler are *independent* from one to another, and permits us to arrive at the expression in eq. 17.

The second question which follows is how about the total dynamic aperture of the storage ring including many wigglers and other nonlinear components. Assuming that the dynamic aperture of the ring without the wigglers' effects is A_y and that there are M wigglers to be inserted inside the ring at different places, one has the total dynamic aperture expressed as:

$$A_{total,y}(s) = \frac{1}{\sqrt{\frac{1}{A_y(s)^2} + \sum_{j=1}^M \frac{1}{A_{j,w,y}(s)^2}}} \quad (23)$$

where $A_{j,w,y}$ denotes the dynamic aperture limited by the j th wiggler.

NUMERICAL EXAMPLE

Now we take TESLA damping ring for example with permanent magnet wigglers [2], where one has $E_0 = 5\text{GeV}$, $B_0 = 1.68\text{T}$, $\lambda_w = 0.4\text{m}$, $N_w = 12$, $\beta_{y,1} = 9\text{m}$, $\beta_{y,2} = 15\text{m}$, and total wiggler number $M = 45$. Without considering the dynamic aperture limited by other nonlinear components, by applying eqs. 19 and 23, one finds that $A_{total,y}(s_{w0}) = 21\text{mm}$. Recalling the gap of the wiggler [2], $g = 25\text{mm}$. It should be noted that eqs. 19 and 23 correspond to ideal wigglers. If the octupole components of a real wiggler is measured to be a factor of "g" larger than that of the ideal wiggler, the values of the dynamic apertures of real wigglers should be those evaluated by eqs. 19 and 23 divided by \sqrt{g} .

CONCLUSION

In this paper we have developed the analytical dynamic aperture formulae limited by wigglers in storage rings, which are very efficient and powerful in designing and operating damping rings and synchrotron radiation facilities.

ACKNOWLEDGEMENTS

The author thanks T. Garvey and P. Bambade for their encouragements.

REFERENCES

- [1] J. Gao, "Analytical estimation of the dynamic apertures of circular accelerators", *Nucl Instr. and Methods*, **A451** (3) (2000), p. 545.

- [2] W. Decking, "Optical layout of the TESLA 5 GeV damping ring", TESLA report 2001-11.
- [3] A. Ropert, "Lattice and emittances", CERN 98-04, p. 91.
- [4] T. Lee, et al., "Analysis of the effects superconducting wiggler on beam dynamics in storage rings", Proceedings of EPAC2000, Vienna, Austria, p. 1030.
- [5] J.M. Jowett, "Emittance control with wigglers", LEP Note 389, 1982.
- [6] A. Fedorova, et al., "Nonlinear beam dynamics and effects of wigglers", Proceedings of EPAC2000, Vienna, Austria, p. 2325.
- [7] M. Katoh and Y. Kamiya, "Effect of insertion devices on beam parameters", Proceedings of PAC87, p. 437.

LATTICE DESIGN OF SAGA SYNCHROTRON LIGHT SOURCE

Y. Iwasaki[#], S. Koda, T. Tomimasu, Saga Synchrotron Light Source, Tosu, 841-0002, Japan

H. Ohgaki, IAE, Kyoto University, Gokasho, Kyoto 611-0011, Japan

H. Toyokawa, M. Yasumoto, National Institute of Advanced Industrial Science and Technology,

Umezono 1-1, Tsukuba, Ibaraki 305-8568, Japan

Y. Yamatsu, T. Kitsuka, Y. Hashiguchi, Y. Ochiai,

Saga Prefectural Government, Saga, 840-8570, Japan

Abstract

The SAGA Synchrotron Light Source is a compact third generation synchrotron light source with a 1.4GeV electron storage ring, and being constructed in Tosu City, Saga prefecture Japan. A distributed dispersion system, the dispersion function is non-zero in long straight section, is adopted for the lattice design to make the ring to be compact. At the typical working point (5.796, 1.825) the emittance without insertions is 25nm-rad and the beam size at the middle of the long straight section is about 0.58 mm in horizontal and 0.13mm in vertical (10% coupling is assumed). One of merits of distributed dispersion system is reduction of sextupole strength required for chromaticity correction. Consequently, a large dynamic aperture can be obtained. We have performed beam dynamics studies by using TRACY2 to estimate tolerable magnetic errors and magnetic misalignments and found that the designed lattice has an enough dynamical aperture to operate the ring.

INTRODUCTION

SAGA Synchrotron Light Source is the middle-scale light source with 262MeV linac and 1.4GeV storage ring [1]. The construction started from the fall of 2001. We will start the commissioning in October 2004. Active X CA based control system will be applied from the commissioning phase [2]. The light source will be opened March 2005. Since the budget and space is tightly restricted, it is reasonable to design the ring with existing accelerator technologies.

The lattice was designed to satisfy the maximum number of user requirements. The number of beamline is more than twenty. A high brightness and wide range of wavelength (from infrared [3] to hard X-ray [4]) of the synchrotron light is required. So, the energy of the stored electron beam and circumstance of the electron storage ring was chosen as 1.4GeV and 75m respectively. We adopted eight symmetries to the electron storage ring to install more than twenty beamlines. Each cell has two bending magnet (DB). Among eight long straight sections, two sections are used for the injection and RF cavity, and six sections are used for insertion devices. In order to make a high brightness synchrotron light, we first examined the Chasman-Green (DBA) type lattice. Optimizing the arrangement of the magnets and strengths of quadrupoles, we found a working point of which

natural emittance was lower than 30nm-rad. However, we also found that the natural chromaticity was large and the small dispersion in the chromaticity correction section at that working point. Furthermore the interference with sextupole magnet and beamline was problem. Therefore, a distributed dispersion system, the dispersion function is non-zero in insertion device section, was examined, because several distributed dispersion type machines have been designed and operated with low chromaticities and low emittances [5].

In this paper, we will describe the design of the distributed dispersion lattice for SAGA-SL and the beam dynamics studies on it.

LATTICE DESIGN

The design of the distributed dispersion lattice has been done as following procedure: At first, we roughly defined the physical sizes of magnet (bending, quadrupole and sextupole). The number of magnet was determined to that two family quadrupole for the tune control and 1 family quadrupole for dispersion control just as Chasman-Green lattice. Two family sextupole were also employed for the chromaticity correction. The next step, we arranged them to keep the length of the long straight section as long as possible. Then, a linear optics calculation was performed to evaluate the machine function. To optimise the machine function, above procedure was iteratively repeated and we obtained acceptable arrangement. After that, the magnets were designed to generate an enough magnetic field with proper accuracies. Then, a fine tune of the magnet arrangement and the linear and non-linear calculations were performed. TRACY2 [6] was used for these calculations. Figure 1 shows the lattice structure of the half cell and the machine parameters at a typical working point are listed in Table 1. It is noted that the horizontal and the vertical beta functions of below 20 m are achieved. However, the dispersion function reaches to be 0.6 m at the long straight section. This will cause the emittance growth from the insertion devices. Preliminary calculations show that the 7.5 T superconducting wiggler enlarge the emittance to 47nm-rad, which is still small enough for the SAGA users.

The dynamical aperture with the bare lattice is shown in Figure 2 and one can see that the dynamical aperture is quite large for the distributed dispersion lattice. It could be emphasized that the natural emittance is 25.1nm-rad

[#]iwasaki@saga-ls.jp

Table 1: Machine parameters and magnets strengths
*10% coupling was assumed

Energy[GeV]	1.4
Circumference[m]	75.6
Superperiod	8
Bending Radius[m]	3.2
Betatron Tunes[ν_x, ν_y]	5.796, 1.825
Synchrotron Tune	0.0093
Momentum Compaction	0.0134
Energy Spread	6.7×10^{-4}
Longitudinal Damping Time[ms]	3.346
Horizontal Damping Time[ms]	6.563
Vertical Damping Time[ms]	6.649
Natural Chromaticity[ξ_x, ξ_y]	-6.54, -9.64
Natural Emittance[nm-rad]	25.1
Horizontal Beam size[mm]	0.58
Vertical Beam size[mm]*	0.13
QF[T/m]	25.1
QD[T/m]	-24.4
QFA[T/m]	18.4
SF[T/m ²]	80.5
SD[T/m ²]	-115

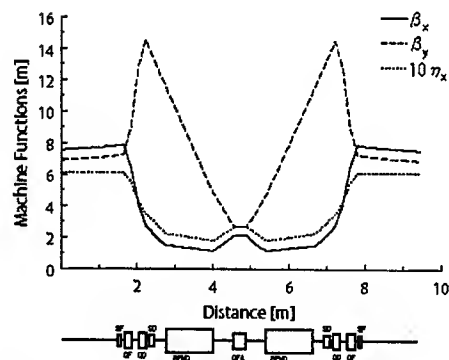


Figure 1: Machine functions and magnets arrangement.

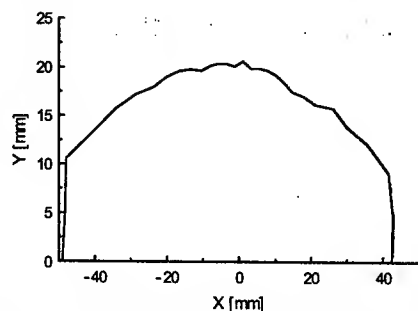


Figure 2: Dynamical aperture of the bare lattice.

We also calculated the beam lifetime using ZAP [7]. The required lifetime is 5 hours with 300mA stored current. The lifetime at the working point is dominated by Touschek half-life and 15hours lifetime was obtained at 500kV RF voltage.

MISALIGNMENT AND MULTIPOLES

The designed lattice satisfies several demands on the SAGA-LS. However, the effect of misalignment of the magnets should be evaluated, because we will use the usual alignment technique. The maximum transverse tilt of the bends of 0.2mrad and the maximum transverse shift of each quadrupoles of 0.2mm were achieved without special alignment technique. Moreover, magnetic field imperfection, dipole strength error of 2×10^{-4} , quadrupole error of 1×10^{-3} , and sextupole strength error of 3×10^{-3} , should be taken into account for the COD evaluation. TRACY2 was used for the evaluation of the COD. The optimum steering position was also investigated for the COD correction at the same time. Figure 3 shows the COD distribution calculated by TRACY2. We can see the maximum 4 mm in horizontal and 10 mm in vertical CODs. Using the 40 steering magnets, 32 combined steerings in the sextupoles and 8 normal steerings, the COD can be suppressed less than $10 \mu\text{m}$ both in horizontal and vertical. At the COD correction, maximum 1mm-rad

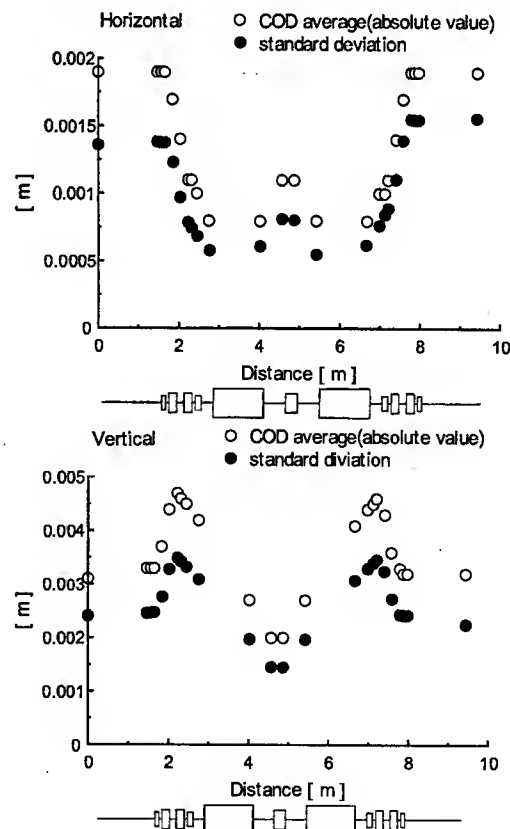


Figure 3: Horizontal and vertical COD distribution.

kick angle was assumed. Figure 4 shows the dynamical aperture after the COD correction. The dynamic aperture is clearly recovered with the COD correction.

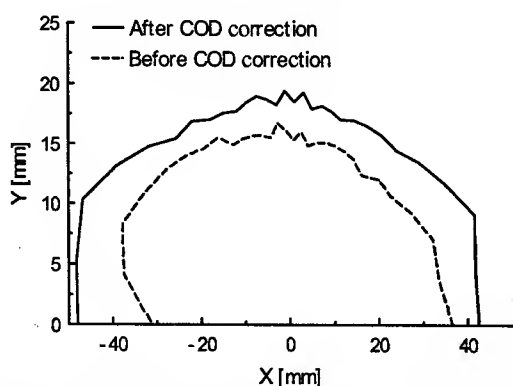


Figure 4: Dynamical aperture before COD correction and after COD corrections.

Under the realistic condition, the multipole effect will be shrink the dynamical aperture. We can define n -th multipole component β_n as the coefficient of Talyor expansion for the field on the mid-plane. The vertical components of the multipole field α_n can also be expressed in the cylindrical coordinate. The relation between them is express as $\beta_n = \alpha_n/r^n$, where r is the distance from the central orbit. By using cylindrical coordinate, the condition to the multipole can be expressed simply and convenient to compare to the experimental data. Table 4 illustrates the multipole conditions for α_n .

BEND	$\alpha_n/\alpha_0 < 2 \times 10^{-4}$
QUAD	$\alpha_n/\alpha_1 < 1 \times 10^{-3}$
SEXTU	$\alpha_n/\alpha_2 < 3 \times 10^{-3}$

Table 4: Multipole conditions expressed in the ratio to the main component.

We examined the multipole effect to the dynamic aperture by using TRACY2. Figure 5 shows the result of the calculation with the multipole conditions illustrated in the table 4. It is clear that the distortion of the dynamic aperture is appeared in the horizontal axis. However, the survived dynamical aperture it is still large enough for the ring operation. The required magnetic construction accuracy is achievable with a standard magnet manufacturing technique. Therefore, we can conclude that the designed lattice has an enough multipole tolerance for the operation.

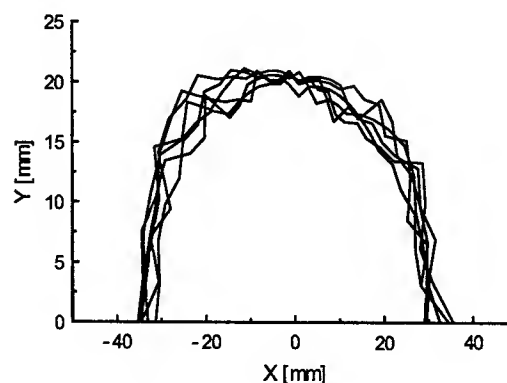


Figure5: Dynamical aperture including systematic multipoles

CONCLUSION

We have designed the lattice of SAGA Synchrotron Light Source electron storage ring. A distributed dispersion system is adopted to make the ring be compact. Optimising the magnet arrangement and searching working point, the natural emittance is obtained to be 25 nm-rad with a bare lattice. We found that the dynamic aperture is still large with achievable misalignments and multipole components.

Since a 7.5T superconducting wiggler will be installed in near future, preliminary calculations have been performed to evaluate the effect of the wiggler. The result shows the emittance grows up to 47nm-rad and it is small enough for user requirements in this facility. The dynamical aperture is also recovered by a tune correction which is executed by quadrupoles located both end of the wiggler.

The authors would like to thank Y. Oku and M. Kuroda (Kawasaki Heavy Industries co. Ltd.,) for their helpful comments on this work.

REFERENCES

- [1] T. Tomimasu et al., Proc. of APAC01, Beijing (2001) p.340.
- [2] H. Ohgaki et al., this Proceedings
- [3] M. Yasumoto et al., Proc. of APAC01, Beijing (2001) p.349.
- [4] Y. Kondo, et al., RFSE of SAGA Univ. Vol. 31, No.2, December, 200.
- [5] M. Eriksson, Novel Techniques Used in MAX II, Proc., EPAC 96, Barcelona (1996) p.73
- [6] J. Bengtsson, E. Forest and H. Nishimura, "Tracy Users Manual", unpublished.
- [7] M. Zisman, et al., "ZAP User's Manual", LBL-21270

LINEAR AND NONLINEAR OPTICS STUDIES IN THE ANKA STORAGE RING

A.-S. Müller, I. Birkel, E. Huttel, F. Pérez, M. Pont, R. Rossmanith,
Institute for Synchrotron Radiation, Forschungszentrum Karlsruhe,
P.O. Box 3640, D-76021 Karlsruhe, Germany

Abstract

The ANKA electron storage ring operates in the energy range from 0.5 to 2.5 GeV. In order to improve machine performance a precise modelling of linear and nonlinear optics is mandatory. At the maximum energy, the dipole magnets show multipolar components due to saturation effects. A new optics model should take higher order fields of the installed magnets into account. In the framework of the model upgrade, extensive optics studies have been done, including a study of the beta function beating and a measurement of higher order chromaticity. Furthermore an energy calibration of the storage ring was done.

INTRODUCTION

ANKA is an electron storage ring for synchrotron radiation located at Forschungszentrum Karlsruhe, Germany (see for example [1]). It is operated in the energy range from 0.5 (injection) to 2.5 GeV (user operation). For a better understanding of the machine the linear and nonlinear optics model was revised. Information about the linear optics can be extracted from "classical" measurements of the β -function and from measurements of the orbit response matrix. At top energy the dipole magnets are close to saturation which causes nonlinear field components that should be accounted for in a model. Field maps of the higher orders do not exist for the exact beam energy, only for slightly lower excitation currents where the saturation is already 7% [2]. Beam based measurements must therefore be used to extract the effective multipolar fields acting on the beam.

β -FUNCTIONS, GRADIENTS AND THE ORBIT RESPONSE MATRIX

Optics Determination from the Response Matrix

The measured orbit response matrix (ORM), reflecting the change in orbit at beam position monitors (BPMs) with changes in the excitation of orbit corrector dipoles, contains a multitude of precise data points imprinted with the focusing structure of the storage ring. The LOCO program [3] provides an elegant way to extract information about the linear optics of the storage ring from the ORM.

Among the fit parameters in LOCO is the strength of the individual corrector kick. The individual strength for all horizontal and vertical corrector magnets resulting from the ORM analysis are shown in Fig. 1 for the same setting of the excitation current. Because of (geometrical) interferences with the ANKA storage ring vacuum chamber, eight

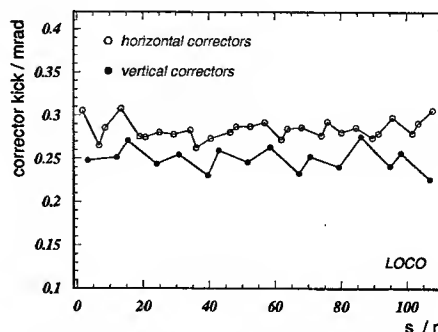


Figure 1: Strength of horizontal and vertical orbit corrector magnets for the individual correctors at the same excitation current. The alternating strength of the vertical correctors is clearly visible.

of the 16 vertical orbit correctors have a different layout. This results in a loss of about 10% of the steering capability for every second corrector. As can be seen in Fig. 1 this alternating structure is nicely reproduced by LOCO. Also the results showed slightly larger kicks for a given excitation than previously assumed. A new corrector calibration based on recent field measurements and the inclusion of fringe fields in the corrector dipoles explain this effect (see listing of average corrector kicks in Tab. 1). Including the new corrector calibration in the ANKA control system has improved the speed of convergence of the orbit correction.

The normalised quadrupole gradients averaged within each of the five families found by LOCO are displayed in Fig. 2. The error bar is a measure for the scatter of the individual gradients within a family. The gradients derived from magnetic measurements under the assumption of the nominal beam energy of 2.500 GeV and for a lower energy (2.477 GeV) are also shown. With respect to the nominal energy gradients, the values extracted from the ORM are systematically increased by about 1 %. This could be explained if the true beam energy was about 1 % lower than its nominal value: The gradients from magnetic measure-

corrector	old	new	meas.
horizontal	0.19	0.26	0.28
vertical	0.21	0.25	0.25

Table 1: Average corrector kicks for a given excitation current for old calibration, new calibration with inclusion of fringe field in the field integral and the effective kicks found by LOCO. All corrector kicks are given in mrad.

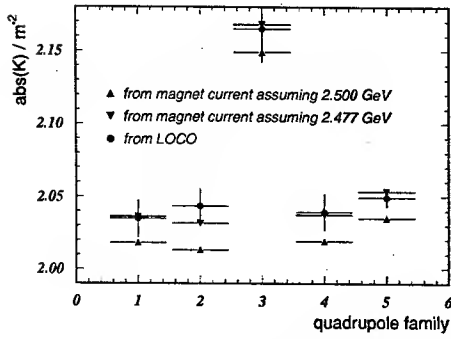


Figure 2: Normalised quadrupole gradients for the five families. Gradients derived from magnetic measurements are shown for a beam energy of 2.500 GeV, for the (true) beam energy of 2.477 GeV as well as those obtained with the LOCO program [3]. For the latter, the error bar is a measure for the scatter of the individual gradients within a family.

ments for the lower energy show a much better agreement with the ORM results. To verify this deviation in beam energy an energy calibration was done using resonant depolarisation (RDP) [4]. As a measure for polarisation change, the Touschek loss rate dependence on electron beam polarisation was used [5, 6]. For RDP, the beam energy is determined by slowly varying the frequency of the depolariser field with time over a given frequency range. If a depolarisation occurs during such a scan, the loss rate will increase suddenly and the beam energy can be determined from the corresponding frequency. The true beam energy could be confirmed to be (2.4774 ± 0.0001) GeV which is in good agreement with the findings from LOCO.

Figure 3 shows an example for depolarisation scans at different RF frequencies (and therefore energies). Using

$$\alpha_c = - \frac{f_{RF} - f_{RF}^c}{f_{RF}^c} \frac{E_c}{E - E_c}$$

where f_{RF} is the RF frequency, E the beam energy and the index c stands for energy and frequency at the central orbit, allows to extract an estimate for the momentum compaction factor α_c from the measurements at different RF

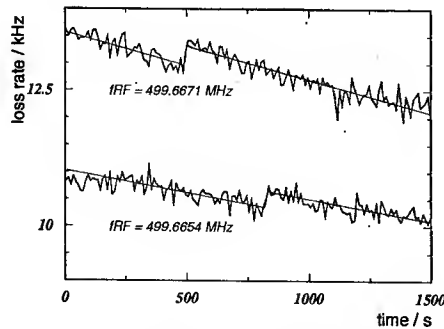


Figure 3: Loss monitor counting rate during two scans of the depolariser frequency at different RF frequencies. The shift in depolarising frequency and therefore in energy is clearly visible

frequencies: $\alpha_c = (7.1 \pm 0.1) \cdot 10^{-3}$. The quoted uncertainty is based on a frequency uncertainty of 10 Hz. This value is in good agreement with the theoretical value obtained from the MAD program [7] with the LOCO derived linear optics model of $7.2 \cdot 10^{-3}$.

Measurement of the β -Function

The β -function is measured by detecting the shift of the betatron tune, $\Delta Q_{x,y}$, resulting from a change in the strength of an individual quadrupole magnet, Δk . Alternatively to this *local* measurement, the β -function can also be derived from the change in the strength of an entire quadrupole family (*global* measurement). Far from half integer and integer resonances and for small changes in tune, the β -function can be estimated from the well known relation

$$\beta_{x,y} \approx \pm 4\pi \Delta Q_{x,y} / \Delta k$$

Figure 4 shows the horizontal and vertical β -function as a function of longitudinal coordinate in one sector. The symbols show local and global measurements, the curves represent the optics model. Global and local measurements are in reasonable agreement. Residual differences between the measurements and the theoretical model could arise from small tune shifts caused by not fully compensated changes in the closed orbit: if the change in quadrupole strength alters the orbit in sextupole magnets, a change in tune results.

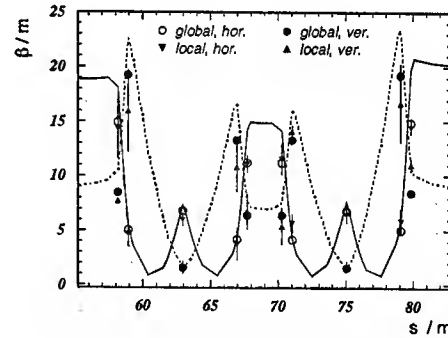


Figure 4: Horizontal and vertical β -function as a function of longitudinal coordinate in sector 3. The symbols show local (gradient variation of individual quadrupole) and global (gradient variation of quadrupole family) measurements. The curves represent the optics model derived from LOCO [3].

CHROMATICITY MEASUREMENTS AND MODELLING

To gain information about nonlinear magnetic field components, the horizontal and vertical tunes are measured as a function of a momentum deviation produced by appropriate changes in the RF frequency. A parabolic fit yields the effective linear and nonlinear chromaticities according to

$$Q_{x,y} = Q_{0,x,y} + Q'_{x,y} \left(\frac{\Delta p}{p} \right) + \frac{1}{2} Q''_{x,y} \left(\frac{\Delta p}{p} \right)^2$$

Figures 5 and 6 show examples of such measurements for different sextupole currents. The solid curves are fits of the previously mentioned parameterisation to the measurements. It is easily visible that a modelling up to the second order is sufficient to describe the data. As a first approach the strengths of the existing sextupole magnets are fitted to reproduce the measured parameters. For this the STATIC command of the MAD program [7] is used. The results of these fits can be seen as dashed curves in Fig. 5. Obviously the behaviour cannot be understood from sextupolar fields only. The measurements seem to suggest the presence of octupolar fields. Those octupolar components could for example be generated by a decapole component in the bending dipole field with an offset. To test the assumption of the presence of octupoles, virtual nonlinear elements were inserted in the machine model in the form of thin multipoles at entry and exit of each dipole magnet. The strength of those virtual octupoles was then adapted to fit the measured data. The results are displayed as dash-dotted curves in Fig. 5 which fit the measurements nicely. The virtual octupoles at both ends of a dipole were found to be of approximately equal size and opposite sign.

For a change in sextupole strength (Figures 5 and 6) the first order chromaticity is changed whereas the second order chromaticity stays almost the same. This is a further confirmation of the presence of higher order nonlinear components.

SUMMARY

Detailed studies have shown that at the highest magnet currents the beam energy is lower by about 1% than expected. This was diagnosed indirectly by extracting the normalised quadrupole gradient using LOCO to analyse measurements

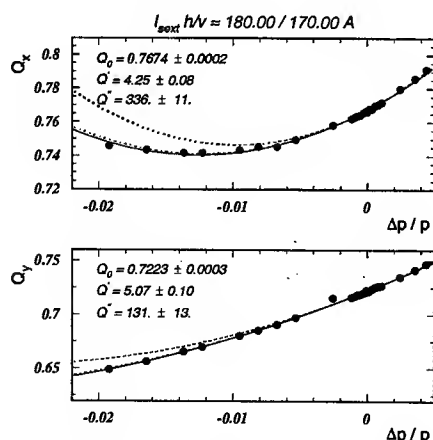


Figure 5: Tune as a function of momentum deviation. The upper plot shows the horizontal, the lower plot the vertical tune. The solid curves are parabolic fits whose parameters are quoted. The dashed curves are best fits with sextupoles only, the dash-dotted curves that almost coincide with the parameterisations are best fits with sextupoles and assumed octupolar components.

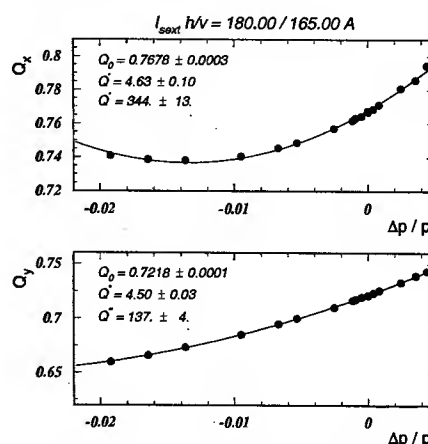


Figure 6: Tune as a function of momentum deviation. The upper plot shows the horizontal, the lower plot the vertical tune. The solid curves are parabolic fits whose parameters are quoted. In contrast to Fig. 5 the vertical sextupole strength was modified. It is clearly visible, that whereas the first order chromaticity changes, the second order stays almost constant.

of the orbit response matrix, and confirmed independently by resonant depolarisation. A closer investigation of the chromaticities indicates that higher order multipole components, possibly related to saturation effects in the dipole magnets, may be the reason.

ACKNOWLEDGEMENTS

Sincere thanks to all who have contributed to the results presented here. Especially we would like to thank M. Böge, S.C. Leeman and J. Wenninger for interesting and instructive discussions and H. Schieler and M. Schmelling for kindly providing the scintillator loss monitors for our energy studies.

REFERENCES

- [1] D. Einfeld et al. Commissioning Results of ANKA. In *Proceedings of PAC2001*.
- [2] M. Pont et al. Magnetic Measurements of the ANKA Storage Ring Magnets. In *Proceedings of PAC99*.
- [3] J. Safranek. Experimental Determination of Storage Ring Optics Using Orbit Response Measurements. In *NIM A388*, pages 27–36, 1997.
- [4] I. Birkel et al. Energy Calibration of ANKA. ANKA-AP Note 2003-03, Forschungszentrum Karlsruhe, ISS.
- [5] P. Kuske et al. High Precision Determination of the Energy at BESSY II. In *Proceedings of EPAC2000*.
- [6] S.C. Leeman et al. Precise Beam Energy Calibration at the SLS Storage Ring. In *Proceedings of EPAC2000*.
- [7] H. Grote and F. C. Iselin. The MAD Program, User's Reference Manual. SL Note 90-13 (AP) (Rev. 4), CERN, March 1995.

BEAM SIZE AND BUNCH LENGTH MEASUREMENTS AT THE ANKA STORAGE RING

F.Perez, I. Birkel, E.Huttel, A.S.Müller and M.Pont

Institut für Synchrotron Radiation - ANKA

Forschungszentrum Karlsruhe, P.O. Box 3640, D-76021, Karlsruhe, Germany

Abstract

ANKA is an electron storage ring working at a nominal energy of 2.5 GeV. The beam is injected at 500 MeV into the storage ring and ramped to the final energy. The beam size and bunch length have been measured in the range from 500 MeV to 2.5 GeV. The beam size measurements were performed with two synchrotron light monitors, one in a dispersion region and the other in a zero dispersion one. The bunch length was measured using the bunch spectrum with an Annular Electrode and a spectrum analyser up to 8 GHz [1]. The bunch length as a function of the momentum compaction factor, the growth rate of a longitudinal instability as a function of beam current and the Intrabeam Scattering have been analysed.

INTRODUCTION

Bunch length and beam size have been measured between 500 MeV and 2.5 GeV; for different bunch currents. The filling pattern has been always the same, 25 bunches filled out of 184 possible.

From the analysis of the results we have seen that the bunch length is mainly determined by the presence of a longitudinal instability that increases the energy spread of the beam below 2.5 GeV.

The beam size measurements were not fully satisfactory since that longitudinal excitation at lower energies, which could not be avoided, is hiding any trace of Intrabeam Scattering or Microwave Instabilities.

BUNCH LENGTH

The bunch length has been measured using the bunch spectrum up to 8 GHz coming from an Annular Electrode [1]. The system has to be calibrated to a reference low current bunch length, which is assumed to be the natural bunch length. We have calibrated the system with 0.04 mA per bunch (1 mA in 25 bunches) at 2.5 GeV, where the beam is completely stable, the energy spread is the natural one and neither Intrabeam Scattering nor Microwave Instabilities are present.

Natural Bunch Length

With 1 mA in 25 bunches and a constant RF voltage, the synchrotron frequency has been measured as a function of the energy, it is shown in figure 1.

By fitting the curve to:

$$f_s = f_o \sqrt{\frac{\alpha h \cos \phi_s}{2\pi} \frac{eV_{RF}}{E}} \quad (1)$$

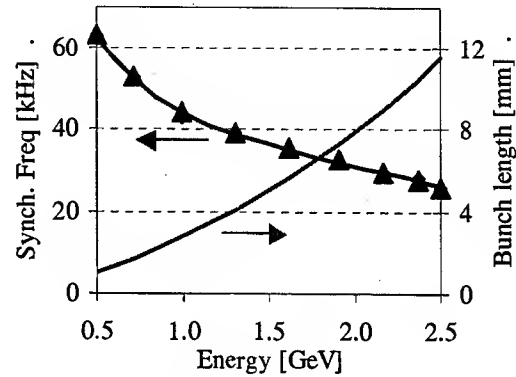


Figure 1: Synchrotron frequency (measurement: points, and fit: line) and bunch length calculation.

Where f_s is the synchrotron frequency, f_o the revolution frequency, α is the momentum compaction factor, ϕ_s is the synchrotron phase, V_{RF} the RF voltage and E the energy, the momentum compaction factor is found to be:

$$\alpha = 0.0070 \pm 0.0004$$

This is in good agreement with the optics model of the ANKA storage ring [2]. The natural bunch length can be then calculated:

$$\sigma_o = \frac{\alpha c}{2\pi f_s} \frac{\sigma_E}{E} \quad (2)$$

Where σ_o is the natural bunch length, c is the light speed and σ_E is the energy spread.

The natural bunch length as a function of energy is shown as well in figure 1. The natural bunch length at 2.5 GeV is 11.5 mm.

Measurement Method

The measurement is done by recording the RF frequency harmonics of the bunch spectrum, the Fourier transform of it is then related to the bunch length in the time domain. Assuming a Gaussian distribution, one only needs to evaluate the spectrum at two frequencies.

In order to get an absolute measurement it is necessary to have a reference or calibration point, for which a beam of 1 mA current at 2.5 GeV was used.

The procedure is, first measure the amplitude of two (or more, for statistics) harmonics of the RF frequency (f_n, f_1) at the reference point $(P_n - P_1)_0$ and use this measurement as a calibration factor. Then, measure the same set of frequencies in any other condition $(P_n - P_1)$, i.e. different bunch current, beam energy, RF voltage or the machine

optics. We can then get the bunch length from the relative change as follows [1]:

$$\sigma_L = \sqrt{\frac{(P_n - P_1)_o - (P_n - P_1)}{171.4 (f_n^2 - f_1^2)} + \sigma_o^2} \quad (3)$$

Where P_n and P_1 are the amplitude of the spectrum in dBm at the frequencies f_n and f_1 in Hz. Subindex "o" means the values for the reference bunch length. Figure 2 shows a typical spectrum of the beam, with markers at the harmonics of the RF frequency.

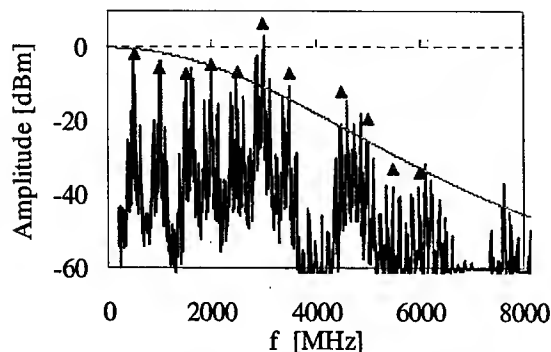


Figure 2: Beam spectrum. Markers point out the harmonics of the RF frequency.

As an example, figure 3 shows the bunch length as a function of the momentum compaction factor, for different optics with negative dispersion in the straight sections.

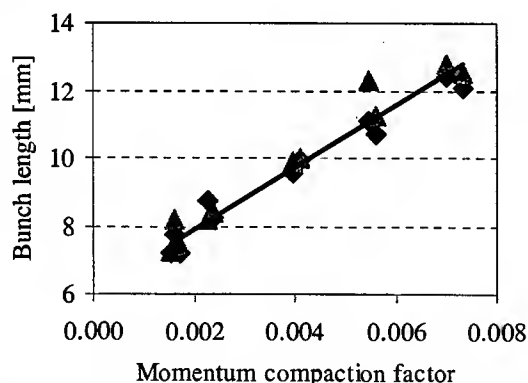


Figure 3: Bunch length as a function of the momentum compaction factor

In these measurement f_1 is 1 GHz and f_n is taken at 3.5 and 5.5 GHz (points). The bunch length is then calculated as an average of these values (line). The measurement was repeated twice with the same results.

Longitudinal Instability

By measuring the bunch length as a function of the energy and the current we have determined the threshold of a longitudinal instability created by one high order mode in the RF cavities.

In figure 4, the bunch length as a function of the energy for a 1mA beam current is shown. One can observe that above 1 GeV the bunch length collapses to the theoretical prediction of the natural bunch length, i.e. the beam is longitudinally stable.

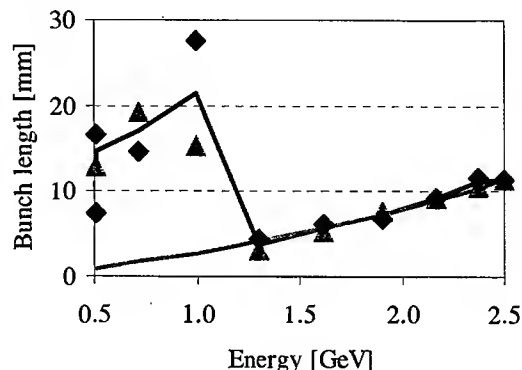


Figure 4: Bunch length as a function of beam energy for a 1 mA beam.

By increasing the beam current, the energy at which the bunch length collapses to the natural one increases, always following:

$$\alpha_{\text{HOM}} < \alpha_{\text{Damping}} \quad (4)$$

Where α_{HOM} is the growth rate of the instability and α_{Damping} is the damping rate of the machine.

By calculating the damping rate for each energy, one can derive the growth rate of the instability as a function of the beam current, shown in figure 5.

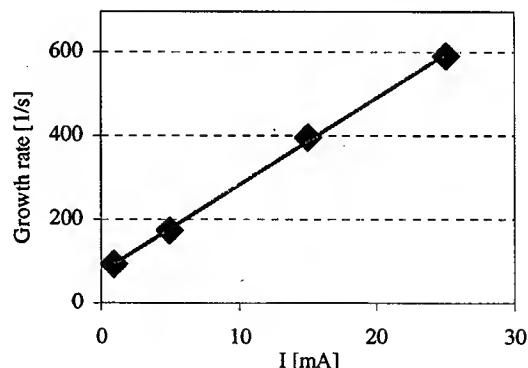


Figure 5: Growth rate of the longitudinal instability as a function of the beam current.

As can be seen the growth rate increases linearly with current, as expected. The extrapolation of the linear fit to zero current ($\alpha_{\text{HOM}} = 74.5 \text{ s}^{-1}$) also indicates that the beam would be unstable always at 500 MeV ($\alpha_{\text{Damping}} = 5.4 \text{ s}^{-1}$).

Another information extracted from the measurement of figure 4 is that at low energies, when the beam is longitudinal unstable, the values of the bunch length show a high spread. To analyse that, we have recorded the

bunch length as a function of time by sitting on one RF harmonic with span zero and sweep time of 2 seconds. The extracted bunch length is shown in figure 6.

One can see that the bunch length is oscillating between 10 and 18 mm. The instability is "unstable", meaning that it does not reach an equilibrium. A similar effect has also been observed at the SPEAR ring [3].

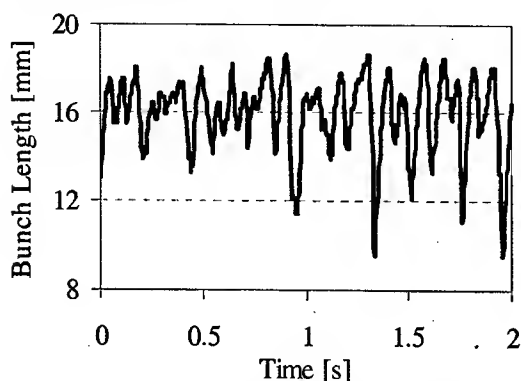


Figure 6: Bunch length vs. time of a 15 mA beam excited by a longitudinal mode at 500 MeV.

BEAM SIZE

An attempt to measure the beam size as a function of current and energy has been done in order to determine the role of the Intrabeam Scattering and the Microwave Instability at low energy.

Two beam line monitors using the visible part of the spectrum have been used. One is located in a non-dispersive section and the other in a dispersive one.

The measurements done with the monitor in the dispersive section are completely random and could not be fitted. This can be explained by the behaviour of the beam in the presence of the longitudinal instability. As shown in the figure 6, the bunch length is oscillating since the energy spread of the beam is as well oscillating. In the dispersive monitor the beam size has a contribution of the dispersion times the energy spread, so the beam size is oscillating as the energy spread. This effect does in fact suppress (or hide) any Microwave Instability that could appear.

On the other hand the monitor in the non-dispersive section is not affected by these oscillations. So we tried to use this one to analyse the effect of the Intrabeam Scattering at low energy.

Intrabeam Scattering

The Intrabeam Scattering has been calculated with the code ZAP [4] for different currents per bunch as a function of the energy, from 500 MeV to 2.5 GeV.

The results are shown in the figure 7, together with the calculated emittances obtained from the measured beam sizes, figure 8. A problem with the calibration of the system did force us to normalise the data to fit with the emittance found by the optics analysis at 2.5 GeV.

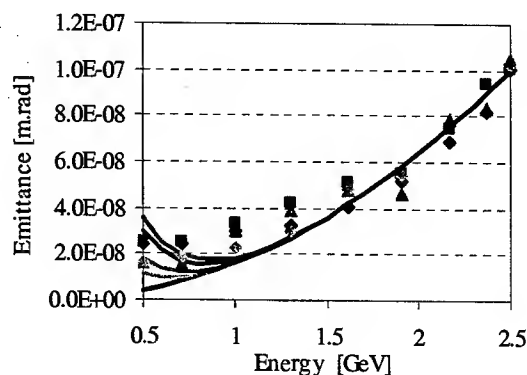


Figure 7: Intrabeam scattering calculations (lines) and emittances calculated from beam size measurements (points). For 0.04 (pink), 0.2 (red), 1 (violet) and 2 (blue) mA per bunch. Black line: natural emittance.

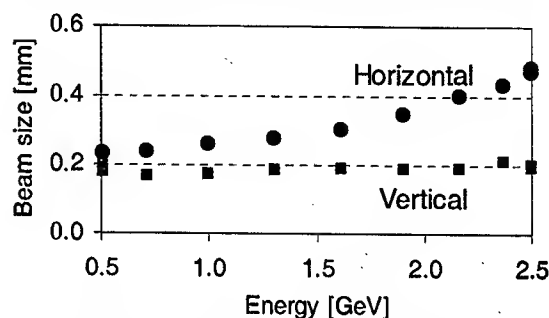


Figure 8: Beam size as a function of the energy for a 2 mA per bunch beam (50 mA in 25 bunches).

As can be seen from the graph, after normalisation, the measured emittances fit quite well the nominal ones for energies over 1.8 GeV. But at lower energies they tend to be higher than the natural ones.

On the other hand the Intrabeam Scattering should not affect the emittance for energies over 1.2 GeV in the range of the measurements.

In conclusion, even if the longitudinal instability should not affect the measurement done at this monitor (with non dispersion), it seems to affect the transverse equilibrium of the beam. Not plausible explanation has been found until now.

REFERENCES

- [1] Z.Greenwald et al., „Bunch length measurement using bunch spectrum“, Proc. of IEEE PAC, San Francisco (1991) p.1246.
- [2] A.S.Müller et al. "Linear and non linear studies in the ANKA storage ring", these proceedings.
- [3] C.Limborg, J.Sebe. "Measurement and simulations of longitudinal relaxation oscillations induced by HOMs", Proceedings PAC 1999, New York, p.3104..
- [4] Zisman,M.S., Chattopadhyay,S., Bisognano,J.J., ZAP User's Manual, LBL-21270 UC-28, December 1986

SINGLE-BUNCH INJECTION SYSTEM FOR THE LNLS BOOSTER INJECTOR

S.R. Marques[#], H.J. Onisto, P. F. Tavares, LNLS, Campinas, Brazil, SP 13083-100

Abstract

A system was developed at LNLS to perform bunch cleaning in the booster synchrotron injector to satisfy the requests for single-bunch runs either for time-resolved experiments or machine studies. This system eliminates all but one electron bunch through the excitation of a horizontal betatron resonance. In this process it is necessary to switch off the RF excitation signal for less than 2.10 ns ($1/f_{RF}$) to obtain a single-bunch. This fast switching is achieved through the utilization of a double balanced mixer. The switched excitation signal is amplified and applied to a stripline kicker. A PECL timing card supplies the gating signal, synchronized to the f_{RF} , which (negatively) modulates the excitation carrier. A local processor card and an FPGA interfacing board provide the bunch cleaner with seamless integration to the storage ring control system, which controls the parameters of the process, namely: the carrier power and the fine gating time. The system performance and operational results are presented.

INTRODUCTION

The LNLS synchrotron light source [1] is composed of a 120-MeV linear accelerator, a 500-MeV booster synchrotron injector and a 1.37-GeV storage ring.

The RF frequency of both storage ring and booster is 476.066 MHz and the booster harmonic number is 54.

The electron gun produces 200 ns current pulses that fill the entire booster during the injection process at a 0.17 Hz rate. In each booster cycle, about 5 mA are injected in the storage ring, therefore, in the multi-bunch mode, a 250 mA accumulation usually takes five minutes.

We realized that producing the single-bunch mode by eliminating undesired bunches at the booster [2] would be easier and less costly than modifying the LINAC electron gun pulser.

SYSTEM DESCRIPTION

A DSP C6711¹ evaluation board is used to manage the system internal circuits and integrate it with the LNLS control system. A card based on a XILINX FPGA (Spartan family model XC2S50E) provides digital integration between the internal modules and DSP board.

In fact, the booster "bunch cleaner" or the "bunch killer" is one of the RF front-ends that the DSP-FPGA back-end controls in this instrument. There is another front-end that measures the storage ring filling-pattern (also reported in these proceedings).

An external RF generator (Fluke 6061A) provides the

RF carrier signal that is applied directly to the double balanced mixer (DBM). The DBM employed was the Minicircuits rms-30.

A homemade PECL programmable divider was developed to produce a signal with 8.816 MHz, which is the booster revolution frequency. This card has also a programmable delay generator with 20 ps resolution and rms jitter inferior to 5 ps. This last feature is very useful to align the blanking on the carrier with the RF bucket, which contains the bunch to be preserved.

The fast DBM aperture pulse (800 ps FWHM) is obtained with a simple PECL digital circuit through the delay introduced by a transmission line. Figure 1 shows the block diagram of this circuit and the Figure 2 shows the block diagram of the instrument.

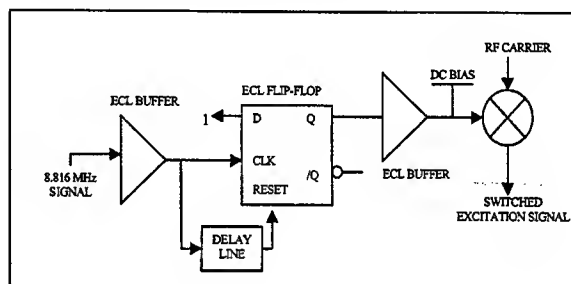


Figure 1 – Block diagram of the DBM aperture circuit

A programmable attenuator placed after the DBM is used to adjust the output power level and turns the excitation off when multi-bunch injection is desired.

PRACTICAL DETAILS

We had some previous knowledge about DBMs operated with fast pulses when we started to work on the single-bunch mode. It was a natural choice to use the DBM as a fast switch in order to save some development time.

After some empirical work to match the IF input of the DBM, the initial tests showed that it was possible to switch the DBM fast enough to preserve only one bunch.

Once the instrument was installed in the booster, we noticed that about 3 seconds of betatron excitation were necessary to kill the undesired bunches, so the duration of the injection cycles increased from 6 to 9 seconds.

In an attempt to obtain a shorter duration for the single-bunch injection cycles, the excitation power was increased from 1 W to 5 W. The result showed that the isolation of this DBM becomes the limiting factor at this power level. By increasing the excitation power, instead of decreasing the single-bunch purification time, we could

[#]sergio@lnls.br

observe that the main bunch preservation was negatively affected, therefore we decided to maintain the system operating with 1 W RF power amplifiers at the expense of the cycle time.

The bunches are spaced by 2.1 ns intervals, however, in

The undesired electron bunches are knocked out from the booster through excitation of a horizontal betatron resonance line. The lower sidebands measured in f_{RF} (476.066 MHz) are at 2.056 MHz (f_H) and 1.410 MHz (f_V), and are related to the horizontal and vertical tunes,

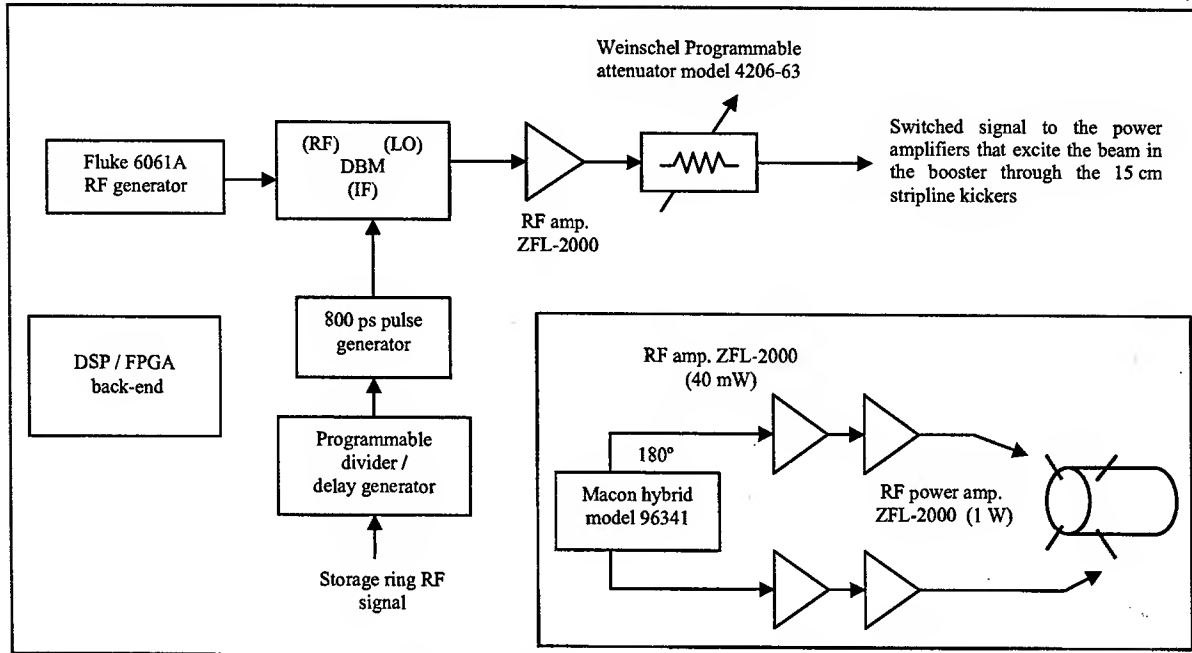


Figure 2: Block diagram of the bunch cleaner.

order to preserve a single-bunch, fast pulses (800 ps) are necessary to switch the DBM. This is due the filter effect produced by the cables and devices, which are placed after the mixer. Figure 3 shows the signal after crossing the programmable attenuator and some meters of coaxial cable.

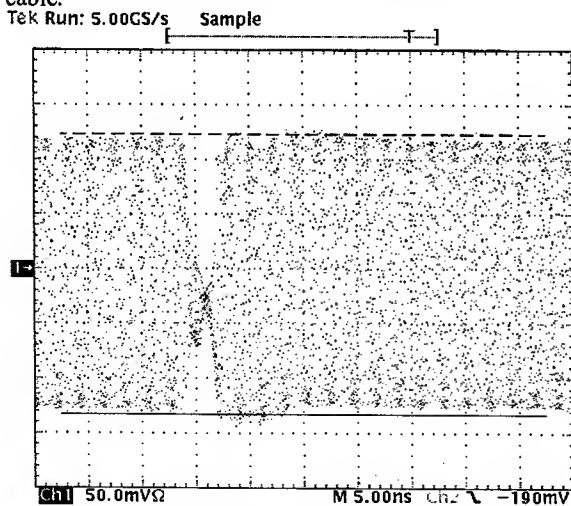


Figure 3 - Excitation signal after crossing the programmable attenuator and some meters of coaxial cable. The valley at this point is larger than 800 ps. (50 mV / division, 5 ns / division).

respectively. The chosen excitation frequency (f_{EX}) is 474.010 MHz; $f_{EX} = f_{RF} - f_H$.

RESULTS

Figure 4 shows the signal from a stripline pick-up in the booster after about 3 seconds of resonant excitation. The revolution period of the booster is 113 ns.

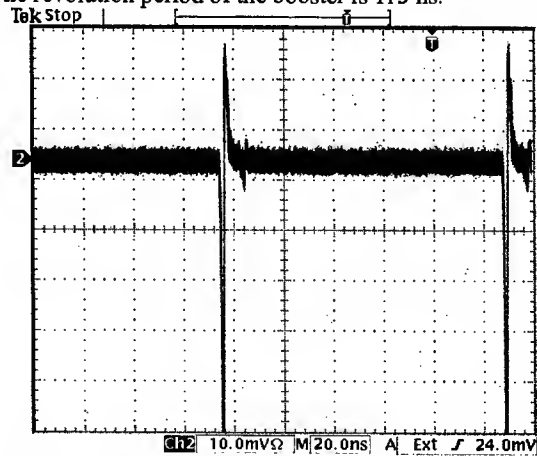


Figure 4 - Signal from a stripline pick-up in the booster 3 seconds after the beam had been injected. We determined that the small signal after the pulse is due to a reflection. (10 mV / division, 20 ns / division).

The duration of the single-bunch injection depends on the LINAC conditions. Typically it takes about one hour to reach 15 mA. We have not observed instabilities which showed us the upper limit of the single-bunch storage current. The limitation seems to be the lifetime, which is about 6 hours @ 10 mA / 1.37-GeV.

Figure 5 shows a typical signal from a stripline pick-up in the storage ring with a single-bunch beam stored.

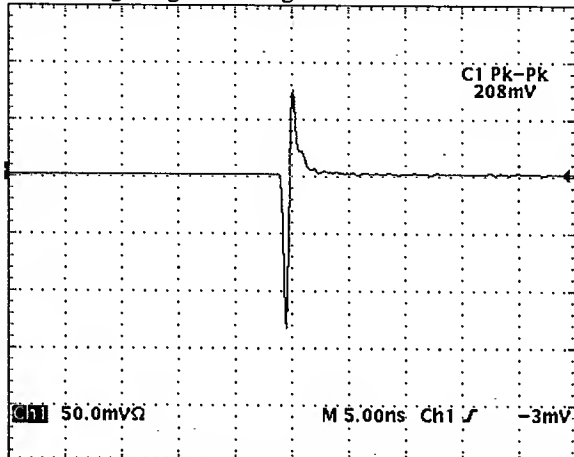


Figure 5 – Typical signal from a stripline pick-up in the storage ring. The accumulated current was about 4 mA. (50 mV / division, 5 ns / division).

The use of a DBM as a fast switch proved to be a good method to provide coarse cleaning in the booster injector, and electrical measurements such as the one shown above indicate a purity factor better than 2×10^3 [3]. In order to improve the purity factor to the $10^5 - 10^6$ range, a bunch fine cleaning system can be designed and installed in the storage ring. Probably this system will be based on the same principle: betatron resonant excitation, switched or not. The shift in the betatron frequency for bunches with different charges [4], enables either a fine cleaning in the storage ring at 500-MeV before the energy ramp or the maintenance of excitation on at 1.37-GeV during users' runs.

The single-bunch beam was provided for users for 2 weeks last March. Three different beam lines utilized synchrotron light [5] [6] [7], among them, we can mention a very innovative experiment using synchrotron excitation in a sample of ultra-cold atoms. In this experiment, neutral cesium atoms were spatially confined into a magneto-optical trap. The purity achieved was enough for all the users to perform their TOF (time of flight) spectrum based experiments.

CONCLUSIONS

The LNLS purification system was developed and installed in the booster synchrotron injector in a relatively short period of time (about 4 months). The results showed us that the purity factor achieved (2×10^3) could be improved by either using a fast switch with better isolation or with a single-bunch fine cleaning system in the storage ring. The objective of providing the users with single-bunch beams for TOF experiments was achieved successfully.

ACKNOWLEDGEMENTS

The authors are in debt with Dr. A.N. de Brito and the TGM beam line staff for the help with the photon counting experiment. We also want to acknowledge L.C. Jahnelt for the software development and all the others involved with the single-bunch run, mainly E. Gilmar L.S. from the synchrotron beam lines instrumentation group. We also express our thanks to C.R. Scorzato for the interesting discussions about using mixers as switches.

REFERENCES

- [1] P. Tavares et al., "Commissioning of the LNLS 500-MeV booster synchrotron", PAC'2001, Chicago, June 2001, p. 2701.
- [2] T. Obina et al., "A new purification method for single bunch operation at the photon factory storage ring", PAC'1999, New York, March 1999, p. 2310.
- [3] We have also performed preliminary photon counting experiments aimed at an optical determination of the purity factor.
- [4] N.S. Sereno, "Bunch cleaning strategies and experiments at the advanced photon source", PAC'1999, New York, March 1999, p. 2322.
- [5] L.H. Coutinho et al., "First results on synchrotron radiation spectroscopic studies in laser cooled atoms", XXVI ENFMC, Caxambu, May 2003.
- [6] I. Iga et al., private communication.
- [7] M.L.M. Rocco et al., private communication.

POLARIZED H⁻ ION SOURCE PERFORMANCE DURING THE 2003 RHIC RUN*

James Alessi, Anatoli Zelenski, Brian Briscoe, O. Gould, Ahovi Kponou, Vincent LoDestro,
Deepak Raparia, John Ritter (BNL);
Viktor Klenov, Sergei Kokhanovski, Valeri Zubets (INR, Moscow)

Abstract

The performance of the RHIC Optically-Pumped Polarized H⁻ Ion Source (OPPIS) for the 2003 run in AGS and RHIC is reviewed. The OPPIS met the RHIC requirement for the beam intensity with the reliable delivery of ~0.5 mA polarized H⁻ ion current in 400 microsecond pulses (maximum current was 1.5 mA). The beam intensity after the 200 MeV linac was $5-6 \times 10^{11}$ H⁻/pulse, which exceeded present RHIC program requirements, even after considerable controlled beam scraping in the Booster to reduce the 6-D emittance in the AGS. Magnetic field shape optimization at the source ionizer cell entrance greatly reduced the extraction high-voltage discharge current in the crossed electric and magnetic fields. As a result, reliable spark free operation was achieved at 7 Hz repetition rate. Polarization optimization studies have resulted in $82 \pm 2\%$ beam polarization as measured in a 200 MeV polarimeter.

INTRODUCTION

The OPPIS has been operating since early January, 2003, for RHIC polarized beam setup and commissioning, followed directly by a RHIC spin physics run. Therefore, we are now nearing the end of ~4½ months of continuous running of the source. During this time, source reliability has been very good. The intensity can easily exceed the requirement for RHIC, so the source is typically operating at ~400-500 µA, which is less than the maximum output current. Polarization is typically 75-80%. An ~8 hour weekly maintenance period has been required for the source, but one can be flexible in the scheduling of the maintenance, so it can be done either along with other machine maintenance, or during a long RHIC store. This maintenance has primarily been on the ECR primary proton source, while laser systems and vapor cells have been trouble free.

OPPIS SOURCE

The OPPIS is shown schematically in Fig. 1. This source was developed in a collaboration between Brookhaven, KEK, INR (Moscow), and TRIUMF. It is based on components from the KEK OPPIS, was upgraded at TRIUMF for high current operation, shipped to BNL in the fall of 1999, and has undergone

considerable further optimization at BNL. The source has a 115 cm long superconducting solenoid with three separately adjustable coils. An ECR source operating at 29 GHz, ~0.8 kW, sits in the solenoid in a resonant field region of 10 kG. It produces the primary proton beam of ~80 mA at an energy of ~3 keV, with a multi-aperture extraction system (120 holes). Also located in the solenoid, in a field of 27 kG, is a Rb vapor cell. This vapor is polarized via optical pumping using circular polarized light from a 1 kW, flashlamp pumped Cr:LiSAF laser. Protons are converted to polarized hydrogen atoms via pickup of a polarized electron from the Rb. These 3 keV atoms are then converted to H⁻ by electron pickup in a Na vapor jet cell, located in a separate solenoidal field of 1.4 kG. The entire Na jet assembly is biased to a voltage of -32 kV, so the H⁻ ions are accelerated to a final total energy of 35 keV while leaving the source, for injection into the RFQ. Details on the source can be found in [1].

A new 35 keV low energy beam transport (LEBT) was designed to allow injection into the existing RFQ without interfering with high intensity, unpolarized beam operations, while preserving polarization and giving the desired vertical spin alignment. The 35 keV beam from OPPIS passes through a pulsed dipole, so one is able to interleave at ~7 Hz rep rate polarized and high current unpolarized beam pulses before injection into an RFQ. (High current pulses go to an isotope production facility at the end of linac). Transmission from the polarized source to the end of the linac is typically ~50%. One is able to monitor beam polarization at 200 MeV with both p-carbon and p-deuteron polarimeters. When polarized beam is injected into Booster at ~0.25 Hz, a second source pulse is sent to the 200 MeV polarimeter for continuous online monitoring of polarization. The design and performance of this new injection line is described in [2,3].

The control system allows one to produce source pulses in an arbitrary spin sequence. For example, bunches in one RHIC ring are filled with the sequence ++---++-, and bunches in the other ring are filled as +-+--+-. Also, it is convenient that one can produce unpolarized beam pulses with no change in beam parameters by merely inhibiting the laser pulses.

*Work performed under Contract Number DE-AC02-98CH10886 with the auspices of the US Department of Energy.

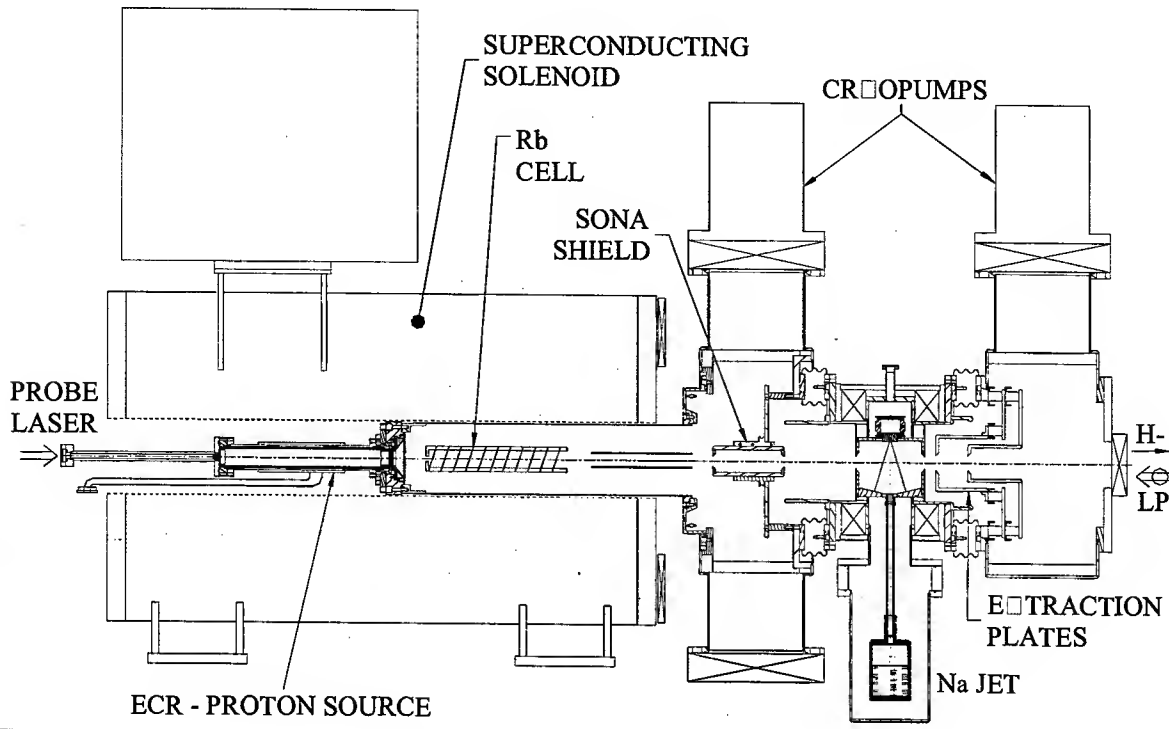


Figure 1: Schematic of the OPPIS source.

OPPIS PERFORMANCE

The source performance has been very good. The ~ 0.5 mA current that we are typically running is quite a bit less than what we can achieve when ECR power, vapor cell temperatures, etc. are all at their peak values, but this current satisfies the program requirements while reducing demands on the source. Indeed, the current is high enough that 80-90% of the current is scraped in a controlled fashion in the Booster in order to reduce both the transverse and longitudinal emittance of the beam in the AGS. This smaller emittance results in less depolarization in the AGS.

With the long continuous runs for RHIC setup/physics, much of the development effort has gone towards refinements to improve long term stability, reliability, and maintainability. Some of the improvements have happened during the course of the run.

Laser System

The 1 kW, flashlamp pumped Cr:LiSAF laser has operated maintenance free for the entire 4.5 month period. The Rb vapor thickness and polarization is measured by the Faraday rotation technique. The measurement provides a continuous polarization confirmation signal for the spin direction pattern of bunches injected into RHIC.

Auxiliary Solenoid Coil

It had been noticed that there was a sensitivity of extractor voltage holding to the precise positioning of the main superconducting solenoid coil. In order to allow an

independent control of this sensitivity to the detailed magnetic field shape in the extraction region, a room temperature coil was added at the end of the superconducting solenoid. This 40-turn pancake solenoid (2 turn, 20 layers) has proved very effective in eliminating sparking of the 32 keV extraction voltage. The correction coil field direction is opposite to the superconducting solenoid field. It helps to reduce significantly the superconducting solenoid stray field at large radii (~ 10 cm). Magnetic field calculations suggest that one is eliminating a region of crossed E and B fields at these large radii, where there was a tendency for a glow discharge to be sustained. The drain current on the extractor power supply can be reduced from ~ 400 mA when the coil is off, to essentially zero with the coil at ~ 130 A.

The coil also allows one to control the Sona transition position, which has resulted in smaller longitudinal field gradient. For maximum polarization, this gradient must be less than 0.5 G/cm at the zero crossing point. With the correction coil the gradient was reduced to less than 0.15 G/cm.

ECR Source Performance

The ECR source operates at 29 GHz, ~ 0.8 kW, and produces the primary proton beam of ~ 80 mA at an energy of ~ 3 keV, with a 120 aperture extraction system. The source has no hexapolar field, and the discharge chamber of the source has a quartz liner. This source has evolved from its original configuration, in which it was operated cw. Since we require only very low duty factor, pulsed operation of the ECR has been explored. A $\sim 30\%$

enhancement in output can be observed in pulsed operation, and the gas flow from the source can be reduced. In addition, the ratio of atomic to molecular ions from the ECR was improved in pulsed operation (resulting in higher beam polarization). An additional enhancement in performance comes from running with a slight admixture (a few percent) of oxygen with the hydrogen feed. Starting with the optimized conditions of a newly cleaned and installed ECR source, however, one observed a reduction in the pulsed output over time, and so the source would periodically be switched back to cw mode for a "re-conditioning". This has only limited effectiveness, and there has been a 30-60% reduction in output on about a 1 week time scale. Since the source output exceeds our requirements for RHIC, we start with the current cut back from the maximum achievable, by reducing the Rb vapor cell thickness below its optimum. As the ECR output degrades, we make up for this by increasing the Rb thickness. After ~7 days, we can no longer compensate for the reduced ECR output, and have to remove and clean the ECR (~8 hour maintenance, which is scheduled to fit with either a machine maintenance, or during a long RHIC store). The reduction in output seems to be coming primarily from a gradual contamination of the inner quartz wall of the ECR chamber, and much of it seems to be sputtered Mo coming back from the extraction grids. Most recently, we have found some improvement in stability by operating the ECR with a cw power of ~ 500 W, which is bumped up to ~ 750 W during beam time to enhance the output current.

Reducing H_2^+ ions from the ECR

We have found that there is some reduction in H^- polarization coming from the H_2^+ ion component extracted from the ECR along with the H^+ . When these molecular ions break up, with half the 3 keV H^+ energy, they can be ionized in the Na cell, resulting in a 33.5 keV

H^- component along with the 35 keV H^- beam. This lower energy component has low polarization. It has been shown both in simulations and experimentally that under many conditions the LEBT tune will match both energy components into the RFQ, resulting in a reduced beam polarization.

We have managed to increase the rejection of the unwanted lower energy ions by replacing a magnetic quadrupole triplet at the exit of the source by an einzel lens, operating in the decelerating mode. Also, with careful setting of the voltages on the 3-gap extraction electrodes, the lower energy ions can be rejected further. These changes have resulted in a suppression in the transport line of H^- ions coming from H_2^+ by almost an order of magnitude. In addition, as mentioned earlier, H_2^+ output from the ECR is reduced in pulsed operation, and in dc operation an O_2 admixture reduces the molecular ions.

REFERENCES

- [1] A. Zelenski, J. Alessi, B. Briscoe, G. Dutto, H. Huang, A. Kponou, S. Kokhanovski, V. Klenov, A. Lehrach, P. Levy, V. LoDestro, Y. Mori, M. Okamura, D. Raparia, J. Ritter, T. Takeuchi, G. Wight, V. Zoubets, *Rev. Sci. Instrum.* **73** (2002) 888.
- [2] J. Alessi, B. Briscoe, O. Gould, A. Kponou, V. LoDestro, D. Raparia, J. Ritter, A. Zelenski, V. Klenov, S. Kokhanovski, V. Zoubets, M. Okamura, *Proceedings of the 2002 Linear Accelerator Conference*, August 19-23, 2002, (Gyeongju, S. Korea).
- [3] J. Alessi, M. Okamura, D. Raparia, T. Toser, P. Levy, A. Zelenski, T. Takeuchi, Y. Mori, *Proceedings 1999 Particle Accel. Conf.*, New York (1999) 1964.

THE SPARC PROJECT: A HIGH BRIGHTNESS ELECTRON BEAM SOURCE AT LNF TO DRIVE A SASE-FEL EXPERIMENT

D.Alesini, S.Bertolucci, M.E.Biagini, C.Biscari, R.Boni, M.Boscolo, M.Castellano, A.Clozza, G.Di Pirro, A.Drago, A.Esposito, M.Ferrario, V.Fusco, A.Gallo, A.Ghigo, S.Guiducci, M.Incurvati, C.Ligi, F.Marcellini, M.Migliorati, C.Milardi, L.Palumbo, L.Pellegrino, M.Preger, P.Raimondi, R.Ricci, C.Sanelli, M.Serio, F.Sgamma, B.Spataro, A.Stecchi, A.Stella, F.Tazzioli, C.Vaccarezza, M.Vescovi, C.Vicario, M.Zobov, *INFN-Frascati*

F.Alessandria, A.Bacci, I.Boscolo, F.Broggi, S.Cialdi, C.DeMartinis, D.Giove, C.Maroli, V.Petrillo, M.Romè, L.Serafini, *INFN-Milano*

D.Levi, M.Mattioli, G.Medici, *INFN-Roma1*

L.Catani, E.Chiadroni, S.Tazzari, *INFN-Roma2*

R.Bartolini, F.Ciocci, G.Dattoli, A.Doria, F.Flora, G.P.Gallerano, L.Giannessi, E.Giovenale, G.Messina, L.Mezi, P.L.Ottaviani, L.Picardi, M.Quattromini, A.Renieri, C.Ronsivalle, *ENEA-Frascati*

A.Cianchi, A.D'Angelo, R.Di Salvo, A.Fantini, D.Moricciani, C.Schaerf, *Università Roma Tor Vergata*

J.B. Rosenzweig, *UCLA - Dept. of Physics and Astronomy*

Abstract

The Project SPARC (Sorgente Pulsata e Amplificata di Radiazione Coerente), proposed by a collaboration among ENEA-INFN-CNR-Università di Roma Tor Vergata-INFN-ST, was recently funded by the Italian Government. The aim of the project is to promote an R&D activity oriented to the development of a coherent ultra-brilliant X-ray source in Italy (SPARX proposal [1]). The SPARC collaboration identified a program based on two main issues: the generation of ultra-high peak brightness electron beams and experimental study of SASE-FEL process with generation of resonant higher harmonics. The SPARC project is being designed in order to encompass the construction of an advanced photo-injector producing a 150-200 MeV beam to drive a SASE-FEL in the optical range. The machine will be built at LNF, inside an underground bunker: it is comprised of an rf gun driven by a Ti:Sa laser, injecting into three SLAC accelerating sections. We foresee conducting investigations on the emittance correction[2] and on the rf compression techniques[3], which are expected to increase the peak current achievable at the injector exit up to kA level, with proper preservation of the transverse emittance. Although the system is expected to drive a FEL experiment, it can be used also to investigate beam physics issues like surface-roughness-induced wake fields, bunch-length measurements in the sub-ps range, emittance degradation in magnetic compressors due to CSR, and Compton backscattering production of sub-ps X-ray pulses.

PROJECT OVERVIEW

The overall SPARC Project consists of 4 main lines of activity:

- 1) *150 MeV Advanced Photo-Injector*: the performances of X-ray SASE-FEL's are critically dependent on the peak brightness of the electron beam delivered at the undulator entrance. Two main issues to investigate: generation of the electron beam and compression via magnetic and/or velocity bunching.
- 2) *SASE-FEL Visible-VUV Experiment*: this is aimed to investigate the problems related to the beam matching into an undulator and the alignment with the radiation beam, as well as the generation of non-linear coherent higher harmonics. The SASE FEL experiment will be performed with the 150 MeV beam, using a segmented undulator with additional strong focusing to observe FEL radiation at 500 nm and below.
- 3) *X-ray Optics/Monochromators*: the X-ray FEL radiation will provide unique radiation beams in terms of peak brightness and pulse time duration (100 fs). This project will pursue a vigorous R&D activity on the analysis of radiation-matter interactions in the spectral range of SASE X-ray FEL's (from 0.1 to 10 nm), and on the design of new optics and monochromators.
- 4) *Soft X-ray table-top Source*: to test these optics and start the R&D on applications the project will undertake the upgrade of the presently operated table-top source of X-rays at INFN - Politecnico Milano, delivering 10^7 soft X-ray photons in 10-20 fs pulses by means of high harmonic generation in a gas.

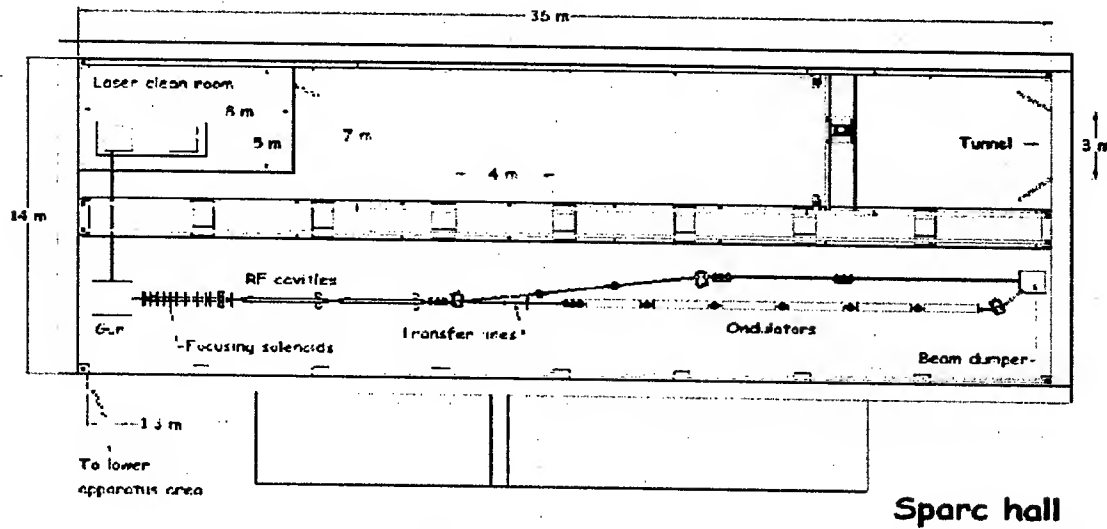


Figure 1 : Lay-out of SPARC Advanced Photo-Injector and SASE-FEL Experiment

In the following we present an overview of the design for the system under construction at the Frascati National Laboratories of INFN, by a collaboration between two national research institutions, INFN and ENEA namely, aiming at reaching the scientific and technological goals indicated in the first two topics listed above, *i.e.* the production of a high brightness electron beam and the operation at saturation of a SASE-FEL experiment driven by such an electron beam.

ADVANCED PHOTO-INJECTOR

The main goals of this activity are the acquisition of expertise in the construction, commissioning and characterization of an advanced photo-injector system and the experimental investigation of two new ideas that have been recently conceived and presented by the study group: the optimum working point for high brightness RF photo-injectors and RF bunch compression technique.

The 150 MeV injector will be built inside an available bunker of the Frascati INFN National Laboratories: the general layout of the system is shown in Fig. 1. The system consists of a 1.6 cell RF gun operated at S-band (2.856 GHz, of the BNL/UCLA/SLAC type) and high peak field on the cathode (120 MeV/m) with incorporated metallic photo-cathode (Cu or Mg), generating a 6 MeV beam[4]. The beam is then focused and matched into 3 accelerating sections of the SLAC type (S-band TW) which accelerates the bunch up to 150-200 MeV. For the Laser system it is planned to use the third harmonic of the radiation from a Ti:Sa laser with the oscillator pulse train locked to the RF. To obtain the time pulse shape we are going to test the manipulation of frequency lines in the large bandwidth of Ti:Sa, in order to produce the 10 ps flat top shape. We can use a liquid crystal mask in the Fourier plane for nondispersive optic arrangement or a collinear acousto-optic modulator for line frequency

manipulation. The goal of these tests is to obtain a pulse rise time shorter than 1 ps with intensity ripples along the 10 ps pulse smaller than 30% (peak to peak); under such a condition the beam emittance achievable at the end of the photo-injector is foreseen to be smaller than $1 \mu\text{m}$.

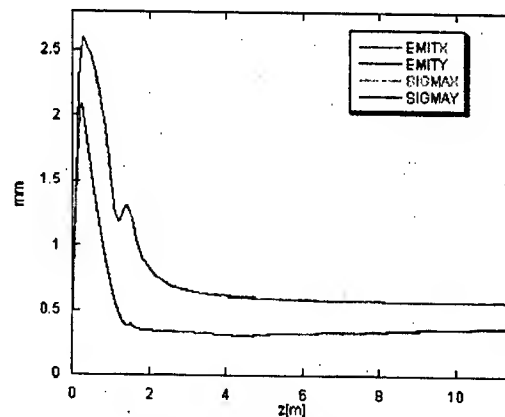


Figure 2: Parmela simulation of emittance and envelope evolution along the SPARC photo-injector (only two accelerating sections taken into account)

The first experiment is planned to verify the beam emittance compensation process. The key point is the measurement, at different bunch charges, of the emittance oscillation in the drift after the gun where a double minima behavior is expected. The optimum beam matching to the booster is predicted on the relative maximum, see Fig. 2. A dedicated movable emittance measurement station has been designed, as shown in Fig. 3. Our simulations using PARMELA indicate that we can generate in this way a beam as required by the FEL experiment at 150 MeV. The rms correlated energy

spread is 0.2% with a rms norm. emittance lower than 2 μm (at 1 nC bunch charge, 85 peak current). The slice energy spread and the slice norm. emittance, calculated over a 300 μm slice length, are below 0.05% and 1 μm respectively, all over the bunch. A complete investigation over the parameter range of the system is in progress, in particular tolerances and sensitivities are being considered in the beam dynamics simulations [5].

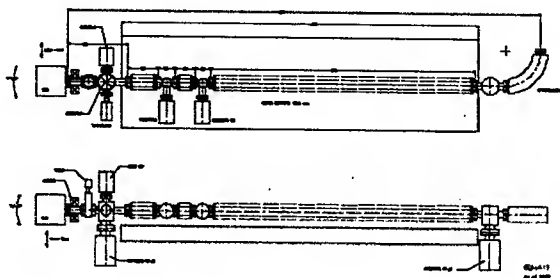


Figure 3: movable emittance measurement station. A pepperpot and a screen are connected with three bellows in order to scan the emittance along 1m long drift

SASE FEL EXPERIMENT

The FEL SASE experiment will be conducted using a permanent magnet undulator made of 6 sections, each 2.13 m long, separated by 0.36 m gaps hosting single quadrupoles which focus in the horizontal plane. The undulator period is set at 3.0 cm, with an undulator parameter $k_w = 1.4$. A simulation performed with GENESIS is reported in Fig. 4, showing the exponential growth of the radiation power along the undulator. Almost 108 Watts can be reached after 14 m of total undulator length. Preliminary evaluations of the radiation power generated into the non-linear coherent odd higher harmonics show that 10^7 and 7×10^5 W can be reached on the third and fifth harmonics, respectively.

FURTHER EXPERIMENTS

Two main upgrades will be implemented in a second phase of the project. A dedicated accelerating section will be inserted downstream the RF gun in order to exploit the full potentialities of the velocity bunching technique. Furthermore, in the parallel beam line a magnetic chicane will be installed to allow the experimental investigation of CSR induced effects on emittance degradation and surface roughness wake-field effects. Its design and construction will proceed in parallel to the commissioning of the SPARC injector system (RF gun + 3 standard SLAC-type 3 m sections). These tests are of great relevance in our R&D program in view of the development of a coherent X-ray source according to the

SPARX proposal[1], the general layout of which foresees a mixed compression scheme: RF compression in the photo-injector and one single stage magnetic compression at 1 GeV up to the final peak current of 2.5 kA.

Applying velocity bunching in the SPARC photo-injector with low charge bunches (about 15 pC) will allow the production of ultra-short electron bunches, in the range of a few μm rms bunch length, fully synchronized to the Ti:Sa laser pulses. A further upgrade of the laser system to produce multi-TW pulses, by means of a third stage of amplification and an under vacuum plasma compressor, will allow to conduct laser wake-field plasma acceleration experiments with external injection of high quality ultra-short bunches into the plasma wave, for ultra-high gradient acceleration of electron beams.

This naturally projects SPARC as a more general test facility to conduct advanced beam physics and new acceleration technique experiments at LNF in the near future.

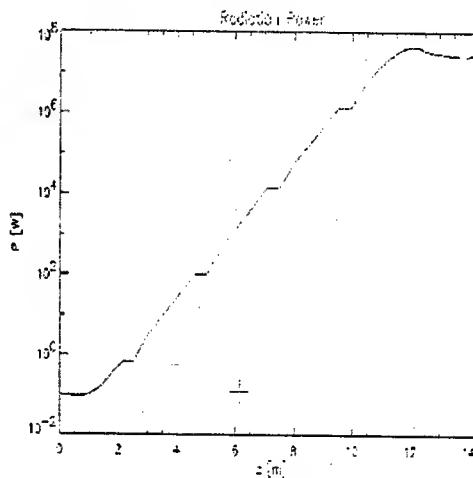


Figure 4: FEL radiation power growth along the undulator

REFERENCES

- [1] D. Alesini *et al.*, *Conceptual design of a High Brightness Linac for Soft X-Ray SASE-FEL Source*, Proceedings of the FEL-2002 Int. Conference
- [2] M. Ferrario *et al.*, *Recent Advances and Novel Ideas for High Brightness Electron Beam Production based on Photo-Injectors*, INFN Rep. LNF-03/06 (P), May 2003
- [3] L. Serafini and M. Ferrario, *Velocity Bunching in Photo-Injectors*, AIP CP 581 (2001) 87
- [4] D.T. Palmer, PhD. Thesis, Stanford University
- [5] M. Biagini *et al.*, *Beam Dynamics Studies for the SPARC Project*, this conference

A SIMULATION STUDY OF THE JLC POSITRON SOURCE

T. Kamitani*, Y. Ohnishi, KEK, Tsukuba, Ibaraki, Japan
S. Kashiwagi, Waseda University, Tokyo, Japan

Abstract

This paper describes a parameter optimization of the JLC positron source design by detailed particle tracking simulations. The design parameters are modified from those of the previous JLC design study [1], considering the energy-density limit of the converter-target damage and the recent change in the specifications, especially the twice increase of a charge intensity of a beam pulse [2]. It is shown that a multiple target system to share the deposition energy is inevitable and at least three targets are necessary to yield sufficient positrons within the energy-density limit.

INTRODUCTION

The design of the JLC positron source [1][2] is based on a conventional scheme of positron production using high-Z material target irradiated by a high-energy electron beam as shown in Fig.1. A combination of a pulsed solenoid (flux

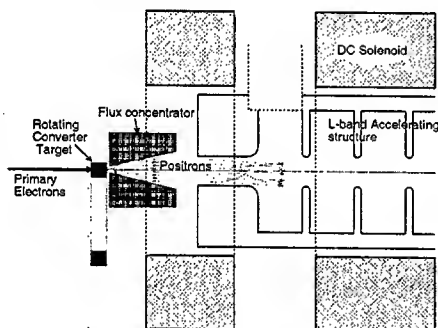


Figure 1: JLC positron source

concentrator) and DC solenoids is used for the transverse phase space matching. The solenoid field is varied slowly from 7.0 T to 0.5 T to achieve an adiabatic matching so as to have a wide energy acceptance. A long flat solenoidal field of 0.5 T extends in the several meters to cover the accelerating structures in the capture section. Only the positrons which can pass through the aperture of the accelerating structure are captured and accelerated. L-band accelerating structures are used here, because it has large aperture (20 mm in radius) and long RF wave length (210 mm), thus having large acceptance both in transverse and longitudinal phase space. The positrons are accelerated up to 180 MeV with the L-band structures in the solenoid focusing region and are transferred to the quadrupole focusing system. In the downstream, the positrons are accelerated by a S-band linac up to 1.98 GeV for injection to the pre-damping ring (PDR).

* takuya.kamitani@kek.jp

An intensity of 14.4×10^{11} positrons/pulse, which is equivalent to that of electrons, is required in the present JLC design. It was increased more than twice, compared with the previous design (6.0×10^{11} particles/pulse) [1]. A beam pulse has a structure like a train of 192 bunches in 1.4 nsec interval, each having 0.75×10^{10} positrons. A repetition rate of the beam pulse is 150 Hz. A primary electron beam, whose intensity is 19.2×10^{11} electrons/pulse, is accelerated up to 10 GeV at the converter target to produce positrons. A performance of the positron source is evaluated by the positron yield which is defined by a ratio of the positron intensity to that of the primary electrons. Assuming a loss of the positron beam from the PDR to the interaction point is negligible, the positron yield is estimated by calculating a conversion ratio from electrons to positrons in the converter target and a fraction of positrons which survive during a transmission from the capture section to the PDR injection. A design goal of the positron yield is $N_{e^+}/N_{e^-} = 0.75$.

ENERGY-DENSITY ESTIMATION

Tungsten-Rhenium alloy has been chosen as a converter-target, because of the high melting point and the high tensile strength. The thickness of the target was determined to be 21 mm (6.0 radiation lengths) for the optimum positron yield with the 10-GeV primary electron beam. A rotating structure is used so that each beam pulse hits a different part of the target to prevent concentrated heat deposition. Nevertheless, the energy deposition by a single beam pulse may exceed the threshold for target damage due to fatigue. From analysis of the cracked SLC positron source target, the threshold for damage is estimated to occur when the local density of the energy deposition is 35 J/g, as reported in the NLC positron source design [3]. This limit is used as a reference in the design of the JLC positron target. Increasing the transverse size of the primary beam helps reduce the energy density in the target. Examples of the energy-density in the target are shown in Fig.2, for two cases of the incident beam sizes of 2.0 and 3.0 mm. The densities grow as the beam goes deeper in the target and the peaks are at the exit. By increasing the beam size from 2.0 to 3.0 mm, the peak energy density becomes almost half. It is because the energy deposition is smeared out in wider region as shown in the contour plots in Fig.2. The energy densities in the plots are for the case of the beam intensity which is one-third of the JLC specification.

Though increasing the beam size reduces the energy density, it also reduces the positron yield, because larger fraction of the produced positrons go out of the acceptance aperture. As shown later, if the incident beam size is suf-

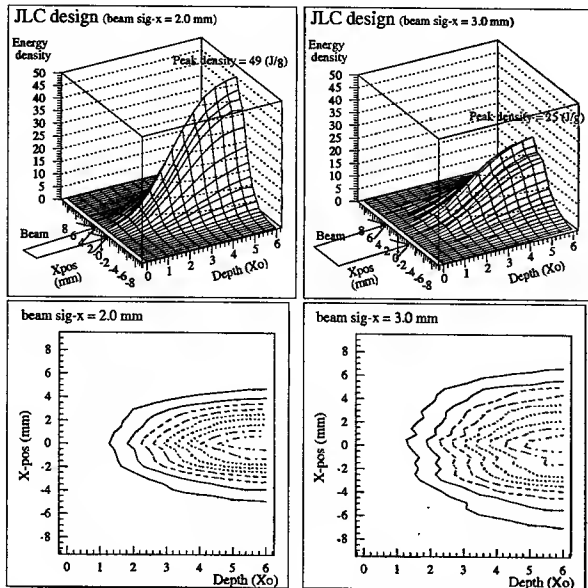


Figure 2: Energy density distribution

ficiently large concerning the energy density, the positron yield is far below the requirement. To keep the density well below the threshold with sufficient positron yield, multiple target system is used for the energy deposition to be shared as proposed for the NLC [3]. A candidate multiple tar-

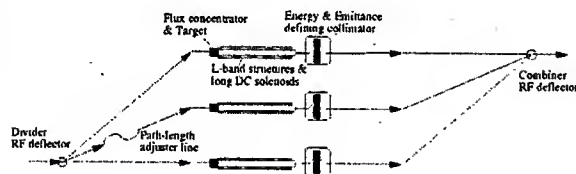


Figure 3: Multiple target system

get system for the JLC is shown in Fig.3. To divide the bunches in a beam pulse into three, an RF deflector cavity whose oscillation is synchronized to every third bunch is used. The three groups of the sparse bunches go towards the different target. Each target is followed by a positron capture section and a collimator to define energy and emittance. The three groups of the produced positrons are then merged with another RF deflector cavity. To see the effect of using the multiple targets, the peak energy density and its dependence upon the incident beam size is evaluated for the case of one to four targets. The result is shown in Fig.4. The EGS4 shower simulation code [4] was used to calculate the energy depositions in small volumes in the target. The acceptable minimum beam sizes to clear the density limit are 4.8, 3.2, 2.5, 2.1 mm for single, 2, 3, 4 target systems, respectively. By using multiple target, the acceptable beam size become smaller.

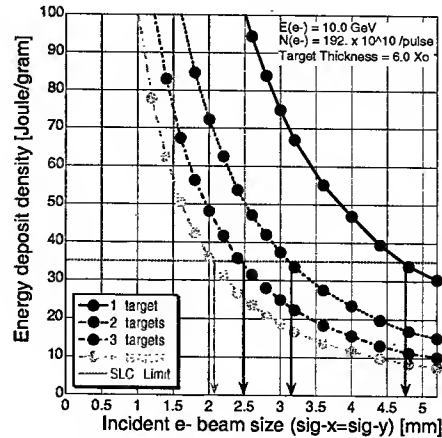


Figure 4: Energy density as a function of beam size

POSITRON YIELD ESTIMATION

In order to estimate the positron yield for each case of the multiple target systems, detailed particle tracking simulations were performed.

As a first step, positron production in the target was simulated using the EGS4 code. Approximately, twenty-thousand positrons were generated in the 21-mm thick tungsten-rhenium target from a thousand initial electrons of 10-GeV beam energy. Samples for different incident beam sizes were generated, assuming the transverse incident particle distribution is a two-dimensional gaussian and were used as input data for later simulations.

Capture efficiency of the solenoid focusing system was evaluated by tracking simulations with a step-by-step integration of the equation of motion, including a focusing magnetic field, an accelerating field and a detailed aperture constraints in the capture section [5]. The step size was 0.25 - 1.0 mm. Typical number of the particles after the capture section was three thousand.

To estimate a beam transmission efficiency of the 1.98-GeV positron injector linac, particle tracking was performed with the SAD code [6] in a six-dimensional symplectic manner. The positron focusing system in the linac is a combination of a FODO of singlets and periodic triplet quadrupoles. In Fig.5, a preliminary design of the beam optics and the layout in the linac is shown, as well as an example of the beam transmission efficiency along the linac. Here, the beam optics from the defining collimator till the junction of the three beams and that for the transfer line to the PDR were omitted. In this simulation, an aperture radius in the linac was assumed to be 10 mm and an acceptance cut by the energy and emittance defining collimator, located just after the capture section, were also taken into account.

Finally, PDR acceptance cuts were applied to the sample particles after the tracking simulation in order to estimate the positron yield. The acceptances for PDR injection were assumed to be 0.027 rad.m in the transverse emittance, ± 1 percent in the particle energies and 24 mm in the longitudi-

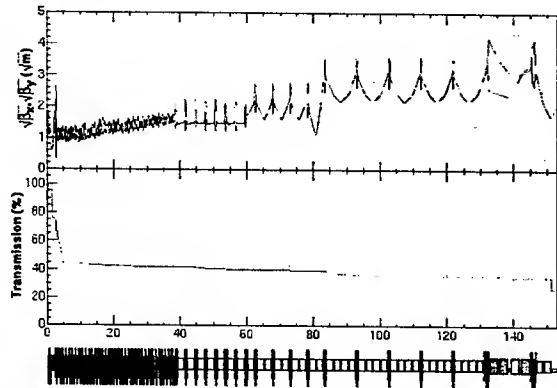


Figure 5: Positron Injector Linac Beam Optics and Beam Transmission

nal position in a bunch. Due to large energy spread of the positrons, approximately 50 % of them were eliminated by the PDR energy acceptance. To improve this efficiency, the single-bunch energy-spread compression system (SBECS) was considered, which has already been used in the KEK B-factory injector linac [7]. This system is composed of the chicane to produce path difference for the particles with different energies and an accelerator section which gives acceleration (or deceleration) to compensate the energy difference in a bunch. As shown in Fig.6, the energy-spread can be compressed with this system and the injection efficiency to PDR was expected to be more than 70 %.

Not only the energy-spread of the positrons in a bunch, but an energy deviations between the bunches due to the transient beam loading along the bunch train is also large. In the positron linac, ΔT multi-bunch energy compensation system (ΔT ECS) is used as in the JLC electron injector linac [2]. Here, the amplitude modulation technique is applied to an input rf pulse into the SLED cavities to obtain the desirable slope of unloaded voltage in the accelerating structure. A combination of two klystrons are needed to modulate the amplitude of rf pulse for the SLED cavities with a constant phase. By using the ΔT ECS, the multi-bunch energy deviation can be negligible compared to the PDR energy acceptance and therefore, it was not included in the tracking simulation.

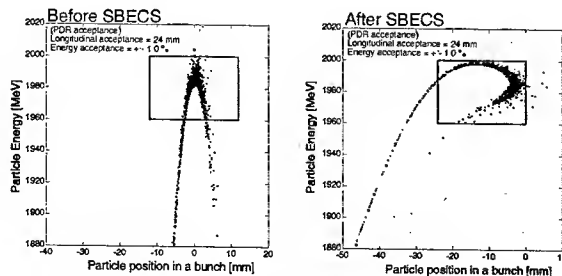


Figure 6: Single-Bunch Energy-spread Compression System

After all the simulations, the positron yield for different

numbers of the targets is shown in Fig.7 at each acceptable minimum beam size. The single or two target systems cannot yield sufficient number of positrons. In the case of three target system, the incident beam size can be 2.5 mm in radius and the estimated positron yield at PDR is $Ne^+/Ne^- = 0.99$ and the requirement of the $Ne^+/Ne^- = 0.75$ is satisfied.

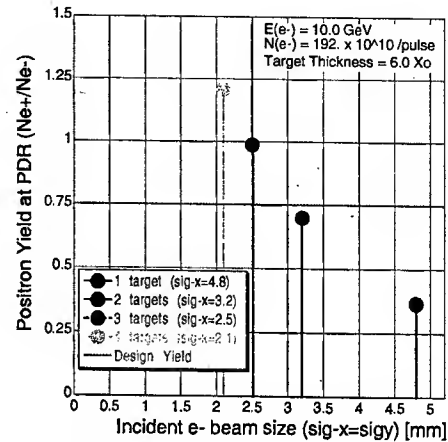


Figure 7: Positron yield as a function of beam size

CONCLUSION

The tracking simulations of the JLC positron source shows that, the multiple target system is inevitable to make the energy density below the threshold of the target damage and to yield sufficient intensity of the positrons. The simulation shows the minimum number of the targets are three. The single bunch energy compression system is effective in improving the injection efficiency to the pre-damping ring.

REFERENCES

- [1] "JLC design study", By N. Akasaka, *et al.*, KEK Report 97-1, 1997 April
- [2] "JLC Roadmap Report", February 12, 2003 see <http://lcdev.kek.jp/RMdraft/>
- [3] "2001 Report on the Next Linear Collider (A report submitted to Snowmass '01)", By the NLC collaboration, SLAC-R-571, 2001 June
- [4] "The EGS4 Code System", By W. R. Nelson, H. Hirayama, D. W. O. Rogers, SLAC-Report-265, December 1985
- [5] "Positron Production at CLIC", By T. Kamitani, L. Rinolfi, CLIC Note 465, March 2001
- [6] "SAD (Strategic Accelerator Design) Home Page", By K. Oide, *et al.*, <http://www-acc-theory.kek.jp/Accelerator/index.html>
- [7] "The KEKB injector linac", By I. Abe, *et al.*, Nuclear Instruments and Methods in Physics Research Section A, Volume 499, Issue 1, 21 February 2003, Pages 167-190

DIFFUSION OF ALKALI SPECIES IN POROUS TUNGSTEN SUBSTRATES USED IN CONTACT-IONIZATION SOURCES*

E. Chacon-Golcher¹, J.W. Kwan² and E. C. Morse³
¹ LANL, ² LBNL, ³ UC-Berkeley

Abstract

Contact ionization (doped) sources used in current Heavy Ion Fusion (HIF) experiments consist of a porous tungsten substrate doped with an alkali carbonate. During the early stages of the heating cycle ($T \sim 600^\circ\text{C}$), the carbonate breaks down and releases the alkali atoms that then diffuse through the substrate. At the emitter surface there is a balance between the fast desorption rate of the alkali atoms (mostly as neutrals) and the slower replenishment rate from the substrate by diffusion. Time-resolved measurements of neutral particle evaporation rates at the emitter surface have been used to estimate the effective diffusion coefficient (D) that characterizes the migration of alkali species in the substrate. These estimates are consistent with the observed source lifetimes (tens of hrs.) and establish the alkali migration in the bulk as a diffusion-limited process. The measurements suggest that the faster migration rates ($D \approx 10^{-5} - 10^{-6} \text{ cm}^2/\text{s}$) occur early during the heating cycle when the dominant species are the neutral alkali atoms. At operating temperatures there is a slower migration rate ($D \approx 10^{-7} \text{ cm}^2/\text{s}$) due to the dominance of ions, which diffuse by a slower surface diffusion process.

1 INTRODUCTION

Original studies carried out in the field of surface physics of alkali atoms on tungsten can be traced back to the definitive work by Langmuir [1]. Subsequent technological applications of those fundamental principles include space propulsion applications and their continued use as a source of heavy ions for inertial fusion energy drivers. Despite the wealth of information accumulated in the ion thruster research, there have been diverse needs to explore the performance of these ion sources for HIF research given the very different regimes of operation present in these two applications. Among the differences for HIF we have: higher ion current density demand, desire for lower neutral particle emission, and a requirement of a lower effective ion temperature (low beam emittance). Previous investigations carried out in LBNL have shown the capability of these ion sources to deliver μs -length pulses of approximately $100 \text{ mA}/\text{cm}^2$ for a potassium beam under typical experimental conditions. This and a description of the basic preparation of these ion sources are elaborated in a previous report [2]. One of the main research interests in HIF applications relate to the ion source lifetime and the atomic processes that

determine it. This report summarizes a simple methodology applied to understand the importance of diffusive processes in the performance of this type of sources. Using previously measured [3] rates of neutral alkali atom desorption to match theoretical curves it was possible to estimate the diffusion constant of the alkali species in the porous tungsten substrate, in good agreement with the observed ion source lifetimes.

2 ONE DIMENSIONAL DIFFUSION MODEL

2.1 Physics Issues

It is known that the mean residence lifetime (τ) of an alkali atom on a tungsten surface decreases exponentially with temperature (T). For instance, in the Arrhenius-type relation

$$\tau = \tau_0 e^{Q/kT} \quad (1)$$

the parameter τ_0 has a magnitude of approximately 10-13 s and the energy desorption parameter, Q , is on the order of 1 eV. These values amount to desorption times of a fraction of a nanosecond over the range of temperatures of interest for ion emission. The porous tungsten substrates used in HIF experiments are doped with an initial amount of alkali atoms (Cs or K). Considering the desorption times, it can be concluded that it is the slow diffusion of the alkalis towards the emitting surface what determines the observed ion source lifetimes.

Even when considering the case of the diffusion of a single species, the process is highly dynamical and somewhat complicated. Initially, the concentration of potassium or cesium in the emitter substrate is relatively large, given the dose of carbonate used, which provides enough alkali atoms to have a full monolayer of coverage throughout the internal surfaces of the emitter. It is expected that the initial distribution of the alkali atoms will become more uniform upon the breaking down of the chemical compounds and the natural diffusion of the alkalis in the bulk. Several stages can be identified:

I. An initial stage of an alkali rich bulk. This stage should be identified at temperatures beyond 600°C . At this stage, the high concentration of alkali atoms highly favors their existence as neutral particles which have a smaller surface affinity with the tungsten than the alkali ions. Therefore, a neutral particle diffusion dominated process is expected. This does not occur at very fast rates

*Work supported by the Office of Fusion Energy, US DOE under contract No. DE-AC03-76SF00098.

since this stage usually happens while the emitter is at relatively low temperatures during the warm up cycle.

II. A mid-stage where sufficient alkali atoms have been desorbed so that there starts to appear a significant ion population. The neutral atoms will continue to diffuse through like in a Knudsen-type flow (given that the mean free path of the atoms is much larger than the characteristic dimensions of the pores), being slowed down by the fact that the gas atoms do not elastically collide with the emitter internal surfaces and bounce right off, but become adsorbed, spend some time on the surface and then become desorbed again. The ions, on the other hand, due to their binding force to the surface, are limited to a slower diffusion speed, as their movement is through surface migration along the grain surfaces.

III. A final stage where the alkali content is sufficiently low to favor the existence of ions, which as said in point b., move by surface diffusion. It is at this stage that the source is fully operational and capable of its higher current yields. It is also this slow surface diffusion mechanism that explains the observed lifetimes of the surface ionization sources.

The above stages may be interpreted from neutral desorption rate data during the heating cycles of doped tungsten substrates [3]. Given the diffusion dynamics described above, the estimated effective diffusion constants ('D') at different temperatures do not scale simply with an Arrhenius-type formula.

2.2 Mathematical Model and Data Fitting

The porous W substrates used in these measurements were small cylindrical pellets (diameter = 0.6 cm, length = 0.64 cm) surrounded by a molybdenum holder. Only one of the circular ends was exposed to the vacuum chamber. Once the dopant was included in the pellet, the diffusive flow would only occur in a single direction. The equation that relates the concentration 'c' with the distance from the back of the emitter 'x' and the time 't' is the known diffusion equation.

$$\frac{\partial c(x,t)}{\partial t} - D \frac{\partial^2 c(x,t)}{\partial x^2} = 0 \quad (2)$$

The solution of this equation was subject to the following boundary conditions.

$$c(x,0) = c_0 \quad (3)$$

$$\left. \frac{\partial c}{\partial x} \right|_{x=0} = 0 \quad (4)$$

$$c(L,t) = 0 \quad (5)$$

which represent the conditions of initial uniform concentration, no flow at the back end of the emitter and an artificial boundary condition of zero concentration at x

= L respectively. L is just at a very small distance from the actual emitting surface to which the experimental data was fitted.

The exact solution to this problem is given by equation (6). This can be obtained in direct analogy with a heat diffusion problem [4].

$$\frac{c}{c_0} = \sum_{n=1}^{\infty} C_n \exp\left(-\frac{\zeta_n^2 D t}{L^2}\right) \cos\left(\frac{\zeta_n x}{L}\right) \quad (6)$$

Here 'c₀' is the concentration at the beginning of the interval in which the data is fit, and the coefficients 'C_n' and 'ζ_n' are related by equations (7) and (8). The condition in equation (8) reflects the fact that the desorption rate of the particles at the surface is much faster than the diffusion rate towards the surface.

$$C_n = \frac{4 \sin(\zeta_n)}{2\zeta_n + \sin(2\zeta_n)} \quad (7)$$

$$\zeta_n \tan(\zeta_n) = \infty \quad (8)$$

Figure 1. shows the curves predicted by equation (6) using the first four terms of the series. The graph shows the decrease in concentration in the bulk with time.

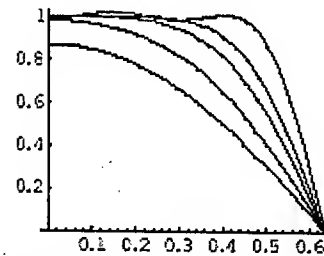


Figure 1: Concentration profile (with respect to original value) as a function of position (in cm) with increasing time as a parameter (lower concentration curves).

Equation (6) was used to fit the experimental measurements of neutral atom desorption of cesium and potassium atoms. These data exist for a collection of operating temperatures and at different points of the heating cycle of the emitter [3]. After applying an appropriate normalization factor to adjust the magnitude, the curve is fitted by varying a single parameter, the effective diffusion coefficient 'D'.

The clear assumption of this method is that the neutral particle desorption rate at the emitter surface varies linearly with the concentration of particles at the surface.

Figure 2 shows an example the fitting of experimental data with the theoretical model. The discontinuities of the data correspond to the background level signal, when the detector was moved out of the line of sight of the emitter.

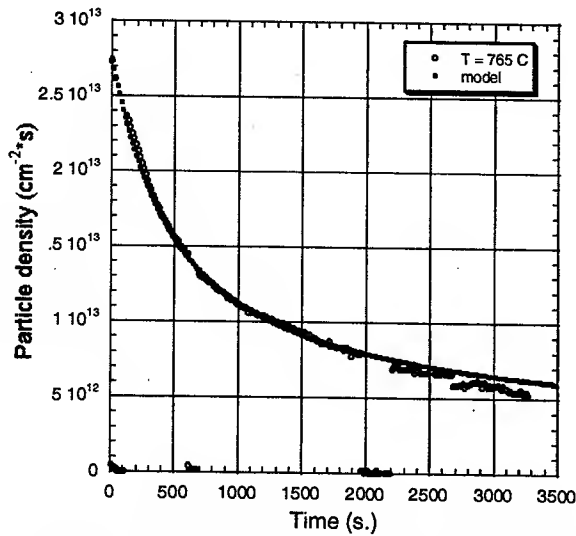


Figure 2. Fitting of the measured neutral particle desorption rate from a cesium source at $T = 765\text{ }^{\circ}\text{C}$. Effective $D = 1.2 \cdot 10^{-5}\text{ cm}^2/\text{s}$.

With a similar procedure a series of effective diffusion coefficients was estimated during the heating cycle of Cs and K ion sources and at different operating temperatures. A summary is presented in Table 1. The cells with a gray color represent the temperatures and conditions normally encountered in the operation stage of these ion sources.

Temperature ($^{\circ}\text{C}$)	Diffusion Coefficient (cm^2/s)	
	Cesium	Potassium
680	$5.9 \cdot 10^{-06}$	
765	$1.2 \cdot 10^{-05}$	
800	$3.7 \cdot 10^{-06}$	$4.0 \cdot 10^{-06}$
815		$5.0 \cdot 10^{-06}$
840	$1.0 \cdot 10^{-05}$	
885	$6.0 \cdot 10^{-06}$	
955	$4.0 \cdot 10^{-06}$	$4.0 \cdot 10^{-06}$
955	$1.1 \cdot 10^{-06}$	$2.0 \cdot 10^{-06}$
955	$6.5 \cdot 10^{-07}$	$1.4 \cdot 10^{-06}$
955	$5.0 \cdot 10^{-07}$	$3.0 \cdot 10^{-07}$
1,025	$1.0 \cdot 10^{-06}$	
1,030		$1.6 \cdot 10^{-06}$
1,055	$1.2 \cdot 10^{-06}$	
1,075	$8.0 \cdot 10^{-07}$	$1.8 \cdot 10^{-06}$
1,095		$1.5 \cdot 10^{-06}$
1,110	$1.35 \cdot 10^{-06}$	
1,130	$5.7 \cdot 10^{-06}$	
1,150		$1.9 \cdot 10^{-06}$
1,185		$3.5 \cdot 10^{-06}$

Table 1. Estimated diffusion constants of Cs and K through a nominal $12\text{ }\mu\text{m}$ grain size porous W substrate. Several values for D are listed for the temperature of $955\text{ }^{\circ}\text{C}$ as at this temperature the source is allowed to eliminate the surplus of alkali atoms and during a period that lasts ~ 17 hours. Diffusion becomes slower with time at this stage. Gray color represents typical operating T 's.

In general, the uncertainty of the values can be estimated to ± 5 in the first decimal place to have curve fits with the type of agreement shown in Figure 2.

3 DISCUSSION AND CONCLUSIONS

From the estimates in Table 1 it can be seen how at the lower temperatures, while the diffusion of the particles is dominated by neutral atoms, there is not much sensitivity to ' T '. This may be explained qualitatively by knowing that the expected faster diffusion rate (at higher T) is opposed by the decrease in concentration of alkalis. This decrease results in a larger fraction of particles migrating as ions, which due to their stronger affinity with the surface, migrate at a slower rate. This effect may be more clearly appreciated after the emitters have been allowed to eliminate their surplus alkalis (at $T = 955\text{ }^{\circ}\text{C}$). At this temperature, the diffusion becomes slower with time, until the temperature starts to rise again. Then, there is still not a clear increase of the flow with T (proportional to ' $\exp(E/kT)$ ', for some activation energy ' E ') since the ratio of ions to neutrals starts decreasing with T as well in accordance with the Saha-Langmuir equation [2].

The estimates of ' D ' are valid for the specific substrates used in these experiments, i.e. sintered tungsten made with nominal $12\text{ }\mu\text{m}$ grain size. While it was found that D varies with T and the alkali content of the emitter, the values found are a good indication of the magnitude of D to be expected in similar conditions.

With regard to ion source lifetimes, consider a Cs source operating at $1,150\text{ }^{\circ}\text{C}$. Taking a diffusion length of $L = 0.64\text{ cm}$, the associated time scale would be $\tau_d \sim L^2/D = (0.64\text{ cm})^2/(5.7 \cdot 10^{-6}\text{ cm}^2/\text{s}) \approx 20\text{ hrs}$. This is consistent with the observed source lifetimes of $\sim 5\tau_d$. This suggests that for the duty factors used in these experiments, ($\sim 2\text{ }\mu\text{s}$, every 20s, or $\sim 1 \cdot 10^{-7}$) the main loss mechanism for alkali atoms is indeed neutral particle loss.

With these results is also possible to estimate the replenishment rate at the emitter surface. By assuming a "surface thickness", ' l ', of the order of the grain size, one can propose a formula like (9) for estimating the maximum pulse repetition rate (MPRR) that would allow a particle balance at the surface for a given current density demand sufficient to significantly affect the surface concentration. This is of interest to HIF applications.

$$MPRR = \frac{1}{5\tau_d} = \frac{D_{bulk}}{5l^2} \quad (9)$$

4 REFERENCES

- [1] Taylor, J.B. and Langmuir, I. Phys. Rev. 44. No. 6. Sept. 1933. p. 423.
- [2] Chacon-Golcher, E. et al. Proceedings of the Particle Accelerator Conference, Chicago, IL. 2001. p. 2102.
- [3] Chacon-Golcher, E. et al. Rev. Sci. Instrum. Vol. 73. No. 2. Feb. 2002. p. 1036.
- [4] Incropera, F.P. and DeWitt, D.P. Fundamentals of Heat and Mass Transfer. 5th Ed. John Wiley & Sons. 2002.

FABRICATION OF LARGE DIAMETER ALUMINO-SILICATE K^+ SOURCES*

D. Baca, J. W. Kwan, J. K. Wu

Lawrence Berkeley National Laboratory, Berkeley, California 94720

E. Chacon-Golcher, Los Alamos National Laboratory, Los Alamos, NM 87544

Abstract

Alumino-silicate sources that are used for Heavy Ion Fusion (HIF) drivers can produce high current beams, and have a long lifetime, typically many months of normal operation. The usual ion source diameter is about 10 cm with a curved emitting surface. Recently we achieved reliable fabrication of such large diameter sources with high quality alumino-silicate coating on tungsten substrates. The effects of substrate porosity, powder size distribution, coating technique, particle packing density, drying, and heat firing temperature have been investigated.

INTRODUCTION

Alumino-silicate K^+ sources have been used in HIF experiments for many years [1,2]. These sources have a typical current density of $\sim 10\text{--}15\text{mA/cm}^2$, for 5-10 μs , but much higher current density has been observed (using smaller size sources). In comparison to ionizers, alumino-silicate sources have a considerably long experimental run time, on the order of months, and lower neutral emission levels. Recently we have improved our fabrication techniques and are able to reliably produce large diameter ion sources with high quality emitter surface without defects. This note provides a detailed description of the procedures employed in the fabrication process. The variables in the processing steps affecting surface quality are substrate porosity, powder size distribution, coating technique on large area concave surfaces, drying, and heat firing temperature.

SUBSTRATE PREPARATION

Alumino-silicate K^+ ion sources are made by melting a layer of synthetic alumino-silicate onto a tungsten substrate, the process is similar to working with ceramics [3]. Since the ion source will be operated at temperatures above 1050 degree C and the melting process is around 1550 degree C, the substrate is usually made of a refractory metal such as tungsten. 80% dense porous tungsten is suitable for ion source application, anything of lighter density is usually too fragile.

There is another very important reason to use porous tungsten substrates. In comparison to a solid substrate, the absorption of molten ceramic material and a rough surface provides the basis for mechanical gripping of alumino-silicate during the melting stage. The HCX source has a dimension of 10cm diameter with a concave surface of

20.32cm spherical radius. The emitting concave surface area is 82.4cm^2 ($\pm 1\text{-mil}$ tolerance). The tungsten substrates supplied by the vendor have pores closed by the finishing machining process so the first step is to reopen the emitting surface pores by electrolysis etching.

Tungsten etching is accomplished by a DC electro-chemical process. A 5 molar KOH solution is produced by mixing 2 liters of high purity deionized water and 500g of potassium hydroxide (KOH). A tungsten substrate is attached to a positive electrode with the region to be etched exposed and facing the negative electrode. The negative electrode has the shape of a convex spherical cap with a smaller spherical radius of 19.05cm, to fit the concentric contour of the substrate etching area and retain uniform electric field line distance across the entire etched surface at a separation of $\sim 1.2\text{cm}$. In etching the 10cm diameter source, a 20A DC current with $\sim 2.5\text{V}$ applied across the electrodes for 40 minutes will etch away $\sim 8\text{-mil}$ of tungsten material and is enough to re-open the pores and produce a uniform surface free of any remaining machining marks. SEM photos (Fig. 1) show that the surface pore average size is typically $\sim 15\mu\text{m}$.

After electro-chemical etching, residual KOH electrolytic solution must be removed from the substrate. Typical practice is to soak and dilute the tungsten substrate in deionized water for a few days until the pH value reaches ~ 6.0 or higher. Drying can be done in a vacuum oven at a temperature of ~ 100 degree C to remove all remaining water vapor. Finally, the substrate is clean fired at 1750 degree C in a vacuum furnace at a pressure of $\sim 10^{-6}$ Torr.

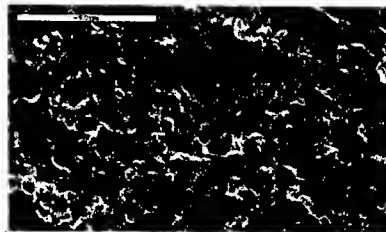


Figure 1: SEM photo of etched, porous, 80% dense tungsten surface (50 μm scale) with $\sim 15\mu\text{m}$ pore size.

ALUMINO-SILICATE PREPARATION

This procedure describes the preparation of synthesizing potassium-aluminosilicate, as it is heated to ~ 1450 degree C to produce the Leucite crystalline phase, $K_2\text{OAl}_2\text{O}_3 \cdot 4\text{SiO}_2$ [4]. It begins with thoroughly mixing raw high purity chemicals followed by a two-step reaction process in an atmospheric air furnace.

*This work has been performed under the auspices of the US DOE by UC-LBNL under contract DE-AC03-76SF00098, for the HIF Virtual National Laboratory. <http://hifweb.lbl.gov/webpages/>

The chemicals, all in powder form, are 99.995% Potassium Carbonate (K_2CO_3), 99.9% Silicon Oxide (SiO_2), and 99.8% Aluminum Oxide (Al_2O_3). The respective stoichiometric ratio by weight is 1.0:1.739:0.738. Since potassium carbonate is hygroscopic, the mixing process begins in a controlled low humidity environment, such as, flowing dry nitrogen gas through a glove box and keeping the humidity below 5%. After mixing by weight, the mixture is tape-sealed in a jar before removing from glove box to trap in the dry nitrogen gas.

The next step is to use a ball mill process to thoroughly blend the chemicals for several hours. Afterward the mixture is transferred to a platinum crucible. Chemical reactions occur when the mixture is heated in an air furnace for 4 hours at 1100 degree C. The reaction product expands and froths as CO_2 gas is released, and then shrinks to form a solid mass when cooled.

The comminution processes that follow after cooling consist of crushing and milling to further disperse the mixture and to reduce the average particle size of the material [5]. The solid mass is carefully removed from the crucible and the dry material ground with mortar and pestle to a fine powder, ~ 200-mesh (75 μ m) size, before placing in a planetary ball mill for one hour minimum reducing it to a finer powder size as a final mixing step. The entire mixture is again transferred to the platinum crucible for re-heating in an air furnace for 2 hours at 1450 degree C, completing the reaction, releasing any remaining CO_2 , producing the Leucite crystalline phase, and cools to a solid mass. After removal from the crucible, the material is ground once more to produce the final particle-size powder distribution.

The particle-size powder distribution was found to be an important factor in minimizing defects, such as, warping, distortion, and cracks on the alumino-silicate layer. Two principal particle sizes for the coating process are separated using wire sieves. Fine particle-size 400-mesh (<37 μ m) powder is chosen as an initial pre-coat layer on porous tungsten substrates to penetrate, and lodge into the ~15 μ m diameter pores of the tungsten substrate. The main coating layer consists of a coarser particle-size distribution between 200-mesh (75 μ m) and 270-mesh (53 μ m) powder.

COATING TECHNIQUE

A thin layer of ceramic may be formed by pouring aqueous slurry onto a surface and then moving a blade over the material to produce a thin film [5]. This coating method was used to apply a uniform adhering finish of 15-mil potassium alumino-silicate to cover large area concave and planar porous tungsten substrates.

The coating process occurs in two steps. Starting with 400-mesh powder, an aqueous slurry suspension is produced by mixing with high purity de-ionized water. Droplets of the 400-mesh aqueous mixture are then distributed over the entire surface, effectively imbedding small particles of fine 400-mesh alumino-silicate powder

into the pores of the tungsten substrate as a pre-coat layer. After a 12-hour drying period, the top layer of 400-mesh dry powder is gently brushed off and discarded.

Second step is to apply the main 15-mil coating layer, consisting of a coarser particle-size distribution between 200 and 270-mesh potassium alumino-silicate powder, and mixing with de-ionized water to form a thicker slurry.

Difficulties can arise in applying this main coating to large diameter and non-planar surfaces. A blade-scraping tool was designed to match the spherical radius of the concave shaped substrate with a smooth knife-edge down the center, and a 30-degree taper from the horizontal on both sides (Fig. 2).

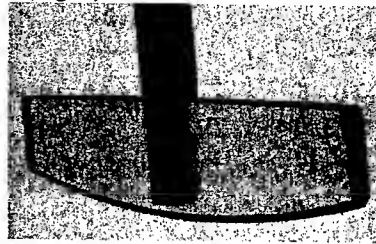


Figure 2: Blade-scraping tool, knife-edge has a 30-degree taper from the horizontal on both sides.

The main coating process begins by pouring alumino-silicate slurry to cover the emitting surface of the tungsten substrate. Because porous tungsten absorbs water readily, it is necessary to frequently apply de-ionized water droplets to keep the mixture near aqueous in viscosity. The scraping tool action is initiated by rotating slowly at the base of the support rod and applying de-ionized water droplets and adding slurry as needed to cover depleted areas. Alignment tolerance is held to ~1-mil in a milling machine. The wet coated material gradually increases in viscosity as it dries and is nearly ready for the final lifting of the knife-edge tool off the surface. An ~1-mil high thin track is typically left by the knife edge tool during final lift off. This is usually not a concern because the track will disappear when the layer of alumino-silicate melts during the heat firing process. With accurate digital vertical position control provided by a milling machine, it is possible to reset the scraping tool each time after removing excess slurry material, and then continue to form the layer until achieving uniform thickness. By slowly rotating the scraping tool and allowing the slurry to increase in viscosity before removing, uniform 15-mil coatings have routinely been achieved. After the coating process has been completed, the drying process should start immediately.

DRYING

The rate of drying and the particle packing density are essential factors of the forming process [6]. If the rate of drying is too fast, shrinkage of the ceramic slurry will cause coating defects to occur. A ceramic part dried too rapidly forms a hard surface film, which traps the moisture and leads to tearing at the surface. Hydrostatic forces, imparted to the mixture by water, are removed through the drying process. During the wet forming

process, the distribution of particle shapes and sizes is known as particle packing density. A higher particle packing density will effectively reduce shrinkage. Shrinkage will occur during drying as the liquid between the particles is eliminated and the interparticle separation distance decreases. Forming the ceramic material at a lower liquid content and increasing the mean particle size will reduce drying shrinkage and thus reduce coating defects. Shrinkage defects occurred using smaller particle size 400-mesh alumino-silicate powder for the main 15-mil coating layer, while shrinkage defects did not occur using increased particle size 200-mesh powder with proper drying techniques.

A basic method requiring limited effort is to control the drying rate by regulating humidity. For this task, a humidifier chamber was built by flowing air through a de-ionized water-filled flask to create water vapor flowing in parallel with dry air into a manifold and combining into a chamber. The air velocity is kept low for slower drying rates. Humidity is monitored at the output tube of the chamber with a humidity sensor. Immediately after wet coating, substrates are placed in the humidifier chamber and slow dried over a period of several days starting with >90% humidity, gradually lowering the humidity and ending with <10% humidity. A completed drying process is essential before heat firing in a vacuum furnace.

HEAT FIRING

Heat firing is the final process step that produces a melted layer of alumino-silicate that mechanically bonds to the tungsten substrate. Since bonding is mechanical, substrate porosity and surface roughness is essential to provide the basis for mechanical gripping. Also, there is thermal expansion mismatch to consider, metals usually have a higher thermal expansion coefficient than ceramics. Poor coating thermal shock resistance can lead to cracking and chipping at the surface. An effective way to enhance thermal shock resistance is to apply as thin a coating as possible with a high ceramic to metal bond. Defects can occur, such as craters and blowholes, from contamination of dust or metal flakes within the material vaporizing during heat firing.

A dry coated substrate is centrally placed in a vacuum furnace to reduce inherent temperature gradients. During the heat firing process, the vacuum furnace pressure is maintained in the 10^{-5} - 10^{-6} Torr range. Potassium alumino-silicate starts to melt at 1550 degree C. Typically, the heat firing process consist of bringing the temperature up to ~1565 degree C and holding for 45 minutes, with a heat-up and cool-down rate of 10 degree C per minute. Temperature control is achieved with thermocouples up until ~1500 degree C, then two optical pyrometers are utilized to achieve accurate temperature control near the melting point. The potassium alumino-silicate surface emissivity, equal to ~0.91, was calibrated by focusing on a blackbody in the vacuum furnace and then compared with a coated substrate at the same temperature, 1570 degree C, in the heat zone region.

Utilizing two optical pyrometers improved the accuracy of the temperature measurements to ± 5 degrees C. The resultant phase structure is dependent upon the maximum heat firing temperature and the aluminosilicate coating thickness. Observed phase transformations, for uniform 15-mil coatings, range from glassy vitreous structure, ~1555 deg C, dull snowy bubble structure, ~1565 deg C, to crystalline needle-like structure, >1570 deg C. After heat firing, alumino-silicate coated layers have typically been reduced by ~30% in thickness due to shrinkage.

The maximum heat firing temperature must be approached slowly to avoid overfiring temperatures. According to SEM analysis, overfiring causes crystal growth and depletion of potassium. The glassy vitreous structure has desirable characteristics of lower defects and high current emission properties. Absorption depth of molten ceramic material into porous tungsten substrates has been detected to depths of ~25-mil to ~50-mil.

CONCLUSIONS

Previous attempts at fabricating ion sources have resulted in coatings displaying various defects, such as, shrinkage cracking, blistering, and craters (Fig. 3). After applying these coating techniques, the surface quality has significantly improved to produce smooth, uniform, and fully coated large diameter emitting surfaces with virtually a single-phase structure. As with most techniques, optimization of these processes is far from complete. For instance, the drying rate and the heat firing duration have not been fully optimized. The effect on surface quality will be a determining factor.

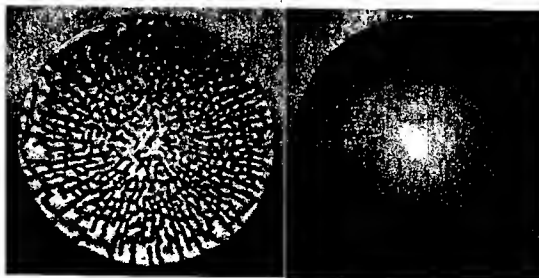


Figure 3: Comparison of significant coating technique improvements fabricating 10cm diameter, 0.4mm K^+ alumino-silicate coatings on porous tungsten substrates.

REFERENCES

- [1] P.A. Seidl, et al., "The High Current Transport Experiment for Heavy Ion Inertial Fusion", these proceedings.
- [2] S. Eylon, et al., "High Brightness Potassium Source for the HIF Neutralized Transport Experiment", these proceedings.
- [3] Ceramic Film and Coatings, Wachtman & Haber, 1993
- [4] Phase Diagram for Ceramists, Amer. Ceramic Society, E.M. Levin, C.R., Robbins, H.F. McMurdie, 1964
- [5] Ceramic Processing, James Reed, 1995
- [6] Introduction to Ceramics, W.D. Kingery, 1960

BEAM OPTICS OF A 10-CM DIAMETER HIGH CURRENT HEAVY ION DIODE *

J.W. Kwan, J.L. Vay, F.M. Bieniosek, Lawrence Berkeley National Laboratory;
E. Halaxa, G. Westenskow, Lawrence Livermore National Laboratory; I. Haber, Univ. of Maryland

Abstract

Typically a large diameter surface ionization source is used to produce > 0.5 A K^+ current with emittance $< 1 \pi$ -mm-mrad for heavy ion fusion experiments. So far we have observed aberrations that are slightly different from those predicted by computer simulations. We have now set up an experiment to study in detail the beam optics of such a large diameter ion diode and to benchmark the simulation code.

INTRODUCTION

Heavy ion driven inertial fusion (HIF) requires about 3-7 MJ to achieve ignition with a D-T target [1]. At 2-4 GeV ion kinetic energy, the corresponding beam charge is ~ 1 mC. Induction linacs can accelerate and compress these beams from ~ 10 μ s at injection to ~ 300 ns by the end of the driver and further drift compress the duration down to ~ 10 ns at the target. The total beam current from the ion source is ~ 50 -100 A. In order to overcome the space charge problem associated with high current heavy ion beams, an HIF driver is usually designed to contain an array of $N \sim 100$ parallel ion beam channels at ~ 0.5 A each.

In order to focus the ion beams onto a mm-size fusion target the beam emittance must be small, thus HIF requires beams with both large current and high brightness. Since the beam brightness is proportional to J/T , where J is the current density and T is the effective ion temperature, high brightness demands either high current density and/or low effective ion temperature. Furthermore, a heavy ion injector must have an adequate low energy beam transport (LEBT) system that can handle the severe space charge force. The LEBT often limits the maximum current density in the injector and therefore dictates the type of ion source that can be used.

According to high voltage breakdown and Child-Langmuir space-charge flow scalings, the current density of a diode decreases as the beam current increases [2]. Thus producing large current and high brightness from a single large aperture implies low ion temperature because the current density must be low. This condition can be met by a surface ionization sources because their typical effective ion temperature is < 1 eV and the solid emitter surface provides a way to design large diameter beam optics.

Although heavy ions such as Cs^+ are ultimately needed

for fusion drivers, lighter ions such as K^+ can be useful in the near future because they provide an opportunity to do experiments at high ion velocities on medium length accelerator facilities during the early development phases.

Figure 1 shows the "2-MV" injector that was developed for the previous ILSE project [3] which consists of a 750 kV triode followed by an electrostatic quadrupole (ESQ) section. Recently the ion source and extraction gap was modified in order to improve the beam optics for meeting the requirements of the High Current Transport (HCX) experiment [4]. So far the experimental results from the HCX experiments have shown qualitative agreement with the computer simulation. The discrepancy in beam current and in beam optics between the measurement and simulation predictions were significant enough to cause uncertainty in future beamline designs. This is especially true if the design relies heavily on "end-to-end simulation" or the experiment requires a high degree of phase space control accuracy.

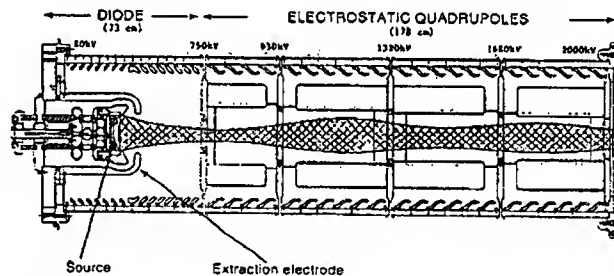


Fig. 1: Schematic Diagram of the 2-MV injector.

At present, our strategy is to use a two-pronged approach for the injector program [2]. On one hand we are exploring a new approach to built compact injectors, that are suitable for multiple beams HIF drivers, using an array of high current density beamlets. On the other hand, we continue to improve the large diameter surface source so it can provide a single-beam injector for near-term HIF projects such as the Integrated Beam Experiment (IBX). Recently we have mastered the techniques to fabricate large diameter alumino-silicate sources with a uniform emitting surface [5].

The main objective of the experiment described in this paper is to study how to produce a high quality ion beam from a large diameter surface ionization source. By carefully comparing the results from experiment against that from computer simulation, we will benchmark the simulation code(s) and also determine if the necessary physics are included in the simulations.

**This work is supported by the Office of Fusion Energy Science, US DOE under contract No. DE-AC03-76SF00098 (LBNL) and W-7405-ENG-48 (LLNL). Email: jwkwan@lbl.gov

RECENT DEVELOPMENT

Previous injector experiment with the ILSE project have produced up to 0.8 A of K^+ ion beam at 2.0 MeV by using a 17-cm diameter ion source [3]. However the beam profile was found to be hollow with significant current density non-uniformity. Since spherical aberration occurs near the edge of the emitter and is more pronounced when the source diameter is large, we reduced the ion source diameter down to 10 cm, and modified the extraction electrode. The result was a lower beam current at 0.6 A, but the beam optics was significantly improved [4,6].

Figure 2a shows a Kapton film image of the beam spot at the injector exit (accumulated exposure of 100 beam pulses). Previous calibration confirmed that the darkening on a Kapton film was proportional to beam exposure at the 2-MV energy range [7]. Since the image was time-integrated over the entire pulse length, it also recorded (superimposed) the beam head and tail that were responsible for the complicated pattern inside the ellipse. In comparison to the corresponding time-integrated image generated by computer simulation, as shown in Fig. 2b, we found a ~15% discrepancy in the rms envelope size and a ~20% discrepancy in the beam current. We found the discrepancy was minimized if the extraction voltage used in the simulation was empirically re-calibrated from the measured value. This finding suggested that there could be a possible error in the extraction voltage measurement but so far we were not able to confirm that assumption.

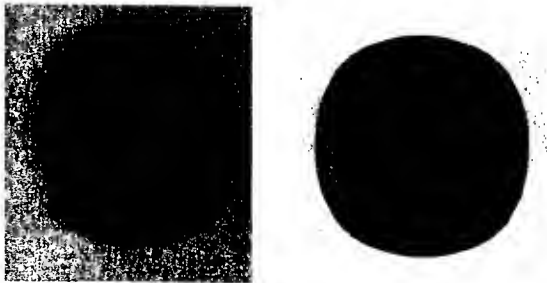


Fig. 2a. Kapton image of beam spot at the injector exit. 2b. Images obtained from time-dependent simulation.

COMPUTER SIMULATIONS

In order to minimize current density non-uniformity and aberrations, the extraction diode must be designed by using reliable computer codes. In the HIF program we have used both EGUN and WARP-3D. Figure 3 shows the result from WARP-3D simulation of a beam extracted from a curved emitter (10 cm diameter). Figure 4a is the corresponding current density profiles at two axial locations and Fig. 4b is the results from a flat emitter. In comparison, the flat emitter produces a more uniform current density beam.

When comparing results between different simulation codes, and also results from the same code but using different mesh sizes or numerical convergent criteria, we often found that the fine details of the beam profile may

vary. For example, the "ripples" on the beam profile in Fig. 4a should not be taken too seriously and the absolute height of the spikes at the beam edge can be very sensitive to small variation. This kind of error can result in up to 10% uncertainty in the total beam current.

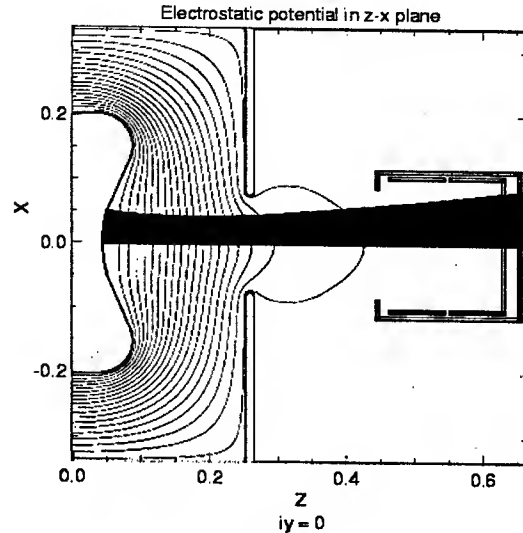


Fig. 3: WARP-3D simulation of a diode producing an ion beam entering a Faraday cup (only trajectories on upper-half plane are shown).

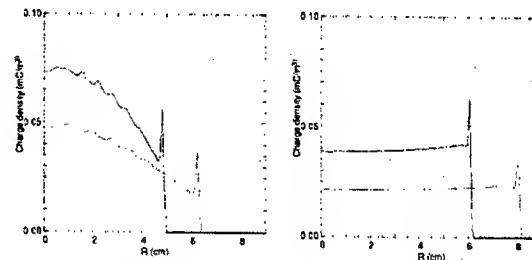


Fig. 4a Current density profiles of a curved source at $z=0.3m$ and $z=0.45m$. Fig. 4b: corresponding profiles for a flat source.

Part of the errors may be due to mesh size being too coarse at critical regions such as the gap between the emitter edge and the tip of the Pierce electrode. An effective way to deal with this problem is to use adaptive mesh [8]. Another possible source of error is the method used to determine the local current density at the emitting surface. Each code seems to have its own unique way of dealing with this boundary condition.

Aside from numerical errors, the simulation can still be inaccurate if the physics is incomplete. For example, the code may ignore effects such as secondary electrons, alignment errors, ion temperature, work function and roughness of the emitting surface. In our case, HIF beams are both high current and low emittance. With high current, the space charge effect is severe, so the secondary

electron problem can be significant. With low emittance, the effective ion temperature is only a small fraction of an eV, therefore the work function and surface roughness can be important.

In electrostatic devices, the charged particle trajectories remain similar if $J \sim V^{1.5}/L^2$ where J is the current density, V is the voltage, and L is the characteristic length. Since the ion temperature, the work function, and the surface roughness are fixed parameters determined by the ion source surface condition, they do not scale according to the diode voltage or the source diameter. Likewise, production of secondary electrons increases rapidly with the beam potential. The important point here is that while reduced size experiment can be useful for proof of principle purpose, only real size experiment can study the "dirty physics" which is critical for a practical driver.

NEW EXPERIMENTAL SETUP

Figure 5 shows the schematic diagram of a new experiment at LLNL dedicated to study the large-diameter ion source and extraction diode problem. Figure 6 is a picture of the 10-cm source mounted on a large Pierce electrode. The test stand can provide up to 500 kV and 20 ms of diode voltage. Beam diagnostics will include Faraday cup, beam spot imaging, slit-scanner and pepper-pot for emittance measurements.

Our goal is to use the experimental results from this experiment for benchmarking the computer simulation codes. Once we have a reliable code, with all the necessary physics included, we hope to improve the beam optics and therefore enhance our ability to observe subtleties in future large-aperture-fill HIF experiments. At the time of writing this paper, the experiment has just begun commissioning. The ion source was heated to 1000 deg C and we saw no relative movement between the ion source and the Pierce electrode that could cause alignment errors. We expect to publish the experimental results, in comparison with computer simulations, by the end of this year.

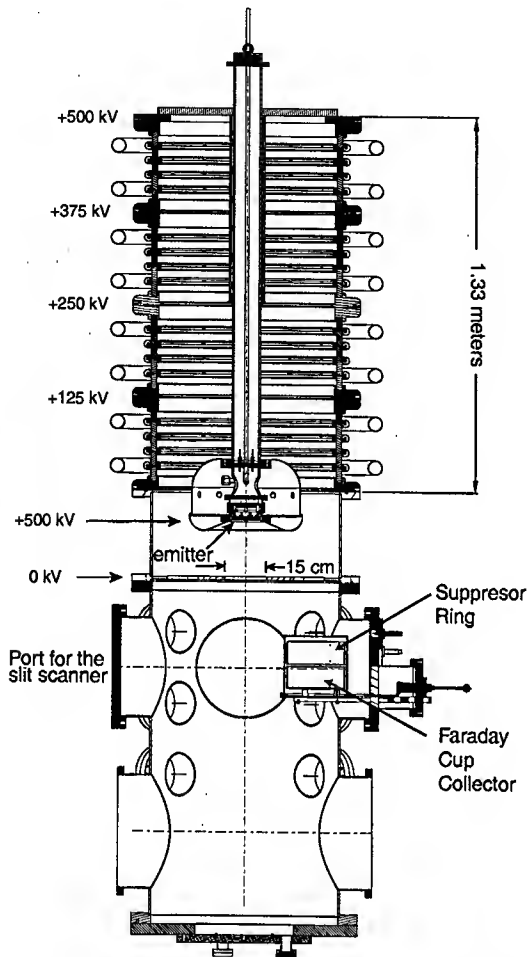


Fig. 5: Schematic diagram of a 10-cm alumino-silicate ion source/diode experiment showing the Faraday cup in the retracted position.

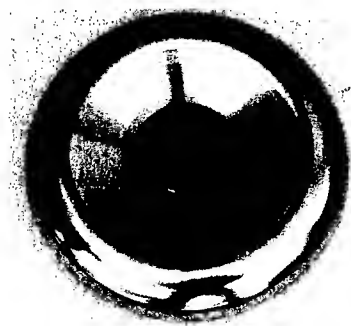


Fig. 6: Photograph of the 10-cm diameter alumino-silicate ion source mounted on a Pierce electrode.

REFERENCES

- [1] D. A. Callahan-Miller, M. Tabak, Nuclear Fusion 39, 1547 (1999).
- [2] J.W. Kwan, Rev. Sci. Instrum, 71(2), p807, (2000).
- [3] S. Yu, et al, Fusion Engineering and Design, 32-33, p309, (1996)
- [4] J. W. Kwan, F. M. Bieniosek, E. Henestroza, L. Prost and P. Seidl, Laser and Particle Beams, 20, p 441-445, (2002).
- [5] D. Baca, E. Chacon-Golcher, J. W. Kwan, J. K. Wu, see this proceeding.
- [6] F. M. Bieniosek, E. Henestroza, and J.W. Kwan, Rev. Sci. Instrum, 73, p1042, (2002)
- [7] F. M. Bieniosek, J.W. Kwan, L. Prost, and P. Seidl, to be published in Rev. Sci. Instrum. August, (2002). Kapton calibration
- [8] J.-L. Vay, P. Colella, P. McCorquodale, B. Van Straalen, A. Friedman, and D.P. Grote, Laser and Particle Beams, 20, p569-575, 2002

CHARACTERIZATION OF AN RF-DRIVEN PLASMA ION SOURCE FOR HEAVY ION FUSION*

G. Westenskow, R. P. Hall, E. Halaxa, Lawrence Livermore National Laboratory;
J. W. Kwan, Lawrence Berkeley National Laboratory

Abstract

We are testing a high-current-density high-brightness Argon-Ion Source for Heavy Ion Fusion applications. The 100-kV 20- μ s source has produced up to 5 mA of Ar^+ in a single beamlet. The extraction current density is 100 mA/cm². We have measured the emittance of the beamlet, and the fraction of Ar^{++} ions under several operating conditions. We present measurements of the extracted current density as a function of RF power and gas pressure (~ 2 mT), current density uniformity, and energy dispersion (due to charge exchange). We are testing a 80-kV 61-hole multi-beamlet array that will produce a total current > 200 mA. In the current experiments the beamlets are not merged into a single beam. A 500-kV experiment where the beamlets will be merged to produce a 0.5-A beam is being planned.

BACKGROUND

Following a proposal that the usual limits on brightness for compact ion-beam sources used in Heavy Ion Fusion can be circumvented by using a multi-beamlet injector [1] we have started an experimental program to examine practical issues. The final source envisioned will start with ~ 100 5-mA beamlets across a 100-kV gap. The beamlets will be focused by Einzel Lens while their energy is increased to about 1.6 MeV. The beamlets are then merged to produce a 0.5-A beam with a normalized emittance below 1π -mm-mrad.

Beyond providing a low-temperature source that can provide ion emission densities of ~ 100 mA/cm²[2], the main physics issues involved in the multi-beamlet approach are emittance growth and envelope matching in the merging process. In computer simulations, if the initial emittance is in the range of measured values, the final emittance increases only weakly with the initial emittance of the individual beamlets.

We have available three test stands for developing the concept. The first has a small chamber with voltages below 50 kV. The second has increased diagnostics and 100 kV. The third larger system is capable of 500 kV with a 20 μ sec pulse [3].

We will first describe the characteristics of a single beamlet. We will then give early results from a "61-beamlet" array. During the next year we have a series of planned experiments that move the design closer to a source that could be used in the driver.

*This work has been performed under the auspices of the US DOE by UC-LBNL under contract DE-AC03-76SF00098 and by UC-LLNL under contract W-7405-ENG-48, for the Heavy Ion Fusion Virtual National Laboratory. Email: westenskow1@llnl.gov

STUDYING INDIVIDUAL BEAMLETS

We are using an rf plasma source to produce the Argon ions. The plasma chamber is 33 cm in diameter with multicusp permanent magnets to confine plasma. RF power (~ 11 MHz, > 10 kW) is applied to the source via a 2-turn, 11-cm diameter antenna inside the chamber for producing beam pulses of 20 μ s at up to 10 Hz. We have shown that we can extract 100 mA/cm² from the chamber. Optimum performance has been with ~ 2 mT gas in the plasma chamber.

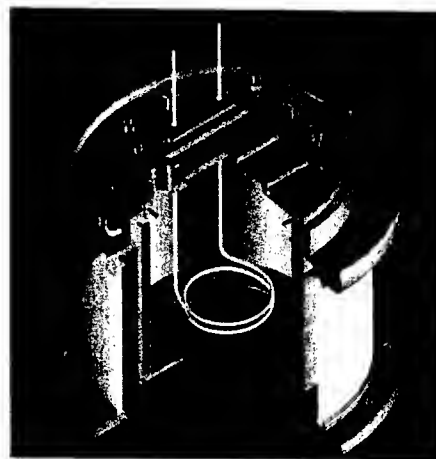


Fig. 1: RF plasma source used in the experiments.

Beam Current

Our first step was to characterize the current in a single beamlet from the rf plasma source (see Fig. 2).

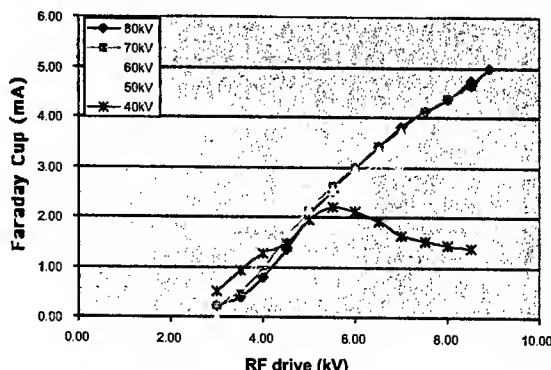


Fig. 2: Extracted current in a single beamlet at 2 mT source pressure. The aperture was 2.5 mm diameter. The curves are different gap potentials. The "10 kV RF drive" is about 12 kW of power from the rf source.

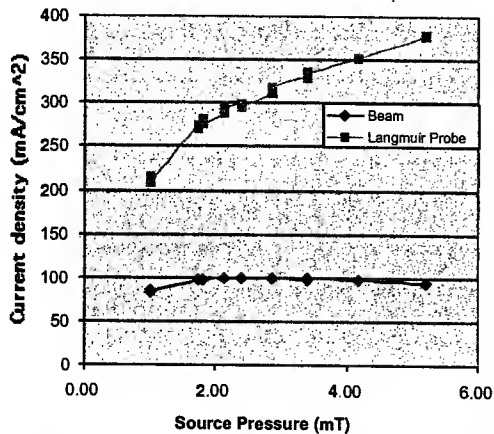


Fig. 3: Effect of source pressure on extracted current and the ion density in the chamber. Gap voltage was 80 kV and the RF drive was 8.5 kV.

As shown in Fig. 3 increasing the source pressure above 2 mT continued to increase the ion density in the chamber, but did not yield higher extracted currents from the gap. Increasing the source pressure increases charge exchange in the gap.

Charge state and charge exchange

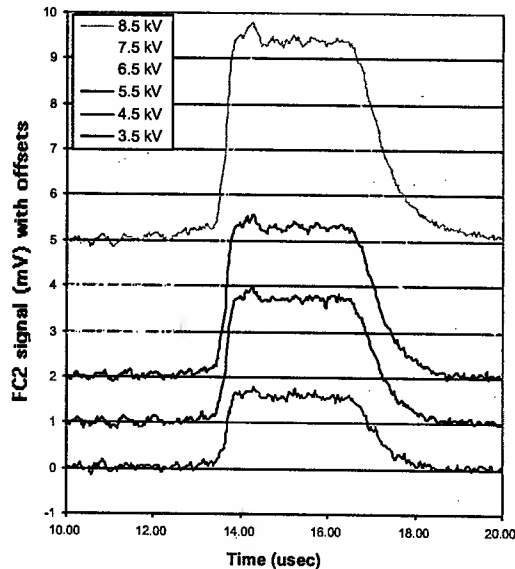


Fig. 4: Arrival time of ions at the back Faraday Cup.

A crude measurement of the ionization state was done by using time-of-flight information. We have a 1.5 meter drift section between pulsed dipole plates and a Faraday Cup. Since there was no focusing, the beam diameter at the cup was larger than it's acceptance. We switched the beam into the Faraday Cup during the center of the pulse. The Ar^{++} ions will have higher momentum, and the front edge of the pulse will arrive at the Faraday Cup before the Ar^+ ions. At drive powers higher than 5 kW, we did see a "front step" in the ion current at the cup (see Fig. 4). We

estimated that less than 5% of the extracted ions were in the Ar^{++} state.

An early concern was that collisions between the extracted ions and the background gas would yield an excessive amount of charge exchange. The newly created ions would leave the gap with lower energies and different transverse motion. Using the dipole plates as an "energy analyzer" we looked for a shift in the profile at the slit cup. We even increased the background gas pressure in the gap to enhance the effect. Our preliminary conclusion is that the energy spread is small. It is conceivable that most of the ions that undergo collisions do not reach the Faraday Cup. Further experiments are planned to improve our ability to resolve energy spread.

Emittance

We used a narrow slit and slit cup to examine the $x - x'$ phase space of a beamlet. An example is shown in Fig. 5.

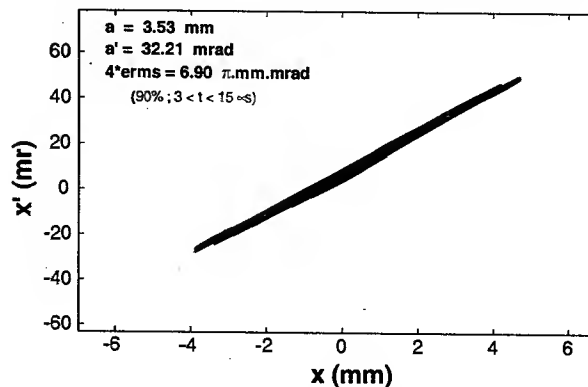


Fig. 5: Phase space of a beamlet 12 cm from the extraction plate. Operation at 80kV, 2.1 mT source pressure, 6.5 kV RF drive. Cut taken at 90% of the peak valve. Early values removed to reduce noise from the spark gaps.

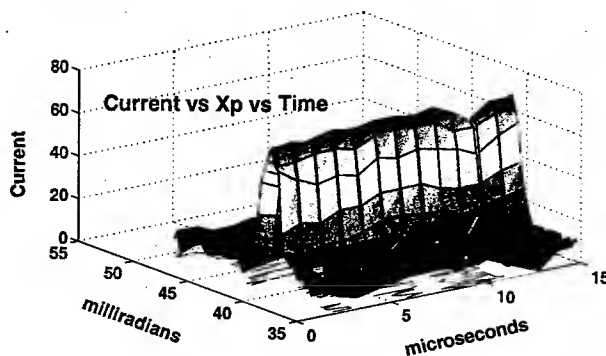


Fig. 6: The current at the slit cup verses angle from the slit as a function of time. Same parameters as in Fig. 5.

The beam parameters were stable over the 3 to 15 μs period as shown in Fig. 6. The deviation at 12 μs is believed to be from a problem with the diagnostics. The normalized emittance for the beamlet was $\sim 0.015 \pi\text{-mm-mrad}$.

CURRENT EXPERIMENTS

We are presently investigating a multi-beamlet extraction array. The 1.6-cm gap is held with three high-gradient insulators. The bottom beam-forming plate in Fig. 7 has Pierce Cones for each of the beamlets. The apertures in the bottom plate are 2.2 mm diameter. The holes in the top plate are 4.0 mm diameter. Figure 8 shows the change in the opacity of a kapton sheet hit with 50-kV 20- μ s beamlets from the array. The kapton sheet was 2 cm from the extraction plate. Figure 9 is a lineout of the image shown in Fig. 8.

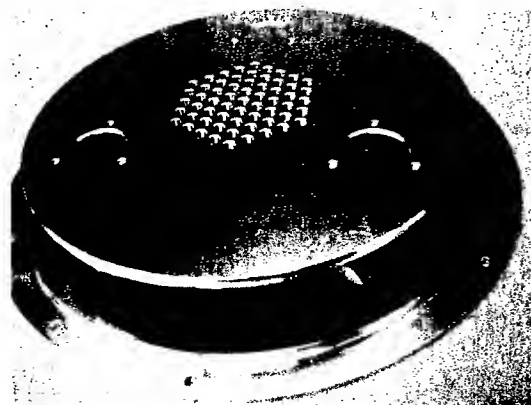


Fig. 7: Extraction plate for the 61-beamlet array.

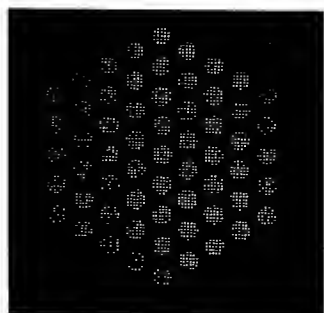


Figure 8. Image produced by ions hitting a Kapton sheet.

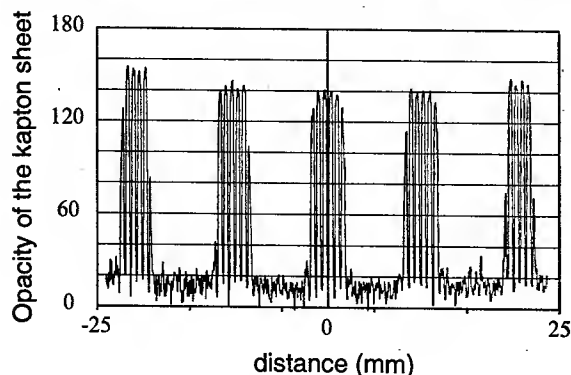


Fig. 9: Line out of the above image taken at the first row of complete beamlets. The fine structure is from a metal screen placed in front of the Kapton sheet to stop ion charge buildup.

NEXT STEPS

After further characterization of the beamlets, our next step will be to add Einzel Lens to the present configuration (shown in Fig. 10). In latter versions the lens will be used to boost the energy of the beamlets. We plan to separate the lens with high-gradient insulators. The separation of the lens is about 1 cm.

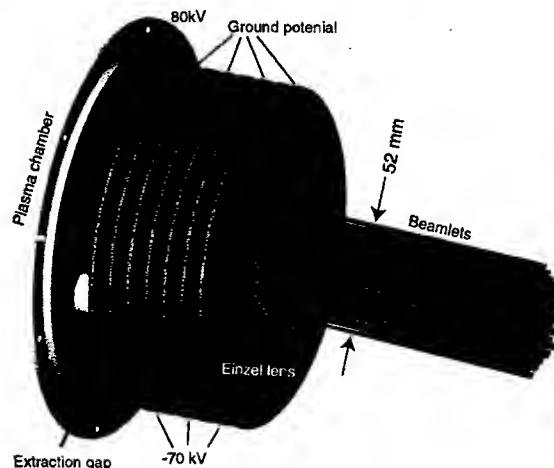


Fig. 10: Next experiment with extraction gap and Einzel Lens.

Merging of the beamlets will not be done at this stage because the perveance is too high. Also, minimizing the final transverse phase space will require curved plates for the Einzel Lens. We are designing an experiment with the extraction gap at ~ 100 kV with post acceleration up to 500 keV.

ACKNOWLEDGEMENT

We would like to thank Gary Freeze and Will Waldron for their assistance with the experiments. Also wish to thank Larry Ahle for his preparation work on the experiment.

REFERENCES

- [1] D.P. Grote, E. Henestroza, J.W. Kwan, PRST Accelerators and Beams, Vol. 6, 014202 (2003).
- [2] L. Ahle, et al., R. of Sc. Inst., Vol. 73 #2, p. 1039, (2002)
- [3] L. Ahle, D.P. Grote, J.W. Kwan, Laser and Particle Beams, Vol. 20 (2002).

STABILITY OF ELECTRON BEAM PARAMETERS IN SOURCES WITH COLD SECONDARY-EMISSION CATHODES

A.N.Dovbnya, N.I.Aizatsky, V.N.Boriskin, V.V.Zakutin, V.A.Kushnir, V.A.Mitrochenko,
N.G.Reshetnyak, Yu.Ya.Volkolupov, M.A.Krasnogolovets
National Science Center 'Kharkov Institute of Physics & Technology'
1, Academicheskaya St., NSC KIPT, 61108 Kharkov, Ukraine

Abstract

The investigation into the generation of tubular electron beams and their parameters in a system of secondary-emission cathodes was carried out. The parameters of electron beams in a multi-cathode secondary-emission source and a single magnetron gun with the use of a multi-channel measuring system were measured. The stability of the beam current amplitude and a net charge in the beam (pulse to pulse), current distribution on the azimuth were studied. In the 8-cathode system at a cathode voltage of ~ 34 kV and a magnetic field strength of ~ 3500 Oe the total current of all beams was ~ 35 A and its stability was $4\pm 5\%$. In the single magnetron gun at a cathode voltage of ~ 30 kV and a magnetic field strength of ~ 2500 Oe the beam current was ~ 60 A. And its stability was $2\pm 4\%$.

1 INTRODUCTION

The electron sources with cold metallic secondary-emission cathodes in crossed fields are of interest as sources of tubular multi-beam electron beams for the

measured the beam parameters in the system with a very non-uniform electric field and in a single magnetron gun. The parameters such as a stability of the electron beam current amplitude and a shape of the electron beam cross-section were studied.

2 EXPERIMENTAL INSTALLATION AND PROCEDURE

The system with a common coaxial anode (1,2) inside which the secondary emission cathodes are arranged is shown in fig.1a. The system comprises 8 copper cathodes (3) of 5 mm diameter. The cathodes are arranged uniformly inside the common coaxial anode on the circle of 44mm diameter. The diameter of the external cylinder of the anode (1) is 68 mm, the diameter of the internal cylinder (2) is 20 mm. The anode cylinders are made from stainless steel and are connected between them with a metallic flange with holes through which the cathodes are put in. The experiments were carried out at the installation [1] the layout of which is presented in Fig.1b.

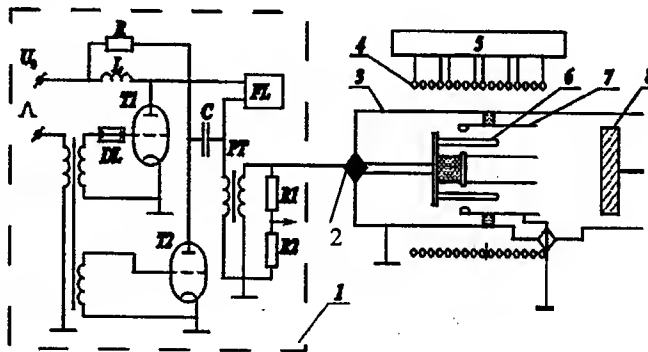
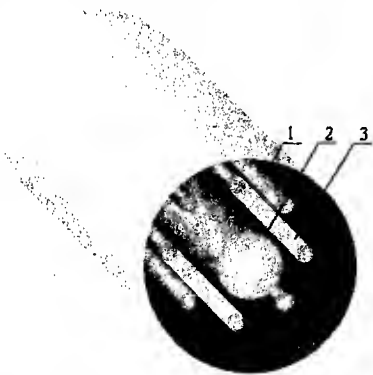


Figure 1 a) Multicathode system. 1,2-anode cylinders; 3-secondary emission cathodes, b) Experimental installation arrangement

microwave high-voltage pulse electronics. Arrangement of cathodes and anodes in the system determines the electric field uniformity and, respectively, the beam generation conditions in it [1]. Till recently, the investigations were carried out with the secondary-emission magnetron sources having a non-uniform electric field distribution on the azimuth [1-3]. In paper [4] studied are the processes of the spatial-periodic beam generation in a multi-cellular system with a non-uniform electric field distribution. Another configuration of a non-uniform system is a multi-cathode system in which the cathodes made in the form of metallic rods are arranged inside the common cylindrical anode. In the present work we have investigated the electron beam generation and

A voltage pulse necessary for the beam generation was shaped in pulse modulator 1 by adding the pulses from two pulse generators in thyristors T1 and T2 [5]. To cathodes 6 of the system through isolator 2 the voltage pulses were applied with an amplitude overshoot up to 100 kV and a pulse flattop duration of $\sim 5\mu s$ (of a controllable amplitude) with a repetition rate of 15 Hz. Anode 7 of the system is grounded. The onset of the secondary-emission process was taking place at the peak decay (duration of $\sim 0.3\mu s$, slope of ~ 150 kV/ μs).

The multi-cathode electron source was placed in vacuum chamber 3 where a discharging of $\sim 10^{-6}$ Torr was maintained. The magnetic field for beam generation and beam transport was created by solenoid 4 supplied from source 5.

To study the parameter of each of beams we used sectionalized cooled Faraday cup 8 (each section of which, of 10mm diameter, recorded the beam from one cathode) disposed at a distance 40 mm from the anode cut. The scattered electrons come onto the block of Faraday cups enveloped by the mask. To investigate the spatial and time uniformity of a beam one of the Faraday cups was covered by the silver shield with a thin radial slit. ($D \sim 0.5$ mm) that allowed observing the beam glow and evaluating visually its transversal dimensions.

The pulses from the Faraday cups, masks, cathode voltages (from the high-voltage divider) arrive into the computer. The measuring system allows one to process (with a discreteness of 100 ns) 32 pulses following one after another by 12 channels: 10 beam channels, the voltage pulse channel and the microwave signal channel. We have measured the current amplitude for each of beams, the mean cathode voltage amplitude, the total beam current and the coefficients of maximum pulse amplitude deviation from the mean value (that is equivalent to the stability of beam currents and cathode voltages). These parameters were measured in the given time point – at the beam current pulse flattop and were averaged for 32 pulses. The measurement error is $1 \pm 2\%$. Besides, the mathematical processing of a pulse sequence (determining their area) was performed to determine the voltage stability and the net charge of beams.

3 EXPERIMENTAL RESULTS AND DISCUSSION

In the system under consideration the generation of 8 electron beams was obtained. At a cathode voltage of 34 kV and a magnetic field strength of ~ 3500 Oe the average value of the current from each of 8 beams positioned on the azimuth changed from 3.15 A to 3.48 A ($\pm 5\%$), and at a voltage of 28 kV it was from 2.5 A to 2.8 A ($\pm 6\%$). This difference is caused by the unequal conditions of beam generation by each cathode that can take place because of the inaccuracy of assembling the system and upsetting the centering of each of cathodes relatively to its Faraday cap.

Fig.2 shows the beam currents (averaged for 32 pulses), recorded by the measuring systems, from 7 cathodes (I1 ... I7) in one voltage pulse U (beam current pulses from the 8th Faraday cup and from the mask are not shown). From the figure one can see that the beam currents from each cathode are insignificantly different by the amplitude, and the pulse shapes are almost coinciding with each other. The electron beam current reaching the mask in this case is ~ 10 A, and the total beam current is ~ 36 A.

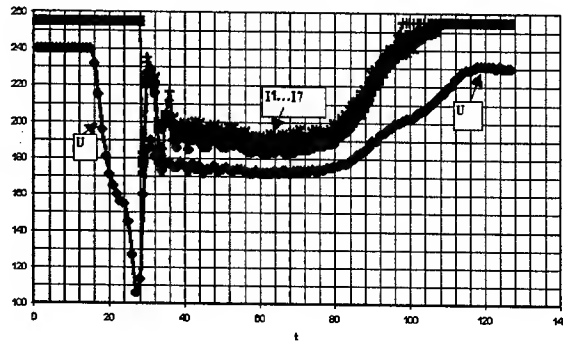


Figure 2. Beam current pulses (I1 ... I7) and cathode voltage pulse (U)

The processing of the results obtained in several series of measurements showed that at a cathode voltage of 34 kV the current stability was from 1 to 4% for current I1, from 1 to 5% for current I2, and the stability of the total current of all beams was from 2 to 5%. The stability of the voltage amplitude in this case was from 1 to 2%. When processing the results of beam current measurements using another method, i.e. by the total beam current, we have obtained the similar results.

The beam current stability of a short duration, with taking into account three pulses following one after other for current I1, was $1 \pm 3\%$ at the voltage amplitude instability of $\sim 1\%$. This value characterizes the limited possibilities of the multi-cathode secondary-emission system in the given concrete experimental conditions.

The experiments have been performed under conditions of the magnetic field instability (pulse-to-pulse) of $\sim 2\%$. The axis of the system was displaced approximately by 4 mm relatively to the axis of the magnetic field and had the tilt angle $\sim 1^\circ$, the misalignment of the cathode and the anode was $\sim 0.1 \pm 0.2^\circ$.

In the secondary-emission system the beam generation stability is determined by the following factors: number of primary electrons bombarding the cathode surface, their energy accumulation stability, presence of steady processes of the secondary-emission multiplication at the stationary stage of beam generation [1], stability of electric and magnetic fields in time and space, etc. These conditions should be satisfied in each of pulses following one after other. The above given experimental results show that the beam current amplitude stability and, consequently, the total stability of all the factors providing the beam generation can have the value of ~ 1 to 2% .

The electron beam generation with the use of secondary-emission cathodes in non-uniform electric fields has some features. This is concerned, in particular, with a transverse beam current distribution. In paper [4] one considers the shaping of four electron beams in the system of rod cathodes and anodes. Calculations of the electric field non-uniformity on the azimuth showed that near the cathode surface it was $\sim 5\%$. The imprint of each beam on the Faraday cap was in the form of a ring close

to a circle. In our case, because of the cylindrical geometry of the anode, the calculated electric field non-uniformity on the azimuth near each cathode is $\sim 40\%$. Here, the electron drift on the radius, determined by the electric field value, leads to shaping the beam of an elliptic cross-section and to turning the ellipse axis. Then a considerable beam corona is formed that creates conditions for a large current of the mask (~ 10).

Fig.3 presents the photo of electron beam glow at the Faraday cup covered with the silver shield. In the photo there is shown the line of a section of 0.5mm width. The glow was in the form of an ellipse turned at an angle $\sim 45^\circ$ with a wall thickness from 0.5 to 1 mm. When the magnetic field is changing the ellipse axis turns at an angle 90° . The major half-axis of the ellipse was 6.5 ± 7 mm, the minor half-axis was $\sim 5.5 \pm 6$ mm. This result, practically, coincides with the results obtained in [6]. It should be noted that at such a significant value of the field non-uniformity the beam ellipticity is not great and equals to 1.2 ± 1.3 . The processing of measurement results from the Faraday cup sectioned into two isolated parts has shown that the ratio of currents taken from these isolated parts remains constant and has a stability of $5 \pm 15\%$. This indicates on the rather high stability of a beam position at the target.

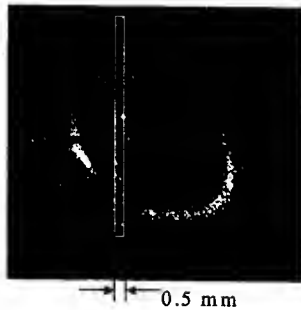


Figure 3. Photography of the beam glow

In the system we observed also the generation of microwave oscillations developed in the course of electron beam shaping. Probably, the microwave oscillations are related with oscillations of the spatial discharge of the electron cloud.

Also, the investigations of the beam current stability in the single magnetron gun with a copper cathode of 40mm diameter and a cylindrical cathode of 50mm diameter

were carried out. At a cathode voltage amplitude of ~ 30 kV and a magnetic field strength of 2500 Oe the beam current was ~ 60 A. The investigation undertaken showed that the current stability of each section in the Faraday cylinder is $2 \pm 4\%$ at a cathode voltage amplitude stability of $1 \pm 2\%$.

4 CONCLUSION

The investigation performed showed, for the first time, a possibility of electron beam generation stabilization in secondary-emission systems. In the multi-cathode electron source the stability of the anode current of each of 8 beams on the azimuth was changing within $\pm 5\%$. It is shown that the beam current stability is $\sim 1 \pm 3\%$ and can reach $\sim 1\%$ under optimum conditions. In the single magnetron gun the beam current stability is $2 \pm 4\%$. Such sources of tubular electron beams can be used in the accelerator technology and in powerful microwave devices.

The work is fulfilled with the support of the University of St. Andrews, Scotland.

REFERENCES

- [1] Volkolupov Yu.Ya., Dovbnya A.N., Zakutin V.V. et al.// Zhourn.Tekhn.Fiz.2001. V.71. N.2. P.98-104 (in Russian).
- [2] Saveliev Y.M., Zibbert W., Parkers D.M.// Physics of Plasmas. 1997. V4. N.7. P.2319-2321.
- [3] Volkolupov Yu.Ya., Dovbnya A.N., Zakutin V.V. et al.// Zhourn.Tekhn.Fiz.2001. V.71. N.7. P.88-91 (in Russian).
- [4] Aizatsky N.I., Volkolupov Yu.Ya., Dovbnya A.N., et al. Pis'ma v Zhourn. Tekhn. Fiz. 2001. V.27. N.23. P.25-30 (in Russian).
- [5] Dovbnya A.N. Reshetnyak N.G., Romas'ko V.P. et al.//Proc. of the Part.Accel.Conf., Chicago, USA, 18-22 June, 2001. V.5. P.3759-3761.
- [6] Aizatsky N.I., Boriskin V.N., Dovbnya A.N. et al.// Zhourn.Tekhn.Fiz.2003. V.73. N.2. P.113-117 (in Russian).

DEVELOPMENT AND STATUS OF THE SNS ION SOURCE

R. F. Welton, M. P. Stockli, S.N. Murray

Accelerator Systems Division, Spallation Neutron Source*
Oak Ridge National Laboratory, Oak Ridge, TN, 37830-6473

R. Keller

Lawrence Berkeley National Laboratory, Berkeley, CA 94720

Abstract

The ion source for the Spallation Neutron Source (SNS) is a radio-frequency, multicusp source designed to deliver 45 mA of H^- with a normalized rms emittance of less than 0.2π mm mrad to the SNS accelerator. The ion source—designed, constructed, and commissioned at Lawrence Berkeley National Laboratory (LBNL)—satisfies the basic requirements of commissioning and early operation of the SNS accelerator. To improve reliability of the ion source and consequently the availability of the SNS accelerator, we are undertaking a comprehensive ion source development program at Oak Ridge National Laboratory (ORNL). To date, this program has focused on design and development of internal and external ion source antennas having long operational lifetimes, development and characterization of efficient RF matching networks, simulation and measurement of the extracted ion beam and, optimization of the beam extraction and Cs systems. This report will outline progress made in some of these areas as well as summarize the current state of the SNS ion source discussing specifically source performance during front end re-commissioning at ORNL.

INTRODUCTION

The Spallation Neutron Source (SNS) is a second-generation pulsed neutron source dedicated to the study of the dynamics and structure of materials by neutron scattering and is currently under construction at Oak Ridge National Laboratory (ORNL). Neutrons will be produced by bombarding a liquid Hg target with a 1.4-MW, 1-GeV proton beam produced using several types of linear accelerators and an accumulator ring [1,2]. In order to meet this baseline requirement, the ion source must deliver approximately 45 mA of H^- within a 1-ms pulse (60 Hz) into a normalized rms emittance of 0.2π

mm mrad. SNS performance upgrades are being discussed which will require 3-5 MW of beam power and consequently demand higher beam currents from the ion source. This report discusses some highlights of our ion source development program as well as ion source performance during the re-commissioning of the front end at ORNL.

THE H^- MULTICUSP ION SOURCE

A schematic diagram of the H^- ion source is shown in Fig. 1. The source plasma is confined by a multicusp magnet field created by a total of 20 samarium-cobalt magnets lining the cylindrical chamber wall and 4 magnets lining the back plate. RF power (2 MHz, 20-50 kW) is applied to the antenna shown in the figure through a transformer-based impedance-matching network. A magnetic dipole (150-300 Gauss) filter separates the main plasma from a smaller H^- production region where low-energy electrons facilitate the production of large amounts of negative ions. A heated collar, equipped with eight cesium dispensers, each containing ~ 5 mg of Cs_2CrO_4 , surrounds this H^- production volume. The RF antenna is made from copper tubing that is water cooled and coiled to 2 $1/2$ turns. A porcelain enamel layer insulates the plasma from the oscillating antenna potentials. More details of this source design can be found in reference 3.

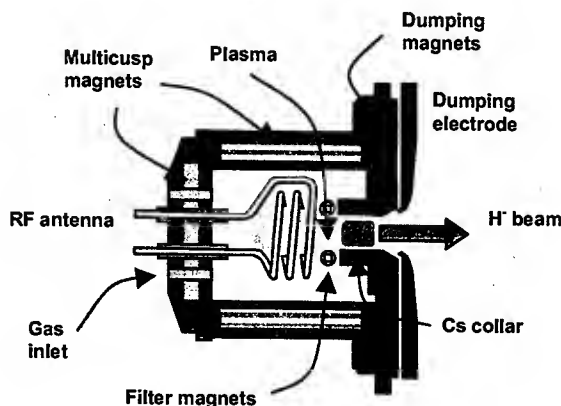


Figure 1: Schematic diagram of the SNS ion source.

*SNS is a collaboration of six US National Laboratories: Argonne National Laboratory (ANL), Brookhaven National Laboratory (BNL), Thomas Jefferson National Accelerator Facility (TJNAF), Los Alamos National Laboratory (LANL), Lawrence Berkeley National Laboratory (LBNL), and Oak Ridge National Laboratory (ORNL). SNS is managed by UT-Battelle, LLC, under contract DE-AC05-00OR22725 for the U.S. Department of Energy.

RF ANTENNA DEVELOPMENT

The multicusp, RF-driven, positive/negative ion sources developed at LBNL have performed quite well in a wide variety of applications [4]. Most of these applications have involved pulsed, low duty-factor operation in which thinly coated (100- to 200- μ m) porcelain enamel coatings were sufficient to guarantee a long operational lifetime. The SNS ion source, on the other hand, requires long pulses (~ 1 ms) and high repetition rates (~ 60 Hz) as well as high peak RF powers (20-50 kW) and therefore tends to destroy these antennas rapidly, usually within a few hours of operation. In a collaborative effort between LBNL and ORNL, we began to improve the lifetime of this ion source component. Detailed accounts of this effort can be found in earlier work [5], and we will only summarize here.

Electromagnetic modeling has shown that a 1- to 2-kV RF potential develops across the length of the antenna because of its inductance. Large RF electric fields can develop between different parts of the antenna and between the antenna and the plasma chamber, since one leg of the antenna is grounded to the plasma chamber through a resistor. If the antenna coating is not sufficiently thick or has too large a dielectric constant the majority of this electric field will exist within the plasma sheath as opposed to within the insulating coating. Large electric fields in the plasma sheath accelerate charged plasma particles into the coated antenna, causing sputter ejection of the coating materials as well as vaporization of the coating material from localized heating. Eventually, a thin spot in the coating develops that enhances the electric field, driving the process until a hole is burnt through the coating. Once bare conductor of the antenna is exposed to the plasma, the plasma itself can conduct a significant portion of the RF current normally carried by the antenna and thereby greatly reduce the inductive power coupling to the plasma. This process can be greatly accelerated if a manufacturing defect already exists porcelain coating.

Quantitative models have been developed and applied to fusion plasmas to determine the fraction of a given electric field that exists within the plasma sheath, versus the field inside a dielectric wall material [6]. Using the plasma parameters of the SNS source and material properties of the porcelain enamel coating, it has been shown that essentially all of the electric field within the plasma sheath can be eliminated provided the following two conditions are met [6]. First, the coating is sufficiently thick, greater than 0.5 mm, several times the thickness of the original coating. Second, the dielectric constant of the porcelain is reduced by removal of the TiO_2 ($K=86$) component from the porcelain mixture.

Based on these calculations, a local company [7] developed a multi-layer coating technique to achieve the specified coating thickness and composition. Since TiO_2 is added to porcelain enamel mixtures purely as a color pigment with no structural importance, it was easily eliminated from the mixture resulting in a coating that appears clear. This approach has yielded coatings as thick as 1 mm which was achieved through the successive

application of ~ 10 enamel layers. Increasing the number of layers also improves antenna lifetime by reducing the chance that a single layer defect will cause an electric breakdown through the coating.

To date antennas fabricated in this fashion have allowed the successful commissioning of the front end of the SNS at LBNL (~ 500 hours of operation) and again at ORNL (~ 1000 hours of operation) [8]. In addition to these accelerator-commissioning activities, which have generally required low duty-factor operation, we have also performed several high duty-factor lifetime tests. On one occasion, the source operated continuously for 107 hours with ~ 25 kW of applied RF power at the full 6% duty factor with no visible damage to the antenna observed. During the last few hours of the test, a ~ 25 mA beam was extracted from the source. Another such test also occurred at LBNL on the front-end system, where the source was operated for 125 hours at 2-3% duty factor, again producing ~ 25 mA with no antenna damage visible.

To ensure an adequate ion source lifetime at the nominal SNS beam current and duty factor, in the absence of specific lifetime tests, we have developed a contingency strategy for coupling RF power into the source: use of an external antenna. This approach is similar to that employed at DESY for their very low duty factor application [9]. To date, thermal and mechanical finite-element analysis has been performed on an Al_2O_3 plasma chamber to determine an optimal design. One such design, shown in Fig. 2, was developed in conjunction with designers at ISI Corporation. The design features an alternative ion source backflange where the helical antenna is submerged in de-ionized water surrounding an Al_2O_3 plasma chamber. This system is currently under consideration for development.

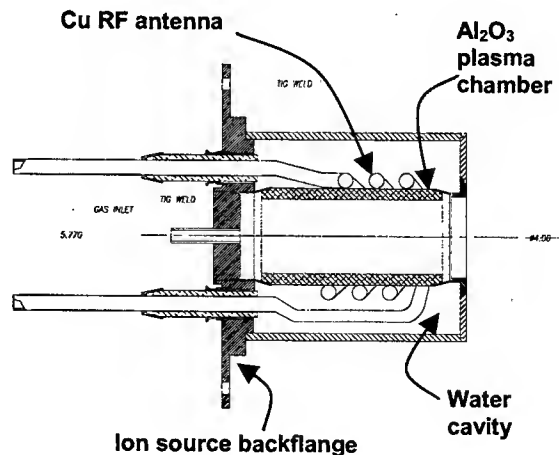


Figure 2: Initial design of an external antenna for the SNS ion source.

SOURCE PERFORMANCE

The SNS front end was recommissioned at ORNL from Nov 5, 2002, to Jan 31, 2003. The ion source performed

quite well over this period and allowed accomplishment of most of our commissioning goals [8].

Initially, a beam-intercepting flag (biased to +300V to suppress secondary electrons) was installed just downstream of the extractor electrode and was used for initial ion source check out as well as operator training. Beam currents as high as 35 mA were produced during this early commissioning period. Fig. 3 shows the dependence of the ion current, intercepted by the flag, on the applied RF power for an un-cesiated source (squares) and after 1 successful cesiation of the source (diamonds). Source cesiation was accomplished by raising the temperature of the 8 Cs dispensers to ~550 C for ~1/2 hour and then maintaining a collar temperature of ~275 C.

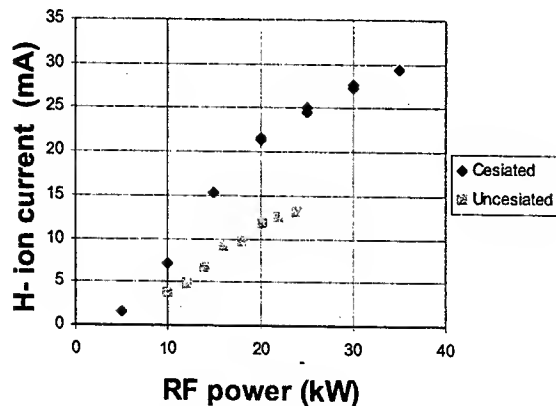


Figure 3: Ion current versus applied RF power from both cesiated and uncesiated sources.

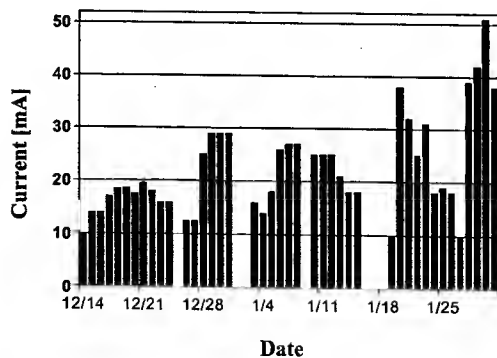


Figure 4: Typical beam currents produced during front-end commissioning at ORNL.

On Dec 14 we began injecting beam into the front-end system [8]. Fig. 4 shows typical beam currents measured over the accelerator-commissioning period by current transformers located near the entrance and exit of the medium-energy beam transport (MEBT). Since most of our commissioning tasks did not require large beam currents, we ran at modest current levels of 15- to 30-mA for much of the commissioning period.

The commissioning period also served as a shakedown of the front-end system delineating weaknesses. The ion source and low-energy beam transport (LEBT, between the ion source and RFQ) systems were available 68% of the time. Much of the down time was attributed to mechanical failures of the LEBT, problems with the ion source RF amplifiers induced by high-voltage sparks, and not having a readily available backup source. Most of these problems have been corrected over the last several months. Near the end of this period when we aimed for higher beam currents, consistent with the commissioning schedule, we were able to achieve currents in excess of 51 mA from a newly cleaned source with fresh Cs operating at higher collar temperatures (300 C) than were maintained during earlier operations.

REFERENCES

1. N. Holtkamp, et al., "The SNS Linac and Storage Ring: Challenges and Progress Towards Meeting Them," EPAC'02, Paris, France, ID: 191 - TUZGB002.
2. M. White, "The Spallation Neutron Source (SNS)," LINAC'02, Gyeongju, Korea, ID: MO101.
3. R. Keller et al., "Ion-source and LEBT Issues with the Front End Systems for the Spallation Neutron Source," Rev. Sci. Instrum. 73 (2002) 914.
4. K. N. Leung, "The Application and Status of the Radio Frequency Multicusp Source," Sci. Instrum. 71 (2000) 1064.
5. R. F. Welton et al., "Ion Source Antenna Development for the Spallation Neutron Source," Rev. Sci. Instrum. 73 (2002) 1008.
6. J. R. Myra et al., J. Nucl. Mater. 249 (1997) 190.
7. Cherokee Porcelain Enamel Corporation, 2717 Independence Lane, Knoxville, TN 37914.
8. A. Aleksandrov, "Commissioning of SNS Front End Systems at ORNL," PAC 2003.
9. J. Peters, "Internal versus External RF Coupling into a Volume Source," EPAC'02, Paris, France, ID: 710 - THPRI025.

PROOF-OF-CONCEPT EXPERIMENTS FOR NEGATIVE ION DRIVER BEAMS FOR HEAVY ION FUSION*

L. R. Grisham, Princeton Plasma Physics Laboratory, P.O. Box 451, Princeton, N.J. 08543
 S. K. Hahto, S. T. Hahto, J. W. Kwan, K. N. Leung, Lawrence Berkeley National Laboratory,
 1 Cyclotron Rd, Berkeley, CA 94720

Abstract

Negative halogen ion beams have recently been proposed as heavy ion fusion drivers. They would avoid the problem of electron accumulation in positive ion beams, and could be efficiently photodetached to neutrals if desired [1]. Initial experiments using chlorine produced a current density of 45 mA/cm² of 99.5% atomic negative Cl with an e/Cl⁻ ratio as low as 7:1 and good emittance.

INTRODUCTION

Driver concepts for heavy ion fusion have traditionally relied upon positive ions, which suffer the possible drawback of accumulating electrons in their deep potential wells. Negative ions would preclude electron accumulation, and if desired, could be converted to atoms by photodetachment with technically feasible lasers before entering the target chamber. The halogens bromine and iodine are the most appropriate masses for a driver, but chlorine, which has a similar electron affinity and is a gas at room temperature, is ideal for proof-of-concept experiments of the source [2].

EXPERIMENTAL ARRANGEMENT

In a process similar to that by which hydrogen forms negative ions in plasmas, halogens can be expected to form negative ions by dissociative attachment of electrons to vibrationally excited diatomic molecules. Thus, an RF driven (12.56 MHz) source previously used for H⁻ production was used with Cl₂ for these experiments. A movable 135 gauss magnetic filter divided the plasma into a vibrational excitation region and an extraction region. A fuller discussion of the setup and the experiments is provided in ref. [3]. Permanent magnets deflected electrons from the beam for measurement. Ion currents were measured with a secondary-suppressed Faraday cup, and a magnetic mass spectrometer analyzed the ion species. Hydrogen, with an electron affinity of 0.75 eV, requires the addition of Cs to produce significant negative ion currents. The halogens have electron affinities of 3.06 – 3.62 eV, so no Cs was needed.

EXPERIMENTAL RESULTS

Oxygen Tests

With an electron affinity of 1.27 eV, oxygen was a convenient non-toxic comparison gas before trying Cl (electron affinity of 3.61 eV). With 2 kW of RF power, a maximum of 5.7 mA/cm² of O⁻ was extracted under the same discharge conditions which yielded 22 mA/cm² of

O⁺ and an electron-to-negative-ion ratio of 300. The negative/positive ion ratio of 0.25 is much better than is achievable in uncesiated H discharges, where it is typically of order .01 – .03. Figure 1 shows oxygen currents extracted versus extraction voltage with 1.5 kW of RF and a source pressure of 10 mTorr, with 40% of the positive ions O⁺ and 90% of the negative ions O⁻.

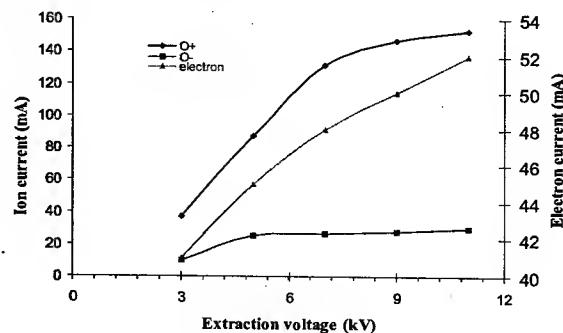


Figure 1: O⁻, O⁺, and e⁻ currents vs extraction voltage.

Chlorine Results

The positive ion spectrum with chlorine was 82% Cl⁺, with the rest in Cl₂⁺ and impurities such as nitrogen and oxygen. At the same RF power of 1.5 kW, the negative spectrum was 99.5% atomic Cl⁻, 0.5% Cl₂⁻, and no detectable impurities. Figure 2 shows the Cl⁻, Cl⁺, and e⁻ current densities versus extraction voltage with arc conditions of 1 kW RF and 25 mTorr. With chlorine's greater electron affinity, the ratios of negative/positive ions and of negative ions to electrons are much more favorable than was the case for oxygen.

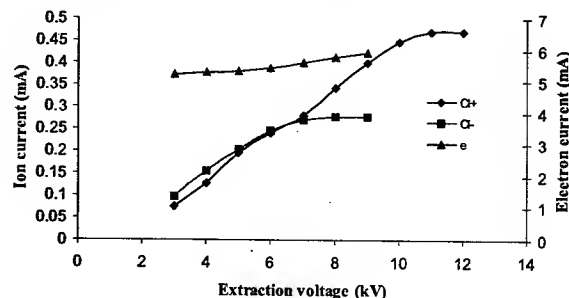


Figure 2: Cl⁻, Cl⁺, and e⁻ currents vs extraction voltage.

The Cl⁻ current density was only weakly dependent upon source pressure across the measured range of 20 – 35 mTorr but began to decline below 20 mTorr. As was the case with O⁻, the Cl⁻ current density scaled linearly with RF power, where it should be noted that the RF

power levels given in this paper are the output power of the RF supply; the actual power coupled into the discharge plasma would have been less.

At an RF power of 2.2 kW (the maximum of the supply) and a source pressure of 28 mTorr, the Cl^- current density was 45 mA/cm^2 and the e^-/Cl^- ratio was 7. Under the same discharge conditions the Cl^+ current density was 53 mA/cm^2 , so the ratio of Cl^- to total positive ion current was 0.69. Since more of the Cl^- would be lost through stripping in the extractor and modestly-pumped analyzer system than would be the case for positive ion loss due to charge exchange, the actual density of Cl^- in the extraction plane plasma was probably greater than 69% of the total positive ion density. Because of their large electron affinities, halogens can form ion/ion plasmas which leave very little room for electrons in phase space [4]. This is substantiated by the low e^-/Cl^- ratio that was obtained without the extractor plane magnets used to reduce the copious co-extracted electrons from H^- sources. Based upon the difference in mobilities, one would expect an e^-/Cl^- ratio of about 240 instead of 7 if the electrons and ions had the same temperature, and in fact, the electron temperature was probably higher than that of the ions, which would make the expected ratio even larger. In the case of oxygen, the e^-/O^+ ratio of 300 exceeded the mobility ratio of about 160 for the same temperatures, implying a higher electron temperature.

In H^- volume sources, biasing the plasma grid positive relative to the plasma reduces the co-extracted electron current and can increase the extracted negative ion current [5]. With oxygen, the bias induced a noticeable effect, augmenting the O^- current by 20% while diminishing the e^- current by 25% as the bias increased from 0 to 15 volts; higher voltages reduced both species. In chlorine plasmas, varying the bias from 0 to 35 volts had almost no effect upon the Cl^- current, and reduced the e^- by less than 5%. This probably reflects the scarcity of electrons in the ion/ion chlorine plasma at the extractor plane.

Figure 3 shows Cl^- and e^- currents as functions of source pressure. The e^- current is much more sensitive to pressure than the Cl^- current, declining strongly with pressure. This may be due to a decrease in the extractor-region electron temperature at higher pressure, which would reduce the electron mobility.

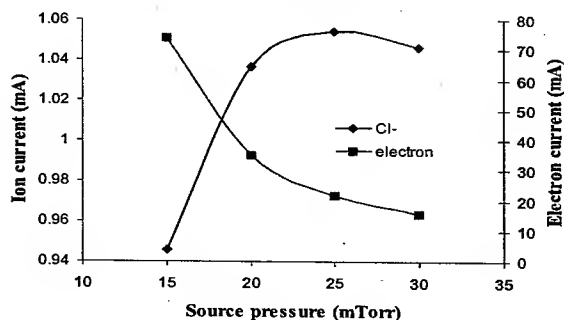


Figure 3: Cl^- and e^- versus pressure

Figure 4 shows the Cl^- and e^- extracted currents as a function of the distance from the plasma grid of the magnetic filter which partitions the plasma. The electron current is significantly more sensitive to filter position than is the Cl^- current. The rapid rise in electron current for the largest distances from the extraction plane might be partly due to the fact that this movable filter may have allowed leakage of energetic electrons around its edges; with more distance, a greater number of these electrons may have reached the axis, where the extraction aperture was located. Alternatively, the filter may have been positioned too close to the RF antenna, allowing electron heating beyond the filter.

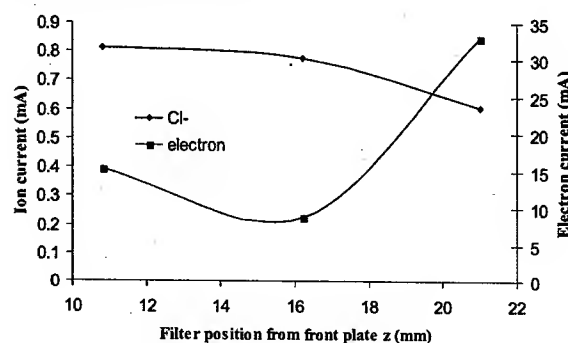


Figure 4: Cl^- , e^- versus filter distance from plasma grid

A pepper pot measurement was done to obtain an approximate measure of the effective beam temperature in the directions transverse to the beam propagation axis. Measurements were done in the directions parallel and perpendicular to the electron deflection magnetic field. The effective beam temperature is larger in the perpendicular direction due to the magnetic deflection of the ions. The effective temperatures in the perpendicular direction were 0.5 eV for both Cl^- and Cl^+ ; in the parallel direction they were 0.3 eV for Cl^- and 0.2 eV for Cl^+ .

Implications for Heavier Halogens

The more massive halogens, bromine (mass 79 and 81) and iodine (mass 127), are most likely to fit the mass requirements presently being considered for heavy ion driver beams. Experiments with these elemental feedstocks will require ion sources at moderately elevated temperatures (the boiling points of Br and I are 59 C and 114 C, respectively). Since they should form negative ions through the same mechanism as Cl (dissociative attachment of electrons to vibrationally excited dimers), results with the heavier halogens should be similar to the Cl experiments. The achievable current density at a given RF power may be somewhat lower for Br, with an electron affinity of 3.36 eV, and for I, with an electron affinity of 3.06 eV, than they were for Cl. However, this should not be a problem if the observed linear scaling of negative ion current density with RF power continues to higher levels. For instance, the 45 mA/cm^2 of Cl^- found at 2.2 kW extrapolates to about 100 mA/cm^2 at 5 kW, which was the planned power level for this source before problems were found with the intended power supply.

Although one would normally expect the co-extracted electron component to be greater for Br and I than for Cl, both because of their greater mass and their somewhat lower electron affinities, this may be compensated to an unknown degree by a competing effect: the greater mass of Br^+ and I^+ compared to Cl^+ . The addition of cesium to H sources not only increases the production of H^- ; it also significantly reduces the co-extracted electron current. The electron suppression is thought to occur because the massive (133 amu) Cs^+ in plasma near the extraction plane provides a drag on the flow of the low energy electrons in that region to the extraction meniscus. If this hypothesis is correct, then the same effect could be expected to occur in halogen plasmas. Thus, the low level of electrons co-extracted with Cl^- might be partly attributable to the mass (37 amu) of Cl^+ , in which case the electron suppression could be expected to be even more favorable for Br and I. Iodine has almost the same mass as cesium (127 versus 133), and the density of I^+ in an iodine plasma should be significantly higher than the density of Cs^+ in a dominantly hydrogen plasma.

H^- ion sources commonly remove their much more abundant co-extracted electrons by mounting permanent magnets inside the extractor grid to deflect the electrons onto the extractor aperture walls while they are still at low energy. The effect upon the optics of the H^- is small because of its much greater mass. While this technique works well, the space required for the placement of magnets reduces the maximum grid transparency available to a multi-aperture beamlet array.

This same technique could be used for multi-aperture Br^- or I^- beamlet arrays; because they are both much more massive than H^- , the effect upon ion optics should be even less than in today's H^- sources. However, it might not be necessary if the electron component remains as small as was found with Cl. Unlike the current applications of multi-aperture H^- sources, which must dump the electrons because the beam pulses last for seconds, and the electrons would otherwise reach the full acceleration energy, heavy ion fusion sources will fire microsecond pulses, and the electrons could be dumped further down or after the injector before they reach the main accelerator, since the short pulses and low duty factor would limit the heat load.

CONCLUSION

Heavy negative ions would have some appealing characteristics as driver beams for inertial confinement fusion [1]. Because the halogens have large electron affinities they are the most natural candidates for high brightness heavy negative ion sources [2]. A proof-of-concept experiment was conducted using chlorine, which can be used in a room temperature source, and should be a good surrogate for bromine and iodine, which have masses more appropriate for driver beams, but require moderately elevated source temperatures.

In contrast to ion sources using hydrogen, which has an electron affinity of 0.75 eV, it was not necessary to add cesium to obtain high negative ion current densities. In order to evaluate the effect of electron affinity upon yield, the source was first operated with oxygen (electron affinity of 1.27 eV), producing an O^- yield of 5.7 mA/cm², an O^- to positive ion ratio of 0.25, and an electron-to-negative-ion ratio of 300. Chlorine (electron affinity of 3.62 eV) yielded a negative ion spectrum which was 99.5% Cl^- , 0.5% Cl_2^- , and no detectable impurities. Under the most optimized conditions, the Cl^- negative ion current was 69% of the total positive ion current, suggesting a mostly ion-ion plasma near the extraction plane (probably with an even higher fraction of negative ions than the current ratios indicate, because of higher negative ion loss rates at low energy). Under these conditions, the electron current to negative chlorine ratio was 7, much less than the mobility ratio of about 240 for equal temperatures, which also suggests the presence of few electrons in the extraction plane plasma. Biasing the plasma grid positive relative to the plasma reduced co-extracted electrons and increased O^- with oxygen, but had little effect with chlorine, again suggesting a scarcity of electrons in the extraction plane plasma. Preliminary emittance measurements gave effective beam temperatures of 0.2 eV for Cl^+ and 0.3 eV for Cl^- in the direction parallel to the electron analysis magnets, and 0.5 eV for both species in the direction perpendicular to the analysis field; these values appear acceptable for drivers.

In both oxygen and chlorine plasmas, the negative ion current density scaled linearly with RF supply output. At the maximum RF supply power of 2.2 kW, the Cl^- current density was 45 mA/cm², which would extrapolate to about 100 mA/cm² at 5 kW (the intended level before problems with the RF supply). This level is fully adequate for driver applications. Since halogens permit negative ion current densities similar to positive ion densities, the extractable current densities of heavier driver ions such as I^- or Cs^+ will depend upon the extraction voltage which can be applied. This will be a function of the extractor design, and not the polarity of the ion. Thus, achievable ion source parameters appear acceptable for halogen negative ion driver beams.

REFERENCES

- [1] L. R. Grisham, Nucl. Instrum. & Meth. **A464**(2001) 315.
- [2] L. R. Grisham, Fus. Sci. & Tech. **43** (2003) 191.
- [3] S. K. Hahto, S. T. Hahto, J. Kwan, K. N. Leung, L. R. Grisham, Rev. Sci. Instr., in press (2003).
- [4] M. Bacal, H. Doucet, IEEE Trans on Plas. Sci. **PS-1** (1973) 91.
- [5] K. Leung, K. Ehlers, R. Pyle, Rev. Sci. Instr. **56** (1985) 11.

* Work supported by U.S. Department of Energy

3D MODELING ACTIVITY FOR NOVEL HIGH POWER ELECTRON GUNS AT SLAC

V. Ivanov, A. Krasnykh, G. Scheitrum, and D. Sprehn, SLAC, Stanford, CA 94025
L. Ives, and G. Miram, Calabazas Creek Research, Inc., 20937 Comer Dr., Saratoga, CA 94070

Abstract

The next generation of powerful electronic devices requires new approaches to overcome the known limitations of existing tube technology. Multi-beam and sheet beam approaches are novel concepts for the high power microwave devices. Direct and indirect modeling methods are being developed at SLAC to meet the new requirements in the 3D modeling. The direct method of solving of Poisson's equations for the multi-beam and sheet beam guns is employed in the TOPAZ 3D tool. The combination of TOPAZ 2D and EGUN (in the beginning) with MAFIA 3D and MAGIC 3D (at the end) is used in an indirect method to model the high power electron guns. Both methods complement each other to get reliable representation of the beam trajectories. Several gun ideas are under consideration at the present time. The collected results of these simulations are discussed.

INTRODUCTION

It is advantageous for multi-beam high power devices that the external magnetic flux guides each individual beam that is emitted from the cathode. This is known as confined flow focusing. The challenge is to develop electron guns and the associated magnetic optic system to confine and compress the electron beams and transport them through the separate beam tunnels to the spent beam collector. This is fundamentally a three-dimensional problem. Asymmetry of the focusing magnetic field can lead to partial interception of the beam. The beam interception creates the power losses and leads to the thermal deformations. To avoid these limitations it is necessary to develop methods of 3D computer simulation and create the mathematical model. A new approach for 3D analysis of the electron guns and beam optics utilizes a combination of MAFIA 3D and TOPAZ 3D. An algorithm based on perturbation theory provides a 3D correction to the 2D, self-consistent field solutions. The combination of TOPAZ 2D or EGUN (in the beginning) with MAFIA 3D and MAGIC 3D (at the end) is used as an indirect method to model the high power electron guns also.

3D MODELING OF MULTIBEAM GUNS **

The amount of RF power that can be produced in a linear beam microwave tube is dependent on the amount of beam power that can be transmitted through the device. Space charge forces that occur as the beam is bunched in device, limit the amount of current that can be transmitted. In order to increase the power, it is necessary to increase the beam voltage. This leads to reduced efficiency and complicates the power supply. One way to

reduce the space charge forces is to use a multiplicity of electron beams. They will travel through individual beam tunnels. This allows operation at significantly lower voltage while enhancing the RF performance. Additionally multi beam mode operation reduces the required magnetic power. For example, the reduction in beam voltage for the same level of rf power for the multi-beam klystron as compared to single-beam design is shown in Fig. 1. Here N is a number of the beamlets.

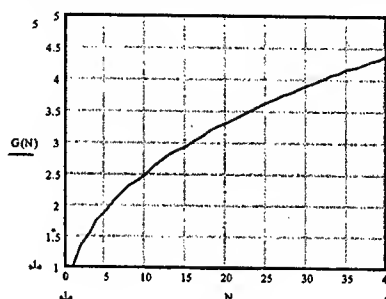


Figure 1

It is seen that the beam voltage can be reduced by factor 2.5 if the ten-beam configuration of klystron is employed.

The SLAC algorithm for a design of the MBG optical system was described in [1]. This algorithm was used for design of MBGs under SBIR grants (see footnote **). Additionally, the MBG for TESLA L-band klystron with initial triode configuration and post acceleration stage was investigated. The advantage feature of proposed klystron gun is a fact that the klystron is connected with DC power supply directly, i.e. without klystron modulator. Only the grid control pulser is required. This pulser has a DC grid bias that shuts off the multi beam gun between pulses. The intermediate electrode (modulating anode) separates the grid controlled region and the post acceleration stage and plays a role as a klystron gun arc protection.

Some of the results of the 3D MBG design, which were performed for Calabazas Creek Research, Inc, are presented. The sketch of MBG is shown in Fig. 2. Here the cross section of the iron dome behind the cathode is shown. The shape of the dome is made in such a way that the magnetic flux distribution in the region between a pole piece and the cathode duplicates the distribution for the case when the cathode is on the axis. A 3D cutaway picture of the iron dome is shown in Fig. 3. The presence of radial magnetic field (B_r) in the beam optical system is the result of the beamlet shear in accordance with $[\vec{v}_z \times \vec{B}_z]$ azimuthal component. The behavior of the off-axis confined flow beamlet is presented in Fig. 4.

** This part of work was performed for Calabazas Creek Research, Inc with funding provided by DoE SBIR program DE-FG03-00ER82964 and DoD SBIR program N00014-02-M-016.

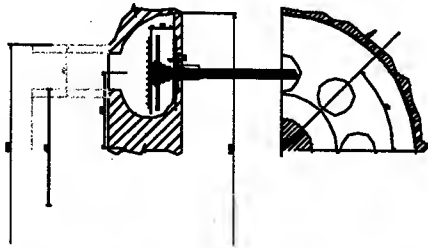


Figure 2



Figure 3

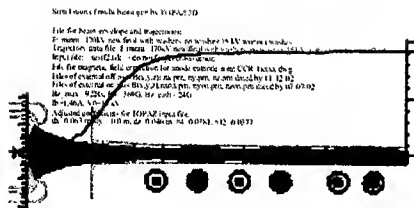


Figure 4

This beam envelope and its cross sections correspond to the case where the ratio between radius of the solenoid and the radius of the bore circle is approximately 2. The designed shape of the iron dome was insufficient to provide 100% transmission through the whole length of the device. A Fig. 5 illustrates B_r distribution along beam axis.

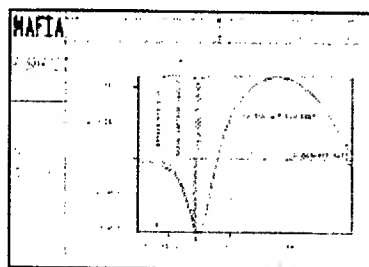


Figure 5

In this case, the fringe solenoid field contains large enough area with B_r . There are several methods to compensate this field. It was found that the field straighteners in the solenoid part effectively suppress the beamlet shear and allows the beam transmission to reach 100% (see Fig. 6).

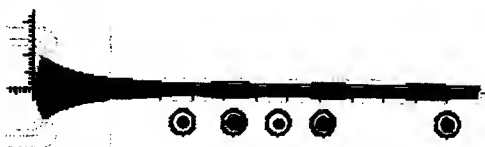


Figure 6

The iron dome shape around the cathode region and the field straighteners in the solenoid part provide the excellent duplication of on-axis magnetic field [2]. The MBG test bench is under construction. The results of the experimental study of this geometry are expected during this year.

3D MODELING OF SHEET BEAM GUNS

Studies of MBG for the high power X-band electron devices show that cathode current is high (more than 15 A/cm² in our example) reducing the cathode lifetime. The klystron with a sheet beam can overcome some limitations of the multi-beam devices. The design of sheet-beam guns (SBG) is fundamentally a three-dimensional problem. Two methods are currently used to design the SBG at SLAC. Direct and indirect modeling methods are developed to meet the new requirements in 3D modeling. The direct method of solving of Poisson's equations for the SBGs is employed in the TOPAZ 3D tool. The combination of TOPAZ 2D and/or EGUN (in the beginning) with MAFIA 3D and MAGIC 3D (at the end) are used in an indirect method to model the high power electron guns. Both methods compliment each other to get reliable representation of the beam trajectories. Currently two SBG geometries are under study. They are shown as quarter model of the whole geometry in Fig. 7 and 8.

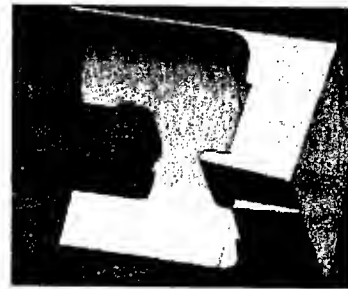


Figure 7

The gun of Fig. 7 represents the diode type gun with three elements: cathode (red), focus electrode (yellow), and anode (grey). This is $V_b=490$ kV and $I_b=250$ A gun with the 100×72 mm² cathode area.



Figure 8

The gun shown in Fig. 8 represents the triode configuration with the intermediate electrode (green). This electrode separates the beam formation region and post accelerating stage. The purpose of this electrode is to protect the cathode area against arcs. It can be also used as the modulating anode for some applications. The

pulsed control voltage in this case is smaller than the beam voltage and isolated x-fmr is necessary in this configuration. The most attractive modification of proposed gun is the gridded version gun that is shown in Fig. 8. This version is being developed for Calabazas Creek Research, Inc with funding from DoE. The current design parameters are as follows: $V_b=415$ kV, $V_1=150$ kV, $I_b=270$ A ($V_g=9$ kV for grid control of SBG). The cathode area is 100×84 mm². Both SBGs have the beam compressive and non-compressive planes. The problem was to find a shape of focus electrode, so the beam trajectories were similar to the 2D trajectories in the beam compressive plane. Especially it was necessary to pay attention for the trajectories at the corner of the cathode. Some of the studied focus electrodes for the diode version of SBG are shown in Fig. 9.

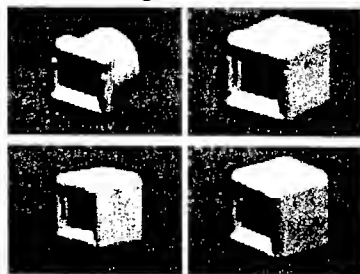
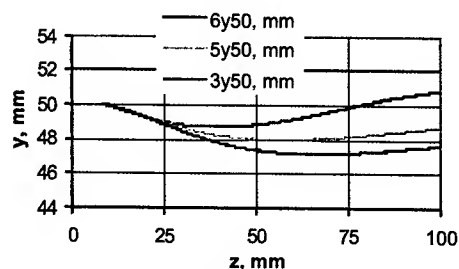
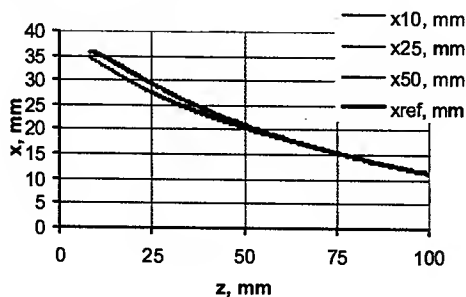


Figure 9

The difference in the shapes takes place mainly for the corner area and the non-compressive plane.

The MAFIA 3D static solver simulates the electric and magnetic fields for SBG geometry. The beam space charge has been extracted from 2D run and introduced into input MAFIA file together with the electrode potentials. The sign of the electric fields from electrodes and the beam space charge are matched to get the physical correct action on the test particle. The same takes place for the beam self magnetic field. The result of MAFIA static solution was six files with **E** and **B** components in the gun space. It was possible to get a visualization of the electric and magnetic Faraday's lines after MAFIA simulation. This feature of the indirect method is useful to get some insight regarding what the electron trajectory would look like. The components **E** and **B** are introduced into MAGIC 3D together with the initial particle momentum distribution on the cathode surface. The trajectories of test electrons are traveling into gun space and can predict the quality of the SBG geometry. The output file of MAGIC 3D contains the trajectory data that can be compared with 2D trajectories in the middle plane. The result of the comparison for the diode type of SBG with the fourth focus electrode is shown in Fig. 10 a) and b).



Figures 10 a) and b)

The picture of Fig. 10a represents the comparison between the reference outer trajectory (red curve) and trajectories of electrons, which are emitted from the cathode corner. There is practically perfect duplication of the corner trajectories with reference trajectory. The trajectories for non-compressive plane are shown in Fig. 10b where 6% deviation takes place. The method described above was employed to study the gridded version of three-electrode gun. Studies show that the original version of the SBG shown in Fig. 8 has the diverging trajectories in non-compressive plane. The new version of this gun is shown in Fig. 11.

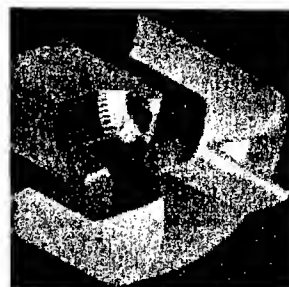


Figure 11

The shape of the focus electrode in the non-compressive plane and its corner were adjusted to meet the beam requirements for the PPM focusing channel. More results and data are available at the PAC2003 FPAB011 poster.

CONCLUSION

The 3D gun design tools have been under development at SLAC. Indirect method has been employed to model different 3D gun geometries and allows to optimize their focus electrodes. The combination of TOPAZ 2D and EGUN (in the beginning) with MAFIA 3D and MAGIC 3D (at the end) is used in an indirect method to model the high power electron guns. This method is effective to get the trajectory deviation from the reference particle.

ACKNOWLEDGEMENTS

This work supported by Department of Energy under contract DE-AC03-76SF00515 and DoE SBIR grants DE-FG03-00ER82964, DE-FG03-01ER83209 and DoD grant N0014-02-M0016. Authors would like also to thank everybody from the Klystron and Microwave Department of SLAC who was involved in the discussed subject.

REFERENCES

- [1] V. Ivanov, et al. 3D Method for the Design of Multi or Sheet Beam RF sources, PAC2001, p.1213.
- [2] E. Gelvich, et al., The new generation of high-power MBK, IEEE-MTT, v. 41 #1, p.15, 1993

AN IMPROVED VERSION OF TOPAZ 3D *

V. Ivanov, A. Krasnykh, G. Scheitrum, SLAC, Stanford, CA 92025
A. Jensen, Oregon Institute of Technology, Klamath Falls, OR 97601

Abstract

An improved version of the TOPAZ 3D gun code is presented as a powerful tool for beam optics simulation. In contrast to the previous version of TOPAZ 3D, the geometry of the device under test is introduced into TOPAZ 3D directly from a CAD program, such as Solid Edge or AutoCAD. In order to have this new feature, an interface was developed, using the GiD software package as a meshing code. The article describes this method with two models to illustrate the results.

INTRODUCTION

The problem of simulating high-current electron devices can be formulated into a set of field equations, particles motion equations, and the conservation law for the total charge. The EGUN [1] 2D code has been available at SLAC for several years and is designed to simulate trajectories of charged particles in electrostatic and magnetostatic fields. The modern development of high power electron devices is bound up with the multi-beam and sheet beam microwave sources. They are attractive for the design of gigawatt range free electron masers, pumping systems of gas lasers, and quasi-optical gyrotrons. For example, multi-beam [2] and sheet beam [3] X-band klystrons may be good candidates for R&D of the Next Linear Collider program. The design of such devices is practically impossible without the development of 3D computer codes. TOPAZ 2D [4] and TOPAZ 3D [5] are computer codes, which have been orientated for the simulation of relativistic charged particle optic problems using the Boundary Element Method. This method provides more precise solutions to complex geometries. The TOPAZ codes are available at SLAC now. Both versions of TOPAZ were revised for the modern computer platform and its shells. More details about the TOPAZ code are available in [5]. The new TOPAZ 3D adds the ability to import a 3D geometry directly and to compute the trajectories of particles in the external electromagnetic fields, including space charge effects, self-magnetic fields, and relativistic effects.

FROM SOLID EGDE INTO GID

The original version of TOPAZ 3D had an expansive set of standard geometric objects (plane, cone, sphere, cylinder, torus, triangle, quadrangle, ring, etc.). These objects could then be operated upon (shift, rotate, stretch, reflect, etc.). This was the original approach used prior to simulation. Typically, the designer had to spend an appreciable amount of time to create a working input file without any errors. However, the visualisation of objects and the ability to work with them was not as user-friendly as preferred. The above disadvantages were the major

motivation for improving TOPAZ 3D. There are several 3D CAD programs, which are available at SLAC. The most sophisticated is the Solid Edge CAD software. This software is powerful and effective to work with 3D objects. However, there is no option to mesh three-dimensional geometries.

GiD [6] is a powerful and reasonably priced software package. It was designed as a universal, adaptive and user-friendly graphical interface for geometrical modelling, data input and visualisation of results for all types of numerical simulation programs. Typical problems that can be successfully tackled with GiD include most situations in solids and mechanics. This program is used as the main interface between Solid Edge and the new version of TOPAZ.

The design of a sheet beam gun can be used to illustrate the new features of TOPAZ. The sheet beam gun consists of three electrodes: anode, focus electrode, and cathode. The results of the Solid Edge gun design and the meshing of this geometry using GiD are presented in Fig. 1 a) and b) accordingly.

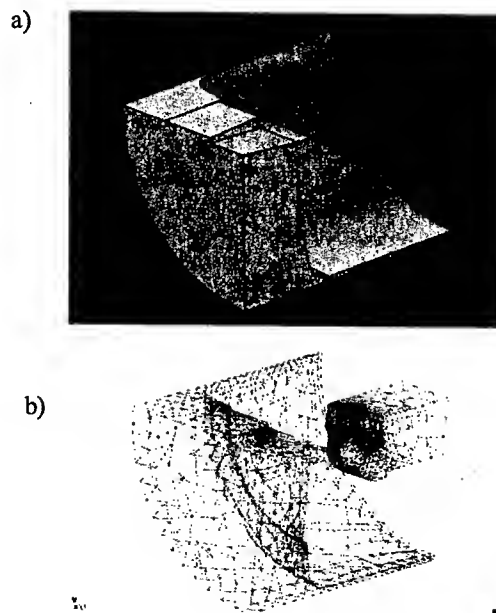


Figure 1:

- a) Sheet beam gun design: anode in grey, cathode in red, and focus electrode in yellow
- b) Unstructured mesh of the geometry using GiD

* Work supported by Department of Energy under contract DE-AC03-76SF00515

The volume, where the beam is going to be propagated, can be split into small discrete distances for each type of coordinate system. The charge and beam current are equally spread inside cells. Fig. 5 shows the result of the sheet beam simulations for the gun geometry shown in Fig. 1. The trajectories for two planes are shown here. Approximately 100 trajectories are shown.

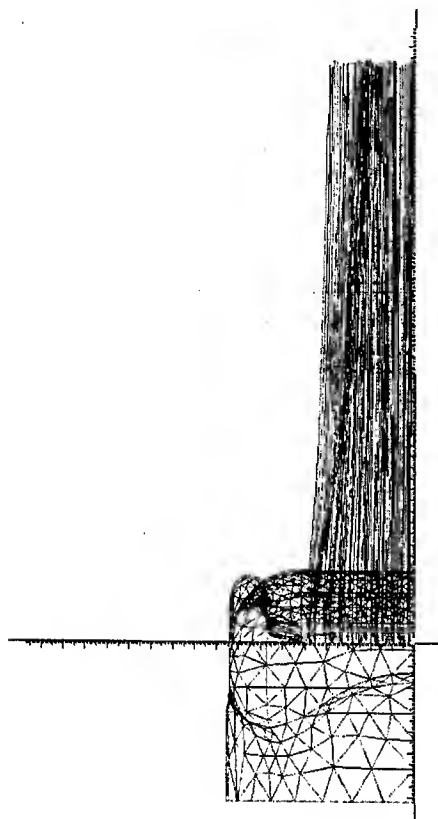


Figure 5: Result of sheet beam gun simulation

It is seen from the above simulation that the shape of the focus electrode for the gun is not optimized. The sheet beam has converged too much for the non-convergence plan. The region of the focus electrode, that is not optimized, is shown in Fig. 6. Similar beam behaviour is

seen for this shape of focus electrode when the indirect method [6] is used.



Figure 6: Focus electrode and cathode of sheet beam gun

The numerical result of the electron gun simulation shows the ability to simulate the complicated sheet beam geometries directly from Solid Edge. The pre-processor stage for preparation of the geometry for simulation is simpler and more user-friendly. In this case Solid Edge and GiD features are used. The geometry is edited and converted into the digital text format after creation of the solid model.

CONCLUSIONS

There are several codes to simulate the behavior of a sheet beam. Some of them are focused on the analysis of the confinement characteristics of sheet beams focused by periodically permanent magnets. The TOPAZ 3D code is optimized to run fully three-dimensional stationary problems such as the design of a relativistic beam gun and following after the gun the beam optics system. Solid Edge CAD and GiD software were adopted as the TOPAZ 3D pre-processor for the preparation of the geometry for simulation and the creation of the input file.

ACKNOWLEDGEMENTS

This work supported by Department of Energy under contract DE-AC03-76SF00515.

REFERENCES

- [1] W. B. Herrmannsfeldt, "EGUN- An Electron Optics and Gun Design Program", SLAC 331, 1988
- [2] L. Ives, et al., "Multiple Beam Guns For High Power RF Applications", IVEC-2002, April 23-25, 2002, Monterey, CA.
- [3] E. Colby, "RF- Power Sources III: Beyond X-Band", The US-CERN-Japan-Russia Joint Accelerator School on Frontier of Accelerator Technology in Linacs, November, 2002, Long Beach, CA
- [4] V. Ivanov. The code POISSON-2. User's Guide, Novosibirsk, Russia, 1992
- [5] V. Ivanov. The code POISSON-3. User's Guide, Novosibirsk, Russia, 1992.
- [6] A. Krasnykh et al., "3D Modelling Activity for Novel High Power Electron Guns at SLAC", article is presented in this conference

FIRST TEST OF THE CHARGE STATE BREEDER BRIC

V. Variale, V. Valentino, INFN sezione di Bari, Bari, Italy, A. Boggia, G. Brautti, T. Clauser, A. Rainò, Dipartimento di fisica Università di Bari e INFN sezione di Bari, Bari, Italy
P. Bak, Y. Boimelshtein, P. Logatchov, B. Skarbo, M. Tiunov, BINP, Novosibirsk

Abstract

The "charge state breeder" BRIC (BREeding Ion Charge) is based on an EBIS device and it is designed to accept Radioactive Ion Beam (RIB) with charge state +1, in a slow injection mode, to increase their charge state up to +n. BRIC has been developed at the INFN section of Bari (Italy) during these last 3 years. Now, it has been assembled at the LNL (Italy) where are in progress the first tests as stand alone source and where, for the end of the year, it will be tested as charge breeder at ISOL/TS facility of that laboratory.

BRIC could be considered as a solution for the charge state breeder of the SPES project under study also at the LNL.

The new feature of BRIC, with respect to the classical EBIS, is given by the insertion, in the ion drift chamber, of a RF - Quadrupole aiming to filtering the unwanted masses and then making a more efficient containment of the wanted ions. In this paper, the charge breeder BRIC first test will be reported and discussed.

INTRODUCTION

The physics with energetic Radioactive Ion Beams (RIB) represents one of the foremost frontiers in Nuclear Physics. For this reason, many laboratories in the world have start to project and build new facilities for the production of RIB accelerated up to several MeV/u (see for ex. ref. [1]). Among them can be mentioned the SPES project which is in an advanced phase of study at the Legnaro National Laboratory (LNL) (Padua, Italy) [1]. This kind of project is based on the ISOL technique. With this technique, two beam acceleration stages are used. The primary accelerator is intended to provide a proton, or a light ion, beam incident on a target to induce nuclear reactions. Then radioactive species will be produced inside. These radioactive elements need to be ionised for acceleration and then a secondary stage is intended to accelerate the radioactive ions at the desired energy before they reach the experimental area. Since the cost of an accelerator is roughly related to the inverse of the charge state of the beam to be accelerated, a higher ion charge state beam can allow a sensitive lowering of the accelerator cost. This problem can be solved by using, before the post-acceleration of RIB, an appropriate device capable of increase the charge ion state of the radioactive element that must be accelerated. In the framework of the LNL SPES project, our INFN group, in Bari, has been involved in the development and testing of a "charge state breeder" device based on an EBIS source type: BRIC. The BRIC features have been presented in a

detailed way in ref. [2,3]. The main feature of BRIC is the using of a RF quadrupolar field to obtain a selective containment of the wanted ions. In this way, a more efficient high charge state ion production could be reached. The BRIC device, before to be used as charge breeder, will be tested as stand alone high charge ion source to verify this idea and then study the radio frequency effects in the ion production. In this paper, the test of the selective containment of the BRIC as high charge state ion source will be presented and discussed.

THE CHARGE BREEDER BRIC

As mentioned before, the detailed design of the device has been already presented in ref. [2,3]. However, for sake of clarity, a shortly description of the device here will be done to recall its main features. As can be seen from fig.1, the BRIC experimental set up is practically the same of a classical Electron Beam Ion Source (EBIS). In fact, in that figure, as in an usual EBIS, the electron gun, the ion drift chamber and the typical electron collector with the hole for the ion extraction are shown.

The main difference between BRIC and a usual EBIS can be observed from the inside of the ion drift chamber of the fig.1. In that chamber, RF electrodes of cylindrical shape, placed around the symmetry axis in such a way to form a quadrupolar RF field, are shown. This RF field, which is added to the electron beam space charge potential, can give the above mentioned transverse selective containment to the wanted ions. Furthermore, the same cylindrical shaped RF electrodes are used to create the longitudinal trap for the ions before they could be extracted for the acceleration.

As electron beam focusing system two short solenoids made of special coils are used. They are suitable to be mounted together in such a way to form a solenoid [4]. These coils have been designed and built by the BINP institute of Novosibirsk. The construction of these coils has finished at the end of the last year with a very big delay with respect to our experiment schedule. Meanwhile, however, few home made coils have been built to test all the system (e-gun, collector and ion trap) at low power [3]. Furthermore, a TOF system to study the ion charge state of the extracted ion beam, for different RF parameter, has been designed and built [4]. The home made coils have been also used to test the TOF system. For this test the vacuum measured was 3.5×10^{-8} Torr, the electron beam current, used to produce ions, measured on the collector was 13 mA (practically all the electron current has been recovered at the collector). The ion pulse measured at the end of the TOF is shown in fig. 2.

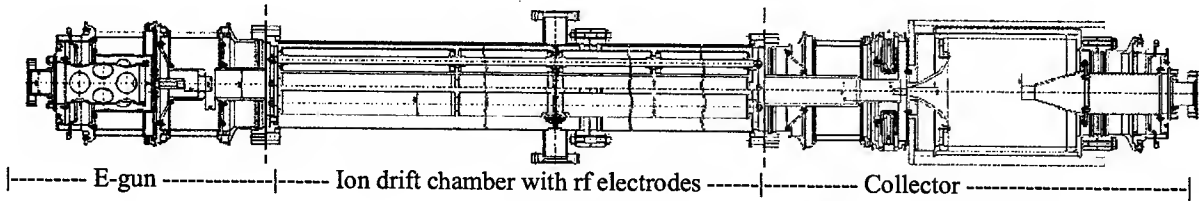


Figure1: BRIC mechanical design without electron focusing solenoid.

From that figure it can be seen that the extracted ion pulse length is of about 350 μ s and the signal amplitude, of 3 V, correspond to an ion current of 3 μ A. Since the charge contained in our trap for this test can be evaluated as about 1 nC ($\Delta Q = I_e \Delta t / v_e$ where $\Delta t = 0.8$ ms is the trap length) and the area inside the pulse signal (in 2a)) gives a higher charge value, the reason why an extra charge has been measured needed to be explained. In order to clarify this effect, the width of the voltage extraction pulse has been increased, as shown in fig. 2b) (yellow line). From that figure, it can be seen that the ion pulse, extracted from the source, was composed by two signals, as shown by the dashed lines: The first signal is given by the ion pulse trapped in the source and then released when the trap potential is down and this pulse must have total charge less than the trap capacity (1 nC). The latter is given by the starting of new ionisations after the pulse has been extracted and the extracted voltage level remains down allowing also to the new ions to go towards the TOF system.

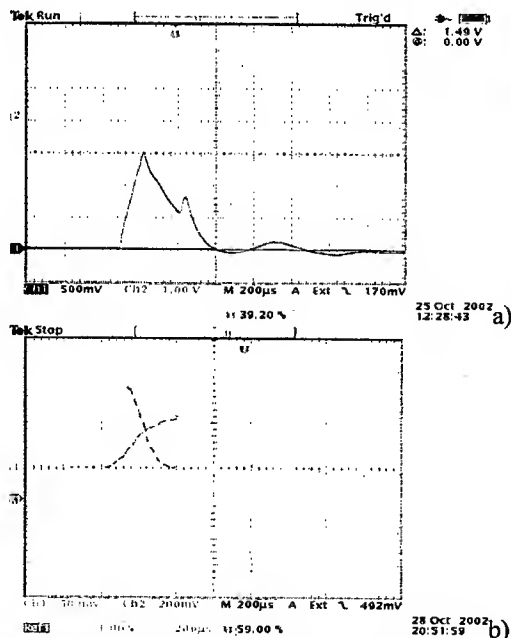


Figure 2: ion pulse measured on the FC at the end of the TOF system. a) cyan line is the voltage pulse for ion extraction with $V_{ex} = -80$ V and $\tau_{ex} = 320$ μ s and blue line indicates the ion pulse. b) yellow line: pulse voltage with $V_{ex} = -80$ V and $\tau_{ex} = 1$ ms, cyan line indicates the ion beam pulse.

Notice that this signal after a while reach a saturation, given by the ionisation rate, and then it remains at constant value up to the closing of the trap.

In these last months, after the arrival of the coils for the solenoid from Novosibirsk, it is started the test of the source at nominal power, which is with an electron current of $I_e = 0.5$ A and a kinetic energy of $E_k = 5$ keV. Since, for this test, a solenoid magnetic field of 1.6 kG will be used a water cooling system has been prepared at LNL where the test is underway. All the coils have been mounted together to form the solenoids and then aligned as shown in fig.3 where the system to measure the axial magnetic field is also exposed. The solenoid has been aligned in the vertical plane by tilting the single coils around the vertical axis by acting on the special wings placed on the coil sides (see fig.3) in such a way to minimize the transverse magnetic field read on the 3D Hall probe.

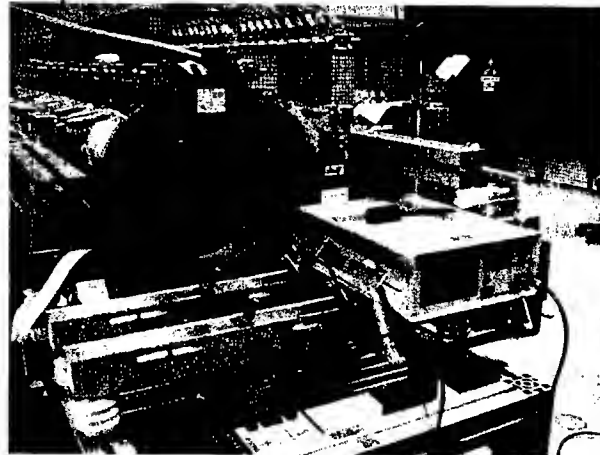


Figure 3: Coils mounted on BRIC to form the suitable solenoid for electron beam focusing. The axial magnetic field measurement system for the coils alignment is also shown.

The magnetic field precision reached with this system has been of about 5×10^{-4} . furthermore, although the water cooling system was still not ready during the magnetic measurement, we measured the maximum axial magnetic field reachable with our solenoid and obtained a value of about 1.2 kG. However, we hope that when the coils water cooling will be operating (at the beginning of May) B_{max} will reach 1.6 kG as foreseen. In conclusion, for the end of the month of May, the first test measurement at nominal power to produce ions of Ar with high charge

states, taking into account the effect of the RF quadrupole containment, will start.

TEST AS HIGH CHARGE STATE ION SOURCE

To find out what are the RF parameters that give stable motion condition for the wanted ions with the aim of improve the containment efficiency a code package, called BRIC-code, have been developed [5]. As described in the ref. [5], once fixed the element of interest, one of the codes can be used to find the stability region in the plane (q,a) .

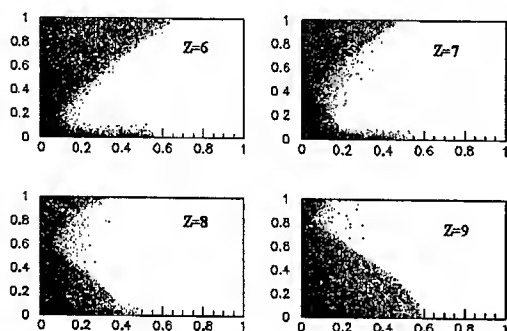


Figure 4: Stability zones (dotted regions) for different charge states of Ar ions in the plane (q,a) .

The parameter q and a are typically used in the theory of the RF quadrupole spectrometry and are defined as:

$$a = a_x = -a_y = \frac{4eU}{m\omega^2 r_0^2}$$

$$q = q_x = -q_y = \frac{2eV}{m\omega^2 r_0^2}$$

here ω is the RF signal used and V its amplitude, U is the DC component, r_0 is the distance from the axis to the RF electrodes and e/m is the charge over mass ratio of the element considered. The simulation results of figure 4 show stable regions for different charge states Z of Ar.

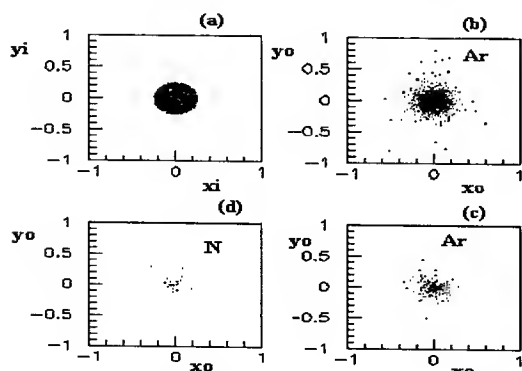


Figure 5: Ion beam spots of (a) initial conditions, (b) final results for Ar with stable value of (q,a) at Ar^{+8} , (d) final results for N.

results for Ar with instable point, (c) final results for N with the same (q,a) of (b) case.

From the ion charge state evolution during the electron beam bombardment (see for ex.[6]), it can be seen that the charge state distribution of one element has, at a certain confinement time τ_c , the simultaneous presence of very different charge state ions. However, for a value of $j_e \tau_c$ of about 2 the main fraction of charge state of Ar are $Z=7$, $Z=8$, $Z=9$. By looking at the stable regions in the plane (q,a) shown in figure 4, a working point, stable for the ions Ar^{+8} and instable for the other charge state ions, can be chosen. In our case, the point $(0.3,0.2)$ has been chosen as RF parameters for the simulations of the Ar ion motion in BRIC. In the code that simulates that motion it is also taken into account Ar ion charge state evolution and the space charge compensation [5]. The results shown in fig. 5 (b) show the beam spot of the Ar ions after a $j_e \tau_c$ of about 2 corresponding at a charge state distribution with a maximum pick for Ar^{+8} [6]. In the fig. 5 (c) it is shown also a beam spot of the N (typical residual gas element) ions after the same value $j_e \tau_c$. Notice that from the simulation results shown in fig. 5, it seems that, for the chosen stable point, a large fraction of the initial Ar ions is preserved only in the case (b). The residual gas elements, as N, are expelled as seen in 5(c). In fig. 5(d) it is shown the case of Ar ions but for a working point, $(q,a) = (0.6,0.4)$, which is external to all the stability regions shown in fig. 4. In that case a very small fraction of Ar ions remain stable up to the end of simulation.

In conclusion we can say that the simulation results seem to confirm the hypothesis of a selective containment effect. However, the simulation codes make several approximations [5] and then an experimental test is needed to be sure of this effect. That experiment is underway at LNL (PD, Italy).

REFERENCES

- [1] SPES Project study, LNL-INFN (REP), 145/99.
- [2] G. Brautti et al., 'BRIC: An EBIS design for charge state Breeding in RIB', EBIS/T 2000, Upton, New York.
- [3] V. Variale, G. Brautti, T. Clauser, A. Rainò, V. Stagno, G. La mánna, V. Valentino, A. Boggia, Y. Boilmelshtein, P. Logatchov, B. Skarbo and M. Tiunov, "An EBIS for charge state breeding in the SPES project", PRAMANA- journal of physics, Vol. 59 (2002) 765.
- [4] V. Variale et al. "The Charge State Breeder BRIC: Status Report", Conference Proceedings of LINAC2002, Gyeongju August 2002, Sud Korea.
- [5] V. Variale et al., 'BRICTEST: A Code For charge Breeding Simulations', EPAC2002, Paris, June2002.
- [6] Handbook of ION SOURCES, ed. B. Wolf, CRC Press, (1995) 12.

DESIGN AND OPERATION OF PEGASUS THERMIONIC CATHODE

P. Frigola, G. Andonian, S. Reiche, J.B. Rosenzweig, S. Telfer, G. Travish,
UCLA, Los Angeles, CA 90095, USA

Abstract

A new thermionic cathode has been developed and installed for use on the PEGASUS plane wave transformer injector. The novel design of the LaB_6 cathode allows for thermionic emission as well as photoinjector operation. Both test-stand measurements and in situ operational experience are reported.

INTRODUCTION

The PEGASUS (Photoelectron Generated Amplified Radiation Source) was commissioned at UCLA as a linac-based electron beam radiation laboratory [1]. The injector is a PWT (Plane Wave Transformer) originally designed to operate strictly as a photoinjector. The virtues of photocathodes are much cited. Their ability to produce short electron pulses for applications such as free electron lasers (FELs) is superior [2]. However, the operation of photocathodes is not always possible or even desirable. In fact for high average charge applications, such as planned optical transition radiation (OTR) experiments [3], a thermionic cathode becomes more desirable.

A thermionic cathode assembly was developed, tested, and installed for use in the PEGASUS PWT injector. The PEGASUS thermionic cathode assembly uses a lanthanum hexaboride (LaB_6) cathode heated by a UHV button heater. The assembly can be installed with little modification to the PWT, and it can operate as a photocathode as well as a thermionic emitter.

APPARATUS

The PEGASUS thermionic cathode is a compact and cost efficient emitter designed to provide beam charges of up to 1 nC. By virtue of its simple design, the thermionic cathode can also operate as a photocathode. The thermionic cathode assembly consists of a cylindrical LaB_6 cathode conductively heated by a UHV cartridge heater, all incased in a molybdenum body. The LaB_6 cathode is 3.5 mm in diameter, with an active area of approximately 0.28 cm^2 , and 1 mm thick. The heater is a commercially available HeatWave UHV Standard Series cartridge heater rated at 1200 C at 7.5 Watts. Two versions have been constructed. A schematic of the major components of the later version is shown in Figure 1.

Test-Stand Setup

For the test-stand measurements, the thermionic cathode assembly is housed in a cylindrical holder whose geometry duplicates that of the cathode mounting plate of the PWT. The entire assembly is located within a vacuum chamber. With the cathode held at ground potential, a voltage of 2 kV is applied to a collector 3 mm from the

cathode. The thermionic current is measured with an Amp meter.

PWT Installation

The PWT's design allows for insertable and removable cathodes. The thermionic cathode assembly is designed to operate as a replacement cathode without the need to modify the PWT structure. A schematic of the cathode assembly is also shown in Figure 1.

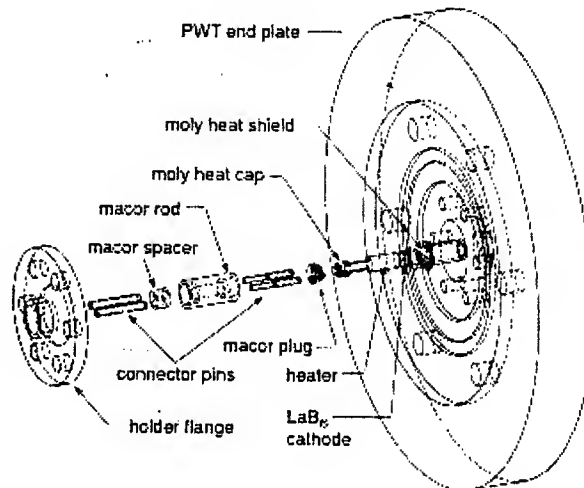


Figure 1: Schematic of thermionic cathode assembly.

EXPERIMENTAL RESULTS AND DISCUSSION

Test-Stand Measurements

With the collector bias at up to 2.0 kV and a maximum operating heater power of 12 Watts, a thermionic DC current of approximately 400 μA was measured. The temperature of the cathode was estimated at approximately 1000-1100 C. This result is consistent with published measurements of thermionic emission of LaB_6 [4]. Further enhancement, when operating under RF power ($E=50 \text{ MV/m}$), will result in an increased Schottky Current well into the mA range.

Operational Experience

With the thermionic cathode assembly installed in the PWT, the system was evacuated and a base pressure below 10^{-9} Torr was reached. Cathode heater power was supplied by a remotely controlled power supply. The cathode was slowly heated and allowed to outgas. The temperature of the cathode was qualitatively measured by imaging the surface of the LaB_6 cathode using a mirror

and camera installed on the beamline. The temperature was estimated to be 900-1000 C based on its color and intensity. Unfortunately, the small size of the cathode and its distance from the imaging mirror made measurement using our pyrometer unreliable.

The thermionic cathode assembly was RF tested to approximately 15 MW. On a number of limited runs, the cathode was brought close to emission temperature (~1000 C) and RF power was applied to the PWT. YAG crystal beam position monitors and a faraday cup were used to observe and measure operation. Initial results indicate that the LaB₆ cathode is not emitting as expected. The problem is likely the result of the cathode not reaching emission temperature. This was in part due to the heater losing contact with the LaB₆ cathode caused by repeated heating and cooling cycles. A new assembly

was designed and constructed to address this problem. Further testing is currently underway.

ACKNOWLEDGEMENTS

This work supported by DOE grant DE-FG03-98ER45693.

REFERENCES

- [1] G. Andonian, et al., These proceedings.
- [2] S. G. Anderson. Creation, Manipulation, and Diagnosis of Intense, Relativistic Picosecond Photoelectron Beams. Ph.D. thesis, UCLA (2002).
- [3] S. Reiche, et. al., Proceedings of 2001 Particle Accelerator Conference, Chicago (2001) 1282.
- [4] J.M. Lafferty, "Boride Cathodes", J. of Appl. Phys. 22 299 (1951).

DEVELOPMENT OF DISPENSER PHOTOCATHODES FOR RF PHOTOINJECTORS

D. W. Feldman, P. G. O'Shea, M. Virgo, IREAP, U. Maryland, College Park, MD, 20742 USA
K. L. Jensen[#], Code 6841, NRL, Washington, DC 20375 USA

Abstract

Nonlinear photoelectric emission from Scandate dispenser cathodes using 1.06 μ m radiation in nanosecond scale pulses has been observed. Unlike single photon emission, the photocurrent is a strong function of both the initial lattice temperature and the applied electric field as well as laser intensity. Quantitative agreement is found between experimental data and the proposed model, especially with regards to temperature, field, laser intensity, and laser wavelength (λ) dependence. In particular, for long wavelength incident lasers, the majority of the absorbed photon energy heats the electron gas and background lattice, and photoemission from that electron distribution constitutes the emitted current.

INTRODUCTION

Photoemission sources for Free Electron Lasers¹ under development for a variety of scientific and industrial applications face unprecedented operational demands. FELs need photocathodes to be long-lived, reliable, produce nanoCoulomb (nC) bunches in picosecond (ps) time scales, and operate using the longest wavelength permissible. Such requirements often conflict. Low work function coatings on semiconductors have excellent quantum efficiency (QE), but degrade prematurely and have response times that are too great². Metal photocathodes are rugged, long-lived, and prompt but have low QE and require ultraviolet (UV) drive lasers³. The wavelength of drive laser is obtained by non-linear conversion crystals. For the UV case, therefore, a great deal of waste heat (90%) will be dumped into the crystals, altering their operation. Moreover, the non-linear conversion process introduces fluctuations that scale as (Laser intensity)ⁿ, where n is the harmonic number (4 for UV), and such fluctuations appear in the resulting electron pulses, resulting in degraded FEL operation. Nevertheless, photocathodes remain the only viable option for high power, short wavelength FELs.

We report on our investigations of the photoemissive properties of thermal dispenser cathodes, the traditional electron source of rf vacuum electronics devices where ruggedness and reliability are paramount. The low work function coating is maintained by the diffusion of, e.g., barium, to the surface, replacing that which is lost due to desorption, evaporation, and sputtering. Such cathodes can be rehabilitated even when operating in non-ideal conditions. The work function is on the order of 2 eV, and scandate cathodes have shown an even lower work

function of 1.8 eV.⁶ Here, theoretical models are developed and applied to analyze experimental results. The modeling effort is directed to predict the performance of such cathodes in an FEL rf gun environment, where the laser intensities are orders of magnitude higher, the pulse lengths orders of magnitude shorter, and the applied fields larger, than are found in the present experimental arrangement.

THEORETICAL MODEL

Relationships exist relating the lattice temperature to the electron temperature under laser illumination⁴. Some approximations and observations simplify the calculation of the electron temperature used to estimate the emitted charge. First, the time scale of the laser pulse is 1 ns, but electron-electron and electron-phonon relaxation times are much smaller so that the electron and lattice temperatures are equal. Second, the temperature exponentially decays into the bulk with a decay length parameter L , e.g. $(T(x) - T_0)/(T(0) - T_0) = \exp(-x/L)$, where the length scale is L is a multiple of the Fermi velocity and the total scattering relaxation time: the multiplicative factor should be on the order of the square root of the ratio of the laser pulse time scale with the scattering time scale, or $n = \sqrt{(1 \text{ ns} / 0.1 \text{ ps})} \approx 100$. Third, given that the cathode is predominantly tungsten grains, the heating of the electron gas by the laser can be approximated using bulk tungsten parameters. We have found that, invoking these approximations, the electron temperature is the solution of

$$T_e^2(T_e - T_0) = \frac{3n^2}{\gamma} \left[\frac{G_0(t)}{B_{ep} + A_{ee}T_0} \right] \quad (1)$$

where T_e and T_0 are the surface and bulk temperature $G(t)$ is the energy per unit volume deposited by the laser as a function of time (presumed to be a Gaussian with a time parameter of 2.7 ns), γ is the ratio of the electron specific heat and the temperature (presumed constant), and B_{ep} and A_{ee} are the coefficients of the relaxation times

$$\tau_{ee}(T) = \frac{\hbar\mu}{A_0} \left(\frac{1}{k_B T} \right)^2 = \frac{A_{ee}}{T^2}; \tau_{ph}(T) = \frac{\hbar}{2\pi\lambda_0} \left(\frac{1}{k_B T} \right) = \frac{B_{ep}}{T} \quad (2)$$

where μ is the chemical potential, A_0 and λ_0 are material-dependent (dimensionless) parameters for tungsten [see Ref. 4], and other symbols have their usual meaning. With the electron temperature and photon wavelength λ in hand, the emitted current can be evaluated. The detailed formulae to do so shall be presented separately; here, in the limit $\beta(\phi - \hbar\omega) \gg 1$ and $\beta\mu \gg 1$, it is approximated by

[#]kevin.jensen@nrl.navy.mil

$$J_\lambda(T, \Phi) \Rightarrow (1-R) \frac{(2\pi\hbar)^2}{m\omega\mu^2} I_\lambda(t) J_{RLD}(T, \phi - \hbar\omega) \quad (3)$$

where J_λ is the photocurrent, β is the inverse temperature $1/k_B T$, $\hbar\omega$ is the photon energy, $I_\lambda(t)$ is the laser intensity, J_{RLD} is the Richardson-Laue-Dushman equation for thermionic emission, ϕ is the barrier height above the chemical potential (i.e., work function minus Schottky factor), and R is the reflection coefficient (taken as 50% hereafter). The electron is assumed to be transmitted if its energy after photon absorption exceeds the surface barrier height: quantum mechanical tunneling via a modified transmission probability calculation⁷ will be deferred to a future work. A detailed theoretical analysis, has shown that asymptotically the QE is

$$QE(\hbar\omega > \phi) = \theta(1-R) \left(\frac{\hbar\omega - \phi}{\mu} \right)^2$$

$$QE(\hbar\omega < \phi) = \frac{\theta(1-R)}{(w+1)^{3/2}} \left(\frac{\Delta t_e}{\Delta t_\lambda} \right) \left(\frac{\hbar\omega}{q} \right) \left(\frac{J_\lambda(T_{\max})}{I_\lambda(0)} \right) \quad (4)$$

$$w = \left(1 - \frac{T_e}{T_{\max}} \right) \left(2 + \frac{(\phi - \hbar\omega)}{k_B T_{\max}} \right)$$

where θ is the fractional coverage of the surface by the low work function coating and Δt is the time constant of the electron or laser pulse. The proportion of the surface covered by low work function material on a dispenser cathode is a thermally regulated phenomenon: temperatures within this study are considerably lower than those generally used when the cathode is run as a thermionic emitter. Surface coverage factors are therefore presumed low. The field used in the Schottky factor is enhanced due to surface roughness (Figure 2): a simple model easily generates enhancement factor of 4x.

EXPERIMENTAL PROCEDURE

Scandate cathodes fabricated by Spectra-Mat Inc.⁵ were illuminated by a Q-switched Nd:YAG laser with full width at half maximum (FWHM) pulses of $\Delta t = 4.5$ ns. The field between the cathode and anode was varied from 0 to 2.5 MV/m. The laser was focused to a circular spot on the cathode with a FWHM area of approximately $\Delta A = 0.3$ cm²; "current density" below is defined as the ratio of total emitted charge with Δt and ΔA . The photon wavelengths (in nm) of the 1st, 2nd, 3rd, and 4th harmonics of the Nd:YAG laser are 1064, 532, 355, and 266, respectively. The electron emission from 2nd, 3rd, and 4th harmonics exhibited "normal" photoemission characteristics, that is, the emission was proportional to the incident laser intensity and independent of electric field low (0.1 to 2.0 MV/m) field gradients: the QE at these wavelengths are shown in Figure 1

The FWHM illumination area of the incident laser was 0.3 cm² implying the e⁻² simulation radius is 0.5249 cm. The cathode was a 1.27 cm diameter rod. The anode was a tube with a 1.27 cm inner diameter and a 2.54 cm outer diameter. The edges of the anode facing the cathode were

rounded, and sat inside a dielectric tube with an inner diameter of 3.175 cm. The anode-cathode separation was 0.4 cm. Simulation showed that with a 1 kV anode potential, the tangential and perpendicular fields were, at the center, 0 MV/m and 0.17 MV/m, respectively, while at the edge (where the illumination was weak), they were 0.2 MV/m and 0.45 MV/m, respectively. The electron temperature is therefore greatest where the laser intensity is strongest, and occurs near the center of the beam spot. The cathode surface, shown in Figure 2, was corrugated due to machining, and therefore field enhancement occurs. Except for Figs. 1&2, $\lambda = 1064$ nm in all figures.

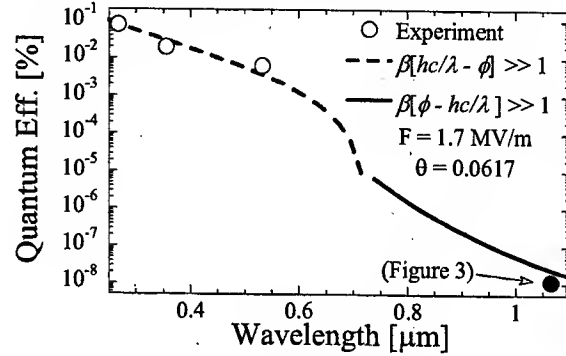


Fig. 1: Measured QE at various λ for Scandate dispenser cathode. Lines refer to Eq. 4. Black dot = same in Fig. 3.

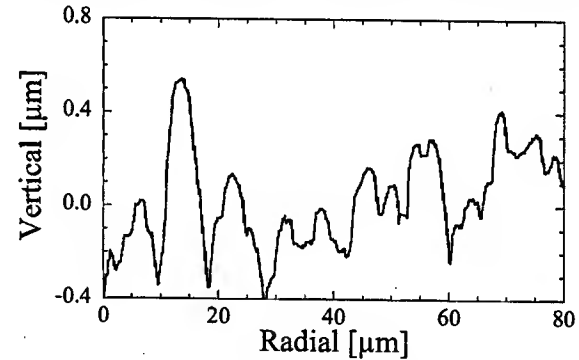


Fig 2: Cathode surface cross-section profilometry plot.

RESULTS

The experimental parameters varied are laser intensity, macroscopic field, and bulk temperature. The QE of various metals reported in the literature serve as an independent confirmation of the values used in the theoretical analysis. Parameters which are unknown, such as the exact value of the reflectivity, work function at the emission site, proportion of the emission sites participating, thermal factors of the dispenser cathode, etc., use appropriate generic parameters (e.g., $R = 50\%$ $\Phi = 1.8$ eV) or are treated as effective parameters.

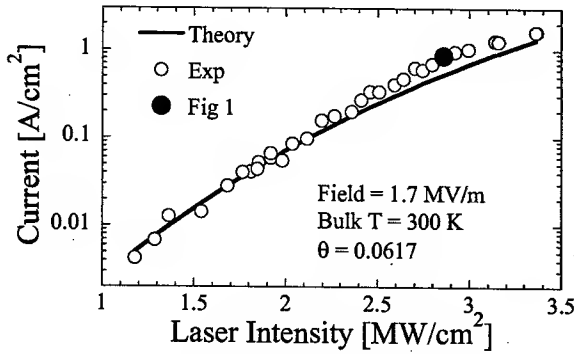


Fig. 3: Current Density vs. laser intensity.

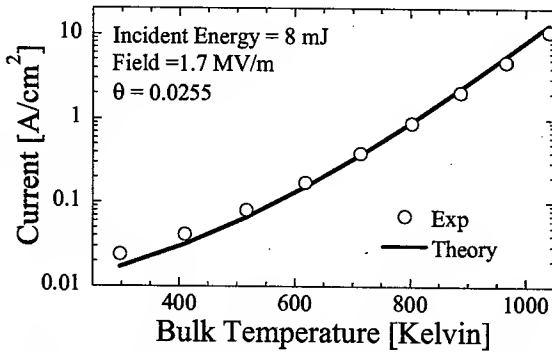


Fig. 4: Same as Figure 3, but for variation in temperature

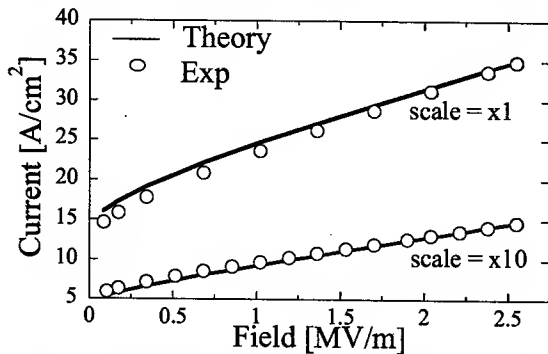


Fig. 5: Same as Figure 3, but for variation in field (top) 5.3 MW/cm², 713 K; (bottom) 2.9 MW/cm², 633K

CONCLUSION

We have found that the theoretical model of a laser-heated electron gas giving rise to photo-thermal-field emission is consistent with experimental findings of infrared laser illumination of a Scandate dispenser cathode. The surprisingly good quantitative agreement between experiment and simulation, seen in the Figures, bodes well for theoretical extrapolation to parameters not achieved experimentally but nevertheless representative of future devices. Temporal characteristics of the laser and the limitations of the test cell constrain the power density and electric fields achieved to well below those characteristic of an rf photoinjector. Nevertheless, extrapolations based on the present study clearly indicates

that dispenser cathodes function as a promising photocathode candidate, as indicated by the theoretical extrapolations performed in Fig. 7.

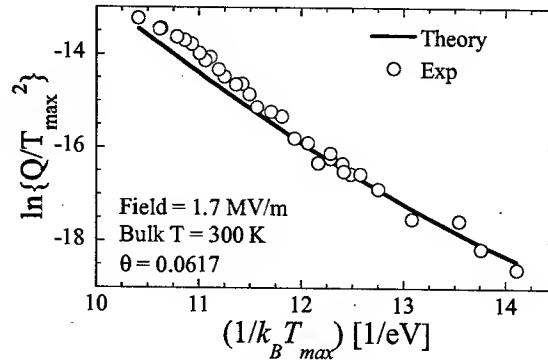


Fig. 6: Demonstration that current follows field & photo-enhanced thermal emission model (Eq. (3)). Max temperature evaluated via Eq. (1) for center of laser pulse.

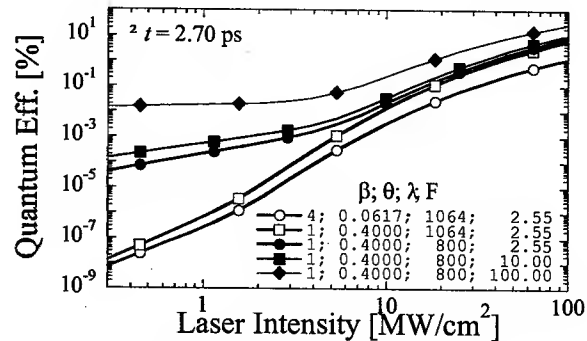


Fig. 7: Extrapolation for other θ , λ [nm] and F [MV/m] for Scandate cathode. $\beta=1$ means no field enhancement

Acknowledgements: We most gratefully acknowledge support provided by the Joint Technology Office and the Office of Naval Research.

REFERENCES

- [1] P. G. O'Shea, H. Freund, *Science* **292**, 1853 (2001).
- [2] W. E. Spicer, A. Herrera-Gómez, SLAC-PUB-6306 & SLAC/SSRL-0042, Aug 1993; P. Michelato, *Nucl. Inst. Meth. Phys. Res.* **A393**, 455 (1997).
- [3] J. A. Nation, L. Schächter, F. M. Mako, L. K. Len, W. Peter, C.-M. Tang, T. Srinivasan-Rao, *Proc. of the IEEE* **87**, 865 (1999)
- [4] N. A. Papadogiannis, S. D. Moustazis, J. P. Girardeau-Montaut, *J. Phys. D: Appl. Phys.* **30**, 2389 (1997); N. A. Papadogiannis, S. D. Moustazis, *J. Phys. D: Appl. Phys.* **34**, 499 (2001).
- [5] Spectra-Mat, Inc., 100 West Gate Drive, Watsonville, CA 95076. <http://www.spectramat.com>
- [6] R. Thomas, *Naval Research Laboratory* (unpublished data obtained from A. Shih and J. Yater).
- [7] K. L. Jensen, P. G. O'Shea, D. W. Feldman, *Appl. Phys. Lett.* **81**, 3867 (2002).

THE RESEARCH ON THE CARBON NANO TUBE CATHODE

A. Yamamoto, H. Nakai, N. Kaneko, T. Nakashizu, IHI Co.Ltd., Yokohama, Japan
S. Ohsawa, T. Sugimura, M. Ikeda, KEK, Tsukuba, Japan

Abstract

Joint experiment, the research of new carbon material, started in collaboration of KEK (High Energy Accelerator Research Organization) and IHI (Ishikawajima-Harima Heavy Industries Co.,Ltd.). Main target is new carbon material, CNT (Carbon Nano Tube) and related materials like GNF (Graphite Nano Tube). The purpose is developing high-current, high-duty electron gun with cold cathode for injectors of accelerators. From the beginning, relatively high current was observed. It seems to have a high potential.

INTRODUCTION

It is well known that field emission from a CNT makes quite high current density (around 10^6A/cm^2 was reported [1]). But many of those measurements were performed as a development of FPDs, total current was not enough to use for an accelerator. Electron current of 1-100A/ cm^2 is needed. One difficulty of cathode is less field enhancement with a flat surface. So, the first step of this research was to find a suitable material.

In this paper, main results of the first experiments were reported.

CATHODE MATERIALS

Samples of CNT and GNF (Graphite Nano Fiber) were employed. Typical microscopic image of the CNT is shown in fig. 1.

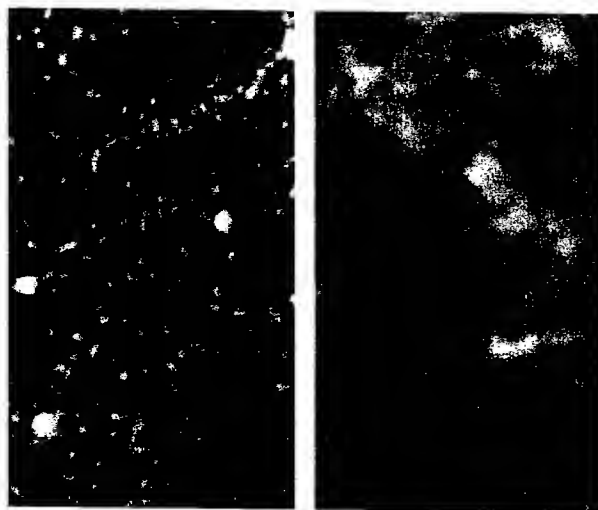


Figure 1: Surface of CNT(left) and GNF(right)

Table 1 shows tested materials. CNTs were employed from three different manufactures. CNT#3 and GNF were the same manufacture. Therefore measurement

condition was almost the same, results were much different. Following results were focused on two remarkable material, CNT#3 and GNF.

Table 1: tested cathodes

No	Emission Area	Substrate	Emission	Remark
CN T#1	i) 10mm square ii) $\phi 6\text{mm}$ circle	Inver i) 10mm square ii) $\phi 25\text{mm}$ circle	10mA/ cm^2	tube / vertical to substrate
CN T#2	10x20mm	Inconel	few μA / cm^2	tube / random
CN T#3	$\phi 6\text{mm}$	Stainless	150mA/ cm^2	tube / random
GN F	i) $\phi 20\text{mm}$ ii) $\phi 6\text{mm}$	Inver i) $\phi 20\text{mm}$ ii) $\phi 25\text{mm}$	40 mA/ cm^2	fiber / random

EQUIPMENTS

Triode electron gun with few kV voltage was employed. Electrodes were adjustable to use various cathodes. Conductive and luminous glass was placed in the anode. Cathode was bound by insulators. Some cathode, which had large emission area, was covered by film with $\phi 6\text{-}8\text{ mm}$ hole, to adjust emission area.

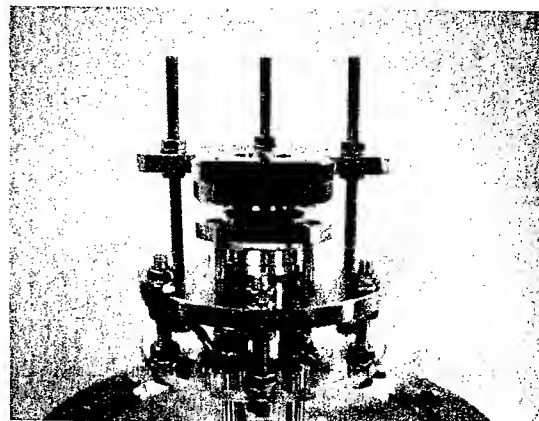


Figure 2: Triode gun with adjustable electrodes

- Grid-Cathode voltage: 0-3.5kV pulse or dc.

- Grid-Cathode gap: around 0.2mm
- Cathode-Anode voltage: 8kV dc fix.
- Cathode-Anode gap: 8mm

RESULTS

Measurements had been performed during a few days - weeks for every sample. Peak currents and long time stabilities were recorded. Summaries are as follows. These characteristics are common for all material.

- 1) Higher current could be obtained by increasing grid voltage. But it is limited by break downs. Frequent discharge made damages on a cathode surface (see fig. 3). That damage led decrease of a current.



Figure 3: Damage of the cathode surface
CNT was processed in the center.

Left: new cathode (black circle)
Right damaged by discharge

- 2) Decay of a current was observed at the starting of every measurement. But then it became stable and the current was constant, while all conditions were kept.
- 3) Currents were stable, while no discharge took place.
- 4) By those measurements, maximum currents were far to saturation with grid voltage. So, it is possible to obtain higher current, with preventing discharges. Following improvements seems to be effective.

- Pulse width : shorter
- Grid mesh : smoother
- Cathode surface : smoother
- Electrodes : optimisation of materials

Following descriptions were results of two materials. Those cathodes marked relative high current and long time stability.

CNT#3

For this cathode, two samples were tested by improvement of equipments.

Figure 4 shows the record of CNT#3 at 1st time measurement. Current change vs. grid voltage and time were plotted. The stable current value was around

140mA/cm². This value was observed after several discharges with higher grid voltage. After 1st measurement, cathode damaged like fig.3. For the 2nd sample of this cathode, measurement was performed carefully not to lead discharge. Figure 5 shows the latest result. The highest current density was recorded as 2.5A/cm² at 3.27kV. Few discharges took place, no apparent reduction of current was observed. It seemed to be possible to exceed few 10A/cm² with development of this cathode.

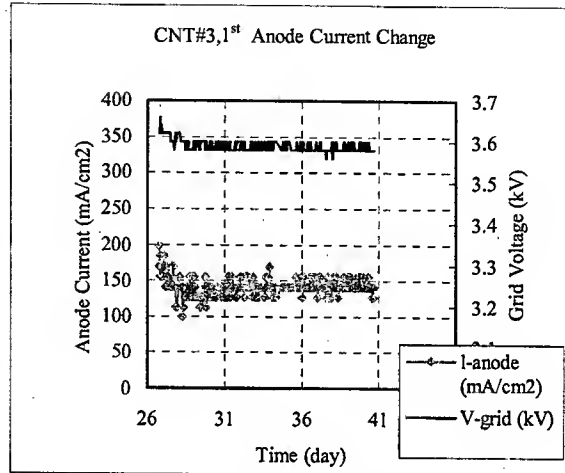


Figure 4: Characteristics of CNT#3, 1st sample.
Long time current change.

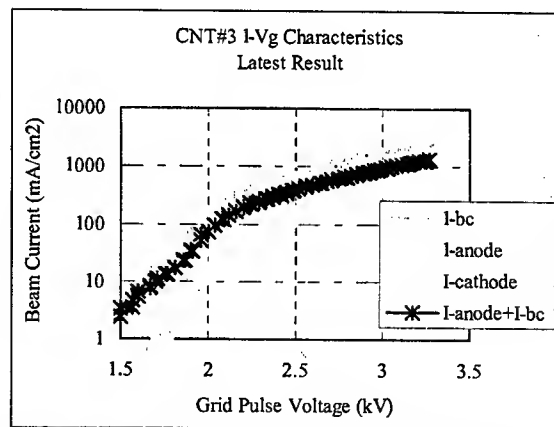


Figure 5: CNT#3, 2nd Grid voltage vs. Emission current.
With improved measurement.

GNF

Figure 5 shows current change of GNF. Peak current was around 150mA/cm², and stable current was around 50mA/cm². This cathode was very stable and it could be used for middle current application. Higher current also seemed to be possible with higher grid voltage.

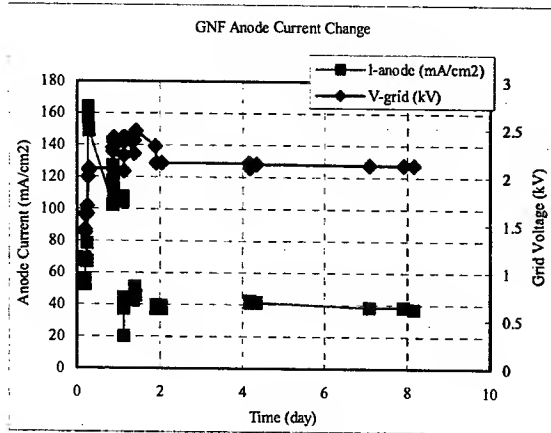


Figure 5: Characteristics of GNF

DISCUSSION

Discharge caused a reduction of emission area. One reason was decrease of emission area. The discussion of the other effects have been started. Molecular structures have analysed by raman shift. From the analysis of the first sample (CNT#1), some interesting data was observed. In figure 6, it is brand-new CNT#1, the spectrum shows two clear peaks. And figure 7 shows the used CNT, it was damaged by discharges. The spectrum shows much different structure. Those change might effect emission characteristics.

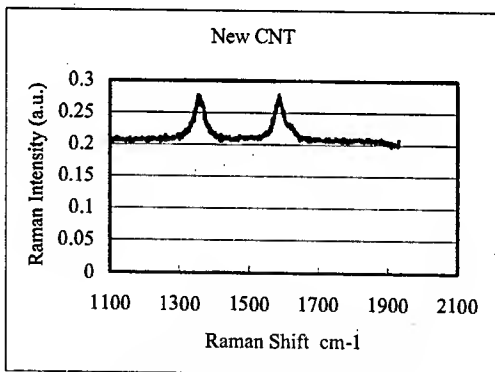


Figure 6: Analyze of CNT#1
Brand-New

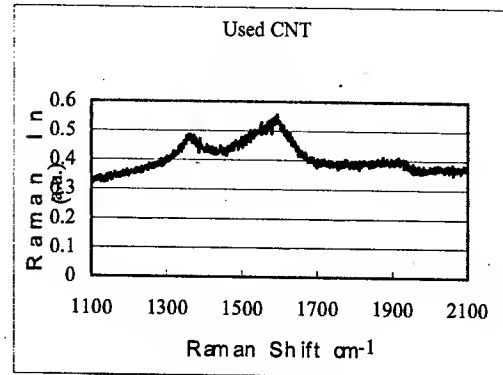


Figure 7: Used cathode damaged by discharge.

ACKNOWLEDGEMENT

Authors would like to thank ULVAC Corp. for useful discussions, supplying some samples.

REFERENCES

- [1] Y.Saitoh, et al. "Synthesis, Structure and Field Emission of Carbon Nanotubes," *Fullerene Science and Technology*, 7(4), 635-664(1999)

CRYSTAL-BASED SPIN ANALYZER FOR FAST NEUTRON BEAMS

N. Bondarenko and N. Shul'ga, KIPT, Kharkov, Ukraine

Abstract

Possibility of construction of a spin analyzer for fast neutron beams is discussed, based on the conception that inter-crystal electric fields may act upon passing neutron via its magnetic moment. Such an influence might be substantial provided that proper crystal orientation is held and coherence conditions are organized. Numerical estimates of the beam and target parameters are performed, confirming possibility of realizing this technique under the condition of the incident beam high collimation degree.

INTRODUCTION

In modern experimental particle physics fast neutron beams are classified as a rather special experimental tool. The need in them is largely suppressed due to use of protons, which have all strong interaction properties almost identical with that of neutrons, but are advantageous technically, allowing for beam operation by means of external electromagnetic fields. Problems, for which use of neutron beams can not be avoided (apart from material research, where rather cold neutrons are proper), are investigation of spatial structure of nuclei and inter-nucleus forces [1], T-invariance precision tests [2] etc. As a whole, today fast neutron experimental physics is a progressing field, with beam quality and particle energies gradually raising.

Parameters of neutron beams available today in general depend on method of the neutron production, which may be basically of two kinds: knock-out reactions caused by fast protons or electrons on neutron-rich nuclei, and diffractive dissociation of neutron-rich light nuclei (D, T). Typical neutron energies achieved by both of the methods are of order 100 MeV. The advantage of knock-out reactions is a high outcoming neutron intensity in a pulsed regime, while the diffractive dissociation provides a better beam quality at high energy, since this process is closer to elastic and its differential cross-section is naturally peaked near the forward direction.

Additional difficulties arise at preparation of polarized fast neutron beams. In knock-out reaction methods a neutron polarization may be obtained by registering the outcoming particles at wide angles, while in diffractive dissociation – by polarization transfer from polarized initial deuterons. Measurement of fast neutron polarization degree is usually performed via measuring their attenuation asymmetry in cryogenically nuclear-spin-aligned targets. Typical polarizations achieved by those methods are of order 0.25.

In the present contribution we describe an alternative method for polarized neutron beam formation under conditions when a good unpolarized primary neutron beam is available. The method bases on the coherent amplification of the electromagnetic interaction at

passage of fast particles near crystal axes or planes. This effect is often exploited in experimental high-energy physics for conversion of charged particle beams. As for neutron, despite its electric neutrality, it possesses a non-vanishing magnetic moment, and thus its interaction with atomic fields is not zero and might be amplified through the coherent mechanism.

MECHANISM

Imagine a neutron with a definite momentum p , impact onto a finite-thickness mono-crystal, whose some strong crystallographic plane is aligned precisely parallel to the neutron initial momentum (z direction). Suppose that the neutron is fast enough as to scatter only through small angles under typical momentum transfers supplied by atomic fields. So, within the crystal the neutron moves approximately straight along a crystal plane. At that, the major impact on the neutron comes from an average electrostatic potential $\Phi(x)$, which depends only on the coordinate x , orthogonal to the oriented crystal planes.

Potential energy of the neutron in such a field depends on the sign of the neutron spin projection $\sigma_y = \pm 1$ on the y axis, the latter thus playing role of a quantization axis:

$$H_\mu = \mu v \sigma_y \frac{\partial}{\partial x} \Phi(x) \quad (1)$$

($\mu = -1.9|e|/2M$, M is the neutron mass, v its velocity). Accordingly, a quantum-mechanical phase, acquired by the neutron after passage through the crystal along a line at an impact parameter x , equals

$$S(x) = -\frac{L}{v} H_\mu(x), \quad (2)$$

where L is the crystal thickness. The scattering amplitude with a momentum transfer q reads

$$a = \frac{P}{2\pi i} \int dx e^{iqx} e^{iS(x)} \quad (3)$$

(we include the initial wave to consideration, too).

In view of identity of all the inter-plane intervals, constituting the crystal, this expression splits into two factors: the Bragg factor

$$F_B = \frac{\sin N_x q d}{\sin q d} \approx \frac{\pi}{d} \sum_n (-1)^n \delta\left(q - \frac{\pi n}{d}\right), \quad N_x \gg 1 \quad (4)$$

(d – the inter-plane distance, N_x – the number of planes, constituting the crystal) and the cell eikonal structure factor

$$F_c = \int_{-d/2}^{d/2} dx e^{iqx} e^{iS(x)}. \quad (5)$$

For a qualitative illustration, let the inter-plane potential $\Phi(x)$ be approximated by a quadratic function

$$\Phi(x) \approx \frac{2\pi\rho Ze}{d} x^2, \quad -\frac{d}{2} \leq x \leq \frac{d}{2}, \quad \Phi(x+d) = \Phi(x) \quad (6)$$

where ρ is the density of nuclei with the charge Z belonging to the chosen crystal plane. With the potential (6) the eikonal scattering phase (2) exhibits a "saw" structure

$$S(x) = \alpha x, \quad -\frac{d}{2} \leq x \leq \frac{d}{2}, \quad S(x+d) = S(x) \quad (7)$$

$$\alpha = \frac{4\pi\rho Ze\mu L}{d} \sigma_y$$

with the sign depending on the σ_y , and the cell structure factor is

$$F_c = \frac{2}{q+\alpha} \sin \frac{(q+\alpha)d}{2}.$$

This is a function with a dominant maximum at $q = -\alpha$. And in order to attain the largest positive effect and sharpness in the total amplitude and the cross-section $d\sigma/d\Omega = |a|^2$, obviously, it is profitable to make the main maximum of F_c coincide with one of the maxima of F_B , distinct from the zeroth (cf. Fig. 1).

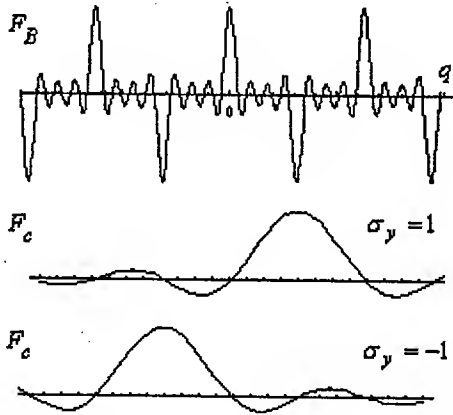


Fig.1 Schematics of Bragg and cell structure factors fitting.

Now let us turn to numerical estimates, which would help us decide, whether the given scheme is realizable and indeed efficient.

ESTIMATES

Let us start from estimating the target parameters and the beam energy, at which the best observable effect may be foreseen.

First, by choosing the F_c main maximum coincide with the first Bragg maximum, we come to the condition $\alpha = \pi/d$, which through (7), $L = N_z d$ determines the crystal thickness:

$$N_z = \frac{L}{d} \approx \frac{M}{4\rho d Ze^2}. \quad (8)$$

As we shall see below, it is advantageous to use materials with large Z , in order to achieve the desired effect at a shorter distance, before any negative effects can evolve.

At $Ze^2 \sim 1$, $\rho \sim 1/d^2$ (8) roughly means

$$N_z \sim 10^5, \quad L \sim 0.1 \mu\text{m}. \quad (9)$$

So, quite a thin (though macroscopic) monocrystal target is required here, and certain subtleties in preparation and setup must be expected. At such a thickness, of course, the target will be transparent to the beam, in the sense that shadows from atomic nuclei are negligible. The effect of the target influence, thus, indeed practically reduces to a pure elastic scattering (through small angles).

Next, the assumed mode of a nearly straight-line passage is dynamically sustainable if

$$p > \frac{N_z}{d}. \quad (10)$$

This entails a lower bound for the energy, which at $Ze^2 \sim 1$ proves to be non-relativistic:

$$E > \frac{(N_z/d)^2}{2M} \sim \frac{1}{2} M \left(\frac{1}{4Ze^2} \right)^2 \sim 30 \text{ MeV}. \quad (11)$$

So, the energies required here are quite accessible with modern neutron facilities. (11) also confirms that larger Z are more appropriate here.

Sensitivity to changes of the energy and the incident angle in the described pattern is not strong. As follows from (2) through (1), the eikonal phase, even in a non-relativistic regime, basically does not depend on velocity. This guarantees that the same grid shall work equally well at all energies. The pattern also does not alter substantially under a non-zero (but small) incident angle between the neutron velocity and crystal planes, even if neutron crosses a few planes in course of its passage – because the "saw" structure of the eikonal phase is conserved.

But a most severe physical condition comes from the notion that under the typical scattering angles being of the order

$$\theta = \frac{q}{p} \sim \frac{1}{pd} < \frac{1}{N_z} \sim 10^{-5}$$

collimation of the beam in x direction must be better or about such a degree. This is not an insuperable difficulty, say, if use a 0.1 mm aperture at a 10 m distance from the neutron source. The reduction of intensity may be compensated by augmentation of the collimating slit length in y direction. Nonetheless, it must be recognized that there are no beams with such a quality of collimation at present – probably because there was no sensible motivation for that so far.

SUMMARY

As we have shown in the present contribution, at certain conditions a thin oriented monocrystal can split a monochromatic neutron beam into two parts, each being completely or almost completely polarized. In this sense the action of the crystal is equivalent to that of the renowned Stern-Gerlach apparatus (which in its conventional construction can not essentially manage with neutrons, since magnetic fields are not strong enough for that). Accordingly, the experiment described by us may also be suggested as a spin analyzer with the same advantages – polarization degree close to 1 and basically conservation of all the primary beam properties.

A salient feature of the oriented-crystal-based neutron spin analyzer, however, is the requirement of quite a high collimation degree for the incident neutron beam. Such a collimation may be planned in itself only in case of precision measurements. Possibility of moderating this

requirement needs more involved theoretical analysis and computer simulations. Tentatively, one may expect one order of magnitude to be reduced. Then the suggested method might be enough easily introduced to practice at existing fast neutron facilities, such as ORELA at ORNL and TSL at Uppsala, or the forthcoming SNS.

ACKNOWLEDGEMENT

Partial support by STCU-1746 grant is acknowledged.

REFERENCES

- [1] Proceedings of Beijing-1991 International Symposium on Fast Neutron Physics, ed. J. Zhang (World Scientific, 1992).
- [2] Time Reversal Invariance and Parity Violation in Neutron Reactions, ed. by C.R. Gould, J.D. Bowman and Yu.P. Popov (World Scientific, 1994).

PULSED HV ELECTRON GUN WITH THERMIONIC CATHODE FOR THE SOFT X-RAY FEL PROJECT AT SPRING-8

K. Togawa, H. Baba, K. Onoe, T. Shintake, SPring-8 / RIKEN Harima Institute, Hyogo, Japan
T. Ishizuka, Sumitomo Heavy Industries, Ehime, Japan

Abstract

A pulsed high-voltage electron gun with a thermionic cathode is under development for the injector system of the SASE-FEL project at SPring-8 (SCSS project) [1]. A CeB_6 single crystal is chosen as a thermionic emitter, because of its excellent emission properties, i.e., high resistance against contamination, uniform emission density and smooth surface [2]. Since we need to apply a -500 kV pulse to the cathode, all gun related high-voltage components; ceramic insulator, step-up transformer, dummy load etc. are immersed in insulating oil to avoid discharge problems. A same model of the C-band klystron modulator is used to provide -500 kV through a step-up transformer. We report on recent progress in the gun development.

ELECTRON INJECTOR CONCEPT

For the SCSS project, we chose a pulsed high-voltage electron gun with a thermionic cathode instead of a photocathode RF-gun. As is well known in SASE-FEL theory, the quality of the internal structure of the bunched beam dominates the FEL gain, that is, the sliced emittance of the beam should be very low to saturate SASE-FEL. Also from the FEL users point of view, the FEL light should be stable with low jitter over long time periods. Therefore, stability is essential for the electron gun. We believe that a cathode made from a single crystal of CeB_6 is suitable to produce such a low emittance, extremely

stable beam, because its surface maintains fairly flat at the nano-meter scale due to material evaporation.

The CeB_6 cathode 3 mm in diameter will produce a 3 A beam with 2 μsec FWHM. The gun voltage of -500 kV was chosen as a compromise between HV breakdown technical problems versus the emittance growth due to space charge with lower voltages. Beam parameters at the gun exit are summarized in Table 1.

A beam chopper will be installed after the gun which will cut out the rising and falling parts of the pulse, and thus create a 2 nsec beam pulse. A 476 MHz pre-buncher modulates the beam energy to form a short bunch. The followed energy filter removes the energy-tails (top and bottom). Finally an L-band accelerator captures the bunch, and accelerates it to 20 MeV. Fig. 1 shows the layout of the injector system of the SCSS project.

Beam Energy	500 keV
Peak Current	3 A
Pulse Width	2 μs FWHM
Repetition Rate	60 Hz
Normalized RMS Emittance	0.4 $\pi\cdot\text{mm}\cdot\text{mrad}$

Table 1: Beam parameters at the gun exit

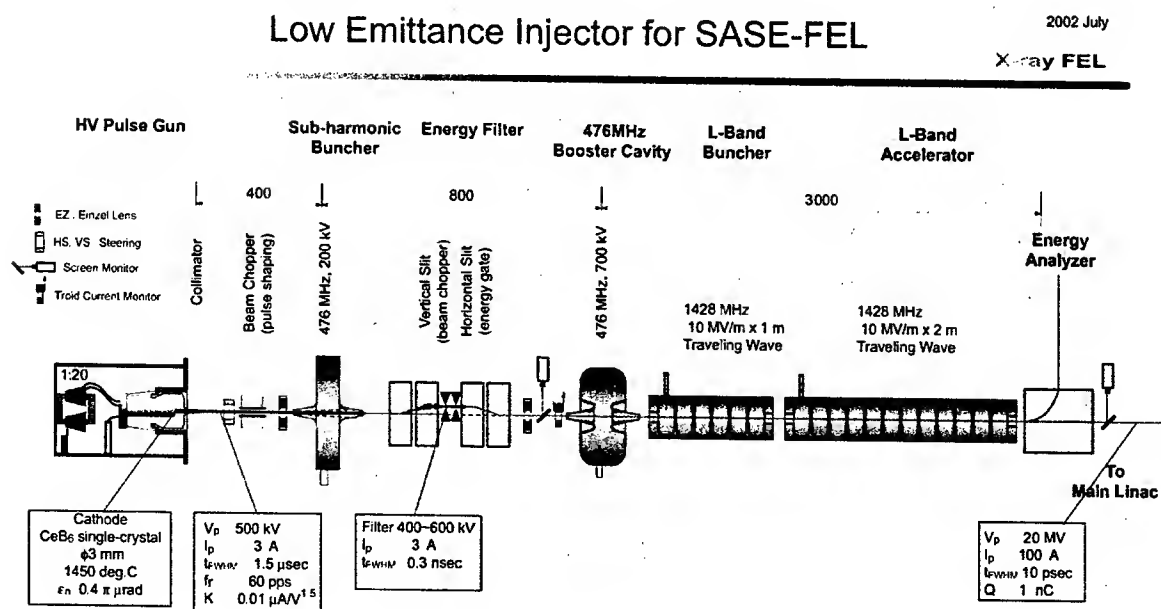


Figure 1: Injector system of SCSS project

CATHODE DEVELOPMENT

The normalized RMS emittance of an electron beam emitted from a hot cathode is described by

$$\varepsilon_{n,RMS} = \frac{r_c}{2} \sqrt{\frac{kT}{m_0 c^2}}$$

where r_c is the cathode radius and T is the cathode temperature. It is obvious from the above relation that a small cathode is necessary to obtain a low emittance beam. The single crystal CeB_6 cathode with a 3 mm diameter will produce a 3 A peak current when heated to 1450 deg.-C. In this case, the beam emittance becomes as low as $0.4 \pi \cdot \text{mm} \cdot \text{mrad}$, which is much lower than the requirement of $2 \pi \cdot \text{mm} \cdot \text{mrad}$ emittance for FEL operation at the undulator section.

Fig. 2 shows the cathode assembly. The CeB_6 crystal is mounted in a graphite sleeve. This produces a surface electric field uniform over the whole cathode area. This is quite important to eliminate halo beam emission from the cathode edge which can cause damage to the undulator magnets.

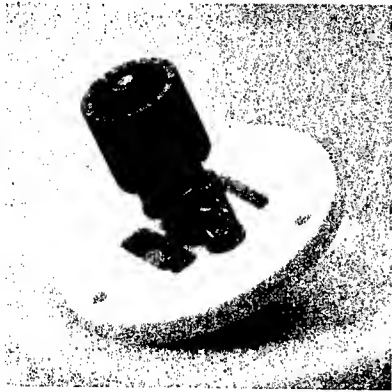


Figure 2: CeB_6 cathode assembly

We use a graphite heater rather than the conventional metallic filament made of tungsten or the like. Graphite is mechanically and chemically stable even at very high temperatures and does not evaporate like metal. Since its electric resistance does not change much as a function of temperature, it is easy to control the heater power. Fig. 3 shows the graphite heater in operation in the vacuum chamber. The cathode was heated up to more than 1450 deg.-C.



Figure 3: Heating test for the graphite heater

GUN GEOMETRY DESIGN

We chose a flat wehnelt rather than the common Pierce-type electrode. Our reasons are as follows. (1) The Pierce electrode has a strong focusing electric field which acts against the radial space charge force of the beam. If the cathode is not exactly centered on the axis of the gun, as may be caused by misalignment of cathode mount or movement of cathode position due to heating, the focusing field does not act on the beam symmetrically. This may cause emittance growth. The flat wehnelt do not have such an effect. (2) We plan to vary the beam current over a wide range in order to tune the accelerator system. The gun will be operated in a temperature limited region. The Pierce electrode is not suitable for such operation because a low intensity beam is over-focused at the electrode. The flat wehnelt never over-focuses the beam because there is no external focusing field.

In order to check emittance growth of the beam from the flat wehnelt, we have performed a computer simulation using the EGUN code. The beam trajectory and the phase space plots in a temperature limited region are shown in Fig. 4 and Fig. 5, respectively. The beam does not diverge much and the slope of the phase space plot becomes straight. The estimated emittance for a rough mesh size is deemed to be non-physical and to be caused by a simulation error. The emittance converges to $0.1 \pi \cdot \text{mm} \cdot \text{mrad}$ at a mesh size of 0.05 mm. We conclude that emittance growth due to space charge in the gun region can be ignored.

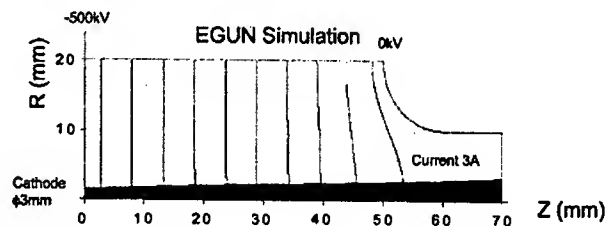


Figure 4: Beam trajectory simulated by the EGUN code

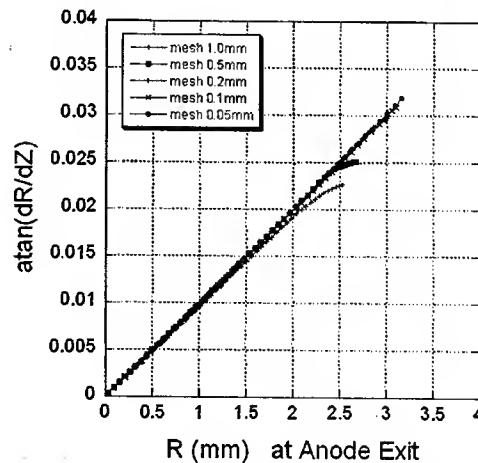


Figure 5: Phase space plot for various mesh sizes

500 KV GUN TEST STAND

We have constructed a 500 kV electron gun test stand and started performance tests. A side view of the test stand is shown in Fig. 6. It consists of the 500 kV electron gun and an emittance measurement system.

Since we need to apply a -500 kV pulse voltage to the cathode, all of the high-voltage components; ceramic insulator, pulse transformer, dummy load etc. are immersed in insulating oil to reduce discharge problems.

We use a same model of the C-band klystron modulator to feed -24 kV pulsed voltage to a pulse transformer, which steps-up the input voltage to -500 kV. In order to match the impedance of the gun to the modulator PFN circuit, a 1.9 k Ω dummy load is connected in parallel with the cathode.

We will measure the beam emittance by the so-called double slit method. Two sets of movable slits are installed in the beam line, one is for vertical emittance and the other for horizontal. The width and position of the slit gate can be controlled with an accuracy of 10 μ m. Fig. 7 shows a photograph of the horizontal slit. The temporal profiles of beam currents are measured by means of core monitors. We also measure a time-resolved beam profile using a YAP:Ce fluorescent screen. We plan to measure emittance of a 500 keV beam from the CeB₆ cathode in this summer.

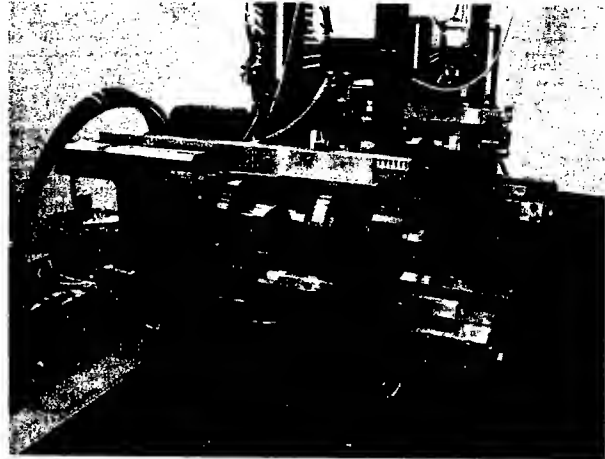


Figure 7: Photograph of the horizontal slit (the vacuum pipe has been removed)

REFERENCES

- [1] <http://www-xfel.spring8.or.jp/>
- [2] <http://www.feibeamtech.com/>

SCSS

500kV Electron Gun Test Stand

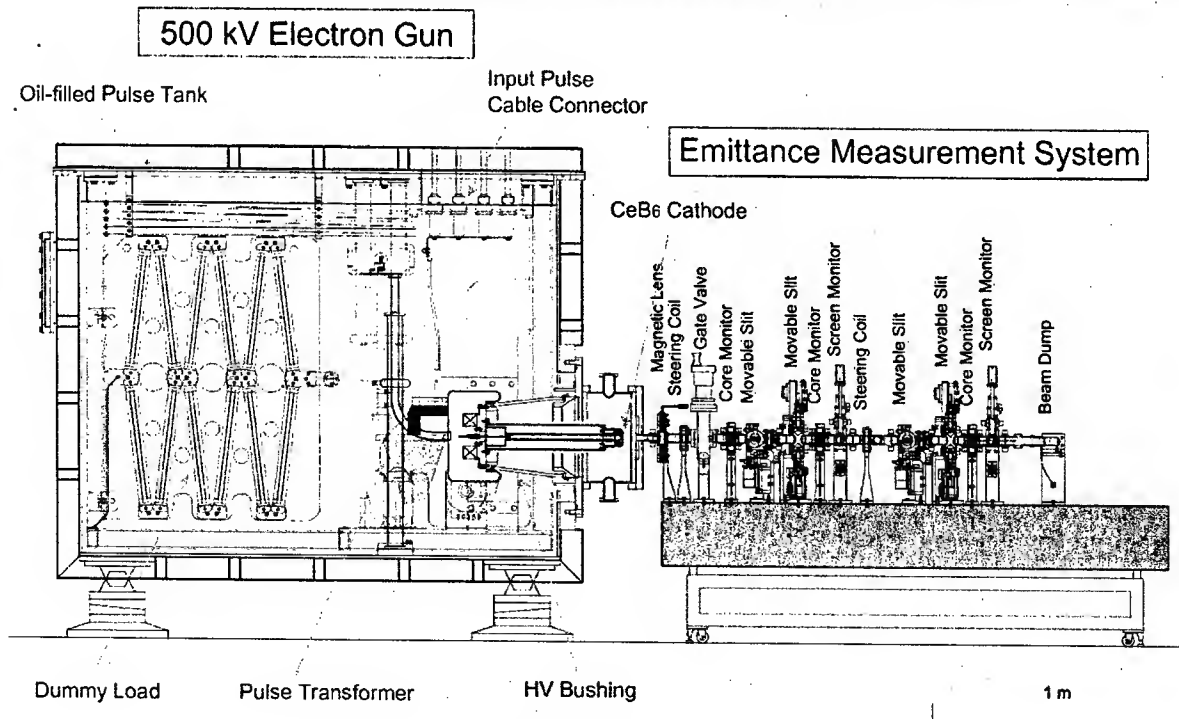


Figure 6: 500 kV Electron Gun Test Stand

ION AND NEUTRAL BEAM GENERATION BY 1 TW, 50 fs LASER IRRADIATION OF THIN FOILS

Y. Wada, T. Kubota, and A. Ogata

AdSM, Hiroshima University, 1-3-1 Kagamiyama, Higashi-Hiroshima 739-8530, Japan

Abstract

Thin ($< 10 \mu\text{m}$) plastic and metal foils were irradiated by a 1 TW, 50 fs laser pulses. The foil surface was located at $\pi/4$ to the laser injection. Particle beams were obtained on both sides of the foil with respect to the laser injection. The laser intensity under $10^{17} \text{ W cm}^{-2}$ produced only neutral particle beams on the rear side of the laser illumination, flowing to the direction perpendicular to the foil surface with small ($\sim 15^\circ$) divergence. The laser intensity over $10^{17} \text{ W cm}^{-2}$ produced also ion beams with larger ($> 45^\circ$) divergence. The components of the neutrals and ions were contaminants of the foil surface. To the contrary, mainly ions were observed on the laser-illuminated side, which were components of the target foils. The most energetic particles were protons on both sides, whose energy was about 550 keV.

INTRODUCTION

In recent years, interaction between high-intensity laser and matter has been actively studied. Especially, the generation of multi-MeV ions produced by the interaction between a short ($< 1 \text{ ps}$) and high-power ($> 10 \text{ TW}$) laser pulse and thin foils is a rapidly growing research area [1-9]. If this phenomenon is reproduced by a T^3 laser, it will enable construction of a compact ion source of an accelerator. Although Zhidkov *et al.* [10] have shown the possibility of MeV proton generation using a laser with $10^{17} \text{ W cm}^{-2}$ intensity, few experiments have been carried out so far using lasers with intensity below $10^{18} \text{ W cm}^{-2}$, except the work of Badziak *et al.* [11] who obtained the 300 keV proton energy with a double-layer foil target using a 1 ps laser with $10^{17} \text{ W cm}^{-2}$ intensity.

This paper reports experiments to irradiate thinner ($< 10 \mu\text{m}$) plastic and metal foils by a laser with smaller power (1 TW) and shorter pulse width (50 fs) than the hitherto experiments. We define the laser-illuminated side and the other side by "backward" and "forward", respectively. It was found that the intensity threshold of the ion generation was $10^{17} \text{ W cm}^{-2}$ on the forward side. Under the threshold, neutral beams with small divergence are generated. However, there were no definite thresholds on the backward side. The most energetic particles were protons on both sides, whose energy was about 550 keV.

In the next section, we describe the experimental apparatus and in the third section, we describe the experimental results and their discussions. The final section gives summary.

EXPERIMENTAL APPARATUS

The experiments were performed with a Ti:Sapphire laser, 50 mJ in pulse energy, 50 fs in pulse width (1 TW in pulse power), 800 nm in wavelength and 10 Hz in pulse frequency. A main pulse was accompanied with a pre-pulse in the ns range, whose total power was $\sim 1/2,000$ of the main. The surface of the target foil was located at $\pi/4$ to the laser injection. An $f=120 \text{ mm}$ lens located inside of a vacuum chamber focused the laser to a target in the chamber. The delivered energy to the interaction point was about 38 mJ. A single shot autocorrelator tells that typical pulse duration was $\sim 40 \text{ fs}$ in FWHM before the laser pulse goes through the window and the lens, which give the laser intensity on the target as about $2 \times 10^{17} \text{ W cm}^{-2}$. Two types of materials were tried as the target foils; mylar $(\text{C}_{10}\text{H}_8\text{O}_4)_n$ and aluminum (Al). Their thickness was mostly less than $10 \mu\text{m}$. Typical vacuum in the chamber was $\sim 10^{-3} \text{ Pa}$.

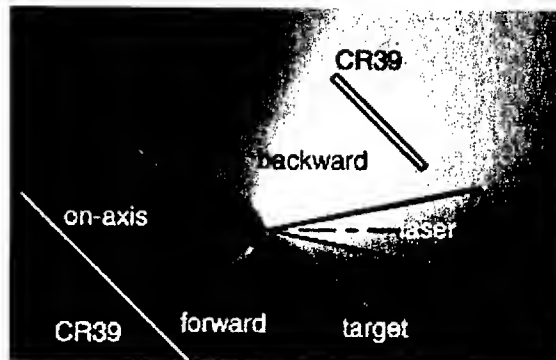


Figure 1: Picture of the interaction between the laser with intensity of $\sim 4 \times 10^{16} \text{ W cm}^{-2}$ and $3 \mu\text{m}$ -thick Al target foil with schematic of the experimental setup. Definitions of "backward" and "forward" sides are also given.

Figure 1 shows a picture taken at the moment of the laser irradiation, from the direction parallel to the laser axis and perpendicular to the foil surface, Al in $3 \mu\text{m}$ -thick in this case. It shows a fine but bright trace to the forward direction, besides the backward laser refraction. A CR39 and a Thomson parabola spectrometer were used to detect generated particles. The CR39 is a track detector sensitive only to ion (and neutron generated by recoil protons or carbons) [12]. The Thomson parabola spectrometer consists of an aperture ($0.5 \text{ mm } \phi$) and a pair of dipole magnets (0.48 T). The pair magnets have also the role of electrodes (2.9×10^5

V m^{-1}). The computer code MAFIA¹ was used to calculate the field distributions, and particle tracking code was used to estimate the deflection of the charged particles.

RESULTS AND DISCUSSIONS

In order to measure particle distributions, we placed the CR39 plates on both forward and backward sides across the target, and also in the direction on the laser axis as shown in Fig. 1. Each CR39 plate is located with distance of 30 mm away from the interaction point. Figure 2(a) and (b) show photographs of CR39 tracks at the forward direction obtained by an Al target in $3\text{ }\mu\text{m}$ -thick in case that the laser intensities are $2.1 \times 10^{17}\text{ W cm}^{-2}$ and $1.1 \times 10^{17}\text{ W cm}^{-2}$, respectively. They show that particles concentrate in the direction normal to the target surface and that few particles are observed on the laser axis. In Fig. 2(a), the particle distribution has two components; one is narrow ($\sim 15^\circ$ in FWHM), another is wide ($> 45^\circ$). In Fig. 2(b), the distribution has only the narrow component. The narrow component consists of neutrals, while the wide component consists of ions as described in the following.

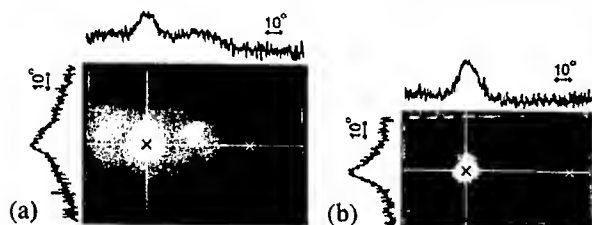


Figure 2: Typical CR39 images of generated particles in the forward direction. Target was Al in $3\text{ }\mu\text{m}$ -thick. Black cross indicates the direction normal to the target surface and white cross indicates on-axis direction. Curves show distributions of etch pits along the path indicated in white lines. Laser intensities were (a): $2.1 \times 10^{17}\text{ W cm}^{-2}$ and (b): $1.1 \times 10^{17}\text{ W cm}^{-2}$.

Figure 3 shows the result of Thomson parabola measurement on the forward side obtained by an Al target in $3\text{ }\mu\text{m}$ -thick. The spectra in (a) and (b) are results of sum of 60 laser shots in the forward direction in case that the laser intensity is $2.0 \times 10^{17}\text{ W cm}^{-2}$ and $5.8 \times 10^{16}\text{ W cm}^{-2}$, respectively. Lines are results of calculation by MAFIA. Neutral particles are concentrated on the $x = y = 0$ point in both figures. The darkest curve is in fine agreement with the theoretical proton parabola. Figure 3(c) shows three energy spectra of protons; two were given by the $3\text{ }\mu\text{m}$ -thick Al target at two laser intensities over 10^{17} W cm^{-2} , and one was given by a $5.7\text{ }\mu\text{m}$ -thick mylar target at the laser intensity of $2.1 \times 10^{17}\text{ W cm}^{-2}$. Maximum proton energy was about 550 keV in the mylar target, and 150 keV in the Al target. Figure 3(d) shows the dependence of the number of particles on the laser intensity. Both ions and neutrals

were detected above 10^{17} W cm^{-2} , but few ions were detected below 10^{17} W cm^{-2} . We therefore conclude that the threshold intensity of the ion generation is around 10^{17} W cm^{-2} .

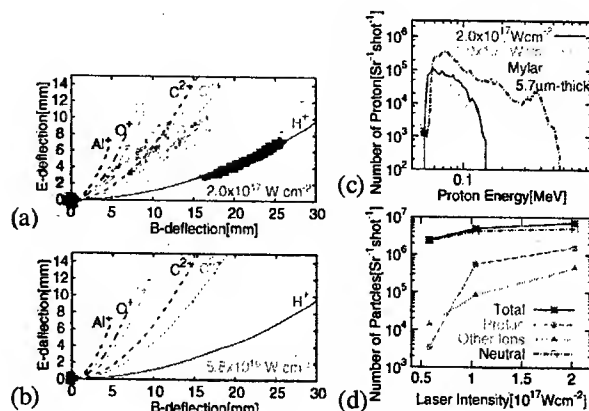


Figure 3: (a) and (b) Thomson parabola spectra from Al $3\text{ }\mu\text{m}$ -thick targets in the forward direction. (c) Proton spectra obtained at laser intensities above 10^{17} W cm^{-2} from the Al targets. A dot-dash line shows the case of mylar in $5.7\text{ }\mu\text{m}$ -thick with $2.1 \times 10^{17}\text{ W cm}^{-2}$ laser intensity. (d) Dependence of the number of particles on the laser intensity.

On the backward side, particles distribute between the laser axis and the direction normal to the target surface, with an angle of $> 45^\circ$. Figure 4 shows the Thomson parabola spectra on this side. Figure 4(a) and (b) show these given mylar target in $8.7\text{ }\mu\text{m}$ -thick. The laser intensities were $2.1 \times 10^{17}\text{ W cm}^{-2}$ and $5.9 \times 10^{16}\text{ W cm}^{-2}$, respectively. Even the laser intensity under 10^{17} W cm^{-2} produced ions but few neutrals. Figure 4(c) shows the spectra of the Al target in $3\text{ }\mu\text{m}$ -thick at $2.1 \times 10^{17}\text{ W cm}^{-2}$ laser intensity. The main components of particles are Al ions and few protons and neutrals are found. Figure 4(d) shows the proton spectra and (e) shows dependence of the number of particles on the laser intensity. Maximum proton energy was about 550 keV in mylar target.

Let us compare the Thomson parabola spectra of Al, Fig. 3(a)-(b) measured on the forward side and Fig. 4(c) on the backward side. The superior particles in the forward direction are neutrals. Protons and carbon ions were not found below the threshold of 10^{17} W cm^{-2} . Note that no Al ions were obtained on this side. The protons must be originated from water vapor and/or hydrocarbons contaminating the target surface as indicated in the hitherto experiments [1-6]. Both sides of the mylar targets generate similar species, but we can deduce that the protons on the backward side are components of the targets while those on the forward side are contaminants, because Al targets do not generate protons on the backward side.

Spectra of visible radiation emitted at the interaction were measured by an asymmetric Czerny-Turner type poly-

¹See <http://www.cst.de>

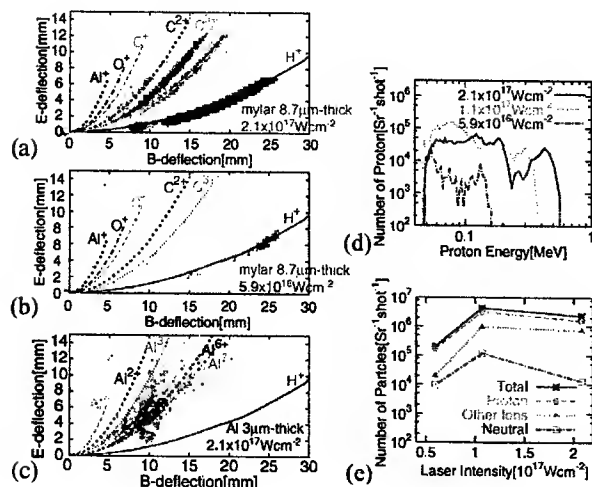


Figure 4: (a)-(c) Thomson parabola spectra in the backward direction. (a) and (b) from 8.7 μm -thick mylar target with laser intensities of $2.1 \times 10^{17} \text{ W cm}^{-2}$ and $5.9 \times 10^{16} \text{ W cm}^{-2}$, respectively. (c) from 3 μm -thick Al target with laser intensity of $2.1 \times 10^{17} \text{ W cm}^{-2}$. (d) Proton energy spectra obtained from 8.7 μm -thick mylar target. (e) Dependence of the number of particles on the laser intensity.

chrometer. Two lenses transferred image of the radiation at a specific position to the polychrometer slit outside of the vacuum chamber with resolution of 1 mm. The range between 413 and 928 nm was detectable with the resolution of 0.07 nm. We identified the observed spectral lines with NIST Spectra Line Database². The measurement found different species between Al and mylar targets on the backward side. The Al targets gave lines of Al, H, C, O atoms and $\text{Al}^{1+,2+,3+}$, C^{1+} , O^{1+} ions, while the mylar targets gave those of H, C, O atoms and $\text{C}^{1+,2+,3+,4+}$, $\text{O}^{1+,2+}$ ions. This also supports the assumption that the particles on the forward side are originated from contaminants and those on the backward side are mainly components of the targets.

Previous works have not reported the generation of neutral particles explicitly, including the paper of Gitomer *et al.*[14] whose laser intensity was under $10^{17} \text{ W cm}^{-2}$ in most cases. This is probably because the mechanism caused by their long ($\sim \text{ns}$) laser pulse is different from that caused by our short ($\sim 50 \text{ fs}$) laser pulse. The CR39 measurements of the neutral particles generated at the laser intensity around $4 \times 10^{16} \text{ W cm}^{-2}$ have been previously described in detail [13].

The number of particles generated was estimated to be under $10^7 [\text{Sr}^{-1} \text{ shot}^{-1}]$ in all cases. This value is lower than the interpolation based on the previous experiments obtained using the laser intensity around $10^{18} \text{ W cm}^{-2}$ with longer pulse width [1–6]. This is because our laser energy is small; it is not the laser power but the laser en-

ergy that is more closely related to the particle generation. Though the energies could be useful, the number of particles obtained by our T^3 laser is too small and their emittance is too large for practical use as an accelerator ion source. Appropriate shaping or conditioning of the target will improve the situation [4, 5, 7, 11]. The neutral beams with high energy and small emittance will be able to find their own applications.

SUMMARY

In summary, we have detected neutral particles and ions in the interaction between a T^3 laser and thin foils. The neutral particles with a small divergence were detected on the forward side with the laser intensity under $10^{17} \text{ W cm}^{-2}$, and ions, mainly protons, were also detected with the laser intensity over $10^{17} \text{ W cm}^{-2}$. In this direction, the generated particles originate from contaminants of the target surface. On the backward side, ions characteristic to the target materials were obtained but no neutrals were stably detected. The maximum proton energy was 550 keV in mylar targets on both sides.

ACKNOWLEDGEMENTS

We would like to thank Fumitaka Nishiyama, Koji Matsukado, Ryoko Katsube, Akio Seiki, Yuji Tsuchimoto, Daisuke Fukuta, Masahiro Sawayama and Masato Tanaka for their help in experiments, Osamu Kamigaito, Naruhiko Sakamoto and Makoto Tobiyama for running the MAFIA code. This work was supported by Nuclear Research Promotion Program of JAERI, Advanced Compact Accelerator Development Project of MEXT and NIRS.

REFERENCES

- [1] E. L. Clark *et al.*, Phys. Rev. Lett. **84** (2000) 670.
- [2] A. Maksimchuk *et al.*, Phys. Rev. Lett. **84** (2000) 4108.
- [3] R. A. Snavely *et al.*, Phys. Rev. Lett. **85** (2000) 2945.
- [4] M. Roth *et al.*, Phys. Rev. ST Accel. Beams **5** (2002) 061301.
- [5] M. Hegelich *et al.*, Phys. Rev. Lett. **89** (2002) 085002.
- [6] P. McKenna *et al.*, Rev. Sci. Instrum. **73** (2002) 4176.
- [7] S. C. Wilks *et al.*, Phys. Plasmas **8** (2001) 542.
- [8] A. Pukhov, Phys. Rev. Lett. **86** (2001) 3562.
- [9] T. Nakamura and S. Kawata, Phys. Rev. E **67** (2003) 026403.
- [10] A. Zhidkov *et al.*, Phys. Rev. E **61** (2000) R2224.
- [11] J. Badziak *et al.*, Phys. Rev. Lett. **87** (2001) 215001.
- [12] B. G. Cartwright *et al.*, Nucl. Instr. and Meth. **153** (1978) 457.
- [13] Y. Wada, T. Kubota and A. Ogata, AIP Conf. Proc. **634** (2002) 329.
- [14] S. J. Gitomer *et al.*, Phys. Fluids **29** (1986) 2679.

²The NIST Spectra Line Database is available at http://physics.nist.gov/cgi-bin/AtData/main_asd

TOPOLOGY FOR A DSP BASED BEAM CONTROL SYSTEM IN THE AGS BOOSTER*

J. DeLong, J.M. Brennan, T. Hayes, Tuong N. Le, K. Smith
Brookhaven National Laboratory, Upton N.Y. 11973

Abstract*

The AGS Booster supports beams of ions and protons with a wide range of energies on a pulse-by-pulse modulation basis. This requires an agile beam control system highly integrated with its controls. To implement this system digital techniques in the form of: Digital Signal Processors, Direct Digital Synthesizers, digital receivers and high speed Analog to Digital Converters are used. Signals from the beam and cavity pick-ups, as well as measurements of magnetic field strength in the ring dipoles are processed in real time. To facilitate this a multi-processor topology with high bandwidth data links is being designed.

1 SYSTEM OVERVIEW

The AGS Booster acceleration system consists of two pairs of RF cavities with two frequency bands. The first group of cavities has a bandwidth of 2.5MHz and is capable of providing 45kV per station, the second group has a wider bandwidth of 5.5MHz and each cavity can provide up to 17kV [1].

To use these systems effectively the voltage and frequency of each individual accelerating station must be changed dynamically. Different ion species require very different acceleration cycles and bunch manipulations such as merging, rotating and squeezing require the low level RF drive system to be fast and flexible. This speed and flexibility is realized by using DSP controlled direct digital synthesizers with frequency, phase and amplitude modulation.

The beam control system must calculate the revolution frequency of the beam in real time as a function of dipole field and radial steering. This frequency program is corrected by feedback from measurements of the beam phase and radial position. The beam position and phase are measured using digital receiver technology [2]. The beam control system will also synchronize the Booster and the AGS to enable bunch to bucket transfer of beam between the two machines.

2 DSP TOPOLOGY

To accomplish all the required tasks in real time it is necessary to divide the problem into smaller pieces, the block diagram in figure 2 shows how the tasks are split among five Analog Devices ADSP-21160 DSP processors and how each task communicates with the others.

Data transfer between DSPs use the six available Link Ports [3] on each processor. The link ports are bi-

directional byte serial communication ports that run at the 80 MHz core clock speed of the DSP. All data in the system is 32 bits wide and each port can transfer 80MB per second. The architecture of the DSP allows all six ports to run at this rate simultaneously without impacting the core process. This high-speed data IO architecture in addition to the 64bit global bus was the primary reason for choosing this DSP.

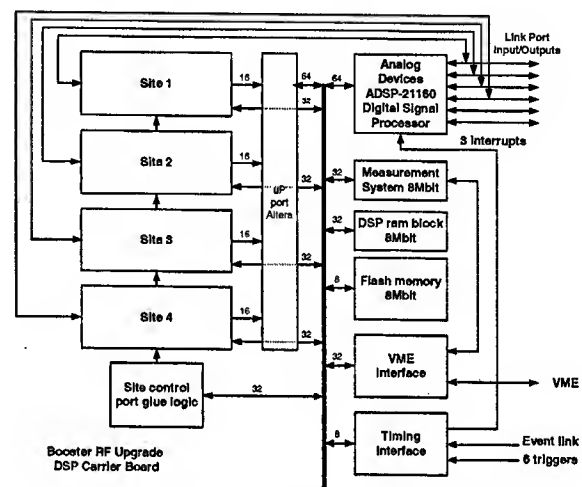


FIGURE 1. DSP carrier board block diagram.

To effectively utilize the capabilities of the DSP processor a carrier card has been designed (FIGURE 1). This printed circuit uses the VME bus form factor with a 32bit VME slave interface. Each carrier card can hold up to four peripheral devices such as digital synthesizers or analog to digital converters. Each peripheral has access to the DSP global bus and one link port as well as power supplies and flexible digital control signals. The DSP boots from an on board flash memory and the carrier also provides 4MB of zero wait state static RAM. Three field programmable gate arrays that are connected to the DSP global bus and each of the four peripheral sites further enhance this flexibility.

The DSP carrier board VME slave interface includes interrupter capability. This allows for tight integration into the control system. The host processor, a Motorola Power PC running the VxWorks operating system, has access to the internal memory space of the DSP as well as control of the peripherals and on board SRAM. Storing user specific program data in local memory and changing a pointer when the context of the machine changes can easily implement pulse-by-pulse modulation or changing of operating parameters of the machine on a system event.

* Work performed under auspices of the US Department of Energy
Contract Number DE-AC02-98CH10886.

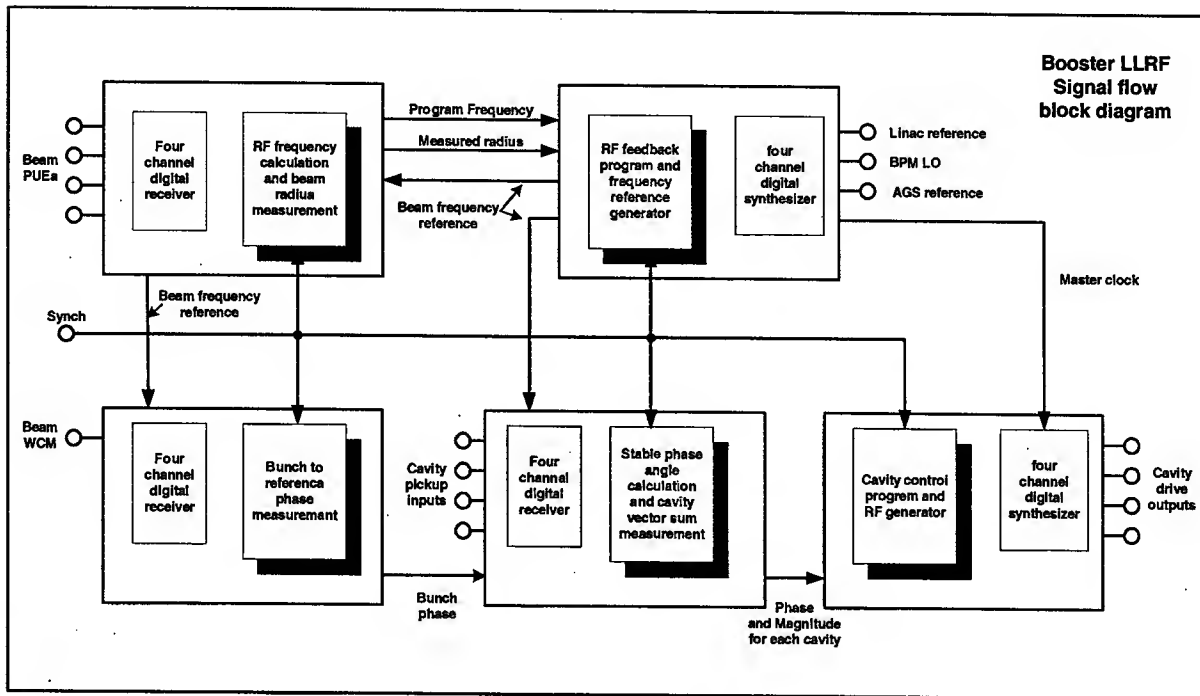


FIGURE 2. shows the general layout of the RF system as well as the programming tasks and interprocessor communication paths.

3 SYSTEM PROGRAMMING TASKS

As shown in figure 2 the programming tasks are divided among the five processors. Each task is synchronized with an external strobe that executes an interrupt service routine on the DSP. This synchronization ensures that all calculations across the system processors are using the most current data.

3.1 Frequency program

The revolution frequency of the beam is calculated at a rate of 500kHz. This rate is sufficient to ensure frequency steps that are small compared to the RF bucket height. A memory-mapped accumulator on the DSP carrier board integrates the Gauss Clock (B train) and a radial steering function downloaded into local memory provide the two dynamic independent variables for this calculation. The control software calculates an acceleration parameter based on the mass and charge of the ion to be accelerated and stores this constant in DSP memory. The result of this calculation is passed to the feedback program via a link port.

3.2 Phase measurement

The bunch to bucket phase is the result of two separate measurements. The wall current signal from the ring is digitized and translated to DC by a digital receiver. The frequency translation is maintained at DC by the feedback program, which provides the Local Oscillator frequency. The phase measured by this receiver is compared to that measured by a four channel receiver connected to the Booster accelerating cavities. This receiver measures the

vector sum of the cavities. As shown in FIGURE 3 the difference is sampled by the DSP. Phase offsets to compensate for the stable phase angle and cable lengths are added by the DSP and a phase error signal is transmitted to the feedback DSP using a link-port.

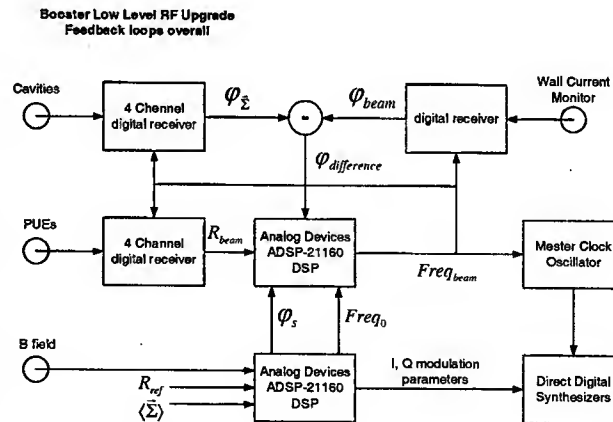


FIGURE 3. Phase loop signal flow diagram.

3.3 Radial position measurement

The radial position of the beam is measured using a four channel digital receiver. The positions at two points in the ring, 180 degrees apart in betatron phase, are averaged to remove any errors caused by distortions in the beam orbit. The signals from the PUEs are digitized and translated to base-band the normalized difference in magnitude between the two plates in the horizontal plane are calculated. This radial signal is transmitted to the feedback DSP using a link-port.

3.4 feedback program

The feedback program calculates the beam frequency from data received from the program and vector sum DSPs. The phase loop damps coherent synchrotron oscillations while the radial loop maintains the horizontal position of the beam according to a programmed function. The radial position measurement and calculated frequency are received from the program DSP and the bunch to bucket phase from the vector sum DSP. The integral of the radial error is calculated locally and is summed with the phase and radial errors. The instantaneous frequency of the beam is the sum of the error terms and the frequency program.

3.5 cavity voltage feedback

The four ferrite loaded cavities in the Booster ring require dynamic tuning to stay on resonance during the acceleration cycle. Imperfections in this tuning as well as characteristics of the amplifier chain require an automatic gain control circuit to flatten the response. To realize this in the LLRF drive chain the voltage of each cavity is measured in the vector sum DSP and compared to a command function downloaded into its local memory. The amplitude of that station's synthesizer is modulated to compensate for errors detected at the cavity.

3.6 synchronization

Synchronization for extraction is implemented in the feedback DSP. The Booster beam is extracted without a flattop, requiring synchronization while the frequency in the booster is still changing. To implement this we will take advantage of the repeatability of the Booster dipole field. The beam frequency, as applied to the master oscillator, during first Booster pulse will be recorded in memory. The total phase accumulated in this cycle will be calculated and subsequent pulses in an AGS fill will be forced to accumulate the same amount of phase, plus the amount required to move to the next AGS bucket. A synchro loop will be imposed to lock the beam to the recorded table. Extraction will occur when the table reaches the correct phase.

4 DSP MEASUREMENT SYSTEM

One of the most difficult tasks in designing a digital beam control system is building in a measurement system capable of both verifying system operation and debugging problems. Data transfer from the target hardware to the control system client is slow compared to the Booster repetition frequency. To allow for this slow transfer, system memory on the DSP carrier board has dual port access. The DSP can write data to the RAM and the front-end computer can read that data without impacting the operation of the DSP.

In addition to the measurement system RAM an FPGA dedicated to timing tasks is implemented on the carrier. Timing information for the Booster is distributed on a serial data link. The data link is decoded in the FPGA and

selected events will cause interrupts to the DSP. Each event is associated with a case statement in the software and is used to trigger different processes in the DSP including triggering measurements.

4 CONTROLS INTEGRATION

The Booster RF upgrade will take advantage of the tools built for RHIC. A rapid application development environment was designed for RHIC that gives non-expert programmers the ability to quickly design applications and control hardware under development. These programs running on the front-end computer interface with client applications running on workstations throughout the complex.

The Booster RF application will manage the pulse-by-pulse modulation of the machine. Functions such as radial steering and voltage command functions can be edited and downloaded to hardware from this application. The measurement system can be controlled by this software, triggering can be manipulated and most variables in the DSP code can be queried. Waveforms from the remote system can be processed and displayed by the application reducing the load on the real time system.

Managing the DSP code will also be done within the application. Code can be downloaded into flash from the application and the DSP can be rebooted remotely.

5 CONCLUSIONS

Many of the building blocks for this system are currently being tested. Prototypes of the DSP carrier board, digital receiver and DDS are now being evaluated. Preliminary results are very promising.

The interconnection of multiple processors using high-speed data links has been successful in the Brookhaven Relativistic Heavy Ion Collider. The Booster upgrade leverages many of the techniques learned in the design and operation of RHIC [4].

The use of digital receivers and improvements to digital synthesizers in the booster design will enhance the flexibility and reliability of this machine.

6 REFERENCES

- [1] J. M. Brennan, "RF Beam Control For The AGS Booster," BNL Formal Report BNL-52438 September 1994.
- [2] J. DeLong et al, "A Bunch to Bucket Phase Detector using Digital Receiver Technology", These proceedings.
- [3] "Analog Devices SHARK DSP Microcomputer ADSP-21160 data sheet", analog Devices, Norwood Ma.
- [4] J. M. Brennan et al, "RF Beam Control System For The Brookhaven Relativistic Heavy Ion Collider," EPAC'98, Stockholm, June 1998, p. 1705.

A BUNCH TO BUCKET PHASE DETECTOR USING DIGITAL RECEIVER TECHNOLOGY*

J. DeLong, J.M. Brennan, T. Hayes, Tuong N. Le, K. Smith
Brookhaven National Laboratory, Upton N.Y. 11973

Abstract*

Transferring high-speed digital signals to a Digital Signal Processor is limited by the IO bandwidth of the DSP. A digital receiver circuit is used to translate high frequency RF signals to base-band. The translated output frequency is close to DC and the data rate can be reduced, by decimation, before transfer to the DSP. By translating both the longitudinal beam (bunch) and RF cavity pick-ups (bucket) to DC, a DSP can be used to measure their relative phase angle. The result can be used as an error signal in a beam control servo loop and any phase differences can be compensated.

INTRODUCTION

The AGS Booster is designed to accelerate protons and ions injected from a LINAC and tandem Van de Graff respectively. Once injected the beams are captured in the RF bucket, accelerated and extracted to the AGS. While the motion of hadrons in the RF potential well is inherently stable it is not strongly damped [1]. Damping coherent synchrotron oscillations is the job of the phase loop and the phase detector is at the heart of this system.

Advances in speed and complexity of digital integrated circuits have changed the basic building blocks of Low Level RF design. Digital Signal Processors are commonly used in feedback loops as well as high speed Analog to Digital Converters. A bottleneck exists though in the transfer of data from high speed ADC to the computational units inside the DSP chip.

Digital receiver circuits take advantage of the relatively narrow bandwidth of the beam signal required by a phase detector. The center of mass of the bunch can be defined by the single spectral component of the beam at the RF frequency. If this spectral component is shifted to DC and band limited the sample rate can be significantly reduced. This technique will in turn reduce the IO bandwidth requirements of the DSP by shifting the burden to a dedicated signal processor designed to handle this high-speed data.

Off-the-shelf digital receivers have some distinct tradeoffs that will be discussed as well as how these tradeoffs may be eliminated by designing a custom receiver in an FPGA.

BASIC BLOCK DIAGRAM OF A DIGITAL RECEIVER

The block diagram in figure 1 is typical of a receiver channel. An RF input is passed through an anti-alias filter

to remove frequencies above the Nyquist limit. The signal is then digitized and the data stream enters the receiver IC. A complex Numerically Controlled Oscillator generates the Local Oscillator frequency for translation. The output of the NCO and the ADC are digitally multiplied (mixed). Two stages of filtering remove the unwanted sidebands and reduce the output sample rate. The circuit outputs complex base-band data at the decimated rate.

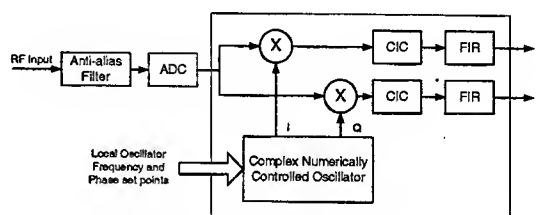


FIGURE 1: Block diagram of a digital receiver channel.

The NCO frequency set point can change dynamically as well as the phase offset of the channel. The order and decimation rate of the Cascaded Integrating Comb filter [2] can be adjusted and the Finite Impulse Response Filter coefficients can be downloaded. In addition to these basic structures Automatic Gain Control circuitry and a Cartesian to polar coordinate transform are provided.

PHASE DETECTOR CONFIGURATION

To implement a phase detector with digital receivers two signals need to be derived: the phase of the beam which is extracted from the wall current monitor and the phase of the RF potential well which is derived from the vector sum of the accelerating stations.

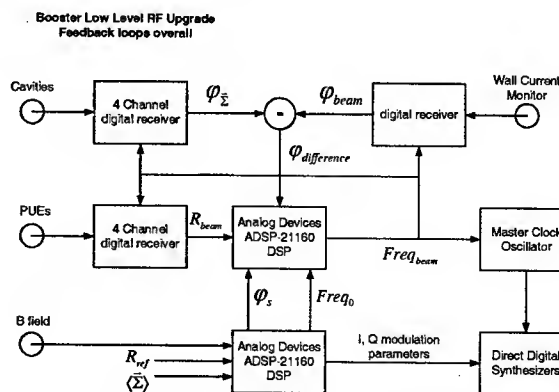


FIGURE 2: Block diagram of the phase detector configuration.

A four channel digital receiver will be used in the Booster Low Level RF design to measure the vector sum

* Work performed under auspices of the US Department of Energy Contract Number DE-AC02-98CH10886.

of the four accelerating stations. Each channel has individual phase control to compensate for the physical location of the cavity on the ring. The effective voltage gain received by the beam on each turn is the sum of the individual cavities rotated according to their physical position. The phase of the vector sum varies relative to the low level RF drive due to dynamic tuning of the ferrite loaded cavities and characteristics of the amplifier chain. This receiver will measure the deviation of the vector sum from the reference oscillator phase.

The phase of the beam is measured with one channel of a four channel digital receiver. The longitudinal beam pick-up is a resistive wall gap detector or wall current monitor this signal is brought out from the ring on high quality 7/8-inch semi-rigid coaxial cable. The coaxial cable preserves the bandwidth and reduces loss of signal amplitude. The beam receiver requires a large dynamic range to work with beam intensities from as low as 10^8 and as high as 3×10^{13} charges per pulse. The front-end electronics and processing gain give the receiver a dynamic range of ~90db.

The two phase measurements are taken with respect to a reference oscillator the frequency of which is updated by feedback from the beam. Any deviation at the output of the receiver from DC will be corrected by feedback through the master oscillator and slave DDS chain (FIGURE 2). To ensure a consistent measurement the NCO in both receiver circuits and the master oscillator are updated simultaneously using an external synch pulse.

HARDWARE IMPLEMENTATION

The first prototype circuit has been built using an Intersil ISL5216 [4] digital receiver IC (figure 3). This chip offers several features:

- 95 MSPS input sample rate
- Four independent receiver channels
- 32-Bit numerically controlled oscillator
- Digital Automatic Gain Control
- 16-Bit uP interface

The output format can be phase, magnitude, I and Q, or frequency and the AGC circuitry boasts a 96db range. The increment value in the phase accumulator of the internal NCO can be updated with an external pulse, allowing all NCOs in the system to be updated synchronously.

The front-end circuit includes a low pass anti-alias filter followed by variable gain amplifier, RF transformer and an Analog Devices AD6644 A to D converter. The filter has been selected to pass only the highest bunch frequency in the Booster approximately 5MHz. The variable gain amplifier was added to ensure that low amplitude signals could be boosted to excite the most significant bits of the ADC. An RF transformer couples the AGC Amplifier to the A to D converter differentially and the outputs of the four converters connect in parallel to the Intersil receiver.

The circuit board is a modular daughter card designed to mate with a DSP carrier board also built at Brookhaven [3]. To communicate with the carrier board an Altera PLD

interfaces the Intersil receiver chip to the DSP global bus. The DSP global bus can transfer data at 40MHz, this is sufficient for updating the dynamic parameters of the receiver in real time as well as reading the output data.

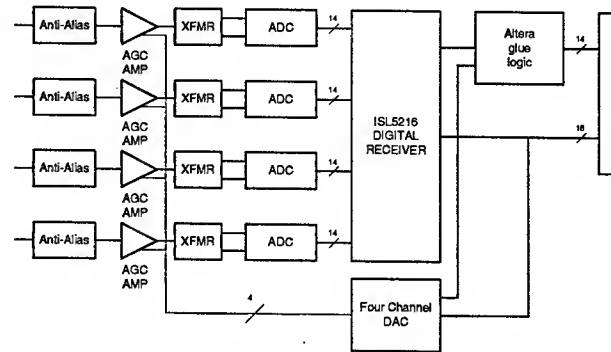


FIGURE 3: Intersil four-channel receiver block diagram.

PERFORMANCE

The prototype receiver has shown a usable dynamic range of 90db. Signal amplitudes of +10dbm down to -80 dbm were successfully measured. The AGC circuit maintained the amplitude of the output signal to within 6db over this range. Lowering the amplitude of the input signal further caused the AGC circuit to go out of regulation.

Out of band frequency rejection agreed with the data in the Intersil documentation [4]. During all tests the filter used was a 7-tap half-band FIR (HBF1) the coefficients of which are stored in Read Only Memory on the receiver IC. This filter provides rejection of approximately -120db at $F_s/2$ and a 3db point at $F_s/4$. Other filters are also available with coefficients stored in ROM. These filters have a faster roll-off at the expense of more taps and a longer delay.

Group delay through the circuit is critical to using this technology in a feedback loop. To calculate the delay each stage must be evaluated. This is best shown by example.

Example delay calculation

We will design a system that has an input sample rate of 40MHz and an output rate of 1MHz. In the CIC filter we will decimate by twenty and then decimate by two in the output FIR Filter. The CIC filter has six taps therefore 3.5 clock cycles to the middle tap. With the decimation set to twenty the delay through this section will be: $3.5 \times 20 = 70$ clock cycles. We follow that with a 7-tap half band decimating filter with a decimation rate of 2. The delay due to the number of taps is four clock cycles we need two more clock cycles for data read and writes. The decimation is two and the sample rate has been reduced in the CIC filter by a factor of twenty this results in: $(4 + 2) \times 2 \times 20 = 240$ clock cycles. Finally pipeline delays and delays through the AGC circuit contribute 30 to 50 extra clock cycles. The total delay with this

arrangement is $70 + 240 + 50 = 360$ clock cycles or $9\mu s$ through the device.

Figure 4 shows an FFT of the data returned by the device with the input signal set to 10kHz offset carrier and an amplitude of -60dbm.

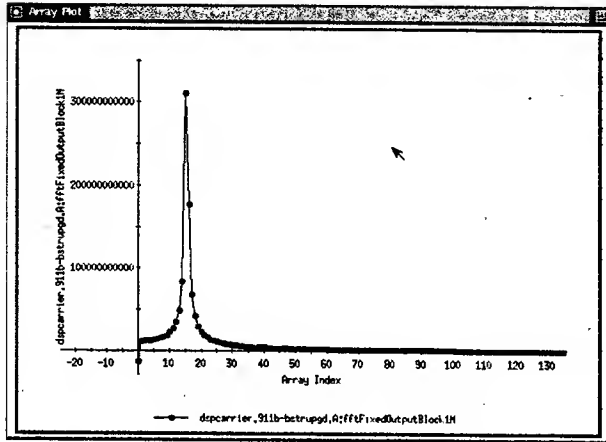


FIGURE 4: Frequency spectrum of a signal 10kHz offset carrier at -60dbm.

INTEGRATION

The digital receiver requires a support system that includes both hardware and software. A program provided by the manufacturer is used to define the internal registers of the receiver IC. After a configuration has been defined another program has been developed to translate the register description file into a format that can be used by the DSP to configure the receiver. This software has been tested successfully. In addition to DSP control software an application is being developed to read measurement data generated by the receiver and display these results graphically. The graph in figure 4 shows the output of this program.

The topology of the Booster beam control system uses several DSP carrier boards connected by high-speed data links to compartmentalize system functions. To test the receiver in-system a program running on another carrier card will calculate the beam frequency as a function of dipole field strength. This data stream is used to update the local oscillator in the receivers. This code has been developed and tested. Once the frequency program and receiver control program have been integrated measurements with beam can commence.

CONCLUSIONS

The prototype receiver has produced the expected results and finding an optimum filtering solution with minimal delay is ongoing. The immediate goal is to integrate the receiver into the Booster Low Level RF system. Once integrated, the booster RF frequency sweep

can be used to drive the receiver LO and beam signals can be observed during the acceleration cycle.

In addition to measuring the bunch to bucket phase this receiver will also be used to measure the radial position of the beam. The normalized beam position will be detected using two receiver channels connected to the horizontal plates of a pick-up electrode. This will provide the radial position input to the LLRF feedback loops [5].

While the Intersil device has a high level of integration the data path is not optimal for the DSP used in our system. In order to take full advantage of the high speed data links available on the Analog Devices ADSP-21160 DSP an FPGA based receiver is being designed. This design will have a full 32-bit interface to the host DSP for changing dynamic variables and result data will be passed to the DSP using a pair of high-speed Link-Ports [6].

In addition to improvements to the IO structure the FPGA based design will use a single phase accumulator for the four channels reducing the complexity of data transfer and synchronization. The current design requires three write cycles to update the frequency or phase of each channel. Reading the measured data from the receiver requires two read cycles per parameter. This overhead will limit the useful bandwidth of the device.

Digital receiver technology along with digital beam control systems will greatly improve the flexibility and reliability of this and future accelerators.

REFERENCES

- [1] J. M. Brennan, "RF Beam Control For The AGS Booster", BNL Formal Report BNL-52438 September 1994.
- [2] E. B. Hogenauer, "An Economical Class of Digital Filters For Decimation and Interpolation", IEEE Transactions on Acoustics, Speech and Signal Processing, ASSP-29(2):155-162, 1981.
- [3] J. DeLong et al, "Topology For a DSP Based Beam Control System in the AGS Booster", These Proceedings.
- [4] "Four-Channel Programmable Digital Down Converter", Intersil inc.
- [5] B. E. Chase, K. G. Meisner, "A Digital Signal Receiver VXI Module For BPM And Phase Detection Processing", Beam Instrumentation Workshop, New York, May 2002, p. 368-375
- [6] "Analog Devices SHARK DSP Microcomputer ADSP-21160 data sheet", Analog Devices inc. Norwood Ma.

PROGRESS ON THE SNS RING LLRF CONTROL SYSTEM*

K. Smith, M. Blaskiewicz, J. M. Brennan, J. DeLong, F. Heistermann, A. Zaltsman
BNL, Upton, New York 11973, USA

T. L. Owens
ORNL, Oak Ridge, TN 37830, USA

Abstract

The SNS Ring RF System[1,2] will comprise three $h=1$ ($f_{rev} = 1.05$ MHz) cavities and one $h=2$ cavity, each with individual digital LLRF control electronics. During each 1ms accumulation of 1 GeV protons in the SNS ring cycling at 60Hz, circulating intensity increases to $1.5E14$ particles. This intensity translates to an average circulating current (at the end of accumulation) of 35A and a peak $h=1$ current of 50A. The LLRF system primary task is to regulate the phase and amplitude of the RF gap voltage in order to maintain a smooth bunch with minimum peak current and a sufficient beam free gap to accommodate the extraction kicker rise time. Maintaining stable control of the cavity-beam system with such intense beam loading is non-trivial, and to do so, the LLRF system will use a combination of techniques including cavity voltage I&Q feedback, beam current feed-forward compensation, dynamic tuning and cycle to cycle adaptive feedback. This paper describes the progress on the LLRF control system to date.

INTRODUCTION

The SNS Ring LLRF Control System is being designed to provide individual digital LLRF control for each of the four cavities in the ring. To date, a number of prototype and first article boards have been designed and tested, and the first integrated test of the cavity IQ control loop with the production HLRF cavity and PA was recently completed. This paper will discuss the concept and architecture of the ring LLRF system and present performance data acquired for the particular case of the cavity IQ control loop. Details of the RF related machine parameters, the theory of the ring LLRF control and the HLRF system design are found in the references [1] and [2].

* SNS is managed by UT-Battelle, LLC, under contract DE-AC05-00OR22725 for the U.S. Department of Energy. SNS is a collaboration of six US National Laboratories: Argonne National Laboratory (ANL), Brookhaven National Laboratory (BNL), Thomas Jefferson National Accelerator Facility (TJNAF), Los Alamos National Laboratory (LANL), Lawrence Berkeley National Laboratory (LBNL), and Oak Ridge National Laboratory (ORNL).

SYSTEM ARCHITECTURE

Discussion will be limited to the core of the digital LLRF system, configured from three basic components: the Cavity Controller Card, the VME Carrier Card, and Carrier Daughter Cards providing application specific IO functions. The design goal has been to develop an architecture which satisfies all current requirements, but is flexible and easily reconfigurable in order to meet changing demands, both during system development and throughout commissioning and operation. To accomplish this, the system is designed to be modular, and different control loops are configured by simply selecting appropriate carrier daughter cards and writing the firmware to implement a particular control algorithm. A simplified block diagram of the implementation of a representative loop, the cavity IQ control loop, is shown in Figure 1. Similar channels provide the other LLRF functions such as feed-forward compensation and dynamic tuning control.

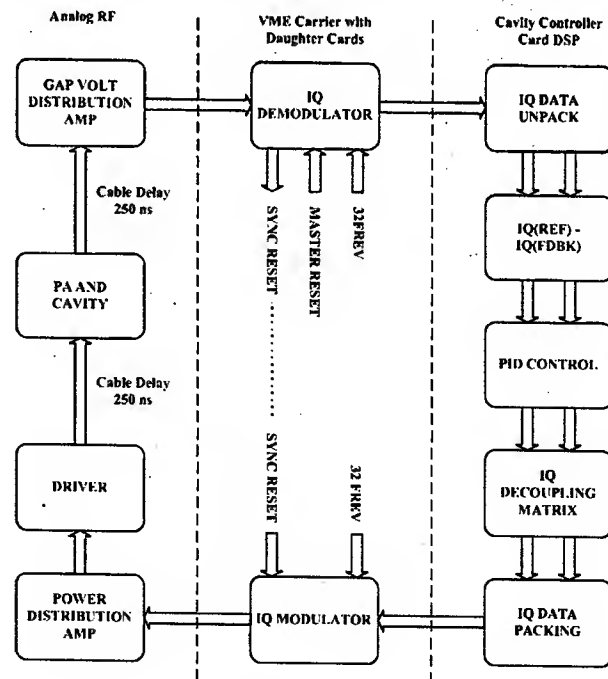


Figure 1: Cavity IQ Control Loop.

Cavity Controller Card

The Cavity Controller Card utilizes all commercial off the shelf (COTS) hardware. A standard SNS VME based Input Output Controller (IOC), the Motorola MVME-2100, hosts a Bittware Hammerhead-PMC+ module. The Hammerhead-PMC+ is a PCI Mezzanine Card (PMC) with four ADSP-21160 processors. Table 1 outlines some basic specifications.

Table 1: Some Hammerhead PMC+ Specifications

DSP	4 x ADSP-21160, 32 bit fixed and floating point
DSP Clock, Speed	80 MHz, 480 MFLOPS
DSP Core Architecture	Single Instruction Multiple Data (SIMD)
DSP Internal SRAM	4 Mbit dual port
DSP External IO Bandwidth	640 MB/s uP port (shared) 6 x 80 MB/s link ports Autonomous IO Controller
Board Shared SDRAM	64 MB (256 MB max)
Board FLASH	2 MB
Board External IO Bandwidth	64bit, 66 MHz PCI (Host to DSP, Host to SDRAM) 4 link ports (F.P.) 4 link ports (VME P2)

The ADSP-21160 provides a combination of good processing power and as important, the considerable external IO bandwidth required for real-time feedback control. In particular, each DSP has six 80 MB/s "link ports" (two to each of two nearest neighbor DSPs and two external) providing high speed point to point IO. While active, the LLRF loops use only these links to provide minimum delay, deterministic connections between the DSPs and carrier daughter cards. Because the DSPs have large internal SRAM, the loops need not make access to DSP external resources (e.g. uP bus and SDRAM) during the accumulation cycle. For each cycle, all necessary loop parameters, function tables, and diagnostic history data are stored in DSP internal SRAM. Access to external resources only occurs during the roughly 10ms dead-time between accumulation cycles when loops are inactive.

Via a direct Ethernet connection to the controls network and a PCI local bus connection to the DSP PMC card, the MVME-2100 IOC provides the necessary bandwidth to exchange all necessary diagnostic and system configuration data on a cycle to cycle basis.

VME Carrier Card

The VME Carrier Card [3] is a custom designed VME host board which provides power, a VME interface and other resources for up to four daughter cards. These include an on-board ADSP-21160, FPGAs, SRAM and FLASH to provide extra processing power and functionality as needed. The board design also supports the use of a mating VME P2 rear transition module providing a convenient means of supplying external clock and trigger signals as well as DSP link port connections for both the on-board DSP and the daughter sites.

Carrier Daughter Cards

The Carrier Daughter Cards provide an easily configurable interface between the digital and analog portions of the LLRF system. While original prototype system testing was based on daughter cards providing single channel functionality (e.g. one A/D channel), the latest architecture employs just two daughter cards (in development), a four channel 14 bit A/D and a four channel 14 bit D/A card, each sharing a common FPGA based digital section designed around an Altera Stratix FPGA. The Stratix FPGA provides tremendous processing power and functional flexibility to the cards. We have already developed A/D FPGA cores to provide direct A/D and IQ demodulation, and a digital receiver core is in development. Similarly, D/A cores have already been developed for direct D/A, IQ modulation and Direct Digital Synthesis (DDS). Commercial IP cores are of course an option as well. The analog front ends of the cards can be configured to use either baseband or RF signals, DC or AC coupled as needed. The VME Carrier Card can host two each of either four channel card ("double width"), or four single channel cards ("single width").

CAVITY IQ CONTROL LOOP

Configuration

The recently completed Cavity IQ control loop test was the first test of a fully integrated loop utilizing all the core LLRF and HLRF hardware together. The cavity was driven closed loop, ramping from 0 to 10kV in 0.5ms and holding at 10kV for a 1.5ms flat-top. No attempt was made to include dynamic tuning or simulated beam loading, though it is planned to do so as soon as practical. For this test, an IQ demodulator card, a single DSP on the Cavity Controller card, and an IQ modulator card were configured as shown previously in Figure 1.

The IQ demodulator samples the $h=1$ cavity RF to 14 bits at $32 \times \text{frev}$, and correlates the samples with 32 sample $h=1$ sine and cosine sequences to produce baseband I & Q values updating at frev . 16 bit I & Q values and the turn number (tracked from reset time) are packed into 32 bit words and sent to the DSP via a link port. The link ports are 8 bit parallel point to point links capable of clocking bytes at 80MHz, but were only clocked at 32 frev for simplicity during the test.

The DSP unpacks the I & Q data and based on a stored I & Q function table (I & Q vs. turn number), processes the I & Q errors in parallel PID algorithms. For simplicity, the decoupling matrix was implemented as a simple rotation accounting only for pure loop delay at the cavity center frequency. No attempt was made to correct coupling of the I & Q modulations arising from the cavity RLC response[4] or the change in cavity center frequency vs. drive level. Efforts are underway to include these corrections. The corrected I & Q drive values are then sent to the IQ modulator via a second link port and the loop closes through the analog signal chain.

A key constraint on the cavity IQ control loop bandwidth is the loop delay. Total pure loop delay is about 2.6 μ s, contributed from: cable delays (500ns), driver, PA and analog filters (250ns), correlation group delay (500ns), other FPGA pipeline delays (250ns), link ports (375ns), and DSP loop code execution (750ns). With a loaded Q of about 25 at 1.05 MHz, the phase slope of the cavity response corresponds to a group delay of about 6.25 μ s, yielding a total effective loop delay of about 9 μ s. However, since the cavity group delay only represents the response from the cavity complex poles, it can be compensated. The pure delay of 2.6 μ s is fundamental in limiting the control bandwidth achievable. Thus, much of the effort aimed at developing the latest hardware includes moving to higher clock rates to reduce pipeline delays in the FPGAs and the link ports. The daughter cards currently in development will easily clock at 128 x freq reducing processing pipeline delays by a factor of four. It is also planned to investigate other IQ demodulation algorithms (4 x RF IQ sampling, etc.) to increase throughput. DSP code optimization continues in an effort to minimize latency in the loop processing algorithm, though it is not likely that the processing time could be reduced below 0.5 μ s (40 DSP clock cycles). With higher FPGA clock speeds and optimizing of the IQ demodulation algorithm, pure loop delay should ultimately be reduced to about 1.5 μ s. Although the DSP offers certain advantages over FPGA, particularly when making frantic code changes during initial testing and debugging, the penalty paid in terms of processing delay can easily outweigh this. Thus, the LLRF system architecture will also permit bypassing the IQ loop DSP if this becomes desirable.

Test Results

As a preliminary attempt to characterize the loop, a test of the closed loop impulse response was performed. The cavity was brought to 10kV, and then a single turn I command for 9kV was issued to the loop, followed by a return to 10kV. Figure 2 shows the I & Q transient responses and Figure 3 shows the corresponding closed loop frequency response for the I loop. The loops were "optimized" by adjusting gains for the P, I and D terms of the controller while observing the transient response in the I channel. Both the I and Q loops were active with the same gain coefficients used on corresponding I and Q gain terms.

In Figure 2, the I command and I & Q responses have been normalized to the 10kV steady state command. The Q response has been offset to 1.0 for clarity.

In Figure 3, the horizontal axis is shown as the index of a 512 point FFT of the data in Figure 3. The 1dB bandwidth is approximately 70kHz = 1MHz * (38/512).

Though the closed loop bandwidth observed is likely sufficient for our system, consideration must be given to the effect of beam cavity interaction under the high beam loading conditions that will exist.

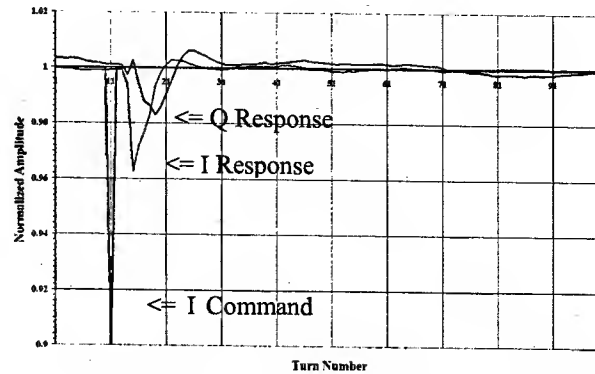


Figure 2: Cavity IQ Control Loop CL Transient Response.

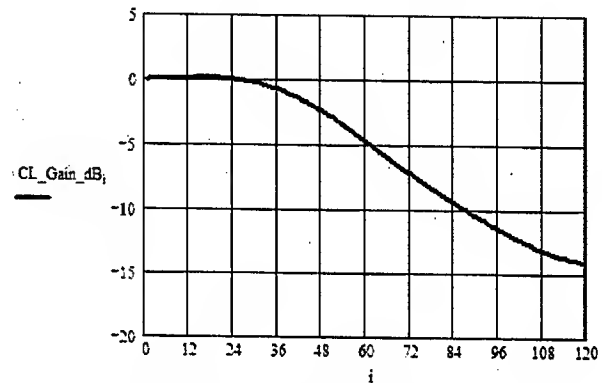


Figure 3: IQ Loop CL Frequency Response (Icav/Icmd).

The relative beam loading parameter ($Y=I_b/I_o$) rises to around 3 at the end of accumulation. Even for optimal detuning, the system operates close to the high current Robinson unstable area [5][6][7]. Direct RF feedback around the cavity was considered in the early stages of the ring RF system design. However, cost and space constraints would not permit the installation of feedback amplifiers in the ring or a nearby structure, and the long cable delays between the LLRF and cavity make it otherwise unfeasible. Options for dealing with this include using somewhat higher than optimal detuning to move further away from the Robinson unstable area, beam current feed forward compensation to dramatically reduce the effective cavity shunt impedance seen by the beam, and investigating IQ loop gain bandwidth tradeoffs. Current plans include using all these techniques and we hope to begin tests in the near future.

REFERENCES

- [1] M. Blaskiewicz, et al., Proc. 2001 PAC, pp 490-494.
- [2] A. Zaltsman, et al., these proceedings.
- [3] J. DeLong, et al., these proceedings.
- [4] R. Garoby, "Low Level RF And Feedback", CERN PS/RF Note.
- [5] F. Pederson, IEEE, TNS, Vol. NS-32, No. 5, pp 2138-2140 (1985) and references therein.
- [6] D. Boussard, CERN 92-03, Vol. II (1992).
- [7] F. Pederson, private communication.

A NEW DIGITAL CONTROL SYSTEM FOR CESR-C AND THE CORNELL ERL*

M. Liepe[†], S. Belomestnykh, J. Dobbins, R. Kaplan, C. Strohman,
LEPP, Cornell University, Ithaca, NY 14853, USA

Abstract

Recent progress in developing digital low-level RF controls for accelerators has made digital systems an option of choice. At Cornell we are presently working on two projects: upgrading the RF controls of the Cornell Electron Storage Ring (CESR) for charm-tau operation (CESR-c) and developing a new low-level RF system for the proposed Cornell energy-recovery linac (ERL).

The present CESR RF control design is based on classic analog amplitude and phase feedback loops. In order to address the required flexibility of the RF control system in the CESR-c upgrade and to implement a true vector sum control we have designed and built a new digital control system. The main features of the new controller are high sampling rates, high computation power and very low latency. The digital control hardware consists out of a powerful VME processing board with a Xilinx FPGA, an Analog Devices digital signal processor (DSP) and memory. A daughter board is equipped with four fast analog-to-digital converters (up to 65 MHz sampling rate) and two digital-to-analog converters (up to 50 MHz update rate). The first set of new electronics will be used in the CESR RF system. However, the described digital control hardware can also be used for the Cornell ERL as it was designed to meet its challenging field stability requirements (see [1]).

THE NEED FOR DIGITAL RF CONTROLS FOR CESR-C

With CESR changing from a single-energy to a multi-energy regime [2], it will be more challenging for the RF system to provide stable and reliable operation as the low-energy sets of operating parameters differs significantly from the high-energy ones [3].

There are new demands to RF controls associated with this:

1) The superconducting cavities will operate in an active or passive mode [4], i.e. driven by beam and generator or just driven by the beam respectively. Switching from one mode of operation to another will be performed routinely and must be done in a straightforward way, efficiently and quickly. 2) The external quality factor of the cavities will need to be adjusted in a wide range from $\approx 2 \cdot 10^5$ at high energy to $\approx 1 \cdot 10^6$ at low energy. For superconducting cavities the cavity transfer function pole is usually the lowest pole in the system and should to be compensated by feedback loops to optimize the performance of the controller [5]. However, a change in the cavity coupling will change the position of the pole and therefore its compen-

sation will have to be adjusted accordingly. Moreover, this compensation may have to be adjusted with the beam current. 3) Good instrumentation for problem diagnostics is a must. 4) Microphonic noise tolerance is stricter at low energy and may require developing a complex feedback system to suppress it [6].

Satisfying these new demands with the present control electronics is partly difficult and cumbersome and to some extent even impossible. This necessitated developing a new, more flexible and easily upgradeable RF control system, and a digital controller is the best choice for this.

THE NEED FOR DIGITAL RF CONTROLS FOR THE CORNELL ERL

The requirements on the RF control system of the proposed CORNELL/TJNAF ERL prototype [7, 8] are demanding [1]. In the injector cavities the strong beam loading of a 100 mA beam needs to be compensated with high accuracy. In main linac cavities ($Q_{ext} = 2.6 \cdot 10^7$) high field stability of $2 \cdot 10^{-4}$ in amplitude and 0.06° in phase needs to be achieved in the presence of a microphonics level similar to the cavity bandwidth. In addition microphonics compensation via a fast cavity frequency tuner is envisioned. These challenging control loops and the associated required flexibility are best addressed by a digital control approach.

While the digital RF control hardware described in the following is primarily designed for the CESR-c RF system and its requirements, it will also serve as a prototype for the ERL RF control system. The digital parts are generic and flexible and have the computation resources to be used in both RF systems.

HARDWARE

OVERVIEW

Figure 1 (left side) shows the schematic of the new digital RF control system for CESR-c. All low-level subcomponents including the digital boards have been designed in house to minimize cost and optimize performance of a fast digital controller. The controller is designed to stabilize the in-phase (I) and quadrature (Q) component of the cavity field. The RF field signals are converted to an IF frequency of 11.9 MHz and then sampled at a rate of 4×11.9 MHz. Accordingly two subsequent data points describe the I and Q component of the cavity field. The digital data are calibrated and filtered, and a fast proportional-integral (PI) controller calculates the new settings for the IQ-vector modulator input. The overall data processing latency will be below $1 \mu s$.

* Work is supported by the National Science Foundation.

[†] mul2@cornell.edu

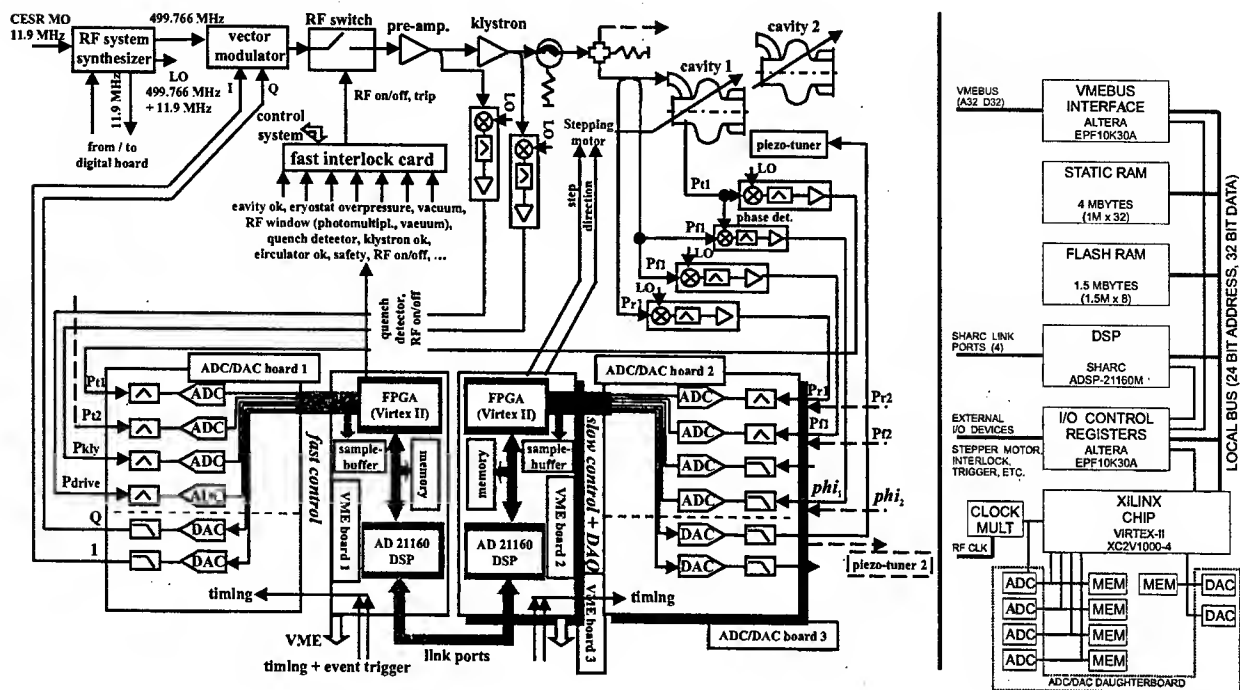


Figure 1: Left: Schematic of the digital RF system for CESR-c. Right: Block diagram of the FPGA/DSP board.

DIGITAL CONTROL BOARD

The FPGA/DSP VME board is shown in Figure 2. A block diagram of the board is shown in Figure 1 (right side). The various subsections are connected by a 24-bit address bus and a 32-bit data bus. All data transfers are 32 bits wide and the addresses are for 32-bit entities. Normally there are three possible bus-masters: the VMEbus interface, the DSP, or the XILINX chip. Additionally, a special controller is provided which uses the local bus to configure the XILINX chip by transferring data from the FLASH RAM or STATIC RAM. A bus arbiter determines which bus master can transfer data.

VME INTERFACE

The VME interface is implemented in an Altera EPF10K30 PLD.

STATIC RAM

The board provides 4 Mbytes of fast static RAM, organized as 1M by 32-bits. The static RAM is accessible from any of the bus masters and can be used to pass data between the various devices. The board can be configured so that either the DSP or the XILINX chip can be configured from static RAM. This is useful for experimenting with different programs without having to reprogram the FLASH memory.

FLASH RAM

The board provides 1.5 Mbytes of FLASH memory, organized as 1.5M by 8-bits. The FLASH memory is accessible from any of the bus masters. Normally, the first third of the FLASH memory is reserved for the DSP code, and the remaining two-thirds are for the XILINX chip configuration.

DSP

The DSP is an Analog Devices ADSP-22160M. This is an SIMD (single-instruction, multiple data) processor with 4 Mbits of internal memory. It can be both a local-bus master and a local-bus slave. The DSP has link ports that can be used to provide a direct path to other DSPs or to other hardware. Four of the six link ports are routed through differential transceivers to connectors on the front panel, and each port may be configured as in input or output port. This allows us to make connections between RF-DSP boards in the same crate or in different crates without needing to use the VME backplane. All of the peripheral control lines on the DSP, such as DMA control, interrupt inputs, I/O flags, and reset, are routed to the I/O CONTROL REGISTER chip.

I/O CONTROL AND STATUS REGISTERS

The CSR (Control and Status Register) chip is a local-bus slave that provides control and reports status of both on-board and off-board resources. On-board resources include reset lines for the DSP and XILINX chip, front panel LEDs and a configuration dipswitch, DSP peripheral control signals, and uncommitted connections to the VME interface and the XILINX chip. Off-board resources include a stepper motor interface for cavity tuning, a serial (SPI) interface to the frequency synthesizer, CESR clock and turn-marker, interlock system interface, and event triggers.

XILINX CHIP

The XILINX chip is Virtex-II XC2V1000-4 in a 456 pin BGA package. The fast RF control loops and data acquisition control run in this chip. Included in the internal resources of this chip are 40 hardware multipliers (each for

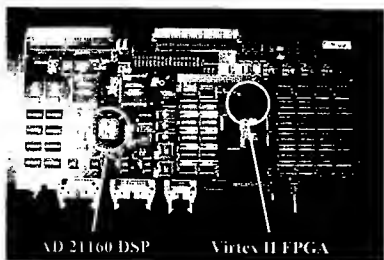


Figure 2: Digital board with FPGA and DSP.

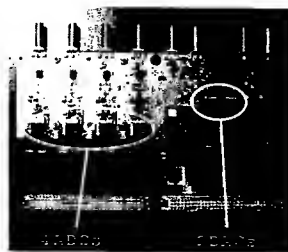


Figure 3: ADC/DAC daughter board.

2 18-bit words) and over 10k flip-flops. The XILINX chip has separate busses for each ADC channel. It has a shared bus for the DACs and a lookup table. It acts as either a master or a slave on the local-bus. The chip provides PIO (programmable I/O) access to the ADC and DAC memory buffers, so data in these buffers can be accessed without interfering with the control algorithms.

MEMORY BUFFERS / LOOK-UP TABLE

Each ADC channel is provided with 2 Mbytes of buffer memory, organized as 1M by 16-bits. Incoming data from the ADC can be stored in this buffer. The XILINX chip provides logic to use an external trigger or a software trigger to start storage, to stop storage, or to wait before stopping. This allows capture of transient events. The memory can be read out under program control using a different data path, so that the feedback control function is undisturbed. Additionally, the buffer can be filled with simulated ADC data and the control algorithm can be run using stored data, rather than ADC data. This is useful for testing control algorithms under controlled conditions. Data can be clocked into the buffers at a maximum rate of 50 MHz. A separate memory buffer is provided for the dual functions of storing data directed to the DACs and for a LUT (Look-Up Table) for feed-forward constants. This buffer is organized as 1M by 16-bits for DAC data and 1M by 16-bit for LUT data. As with the ADC buffer, the DAC buffer can capture a stream of data that is going to the DACs. It can also supply data to the DACs, which is useful for exercising downstream components with know data. Data frozen in the DAC buffer can be read out under program control without interfering with the control algorithm.

CLOCK CIRCUITRY

The control algorithm calls for a 4 times oversampling of the ADCs IF input. The incoming RF clock is 11.9 MHz. A PLL (ICS670-01) multiplies this by a factor of 4. Jumpers are provided for other multiplication factors in different applications. The circuitry is designed to minimize jitter, since jitter translates into a phase error. By moving jumpers, other clock sources can drive individual ADCs.

ADC/DAC BOARD

Analog input and output is implemented as a daughter board; see Figure 3. This board has four 14-bit analog to digital converters (ADCs) and two 16 bit digital to analog converters (DACs). The ADCs can be read simultaneously

at sample rates up to 65 MHz. The ADCs are preceded by a signal conditioning chain consisting of a buffer amplifier, a band-pass filter and a differential ADC driver. The DACs are updated over a shared bus at sample rates up to 50 MHz. Initial tests indicated that the ADCs perform to expectations with a signal to noise ratio of approximately 74 dB. Aperture jitter measurements for the ADCs set an upper limit of 5 ps rms. Ultimately jitter will be determined by the quality of the clock delivered to the board. DAC outputs are differential, buffered and level shifted. The board draws its power from dedicated linear power supplies.

FUTURE PLANS

After developing and building the hardware for the digital CESR-c control system, we are writing the software for the PI-control loop in the FPGA and for the interface with the CESR control system. We plan to have a first digital RF control system in operation in CESR by late summer this year. Detailed tests will be done to study the performance and reliability of the new RF field controller.

CONCLUSIONS

We have designed and built the hardware for a fast digital low-level RF controller with high sampling rates, high computation power and very low latency. The digital boards are generic and flexible enough to be useable for a variety of control and data processing applications.

REFERENCES

- [1] M. Liepe and S. Belomestnykh, this conference, paper TPAB056.
- [2] D. Rice, Proceedings of the 8th European Particle Accelerator Conference 2002, Paris, June 2002, p. 428.
- [3] S. Belomestnykh, Report SRF020918-06, Cornell Laboratory for Elementary-Particle Physics (2002).
- [4] S. Belomestnykh et al., this conference, paper TPAB048.
- [5] R. Garoby, Proceedings of the Joint US-CERN-Japan International School Frontiers of Accelerator Technology, Ed. S. I. Kurokawa, M. Month & S. Turner, World Scientific, 1999, pp. 455-489.
- [6] M. Liepe and S. Belomestnykh, this conference, paper TPAB055.
- [7] Study for a proposed Phase I ERL Synchrotron Light Source at Cornell University, ed. by S. Gruner and M. Tigner, CHESSTech. Memo 01-003, JLAB-ACT-01-04 (July 2001)
- [8] G. Hoffstaetter et al., this conference, paper TOAC005.

LONGITUDINAL DAMPING SYSTEM WITH TWO TRANSVERSE KICKERS

A. Mikhailichenko, Cornell University, LEPP, Ithaca NY 14853, USA

Abstract

We describe here a scheme for damping of longitudinal oscillations of a bunch of charged particles in a storage ring. This scheme uses two transverse kickers operating in push-pull mode for pass lengthening in accordance with instant energy deviation of bunch energy from its equilibrium value. By this way the main cavity of the ring damps the energy oscillations.

INTRODUCTION

In [1] the Transit-time method applicable to Stochastic Cooling was described. General idea is that action of the kicker is a matter of transient time delay associated with particle's momentum. In the method described below, transit-time variation is arranged with two kickers, but action to the particle is going through the main RF cavity of the ring. In some sense one can say that acting kicker spitted in two ones and they act together in such a way, that the path lengthening is a function of particles parameters identified by pickup [2].

SCHEME

Let us consider two transverse kickers K_0 and K_1 what are installed along the particle trajectory in a damping ring, Fig 1. Let the point $s = s_1$ is a focal point for sine-like trajectory, what starts at point $s = s_0$ where the first kicker is installed. Basically, this means that the distance $s_2 - s_1$ corresponds to an integer and a half of a betatron wavelength in a damping ring.

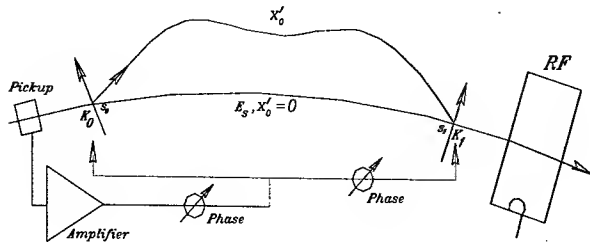


Figure 1: Kicker K_0 installed at longitudinal position $s = s_0$ and the kicker K_1 installed at longitudinal position $s = s_1$ in the focal point of sine-like trajectory, what starts at the point $s = s_0$.

In Figure 1, RF is a RF cavity of the ring. This may be also an additional RF cavity operating at higher frequency

than the main RF cavity of the ring. There are also shown Pickup, Amplifier and phase adjustment elements (time delay).

Let the amplitudes of the kicks arranged so that there is no residual oscillations after one pass over this system of kickers. Let the transverse motion is represented by the following [3]

$$x(s) = x_0 \cdot C(s, s_0) + x'_0 \cdot S(s, s_0) + D(s, s_0) \frac{\Delta p}{p}, \quad (1)$$

where $C(s)$ and $S(s)$ -- are cosine and sin-like solutions of equation of motion, $D(s)$ -- is the dispersion function and the derivative is taken over longitudinal coordinate s . The path length variation between two points can be represented in this case as [3]

$$\Delta l = -x_0 \int_{s_0}^{s_1} \frac{C}{\rho} ds - x'_0 \int_{s_0}^{s_1} \frac{S}{\rho} ds - \frac{\Delta p}{p} \int_{s_0}^{s_1} \frac{D}{\rho} ds. \quad (2)$$

So if x'_0 , for example, is modified by the kicker K_0 (and eliminated by K_1), with correspondence to the energy variation of the particle by appropriate way, one can change the phase of arriving into the RF cavity and, hence, tolerate to the phase motion of the (macro)particle¹ without perturbation to the betatron oscillations.

One can obtain the equation of motion for individual (macro) particle in the damping ring in the same manner as description of ordinary longitudinal motion [4]. Namely, variation of the phase and energy deviation from turn to turn will be

$$\phi_{n+1} = \phi_n + \omega_{RF} T_0 \cdot \eta \frac{\Delta E}{E} + \Delta l(x_0, x'_0) \frac{\omega_{RF}}{c}$$

$$\Delta E_{n+1} = \Delta E_n + eV(\sin \phi_n - \sin \phi_s), \quad (3)$$

where T_0 is the period of revolution, and the factor η can be expressed as

$$\eta \cong \frac{1}{c T_0} \oint \frac{D}{\rho} ds \cong (1/\gamma_r^2 - 1/\gamma^2), \quad \gamma = E/mc^2, \quad (4)$$

$\gamma_r \cong \alpha^{-1/2}$ is the gamma factor, corresponding the transition energy. The last term in the first equation arising from the path length variation according to initial

¹ That defined by the bandwidth of the feedback system. Basically the number of the particles in the bandwidth W are $N_W \cong Nc / (\sigma_1 W)$

conditions at the position of the first kicker. Basically, the general term in our case is

$$\Delta l(x_0, x_1) = -x'_0 \cdot \int_{s_0}^{s_1} \frac{S(s, s_0)}{\rho} ds = -x'_0 \cdot I(s_0, s_1), \quad (5)$$

where we defined the integral

$$I(s_0, s_1) = \int_{s_0}^{s_1} S(s, s_0) / \rho \cdot ds, \quad (6)$$

what is a dimension constant (with the dimension of a length), depending only from positions of initial and final points in a damping ring. Treating the number of turns n as independent variable, one can obtain

$$\begin{aligned} \frac{d\psi}{dn} &= \frac{\omega_{RF}}{c} cT_0 \cdot \eta \frac{\Delta E}{E_s} + \frac{\omega_{RF}}{c} I(s_0, s_1) \cdot x'_0 \\ \frac{d\Delta E}{dn} &= eV \cdot \cos \phi_s \cdot \psi. \end{aligned} \quad (7)$$

We also suggested, that the difference $\psi = (\phi - \phi_s) \ll 2\pi$. From the last equations one can obtain

$$\frac{d^2\psi}{dn^2} = \frac{\omega_{RF} T_0 \cdot \eta \cdot eV \cdot \cos \phi_s}{E_s} \psi + \frac{\omega_{RF}}{c} I(s_0, s_1) \frac{dx'_0}{dn}. \quad (8)$$

If we suggest, that $x'_0 \cong k \cdot \psi$, the equation of motion for the phase becomes

$$\frac{d^2\psi}{dn^2} = -(2\pi\nu_s)^2 \psi + \frac{\omega_{RF} I(s_0, s_1) \cdot k}{c} \cdot \frac{d\psi}{dn}, \quad (9)$$

$$\text{where } (2\pi\nu_s)^2 = -\frac{\omega_{RF} T_0 \cdot \eta \cdot eV \cdot \cos \phi_s}{E_s}.$$

One can see, that the last term describes the decrement. If we define as usual

$$\lambda = -\frac{\omega_{RF} I(s_0, s_1) \cdot k}{2c}, \quad (10)$$

then the equation of motion can be rewritten as the following

$$\frac{d^2\psi}{dn^2} + 2\lambda \cdot \frac{d\psi}{dn} + (2\pi\nu_s)^2 \psi = 0. \quad (11)$$

The last equation has standard solution

$$\psi = c_1 \cdot \exp\{n \cdot [-\lambda - \sqrt{\lambda^2 - (2\pi\nu_s)^2}]\} + c_2 \cdot \exp\{n \cdot [-\lambda + \sqrt{\lambda^2 - (2\pi\nu_s)^2}]\}.$$

If $\lambda > 2\pi\nu_s$ the motion is aperiodic. For this one needs

$$\text{to have } k > 2 \frac{cT_0}{I(s_0, s_1)} \frac{\eta \cdot eV \cdot \cos \phi_s}{E_s}.$$

The factor $cT_0/I(s_0, s_1)$ is the ratio of the circumference of the damping ring and the path length integral. The last relation can be rewritten as

$$k > 2 \frac{cT_0 \cdot \alpha \cdot eV \cdot \cos \phi_s / E}{I(s_0, s_1)}, \quad (12)$$

what has a clear physical sense, as the $(cT_0 \cdot \alpha \cdot eV \cdot \cos \phi_s / E)$ is the path length difference, arising from the energy variation, produced by one pass through the RF cavity.

Now let us discuss more detailed the nature of the relation $x'_0 \cong k \cdot \psi$. As one can see this term indicates that the kick is proportional to deviation of the bunch position from equilibrium azimuthal position $\psi = \phi - \phi_s$.

So the signal from a pick-up electrode needs to be processed through the phase detector, with the RF phase as a reference one. This is a standard technique and we will not discuss it here.

The other possibility is the notch-filter scheme, see Figure 2.

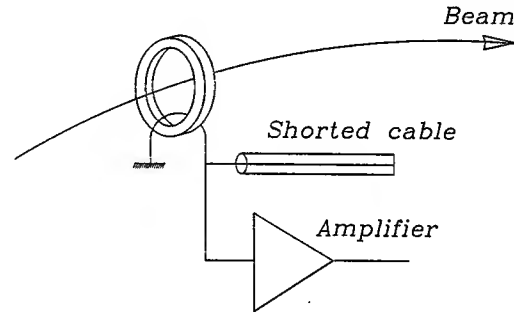


Figure 2: The notch-filter scheme (Lars Thorndahl, CERN, 1975).

In this scheme, the signal, induced by the current $J(t)$, passing through pick-up, induces the voltage

$$U(t) \cong \int_{\omega} J_{\omega}(\psi) Z_{\omega} e^{-i\omega t} d\omega^2. \text{ As the pick-up loop and}$$

the cable are connected in parallel, $Z_{\omega} \cong \frac{-i\omega L \cdot Z}{Z - i\omega L}$,

where L is the inductance of the loop, $Z \cong iZ_0 \tan(\omega l / c)$, l -- is the length of the cable, Z_0 -- is the impedance of the cable. Representing $J_{\omega} \cong J_{0\omega} \cdot \cos(\nu_s \omega t)$ and considering the signal

² Details of the scheme depend on the design of the pick-up. We consider the pick-up with inductive type, but considerations still valid in general for any type of pick-up electrode.

around harmonic with the number m , $\omega \cong m\omega_0$, where ω_0 -- is the revolution frequency, one can estimate

$$U(t) \cong J_\omega \cong J_{\omega_0} \cdot \cos(\nu_s \omega_0 t) \frac{-im\omega_0 L \cdot Z}{Z - im\omega_0 L} e^{-im\omega_0 t}.$$

The length of the cable l is chosen so, that $\frac{2l}{c} = T_0$, or

$$\frac{l}{c} \cong \frac{\pi}{\omega}, \quad Z \cong iZ_0 \tan[(m\omega_0 \pm \nu_s \omega_0)l/c] \cong iZ_0 \cdot (-1)^m \tan(\pi \nu_s).$$

If inductance of the loop is small enough, so the $Z_0 \cdot \tan(\nu_s \pi) \geq m\omega L$, than the amplitude of the signal from pick-up is proportional.

$$U(t) \cong J_\omega \cong -iJ_{\omega_0} m\omega_0 L \cdot \cos(\nu_s \omega_0 t) \cdot e^{-im\omega_0 t} \propto \cos(\nu_s \omega_0 t) \propto \Psi.$$

DISCUSSION

One can see, that there is no visible restriction for the speed of damping in this scheme, depending only on bandwidth of the pick-up, amplifier and kickers. So this scheme can be easily implemented for stochastic cooling of the longitudinal emittance as well.

The scheme considered, does not excite the transverse motion of the beam after passing the pair of kickers. Small residual transverse oscillations can be eliminated by tuning the amplitude of the second kicker *in situ*.

One interesting possibility of the scheme described is the following. As one can pick-up the signal what is proportional to the amplitude of phase oscillations and, hence, the instant deviation of the beam energy from equilibrium, $U \propto \psi \propto \Delta p / p$, one can see, that the difference in the path length could be made as following

$$\Delta l = -x_0 \int_{s_0}^{s_1} \frac{C}{\rho} ds - \left(K \int_{s_0}^{s_1} \frac{S}{\rho} ds + \int_{s_0}^{s_1} \frac{D}{\rho} ds \right) \frac{\Delta p}{p},$$

where we supposed, that $x'_0 \cong K \frac{\Delta p}{p}$, K -- is an appropriate

coefficient of proportionality. So if the sum of the terms in the brackets made equal to zero, the channel, connecting s_0 and s_1 will not depend on the energy deviation at all.

One can see, that the scheme proposed is not sensitive to the dispersion at the points of the actual location of the kickers.

REFERENCES

- [1] W. Kells, "New Approach to Stochastic Momentum Cooling", TM-942, FERMILAB, 1980.
- [2] A. Mikhailichenko, "Longitudinal damping scheme with two transverse kickers", Cornell CBN 96-10, 1996.
- [3] Klaus G. Steffen, "High Energy Beam Optics", Interscience Publishers, 1964.
- [4] D.A. Edwards, M.J. Syphers, "An Introduction to the Physics of High Energy Accelerators", a Wiley-Interscience Publishing 1993.

Work supported by National Science Foundation.

53 MHZ FEEDFORWARD BEAM LOADING COMPENSATION IN THE FERMILAB MAIN INJECTOR *

J. Dey[#], I. Kourbanis, J. Reid, J. Steimel, FNAL, Batavia, IL 60510, USA

Abstract

53 MHz feedforward beam loading compensation is crucial to all operations of the Main Injector. Recently a system using a fundamental frequency down converter mixer, a digital bucket delay module and a fundamental frequency up converter mixer were used to produce a one-turn-delay feedforward signal. This signal was then combined with the low level RF signal to the cavities to cancel the transient beam induced voltage. During operation we have shown consistently over 20 dB reduction in side-band voltage around the fundamental frequency during Proton coalescing and over 14 dB in multi-batch antiproton coalescing.

HARDWARE

The purpose of the hardware (Fig. 1) is to take the Main Injector resistive wall current monitor and delay it by one turn and combine it with the 53 MHz low level RF (VCO) fan-out sent to the cavities. This signal is down converted and up converted (In-Phase) because the Digital Bucket Delay A/D clock is operated at the VCO frequency. After the down convert, the fundamental frequency (DC component) is removed with a capacitor leaving the 90 kHz spaced transient mode lines to be digitized and delayed. The Digital Bucket Delay consists of an A/D converter, a FIFO, and a D/A converter that all operate off of the VCO frequency. The A/D and D/A are both 14-bit and operate between ± 1 volt. With the FIFO, the signal is delayed by an integer numbers of rf cycles. The Main Injector harmonic number is 588 and taking into account cable delays and component positions we use the FIFO to delay the signal 531 buckets. Once delayed, the signal is cleaned up with a 30 MHz low pass filter and up converted with the VCO. In order to run this system from 52.8 MHz to 53.1 MHz up the ramp, 6 ns of phase shift is used of the 180 degree 53 MHz phase shifter. A mixer

was used to electronically attenuate the signal for different gains and number of bunches. A Mini-Circuits ZFSC-24-11 24 way-0° splitter was used to fan-out the signal to each of the 18 Main Injector stations. This signal was then combined with the low level rf just after the limiter [1] in the solid state metering chassis using a Mini-Circuits ZFSC-2-1 2 way combiner. In doing fan-out and fan-back for Feedforward BLC, one must take into account the time of flight for the particles to pass each station. The fan-back also uses the Mini-Circuits ZFSC-24-11 to vectorially sum up all of the Main Injector Cavity gap monitors. Since the Pbars spin in the opposite direction, Station 18 now becomes the first cavity, a whole separate time of flight fan-out and fan-back system was created for Pbar Feedforward BLC.

OPERATION

Feedforward (FF) Beam Loading Compensation (BLC) was first done during Proton Coalescing at 150 GeV. Later, it was also implemented during Pbar Coalescing at 150 GeV. Presently we are in the process of commissioning Feedforward BLC to work up the Ramp from 8 GeV to 150 GeV.

Proton Coalescing

Figure 2 shows a Mountain Range of typical seven bunch Proton Coalescing using both feedforward and feedback [1] BLC. The HP 89441A Vector Signal Analyzer (VSA) plot (Fig. 3) at 150 GeV shows a reduction in the transients by 26 dB. The VSA plot was made from the fan-back of all eighteen stations. In adding feedforward BLC, Proton Coalescing efficiency improved by 5% and day-to-day reliability has been greatly enhanced.

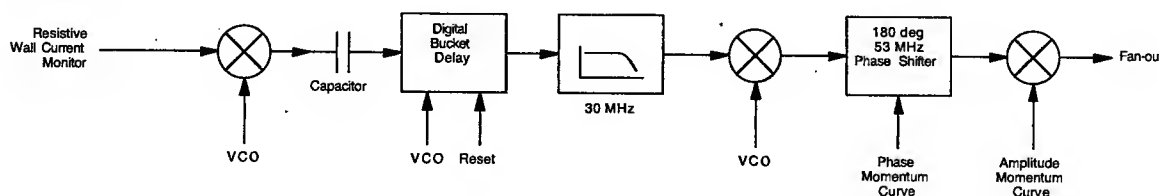


Figure 1: Block Diagram of Feedforward Beam Loading Compensation

*Operated by Universities Research Association, Inc. for the U.S. Department of Energy under contract DE-AC02-76CH03000.
[#]dey@fnal.gov

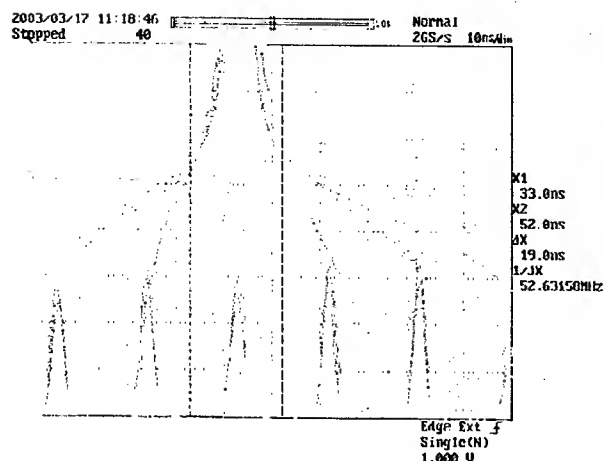


Figure 2: Proton Coalescing of 283E9 Protons

Pbar Coalescing

Pbar Coalescing consists of multi-bunch coalescing. Each of the four bunches only consists of 30E9 Pbars so intensity is not the issue here but alignment during recapture of all four bunches is. Figure 4 shows a reduction in the transient modes of 15 dB. One can clearly see in Figure 5 the multi-bunch alignment problem that occurs with feedback BLC only being applied. In Figure 6, the coalesced beam was recaptured properly and no beam appears outside the bucket on the right side when both Feedback and Feedforward BLC are applied. Overall Pbar Coalescing efficiency rose from 75% to 87% because of this improvement.

Feedforward BLC up the Ramp

Early promising results are shown for FF BLC up the Ramp. A Merrimac PMP-3R-53B 180 degree 53 MHz phase shifter is used to track the 6 ns time of flight difference from 8 GeV to 150 GeV. The difference of only 6 ns is attributed to the 531 buckets of delay that is removed by the Digital Bucket Delay being clocked off the VCO. A mixer was used after the phase shifter to

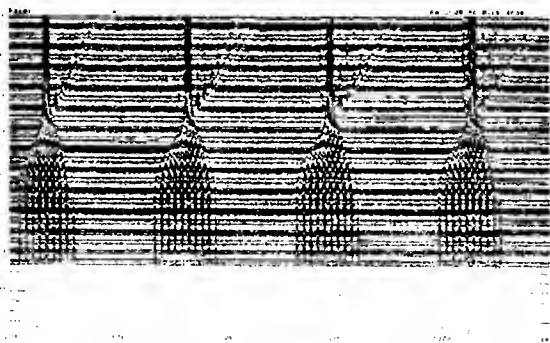


Figure 5: Without FF BLC on Pbar Coalescing

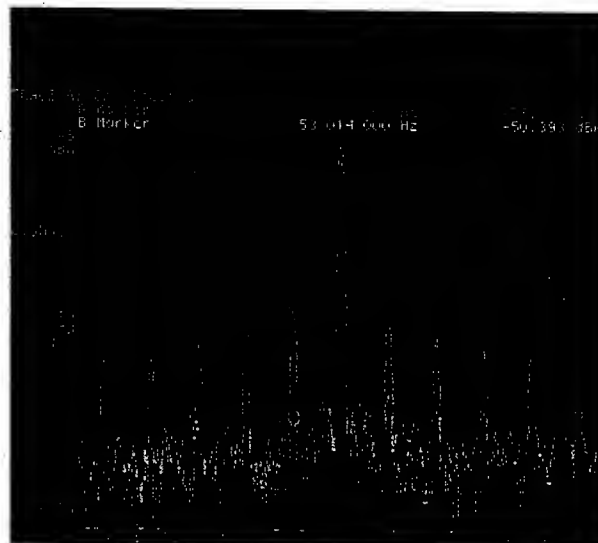


Figure 3: Main Injector Cavity Gap Response with (green) and without (blue) Feedforward BLC during Proton Coalescing

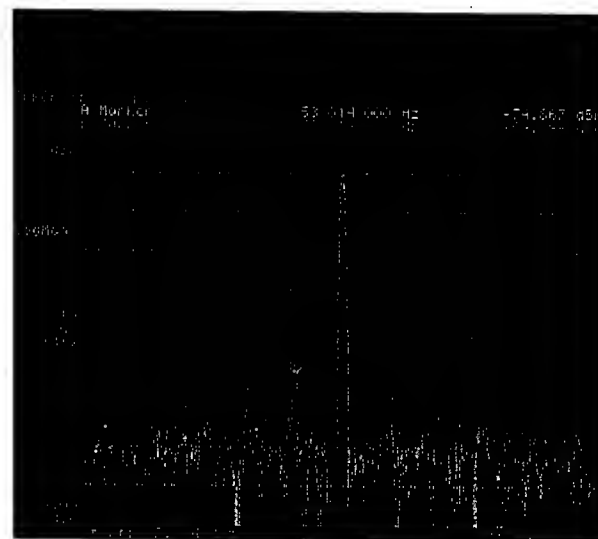


Figure 4: Main Injector Cavity Gap Response with (green) and without (blue) Feedforward BLC during Pbar Coalescing

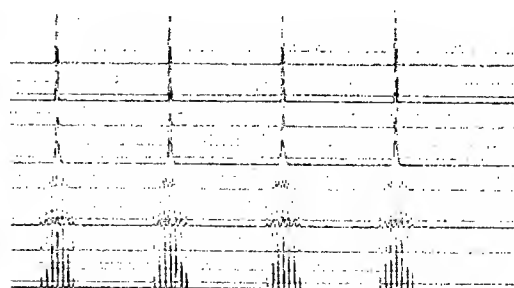


Figure 6: With FF BLC on Pbar Coalescing

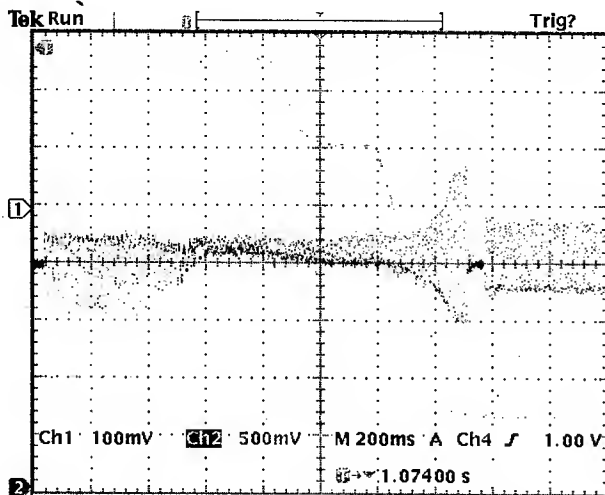


Figure 7: Without Feedforward BLC up the Ramp

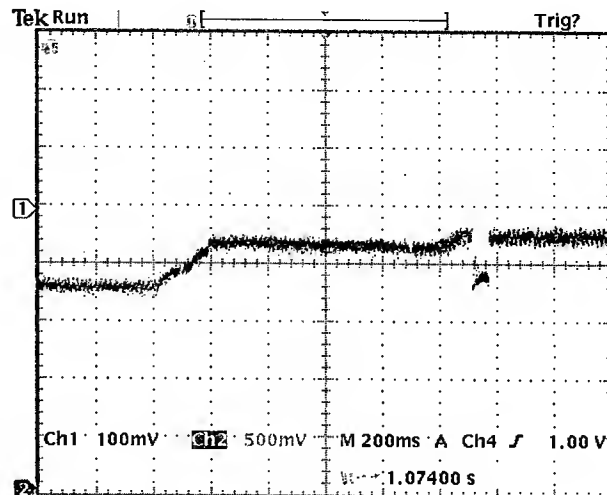


Figure 8: With Feedforward BLC up the Ramp

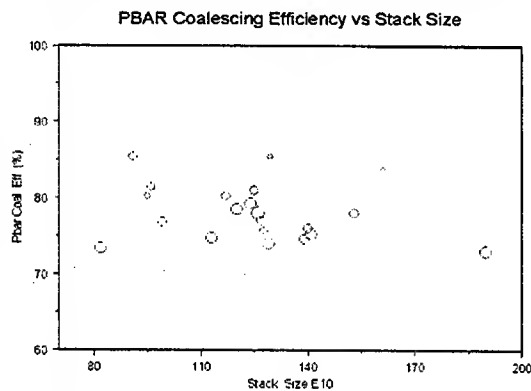


Figure 9: Coalescing without Feedforward BLC

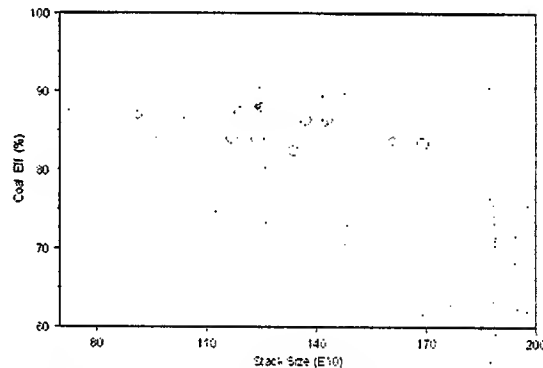


Figure 10: Coalescing with Feedforward BLC

electronically attenuate the FF BLC for different gains up the ramp. Figure 7 and 8 show the Local Station Phase Detector ($0.9^\circ/\text{div}$) response (blue trace) and the Detected RF Gap Envelope (aqua trace) for Main Injector Station #1 during Proton Coalescing. We also plan to use FF BLC up the Ramp during a Main Injector Pbar Stacking Cycle where it is expected to help us reduce the longitudinal emittance blow-up (especially through transition.)

RESULTS

Figure 9 shows the average Pbar Coalescing Efficiency as a function of Stack Size without FF BLC. The size of

the circles is proportional to the longitudinal emittance of the Pbar bunches before coalescing. Average Coalescing efficiency was about 75% and was getting lower with the larger stack size. Figure 10 is with Feedforward BLC. The average Coalescing efficiency was about 87% and no dependence with stack size is observed.

REFERENCES

- [1] J. Dey, J. Steimel, J. Reid, "Narrowband Beam Loading Compensation in the Fermilab Main Injector Accelerating Cavities," 2001 PAC, p. 876, Chicago, June 2001.

2.5 MHZ FEEDFORWARD BEAM LOADING COMPENSATION IN THE FERMILAB MAIN INJECTOR *

J. Dey[#], I. Kourbanis, J. Steimel, FNAL, Batavia, IL 60510, USA

Abstract

There are five 2.5 MHz ferrite cavities ($h = 28$) in the Main Injector with an R/Q of 500 that are presently used for coalescing for the Tevatron. For use with the Fermilab Recycler, feedforward (FF) beam loading compensation (BLC) is required on these cavities because they will be required to operate at a net of 2 kV. Under current Recycler beam conditions, the beam-induced voltage is of this order. Recently a system using a digital bucket delay module operating at 53 MHz ($h = 588$) was used to produce a one-turn-delay feedforward signal. This signal was then combined with the low level RF signal to the 2.5 MHz cavities to cancel the beam induced voltage. During current operation we have shown consistently to operate with over a 20 dB reduction in beam loading.

HARDWARE

The purpose of the hardware (Fig. 1) is to take the Main Injector resistive wall current monitor and delay it by one turn and combine it with the 2.5 MHz low level rf fan-out sent to the cavities. In digitizing at 53 MHz (VCO), we are sampling at 21 times the fundamental mode of the cavities with the Digital Bucket Delay. The signals of interest are the fundamental and the 90 kHz spaced transient mode lines, so a 10.7 MHz and 5 MHz low pass filter are used to remove the unwanted upper frequency response of the resistive wall current monitor. The Digital Bucket Delay consists of an A/D converter, a FIFO, and a D/A converter that all operate off of the VCO frequency. The A/D and D/A are both 14-bit and operate between ± 1 volt. With the FIFO, the signal is delayed by an integer numbers of rf cycles. The Main Injector harmonic number is 588 and taking into account cable delays and component positions we use the FIFO to delay the signal 536 buckets. A Mini-Circuits ZFSC-8-6 8 way-0° splitter was used to fan-out the signal to each of the five 2.5 MHz cavities. This signal was then combined with the low level RF (Fig. 2) just after the

fundamental feedback [1] splitter/combiner using a Mini-Circuits ZFRSC-2050 2 way splitter/combiner. Presently the fan-out is only setup to act on proton transfers to the Recycler. A new fan-out is in the works to take into account Pbars spinning in the opposite direction and the position of the resistive wall current monitor in reference to the cavities.

OPERATION

The present mode of operation is to take a multi-batch injection of protons from the Booster into the Main Injector and create four 100E9 2.5 MHz proton bunches. These four bunches are then transferred from the Main Injector at 8 GeV with 2 kV of 2.514 MHz RF to match the Recycler. Reducing beam loading on the latter bunches is critical for an efficient transfer.

In all cases, fundamental feedback BLC is operating on each individual cavity with a gain of 5.

RESULTS

In Figure 3, the red trace shows the vector summation of the five 2.5 MHz cavities using the vlog output from an Analog Devices AD8309 Logarithmic Amplifier. The green trace is four batches of Protons being injected from Booster. Since the cavities have not been turned on at this point one can see the beam induced voltage on the cavities. At about 2.5 seconds the FF BLC was turned on for one second and the red trace goes down by a factor of 8 until the cavity is turned on to 2.2 kV. The 2.2 kV part of the trace is flat until FF BLC is turned off and then one can see the effects of beam loading take over again. In normal operations, the FF BLC is left on during the entire length of a proton injection into the Recycler (\$2D cycle.) Figure 4 shows a plot from a HP 89441A Vector Signal Analyzer (VSA) at 2 seconds in the cycle. The blue trace is beam-induced voltage on cavity number five's gap monitor. The green trace is with FF BLC applied.

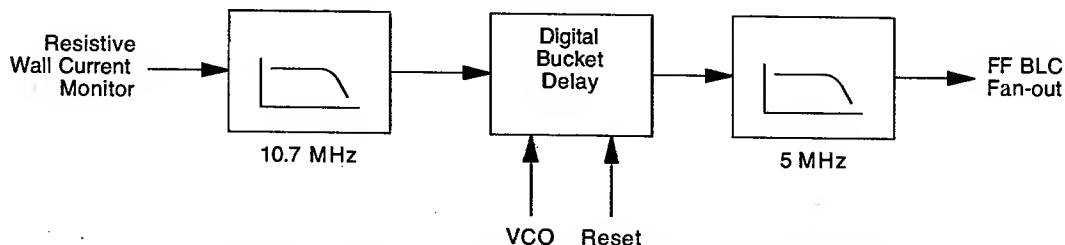


Figure 1: Block Diagram of Feedforward Beam Loading Compensation

*Operated by Universities Research Association, Inc. for the U.S. Department of Energy under contract DE-AC02-76CH03000.

[#]dey@fnal.gov

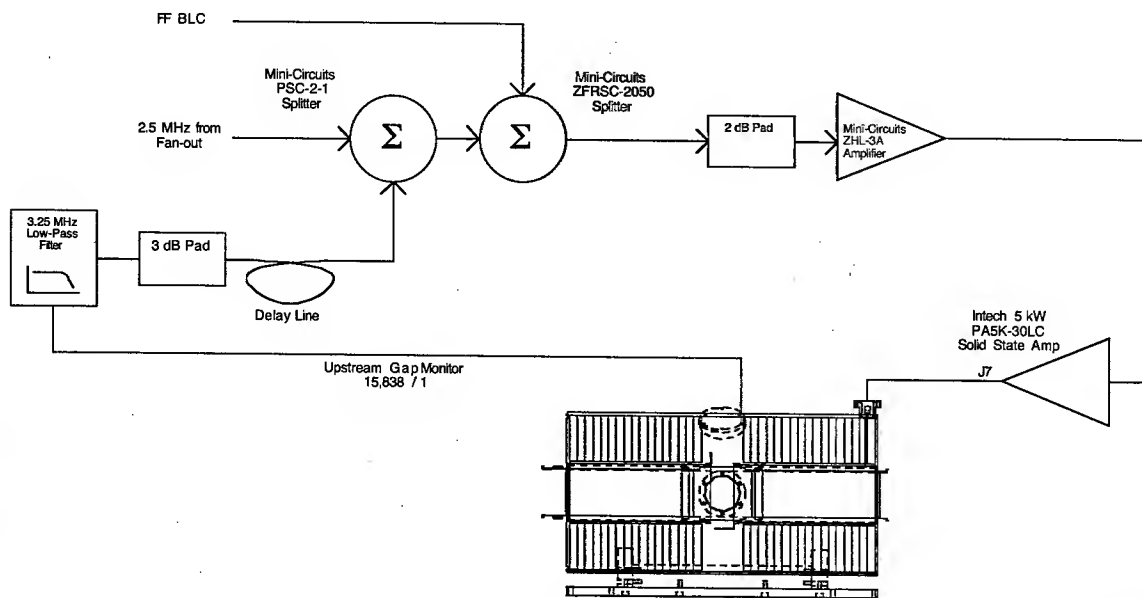


Figure 2: 2.5 MHz Coalescing Station Block Diagram

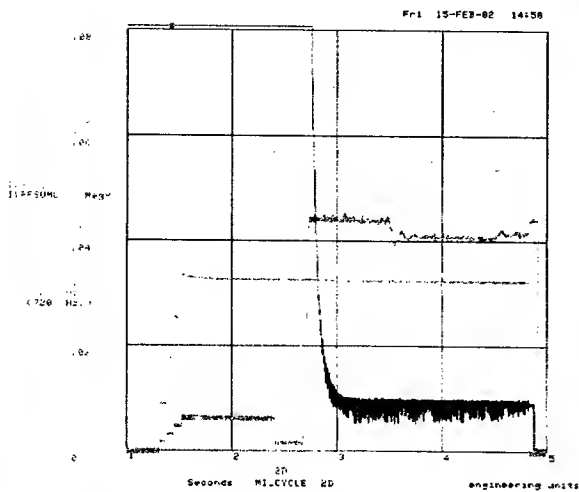


Figure 3: FF BLC on for a portion of a 2D cycle.

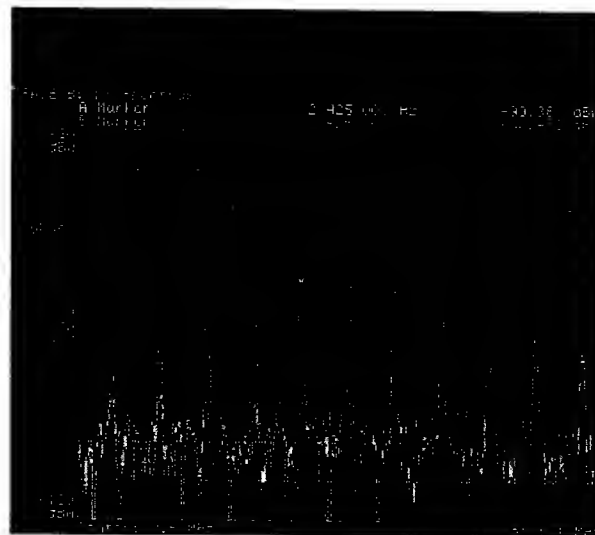


Figure 4: VSA plot of the gap monitor on Cavity #5

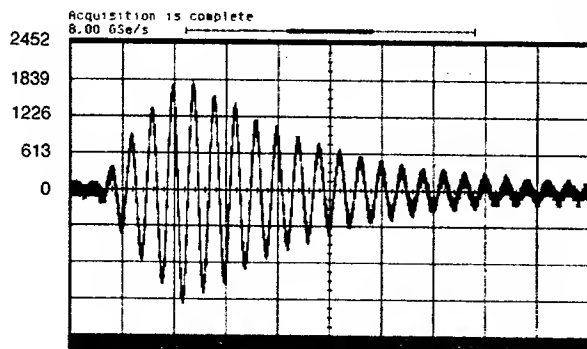


Figure 5: FF BLC off

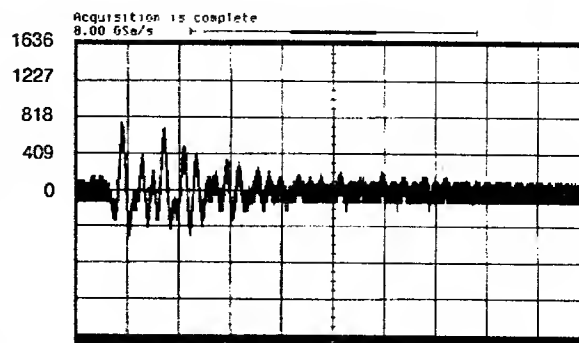


Figure 6: FF BLC on

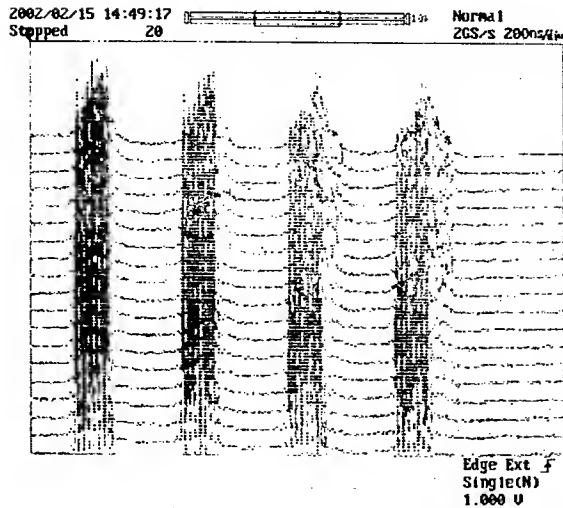


Figure 7: FF BLC off

Almost 30 dB of reduction is seen on the first lower transient beam loading line of Figure 4.

Figure 5 shows the vector summation of beam induced voltage on the five 2.5 MHz cavities from four 100E9 proton bunches. The time domain plot is for a single turn when no induced voltage is applied at 2 seconds on a \$2D cycle. Note that almost 1840 volts is shown of beam loading. Figure 6 is under the same conditions as Figure 5, but with the FF BLC turned on. The reduction in beam loading voltage is very apparent. Figure 7 shows a mountain range of each of the four 100E9 proton bunches on a \$2D cycle. Each of the bunches following the first are beginning to get wider on the left hand side from beam loading. In Figure 8, FF BLC is turned on and each of the bunches keep their original width. This allows for an efficient multi-bunch transfer to Recycler without any alignment errors.

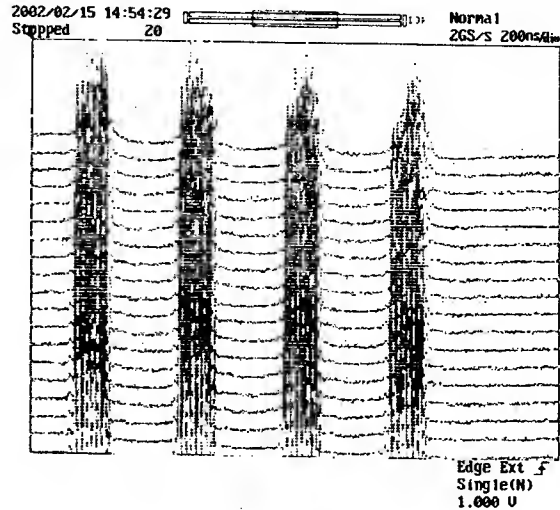


Figure 8: FF BLC on

CONCLUSIONS

Feedforward BLC has greatly reduced the amount of beam loading on the five 2.5 MHz Ferrite Loaded Cavities. The compensation system has been operational for over a year now and overall stability has been excellent.

REFERENCES

- [1] J. Dey, J. Steimel, "Improving the Linearity of Ferrite Loaded Cavities Using Feedback," 2001 PAC, p. 873, Chicago, June 2001.

TUNE AND COUPLING DRIFT COMPENSATION DURING THE TEVATRON INJECTION PORCH *

M. Martens[†], G. Annala, P. Bauer, Fermilab, Batavia, IL, USA

Abstract

During Collider Run II operations drifts in the betatron tunes and coupling are observed over a several hour period while the Tevatron is on its injection front porch. Associated with these drifts is a so-called snapback of the tune and coupling at the beginning of the Tevatron energy ramp from the injection porch. The magnitude of the drifts and snapback has added to the efforts to keep the Tevatron tuned for optimal beam conditions and has made it more difficult to understand beam behaviour. Therefore a feed-forward system was implemented to compensate for the tune and coupling drifts and snapback. The cause of the drifts has not been conclusively identified but the leading hypothesis is persistent current effects in the Tevatron superconducting magnets. We have begun experimental investigations to verify this hypothesis and some of the results are presented in this paper.

MEASURED TUNE DRIFT

In Collider Run II drifts of the betatron tunes and the transverse coupling are observed while the Tevatron is at its injection front porch energy of 150 GeV. Fig. 1 shows plots of the measured horizontal and vertical tunes as a function of time at 150 GeV. Because a significant change in the coupling was also observed, each of these tune measurements was made after the Tevatron was decoupled using the trim skew quadrupole magnets.

Similarly, Fig. 2 shows plots of the measured coupling as a function of time at 150 GeV. The amount of coupling was determined by measuring the minimum tune split as the trim tune quadrupole circuits were used to push the horizontal and vertical tunes as close together as possible. We also measured the strength of two families of skew quad circuits that were required to decouple the Tevatron to a minimum tune split of 0.002 or better.

If these tune drifts are related to persistent current effects in the Tevatron magnets then the history of the previous energy ramp is an important factor determining the amount of drift. This factor was not examined in detail. Instead we focussed on the behaviour of the tunes and coupling after a standard Tevatron ramp pre-cycle. Presently the standard pre-cycle is essentially a ramp of the Tevatron magnets in the same sequence used during a collider store but without beam and with only a 20-minute duration at the flattop energy of 980 GeV (as compared to the ~12-24 hour flattop duration during a collider store.) Figs. 1 and 2 include measurements taken on several occasions over a one-year period. In each case the

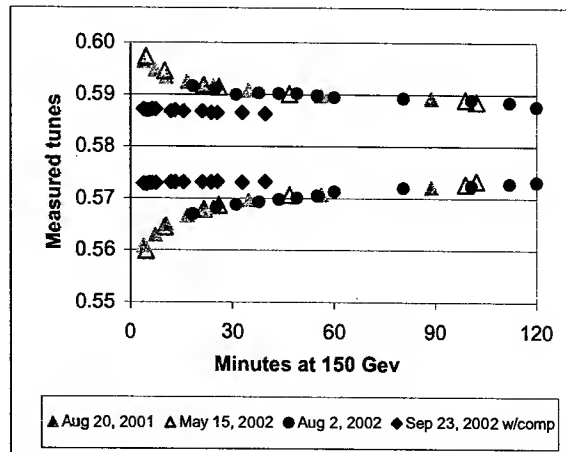


Figure 1: Measured horizontal (upper) and vertical (lower) tunes as a function of time at 150 GeV on three different days. Included is a plot of the measured tunes after the compensation was implemented in Sept. 2002.

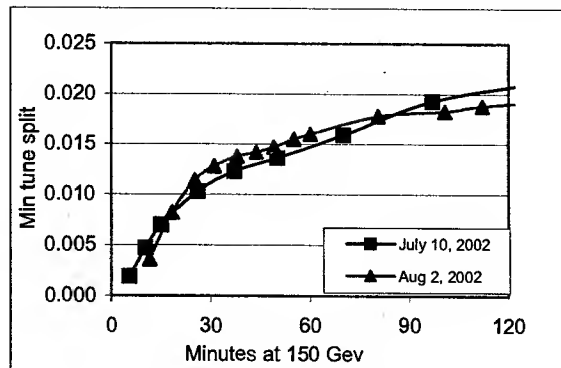


Figure 2: Measured minimum tune split as a function of time at 150 GeV on two different days.

standard ramp pre-cycle was performed and the results demonstrate the repeatability of the drifts.

Associated with the drifts at 150 GeV is a so-called snapback of the tune and coupling that occurs at the beginning of the Tevatron energy ramp from the injection porch. The magnitude of the tune and coupling snapback has not been measured as accurately as the tune drift at 150 GeV. However, from observations of the tunes near the start of the Tevatron ramp it is clear that tune variations of ~0.01 are present.

For Tevatron operations we prefer to maintain the tunes within a tolerance of about ~0.002 and to keep the transverse coupling below ~0.003 units. Thus these large drifts were a problem and a feed-forward system was implemented to counter act these drifts.

*Work supported by the U.S. Department of Energy

[†]martens@fnal.gov

DRIFT COMPENSATION

The drift compensation system applies a correction to the tune and coupling circuits on the 150 GeV front porch in the form a logarithm function. The change in the tune circuits follows the equations

$$\Delta v_x(t) = -0.00778 + 0.0019 * \ln(t) \quad (1)$$

$$\Delta v_y(t) = +0.0127 - 0.0031 * \ln(t) \quad (2)$$

$$\Delta \kappa_{SQ}(t) = +0.0250 - 0.0061 * \ln(t) \quad (3)$$

where t is the time in seconds since the start of the injection porch and the coefficients were determined from fits to the measured data shown in Figs. 1 and 2.

After implementing the correction algorithm the tunes and coupling were measured again as a function of time on the front porch and these are plotted in Fig. 1. We also measured the coupling as a function of time and found that the minimum tune split remained below 0.002 during this time.

In addition to the drifts at 150 GeV, there is also a snapback effect that causes large coupling and tune changes at the start of the energy ramp. It is time consuming to measure the tunes and coupling at the start of the Tevatron ramp so the snapback has not been investigated as thoroughly as the drift on the front porch. Instead we chose to implement the snapback correction the same manner as the chromaticity snapback correction. The correction that is applied at the start of the Tevatron energy ramp has a polynomial form

$$\langle x^2 \rangle = x_{2,start} [1 - (t/T)^2]^2$$

where $\langle x^2 \rangle$ represents one of the tune or coupling variables $\langle \Delta v_x \rangle$, $\langle \Delta v_y \rangle$, or $\langle \Delta \kappa_{SQ} \rangle$. The value of $x_{2,start}$ is the value of $\langle x^2 \rangle$ at the time of the start of the Tevatron energy ramp. The values of $x_{2,start}$ are determined just before commencing the energy ramp and the corresponding corrections are loaded into hardware. The time constant for the snapback correction, T , is presently set to 6 seconds. This choice was based on the hypothesis that the source of both the chromaticity and the tune/coupling coupling drifts are related to persistent currents and would therefore have similar time variations.

Without the snapback compensation we observed tune changes of about 0.01 at the start of the Tevatron ramp. With the snapback compensation in place the tunes at the start of the ramp deviate by less than ~ 0.003 tune units.

SOURCE OF THE TUNE DRIFT

It has been known for some time that persistent current effects in the Tevatron dipoles create time-varying sextupole fields that cause drifts in the chromaticity on the injection front porch and a snapback at the start of the energy ramp [1,2,3]. Furthermore the magnitude of the time-varying sextupole fields depends on the previous

Tevatron energy ramp cycle and parameters such as: the energy of the previous flattop, the time spent on the previous flattop, and the time spent on the previous front porch. In order to compensate for the drifting sextupole fields a correction algorithm is used to control the trim sextupole correctors while the Tevatron is at 150 GeV and during the snapback at the start of the ramp [2,3].

It is reasonable to hypothesize that tune and coupling drifts and snapback are also related to persistent currents. We have been investigating this possibility with both beam based measurements and magnetic field measurements in the Tevatron superconducting magnets. We have not reached a conclusion regarding the source of the drifts but we have begun analysis and we report some to the results in this section. The three main possibilities being considered are a feeddown effect from the drifting sextupole field in the Tevatron dipoles and an orbit offset, drifting quadrupole component in the Tevatron dipoles, and drifting quadrupole strength in the Tevatron quadrupoles.

Tune drift from sextupole feeddown effect

One possible explanation for the tune and coupling drifts is a feeddown effect from orbit offsets and the time-varying sextupole fields in the dipole magnets. The horizontal tune change from horizontal orbit offsets in sextupole magnetic fields is given by the formula

$$\Delta v_x = \frac{1}{4\pi} \sum ((\beta_x L \Delta K_2) ((\Delta p/p) D_x + x_0)) \quad (4)$$

where β_x is the horizontal beta function, L is the length of the magnet, ΔK_2 is the change in sextupole field gradient, and $((\Delta p/p) D_x + x_0)$ is the horizontal orbit position due to position and momentum errors. The sum is over all sextupole fields which, in the case of the Tevatron, includes the sextupole component, b_2 , of the Tevatron dipoles and the two families of chromaticity correction sextupole magnets (which we refer to as T:SF and T:SD in the Fermilab nomenclature.)

We make use of Eq. 4 by assuming: 1) that we know the lattice functions β_x and D_x at the locations of the sextupole fields, 2) the sextupole gradient strength in the chromaticity sextupoles are known from the current in these circuits, and 3) that we can determine the average time varying sextupole component in the Tevatron magnets from chromaticity measurements. As for item 3) above, we know that the chromaticity does not change, $\Delta \xi = 0$, when the chromaticity compensation is active. Since the total variation in the chromaticity is the sum of the change from the b_2 in the dipoles and sextupole correctors, and the applied correction is known, we can estimate the average time-varying b_2 field in the Tevatron dipoles. With these assumptions the undetermined variables in Eq. 4 are the average horizontal orbit offsets in the dipoles and chromaticity sextupoles.

To determine the average offset in the sextupole correctors we measure the tune shift from a change in the strength of the sextupole field, ΔK_2 , in the T:SF or T:SD magnets. If we make this measurement as a function of

momentum offset $\Delta p/p$ then we can determine the average value of the horizontal orbit offset in T:SF and T:SD circuit. Using the relationship between the RF frequency and the beam momentum, $(\Delta f/f) = -\eta(\Delta p/p)$ where η is the slip factor, we can extract this tune change from Eq 4 as

$$\Delta \nu_x = (\Delta K_2 L) \frac{N}{4\pi} \left(-\frac{1}{\eta} \langle \beta_x D_x \rangle (\Delta f/f) + \langle \beta_x x_0 \rangle \right)$$

where N is the number of magnets in the circuit and $\langle \rangle$ denotes the average value.

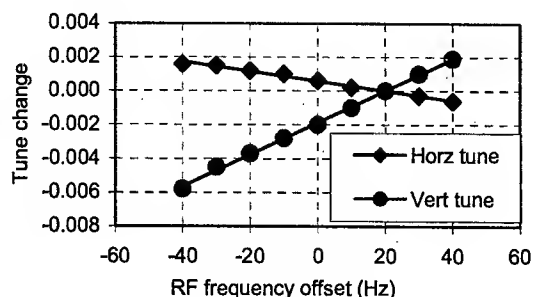


Figure 4: Measured tune change from a 0.5 amp change in the sextupole circuit T:SD versus the RF frequency offset.

An example measurement is shown in Fig. 4 for the T:SD sextupole family. In this case we see that a +20 Hz offset from the nominal RF frequency is needed in order to observe no tune shift from the T:SD circuit. This corresponds to an average horizontal orbit offset of +0.34 mm to the radial outside. A similar measurement for the T:SF circuit shows that an RF frequency offset of 0 Hz is needed corresponding to no average horizontal orbit offset in the T:SF magnets. The average orbit offset in T:SF and T:SD, along with the measured tune drift, can be used in Eq. 4, to determine the average orbit offset in the Tevatron dipoles that is required to explain the feeddown hypothesis.

An analysis along these lines would require a -0.68 mm average orbit offset in the Tevatron dipoles if the horizontal tune drift is used and would require a -0.95 mm horizontal orbit offset if the vertical tune drift measurement is used. Thus the horizontal and vertical tune data are not consistent for this hypothesis. In addition to these measurements, we also have Beam Position Monitor data of the orbits. In particular the average horizontal BPM position at the location of the T:SF magnets is -0.71 mm. This is inconsistent with the value of 0 mm determined from the feeddown measurements. If we choose to use the BPM data as the position in the T:SF magnets then an even larger average horizontal orbit offset in the dipoles is needed to explain the observed tune drift.

In addition to the tune drift, there is a time varying coupling change that, if left uncorrected, results in a minimum tune split of about 0.02 tune units after about 2 hours. Explaining this drift with the feeddown hypothesis requires an average vertical orbit offset of about +0.94 mm in the Tevatron dipoles. Recent survey results have

shown that there are systematic mechanical rolls of many Tevatron dipoles which result in vertical kicks of the beam. Although the orbits are corrected using trim dipole magnets the relatively large spacing between vertical correctors (8 dipoles between correctors) produces a scalloped orbit that results in a net vertical orbit offset in the dipoles even though the BPMs record no net vertical offset. An analysis of this effect has been done but the vertical orbit offset resulting from the rolled dipoles explains only about 1/3 of the coupling drift [4].

Drifting quadrupole fields in the Tev magnets

Another possible source of the tune drift is a time-varying quadrupole field in the Tevatron, for example a drift of the main field in the arc quadrupoles. In order to explain the tune drifts at 150 GeV we find that an integrated gradient of $\Delta K_1 L = 0.0033$ is needed, which is equivalent to ~ 2 b_1 units (of 10^{-4} of the main quad gradient) per Tevatron arc quadrupole. This is of the same order as the main field decay observed in HERA and LHC dipole magnets. It can therefore not be excluded that main field decay in the Tevatron quadrupoles explains part of the tune drift. Experimental verification of this issue is in the planning stages. These drifts can presumably be explained by the same phenomena that cause the drift in the sextupole and other allowed harmonics. Although a significant b_1 component should not be present in the dipole magnets, there is also the possibility of a b_1 drift in Tevatron dipole magnets. A very small drift of ~ 0.1 units in b_1 would be required.

Similarly the coupling drift can be related to a drifting skew quadrupole, a_1 . A derivation of the a_1 needed to produce the observed change of minimum tune split over a 2 hrs injection, indicates that ~ 70 units of a_1 distributed over all dipoles would be required, again a very small effect. Although a significant a_1 component should not be present in the dipole magnets, there is some experimental evidence of such a_1 drifts exist in Tevatron dipole magnets. Although hard experimental evidence is still missing, the possibility of explaining part of the tune and coupling drift by drifting b_1 and a_1 in the Tevatron main magnet should not be excluded.

REFERENCES

- [1] G.V. Velez, et. al, "Measurements of Field Decay and Snapback Effect on Tevatron Dipole Magnets," WPAE016, this conference.
- [2] M. Martens and J. Annala, "Chromaticity, Tune, and Coupling Drift and Snapback Correction Algorithms in the Tevatron," Internal Fermilab Memo, Beams-doc-467, March 3, 2003, available on-line at <http://beamdocs.fnal.gov/cgi-bin/public/DocDB/ShowDocument?docid=467>.
- [3] P. Bauer, et. al. "Analysis of the b2 Correction in the Tevatron." TPPB055, this conference.
- [4] M. J. Syphers, "Effects of Systematic Rolls of Tevatron Magnets," Internal Fermilab Memo, Beams-doc-429, February 11, 2003.

BEAM LOADING COMPENSATION FOR SLIP STACKING*

J. Steimel, T. Berenc, C. Rivetta, FNAL, Batavia, IL 60510, USA

Abstract

This paper discusses the beam loading compensation requirements to make slip stacking practical in the Fermilab main injector. It also discusses some of the current plans for meeting these requirements with a digital, direct RF feedback system.

INTRODUCTION

Slip stacking takes advantage of the extra longitudinal phase space in the main injector. It is a method of injecting two batches of beam into the main injector and combining the two batches into one double charged batch before extracting to the antiproton target. Two batches of beam are injected consecutively into the main injector with slightly different momenta. The different momentum batches have slightly different velocities, and one batch eventually overtakes the other batch. When the two batches completely overlap, the RF voltage is increased to provide a bucket big enough to contain the entire momentum space of the two batches.

The momentum separation between the batches must be large enough, compared to the bucket size, to minimize the interference between the two batches but not larger than the momentum acceptance of the main injector. For optimal slip stacking, the bucket size should be just big enough to contain the longitudinal emittance of the injected beam. Maintaining small bucket sizes becomes difficult for high intensity beams in the presence of beam loading on the cavities.

Low intensity slip stacking has already been demonstrated in the main injector [1]. With a total beam intensity of 0.8×10^{12} protons, two batches were combined with a total emittance dilution of about 60%. Unfortunately, the main injector must slip stack 9.0×10^{12} protons/cycle, and beam loading already greatly degrades slip stacking performance at 3.0×10^{12} . Beam loading compensation is required for practical slip stacking performance.

Slip stacking simulations have been studied to determine how much beam loading compensation is required for full intensity with emittance preservation [2]. The simulations show that the beam loading compensation must reduce the effect of beam current by 40dB at the fundamental resonance of the cavity and by 26dB at the first revolution harmonic. The rest of the paper discusses the present beam loading compensation system in the main injector and how to modify the system for the slip stacking specifications.

* Work supported by the Universities Research Assoc., Inc., under contract DE-AC02-76CH03000 with the U.S. Dept. of Energy.

PRESENT SYSTEM

The purpose of the present beam loading compensation system is to improve the reliability of the RF system under beam loaded conditions, and it also improves low voltage manipulations like coalescing. The system consists of direct RF feedback systems at each RF station, and a global feedforward system derived from a wideband beam intensity detector.

Direct RF Feedback System

The main injector is equipped with a direct RF feedback system [3]. Each cavity in the main injector has an independent feedback system. The system consists of a module that converts the signal from the cavity gap monitor to baseband.

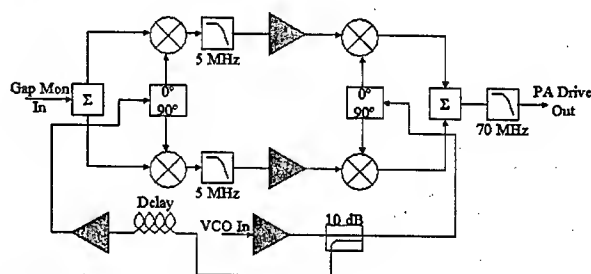


Figure 1: Block diagram of the beam loading module. The superheterodyne structure is designed to track the phase response with the changing VCO frequency. The downconvert reference is synchronized with the cavity gap signal, and the upconvert reference is synchronized with the fanout.

The signal is low-pass filtered, up-converted, and combined with the fundamental amplifier drive signal. It is important that the phase of the open loop response remain 180° at the fundamental frequency for maximum stability margin. The system maintains the proper phase by using different delays for the up-convert and down-convert RF references in the feedback module. The up-convert reference delay is matched to the LLRF fanout delay to the cavity, and the down-convert delay is matched to the cavity gap signal from the tunnel. With the proper delays on the references, the feedback module will adjust its delay to maintain the proper phase intercept for the system.

Maintaining proper phase intercept improves the stability margin, but there is still a stability limit on the allowable open loop gain on the system. The current main injector system will only allow an open loop gain of about 26 dB with a reasonable gain margin. Equation (1)

shows the relationship between maximum gain and the Q of the cavity, the cavities resonant frequency, and the open loop delay of the system [4].

$$G_{\max} = \frac{\pi Q}{2\omega_r \tau} \quad (1)$$

The feedback module has a fixed gain profile, in frequency, over many revolution harmonics, so the cavity response dictates the open loop bandwidth. Because of the high Q of the cavity, the open loop gain of the system rolls off quickly. Thus, the system performs insufficient beam loading compensation at any revolution harmonics other than the fundamental.

Feedforward System

The feedforward system currently being tested in the main injector uses a wall current monitor for its beam current source [5]. The signal from the wall current monitor is down-converted, filtered, and delayed digitally. The output of the digital delay drives a special cavity fanout system. Instead of having a system of equal length cables, this fanout system is designed to have delays different by the beam transit time between cavities. At each of the cavities, the signal is upconverted and combined with the drive.

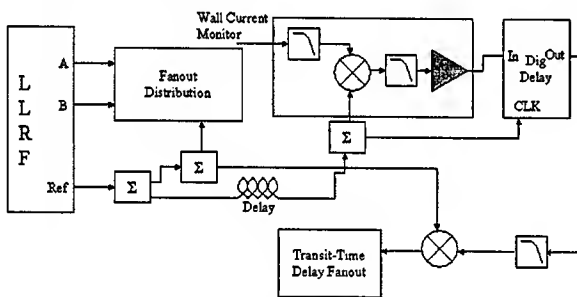


Figure 2: Block diagram of feedforward system low level processing. The output of the delay fanout is combined with the cavity drive.

The disadvantage of the feedforward system is the beam signal and power amplifier current must match very closely. There is no inherent correction mechanism like there is in a feedback system. Therefore, the system can only operate in very well defined conditions. It cannot track energy changes or changes in RF amplitude or operating conditions. Also, it is extremely important that the signal path be completely linear, otherwise the feedforward signal will be too distorted to cancel out the beam signal when the two meet in the cavity. The power tube is a major source of nonlinearity in the signal path.

SLIP STACKING FEEDFORWARD

Slip stacking brings a different challenge to feedforward that does not exist in the present system. The first difference is the 100% amplitude modulation of the fundamental component of the beam spectrum. The second difference is the phase modulation of the fundamental component relative to the acceleration

frequency. Compensating for these differences places a strain on the linearity of the power amplifier and produces new hazards in the feedforward system.

Amplitude Modulation Compensation

As the batches of approximately equal charge amplitude slip past each other, there will be a change in the amplitude of the fundamental beam component. When the RF phases of the two batches are coincident, the fundamental amplitude will be twice that of a single batch. When the phases are opposing, the fundamental amplitude goes to zero. This means that the feedforward compensation will operate over a very large dynamic range.

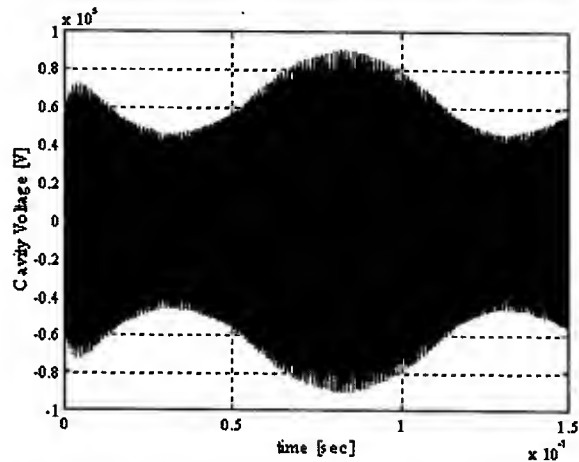


Figure 3: Simulated RF voltage in operating cavity with two batches of beam slipping against each other.

The RF power tube does not have perfect linearity over its operating range. Large signal variations in its grid drive will reveal its non-linearity. Proper cancellation of the beam loading current requires that the feedforward system produce a current pulse that closely resembles the beam pulse. If the net system is non-linear, then there will be an amplitude mismatch in the cavity that will limit the cancellation.

Phase Modulation Compensation

Another problem with the current feedforward system is that the resultant phase of the two fundamental components rotates with respect to a particular cavity drive. This means that the current system will try to compensate the cavities with the wrong amplitude and phase of beam signal. There are three possible solutions to this problem. One solution involves deriving both the in-phase and quadrature component of the beam signal from the pickup. Then, phase information is preserved. Another solution would be not to downconvert at all, but sample at a fast enough rate to preserve the data at and around the fundamental with the required bandwidth. The third solution would be to distribute a reference frequency that is phase matched to the amplitude modulated carrier of the beam frequency while slipping. This frequency would be the mean of the two fundamental frequencies.

The result of downconverting with this reference would be the pure amplitude modulation of the slipping buckets.

The disadvantage of using a method that preserves phase is that a parasitic longitudinal feedback loop develops. The system has significant delay, and if the gain required for proper compensation is high enough, the synchrotron oscillations could be driven unstable.

SLIP STACKING FEEDBACK

The current direct RF feedback modules in the main injector already provide fundamental frequency compensation during slip stacking without modification. However, to make slip stacking practical, the gain of the system must be increased by a factor of 10, and the system must provide transient beam loading compensation. The increased gain will put the current system well beyond its stability limit. In order to provide more gain at the fundamental as well as transient beam loading compensation at the revolution harmonics, the feedback module must be modified. First, to insure the proper open loop phase intercept for multiple revolution harmonics, the system must have a delay equal to some multiple of the revolution period [6]. Second, the bandwidth of the filter should not be dictated by the cavity, since this is not optimal for stability. The bandwidth of the system could be reduced to the point of just containing the frequency difference between the two batches in a slip stacking cycle. Of course the filter would necessarily have the same shape around the fundamental frequency as well as multiple revolution lines. This implies some kind of digital filter sampling at the fundamental frequency with taps at multiples of the revolution frequency.

One possible design uses a DSP with a highly parallel architecture, clocked at a multiple of the fundamental frequency. The down-converted signal from the cavity gap is digitized and stored in FIFO memory blocks. Data

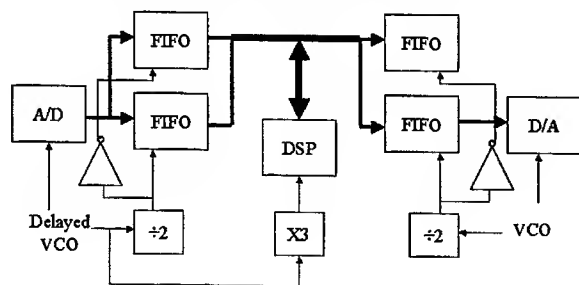


Figure 4: Block diagram of digital direct RF feedback filter.

from the memory blocks are burst into the DSP, and the DSP performs the filtering calculations. Output data from the DSP is burst into another set of FIFO memory blocks that drive a DAC. The FIFO memory blocks maintain the system delay at one revolution period. The output of the DAC is up-converted and combined with the cavity

fanout drive. Calculations done for an IIR filter in the

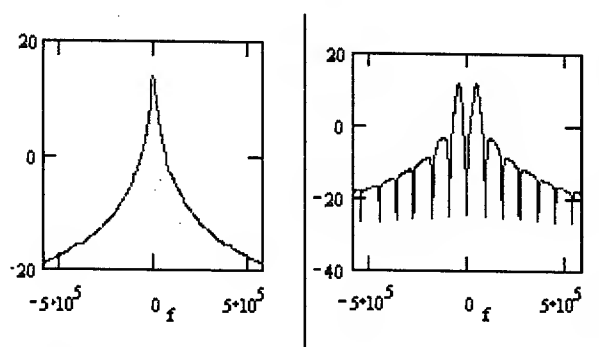


Figure 5: Comparison of cavity response without compensation and with IIR filter compensation. Horizontal scale is in Hz offset from fundamental. Vertical scale is in dB.

DSP show that open loop gains on the order of 40dB are achievable. To maximize the gain margin for the revolution harmonics, the signals for the revolution harmonics will follow a different path than the fundamental, so that they can receive a 90° phase shift. This is to compensate for the cavity response, which is reactive at the revolution harmonics.

CURRENT STATUS

The current feedforward system is being modified to include both inphase and quadrature beam signals. Once installed, the stability threshold will be investigated. Ways of regenerating the carrier frequency from the two RF frequencies are also being investigated.

A very detailed model of the RF cavity system is being produced. It should reveal conflicts between different feedback loops in the cavity system. Once completed, different types of filters can be simulated in the direct RF feedback system. If an appropriate digital filter can be simulated inside the cavity system that meets the slip stacking requirements, design and construction will begin.

REFERENCES

- [1] Kiyomi Kobe, et al, "Slip Stacking at Fermilab Main Injector," PAC'03, These proceedings.
- [2] J. MacLachlan, "The Beam Dynamics of Slip Stacking," FERMILAB-FN-0711 (Nov 2001).
- [3] J. Dey, J. Steimel, J. Reid, "Narrowband Beam Loading Compensation in the Fermilab Main Injector Accelerating Cavities," 2001 PAC, p. 876, Chicago, June 2001.
- [4] R. Garoby, "Beam Loading in RF Cavities", Joint US-CERN School, CERN/PS 91-33 (RF) (1990).
- [5] J. Dey, et al, "53 MHz Feedforward Beam Loading Compensation in the Fermilab Main Injector," PAC '03, These proceedings.
- [6] F. Pedersen, "Beam Loading Aspects of TRIUMF KAON Factory FR Systems", TRI-DN-85-15 (1985).

ANALYSIS OF THE FEEDBACK SYSTEM USED TO DAMP LONGITUDINAL QUADRUPOLE-MODE BUNCH OSCILLATIONS

S. Sakanaka and T. Obina, Photon Factory, High Energy Accelerator Research Organization (KEK),
1-1 Oho, Tsukuba, Ibaraki 305-0801, Japan

Abstract

Longitudinal quadrupole-mode oscillations of the electron bunches sometimes limit the beam quality in storage-ring FEL's or in other storage rings. Such oscillations can be damped by using a feedback system. In this paper, we analyze how the feedback system damps the longitudinal quadrupole oscillations. We also present a result of the feedback test experiment, which was carried out at the KEK Photon Factory.

INTRODUCTION

In high-intensity storage rings for free-electron lasers (FEL's) or for particle factories, higher-order bunch oscillations sometimes limit the ring performance. Problems due to longitudinal quadrupole-mode oscillations have been reported in the Super-ACO under FEL experiments [1] or in the DAΦNE Φ-factory [2]. Such quadrupole-mode oscillations can be damped by using a feedback system [1]. We analyze in this paper how the longitudinal feedback can damp the quadrupole oscillations. We limit our analysis to a single-bunch case, assuming that a single bunch is made up of two macroparticles. An approximate expression for describing damping oscillations is then derived. This analysis will be useful for understanding the feedback mechanism for the quadrupole oscillations, although its effectiveness has been reported. The same analysis can be used to understand the feedback damping of a π-mode coupled-bunch oscillation in a two-bunch system, where we assume that two macroparticles are stored in separate rf buckets.

FEEDBACK MECHANISM

Detection of Quadrupole Oscillation

A typical feedback system for damping the longitudinal quadrupole oscillations is shown in Fig. 1. We suppose that a single bunch is made up of two point-like macroparticles, each of which executes synchrotron oscillation having an opposite phase to each other. This situation is illustrated in Fig. 2. Let τ_1 and τ_2 be the time advances of these macroparticles, which are relative to the synchronous particle, and δ_1 , δ_2 be the relative energy deviations, respectively. Small-amplitude synchrotron oscillations for these particles are then approximately described by

$$\tau_1(t) = r(t) \cos[\omega_s t + \psi(t)], \quad (1)$$

and $\tau_2(t) = -\tau_1(t)$, where ω_s is the synchrotron-oscillation frequency. We assume that the amplitude $r(t)$ and the phase $\psi(t)$ vary slowly with time. When each particle has an equal charge of $q_b/2$, the beam current is given by

$$i_b(t) = (q_b/2) \sum_{n=-\infty}^{\infty} [\delta(t - nT_0 + \tau_1) + \delta(t - nT_0 + \tau_2)], \quad (2)$$

where $\delta(t)$ is the delta function and T_0 is the revolution time, respectively. Using Poisson's sum formula, it

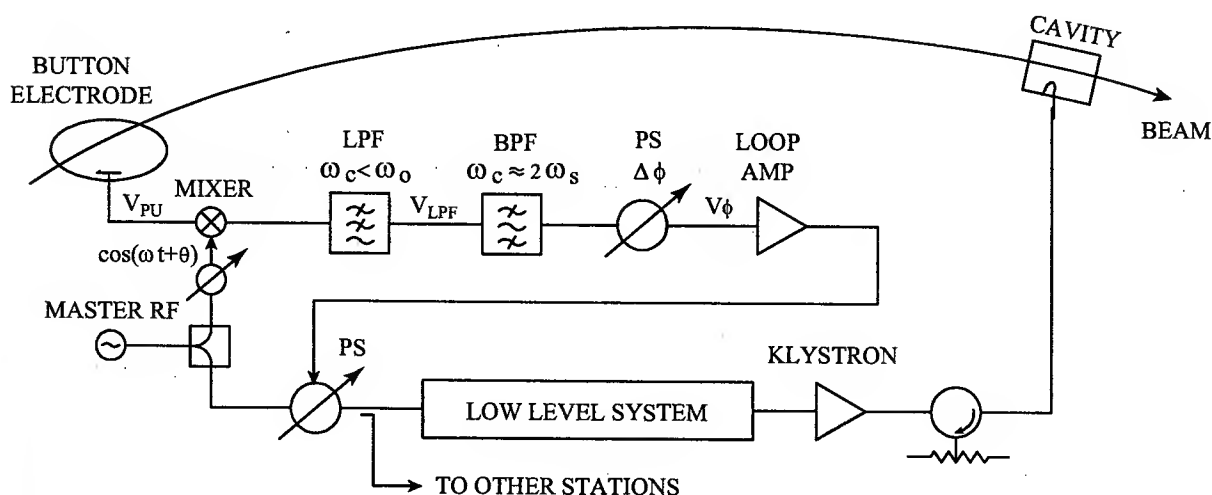


Figure 1: Typical feedback system for damping longitudinal quadrupole oscillations.

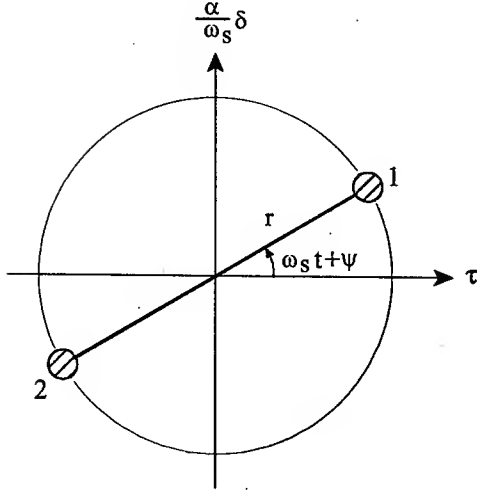


Figure 2: Two macroparticles in the longitudinal phase space.

follows

$$i_b(t) = I_0 \sum_{p=-\infty}^{\infty} \sum_{m \text{ even}} i^m J_m(p\omega_0 r) e^{i(p\omega_0 + m\omega_s)t + im\psi}, \quad (3)$$

where I_0 is the average beam current and $\omega_0 = 2\pi/T_0$ is the angular revolution frequency, respectively. When the frequency response (transfer function) for a pick-up electrode is given by $H(\omega)$, the output voltage from the electrode is given by

$$V_{PU}(t) = I_0 \sum_{p=-\infty}^{\infty} \sum_{m \text{ even}} i^m J_m(p\omega_0 r) H(p\omega_0 + m\omega_s) e^{i(p\omega_0 + m\omega_s)t + im\psi}.$$

In order to detect the phase oscillations, we multiply this signal by a distributed signal from a master rf oscillator:

$$V_{LO} = \cos(\omega_{rf}t + \theta), \quad (4)$$

where the ω_{rf} is an rf frequency, and the θ is a certain phase angle which is adjusted later. Selecting low-frequency ($\omega < \omega_0$) signals using a low-pass filter (LPF), we have

$$V_{LPF}(t) = (I_0/2) \sum_{m \text{ even}} i^m J_m(h\omega_0 r) \times [H(h\omega_0 + m\omega_s) e^{-i\theta} + H^*(h\omega_0 - m\omega_s) e^{i\theta}] e^{im(\omega_s t + \psi)}, \quad (5)$$

where $h = \omega_{rf}/\omega_0$ is the harmonic number, and the relation $H(-\omega) = H^*(\omega)$ was used. In most cases, we can think that the $H(\omega)$ is nearly constant ($\approx H_0 e^{i\theta_0}$) within a narrow frequency range of $|\omega - h\omega_0| \ll \omega_0$. We can then approximate eq. (5) by

$$V_{LPF} \approx I_0 H_0 \cos(\theta - \theta_0) \sum_{m \text{ even}} i^m J_m(h\omega_0 r) e^{im(\omega_s t + \psi)}. \quad (6)$$

In order to maximize the quadrupole-oscillation ($m=2$) signal, we adjust a phase angle θ of the local rf signal, so that $\cos(\theta - \theta_0) = -1$ holds. This can be experimentally done by adjusting a DC level in the V_{LPF} to its minimum value.

Next, we input the above signal to a bandpass filter (BPF) which can pass the frequency component around the frequency of $2\omega_s$, and then, apply a phase shift of $\Delta\phi$ using an electrical phase shifter. The output signal is given by

$$V_\phi = 2I_0 H_0 J_2(h\omega_0 r) \cos(2\omega_s t + 2\psi + \Delta\phi). \quad (7)$$

After amplification by G_0 -times, we apply this feedback signal to a phase shifter, which is used to modulate the phase of an rf accelerating voltage. When the amplitude r is small ($h\omega_0 r \ll 1$), we can approximate $J_2(x)$ by $x^2/8$. Then, the phase modulation is approximately given by

$$\phi_m(t) \approx Gr^2(t) \cos(2\omega_s t + 2\psi + \Delta\phi), \quad (8)$$

with a feedback gain given by

$$G = G_0 I_0 H_0 (h\omega_0)^2 / 4. \quad (9)$$

Damping quadrupole oscillation by feedback

When we apply a small phase modulation (ϕ_m) at a frequency of about $2\omega_s$, the synchrotron oscillation of a single macroparticle is approximately described by

$$\ddot{\tau} + 2\lambda\dot{\tau} + \omega_s^2(1 + \phi_m \cot \phi_0)\tau = 0, \quad (10)$$

where λ is the radiation damping rate, ϕ_0 is the synchronous phase ($\cos\phi_0 = U_0/eV_c$), ϕ_m is given by eq. (8), and the dot denotes the differentiation with respect to time. Here, we have ignored a less-important term of $\phi_m \omega_s^2/\omega_{rf}$ on the right hand side.

We can see that if the τ_1 for one of the macroparticles follows eq. (10), the other τ_2 automatically follows the same equation. We assume that the solution of eq. (10) is approximately given by eq. (1), which gives the first-order approximation by neglecting higher-frequency terms. Then, we substitute eq. (1) into eq. (10), and leave the terms having a fundamental frequency of ω_s . Because both the r and the ψ are assumed to be slowly varying functions of time, we omit higher-order terms of $\dot{\psi}$, \dot{r} and λ . We then have

$$\dot{r} + \lambda r + kr^3 \sin \Delta\phi = 0, \quad (11a)$$

$$r\dot{\psi} - kr^3 \cos \Delta\phi = 0, \quad (11b)$$

with $k = (\omega_s G \cot \phi_0) / 4$. Integrating eq. (11a), we obtain a solution for the r :

$$r(t) = \frac{r_0 e^{-\lambda t}}{\sqrt{1 + \frac{k r_0^2 \sin \Delta \phi}{\lambda} (1 - e^{-2\lambda t})}}, \quad (12)$$

where $r_0 = r(0)$ is the initial condition. When the feedback gain is zero ($k = 0$), the above equation (12) reduces to

$$r(t) = r_0 e^{-\lambda t}, \quad (13)$$

which gives the radiation damping effect. When we apply a negative feedback ($\sin \Delta \phi > 0$), we can enhance the damping effect of the oscillation. A typical damping of the oscillation is shown in Fig. 3. The feedback is most effective when the phase shift is adjusted to be $\Delta \phi = \pi/2$. In this case, the above eq. (11b) gives

$$\psi(t) = \psi(0), \quad (14)$$

which means that there is no change in the oscillation phase. Note that somewhat unfamiliar expression in eq. (12) comes from the fact that the feedback signal is proportional to the square amplitude of the oscillation.

In the above analysis, we have assumed that there are two macroparticle in the same rf bucket, and that each macroparticle oscillates out-of-phase to each other. This analysis still holds under a different situation where two macroparticles are stored in different rf buckets. In this case, two macroparticles represent two bunches which oscillate out-of-phase to each other, indicating a π -mode coupled-bunch oscillation. Then, we can show that the π -mode coupled-bunch oscillation in this two-bunch system can be damped by using the same feedback system. This damping mechanism is essentially the same as the one used in the SLC damping ring [3]. Note that in case of the π -mode coupled-bunch oscillation, one can detect the oscillation more effectively by detecting $\pm \omega_k$ sidebands ($m=1$ mode) beside odd revolution harmonics, or by detecting each bunch oscillation independently, rather than by detecting $\pm 2\omega_k$ sidebands beside even revolution harmonics as shown in this paper.

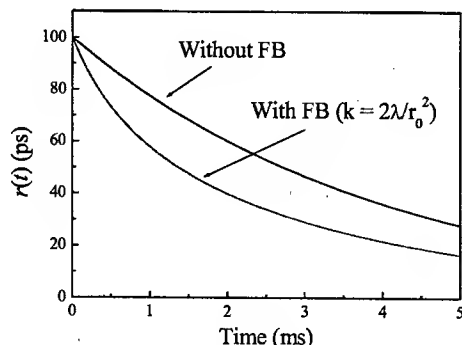
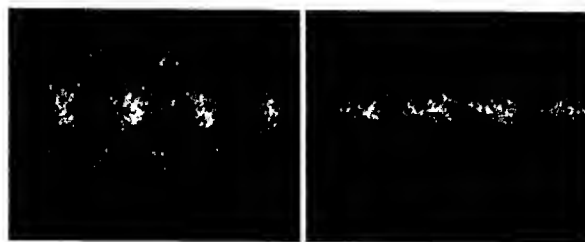


Figure 3: Calculated damping effect due to the feedback. Assumed $r_0 = 100$ ps, $\lambda = 255$ s⁻¹, and $\Delta \phi = \pi/2$.

EXPERIMENT

We carried out a feedback test experiment in the 2.5-GeV Photon Factory storage ring at KEK. While storing a single bunch of electrons, we artificially induced

longitudinal quadrupole oscillations by exciting one of four rf cavities at a frequency of about $(\omega_{rf} - 2\omega_s)$. Then, we tried to damp induced oscillations using a feedback system which is shown in Fig. 1. Most of the electronics were reuse of our old bunch-by-bunch feedback system [4]. Longitudinal bunch oscillations were observed using a dual-sweep streak camera. The results are shown in Fig. 4. The quadrupole oscillation was considerably reduced by using this feedback, as shown in Fig. 4(b).



(a) Without feedback. (b) With feedback.

Figure 4: Longitudinal quadrupole oscillations without and with the feedback, respectively, which were observed using a dual-sweep streak camera. Vertical axis: longitudinal bunch profile (1 ns full scale), horizontal axis: slow sweep (100 μ s full scale). Beam current: 10 mA.

CONCLUSION

A feedback mechanism, which can damp longitudinal quadrupole-mode oscillations, was analyzed. It was shown that small-amplitude oscillation follows eq. (11), and its solution (12) gives the damping oscillation under both the feedback and the radiation damping. This analysis will be useful for designing such feedback systems, as well as for understanding its operations. Additionally, it was also shown that a π -mode coupled-bunch oscillation in two-bunch systems can be damped by using the same feedback system.

REFERENCES

- [1] M. Billardon, R.J. Bakker, M.E. Couprie, D. Garzella, D. Nutarelli, R. Roux, F. Flynn, "Operation of the Super-ACO Free Electron Laser with a Feedback Damping Quadrupolar Coherent Synchrotron Oscillation", EPAC'98, Stockholm, 1998, p. 679.
- [2] A. Drago, A. Gallo, A. Ghigo, M. Zobov, "Longitudinal Quadrupole Instability in DAΦNE electron ring", EPAC 2002, Paris, 2002, p. 239.
- [3] J.D. Fox and P. Corredoura, "Amplification and Damping of Synchrotron Oscillation via a Parametric Process," EPAC'92, Berlin, 1992, p. 1079.
- [4] S. Sakanaka, A. Ueda, K. Haga, H. Kobayakawa, "A Longitudinal Feedback System used under Low-Energy 4-Bunch Operation of the Photon Factory Storage Ring," Proc. 9th Symposium on Accelerator Science and Technology, Tsukuba, Aug. 25-27, 1993, p. 395.

TWO-BUNCH ORBIT CORRECTION USING THE WAKE FIELD KICK

M. Satoh[†], T. Suwada, K. Furukawa, Y. Ogawa, M. Kikuchi and H. Koiso
Accelerator Laboratory, KEK, Ibaraki 305-0801, Japan

Abstract

In the KEKB injector linac, a two-bunch acceleration scheme has been used for doubling the positron injection rate to the KEKB Low-Energy-Ring (LER). In this operation mode, the multi-bunch transverse wake field caused by the first bunch affects the beam orbit of the second bunch. In the KEKB linac, an orbit correction method based on the average minimum of two-bunch orbits has been adopted, and has worked stably. However, a new two-bunch orbit correction method is strongly required to make the loss of charge less. We propose a new two-bunch orbit correction method based on a local bump method. In this scheme, some local bumps are intentionally constructed in a low-energy area. Adjusting the local bump height can control the wake field strength affecting the second bunch. In this paper, we report on the results of a preliminary beam test to confirm that this new method is useful.

1 INTRODUCTION

The KEKB project started in 1994 to investigate CP-violation in B-meson decays with the double-ring collider [1]. It consists of 8-GeV electron and 3.5-GeV positron storage rings. The beam-injection efficiency from the injector linac to the ring should be boosted as high as possible since the performance of the experiment depends strongly on the integrated luminosity. In order to achieve efficient full-energy injection, the original 2.5-GeV electron linac was upgraded up to 8-GeV, while enforcing the acceleration gradient by a factor of 2.5 and by extending the length of the linac. The layout of the KEKB linac is shown in Fig. 1. Because of the site limit, two linacs with 1.7-GeV and 6.3-GeV were combined using a 180-degree bending magnet system to form a J-

shape linac. In the J-arc section, the beam optical parameters are determined so that the achromatic and isochronous conditions are fulfilled [2].

A beam starting from an electron gun passes two subharmonic bunchers (SHB1: 114.24 MHz and SHB2: 571.2 MHz) and an S-band bunching section (2856 MHz) to accomplish a single-bunched beam with a bunch width of about 10 ps (FWHM). After acceleration to the end of sector B (1.5-GeV), it enters into the J-arc section. It is then re-accelerated either to the end of the linac (8.0-GeV) or to the positron production target (3.3-GeV), depending on the operation mode. In order to obtain high-intensity positrons, a large amount of primary electrons should be transported to the positron production target. The primary electron beam was designed to be 10 nC per bunch to produce 3.5-GeV positrons with 0.64 nC. We therefore doubled the bunch number to increase the positron beam intensity per pulse and to halve the injection time [3]. Figure 2 shows the orbit and current status display for two-bunch operation. The bunch interval time must be 96.29 ns, which corresponds to the common period of the frequencies of the linac and the ring.

In the KEKB linac, the orbit correction method, based on the average minimum, has been successfully used for daily operation. The orbit distortion causes beam loss, especially in the J-arc section. Using this method, the orbit correction is carried out so that the average orbit distortion of both bunches can be minimized. Figure 2 shows the orbit and charge status panel in two-bunch operation. This example shows that the charge loss of the second bunch is larger than that of first bunch because of a deterioration of the second bunch orbit. In order to avoid such beam loss due to orbit distortion and to obtain more high-intensity positrons, a new orbit correction method is

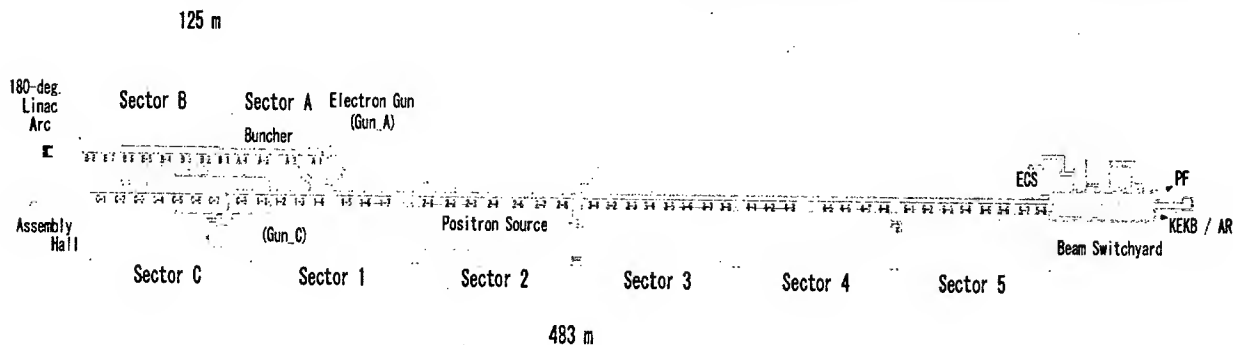


Figure 1: Layout of the KEKB injector linac. The J-arc section combines two straight sections.

[†]masanori.satoh@kek.jp

strongly required.

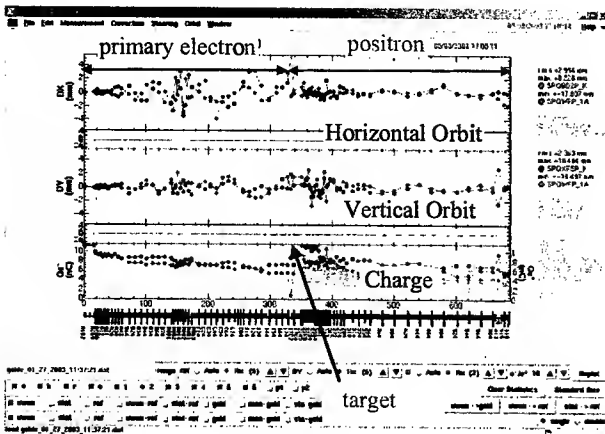


Figure 2: Orbit and charge status panel for the two-bunch operation mode. Top and middle show the horizontal and vertical orbit respectively. Bottom shows charges of each bunch. Blue and light green indicate first and second bunches.

2 TWO-BUNCH ORBIT CORRECTION METHOD

In a new two-bunch orbit correction method, which we have proposed, the beam position of first bunch is corrected by using the wake field kick of first bunch. When the first bunch beam traverses the off-center of an accelerating structure, the long-range transverse wake field caused by first bunch kicks the second bunch. Figure 3 shows a schematic drawing of this correction method. If the bump height is adjusted to a suitable value, the orbit of the second bunch can be controlled arbitrarily. If both the beam positions and angles of each bunch can be corrected to zero in a low-energy section, the beam orbit keeps constant in the following beam line. Accomplishing such a high-quality orbit correction will

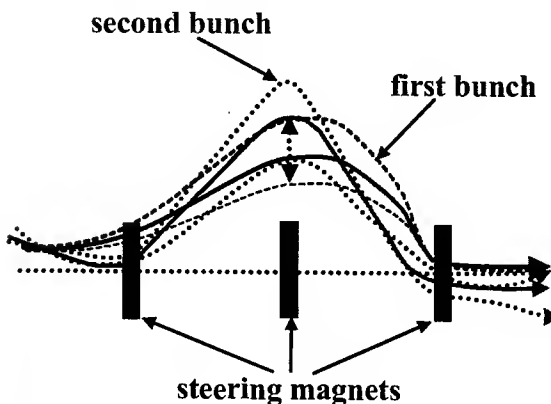


Figure 3: Schematic drawing of a new two-bunch orbit correction method using the transverse wake field kick caused by first bunch.

result in reducing the charge loss in the J-arc section of the KEKB injector linac.

3 RESULTS OF BEAM TEST

In this section, the results of a beam test are presented. Only a horizontal beam-orbit correction was carried out in this experiment. The procedure of this test is as follows:

- Construct a first local bump at a beam position monitor (BPM) where the orbit difference between first and second bunch is becoming larger. Adjust its bump height so that the orbit difference is minimized at the downstream side of the bump.
- Step (a) will deteriorate the beam orbits of each bunch further at the downstream side. With keeping the first bump, construct a second local bump downstream of the previous bump. Then, iterate the above procedures in order to squeeze out the orbit difference toward the downstream side of the linac, and minimize the beam position and angle of each simultaneously.

If the orbits of each bunch are corrected in Sector A or B without an optics mismatch, it can be expected that the charge loss in the J-arc section will be decreased.

Figure 4 shows the software panel for constructing a local bump. This software can construct a local bump at an arbitrary BPM position in the KEKB linac. In this beam test, three local bumps were successively constructed for an orbit correction. In Fig. 4, local bumps (1), (2) and (3) were constructed by changing the bump heights of the SPA11, SPA32 and SPB14 BPMs, respectively. First of all, the bump height of SPA11 was set to 1 mm, so that the orbit difference would be reduced at SPA32. However, the orbit difference in the downstream area of SPA32 became worse after first bump was constructed. In the next step, in addition to bump (a), a bump height of SPA32 was varied in order to reduce the orbit difference of each bunch downstream of the second bump (b). After the height of the bump (b) was set to 2.5 mm, bump (c) was constructed, while

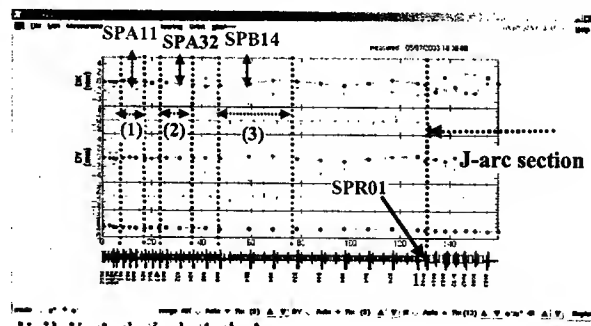


Figure 4: Software panel to construct a local bump. The dotted plot shows the range of local bumps. Three local bumps are successively contracted.

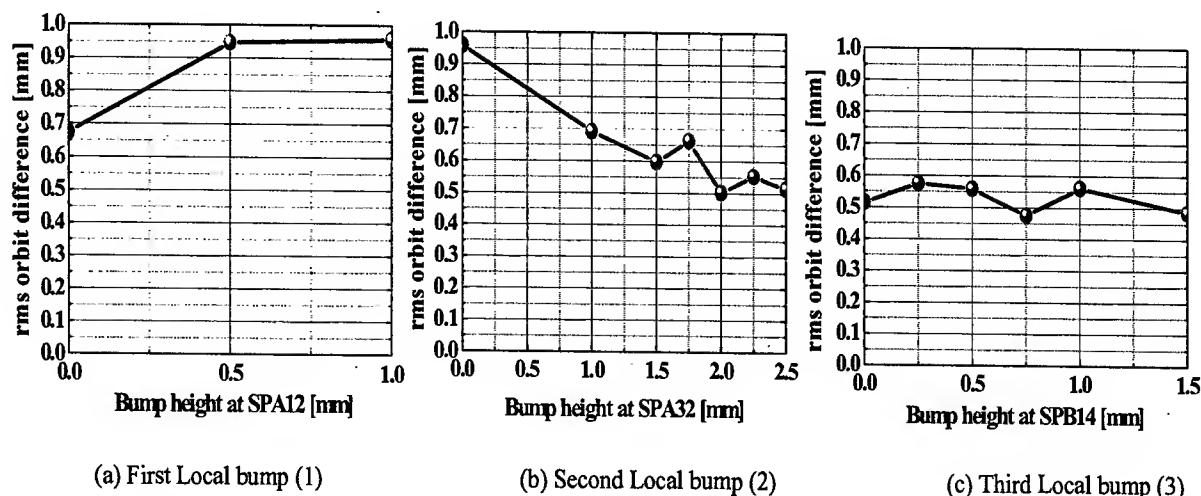


Figure 5: Rms orbit difference between first and second bunches versus bump height. The rms orbit difference calculated from the all BPMs between SPA12 (first bump position) to SPR01 (entrance of J-arc section). Three local bumps were constructed successively. In the case of (c), therefore, three local bumps were simultaneously constructed.

bumps (a) and (b) were kept.

Figure 5 shows the results of the rms orbit differences between first and second bunches. The rms orbit difference was calculated from all of the BPMs between SPA12 (first bump position) to SPR01 (entrance of J-arc section). These three local bumps were constructed successively. In the case of (c), therefore, three local bumps were simultaneously constructed. The result of varying the bump height of first bump (1) is plotted in Fig. 5-(1). The rms orbit difference is increased after the bump is constructed because the orbit at the further downstream of SPA32 is deteriorated. Increasing the bump height of the second bump (2) can reduce the orbit difference, as shown in Fig. 5-(b). Figure 5-(c) shows that varying the bump height of bump (3) cannot adjust the rms orbit at the downstream side. The beam energy in Sector B is higher than that in Sector A. For that reason, the long-range wake field of first bunch cannot fully kick the second bunch. In addition, bump (3) was constructed in a relatively long area where three different types of accelerating structures are used for compensating the transverse wake field.

With regard to the beam loss after an orbit correction, the transmission rate decreased to a great degree. To recover the transmission rate, we tried optics matching. However, the emittance could not be measured, since the large emittance growth prevented a wire scanner measurement. If the bump positions are selected by those betatron phases, some suitable bump combinations will be found without any emittance growth.

4 SUMMARY AND FUTURE PLAN

A new orbit correction method was proposed for two-bunch operation in the KEKB injector linac. This method uses the long-range transverse wake field kick caused by the first bunch. To confirm this correction

method, a preliminary beam test was carried out in the KEKB injector linac. The results of a beam test shows that this correction method can be useful for a two-bunch orbit correction when the bump positions are suitably selected.

On the other hand, the emittance growth due to a local bump also caused an optics mismatch between the straight and J-arc sections. It became an origin of charge losses. In order to avoid such emittance growth, constructing an additional bump at the 180-degree phase difference is very effective. With all of these conditions fulfilled, the two-bunch beam orbit can be corrected without any emittance growth. Therefore, this new orbit correction method can be used for daily operation. A more detailed beam test and a numerical simulation will be carried out in the near future. We will present its result, elsewhere.

ACKNOWLEDGMENTS

The authors would like to thank the members of LCG (Linac Commissioning Group) for their useful discussions and advice. We would like to thank the linac operators for their great help in our experiments.

REFERENCES

- [1] H. Koiso et al., "Present Status of the KEKB B-Factory", EPAC2002, Paris, France, June 3-7, pp.2772-2773.
- [2] T. Kamitani et al., "Beam Optics Matching in the KEKB Injector Linac", APAC'98, Tsukuba, Japan, March 23-27, 1998. pp.429-431.
- [3] Y. Ogawa et al., "Two-Bunch Operation of the KEKB Linac for Doubling the Positron Injection Rate to the KEKB Ring", APAC2001, Beijing, China, September 17-21, 2001, pp.112-114.
- [4] K. Furukawa et al., "Beam Feedback Systems And BPM Read-Out System for the Two-Bunch Acceleration at the KEKB Linac", ICALEPCS2001, San Jose, U.S., November 27-30, 2001, pp.266-268.

NEWLY DESIGNED FIELD CONTROL MODULE FOR THE SNS*

A. Regan[#], K. Kasemir, S. Kwon, J. Power, M. Prokop, H. Shoaee, M. Stettler, LANL, Los Alamos, NM 87544 USA; L. Doolittle, A. Ratti, LBL, Berkeley, CA 94720 USA; M. Champion, ORNL, Oak Ridge, TN 37831; C. Swanson, Alpha Cad, Inc. Alpharetta GA USA

Abstract

The low-level RF (LLRF) control system for the Spallation Neutron Source has undergone some recent hardware changes. The intended Field and Resonance Control Module (FRCM) design has been re-vamped to minimize functionality and ease implementation. This effort spans a variety of disciplines, and requires parallel development with distinct interface controls. This paper will discuss the platform chosen, the design requirements that will be met, and the parallel development efforts ongoing.

OVERVIEW OF THE NEW FCM

Performance specifications were eased late last year for the LLRF control system for SNS. Physics simulations indicated that the field control requirement could be reduced from from $\pm 0.5\%$, $\pm 0.5^\circ$ to $\pm 1.0\%$, $\pm 1.0^\circ$. In addition required functions were changed such that on-board processing for resonance control was moved to the crate controller (IOC), as well as feedforward table update and access; fewer RF channels were required (no need to provide for possible beam information via a beam diagnostics channel); no real time data link needed between the control system and the operators; and much less memory per channel was deemed appropriate. By moving the iterative learning controls onto the IOC as well, we completely eliminated the need for DSPs on the module. A collaborative effort was established between Lawrence Berkely, Los Alamos, and Oak Ridge national labs in order to develop a control system that meets these specifications [1].

Due to these relaxed system performance specifications, and a new staged approach to implementation and integration of control system functions, the original complicated, meet-all-performance-specifications-at-once FRCM de-sign has been greatly simplified. The new Field Control Module (FCM) is still a basic VXIbus-based module with multiple daughter cards. The infrastructure for a VXIbus-based RF Control System (RFCS) was already in place at the SNS: VXIbus crates had been purchased and other modules within the system are VXIbus, so it only made sense to remain consistent. However the new FCM has three new daughter cards which minimize the functionality of the FCM; and the implementation of the firmware is in a staged approach where progressive phases will be achieved as the accelerator grows from one cavity to many and functional requirements of the RFCS increase [1]. A block diagram of the module hardware is given in figure 1.

*Work supported by the Office of Science of the US Department of Energy
#aregan@lanl.gov

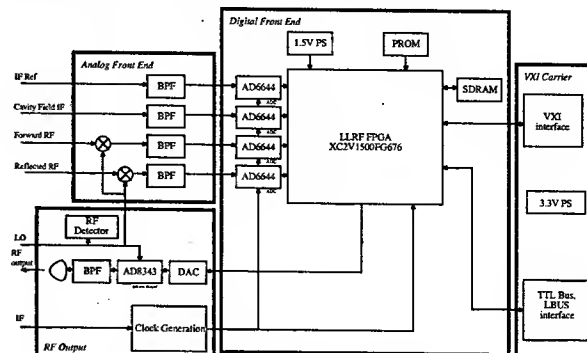


Figure 1: FCM Block Diagram

PRINTED CIRCUIT CARDS

The basis for the re-designed FCM is the successful SNS Diagnostics PCI-based electronics, specifically the Beam Position Monitors (BPMs) [2]. In that vein, we attempted to make use of as much of the foundation provided by the Diagnostics BPMs as possible. The BPMs have an Analog Front End daughter card manufactured by Bergoz Instrumentation of France. Likewise, we specified a very similar LLRF AFE for use on the FCM. The BPMs have a Digital Front End (DFE) processing card. We, too, utilize a DFE for providing the analog-to-digital conversion of the input RF and IF signals, as well as for providing an interface to the host computer. In this case, however, the LLRF system continues to utilize an MVME2101-1 slot zero controller for its CPU. Unlike the diagnostic BPM, the LLRF system requires an RF output for driving the correctly controlled signal to the klystron, hence another daughter card: the RF Output (RFO).

Two primary reasons drove us to utilize the BPMs as a foundation for the new FCM. The first is the similarity between the BPM AFE and the requirements for the LLRF AFE. By essentially removing two downconverting stages for IF channels on the LLRF AFE, and eliminating extra diagnostic switches on the BPM AFE, the design for the LLRF AFE was complete. Therefore with minimal change, we incurred very little design risks and expected to achieve performance expectations on the first pass. Secondly, by using the PCI mother board as a test platform for the newly designed LLRF daughter cards, we took advantage of the existing board tests already written for testing the BPM performance, thereby reducing extensive test development time. LabVIEW programs have already been written for easy measurement of channel isolation, ADC performance analysis and the like.

AFE

An AFE daughter board photo is shown in figure 2.

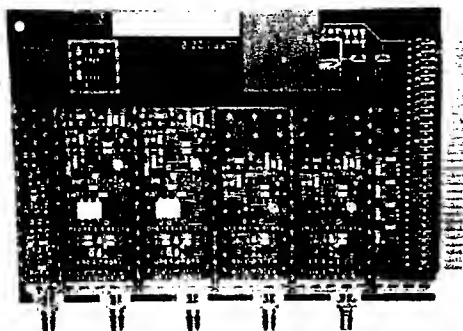


Figure 2: LLRF Analog Front End daughter board from Bergoz Instrumentation.

The key requirements for the AFE are channel to channel isolation and dynamic range (30 dB). Bergoz was able to meet all specifications on the first prototype board, with the exception of isolation on the IF channels. A simple bypass capacitor and filtering scheme on some power lines, however, solved the problem.

DFE

A photo of the DFE is shown in figure 3.

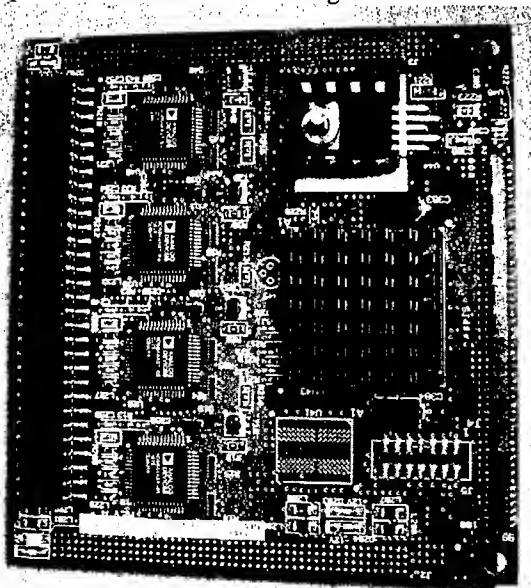


Figure 3: SNS LLRF Digital Front End daughter board.

The chief component of the DFE is a Xilinx Virtex-II XC2V1500FG676, shown in the photograph with its large finned heat sink on top. The DFE essentially receives the analog IF signals from the AFE and translates them to digital signals for processing through Analog Devices AD6644 14-bit ADCs. The FPGA provides the path through which the feedback control algorithms are implemented. In addition, it is the key component that

provides an interface between the control system and the operator: registers, history buffers, data multiplexers...

RFO

A photo of the RFO is shown in figure 4.

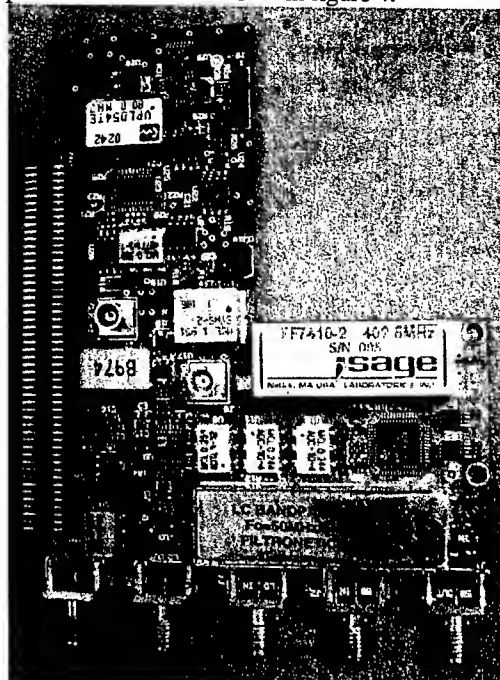


Figure 4: RF Output daughter board.

The primary purpose of the RFO is to translate the 50 MHz baseband control signals from the Digital Front End (DFE) from digital to analog signals and then upconvert them to the RF frequency. In addition it is the home for the phase locked loop clock generation circuitry, which is the basis for all of the coherent sampling on the module. Essentially the RF Output board core components are a 14-bit DAC, an upconverting Analog Devices active mixer AD8343, and some filters. However, it also acts as the distribution center for the 50 MHz Reference and the LO required by the other daughter cards

The key requirements for the RFO is its spectral response, dynamic range (30 dB from -20 to +10 dBm), and clock generation. Important to the success of the FCM is its ability to maintain tight synchronization between the external 50 MHz IF reference, and the on-board generated 40 MHz ADC clock and the 80 MHz FPGA clock. Larry Doolittle built and tested such a circuit for use on his Berkeley LLRF system [3], and it works well. This same circuit, reliant on the Analog Devices ADF4001 clock generator chip, is now in use on the RFO as well as the SNS Diagnostic BPM boards. Initially there was concern over jitter in the clock system. However, white noise averages out rather nicely on the time scales of the closed-loop-bandwidth of the cavity. Therefore a jitter goal of 2 or 3 ps RMS from 2 kHz to 40 MHz is perfectly reasonable. The low frequency, DC to 2 kHz jitter is taken out by the phase locked-loop, although here the performance is limited by the PLL phase

comparator, which itself presumably has a $1/f$ term. The software and phase reference line should be able to correct that error down to DC.

MOTHER BOARD

The VXIbus mother board is very basic. Its primary purpose is to provide a platform for the AFE/DFE/RFO combination, and to provide for communication with the VXIbus backplane. In addition it receives system timing signals from the Brookhaven Laboratory-designed Timing Module (model V124S) and translates them to the DFE and VXI backplane for system synchronization.

Figure 5 shows the fully populated Field Control Module: a mother board VXI carrier with mounted AFE, DFE, and RFO. Interconnect cables are not mounted, neither is the front panel. A front-panel mounted blind-mate sub D housing is used to complete the cable routing from the daughter cards to the front panel. The board is a single-wide VXIbus module.

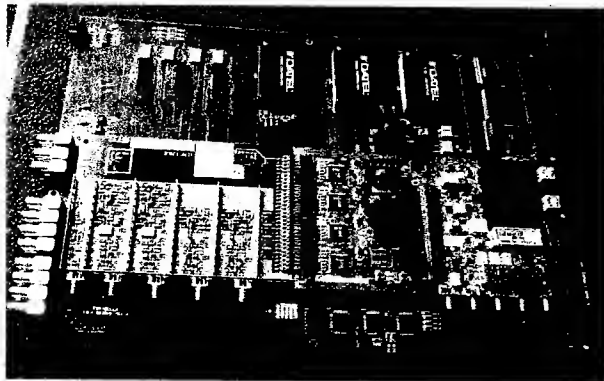


Figure 5. Field Control Module

FIRMWARE

The foundation for all of the phase I control algorithms was written in verilog for a 12-bit system by Larry Doolittle [3]. In order to produce a control system which has a common language that can be maintained by more people, these algorithms have been converted to VHDL by Craig Swanson. The hardware wrapper is also written in VHDL by Matt Stettler. A firmware specification was written at the outset of the conversion process in order to make sure that the interfaces are complete and various people can all work on the same end product. Close communication between the firmware designers has helped close any gaps. The firmware is written in a modular format and test benches have been written for a ModelSim simulation of each step.

As previously reported [4,5], we have performed extensive modeling of the SNS RF control system. This model has been developed in MATLAB/Simulink. Part of the validation of the overall firmware design is to utilize the MATLAB model to generate input test vectors for the DFE's FPGA VHDL code. Then the FPGA firmware will be simulated with ModelSim using the given input test vectors and will generate outputs. The ModelSim outputs

will be compared to MATLAB/Simulink outputs. Any discrepancies between the two will be analyzed and used to modify the firmware code accordingly. This work is in progress now.

While the firmware is being developed, a register map has been created and provided for EPICS development. Because this system utilizes much of Larry's code as well as has the same inputs and output, much of the EPICS screen development and some of the scripts that have been utilized in the past are still applicable.

WHERE WE ARE TODAY

At this point in time we are in the process of validating each of the daughter boards individually. The AFE and mother board have been certified. Design validation of the RFO is nearly complete. Tests on the RFO are being run via a DFE on a Diagnostics PCI mother board, and hence that interface is also being worked. The DFE hardware works, and the FPGA code is more than 70% complete and simulated. We intend to integrate the module in the lab with a dummy cavity and the EPICS global controls, and will be given a chance to try it out on a real DTL cavity at SNS this summer.

REFERENCES

- [1] M. Champion, "The Spallation Neutron Source Low Level RF Control System," these proceedings.
- [2] J. Power, et al, "Beam Position Monitors for the SNS Linac," PAC'01, Chicago, IL, June 2001.
- [3] L. Doolittle, et al, "The SNS Front End LLRF System," Linac 2002, Gyeongju, Korea, August 2002.
- [4] Kwon, S.I. and Regan, A. "Control System Analysis for the Perturbed Linear Accelerator RF System," Los Alamos National Laboratory Technical Report LA-UR-02-2100, 2001.
- [5] Kwon, S.I., et al, "Uncertain System Modeling of the SNS RF Control System," PAC'01, Chicago, IL, June 2001.

COMMISSIONING RESULTS OF THE FAST ORBIT FEEDBACK AT THE ALS*

C. Steier[†], A. Biocca, E. Domning, S. Jacobson,
G. Portmann, T. Scarvie, E. Williams, LBNL, Berkeley, CA 94720, USA

Abstract

A new fast global orbit feedback system has been designed at the ALS and is in commissioning since last September. The system has two main purposes. The first is to meet the demands of some users for even improved short term orbit stability. The second is to enable the use of more sophisticated insertion device compensation schemes (e.g. tune, beta-beating, coupling) for fast moving insertion devices like elliptically polarizing undulators, without deteriorating the orbit stability. One feature of the fast orbit feedback (with 1 kHz update rate) is the use of standard computer and networking equipment.

INTRODUCTION

The ALS is a third generation synchrotron light source and has been in operation since 1993. Many of the experiments carried out nowadays require very high resolution or measure very small asymmetries and therefore require extremely high orbit stability. On the other hand there are new sources of orbit distortions created with the installation of additional (fast moving) insertion devices [1] and the implementation of more and more feedback or feed-forward loops (e.g. optics and coupling compensation).

Over the years there have been continuous upgrades of the orbit stability at the ALS, by improving the passive stability, using feed-forwards or slow (and most recently fast) feedbacks. One of the improvements in the last year was the installation of new chicane magnets. The second was the inclusion of additional stable, high-resolution beam position monitors around the center bend magnets, and the third were improvements in the slow orbit feedback algorithm. Last, there was the initial commissioning of a fast orbit feedback system.

New Chicane Magnets

The chicane magnets at the ALS are used to allow the use of two short (2 m) undulators in a long (5 m) straight section feeding two independent beamlines. The original set of chicane magnets in one straight section were iron core magnets and unfortunately they had larger than acceptable hysteresis and low bandwidth. To solve this problem a new low hysteresis chicane magnet was constructed based upon a novel design (see Fig. 1). The new chicane consists of permanent magnet cylinders and air core coils.

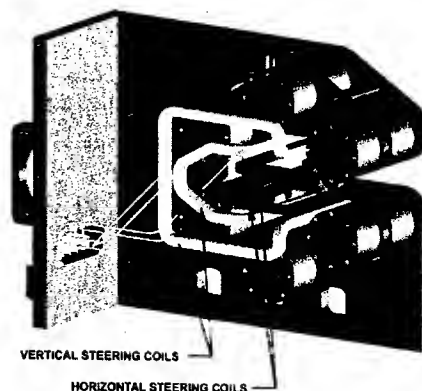


Figure 1: New permanent magnet/air coil chicane magnets.

Now the field integral errors of the fast moving APPLE-II type undulators can be corrected more locally, allowing them to shift from left to right circular polarization with significantly less than 1 μ rad local angular distortion. Last year two of these new chicane magnets were installed in the ALS.

RF-Frequency Feedback

Starting in September 2001, RF frequency feedback was routinely included in the orbit feedback [2]. The orbit feedback now compensates changes in the ring circumference by adjusting the RF frequency once a second. Fig. 2 shows how the ring circumference changed since RF frequency feedback was implemented.

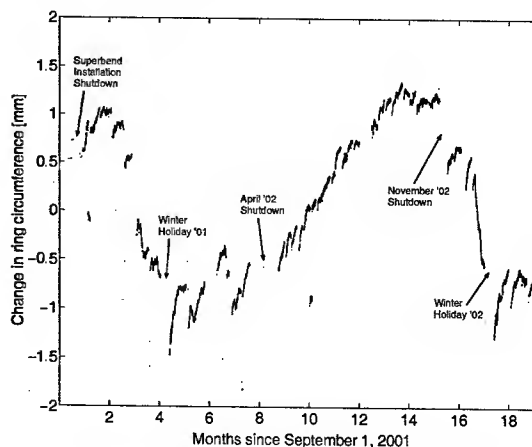


Figure 2: Change in circumference of the ALS over 1.5 years.

What can be seen is that there are substantial circumference variations. Some of the variations are seasonal and are due to temperature and ground water levels. These changes

* This work was supported by the U.S. Department of Energy, under Contract No. DE-AC03-76SF00098.

[†] CSteier@lbl.gov

correspond to a variation of about 3 mm over the year and the variation appears to be cyclic. The ALS circumference changes for example rapidly when the rainy season begins in November (months 3 and 15) which is the dominating external factor influencing the circumference. There are also changes that occur on faster time scales such as changes in the thermal load corresponding to the three daily fills. Frequency analysis shows even smaller effects due to the tides and the daily outside air temperature variations. Using resonant depolarization it was verified that the RF-frequency feedback keeps the beam energy very stable.

There was also continuous further development of the slow orbit feedback system. Of particular note was the inclusion of more stable, high resolution beam position monitors in several arcs. The result was a marked improvement in the orbit stability at some especially sensitive bending magnet beamlines.

FAST GLOBAL ORBIT FEEDBACK

Employing a combination of good passive measures and careful engineering of noise sources like power supplies and the cooling system, the short term closed orbit stability in the ALS fulfills the user requirements up to now. In the range between 0.1 and 500 Hz the integrated closed orbit motion in the insertion device straights is below 2 μm in the vertical plane and about 3 μm in the horizontal plane (one sigma beam sizes at 1.9 GeV at that position are about 23 μm vertical and 300 μm horizontal).

The constant expansion of the ALS creates new sources of closed orbit noise. Elliptically Polarizing Undulators [1] for example require fast focusing and coupling compensation, to minimize their influence on the beam size, which in turn creates fast distortions of the orbit. Other noise sources are active tune/chromaticity compensation schemes, the cryogenics of superconducting magnets or beamlines, etc. To prevent a deterioration of the current orbit stability due to those upgrade projects and ultimately provide a short term submicron orbit stability a fast, global orbit feedback system was designed similar to the approach at several other light sources [3, 4, 5]. The initial goal was to operate at an update rate of up to 1 kHz.

Transfer Function Measurements

In preparation for the commissioning of the fast orbit feedback, many transfer function measurements were carried out. The transfer functions of all power supplies, magnets, vacuum chambers, and BPMs were measured (compare Fig. 3) and the results were put into a Matlab Simulink model of the feedback system.

In addition the noise performance of all components (BPMs, ADCs, DACs, power supplies) was measured. To improve the resolution of the system, the DACs were upgraded to a higher resolution dual DAC system with effectively about 20 Bit of resolution.

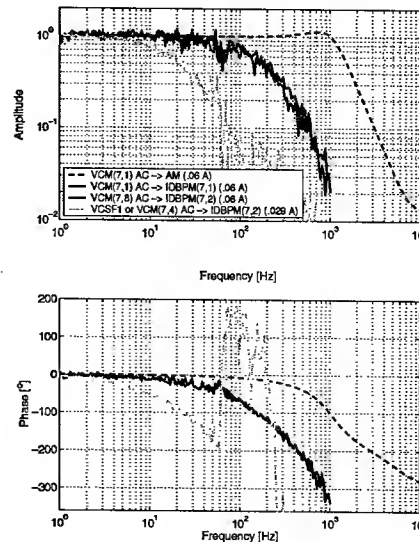


Figure 3: Transfer function of an ALS corrector magnet power supply and combined transfer function of power supply, magnet, vacuum chamber and beam.

Feedback System Layout

With the advent of higher performance networking it is practical to use it directly for medium performance distributed control systems. This system consists of 12 Compact PCI chassis distributed around the ring on a private, switched 100 Mbit/s network. Each chassis handles four BPM inputs and four corrector magnet outputs. Each crate has a timing board to provide the interrupt synchronizing the inputs and outputs of the control algorithm. Initially network packets are used to synchronize these timers. If necessary, there is a backup plan to distribute a precision timing signal to the cards via hardware. More details can be found in [6].

Commissioning Results

The commissioning of the fast orbit feedback started late last year. Initially the system was configured as a single channel local feedback to simplify the optimization. Later it was tested in its full configuration with 24-40 BPMs in each plane and 22 corrector magnets in each plane distributed at 12 distinct locations.

After solving many software and hardware problems a reasonable performance of the system could be achieved, correcting all orbit noise below 15 Hz down to the BPM noise floor (compare Fig 4), without exciting higher frequencies in a significant way (compare Fig 5).

The performance is limited by the fact that it is currently impossible to operate the system reliably with update rates above 700 Hz. At higher rate, the communication becomes unreliable. This effect did not occur in our network benchmarks with a test setup, so we are currently investigating the exact cause. A possible reason is a priority inversion problem with the other EPICS functions running on the same local computers.

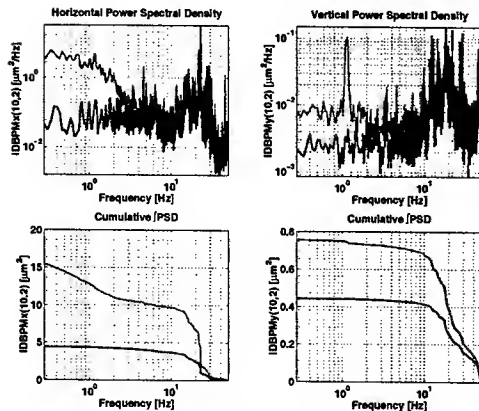


Figure 4: Power spectral density of the closed orbit motion between 0.1 and 50 Hz with the fast orbit feedback in open and closed loop. The measurements were taken with an independent acquisition system connected to a BPM which is not included in the feedback system. At low frequencies the orbit motion is corrected close to the noise floor of the BPMs.

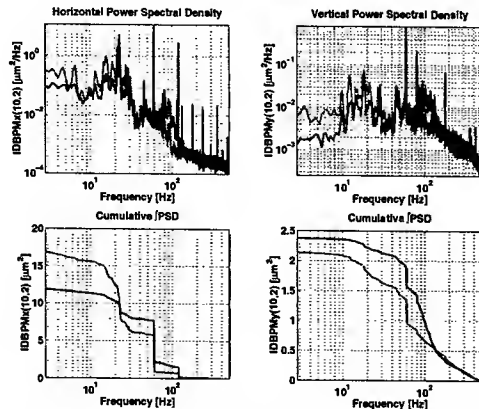


Figure 5: Power spectral density measurement between 1 and 500 Hz. The gain of the feedback changes sign at about 50 Hz and some measurable excitation of orbit oscillations is observed above 100 Hz.

Once the feedback system was operating, we measured closed loop transfer functions, step responses, and disturbance rejection and compared the results with predictions of the Simulink model. The agreement of the measurements and the model predictions is very good (see Fig. 6).

Future Plans

Further work in the commissioning will include improving the controller algorithm, including a notch filter to directly target steady 60 Hz noise, debugging and resolving the communication problems at higher update rate, improving the timing system (which is currently completely network based) and making the slow and the fast feedback system work together.

Planned upgrades for the next year include the switch to faster network (gigabit), use of ADCs with higher speed (which will allow digital filtering to improve the BPM resolution and noise), use of DACs with shorter access times and further improvements to the timing system. There are

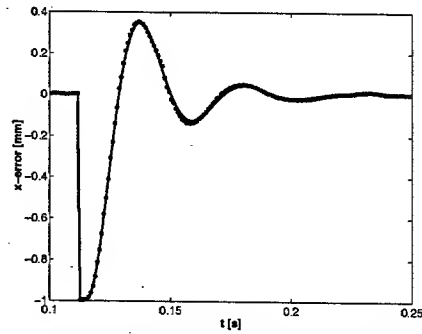


Figure 6: Comparison of the error signal of a measured closed loop stepresponse of the feedback system (dots) with the predictions of the Simulink model (solid line) for the same settings of the PID controller. The PID settings for this example were intentionally chosen to exhibit some oscillatory behaviour.

plans to integrate the slow and fast orbit feedback systems into one system in the long term.

To improve the slow orbit stability it is planned to install monitors to measure the physical location of BPM buttons (pickups placed on invar rods).

SUMMARY AND OUTLOOK

The orbit stability at the ALS has been continually improved. Recent improvements included new chicane magnets for the EPU straights, installation of additional high precision BPMs in several arc sectors, improvements to the slow orbit feedback algorithm and the initial commissioning of the fast feedback system. Even without the fast orbit feedback system, the orbit stability is comparable to the best other light sources. The commissioning of the fast feedback encountered several problems and the performance of the system so far is satisfactory up to about 15 Hz. The current work focuses on solving the communication problems to allow higher update rates. In addition work is spent to make the slow and fast orbit feedbacks cooperate. Once that challenge is solved, the fast feedback in its current state will already provide a significant improvement in orbit stability especially for transient effects of insertion device motion.

REFERENCES

- [1] C. Steier et al., Proceedings of EPAC2000, p. 2343, Vienna, Austria (2000).
- [2] C. Steier et al., Proceedings of EPAC 2002, p. 2103, Paris, France (2002).
- [3] G. Decker et al., Proceedings of DIPAC 2001, p. 177, ESRF Grenoble, France (2001).
- [4] M. Boege et al., Commissioning of the fast orbit feedback at the SLS, these proceedings
- [5] B. Podobodov, et al., Proceedings of PAC 2001, p. 396, Chicago (2001).
- [6] C. Steier et al., Proceedings of PAC 2001, Chicago p. 1253 (2001).

THE SPALLATION NEUTRON SOURCE ACCELERATOR LOW LEVEL RF CONTROL SYSTEM*

M. Champion, M. Crofford, H. Ma, M. Piller, ORNL, Oak Ridge, TN

A. Ratti, L. Doolittle, M. Monroy, S. DeSantis, LBNL, Berkeley, CA

H. Shoaee, K. Kasemir, S. Kwon, J. Power, M. Prokop, A. Regan, M. Stettler, D. Thomson, LANL, Los Alamos, NM

Abstract

The Spallation Neutron Source Low Level RF Team includes members from Lawrence Berkeley, Los Alamos, and Oak Ridge national laboratories. The Team is responsible for the development, fabrication and commissioning of 98 Low Level RF (LLRF) control systems for maintaining RF amplitude and phase control in the Front End (FE), Linac and High Energy Beam Transport (HEBT) sections of the SNS accelerator, a 1 GeV, 1.4 MW proton source. The RF structures include a radio frequency quadrupole (RFQ), rebuncher cavities, and a drift tube linac (DTL), all operating at 402.5 MHz, and a coupled-cavity linac (CCL), superconducting linac (SCL), energy spreader, and energy corrector, all operating at 805 MHz. The RF power sources vary from 20 kW tetrode amplifiers to 5 MW klystrons. A single control system design that can be used throughout the accelerator is under development and will begin deployment in February 2004. This design expands on the initial control systems that are currently deployed on the RFQ, rebuncher and DTL cavities. An overview of the SNS LLRF Control System is presented along with recent test results and new developments.

INTRODUCTION

The SNS LLRF Control System is comprised of three main components: the RF control chassis, the High Power Protection Module (HPM), and the reference system. The RF control chassis is a digital feedback controller that uses a Field Programmable Gate Array (FPGA) for fast data processing. Three generations of control chassis are planned for supporting the near- and long-term goals of the SNS project: the 1st generation control chassis (Fig. 1) was designed at LBNL for use with the 402.5 MHz rebuncher cavities in the Medium Energy Beam Transport (MEBT) beamline downstream of the RFQ [1]. The 2nd generation control chassis (Fig. 2) is a refinement of the MEBT control chassis and will serve the RFQ and DTL sections of the linac through DTL commissioning [2]. The 3rd generation control chassis is under development and will begin deployment in the CCL, SCL and HEBT in early 2004. It is planned to eventually retrofit the RFQ and DTL with the

3rd generation control chassis. The HPM provides for fast shutoff of the RF drive to the klystron in case of RF over power, arc detection, and vacuum system interlocks [3]. The reference system provides for distribution of the phase-synchronous RF signals necessary to operate the linac and includes cavity and reference signal transport and downconversion (Fig. 3).

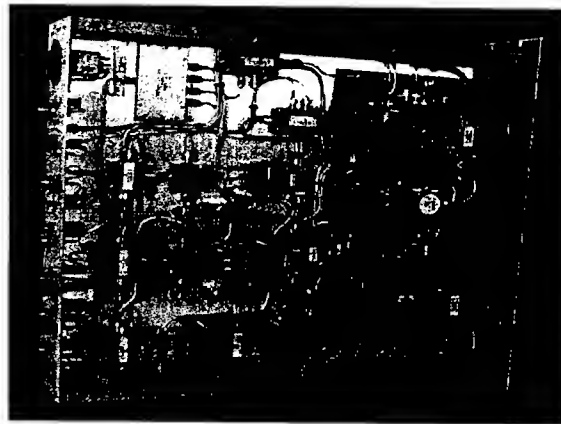


Figure 1. The 1st generation RF control chassis that is used for the MEBT rebuncher cavities.

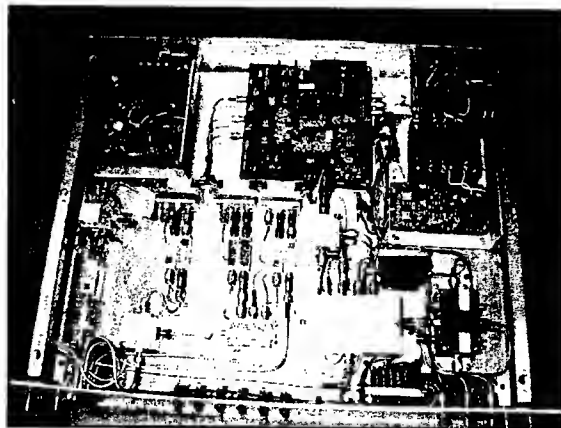


Figure 2. The 2nd generation RF control chassis that is used for the RFQ and DTL.

The 1st and 2nd generation RF control chassis have been used already in Dec.-Jan. for beam commissioning of the RFQ and MEBT rebunchers. Installation of RF control systems for DTL tanks 1 and 3 is complete; tank 3 was tested without beam in early May. Tank 1 will be tested and commissioned with beam during Summer

*SNS is a collaboration of six US National Laboratories: Argonne National Laboratory (ANL), Brookhaven National Laboratory (BNL), Thomas Jefferson National Accelerator Facility (TJNAF), Los Alamos National Laboratory (LANL), Lawrence Berkeley National Laboratory (LBNL), and Oak Ridge National Laboratory (ORNL). SNS is managed by UT-Battelle, LLC, under contract DE-AC05-00OR22725 for the U.S. Department of Energy.

2003. The HPM has been used successfully for high power protection during operation of the RFQ and DTL.

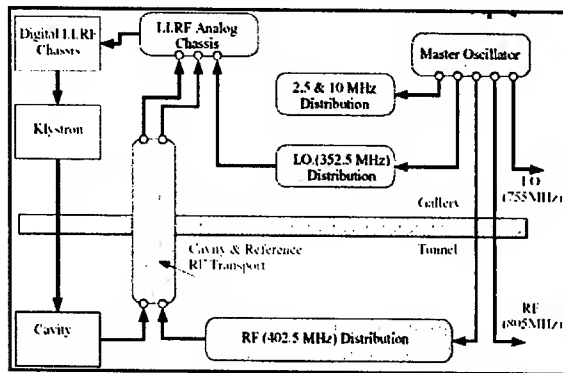


Figure 3. The reference system for the SNS linac.

NEW HARDWARE DEVELOPMENT

The 1st and 2nd generation RF control chassis have been and will continue to be essential to meeting the near-term testing and commissioning schedule. However, these systems are based on relatively small FPGAs (150k gates) and feature rather limited memories. Therefore it was decided last October to design a new RF control chassis that would overcome these limitations and provide a suitable platform for long-term SNS linac operations. The schedule for developing and producing this chassis is very tight; prototypes were due (and received) in March, and first high power tests are planned for Summer 2003. Production is scheduled to commence in September, and installation should begin in February 2004. This aggressive schedule forced a conservative design approach that called for conciseness and an evolution of existing hardware rather than a green field design. This 3rd generation RF control chassis is implemented as a VXI motherboard with three daughtercards: Analog Front End (AFE), Digital Front End (DFE) and RF Output (RFO). The AFE is nearly identical to the SNS Diagnostics Beam Position Monitor (BPM) AFE and was procured from the same vendor. The DFE is an evolution of the digital boards used in the 2nd generation RF control chassis and the BPM hardware; it consists mainly of four A/D converters and a 1.5M gate FPGA. The FPGA can be loaded with a soft core processor that may be useful in the future if more local processing is needed (as compared to the slot-0 controller). The RFO circuitry is a copy of that already proven in the 2nd generation chassis. This package, being a VXI module, has been dubbed the Field Control Module (FCM) and is further documented in a companion paper [4].

The software and firmware is key to the success of this development effort. Following the hardware design philosophy, we chose to re-use the existing code base to the extent possible. Hence the FPGA code implemented on the 2nd generation RF control chassis has been ported to the FCM. Similarly, the slot-0 controller code and EPICS interface have been retained. The VXI motherboard uses a proven VXI-bus interface. The code

development is backed up by system simulations and FPGA code simulations. The standard SNS code repository is used for revision control.

The FCM is presently undergoing bench testing. The FPGA code has been downloaded via the JTAG interface, and basic read/write capability to FPGA registers and block RAM has been demonstrated via the VXI backplane. The AFE has been characterized separately and meets performance requirements. A few RFO parameters have been measured already. The RFO will be more fully characterized in integrated testing of the FCM. The VXI motherboard was tested prior to installing the daughterboards.

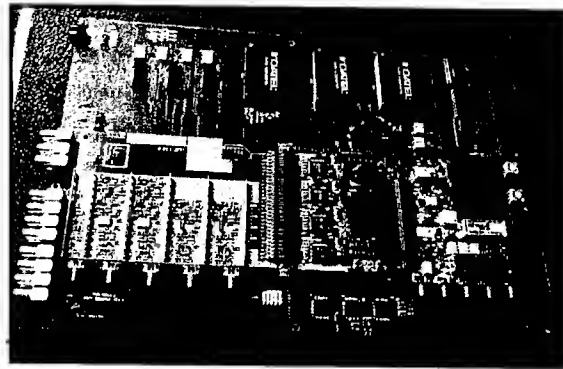


Figure 4. The prototype Field Control Module. The Analog Front End, Digital Front End, and RF Output daughtercards (left to right) are mounted on the VXI motherboard.

PERFORMANCE MEASUREMENTS

The superconducting cavities of the SNS linac are subject to Lorentz force and microphonics detuning. Regulation of the cavity fields therefore requires RF power above and beyond the beam power. Fast acting piezoelectric tuners are being installed on all of the superconducting cavities to mitigate Lorentz force detuning effects if necessary and to allow for future operation of the SCL at increased accelerating gradients. Because of concern about these detuning effects, a long-planned test of the LLRF control system with the first production medium-beta cryomodule was carried out at Jefferson Lab in early March with very encouraging results. The 2nd generation RF control chassis was used for this test. The primary goal was to demonstrate field regulation within the specification of $\pm 1\%$ and $\pm 1\text{deg}$ at the design parameters of 10 MV/m accelerating gradient, 60 Hz repetition rate, and 1.3 ms pulse length. First feedback control was demonstrated on March 1; follow-on testing showed that we can indeed meet the field regulation requirements (Fig. 5). Typical amplitude and phase waveforms are shown in Figure 6 for open and closed loop control of the cavity fields. Feedforward control is necessary to minimize ringing due to the turn-on transient and was used to obtain the results shown in Figure 5. Our long term plans call for automatic adaptive feedforward in addition to feedback control.

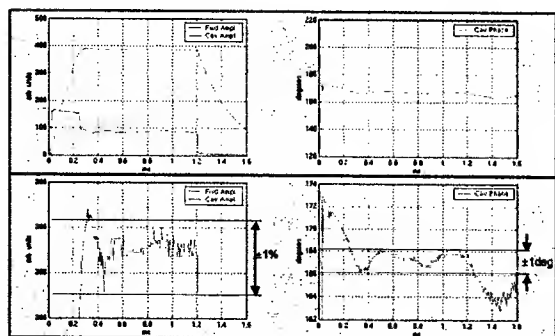


Figure 5. First demonstration of required amplitude and phase regulation on a production medium-beta cryomodule.

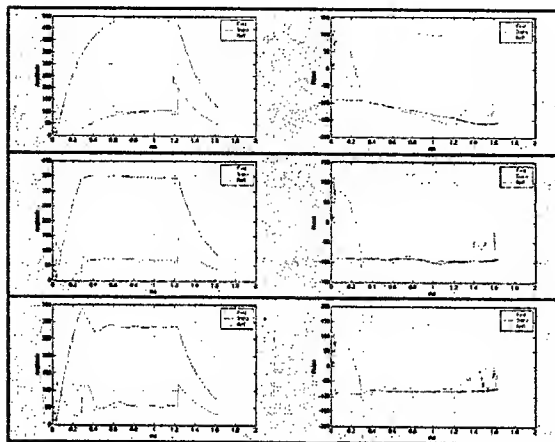


Figure 6. Amplitude and phase responses for three cases: open loop, closed loop with proportional gain only, closed loop with proportional and integral gain. Cavity field, forward power, and reflected power are shown in blue, green, and red, respectively.

Several other features of the LLRF control system were tested in March and April with the first production cryomodule. Two resonance detection algorithms were tested: 1) in the case where the detuning is only a few bandwidths, the frequency error is determined from the decay of the cavity field after the end of the RF pulse; 2) in the case of larger detuning, a single-pulse burst-mode technique has been demonstrated up to a detuning error of about 15 bandwidths. More recently, the decay technique has been applied in testing of DTL tank 3 at Oak Ridge. The detuning information was used to control the stepper motor tuner in the cryomodule tests, and it is presently being implemented for control of the water temperature on the DTL.

The performance of the superconducting cavities must be confirmed following the installation and cooldown of the cryomodules at Oak Ridge. This will be done by calorimetric measurements of Q_0 as a function of accelerating gradient under pulsed conditions. The LLRF control system was used to perform this test at Jefferson Lab with good results.

The piezo tuner was operated in conjunction with the LLRF control system. The piezo power supply was

driven with a pulse generator. One example (Fig. 7) is given where the piezo drive pulse was manually adjusted to flatten the phase response of the cavity field. Optimization of the piezo drive parameters and the interplay between the piezo tuners and the LLRF control system will be an interesting task.

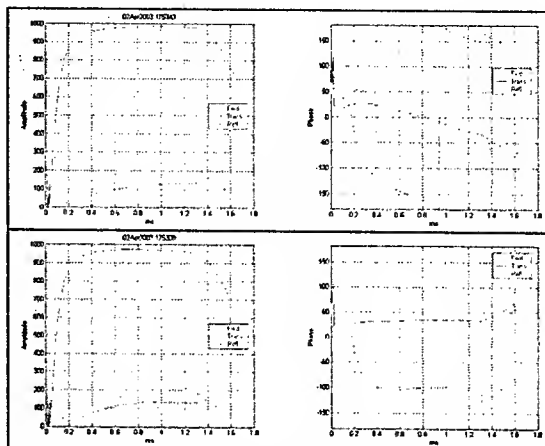


Figure 7. Demonstration of effect of piezoelectric tuner on dynamic cavity performance. Open loop operation at 12.5 MV/m for two cases: piezo tuner inactive, and piezo tuner driven with rectangular pulse having width=860 μ s, amplitude=220 V, and lead=580 μ s.

SUMMARY

The testing and commissioning of the FE and DTL is being supported by the 1st and 2nd generation SNS LLRF control systems. The 3rd generation system, that will ultimately serve the FE, Linac and HEBT, is under development and will begin deployment on the CCL and SCL beginning in early 2004. A successful proof-of-principle test has recently been completed with the first production cryomodule; the performance requirement of $\pm 1\%$ and $\pm 1\text{deg}$ amplitude and phase regulation has been demonstrated. The LLRF Team, which is distributed across three laboratories, is well on its way to providing a flexible control system that will meet the performance requirements of the SNS accelerator.

ACKNOWLEDGEMENTS

We thank the many individuals who have aided us in achieving our goals, and we thank the following groups for their support: SNS Controls, SNS Diagnostics, LANL E-CAD and Electronics Assembly, and the Jefferson Lab SRF Institute.

REFERENCES

- [1] L. Doolittle et al, The SNS Front End LLRF System, Linac 2002, Kyongju, Korea.
- [2] L. Doolittle et al, these proceedings.
- [3] http://www.sns.gov/projectinfo/llrf/lan/llrf_system_documentation/hpm.pdf
- [4] A. Regan et al, these proceedings.

CONTROL OF HEAVILY-BEAM-LOADED SNS-RING CAVITIES

T. L. Owens, ORNL,* Oak Ridge, TN 37830, USA
K. Smith and A. Zaltsman, BNL, Upton, NY 11973, USA

Abstract

In each of four rf stations that make up the rf buncher system in the SNS accumulator ring, cavity voltage and phase are control led through a negative-feedback system employing digital electronics. With peak beam currents as high as 75 Amperes near the end of each 1.1 ms machine cycle, the rf cavities in the SNS ring are strongly driven by the beam. To provide adequate regulation of cavity fields in the presence of high SNS beam currents, basic feedback loop parameters are pushed to levels where stability becomes a major concern. This note presents a LabVIEW simulation of the ring rf system that demonstrates how Smith compensation can be used to mitigate the destabilizing effect of dead-time delay in the feedback loop and assure adequate regulation of cavity fields. A digital implementation of Smith compensation is outlined that could be incorporated into the LLRF system being provided by BNL.

BACKGROUND

In any feedback system, unstable conditions exist whenever signal-delays in the feedback loop become long enough to produce positive-feedback for loop gains exceeding unity. Mechanisms for compensating delays are usually essential for the attainment of required regulation levels together with acceptable stability margins.

There are two general types of delay in any feedback system. The first type of delay is associated with dead time from signal propagation delays and timing delays. In the SNS system, a major source of propagation delay arises from the round-trip signal-transit-time between signal sources in the rf control room and receiver amplifiers in the ring tunnel. The second type of delay results from energy build-up in energy-storage elements in the feedback path. This second type of delay is associated with poles in the system response. While the delay mechanisms differ, the two types of delay are indistinguishable in the processed signal. However, the delay types differ markedly in their responses to various compensation methods.

Anticipating the effect of delay by adding a predictive signal into the feedback path can mitigate degradation in stability caused by dead-time delays. This compensation technique forms the basis for the Smith compensator [1] that will be described in this report. Other compensation devices, such as the lead-lag network used in PID controllers, are effective in compensating delays resulting

from energy-storage elements, but they must be de-tuned to compensate dead-time delays, compromising performance of PID controllers. The simulations presented in this report show that the Smith compensator makes a substantial improvement in stability for the SNS ring buncher system by essentially moving dead-time delays outside of the feedback loops. Additional details are contained in a separate report [2].

SMITH-COMPENSATED FEEDBACK

Figure 1 is a block diagram of the feedback control system that has been simulated in the present study. The diagram contains the basic elements of the Smith compensator. In principle, the compensator forms a signal path in parallel with the actual cavity and delay lines of the SNS ring-rf system. The parallel path contains the cavity analogue and a delay-line analogue that together produce a signal response as close as possible to that of the actual cavity and the actual system delays.

At the differencing ports to the right of the middle $I&Q$ demodulator in figure 1, the delayed signal from the cavity analogue is subtracted from the delayed signal from the actual cavity. For a precisely constructed analogue, the resulting difference signal equals the beam-induced signal, or the beam "disturbance," which drives the actual cavity but not its analogue. If the analogue construction is imprecise, the difference signal is only an estimate of the beam disturbance.

At the $I&Q$ summing junctions in figure 1, the cavity-analogue output is added to the estimated beam disturbance from the previous differencing ports, producing a predicted cavity signal plus the estimated beam disturbance. This composite signal is then compared to the reference $I&Q$ input to form a short, fast feedback loop that does not contain the delay, yet regulates the system based upon an estimated beam disturbance. In effect, the delay has been moved outside of the feedback loop. The demodulators convert rf signals from the delayed cavity, the delayed cavity analogue and the undelayed cavity analogue into digitized envelope signals representing the in-phase, I , and quadrature, Q , components of the rf signals. The rf signals are sampled at a rate of four times the applied frequency. Samples are de-multiplexed into even and odd samples and retained between consecutive samples (sample and hold feature). Odd samples are multiplied by $\cos(2\pi ft)$ and even samples are multiplied by $\sin(2\pi ft)$ to

* SNS is a collaboration of six U.S. national laboratories: Argonne National Laboratory (ANL), Brookhaven National Laboratory (BNL), Thomas Jefferson National Accelerator Facility (TJNAF), Los Alamos National Laboratory (LANL), Lawrence Berkeley National Laboratory (LBL), and Oak Ridge National Laboratory (ORNL). SNS is managed by UT-Battelle, LLC, under contract DE-AC05-00OR22725 for the U.S. Department of Energy.

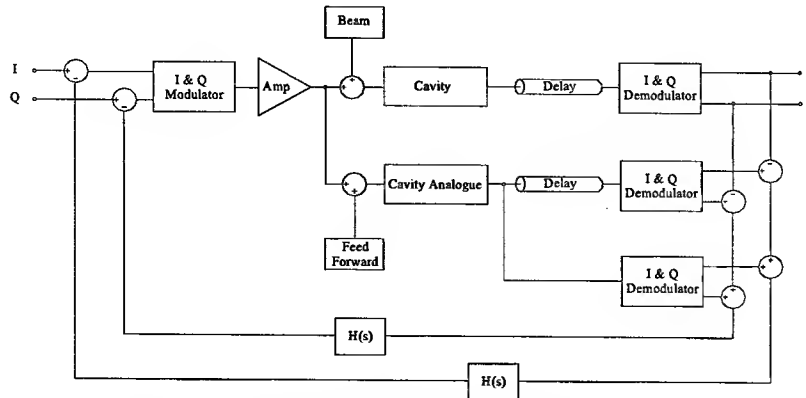


Figure 1. Ring RF Feedback System Utilizing Smith Corporation

produce the desired I and Q values. Because the sampling rate is four times the applied frequency, f , the sine and cosine multiplications are accomplished in the digital domain by simply changing the sign of alternate samples.

The buncher cavity is treated as a parallel RLC circuit. The inductor in the model comprises a ferrite-loaded coaxial transmission line having a time-varying permeability, μ , in order to simulate dynamic tuning of the cavity. The presence of a time-varying inductive element transforms the circuit equations from linear-time invariant forms to non-linear forms given by,

$$C\lambda\mu\frac{d^2i}{dt^2} + \left(2C\lambda\frac{d\mu}{dt} + G\lambda\mu\right)\frac{di}{dt} + \left(C\lambda\frac{d^2\mu}{dt^2} + G\lambda\frac{d\mu}{dt} + 1\right)i = i_d \quad (1)$$

$$V_s = \lambda\left(\mu\frac{di}{dt} + i\frac{d\mu}{dt}\right), \quad (2)$$

$$\lambda = \frac{l \cdot \ln\left(\frac{b}{a}\right)}{2\pi} \quad (3)$$

where C is the capacitance across the buncher gap, i is the current in the inductive element of the buncher cavity, G is the shunt conductance across the gap, l is the length of the coaxial line representing the inductive element, b is its outside diameter, and a is its inside diameter. The quantity, i_d , is the drive current consisting of a linear superposition of currents from the rf power amplifier and the SNS beam.

The power amplifier is treated as a non-linear tetrode in which the output current depends upon both the grid excitation and the anode voltage of the tetrode in accordance with data supplied by the tube manufacturer. The SNS beam is treated as a rigid body of charge, having a longitudinal beam current profile calculated by M. Blaskewitz [3].

The simulation model described above was implemented using LabVIEW. While LabVIEW is most commonly known for applications in instrument control and data acquisition, LabVIEW also includes software tools for control-loop simulations.

SIMULATION RESULTS

Open Loop Response

Without dynamic tuning, but with full beam current, the gap voltage rises to about 60-70 kV at the end of the cycle, implying an effective shunt impedance of approximately 1,000 Ohms per gap, determined largely by the output impedance of the power amplifier.

When dynamic tuning that is linear with respect to time is included, the gap voltage rises rapidly at first, and then falls off slowly as the resonant frequency of the gap separates from the ring revolution frequency. The frequency separation for SNS parameters is large enough that gap voltage is out of phase with the beam by about 87 degrees at the end of the beam cycle. In effect, with dynamic tuning, the beam excites a gap voltage that nearly sustains beam bunching without an active drive signal. Therefore, only a small amount of power is required in the active drive. From another viewpoint, dynamic tuning maintains the gap voltage and anode current at or near their unloaded values, thereby minimizing drive-power requirements.

Closed-Loop Response

When dead-time delays are added to the feedback path, cavity regulation and system stability become inadequate without some form of compensation. Figure 2 shows the system response when a Smith compensator and a single pole filter are added to the basic feedback system. In this case, the cavity analogue is identical to the actual cavity.

A delay of 750 ns has been applied to both the actual feedback path, and the analogue path to test the effectiveness of the compensator. This much delay equals about 80% of the rf period and goes well beyond the threshold for instability in a typical uncompensated network having comparable loop gain. In spite of the presence of this relatively large delay, it is clear from figure 2 that stability is maintained when the Smith compensator is added to the network.

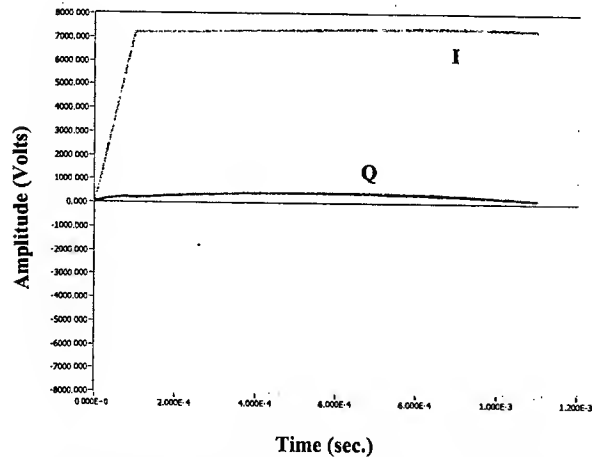


Figure 2. In-phase, I, and quadrature, Q, components of gap voltage with Smith compensation at full beam current.

For a perfectly constructed analogue, the response with 750 ns of delay is identical to the response of an uncompensated network that has no delay. This behaviour is expected, since the Smith compensator places the delay completely outside the feedback loop in this situation.

In a practical feedback system there will be errors in the cavity and delay analogues. For the SNS, the largest analogue error will occur in the characterization of dynamic tuning in the fast-feedback leg of the Smith compensator. Figure 3 shows the effect of this type of error on gap voltage regulation and stability for the ring buncher system. Stability is maintained when errors in the time dependence of the dynamic tuning is within the range, -5% to +25%. In addition, gap voltage variations are less than 4.5% as long as dynamic tuning errors are less than $\pm 5\%$.

Conclusions

The simulations presented in this report demonstrate that a Smith compensator can stabilize the SNS ring-rf feedback-control system in spite of long delays in signal transmission around the feedback loop. The simulations also demonstrate that an effective Smith compensator can be implemented using only a modest level of care in the construction of the necessary compensator elements.

While the simulations have been carried out using high-frequency compensator elements, similar results should be obtained using equivalent low-frequency base band elements [4]. These base band elements can be readily implemented using reasonably simple algorithms in a digital signal processor. Since the control system being provided by BNL is already digitally based and highly flexible, addition of a Smith compensator with base band analogue elements appears practical.

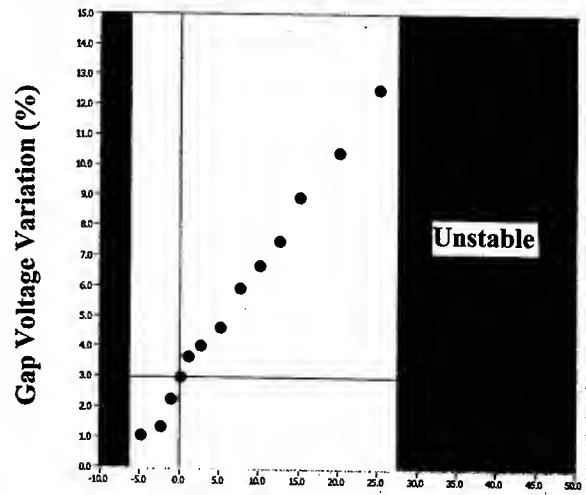


Figure 3. Buncher-cavity gap-voltage variation over SNS beam cycle due to errors in time dependence of the dynamic tuning analogue of the Smith compensator.

REFERENCES

- [1] O. J. M. Smith, "A Controller to Overcome Dead Time," ISAJ, Vol. 6, pp 28-33, 1970.
- [2] T. L. Owens, "Smith Compensation for Stabilization Of the Ring RF Feedback System," SNS Tech Note SNS-NOTE-CNTRL-97, March 6, 2003.
- [3] M. Blaskiewicz, J. M. Brennan, J. Brodowski, J. Delong, M. Meth, K. Smith and A. Zaltsman, "RF System for the SNS Accumulator Ring," in Proceedings of the 2001 Particle Accelerator Conference, Chicago, pp 490-494.
- [4] B. R. Cheo, and Stephan P. Jachim, "Dynamic Interactions Between RF Sources and LINAC Cavities with Beam Loading," IEEE Trans. On Electron Devices, Vol. 38, No. 10, Oct., 1991, pp 2264-2274.

ANALYSIS OF SLOW ORBIT MOVEMENT IN PLS STORAGE RING*

H. S. Kang[#], H. J. Park, J. Choi, Y. J. Han, PAL, Pohang 790-784, Korea

Abstract

Slow orbit movement in the horizontal and vertical planes at the Pohang Light Source (PLS) storage ring is analysed with the accumulated data of BPM and environment variables such as the ambient temperature of the storage ring tunnel, the LCW temperature, the outside weather condition, and the tunnel floor elevation. Each factor causes an orbit variation with different pattern and magnitude in the horizontal and/or vertical planes. Facts and causes of slow orbit movement are described as well as the orbit feedback in use or under preparation.

1 INTRODUCTION

The PLS lattice is a triple bend achromat with 12 superperiods and 280.56m circumference, and each superperiod has 12 quadrupole magnets. The operating beam energy is 2.5GeV and the maximum beam current is 200mA. In the usual user-service operation the beam is directly injected from the 2.5GeV electron linac twice a day, which was changed from the energy ramping from 2GeV in October 2002. For the PLS with the natural emittance of 18.9 nm-rad, assuming a 1%-betatron coupling, the orbit stability requirements in position for 0.1% photon intensity fluctuation at beam lines are 20 μ m for the horizontal plane and 3 μ m for the vertical plane.

From the operation data of two years since 2000, it was clearly seen that the magnitude of the slow orbit movement, which is below 0.1 Hz in the frequency range, is much larger than that of the fast one that is mainly due to magnet power supply ripple, and particularly the orbit movement in the vertical plane is an order of magnitude larger than the orbit stability requirement. A simultaneous change in both horizontal and vertical planes is typical in the slow orbit movement: the average change in the horizontal plane and the rms change in the vertical plane, and the slow orbit movement is correlated with the outside temperature change and dominates during the change of season like spring and fall.

There is also an orbit movement only in the vertical plane, while no movement in the horizontal plane, in case of rainfall or a localized change of the ambient temperature of the storage ring tunnel. Even though regular survey alignment is performed twice a year at the PLS, ground settling and ground diffusion result in changes of the position of each magnet during the machine operation time.

This paper describes the effects of various environmental factors on the slow orbit movement at the PLS storage ring by analysing the accumulated orbit data since 2000. Factors are investigated in detail such as outside temperature, rainfall, tunnel air temperature, LCW

temperature. In particular, the issue of differential ground settlement is emphasized.

2 ENVIRONMENTAL FACTORS

The horizontal and vertical movement of the beam relative to the quadrupoles can be observed directly with the BPMs. The number of BPMs installed per superperiod (hereinafter "cell") is 9, and totally 108 BPMs. Several BPMs show frequent problems or suspicious behaviours. Such BPMs (about 14 out of 108) are removed from the analysis.

2.1 Tunnel Air Temperature

For ambient temperature control the tunnel area is divided into six zones each of which covers two cells. The tunnel air temperature of each zone is independently controlled with a stability of $\pm 0.1^\circ\text{C}$ by a temperature-controlled circulating airflow. The temperature control system for each zone controls the average temperature of eight temperature sensors that are installed close to the quadrupole magnets. Therefore, the ambient tunnel temperature must be different from the sensor temperatures and not uniform, and a temperature gradient along the tunnel or around magnets is unavoidable because the airflow is different everywhere and even around a single dipole magnet. The ambient temperature non-uniformity depends on the airflow rate and flow mixing in the tunnel.

Figure 1 shows the sensor temperatures at cell 9, 10, and 11, and BPM readings in the vertical plane at cell 5 when the supply air temperature for cell 10 and 11 changed abruptly by about $+1^\circ\text{C}$ for 3 hours. At the event the tunnel air temperature at cell 10 increases by 0.42°C , a very small change in cell 9 and 11, and no change in other cells. The BPM readings started to change at the onset of change of supply air temperature, around 5:30 AM. The resultant rms change in the vertical orbit is about 20 μ m. However, no change is observed in the horizontal plane.

At the temperature-changing area there might be a position change of quadrupole magnet in the vertical direction rather than the horizontal direction. Each cell has two sector girders on which 12 quadrupole magnets are installed. It is difficult to estimate the accurate position change of each quad when the ambient tunnel temperature changes. The deformation of the 10-m long sector girder is so complex that each quad on the sector girder changes its position very differently.

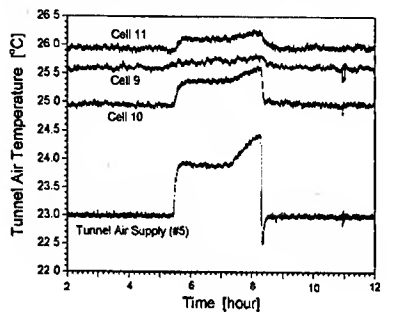
*Supported by Ministry of Science and Technology, Korea.

[#]hskang@postech.ac.kr

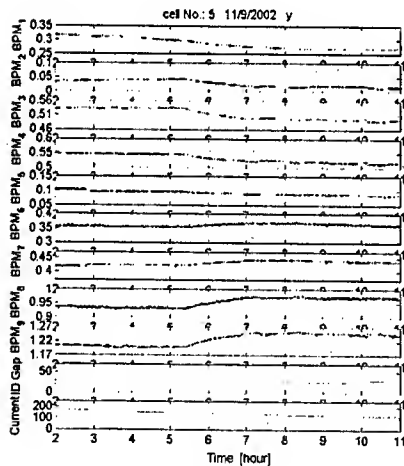
2.2 LCW Temperature

The LCW control system supplies the cooling water with a stability of $\pm 0.1^\circ\text{C}$ to all magnets, vacuum chambers, and photon stops. The closed orbit looks like to be affected by magnet temperature change that is directly related to the LCW temperature. The structural change of magnet poles, especially, of quadrupole magnet contributes to orbit movement.

It is observed that the horizontal orbit is much more dependent on the LCW temperature than the vertical orbit. However, in the BPM reading there is also a contribution from the vacuum chamber movement due to the temperature change of the vacuum chambers, especially the photon stops where most of photon power is absorbed.



(a)



(b)

Figure 1: The tunnel air temperature at cell 9, 10, 11 (a) and BPMs in the vertical plane at cell 5 (b) when the supply air temperature for those cells increases rapidly about 1°C for 3 hours. The unit of BPMs in (b) is mm.

2.3 Weather Effect

1) Outside Temperature Change

The differential ground movement is closely related to the temperature variation of the surface ground. A substantial change of outside temperature can cause a temperature variation of the surface ground, which results in a differential ground movement. "Substantial change of

outside temperature" means a continuous change for at least a few days, which can induce a ground movement, while a diurnal big change for only one day cannot do.

Even though the tunnel air temperature is well controlled by a forced airflow system, which is normally a sort of cooling system with a limited flow capacity, the outside temperature may affect the tunnel air temperature by the increase of heat transfer to the building wall. A diurnal change of the outside temperature can affect in this case.

Figure 2 shows the average and rms of the orbit in the horizontal and vertical planes without the RF frequency feedback. Without the RF frequency feedback the average in the horizontal plane changes as much as $100\mu\text{m}$ and the rms in the vertical orbit changes about $40\mu\text{m}$, which exactly follow the change of daily average temperature in local area, about 9°C for five days as shown in Fig. 3.

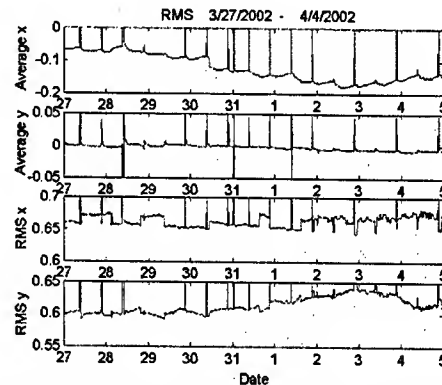


Figure 2: The average and rms of the orbit without the RF frequency feedback. X and y represent the beam position in the horizontal and vertical plane, respectively. The ordinates are in mm.

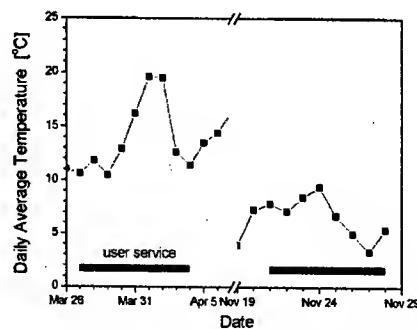


Figure 3: The daily average of outside temperature from March 26 - April 6, and November 19-28, 2002.

The rms in the vertical plane changes slowly about $40\mu\text{m}$ with the same time-correlation as the average in the horizontal plane as shown in Fig. 2. The time-correlation between the horizontal orbit drift and the COD in the vertical plane implies that both are caused by the same source. The COD in the vertical plane is mainly affected by two factors: one is the quadrupole magnet alignment

errors which vary as the ground movement and the tunnel air temperature, and the other is skew quadrupole field.

A measurement of the rms of vertical orbit and the average of horizontal orbit as a function of RF frequency shows that when the horizontal orbit moves about $100\mu\text{m}$ by changing the RF frequency, simulating the same change of Fig. 2, the rms in the vertical plane changes only $4\mu\text{m}$, very small compared to $40\mu\text{m}$ of Fig. 2.

The changes of the rms in the vertical plane as shown in Fig. 2 result mainly from the change of quadrupole magnet positions which seem to be affected by the outside temperature change. However, it is difficult to estimate the differential ground movement with respect to the outside temperature because geological problem is complex and too many variables are unknown.

2) Rainfall

When it rains, some movement of orbit in the vertical plane is frequently observed at the PLS. Some of the ground movements are clearly correlated to fluctuations in the underground water table height. However, the average of horizontal and vertical orbit, and the rms of horizontal orbit almost unchanged. The changes of rms in the vertical plane seem to be due to differential ground settlement of the ring tunnel caused by rainfall.

3 DIFFERENTIAL GROUND SETTLEMENT

The changes of vertical offset between the beam position and the centre of quadrupole magnet mainly come from differential ground settlement. Ground motion is classified as wave dominated, ATL dominated and systematic motion dominated [1]. The sources of the slow ground motion are atmospheric activity, change of underground water, ocean tide, temperature variation of the surface ground and so on [2].

The very slow ground motion observed in the PLS appears to be systematic in time. The tunnel elevation of the PLS storage ring has changed continuously. It is seen that the peak-to-peak of elevation deviation has increased since June 1993, which reached the accumulated value of about 22mm as of July 2002. The tunnel floor elevation changes in average by about 1.2mm per year. The ground settlement is relatively worse at cell 1, cell 6 and cell 9. The rate of this ground motion has decreased over time, but preserving the direction of motion.

From the survey data of almost ten years it is known that the ground settlement occurs dominantly between July and February of the next year, which implies the most change is activated during the period of cold winter months. It seems reasonable to think that the differential ground settlement is mostly activated by the soil shrinkage during the cold winter months after heavy rainfall during the rainy months of July to September.

The vertical positions of quadrupole magnets change in a systematic way by the differential ground settlement.

Figure 4 shows the vertical position changes of quadrupole magnets and the tunnel floor elevation between February and July 2002, which are the differences of the survey data in February and July. The positions of quadrupole magnets change smoothly in-group and step changes between groups are clearly seen because magnets are installed on the sector girders. The magnet-to-magnet alignment on each girder stays relatively constant over time, but the girders move independently with respect to each other.

The slow orbit movement in the vertical plane in the PLS storage ring is mainly due to the differential ground settlement.

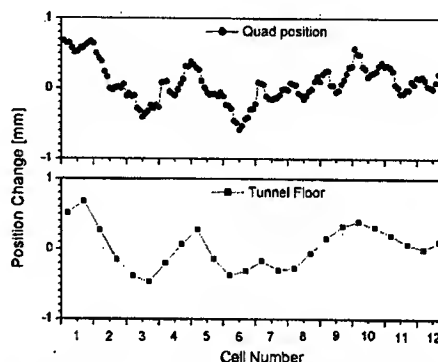


Figure 4: The vertical position change from February to July 2002; upper figure: quadrupole magnets, lower figure: SR tunnel floor elevation.

4 FEEDBACK SYSTEM

In order to achieve the orbit stability of a few μm , a global orbit feedback system is absolutely necessary. A slow global orbit feedback system using a SVD algorithm is being prepared. The RF frequency feedback has been in operation since November 2002 to compensate the circumference change. With the RF frequency feedback the average in the horizontal orbit is bounded within $\pm 2\mu\text{m}$.

As for the implementation of global orbit feedback system, the reference orbit for the feedback is very important and should be re-established at a proper time; the analysis of the tunnel ground movement data helps to decide when the reference orbit should be re-established. And it is important to know the correlation between environment factors and those effects on orbit. A better understanding of slow orbit movement, sources and temporal behaviours, is essential for the orbit feedback.

REFERENCES

- [1] Andrei Seryi et al., Proc. of the 20th Linac Conference, Monterey, USA, 2000, p. 68.
- [2] Shigeru Takeda et al., Proc. of the 2000 EPAC, Viena, Austria, 2000, p. 2394.

COMMISSIONING OF THE FAST ORBIT FEEDBACK AT SLS

T. Schilcher, M. Böge, B. Keil, V. Schlott, Paul Scherrer Institut, Villigen, Switzerland

Abstract

At the SLS a Fast Orbit Feedback (FOFB) has been designed to stabilize the closed orbit to the $1 \mu\text{m}$ level up to frequencies of 100 Hz. The feedback is integrated into the digital BPM system [1] by means of 12 dedicated digital signal processors (DSP) and a fiber optic network. Submatrices of the "inverted" corrector/BPM response matrix are distributed to the BPM stations and corrections are performed in parallel. First promising commissioning results of the FOFB running at 4 kHz orbit sampling rate are presented. It is demonstrated that the chosen FOFB concept is appropriate and has the potential to reach or even exceed the design goals.

INTRODUCTION

Orbit stability and reproducibility of the electron beam at the location of the radiation source points is a crucial requirement at the Swiss Light Source. It is desirable to suppress the photon beam fluctuations by at least one order of magnitude below the spot size at the experiments. At the SLS this translates into electron beam angular stability along the insertion device straights below $1 \mu\text{rad}$ and into beam position stability below 1/10th of the vertical beam size which corresponds to $\approx 1 \mu\text{m}$. A Slow Orbit Feedback (SOFB) working with less than 1 Hz correction rate is in operation since August 2001 and succeeded to stabilize the orbit in both planes to $1 \mu\text{m}$ RMS [2]. At the low beta short straight insertion devices the electron beam oscillations could even be reduced to a sub-micron level of $\sigma_{x/y} \approx 0.5 \mu\text{m}$. Measurements of the power spectral densities at the tune BPM have shown that the main contributions to orbit perturbations lie in a frequency range below 100 Hz (see Tab. 1). Integration up to 100 Hz results in beam motions of $0.5 \mu\text{m}/\sqrt{\text{m}}$ horizontally and $0.4 \mu\text{m}/\sqrt{\text{m}}$ vertically (normalized to the beta function) without any fast feedback. The average machine beta values for the SLS storage ring are $\beta_{x/y} \approx 10 \text{ m}$ at the locations of the BPMs. The residual beam motion caused by sources given in Tab. 1 as well as additional orbit perturbations introduced by an increasing number of insertion devices (ID) and experimental stations require stabilization by a fast orbit feedback.

FOFB IMPLEMENTATION

General Layout

The layout of the SLS FOFB is based on the structure of the "inverted" beam response matrix where only the diagonal and their adjacent coefficients have non zero values.

Frequency	Noise Source	RMS contribution	
		horizontal	vertical
3 Hz	booster ramp	$0.5 \mu\text{m}$	$0.35 \mu\text{m}$
20-35 Hz	girder eigen frequencies	$0.85 \mu\text{m}$	$1.4 \mu\text{m}$
50 Hz	line frequency, vacuum pumps (async.)	$1.2 \mu\text{m}$	$0.45 \mu\text{m}$
85 Hz	unidentified		$0.35 \mu\text{m}$

Table 1: Main contributions to orbit oscillations at SLS without feedback measured at the location of the tune BPM with $\beta_x \approx 11 \text{ m}$ and $\beta_y \approx 18 \text{ m}$. The quadratic sum of the contributions yields a RMS value of $1.6 \mu\text{m}$ horizontally and $1.55 \mu\text{m}$ vertically.

Therefore, steerer magnet settings are only determined by position readings from their closest BPMs [3]. As a result, the feedback calculations can be decentralized allowing to implement the FOFB throughout the twelve BPM stations. Each of the twelve stations handles six direct BPM inputs and six corrector magnet outputs. The data between adjacent BPM stations are transmitted over a fiber optic point-to-point network which reflects the localized structure of the "inverted" beam response matrix.

Integration Issues

Basis for the FOFB is the real time operation mode of the digital BPM (DBPM) system where each BPM electronics continuously delivers data at a rate of 4 kHz. This rate is the result of down conversion and decimation in the digital receivers with their 31.2 MHz ADC clocks locked to the 500 MHz ring RF frequency. Presently, the 4 kHz data streams of the 72 digital BPMs are not synchronous to each other. Thus, the FOFB has to wait for the latest data acquisition before a new orbit correction can be calculated although the transfer time for BPM data between the different sectors takes only $8 \mu\text{s}$. The asynchronous data rate introduces an additional delay of maximal one feedback cycle which amounts to $250 \mu\text{s}$. This delay will be eliminated by a DBPM firmware upgrade. The passband width of each BPM is set to 2 kHz by means of programmable filters on the digital receiver. It results in a resolution of $1.2 \mu\text{m}$ and typical group delays of about $300\text{-}600 \mu\text{s}$. The numerical controlled oscillator (NCO) frequencies on the DDCs are adjusted to the main RF frequency. An automatic loop on the BPM low level control system tracks the ring RF frequency and reprograms the NCO frequencies to keep the BPM signal in the passband width of the DDCs. This be-

comes important when even smaller passband widths of the BPMs are envisaged in order to reduce noise and group delays in the DDCs and hence to increase the bandwidth of the feedback loop. Frequency changes are necessary since horizontal path length effects are taken into account by the FOFB as well. Off-energy orbits are not corrected by the steerer magnets but by adjustments of the RF frequency. It is therefore necessary to subtract the dispersion orbit from the measured orbit before a correction is applied. The dispersion orbit is extracted on the DSP level by a one dimensional SVD fit on the position data from three sectors, which corresponds to 18 BPM readings. Whenever the fitted RF frequency error exceeds 5 Hz (equivalent to $dP/P \sim 2 \cdot 10^{-5}$) a high level application on the beam dynamics model server [4] corrects the RF frequency.

The start of the fast orbit feedback is performed in a sequence where the central high level orbit correction application (former 'slow orbit feedback, SOFB') corrects the electron beam to the required reference orbit within 5 μm and adjusts the RF frequency. Subsequently, all necessary feedback parameters including the inverted response submatrices and PID control parameters are downloaded to the DSPs at the twelve BPM stations. A global trigger from the timing system starts the FOFB on all BPM stations synchronously. Since the same number of correctors and BPMs are used to constrain the orbit to the "Golden Orbit" at each of the 72 BPM locations, it is indispensable to rely on each single position reading. BPM pickup cross checks of the four RF buttons have therefore been implemented on the DSP in order to detect BPMs with spurious bad readings. If the sums of the two diagonal BPM button raw values do not agree within a predefined level (default 20%) the reading is considered to be faulty. In such a case, the DSP disables the BPM and stops the feedback in this particular sector because the structure of the "inverted" response submatrices are not appropriate anymore. The halt of the feedback loop on one BPM station also directly affects the two adjacent sectors which do not get position readings over the fiber links anymore and consequently skip the correction cycles with 'data timeouts'. The localized structure of the fast orbit feedback allows this type of asymmetric operation mode. Nevertheless the feedback is then automatically stopped by the EPICS control system which permanently monitors the status of all sectors. The high level orbit control application reloads a new set of sub-matrices where the particular faulty BPM is disabled and finally restarts the feedback. This scenario has already been successfully tested during machine development shifts.

Feedback Characterization

Besides the different components in the feedback loop like corrector magnets, vacuum chambers, BPM system and global BPM data distribution, the overall performance of the feedback system depends on the type of the digital controller. Presently, a simple PID controller has been implemented. The horizontal and vertical open loop trans-

fer functions from a corrector magnet to its closest BPM (nearly no phase advance) have been measured (see Fig. 1) in order to optimize the feedback parameters. The underly-

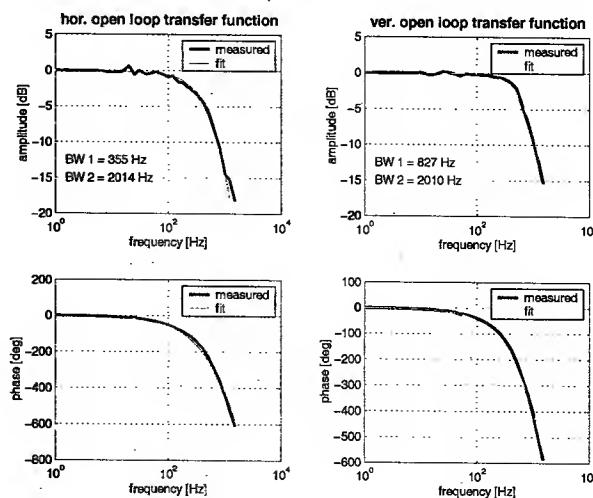


Figure 1: Horizontal and vertical open loop transfer functions of the fast orbit feedback. The model of the fit consists of a series of a first (bandwidth 1) and fifth order (bandwidth 2) low pass filters and a time delay.

ing model of the fitted data comprises a first order low pass filter representing DDC filters, corrector magnet, vacuum chamber and eddy currents, a fifth order low pass filter for the digital power supplies and a time delay for the digital processing. The fit predicts first order low pass bandwidths of ≈ 355 Hz horizontally and ≈ 830 Hz vertically indicating the asymmetry of the SLS storage ring vacuum chamber. Independent laboratory measurements of the digital power supplies showed a fifth order low pass filter characteristics with a small signal bandwidth [5] of 2 kHz. Delay times through the digital processing chain were determined to ≈ 300 μs for the digital receivers, ≈ 60 μs for the first DSP for beam position calculations, ≈ 70 μs for the feedback algorithm in the second DSP and 160 μs to transfer the correction values to the power supplies. A maximum of 250 μs have to be accounted for the global data exchange due to the asynchronous transfer. Therefore a total digital time delay of around 700 μs corresponding to 3 correction cycles were used in the fit.

RESULTS

Up to now, the FOFB was operated only during machine development shifts. The tune BPM has been chosen for monitoring the FOFB performance since it is not part of the feedback loop and therefore allows a more objective analysis of beam oscillations. Although the observed orbit excitations vary over time, Tab. 1 gives an overview of the main beam noise sources and their typical contributions to the position RMS value at the location of the tune BPM. Note, the beta functions at this BPM amount to $\beta_x \approx 11$ m

and $\beta_y \simeq 18$ m while the average machine beta values are $\beta_{x/y} \simeq 10$ m at the location of the BPMs. The measured power spectral densities of both planes (see Fig. 2) show snapshots of the orbit excitations at the tune BPM with and without feedback. The dominant noise sources in the fre-

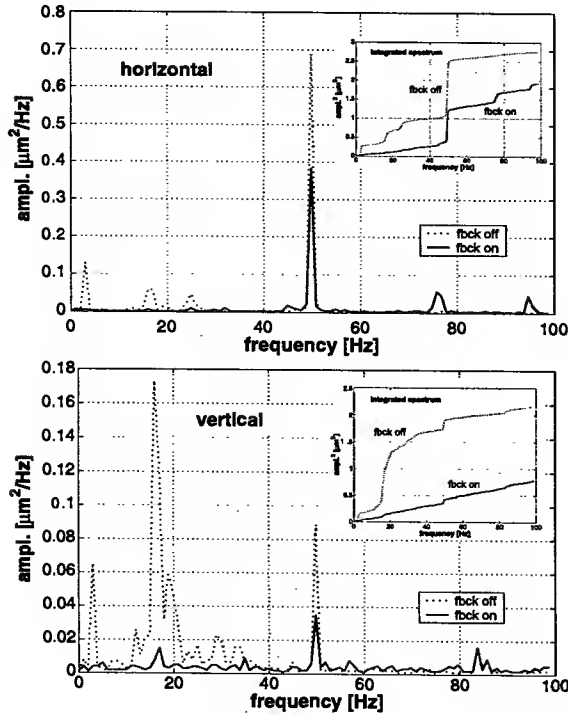


Figure 2: Snapshots of the horizontal and vertical power spectral densities measured with the digital BPM system at the location of the tune BPM.

quency range up to 100 Hz as indicated in Tab. 1 could be suppressed from $1.7 \mu\text{m}$ to $1.4 \mu\text{m}$ horizontally and from $1.5 \mu\text{m}$ to $0.9 \mu\text{m}$ vertically. Fig. 3 shows the measured vertical closed loop transfer function for non-optimized PI start parameters. The differential control has not been ap-

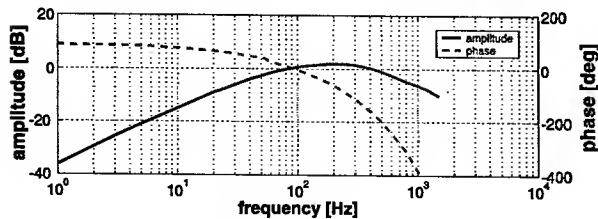


Figure 3: Measured vertical closed loop transfer function with moderate PI parameter settings. The amplitude curve shows the maximal suppression of orbit perturbations at the locations of the BPMs.

plied so far. According to the transfer function unity gain is reached at 80 Hz and moderate amplifications can be observed up to 400 Hz. The integrated RMS orbit motions were enlarged from $0.95 \mu\text{m}$ to $1.1 \mu\text{m}$ horizontally and from $0.95 \mu\text{m}$ to $1.2 \mu\text{m}$ vertically.

Two excitations of the electron beam at frequencies of 76 and 95 Hz are most likely due to numerical rounding errors in the digital receivers. This effect can be eliminated by adjusting the internal gain settings in the DBPM system. The integrated position RMS values with and without feedback are summarized in Tab. 2.

FOFB	horizontal		vertical	
	off	on	off	on
0.5-100 Hz*	$1.7 \mu\text{m}$	$1.4 \mu\text{m}$	$1.5 \mu\text{m}$	$0.9 \mu\text{m}$
100-400 Hz*	$0.95 \mu\text{m}$	$1.1 \mu\text{m}$	$0.95 \mu\text{m}$	$1.2 \mu\text{m}$

Table 2: Integrated position RMS values at the location of the tune BPM ($\beta_x \simeq 11$ m, $\beta_y \simeq 18$ m).

*These figures still contain the sensor noise contribution which is not clearly quantified yet.

CONCLUSION AND PERSPECTIVES

The commissioning of the SLS FOFB has just started and first results have been presented. Its conceptional design could be successfully demonstrated. Focus during the first measurements was the commissioning of the feedback components rather than optimization of the performance.

To reach the FOFB design goals of integrated sub-micron orbit stability up to 100 Hz in both planes, several improvements will be accomplished during the further commissioning. An upgrade of the DDC firmware to synchronize the 4 kHz BPM outputs will reduce the digital feedback delay by $240 \mu\text{s}$. Beside this, the data transfer from the DSP to the power supply controller which presently takes place via the IOC of the control system will be short cut. Both upgrades will reduce the digital latency and consequently increase the loop bandwidth. Optimizations of PID parameters are required to achieve increased feedback performance. Recent laboratory studies have shown the potential to reduce the BPM noise clearly below $1 \mu\text{m}$ even at 2 kHz bandwidth. Furthermore, long term and power spectral densities measurements at several locations especially close to the insertion devices as well as X-ray BPM measurements will be necessary in order to quantify the residual position RMS values of the orbit.

REFERENCES

- [1] V. Schlott et al., "Performance of the Digital BPM System for the Swiss Light Source", DIPAC'01, Grenoble 2001.
- [2] M. Böge et al., "Orbit Control at the SLS Storage Ring", EPAC'02, Paris 2002.
- [3] M. Böge et al., "Fast Closed Orbit Control in the SLS Storage Ring", PAC'99, New York 1999.
- [4] M. Böge, J. Chrin, "Integrating Control Systems to Beam Dynamics Applications with CORBA", Contribution to this conference.
- [5] F. Jenni, Private Communications, 2002.

LOW-MODE COUPLED BUNCH FEEDBACK CHANNEL FOR PEP-II*

L. Beckman[†], N. Hassanpour, L. Sapozhnikov, D. Teytelman, J. Fox
Stanford Linear Accelerator Center, Menlo Park, CA 94025, USA

Abstract

Both the HER and LER of PEP-II use broadband longitudinal multi-bunch feedback systems which process all coupled-bunch modes in the machine spanning a 119 MHz bandwidth. Roughly 1 MHz of this bandwidth includes modes driven by impedance related to the RF cavity fundamental.

The longitudinal modes within the cavity bandwidth are processed by the all-mode broadband systems, though the correction signal is applied to the beam via a path through the broadband kicker, as well as through a special woofer channel which uses the RF system to apply low-mode correction signals to the beam. As there are two correction paths, with differing group delay and frequency response, yet only one adjustable processing channel, it is difficult to get an optimal low-frequency ("woofer") response if the broadband feedback path is configured to best control HOM driven instabilities.

A new low-mode processing channel has been designed to provide an independent means of providing the low-mode correction signal. It is a digital channel, operating at a 10 MHz sampling rate, and incorporating programmable 12 tap FIR control filters. This channel, implemented using EPLD technology, allows more optimal gain and phase adjustment of the woofer control path, with lower group delay allowing higher gain. This extra flexibility and higher gain will be useful in future high-current PEP-II operation. The design of the control channel is illustrated, and a possible control filter with system dynamics is described.

INTRODUCTION

The RF systems in PEP-II use room temperature copper cavities, with HOM damping and complex LLRF feedback loops to control the impedances seen by the circulating beam [1, 2]. This RF system has been successfully operated at design currents, though the growth rates of low longitudinal modes within the RF system bandwidth have been measured to be significantly (factors of 5 to 20) higher than estimated by simulations during system design [3]. To control these low longitudinal modes the systems have been using a processing channel [4] to extract low mode longitudinal motion signals from the broadband control path and inject this correction signal in the RF system itself, using the klystrons as a power source to make correction fields.

The maximum damping rate that this "woofer" can provide is limited by the combination of the bandwidth of control required, the gain required, phase non-linearities in the

control path and the time delay around the control path, which physically spans several sections of the 2.2 kilometer machine circumference. The broadband multi-bunch feedback control filters are optimized to have best damping for signals applied to the beam via the broadband all-mode kickers and power amplifiers. Using the RF cavities as a kicker path requires extra time delays to align the correction signal with the proper bunches (which can be up to 12/3 of a revolution), and the phase response of the control filter is not optimum for this longer path. Figure 1 shows the maximum damping rate the existing woofer implementation can provide as a function of feedback path gain. The maximum damping rate of -1.5 ms^{-1} at the 1580 mA current limits the allowable instability growth rates of the low modes – turning up the gain in the channel simply reduces the damping while adding a large reactive tune shift. As the growth rates increase with current, the measured results suggest that the existing implementation will become marginal in effectiveness at operating currents much above the design level.

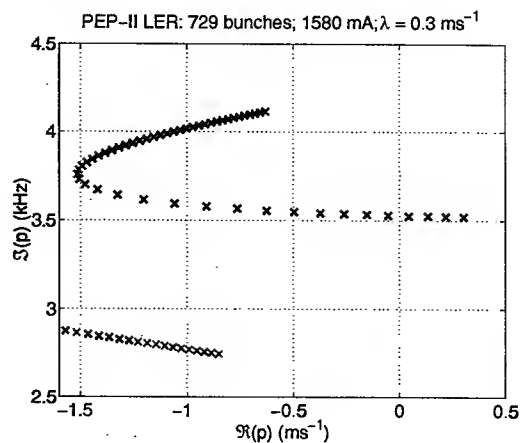


Figure 1: Gain-locus plot showing the maximum damping possible through the woofer in the PEP-II LER. With no gain the instability growth rate for the most unstable mode is 0.3 ms^{-1} . With increasing woofer gain a maximum damping of -1.5 ms^{-1} is reached. Increasing the channel gain beyond this point simply produces greater reactive tune shift, as well as less resistive damping.

A LOW-GROUP DELAY WOOFER

One path to achieving control at higher operating currents is to reduce the time delay around the feedback loop, which allows higher loop gain. To implement this path requires a control channel independent of the existing downsampled DSP farm. This non-downsampled path can sam-

*Work supported by Department of Energy contract DE-AC03-76SF00515.

[†]lbeckman@slac.stanford.edu

ple at a rate lower than the bunch crossing rate if it is only to control a fraction of the 119 MHz bandwidth (just the low-modes within the cavity bandwidth), rather than the full span of coupled-bunch modes. Such a channel is also advantageous in that it can be independently adjusted to optimize the control loop gain and phase to achieve best damping using the RF cavities in the control loop.

The low group delay woofer is based around a 10 MHz sampling rate FIR filter, structured so that the delay between taps is exactly one revolution period at the sampling rate. The system can be thought of as a macrobunch-by-macrobunch feedback system, where the information on the oscillation coordinates of a group of bunches is averaged into a "macrobunch". In essence the lowest normal modes of bunch motion involve small variations in oscillation phase between neighbor bunches, so that the motion of a "macrobunch" is a good measure of the collective low-mode motion of that sub-group of bunches.

DESIGN FEATURES

The sampling clock is derived from the RF system master oscillator in the existing back-end module, using a PLL to generate a bunch synchronous sampling clock at 72x the revolution frequency. The baseband bunch phase oscillation signal from the broadband longitudinal system is split off, low pass filtered and digitized with 12 bit resolution. The output data path is converted back to baseband in a 12 bit D/A, and this computed correction is then re-sampled in the existing back-end module and transmitted to the RF stations. [5]

As shown in Figure 2 the data path is 8 bits wide, and the filter implements 16 bit coefficients with a 28 bit output accumulator. To allow final gain adjustment, independent of the coefficient values, the design includes a "shift gain" output register that allows post-computation shifting of the output result of up to 15 bits (scaling the gain by 2^N), and includes arithmetic saturation in the output logic.

The filter coefficients are stored as a set of 2 possible coefficient sets, so that the filter can be changed on the fly by selecting a filter set. This structure allows a number of transient-domain measurements of the dynamics to be made [6]. A 128 KB block of diagnostic memory is included in the design, and this memory can either record beam motion while the filter runs (or switches), or play back sequences through the output D/A to drive the system for diagnostic or measurement purposes.

The prototype is controlled via a parallel interface from a host computer, and the interface memory maps the various control registers, coefficient registers, and diagnostic memory. A simple user interface has been prototyped allowing the selection of filter coefficient sets, shift gains, etc. via a graphical panel.

The design has been prototyped using a commercial Xilinx evaluation board from GV Associates [7], which includes a pair of Xilinx XC4085XLA FPGA devices, the A/D and D/A components, diagnostic memories and a gen-

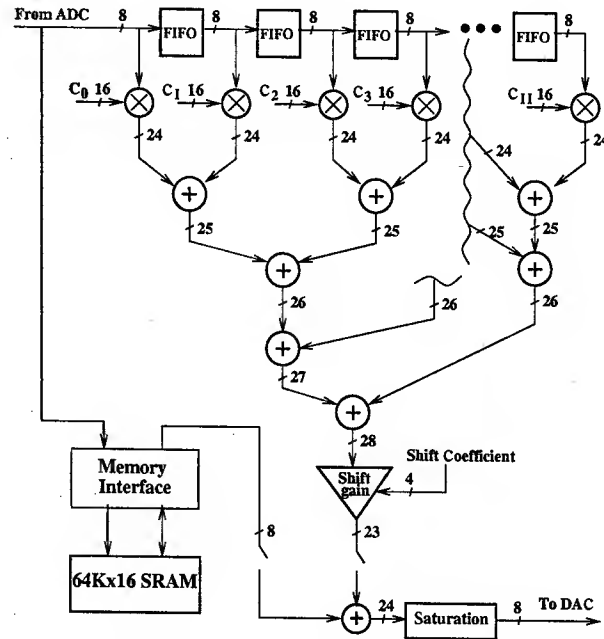


Figure 2: Block Diagram of the EPLD implemented 12 tap FIR filter. The figure explicitly shows 5 taps; the structure of the adder tree is shown where it is extended for the 12 tap filter, with 12 coefficients and multipliers. Also shown is a diagnostic memory used for transient domain measurements.

eral purpose parallel interface. The evaluation board environment is an excellent platform to evaluate various architectures and test this approach on real beam signals.

SIMULATIONS OF THE DYNAMICS OF LOW-MODES

To estimate the performance of this system, a simple dynamic model has been constructed, which models the low-mode feedback filter, RF system and beam, though the beam model is a simplified treatment of an unstable harmonic oscillator with parameters derived from measurements of the actual machine. There are numerous possible control filters, and Figure 3 presents the baseband frequency response for the filter used in our initial simulations. This baseband control filter is then folded around all the 36 revolution harmonics in the system bandwidth. The frequency response of this filter peaks at 12 KHz, a frequency well above the 5.5 KHz synchrotron frequency. This high-frequency gain is a consequence of the low-group delay processing. A filter more narrowly peaked around the synchrotron frequency must inherently have a longer processing or group delay as it must take more samples and time to define the synchrotron frequency. Hence this processing approach achieves the low group delay, as desired, but the system is now sensitive to extraneous noise or beam signals above the synchrotron frequency, and the system must not saturate on these signals, even though the filter has 10 dB more gain at these high frequencies compared to the synchrotron frequency.

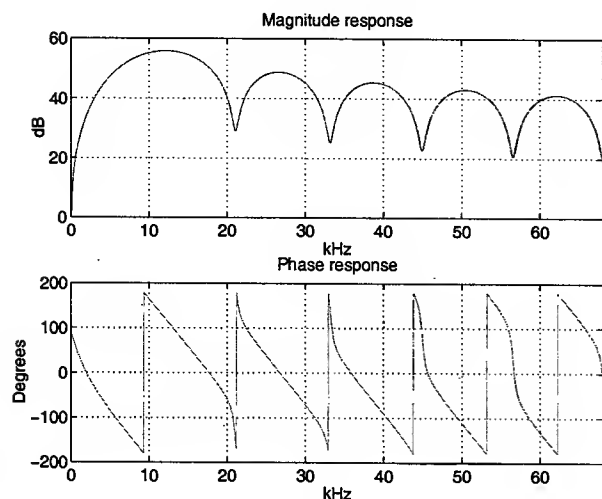


Figure 3: Magnitude and phase responses for a proposed 12 tap FIR filter for the low group delay processing channel. This filter is designed for the PEP-II HER, with a synchrotron frequency of 5.5 KHz. The low group delay filter provides the damping phase shift of 90 degrees with 44 dB of gain at this frequency, though the 54 dB maximum gain of the filter is found at 12 KHz

A LOW-GROUP DELAY WOOFER

Figure 4 presents a gain locus plot for a possible filter candidate. The filter shows the unstable pole with no feedback, and shows the damping increasing with increasing system gain. There is a maximum useful gain, above which the damping decreases with significant tune shifts. This simulation result suggests this type of filter could provide damping rates in the PEP-II HER of the order of 4 ms^{-1} before excessive tune shifts are created, or roughly a factor of three better than the existing implementation. Such an improvement would be a significant increase in the operating margins and headroom at the design current, though exactly what ultimate higher operating current such a filter might control requires more study.

CONCLUSIONS AND FUTURE DIRECTIONS

The core processing functions are compiled and functioning, as is the interface to the FIR filter functions from a host PC. We are in the process of verifying the dynamic range and functioning of the processing channel, and comparing the measured behavior to that expected from simulations. We expect to be able to run the low-mode woofer as a control element of the PEP-II LER in summer machine physics opportunities. A careful study is necessary to verify that this approach is feasible, given the concerns about noise saturation of the filter, and that it actually offers a damping rate improvement over the existing control path in the broadband feedback. Finally, there is considerable room to develop optimized filters, of various forms, that may well offer better control dynamics and allow higher

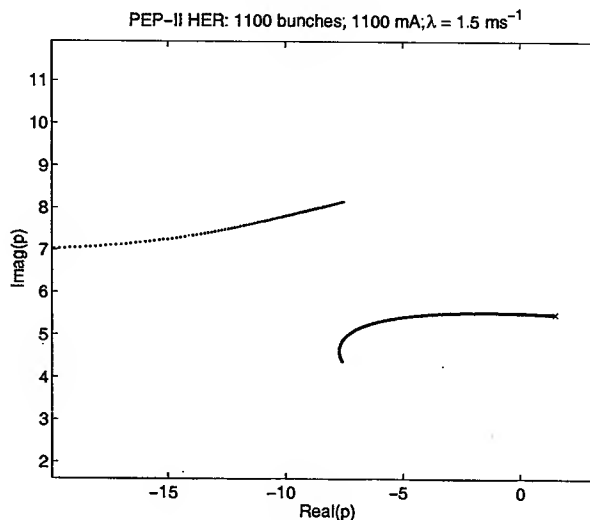


Figure 4: Gain locus study for a proposed woofer filter for the PEP-II HER. The unstable growth rate without feedback is 1.5 ms^{-1} at 1100 mA. Increasing the woofer gain to the 44 dB of Figure 3 produces damping rates of -4 ms^{-1} .

gain. Efforts to understand these options are at very preliminary stages.

ACKNOWLEDGMENTS

The authors thank Boni-Cordova Grimaldi for her patient fabrication of the prototype chassis, and A. Young (SLAC) for his suggestions on integrating the low-group delay woofer into the existing PEP feedback systems. We also thank Dr. Makoto Tobiyama of KEK for his numerous technical suggestions and help in preparing the poster and paper for the conference.

REFERENCES

- [1] P. Corredoura, et al., "Experience with the PEP-II Rf System at High Beam Currents", Proc. EPAC'2000, Vienna, Austria, 2000
- [2] F. Pedersen, "RF Cavity Feedback", Proc. of B-Factories-The State of the Art in Accelerators, Detectors and Physics, Stanford, CA 1992
- [3] R. Tighe, P. Corredoura, "RF Feedback Simulation Results for PEP-II", Proc PAC'95, Dallas, TX, May 1995
- [4] J. Fox, et al "Programmable DSP based Multi-Bunch Feedback: Operational Experience from Six Installations", Proc Beam Instrumentation Workshop, Cambridge MA 2000
- [5] A. Young, et al "VXI based Multibunch Detector and QPSK modulator for the PEP-II/ALS/DAFNE Longitudinal Feedback System", Proc PAC'97, Vancouver, BC June 1997
- [6] D. Teytelman, et al, "Beam Diagnostics Based on Time Domain Bunch by Bunch Data," Proc. Beam Instrumentation Workshop, 1998
- [7] GV & Associates, Inc. Ramona, CA

execute various applications in every VME node in the same operating system environment. The system timing was improved to one millisecond using a VME interrupt. The bus adapter is fit into slot 1 of the VME crate, to be as a system controller. All programs were developed and debugged on a PC and downloaded to the DSP board. The DSP board, carrying a TMS320C40 module, handled all signal processing, and included a digital low pass filter (LPF) and PID controller.

UPGRADE ISSUES

The existing orbit feedback system was a C'4x DSP based system. The DSP module was installed in the corrector control VME crate. The host computer of the corrector node handled interrupt requests and generated two trigger events that were sent to DSP. One was for vertical orbit feedback; other was for horizontal orbit feedback. The system was nearly ten years old and outdated in terms of performance, features and integration.

The demand of orbit feedback system have increased dramatically during the last decade. More BPM signals and correctors are required in the feedback loops. In particular, several insertion devices had to be able to be moved at the same time. A simple look-up table correction scheme does not suffice for this dynamic request. The orbit feedback system had to be upgraded for several reasons, to improve the maintainability and stability of the system. The DSP board of the original feedback system is embedded in the corrector control VME crate, which situation is inconvenient for developing a feedback system. The impact of machine operation and research on the control algorithm development was a problem. Secondly, the system was implemented in 1995 with a slow DSP board; the functionality of the feedback loop was therefore limited. Not enough computing power was available to meet the increasing demand of the increasing number of BPMs and correctors. The control algorithm implement was also limited due to the computing power. In the new implementation, the feedback calculation will be performed on a separate VME crate. The feedback controller is decoupled to the feedback node processor from corrector node. The upgraded system includes three VME crates – the BPM node, the corrector node and the feedback node, as shown in the figure 5. These three nodes are connected by reflective memory. Several of the fiber link reflective memory cards are tied together by one dedicated reflective hub that simplifies the routing of the fiber link. The corrector node handles the power-supply control. The existing DSP systems have migrated to PowerPC 7410 (G4) architectures for greater performance, ease of use, and access to opening standards. The PowerPC handles feedback control, the calculation of the control algorithm and the conversion of the orbit information signal to the corrective action of the corrector. The correction value results are sent to the

corrector node with fiber link. In the same time, the synchrotron event is broadcasted from BPM node and sends to corrector node and feedback node with fiber link.

The processor of feedback node handles more multi-input and multi-output controller loops in each mill-second period. Although the new-generation DSPs, such as TMS320C6201 or TMS320C6701 from Texas Instruments, can meet this request, maintenance is problematic and parts are expensive. The general-purpose CPU with a real-time OS also met our specification of feedback control, but isn't the disadvantage of DSP. The more important issue is that save time in the developing the upgrade.

The PowerPC is belong to a kind of general purpose CPU that is based on Motorola's AltiVec technology, specifically on the fourth-generation MPC74xx. Digital signal processing applications are beginning to migrate from a traditional DSP environment to a RISC environment, Motorola has been increasing the processing power of the PowerPC, to increase the speed and flexibility of an already impressive portfolio of DSPs, such as by introducing new parts from the C6000 family of Texas Instruments. Table 1 presents some of the processors available from Texas Instruments and Motorola that can be used to meet upgrade requirements in the future.

Table 1: List of processors for orbit feedback.

Manufacturer	Processor	Part Number
Texas Instruments	C6415	TMS320C6415
Texas Instruments	C6203	TMS320C6203
Texas Instruments	C6701	TMS320C6701
Motorola	7410	MPC7410

Table 2: Speed and benchmarks of DSP and PowerPC. The 7410 can perform up to 16 parallel integer calculations on 8-bit data per cycle, so the MIPS number: is 16 multiplied by 500 MHz to 8000 MIPS. Some 7410 instructions involve 8 calculations per cycle.

	C6415	C6203	C6701	7410
Clock(MHz)	600	300	167	500
Instruction Cycle (ns)	1.67	3.33	6	2
Instruction Per Cycle	1~8	1~8	1~8	1~3
Peak MIPS	4800	2400	1336	917 ¹
Floating-Point Operations Per Cycle	-	-	1~6	4 ²
Peak MFLOPS	-	-	1000	2000

A first view of the performance of the processor can be obtained by comparing clock speeds and peak processing power, as shown in Table 2. Both DSP and the PowerPC solution can meet the requirements of orbit feedback. However, the PowerPC was chosen since it is to be compatible with the existing control system.

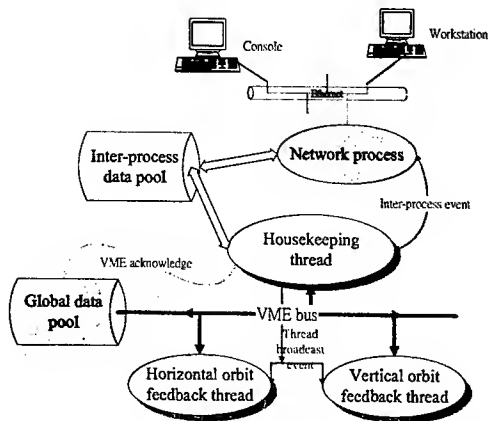


Figure 2: Relationship between software processes.

SOFTWARE TASK MANAGEMENT

The main tasks of the software in the feedback node include housekeeping, horizontal orbit control and vertical orbit control thread process. The housekeeping thread handles the transportation of control parameters; the VME interrupts acknowledge and thread broadcast events. Two orbit control threads handle global data access, digital filtering and the PID controller. The control parameters include the PID coefficient, the filter coefficient, feedback on/off and other special applications. The network process receives these parameters and saves them to the inter-process data pool from the console over the Ethernet. The inter-process data pool supports data exchange between different tasks. The global data pool handles data exchange between different VME crates and different threads. The housekeeping thread broadcasts an event to other threads when the interrupt is acknowledged from the VME bus. Two orbit feedback threads are always waiting until such an event is received. The threads are synchronized at the same time to prevent two the feedback controls of plane in the data access specifically.

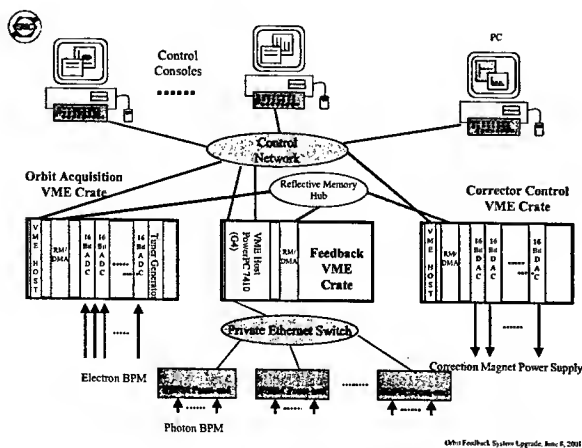


Figure 3: Hardware structure of the orbit feedback system.

CURRENT STATUS

The new hardware structure is based on the old system. The feedback loop is divided into a VME crate separate from the original corrector node. The sub-components of the feedback node were tested successfully. These components support VME interrupt requests, VME bus access, signal processing and the controller loop. Figure 2 presents the new system block diagram. The system process rate is close to 1KHz, with two-planes orbit feedback. Figure 3 shows details the process timing. The signal in line 1 is close to 1 millisecond, which is the sampling rate of the system. Two feedback loops are processed timing simultaneously as shown in line 2 of figure 3, take 70 microseconds in two planes. This period time includes filtering, PID calculation and 60 BPM readings and 36 corrector settings. The multi-thread technique is applied to the feedback control. The latency time in the line2 of figure 3 is 50 microseconds due to bus arbitration of CPU. The threads technique keeps from processes are interfered each other. Optimization of the orbit feedback system is ongoing.

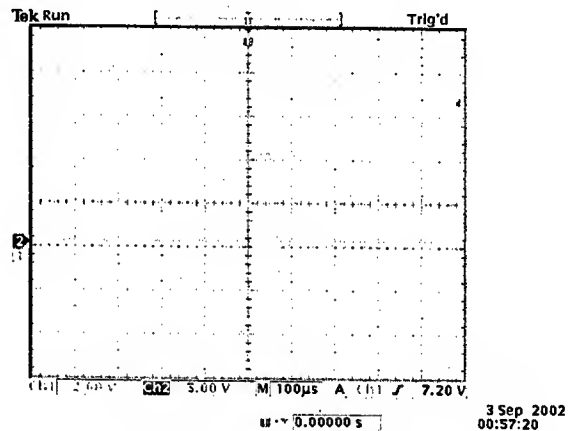


Figure 4: Timing measurement.

REFERENCES

- [1] C. H. Kuo, et al., "Local Feedback Experiment in the Taiwan Light Source", Proceedings of 1997 IEEE Particle Accelerator Conference, Vancouver, 1997.
- [2] C. H. Kuo, et al., "Digital Global Orbit Feedback System Developing in SRRC", Proceedings of 1997 IEEE Particle Accelerator Conference, Vancouver, 1997.

OPERATION OF THE DIGITAL MULTI-BUNCH FEEDBACK SYSTEMS AT ELETTRA

D. Bulfone, V. Forchi', M. Lonza, L. Zambon, Sincrotrone Trieste, Trieste, Italy
M. Dehler, Paul Scherrer Institut, Villigen, Switzerland

Abstract

Bunch-by-bunch feedback systems have been installed at ELETTRA to counteract coupled-bunch instabilities. Following a novel approach both the transverse and the longitudinal systems rely on the same type of programmable digital processing electronics executing the proper software. After a description of the overall machine scenario in which the transverse systems are operated, the status of the longitudinal feedback commissioning is given.

OPERATION OF THE TRANSVERSE FEEDBACK SYSTEMS

Digital bunch-by-bunch Transverse and Longitudinal Multi-Bunch Feedback (TMBF and LMBF) systems have been developed in collaboration between ELETTRA and the Swiss Light Source (SLS). Their characteristics and diagnostic capabilities are described in [1, 2].

The first TMBF acting on the vertical plane has been routinely operating since November 2001 during the users shifts at 2.4 GeV (140 mA). At this energy a suitable setting of the cavity temperatures and higher order mode shifters can damp longitudinal instabilities. Horizontal instabilities are removed by increasing the strength of the harmonic sextupoles, which broaden the tune spread with amplitude of the electrons within the bunch. The resulting reduction in dynamic aperture affects the beam lifetime that nevertheless is still about 26 hours at 140 mA.

The 2 GeV (330 mA) scenario has significantly improved after the recent installation and cool down of the Superconducting 3rd Harmonic Cavity (S3HC) [3]. In addition to providing a better lifetime, the S3HC has a damping effect on the longitudinal instabilities, which can be completely eliminated by increasing the multi-bunch contiguous filling adopted during user shifts from 80 to 90%. The installation of a second TMBF system for the horizontal plane has further enhanced the 2 GeV scenario. The harmonic sextupoles setting could be restored to the nominal value with a considerable gain in lifetime. In this configuration a coupled-bunch instability free beam is delivered to the users also at 2 GeV and the lifetime at 300 mA is about twice the theoretical value. Further optimizations are in progress together with the full characterization of the S3HC.

Since their installation the operation of the TMBF systems has been effective and reliable. They are integrated in the ELETTRA control system with the *init*, *run* and *standby* procedures fully automated and easily activated from the control room panels running on the UNIX consoles.

LONGITUDINAL FEEDBACK SYSTEM COMMISSIONING

Back-End

Figure 1 shows the block diagram of the LMBF back-end. The 250 MHz bandwidth base-band signal generated by the DAC, which contains the longitudinal kick values for each of the 432 ns spaced bunches, is amplitude modulated (SSB modulation) using a coherent carrier at $3 \cdot f_{RF}$. The broadband signal is then amplified by a 250 W TWT (Travelling Wave Tube) power amplifier followed by a circulator that protects the amplifier against backward power coming from the kicker. The power signal is brought into the accelerator tunnel by a 7/8" coaxial cable and then split to drive the four wave-guide input ports of the kicker. The four output ports are terminated with 50 Ohm power loads installed nearby the kicker.

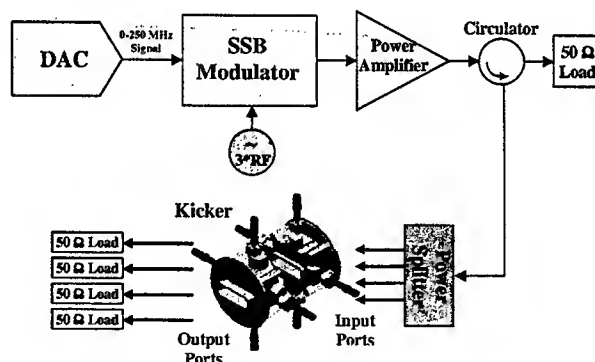


Figure 1: Block diagram of the longitudinal feedback back-end.

The installation of the longitudinal kicker (figure 2) was smooth and no additional coupled bunch modes have been observed in the beam, proving that it behaves as expected with respect to Higher Order Modes (HOMs) [4].

Particular care has been taken to optimize the operation of the back-end considering that the kicker behaves like a resonant cavity at $11/4 f_{RF}$ frequency. The bunch-by-bunch approach adopted by the digital multi-bunch feedback systems considers each bunch as an independent oscillator that can be damped by applying a dedicated feedback loop. This implies that the correcting kick for each bunch must not perturb the adjacent bunches, i.e. the voltage signal must have a maximum when the selected

bunch passes through the kicker and must be zero for the preceding and following bunches.

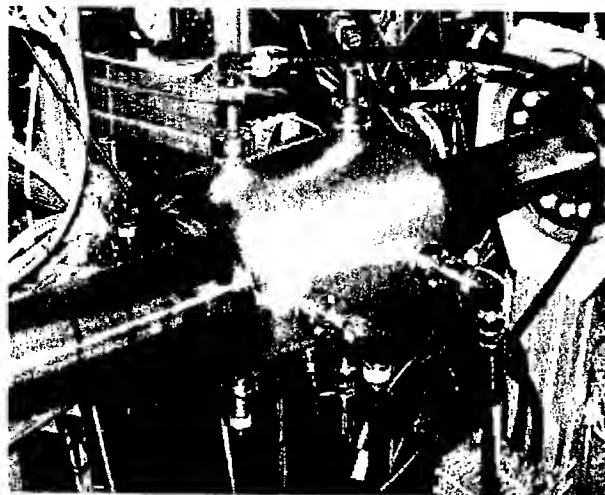


Figure 2: The longitudinal kicker installed at ELETTRA.

Starting from the SSB modulation scheme as described in [2], a number of modifications have been carried out to improve the time domain response of the back-end. The resulting response to a 2 ns long square pulse (i.e. the correction value for a given bunch generated by the DAC) measured on the kicker HOM coupler output is shown in figure 3. The signal features zero crossings at 2 ns from the maximum, while before/after 4 ns the voltage is negligible.

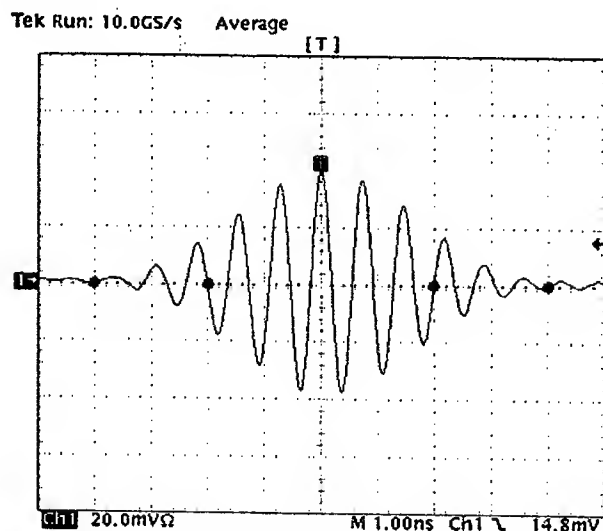


Figure 3: Back-end response to a 2 ns long square pulse generated by the DAC measured on the kicker HOM coupler output.

Longitudinal Feedback DSP Software

The same type of digital processing electronics used for the TMBF systems can be employed also for the LMBF by simply running different DSP (Digital Signal Processor) software. In the transverse planes the betatron fractional tunes are relatively high (at ELETTRA they are

about 0.2 in the vertical and 0.3 in the horizontal plane) and the position samples acquired at each machine revolution must be processed in order to calculate the correction signal used to damp the oscillation of a given bunch. In the longitudinal plane the lower synchrotron tune (0.0092 at 2 GeV) allows to down sample the digital phase error signal from each bunch and to use only one over n of the incoming samples to feed the digital filter; the correction signal is accordingly updated once every n revolution periods. The down sampling technique increases the time the DSPs have to calculate the correction values and more sophisticated digital filters can be implemented.

Thanks to the programmability of the system, the down sampling is carried out via software. The samples at full data rate (500 MSample/s) are acquired by the array of DSPs, which can concurrently record all of them for diagnostic purposes, but only one out of n is used by the feedback algorithm, the rest of them being discarded. After the processing, the DSPs' output buffer is filled with the same calculated value for n times.

At ELETTRA a down sampling factor $n = 10$ has been chosen resulting in a down sampled synchrotron tune of 0.092, which allows the digital filter to reject the DC component of the signal and to have at the same time a pretty high gain at the synchrotron tune. A 4th order digital IIR (Infinite Impulse Response) filter is currently implemented.

Commissioning Techniques

The commissioning of the LMBF is taking full advantage of the diagnostics capabilities provided by the digital processing system.

One of the most important tasks when setting up the feedback is the synchronization of the kicks with the bunches. The feedback system itself can be used for this purpose. By kicking only one bunch with an excitation signal and analyzing the spectrum of each bunch, the actually excited bunch is determined and the system delay is then adjusted until the chosen bunch is kicked. The excitation signal can be generated in Matlab, which runs on the control room workstations, and is downloaded through the control system directly into the DSPs' memory. In the transverse planes excitation with pink noise featuring a frequency band around the fractional betatron tune has been employed. In the longitudinal plane the lower efficiency in kicking the beam led us to excite the bunch with a sinusoid at the synchrotron tune. Using fine adjustments (10 ps resolution) the timing can be further optimized by maximizing the excitation amplitude of the selected bunch while minimizing the spurious excitation of the adjacent ones. Figure 4 shows an example of bunch excitation and demonstrates the selectivity of the system.

Another technique used to optimize the feedback settings (timing, gain, filters, etc.) and to evaluate the feedback performance in terms of damping capabilities is the generation of transients.

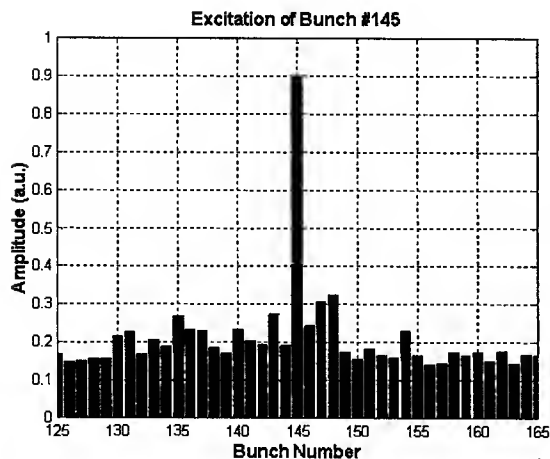


Figure 4: Amplitude of the synchrotron tune spectrum component of a number of bunches when selectively exciting only bunch #145.

Figure 5 shows examples of transients created by the LMBF system, which can record up to 192 ms of bunch-by-bunch samples during the transients. The data are immediately uploaded in Matlab and analyzed. In this experiment the beam is originally stable, being the potential longitudinal coupled-bunch modes due to cavity HOMs below their excitation threshold. By properly setting the feedback filter coefficients an anti-damping effect is produced and the coupled-bunch mode #91 gets steadily excited with 11.5 degrees oscillation amplitude.

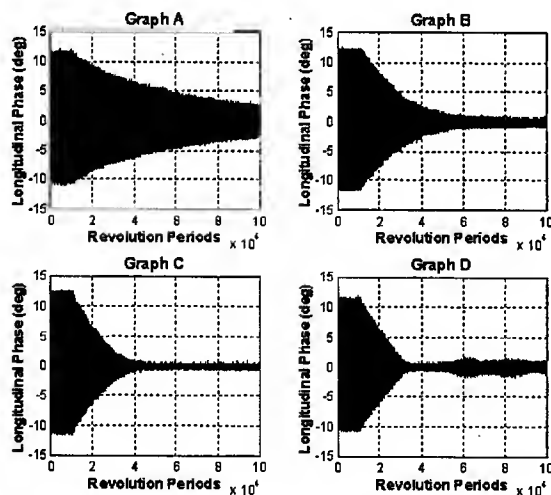


Figure 5: Longitudinal oscillation of one bunch during four different transients generated by the feedback system. A: natural plus Landau damping. B: damping with feedback at half gain. C: damping with feedback at full gain. D: damping with saturated feedback.

After 12000 revolution periods from the beginning of the data acquisition the filter coefficients are changed to create four damping transients of different type:

- A: filter coefficients set to zero. The decay is due to natural and Landau damping.
- B: filter coefficients set to damping values. The filter is linear producing an exponential damping.
- C: filter coefficients set to damping values and filter gain set to twice the value of case B. The filter is still linear producing a shorter exponential damping.
- D: filter coefficients set to damping values and filter gain set to its maximum. The filter is saturated and the decay is linear.

The combination of the linear equations obtained from the cases above allows to easily determine the LMBF performance.

Status and Plans

The LMBF equipment and electronics have been installed and the commissioning is in progress. Due to the cessation in the construction of the commercial 500 MSample/s ADC and DAC boards adopted by the system, the digital processing electronics of one of the two TMBF systems running the appropriate software is used for the commissioning of the LMBF. A new family of conversion boards developed in collaboration with SLS will be ready soon [5].

By activating the LMBF from the beginning of the injection process, up to 280 mA of a longitudinally stable beam at 0.9 GeV have been accumulated.

REFERENCES

- [1] D. Bulfone et al., "Exploitation of the Integrated Digital Processing and Analysis of the ELETTRA/SLS Transverse Multi-Bunch Feedback System", PAC'01, Chicago, June 2001.
- [2] D. Bulfone et al., "The ELETTRA Digital Multi-Bunch Feedback Systems", EPAC'02, Paris, June 2002.
- [3] M. Pedrozzi et al., "First Operational Results of the 3rd Harmonic Super Conducting Cavities in SLS and ELETTRA", these Proceedings.
- [4] M. Dehler, "Kicker Design for the ELETTRA/SLS Longitudinal Multi-Bunch Feedback", EPAC'02, Paris, June 2002.
- [5] M. Dehler et al., "Capabilities of the ELETTRA/SLS Multi-Bunch Feedback Electronics", DIPAC'03, Mainz, May 2003.

STRONG-STRONG SIMULATION OF BEAM-BEAM INTERACTION FOR ROUND BEAMS

A. Valishev*, E. Perevedentsev, Budker Institute of Nuclear Physics, 630090, Novosibirsk, Russia
K. Ohmi, KEK, 1-1 Oho, Tsukuba, 305-0801, Japan

Abstract

This paper presents the results of numerical simulations of beam-beam interaction in a e^+e^- machine with round colliding beams. The calculations were done with the Particle-in-Cell computer code which was developed for the KEKB B-Factory [1]. The code was modified to include the effect of the machine nonlinearity and dynamical radiation emittance. A simulation study of the round beam collider VEPP-2000 justified the choice of the chromaticity correction scheme, working point and optics capable of achieving the design luminosity.

INTRODUCTION

The single bunch luminosity at present circular e^+e^- colliders is limited by the beam-beam interaction. The nonlinear force of the counter-rotating bunch disturbs the betatron motion leading to the betatron coupling resonances. At some threshold beam intensity the resonances overlap, making the motion chaotic and causing the beam blow-up and life time degradation detrimental to the luminosity. The intensity of the beam-beam interaction is characterized by the dimensionless parameter ξ . In a collider with flat beams the beam-beam parameters for two transverse oscillation modes (x and y) differ, and the threshold value for ξ currently does not exceed 0.09.

Hence, various methods are proposed to overcome this limit. One of them makes use of the Round Colliding Beams. The first straightforward advantage of round beams is that ξ_x is equal to ξ_y and the cross-section of beams at the Interaction Point (IP) is round. This geometric property gives at least a factor of two increase in luminosity at constant ξ [2].

But the main idea of the method is aimed at enhancement of the maximum attainable beam-beam parameter. This can be achieved because of elimination of the betatron coupling resonances by introducing an additional integral of motion, namely the longitudinal component of the particle's angular momentum [3, 4]. Analytical models show the possibility to construct an integrable optics and predict the advantage of the round beams [4]. Some experimental tests of a Möbius accelerator [5] which is an option of round beam machine, were done at CESR (Cornell, USA) demonstrating accessibility of the beam-beam parameter as high as 0.1 [6]. However, the round beams in high luminosity regime were not obtained to this moment. The collider VEPP-2000 (BINP, Novosibirsk) with the design luminosity of 1×10^{32}

$\text{cm}^{-2}\text{s}^{-1}$ at 1 GeV will use round beams as one of its operation options, thus presenting an opportunity to check the method [7].

In the past decade a number of computer codes appeared [1, 8, 9] using advanced models of the beam-beam interaction and allowing to perform numerical simulations of colliding bunches with sufficient accuracy. Although the computer simulations do not reproduce the experimental results precisely, they give a good answer about the main characteristics of the system: beam size and the beam-beam limit, coherent beam-beam tune shift, etc. Thus, a comprehensive numerical simulation of beam-beam effects for a new collider is highly advisable.

This report presents some results of simulation of beam-beam interaction for the VEPP-2000 optics using a modified PIC code which has been originally developed for KEKB [1]. The calculations show availability of very high values of ξ in ideal optics and reveal some problems in a more realistic case. Based on this simulation, a corrected machine optics has been chosen.

THE CODE

The code for calculating the beam-beam force is described in detail in [1]. This part did not need modification for our purposes. Here we describe only the main features of the algorithm.

Each colliding beam is represented with N_p macroparticles forming a 3-dimensional distribution in space, where N_p is taken big enough to avoid statistical effects and in our case was 5×10^4 . The code uses 2D mesh to evaluate the transverse field which is calculated via the Poisson equation using FFT. Particles of the opposite bunch are tracked through the field. We used 128×128 mesh with coordinate region covered approximately ± 10 of the transverse beam σ . Due to a comparatively long radiation damping time in VEPP-2000 (5×10^4 turns) we did not use longitudinal slicing of the beam, hence the beam-beam interaction was substantially 2-dimensional.

Modifications of the code concern particle tracking over the accelerator arc and radiation damping/quantum excitation. Nonlinearities of the machine optics are known to influence the beam-beam effect, therefore we included the chromaticity correction sextupoles as thin elements with linear transformations of betatron coordinates between them. Simulated dynamical aperture in the absence of beam-beam interaction reproduces very well the results of special codes.

Another important effect for electron machines consists

* valishev@inp.nsk.su

in dynamical change of the beam emittance due to deformation of the machine lattice by linear part of the beam-beam force. In the original code the equilibrium emittance was simulated by applying radiation damping and random quantum excitation once per turn:

$$X = \lambda X_0 + \sqrt{(1 - \lambda^2)\epsilon} \hat{F}.$$

Here X is 2-vector of dynamic variables of one normal mode, $\lambda = e^{-\delta}$ with δ being the damping decrement, ϵ is the nominal equilibrium beam emittance, and \hat{F} is a vector of two Gaussian random numbers with the mean value equal to 0 and $\sigma = 1$. This mapping did not give the correct deformation of the beam emittance. To repair it, we introduced the modified mapping

$$X = \lambda X_0 + \sqrt{(1 - \lambda^2)\epsilon} M_d \hat{F},$$

where

$$M_d = \begin{pmatrix} a + d & b \\ b & a - d \end{pmatrix},$$

with

$$a = \sqrt{\frac{1}{2} - \frac{1}{2}\sqrt{1 - c^2 - s^2}}, \quad d = c/2a, \quad b = -s/2a.$$

The excitation coefficients c and s are calculated from the quantum excitation (or *diffusion*) matrix Q [10]. In the normal mode basis the matrix has the form

$$\tilde{Q} = 2\delta\epsilon \begin{pmatrix} 1 + c & -s \\ -s & 1 - c \end{pmatrix}.$$

Figure 1 shows comparison of tracking using weak-strong linearized beam-beam interaction and the modified quantum excitation with calculation using conventional optics code, namely, SAD [11]. In SAD, the axisymmetric beam-beam lens was modelled using a pair of thin solenoids placed at the IP.

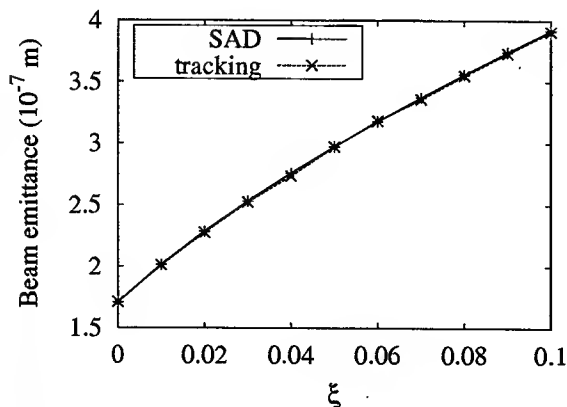


Figure 1: VEPP-2000, one IP. Beam emittance vs. ξ . Weak-strong linearized beam-beam interaction.

RESULTS FOR LINEAR OPTICS

VEPP-2000 has the design with two IP's and symmetrical arcs between them [7]. Maximum operation energy is 1 GeV per beam, but all calculations were carried out at injection energy of 900 MeV. Final focus is formed by superconducting solenoids making beams round at IP and rotating the betatron oscillation plane by $\pi/2$ per IP. The design parameters are $\beta_x^* = \beta_y^* = 6.3$ cm, $\epsilon_x = \epsilon_y = 1.7 \cdot 10^{-7}$ m and fractional tunes $\nu_x = \nu_y = 0.1$. Results for the case of accelerator arc represented by linear transformation are presented in Figs. 2,3. For linear arc optics no luminosity degradation is observed until $\xi = 0.15$, where increase in the beam size is approx. 20%, mainly due to tails of the distribution. The spectrum of dipole oscillations with infinitesimally small amplitude is clean, showing no lines except the expected σ and π modes (the tune shift is twice the ξ due to two IPs).

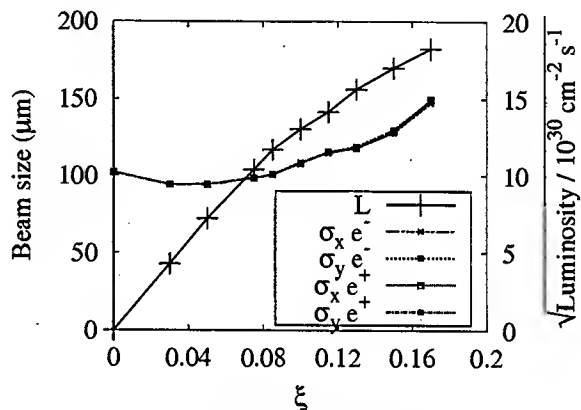


Figure 2: Beam size at IP and square root of the luminosity per 1 IP vs. the nominal beam-beam parameter. Linear machine optics.

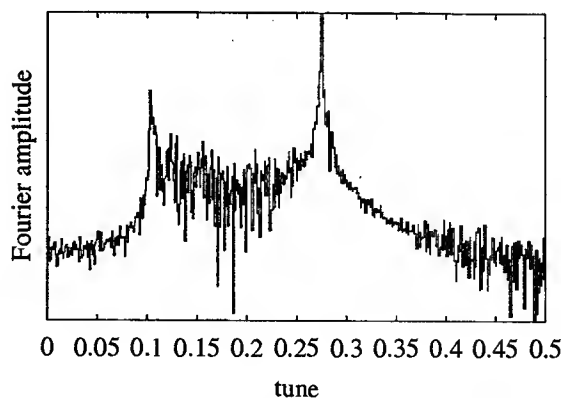


Figure 3: Fourier spectrum of the transverse dipole signal at $\xi = 0.17$ (logarithmic scale).

EFFECT OF SEXTUPOLES

Installing sextupoles (4 per half) in the accelerator arc leads to significant change in the beam-beam system behavior. Although the beam size growth (Fig. 4) is not

very large as compared, for example, with the flat-beam collision, particle losses arise at rather moderate values of ξ (0.06-0.07, Fig. 5). Apparently, this happens because of 'shrinking' of the dynamical aperture in the optics distorted by the beam-beam force. This was justified by tracking simulation using SAD, where the dynamical aperture of the distorted lattice was as low as 6σ .

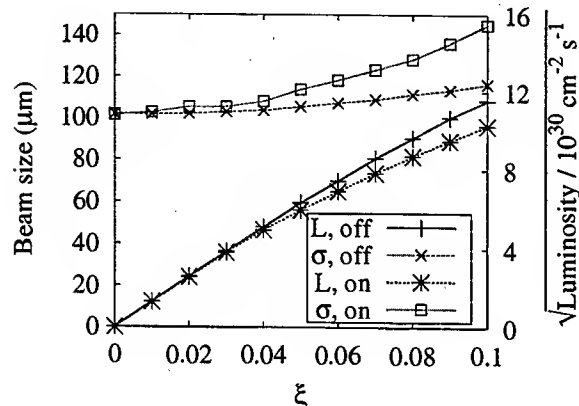


Figure 4: Beam size at IP and square root of the luminosity vs. the beam-beam parameter. Comparison of the sextupoles on and off options, $\beta^*=6.3$ cm.

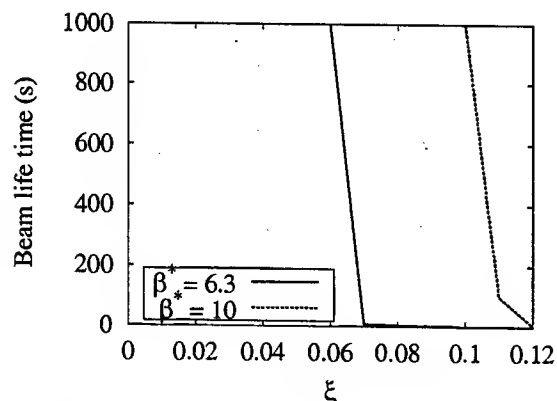


Figure 5: Simulated beam life time vs. ξ . Sextupoles on.

To overcome this problem, a new optics was adopted with improved phase relations between sextupoles and initial dynamical aperture increased to 25σ . This optics has $\beta^*=10\text{cm}$ (6.3 cm in the original one), but due to smaller beam emittance the beam size σ^* was conserved thus allowing to have the same luminosity at available beam intensity. The betatron working point was tuned closer to the integer resonance and now $\nu=0.05$. Simulation for this parameters does not show particle losses up to $\xi=0.1$ (Fig. 6, 5). Further increase of the dynamical aperture may be achieved by lowering betatron tunes or tuning harmonic sextupole correctors.

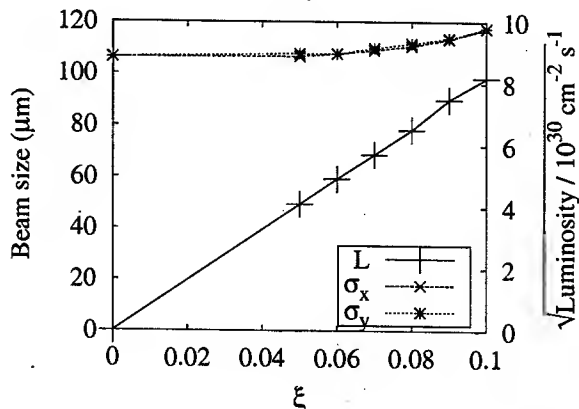


Figure 6: Beam size at IP and square root of the luminosity vs. the beam-beam parameter, $\beta^*=10$ cm.

SUMMARY

Simulation of beam-beam effects for round colliding beams at the VEPP-2000 e^+e^- collider using the strong-strong 2D PIC code predicts values of the maximum attainable ξ up to at least 0.15 in a lattice without nonlinearities. Inclusion of the machine sextupoles does not cause a serious beam blowup and reduction of luminosity. However, reduction of the dynamical aperture limits the beam life time in the optics with $\beta^*=6.3$ cm. Modification of optics with $\beta^*=10$ cm conserving the beam size at IP allows to enhance the dynamical aperture and reach the design luminosity.

ACKNOWLEDGMENTS

One of the authors (A. Valishev) is grateful to Professor S. Kurokawa for providing the opportunity to work at KEK on this subject. We thank I. Koop, I. Nesterenko and Yu. Shatunov for cooperation.

REFERENCES

- [1] K.Ohmi, Phys. Rev. E **59**, 7287 (2000)
- [2] Yu.M.Shatunov, Frascati Physics Series Vol. X (1998), 49
- [3] V.V.Danilov et al., in *Proceedings EPAC'96*, **2**, 1149
- [4] V.V.Danilov and E.A.Perevedentsev, Frascati Physics Series Vol. X (1998), 321
- [5] R.Talman, Phys. Rev. Lett. **74**, 1590 (1995)
- [6] E.Young, S.Henderson, R.Littauer, et al., in *Proceedings PAC'97*, 1542
- [7] Yu.M.Shatunov, A.V.Evstigneev, D.I.Ganyushin, et al., in *Proceedings EPAC'2000*, 439
- [8] S. Krishnagopal, Phys. Rev. Lett. **76**, 235 (1996)
- [9] Y.Cai, A.W.Chao, S.I.Tzenov, and T.Tajima, Phys. Rev. ST Accel. Beams **4**, 011001 (2001)
- [10] K.Ohmi, K.Hirata, and K.Oide, Phys. Rev. E **49**, 751 (1994)
- [11] <http://acc-physics.kek.jp/SAD/sad.html>

MACROPARTICLE SIMULATIONS OF ANTIPROTON LIFETIME AT 150 GeV IN THE TEVATRON

J. Qiang*, R. D. Ryne, LBNL, Berkeley, CA 94720, USA
T. Sen, M. Xiao, FNAL, Batavia, IL 60510, USA

Abstract

In this paper we report on a systematic study of antiproton lifetime at the injection energy of 150 GeV in the Tevatron. Our parallel beam-beam model can handle both strong-strong and weak-strong beam-beam collisions with arbitrary beam-beam separation and beam distributions. In this study, we have only used the weak-strong capability due to the fact that the antiproton intensity is much smaller than the proton intensity. We have included all 72 long-range beam-beam collisions with a linear transfer map between adjacent collision points and taken into account linear chromaticity. The effects of antiproton emittance, beam-beam separation, proton intensity, and machine chromaticity have been investigated. Initial results show that the antiproton lifetime as a function of the proton intensity from the simulation is in good agreement with that from the experimental measurements. The antiproton lifetime can be significantly improved by increasing the beam separation and by reducing the antiproton emittance.

INTRODUCTION

The Tevatron has been upgraded in recent years to increase the luminosity of the proton-antiproton collisions. One of the most important factors limiting luminosity in the past and in Run II is the antiproton availability. It has been observed that the luminosity in the Tevatron is proportional to the total antiproton intensity, where the total antiproton intensity is determined by the antiproton production rate, the transmission efficiency from the antiproton accumulator to the Tevatron, and the store lifetime. A study of the antiproton lifetime subject to the effects of a range of physical parameters will help to minimize the antiproton losses during the machine operation and to improve the luminosity. In this paper, we focus our study on the antiproton lifetime during the injection stage with energy of 150 GeV. At this stage, the major factor causing the antiproton loss is the 72 long range beam-beam interactions between the proton bunches and the antiproton bunches.

COMPUTATIONAL MODEL

The computational tool used in this paper is a parallel program, BeamBeam3D, developed at Lawrence Berkeley National Laboratory for strong-strong and strong-weak beam-beam modeling [1]. This tool calculates self-consistently the electromagnetic beam-beam forces for arbitrary distributions during each collision when a strong-strong beam-beam interaction model is used. When a

strong-weak model is used, the code has the option of using a Gaussian approximation for the strong beam. BeamBeam3D uses a multiple-slice model, so finite bunch length effects can be studied. The code also includes a Lorentz boost and rotation to treat collisions with finite collision crossing angle. It handles arbitrary closed-orbit separation (static or time dependent) and models long-range beam-beam interactions using a newly developed shifted Green function approach. It can also handle multiple interaction points using externally supplied linear maps between interaction points in the strong-weak model. The linear machine chromaticity is represented using a one-turn kick. The diffusion due to the random noise is emulated using a one-turn random kick in momentum space with adjustable noise amplitude.

In the calculation of the antiproton lifetime, we have assumed a strong-weak beam-beam interaction model since the antiproton intensity is much smaller than the proton intensity (typically a factor of 10). We first perform a MAD simulation using the Tevatron lattice at the injection energy of 150 GeV. From there, we extract 73 linear transfer maps, starting at B0, for the 72 long-range beam-beam interactions. These linear transfer maps are symplectified before being used to track antiprotons in the beam-beam simulation. Information related to the proton-antiproton separation, machine bare tune, and linear chromaticity is also extracted. Fig. 1 shows the normalized proton-antiproton separation as a function of distance along the proton trajectory in the Tevatron. There are three locations where

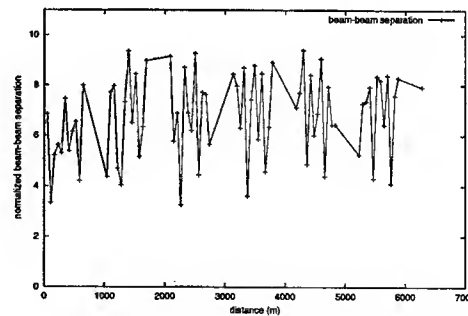


Figure 1: Normalized beam-beam separation as a function of the distance along proton trajectory in the Tevatron.

the beam-beam separations are below four sigma. Given the initial antiproton emittances and Twiss parameters, we generate an initial 6D Gaussian distribution of particles for the antiproton beam using a weighted sampling technique. Here, instead of sampling the Gaussian distribution directly, we sample a uniform distribution within the given aperture size. Then, each particle is given a weight based

*jqiang@lbl.gov

on the function value of the Gaussian distribution at the particle position. Using a weighted sampling technique, we can increase the resolution of the calculated antiproton intensity and reduce the minimum number of particle-turns required for the simulation.

The antiprotons are then transported from one long-range beam-beam collision point to the next using the symplectified linear map. Before each collision, the transverse amplitudes of each particle are checked against a specified "aperture" size. If the amplitude is larger than the aperture size, that particle is lost and no longer tracked in the simulation. At the collision point, every antiproton receives a kick from the beam-beam force generated by the proton beam. The beam-beam force is calculated assuming a Gaussian distribution for the proton beam. Within each turn, the antiproton bunch will receive 72 such long range beam-beam kicks from 36 proton bunches. After each turn, a linear chromaticity map and a random diffusion map are applied to all antiproton particles. The amplitude of the noise has been adjusted so that the emittance growth of the antiproton beam without beam-beam collisions is several pi-mm-mrad after one hour of machine operation. The intensity of the antiproton beam is calculated from the summation of the weights of individual particles. Most of our simulations, performed on an IBM SP parallel computer at the National Energy Research Scientific Computing Center (NERSC), are run for 100,000 turns, which corresponds to about 2 seconds of real machine operation. The antiproton lifetime τ is estimated from fitting the antiproton intensity with the function $I_0 \exp(-t/\tau)$ using a least square method. Here, I_0 is the initial antiproton intensity.

PARAMETER SCAN STUDY

We have carried out a systematic parameter scan study of the antiproton lifetime as a function of the proton intensity, antiproton emittance, beam-beam separation, and the machine vertical chromaticity. We have defined a reference case for all parameter scans. In the reference case, the proton beam has an intensity of 2.2×10^{11} per bunch, a 95% emittance of 25 pi-mm-mrad, a momentum spread of 7×10^{-4} , and an rms bunch length of 0.9 meters. The antiproton beam has an emittance of 20 pi-mm-mrad, a momentum spread of 4.31×10^{-4} , and an rms bunch length of 0.6 meters. The Tevatron horizontal bare tune is 0.581, vertical tune is 0.576, horizontal chromaticity is 2, and vertical chromaticity is 8. In the simulation, we have assumed an "aperture" size of 3.25σ , where σ is the horizontal or vertical rms size at each collision point. The choice of the aperture size is based on a particle tracking study of the dynamic aperture in the Tevatron [2]. The noise amplitude is set as 2×10^{-8} which gives a few pi-mm-mrad antiproton emittance growth after one hour of machine operation. To check the sensitivity of the estimated lifetime versus the number of particles used in the simulations, we have run a test simulation using 100,000, 200,000, and 1,000,000 particles for the reference case. The variation of the estimated

lifetime in these three simulations is within 2%. In this paper, we have used 1,000,000 particles for all parameter scan studies.

Fig. 2 shows a plot of the antiproton lifetime at the injection energy of 150 GeV as a function of the proton intensity from simulations and from measurements. We see that the

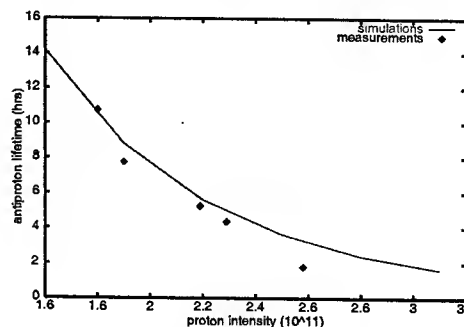


Figure 2: Antiproton lifetime as a function of proton intensity at 150 GeV in the Tevatron.

simulations have reasonably predicted the antiproton lifetime as a function of proton intensity. With a factor of 2 increase of the proton intensity, the antiproton lifetime has dropped by about a factor of 7. The rapid loss of antiprotons with increasing proton intensity observed here might overestimate the dependency of the antiproton lifetime on the proton intensity due to the fact that in the measurements the antiproton emittance had a growth from one data point to another data point. Particle tracking study of dynamic aperture size as a function of proton intensity suggests that there seems to be a threshold proton intensity above which the antiproton losses depend weakly on the intensity [3].

Fig. 3 shows the antiproton lifetime as a function of the initial antiproton emittance. With a factor 2 increasing of the antiproton emittance, the antiproton lifetime has decreased drastically by more than a factor of 100. The strong antiproton emittance dependency of the lifetime may be due to the following two effects: First, the larger antiproton emittance gives a larger antiproton beam size and results in a faster loss out of the aperture. Second, the larger antiproton beam size reduces the distance between the proton beam and the antiproton particles, which results in stronger beam-beam interactions.

Fig. 4 shows the antiproton lifetime as a function of the fractional nominal beam-beam separation. The nominal beam-beam separation is given in Fig. 1. We see that the antiproton lifetime is quite sensitive to the beam-beam separation. When the two beams are 20% closer, the antiproton lifetime has dropped by more than a factor of 2. When the two beams are further moved to approximately 50% of the nominal separation, the antiproton lifetime drops from 5 hours to about 10 minutes. The strong separation dependence of the antiproton lifetime is a result of strong beam-beam forces from the proton bunches. Fig. 5 shows the antiproton lifetime as a function of the Tevatron vertical chromaticity. The antiproton lifetime does not change sig-

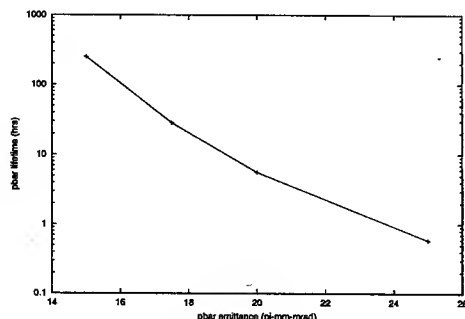


Figure 3: Antiproton lifetime as a function of antiproton emittance at 150 GeV in the Tevatron.

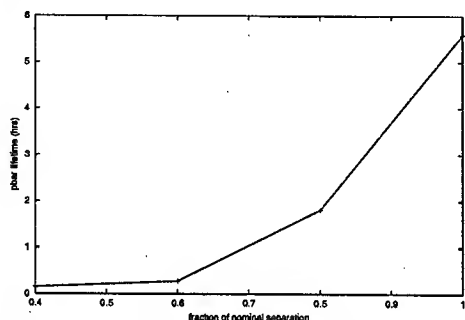


Figure 4: Antiproton lifetime as a function of fractional nominal beam-beam separation at 150 GeV in the Tevatron.

nificantly when the chromaticity varies between 2 and 8. However, in the Tevatron operation, the antiproton lifetime shows a strong dependency on the machine chromaticity. This discrepancy might be due to the fact the current computational model does not include the effects from the non-linear external fields.

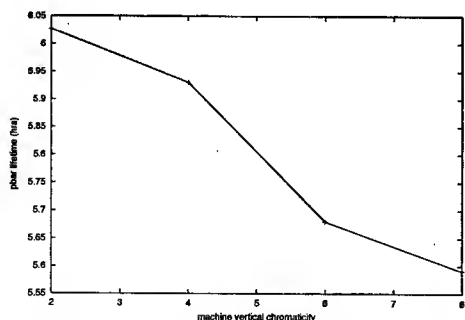


Figure 5: Antiproton lifetime as a function of machine vertical chromaticity at 150 GeV in the Tevatron.

SUMMARY

In this paper, we have presented a parameter scan study of the antiproton lifetime at the injection energy of 150 GeV in the Tevatron as a function of proton intensity, antiproton emittance, beam-beam separation, and machine

vertical chromaticity. The antiproton lifetime as a function of the proton intensity from the simulation is in good agreement with the experimental measurements. For the given proton intensity, the antiproton lifetime shows strong dependence on the antiproton emittance and the beam-beam separation. This suggests that the antiproton lifetime can be significantly improved by increasing the beam separation and with smaller antiproton emittance.

ACKNOWLEDGMENTS

We would like to thank Drs. Y. Alexahin, M. Furman, P. Lebrun, P. Spentzouris, V. Shiltsev, A. Wolski, A. Zholents, and M. Zisman, for helpful discussions. This research used resources of the National Energy Research Scientific Computing Center, which is supported by the Office of Science of the U.S. Department of Energy (US DOE/SC) under Contract No. DE-AC03-76SF00098, and the resources of the Center for Computational Sciences at OAK Ridge National Laboratory. This work was performed under the auspices of a Scientific Discovery through Advanced Computing project, "Advanced Computing for 21st Century Accelerator Science and Technology," which is supported by the US DOE/SC Office of High Energy and Nuclear Physics and the Office of Advanced Scientific Computing Research.

REFERENCES

- [1] J. Qiang, M. A. Furman, and R. D. Ryne, Phys. Rev. ST Accel. Beams 5, 104402 (2002).
- [2] T. Sen, "New Aspects of Beam-Beam Interactions in Hadron Colliders," PAC2003 proceedings.
- [3] T. Xiao, T. Sen, and B. Erdelyi, "Tevatron Beam-Beam Simulation at Injection Energy," PAC2003 proceedings.

PARALLEL COMPUTATION OF BEAM-BEAM INTERACTIONS INCLUDING LONGITUDINAL MOTION

F.W. Jones, TRIUMF, 4004 Wesbrook Mall, Vancouver, Canada V6T 2A3
W. Herr, CERN, CH-1211 Geneva 23, Switzerland

Abstract

In beam-beam macroparticle simulations for collider rings, the accurate determination of the incoherent spectrum and potentially unstable coherent modes requires (1) large numbers of collisions, and (2) accurate electric field solutions at each collision. On a single processor, a self-consistent simulation typically uses a 2D model of the beam-beam interaction in order to achieve a reasonable computation time, however for the long ($\sim 0.3\text{m}$) bunches in the LHC we wish to include the third dimension in order to account for effects such as longitudinal motion, crossing angle, and the beam size and density variations. We describe here a parallel algorithm, developed with MPI on a small commodity Linux cluster, to extend our simulation code BeamX from 2D to 3D using longitudinal subdivision (slicing) of the bunches. Although this paper concentrates on the computing methods, some performance trials and example results will also be shown.

INTRODUCTION

In investigating coherent beam-beam effects in colliders, one goal of simulations is to identify potentially unstable modes and possible damping mechanisms. In this respect, useful qualitative descriptions can be obtained by simplifications such as rigid-bunch and soft-gaussian models, but herein we restrict ourselves to "self-consistent" simulations in which the electric fields are computed directly from the ensemble of macroparticles without assumptions as to the nature of their distribution.

For a 2D model of the beam-beam forces, such simulations are feasible on today's desktop computers using conventional particle-mesh field solvers or, for parasitic collisions, grid-multipole[1] and shifted Green's function methods[2]. However, the 2D treatments omit longitudinal effects such as: (1) longitudinal variation in transverse beam size (hourglass effect); (2) variation of longitudinal density (affects the strength of the beam-beam forces); (3) the effect of beams crossing at an angle instead of head-on; and (4) the coupling of longitudinal motion with these effects. It is therefore of interest for the LHC and other colliders to extend our simulations to 3D if it can be done without prohibitive computational cost.

EXTENSION TO 3D

As in space-charge simulations, there are various numerical methods by which one can compute the bunch-to-bunch forces in 3D, and these methods are generally practi-

cal only for parallel computation. In our case, to show sufficient detail in the coherent frequency range requires $\sim 10^5$ or more simulated collisions, suggesting that the problem lies in the supercomputer realm. However, the small transverse-longitudinal aspect ratio of the LHC bunches allows us to seek economies by using a rather coarse-grained subdivision of the solution domain in the longitudinal direction. In conjunction with a 36×36 or more computational mesh in the transverse plane, we divide the beam longitudinally into ~ 10 segments. This "bunch slicing" approach[3, 4] is applied to both beams, and the beam-beam collision is treated as a series of 2D slice-slice interactions (see Figure 1).

For particle-mesh solvers it is natural to parallelize the field solver in the mesh computation stage. For the BeamX code, however, the fast-multipole solver in use does not lend itself readily to parallel decomposition because of its adaptive subdivision and hierarchical data structures. Hence, we have pursued a more fundamental parallelism, that of the pairwise slice interactions, which may be done independently on different processors provided the causal relationships are maintained. For N slices in each beam, the number of overlapping slices during the collision varies from 1 to N , allowing a parallel speed-up of roughly $N/2$ by the application of N processors.

PARALLEL ALGORITHM

The design and implementation of the parallel version of BeamX were done using a small commodity Linux cluster, representing a low-cost resource which is able to handle small numbers of slices. Utilizing the MPI toolkit for inter-process communication, the fundamental division of labour is between a *master* process and several *slave* processes, as follows:

Master:

- Filling of slice data structures (longitudinal binning)
- Dispatch of slice-data to Slaves
- Receipt of slice-data to Slaves and un-binning
- Longitudinal transport to next IP
- Compiling statistics and all program output

Slave:

- Receipt of slice-data from Master
- Computation of electric fields
- Application of beam-beam forces via symplectic map
- Transport in transverse plane to next IP
- Dispatch of slice data to other Slaves and Master

As described in the next section, the Slaves require a nearly complete set of coordinates $(x, x', y, y', \epsilon = \Delta E/E)$ for the macroparticles in a slice-pair to do their work, entailing $\sim 0.5\text{MB}$ of data per 10k particles. With this communication overhead it is imperative to minimize the message volume between processes, and to this end a topology has been devised in which one beam's slices "stay at home", i.e. are resident in the Slave processes, and the other beam's slices "go visiting", i.e. are passed between Slave processes. This is illustrated schematically in Figure 1. Once a Slave has received its assigned Beam 1 slice from the Master, it is ready to receive Beam 2 slices to interact with it. The Master (process 0) sends Beam 1 slices $1, \dots, N$ to Slave processes $1, \dots, N$ respectively. It sends all the Beam 2 slices to Slave 1 in sequence. When Slave 1 receives a Beam 2 slice, it does the pair-interaction, updates the coordinates of each slice, and passes the Beam 2 slice on to Slave 2. Slave n , $1 < n \leq N$, receives a Beam 2 slice from Slave $n-1$, does the pair-interaction, and passes it on to Slave $n+1$, or to the Master if $n = N$. Once a Slave has dealt with the last Beam 2 slice, it is finished with slice-interactions for this collision and can send its resident Beam 1 slice data to the Master.

In this scenario the Master does not have to perform any control or synchronization functions for the Slaves. All processes are essentially free-running and the data flow itself imposes and maintains the proper ordering of events.

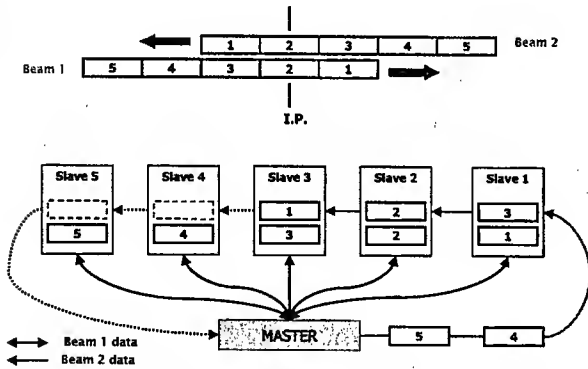


Figure 1: Inter-process communication scheme for parallel computation (case of 5 slices per bunch)

DETAILS OF SLAVE WORK

The interaction of a slice-pair $i-j$ occurs at the interaction point (IP) if $i = j$, but otherwise occurs at distance $s = (j - i) * H/2$, the collision point (CP), where H is the slice length. Since macroparticle transport through the rings is done by an IP-to-IP map, it is convenient to "drift" the particles forward or backward to the CP, evaluate and apply the beam-beam forces, and drift them to the IP again. In extending to 3D the angular kicks due to transverse forces are now accompanied by energy kicks due to longitudinal forces. To preserve symplecticity in the

6 phase-space variables the "synchro-beam" mapping[5] is employed:

$$\begin{aligned} x^{\text{new}} &= x - sF_x/2 \\ x'^{\text{new}} &= x' + F_x \\ y^{\text{new}} &= y - sF_y/2 \\ y'^{\text{new}} &= y' + F_y \\ \epsilon^{\text{new}} &= \epsilon + F_x(x' + F_x/2)/2 + F_y(y' + F_y/2)/2 \\ &\quad - s(\sigma_x^2 F_x + \sigma_y^2 F_y) \end{aligned}$$

where F_x and F_y are the angular deflections of a particle which has coordinates (x, y) when it passes the IP and encounters a given slice of the opposing beam at distance s from the IP, and σ_x^2 and σ_y^2 are the variances of the opposing beam.

The above mapping applies to beams moving on parallel trajectories. If the beams cross at an angle then a Lorentz transformation[6] is applied to each slice in turn so that it is oriented parallel to the opposing slice, after which the electric fields are computed, the synchro-beam mapping is done, and then the inverse transformation is performed.

After these iterated series of transformations for slice-pairs, all coordinates are transformed back to the IP in that their relative positions are consistent with the opposing bunches being in the middle of their collision, i.e. centered at the IP. It is then straightforward to transform all coordinates to the next IP by the conventional transfer matrix and longitudinal difference equations, according to the lattice optics and the applied RF voltage.

PERFORMANCE

We performance-tested the parallel BeamX code on three different platforms:

1. Linux, Pentium IV 1.6 GHz, 100Mb Ethernet, MPICH toolkit
2. Linux, Pentium III 1.4 GHz, 1Gb Ethernet, LAM MPI toolkit
3. Linux, Pentium III 1.4 GHz, Dolphin Scalable Coherent Interconnect (SCI), SCALI MPI toolkit

On each platform, 1000 collisions were executed for varying numbers of slices N , where the number of parallel processes was $N + 1$. In order to estimate both the communication overhead and the parallel speedup, each job was run normally with each process running on a separate CPU, and with all processes running on a single CPU. As seen in Figure 2, there is significant communication overhead but the N^2 complexity is reduced to nearly linear scaling by the parallel algorithm.

With conventional ethernet communications, increasing the bandwidth by a factor of 10 yielded a significant performance improvement for small numbers of slices, even with somewhat slower processors. For larger numbers of slices, the communication burden becomes proportionally smaller and the parallel efficiency becomes about the same for the three communication hardware/software configurations. In

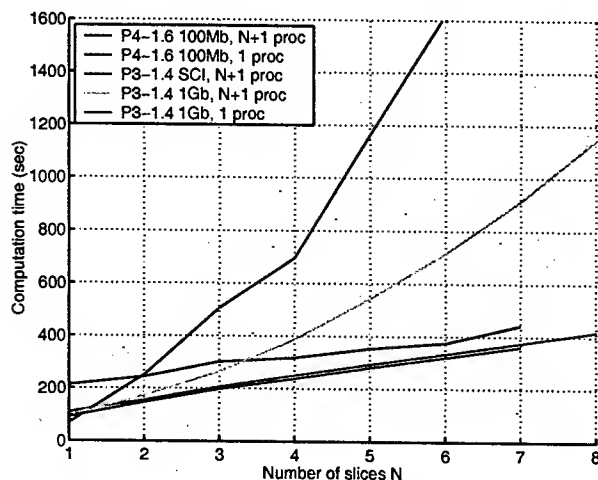


Figure 2: Parallel and single-node performance timings

particular the SCI showed no benefit over Ethernet in our trials. This may be a matter of tuning and remains to be investigated.

EXAMPLES

The 3D-extended BeamX code has been applied to some test cases for the LHC with a single interaction point. For the LHC there is no dispersion in the interaction region and the variation of beam size along the bunch length (hour-glass effect) is quite small. The dominant longitudinal effects are due to the synchrotron motion and the crossing angle. Figure 3 shows the FFT spectra of the coherent frequencies (beam centroid motion) for runs of $2^{17}=131072$ turns with 5 longitudinal slices and 50000 macroparticles, with an applied RF of 40 MV/turn (nominal synchrotron tune $Q_s=0.00335$) and with crossing angles of 0, 150, and 300 μ rad. The crossing angle induces a relativistic projection of the beam-beam force and hence reduces the beam-beam tune shift as seen by the π mode frequency which shifts from its normal value of -1.21 to -1.10 and -0.92 , respectively. With RF on, the synchrotron tune is comparable in size to the beam-beam tune shifts as revealed by the multiple sidebands.

As in soft-Gaussian simulations with bunch slicing[4] a relatively modest number of slices and macroparticles suffice to model these basic phenomena. Running the same cases with >5 slices and >50000 macroparticles showed little difference in the coherent spectra, with the relevant features being essentially unchanged.

CONCLUSIONS

A three-dimensional self-consistent multiparticle beam-beam simulation has been developed using coarse-grained longitudinal subdivision and parallel programming techniques. The implementation via MPI, with a master-slave/slave-slave message-passing algorithm, reduces the computational cost from N^2 to linear scaling with the number of slices N and makes it feasible to run simulations on

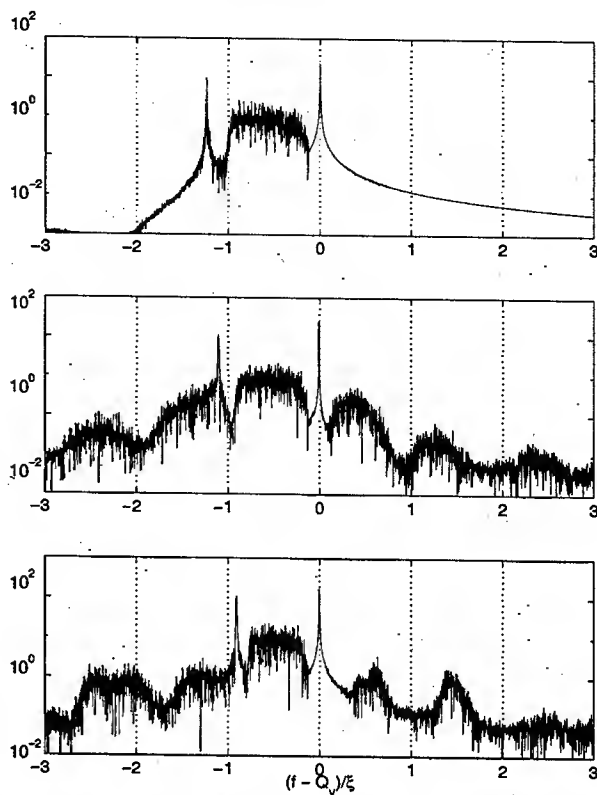


Figure 3: Spectra with 0, 100, and 300 μ r crossing angle

small low-cost Linux clusters with ethernet. To further decrease computation times, the use of more advanced MPI and/or SCI features may decrease communication overhead, and further parallelism can be sought, such as a parallelized multipole solver. In this work we have confined ourselves to commodity-based hardware/software solutions. The use of shared-memory parallel systems could yield greater parallel efficiency, although at considerably higher cost.

ACKNOWLEDGEMENTS

We would like to thank Corrie Kost and Steve McDonald for establishing a test-bed Linux cluster at TRIUMF on which we could develop and test the code, and James Pinfold and Bryan Caron for arranging access to the THOR cluster at the University of Alberta Physics Department.

REFERENCES

- [1] W. Herr, M.P. Zorzano and F. Jones, *Phys. Rev. S.T. Accel. Beams* **4**, 054402 (2001).
- [2] J. Quiang, M.A. Furman and R.D. Ryne, *Phys. Rev. S.T. Accel. Beams* **5**, 104402 (2002).
- [3] A. Jejcic et al., *XVII Int. Conf. on High Energy Accelerators*, Dubna 1998, 220.
- [4] W. Herr and R. Paparella, LHC Project Note 304, CERN 2002.
- [5] K. Hirata, H. Moshhammer and F. Ruggiero, *Part. Accel.* **40**, 205 (1993).
- [6] K. Hirata, *Phys. Rev. Lett.* **74**:12, 2228 (1995).

MEASUREMENT AND APPLICATION OF BETATRON MODES WITH MIA*

Chun-xi Wang[†], Argonne National Laboratory, Argonne, IL 60439, USA

Abstract

We present Model-Independent Analysis (MIA)-based methods for measuring lattice properties of a storage ring such as phase advance, beta function, chromaticity, and tune shift with amplitude. Using beam position histories of excited betatron oscillations that are simultaneously measured at a large number of beam position monitors (BPMs), the spatial-temporal modes of betatron oscillation can be extracted with MIA-mode analysis. The resulting spatial vectors are used to determine linear phase advance and beta function, and the temporal vectors are used to determine nonlinear chromaticity and tune shift with amplitude. Measurements done at the Advanced Photon Source are reported.

INTRODUCTION

Assuming weak coupling and nonlinearity, the betatron oscillation of a single particle can be described by

$$x_\beta(s) = \sqrt{2J\beta(s)} \cos[\phi + \psi(s)], \quad (1)$$

where $\{J, \phi\}$ are the action-angle variables specifying a specific trajectory, $\beta(s)$ is the beta function, and $\psi(s)$ is the phase advance. In a perfectly linear machine and on a time scale much shorter than the radiation damping time, the action J is conserved and the angle evolves as $\phi = \phi_0 + 2\pi\nu_0 p$, where ν_0 is the lattice tune and p is the number of turns. However, weak nonlinearities generate energy-dependent and amplitude-dependent tune shifts $\Delta\nu = \xi\delta + aJ$, where ξ is the chromaticity and a is the coefficient of amplitude-dependent tune shift. For a bunched beam, particles' energies and amplitudes have certain distribution, thus the bunch centroid observed at the BPMs is the phase-space average of Eq. (1). The resulting centroid oscillation of an excited beam may not follow Eq. (1), for example when decoherence occurs. However, for each turn the centroid is expected to follow single particle behavior closely, i.e., the centroid oscillation can still be written as

$$b_p^m = \sqrt{2J_p\beta_m} \cos(\phi_p + \psi_m), \quad (2)$$

where b_p^m is the beam centroid position at the m -th monitor for the p -th turn. Note that both action and angle are carrying the turn index so that Eq. (2) can accommodate much more complicated centroid motion.

In recent years, Model-Independent Analysis (MIA) [1, 2] has emerged as a new approach to study beam dynamics by analyzing beam histories simultaneously recorded at

a large number of BPMs, i.e., the data matrix $B_{P \times M} = (b_p^m)/\sqrt{P}$, where P is the number of turns and M is the number of BPMs. B is normalized such that $B^T B$ is the variance-covariance matrix of BPM measurements. A basic MIA technique is the spatial-temporal mode analysis via singular value decomposition (SVD) of B , which yields

$$B = U S V^T = \sum_{\text{modes}} \sigma_i u_i v_i^T, \quad (3)$$

where $U_{P \times P} = [u_1, \dots, u_P]$ and $V_{M \times M} = [v_1, \dots, v_M]$ are orthonormal matrices comprising the temporal and spatial eigenvectors, and $S_{P \times M}$ is a rectangular matrix with nonnegative singular values σ_i along the upper diagonal. Similar to the Fourier analysis, this mode analysis decomposes the spatial-temporal variation of the beam centroid into superposition of various orthogonal modes by effectively accomplishing a major statistical data analysis, namely the Principal Component Analysis. A pair of spatial and temporal vectors $\{v_i, u_i\}$ characterizes a spatial-temporal eigenmode, and the corresponding singular value σ_i gives the overall amplitude of the mode. It can be shown that when beam motion is dominated by betatron oscillations, there are two orthogonal eigenmodes (referred to as betatron modes) that correspond to the normal coordinates of betatron motion. In the following, we give the explicit expression of the betatron modes and their measurements, then show how to use them to determine phase advances, beta function, chromaticity, and tune shift with amplitude.

BETATRON MODE MEASUREMENT

When B is dominated by the excited betatron motion given by Eq. (2) with action and angle independently distributed, it can be decomposed into [2]

$$B \simeq \sigma_+ u_+ v_+^T + \sigma_- u_- v_-^T, \quad (4)$$

where the spatial and temporal vectors are given by

$$\begin{cases} v_+ = \frac{1}{\sigma_+} \left\{ \sqrt{\langle J \rangle} \beta_m \cos(\phi_0 + \psi_m), m = 1, \dots, M \right\} \\ v_- = \frac{1}{\sigma_-} \left\{ \sqrt{\langle J \rangle} \beta_m \sin(\phi_0 + \psi_m), m = 1, \dots, M \right\} \end{cases} \quad (5)$$

and

$$\begin{cases} u_+ = \left\{ \sqrt{\frac{2J_p}{P\langle J \rangle}} \cos(\phi_p - \phi_0), p = 1, \dots, P \right\} \\ u_- = \left\{ -\sqrt{\frac{2J_p}{P\langle J \rangle}} \sin(\phi_p - \phi_0), p = 1, \dots, P \right\}. \end{cases} \quad (6)$$

Here $\langle \rangle$ means sample average. Note that the spatial vectors are orthogonal single-particle trajectories of Eq. (1) even though the centroid follows the more complicated

* Work supported by U.S. Department of Energy, Office of Basic Energy Sciences, under Contract No. W-31-109-ENG-38.

[†] wangcx@aps.anl.gov

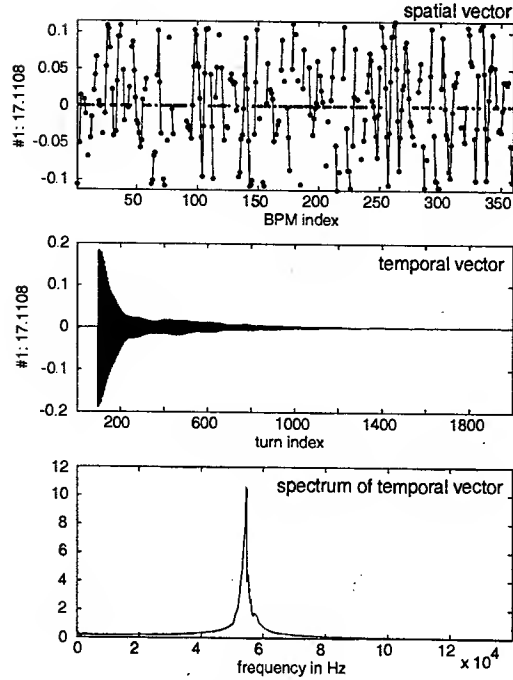


Figure 1: The first betatron mode of a kick excitation. Measured values are solid dots and joined by lines for consecutive BPMs. Bad BPMs are dots at zero. The mode number and its singular value are shown on the left-side label.

Eq. (2). Furthermore, the temporal vectors clearly relate to the normal coordinates that depict time-evolution in phase space.

As an example, Fig. 1 shows the first betatron mode of a horizontally kicked beam in the APS ring. The second is very similar and not shown for lack of space. The spatial vector is a betatron orbit, although due to the unusable BPMs the orbit is broken into pieces and looks irregular. The temporal vector clearly shows a beam that is kicked at about the 100th turn then decohered and damped. The Fourier spectrum of the temporal vector shows the betatron frequency with a broadened peak due to decoherence. Note that the synchrotron and vertical tunes as well as other nonlinear resonance frequencies are invisible, even though they do exist and show up in other modes [3]. This indicates the quality of the betatron modes.

PHASE ADVANCE AND BETA FUNCTION

From the spatial betatron vectors, Eq. (5), the phase advances can be determined as

$$\psi = \tan^{-1} \left(\frac{\sigma_- v_-}{\sigma_+ v_+} \right), \quad (7)$$

where the phase ϕ_0 is absorbed by shifting the reference point. Since we are interested in only the phase advance between BPMs, the reference point does not matter. The beta function can be written as

$$\beta = \langle J \rangle^{-1} [(\sigma_+ v_+)^2 + (\sigma_- v_-)^2]. \quad (8)$$

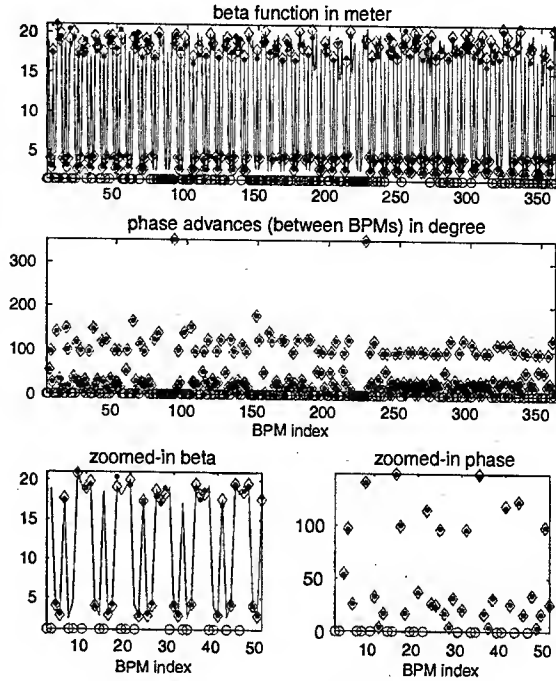


Figure 2: Horizontal beta function and phase advance. The solid dots are MIA measurements. The solid lines are calibrated machine model. Diamonds are model values at used BPMs. Circles are bad BPMs. Figures in the third row are blowups of the above figures for the first 50 BPMs.

Note that, except for an overall scaling factor $\langle J \rangle$ in β , the phase advance and beta function can be computed from the spatial betatron vectors. The phase measurement can tolerate BPM gain errors, but the beta function measurement cannot.

Using the measured spatial betatron vectors as shown in Fig. 1, the beta function and phase advances are computed and shown in Fig. 2. For comparison, the values from a model fitted with response-matrix measurements is also shown, which agrees well with the MIA measurements. See [4] for more details on phase advance and beta function measurements.

CHROMATICITY AND TUNE SHIFT WITH AMPLITUDE

Chromaticity and tune shift with amplitude are basic parameters describing the nonlinear energy- and amplitude-dependent tune shifts. Usually they are determined by directly measuring the tune slope versus different beam energies and kick amplitudes. One major limitation of such measurements is that machine tunes often wobble around from measurement to measurement such that the chromatic and nonlinear tune shifts may be obscured. An alternative approach is to measure chromatic decoherence [5] and nonlinear decoherence [6] of the beam centroid due to the tune shift $\Delta\nu = \xi\delta + aJ$. Assuming the initial state is a well-

damped Gaussian distribution in (x, x') and δ , the centroid position is given by Eq. (2) with [7]

$$\sqrt{J_p} = \sqrt{J_{\max}} \frac{1}{1 + \theta^2} e^{-\frac{Z^2}{2} \frac{\theta^2}{1 + \theta^2}} e^{-2 \left(\frac{\xi \sigma_\delta}{\nu_s} \right)^2 \sin^2(\pi \nu_s p)} \quad (9)$$

and

$$\phi_p = \phi_0 + 2\pi \nu_0 p + \frac{Z^2}{2} \frac{\theta}{1 + \theta^2} + 2 \tan^{-1} \theta, \quad (10)$$

where $\theta = 2\pi a \epsilon p$, ϵ is the emittance, $Z = \sqrt{2J_{\max}}/\epsilon$ is the kick strength, σ_δ is the energy spread, and ν_s is the synchrotron tune. Fitting these with measured centroid evolution gives the products $a\epsilon$ and $\xi\sigma_\delta$.

The temporal betatron vectors such as the one shown in Fig. 1 can be used in both approaches and may result in significant improvement by reducing the random noise by a factor of about $1/\sqrt{M}$. (Differences in BPM resolutions and beta values at BPM locations must be taken into account for better estimate.) For the direct tune measurement approach, one simply does a spectrum analysis of the temporal vectors. Since the signal often decoheres very fast, one may need to apply the NAFF technique [8] on a small number of turns to determine the tune for each kick. For decoherence measurement, J_p and ϕ_p can be simply obtained from the temporal vectors of Eq. (6) as

$$J_p = P\langle J \rangle \frac{u_+^2 + u_-^2}{2}, \quad \phi_p = -\tan^{-1} \left(\frac{u_-}{u_+} \right). \quad (11)$$

Note that both J_p and ϕ_p are smooth functions without fast betatron oscillation. They provide independent constraints for fitting the decoherence parameters.

As examples, we show preliminary results of two sets (at 0.2 and 1.5 mA) of horizontal measurements using horizontally kicked single bunches (at five different amplitudes in each set) in the APS ring. We choose the low current in order to minimize the wakefield effect since the above decoherence model does not take such an effect into account. The temporal vectors at the lowest kick are shown in Fig. 3,

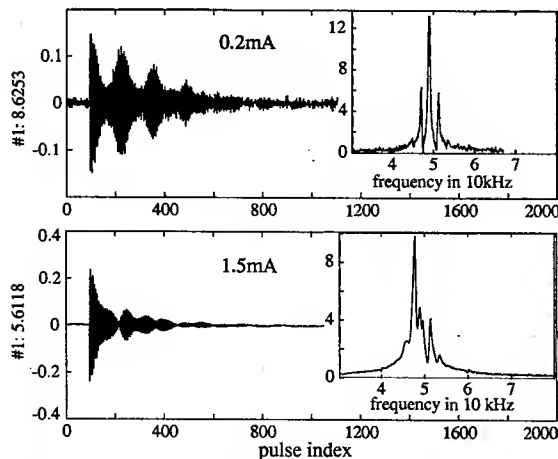


Figure 3: The temporal betatron vectors of 0.3 kV kick excitation ($Z = 3.2$) at 0.2 mA (top) and 1.5 mA (bottom).

where the wake effect is obvious. Since the APS BPM system is not intended for measuring such a low current, the resolution at 0.2 mA is very poor (five times worse than at 1.5 mA). Thanks to MIA noise reduction, we are still able to obtain decent decoherence measurements.

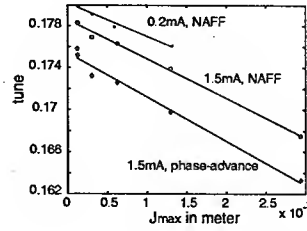


Figure 4: Tune slopes versus kick amplitudes.

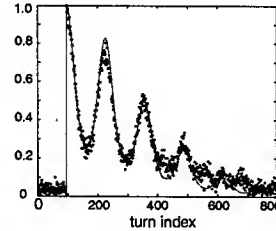


Figure 5: Measured and fitted decoherence.

The results of tune slope measurements are shown in Fig. 4, where the NAFF results are based on the first 20 turns of temporal vectors, which yield $a \simeq -3.2 \times 10^{-4} m^{-1}$ and $-3.8 \times 10^{-4} m^{-1}$ for 0.2 mA and 1.5 mA, respectively. The phase-advance results are based on Eq. (7), which yields $a \simeq -4.2 \times 10^{-4} m^{-1}$ for 1.5 mA and failed at 0.2 mA due to noise. The apparent offset is unclear at this point. The result of fitting decoherence at 0.2 mA is shown in Fig. 5. Fitting for 1.5 mA failed due to the wakefield effect. Since the beam completely decohered well before θ reached 1, the phase cannot constrain θ due to uncertainty in ν_0 . Thus, only the fit for J_p is shown, which yields $\xi\sigma_\delta \simeq 6.2 \times 10^{-3}$ and $a\epsilon \simeq 1. \times 10^{-4}$. With $\sigma_\delta = 0.9 \times 10^{-3}$ and $\epsilon = 2.4 nm$, we have $\xi \simeq 6.9$ and $|a| \simeq 4 \times 10^4 m^{-1}$. The measured chromaticity and tune shift with amplitude are consistent with the model.

Thanks to V. Sajaev for providing information about the APS storage ring model.

REFERENCES

- [1] J. Irwin, C.X. Wang, Y. Yan et al., Phys. Rev. Lett. **82**(8), 1684 (1999).
- [2] Chun-xi Wang, Model Independent Analysis of beam centroid dynamics in accelerators, Ph.D. dissertation, Stanford University (1999). Also available as SLAC-R-547.
- [3] Chun-xi Wang, "Spatial-Temporal Modes Observed in the APS Storage Ring using MIA," in this proceedings.
- [4] Chun-xi Wang, Vadim Sajaev, and Chih-Yuan Yao, "Phase advance and beta function measurements using Model-Independent Analysis," to be published.
- [5] See, for example, I. Hsu, Particle Accelerators **34**, 43 (1990).
- [6] See, for example, J.M. Byrd and D. Sagan, Proc. of the 1991 Part. Accel. Conf., p. 1080 (1991).
- [7] A. W. Chao and M. Tigner, Eds., *Handbook of Accelerator Physics and Engineering*, World Scientific, River Edge, NJ (1998).
- [8] J. Laskar et al., Physica D **56**, 253 (1992).

SPATIAL-TEMPORAL MODES OBSERVED IN THE APS STORAGE RING USING MIA*

Chun-xi Wang[†], Argonne National Laboratory, Argonne, IL 60439, USA

Abstract

Singular-value decomposition of the data matrix containing beam position histories yields a spatial-temporal mode analysis of beam motion by effectively accomplishing the statistical Principal Component Analysis. Similar to the Fourier analysis, this mode analysis decomposes the spatial-temporal variation of the beam centroid into a superposition of orthogonal modes that are informative. We briefly review this mode analysis technique and show some interesting modes observed at the APS storage ring.

INTRODUCTION

Fourier analysis is commonly used to extract basic beam dynamics information in a storage ring. Generally it is a 1D harmonic mode analysis of beam temporal motion. In recent years, as a major part of Model-Independent Analysis (MIA), a spatial-temporal mode analysis technique has emerged for studying beam dynamics [1,2], where the spatial information comes from a large number of BPMs and the temporal information comes from turn-by-turn beam position histories at all BPMs. All the beam histories form a data matrix $B = (b_p^m)/\sqrt{P}$ where the column index m indicates the monitor, the row index p indicates the pulse or turn, and P is the number of turns. Usually B is normalized such that $B^T B$ is the variance-covariance matrix of BPM readings. The spatial-temporal mode analysis uses the singular value decomposition (SVD) of B to decompose beam motion into a superposition of orthogonal spatial-temporal modes according to the Principal Component Analysis. We introduce the technique first, then show, with data from the Advanced Photon Source (APS) storage ring, that the spatial-temporal modes are interesting and informative.

SVD Mode Analysis

Mathematically, an SVD of the matrix B yields

$$B = USV^T = \sum_{i=1}^d \sigma_i u_i v_i^T, \quad (1)$$

where $U_{P \times P} = [u_1, \dots, u_P]$ and $V_{M \times M} = [v_1, \dots, v_M]$ are orthogonal matrices, $S_{P \times M}$ is a diagonal matrix with nonnegative σ_i along the diagonal in decreasing order, $d = \text{rank}(B)$ is the number of nonzero singular values, σ_i is the i -th largest singular value of B , and the vector u_i (v_i) is the i -th left (right) singular vector. The singular values reveal the number of independent variations and their magnitudes, while each set of singular vectors form an orthogonal basis of the various spaces of the matrix. These

properties make SVD extremely useful. An SVD routine is commonly available in numerical packages. Thus it is as easy as Fourier analysis to obtain the SVD of B that yields a large set of $\{\sigma_i, u_i, v_i\}$. Each set of $\{u_i, v_i\}$ defines a spatial-temporal mode, where u_i gives the temporal variation, v_i gives the spatial variation, and σ_i gives the overall strength of this mode.

Principal Component Analysis

Principal Component Analysis is a major multivariate statistical data analysis technique. It is used to reduce a large set of observed variations to a minimum set of variables that account for the correlations observed in the sample variance-covariance matrix. The basic idea is to find the first "principal axis" in the data-point space such that the sample variance of the components of all data points along this axis is maximum, then find the next such axis that is orthogonal to the other principal axes, and so on. In our case, each BPM is one variable and the readings at the M BPMs for one turn become a data point in an M -tuple space. To find the first principal axis $v_1 = \{v_{11}, v_{12}, \dots, v_{1M}\}^T$ with $v_1^T v_1 = 1$, we need to maximize the variation projected onto this axis, i.e., $\text{var}(\sum_m v_{1m} b_p^m) = \text{var}(Bv_1) = v_1^T B^T B v_1 = \max$. This maximization requires that the maximum variance is equal to the largest eigenvalue λ_1 of $B^T B$, and v_1 is the corresponding eigenvector. After finding the first principal axis, the associated variations can be subtracted out and the residual variation $\Delta B = B - (Bv_1)v_1^T$ is orthogonal to v_1 . In the same way, we can find the principal axis v_2 for the residual variation ΔB . Since v_2 is orthogonal to v_1 , v_2 must be an eigenvector of $B^T B$ as well. By repeating this procedure we can find all the principal axes and all are eigenvectors of $B^T B$. Let the variations along the principal axes be $w_i = Bv_i$. It is easy to see that they are orthogonal to each other as well because $w_i^T w_j = v_i^T B^T B v_j = \lambda_i \delta_{ij}$. Furthermore, the variance of w_i is λ_i . Normalizing w_i by its standard deviation $\sigma_i = \sqrt{\lambda_i}$, we have orthonormal vector $u_i = w_i/\sigma_i$ with $u_i^T u_j = \delta_{ij}$. Putting the spatial vector v 's into matrix $V = [v_1, v_2, \dots]$, temporal vector u 's into $U = [u_1, u_2, \dots]$, and the standard deviations into diagonal matrix $S = \text{diag}(\sigma_1, \sigma_2, \dots)$, we get $B = USV^T$. Therefore, the SVD of B in fact accomplishes the statistical Principal Component Analysis of beam histories. In other words, statistical analysis is the foundation of the spatial-temporal mode analysis and SVD is the tool.

For more discussion on the technique and characteristics of the singular-value spectrum, see [2]. Usually a large number of modes are generated, but less than a dozen leading modes are due to beam motion; the rest are due to BPM noises. In the next section, we present a set of interesting spatial-temporal modes observed at the APS.

* Work supported by U.S. Department of Energy, Office of Basic Energy Sciences, under Contract No. W-31-109-ENG-38.

[†] wangcx@aps.anl.gov

MODES OBSERVED

The following modes are from horizontal BPMs with a horizontally kicked beam in the APS ring. There are nine modes above the noise floor. The first two are dominating betatron modes that are well understood and used for beam measurements. We skip these two modes here for lack of space. The next seven modes are shown in Figs. 1-7. In each figure, the spatial vector is on the top, the temporal vector is in the middle, and the Fourier spectrum of the temporal vector is at the bottom. The red dots are bad BPMs. Shown on the left-hand labels are the mode number and singular value in units of BPM count ($7 \mu m$). Brief comments are given in the figure captions. Note that the magnitudes of these modes are on the order of microns.

Remarks

The spectra of the temporal vectors indicate that each mode corresponds to certain excitations that have characteristic features in the frequency domain. This is remarkable since the statistical analysis knows nothing about the frequency domain. This also indicates that the associated spatial vectors should provide useful spatial information about the excitation, though more studies are required to fully understand and make use of such information. (In our case, bad BPMs make it even harder by breaking spatial periodicity.) What we have shown here are just more examples demonstrating that spatial-temporal mode analysis provides a useful way to investigate beam motion.

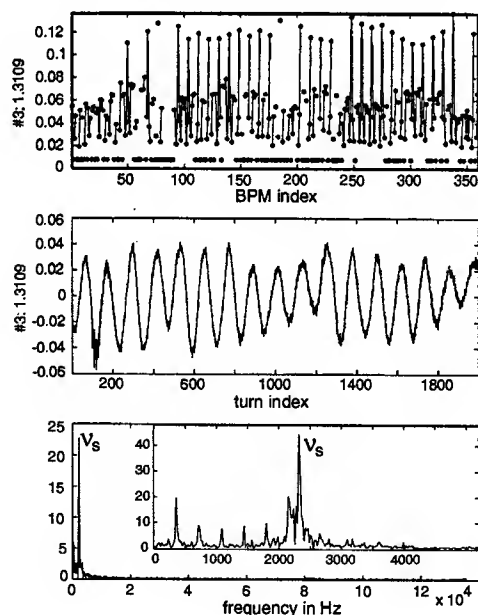


Figure 1: The third mode shows an oscillation unrelated to the kick. Its spectrum sharply peaked at the synchrotron tune and its spatial vector is consistent with dispersion. Thus this mode is due to residual synchrotron oscillation of magnitude $10 \mu m$. The insert is the lower end of the spectrum that shows various power-line harmonics, which are the cause of the undamped synchrotron motion.

Thanks to K. Harkay and L. Emery for their comments.

REFERENCES

- [1] J. Irwin et al., *Phys. Rev. Lett.* **82**(8), 1684 (1999).
- [2] Chun-xi Wang, SLAC-R-547 (1999).
- [3] Chun-xi Wang, "Measurement and Application of Betatron Modes with MIA," these proceedings.

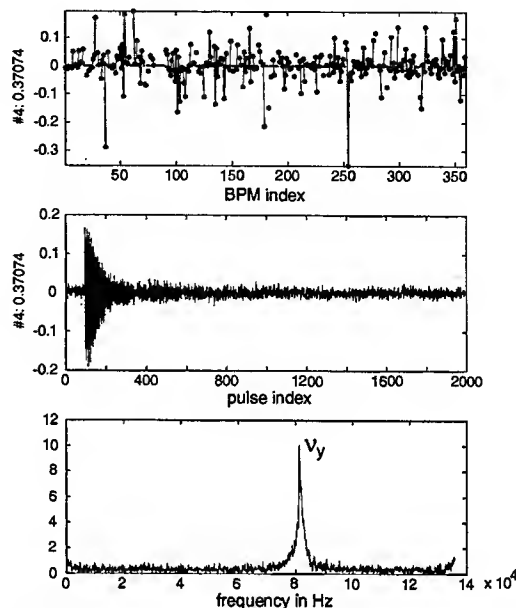


Figure 2: The fourth mode shows a kicked beam oscillating at the vertical tune. Since both the kick and observation are in the horizontal plane, this leads to transverse coupling. Misalignment of the kicker and BPMs might also contribute.

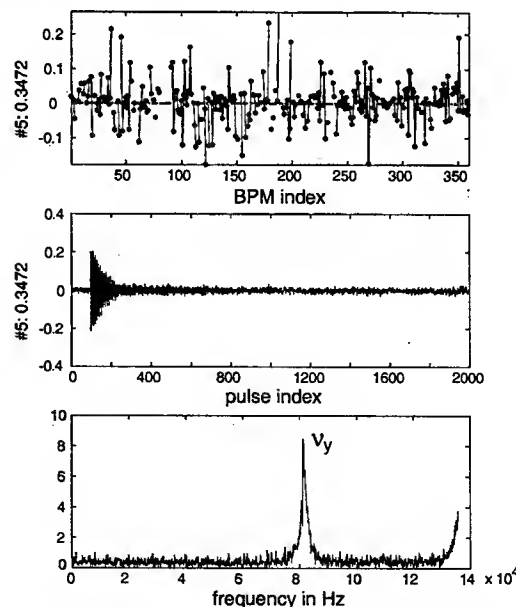


Figure 3: The fifth mode is the other vertical betatron mode paired with mode 4. See Fig. 5 for more comments.

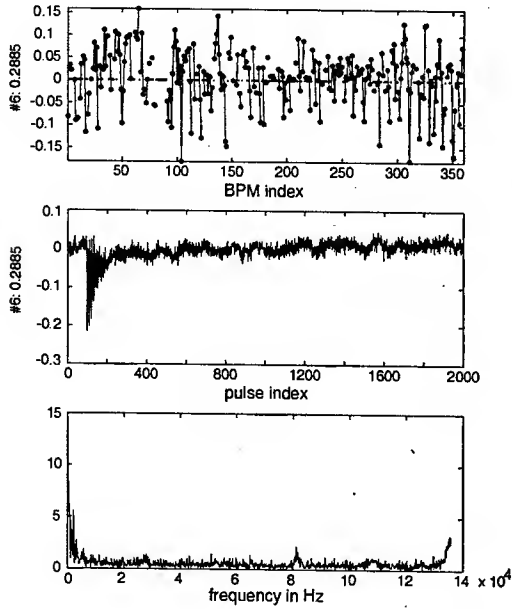


Figure 4: The sixth mode is rather different from others. The signal is excited by the kick and then smoothly damped instead of oscillating. Mixed with it are small oscillations at various frequencies.

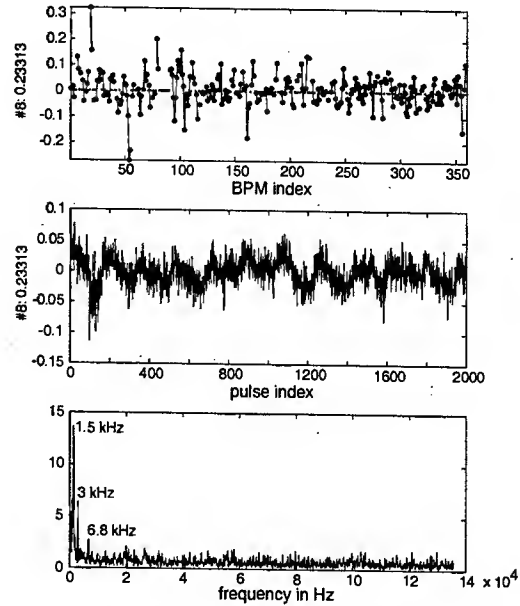


Figure 6: The eighth mode is unrelated to the horizontal kick. Its spectrum shows peaks around 0.36, 1.5, 3, and 6.8 kHz. The zig-zag motion suggests that it may be due to feedback. In fact, some of these frequencies are connected with the real-time feedback system. Power line noise could be a factor as well.

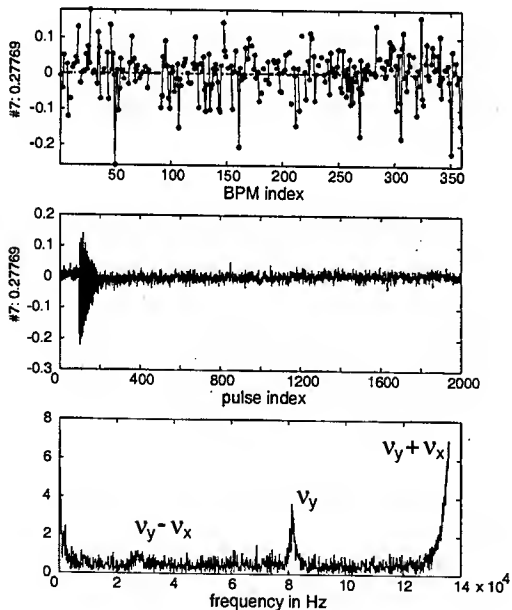


Figure 5: The seventh mode shows oscillation with frequencies y , $y - x$, and $y + x$ ($x \approx 3520$, $y \approx 1926$, and $\text{rev} = 271$ kHz). The right-most sum line is particularly strong, which suggests that sum resonance is much stronger than the difference resonance. Note that the sum signal also appeared in the vertical betatron modes, especially in Fig. 3. Thus the sum resonance might be the main driving force for transverse coupling.

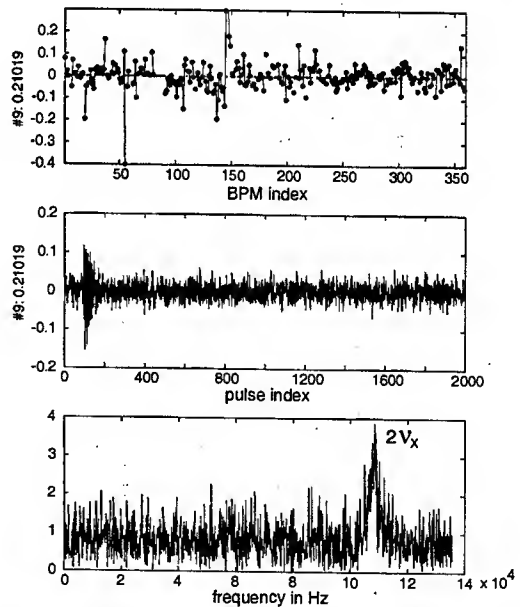


Figure 7: The ninth mode oscillates at $2x$ indicating non-linear effects due to either lattice or BPM nonlinearity. The spatial vector suggests large effects around BPM 50 and 150. It is remarkable that the spatial-temporal mode analysis can clearly resolve this mode even at such a low signal level.

FFAGS FOR MUON ACCELERATION

J. Scott Berg, Stephen Kahn, Robert Palmer, Dejan Trbojevic,

Brookhaven National Laboratory*, Upton, NY 11973, USA

Carol Johnstone, Eberhard Keil, Fermilab†, Fermilab, Batavia, IL, USA

Masamitsu Aiba, Shinji Machida, Yoshiharu Mori, Toru Ogitsu, Chihiro Ohmori,
KEK, Tsukuba, Japan

Andrew Sessler, LBNL‡, Berkeley, CA, USA

Shane Koscielniak, TRIUMF, Vancouver, B.C., Canada

Abstract

Due to their finite lifetime, muons must be accelerated very rapidly. It is challenging to make the magnets ramp fast enough to accelerate in a synchrotron, and accelerating in a linac is very expensive. One can use a recirculating accelerator (like CEBAF), but one needs a different arc for each turn, and this limits the number of turns one can use to accelerate, and therefore requires significant amounts of RF to achieve the desired energy gain. An alternative method for muon acceleration is using a fixed field alternating gradient (FFAG) accelerator. Such an accelerator has a very large energy acceptance (a factor of two or three), allowing one to use the same arc with a magnetic field that is constant over time. Thus, one can in principle make as many turns as one can tolerate due to muon decay, therefore reducing the RF cost without increasing the arc cost. This paper reviews the current status of research into the design of FFAGs for muon acceleration. Several current designs are described and compared. General design considerations are also discussed.

INTRODUCTION

An FFAG accelerates muons using a single arc with magnets whose fields do not vary with time. The arc must be able to transmit a beam over a wide range of energies. The first difficulty encountered in designing such an arc is ensuring that there are no single-cell linear resonances in the energy range of interest. There are three ways of achieving this:

- The arc has a tune which is independent of energy. This is what occurs in the original conception of an FFAG [1], what we are here calling a "scaling FFAG." Other designs are referred to as "non-scaling FFAGs."
- The single-cell tune at the lowest energy is less than 0.5, and decreases as the energy increases [2].
- Have a single-cell tune above 0.5, and use sextupoles to control chromaticity and maximize the energy range determined by the linear resonances [3].

* Work Supported by US Department of Energy contract DE-AC02-98CH10886

† Work Supported by the US Department of Energy contract DE-AC02-76CH03000

‡ Work supported by the Director, Office of Science, Division of High Energy Physics, of the U.S. Department of Energy under Contract No. DE-AC03-76SF00098

Acceleration is generally achieved by distributing RF cavities relatively uniformly around the ring. Since the muons are decaying, acceleration must be rapid (generally on average at least 1 MV/m). This means that in non-scaling FFAGs, one accelerates rapidly through any nonlinear resonances, and thus these are of little concern. Acceleration is still sufficiently gradual, however, that the bunch will adiabatically follow the energy-dependent closed orbit in the machine.

Due to the rapid acceleration, it is impractical to restore energy to the cavities at the rate that the beam is extracting it, or to change the phase of the RF as the beam accelerates. Since no FFAG design is perfectly isochronous, there is the problem that the beam does not stay at the same phase of the RF from one turn to the next. The result is that there is a minimum installed RF voltage needed to accelerate over the desired energy range. For a given type of relationship between time-of-flight and energy, that minimum voltage is proportional to the difference between the minimum and maximum time-of-flight over the energy range [4]. In addition, the longitudinal phase space area transmitted increases as the voltage increases above that minimum voltage, or equivalently as the time-of-flight range decreases.

In general, reducing the cell length reduces both the time-of-flight range and the required magnet aperture, as does increasing the number of cells in the ring.

RF CAVITIES

One of the primary reasons for using an FFAG for acceleration is the reduction in RF costs. This is achieved by making many passes (10 to 20) through the same cavities.

In the US neutrino factory designs [5, 6], 201.25 MHz (or a multiple thereof) RF must be used for acceleration. One can use superconducting or room-temperature RF for this purpose. Either type of cavity must be run near its maximum gradient (12 MV/m or more) so that the voltage does not drop too much due to beam loading. This causes the costs of room-temperature RF to far exceed that of superconducting RF, due to the substantial peak power requirements for the former.

The disadvantage of superconducting RF is the need to maintain low magnetic fields on the superconducting surfaces of the cavities. This requires space to be placed between the magnets and the cavities that would not need to be there were room-temperature RF being used. Under

normal circumstances, that field would need to be around 0.1 Gauss. However, if the cavities are cooled down before the magnets are powered, that field can be as high as 0.1 T [7]. There is little danger of inadvertent quenching, since 200 MHz cavities are made of Niobium sputtered on copper, and the volume of copper will prevent the quenching [8].

Preliminary studies have indicated that 50 cm is a sufficient cavity-magnet distance to bring the fields down to the desired levels. Thus, 200 Mhz cavities will require a roughly 2 m drift, whereas room-temperature cavities would only require around 1 m.

For the NufactJ scaling FFAG designs [9], lower frequency RF is required. Due to their low frequency, they have a large amount of stored energy. Relatively high gradients for that frequency are required. Due to the extremely low duty factor for the power sources, the large amount of peak power should be relatively inexpensive.

SCALING FFAGS

Scaling FFAGs are the only type of FFAGs that have ever been built [10, 11, 12]. A neutrino factory design using scaling FFAGs has been produced by the NufactJ working group [9]. The design has no cooling, and uses four successive FFAG rings to reach an energy of 20 GeV.

The design uses 24 MHz RF (other frequencies in this range may also be used). An RF bucket is created which encompasses both the initial and final energies for the acceleration stage, and the bunch undergoes half a synchrotron oscillation in that bucket to get from the lowest to highest energy. There has also been preliminary success with a scheme using something resembling two RF buckets, one accelerating from the lowest energy to an intermediate energy, then the second accelerating to the final energy [13].

In a scaling FFAG, the midplane vertical magnetic field is of the form $B_{y0}(\theta)(r/r_0)^k$, where r and θ are cylindrical coordinates centered at the center of the ring, and r_0 is a reference radius. As k increases, the dispersion decreases, reducing the required magnet aperture. The time-of-flight range also decreases with increasing k . Thus, maximizing k seems to be advantageous. The difficulty with this is that for larger k , the fields become more nonlinear, and the dynamic aperture becomes reduced.

Preliminary designs for superconducting magnets for the highest energy accelerator (10–20 GeV) have been made. They use a $\cos \theta$ style of design (with an elliptical vacuum chamber), but the coils are distributed highly asymmetrically to give the r^k field dependence. In addition, a trim coil has been included to allow the adjustment of k over a limited range [14].

NON-SCALING FFAGS

There has been work on a number of non-scaling lattice designs. These all share the common property that their time-of-flight varies parabolically as a function of energy.

The lattices are tuned so that the minimum of that parabola is placed at the central energy, so as to minimize the time-of-flight range.

Low Emittance Lattice

This lattice is based on a lattice cell which would give a low emittance for an electron ring [3]. Both the dispersion and beta functions are small at the bending magnet. The primary appeal is that the closed orbit variation and the time-of-flight range are small. These properties allow the ring to be made relatively short. Such a ring seems to be very inexpensive.

Unfortunately, this lattice has a very poor dynamic aperture due to the sextupoles required to control the chromaticity in this lattice, since its tune is above 0.5.

FODO Lattice

The original non-scaling FFAG design was based on a FODO lattice [2]. The lattice consists of two gradient dipoles with drifts between them. A simple procedure has been developed to design these lattices using standard nonlinear minimization and/or equation solving algorithms: vary the lattice parameters so that the frequency slip factor at the central energy is zero and the tunes at the minimum energy are some fixed value below 0.5. There are degrees of freedom remaining to optimize costs or insure that the lattice meets certain minimum requirements, such as a maximum amount of decay, a maximum number of turns (beam loading considerations), maximum pole tip fields, or a minimum longitudinal acceptance. These techniques have been used to demonstrate various properties of the lattice such as

- The time-of-flight range is linear in the cell length. The drifts should therefore have the minimum length compatible with the space requirements for cavities.
- The time-of-flight range is roughly inversely proportional to the number of cells.
- The time-of-flight range decreases as the minimum tune increases, but at the cost of an increasing beta function at low energy. The former decreases the cost, while the latter will increase costs.

The ability to generate these lattices automatically and rapidly has become a useful tool in performing cost optimizations and comparisons.

Triplet Lattice

The triplet lattice has arisen as a candidate lattice from two directions. Since the dynamic aperture of the low-emittance lattice was so poor, the sextupoles were removed. The tune needed to be brought below 0.5 for this lattice to work, and so a pair of quadrupoles was removed, leaving the triplet lattice. From the other direction, the two long drifts in the FODO lattice were often unnecessary, so making a lattice cell with only one drift seemed logical.

Table 1: Accelerating system costs for various designs.

	Range GeV	# Cells	Voltage GV	Magnet Cost	RF Cost	Other Costs	Total Cost	Per GeV
Study-II RLA	2.5–20	218	4.38	63	263	58	384	21.9
Scaling	10–20	180	1.26	178	89	32	299	29.9
FODO	10–20	108	0.91	54	55	15	124	12.4
Triplet	10–20	89	0.8	28	48	12	87	8.7
Triplet	5–10	70	0.47	30	28	8	66	13.2
Triplet	2.5–5	58	0.19	25	39	3	67	26.8

The triplet lattice is designed just as the FODO lattice is: all three magnets are combined-function magnets, the frequency slip factor at the central energy is set to zero, and the tunes at the minimum energy are set to values somewhere below 0.5. For a given drift length, the triplet lattice seems to have a lower time-of-flight range.

Racetrack

Any of these lattices can be used to create an even lower time-of-flight range as a function of energy by using a racetrack configuration. The RF is placed in the straights, where there is almost no time-of-flight variation with energy. Time-of-flight range in the arcs is minimized by minimizing the drift space: none is needed for the RF. Adiabatic transitions are made between the arcs and the straights. The greatest difficulty is in the adiabatic transitions; some preliminary work has been done [15].

COST ANALYSIS

Starting with approximate cost formulas for magnets and RF cavities, we have attempted to compare the costs of various designs. Table 1 summarizes these comparisons. Note that the triplet lattices are the result of inexact attempts at optimizing the lattice cost (the lattice costed is not a lattice that was actually designed), but are expected to be a good reflection of the actual cost trend.

The increased magnet cost in the scaling lattice over the FODO lattice results from the larger number of cells required and the fact that the defocusing quadrupole in the FODO lattice has a smaller aperture than the corresponding quad in the scaling lattice (the focusing quads have similar aperture). Furthermore a larger RF voltage is required in the scaling lattice, thus increasing the RF costs. Improving the performance of the scaling lattice would require increasing the k , or maybe even increasing the number of cells (thus reducing the apertures and maybe lowering the RF requirements).

The triplet lattice appear to be more cost effective than the FODO lattice, but this may be deceptive, since different attempts at optimization have been performed on the triplet lattice than on the FODO lattice. A more systematic comparison needs to be performed.

Note the increased cost per GeV as the energy range of the FFAG is lowered. This largely results from larger aper-

ture requirements at the lower energies. The increased RF costs in the lowest energy range result from the need to reduce the drift in that lattice, and thus use room-temperature instead of superconducting RF.

Finally, note that the costs of the triplet lattices were minimized by choosing a larger number of cells that what was initially thought necessary, and by using relatively modest superconducting pole-tip fields (around 4 T). Larger pole tip fields drive up the magnet cost rapidly, and the larger apertures required for a short ring (due to dispersion) also drive up the cost significantly.

REFERENCES

- [1] K. R. Symon *et al.*, Phys. Rev. **103**, 1837 (1956).
- [2] C. Johnstone and S. Koscielniak, in *Proc. of the APS/DPF/DPB Summer Study on the Future of Particle Physics (Snowmass 2001)*, ed. N. Graf, SNOWMASS-2001-T508.
- [3] D. Trbojevic *et al.*, in *Proceedings of EPAC 2002, Paris, France* (EPS-IGA/CERN, Geneva, 2002), p. 1199.
- [4] J. S. Berg, in *Proceedings of EPAC 2002, Paris, France* (EPS-IGA/CERN, Geneva, 2002), p. 1124.
- [5] N. Holtkamp and D. Finley, eds., Fermiab-Pub-00/180-E (2000).
- [6] S. Ozaki *et al.*, BNL-52623 (2001).
- [7] M. Ono *et al.*, in *9th Workshop on RF Superconductivity 1999* (Los Alamos, NM, 2002), Los Alamos National Laboratory report LA-13782-C.
- [8] Hasan Padamsee, private communication.
- [9] NufactJ Working Group, "A Feasibility Study of a Neutrino Factory in Japan," <http://www-prism.kek.jp/nufactj/> (2001).
- [10] F. T. Cole *et al.*, Rev. Sci. Instrum. **28**, 403 (1957).
- [11] D. W. Kerst *et al.*, Rev. Sci. Instrum. **31**, 1076 (1960).
- [12] M. Aiba *et al.*, in *Proceedings of EPAC 2000, Vienna, Austria*, p. 581.
- [13] T. Uesugi and C. Ohmori, presentations given at the Neutrino Factory and Muon Collider Collaboration Workshop on FFAG Acceleration, Berkeley, CA, Oct. 28–Nov. 8, 2002.
- [14] T. Ogitsu, presentation given at the Neutrino Factory and Muon Collider Collaboration Workshop on FFAG Acceleration, Berkeley, CA, Oct. 28–Nov. 8, 2002.
- [15] Eberhard Keil, unpublished note, <http://keil.home.cern.ch/keil/MuMu/Doc/FFAG02/adiabatic.pdf> (2002).

BEAM DUMP OPTICS FOR THE SPALLATION NEUTRON SOURCE *

D. Raparia, Y. Y. Lee, J. Wei, Brookhaven National Laboratory
S. Henderson, SNS, Oak Ridge National Laboratory

Abstract

The Spallation Neutron Source accelerator complex will have three beam dumps for beam tuning and for the collection of controlled losses. The linac and extraction beam dumps will be used for beam tuning purposes and are designed for 7.5 kW of beam power. The optics issues for these dumps are i) the beam size at the vacuum window which is near the last quadrupole and ii) guaranteeing the beam size at the dump due to multiple scattering in the presence of potentially large variations in the linac and accumulator ring emittances. The injection dump will collect the partially stripped H^0 ions as well as H^- ions which have miss the foil and is designed to absorb up to 200 kW of beam power. The closed orbit for these ions are much different in the injection area and have to be collected in the injection beam dump with a certain beam size.

INTRODUCTION

For Spallation Neutron Source (SNS) accelerator complex [1], a major requirement of all parts of this accelerator is to have low uncontrolled beam losses (≤ 1 Watt/m), to allow hands on maintenance. There will have three beam dumps for beam tuning and for the collection of controlled losses. The linac and extraction beam dumps will be used for beam tuning purposes and are designed to absorb 7.5 kW of beam power. The injection dump will collect the partially stripped H^0 ions as well as H^- ions which have miss the foil and is designed to absorb up to 200 kW of beam power. Figure 1 shows these all three dumps.

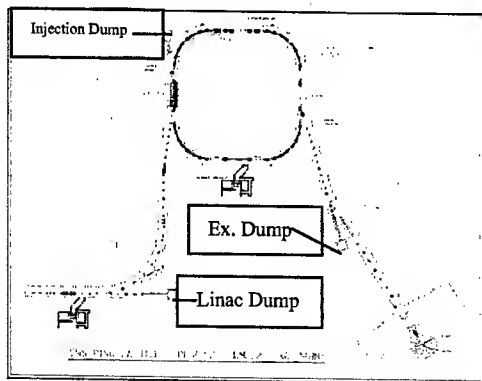


Figure 1: Layout of beam dumps.

LINAC BEAM DUMP

Linac beam dump is located after linac to achromat matching section of the High Energy Beam Transport

*SNS is managed by UT-Battelle, LLC, under contract DE-AC05-00OR22725 for the U.S. Department of Energy.

(HEBT) [2], this dump will be used for linac beam characterization of the linac beam from 200 MeV to 1.3 GeV and for collecting singly stripped H^0 particle from the linac. This line is about 35 meters long and has six quadrupoles and one vacuum window. Vacuum window is located just after the last quadrupole. This window is made of Inconel and 2 mm thick. The advantage of the window at this location is that it guarantees the beam size at the dump. The requirement for the dump is that beam size should be 60 mm in radius and beam power outside 8 inch diameter circle should be less than 750 watts.

As H^- traverse through the window [3], it deposited two electrons and some energy due to straggling and suffer from multiple and nuclear scattering. The average energy deposited by H^- ions due to two electrons is 1.12 MeV at 1000 MeV and 0.22 MeV at 200 MeV in relatively short distance in the window. Figure 2 shows the rms multiple scattering angles as function of energy and Figure 3 shows the energy loss per proton as function of energy for 2 mm of Be, Al, and Inconel.

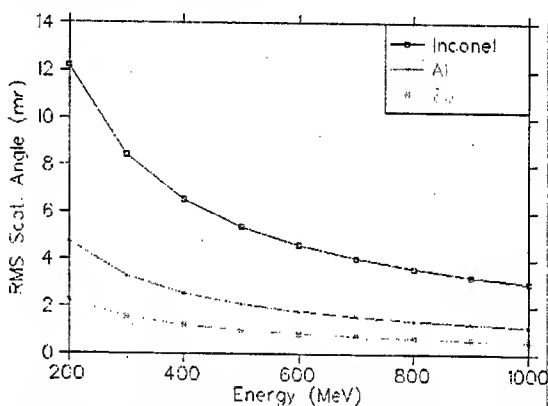


Figure 2: RMS multiple scattering angle as function of the proton energy for 2.0 mm thick window for Be, Al, and Inconel.

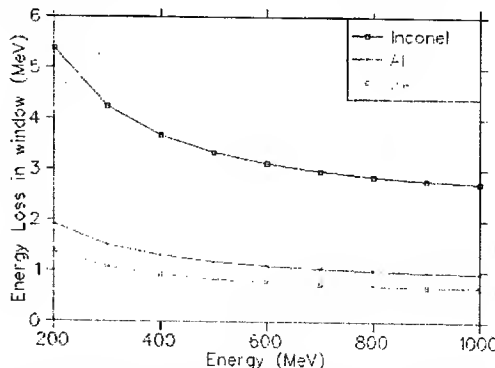


Figure 3: Average energy loss in window per proton in 2 mm thick window as function of proton energy.

To minimize the temperature in the window the beam size is kept 30 mm in diameter for 95% of beam for all the energies and various emittances. Figure 4 shows the TRANSPORT out put for the 200 MeV and Figure 5 shows the TRANSPORT out put for the 1000 MeV.

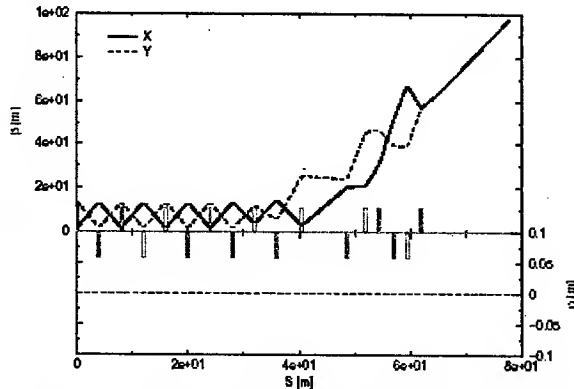


Figure 4: Beta function along linac dump for thick window (2.0 mm of Inconel) at 200 MeV.

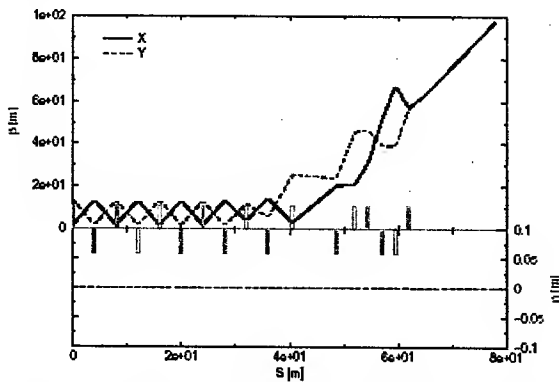


Figure 5: Beta function along the linac dump for 2.0 mm Inconel vacuum window and four times normal emittance at 1000 MeV.

As shown in Figure 2, at lower energies the rms scattering angle is higher therefore more particles will be outside 8 inches diameter circle. Linac has to operate at lower power at the time of commissioning for lower energies. PARMILA (which was modified for multiple and nuclear scattering) simulations show losses in the flight tube and dump. Table I shows the require operating power for different energies.

Table I: Maximum power for different energies.

E, GeV	0.2	0.4	0.6	0.8	1.0
β	0.56	0.71	0.79	0.84	0.87
γ	1.21	1.43	1.64	1.85	2.06
$\beta\gamma$	0.69	1.02	1.30	1.56	1.81
Loss in FT, %	40	7.6	3.3	2.6	2.3
$P_{\text{outside}}, \%$	39.0	39.0	21.1	10.9	5.9
Max. P, kW	1.92	1.92	3.55	6.88	7.5

INJECTION BEAM DUMP

Injection beam dump is designed to absorb 200 kW of beam power and requires that 99% of the beam should lie in 200 mm diameter circle. It will collect unstripped H^- and partially stripped H^0 ions. Figure 6 shows the layout of the injection region.

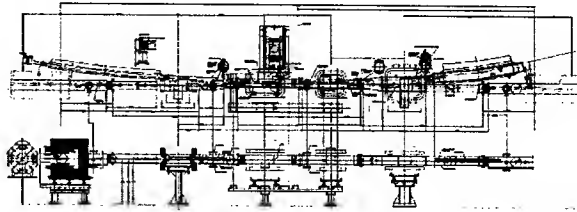


Figure 6: Layout of the injection region.

H^- ions which have missed the foil will emerge from the injection bump magnet # 2 as 2.1 mrad toward left, H^0 will go straight and proton will bend 2.1 mrad right. The injection bump magnet # 3 will bend further H^- ions by 42 mrad while H^0 ions will go straight. There will be a thick foil before the injection bump magnet #4, which will convert H^- and H^0 ions to proton by stripping two and one electrons respectively. After injection bump magnet #4 both trajectory goes through an injection dump gradient magnet and finally through an x-defocusing quadrupole magnet. The optics is such that that the both trajectories coincide at the injection dump. Figure 7 shows the H^0 centroid displacement with respect to the close orbit. H^- trajectory will be just mirror of the H^0 trajectories in Figure 7.

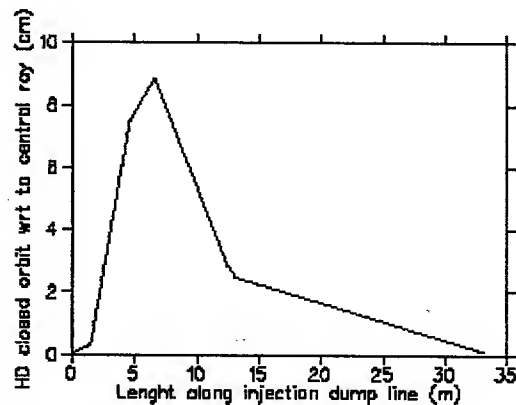


Figure 7: H^0 trajectory displacement with respect to the central closed orbit.

PARMILA was modified to track three species (P , H^- , H^0) and included multiple and nuclear scattering. Figure 8 shows the all three species after the foil. Foil will be carbon about $300 \mu\text{g}/\text{cm}^2$, about 2-4 % H^- will be partially stripped and about 1-2% H^- ion will miss the foil. Figure 9 shows the particle distribution at dump, middle particle are the H^0 and outer particle are H^- when they started at

the foil. Figure 10 shows the TRANSPORT out for the injection beam dump beam line.

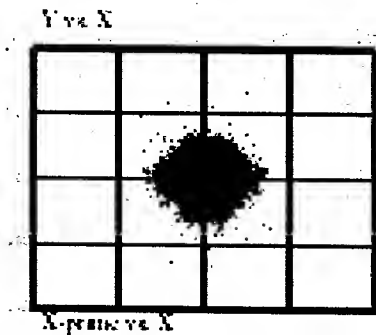


Figure 8: Particle distribution at the foil. Red are the fully stripped protons, black are the H^- ions, which have missed the foil and blue are the partially stripped H^0 ions.

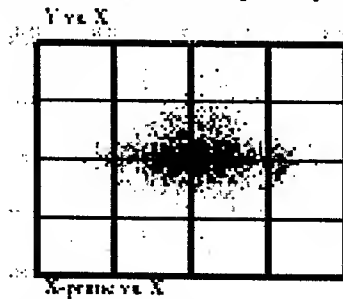


Figure 9: Particle distribution at the injection dump. In the middle (blue) are the particles, which started H^0 at the foil. The outer (red) are the particles which started as H^- at the foil.

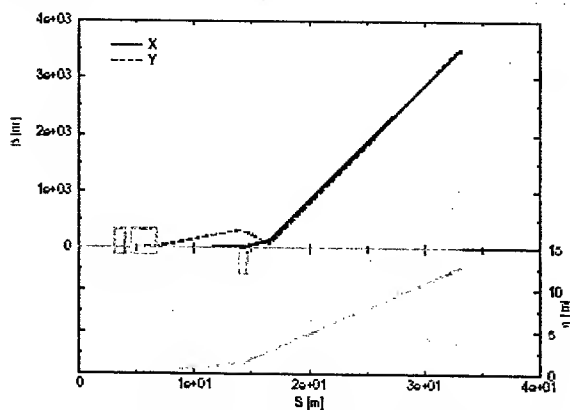


Figure 10: TRANSPORT output for the injection beam dump beam line.

EXTRACTION BEAM DUMP

The extraction dump will be used for ring tuning purposes and will have the capacity of 7.5 kW. The extraction dump requirement is that 99% beam should be within 8

inch of diameter circle and only 750 Watts of beam can lie out side of this circle. The extraction dump is located after the 16.8 degrees dipole in the Ring Target Beam Transfer (RTBT) [2] line. If the dipole is off beam will get o the dump hence failsafe. There are two quadruples in this line and vacuum window is located just after the last quad in the line. The vacuum window will be 0.5 mm thick of Inconel. The line is designed to accommodate single turn to full 1060 turns injection into the ring. Again like the linac dump line vacuum window guarantee the beam size at the dump. Figure 11 shows the TRANSPORT output for this line.

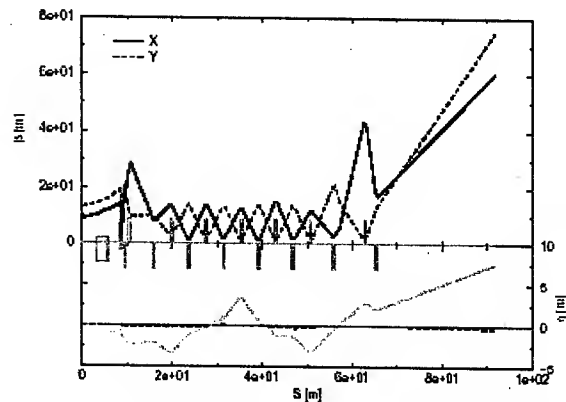


Figure 11: Transport output for extraction dump beam line.

Figure 12 shows the current distribution at the extraction beam dump only $\frac{1}{4}$ of the beam footprint is shown.

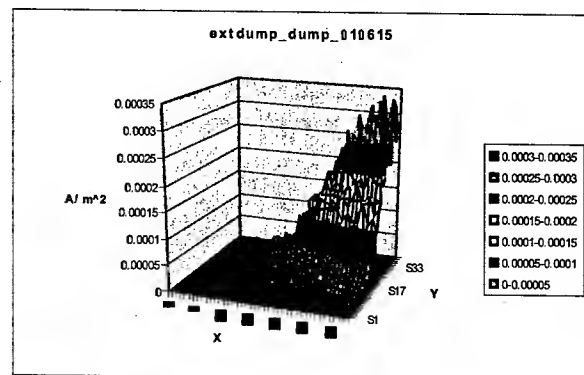


Figure 12: beam current density at the extraction dump, only $\frac{1}{4}$ of the beam footprint is shown.

REFERENCES

- [1] N. Holtkamp, Proc. EPAC 2002, p. 164.
- [2] D. Raparia et al., Proc. AIP #642, p. 130.
- [3] G. R. Murdoch, SNS-NOTE-ENGR-40, 28 January 2002.

BEAM SCRUBBING STRATEGY FOR ELECTRON-CLOUD SUPPRESSION IN THE SPALLATION NEUTRON SOURCE RING*

S.Y. Zhang, M. Blaskiewicz, H.C. Hseuh, and J. Wei, BNL, R. Macek, LANL, USA

Abstract

Electron cloud is still an unsettled issue for the high intensity SNS storage ring. Studies are undergoing, especially on the electron multipacting condition, beam instability threshold, electron density and the electron dose on the wall. It has been simulated that the electron multipacting may generate very large electron dose that the pressure rise might become unacceptable. Chamber sections with high secondary electron yield and/or locations having large numbers of primary electrons, such as the injection region or the collimation area, are likely to have higher pressure rise. Beam scrubbing is proposed as one of the principle mitigations for the electron multipacting problem in the SNS. In this article, experiments of the beam scrubbing on existing machines will be reviewed, and specifics of the SNS ring beam scrubbing will be discussed.

INTRODUCTION

The secondary electron yield (SEY) of the vacuum chamber can be reduced by the beam scrubbing through the electron bombardment, but the required dose is very large [1]. For most machines that encountered electron cloud (EC) problem, beam instability and emittance blowup have already become serious problem before reaching such a high dose rate. Therefore, the beam instability and emittance growth are usually the first consequences of the electron cloud, and the effect of scrubbing was only observed over a long period of time. These machines include the LANL PSR, CERN SPS, and the B-factories.

After several years of struggling with the electron cloud of LHC beam at the CERN SPS, intentional beam scrubbing aiming at the vacuum chamber conditioning has shown clear effect, and the LHC beam requirement has been achieved at the SPS in the first time [2].

With very high beam intensity in SNS storage ring [3], it has been simulated that the electron multipacting may generate very large electron dose on the chamber wall [4]. The pressure may rise to an unacceptable level, due to the electron stimulated gas desorption. Also, chamber sections with high secondary electron yield, and/or locations having large numbers of primary electrons, such as the injection region or the collimation area, are likely to have higher pressure rise.

* SNS is managed by UT-Battelle, LLC, under contract DE-AC05-00OR22725 for the U.S. Department of Energy. SNS is a partnership of six national laboratories: Argonne, Brookhaven, Jefferson, Lawrence Berkeley, Los Alamos, and Oak Ridge.

Beam scrubbing is, therefore, proposed as one of the principle mitigations for the electron multipacting problem in the SNS. In this article, experiments of the beam scrubbing on existing machines will be reviewed, and specifics of the SNS ring beam scrubbing will be discussed.

BEAM SCRUBBING

It was shown in [1] that with the electron dose of about 1mC/mm^2 , SEY can be reduced from 2.2 to 1.2 for stainless steel surface. To see how large this dose is, one may look at the one of the most pronounced effect in the beam chamber, which is the vacuum pressure rise.

Usual pumping capability is calculated by

$$M = kSP \quad (1)$$

where $k = 3.3 \times 10^{22} / \text{m}^3$ is the gas molecule density per Torr, S is the average pumping speed, and P is the pressure in Torr. Using average pumping speed of $S = 13\text{ls}^{-1}\text{m}^{-1}$, i.e. 13 liters per second per meter, which is close to the situation of RHIC, SPS, PSR, and SNS, the gas molecules pumped out of the chamber are $M = 4.3 \times 10^{20} \text{Ps}^{-1}\text{m}^{-1}$.

On the other hand, for a typical round chamber with radius of 5 cm, with the dose of 1mC/mm^2 applied in 24 hours, 2.3×10^{16} electrons will be generated in a 1 meter long chamber per second. Using electron gas desorption rate of 0.1, $N = 2.3 \times 10^{15}$ N_2 -equivalent molecules will be produced.

The equilibrium pressure rise will be reached by equating the electron desorption generated molecules with the pumping capability, which is

$$P = N(kS)^{-1} \quad (2)$$

and one gets $P = 5.3 \times 10^{-6} \text{Torr}$. Usually the ion pump will stop work at this pressure level, and vacuum valve will be closed to protect the equipment.

For most machines with electron cloud, the EC induced beam instability and associated emittance blowup have prevented the higher beam intensity, the pressure rise was usually less than 10^{-7}Torr , therefore, the beam scrubbing effect was not obvious. Only exception is perhaps the RHIC, where electron cloud takes place only in part of the warm sections, which is in total 1,300 m in two rings over the machine circumference of 3,834 m. The pressure rise sometimes was so high that the vacuum valve closed, yet the beam instability had not become a serious problem [5].

In principle, using electron dose as the criterion for the beam scrubbing is not very proper, since the energy of these electrons is very important in terms of scrubbing

effect. For example, the electrons with energy less than 20 eV contribute very little in scrubbing, while the ones with 500 eV are probably having the largest effect. Fortunately, similar relation exists also to the projectile electron's energy and the gas desorption rate. Therefore, instead of the complicated procedure of estimating the electron dose on the chamber wall, the pressure rise has emerged as a more useful criterion for the beam scrubbing effect. If the pressure rise induced by the electron cloud is higher, then the beam scrubbing is more effective.

MACHINE EXPERIENCES

In this section, existing machines' practice and study experiences will be reviewed. The relation between the electron dose, associated pressure rise and the scrubbing effect seems to approximately agree with the prediction.

PSR

In the PSR, detected peak electron flux on the wall, in a high intensity study, is 0.14 mA/cm^2 [6], but in normal operation, it was more like 0.014 mA/cm^2 . This flux takes place at about 40 ns in the 357 ns revolution time in each turn, and in 300 turns of the usual 1,800 injection turns. For 20 Hz repetition rate, the average electron current on the wall is 0.034 nA/mm^2 . Therefore, the accumulated dose in 24 hours is $2.9 \mu\text{C/mm}^2$. For the round chamber radius of 5 cm, the pressure rise is, using equation (2), $1.6 \times 10^{-8} \text{ Torr}$. The observed pressure rise in PSR is from 2 to $4 \times 10^{-8} \text{ Torr}$, approximately agreeable with the calculation.

In a period of longer time, the scrubbing effect, nevertheless, was obvious [7].

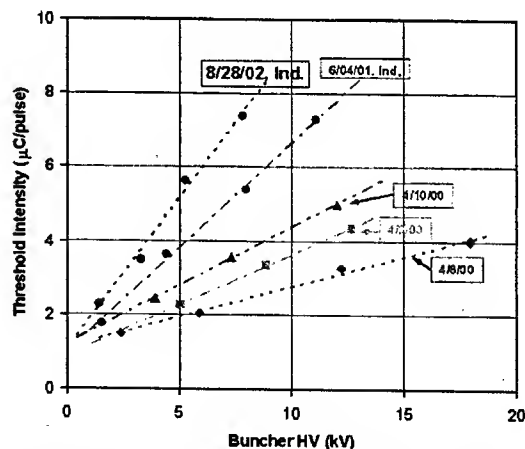


Fig. 1. Instability threshold intensity curves during 2000-2002 operations. The data for 2001 and 2002 also include the effect of inductive inserts, which cause an ~30% increase in the slope of the curves for those dates.

Fig. 1 shows the PSR beam scrubbing effect in terms of instability threshold vs. RF voltage. Excluding other

factors, such as the inductive inserts, there is a factor of 2 improvement during the period.

In Fig. 2, the prompt electron signals and ion pump pulse during 2002 operation are plotted. The electron signal diminished rapidly at first and more slowly after a few weeks, and tends to reach a plateau after 3 months.

Among other indicators of the beam scrubbing effect, the electron signal at the extraction transfer line did not change much, and it offers now the strongest electron signal at the PSR, presumably because of lack of scrubbing.

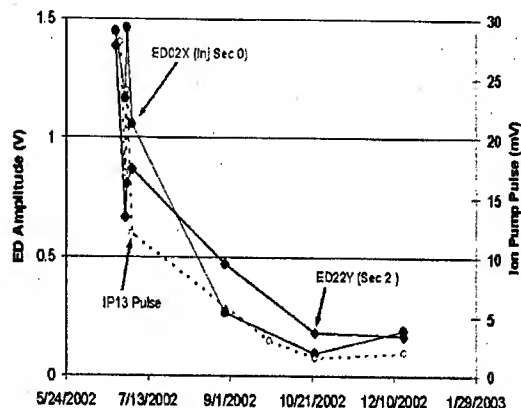


Fig. 2. Prompt electron detector signals and ion pump pulse for $8 \mu\text{C}$ beam pulse as a function of time in the run cycle.

SPS 2000

In 2000, a beam scrubbing of 2.5 days was tested in the SPS, with modest pressure rise and the electron dose [8]. The bunch intensity was 0.43×10^{11} proton, and 72 bunches (1 batch) was injected. The collected electrons by a pick up showed that about 10^{11} electrons hitting the wall in a meter long pipe for 1 batch of beam passing. Using the electron gas desorption rate of 0.1, with the revolution frequency of 43 kHz , this implies that $4.3 \times 10^{14} \text{ s}^{-1} \text{ m}^{-1} \text{ N}_2$ -equivalent molecules were produced. For the duty cycle of 45%, total electron dose in 24 hours is about 0.1 mC/mm^2 , the observed typical pressure rise was $< 7 \times 10^{-7} \text{ Torr}$, close to the calculated pressure rise, $5.3 \times 10^{-7} \text{ Torr}$. As the result of the beam scrubbing, the pressure rise was reduced by a factor of 5 in the first 24 hours for the same beam.

SPS 2002

In 2002, it was decided to have a dedicated beam scrubbing run for SPS, which lasted 10 days [8]. The bunch intensity was raised to between 1×10^{11} to 1.4×10^{11} protons, with 1 to 4 batches injected. The pressure rise was pushed to as high as $5 \times 10^{-6} \text{ Torr}$, barely below the valve close threshold. Various patterns of the beam injections with increasing bunch intensity were used to maximize the beam scrubbing effect. The duty cycle was about 45% in first 24 hours, and the accumulated electron dose, estimated from the pressure rise, was about 0.5 mC/mm^2 . Correspondingly, the pressure rise for the same beam was reduced by a factor of 100 in 24 hours.

Table1: Beam scrubbing parameters comparison, with the electron dose, associated pressure rise and result in 24 hours of period

	Dose	Pres. Rise	Result
PSR	0.003	2e-8	Ins. thre. modest incr.
SPS00	0.1	7e-7	PR reduced, factor 5
SPS02	0.5	5e-6	PR reduced, factor 100
	<i>mC/mm²</i>	<i>Torr</i>	

SNS BEAM SCRUBBING

SNS Electron cloud and counter measures

With 2.08×10^{14} protons in the SNS ring of the 2 MW operation, large numbers of electrons may be produced by the bunch tailing edge multipacting. Simulation [4] shows that the peak electron flux at the beam tail may reach $5mA/cm^2$. Given the flux duration of 70 ns over 945 ns per turn, assuming that the electron cloud takes place in the last 100 turns of total 1,200 injection turns, with 60 Hz operation cycle, the electron dose on the wall is $1.6mC/mm^2$ in 24 hours. For the SNS chamber with radius of 10 cm, the pressure rise of $1.7 \times 10^{-5} Torr$ is calculated using equation (2), which is well above the vacuum valve close threshold, $5 \times 10^{-6} Torr$. As the result, there is a possibility that the SNS ring will encounter difficulties for full power operation without a proper beam chamber conditioning.

In addition to conventional electron cloud induced problems, such as the beam instability, the vacuum valve may close due to high pressure rise. The later is different from the former that it may happen locally at a few locations. In general, a high pressure rise in a limited length of pipe affects not much the beam stability and emittance.

For the counter measure, the SNS ring chamber is coated by TiN alloy, several electron collectors will be placed at the most troublesome locations, such as the injection area, and also solenoids will be installed between the collimators [3]. In addition, SNS ring has reserved empty ports to later install high throughput pumps if needed in the future.

For further electron cloud suppression in the SNS ring, the beam scrubbing is proposed. In the following, some possible scenarios are discussed.

Scenarios of beam scrubbing

To prepare for the worst case scenario, the beam scrubbing fits this need very well as one of the principle mitigations for the electron multipacting problem in SNS ring.

1. First scenario is that at the early commissioning, the electron multipacting may take place, and at one or more locations, the local pressure rise might be too high to tolerate. For beam scrubbing, the beam may be injected until the local pressure rises to about $5 \times 10^{-6} Torr$, and to run the machine until the pressure

rise reduces, then increase the injection turns, and/or increase the Linac beam current. It is possible that the locations with highest pressure rise are scrubbed more than others, which means that more time is needed to conditioning the whole ring.

2. The second scenario is that in the early operation, the electron cloud induced beam instability may prevent the higher intensity operation, similar to PSR's situation. In the proposed operation mode, which is similar to the PSR, the Linac beam will be injected by 1,200 turns, followed by prompt beam extraction. The electron cloud is likely to develop at the end of the injection, probably the last 100 turns within the total 1,200 turns of the beam accumulation. At the end of the injection, 0.5 ms to 1 ms additional store time may increase the electron dose by about factor of 20. According to the PSR experience, the conditioning period may be reduced by the same factor. There is no major stopper in this scenario. Existing RF power supply, which is a resonance type and hence cannot hold up the voltage for too long, can support this period of time with tolerable voltage drooping. Beyond this store time, a \$250K upgrade of the power supply system can extend the store time much longer [9]. It is of interest to know, of course, if the beam loss, etc. can be tolerable.

SUMMARY

Review of existing machine cases has shown consistent relation between the electron dose, pressure rise, and the beam scrubbing effect. The pressure rise caused by the electron cloud is a good indicator of the effective electron dose, and it can be used in the beam scrubbing operation.

The SPS dedicated beam scrubbing experiment has changed the conventional thinking about mitigation of the electron cloud effects, which is to directly counteract the EC induced beam instability and emittance blowup. One now can see a strong role for conditioning the beam pipe to reduce the beam induced electron multipacting. With hindsight, more attention should be given to beam scrubbing as part of the mitigation strategy.

For the very high power SNS ring, therefore, the beam scrubbing has been proposed as one of the principle mitigations for the electron multipacting problem.

REFERENCES

- [1]. N. Hilleret et al, p. 2629, PAC, New York, 1999.
- [2]. J.M. Jimenez, Mini-Workshop on SPS Scrubbing run, CERN, 2002.
- [3]. J. Wei and R. Macek, ECLOUD'02, CERN, April, 2002.
- [4]. M. Pivi and M.A. Furman, p. 1547, EPAC, Paris, 2002.
- [5]. S.Y. Zhang et al, these proceedings.
- [6]. R. Macek, ECLOUD'02, CERN, April, 2002.
- [7]. R. Macek, LANL PSR Tech. Note, in preparation.
- [8]. J.M. Jimenez, Chamonix XI, CERN, 2001.
- [9]. A. Zaltsman, private communication.

THE AGS ELECTROSTATIC SEPTUM

J. Hock, T. Russo, J. Glenn, K. Brown

INTRODUCTION

The previous slow beam extraction electro static septum in the AGS was designed in 1981. Research documented at the Fermi Laboratory was used as the base line for this design. The septum consisted of a ground plane of .002" diameter wire tungsten-rhenium alloy (75%W 25%Re) with a hollow welded titanium cathode assembly. The vacuum chamber is stationary and the septum is moved with a pair of high vacuum linear feed throughs.

After years of beam time, the frequency of failures increased. The vacuum system design was poor by today's standards and resulted in long pump down times after repairs. The failures ranged from broken septum wires to a twisted cathode. In addition to the failures, the mechanical drive system had too much backlash, making the operating position difficult to repeat. The new septum needed to address all of these issues in order to become a more reliable septum.

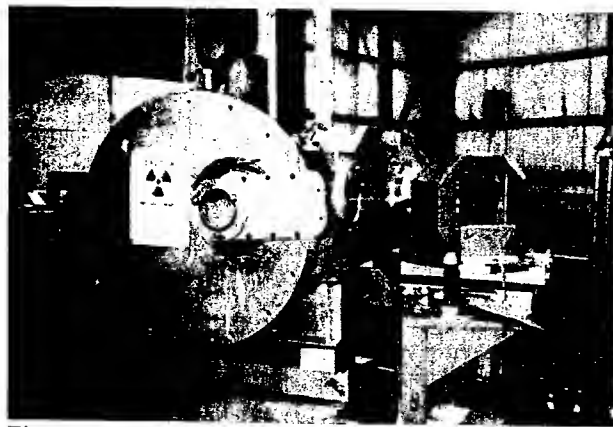


Figure 1: The Old AGS Electro Static Septum

VACUUM CHAMBER

The vacuum chamber material was changed to stainless steel with knife-edge flanges and copper gaskets. The septum assembly was slid into the chamber on linear bearings, so the septum could be removed quickly from the chamber during maintenance. All materials used in the septum were compatible for high vacuum. All mating surfaces were vented and all blind tap holes were assembled with vented bolts. The pump down time was reduced from 6 hours to less than an hour.

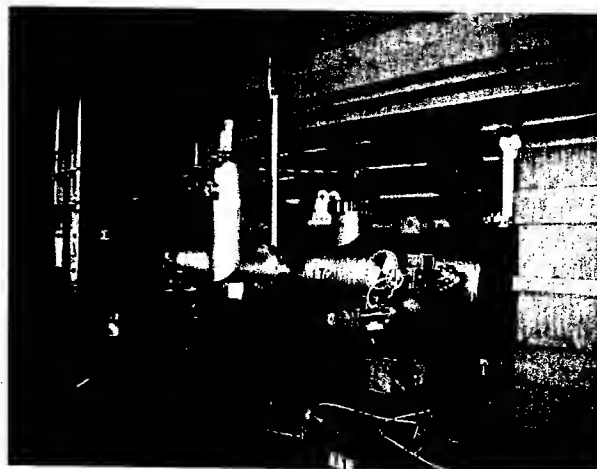


Figure 2: The New AGS Electro Static Septum

LINEAR ACTUATORS

The mechanical linear actuators were designed with all the control components (limit switches, feedback potentiometer, and drive motor) mounted to the same unit. The actuator is attached to the vacuum with a flange, and the septum with a pin, for quick removal from the high radiation area. The backlash was minimized by adding a tension spring on the septum assembly, opposite the linear drives, thus always loading the drive system in one direction. The feedback potentiometer was mounted directly to the actuator shaft with an anti-backlash gear.

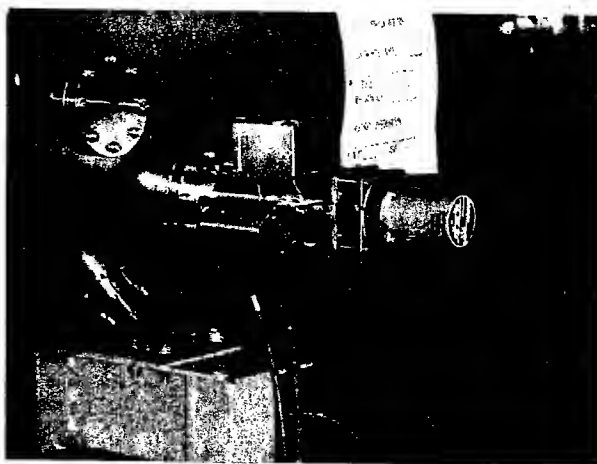


Figure 3: The Linear Drive Installed On The Septum

CATHODE

The old cathode was a welded assembly made from tubular titanium, which was twisted, possibly from over heating during conditioning. The new cathode was made from a solid titanium rod, able to carry more current during conditioning.

GROUND PLANE

In an effort to prevent the proton beam from breaking the septum wire, the geometry and material of the wire was addressed. The wire was mounted to the septum on a c-shaped support between two tension springs. The spring tension provided stiffness to the fragile wire, minimizing its deflection induced by the electrical field, and pulls the wire away from the cathode if it breaks. The tensile load on the wire from the springs is small (.25#) due to the small cross sectional area of the wire. The wire is attached to the springs by twisting a loop in the end of the wires, causing slight slippage at initial tensioning of the wire. A consistent wire length was difficult to maintain. The varying lengths of the wire, coupled with the varying properties of the springs yield different tensile load on the wires, hence different displacements caused by the 60 kV electro static field. The different deflections of the wire meant that the ground plane was thicker then .002".

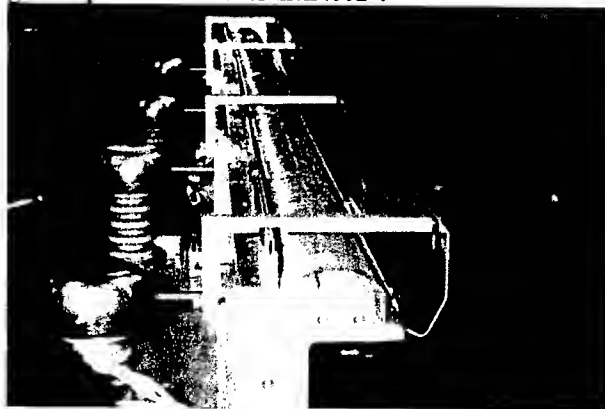


Figure 4: AGS Old Electro Static Septum

Several different shapes and materials were heat load tested using a defocused electron beam welder in a vacuum. Five tests were performed for each of the following test samples: .002" diameter W 75% Re 25% alloy wire (the existing design), .002" by .035" W 75% Re 25% alloy foil strip, .001" by .035" W 75% Re 25% alloy foil strip, .002" by .035" 3Al-2.5V Ti alloy foil strip, and .001" by .035" 3Al-2.5V Ti alloy foil strip. The test fixture consisted of four foils of the same type, installed between a pair of springs, evenly spaced at .125", and orientated so that the edge of the foil shadows

electron beam. The .002 diameter wire test samples were set up the same as the foils except eight wires were evenly spaced at .063". The beam was set at different power settings and the exposure time was recorded. From the results of this test (listed in Table 1), the .001" thick by .035" W 75% Re 25% alloy was the best choice. Further research of the tungsten rhenium alloy showed the W 95% Re 5% had the highest tensile strength of this alloy.²

The new AGS electro static septum uses a .001" thick by .035" wide W 95% Re 5% alloy foil strip. The large cross sectional area allows the foil to have a higher tensile load than the wire, yielding less displacement from the electro static force. The theoretical displacement for the foil is .0003" as compare to the wire .003". The stiffer foil also reduces the displacement due to the different spring properties and lengths of the foil.

Although the foil strip septum is thinner, the total length of material is 26.25" as compared to the wire, which is 3". The predicted losses at the septum will increase, but reduce the losses for the downstream slow beam extraction devices.

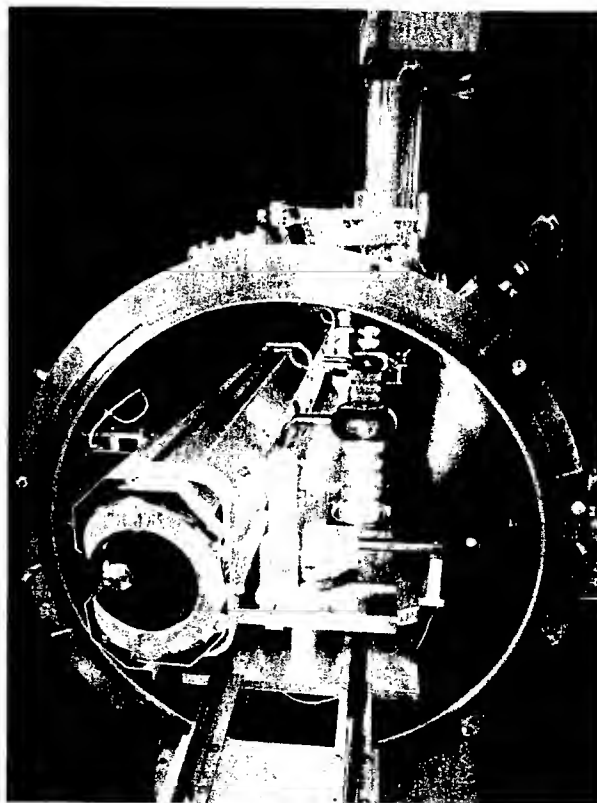


Figure 5: The New AGS Electro Static Septum

TABLE 1: SEPTUM HEAT LOAD TEST

TEST SPECIMAN	BEAM CURRENT (mA)	VOLTAGE (kV)	BEAM DIA. (cm)	BEAM FLUX (W/cm ²)	TIME (s)	OBSERVATION
.002" BY .035"	0.7	90.6	0.2	2,020	2.5	NO FAILURE
W 75% Re 25%	0.7	90.6	0.2	2,020	3.5	3 RD FOIL FAILED
FOIL STRIP	0.6	85.0	0.2	1,624	30.0	NO FAILURE
	0.7	90.6	0.2	2,020	3.0	1 ST FOIL FAILED
	0.6	88.0	0.2	1,682	9.5	2 ND FOIL FAILED
	0.6	87.0	0.2	1,662	38.0	4 TH FOIL FAILED
.001" BY .035"	0.6	85.0	0.2	1,624	9.0	1 ST FOIL FAILED
W 75% Re 25%	0.6	87.0	0.2	1,662	60.0	NO FAILURE
FOIL STRIP	0.6	88.0	0.2	1,682	60.0	NO FAILURE
	0.7	90.6	0.2	2,020	60.0	NO FAILURE
	0.7	91.0	0.2	2,028	300	NO FAILURE
.002 DIA. WIRE	0.6	85.0	0.2	1,624	0.0	ALL 8 WIRES FAILED
W 75% Re 25%	0.3	60.0	0.5	92	8.0	ALL 8 WIRES FAILED
.002" BY .035"	.06	85.0	0.2	1,624	1.0	ALL 4 FOILS FAILED
3A1-2.5V Ti ALLOY						
FOIL STRIP						
.001" BY .035"	0.6	85.0	0.2	1,624	1.0	ALL 4 FOILS FAILED
3A1-2.5V Ti ALLOY	0.2	50.0	0.76	22	60.0	NO FAILURE
FOIL STRIP	0.3	50.0	0.5	76	60.0	NO FAILURE
	0.3	50.0	0.25	306	5.0	1 ST FOIL FAILED
	0.3	50.0	0.4		60.0	NO FAILURE
	0.3	60.0	0.50	119	110.0	2 ND FOIL FAILED
	0.3	60.0	0.50	92	40.0	3 RD FOIL FAILED
	0.3	60.0	0.50	92	188.0	4 TH FOIL FAILED

CONCLUSION

The new foil strip septum performed similar to the wire septum. As predicted the losses increased at the septum and was slightly reduce at the downstream extraction devices, but the overall extraction efficiency was unchanged. Due to problems with the positioning control circuit, caused by noise, it is unclear if the backlash was reduced. In addition, the leakage current gradually increased with beam time. During the 2003 shutdown the AGS electrostatic septum will be removed, inspected and repaired. Also the positioning control circuit will be fixed.

REFERENCES

1. J. Walton, et al, "An Improved Design For The Fermilab Septa", IEEE Transactions on Nuclear Science, Vol. NS-22, No.3, June 1975.
2. ASM Handbook, "Properties And Selection: Nonferrous Alloys and Special-Purpose Materials", Vol. 2, p.580, October 1995.

BEAM BASED CHARACTERIZATION OF A NEW 7-POLE SUPERCONDUCTING WIGGLER AT CESR*

A. Temnykh[†], J. Crittenden, D. Rice and D. Rubin
Laboratory of Nuclear Studies
Cornell University, Ithaca NY 14953, USA

Abstract

The paper describes the beam based measurements of the magnetic field characteristics of the first 7-pole superconducting wiggler recently installed in CESR. The results are compared with the model prediction and with the estimates based on magnetic field measurements. It also presents results of the beam resonance mapping which was done by a 2D scan of betatron tunes while recording vertical beam size. The scan clearly exposed resonances excited by the wiggler nonlinear magnetic field components. In conclusion, the ways to optimize the wiggler magnetic field in order to reduce destructive effects on beam dynamics are discussed.

INTRODUCTION

The CESR low energy upgrade project calls for 12 superconducting wigglers installation to provide adequate radiation damping. The first 7-pole superconducting wiggler [1] was built [2] and, after magnetic measurement [3], in the fall of 2002 was installed in CESR. A number of machine study periods were devoted to a beam based characterization of the wiggler magnetic field. Results of this characterization in comparison with the magnetic measurement and model prediction are described below.

MODEL CALCULATION AND MAGNETIC MEASUREMENT RESULT

The wiggler field integrals along straight lines and along wiggling beam trajectories are used for wiggler field characterization. Depending on the wiggler design, the difference between those integrals can be substantial. The straight line integrals calculated from model can be easily verified by a long flipping coil measurement. The measurement of the field integrals along beam trajectory can be done by using modified vibrating wire technique [6] or with a beam after wiggler installation in the ring.

Magnetic measurement results for 2.1T and 1.9T wiggler peak fields in comparison with a model calculation are presented in the Table 1. Moments a_n and b_n are the coefficients of the polynomial fit of the horizontal and vertical field integral dependence on horizontal position: $I_{x,y}(x) = \sum (a_n, b_n) \times x^n$. Columns "str.line" and

"str.coil" refer to calculated and measured straight line integrals. Columns labeled with "wgl.line" and "wgl.wire" are for integrals calculated and measured along wiggling trajectory of beam of 1.8GeV energy. The measurement technique is described in [3].

a_n, b_n $\frac{Gm}{cm^n}$	Model		Magnetic measurement	
	str. line	wgl. line	str. coil	wgl. wire
Wiggler peak field $\sim 2.1T$				
a_1	0.0	0.0	1.53 ± 0.01	N/A
b_1	0.0	1.33	-0.19 ± 0.02	2.5 ± 0.15
b_2	-0.29	-0.28	-0.28 ± 0.004	-0.51 ± 0.03
b_3	0.00	-0.11	0.004 ± 0.002	-0.19 ± 0.02
Wiggler peak field $\sim 1.9T$				
a_1	0.0	0.0	1.37 ± 0.01	N/A
b_1	0.0	0.83	-0.21 ± 0.03	N/A
b_2	-0.06	-0.18	-0.02 ± 0.001	N/A
b_3	0.01	-0.10	0.007 ± 0.003	N/A

Table 1: Calculated and measured the wiggler integrated field characteristics.

Because of the model symmetry, the skew and normal quadrupole moments a_1 and b_1 of straight line integrals are equal to zero. However the straight coil magnetic measurement reveals non-zero but negligible normal quadrupole moment $b_1 \sim -0.2Gm/cm$ and significant for beam dynamics skew quadrupole component $a_1 \sim 1.57 \div 1.37Gm/cm$. While the b_1 occurrence can be explained by a small error in pole geometry, the cause of relative large a_1 is not understood. The normal sextupole moment b_2 measured with straight coil is in good agreement with model calculation for both 2.1T and 1.9T wiggler fields. For 2.1T it is $\sim -0.28Gm/cm^2$ and for 1.9T it is close to zero. The change in b_2 with a field level is due to specifics of the wiggler design. In the 7-pole design, the central pole is compensated by the two opposite polarity end poles. Because the magnetic field environment in the middle of the wiggler is different from the wiggler ends, the compensation can be provided in a limited range of excitation. Calculated and measured octupole moments b_3 are negligible.

Although the comparison between calculated and measured straight line integrals is the most convenient way

for integrated magnetic field representation in form $B_y + iB_x = \sum (b_n + ia_n)(x + iy)^n$. In the case of integrals along wiggling beam trajectory this representation is not valid.

* Work supported by National Science Foundation

[†] e-mail: abt6@cornell.edu

¹ In the case of straight line integrals the moments a_n, b_n can be used

to verify the model, the beam dynamics depends on the field integrals along *wiggling beam trajectories*. In [4] it was noticed that interference between the beam trajectory wiggles and field variation across the single pole, $B_y(x)$, results in an additional integrated field: $\Delta I_y(x) \simeq -\frac{1}{2} L x_p \frac{dB_y(x)}{dx}$. Where x_p and L are the wiggling amplitude and the wiggler length. As $B_y(x)$ is a symmetric function, $dB_y(x)/dx$ and $\Delta I_y(x)$ are odd function of x . The latter generates the odd order moments (normal quadrupole b_1 , normal octupole b_3) seen in column "wig.line" of the table 1. Magnetic measurement with a vibrating wire (column "wig.wire") confirmed existence of these moments but gave approximately two times bigger amplitudes. This inconsistency is likely to be a result of a not accurate calibration of the used vibrating wire technique.

BEAM BASED CHARACTERIZATION

Wiggler generated coupling.

Beam based measurement of the local coupling around the ring indicated $\sim 2\text{Gm/cm}$ skew quadrupole moment generated by the wiggler, which is in good agreement with a magnetic measurement result. This component was compensated with skew quadrupole magnet installed near the wiggler.

Wiggler generated betatron tune variation

Vertical and horizontal betatron tunes were measured as a function of horizontal beam position in the wiggler at several wiggler field levels. For the beam displacement a closed orbit bump was used. The result of the measurement at 2.1T and 1.9T fields in comparison with tune variation obtained from the model tracking are plotted in Figures 1 and 2. In all cases one can see a reasonable consistency between calculation and measurement. The sextupole and

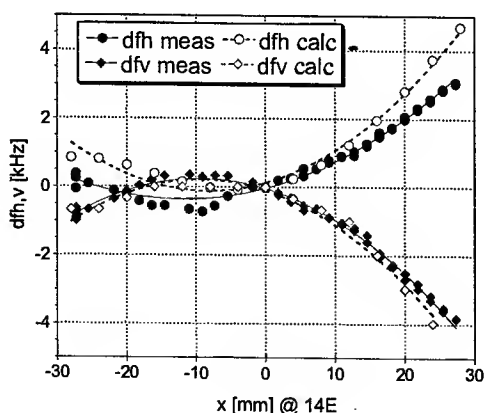


Figure 1: Measured and calculated betatron tune variation versus horizontal beam position in the wiggler at 2.1T wiggler peak field.

octupole moments calculated from the coefficients of the

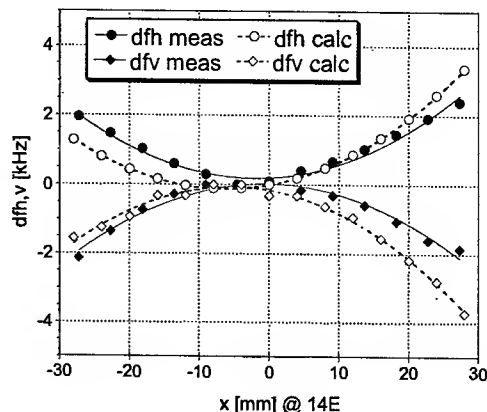


Figure 2: Measured and calculated betatron tune variation versus horizontal beam position in the wiggler at 1.9T wiggler peak field.

polynomial fit of the measured horizontal tune variation are given in table 2. They are in good agreement with calculated, see column "wgl.line" in Table 1.

Moment	2.1T	1.9T
$b_2[\text{Gm/cm}^2]$	-0.29 ± 0.01	-0.059 ± 0.011
$b_3[\text{Gm/cm}^3]$	-0.082 ± 0.002	-0.10 ± 0.004

Table 2: The moments calculated from the measured dependence of horizontal tune on horizontal beam position in the wiggler.

Nonlinear resonances excitation and tune plane appearance.

The machine performance (luminosity, injection efficiency, beam life time and etc.) often critically depends on the appearance of the betatron tune plane. The tune scan, a measurement of beam characteristics as a function of the betatron tunes, exposing the tune plane resonance structure facilitates the choice of the working point and the structure analysis may help to reveal the cause of magnetic field nonlinearities affecting machine performance. To explore effect of the wiggler magnetic field on the nonlinear beam dynamics we made a series of tune scans with a vertical beam size measurement. Two examples are shown in Figures 3 and 4. Here is depicted the vertical beam size as a function of betatron tunes on a 40x40 grid measured with zero and 2.1T wiggler peak field and a flattened orbit. Both plots have the same vertical beam size scale. Vertical beam size was measured using synchrotron light monitor. To help identify resonances Figure 5 shows a resonance map corresponding to the experimental condition. On the map, only resonances seen in measurement are shown. The effect of the wiggler field on the beam dynamics can be clearly observed by comparison of these two measurements. With wiggler field turned off, the scanned area

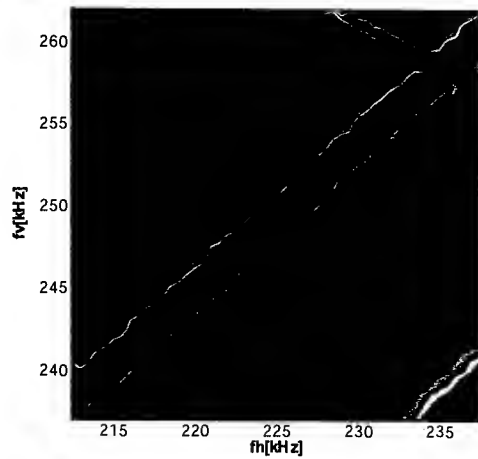


Figure 3: Vertical beam size versus betatron tune measured with CESR-c wiggler turned OFF.

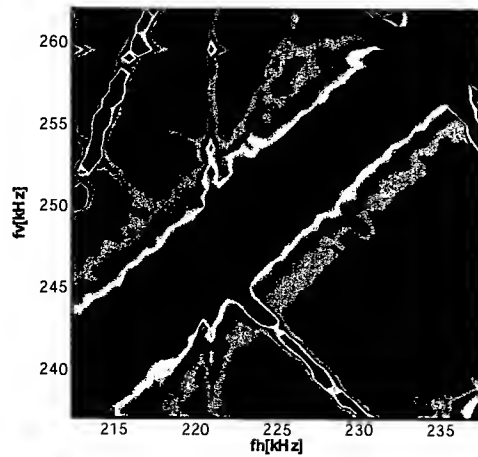


Figure 4: Vertical beam size as a function of betatron tunes measured at 2.1T wiggler magnetic field.

is relatively clean. There are only 3 resonance lines: $-fh+fv=0$, $-fh+fh-fs=0$, $fh+2fv+fs=2f_0$. With 2.1T wiggler field one can see 8 additional "working" resonances: $-3fh+fv=f_0$, $fh+fv-3fs=f_0$, $3fv=2f_0$, $fh+2fv+2fs=2f_0$, $4fh+fv=3f_0$, $2fh+fv+2fs=2f_0$, $2fh-2fs=f_0$ and $-3fh+fv+fs=-f_0$ covering much bigger area then the previous. Based on this observation one can conclude that in the given case the wiggler nonlinearity is a major player in a nonlinear beam dynamics.

A tracking simulation of the observed effect of the wiggler field on beam dynamics is progress.

CONCLUSION

The magnetic field of the first 7-pole super-conducting wiggler was characterized by the magnetic and beam based measurements. Reasonable agreement has been found between these measurements and the model calculations. Results of tune plane scanning suggest that the effect of the

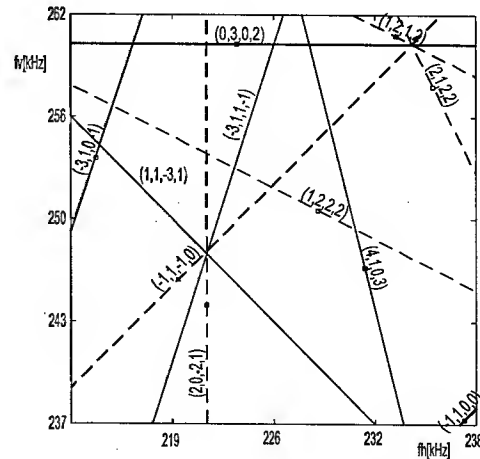


Figure 5: Resonance map for a scanned tune plane area. Shown are resonances seen in measurement. Labels (p, q, r, n) indicate $pf_h + qf_v + rf_s = nf_0$ resonance lines.

wiggler field nonlinearity on beam dynamics dominates over the effect from the rest of the ring and could compromise machine performance.

The part of the wiggler nonlinearity problem can be associated with the design specific. In symmetric 7-pole configuration the central pole is compensated by two opposite polarity end poles. But because of very different magnetic environment at the ends and in the middle of the magnet this compensation can not be fulfilled completely. The corroboration of the modeling of the CESR-c wigglers by the measurements presented above was an important step in the decision for the final 8-pole configuration of the wigglers. In 8-pole design each pole is compensated by the identical pole of opposite polarity. This provides better field nonlinearity compensation in a wider range of the wiggler field excitation.

REFERENCES

- [1] James Crittenden et al., *Design Considerations for CESR-c Wiggler Magnets*, to be published in PAC2003 proceedings.
- [2] David Rice, Richard Gallagher et al., *Production and Testing Considerations for CESR-c Wiggler Magnets*, to be published in PAC2003 proceedings.
- [3] A. Temnykh, *Vibrating Wire and Long Integrating Coil Based Magnetic Measurements of a 7-pole Super-Conducting Wiggler for CESR*, to be published in PAC2003 proceedings.
- [4] J. Safranek et al., *Nonlinear Dynamics in SPEAR Wigglers*, EPAC' 2000, p.295
- [5] This measurement technique was first developed by the ID group at ESRF. See *Developpement de Banc de mesures magnetiques pour undulateurs et wigglers*, D. Frachon Thesis, April 1992.
- [6] A. Temnykh, *Some aspects of the use of Vibrating Wire Technique for a wiggler magnetic field measurement*, Preprint CBN 01-17, Cornell 2001.

STATUS OF THE COOLER SYNCHROTRON COSY-JUELICH

D.Prasuhn, U.Bechstedt, J.Dietrich, R.Gebel, K.Henn, A.Lehrach, B.Lorentz, R.Maier, A.Schnase, H.Schneider, R.Stassen, H.J.Stein, H.Stockhorst, R.Toelle, Forschungszentrum Juelich GmbH, Postfach 1913, D-52425 Juelich, Germany

Abstract

The cooler synchrotron COSY delivers unpolarized and polarized protons and deuterons in the momentum range 300 MeV/c up to 3.65 GeV/c. Electron cooling at injection level and stochastic cooling covering the range from 1.5 GeV/c up to maximum momentum are available to prepare high precision beams for internal as well as external experiments in hadron physics. The beam is fed to external experiments by a fast kicker extraction or by stochastic extraction. Results of extracted electron cooled beams and developments to increase the number of stored particles and to increase the degree of polarization during acceleration are reported.

INTRODUCTION

The accelerator facility COSY [1] consists of the injector cyclotron and the synchrotron and storage ring with 184 m circumference. It accelerates unpolarized and polarized protons and deuterons in the momentum range between 300 and 3650 MeV/c. The floor plan of COSY with the 4 internal and 3 external experimental areas is shown in figure 1. The main topic of research is the production and interaction of strange mesons close to threshold.

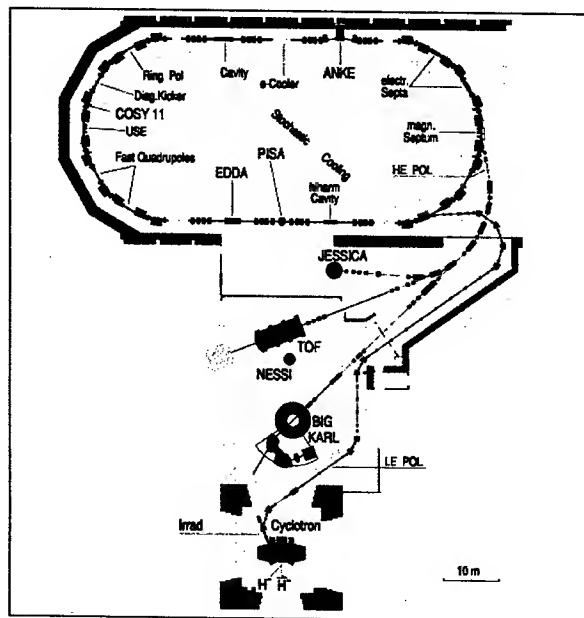


Figure 1: The COSY floor plan

BEAM TIME STATISTICS

COSY has improved its yearly running over the 10 years of operation from 3500 h per year in 1993 up to 7500 h in 2002. And for the year 2003 more than 7700 operational hours are scheduled. The past reliability of COSY increased from 80% in the first year of operation to more than 90% afterwards. More than 2/3 of the available time is dedicated to user operation.

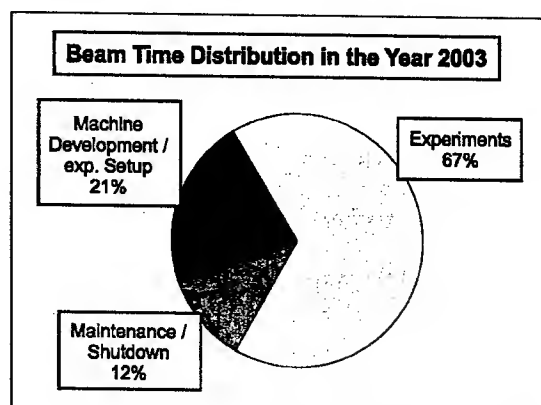


Figure 2: Distribution of the available time in the COSY operation

During the first years of operation only unpolarized protons were asked for by the COSY user community. But this has changed during the last years. Besides polarized protons the demand for unpolarized and polarized deuterons is increasing. The ratio of different requested ion species in the year 2002 is shown in figure 3.

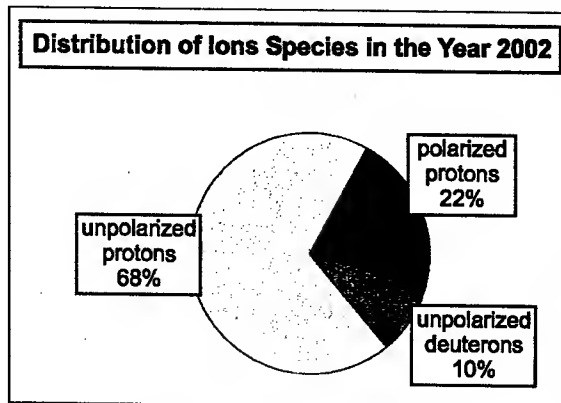


Figure 3: Demand for the different ion species in the COSY operation

ELECTRON AND STOCHASTIC COOLING

Increasing the phase space density by electron cooling at injection momentum and conservation of beam emittance in internal experiments at high momenta are outstanding features at COSY [2].

The electron cooler, designed for an electron energy up to 100 keV and an electron current up to 4 A, is nowadays only used at injection energy, i.e. at 22 keV and with an electron current between 170 mA and 250 mA. It is used with a single injection to decrease the beam emittance and momentum spread without major beam losses. By this we can accelerate $1.5 \cdot 10^{10}$ protons (or deuterons). This is needed for external experiments. In the case of slow stochastic extraction the pre-cooling decreases the amount of "halo-particles" of the extracted beam by a factor of 50 relative to the uncooled beam, which is important for the high resolution experiments with small hole veto detectors at the target location. For the one-turn kicker extraction the beam has to be pre-cooled, so that the small beam can be steered closed enough to the extraction septum foil and a small kick amplitude kicks the whole beam across the foil within one turn. This is necessary at COSY because no extraction kicker is installed in COSY and a rather small diagnostic kicker has to take over the task of extraction.

Another need for the electron cooler came up with the demand of polarized protons. The intensity of the polarized ion beams is limited by the intensity of the ion source to a factor 10 less than the intensity of the unpolarized beams. And especially internal experiments with thin cluster or atomic beam targets suffer from low counting rates. On the other side the internal experiments show a long cycle time with long beam lifetimes. So a combined cooling and stacking injection can increase the intensity of the polarized ion beams. Figure 4 shows the intensity increase due to 500 injections every 2 sec with an injected intensity which is comparable to that of the polarized ion source. The intensity of the stacked beam can be increased from $2 \cdot 10^9$ to $3 \cdot 10^{10}$.

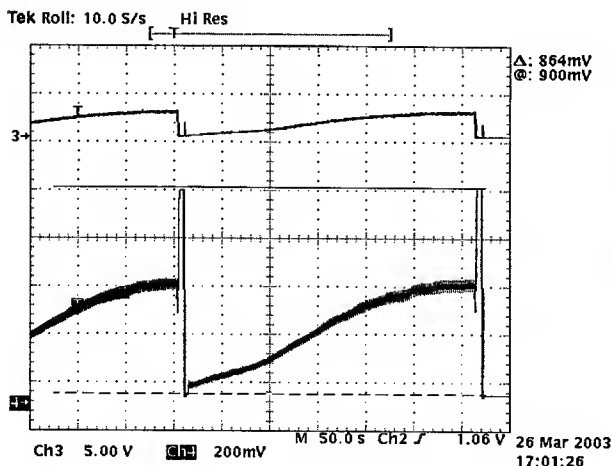


Figure 4: Intensity increase due to electron cooling and stacking

The transverse stochastic cooling at COSY compensates the emittance growth due to small angle Coulomb scattering for internal experiments with cluster targets, the longitudinal system compensates the momentum loss and momentum spread due to target heating. By this the beam-target overlap and thus the luminosity for the experiment stays constant over one hour. Figure 5 illustrates the contrast in counting rate behaviour with and without stochastic cooling.

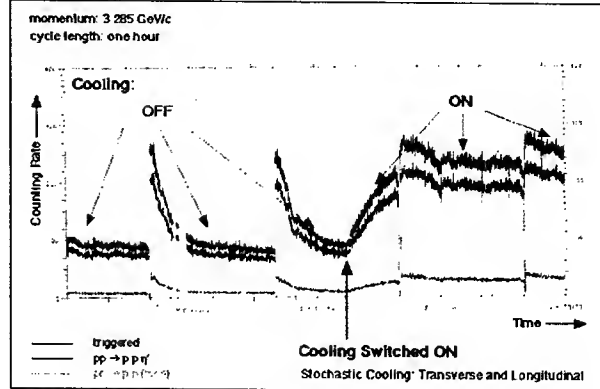


Figure 5: Counting rate of an internal target experiment without and with stochastic cooling

POLARIZATION

Some COSY experiments investigate the spin observables in the nucleon-nucleon scattering. Thus there is a need to conserve the polarization of protons during the acceleration. In the momentum range of COSY there are 5 imperfection and 10 intrinsic resonances. The imperfection resonances which depend only on the momentum are increased in strength by a vertical orbit bump to excite a total spin flip. The momentum and tune dependent intrinsic resonances are compensated by a fast tune jump which increases the speed of resonance crossing [3]. In figure 6 we show a typical acceleration cycle of polarized protons with the necessary tune jumps and vertical orbit bumps.

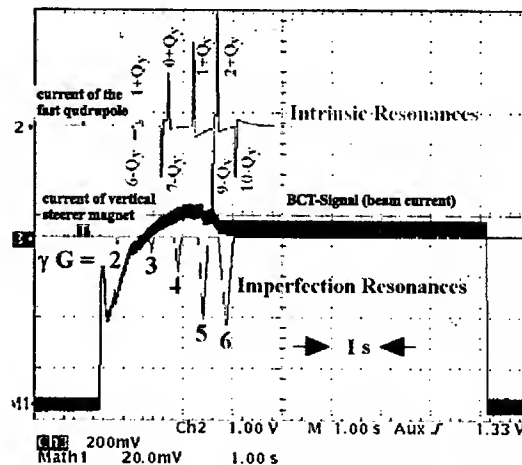


Figure 6: The acceleration with polarized protons

In figure 7 the polarization of protons as a function of the momentum, measured by EDDA during the acceleration ramp, is shown. The strongest $(8-q_y)$ -resonance may either be compensated by a tune jump, which usually leads to beam losses, or can be increased in strength by a special tune setting in the acceleration ramp to excite a total spin flip without beam losses.

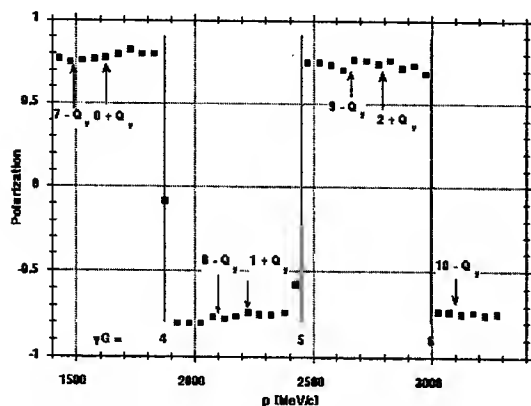


Figure 7: Polarization of protons as a function of the momentum

In February 2002 for the first time vertically polarized deuterons have been accelerated in COSY. For the acceleration of polarized deuterons, additional correction provisions are not necessary to preserve polarization during acceleration because depolarizing resonances do not occur within the momentum range of COSY at ordinary transversal betatron tunes. Asymmetries of polarized deuterons have been measured with the EDDA detector.

SUMMARY

COSY is a unique accelerator in the medium energy range for (un-) polarized proton and deuteron beams with the combination of electron and stochastic cooling, with both internal and external experiments. It delivers beam to users for more than 5400 hours per year with a high reliability of more than 90%. A super conducting LINAC [4] was proposed as a new injector to increase the intensity of polarized ions up to the space charge limit.

REFERENCES

- [1] H.Stockhorst, U.Bechstedt, J.Dietrich, R.Gebel, K.Henn, A.Lehrach, B.Lorentz, R.Maier, D.Prasuhn, A.Schnase, H.Schneider, R.Stassen, H.J.Stein, R.Tölle, "Progress and Developments at The Cooler Synchrotron COSY", Proceedings of the 8th European Particle Accelerator Conference (EPAC 2002) -92-9083-198-7, p. 629
- [2] D.Prasuhn, J.Dietrich, K.Fan, V.Kamerdjiev, R.Maier, H.J.Stein and H.Stockhorst, "Cooling at COSY", Proceedings of the Workshop Beam Cooling and Related Topics (ECOL 2001), Schriften des

Forschungszentrums Jülich, Reihe Materie und Material, Vol. 13, 3-89336-316-5

- [3] A.Lehrach, "Acceleration of Polarized Protons and Deuterons in the Cooler Synchrotron COSY", 15th International Spin Physics Symposium, Brookhaven, 2002
- [4] R.Tölle, U.Bechstedt, N.Bongers, J.Dietrich, R.Eichhorn, O.Felden, R.Gebel, K.Henn, H.Jungwirth, A.Lehrach, R.Maier, U.Pfister, D.Prasuhn, P.v.Rossen, A.Schnase, H.Schneider, Y.Senichev, R.Stassen, H.Stockhorst, E.Zaplatin, A.Schempp, "COSY-SCL, The Super conducting Injector LINAC for COSY", contribution to this conference

FERMILAB RECYCLER STOCHASTIC COOLING COMMISSIONING AND PERFORMANCE

D. Broemmelsiek*, R. Pasquinelli, FNAL, Batavia, IL 60510, USA

Abstract

The Fermilab Recycler is a fixed 8GeV kinetic energy storage ring located in the Fermilab Main Injector tunnel near the ceiling. The Recycler has two roles in Run II. First, to store antiprotons from the Fermilab Antiproton Accumulator so that the antiproton production rate is no longer compromised by large numbers of antiprotons stored in the Accumulator. Second, to receive antiprotons from the Fermilab Tevatron at the end of luminosity periods. To perform each of these roles, stochastic cooling in the Recycler is needed to preserve and cool antiprotons in preparation for transfer to the Tevatron. The commissioning and performance of the Recycler stochastic cooling systems will be reviewed.

INTRODUCTION

Each role of the Recycler represents different constraints on the design of a stochastic cooling system. The design [1] of the Recycler stochastic cooling systems represents a compromise between the tasks of maintaining the phase space densities of accumulated antiprotons and pre-cooling antiprotons recycled from the Tevatron.

The cooling rates for momentum and emittance are given by,

$$\frac{1}{\tau} = \frac{W}{N} [2g(1 - \tilde{M}^{-2}) - g^2(M + U)] \quad (1)$$

where W is the system bandwidth, N is the number of particles, g is the so called "cooling gain", M and \tilde{M} are the mixing factors from the kicker to pickup and pickup to kicker respectively and U is the system noise to signal ratio. M is approximately 6, which implies that stochastic cooling is dominated by bad mixing in the Recycler.

Momentum Cooling

There are two different approaches to stochastic momentum cooling, the Palmer and filter methods. The design of the Recycler lattice prohibits the use of Palmer cooling. There is no appropriate location with the required high dispersion and small beam size for this technique to be feasible.

The choice of filter cooling in the frequency bands 0.5 – 1.0GHz and 1 – 2GHz was made to provide the required bandwidth. Such a system also retains a larger momentum acceptance than higher frequency systems by being less sensitive to errors that would cause feedback gain instability. However, a disadvantage is the dispersion caused by the imperfections in any notch filter

system, which will cause additional heating from the momentum cooling systems.

Betatron Cooling

The initial design included the assumption of a 2π mm-rad/hr [2] transverse heating rate. Again, a higher bandwidth system would be preferred for cooling rate. However, a larger momentum acceptance was desired for the purpose of recycling antiprotons.

A 2 – 4GHz bandwidth system, one for each transverse dimension, was chosen to implement betatron cooling in the recycler and maintain a large momentum acceptance. The pickups and kickers are located in zero dispersion regions with the betatron phase advance an odd multiple of 90° .

TECHNOLOGY

Pickups & Kickers

Room temperature phased planar loop array electrode technology [3] was chosen for the Recycler stochastic cooling pickups and kickers. Figure 1 depicts a 2 – 4GHz

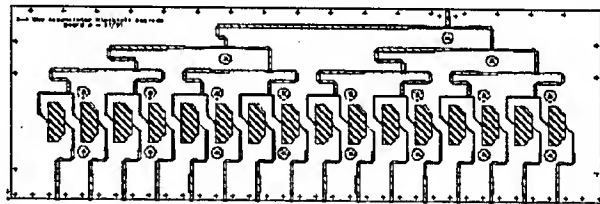


Figure 1: 2-4 GHz Planar Loop Array

planar loop array composed of sixteen 100Ω loops. Half the momentum pickups operate as horizontal pickups and half as vertical pickups and placed in a high dispersion region in the Recycler lattice. The momentum kickers are similarly grouped and placed in a zero dispersion region. Therefore, it is possible to use the momentum electrodes for betatron cooling if it becomes expedient to increase the betatron cooling bandwidth (decrease the betatron cooling time) in the future. In principle, placing the pickups in a high dispersion region makes Palmer cooling possible. However, the beam size is still dominated by betatron motion where the pickups are located.

Both the pickups and kickers are placed in vacuum tanks mounted on moveable stands. Centering the pickups with respect to the beam is important for both the pickups and kickers. The Recycler beam is normally bunched into a barrier bucket system. Centering the betatron pickups removes the common mode signal improving performance. Centering the momentum kickers

*broemmel@fnal.gov

minimizes whatever betatron heating is caused by a modulation of orbit length when the beam is bunched.

Transmission Line

Amplitude modulated infrared lasers [4] are used to transmit the error signals generated by the pickups to the kickers. The distance is approximately 2000ft. These optical links provide flat amplitude and phase response. For timing stability, the laser light is transmitted through a vacuum.

COMMISSIONING

There were two principal goals while commissioning the stochastic cooling systems, finding a stable operating point and increasing the bandwidth of each system. Any possible reductions in heating terms coming from the stochastic cooling systems themselves are also resolved.

One of the most important diagnostics is the beam transfer function measurement. This is a network analysis of the entire feedback circuit including the antiproton beam.

Transfer Function Measurements

A beam transfer function measurement, BTF, gives both the magnitude and phase response of the system. Figure 2 depicts a typical BTF for the horizontal betatron

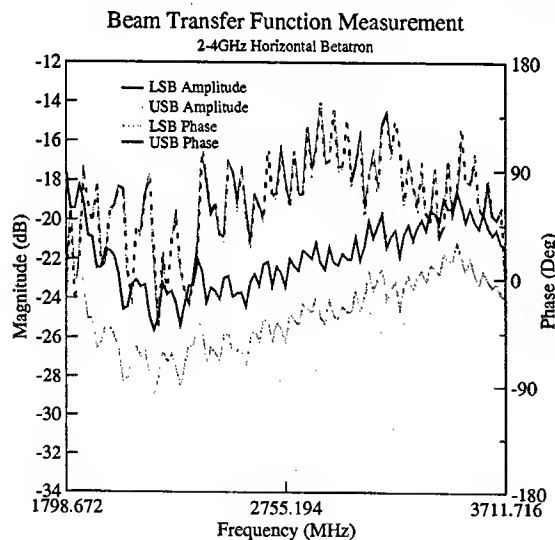


Figure 2: A "BTF" measurement. The average phase advance through the available bandwidth is zero.

system. System delay between pickup and kicker is modified to make the average phase response zero across the sensitive bandwidth (3dB of maximum).

BTF measurements also reveal the faults in the system. Figure 3 depicts two transfer functions. Before the installation of filters and equalizers, beam heating occurred due to low frequency system sensitivity where the phase behavior provides significant positive feedback. All systems, not just the one pictured in Figure 4, were modified several times to maximize the bandwidth and increase system stability, i.e. improve the phase response.

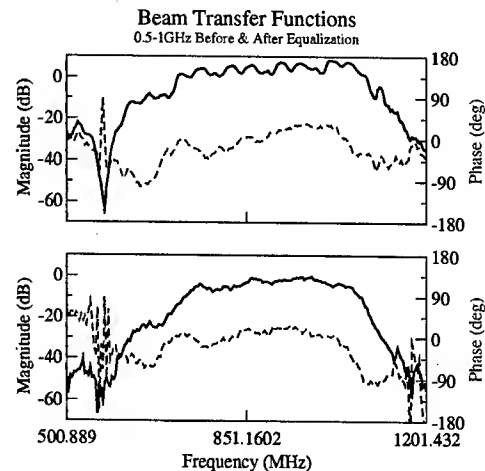


Figure 3

Tank Centering

Using the moveable stands, the cooling pickups are positioned to minimize the power output at the kickers. In addition, minimizing the common mode signal detected may also align the transverse pickups.

There are also two methods to center the kickers. Either by physically centering the kickers while monitoring beam loss, or by minimizing the signal induced out of plane. That is, by moving a momentum kicker to minimize any induced transverse signal and *vice versa*. This can again be done using a network analyzer.

PERFORMANCE

The cooling performance may be characterized by several measurements. The useful bandwidth for each system is determined from the BTF measurements. Measurement of the cooling rates combined with the BTF measurements characterizes the system performance. The cooling gain should be consistent with signal suppression measurements.

Signal Suppression

Signal suppression, the difference in the Schottky noise signals of the beam with the feedback loop opened and closed, is used as a diagnostic during operations. Figures 4 and 5 clearly show signal suppression measured at particular harmonics in both betatron and momentum cooling systems. Figure 4 also indicates one of the interesting aspects of betatron cooling in the Recycler. For the smallest momentum widths foreseeable, the betatron side bands begin to overlap at ~3GHz. These measurements, when calibrated, allow operations to fine tune the system performance regardless of the presence of systems experts.

For filter momentum cooling, the measurements are made where the Schottky signal is convoluted with the notch filter. Figure 5 shows the effect of the convolution at a particular harmonic of the revolution frequency.

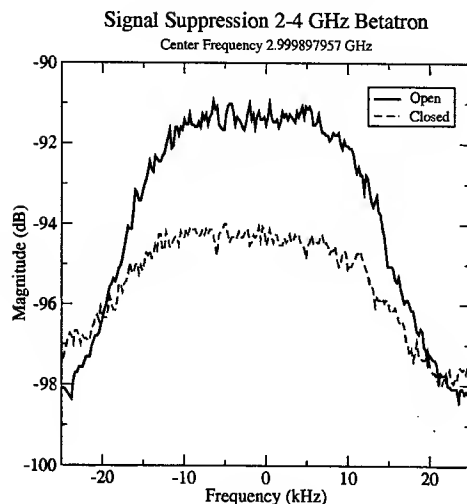


Figure 4

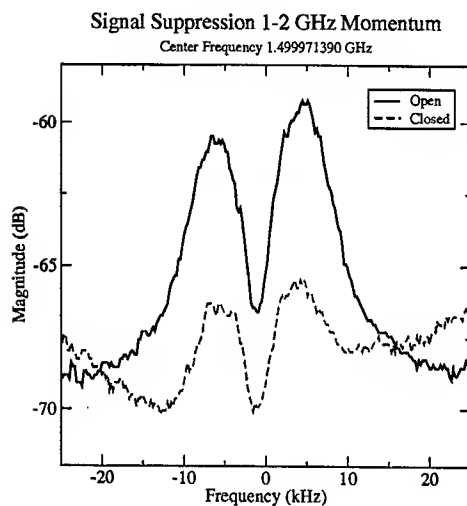


Figure 5

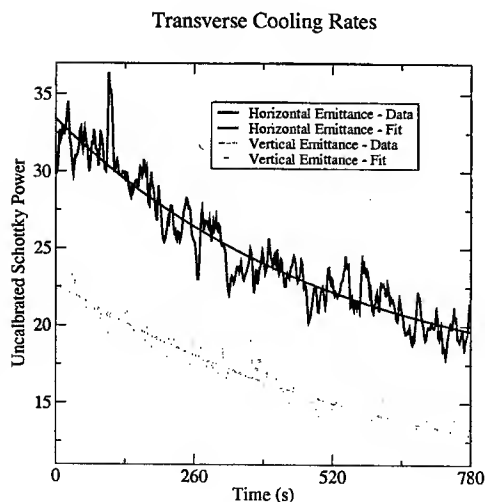


Figure 6

RMS Frequency Width Time Evolution

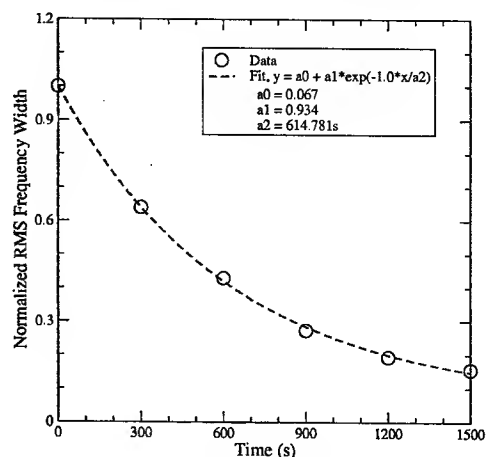


Figure 7

Cooling Rates

Recording the time evolution of the transverse emittances and RMS frequency width is a measure of the cooling rates defined in Equation (1). Figures 6 and 7 show both data and fits for transverse and momentum cooling respectively. The fit function in all cases is a constant plus an exponential decay as shown in the legend of Figure 7.

SUMMARY

Table 1 summarizes the bandwidth measurements and the cooling rates for the given number of particles. The other interesting performance parameters are the 95% asymptotic emittances. Over many attempts, the Recycler has averaged $<10\pi$ mm-mrad transverse emittances and ~ 100 eV-s longitudinal emittances for antiproton intensities from $4 \cdot 10^{10}$ to $70 \cdot 10^{10}$.

Table 1: Parameter Summary

	Betatron		Momentum	
	H2-4 GHz	V2-4 GHz	0.5-1 GHz	1-2 GHz
W (MHz)	495	715	260	674
τ (s)	516	644	615	
N	$7 \cdot 10^{10}$		$4 \cdot 10^{10}$	

REFERENCES

- [1] J.P. Marriner, Fermilab MI Note 168 & 169, April, 1996.
- [2] All emittances in this note are 95% normalized.
- [3] "Novel Stochastic Cooling Pickups and Kickers," J. Petter, D. McGinnis and J. Marriner, Proceedings of the 1989 IEEE Particle Accelerator Conference, Vol. 1, 636, March 1989.
- [4] R. Pasquinnelli, "Wide Band Free Space Transmission Link Utilizing a Modulated Infrared Laser," PAC'99, New York, March 1999, p. 7984.

TIME EVOLUTION OF BEAM CURRENT IN THE RECYCLER RING

K. Gounder *, J. Marriner and S. Mishra
FNAL, Batavia, IL 60510, USA.

Abstract

We study the time evolution of the beam current in the Fermilab Recycler Ring due to abrupt physical processes (single coulomb scattering, nuclear scattering) that cause sudden loss of beam, and diffusive processes (multiple coulomb scattering, lattice dependence, etc.) which cause emittance growth. This emittance growth combined with finite aperture of the beam pipe will lead to eventual loss of most beam. We develop a fitting technique to the time evolution of beam current to estimate emittance growth. Finally we compare the directly measured growth with the fitted value. Work supported by the U.S. Department of Energy under contract No. DE-AC02-76CH03000.

INTRODUCTION

The Recycler Ring [1] located in the Main Injector tunnel at Fermilab is designed to store antiprotons from the Accumulator and the residual Tevatron stores as a part of Run II luminosity upgrade program. The Recycler Ring (RR) is expected to improve the luminosity by increasing the antiproton accumulation efficiency and recycling the residual Tevatron antiprotons after colliding stores [2]. Presently, the RR is being commissioned using protons as well as antiprotons. The successful operation of the Ring requires a beam lifetime of > 100 hours with stochastic cooling and high stacking efficiency. Therefore the study of beam evolution and emittance growth rate is essential for the RR to be an efficient storage ring. The basic parameters for RR are listed in Table 1.

Parameter	Value
Acceptance (mm-mr)	40.0π
Average β (m)	42.0
Average beam pipe radius (in m)	0.023
Beam energy (GeV)	8.89
Average beam β	0.998
Average beam γ	9.48
Maximum energy loss (GeV)	0.089

Table 1: The basic Recycler Ring parameters relevant for the computations detailed in this note.

BASIC FORMULATION

For most lifetime measurements, we introduce a thin approximately Gaussian beam of known intensity in the mid-

*gounder@fnal.gov

dle of RR aperture. In such cases, the beam lifetime and evolution are determined by two classes of processes: (1) Processes like single coulomb scattering, nuclear scattering or ionization by which the beam loses a particle abruptly at any given time and region of the beam; (2) Diffusion processes like multiple coulomb scattering, intrabeam scattering or some form of noise where the beam emittance grows and eventually the beam loses particles by hitting the aperture of the beam pipe. Assuming these two classes of processes are independent [6], we write the beam current at any given time as:

$$I(t) = I_0 N_{ab}(t) N_{df}(t)$$

where I_0 is the initial beam introduced, $N_{ab}(t)$ denotes time evolution due to abrupt loss of beam particles as in the first case, and $N_{df}(t)$ denotes the time evolution due to diffusion processes as described in the second case. For most cases, we can write:

$$N_{ab}(t) = e^{-\frac{t}{\tau_{ab}}}$$

where τ_{ab} characterizes the lifetime due to processes belong to the first case and assumed to be constant during the evolution. To describe the diffusive processes, we have to solve the Foker-Planck equation [3]:

$$\frac{\partial f}{\partial \tau} = \frac{\partial}{\partial Z} \left(Z \frac{\partial f}{\partial Z} \right)$$

where f describes the particle distribution and subject to the boundary conditions:

$$f(Z, 0) = f_0(Z)$$

$$f(1, \tau) = 0$$

$$\frac{\partial f}{\partial Z} \Big|_{Z=0} = 0$$

where $Z = \epsilon/\epsilon_a = \text{emittance/acceptance}$, and $\tau = tR/\epsilon_a$ with R , the diffusion coefficient. Here f_0 denotes the beam distribution at $t = 0$. In the case of pure multiple coulomb scattering phenomena, the diffusion coefficient R is given in terms of the mean scattering angle θ by:

$$R = \beta_{avg} \langle \dot{\theta}^2 \rangle$$

The general solution of the above equation can be written as:

$$f(Z, \tau) = \sum_n C_n J_0(\lambda_n \sqrt{Z}) e^{-\lambda_n^2 \tau/4}$$

with coefficients C_n :

$$C_n = \frac{1}{J_1(\lambda_n)^2} \int_0^1 f_0(Z) J_0(\lambda_n \sqrt{Z}) dZ$$

where λ_n is nth root of the Bessel function $J_0(Z)$. We obtain the total beam particles as a function of time:

$$N_{df}(t) = \int_0^1 f(Z, \tau) dZ = 2 \sum_n \frac{C_n}{\lambda_n} J_1(\lambda_n) e^{-(\lambda_n^2 R / 4 \epsilon_a) t}$$

The beam lifetime at any time can be computed using:

$$\tau_{mc} = - \frac{N(\tau)}{dN(\tau)/d\tau}$$

The beam life time varies with time but reaches an asymptotic value:

$$\tau_a = \frac{4 \epsilon_a}{\lambda_1^2 R}$$

The emittance growth can be obtained from:

$$\frac{d\epsilon_N}{dt} = \frac{\pi \beta \gamma}{2} R$$

Now combining the expressions for N_{ab} and N_{df} , we cast the time evolution of beam current as:

$$I(t) = I_0 e^{-\frac{t}{\tau_{ab}}} 2 \sum_n \frac{C_n}{\lambda_n} J_1(\lambda_n) e^{-(\lambda_n^2 R / 4 \epsilon_a) t}$$

Since the beam current measurement as a function of time is one of the most accurate measurement we can make in the Recycler Ring, we can fit the measurements for two parameters - for the diffusion constant R and the lifetime due to abrupt processes τ_{ab} . From these, further information about the vacuum residual gas scattering or other processes causing emittance growth can be extracted. This method also provides an alternative to other emittance growth measurements such as using Schottky detectors or techniques based on beam scrapers. Or simply, this could be a cross check on understanding of the relevant physical quantities as well as systematics of other measurement methods.

FITTING PROCEDURE

To apply the above formalism to real Recycler Ring data, we develop a fitting procedure. From the above formalism, the beam current at a given time t after $t = 0$ can be written as:

$$I(t) = I_0 e^{-\frac{t}{\tau_{ab}}} \sum_n Y_n e^{-R \alpha_n t} \quad (1)$$

with the coefficients $Y_n = Y_n(\frac{\sigma}{a}, \epsilon_a)$, and $\alpha_n = \alpha_n(\epsilon_a)$. The coefficients Y_n, α_n can be generated numerically for most cases once knowing the initial beam distribution σ , the RR acceptance ϵ_a and half aperture a . We can obtain

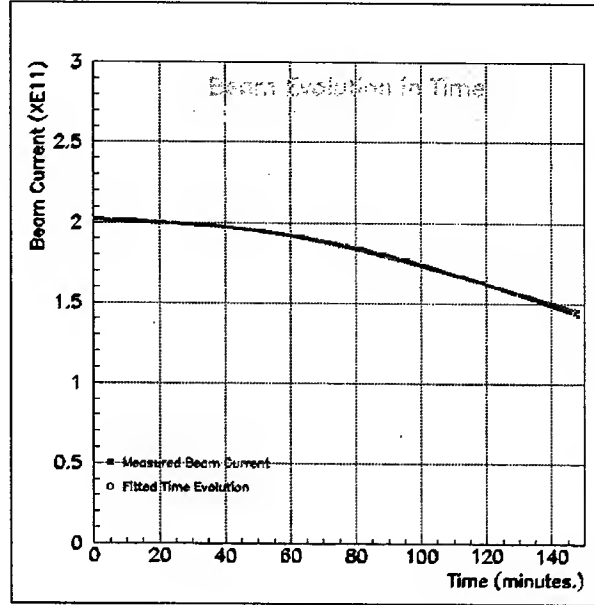


Figure 1: Time evolution of antiproton beam in the Recycler Ring. The dots denote the measured beam current values while the smooth curve is a fit using the first five terms of the expansion for $I(t)$ as discussed above. The fitted value for the diffusion constant determines the emittance growth rate as $9.75 \pm 2.2 \pi$ -mm-mr/hour while the measured value is $9-11 \pi$ mm-mr/hour.

$I(t)$ - from beam current monitors. We can fit $I(t)$ for τ_{ab} and R using any normal fitting technique. Once knowing R , we can extrapolate to many quantities such as computing the emittance growth using:

$$\frac{d\epsilon_N}{dt} = \frac{\pi \beta \gamma}{2} R$$

For most practical purposes, the sum in the above expression for $I(t)$ can be limited to first 5 terms or less. This can be easily seen from zeros of the Bessel function $J_0(X)$ in increasing order: 2.405, 5.520, 8.654, 11.792, and 14.931. Here we use first five terms of the above expansion.

ANTIPROTON BEAM TIME EVOLUTION

The antiproton beam in the RR is cooled using stochastic cooling methods [4]. The well cooled beam provides an ideal situation for the beam time evolution studies as it has a Gaussian distribution whose initial width can be determined using scraping techniques or a Schottky detec-

tor. After 2003 January shutdown, the RR vacuum residual gases were unusually dominated by leaks and contamination. An initial Gaussian beam of 2.2×10^{11} antiprotons (width 3.7mm) was allowed to evolve in time when no Main Injector ramping was present [5]. The above figure illustrates the beam evolution where the dots denote the beam current measured for 2.5 hours. The data was fitted using the first five terms of the expansion (equation 1) for $I(t)$ for τ_{ab} and the diffusion constant R . The fitted values of $\tau_{ab} = 37.8 \pm 1.7$ hours $R = 0.65 \times 10^{-10}$, $d\epsilon/dt = 9.75 \pm 2.2\pi\text{mm-mr/hour}$ [7] is consistent with directly measured values of 40 hours and $9\text{-}11\pi\text{-mm-mr/hour}$.

REFERENCES

- [1] Gerry Jackson, "The Fermilab Recycler Ring Technical Design Report", November 1996, Fermilab-TM-1991; Mishra, "Status of Fermilab Recycler Ring", EPAC2002, Paris, June 2002.
- [2] J. Marriner et. al., "Run II Handbook", at <http://www-bd.fnal.gov/runII/index.html>. Also see M. Church, "Tevatron Run II Performance and Plans", EPAC2002, Paris, June 2002.
- [3] D. Edwards and M. Syphers, "An Introduction to Physics of High Energy Accelerators", John Wiley and Sons, 1993.
- [4] D. Mohl in Advanced Accelerator Physics Course, Proceedings of 1985 CERN Accelerator School, CERN 87-03 (1986).
- [5] As the Recycler Ring is located in the MI tunnel, the RR beam is affected by the stray fields while the Main Injector is ramping. More beam pipe shielding and ramping power supplies are installed to minimize this effect.
- [6] This is only an approximation as the threshold scattering angle for single coulomb scattering depends on the size of the beam and beam pipe aperture.
- [7] The emittance quoted here is the normalized 95%, i.e., $\epsilon_{N95\%} = 3.0\epsilon_{rmsN}$

RESIDUAL GAS PRESSURE PROFILE IN THE RECYCLER RING

K. Gounder *, J. Marriner, S. Mishra, and Terry Anderson
FNAL, Batavia, IL 60510, USA

Abstract

We simulate the pressure profile of residual gases from basic principles using detailed beam pipe geometry and the relevant physical parameters. These profiles are compared with the actual ion gauge measurements and is being used to predict the vacuum contribution to the Recycler Ring beam lifetime. Work supported by the U.S. Department of Energy under contract No. DE-AC02-76CH03000.

INTRODUCTION

The Recycler Ring [1] located in the upper portion of the Main Injector tunnel at Fermilab is designed as a storage ring for antiprotons. Antiprotons transferred from the Accumulator and the residual Tevatron stores will be cooled and stored in the Recycler before reinjection into the Tevatron. The stacking rate of the antiprotons in the Accumulator is improved by steady transfer of antiprotons to the Recycler Ring when the stack size becomes sufficiently large. Thus, as a part of Run II upgrade, the Recycler Ring will provide a factor of 2-3 improvement in luminosity. Presently, the Recycler Ring (RR) is being commissioned using protons as well as antiprotons. Here we describe the design of the RR vacuum, compute the pressure profile for the residual vacuum gases around the ring and compare with measured partial pressures of residual gases. The simulated partial pressures of gases can be used to estimate the RR beam life time and emittance growth due to the interaction of residual gases with the beam particles. The relevant RR parameters used are listed in Table 1. More detailed description of the Recycler Ring can be found elsewhere [1].

Table 1: Recycler Ring Parameters

Parameter	Value
Acceptance (mm-mr)	40.0 π
Average β (m)	40.0
Average beam pipe radius (in m)	0.023
Beam energy (GeV)	8.89
Average beam β	0.998
Average beam γ	9.48
Maximum energy loss (GeV)	0.089

RECYCLER RING VACUUM SYSTEM

The RR vacuum design was motivated by the requirement of storing about 2.5×10^{12} antiprotons with less

than 5% loss for stores of duration 8 hours or more. This requires a beam life time of greater than 100 hours and a transverse emittance growth rate less than 2π mm-mr/hour. In turn, this imposes very stringent requirements on the amount of residual gases allowed in the RR vacuum. Therefore the vacuum design is expected to support only a few tenths of nano Torr of total gas pressure with only a minute amount of heavy gases such as Argon, CO_2 etc..

The RR beam pipe is made up of stainless steel and is mostly elliptical in shape with horizontal major axis 9.67 cm and vertical minor axis 4.44 cm. It also has 3 and 4 inch radii circular portions (for about 7% of the total length) in the straight sections of the ring. There are over 640 Titanium Sublimation Pumps (TSP) distributed periodically around the Ring with a distance of 4-5 m between the pumps depending on the location. These were custom designed and built by Fermilab with a maximum pumping speed of 10460 liters/second for Nitrogen. These are fired manually every 6-12 months depending on the gas pressure needs. There are also 226 Ion Pumps (IP) located around the Ring most of them fitted directly to a TSP. A fraction of the Ion pumps are specifically located around special devices such as Lambertson magnets, Schottky detectors and stochastic cooling tanks etc. All the Ion pumps are diode pumps made by Varian [3] and a large fraction of them have a Nitrogen pumping speed of 30 liters/second. The rest are specifically modified to pump noble gases such as Argon more efficiently. The details of the beam pipe geometry and vacuum pump specifications are provided in Table 2.

The vacuum pressure is readout and monitored by 30 Ion gauges along with ion pumps located through out the Ring. There are also 8 Residual gas analyzers (RGA) installed at strategic locations providing partial pressures of residual gases present. The schematics of the pump configuration is shown in the figure below. The RR vacuum is divided into 30 sections separated by control valves. This configuration helps to isolate parts of the vacuum when necessary during maintenance, repairs, leaks or installation of new devices.

RECYCLER RING VACUUM RESIDUAL GASES

The RR ultra high vacuum is maintained by arrays of TSPs and ion pumps has a total pressure of a fraction of a nano Torr. The types of gases present in the vacuum and their partial pressures can be obtained by RGA measurements done often around the ring. The major constituents of the vacuum (average of RGA readings) are listed in Table 3. We have also detected some very minor quantities of hydro carbons such as Ethane, Ethylene etc.

* gounder@fnal.gov

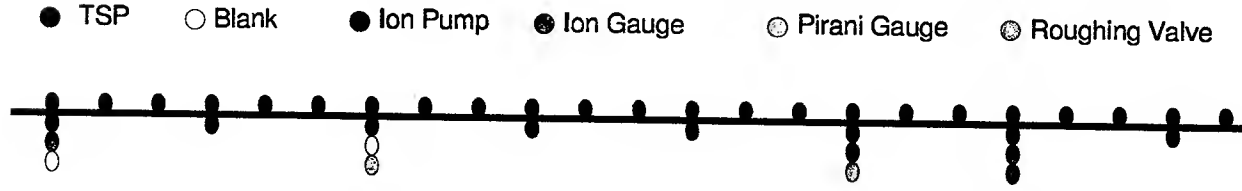


Figure 1: The Recycler Ring Vacuum pump configuration for major portions of the Ring. The remaining portions are being upgraded to have the same configuration. Besides the periodic array of pumps, there are special ion pumps and TSPs installed at critical locations such as Lambertson magnets, stochastic cooling tanks, Schottky detectors etc.

Parameter	Value
Vacuum Temperature	293 K
TSP Pumping Efficiency	≈ 0.05
Ion Pump Efficiency	1.0
Ring Length [m]	3319.4
Number of TSPs	644
Number of Ion Pumps	226
Number of Ion Gauges	30
Number of Vacuum Sectors	30
Number of RGAs	8
Elliptical Sections	[MKS Units]
Major axis [m]	9.667×10^{-2}
Minor axis [m]	4.444×10^{-2}
Area of TSP Aperture [m^2]	34.90×10^{-4}
Area of Ion Pump Aperture [m^2]	28.60×10^{-4}
Length of Ion Pump [m]	6.033×10^{-2}
Circular Sections	[MKS Units]
Diameter of 3' Beam Pipe [m]	7.303×10^{-2}
Diameter of 4' Beam Pipe [m]	9.8425×10^{-2}

Table 2: Beam pipe geometry and vacuum pump data for the Recycler Ring.

PRESSURE PROFILE SIMULATION

Knowing the complete beam pipe geometry, the vacuum pump configuration and the details of gas parameters such as outgassing rates, conductances etc., we can simulate the pressure profile of each gas around the ring. For simulation purposes, we treat the 'unknown' component as Nitrogen. The TSPs do not contribute to pumping out Argon or Methane while pumping other gases such as Hydrogen, Water, Carbon Monoxide, Carbon Dioxide and Nitrogen. The ion pumps pump all gases including Argon and hydrocarbons such as Ethylene, Methane etc.

The vacuum pressure P , the pumping speed s , the conductance of the beam pipe c and the outgassing rate q at a given location are related by:

$$\frac{d}{dz} \left\{ c \frac{dP}{dz} \right\} - sP + q = 0$$

A technique based on the approximation of *finite differences* is used to solve the above differential equation [4]. This method has the advantage of being numerically stable

Gas	Pump. Speed [liter/s]	Outgassing Rate [(nTorr.liter)/(s m^2)]	Avg. Press. [nTorr]
H_2	3490.000	4.500	0.354
H_2O	3490.000	0.290	0.038
CO	10460.000	0.190	0.019
CO_2	8775.000	0.110	0.015
CH_4	30.000	0.003	0.005
N_2	10460.000	0.081	0.105
Ar	1.700	0.001	0.001
Total		5.185	0.537

Table 3: The relevant gas parameters required for simulation of the pressure profile around the ring. The 'unknown component' of gases is treated as Nitrogen.

when the system is very long such as the Recycler Ring. We cast the first term as:

$$\frac{d}{dz} \left\{ c_i \frac{dP}{dz} \right\} = \frac{(c_{i+1} + c_i)P_{i+1} + (c_i + c_{i-1})P_{i-1}}{2\Delta z^2} - \frac{(c_{i+1} + c_{i-1} + 2c_i)P_i}{2\Delta z^2}$$

The above equation becomes:

$$\left\{ \frac{-(c_{i+1} + c_{i-1} + 2c_i)}{2} - s_i \Delta z^2 \right\} P_i + \frac{c_i + c_{i+1}}{2} P_{i+1} + \frac{c_i + c_{i-1}}{2} P_{i-1} = q_i \Delta z^2$$

The boundary conditions at each end of the segment should be specified:

$$Q_i = -c_i \frac{P_{i+1} - P_{i-1}}{2\Delta z}$$

This allows us to solve for either P_{i+1} or P_{i-1} in terms of the flow in the i th segment. In fact we can form a tridiagonal matrix as shown below. This system of equations can be solved by Gaussian elimination technique and back substitution. A simpler alternative approach for an array of pumps was used to verify the numerical accuracy of this method.

For each constituent gas, the pressure profile around the ring has been simulated. The results for Hydrogen and

Methane are shown in Figure 2 for region in the 400

$$\left\{ \begin{array}{l} -\frac{c_2+3c_1}{2} - s_1 \Delta z^2 \quad \frac{c_2+3c_1}{2} \\ \frac{c_i+c_{i-1}}{2} - \frac{c_{i+1}+c_{i-1}+2c_i}{2} - s_i \Delta z^2 \quad \frac{c_{i+1}+c_i}{2} \\ \frac{c_n-1+3c_n}{2} \quad \frac{c_n-1+3c_n}{2} - s_n \Delta z^2 \end{array} \right\} \left\{ \begin{array}{l} P_1 \\ P_i \\ P_n \end{array} \right\} = \left\{ \begin{array}{l} -q_1 \Delta z^2 - 2Q_1 \Delta z \\ -q_i \Delta z^2 \\ -q_n \Delta z^2 - 2Q_n \Delta z \end{array} \right\}$$

section of the RR. Note the Hydrogen is pumped by the TSPs and Methane by the Ion pumps. The x-axis of these figures are location of various sectors from the point of proton injection into the Recycler at the location 328 in units of meters. The TSPs and Ion Pump locations are also shown along with beam pipe geometry. The RR simulated gas pressure averages are listed in Table 4.

Gas	Avg. Pressure (nTorr)
Hydrogen	0.355
Water	0.038
Carbon Monoxide	0.022
Carbon Dioxide	0.016
Nitrogen	0.050
Argon	0.002
Methane	0.005
Total	0.498

Table 4: The Ring wide average of the simulated pressure of residual gases. The 'unknown' gas component is treated as Nitrogen.

COMPARISON WITH MEASUREMENTS

The ring wide average partial pressures shown in Table 3 were obtained from RGA measurements and nearby Ion Gauge readings (normalization) taken at 7 different locations around the ring. The raw RGA/IG readings were corrected for each gas for calibration, conductance of the connecting assemblies as well as the measurement location with respect to the relevant pump locations. On the other hand, the simulated values shown in Table 4 greatly depends on knowledge of the beam pipe geometry, outgassing rates measured in mockups and pumping efficiencies of TSPs (time varying) and Ion pumps. To obtain predictive power for the simulation techniques, we have adjusted the outgassing rates to reasonably produce the observed partial pressures. This is evident by comparing Tables 3 and 4. The partial pressures of residual gases can be used to determine the contribution of beam-gas scattering for the RR beam lifetime [5].

REFERENCES

- [1] Gerry Jackson, "The Fermilab Recycler Ring Technical Design Report", November 1996, Fermilab-TM-1991; Mishra, "Status of Fermilab Recycler Ring", EPAC2002, Paris, June 2002.

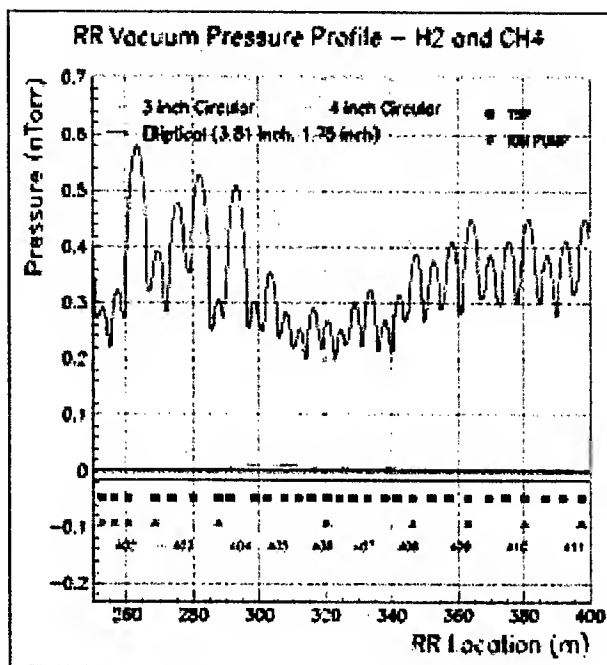


Figure 2: The simulated pressure profiles for Hydrogen (red - upper) and Methane (green - lower) are shown for region in the 400 section of the RR. Note the Hydrogen is pumped by the TSPs and Methane by the Ion pumps. The x-axis is location of various sectors from the point of proton injection into the Recycler at the location 328 in units of meters. The TSPs and Ion Pump locations are also shown along with beam pipe geometry.

- [2] J. Marriner et. al., "Run II Handbook", at <http://www-bd.fnal.gov/runII/index.html>; Also see K. Gounder, "The Status of Run II at Fermilab", in the 2002 proceedings of ICHEP, Amsterdam, July 2002.
- [3] Varian Vacuum Products Lexington, 121 Hartwell Avenue, Massachusetts, 02173 USA.
- [4] M. K. Sullivan, "A Method for Calculating Pressure Profiles in Vacuum Pipes", SLAC, 1993.
- [5] K. Gounder et al., "Recycler Ring Beam Lifetime", Fermilab-Conf-01-186-E, PAC-2001-RPPH055, July 2001.

LATTICE FUNCTION MEASUREMENTS OF FERMILAB RECYCLER RING[†]

M.J. Yang[‡], C.S. Mishra, A. Marchionni, Fermilab

Abstract

The Fermilab Recycler ring, designed and built as an 8-GeV anti-proton storage ring, is at the final stage of its commissioning. Once integrated into the accelerator complex it is expected to help achieve the luminosity goal of Run II at Fermilab. The Recycler Ring is made up mostly of combined function magnets with a substantial sextupole component. Any orbit error could cause higher order feed-down and potentially change the machine. Lattice function measurements had been done at various stages of the machine and the results is presented here.

INTRODUCTION

Several modifications to the Recycler were made during commissioning. The magnet end-shims[1] were replaced to correct for sextupole feed-down. Heater tapes around the ring, used for baking the beam pipe at high temperature, had to be replaced because they were found to be magnetic. A high beta straight section was replaced with one of medium beta when it was decided not to have Electron Cooling in transverse space [2]. Dipole correctors were installed at every location to control closed orbit. Vertical re-alignment of gradient magnets was necessary to correct for a problem in the fiducial reference of the magnets. Any of these modifications could have significant impact on the machine.

Lattice function and dispersion function measurements had been taken throughout the commissioning and results will be presented here.

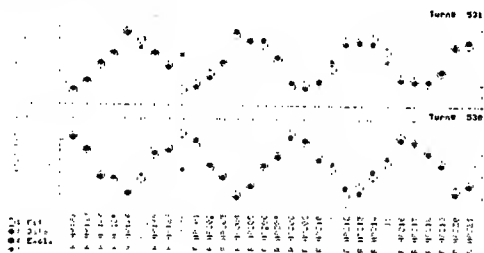


Figure 1. Two turns of BPM data from Recycler BPM house 20. Solid dots are data points and open circles are the calculated position based on the fitted $x-x'$.

DATA

The Recycler Ring Beam Position Monitor (BPM) system, in spite of its problems and limitations, has been used regularly to study the machine properties. First turn and circulating beam orbit data were used to extract phase advances. Beta function measurements from BPM orbit data, which are sensitive quadratically to calibration uncertainties, will not be presented. The dispersion function, also measured from orbit data, is instead sensitive to calibration only linearly.

[†] Work supported by the US Department of Energy under contract DE-AC02-76CH00300.

[‡] E-mail: YANG@FNAL.GOV

The Turn-by-Turn (TBT) lattice function analysis [3], which is less sensitive to calibration error, is used for beta and alpha lattice function measurements. The Recycler BPM system precludes taking ring-wide TBT data simultaneously, instead data was taken over repeated injections. The injection reproducibility is likely a source of systematic error. Fig. 1 is an example of TBT BPM data in two consecutive turns. The TBT analysis also provides diagnostic information, such as RMS deviation which is used to gauge the quality of data.

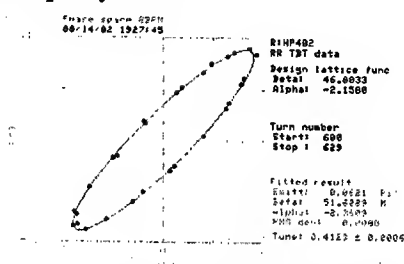


Figure 2. 30 turns of phase space points are plotted and fitted to an ellipse which gives lattice functions at the BPM location.

ANALYSIS

TBT lattice function analysis

The first step in TBT lattice analysis is to get the phase space coordinates, i.e. position and angle, at a reference location for every turn. Transfer matrices between the reference and the BPM locations, calculated based on known machine focusing properties, are used to fit for the coordinates which best match data from the selected number of BPMs. Fig. 1 shows BPM data with projected positions based on fitted coordinates at the reference location. Next step is to fit for an ellipse using the fitted phase space points over a number of turns (Fig. 2). The parameters of the ellipse give lattice functions β and α .

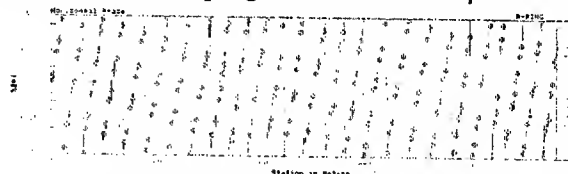


Figure 3. Horizontal phase advance measured from closed orbit and plotted in modulo of 2π . Data points are in green and model calculation is the magenta line. End-shim effects were included in the calculation and adjusted to match the data.

Phase advance

Phase advance at the BPM is calculated from orbit displacements using two correctors, approximately 90° apart in phase advance [4]. Fig. 3 shows a closed orbit data example. All other phase advance results presented will be from first turn orbit data. Sources of systematic errors include corrector strengths, beta functions at the correc-

tors, and phase advance between them. This analysis is inherently insensitive to BPM calibration.

Dispersion function

The dispersion function is measured by observing position changes as a function of $\Delta p/p$. Likely systematic errors are the calculated $\Delta p/p$, based on the phase slip factor, and BPM positions which are sensitive to calibration errors.

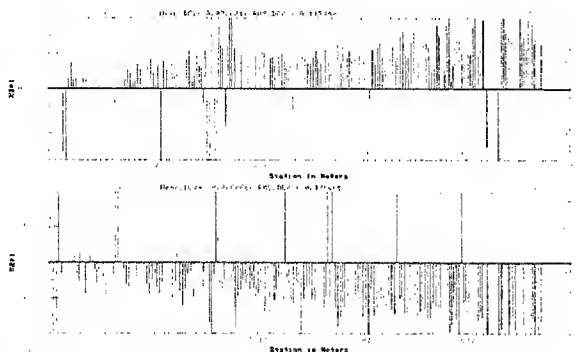


Figure 4. The phase advance errors as measured before the end-shim replacement using first turn orbit data. The cumulated phase advance error is about $+0.15$ in the vertical plane (top plot) and -0.18 for horizontal plane, in units of 2π .

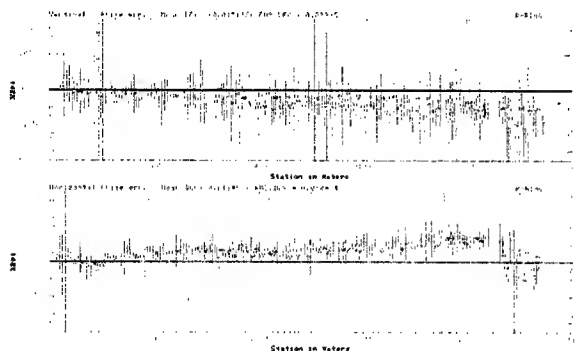


Figure 5. Phase advance error after end-shim and heater tape replacement.

LATTICE RESULTS

The results are shown with reference to specific issues during the commissioning and in chronological order.

End-shim feed-down

Each permanent gradient dipole installed in the Recycler Ring has two end-shims to correct for magnetic errors. With a large fraction of the body sextupole component being corrected at the end and with a sagitta offset of about 7.5 mm, the feed-down from sextupole is significant. Fig. 4 shows the deviations of the measured phase advances from that calculated from the machine model. The deviations are consistent with tune measurements using Schottky detectors. A quadrupole component was added to the end-shims to cancel the feed-down during the January 2000 shut-down. The heater tapes, made of magnetic stainless steel, were also replaced.

Recycler with high beta straight section

The new end-shims had over corrected the phase advance by about 10% or so. Fig. 5 shows the horizontal phase

advance going faster and the vertical slower than expected, opposite of Fig. 4. The errors are well within the range of the phase trombone for tune adjustment.

At the 3000 m location in Fig. 5, after the high beta straight, a drop in phase advance error is seen. This is consistent with high beta quadrupole gradients being -1% off from design. This deviation predicts beta functions that compare well with beta functions measured with TBT lattice analysis (see Fig. 6 and 7, where the solid green line is the design lattice calculation and the dashed cyan line includes the -1% gradient error in the calculation).

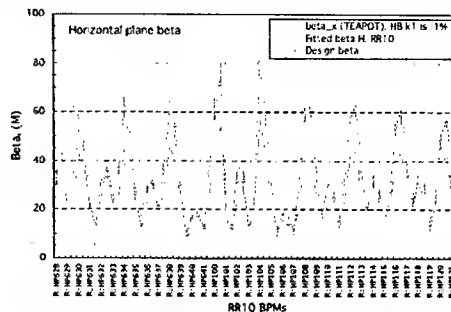


Figure 6. Measured horizontal beta function of RR10 BPMs.

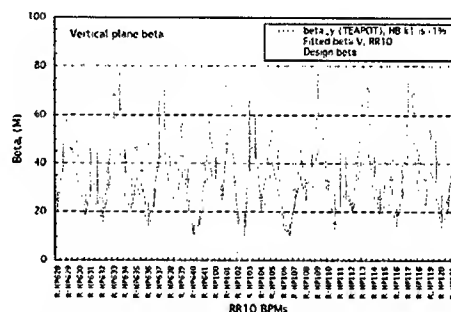


Figure 7. Measured vertical beta function of RR10 BPMs.

With medium beta straight section

With the medium beta straight, installed in July 2001 shut-down, the measured phase advance error (shown in Fig. 8) was consistent with expectations.

The measured lattice functions compared to calculations are shown in Fig. 9 and Fig. 10, which shows the error for the whole ring. While the vertical beta appears to be in good agreement with the model, the horizontal beta function does not.

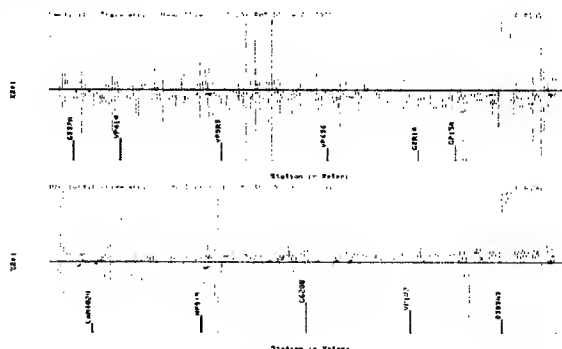


Figure 8. Measured horizontal and vertical plane phase advance error with the medium beta straight in place.

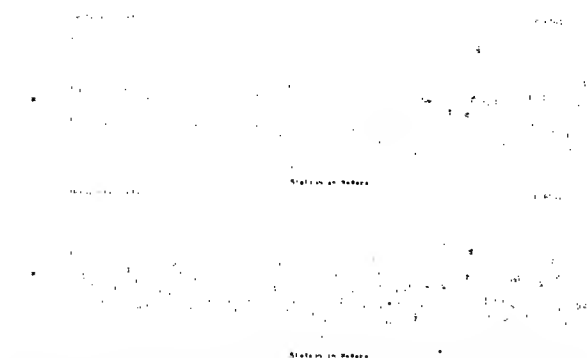


Figure 9. Measured horizontal and vertical beta functions compared with model calculations over a stretch of 800 m, including the medium beta straight region.

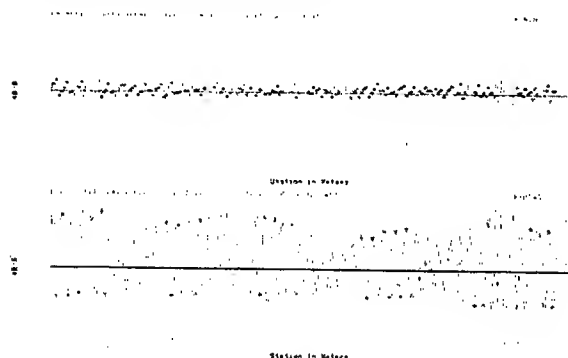


Figure 10. Plots of ring-wide $\Delta\beta/\beta$ for horizontal and vertical planes. As in Fig. 9 the horizontal beta error was substantial.

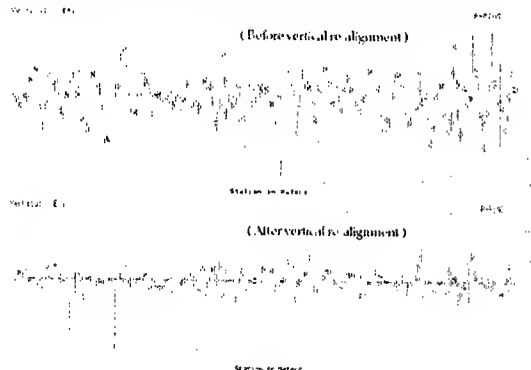


Figure 11. Ring-wide vertical dispersion function measured before (top) and after (bottom) vertical plane re-alignment.

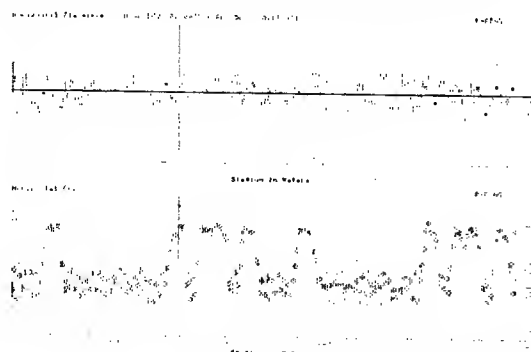


Figure 12. Measured ring-wide horizontal dispersion function. Bottom plot shows both data and calculation (cyan line), and the top plot their difference.

Vertical alignment and corrector installation

During the October 2001 shut-down Recycler was re-aligned to correct for the vertical fiducial problem. Dipole corrector were also installed at every location in the ring. A dramatic improvement was observed in the measured vertical dispersion function as shown in Fig. 11. For completeness the horizontal dispersion function is also shown in Fig. 12. The dispersion-free region is well preserved.

The measured beta functions after the re-alignment are shown in Fig. 13. The horizontal plane beta is close to design, to within 10%, while the vertical beta shows deviation up to 30%.

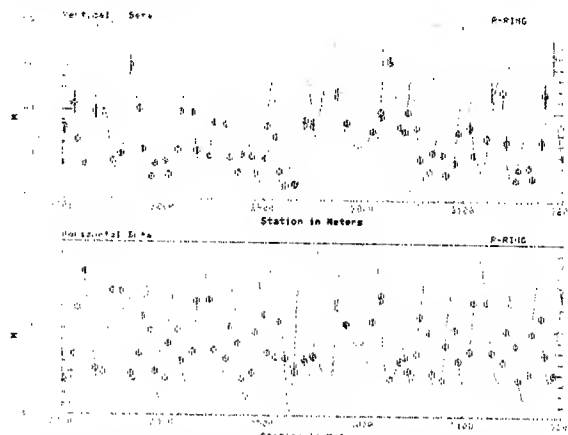


Figure 13. Up-to-date measured Recycler beta functions for a portion of the Recycler ring: bottom plot is the horizontal and top the vertical. Green circles are the measurements and magenta line is the model calculation.

CONCLUSION

Lattice measurement is an important tool to understand the machine. Disagreements between measurements and model calculations have been shown to point to problems which in some cases were independently known.

The reliability of Recycler BPMs has always been an issue. The system is in the process of being upgraded [5] to improve its stability and absolute calibration. A robust BPM system is critical in keeping track of the closed orbit which is important to the consistency and stability of the machine. Improvements to the accuracy of the lattice function measurements are expected.

REFERENCES

- [1] D.E. Johnson et al, "Corrections to the Fermilab Recycler Focusing with End Shim", PAC '01, p.2575.
- [2] W. Wan et al, "Design and Implementation of the Medium Beta Insert for the Fermilab Recycler", Proc. PAC '01, p.2575.
- [3] M.J. Yang, "Lattice Function Measurement with TBT BPM Data", Proc. PAC '95, p. 2500
- [4] M.J. Yang, "A Beam Line Analysis Program for Main Injector Commissioning", Proc. PAC '99, p723.
- [5] Fermilab document RR-BPM-0001.rev1.1

LINAC OPTICS OPTIMIZATION FOR ENERGY RECOVERY LINACS

R. Nagai[#], R. Hajima, N. Kikuzawa, E. Minehara, N. Nishimori, M. Sawamura,
JAERI, Tokai, Ibaraki, Japan

Abstract

Linac optics of an energy recovery linac (ERL) is optimized to ensure the high average current electron beam to drive synchrotron light sources and free-electron lasers. Genetic algorithm is utilized to search globally optimum parameters of the linac optics. Multi-pass transverse beam-break-up (BBU) threshold current is estimated by numerical simulation with the optimized optics parameters. It is shown by numerical simulations that over 100 mA of multi-pass transverse BBU threshold current can be achieved in a simple one-pass ERL with cavity gradient of less than 15 MV/m.

INTRODUCTION

A superconducting linac based ERL is an extremely efficient accelerator for synchrotron light sources and free-electron lasers. The performance of the ERL light sources is improved as the beam average current is increased. The average current, however, is limited by instabilities such as multi-pass transverse BBU. It was shown by an analytical solution [1] that the BBU threshold current is inversely proportional to the Q factor of the higher-order-mode (HOM) and transfer matrix elements of divergence to transverse position (R_{12} and R_{34}). To suppress the BBU instability, the HOM should be damped sufficiently. The HOM damping should be incorporated into the superconducting cavity design. To achieve high BBU threshold current, transport optics along the superconducting linacs should be optimized to minimize R_{12} and R_{34} . This optimization can be performed through a numerical design of the linac optics.

Result of local optimization method such as Newton method strongly depends on starting parameters. A set of initial parameters to start the optimization cannot be fixed a priori for a system with a lot of free parameters such as linac optics design of the ERL. The linac optics has many free parameters because of the lengthy structure of the linac. The local optimization method is therefore not suitable to find directly the optimum parameters of the linac optics. Genetic algorithm [2] is well known as an optimum parameter global search method. In the case of many free parameters, however genetic algorithm spends a lot of computation time. Hence we employ two-step optimization utilizing the local and global optimization methods. Genetic algorithm is only used to find the starting parameters of the local optimization, and the parameters are refined by the following local optimization. The optimum parameters of the linac optics for a simple one-pass configuration ERL are easily found using the two-step optimization method.

LINAC OPTICS OPTIMIZATION

In this optimization, we assume a conceptual ERL with a simple one-pass configuration and external quadrupole triplets between cryomodules as shown in Fig. 1. Each cryomodule includes eight cavities, which are 9-cell 1.3 GHz TESLA cavities [3]. A 10 MeV electron beam with small transverse emittance is injected to the main linac. The main linac accelerates the beam to 6 GeV. Subsequently, the beam is transported through the recirculation loop where it is used to produce high brightness X-rays. The beam is then returned to the main linac with decelerating rf phase for energy recovery. In the linac the recirculated beam gives back its energy, which is used for the acceleration of successive beams. The low energy beam after energy recovery finally goes to the dump.

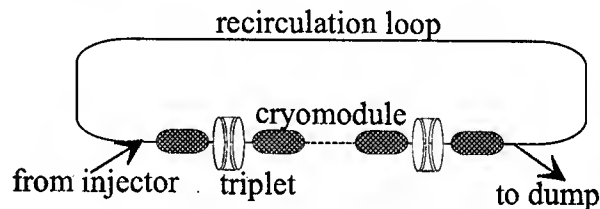


Fig. 1: Conceptual ERL layout.

The linac optics is numerically optimized based on Bazarov's guideline [4] as following:

- 1) Minimize the β -function in the linac by adjusting the strength of the quadrupole triplets and by matching the envelope of the injected beam.
- 2) Set the phase advance of the recirculation transport loop to minimize R_{12} and R_{34} .

The optimization code takes the two-step optimization method to find quickly and globally optimum parameters. At first step, proper starting parameters for the local optimization are found by genetic algorithm. The parameters are then refined in the local optimization step by BFGS method [5].

In the optimization code, the β -function and R_{12} and R_{34} are calculated by transport matrix of the optic element, which is basically same as TRANSPORT [6]. Unfortunately, TRANSPORT does not support standing-wave cavity such as the superconducting cavity. In order to simulate transverse beam dynamics in the linac, it is indispensable to include rf focusing of the cavity. The transport matrix of the standing-wave cavity was derived by the study of transverse particle motion in the cavity [7].

RESULTS OF THE OPTIMIZATION

As a result of the optimization for the simple one-pass ERL with cavity gradient of 15 MV/m, β -function of the

[#]r_nagai@popsvr.tokai.jaeri.go.jp

linac is presented in Fig. 2. The linac contains 48 cryomodules and 47 external quadrupole triplets, and its length is about 600 m. The strength of quadrupole triplets, which is field gradient normalized by beam rigidity, is shown in Fig. 3. All quadrupoles in the triplet are of the same strength. The middle and the end quadrupole of the triplet are 50 cm length and 25 cm length, respectively. It can be seen in Fig. 3 that triplets are set in such a way as to produce a nearly constant focusing length for lower energy beam at the same triplet.

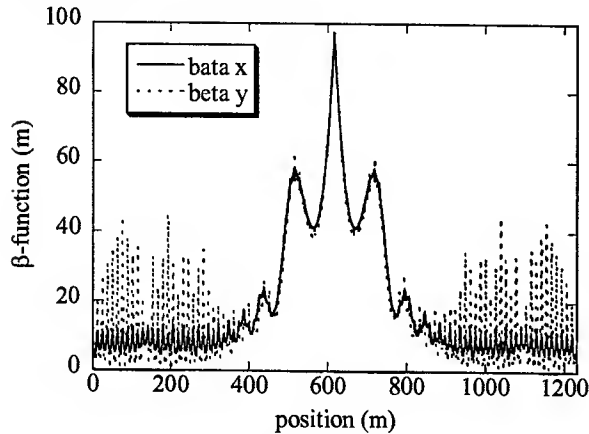


Fig. 2: β -function in the linac as a result of the optimization.

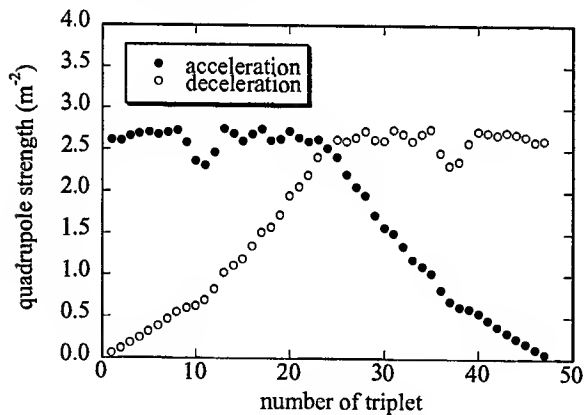


Fig. 3: Strength of the quadrupoles along the linac corresponding to Fig. 2.

Numerical simulation code BBU-R [8], which is similar to TDBBU [9] is used to determine the BBU threshold current. Calculated HOM data [10] as shown in Table 1 are taken into BBU-R. To mimic the expected frequency spread of the HOMs in the actual cavities, the HOM frequencies are chosen to be random. The BBU threshold current for the linac optics optimized ERL is presented in Fig. 4. As shown in Fig. 4, by increasing frequency spread of the HOM it is possible to increase the BBU threshold current up to 100 mA or more. It is found that the threshold current depends much on the sorting order of the randomized HOM frequencies. The error bars seen in Fig. 4 correspond to different sorting orders.

Table 1: HOM parameters used in BBU-R

f [MHz]	Polarization	R/Q [Ω]	Q
1734	x/y	116.7	3400/4500
1865	x/y	42.4	50600/26500
1874	x/y	56.8	50200/51100
1880	x/y	11.8	95100/85500
1887	x/y	1.2	633000/251000

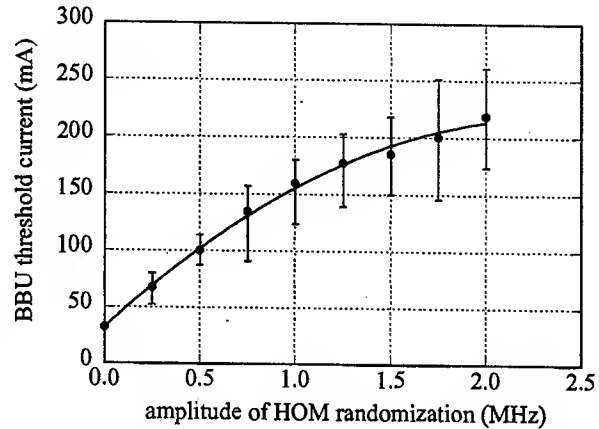


Fig. 4: BBU threshold current vs. amplitude of HOM randomization.

In the linac optics optimization of the ERL, the cavity gradient is a principal parameter. The linac optics is optimized with various cavity gradients and the threshold current is estimated with 1 MHz HOM frequency spread. As shown in Fig. 5, the threshold current is increasing with the cavity gradient. It is found that it is possible the threshold current of more than 100 mA even if the cavity gradient is less than 15 MV/m.

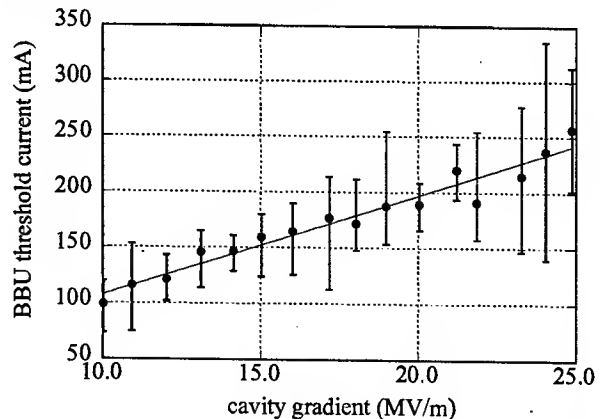


Fig. 5: BBU threshold current vs. cavity gradient.

CONCLUSION

The optimum parameters of the linac optics for a simple one-pass configuration ERL have easily found utilizing genetic algorithm. As a result of the optimization, the BBU threshold current more than 100

mA is reasonably available with cavity gradient of 15 MV/m. The cavity gradient of 15 MV/m is the most economical so far as 10-year running cost is concerned [11].

The optics has been optimized only for a one-pass simple configuration and single-parameter triplets. It will be expected to increase the threshold current by the other configurations such as cascade configuration and by two-parameter triplets or FODO like optics.

REFERENCES

- [1] J.J. Bisognano, G.A. Krafft, Proc. of the 1986 Linear Accel. Conf. (1986) 452-454.
- [2] M. Mitchell, "An Introduction to Genetic Algorithms", MIT Press (1996).
- [3] B. Aune, et al., Proc. of the 1999 Part. Accel. Conf. (1999) 245-249
- [4] I. Bazarov, et al., CHES Technical Memo 01-003 (2001).
- [5] C.G. Broyden, J. of the Inst. for Math. and Applications **6** (1970) 222-231, R. Fletcher, Computer Journal **13** (1970) 317-322, D. Goldfarb, Mathematics of Computation **24** (1970) 23-26, D.F. Shanno, Mathematics of Computation **24** (1970) 647-656.
- [6] K.L. Brown, et al., SLAC-91 (1970).
- [7] J. Rosenzweig, L. Serafini, Phys. Rev. **E49** (1994) 1599-1602.
- [8] M. Sawamura, et al., these proceedings (2003), M. Sawamura, et al., Proc. of the 27th Linear Accel. Meeting in Japan (2002) 275-277, in Japanese.
- [9] G.A. Krafft, J.J. Bisognano, Proc. of the 1987 Part. Accel. Conf. (1987) 1356-1358.
- [10] J. Sekutowicz, TESLA 94-07 (1994).
- [11] M. Sawamura, et al., these proceedings (2003).

PERFORMANCE AND UPGRADE OF THE JAERI ERL-FEL

M.Sawamura, R.Hajima, N.Kikuzawa, E.J.Minehara, R.Nagai, N.Nishimori,
JAERI, Tokai, Ibaraki 319-1195 Japan

Abstract

The free-electron laser (FEL) linac has been modified to the energy recovery linac (ERL) at the Japan Atomic Energy Research Institute (JAERI) to achieve the higher power FEL of the next stage of 5-10kW. Energy recovery has been successfully demonstrated up to 5mA of average current. Upgrade of the injector is in preparation to accelerate the higher average current of 40mA. We review transverse instabilities and present experimental data on transverse beam breakup (BBU) obtained at the JAERI ERL-FEL. We compare measurement with simulation.

INTRODUCTION

JAERI has been developing a high-power FEL with a superconducting linac. After the initial goal of kilowatt FEL lasing was achieved in 2000 [1], the linac has been modified into an ERL. Energy recovery is the process by which the energy invested in accelerating a beam is returned to the rf cavities by decelerating the beam. Energy recovery of an FEL beam driven by a superconducting linac is a possible way of greatly increasing the efficiency of the laser since most of the beam energy remains after lasing occurs. This energy-recovery technology with a superconducting linac is the most promising for the next stage of 10kW FEL lasing owing to increasing the beam current without additional rf power sources.

In a recirculating linac, a feedback system is formed between the beam and the rf cavities, so that instabilities can arise at high currents. These instabilities become important and can potentially limit the average beam current especially for the high-Q superconducting cavities. Instabilities can result from the interaction of the beam with transverse higher order modes (HOMs) (transverse beam breakup (BBU)), with longitudinal HOMs (longitudinal BBU) and with the fundamental accelerating mode (beam loading instability). Of the three types of instabilities, transverse BBU appears to limit the average current in the ERL [2].

In the present paper we will describe the recent result

and upgrade plan of the JAERI ERL-FEL, and transverse HOM instability research by simulation and measurement.

JAERI ERL CONFIGURATION

The JAERI original FEL superconducting linac consisted of an injector, two main modules of 499.8MHz 5-cell superconducting accelerators, a 180-degree bending arc and an undulator. The injector consists of a 230kV thermoionic electron gun driven by a grid pulser, an 83.3MHz normalconducting subharmonic buncher (SHB) and two modules of 499.8MHz single-cell superconducting accelerators. The JAERI ERL-FEL has been constructed by adding an injector merger, a half-chicane before the undulator and the second arc to the original FEL linac. Figure 1 shows the layout of the JAERI ERL-FEL.

Electron microbunches with a charge of 0.5nC at repetition of 10.4125MHz are produced and accelerated to 230keV in a DC electron gun. The average current corresponds to 5mA. The bunches are compressed by the SHB, pass through the two single-cell modules and are accelerated to 2.5MeV. The output beam is injected into the two 5-cell main modules where it is accelerated up to 17MeV. The beam then passes through the first arc, the half-chicane and the undulator. Afterward it is recirculated through the second arc, returned into the main modules in the decelerating rf phase and dumped at the injection energy of 2.5MeV.

ENERGY RECOVERY EXPERIMENT

Energy recovery has worked well in the JAERI ERL-FEL with beam current of 5mA. We measured the rf forward power from the rf power source to the cavity to estimate the energy-recovery ratio, which is defined as the ratio of the recovered rf power to the beam energy. Figure 2 shows the rf forward power signal for one of the main modules with and without energy recovery. When a 100μsec beam pulse is injected into the cavity in the absence of energy recovery, the forward power signal reaches to -343mV to compensate for beam loading. With

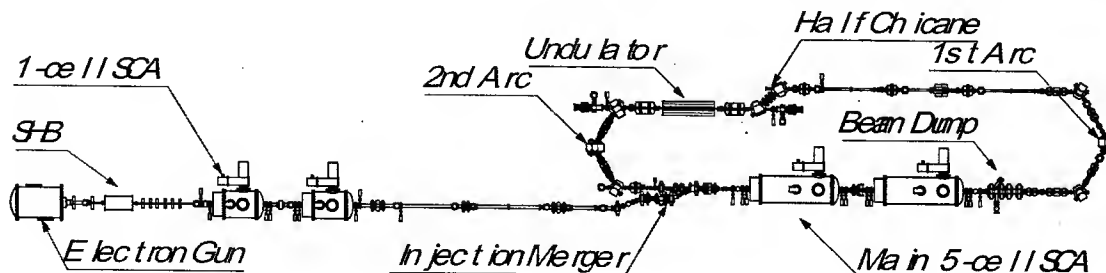


Figure 1: Layout of the JAERI energy-recovery linac

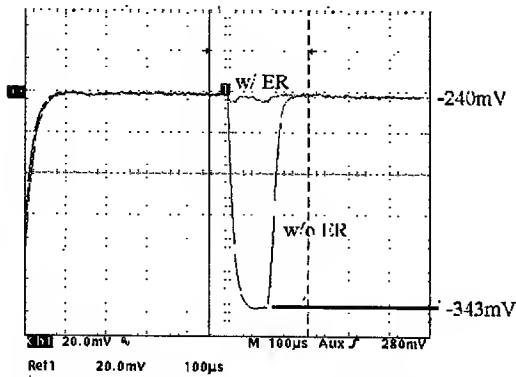


Figure 2: Energy recovery with a 100 μ sec beam pulse: Response of the rf forward power signal with (-240mV) and without (-343mV) energy recovery

energy recovery, this signal is close to -240mV (where -240mV corresponds to the DC voltage required to drive the accelerating field in the cavity), as the accelerating and the decelerating beam vectors cancel each other resulting in nearly zero net beam loading. The level of the forward power with energy recovery has small fluctuation so that we estimate the energy-recovery ration to 98%.

TRANSVERSE BBU

Transverse BBU has been long known to be a potential limiting factor in the operation of high current linac-based recirculating accelerators. Transverse beam displacement on successive recirculations can excite HOMs that further deflect the initial beam. The effect is worse in superconducting rf cavities because of higher Q values of HOMs. The threshold current depends on the various parameters of cavity and beam optics such as Q values, frequencies and R/Q of the HOMs, beam energy, beta functions and phase advance in the paths and recirculation path length.

HOM Instability Simulation

A simulation code, named BBU-R, has been developed to calculate the threshold current at an actual machine configuration. Analytic model for simulation is impulse approximation, where the transverse position of the bunch is treated as one point and the transverse deflection through the cavity as single deflecting force [3].

This simulation code requires the transfer matrices between the adjacent cavities and the HOM parameters such as frequency, R/Q and loaded Q value. The HOM frequencies and R/Q of the JAERI superconducting cavity was calculated with the 2.5-D rf cavity code PISCES II, which can evaluate all the eigenfrequencies and fields for arbitrarily shaped axially symmetric rf cavity [4]. The loaded Q values and frequencies of the HOMs were measured with a network analyzer connected to the HOM coupler, from which reflection power was measured. The transfer matrices were calculated with the code TRANSPORT.

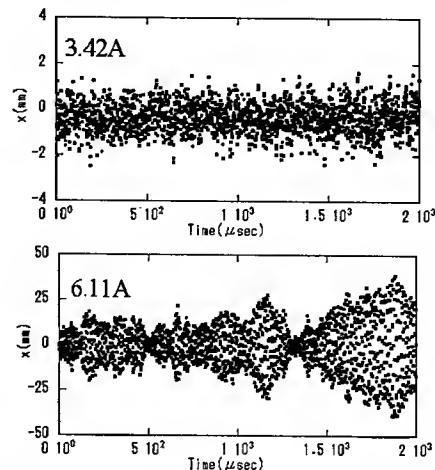


Figure 3: Bunch position vs. time for 3.42A beam current, approximately threshold (top), and for 6.11A beam current, above threshold (bottom)

In the JAERI ERL-FEL two main modules of 5-cell superconducting accelerators are used for energy recovery. The microbunch interval is 10.4125MHz corresponding to 96 times and recirculation period is to 131 times of half period of the fundamental frequency of 499.8MHz. Figure 3 shows the calculated beam positions in the second main module as a function of the time at the various average current. The initial beam has 1mm diameter and 0.5mm offset from the axis. The beam diameter increases with the current. The threshold current is defined as the current where the beam can be transported within 5 times of diameter of the initial. Table 1 lists the threshold currents when one of 10 HOMs is excited and all of 10 HOMs are excited. The threshold current when all of 10 HOMs are excited is 3.42A, which is large enough to increase the beam current for the next stage of our plan.

HOM Power Spectrums

Each module has five rf couplers such as a main power coupler, a pick-up coupler and three HOM couplers. Two HOM couplers are designed to damp transverse modes and the other to damp longitudinal modes. All HOM

Table 1: Threshold current

No.	Mode	Threshold Current (A)
#1	TE111 $\pi/5$	666.40
#2	TE111 $2\pi/5$	487.31
#3	TE111 $3\pi/5$	34.36
#4	TE111 $4\pi/5$	10.74
#5	TE111 $\pi/5$	578.94
#6	TM110 π	32520.32
#7	TM110 $4\pi/5$	16.79
#8	TM110 $3\pi/5$	5.47
#9	TM110 $2\pi/5$	7.03
#10	TM110 $\pi/5$	1482.74
#1-#10	All modes	3.42

couplers are terminated to the dummy loads out of the cryomodels. This makes it possible to measure the excited HOM powers inside the cavity through the HOM couplers. The terminator was exchanged for a real-time spectrum analyzer to measure frequencies and powers of the HOMs. Figure 4 shows the power signals from the HOM couplers. When a 120 μ sec beam pulse is injected into the cavity with and without energy recovery, the power signals rises. Although the signals seem to be large, they include many spectrums with harmonic frequencies of the microbunch repetition of 10.4125MHz. These spectrums are thought to be induced in the couplers by the electron bunches on the grounds that the HOM power signals fall rapidly after beam-off. Figure 5 shows the amplitude of the HOMs after removing the harmonic frequencies of the microbunch repetition. There seems to be four groups of the HOMs or more. The group near 630MHz is considered to be TE111 mode and that near 700MHz to be TM110 mode. The groups over 850MHz have not been identified yet.

The mode of the highest power of TE111 is considered to be $3\pi/5$ mode of 634MHz and that of TM110 to be $4\pi/5$ mode of 715MHz. The calculated threshold current is 34.36A for TE111- $3\pi/5$ mode and 16.79A for TM110- $4\pi/5$ mode. While these modes of small threshold current show high HOM powers, the modes of the smaller threshold current for such as TM110- $3\pi/5$ and TM110- $2\pi/5$ modes show fairly low HOM powers. Measurement of HOM coupling factors is required to estimate more precise HOM powers in the cavity and to investigate the HOM instabilities in further detail.

5-10KW UPGRADE

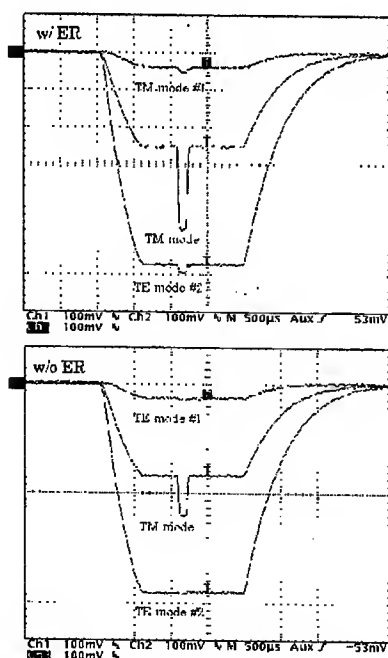


Figure 4: Power signals from the HOM couplers with (top) and without energy recovery (bottom)

To achieve the higher FEL power of 5-10kW, we must increase the beam current and FEL efficiency. The operation of the higher beam current is available at the main modules owing to energy recovery and not sufficient at the injector where the energy recovery does not work. The rf amplifier of 6kW, which is sufficient for 5mA acceleration through the single-cell cavity, is replaced to the rf power source of 50kW IOT to accelerate 40mA electron beam. Modification of the grid pulser is now in progress to increase the repetition from 10.4125MHz to 83.3MHz and beam current from 5mA to 40mA. The higher beam current experiment will start soon.

CONCLUSION

The original JAERI FEL has been modified to ERL-FEL to result in 98% energy recovery. Additional elements of the injector are being prepared to increase the beam current and the FEL power. The threshold current of the JAERI ERL-FEL limited by the HOM instability is calculated to 3.42A, which is large enough to increase the beam current from 5mA to 40mA of our next stage. The HOM spectrums were measured from three HOM couplers. The mode of the smallest threshold current by calculation is not detected from the HOM couplers. The more precise measurement is required to well-understand the HOM instabilities.

ACKNOWLEDGMENTS

We are grateful to Dr. Iwashita (Kyoto University) for calculating the HOM parameters of the JAERI superconducting cavities with PISCES II.

REFERENCES

- [1] N.Nishimori et al., Nucl. Instr. Meth. A 475 (2001) 266-269
- [2] L.Merminga, Nucl. Instr. Meth. A 483 (2002) 107-112
- [3] J.Bisognano, et al. CEBAF-PR-87-007 (1987)
- [4] Y.Iwashita, Computational Accelerator Physics, Williamsburg, VA, AIP conference proceedings No.361 Sept. 1996, 119-124

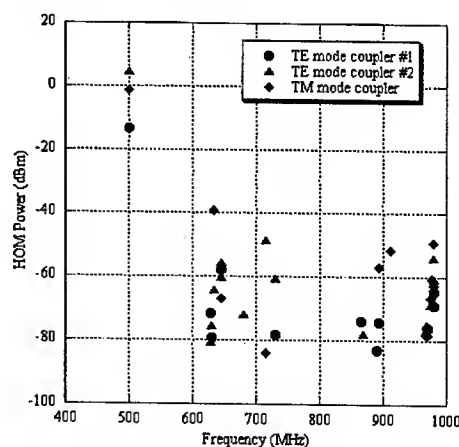


Figure 5: HOM power spectrums

COST ESTIMATION OF AN ENERGY RECOVERY LINAC LIGHT SOURCE

M.Sawamura, R.Hajima, N.Kikuzawa, E.J.Minehara, R.Nagai, N.Nishimori,
JAERI, Tokai, Ibaraki 319-1195 Japan

Abstract

A cost estimation model for scaling energy-recovery linacs (ERLs) has been developed for estimating the impact of system-level design choices in scaling superconducting accelerator facilities. The model consists of a number of modules which develop subsystem costs and derive as a budgetary criterion. The model does not include design engineering or development costs. Presented in the paper is the relative sensitivity of designs to the accelerators and the refrigerators while allowing the accelerating field to optimize.

INTRODUCTION

Light source has become an integral part of the experiment in most science concerned with the structure of matter on the atomic scale. This impact is felt over a broad range of science from protein crystallography in the biological science to studies of atomic and electronic structure in systems ranging from high temperature superconductors to toxic elements in soil. The impact of this research has grown exponentially as the sources have evolved. Although synchrotron radiation is produced by about 70 storage-ring based facilities in the world, the performance is nearly at its ultimate level. Superconducting ERLs can be extremely efficient accelerators for free-electron lasers, synchrotron radiation light sources. In an ERL, a beam is accelerated to the energy required for the application, and returned to the linac 180 degrees out of phase with respect to the accelerated electrons. In this way the returning high-energy electrons are decelerated, and they recycle their energy to the rf field to provide most of the power necessary to accelerate the entering electrons. Besides the high efficiency, ERLs offer crucial advantages for a new user-oriented light sources, including very high brightness, a large degree of spatial coherence, and ultra-fast temporal structure.

A spreadsheet-based cost estimation model for ERLs has been developed motivated by a desire to uncover the element of the highest cost and to determine the ERL parameters with which the construction and running costs become reasonable. The point of comparison in the present paper is the total cost – the primary budgetary criterion used to judge the advantage of an ERL.

PARAMETERS FOR COST ESTIMATION

In the present model we have assumed the ERL is based on a continuous wave (CW) rf superconducting accelerator (SCA), the final energy of 6GeV, the current

of 0.1A and 40 sections of light sources. The injector installed before the recirculating SCA is not included in the cost because the design of the injector has not examined in detail yet. The cost of the site is not included neither because the cost widely changes with the choice of the site. The model can optimize cost on the accelerating field of SCA.

The subsections below discuss the cost estimating modules for each element. We use the exchange rate to \$1=1Euro=130JPY.

SCA Cavities Model

SCA cavities represent a major fraction (16%-34%) of the system capital costs. Fortunately we can refer to the TESLA design [1,2]. We assume to use the TESLA-type cavities and cryo modules. The TESLA module is 12.2m long including 1.3GHz eight 9-cell cavities. The unloaded Q value is 1×10^{10} . The cost of the SCA module is evaluated to \$1M including a cavity assemble and a cryo vessel.

Refrigerator System Model

Required cooling power of the refrigerator system is estimated from static heat leak, dynamic heat leak and rf wall loss. Since cost of the refrigerator system depends on number and capability of the refrigerators, we assume the cost of refrigerator system is proportional to the cooling power for 2K and 4.5K. It is assumed to cost \$3.4k/W for refrigerator operating at 2K and \$1.7k/W at 4.5K in accordance with the Very Large Hadron Collider (VLHC) [3]. The electrical power consumption of 1W refrigerator is assumed to 600W at 2K and 245W at 4.5K in accordance with the TESLA cryogenic system [4].

RF Power Source Model

The rf power is small owing to energy recovery, but it is necessary to supply rf power for compensating the beam power loss due to light generation and correcting the amplitude and phase errors. Required rf power is estimated from the parameters such as beam current, cavity shunt impedance, unloaded Q value, accelerating field, current error and phase error [5]. Since the cost and the efficiency depend on a type of the rf source, the cost is assumed to be proportional to the rf power with the factor of \$1.15/W and the efficiency from AC power to rf power to 0.5 for calculation of the power consumption.

Magnetic System Model

ERL optics is designed to suppress the beam breakup (BBU) instability by obtaining small pass-to-pass matrix elements of R12 and R34. Required magnetic parameters depend on accelerator design. We assume that a

quadrupole triplet magnet of 25T/m is installed between adjacent SCA modules. The middle magnet of the triplet has length of 50cm and the others of 25cm. The back-straight beam line has half the number of triplets in the accelerator line.

One section of the arc, where an insertion device is installed, is assumed to have three bending magnets, four quadrupole triplet magnets, two quadrupole doublet magnets and an undulator.

Since it is difficult to estimate the cost of magnets precisely without beam optics design, we roughly estimate the magnet cost to be proportional to the weight of magnet. Referring to the magnet cost of several accelerator facilities such as the JAERI-FEL, the Spring-8 and the TESLA, we assume the cost to \$60/kg for quadrupole and bending magnets.

The cost of the DC power supply is assumed to be proportional to the DC power with the factor of \$1410/kW. The conversion ratio from AC to DC of the DC power supply is typically 0.85.

The cost of an undulator is assumed to \$230k in accordance with the JAERI-FEL undulator.

Building Model

The straight parts of the SCA modules and back-straight beam line including the auxiliary components are assumed to be installed in the tunnel same as that of the TESLA. The parts of the light sources are installed in the buildings along the arc with concrete wall of 1m thickness to shield the radiation caused by beam loss of 1×10^{-5} . The tunnel cost is estimated to \$9k/m and the arc building \$55k/m. The arc building includes the experimental rooms.

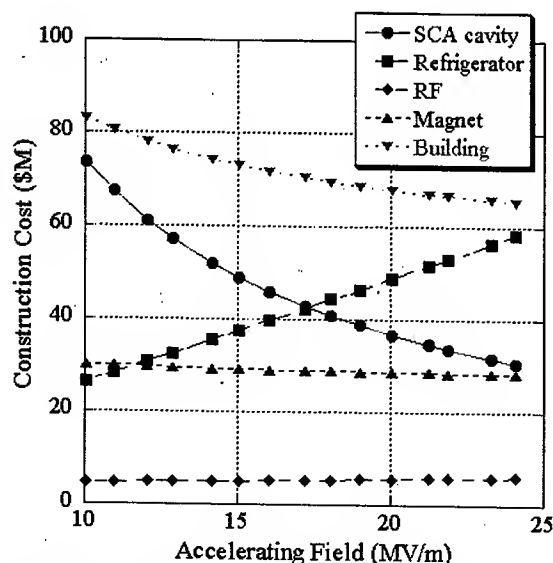


Figure 1: Construction cost of each model as a function of the accelerating field

RESULT

Two types of costs are discussed below. The first is a construction cost. Figure 1 shows the each cost of models as a function of the accelerating field. As expected, the costs of the SCAs and building decrease monotonically with increasing the accelerating field. The high accelerating field decreases number of the SCA modules and the length of the tunnels. On the other hand the cost of the refrigerators increases with the accelerating field since the number of the SCAs decrease inverse-proportionally and the heat load, dynamic heat leak and rf wall loss, increases square-proportionally with the accelerating field. The costs of the magnets and rf system vary slightly enough to be considered to be constant. Since the major parts of ERL, SCAs and refrigerators, vary inversely, the optimum accelerating field exists as shown in Figure 2. The construction cost at the accelerating field of 21MV/m is minimum and the increase over 20MV/m is very small.

The second is a running cost. Figure 3 shows the electrical power consumption of the refrigerator system, the rf power source and the magnet system. The power consumption of the refrigerator and the rf power source increases with the accelerating field. Typical electric charge is about \$9k/MW per month for maximum power of the facility and \$75/MWh for electrical power consumption at a typical rate of Japanese electric companies. The running cost increases monotonically with the accelerating field as shown in Figure 4.

If the running cost includes a depreciation expense of the construction cost as the 10-year useful life of the ERL machine, the running cost has optimum accelerating field near 13MV/m as shown in Figure 5. This means that the ERL does not require as high gradient cavities as a linac for nuclear physics. The higher unloaded Q value is expected at the low accelerating field than at the high field. The high Q value can reduce the required cooling power of the refrigerator and the running cost as shown in Figure 6. The optimum accelerating field increases with the Q value for dominant of the construction cost over the running cost. The ERL requires the SCAs with high Q value than with high accelerating field.

REFERENCES

- [1] "TESLA Technical Design Report", March 2001, http://tesla.desy.de/new_pages/TDR_CD/start.html.
- [2] "Report on the TESLA Engineering Study/Review", July 2002, <http://home.fnal.gov/~peterg/report/>.
- [3] S.Belomestnykh, "RF Considerations", Workshop on an e+e- Ring at VLHC, 2001.
- [4] S.Wolff, "Cryogenic system for TESLA", <http://conference.kek.jp/heacc2001/pdf/tu06.pdf>.
- [5] S.M.Gruner and M.Tigner, eds, CHESST Technical Memo 01-003, 2001.

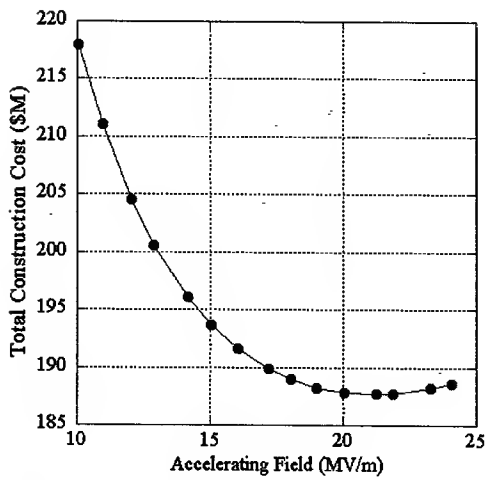


Figure 2: Total construction cost

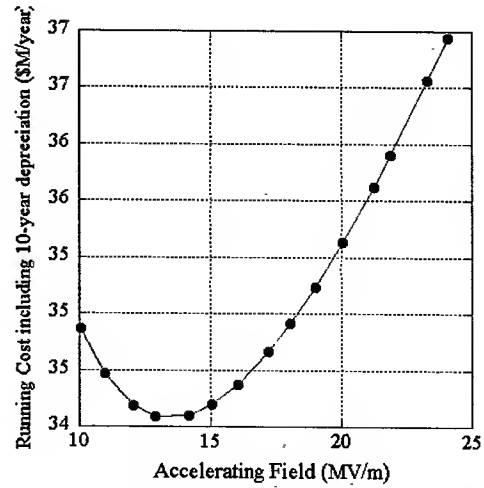


Figure 5: Running cost including a depreciation expense of the construction cost as 10-year useful life

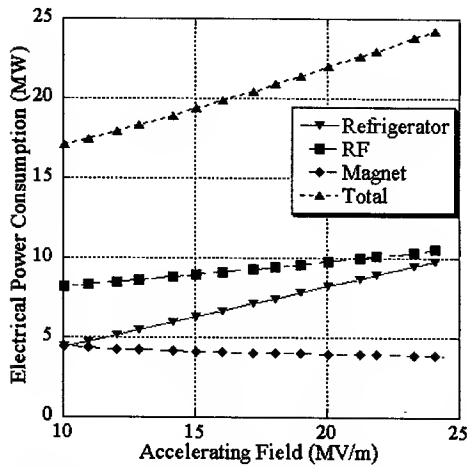


Figure 3: Electrical power consumption

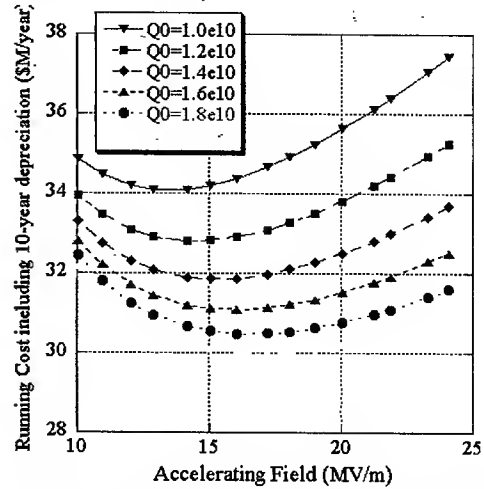


Figure 6: Running cost including a depreciation expense of the construction cost as 10-year useful life for various Q values

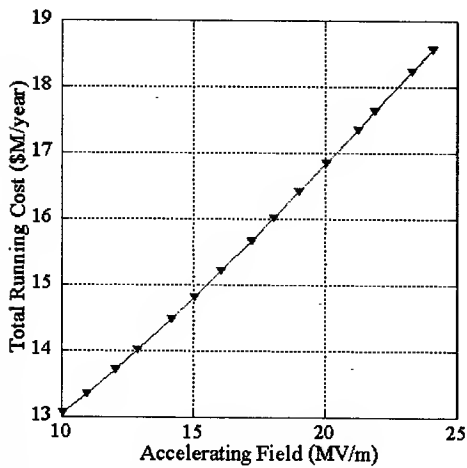


Figure 4: Running cost

STATUS OF 150MeV FFAG SYNCHROTRON

Shinji Machida, Yoshiharu Mori, Atsutoshi Muto, Jo Nakano, Chihiro Ohmori, Izumi Sakai,
Yasuo Sato, Akira Takagi, Tomonori Uesugi, Akiyoshi Yamazaki, Takeichiro Yokoi*,
Masahito Yoshii, Masahiro Yoshimoto, Yoshimasa Yuasa KEK, Ibaraki, Japan
Masaru Matoba, Yujiro Yonemura Kyushu-univ., Fukuoka, Japan
Masamitsu Aiba, Masahiro Sugaya Univ of Tokyo, Tokyo, Japan

Abstract

The 150MeV proton FFAG (Fixed Field Alternating Gradient) synchrotron has been developed for aiming to investigate the possibilities of various applications such as proton beam therapy. The construction started in September 2002, and almost completed recently. In the proceedings, the overview of construction and status of commissioning is to be reviewed.

As the beam injector, a cyclotron which can generate 10MeV proton beam was employed. Because of the pulse operation of the FFAG accelerator, the duty factor of the cyclotron was reduced to, typically, 1/100, by modulating the RF voltage of the cyclotron to reduce the beam loss at the injection stage. With the treatment, a pulsed beam of about 100 μ sec wide was injected into the ring.

INTRODUCTION

Based on the achievements of PoP FFAG(Fixed Field Alternating Gradient), the project to construct a 150MeV proton FFAG started in 2000[1]. The project aims to build a prototype of FFAG synchrotron for a practical usage and to investigate the possibilities of FFAG for various applications such as proton beam therapy[2].

OVERVIEW OF 150MEV FFAG

The main parameters of the 150MeV FFAG are summarized in Table 1, and Figure 1 shows the schematic layout of the accelerator. Compared to the PoP FFAG, in the 150MeV FFAG, two technical challenges are to be tried. One is the employment of the yoke free magnet for the FFAG magnet[2]. The employment of the yoke free magnet is expected to make the beam injection and extraction easier than the case of the conventional FFAG triplet magnet. The other challenge is the beam extraction from the ring. The completion of them should be a milestone for a practical FFAG accelerator.

Table 1: Main Parameters of 150MeV FFAG

Type of Magnet	Triplet Radial (DFD)
Num. of Sector	12
k-value	7.6
Beam Energy (MeV)	12→150 (proton)
Average Radius (m)	4.47→5.20
Betatron Tune	Hor. 3.69~3.80 Ver. 1.14~1.30
Maximum Field (T) (on orbit)	Focus 1.63 Defocus 0.78
Repetition (Hz)	250

*yokoi@post.kek.jp

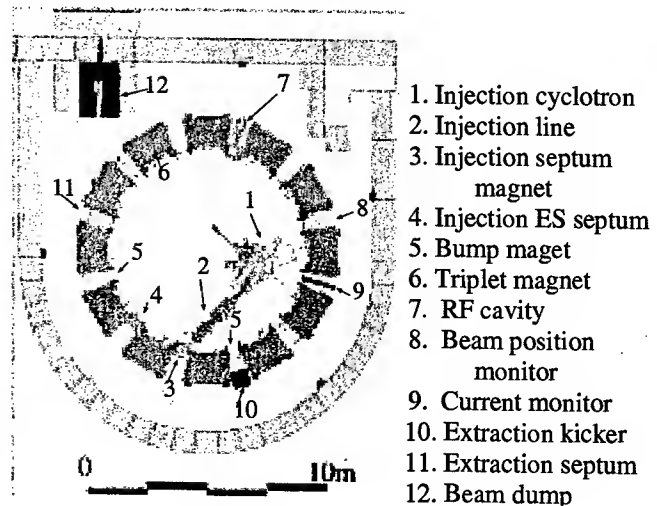


Figure 1: Schematic view of 150MeV FFAG

CONSTRUCTION

The construction of the 150MeV FFAG has started in September 2002 at the east counter hall in KEK, and almost completed in March 2003. Figure 2 shows a picture of the 150MeV FFAG ring and the injection cyclotron.

In the construction of the accelerator, one of the most important issues is careful alignment of the accelerator elements, especially of the sector magnets. From beam tracking simulation, it was found that the misalignment of magnet position should be suppressed below 0.5mm in order to avoid a serious COD.

To achieve such an accuracy, magnet alignment with laser theodolites was carried out. After the alignment, it was found that the positioning accuracy of the markers for the magnet alignment was below 0.2mm. From the accuracy, the final accuracy of the magnet position is expected to be below 0.5mm. This is within a satisfactory level for the

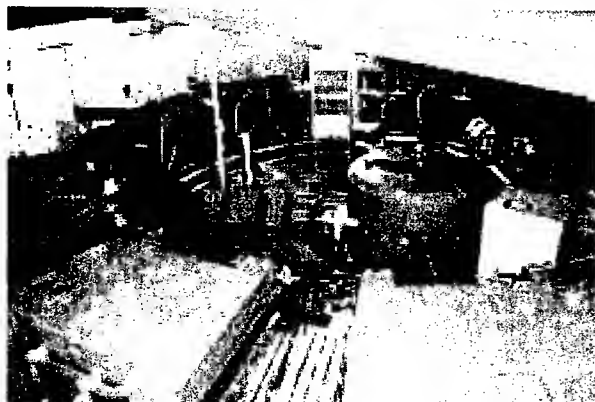


Figure 2: 150MeV FFAG ring and injection cyclotron

initial stage of the commissioning. The final, more precise, alignment will be done using a laser tracking system in this summer.

As the radiation shield, concrete shield walls covers the accelerator. The thickness of the shield is 1m for the side wall and 0.5m for the ceiling. Even with these shields, the beam intensity of 40nA is allowed.

COMMISSIONING

After the construction of the ring was completed, the beam commissioning has started. In the commissioning, the first thing to be done is to beam injection. Figure 3 shows the injection orbit of the 150MeV FFAG and the location of the elements for the beam injection.

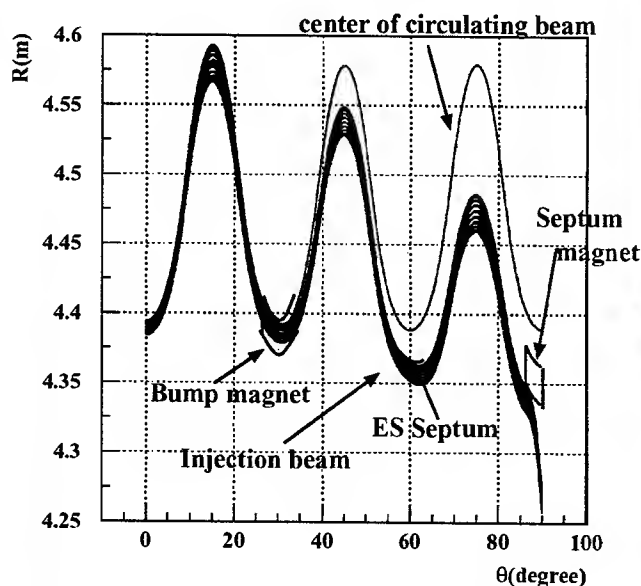


Figure 3: Injection Orbit of 150MeV FFAG

Three elements are installed for the beam injection. Those are, from upstream, injection septum magnet, injection electrostatic(ES) septum and a pair of bump magnet. Required field strength of the injection septum magnet is 1 Tesla for 10MeV injection, and for the ES septum, 35kV/cm. The required field of the bump magnet is 300 gauss and it decays with the time constant of $5\mu\text{sec}$. With these apparatus, the multi-turn injection with phase space painting for 10 turns is capable.

To find out the injection condition, the beam position was measured by a Faraday cup from the upstream of the injection orbit. For each step, the field strength of the septum magnet and the setting of injection beam line was tuned so that beam passed through the correct position with maximum intensity.

Finally, after tuning the injection condition by measuring the beam position at the bump magnet, the circulating beam of one turn was observed with the Faraday cup installed outside of the injection septum magnet. In this time, to measure the beam position at the bump magnet, in the position of the bump magnet, a Faraday cup was installed and the bump magnet itself was not installed. Figure 4 shows the signal observed with the Faraday cup. It should be noted that the beam intensity after one turn was almost the same as that observed at the position of the bump magnet. That means there observed no beam loss along one turn.

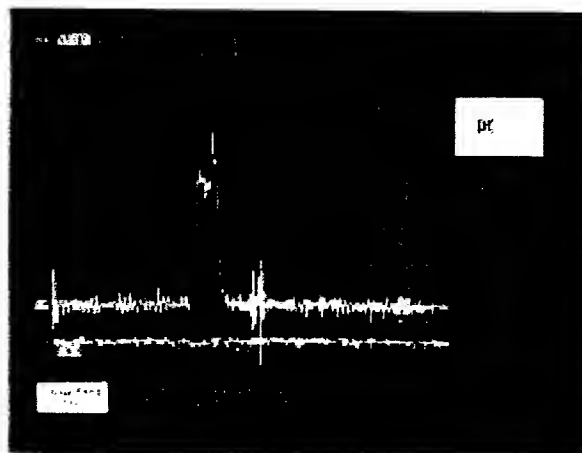


Figure 4: Beam signal observed by Ring Faraday Cup at the point of 1turn

From the result, we found that the FFAG magnet and the injection system are working mostly as expected.

The beam commissioning is still going on intensively. The next step is to install the bump magnet and to accelerate the beam. The preparation for the study is now under-going.

SUMMARY

The construction of the 150MeV FFAG was completed in March 2003. After that, the commissioning run is under going. Up to now, the circulating beam for one turn was successfully observed.

REFERENCES

- [1] Y. Sato et al. 'Development of a FFAG proton synchrotron', Proceedings of EPAC 2000, p.299.
- [2] M. Aiba et al., 'A 150MeV FFAG with return-yoke free magnet' Proceedings of PAC 2001

STRIPPER FOIL TEMPERATURES AND ELECTRON EMISSION AT THE LOS ALAMOS PROTON STORAGE RING*

T. Spickermann†, M. Borden, A. Browman, D. Fitzgerald, R. Macek, R. McCrady, T. Zaugg,
Los Alamos Neutron Science Center, LANL, Los Alamos, NM 87545, USA

Abstract

We have modeled the heating process of the PSR stripper foil and compared our results to observations that depend on the foil temperature. The foil is heated by the energy deposited by injected H⁺ ions and stored protons passing through the foil. Secondary emission of electrons due to these foil hits results in a measurable current that we can use to benchmark our model. At higher beam intensities thermionic emission of electrons dominates the foil current. Due to the extreme temperature dependence of the thermionic current this is a very sensitive indicator of the foil temperature and will be used to safeguard against overheating the foil in extreme beam conditions. We will present our best estimates of the foil temperature for different beam intensities.

SIMULATION OF FOIL HEATING

To inject protons into the Proton Storage Ring (PSR) H⁺ ions with a kinetic energy of 800 MeV pass through a carbon foil [1], typically of an area density of 400 µg/cm², where the two electrons are stripped off. Injection pulse lengths are typically of the order of a millisecond, or several thousand turns of 359 ns duration. Injection is "off-axis", i.e. off the closed orbit in the ring ("On-axis" injection is occasionally used during beam studies). A four-magnet vertical closed orbit bump is used to "paint" the injected beam over the available phase space in the ring to reduce space charge effects and to reduce the number of foil hits by the circulating beam. The stripper foil position is adjusted to cover about 97-98 % of the injected beam. Totally covering the injected beam would approximately double the number of foil hits by the circulating beam and consequently double the beam loss rate. Observing the stripper foil with a video camera shows bright flashes during the accumulation cycle, indicating that the foil gets "red-hot". Presently installed equipment does not allow, however, measurement of the foil temperature with any precision. Instead, we use the ORBIT [2] code to simulate the accumulation and storage of protons in the PSR. This provides us with the number of foil hits per time. Each circulating proton hits the foil about 30-80 times (depending on beam conditions) during the accumulation cycle. The average energy deposited per foil hit can be obtained from stopping power tables [3].

* Work conducted at the Los Alamos Laboratory, which is operated by the University of California for the United States Department of Energy under contract W-7405-ENG-36.

† Email: spickermann@lanl.gov

FOIL CURRENT

While we lack a direct measurement of foil temperature we do measure the foil current. Figure 1 shows the measured current for a final beam charge of 8.7 µC injected over 1225 µs.

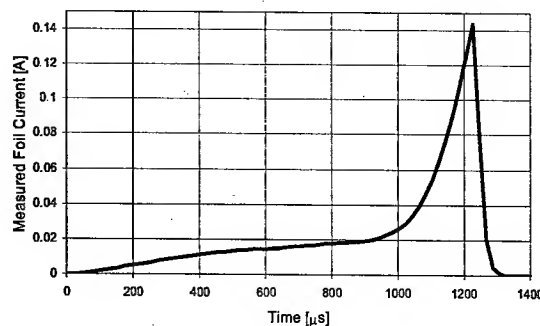


Figure 1: Measured foil current. Beam is extracted immediately after injection at 1225 µs.

From start of injection to ~ 900 µs the current is dominated by secondary emission. It is therefore directly proportional to the total number of foil hits per time and can be used as a check on the ORBIT simulation. The secondary emission yield Y, i.e. the average number of electrons emitted per proton hitting the foil can be estimated with the Sternglass formula [4]:

$$Y = \frac{P d_s}{E_*} \cdot \frac{dE}{dx} \quad (\text{per surface}),$$

where P is a probability (~ 0.5), d_s is the average depth from which secondaries arise (~ 1 nm) and E_{*} is the average amount of kinetic energy lost by a proton per ionization (~ 25 eV). Here, dE/dx is in eV/nm. At t > 900 µs thermionic emission (TE) becomes the dominant contributor to the foil current.

ENERGY EQUATION

To calculate the maximum temperature we have divided the foil area in the model into bins of 1.5 · 1.5 mm². The peak temperature in the "hottest bin", i.e. the bin with the maximum number of hits can be calculated by solving the energy equation

$$\Delta E \frac{dN_{\text{hits}}}{dt} = \rho V c(t) \frac{dT}{dt} - 2A \epsilon \sigma (T^4 - T_{\text{amb}}^4) - 2A J_{\text{TE}}(A_R, \phi, T) \cdot \left(\phi + \frac{2kT}{q} \right) \quad (1)$$

Table 1 shows the variables used in Eq. 1.

Table 1:

Var.	Value	Description
ρ	2.0 g/cm ³	Density of carbon
c	function of temperature	Heat capacity of carbon
σ	$5.67 \cdot 10^{-8} \text{ J/(s m}^2 \text{ K}^4)$	Stefan-Boltzmann constant
ϵ	0.8	Emissivity
q	$1.602 \cdot 10^{-19} \text{ C}$	Electron charge
A_R	120 A/K ² cm ² (theoretical value)	Richardson constant
ϕ	~ 4.5 eV	Work function
k	$1.38 \cdot 10^{-23} \text{ J/K}$	Boltzmann constant
ΔE	825 eV	Energy deposited per hit
N_{hits}	function of time	Number of hits in bin
A	2.25 mm ²	Area of one bin
V	$4.5 \cdot 10^{-3} \text{ mm}^3$	Volume of one bin
T_{amb}	297 K	Ambient temperature
J_{TE}	Function of temperature	Thermionic current density

Cooling via heat conduction was not included in the calculation. However, solving the heat equation for a simplified geometry shows that conduction would lower the peak temperature by less than 1%.

Foil Heating

From the ORBIT simulation we obtain the number of hits per turn to which we fit a piecewise linear function to obtain the number of hits as a function of time. The simulation also tells us where on the foil each hit occurs. This allows us to divide the foil into bins and to calculate the number of foil hits in each bin. Multiplied with the average energy deposit per foil hit ΔE this gives the energy deposited per time for each bin.

Heat Capacity

The heat capacity of carbon is a strong function of temperature [5,6]. This must be taken into account when solving the energy equation. The sharp increase of the heat capacity with temperatures above room temperature (297 K) results in a slower rise in the foil temperature, but also in a slower cooling process after beam extraction.

Thermionic Emission

Thermionic Emission is expected to play a role at extreme foil temperatures, due to the very strong temperature dependence of thermionic currents. The thermionic current density can be calculated as

$$J(A_R, \phi, T) = A_R T^2 e^{\frac{-\phi}{kT}}$$

The power dissipated by thermionic emission is given by [7]

$$\frac{dE_{\text{TE}}}{dT} = 2A \cdot \left(\phi + \frac{2kT}{q} \right) \cdot J_{\text{TE}}(A_R, \phi, T).$$

PEAK FOIL TEMPERATURES

Solving the energy equation Eq. 1 is an iterative process because some parameters are not well known, e.g the number of foil hits, which depends on the exact foil position with respect to the injected beam, or the parameters that go into the calculation of the thermionic current. These have to be adjusted to obtain the best possible agreement between the measured foil current and the current calculated as the sum of secondary emission and thermionic emission currents. Figure 2 shows a comparison between a measured current and the current obtained from the model for a beam intensity of 8.7 $\mu\text{C/pulse}$ injected over 1225 μs with a pulse repetition rate of 4 Hz.

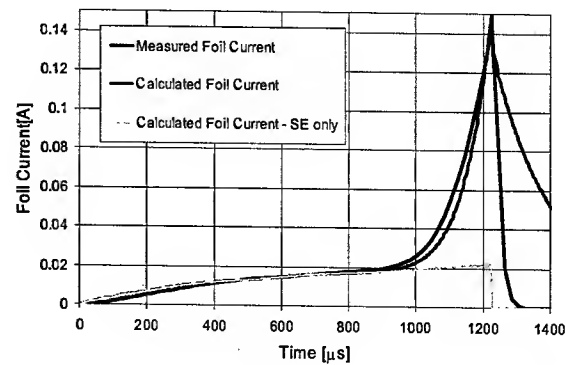


Figure 2: Comparison of measured and calculated foil currents.

The TE current was calculated with $\phi = 4.5 \text{ eV}$ and $A_R = 2.2 \text{ A/(cm}^2 \text{ K}^2)$. Better agreement between the measured and calculated currents could be achieved with lower values for the work function ϕ , but these are not supported by literature. One also notices that after beam extraction the measured current drops much faster than the calculated one. We believe that this may be due to space charge built up around the foil by TE electrons as these are no longer removed by the strong potential of the circulating beam. We plan to test this hypothesis in the coming run period by biasing the foil. One should note that, unless the measured current is from the very first injected beam pulse, one has to solve the energy equation for consecutive pulses and cool down times (given by the pulse repetition rate) because the initial foil temperature on subsequent pulses will be higher than the ambient temperature. For this case we calculate a maximum temperature of 3122 K in the hottest bin in the foil. Neglecting thermionic emission yields a value only ~1 K

higher. Although it may dominate the foil current, TE is not a significant source of cooling for the foil.

Peak Temperatures for Production Beams

With the parameters of the simulation and calculation adjusted one can compute the foil temperature for different beam conditions. Figure 3 shows the temperature in the hottest bin for a production beam, i.e. 125 μA with a pulse repetition rate of 20 Hz and for beam conditions expected in a potential upgrade, i.e. 200 μA at 30 Hz. Although the beam intensities are not too different (6.25 $\mu\text{C/pulse}$ vs. 6.7 $\mu\text{C/pulse}$) the higher repetition rate leads to a significantly higher peak temperature.

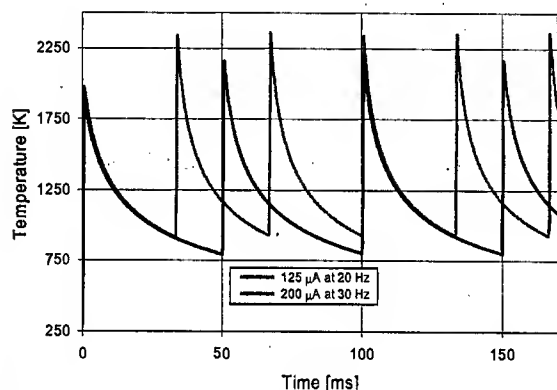


Figure 3: Temperatures in hottest bin for a production-type beam and for a planned upgrade.

The peak temperatures are 2182 K for the production-type beam and 2361 K for the upgrade. Both peak temperatures are well below the sublimation temperature of carbon of about 4000 K.

Extreme Beam Conditions

Figure 4 shows the measured foil current for a beam intensity of 5.2 $\mu\text{C/pulse}$, injected over 625 μs . The storage time was increased from 0 μs (no storage) to 400, 600 and 800 μs . Consequently, the number of foil hits and the foil temperature were also increased. The measured foil current is very sensitive to the increase in foil temperature and is thus a valuable monitor of the strain put on the foil by extreme beam conditions.

We also deliberately damaged the foil by increasing the storage time to 1200 μs . There the TE current was about 25 times higher than the SE current. For these conditions we calculate a peak temperature in the hottest bin of about 4000 K, i.e. the sublimation point of carbon in vacuum. Thermionic emission in this case lowers that temperature by about 100 K. However, these numbers are preliminary as the calculation needs yet to be refined for this case.

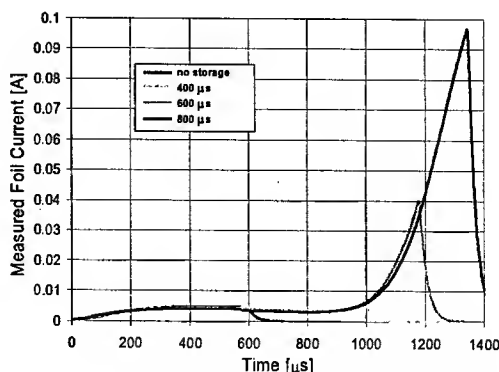


Figure 4: Measured foil current for different beam storage times.

CONCLUSION

Peak foil temperatures for PSR production beams (including future upgrades) are safely below the sublimation point of carbon.

At higher beam intensities or extended storage thermionic emission dominates the foil current, but does not seem to provide much additional cooling.

Thanks to the strong temperature dependence of TE monitoring the foil current can provide a very sensitive signal for safeguarding the foil from potentially severe beam conditions.

Improvements can be expected from a better understanding of the measured signals and refinements to the model and calculations.

REFERENCES

- [1] M. Borden et al., "Carbon Stripper Foils Used in the Los Alamos PSR", Proceedings of PAC 1997.
- [2] J. D. Galambos et al., "The ORBIT User's Manual", <http://www.sns.gov/APGroup/Codes/orbit.htm>.
- [3] National Institute of Standards and Technology, <http://physics.nist.gov>.
- [4] J. E. Borovsky and D. M. Suszcynsky, "Experimental Investigation of the z^2 Scaling Law of Fast Ion-produced Secondary Electron Emission", *Physical Review A*, Volume 43, Number 3, page 1416 (1991).
- [5] A.T. Dinsdale, "SGTE Data for Pure Elements", *CALPHAD* 15, 317-425 (1991).
- [6] High temperature data from "Thermophysical Properties of Matter - Nonmetallic Solids", TPRC Data Series.
- [7] B. C. Lough et al., "Numerical Calculation of Thermionic Cooling Efficiency in a Double-Barrier Semiconductor Heterostructure", *Physica E* 11 (2001) 287-291.

TESTING AND COMMISSIONING OF THE ALS ADJUSTABLE, HYSTERESIS-FREE CHICANE MAGNET

J. Y. Jung, S. Marks, R. Schlueter, LBNL, Berkeley, CA 94720 USA

Abstract

The magnetic performance and commissioning of a new Advanced Light Source (ALS) chicane magnet are presented. The new magnet is iron free using permanent magnet rotors and trim coils, resulting in hysteresis-free operation. The theory and method for magnetic adjustments are discussed. Results of adjustments are presented that produce a maximum dipole field and reduce unallowed harmonics to below the required level of $|b_n/b_1| < 3 \times 10^{-3}$.

INTRODUCTION

Chicane magnets are used in Advanced Light Source (ALS) straights where two insertion devices are installed. The chicane provides an approximately 2.5 mrad angular separation between the two photon fans. A new iron free chicane magnet has been installed which employs a ring of counter-rotating permanent magnet pairs to create an adjustable dipole field for operation between 1.5 and 1.9 GeV. A previous iron core chicane magnet did not achieve the required precision for fast steering corrections due to magnetic hysteresis.

The theory and design of the new chicane have been previously reported [1, 2]. This paper presents the concepts and results of the procedure for magnet adjustments to maximize dipole and minimize unallowed multipoles.

Summary of Magnet Features

The chicane magnet design is iron free to eliminate magnetic hysteresis. Fig. 1 shows the magnet tuners and coil configuration. Coils are used for fast feed back steering correction. The primary field is provided by six NdFeB permanent magnet (PM) pairs. A cylindrical pair consists of two coaxial cylindrical magnets oriented parallel to the beam axis. The magnetic orientation is perpendicular to the axis. Two cylinders can be counter rotated to adjust the effective strength of the pair. Each magnet is enclosed in an aluminum case. The total magnetic length of a pair, L , is 7 cm (each magnet is 3.5 cm). The six magnet pairs are equally spaced in azimuth. A system of two chain drives with independent micro-stepping motors and encoders connects six rotor sets to control cylinder pair counter rotation. Chain sprocket clamps are used at each rotor to allow for relative orientation adjustment. After final adjustments, the clamps are spot welded to the sprockets to hold them permanently. The drive system insures that changes in counter rotation is the same for each cylinder pair.

Requirements

Table 1 shows the integrated dipole fields corresponding to a 2.5 mrad bend for the storage ring

operating energies of 1.5 and 1.9 GeV. The required multipole tolerance is $|b_n/b_1| < 3 \times 10^{-3}$. The required fast feed back correction of magnitudes are $\pm 2 \times 10^{-4}$ T-m for vertical steering and $\pm 7 \times 10^{-5}$ T-m for horizontal steering.

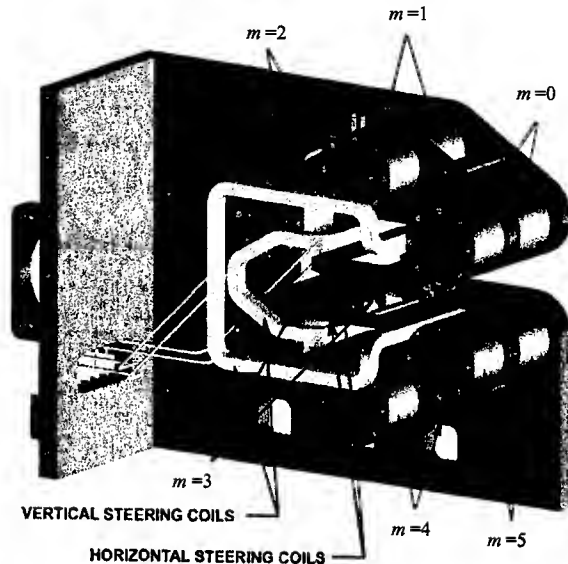


Figure 1: Chicane magnet tuners and steering coils

Table 1: Integrated dipole field corresponding to 2.5 mrad

Beam (GeV)	Integrated Dipole field (T-m)
1.5	1.251×10^{-2}
1.9	1.584×10^{-2}

Ideal Magnet Configuration

Table 2 shows the ideal dipole rotor configuration. Rotor azimuth relative to beam center is designated as β_m . Rotor angular magnetic orientation, or rotation, about the rotor center is designated as ϕ_m . The rotor number designation is shown in Fig. 1. Note that in this context a cylinder pair is designated as a rotor.

Table 2: Magnetic configuration

rotor, m	0	1	2	3	4	5
azimuth, β_m (deg.)	30	90	150	210	270	330
easy-axis orient., ϕ_m (deg.)	330	90	210	330	90	210

The ideal dipole configuration also generates allowed higher order multipoles. The multipole expansion of

magnetic field integral $I^*(z)$ for the corrector ring of rotors with M cylinder pairs spaced uniformly in azimuth with pairs counter rotated $\pm\eta$ is

$$I^*(z) = \sum_{n=1}^{\infty} b_n z^{n-1}, \quad b_n = \frac{B_r L n r_c^2}{2R^{n+1}} \sum_{m=0}^{M-1} e^{-i(n+1)\beta_m + i\phi_m} \cos\eta_m \quad (1)$$

per Eq. 4, Ref. [1]. For the magnet considered here $M=6$, $L=7$ cm, rotor radius $r_c=2.03$ cm, and $R=7.5$ cm. Using these values in Eq. 1 with an assumed $B_r=1.2$ T, the maximum dipole is $b_1=i1.85 \times 10^{-2}$. The first two allowed multipoles are: $b_7/b_1=i3.69 \times 10^{-5}$ and $b_{13}/b_1=i3.85 \times 10^{-10}$ at reference radius $r_p=1$ cm. The dipole strength can be reduced relative to the maximum by a factor of $\cos(\eta)$, where η is the counter rotation angle of all cylinder pairs.

SOURCES OF ERROR

The above discussion pertains to the ideal device where perfect six fold symmetry is maintained. Deviations from symmetry will result in a reduction in dipole strength as well as the introduction of new higher order multipoles. In particular, nonuniformity in the either the magnetic strength or length of rotors will result in errors. Backlash in the drive system will result in orientation and counter rotation errors.

Perturbations to the magnetic structure can be considered in the context of Eq. 2 below, per Eq. 19, Ref [1].

$$\delta P \frac{dI^*(z)}{dP} = \sum_{n=1}^{\infty} \left\{ g_n \left(\frac{r_p}{R_m} \right)^{n-1} B_{r_m} L_m \left(\frac{r_{cm}}{R_m} \right)^2 \right\} e^{i(\phi_m - (n+1)\beta_m)} \left(\frac{z}{r_p} \right)^{n-1} \quad (2)$$

The kernel, g_n , is specific to the particular error type. We will consider three error types, tabulated below with the specific kernel definitions.

- Strength errors: $g_n = (n/2)(\delta B_r/B_r)$,
- Orientation errors: $g_n = (n/2)\delta\phi_m$,
- Counter rotation errors: $g_n = (n/2)\delta\cos\eta_m$.

For example, consider a 1% perturbation, due to either $\delta B_r/B_r$, $\delta\phi_m$ or $\delta\cos\eta_m$, at rotor $m=0$. This will result in an integrated dipole error of $\delta I^*/|I^*|=0.002$, and a quadrupole error of $\delta I^*/|I^*|=0.002-0.003i$

MEASUREMENT RESULTS

To maximize the dipole and minimize unallowed multipoles, each rotor is first carefully adjusted to the orientation ϕ_m given by Table 2, with counter rotation $\eta_m=0^\circ$. Using a rotating field measurement coil, the multipoles are measured. Adjustments and measurements are iterated until the maximum dipole field is achieved.

The measured maximum dipole field, 1.78×10^{-2} T-m is 3.4% less than the analytical expectation, as given above. This difference can arise from an inaccurate B_r assumption, the deviation from unity of dB/dH in the permanent magnet, or from measurement inaccuracy.

Over the range of interest of strength variation, corresponding to $25^\circ < \eta < 45^\circ$, it was found that the largest error term was the skew quad, which assumed its largest normalized value $B_2/C_1 = 3 \times 10^{-3}$ at $\eta = 40^\circ$ (See Table 3, left half). An advantageous feature of the PM ring is that unallowed harmonics may be nulled via slight adjustments of rotor orientations and counter rotations, so as to add vectorially to the existing magnetization vectors a new [e.g. skew quad] multipole contribution that is the negative of the existing error term.

This could effectively be a superposed Halbach six element PM quadrupole [3] per Eq.8, ref [1] with higher harmonics $n=8, 14$, etc. Though such a set of vectoral additions would themselves be symmetric, application to the exiting dipole configuration orientation would entail slight adjustments in both $\delta\phi_m$ and $\delta\eta_m$ unique to each individual rotor pair. Moreover, these are of the same order of magnitude as the orientation accuracy of the cylinders, which makes their adjustment a delicate task.

Table 3: Normalized multipoles before and after nulling the skew quadrupole at $\eta = 40^\circ$. Dipole strength $C_1/r_p = 1.31 \times 10^{-2}$ T-m before and 1.33×10^{-2} T-m after nulling.

N	Before ($\times 10^{-3}$)		After ($\times 10^{-3}$)	
	A_n/C_1	B_n/C_1	A_n/C_1	B_n/C_1
2	-1.57	-9.92	0.87	-1.37
3	-3.52	2.35	-1.86	0.51
4	0.72	1.98	-0.03	0.55
5	-0.81	0.67	-0.33	-0.13
6	0.48	0.08	0.21	-0.02
7	-0.05	0.33	0.06	0.12

Alternatively, the skew quad can be modulated as shown below, utilizing only equal counter rotations $\delta\eta_m$ of perturbed cylinder pairs 1&4 and/or pairs 0,2,3,&5 with existing orientations $\delta\phi_m$ unchanged.

Nulling the skew quad with magnetization perturbations ϵ_1 via identical counter rotations of cylinders in pair $m=1$ and in pair $m=4$ and/or perturbations ϵ_2 for identical counter rotations of pairs $m=0, 2, 3$ and 5 as shown in Fig. 2 generates a [skew] quadrupole (Eq. 1):

$$b_2 = \sum_{m=0,4} b_{2|m} + \sum_{m=0,2,3,5} b_{2|m} = 0.14 \epsilon_2 - 0.14 \epsilon_1 \quad (3)$$

Perturbation adjustments can be iterated to fully null the resultant skew quadrupole term at the energization excitation strength corresponding to the initial $\eta = 40^\circ$. Higher order harmonics introduced, $n = 4, 6, 8$ etc. are smaller in magnitude.

$$I^*(z) = \sum_{n=1}^{\infty} i \frac{n C_n}{r_p} \left(\frac{z}{r_p} \right)^{(n-1)}, \text{ where } C_n \equiv A_n + i B_n \quad (4)$$

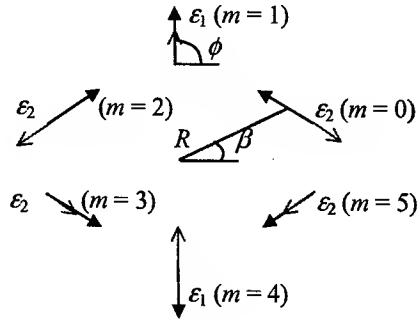


Figure 2: Skew quad nulling scheme, with field with design dipole orientation shown with red arrows and the nulling magnetization perturbations show in black.

Table 3 shows normalized multipoles before and after adjustment at $r_p = 1$ cm, $\eta = 40^\circ$ where integrated field, $I^*(z)$ (Eq. 4). As can be seen, after the adjustment the normalized skew quadrupole B_2/C_1 meets the requirement as well as other higher multipoles. For $n = 7$, $b_7/b_1 = i5.901 \times 10^{-5} - 1.230 \times 10^{-4}$ which is higher than the expected design value $b_7/b_1 = i3.933 \times 10^{-5}$ by Eq. 1. Part of the reason is because the measurement accuracy including electronic noise ($\sim 5 \times 10^{-6}$ T-m) is the order of 1×10^{-5} T-m.

Table 4 shows normalized multipoles at $\eta = 25^\circ$, corresponding to a 2.5 mrad kick at ~ 1.5 GeV operation, before and after adjustment. All multipoles meet the requirement after adjustment.

Table 4: Normalized multipoles at $\eta = 25^\circ$ before and after the $\eta = 40^\circ$ skew quadrupole nulling. The dipole $C_1/r_p = 1.58 \times 10^{-2}$ T-m before and 1.60×10^{-2} T-m after nulling.

N	Before ($\times 10^{-3}$)		After ($\times 10^{-3}$)	
	A_n/C_1	B_n/C_1	A_n/C_1	B_n/C_1
2	-1.48	-4.95	0.39	-1.52
3	-3.88	2.19	-2.24	0.85
4	0.88	1.85	0.05	0.69
5	-0.89	0.61	-0.22	-0.08
6	0.35	0.14	0.23	-0.07
7	0.04	0.41	0.03	0.01

More exactly, It is found that 2.5 mrad kick at 1.9 GeV can be obtained at 26.1° of counter rotation, while 43.9° produces the same kick at 1.5 GeV. Table 5 shows normalized multipoles at counter rotations $\eta = 0^\circ$, where the dipole field is maximized.

During the counter rotation from $\eta = 0^\circ$ to $\eta = 90^\circ$, the chain slack/backlash reduces the reproducibility of the magnetic field around $\eta = 90^\circ$.

There are some limitations for adjusting tuners. Sprockets are rotated by wrench. Since the wrench is not perfectly fit to the sprockets, it generates about 1° error which is acceptable. Instead of using a chain driving system for counter rotation of magnets, motors can be directly attached to the tuners so that each tuner can be adjusted by the motor. This driving system may have electronic noise problem due to motors and motor drives. Motor drives for operating counter rotation of the tuners generate the noise to the measurement system. This noise can affect and interrupt the measurement. But in the current operation, since the motor drives are far from the magnets, there is no noise problem of motor drives.

Table 5: Normalized multipoles at $\eta = 0^\circ$. Dipole strength $C_1/r_p = 1.78 \times 10^{-2}$ T-m.

n	$A_n/C_1 \times 10^{-3}$	$B_n/C_1 \times 10^{-3}$
2	0.66	-3.64
3	-2.92	1.46
4	0.15	0.59
5	-0.36	-0.17
6	0.16	-0.09
7	0.13	0.10

CONCLUSION

After the magnetic adjustment of rotors, the new hysteresis-free chicane magnet can generate the required dipole field. Also, the multipoles of the magnet meet the requirement. The existing iron core chicane magnet is replaced with the new iron free chicane magnet.

ACKNOWLEDGEMENT

This work was supported by the Director, Office of Energy Research, Office of Basic Energy Sciences, Materials Sciences Division, of the U. S. Department of Energy, under Contract No. DE-AC03-76F00098.

REFERENCE

- [1] R. D. Schlueter, D. Humphries, J. Tanabe, Pure Permanent Magnet Harmonics Corrector Ring, Nuclear Instruments and Methods in Physics Research A 395 (1997) pp.153-158
- [2] S. Marks, R. Schlueter, D. Anderson, W. Gath, J. Y. Jung, D. Robin, C. Steier, T. Stevens, New Chicane Magnet Design for Insertion Device Straights at the Advanced, Light Source, IEEE Transactions on Applied Superconductivity, Vol. 12, No. 1 (2002) pp.153-156
- [3] Halbach, K, Design of Permanent Multipole Magnets with Oriented rare Earth Cobalt Material, Nuclear Instruments and Methods 169 (1980).

SDDS-BASED SOFTWARE TOOLS FOR ACCELERATOR DESIGN*

M. Borland, L. Emery[†], H. Shang, R. Soliday, ANL, Argonne, IL 60439, USA

Abstract

The Self-Describing Data Set (SDDS) file protocol is a standardized way to store and access data and is the basis of an extensive toolkit. It is also the file protocol used for many accelerator design tools. Over the years, several of these SDDS-compliant accelerator programs (e.g., *clinchor*, *elegant*, *estat*, *shower*, and *spiffe*) have been developed at the Advanced Photon Source. Also, existing accelerator design tools for which the source code is available (e.g., ABCI, GENESIS, GINGER, MAFIA, and URMEL) have been converted to read and write SDDS files. As a result, we now have a capable set of accelerator codes that make use of the same data format and the same pre- and postprocessing suite. Further, the SDDS toolkit program *sddsoptimize* can be used around any of these tools or around a script that runs one or more of these tools. This provides the capability of very general, multicode optimization. In this paper, we discuss the capabilities of the existing SDDS-compliant accelerator codes, then provide examples of applications of these tools.

INTRODUCTION

The accelerator field is well supplied with simulation codes. Accelerator designers frequently need to make use of codes by many authors, developed in different programming languages. Although this need is common, it is usually not easy to integrate the results of these codes. Part of the reason for this is that codes do not share a common, stable data protocol. Instead, each code (or group of codes) has a custom data protocol that may change from one version to the next. Another reason is that each code has its own pre- and postprocessor, which typically don't recognize data from other codes.

This means that integration of two or more codes requires writing a custom translation program. Such translators tend to be fragile as the developers of the simulation code don't support them and may change their protocols without notice in new code versions. This fragility is largely due to the widespread failure to use robust self-describing data protocols.

At APS, we developed a common self-describing data standard [1] for used by codes and controls systems. This standard is called SDDS, for Self-Describing Data Sets. SDDS datasets, very briefly, consist of a header that describes the contents of the file, including names, data types, and units. The header describes a data structure containing parameters, a table, and arbitrarily-dimensioned arrays.

Access to data in SDDS files is *by name only*. This is the key feature for a robust protocol.

In addition to requiring accelerator codes to read and write SDDS files, we created a suite of data processing and display tools that work with SDDS files. In effect, we created a common pre- and postprocessing toolkit that is used by our codes and codes we have modified. This set of approximately 80 generic programs is referred to as the SDDS Toolkit [1].

As indicated, a major advantage of using SDDS files is that data from any code can be used with any other code. This is robust due to the use of SDDS files, meaning that one code can be upgraded without requiring a change of the other code. In addition, with SDDS it is straightforward to process and display data from several codes together. The SDDS Toolkit also provides the ability to make transformations of data, which is useful when codes have different conventions (e.g., for phase-space quantities). Finally, using SDDS means that adding capabilities to a simulation code is faster and easier. The new data is simply placed in SDDS files where it can be accessed with the existing suite of tools.

In addition to the SDDS Toolkit, users can import SDDS data directly into programming environments like C/C++, FORTRAN, IDL, Java, MATLAB, and Tcl/Tk, using libraries created and supported by APS. These libraries, like the rest of the SDDS software and our simulation codes, are covered by an Open Source license and available for download from our web site. The codes discussed are all available for UNIX environments, including LINUX, Solaris, and MAC OS-X, and also (usually) for Windows.

SDDS-COMPLIANT CODES AND THEIR CAPABILITIES

In this section, we briefly review the capabilities of some of the existing SDDS-compliant codes. We also attempt to briefly indicate how these codes can be used together. Detailed examples of this will appear in the next section.

General Accelerator Simulation with elegant

The program *elegant* [2] was the first of the SDDS-compliant accelerator codes. Because it performs general-purpose accelerator simulation, it is at the center of the SDDS-compliant code set. *elegant* performs optics calculations, errors and lattice correction, various types of particle tracking, and many other functions. Multidimensional scans may also be performed.

In addition, *elegant* provides a general-purpose optimization capability that may be unique: the user-defined

* Work supported by U.S. Department of Energy, Office of Basic Energy Sciences under Contract No. W-31-109-ENG-38.

[†] emery@aps.anl.gov

penalty function may include the usual quantities such as Twiss parameters and matrix elements (at any point in the system), but also quantities like the equilibrium emittance or momentum compaction. In addition, properties (e.g., centroids, beam sizes) of tracked particle distributions may be optimized.

Besides the typical beamline optical components, *elegant* provides some unusual elements. These simulate various collective effects, such as longitudinal and transverse short-range wakefields (or impedances), longitudinal and transverse resonator impedances, coherent synchrotron radiation, and intrabeam scattering. There are also time-dependent elements such as rf cavities, rf deflectors, kickers, and single-bunch digital feedback.

The *SCRIPT* element allows the user to add a custom-defined element for tracking in *elegant* by specifying an external program that is used to transform the beam distribution. The program must be *SDDS*-compliant. For noncompliant programs, a wrapper script must be written to translate between *SDDS* and the program's unique data format. Such scripts are easily written using the *SDDS* Toolkit, which features several programs (*sddsprintout*, *sdds2stream*, and *sdds2plaindata*) designed to convert *SDDS* data into plain ASCII or binary data.

Specialized Tools for Use with elegant

As mentioned above, the generic *SDDS* Toolkit can be used to process and display data from *SDDS* files produced by *elegant* or any other *SDDS*-compliant code. In addition, there are some specialized *SDDS* tools that are designed to support or work with *elegant*. Of course, they can be used with other *SDDS*-compliant codes as well.

ibsEmittance — Computes intrabeam scattering (IBS) growth rates using Twiss parameter data from *elegant*. The algorithm is based on an improved version of IBS code in the program *ZAP* [3]. **ibsEmittance** will also compute transverse and longitudinal emittance evolution by integrating the differential equations for the emittances. Growth rates are recomputed as the emittances change.

sddsanalyzebeam — Analyzes particle distributions produced by *elegant* or other codes that use the same naming convention. Output includes Twiss parameters, emittance, and beam sizes. Output can be used as input to Twiss parameter propagation in *elegant*.

sddsbrightness — Computes undulator brightness curves using Twiss parameter and emittance data from *elegant*. Supports several methods, from very simple estimates to full-blown calculations based on the program *xop* by Dejus [4].

sddsemitmeas — Analyzes quadrupole scan data to find the sigma matrix of a beam. *elegant* is used to compute the transfer matrix of a beamline as one or more quadrupoles are varied. **sddsemitmeas** uses this data along with beam size data from simulation or experiment to determine the sigma matrix. Error analysis is included.

sddsmatchtwiss — Performs phase-space transformations of particle distributions. For example, the beta functions can be changed to match a beam into a simulation even if the matching optics haven't been developed yet. **sddsmatchtwiss** will also take output of *elegant* Twiss computations or *sddsanalyzebeam* computations to specify which Twiss parameters to match to the beam.

sddssasefel — Performs computations of self-amplified spontaneous emission free-electron lasers using the method of M. Xie [5]. The beam properties can be those computed by an *elegant* tracking run or prepared in some other fashion. Xie's method is also used internally to *elegant*, but **sddssasefel** has additional features such as optimization of parameters that are not specified in the input data.

sddsrandmult — Prepares data giving the multipole content of quadrupoles or sextupoles in the presence of various construction errors. This data is accepted by *elegant* for tracking (e.g., dynamic apertures).

Free-Electron Laser Simulation

As mentioned above, *elegant* performs a simple FEL calculation using M. Xie's parametrization, which gives a good estimate of FEL behavior. For more exact results, or to perform start-to-end simulations [6], the user needs to use an FEL code such as *GENESIS* [7] or *GINGER* [8]. At APS, we have modified *GENESIS* [9] to read and write *SDDS* files, making it easy to evaluate FEL performance for a given particle distribution from *elegant*. To do this, we made use of the existing *BEAMFILE* feature of *GENESIS*, which allows specifying centroid and rms properties of a series of independent beam slices. The necessary slice analysis is performed with the program *elegant2genesis* [9]. *GENESIS* can then simulate each slice in turn, producing *SDDS* files with radiation properties for each slice along the undulator. As discussed in more detail in [6], this data is readily associated with the input slice properties and the settings or errors in the accelerator, making quantitative understanding of slice-to-slice output variations possible. This is made easy by the fact that all the input and output data is in *SDDS* files. An *SDDS*-compliant version of *GINGER* has also been produced [10].

Other Codes

ABCI/APS — Our version of *ABCI* [11] produces an *SDDS* file giving the longitudinal or transverse wakes. These wakes can be used directly with the *WAKE* and *TRWAKE* elements, respectively, in *elegant*. These elements perform simulation of beam interaction with single-pass wakefields. If necessary, the output from *ABCI* can be processed with the *SDDS* Toolkit before using the data with *elegant*. This might be necessary, for example, to deconvolve the effects of nonzero bunch length in *ABCI*.

clinchor [12] — This program simulates single- or coupled-bunch instabilities driven by resonant modes. The

mode properties are taken from the SDDS output file generated by our version of URMEL (see below). Lattice information is taken from the `elegant` Twiss parameter output file.

`estat` [13] — This is a simple 2-dimensional electrostatic solver. Output from `estat` can be used in tracking with the `BMAPXY` element in `elegant`. This is a good example of a fairly small, simple code that becomes much more useful by virtue of the SDDS Toolkit (which obviates the need for a postprocessor) and interaction with `elegant`.

MAFIA/APS — We have modified the MAFIA version 2.04 [14] T3 calculator to write SDDS output of wake potentials. Program `mafiaTimeData` converts the T3 internal format file into several SDDS files of wakefield and electromagnetic field data. The field data from the frequency-domain solver are converted to SDDS by program `mafia2sdds`.

`shower` [15] — We developed an EGS4 [16] wrapper program called `shower` that simplifies use of the EGS4 electron-gamma shower simulation code. Instead of writing MORTAN macros, the user specifies the geometry using a simple text file. `shower` accepts input and output particle distributions in SDDS files. Hence, one can easily simulate interaction of an accelerator beam with matter and the subsequent behavior of shower products in the accelerator. Postprocessing to obtain dose rates is also straightforward with the SDDS Toolkit.

`spiffe` [13] — This is a 2.5-dimensional particle-in-cell code written at APS, intended for rf gun design. `spiffe` produces SDDS particle output files that are read directly by `elegant`. `spiffe` will use field profiles generated by URMEL/APS to impose cavity fields on the beam.

URMEL/APS — Our version of URMEL produces an SDDS file giving the on-axis field profiles for all modes. This data can be used with `spiffe` to simulate the accelerating mode of an rf gun, for example. URMEL/APS also produces a file giving the frequency, shunt impedance, and Q for each mode. This file can be used with the `FRFMODE` and `FTRFMODE` elements in `elegant`, which simulate longitudinal and transverse resonant cavity modes.

APPLICATION EXAMPLES

Here we briefly mention several applications of the above suite of simulation codes.

- `elegant` and `shower` were used to simulate beam losses and radiation production in the APS injector and ring, for evaluation of shielding design and radiation dose to undulators [15].
- `shower` was used as a part of an `elegant` beamline using the `SCRIPT` element for evaluation of a beam collimation system for the APS booster-to-storage-ring transport line.
- `spiffe` and `elegant` were used to simulate the APS thermionic rf guns, transport lines, and subsequent acceleration. These simulations helped to solve beam

transport problems with one of the rf guns that had prevented use of the gun for top-up.

- PARMELA, `elegant`, `sddsmatchtwiss`, `elegant2genesis`, and GENESIS were used for start-to-end jitter simulation [6] of the Linac Coherent Light Source [17]. PARMELA [18] and `elegant` were used to simulate the APS photoinjector.
- URMEL and `clinchor` were used to evaluate staggering of APS resonant cavity modes to avoid multi-bunch instabilities [12]. This work was done prior to the development of the SDDS system, but the codes have been made SDDS-compliant and are used for similar computations.
- MAFIA and `elegant` are being used for simulation of the bursting mode instability in the APS [19].
- `elegant` and `sddsemitmeas` are used to analyze emittance measurement quadrupole scans for APS linac experiments. The experiments are performed and analyzed by a Tcl/Tk script. Data collection is performed with the SDDS-compliant EPICS Toolkit [20].
- `elegant` and `sddsbrightness` are used to provide brightness curves for APS users, updated every 15 minutes.

REFERENCES

- [1] M. Borland, "A Self-Describing File Protocol for Simulation Integration and Shared Postprocessors," 1995 PAC, Dallas, Texas, 2184 (1996).
- [2] M. Borland, "elegant: A Flexible SDDS-Compliant Code for Accelerator Simulation," Advanced Photon Source LS-287, September 2000.
- [3] M. Zisman, PAC 1987, 991 (1988).
- [4] M. Sánchez del Río and R. J. Dejus, "XOP: Recent developments" SPIE proceedings 3448 (1998).
- [5] M. Xie, <http://epaper.kek.jp/p95/ARTICLES/TPG/TPG10.PDF>.
- [6] M. Borland *et al.*, PAC 2001, Chicago, 2707 (2002).
- [7] S. Reiche, NIM A 429, 242 (1999).
- [8] W.M. Fawley, LBNL CBP Tech Note-104 (1995).
- [9] Y. Chae and R. Soliday, PAC 2001, Chicago, 2710 (2001).
- [10] W.M. Fawley, private communication.
- [11] Y. Chin, PAC 1993, Washington D.C., 3416 (1994).
- [12] L. Emery, PAC 1993, Washington D.C., 3360 (1994).
- [13] M. Borland, private communication.
- [14] R. Klatt and T. Weiland, SLAC Report 202 (1986), Version 2.04.
- [15] L. Emery, 1995 PAC, Dallas, Texas, 2039 (1996).
- [16] W.R. Nelson *et al.*, SLAC 265, 1985.
- [17] "LCLS CDR," SLAC-R-593, April 2002.
- [18] J. Billen, Los Alamos National Laboratory report LA-UR-96-1835 (1996).
- [19] Y. Chae, "The Impedance Database and its Application to the APS Storage Ring," these proceedings.
- [20] H. Shang *et al.*, "New Features in the SDDS-Compliant EPICS Toolkit," these proceedings.

APPLICATION OF MODEL-INDEPENDENT ANALYSIS USING THE SDDS TOOLKIT*

L. Emery[†], Argonne National Laboratory, Argonne, IL 60439, USA

Abstract

The model-independent analysis (MIA) method in accelerators has not yet come into widespread use, unfortunately. This is perhaps due to a lack of convenient tools to bring the measurement data to the results stage. At the Advanced Photon Source, we used the SDDS Toolkit and the SDDS-compliant EPICS Toolkit in simple and not-so-simple applications for diagnosing operational problems from beginning to end in a short time. We were able to make quantitative measurements of pulsed power supply noise and beam position monitor noise, and identify an unstable power supply.

INTRODUCTION

Model-independent analysis (MIA) was introduced a few years ago as an implementation of Principal Component Analysis, a statistical analysis method that extracts essential signals from noisy but correlated sampled data [1]. MIA has been applied to the SLAC linear accelerator [1] and the PEP-II [2] and Advanced Photon Source (APS) rings [3] to identify spatial modes (trajectory-like patterns) in beam position monitor (BPM) data and their time dependence. Since this type of study involves both data acquisition and numerical analysis, it is natural to integrate these parts using the SDDS Toolkit [4] and the SDDS EPICS Toolkit [5].

This paper will give examples of the SDDS Toolkit implementation in quantifying some operational problems at APS. The theory of MIA has already been covered in [1], so we won't repeat it here. We'll simply give a description of the steps.

Using the notation of [6], we take P samples of M synchronized BPMs, $\mathbf{b}(t_p) = (b_p^1, b_p^2, \dots, b_p^M)$, and arrange the data as a matrix,

$$\mathbf{B} = \begin{pmatrix} b_1^1 & b_1^2 & \dots & b_1^M \\ b_2^1 & b_2^2 & \dots & b_2^M \\ \vdots & \vdots & \ddots & \vdots \\ b_P^1 & b_P^2 & \dots & b_P^M \end{pmatrix}. \quad (1)$$

Using singular value decomposition (SVD), this matrix \mathbf{B} is factored into a product of matrices $\mathbf{U}\mathbf{\Lambda}\mathbf{V}^T$, where the columns of \mathbf{U} and \mathbf{V} are orthonormal, and $\mathbf{\Lambda}$ is a diagonal matrix of positive eigenvalues or singular values (SV) with values λ_m , $m = 1, \dots, M$. The columns of \mathbf{V} , \mathbf{v}_m , are the spatial modes, or trajectory-like pattern modes. Typically for BPM data from a transport line or a ring, the most

two important modes (i.e., modes associated with the two largest SVs) are the sine-like and cosine-like trajectories. The columns of \mathbf{U} , \mathbf{u}_m , are the time patterns of each of the M trajectories (spatial modes). The length of the \mathbf{u}_m is the number of sample points, P . The pair of vectors \mathbf{u}_m and \mathbf{v}_m is referred to as the temporal-spatial mode m . Note that the inverse of \mathbf{B} is not used for anything.

The next step is to make an interpretation of the modes based on the value of their SVs or simply based on the appearance of the spatial or temporal part. Any sources of trajectory jitter (i.e., real trajectory, not readback noise) will show up as a temporal-spatial mode with a significant singular value. Because there is usually more BPMs than independent sources of trajectory jitter, the extra temporal-spatial modes represent BPM readback noise. Typically we do not know in advance how many sources of trajectory jitter there are, or equivalently, how many modes will be associated with BPM readback noise. A useful result of MIA [2] is that the SVs for the BPM readback noise modes are clustered at the bottom of the distribution of singular values. This allows the identification of the known sources of trajectory jitter and the quantification of the BPM noise for engineering purposes. If we discover more SVs above the noise floor than the expected number of independent sources, then some sources have been overlooked, and should be investigated.

SDDS TOOLKITS

It is crucial that the data in each row of the matrix \mathbf{B} belong to the same physical sample (i.e., same beam pulse) otherwise the analysis will produce unclear signals. Unfortunately, the EPICS control system at APS does not guarantee that BPM data collected from different input/output controllers (IOCs) will be synchronized. Typically we use the generic SDDS monitoring tool `sddsmonitor`, which collects data from several IOCs and write them to a file. For beam pulses of repetition rate 2 Hz or lower, the data written to the file is synchronized to the same beam pulse. For the higher repetition rate of 10 Hz, such as from the APS linac, the data is not synchronized. A more sophisticated monitoring tool `sddssynchlog` was written, which internally records the EPICS time-stamp data for each monitored quantity of a given time step. If the time-stamp data for a time step fall outside a specified time spread tolerance, then the data for the sample is discarded.

We use the SDDS Toolkit for the analysis of the \mathbf{B} data. Some data preparation is required, such as removing the average values and linear time trends, which is done by the polynomial fitting application `sddsmppfit`. The `sddspseudoinverse` application does the SVD decompo-

* Work supported by U.S. Department of Energy, Office of Basic Energy Sciences under Contract No. W-31-109-ENG-38.

[†] emery@aps.anl.gov

sition and produces the U and V matrices and a list of λ_m in SDDS files. `sddspseudoinverse` can also reconstruct the data with the modes of the largest SVs specified by the user. A Tc/Tk procedure using other toolkit applications can optionally remove BPMs from the original data after determining which ones are obviously bad or malfunctioning from a first-pass MIA analysis.

To further the MIA analysis, one can do particle trajectory simulations with the SDDS-compliant tracking code elegant [7] with beam jitter and BPM readback noise included. The simulated particle trajectories are analyzed the same way as the experimental data. The goal is to find the simulation parameters (e.g., the amplitudes of power supply and BPM noise) whose resulting λ_m spectrum best fit the experimental λ_m . When a match of simulation parameters is found, one has to make sure that the simulated and experimental spatial modes (V) are in agreement as well and have the same ordering. Any disagreement in the v_m indicates an incorrect model, while a difference in the ordering of the spatial modes indicates that the source amplitudes are not really a match. The use of SDDS file protocol enabled such complex integration of simulation and measurement.

APPLICATIONS

The first application of MIA at APS was the characterization of the beam jitter in the linac in June 1999 for the commissioning of the bunch compressor. The data obtained by `sddssynchlog` was used to make an obvious determination that dipole magnets that were set to zero current were the source of a strong trajectory jitter.

The next application was the characterization of the horizontal trajectory jitter in the booster-to-storage ring (BTS) transport line measured by beam position monitors (BPMs) for the purpose of improving injection efficiency. The source of the jitter was two pulsed extraction septum magnets at the start of the beamline. For the original characterization the BPMs were not yet upgraded and were very noisy. The goal was to provide the engineers with BPM noise levels and the output jitter of the septums' charging supplies. An optics model was required after MIA to calculate the actual septum output current jitter.

Only one SV dominated, with its spatial mode resembling the trajectory produced by either of the two septum magnets. Therefore, the source was ambiguous. The rms amplitude of the mode at the entrance of the storage ring (SR) was 0.67 mm. The mode was subtracted from the original data, giving only the noise. The resulting rms noise level of 0.45 mm was uniform across the BPMs. The same analysis was done for the vertical plane, which produced no trajectory jitter (as expected) and the same rms noise, which confirmed the validity of the BPM electronics noise estimate.

At a later date, the BPMs electronics were upgraded to reduce the noise level by a factor of 30. MIA was applied again in the same way to reveal a much-reduced BPM noise

level of 0.025 mm. Figure 1 shows the reduced noise level after the BPMs were upgraded, and Figure 2 shows the corresponding reduction in SV spectrum.

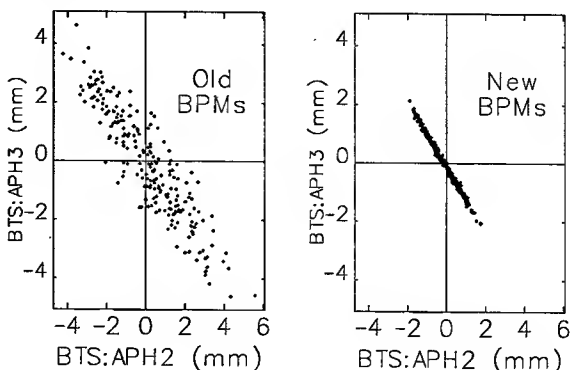


Figure 1: Correlation between two BTS BPMs showing change in electrical noise after upgrade.

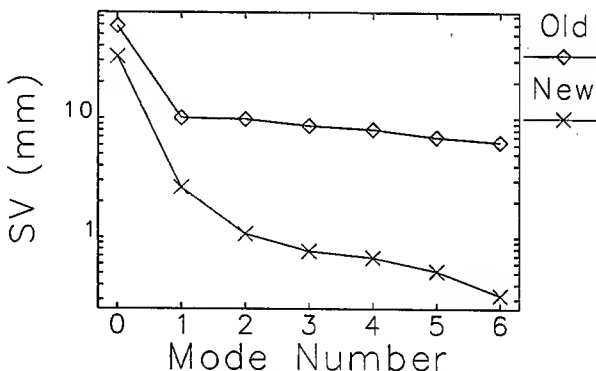


Figure 2: Comparison of SV spectrum after the BPM upgrade.

MIA revealed three modes instead of one. The strongest mode was the same as before, and two new modes appeared clearly above the noise floor. The second spatial mode originated because the two septums are independent and can create a cosine-like trajectory pattern to complement the sine-like trajectory of a single-septum angle error. The third spatial mode is an energy jitter that is caused by the booster dipole ramping supply. The correct identification of these two new spatial modes was confirmed by tracking simulations. Actually, the two spatial patterns don't look like the pure cosine-like trajectory or dispersion trajectory because these trajectories are necessarily orthogonal to the main angle trajectory, forcing a certain mixing of the pure physical trajectories.

The same number of data points were used in the MIA analyses that produced the spectra of Figure 2, which allowed the direct comparison of the spectra. If the septum noise was unchanged, then we would expect the largest SV in each curve to be equal. However, it appears that the septum noise was reduced by almost a factor of two. It is possible that in the two years between measurements that

improvements were made to the septum.

The SVs of the experimental data (λ_m^{exp}) for the three modes can be fitted to those of a beamline model. The main parameters of the model were the amplitudes of the septum relative strength errors, which were scanned over a 10×10 grid. The grid calculation was repeated for a few values of energy jitter. For simplicity, a uniform distribution of error was adopted, which is probably more realistic for power supply regulation and energy jitter. The BPM noise amplitude was fixed at 0.050 mm for the simulations, which closely reproduced the observed rms of 0.025 mm. We already had an idea of what the energy jitter would be due to the booster ramp data. Measurements of the 360-Hz ripple produces a relative dipole current error of typically 10^{-4} at the extraction time. The SVs calculated for each simulation (λ_m^{sim}) were written to an SDDS file, which facilitated calculating the quantity $\Delta = \sum_m^3 (\lambda_m^{\text{exp}} - \lambda_m^{\text{sim}})^2$ for each simulation. One such set of Δ is displayed in a contour plot in Figure 3. In this particular contour plot, there may be more than one solution. At the very least one can conclude that both septums contributed to the jitter of the trajectory.

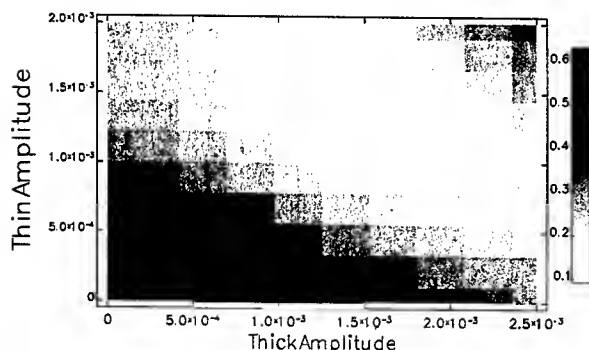


Figure 3: Contours of the differences of the experimental and simulated SVs.

We also analyzed the BTS trajectory noise with all quadrupole magnets turned off. Since the trajectory sources do not change, we expected the same solution for the septum noise amplitude from a different contour plot of Δ . Because the beam size eventually grew to the dimension of the beam pipe, most of the BPMs stopped functioning normally, which made the use of a model simulation difficult.

Also, we temporarily installed a different (lower noise) pulsed supply for the thin septum. We did this at a time when only two new low-noise BPMs had been installed in the BTS. Unfortunately the new and old BPMs have different timing systems and are not synchronized in general (sddssynchlog wouldn't have helped), so they could not be used together in MIA. We attempted to do MIA with two new BPMs only and with the five old BPMs only with two sets of data (one with the old supply and another one with the new supply). The spatial modes do not change with the supply, but the SVs are reduced by about 10% with the new supply, suggesting that the new supply really had reduced

jitter. In May of 2003, the booster extraction septums will have improved charging supplies, and MIA will be able to quantify the improvement.

We extended the problem to analyzing the BTS trajectory plus the SR trajectory using the single-pass capability of the SR BPM system. The analysis is expected to produce the additional trajectory noise contributed by the two SR injection septum magnets. There will be five sources of noise in all. We had to remove the bad SR BPMs using a threshold criterion on the elements of V , and repeat the MIA analysis with the bad BPMs removed. The strongest mode was the combination of the original strongest BTS spatial mode plus an oscillatory trajectory throughout the whole SR. It was expected that the SV spectrum would have five SVs standing out. However, as Figure 4 shows, there is one dominant mode, but the other SVs do not stand out clearly even though the spatial patterns have reasonable trajectories. We have not yet done elegant simulations of the trajectory. It is hoped that the modes will be better understood through a comparison with simulations.

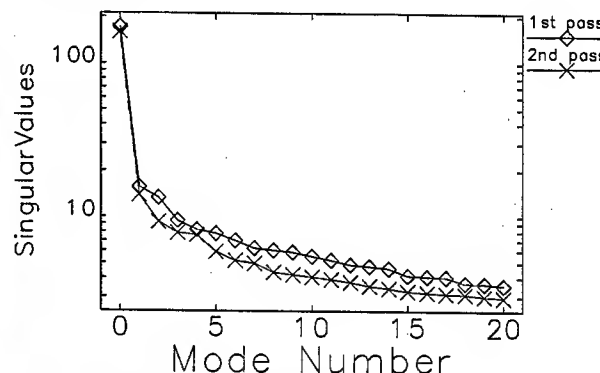


Figure 4: Part of spectrum of SVs for combined BTS-SR beamline before and after removing bad BPMs.

REFERENCES

- [1] J. Irwin and C. Wang, Y. Yan et al., Phys. Rev. Lett. 82, 1684 (1999).
- [2] Y. Cai, J. Irwin, M. Sullivan, and Y.T. Yan, "Application of Model-Independent Analysis to PEP-II Rings," PAC 2001, Chicago, 3555 (2002).
- [3] C.-X. Wang, "Spatial-Temporal Modes Observed in APS Storage Ring with MIA," these proceedings.
- [4] M. Borland, "A Self-Describing File Protocol for Simulation Integration and Shared Postprocessors," 1995 PAC, Dallas, Texas, 2184 (1996).
- [5] H. Shang et al., "New Features in the SDDS-Compliant EPICS Toolkit," these proceedings.
- [6] J. Irwin, *Handbook of Accelerator Physics and Engineering*, World Scientific, Edited by A. Chao, M. Tigner, 278 (1999).
- [7] M. Borland, "elegant: A Flexible SDDS-Compliant Code for Accelerator Simulation," Advanced Photon Source Light Source Note LS-287, September 2000.

BEAM DYNAMICS OPTIMIZATION IN THE RARE ISOTOPE ACCELERATOR DRIVER LINAC*

Eliane S. Lessner and Petr N. Ostroumov

Argonne National Laboratory USA

Abstract

A preliminary design of the superconducting linear accelerator of the Rare Isotope Accelerator (RIA) facility has been previously reported. The driver linac consists of about 400 superconducting independently-phased rf cavities, and is able to accelerate beams of any ion, including uranium, to energies of 400 MeV per nucleon and beam power of 400 kW. The linac has the novel capability of accelerating multiple-charge-state beams, which results in a significant increase in available beam current. Use of multiple-charge states imposes strict requirements on the steering procedure to avoid effective emittance growth. A program of detailed beam dynamics studies has been initiated to simplify the accelerator design, enhance its performance, and develop specifications for the engineering design of the accelerator systems. As part of the program, a correction algorithm has been developed that takes into consideration solenoid induced couplings. The correction method and initial results of corrections applied to the low- and medium-energy driver linac sections are presented.

TRANSVERSE EMITTANCE GROWTH

The effective transverse emittance of a multiple-charge-state beam oscillates along the linac due to the small mismatch in the focusing properties of each beam [1]. In the RIA driver linac the multi-charge beam emittance is well within the lattice aperture and the lattice is designed to preserve the beam quality. However, misalignments of SC resonators and focusing elements, passage through the strippers, and non-linear terms in the transport elements, can be sources of effective transverse emittance growth. In particular, misalignments of focusing components induce different deflections on beam particles of different energies or charge states, causing dilution of the transverse emittance. In addition, large trajectory excursions may lead to beam loss. In the RIA project, losses are to be limited to a factor of 10^{-4} . An effective trajectory-correction mechanism needs to reduce the emittance growth and limit the trajectory oscillations. We present a correction algorithm and initial results of its application to the low- and medium- β sections of the driver linac. Our algorithm is based on the dispersion-free correction technique developed by Raubenheimer and Ruth, whereby trajectory information from two or more different focusing configurations is used to correct lattice component misalignments [2]. Specifically, the trajectory

for a given magnet setting is measured, and then the trajectory is measured again, for a different magnet setting. The difference trajectory is less dependent on beam position monitor (BPM) misalignments. The method consists of establishing a goal function that minimizes the trajectory. As shown in [2], the method is more effective in reducing the emittance than attempting to zero the trajectory at the BPMs in a "one-to-one" correction.

CORRECTION ALGORITHM

Particle trajectories near the design trajectory can be described by transport matrices that map the particle initial phase-space coordinates at s_0 to its coordinates at a point s along the linac. A similar mapping can be defined for the centroid of a beam of non-zero emittance, which describes the beam central trajectory. To correct the trajectory one applies additional deflections induced by dipole correctors. In the low- and medium- β sections of the RIA driver linac focusing is provided by SC solenoids that rotate the beam and couple the horizontal and vertical beam motion. In this case, one needs to take the full transverse transport matrix into account. Considering only displacements of solenoids, the centroid horizontal coordinates at a position s can then be expressed as:

$$X(s) = x(s) + \sum R_{12}(s, s_j) \theta_H(s_j) + \sum R_{14}(s, s_j) \theta_V(s_j) \quad (1),$$

$$X'(s) = x'(s) + \sum R_{22}(s, s_j) \theta_H(s_j) + \sum R_{24}(s, s_j) \theta_V(s_j) \quad (2),$$

where X, X' represent the corrected trajectory coordinates and x, x' are the uncorrected measured coordinates:

$$x(s) = x(s_0) R_{11}(s_0, s) + x'(s_0) R_{12}(s_0, s) + y(s_0) R_{13}(s_0, s) + y'(s_0) R_{14}(s_0, s) + \sum d_k D(s_k, s), \quad (3),$$

$$x'(s) = x_0(s_0) R_{21}(s_0, s) + x'(s_0) R_{22}(s_0, s) + y(s_0) R_{23}(s_0, s) + y'(s_0) R_{24}(s_0, s) + \sum d_k D'(s_k, s). \quad (4)$$

In (1) and (2), θ_H and θ_V are horizontal and vertical functions representing the distortions at s induced by dipole correctors at positions s_j . In both equations, \sum represents a sum over j dipoles. The components of R represent the lattice transfer functions. In (3) and (4), $D(s_k, s)$ and $D'(s_k, s)$ relate the misalignments of a solenoid at s_k to the induced position and slope at s , and the sum is over N solenoids. Similar equations describe the vertical coordinates.

We need $(2N+4)$ BPMs to solve for the misalignments and initial conditions. In the RIA driver, where space is

* Work supported by the U.S. Department of Energy, Nuclear Physics Division, under Contract W-31-109-ENG-38.

†esl@phy.anl.gov

limited due to beam dynamics considerations, BPMs must be placed between cryostats, and there are two or more solenoids per cryostat. Therefore the equations cannot be solved exactly and we seek least-square solutions for the trajectory equations.

The Optimization Function

We establish a goal function, Φ , whose minimum is found by sweeping the corrector strength parameter space. The function Φ is expressed as:

$$\Phi = \sum_j \left[\frac{(X_j + C_j)^2}{(\sigma_p + \sigma_b)^2} + \frac{(\Delta X_j + \Delta C_j)^2}{(2\sigma_p)^2} \right], \quad (5)$$

where X_j , C_j denote measured and calculated deflections at position j , at nominal magnetic settings, and ΔX_j and ΔC_j are the measured and calculated deflections at non-nominal magnetic settings. Specifically, C_j and ΔC_j represent the sum terms in the right-hand sides of Eqs. (1) and (2), and depend on the lattice transfer functions. σ_p and σ_b are the BPM's rms precision and alignment errors, respectively. The minimization uses the measured trajectory and the difference trajectory with appropriate weights. We found that when BPM misalignments can be neglected the best optimization is obtained by excluding the difference trajectory in the algorithm.

LOW-ENERGY LINAC SECTION

A detailed layout of the low-energy section of driver linac can be found in [1]. This section precedes the first stripper and accelerates uranium atoms of charge states 28 and 29, from 190 keV/u to 10 MeV/u. Table I shows the initial and final values of some basic focusing-lattice parameters of the section.

Table 1: Some Basic Parameters of the Prestripper Lattice

Beam energy (MeV/u)	0.19 – 10.03
Frequency (MHz)	57.5 – 115.
Number of cavities	85
Number of cryostats	10
Focusing period (cm)	54.9 – 177.3
Solenoid effective length (cm)	10 - 30
Focusing field (T)	7.0 – 10.2
rms misalignm. at sol. (mm)	0.09 – 0.17
rms misalignm. at cavities (mm)	0.17 – 0.17

A modification of the code TRACK was used in simulations of random error misalignments of the solenoids. The code calculates the response functions in Eqs. (1) and (2) at the BPMs in terms of delta-function kicks at the correctors, and looks for values of the corrector strengths that minimize Eq. (5).

In our simulations, we investigated two different corrector-placement options. In one option, we placed thin-element correctors inside the cryostats, after every two solenoids. In the RIA case, this option can only be

realized if non-conventional correctors are used, given the lack of available free space in the cryostats. We have proposed the development of dipole coils superimposed on solenoids in a compact corrector element as a possible solution [3]. The simulations presented here use thin dipoles as a test of the effectiveness of the option. In the second scheme, the correctors were placed outside each cryostat. In both schemes, the BPMs were placed outside the cryostats.

Fig. 1 shows the horizontal and vertical emittance of the two-charged-state beam along the prestripper, before and after trajectory optimization. The uncorrected emittance growth results from simulations of 0.03-cm random uniform misalignment errors in solenoids and cavities. For this particular set of misalignments the uncorrected emittance grows fast with distance. There is no emittance growth after correction with thin-dipole placed after every set of two solenoids. The oscillation of the "corrected" emittance is the natural oscillation of a multi-charged state beam in a solenoidal focusing channel.

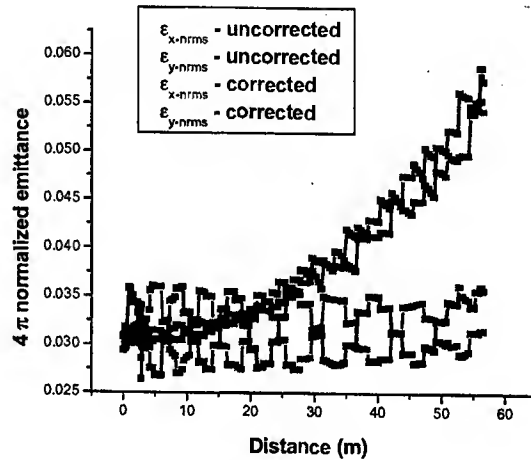


Figure 1: Emittance growth of a two-charged-state uranium beam in the low-energy linac section, resulting from ± 0.03 -cm random misalignments of cavities and solenoids.

In Fig. 2 we compare the horizontal position and slope coordinates at the BPMs before and after trajectory correction. The corrected values are plotted on the right side of the figure and are shown in a larger scale than the uncorrected values, for clarity. The corrector field distribution for the horizontal plane is shown in Fig.3. The required integrated-field strengths for the correction shown in Fig. 2 do not exceed a pre-estimated value.

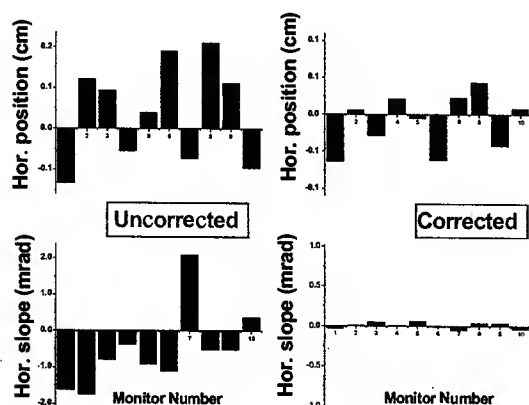


Figure 2: Comparison of the uncorrected (left) and corrected (right) BPM position (top) and slope (bottom). The corrected values are plotted at a larger scale, for clarity.

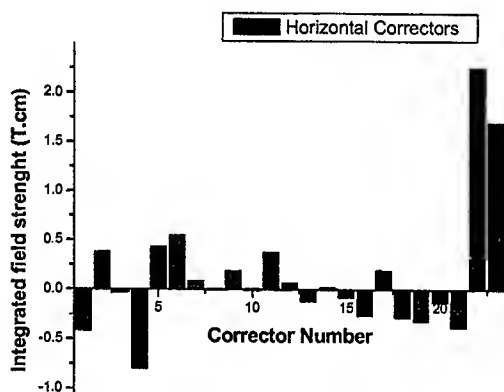


Figure 3: Required integrated-field strength for the correction shown in Fig. 2.

MEDIUM- ENERGY LINAC SECTION

Table 2 contains some of the basic transverse focusing parameters for this section of the RIA driver, located between two strippers. It is designed to transport five-charge-states of uranium beam from 10 to 86 MeV/u.

Table 2: Some Basic Parameters of the Medium-Energy Linac Section

Beam energy (MeV/u)	10.03 – 86.24
Number of cryostats	26
Focusing period (cm)	173.4– 258.9
Solenoid effective length (cm)	30
Focusing field (T)	6.0 – 10.4
rms misalignm. at sol. (mm)	0.17
rms misalignm. at cavities (mm)	0.17

As shown in [1], in the absence of errors, there is no transverse emittance growth in the multi-charge beam. In the presence of errors, the growth can be very large. For

the case of 0.03-cm random solenoid misalignments, the emittance dilutes by a factor of five. By optimization correction, the growth is reduced to a factor of 1.5, for this particular set of random misalignments, and with correctors placed outside the cryostats. The uncorrected and corrected emittances are depicted in Fig. 4, where we also plotted the nominal emittance values for comparison.

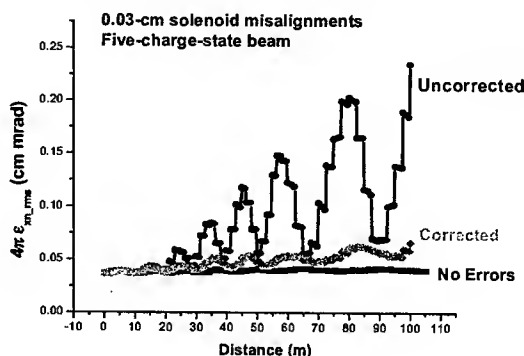


Figure 4: Transverse emittance without errors, and with solenoid misalignments, uncorrected, and after optimization.

SUMMARY

The optimization correction method effectively reduces the misalignment-induced emittance growth of a multi-charge-state beam. The method takes into account the coupling of horizontal and vertical motions in the solenoids and corrects for both position and angle errors.

The compactness of the lattice, required for optimal beam-dynamics, does not allow many choices for the placement of correctors. In a previous paper, we have proposed to develop combined-field solenoids that incorporate dipole steering coils. To confirm the effectiveness of using steering coils, we applied the optimization algorithm to a lattice containing fictitious thin-dipole correctors placed next to every other two solenoids. We found that the optimization restored the emittance to the nominal values and the corrected trajectory was much smoother than the ones resulting from the lattice with correctors placed outside the cryostats. This result reinforces the advantages of using the combined-solenoids-plus-steering-coils design option. Further studies in terms of a) optimal set of correctors, and b) sensitivity of the effective emittance growth to alignment errors will be undertaken.

REFERENCES

- [1] P.N. Ostroumov, Phys. Rev. STAB Vol. 5, 0030101 (2002).
- [2] T. O. Raubenheimer and R. D. Ruth, "A Dispersion-Free Trajectory Correction Technique for Linear Colliders," SLAC-PUB-5222, October 1990.
- [3] P. N. Ostroumov et. al., Gyeongju, Korea, Paper TU413, Aug 19-23, Linac 2002 Conf. Proc. (2002).

NEW FEATURES IN THE SDDS-COMPLIANT EPICS TOOLKIT *

H. Shang, R. Soliday, L. Emery and M. Borland
Argonne National Laboratory, Argonne, IL 60439, USA

Abstract

This paper introduces new features and programs developed to enhance various aspects of the SDDS-compliant EPICS toolkit. A new optimization program, **sddsoptimize**, was added to the toolkit; it employs the Simplex and 1-D scan methods and can be used for both EPICS and non-EPICS optimizations. Several new data logging programs were also developed, including a new, more flexible glitch logger that logs data before and after a glitch occurs. Another new data logger logs data every time the value of a process variable changes. With the data generated from this program, it is now possible to restore settings from any arbitrary time without the need for a snapshot of the system. Another new addition is the capability of saving and restoring waveform process variables. In addition to these new features, performance improvements have been realized in all the toolkit programs by replacing EZCA calls with low-level channel-access calls. Some of the toolkit programs have been upgraded to run on vxWorks to achieve higher performance.

INTRODUCTION

The SDDS-compliant EPICS toolkit is a set of software applications (tools) for the collection or writing of data collected from Experimental Physics and Industrial Control System (EPICS) database records. Although most of the applications essentially do rather simple operations, the combination of these applications and others from the SDDS postprocessing toolkit allows arbitrarily complicated analysis of data and control of the accelerators at the Advanced Photon Source (APS). These tools are general enough to be applied to devices other than accelerators, provided that the devices are under control of EPICS. One can regard the EPICS tools as the layer between the EPICS control system and more functional analyzing tools and scripts, with the SDDS protocol files as an intermediary. EPICS database records are referred to as process variables (PVs), each one having a unique name. PVs can be analog, digital (two or more states), or entire waveforms, depending on the I/O configuration. APS has developed over twenty SDDS-compliant EPICS programs. These programs can be categorized into three functional groups: (1) configuration save and restore, (2) data collection, and (3) process control [1]. The purpose of this paper is to review enhancements, new features, and new programs developed for the SDDS-compliant EPICS toolkit.

ENHANCEMENT OF CHANNEL ACCESS

EZCA (Easy Channel Access) provides a simplified interface to channel access for C programs. As a generic channel access facility, EZCA is used in many EPICS programs. The main shortcomings of EZCA are instability and speed: using EZCA, channel access errors occur unpredictably and channel access can be very slow. To overcome these problems, all EZCA calls in the SDDS-compliant EPICS toolkit have been replaced by low-level channel-access calls.

NEW FEATURES AND PROGRAMS FOR PROCESS CONTROL

This section describes new features added to the program **sddscontrollaw** and a new optimization program, **sddsoptimize**. Both of these programs are used for process control.

sddscontrollaw

This program provides a generic feedback capability for EPICS. As an accelerator control tool, **sddscontrollaw** is applied to (1) maintain constant energy and trajectory from the linac using an experimentally-derived matrix, (2) correct the orbit in the particle accumulator ring (PAR), (3) steer and maintain the storage ring (SR) orbit using a theoretical matrix and an orbit despiking filter, (4) maintain the APS ring injection trajectory, (5) regulate power levels from linac klystrons, and (6) regulate output of pulsed magnets using pulsing history. It is also used by a Tcl/Tk script that allows on-the-fly creation of one-readback, one-actuator control loops [1].

However, **sddscontrollaw** could not perform fast orbit correction because it was workstation-based and connected to each control and readback PV as a scalar. In order to perform fast orbit correction, the following new features were added:

- Frequency-band overlap compensation [2]

The APS real-time orbit feedback system (RTFS) operates in parallel with the DC orbit correction (DC OC) **sddscontrollaw**. The output of the RTFS is high-pass filtered with a cut-off frequency of 0.02 Hz to avoid interfering with the DC OC. If the DC OC has a bandwidth lower than that of the RTFS high-pass cut-off frequency, then a part of the orbit noise spectrum is not corrected. If the DC OC has a bandwidth higher than the RTFS high-pass filter cut-off, then the bands overlap (i.e., corrections doubled) and the orbit noise increases in the overlapping region. We developed a feedforward scheme in **sddscontrollaw** to allow operation in the latter overlap condition. At each iteration the expected orbit change from the DC OC is added to the value of the RTFS BPM

* Work is supported by U.S. Department of Energy, Office of Basic Energy Sciences, under Contract No. W-31-109-ENG-38.

set points, thus preventing the RTFS from reacting to the DC OC corrector change. An additional file for the corrector-to-BPM set point matrix is required, since the set of BPMs in the RTFS may be different from those in the DC OC. Digital filtering of the BPM set points is also possible to account for corrector response. With this compensation, a large amount of frequency-band overlap is now workable and serves to eliminate the possibility of a gap in the total OC response spectrum.

- The ability to read and set waveform PV values was added to the program. Waveform PVs can be used to provide rapid access to arrays of scalar PVs of similar properties. In this case, waveform PVs are used to provide collections of corrector power supply set points and of beam position monitor readbacks.

- EZCA channel access function calls were replaced with the low-level channel access functions. Testing has shown that low-level channel access is more efficient and reliable compared to the EZCA channel access.

- The workstation version of the program **sddscontrollaw** is limited in performing DC OC for the APS storage ring (SR) because it has to contact many different IOCs at each iteration to send and receive the BPM and corrector data. To overcome this limitation, the program was ported to VxWorks and hence can run in IOCs using that operating system. For the APS DC OC application [3], the IOC in question has special hardware to send and receive vectorized corrector and BPM values to and from a memory backplane, which moves the data to and from the other related IOCs at a very high rate.

- **sddscontrollaw** has a feature that suspends or resumes correction based on whether test conditions are satisfied by a group of PVs. For example, DC OC is inhibited when beam is lost, when a corrector changes by a large amount, when a BPM has a bad status, etc. The necessary testing of so many PVs is time-consuming, so we developed a special-purpose program, **sddspvtest**, that performs this function and sets a single PV with the result. **sddscontrollaw** then need only test this one PV.

As a result of these new features, **sddscontrollaw** is able to correct the APS orbit at a rate of 20 Hz [3]. In addition, **sddscontrollaw** is used in linac IOCs to perform klystron power regulation. Having the same code running on a workstation and in the IOC both reduces code maintenance requirements and expedites development of new features and control loops.

sddsoptimize

This is a new addition to the SDDS control tools. It provides a generic optimizer that can be used for cases where feedback is not applicable. The main features of the optimizer are detailed below:

- The optimization criterion is the rms value of one or more PVs, or else the value obtained by running a script. In the former case, one may optionally assign weights, target values, and tolerances for each PV. In the latter case, the measurement script can be used to perform more general operations, which may or may not involve accessing PV values.

- Two optimization methods are provided: simplex and successive 1D optimization (also called 1D scan). Simplex is a multidimensional minimization method that requires only function evaluations [4]. It is frequently the best method if the computational burden is small. By default, our simplex method makes explicit use of a one-dimensional minimization algorithm as a part of the computational strategy, since this often will make the optimization proceed faster; this can be disabled in cases where it is found not to help. The successive 1D scan method allows minimization of the target with respect to each parameter separately and in turn. The main disadvantage is that if the optimal changes of the parameters are mutually dependent, this method may converge very slowly toward the minimum. Nevertheless, it runs efficiently when the variations are quasi-independent.

- Setting the values of PVs can be replaced by running a "variable script" (given by the `varScript` option) so that the program can effectively set PVs in an arbitrarily complicated fashion or even perform optimizations that do not involve PVs. There are no CA calls in **sddsoptimize** if both variable and measurement script are provided, so non-EPICS optimizations are possible. For example, one can optimize the results of a simulation.

- The program performs minimization by default and will perform maximization if the `"-maximize"` option is given.

- **sddsoptimize** can be used to adjust knob PVs, which are predefined linear combinations of PVs. Examples are knobs for orbit bumps or ganged timing control for a set of kicker magnets.

- To make the optimization robust, a series of validity tests on PV values are implemented by means of an additional SDDS file containing the names of PVs and their corresponding limit values. The optimization is suspended if one of the tests fails. This can be used to avoid processing invalid data and to terminate the program if it adjusts settings beyond a safe or reasonable range.

- The optimization can be stopped at will by the user using `ctrl-c` (i.e., the UNIX SIGINT signal). The best settings obtained so far will then be implemented before the program terminates.

- **sddsoptimize** optionally logs settings and results to an SDDS file. This file can be used to view results during or after an optimization, and also to set up a new optimization.

As a result of these features, **sddsoptimize** has been applied to the APS SR for (1) maximizing injection efficiency, (2) storage ring beam x-y coupling minimization, (3) booster-to-SR rf phase adjustment to center injected beam in the rf bucket, and (4) on-axis injection setup and closed bump setup. **sddsoptimize** has also been used in the APS linac for beam-based optimization of rf phase and power, and in the PAR for maximizing capture efficiency. It was also employed for fitting APS linac bunch compressor measurements using

the simulation code elegant to evaluate the values of the fit (through particle tracking) at the experimental points.

NEW PROGRAMS IN THE DATA COLLECTION TOOLKIT

Data collection programs provide various types of data logging into SDDS files [1]. Three new programs, **sddsglitchlogger**, **sddslogonchange**, and **sddssynchlog** have been developed and are discussed in this section.

sddsglitchlogger—This program is able to log data before and after a glitch occurs, where a glitch is a sudden change in readings from a process variable. Although another data logging program, **sddsmonitor**, provides a similar capability, **sddsglitchlogger** is much more flexible. For example, with **sddsglitchlogger** one can specify multiple glitch conditions and corresponding multiple output files. This allows one **sddsglitchlogger** process to do the work of many **sddsmonitor** processes, thus decreasing loads on IOC's. As in **sddsmonitor**, the PVs to be logged are defined in an input file. The trigger PVs can be defined either in the input file as parameters or in a separate trigger file. In the former case, many output files may be specified for different sets of logged PVs, each triggered by a different, single PV. If multiple trigger PVs are required, then a separate trigger file is used. There are three types of triggers, detailed use of which is described in the manual page: (1) Alarm-Based Trigger – Occurrence of an alarm of a specified severity or severities results in dumping of data; (2) Transition-Based Trigger – Data is dumped when the specified PV transitions through a certain level from above or below (as selected); and (3) Glitch-Based Trigger – The trigger fires when the difference of the PV value from the average of recent values is greater than the glitch threshold. To make **sddsglitchlogger** more robust, a conditions file is supported that lists conditions that must be satisfied at each time step before the data can be logged. This prevents accumulating and logging invalid data.

sddslogonchange—The program **sddslogonchange** logs data every time a PV's value changes. With the data generated from this data logger it is possible to restore settings from an arbitrary time without a snapshot from the system. With the introduction of the program **sddslogonchange** it is now possible to log slowly-changing PVs more efficiently than previous SDDS data loggers. Data loggers such as **sddsmonitor** and **sddslogger** log every PV at a specified iteration, while **sddslogonchange** logs a PV only when its value changes. Therefore no unnecessary data is logged. By logging the initial values of every PV it is possible to determine each PV's value at any given time from **sddslogonchange**'s output file. As in **sddsalarmlog**, disk space efficiency is enhanced by using the SDDS array feature to store PV names in a coded format, obviating the need to store the same string each time a PV changes.

sddssynchlog—EPICS is by its nature an asynchronous control system. This can present problems in data collection and correlation analysis. The program **sddssynchlog** addresses this issue by collecting time-stamped data from many PVs, then organizing the data to line up the time stamps. This is necessary given that different IOC's may have different loads and hence serve data at different rates or even with gaps. Even in such an environment, **sddssynchlog** provides data suitable for reliable correlation analysis. The program was used extensively in the APS linac, helping to pinpoint problems with BPMs and to find sources of beam motion.

NEW PROGRAMS IN THE CONFIGURATION SAVE AND RESTORE TOOLKIT

Previous SDDS-based configuration save and restore programs only work for scalar PVs. In order to be able to handle waveform PVs, two new programs **sddswget** and **sddswput** have been developed for the configuration save and restore toolkit, as will be described in this section.

sddswget—This program is developed to provide a convenient and fast method for collecting waveform data, including character and string types. The input file to **sddswget** specifies the waveforms to be read; this may be done with a file that is compatible with **sddswmonitor**, or using a **sddswget**-specific SDDS file. The latter is formally identical to the *output* file produced by **sddswget**, which is convenient in many cases. Optionally, one may specify the names of the PVs on the command line.

sddswput—This program was developed to provide a convenient and fast method for setting waveform data from SDDS files. Like **sddswget**, it supports character and string types. It accepts as input the output files from **sddswget**.

sddswget and **sddswput** are used to retrieve booster corrector ramp tables, initialize waveform PVs in the DC OC, and save and restore waveform PVs in the data pool IOC's. **sddswget** and **sddswput** are also used in the rapid reconfiguration of the APS monopulse BPM trigger timing systems for different bunch patterns.

REFERENCES

- [1] M. Borland, L. Emery, Proceedings of the 1995 ICALEPS Conference, Chicago, Illinois, pp. 653-662 (1996).
- [2] C. Schwartz, L. Emery, Proceedings of the 2001 Particle Accelerator Conference, Chicago, IL, pp. 1234-1236 (2001).
- [3] R. Soliday, M. Borland, L. Emery, H. Shang, "Use of a Simple Storage Ring Simulation for Development of Enhanced Orbit Correction Software," these proceedings.
- [4] W. Press, S. Teukolsky, W. Vetterling and B. Flannery, "Numerical Recipes in C," Cambridge University Press, p. 408 (1992).

NEW FEATURES IN THE SDDS TOOLKIT*

R. Soliday, M. Borland, L. Emery, H. Shang,
Argonne National Laboratory, Argonne, IL 60439 USA

Abstract

Self-Describing Data Sets (SDDS) and the corresponding SDDS tools have long been used at the Advanced Photon Source (APS) and other laboratories for data storage and analysis. Various programs in the toolkit have been added or improved recently. Support for the Mac OS X operating system has been added. Automated testing scripts are being used to reduce bugs prior to software upgrades. The Java version of the SDDS Toolkit has been used to integrate standard SDDS functions into MATLAB. The fitting of generic functions to SDDS data has been improved. Conversion of array data to column data has been added to allow analysis of array data with existing programs. The display of sddsplot movies by saving plots to files for rapid playback has been improved.

NEW PORTS

Macintosh OS X

The SDDS Toolkit [1], which was written to store and manipulate accelerator data at the Advanced Photon Source (APS), continues to evolve to meet new requirements at different facilities. The toolkit was previously available on Solaris, Linux, Windows, and VxWorks [2] operating systems. With the introduction of OS X (a variant of Unix) for Macintosh computers, we were able to make SDDS available on Macintosh computers. Since all of the toolkit programs, with the exception of the SDDS plotter, do not require graphics libraries, the port was relatively straightforward. The SDDS plotter uses X11 libraries and thus requires that XDarwin and Lesstif be installed on the system. The SDDS Toolkit source code and OS X binaries are available on the OAG web site, along with the installation instructions.

MATLAB

The Java version of the SDDS Toolkit has been used to add SDDS compatibility to MATLAB. This provides MATLAB users with a stable and reliable way to access SDDS datasets, which, being self-describing and uniform in structure, provide a more organized way of storing data than MATLAB's own data formats. In addition, the SDDS toolkit has data manipulation features similar to a database, which supplements the capabilities of MATLAB. This port also allows SDDS users to take advantage of plotting and analysis features of MATLAB that may be lacking in the SDDS Toolkit.

We created new MATLAB commands that can be used to produce complex plots from data stored in SDDS files.

The `sdds3d` command reads an SDDS data file and converts it into a MATLAB 3D mesh including the X, Y, and Z data points and the corresponding labels. This mesh can then be passed to `sddspcolor` to create a flat colored contour plot. These plots can be stacked on top of each other if there are multiple pages of data to be plotted. The 3D mesh can also be passed to `sddssurf` to create a 3D shaded surface plot (see Figure 1). Other new MATLAB commands are `sddscontour`, `sddsmesh`, and `sddsplot3`. These can be used to create contour plots, 3D shaded surface plots with mesh lines, and plots of points in 3D space, respectively.

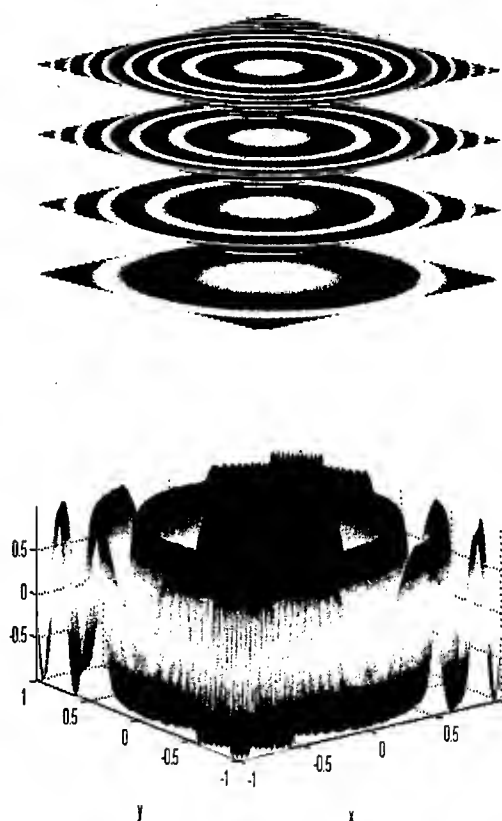


Figure 1: SDDS data plotted in MATLAB.

IMPROVEMENTS

Data Fitting

Fitting of generic functions to data can now be accomplished with `sddsgenericfit`. The user simply provides an arbitrary functional form, the range, and step

* Work is supported by U.S. Department of Energy, Office of Basic Energy Sciences, under Contract No. W-31-109-ENG-38.

sizes for the variables in the fitting function. The versatility of this program greatly reduces any need to design new fitting software for specific tasks. This will allow the user to create and modify high-level data analysis tools faster since it will not be necessary to create low-level data fitting routines.

Signal Analysis

The new program **sddsnaff** performs Numerical Analysis of Fundamental Frequencies (NAFF), which is Laskar's algorithm for accurate determination of the frequency components of a signal. NAFF is much more accurate than fast Fourier transforms (FFTs). The algorithm starts by removing the average value of the signal and applying a Hanning window. Next, the signal is FFT'd, and the frequency at which the maximum FFT amplitude occurs is found. This provides a starting frequency for numerical optimization of the "overlap" between the signal and $e^{i\omega t}$, thus determining ω to a resolution less than the frequency spacing of the FFT. Once ω is determined, the overlap is subtracted from the original signal and the process is repeated, if desired, to find another frequency component. Output from **sddsnaff** includes the frequency, amplitude, and phase of the frequency components.

Array Data Conversion

The SDDS file protocol allows storing data in both arbitrarily dimensioned arrays and one-dimensional columns of a common length. However, most of the SDDS data analysis tools work on column data. To support array manipulation without altering each program, **sddsarray2column** was created. This program converts SDDS array data to SDDS column data. In addition, it allows taking slices out of multidimensional arrays. The array data to be converted must meet two requirements: the number of elements taken from multiple arrays must be equal to each other and also equal to the number of rows in the data file if columns already exist. While not every SDDS data file with arrays will fit these requirements, **sddsarray2column** has been very useful at the APS and elsewhere.

Image Analysis

In order to develop automated analysis of image data from the LEUTL FEL, we developed the program **sdsspotanalysis**. This program analyzes a series of images to find beam spots. It performs noise reduction and background subtraction, and then determines the centroid, intensity, rms parameters, and degree of saturation. It allowed rapid, automated analysis of thousands of beam images from the FEL.

Frequently it is more efficient to store only the horizontal and vertical profiles of images rather than complete images, so we developed new tools for this case. The program **sddsbaseline** provides various methods of determining and removing baselines from such profiles. **Sddscloptails** provides various methods of clipping the tails from image profiles, where the tail is a dubious

feature extending to the right or left of a peak. These programs can be used in sequence to process profiles, which can then be analyzed using **sddsprocess** to determine, for example, rms spot properties.

Along the same lines, a new image converter has been created called **tiff2sdds**. This program converts a TIFF image to an SDDS data file by summing the red, green, and blue color intensities for each pixel and storing the values as SDDS columns.

SDDS Plotter

Many improvements have been made to the SDDS plotting software. A new native Windows graphic interface obviates the need to have an X-windows emulator on Windows platforms. Another new feature of the SDDS plotter is the ability to write the binary plotting instructions to a file. This allows the user to store **sddsplot**-generated movies in a compact file for later replay, even if the original data is unavailable. A related improvement is an interval control in the SDDS plotter that allows changing the playback rate.

Other improvements to **sddsplot** include: the ability to display parameters of any data type on labels; support for wildcards in the independent variable data names and templates for the dependent variable names; support for PNG (portable network graphics) files; addition of a common-offset feature helpful for plotting data from many files at once; and addition of a "spectral" mode for more intuitive color-coding of large amounts of data.

Library and Miscellaneous Improvements

Many improvements have been made to the SDDS libraries. The SDDS library now supports platform-independent binary files, which allows mixing of hardware platforms (e.g., PC and SPARC). It supports synching of files over a network to improve reliability of fast data loggers. One can now work with an unlimited number of active SDDS files even if the operating system has a limit on the number of open files.

A function was added that converts algebraic expressions into reverse polish notation expressions; this has allowed the use of algebraic expressions in programs like **sddsprocess** with only minor coding changes. Data types of elements in SDDS files can now be changed using a new program called **sddscast**. We wrote and released **sddspoly**, a program for polynomial transformation of large quantities of input data. This program is used at APS for translation of BPM set points and offsets between various polynomial sets. The new program **sddsmultihist** allows creating histograms of arbitrary numbers of columns. The new program **sddseventhist** allows histogramming tagged data (e.g., alarms identified by channel name). Savitzky-Golay filters are now available for smoothing in **sddsmooth** and for taking numerical derivatives in **sddsderiv**. A variant of **sddsinterp** called **sddsinterpset** was created to perform multiple polynomial interpolations. This tool simplified calculating set points for individual magnets that have separate magnetic measurement files. Another

new tool called **sddsmakedataset** is used to create SDDS files from data entered in the command line arguments. This can save programming effort when a short file is created within a script.

Java

We continued improvement of a Java-based three-dimensional plotting program for SDDS files. It can now plot all the file types that **sddscontour** can plot, as well as performing 3D color-coded scatter plots. Some of the usefulness of this program has been diminished with the release of the SDDS-to-MATLAB interface but it still is the best choice for three-dimensional plotting if MATLAB is unavailable. Another recent improvement to the native Java version of SDDS is the addition of SDDS array support. With this addition the Java version of SDDS is totally compatible with the latest version of SDDS libraries written in C.

STABILITY

Testing Scripts

To help increase stability and reliability, various testing scripts and simulators are routinely used to test and debug SDDS software prior to a release. Two types of storage ring simulators have been used. The first is a portable channel access server that simulates a storage ring orbit. This version does not require much memory but it has been hard to customize to fit new uses. The second is set up as a workstation IOC. This version accepts standard EPICS database files to create process variables and has shown itself to be highly customizable. Both of these simulators include quasi-Gaussian noise on BPMs and correctors. The workstation IOC version of the simulator has been used recently to test and debug the new SDDS

waveform programs **sddswget** and **sddswput** [3]. A third simulator is running on vxWorks in an IOC. This simulator was used extensively during the porting and testing of SDDS/ EPICS software [4].

AVAILABILITY

OAG Web Site

The majority of SDDS applications are available though the Operations Analysis Group (OAG) web site (www.aps.anl.gov/asd/oag/software.shtml). Here the source code for the various programs can be downloaded. This code is offered under the terms of the EPICS Open License (www.aps.anl.gov/epics/license/open.php). We also offer precompiled versions for Linux, OS X, and Windows. These packages are offered under the same license with the exception of any packages that are compiled against EPICS 3.14 and contain channel access routines. This subset of packages is offered under the terms of the EPICS BASE License (www.aps.anl.gov/epics/license/base.php).

REFERENCES

- [1] M. Borland and L. Emery, "The Self-Describing Data Sets File Protocol and Program Toolkit," Proc. ICALEPCS 1995, Chicago, Illinois, pp. 653-662 (1996).
- [2] R. Soliday, "Proliferation of SDDS Support for Various Platforms and Languages," Proc. ICALEPCS 2001, San Jose, California, pp. 545-547 (2002).
- [3] H. Shang et al., "New Features in the SDDS-Compliant EPICS Toolkit," these proceedings.
- [4] F. Lenkszus et al., "Integration of Orbit Control with Real-Time Feedback," these proceedings.

USE OF A SIMPLE STORAGE RING SIMULATION FOR DEVELOPMENT OF ENHANCED ORBIT CORRECTION SOFTWARE*

R. Soliday, M. Borland, L. Emery, H. Shang,
Argonne National Laboratory, Argonne, IL 60439 USA

Abstract

At the Advanced Photon Source (APS) most of the testing of minor operational software is done during accelerator studies time. For major software changes, such as the porting of the complex workstation-based orbit control software to an EPICS IOC, much of the testing was done "offline" on a test IOC. A configurable storage ring simulator was created in a workstation with corresponding control system records for correctors and orbit readbacks. The simulator's features will be described as well as the method used to develop and debug the most recent improvement of the APS orbit control software, among others. The simulator is also useful in general-purpose software testing.

BACKGROUND

With the increasing percentage of time dedicated to user operations at APS and accelerator physics studies, less and less time is available for testing new or updated controls software. With the advent of extended top-up operation [1], the amount of software testing that can be accommodated for the injector subsystems has continued to decrease. Faced with limited software testing time and striving to maintain high reliability, we have created new methods for testing software. These include using simulations of accelerator systems that interact with normal channel-access applications. These simulations have continued to evolve and have helped us develop more sophisticated high-level applications, the latest example being an enhanced version of our orbit correction software.

SIMULATED LINAC

VxWorks IOC

The first simulation created was of a simple linac. It runs on a VxWorks EPICS input/output controller (IOC) that is used exclusively for testing. This simulation includes an rf gun cathode, beam correctors, and beam position monitors (BPMs). While this simulation is quite simple, it has been very useful in debugging various EPICS applications while in an office environment. The simulation includes various types of process variables, including analog inputs, analog outputs, and binary outputs. A simple response matrix connects the BPMs and correctors, allowing testing of feedback software, such as *sddscontrollaw*.

This simulator has been used in the testing of one of the components of our enhanced orbit correction software,

namely, the VxWorks port of *sddscontrollaw*. However, there are limitations to this type of simulation. In particular, as it was modified to simulate the storage ring, we found that the memory in the IOC was quickly consumed before an adequate simulation could be created. We also found that large-scale simulations required more processing power than was available in the IOC that was being used. Avoiding these two limitations led to the creation of a workstation-based version of a storage ring simulator.

SIMULATED STORAGE RING

Workstation with EPICS 3.13

The second simulation created was of a storage ring that runs on a Solaris workstation. This simulation was created by extension modifications of the portable EPICS CA server [2], which is available with EPICS 3.13. This simulation, like the previous linac simulation, also interacts with standard channel-access applications but it is not running on an IOC. Instead it is a standalone application that mimics some of the behavior of an IOC. Two SDDS files, giving the horizontal and vertical response matrix for the storage ring, configure this simulation. The response matrices can be generated by the accelerator code *elegant* [3], meaning that one can simulate any accelerator for which an *elegant* input lattice is available. In addition, the response matrices can be generated by actual measurements on an accelerator.

One of the features of this simulator and the other simulators described here is that randomness that can be added to the corrector strengths and/or the BPM readbacks. This permits much more realistic simulation of feedback processes, which are strongly affected by noise. It also allows development of data analysis algorithms, for example, algorithms for finding the source of unexpected orbit motion.

While this simulation removed the memory limitations of the VxWorks EPICS IOC simulation and is flexible enough to simulate different accelerators, it does have limitations. The major limitation is that it was very time-consuming and error-prone to add new types of process variables (PVs). Since it was not an EPICS IOC there were no such things as database DB or DBD files, which are normally used to define PVs. This meant all the behavior of new PVs has to be programmed into the code. With the wide range of different types of PVs for the various accelerator systems, this limitation meant that developing more detailed simulations would require

* Work is supported by U.S. Department of Energy, Office of Basic Energy Sciences, under Contract No. W-31-109-ENG-38.

extensive programming work. With the release of the latest version of the EPICS source code it was possible to overcome this limitation by developing a new kind of simulator.

Workstation with EPICS 3.14

The release of EPICS 3.14 enabled us to run an IOC on a Solaris workstation [4]. This meant we could develop an improved simulation by taking advantage of the ease-of-development of the VxWorks IOC simulation combined with the increased available memory and processor speed from the workstation. Like the original workstation-based simulation, this new simulation also uses response matrices. Hence, the simulation is easily configured for different accelerators.

This simulator makes it easy to add waveform process variables. Such process variables are used in the enhanced orbit correction software for the APS storage ring. The values in the waveforms represent vectorized corrector and BPM values for the storage ring. The simulation was created by using a combination of EPICS database records to create bending magnets, correctors, quadrupole magnets, sextupole magnets, trim magnets, and waveforms of vectorized correctors, along with special PVs to dynamically change the level of randomness. Most simulated PVs have related calc and sequence PVs that are used to calculate the simulated values.

One of the first uses of this simulator was to improve storage ring power supply startup, condition, and shutdown Procedure Execution Manager (PEM) procedures. By artificially decreasing the time needed for conditioning, it was possible to rapidly test modifications to the procedures.

ENHANCED ORBIT CORRECTION SOFTWARE

The main goal of the enhanced orbit correction software [5] is to more precisely control the position of the beam in the storage ring. To accomplish this, the correction software has to run at a faster rate than is possible with the workstation version. The workstation version is limited because it has to contact many different IOCs at each iteration to send and receive the BPM and corrector data. To overcome this limitation, the orbit correction software has been ported to VxWorks and is running on a dedicated IOC. This IOC has special hardware that it uses to send and receive vectorized corrector and BPM values to and from a memory back plane, which almost instantaneously moves the data to and from the other related IOCs. The orbit correction software then reads and writes these waveform PVs using optional direct database access routines. When all these systems are put together, the orbit can be corrected up to twenty times per second.

The process of porting this software to run on a VxWorks EPICS IOC was greatly aided by the use of the simulators described above. Beyond the benefits of using

a VxWorks EPICS IOC simulator to port software that was never intended to run on VxWorks when it was originally written, these simulators were used to track down problematic race conditions that did not occur on the Solaris version. The VxWorks version of the orbit correction software was only able to run on the linac simulator as opposed to the two newer simulators because the target platform was VxWorks. However, by turning off the optional direct database access routines and using channel access instead, it was possible to use the latest workstation version of the simulator to run more detailed tests.

GENERAL SOFTWARE TESTING

Different combinations of these simulators have been used to test and debug other channel-access software here at the APS. The high-level accelerator applications at APS make use of the SDDS/EPICS toolkit. This consists of a collection of about 20 separate programs that can be configured to perform various data collection and process control tasks. Upgrades to the toolkit programs obviously must be thoroughly tested prior to releasing new versions into operation. To accomplish this, various testing scripts have been written that test most of the capabilities of the toolkit.

In addition, new programs such as `sddslogonchange`, `sddsglitchlogger`, `sddswget`, and `sddswput` have been developed with the help of these simulators [6]. The first program is used to log PV changes in efficient SDDS array data format. The second is used to log data when user-specified glitch events occur. The latter two programs are used to read and write waveforms to and from SDDS files.

SDDS/EPICS DEMONSTRATION SOFTWARE

The storage ring simulator based on the Portable Channel Access Server has also been used to develop a set of Tcl/Tk scripts that demonstrate the capabilities of the SDDS/EPICS toolkit. The demonstration software allows one to choose from among several accelerator configurations, from a small FODO transport line to a large ring. The simulator is fast enough that most of these configurations can be simulated with good results on a laptop. (Simulating the large ring requires a fast PC.) Whichever configuration is chosen, the simulation is configured from an *elegant* input lattice along with several extra parameters, such as the noise level for BPMs and correctors. In particular, *elegant* provides the horizontal and vertical response matrices, from which the PV names for the BPMs and correctors are determined. The SDDS toolkit (a general-purpose data analysis and display suite) is used to create input files for data logging.

The purpose of the demonstration scripts is to show how SDDS/EPICS tools can be used for data collection and how the SDDS tools can then be used for data analysis and display. To provide some interesting signals, one of the scripts imposes a small oscillation on two of

the correctors. Another script collects data from the simulation and illustrates use of the SDDS toolkit to find the frequency, relative amplitude, and the location of the oscillating correctors. The final step is performed using singular value decomposition and comparison of the singular vectors to the response matrix.

The scripts generate an input file for the Array Display Tool (ADT) program to allow the user to view the orbit in real time. In addition, the scripts allow measurement of the response matrix and comparison to the ideal matrix. Following this, the user can perform orbit correction using the measured matrix. An MEDM screen allows the user to change the gain of the orbit correction while it runs, to start and stop the correction, and to change several corrector values. The programs `sddsstatmon` and `sddsplot` are used to create a stripchart of the rms orbit. The demonstration scripts are intended to be tutorial in nature. All SDDS commands are displayed as they are performed. The software is available for download from the Operations Analysis Group web site at APS (www.aps.anl.gov/asd/oag/oaghome.shtml). Adding a new accelerator to the demonstration is very simple, provided an elegant lattice is available.

FUTURE PLANS

In the future we hope to use these simulators to train the accelerator operators. Operator training takes a

significant amount of time and has some of the same problems allocating time from user operations, similar to software testing. By using the simulated accelerator it would be possible to teach basic operations and problem solving skills.

REFERENCES

- [1] L. Emery and M. Borland, "Upgrade Opportunities at the Advanced Photon Source Made Possible by Top-Up Operations," Proc. EPAC 2002, Paris, France, pp. 218-220 (2002).
- [2] J. Hill, "A Server-Level API for EPICS," Proc. ICALEPCS 1995, Chicago, Illinois, USA, pp. 136-141 (1996).
- [3] M. Borland, "elegant: A Flexible SDDS-compliant Code for Accelerator Simulation," Advanced Photon Source LS-287, September 2000.
- [4] M. Kraimer, J. Anderson, J. Hill and E. Norum, "EPICS: A Retrospective on Porting iocCore to Multiple Operating Systems," Proc. ICALEPCS 2001, San Jose, California, pp. 238-240 (2002).
- [5] F. Lenkszus et al., "Integration of Orbit Control with Real-Time Feedback," these proceedings.
- [6] H. Shang, R. Soliday, L. Emery, M. Borland, "New Features in the SDDS-Compliant EPICS Toolkit," these proceedings.

EVALUATION OF THE HORIZONTAL TO VERTICAL TRANSVERSE IMPEDANCE RATIO FOR LHC BEAM SCREEN USING A 2D ELECTROSTATIC CODE

U. Iriso-Ariz, BNL, Upton, NY - 11973, USA

F. Caspers, CERN, Geneva, Switzerland; A. Mostacci, U. La Sapienza, Roma, Italy

Abstract

The classical 2 wires method is not suitable for high precision transverse impedance measurements on a homogeneous copper beam-pipe with non circular cross-section due to measurement noise limitations in case of narrow wire spacing. Thus we tackled the problem by simulating the 2D electrostatic field and image charge distribution of that setup and subsequently calculating the corresponding surface current for a TEM wave excitation. In this computer simulation the 2 wires can be assumed lossless, which is not possible in a practical bench setup. The theoretical justification for the method and certain limitations are discussed. The results compare very well to several independent numerical and analytical results.

1 INTRODUCTION

We discuss a method to calculate the ratio between the horizontal and vertical transverse impedances (Z_h and Z_v) for a given beam pipe cross-section. In particular, we consider the case of a cylindrical homogeneous metallic beam pipe, such as the LHC beam screen (BS) geometry (the effect of the pumping slots present in the beam pipe wall will be neglected). Our results may become a useful tool to calculate the transverse impedance for non-analytical solution cases.

The basic principle is that an ultra-relativistic off center beam produces a surface current distribution in the inner surface of the beam pipe similar to a (statically) charged off center inner conductor. It is possible to reproduce the beam pipe cross section geometry and the inner conductor for use in an electrostatic field code which can then be used to obtain the surface current distribution.

Using the electrostatic field code *Superfish* [1], one can obtain the normal electric field (E) at each point on a perfectly conducting surface for a given 2-D geometry. Two inner conductors in an odd mode are placed inside the beam screen geometry of the LHC (Fig. 2) to simulate the dipole component of the beam field. Since the transverse impedance (Z) is proportional to $\int E^2 dl$ (losses in the surface wall), the ratio between the Z_h and Z_v is given by the ratio of $\int E^2 dl$ for the horizontal and vertical excitations.

The BS is expected to be the main contributor to the resistive wall effect in the LHC [2]. In order to properly calibrate this method, some cases with a known analytical solution have been simulated. We describe here the method used to calculate $\int E^2 dl$ from the *SuperFish* output and compare numerical and analytical results for the BS.

2 MATHEMATICAL METHOD AND THE USE OF SUPERFISH

For an arbitrary pipe cross section the ratio between Z_h and Z_v can be computed by [3]:

$$\frac{Z_v}{Z_h} = \frac{\int |J_v|^2 dl}{\int |J_h|^2 dl}, \quad (1)$$

where J is the surface current in the inner surface of the outer conductor, and J_v and J_h stand for an off center beam displaced in the vertical axis and horizontal axis, respectively. In order to compute J , the first step is to solve the Poisson equation using *SuperFish* and obtain the static electric field (E_x, E_y) for any position of the inner wires. Then, the dynamic solution of the TEM wave can be obtained by the electrostatic transverse field distribution:

$$E = (E_x, E_y) \cdot e^{j(\alpha x - \beta z)}. \quad (2)$$

In a TEM line, at any point of the outer conductor inner surface, the electric field (E) is always orthogonal to the magnetic field (H), and both are related by:

$$\frac{|E|}{|H|} = Z_0, \quad (3)$$

where $Z_0 = 377\Omega$ is the vacuum impedance. For very high frequencies, and considering perfect conductors, J in the inner surface of the outer conductor is equal to the tangential H in the same surface:

$$J = H_t \hat{\phi}. \quad (4)$$

Joining Eqs. 3 and 4 to Eq. 1 leads us to:

$$\frac{Z_v}{Z_h} = \frac{\int |E_v|^2 dl}{\int |E_h|^2 dl}, \quad (5)$$

where E has to be considered normal to the outer surface, since we are assuming a perfectly conducting beam pipe.

In such a perfect conductor the skin depth is null and therefore the transverse impedance (Z_T) will not depend on the frequency. This dependence can be introduced as a perturbation in a second order calculation, but the first order field distribution is not affected by the conductivity of the material. Therefore, the J distribution is related only to beam parameters, such as the beam displacement, i.e. the wire displacement in our model. One way to measure Z_T (and also the longitudinal impedance, Z_L) is to measure the variation of J versus the lateral displacement of the beam (wire) [3]. For that reason, we use the classical method of the two wires (polarized in the odd mode) to do bench measurements and calculations. In a

first order approximation, the field distribution produced by an offset wire can be assumed to be generated by a centered wire plus the effect of a dipole field, which is illustrated in Fig. 1. The ratio of $\int E^2 dl$ for the total electric field (centered wire plus dipole) is the same as the ratio of the $\int E^2 dl$ for a dipole: a single offset wire (beam) can be represented for the surface charge or current distribution by a centered wire plus the contribution of a dipole moment. Since we are only interested in Z_T , we only consider the dipole moment (wire pair).

SuperFish provides the normal E at each point of the surface. The number of points into which the surface is divided is given by the mesh size. In order to get good resolution, the optimum value for the mesh size has been set to 0.1 mm for a total length ranging from 36 and 44mm (*BS* dimensions). Different values for the inner conductor diameter (Φ_{int}) and the separation between the inner wires (s) have been used (Fig. 1) in order to find the best combination for the dipole size.

When calculating $\int E^2 dl$, it is worth mentioning that the differential length fixed by the mesh size, dl , is not constant in the circular as in the flat zones of the *BS* geometry (Fig. 2). In order to ensure all points have the same specific weight when computing the $\int E^2 dl$, normalization for the 'bin' length has been implemented.

3 RESULTS FOR THE DIFFERENT GEOMETRIES

We are interested in calculating the ratio Z_ν/Z_h for the *BS* following Eq. 5. In order to calibrate the method, some cases with a known analytical solution have been evaluated. Each case involves a cylindrical tube with a circular cross section (see Fig. 1) and a different radius ($R=18, 20$, and 22 mm). In each case, neglecting the skin depth, it turns out that Z_T depends inversely on the third power or R (see Ref. [4]). For a set of two different external radii, R_1 and R_2 , this ratio is:

$$\frac{Z_T(R_1)}{Z_T(R_2)} = \frac{R_2^3}{R_1^3}. \quad (6)$$

Since the *SuperFish* output will be $|E_i^2|$, the calibration of this method will be done joining Equations 5 and 6:

$$\frac{\int |E_{R_1}^2| dl}{\int |E_{R_2}^2| dl} = \frac{R_2^3}{R_1^3}. \quad (7)$$

3.1 Two Inner Conductors in a Round Geometry

Figure 1 describes the general calibration geometry. The two inner conductors are numerically polarized to +1V and -1V respectively. The dimensions and the corresponding results for these cases are given in Table 1. Basically, the goal is to check how well the method agrees with the theoretical results and find an optimum value for the dipole size, i.e., an optimum combination of Φ_{int} and s .

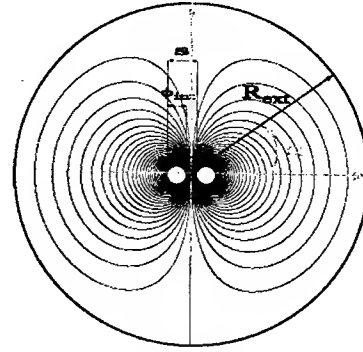


Figure 1. General round geometry used to calibrate the method. R_{ext} stands for the external radius (in the text stated as R); Φ_{int} is the diameter of the internal wire; s is the distance between the inner conductors; and α marks the angle. The two lossless inner conductors are numerically polarized to +1V and -1V, and the internal lighter lines represent the equipotential lines.

Table 1: Ratio $\int E_{R_2}^2 dl / \int E_{R_1}^2 dl$ for different combinations of R_1 and R_2 and the different dipole sizes. Last row shows the theoretical value according to Eq. 7.

	$R_1=18\text{mm}$ $R_2=20\text{mm}$	$R_1=20\text{mm}$ $R_2=22\text{mm}$	$R_1=18\text{mm}$ $R_2=22\text{mm}$
$\Phi_{int}=2\text{mm}$ $s=3\text{mm}$	1.3780	1.3352	1.8399
$\Phi_{int}=2\text{mm}$ $s=6\text{mm}$	1.3888	1.3430	1.8653
$\Phi_{int}=4\text{mm}$ $s=6\text{mm}$	1.4035	1.3531	1.8992
Theoretical value: R_2^3/R_1^3	1.3717	1.3310	1.8258

Table 1 shows the results of the calibration done using Eq. 7. Results for the smallest dipole case ($\Phi_{int}=2\text{mm}$ and $s=3\text{mm}$) show very good agreement: the maximum error for this geometry is within 1%. For a given combination of R_1 and R_2 , the error increases with the dipole size. We can see that the discrepancy in the case of the largest dipole, i.e., $\Phi_{int}=4\text{mm}$ and $s=6\text{mm}$, can be as big as 8%. Note that for a fixed combination of Φ_{int} and s , the maximum error corresponds to the maximum difference between R_1 and R_2 . Table 1 gives also an indication of the mistake one makes with the classical 2 wires method for Z_T measurements as a function of s and Φ_{int} .

According to results shown on Table 1, the best configuration when computing the ratio Z_ν/Z_h for the *BS* geometry, is the combination of $\Phi_{int}=2\text{mm}$ and $s=3\text{mm}$.

3.2 Results for the Beam-Screen Geometry

Figure 2 shows the *BS* cross section with the two inner conductors placed in the horizontal plane. For the calculations in the vertical case, the dipole is rotated 90°.

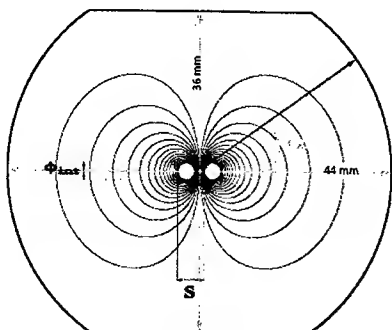


Figure 2. Cross section of the *BS* geometry with two wires inside simulating the dipole field. The inner wires are placed in the horizontal plane and held to +1V and -1V. The closed lighter lines represent the equipotential lines. For the vertical case, the dipole is rotated 90°.

In this case, we will use Eq. 6 to evaluate the Z_v/Z_h . Figure 3 shows the $|E_i^2|$ distribution for both vertical and horizontal configurations. The final results can be found in Table 2.

Table 2. Final results used to compute Z_v/Z_h and the value of the ratio of the horizontal and vertical Z_T 's.

$\int E_{VER}^2 dl$	11.2830 (V/cm) ²
$\int E_{HOR}^2 dl$	7.8678 (V/cm) ²
Z_v/Z_h	1.43

The prediction for Z_v/Z_h is in a good agreement with other methods, such as the Boundary Element Method (BEM) from H. Tsutsui in [5], who recently obtained $1.42 \pm 1\%$. Our error bar is estimated to be 1%, as stated in Sec. 3.1.

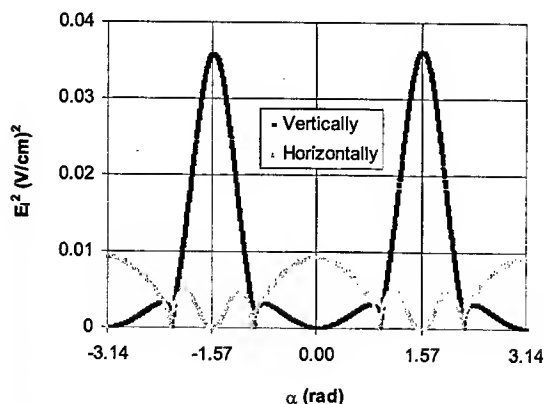


Figure 3. Distribution of $|E_i^2|$ at the surface of the external conductor of the *BS* surface as a function of the angle α when the inner conductors are placed vertically (blue trace) and horizontally (orange).

4 CONCLUSIONS

By means of an electrostatic computer code, one can compute a reasonable approximation for Z_v/Z_h for any beam pipe cross section. Assuming 2 lossless wires, the classical two wire method has been implemented by simulating the 2D electrostatic field and image charge distribution of the *BS* geometry, and subsequently calculating the corresponding surface current for a TEM wave excitation. The electrostatic computer code used was *SuperFish*, which as mentioned in Sec. 2, requires length normalization, especially for non-circular surfaces. The appropriate dipole size is critical to get reasonable results, and it should be as small as possible. Theoretical justification to compute the ratio Z_v/Z_h from the ratio of $\int E^2 dl$ is given. For the LHC *BS* geometry we predict $Z_v/Z_h = 1.43 \pm 1\%$, which is in a good agreement with other theoretical results [5]. The calculation of coupling impedance of beam pipes of general cross section has also been solved by Yokoya [6] by means of a field formula perturbation solution, which is not always applicable. However, the use of this method is only restricted by the use of the electrostatic computer code. In the case of *SuperFish*, all arbitrary surfaces can be simulated and therefore, this can become a useful tool to calculate the transverse impedance.

5 ACKNOWLEDGMENTS

The authors would like to thank F. Ruggiero, L. Vos, and B. Spataro for their helpful and useful discussions. K. Zeno and N. Luciano made the English in this paper readable.

REFERENCES

- [1] J.H. Billen, L.M. Young. Poisson Superfish on PC compatibles. PAC'93, Washington, May 1993.
- [2] D. Brandt and L. Vos. Resistive wall instability for the LHC: intermediate review. LHC Project Note 257, CERN, Geneva, June 2001.
- [3] Regenstreif, E. Electrostatic beam potential created by a uniform round beam coasting off center in a circular vacuum chamber. CERN/PS/DL 76-2. Geneva, 1976.
- [4] G. Nassibian and F. Sacherer. A method for measuring transverse coupling impedance. CERN, PS/BR 77-40. Geneva, 1977.
- [5] H. Tsutsui. Using boundary element method for calculation of coupling impedance of beam pipes of general cross section. LHC project note. Geneva, September 2002.
- [6] Yokoya, K. Resistive wall impedance of beam pipes of general cross section. KEK 92-196, Oho, Tsukuba-shi, Ibaraki, Japan. February 1993.

CONFIGURABLE UAL-BASED MODELING ENGINE FOR ONLINE ACCELERATOR STUDIES

N. Malitsky, T. Satogata, BNL, Upton, NY 11973, USA,
R. Talman, Cornell University, Ithaca, NY 14853, USA

Abstract

The diversity of online accelerator modeling tasks poses a considerable challenge for accelerator physicists and software developers. Compromises between performance and completeness are always required. For example, modeling of chromatic effects requires second-order calculations, while speed favors first-order matrix multiplication. This paper presents our solution: a configurable computational modeling engine based on the UAL Accelerator Propagator Framework (APF). The choices of evolution algorithms are defined in an external Accelerator Propagator Description Format (APDF) file, permitting a flexible mechanism for employing different approaches within the context of machine studies and operation.

RATIONALE

Demands on online modeling during commissioning and routine operation of an accelerator are fairly predictable. Often a single model (possibly only the design model) services the physicist's needs. However, more flexibility is often required while planning studies and a flexible, easily configurable model is most necessary during accelerator studies, to efficiently deal with improvisation and unanticipated beam conditions.

Previous approaches to online model flexibility[1] have wrapped model engines, ranging from simple to complex, in a single modeling environment. Though this unifies client and server layers for various models, reconfiguration of modeling layout of the underlying model engines requires architecture changes or recompilation.

The UAL framework[2] within the RHIC/AGS online model already incorporates most relevant physics, and UAL is easily extensible. We have therefore designed and implemented a flexible configuration format for UAL, to allow dynamic specification of modeling propagators and to permit evaluation of tradeoffs between speed and completeness in online modeling applications for machine studies.

ACCELERATOR PROPAGATOR FRAMEWORK

The Accelerator Propagator Framework (APF) is the next logical step of the UAL evolution. APF aims to provide a consistent mechanism for building configurable accelerator modeling engines. The first phase of the UAL infrastructure was associated with development of the Standard Machine Format (SMF) which introduced a compact and generic accelerator model for implementing various accelerator structures. The organization of SMF is exhibited graphically in Fig. 1.

Lattice Input File (MAD, SXF, ADXF)

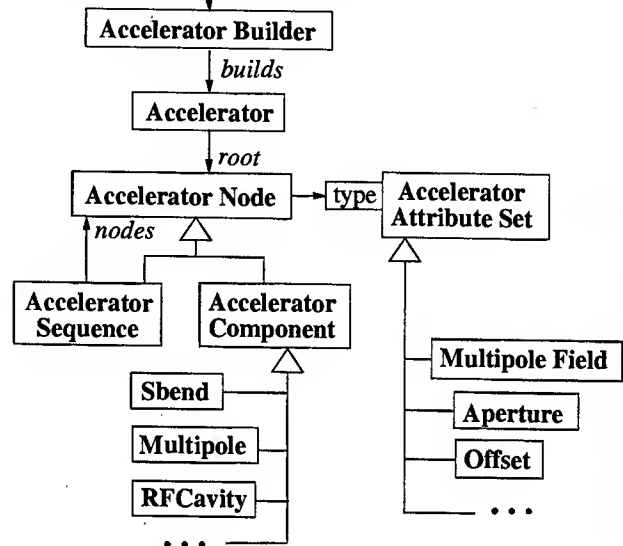


Figure 1: Standard Machine Format object model.

SMF, the result of analysis and generalization of several accelerator modeling formats, has been successfully tested by several accelerator projects. Its data structures have also been optimized from different implementation perspectives, facilitating the employment of formal methodologies for mapping SMF objects into various physical representations, such as Java classes, XML, relational databases tables, and GUI components. The second part of the UAL infrastructure, the Accelerator Propagator Framework (APF), has been based on proven SMF design patterns. Fig. 2 shows the APF model.

In APF, *Accelerator Propagator* replicates the hierarchical organization of the Accelerator structure with one important distinction. Each *Propagator Node* may be associated with an entire accelerator sector identified by begin and end *Accelerator Nodes*. This scheme allows us to accommodate most accelerator modeling algorithms and to bridge the gap between element-by-element and map-based approaches. The structure of the configurable Accelerator propagator is described in the Accelerator Propagator Description Format (APDF). Then one can consider the APDF file as a complement to the MAD and SXF lattice input files.

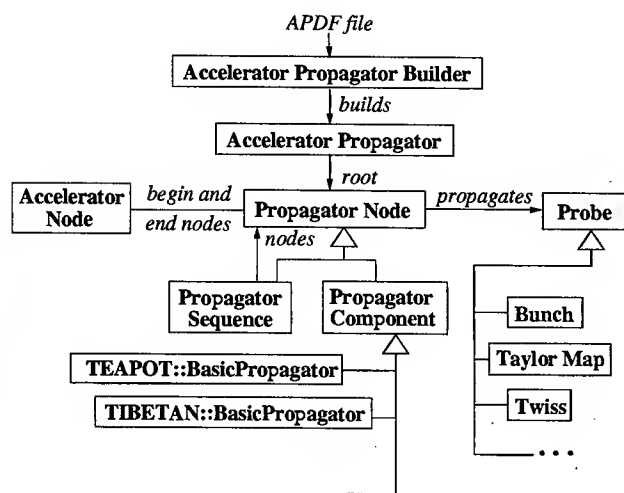


Figure 2: Accelerator Propagator Framework

APDF SPECIFICATION

The structure of the Accelerator Description Format (APDF) is determined by a single conceptual statement: *Accelerator Propagator is a sequence of links between accelerator nodes and corresponding accelerator algorithms.* This statement introduces two entities, *Accelerator Propagator* and *Link*, and their relationship. According to the formal methodologies, like the lattice description, this model should be naturally represented by an ordered list of all elements with their element-algorithm associations. However, for the sake of brevity, we favor a command-oriented SQL-like approach that allows one to define many associations in a very compact way. The following sections describe the structure and semantics of the APDF elements.

APDF Propagator

Accelerator Propagator is a sequence of element-algorithm links that can be created, inserted, and deleted in the APDF file:

```

<!ELEMENT propagator (create|insert|delete) >
<!ELEMENT create (link)*>
<!ELEMENT insert (link)*>
<!ELEMENT delete (link)*>

```

The `<create>` procedure builds a propagator instance from scratch. The `<insert>` and `<delete>` elements aim to facilitate user's extensions of some common and sharable accelerator propagator version.

APDF Link

The APDF link, the key element of the APDF specification, provides the mechanism for associating a selected family of accelerator nodes with appropriate accelerator algorithms:

```

<!ELEMENT link>

```

```

<!ATTLIST link
  algorithm CDATA #REQUIRED
  sector    CDATA #IMPLIED
  elements  CDATA #IMPLIED
  types     CDATA #IMPLIED
>

```

The following table contains a brief description of link attributes:

sector	a pair of begin and end accelerator element design names, e.g. "d1, qf1"; (sector includes d1 but not qf1)
elements	a regular expression for selecting accelerator nodes with specified design names, e.g. "q1 q2"
types	a regular expression for selecting accelerator nodes with specified element types, e.g. "Quadrupole Sextupole"
algorithm	a full class name of the associated propagator, e.g. "TEAPOT::MltTracker"

Sector, elements, and types define three different approaches for selecting families of accelerator elements. In case of overlapping, sector-based priority is first, element-based priority is second, and type-based priority is third.

APPLICATIONS

This approach addresses the spectrum of applications ranging from small special tasks to full-scale realistic beam dynamics studies encompassing heterogeneous algorithms and special effects. This will be illustrated by several models that exhibit different features of APDF description.

Longitudinal Tracker

A traditional accelerator longitudinal model is usually represented by a combination of 2D sector matrices and RF cavity nodes. In the APF framework, this structure can be described by the following (complete) APDF file:

```

<apdf>
  <propagator>
    <create>
      <link algorithm="TIBETAN::SectorTracker"
        sector= "Default" />
      <link algorithm= "TIBETAN::RFCavityTracker"
        elements="rfac1" />
      <link algorithm="TIBETAN::WCMonitor"
        elements="mend" />
    </create>
  </propagator>
</apdf>

```

In contrast with traditional programs, linear coefficients and nonlinear momentum-compaction factors of TIBETAN *SectorTracker* are not part of the new input file; they are calculated during an initialization phase from a common lattice description (such as MAD or SXF input file) shared by other modeling engines. This approach facilitates the synchronization of input parameters among various project

applications and the consistent transition between different simulation scenarios. In addition to longitudinal tracking algorithms, the above model is also able to accommodate a diagnostics device, Wall Current Monitor, which accumulates beam profiles after each turn and forwards them to an intermediate buffer. The extensibility of the APDF-based longitudinal tracker also permits the addition of longitudinal space charge and various impedance effects as associations of corresponding algorithms with arbitrary elements or markers of the accelerator lattice.

Conventional Element-by-Element Tracker

In traditional accelerator codes, tracking algorithms have been uniquely associated with particular element types. This functionality can, of course, be replicated by APDF. The following file represents the original TEAPOT element-by-element tracking engine:¹

```
...
<create>
  <link algorithm="TEAPOT::DriftTracker"
    types= "Default" />
  <link algorithm="TEAPOT::DriftTracker"
    types="Marker|Drift|[VH]monitor|Monitor" />
  <link algorithm="TEAPOT::DipoleTracker"
    types="SBend" />
  <link algorithm="TEAPOT::MltTracker"
    types="Quadrupole|Sextupole|Multipole|
      [VH]kicker|Kicker" />
  <link algorithm="TEAPOT::RfCavityTracker"
    types="RfCavity" />
</create>
...
```

As well as preserving this traditional scheme, the APDF approach provides a consistent mechanism for combining algorithms from different UAL modules and for adding application-specific extensions. The following APDF file describes an updated model for collecting turn-by-turn BPM data in the Model Independent Analysis (MIA) application:

```
...
<create>
  <link algorithm="TEAPOT::DriftTracker"
    types= "Default" />
  <link algorithm="TEAPOT::DriftTracker"
    types="Marker|Drift|[VH]monitor" />
  <link algorithm="TEAPOT::DipoleTracker"
    types="SBend" />
  <link algorithm="TEAPOT::MltTracker"
    types="Quadrupole|Sextupole|Multipole|
      [VH]kicker|Kicker" />
  <link algorithm="TIBETAN::RfCavityTracker"
    types="RfCavity" />
  <link algorithm="MIA::BPM"
    types="Monitor" />
</create>
...
```

¹For brevity, beginning and ending "apdf" and "propagate" tags are suppressed from the remaining examples.

In this example, MIA::BPM is a temporary application-oriented class that collects data and writes them into a global container analyzed by the MIA post-processing tool.

Fast TEAPOT

Chromatic effects are a typical accelerator feature modeled by many conventional element-by-element and differential algebra-based accelerator codes. However, the power of all-purpose accelerator programs significantly diminishes their computation speed, tending to make them unacceptable for online applications. The APDF fine-grained selection mechanism allows us to build "custom-made" models from a combination of sector linear matrices and TEAPOT symplectic integrators for chromatic elements such as the main quadrupole and sextupole elements—the so-called Fast TEAPOT:

```
...
<create>
  <link algorithm="TEAPOT::MatrixTracker"
    sector= "Default" />
  <link algorithm="TEAPOT::MltTracker"
    types="Quadrupole|Sextupole" />
</create>
...
```

The same approach can be applied to other applications for studying localized dominant effects (for example, interaction regions) or combining traditional algorithms with application-oriented, efficient approximations.

ONLINE MODELING

The RHIC/AGS model server provides CDEV access and namespace support for multiple concurrent online models. With the APDF specification in UAL, these online model instances are uniquely specified by the SMF lattice and the APDF algorithm specification. Work is in progress to extend the CDEV access to permit dynamic model instantiation with user-specified APDF files customized for specific beam studies, such as nonlinear dynamics and roll of interaction region triplets. Standard operations applications can then retrieve optics and lattice information from these customized models for study planning and feedback.

Though flexibility is paramount in an offline modeling environment where hypotheses are constantly being tested and reinterpreted, model stability is also important for machine operations and reproducibility. There is therefore also a canonical operations model that is the default source of all application modeling data for RHIC, and the APDF for this model is under strict configuration control.

REFERENCES

- [1] T.Satogata, et al. The RHIC Online Model Environment: Design and Overview, PAC 99.
- [2] See <http://www.ual.bnl.gov>.

A COMPARISON OF SEVERAL LATTICE TOOLS FOR COMPUTATION OF ORBIT FUNCTIONS OF AN ACCELERATOR *

Ernest D. Courant, Scott J. Berg, and Dejan Trbojevic, BNL, Upton, New York
 Richard Talman, Cornell University, Ithaca, New York
 Al A. Garren, LBL, Berkeley, California

Abstract

The values of orbit functions for accelerator lattices as computed with accelerator design programs may differ between different programs. For a simple lattice, consisting of identical constant-gradient bending magnets, the functions (horizontal and vertical betatron tunes, dispersions, closed orbit offsets, orbit lengths, chromaticities etc.) can be evaluated analytically. This lattice was studied with the accelerator physics tools SYNCH [1], COSY INFINITY [2], MAD [3], and TEAPOT [4]. It was found that while all the programs give identical results at the central design momentum, the results differ substantially among the various lattice tools for non-zero momentum deviations. Detailed results and comparisons are presented.

1 INTRODUCTION

The neutrino factory or muon-collider project requires very fast muon acceleration due to a short muon lifetime. The non-scaling FFAG: fixed alternating gradient field synchrotron in recent analyses has been shown to be a promising solution [5]. The lattice design of such a synchrotron requires coverage of a very large range of momentum in the fixed magnetic field ($\delta p/p \sim \pm 40\%$). A simple test case was used to compare various lattice design codes. For this case the Courant-Snyder lattice functions can be calculated analytically, and the results compared to results obtained using the accelerator physics codes SYNCH, MAD, COSY, and TEAPOT over a wide momentum range ($\delta p/p < 40\%$). We use the equations of particle motion as presented, for example, in the first lecture in the 1981 accelerator physics school [6]. In the third section, we show the results for the dependence on momentum of the lattice functions. The fourth section is a summary of the results.

2 A SIMPLE CYCLOTRON

2.1 Accelerator physics relations

The equations of motion [2] are:

$$\frac{\partial^2 x}{\partial s^2} = -\frac{x}{\rho^2} + \frac{B_y - B_0(s)}{B\rho} \quad (1)$$

$$\frac{\partial^2 y}{\partial s^2} = -\frac{B_x}{B\rho} \quad (2)$$

We take the magnetic field to be:

$$B_y = B_0 \left(1 - \frac{n_0 x}{\rho_0} \right) = B_0 + Gx \quad (3)$$

$$B_x = B_0 \frac{n_0 y}{\rho_0} \quad (4)$$

Where ρ_0 is the central radius, B_0 the central field, and we assume the field depends linearly on the radius with gradient $G = -n_0 B_0 / \rho_0$, with no nonlinearity. The central radius is equal to $\rho_0 = p_0 / eB_0$. With a momentum offset δ defined by $\delta = \Delta p / p_0$, the closed orbit is a circle of radius $\rho_0 + x_0$, where the magnetic field B_y equals $B_0 + Gx_0$; we have the equation:

$$e(B_0 + Gx_0)(\rho_0 + x_0) = p_0(1 + \delta) \quad (5)$$

To simplify the equation (5) we introduce a new variable $u = x_0 / \rho_0$ and define $\lambda = (1 - n_0) / 2n_0$. We obtain the equation:

$$n_0 u^2 - (1 - n_0)u + \delta = 0 \quad (6)$$

The solutions of which are:

$$u_{1,2} = \lambda \pm \sqrt{\lambda^2 - \frac{\delta}{n_0}} \quad (7)$$

(The minus sign should be chosen) The two transverse equations of motion for oscillations about the circle of radius $\rho = \rho_0 + x_0$ are as usual:

$$\frac{\partial^2 x}{\partial s^2} = -\frac{(1-n)}{\rho^2} x \quad (8)$$

$$\frac{\partial^2 y}{\partial s^2} = -\frac{n}{\rho^2} y, \text{ The local field index } n \text{ is:} \quad (9)$$

$$n = n_0 \frac{1+u}{1-n_0 u} \quad (10)$$

The condition for stable solutions is $0 < n < 1$. The analytical solutions for the Courant-Snyder lattice parameters like horizontal and vertical tunes ν_x and ν_y , amplitude functions β_x and β_y , are:

$$\nu_x = \sqrt{1-n}, \nu_y = \sqrt{n}, \beta_x = \frac{\rho}{\sqrt{1-n}}, \beta_y = \frac{\rho}{\sqrt{n}}.$$

The horizontal and vertical chromaticities ξ_x , and ξ_y , are defined to be the derivatives of the tunes with respect to the relative momentum offset δ : $\xi_x = \partial \nu_x / \partial \delta$ and $\xi_y = \partial \nu_y / \partial \delta$.

*Work performed under Contract Number DE-AC02-98CH10886 under the auspices of the US Department of Energy

The dispersion D_x and the momentum compaction factor α_c are: $D_x = \partial x_0 / \delta = \rho / (1 - n)$ (as $\partial x \equiv D_x \delta p / p = D_x \delta$) and $\alpha_c = D_x / \rho = 1 / (1 - n)$.

2.2 The test case-cyclotron 100 meters long

To make the easiest comparison for the large off momentum offsets we used a ring with a circumference of $C_0 = 100$ m, made up of five combined-function constant-gradient magnets, each 20 m long, with the central rigidity of $B\rho = 50$ Tm, and with the field index $n_0 = 0.5$. All other ring parameters like the central bending radius ρ_0 , the vertical bending magnetic field B_0 follow as $\rho_0 = C_0 / 2\pi$ and $B_0 = 50 / \rho_0$. The betatron functions for the central energy are calculated correctly in all of the codes (MAD, SYNCH, COSY, TEAPOT).

3 RESULTS

A few details of use of the accelerator physics codes should be noted. The COSY INFINITY code was set up to do the transfer matrix calculation with an 8th order polynomial expansion in momentum. MAD was used in the version MAD8c as implemented on the BNL computer system. The magnets are defined as sector dipoles with gradients. TEAPOT is a thin element approximation code, so the 20 m long dipole was divided into 8000 pieces. The SYNCH code was used with a sector dipoles definition with gradients. The analytical results for various parameters as a function of momentum, together with results from the four different codes are presented in Figs. 1. to 7. Note that all the codes agree for $-0.08 < d < 0.08$, but only SYNCH agrees with the analytical results over the whole range. The orbit offsets ($x_0 = \rho - \rho_0$) as a function of momentum are shown in Fig. 1.

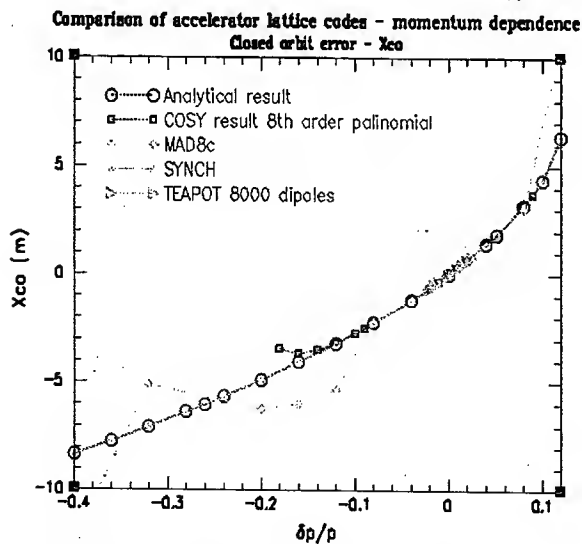


Figure 1: Orbit offset dependence on momentum. Fig.2 shows the change in circumference; this should of course be just $2\pi x_0$, but comparing Fig.1 and 2 we see that MAD has a discrepancy.

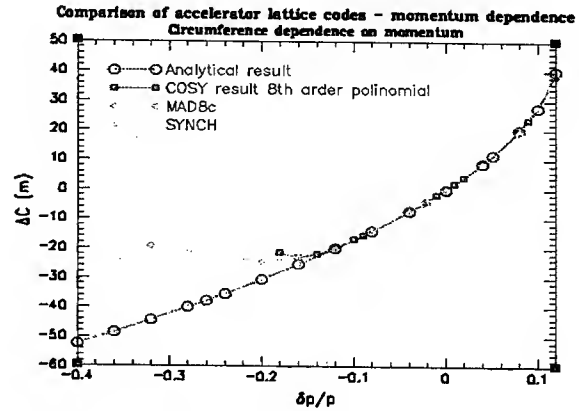


Figure 2: Change in circumference vs. momentum.

The results for the horizontal and vertical betatron are presented in Fig. 3 and Fig. 4.

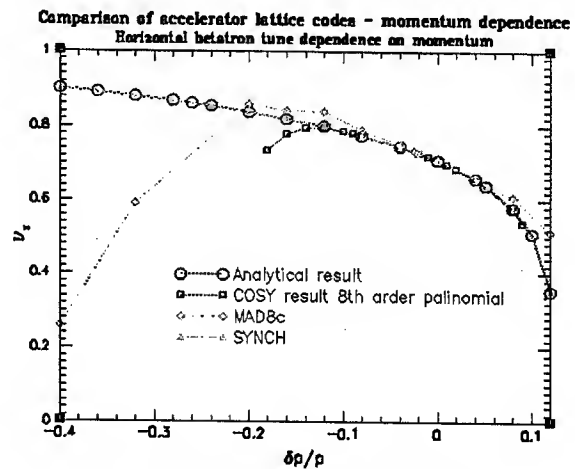


Figure 3: Horizontal betatron tune vs. momentum.

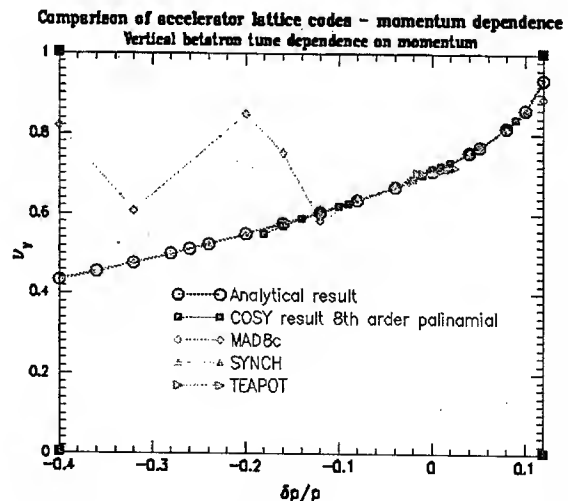


Figure 4: Vertical betatron tune vs. momentum.

The betatron functions β_x and β_y vs. momentum are presented in Fig. 5 and Fig. 6, respectively.

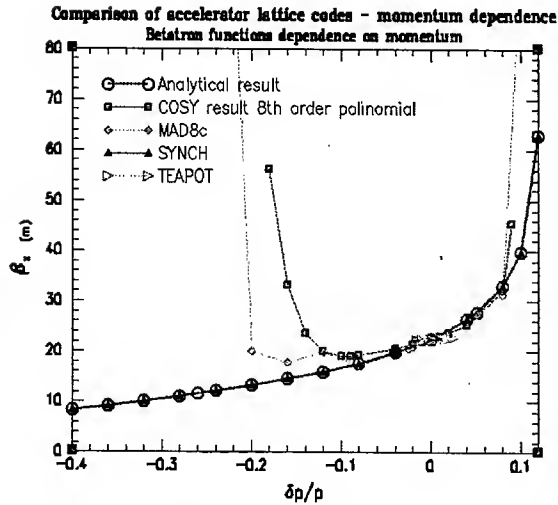


Figure 5: β_x vs. momentum.

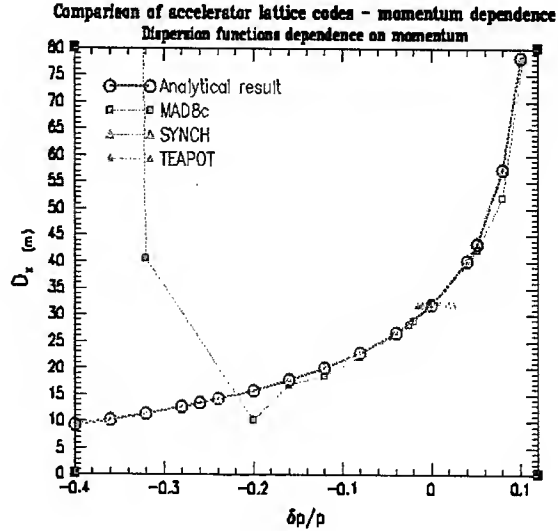


Figure 7: Dispersion function vs. momentum

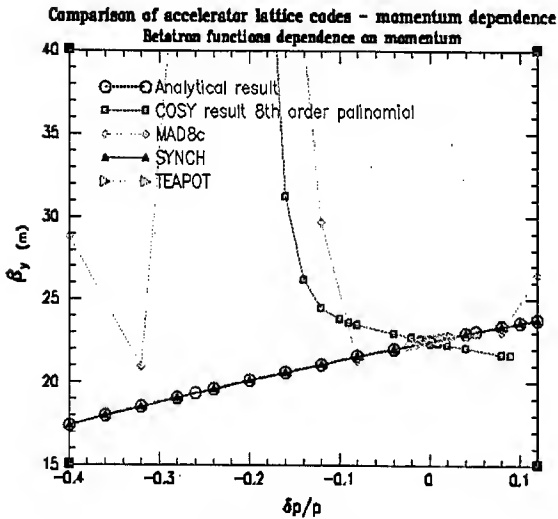


Figure 6: β_y vs. momentum.

One of the most important parameters for the large momentum offsets in the lattice design is the dispersion function. The analytical prediction for the dispersion function, defined as $D_x = \rho / (1 - n)$ in this example, together with the code results is shown in Fig. 7. The momentum compaction $\alpha_c = D_x / (\rho_0 + x)$ in this example divided by the horizontal tune should be equal to $\alpha_c / \nu_x = \text{one}$. This was confirmed by SYNCH and within a limited momentum range by the other codes. The dispersion function dependence on momentum calculated analytically together with the codes results is shown in Fig. 7.

4 SUMMARY

Large momentum offset calculations occur in some applications such as the Fixed Field Alternating Gradient synchrotron (FFAG). There is a concern with the accuracy of the existing codes for the large momentum offsets of the order of $\pm 33\%$ and more. An easily analytically calculable example, made of five combined-function magnets, shows limitations in the momentum range of codes like MAD, TEAPOT, COSY INFINITY. The SYNCH code has shown perfect agreement between the analytical predictions and the code results for every lattice function examined.

5 REFERENCES

- [1] A. Garren, A. S. Kenney, E. D. Courant, A. D. Russell, and M. J. Syphers, SYNCH-A Program for Design and Analysis of Synchrotrons and Beam Lines, User's Guide 1993.
- [2] K. Makino and Martin Berz, "COSY INFINITY", Nuclear Instruments and Methods, A427, pp. 338-343, 1999, <http://cosy.pa.msu.edu/>.
- [3] F. C. Iselin and H. Grote, MAD, "Methodical Accelerator Design", CERN/SL, 90-13 (12991).
- [4] Richard Talman and Lindsay Schachinger, "Teapot: Thin Element Accelerator Program for Optics and Tracking", Particle Accelerators, 22, 35 (1991).
- [5] E.D. Courant, M. Blaskiewicz, J.S. Berg, R. Palmer, D. Trbojevic, A.A. Garren, "AN UPDATE ON THE FFAG LATTICE DESIGN WITHOUT OPPOSITE BEND AND WITH DISTRIBUTED RF", at this conference, TPPG003.
- [6] E. Courant, R.D. Ruth, W.T. Weng, "Introduction to Accelerator Theory", AIP Conference Proceedings, 87, American Institute of Physics, New York, 1982, pp. 4-14.

LIONS_LINAC : A NEW PARTICLE IN CELL CODE FOR LINACS

P. Bertrand[#], GANIL, Caen, France

Abstract

In the frame of the SPIRAL II project at GANIL, a new particle-in-cell code called LIONS_LINAC has been developed. It is written in pure Fortran 95, and can work either on PCs and workstations or on vectorial/parallel computers. We present the main characteristics of the code, in particular the treatment of the space charge effects, using the multigrid method with conjugate gradient smoothing iterations.

INTRODUCTION

A detailed study on a new facility at GANIL for the production of high intensity exotic beams is underway. The SPIRAL II project, based on the LINAG I preliminary conceptual design [1], and using the Uranium target fission method, requires the acceleration of $q/A=1/3$ ions (1mA) and Deuterons (5mA) at 40Mev. It will consist of 2 dedicated ECR sources, a warm RFQ, and a linac composed of independently phased superconducting QWR and/or HWR cavities [2][3]. Accurate beam dynamics calculations using various codes are needed to optimise the linac and minimize the losses. In this context, we have developed a new code, LIONS_LINAC, using very precise 3D electromagnetic maps, able to solve huge space charge problems and study the halo dynamics.

LANGUAGE AND IMPLEMENTATION

We have chosen the Fortran 95 language and optional HPF directives, without any specific library, in order to ensure perfect portability and high efficiency on vectorial or parallel computers. In particular this allows one to use intensively the array notation, and the main object-oriented features (dynamic allocation, recursivity, derived type, etc), which makes the program easy to maintain and improve, and facilitates the multigrid method of coding.

INPUT FILES AND LINAC DESIGN

The code uses 2 main ASCII input-files : the first gives the ion characteristics (q , m , I , initial conditions...) and the algorithmic options (discretization scheme, time step, space charge solver...). The second file gives the list of elements (one per line) describing the MEBT and the linac (drifts, quadrupoles, solenoids, cavities...). The elements are included in boxes with extra-drifts so that it is easy to replace analytical fields by realistic field maps.

INITIAL CONDITIONS

The initial beam characteristics can be introduced in two ways: by giving the Twiss parameters in the different planes and generating a 6D uniform particle distribution, or by reading a portable binary file coming for example

from realistic output results given by an RFQ TOUTATIS computation [4]. This allows us to compare the behaviour of LIONS_LINAC with that of TRACEWIN [4].

DISCRETISATION IN TIME

In dealing with space charge effects, we have chosen the time as the evolution variable [5], and (x, P_x, y, P_y, z, P_z) as the phase space variable, where P is the generalised momentum. Leap-Frog and RK4 schemes are both implemented, which allows us to know the influence of the discretisation algorithm on the precision obtained.

ELECTROMAGNETIC FIELDS

Solenoids and incorporated steerers

Each solenoid can be chosen to be hardedge of analytical, with optional (x,y) steerers. In the hardedge case, the time step must be chosen small enough to avoid artificial emittance growth. In the analytical case, the solenoid is composed of a main coil and inverse correction coils on each side, following the suggestion in [6]. Using a 3rd order development of the 3 fields, we can chose the length, radius and B_z correction values with respect to the main coil, in order to minimize the resulting fringe field.

Cavities

The cavities can be QWR or HWR, and we use analytical or 3D (E,B) realistic field maps coming from SOPRANO [7]. In the case of QWR resonators, the vertical steering, due mainly to the B_x component, can be an issue and must be studied carefully. Knowing that the $B_x(z)$ function is generally close to that of $E_z(z)$, within a multiplicative constant, we introduce the parameter:

$$\delta = \frac{B_x}{E_z}$$

This also allows us to define useful "double-sinus" analytical fields including the magnetic steering component, and defined as follows:

$$V = \frac{9}{16} V_{stem} (\cos(kz) - \frac{1}{9} \cos(3kz) + \frac{8}{9} \sin(\omega t + \varphi))$$

$$E_z = \frac{9}{16} k V_{stem} (\sin(kz) - \frac{1}{3} \sin(3kz)) \sin(\omega t + \varphi) + \dots$$

$$E_r = -r \frac{9}{32} k^2 V_{stem} (\cos(kz) - \cos(3kz)) \sin(\omega t + \varphi) + \dots$$

$$B_x = \delta E_z \cot g(\omega t + \varphi) \quad ; \quad \omega = 2\pi f_{rf} \quad ; \quad k = \frac{2\pi}{\beta_0 \lambda}$$

Integrating this formulae along the cavity, we can obtain analytical expressions of the Transit Time Factor, the energy gain, the magnetic steering angle, the emittance

[#]bertrand@ganil.fr

growth induced by such a steering and the negative cavity shift Δy needed for a good compensation:

$$u = \frac{\beta}{\beta_0} ; T(u) = \frac{16 \sin(\pi/u) u^4}{\pi(1-u^2)(1-9u^2)} ; T(1)=1$$

$$\Delta W = \frac{9\pi}{16} q V_{stem} T(u) \cos(\varphi)$$

$$\frac{\Delta p_y}{P_{mag_steering}} = \frac{9\pi}{16} \frac{q V_{stem}}{m \beta c} \delta T(u) \sin(\varphi)$$

$$\frac{\Delta p_y}{P_{cavity_shift}} = \frac{9\pi}{32} \frac{q V_{stem}}{m \beta^2 c^2} k \frac{T(u)}{u} \sin(\varphi) \Delta y$$

$$\frac{E_{cavity_exit}}{E_{cavity_entrance}} = 1 + \frac{1}{2} \left(\frac{9\pi}{16} \frac{q V_{stem}}{m \beta c} \delta T(u) \cos(\varphi) \frac{\Delta \phi_{max}}{\Delta y_{max}} \right)^2$$

These calculations are very useful to compare the motion evolution in analytical or realistic fields, and understand the origin of emittance growths and anomalies.

SPACE CHARGE EFFECTS

The space charge force can be computed using analytical formulae or a 3D multigrid Poisson solver. The first method allows us to tune rapidly the various parameters using a limited number of particles; the second produces realistic results in the case of a mismatched initial beam and misalignments of elements.

Analytical method

In this case, we use an initial particle distribution which is *uniform in the 6D phase space*, and consider this property maintained along the acceleration. At a given time t , we calculate the second order space momenta and RMS values, which multiplied by $\sqrt{8}$ give a realistic evaluation of the marginal ellipsoidal envelopes. Then we apply to each particle the analytical fields corresponding to an ellipsoidal *3D uniform distribution* whose RMS parameters are the same: the internal and external analytical fields are of course necessary (fig (1)).

Multigrid solver

The multigrid method is a very powerful tool to accelerate the convergence of a 3D Poisson solver [8]. However some precautions have to be taken in order to obtain good results on a vectorial/parallel computer. We have chosen the Conjugate Gradient algorithm as the pre- and post-smoothers. It is highly parallel even if we put Dirichlet boundary conditions inside the 3D computing box (e.g. a tube). The restriction and prolongation use 27 points. The grids are nested in the natural way using the finite-difference scheme. The object-oriented data structures are defined in terms of user-defined types with chained lists, using pointers. The multigrid routine itself is recursive. All the parameters defining the nested meshes can be chosen in the initial data-file, and the different 3D arrays are dynamically

allocatable. In order to avoid CPU and memory consuming duplications when passing parameters to the specific calculation routines (conjugate gradient, restriction, prolongation), just the address of the huge arrays ($A(0,0,0)...$) are transmitted.

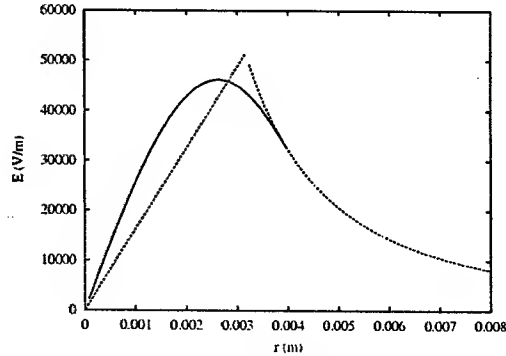


Figure 1: Theoretical electric fields for in a uniform 6D distribution and a uniform 3D one having the same RMS value, the space envelope being a sphere.

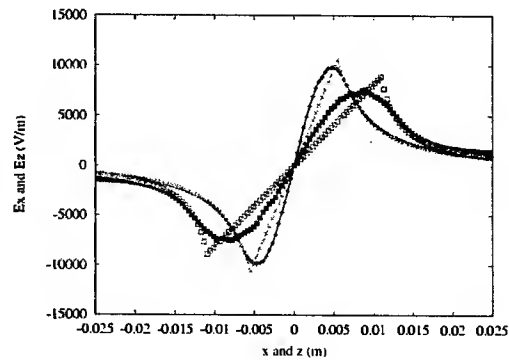


Figure 2: Analytical and Poisson electric fields deduced from a uniform 6D distribution of 200000 particles with a longitudinal length greater than the transverse size, using a 127x127x127 mesh.

For a bunch size of 1 cm in each direction, we choose a typical box of 3x3x3 cm, with about 2 million unknowns on the finer mesh, corresponding to a space step of 0.236 mm. With one CPU on a vectorial FUJITSU VPP-5000 computer, we obtain 0.3 second for 20 complete V-cycle multigrid iterations with a rate of 2.5 Gigaflops/s.

MISALIGNMENT TESTS

The misalignment of the cavities and the solenoids can be a problem in a linac. We can study these effects by applying to each element small misalignments in x and y and Euler angles in the case of solenoids. A misalignment-random generator for such misalignments will be added soon.

TUNING AND PHASE ADVANCE

An optional ASCII input-file can be read to activate the optimisation of the linac parameters. The linac is divided into successive sections. A Newton's method tunes the B_z value of each solenoid, according to a chosen envelope radius. A similar philosophy will be used for the optimisation of the cavity voltage and synchronous phase.

In order to evaluate the phase advances for each section we proceed as follows:

Once the *initial* bunch of n particles is randomly generated, and the beam matrix σ calculated with the 2nd momenta, we determine the subset of \tilde{n} particles corresponding to the beam core, having in mind the evaluation of the 1st order transfer matrix. The complete tracking being achieved for a given section, let P_0 and P the input and output $(6, \tilde{n})$ matrices giving the $(\Delta x, \Delta x', \Delta y, \Delta y', \Delta z, \Delta z')$ phase space positions. Then we calculate the $(6,6)$ transfer matrix T , which is numerically close to the symplecticity:

$$P = T P_0 \quad ; \quad \frac{P P_0^t}{\tilde{n}} = T \frac{P_0 P_0^t}{\tilde{n}} = T \tilde{\sigma}_0 \quad ; \quad T = \frac{P P_0^t}{\tilde{n}} \tilde{\sigma}_0^{-1}$$

The transverse and longitudinal planes being decoupled, the longitudinal phase advance is easy to deduce from T by finding the Twiss parameters. The situation is more complex in the transverse planes due to the coupling induced by the solenoids. Following [9], we decouple the (x, x') and (y, y') planes by a change of basis. This leads in fact to the determination of 2 *characteristic transverse phase advances*.

OUTPUT FILES

LIONS_LINAC generates a set of ASCII files compatible with the GNUPLOT package and giving various quantities as a function of the z value: particular (x, y, z) trajectory with electromagnetic applied components, beam envelopes and emittances, maximum spatial extensions, maximum space charge forces, etc. In order to compare the results with TRACEWIN calculations, LIONS_LINAC also generates binary files compatible with the PLOTWIN viewer (fig.3).

CONCLUSION

We have developed a new Particle In Cell code for linacs having in mind 2 main issues: the *emittance growth* and the *space charge* effects. The emittance growth may have various origins : longitudinal halo from the RFQ, random generation and number of particles, precision of the finite-element mesh in (E, B) field maps, time step, discretization method, non-linearities due to MEBT bunchers, $\Delta z \Delta x$ and $\Delta z \Delta y$ second-order effects through cavities, magnetic steering, misalignments, resonance coupling, space charge, etc. The space charge itself is very CPU and memory consuming when the halo

evolution has to be correctly simulated, which is the case in superconducting accelerators. The numerous options and the vectorial and parallel implementation of LIONS_LINAC will help to simulate all these effects in the best conditions.

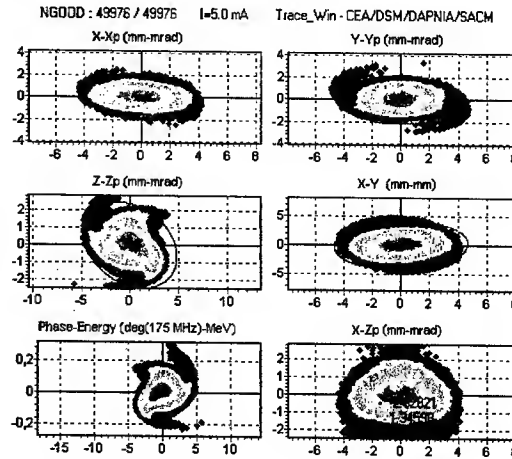


Figure 3 : Example of figures obtained at the linac exit.

ACKNOWLEDGMENTS

We would like to thank the student Yvan Gauthier, for its participation in the coding of the multigrid solver.

REFERENCES

- [1] http://www.ganil.fr/research/sp/reports/files/LINAG_PhaseI.pdf
- [2] A. Mosnier, SPIRAL II : "A High Intensity Deuteron and Ion Linear Accelerator for Exotic Beam Production", PAC2003, Portland, May 2003.
- [3] R. Duperrier et Al. , "Beam Dynamics Studies in SPIRAL II Linac" , PAC2003, Portland, May 2003.
- [4] R. Duperrier, N. Pichoff, D. Uriot, "CEA Saclay codes Review for High Intensity Linacs Computations" , ICCS2002, Amsterdam.
- [5] J. Qiang, R.D. Ryne, "Systematic comparison of position & time dependant macroparticle simulations in beam dynamics studies", Physical Review special topics, Accelerators and Beams, Vol .5. (2002).
- [6] P.N. Ostroumov, K.W. Shepard, S.H. Kim, E.S. Lessner, R. Laxdal, R. Wheatley, "A New Generation of Superconducting Solenoids for Heavy-Ion Linac Application", LINAC2003, Gyeongju.
- [7] OPERA-3D, Vector Fields. Ltd.
- [8] W. Hackbusch, "Multigrid Methods & Applications", Springer-Verlag, (1985).
- [9] D.A. Edwards and L.C. Teng, "Parametrization of linear coupled motion in periodic systems", IEEE Trans. Nucl. Sci 20, 3, pp 885-889 (1973).

NEW IMPLEMENT IN TRACEWIN/PARTRAN CODES: INTEGRATION IN EXTERNAL FIELD MAP

D. Uriot, CEA Saclay, 91191 Gif sur Yvette cedex, France,

N. Pichoff, CEA Bruyères-le-Châtel, BP 12, 91680 Bruyères-le-Châtel, France.

Abstract

The calculation of particle trajectories in external dynamic and/or static electromagnetic fields has been implemented in TraceWIN and PARTRAN codes [1]. The four field maps can be superposed. In TraceWIN (envelope code), the field is linearised around the synchronous trajectory. In PARTRAN, a RK4 integration in a measured or calculated field map is made. Results are produced for various projects like SPIRAL2, PISI and AIRIX.

INTRODUCTION

The TraceWIN/PARTRAN codes package has been developed in CEA and is used in various linac projects. TraceWIN is an envelope code capable to perform various functions like automatic matching or linac errors studies. It has a powerful and user-friendly interface. It is also able to run automatically PARTRAN and TOUTATIS, multiparticle codes and to process graphically its results [1].

Until then, both codes were using classical elements where the beam dynamic was issued from analytical calculations. Recent needs have pushed us to implement the dynamic of beams in external magnetostatic, electrostatic or electromagnetic field maps. These field maps can be 1D (on the axis in cylindrical symmetry, using an expansion of the field out of the axis), in 2D ((r,z) in cylindrical symmetry configuration or (x,y) in transverse fields), or in 3D. Moreover, these 3 kinds of field maps can be superposed.

These new possibilities have been extensively used recently:

- for SPIRAL2 project, to put in evidence the transverse kick of quaterwave resonator, and its coupling with solenoid focalisation.
- for PISI project, to calculate the extraction of a low current heavy ions beam from an electrostatic source, through a Einzel lens and a Wien filter,
- for AIRIX project, to calculate the transport of a 2 kA beam focalised with solenoids through an induction machine.

SPIRAL 2 PROJECT [2]

The proposed LINAG driver for the SPIRAL 2 project aims to accelerate a 5 mA D^+ beam up to an energy of 20 A.MeV and an 1 mA beam for $Z/A=1/3$ up to 14.5 A.MeV. It consists in an injector (two ECRs sources + Radio Frequency Quadrupole) followed by a

superconducting section based on an array of independently phased cavities [3]. The QWR description is carried out by 3D electric and magnetic field maps. The transverse focalisation is carried out by superconducting solenoids described by a 1D magnetic field map. All the matching and correctors calculations between the four tanks have been performed using TraceWIN functionalities giving 1 mm misalignment error randomly distributed on cavities and solenoids. The final multiparticle simulation is made with PARTRAN. The simulation has been performed with a 100.000 macro-particles Gaussian distribution at the first tank input. The whole computation requires about half an hour, considering a two millimetres step for extern fields and one centimetre step for space-charge computations. Figure 1 shows transverse envelopes for the deuteron beam (green). The beam centroid motion due to the QWR steering and misalignment is clearly visible (pink).

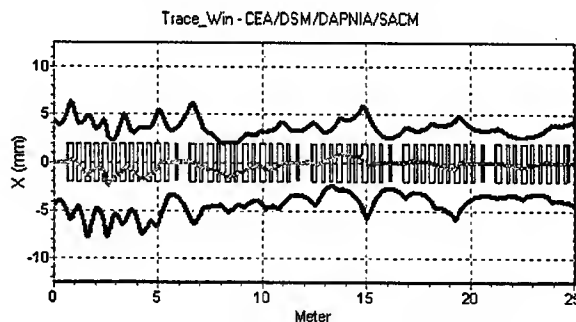


Figure 1: Transverse beam envelope behaviour

The multiparticle distribution along the structure is very close to the envelope behaviours (figure 2). The output space phase distributions are shown figure 3.

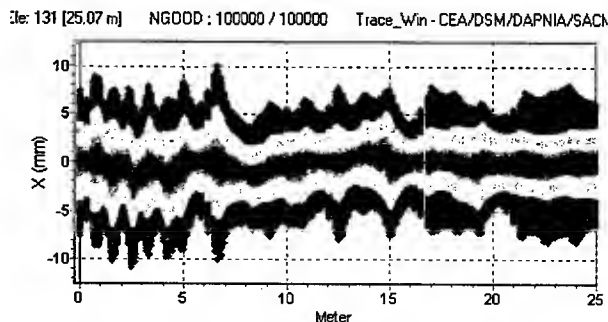


Figure 2: Transverse multiparticle distribution along the linac for deuteron beam.

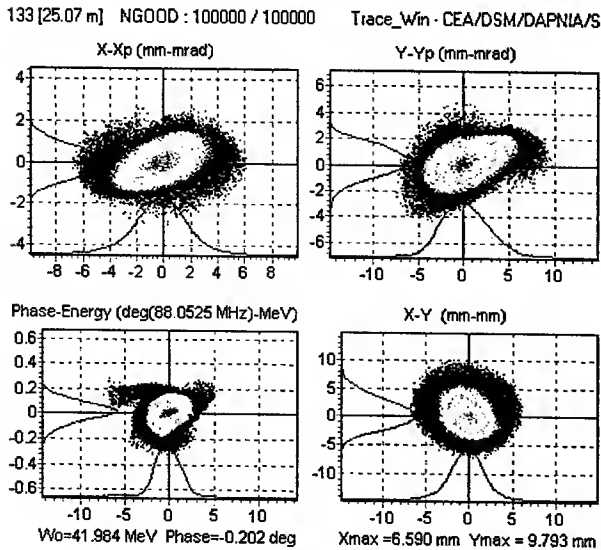


Figure 3: Output distribution for deuteron beam.

Most of emittance growth is due to the phase dependence kick in QWR and transverse solenoid coupling. And these effects are both visible in envelope and multiparticle codes.

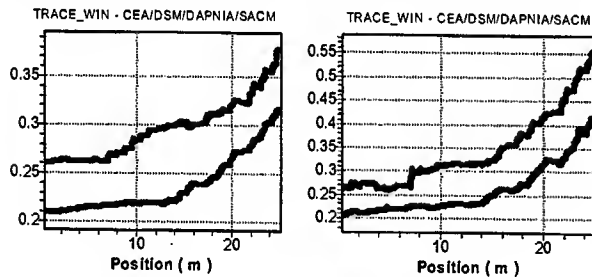


Figure 4: Transverse (violet) and longitudinal (green) rms emittance growths in envelope (left) and multiparticle simulation (right).

In this example, the full linac is described by field maps and the linac tuning computations have been performed with envelope formalism. The results stay very similar in multiparticle simulations allowing to save a lot of computation time.

PISI EXPERIMENT

PISI is an experiment which aims in measuring the photo-ionisation cross section of multi-charged heavy ions. The ions beams are produced with an ECR source. The beam is then focalised with an Einzel lens and goes through a Wien filter mass separator. The beam is then transported toward an "interaction region" where it is kept parallel to a photon beam delivered by the Super-ACO synchrotron light source.

The electrostatic field map in the extraction region has been calculated in 2D using POISSON code [4]. The beam is then transported in this map with PARTRAN.

The influence of the source ions temperature and plasma potential has been evaluated.

The figure 5 represents the beam propagation through the extraction geometry of PISI source. The plasma temperature is 10 eV.

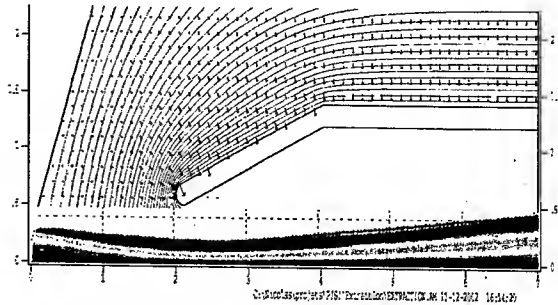


Figure 5: PISI source extraction configuration.

The beam output (x, x') phase-space distribution is plotted in figure 6. In these conditions (very low beam current, and beam far from the extraction hole border), the larger contributor to the final emittance is the plasma temperature.

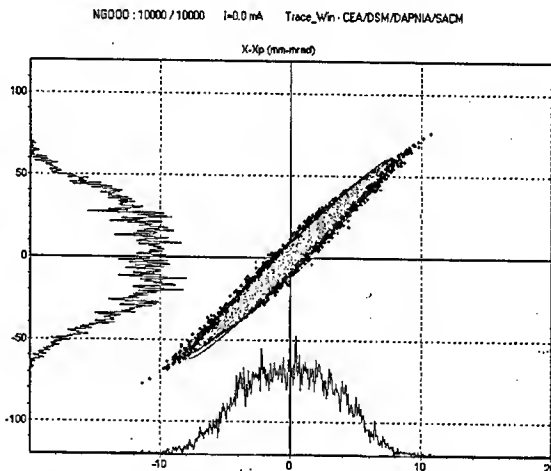


Figure 6: Output beam distribution in (x, x') phase-space.

AIRIX LINAC

AIRIX [5] is a high current (up to 3 kA) electron linac aiming in x-ray production for radiography. The beam is produced by a 4 MV diode and accelerated to 20 MeV with induction cells. The transverse focalisation is done with solenoids. AIRIX has been successfully calculated and designed with an 1D envelop code, ENV [6]. Nevertheless, the measured focal spot is still bigger than the predicted one. This could arise from different effects which would not be taken into account with a simple 1D envelope model. For this reason, the calculation of AIRIX beam transport has been implemented in the TraceWIN and PARTRAN codes. The PARTRAN calculation has been done using 10,000 particles with a 2 mm step size. The field of the solenoids and the accelerating cells are superposed. The behaviour of the particle transverse

distribution in the linac is plotted on figure 7. The beam is finally focused with a solenoid to a millimetric size.

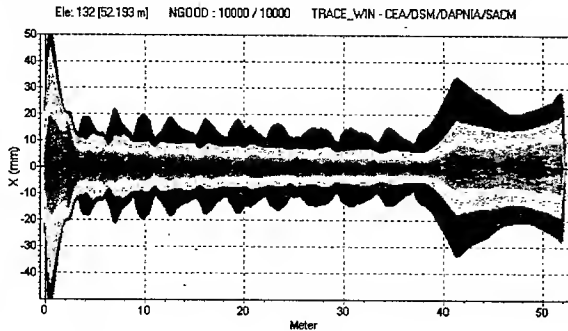


Figure 7 : Beam transverse distribution along AIRIX.

The behaviour of the 4D transverse rms normalised emittance is plotted on figure 8. The growth is about 60%, mostly at low energy. The beam size on target is about twice this obtained by 1D envelope code.

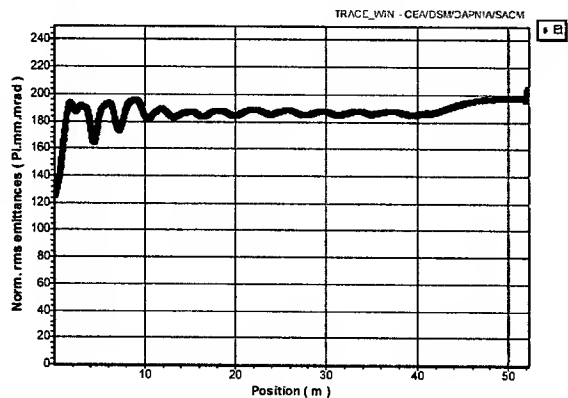


Figure 8: Emittance behaviour in AIRIX.

CONCLUSION

TraceWIN and PARTRAN codes now permit simulations in field maps keeping the user-friendliness and speed advantages of the TraceWIN envelope code. This new functionality has allowed to obtain a better representation of external fields in a linac, especially coupling terms and non-linearity.

REFERENCES

- [1] R. Duperrier, N. Pichoff and D. Uriot, "CEA Saclay Codes review for high intensity linac", ICCS conference, Amsterdam, 2002.
- [2] R. Duperrier et al, "Beams dynamics studies in spiral 2 linac", PAC 2003, Portland USA
- [3] M. Duval, private communication, GANIL, France.
- [4] J. H. Billen, L. M. Young, "Poisson, Superfish documentation", LA-UR-96-1834.
- [5] J. Bardy, "Codes ENV - Résolution de l'équation d'enveloppe", internal communication.
- [6] E. Merle et al., "Progress with the 2-3 kA AIRIX Electron Beam", EPAC Proceedings, Paris, 3-7 June 2002.

TOOLS FOR PREDICTING CLEANING EFFICIENCY IN THE LHC

R. Aßmann, M. Brugger, M. Hayes, J.B. Jeanneret, F. Schmidt, CERN, Geneva, Switzerland

I. Baichev, IHEP, Protvino, Russia

D. Kaltchev, TRIUMF, Canada

Abstract

The computer codes Sixtrack and Dimad have been upgraded to include realistic models of proton scattering in collimator jaws, mechanical aperture restrictions, and time-dependent fields. These new tools complement long-existing simplified linear tracking programs used up to now for tracking with collimators. Scattering routines from STRUCT and K2 have been compared with one another and the results have been cross-checked to the FLUKA Monte Carlo package. A systematic error is assigned to the predictions of cleaning efficiency. Now, predictions of the cleaning efficiency are possible with a full LHC model, including chromatic effects, linear and nonlinear errors, beam-beam kicks and associated diffusion, and time-dependent fields. The beam loss can be predicted around the ring, both for regular and irregular beam losses. Examples are presented.

INTRODUCTION

The collimation system of the LHC [1] requires an excellent cleaning efficiency in order to avoid quenches of the super-conducting magnets. Various numerical tools used for prediction of cleaning efficiency were compared. The programs include generation of a primary beam halo, scattering of high energy protons through material and tracking of beam halos in the storage ring. The degree of agreement between different codes is discussed. Differences are used to assess possible systematic errors.

SCATTERING CODES

The physics of proton scattering in the material of collimator jaws has been implemented in various computer codes. The scattering routines track the protons through some length of a given material having them interacting with the proper cross-sections. The protons receive transverse kicks $\Delta\theta_x$, $\Delta\theta_y$ and offsets Δx , Δy and some momentum loss $\delta = \Delta p/p_0$. Note that a full shower calculation is not required for predicting the cleaning of "primary" beam protons. The primary protons in the LHC have energies from 450 GeV at injection to 7 TeV at top. The scattering routines must correctly describe the interactions over the full range of energies, allow for different jaw materials, and include the correct jaw geometry, as protons impact at very close distance from the edge of the jaw.

Three different scattering routines were compared:

1. K2 was developed in the 1990's by Jeanneret and Trenkler for studies of LHC collimation [2].

2. STRUCT was developed in the 1980's by Baichev et al, among others for studies of LHC and SSC collimation [3].

3. FLUKA is a general purpose scattering and showering code ([4] and references therein).

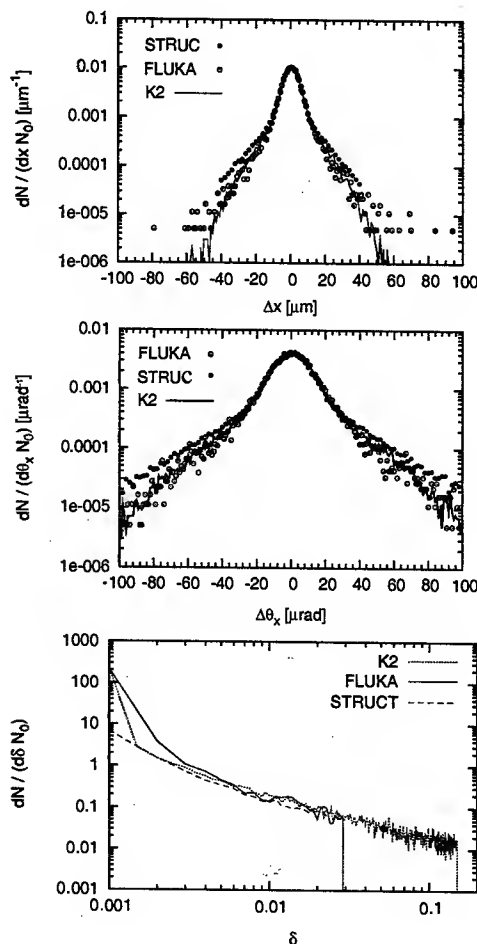


Figure 1: Scattering probabilities for one 7 TeV proton impacting on a 0.5 m long Cu jaw. Change in position (top), angle (middle) and energy (bottom).

A test case was defined: A 7 TeV pencil beam with zero angle ($y' = 0$) impacting $y = 1 \mu\text{m}$ from the edge of a 0.5 m long vertical collimator, made of Cu. The changes in particle offsets, angles and momentum were recorded. The comparison of the different scattering routines shows good agreement, Fig. 1. Note that for FLUKA a 6.8 TeV energy cut was used. A probability function $dN/(dx N_0)$ is intro-

duced with N_0 being the number of protons impacting on the jaw. Only a fraction of protons "survive" the passage through the jaw, the others are fragmenting. The results shown here refer to the horizontal plane which is symmetric contrary to the vertical plane where the $1 \mu\text{m}$ impact parameter introduces a pronounced asymmetry. The symmetry in the horizontal plane allows more easy interpretation of the effect on cleaning efficiency.

The differences in the results were analyzed in detail. It was found that the momentum loss shows a variation of $\pm 15\%$ between different codes which is used to assign a systematic error on this observable. Large scattering angles and offsets exhibit differences of up to a factor of 3, as visible in Fig. 1. The large angle probabilities (above $25 \mu\text{rad}$) affect cleaning efficiency and were approximated by fitting them, as shown in Fig. 2:

$$dN/d(d\theta_x N_0) = -6.25 - 0.058\theta_x \quad \text{K2} \quad (1)$$

$$= -6.70 - 0.042\theta_x \quad \text{STRUCT} \quad (2)$$

Note that θ_x is to be given in units of μrad . The fraction of particles above a given angle θ_x^0 is easily obtained from the integral:

$$\frac{N}{N_0}(\theta_x > \theta_x^0) = -0.033 \cdot -0.058\theta_x^0 \quad \text{K2} \quad (3)$$

$$= -0.029 \cdot -0.042\theta_x^0 \quad \text{STRUCT} \quad (4)$$

Integrating above $10 \mu\text{rad}$ it is seen that in K2 about $7.8 \cdot 10^{-3}$ of the impacting protons would be kicked to above $10 \mu\text{rad}$, while in STRUCT $10.3 \cdot 10^{-3}$ of the impacting protons would reach $10 \mu\text{rad}$. It is seen that the factor three difference in large angle probabilities would at maximum amount to a 30% difference in cleaning efficiency.

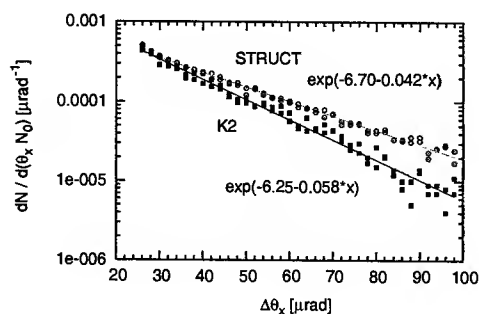


Figure 2: Large angle scattering probabilities for a 7 TeV proton impacting on a 0.5 m long Cu jaw with STRUCT and K2. The functional dependence is fitted.

TRACKING WITH COLLIMATORS

Halo cleaning is a multi-turn process. Particles can have multiple interactions in collimator jaws and in addition can perform many turns between subsequent hits of a collimator jaw. Speed requirements are important: The target

cleaning efficiency ($10^{-3} - 10^{-4}$) requires large particle ensembles ($10^5 - 10^6$) that must be tracked for many turns (20-1000). Several tools have been set-up, each with specific advantages and limitations.

Colltrack with K2

Historically the design of the LHC collimation system relies on the K2 scattering procedure and linear transfer matrices (obtained from Twiss functions calculated with MAD). Recently an updated COLLTRACK program was written, relying on K2. The advantage of this approach is a very fast algorithm, allowing to track very large particle ensembles over many turns. Multiple imperfections are implemented. This allows for example the study of very short primary collimators, where halo protons stay in the machine for up to thousand turns after the first interaction in a primary collimator. Drawbacks are the limited description of chromatic and dispersive effects, the absence of nonlinearities, coupling, and beam-beam effects. Results from linear tracking with K2 can for example be found in [5].

Sixtrack with K2

The Sixtrack program [6] is the standard tracking tool for the LHC. For example, the LHC dynamical aperture is calculated with Sixtrack that includes all relevant imperfections, linear and non-linear fields, beam-beam kicks, and other errors for the LHC. It performs fully chromatic and coupled tracking, allowing the treatment of time-dependent field errors and the inclusion of the LHC aperture. The K2 scattering module has been included for proper treatment of beam scattering in collimators. Results of SIXTRACK with collimators are published in [7] for collimation efficiency during the snapback at the start of the LHC ramp.

Dimad with STRUCT

Dimad is based on second order Transport maps with kicks describing the action of higher order multipoles and also accepts symplectic ray tracing [8]. To describe propagation of TeV protons in materials a new collimator element was created, based on the main block of STRUCT[3], and also a new set collimator operation which exists along with standard Dimad operations: field errors, misalignment, orbit correction and analysis of geometric and chromatic aberrations¹. The original Dimad source is kept, with the new executable provisionally named Dimcol.

A highlight of Dimad is the possibility to study beam loss distributed in an aperture. An example radial aperture $R=2 \text{ cm}$ was set at all drift entrances.

Since in reality the chamber geometry varies along the ring and the losses do not occur in one point, the exact per-meter occupancy cannot be found in this way. One can however estimate losses over large sections of the ring, and

¹Scattering of GeV protons was first introduced in Dimad during the KAON factory studies with the collimator treated during tracking as an arbitrary element [9], [10]

Ideal system – fraction of halo lost				
in collimators	on the 2 cm aperture			
	RDS7	IP6	IP1,2,5	arcs
Collision: 10^6 part., 300 turns				
0.9986	$6 \cdot 10^{-4}$	0	$4 \cdot 10^{-4}$	0
Injection: 10 seeds $\times 10^5$ part., 150 turns				
0.9985	$1.3 \cdot 10^{-3}$	$8 \cdot 10^{-5}$	0.	$8 \cdot 10^{-5}$

Table 1: Halo fractions absorbed in collimators and lost on the 2-cm radial aperture (drift entrances) in different ring sections. The injection values are averages of 10 seeds.

such were chosen to be: the two collimator occupied sections in IR7 and IR3, the Right Dispersion Suppressor in IR7 (RDS7), the IP6, the high-beta IP-s (IP8,1,2,5) and all the arcs. The resulting losses are summarized in Table 1. It is seen that at collision no particles reach the arcs and a fraction $4 \cdot 10^{-4}$ reaches high-beta locations in the IP-s. Here, however, the real chamber size will be larger. More detailed studies are underway.

COMPARING INEFFICIENCY

The cleaning efficiency for the 7 TeV LHC has been studied in detail with the linear Colltrack(K2) code and Dimad [11]². The goal was to assess the size of possible differences. K2 and Sixtrack were compared for injection energy. No aperture limitations are set besides collimators. Coordinates and momenta are stored at some location, which yields the *integrated inefficiency* curve (r), defined to be the fraction of halo lost on an absorber standing at radial amplitude $r = \sqrt{\frac{x^2}{2} + \frac{y^2}{2}}$, where $\frac{x^2}{2} = 2 \cdot x / (x_{y,y})$ (similar for y). Here $x_{y,y}$ are the transverse action invariants, hence (r) is independent on the lattice location chosen. The following results were obtained for the integrated inefficiency at radial amplitudes of $r > 10\sigma$:

Energy	Disp.	Dimad	Colltrack	Sixtrack
7 TeV	0 m	$0.6 \cdot 10^{-3}$	$0.6 \cdot 10^{-3}$	-
7 TeV	2 m	$3.0 \cdot 10^{-3}$	$1.2 \cdot 10^{-3}$	-
.45 TeV	0 m	-	$1.6 \cdot 10^{-3}$	$4.7 \cdot 10^{-3}$

Note that the SIXTRACK result is for the LHC with realistic errors and non-linear fields. The Dimad results refer to a machine with corrected linear chromaticity. The other results refer to an unperturbed machine.

An exact agreement is seen between Colltrack and Dimad at a location with zero dispersion. At a 2 m dispersion location the predicted inefficiency is larger by a factor 2.5 in Dimad than in the simplified Colltrack approach. The scattering routine could explain a factor of about 1.3. The rest is due to the more realistic Dimad tracking of off-momentum particles.

At injection Sixtrack predicts a 3 times larger inefficiency than Colltrack, relying on the same K2 scattering

²the results in [11] are obtained in the case of a detuned optics i.e. injection optics with collision emittance.

routine. This may be explained by the realistic tracking in Sixtrack and the errors on the LHC settings (orbit, coupling and non-linear field errors).

CONCLUSION

A number of numerical tools have been set up to predict the LHC cleaning efficiency. They rely on different scattering routines that transport the protons through the collimator jaw. These routines show discrepancies of up to a factor of three for large angle scattering. This can amount to changes of up to 30% in predicted cleaning inefficiency. In addition variations of up to $\pm 15\%$ are seen in the predicted momentum loss, with resulting systematic errors of $\pm 7\%$ in inefficiency.

The direct comparison of predicted cleaning inefficiency, however, shows more important differences. It is seen that the simplified linear tracking underestimates cleaning inefficiency by a factor of 2 to 3. The more accurate tracking in Dimad and Sixtrack finds larger inefficiencies. In addition, Sixtrack includes realistic LHC errors (coupling, orbit, non-linear field errors). The errors moderately increase the inefficiency. Note that the imperfections in the Sixtrack study did not include imperfect set-up of the collimation system.

The Dimad program was used to analyze the distribution of losses around the ring. It was shown that less than 10^{-4} of the primary halo is lost in the high-beta insertions. A more accurate model of aperture is expected to show even smaller losses.

The overall agreement in the results is quite reasonable. The available tools can be employed with decent certainty in the reliability of results, choosing the most appropriate tool for a particular study.

REFERENCES

- [1] R. Aßmann et al. These proceedings.
- [2] T.Trenkler, J.B. Jeanneret, CERN SL/Note94-105(AP), 1994.
- [3] I. Baichev, D. Kaltchev, *Implementation in Dimad of a new Collimator Element (STRUCT module)*, TRIUMF Report (in preparation)
- [4] A. Fasso, A. Ferrari, J. Ranft, P.R. Sala. Proc. of Int. Conf. Monte-Carlo 2000, Lisbon, Oct. 2000, p.95, Springer-Verlag Berlin Heidelberg (2001).
- [5] R. Aßmann. Proc. Chamonix 2003. CERN-AB-2003-008 ADM.
- [6] F. Schmidt. CERN SL/94-56 (AP).
- [7] M. Hayes et al. Proc. EPAC02. CERN-LHC-Project-Report-589.
- [8] R.V.Servranckx. TRIUMF Design Note, TRI-DN-93-K233, (1993).
- [9] R.V.Servranckx, private communication.
- [10] U. Wienands, C.P. Parfitt, F.W. Jones. TRI-PP-91-42, May 1991 and Part. Acc. Conf., San Francisco, CA, May 6-9, IEEE 1991.
- [11] D.Kaltchev. LHC Project Note 294, Nov. 2002.

MAD-X – AN UPGRADE FROM MAD8

H. Grote and F. Schmidt, CERN, Geneva, Switzerland

INTRODUCTION

During the central period of the LHC design the accelerator design group at CERN had to face a serious bottleneck concerning our optics design code. Since years we had been using the MAD8 [1] code at CERN and it is still heavily used world wide. This old code has been very well debugged and most of the MAD8 performed rather well. However, due to the lack of essential features for the LHC design, e.g. operating on 2 rings simultaneously, involved Zebra [2] data bank management and the fact that the modules are rather interdependent larger upgrades of the code MAD8 are basically excluded, in particular if one wants to achieve a better physics description of the thick elements and make use of more modern map related tools à la Berz-Forest [3]. On the other hand, the C++ implementation used for the MAD9 program [4] turned out to be too complex for a fast development as it was needed for the LHC design. After a lengthy and frustrating trial period with MAD9 it was decided to suspend the MAD9 development and to start a new project called MAD-X with the following design criteria:

- Core part in C with dynamic memory allocation.
- Truly independent modules with interfaces to the core for data access.
- Make use of existing and debugged modules of MAD8 in Fortran77.
- Retain only those features of MAD8 that are sound and concentrate on those modules that are needed for the LHC design.
- Spread responsibility for development and maintenance of modules between a large group of module keepers inside and outside of our group organized by one code custodian.
- Use E.Forest's PTC [5] as external module to provide map techniques and better physics description of the elements.
- CVS version management.
- Adding powerful constructs to the input language like: WHILE and IF .. ELSE .. ENDIF .

Presently, we are at MAD-X version V1.11 and all modules and features needed for the LHC design are debugged and tested. There is a rather complete documentation on the web together with code, binaries and examples.

In the following we will present the module keepers and describe the documented modules. The major extension of MAD-X by the PTC code will be outlined. A simple example will be given and it will be described what kind of documentation can be obtained. Lastly, an outlook will be given about the next steps in the development of MAD-X.

MODULE KEEPERS

Table 1: Module Keepers

Module	Keeper	Tested	Docu.	Exam.
C6T	M.Hayes F.Schmidt	yes	yes	yes
CORORBIT	W.Herr	yes	yes	yes
DYNAP	H.Zimmermann H.Grote	yes	yes	yes
EMIT	H.Grote F.Pilant	no	no	no
ERROR	W.Herr	yes	yes	yes
IBS	F.Bonifazi	yes	yes	yes
MAKETHIN	M.Hayes H.Burkhardt	yes	yes	yes
MATCH	O.Bierling	yes	yes	yes
PLOT	H.Grote D.Amaldi	yes	yes	yes
SURVEY	A.Amaldi	yes	yes	yes
SXF	H.Grote F.Pilant	no	no	no
THREADER	H.Grote W.Herr	no	no	no
TWISS	F.Schmidt	yes	yes	yes
THINTRACK	A.Amaldi	yes	yes	yes

In Tab. 1 a list is given of all modules with their original and present module keepers depicted in "blue" and "green" respectively. Moreover, we have one first example of an external module, i.e. the F.Pilant from BNL who has agreed to look after the SXF [6] module. The table also shows which modules have been sufficiently tested and for which modules there are documentation and/or examples.

THE DOCUMENTED MAD-X MODULES

C6T

In dynamic aperture studies SixTrack [7] is often used because of its speed and controllability. However, the input files are notoriously difficult to produce by hand. This command may be used to produce SixTrack input files from any MAD-X preparation file.

CORORBIT

This module can be used to correct the closed orbit or a trajectory. The distorted orbit, the model and if required the target orbit are calculated with one or more TWISS commands.

DYNAP

For each previously entered start command, DYNAP tracks two close-by particles over a selected number of turns, from which it obtains the betatron tunes with error, the action smear, and an estimate of the Lyapunov exponent.

ERROR

It is possible to assign alignment errors and field errors to single beam elements or to ranges of beam elements. Errors can be specified both with constant or random values. They may be entered after having selected a beam line or sequence by means of a USE command.

MAKETHIN

This module converts a sequence with thick elements into one composed entirely of drifts and thin multipole elements as required e.g. by the default MAX-X tracking.

MATCH

Before a match operation at least one sequence must be selected by means of a USE command. Matching is then initiated by the MATCH command. The matching module can act on more than one sequence simultaneously by specifying more than one sequence when initiating the matching mode. From this command to the corresponding END-MATCH command MAD accepts various matching commands.

PLOT

Values contained in MAD-X tables can be plotted in the form column versus column, with up to four differently scaled vertical axes; furthermore, if the horizontal axis is the position "s" of the elements in a sequence, then the symbolic machine can be plotted on the top of the figure. The "environment" (line thickness, annotation size, PostScript format) can be set with the setplot command.

SURVEY

The SURVEY command computes the coordinates of all machine elements in a global reference system. These coordinates can be used for installation. In order to produce coordinates in a particular system, the initial coordinates and angles can be specified. The computation results are always written to an internal table but they can also be written to an external file.

SXF

Read and writes SXF format[6] from or to the currently USED sequence with all alignment and field errors.

TWISS

The TWISS command causes computation of the closed orbit and of the coupled Courant and Snyder [8] linear lattice functions, and optionally of the chromatic functions, either as the periodic solution or starting with initial values of the lattice functions. It operates on the working beam line defined in the latest USE command: i.e. either a SEQUENCE="sequence_name" or a LINE="line_name" on the TWISS command. Moreover, one can restrict the TWISS calculation to a desired RANGE.

THINTRACK

Particle trajectories can be tracked either for single passage (option onepass in the command), or for many turns (default option). In all cases the tracking is performed element per element. Only thin elements are allowed, which guarantees the symplecticity of the coordinate transformation. Any lattice can be converted into a "thin element" lattice by invoking the MAKETHIN command.

PTC

E.Forest's Polymorphic Tracking Code (PTC[5]) is a kick code or symplectic integrator and therefore ideally suited to describe all elements symplectically and to arbitrary exactness. The degree of exactness is determined by the user and the speed of his computer. The code is written in an object oriented fashion using Fortran90. Therefore, it becomes much easier to describe arbitrarily complex accelerator structures. The other main advantage is that the code is inherently based on map formalism [3] and a linking with MAD-X will provide all the sophisticated tools, e.g. Normal Form. There is already an experimental MAD-X version that calculates successfully the fully 6d coupled lattice functions like in MAD8 but using PTC tools. MAD-X version 2.0 will include PTC and then many additional modules are conceivable that are based on this tool.

DOCUMENTATION

The MAD-X website [9] is accessible either via a "google" search for "CERN MAD-X" or directly via: <http://frs.home.cern.ch/frs/Xdoc/mad-X.html>. On this website you can find a "News" link which shows the changes between versions, the documentation based on "html" files and derived from them a "ps" and a "pdf" version, a "Keyword and Subject Index", a link to "Source and binaries" and one link to "Examples" for all modules and a facility to report bugs found in MAD-X by its users. Lastly, it is planned to provide a MAD-X mailing list "Subscribe" button.

EXAMPLE

As an example a simple FODO lattice has been used: it shows how elements are defined and located in a sequence. Notice the two symbols “=” and “:=”, the former evaluates the variable with the present value while in the second form this evaluation is deferred to the moment when it is needed and with the momentary value. The example shows how a “WHILE” loop is used to build the structure of “ncell” cells. After applying the “BEAM” command, “USE”ing the sequence and “SETPLOT”ing the plot parameters “TWISS” is executed twice. The first “TWISS” is used to produce Fig. 1 with the “PLOT” command. The second time “TWISS” is done for a number of momentum deviations

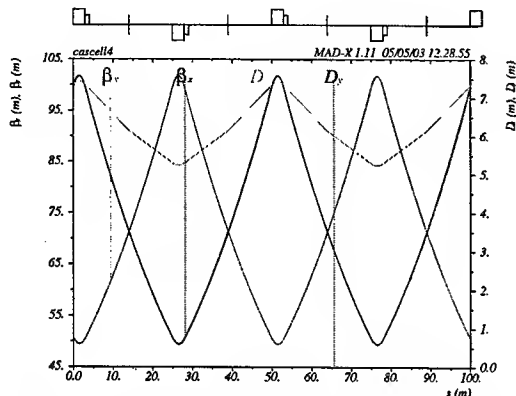


Figure 1: Lattice function for a simple FODO structure.

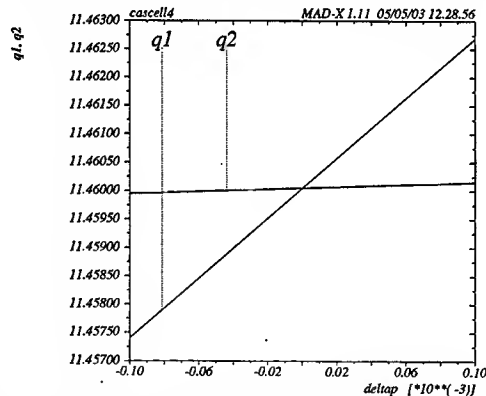


Figure 2: Mode I and II Tunes versus momen. deviation.

```
// element definitions;
lsex = 1.1; mq: quadrupole, l=3.0;
mb3:multipole, lrad:= 5.0,
knl:={.031415927}; qf: mq, k1:=kqf;
qd: mq,k1:=kqd; mscbh:
sextupole, l=lsex, k2:=ksf;
mscbv: sextupole, l=lsex, k2:=ksd; kqf
=.9795014e-2; kqd=-.9795014e-2;ksf=.01; ksd=-.01;
circum=5000.0;ncell=100;
lcell=circum/ncell;lcell2=lcell/2.;lquad=3.00;
lquad2=lquad/2.;lsex=1.1;
// sequence declaration;
casell4: sequence, refer=centre, l=circum;
start_machine: marker, at = 0;
n = 1;
while (n < ncell+1) {
  qf:qf,at=(n-1)*lcell+0.00*lcell+lquad2;
```

```
mscbh:mscbh,at=(n-1)*lcell+0.00*lcell+lquad+lsex/2.0;
mb3:mb3,at=(n-1)*lcell+0.25*lcell+lquad2;
qd:qd,at=(n-1)*lcell + 0.50*lcell+lquad2;
mscbv:mscbv,at=(n-1)*lcell+0.50*lcell+lquad+lsex/2.0;
mb3:mb3,at=(n-1)*lcell+0.75*lcell+lquad2;
n=n+1;
}
end_machine: marker at=circum;
endsequence;
// using sequence
eg:=100;bg:=eg/pmass;
en:=3.75e-06;epsx:=en/bg;epsy:=en/bg;
beam, sequence=casell4,
  particle=proton,energy=eg,sigt=0.077,
  size=1.1e-4,npart=1.05e11,exn=4*en,eyn=4*en,
  kbunch=10,et=0.002,bv=1,ex=epsx,ey=epsy;
setplot,post=2,ascale=1.5,lscale=1.5,
  rscale=1.5,sscale=1.5,lwidth=3;
use,period=casell4;
twiss;
plot,haxis=s,hmin=0.,hmax=100.,spline,vaxis1=betx,
  bety,vaxis2=dx,dy,colour=100;
twiss,deltap=-0.0001:0.0001:0.00005;
plot,table=summ,haxis=deltap,vaxis=q1,q2;
stop;
```

OUTLOOK

At version V1.11 MAD-X is now advanced enough to be presented as CERN's official replacement for MAD8. MAD-X has the most useful features of MAD8 but those features that were flawed and difficult to improve have been removed. On the other hand, MAD-X is now so much better organized into independent modules which are nicely interfaced with the “C” core that external modules can easily be added and maintained. The proper integration of MAD-X with the very versatile map based tool PTC is imminent. A release of MAD-X for the 32-bit Windows platform is in preparation. For fall 2003 a review is planned to discuss how MAD-X should be developed further to bring best service to the accelerator community.

REFERENCES

- [1] H.Grote and F.C. Iselin, CERN/SL/90-13(AP) (Rev. 5), <http://hansg.home.cern.ch/hansg/mad/mad8/mad8.html>.
- [2] R. Brun, M. Goossens and J. Zoll, Program library Q100, CERN, 1993.
- [3] M. Berz, É. Forest and J. Irwin, Part. Accel., 1989, Vol. 24.
- [4] F.C. Iselin, J. Jowett, J. Pacin and A. Adelmann, “MAD Version 9”, in the proceedings of EPAC2000;
- [5] E. Forest, E. McIntosh and F. Schmidt, KEK Report 2002-3, CERN-SL-2002-044 (AP).
- [6] H. Grote, et al., RHIC/AP/155.
- [7] F. Schmidt, CERN SL/94-56 (AP) (1994) (Rev.11.2001), <http://cern.ch/Frank.Schmidt/Documentation/doc.html>.
- [8] E.D. Courant and H.S. Snyder, Ann. of Phys., 3, 1958.
- [9] H. Grote and F. Schmidt, <http://frs.home.cern.ch/frs/Xdoc/mad-X.html>.

RECENT IMPROVEMENTS TO THE ASTRA PARTICLE TRACKING CODE

K. Flöttmann, DESY D 27603 Hamburg, Germany
 S. M. Lidia, LBNL, CA 94720, USA
 P. Piot, FNAL, Batavia, IL 60510, USA

Abstract

The Astra simulation code has been successfully used in the design of linac and rf photoinjector systems utilizing beams with azimuthal symmetry. We present recently implemented changes to Astra that allow tracking of beams in beamlines without the assumption of any symmetry. The changes especially include a 3D mesh space charge algorithm and the possibility to import 3D electromagnetic field maps from eigensolver programs.

INTRODUCTION

Program description

The computer program Astra (A space charge tracking algorithm) originally developed by one of us (K.F.) has been extensively used in the framework of photoinjector designs [1] and benchmarking of experimental data [2]. The program executables are freely available on various operating systems (Linux, Mac X, Solaris and Windows) from the world wide web page <http://www.desy.de/~mpyf10/Astra>. The Astra suite of programs consists of the particle tracking code together with an input distribution generator and several graphical user interface post-processors based on the PGLOT library [4]. Astra tracks point-like macroparticles (currently possible species are electrons, positrons, protons and hydrogen ions) through a user defined external fields taking into account the space charge field of the particle cloud. The tracking is based on a Runge-Kutta integration of fourth order with fixed time step. The beam line elements are set up w.r.t. a global Cartesian coordinate system. The program is a three-dimensional code, but its first version allowed the calculation of the space charge field only for round beams on a cylindrical grid and all the external fields (apart from quadrupoles) were cylindrical symmetric.

Note on particle emission

The dependence of the charge emission on the electric field at the cathode surface due to the Schottky effect can be simulated. At any time step during the emission, the charge of the macroparticles is calculated according to the relation: $Q_{\text{Macroparticle}} = (Q_{\text{Total}} + Q_{\text{Schottky}} E_{\text{acc}}) / N_{\text{Particles}}$ wherein E_{acc} is the actual accelerating field (including both RF and space charge) in the center of the cathode, Q_{Schottky} is a user defined parameter, Q_{Total} and $N_{\text{Particles}}$ is the bunch charge and number of macroparticle used to model the bunch. Thus a self-consistent emission is simulated.

The linear parameterization w.r.t. the accelerating field is motivated by measurements performed on Cs₂Te photocathodes reported in Ref. [3].

3D CAVITY ELECTROMAGNETIC FIELD

In the case of cylindrical-symmetric field, the radio-frequency field for a standing wave accelerating structure (TM modes) are described by the on-axis longitudinal electric field $E_z(z, r=0)$ the radial electric and azimuthal magnetic fields are then computed from $\nabla E = 0$ and $\nabla \times B = dE/dt$ respectively.

To accommodate more general problem, e.g. simulation of deflecting mode cavity or asymmetric rf-field, arbitrary external fields defined on a three-dimensional mesh can directly be loaded into Astra. Such fields are generally obtained from electromagnetic eigensolvers. Given the six components of the electromagnetic field vector $[\text{Re}(\mathbf{E}), \text{Im}(\mathbf{B})](x_i, y_j, z_k)$ tabulated on a grid node (i, j, k) , the field experienced by a particle with coordinate $\mathbf{x} = (x, y, z)$ is obtained via a tri-linear interpolation of the tabulated field, and the time dependence is introduced following

$$\begin{bmatrix} \mathbf{E} \\ \mathbf{B} \end{bmatrix}(\mathbf{x}; t) = \begin{bmatrix} \text{Re}(\mathbf{E}) \sin(\omega t + \varphi) \\ \text{Im}(\mathbf{B}) \cos(\omega t + \varphi) \end{bmatrix}(\mathbf{x}), \quad (1)$$

wherein $\omega/(2\pi)$ and φ are respectively the frequency of the rf-structure and the phase of the electric field. Practically, each of the field components is given in a separate ASCII file whose header describes the mesh geometry. Such a description enables the user to defined the different field components not *a fortiori* on the same mesh.

Since Astra allows the overlap of cavity fields onto the same position, the simulation of traveling wave structures described by 3D fields is straightforward if included as a superimposition of two standing wave fields with the proper phase and amplitude relations [5].

An example of application of the 3D rf-field map option has been the simulation of the beam dynamics in the L-band rf-gun cavity used at TTF 1 and FNPL facilities. This 1+1/2 cell cavity has an input power coupler that induces rf-field asymmetry in the full cell; the 3D electromagnetic field map has been simulated using HFSS [6] and was used in ASTRA to study the impact of the induced asymmetry. In Fig. 1, we compare the vertical phase space obtained

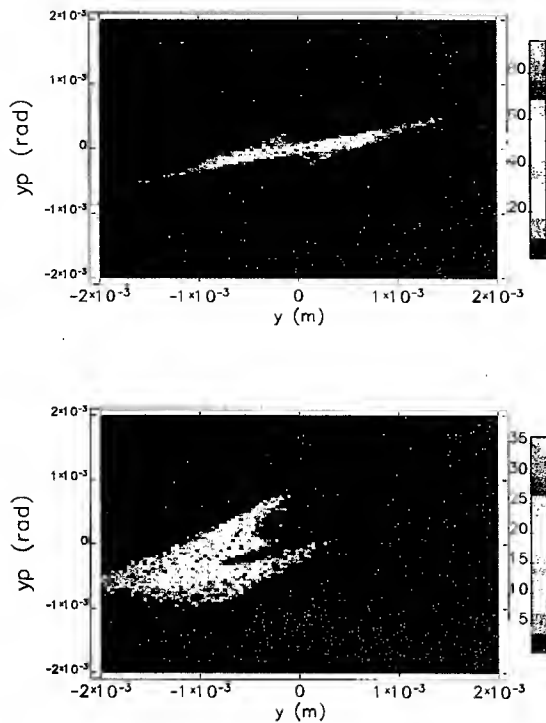


Figure 1: comparison of the vertical transverse phase spaces (y, y') with (top) and without (bottom) considering the 3D-rf field map in a L-band RF-gun.

after tracking the particle distribution in the case of (1) a cylindrical symmetric field and (2) the HFSS 3D field map.

3D SPACE CHARGE PARTICLE-MESH ALGORITHM

We have implemented a 3D space charge algorithm to handle beam distributions without the assumption of azimuthal symmetry. The algorithm does make the usual assumptions: that no dipole or bending magnet element exists along the beamline, so that the geometry is essentially Euclidean; that conducting walls are located far from the beam, so that free space boundary conditions apply in all directions; and that the velocity distribution in the beam rest frame is non-relativistic, so that an electrostatic approximation is valid. With these assumptions, the underlying Poisson equation is solved by a simple, volume-weighted particle-mesh (PM) algorithm. The PM algorithm is well known [7]. We use a variant of the field solver that is based on Fourier expansion, convolution with a grid Green function, and Fourier synthesis to determine the electrostatic potential on the grid nodes [7, 8]. The rest frame electric field components are calculated by second-order differencing, and tri-linear interpolation calculates the field values at the individual particle locations. The resulting electric and magnetic fields (neglecting the lon-

gitudinal B-field component) are applied in the laboratory frame with the remainder of the external fields.

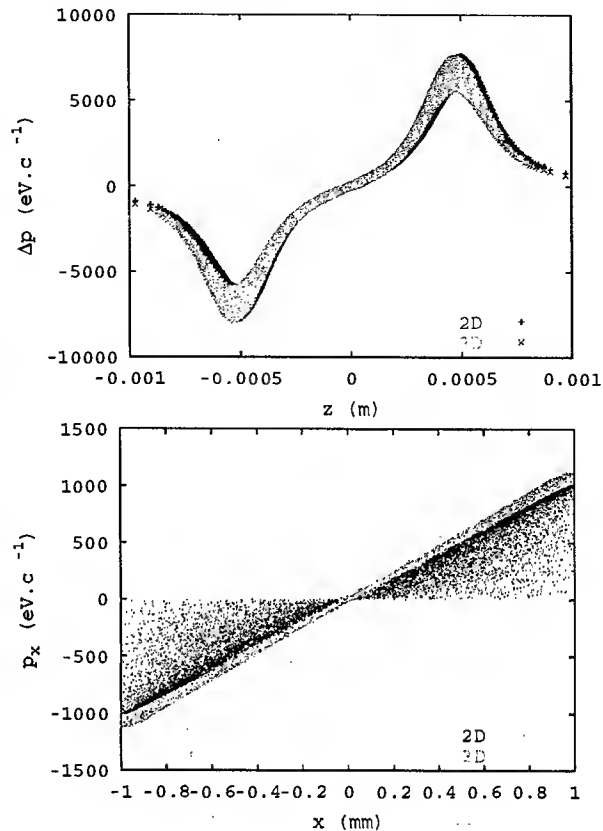


Figure 2: Comparison of the longitudinal (top) and transverse phase spaces (bottom) obtained with the cylindrical-symmetric mesh and the 3D mesh algorithm. The initial beam is a cylindrical symmetric beam with a Gaussian longitudinal distribution.

This algorithm is known to suffer from errors due to aliasing effects from the use discrete Fourier transforms. There are several known methods for dealing with this error. The issue may be successfully handled with the brute force technique of using very large meshes and correspondingly large number of particles. By ensuring that fine details in the beam distribution vary over at least several mesh cells, the highest frequency error components are excluded. Widely used [7, 9] is the method of truncating the Green's function at the edge of the first Brillouin zone, or otherwise introducing a cutoff mechanism in the frequency domain to remove these high-frequency errors. We employ a similar technique by applying a charge-conserving smoothing kernel to the mesh nodes after the charges have been distributed onto the grid. We also apply a technique where the solution for the scalar potential is then differenced twice to obtain the charge distribution. This 'new' distribution is compared with the original one. The difference is computed and fed back into the field solving algorithm with the original charge distribution to counter the errors. In effect we are executing the field solver twice (or more, if addi-

tional iterations are warranted). However, the Astra particle tracking engine utilizes an algorithm that rescales the solution to Poisson's equation, and need not execute the complete field solver at every time step.

In Figure 2 we compare the phase spaces calculated with the 2-d and 3-d mesh algorithm for the case of a cylindrical symmetric beam; the agreement between the two algorithms is good.

OUTLOOK

The 3D space charge algorithm will be released in a forthcoming new version of Astra. In a close future we also plan to introduce the dipole magnet element to enable simulation of magnetic bunch compression systems and analyzing spectrometers.

REFERENCES

- [1] See for example: K. Flöttmann and P. Piot, *Proceedings of EPAC 2002* (Paris), 1798-1800 (2002); F. Zhou et al., *Proceedings of PAC 2001* (Chicago), 2266-2268 (2001); S. Lidia, et al. "An Injector for the Proposed Berkeley Ultrafast X-Ray Light Source", these proceedings.
- [2] See for example: M. Hüning and H. Schlarb "Measurement of energy spread at the TTF injector" these proceedings; P. Piot et al., *Proceedings of PAC 2001* (Chicago), 86-88 (2001); P. Piot et al., *Phys. Rev. ST Accel. Beams* 6, 033503 (2003); J.-P. Carneiro et al., "Transverse and longitudinal beam dynamics studies at the FNPL photoinjector", submitted to *Phys. Rev. ST Accel. Beams*.
- [3] G. Suberlucq, Report CLIC-Note 299, CERN, Geneva (1996).
- [4] The PGPLOT library is freely available from the world wide web: <http://astra.caltech.edu/~tjp/pgplot>
- [5] G. Loew, et al., SLAC-PUB-2295 (1979).
- [6] T. Khabibouline, private communication, (FNAL, Jan. 2003).
- [7] R.W. Hockney, J.W. Eastwood, *Computer Simulation Using Particles*, Adam Hilger: New York, 1988.
- [8] J.W. Eastwood, D.R.K. Brownrigg, *J. Comput. Phys.* 32 (1979), pp. 24-38.
- [9] C.K. Birdsall, A.B. Langdon, *Plasma Physics Via Computer Simulation*, Adam Hilger: Bristol, 1991.

PyORBIT: A PYTHON SHELL FOR ORBIT

J.-F. Ostiguy* Fermi National Accelerator Laboratory, Batavia, IL

J. Holmes, ORNL Oak Ridge, TN †

Abstract

ORBIT is code developed at SNS to simulate beam dynamics in accumulation rings and synchrotrons. The code is structured as a collection of external C++ modules for SuperCode, a high level interpreter shell developed at LLNL in the early 1990s. SuperCode is no longer actively supported and there has for some time been interest in replacing it by a modern scripting language, while preserving the feel of the original ORBIT program. In this paper, we describe a new version of ORBIT where the role of SuperCode is assumed by Python, a free, well-documented and widely supported object-oriented scripting language. We also compare PyORBIT to ORBIT from the standpoint of features, performance and future expandability.

INTRODUCTION

The philosophy of either embedding or extending a high-level scripting language has become popular for scientific applications. Typically, scientific simulation code execution time is dominated by a few computationally intensive tasks. On the other hand, bookkeeping operations such as data analysis and presentation represent a large portion of the overall development effort. This effort can potentially be significantly reduced by implementing this functionality in an interpreted language, without significantly affecting overall performance. It is in this spirit that ORBIT, a code to model the dynamics of a synchrotron in the presence of space charge, was developed at the SNS [1]. ORBIT is structured as a collection of extension modules for SuperCode, an interpreted array-oriented scripting language with a C++-like syntax originating from the early 1990's Fusion research program at LLNL. Unfortunately, SuperCode is no longer actively developed and supported. In recent years, a number of free, well-documented and stable alternative scripting languages have emerged: Perl, Python, Tcl, Ruby, Guile etc. All these languages have strengths and weaknesses. Perl has already been used successfully to build a framework integrating existing accelerator codes [2].

WHY PYTHON ?

Among the many scripting languages, Python has the distinction of being fundamentally object-oriented. It supports concepts such as classes, inheritance and operator overloading. Python scripts are compiled into interpreted bytecode. Python and C++ syntax and semantics both

map very well into each other, making Python a particularly good choice as middleware language to integrate functionality implemented in C++. Commonalities between Python and C++ can be summarized as follows [3]:

- both languages use C-family of control structures
- support for object-orientation, functional and generic programming
- comprehensive operator overloading facilities
- collections and iterators
- support for namespaces (Python modules)
- exception handling
- Python reference semantics mirrors common C++ idioms (handle/body classes, reference-counted smart pointers)

MODULE INTERFACE CODE GENERATION

Although Python and C++ overlap conceptually, from a low-level implementation standpoint they differ substantially. Python is implemented in C and naturally offers a C-based API for extension. Compared to C++ and Python, C has rudimentary abstraction facilities and no support for exception-handling. Writing interface code for extension modules using the C-API requires specialized knowledge; furthermore, the code tends to be complex and hard to maintain. This has stimulated the development of automated interface code generation or "wrapping" systems. The exported module interface is specified in a file processed by a specialized program which generates the necessary interface code without further user intervention. There exists at least five systems to generate python/C++ wrappers [4, 5, 6, 7, 8]: SWIG, SIP, CXX, SCXX and Boost.python. SWIG was one of the first and is probably the most widely known interface generator. It offers comprehensive support for most of the popular scripting languages including Python. Although support for the Python/C++ combination has been continuously improving, important limitations remain, one of them being the requirement that all exported templated functions and classes be explicitly instantiated. The inter-language binding code produced by SWIG is also an inelegant mixture of Python scripts and C code. SIP is very similar in philosophy to SWIG – from which it was originally inspired – but is strictly Python/C++ specific. It was developed as a tool to produce python wrappers for the Qt library, a popular open source GUI framework. Although the results are impressive, the SIP interface specification can be complex and requires the programmer to write some low-level code. CXX wraps some part of the Python C-API in C++, managing the complexity using static meta-programming tech-

* ostiguy@fnal.gov

† Work supported by the US Department of Energy under contract number DE-AC02-76CH03000.

niques. SCXX started as a lightweight version of CXX. It does not use templates and as such cannot hide as many details of the low-level Python C-API. On the other hand, it automates tedious error-prone tasks such as reference counting. Boost.python has features and goals that are similar to all the other systems. However, remarkably, it does not introduce a separate wrapping language and interface code generator. Rather, it makes use of C++ compile-time introspection capabilities and advanced meta-template programming techniques to allow interface specification to be done in pure C++. Boost.python also goes beyond the scope of other systems by providing the following features:

- support for C++ virtual functions that can be overridden in python
- lifetime management facilities for low-level C++ pointers and references
- a safe and convenient mechanism for tying into Python's powerful serialization engine
- support for organizing extensions as Python packages with a central registry for inter-language type conversions
- automatic coherent handling of C++ lvalues and rvalues

Because of its comprehensiveness and elegance, Boost.python was selected to implement PyORBIT.

PYORBIT IMPLEMENTATION

To facilitate the transition for users already familiar with ORBIT, an important objective was to make the feel of the new PyORBIT as close as possible to the existing one. This is mostly the case, but some important differences remain. While SuperCode is strongly typed, Python is a dynamically typed language. Variables are not declared; assigning an object to a variable creates it. All Python variables are references to PyObjects. The practical consequence is that an assignment statement such as `a = b` does not result in `a` holding a copy of `b` but rather in both `a` and `b` referring to the same object on the heap. References are counted and objects are marked for automatic deletion when no variable refer to them (automatic garbage collection). Another significant difference between Python and SuperCode the fact that in Python numbers and strings are immutable objects. If a function has arguments whose types are immutable, the values of these arguments cannot be changed by the function. Immutability of basic data types is not as restrictive as it might seem since Python also provides a mutable container type (`list`). While the container itself cannot be modified, the elements it contains can be.

Array Types

SuperCode defines the built-in array types `Vector`, `Matrix`, and `Array3D` (separately for integers, double and complex) patterned after Fortran arrays (stored in column-major order and 1-based). These types are extensively

used in the ORBIT code and therefore have been emulated. In PyORBIT, the SuperCode implementation of the built-in array types is replaced by a new simplified templated version. Fig. 1 provides an example of how the `ComplexMatrix` type interface is exported to Python using boost.python. At first glance, this may not seem like

```
#include <boost/python.h>
using namespace boost::python;
typedef Matrix<complex<double>
    ComplexMatrix;

...

class_<ComplexMatrix > >
    ("ComplexMatrix", init<int,int>())
    .def(init<const ComplexMatrix > >())
    .def("get",      &ComplexMatrix >::get)
    .def("set",      &ComplexMatrix >::set)
    .def("__repr__", &ComplexMatrix >::print)
    .def("clear",    &ComplexMatrix >::clear)
    .def("resize",   &ComplexMatrix >::resize)
    .def(self + self)
    .def(self - self)
    .def(self * self)
    .def(self ^ self)
    ;
...

```

Figure 1: Exporting the interface of an array datatype using boost.python

C++ and a few explanations are in order. The construct `class_<type>(name)` is simply an anonymous instantiation of a templated class named `class_`. This instantiation calls the `class_` constructor and passes the C++ type to it. A new python class type is created and associated with name in the Python registry. The syntax `.def` simply denotes a call to a member function named `def`. Because `object.def()` returns a reference to object, multiple calls can be chained. The resulting expression is made more readable by taking advantage of the fact that the compiler ignores whitespace. Note the last four `.def` statements which define operator overloads.

ORBIT Modules

Exporting existing ORBIT modules to Python with boost.python is a relatively mechanical task. The following (simplified) code provides an example. This defines the Python class `Particles` and exposes its method `addMacroHerd` and its data `nHerds`. Note that the variable `nHerds` is mirrored in Python by a special boost.python object which does not have the type `int`. The expression `Particles.nHerds = 1` in Python does not result in the creation of an immutable `int` object. Rather, for objects of type `Particles`, assigning a value to the attribute `nHerd` calls a method that sets the C++ variable `Particle::nHerds`. All this mechanics is completely transparent to the programmer and generated by the boost.python library. Compiling the code in Fig. 2 ultimately produces a shared object module that can be dynam-

```
#include <boost/python.h>
...
class_<Particles>("Particles")
    .def("addMacroHerd",
        &Particles::addMacroHerd,
        "Make a main herd of macro particles")
    .staticmethod("addMacroHerd")
    .def_readwrite("nHerds", &Particles::nHerds)
;
...
```

Figure 2: Exporting the interface of an ORBIT module using boost.python

ically imported by Python, making its classes and methods available to the interpreter.

Strings

SuperCode defines its own private string class. While semantics of this class are close to that of `std::string`, they are not identical. By default, Boost.python provides automatic conversion between Python `str` type and C++ `std::string`. However, it is also possible to define and register other type conversions. This approach is used in PyORBIT to avoid modifying the substantial amount of code that refers to the private string class.

Function Pointers

Some ORBIT functions expect a function as an argument. Typical examples are functions used to generate initial macroparticles phase space distributions or functions used to define an RF cavity voltage program. Using the latter as an example, it is convenient to define a voltage program at the interpreter level since this is a function which is typically called once per turn. In SuperCode, function pointers are basically C-style `void (*)()`. In Python, all variables and functions are references to dynamically allocated objects. When a call to an ORBIT function such as `AddRampedRFCavity` is executed from Python, the arguments are effectively a list of `PyObject*`. Boost.python introspection allows basic data types to be converted before the C++ version of `AddRampedRFCavity` gets called. However, references to functions cannot be converted i.e. there is no unambiguous way to go from a `PyObject*` to a `void (*)()`. To emulate SuperCode syntax and behavior, it is necessary to introduce an additional C++ wrapper function. How this is done is illustrated in Fig. 3 where for clarity, function arguments that are not relevant have been omitted. Python calls `addRampedRFCavity` with a `PyObject*` argument. This argument is passed through a private static variable to a private function which in turn uses the boost.python facility `call<>` to interpret the python function. Finally, the private function is passed as regular C-style function pointer to the original version of `addRampedRFCavity`.

```
void addRampedRFCavity( (void(*)()) sub);

using boost::python::call;

static PyObject* RampedRFVolt_pyobjptr = 0;

static void private_RampedRFVolt()
{
    call<void>(RampedRFVolt_pyobjptr);
    return;
}

void addRampedRFCavity(PyObject* po )
{
    RampedRFVolt_pyobjptr = po;
    addRampedRFCavity(&private_addRampedBACcel);
}
```

Figure 3: Passing a reference to a function defined in Python to a C++ extension module.

OUTLOOK AND CONCLUSION

Using Boost.python we have successfully transformed ORBIT into a collection of Python modules. This has been accomplished with minimal modifications to the original code. PyORBIT performance is basically the same as that of the original ORBIT since the computationally intensive work is performed by virtually identical C++ code. A vast amount of high quality third party libraries and modules developed for Python have now become available to ORBIT users. In principle, this should allow accelerated development of new data analysis and display facilities. Finally, through boost.python, adding new C++ modules is a well-defined, well-documented and straightforward matter that does not require specialized programming knowledge. At the time of this writing, PyORBIT remains a work in progress. While it is certainly usable as it stands, some work remains to be done before it can be considered a production tool, mostly in connection with exception handling and error recovery.

REFERENCES

- [1] J. Galambos et al., "ORBIT - A Ring Injection Code with Space Charge", Proceedings of the 1999 PAC Conference, pp. 3143-3145
- [2] N. Malitsky and R. Talman, AIP 391, 1996
- [3] D. Abrahams and R.W. Grosse-Kunstleve, "Building Hybrid Systems with Boost.Python", PyCON 2003, Washington DC, March 2003
- [4] <http://www.swig.org>
- [5] <http://www.riverbankcomputing.co.uk/sip>
- [6] <http://sourceforge.net/projects/cxx>
- [7] <http://www.macmillan-in.com/scxx.html>
- [8] <http://www.boost.org/scxx.html>

A FRAMEWORK DESIGN FOR A CYCLOTRON VIRTUAL CONTROL PLATFORM BASED ON OBJECT-ORIENTED METHODOLOGY *

Bin Qin, Yongqian Xiong, Xiong Jian, Dezhi Chen, Tiaoqin Yu, Mingwu Fan
Huazhong University of Science and Technology, Wuhan, P. R. China

Abstract

This paper introduces a new software solution for cyclotron control system design and validation that named Cyclotron Virtual Control Platform (CVCP) and gives implementations in framework design. This software platform has abilities to simulate the processes and conditions in normal cyclotrons such as start up and shut down, routine operations, beam current regulation with combination of built-in component models and sequential control logic. A Human Machine Interface (HMI) with Supervisory Control and Data Acquisition (SCADA) functions and 3D interaction features provides a good operation channel. And an intelligent fault diagnosis module that can both generate errors and give solutions will be integrated into the platform in further plans. We use Object-Oriented technology to build this complex system and represent it in Unified Modeling Language (UML). It is easy to extend the functions in this open system. The platform is applied to Cyclotron Virtual Prototyping technology.

INTRODUCTION

Virtual Prototyping (VP) is a new design paradigm being developed these years with the increasing demand for manufacturing products in a short period of time and in a cost effective manner. During the complex system's entire life circle, Virtual Prototype based on CAD/CAM data is applied to replace the physical prototypes for system design, modeling, analysis and validation.

Cyclotron is a sort of very important facilities used in fundamental physics researches and some civil medical applications. How to establish an integrity cyclotron prototype is an urgent problem we must face to. Considering the system complexity and cost-effective design, VP is a more appropriate way to achieve this. This paper describes control system design and simulation issues in Cyclotron Virtual Prototyping.

Control system is a vital section in cyclotrons, which provide a safe and effective way to manipulate the machine. Correspondingly, CVCP was put forward to take roles for control system design, modeling and simulation, logic validation, intelligent diagnosis and Human-Machine Interface design in Cyclotron Virtual Prototype. Using the platform, Engineers can test their ideals, find defects and then make modifications in earlier time that far reduces design works. As known, cyclotron control system is complicated with interaction subsystems and a number of feedbacks and logic interlocks. Traditional process-oriented method is difficult to build or extend this complex system, so we adopt object-oriented

methodology. It makes system easier to be modeled, organized, maintained and extended by using encapsulation, inheritance and polymorphism features of objects. UML is used to describe the framework of CVCP and also applied in the entire software engineering.

GENERAL DESIGN FOR CVCP

The control of Cyclotron is a typical complex real-time system. Generally, it is a hybrid system including both continuous control and dynamic discrete events. But for time response requirements, closed-loop controls are implemented by hardware such as PLC and DSP in most cases of Cyclotron. The purpose of computer control system is mainly to carry out the SCADA functions.

Conceptual Model

As a good example, EPICS (Experimental Physics and Industrial Control System) [2] is a powerful architecture and software toolkit to build distribute real-time control systems applied in accelerators, telescopes or industrial processes. But different from the real industrial application, we need a specific control platform to accomplish tasks for Cyclotron Virtual Prototyping. Therefore CVCP is advanced with some explicit goals below:

- Control principles and mechanisms simulation
- Control logic and interlocks establishment
- Start-up and routine operations simulation
- Beam current monitoring and regulation
- Intelligent diagnosis

Based on these purposes, Figure 1 shows the conceptual model of CVCP.

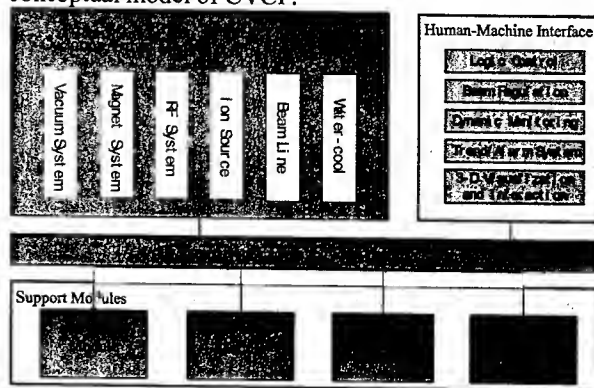


Figure 1: Conceptual Model of CVCP

CVCP Framework Using Object-Oriented Methodology

Considering the complexity and extensibility of the

*Supported by National Nature Science Foundation of China

platform in Figure 1, we used object-oriented design methodology to decompose this complex system and defined classes to describe different levels of cyclotron models, HMI factors and I/Os with hierarchy architecture as shown in Figure 2. In this diagram, we comply with the *Unified Modeling Standard* [3] and three relationships are used to represent organization among classes: *Composition*, *Generalization* (or inheritance) and *Usage*. Specific components in cyclotron such as vacuum subsystem or stripper are instances of these classes' inheritance or combination.

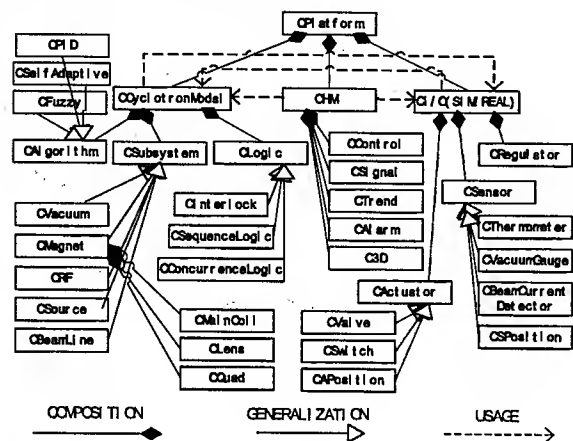


Figure 2: Class Structure Diagram

Figure 2 only illustrates the brief static model of the system, and some classes and their details in properties and methods are omitted. *Interaction Diagram* and *State Machine Diagram* are applied for dynamic level design of the system. Both the static model and the dynamic model constitute the framework of CVCP.

CYCLOTRON VIRTUAL MODELS

Cyclotron Virtual Models is the kernel of the platform, which represents entities for simulation and shows evaluation for control strategy design. It is divided into three parts in the framework: subsystems, logic and control algorithm that shows below:

- **Subsystems and Controllable Components:** It mainly includes cyclotron control subsystems like vacuum, magnet, RF etc. and all controllable components such as gas valves, electro motors and stripper. These models have information on objects' control methods, I/O, geometrical and physical characters.
- **Control Logic and Interlocks:** It is a regulation library including interlocks that promise correct and safe system running and sequential logic for cyclotron routine operation such as system startup and shutdown in automatic/manual modes.
- **Control Algorithm:** This is a software library covers control-system algorithms most widely used in engineering, which can be embed into particular component model.

HMI DESIGN

Human factors [4] are important in semiautomatic control systems like cyclotron. The system need human to make some pivotal decisions in supervisory control, and machine plays a clear role in accomplishing dangerous real-time operations safely and efficiently. A Good HMI design can make an easier and more effective way for Human-Machine interaction. In the following, we separate the HMI of CVCP into three sections and give a functional representation.

SCADA Interface

Supervisory control and data acquisition is the basic requirements for distributed control system of industrial process and large-scale equipment like cyclotron, which has high channel counts that demands for keeping track of a large number of data points. Normally, SCADA provides effective approaches to system's high-level monitor and control by combining real-time/historical data collection, logging and trending with friendly dynamic graphic indicators. Correspondingly, alarm system, event report and security are important assistant components. We plan to achieve the interface by combining *Visual C++* with *Measurement Studio*.

Specific Cyclotron Manipulation Interface

Especially CVCP is applied in cyclotron control. Therefore, found on SCADA, some specific operations such as beam current regulation, stripper location and interlocking of cyclotron components should be available on GUI. Clear-cut and full-function graphic interface makes the operations more easily and safely. *Virtual Instrumentation* is applied for this interface.

3-D Visualization and Interaction Interface

The *CAD/CAE Data Import Module* in CVCP provides a dynamic channel to load 3-D format data created or computed in CAD/CAE system. It is useful to visualize and handle these data interactively because this method offers extra information to engineers who deal with the optimization works in cyclotron prototyping. For example, the CAE experts utilize *Finite Elements Method (FEM)* to compute the beam track under current virtual conditions, and then we can see the track in an intuitive way and make some adjustments through control system to maintain good beam status.

OpenGL [6] is a widely used industrial-standard 3-D graphic library with good compatibility to C++ language. It can be used to accomplish the visualization and interaction tasks with high performance and quality.

SUPPORT MODULES AND DYNAMIC DATA EXCHANGE

Simulation Module

Substantially CVCP we implements in the first step is a *virtual system* that has no connections to external physics sensors and actuators like PLC, DSP and other hydraulic

or pneumatic equipments. For the purposes in simulation and validation of the control system, we use software method to generate internal signals and then give stimulates to cyclotron virtual models. This module is designed to have the following abilities.

- **Signal Source:** In order to construct a real external environment, mathematic method is used to generate two types input signals including analog measurement data and digital status data.
- **Control System Feedback:** We endow a simplified mathematic model to each cyclotron controllable components with close-loop or open loop methods. Thus responses that simulate real cyclotron can be achieved with input from signal source.
- **Parameters Initialization:** The function mainly sets up conditions for system start-up.

Experiment Module

At the final real prototyping level, external sensors and actuators distributed in industrial field bus will replace simulation codes. In the same way, *Experimental Module* is a transformation of *Simulation Module* at this time. This module provides hardware I/O interface and drivers of CVCP that communicate with measurement instrumentations and controllers.

Diagnosis Module

The role of this module is to establish schemes that can validate control system designed for cyclotron and solute problems on fault detection and correction. Diagnosis mainly considers logic and interlocks because we focus on macro correlations of the distributed cyclotron components.

In virtual mode, faults will be generated in a random way firstly. Then the module use the pre-defined logic regulations to find the position that error occurs and provide a suggest solution to user.

CAD/CAE Data Import Module

Cyclotron Virtual Prototyping needs multiple specialties' co-operation and interaction to achieve system-level optimization. As discussed in *3-D Visualization and Interaction Interface*, CAD/CAE data is useful for CVCP. Therefore this module sets up a channel that imports data and provides to HMI.

Dynamic Data Exchange/Real-Time Database

As illustrated in *conceptual model*, we segment the platform into three sections: *Cyclotron Virtual Model*, *HMI* and *Support Modules*. Predictably huge data will exchange among these sections. We must find a method to solute requirements on date throughput and time-response limitation.

Dynamic Data Exchange (DDE) supported by *Win32 Platform SDK* is adopted to implement data exchanging by a Server/Client mode. Considering the future requirement for data exchange efficiency, a *real-time database* will replace DDE.

FUTURE DEVELOPMENTS

Codes Implementation

C++ is a widely used object-oriented programming (OOP) language with many advanced features and concepts of contemporary OOP supported. In addition, C++ codes can be easily transplanted among different Operation Systems. Accordingly we use it for CVCP codes implementation. Considering the complexity of CVCP, codes implementation is a hard work that needs team collaboration and proper software engineering method. UML is also a good tool for software full life cycle design.

Industrial Application

Industrial prototyping normally includes three levels: Virtual Prototyping, Simulation and Real Prototyping thus the ultimate purpose of CVCP is for engineering control application. With less modifications to the core codes, CVCP can be embed into real-time system and take on control missions on the real cyclotron. Experiment Model plays an important role in implementing hardware interfaces to the outside sensors and actuates. Many factors such as the instrumentations and Electromagnetic Compatibility problems should be well considered.

CONCLUSION

We introduce a virtual control concept in cyclotron virtual prototyping and use object-oriented methodology to establish a conceptual model and framework design of CVCP. Three sections Cyclotron Virtual Model, HMI and Support Modules are demonstrated in succession.

Our works give a clear direction for future implementation of CVCP. And this design method can be adapted and used in other nuclear engineering applications and generic virtual control system development.

REFERENCES

- [1] Z. Wei, L. Baochun, W. Huizhong, "Modelling and Simulation Approach for Multi-disciplinary Virtual Prototyping", Proc. of the 4th World Congress on Intelligent Control and Automation.
- [2] S. A. Lewis, "Overview of the Experimental Physics and Industrial Control System: EPICS", Lawrence Berkeley National Laboratory, April 2000.
- [3] Booch G, Rumbaugh J, Jacobson I, "The Unified Modelling Language User Guide Reading", Addison-Wesley, 1998.
- [4] P. C. Cacciabue, "A Methodology of Human Factors Analysis for System Engineering: Theory and Applications", IEEE Trans. Systems, Man, And Cybernetics, vol.27, pp. 325-339, 1997.
- [5] J. Neider, T. Davis, M. Woo, "OpenGL Programming Guide", Addison-Wesley, 1994.

MODELING AND BEAM DYNAMIC VISUALIZATION IN CYCLOTRON VIRTUAL PROTOTYPING*

Xiong Jian, Bin Qin, Yongqian Xiong, Dezhi Chen, Tiaoqin Yu, Mingwu Fan
HuaZhong University of Science and Technology, CHINA

Abstract

Cyclotron virtual prototype improves design quality, reduces the number of costly physical cyclotron prototypes and the time of product development, and delivers innovative new designs faster. This paper describes the overall lifecycle models of cyclotron via CAD system, which can be used in cyclotron virtual design, virtual assemble, virtual manufacture and other relevant domains. The 3-dimension models with physical information help designers in the research of cyclotron construct, and empower designers with the flexibility of parametric or alternative design. This paper introduces applications in virtual assembly and automated modeling and describes particle moving animation and beam dynamic analysis result visualization expression in cyclotron virtual prototyping.

INTRODUCTION

Traditional cyclotron design is based on a mass of experimentation. People first work from conception design to decide general performance of the cyclotron, then distribute performance features to the components of the cyclotron for technology design, finally, after having decide the parameters of the components, they would work at detail design, manufacture of trial-components, and validation by testing. In this process, it has been a tendency to study individual components in isolation, with relatively little emphasis on the often-intimate relationships between the various components, and the detection of the problems lied in the design mainly depends on testing. Because the testing of each components of the cyclotron hardly can reflect the actual situation of the whole cyclotron, the interaction of all the components can be found only after the whole is tested. Thus, the traditional design, including design, manufacture, testing, modification, remanufacture etc, is generally a very long process which makes developing cyclotrons with high cost and risk.

Virtual prototyping (VP) Technology is a digital-design way of developing products, based on computer simulation models. These digital models or virtual prototypes simulate the appearance, functions and activities of real objects. Thus virtual prototypes can be used to replace physical prototypes for realizing innovative design, manufacture, testing and evaluation. Due to optimization possibilities, main working functions of the designed objects can be enhanced.

The use of VP of products and devices has heavily influenced other industries, for example, in automobile

and aircraft design, here we introduce this technology into developing cyclotrons. Our goal is to develop a VP system for cyclotrons, in which we can design, analyse, manufacture, assemble, control, and debug virtual cyclotrons in computer environment. It is necessary to validate the capability of this technology through rigorous and extensive comparison with data for known situations of real cyclotrons to confidence in its reliability for developing new type cyclotrons. It is unlikely that VP will ever totally replace traditional methods, but it certainly can reduce their cost by identifying the best approaches before building actual hardware.

Modeling and simulation visualization are very important in the whole VP architecture. VP model should be involved in product overall lifecycle of development and support applications in different domains. Science data visualization techniques are used to allow better understanding of VP performance.

VIRTUAL PROTOTYPE MODELING

The virtual prototype is defined as a function, photo realistic, and three-dimensional digital model. Besides visualization, designers need to know the physical attributes, such as dimensions, weight and material [1]. Our cyclotron virtual prototype models are generated from CAD system since the current CAD system has had a very long developed history with a powerful capacity. Although they are often not as accurate as physical ones, improvement in CAD system is narrowing the gap, which can provide enough of key features to allow analysis, testing, and manufacture for the requirements of developing cyclotrons.

Modeling Characteristics

In modeling environment, we can directly build three-dimension cyclotron models according to the imagination of the designers. They have some basic characteristics including:

- Feature-based modeling;
- Parametric driving;
- Uniform database.

In product overall lifecycle, there are different types of information, for example, design information, manufacture information, management information, etc. We require cyclotron models include not only geometric data but also other data. The feature-based modeling is a way of expressing information, and the use of feature allows the association between the shape and functionality. For example, a shape feature is a special shape composed of a group of geometric elements with topological relationship such as cylinder and cone, an

*Work supported by the National Natural Science Foundation of China.

assembly feature describes the information of assembling parts, an attribute feature may express mass and material, and a technological feature may express design tolerance. Actually, A model is composed of all kinds of features, which can create high-level representations of product.

The primary model is generated from the conception of designers, and in product overall lifecycle, it need continually to be modified and consummated by experts from different disciplines together, because the same model can be expanded later as more detail is required. The modeling is the process that all kinds of features are continually created and modified according to planning feature tree.

As mentioned above, each model can be disassembled into finite types of features. But each type of feature can be constrained by finite parameters in the same way. That is a parametric driving characteristic. In three-dimension CAD system, we constrain the dimensions of cyclotron parts by parameters, so a desired new model will immediately be product only by changing the value of these parameters. In this case, cyclotron models are more easily and quickly modified and controlled, and the ideas of designers are expressed better.

Model data is managed by uniform database, which make a model be shared in modeling environment. It means that in modeling process, when designers modify a model in any place, all data associated with the model will refresh. For example, if a sector pole changes, the cyclotron assembly will show the change at one time. It is clear that we must do more work in limited time for shorting the cycle of developing product. The database management supports concurrent design that allows several engineers to take part in modeling together by local area network (LAN).

We express abundant product information by the greatest extend, which meets the needs in different phases of developing cyclotrons. The same model in different application domains has consistent information description for share. The modeling way also supports top-down and down-top designs.

Applications of Cyclotron Models



Figure 1: 10MeV cyclotron parts.

We have built cyclotron parts (see figure 1), and a proficient CAD engineer can almost create any complicated part. For convenience of other researchers, we have created program automated modeling based on model feature-program. If we reedit it, it can automatically create the same type of models without trouble drawing. Therefore, an ordinary researcher can also create a complicated part only by inputting some parametric value in interactive interface. Due to similarity of one type of parts, we can conveniently create a serious of part family. Therefore, it avoids a great deal of work of repeated modeling and provides a possibility of multi-project comparison and evaluation with a serious of similar models.

An assembly is a collection of bodies (also called parts or subassemblies) in some given placements. We have assembled parts together with constraint relationships, and finally become a cyclotron VP assembly model (see figure 4). Designers have often made a mistake in product assembly before. They couldn't find the problem until products were manufactured. With virtual assembly technology, we can simulate assembling process, check interference and optimize assembly planning in computer. Now we can ensure the validity of design early in design phase.

We can research cyclotron from different viewpoints by the VP model. In VP environment, the model should support design, analysis, manufacture, and simulation. When we project tree-dimensional solid models to plane for drawing, we can get all kinds of drawings such as section drawing, assembling drawing, detail drawing and perspective drawing. And besides, we input technological data and explanation in these drawings in order to meet the engineering requirements completely. In cyclotron analysis, there are mainly magnetic analysis, RF analysis and beam dynamic analysis, which all use three-dimension solid models to replace hardware analysis. For example, in magnetic analysis, the main body model is meshed into a lot of grids and then we analyse magnetic field in ANSYS. Through feedback from these analyses, we evaluate the virtual prototype, then if we dissatisfy it, we may modify and analyse it again. The satisfied VP model will continue to research his feasibility of manufacture. For example, we may simulation the manufacture process in computer environment. Therefore the cyclotron model should support the product overall lifecycle management (see figure 2).

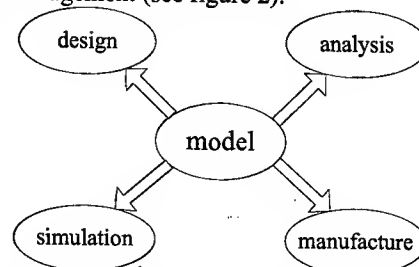


Figure 2: Cyclotron modeling framework.

We have already known that VP system is composed of these application modules above. Each module needs to utilize the VP model. It brings a question: How the model data can be exchange into each module? Because currently each module is independent relatively with own data format, the preferred technology for exchange of product model is based on using a neutral format, which is capable of capturing design intent, or in more recent terminology, product model [2]. STEP, the international standard for external representation of product data, aims to represent a compatible and integrated model data with a neutral format in product lifecycle, which is independent of any CAX system. We have used it to exchange model data between CAD module and other modules, and proven reliability of STEP. For example, figure 4 shows the VP model in simulation module.

BEAM DYNAMIC VISUALIZATION

Experimental methods remain the primary source of design information. On the other hand, because of the advance in computational technology, numerical predictions of cyclotron performance have become feasible and are beginning to produce results consistent with experiments. Appropriate visualization methods are needed to monitor and verify the results from numerical simulation. It transforms numerical data into computer-generated images. It includes three-dimensional computer graphics rendering, time series animations, and interactive display on computers. An example of beam dynamic visualization is introduced here.

We first import the cyclotron model into simulation module. Through beam dynamic analysis software, we obtain the numerical results of beam acceleration. To designers, the most concerned result is total phase excursion of beam, which shows a tendency chart with sector pole radius in Fig. 3.

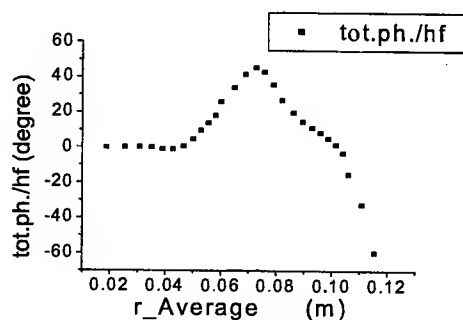


Figure 3: Total phase excursion

It is hard to create a actual motion equation of beam in beam dynamic simulation. Considering we don't take care of any special velocity and acceleration of beam, it become simply by beam track. In simulation module, beam is driven by the track spline. We can observe beam accelerate process in three-dimensional environment. Meanwhile, the total phase excursion change is displayed

in graphic way. The figure 4 is a picture of beam movement, in which we can see a total phase excursion.

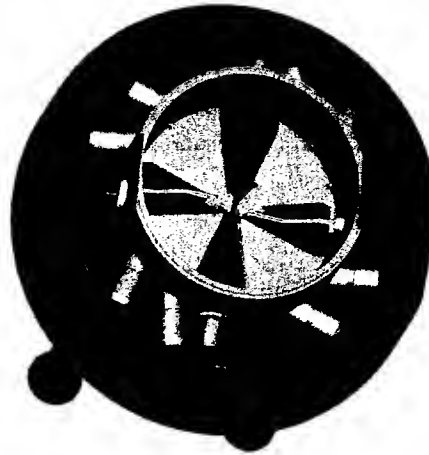


Figure 4: Beam dynamic visualization.

However, we purposely chose an imperfect result that most of beam cannot accelerate final energy in this simulation because of too large total phase excursion. It obviously shows the magnetic field of the cyclotron should be shimmed to close the isochronous. We should modify the sector pole edge for the magnetic field adjustment in modeling environment, and evaluate the performance again to get the most promising cyclotron. It also expresses an advantage of evaluating cyclotron with virtual prototypes.

CONCLUSION

This paper mainly describes CAD and visualization aspects in Cyclotron VP system. Modeling technology has already met the requirement of developing cyclotron. Visualization provides an aided method for understanding design intent better. Future work will focus on verifying VP with measurement data of real cyclotrons.

REFERENCES

- [1] Virttu Halttunen, Tuomo Tuikka, "Augmenting virtual prototyping with physical objects," Proceedings of the Working Conference on Advanced Visual Interfaces, May 2000.
- [2] Bloor, M.S., "STEP-standard for the exchange of product model data," Standards and Practices in Electronic Data Interchange, IEE Colloquium in 1991.

SELF-CONSISTENT 3-D PIC CODE FOR MODELLING OF HIGH-BRIGHTNESS BEAMS

Alberto Bacci, Cesare Maroli, Vittoria Petrillo and Luca Serafini

INFN-Milan and University of Milan

Abstract

The 3D numerical code RETAR has been developed to model the beam dynamics of high-brightness electron beams in photoinjectors and in magnetic compressors, where the interaction of the beam with its self-field is of crucial relevance to optimize the performances of these devices, either in the case of space charge dominated dynamics or under strong coherent synchrotron radiation effects, respectively. The code is fully relativistic and calculates the self-fields directly from convenient integral forms that can be obtained from the usual retarded expressions. Numerical results are presented so far for the dynamics of an electron bunch in a radio-frequency photo-injector taking into account solenoidal magnetic focusing fields, RF focusing, thermal emittance, image charges inside the cathode surface, acceleration and space-charge effects.

INTRODUCTION

RETAR is a 3D code for the description of the motion of an electron beam under any kind of (given) external electromagnetic (em) fields plus the fields created by the beam itself (space-charge and radiation-fields). At the present time, the code is limited to consider only propagation in vacuum. Metallic or other kind of boundaries will be added in the future.

The trajectory of each single electron of the beam satisfies the following equations:

$$\frac{d\mathbf{x}_j}{dt} = \mathbf{v}_j ; \quad \frac{d\mathbf{p}_j}{dt} = -e(\mathbf{E}_{tot} + \frac{\mathbf{v}_j}{c} \times \mathbf{B}_{tot})$$

where \mathbf{E}_{tot} and \mathbf{B}_{tot} are the total fields acting on each electron, taking into account both external and self fields. The equations of motion are integrated by means of a second-order Runge-Kutta scheme: this does not cause any particular difficulty provided all forces acting on the electrons are known at each time step. The electron itself is actually a *macro-electron*, with total charge and mass that are several orders of magnitude larger than the charge and mass of a true electron. These macro-electrons are considered as point like particles but their number everywhere within the bunch is supposed to be sufficiently large as to allow suppression of divergent or very large contributions to the em self-fields, when they happen to be calculated at points very near to the electrons or exactly on the electrons. As regards the external forces, they are obviously considered to be

known as functions of time and everywhere within the region of space crossed by the beam in its motion outside the cathode surface. The em self-fields are calculated directly (*i.e.* without calculating first the em potentials) in terms of the values of the charge density $\rho(\mathbf{x}, t)$ at time t and at all preceding times, through the following equations that can be readily obtained by an easy manipulation of the usual retarded forms

$$\mathbf{E}(\mathbf{x}, t) = \int d\mathbf{x}' \rho(\mathbf{x}', \tau) \mathbf{Q}_E(\mathbf{x} - \mathbf{x}', \tau) \quad (1)$$

$$\mathbf{B}(\mathbf{x}, t) = \int d\mathbf{x}' \rho(\mathbf{x}', \tau) \mathbf{Q}_B(\mathbf{x} - \mathbf{x}', \tau) \quad (2)$$

where $\tau = t - \frac{1}{c} |\mathbf{x} - \mathbf{x}'|$ and

$$\mathbf{Q}_E = \frac{\mathbf{n} \times ((\mathbf{n} - \boldsymbol{\beta}) \times \dot{\boldsymbol{\beta}})}{c |\mathbf{x} - \mathbf{x}'| (1 - \mathbf{n} \cdot \boldsymbol{\beta})^2} + \frac{(\mathbf{n} - \boldsymbol{\beta})(1 - \mathbf{n} \cdot \boldsymbol{\beta})^{-2}}{\gamma^2 |\mathbf{x} - \mathbf{x}'|^2} \quad (3)$$

$$\mathbf{Q}_B = -\frac{\mathbf{n} \times (\dot{\boldsymbol{\beta}}(1 - \mathbf{n} \cdot \boldsymbol{\beta}) + \boldsymbol{\beta}(\mathbf{n} \cdot \dot{\boldsymbol{\beta}}))}{c |\mathbf{x} - \mathbf{x}'| (1 - \mathbf{n} \cdot \boldsymbol{\beta})^2} - \frac{(\mathbf{n} \times \boldsymbol{\beta})(1 - \mathbf{n} \cdot \boldsymbol{\beta})^{-2}}{\gamma^2 |\mathbf{x} - \mathbf{x}'|^2} \quad (4)$$

In addition, $\mathbf{n} = (\mathbf{x} - \mathbf{x}')/|\mathbf{x} - \mathbf{x}'|$, $\boldsymbol{\beta} = \mathbf{v}(t)/c$, and all time dependent quantities in (3) and (4) are calculated at the retarded time τ .

The 3D integrals in (1) and (2) are calculated in the following way:

- i) The whole space around the point \mathbf{x} at which the fields are to be computed, is divided into a set of spherical shells of a conveniently small thickness.
- ii) In each shell the code sums the values of the vector \mathbf{Q}_E (and those of \mathbf{Q}_B) at all points that happen to be occupied at the corresponding retarded time by one of the electron of the beam. The retarded time itself depends only on the radius of the shell and is the same everywhere inside each shell.
- iii) The integrals giving the electric field \mathbf{E} and the magnetic induction \mathbf{B} at the position \mathbf{x}

and time t , are then obtained by summing the contributions from all spherical shells.

The basic advantages of this method seem to consist in i) the absence of convergence difficulties that may arise when one chooses to calculate the em self-fields from direct numerical integration of the relevant propagation equations and ii) in the fact that the retardation is very simply taken into account instead of having to find by means of a Newton iteration, for instance, the root of a complicated equation, when one chooses to calculate the em self-fields by summing the fields produced by each single electron as given by the Liénard-Wiechert equations. The CPU time is expected to scale as the product of the number of macro-electrons times the number of spherical shells, implying a linear scaling with the number of macro-electrons: we are in the process of checking in details this scaling law which represents a clear advantage over particle-to-particle integral codes based on Liénard-Wiechert retarded potentials.

The values of the self-fields obtained inside and outside the electron beam have been accurately tested by comparing them with well-known analytical and numerical estimates in various situations where space charge field is dominant (cylindrical and elliptic cross-section bunches with relativistic velocities) and the results have always shown fairly good agreement.

This algorithm is fully self-consistent in a 3D fashion, so it is suitable for the study of a class of beams strongly interacting with space charge and radiation fields: since it is based on an integral description for the field components, there is no mesh discretization, hence no limitations arising from space discretization of the field propagation like in case of differential PIC codes. Time (frequency) and space resolutions are only set by the number of spherical shells used in the simulation to reconstruct the retarded times.

NUMERICAL RESULTS

We are applying the code to the specific purpose of simulating numerically the relativistic motion of the electrons that are emitted by short laser pulses from the photo cathode surface and immediately subjected to a strong acceleration and focusing by suitable given electromagnetic fields.

The analysis includes the self-fields of the electrons that leave the cathode, as well as the fields produced by the image charges inside the cathode. The electron injection is simulated by fixing the electron flux at the cathode surface (for instance the plane $z=0$), i.e. by giving the number of electrons streaming out of the cathode per time interval and surface element. Thermal fluctuations in both spatial locations and velocity distribution of the electrons emitted are taken into account.

The photoinjector lay-out considered in these simulations is that of SPARC, described in a separate paper [1]: the external magnetic field has a solenoidal

shape with the maximum value $B_z = 0.27 \text{ T}$ on the axis at $z = 20 \text{ cm}$, while the axial component of the electric field is applied with a peak field on the cathode $E_0 = 120 \text{ MV/m}$. The beam is accelerated in the RF gun up to about 6 MeV and propagated along 1.2 m of downstream drift space. 2000 macro-electrons and 100 spherical shells have been used in this simulation with an integration time step of 0.5 ps : the CPU time was about 3 hours on a 1.8 Ghz processor.

In Figure 1 the time evolution of the beam is presented at different times. Significant values of the beam parameters are: the total beam charge $Q=1 \text{ nC}$, the laser pulse length 10 ps (uniform flat top time distribution for the laser pulse intensity), initial beam radius $R=1 \text{ mm}$, initial thermal emittance $\epsilon_n = 0.3 \text{ } \mu\text{m}$, launching phase 30° RF .

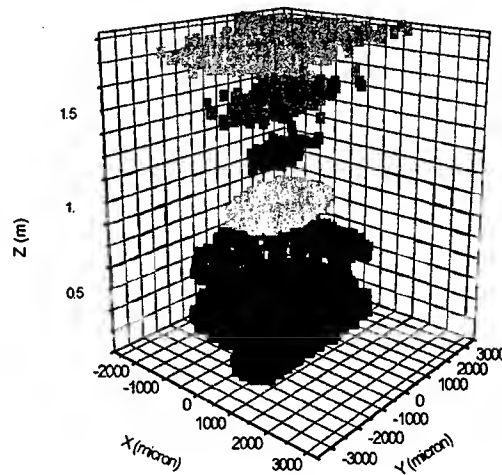


Figure 1: temporal evolution of the beam through the SPARC photoinjector

In figure 2 the rms radius σ_r and the rms normalised emittance:

$$\epsilon_x = \sqrt{\langle x^2 \rangle \langle p_x^2 \rangle - \langle x p_x \rangle^2}$$

are plotted as functions of z for the values of the parameters given previously showing that the minimum value of ϵ_x takes place at $z = 105 \text{ cm}$ in correspondence of the minimum of the rms radius.

No systematic investigations has been done yet on the optimum parameter set in order to minimize the emittance according to the Ferrario criterium for the working point of integrated photo-injectors [4]. Therefore, the comparisons to other simulations are quite preliminary, with the aim just to test the absence of errors in the code.

In Figure 3 the $r-p_r$ phase space is shown at the same time instants as in Figure 1.

After the focusing, a degradation of the beam quality can be seen, apparently due to non linear space charge effects in combination to an incorrect matching into the invariant envelope [3,4] conditions.

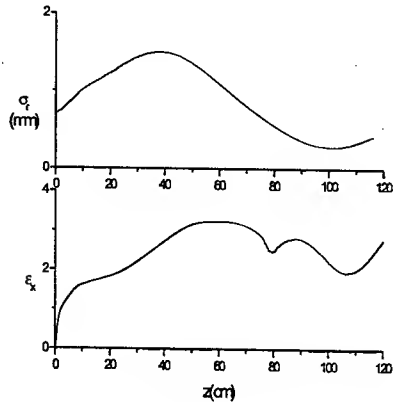


Figure 2: rms radius σ_r in mm and normalised emittance ϵ_x in μm vs z in the case of SPARC parameters

The RETAR code has been compared with other beam evolution codes as for instance Homdyn [2] based on the envelope approximation [3].

In Figure 4 the comparison between the average kinetic energy as given by RETAR (black curve) and Homdyn (red curve) for the same parameters is shown for the first 12 cm.

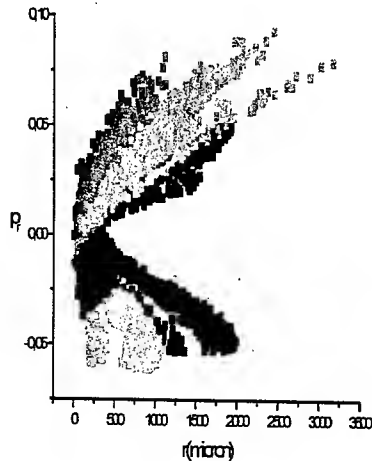


Figure 3: beam evolution in the $r-p_r$ phase space

As for the beam envelope and the rms transverse emittance, we found a slight discrepancy with Homdyn, which predicts an emittance minimum located at 1.5 m with a minimum value of 0.6 μm . We believe most of this discrepancy is due to an incorrect setting of the most

critical parameters (solenoid peak field, launching phase, cathode spot size) and we are in the process of investigating it thoroughly.

In conclusion, the code RETAR is under test in the context of a class of general beam phenomena where beam-field interaction is of crucial relevance: we reported here the preliminary results of testing the code in photoinjector beam dynamics. Next step will be the study of CSR effects in magnetic compressors.

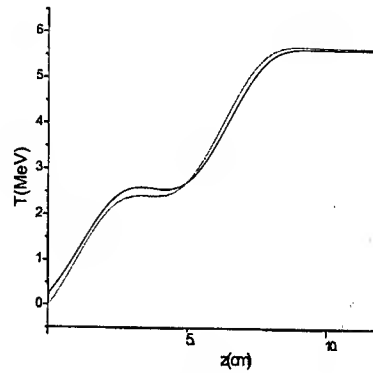


Figure 4: comparison between RETAR and Homdyn

REFERENCES

- [1] M. Biagini *et al.*, *Beam Dynamics Studies for the SPARC Project*, this conference
- [2] M. Ferrario *et al.*, *Particle Accelerators* **52** (1996) 1
- [3] L. Serafini, J.B. Rosenzweig : *Phys.Rev. E* **55** (1997) 7565
- [4] M. Ferrario *et al.*, *Recent Advances and Novel Ideas for High Brightness Electron Beam Production based on Photo-Injectors*, INFN Rep. LNF-03/06 (P), May 2003

RF COUPLER FOR HIGH-POWER CW FEL PHOTOINJECTOR*

S.S. Kurennoy and L.M. Young, LANL, Los Alamos, NM 87545, USA

Abstract

A high-current emittance-compensated RF photoinjector is a key enabling technology for a high-power CW FEL. The design presently under way is a 100-mA, 2.5-cell π -mode, 700-MHz, normal conducting demonstration CW RF photoinjector. This photoinjector will be capable of accelerating 3 nC per bunch with an emittance at the wiggler less than 10 mm-mrad. The paper presents results for the RF coupling from ridged waveguides to the photoinjector RF cavity. The LEDA and SNS couplers inspired this "dog-bone" design. Electromagnetic modeling of the coupler-cavity system has been performed using both 2-D and 3-D frequency-domain calculations, and a novel time-domain approach with MicroWave Studio. These simulations were used to adjust the coupling coefficient and calculate the power-loss distribution on the coupling slot. The cooling of this slot is a rather challenging thermal management project.

INTRODUCTION

The project is underway to build a demonstration 700-MHz RF emittance-compensated CW photoinjector (PI) capable of accelerating 100 mA of the electron beam (3 nC per bunch at 33.3-MHz repetition rate) to about 5 MeV with the transverse emittance at the wiggler below 10 mm-mrad, see [1] and references therein. The PI consists of a 2.5-cell cavity with the accelerating gradient $E_0=7$ MV/m (the PI proper) that brings the electron beam energy to 2.7 MeV, followed by a 4-cell booster with $E_0=4.5$ MV/m, where the beam is accelerated to 5.5 MeV. This gradient choice is a trade-off between the beam-dynamics requirements and challenges of the cavity thermal management [2,1].

The injector is designed to be scalable to even higher beam currents, up to 1 A, and therefore, to higher beam power by increasing the bunch repetition rate. The high beam power plus a significant wall power loss in the normal-conducting PI cavity lead to serious challenges for cavity cooling. In addition to a large total RF power needed, there are regions of rather high loss power densities on the cavity walls. Therefore, we need to provide an effective RF power feeding to the PI cavity with the lowest possible increase of the surface power density. Here we present the design and electromagnetic modeling of the RF power couplers for the PI cavity.

RF COUPLER

The RF feeds are in the 3rd (the 2nd full) cell of the 2.5-cell PI cavity; see Fig. 1. Two symmetrically placed ridge-loaded tapered waveguides are connected to the cavity via "dog-bone" coupling irises – consisting of a long narrow slot with two circular holes at its ends – in a 0.5"-thick copper wall. This RF coupler design is based on the

experience for the LEDA RFQ and SNS high-power RF couplers, e.g., see [3]. The required cavity-waveguide coupling is given by the coupling coefficient $\beta_c = (P_w + P_b)/P_w \approx 4/3$, where $P_w=780$ kW is the CW wall power loss [1], and $P_b=270$ kW is the beam power of a 100-mA beam at the 2.5-cell cavity exit. The coupling is adjusted by changing the radius of the holes at the ends of the coupler slot.

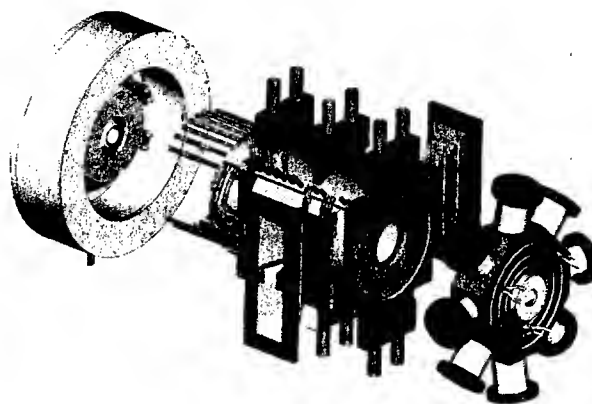


Figure 1: Schematic of 2.5-cell cavity with emittance-compensating magnets (left) and vacuum plenum (right).

Coupler Model

To study the waveguide-cavity system we use a simplified model shown in Fig. 2: a short pillbox cavity, which can be considered as a slice of the 3rd cell in the 2.5-cell PI cavity, with two attached short sections of the ridge-loaded waveguides. The picture shows only the internal (vacuum) part of the coupler model as used in simulations with the CST MicroWave Studio (MWS) [4].

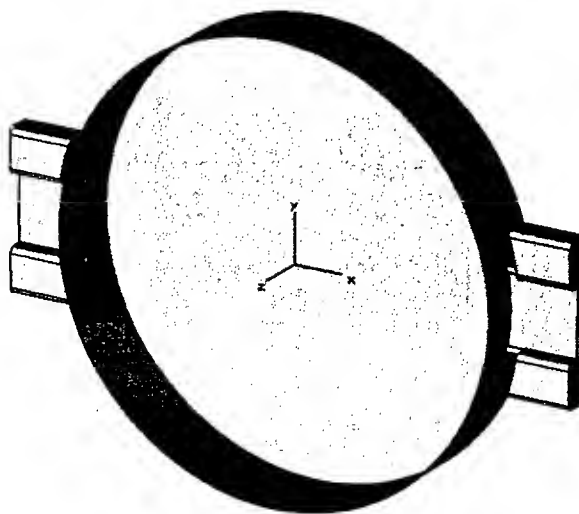


Figure 2: Model of pillbox cavity with two waveguides.

*Supported by the DoD High Energy Laser Joint Technology Office through a contract from NAVSEA.

The pillbox radius is slightly adjusted to provide the correct resonant frequency 700 MHz. Some model dimensions are listed in Table 1.

Table 1: Model dimensions

Parameter	Value, mm
Pill-box cavity radius	163.922
Pill-box length	60
Coupler slot length	50.8
Coupler slot width	1.434
Coupler end-hole radius	2.5

Obviously, for the pillbox cavity the waveguide-cavity coupling will be different than for the 2.5-cell PI cavity. It is related to the required β_c as

$$\beta_{pb} = \beta_c \frac{W_c}{W_{pb}} \frac{Q_{pb}}{Q_c}, \quad (1)$$

where W_i , Q_i are the field energies and unloaded quality factors of the pill-box TM_{010} mode and the operating π -mode in the 2.5-cell cavity. We assume that W_{pb} is scaled such that the surface magnetic field far from the coupler iris in the transverse cross section at the coupler location is equal to one at the same location in the 3rd PI cell (14.8 kA/m) for the nominal PI gradient. From (1) the required waveguide-pillbox coupling is $\beta_{pb} \approx 6.1$.

Time-Domain Simulations with MWS

The waveguide-pillbox coupling is calculated directly with MWS time-domain simulations: the fields excited in the cavity with perfectly conducting walls decay due to radiation into the open waveguides. Due to the model symmetry, we restrict our simulations to 1/8 of the model, imposing the electric boundary conditions in xy -plane, and magnetic ones in xz - and yz -planes, cf. Fig. 2.

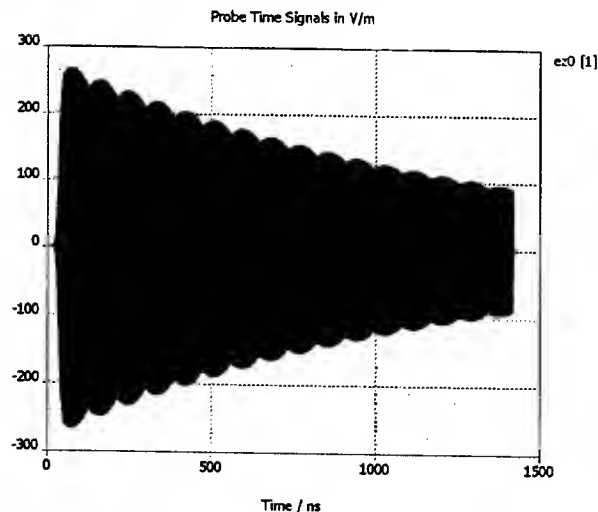


Figure 3: Electric field decay due to radiation into open waveguides as calculated by MWS.

The decay of the on-axis electric field excited in the cavity center by a short pulse from the waveguide is illustrated in Fig. 3. This particular computation on a mesh of about 50K points took 3.5 hours on a dual 1-GHz Pentium III Xeon PC. Inverting the calculated decay time constant gives us the external quality factor Q_e of the system, and then we find $\beta_{pb} = Q_{pb}/Q_e$ [4]. Starting from large slot-end holes (shorter computation times), we found that the required coupling $\beta_{pb} = 6.1$ is achieved for a hole radius of 2.5 mm, cf. Tab. 1 and Fig. 3.

An exact resonance frequency of the pillbox-waveguide system is conveniently calculated with the auto regressive (AR) filter feature in MWS time-domain simulations. It allows one to analyze spectra of time signals that have not reached a steady state yet. With this technique we found the pillbox-waveguide resonance at $f_r = 699.575$ MHz.

To calculate the power density distribution around the coupler during its nominal operation, we simulate the RF feeding of the model via the waveguides with a TE-mode at frequency f_r . The waveguide-mode fields are mostly concentrated in the narrow gap between the waveguide ridges, as shown in Fig. 4. The field scale corresponds to 1 W of the peak RF power fed through the waveguide.

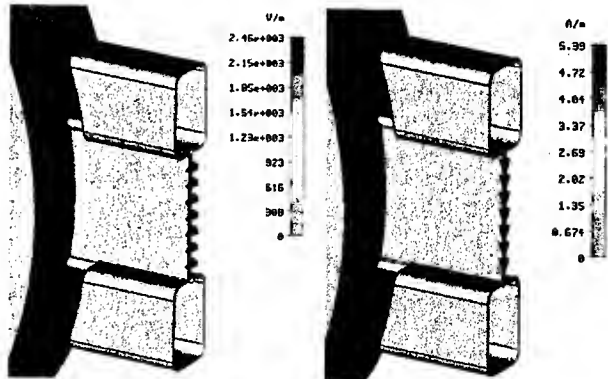


Figure 4: Electric (left) and magnetic (right) fields of the waveguide RF input mode.

The model symmetry means that the system is driven by two waveguides in phase. Calculated normalized time signals are plotted in Fig. 5. This plot, as well as one in Fig. 3, includes hundreds of oscillation periods; we see only signal envelopes. While the waveguide input remains constant, the output decreases reaching a point ($t=956.6$ ns) where it vanishes, and increases again after that. The output decrease is due to a destructive interference of two waves: one is reflected from the coupler aperture, and the other is radiated into the waveguides from inside the cavity. The reflected-wave amplitude remains constant when the input is constant, while the radiated-wave amplitude increases as the cavity field increases. These two waves are always in opposite phases [5]. As a result, at certain moment the two waves cancel each other, so that the reflected power vanishes at that particular moment. This situation corresponds to an exact match; therefore, the field snapshots at that moment give us field distributions for the matched case.

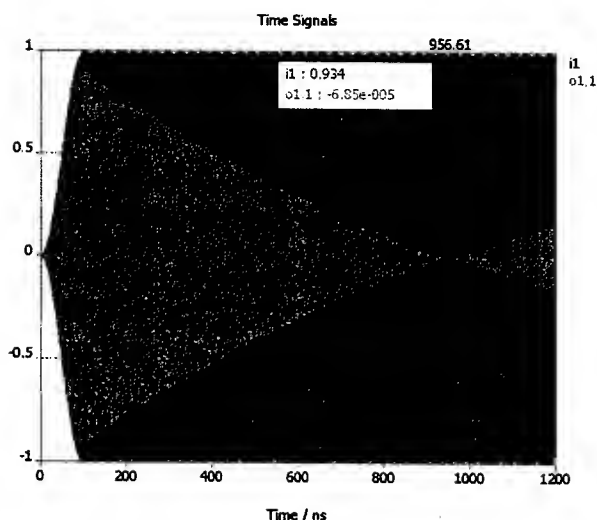


Figure 5: Input (red) and output (green) waveguide signals from MWS time-domain simulations.

The peak surface current magnitude at this moment is shown in Fig. 6. This picture was obtained using field monitors in MWS time-domain solver. The field scaling here is the same as for Fig. 4, i.e. 1-W peak RF power input into each of two waveguides.

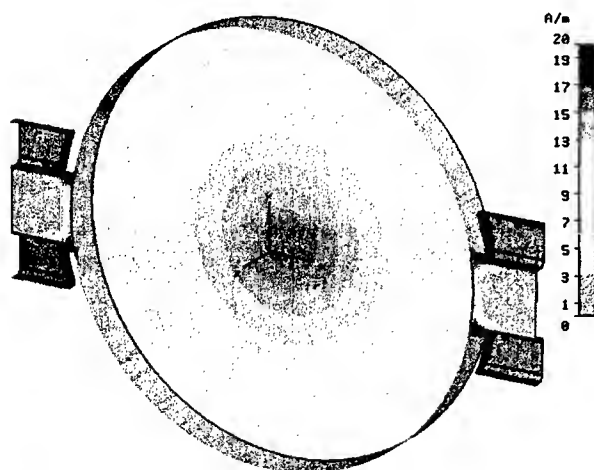


Figure 6: Peak surface current distribution at the moment of zero reflected power (view cut in xy-plane).

One can see that the surface power densities are the highest near the ends of the slot aperture. Comparing the magnetic field on the cylindrical wall far from the coupler with one at the coupler location in the 2.5-cell cavity for the nominal field gradient, we find a field-scaling factor. Some results for rescaled fields and power values are presented in Tab. 2. The rescaled averaged RF power transferred through each of the two waveguides is about 525 kW, as should follow from the energy balance for the matched waveguide-cavity coupling.

Table 2: Fields and power in 2.5-cell cavity with couplers

Parameter	Value
Surface magnetic field on the wall in the 3 rd cell far from the coupler*	14.8 kA/m
Power density on the smooth wall in the 3 rd cell far from the coupler*	76 W/cm ²
Maximal surface magnetic field near the coupler slot ends	24.4 kA/m
Maximal power density near the coupler slot ends	205 W/cm ²
Maximal power density elsewhere in the 2.5-cell PI cavity w/o RF couplers**	107 W/cm ²

* In the transverse cross section at the coupler location.

** On the upstream wall of the 1st half-cell [1].

CONCLUSIONS

Electromagnetic modeling of the coupler-cavity system has been performed using 2-D (Superfish) and 3-D (MWS) frequency-domain calculations, plus a novel time-domain approach using the MicroWave Studio. These simulations were applied to adjust the coupling coefficient and calculate the power-loss distribution on the coupling slot.

The cooling of the regions around the coupling irises is a challenging thermal management issue due to the surface power density exceeding 200 W/cm² at some points. However, since the hot spots are localized in small regions around the slot ends, they can be cooled effectively with cooling channels placed properly around the slots in the thick cavity wall.

The authors would like to acknowledge useful discussions with F. Krawczyk, D. Schrage, and R. Wood (LANL), as well as with J. Rathke and T. Schultheiss of Advanced Energy Systems.

REFERENCES

- [1] S.S. Kurennoy, et al. "Photoinjector RF Cavity Design For High Power CW FEL", these proceedings.
- [2] S.S. Kurennoy, et al. "CW RF Cavity Design for High-Average-Current Photoinjector for High Power FEL", FEL'02, Argonne, IL, Sep. 2002.
- [3] L.M. Young, et al. "High Power RF Conditioning of the LEDA RFQ", Proceed. 1999 PAC, NY, p. 881.
- [4] MicroWave Studio v. 4.2, CST GmbH (Darmstadt, Germany), 2003. www.cst.de.
- [5] T.P. Wangler, *RF Linear Accelerators*, Wiley, NY, 1998.

RECENT IMPROVEMENTS IN THE PARMILA CODE*

H. Takeda, J. H. Billen, LANL, Los Alamos NM 87545

Abstract

We discuss capabilities, computational procedures, and recent improvements in the accelerator design code PARMILA. The name PARMILA stands for Phase and Radial Motion in Ion Linear Accelerators. We discuss the algorithms used in PARMILA, how the code designs individual linac sections to achieve efficient acceleration, and how it determines the distance between linac segments. We also discuss the restructuring and transformation of code from the Fortran 77 standard to the Fortran 90 standard.

INTRODUCTION

Program PARMILA originated in the early 1950s for the design drift-tube linear accelerators.[1] The code came to Los Alamos with D. E. Swenson in the mid 1960s and since then many author have contributed to the development of PARMILA. We report here on the current status of the code distributed by the Los Alamos Accelerator Code Group (LAACG) since 1993.

PARMILA performs two distinct tasks: accelerator design and beam-dynamics simulation. Though these tasks are closely related, the code can be used for either one separately or for both together in a single run. In a previous paper [2], we described code organization from the user's point of view. In this paper we concentrate more on computational algorithms.

ALGORITHM FOR GEOMETRICAL β

To achieve efficient acceleration, cell lengths must continuously increase as particles gain energy. However, to build the actual hardware, it is easier to design and engineer sections with a few identical cells. In this case, the rf fields are not exactly synchronous with the particles' arrival at the gap centers. The synchronous particle would have a constant velocity that we call β_g , or the "geometrical beta." To determine β_g for a sequence of equal-length cells, PARMILA uses an extension of Lapostolle's original formulation [3]. For simplicity in this discussion, we assume that the geometrical center of each gap coincides with its electrical center, which has equal potential differences on both sides of the gap.

We describe the acceleration through a cell by a "gap transformation" consisting of three elements: a field-free drift, an impulse kick at the gap center, followed by a field-free drift. The gap transformation derives from the approximation of constant particle velocity across the cell, which is accurate for ions subjected to electric fields achievable in typical accelerating structures. The impulse

in each gap has no length and applies the energy gain through the entire cell instantaneously at the gap center.

Particle acceleration computed by PARMILA agrees closely with results of time-step integration using 3-dimensional field maps. The transit-time factor and its derivatives with respect to wave number represent the cumulative effect of the electromagnetic field through the cell. Particle velocities at the entry, electrical center, and exit of a cell are β_i , β_c and β_o . The phases of the rf fields "seen" by the design particle at these locations are ϕ_i , ϕ_c , and ϕ_o .

Consider the coupled-cavity drift-tube linac (CCDTL) shown in Figure 1 and a particle traveling from left to right. The drift tube centered in the cavity creates two asymmetric cells. For each cell, we designate the left and right halves by L and R subscripts. For the first cell, the drift lengths are $\beta_g \lambda n_L$ and $\beta_g \lambda n_R$, where $n_L = 1/4$ and $n_R = 1/2$. If a particle is synchronous with the rf for this structure, the phase difference between the entry and exit must satisfy the condition $\phi_o - \phi_i = 2\pi(n_L + n_R)$.

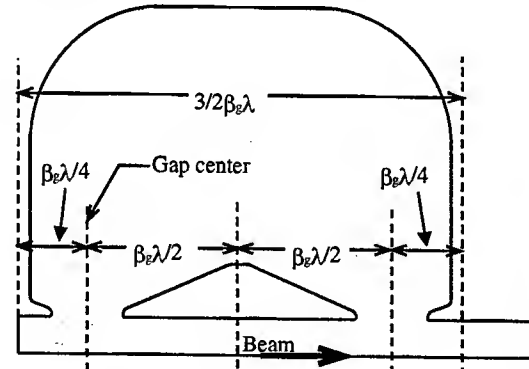


Figure 1. A 2-gap CCDTL cavity.

The structure design accounts for the different entry and exit velocities through the energy-gain equation. For cell j , the energy gain is

$$\Delta W_j = E_0 T_j (n_{j,L} + n_{j,R}) \beta_g \lambda \cos(\phi_d + \Delta\phi_{Pr}),$$

where E_0 is the average axial electric field, T_j is the transit-time factor, ϕ_d is the design phase, and $\Delta\phi_{Pr}$ is the Promé phase correction term [4]. For a single cell with drift lengths Δz_L and Δz_R , the total phase change is

$$\phi_o - \phi_i = 2\pi(n_L + n_R) = \Delta\phi_L + \Delta\phi_R + \Delta\phi_{Pr}, \text{ where}$$

$$\Delta\phi_L = 2\pi\Delta z_L / \beta_i \lambda, \text{ and } \Delta\phi_R = 2\pi\Delta z_R / \beta_o \lambda.$$

PARMILA interpolates the transit-time factor T_j from a table of values computed for a series of

*Work supported by the US Department of Energy, Office of Science, Division of High Energy Physics.

representative cavities of increasing length. To design a symmetric structure containing several identical cavities we can satisfy the requirement for synchronism from end to end of the entire structure as follows:

$$2\pi \sum_j (n_{j,L} + n_{j,R}) = \sum_j \left(\frac{2\pi}{\beta_{j,i}\lambda} n_{j,L} \beta_g \lambda + \frac{2\pi}{\beta_{j,o}\lambda} n_{j,R} \beta_g \lambda \right) + \sum_j \Delta\phi_{j,Pr}$$

The Promé correction depends on the particle velocity $\beta_{j,c}$ at the center of the gap, and is computed for each cell. This equation can be written as follows:

$$\beta_g = \frac{\sum_j (n_{j,L} + n_{j,R})}{\sum_j \left(\frac{n_{j,L}}{\beta_{j,i}} + \frac{n_{j,R}}{\beta_{j,o}} \right) + \sum_j \frac{\Delta\phi_{j,Pr}}{2\pi\beta_g}}$$

which can be solved iteratively for β_g in a few cycles. Because the Promé correction term is normally positive, its effect is to reduce slightly the result for β_g .

REFERENCE PARTICLE DYNAMICS AND RF STRUCTURE DESIGN

PARMILA designs individual drift-tube linac cells and also rf structure segments separated by drift spaces. We use the term segment to refer to a contiguous section of one or more cavities, usually of the same length. The drift space may contain transverse focusing elements. There are differences in design procedures for normal-conducting and superconducting structures.

Normal-conducting structures often consist of many cavities of varying length, but locked in phase because they are driven by single power source. Examples include the drift-tube linac (DTL) and the coupled cavity linac (CCL). The CCL for the Spallation Neutron Source (SNS) has 48 eight-cavity segments, each segment of a different length, and spanning the velocity range from $\beta_g = 0.40$ to 0.55 .

In contrast, a superconducting linac typically has only a few different cavity types, with an rf power source for each individual cavity or for small groups of cavities. The layout of the accelerator comes from practical considerations related to the packaging of cavities within cryostats. For SNS, there are two superconducting cavity types, one with $\beta_g = 0.61$ and the other with $\beta_g = 0.81$.

Transit-time factors

The transit-time factor T for internal cavities of a multicell segment may differ from T for cavities at the end of the segment, especially if the segment has a large bore radius. The user supplies PARMILA with multiple sets of transit-time factor tables, one table for each type of boundary between cells and at the ends of segments. For example, the extended bore tube on the right side of

Figure 1 implies the end of a segment while the left side abuts another cavity whose fields are of opposite sign.

For normal-conducting structures, the transit-time data corresponds to a series of representative cavities, each with a different β_g . For superconducting structures, the data correspond to many particle velocities β for each individual cavity.

PARMILA linearly interpolates needed values from the supplied transit-time factor tables and warns if a requested β value is outside the table range. During the design part of the PARMILA run, the code stores interpolated transit-time data for each cell for later use in the dynamics simulation. If β_g of a designed segment differs appreciably from the particle velocity, PARMILA expands the equation for the transit-time factor and its derivatives in terms of the particle wave number $k (= 2\pi/\beta\lambda)$ to compute T , $\partial T/\partial k$, etc. for the β of interest.

Normal-conducting structures

To design a segment, the user specifies a design phase ϕ_d and an effective accelerating field $E_0 T$. The code performs single-particle dynamics simulations iteratively to compute cell lengths or segment lengths and the spacing between them. This particle is called the reference particle. For segments containing same-length cavities, the reference particle arrives at each cell center at a different phase of the rf fields. The goal in PARMILA is to make the average of these phases for the segment equal to the user-specified design phase ϕ_d . The code iterates a calculation of the reference particle dynamics over the segment to achieve this goal. The iteration loop can include additional restrictions, for example, if the user requires a particular energy gain for the segment. Convergence of this process determines the segment length, at which point the code records the entry phase ϕ_i and exit phase ϕ_o for the next step: determining the intersegment spacing.

If two consecutive segments are part of the same coupled structure, the cavity fields are locked in phase. Therefore, the particle phase advance over the intersegment length is restricted to $m\pi/2$, where m is an integer. For a given segment n , phases $\phi_{i,n}$ and $\phi_{o,n}$ generally differ from one another and from phases $\phi_{i,n+1}$ and $\phi_{o,n+1}$ of the next segment. PARMILA computes the spacing between segments n and $n+1$ after it has determined both segment lengths and makes a small correction equal to $(\phi_{i,n+1} - \phi_{o,n})\beta\lambda/2\pi$, where βc is the particle velocity between segments. Because of this method, the user normally designs one extra segment intersegment length between two different rf structures.

Superconducting structures

For a superconducting linac, the design procedure does not include finding cavity lengths. The layout of the linac is fixed, and we know each segment's β_g , and the spacing between segments. In the simplest case, a single independently-phased power source drives each segment. For efficient acceleration, we adjust the cavity phases for each segment.

Because a particular superconducting cavity may accelerate particles over a wide range of velocities, the individual cell lengths differ significantly from $\beta\lambda/2$ at the ends of the velocity range. PARMILA uses the exit phase $\phi_{o,n}$ from cavity n and the entry phase $\phi_{i,n+1}$ for cavity $n+1$ to calculate the drive phase for cavity $n+1$ that satisfies the design requirements.

CODE IMPROVEMENTS

3-D space charge

During the particle dynamics simulation, PARMILA applies space charge forces in a linac. Previous versions of PARMILA used exclusively the 2-D space-charge subroutine SCHEFF. The latest version of the code includes an option to use either SCHEFF or the 3-D code PICNIC.[5] PARMILA applies space-charge impulses once per cell at the center of each gap for the entire cell. In a quadrupole lens, the space charge is applied once at the center of each quadrupole for the entire lens. In transport structures, the code applies space charge at least once per $\beta\lambda$ in each drift. The user can specify the number of space charge kicks in the input file.

Code modernization

Recently, PARMILA went through a large structural reorganization. The source code now conforms to the Fortran 90 standard with free format. We eliminated obsolete language features and use Fortran modules rather than the older common block for storing variables. All of the code modules, subroutines, and functions declare IMPLICIT NONE and define the type and kind of all variables. We use more descriptive names for important variables. With these changes, the code is more robust and easier to maintain.

File names are no longer limited to eight characters. PARMILA reads an initialization file, which may include names of input and output files, and also some program limits. The user can declare the maximum numbers of linac cells, tanks, and simulated particles.

Code organization

The input file for PARMILA contains keywords to define linac properties, initiate the linac design, and start the particle simulation. (We use quoted lower case strings for these keywords in this discussion.) At the highest level, a PARMILA input file is divided into sections by the "structure" keyword. Some structure sections design

and simulate the performance of a particular accelerator type (for example, DTL, CCL, or superconducting linac). A separate structure section may define components for a transport beam line. Before the first "structure" line, the input file defines the beam particle distribution or provides the name of a binary file containing a distribution. Certain global keywords define parameters that pertain to the entire design and simulation calculation.

In structure sections that design a linac, keyword lines placed before the transit-time factor tables define properties of the linac. These properties include accelerating field E_0 , design phase ϕ_d , and the transverse focusing lattice. After reading all the transit-time factor data, PARMILA designs the linac. At this point in the file, the user can modify some of the linac properties (e.g., quadrupole lens settings or accelerating field) before the code starts the simulation part of the run.

The "scheff" line provides information for applying space charge impulses. The beam dynamics simulation starts after the "begin" line. The code generates an output text file that logs progress of the calculation. Certain options may generate other text files. PARMILA creates a binary file containing particle coordinates at locations specified by the "output" line. The postprocessor LINGRAF plots data read from the binary file. This file can be read as an input distribution to another PARMILA run.

CONCLUSION

We have described the latest version of the PARMILA program. For more information and to obtain a copy of PARMILA, send email to laacg@lanl.gov.

REFERENCES

- [1] W. K. H. Panofsky, "Linear Accelerator Beam Dynamics," UCRL-1216 (February 1951).
- [2] H. Takeda et al., "Recent Developments in the Accelerator Design Code PARMILA," Proceedings of the 1998 Linear Accelerator Conference, Chicago, IL, August 23-28, 1998.
- [3] P. Lapostolle et al., Numerical Methods. Acceleration by a Gap, Linear Accelerators p. 747-783, J. Wiley & Sons, 1970.
- [4] M. Promé, "Effects of the Space Charge in Proton Linear Accelerators," CEA-N-1457, 1971.
- [5] N. Pichoff et al., "Simulation Results with an Alternate 3D Space Charge Routine, PICNIC," Proceedings of the 1998 Linear Accelerator Conference, Chicago, IL, August 23-28, 1998.

THE PARTICLE TRACKING CODE PARMELA *

Lloyd Young and James Billen

Los Alamos National Laboratory, Los Alamos, NM 87545, USA

Abstract

The name PARMELA came from the phrase "Phase And Radial Motion in Electron Linear Accelerators," which described its earliest applications[1]. However, a decade ago, the code's capabilities were expanded to track particles of any mass and charge. A more recent addition was the ability to track particles of three different masses and any charge simultaneously. PARMELA uses time as the independent variable. PARMELA is a simulation code, and does not design a linac or beam transport channel. PARMELA can use electromagnetic fields calculated by other codes. These fields can be RF electromagnetic, static magnetic, or electrostatic. Both 2D cylindrically symmetric and fully 3D field maps can be used for all three types. The RF fields are confined to the rf cavity elements that describe standing-wave or traveling-wave structures. The static fields are treated as a background field that is superimposed over drift spaces and rf cavity elements. PARMELA includes options for selecting either 2D or 3D space-charge effects. The code's input file can supply data for most common beam-line components and accelerator structures. This paper describes some of the capabilities of PARMELA and a few examples of PARMELA simulations.

INTRODUCTION

Parmela takes a collection of particles and follows their path through a "beam line". The path a particle takes is influenced by electromagnetic fields including the self-fields. The self-fields are usually called "space charge" and are caused by the charge on the particles. Gravity is ignored. The electromagnetic fields are described by a control file called the input file or by files containing a field map generated by another code. The "beam line" is described in the input file by a series of keywords. The beam line is made up of a series of elements. The keywords associated with the elements are followed by a series of parameters that describe the element. For example, the keyword "DRIFT" is followed by 3 numbers that represent the length of the element, the radial clear aperture, and a flag that tells PARMELA if you want to write the particle coordinates into an output file at the end of the "DRIFT" element. All keywords that represent elements have these same parameters as the first three followed by additional parameters that depend on the type of element.

To make the collection of particles visible, a second code call PARGRAF reads the output files produced by PARMELA and displays them in various formats. A

simple control file and tabs on the graphics display control the action of PARGRAF. PARGRAF can generate hard copy or graphic files with a choice of formats.

THE INPUT FILE

The first line of the input file uses the keyword "RUN" that is followed by several parameters describing some basic parameters of the accelerator; namely, frequency, starting position and energy of the reference particle. Figure 1 shows an example of a Parmela input file with the various types of keywords. The mass of up to 3 particle types can also be defined on the run line. The default mass is 0.5110034 MeV which represents an electron. The optional keyword "TITLE" is followed by text on the next line that may be a description of the beam line. "TITLE" and its following line of text may be placed anywhere in the input file. The keyword "INPUT" generates the distribution of particles. In this case the particles are electrons because the run line does not have a

```
run 1 2 2856. -.00113 1.e-5
title
PHOTOCATHODE RF GUN + SLAC Linac.
INPUT 9 9999 9. 1 30. 5 0 3 5
Cathode 0 1 1 0 -.5
poisson 0.00 0.5 0 0 0 0 1
ecompl0.po7
CELL 2.625 1. 1 0. 63.75 1 5 -1
cfield 1
atfmm.t7
cell 2.625 1. 1 180. 63.75 1 5 1
cell 5.2464 1. 1 180. 32.05 2 5 -1
drift 10.0 5 1
drift 10.0 5 1
cell 5.2464 0.9547 1 90.0 4.7452 2 5 1 2856.
cfield 2
slac1.t7
trwave 1.75 0.9547 1 0.0 10.6289 1 5 2856. 1 -5 5 .666667 84
trwave 3.50012 1.311 1 0.0 10.6289 1 5. 2856. 1
...
trwave 3.50012 0.955 1 0.0 10.6289 1 5. 2856. 1
trwcfield 1
slac2.t7
slac2b.t7
adjust 4 7 7 120 7
adjust 4 8 97 120 9
zout 1000 30 0 80.8
OUTPUT 5
scheff 2.86 .33 3 20 1000 0 0 7 1.5 0
start 39. 1. 330 1 10
continue 15 1500 1 3
end
```

Figure 1 Example of PARMELA input file.

* Work supported by the US DOE, Office of Energy Research.

mass specified. Figure 2 shows a snap shot of the fields in the first 100 cm of the linac described in the above input file. This figure is produced by "TABLPLOT" from a text file written by PARMELA. The TABLPLOT program and it's companion QUIKPLOT are general purpose window plotting codes distributed with both PARMELA and the Poission Superfish code distribution[2]. This file is produced by the "ZOUT" line that calls for a snap shot of the fields every 30 degrees of the master clock.

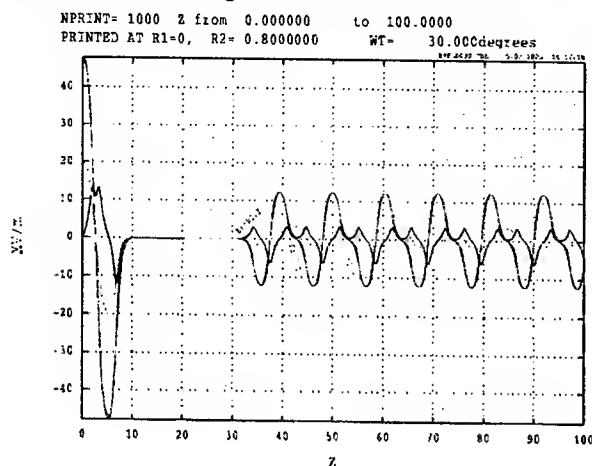


Figure 2: Plot of fields with master clock at 30 degrees.

PARGRAF

Pargraf is the graphics code that uses the coordinates of the particles that PARMELA writes to two output files. One file is the particle coordinates at the end of each

```
subnum 8
output 2 1 1 500
optcon 11 12 0 340 10 0 5 1 200 1
begin
subnum 7
output 2 1 1 500
optcon 2 0 1 0 0 0 0 0
begin
subnum 5
output 2 1 1 2000
optcon -1. 1.0 8 1. 2 1. 2 200 0
begin
end
```

Figure 3: Sample control for PARGRAF.

element for which the input file requests output. The other file contains the particle coordinates at the end of a time step. The time steps at which output is desired is set on the appropriate "START", "CONTINUE", or "RESTART" lines. A sample control file for PARGRAF appears in Figure 3. One of the pictures PARGRAF generates with this control file is shown in Figure 4.

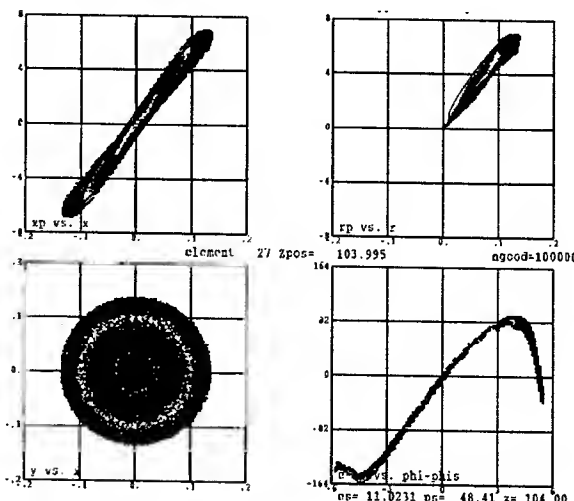


Figure 4: Sample picture from Pargraf.

NEW FEATURES IN PARMELA V3.XX

- Unlimited number of particles. But in practice the number of particles is limited to about two million because of memory limitations.
- 3D space-charge routine. Invoke by using the SPCH3D line.
- 3-D field maps can now be used with the CFIELD line that reads in electromagnetic field maps for use by a CELL line.
- Coherent synchrotron radiation (CSR) calculation is available for use with SCHEFF and SPCH3D
- Unlimited number of cell types.
- Nearly unlimited number of elements. The limit is 2708 elements. This limit will increase when PARMELA is compiled with the Lahey LF95 compiler[3].
- Unlimited numbers of mesh intervals in cell fields maps. In 2D field maps, only, the number of intervals must be the same in all 2D field maps.
- Unlimited number of traveling-wave accelerators.
- Field maps are available for traveling-wave accelerators.
- Drift-tube-linac cell; RF field maps overlap quadrupole fields.
- 3D electrostatic and 3D static magnetic field maps can be read in with the POISSON line.
- The default extension on the PARMELA input file is ".acc". In windows, PARMELA can be invoked by double clicking on the input file.
- An optional TABLPLOT file of time-step-data can be generated.

Figure 5 shows an example of a TABLPLOT file of time-step-data from running the PARMELA input file in Figure 1. PARMELA creates the optional time-step-data as input for TABLPLOT if the keyword TimeStepEmittance appears in the initialization file LANL.INI and if this keyword specifies the name of a TABLPLOT input file in the form filename.TBL. If this

keyword is present (and has a value other than None), then Parmela will write the Time-Step-data file. The Data in this file includes the following columns:

- T(deg) Time step in degrees
- Z(cm) Reference particle position
- Xun(mm-mrad) Un-normalized rms X-Xp emittance
- Yun(mm-mrad) Un-normalized rms Y-Yp emittance
- Zun(mm-mrad) Un-normalized rms Z-Zp emittance
- Xn(mm-mrad) Normalized rms X-Xp emittance
- Yn(mm-mrad) Normalized rms Y-Yp emittance
- Zn(mm-mrad) Normalized rms Z-Zp emittance
- Xrms(mm) Rms beam size in X direction
- Yrms(mm) Rms beam size in Y direction
- Zrmz(mm) Rms beam size in Z direction
- <kE>(MeV) Average energy
- Del-Erms Rms energy spread

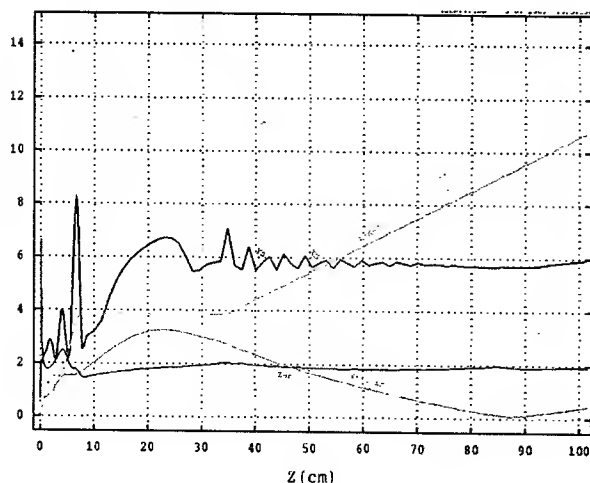


Figure 5: Example plot of data in TABLplot file produced by PARMELA

NEW FEATURES IN PARGRAF V 3.XX

- Higher resolution graphics in Windows.
- Mouse control.
- Pull-down menus.
- More hard copy options.
- More information in the output file.
- Display the previous screen (Back up).
- Skip current SUBNUM series.
- Slice emittance calculations.
- LANL.INI file controls some initial display options (Background, Movie, Slice).
- The default extension of the PARGRAF control file is ".pgf". When the user double clicks on a control file with this extension, PARGRAF will open the file and plot the data requested.

PARMELA DOCUMENTATION

The PARMELA installation comes with a Microsoft Word document containing the Parmela documentation. This documentation is currently 116 pages long. Highlighted links are used extensively in this document to conveniently move to the location in the file of interest.

ACKNOWLEDGMENTS

The authors of PARMELA version 3 wishes to acknowledge the extremely important contribution of Kenneth R. Crandall, who wrote the original version of PARMELA in 1980. He introduced the use of time (or phase angle) as the independent variable, which is retained in the present version. Even after retiring from Los Alamos National Laboratory in the mid 1980s, Ken Crandall contributed to the further development of PARMELA. Working as a consultant, he wrote new sections of the code for a traveling-wave accelerator tank and a wiggler element.

The author is also grateful to the many users of these codes who have pointed out bugs and made suggestions for additional features. This code is maintained by the Los Alamos Accelerator Code Group (LAACG)[4] at Los Alamos National Laboratory. The activities of the LAACG are supported by the US Department of Energy, Office of Energy Research, through the Division of High Energy Physics, Division of Nuclear Physics, and Division of Mathematics, Information, and Computational Sciences.

REFERENCES

- [1] L. M. Young, "PARMELA," Los Alamos National Laboratory report LA-UR-96-1835 (Revised April 22, 2003).
- [2] J. H. Billen and L. M. Young, "Poisson Superfish," Los Alamos National Laboratory report LA-UR-96-1834 (Revised February 6, 2003).
- [3] Lahey Computer Systems, Inc. 865 Tahoe Blvd. Box 6091 Incline Village NV 89450
- [4] <http://laacg1.lanl.gov/>

PARSEC: PARALLEL SELF-CONSISTENT 3D ELECTRON-CLOUD SIMULATION IN ARBITRARY EXTERNAL FIELDS*

Andreas Adelmann† and Miguel A. Furman, LBNL, Berkeley CA 94720, USA

Abstract

We present PARSEC, a 3D parallel self-consistent particle tracking program which allows electron-cloud calculations in arbitrary external fields. The program is based on an general particle tracking framework called GenTrackE [5]. The Lorentz force equation is integrated with time as the independent variable. A 3D parallel Multigrid solver computes the electric field for the drive beam in the beam frame, while the space-charge field of the electrons is computed in the lab frame. The resulting total field, obtained by superposition, acts on both the beam particles and the cloud electrons. Primary and secondary emission takes place at each time step of the calculation. This sort of computation is only possible by the use of massive parallelization of the particle dynamics and the Poisson solver in combination with modern numerical algorithms such as the Multigrid solver with Gauss-Seidel smoothing.

INTRODUCTION AND MOTIVATION

The electron-cloud effect (ECE) has been investigated in various storage rings for several years now [1]. The ECE arises from the strong coupling of a two-species plasma with the surrounding vacuum chamber. Several analytical models and simulation programs have been developed to study this effect [2]. Owing to the complexity of the problem, these simulation codes typically make one or more simplifying assumptions, such as: (i) the electrons are dynamical but the beam is a prescribed function of space and time; (ii) the beam is dynamical but the electron cloud is a prescribed function of space and time; (iii) both the beam and the electrons are dynamical, but the electron-wall interaction, particularly the secondary emission process, is either absent or much simplified; (iv) the geometry of the beam and/or vacuum chamber is much simplified (eg. round beams and/or cylindrical chambers); (v) the simulation “looks” at only one specific region of the machine, typically a field-free region or one magnet of a specific kind; (vi) the forces on the particles, both from, and on, the electrons and the beam, are purely transverse. Computer codes involving these approximations, when applied in the proper context, have shed valuable information on one or more aspects of the ECE.

There are problems, however, in which any of these approximations may render the reliability of code inadequate for a quantitative understanding of the dynamics. One such example concerns problems involving very long, intense,

bunches with significant variation in the longitudinal profile, which require a self-consistent, fully 3D simulation, including a full description of the storage ring lattice (or at least, a section of the lattice at least as long as the bunch). Another example might be the simulation of damping rings for future linear colliders, which make significant use of wigglers. In this article we report on progress towards the goal of a fully self-consistent and realistic simulation of the ECE which, in its final stage, will not invoke any of the above-mentioned simplifications.

THE OVERALL SIMULATION MODEL

Self-consistent Formulation

Let the particle coordinates of particle k be $\vec{x}_k = (q_1, q_2, q_3)_k$, and the normalized velocity be $\vec{\beta}_k = (v_x/c, v_y/c, v_z/c)_k$ where c is the speed of light (all quantities in MKS units unless explicit stated otherwise). We consider $\ell = 1, 2, \dots$ magnetic elements which makes up what is called the lattice L . Defining $I = \{1, 2, \dots\}$ and $J = \{1, 2, \dots\}$ the index sets for the beam particles and electrons, respectively as unique identifiers, we are able to distinguish beam particle ($i \in I$) and electron coordinates ($j \in J$) in a natural way (see Figure 1 as an illustration). For each particle $k \in I \cup J$ we solve formally

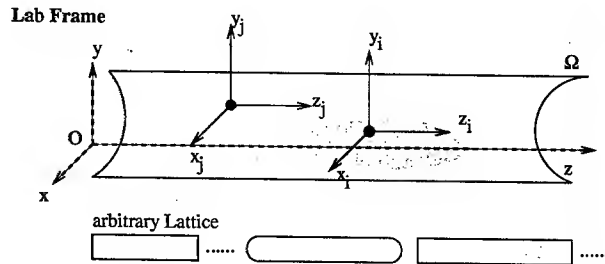


Figure 1: (color) Geometry and Particle domains.

$$\frac{d(m_k \gamma_k c \vec{\beta}_k)}{dt} = \vec{F}(\vec{x}_k, t) \quad (1)$$

$$\vec{F}(\vec{x}_k, t) = \frac{q_k}{\gamma_k m_k} (\vec{E}(\vec{x}_k, t) + \vec{\beta}_k \times \vec{B}(\vec{x}_k, t)) \quad (2)$$

where m_k and q_k is the mass and charge of the particle, respectively, and γ_k its usual relativistic factor.

The lattice magnetic field \vec{B}_{ext} in cylindrical coordinates

* Work supported by the US DOE under contract DE-AC03-76SF00098.

† AAAdelmann@lbl.gov

is represented by:

$$\begin{aligned} B_\rho &= \sum c_{m,n} I'_m(nk_z \rho) \sin(m\phi) \cos(nk_z z) \\ B_\phi &= \sum c_{m,n} \frac{m}{nk_z \rho} I_m(nk_z \rho) \cos(m\phi) \cos(nk_z z) \\ B_z &= - \sum c_{m,n} \frac{m}{nk_z \rho} I_m(nk_z \rho) \sin(m\phi) \cos(nk_z z). \end{aligned} \quad (3)$$

where I_n is the usual modified Bessel function, which satisfies $I'_m(nk_z \rho) = \frac{1}{2}[I_{m-1}(nk_z \rho) + I_{m+1}(nk_z \rho)]$. In this formulation we will treat coasting beams only although it is straightforward to include acceleration. The potential ϕ is obtained by solving two Poisson problems with $\rho_e(\vec{x}_j)$ and $\rho_b(\vec{x}_i)$ the electron and beam charge density. Let $\vec{x}'_i = \mathcal{L}(\vec{x}_i)$ with \mathcal{L} denoting the proper Lorentz transformation from the laboratory to the beam rest frame. The first Poisson problem, in which the beam charge density ρ_b is the source, reads:

$$\begin{aligned} \Delta \phi(\vec{x}'_i) &= -\frac{\rho_b(\vec{x}'_i)}{\epsilon_0}, \quad \vec{x}'_i \in \Omega \subset \mathcal{R}^3 \\ \phi(\vec{x}'_i) &= 0, \quad \vec{x}'_i \in \partial\Omega. \end{aligned} \quad (4)$$

Upon Lorentz-transforming back to the Lab frame, this yields both an electric (\vec{E}_b) and magnetic field (\vec{B}_b). Assuming that the electrons are sufficiently non-relativistic, which is typically a good approximation, we can neglect their contribution to the magnetic field, and we can solve in the laboratory frame for the second Poisson problem, in which the electron-cloud density ρ_e is the source,

$$\begin{aligned} \Delta \phi(\vec{x}_i) &= -\frac{\rho_e(\vec{x}_i)}{\epsilon_0}, \quad \vec{x}_i \in \Omega \subset \mathcal{R}^3 \\ \phi(\vec{x}_i) &= 0, \quad \vec{x}_i \in \partial\Omega \end{aligned} \quad (5)$$

thus the full answer is obtained by superposing the two fields:

$$\begin{aligned} \vec{F}(\vec{x}_k, t) &= \frac{q_k}{\gamma m_k} (\vec{E}_e(\vec{x}_j, t) + \vec{E}_b(\vec{x}_i, t) + \\ &\quad \vec{\beta}_k \times (\vec{B}_{ext}(\vec{x}_k, t) + \vec{B}_b(\vec{x}_j, t))) \end{aligned} \quad (6)$$

where \vec{E}_e is the electric self-field of the electrons.

Secondary Emission Model

When an electron strikes the vacuum chamber wall, it can be absorbed or can generate one or more secondary electrons. In our computations we simulate this process by a detailed probabilistic described elsewhere [3]. This process incorporates, as inputs, the measured secondary electron yield (SEY) δ and the energy spectrum of the emitted electrons, $d\delta/dE$ for a given vacuum chamber surface material. The three main subprocesses, namely elastical reflection, rediffusion, and true secondary emission, are included. We are not concerned for the moment with the processes responsible for the generation of primary electrons (chiefly the photoelectric effect, ionization of residual

gas, and stray beam particles striking the vacuum chamber wall), since these process is simpler to simulate with phenomenological models.

Time Integration

The code integrates (1) using a 4th-order Runge-Kutta method, with adaptive time step control for the electrons. We estimate the time step T_j by considering the cyclotron frequency $\omega_c = eB/m_e$, consequently

$$T_j = \frac{2\pi}{\omega_c K}. \quad (7)$$

is defined upon the factor K . Defining ϵ_{min} and ϵ_{max} the minimum and maximum error tolerated we estimate K using two Runge-Kutta steps and Richardson Extrapolation [6]. Choosing an initial step size T_j by setting $K = 1$ and let u_1 be the result of an Runge-Kutta step of length T_j . Let u_2 is the result of two subsequent Runge-Kutta steps of length $T_j/2$. We then estimate the error by $\epsilon = |u_1 - u_2|$. Richardson Extrapolation is then be used to set K corresponding to an error-range as defined. This procedure will guarantee the minimal work in order to achieve a desired accuracy, considering the dynamic of the individual particle.

```
#1   $\forall i \in I$ 
#2    for  $m = 1$  to  $N$ 
#3      Integrate equation of motion
#4    end for
#5  calculate  $\rho_z$  drive beam
#6  generate electrons
#7   $\forall j \in J$ 
#8    while  $timeLeft_j > 0.0$  AND NOT ATTHEWALLj
#9      Integrate equation of motion
#10     if ( $\vec{x}_j \notin \Omega$ )
#11       status of particle  $j$  equal to ATTHEWALL
#12     end if
#13   end while
#14   $\forall j \in J$ 
#15   if status of particle  $j$  equal to ATTHEWALL
#16     generate secondaries
#17   end if
#18   if secondary generated goto #7
#21  calculate space charge
```

Figure 2: Tracking Algorithm

Particle Tracking Procedure

As a first step towards a full lattice simulation, we model a portion of the magnetic lattice by imposing periodic boundary conditions in the z coordinate, for example one half of the PSR circumference or one FODO cell of the LHC arc. Further, we assume a constant number of particles in the drive beam, and a fixed number N of time steps of size ΔT . All electrons $i \in I$ and protons $j \in J$ are advanced by $N\Delta T$ followed by a space-charge

calculation. The simplified algorithm for advancing all particles by $N\Delta T$ in time is pictured in Figure 2, where $timeLeft_j = N\Delta T - t_j$ and ATTHEWALL indicate that a particles hits the vacuum chamber (we left out some of the indexes where the meaning is deducible from the contents). ρ_z is the longitudinal charge density of the drive beam which determines the distribution of the generated primary electrons.

Poisson Solver

For the Poisson solver, this type of simulations is very demanding. First of all, the computational domain Ω is very large *and* almost completely filled with simulation particles. Second, the number of macro particles (or simulation particles) is huge (many times 10^6) and the number of time steps is large as well. The Poisson solver uses a semi-unstructured grid as shown in Figure 3 to decompose Ω . Linear bases function are used to assemble the stiffness matrix \mathcal{A} and the right hand side f_h (discrete charge density) is constructed using a area wighting scheme. The resulting linear system of equations

$$-\Delta\phi = \frac{\rho}{\epsilon_0}, \phi = 0 \text{ on } \partial\Omega \implies \mathcal{A}u_h = f_h \quad (8)$$

is solved using parallel Multigrid. From the solution u_h we back-interpolate and use a second-order finite-difference scheme in order to obtain the two electric fields used in equation (6). Preliminary performance of the parallel Pois-



Figure 3: (color) Finite Element Discretization of Ω

son Solver [4] and the parallel grid generators is shown in Table 1 for an toy Poisson problem in S^3 (sphere). We show in Table 1 the scalability of the grid generator and the solver. A method is said to be scalable, if the time (T) times the number of processors used (P) divided by problem size (M) remains bounded as P and M gets increased. The data in Table 1 is given for the grid generation (in column 3) and for one multigrid iteration (in column 5) with an Gauss-Seidel smoother. Table 1 shows excellent scalability with respect to the problem size M which is equivalent to say we can handle in the order of 10^{11} **macro particles** in a simulation with reasonable computing time. For this

scaling study we use the Seaborg (IBM SP-3) computer at NERSC.

P	M	$T_g P/M$	T	TP/M
8	625,464	3.5e-3	3.1	3.9e-5
32	306,080	8.5e-3	0.78	8.1e-5
248	4,751,744	5.90e-3	1.2	6.2e-5
248	36,998,619	7.50e-3	7.7	5.1e-5
960	23,312,735	4.85e-3	4	1.64e-4
2025	405,242,845	6.60e-3	10.7	5.3e-5
4075	7,166,171,845	8.76e-3	160	9.9e-5

Table 1: Scalability of the parallel grid generator $T_g P/M$ and the Poisson solver showing also T , the time in seconds for one Multigrid step

CONCLUSION

The presented code PARSEC is based on GenTrackE, which is written in C++ and is fully parallelized using MPI. PARSEC advances macro particle of the drive beam and the electrons using a 4th-order Runge-Kutta method. Variable time steps for the electrons according to their dynamics are used. The arbitrarily shaped computational domain is discretized using linear finite elements, the resulting linear system of equation is solved efficiently by the use of an massive parallel and scalable Multigrid solver.

We are finalizing the code construction and are about to start simulation of a simplified LHC FODO cell, as well as some part of the Los Alamos proton storage ring. The issue of large aspect ratios in the computational domain and the impact of the accuracy of the Poisson solver will be investigated in detail, a subject which is of general importance in many space charge dominated problems.

ACKNOWLEDGMENTS

We thank Robert Ryne, Mauro Pivi and Andy Wolski for enlightening discussions and NERSC for supercomputer support.

REFERENCES

- [1] Various contributions to these proceedings.
- [2] Various contributions to the Proceedings of the ECLLOUD-02 Workshop [CERN Yellow Report no. CERN-2002-01], <http://slap.cern.ch/collective/ecloud02/>.
- [3] M. A. Furman and M. T. F. Pivi, PRST-AB **5** 124404 (2002).
- [4] A. Adelmann and Ch. Pflaum, LBNL Report to be appear (2003).
- [5] A. Adelmann, GenTrackE: General Tracking Engine, LBNL Report to be appear (2003).
- [6] R. Bulirsch and J. Stoer, Introduction to Numerical Analysis. New York: Springer-Verlag, 1991.

A MODULAR ON-LINE SIMULATOR FOR MODEL REFERENCE CONTROL OF CHARGED PARTICLE BEAMS*

C.K. Allen[#], C.A. McChesney, LANL, Los Alamos, NM, USA

N.D. Pattengale, Sandia National Laboratory, Albuquerque, NM, USA

C.P. Chu, J.D. Galambos, W.-D. Klotz, T.A. Pelaia, A. Shishlo, ORNL, Oak Ridge, TN, USA

Abstract

We have implemented a particle beam simulation engine based on modern software engineering principles with intent that it be a convenient model reference for high-level control applications. The simulator is an autonomous subsystem of the high-level application framework XAL currently under development for the Spallation Neutron Source (SNS). It supports multiple simulation techniques (i.e., single particle, multi-particle, envelope, etc.), automatically synchronizes with operating accelerator hardware, and also supports off-line design studies. Moreover, since it is implemented using modern techniques in the Java language, it is portable across operating platforms, is maintainable, and upgradeable.

INTRODUCTION

To support the operation of the SNS accelerator we have built a development framework for high-level control applications called XAL (for a description of XAL see [2]). The framework includes a simulation engine that we call the XAL model subsystem. This subsystem works in conjunction with the application framework, or as a stand-alone particle beam simulator. XAL contains a utility for automatically generating modeling lattices and synchronizing them with the operating machine. Here we outline the architecture of the model subsystem and the mathematical models upon which it is based.

DYNAMICS

In all simulations we parameterize phase space using homogeneous coordinates in $\mathbb{R}^6 \times \{1\}$. Letting z denote a point in phase space it has the representation

$$z \equiv (x \ x' \ y \ y' \ z \ z' \ 1)^T \quad (1)$$

where the prime indicates differentiation with respect to the design path length parameter s . Note that we use (z, z') as the longitudinal phase coordinates rather than $(z, \Delta p/p)$. Mathematicians typically use homogeneous coordinates to parameterize the real projective spaces $\mathbb{R}P^n$; they are also widely used in computer graphics for three-dimensional rendering because translation, rotation, and scaling can all be performed by matrix multiplication.

Single Particle Simulation

In single-particle simulations we propagate the phase space coordinates z of the particle. Each beamline

element n is obligated to provide a transfer map \mathcal{M}_n (embodied by the PhaseMap class) that represents the action of the element. Note that the characteristics of this map typically depend upon the parameters of the beam being propagated. In any case, the particle coordinates are propagated according to the transfer equation

$$z_{n+1} = \mathcal{M}_n(z_n). \quad (2)$$

Although provisions for high-order dynamics are included in the PhaseMap class, currently most of the beamline elements simply provide a transfer matrix to represent its dynamics. This transfer matrix $M_n \in \mathbb{R}^{7 \times 7}$ is just the linear part of \mathcal{M}_n , or $M_n = \partial \mathcal{M}_n / \partial z$ and we have

$$z_{n+1} = M_n z_n. \quad (3)$$

Note that because we employ homogeneous coordinates it is still possible to perform translations, such as those produced by steering magnets, using a transfer matrix. Such matrices have the form

$$M_n = \begin{pmatrix} m_{xx} & m_{xx'} & \cdots & \Delta x \\ m_{x'x} & m_{x'x'} & & \Delta x' \\ \vdots & \vdots & \ddots & \vdots \\ 0 & 0 & \cdots & 1 \end{pmatrix}, \quad (4)$$

where Δx , $\Delta x'$, Δy , ... are the translations along the respective coordinate axes. This fact is especially useful when performing rms envelope simulations where only the linear part of the transfer map is used.

RMS Envelope Simulation

For rms envelope simulations we propagate the (homogeneous) correlation matrix $\sigma \in \mathbb{R}^{7 \times 7}$ defined by

$$\sigma \equiv \langle zz^T \rangle = \begin{pmatrix} \langle x^2 \rangle & \langle xx' \rangle & \cdots & \langle x \rangle \\ \langle xx' \rangle & \langle x'^2 \rangle & & \langle x' \rangle \\ \vdots & \vdots & \ddots & \vdots \\ \langle x \rangle & \langle x' \rangle & \cdots & 1 \end{pmatrix} \quad (5)$$

where $\langle \cdot \rangle$ is the phase space moment operator with respect to the beam distribution. Substituting Eq. (3) into the above then unwinding the definitions forms the state transfer equation for rms envelopes

$$\sigma_{n+1} = \langle (M_n z_n)(M_n z_n)^T \rangle = M_n \sigma_n M_n^T. \quad (6)$$

Note that these operations do not commute for the full transfer map \mathcal{M}_n . Thus, to account for space charge we must linearize the self electric fields of the beam. To this end we employ a weighted linear regression of the true fields. Considering the x -plane, we proceed by assuming a self electric field E_x of the form

$$E_x \approx a_0 + a_1 x. \quad (7)$$

* Work supported by the US Department of Energy
ckallen@lanl.gov

Weighting the regression with the beam distribution itself yields the following approximation:

$$E_x \approx \frac{\langle x E_x \rangle}{\langle x^2 \rangle} (x - \langle x \rangle), \quad (8)$$

(the moment $\langle E_x \rangle$ is zero by Newton's third law). For beams with ellipsoidal symmetry, that is, having distributions $f(z)$ of the form

$$f(z) = f(z^T \sigma^{-1} z), \quad (9)$$

the moment $\langle x E_x \rangle$ can be computed analytically in terms of elliptic integrals whose arguments are elements of the matrix σ . These expressions can be found in the literature [1]. Note that Eq. (8) will yield a transfer matrix form for space charge effects that may be applied in the same fashion as Eq. (6).

Ensemble Simulations

The state E of a particle ensemble is represented as a collection of phase space coordinates

$$E = \{z_\alpha \in \mathbb{R}^6 \times \{1\} \mid \alpha \in I_E\}, \quad (10)$$

where I_E is an index set. The transfer equation for this state object is

$$E_{n+1} = \mathcal{M}_n(E_n) \equiv \{\mathcal{M}_n(z_\alpha) \mid \alpha \in I_{E_n}\}. \quad (11)$$

Although this state can be represented as a point in the Cartesian product of phase spaces $(\mathbb{R}^6 \times \{1\})^N$ where $N=|E|$, it is more constructive to think of it as a set with collective properties. This process is most easily captured as a software object, which we have done with a class *Ensemble*. Ensemble objects are responsible for calculating self-fields and other collective properties. There are many ways to compute these fields, including grids, finite elements, and direct summation. These computation techniques are currently under development. We point out that the software is so designed such that specific self-field calculations may be swapped at run time. Once the self electric fields are computed, the ensemble state can be advanced according to the equations of motions. Considering the x phase plane, we have the approximation

$$\Delta p_x \approx \frac{q}{\gamma^2} E_x \Delta t, \quad (12)$$

where the relativistic factor γ accounts for the collective magnetic fields and Δt is the time step. From the above we infer

$$\Delta x' = \frac{\Delta p_x}{p} \approx \frac{1}{\beta \gamma m c} \frac{q}{\gamma^2} E_x \frac{1}{\beta c} \Delta s, \quad (13)$$

where m is the particle mass and β is the synchronous velocity normalized to the speed of light c , and Δs is the distance traveled along the design trajectory during Δt .

SOFTWARE ARCHITECTURE

We are able to support the various particle beam simulation techniques due to a novel approach in software architecture. By employing a variant of the Element/Algorithm/Probe design pattern introduced by

Malitsky and Talman [3], we separate the machine representation from the beam representation and the dynamics calculations. In this scheme, systems for representing the accelerator, the beam, and the beam dynamics are decomposed into separate software components that communicate through the well-defined

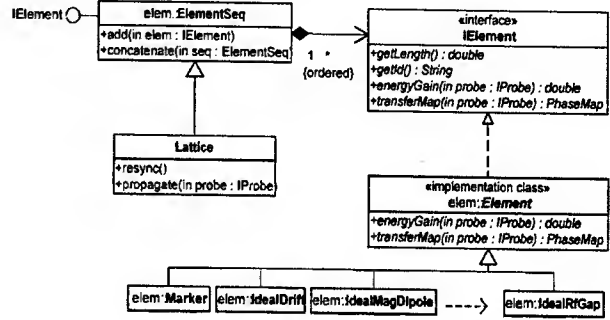


Figure 1: machine representation component software interfaces *IElement*, *IProbe*, and *IAlgorithm*, respectively.

Machine Representation

A major effort in accelerator simulation is simply representing the machine. By decoupling the machine representation from the machine's action on the beam, the representation then can be used to support any number of simulation techniques. Figure 1 is a UML structure diagram outlining the machine representation component of the simulator. At the heart of this component is the *IElement* interface, which is exposed by any object representing a modeling element of the machine. Note that we provide the (abstract) implementation class, *Element*, which provides a variety of common functions that modeling element must accommodate in support of the *IElement* interface. Most objects representing beamline elements are derived from this convenience base class. In the figure we see derived classes must provide energy gains and transfer maps specific to the modeling element, done by implementing the abstract methods *energyGain()* and *transferMap()*.

Shown in Figure 1 is the aggregation *ElementSeq*, which is an ordered sequence of *IElement* objects. It, too, exposes the *IElement* interface, since it may be considered a composite modeling element. The values obtained here, however, would be the aggregate results of all members in the sequence. We also see that the *Lattice* object is just a specialized sequence. Much of the *Lattice* class function is conceptual, however, it also provides access to the important mechanisms of probe propagation and online synchronization. Through the method *propagate()* the *Lattice* object coordinates the operation of the machine representation, beam representation, and beam dynamics. The online synchronization mechanism, which automatically synchronizes the *Lattice* object to the parameters of the operating hardware, is accessed via the method *resync()*.

Beam Representation

Figure 2 depicts the basic architecture of the beam representation component. The interface to this component is called *IProbe*, as seen in the figure. Note that the interface for the dynamics subsystem, *IAlgorithm*, is associated with *IProbe*. Thus, each probe object, representing some aspect of a charged particle beam, also specifies its own dynamics. There may be several types of dynamics calculations available for any particular probe (e.g., linear, third-order, etc.).

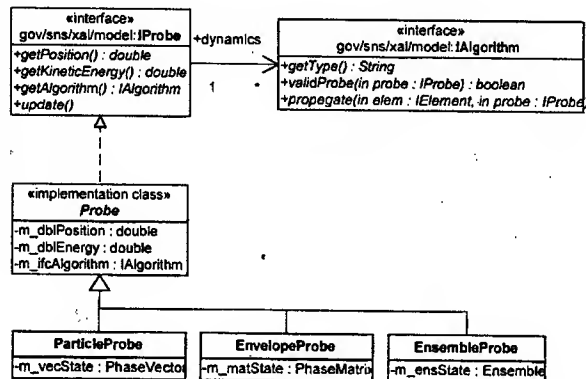


Figure 2: architecture of beam representation component

In Figure 2 we see that the (abstract) implementation class *Probe* is provided to assist in the implementation of particular probes. It provides necessary bookkeeping as well as access to trajectory objects (not shown), which store probe histories along the lattice. The maintenance of actual probe states is left to the particular probe implementation. In the figure we see that the state of a *ParticleProbe* is the vector of particle phase space coordinates, the state of an *EnvelopeProbe* is the correlation matrix of moments up to second order, and the state of an *EnsembleProbe* is an ensemble object.

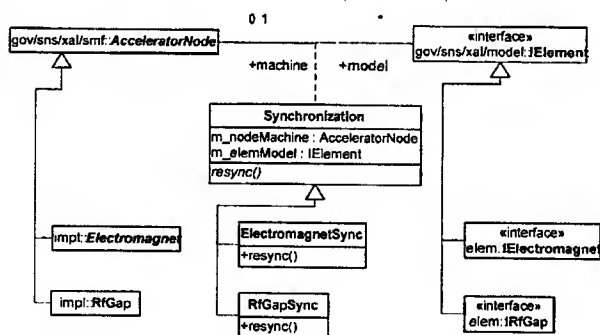


Figure 3: synchronization mechanism

Machine Synchronization

Synchronization with the operating hardware is accomplished through a subsystem based on the (abstract) association class *synchronization*. It supports communication between the XAL model system and the XAL SMF (Standard Machine Format) system, which otherwise have no knowledge of one another.

Shown in Figure 3, these synchronization objects understand the vernacular of both XAL subsystems. The children of the *AcceleratorNode* class, belonging to SMF, represent actual accelerator components and supports communication with these devices. The interfaces derived from *IElement* represent modeling elements. Note that is a one/none-to-many association between accelerator devices and their modeling counterparts. This condition is necessary because, for example, "drifts" are not controllable devices of the accelerator and actual devices may require several modeling elements to represent (e.g., quadrupoles with trim windings for steering, etc.). Referring to the figure we see that each type of accelerator device requires the implementation of a particular synchronization class that understands how to communicate with both the device and the modeling element. Once implemented, any synchronization request is carried out by invoking the abstract method *resync()* in the base class. Thus, to remain synchronized with the operating machine the Lattice object maintains a set of synchronization objects, invoking *resync()* on each whenever required.

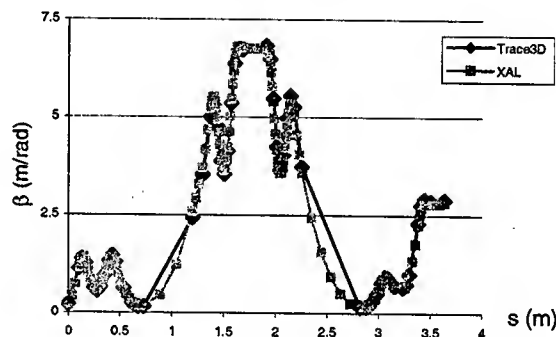


Figure 4: transverse beta simulations of the SNS MEBT

VERIFICATION

To verify the operation of the XAL modeling subsystem we have compared the results for single particle and envelope simulations against those of Trace3D. Figure 4 shows such a comparison for a simulation of the SNS Medium Energy Transport (MEBT) system. The figure plots the Twiss parameter beta in the (horizontal) transverse plane computed by each code. There we can see that the results are essentially equivalent.

REFERENCES

- [1] C.K. Allen and N.D. Pattengale, LANL Internal Report LA-UR-02-4979.
- [2] C.M. Chu, *et. al.*, "Applications Programming Structure and Physics Applications", these proceedings.
- [3] N. Malitsky and R. Talman, "The Framework of Unified Accelerator Libraries", ICAP 1998.

MONTE-CARLO SIMULATION MODULE FOR LIDOS.RFQ.DESIGNER CODE

Bondarev B.I., Durkin A.P., Ivanov Yu.D., Shumakov I.V., Vinogradov S.V.

Moscow Radiotechnical Institute

113519, Russia, Moscow, Warshawskoe shosse, 132 e-mail: lidos@aha.ru

New criteria arise when high-current CW linacs are considered. The main requirements for such linacs are maximal RF intensity reduction, very small beam losses.

Minimization of CW beam losses in RFQ linac places more stringent requirements upon beam perturbations. Instrumental errors in vane manufacturing, installation and adjustment are sources of such perturbations. Even with very small cell parameter deviations the potential of such perturbations is high enough both for beam transmission reduction and beam quality degradation. A reason enough to such statement is provided by the fact that trajectories even for "ideal" (without perturbations) RFQ channel are spaced in the immediate vicinity of vane surfaces.

Hence to choose RFQ channel optimal parameters random perturbation influence have to be taken into account and estimation of tolerances must be given. The goal of the LIDOS.RFQ.Designer package [1-5] development is to help user to solve this problem. It will be recalled that the package contains codes with three levels of mathematical model complexity.

The first-level codes make only a preliminary choice of the main parameter arrays on the basis of a simplified physical model. These codes are richly supplied with visual information that helps to find the best linac version quickly. Separate algorithm branch allows using output parameter table obtained by PARMTEQ codes as initial information

The second-level codes are used for channel data calculations with the real shape of the RFQ vanes and real RF fields. Information from the first level codes is used here as input data.

The third-level codes are based on information from the first and second level codes and on complex PIC-models that are needed for a correct beam simulation in the chosen channel version.

New version of the package contains the fourth level - "Statistics". Random realizations of channel taking into account deviations of vanes from their ideal positions are generated. From cell to cell the random deviations are statistically independent. To compute the position of vane surface we base on the parameters: r - the distance from axis to cell beginning, m - vane modulation and L - cell length. With perturbations the parameter r is changed over a random value Δ . For cell numbered k we use $\tilde{r}_k = r_k + \Delta_k$. In turn the deviations of any vane inside cell are statistically independent also. Such perturbation leads to changes in focusing field gradient, deviation of accelerator axis from ideal line (axis may be presented as

polygonal line), quadrupole symmetry violation. As a result there are transverse beam mismatching, coherent beam oscillations about real accelerator axis and transverse phase volume increase produced by its.

If the channel is divided into sections then another perturbation are independent deviations of any vane ends inside section.

The code simulates beam dynamics for every version of channel. To decrease the time, taken to statistic calculation, the visualization of current version can be switched off. Because it takes the calculation of many random version for sufficient statistic (as a rule no less than 50), this procedure is very time consumed, so it is possible to stop calculations and to continue it after any time beginning from last version.

The part Advisor offers the supplementary visual information for tolerance estimation. In [6] we define parameter S - sensitivity of period to perturbations. In this case this parameter is determined by relation

$$S = \left(B \int_0^1 \rho(\tau) |\cos 2\pi\tau| d\tau \right)^2,$$

where B is focusing parameter, ρ is the envelope of matched beam with the emittance of unity in the ideal channel.

Visual information presents the plot of sensitivity versus number of cell as well as statistic estimation of effective emittance growth and beam center transverse displacement. The error integrals are calculated in according with relations given in [6]: if σ^2 is mean square value of focusing field gradient relative error then the probability that effective emittance growth would be no more than x is determined by function

$$P(x) = 1 - e^{-(\ln x)^2 / \Delta^2}, \text{ where } \Delta^2 = \frac{\sigma^2}{4} \sum_{k=1}^N S_k. \text{ If } \sigma^2 \text{ is error}$$

of axis transverse displacement then the probability that center of output beam displacement would be no more than x is determined by function $P(x) = 1 - e^{-x^2 / \Delta^2}$, where

$$\Delta^2 = \sigma^2 \sum_{k=1}^N S_k. \text{ For both cases } S_k \text{ is sensitivity of cell}$$

numbered k , N is total number of cells. The general view of picture is shown in the Fig.1.

The examples of output pictures of new part "Statistics" are shown in the Fig.2-5. The RFQ channel with the frequency 175 MHz, accelerating protons from energy 0.05 MeV to energy 2 MeV have been used as example. The statistic have been calculated for two values of tolerance - 10 μm (Figs.2,4) and 25 μm (Figs.3,5).

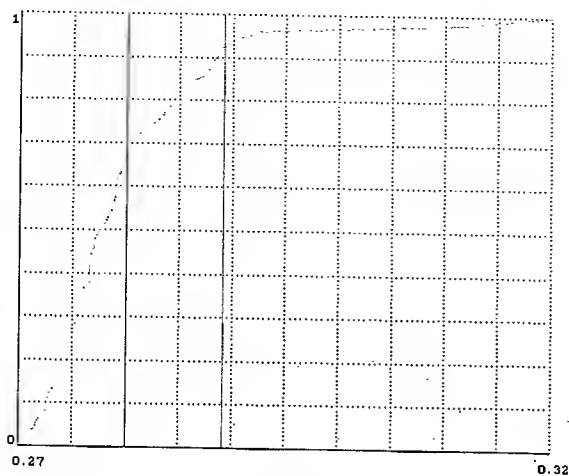


Fig.2.

Statistics of *RMS-Emittance XX'*
Mean - 0.28, Sigma - 0.01, Ideal - 0.28

Probability	Value
0.7	0.28
0.8	0.29
0.9	0.29
0.95	0.29

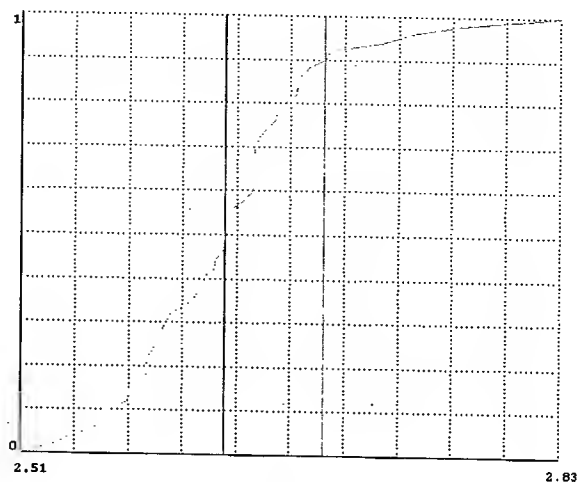


Fig.4.

Statistics of *Total Emittance XX'*
Mean - 2.63, Sigma - 0.06, Ideal - 2.60

Probability	Value
0.7	2.65
0.8	2.66
0.9	2.69
0.95	2.73

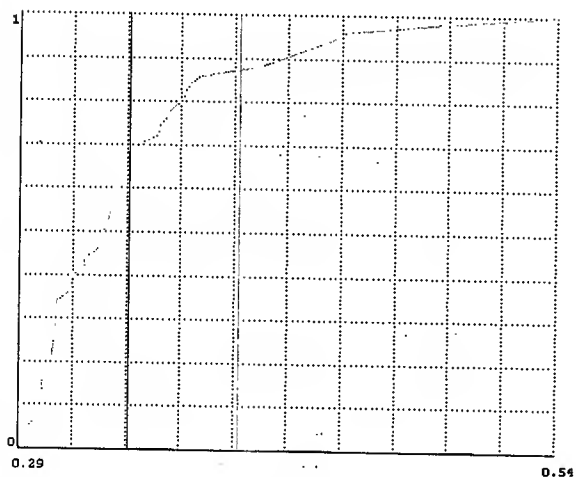


Fig.3.

Statistics of *RMS-Emittance XX'*
Mean - 0.34, Sigma - 0.05, Ideal - 0.28

Probability	Value
0.7	0.35
0.8	0.37
0.9	0.41
0.95	0.44

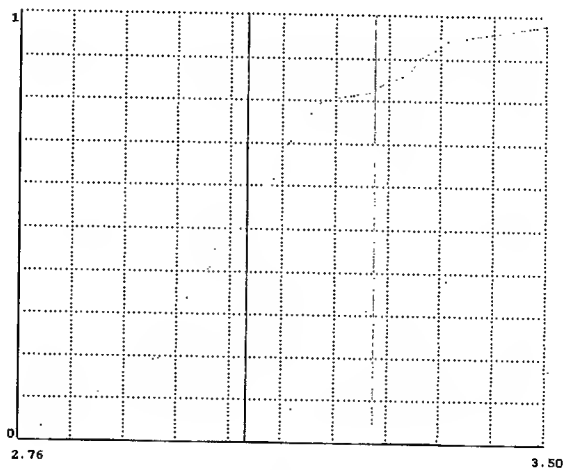


Fig.5.

Statistics of *Total Emittance XX'*
Mean - 3.08, Sigma - 0.18, Ideal - 2.60

Probability	Value
0.7	3.13
0.8	3.18
0.9	3.32
0.95	3.39

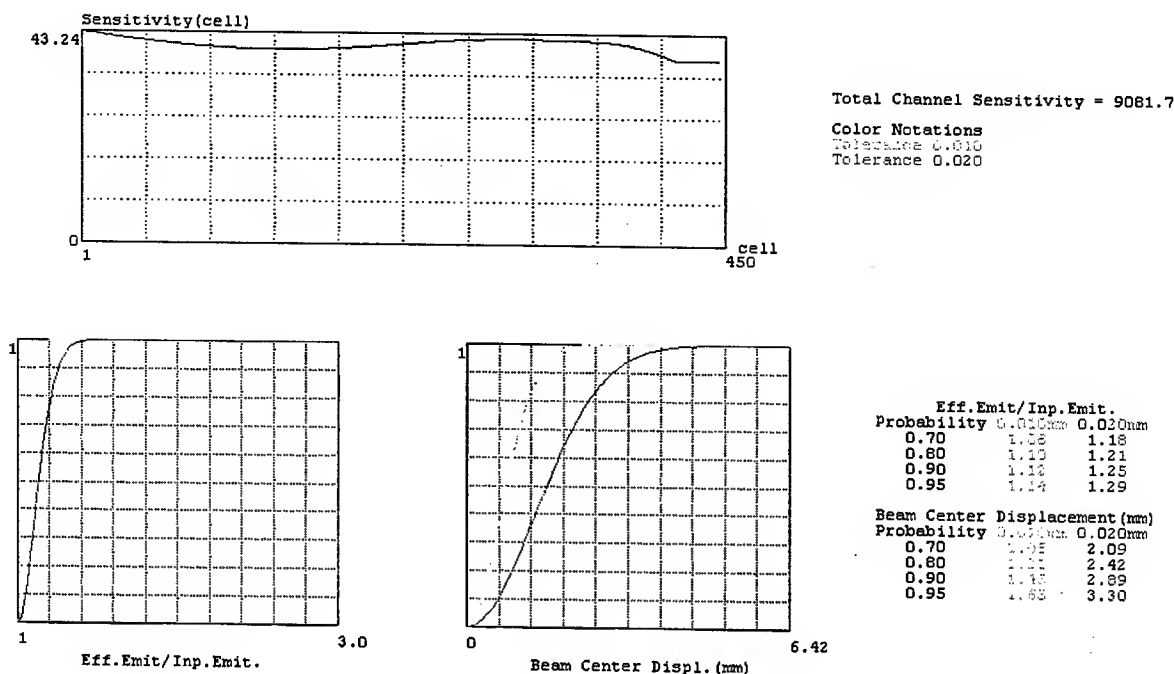


Fig.1.
"Statistics" module general view

REFERENCES

- [1] B.P.Murin, B.I.Bondarev, A.P.Durkin et al. A Computing Optimization System for Ion Linac Accelerating/Focusing Channels. *Proceedings of 1992 Linear Accelerator Conference*, AECL-10728, v.2, pp.734-736. (1992, August 24-28, Ottawa, Ontario, Canada).
- [2] B.I.Bondarev, A.P.Durkin, et al. LIDOS- Unconventional Helper for Linac Beam Designing. *Computational Accelerator Physics Conference, AIP Conference Proceedings 297*, Los Alamos, NM 1993, pp.377-384.
- [3] B.I.Bondarev, A.P.Durkin, G.H.Gillespie. Beamline Parameter Optimization in the Framework of the Lidos.Advisor. *Proceedings of Second International Workshop Beam Dynamics&Optimization*, pp.61-64. (July 4-8, 1995, St. Petersburg, Russia).
- [4] B.Bondarev, A.Durkin, S.Vinogradov, J-M.Lagniel, R.Ferdinand, CW RFQ Designing Using The LIDOS.RFQ Codes, *Proceedings of the XIX International Linac Conference, LINAC'98*, August 23-28, 1998 Chicago, Illinois, USA, pp.502-504.
- [5] B.Bondarev, A.Durkin, S.Vinogradov, I.Shumakov, New Tasks And New Codes For RFQ Beam Simulation, *Proceedings of the XX International LINAC Conference, Monterey, California, August 21-25, 2000*, pp.830-832.
- [6] B.Dondarev, A.Durkin, Non-Coulomb Perturbations Influence on Beam Dynamics in Extended Accelerating/Focusing Channels. This Conference.

TEMPLATE POTENTIALS TECHNIQUE WITH FULLY-PARAMETERIZED FIELD SOLVER FOR HIGH-CURRENT BEAMS SIMULATION*

L.G. Vorobiev and R.C. York, NSCL/MSU, East Lansing, MI 48824, USA

Abstract

A three-dimensional (3D) particle-in-cell (PIC) code based on the template potential concept [1-6] has been upgraded by inclusion of a fully parameterized model for 3D space charge force calculations. The dynamics of a bunched 3D beam were studied for FODO channels having a conducting chamber with an arbitrary elliptical symmetry. The simulation results were in a good agreement with conventional 3D PIC models, but were obtained with ten to one hundred shorter computational times.

1 INTRODUCTION

Envelope (KV) equations are adequate for modeling a coasting two-dimensional (2D) beam with elliptical symmetry through linear FODO channels in free space [7]. Adaptation of the KV model for rms sizes [8-10] provides inclusion of image forces and momenta dispersion [11-12]. However, extension of the envelope formalism to 3D beam configurations [13] can be inappropriate for non-linear image forces.

General 3D PIC codes provide the most complete model, but require significant computational times. An alternative approach using templates has been developed providing a nearly complete model with dramatically reduced computational times [1-6]. Similar to analytical models, this approach operates with macro objects and expresses the solution for field components via special functions, the template potentials, maintaining a good generality of dynamics simulation on a micro level.

2 HIERARCHY OF TEMPLATE METHODS

The grid density is the most time-consuming subroutine in general 3D PIC codes. The template approach does not require calculation of the 3D grid density. Instead, the space charge fields are derived from the convolution of template potentials, corresponding to beam shape functions $S_{x,y}(z)$, scaled by the charge density $\Lambda(z)$ [1,5].

The theory of templates was published in [1-6]. These template-based field solvers were included as subroutines into PIC codes to model dynamics of 3D intense beams.

1. One approach [6] used the transverse fields $E_{x,y}$ found from the 2D Poisson equation with the longitudinal field E_z determined by superposition of on-axis template potentials or uniformly charged round discs (slices).

2. A more general approach [3-5] obtained $E_{x,y}$ from a series of 2D Poisson equations with a "corrected density": $\Delta u = -4\pi\rho_{\text{corr}}$ and $\rho_{\text{corr}}(x,y,z) = \rho + \partial^2 u / \partial z^2 / 4\pi$. The latter term was evaluated via an off-axis longitudinal field E_z derivative: $\partial^2 u / \partial z^2 = -\partial E_z / \partial z$, found from the superposition of round template potentials with arbitrary transverse density.

3. An improvement [1-2] was made with the inclusion of the driving terms $\partial^2 u / \partial z^2 = -\partial E_z / \partial z$ and corrected density for all off-axis coordinates for any templates with elliptical symmetry. The code also used a parameterization for E_z field representation. This version approaches the generality of a conventional 3D PIC algorithm and is appropriate for 3D modeling of a bunched beam without axial symmetry, propagating in an arbitrary focusing doublet, as shown schematically in Fig. 1.

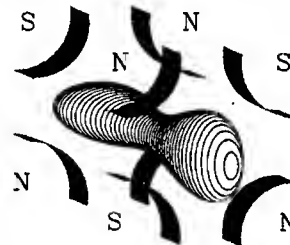


Figure 1: Non-ellipsoidal 3D bunched beam in a quadrupole doublet (different polarities are indicated).

3 PARAMETERIZATION

For the template technique [1-6], the beam is represented as a sequence of templates and the total potential $u_{\text{beam}}(x,y,z)$, including space charge and image fields, is represented as a superposition of individual template potentials $u_{\text{mp}}(x,y,z)$.

Template potentials for geometries of different sizes and aspect ratios, as shown in Fig. 2, are stored and tabulated prior to simulations and will reconstruct the potential of a beam with an evolving distribution.

Since direct storage of all 3D template potential functions could require excessive memory demands and possibly slow the simulation process, an alternative approach was used. The approximation of individual template potentials allows an analytical representation [1]: $u_{\text{mp}}(x,y,z) = \exp(a_0(x,y) + a_1(x,y)z + a_2(x,y)z^2)$ with the longitudinal field derived as $E_{z,\text{tmp}} = -(a_1 + 2a_2z)u_{\text{mp}}(x,y,z)$. The three coefficients a_i , $i=0,1,2$ define both potential and field from a template for specific x, y as a function of "z".

*Work supported by Michigan State University

The approximation for the transverse fields $E_{x,tmp}$ and $E_{y,tmp}(x,y,z)$ are obtained with a similar approach.

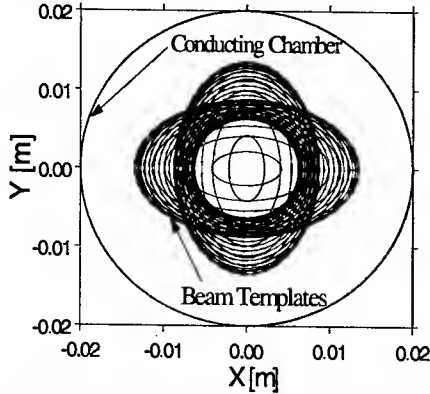


Figure 2: Elliptical templates with different sizes and aspect ratios, used to reconstruct the 3D beam of Fig. 1.

The approximating coefficients $\{a_i\}$ for all three field components $E_{x,tmp}$, $E_{y,tmp}$, $E_{z,tmp}$ can be stored in a library of modest memory size. The template fields are now represented by a smooth continuous function providing faster numerical evaluations for total field ($E_{x,y,z}$) reconstruction and the avoidance of computational errors.

4 ILLUSTRATION OF 3D FIELD SOLVER

As an example of the 3D parameterization, we evaluated the beam shown in Fig. 1, carrying a total charge of 10^{-11} C in a conducting cylindrical pipe 4 cm in diameter.

The beam was represented by $N_p=10^4$ macroparticles. Figs. 3 and 4 illustrate the procedure.

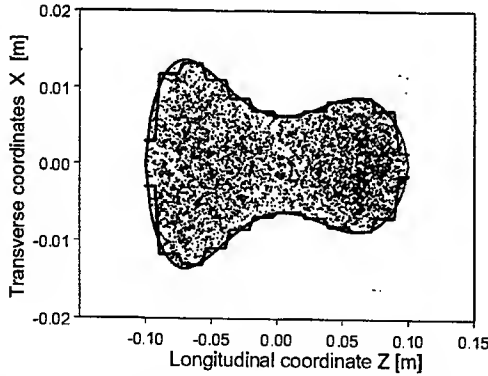


Figure 3: Macro-particle $\{x\}$ -coordinates (dots), the envelopes (step-wise lines) and smoothed profiles (solid).

For the vertical direction the algorithm is similar.

From particle coordinates, we find rms envelopes $\langle x^2 \rangle^{1/2}(z,p)$, $\langle y^2 \rangle^{1/2}(z,p)$ and the shape functions $S_{x,y}(z,p)$, scaled by $\Lambda(z,p)=\lambda_0 \cdot \lambda(z,p)$ for each i -th thick slice, having a width H_z^T in z -direction.

$$\lambda(z_i) = \frac{N_i}{\pi \cdot r_{m,x} \cdot r_{m,y} \cdot H_z^T} \quad \text{and} \quad \lambda_0 = \frac{\int dz \int \sigma(x,y,z,p) dx dy}{N_p}$$

with $r_{m,x}=S_x(z)$, $r_{m,y}=S_y(z)$, $r_m^2=r_{m,x}^2+r_{m,y}^2$ and $\sigma(x,y,z,p)=\sigma_0(z)[1-(x^2(z)+y^2(z))/r_m^2]^p$, see [1,5] for details.

A superposition of template potentials yields the total beam potential u_{beam} and $E_{x,y,z}$ fields, as shown in Fig.5.

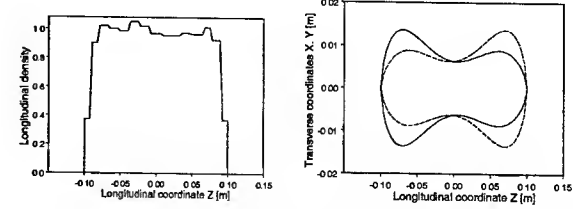


Figure 4: Charge density $\lambda(z)$ (left) and the shape functions for horizontal and vertical directions (right).

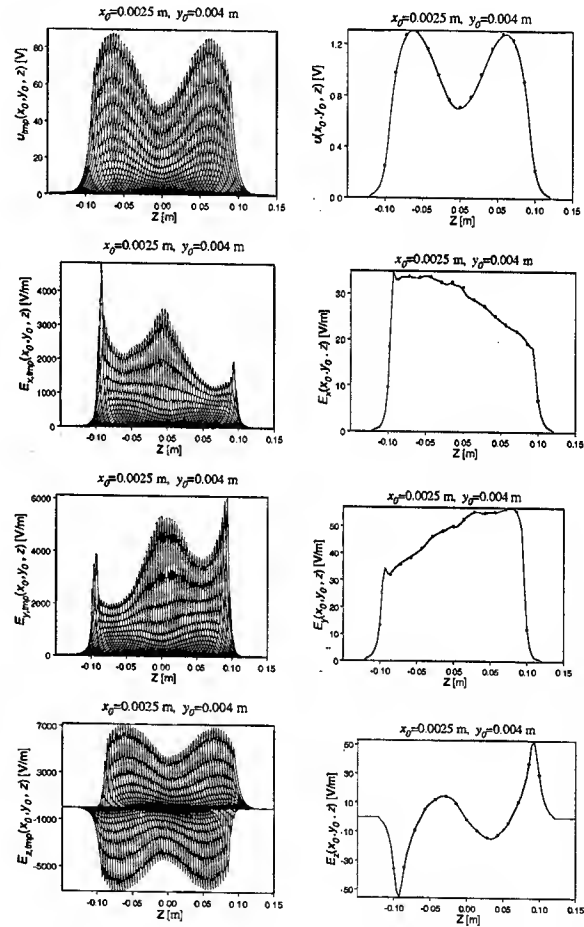


Figure 5: Template potentials and fields (left). The total potential and total fields (right, solid lines) found for off-axis coordinates, as functions of "z" and the cross-checking results obtained by SOR 3D algorithm (dots).

The number of coefficients $\{a_i\}$ for the potential and each field component is less than 9×10^3 (see [1] for details). The total array providing a full $E_{x,y,z}$ parameterization is of 2.7×10^4 in size. With the inclusion of different charge densities $\sigma(x,y,z,p)$, say for $p=0,1,2,4$ the total number of coefficients would be about 10^5 .

5 BEAM SIMULATION BY 3D PIC CODE

The parameterized field solver was implemented in the 3D PIC code and the beam dynamics modeled for one full turn in the E-Ring [14] with a focusing lattice consisting of 36 FODO periods of length 32 cm and 36 dipole magnets each deflecting beam by 10° . The initial electron beam was assumed to have an energy of 10 KeV and a current of 10 mA (the equivalent generalized perveance for a 2D beam would be $Q=1.5 \times 10^{-4}$). As an example, we considered a beam bunch with rms semi-axes $0.35\text{cm} \times 0.67\text{cm}$ and a semi-length of 5cm, with initial rms emittances $\epsilon_{x,y}=5 \cdot 10^{-5}\pi$ m-rad, $\Delta p/p=0$ (i.e. $\epsilon_z=0$), propagating along a metal pipe 4 cm in diameter through a FODO lattice. No longitudinal focusing was applied.

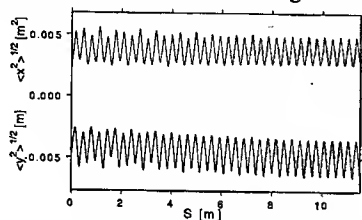


Figure 6. Rms-envelopes in the E-Ring.

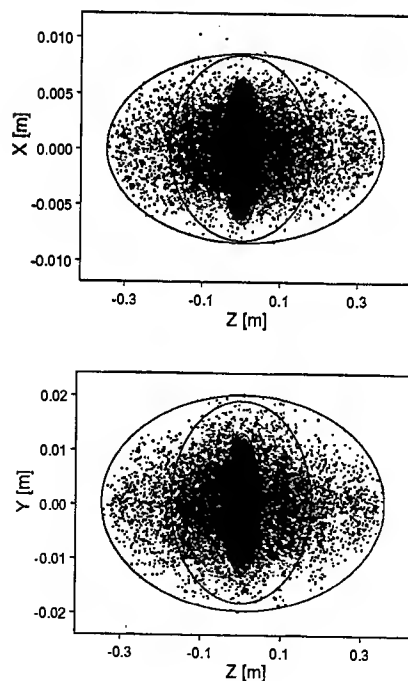


Figure 7. (Color) Particle distributions (x,z) and (z,y) for $s=0$, $s=6.4$ m (20 periods) and $s=11.52$ m (36 periods=1 full turn). Contour lines include 98% of the beam particles for each cross-section. Due to the absence of longitudinal focusing the beam dilutes in “ z ” direction and space charge forces subside.

Beam particles were tracked through one full turn of 11.52 m with the initial, intermediate and final (z,x) , (z,y) distributions given in Figs. 6-7. The number of particles

used for simulation was $5 \cdot 10^4$ and the number of templates used to reconstruct the beam potential was 50. The dipole magnet chambers were approximated by a straight chamber. In addition, the 2D charge density $\sigma(x,y,z,p)$ was assumed to have a fixed parameter “ p ”. The typical calculation time was 30 minutes on a 600 MHz Alpha machine. To the best of our knowledge this is one to two orders of magnitude faster than using conventional 3D PIC methods.

6 DISCUSSION AND CONCLUSION

General PIC codes may be used to model nearly any beam distribution. The template-based formalism is less general and would not be appropriate for e.g., filamenting beam distributions. The template approach is, however, appropriate for those beams which have *a priori* regular shapes and when their 3D geometry may be approximately reconstructed by elliptical slices such as shown in Figs. 1,2.

Some of the template limitations can be overcome. E.G., the inclusion of changing chamber geometry (bends, etc.), off-centered beam bunches and varying parameter “ p ” in $\sigma(x,y,z,p)$, are feasible simply by an extension of the tabulated data and the implementation of this upgrade is planned. However, clustered, filamenting, or disintegrating beam simulation requires a standard 3D PIC algorithm with adaptive mesh refinement.

Preliminary comparisons with standard 3D PIC codes give a confidence in a validity of template-based algorithms for a large class of beam configurations with calculation times one to two orders of magnitude shorter.

7 REFERENCES

- [1] L.G.Vorobiev and R.C.York, EPAC'02, Paris, June 2002, p. 1679.
- [2] L.G.Vorobiev and R.C.York, ICCS 2002, LNCS 2331, Springer-Verlag, pp. 315-324 (2002).
- [3] L.G. Vorobiev and R.C. York, Phys. Rev. ST Accel. Beams **3**, 114201 (2000).
- [4] L.G. Vorobiev and R.C. York, PAC'01, Chicago, June 2001, pp. 3072-3075.
- [5] L.G. Vorobiev and R.C. York, *ibid.*, pp. 3075-3077.
- [6] L.G. Vorobiev and R.C. York, PAC'99, New York, March 1999, p. 2781.
- [7] I. M. Kapchinskij and V. V. Vladimirkij, Proc. Int. Conf. on High-Energy Accelerators (CERN, Geneva, 1959), p. 274.
- [8] P. Lapostolle, CERN Report AR/Int SG/65-15, 1965.
- [9] F. J. Sacherer, IEEE Trans. NS **18**, p. 1105 (1971).
- [10] P. Lapostolle, IEEE Trans. NS **18**, p. 1101 (1971).
- [11] B. L. Qian, J. Zhou, and C. Chen, Phys. Rev. ST Accel. Beams **6**, 014201 (2003).
- [12] M. Venturini and M. Reiser, Phys. Rev. E **54**, p. 4725 (1998).
- [13] T. Wangler “RF Linear Accelerators”, John Wiley & Sons, New York (1998).
- [14] M.Reiser et al. PAC'99, New York, March 1999, p. 234. Web site: <http://www.ireap.umd.edu/ebte/ring/>.

ON-LINE MODEL OF THE SNS MEDIUM ENERGY BEAM TRANSPORT LINE*

A. Aleksandrov, SNS, ORNL, Oak Ridge, TN 37830 USA
V. Alexandrov, Branch of INP, Protvino, Russia

Abstract

An on-line model of the beam dynamics in the SNS Medium Energy Beam Transport line (MEBT) has been developed using MATLAB Graphics User Interface. The model performs beam simulation using TRACE-3D and/or PARMILA codes. The input data for the simulation are generated on-line using settings of the transport line elements read from the EPICS control system. Simulated beam profiles are compared with wire scanner measurements on-line. Various tools are provided for estimating and fitting input beam parameters, which are not measured in the MEBT. This paper provides a description of the model and presents results of experimental tests during commissioning of the SNS Front End.

INTRODUCTION

The Front End Systems (FES) of the SNS accelerator is discussed in details elsewhere [1]. The medium-energy beam-transport section (MEBT) is part of the FES beam-line serving to transport 2.5 MeV 38 mA beam of H⁻ from the RFQ exit to the drift-tube linac (DTL) entrance. The MEBT is a fairly complicated 3.6 m transport line consisting of 14 quadrupole focusing magnets, 4 buncher cavities, chopper system and suite of diagnostics devices.

The nominal transverse beam beta-function in the MEBT is not periodic but rather irregular with three distinct regions: input matching section of 4 quadrupole magnets, chopper section of 6 quadrupole magnets in a symmetric configuration and output matching section of 4 quadrupole magnets. Transverse beam size can be measured at 5 locations along the MEBT using dual plane wire scanners [2]. Longitudinal focusing is rather periodic. There are no in-line instruments for direct measuring of the longitudinal beam size. Space charge is strong enough to provide coupling between horizontal, vertical and longitudinal planes and must be taken into account in beam dynamics simulations.

During commissioning beam current and input beam Twiss-parameters in the MEBT can deviate significantly from the design values. Optical functions required for particular experiments can be different from the nominal one. Therefore an operator needs a beam dynamic simulation tool available on-line in the control room to facilitate tuning of the MEBT parameters. The MEBT on-line model was written in Oak Ridge and tested during the SNS FES commissioning. Details of the implementation and test results of the model are presented.

* SNS is managed by UT-Battelle, LLC, under contract DE-AC05-00OR22725 for the U.S. Department of Energy. SNS is a partnership of six national laboratories: Argonne, Brookhaven, Jefferson, Lawrence Berkeley, Los Alamos and Oak Ridge.

THE SNS MEBT ON-LINE MODEL IMPLEMENTATION

General Structure

The MEBT on-line model consists of graphical user interface (GUI) for controlling model parameters and representing output information; beam dynamics simulation engine performing actual calculation of beam dynamics; input/output module providing data exchange between the model and beam dynamics calculation engine; EPICS access library providing data exchange between the model and the accelerator hardware; and several high-level algorithms performing MEBT-specific functions described later. Schematic diagram of the model is shown in figure 1.

All elements except beam dynamics simulation engine are written in the MATLAB [3].

Beam Dynamics Simulation

The core of the on-line model is a beam dynamics simulation routine. In order to minimize development time and efforts we decided to use the same simulation codes that are used for the SNS linac design and off-line simulations within the SNS collaboration. For faster calculations TRACE-3D beam envelope code is well suited; particle-tracking code PARMILA can be selected for more accurate simulation. Operator using the GUI screen does selection of the simulation code. Standard TRACE-3D/PARMILA input and output files are used for data exchange between the model program and the simulation program. Simulation program is called from the MATLAB using the standard OS command call.

Communication with Accelerator Hardware

The MEBT on-line model can create input file for the simulation engine using input from the GUI or reading actual settings from the accelerator hardware. The GUI input can also be used for controlling settings of the quadrupole magnets and bunchers in the MEBT. Measured data from the wire scanners can be read into the model for comparison with simulation results. This type of data exchange is done through the EPICS control system using MATLAB Channel Access (MCA) library, which is supported for Linux and Windows operating systems [4].

HIGH LEVEL ALGORITHMS

What gives the on-line model its power and flexibility is the possibility to write data processing layer between

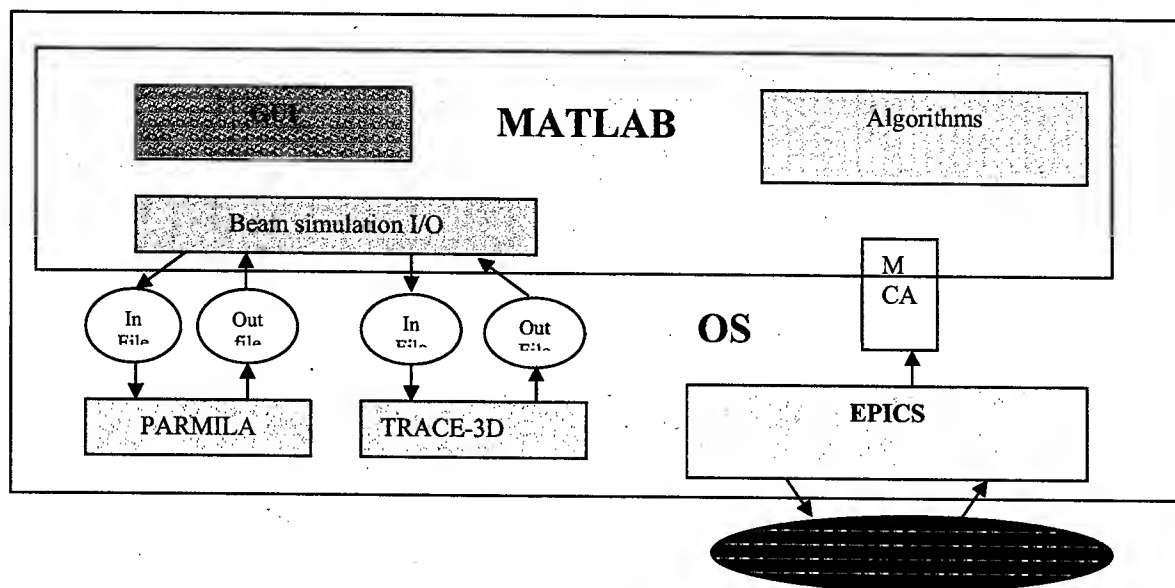


Fig 1 Schematic diagram of the MEBT on-line model.

the hardware and the simulation engine using very efficient MATLAB language. Using this mechanism one can include in simulation important hardware specific features, which is difficult or impossible to describe in terms of standard TRACE-3D or PARMILA input language. The same mechanism allows building of various optimization algorithms combining both measured and simulated data. There are two high level algorithms currently implemented in the MEBT on-line model: correction of quadrupole magnets strength due to proximity effect and input parameters search routine.

Correction of the Quad Proximity Effect

Quadrupole magnets surrounding chopper target in the MEBT are so close to each other that their fringe fields overlap. Correction to integrated focusing strength due to this effect is significant and has to be taken into account in simulation [5]. Unfortunately correction can't be described by static constant because it depends on the strengths of neighboring quads and should be calculated each time when current in the magnet coil is changed. Calculation of the correction term based on measured magnetic field distribution is included in the on-line model and can be switched on and off from the GUI.

Input Beam Twiss-Parameters Search

Twiss-parameters of the beam at the MEBT entrance are generally unknown. Those parameters are calculated using beam dynamic simulations but accuracy of the result can't be confirmed by direct measurements due to absence of any beam diagnostics upstream of the MEBT. This is a common problem in beam dynamic simulations because any model requires right input parameters in

order to produce results close to measured values. Simultaneous measurements of beam profile at 5 locations in the MEBT are used to find best approximation for the input parameters. Optimization algorithm embedded in the on-line model minimizes the difference between measured beam sizes and one calculated in beam simulation by varying input Twiss-parameters. Set of input parameters corresponding to the minimum difference is used in all subsequent simulations unless parameters of the beam line upstream of the MEBT change. When the ion source or RFQ settings change, optimization procedure should be repeated to find new set of input parameters. The procedure described above represents a way of indirect measurement of input beam parameters. In principle, it always converges to right values provided sufficient number of profile measurements along the beam line is available.

GRAPHICAL USER INTERFACE

The interface for the MEBT on-line model is written using the MATLAB and destined for the operative and convenient modeling of the beam dynamic both during the accelerator operation and for the theoretical researches.

Screenshot of the GUI screen is shown in fig. 2. The interface consists of two main parts: MEBT parameters values assignment and results representation. The quads strengths and cavities parameters can be read from file, loaded directly from the hardware or assigned manually

by operator. The interface enables to choose the simulation code. The quad proximity effect correction can be switched on or off from the GUI. The calculated values of the beam profile can be compared with the measured ones. Optimal Twiss-parameters of the input beam can be found by fitting model prediction to the measured beam profiles.

On-line model proved to be a useful tool during the Front-end commissioning. Measured beam size agreed with model prediction within wire scanner measurement accuracy when initial Twiss-parameters for the model were found using the best fit to the measured data [1]. Accuracy of the fit is demonstrated in fig. 3, where spread of β and α found from the fit is shown.

Many thanks to Ernest Williams and Carl Lionberger for help with implementation of reliable communication between MATLAB and EPICS.

[1] A. Aleksandrov, ‘Commissioning of the SNS Front End Systems’, Procs. of this conference, PAC2003
 [2] S. Assadi, ‘The Spallation Neutron Source diagnostics’, Procs. of this conference, PAC2003
 [3] www.mathworks.com

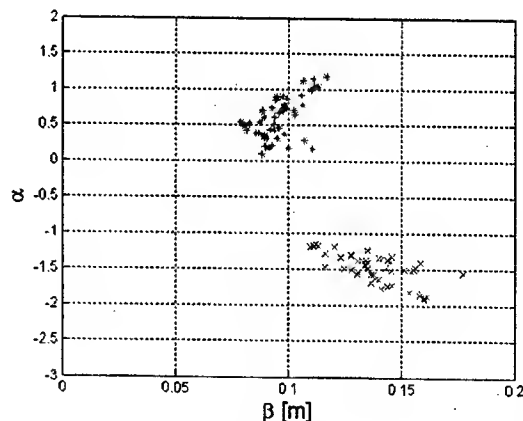


Figure 3. Spread of the input beam Twiss-parameters found using fitting algorithm for different MEBT settings. Red stars – vertical plane; blue crosses – horizontal plane.

- [4] <http://www-csr.bessy.de/control/Epics02/WED-PM/pdf/MCA-sns3.pdf>
[5] A. Aleksandrov, J. Staples, '3-D Calculations of Field Distribution in the MEBT Quad and Effect of the Fringe Field on Beam Dynamics', procs. of PAC2001, Chicago, 2001

PARTICLE TRACKING AND BUNCH POPULATION IN TraFiC⁴ 2.0

Andreas C. Kabel*

Stanford Linear Accelerator Center, Stanford, CA, USA

andreas.kabel@slac.stanford.edu

Abstract

Coherent Synchrotron Radiation (CSR) plays an important role in the design of accelerator components with high peak currents and small bending radii, such as magnetic bunch compressors, wigglers, and compact storage rings. The code TraFiC⁴ has been developed to design such elements [1, 2, 3, 4, 5, 6, 7, 8, 9, 10, 11, 12]; it simulates CSR effects from first principles. We present a re-write of the tracking and user interface components of TraFiC⁴. Extensions and corrections include: expanded input language; generalized bunch populations (rectangular, Gaussian, user-specified function); new element types; truly three-dimensional dynamics (i. e., the restriction to a single plane of motion has been abandoned), vastly expanded documentation; documented C++ class interface; and improved dynamic load-balancing for parallel computers.

FULLY THREE-DIMENSIONAL TREATMENT

Generalized Local Coordinates

TraFiC⁴ now handles fully three-dimensional problems; there is no limitation to one plane of movement. This makes it necessary to choose a more general system of local coordinates: while TraFiC⁴ does all of its tracking in laboratory coordinates, as it needs to store the history of all particles to calculate the retarded fields, accelerator physics is usually done in a co-moving frame.

As a local system, we choose the Frenet coordinate system associated with an orbit particle's trajectory $\vec{r}_0(s)$, where s is the arc length. The co-moving frame is spanned by $\vec{r}_0'(s)$, $\vec{r}_0''(s)$, and $\vec{r}_0'(s) \times \vec{r}_0''(s)$; the associated normalized vectors are $\vec{t}(s)$, $\vec{n}(s)$, and $\vec{b}(s)$. Given another particle trajectory $\vec{r}(s(t))$, parametrized by the lab time t , we find that particle's local coordinates x, y, l by $\vec{r}(s(t)) = x\vec{n}(s(t) + l) + y\vec{b}(s(t) + l)$. Note that this decomposition is not unique, as there might be several l for which $\vec{t}(s_0(t) + l) \cdot (\vec{r}(s(t)) - \vec{r}(s_0(t) + l)) = 0$. TraFiC⁴ starts looking around $l = 0$, however.

Note that this generalized prescription leads to some unfamiliar effects, such as x and y coordinate flipping their sign when the curvature does or switching roles when a sideways bend turns into an upward bend.

Also note that the prescription is not unique on drifts, as $\vec{r}'' = 0$. We use the parallel-transported \vec{n} from the last

curved section in these cases; by convention, we start our beamline with $\vec{t}(0) \parallel x_{Lab}$ and $\vec{n}(0) \parallel y_{Lab}$.

Generalized Dipoles

It is now possible to rotate Bending magnets around the axis of the incoming particle by an arbitrary angle. This makes TraFiC⁴ fully three-dimensional, as the movement of the orbit particle is not restricted to a plane any more.

Furthermore, a dipole can be tilted upward and downward, i. e., rotated around the curvature vector. This turns the trajectory of the orbit from a circular arc into a helix segment; this generalization might be useful for studying the behavior of bunches moved out of the radiation cone of their own CSR by such an arrangement.

Also, the magnet's entry and exit faces may be rotated away from a sector-bend setup; the (de)focusing effects induced by fringe fields components occurring by tilting the magnet and its faces in the x and y phase-space planes, resp., is modeled by sandwiching the dipole between thin-lens (de)focusing elements. Neighboring wedge elements of the same strength, but opposite signs, are canceled automatically. Neighboring dipoles need to have compatible exit and entry faces; otherwise, an arbitrarily small drift space in between is required.

OBSERVER GRIDS

Sometimes it is of interest to calculate the fields due to CSR not only within the bunch, but at observation points far away from the bunch. TraFiC⁴ now allows to specify such observation points. It is most convenient to do that with reference to the beam-line coordinates. A new beam-line element type `ObserverGrid` was introduced for this purpose; it has parameters $n_t, t_{min}, t_{max}; n_s, s_{min}, s_{max}; n_x, x_{min}, x_{max}; n_y, y_{min}, y_{max}; \beta_s, \beta_x, \beta_y$. It will create four-dimensional lattice of size n_t, n_s, n_x, n_y , spanning the spacetime interval $[t_{min}, t_{max}] \otimes [s_{min}, s_{max}] \otimes [x_{min}, x_{max}] \otimes [y_{min}, y_{max}]$, where t refers to the laboratory time and s, x, y refer to the local tangential, radial, and transverse direction, resp. The observation grid moves with a speed of $c\vec{\beta}$. The quantities calculated are the total force per charge $\vec{E} + c\vec{\beta} \times \vec{B}$ and the energy change per charge $\vec{E} \cdot \vec{\beta}$. An arbitrary number of `ObserverGrid`s can be defined.

Fig. and show field profiles over time and transverse (i. e., perpendicular to the curvature of the magnet) coordinates in the middle of a dipole of curvature $1/m$ and length $2m$. The 100×100 grid was specified by writing the beam-line as

*Work supported by Department of Energy contract DE-AC03-76SF00515.

```
param Beamline=Group(Bend(1., 1.),
  ObserverGrid(100, -bunchlength, 5.*bunchlength,
    1, 0., 0.,
    1, 0., 0.,
    100, -bunchlength, bunchlength,
    0., 0., 0.
  ),
  Bend(1., 1.)
);
```

The first field profile is due to a Gaussian bunch, the second is caused by a rectangular bunch, softened by a Fermi-Dirac distribution.

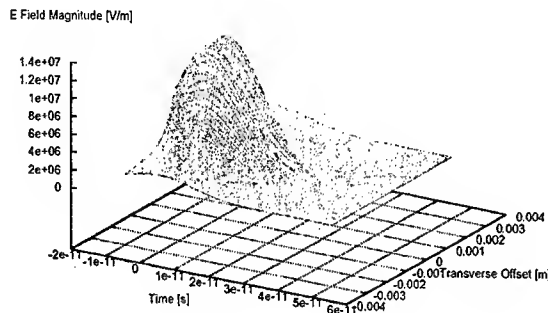


Figure 1: Field vs. time, transverse offset plot Beam parameters: $E = 150\text{ MeV}$, $Q = 1.0\text{ nC}$, $\sigma_s = 3\text{ mm}$, $\sigma_y = \sigma_s/10$

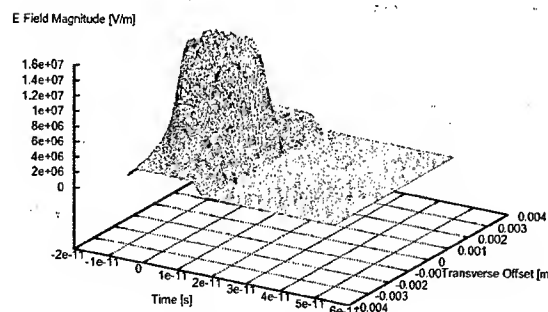


Figure 2: Same as , but for an almost rectangular charge distribution (softened by a Fermi-Dirac distribution with $T=1/15$)

BUNCH SETUP

One of the biggest hurdles to successfully use TraFiC⁴ in its previous versions was the awkward way of setting up

bunches. TraFiC⁴ knows three kinds of bunches: *generating* bunches, comprising weighted, smoothed-out macro particles which generate the fields and may or may not move under the influence of their own fields, depending on whether or not the user expects these effects to be important; *optical* bunches, which do not generate fields, but feel the perturbations of the fields caused by the generating bunch(es), and *sampling* bunches, which sample the fields of the generating bunches, but are not influenced by them (they can be viewed as co-moving ObserverGrids).

Generating bunches consist of one-, two-, or three-dimensional extended Gaussian charge distributions whose centroids are tracked according to the magnetic lattice and possibly the bunch's fields. All other bunches comprise point particles, which can bear a charge (or statistical weight), which will be used in calculating collective quantities such as dissipated power, rms values, Twiss parameters. As sampling and optical bunches do not contribute to the fields, their setup needs not coincide with the setup of the generating bunch(es), so they can be used to study the behavior of sub-ensembles of the bunch.

A bunch in TraFiC⁴ is now set up by specifying a particle class (point, pencil, sheet, or cylinder) and a Generator. A Generator is a sequence of extended phasespace vectors (extended meaning 6 phasespace coordinates + 1 statistical weight); pre-defined generators are cartesian Grids, quasi-random sequences, and input from a text file. Generators can be transformed into new Generators using a set of predefined functions (transform to beam ellipses with given Twiss parameters, Scale, Shift, transform to gaussian normal distribution), Selectors (first n particles from a generator, particles lying on either side of a hyperplane), and arbitrary user-defined functions. All transformations can be concatenated, allowing for high flexibility in populating the bunch.

SELF-CONSISTENT CALCULATIONS

TraFiC⁴ has been augmented by a new algorithm for self-consistent calculations. The user now has the choice of two algorithms:

- A "pong" algorithm, in which two initially identical copies of the generating bunch correct their trajectories by applying the field of the respective other bunch. This mutual correction is repeated a user-defined number of times for each timestep. The deviation of the copies' trajectories give a rough estimate of the error made in the process. This algorithm, however, sometimes will converge only for ungainly small timesteps or high particle numbers [].
- A self-correcting algorithm, in which all fields of a bunch on itself in a given timestep are collected and subsequently applied at once to all particles. The trajectories are then corrected up to the end of the beamline, and the process repeats (again, the number of iterations is user-defined) or advances to the next

timestep. This does not give an error estimate, but avoids having macroparticles of the generating and receiving bunch have a very small but finite distance (as generating and receiving bunch coincide).

OTHER NEW FEATURES

Memory Requirements

Memory requirements for TraFiC⁴ have drastically reduced, as a number of quantities that had to be stored in the previous version are now computed on the fly and discarded. This was made possibly by an overall restructuring of the code. The asymptotic memory requirements are now $11 \times \text{sizeof}(\text{double}) + \text{sizeof}(\text{void}^*)$ (=92 bytes on most machines) per particle and timestep, as opposed to 234 bytes in previous versions.

Load Balancing

The automatic load balancing in the multi-processing version has been improved. TraFiC⁴ allows for the automatic distribution of particles to processors according to the measured speeds in previous timesteps. The load balancer will react to changes in speed according to a user-selectable inertia. Moreover, the load balancer associated with each bunch and ObserverGrid can learn from the speed behavior of calculations for bunches treated before, distributing particles accordingly.

Documentation and Source Code

The documentation of the user interface and tracking part has been vastly extended [13]. Also, the class structure of the tracking part has been extensively documented, which should make it possible for programmers to add their own element types or transformer functions [14, 15].

The source code for TraFiC⁴ is available from [16]. TraFiC⁴ requires a recent, ANSI-compliant C++ compiler, a Fortran 77 compiler, some components of the "boost" extension library [17], and an MPI multiprocessing library.

Acknowledgements

I wish to thank T. Limberg, H. Schlarb and F. Stulle for useful discussions. I also wish to thank M. Dohlus to make his new field calculation algorithm available to me.

REFERENCES

- [1] A. Kabel. Coherent synchrotron radiation calculations using traffic4: Multi-processor simulations and optics scans. Presented at IEEE Particle Accelerator Conference (PAC2001), Chicago, Illinois, 18-22 Jun 2001.
- [2] M. Borland, H. Braun, S. Doebert, L. Groening, and A. Kabel. Recent experiments on the effect of coherent synchrotron radiation on the electron beam of ctf ii. Presented at IEEE Particle Accelerator Conference (PAC2001), Chicago, Illinois, 18-22 Jun 2001.
- [3] A. Kabel, M. Dohlus, and T. Limberg. Numerical calculation of coherent synchrotron radiation effects using TraFiC4. *Nucl. Instrum. Meth. A*, A455:185-189, 2000.
- [4] A. Kabel, M. Dohlus, and T. Limberg. Numerical calculation of coherent synchrotron radiation effects. 1999. Invited talk given at the International Symposium on New Visions in Laser Beam Interactions: Fundamental Problems and Applications of Laser Compton Scattering, Tokyo, Japan, 11-15 Oct 1999.
- [5] H. H. Braun, R. Corsini, L. Groening, F. Zhou, A. Kabel, T. Raubenheimer, R. Li, and T. Limberg. Coherent synchrotron radiation measurements in the CLIC test facility (CTF II). *eConf*, C000821:TH206, 2000.
- [6] H. H. Braun, R. Corsini, L. Groening, F. Zhou, A. Kabel, T. Raubenheimer, R. Li, and T. Limberg. Emittance growth and energy loss due to coherent synchrotron radiation in a bunch compressor. *Phys. Rev. ST Accel. Beams*, 3:124402, 2000.
- [7] M. Dohlus, A. Kabel, and T. Limberg. Efficient field calculation of 3D bunches on general trajectories. *Nucl. Instrum. Meth.*, A445:338-342, 2000.
- [8] M. Dohlus, A. Kabel, and T. Limberg. Coherent effects of a macro bunch in an undulator. *Nucl. Instrum. Meth.*, A445:84-89, 2000.
- [9] M. Dohlus, A. Kabel, and T. Limberg. Optimal beam optics in the TTF-FEL bunch compression sections: Minimizing the emittance growth. In *Proceedings of the IEEE Particle Accelerator Conference (PAC 99)*, New York, NY, 29 Mar - 2 Apr 1999, 1999.
- [10] M. Dohlus, A. Kabel, and T. Limberg. Uncorrelated emittance growth in the TTF-FEL bunch compression sections due to coherent synchrotron radiation and space charge effects. In *Proceedings of the 6th European Particle Accelerator Conference (EPAC 98)*, Stockholm, Sweden, 22-26 Jun 1998, 1998. DESY-M-98-0601.
- [11] M. Dohlus, A. Kabel, and T. Limberg. Design consequences of coherent synchrotron radiation beam dynamic effects on the TTF-FEL bunch compression system. In *Proceedings of the 19th International Conference on Free Electron Lasers, Beijing, China, 18-21 Aug 1997*, 1997. DESY-TESLA-FEL-97-06B, Oct. 1997.
- [12] M. Dohlus, A. Kabel, and T. Limberg. Wake fields of a bunch on a general trajectory due to coherent synchrotron radiation. In *Proceedings of the 17th IEEE Particle Accelerator Conference (PAC 97): Accelerator Science, Technology and Applications, Vancouver, Canada, 12-16 May 1997*, 1997. DESY-M-97-10J.
- [13] A. Kabel. A short guide to traffic4 2.0. 2003. <http://www.slac.stanford.edu/~akabel/TraFiC4-2.0/doc.pdf>.
- [14] A. Kabel. Traffic4 2.0 - programmer's manual. 2003. <http://www.slac.stanford.edu/~akabel/TraFiC4-2.0/TraFiCdoc/latex/refman.pdf>.
- [15] A. Kabel. Traffic4 2.0 - programmer's manual. 2003.
- [16] <http://www.slac.stanford.edu/~akabel/TraFiC4>.
- [17] <http://www.boost.org>.

A PARALLEL CODE FOR LIFETIME SIMULATIONS IN HADRON STORAGE RINGS IN THE PRESENCE OF PARASITIC BEAM-BEAM INTERACTIONS

A. Kabel*, Y. Cai; SLAC
B. Erdelyi, T. Sen, M. Xiao; FNAL

Abstract

The usual approach to predict particle loss in storage rings in the presence of nonlinearities consists in the determination of the dynamic aperture of the machine. This method, however, will not directly predict the lifetimes of beams. We have developed a code which can, by parallelization and careful speed optimization, predict lifetimes in the presence of 100 parasitic beam-beam crossings by tracking $> 10^{10}$ particles-turns. An application of this code to the anti-proton lifetime in the Tevatron at injection is discussed.

BEAM-BEAM EFFECTS IN THE TEVATRON

In its current setup, the Tevatron operates with 36×36 proton/anti-proton bunches, which share the beam pipe in a helical scheme. During the injection stage, which takes place at 150 GeV, all 72 interaction points are parasitic.

During injection, a relatively fast decay of the anti-proton current is observed; the lifetimes obtained by fitting to an exponential decay behavior are of the order of 1 hour. In the absence of the proton beam, the anti-proton lifetime is well beyond 20 hours. The proton beam itself is unaffected, having a vastly higher charge. Thus, it seems justified to assume that the lifetime behavior is due to weak-strong beam-beam effects.

LIFETIME CALCULATIONS

The beam lifetimes we would like to simulate are of the order of 1 hour. For the Tevatron, this corresponds to a loss rate of $< 5.8 \cdot 10^{-9} N/\text{turn}$, where N is the number of particles in a weak bunch.

We choose a direct particle tracking approach to lifetime calculations, as opposed to the usual dynamic aperture calculations. As we are dealing with a proton machines, synchrotron radiation damping mechanisms are absent, so there is no natural limit on the number of turns one needs to track. Assuming that we need to observe 10^2 particles being lost during the tracking procedure to get decent statistics, we need to simulate $> 1.7 \cdot 10^{10}$ Particles · Turns. As we are interested in the injection stage, where we assume that all parasitic crossings will contribute to the dynamics of the beam, $> 1.2 \cdot 10^{12}$ weak-strong interactions need to be simulated. The computational effort necessary is clearly out of the range of single processor machines.

Parallelization clearly is needed to tackle the problem described above. But even when parallelized, the computational demands of a proton tracking code for lifetime calculations are pushing the limits of the computing resources available to us. Thus, a carefully designed, speed-optimized code is necessary; only the physics relevant to the problem should be included.

The code `PLiBB` (Parallel Lifetime Calculations with beam-Beam) was written with this goal in mind. It is not an optics code; rather it assumes a machine description prepared for it using `MAD8`, using a defined convention of marking the interaction points within the beamline.

Using the `MAD` input file, a `PERL` script then runs `MAD` several times to (1) calculate the closed orbit of both beams (2) calculate the linear transfer matrices for the anti-proton beam between interaction points with respect to the closed orbit and (3) calculate the one-turn matrix for the proton beam with respect to each interaction point. The Twiss parameters and transfer matrices are then used by the script to generate a C++ program file, containing an alternating sequence of beam-beam kick elements and linear transformations, as well as a single 'aperture', 'twiss', and 'one-turn chromaticity' element each (see below). This file is then compiled and linked into the main code.

In the code, we consider fully coupled motion, which is handled the following way: (Roman indices run over $1 \dots 2N$, Greek ones over $1 \dots N$.) Let M be the one-turn matrix with respect to a given interaction point, it is assumed to describe stable motion, i.e. all its eigenvalues are of unit modulus and pairwise complex conjugate, belonging to complex conjugate eigenvectors: $\vec{\lambda}_{(\mu)} = \lambda_{(\mu)}$, with normalization $\vec{\lambda}_{(\mu)}^+ J \vec{\lambda}_{(\mu)} = i$, where J is the symplectic pseudometric. We can now find correlation matrices of eigendistributions $C^{(\mu)} = M C^{(\mu)} M^T$ where C is a real, symmetric, positive semidefinite matrix. Introducing $z_{(\mu)} = \vec{\lambda}_{(\mu)}^T \vec{\lambda}_{(\mu)}$, it is easy to check that $C_{(\mu)} = \frac{\vec{\lambda}_{(\mu)} \vec{\lambda}_{(\mu)}^+}{2} + c.c.$ forms a set on N such correlation matrices. The real normalized vectors $\vec{v}_{(\mu)}^{\pm} = \frac{\vec{\lambda}_{(\mu)} \pm \vec{\lambda}_{(\mu)}^*}{\sqrt{2}}$ are real vectors and span eigenplanes to which the motion associated with the tune ν_{μ} is restricted. We can construct matrices $D_{\mu, \pm}^{\pm} = v_{(\mu)}^{\pm}$ and $D^{-1} = J D J^T$ which transform to a diagonal basis in which $D M D^{-1}$ is a decoupled rotation matrix and $D C D^T$ are projectors onto the eigenplanes. Our code determines the matrices D, D^{-1}, C^{μ} from the one-turn matrix of protons and anti-protons. The μ indices are sorted according to the eigenvalue, so coordinates are labeled by the associated tune. Emittances are then chosen as to have the spatial diagonal elements of the total correlation matrix

* Work supported by Department of Energy contract DE-AC03-76SF00515.

$C = \sum_{\mu} \epsilon_{\mu} C^{(\mu)}$ coincide with the known beam dimensions. For the Tevatron at injection, $\epsilon_0 \approx \epsilon_y, \epsilon_1 \approx \epsilon_x, \epsilon_2 \approx \epsilon_s$ to within a few percent.

Chromaticity can be artificially inserted by reading off the eigenchromaticities by analyzing the eigenvalue dependence of M with energy (in the case of the Tevatron, this is in good agreement with the x,y chromaticity output by MAD). Then, the appropriate phase advance is applied each turn to each particle by going to the eigenbasis, rotating by a phase of $2\pi \xi \delta_i$, and going back to the usual basis.

ANALYTIC TREATMENT OF THE BEAM-BEAM KICK

The integrated transverse kick of a gaussian bunch can be expressed by the Bassetti-Erskine Formula[1] in terms of the complex error function $w(z)$.

The evaluation of w turns out to be the most time-critical component of the code. Thus, we surveyed a number of implementations, (for a comprehensive list, see [2]); the fastest we found are the Chiarella-Matta-Reichel algorithm ([3]) and brute force, namely, a pre-calculated 2-D lookup table and bilinear interpolation. This is good for 10^{-6} accuracy. The lookup method works very well on the IBM SP, which has a large data cache; on the PC platform, the first method turns out to be faster.

The implementations were checked with a reference implementation ([4]). Numerical experiments showed that a 10^{-5} relative accuracy or better everywhere is sufficient for typical simulation lengths; lifetime estimates (see below) are in excellent agreement with code using 10^{-16} accuracy implementations; test particles begin to showed visible deviation from the reference implementation not before $10^5 \dots 10^6$ turns.

Currently, the speed achieved is 10^6 (kicks,transforms)/second on Intel Xeon and $6.7 \cdot 10^5$ (kicks,transforms)/second on IBM SP.

Parallelization

The Weak-Strong is embarrassingly parallelizable; a parallel code merely assigns different chunks of particles of a common particle pool to each processor. Communications between processes is only necessary when collective quantities (lost particles, beam sizes, ...) are calculated.

Simplified Distributions

Usually, one would not expect particles in the core of the beam being lost. Therefore, one can use 'de-cored' distributions where particles near the center of the distribution are left out, thus increasing the effective speed of the simulation. Different strategies are possible. Clearly, a simple cutoff in each phasespace dimension is not sufficient, as it will not be a matched distribution. In action space, different cutoffs are possible, the limiting cases of which are (with an obvious notation referring to phasespace coordinates normalized to unity)

- An all-dimensional cutoff, i.e., a $2d$ -hypersphere of radius R cut out: $\rho(\vec{x}) \propto \Theta(|\vec{x}| - R) e^{-|\vec{x}|^2/2} d(|\vec{x}|^{2d}) d\Omega$; the ratio of particles within that distribution is

$$N/N_0 = e^{-R^2/2} \sum_{i=0}^{d-1} \frac{R^{2i}}{2^{2i} i!}$$

- pairwise radial cutoff, i.e., the direct product of distributions with a disc of radius R cut out: $\rho(\vec{x}) \propto \prod_i \Theta(x_i^2 + p_i^2 - R^2) e^{-(x_i^2 + p_i^2)/2} d^d x d^d p$, here

$$N/N_0 = (1 - \exp(-R^2/2))^n$$

For $d = 3$ (six-dimensional phasespace), the latter choice (which we use in our code) eliminates more particles for typical choices ($R \approx 1\sigma \dots 2\sigma$) of the cutoff. Typically, we use 2σ in both transverse direction, corresponding to a savings factor of ≈ 4.0 .

Optimized Transport in Beam-Beam Kicks

The eigendistributions obtained from the one-turn proton matrices in each interaction points are used to calculate the transverse proton beam profile ellipse. Depending on the quantities $\sigma_{long}/\sigma_{trans}, -2\langle xy\rangle/\langle x^2\rangle - \langle y^2\rangle$, and its derivative, the transport of a particle with non-zero longitudinal coordinate or the strong beam's ellipse into the actual interaction point may require to consider (1) the hourglass effect (2) the tilt of the beam ellipse (3) an s -dependent tilt of the beam ellipse. Consequently, 6 different routines were written to handle the possible cases in a speed-optimized fashion. The appropriate routine for a given interaction point is determined at the initialization stage of the code.

LIFETIME ESTIMATES

During the tracking procedur, the 3 action variables of the particle are determined (in the "Aperture" element). The action is recorded in the particle's data structure if it is greater than actions recorded before. Thus, after completion of each turn, one has a record of the maximum action for each particle.

Scanning through I_x, I_y -action space, one can count the number of particles beyond a certain I_x, I_y . Assuming that this action pair represents the physical aperture of the machine, one gets a number $N_{Lost}(I_x, I_y; t)$ (where t represents the number of turns), which is a monotonously falling function with respect to I_x, I_y for fixed t and a monotonously rising function with respect to t for fixed I_x, I_y . In order not to slow down the code, this scan is typically run after each $10^3 \dots 10^4$ turns. The instable particles are identified and its tag number printed out; in a subsequent run, the code can be run with only the instable particles in the initial distribution; phase space dumps then are used to help; identify the instability mechanism.

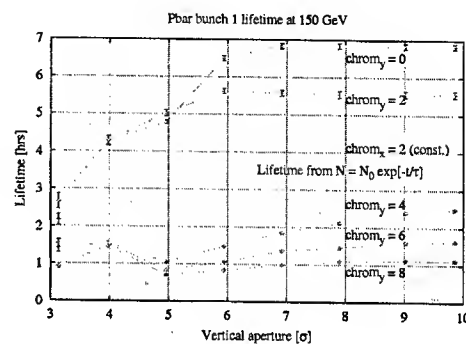
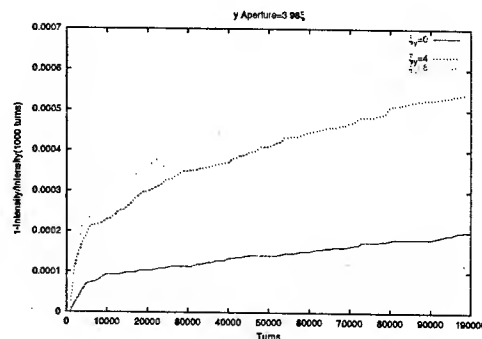
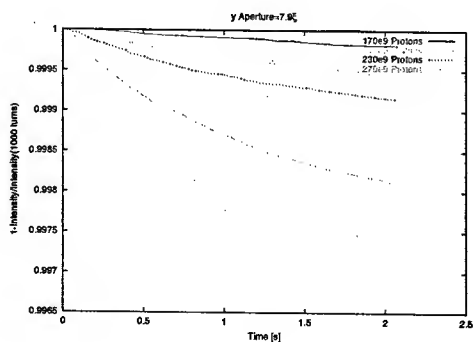
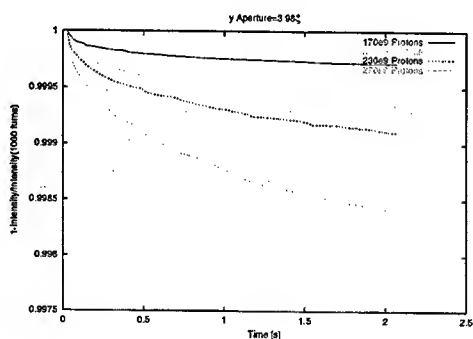
Looking at N_{Lost} for fixed I_x, I_y , one can observe typical lifetime patterns: a quick loss of particles (due to fast resonances or mismatching effects), going over into a linear

behavior for large turn numbers. Extrapolating the linear behavior, one can estimate the lifetime, assuming a certain aperture, by looking at the slope of the linear part of N_{Lost} . The advantage of this procedure is, of course, the fact that it allows to check the connection between physical aperture and lifetime for a number of apertures with a single run.

PARAMETER SCANS

We run a series of studies, varying proton current and chromaticity. The intensities were normalized to unity at 1000 turns (disregarding, in effect, fast losses due to mismatching). Typical results are given in figures The x aperture was fixed at $> 9\sigma$. Fig. (plot courtesy T. Sen) shows the results of an exponential fit for the intensity results for the chromaticity scan. The apparently decreasing lifetimes for increasing apertures near 3σ can be explained by the choice of the fit, only for large apertures can the intensity be approximated by an exponential function; for smaller apertures, $I(t) \approx \exp(-\sqrt{t/\tau})$. Clearly, a better model for the $I(t)$ is needed to accurately predict actual lifetimes.

An interesting observation is the increase in lifetime with decreasing y chromaticity. This signature is indeed observed experimentally¹. However, the region of the predicted jump in lifetime has not been accessed experimentally so far.



CONCLUSION AND FURTHER DIRECTIONS

Through parallelization and optimized implementation of tracking procedures, the P11bB code is able to calculate finite lifetimes caused by parasitic beam-beam crossings based on the tracking simulation of $\approx 10^{10}$ particles·turns, which, as it produces measurable quantities, can be viewed as a distinct advantage over dynamical aperture results produced by other tracking codes. While we are able to reproduce the signatures of anti-proton loss in the injection stage of the Tevatron, the model is not complete.

The possibly most important physics we are missing is magnet nonlinearities. The natural chromaticity of the Tevatron due to sextupole elements is extremely high (it is compensated down to 8 units, however). While we have implemented the effective global lattice chromaticity, the high local sextupole content may lead to strong non-linear effects. To handle this effects, we have implemented a fast truncated power series evaluator and a chain of tools, involving MAD and COSY infinity, which allows us to extract high-order maps between interaction points and compile them into P11bB.

REFERENCES

- [1] G. A. Erskine M. Bassetti. *CERN-ISR-TH/80-06*, 1980.
- [2] J. A. C. Weideman. *SIAM J. Numer. Anal.*, 31:1497, 1994.
- [3] F. Matta and A. Reichel. *Math. Comp.*, 25:339, 1971.
- [4] W. Gautschi. *SIAM J. Numer. Anal.*, 7:187, 1970.

¹T. Sen, personal communication

PARALLEL SIMULATION ALGORITHMS FOR THE THREE-DIMENSIONAL STRONG-STRONG BEAM-BEAM INTERACTION

Andreas C. Kabel*, SLAC

Abstract

The strong-strong beam-beam effect is one of the most important effects limiting the luminosity of ring colliders. Little is known about it analytically, so most studies utilize numeric simulations. The two-dimensional realm is readily accessible to workstation-class computers (cf., e.g., [1, 2]), while three dimensions, which add effects such as phase averaging and the hourglass effect, require vastly higher amounts of CPU time. Thus, parallelization of three-dimensional simulation techniques is imperative; in the following we discuss parallelization strategies and describe the algorithms used in our simulation code, which will reach almost linear scaling of performance vs. number of CPUs for typical setups.

TWO DIMENSIONS

For the simplest parallelization of the strong-strong problem, both beams are represented by macro particles. We have two parallelizable tasks: the application of fields to the particles and the calculation of the fields due to the particle distribution. The latter problem is addressed by a particle-on-grid algorithm: A discretized charge density ρ_i is used to calculate the electric potential ϕ_i by solving the discretized Poisson equation. A particle is deposited on ρ_i (i, \vec{k}, \dots are two-dimensional integer vectors, corresponding to positions $x = x_0 + h_x i_1, y = y_0 + h_y i_2$ on the grid) by adding charge to the lattice sites nearest to it with distance-depending weights. We use a third-order momentum-conserving deposition scheme [3]. For the two-dimensional sub-problem, we make use of algorithms introduced and validated in [1, 2].

We divide the particles into pools local to processors. For the two-dimensional problem, a single grid is placed in the interaction point, perpendicular to the directions of motion. A parallelized solver step now is a sequence of: (1) collecting ρ_i from test particles (2) add all ρ_i from particle pools (3) distribute sum ρ_i to solver processors (4) calculate \vec{E}_i from ρ_i (5) distribute \vec{E}_i to particle pools (6) apply \vec{E} to test particles (7) transport particles around the complete ring or to the next interaction point. The transport operation involves all of the particle dynamics between IPs (usually linear transport (hadron machines) or linear transport + damping (e^\pm machines)).

THREE DIMENSIONS

For the solution of the three-dimensional problem, we divide the bunches into n_z longitudinal slices of equal lengths h_z and slice numbers $i_z \in [0, n_z)$, 0 representing the leading slice. We now need to place (for both bunches) $2n_z - 1$ grids numbered $1 - n_z \dots n_z - 1$ at positions $\frac{1-n_z}{2}, \dots, \frac{n_z-1}{2}$ around the IP.

For each encounter of bunches, $2n_z - 1$ steps need to be executed, numbered $s \in [0, 2n_z - 2]$. In step s , particles in slice $k \in [\max(0, s - n_z + 1), \min(s, n_z - 1)]$ are deposited on grid $\pm(k - s)$ (sign according to the direction of flight). All updated grids are then used to calculate fields, and the resulting fields are applied to the opposing bunch's particles longitudinally nearest to the respective grid. Each bunch encounter thus consists of n_z^2 slice encounters comprising 1 two-dimensional deposit/solve/kick step each.

When the bunch length is comparable to the β function in the IP, the hourglass effect becomes significant, meaning that the grids far away from the IP have to accommodate a larger bunch diameter than the grids close to it. To optimize resolution, we scale the grid resolutions according to $h_{x,y} \propto \sqrt{1 + \frac{z^2}{\beta_{x,y}^2}}$.

Field Calculation

The field calculation is based on a convolution algorithm. The discretized charge distribution ρ_i is convoluted with the discretized Green's function $G_{i-\vec{k}} \propto \log \sum_i \frac{(i_i - k_i)^2}{h_i^2}$ for the two-dimensional Coulomb problem. The convolution can be done efficiently by Fast Fourier transforming ρ , doing a point-wise multiplication with the Fourier transform \tilde{G} of G , and transforming back. If we choose a lattice of dimensions $L = [0, 2h_x n_x) \otimes [2h_y n_y)$, but restrict the support of ρ to $L' = [0, h_x n_x) \otimes [0, h_y n_y)$, the $(2n_x, 2n_y)$ periodicity of \tilde{G} will not modify the potential in L' , i.e. the method will obtain the correct potential for open boundary conditions. This is the famous Hockney trick [3]. To avoid the singularity of the Green's function at the origin, we choose a natural smoothing prescription: we shift the Green's function by $\frac{1}{2}\vec{h}$, such that $G_0 = 0$, and evaluate the fields at a position shifted by $-\frac{1}{2}\vec{h}$.

The Green's function is pre-calculated at program start. As G obeys no simple scaling law for the case of $\beta_x^* \neq \beta_y^*$, this precalculation needs to be done for each encounter point. The method is easily generalized to non-concentric lattices, different resolutions for different beams, and dynamic rescaling of lattices, should the beam dimensions change.

*Work supported by Department of Energy contract DE-AC03-76SF00515.

Parallelizing the convolution method amounts to parallelizing the local multiplication with \tilde{G} , which is trivially done, and parallelizing the Fast Fourier Transform. For the latter, we use the high-performance, open-source parallel FFT library 'FFTW'[4]. Calculation of the electric field is done by discretized differentiation with an appropriate weight algorithm[2]. The fields can be applied to particles by scattering particles to the appropriate slices or by gathering the fields into the particle pools; we choose the latter solution in our code.

We can make use of an additional symmetry property of the system: as there are two rings involved, we split the processors into two subgroups, each assigned to one of the bunches. The only communication necessary between these subgroups is then the exchange of the charge density ρ_i , which can be done after collecting it to the root process of the solver. Thus, only a single pair of communicators between processes assigned to different bunches is necessary.

The advantage of this procedure is due the hardware configuration of the computer system available to us. On the IBM SP at NERSC, 16 processors share a node and can communicate via shared memory. Communications between nodes will be over a fast network, but still be substantially slower. Thus, it is advantageous to limit the distribution of the Poisson solver, which will involve a large amount of all-to-all communications, to one node. By the bisection of the problem the communications overhead penalty will start to set in at 32 processors instead of 16 processors.

Communications overhead can be further reduced by using another possible parallelization. As soon as the longitudinal slice number $n_z > 1$, each encounter will involve the independent encounters of several slices. Particle deposition and solving the Poisson equation can then be done in parallel, making it possible to keep both local to a single node by setting the number of processors in a solver to $n_{sp} < n_p/2$. However, not every encounter step involves the encounter of an integer multiple of n_{sp} , so some solvers will have been idling during one encounter. The optimum choice for n_{sp} depends on the hardware setup and the ratio of CPU time usage for solving the Poisson equation and particle-grid-dynamics, resp., so it has to be found experimentally for each given number of particles and grid size.

THE SLICE ALGORITHM

While the algorithm described above allows for a great flexibility with respect to variable computer parameters such as number of processors, number of processors in a fast sub-cluster etc., its performance for a higher number of processors is disappointing; test runs on the NERSC facility show it to go into saturation at $\approx 32 \dots 64$ processors. This is due to the choice of a common "pool" of particles, shared among all processors, with no attempt at localization in physical space. Thus, particle localization is desirable, however, the dynamics between interaction will

move a particle from one processor's responsibility into another's. Care must be taken not to lose in particle management communication what was gained by saving field communication.

Consequently, particles should be assigned to processors according to their longitudinal coordinate: The longitudinal dynamics in a storage ring usually is much slower than the transverse one, meaning that a relatively small number of particles will change processors during a single turn.

A simple equidistant slicing will lead to a very uneven distribution of particles, leaving most of the tracking work to the processors responsible for the center slices. This can be cured by a Hirata-type slicing [5], choosing borders $\zeta_i, \zeta_0 = \infty, \zeta_{z_n} = -\infty$ such that the number of particles in $[\zeta_i, \zeta_{i+1}) = N_p/n_z$; the encounter points between slices i and k are chosen at a distance $\frac{z_i - z'_k}{2}$ from the IP, where z_i, z'_k are the centers of gravity of the slices in the respective bunch. Again, the grids' resolutions are scaled according to z_i and β .

The Wraparound Algorithm with Idle Cycles

The processors assigned to the head of the bunch will be idle after the centers of the bunches have passed each other, as there are no collision partners left.

One can, however, apply the transfer map of the lattice up to the next IP (or to the beginning of the same IP) in the first of these idle steps, and do the next collision in the next step. Pparticles from trailing slices may still move into a leading slice when they are transported through the ring after they have encountered their last collision partner. This can be partially cured by inserting a 'cool-down cycle', i.e., a slice, after having been transported, waits for one or several additional idle steps, leaving CPUs unused, for particles from its trailing slices to catch up.

Assuming a matched distribution (i. e., $\rho(p, q) = \tilde{\rho}(H(p, q))$) and a quadratic Hamiltonian, and scaling the canonical variables to $\sigma_{p,q} = 1$, the number of particles moving from a slice $q_1 < q \leq q_2$ to a slice $q_3 < q \leq q_4$ in two-dimensional phasespace during a phase advance $\Delta\phi = 2\pi\Delta\nu$ (or vice versa, as the distribution is invariant under rotations) is given by the integral over the parallelogram obtained by overlapping one slice with the other, rotated slice:

$$\Delta N = N_P \int_{q_3}^{q_4} dq \int_{q_1 / \sin \Delta\phi + q \cot \Delta\phi}^{q_2 / \sin \Delta\phi + q \cot \Delta\phi} dp \rho(H(p, q)) \quad (1)$$

For a gaussian distribution, this integral has to be evaluated numerically.

The acausal leakage rate can now be calculated by use of (1), a plot of the maximum acausal leakage rate per turn vs. the number of inserted idle cycles is given in Fig. 1. The synchrotron tunes are 0.04, 0.02, and 0.00072 (PEP II HER, PEP II LER, and Tevatron, resp.), the number of slices is 11. For the Tevatron, the leakage rate is completely benign even for just 1 idle cycle, resulting in near-optimal CPU utilization. For the sake of clarity, we give

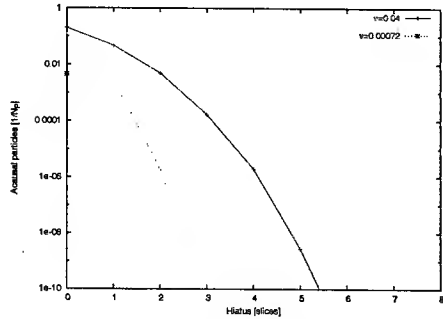


Figure 1: Acausal leakage rate for typical machines and a longitudinal decomposition into 11 slices

the wraparound algorithm in some detail for a configuration of 5 slices and a hiatus of 2. We get the following table of operations: Here, K_i stands for a kick due to slice

Table 1: Sequence of parallel operations for 5 slices and a hiatus period of 2; column number=slice number, row number=step number

0	1	2	3	4	5	6
$K_4 L$	F_0^2	$F_0^2 B_0^2$	$K_0 F_0^2$	$K_1 F_0^2$	$K_2 F_0^2$	$K_3 F_0^2$
K_3	$K_4 L F_0^2$	$F_0^2 B_0^2$	$F_0^2 B_0^2$	$K_1 F_0^2$	$K_2 F_0^2$	$K_3 F_0^2$
K_2	K_3	$K_4 L F_0^2 B_0^2$	$F_0^2 B_0^2$	$F_0^2 B_0^2$	$K_1 F_0^2$	$K_2 F_0^2$
K_1	K_2	K_3	$K_4 L F_0^2 B_0^2$	$F_0^2 B_0^2$	$K_1 F_0^2$	$K_2 F_0^2$
K_0	K_1	K_2	K_3	$K_4 L F_0^2 B_0^2$	B_0^2	1

i of the opposing bunch, K_i' for a kick due to slice i of the opposing bunch in the next IP, L for the transport to the next IP, $F(B)_i^k$ for a forward (backward) re-shuffling operation involving slices $[i, k]$ ($k(i)$ being the originating slice). Each K operator involves the transport to the appropriate encounter point and the (un)projection on/off the slice before/after the actual kicks step. Each L operator involves the transport into the IP. The sequence expects and releases the particles in completely overlapping bunches, transported into the IP. The sequence is synchronized by collective operations and leaves no collective operation open after the encounter. The B 's scope is different from the F 's: while one has to accept the occasional causality-violating particle being transported forward, causality violations for B can be avoided by transporting no further backwards than to the youngest slice in hiatus. Particles not belonging there will move out when it is that slice's turn to be originator of a backwards re-shuffling operation.

We have test-run the code on the NERSC facility; this time, we observe an almost linear behavior of the CPU time vs. CPU number (Fig. 2). Due to the much more favorable localization of particles on CPUs as opposed to the pool algorithm, a breakdown of this behavior will not set in before the most communication-intensive process, field solving, is distributed among more than 16 CPUs. Thus, for a typical slice number of 32, we expect this point to be reached for 1024 CPUs.

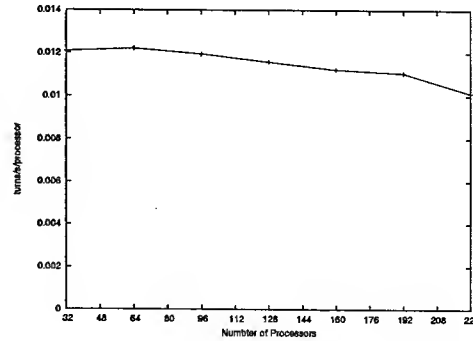


Figure 2: Scaling of a simulation run on NERSC; $n_x = n_y = 64, n_z = 16, \nu_s = 7.2 \cdot 10^{-4}$

Bunch Setup and Random Number Generation

The simulation code makes use of pseudo-random numbers during the initial setup of the particles and, in the case of electrons, for the simulation of noise induced by synchrotron radiation. The code's result have to be transparent with respect to the number of processors used; this means that initial conditions and the history of noise should be the same for a given particle, no matter what processor it is assigned to. As that assignment may change in our algorithm, a simple solution is to have each particle carry its own unique RNG. We use a 64-bit linear congruential generator, with $X_{k+1} = aX_k + p \mod m$, where a is an integer constant, $m = 2^{64}$. The generator can be made unique by choosing p the i th prime for the i th generator; this prescription will work for all particle numbers we can expect to be practically feasible.

Conclusion and Outlook

We have developed a three-dimensional strong-strong beam-beam simulation code which makes use of a novel parallelization scheme. For machines with small synchrotron tune, CPU utilization is almost optimal. The parallelization is completely transparent. We have verified the code's correctness for analytically approachable cases. We plan to use it to run precision simulation studies for PEP-II and the Tevatron.

REFERENCES

- [1] S. Tzenov T. Tajima Y. Cai, A. Chao. Simulation of the beam-beam effect in e^+e^- storage rings with a method of reduced region of mesh. *PRSTA*, 4:011001, 2001.
- [2] Y. Cai. Simulation of beam-beam effects in e^+e^- storage rings. *SLAC-PUB-8811*, 2001.
- [3] R. W. Hockney and J. W. Eastwood. *Computer Simulation Using Particles*. Institute of Physics Publishing, 1988.
- [4] M. Frigo and S. G. Johnson. Fftw: An adaptive software architecture for the fft. In *1998 ICASSP conference proceedings*, page 1381. <http://www.fftw.org>.
- [5] H. Moshhammer K. Hirata and F. Ruggiero. *Particle Accelerators*, 40:205, 1993.

CODE COMPARISON FOR SIMULATIONS OF PHOTO-INJECTORS

C.Limborg*, Y.Batygin, SLAC 2275 Sand Hill Road, Menlo Park, 94025 CA, USA

M.Boscolo, M.Ferrario, V. Fusco, C.Ronsivalle,

INFN-LNF, Via E. Fermi 40. I-00044, Frascati (Roma), Italy

L.Giannessi, M.Quattromini, ENEA Research Center Via Enrico Fermi 45, 00044 Frascati, Italy

JP.Carneiro, K.Floetmann, DESY, Notkestrasse 85, 22603 Hamburg, Germany

Abstract

RF photo-cathode injectors constitute one of the key components of many future single pass FEL based synchrotron radiation sources. The possibility of reaching very high brightness beams had been anticipated by using various simulations tools. Several experiments have proven that the 1mm.mrad normalized projected emittance for 1 nC, 10 ps pulses is within reach. For optimizing these photo-injectors, a first search of parameters is efficiently performed with HOMDYN. Further refinement in the tuning is usually obtained using a multi-particle tracking code such as ASTRA, PARMELA or BEAMPATH. In this paper, we compare results from HOMDYN, ASTRA, PARMELA, and BEAMPATH for the cases of an S-Band photo-injector. Limitations in their accuracy and differences between the codes are discussed.

1 MOTIVATION

Many codes are available for studying the dynamics of intense electron bunches at low energy in the space charge dominated regime. Newcomers in the field often ask which code to use to start studying a system based on a photo-cathode RF gun. In this paper, we compare codes which use five very different algorithms to compute the space charge: a code which solves the envelope equation HOMDYN [1], a Cloud-In-Cell (CIC) code BEAMPATH [2], a ring based algorithm PARMELA[3] and ASTRA[4], a fast Particle-In-Cell (PIC) algorithm for PARMELA spch3d and a Lienard-Wiechert potentials approach for TREDI [5]. The test problem studied consists in an S-Band RF gun, a compensation solenoid and a drift. Quantities of interest such as rms beam size, emittance bunch length could be matched for all those codes when optimal running conditions.

2 DESCRIPTION OF CODES

HOMDYN

HOMDYN relies on a multi-envelope model based on the time dependent evolution of a uniform bunch[1]. The basic approximation, in the description of the beam

dynamics, lies in the assumption that each bunch is represented by a uniformly charged cylinder whose length and radius vary, assuming a uniform charge distribution inside the bunch. The HOMDYN algorithm is very efficient and despite some strong simplifying assumptions it allows the quick relaxation of the large number of parameters involved in parameter studies, to quickly find a reasonably optimized configuration.

BEAMPATH

BEAMPATH is used for 2D and 3D simulation of axial-symmetric, quadrupole-symmetric and z-uniform beams in a channel containing RF gaps, radio-frequency quadrupoles, multipole lenses, solenoids, bending magnets, and user-defined elements. The space charge potential of the beam is calculated from the direct solution of Poisson's equation by cloud-in-cell method in a moving system of coordinates with Dirichlet boundary conditions at the aperture and periodic conditions in z-direction. Simulation of the beam with large energy spread is performed utilizing Green function method for interaction of particles with individual energies. To simulate particle emission in RF photoinjector, the code was updated by an additional space charge routine which solves Poisson's equation inside a cylindrical iron box. This approach automatically takes into account image charges arising both from injection plane and from surrounding aperture.

PARMELA / ASTRA

PARMELA and ASTRA compute the space charge force by Lorentz-transforming the particles positions and field maps into the average rest frame of the beam. It then applies static forces to the various rings of the cylindrical map assuming a constant charge density inside a ring. This algorithm requires to have at least 5 particles in each of the cell of the cylindrical grid.

PARMELA / SPCH3D

The SPCH3D algorithm of PARMELA-LANL is based on a fast Fourier Transform set on a 3D grid over which the electric field is solved to verify Poisson's equation [6]. It is quite time consuming as it requires running at least

* Contact : limborg@slac.stanford.edu.

SLAC is operated by Stanford University for the Department of Energy under contract number DE-AC03-76SF00515

100k particles and small aspect ratios of the cell dimensions. This algorithm is nevertheless necessary to be used when the aspect ratio horizontal to vertical of the beam is more than 2 and when the transverse profile does not have a cylindrical symmetry. The automated remeshing is included when using this algorithm.

TREDI

TREDI is a fully three dimensional Monte Carlo code devoted to the simulation of beam dynamics. Space charge fields can be evaluated in a point to point or point to mesh & interpolation mode, calculating the fields according to the Lienard Wiechert formalism and taking into account the effects due to the finite propagation velocity of signals. This is accomplished by storing the histories of macro-particles, and by tracking back in time the source coordinates until a retarded condition is fulfilled. Short bunch injector simulations (as the test case) can be run also in a faster "Static" mode, where instantaneous signal propagation is assumed. The "Retarded" mode allows the simulation of a wider class of problems such as CSR effects in bendings.

3 PROBLEM DESCRIPTION

The test problem consisted of simulating a S-Band gun with an emittance compensation solenoid and a drift for a 10ps square pulse, 1 mm uniform transverse laser pulse producing a 1 nC charge. No thermal emittance was included. The solenoid was set to 2.541 kG.

The first difficulty in performing such comparisons consists in implementing exactly the same maps of fields (electromagnetic for the gun field and magnetostatic for the solenoid). All of the five codes studied can translate outputs from SuperFish and Poisson. So identical maps were used. The second difficulty consists in using the same starting conditions. Each of the codes has its own launching conditions. To check that starting parameters were in agreement for all codes, we compared energy and beam sizes output for cases run without space charge. A very good overlap was obtained with the 5 codes. We could then study the single impact of the different space charge algorithms.

4 RESULTS OF COMPARISONS

Good agreement inside gun

The rms quantities beam size, emittance, bunch length and energy spread could be matched exactly for all the 5 codes inside the gun. The rms beam size obtained at the gun exit was slightly smaller with HOMDYN, see figure 1. The differences become larger in the drift which follows.

Some disagreement in drift

The local maximum in emittance around 1.5 m shows at 1.2 m in HOMDYN but around 1.5 for all the other codes, See figure 2. The first local emittance minimum is nearly

identical for the multiparticle codes and the agreement is not as good for the second minimum. The energy spread from HOMDYN is closer to that of the other codes if only the core slices are taken into account for the comparison.

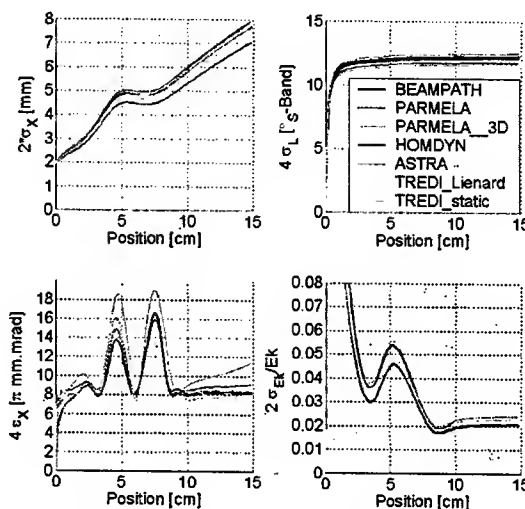


Figure 1. Comparison of evolution of rms beam size, bunch length, emittance and energy spread inside gun for the 5 codes

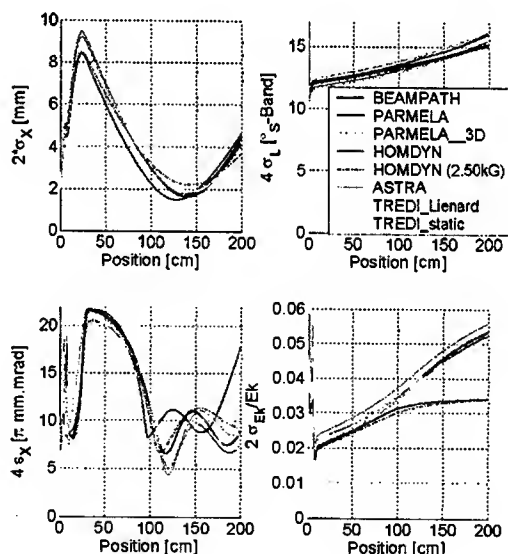


Figure 2. Comparison of evolution of rms beam size, bunch length, emittance and energy spread up to 200 cm for the 5 codes; second HOMDYN case run with solenoid reduced from 2.541kG down to 2.5 kG

5 MESHING IN TIME AND SPACE

Results depend strongly on the meshing used for the CIC code and for the SCHEFF algorithm. As a rule of thumb, each mesh should contain about 5 particles.

Table 1 – Comparison CPU time

Code	Platform	CPU	Num. particles	Mesh points $N_r \times N_z$	Mesh size $h_r \times h_z$	Integration step	CPU time (s)
HOMDYN	PC Win		75 slices			0.13°	45
BEAMPATH	PC Win	1 GHz	10^4	256 x 2048	$50 \times 50 \mu\text{m}^2$	$0.1^\circ, 1^\circ$	8000
PARMELA	"	1 GHz	$2.5 \cdot 10^4$	25 x 75	"	"	9846
" spch3d	"	1 GHz	$10 \cdot 10^4$	32 x 32 x 1024	Automatic	"	$1.4 \cdot 10^4$
ASTRA	"	1.8 GHz	$1.5 \cdot 10^4$	20 x 60	Automatic	Adaptative	420
Tredi Stat.	16 nodes	1.8 GHz	$5.0 \cdot 10^4$	20 x 30	Automatic	Adaptative	$7.5 \cdot 10^3$
Tredi Lien.	PC Win	1.8 GHz	$5.0 \cdot 10^4$	20 x 30	Automatic	Adaptative	$7.4 \cdot 10^4$

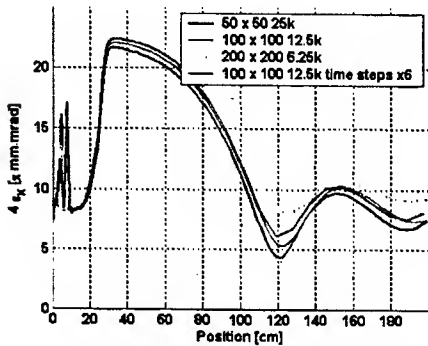


Figure 3. PARMELA results for the different meshes described in Table 2; Only the emittance varied for those 4 different cases, other parameters stayed constant

Table 2: PARMELA CPU Time on 1GHz PC

time	SPACE Mesh.	TIME Mesh.	Particles
9846 s	$50 \times 50 \mu\text{m}^2$	1100, 0.1° then 1°	25 k
1286 s	$100 \times 100 \mu\text{m}^2$	1100, 0.1° then 1°	12.5 k
445 s	$200 \times 200 \mu\text{m}^2$	1100, 0.1° then 1°	6.25 k
345 s	$100 \times 100 \mu\text{m}^2$	505, 0.2° then 1°	12.5 k

6 PHYSICS REPRESENTED

INITIAL ACCELERATION

A comparison of the dynamics between PARMELA and PIC codes [7], has shown that:

- 1- the image charge model is good enough to represent the boundary conditions at the origin
- 2- the computation of space charge forces, performed in the frame of the center of mass of the bunch in PARMELA type codes, when the Lorentz factor is small give good enough results compared with PIC or Lienard-Wiechert codes
- 3- neglecting the radial force generated from the beam self-induced azimuthal magnetic field does not affect the results

It was confirmed with BEAMPATH and TREDI that the approximation described in the second is correct. In TREDI the approximation is simply not used and BEAMPATH can perform computations using a Poisson solver for which individual energies are taken into

account. The use of this solver for the first few mm is very time consuming but did not change the results at the end of the gun.

THERMAL EMITTANCE

In each of these codes the initial distribution can be given such that a thermal emittance is included. None of the codes include the physics involved in the generation of that thermal emittance. This is one of the key issues of the RF-Cathode gun to be tackled.

SHOTTKY EFFECT

ASTRA is the only code which includes this effect.

LONGITUDINAL PROFILE

Each of the codes can include the rise and fall time of the initial pulse but HOMDYN.

TRANSVERSE NON-UNIFORMITY

When the transverse profile does not have cylindrical symmetry, only 3D space charge algorithm should be used as in TREDI or PARMELA in the spch3d mode. ASTRA is being upgraded to offer a similar possibility.

PARMELA-UCLA and PARMELA-LANL include the possibility of using 3D maps of fields. It was checked [7] that the quadrupole moment present in the S-Band gun to be used for LCLS has negligible effects in the dynamics of the beam.

REFERENCES

- [1] M.Ferrario, HOMDYN code : <http://www.slac.stanford.edu/pubs/slacpubs/8000/slac-pub-8400.html>
- [2] Y.Batygin, "Particle-in-cell code BEAMPATH for beam dynamics simulations with space charge", ISSN 1344-3877, RIKEN-AF-AC-17 (2000), 81 p.
- [3] L.Young, J.Billen, PARMELA, LANL Codes, laacg1.lanl.gov/laacg/services/parmela.html
- [4] K.Floetmann, ASTRA, http://www.desy.de/~mpyflo/Astra_dokumentation/
- [5] F. Ciocci, L. Giannessi, A. Marranca, L. Mezi, M. Quattromini, Nucl. Instr. & Meth. A 393, 434 (1997)., Web site: <http://www.tredi.enea.it>
- [6] R.Ryne et al., Proc. 1998 Linac Conf., Chicago, IL
- [7] E.Colby, et al. "Simulation Issues for RF Photoinjectors" 7th Computational Accelerator Physics Conference, Michigan State U. Oct15-18-2000

SIMULATION OF PARTICLE DYNAMICS IN ACCELERATORS USING THE ENSEMBLE MODEL*

W. Ackermann, M. Krasilnikov, T. Weiland, TEMF, TU Darmstadt, Germany
W. Beinhauer, H.-D. Gräf, A. Richter, IKP, TU Darmstadt, Germany

Abstract

In beam dynamics simulation a particle beam is usually considered as a set of numerous macroparticles. As each macroparticle is described by six phase space coordinates an enormous amount of computational effort has to be performed for accurate studies. In order to reduce simulation time an ensemble model which also considers the motion of individual particles inside the regarded subspace is introduced. This so-called ensemble model is derived from the VLASOV equation and includes the average values of the coordinates and momenta as well as the second-order correlation parameter. Therefore the number of involved particles can be reduced significantly. Based on the ensemble model the V-Code was developed to perform fast and accurate calculations for complete accelerator simulations. Its database had been initially designed for the TESLA Test Facility accelerator component description but was modified to meet also the requirements of the S-DALINAC injector simulations. In a further step the object-oriented code has been successfully extended to enable the simulation of recirculation. In this paper the results for the beam simulation at the S-DALINAC are presented.

INTRODUCTION

A large amount of single particles is required for careful examination of the beam dynamics' behavior in accelerators. Since it is impossible to handle real particles effectively so-called macro particles are to be introduced to reduce the simulation time and to save computer resources. Usually, such a macro particle is composed of numerous individual particles interacting with the external fields and consequently less NEWTON equations for the coordinates and momenta have to be solved.

ENSEMBLE MODEL

In contrast to the common stiff macro particles there is a possibility to include also the internal movements inside such a macro particle using the ensemble model [1]. Instead of solving the VLASOV equation immediately to obtain the phase distribution function f of the particle density in the space of the coordinates and momenta it is convenient to consider additionally to the first order moments

$$M_u = \langle u \rangle = \int u f d\vec{r} d\vec{p} \quad (1)$$

also second and even higher order moments in the model. The first order moments represent the corresponding values of a single particle as a whole while the second order moments

$$M_{u,v} = \langle (u - \langle u \rangle)(v - \langle v \rangle) \rangle \quad (2)$$

allow to describe the behavior of the particle distribution due to its finite dimensions. The values u and v can be any coordinates from the phase space $\{x, y, z, p_x, p_y, p_z\}$ with the normalized momentum $\vec{p} = \vec{P}/(mc)$ in cartesian components.

General Approach

To calculate the beam parameter along the beam line for its different parts it is necessary to obtain appropriate time relations for the individual ensemble parameter. If the energy spread in the particle cloud is small enough compared to the mean energy

$$\gamma_m = \sqrt{1 + \langle p_x^2 \rangle + \langle p_y^2 \rangle + \langle p_z^2 \rangle} \quad (3)$$

it is reasonable to implement a linear approximation of the encountered energy in a given operating point. Whenever the beam is exposed to forces which satisfy the condition

$$\langle \mu \operatorname{div}_{\vec{p}} \left(\frac{\vec{F}}{mc^2} \right) \rangle = 0 \quad (4)$$

for each ensemble parameter $\mu \in \{M_u, M_{u,v}\}$ it is possible to obtain the differential equations

$$\frac{\partial \langle \mu \rangle}{c \partial t} = \langle \operatorname{grad}_{\vec{r}}(\mu) \cdot \frac{\vec{p}}{\gamma} \rangle + \langle \operatorname{grad}_{\vec{p}}(\mu) \cdot \frac{\vec{F}}{mc^2} \rangle \quad (5)$$

from VLASOV equation to calculate the time-dependent ensemble parameter [2]. Starting from a given set of parameters as an initial condition it is then possible to determine the beam characteristics along the whole beam line.

Time Relations

In order to implement an algorithm based on the ensemble model it is mandatory to derive a proper time equation for each involved ensemble parameter. The available degrees of freedom are apparently linked to the maximum order of moments. For an ensemble model which utilizes the statistical values up to the second order moments to describe the beam characteristics in an accelerator substructure it is proposed to formulate the individual time relations in the following way:

* Work supported by Graduiertenkolleg 410/2
"Physik und Technik von Beschleunigern"

- coordinate relations

$$\frac{\partial M_u}{c \partial t} = \frac{p_u}{\gamma_m} - \frac{1}{\gamma_m^3} \sum_k \langle p_k \rangle M_{p_u, p_k} \quad (6)$$

- momentum relations

$$\frac{\partial M_{p_u}}{c \partial t} = \langle \frac{F_u}{mc^2} \rangle \quad (7)$$

- coordinate coordinate relations

$$\begin{aligned} \frac{\partial M_{u,v}}{c \partial t} &= \frac{1}{\gamma_m} (M_{u,p_v} + M_{v,p_u}) \\ &- \frac{\langle p_u \rangle}{\gamma_m^3} \sum_k (\langle p_k \rangle M_{v,p_k}) \\ &+ \frac{\langle p_v \rangle}{\gamma_m^3} \sum_k (\langle p_k \rangle M_{u,p_k}) \end{aligned} \quad (8)$$

- coordinate momentum relations

$$\begin{aligned} \frac{\partial M_{u,p_v}}{c \partial t} &= \frac{M_{p_u, p_v}}{\gamma_m} \\ &- \frac{\langle p_u \rangle}{\gamma_m^3} \sum_k (\langle p_k \rangle M_{p_v, p_k}) \\ &+ \langle (u - \langle u \rangle) \frac{F_v}{mc^2} \rangle \end{aligned} \quad (9)$$

- momentum momentum relations

$$\begin{aligned} \frac{\partial M_{p_u, p_v}}{c \partial t} &= \langle (p_u - \langle p_u \rangle) \frac{F_v}{mc^2} \rangle \\ &+ \langle (p_v - \langle p_v \rangle) \frac{F_u}{mc^2} \rangle \end{aligned} \quad (10)$$

These general time relations have to be applied to the different parts of the investigated accelerator structures. Special attention has to be paid to Eqs. (7,9,10) because of the ability to provide an interaction point with the essential external fields. All remaining Eqs. (6,8) are used to establish proper update relations.

V-CODE

Based on the ensemble model the simulation tool V-Code has been constructed [3]. It is organized to handle even a very long beam line with a large amount of individual beam line elements. Each element covers typical beam line properties without any interference to each other.

Beam Line Elements

So far a reliable database has been established to provide various beam line elements like cavities, drift spaces, steerers, quadrupoles, and bending magnets. Each part can be described by its geometry and by the predominant electric and magnetic field along the axes. It is possible to simulate the whole system in a step-by-step procedure. The software package had been initially designed for the TESLA Test Facility linear accelerator but was modified to meet also the requirements of a S-DALINAC injector simulation. The installed beam guiding system there allows to use the main linac several times and this emphasizes the necessity of the simulation code to handle even recirculation.

Recirculation

To illustrate the recirculating configuration of the S-DALINAC a principle layout is given in Fig. 1. It shows the injector part together with the main linac and the two established loops. The requirement to implement some modifications to the simulation code is obvious if the well proven linear approach of the program used so far is to be utilized further on.

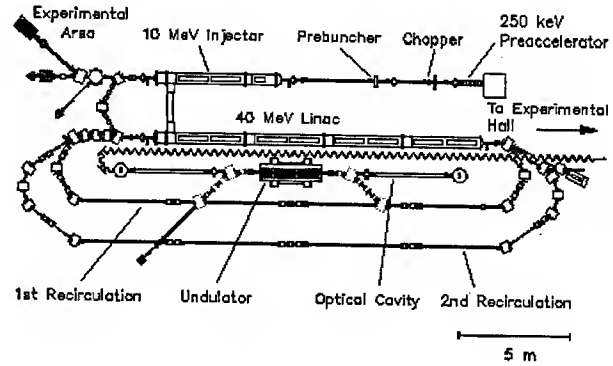


Figure 1: Layout of the S-DALINAC

Bending Magnets

The first approach to simulate a bending magnet is to assume a hard edge model with a constant magnetic flux density inside the magnet and a zero field outside. Some modifications have to be done if the effects caused by the finite extend of the fringe fields are to be also taken into account. All regarded external magnetic fields contribute to Eqs. (7,9,10) whereas the LORENTZ law $\vec{F} = \vec{v} \times \vec{B}$ acts as the only force to calculate the particular contributions:

$$\frac{\partial M_{p_u}}{c \partial t} = \vec{u} \cdot \frac{1}{mc} \langle \frac{\vec{p}}{\gamma} \rangle \times \vec{v} \quad (11)$$

$$\frac{\partial M_{u,p_v}}{c \partial t} = \vec{v} \cdot \frac{1}{mc} \langle (u - \langle u \rangle) \frac{\vec{p}}{\gamma} \rangle \times \vec{v} \quad (12)$$

$$\begin{aligned} \frac{\partial M_{p_u, p_v}}{c \partial t} &= \vec{u} \cdot \frac{1}{mc} \langle (p_v - \langle p_v \rangle) \frac{\vec{p}}{\gamma} \rangle \times \vec{v} \\ &+ \vec{v} \cdot \frac{1}{mc} \langle (p_u - \langle p_u \rangle) \frac{\vec{p}}{\gamma} \rangle \times \vec{v} \end{aligned} \quad (13)$$

Coordinate System

Originally the V-Code was created to simulate the beam dynamics in a linear accelerator. To meet the new requirements as close as possible a fixed cartesian coordinate system with its origin located in the gun of the accelerator and its z-axis oriented along the beam tube is used. Unfortunately, this approach does not fit the needs of a recirculating accelerator structure and a more convenient moving curvilinear system has to be used instead.

SIMULATION

All efforts to enable recirculating of the V-Code can concentrate on the study of the bending magnets. In order to obtain a comparison with a calculational approach entirely different from the ensemble model a usual tracking routine has been set up additionally. The obtained results refer to an ideal bending magnet with a reference path length of 0.25 m and a bending angle of 45° . Into its homogeneous field a single bunch with the kinetic energy of 10 MeV is injected along the reference path. As an additional step a second bunch is tracked with an offset of 5 mm to simulate off-axes behavior. For detailed studies a subsequent drift space of 0.25 m is attached to the magnet.

In order to implement a moving coordinate system to the simulation code two different strategies were examined:

- fixed coordinate system for simulations inside the bending magnet and a one-time rotation after a particle reaches the end of the magnet;
- moving curvilinear coordinate system with successive rotations in every simulation step.

The results for the first approach are illustrated in Fig. 2. Due to the proposed fixed coordinate system even the particles on the reference path with no offset appear to possess a non-neglecting transverse component.

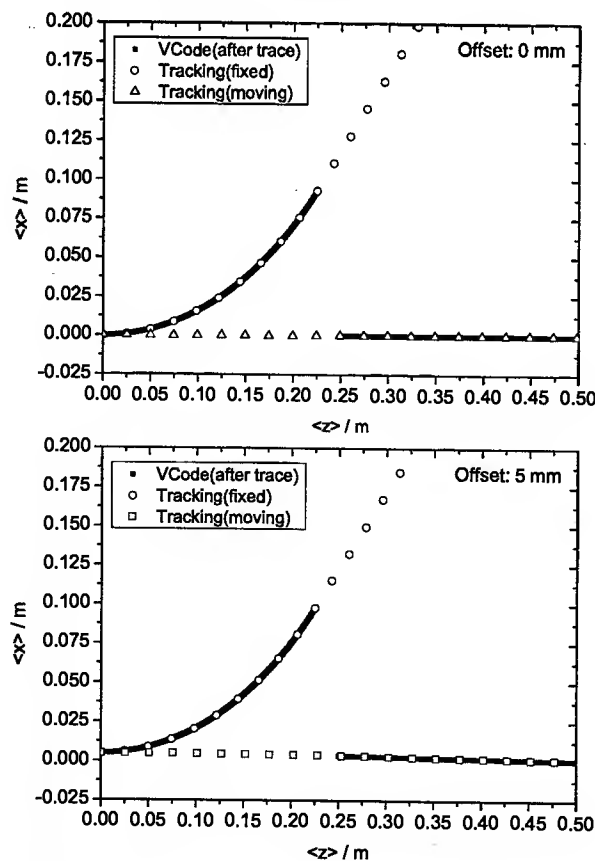


Figure 2: Beam location on a fixed coordinate system

The simulation data for the unshifted and the intentionally shifted bunch in the case of a rotated coordinate system can be seen in Fig. 3. Ultimately, if one is interested in studies related to the longitudinal and transverse behavior of the beam within the magnet it is advisable to use a moving coordinate system. The simulation data also show that the output which has been acquired on a fixed coordinate system can be regarded as intermediate results only. The necessary corrections for further usage of the data are then carried out with a one-time rotation after the ensemble reaches the end of the magnet.

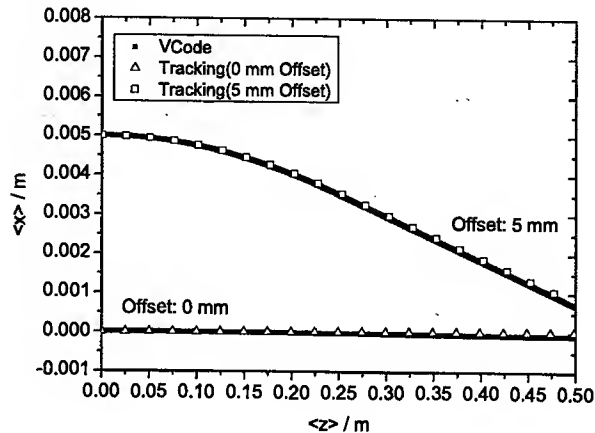


Figure 3: Beam location on a moving coordinate system

CONCLUSION

To enable the simulation of accelerator structures with V-Code with respect to recirculation the corresponding update equations for bending magnets are demonstrated. Two different possibilities to handle the rotation of the corresponding coordinate system are examined and the relevant numerical results are shown. In order to verify the results obtained by the V-Code, an additional tracking program was established. Both codes operate on the basis of a hard edge model for the bending magnet whereas no losses due to radiation are taken into account. The simulation data show that with a rotated coordinate system it is possible to unwrap the recirculating beam line configuration of the S-DALINAC and to apply the whole database from V-Code to further beam line elements beyond the injector part.

REFERENCES

- [1] A. Novokhatski and T. Weiland, "Self-consistent Model for the Beams in Accelerators", *Proc. of ICAP*, Monterey, 1998
- [2] A. Novokhatski and T. Weiland, "The Model of Ensembles for the Beam Dynamics Simulation", *Proc. of PAC1999*, New York, 1999
- [3] M. Krassilnikov, A. Novokhatski, B. Schillinger, S. Setzer, T. Weiland, W. Koch, P. Castro, "V-Code Beam Dynamics Simulation", *Proc. of ICAP2000*, Darmstadt, 2000

PERIODIC BOUNDARY CONDITIONS IN THE PARALLEL EIGENSOLVER OM3P: APPLICATION OF THE INEXACT LANCZOS PROCESS TO HERMITIAN SYSTEMS*

J. F. DeFord and B. Held, Simulation Technology & Applied Research, Inc., Mequon, WI, USA

Abstract

This paper details the development of periodic boundary condition support in the parallel finite-element eigensolver OM3P. OM3P is based on the inexact Lanczos/JOCC hybrid method, and it uses the vector-scalar (A-V) basis set that has previously been shown to dramatically reduce the computational requirements of the method. We will discuss the implementation challenges, including proper handling of problem partitioning/load balancing for periodic problems. The use of A-V basis introduces additional difficulties in the parallel domain, and we will show solutions to these problems as well omega-beta diagrams for the RDDS structure generated on a modest computer cluster using the software.

THE INEXACT LANCZOS METHOD

The shift-invert Lanczos method is a standard technique for solving the generalized eigenvalue problem

$$Ax = \lambda Bx \quad (1)$$

when the coefficient matrices are large and sparse, such as arise in eigenmode analysis of rf cavities using the finite-element method. In the standard approach, a shifted linear system is formed to facilitate the rapid convergence of eigenvalues near the shift point,

$$(A - \sigma B)^{-1} Bx = \frac{1}{\lambda - \sigma} x \quad (2)$$

and at each Lanczos step the shifted system $A - \sigma B$ must be solved to high accuracy. The shifted system is often highly ill-conditioned, leading to very poor convergence of iterative solvers such as conjugate gradient that are used for large systems that cannot be factored. Consequently, solution times can be unacceptably long even for relatively small problems.

The coupling of inexact solutions to the shifted linear system (Inexact Shift-Invert Lanczos - ISIL) followed by Jacobi Orthogonal Component Correction (JOCC) steps was proposed by Y. Sun, et al.[1], to address this problem. The method was first implemented in the Omega3P code developed at Stanford Linear Accelerator Center, and later in the OM3P solver developed by Simulation Technology & Applied Research [2]. The technique has been shown to be much faster than the traditional Lanczos process for large systems, is highly efficient on parallel computers, and has been further developed by the original authors for complex symmetric (lossy) systems. In this paper we discuss an additional extension to Hermitian systems that arise from the application of periodic boundary conditions.

PERIODIC BOUNDARY CONDITIONS

The need for periodic boundary conditions arises in the design of rf beamline cavities, where it is of interest to know the resonant behavior of a periodic (or approximately periodic) system of cavities with a specified phase advance per cell. When the phase advance is a rational fraction of 360 degrees, one can in principle obtain the desired mode by including enough cavities in the analysis. A much more computationally efficient approach is to model one cavity but enforce the requirement that the fields on the entrance and exit planes (periodic boundaries) differ only by the desired phase advance, i.e.,

$$\vec{E}|_{plane 1} = e^{-j\phi} \vec{E}|_{plane 2} \quad (3)$$

If the matrix equation obtained via the finite element method without periodic boundaries is given by (1), then the application of periodic boundaries transforms the equation as follows:

$$P^T A P x^p = \lambda P^T B P x^p \quad (4)$$

where superscript "T" indicates conjugate transpose, x^p is the subset of unknowns that excludes those that occur on one of the periodic planes (referred to as "dependent" unknowns/sources). Assuming the volume unknowns are enumerated first, followed by those on the independent periodic plane, followed by those on the dependent plane, the matrix P is given by

$$P = \begin{bmatrix} I_n & 0 \\ 0 & I_m \\ 0 & e^{-j\phi} I_m \end{bmatrix} \quad (5)$$

where $n + m$ is the total unknown count, and m is the number of unknowns on the independent periodic plane. I_m is the identity matrix of order m , and ϕ is the phase advance across the cell.

APPLICATION TO A-V FORMULATION

In finite-elements used for electromagnetics the basis set is composed of vector functions tied to specific element entities, including edges, faces, and cells (depending on the order of interpolation). Recent work [3] has shown that the addition of scalar functions that are tied to the nodes yields substantial improvements in the convergence rate of iterative solvers such as conjugate

gradient, and this approach has been implemented in OM3P. The resulting matrix equation can be written in the form

$$G^T AGx = \lambda G^T BGy \quad (6)$$

where G is very sparse (at most 3 entries per row). Converting to the periodic case yields,

$$P^T G^T AGPx = \lambda P^T G^T BGP_y \quad (7)$$

By eliminating the scalar unknowns on the periodic faces, we can interchange the order of G and P in Eqn. 7, which allows us to express the shifted form as

$$G_p^T B_p G_p x^p = \frac{1}{\lambda - \sigma} G_p^T (A_p - \sigma B_p) G_p x^p \quad (8)$$

where

$$A_p = P^T AP \quad B_p = P^T BP \quad (9)$$

and the rows of G that correspond to unknowns on the dependent periodic surface have been removed to form G_p . To improve efficiency in OM3P the A_p and B_p matrices are formed explicitly.

PERIODIC PARTITIONING

To run a problem on a parallel computer, the mesh must be partitioned into parts that can be analyzed on each process. An efficient partition is one that minimizes the amount of communication between processes as compared to the amount of computational work each process must perform. For this reason, good partitioners tend to create mesh partitions that are blocks of contiguous elements. This is not necessarily appropriate for periodic problems because the periodic planes are logically connected, even though they are physically separated in the mesh.

Fig. 1 shows the procedure used in OM3P for partitioning periodic problems. The mesh is initially distributed by sending an equal number of nodes to each process, and then sending full element support for each node set, i.e., a given process receives all elements that connect to any of the nodes that are owned by the process.

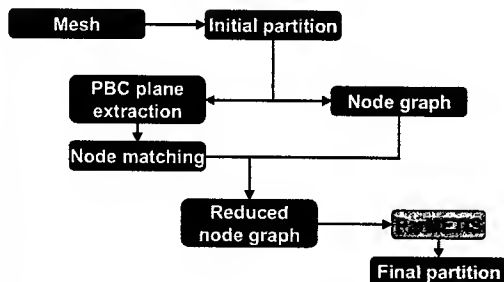


Fig. 1: Periodic partitioning flowchart.

A node graph is created from the initial partition, which is a list of nodes connected to each node via an edge.

Nodes on the independent periodic plane are then matched with the corresponding nodes on the dependent plane, and this information is used to reduce the node graph to one that excludes the nodes on the dependent surface (nodes connected to dependent nodes are connected to the corresponding independent nodes in the reduced graph). The reduced graph is used by ParMETIS [4] to create a load-balanced partition in which independent-dependent node pairs are always found on the same process. In OM3P, all of these steps (after the initial partition) occur on the distributed mesh because we assume that no one process can hold the entire mesh even for pre-assembly processing. Thus, even matching of nodes between dependent and independent planes requires inter-process communication.

A comparison of the results of this partitioning procedure as compared to the non-periodic case is illustrated in Fig. 2.



Fig. 2: Two-processor partitions for non-periodic case (left), and periodic case (right). Periodic boundary conditions were applied on the small faces on both ends of the model.

COMPUTATIONAL RESULTS

OM3P has been applied to a variety of periodic structures, with one example shown in Figs. 3-4. The ISIL-JOCC procedure works well for periodic problems formulated with the A-V basis, and we have been able to run problems with in excess of 400K elements on dual processor high-end workstations in a few minutes of cpu time. The floating-point operation count is greater by a roughly a factor of two for the periodic case because the solution vectors are now complex (the matrix is still mostly real, and since the real and imaginary parts are stored separately we incur only a small increase in storage requirements for the coefficient matrix). A modest decrease in convergence rate of the iterative solver has been observed as compared to similar cases where periodic boundaries are not present (for instance, comparing the non-periodic case to the zero phase advance case). This behavior is attributed to the elimination of scalar unknowns on the periodic faces.

CONCLUSIONS

Support for periodic boundary conditions has been implemented in OM3P. Testing indicates no significant problems in using ISIL-JOCC method on the resulting

Hermitian matrices. Some degradation in performance is seen due to elimination of scalar unknowns on periodic surfaces, and future work will re-examine this requirement.

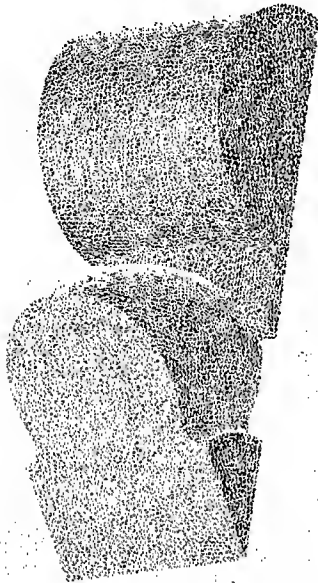


Fig. 3: 1/8 model of RDDS structure (one cell axial width). Periodic boundary conditions applied to axial faces. Approximately 400K elements.

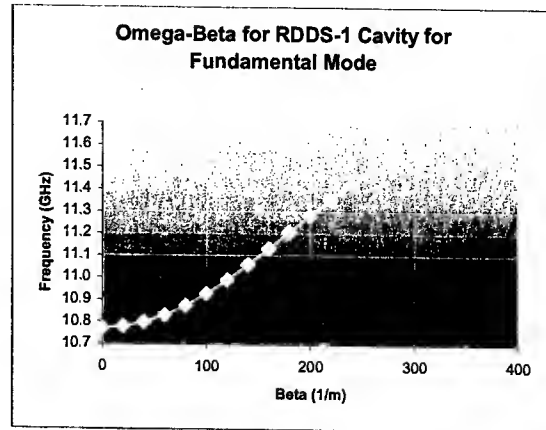


Fig. 4: Dispersion diagram for RDDS cavity.

REFERENCES

- [1] Y. Sun, N. Folwell, Z. Li, and G. Golub, "High precision accelerator cavity design using the parallel eigensolver Omega3P," *Proceedings of The Annual Review of Progress in Applied Computational Electromagnetics 2002*.
- [2] J. F. DeFord and B. Held, "Enhancements to iterative inexact Lanczos for solving computationally large finite element eigenmode problems," *Proceedings of the 2002 International Conference on Computational Accelerator Physics*, Oct. 15-18, 2002, Michigan State University, East Lansing, MI.
- [3] R. Dyczij-Edlinger, G. Peng, and J. F. Lee, "A fast vector-potential method using tangentially continuous vector finite elements," *IEEE-MTT*, **46**, June, 1998, pp.863-868.
- [4] ParMETIS is a parallel, graph-theory based, unstructured grid partitioner developed/maintained by G. Karypis, et al., at the University of Minnesota.

SIMULATION TOOLS FOR HIGH-INTENSITY RADIOGRAPHIC DIODES*

Stanley Humphries, Field Precision, Albuquerque, NM 87192 USA and
Thaddeus Orzechowski and James McCarrick, Lawrence Livermore National Laboratory,
Livermore, CA 94551 USA

Abstract

Version 6.0 of the Trak 2D ray-tracing code has new features to address simulations of intense electron beam diodes for radiography. The modifications support a program at LLNL to develop small radiographic sources for interior illumination. The application requires a pulsed electron beam (>15 kA, 30 ns, 1.2 MeV) confined to a three-dimensional focus less than 1 mm in dimension. Two key concepts make the application feasible: a magnetically-insulated transmission line for connection to the pulsed-power generator and a coaxial pinched-beam diode for axial localization of electrons. New capabilities in Trak include high-accuracy calculations of beam-generated magnetic fields with the effects of non-laminar or reflex electron orbits and current flow in the anode target. The program supports multiple space-charge emission surfaces to model effects of ion backflow. Models for electron backscatter from the tungsten target have also been implemented. Simulations indicate that the requirements can be achieved with reasonable anode/cathode gaps (>4 mm).

CRAD -- COMPACT RADIOGRAPHIC DIODE

We describe computation work in support of a project at Lawrence Livermore National Laboratory to develop pulsed X-ray sources for radiography with internal illumination. Experimental work is currently in progress at LLNL under the direction of Timothy Houck. The application requires the transport of about 20 GW of pulsed power to an electron diode over lengths greater than 1 m with a maximum available transverse dimension less than 8 cm. The diode must generate more than 15 kA of electrons at 1.2 MV with transport to a spot less than 1 mm in width. Our approach has three key components:

- an applied-field magnetically-insulated transmission line for power transport,
- a narrow anode rod for small radial spot size, and
- a diode geometry that ensures electron self-pinching to achieve a small axial spot size.

Figure 1 shows the transmission line cross-section. With an applied field of 0.6 tesla the assembly has been shown to withstand pulsed electric fields exceeding 1 MV/cm.

The computations discussed in this paper address the third issue, optimum diode geometries to ensure electron pinches at relatively high impedance (50Ω).

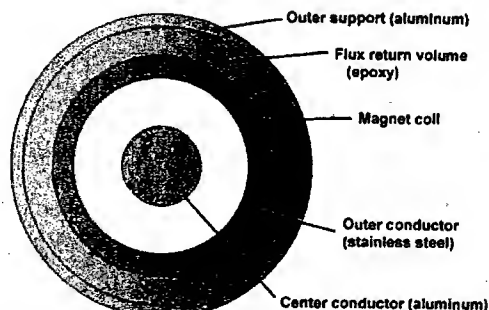


Figure 1. Magnetically-insulated transmission line, outer diameter 7.6 cm

FEATURES OF TRAK

The Trak 2D ray tracing code has been under development for over 10 years and is now in Version 6.0. Trak is an integrated package for mesh generation, electric and magnetic field solution and orbit tracking with self-consistent effects of beam fields. The programs constitute a fully interactive graphical working environment. The foundation of the codes is the application of finite-element methods on conformal meshes. The approach gives precise field calculations on material surfaces for accurate simulations of space-charge-limited and field emission. The following new features of Version 6.0 address CRAD simulation requirements:

- increased flexibility for multi-species particle generation,
- advanced methods to find the magnetic fields of relativistic beams on conformal meshes, and
- inclusion of electron backscatter from the tungsten target.

Regarding the first feature, users can now enter particle parameters manually from a list and/or request automatic generation from emission surfaces in any of the particle tracking modes. In the space-charge mode current is assigned to emission-surface particles following the Child-law prescription with the option for local source limits. An emission surface in Trak is a set of contiguous nodes on an electrode that have a unique region number. Emission facets are the boundaries between material and vacuum elements that connect the nodes. Trak automatically identifies and organizes facets and then divides them into segments associated with model particles. The code supports up to twenty emission surfaces that can each be assigned a particle species, a source limit and an angular divergence. With this

*This work was performed under the auspices of the U.S. Department of Energy by the University of California, Lawrence Livermore National Laboratory under Contract No. W-7405-Eng-48.

flexibility it is straightforward to model the space-charge-limited counter-flow of ions and electrons. Trak uses an adjustable time step for particle integration so there is no penalty for a large difference in mass.

The calculation of beam-generated magnetic fields is based on the assignment of model particle currents to element facets intersected by the orbits. Current enclosed within a node can be determined by taking an integral along facets to the axis. Current assignment on the conformal mesh preserves zero divergence of current density and unambiguously defines the sense of current with respect to the axial direction. These features are necessary to model the complex reflex orbits of electrons in a pinched beam. The program also assigns current to the source and target facets intersected by the orbits. The values are used to determine surface current flow on conducting boundaries and structures. In addition, the facet currents on the target provide a useful diagnostic of axial beam spot size.

METHODS FOR ELECTRON BACKSCATTER

In the radiography application we seek the maximum electron current for a given anode-cathode gap. Therefore current-enhancement effects from ion flow and electron backscatter are of considerable interest. The Trak code was modified to handle electron backscatter from tungsten in the energy range 0.0-1.2 MeV. The Monte Carlo radiation transport code MCNP was used to generate lookup data under the simplifying assumption that the electron emission point was close to its entrance point. We further assumed that the incident electron distribution would be almost symmetrical in azimuth with respect to the local target surface so that variations could be ignored. In this case incident electrons could be described with two parameters: kinetic energy E and $\mu = \cos(\theta)$, where θ is the polar angle with respect to the surface. Similarly, the exit electron is parametrized by E' and μ' . The total backscatter probability P_b was calculated on a 10×10 grid of (E, μ) values. We also calculated marginal probability distributions $P(E, E, \mu)$ and $P(\mu', E, \mu)$ from the coupled probability distribution with similar bins. The data were organized into a standard table format for input to Trak to facilitate future expansion of materials and energy range in the database.

Figure 2 shows how the backscatter data is applied on a conformal mesh. When an incident electron enters a tungsten element, Trak searches for the material/vacuum surface facet intersected by the orbit vector. The incident electron energy E is known while the dot product of orbit and surface normal vectors at the entrance point gives μ . The model particle current is multiplied by P_b . The program determines emission energy and direction by sampling the marginal distributions. The particle is then regenerated with energy E' and direction μ' (relative to the surface normal) at a random value of azimuth.

Electron backscatter may significantly influence current flow in a pinched beam radiation diode. Ion flow is

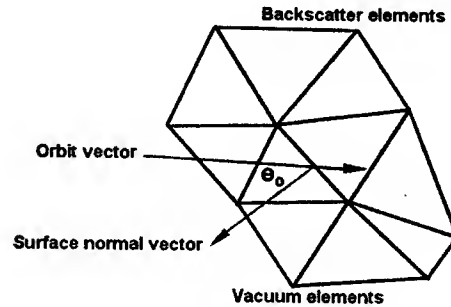


Figure 2. Representing backscatter on a conformal mesh

necessary to support a pinch — the negative space charge of backscattered electrons enhances the flux of ions emitted from the target. Figure 3 shows Trak results for a planar diode (1.0 cm gap, 1.2 MV applied potential) with a tungsten anode. The variation of electric field across the gap is plotted for four cases: 1) bare electrons, 2) electrons and ions, 3) electrons and backscattered electrons and 4) incident and backscattered electrons with ion flow. The presence of ions in the relativistic diode gives an electron-current enhancement factor of 1.96. Without ions the inclusion of the space charge of backscattered electrons gives a suppression factor of 0.85. In contrast, with the feedback mechanism of ion flow the presence of backscattered electrons gives an incident electron current enhancement of 2.89.

NESTED COAXIAL DIODE SIMULATIONS

In the small radiographic diode the goal is to generate high current within the constraints of a practical geometry. The anode-cathode gap must be large enough to avoid plasma closure and to allow latitude for alignment errors. Alignment is a concern because the anode is attached to the cantilevered center-conductor of the magnetically-insulated transmission line. It is also desirable that the diode operates consistently for two or more shots. This feature would allow at least one test shot for a setup. Because the deposited energy density at the anode tip (>10 MJ/kg) is sufficient to vaporize tungsten, the diode design must be tolerant to changes in the anode length.

We studied several cathode configurations for a fixed anode diameter of 1 mm. A hemispherical cathode gave promising results but had several drawbacks. The part required some fabrication effort and the diode performance was sensitive to the relative axial position of the anode tip. Figure 4 shows our present baseline design, the nested coaxial diode. Here the cathode is a thin cylinder of light metal to minimize X-ray attenuation, and there is significant cathode/anode overlap (~ 5 mm). With the correct choice of cathode radius, electron flow is dominated by magnetic pinching effects creating an anode spot less than 1 mm in length independent of the overlap.

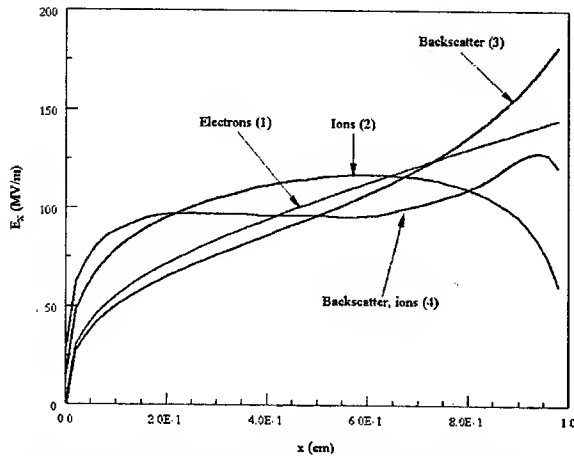


Figure 3. Variation of electric field in a planar diode with incident electrons, ions and backscattered electrons.

In Trak simulations of diode performance a space-charge-limited electron flux was initiated over an extended section of the cathode interior and edge. Ions were emitted from a 2.0 mm length of the anode near the tip. Regarding the origin of the ions, plasma generation is inevitable at the energy densities involved. On the other hand, the plasma initiation time and the ion transit time (3 ns for W^D) may delay the onset of a pinch. It may be necessary to coat the anode with light-ion contaminants. Note that the steady-state simulation results are independent of ion mass.

Table 1 shows scaling of diode behaviour with cathode/anode overlap for a cathode inner-diameter of 10.0 mm and 1.2 MV applied voltage. Electron orbits and variations of the beam-generated magnetic field are shown in Fig. 4. We can draw several conclusions:

1) Even though the overlap and the effective area of the diode varies by a large factor, the total current remains almost constant. The implication is that electron flow in the diode is dominated by magnetic pinch effects.

2) The current initially rises with increasing overlap and then falls. The decrease reflects the fact that ion emission is limited to a small region near the anode tip. At high overlap the ion spray does cover the region of enhanced electric field at the cathode edge.

3) Axial localization of electron deposition improves with both increasing overlap and increasing total current.

4) At 1.2 MV, the critical pinching current in the coaxial diode is about 17 kA.

Table 2 shows results from a set of runs with large anode/cathode overlap (-6.0 mm) as a function of cathode inner diameter. The results have the following implications:

1) The total current does not follow the simple diode scaling with current approximately proportional to the inverse of the square of the gap width. This law predicts that current should increase by a factor 2.25 as the cathode diameter changes from 12.0 mm to 8.0 mm. The simulations show an increase by a factor of only 1.2.

2) Although the change in current with decreasing radius is small, the difference in magnetic pinching force is sufficient to change the electron focal properties substantially. The electron deposition length on the anode drops by a factor of 3.3 at the smaller radius.

In conclusion, the simulations indicate that the nested coaxial diode with a cathode radius $\square 10.0$ mm can generate high currents if anode ion generation occurs quickly. The current levels observed (18 kA) are approximately matched to the pulsed-power generator and magnetically-insulated transmission line. At high current electron motion is dominated by magnetic pinching and the axial spot size is less than 1 mm in length.

Table 1. Diode variation with axial overlap

A/K overlap (mm)	I (ka)	Axial size (mm)
0.0	16.58	2.73
1.0	16.16	1.83
2.0	17.19	1.13
3.0	17.29	0.73
4.0	16.67	0.63
5.0	16.52	1.83

Table 2. Diode variation with cathode radius

Cathode radius (mm)	I (kA)	Axial size (mm)
6.0	15.19	2.44
5.0	16.14	1.63
4.0	18.17	0.73

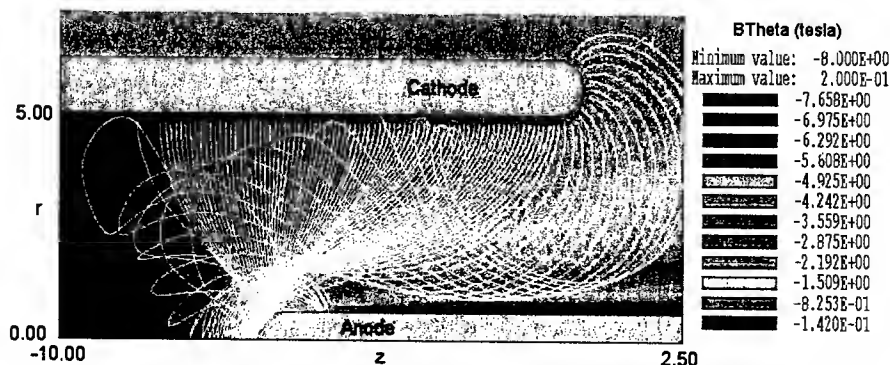


Figure 4. Electron orbits and beam-generated magnetic field in the nested coaxial diode.

DEVELOPMENT OF 3D FINITE-ELEMENT CHARGED-PARTICLE CODE WITH ADAPTIVE MESHING

L. Ives, T. Bui, W. Vogler, Calabazas Creek Research, Inc., Saratoga, USA

Mark Shephard, Debyendu Datta, Scientific Computational Research Center, Rensselaer Polytechnic Institute, NY

Abstract

A number of new RF sources are in development that require complex analysis of steady-state, charged particle trajectories. A few codes are currently available; however, they are difficult to use and place severe demands on computational resources. A new program is nearing completion that addresses issues of problem setup and significantly reduce the computational requirements. In particular, the code accepts geometrical input from standard CAD of solid modeling programs, provides an intuitive graphical user interface for attribute assignment, and requires no user setup of the computational mesh. Meshing is fully automatic and adaptive. The mesh adaptation dramatically reduces the size of the computational problems, often by three orders of magnitude, while maintaining or increasing the accuracy over conventional fixed mesh codes. The program includes both electrostatic and magnetostatic field solvers and a fully relativistic particle pusher. The code is intended for engineers and scientist involved in design of the next generation of complex, 3D, charged particle devices.

INTRODUCTION

Calabazas Creek Research, Inc. (CCR), in coöperation with the Scientific Computational Research Center (SCOREC) at Rensselaer Polytechnic Institute, and Simmetrix, Inc., is completing development of a 3D, finite element, adaptive mesh program for designing electron guns, collectors, and other charged particle devices. The program is called *Beam Optics Analysis* (BOA) and includes an intuitive, user-friendly, graphical user interface (GUI) and integral, 3D, magnetostatic solver. The adaptive meshing eliminates requirements for user input of mesh information, dramatically simplifying problem setup, especially for 3D problems. The adaptive meshing also reduces the number of nodes to the minimum necessary for problem solution, significantly reducing the computational requirements and problem execution time.

PROGRAM STRUCTURE

The GUI provides input of geometrical information from any program that outputs ACIS or ParaSolid formatted files, which includes most all commercially available CAD programs. The geometrical information is transferred to a display program for assignment of attributes to objects and surfaces. Typical attributes

include voltages, emission surfaces, and material properties. Material properties include conductivity, dielectric properties, work function, secondary emission properties, and magnetic properties. For emitters, the user will be able to input work function and temperature information. Future versions will allow variation of these parameters across the emitting surface. Properties for commonly used materials will be built into the GUI. Prototype GUI screens are shown in Figure 1.

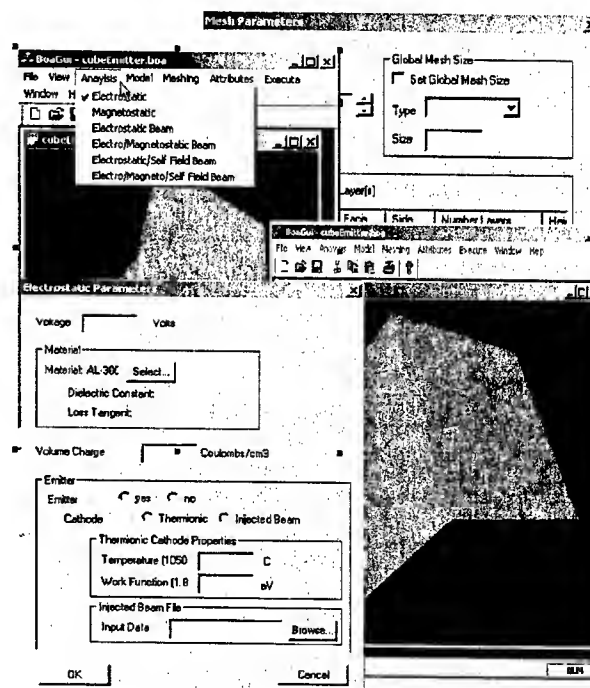


Figure 1. Prototype GUI screens in BOA

Once the attribute information is assigned, the user inputs programmatic information, including the accuracy requirements, number of iterations, and convergence criteria. The program will also have a restart capability. Upon initiation of program execution, the geometrical information is transferred to *MeshSim*, the mesh generator, which creates the initial mesh based on user and geometrical information. A simple example is a charged cylinder in a square box, shown Figures 1 & 2.

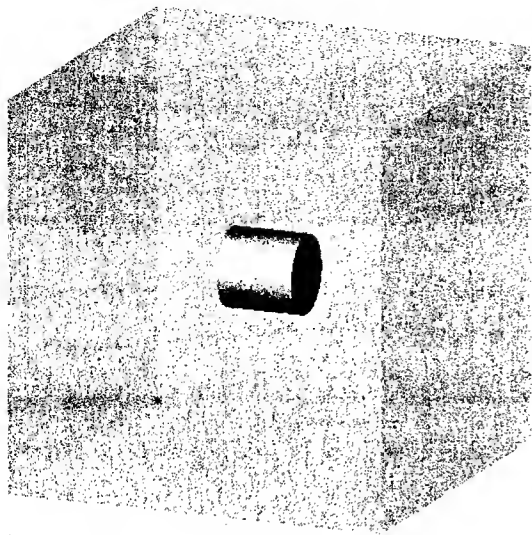


Figure 2. Single cylinder in a box

The initial mesh is used to solve Laplace's Equation throughout the region preparatory to emitting electrons and solving Poisson's Equation. For the example problem, electrons are emitted from the left boundary and accelerated to the right. As the problem evolves, the mesh is adapted based on the electric field values and the space charge of the electrons. Figure 3 displays the initial mesh and the final mesh for the sample problem. In addition to refining the mesh in regions with high electric field gradients and space charge, the element density is reduced where the accuracy criteria is exceeded, such as at the problem boundaries. Consequently, the number of elements is reduced to the minimum necessary to solve the problem. For the sample problem, the number of initial elements was 1641, and the final iteration contained 2690, despite the fact that the element density at the central cylinder increased by more than one order of magnitude. Equivalent accuracy with a fixed mesh code would require more than 55,000 elements, approximately 20 times the number required by BOA.

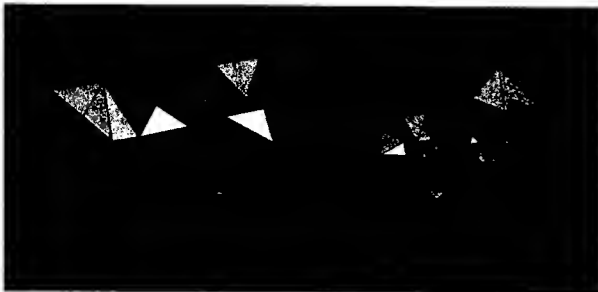


Figure 3. For the example problem, the initial mesh is shown on the left and the final mesh is shown on the right. These are slices through the tetrahedral mesh perpendicular to the direction of electron emission.

The trajectories for the sample problem are plotted in Figure 4. The BOA results are being compared with analytical problems to verify the accuracy and optimize the performance. The GUI is also being completed to facilitate generation of input data and provide post processing. Problem setup is being tested with AutoCAD and SolidWorks.

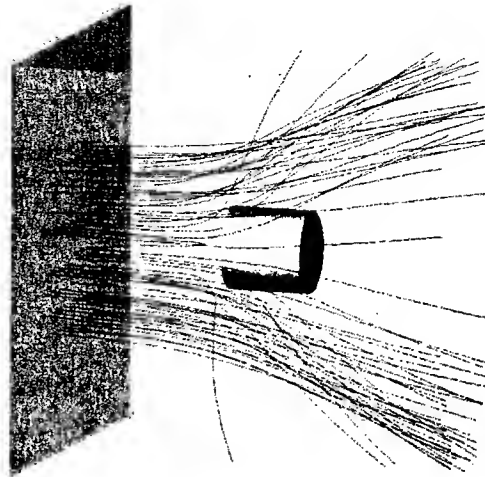


Figure 4. Electron trajectories for sample problem.

The program includes an integral, 3D, magnetostatic solver. This allows design of the magnetic circuit in parallel with the electrostatic configuration and eliminates import of magnetic field information from other 3D programs, though the code will have capability to import field information from Maxwell 3D and MAFIA. Calculation of self magnetic fields is included.

Development of the magnetostatic solver required considerable effort, including development of a new class of tetrahedral element to allow precise matching of boundary conditions across element faces. This was a joint development between CCR and researchers at SCOREC. Information on the components and performance of BOA will be presented. The magnetostatic solver is currently undergoing final testing. A comparison with theoretical results is shown in Figure 5 for a sample case.

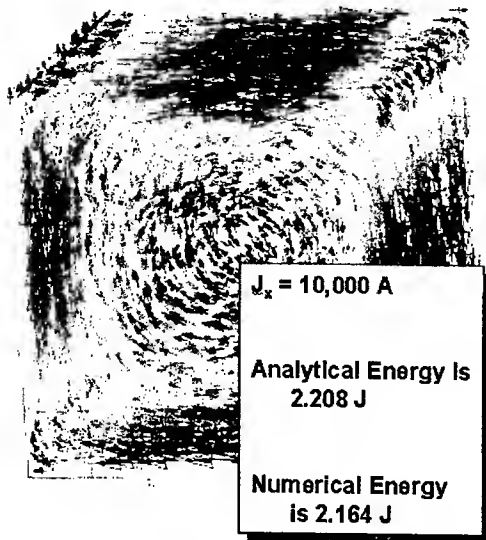


Figure 5. Sample test results for simple magnetostatic problem

FUTURE DEVELOPMENTS

Following completion of the basic code, a number of enhancements are planned. These include:

- parallel processing,
- secondary electron emission,
- performance optimization
- enhanced post processing,
- template generation.

Additional features will be incorporated as suggested by users.

SUMMARY

An advanced 3D trajectory code with adaptive meshing is undergoing final testing. The program accepts geometrical input from standard CAD programs with parametric input from a user-friendly, intuitive, graphical user interface. With adaptive meshing, no user input is required for the mesh. The initial mesh is generated automatically, then coarsened or refined based on the computational results. This minimizes the computational requirement and allows analysis of complex, 3D problems on common personal computers.

ACKNOWLEDGEMENTS

This research is funded by U.S. Department of Energy Grant No. DE-FG03-00ER82966.

CONFORMAL MODELING OF SPACE-CHARGE-LIMITED EMISSION FROM CURVED BOUNDARIES IN PARTICLE SIMULATIONS

E. Gjonaj, T. Lau* and T. Weiland,

Darmstadt University of Technology, TEMF, Schloßgartenstr. 8, D-64289, Darmstadt, Germany

Abstract

The reliability of Particle-In-Cell simulations depends on the accuracy of field and charge characterization at emission boundaries. In this work a novel approach to the modeling of curved emission boundaries in 3D-PIC simulations is presented. The method uses a boundary-conformal discretization for the electrostatic field equations, based on the orthogonal grid formulation of the Finite Integration Technique [1]. It also implements a consistent procedure for injecting particles at arbitrarily curved emission surfaces. The efficiency of the method is shown in 3D-simulations for the space-charge-limited emission in a Pierce gun model.

INTRODUCTION

Motivation

Electromagnetic PIC codes are commonly used for investigating the physics of charged particles in accelerators. A typical PIC simulation consists of a coupled computation of the dynamic particle equations and of the electromagnetic field solution on a computational grid. Among several techniques used for the solution of the field equations, the FD, FDTD and FIT applied on orthogonal, spatially staggered grids are the most popular. This is due to the capability of orthogonal grids of efficiently handling large to huge problems, and to the simplicity of the underlying data structure and implementation. However, the modeling of geometries with curved material boundaries on orthogonal grids, poses principal difficulties in maintaining solution accuracy close to such boundaries. The often used staircase approximation introduces large discretization errors, even when the grid size is very small. The low accuracy of boundary fields at curved emission surfaces strongly affects the overall performance of PIC simulations in two more particular ways. First, the local space-charge-limited emission model will predict inaccurate emission currents at staircase boundaries. Second, the large number of grid nodes needed for resolving geometry details leads to serious restrictions on the time step used in the simulation. This paper introduces a boundary-conformal approach to 3D-PIC simulations which retains the advantages of orthogonal grid modeling while providing accurate solutions for arbitrarily curved emission boundaries.

Mathematical Model

The model equations considered, consist of the set of equations of motion for N computational particles,

$$\frac{d\mathbf{r}_i}{dt} = \mathbf{v}_i, \quad \frac{dm_e \mathbf{v}_i}{dt} = e(\mathbf{E} + \mathbf{v}_i \times \mathbf{B}), \quad (1)$$

with $i = 1 \dots N$, where e is the electron charge, m_e is the relativistic electron mass; particle positions and velocities are given by \mathbf{r}_i and \mathbf{v}_i , respectively. Assuming only electrostatic particle-particle interactions the space-charge field \mathbf{E} is obtained by

$$\nabla(\epsilon \mathbf{E}) = \frac{1}{\epsilon_0} \sum_i^N q_i \delta(\mathbf{r} - \mathbf{r}_i), \quad \mathbf{E} = -\nabla\varphi, \quad (2)$$

where ϵ is the material dielectric constant and q_i the charge carried by the i -th particle.

The set of equations (1,2) is completed by specifying boundary conditions for the electrostatic potential φ , and initial conditions for the particle positions \mathbf{r}_i and velocities \mathbf{v}_i . In the case of space-charge-limited emission particle initial conditions can be derived by locally applying the Child-Langmuir diode equation [2],

$$J_{CL} = \left(\frac{4\epsilon_0}{9} \right) \sqrt{\frac{2e}{m_e}} \frac{\delta\varphi_b^{3/2}}{\delta d^2}, \quad (3)$$

where J_{CL} is the current at the emission surface, and $\delta\varphi_b$ denotes the local potential difference at a small distance δd from the emission surface. Thus, the space-charge-limited emission condition is completely determined by the electrostatic potential solution obtained in (2).

CONFORMAL METHOD

Discrete Field Equations

Equations (2) are discretized in space using the Finite Integration Technique (FIT) [1]. This technique uses an orthogonal doublet of staggered grids, with grid potential values Φ_i defined on the primary grid nodes (cf. Fig. 1).

Denoting, $\vec{\mathbf{d}} = (\vec{\mathbf{d}}_1, \vec{\mathbf{d}}_2, \dots)^T$ the vector of electrostatic fluxes through each of the elementary facets of the dual cells, the discrete equations counterpart to (2) read,

$$\mathbf{S}\vec{\mathbf{d}} = \mathbf{q}, \quad \vec{\mathbf{d}}_i = \iint_{\Delta A_i} \epsilon(\nabla\varphi) d\mathbf{A}, \quad (4)$$

where \mathbf{S} is the discrete div-operator, \mathbf{q} is the vector of total charge contained in each of the dual cells and ΔA_i is the area element corresponding to the i -th dual cell facet.

*lau@temf.de

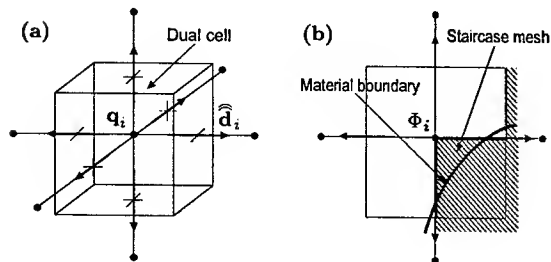


Figure 1: (a) Primary grid and a dual cell in the FIT. (b) Staircase vs. conformal discretization.

Equations (3) are the *exact* representation of (2) in terms of the finite fluxes \bar{d}_i . A discretization error arises first, when the flux integrals \bar{d}_i are approximated using potential grid values Φ_i . The conformal approach used in this paper for evaluating the flux integrals was first proposed for high frequency applications [3]. It minimizes the discretization error by taking into account the geometry of the material boundary within inhomogeneously filled cells containing curved material transitions (cf. Fig. 1b). In contrast to the staircase approximation, the conformal method requires no additional mesh refinement at curved boundaries, because subcellular material information is already contained in the formulation.

Particle Injection

Injecting computational particles at emission boundaries involves a) identifying appropriate geometrical samples for the initial particle positions and b) determining charge and velocity values for the emitted particles, which are consistent to the emission current (3).

In this implementation, the first step is realized by means of a triangular mesh of specified size which is generated on the emission surface. Then, static emission samples are located at the triangle barycenters. The algorithm selects all or a random part of these samples, assigning their positions to the emitted particles. In this procedure, uniform as well as locally refined distributions for the particle initial positions (e.g., at sharp emission tips) are obtained.

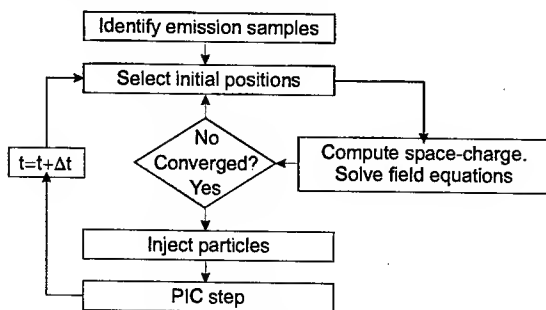


Figure 2: Simulation flow chart with particle injection.

The second task is to compute the charge carried by the emitted particles according to the space-charge-limited

emission model. For this purpose, a small constant distance span δd from the emission samples in the direction normal to the source surface is introduced. This allows of determining local currents (3) associated to the emitted particles. The consistency between the computed currents and the field solution is enforced by performing a fixed point iteration as shown in the flow chart of Fig. 2. Here, the particle charges predicted by (3) are assigned to the grid during each iteration using a Cloud-In-Cell (CIC) interpolation scheme [4]. The resulting field equations (4) are repeatedly solved until no additional charge can be extracted from the source surface, i.e., a consistent emission current is established.

RESULTS

In order to demonstrate the performance of the method, test simulations for a Pierce gun model are performed. The fully 3D-model of the gun [5] contains a spherical Dispenser-cathode with Os-coating (M-type), anode and focus electrode with specific parameters listed in Table 1. Additionally, a focusing, static magnetic field of strength 90mT on the gun axes was externally computed with the commercial simulation package CST EM StudioTM [6] and loaded into the simulations.

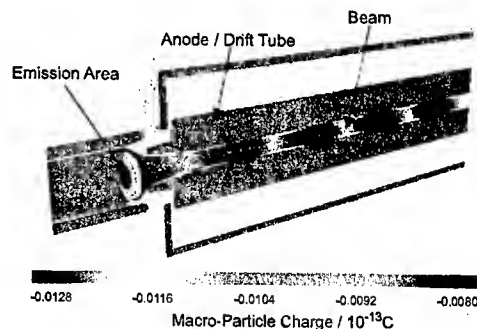


Figure 3: Geometry of the Pierce gun and simulated beam.

Figure 3 shows the geometrical gun arrangement and the simulated electron beam 2.5 ns after the beginning of the emission process. A total of 1.5 mio. computational particles were used in the simulation, corresponding to an average of 3.000 particles per time step, injected into the emission area according to the above procedure. The beam envelope develops transversal oscillations, which are due to a slight mismatch between accelerating voltage the focusing magnetic field [5]. The computed charge distribution and potential along the gun axes are shown in Fig. 4.

Table 1: Pierce Gun Parameters [7]

Voltage	90kV	Cathode disc radius	33.1 mm
Convergence angle	37.15°	Anode disc radius	16.8 mm
Anode angle	47.0°	Focus angle	45.0°
Waist distance	62.0 mm	Waist radius	8.0 mm

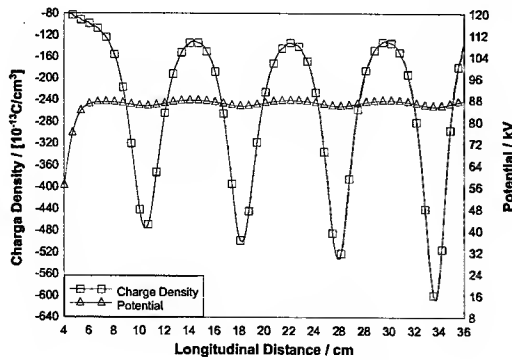


Figure 4: Charge density and potential on the gun axes.

The main result of this investigation is illustrated in Fig. 5–6. The steady state emission current is monitored on the source surface using several discrete models of different mesh resolutions. The numerical convergence of simulations using the staircase approximation is shown in Fig. 5. In this case, the relative error obtained for fine to moderate mesh sizes varies between 10–25%. Only at the very fine discretization of 1.5 mio. mesh nodes, the emission current approaches the correct curve. Despite the slow convergence, the staircase models introduce numerical oscillations in the current curves, resulting from the low order field approximation at the emission surface.

Figure 6 shows the simulation results using the conformal method. The emission current curves do already converge at the lowest mesh resolution. For emission dominated problems, the high accuracy of the conformal method implies better numerical performance. Recalling the solution algorithm shown in Fig. 2, a consistent modeling of space-charge-limited emission requires several solutions of the grid-field-equations (4) at every time step; the number of iterations depending on the share of space-charge-fields in the total particle forces. The computational effort for the solution of these equations, typically involving an iterative solver, can therefore be reduced by using the conformal model, since the number of mesh nodes can be decreased without accuracy loss. Note also, that using larger cell sizes in conformal models, improves the stability bounds imposed on the explicit integration of (1). This issue, however, will be discussed in a forthcoming publication.

CONCLUSIONS

The conformal method for the modeling of space-charge-limited emission from curved surfaces is based on a) a boundary conformal discretization of the electrostatic field equations and b) on a boundary conformal technique for particle injection at emission time. The method enforces the field-space-charge consistency implied by Child's law, by iterating the field solution equations until a consistent current is established.

The numerical simulation of a Pierce gun model shows that the conformal method is considerably superior to the

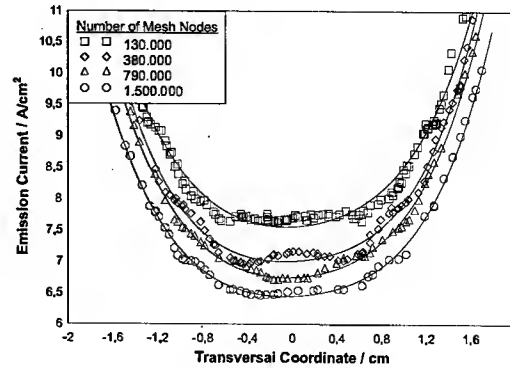


Figure 5: Emission currents on the source surface using staircase modeling.

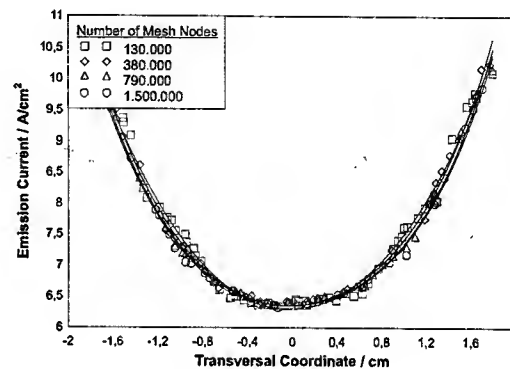


Figure 6: Emission currents on the source surface using the conformal method.

staircase approximation. In the presented simulation, the fast numerical convergence of the method allows of reducing the number of mesh nodes by at least 10 times compared to the staircase simulation.

REFERENCES

- [1] T. Weiland, "A discretization method for the Solution of Maxwell's Equations for Six-Component Fields", *Electronics and Communication (AEÜ)*, Vol. 31, 116 (1977)
- [2] C.D. Child, "Discharge from Hot CaO", *Phys. Rev.* **32**, 492 (1911). I. Langmuir, "The Effect of Space Charge and Residual Gases on Thermionic Currents in High Vacuum", *Phys. Rev.* **2**, 450 (1913).
- [3] B. Krietenstein, P. Thoma, R. Schuhmann, and T. Weiland, "Facing the big challenge of high precision field computation", in *Proc. 19th LINAC Conf.*, Chicago, IL, August 1998.
- [4] C.K. Birdsall, D. Fuss, "Clouds-in-Clouds, Clouds-in-Cells Physics for Many-Body Plasma Simulations", *J. Comp. Phys.* **135**, 141 (1997)
- [5] S. Setzer, private communications, Darmstadt University of Technology, TEMF, Darmstadt, Germany (2003)
- [6] CST EM StudioTM, "User's Guide", Bädingerstr. 2a, D-64289 Darmstadt, Germany
- [7] J. Rodney, M. Vaughan, "Synthesis of the Pierce Gun", *IEEE Trans. on Electron Devices*, Vol. Ed-28, No. 1, 37 (1981)

SIMULATION OF DARK CURRENTS IN A FEL RF-GUN*

S. Setzer[§], W. Ackermann, T. Weiland, Technische Universität Darmstadt
M. Krasilnikov, PITZ, DESY-Zeuthen

Abstract

Dark currents caused by field emission are dramatically limiting the lifetime of photocathodes used in RF-guns needed for successful FEL operation. Due to the mismatch of the dark current electrons to the transport channel they are also a serious hazard to beam diagnostic systems and may cause severe radiation damage. In the past high dark currents emitted from the laser driven RF-guns have been observed during substantial time of linac operation. For a better understanding of the dark current dynamics the transport through the injector part of the PITZ accelerator has been investigated with the help of an appropriate tracking algorithm. Additionally, potential emission spots inside the rf-gun have been located by RF field mapping. Furthermore, the dependency of the dark current on the accelerating field inside the RF-gun as well as on the strength of the focusing solenoid has been studied.

INTRODUCTION

For the successful operation of future linear colliders as well as free electron lasers the generation of a low emittance electron beam with bunch charges is of fundamental importance. Therefore rf-guns employing laser driven photocathodes are used as particle sources. The main contribution to the beam emittance is caused by space charge dominated processes in the vicinity of the cathode [1]. To minimize these effects, high accelerating gradients are favorable, resulting in large amplitudes of the electric field inside the rf-gun which benefits the generation of dark currents. The dark current density for a specific electric field on a metallic surface can be calculated from the well known FOWLER-NORDHEIM equation [2]

$$j = \frac{1.54 \cdot 10^{-6} \cdot 10^{4.52\phi^{-0.5}} (\beta E)^2}{\phi} \exp\left(-\frac{k\phi^{1.5}}{\beta E}\right), \quad (1)$$

where $k = 6.53 \cdot 10^9$ and ϕ corresponds to the work function of the metal in eV. Due to geometrical imperfections of the metal surface, the electric field is enhanced by a factor β . Usually only the time averaged dark current of an rf driven structure is measured. In this case equation (1) has to be slightly modified:

$$\bar{j} = \frac{5.7 \cdot 10^{-12} \cdot 10^{4.52\phi^{-0.5}} (\beta E)^{2.5}}{\phi^{1.75}} \exp\left(-\frac{k\phi^{1.5}}{\beta E}\right). \quad (2)$$

* Work supported in part by DESY
[§] setzer@temf.de

In an actual measurement of the dark current only the electrons leaving the structure are taken into account. To gain better insight into the dark current dynamics inside the complete structure a numerical tracking method has to be applied.

TRACKING ALGORITHM

For the tracking of the dark current electrons a fast and efficient three dimensional leap-frog algorithm, being second order accurate, has been implemented [3]. Based on the equations of motion

$$\frac{\partial \vec{u}}{\partial t} = \frac{q}{m_0 c} (\vec{E} + \vec{v} \times \vec{B}) \quad (3)$$

$$\frac{\partial \vec{x}}{\partial t} = \vec{v} \quad (4)$$

$$\vec{u} = \frac{m\vec{v}}{m_0 c} = \gamma \vec{\beta} \quad (5)$$

the discrete time integration scheme

$$\vec{u}^{n+1} = \vec{u}^n + \Delta t \frac{q}{m_0 c} (\vec{E}^{n+1/2} + \vec{v}^{n+1/2} \times \vec{B}^{n+1/2}) \quad (6)$$

$$\vec{x}^{n+3/2} = \vec{x}^{n+1/2} + \Delta t \frac{c}{\gamma^{n+1}} \vec{u}^{n+1} \quad (7)$$

can be derived. To avoid an implicit formulation in equation (6), an explicit approximation is introduced [4]:

$$\vec{u}^- = \vec{u}^n + 0.5 \Delta t \frac{q}{m_0 c} \vec{E}^{n+1/2} \quad (8)$$

$$\vec{u}^* = \vec{u}^- + \vec{u}^- \times \vec{T} \quad (9)$$

$$\vec{u}^+ = \vec{u}^- + \vec{u}^* \times \vec{S} \quad (10)$$

$$\vec{u}^{n+1} = \vec{u}^+ + 0.5 \Delta t \frac{q}{m_0 c} \vec{E}^{n+1/2} \quad (11)$$

where

$$\vec{T} = \Delta t \frac{q \vec{B}^{n+1/2}}{2 m_0 \gamma^{n+1/2}}, \quad (12)$$

$$\vec{S} = \frac{2 \vec{T}}{1 + |\vec{T}|^2}, \quad (13)$$

$$\gamma^{n+1/2} = \sqrt{1 + |\vec{u}^-|^2}. \quad (14)$$

The charges of the individual particles used for the tracking are adjusted individually according to equation (1) for a given field enhancement factor β .

SIMULATION RESULTS

The dark current tracking algorithm has been applied to the normal conducting rf-gun operated at 1.3 GHz which is installed at DESY Zeuthen (PITZ). The electromagnetic fields of the accelerating mode inside the complete gun cavity as well as the external static magnetic fields have been calculated with the help of the electromagnetic simulation package MAFIA [5]. The rf-gun is capable of providing accelerating fields on the cathode of up to 40 MV/m. To minimize the resulting beam emittance a solenoid based emittance compensation scheme is applied [6]. The maximum of the magnetic flux density is located at $z = 27.85$ cm with respect to the cathode. Additionally, a bucking coil ensures that the magnetic flux density vanishes at the cathode. The absolute value of the accelerating electric field distribution inside the rf-gun is shown in fig. 1. Inside the gun cavity

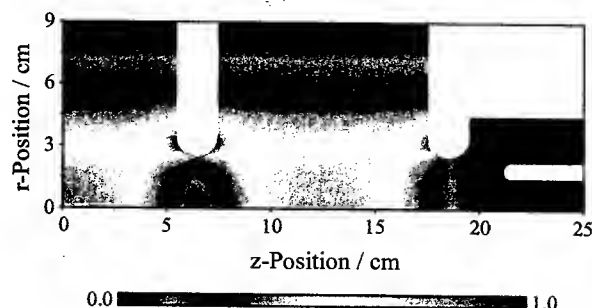


Figure 1: Normalized absolute value of the accelerating electric field inside the rf-gun.

areas of high electric fields are located at the irises. The results of a tracking simulation for particles starting at the iris are depicted in fig. 2. The maximal electric field on the cathode was set to 30 MV/m and a magnetic flux density of 100 mT has been applied while the particles are started at arbitrary phases and positions.

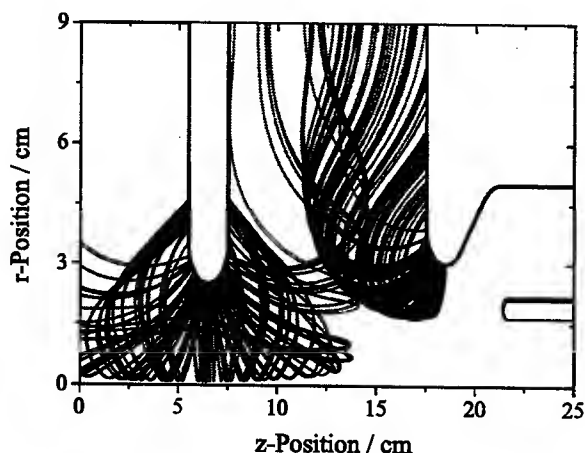


Figure 2: Trajectories of dark current electrons starting at the irises for an accelerating field of 30 MV/m on the cathode and a maximal magnetic flux density of 100 mT.

The trajectories of the dark current electrons originated at the irises reveal that those particles can not leave the rf-gun and therefore do not contribute to the dark current measurements taken at a longitudinal position of $z = 79$ cm with respect to the cathode. Additionally, the kinetic energy of the particles hitting the rf-gun structure is greater than several tens of keV. This is why they are a potential hazard to the Cs_2Te cathode. Due to the high impact energy the secondary electron emission yield is very low, therefore the generation of secondary electrons is neglected in the presented studies. Only particles starting at the cathode (16 mm diameter) can leave the rf-gun close to the axis. This coincides with the fact that the measured dark current is reduced by a factor of 2.5 if the Cs_2Te cathode is exchanged with a molybdenum dummy [7]. Additionally, there is a strong dependency of the dark current on the strength of the external magnetic field for higher solenoid currents. The values obtained by a dark current measurement [7] as well as the corresponding simulation results for an electric field of 40 MV/m on the cathode at different solenoid currents are shown in fig. 3.

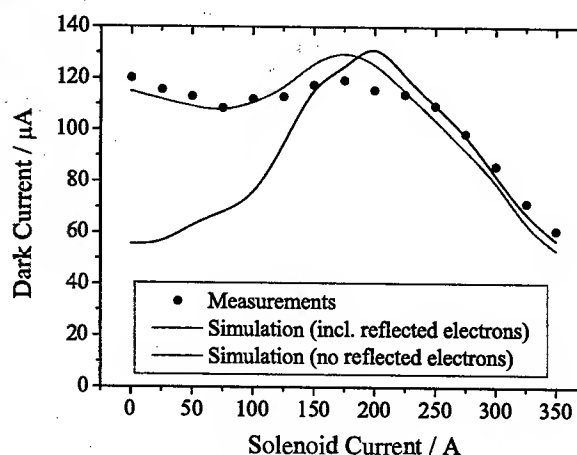


Figure 3: Comparison between simulated and measured dark current as a function of the solenoid current with and without reflected electrons taken into account. The electric field on the cathode was set to 40 MV/m.

The measured dark currents show no significant dependency on the solenoid current up to 175 A and do not fit very well to the simulation results in this range. This can not easily be understood because the trajectories of the electrons for both cases are quite different. The simulated trajectories for a solenoid current of 0 A and 175 A of dark current electrons starting at the cathode at different rf phases are shown in fig. 4. In absence of a magnetic field some of the electrons hit the beam tube and do not contribute to the dark current in the simulations. When the solenoid current is set to 175 A all particles reach the end of the calculation area resulting in a much higher current. The discrepancy between measurements and simulations for low solenoid currents can be overcome if those electrons hitting the beam tube at a very low angle are con-

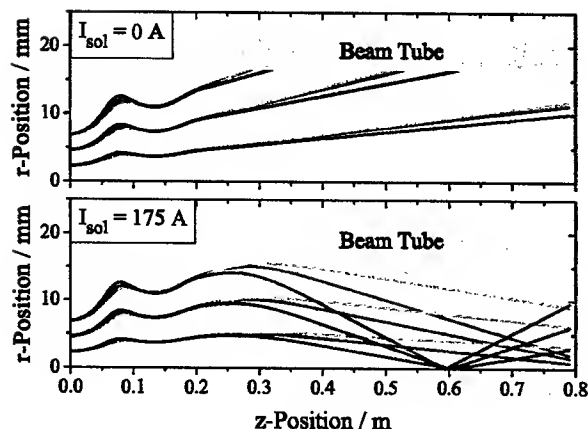


Figure 4: Trajectories of dark current electrons starting at the cathode at different rf-phases for two different solenoid currents. The electric field on the cathode was set to 40 MV/m.

considered to be scattered at the surface. In this case the simulation results fit very well to the measurements (see fig. 3). By fitting the simulated and measured data it is possible to calculate a field enhancement factor of $\beta = 23$. With the help of the assumption that electrons might be scattered at the tube the dependency of the dark currents on the electric field on the cathode for different solenoid currents has been calculated. A comparison between simulated and measured [8] dark current is shown in fig. 5. Once again the simulated values are in very good agreement with the measurements. The field enhancement factor calculated from the results is $\beta = 18$ and fits well with the value extracted from the data at 40 MV/m.

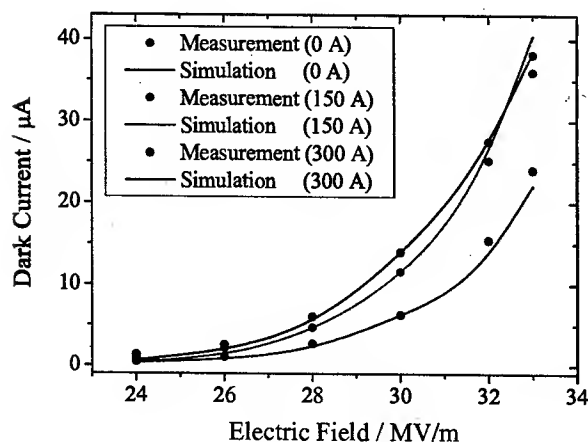


Figure 5: Comparison between simulated and measured dark current as a function of the electric field on the cathode for different solenoid currents.

CONCLUSIONS

With the help of detailed numerical tracking studies the dynamics of dark current electron inside an rf-gun have been investigated. Particles emitted at the high electric field areas located in the vicinity of the irises hit the walls of the rf-gun with energies of up to several tens of keV and are therefore a potential hazard to the Cs_2Te cathode. It was shown that the main part of the particles contributing to the measured dark current are originated at the cathode. By fitting the simulation data to the measured values a field enhancement factor of $\beta \approx 20$ has been estimated. Furthermore the dependency of the dark currents on the external magnetic field as well as on the electric field on the cathode can be predicted by simulations if electrons hitting the beam tube at very low angles are considered to be scattered. To confirm this assumption further studies have to be carried out.

REFERENCES

- [1] R. Cee, M. Krassilnikov, S. Setzer, T. Weiland, A. Novokhatski, "Detailed numerical studies of space charge effects in a FEL RF gun", Nucl. Instr. and Meth. A 483 (2002), p. 321.
- [2] R.H. Fowler, L. Nordheim, "Electron emission in intense electric fields", Proc. R. Soc. London A 119 (1928), p. 173.
- [3] R.W. Hockney, J.W. Eastwood, "Computer Simulation using Partricles", Institut of Physics Publishing, Bristol and Philadelphia, 1994.
- [4] J. Boris, "Relativistic Plasma Simulation - Optimisation of a Hybride Code", Proc. 4th Conf. on Numer. Simulation of Plasmas (1970), Office of the Naval Research, Arlington, Va., p. 3
- [5] "MAFIA User Manual", CST GmbH, BÜdinger Strasse 2a, D-64289 Darmstadt.
- [6] B.E. Carlsten, "New photoelectric injector design for the Los Alamos National Laboratory XUV FEL Accelerator", Nucl. Instr. and Meth. A 285 (1989), p. 313
- [7] "Dark current measurements at the PITZ gun", Proc. DIPAC2003, Mainz, May 2003
- [8] Measurements by S. Schreiber, data taken from Pitz-Logbook.

INVESTIGATION OF DARK CURRENT IN A S-DALINAC SUPERCONDUCTING CAVITY*

M. Gopych, H.-D. Gräf, U. Laier, M. Platz, A. Richter, A. Stascheck,
S. Wazlawik, Institut für Kernphysik, TU Darmstadt, Germany
S. Setzer, T. Weiland, TEMF, TU Darmstadt, Germany

Abstract

During the operation of the S-DALINAC [1], light emission associated with field emission on the surface from a 20 cell 3 GHz superconducting niobium rf cavity has been observed. The optical spectrum of the light spots has been measured by a photomultiplier using a set of filters. The obtained spectral density distribution is close to a black body radiation spectrum. In order to determine the maximum energy of the dark current electrons, measurements of bremsstrahlung spectra at the beam line exit of the accelerator have been carried out. For the interpretation of these data electron trajectory simulations based on field distributions calculated by MAFIA [2] have been performed. Additionally, the behavior of dark current has been investigated for different rf frequencies by means of numerical calculations for TESLA and S-DALINAC cavities.

INTRODUCTION

In this paper we present a detailed description of experiments on investigation of field emission accompanied by emission of light and results of simulations. The initial goal was to understand the reason for this phenomenon in a S-DALINAC cavity [1] means of extensive diagnostic measurements in order to avoid this problem in the future. The measurements were performed downstream of the last superconducting cavity (#11) of the main linac. The design parameters of the cavity are summarized in Tab. 1. For the

Table 1: Design parameters of the S-DALINAC accelerating structure

Material	Nb
Number of cells	20
Frequency	2.9975 GHz
Mode	π
Temperature	2 K
Quality Factor	$3 \cdot 10^9$
Accelerating Gradient	5 MV/m
RF Losses at 5 MV/M	4.2 W

experiments the cavity remained installed in the accelerator cryostat, it was powered by a 500 W klystron and operated at a bath temperature of 2 K. Optical measurements were performed through the viewport in the straight beam line using a CCD camera, a monochromator, or a set of filters together with a photomultiplier. Bremsstrahlung spectra

were taken with a BGO detector positioned directly above the beam line. According to preliminary experimental results reported in [3] the optical spectra measured using a spectrometer set up with high resolution was identified as a fluorescence spectrum of Cr^{3+} in chromium doped Al_2O_3 . Further investigations have shown that the observed spectrum was due to scattered light from a fluorescence view screen behind the main linac. Although it was not positioned in the beam line during the measurements, the view screen was excited by dark current electrons from the cavity. Subsequently this target was replaced by a species fabricated from BeO and equipped with an improved shielding. In the following the determination of the maximum energy of dark current electrons via bremsstrahlung spectra is described, followed by an analysis of these results through extensive calculation of electron trajectories in the superconducting 20 cell cavity, using a combination of different numerical codes. Finally, the spectral distribution of the light, emitted from the bright spots inside the cavity, is presented and explained.

BREMSSTRAHLUNG MEASUREMENTS

A significant part of field-emitted electrons is bent in the rf magnetic field and impacts on the cavity surface near the own emission site. But some electrons can be captured by the accelerating field and can traverse the entire cavity. The energy of these electrons can help to localize the cavity cell, where they started from. Bremsstrahlung produced by impacting electrons can be used to determine their maximum energy. It is the endpoint energy of the corresponding bremsstrahlung spectrum. The experimental set up is shown in Fig. 1. In order to produce bremsstrahlung,

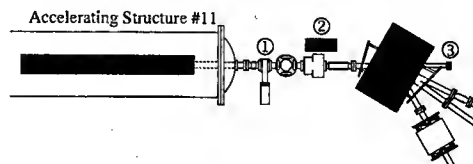


Figure 1: Experimental set up downstream of main linac. The figures denote: (1) view screen, (2) BGO detector, (3) viewport for optical measurements.

the electrons, which were able to exit the cavity, are scattered from the view screen ((1) in Fig. 1) and hit the wall of the vacuum chamber. Bremsstrahlung spectra have been taken at accelerating gradients E_{acc} of 6.84, 6.66, 6.48 and 6.12 MV/m using a BGO detector ((2) in Fig. 1) located directly above the beam line. The values of the accelerating

* Supported by the DFG (FOR 272/2-1 and GRK 410/2)

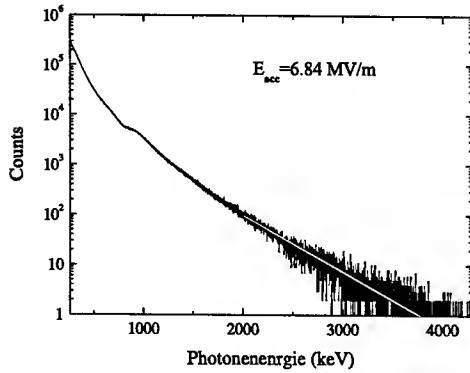


Figure 2: Bremsstrahlung spectrum taken with the BGO detector for $E_{acc}=6.84$ MV/m. The white line shows the exponential fit determining the endpoint energy.

gradients are known very accurately through calibrations from regular accelerator operation. As an example, the background corrected bremsstrahlung spectrum measured at $E_{acc} = 6.84$ MV/m is shown in Fig. 2. To evaluate the endpoint energy value an exponential fit has been used. For the spectrum in Fig. 2 the endpoint energy has been determined to 3.75 MeV. For other the spectra energies of 3.4, 3.05 and 2.3 MeV corresponding to decreasing accelerating gradients have been obtained. The experimental accuracy for the obtained energies is about 100 keV.

SIMULATION

In order to explain the electron energies at the end of the cavity a simulation program for particle trajectories inside the cavity has been written. The trajectories of the field-emitted electrons in the accelerating structure are calculated numerically by integration of the relativistic equation of motion in electromagnetic fields using the Leap-Frog method. An initial field distribution in the accelerating structure was calculated using the MAFIA eigenmode solver [2] and used as an input file for the simulation code.

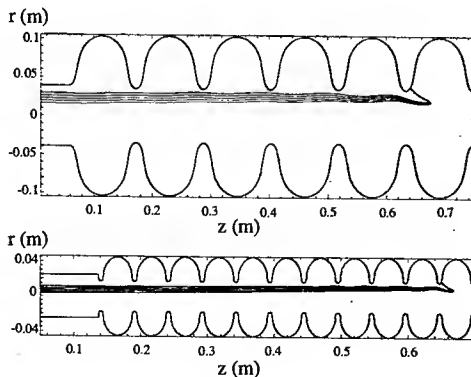


Figure 3: Electron trajectories in a TESLA (top) and in a S-DALINAC (bottom) structure for gradients of 10 and 23 MV/m respectively

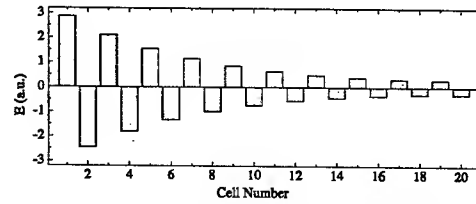


Figure 4: Field profile of a 20 cell S-DALINAC structure with the first cell detuned by 5 MHz

Because of the rotational symmetry of the considered cavity the simulation is performed in r - z plane. The electron energy is saved for every integration step. Calculation of the trajectory is terminated when the electron hits the cavity wall. Space charge effects and the secondary emission process are not taken into account in the simulation program.

In a first attempt, a flat field distribution (i.e. field amplitude of the accelerating π -mode have equal magnitudes but opposite signs in neighboring cells) was assumed. Electrons were started with a zero velocity in a phase interval from -30° to 30° and scanning the entire region of an iris, where field emission occurs most likely. A time integration step of $5 \cdot 10^{-13}$ seconds was used to corresponding to 660 steps per rf period. An rf phase of 0° corresponds to the maximum electric field in the cell. These simulations have shown, that there were not any electrons which were able to gain an energy of more than 600 keV. The numerical calculations repeated for other irises provided the same result.

Because the calculated energies did not agree with the experimental ones, similar simulations were performed for a TESLA cavity with an operating frequency of 1.3 GHz to check the correctness of the code. The numerical results for an accelerating gradient of 10 MV/m presented in [4] were exactly reproduced. Comparison between electron trajectories for TESLA and S-DALINAC cavities have shown that due to the higher frequency in the S-DALINAC considerably higher accelerating gradients are necessary to produce

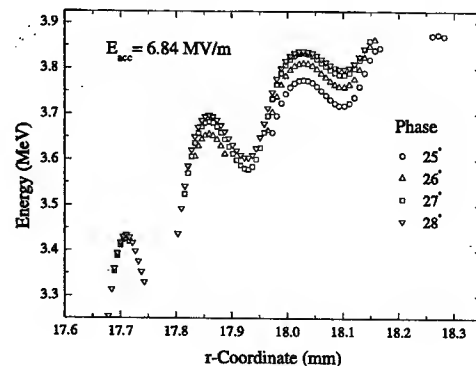


Figure 5: Energies of electrons at the end of the cavity as a function of the r coordinate of their start position on the iris for $E_{acc}=6.84$ MV/m.

similar trajectories to the ones in the TESLA cavity. The electrical field strengths must differ by a factor of 2.3 (the ratio of operating frequencies). Figure 3 shows electron trajectories in both cavities for gradients of 10 and 23 MV/m respectively. Remaining differences in the trajectories are attributed to the different cell shapes of the TESLA and S-DALINAC structure. Thus the assumption of a flat field profile had to be dropped in order to explain the observed electron energies.

After initial fabrication all accelerating structures were tuned for flat field profiles. The operating π -mode, however, is extremely sensitive to perturbation of single cells (particularly the end cells) of multicell structures. As an example, a field profile of a 20 cell S-DALINAC structure with the first cell detuned by 5 MHz calculated from a simple lumped circuit model is shown in Fig. 4.

Table 2: Comparison of the energies obtained experimentally with the calculated ones.

E_{acc} (MV/m)	E_{kin} (MeV) Experiment	E_{kin} (MeV) Simulation
6.12	2.3 ± 0.1	2.16 ± 0.08
6.48	3.05 ± 0.1	3.1 ± 0.05
6.66	3.4 ± 0.1	3.45 ± 0.05
6.84	3.75 ± 0.1	3.8 ± 0.05

Under the assumption of such a field profile with the electron emission site located in a cell with high electric field it should be possible to explain the energies obtained from the bremsstrahlung spectra. Therefore the same simulations have been carried out for a cavity with a detuned first cell. Electrons started from the iris between the first and second cell because of the high electric field in this region. The field profile was obtained from the flat field distribution calculated with MAFIA scaled with the respective field amplitudes from cell to cell. Simulations for an accelerating structure with the first cell detuned by 5.4 MHz have succeeded in reproducing the experimental energies most suitably. Figure 5 shows energies of dark current electrons emerging from the cavity as a function of the r coordinate of their starting position on the iris between the first and second cell for accelerating gradient of 6.84 MV/m. The rounded part of the iris covers r coordinates from 17.325 to 20.525 mm. A comparison of experimentally observed and corresponding calculated energies is given in Tab. 2. The excellent agreement shows, that under the hypothesis of a detuned end cell (causing a non-flat field profile) the observed dark current energies can be explained.

OPTICAL MEASUREMENTS

After replacement of the chromium doped Al_2O_3 target the monochromator set up was no longer able to measure optical spectra due to lack of intensity, even though the

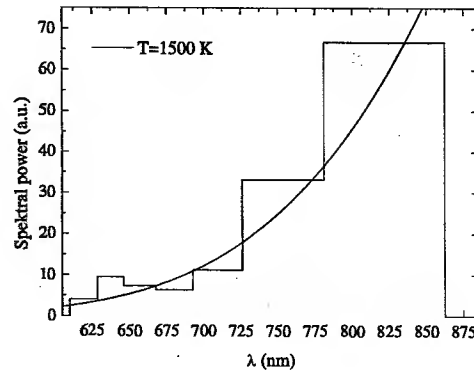


Figure 6: Spectrum of the light radiation emitted by the light spots.

bright, light emitting spots inside the cavity (reported earlier [3]) was clearly visible. Thus a set up of optical high-pass-filters, with cut-off-wavelengths ranging from 600-850 nm (in steps of 15 to 70 nm) together with a photomultiplier (Hamamatsu R1547) was used to determine the spectrum displayed in Fig. 6.

It shows increasing power starting at 600 nm toward the IR region, similar to a black body radiation spectrum. This result can be explained by a thermal model [5] according to a small particle thermally insulated from the surface of the cavity being heated by electric or magnetic field and losing its energy by black body radiation. The curve giving in Fig. 6 for comparison shows the radiation power corresponding to a black body temperature of 1500 K.

The observation of light spots with a CCD camera placed at the exit of the accelerator has shown that all light spots were located in the second half of the cavity. On the other hand as shown by trajectory calculation, the sources of field emission must be located in the first cell of the cavity. This leads us to conclusion that the light spots are not associated with the field emission sites.

REFERENCES

- [1] A. Richter, Proc. 5th Europ. Part. Acc. Conf., Eds. S. Myers, A. Pacheco, R. Pascual, Ch. Petit-Jean-Genaz and J. Poole, IOP Publishing, Bristol, (1996) 110.
- [2] "MAFIA User Manual" CST-GmbH Bldinger Strasse 2a, D-64289 Darmstadt.
- [3] "Latest developments at the S-DALINAC" 8th Europ. Part. Acc. Conf. (2002) 2007.
- [4] U. Becker, M. Zhang, T. Weiland "Two and Three Dimensional Simulations of Dark Current in TESLA-Cavities" 7th Workshop on RF-Superconductivity, Paris (1995) 397.
- [5] W. Bauer, A. Citron, G. Dammertz, M. Grundner, L. Husson, H. Lengler, E. Rathgeber, IEEE Trans. NS-22 3 (1975) 1444.

- Abbott, S.R. 86
 Abell, D. 1059
 Aberle, O. 45, 878
 Abeyta, E.O. 558
 Ablett, J.M. 241
 Abo-Bakr, M. 3020, 3023
 Abrahamyan, K. 2114
 Achard, C. 495
 Ackermann, W. 3551, 3566
 Adachi, T. 1679
 Adams, D.J. 1527
 Adelman, A. 3524
 Adolphsen, C. 668, 678,
 1264, 2664, 2763
 af Ugglas, M. 1590
 Agarwal, D. 278
 Agustsson, R. 944
 Ahle, L. 989
 Ahrens, L. 51, 405, 1542,
 1545, 1640, 1685, 1697,
 1706, 1715, 2441
 Aiba, M. 1679, 3413, 3452
 Aizatsky, N.I. 1107, 3303
 Ajima, Y. 1978
 Akai, K. 356
 Akiyama, A. 2351
 Akre, R. 235, 2107, 2285,
 3141
 Aladwan, A. 238
 Alber, R. 983
 Albrecht, C. 467
 Al-Dmour, E. 238
 Alduino, J. 2138, 2156
 Aleksandrov, A. 65, 1524,
 2598, 2706, 3536
 Alekseev, I. 51
 Alesini, D. 366, 2080, 2279,
 2500, 2742, 3285
 Alessandria, F. 2080, 3285
 Alessi, J. 51, 89, 1637, 1715,
 2793, 3282
 Alexahin, Y. 1757
 Alexandrov, V. 3536
 Al-Khateeb, A. 2607
 Allen, C.K. 2360, 3527
 Allison, S. 235
 Allison, T. 1485, 2379
 Alsharo'a, M. 1792
 Altmark, A. 1891, 1894,
 1897
 Alton, G.D. 995, 998, 1001
 Ambrosio, G. 1966
 Amemiya, Y. 530
 Ames, F. 2869
 Ammigan, K. 1452
 Amundson, J. 2939, 3195
 Anami, S. 1509
 Anderberg, B. 2318, 2321
 Anders, A. 98, 2622
 Anders, W. 1186, 3020
 Anderson, D. 3141
 Anderson, D.E. 553
 Anderson Jr., J. 1652
 Anderson, R. 2390
 Anderson, S.G. 95, 2957
 Anderson, T.G. 1649, 3437
 Andersson, A. 2318, 2321
 Andler, G. 1590
 Ando, L. 81
 Andonian, G. 944, 947,
 2110, 2112, 3321
 Andreev, N. 1966
 Andreoli, S. 470
 Andresen, N. 869
 Anerella, M. 164, 1939,
 2162
 Anferov, V. 699, 1563
 Ang, Z. 1285
 Anghel, A. 878
 Angoletta, M.E. 2461
 Ankenbrandt, C. 1792,
 2936
 Annala, G. 1730, 1972,
 3062, 3359
 Antokhin, E. 2198
 Anzalone, E. 2382
 Ao, H. 2826
 Aoki, M. 1993, 2198
 Aoki, N. 530, 713
 Aoki, T. 2551
 Apgar, S.E. 553
 Arai, S. 1509
 Arakida, Y. 568, 1512,
 1784, 1807
 Arduini, G. 307, 1718,
 1727, 2240, 3038
 Arkan, T. 1210
 Arnold, N.D. 2327
 Artoos, K. 1434
 Aryshev, A.S. 2709
 Asano, H. 1338
 Asano, Y. 782
 Aseev, V.N. 2875
 Ashmanskas, W. 323
 Asiri, F. 2748
 Aspart, A. 1303
 Assadi, S. 498, 1524, 1569,
 2444, 2706
 Assmann, R. 45, 665, 3494
 Attal, M. 238
 Autin, B. 444
 Averboukh, I.I. 1074
 Avilov, A. 1619
 Ayvazyan, V. 467, 2342,
 2730
 Ayzatsky, M.I. 1605, 2098,
 2878, 2969
 Baartman, R. 1578, 1584
 Baba, H. 3332
 Baba, Y.H. 487
 Baboi, N. 467, 1086, 1261,
 1270
 Babzien, M. 944, 1909
 Baca, D. 312, 536, 553,
 3294
 Bacci, A. 2080, 3285, 3512
 Bäcker, H.-J. 836
 Badea, S.V. 2138, 2156
 Bae, Y.S. 2539
 Bagge, L. 1590
 Baggett, K. 2183, 2186,
 2189
 Baglin, V. 307, 1727
 Bähr, J. 2114
 Bahrdt, J. 836
 Bai, M. 51, 54, 405, 1697,
 1706, 2204, 2207
 Baichev, I. 3494
 Bailey, C.P. 1527
 Baishev, I. 45
 Bajko, M. 1942
 Bak, P. 3318
 Bakker, R.J. 214

- Balbekov, V.** 1751, 2014, 2017
Balkcum, A. 1144
Ball, M.J. 1996
Balleyguier, P. 2053, 2458, 2601, 2799
Bandelmann, R. 467
Bandura, L. 1999
Bane, K. 126, 3126, 3252
Banna, S. 722, 1879
Bao, X. 2357
Baptiste, K. 869, 1240, 1252
Bär, R. 694
Barber, D.P. 372
Barletta, W.A. 186, 923
Barlow, D. 702, 1664
Barnard, J.J. 1521, 1990, 2658
Barnes, B. 1736
Barnes, C.D. 1530, 1933, 2101
Barnes, M.J. 1162
Barnes, P. 1309, 1323
Barni, D. 1341, 1506
Barov, N. 1870, 2682
Barr, D. 2512
Barr, G. 1987
Barstow, B. 192, 1317, 1320
Barsz, T. 2029
Bartolini, R. 914, 2077, 3285
Barton, D. 1637
Barty, C.P.J. 95
Baskiewicz, M. 302
Batchelor, K. 541
Batrakov, A. 250
Batygin, Y.K. 2751, 3548
Baudrenghien, P. 1718, 3050
Bauer, P. 1730, 1972, 3359
Bauer, S. 1410, 2887
Baum, D. 2527
Baynham, D.E. 1987
Bazarov, I. 192, 842, 848, 1201, 1317, 1323, 2062
Beard, K. 195, 332, 1104, 1575
Beaudoin, B. 426, 2312, 2571
Beche, J.-F. 2530
Bechstedt, U. 598, 3428
Bechtold, A. 1062
Beck, M. 2189
Beckert, K. 434
Beckman, L. 3389
Beczek, K. 2038
Beebe, E. 89
Beebe-Wang, J. 51, 1706
Beinhauer, W. 3551
Belgroune, M. 896
Bellavia, S. 1542
Bellenger, D.W.J. 1527
Beller, P. 434
Bellodi, G. 1527
Bellomo, P. 235
Bellucci, S. 917, 986
Beloglasov, V.I. 2878
Belohrad, D. 2461
Belomestnykh, S. 192, 1198, 1201, 1306, 1317, 1323, 1326, 1329, 1410, 1437, 2059, 3347
Beltran, C. 326, 3086
Bender, H. 558
Benedetti, G. 366, 2279, 2945
Benedetto, E. 1727, 3053
Benedikt, M. 1548
Bengtsson, J. 195
Benjamin, J. 1715
Bennett, J.R.J. 1527
Bennett, S.L. 189
Ben-Zvi, I. 39, 92, 944, 1300, 1909, 2005, 3186
Berden, G. 519
Berenc, T. 1736, 3362
Berg, J.S. 1804, 1816, 2002, 2210, 2213, 2216, 2219, 3413, 3485
Berg, S. 1416, 1422, 2029, 2038
Berg, W.J. 2417, 2420
Bergqvist, M. 2321
Berio, R. 989
Berkaev, D.E. 372
Berkvens, P. 854
Berman, L. 241
Bernal, S. 426, 1673, 1676, 2312, 2571, 2574, 2577, 2673
Bernard, A. 195
Bernardin, J. 1461
Bernaudin, P.-E. 2799
Bernstein, L. 989
Bertolucci, S. 3285
Bertrand, P. 2802, 3488
Bessonov, E. 1963
Bhashyam, S. 1966
Bhat, C.M. 514, 1769, 2345, 2348, 3180
Bhatt, R. 2643
Biagini, M. 366, 914, 2077, 2279, 2297, 2300, 2945, 3285
Biallas, G. 2123, 2135, 2183, 2186, 2189
Biarrotte, J.L. 1303, 2802
Biasci, J.C. 854
Bieler, T.R. 1359
Bieniosek, F.M. 98, 275, 312, 536, 1518, 2524, 2619, 3297
Bierwagen, J. 1353
Bilderback, D. 192
Bilheux, H. 998
Billen, J. 1461, 1515, 2844, 3518, 3521
Biller, E.Z. 1605, 2878
Billing, M. 3059
Binello, S. 1542, 1703
Bini, S. 917
Binkley, M.E. 2497
Biocca, A. 3374
Birkel, I. 893, 3273, 3276
Biryukov, V.M. 917, 986, 1655, 1691
Biscardi, R. 241
Biscari, C. 335, 366, 684, 2279, 2742, 2945, 3285
Bishofberger, K. 57, 1778, 1781
Bisognano, J.J. 3147
Bizen, T. 487
Björkhage, M. 1590

- Bjorklund, E.** 2354
Black, E. 983, 1792, 1834, 1999
Blair, G. 2739
Blanco-Vinuela, E. 1945
Blasche, K. 589
Blaskiewicz, M. 54, 135, 272, 394, 476, 797, 1195, 1569, 1706, 1715, 1816, 2595, 2598, 3026, 3029, 3035, 3344, 3419
Blind, B. 702, 1664, 2948
Bliss, N. 189, 1029
Blivet, S. 1303
Blokland, W. 1524, 2444, 2491, 2706
Blom, M. 1590
Blomqvist, I. 220
Blue, B.E. 731, 1530, 1864
Bluem, H. 92, 977
Bocchetta, C.J. 214
Boege, M. 3386
Boffo, C. 1210
Bogacz, A. 195
Böge, M. 291
Boggia, A. 3318
Bohl, T. 1718, 3050
Bohlen, H. 1144
Bohn, C.L. 2676
Bohnet, I. 2114
Boilot, D. 1332
Boimelshtein, Y. 3318
Boine-Frankenheim, O. 589, 2607
Bojtar, L. 2461
Boller, K.-J. 1900, 1903
Bolton, P.R. 2104, 2709, 3216
Bondarenco, N. 3329
Bondarev, B.I. 2679, 3002, 3530
Bongers, H. 2872
Bongers, N. 598
Boni, R. 366, 2279, 2742, 3285
Bookwalter, V. 1494
Borburgh, J. 1643
Borchard, P. 1113, 1116
Borden, M. 508, 2521, 3089, 3455
Bordry, F. 1945
Boriskin, V.N. 1107, 2878, 3303
Borissov, E. 1210
Borland, M. 247, 256, 283, 2330, 2417, 2420, 3138, 3461, 3470, 3473, 3476
Borovina, D.L. 553, 1168
Borrion, H. 2458
Bosch, R.A. 887, 929, 932, 935, 2373, 3147
Boscolo, I. 3285
Boscolo, M. 366, 914, 2077, 2279, 2945, 3285, 3548
Bosland, P. 878, 1332
Bosotti, A. 1341
Bossert, R. 1969
Bottura, L. 173, 1730, 1945
Bourcey, N. 1434
Bousson, S. 1303
Bowden, G. 1261, 1264
Bowler, M.A. 189
Boyce, J.R. 938, 941
Boyce, R. 235, 2174
Bozzini, D. 1945
Bradley III, J. 553, 1095, 1168, 1458
Brajuskovic, B. 830, 1017
Brarvar, S. 51
Braud, D. 1303
Braun, H. 495, 1156, 2721
Brautti, G. 3318
Bravin, E. 2464
Bredy, P. 878, 1332
Brelsford, B. 1542
Brenger, A. 2476
Brennan, J.M. 39, 51, 135, 394, 476, 1195, 1545, 1706, 1715, 3026, 3029, 3338, 3341, 3344
Bricault, P. 439, 1584, 1670
Bricker, S. 1353
Briddick, D. 2029, 2038
Bridges, F. 1092
Briggs, R. 3098
Brinkmann, A. 1374, 1395
Briscoe, B. 3282
Britvich, G.I. 917
Brodowski, J. 1195, 2156, 2444, 2598
Broemmelsiek, D. 3431
Broggi, F. 3285
Bromberek, D. 1416
Bross, A. 983, 1183
Broste, W. 558
Browdowski, J. 1428
Browman, A. 326, 508, 2521, 3086, 3089, 3455
Brown, B.C. 2165
Brown, C. 1446
Brown, K.A. 51, 405, 746, 1542, 1545, 1706, 1715, 2441, 2595, 3422
Brown, W. 95, 938, 2192, 2957
Browne, M. 2297
Bru, B. 2802
Brugger, M. 45, 3494
Bruhwieler, D.L. 719, 734
Brumwell, F.R. 592
Brunelle, P. 229, 896
Brunner, O. 473
Bruno, D. 743, 1700, 1706
Bruno, L. 45
Brüning, O.S. 42, 1748
Bui, T. 3560
Bukh, B. 2631, 2634
Bulfone, D. 3395
Bullard, D. 2183
Bultman, N. 1461, 2844
Bunce, G. 51
Burgazzi, L. 1506
Burgmer, R. 1948
Burke, D.L. 1264
Burkhardt, H. 45, 1721, 3041, 3044
Burns, M. 2354
Burov, A. 2020, 3062
Burrill, A. 39, 92
Burrows, P.N. 687
Busch, M. 2273
Bussmann, M. 112
Butler, C. 195

- Butler, J. 1195
 Büttner, T. 467
 Byer, R. 722, 728, 1858
 Bylinsky, I. 1285, 1584
 Byrd, J. 863, 869, 1240, 2530
 Cacciotti, L. 2476
 Cadapan, L. 235
 Cadorna, A. 2348
 Cai, Y. 350, 2288, 2291, 2297, 2300, 3542
 Calaga, R. 39, 272, 2207
 Calatroni, S. 1309
 Callahan, D.A. 2637
 Calvet, O. 1434
 Calzas-Rodriguez, C. 1945
 Cameron, P. 54, 135, 394, 524, 1703, 1706, 2444, 2447, 2598, 2691, 2697, 3026, 3029
 Campbell, L.P. 1909
 Campisi, I. 457, 977, 1104, 1377
 Cao, L. 2852
 Capatina, O. 1434
 Capista, D.P. 2165
 Caporaso, G. 563
 Cappi, R. 388, 2910, 2913
 Carcagno, R. 1969, 1972
 Cardona, J. 1059, 1706, 2901
 Carey, D. 1446
 Carli, W. 2872
 Carlier, E. 1945
 Carlson, C. (Bechtel) 558
 Carlson, C. (BNL) 1715
 Carlson, K. 2020
 Carneiro, J.-P. 2065, 2068, 2114, 3548
 Carr, G. 2354
 Carr, G.L. 241, 1497
 Carr, L. 329
 Carroll, A. 1709, 3255
 Carron, G. 1156
 Carson, J. 1969
 Carter, H. 1210, 1813
 Cary, J.R. 719, 734, 1536, 1885, 1918, 2026
 Casarin, K. 2309
 Casey, B. 241
 Casey, J.A. 547, 1500
 Caspers, F. 1801, 2470, 2700, 3479
 Caspi, S. 42, 170, 1984
 Cassel, R. 235
 Castellano, M. 2476, 3285
 Castro, P. 198, 467, 1086, 2730
 Catalan-Lasheras, N. 1428, 2144, 2225, 2598, 3026
 Catani, L. 2476, 3285
 Cattelino, M. 1144
 Caudill, L. 558
 Cederkfll, J. 2869
 Cee, R. 2114
 Celata, C.M. 275, 536, 1518, 1521
 Celona, L. 81
 Cerniglia, P. 2444, 2697
 Chacon-Golcher, E. 73, 3291, 3294
 Chae, Y.-C. 3008, 3011, 3014, 3017
 Chambers, F. 563, 2960
 Champion, M. 1464, 3371, 3377
 Chan, K.C.D. 558, 3210
 Chang, C.H. 1041, 1044, 1047
 Chang, C.K. 2376
 Chang, H.P. 890, 1044
 Chang, J.C. 1476, 1479, 1482, 2402, 2405
 Chang, L.H. 1371, 2670
 Chang, S.H. 2402, 2405
 Chang, X. 39, 1300, 2005, 3186
 Chao, A. 126
 Chao, Y. 195, 294, 3243
 Chao, Z. 487
 Chapman, S. 167
 Chaput, R. 229
 Charrier, J.P. 1303
 Chase, B. 1736, 1769
 Chattopadhyay, S. 195
 Chavanne, J. 253, 854
 Chazot, G. 851
 Cheever, D. 2324
 Chel, S. 878, 1332
 Chen, A. (FNAL) 623
 Chen, A. (YY Labs) 2586
 Chen, C. 1255, 1258, 2643, 2646, 2966
 Chen, C.I. 3234
 Chen, D. 1560, 3506, 3509
 Chen, G. 2586
 Chen, H. 467
 Chen, J. 1044, 2376, 2554, 2557, 2580, 3237, 3392
 Chen, J.R. 821, 1476, 1479, 1482, 2402, 2405
 Chen, L. 2357
 Chen, S. 1921
 Chen, Y.-J. 558, 563, 2960, 3210
 Chen, Z. 2844
 Chen-Yao, L. 764
 Cherbak, E. 1177
 Chesnokov, Y. 917, 986, 1655, 1691
 Cheung, H.W.K. 2488
 Chevtsov, P. 2560
 Chiadroni, E. 914, 3285
 Chiaveri, E. 45, 878, 1309, 1332
 Chiba, J. 1509
 Chichili, D. 1969
 Chien, Y.-C. 764, 767
 Chiesa, L. 170, 1984
 Chin, M. 869
 Chin, Y.H. 479
 Chiou, J. 764
 Chishiro, E. 1338
 Cho, Y.S. 1219, 1222, 2539, 2832, 2857, 2884
 Choi, B. 235
 Choi, B.H. 1219, 1222, 1602, 2539, 2832
 Choi, J. 875, 3383
 Choroba, S. 467
 Chou, P.J. 1368, 3150
 Chou, W. 604, 623, 1551, 1554, 1557, 2922, 2925, 2936

- Chouhan, S. 899
 Chrin, J. 291
 Christensen, W. 2485
 Christina, V. 920, 977, 2186
 Christoph, M. 39
 Chu, C. 2360, 2363, 3527
 Chu, P. 2366
 Chun, M.H. 1470, 2857
 Chung, Y.C. 1479
 Chupyra, A. 2769
 Cialdi, S. 3285
 Cianchi, A. 2476, 3285
 Ciavola, G. 81
 Cimino, R. 1727
 Ciocchi, F. 3285
 Ciovati, G. 1362, 1374, 1395
 Citver, G. 39, 92
 Clark, G. 601
 Clarke, D.G. 1029
 Clarke, J.A. 189, 1029
 Clarke-Gayther, M.A. 1473
 Clauser, T. 3318
 Clayton, C. 731, 1530, 1864, 1873, 1933
 Clendenin, J. 2104, 2126, 2129, 3216
 Clift, B.E. 2426
 Cline, D. 1787, 1876, 1909, 2008, 2709
 Clozza, A. 366, 2279, 2742, 3285
 Cobb, J.H. 1834
 Codner, G. 2399
 Cohen, R. 132, 312, 536
 Colby, E. 722, 1858, 2101
 Cole, J.M. 998
 Cole, M. 92, 977, 2047, 2050
 Coleman, J. 1485
 Colestock, P. 977, 3086
 Collier, M. 2844
 Collier, P. 307, 1718, 1727
 Collins, I. 1727
 Collins, J. 699
 Collins, S. 1661
 Colocho, W. 2297
 Compton, C. 1353, 1359, 1362
 Conde, M.E. 2032
 Coney, L. 1587
 Congretel, G. 2799
 Connolly, R. 135, 1706, 2444
 Cook, E.G. 544
 Coosemans, W. 665
 Corbett, J. 2369, 2372
 Corbett, W. 235
 Corlett, J. 186, 812, 866, 923, 1246, 1249, 2086, 2408, 3198
 Cornelis, K. 1718, 1727, 3038
 Cornelis, M. 1942
 Corniani, G. 1341
 Corsini, R. 684, 2742
 Courant, E.D. 405, 1697, 1816, 3485
 Cousineau, S. 117, 259, 1428, 1569, 1572, 2598
 Cowan, B. 722, 1855
 Cox, L. 1144
 Craddock, M.K. 1581
 Craft, B. 1053, 2382
 Craievich, P. 214, 878
 Crandall, K. 1515, 2855
 Crandall, K.R. 2889
 Crane, J.K. 95
 Crappell, A. 2382
 Crawford, A. 1312
 Crisp, J. 1781, 2348, 2491
 Crittenden, J. 1023, 1954, 3425
 Crofford, M. 3377
 Cross, R.R. 95
 Cui, Y. 426, 511, 3156
 Cullerton, E. 3068
 Cummings, K. 1095, 1237
 Cummings, M.A. 1834
 Cummings, M.A.C. 983, 1798, 1999
 Cupolo, J. 524, 2444, 2697
 Cusick, M. 1144
 Cutler, R. 550, 617
 Czyz, W.S. 592
 Da'l, A. 229
 Dail, J. 2183
 D'Alessio, C. 2500
 Dallin, L. 220, 2195
 Dalmas, D. 558
 Daly, E. 457, 977, 1377, 2866
 Danailov, M. 214, 2306
 Danared, H. 1590
 D'Angelo, A. 3285
 Danilov, V. 117, 1569, 1572, 2598, 3032
 Danilova, E. 2363
 Daté, S. 250, 881
 Datta, D. 3560
 Datte, P. 2530
 Dattoli, G. 914, 3285
 D'Auria, G. 214
 Davidson, R.C. 1667, 2655, 2658, 2661, 2975, 2978, 3117, 3120, 3123
 Davino, D. 1428, 2147, 2598, 3035
 Davis, G.K. 457, 1383
 Davis, H. 120
 Dawson, C. 2444, 2453, 2697, 3026
 Dawson, W. 524
 Day, L. 2429
 De Baca, J.M. 1237
 DeBarger, S. 3141
 DeCarlo, A. 1467, 2706
 De Conto, J.-M. 2802
 Decker, F.-J. 423, 731, 1530, 1864, 1933, 2282, 2285, 2297, 2300, 2754, 3126, 3129
 Decker, G. 833, 2688
 Decking, W. 652
 Decyk, V. 3174
 DeFord, J.F. 3554
 Degen, C. 524, 2444, 2697, 3026
 Dehler, M. 3395
 Dehning, B. 45, 2470
 Deibele, C. 1524, 2706
 Deitinghoff, H. 1335, 2942
 de Jong, M. 220

- Dejus, R.J. 1020
 DeKamp, J.C. 161
 Delaney, T. 690
 Delayen, J. 92, 457, 992,
 1098, 1291, 1380, 1383,
 2379, 2860
 DellaPenna, A. 524, 2444
 Delle Monache, G. 366,
 2279, 2742
 Dell'Orco, D. 235, 2174
 DeLong, J. 476, 1715, 3338,
 3341, 3344
 De Martinis, C. 2080, 3285
 Demidov, N.V. 2878
 Demirkan, M. 2318
 Demma, Th. 2993, 2996,
 2999
 Demske, D. 1497
 Denard, J.-C. 229, 2560
 Denes, P. 2530
 Deng, S. 1530, 1933
 Den Hartog, P. 824, 830,
 833, 1017
 De Ninno, G. 214, 2306,
 2309
 Denz, R. 1945
 Derbenev, Y. 941
 Derenchuk, V.P. 1563
 De Rijk, G. 1942
 Deriy, B. 2261
 Deryuga, V. 1619
 De Santis, S. 186, 866,
 2530, 2745, 3377
 Deslandes, D. 2458
 Desler, K. 2682
 Devanz, G. 878, 1086
 DeVoy, J. 2934
 Devred, A. 42, 146, 173
 Dewan, S. 770
 Dey, J. 1204, 1769, 3353,
 3356
 Diao, C.Z. 968
 Dickson, R. 2563
 Diebele, C. 2444
 Diep, A. 2312, 2571, 2577
 Dierker, S. 241
 Dietderich, D.R. 170, 1032,
 1984
 Dietrich, J. 598, 3428
 Dilley, C.E. 1909
 DiMarco, J. 1730, 1969,
 1972
 DiMauro, L. 217
 Di Mitri, S. 214, 1050
 Dimitrov, D.A. 734
 Ding, Y. 2580
 Di Pirro, G. 366, 2279,
 2476, 3285
 Di Salvo, R. 3285
 Diviacco, B. 214, 1050,
 2306
 Diwan, M. 429, 1709, 3255
 Dohhins, J. 2473, 3347
 DÅbert, S. 495, 1156
 Dodson, G. 1569
 Doelling, D. 899
 Dohan, D.A. 2327
 Doleans, M. 1599
 Dolgashev, V.A. 1264,
 1267, 1276, 2763
 Dolinskii, A. 434, 694
 Domhsky, M. 439, 1584
 Domning, E. 3374
 Donald, M. 2288, 2297
 Dong, H. 195
 Dong, S. 758
 Donley, L.I. 1159
 Dooling, J.C. 592, 1159
 Doolittle, L. 186, 1464,
 2408, 3371, 3377
 Doose, C. 1020
 Doria, A. 3285
 Dormiani, M. 3141
 Dortwegt, R. 630, 2038
 Doss, J.D. 553
 D'Ottavio, T. 1715
 Douglas, D. 195, 938, 977,
 2183, 2186, 2189, 3243
 Dovhnya, A.N. 1107, 2878,
 3303
 Dowell, D. 2104, 3216
 Dowling, A. 439
 Doyle, E. 644
 Doyuran, A. 217, 241,
 1192, 2455
 Drago, A. 366, 2279, 2742,
 3285
 Dragt, A. 2772
 Drees, A. 51, 54, 794, 797,
 1685, 1688, 1691, 1706,
 2691, 2904
 Drees, K. 3026
 Dris, S. 1204
 Drozdoff, J. 638
 Drozhdin, A. 1503, 1557,
 1733, 1742, 2739, 2925,
 2936
 Drury, M. 457
 Ducar, R. 1652
 Ducimetiere, L. 1162
 Dugan, G. 737
 Duke, J.P. 2542
 Du Mont, D. 1542
 Dunkel, K. 2887
 Duperrier, R. 2802, 2805
 Durante, M. 1948
 Durkin, A.P. 2679, 3002,
 3530
 DËrr, H.A. 836
 DËrr, V. 836
 Durtschi, G. 558
 Duru, P. 854
 Dutto, G. 601, 638, 1584
 Dwinell, R.D. 86
 Dykes, D.M. 189
 Eherhardt, W. 836
 Ebihara, K. 860, 1228
 Ecklund, S. 2297, 2300
 Edwards, D. 2068, 2682
 Edwards, H. 447, 1213,
 2682
 Edwards, R.L. 1341, 1344
 Efthimion, P. 98, 2622,
 2655, 2661
 Egawa, K. 1071, 1074
 Ego, H. 250, 487
 Ehrlich, R.D. 2399
 Eichhorn, R. 598
 Eickhoff, H. 694
 Einfeld, D. 238
 Eisen, E. 1122
 Eisert, D.E. 887, 2373
 Ekdahl, C. 558, 3210

- Elioff, T. 235
 Elleaume, P. 854
 Ellis, S. 2841
 Emamian, M. 2273
 Emery, L. 256, 283, 833,
 2261, 2330, 2423, 2438,
 3461, 3464, 3470, 3473,
 3476
 Emhofer, S. 2869, 2872
 Emma, P. 211, 423, 914,
 926, 965, 1530, 1933,
 3126, 3129, 3138
 Endo, K. 1071, 1074
 Eng, W. 743, 770, 1542,
 2144
 England, R.J. 3258
 Enomoto, A. 2838
 Erdelyi, B. 1760, 1772,
 3542
 Erdem, O. 1933
 Ereameev, G. 1312
 Erickson, R. 2297
 Eriksson, L. 644
 Eriksson, M. 2318, 2321
 Ernst, D. 2174
 Erokhin, A. 2769
 Errede, D. 983, 1999
 Esarey, E. 719, 734, 1885
 Escallier, J. 164
 Eschke, J. 467
 Espinoza, C. 1664
 Esposito, A. 3285
 Esser, F.M. 598
 Estrada, J. 1763
 Evangelakis, G. 1709
 Evans, I. 235
 Evans, L.R. 19
 Evans, R. 1485
 Eversole, S. 558
 Eylon, S. 98, 558, 1171,
 2533, 2616, 2619, 2622,
 2625, 2628, 2646, 3098
 Ezura, E. 860, 1228
 Faatz, B. 467
 Fabbriatore, P. 1987
 Fabris, A. 878
 Facco, A. 470
 Falabella, S. 563
 Falce, L. 1113, 1116
 Faltens, A. 536, 1990
 Fan, L. 815
 Fan, M. 1560, 3506, 3509
 Fan, T.C. 1041, 1047
 Fang, J.-M. 1882, 1924
 Fang, S. 1285, 1404
 Fang, Z. 1071, 1074
 Fann, C.-S. 767
 Fantini, A. 3285
 Farinon, S. 1987
 Farkhondeh, M. 956, 959,
 980, 2324
 Farrell, J.P. 541
 Farrow, R.C. 189
 Fartoukh, S. 2225
 Farvacque, L. 854, 3189
 Faucett, J. 2354
 Faure, J. 1840
 Faus-Golfe, A. 2240
 Favale, A. 92
 Fawley, W. 186, 558, 923,
 959, 3098
 Fedotov, A. 39, 117, 383,
 1572, 2589, 2592, 2598,
 3032
 Fedurin, M. 1053, 2382,
 2892
 Feher, S. 1969
 Feigerle, C.S. 617
 Feikes, J. 845, 3023
 Felden, O. 598
 Feldman, D. 426, 3323
 Feldman, R. 426
 Fellenz, B. 2348, 2491
 Ferguson, P. 1110
 Ferianis, M. 214
 Ferioli, G. 307
 Fernow, R.C. 2002
 Ferracin, P. 170, 1984
 Ferrari, A. 45, 684
 Ferrario, M. 467, 914,
 2077, 2080, 2730, 3285,
 3548
 Fessenden, T.J. 2533
 Fessia, P. 1942
 Filhol, J.-M. 229, 1332
 Filip, C.V. 1873
 Findlay, A. 2461
 Findlay, D.J.S. 2542
 Finley, D. 1207, 1210, 1813
 Fiorito, R. 1497, 2712
 Fischer, R. 2476
 Fischer, W. 51, 54, 135,
 476, 794, 797, 1625, 1697,
 1706, 1754, 2222, 2228,
 3026, 3029
 Fisher, A. 2285, 2297, 2300
 Fisher, M. 887, 2303
 Fittinghoff, D.N. 95
 Fitzgerald, D. 508, 2521,
 3089, 3455
 Fitzgerald, J. 1781
 Flanagan, J.W. 2503
 Flanz, J. 690
 Fliflet, A.W. 1128
 Filler III, R. 272, 1685,
 1691, 1706, 2904
 Floettmann, K. 965, 2114,
 3500, 3548
 Flora, F. 3285
 Flora, R. 2491
 Foley, M. 983, 1213
 Folwell, N. 2664
 Fong, K. 601, 1285, 1404,
 1488
 Fontenille, A. 2799
 Fontus, R. 138
 Forchi', V. 3395
 Ford, R. 1652
 Forest, E. 397, 1023, 2249
 Foster, G.W. 323, 1649,
 1766
 Fox, B. 1688
 Fox, J. 2297, 2300, 3141,
 3389
 Fox, W. 1461, 2841
 Frak, B. 1715
 Franchetti, G. 129, 589
 Francis, V. 1029
 Franczak, B. 589
 Franklin, W.A. 2324
 Franzke, B. 434
 Frawczyk, F.L. 2083
 Frayer, D. 558

- Freyberger, A. 195, 2560, 2565, 3243
 Friedlander, F. 1144
 Friedman, A. 132, 275, 312, 536, 1518, 2673
 Friesel, D.L. 699, 1065, 1563
 Frigola, P. 947, 2110, 2112, 2192, 3321
 Frisch, J. 644, 1279, 2545, 2548
 Frischholz, H. 473
 Froidefond, E. 2799, 2802
 Fruneau, M. 2799
 Fu, S. 1455, 1509
 Fu, W. 1685
 Fubiani, G. 719, 1885
 Fuerst, J.D. 1291, 1294, 1297
 Fujii, T. 1978
 Fujita, T. 860, 3077, 3080, 3261
 Fukami, K. 2551
 Fukuda, S. 1509
 Fukui, T. 250
 Fukui, Y. (KEK) 1509
 Fukui, Y. (UCLA) 1787, 1790, 2008, 2709
 Fukuma, H. 860, 3056
 Fuller, R. 235
 Furman, M. 132, 297, 312, 350, 2598, 3219, 3222, 3524
 Furukawa, K. (KEK) 533, 3368
 Furukawa, K. (Osaka U) 755
 Fusco, V. 914, 2077, 3285, 3548
 Gagliano, J. 1416
 Gai, W. 492, 1156, 1810, 1813, 1819, 1888, 1894, 2032
 Galambos, J. 1569, 2360, 2363, 2366, 3527
 Gallagher, R. 167
 Gallardo, J.C. 1909, 2002, 3255
 Gallegos, F. 2515, 2518
 Gallegos, R. 558
 Gallerano, G.P. 3285
 Gallo, A. 366, 2080, 2279, 2742, 3285
 Gamma, F.S. 3285
 Gammino, S. 81
 Ganetis, G. 164, 743, 1431, 1637, 1700, 1706, 2162
 Gao, J. 3264, 3267
 Gardner, C. 51, 1542, 1706, 1715
 Gardner, I.S.K. 1527
 Garnett, R.W. 2613
 Garoby, R. 1724, 2336
 Garrel, N. 1162
 Garren, A.A. 1557, 1787, 1804, 1816, 2008, 2213, 2219, 3485
 Gasser, Y. 1303
 Gassner, D. 54, 794, 1425, 1542, 1691, 2444, 2447, 2450, 2694, 2904
 Gattuso, C. 1649, 1766, 2931
 Gaudreau, M.P.J. 547, 1500
 Gaupp, A. 836
 Gavrillov, N. 2273
 Ge, L. 2664
 Gebel, R. 598, 3428
 Geddes, C.G.R. 1840
 Geer, S. 983, 1183
 Geisler, A. 899
 Gelfand, N. 1557
 Geng, R. 2580
 Geng, R.L. 264, 1309, 1312, 1314, 1317, 1323, 2059
 Genoni, T.C. 3165
 Gensch, U. 2114
 Genser, K. 1763
 Gentzlinger, R. 1341, 2841
 Gerigk, F. 1527
 Geros, E. 73
 Gerth, C. 189
 Gerth, Ch. 911
 Ghalam, A.Z. 3174
 Ghigo, A. 366, 684, 1658, 2279, 2742, 3285
 Ghiorso, W. 2524
 Ghosh, A. 164, 2162
 Giaccone, R. 719, 1885
 Giannessi, L. 914, 2077, 3285, 3548
 Giannini, G. 917
 Gibson, D.J. 95
 Gibson, P. 2706
 Gierman, S. 2104, 2667, 3216
 Gillespie, W.A. 519
 Gilpatrick, J.D. 2512, 3086
 Gilson, E. 98, 2622, 2655, 2661
 Giovannozzi, M. 129, 388, 2910, 2913, 2916
 Giove, D. 2080, 3285
 Giovenale, E. 3285
 Girard, A. 81
 Givens, M. 2029, 2038
 Gjonaj, E. 3563
 Glanzer, M. 426, 2571, 2577
 Glass, H. 1766, 1969, 1972, 2168
 Gl  ner, C. 1622
 Glenn, J. 51, 405, 746, 1542, 1545, 1706, 1715, 2595, 3422
 Gloor, W. 878
 Gluckstern, R.L. 2592
 Goddard, B. 45, 1646, 1721
 Godlove, T. 426, 1673, 1676
 Goepfner, G. 1416, 2029
 Gold, S.H. 492, 1128, 1147
 Goldin, F. 563
 Golovko, N.G. 1605
 Golub, Yu.Ya. 3101, 3103
 Gomez, J. 1664
 Gonin, I. 48, 1207, 1210, 1213, 2068
 Gonzales, J.M. 553
 Gonzalez, R. 2444
 Goodzeit, C.L. 1996
 Gopych, M. 3569
 Gorbachev, A.M. 1147
 Gordon, D.F. 716, 1846
 Gordon, J. 2860

- Gorelov, D. 2805, 2849, 2972
- Gössel, A. 467, 1086, 1392
- Gottschalk, S.C. 1909
- Gould, H. 1837
- Gould, O. 794, 3282
- Gounder, K. 2928, 3434, 3437
- Gourlay, S.A. 42, 170, 1032, 1984
- Grabosch, H.J. 2114
- Graef, H.-D. 3551, 3569
- Graham, D. 89
- Granata, V. 1945
- Granatstein, V. 1140
- Grau, M. 2444
- Graves, W.S. 217, 329, 956, 959, 980, 1192
- Gray, J.W. 1527
- Green, M.A. (LBNL) 186, 1834, 1987
- Green, M.A. (SRC) 887, 929
- Greenwald, Z. 2056
- Greenway, W. 1171
- Grelick, A. 1416, 1422, 2029, 2038
- Grenoble, C. 457
- Gribble, R.F. 553
- Grice, W. 1524, 2706
- Griep, B. 2887
- Grier, D. 1724
- Griffin, J. 1554, 2922
- Grimm, T. 1350, 1353, 1356, 1359, 1362, 1407, 2849, 2972
- Grippo, A. 1485
- Grisham, L. 2661, 3309
- Grishin, V. 1007, 1010
- Grote, D.P. 70, 275, 1518, 2637, 2673
- Grote, H. 3497
- Gruber, P. 1183, 1413
- Gruner, S. 192
- Gu, A. 2580
- Guan, C.Y. 815
- Guenzel, T. 854
- Guerra, A. 195
- Guethlein, G. 563
- Guetz, A. 2664
- Guidi, V. 917, 986, 1655
- Guiducci, S. 366, 914, 2077, 2279, 2945, 3285
- Guignard, G. 665
- Guilhem, D. 2601
- Guimbal, Ph. 2053, 2458
- Gullotta, J. 54, 794, 1425, 2444, 2694
- Gung, C. 1990
- Gunther, K. 1113, 1116
- Gupta, R. 42, 164, 1748, 1936, 1939
- Guy, F.W. 2889
- Gyr, M. 1646
- Ha, K.M. 2857
- Ha, W. 1861
- Haase, M. 1724
- Haber, I. 426, 511, 536, 1673, 2312, 2574, 2577, 2673, 3156, 3297
- Haberer, Th. 694
- Habs, D. 112, 2869, 2872
- Hacker, K. 423
- Hafalia, R.R. 170, 1984
- Hafizi, B. 716, 1846
- Hafz, N. 1849
- Haga, K. 860
- Hahn, A. 2488, 2491
- Hahn, H. 39, 1625, 1706, 2147, 3035
- Hahto, S.K. 3309
- Hahto, S.T. 3309
- Haimson, J. 2095
- Hajima, R. 3443, 3446, 3449
- Halaxa, E. 3297, 3300
- Halbritter, J. 1374
- Hall, R.P. 3300
- Hamatsu, R. 2709
- Hamm, R.W. 1563
- Hammons, L. 1542, 1691
- Han, J.H. 2114
- Han, J.M. 1222, 2539, 2832, 2857, 2884
- Han, S.H. 2539, 2832
- Han, Y.J. 1470, 2857, 3114, 3383
- Hanaki, H. 2838
- Hanft, R. 1730, 1972
- Hanna, B.M. 2497
- Hanna, S.M. 1077
- Hannink, R. 2625
- Hannon, F.E. 1029
- Hansen, R.W.C. 929
- Hansen, S. 323
- Hara, M. 250
- Hara, T. 487
- Harada, K. 857, 860, 3201
- Hardek, T. 553, 1095, 1168, 1458, 1461
- Hardekopf, R. 1461, 1661
- Harding, D. 1730, 2168
- Hardy, L. 854
- Harkay, K. 508, 592, 2438, 3008, 3011, 3014, 3183
- Harris, J. 426, 2312, 2571, 2577
- Harrison, J. 558, 1237
- Harrison, M. 39, 42, 164, 1748
- Hartemann, F. 95, 938
- Hartill, D. 1309, 2339
- Hartline, R.E. 1792
- Hartman, S. 752, 2270, 2273, 2482
- Hartouni, E. 1446
- Hartrott, M.v. 2114
- Hartung, W. 1350, 1353, 1356, 1362, 1395, 2849, 2972
- Harvey, M. 1715
- Harwood, L. 586, 992, 1098
- Hasegawa, K. 1509
- Hashemi, H. 238
- Hashiguchi, E. 1978
- Hashiguchi, Y. 902, 3270
- Hassanein, A. 1180
- Hassanpour, N. 3389
- Hassanzadegan, H. 238
- Hassenzahl, W. 2162
- Hatano, T. 1165
- Hauviller, C. 1434
- Hawkey, T. 547, 1500

- Hawkins, S. 2533
 Hayano, H. 530, 2545, 2548
 Hayashizaki, N. 2826
 Hayden, D. 2354
 Hayes, M. 2231, 3494
 Hayes, T. 476, 1706, 1715, 3338, 3341
 He, D.H. 968
 He, P. 54, 785, 788, 791, 1425, 2598
 He, Y. 167, 2399
 Hechler, M. 2706
 Heese, R. 217, 241
 Heidenreich, D.A. 553
 Heifets, S. 2297, 2300, 3132, 3135
 Heimann, P. 186, 1032
 Heistermann, F. 3344
 Held, B. 3554
 Hemmer, M. 2390
 Henderson, S. 117, 1467, 1569, 1572, 2598, 3416
 Hendrickson, L. 423, 644, 662, 2545, 2757, 3126
 Henestroza, E. 98, 558, 1171, 2616, 2619, 2622, 2625, 2628, 2637, 2646
 Henn, K. 598, 3428
 Henning, W. 16
 Henrist, B. 1727
 Henrist, H. 307
 Henry, J. 1377, 2866
 Heo, H. 3108
 Heppner, G. 1685
 Herbeaux, C. 229
 Herr, A.D. 617
 Herr, W. 3404
 Hershcovitch, A. 39, 92
 Hertel, I. 836
 Herzog, R. 1945
 Hess, M. 2643
 Hettel, R. 235, 761
 Hiatt, T. 2183, 2186, 2189
 Hicks, J.D. 553
 Hicks, R. 195, 2560
 Hicks, W.R. 1377
 Higashi, N. 1978
 Higashi, Y. 2393, 2838
 Hill, A. 235, 1273
 Hill, C. 1029
 Hilleret, N. 307, 788, 1727
 Himel, T. 644, 2757
 Hiramatsu, S. 2503
 Hirashima, T. 1074
 Hirata, K. 2996
 Hirshfield, J.L. 725, 1128, 1131, 1147, 1150, 1882, 1924, 1927, 1930, 2881
 Hitz, D. 81
 Ho, D. 563
 Ho, H.K. 1876
 Ho, S. 620
 Hobl, A. 899
 Hock, J. 1542, 3422
 Hoff, L. 1542, 2444
 Hoffstaetter, G.H. 192, 369, 375, 842, 848
 Höfle, W. 1718, 3038
 Hofler, A. 195
 Hofmann, I. 129, 589, 2592, 2607, 2954
 Hogan, B. 1119
 Hogan, G. 702
 Hogan, J. 457, 1377, 2866
 Hogan, M.J. 731, 1530, 1864, 1933
 Holder, D.J. 189
 Holidack, K. 836, 839, 2527, 3023
 Holloway, M. 426, 2571
 Holmes, J. 117, 1569, 1572, 3503
 Holmes, R. 770
 Holtkamp, N. 11
 Holzscheiter, M. 558
 Honkavaara, K. 467, 911, 2476
 Hopkins, S. 1461
 Horan, D. 1177
 Hori, Y. 809, 860
 Horioka, K. 1807
 Horst, B. 467
 Hosoda, N. 250, 2551
 Hosokai, T. 2258
 Houck, T. 558, 2628
 Hourican, M. 1643
 Hovater, C. 195, 1098, 2379
 Howe, S. 705
 Hseuh, H. 54, 785, 788, 791, 1425, 1715, 2144, 2147, 2390, 2598, 3419
 Hsiao, F.Z. 2402, 2405
 Hsiung, G.Y. 821
 Hsu, K.T. 890, 1044, 2376, 2554, 2557, 3237, 3392
 Hsu, S.-Y. 2376
 Hsu, S.N. 821
 Hu, K.H. 2376, 2554, 2557, 3237, 3392
 Hu, M. 1649
 Huang, C. 1530, 1864, 1933, 3174
 Huang, H. (BNL) 51, 54, 405, 1697, 1706, 1712
 Huang, H. (Yale U) 1688
 Huang, J.Y. 875, 2539
 Huang, M.H. 1047
 Huang, Z. (ANL) 905
 Huang, Z. (SLAC) 329, 3138, 3231
 Hubbard, R.F. 716, 1846
 Hubers, H.-W. 839
 Huelsmann, P. 589
 Huening, M. 467, 2074, 2682, 2730
 Hughes, T. 120, 558, 3210
 Huhn, A. 2444
 Hulbert, S. 241
 Hülsmann, P. 434
 Humphries, S. 3557
 Hung, D.S. 3234
 Hunter, T. 2706
 Huo, Y. 426, 2312
 Hurh, P. 641, 1440, 1443, 1449, 1452
 Hutchinson, E. 1542
 Huttel, E. 893, 3273, 3276
 Hutton, A. 195
 Hwang, C.S. 821, 1041, 1044, 1047, 2376
 Hwang, W.H. 2539, 2857
 Iarocci, M. 1631
 Iazzourene, F. 2306, 2309
 Ieiri, T. 860, 3077, 3080

- Igarashi, S. 568, 755, 1165,
 1807, 2610
 Igarashi, Y. 2838
 Igarashi, Z. 1509
 Igo, G. 51
 Ihee, H. 420
 Ihloff, E. 2324
 Iida, K. 530
 Iida, M. 1978
 Iida, N. 2240
 Ikeda, H. 2503
 Ikeda, M. 3326
 Ikegami, K. 1509
 Ikegami, M. 1455, 1509,
 2393, 2835
 Ilg, T. 2841
 Imai, T. 2829
 Inagaki, S. 568, 1784
 Inagaki, T. 487
 Incurvati, M. 2279, 3285
 Ingrassia, P. 1715
 Irie, Y. 1512, 2509
 Iriso-Ariz, U. 54, 794, 797,
 1706, 1801, 3479
 Isaev, V.A. 1147
 Isagawa, S. 860, 1228
 Ise, T. 755
 Ishi, Y. 1512
 Ishibashi, K. 1784
 Ishikawa, T. 487
 Ishimoto, S. 1834
 Ishizuka, T. 3332
 Ito, T. 1509, 2835
 Ivanov, O. A. 1147
 Ivanov, P.M. 3062
 Ivanov, V. 1137, 2664,
 3312, 3315
 Ivanov, Yu.D. 3530
 Ivanov, Yu.M. 917
 Iversen, J. 467
 Iverson, P. 1530
 Iverson, R. 731, 1864, 1933,
 2285, 2297
 Ives, L. 269, 1110, 1113,
 1116, 1119, 1125, 1127,
 1137, 1140, 1142, 3312,
 3560
 Iwasaki, Y. 902, 2387, 3270
 Iwashita, D. 1807
 Iwashita, Y. 1993, 2198
 Izawa, M. 3201
 Jackson, A. 244
 Jackson, G. 705, 3159, 3162
 Jackson, J. 2153, 2159,
 2390
 Jacob, J. 854, 1332, 3192
 Jacobs, K.D. 887, 929,
 2303, 2373
 Jacobson, E.G. 73
 Jacobson, S. 3374
 Jacques, E. 1303
 Jacquez, E. 558
 Jaeschke, E. 836, 2114
 Jain, A. 39, 164, 1637,
 2159, 2390
 Jamilkowski, J. 1542
 Jamison, S.P. 519
 Jang, J.H. 1219, 2832, 2884
 Jansma, W. 2029
 Jansson, A. 1751, 1763
 Jason, A. 702, 1664, 1966,
 2948
 Javanmard, M. 722, 1855
 Jeanneret, J.-B. 45, 1682,
 3494
 Jennings, B. 307, 1727
 Jensch, K. 467
 Jensen, A. 3315
 Jensen, E. 2467, 2470
 Jensen, J.-P. 749
 Jensen, K.L. 3323
 Jensen, L. 307
 Jeon, D. 107, 1515, 2652,
 2855
 Jeong, K.K. 1222, 2832,
 2884
 Jeong, S.-H. 3114
 Jia, L. 1431
 Jia, Q.K. 968
 Jian, X. 3506, 3509
 Jiang, D. 2852
 Jiang, H. 1359
 Jimenez, J.M. 45, 307, 1727
 Jin, L. 369
 Jines, P. 2382, 2892
 Jing, C. 492, 1810, 2032
 Jing, D.M. 815
 Jinnochi, O. 51
 Jobe, K. 1279, 3141
 Johnson, D. (Bechtel) 558
 Johnson, D. (FNAL) 1649,
 1766, 2931
 Johnson, D. (UCLA) 1530,
 1933
 Johnson, E. 217, 241
 Johnson, G. 2841
 Johnson, J. 558
 Johnson, M. 1350
 Johnson, R.P. 1792
 Johnstone, C. 983, 1446,
 1557, 1649, 1831, 2216,
 2931, 3413
 Jones, F.W. 3404
 Jones, J.K. 2243
 Jones, K. 558
 Jones, R.M. 1261, 1264,
 1270, 2760, 2763
 Jones, T. 716, 1846
 Jones, W.P. 699, 1065, 1563
 Jordan, K. 1485
 Joshi, C. 731, 1530, 1858,
 1864, 1873, 1933
 Joshi, C.H. 1407
 Joshi, P. 2162
 Jowett, J.M. 1682
 Julian, J. 1240
 Julian, R.L. 929
 Jung, J.Y. 3458
 Jungwirth, H. 598, 2811
 Junquera, T. 1303
 Kabel, A.C. 2252, 3539,
 3542, 3545
 Kadokura, E. 1509
 Kaertner, F.X. 959, 980
 Kaganovich, D. 716
 Kaganovich, I.D. 1667,
 2975
 Kageyama, T. 800, 803
 Kahn, S.A. 1709, 3255,
 3413
 Kain, V. 45, 1685
 Kaiser, H. 467
 Kakiyama, K. 2838
 Kako, E. 1338

- Kalantari, B. 238
 Kalinichenko, A.I. 1080
 Källberg, A. 1590
 Kalnins, J.G. 1837, 2951
 Kaltchev, D. 45, 1581, 3494
 Kamikubota, N. 1509
 Kamitani, T. 1225, 3288
 Kamiya, Y. 530
 Kammering, R. 467, 2730
 Kanahara, T. 1978
 Kanareykin, A. 1888, 1891, 1894, 1897
 Kanazawa, K. 806, 2503
 Kandaswamy, J. 167
 Kaneko, N. 3326
 Kang, H. 3180
 Kang, H.S. 1470, 2857, 3383
 Kao, C.C. 241
 Kaplan, D.M. 1183, 1792, 1798, 1834
 Kaplan, R. 1306, 1437, 3347
 Karantzoulis, E. 2306, 2309
 Karataev, P.V. 2709
 Karl, F. 2390
 Karmanenko, S. 1888
 Karpov, G. 250
 Kasemir, K. 3371, 3377
 Kashikhin, V.S. 1966
 Kashikhin, V.V. 1748, 1966, 1969, 1975
 Kashiwagi, S. 3288
 Kashtanov, E. 1781
 Kaspar, K. 589
 Kasper, P.H. 1503, 2936
 Kasuga, T. 860, 1228, 3077, 3080, 3261
 Kato, T. 1455, 1509, 2393, 2835
 Katoh, T. 860, 2351
 Katsouleas, T.C. 731, 1530, 1858, 1864, 1933, 3174
 Katuin, J. 699, 1068
 Kaugerts, J. 2162
 Kawakubo, T. 1165, 1512
 Kawamoto, T. 2351
 Kawamura, M. 1509
 Kawashima, Y. 250, 487
 Kawata, H. 860
 Kedzie, M. 1291, 1294, 1297
 Keeley, D. 235, 2372
 Keil, B. 3386
 Keil, E. 414, 3413
 Keil, R.G. 887
 Kelez, N. 2527
 Keller, L. 2739
 Keller, R. 527, 3306
 Kelley, J.P. 977, 1966
 Kelly, J. 2706
 Kelly, M.P. 1291, 1294, 1297
 Kempkes, M.A. 547, 1500
 Kephart, R. 1972
 Kerby, J.S. 1745, 1969
 Kersevan, R. 854
 Kesar, A.S. 2095, 2536
 Kesselman, M. 524, 2444, 2453
 Kester, O. 2869, 2872
 Kewisch, J. 39, 372, 1300, 1694, 1700, 2005, 2011, 3186
 Khabiboulline, T. 48, 1207, 1210, 1213
 Khachatryan, A.G. 1900, 1903
 Khan, S. 836
 Khodak, I.V. 2098
 Kikuchi, M. 860, 3368
 Kikuzawa, N. 3443, 3446, 3449
 Kim, C. 1849, 1852, 1906, 1912, 2987
 Kim, D.T. 1470, 2857
 Kim, E.-S. 3105, 3108, 3111, 3114
 Kim, G.H. 1849, 1852, 1906, 1912, 2987
 Kim, J.B. 2984, 2987
 Kim, J.U. 1849, 1852, 1906, 1912, 2987
 Kim, K.-J. 905, 1813, 2682, 3138
 Kim, K.R. 1602
 Kim, M.G. 875, 3114
 Kim, S.C. 2857, 3114
 Kim, S.H. (ANL) 1020
 Kim, S.-H. (ORNL) 1365, 1467, 1599
 Kim, T.H. 1539
 Kim, Y. (CHEP) 962, 965
 Kim, Y. (DESY) 962, 965
 Kim, Y.J. 2832, 2884
 Kimura, N. 1978
 Kimura, W.D. 1909
 King, L. 457
 King, Q. 1945
 King, T.C. 2402, 2405
 Kinkead, A.K. 492, 1128, 1147
 Kinoshita, K. 2258
 Kirchgessner, J. 1314
 Kirk, H. 1628, 1631, 1634, 1709, 1787, 2008, 2213, 2219, 3255
 Kishek, R.A. 426, 1673, 1676, 2574, 2577, 2673, 3156
 Kishiro, J. 568, 1509, 1784, 1807
 Kitamura, H. 487, 962, 965
 Kitsuka, T. 902, 3270
 Klein, H. 1335, 2942
 Klein, H.-U. 1948
 Klein, S.B. 699
 Kleman, K.J. 887, 929, 2373, 3147
 Klenov, V. 3282
 Kling, N. 1542
 Klotz, W.-D. 2360, 2363, 3527
 Knapic, C. 1050
 Kneisel, P. 92, 457, 1350, 1362, 1374, 1377, 1395, 1575, 2863
 Knippels, G. 519
 Knobloch, J. 1323
 Ko, I.S. 1852, 2984
 Ko, K. 2664
 Koba, K. 1679, 1736
 Kobayashi, H. 1509
 Kobayashi, M. 860
 Kobayashi, N. 713

- Kobayashi, T. 1509
 Kobayashi, Y. 857, 860, 2171, 3201, 3204
 Kobilarcik, T. 1652, 2934
 Koch, J.M. 851
 Koda, S. 902, 2387, 3270
 Kodera, M. 250
 Koiso, H. 3368
 Kokhanovskii, S. 3282
 Kolomiets, A.A. 2875
 Komada, I. 2351
 Kondaurov, M. 2769
 Kondo, Y. 1509
 Konecny, R. 492, 1156, 1810, 2032
 Konkashbaev, I. 1180
 Koop, I.A. 372, 2898
 Koopman, J. 2470
 Kooy, H. 690
 Korbly, S. 2095, 2536
 Korenev, I. 1013, 1611
 Korenev, S. 1013, 1015, 1608, 1611, 1614
 Koropsak, E. 3026
 Korostelev, M. 2315
 Koschik, A. 3044
 Koscielniak, S. 1488, 1831, 3413
 Koseki, K. 568, 1784, 1807
 Koseki, T. 530, 857
 Kostin, D. 467
 Kostin, M. 1446
 Kotlyar, Y. 1542
 Kotov, V.I. 917, 1655
 Kou, C.H. 1044
 Kourbanis, I. 1736, 3353, 3356
 Koutchouk, J.P. 2225
 Kovach, P. 1939
 Kozanecki, W. (CE Saclay) 2739
 Kozanecki, W. (SLAC) 2297
 Kozub, S. 1781
 Kozyrev, E.V. 1128
 Kponou, A. 89, 3282
 Kraft, G.A. 192
 Kramarenko, K. 1605, 2969
 Krämer, A. 589
 Krämer, D. 836, 1083, 2114
 Kramer, S.L. 241
 Kramper, B. 2020
 Krasilnikov, M. 2114, 3551, 3566
 Krasnogolovets, M.A. 1107, 3303
 Krasnykh, A. 1137, 3312, 3315
 Krause, S. 2324
 Krawczyk, F.L. 1341, 1344
 Krejcik, P. 423, 1530, 1933, 2297, 3126, 3129
 Kreps, G. 467, 1392
 Krinsky, S. 217, 3225
 Krischel, D. 1948
 Krishock, A. 1542
 Kroc, T. 2020
 Kroll, N.M. 1270
 Kroyer, T. 2700
 Krusche, A. 1724
 Kuan, K.C. 821
 Kuba, J. 95
 Kubicki, T. 1204
 Kubota, C. 1509
 Kubota, T. 3335
 Kubsy, S. 899
 Kucharczyk, A. 2787
 Kuchnir, M. 1792
 Kudo, K. (AIST) 2387
 Kudo, K. (KEK) 860, 2351
 Kudo, T. 487
 Kuehnelt, K.-U. 1622, 2817
 Kulikov, A. 2282, 2297
 Kulinski, S. 2787
 Kulipanov, G. 250
 Kumada, M. 1993, 2198
 Kumagai, N. 250, 782, 881, 884
 Kumaran, R. 1285
 Kuo, C.C. 890, 1044
 Kuo, C.H. 764, 2376, 2554, 2557, 3234, 3237, 3392
 Kuo, K.C. 1476
 Kurennoy, S. 920, 977, 1661, 2083, 3515
 Kurita, N. 235
 Kusche, K.P. 1909
 Kushnir, V.A. 1107, 1605, 2098, 2878, 3303
 Kuske, P. 839, 1186, 3020, 3023
 Kustom, R.L. 1020
 Kuzikov, S. V. 1147
 Kuzin, M. 250
 Kuznetsov, A. 2769
 Kuznetsov, G. 57, 1781
 Kwan, J. 70, 3291, 3294, 3297, 3300, 3309
 Kwiatkowski, S. 1240
 Kwon, H.J. 1219, 1222, 2832, 2857, 2884
 Kwon, S. 3371, 3377
 Lach, J. 2769
 Lackey, J.R. 1503, 2168, 2936
 Ladd, P. 2706
 Ladran, A. 1243, 2023
 Lagniel, J.-M. 2601
 Lai, S. 1763
 Laier, U. 3569
 Lamb, D. 426, 2571, 2574, 2577
 Lambertson, G.R. 410, 1837
 Lambiase, R.F. 550, 743, 770, 2144
 Lamm, M. 42, 1730, 1969, 1972
 Lamont, M. 45
 Lange, R. 467
 Langton, J. 235
 LaPointe, M.A. 1131
 Larbalestier, David C. 151
 Larsson, JÅrgen 2321
 Laskar, J. 378, 3189
 Lau, T. 3563
 Lau, W. 1243, 1834
 Laurent, J.M. 307
 Lauze, R. 195
 Laverty, M. 1404
 Lawson, Greg S. 288

- Lawson, W. 1119, 1140
 Lawton, D. 138
 Laxdal, R.E. 601, 1488, 1584
 Lazurik, V.M. 1616
 Lazurik, V.T. 1080, 1616
 Le, Tuong N. 3338, 3341
 Lebedev, V.A. 29, 48, 1733, 1739, 1751, 2497, 3062
 LeBlanc, G. 2318, 2321
 Lebrun, P. 1739, 1754, 1763, 2703
 Ledford, J.E. 1341
 Lee, Demi 2376, 2554
 Lee, E.P. 312, 1521, 2658, 2975
 Lee, H.H. 2832
 Lee, H.J. 1849, 1852, 1906, 1912, 2984, 2987
 Lee, H.R. 1602
 Lee, Jinhyung 2026
 Lee, Peter J. 151
 Lee, R.C. 54, 785, 794
 Lee, S.Y. 1065, 3150, 3240
 Lee, Soon-Hong 824
 Lee, W.-T. 426, 2571, 2577
 Lee, Y.-Y. 550, 571, 617, 1569, 1572, 1637, 2144, 2147, 2150, 2153, 2159, 2390, 2598, 3416
 Leemans, W.P. 719, 734, 1840, 1885
 Lefevre, T. 2464
 Legg, R.A. 887
 Lehrach, A. 598, 2811, 3428
 Lei, S.C. 1476
 Leibfritz, J. 2020
 Leitner, D. 86
 Leitner, M.A. 86, 1521, 1990
 Lemaire, J.-L. 2601
 Lemuet, F. 444
 Lenci, S. 1122
 Lenkszus, F. 283, 2435
 Leone, S. 186
 Leontiev, V.N. 553
 Le Pimpec, F. 1279, 2748
 LeSage, G.P. 95
 Lessner, Eliane S. 3467
 Letchford, A.P. 2542
 Leung, K.N. 3309
 Level, M.-P. 229, 1332
 Leveling, A. 1440
 Levi, D. 3285
 Lewandowski, J.R. 1261, 1264
 Lewellen, J.W. 905, 1813, 2029, 2035, 2038, 2132, 2333, 2417, 2420
 Leyh, G.E. 235, 761, 1174
 Li, C. 2357
 Li, D. 186, 1183, 1243, 1246, 1249, 1389, 2023
 Li, G. 968
 Li, H. 426, 1673, 1676, 2574, 2577
 Li, H.C. 2402, 2405
 Li, J. 391, 2270, 2357, 2479
 Li, Juexin 2715
 Li, N. 2174
 Li, R. 208, 941
 Li, Shaoqing 2852
 Li, Shiqui 1560
 Li, W. 2357, 2715
 Li, Xiaoguang 2852
 Li, Y. (ANL) 905
 Li, Y. (Cornell) 620, 2264, 2399
 Li, Yuxiong 2715
 Li, Z. 1264, 2664, 2760
 Liaw, C.J. 617, 2444
 Lidia, S.M. 186, 2086, 2089, 2092, 2682, 3198, 3500
 Liebermann, H. 1335, 2820, 2942
 Lien, M.K. 592
 Liepe, M. 192, 467, 1201, 1317, 1320, 1323, 1326, 1329, 2059, 3347
 Lietzke, A.F. 170, 1984, 1990
 Ligi, C. 2279, 3285
 Likhachev, S. 1010
 Lill, Robert M. 2435
 Lim, J. 2192
 Lima, R.R. 2201
 Limborg, C.G. 235, 329, 2077, 2104, 2667, 3216, 3548
 Limon, P. 42
 Lin, F.Y. 1047
 Lin, M.C. 1371, 2402, 2670
 Lin, Y.C. 1476
 Lindgren, L.-J. 2318, 2321
 Linnecar, T. 1718, 3050
 Lipka, D. 2114
 Litvinenko, V. 391, 752, 2273, 2479
 Liu, C.Y. 1479, 1482
 Liu, G. 2357
 Liu, J.-F. 1341, 1344, 2083
 Liu, J.Y. 968
 Liu, Kuo-Bin 767
 Liu, P. 1452
 Liu, W. 492, 1156, 1810, 2032
 Liu, Y. 998, 2607
 Liu, Zuping 2715
 Lo, Y.C. 3234
 Lockey, R. 550, 1542
 LoDestro, Vincent 3282
 Loew, G.A. 647
 Loewen, R. 1264
 LÅfgren, P. 1590
 Loftsdottir, A. 863
 Logan, B.G. 1521, 2661
 Logatchov, P. 3318
 Loiacono, L. 3183
 Longcoy, L. 2324
 Longo, C. 1428
 Lonza, M. 3395
 Loos, H. 217, 241, 329, 908, 1192, 1497, 2455
 Lopes, M.L. 1596, 2201
 Lopez, A. 2029
 Lorentz, B. 3428
 Lorkiewicz, J. 467
 Lorman, E. 2494, 3062
 Losito, R. 878, 1309, 1332
 Lou, G.H. 1044
 Louie, W. 743, 1431, 1700
 Loulergue, A. 229

- Low, R.** 1240
Lowe, D. 220, 2195
Lowenstein, D. 1715
Lu, J. 1285
Lu, W. 1870, 1933
Lucas, P. 2925
Luccio, A.U. 51, 272, 405, 1697, 1936
Ludewig, H. 1428, 1628, 1709, 2598, 2796
Ludvig, J. 2625
Ludwig, M. 2461
Lumpkin, A.H. 2411, 2414, 2417, 2420, 2423
Lund, S.M. 132, 312, 536, 1990, 2631, 2634
Luo, G.H. 890, 1041, 1371, 2670
Luo, Y. 2123, 2126, 2129, 2132, 2135, 2186
Luque, A. 3029
Lusk, M. 2354
Lyles, J.T.M. 1092
Lyn, L. 1240
Lynch, M.T. 553, 1095, 1168, 1458
Lyneis, C.M. 86
Lysenko, W.P. 2613
Ma, H. 1464, 3377
MacDonald, M.A. 189
Macek, R.J. 326, 508, 2521, 2598, 3086, 3089, 3419, 3455
MacGill, R. 1246
Machida, S. 1512, 1679, 3413, 3452
Machie, D. 1377, 2866
Macina, D. 1742
MacKay, W.W. 39, 51, 54, 164, 405, 1697, 1706, 1712, 1715, 1936
MacLachlan, J.A. 1554, 1736, 1769, 3180
MacLean, E.J. 708
MacLeod, A.M. 519
MacNair, D. 235
Madre, B. 1494
Maebara, S. 2829
Maesen, P. 1724
Magome, T. 250, 782
Mahler, G. 2156
Maier, R. 598, 2811, 2814, 3428
Maisheev, V.A. 917
Majeski, R. 2655
Makarov, O. 2261
Makita, Y. 1539
Malafronte, A.A. 2201
Malagu, C. 917, 1655
Malitsky, N. 272, 2919, 3482
Malm, K. 2150
Malmgren, L. 2321
Malo, J.F. 2470
Mammarella, F. 638
Mammosser, J. 457, 1104, 1386, 2860
Mansell, J. 1861
Mao, S. 779
Mapes, M. 785, 788, 1542, 2141
Marcellini, F. 366, 2080, 2279, 2742, 3141, 3285
Marchand, D. 2799
Marchand, P. 229, 878, 1332
Marchionni, A. 1649, 3440
Marcouill, O. 229
Marechal, X. 487
Marhauser, F. 1189
Markiewicz, T. 644, 2739
Marks, S. 1032, 3458
Marlats, J.L. 229
Marneris, I. 746, 1542, 1637
Maroli, C. 3285, 3512
Marone, A. 164, 1939, 2162
Marque, S. 878
Marques, S.R. 2583, 3279
Marqversen, O. 2461
Marr, G. 1542, 1715
Marriner, J.P. 514, 2928, 3180, 3434, 3437
Marsden, D. 1110, 1119
Marsh, K.A. 731, 1530, 1864, 1873, 1933
Marshall, T.C. 1882, 1924, 1930
Marsi, M. 2306
Martens, M. (ANL) 2029
Martens, M. (FNAL) 1730, 1972, 3359
Marti, F. 138, 1353, 2649, 2849, 2972
Martin, D. 235
Martin, M.C. 863, 869
Martineau, R. 2841
Martinelli, G. 917, 1655
Martinez, D. 2512
Martini, M. 129, 388, 2913, 2916
Martins, M.N. 1593, 1596, 2201
Martovetsky, N. 1990
Marusic, A. 524, 1706
Maruyama, A. 1539
Maruyama, T. 2739
Masaki, M. 250, 881
Mastovsky, I. 2095
Masuda, T. 250
Masunov, E.S. 2640, 2963
Matheisen, A. 467
Matoba, M. 1679, 3452
Matsui, S. 250, 487, 884
Matsumoto, H. 487
Matsuoka, M. 1338
Mattioli, M. 3285
Matveev, Yu. 2273
Mauri, M. 2080
Mausner, L. 1628
Mavanur, A. 1407
Mazzitelli, G. 366, 1658, 2279
McCarrick, J. 563, 2533, 3557
McChesney, C.A. 2360, 3527
McCormick, D. 1279, 2545, 2548
McCrary, R. 2521, 3086, 3089, 3455
McCrea, M. 2183
McCuistian, B.T. 558
McDonald, J.L. 2385

- McDonald, K.T. 1628, 1631, 1634, 1709
McGahern, W. 2390
McGee, M. 2020
McIntosh, P. 235, 1273, 3141
McInturff, A.D. 170, 1984
McIntyre, G. 39, 1691, 2904
McKinney, W. 869
McManamy, T. 1572
McMichael, G.E. 592, 1159
McNeil, B.W.J. 189, 950, 953
Mc Nerney, A. 746, 1542
Mead, J. 524, 2444, 2697
Mecklenburg, B. 2095
Medici, G. 3285
Medjidzade, V. 167, 2399
Medvedko, A. 2769
Medvedko, E. 235, 761
Meidinger, A. 558
Meinke, R.B. 1990, 1996
Meisner, K. 1736, 1769
Melin, G. 81
Meller, R.E. 2339
Meng, W. 1637, 2144, 2147, 2159, 2598
Meot, F. 444
Merl, R. 2354, 2515, 2518
Merminga, L. 192, 195, 332
Merrill, F. 702
Mertens, V. 1721
Mertins, H.-C. 836
Merz, W. 749
Messina, G. 3285
Meth, M. 1195
Métral, E. 129, 388, 2913, 2916, 3047
Métral, G. 388, 2913, 2916
Meyer, A. 1542
Meyer, B.J. 73
Meyer, F.W. 998
Meyer, T.S. 2491
Meyer Sr., R.E. 2485
Mezentsev, N. 250
Mezi, L. 914, 3285
Mi, C. 2447
Mi, J. 550, 1640, 2147
Michalek, W. 2029
Michelato, P. 1506, 2071, 2114
Michelotti, L. 1557
Michnoff, R. 1706, 2691, 3026
Miglione, G. 2150
Migliorati, M. 2077, 3285
Mihalcea, D. 2682
Mihara, T. 2198
Mikado, T. 713, 971, 974
Mikhailichenko, A. 167, 1822, 1825, 1828, 1954, 1957, 1960, 1963, 2399, 2781, 2784, 3350
Mikhailov, S.F. 391, 752, 2273, 2276, 2482
Milani, D. 1945
Milardi, C. 366, 2279, 2742, 2945, 3285
Miles, J. 1942
Miller, R.H. 1264, 2760, 2763
Miller, T. 2382, 2892
Mills, G.D. 998
Milner, R. 956, 959, 980
Miltchev, V. 2114
Milton, S.V. 905, 1813
Minagawa, Y. 860, 3077, 3080, 3261
Minehara, E.J. 3443, 3446, 3449
Minervini, J. 1990
Miram, G. 1110, 1113, 1116, 1137, 1140, 1142, 3312
Mishra, C.S. 1, 1649, 1766, 2928, 3434, 3437, 3440
Mistry, N.B. 167, 2399
Mitchell, D. 1213
Mitra, A. 601
Mitrochenko, V.A. 1107, 3303
Mitrochenko, V.V. 1605, 2098, 2878
Mitsuhashi, T. 860, 2503, 2506, 3204, 3207
Miura, T. 2509, 2610
Miyajima, T. 860, 2171
Mizobata, M. 1071
Mizrahi, A. 722, 728
Mizuhara, A. 1142
Mizuhara, M. 1110, 1113, 1116, 1119
Modena, M. 1942
Moffitt, J.R. 2473
Mokhov, N.V. 42, 983, 1503, 1733, 1742, 1745, 1748, 2739, 2936
Möller, W.-D. 467
Molvik, A.W. 132, 312, 536
Monaco, L. 1506, 2071
Moncton, D.E. 959, 980
Monroe, J. 1587, 1652
Monroy, M. 1464, 3377
Montag, C. 51, 135, 1300, 1431, 1694, 1697, 1700, 1706, 2005, 2011, 2691, 2907, 3026, 3186
Montoya, D.I. 1341
Montoya, N. 558
Moog, E.R. 156, 1020
Moore, C. 1652, 2934
Moore, R. 1751, 1754, 2497
Moore, T. 167
Moraes, J.S. 2990
Morcombe, P. 752
Moretti, A. 1183, 1246, 1792, 2023
Morgan, G. 1936
Morgan, J. 641, 1443
Mori, W.B. 731, 1530, 1858, 1864, 1870, 1933, 3174
Mori, Y. 1231, 1234, 1679, 3413, 3452
Moricciani, D. 3285
Morishita, T. 2829
Moritz, G. 589, 2162
Moritz, L. 638
Morley, K. 702
Morris, C. 702
Morris, J. 746, 1542, 1715
Morris, W.A. 1527
Morse, E.C. 3291

- Morvillo, M. 1724
 Mosnier, A. 595
 Mostacci, A. 1801, 2500, 3479
 Mostrom, C. 558
 Mottershead, T. 702, 1664
 Mouat, M. 638
 Moy, K. 558
 Mueller, I. 2823
 Mueller, N. 2823
 Mueller, P.E. 1004
 Muggli, P. 731, 1530, 1864, 1915, 1933
 Muir, A.A. 1029
 Mulholland, G. 1631
 Mullany, B. 1428
 Müller, A.-S. 388, 893, 2913, 3273, 3276
 Mulvaney, J.M. 547, 1500
 Murai, S. 1978
 Murasugi, S. 1165
 Muratore, J. 164, 2162
 Muratori, B. 189
 Murdoch, G. 1467, 2706
 Murokh, A. 944, 2568
 Murphy, B.F. 2104, 3216
 Murphy, J.B. 176, 217, 241, 2455, 2808
 Murray, S.N. 3306
 Musser, S.E. 1356
 Mustafin, E. 589
 Musumeci, P. 1867, 1873, 2117, 2957, 3258
 Muto, A. 1679, 3452
 Muto, M. 755
 Muto, T. 2709
 Myakushko, L.K. 2878
 Myneni, G. 1374
 Na, J.H. 2832
 Nadji, A. 229, 896
 Nadolski, L. 229, 397, 896
 Nagahashi, S. 860, 2171, 2351
 Nagai, R. 3443, 3446, 3449
 Nagaitsev, S. 2020
 Nagaoka, R. 229
 Naito, F. 1509, 2835
 Nakai, H. 3326
 Nakamoto, T. 1978
 Nakamura, E. 568, 1165, 1784, 1807, 2610
 Nakamura, N. 530, 857
 Nakamura, S. 1539
 Nakamura, T. 250, 881
 Nakamura, T.T. 860, 2351
 Nakanishi, H. 860, 1228
 Nakanishi, T. 1539
 Nakano, J. 1231, 1679, 3452
 Nakashizu, T. 3326
 Nakayama, K. 530
 Nam, K.Y. 1602
 Nam, S.H. 1470, 2539, 2857, 3108
 Nantista, C.D. 482, 1276
 Napoly, O. 2718, 2739
 Narang, R. 1873
 Nash, B. 126
 Nassiri, A. 1416, 2038
 Nath, S. 1461, 1515
 Naumenko, G.A. 2709
 Naylor, C. 1542
 Naylor, G. 854
 Nehring, T. 550
 Neil, G.R. 181, 977
 Neilson, J. 269, 1119, 1125, 1127
 Nelson, J. 1279
 Nelson, R. 1098
 Nemesure, S. 1542
 Nenasheva, E. 1888, 1894
 Neri, F. 3086
 Neumann, J. 1497
 Newsham, D. 1153, 1156, 2123, 2126, 2129, 2132, 2135, 2186
 Nexsen, W. 2533
 Nezhevenko, O.A. 1128, 1131, 1147, 1150, 2881
 Ng, C.-K. 235, 1264, 2664
 Ng, K.Y. 1751, 2922, 3065
 Nguyen, D. 977
 Nicklaus, D. 323
 Nicol, T. 1969
 Nicolas, L.Y. 1733
 Nielsen, K. 558
 Nieter, C. 719, 1885, 1918
 Nigorikawa, K. 1509
 Nikitina, T.F. 2878
 Nishimori, N. 3443, 3446, 3449
 Nishimura, H. 244, 397, 1837, 2249, 2385
 Noack, F. 836
 Noble, R.J. 722, 1858
 Noda, F. 1512
 Noda, T. 250
 Nogami, T. 809, 860
 Noguchi, S. 1338, 1509
 Nolden, F. 434
 NÅlle, D. 2476
 Nomura, M. 530
 Norbrega, A. 1969
 Nordberg, E. 2399
 Norem, J. 1180, 1183, 1246, 1999
 Norris, B. 983
 Nosochkov, Y. 2288, 2291, 2300
 Novati, M. 1506
 Novokhatski, A. 315, 2294, 2297, 2300, 2981
 Nusinovich, G. 1140
 Nzeadibe, I. 235
 Oakeley, O. 752
 Obina, T. 860, 2351, 3077, 3080, 3201, 3207, 3261, 3365
 Ochiai, Y. 902, 3270
 O'Connell, C.L. 423, 731, 1530, 1864, 1933, 3126, 3129
 Odagiri, J. 2351
 Odajima, W. 1978
 Oepts, D. 519
 Oerter, B. 54, 1640
 Ogata, A. 3335
 Ogawa, H. 713, 971, 974
 Ogawa, Y. 3368
 Ogitsu, T. 1978, 3413
 O'Hara, J.F. 2512
 Ohashi, Y. 250

- Ohgaki, H. 713, 902, 2387, 3270
- Ohhata, H. 1978
- Ohishi, M. 884
- Ohkuma, H. 881
- Ohmi, K. 345, 353, 3053, 3056, 3083, 3398
- Ohmori, C. 1216, 1234, 1679, 3413, 3452
- Ohnishi, Y. 3056, 3288
- Ohnuma, S. 1557
- Ohsawa, S. 2838, 3326
- Ohsawa, Y. 860
- Ohshima, T. 250, 782, 881, 2551
- Ohuchi, N. 1978
- Oide, K. 353, 2604
- Oishi, M. 250, 782
- Okada, M. 1509
- Okamoto, H. 2592
- Okamura, M. 164, 1936
- Oleck, A.R. 1649
- Olsen, J. 235, 761
- Olson, C.L. 2685, 3165
- Olson, M. 1781
- Onishi, Y. 860
- Onisto, H.J. 2583, 3279
- Ono, M. 860, 1228
- Onoe, K. 487, 3332
- Oogoe, T. 2838
- Oothoudt, M. 2354
- Oppelt, A. 2114
- Orikasa, T. 1978
- Oro, D. 558
- O'Rourke, S. 2975
- Orris, D. 1969
- Ortega, M. 235
- Orzechowski, T. 3557
- O'Shea, P.G. 426, 511, 1497, 1673, 1676, 2312, 2571, 2574, 2577, 2673, 2712, 3156, 3323
- Österdahl, F. 1590
- Ostiguy, J.-F. 2168, 2925, 3503
- Ostojic, R. 42
- Ostroumov, P.N. 400, 2426, 2790, 2875, 2963, 3467
- Otboev, A.V. 372, 2898
- Ott, K. 773, 776
- Ottaviani, P.L. 3285
- Ottavio, D. 2360
- Owen, H.L. 189
- Owens, T.L. 3344, 3380
- Oz, E. 1530
- Ozaki, T. 860
- Ozelis, J.P. 1491, 1494
- Paál, A. 1590
- Padamsee, H. 192, 1201, 1309, 1312, 1314, 1317, 1320, 1323, 1410, 2059
- Pagani, C. 467, 1300, 1341, 1506, 2114
- Page, T. 1969
- Pai, C. 550, 2144, 2147
- Pakter, R. 1134, 2990
- Palmer, D.T. 1858, 2107
- Palmer, M.A. 2267, 2473
- Palmer, R. 1816
- Palmer, R.B. 1804, 1834, 1987, 2002, 3413
- Palumbo, L. 944, 2500, 3285
- Pantell, R.H. 1909
- Paoluzzi, M. 1724
- Papaphilippou, Y. 123, 851, 854, 1569, 2159, 3053, 3189
- Paparella, R. 470
- Pappas, C. 235
- Paramonov, V. 2826
- Pardo, R.C. 2426, 2875
- Park, B.R. 1470
- Park, B.S. 1602
- Park, E.S. 875
- Park, H.J. 3383
- Park, J.H. 2539
- Park, M.Y. 1219, 2832, 2884
- Park, S. 235
- Park, S.-S. 3114
- Park, S.J. 2539
- Parker, B. 372
- Parkhomchuk, V. 2769
- Parmigiani, F. 186
- Parodi, R. 1395
- Parsa, Z. 3005
- Partridge, R. 644
- Parzen, G. 2589
- Pasky, S. 1419, 2038, 2333
- Pasotti, C. 878
- Pasquinelli, R.J. 3068, 3431
- Pate, D. 39, 92
- Pattengale, N. 2360
- Pattengale, N.D. 3527
- Patton, J. 2363
- Paul, A.C. 2533, 2960
- Paul, K. 2931
- Paulon, R. 1506
- Payet, J. 2718
- Pearson, C. 1264
- Peatman, W.B. 836
- Pedersen, F. 2461
- Pedrozzi, M. 878
- Peggs, S. 39, 42, 135, 278, 372, 797, 1059, 1691, 2204, 2901, 2904
- Pei, Y.J. 818, 2852
- Peiniger, M. 1410
- Pekeler, M. 1410, 2887
- Pelaia, T.A. 2360, 2363, 2366, 3527
- Pellegrini, C. 211, 944, 1867, 1873
- Pellegrino, L. 366, 2279, 3285
- Pellico, W.A. 1587, 2936, 3177
- Peñano, J.R. 716
- Penco, G. 878
- Penel, C. 253
- Peng, Z.H. 601
- Perevedentsev, E.A. 2898, 3398
- Perez, F. 893, 3273, 3276
- Perezhogin, S.A. 1605
- Peschke, C. 434
- Peters, H.-B. 467
- Peterson, D. 3068
- Peterson, E. 1294
- Peterson, P.F. 2637
- Peterson, T. 1966, 1969
- Petra, M. 1020

- Petracca, S. 2993, 2996, 2999
- Petrillo, V. 3285, 3512
- Petrossyan, B. 2114
- Petrosyan, G. 470
- Petrinin, A.A. 917
- Petry, J.E. 1500
- Peyrot, M. 1948
- Pfeffer, H. 1781
- Pfister, U. 598
- Phillips, D. 1542
- Phillips, L. 1401, 2860
- Phinney, N. 678
- Picardi, L. 3285
- Pichoff, N. 2601, 2802, 3491
- Pieck, M. 1168
- Piekarz, H. 1649, 1981
- Piel, C. 2887
- Pierini, P. 1300, 1506
- Pikalov, V.A. 917
- Pikin, A. 89
- Pilat, F. 42, 51, 1697, 1703, 1706, 1712, 2207
- Pillai, C. 2515, 2518
- Piller, M. 3377
- Pinayev, I. 752, 2273
- Pindak, R. 241
- Piot, P. 911, 2682, 3500
- Pirkel, W. 186
- Pivi, M. 350, 2598, 3219, 3222
- Pjerov, S. 241
- Placidi, M. 186, 2530
- Plan, B. 253
- Planet, M. 2799
- Plant, D. 2769
- Plate, D. 1240
- Plate, S. 164, 1939
- Platz, M. 3569
- Plawski, E. 467, 2787
- Plawski, T. 195, 2379
- Plettner, T. 722, 1861
- Plouviez, E. 851, 854
- Plum, M.A. 2429, 2444, 2485
- Podlech, H. 1335, 2820, 2942
- Podobedov, B. 241, 2808
- Pogge, J. 1524, 2706
- Pogorelsky, I.V. 1909
- Poirier, R. 601, 1285, 1584
- Polozov, S.M. 2963
- Ponnaiyan, V. 54, 794
- Pont, M. 893, 3273, 3276
- Poole, M.W. 189, 950, 953
- Popenko, V.A. 2878
- Popov, G.F. 1080, 1616, 1619
- Popov, V.G. 752, 2273
- Popova, N. 1619
- Popovic, M. 983, 1792
- Pordes, S. 2491
- Portmann, G. 890, 2369, 2372, 3213, 3374
- Potter, J. 2354
- Potter, K. 1467, 2706
- Potylitsyn, A.P. 2709
- Poupeau, J.P. 1303
- Power, J. 1661, 2429, 3371, 3377
- Power, J.G. 492, 1810, 1813, 1888, 1894, 2032, 2432, 2667
- Power, K. 1936, 1939
- Powers, T. 457, 2379
- Pozdeyev, E. 138, 2649
- Prasuhn, D. 598, 3428
- Preble, J. 457, 977, 1104
- Prebys, E.J. 1503, 1587, 1652, 2936
- Preger, M.A. 366, 684, 1658, 2279, 2945, 3285
- Preis, H. 1309
- Prelec, K. 89
- Prestemon, S. 1032
- Prichard Jr., B.A. 73
- Prior, C.R. 1527
- Proch, D. 467
- Prochnow, J. 2467
- Prokop, M. 3371, 3377
- Prom, M. 2601
- Prost, A. 1643
- Prost, L.R. 275, 312, 536, 1518, 2524
- Przeklasa, R.S. 1168
- Ptitsyn, V. 51, 54, 135, 372, 405, 1697, 1703, 1706, 1712
- Pu, Y. 1539
- Puccio, B. 1945
- Pugachev, G.D. 2878
- Pugnat, P. 1942
- Purcell, D. 2444, 2706
- Pusina, J. 2086
- Qian, B.L. 2646, 2966
- Qian, Z. 1183, 1246
- Qiang, J. 1509, 2613, 2954, 3401
- Qin, B. 3506, 3509
- Qin, H. 2655, 2658, 3117, 3120, 3123
- Quan, S. 2580
- Quast, T. 836
- Quattromini, M. 914, 2077, 3285, 3548
- Quigley, P. 1410, 1437
- Quimby, D.C. 1909
- Quinn, B. 426, 1673, 2312, 2571, 2574, 2577, 2673
- Quinn, F.M. 189
- Quirus, M. 2571, 2577
- Rabedeau, T. 235
- Rabehl, R. 1969
- Radovinsky, A. 1990
- Raguin, J.-Y. 2724
- Raimondi, P. 366, 731, 2279, 2766, 2945, 3285
- Raino, A. 3318
- Raja, R. 1446
- Raka, E. 2595
- Rakhno, I.L. 983, 1742, 1745, 1748
- Rakowsky, G. 217
- Ranjbar, V. 3062
- Rank, J. 39, 1467, 2150
- Rao, Y.-N. 1578, 1584
- Raparelli, M. 2476
- Raparia, D. 571, 1428, 1467, 1569, 1572, 1637, 1709, 2150, 2153, 2156,

- 2390, 2598, 2793, 3282, 3416
- Rarback, H.** 235
- Rathke, J.W.** 92, 920, 977, 2186, 2790
- Ratti, A.** 186, 1464, 2530, 3371, 3377
- Ratzinger, U.** 1062, 1335, 2820, 2942
- Raubenheimer, T.O.** 662, 1038, 2739, 2754, 2757, 2760, 2775, 3219, 3231
- Ravel, J.-C.** 2799
- Rawnsley, W.** 601
- Read, M.E.** 1113, 1116, 1119, 1137, 1140, 1142
- Reass, W.A.** 553, 1168
- Redaelli, S.** 665
- Redlin, H.** 2114
- Reece, C.** 1377, 1398, 1494
- Reece, K.** 1569
- Reed, C.A.** 998
- Rees, D.E.** 553, 1095, 1168, 1458
- Rees, G.H.** 1527, 1557
- Regan, A.** 3371, 3377
- Rehlich, K.** 467, 2342, 2476
- Reichardt, G.** 836
- Reiche, S.** 211, 944, 947, 2110, 2112, 3153, 3321
- Reich-Sprenger, H.** 589
- Reid, J.** 48, 1204, 1213, 1769, 3353
- Reilly, J.** 1306
- Reiser, M.** 426, 511, 1673, 1676, 2312, 2571, 2574, 2577, 2673, 3156
- Rej, D.** 1461
- Remondino, V.** 173
- Renieri, A.** 3285
- Rensfelt, K.-G.** 1590
- Repikhov, G.D.** 2878
- Reprintzev, L.V.** 2878
- Reschke, D.** 467
- Resende, X.R.** 1056
- Reshetnyak, N.G.** 1107, 3303
- Reuter, A.** 92
- Revol, F.** 253
- Revol, J.L.** 851, 854
- Rey, J.M.** 1987
- Reynolds, J.** 2354
- Rhee, S.J.** 2177
- Ricci, R.** 366, 2279, 3285
- Rice, D.** 167, 278, 2399, 3425
- Richards, D.** 2844
- Richardson, R.** 563
- Reiche, S.** 203
- Richichi, S.** 167
- Richter, A.** 3551, 3569
- Ries, T.** 601, 1488
- Rifflet, J.-M.** 1948
- Rimmer, R.A.** 186, 977, 1104, 1183, 1243, 1246, 1389, 2023, 2092
- Ringwall, A.** 235
- Rinn, J.** 1942
- Rinolfi, L.** 684, 2742
- Rios, P.B.** 1593, 1596
- Riot, V.** 2530
- Ritson, D.** 1557
- Ritter, J.** 89, 3282
- Rivetta, C.** 3362
- Rizzato, F.B.** 2990
- Robb, G.R.M.** 950, 953
- Robin, D.** 224, 397, 2246, 2249, 3213
- Robinson, K.** 186
- Robinson, T.** 1119
- Roblin, Y.** 195
- Robothom, W.** 2168
- Rock, B.Y.** 2473
- Rockford, J.H.** 1987
- Rode, C.H.** 977, 2863
- Rodriguez, M.** 1237
- Rodriguez, J.** 138, 2649
- Rodriguez, L.** 558
- Rodriguez, P. (LANL)** 558
- Rodriguez, P. (SLAC)** 235
- Rodriguez-Mateos, F.** 1945
- Rogers, G.** 2303
- Rogers, J.T.** 375
- Rogov, Yu.V.** 1616
- Rohlev, A.** 2336
- Rom, M.** 3285
- Romanov, G.** 48, 1210
- Romas'ko, V.G.** 1107
- Romè, M.** 3285
- Romero, D.** 2354
- Roncarolo, F.** 2470
- Ronsiville, C.** 914, 2077, 3285, 3548
- Root, L.** 1584
- Ropert, A.** 851, 854, 3189
- Rose, C.R.** 2485
- Rose, D.V.** 98, 2622, 2637, 2685, 3165
- Rose, J.** 217, 241, 1192, 2455, 2808
- Roseberry, T.** 1467
- Rosenberg, R.A.** 508, 3183
- Rosenthal, S.** 690
- Rosenzweig, J.B.** 95, 914, 944, 947, 1533, 1858, 1867, 1870, 1873, 2110, 2112, 2117, 2192, 2957, 3153, 3258, 3285, 3321
- Roser, R.** 1706
- Roser, T.** 24, 39, 51, 54, 405, 1545, 1637, 1697, 1715, 1936, 2204, 2793, 3026
- Ross, I.N.** 189
- Ross, M.C.** 503, 678, 1279, 2494, 2545, 2548, 2709
- Rossbach, J.** 2114
- Rossen, P.v.** 598
- Rossi, A.** 307, 1727
- Rossi, C.** 1724
- Rossi, L.** 42, 141
- Rossmannith, R.** 899, 3273
- Rotela, E.** 2790
- Roth, I.S.** 547, 1500
- Rothgeb, T.** 1377, 1386
- Roudier, D.** 1303
- Rouleau, G.** 73
- Rowley, L.** 2303
- Rowton, L.** 2841
- Roy, P.K.** 98, 2616, 2619, 2622, 2625, 2628
- Roybal, R.J.** 1341, 1661
- Roybal, W.** 1095, 1458
- Royer, P.** 684

- Rubin, D.L. 1023, 2056,
2267, 3425
 Rudolph, K. 2869, 2872
 Rudychev, V. 1619
 Ruegg, R. 638, 1584
 Ruggiero, A.G. 1637, 2793,
2796
 Ruggiero, F. 42, 45, 123,
1727
 Ruggiero, R. 1748
 Ruggles, S.C. 1168
 Ruland, R. 2769
 Rumolo, G. 123, 1727,
2234, 2607, 3038, 3041,
3044, 3053
 Rusek, A. 1542
 Rusnak, B. 989, 1347
 Russell, A. 1652
 Russell, S. 977
 Russo, T. 1545, 3422
 Rust, K. 550, 770
 Rust, W.W. 635
 Ruth, R.D. 1264
 Ryan, J. 1542, 2595
 Rybarczyk, L.J. 1092, 1566,
3086
 Ryne, R.D. 1509, 2954,
3401
 Saban, R. 1945
 Sabbi, G. 42, 170, 536,
1032, 1521, 1984, 1990
 Sabol, D. 2399
 Saeki, H. 250
 Saewert, G. 1781, 2020
 Safranek, J. 235, 890, 3213
 Sagan, D. 192, 848, 1023,
2267
 Sahuquet, P. 1303
 Saigusa, M. 2829
 Saino, K. 487
 Saito, K. 462
 Sajaev, V. 417, 905
 Sakai, H.R. 530, 857
 Sakai, I. 1512, 1679, 3452
 Sakamoto, Y. 860
 Sakanaka, S. 860, 1228,
3207, 3365
 Sakuda, M. 1807
 Sakumi, A. 312
 Saleh, N. 1921
 Sanchez, B.J. 2515
 Sanchez, M. 558
 Sandberg, J. 550, 571, 743,
746, 770, 1640, 2144, 2147
 Sanderson, D. 138
 Sandner, W. 836, 2114
 Sanelli, C. 366, 2279, 2742,
3285
 Sanfilippo, S. 173
 Sannibale, F. 863, 1658,
2527
 Santucci, J. 2682
 Sapozhnikov, L. 3389
 Sarraf, R.H. 238
 Sasaki, S. (ANL) 2261
 Sasaki, S. (SPRING-8) 250,
782
 Sato, H. 568, 755, 1165,
1807, 1981
 Sato, M. 860
 Sato, Y. (IU) 3240
 Sato, Y. (KEK) 1679, 2509,
3452
 Satogata, T. 51, 54, 272,
278, 405, 1697, 1706,
1712, 1715, 2204, 2207,
2697, 2901, 3026, 3482
 Satoh, M. 533, 860, 3368
 Sauer, A. 1335, 2820, 2942
 Saugnac, H. 1303
 Saunders, A. 702
 Saunders, J. 2860
 Savage, R. 2390
 Savalle, A. 2802
 Savary, F. 1942
 Savatteri, S. 746
 Sawamura, M. 3443, 3446,
3449
 Sazawa, S. 2829
 Scaduto, J. 39, 92, 1631
 Scandale, W. 173, 986,
1655
 Scanlan, R.M. 170, 1032,
1984
 Scarlett, C. 3255
 Scarpine, V. 2414, 2494,
3062
 Scarvie, T. 869, 2527, 3374
 Schächter, L. 722, 728,
1879
 Schaerf, C. 3285
 Schaetz, T. 112
 Schaller, S. 2354
 Schamel, H. 3029
 Schappert, W. 323, 2494
 Schauer, M. 558
 Scheer, M. 836
 Scheidt, K. 854
 Scheitrum, G. 3312, 3315
 Schellong, B. 1948
 Schempp, A. 598, 1062,
1622, 2817, 2823
 Schilcher, T. 3386
 Shimizu, J. 250
 Schindl, K. 1682
 Schirm, K.-M. 1948
 Schlabach, P. 1730, 1969,
1972
 Schlarb, H. 423, 467, 2074,
2730, 3126, 3129
 Schlitt, B. 694, 1062
 Schlott, V. 3386
 Schlueter, R. 1032, 3458
 Schmalzle, J. 1939, 2162
 Schmekel, B.S. 375
 Schmerge, J.F. 2104, 3216
 Schmidt, C.W. 2020
 Schmidt, F. 1754, 1757,
2207, 2228, 2231, 3494,
3497
 Schmidt, P. 1948
 Schmidt, R. 45, 1945
 Schmidt-Bäcking, H. 1622
 Schmidts, F. 1775
 Schmor, P. 6, 439, 1584
 Schnase, A. 598, 1216,
1234, 2817, 3428
 Schneider, H. 598, 3428
 Schneider, W.J. 2863
 Schnitter, U. 2201
 Schoenlein, R. 186, 2408,
2530
 Schrage, D.L. 920, 977,
1341, 1344, 1661, 2083,
2790

- Schramm, U. 112
 Schreiher, S. 467, 911, 1086, 2068, 2071, 2114, 2730
 Schreuder, A.N. 699
 Schroeder, C.B. 1885
 Schuett, P. 589
 Schuh, P. 2297
 Schulte, D. 657, 662, 665, 1727, 2721, 2727, 2733, 2736, 2739, 2757, 3053
 Schultheiss, C. 524, 743
 Schultheiss, T.J. 92, 920, 977, 2186, 2790
 Schultz, D. 2129
 Schultz, J. 1990
 Schultz, R. 1443, 1449, 1452
 Schulze, M. 3086
 Schumann, R. 2114
 Schussmann, G. 2664
 Schwartz, H. 235
 Schwarz, H. 1273, 2297, 3141
 Scott, B. 235
 Scott, D.J. 1029
 Sears, C.M. 2101
 Sears, J. 1309, 1312, 1314, 1323, 1410
 Sebek, J. 235, 2494
 Seberg, S. 2156
 Seddon, E.A. 189
 Seeman, J. 315, 2294, 2297, 2300
 Sei, N. 713, 971, 974
 Seidl, P.A. 275, 312, 536, 1518, 1990
 Seifrid, P. 3068
 Seike, T. 487
 Sekachev, I. 601
 Sekutowicz, J. 467, 977, 1086, 1300, 1374, 1377, 1392, 1395, 1575, 2730, 2866
 Seletsky, S. 2020
 Semenov, A. 323, 1781
 Semertzidis, Y.K. 1625
 Sen, T. 34, 42, 1754, 1757, 1760, 1772, 1775, 3401, 3542
 Senf, F. 836
 Senichev, Y. 598, 2814
 Seo, J.-H. 3114
 Seol, K.T. 2832, 2857
 Serafini, L. 914, 2077, 2080, 3285, 3512
 Serdobintsev, G.V. 2881
 Sereno, N.S. 247, 827, 2420, 2435
 Serio, L. 1945
 Serio, M. 366, 2279, 2742, 3285
 Serrano, J. 2336
 Serriere, V. 3192
 Sertore, D. 1506, 2071, 2114
 Seryi, A. 657, 662, 2739, 2748, 2754, 2757, 2766, 2769
 Sessler, A.M. 414, 3413
 Setzer, S. 2114, 3566, 3569
 Severino, F. 1195, 2441
 Sezaki, K. 487
 Sgamma, F. 366, 2279, 2742
 Shaftan, T. 217, 241, 329, 908, 1192, 1497, 2455, 2808
 Shang, H. 247, 283, 2330, 3461, 3470, 3473, 3476
 Shang, J. 1452
 Shao, L. 1876
 Shapiro, A.H. 1341, 1344, 2083
 Shapiro, M.A. 1255, 1258, 2536
 Shapiro, S. 2796
 Shaposhnikova, E. 1718, 3050
 Sharamentov, S.I. 1291, 2426, 2790
 Sharma, S. 2790
 Sharp, W. 2622
 Sharp, W.M. 98, 2637
 Shatunov, P.Yu. 2898
 Shatunov, Yu.M. 372, 2898
 Shaw, R.W. 617
 Shchelkunov, S.V. 1924
 Shea, T.J. 1569, 2444, 2706
 Sheehy, B. 217, 241, 329, 1192, 1497, 1819, 2455, 2808
 Sheinman, I. 1888, 1891, 1897
 Shelley, F. 2515, 2518
 Shelley, Jr., F. 2354
 Shemelin, V. 192, 1201, 1314, 1317, 2059
 Shemyakin, A. 2020
 Shen, J.L. 519
 Shen, L. 2852
 Shen, S. 1347
 Shen, Y. 217, 2455
 Shendrik, V.A. 2878
 Shepard, K.W. 581, 1291, 1294, 1297
 Shephard, M. 3560
 Sheppard, J.C. 2751
 Sherman, J. 73
 Sherwood, R. 1661
 Shi, J. 369
 Shibata, K. 800, 803, 806
 Shigaki, K. 1512
 Shiho, M. 1807
 Shiltsev, V. 48, 57, 1739, 1751, 1754, 1757, 1778, 1781, 2497, 2769, 3062
 Shimada, T. 1512
 Shimizu, N. 1165
 Shimosaki, Y. 568, 1807, 2610
 Shinoe, K. 530
 Shintake, T. 487, 962, 965, 3332
 Shintomi, T. 755, 1978
 Shioya, T. 860
 Shirakata, M. 568, 1807, 2610
 Shishido, T. 1338
 Shishlo, A. 117, 2360, 2363, 2366, 3527
 Shkaruha, V. 250
 Shkvarunets, A.G. 2712
 Shoace, H. 3371, 3377

- Shoji, M. 250, 782, 2551
 Shrey, T. 1542
 Shubin, E. 2769
 Shul'ga, N. 3329
 Shumakov, I.V. 3530
 Shuman, D. 98, 2625, 2628
 Shurter, R.B. 2512
 Shvedov, D. 2273
 Shvets, G. 3117
 Sibley, C. 607
 Siddons, P. 241
 Sideris, I.V. 2676
 Sieber, T. 2869, 2872
 Siemann, R.H. 722, 728, 731, 1530, 1855, 1858, 1864, 1879, 1933
 Siemko, A. 1942
 Sievers, P. 45
 Sigler, F. 1664
 Sikora, J. 1306, 3059
 Sikora, R. 524, 2444
 Silzer, M. 220
 Simmons, D. 558
 Simmons, L. 1213
 Simoens, F. 1303
 Simon, F. 1948
 Simonsson, A. 1590
 Simos, N. 1428, 1628, 1709, 3255
 Simpson, J. 1813
 Simrock, S. 467, 470, 2342, 2730
 Sims, J. 2841
 Sinclair, C.K. 76, 192, 1317, 2062
 Singatulin, S. 2769
 Singer, W. 467, 1374
 Singer, X. 467
 Singh, O. 283
 Skarbo, B. 3318
 Skaritka, J. 217, 1909, 2455
 Skorobogatov, V.V. 917
 Skrinsky, A. 250
 Slaughter, D.R. 95
 Slaughter, J. 1739, 1763
 Smaluk, V. 214
 Smart, L. 54, 785
 Smedley, J. 541, 2132
 Smirnov, A.V. 1153, 1156, 2123, 2129, 2132, 2135, 2186, 2640, 3171
 Smirnova, E.I. 1255, 1258
 Smith, B. 1210
 Smith, E.N. 2399
 Smith, G. 1715, 2444, 2453
 Smith, H. 423
 Smith, H.V. 558
 Smith, J.C. 2267
 Smith, K. 1377
 Smith, K.S. 476, 1195, 1545, 1706, 1715, 2441, 3338, 3341, 3344, 3380
 Smith, M. 2382
 Smith, S. 235, 761
 Smith, S.L. 189
 Smith, T. 1279
 Smith, T.L. 1416, 1422, 2038
 Smolenski, K. 167, 1317, 2399
 Snowel, M. 2574
 Snydstrup, L. 1542
 Soika, R. 2162
 Soliday, R. 283, 1419, 2261, 3461, 3470, 3473, 3476
 Solyak, N. 1207, 1210, 1213, 1781
 Someya, H. 2509
 Son, D. 962, 965
 Song, L. 1110, 1142
 Sonnad, K.G. 1536
 Sorchetti, R. 2476
 Soutome, K. 250, 782, 881
 Spata, M. 195
 Spataro, B. 914, 2500, 3285
 Spataro, C. 2159
 Spencer, C.M. 779, 2177
 Spencer, J. 779, 1861, 2180
 Spentzouris, P. 2939, 3195
 Spickermann, T. 2521, 3086, 3089, 3455
 Spiller, P. 589, 694
 Spinka, H. 51
 Spitz, R. 1195
 Sprangle, P. 716, 1846
 Sprehn, D. 3312
 Springer, P.T. 95
 Srinivasan-Rao, T. 39, 92, 541, 2047, 2132
 Stanek, M. 423, 2297
 Stanford, G. 601, 1488
 Staples, J. 186, 1243, 1563, 2023, 2086, 2092, 2408, 3198
 Starling, W.J. 2889
 Startsev, E.A. 1667, 2975, 2978, 3120, 3123
 Stascheck, A. 3569
 Stassen, R. 598, 2814, 3428
 Stecchi, A. 366, 2279, 2742, 3285
 Steck, A. 2515
 Steck, M. 434
 Steerenberg, R. 388, 2913, 2916
 Stefancich, M. 917, 1655
 Stefanski, R. 1652
 Steier, C. 397, 869, 2246, 2249, 3213, 3374
 Steimel, J. 48, 1736, 3068, 3071, 3074, 3353, 3356, 3362
 Stein, H.J. 3428
 Stein, W. 2847
 Steinhauer, L.C. 1909
 Stella, A. 366, 2279, 2742, 3285
 Stelzer, J.E. 73
 Stenning, M. 1584
 Stephan, F. 2114
 Stephani, T. 1948
 Stepin, D.L. 2878
 Steski, D. 1715
 Stettler, M. 2429, 2512, 3371, 3377
 Stevens Jr., R.R. 73
 Still, D. 1730
 Stinson, G. 1584, 1670
 Stirbet, M. 457
 Stockhorst, H. 598, 3428
 Stockli, M.P. 527, 3306
 Stockwell, B. 1122, 1144
 Stoltz, P. 132

- Stótt, J.P. 887, 2373
 Stout, D. 2706
 Stovall, J. 1515, 2652, 2855
 Strait, J.B. 42, 1745, 1748, 1969, 1975
 Straumann, T. 235, 761, 2494
 Striganov, S.I. 1733
 Strohman, C.R. 2473, 3347
 Strohmer, S. 899
 Studebaker, J. 558
 Stulle, F. 3129
 Stupakov, G.V. 102, 926, 1038, 3132, 3135, 3225, 3231
 Sturgess, R. 558
 Suetake, M. 860, 1228
 Suetsugu, Y. 612, 800, 803, 806
 Sugahara, R. 860
 Sugai, I. 1512
 Sugawara, S. 1978
 Sugaya, M. 1231, 1679, 3452
 Sugimoto, M. 2829
 Sugimura, T. 3326
 Sugita, K. 1978
 Sugiyama, E. 1993
 Suhring, S. 625
 Suk, H. 1849, 1852, 1906, 1912, 2984, 2987
 Suller, V.P. 189
 Sullivan, G. 558
 Sullivan, J. 2533
 Sullivan, K. 2189
 Sullivan, M. 340, 2282, 2294, 2297, 2300
 Summers, D.J. 1804
 Sun, D. 3068
 Sun, X. 2688, 3008, 3011, 3014
 Sun, Y. 2682
 Sundelin, R. 1398, 1401
 Suwada, T. 533, 1225, 3368
 Suzuki, H. 1338
 Svandrlik, M. 878
 Svirida, D. 51
 Swanson, C. 3371
 Swenson, D.A. 2889
 Swift, G. 2273
 Swinney, C. 558
 Swirsky, J. 2195
 Sylvester, C. 1969
 Symon, K.R. 452
 Syphers, M. 1649, 1754, 2931
 Syratcev, I. 495
 Sytnik, V. 1781
 Szott, Ph. 1303
 Tabak, M. 2637
 Taborelli, M. 495
 Tada, J. 782
 Tadano, M. 860, 2506
 Tai, C.-Y. 1407
 Tajima, T. 1341, 1344, 2083
 Takagi, A. 1216, 1231, 1234, 1679, 2922, 3452
 Takagi, T. 782
 Takahashi, J. 1593, 1596, 2201
 Takahashi, S. 487
 Takahashi, T. 860, 1228
 Takaki, H. 530, 857
 Takala, B.E. 1168
 Takano, S. 250, 881
 Takao, M. 250, 782, 881
 Takasaki, E. 1509, 2835
 Takasaki, S. 860
 Takashima, T. 250, 487
 Takasu, Y. 487
 Takayama, K. 568, 1784, 1807, 1981, 2610
 Takayanagi, T. 1512
 Takebe, H. 250
 Takeda, H. 1515, 2855, 3518
 Takeda, S. 487
 Takeda, Y. 1512
 Takeshita, K. 487
 Takeuchi, H. 2829
 Takeuchi, Y. 803, 860, 2351
 Tallerico, P.J. 553, 1095, 1168, 1458, 1461
 Talman, R. 192, 272, 848, 2919, 3482, 3485
 Tamasaku, K. 487
 Tamura, F. 1216, 1234
 Tamura, K. 250, 881, 2551
 Tan, C.Y. 1751, 2703, 3071, 3074
 Tanabe, J. 2174
 Tanabe, T. 235
 Tanaka, H. (KEK) 1509, 2393, 2835
 Tanaka, H. (Mitsubishi) 1539
 Tanaka, H. (SPRING-8) 250, 881
 Tanaka, K. 1978
 Tanaka, T. 487
 Tang, C. 467
 Tang, Z. 623
 Tanimoto, Y. 809, 860
 Taniuchi, T. 2838
 Taniuchi, Y. 250
 Tantawi, S.G. 482, 1125, 1127, 1261, 1264, 1270, 1276
 Tarakanov, V.P. 1882
 Tarasov, G.E. 2878
 Tarawneh, H. 238, 2318, 2321
 Tariq, S. 641, 1452
 Tartaglia, M. 1730, 1969, 1972
 Tateishi, T. 884
 Tatum, B.A. 995
 Tavakoli, K. 238
 Tavares, P.F. 2583, 3279
 Tawada, M. 353
 Taylor, C. 86
 Taylor, T. 42
 Tazzari, S. 3285
 Tazzioli, F. 3285
 Tecker, F. 684
 Tegenfeldt, F. 1945
 Tejima, M. 860
 Telfer, S. 947, 2110, 2112, 2120, 2192, 3321
 Temkin, R.J. 1255, 1258, 2095, 2536
 Temnykh, A. 167, 1026, 1954, 3425

- Temple, R. 558
 Tenenbaum, P. 657, 662, 681, 2739, 2757
 Teng, L.C. 2895
 ten Kate, H. 42
 Tennant, C. 195, 2189, 3243
 Tepikian, S. 51, 135, 405, 1706, 1712, 2144, 2159, 2390
 Teramoto, A. 1071
 Terashima, A. 1978
 Terebilo, A. 235, 2255, 2369, 2372
 Terekov, V. 1691
 Terremoto, L.A.A. 1593
 Tesarek, R. 2497
 Teytelman, D. 318, 2297, 2300, 3141, 3389
 Theobald, W. 1921
 Thibus, J. 2823
 Thieberger, P. 1628, 1634, 1715
 Thiesen, H. 1945
 Thikim, M. 2303
 Thomas, C. 1575
 Thomas, R. 164, 2162
 Thomas-Madec, C. 1104, 1332
 Thomason, J. 2542
 Thompson, K.M. 1020
 Thompson, M.C. 1870
 Thompson, N.R. 189
 Thomson, D. 3377
 Thorndahl, L. 1156
 Tiede, R. 2942
 Tiefenback, M. 195, 3243
 Tigner, M. 192, 1317
 Tikhoplav, R. 2682
 Timossi, C. 2385
 Ting, A. 716, 1819, 1846
 Tinsley, D. 3068
 Titt, U. 690
 Titus, P. 1631
 Tiunov, M. 1781, 3318
 Tkachenko, L. 1781
 Tobiyama, M. 2709, 3141
 Tochitsky, S.Ya. 1873
 Todd, A. 977
 Todd, R. 788, 791
 Todesco, E. 173, 1942
 Toelle, R. 598, 2811, 2814, 2817, 3428
 Toellner, T. 2411
 Togawa, K. 487, 3332
 Tokuchi, A. 1165
 Tollestrup, A.V. 48, 1733, 2491, 2497
 Tolmachev, S. 1867
 Tom, C.Y. 558
 Tomàs, R. 2207, 2228, 2231, 2234, 2240, 2901
 Tombolini, F. 917
 Tomimasu, T. 902, 2387, 3270
 Tomizawa, H. 2838
 Tomizawa, M. 3083
 Tomlin, R. 2936
 Tompkins, J. 1730, 1966, 1969, 1972
 Tordeux, M.A. 229
 Torii, Y. 884
 Torikai, K. 568, 1784, 1807
 Torrez, P.A. 1237
 Tortschanoff, T. 1948
 Torun, Y. 1183, 1246, 1413, 1795
 Tosi, L. 214, 1050, 2306, 2309
 Totchisky, S. 1867
 Toth, C. 1840
 Touzzolo, J. 1428
 Tovstiak, V.V. 1080
 Towne, N. 241, 3168
 Towns-Andrews, E. 708
 Toyama, T. 568, 1784, 1807, 2610, 3083
 Toyokawa, H. 195, 713, 902, 938, 974, 2387, 3270
 Trakhtenberg, E. 824, 830, 1017
 Trask, W. 167
 Trautwein, A. 235
 Travish, G. 944, 947, 1867, 1870, 2110, 2112, 2192, 3321
 Trbojevic, D. 39, 51, 54, 135, 372, 794, 797, 1425, 1691, 1697, 1706, 1712, 1816, 2204, 2694, 2904, 3413, 3485
 Tremaine, A.M. 95, 2192, 2957
 Tromba, G. 2309
 Trotman, J.V. 1527
 Trovò, M. 2306
 Trujillo, P.G. 553
 Trzeciak, W. 887, 2303
 Tsai, H.J. 890
 Tsai, Z.D. 1479
 Tsakov, I. 2114
 Tsang, T. 541
 Tschalaer, C. 372, 956, 959, 980, 2324
 Tsentalovich, E. 2324
 Tsoupas, N. 51, 405, 550, 1542, 1545, 1637, 1706, 1715, 2138, 2141, 2147, 2150, 2153, 2159
 Tsuchiya, K. 860, 1978
 Tsukishima, C. 1539
 Tsumaki, K. 250, 782, 884
 Tuckmantel, J. 1718, 3050
 Tuozzolo, J. 550, 571, 1637, 2138, 2144, 2147, 2150, 2156, 2390, 2598
 Tupikov, V. 2020
 Tur, Yu.D. 2878
 Turlington, L. 1350
 Turner, J.L. 2297, 2754
 Turner, W. 2530
 Twarowski, K. 467
 Uchiyama, T. 809, 860
 Ueda, A. 860, 3201, 3204
 Ueng, T.S. 3237
 Ueno, A. 1509
 Ueno, R. 1679
 Uesaka, M. 2258
 Uesugi, T. 1216, 1231, 1234, 1679, 3452
 Ullrich, J. 1622
 Umemori, K. 860, 1228
 Umstadter, D. 1921
 Underwood, D. 51
 Urakawa, J. 2545, 2709

- Uriot, D. 2802, 3491
Uvarov, V.L. 2878
Uythoven, J. 45, 1646
Vaccarezza, C. 366, 914, 2077, 2279, 2500, 2945, 3285
Valdiviez, R. 702, 1664
Valente, A.-M. 1401, 2860
Valente, P. 1658
Valentino, V. 3318
Valfells, A. 426, 1673, 2312, 2571, 2574, 2577, 3156
Valishev, A. 3398
Valuch, D. 473, 1089
van der Laan, J.B. 372, 956, 959, 980, 2324
van der Meer, A.F.G. 519
Vanenkov, I. 1951
van Goor, F.A. 1900, 1903
VanKuik, B. 1542
van Tilborg, J. 1840
van Weelderen, R. 1945
van Zeijts, J. 51, 135, 524, 1697, 1706, 1712
Varenne, F. 2802
Varfolomeev, A. 1867
Varfolomeev, Jr., A. 1867
Variale, V. 3318
Varnasery, S. 238
Vascotto, A. 2309
Vasserman, I. 2261
Vasyukhin, N. 2814
Vay, J.-L. 132, 312, 2673, 3297
Vaziri, K. 983
Velev, G. 1730, 1969, 1972
Veness, R. 1646
Venturini, M. 863, 2772, 3144
Venturini-Delsolaro, W. 1948
Verdier, A. 444, 2237
Vermare, C. 2464
Verzilov, V. 214
Vescovi, M. 366, 2279, 3285
Veshcherevich, V. 192, 1198, 1201, 1306, 1317
Vetter, K. 524, 2444, 2697
Vicario, C. 944, 3285
Vidal, R. 2497
Vignola, G. 1053, 1658
Vikharev, A.L. 1147
Vincenzi, D. 917, 1655
Vinogradov, N.E. 2790, 2963
Vinogradov, S.V. 3530
Vinokurov, N. 2273
Viren, B. 3255
Virgo, M. 3323
Virostek, S. 1243, 2023, 2092
Visentin, B. 1303
Vlachoudis, V. 45
Vlogaert, J. 1942
Vobly, P. 2273
Vogel, H. 1410, 2887
Vogel, V. 2545
Vogler, W. 269, 3560
Volk, J.T. 1766, 2180
Volkolupov, Yu.Ya. 1107, 3303
Volkov, V.N. 2041, 2044
Vollinger, C. 173, 1951
vom Stein, P. 1410, 2887
Vorobiev, L.G. 3533
Vos, L. 45, 1801
Wada, Y. 3335
Wahrer, B. 1032
Wait, G.D. 1162
Wake, M. 568, 1784, 1807, 1981
Waldron, W. 98, 536, 1171, 1521, 2628
Waldschmidt, G. 1422
Walker, N. 657, 2396, 2733, 2736, 2739
Walker, R.P. 232
Wallace, D.J. 2303
Wallace, P. 752, 2273
Wall_n, E. 2321
Wallig, J. 1246
Walstrom, P. 544, 1966
Walter, M. 426, 1673, 1676, 2312, 2571, 2574, 2577
Walz, D. 731, 1530, 1858, 1864, 1933
Wan, W. 186, 397, 2246, 2249
Wanderer, P. 164, 1637, 2159, 2162, 2390
Wang, B. 1032
Wang, C. 1927, 1930
Wang, C.J. 2554
Wang, C.X. 3407, 3410
Wang, Ch. 1041, 1371, 2402, 2670
Wang, D. 39, 1300, 2005, 3186, 3228
Wang, D.J. 890
Wang, F. 372, 956, 959, 980, 2324
Wang, H. (ANL) 1813, 2032
Wang, H. (TJNAF) 457, 1098, 1101, 1104, 1389
Wang, J.M. 241
Wang, J.P. 815, 2357
Wang, J.W. 1264, 2664, 2763
Wang, M.H. 890, 3150, 3240
Wang, P. 752, 2479
Wang, S. 1455, 1509
Wang, S.-H. 186, 2682, 3198
Wang, T. 1386, 1398, 2860
Wang, T.S. 508, 3092, 3095
Wang, X. 2174
Wang, X.J. 217, 241, 420, 1819, 2455, 2808
Wang, X.Z. 2586
Wang, Y. (CAMD) 2382, 2892
Wang, Y. (NSRL) 815
Wangler, T.P. 2613
Warburton, D. 550, 1625, 1640, 2147
Warner, A. 2020
Warner, D.K. 1237
Warnock, R. 3144
Warsop, C.M. 1527
Watanabe, Y. 1512
Watson, J.A. 2533, 2960
Wazlawik, S. 3569
Weathersby, S. 2981

- Weaver, M. 2285
 Webber, R.C. 1503, 2936
 Weber, C. 1189
 Weggel, R.J. 1628, 1631, 1634
 Wei, J. 272, 394, 550, 571, 1569, 1572, 2153, 2159, 2390, 2598, 3029, 3032, 3416, 3419
 Wei, W. 815
 Weichert, G. 467
 Weihreter, E. 1189
 Weiland, T. 2114, 3249, 3252, 3551, 3563, 3566, 3569
 Weiner, M. 2664
 Weinrich, U. 694
 Weir, J. 563, 2960
 Weise, H. 673
 Weiss, D. 785
 Weiss, K. 307
 Welch, D.R. 98, 2622, 2637, 2685, 3165
 Welch, J. 3126
 Wells, R.P. 186, 812
 Welsch, C.P. 1622, 2817
 Welton, R.F. 527, 3306
 Wender, S.A. 1168
 Wendt, M. 467, 1086, 2730
 Weng, W.T. 429, 571, 1637, 1709, 2793
 Wenhui, H. 467
 Wenninger, J. 45, 1718
 Werin, S. 2318, 2321
 Werkema, S. 1554
 Wermelskirchen, C. 235, 761
 Wesling, S. 2029
 Westenskow, G. 2533, 3297, 3300
 Weterings, W. 1646
 White, G.R. 2733, 2778
 Whitlatch, T. 457, 977, 1377, 2866
 Widger, D. 2399
 Widjaja, C. 1921
 Widmeyer, M. 235
 Wiemerslage, G. 830
 Wienands, U. 2297, 2300, 3141
 Wilcox, R. 2408
 Wildman, D. 323, 1781, 2922, 3177
 Wildner, E. 173
 Wilinski, M. 2441, 2444, 2691
 Wilke, I. 519
 Will, I. 836, 2114
 Willen, E. 164, 1936, 1939
 Williams, C.L. 998
 Williams, E. 3374
 Williams Jr., E.L. 288
 Wilson, I. 495, 665, 1156, 2724
 Wilson, K.M. 1377, 2866
 Wilson, M. 426
 Wilson, M.N. 2162
 Wilson, P. 1264, 1282
 Win, S.S. 3056
 Wines, R. 2135, 2186
 Wisdom, J. 1861
 Wiseman, M. 457, 977, 1377
 Witkover, R.L. 2444, 2447, 2450
 Wittmer, W. 2237
 Wojtkiewicz, G. 467
 Wolf, M. 2664
 Wolski, A. 186, 652, 657, 866, 2246, 2396, 2745, 2772, 2775, 3213
 Wood, J. 51
 Wood, R.L. 920, 977, 2083
 Woodley, M. 657, 662, 2739, 2757, 2766, 2775, 3126, 3129
 Woods, M. 2754
 Wright, E. 1144
 Wu, A.T. 1386, 2860
 Wu, G. (NSRL) 815
 Wu, G. (TJNAF) 1389, 1395, 1401, 1575
 Wu, J. 126, 1035, 1038, 2775, 3228, 3231
 Wu, J.K. 3294
 Wu, K.C. 164
 Wu, V. 1246, 1769
 Wu, X. 2849, 2972
 Wu, Y. 397
 Wu, Y.K. 391, 752, 2249, 2270, 2273, 2479, 2482
 Wu, Z. 217, 420, 1192, 1497, 1819, 2455
 Wuensch, W. 495, 1156, 2467, 2724
 Westefeld, G. 836, 839, 845, 3020, 3023
 Xiao, A. 2488
 Xiao, M. 1730, 1757, 1760, 1772, 1775, 3401, 3542
 Xie, M. 1843
 Xiong, Y. 1560, 3506, 3509
 Xu, H.L. 968
 Xu, N. 2174
 Xu, Z. (BNL) 1688
 Xu, Z. (IMP) 1288
 Yadav, S. 1748, 1969
 Yakimenko, V. 944, 1909
 Yakovlev, V.P. 1128, 1131, 1150, 1927, 2881
 Yamada, K. 713, 971, 974
 Yamada, R. 1981
 Yamaguchi, S. 1509, 2838
 Yamamoto, A. (IHI) 3326
 Yamamoto, A. (KEK) 1978
 Yamamoto, K. 1512
 Yamamoto, M. 1216, 1234
 Yamamoto, N. 860, 2351
 Yamamoto, S. (KEK) 860
 Yamamoto, S. (Mitsubishi) 1539
 Yamanaka, S. 1165
 Yamatsu, Y. 902, 3270
 Yamazaki, A. 1679, 3452
 Yamazaki, M. 1338
 Yamazaki, Y. 576, 1509
 Yan, X. (IAP) 1335
 Yan, X. (UAD) 519
 Yan, Y. 2297, 2300
 Yang, B.X. 2411, 2423
 Yang, J.S. 1470, 2857
 Yang, M.J. 1649, 1766, 3440
 Yang, S. 1243, 1834
 Yang, X. 1288

- Yanovsky, V. 1921
 Yao, C. 758
 Yao, C.Y. 2411, 2423, 2438
 Yao, J. 2852
 Yarovoi, T. 1867
 Yasumoto, M. 713, 902, 971, 974, 3270
 Yeh, M.K. 1371
 Yin, Y. 2586
 Yocky, J. 2297, 2754
 Yoder, R. 1533, 1867, 1873, 2117, 3258
 Yokoi, T. 1679, 3452
 Yonehara, H. 250, 782, 884, 2551
 Yonemura, Y. 1679, 3452
 Yorita, T. 250, 782
 York, R. 138, 1350, 1353, 1362, 2849, 2972, 3533
 Yoshida, M. 487
 Yoshii, M. 1216, 1234, 3452
 Yoshikawa, H. 1509
 Yoshimoto, M. 1679, 3452
 Yoshimoto, S. 860, 1228
 Yoshino, K. 1509, 2393
 Yoshioka, M. 860
 Yotam, R. 235
 Young, A. 3141
 Young, L.M. 60, 920, 977, 1461, 1515, 2844, 3515, 3521
 Yu, D. 1153, 1156, 2123, 2126, 2129, 2132, 2135, 2186, 3171
 Yu, L.H. 2857
 Yu, J. 2132
 Yu, L.H. 217, 241, 2455, 2808
 Yu, S.S. 98, 558, 1171, 2616, 2619, 2622, 2625, 2628, 2637, 2646, 2661, 2685
 Yu, T. 1560, 3506, 3509
 Yuasa, Y. 1679, 3452
 Yun, J.C. 1763
 Yun, R. 426, 2571
 Yunn, B. 332, 3246
 Yusof, Z. 2032
 Zadorozhny, V. 3005
 Zagorodnov, I. 3249, 3252
 Zahariou-Cohen, S. 1542
 Zajic, V. 89
 Zakutin, V.V. 1107, 3303
 Zaltsman, A. 39, 476, 1195, 3344, 3380
 Zambon, L. 3395
 Zangrando, D. 1050
 Zapfe, K. 467
 Zaplatin, E. 598
 Zaugg, T. 508, 2521, 3089, 3455
 Zelenski, A. 51, 405, 3282
 Zeller, A. 138, 161
 Zeng, J. 770
 Zeno, K. 51, 54, 794, 1542, 1545, 1715
 Zhan, W. 1288
 Zhang, B. 2580
 Zhang, C. 250
 Zhang, H. 818
 Zhang, P. 1921
 Zhang, P.F. 968
 Zhang, S.C. 968
 Zhang, S.Y. 51, 54, 785, 794, 1425, 1706, 1715, 2598, 2694, 3419
 Zhang, W. (BNL) 550, 1640, 2147, 3255
 Zhang, W. (IMP) 1288
 Zhang, W. (YY Labs) 2586
 Zhang, X.L. 57, 1754, 1757, 1778, 1781, 2703
 Zhang, Y. (NSRL) 758
 Zhang, Y. (ORNL) 995, 1001, 1004
 Zhang, Y. (TJNAF) 941
 Zhao, F.Y. 815
 Zhao, H. 1288
 Zhao, K. 2580
 Zhao, Q. 92, 2047
 Zhao, T. 2382, 2892
 Zhao, Y. 39, 92, 1300, 2050
 Zhavoronkov, N. 836
 Zheng, H. 2922
 Zheng, Q. 1404
 Zheng, S. 467, 1392, 1395, 1575
 Zhidkov, A. 2258
 Zhiglo, V.F. 2098
 Zholents, A. 186, 397, 812, 866, 872, 923, 2086, 2132, 2408, 3198
 Zhou, F. 1876, 1909, 2709, 3186, 3228
 Zhou, J. 2646, 2966
 Zigler, A. 716
 Zimmermann, F. 123, 307, 665, 1727, 1730, 1754, 1757, 1778, 2237, 2240, 2315, 2604, 2739, 3038, 3041, 3044, 3053, 3056
 Zimmermann, H. 2823
 Zink, R. 138
 Zinkann, G.P. 2426, 2790
 Zisman, M. 361, 1183, 1243, 1246, 2023, 2297
 Zitelli, L. 1144
 Zlobin, A.V. 42, 1748, 1966, 1969, 1975
 Zobov, M. 366, 914, 2279, 2742, 2945, 3285
 Zolfaghari, A. 956, 959, 980, 2324
 Zolotarev, M. 2530
 Zotter, B. 3044
 Zou, Y. 426, 511, 1673, 2673, 3156
 Zubets, V. 3282
 Zuo, K. 235
 Zviagintsev, V. 470
 Zwart, T. 956, 959, 980, 2324